VOLUME I

Edited by Billy L. Edge

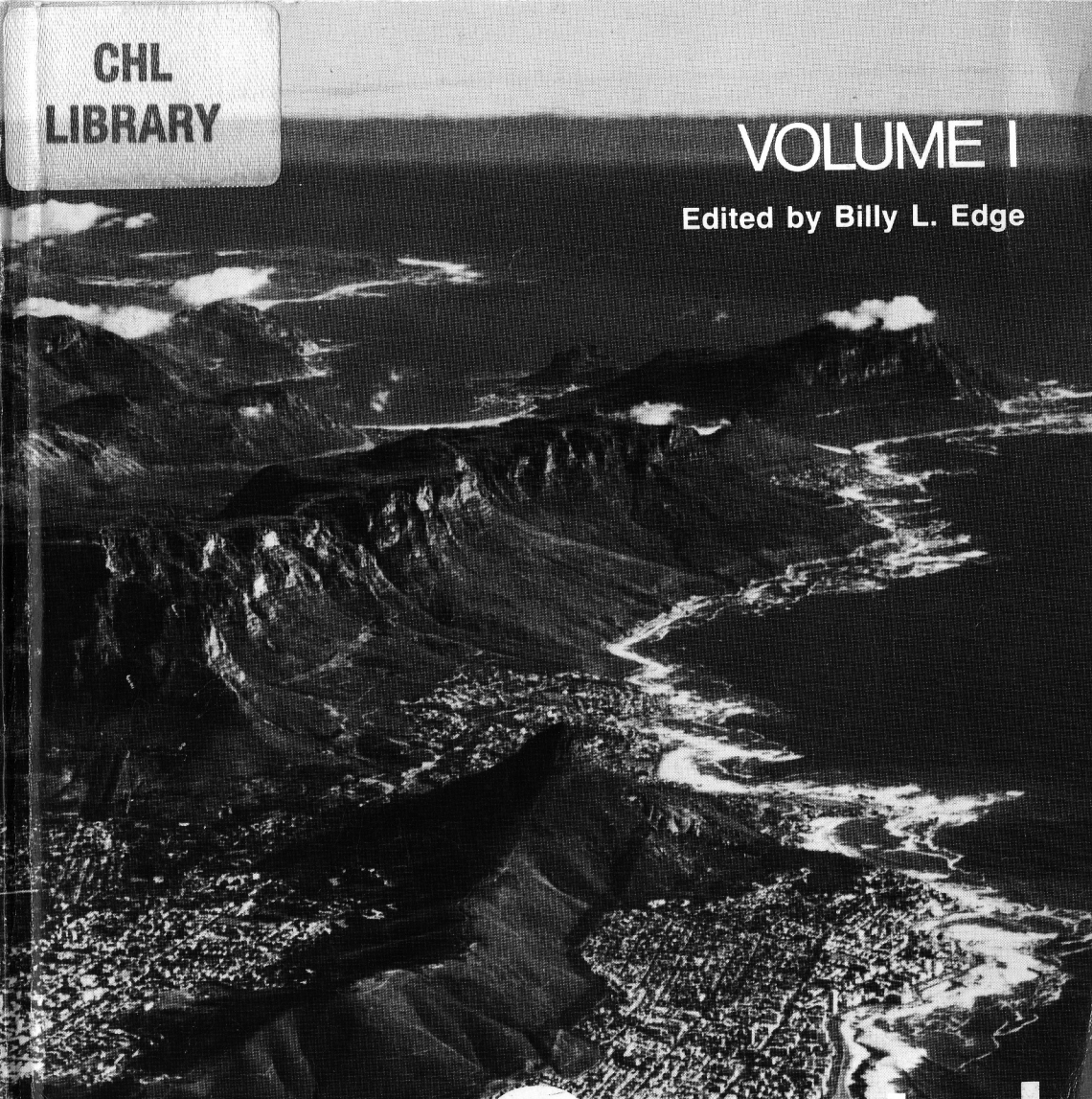

Coastal Engineering

1982 PROCEEDINGS

Proceedings of the

EIGHTEENTH COASTAL ENGINEERING CONFERENCE

Volume I

November 14-19, 1982
Cape Town, Republic of South Africa

Conference held under the auspices of the
Coastal Engineering Research Council
of the
American Society of Civil Engineers,
International Association of Hydraulics Research
and the
Engineering Committee on Oceanic Resources

and organized by the
South African Institution of Civil Engineers
assisted by the
Council for Scientific and Industrial Research

Edited by Billy L. Edge

Published by the
American Society of Civil Engineers
345 East 47th Street
New York, New York 10017

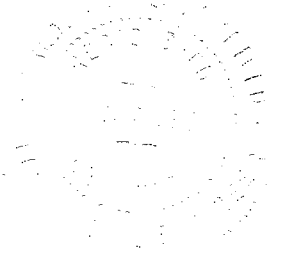

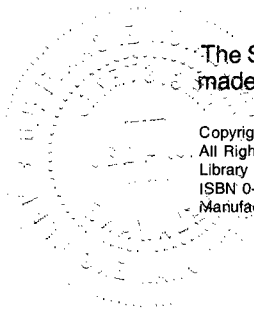

The Society is not responsible for any statements made or opinions expressed in its publications.

Library of Congress Catalog Card No. 83-72167
ISBN 0-87262-373-4
Manufactured in the United States of America.

FOREWORD

Only one International Conference on Coastal Engineering has been held in the same city thus far. Moreover no country has been the venue for more than one Conference except the United States. Although repeat venues are not discouraged, the extremely time consuming activities of planning and conducting a major international conference do not encourage a second effort by the same group. Having the venue in different countries allows the participants to learn first hand about coastal problems and solutions around the world. This approach also allows those engineers and coastal scientists who could not travel to foreign countries to meet the international coastal community.

The papers in this *Proceedings* have been prepared by the authors who made presentations at the 18th International Conference on Coastal Engineering. The authors were asked to make their presentations and submit final papers based on review of the abstracts that were submitted well in advance of the conference. These abstracts were reviewed by a committee of four professionals including representation from the local organizing committee. All papers are eligible for discussion in the Journal of the Waterway, Port, Coastal and Ocean Division. All papers are eligible for ASCE Awards.

Venues for the 19th and 20th conferences are Houston, Texas, and Taiwan, Republic of China, respectively. Countries desiring to host a future conference should contact the Secretary of the Coastal Engineering Research Council to receive information on submitting a proposal.

Billy L. Edge, Secretary
Coastal Engineering Research Council
American Society of Civil Engineers

ACKNOWLEDGEMENTS

NATIONAL ORGANIZING COMMITTEE

Mr. K. G. Witthaus	National Chairman
Mr. J. Rossouw	Deputy Chairman
Mrs. Z. Retief	Ladies Programme Subcommittee
Mr. J. M. Evans	Financial Subcommittee
Dr. D. H. Swart	Papers Subcommittee
Mr. J. F. Kapp	Publicity Subcommittee
Mr. K. S. Russell	Programme Subcommittee
Prof. G. de F. Retief	Social Subcommittee
Mr. J. A. Zwamborn	Technical Tours Subcommittee
Mr. J. P. Möller	Transport Subcommittee
Mr. F. P. Anderson	Other members:
Mr. N. P. Campbell	
Mr. P. Grobbelaar	
Prof. F. A. Kilner	
Mr. D. C. MacLeod	
Dr. A. L. Moss-Morris	
Mr. A. P. M. Vonk	
Mr. R. K. Newman	
Mrs. A. Wissing	Secretariat

SPONSORSHIP

SOUTH AFRICAN INSTITUTION OF CIVIL ENGINEERS (SAICE)

assisted by the

COUNCIL FOR SCIENTIFIC AND INDUSTRIAL RESEARCH (CSIR)

under the auspices of the

Coastal Engineering Research Council (CERC),
American Society of Civil Engineers

International Association for Hydraulics Research (IAHR)

and the

Engineering Committee on Oceanic Resources (ECOR)

SUPPORT

CDM (Pty) Ltd, Oranjemund—Provided free accommodation.
Marine Civil (Pty) Ltd, Cape Town—Sponsored Gans Bay tour.
Borough of Richards Bay, Richards Bay—Entertainment, Richards Bay tours.
Underwater Construction (Pty) Ltd, Cape Town—Sponsored Saldanha Bay tour.
Fisheries Development Corporation of South African Limited, Cape Town.
Land & Marine and Salvage, Cape Town.
Murray & Roberts Civils (Cape) (Pty) Ltd, Cape Town.
The Anglo American and De Beers Chairman's Fund, Johannesburg.
South African Airways, Johannesburg.
SARTRAVEL, Cape Town.
Cape Town City Council, Cape Town—Visit to False Bay coastal development.
Electricity Supply Commission, Cape Town—Visit to Koeberg inlet basin.
National Institute for Oceanology, Stellenbosch—Laboratory visit.
South African Transport Services, Saldanha/Cape Town/Port Elizabeth/Richards Bay—Harbour visits.

PART I
THEORETICAL AND OBSERVED WAVE CHARACTERISTICS

Chapter 1
TURBULENCE GENERATED BY WAVE BREAKING ON BEACH
T. Sakai, Y. Inada and I. Sandanbata 3
Chapter 2
ON THE RELATION BETWEEN CHANGES OF INTEGRAL QUANTITIES OF SHOALING WAVES AND BREAKING INCEPTION
T. Yasuda, S. Goto and Y. Tsuchiya 22
Chapter 3
A FIELD STUDY OF WAVES IN THE NEARSHORE ZONE
S. Hotta, M. Muzuguchi and M. Isobe 38
Chapter 4
WAVE HEIGHT DISTRIBUTIONS AND WAVE GROUPING IN SURF ZONE
H. Mase and Y. Iwagaki 58
Chapter 5
NEARSHORE WAVE SPECTRA MEASURED DURING HURRICANE DAVID
M. K. Ochi and M-H Chiu 77
Chapter 6
A SOUTH AFRICAN WAVE CLIMATE STUDY
J. Rossouw, L. W. Coetzee and C. J. Visser 87
Chapter 7
SYNTHESIS OF HURRICANE RESPONSE HYDROGRAPHS
R. J. Sobey 108
Chapter 8
SECOND ORDER THEORY OF MANOMETER WAVE MEASUREMENT
F. Biesel 129
Chapter 9
HEIGHT DISTRIBUTION OF ESTUARINE WAVES
V. Barthel 136
Chapter 10
ANALOGOUS DISPERSION PROPERTIES OF SURF ZONE AND ELECTROMAGNETIC WAVES
F. Büsching 154
Chapter 11
NUMERICAL CALCULATION OF SEICHE MOTIONS IN HARBOURS OF ARBITRARY SHAPE
P. Gaillard 172
Chapter 12
STATE OF THE ART IN TIDE PREDICTIONS
B. D. Zetler 192

Chapter 13
AUTOMATED DIGITAL SIMULATION OF TIDES AND LONG WAVES
R. F. Henry 203
Chapter 14
LONG WAVES OVER THE GREAT BARRIER REEF
E. Wolanski 219
Chapter 15
CYLINDRICAL LONG WAVE INTO A CYLINDRICAL SHELF
H. Power 228
Chapter 16
A PROPOSAL FOR WAVE ENERGY CONVERSION NEAR CAPE TOWN
G. de F. Retief, G. K. Prestedge and F. P. J. Muller 245
Chapter 17
SOME PROPERTIES OF SWELL IN THE SOUTHERN OCEAN
J. B. Hinwood, D. R. Blackman and G. T. Lleonart 261
Chapter 18
UNUSUAL WAVES ON EUROPEAN COASTS, FEBRUARY 1979
L. Draper and T. M. Bownass 270
Chapter 19
MEASUREMENTS OF TURBULENCE OVER VORTEX-RIPPLE
M. Sawamoto, T. Yamashita and T. Kitamura 282
Chapter 20
INVESTIGATIONS ON ORBITAL VELOCITIES AND PRESSURES IN IRREGULAR WAVES
K-F Daemrich, W-D Eggert and H. Cordes 297
Chapter 21
WAVE INDUCED VELOCITIES CLOSE TO A RIPPLED BED
C. G. Du Toit 312
Chapter 22
MASS TRANSPORT IN VOCOIDAL THEORY
J. W. Gonsalves and D. H. Swart 328
Chapter 23
PROBABILITY DENSITY FUNCTION OF WAVE HEIGHTS OFF THE WESTERN COAST OF TAIWAN
F. L. W. Tang and J.-T. Juang 342
Chapter 24
STUDY OF HURRICANE WAVES AROUND THE TAIWAN COAST
H-S Hou, S. C. Kuo and R. S. Tseng 357
Chapter 25
WIND TURBULENCE OVER SEAS IN TROPICAL CYCLONES
W. H. Melbourne and D. R. Blackman 370
Chapter 26
A COMPUTER MODEL FOR THE REFRACTION OF NON-LINEAR WAVES
J. B. Crowley, C. A. Fleming and C. K. Cooper 384
Chapter 27
WAVE AND CURRENT INTERACTION IN THE NEAR BED REGION
P. H. Kemp and R. R. Simons 404
Chapter 28
EFFECT OF WAVE-CURRENT INTERACTION ON THE WAVE PARAMETER
Y-C Li and J. B. Herbich 413

Chapter 29
RESONANCE IN SOUTH AFRICAN HARBOURS
W. A. M. Botes, K. S. Russell and P. Huizinga 439
Chapter 30
NUMERICAL MODEL STUDY OF TEMPERATURE DISTRIBUTIONS IN A HARBOUR
R. A. Falconer 454
Chapter 31
WAVE ENERGY VARIATION NEAR CAPE TOWN, SOUTH AFRICA
F. A. Shillington 473
Chapter 32
INDIVIDUAL WAVE ANALYSIS OF IRREGULAR WAVE DEFORMATION IN THE NEARSHORE ZONE
M. Mizuguchi 485
Chapter 33
NEW EQUATION OF SURFACE ELEVATION IN WAVE MOTION
Y. C. Ouyang, Y. Y. Chen and F. L. W. Tang 505
Chapter 34
ENGINEERING APPROACH TO NONLINEAR WAVE SHOALING
J. Walker and J. Headland 523
Chapter 35
WAVE REFLECTION FROM UNDULATING SEABED TOPOGRAPHY
A. D. Heathershaw 543
Chapter 36
THE EFFECT OF BED SLOPE ON WAVE CHARACTERISTICS
R. C. Nelson 555
Chapter 37
SENSITIVITY OF PARAMETERS AND APPROXIMATIONS IN MODELS OF TIDAL PROPAGATION AND CIRCULATION
J. J. Leendertse and S-K Liu 573
Chapter 38
A NEW TWO DIMENSIONAL TIDAL MODELLING SYSTEM
J. P. Benque, M. I. Chenin, A. Hauguel and S. Schwartz 582
Chapter 39
A THREE-DIMENSIONAL MODEL OF BERING AND CHUKCHI SEA
S.-K. Liu and J. J. Leendertse 598
Chapter 40
A FINITE ELEMENT METHOD FOR THE SHALLOW WATER EQUATIONS
A. Hauguel, G. Labadie and B. Latteux 617
Chapter 41
TRIDIMENSIONAL NUMERICAL MODEL FOR TIDAL AND WIND GENERATED FLOW
M. C. Burg, A. Warluzel and Y. Coeffe 635
Chapter 42
COMPUTATION OF PARTICLE PATHS USING THE LAGRANGIAN LONG WAVE EQUATIONS
M. A. Savoie and J. van de Kreeke 652
Chapter 43
2- AND 3-DIMENSIONAL DETERMINISTIC FREAK WAVES
S. P. Kjeldsen 677

Chapter 44
LABORATORY PHOTOGRAMMETRIC WAVE HEIGHT MEASUREMENT
J. D. Pos and F. A. Kilner 695
Chapter 45
A NEW APPROACH TO TRANSIENT WAVE GENERATION
E. P. D. Mansard and E. R. Funke 710
Chapter 46
THE CONTROL OF WAVE ASYMMETRIES IN RANDOM WAVES
E. R. Funke and E. P. D. Mansard 725
Chapter 47
THREE-DIMENSIONAL MARINE MODELS FOR IMPACT STUDIES
J. C. J. Nihoul and F. C. Ronday 745
Chapter 48
ANALYSIS OF TIDAL RECORDS OF THE 1964 ALASKAN TSUNAMI
B. W. Wilson 765
Chapter 49
WAVE RUN-UP CAUSED BY NATURAL STORM SURGE WAVES
J. Grune 785
Chapter 50
WAVE RUN-UP AT SEA DIKES UNDER OBLIQUE WAVE APPROACH
E. Tautenhain, S. Kohlhase and H. W. Partenscky 804
Chapter 51
WATER WAVES PROPAGATING ON BEACHES OF ARBITRARY SLOPE
Y. Y. Chen and H. H. Hwung 811
Chapter 52
EXAMPLES OF STORM SURGE PREDICTION MODELS
P. Lencioni, J. P. Benque and Y. Coeffe 823
Chapter 53
WATERWAVES CALCULATION BY NAVIER-STOKES EQUATIONS
O. Daubert, A. Hauguel and J. Cahouet 832
Chapter 54
APPLICATIONS OF A NUMERICAL SHALLOW WATER WAVE MODEL
A. Hauguel and P. Pechon 846
Chapter 55
ON THE VARIATION OF CHARACTERISTICS OF TWO WAVE TRAINS CROSSING IN INTERMEDIATE DEPTH
H. H. Hwung and C. P. Tsai 862
Chapter 56
INTEGRAL PROPERTIES FOR VOCOIDAL THEORY AND APPLICATIONS
G. P. Bleach 887

PART II
COASTAL SEDIMENT PROBLEMS

Chapter 57
ARTIFICIAL MANIPULATION OF BEACH PROFILES
T. W. Kana and M. Svetlichny 903
Chapter 58
FIELD STUDY ON ONSHORE-OFFSHORE SEDIMENT TRANSPORT
M. Hattori 923
Chapter 59
MORPHOLOGY AND DYNAMICS OF CRESCENTIC BAR SYSTEMS
V. Goldsmith, D. Bowman, K. Kiley, B. Burdick, Y. Mart and S. Sofer 941
Chapter 60
LONGSHORE TRANSPORT DETERMINED BY AN EFFICIENT TRAP
R. G. Dean, E. P. Berek, C. G. Gable and R. J. Seymour 954
Chapter 61
FIELD EXPERIMENTS ON LONGSHORE SAND TRANSPORT IN THE SURF ZONE
N. C. Kraus, M. Isobe, H. Igarashi, T. Sasaki and K. Horikawa 969
Chapter 62
LITTORAL PROCESSES IN CAMPELLO COASTS
J. J. Diez and M. Arenillas 989
Chapter 63
BARRIER BEACH FEATURES OF CALIFORNIA
H. Converse 1008
Chapter 64
CHANGES IN THE COASTAL MORPHOLOGY OF VRACHATI, GREECE
C. I. Moutzouris and A. J. Rogan 1028
Chapter 65
COMPUTATIONAL ALGORITHM FOR LONGSHORE ENERGY FLUX INCORPORATING FRICTION
T. L. Walton and J. R. Weggel 1046
Chapter 66
BREACH/INLET INTERACTION AT MORICHES INLET
E. J. Schmeltz, R. M. Sorensen, M. J. McCarthy and G. Nersesian 1062
Chapter 67
SHORE PROTECTION AT VENICE: A CASE STUDY
A. Muraca 1078
Chapter 68
SEDIMENT BYPASSING AT MIXED ENERGY TIDAL INLETS
D. M. FitzGerald 1094
Chapter 69
HARBOUR SEDIMENTATION—COMPARISON WITH MODEL
B. D. Pratte, D. H. Willis and J. Ploeg 1119

Chapter 70
MODELING COASTAL CURRENTS AND SEDIMENT TRANSPORT
Y. P. Sheng and H. L. Butler 1127
Chapter 71
MODELLING OF SEABED EVOLUTION UNDER WAVES ACTION
Y. Coeffe and P. Pechon 1149
Chapter 72
DESIGN AND CALIBRATION OF FALSE BAY SEDIMENT MODEL
J. S. Schoonees and J. P. Moller 1161
Chapter 73
BLOWN SAND ON BEACHES
S. Kubota, K. Horikawa and S. Hotta 1181
Chapter 74
CHANNEL SHOALING PREDICTION: A METHOD AND APPLICATION
R. B. Harley and R. G. Dean 1199
Chapter 75
CONSTRUCTION OF A BREACH CLOSURE IN A BARRIER ISLAND
M. J. McCarthy, E. J. Schmeltz and G. R. Lehan 1219
Chapter 76
HYDROSEDIMENTOLOGICAL STUDIES IN BAHIA BLANCA
R. V. Petroni, D. D. Serman and R. S. Escalante 1231
Chapter 77
SPENDING BEACH BREAKWATER AT SALDANHA BAY
D. Zwemmer and J. Van't Hoff 1248
Chapter 78
SAND MOVEMENT INTO CARMEL SUBMARINE CANYON, CALIFORNIA
J. R. Dingler and R. J. Anima 1268
Chapter 79
SUSPENDED SEDIMENT DISCHARGE ON A NON-TIDAL COAST
J. P. Coakley and M. G. Skafel 1288
Chapter 80
MODEL TESTS ON LITTORAL SAND TRANSPORT RATE
J. W. Kamphuis and O. F. S. J. Sayao 1305
Chapter 81
THE RATE OF LONGSHORE SEDIMENT TRANSPORT AND BEACH EROSION CONTROL
Y. Tsuchiya 1326
Chapter 82
SEDIMENT TRANSPORT UNDER SHEET FLOW CONDITION
K. Horikawa, A. Watanabe and S. Katori 1335
Chapter 83
MEASURED AND COMPUTED COASTAL OCEAN BEDLOAD TRANSPORT
A.W. Niedorada, C.-M. Ma, P. A. Mangarella, R. H. Cross, S. R. Huntsman and D. D. Treadwell 1353
Chapter 84
FIELD INVESTIGATION OF BEACH PROFILE CHANGES AND THE ANALYSIS USING EMPIRICAL EIGENFUNCTIONS
H. Hashimoto and T. Uda 1369
Chapter 85
EXPERIMENTS ON BEACH PROFILE CHANGE WITH A LARGE WAVE FLUME
R. Kajima, T. Shimizu, K. Maruyama and S. Saito 1385

Chapter 86
DESCRIPTION OF BEACH CHANGES USING AN EMPIRICAL PREDICTIVE MODEL OF BEACH PROFILE CHANGES
T. Uda and H. Hashimoto 1405
Chapter 87
MODELING ON-OFFSHORE SEDIMENT TRANSPORT IN THE SURFZONE
J. A. Bailard 1419
Chapter 88
SEDIMENT TRANSPORT AND BEACH TRANSFORMATION
T. Shibayama and K. Horikawa 1439
Chapter 89
A PROCESS-RESPONSE MODEL FOR HURRICANE WASHOVERS
J. R. Suter, D. Nummedal, A. K. Maynard and P. Kemp 1459
Chapter 90
NATURAL BAR BYPASSING OF SAND AT A TIDAL INLET
W. J. Sexton and M. O. Hayes 1479
Chapter 91
SHOALING WITH BYPASSING FOR CHANNELS AT TIDAL INLETS
C. Galvin 1496
Chapter 92
DREDGING TO MINIMIZE WAVE PENETRATION INTO A HARBOUR
H. P. Riedel and A. P. Byrne 1514
Chapter 93
SCOUR BEHIND CIRCULAR CYLINDERS IN DEEP WATER
J. Imberger, D. Alach and J. Schepis 1522
Chapter 94
INCIPIENT MOTION OF PARTICLES UNDER OSCILLATORY FLOW
L. Lenhoff 1555
Chapter 95
RESUSPENSION OF DEPOSITED COHESIVE SEDIMENT BEDS
A. J. Mehta and E. Partheniades 1569
Chapter 96
BED LOAD TRANSPORT OF FINE SAND BY LAMINAR AND TURBULENT FLOW
A. J. Grass and R. N. M. Ayoub 1589
Chapter 97
SURVEY TECHNIQUES/PROCEDURES AND DATA PROCESSING FOR MONITORING NEARSHORE SEDIMENT TRANSPORT
J. Zacks 1600
Chapter 98
FIELD INVESTIGATION OF LONGSHORE TRANSPORT DISTRIBUTION
E. P. Berek and R. G. Dean 1620
Chapter 99
NEW FRAMEWORK FOR PREDICITON OF LONGSHORE CURRENTS
C. A. Fleming and D. H. Swart 1640
Chapter 100
MODELING LONGSHORE CURRENTS FOR FIELD SITUATIONS
S. R. Vemulakonda, J. R. Houston and H. L. Butler 1659
Chapter 101
SHORE-PARALLEL FLOWS IN A BARRED NEARSHORE
B. Greenwood and D. J. Sherman 1677

PART III
COASTAL STRUCTURES AND RELATED PROBLEMS

Chapter 102
FORCES INDUCED BY BREAKERS ON PILES
Robert L. Wiegel 1699
Chapter 103
GANSBAAI FISHING HARBOUR—THE DESIGN AND CONSTRUCTION OF A BREAKWATER ON A HOSTILE COAST
W. S. van Dijk, A. P. M. Vonk and G. de E. Retief 1716
Chapter 104
REPAIR TO A DOLOS ARMOURED BREAKWATER
C.W. Glodowski, D. L. Lajoie and Y. Ropars 1733
Chapter 105
ZEEBRUGGE'S MAIN BREAKWATERS
L. V. Van Damme 1745
Chapter 106
CONSTRUCTION SEQUENCE MODELLING FOR HARBOUR BREAKWATER
R. W. Hendry 1765
Chapter 107
DESIGN AND CONSTRUCTION OE HADERA OEESHORE COAL UNLOADING TERMINAL
S. L. Yaron, J. Shimoni, C. Tzachar and D. Zwemmer 1786
Chapter 108
WAVE EORCES IN PILES OF VARIABLE DIAMETER
B. LeMehaute, J. Walker, J. Headland and J. Wang 1800
Chapter 109
PROTOTYPE TESTS ON RIPRAP UNDER RANDOM WAVE ATTACK
J. D. Pitt and P. Ackers 1820
Chapter 110
OEESHORE ARTIEICIAL STRUCTURES AND THEIR INELUENCE ON THE ISRAEL AND SINAI MEDITERRANEAN BEACHES
Y. Nir 1837
Chapter 111
COASTAL PROTECTION DEVICES—A REVIEW*
D. N. Eoster 1857
Chapter 112
VARIATION OF FORESHORE DUE TO DETACHED BREAKWATERS
O. Toyoshima 1873
Chapter 113
RESULTS OE SHORELINE EROSION DEMONSTRATION PROGRAM
B. L. Edge and J. G. Housley 1893

*This paper is an overview of the papers discussed in the poster session on Shore Protection Devices. The papers discussed are presented in Chapters 112–118.

Chapter 114
PERFORMANCE OF SAND-FILLED TUBE SHORE PROTECTION, TUKTOYAKTUK, NORTH WEST TERRITORIES, CANADA
V. K. Shah 1901
Chapter 115
THE BEHAVIOUR OF PROTOTYPE BOULDER REVETMENT WALLS
A. W. Smith and D. M. Chapman 1914
Chapter 116
SEDIMENTOLOGICAL INFLUENCES OF DETACHED BREAKWATERS
D. S. Rosen and M. Vajda 1930
Chapter 117
LITTORAL PROBLEMS IN THE PORTUGUESE WEST COAST
I. B. M. Oliveira, A. J. S. F. Valle and F. C. C. Miranda 1950
Chapter 118
DURBAN BEACHES RECLAMATION: PRACTICAL ASPECTS
K. A. Barnett 1970
Chapter 119
FLOATING TYRE BREAKWATERS—A CASE HISTORY
R. C. McGregor and C. H. G. Gilbert 1992
Chapter 120
NON-LINEAR WAVE FORCES ON FLOATING BREAKWATERS
C. T. Niwinski and M. de St. Q. Isaacson 2009
Chapter 121
DOLOS STABILITY: EFFECT OF BLOCK DENSITY AND WAIST THICKNESS
D. J. P. Scholtz, J. A. Zwamborn and M. van Niekerk 2026
Chapter 122
IMPROVEMENTS IN MODELLING RUBBLE-MOUND BREAKWATERS
G. W. Timco and E. P. D. Mansard 2047
Chapter 123
PROTOTYPE TESTING OF DOLOSSE TO DESTRUCTION
T. Terao, K. Terauchi, S. Ushida, N. Shiraishi, K. Kobayashi and H. Gahara ... 2062
Chapter 124
A NUMERICAL MODEL OF WAVE/BREAKWATER INTERACTIONS
D. I. Austin and R. S. Schlueter 2079
Chapter 125
FACTORS OF SAFETY FOR THE DESIGN OF BREAKWATERS
J. D. Mettam and J. G. Berry 2097
Chapter 126
BREAKWATER STABILITY-BREAKING WAVE DATA
R. D. Carver and D. D. Davidson 2107
Chapter 127
STABILITY ANALYSIS FOR A RUBBLE-MOUND FOUNDATION THROUGH IRREGULAR WAVE TEST
M. Yamamoto and T. Asakawa 2129
Chapter 128
IRREGULAR WAVE TESTS FOR COMPOSITE BREAKWATER FOUNDATIONS
K. Tanimoto, T. Yagyu and Y. Goda 2144
Chapter 129
THE MONITORING OF RUBBLE MOUND BREAKWATER STABILITY USING A PHOTOGRAPHIC SURVEY METHOD
J. W. J. Kluger 2164

Chapter 130
COMBINED WAVE-CURRENT FORCES ON HORIZONTAL CYLINDERS
B. D. Chandler and J. B. Hinwood 2171
Chapter 131
DISSIPATION OF WAVE ENERGY IN A SEAWATER OUTFALL CHANNEL
K. G. Witthaus, G. De F. Retief, G. K. Prestedge and L. R. Huskins 2189
Chapter 132
TIDAL EROSIONAL EFFECTS ON A BULKHEAD SYSTEM
R. M. Noble, W. H. Roth and U. K. Patil 2204
Chapter 133
BREAKAGE OF CONCRETE ARMOR UNITS
D. G. Markle and D. D. Davidson 2216

PART IV
COASTAL, ESTUARINE AND ENVIRONMENTAL PROBLEMS

Chapter 134
RESPONDING TO AN SOS—SAVE OUR SHORES
E. R. Heiberg III, L. A. Duscha and J. H. Lockhart 2241
Chapter 135
ENVIRONMENT IN COASTAL ENGINEERING: DEFINITIONS AND EXAMPLES*
Cyril Galvin 2264
Chapter 136
STRUCTURAL DESIGN ASPECTS OF A COASTAL BUILDING CODE
R. R. Clark 2285
Chapter 137
THE ESTUARIES OF NATAL: A METHOD OF CLASSIFICATION
J. E. Perry 2300
Chapter 138
ENVIRONMENTAL AND ENGINEERING CONSIDERATIONS IN DESIGNING COASTAL WATER INTAKES
P. Hofmann, Y. G. Mussalli and E. P. Taft 2308
Chapter 139
COASTAL ENGINEERING IN SOUTH AFRICA
K. S. Russell 2322
Chapter 140
YACHT HARBOURS IN THE UNITED KINGDOM
J. D. Mettam, P. C. Mornement, and J. G. Berry 2332
Chapter 141
THERMAL IMPACT STUDIES FOR FRENCH COASTAL NUCLEAR SITES
Y. Coeffe, P. M. Clique and B. Manoha 2342
Chapter 142
STUDY ON SEDIMENT TRANSPORT IN A POWER STATION HARBOR BASIN
K. Maruyama, R. Kajima, A. Narihiro and K. Kondo 2351
Chapter 143
SALINITY INTRUSION INTO MULTI-PORT SEA OUTFALLS
J. A. Charlton 2376
Chapter 144
DRIFT CURRENTS OF CLEAN AND SLICK SEA SURFACE
J. Wu 2386
Chapter 145
LOCAL WIND FORCING AND SMALL SCALE UPWELLING
C. A. R. Bain 2390
Chapter 146
MARINE PIPELINE PROTECTION WITH FLEXIBLE MATTRESS
A. D. Crowhurst 2403

*This paper is an overview of the papers discussed in the poster session on Environmental Aspects in Coastal Engineering Design. The papers discussed are presented in Chapters 136–137.

Chapter 147
SAN FRANCISCO'S SOUTHWEST OCEAN OUTFALL
Y. Eisenberg and D. D. Treadwell 2418
Chapter 148
SEDIMENT TRANSPORT INVESTIGATIONS IN A NEW ZEALAND TIDAL INLET
K. P. Black and T. R. Healy 2436
Chapter 149
ARTIFICIAL BREACHINGS OF BOT RIVER ESTUARY
G. A. W. Fromme 2458
Chapter 150
INTERFACIAL AND BED SHEAR STRESSES IN SALINE WEDGES
V. Dermissis and E. Partheniades 2474
Chapter 151
MORPHOLOGICAL REACTIONS OF TIDAL SYSTEMS DUE TO NEARSHORE CONSTRUCTION WORKS
R. Dieckmann, H. W. Partenscky and H. Schwarze 2494
Chapter 152
A SURVEY OF MAN-MADE TIDAL SWIMMING POOLS ALONG THE SOUTH AFRICAN COAST
D. E. Bosman and D. J. P. Scholtz 2504
Chapter 153
DESIGN OF COASTAL STRUCTURES FOR RECREATIONAL PURPOSES
G. H. O'Connell 2514
Chapter 154
MULTIPURPOSE GATE OPERATION
K. Mizumura 2534
Chapter 155
THE COASTAL WIND FIELD OF THE SOUTHERN CAPE
I. T. Hunter 2551
Chapter 156
TIDAL AND INERTIAL CURRENTS AROUND SOUTH AFRICA
E. H. Schumann and L-A Perrins 2562
Chapter 157
THE RELINING OF SAICCOR'S EFFLUENT OUTFALL
M. Bernstein, H. P. L. Ahrens and M. D. Smart 2581
Chapter 158
CIRCULATION OF TWO MULTIPASS ESTUARIES IN THE GULF OF MEXICO
D. S. Graham 2595
Chapter 159
AUGMENTATION OF URBAN WATER BY ANTARTIC ICEBERGS
J. D. Lawson and D. S. Russell-Head 2610

PART V
SHIP MOTIONS

Chapter 160
MOORED SHIP RESPONSE IN IRREGULAR WAVES
E. P. D. Mansard and B. D. Pratte 2621
Chapter 161
MEASUREMENT TECHNIQUES FOR MOORED SHIP DYNAMICS
J. Moes and S. G. Holroyd 2641
Chapter 162
SHIP MOTIONS RELATED TO DEEP DRAFT CHANNEL DESIGN
S. Noble 2662
Chapter 163
WAVE-INDUCED SHIP MOTIONS IN HARBOUR ENTRANCES—
A FIELD STUDY
A. C. van Wyk 2681
Chapter 164
OPERATIONAL PROCEDURES, RICHARDS BAY HARBOUR
J. A. Zwamborn and P. J. Cox 2700
Chapter 165
THE RESPONSE OF SMALL CRAFT TO WAVE ACTION
M. Isaacson and A. G. Mercer 2723
Chapter 166
THE MOTIONS OF A MOORED SHIP IN A HARBOR BASIN
T. Sawaragi and M. Kubo 2743
Chapter 167
STUDY OF SHIP'S TRACK AND MOTIONS AT PORT TARANAKI
G. Greenstreet 2763
SUBJECT INDEX 2773
AUTHOR INDEX 2777

Skiboat during beach survey in surf waves at Richards Bay

PART I
THEORETICAL AND OBSERVED WAVE CHARACTERISTICS

Victoria Bay, George

TURBULENCE GENERATED BY WAVE BREAKING ON BEACH

by

T. Sakai[1] , Y. Inada[2] and I. Sandanbata[3]

ABSTRACT

Horizontal and vertical velocities are measured with a hot-film anemometer(HFA) and a two-component laser-doppler velocimeter(LDV) in surf zones on uniform slopes of about 1/30 in two wave tanks. The turbulence generated by wave breaking is detected from the records. Following three aspects of the turbulence are discussed : (1) the distribution of the turbulence intensity in the surf zone, (2) the variation of the vertical distribution of the turbulence during one wave period and (3) the variation of the Reynolds stress during one wave period. It is found that the pattern of the distribution of the turbulence in the surf zone depends on the breaker type. A model is proposed, by extending the turbulent wake theory, to explain the variation of the vertical distribution of the turbulence during one wave period.

1. INTRODUCTION

It is recognized that the turbulence generated by wave breaking in surf zone plays an important role in various phenomena such as generation of longshore current, suspension of sediment and dispersion of material in surf zone.

Peregrine and Svendsen(1978) proposed a qualitative model for the flow field in spilling breaker. They concluded that the turbulent flow, immediately following the breaking, resembles a turbulent mixing layer.

Battjes and Sakai(1981) measured a velocity field in a steady breaker generated behind a wing inserted in a uniform open channel flow. The mean flow, the turbulent intensity, the Reynolds stress and their decays with distance downward and downstream were discussed in comparison with the turbulent shear layer and turbulnet wake theories. They concluded that the whole velocity field resembles the turbulent wake rather than the turbulent shear layer.

The steady breaker, in which Battjes and Sakai measured the velocities,

1) Assoc. Prof., Dept. of Civil Engg., Kyoto Univ., Kyoto, Japan
2) Engineer, Tobishima Cooperation, Tokyo, Japan
3) Graduate student, School of Civil Engg., Kyoto Univ., Kyoto, Japan

is not progressive but standing. Stive(1980) measured the velocity due to progressive breaking waves in a surf zone on a uniform slope of 1/40 in a wave tank by using a laser-doppler velocimeter. He also found a wake type flow in the region behind the crest. Flick, Guza and Inman(1981) measured the velocity in a surf zone on a uniform slope of 1/35 in a wave tank by using a hot-film anemometer. They discussed a difference of the turbulence due to the breaker type.

The conclusions and discussions in above mentioned two works are limited to few experimental conditions. In this study, the velocity fields are measured, under conditions different from those of their works, in surf zones on uniform slopes in two wave tanks by using a hot-film anemometer and a two-components laser-doppler velocimeter. At first, the effects of the breaker type on the overall turbulence distribution in the surf zone are discussed.

Secondly the variation of the vertical distribution of the turbulence during one wave period is discussed. A model is proposed, by extending the turbulent wake theory, in order to explain the variation. Finally a cross product of the simultaneous horizontal and vertical velocity fluctuations is calculated. The variation of this cross product during one wave period and its physical meaning are discussed.

2. EXPERIMENTS

2.1. Arrangements

The experiments were done in two wave tanks. Two wave tanks have nearly the same dimensions. The length is about 30m, the width is about 50cm and the height is about 70cm. A uniform slope of about 1/30 was installed in the tanks. The still water depth in the uniform depth part in front of the slope was always 35cm(see Fig.1). X-axis is taken shoreward from the breaking point. Z-axis is taken upward above the still water level. The experimental conditions are listed in Table 1.

The letters "H" and "L" in the case number indicate that the hot-film anemometer and laser-doppler velocimeter was used in the case respectively. h_1 is the still water depth in the uniform depth part in the tank, i is the slope and T is the wave period. H_0/L_0 is the deep-water wave steepness calculated from the wave height in the uniform depth part or at the breaking point. h_b is the still water depth at the breaking point, H_b is the wave height at the breaking point, and W is the width of the surf zone between the breaking point and the still water line (see Fig.1). The word "transient" in the column of breaker type means that the breaker type was a transient type between the spilling and plunging breakers. "HFA" and "LDV" mean hot-film anemometer and laser-doppler velocimeter respectively.

2.2. Measurements

The water surface elevation was measured at the breaking point and

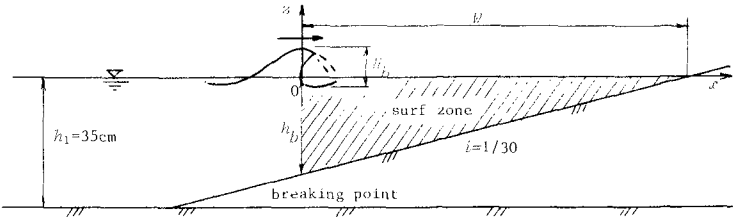

Fig. 1 Experimental Arrangements

Table 1 Experimental Conditions

case	h_1 (cm)	i	T (sec)	H_0/L_0	h_b (cm)	H_b (cm)	W (cm)	breaker type	instrument
H1	35.0	1/31	1.00	0.088	19.4	13.3	600	spilling	HFA
H2	35.0	1/28	1.16	0.066	17.7	12.8	490	spilling	HFA
L	35.0	1/31	1.17	0.063	18.0	12.8	530	spilling	LDV
H3	35.0	1/31	1.32	0.032	14.5	10.4	450	transient	HFA

the velocity measuring point with two capacitance-type wave gauges. In the cases H1 and H3, the water surface elevation was measured in the uniform depth part too.

The hot-film anemometer is DISA type 55M01, and the probe is DISA type 55R13. The hot-film probe was calibrated by using a vertically oscillating plate in still water to which the probe was attached. This probe has a vertical sensor of cylinder type and measures the velocity of the on-offshore direction. In the cases H1 and H3, in which the hot-film anemometer was used, the on-offshore velocity was measured at about 30 points under the level of the wave trough in the surf zone. The recording time at one point was 90sec. In the case H2, it was measured at about 40 points under the still water level in the surf zone. The recording time at one point was 60sec.

The two-components laser-doppler velocimeter is KANOMAX optical system 8143S, and the signal processor is KANOMAX model 8015 of tracker type. It can measure two components of oscillatory flow velocity simultaneouly. The mode of operation was the forward scatter fringe mode. The on-offshore and vertical velocities were measured at about 40 points in the case L under the still water level in the surf zone. The recording time at one point was 60sec.

All outputs from the wave gauges and the velocity meter were recorded in a analog magnetic redorder simultaneously. In the case L , the dropout signals from the laser-doppler velocimeter were also recorded.

3. DATA ANALYSIS

3.1. Distribution of Turbulence in Surf Zone(Cases H1 and H3)

In the cases H1 and H3, the data in the analog recorder were A-D converted every 0.01sec during 60sec for each measuring point. The first part of 24sec in the digital data was plotted graphically. Fig.2 shows two examples of the time profiles of the water level and the on-offshore velocity. In general, hot-film anemometer can not feel the change of the velocity direction. So the output of the measured velocity is rectified.

The figure (1) shows the time profiles at the breaking point. It is clear that the significant turbulence does not yet exist at the breaking point especially in the crest phase. On the other hand, within the surf zone, it is not so easy to find the instance when the direction of the water particle velocity changes in the time record due to the high turbulence(the figure (2)). Waves, in which the instance of the direction change was possible to find, were selected in the record. At most 90% of the waves during 24sec were selected.

The time profile of the velocity varies wave to wave. Turbulence defined as the deviation from the ensemble average of many waves(Stive, 1980) includes above mentioned velocity profile variation. Considering this fact, the measured velocity was smoothed with a moving average method for each selected wave. The time interval of average was 0.1sec.

A root-mean-square of the deviation u' from the smoothed velocity u_w was calculated for each selected wave. This was done separately for the phase of onshore velocity and the phase of offshore velocity(see Fig.3). They are called the horizontal turbulent intensities at the onshore velocity phase and the offshore velocity phase, and are expressed with symbols "$u'_{rms,c}$" and "$u'_{rms,t}$" respectively.

3.2. Variation of Vertical Distribution of Turbulence during One Wave Period(Case H2)

As well as in the cases H1 and H3, the data in the analog recorder were A-D converted every 0.01sec for each measuring point. The first part of 24sec in the digital data was plotted graphically. In order to discuss the variation of the turbulence during one wave period, the velocity record during the full length of 24sec, which contains about 20 waves, was smoothed with the same moving average method as in the cases H1 and H3(see Fig.4).

One wave period was divided into 12 sections of 0.1sec. The first section starts at the phase when the water surface crosses the still water level upward. The length of the last section is shorter than 0.1sec, because the wave period of the case H2 is 1.16sec. Each section of each wave contains 10 data of the deviation u' from the smoothed velocity u_w except for the last section. For each section, a root-mean-square of the deviation u' of all waves was calculated. This is expressed with a symbol "$u'_{rms}(t)$".

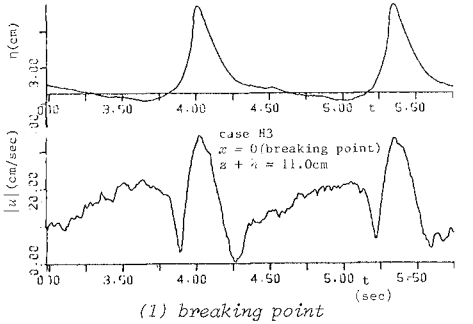

(1) breaking point

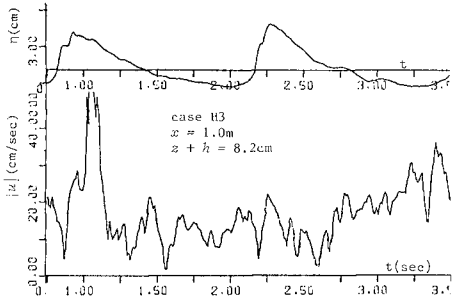

(2) surf zone

Fig. 2, (1), (2) Time Profiles of Water Level and On-offshore Velocity Measured with Hot-Film Anemometer

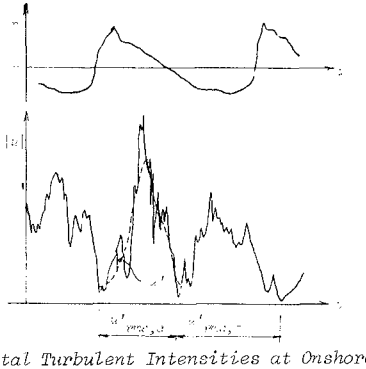

Fig. 3 Horizontal Turbulent Intensities at Onshore and Offshore Vlocity Phases $u'_{rms,c}$ *and* $u'_{rms,t}$

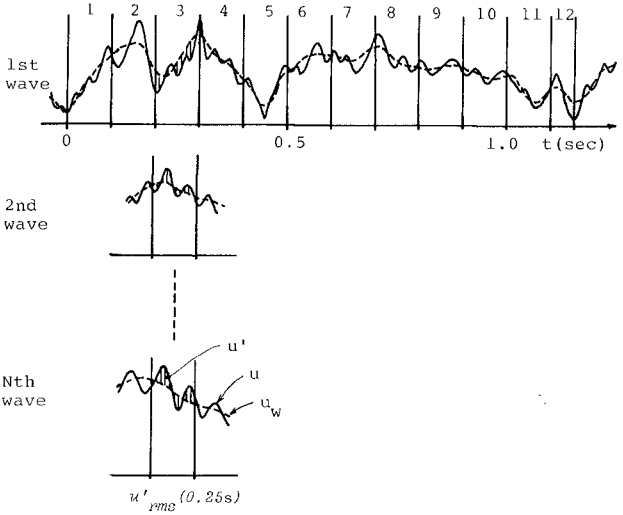

Fig. 4 Variation of Turbulent Intensity "$u'_{rms}(t)$"

3.3. Cross Product of On-offshore and Vertical Deviations u' and w' (Case L)

In the case L, the data in the analog recorder were A-D converted every 0.01sec during 48sec for each measuring point. The water level variations at the breaking point and the velocity measuring point, the on-offshore and vertical velocities and their dropout signals of 48sec were plotted graphically.

In general, laser-doppler velocimeter can not get any information about the flow velocity when no particle is detected by the LDV system. The situation of such no velocity information is called "signal dropout". The signal processor was operated in the so-called track-and-hold mode. The output from the signal processor keeps the value just before the signal dropout(see Fig. 5).

The signal dropout occurs due to several causes. At the measuring point above the trough level, in the trough phase, the laser beam goes out from the water between two glass walls of the tank. Then the dropout occurs. It occurs also when the air bubbles interupt the beams. The time intervals when no signal dropout occurs were selected from the plotted time profiles for the on-offshore and vertical velocities.

The on-offshore and vertical velocities in the no-dropout intervals were smoothed with the same moving average method as in the cases H1, H2 and H3. The product of the simultaneous on-offshore and vertical deviations u' and w' from the smoothed velocities were calculated only

in the time intervals when no dropout occurs both in the on-offshore and vertical velocities(see Fig.5).

The value of the cross product of u' and w' at every 0.01sec in each no dropout interval was smoothed again with the moving average method of 0.1sec. This smoothed value is expressed with a symbol "$\overline{u'w'(t)}$". $-\overline{u'w'(t)}$ is called Reynolds stress here. As the signal dropout occurs sometimes, there are waves in which the data of $-\overline{u'w'(t)}$ are lacked in some part of one wave period.

The Reynolds stress $-\overline{u'w'(t)}$ was ensemble averaged at every 0.01sec for all waves during 48sec. This ensemble averaged Reynolds stress is expressed with a symbol "$<-\overline{u'w'(t)}>$". As mentioned above, there are waves in which the data are lacked in some part of one wave period. Therefore, the number of the ensemble averaging is, in general, equal to or less than the number of total waves during 48sec(about 40).

The time interval of one wave was defined as from the phase 0.5sec after the crest of the preceeding wave to the phase 0.5sec after the crest of the wave. The wave period of the individual wave varies wave to wave. So, near the end of one wave period, the number of the ensemble averaged data decreases rapidly.

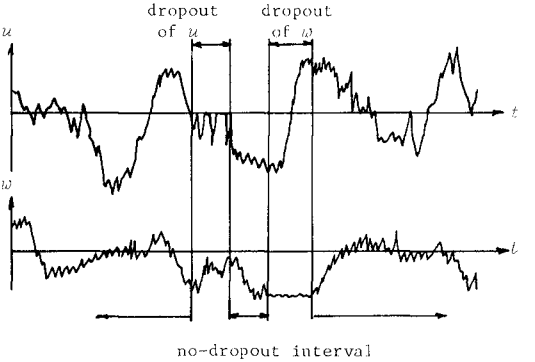

Fig.5 Signal Dropout of Laser-Doppler Velocimeter

4. DISTRIBUTION OF TURBULENCE IN SURF ZONE

4.1. Results

Fig.6,(1) shows the distribution of the horizontal turbulent intensities at the onshore velocity phase and the offshore velocity phase $u'_{rms,c}$ and $u'_{rms,t}$ in the surf zone in the case H1. In the figure, the range of scatter of the value is indicated by connecting the maximum and minimum values of each measuring point. The upper figure shows the on-offshore variation of the measured value at the highest measuring point. Fig.6,(2) shows the similar result in the case H3.

4.2. Error Estimate

In these two cases, the hot-film anemometer was used. The measured values contain some errors. The first error comes from the uncertainty of the calibration curve of the hot-film anemometer. The calibration curve itself has the error of 3cm/sec. This error influences the smoothed velocity u_w directly. But it is thought that it does not influence the deviation u' defined as $u - u_w$ so much.

Another possible cause is the vibration of the probe mouting arm. The natural frequency of the arm was increased to more than 50Hz by shortening the length of the arm. So the fluctuation in the velocity due to the vibration was separated from the turbulence, the frequency of which is thought to be lower than 50Hz.

The probe may feel the vertical component of the velocity too especially near the phase when the on-offshore component becomes 0. This was already discussed(Isobe et al., 1979). It is found, using their result, that the error is about 1cm/sec. The ambiguity in the decision of the phase when the water particle velocity changes its direction is thought not to influence the mean value u'_{rms} so much.

The value of the turbulence defined as the deviation from the smoothed velocity calculated by using the moving average method has one inherent error. The smoothed curve can not follow the abrupt change of the water particle velocity itself at the crest(see Fig.1,(1)). In fact, Fig.6 shows the turbulence of about 1cm/sec at the breaking point. This means that the value of $u'_{rms,c}$ contains the error of 1cm/sec.

The severest error comes from the air bubble interuption of the probe. At present, nothing is done to separate the effect of the air bubble interuption from the velocity measured by using the hot-film anemometer. Only one thing being done to reduce this error was to limit the measuring points under the trough level where the concentration of the air bubble is not so high. Therefore it is impossible to estimate this error quantitatively. The measured value is thought to contain this error to some extent.

4.3. Discussions

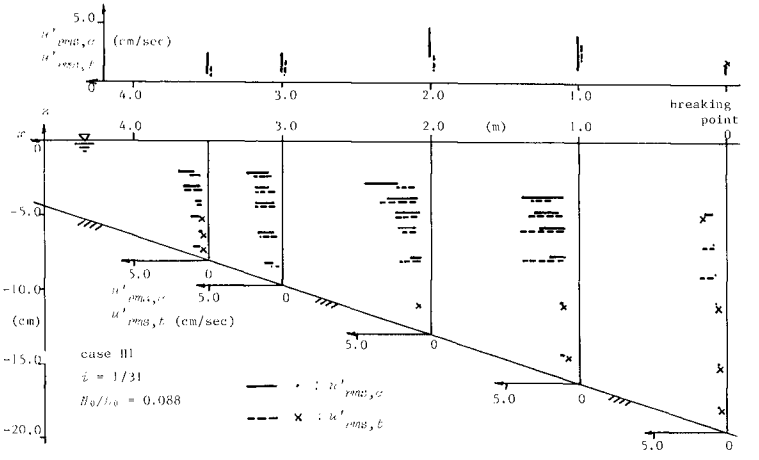

(1) case H1

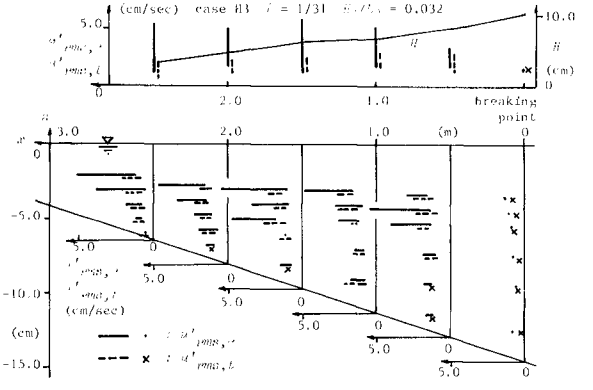

(2) case H3

Fig. 6, (1),(2) Distribution of Horizontal Turbulent Intensities at Onshore and Offshore Velocity Phases $u'_{rms,c}$ *and* $u'_{rms,t}$

From Fig.6, it is found that the turbulent intensity varies largely wave to wave especially in the case H3, in which the breaker type was a transient type from spilling to plunging. The intensity is larger in the case H3 than in the case H1 in which the breaker type was spilling. It should be noticed that the breaking wave height H_b is smaller than that of the case H1(see Table 1).

As already seen in Fig.2,(1), the significant turbulence does not exist at the breaking point. The turbulence begins to grow after the waves propagate some distance from the breaking point. In the case H1, the turbulence damps after it reaches a maximum. But in the case H3, it does not damp so much at least in the measurement region. The wave height H itself decreases monotonically even in the case H3.

The turbulent intensity is larger in the upper part than near the bottom especially in the case H3. It means that the turbulence gererated by wave breaking does not penetrate into the lower part of the water body near the bottom. In the case H3, the turbulent intensity at the offshore velocity phase $u'_{rms,t}$ is smaller than that at the onshore velocity phase $u'_{rms,c}$.

5. VARIATION OF VERTICAL DISTRIBUTION OF TURBULENCE DURING ONE WAVE PERIOD

Fig.7,(1) shows one example of the variation of the horizontal turbulent intensity $u'_{rms}(t)$ during one wave period in the case H2. The $<\eta>$ curve shows an ensemble mean of the time profile of about 20 waves. In this figure t-axis does not coincide with the still water level. Fig. ,(2) shows one example of another representation of the variation of the turbulent intensity during one wave period. In this figure, contour lines are used.

In the case H2, the hot-film anemometer was used. So the measured value contains the same errors as those in the cases H1 and H3. The velocity measurement was done also at the still water level. But, to reduce the error due to the air bubble interuption, the data at the still water level were not used in Fig. .

In this case, the velocity record during the full length of 24sec was smoothed. Therefore, the error due to the fact that the smoothed curve can not follow the abrupt change may occur also near the phase when the water particle velocity changes its direction. At such phase, the velocity becomes zero, and the rectified output drops abruptly to zero. But, as seen in Fig. ,(1), no effect of this error can be seen at the zero crossing phases.

As seen in Fig. ,(1), the phase of the peak in the curve of the variation of the turbulent intensity delays in the downward direction. This is also shown in the contour lines in the figure (2). The similar treand can be seen in Fig.8 of Stive(1980) too.

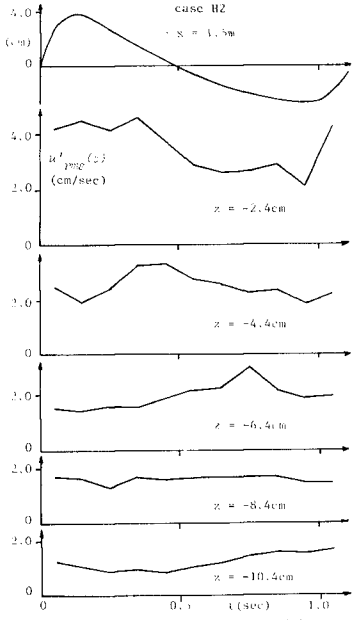

(1) 1.5m shoreward from breaking point

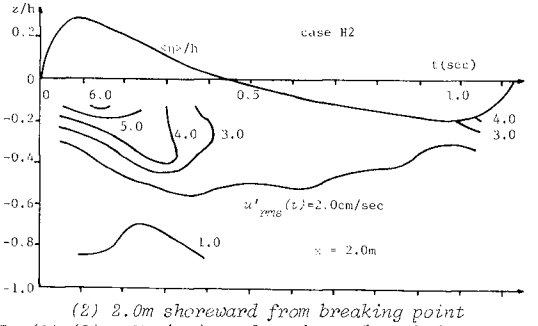

(2) 2.0m shoreward from breaking point

Fig. 7, (1),(2) Variation of Horizontal Turbulent Intensity $u'_{rms}(t)$ during One Wave Period

6. MODELING OF TURBULENCE VARIATION DURING ONE WAVE PERIOD

Fig.8 shows the turbulence variation during one wave period in form of time series of the vertical profile of turbulent intensity, at two positions 1.5m and 2.0m shoreward from the breaking point in the case H2. The crosses indicate the measured values.

The vertical profile of the turbulent intensity resemble that measured by Battjes and Sakai(1981) under an air entraining turbulent water surface generated behind a wing inserted in an open channel flow(see Fig.3 of their paper). The trend of the variation during one wave period in Fig.8 also resembles the streamwise variation of the vertical profile measured by Battjes and Sakai.

They showed that the streamwise variations of the mean velocity defect near the water surface, the length scale of the vertical profile and the turbulent intensity are explained by the turbulent wake theory(Tennekes and Lumley, 1972). In the following, it is tried to explain the turbulence variation during one wave period shown in Fig.8 by extending the turbulent wake theory.

6.1. Turbulent Wake Theory(Tennekes and Lumley, 1972)

Turbulent wake belongs to free turbulence as well as turbulent jet and turbulent shear layer(see Fig.9). Following assumptions are made in the turbulent wake theory : 1) The length scale in the streamwise direction is larger than the length scale l in the lateral direction, 2) Reynolds number is large, and 3) The order of the velocity defect U_s is same as the order of the turbulence. The equations of motion are simplified according to these assumptions.

One characteristic feature of free turbulence is that there is no characteristic length such as the water depth or the channel width. Then the velocity profile in the lateral direction are similar in the streamwise direction("self preservation"). Therefore the velocity U and the Reynolds stress are functions of only the lateral distance y and the scale l.

From above mentioned fact and the steamwise constancy of the velocity defect, it is found that the velocity scale U_s and the length scale l are proportional to the $-1/2$ power and $1/2$ power of the streamwise distance x. Introducing a constant eddy viscosity, it is found that U and the Reynolds stress are proportional to a function $f = \exp(-1/2 \cdot \alpha \xi^2)$ and $-f'$ respectively. Where $\xi = y/l$ and "'" indicates the differentiation with respect to ξ. α is a constant.

The turbulent intensity is thought to be proportional to the Reynolds stress. The shape of f' is shown in Fig.10. f' decreases near $\xi = 0$. This is not the case of the turbulent intensity, which has a nearly constant maximum value near $\xi = 0$.

6.2. Model of Turbulence Variation during One Wave Period

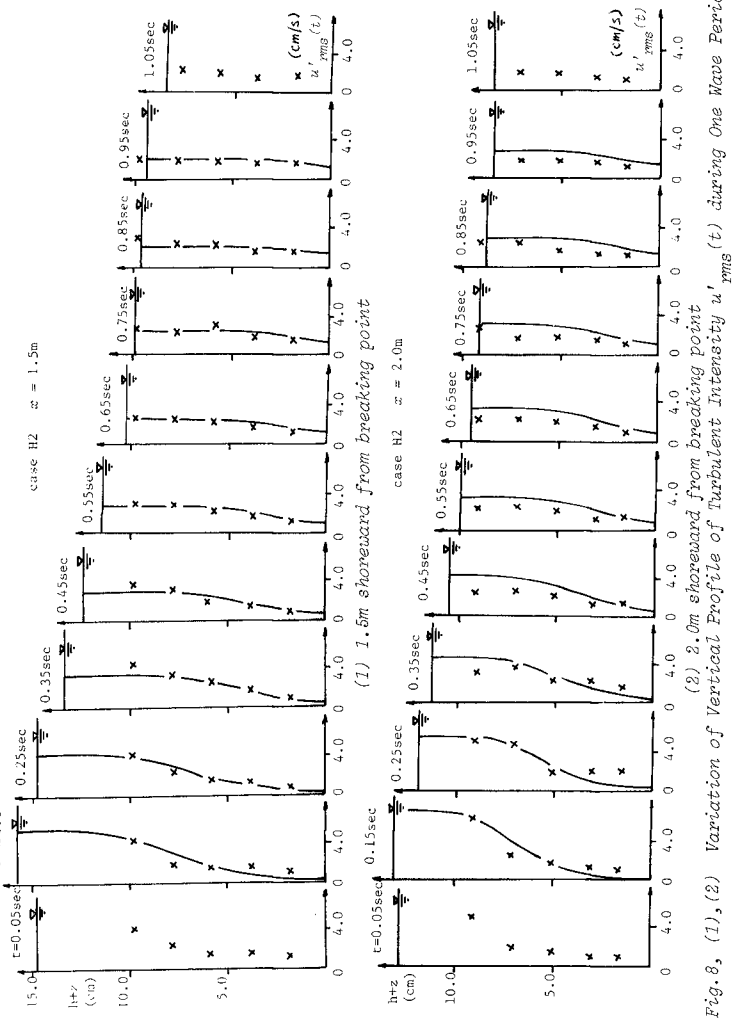

Fig. 8, (1), (2) Variation of Vertical Profile of Turbulent Intensity $u'_{rms}(t)$ during One Wave Period

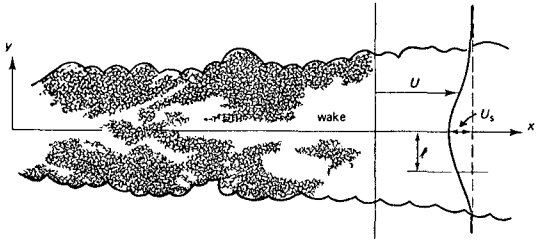

Fig.9 Turbulent Wake(Tennekes and Lumley, 1972)

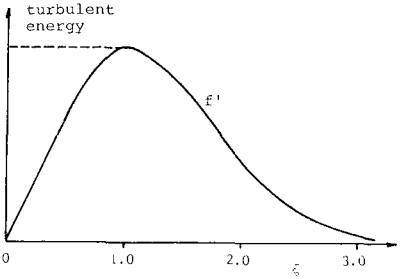

Fig.10 Lateral Profiles of Turbulence and Reynolds Stress(Tennekes and Lumley, 1972)

Before going to modeling, it should be noticed that the phenomenon to be modeled is the variation in time and not the variation in space. The turbulent wake theory itself explains the variation in the streamwise direction. But this model does not treat the variation in the on-offshore direction.

The crest phase is taken as the time origin. The phase to be modeled is limited to the range from the crest to the following trough($t = t_t$).

The instantaneous water level at each phase is taken as corresponding to the center line $y = 0$ of the turbulent wake(see Fig.9). The vertical distribution of the turbulence at each phase is assumed to be expressed by

$$\{u'_{rms}(z,t)\}^2 = \{u'_{rms}(t)_m\}^2 \gamma\{(\eta-z)/l\}, \quad (1)$$

in which η is the water level above the still water level, and l is the vertical length scale explained later. The function γ is assumed to be proportional to a function which takes the value expressed by the solid curve for $\xi > 1.0$ and the peak value of the solid curve in Fig.10 for $0 \leq \xi \leq 1.0$. $u'_{rms}(t)_m$ is a representative turbulent intensity at each phase(explained later).

The functional form of γ is determined by making its maximum value equal to 1.0 as follows :

$$\gamma(z) = \begin{cases} \frac{\eta-z}{l} \exp\left\{-\frac{1}{2}\left(\frac{\eta-z}{l}\right)^2 + \frac{1}{2}\right\} & ; \frac{\eta-z}{l} > 1.0 \\ 1.0 & ; 0 \le \frac{\eta-z}{l} \le 1.0 \end{cases} . \qquad (2)$$

The crest height η_0 above the still water level is taken as the vertical length scale l_0 at $t = 0$(crest phase). According to the turbulent wake theory, l is assumed to increase in proportion to the 1/2 power of the phase :

$$l = l_0\{(t + T)/T\}^{1/2} , \qquad (3)$$

where T is the wave period.

As seen from Eq.(3), $l = l_0 = \eta_0$ at $t = 0$. So $(\eta-z)/l = 1.0$ at $t = 0$ and $z = 0$. Therefore at the crest phase, $\gamma = 1.0$ from the water surface to the still water level. The measured value above the still water level at the crest phase should be taken as $u'_{rms}(0)_m$. Unfortunately there is no data above the still water level. The value of $u'_{rms}(0)_m$ was estimated from the data at the highest point and the profile given by Eq.(2). According to the turbulent wake theory, $u'_{rms}(t)_m$ is assumed to decrease in proportion to the -1/2 power of the phase :

$$\{u'_{rms}(t)_m\}^2 = \{u'_{rms}(0)_m\}^2 \left\{ \frac{\frac{1-K^2}{K^2} t + t_t}{t_t} \right\}^{-1} , \qquad (4)$$

where $K = u'_{rms}(t_t)_m / u'_{rms}(0)_m$.

The maximum measured value at $t = t_t$ was taken as $u'_{rms}(t_t)_m$.

6.3. Comparison with Experimental Results

The phase 0.95sec after the zerp-up crossing phase of the water surface was taken as t_t. The calculated vertical profile of the turbulent intensity is shown with solid lines in Fig. . The model developed here is rather simple. But the vertical profile and the time variation of the turbulence are explained well, at least in the lower part under the still water level.

But it should be recalled that the breaker type of the case H2 is a typical spilling type. Futhermore, the comparisons with the experimental results are limited to the data at the positions 1.5m and 2.0m shoreward from the breaking point. The width of the surf zone is about 500m. In these positions, the waves after breaking propagate just like stable bores. Therefore, it can be said that the model developed here is applicable to the turbulent field in the bore region located at 30 to 40% of the surf zone width shoreward from the breaking point.

7. CROSS PRODUCT OF ON-OFFSHORE AND VERTICAL DEVIATIONS

7.1. Result

Fig.11 shows the variation during one wave period of the ensemble averaged Reynolds stress $\langle -\overline{u'w'(t)} \rangle$ at the location 1.5m shoreward from the breaking point in the case L, in which the two-components laser-doppler velocimeter was used. As explained in 3.3., the ensemble averaged Reynolds stress $\langle -\overline{u'w'(t)} \rangle$ is defined as the ensemble average of the Reynolds stress $-\overline{u'w'(t)}$ at every 0.01sec of all waves during 48sec. But exactly speaking, the value shown in Fig.11 is not the value of this ensemble averaged Reynolds stress.

As explained in 3.3., the time interval of one wave period was defined as the interval from the phase 0.5sec after the preceeding wave crest to the phase of 0.5sec after the present wave crest. This time interval of one wave period was divided into 12 sections of 0.1sec. The value in Fig.11 is an averaged value of the ensemble averaged Reynolds stress in each section.

7.2. Discussions

One simple definition of Reynolds stress is the ensemble average of the product of the deviations u' and w' from the smoothed velocities over many waves. On the other hand, as well known, Reynolds stress is defined originally as a time mean of the product. So the Reynolds stress defined as the ensemble average over many waves is completely different from the original Reynolds stress.

In this study, the Reynolds stress was defined as the time mean. The interval of the time mean is 0.1sec(see 3.3.). The choise of the time length is arbitrary. There is no definite reason to choose 0.1sec. The time interval of no dropout is not always longer than 0.1sec. In a time interval shorter than 0.1sec, the interval of the time mean was reduced. Also in the beginning and end of one interval of no dropout, the interval of the time mean was reduced.

The number attached to each plotted point indicates the number of the averaged data. Near the water surface, it decreases rapidly. If no dropout occurs, it amounts to about 400.

The value itself is small compared with the value of the turbulent intensities $u'_{rms,c}$, $u'_{rms,t}$ and $u'_{rms}(t)$ shown in Fig.s 6 to 8. In many points, it is smaller than $1.0cm^2/sec^2$. $1.0cm^2/sec^2$ is the order of the possible error of the turbulent intensity(see 4.2.). At the position 0.5m shoreward from the breaking point, the calculated value of the ensemble averaged Reynolds stress in each section is less than $0.5cm^2/sec^2$. So, it may be said that the value of the Reynolds stress larger than $0.5cm^2/sec^2$ is meaningful.

As explained in 6.1., the Reynolds stress in the turbulent wake is proportional to $-f'$. Therefore, the cross product itself is proportional

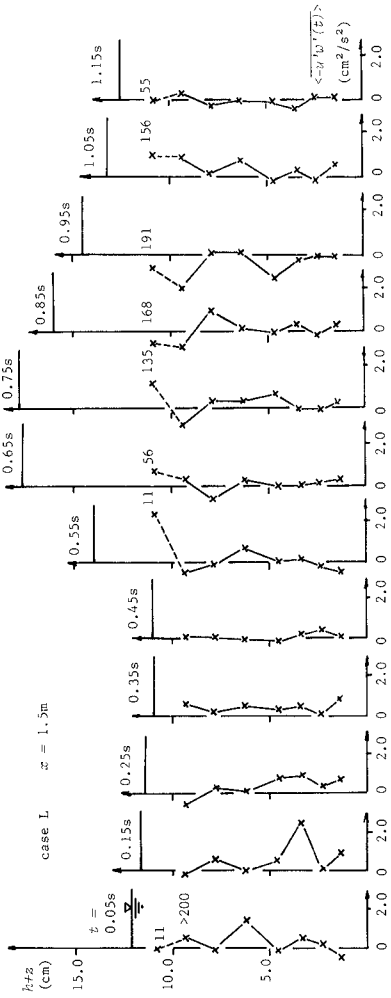

Fig. 11 Variation during One Wave Period of Ensemble Averaged Reynolds Stress $\langle -\overline{u'w'(t)} \rangle$ (1.5m Shoreward from Breaking Point)

to f'. As shown in Fig.4 of Battjes and Sakai(1981), the cross product under a steady breaker generated behind a wing inserted in an open channel flow has a similar vertical profile as f' in Fig.10.

The direction of the positive on-offshore velocity in this study is opposite to that of the turbulent wake in Fig.9. So, if the Reynolds stress obeys the turbulent wake theory, it must be proportional to f'. In Fig.11, there is no such trend. It becomes negative in some parts of the vertical profile. It is also found that at the phase after the crest it has a positive hump in the lower part of the vertical profile.

As mentioned above, the calculated value of the Reynolds stress has many ambiguities. Therefore no definite conclusion is derived from Fig.11. Only thing to be said is that the Reynolds stress field in surf zone may not be explained by the turbulent wake theory which could explain roughly the turbulent intensity generated by wave breaking.

8. CONCLUSIONS

Horizontal and vertical velocities were measured with a hot-film anemometer and a two-components laser-doppler velocimeter in surf zones on uniform slopes of about 1/30 in two wave tanks.

The rectified on-offshore velocity measured with the hot-film anemometer was smoothed with a moving average method of 0.1sec. A root-mean-square of the deviation from the smoothed velocity was calculated for the onshore and offshore velocity phases of individual waves. The following conclusions were obtained : 1) The calculated turbulent intensity varies more and is larger in the case of the transient breaker type between spilling and plunging than in the case of spilling breaker, 2) the turbulent intensity does not damp so much as the waves propagete in the surf zone in the case of transient breaker, while it damps in the case of spilling breaker, and 3) the turbulent intensity is larger in the upper part of the water column than near the bottom.

A root-mean-square of the deviation from the smoothed on-offshore velocity was calculated for every 0.1sec section composing one wave period over about 20 waves in the case of spilling breaker. It was found that the vertical distribution of the calculated turbulent intensity and its variation during one wave period resemble those of the turbulence under a steady breaker generated behind a wing inserted in an open channel flow which was explained by the turbulent wake theory(Battjes and Sakai, 1981). A model was proposed, based on the turbulent wake theory, to explain the variation of the vertical distribution of turbulence during one wave period. It was found that this simple model can explain it roughly.

A time-mean over 0.1sec of the cross product of the on-offshore and vertical deviations from the smoothed values of the velocities measured with the laser-doppler velocimeter was calculated. It was defined as the Reynolds stress. An ensemble average of the Reynolds stress was

taken over about 40 waves. The variation during one wave period of the vertical distribution of the ensemble averaged Reynolds stress was discussed. It was suggested that the turbulent wake theory may not explain the variation of the Reynolds stress in surf zone.

9. ACKNOWLEDGEMENT

This study was partly supported by the Grant-in-Aid for Scientific Research of the Ministry of Education, Science and Culture, Japan, for which the authors express their appreciation.

10. REFERENCES

Battjes, J.A. and T. Sakai (1981) : Velocity field in a steady breaker, Jour. of Fluid Mechanics, Vol.111, pp.421-437.

Flick, R.E., R.T. Guza and D.L. Inman (1981) : Elevation and velocity measurements of laboratory shoaling waves, Jour. of Geophysical Research, Vol.86, No.C5, pp.4149-4160.

Isobe, M., N. Fukuda and K. Horikawa (1979) : Experiment on velocity field in two-dimensional surf zone, Proc. of 26th Japanese Conf. on Coastal Engineering, p.42(in Japanese).

Peregrine, D.H. and I.A. Svendsen (1978) : Spilling breakers, bores and jydraulic jumps, Proc. of 16th Conf. on Coastal Engineering, pp.540-550.

Stive, M.J.F. (1980) : Velocity and pressure field of spilling breakers, Proc. of 17th Conf. on Coastal Engineering, pp.547-566.

Tennekes, H. and J.L. Lumley (1972) : A First Course in Turbulence, The MIT Press, pp.104-145.

ON THE RELATION BETWEEN CHANGES IN INTEGRAL QUANTITIES OF SHOALING WAVES AND BREAKING INCEPTION

Takashi Yasuda,[1] Shintaro Goto[2] and Yoshito Tsuchiya,[3] M. ASCE

ABSTRACT

This paper describes a mechanism of breaking waves over sloping bottoms in terms of changes in integral quantities of the waves. Systematic computations are made of wave profiles of shoaling waves up to the numerical unstable points by using the K-dV equation with variable coefficients and internal properties such as horizontal and vertical water particle velocities by a stream function method satisfying the conservation laws of mass and energy. Applicability of the numerical results is examined and a relation between numerical unstable points and actual breaker points is found. Characteristics of the integral quantities of shoaling waves are investigated in relation to the existence of the extremum of the energy of the shoaling waves and their breaking inception.

INTRODUCTION

A sound knowledge on breaking waves is very important for coastal engineering, as stated by Longuet-Higgins(1980) at the Sydney Conference. However, theoretical elucidation on the mechanism of breaking waves on sloping bottoms is not enough, although many prominent theoretical investigations have been carried out on this problem. A series of studies by Longuet-Higgins et al.(1974 & 1975) obtained the very interesting conclusion that the integral quantities, such as the phase speed, momentum and energy increase with wave-height initially, become maxima and then decrease; that is, these quantities reach their extrema at a wave-height preceding the highest wave. So, a great interest is now being taken in the relation between the existence of the extrema of the integral quantities and breaking inception and in the derivation of the breaking inception from the behaviour of the integral quantities which reflect the properties of the whole wave field, by regarding the wave breaking as an instability of the field.

Because symmetrical wave formes were assumed in their calculation, the conclusion obtained by Longuet-Higgins et al. indicates only that the integral quantity of the highest wave is not usually maximum and does not directly show that extrema arise in the integrals of shoaling waves on sloping bottoms. Therefore, it is necessary to calculate the changes in the integral quantities of shoaling waves in order to investigate the mechanism of wave breaking on a sloping bottom which is important in coastal engineering.

1 Associate Professor, Department of Civil Engineering, Gifu University
2 Research Staff, Mitsubishi Research Institute Incorporation
3 Professor, Disaster Prevention Research Institute, Kyoto University, Kyoto, Japan

Here, based on the results of the authors' studies(1979 & 1982) on the transformation of shoaling waves over sloping bottoms, are made computations on the wave profiles of shoaling waves up to the numerically unstable points by using the K-dV equation with variable coefficients. At the same time, the internal properties such as water particle velocities are computed for the given wave profiles at each water depth by the stream function method, satisfying the conservation laws of mass and energy. The relation between numerically unstable points and the actual breaker points defined by Goda(1980) are also examined, and investigations are made of the characteristics of the integral quantities of shoaling waves over sloping bottoms. It is then shown that whether the energy of shoaling waves has extrema or not is a function of the surf-similarity parameter(1974). Finally, examinations are made of the relation between the existence of the extrema of the energy of shoaling waves and breaking inception or breaker type.

CALCULATION OF INTERNAL PROPERTIES OF SHOALING WAVES ON SLOPING BOTTOMS

1. Reduction of Basic Equation

By considering irrotational wave motion over a uniformly sloping bottom and taking a Cartesian co-ordinate system as Shown in Fig.1, the governing equations are given as

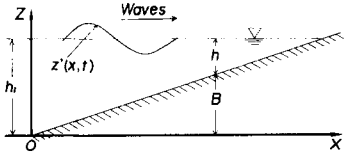

Fig. 1 Co-ordinate system and symbols used

$$\left.\begin{aligned} &\nabla^2\phi=0,\quad \phi_t+(\phi_x^2+\phi_z^2)/2+g(z-h)\big|_{z=h_1+z'}=0,\\ &z'_t+z'_x\phi_x-\phi_z\big|_{z=h_1+z'}=0,\quad \phi_z-B_x\phi_x\big|_{z=B}=0, \end{aligned}\right\}\quad (1)$$

where, the subscripts denote partial differentiation, ϕ is the velocity potential, z' the water surface displacement from the mean water level, B the height of the sea bottom above the horizontal co-ordinate, h_1 the depth of mean water at the origin and g the acceleration of gravity. The above equations can be directly solved by a numerical method, such as the MAC method. However, there arise the problems of the great effort necessary for the computation and the insufficient accuracy of numerical solutions in view of the labour expended, so that the following approach is adopted here.

For our calculations the following four assumptions are made.

i) Bottom slopes are gentle and the water depth changes dependently on $X = \varepsilon x$ in which ε is a small parameter, and therefore,

ii) the wave reflection from the sloping bottom is negligible and mass transport by waves is not bound by a sloping bottom. In addition, according to the conclusion by Stiassnie et al.(1975) that the effect of wave set-down is less than about one percent of the water depth, the third assumption is

iii) the effect of wave set-down is negligible. And lastly,

iv) the effects of nonlinearity and frequency dispersion of waves and bottom slope are of the same order.

By developing Kakutani's approach(1971) to a higher order approximation on the basis of these assumptions, Eq.(1) yields the following tractable wave equation using a new expression of wave profile, η.

$$\eta_\tau + 3\eta\eta_\xi/2c_0^3 + c_0\eta_{\xi\xi\xi} - B^*{}_\tau\eta/4c_0^2 = \epsilon(-c_0^3\eta_{\xi\xi\xi\xi\xi}/15$$
$$-3\eta_\xi\eta_{\xi\xi}/2c_0 - 2\eta\eta_{\xi\xi\xi}/3c_0 - 2c_0\eta_{\xi\xi\tau}/3 + B^*_\tau\eta_{\xi\xi}/2 - 3\eta^2\eta_\xi$$
$$/2c_0^5 - \eta_\xi\Omega_\tau/c_0^2 - 3\eta\eta_\xi/c_0^2 - \Omega_{\tau\tau}/2c_0 - 5B^*_\tau\eta^2/8c_0^4$$
$$+ B^*_\tau\Omega_\tau/2c_0) + o(\epsilon^2) \qquad (2)$$

where

$$\left.\begin{aligned} &c_0 = \sqrt{1-B^*} = \sqrt{h^*},\ \xi = \epsilon^{1/2}(\int dx^*/c_0 - t^*),\ \tau = \epsilon^{3/2}x^*, \\ &B^* = B/h_1,\ x^* = x/h_1,\ z^* = z/h_1,\ t^* = t\sqrt{g/h_1},\ h^* = h/h_1, \\ &\epsilon = (h_1/L_1)^2 \ll 1,\ \zeta = z^* - B^*,\ \epsilon\eta = z'/h_1 \end{aligned}\right\} (3)$$

L_1 is the wave-length at the origin and a new expression of the velocity potential, Ω, has the following relations

$$\Omega_\xi - \eta = \epsilon(c_0\eta_{\xi\xi}/2 + \eta^2/2c_0^2) + o(\epsilon^2) \qquad (4)$$

$$\frac{\Phi}{h_1\sqrt{gh_1}} = \epsilon^{1/2}\left(\Omega - \frac{\epsilon}{2}z^{*2}\Omega_{\xi\xi} + \frac{1}{4!}\epsilon^2 z^{*4}\Omega_{\xi\xi\xi\xi} - \cdots\right) \qquad (5)$$

The applicability of the numerical results of Eq.(2) has already been examined in detail by comparing them with the results of the experiment without the restriction on mass transport by waves due to a sloping end wall of the wave flume and the influence of wave reflection from the end wall. As a result, it was concluded by authors(1979) that the first order solution, which is the numerical solution of the lowest order equation of Eq.(2) given by

$$\eta_\tau + \frac{3}{2}c_0^3\eta\eta_\xi + \frac{1}{3}c_0\eta_{\xi\xi\xi} - \frac{1}{4}c_0^2 B^*_\tau\eta = 0 \qquad (6)$$

is stable and applicable to shoaling waves over sloping bottoms. The second order solution, which is the numerical solution of the second order equation of Eq.(2), however, because of its round-off errors and secular terms, is not as applicable. In Fig.2 is shown an example of the comparisons between the numerical and experimental results of wave profiles of shoaling waves. Here, the thin, broken and solid lines indicate the results of the first and second order solutions, respectively, and the heavy lines indicate the experimental results. Therefore, based on the assumptions i), ii), iii) and iv), and as far as the wave profiles of shoaling waves as concerned, it could be said that the numerical solution of Eq.(6) can be used instead of the direct solution of Eq.(1). Hence, the present problem is reduced to finding the velocity potential ϕ satisfying Eq.

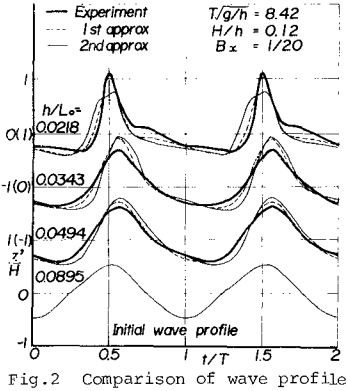

Fig.2 Comparison of wave profiles deter determined from numerical solutions and from experimental data

(1) against the water surface displacement z' derived from Eq.(6). The mathematical formulation of ϕ has already by the authors(1980) as:

$$\frac{\Phi_x}{\sqrt{gh}} = \varepsilon\eta + \varepsilon^2\{\frac{1}{2}\eta^2 + (z^{*2}-1)\eta_{\xi\xi} + B^*_\tau\eta\} + o(\varepsilon^3) \tag{7}$$

The characteristics of the horizontal water particle velocities were numerically examined through Eq.(7), and it was found that the accuracy of the high-order differential quotients computed numerically became lower with shoaling water. So, by paying attention to the physical significance of Eq.(7), i.e., that the velocity potential of shoaling waves is mainly subject to the water surface displacement and suffers the direct effect of bottom slope only in the second order, the following approach is here adopted, where the effect of water surface displacement given by Eq.(6) is evaluated as accurately as possible instead of ignoring the direct effect of bottom slope as assessed in Eq.(7). Therefore, in order to use the WKB method, a fifth assumption must be made:

v) Both water surface displacement and velocity potential depend on two variables, υ and X, expressing the phase change and the gentle change in water depth, respectively:

$$z'(x,t)=z'(\upsilon,X), \quad \phi(x,z,t)=\phi(\upsilon,X,z) \tag{8}$$

where

$$\upsilon=\frac{1}{\epsilon}\int_0^K K(X)dx-\omega t \tag{9}$$

K(X) is the wave-number dependent on the change in water depth and ω, the angular frequency, independent from the change according to the conservation law of wave-number.

This assumption can be sufficiently justified because the expression,

$$z'(\xi,\tau)=z'(\xi-\int c\,d\tau), \qquad c=\frac{3z'}{2\epsilon c_0^3}+\frac{c_0 z'_{\xi\xi\xi}}{3z'_\xi}-\frac{B^*_\tau}{4c_0^2} \tag{10}$$

can be derived by considering that the water surface displacement, z'=$(h_1/\epsilon)\eta$, is a solution of Eq.(6), and then

$$\xi-\int c\,d\tau=\frac{\epsilon^{1/2}}{\omega}\{\int K(X)dx-\omega t\} \tag{11}$$

can be obtained.

Application of the assumptions of i) and v) to Eq.(1) yields the following equation, where the effect of the water depth change rate is explicitly expressed by the small parameter, ε.

$$\left.\begin{aligned}
&K^2\phi_{\upsilon\upsilon}+\phi_{zz}+\varepsilon(K_X\phi_\upsilon+2K\phi_{\upsilon X})+\varepsilon^2\phi_{XX}=0\\
&-\omega\phi_\upsilon+\frac{1}{2}(K^2\phi_\upsilon^2+\phi_z^2)+gz'+\varepsilon K\phi_\upsilon\phi_X+\frac{\varepsilon^2}{2}\phi_X^2=0 \qquad \text{at} \quad z=h_1+z'\\
&-\omega z'_\upsilon+K^2\phi_\upsilon z'_\upsilon-\phi_z+\varepsilon(K\phi_X z'_\upsilon+K\phi_\upsilon z'_X)+\varepsilon^2\phi_X z'_X=0 \ \text{at} \quad z=h_1+z'\\
&-\phi_z+\varepsilon KB_X\phi_\upsilon+\varepsilon^2 B_X\phi_X=0 \qquad \text{at} \quad z=B
\end{aligned}\right\} \tag{12}$$

Here, a final assumption is made concerning the velocity potential ϕ:

vi) The velocity potential ϕ can be expanded as a power series with respect to the small parameter ε as:

$$\phi(\upsilon, X, z)=\phi_0(\upsilon, X, z)+\varepsilon\phi_1(\upsilon, X, z)+\cdots . \tag{13}$$

Moreover, by exchanging υ for a new variable θ and defining the stream function ψ, respectively, as:

$$\frac{\partial}{\partial\theta}=K\frac{\partial}{\partial\upsilon} \quad , \quad \frac{\partial^2}{\partial\theta^2}=K^2\frac{\partial^2}{\partial\upsilon^2} \quad , \quad \theta=x-c(X)t \quad , \tag{14}$$

$$\psi_z=\phi_\theta-c \quad , \quad \psi_\theta=-\phi_z \quad , \tag{15}$$

the following equation, expressed with the stream function, is derived in the lowest order O(1) from Eq.(12).

$$\left.\begin{aligned} &\nabla^2\psi=0 \ , \\ &\frac{1}{2}(\psi_\theta^2+\psi_z^2)+gz'=\frac{1}{2}c^2 \qquad \text{at} \quad z=h_1+z' \ , \\ &\psi=\psi_0 \qquad \text{at} \quad z=h_1+z' \ , \\ &\psi=0 \qquad \text{at} \quad z=B \ , \end{aligned}\right\} \tag{16}$$

where ψ_0 is a constant denoting the total volume rate of flow underneath the steady wave per unit length in a direction normal to the x plane.

As mentioned above, the water depth change rate is of the order ε and from the assumption i) the value of ε could be considered small enough that the velocity potential ϕ can be sufficiently evaluated by the lowest order term ϕ_0, that is, the stream function defined in Eq.(14). Thus, under assumptions i)-v), although ψ is an explicit function of θ and z alone because all terms dependent on the change of water depth, such as bottom slope, are neglected, and although ψ is indirectly affected by water depth change through the conservation laws, the mathematical formulation satisfying both Eq.(15) and the conservation laws against the water surface displacement z' given numerically from Eq.(6) is synonymous with Eq.(1).

2. Examination on Conservation Laws

The effect of wave set-down is ignored by the assumption iii), so that the conservation laws to be satisfied become those of mass and energy alone. They can be expressed in a two-dimensional wave field of steady state, shown in Fig.1, as:

$$\frac{d}{dx}\overline{\left\{\int_B^{h_1+z'}\rho u\,dz\right\}}=0 \tag{17}$$

$$\frac{d}{dx}\overline{\left[\int_B^{h_1+z'}\rho u\left\{\frac{1}{2}(u^2+w^2)+\frac{p}{\rho}+q(z-h_1)\right\}dz\right]}+\rho g\eta_s\frac{d}{dx}\overline{\left\{\int_B^{h_1+z'}u\,dz\right\}}=0 \tag{18}$$

where the bar — indicates averaging over one period, and η_s is wave set-

down. It is found from Eq.(18) that the uniformity of energy flux by waves is satisfied independently from the evaluation of wave set-down when the conservation law of mass is satisfied. Substitution of Eq.(15) into Eq.(17) yields

$$\varepsilon \frac{d}{dX} \{ \int_B^{h_1+z'} K\Phi_{0U}\, dz \} + o(\varepsilon^2) = 0 \tag{19}$$

The conservation law of mass is satisfied unconditionally in the same order O(1) as in Eq.(16), so that it can be considered in the order of ε. Hence, the law is expressed as

$$I = \varepsilon \overline{\int_B^{h_1+z'} (\psi_z + c)\, dz} = \varepsilon \{ \psi_\theta + c(h_1 - B) \} = \text{const.} \tag{20}$$

where I is the mass flux by waves.

By similar examination on the conservation law of energy, the law can be written in the order of ε independently from wave set-down as:

$$W = \varepsilon \overline{\int_B^{h_1+z'} \rho(\psi_z + c) \{ \frac{1}{2}(\psi_z + c)^2 + \frac{1}{2}\psi_\theta^2 + \frac{p}{\rho} + g(z - h_1) \} dz}$$

$$= \frac{\varepsilon}{2} \rho c \{ (3c + \bar{u}) 1 - c\bar{u}(h_1 - B) - 2g\overline{z'^2} \} = \text{const.} \tag{21}$$

where W is the energy flux by waves.

3. Calculation of the Stream Function of Shoaling Waves

By considering the theoretical result(1980) that mass transport velocity $\bar{u}$ is given in Eulerian co-ordinate due to a nonlinear effect when the phase of z' is assumed to agree with that of ϕ, a generalized mathematical formulation of the stream function is assumed as

$$\frac{\psi}{h\sqrt{gh}} = -\{ \frac{1}{X_{(1)} X_{(2)}} - \frac{\bar{u}}{\sqrt{gh}} \} \zeta + \sum_{n=4,6}^{N-1} \frac{\sinh(n-2)\pi X_{(2)} \zeta}{\cosh(n-2)\pi X_{(2)}}$$

$$[X_{(n)} \cos\{(n-2)\pi\chi\} + X_{(n+1)} \sin\{(n-2)\pi\chi\}] \tag{22}$$

where $\zeta = (z-B)/h$, $\chi = (x-ct)/L$, $X_{(n)}$ is the n-th coefficient, especially $X_{(1)} = T\sqrt{g/h}$, $X_{(2)} = h/L$, $X_{(3)} = \psi_0/h\sqrt{gh}$ and T wave-period. The dynamic boundary condition at free surface shown in Eq.(16) can be rewritten with respect $\bar{u}$ as:

$$\frac{1}{2}\bar{u}^2 + (u_w - c)\bar{u} + \frac{1}{2}(u_w^2 + w^2) - cu_w + gz' = 0 \qquad \text{at} \quad z = h_1 + z' \tag{23}$$

where u_w and w are the periodic component of the horizontal and vertical water particle velocities respectively. They are in the following relation with the stream function.

$$\psi_x = -w \qquad \psi_z = \bar{u} + u_w - c \tag{24}$$

Hence, u_w and w are expressed by Eq.(22) and (24), respectively, as:

$$\left.\begin{aligned} u_w &= \sum_{n=4,6}^{N-1} \frac{(n-2)\,X_{(2)}\cosh\{(n-2)\pi X_{(2)}\zeta\}}{\cosh\{(n-2)\pi X_{(2)}\}}\{X_{(n)}\cos(n-2)\pi\chi \\ &\qquad + X_{(n+1)}\sin(n-2)\pi\chi\} \\ w &= -\sum_{n=4,6}^{N-1} \frac{(n-2)\pi\sinh(n-2)\pi X_{(2)}\zeta}{\cosh(n-2)\pi X_{(2)}}\{X_{(n+1)}\cos(n-2)\pi\chi \\ &\qquad - X_{(n)}\sin(n-2)\pi\chi\} \end{aligned}\right\} \quad (25)$$

Moreover, the mathematical formulation of water surface displacement using the stream function is derived through the kinematic boundary condition at free surface:

$$Y_i = \frac{-X_{(1)}X_{(2)}}{1-(\bar{u}/\sqrt{gh})X_{(1)}X_{(2)}}\left[X_{(3)} - \sum_{n=4,6}^{N-1}\frac{\sinh\{(n-2)\pi X_{(2)}(1+Y_i)\}}{\cosh\{(n-2)\pi X_{(2)}\}}\right.$$
$$\left.\{X_{(n)}\cos(n-2)\pi\chi_i + X_{(n+1)}\sin(n-2)\pi\chi_i\}\right] - 1 \quad (26)$$

Hence, as long as the above expression is used, the conditions to be satisfied by Eq.(22) become a binding condition, i.e., the wave profile expressed by Eq.(26) must agree with both the numerical solution given by Eq.(6) and the conservation laws mentioned above. Although these conditions determine the coefficients $X_{(n)}$ uniquely, some of them are subject to nonlinear equations with respect to $X_{(n)}$. So, the determination of the stream function satisfying the above conditions is carried out by a method similar to that used by Rienecker et al.(1981). The unknown coefficients to be determined are $X_{(2)}$, $X_{(3)}\cdots X_{(n)}$, their total number being N-1 quantities.

The conditions to be satisfied by them can be expressed as follows: Firstly, as to the wave profile conditions, the numerical solutions of Eq.(6) and z_c' must agree with the expression shown in Eq.(26), so the conditions written as

$$f_i = z_{ci}/h - Y_i = 0, \quad i = 1, 2, \cdots, N-3 \quad (27)$$

must be satisfied. Here, i indicates the i-th phase during one period divided impartially by N-3. Secondly, the conservation laws of mass and energy expressed in the order of ε are, respectively,

$$f_{N-2} = \varepsilon(I-I_0), \quad f_{N-1} = \varepsilon(W-W_0) \quad (28)$$

where the subscript o denotes the quantity in deep water and I is written by the expression shown in Eq.(22) as:

$$I = \bar{u}h + h\sqrt{gh}\sum_{n=4,6}^{N-1}\tanh\{(n-2)\pi X_{(2)}\}\{X_{(n)}\cos(n-2)\pi\chi_i$$
$$+ X_{(n+1)}\sin(n-2)\pi\chi_i\} \quad (29)$$

Here, the subscript i denotes the pahse giving $Y_i = 0$. The N-1 numbers of equations shown above are solved by Newton-Raphson's method so that the internal properties of shoaling waves can be calculated under the six assumptions mentioned above.

4. Examination of the applicability of Numerical Solutions

An examination by Iwagaki et al.(1974) has already been made of the applicability of Dean's stream function method(1965) to the waves on sloping bottoms. Water surface displacement was given by experimental results at each water depth with normal wave flumes, and its applicability was determined for shoaling waves with deformed wave profiles. Their conclusion was that the stream function method can be applied to waves with asymmetrical wave profiles on sloping bottoms as long as the wave profiles can be accurately calculated, although the method should be primarily developed for uniform waves with symmetrical profiles. Hence, it is thought to be possible to apply the present approach, as well as the calculation by Iwagaki et al.(1974). However, the present approach is different in that the satisfying of the conservation laws, is not required in the usual methods. So, an examination is here made of the applicability of the horizontal water particle velocity computed by the present approach.

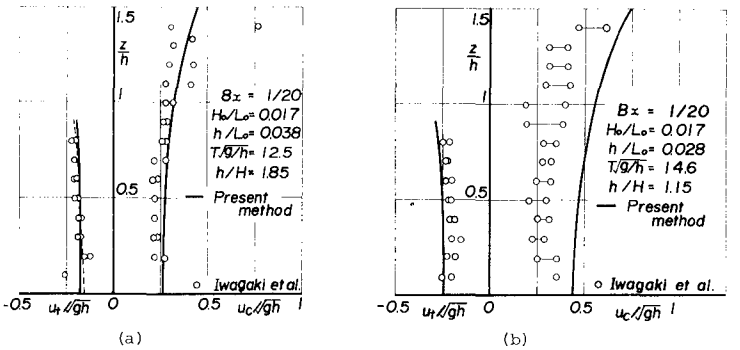

Fig. 3 Comparison between numerical solution and experiment by Iwagaki et al. of vertical distributions of horizontal water particl particle velocities

Fig.3 shows the comparisons between the numerical results obtained by the present approach where the measured wave profile at $h/L_o = 0.069$ was given as initial value and experimental results by Iwagaki et al. of vertical distribution of horizontal water particle velocities of shoaling waves. And Fig.4 shows comparisons of their corresponding wave profiles up to the breaker point noted by $h/L_o = 0.028$ in the figure. Here, the solid line shows the numerical results determined by

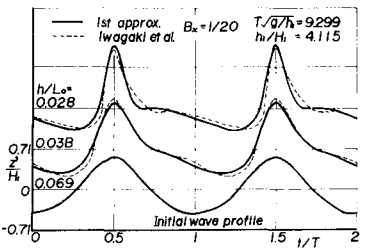

Fig. 2 Comparison of wave profiles determined from numerical solutions and from experimental data

the present approach and both of circles and broken lines show the experimental results. It might be said from the figures that the present approach is applicable for the calculation of the internal properties of shoaling waves up to a breaker point, although the examination was made only of the water particle velocities and wave profiles and although their numerical results seem to give larger values at the breaker point than the experimental ones which probably suffered from the effect of back currents from the end wall of wave flume.

CALCULATION OF INTEGRAL QUANTITIES OF SHOALING WAVES

1. Definition of Integral Quantities

The method used by Longuet-Higgins(1975) can be applied to the present approach, and the expression of the various integrals can be derived as in the following, if the integrals are evaluated in the same order, O(1), as the terms in the equations mentioned above. The potential energy E_p at arbitrary water depth is defined as:

$$E_p = \frac{1}{2}\rho g\bar{z}'^2 \tag{30}$$

and the kinetic energy E_k is defined as:

$$E_k = \int_B^{h_1+z'} \frac{1}{2}\rho\{(\psi_z - c)^2 + \psi_\theta^2\}dx \tag{31}$$

By applying the expression defined by Longuet-Higgins, Eq.(32) can be rewritten as:

$$E_k = \frac{1}{2}\rho\{c^2h - (\bar{u} + c)I\} \tag{32}$$

In the same way, the radiation stress S can be expressed as:

$$S = \int_B^{h_1+z'} (p + \rho u^2)dz - \frac{1}{2}\rho gh^2$$

$$= 2cI - 3E_p \tag{33}$$

Then, the energy flux W shown in Eq.(29) can be expressed as:

$$W = \frac{1}{2}\rho c\{(3c + \bar{u})I - \bar{u}ch - 4E_p\} \tag{34}$$

Therefore, the integral quantities of shoaling waves can easily be calculated within the limits of O(1), as long as the values of the wave celerity, the potential energy and the mass transport velocity can be given at an arbitrary water depth.

2. Definition of Breaker Point

In order to carry out the computation of the integral quantities of shoaling waves up to the breaker point, the breaker points must be reasonably and accurately defined and the computation of the stream function with sufficient accuracy must be possible. The former must be investigated here because the definition of breaker points has not yet been established theoretically, although the latter is satisfied by comparison with experiments including the actual breaker points. So, some

examinations must be made of the breaker points to be used here.

Although the theoretical breaker point is thought to be defined by the singular point of Eq.(6) in the lowest order, the equation has not been yet analytically solved, so the condition for the singularity cannot be obtained theoretically. Therefore, the breaker point is conjectured from the behaviour of the results computed numerically under the conditions of the wave steepness H_o/L_o and bottom slope B_x described in Table 1, where the values of the well-known surf-similarity parameter $\mu = B_x/\sqrt{H_o/L_o}$ are also shown. The computations start from the point of $h/L_o = 0.08$ and the values of L/L_o and H/H_o at the point are computed by the energy flux method(1977).

Table 1 Conditions of wave parameters computed

H_o/L_o	B_x	μ
0.004	1/10	1.58
0.008	1/10	1.12
0.01	1/10	1.00
0.004	1/20	0.79
0.008	1/20	0.55
0.01	1/20	0.50
0.01	1/50	0.20
0.02	1/50	0.14
0.04	1/100	0.05

Fig.5 depicts the changes in wave-heights of shoaling waves computed from Eq. (6) as a function of the surf-similarity parameter. Here, the solid circles indicate the breaker points defined by Goda and expressed as

$$\frac{H_b}{L_0}=0.17\left[1-\exp\left\{-1.5\pi\left(\frac{h}{L_0}\right)\left(1+15\,B_x^{4/3}\right)\right\}\right] \qquad (35)$$

It can be found from the figure that the extrema always exist in the changes in wave-height. The occurence of the extrema is conjectured to be caused by a kind of instability in the numerical solutions, which can be attributed to the excessive value of the curvature of the wave profile at crest. So, the relation between the existence of the extremum noted in the figure and the upper limit of a curvature of water surface displacement at crest of the numerical solution of Eq.(6) were examined to discover the reason for such an extremum. In Fig.6 white circles shows the values of the curvatures at the point of maximum wave-height of the numerical solution, and the points defined by Goda's breaking inception are indicated by solid circles for every value of the surf-similarity parameter. It can be noticed that the upper limit of the curvature exists in the vicinity of the values of 10^4 for every value of the parameter, and the maximum value

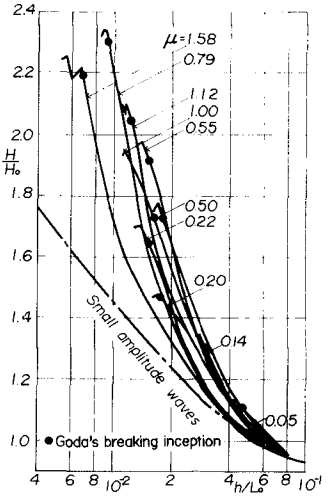

Fig. 5 Changes in wave-height of shoaling waves as a function of the surf-similarity parameter

for wave-height computed by Eq.(6) depends on the upper limit of the curvature of the numerical solution. Therefore, it is assumed that the theoretical breaker point in the numerical simulation generated by Eq.(6) is given by the upper limit.

Fig.7 shows the relation between the theoretical breaker indices, i.e., the ratio of wave-height to water depth at the breaker points, H_b/h_b, and the actual indices defined by Eq.(35). Here, the solid lines

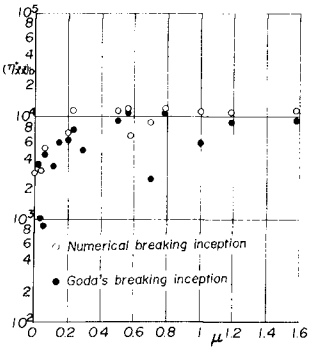

Fig. 6 Curvatures of the heighest waves and the surf-similarity parameter

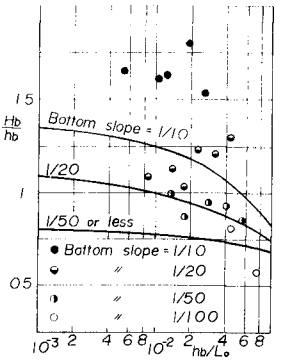

Fig. 7 Comparison between the theoretical breaker indices and the actual ones defined by Goda's breaking inception

describe the breaker indices given by Eq.(35), and circles indicate the theoretical indices for all bottom slope conditions. It could be considered from the results shown in the figure that most of the theoretical breaker indices exceed the actual ones and that the numerical solutions are stable and continue to maintain sufficient accuracy in the shallower water beyond the actual breaker points. And, it is found that the dependency of the theoretical breaker indices on bottom slopes reasonably corresponds to that of the actual breaker indices, although there are a few difference with regard to the

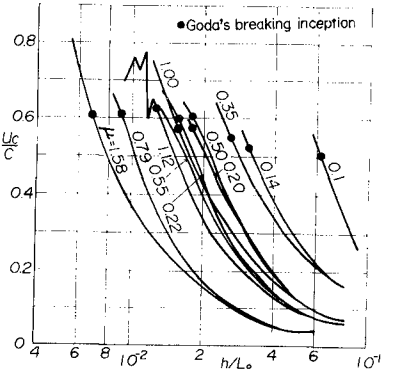

Fig. 8 Changes in the ratio u_c/c of shoaling waves with the surf- similarity parameter

absolute values between them. Thus, the definition of the breaker points as being dependent on the upper limit of the courvature is regarded as reasonable. So, an investigation is made on the relation between the theoretical breaker point and Rankine-Stokes' condition of greatest wave-height.

Fig.8 shows the change in the ratio of the horizontal water particle velocity at crest, u_c, to the wave-celerity, c, of the shoaling waves computed by the present approach up to the theoretical breaker points. It is noticed that all the values of the maximum ratio u_c/c do not exceed 1, although the ratios at the breaker points approach one as the value of the surf-similarity parameter increases. This result means that shoaling waves on sloping bottoms become unstable and begin to break down before Rankine-Stokes' condition is satisfied and that the breaking inception of shoaling waves is controlled by another condition besides Rankine-Stokes' condition.

Fig.9 shows the change in the small parameter σ with the ratio u_c/c definded by Longuet-Higgins(1975) as:

$$\sigma = \frac{1 - (u_c - c)^2 (u_t - c)^2}{c^2 c_o^2} \quad (36)$$

It is found that the parameter σ has a tendency similar to the ratio u_c/c and that any given value of σ does not exceed 1 because of the similarity of the parameter σ to the ratio u_c/c, although the value σ of the highest wave becomes 1 in the calculations by Longuet-Higgins et al..
Therefore, it is to be expected that results considerably different from his will be obtained from the changes in the integral quantities of shoaling waves computed by the present approach.

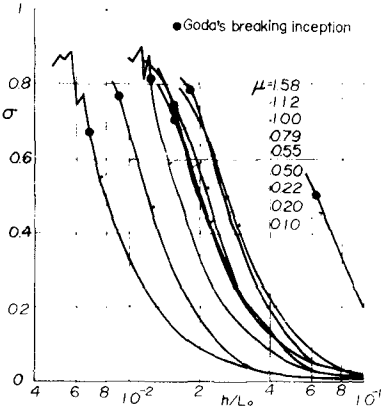

Fig. 9 Changes in the ratio u_c/c of shoaling waves with the surf-similarity parameter

CHANGES IN INTEGRAL QUNATITIES WITH SHOALING WATER

Fig.10 shows the changes in the potential energy of shoaling waves with the surf-similarity parameter up to the theoretical breaker point computed by the present approach. It is found that the extrema of potential energy always exist before both the breaker points are attained and that the integral quantities of the highest wave are not always maxima. This agrees with the result shown by Longuet-Higgins et al.(1974), although the effect of the surf-similarity parameter is not taken into account in their calculation. It is thought that the existence of

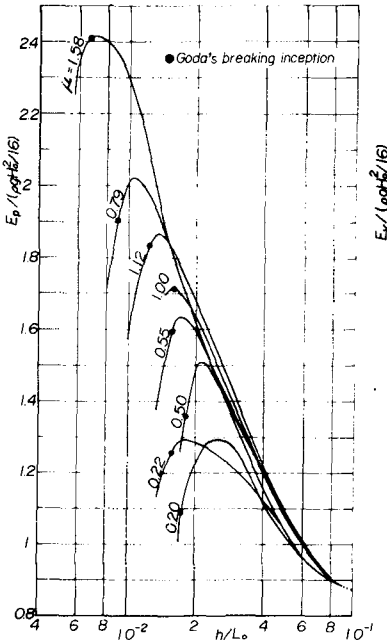

Fig. 10 Changes in the potential energy of shoaling waves with the surf-similarity parameter

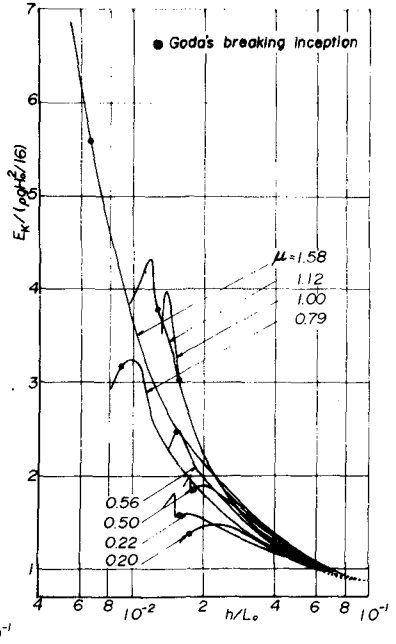

Fig. 11 Changes in the kinetic energy of shoaling waves with the surf-similarity parameter

such extrema is due to the sharpening of the wave crest caused by the tendency of the competition between the nonlinear effect and the dispersive effect to deform the wave profile which is strengthened with shoaling water.

Fig.11 shows the change in the kinetic energy of shoaling waves obtained by the same computation continued to the breaker points. It is found that the extrema of kinetic energy do not always exist before the breaker points are attained, in contrast to the case of potential energy and that the existence of the extrema depends on the value of the surf-similarity parameter. This is very different from the results of Longuet-Higgins(1975) which state that these extrema are always found in both the potential and the kinetic energies. This result indicates that there is a difference in the existence of the extrema of kinetic energy between shoaling waves with asymmetrical wave profiles on a sloping bottom and uniform waves with symmetrical wave profiles on a flat bottom. Therefore, it could be said that there is a difference in the internal properties, such as water particle velocities, between these wave types

and that the conclusion obtained for one cannot be directly applied to the explanation of the wave breaking for the other.

Fig.12 shows the change in the total energy E_t of the same shoaling waves. Several matters are clear from this figure. The existence of the extremum of total energy depends on the value of the surf-similarity parameter just as that of the kinetic energy does. The extrema arise with the value of the parameter μ under 1.12 before the theoretical breaker points are attained and under 0.79 before the actual breaker points are attained. The critical value of the parameter controlling the existence of the extremum seems to be between 1.12 and 1.58 where the theoretical breaker points are applied and between 0.79 and 1 where the actual breaker points are applied. It is well-known from the experiments by Galvin(1969) that the breaker type depends on the value of the surf-similarity parameter and that a spilling breaker occurs when the value of the parameter is less than 0.5. Hence, it could be judged that the existence of the extremum closely relates to the breaker type and that a spilling breaker occurs due to the instability of the transfer of wave energy when the value of the parameter μ is less than the critical value mentioned above. The extremum exists because the conservation law of energy is satisfied in the present approach, the decreasing of the total energy with shoaling water requiring the increasing of the energy transport velocity of shoaling waves.

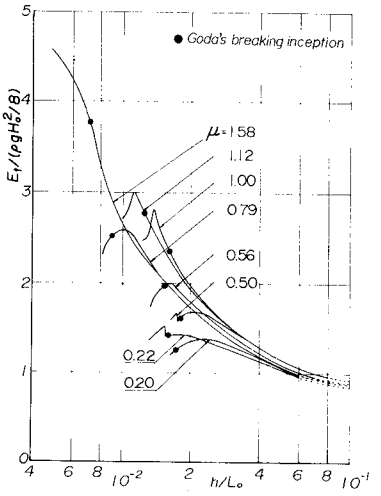

Fig. 12 Changes in the total energy of shoaling waves with the surf-similarity parameter

Fig.13 describes the change in the ratio of the energy transport velocity to the wave-celerity, c_g/c, of shoaling waves continued to the theoretical breaker point. It can be noticed that there is a tendency for the ratios c_g/c at both breaker

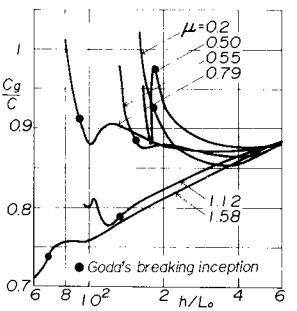

Fig. 13 Changes in the ratio c_g/c of shoaling waves with the surf-similarity parameter

points to decrease away from 1 as the value of the surf-similarity parameter increases, although the computed results scatter considerably of numerical errors in the computed value of wave-celerity. As it is judged that the energy transport velocity cannot physically exceed wave-celerity, instability with regard to energy transfer is considered to occur when the ratio c_g/c exceeds 1. Accordingly, this instability of energy transfer occurs dependently on the parameter and becomes liable to occur as the value of the ratio approaches 1. This instability could be conjectured to be closely related to the mechanism of wave breaking, and, in particular, to the mechanism of the occurence of a spilling breaker, where excess energy not transported by stable waves is exhausted by partial wave breaking. The approach of the ratio to 1 depends on the parameter, as mentioned above, and the instability of energy transfer occurs dependently on the value of the parameter, becoming liable to arise with the approach of the ratio to 1. Thus, it might be said that the instability of energy transfer is closely related to the spilling breaker and that the beginning of the instability is the breaking inception of a spilling breaker.

CONCLUSION

Integral quantities of shoaling waves have been calculated by using the K-dV equation with variable coefficients and the stream function method satisfying the conservation laws of mass and energy, and some investigations have been made on their characteristics. The most significant conclusions of this paper are summarized as follows.

The maximum wave-height of shoaling waves computed by the K-dV equation is controlled by the upper limit of the curvature of wave profiles, where numerical instability arises. Thus, the theoretical breaker point is defined by the limit, and it corresponds reasonably to the actual breaker point defined by Goda's breaking inception. However, Rankine-Stokes' condition of greatest wave-height is not satisfied at the theoretical breaker point of the computed shoaling waves and the wave breaking of shoaling waves seems to occur independently from the condition.

Although the extrema are always found in the potential energy of shoaling waves before the theoretical and actual breaker points are attained and the potential energy of the highest waves is not maximum just as in the results shown by Longuet-Higgins et al., the extrema of the kinetic and total energies are not always found in the shoaling waves with asymmetrical wave profiles before both the breaker points are attained, in contrast to the case of potential energy. In addition, the existence of the extrema depends on the value of the surf-similarity parameter and the extrema occur in the value of the parameter under the critical value controlling the existence. It is found by comparison with the experimental results of Galvin and his examination of the change in the ratio of energy transport velocity to wave-celerity that the existence of the extrema of total energy closely relates to the breaking inception and breaker type, especially to those of the spilling breaker, because it causes the instability of energy transfer of shoaling waves which is conjectured to be the cause of the wave breaking of the spilling type.

REFERENCES

Battjes, J.A.: Surf-similarity, Proc. 14th Intl. Conf. on Coastal Eng., pp.466-480, 1974.

Dean, R.G.: Stream function representation of non-linear ocean waves, Jour. Geophys. Res., Vol.70, pp.4561-4572, 1965.

Galvin, C.J.Jr.: Breaker type classification on three laboratory beaches, Jour. Geophys. Res., Vol.73, No.12, pp.3651-3659, 1968.

Goda, Y.:Deformation of irregular waves due to depth-controlled wave breaking, Rep. Port & Harb. Res. Inst., Vol.14, No.3, pp.59-106, 1975.

Iwagaki, Y. and T. Sakai: Expression of water particle velocity of breaking waves on a sloping bottom using stream function method, Proc. 21st Conf. on Coastal Eng., JSCE, pp.27-32, 1974.

Kakutani, T.: Effect of an uneven bottom on gravity waves, Jour. Phys. Soc. Japan, Vol.30, No.1, pp.272-276, 1971.

Longuet-Higgins, M.S. and J.D. Fenton: On the mass, momentum, energy and circulation of a solitary wave. II., Proc. Roy. Soc. London, Ser. A340, pp.471-493, 1974.

Longuet-Higgins, M.S.: Integral properties of periodic gravity waves of finite amplitude, Proc. Roy. Soc. London, Ser. A342, pp.157-174, 1975.

Longuet-Higgins, M.S.: The unsolved problem of breaking waves, Proc. 17 th Intl. Conf. on Coastal Eng., pp.1-27, 1980.

Rienecker, M.M. and J.D. Fenton: A fourier approximation method for steady water waves, Jour. Fluid Mech., Vol.104, pp.119-137, 1981.

Stiassnie, M. and Peregrine, D.H.: Shoaling of finite-amplitude surface waves on water of slowly-varying depth, Jour. Fluid Mech., Vol.97, pp.783-805, 1980.

Tsuchiya, Y., T. Yasuda and T. Yamashita: Mass transport in progressive waves of permanent type, Proc. 17th Intl. Conf. on Coastal Eng., pp.70-80, 1980.

Yasuda, T. and Y. Tsuchiya: On wave shoaling by finite amplitude wave theories, Annuals of Disas. Prev. Res. Inst., Kyoto Univ., No.20B-2, pp.483-491, 1977.

Yasuda, T., T. Yamashita, S. Goto and Y. Tsuchiya: Wave transformation on a sloping beach by K-dV simulation, Proc. 26th Conf. on Coastal Eng., JSCE, pp.21-25, 1979.

Yasuda, T., S. Goto and Y. Tsuchiya: Water particle velocities of waves on sloping bottoms, Proc. 27th Conf. on Coastal Eng., JSCE, pp.11-15, 1980.

Yasuda, T., T. Yamashita, S. Goto and Y. Tsuchiya: Numerical calculation for wave shoaling on a sloping bottom by the K-dV equation, Coastal Eng. in Japan, JSCE, Vol.25, 1982(in printing).

A FIELD STUDY OF WAVES IN THE NEARSHORE ZONE

by

S. Hotta[1], M. Mizuguchi[2] and M. Isobe[3]

ABSTRACT

Initial results are described of precise observations of waves shoaling in the nearshore zone. The key technique of the experiments is a 16 mm memo-motion camera system by which long term measurements of waves can be made simultaneously at many locations. Six or seven pairs of synchronized cameras were mounted on a research pier crossing the surf zone. The cameras were focused on target poles mounted on sleds which were towed about 200 m outside the breaker line, and on a line of poles jetted into the sea bottom across the surf zone. Waves transforming in the nearshore zone were observed from about 400 m offshore to the shoreline. At present only the characteristics of the statistical waves, wave height distributions, wave period distributions, and the joint distributions of wave height and period are described as part of the initial analysis.

INTRODUCTION

The authors have been carrying out extensive field studies to better understand the characteristics of waves in the nearshore zone. As a method of measuring waves, we have developed and applied a remote sensing photographic technique utilizing synchronized 16 mm memo-motion cameras to record the water surface elevation at fixed time intervals at poles installed in the nearshore zone. The basic function of this system is to take continuous synchronized pictures over a broad area of the nearshore zone. Some results with this method have been already presented (Hotta and Mizuguchi, 1980; Hotta, Mizuguchi and Isobe, 1981; Mizuguchi, 1982).

The observation time of a single camera is limited by the length of the film. Such a short length of time is insufficient for a quantitative discussion of some subjects, especially the statistical characteristics of waves. This problem was overcome by employing cameras in sets of two and running them alternately. Film changing can

1. Research Associate, Department of Civil Engineering, Tokyo Metropolitan University, Tokyo, 158, Japan.
2. Associate Professor, Department of Civil Engineering, Chuo University, Tokyo, 112, Japan.
3. Associate Professor, Department of Civil Engineering, Yokohama National University, Yokohama, 240, Japan.

be done for the camera not in current use, enabling a continuous record without time limitation. Using this method, and poles mounted as targets on sleds, three observation of waves in the nearshore zone were conducted. Data sets long enough to discuss the statistical wave characteristics were obtained at several points from about 400 m offshore and through the breaker zone to a point near the shoreline. In the present article, only the characteristics of the wave height and period distributions and their joint distributions are described as part of the initial analysis.

2. FIELD OBSERVATION

2.1 Study site and observations

The field observation site was at Ajigaura beach facing the Pacific Ocean, and located about 200 km north of Tokyo (Fig. 1). At this beach there is a pier operated by the Public Works Research Institute, Ministry of Construction, for facilitating field studies in the nearshore zone. Observations have been carried out utilizing the pier as a platform for the 16 mm memo-motion camera system. The average tidal range at this beach is about 1.2 m and the beach slope is about 1/60 to 1/70. The beach sand size is in the range of 0.2 to 0.5 mm.

Three observations were carried out. The first was done on Sep. 2, 1980 using six pairs of 16 mm cameras and six sleds. The second and third observaions were done on Sep. 8 and 9, 1981. In the second observation, seven pairs of cameras, six sleds, and a single pole (installed by water jet and positioned near the shoreline) were used. The waves at seven locations from near the shoreline to a position about 400 m offshore were observed. In the third observation, five pairs of cameras were employed to record the shoaling deformation, and the remaining two sets of cameras were used for the observation of wave run-up in the swash zone.

The six sleds were linked together at about 50 m intervals and pulled offshore by a tug boat. The wave conditions were relatively rough and the breaking height of the larger waves was 1.8 to 2.2 m. The width of the surf zone by visual observation was about 200 m, and two or three broken waves existed in the surf zone.

Photo 1 shows the 16 mm camera system in operation on the pier for Ex810908 [The notation is: Ex (beach experiment), 81 (year), 09 (month) and 08 (day)]. Photo 2 shows the sleds before being pulled to sea. Photo 3 shows the sea condition and target poles on the sleds in Ex800902.

Figures 2 and 3 show the positions of the sleds and the beach profiles for the first and second observations, respectively. In Fig. 3, A' to E' are the positions of the sleds for the third observation. The average breaker line by visual observation was between Station C and D for Ex800902 and Ex810908. All stations were positioned seaward of the breaker line for Ex810909.

2.2 Instrumentation

The sleds on which the target poles (8 m high) were mounted are constructed of steel pipe 50 mm in diameter. The sleds are 5.5 m long, 2.4 m wide, and 0.5 m high, and weigh about 200 kgf. The cameras were mounted on the pier. Three kinds of zoom lenses were employed, 150 to 250 mm, 80 to 150 mm, and 17 to 85 mm. Each pair of cameras was equipped with the same type of lens.

The cameras were synchronized by a main control unit and connected by the same number of relay units in pairs. One camera of a set stops operation at a certain frame as directed by the main control unit, and the other camera of the set automatically begins to operate. This procedure is repeated and an observation can continue without time limitation. The sampling interval is variable between 0.1 to 10. In the present observations, a sampling interval of 0.2 s was used. The water surface variation photographed by the cameras is transferred to paper tape using a 16 mm film analyzer and an ultrasonic digitizer graph pen system. Records on the paper tapes are then transferred to magnetic tapes or disk for analysis by computer.

3. RESULTS

3.1 Effective data

Ten rolls of films per set of cameras were taken for Ex800902. Therefore 37,500 frames (7500 s) of data were completely obtained for Stations A to F. During observation Ex810908, it rained after four rolls of film were taken, and the observation had to be terminated early. We had difficulty in handling the film in the rain, and a portion of the data was lost. Effective data were 3800 s for Stations A, B, C, D and E, 3599.4 s for Station F, and 3350 s for Station G. Twelve rolls of film were taken for Ex810909. Data of 9120 s were obtained for Stations A, B, C and D. However, the sled at Station E was moved a few meters shoreward by large waves and went out of frame in the sixth roll. The camera angle was adjusted, but the sled again went out of frame in the twelfth roll. Thus a portion of the data at Station E was also lost. The effective data at Station E was 3508.4 s for the first part of the observation, and 4782 s for the latter part.

3.2 Number of waves defined by the zero-crossing method

Direct application of the zero-crossing methods creates a problem for defining waves in the nearshore zone. That is, many small amplitude short period waves are defined, especially in the surf zone. Figures 4 and 5 show the number of waves defined by the zero-up cross method for the three observations. The number of waves given from limited data were multiplied by the ratios of the total observaton time to the effective time. In Figs. 4 and 5, the number of waves defined with a minimum wave height of 4, 6, 8, 12, 16 and 20 cm are also shown. D indicates this minimum wave height (See also the number of waves defined in Table 1 and Fig. 7). A great number of small amplitude short period waves are defined both inside and outside the surf zone. It does not seem reasonabale to take into consideration such small waves. However, no firm physical criteria has yet been given for excluding small waves.

The problem of how to treat the small waves will not be discussed further here. This and some related matters were treated by Hotta and Mizuguchi (1980). In that reference, waves having a height smaller than 6 cm were ignored, based on accuracy limitations of the measurement process. We further investigated the accuracy of this type of measurement of the sea water surface elevation, and have found that a maximum error of $\pm$ 2.6 cm should be expected. Therefore, we will continue our discussion by ignoring waves lower than 6 cm. The treatment of the time interval associated with the omitted wave is also discussed by Hotta and Mizuguchi. In the present paper, the time intervals of the omitted waves were added to the trailing part of the preceding main wave, referred to as the B-method in the previously-mentioned paper.

Viewing Figs. 4 and 5, it is seen that the number of waves in the surf zone defined by the zero-crossing method is larger than the number in the offshore zone. The number of waves defined is constant in the offshore, although some difference appears at Station E in Ex810909 (attributed to missing data for that station). Therefore, the number of waves is conserved in the offshore zone. The increase in the number of waves defined in the surf zone is produced by the disturbance accompanying wave breaking.

The symbol * in Figs. 4 and 5 is the number of waves defined after applying a numerical filter which cuts waves lower than 0.04 Hz and passes waves higher than 0.05 Hz. Due to filtering, 380 data points (76 s) were cut from the beginning and end of the time series. Because the time periods of the defined waves with and without the filter are not the same, we can not compare the absolute number of waves defined. However, at Station A located near the shoreline in Ex800902 and Ex810908, the number of waves defined after applying the filter is larger than the number defined without the filter. At other stations, (more distant from the shoreline), the difference is small. This result is interpreted as follows. The wave height in the neighborhood of the shoreline is small, and anti-nodes of long period waves, such as edge waves or two-dimensional on-offshore standing waves, can exist there. The amplitudes of these long period waves rapidly decrease in the offshore direction, and the effect of the long period waves on the (ordinary) waves of period less than 20 s is small. We conclude that the long period waves will have a proportionately larger effect on the ordinary waves near the shoreline as compared to offshore.

3.3 Statistically representative waves

Values of the statistically representative waves, the wave grouping parameters, statistics of the sea water surface elevation and spectral parameters for each observation are listed in Tables 1 to 4. Table 2 gives the statistically representative waves defined without cutting the small waves for Ex800902. Table 3(a) (not filtered) shows values obtained by omitting waves lower than 6 cm and adding their time durations to the front part of the following main wave. It can be seen that the average wave heights and periods of the waves in Table 2 are much smaller than those in Table 3, due to the effect of the many small waves defined. However, the respective differences in the one-tenth and significant waves are relatively small. This indicates that the large waves in the wave distribution can be defined with little consideration

of the small waves. Table 3(b) gives the statistically representative waves of Ex800902 after filtering. Concerning the mean wave, only the values for Station A were altered by use of the filter.

Table 4 gives results from Ex810900 and Ex810909. From Tables 3 and 4 it can be seen that in the surf zone, the maximum, one-tenth, and one-third waves defined by the zero-down crossing method are slightly larger than those given by the zero-up crossing method. The zero-down crossing method defines one large wave and one small wave, while the zero-up crossing method defines two waves of almost equal equal height when a wave trails a relatively smaller wave (Hotta and Mizuguchi, 1980). This kind of wave behavior is seen primarily at the breaking point and in the surf zone. This is also the reason why a bi-modal distribution of the wave height, and a double-peaked distribution in joint distribution of wave height and period, are found for waves in the surf zone.

3.4 Shoaling of the statistically representative waves

Figure 6 shows the shoaling deformation of the observed statistically representative waves. The shoaling deformation curve given by linear wave theory is also drawn. The corresponding wave height in deep water was calculated by linear wave theory using the wave period and depth at the furthermost station (Station F for Ex800902, Station G for Ex810908, and Station F for Ex810909). The shoaling coefficient was defined as the ratio of the measured (or calculated) wave height at each station to the wave height in deep water, assuming normal wave incidence. The reason why Station E for Ex810909 was not used is that the periods of the significant, the mean, and the root mean square waves differed somewhat from the respective quantities at the other stations, in spite of the fact that a constant wave period was found for the offshore zone. At present, we can not say why this happened. The one-tenth wave period at Station E for Ex810909 was almost the same as at other stations in the offshore zone.

As can be seen in Fig. 6, the prediction of linear theory agrees well with the shoaling deformation of the statistical waves in this limited distance of approximately 200 m. It is well known that the shoaling deformation given by linear wave theory does not give good agreement with the measured results regular waves in the laboratory and for individual irregular waves on field beaches offshore and in the neighborhood of the breaker line. However, the prediction by linear wave theory agrees very well with the shoaling deformation of statistical waves in the present field observation.

3.5 Wave height and period distributions

The distribution of wave height and period and the marginal distribution of wave height and period at each measuring station are shown in Figs. 7 to 11. Figure 7 shows distributions for Ex800902 including the small waves. Equi-number lines of 10, 30 and 50 waves are drawn respectively with dotted, broken, and solid lines. Figure 7 shows the process of change of the distribution. Figure 8 shows the distributions for Ex800902 omitting waves lower than 6 cm, and applying the filter. Figures 9, 10, and 11 show the distributions for Ex800902, Ex810908 and Ex810909 omitting waves smaller than 6 cm. The distribu-

tions in Figs. 8, 9, 10 and 11 are normalized by the mean wave height and the mean wave period for 1000 waves. Equi-probability density lines of 0.1, 0.5 and 1.0 are drawn with dotted, broken, and solid lines, respectively. The interval of (H/$\bar{H}$) and (T/$\bar{T}$) is 0.2. A probability density of unity requires 40 waves.

From these figures, the following may be pointed out:

1. There is a strong correlation between wave height and period for the waves lower than the mean wave.

2. The marginal distributions of the wave height and period becomes bi-modal, and the joint distribution exhibits two maxima in the neighborhood of the breaking point. This tendency is particularly strong if waves are defined by the zero-down crossing method. The marginal distributions of wave height and period in the offshore approach a distribution similar to the Rayleigh distribution, but one which has a peak on the smaller side of the mean.

3. The range of wave height distribution is broad at the offshore side of the breaking point, whereas the range of wave period distribution is broad in the surf zone. These phenomena can be interpreted from the shoaling and breaking deformation of waves. That is, with approach to the breaking point, the waves increase in height and broaden the range of the distribution. After breaking, the disturbance accompanying the wave breaking generates many secondary waves having small periods, and the range of the period distribution thus broadens.

4. The linear correlation coefficients between individual wave heights and periods for the surf zone are smaller than those at the seaward of the breaking point.

5. From Figs. 8 and 9, it is seen that the long period waves have little influence on the joint distributions.

4. COMMENTS ON THE MEASUREMENT SYSTEM

The photographic technique as described here has the distinguishing merit that the sea water surface elevation can be sampled directly and at closely spaced points over a long observation of time. Also, because the method is direct, the data can be easily reviewed and checked. However, the method has the disadvantage that it takes a great deal of time and much labor to transfer the sea surface elevation from the film to a form suitable for calculation. From the viewpoint of data handling, the 16 mm camera should be replaced by video television in the future. But at the present time, film gives higher resolution than video TV. We would like to suggest to researchers who intend to apply similar methods that a heavier sled than our sled be used to avoid movement as happened in Ex810909.

ACKNOWLEDGEMENTS

The field observations discussed in this paper were carried out under the supervision of Professor K. Horikawa, Department of Civil Engineering, University of Tokyo. The authors would like to thank him for his considerable assistance and advice. We appreciate the permission of the Public Works Institute, Ministry of Construction for use of the pier. We would also like to express our appreciation to our university students who supported the field work. Without their help we could not have carried out these field observations. We would also like to thank Dr. N. C. Kraus and Miss T. Kohno of the Nearshore Environment Research Center for proofreading and typing of the manuscript.

REFERENCES

Ezraty, R., Laurent, M., and Arhan, M.: Comparison with observation at sea of period or height dependent sea state parameters from a theoretical model, OTC 2744, 9th Offshore Tech. Conf., 1977.

Goda, Y.: The observed joint distribution of periods and heights of sea waves, Proc. 16th ICCE, Vol. 1, 1978, pp. 227-246.

Hotta, S. and M Mizuguchi: A field study of waves in the surf zone, Coastal Eng. in Japan, Vol. 23, JSCE, 1980. pp. 59-79.

Hotta, S., M. Mizuguchi and M. Isobe: Observations of long period waves in the nearshore zone, Coastal Eng. in Japan, Vol. 24, JSCE, 1981, pp. 41-76.

Mizuguchi, M.: Individual wave analysis of irregular wave deformation in the nearshore zone, Proc. 19th Coastal Eng. Conf. (in press), 1982.

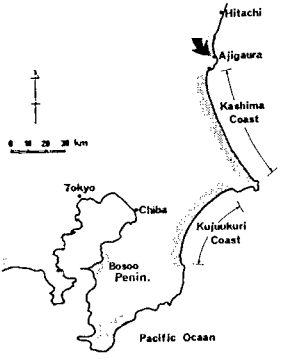

Fig. 1 Location map of the field observation site.

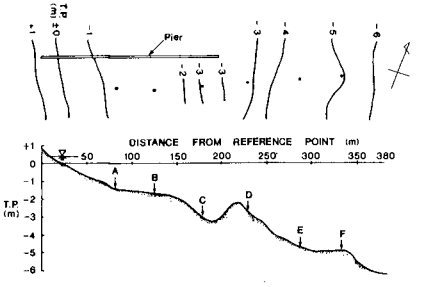

Fig. 2 Beach profile and positions of sleds for Ex800902.

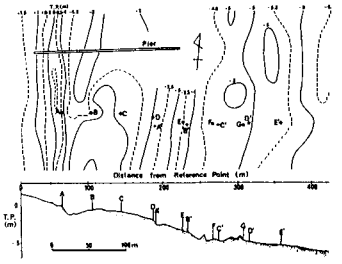

Fig. 3 Beach profile and positions of sleds for Ex810908 and Ex810909.

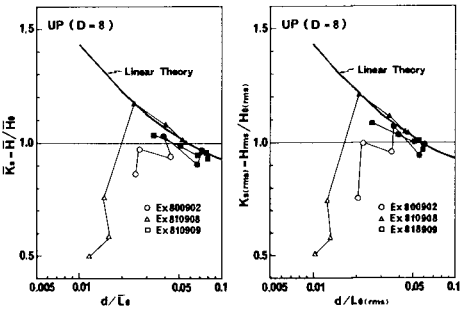

Fig. 6 Shoaling deformation of statistically representative waves.

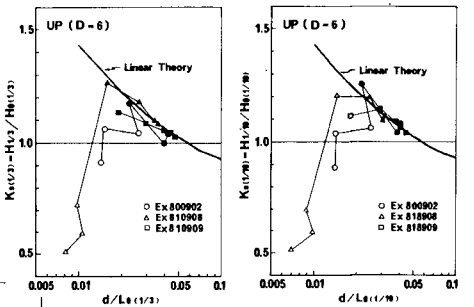

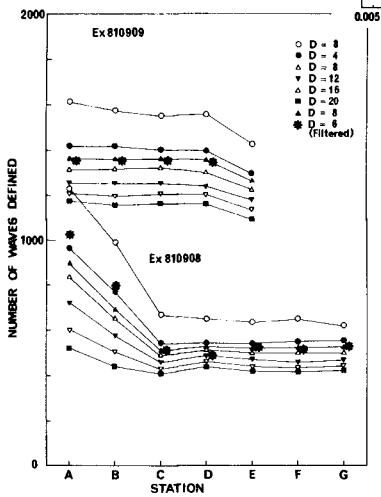

Fig. 4 Number of defined waves obtained by imposing a minimum wave height (D) for Ex800902.

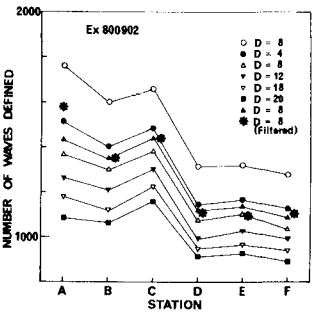

Fig. 5 Number of defined waves obtained by imposing a minimum wave height (D) for Ex810908 and Ex810909.

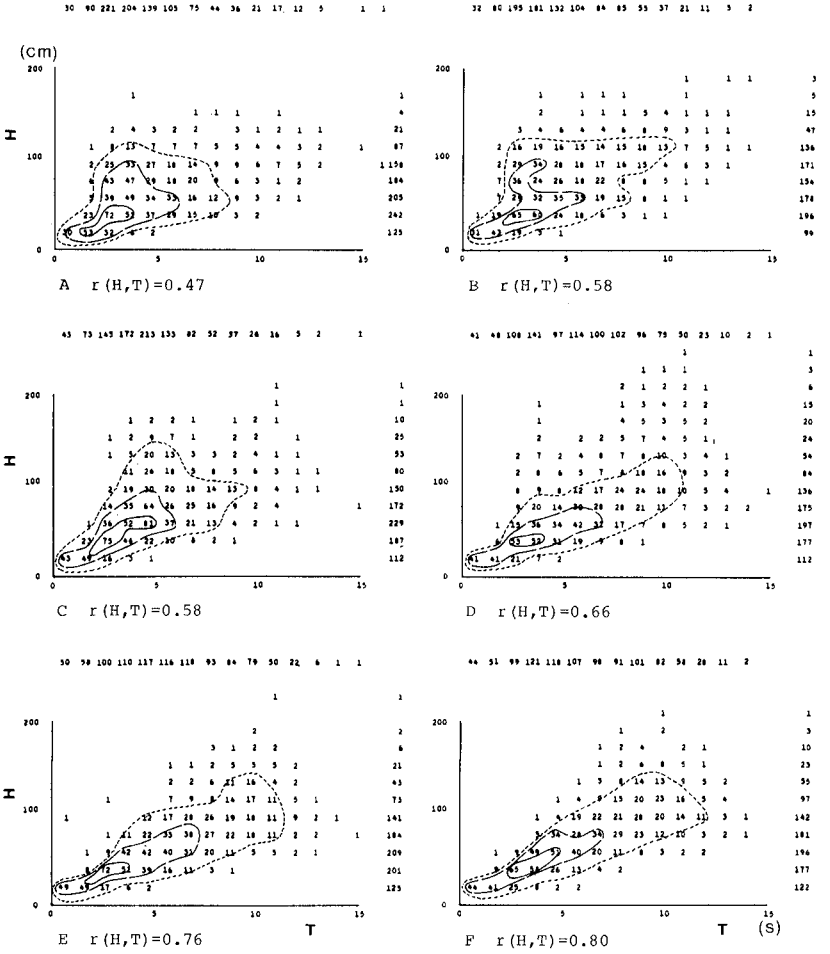

Ex800902 UP-CROSS RAW DATA D=0

Fig. 7 Joint distribution for Ex800902 including small waves.

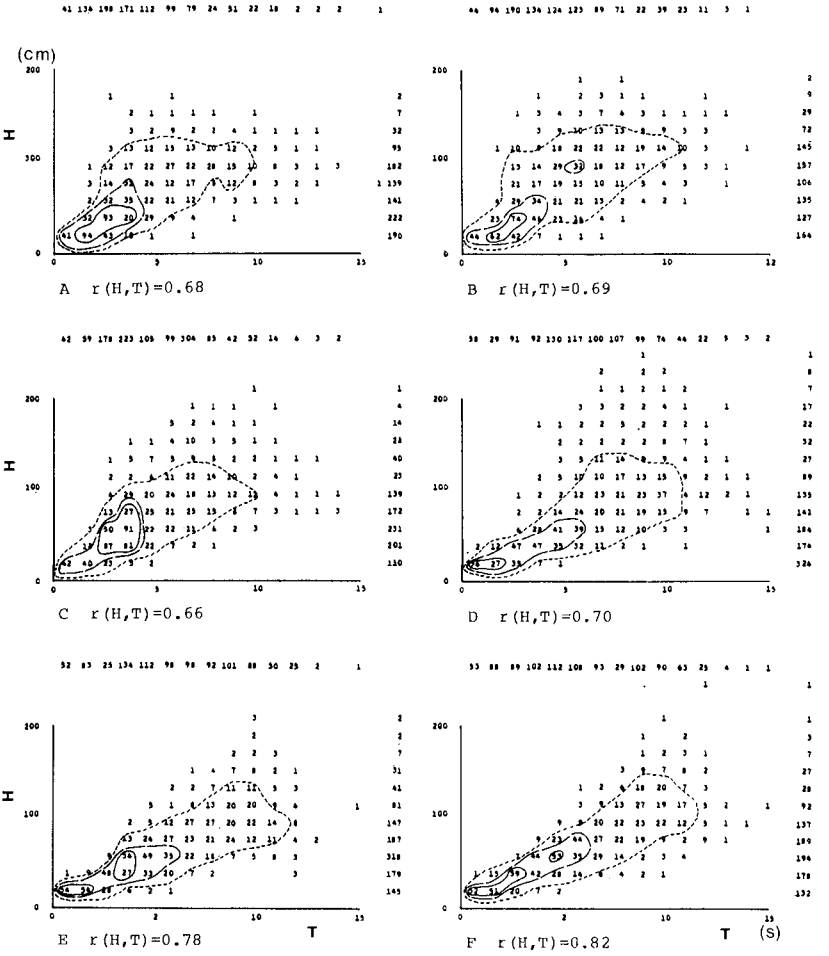

Ex800902 DOWN-CROSS RAW DATA D=0

Fig. 7 Joint distribution for Ex800902 including small waves.

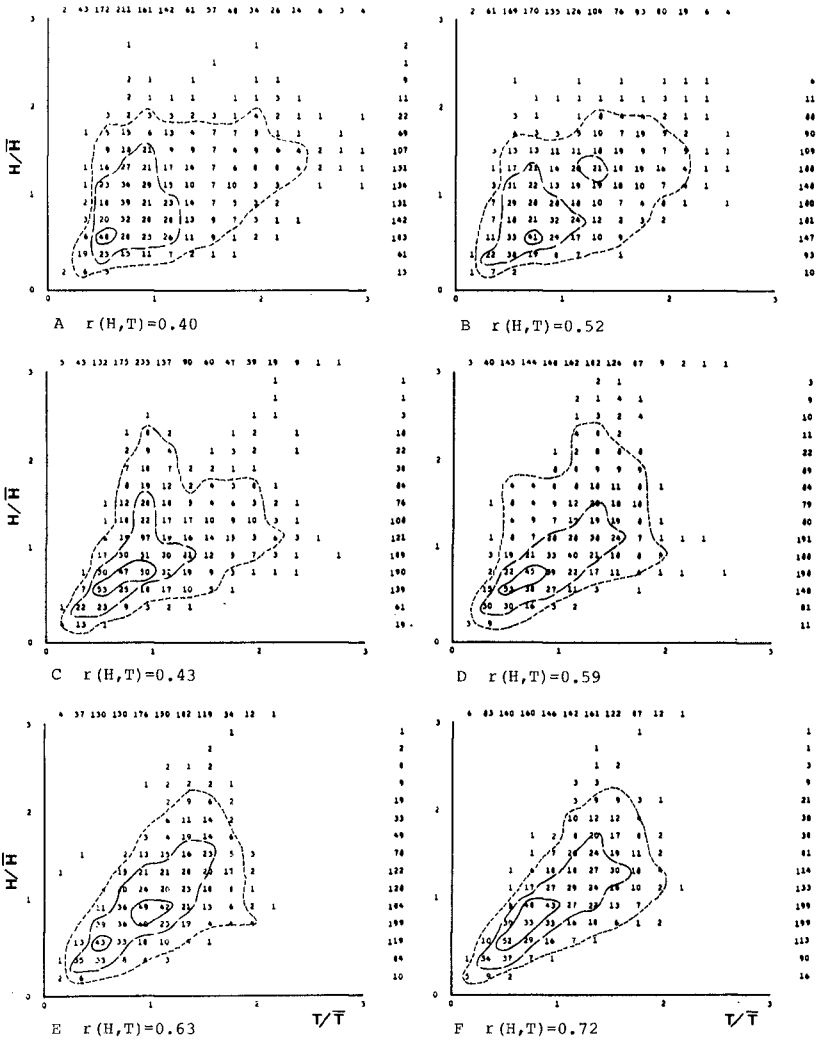

Ex800902 UP-CROSS FILTERED D=6

Fig. 8 Normalized joint distribution after filtering for Ex800902.

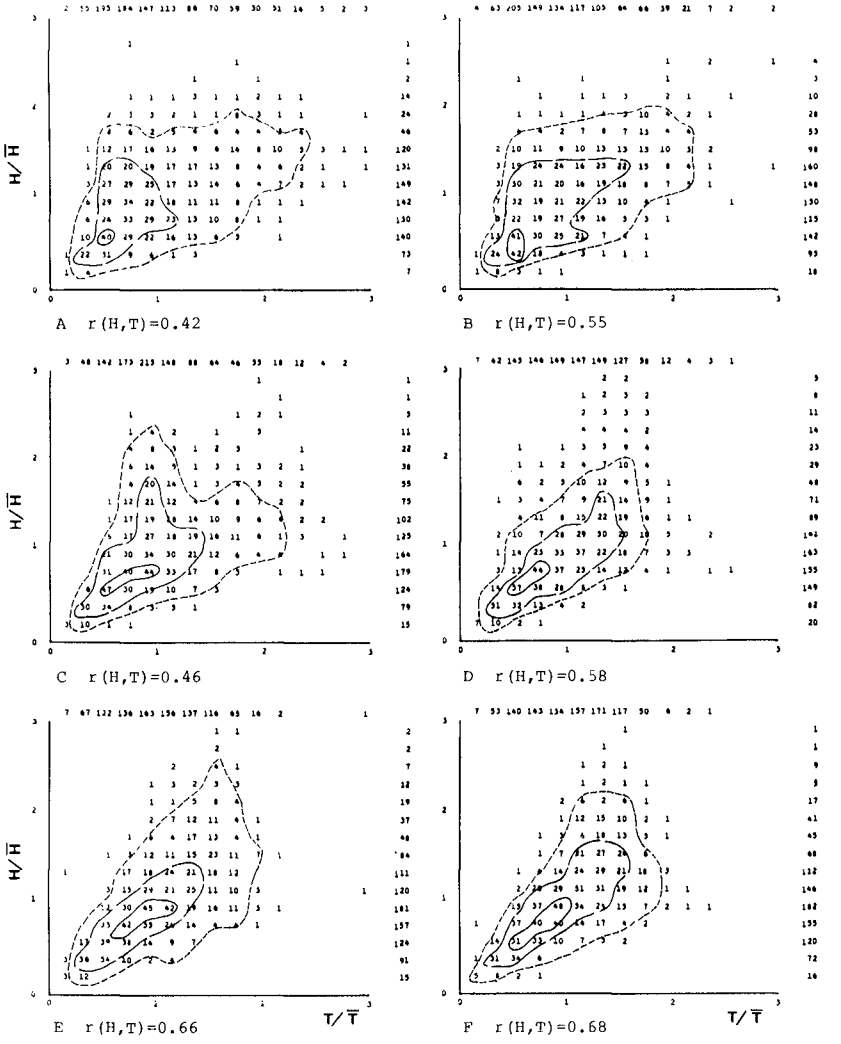

Ex800902 UP-CROSS D=6

Fig. 9 Normalized joint distribution for Ex800902.

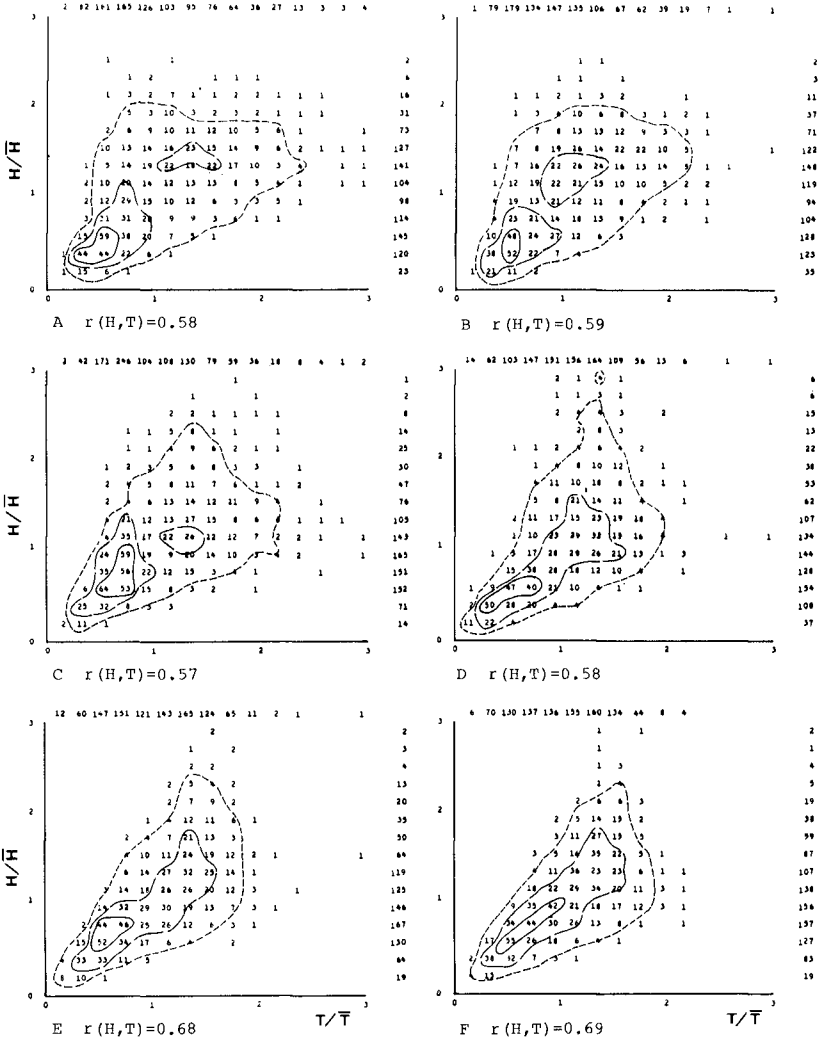

Ex800902 DOWN-CROSS D=6

Fig. 9 Normalized joint distribution for Ex800902.

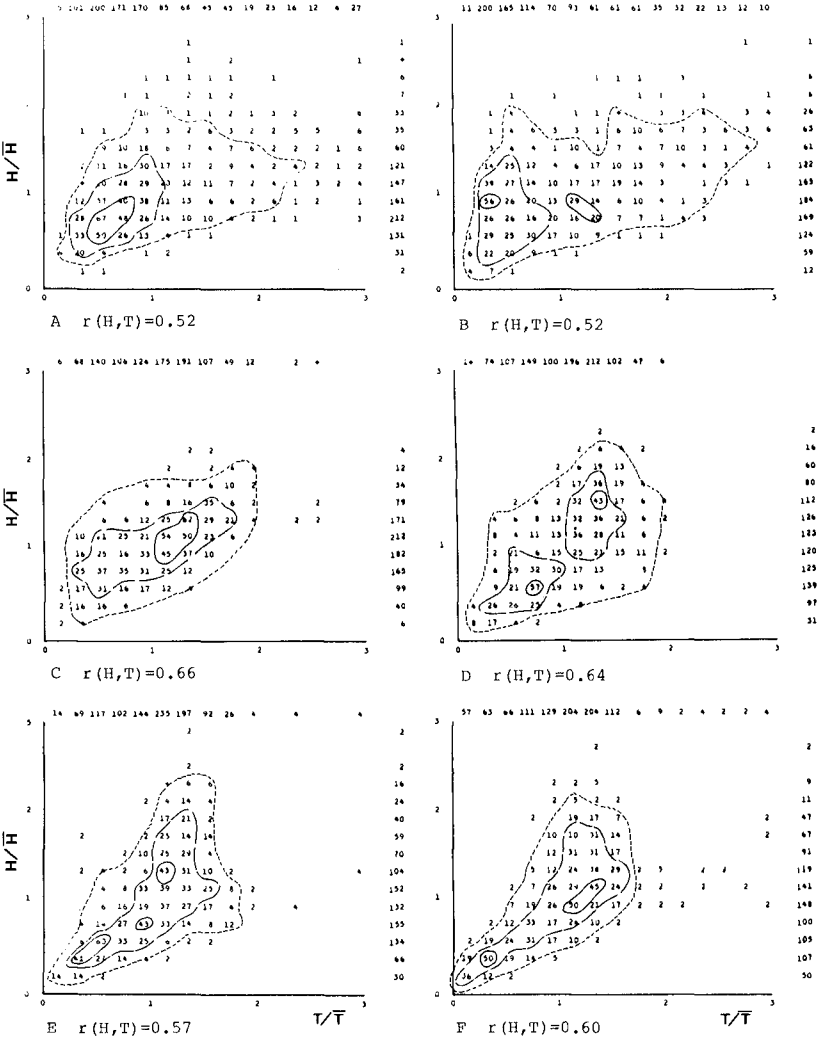

Ex810908 UP-CROSS D=6

Fig. 10 Normalized joint distribution for Ex810908.

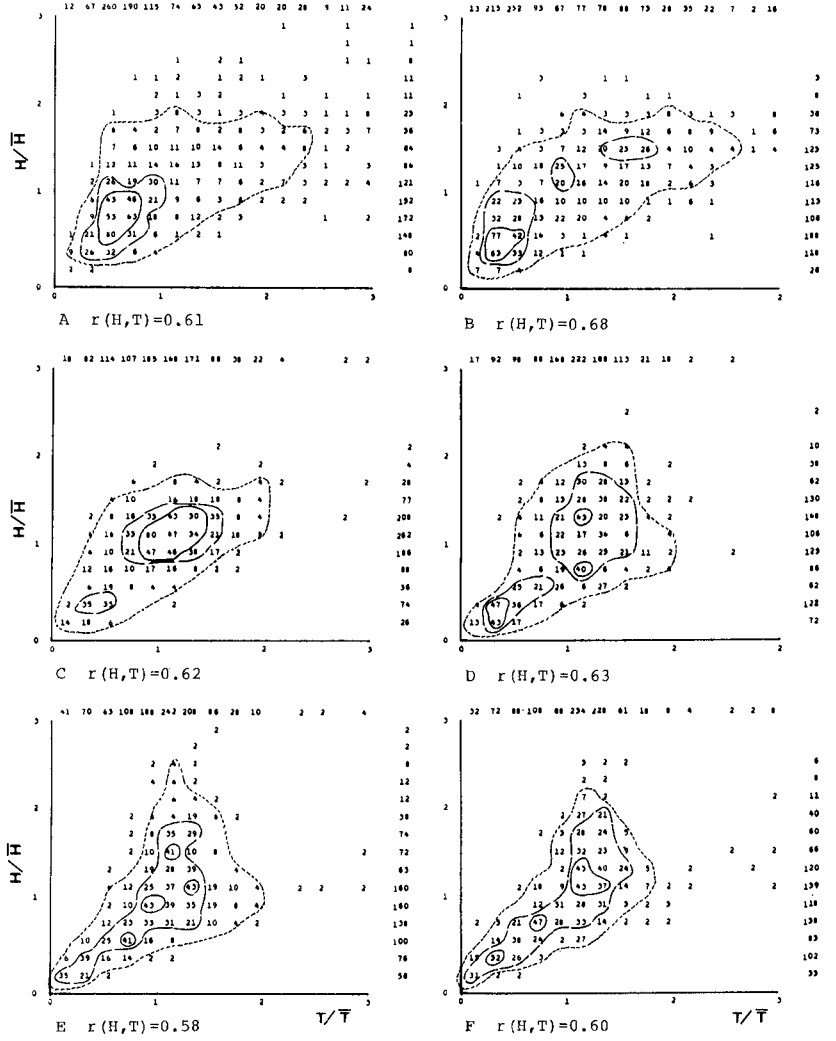

Ex810908 DOWN-CROSS D=6

Fig. 10 Normalized joint distribution for Ex810908.

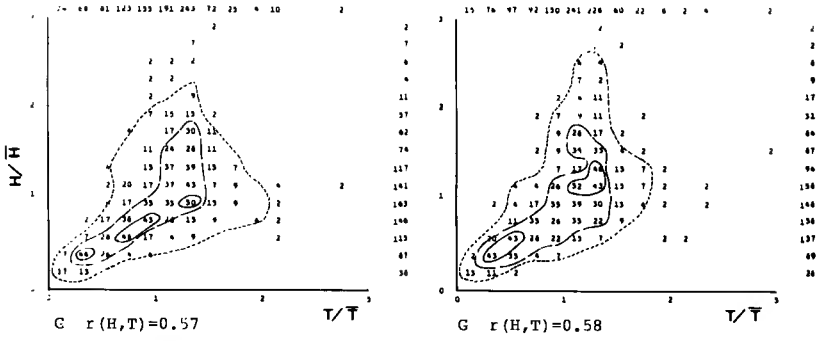

Fig. 10 Normalized joint distribution for Ex810908.

Photo 1 16 mm camera system in operation on pier for Ex810909.

Photo 2 Sleds prior to being pulled out.

Photo 3 Sea condition and target poles.

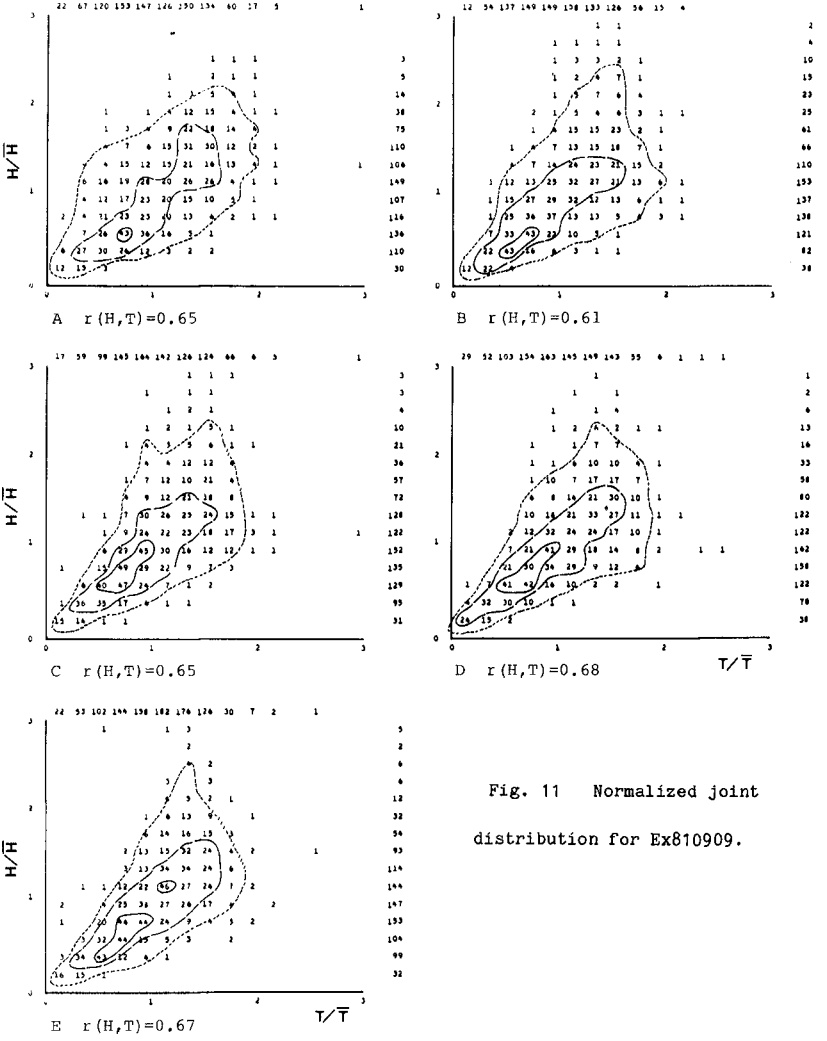

Fig. 11 Normalized joint distribution for Ex810909.

Ex810909 UP-CROSS D=6

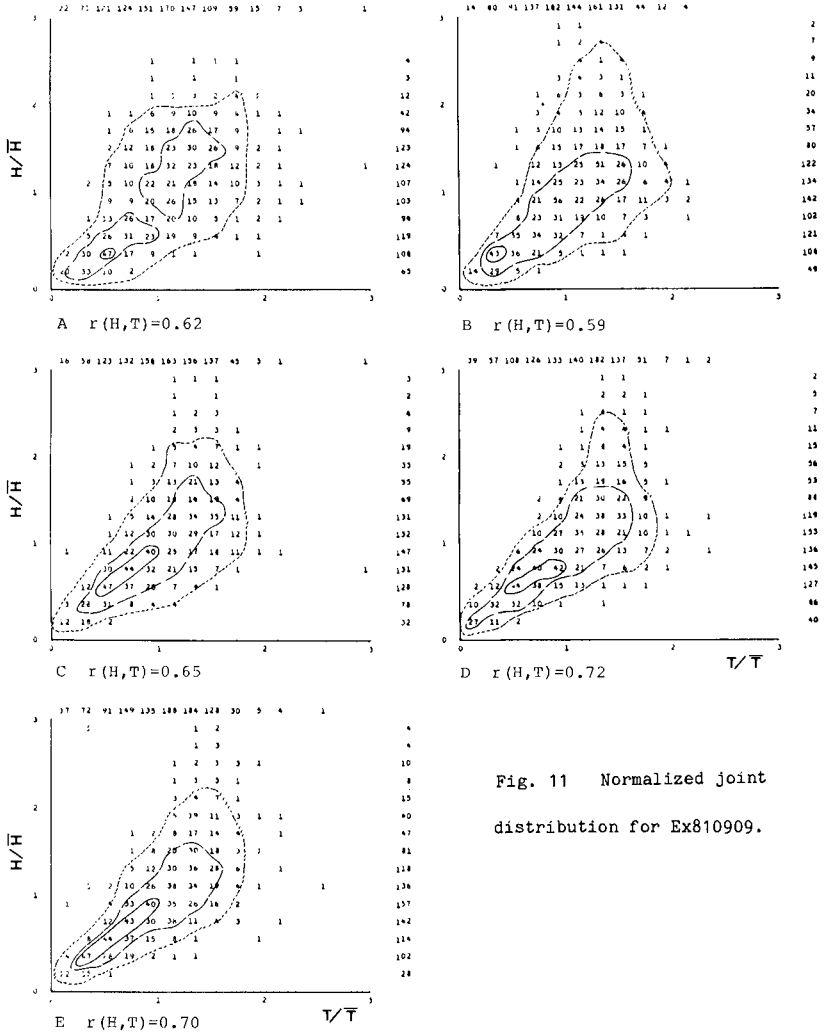

Fig. 11 Normalized joint distribution for Ex810909.

Ex810909 DOWN-CROSS D=6

	Ex800902 (0=0)											
	DOWN						UP					
	A	B	C	O	E	F	A	B	C	O	E	F
d	1.81	1.84	3.22	2.79	4.93	5.14	1.81	1.84	3.22	2.79	4.93	5.14
N	1737	1597	1657	1308	1319	1282	1738	1597	1657	1308	1318	1283
H max	166	189	217	243	217	242	173	186	208	241	228	208
T max	2.94	7.51	9.29	8.21	9.56	12.0	3.17	12.5	10.3	10.2	10.8	9.40
H 1/10	119	137	140	167	135	139	112	131	138	160	135	138
T 1/10	6.53	6.89	6.74	8.18	8.89	9.20	6.11	7.25	5.89	8.35	8.93	9.05
H 1/3	98	114	107	123	105	109	92	108	107	119	104	108
T 1/3	6.36	6.73	6.37	8.04	8.34	8.65	5.50	6.22	5.95	7.88	8.12	8.63
$\bar{H}$	56	65	64	69	61	64	56	65	64	69	61	64
$\bar{T}$	4.31	4.69	4.52	5.73	5.68	5.84	4.31	4.68	4.52	5.73	5.68	5.84
H rms	66	78	74	84	72	75	64	75	74	82	72	74
T rms	5.02	5.37	5.11	6.47	6.43	6.57	4.94	5.34	5.05	6.43	6.39	6.55
r(H,T)	0.68	0.69	0.66	0.70	0.78	0.82	0.47	0.58	0.58	0.66	0.76	0.80
r(H)	-.13	-.14	0.02	0.11	0.25	0.30	0.01	0.00	0.08	0.26	0.29	0.32
r(T)	-.04	-.04	-.05	0.13	0.22	0.24	0.05	0.01	0.05	0.21	0.24	0.28
WG 1/3	217	198	201	131	116	119	205	178	199	121	117	120
$\bar{J}$ 1/3	1.14	1.11	1.13	1.30	1.47	1.48	1.19	1.20	1.14	1.36	1.45	1.49
$\bar{1}$ 1/3	7.95	8.06	8.24	10.0	11.3	10.8	8.47	8.97	8.32	10.9	11.3	10.8
WG a	511	464	421	314	292	265	480	430	407	279	285	248
$\bar{J}$ a	1.58	1.66	1.75	1.88	2.03	2.25	1.72	1.83	1.80	2.04	2.12	2.31
$\bar{1}$ a	3.40	3.44	3.94	4.17	4.51	4.84	3.62	3.71	4.08	4.69	4.62	5.19

Table 2 Statistically representative waves for Ex800902 including small waves.

	Ex810908						
	A	B	C	O	E	F	G
σ	18	19	22	36	34	35	35
$\sqrt{\beta_1}$	0.72	1.02	0.95	1.37	0.98	0.68	0.89
β_2	4.08	4.43	4.06	5.14	4.45	3.55	4.34
$\overline{\eta^2}$	319	344	462	1305	1160	1228	1215
η	40	11	18	-2	-11	-30	-6
ε	0.95	0.95	0.96	0.97	0.98	0.99	0.99
υ	1.22	1.17	1.16	1.00	0.96	1.22	1.08

	Ex800902						Ex810909				
	A	B	C	O	E	F	A	B	C	O	E
σ	23	27	28	30	28	30	41	40	40	43	46
$\sqrt{\beta_1}$	1.26	1.25	0.93	1.16	0.64	0.51	1.37	1.09	0.88	0.81	0.52
β_2	5.05	4.89	4.36	5.43	3.73	3.43	5.05	4.84	4.16	4.03	3.53
$\overline{\eta^2}$	528	748	960	926	777	872	1692	1594	1631	1851	1768
η	27	23	0	-2	13	24	3	-3	-17	18	15
ε	0.94	0.94	0.97	0.97	0.98	0.98	0.97	0.98	0.98	0.99	0.99
υ	0.86	0.86	0.85	0.83	0.85	0.85	1.01	0.86	0.92	1.00	0.99

Table 1 Statistical parameters of sea water surface elevation, and spectral parameters.

LIST OF SYMBOLS

d : water depth (m)
N : number of waves defined by zero-crossing method
H max : maximum wave height (cm)
T max : maximum wave period (s)
H 1/10 : one-theth wave height (cm)
T 1/10 : one-tenth wave period (s)
H 1/3 : significant wave height (cm)
T 1/3 : significant wave period (s)
$\bar{H}$: mean wave height (cm)
$\bar{T}$: mean wave period (s)
H rms : root mean square wave height (cm)
T rms : root mean square wave period (s)
r(H,T) : correlation coefficient between individual wave height and period
r(H) : correlation coefficient between successive two wave height
r(T) : correlation coefficient between successive two wave period
WG 1/3 : number of run exceeding significant wave height
$\bar{J}$ 1/3 : mean length of run for WG 1/3
$\bar{1}$ 1/3 : mean length of total run for WG 1/3
WG a : number of run exceeding mean wave height
$\bar{J}$ a : mean length of run for WG a
$\bar{1}$ a : mean length of total run for WG a
σ : standard deviation of sea water surface variation
$\sqrt{\beta_1}$: skewness of sea water surface variation
β_2 : kurtosis of sea water surface variation
$\overline{\eta^2}$: mean root square of sea water surface variation (variance) (cm^2)
η : mean water level from reference elevation (cm)
ε : spectral width parameter defined by $\varepsilon = [1-m_2^2/(m_0 m_4)]^{1/2}$
υ : spectral width parameter defined by $\upsilon = [m_0 m_2/m_1^2-1]^{1/3}$

$$m_n = \int_{-\infty}^{\infty} f^n S(f)\,df$$

	EX800902 (D=8)												EX800902 (D=8) FILTERED											
	DOWN						UP						DOWN						UP					
	A	B	C	O	E	F	A	B	C	O	E	F	A	B	C	O	E	F	A	B	C	O	E	F
d	1.81	1.84	3.22	2.79	4.93	5.14	1.81	1.84	3.22	2.79	4.93	5.14												
N	1434	1348	1445	1118	1142	1082	1435	1348	1445	1118	1141	1083	1508	1344	1440	1093	1098	1092	1508	1344	1440	1084	1097	1091
H max	166	189	217	243	217	242	173	191	208	241	228	208	173	188	223	244	216	229	172	178	201	236	222	217
T max	2.94	7.51	9.29	8.21	9.56	12.0	3.17	16.2	1.26	9.92	10.8	10.5	5.62	7.41	9.57	9.15	9.29	10.9	3.14	11.1	10.2	10.2	11.1	10.1
H 1/10	122	140	144	173	139	143	117	139	142	168	139	142	121	141	144	172	139	141	115	135	140	165	138	140
T 1/10	7.00	7.26	7.02	8.50	9.13	9.36	7.02	8.33	6.17	9.01	9.07	9.16	6.69	7.30	7.16	8.73	9.13	9.36	6.31	7.95	5.86	8.89	9.04	9.15
H 1/3	103	119	112	130	110	115	98	115	112	127	109	114	101	118	111	130	110	113	95	113	110	126	109	112
T 1/3	6.90	7.21	6.76	8.34	8.71	8.97	6.53	7.19	6.35	8.40	8.49	8.95	6.62	7.22	6.66	8.44	8.68	8.94	6.01	7.03	6.05	8.38	8.52	8.96
$\bar{H}$	65	75	71	79	69	74	65	75	71	79	69	74	62	75	70	79	70	72	62	75	70	79	70	72
$\bar{T}$	5.22	5.55	5.18	6.70	6.57	6.92	5.22	5.50	5.18	6.71	6.56	6.92	4.87	5.46	5.10	6.72	6.69	6.72	4.87	5.46	5.10	6.72	6.69	6.72
H rms	73	85	79	91	78	82	71	83	79	89	78	82	70	84	79	91	78	81	68	82	78	89	78	80
T rms	5.90	6.16	5.74	7.28	7.14	7.46	5.87	6.18	5.69	7.27	7.11	7.45	5.50	6.06	5.63	7.24	7.23	7.27	5.44	6.06	5.56	7.24	7.19	7.25
r(H)	0.58	0.59	0.57	0.58	0.68	0.69	0.42	0.55	0.46	0.58	0.66	0.68	0.60	0.60	0.57	0.60	0.66	0.73	0.40	0.52	0.43	0.59	0.63	0.72
r(H)	-.15	-.14	-.03	0.17	0.24	0.29	-.01	-.03	0.04	0.29	0.29	0.32	-.14	-.14	-.06	0.18	0.26	0.32	0.01	-.01	0.02	0.29	0.32	0.36
r(T)	0.00	0.02	-.03	0.12	0.15	0.20	0.04	0.30	0.08	0.18	0.21	0.23	0.00	0.06	-.09	0.14	0.18	0.22	0.06	0.06	0.05	0.18	0.26	0.26
WG 1/3	182	163	170	110	104	99	158	148	163	107	99	93	136	159	170	109	101	95	174	154	176	105	97	89
$\bar{H}$ 1/3	1.12	1.14	1.19	1.35	1.48	1.52	1.25	1.20	1.20	1.35	1.48	1.48	1.15	1.13	1.13	1.29	1.47	1.57	1.24	1.19	1.16	1.38	1.53	1.60
$\bar{T}$ 1/3	7.84	8.27	8.51	10.2	11.0	11.0	8.98	9.10	8.88	10.5	11.6	11.7	8.05	8.33	8.44	10.0	10.9	11.5	8.67	8.60	8.09	10.4	10.7	11.7
WG a	412	378	379	250	233	206	381	357	363	227	231	211	439	378	385	242	218	207	401	351	372	216	208	200
$\bar{H}$ a	1.75	1.83	1.70	2.02	2.21	2.39	1.85	1.90	1.73	2.13	2.14	2.35	1.68	1.81	1.64	2.02	2.31	2.43	1.81	1.91	1.69	2.19	2.30	2.46
$\bar{T}$ a	3.48	3.56	3.82	4.48	4.91	5.26	3.77	3.78	3.98	4.93	4.95	5.15	3.44	3.55	3.72	4.49	5.05	5.28	3.76	3.83	3.87	5.04	5.28	5.47

(a) (b)

Table 3 Statistical representative waves for Ex800902.

	EX810908 (D=8)														EX810909 (D=8)										
	DOWN							UP							DOWN					UP					
	A	B	C	O	E	F	G	A	B	C	O	E	F	G	A	B	C	O	E	A	B	C	O	E
d	0.95	1.31	1.19	1.95	3.28	4.22	4.34	0.95	1.31	1.19	1.95	3.28	4.22	4.34	2.28	3.52	4.73	5.08	5.45	2.28	3.52	4.73	5.08	5.45
N	898	691	516	530	516	422	460	899	691	515	530	516	421	461	1370	1365	1362	1353	1163	1370	1364	1362	1353	1164
H max	122	117	145	253	265	218	247	114	136	137	242	268	241	255	278	323	316	322	345	288	335	328	328	336
T max	8.66	4.12	11.3	10.1	10.8	7.75	8.89	5.40	15.1	10.0	9.87	9.40	8.74	10.8	8.00	5.44	7.60	9.66	10.6	12.4	9.34	8.63	8.72	8.37
H 1/10	86	93	103	186	189	170	175	81	93	108	188	188	169	174	212	221	206	213	207	213	219	207	207	200
T 1/10	7.29	9.32	9.67	8.61	8.70	9.31	8.56	7.37	9.81	10.5	9.62	9.25	9.80	8.69	8.46	8.13	8.78	9.23	9.82	9.53	8.75	8.80	8.92	9.20
H 1/3	68	79	99	162	150	138	138	64	75	92	160	149	139	137	181	173	162	167	161	178	170	163	165	159
T 1/3	6.29	8.32	8.90	8.53	8.74	9.29	9.02	5.93	7.72	9.85	9.04	8.93	9.37	8.83	8.20	8.23	8.56	8.94	9.29	8.79	8.49	8.53	8.73	9.11
$\bar{H}$	43	50	66	102	94	88	87	43	50	66	102	94	88	87	112	106	102	104	101	113	106	102	104	101
$\bar{T}$	4.22	5.46	7.35	7.16	7.35	7.19	7.27	4.23	5.47	7.36	7.15	7.35	7.19	7.26	6.65	6.68	6.69	6.74	7.17	6.66	6.68	6.69	6.73	7.17
H rms	48	56	71	115	106	98	98	47	55	70	114	105	99	98	128	121	115	118	114	126	120	115	117	113
T rms	5.09	6.54	8.01	7.72	7.98	8.13	7.81	5.08	6.57	8.00	7.71	7.95	8.16	7.82	7.26	7.23	7.22	7.32	7.71	7.26	7.24	7.24	7.30	7.73
r(H,T)	0.61	0.68	0.62	0.63	0.56	0.60	0.58	0.52	0.52	0.66	0.64	0.57	0.60	0.57	0.62	0.59	0.65	0.72	0.70	0.65	0.61	0.65	0.68	0.67
r(H)	-.11	0.11	-.07	0.12	0.30	0.33	0.27	-.00	0.05	0.03	0.22	0.36	0.28	0.29	0.05	0.14	0.27	0.24	0.29	0.15	0.22	0.28	0.29	0.33
r(T)	-.03	-.02	0.09	0.10	0.12	0.20	0.10	0.02	-.02	0.15	0.12	0.20	0.21	0.13	0.12	0.16	0.23	0.19	0.20	0.14	0.19	0.24	0.23	0.22
WG 1/3	116	80	49	64	53	41	48	106	78	56	61	49	40	45	146	136	126	124	112	150	140	126	126	104
$\bar{H}$ 1/3	1.10	1.17	1.31	1.31	1.43	1.39	1.31	1.10	1.24	1.16	1.30	1.55	1.47	1.36	1.31	1.29	1.45	1.38	1.35	1.30	1.36	1.45	1.40	1.39
$\bar{T}$ 1/3	7.67	8.57	10.4	8.06	9.79	10.4	9.62	8.40	8.83	9.27	9.52	10.6	10.3	10.3	9.20	9.98	10.8	10.9	10.1	9.13	9.76	10.6	10.7	10.9
WG a	249	198	131	121	94	76	92	220	170	118	112	92	77	93	325	320	283	283	231	310	299	274	266	224
$\bar{H}$ a	1.59	1.72	2.26	2.25	2.59	2.76	2.30	1.80	1.96	2.23	2.33	2.61	2.68	2.29	2.14	2.02	2.23	2.24	2.31	2.21	2.16	2.27	2.35	2.43
$\bar{T}$ a	3.59	3.50	3.92	4.39	5.48	5.53	4.98	4.06	4.06	4.36	4.75	5.59	5.45	4.92	4.20	4.26	4.87	4.78	5.02	4.42	4.54	4.97	5.08	5.21

Table 4 Statistical representative waves for Ex810908 and Ex810909.

Wave Height Distributions and Wave Grouping in Surf Zone

Hajime Mase[1] and Yuichi Iwagaki, M. ASCE[2]

Abstract

The main purpose of this paper is to propose a model for prediction of the spatial distributions of representative wave heights and the frequency distributions of wave heights of irregular waves in shallow-water including the surf zone. In order to examine the validity of the model, some experiments of irregular wave transformation have been made. In addition, an attempt has been made to clarify the spatial distribution of wave grouping experimentally. Especially the present paper focusses finding the effects of the bottom slope and the deep-water wave steepness on the wave height distribution and wave grouping.

1. Introduction

Battjes (1972) calculated the wave setup of irregular waves by a model of breaking waves that the Rayleigh distribution as the wave height distribution in deep-water is cut off partly by the breaker height determined by the local water depth. Afterwards Battjes (1978a) calculated the changes of the root-mean-square wave height and the wave setup of irregular waves on an arbitrary bottom slope by solving the energy balance equation, and it was reported that the calculated results agreed reasonably with the experimental ones. In that model of wave breaking the energy dissipation due to wave breaking was formulated by the bore model and the wave height distribution was cut off partly similarly to the previous model.

Since it is not realistic that the cumulative distribution function of the wave height is discontinuous at the breaking limit as Battjes's model, Goda (1975) proposed a model of irregular wave breaking that the portion of high waves in the Rayleigh distribution cut off partly is transfered to the portion of low waves with a certain probability due to breaking.

In the models of irregular wave breaking proposed by Battjes (1972) and Goda (1975), the Rayleigh distribution is modified with the breaker height determined by the local water depth, and the spatial propagation of waves with energy dissipation is not considered. On the other hand, it is considered in the model proposed later by Battjes (1978a), but still his model holds a problem that the cumulative distribution function of the wave height is discontinuous at the point of the wave height of breaking limit.

1) Research Associate, Department of Civil Engineering, Kyoto University, Kyoto, Japan
2) Professor, Department of Civil Engineering, Kyoto University, Kyoto, Japan

In this paper, the representative wave heights such as the significant and mean wave heights and the wave height distributions are predicted under the assumption that the wave height change of an individual irregular wave is equal to that of monochromatic waves having the same wave height and wave period and it can be superimposed independently. This method of analysis will be called the individual wave analysis method hereafter.

In addition to the height and period of irregular waves, a phenomenon of wave grouping that large waves continue successively is important, because it seems to be one of main factors for collapses of coastal structures such as rubble mound breakwaters. It was recently reported by Johnson et al. (1978) that even if energy spectra of irregular waves are same, a degree of damage is not same but depends on wave grouping of irregular waves. Accordingly, characteristics of wave grouping in shallow-water must be investigated as an important factor of design waves. The characteristics of wave grouping in shallow-water have not been studied little so far.

2. Calculation method for wave height change of irregular waves in shallow-water

2.1 Formulation for wave height change of individual wave

The wave height change of an individual wave defined by the zero-up-cross method is formulated under the following assumptions: (1) an individual wave among irregular waves is transformed independently, (2) the small amplitude wave theory is applied to wave shoaling before wave breaking, (3) the breaker height is calculated by modifying the breaker index for monochromatic waves proposed by Goda (1970), (4) the bore model adopted by Battjes (1978b) is used in a modified form after breaking, and (5) the temporal change of the mean water level is considered by introducing the effect of surf beats in addition to the spatial change of the mean water level due to wave setup.

The representative wave heights and the wave height distributions are predicted by superimposing the calculated wave height of an individual wave.

Based on the assumption (2), the following equation of the shoaling coefficient K_s is used:

$$K_s = \left[\left\{1 + \frac{4\pi d/L}{\sinh 4\pi d/L}\right\} \tanh \frac{2\pi d}{L}\right]^{-1/2}, \qquad (1)$$

and based on the assumption (3), Goda's breaker index

$$H_b/L_o = A\left[1 - \exp\left\{-1.5\frac{\pi d}{L_o}(1 + 15\tan^{4/3}\theta)\right\}\right], \qquad (2)$$

is applied, in which A=0.17 in the case of monochromatic waves, $\tan\theta$ is the bottom slope, and L_o the deep-water wave length, L the wave length in shallow-water, d the mean water depth, and H_b the breaking wave height.

Concerning the change of the wave height after breaking, the bore model adopted by Battjes (1978b) is used. Both factors of the bottom slope and the deep-water wave steepness can be introduced to this model by using the surf similarity parameter. The non-dimensional wave height in the surf zone is expressed as follows:

$$\left.\begin{aligned} \tilde{H}^{-4} &= (1 - \frac{4}{9}K)\tilde{d} + \frac{4}{9}K\tilde{d}^{-7/2}, \\ K &= (\frac{2}{\pi})^{1/2} B\gamma^{1/2}\xi_o^{-1}, \\ \gamma &= 0.7 + 5\tan\theta \qquad (0.01 \leq \tan\theta \leq 0.1), \end{aligned}\right\} \tag{3}$$

in which $\tilde{H} = H/H_b$, $\tilde{d} = d/d_b$, d_b is the breaking water depth, and $\xi_o = \tan\theta/\sqrt{H_o/L_o}$, the surf similarity parameter in deep-water.

The water depth d in the above equations should be taken as the mean water depth. Battjes (1978b) assumed that the mean water level in the surf zone has a gradient equal to 1/5 of the bottom slope with zero setup at the breaking point; therefore, $\tan\theta$ in Eq. (3) becomes as gentle as 0.8 times of the actual bottom slope.

In this paper, the wave height change is firstly calculated by Eqs. (1), (2) and (3) for the still water depth h, and secondly the wave setup $\bar{\eta}$ is calculated numerically from deep-water to the shoreline by using the obtained wave hiehgts and the following equation:

$$\frac{d\bar{\eta}}{dx} = -\frac{1}{(h+\bar{\eta})}\frac{d}{dx}\left\{\frac{1}{8}H^2\left(\frac{1}{2} + \frac{2k(h+\bar{\eta})}{\sinh 2k(h+\bar{\eta})}\right)\right\} \tag{4}$$

The calculated value $\bar{\eta}$ is added to the still water depth h, and the calculation for the wave height change is repeated for the mean water depth $d = h + \bar{\eta}$. The repeated calculation is closed when the difference of successive wave setup becomes as small as 1% after repeats of several times.

Since the calculated value of $\bar{\eta}$ obtained from Eq. (4) using the measured wave height seem to give an overestimate compared with the experimental results, Eq. (4) is modified with the multiplication factor of 0.6.

Energy dissipation due to wave breaking is composed of various factors such as the horizontal roller, the bottom friction and the tubulence with air entrainment (Sawaragi and Iwata (1974)). Eq. (3) is derived from the energy balance equation in which the energy dissipation due to wave breaking is simplified by simulating that due to a bore. Since Eq. (3) can not always fit the experimental results well in all cases, the value of B in Eq. (3) is determined so that the spatial distributions of the wave height agree with the experimental results by Nakamura et al. (1966), Saeki et al. (1974) and Singamsetti et al. (1978) as follows:

(i) In cases that $\tan\theta > 1/20$,

$$\left.\begin{aligned} &B = 1 && \text{for} \quad 0.9 \leq \tilde{d} \leq 1.0, \\ &B = 13 - 40\tilde{d}/3 && \text{for} \quad 0.6 \leq \tilde{d} \leq 0.9, \text{ and} \\ &B = 5 && \text{for} \quad \tilde{d} \leq 0.6. \end{aligned}\right\} \qquad (5)$$

(ii) In cases that $\tan\theta < 1/20$,

$$\left.\begin{aligned} &B = 11 - 10\tilde{d} && \text{for} \quad 0.6 \leq \tilde{d} \leq 1.0, \text{ and} \\ &B = 5 && \text{for} \quad \tilde{d} \leq 0.6. \end{aligned}\right\} \qquad (6)$$

Fig. 1(a) shows the wave height decay of monochromatic waves with decrease in the still water depth after wave breaking in dimensionless form for the deep-water wave steepness of 0.02 with a parameter of the bottom slope from 1/10 to 1/50, in which the experimental results by Saeki et al. (1974) are plotted herewith. Fig. 1(b) also shows the wave height decay after breaking for the bottom slope of 1/30 with a parameter of the deep-water wave steepness from 0.005 to 0.08. It is seen from these figures that the wave height decay becomes remarkable with decrease in the bottom slope and increase in the deep-water wave steepness.

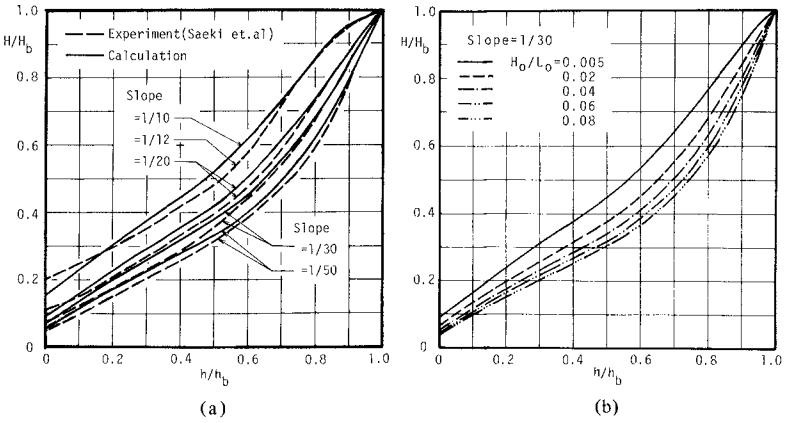

Fig. 1 Wave height decay after wave breaking

2.2 Different points between transformations of breaking irregular waves and monochromatic waves

One of different points between irregular and monochromatic wave transformations in the surf zone is the breaking limit of an individual wave; that is, the breaking wave height of an individual wave of irregular waves is smaller than that of monochromatic waves having the same wave height and period (Kimura and Iwagaki (1978), Sawaragi and Iwata (1981)). The other point is the generation of temporal variations of the water surface having some long-periods, so called surf beats; therefore, they may affect transformations of breaking irregular waves.

With respect to the first point, the reasonable value of A in Eq. (2) is investigated by experiments, and for the second point the following empirical formula of the root-mean-square value of surf beats ζ_{rms} based on the field observation by Goda (1975) is used:

$$\frac{\zeta_{rms}}{H_o} = \frac{0.01\, H_o}{\sqrt{\frac{H_o}{L_o}\left(1+\frac{d}{H_o}\right)}} \quad , \tag{7}$$

in which H_o denotes the significant wave height in deep-water and L_o the wave length in deep-water corresponding to the significant wave period.

In this paper, the surf beat elevation ζ is added to the mean water depth by generating random numbers of the normal distribution with the mean value of 0 and the root-mean-square value of ζ_{rms} by Eq. (7).

2.3 Calculation method for wave height change of irregular waves

As input data, wave heights and periods obtained from the wave record at a constant water depth by the zero-up-cross-method, the bottom slope and the still water depths at all points to predict wave heights are given in this paper.

After calculation of the wave height change of an individual wave for the still water depth and surf beats, the root-mean-square wave heights $\overline{H^2}$ are calculated to obtain the wave setup $\overline{\eta}$ from Eq. (4) with $\overline{H^2}$ instead of H and the wave length corresponding to the significant wave period. Then, the wave height of an individual wave is calculated for the still water depth h, the obtained wave setup $\overline{\eta}$ and the surf beat ζ. Repeating this procedure, the calculation is closed when the difference of successive wave setup becomes less than 1% of the wave setup, and the representative wave heights and the frequency distributions of wave height are obtained. Fig. 2 shows the flow chart for this calculation.

In this calculation program, several supplemental water depths in addition to the water depths of input data are adopted in order to solve Eq. (4) numerically, and many additional water depths are used for determination of the breaking point.

3. Experimental aparatus and procedures

A wave tank, 27m long, 50cm wide and 70cm high, at the Department of Civil Engineering, Kyoto University was used in the present experiments. A wave generator

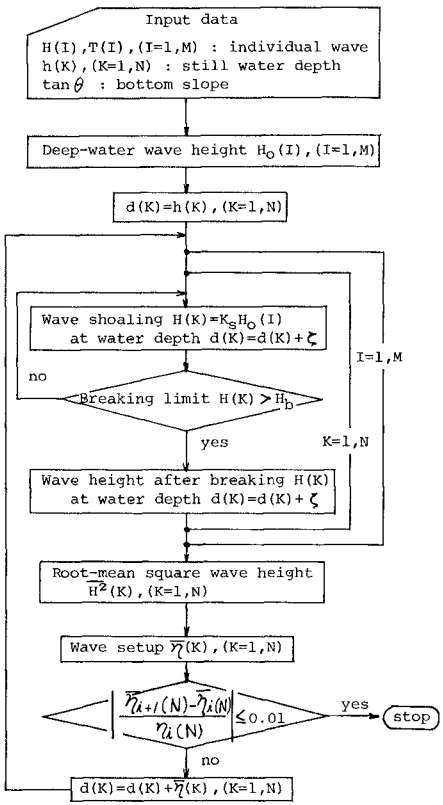

Fig. 2 Flow chart for calculation of wave height change of irregular waves

of irregular waves is installed at an end of the tank.

In order to examine at first the breaker height of an individual irregular wave, some experiments were carried out on the uniform slopes of 1/20 and 1/30 by taking photographs with a 16mm-cinecamera. An experiment for the 1/10 slope was not carried out because the data of breaker height of an individual wave tend to scatter (Kimura and Iwagaki (1978)). In these experiments, the elevation of the top of the slope was ajusted to be equal to the still water level in order to decrease the unsteady back wash which was considered as one of reasons for the difference from the breaking characteristics of regular waves. The range of the breaker depth to be measured by taking pictures was from 10 to 15cm. Irregular waves having the spectra of Pierson-Moskowitz type and two kinds of deep-water wave steepnesses were used. The water depth was kept to be 50cm at the uniform section. The films were analyzed by a film motion analyzer.

In order to examine furthermore the spatial distributions of wave heights and wave grouping of irregular waves with decrease in the water depth, experiments were carried out on the uniform solpes of 1/10 and 1/30 with the water depth of 45cm at the uniform section. Irregular waves having the spectra of Pierson-Moskowitz type and five kinds of deep-water wave steepnesses of 0.005 to 0.07 were used. Water surface elevations were measured by six wave gauges of capacitance type, which were installed at the water depths of 45,20,15,10,5 and 2cm in the case of 1/10 slope and 45,20,12,8,5 and 2cm in the case of 1/30 slope. Additional experiments for the slopes of 1/20 and 1/30 with the water depth of 50cm were carried out by using eleven wave gauges of capacitance type to investigate the change of wave grouping in detail.

Water surface elevations were recorded in a 14-channel analog data recorder. The records were digtized by an A-D converter with 0.04sec time interval and used in analysis.

4. Experimental results and discussions

4.1 Breaking characteristics of individual wave

Figs. 3(a) and (b) show the relationships between H_b/h_b and h_b/L_o on the uniform slopes of 1/20 and 1/30. An individual wave is defined by the spatial zero-up-cross method. The solid lines in the figures represent the results by Eq. (2), and the dashed lines show the results by putting the value of A in Eq. (2) as 0.13,0.14,0.15 and 0.16. The tendency that H_b/h_b decreases with increase in h_b/L_o is similar to that by Eq. (2). However, the experimental data are generally plotted somewhat smaller than the values by Eq. (2). Since the unsteady back wash seems to be weak in the present experiments, the data are plotted a little larger than those by Kimura et al. (1978) and Sawaragi et al. (1981). In determining the breaker height of an individual wave for numerical calculation, the value A in Eq. (2) is taken as 0.16.

4.2 Representative wave heights

Figs. 4(a) and (b) show the changes of the non-dimensional significant wave height $H_{1/3}/H_o$ and mean wave height $\overline{H}/H_o$ with decrease in the water depth on the uniform slopes of 1/10 and 1/30, respectively. An individual wave is defined by the temporal

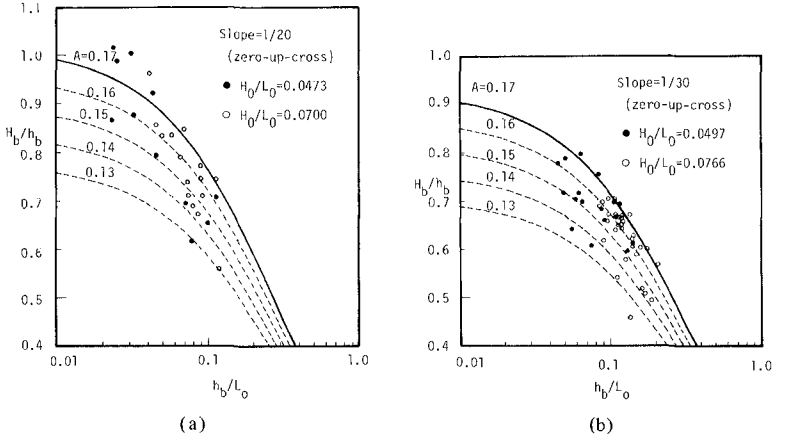

Fig. 3 Relationships between H_b/h_b and h_b/L_o for individual waves

zero-up-cross method, in which the mean water level is determined by simply averaging the water surface elevation. In very shallow water, however, there exist sometimes no intersecting waves with the mean water level. As a result, the significant wave height becomes large and the number of an individual wave decreases compared with the waves obtained from the water surface elevation after the effect of surf beats is eliminated. Therefore, the wave height distributions become different depending on whether the effect of surf beats is eliminated or not, as described later. The curves in Fig. 4(a) and (b) show the calculated results predicted by the individual wave analysis method.

It is found from these figures that the non-dimensional wave heights become large as the deep-water wave steepness, which is estimated from the significant waves at the constant depth by the small smplitude wave theory, becomes small and the bottom slope becomes steep. Concerning the significant wave height, the experimental results are a little larger than calculated ones when the relative water depth h/H_o is less than 1.0, and the calculated results in the region of wave shoaling using the shoaling coefficient by the small amplitude wave theory are a little smaller than the experimental ones. Concerning the mean wave height, the calculated results are somewhat larger than the experimental ones in the case of small deep-water wave steepness. Generally speaking, the predicted curves agree fairly well with the experimental results.

4.3 Wave height distributions

Figs. 5 and 6 show the frequency distributions of wave heights for the cases of

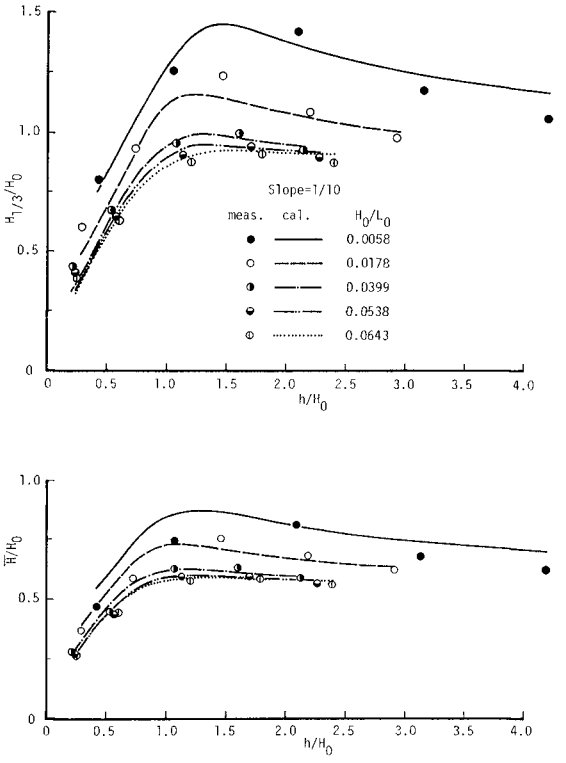

Fig. 4 (a) Change of significant and mean wave heights of irregular waves in shallow-water for 1/10 beach slope

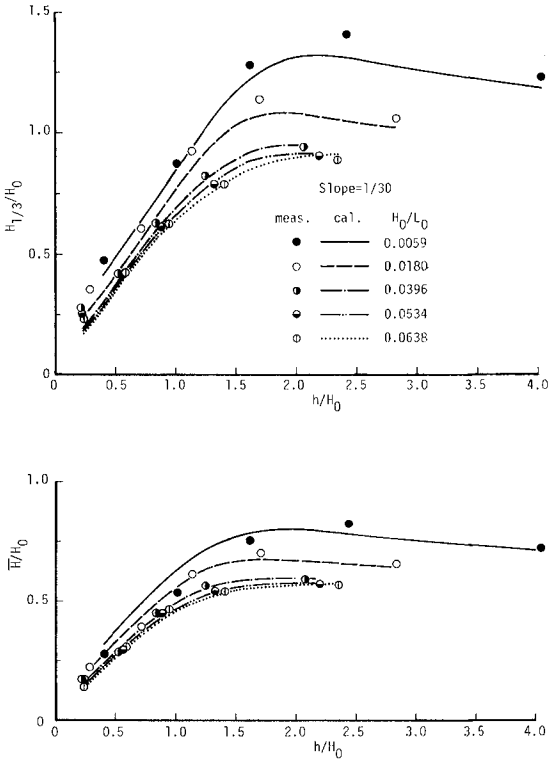

Fig. 4 (b) Change of significant and mean wave heights of irregular waves in shallow-water for 1/30 beach slope

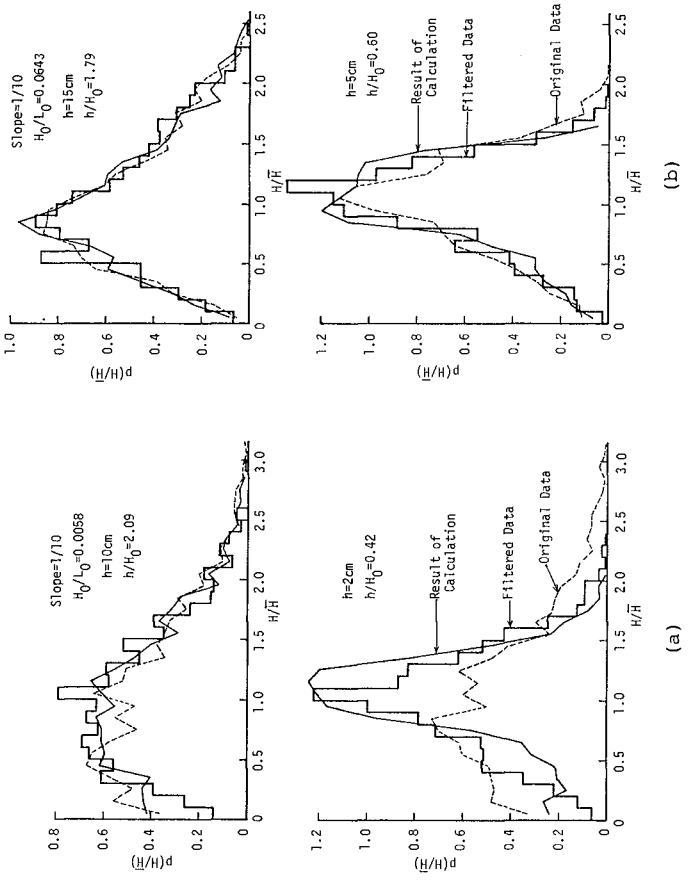

Fig. 5 Wave height distribution in shallow-water for 1/10 beach slope

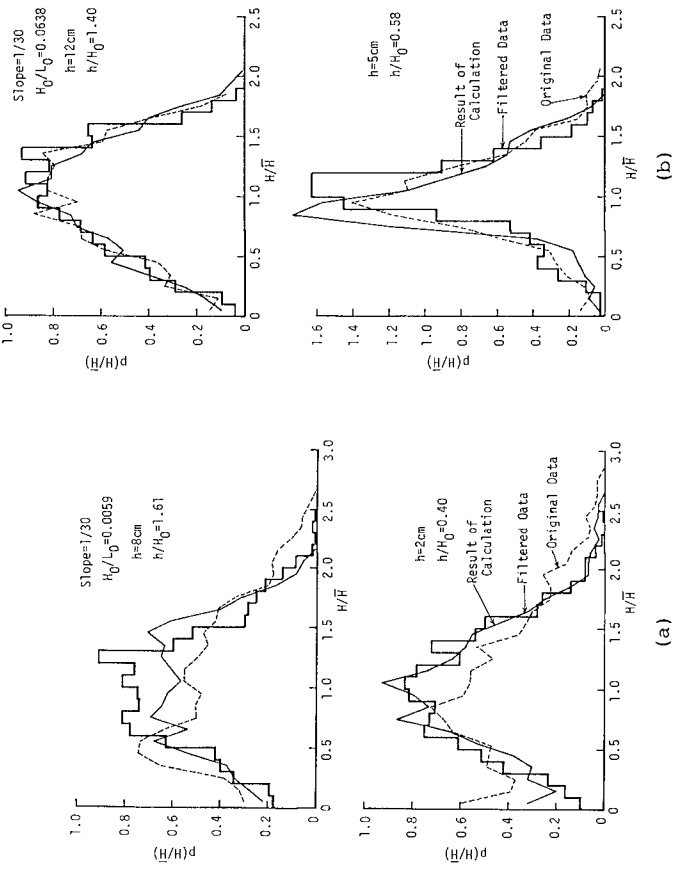

Fig. 6 Wave height distribution in shallow-water for 1/30 beach slope

the smallest and largest wave steepnesses in the experiments on the uniform slopes of 1/10 and 1/30, respectively, in which the wave height is normalized by the local mean wave height. In these figures the bent solid lines show the calculated results by the individual wave analysis method, the bent dashed lines show the experimental results obtained from the simply averaged mean water level denoted by "original data", and the histogram show the experimental results obtained from the "filtered data" of water surface elevations by cutting off the component waves of surf beats having the lower frequency than f_L *Hz* and the component waves having the higher frequency than f_U *Hz*. Cutting off of the high frequency components is for elimination of abrupt rising of the water surface due to splash with breaking and small disturbed waves after breaking. The frequency f_L was determined as $0.5f_p$ (f_p: the peak frequency) from the shapes of energy specta, and f_U was taken as $6f_p$ for convienience. An example of original and filtered water surface variations are shown in Fig. 7.

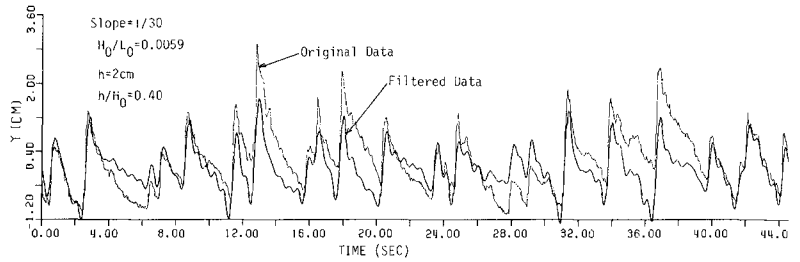

Fig. 7 Original and filtered water surface variations

In the case of large deep-water wave steepness as shown in Fig. 5(b) and Fig. 6(b), the shapes of the dashed line obtained from the original data and the histogram from the filtered date are almost same. It means that the effect of the filter is not so remarkable. However, in the case of small deep-water wave steepness as in Fig. 5(a) and Fig. 6(a), the shapes of the dashed line become flatter than those of the histogram, which means the effect of the filter is remarkable. Comparisons of the calculated wave height distributions with those of original data show fairly good agreement except for the case of small deep-water wave steepness in very shallow water. However, it is found that even in the case of small deep-water wave steepness, if the long-period variation due to surf beats and the high frequency components are removed from the original water surface variation, the calculated results agree well with the experimental ones. In other words, how to define an individual wave in very shallow water becomes important (Hotta (1980)).

4.4 Wave grouping

At present, several indicies are used to represent the degree of wave grouping, Goda (1970) used a run of wave heights $j(H_c)$ defined as the number of sequent waves, the heights of which exceed a definite value H_c and a total run $l(H_c)$ defined as the number

of waves between the first excess over the definite level H_c and the next excess over the same level. Funk et al. (1979) used a Groupiness Factor defined as the coefficient of variation of the time history of wave energy.

In the following, the spatial changes of wave grouping with decrease in the water depth are examined by using the parameter of the mean length of run $\overline{j(H_c)}$ and the mean length of total run $\overline{l(H_c)}$. Figs. 8(a) and (b) show the changes of $\overline{j(\overline{H})}$ and $\overline{l(\overline{H})}$ on the uniform slopes of 1/10 and 1/30, respectively. Figs. 9(a) and (b) show the detailed experimental results of wave grouping for the bottom slopes of 1/20 and 1/30, respectively. The followings can be seen from Figs. 8 and 9: In the case of 1/10 slope the mean length of run $\overline{j(\overline{H})}$ and total run $\overline{l(\overline{H})}$ over the mean wave height are almost constant independently of the deep-water wave steepness when the relative water depth h/H_o is larger than 1.5 and decrease with decrease in the water depth. On the other hand, in the cases of gentle slopes as 1/20 and 1/30, the mean lengths of run $\overline{j(\overline{H})}$ and total run $\overline{l(\overline{H})}$ become large as the deep-water wave steepness becomes large. The mean lengths of total run $\overline{l(\overline{H})}$ in the case of 1/20 and 1/30 slopes decrease with decrease in the water depth in similar way to the case of 1/10 slope. However, the mean lengths of run $\overline{j(\overline{H})}$ take maximum values in the region $1.0 \leq h/H_o \leq 1.5$ and decrease rapidly with decrease in the water depth. This tendency is remarkable in the case of gentle slope and large deep-water wave steepness. The mean lengths of run $\overline{j(H_{1/3})}$ and total run $\overline{l(H_{1/3})}$ over the significant wave height also tend to take maximum slightly as well as $\overline{j(\overline{H})}$ and $\overline{l(\overline{H})}$.

According to the results of numerical simulation by Goda (1970), $\overline{j(H_c)}$ and $\overline{l(H_c)}$ become small with decrease in the spectral peakedness parameter Q_p. From the present experimental results, however, it is noted that $\overline{j(H_c)}$ and $\overline{l(H_c)}$ increase near the relative water depth of 1.5 in spite of decrease in the spectral peakedness parameter due to the rapid decay of a main peak and the grow of the low frequency components of the spectrum by wave breaking.

5. Conclusions

Among the transformation characteristics of irregular waves in shallow-water including the surf zone, the changes of the significant and mean wave heights, the wave height distributions and wave grouping have especially been investigated. In addition to the experiments of irregular waves, a model for prediction of wave heights named the individual wave analysis method has been proposed. The summaries of the results are described bellow.

(1) An individual wave of irregular waves tends to break compared with monochromatic waves having the same wave height and period in the experiments.

(2) Non-dimensional significant wave height $H_{1/3}/H_o$ and mean wave height $\overline{H}/H_o$ become large as the bottom slope becomes steep and the deep-water wave steepness becomes small.

(3) The predicted significant and mean wave heights are in fairly good agreement with the experimental ones.

(4) Comparisons of the predicted wave height distributions with those of the original experimental data show good agreement except for the case of small deep-water wave steepness in very shallow water. Even in such cases, if the long-period variation

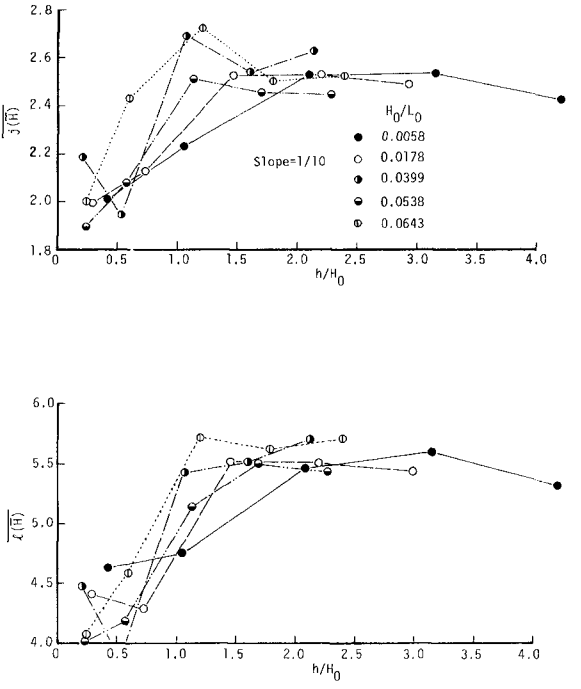

Fig. 8 (a) Change of wave grouping in shallow-water for 1/10 beach slope

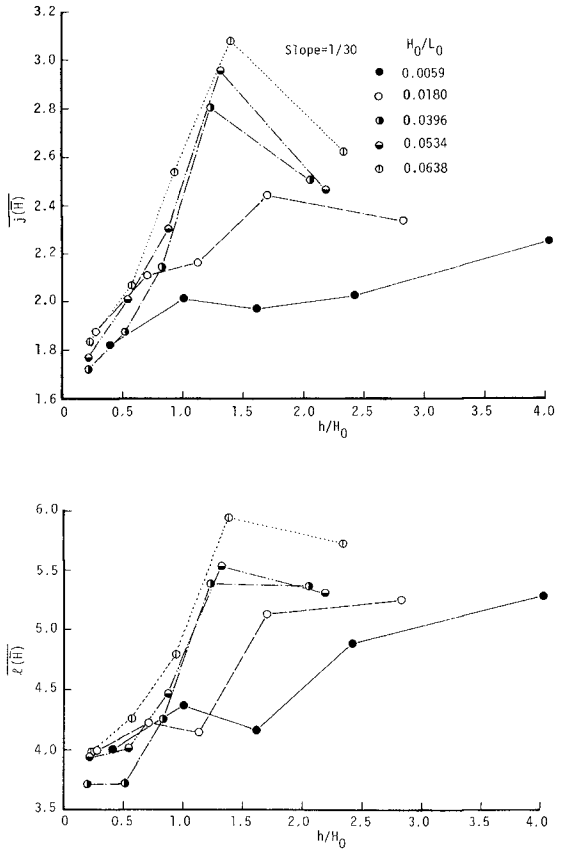

Fig. 8 (b) Change of wave grouping in shallow-water for 1/30 beach slope

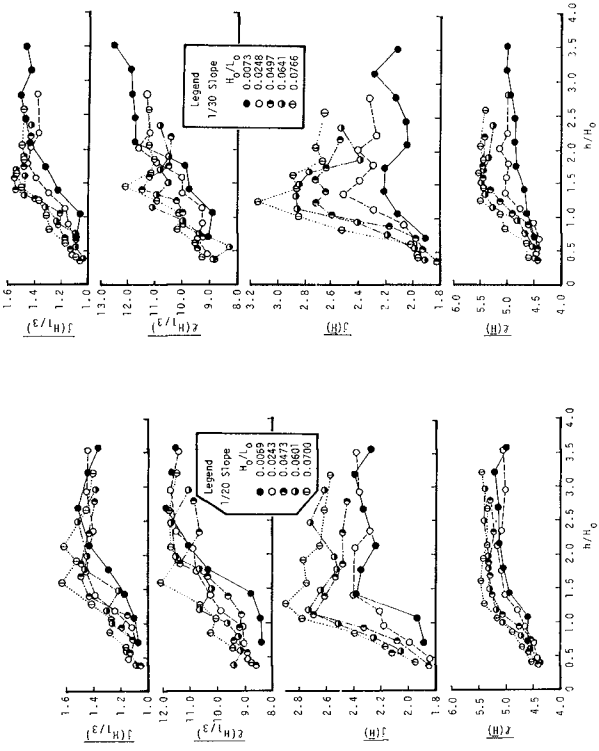

Fig. 9 Change of wave grouping in shallow-water for slopes of 1/10 and 1/30

due to surf beats and high frequency components of the water surface variation are removed, the calculated and experimental results agree well.

(5) Wave grouping becomes remarkable at the range of the relative water depth $1.0 \leq h/H_o \leq 1.5$ with decrease in the bottom slope and increase in the deep-water wave steepness.

Acknowledgement

The authors wish to thank Dr. A. Kimura at Tottori University for his helpfull advice. A part of this investigation is supported by a Grant-in-Aid for Research in Natural Disasters of The Ministry of Education, Science and Culture.

References

1) Battjes, J. A. (1972): Setup due to irregular waves, Proc. 13th Coastal Eng. Conf., pp. 1993–2004.
2) Battjes, J. A. and J. P. F. M. Janssen (1978a): Energy loss and set-up due to breaking of random waves, Proc. 16th Coastal Eng. Conf., pp. 569–587.
3) Battjes, J. A. (1978b): Energy dissipation in breaking solitary and periodic waves, Manuscript, Delft University of Technology.
4) Funk, E. R. and E. P. D. Mansard (1979): On the synthesis of realistic sea states in a laboratory flume, Hydraulics Laboratory Report LTR-HY-66, National Research Council of Canada, p. 54.
5) Goda, Y. (1970): A synthesis of breaker indicies, Proc. JSCE, No. 180, pp. 39–49 (in Japanese).
6) Goda, Y. (1975): Numerical experiments of wave statistics with spectral simulation, Report of Port and Harbour Res. Inst., Vol. 9, No. 3, pp. 3–57.
7) Goda, Y. (1975): Irregular wave deformation in the surf zone, Coastal Eng. in Japan, Vol. 18, pp. 13–26.
8) Hotta, S. (1980): Wave height distribution arround permeable breakwaters, Proc. 17th Coastal Eng. Conf., pp. 221–240.
9) Johnson, R. R., E. P. D. Mansard and J. Ploeg (1978): Effect of wave grouping on breakwater stability, Proc. 16th Coastal Eng. Conf., pp. 2228–2243.
10) Kimura, A. and Y. Iwagaki (1978): Wave length, wave velocity and shoaling characteristics of random waves, Proc. 16th Coastal Eng. Conf., pp. 320–339.
11) Nakamura, M., H. Shiraishi and Y. Sasaki (1966): Wave decaying due to breaking, Proc. 10th Coastal Eng. Conf., pp. 234–267.
12) Saeki, H. and M. Sasaki (1974): Study on wave transformation after breaking, Coastal Eng. in Japan, Vol. 21, pp. 39–44 (in Japanese).
13) Singamsetti, S. R. and H. G. Wind (1980): Breaking waves—characteristics of shoaling and breaking periodic waves normally incident to plane beaches of constant slope—, Delft Hydraulics Laboratory, Report on Investigation, M1371, p. 67.
14) Sawaragi, T. and K. Iwata (1974): On wave deformation after breaking, Proc. 14th

Coastal Eng. Conf., pp. 481–498.
15) Sawaragi, T. and K. Iwata (1981): Experimental study on irregular wave deformation due to depth-contorolled wave breaking, Hydraudynamics in Ocean Eng., Norwegian Inst. of Technology, pp. 166–182.

NEARSHORE WAVE SPECTRA MEASURED DURING HURRICANE DAVID

Michel K. Ochi* and Ming-Hsing Chiu*

ABSTRACT

This paper presents the results of an analysis carried out on wave spectra measured at three nearshore sites along the United States Florida coast when Hurricane DAVID passed these sites in 1979. Included are (a) the variability of the shapes of wave spectra during the stages of growth and decay of the hurricane-generated seas, (b) the presentation of spectra according to various spectral formulations, and (c) a comparison between spectra measured at the coastal sites and those measured in deep water for the same severity (significant wave height) of hurricane-generated seas.

INTRODUCTION

For the design of onshore, nearshore, and coastal structures, it is highly desirable and, from a safety viewpoint, extremely important to have a precise description of nearshore sea severity. In particular, for structures along coasts, wave data measured during hurricanes provide a vital source of information for establishing design criteria.

Although many observations and measurements have been made on wind-generated waves associated with hurricanes over deep water, we have as yet little information as to hurricane-generated sea severity in coastal waters.

This paper presents the results of analysis carried out on wave spectra measured at three locations in shallow water when a hurricane passed through these sites. That is, on September 3rd, 1979, Hurricane DAVID approached the Florida east coast from the eastern Carribbean with a moving speed of about 10 knots. During this period, wave recorders installed by the University of Florida at Miami Beach, West Palm Beach, and Vero Beach successfully recorded the waves throughout the duration of the storm at each site.

In order to obtain an accurate representation of wave spectra associated with sea conditions arising from hurricanes, the variability of the shapes of wave spectra during the stages of growth and decay of

* Coastal and Oceanographic Engineering Department,
University of Florida, Gainesville, Florida, USA

Hurricane DAVID is examined. The wave spectra are represented by various mathematical formulations to provide information for further analysis of coastal waves. Furthermore, comparisons are made between the shapes of wave spectra obtained at the coastal sites and those obtained in deep water for the same severity (significant wave height) of hurricane-generated seas.

WAVE DATA DURING HURRICANE DAVID

Hurricane DAVID (August 26 - September 6, 1979) approached the east coast of Florida from the Carribbean, and its eye passed over several Florida coastal cities as shown in Figure 1. During this period of moving almost due north at about 10 knots (5.1 m/sec), the hurricane moved inland just north of Palm Beach, then later it again

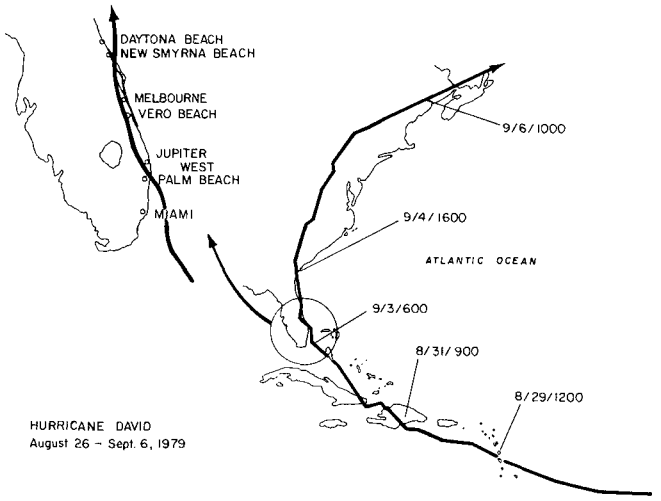

Figure 1 Hurricane DAVID track

moved offshore. The eye diameter was 20 to 30 nautical miles (37 to 56 km) while it was passing over the Florida area, and the highest winds experienced were gusts up to 75 knots (39 m/sec).

The data used in this study were recorded from three measurement sites which are chosen at nearly equally spaced intervals along the Florida east coast. These sites are located at Miami Beach, West Palm Beach and Vero Beach respectively, and are about one kilometer offshore. They are part of the Florida Coastal Data Network system (Howell 1980) which collects long-term diary wave data as well as storm wave data.

The geographic features of these sites and the measured maximum significant wave heights are tabulated in Table 1.

Table 1 Geographic features and measured maximum significant wave heights at three sites

SITE	MIAMI BEACH	WEST PALM BEACH	VERO BEACH
GEOGRAPHIC LOCATION	25°46'06"N 80°07'23"W	26°42'07" 80°01'42"	27°40'20" 80°21'07"
DISTANCE FROM SHORE (km)	0.91	0.61	0.90
WATER DEPTH (m)	6.1	8.5	7.6
SHORTEST DISTANCE TO HURRICANE EYE (km)	70.5	25.0	14.1
MAX. SIG. WAVE HEIGHT (m)	2.65	5.10	3.51

Pressure transducers located about one-half meter above the seabed were used to take data. They were bottom mounted on a completely self-contained electronic cylinder which contains a microcomputer controlled data acquisition system. From surface pressure signals, the pressure energy spectra were computed, and then converted to surface wave spectra by assuming the pressure-wave profile-relation to be linear.

RESULTS OF ANALYSIS

Significant wave height, denoted by H_s, was evaluated from the measured spectra by using the formulation given by $H_s = 4\sqrt{m_o}$, where m_o is the area under the spectrum. The temporal variation of significant wave height and radial distance from the hurricane center measured at sites are shown in Figures 2(a) through 2(c). It can be seen in these figures that the significant wave height decreases rapidly in the decaying stage in comparison with the increase of its intensity in the growing stage.

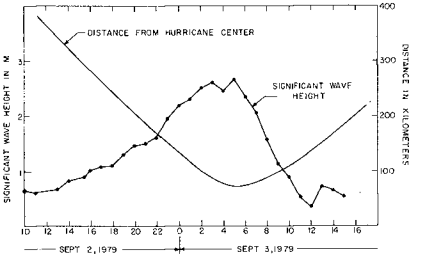

Figure 2 Temporal variations of significant wave height and radial distance (a) Miami Beach

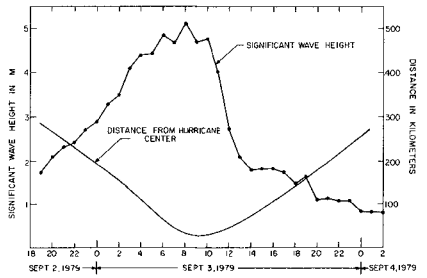

Figure 2 Temporal variations of significant wave height and radial distance
(b) West Palm Beach

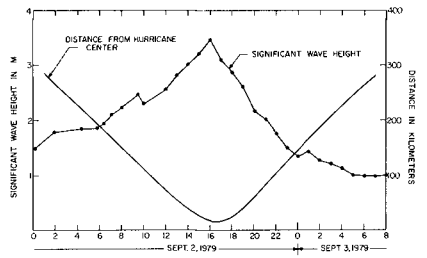

(c) Vero Beach

In order to present the overall picture of the growth and decay status of hurricane-generated seas, contour lines of spectral energy densities are constructed from the entire series of spectra, and are shown in Figures 3(a) through 3(c). Each contour in the figure represents spectral density of a certain level (2.0 m^2-sec, 4.0 m^2-sec, etc.) and the inner portions of the enclosed contours correspond to higher spectral densities. The highest spectral density at the innermost portion of the contour lines corresponds to the severest sea state in which the highest significant wave height was obtained.

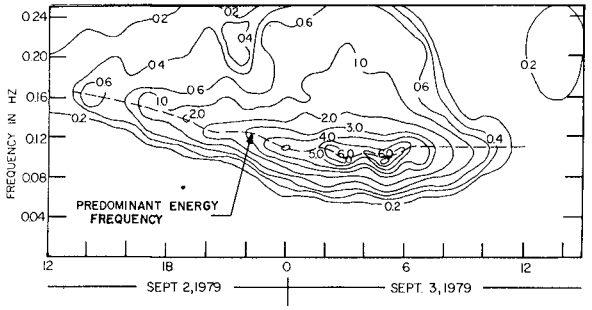

Figure 3 Contours of spectral densities constructed from wave spectra (a) Miami Beach

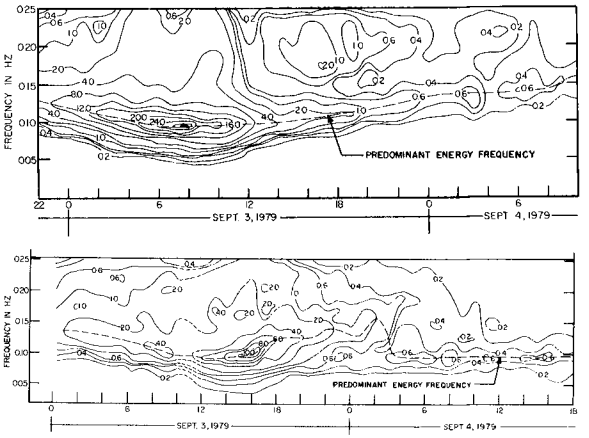

(b) West Palm Beach

(c) Vero Beach

Figure 3 Contours of spectral densities constructed from wave spectra

The severest sea states at the three sites occurred at 5 am, 8 am, and 4 pm, September 3rd, respectively, and the corresponding spectra had approximately the same peak frequency, 0.094 Hz.

It is of interest to compare the shapes of wave spectra obtained in seas of approximately the same significant wave height but under different conditions; one in the growing stage, the other in the decaying stage of the hurricane. As an example, Figure 4(a) shows a comparison of spectra measured at West Palm Beach in a mild sea state of significant wave height of 2.07 m. As can be seen in the figure, the frequency where the spectrum peaks (modal frequency) in the decaying stage is lower than that in the growing stage. This trend holds throughout the storm as can be seen in Figures 4(b) and 4(c). The same trend was also observed for spectra measured in Miami Beach. However, this general trend is reversed when the hurricane passes inland or shoreward of the point of measurements. As Hurricane DAVID

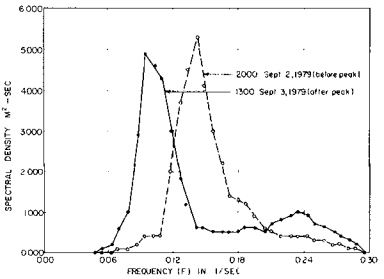

Figure 4 Comparison of wave spectra obtained in the growing and decaying stages of the hurricane, West Palm Beach
(a) Significant height 2.07 m

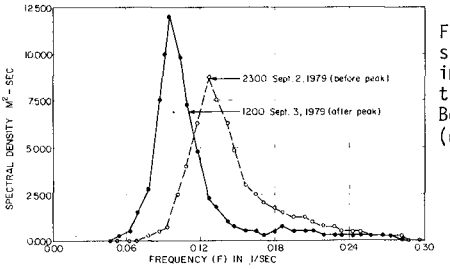

Figure 4 Comparison of wave spectra obtained in the growing and decaying stages of the hurricane, West Palm Beach
(b) Significant height 2.72 m

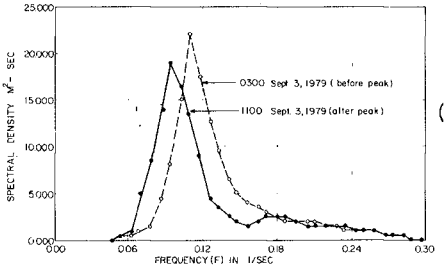

(c) Significant height 3.99 m

passed Miami Beach and West Palm Beach, its path was offshore. After it passed West Palm Beach, it moved inland, then later moved offshore again. The hurricane's path was inland throughout the period when severe seas were observed at Vero Beach. This may account for the modal frequency in the growing stage being lower than that in the decaying stage for the Vero Beach data as shown in the example in Figure 5.

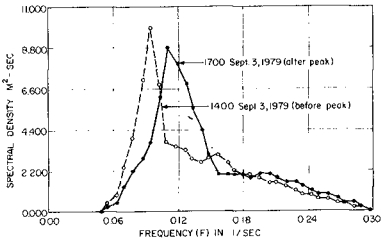

Figure 5 Comparison of wave spectra obtained in the growing and decaying stages of the hurricane, Vero Beach, Significant height 3.08 m

The measured spectra are fitted by various spectral formulations to see how well hurricane-generated nearshore wave spectra can be represented by currently available formulations which have been developed for seas in deep water. These include the one-parameter (Pierson-Moskowitz 1964), and the two-parameter (Bretschneider 1959), three and six-parameter (Ochi and Hubble 1976), and JONSWAP (Hasselmann et al. 1959) spectral formulations. The JONSWAP spectrum used in the comparison is not the mean JONSWAP spectrum; instead it is obtained

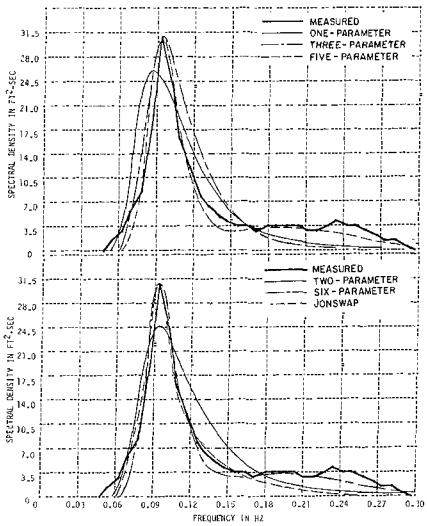

Figure 6 Comparison between measured and mathematical spectra. West Palm Beach, significant height 5.1 m.

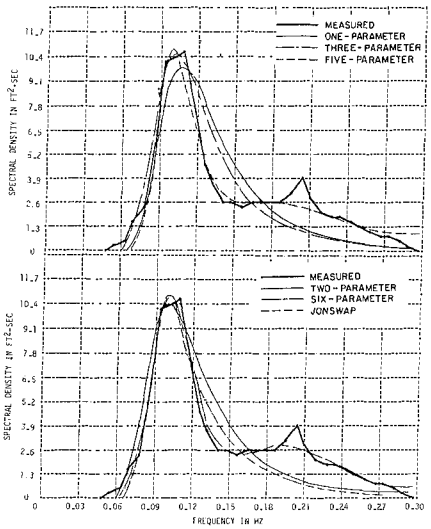

Figure 7 Comparison between measured and mathematical spectra. Vero Beach, significant height 3.5 m

by fitting the measured spectrum through least-square fitting techniques. Included also in the comparison is the five-parameter spectrum which is a combination of a three-parameter formulation representing the lower-frequency range of the spectrum and a two parameter formulation representing the higher frequencies.

The results of the comparison between measured and mathematical spectra show that the five and six-parameter spectra appear to best represent the measured spectra in shallow water areas throughout the various stages of the hurricane. Also, the JONSWAP spectral formulation yields a good fit to the shape of the measured spectra, in general, with the exception of those with a secondary peak or an extended plateau in the high-frequency region. As an example, Figures 6 and 7 show a comparison made for the severest sea state observed at West Palm Beach and Vero Beach, respectively, during the hurricane.

The shapes of hurricane-generated wave spectra obtained at the coastal sites and those obtained during hurricanes in deep water are compared. If the shapes of deep and shallow water hurricane-generated wave spectra are alike under certain conditions, then the results of analysis made on the shapes of deep-water hurricane spectra may be used for those of shallow water. In the comparison of Hurricane DAVID (shallow water) wave spectra with spectra measured in deep water, the results obtained during Hurricane ELOISE in the Gulf of Mexico (Withee and Johnson, 1977) are used, and comparisons are made between spectra having the same significant wave height and the same modal frequency.

As an example, Figure 8(a) shows a comparison between deep and shallow water (8.5 m water depth) wave spectra of significant wave height of 4.8 m with the same modal frequency of 0.098 Hz. Other examples of comparison made in less severe sea states are shown in Figures 8(b) and (c). Although the shapes of hurricane-generated wave spectra measured in deep and shallow water of 7-10 m water depth are significantly different in mild sea conditions (significant wave heights less than 2 meters), the shapes of spectra with the same significant wave height and the same modal frequency appear to be very similar in relatively severe seas as shown in Figure 8.

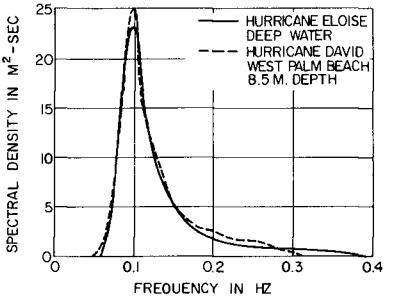

Figure 8 Comparison of hurricane wave spectra measured in coastal and deep waters. (a) Significant height 4.8 m

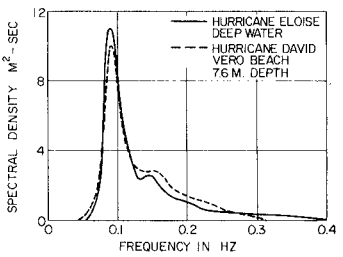

(b) Significant height 3.0 m

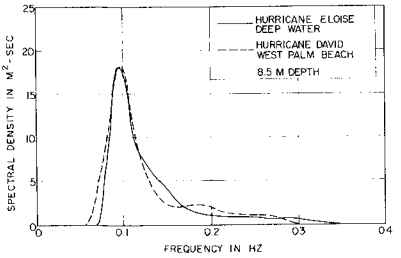

(c) Significant height 3.9 m

CONCLUSIONS

This paper presents the results of analysis carried out on wave spectra measured at three nearshore sites along the United States Florida coast when Hurricane DAVID passed through these sites. It is found from the results of the analysis that the peak frequencies of the spectra in the decaying stage of the hurricane-generated coastal waves are, in general, lower than those in the growing stage. This implies that the wave energy in longer wave lengths is dominant in the decaying stage.

The shapes of the measured wave spectra can best be represented by the five and six-parameter spectral formulations throughout various stages of the hurricane. The JONSWAP spectral formulation also yields a good fit to the shapes of the measured spectra, in general, with the exception of those with a secondary peak or an extended plateau in the high-frequency region.

The shapes of the hurricane-generated wave spectra with the same significant wave height and the same modal frequency obtained in coastal and deep water are very similar in relatively severe seas.

REFERENCES

Bretschneider, C.L. (1959), "Wave Variability and Wave Spectra for Wind-Generated Gravity Waves", Tech. Memo. No. 118 Beach Erosion Board, U.S. Army Corps of Eng.

Hasselmann, K. et al. (1973), "Measurements of Wind-Wave Growth and Swell Decay during the Joint North Sea Wave Project (JONSWAP)", Deutsches Hydro. Inst.

Howell, G.L. (1980), "Florida Coastal Data Network", Proc. 17th Int. Conf. Coastal Eng., Vol. 1, pp 421-431

Ochi, M.K. and Hubble, E.N. (1976), "On Six-Parameter Wave Spectra", Proc. 15th Int. Conf. Coastal Eng., Vol. 1, pp 301-328

Pierson, W.J. and Moskowitz, L. (1964), "A Proposed Spectra Form for Fully Developed Wind Seas Based on the Similarity Theory of S.A. Kitaigorodskii", Journal Geoph. Res. Vol. 69, No. 24, pp 5181-5190

Withee, G.W. and Johnson, A. (1975), "Buoy Observations During Hurricane ELOISE", Data Report, Data Buoy Office, NOAA, Bay St. Louis, Miss.

A SOUTH AFRICAN WAVE CLIMATE STUDY

by

J Rossouw[1], L W Coetzee[2] and C J Visser[3]

ABSTRACT

A study was made, using all the available sources of deep-sea wave data around the South African coast, to establish a statistical representation of the wave climate in this region. Data obtained from clinometer observations, the Datawell Waverider and voluntary observing ships were found to be the most useful.

The most accurate source of height, period and spectral information came from the Waverider which has been in extensive use in the region since 1969. To optimise the information value of these data a sophisticated data qualification technique was developed for digitised Waverider data in order to exclude poor data. This technique was also found to be useful in optimising the operational efficiency of a Waverider station.

A clear pattern was obtained for the general wave climate around the South African coast; this is in accordance with the pattern that may be expected from the weather climate affecting this region. Of interest are the SE'ly winds generating increased wave heights in proportion to the distance offshore from the west coast as well as the effect of the Agulhas current, opposing the SW'ly waves along the east coast, also creating high-wave conditions.

1. INTRODUCTION

Instrumental recording of waves has been done in South African coastal waters since 1961. Initially a wide variety of instruments were used including clinometers, NIO ship-borne wave recorders, inverted echosounders and pressure recorders. The first Datawell accelerometer buoy

[1] University of Stellenbosch, Stellenbosch, RSA.

[2] Hydrodnamics Division, Coastal Engineering and Hydraulics, National Research Institute for Oceanology, CSIR, Stellenbosch, RSA.

[3] Institute of Maritime Technology, Simonstown, RSA.

(Waverider) was installed off Mossel Bay in 1969 and the Waverider has since become the main recording instrument to be used in South African coastal waters. The number of Waverider stations varied over the years, but data representative of the open coast were obtained from 11 stations covering the entire South African and South West African coastline.

The main purpose of this study was to investigate all the possible sources of wave data that might be of use to the design engineer, to analyse the data and to publish the data in a form useful to all possible users. The data were also to be stored in a computer data bank to enable fast retrieval for further analysis by interested researchers and engineers.

This paper presents a summary of the main aspects of the study. It describes the development and application of a standard wave analysis and data qualification computer program for digital Waverider data, the system of data handling and storage, the comparison of the Waverider data with information from other sources and the present knowledge of the wave climate around South Africa.

2. WAVE ANALYSIS AND DATA QUALIFICATION

2.1 Data Collection

Waverider data are usually obtained for periods of 20 minutes every six hours from the various wave recording stations around the South African coastline. A sampling interval of 0,5 s is normally used for digital data and the resolution of the water elevation measured is 10 mm.

2.2 Computer Program

The detailed description of the program WAVES can be found elsewhere (Visser et al., 1980; Visser et al., not yet published). WAVES reads digitized wave records, applies qualification criteria to the data, performs spectral analysis, labels records as good, suspect or bad, and stores the processed records in a data bank. An example of a printout with a brief description is shown in Appendix A.

The procedures for spectral analysis are well documented and numerous computer routines for the fast Fourier transform (FFT) can be found in the literature. Writing a program to perform the basic computations is therefore relatively easy. However, the real problem lies in identifying invalid wave records which can result when, for example, noise due to equipment malfunction is superimposed on the data. Some bad records are easily identified, while in others, deficiencies are elusively masked. The influence

of unidentified invalid results in a data bank needs no elaboration.

2.3 Conventional Data Qualification

Examples of methods being used for the identification of invalid wave records are visual inspection and identification of outliers according to the number of standard deviations they are removed from the mean water level. The first method is deemed unpractical because of the dependence on a trained observer and the large amounts of data involved. The second method is based on the assumption of normality of the instantaneous water elevation $x(t_i)$ as a function of time t_i. Outliers change the shape and position of the distribution. The intensity of this depends on the number of outliers, their magnitude and their bias towards the peak or trough side of the record. In many cases this renders the method useless.

2.4 WAVES-program Data Qualification

A rather random approach was adopted in arriving at the present qualification procedure. As many tests as could be thought of were applied to a large number of wave records. The types of tests ranged from crude empirical models to standard statistical tests. The procedure was refined by comparing, for a large number of records of various localities, the outcome of the tests with the judgement of experienced observers. A wave record (usually consisting of 2 048 digitized $x(t_i)$-values) is split into two halves of 1 024 data points each. This facilitates investigating stationarity and provides results when one half of the record is bad or non-existent. Six tests on time-domain and frequency-domain parameters are performed on each half of the record to identify good ("GOOD"), suspect ("BAD?") or bad ("BAD") data. On the basis of the outcome of each test a severity code is assigned to the test. The severity codes are then used to determine a category ("GOOD", "BAD?" or "BAD") for each half. A further scheme is then used to determine a category for a whole record. For example, "GOOD2B" means that the second half is "GOOD" and the first half is "BAD").

The following tests are used to categorize records.

2.4.1 Flatheads ("P2", "P3", "P4" and ">P4" in Appendix A)

A flathead is identified when consecutive $x(t_i)$ have the same numerical value (to the nearest 10 mm, that is, the resolution of the digitizer). Thus the value of "P2" denotes the number of times two (and no more) consecutive $x(t_i)$ with the same value are detected. Similarly for the "P3", "P4" and ">P4" parameters. (For example, if

">P4" = 2, then two occurrences of flatheads with more than four $x(t_i)$ values occurred.)

2.4.2 Rate of change of wave profile ("ERR" in Appendix A)

If the slope of two consecutive data points is greater than the theoretical maximum slope that the water surface can attain, an erratic point is identified. The value of "ERR" denotes the number of erratic points in the record.

2.4.3 Consecutive erratic points ("CON" in Appendix A)

The value of "CON" denotes the number of times two erratic points (see 2.4.2) next to each other are detected.

2.4.4 The sample correlation coefficient ("CORR" in Appendix A)

A linear trend in the data, which can be caused, for example, by zero-drift in recording instrumentation, is detected when the correlation between $x(t_i)$ and t is statistically significant.

2.4.5 Normality of the $x(t_i)$ ("SKEWNESS" and "KURTOSIS" in Appendix A

Experience shows that the instantaneous water elevation $x(t_i)$ of sea waves follows approximately the normal distribution. Tests for normality are done using slightly adjusted distributions for skewness and kurtosis. (Relaxing slightly on the theoretical distributions.)

2.4.6 Low-frequency detector ("LF.DET" in Appendix A)

Most Waverider buoys used in South Africa will respond only to waves with periods in the range 1 to 33 seconds (band width of 0,03 to 1,0 Hz). This covers the domain for most applications. The buoy is "blind" to waves with periods outside the mentioned range (for example, the tide). Therefore, if the power spectrum contains significant spectral information outside the mentioned band width, invalid data that could not be measured with the buoy are indicated. The sum of the first four power spectral density values 0,006 to 0,035 Hz is denoted by "LF.DET".

The test criteria used to assign severity counts to the six parameters are shown in Appendix B.

3. DATA HANDLING AND STORAGE

The main agency dealing with waves in the RSA is the National Research Institute for Oceanology (NRIO) of the

Council for Scientific and Industrial Research (CSIR) at Stellenbosch.

A Wave Study Group was established within NRIO during mid-1980 with one of its primary purposes to develop a system for the more efficient gathering and analysing of digitized wave data, thus providing more effective quality control and faster feedback of the analysed information. At present this group copes with the management of wave data gathered at seven Waverider stations.

System improvements include the following:

3.1 Waverider Data Logger

An improved micro-computer-based Waverider data logger was developed by the Electronic Systems Division within NRIO (Holroyd, 1982). This system features a real-time full calendar clock with built-in leap-year compensation. Recording times are fixed at 00h00, 06h00, 12h00 and 18h00 GMT with additional facilities to initiate recordings at other chosen intervals as well as single recordings. A stand-by battery will drive the clock for about six hours during a power failure. A Memodyne Model 200 cassette data logger is used together with Philips data cassettes. Storage capacity amounts to about 11 days of 4 × 20 minute recordings per day.

Each wave record contains unique station identification, time, calibration and self-test data. File lengths are recorded at exactly 2 100 words of data, sampled at 2 Hz rate and recorded as 12-bit words. A real-time Draper analysis option can be utilized by connecting an 80-column printer to the data logger. H_S, H_1, T_Z and T_C are printed. The data logger is also supplied with an external Esterline Angus servo recorder providing an analogue trace of each wave record.

3.2 Process Control

The present system of gathering, analysing and storing wave data consists basically of the following steps:

- Waverider data are transmitted to nearby shore stations using the 27 MHz band.
- Cassette and analogue recordings are transported to NRIO using the most suitable means.
- Cassette data are transferred to 9-track magnetic tape using the NRIO in-house computer.

- The 9-track tape data are transmitted to the central CSIR computer in Pretoria using the available remote batch facilities.

- Final analysis and storage of the data are performed.

In order to obtain the maximum possible yield of good data from each recording station every effort is made to speed up and maintain a steady flow of data from the station to its final destination in Pretoria.

3.3 Quality Control

At NRIO several checks are done on the data prior to transferring it to the CSIR central computer. This includes a visual examination of the analogue records and also of suspect digital records on a graphics terminal. Time domain analysis is also done on the digital data and includes tests for normality. Useful fault reports are generated at this stage, although it was found that these tests are not critical enough to detect bad or suspect data in a large number of cases. Figure 1 shows digital records which were rejected by WAVES, although the records had passed the test for normality and were also not rejected during the visual test of the analogue record. At this preliminary check stage it is also difficult to decide whether the performance of a station is actually deteriorating, because a certain level of bad data appears to be inevitable, for example, where the station is exposed to heavy, sporadic R/T traffic.

Once the data have been transferred to the central computer, they are analysed by means of the program WAVES described earlier. At this stage information is obtained which forms the basis of a more critical quality control system.

Regarding each cassette as a "unit of wave data", the data are analysed and statistics plotted of the various tests obtained through WAVES. In order to determine whether a particular fault detected occurs consistently over a period of time, time series plots are made of the results of the data qualification tests.

Figure 2 shows the results of a study which was made of the bad performance at the Slangkop recording station during 1982. A backlog of data had inadvertently been allowed to build up at this station and action was therefore taken only when the problem was revealed during the pre-checks at NRIO. Analysis of 4 342 records collected at Slangkop showed that 12,8 per cent of the records had been rejected (Figure 3). This was due mainly to L.F. Detection and the occurrence of erratics. Further analysis showed that all but 1 per cent of the rejections through the detection of

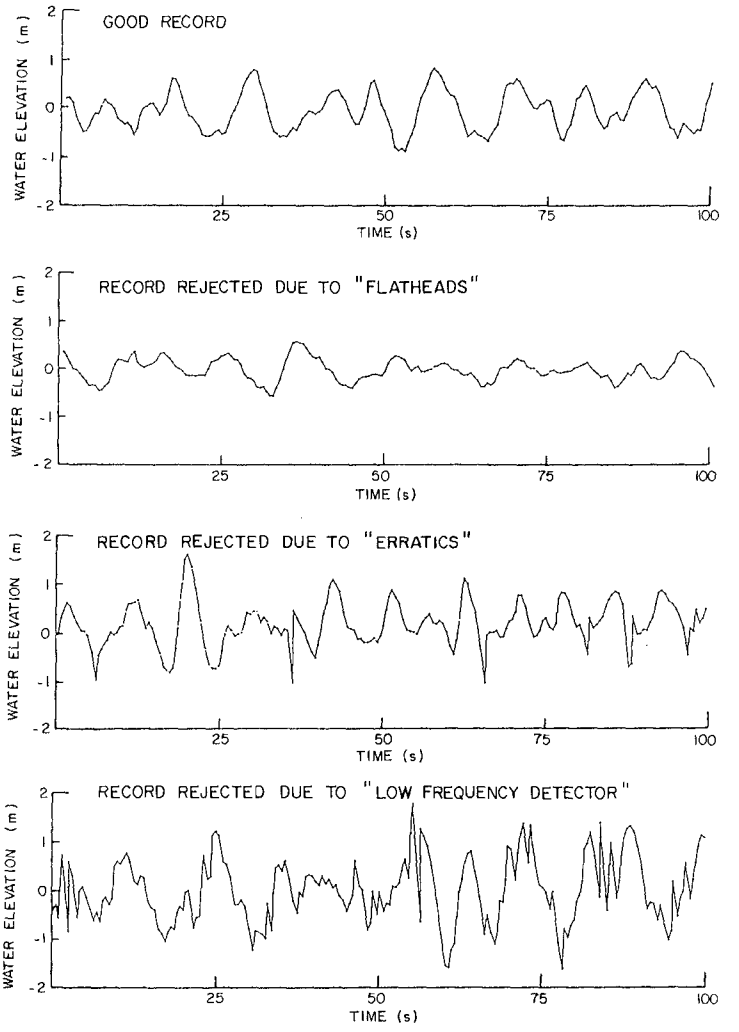

FIG. 1. EXAMPLES OF 100 SECOND PORTIONS OF GOOD AND BAD DIGITAL WAVE RECORDINGS

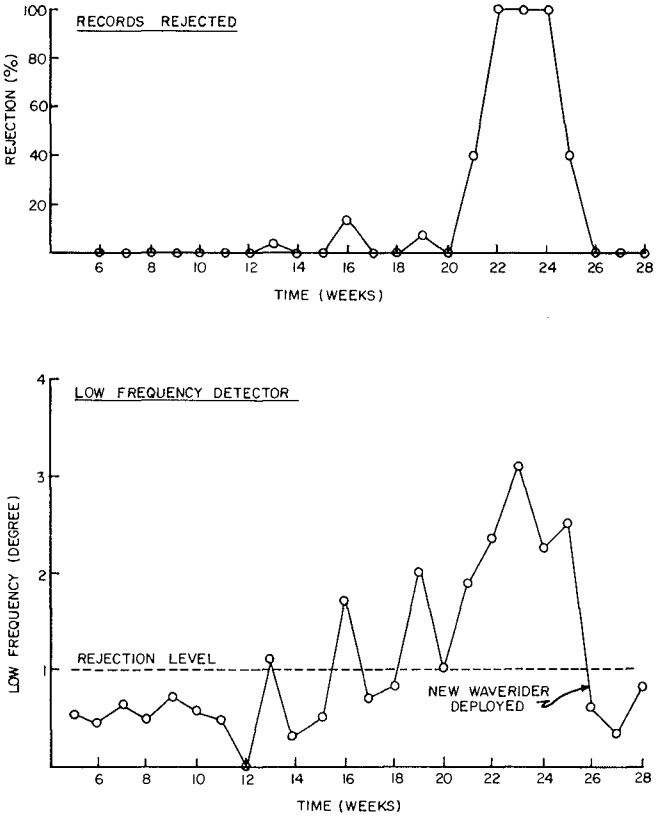

FIG. 2. TREND PLOTS OF LOW FREQUENCY DETECTED AND RECORDS REJECTED (STATION: SLANGKOP, PERIOD: 1982.2.5 TO 1982.7.16)

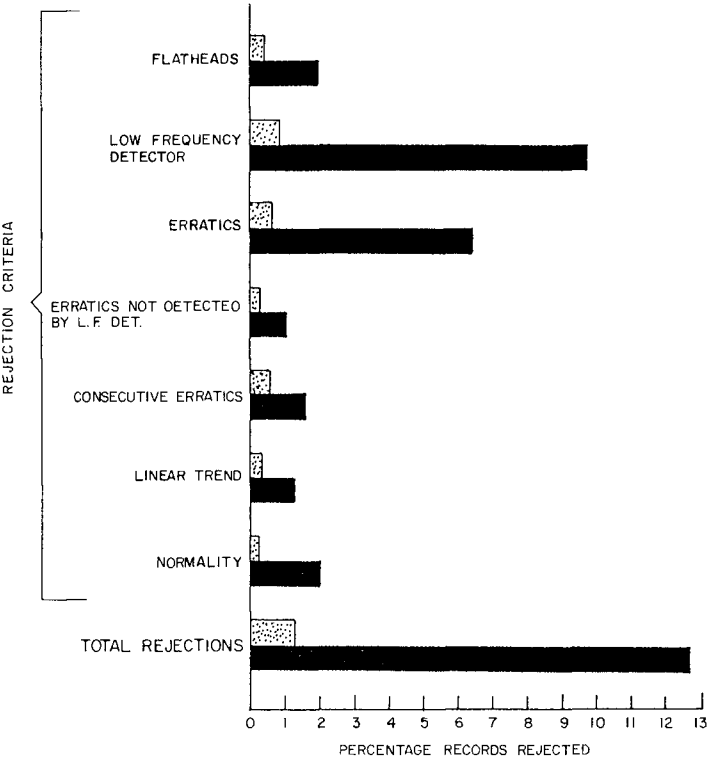

KEY	STATION	PERIOD	NO. OF RECORDS
■	SLANGKOP	OCT. 1978 - AUG. 1982	4352
▒	KOEBERG	NOV. 1977 - FEB. 1982	4386

FIG. 3. WAVE DATA QUALITY ANALYSIS FOR SLANGKOP AND KOEBERG

erratics had also been picked up by the L.F. Detector, thus leaving the main cause for rejection the detection of a low-frequency component. Figure 2 shows that the station performed well up to week 12 after which the L.F. Detector became very unstable. In addition, there is a clear trend indicating that the situation was worsening gradually. Subsequently the Waverider buoy could not be located and it is surmised that it had probably started to drift slowly, dragging its anchor, with a slowly weakening signal and thus became more prone to radio interference. A new buoy was deployed and good records obtained. A similar analysis was done for another station (Koeberg) and the results are included in Figure 3. This waverider is deployed closer inshore and completely away from any normal shipping routes as well as fishing areas, both hazards to which the Slangkop Waverider is exposed. A great improvement in data quality is evident under these improved conditions.

3.4 Data Storage

A prototype scheme for a computerized WAVES data base has been designed and installed on the CSIR central computer. Provision was made to store the entire output of the WAVES program and about three years' data have been stored. The data base is presently being "user-tested" prior to finalising its format.

4. WAVE CLIMATE

4.1 Introduction

In this section the wave climate as evident from all available data sources will be summarised. Wave height and wave period data are based mainly on the analysis of Waverider records since these are considered the most reliable source of such data. Wave direction data are based on clinometer observations that were refracted to deepsea as well as data from voluntary observing ships (VOS).

4.2 Weather Patterns

The major wave-generating system resulting in high waves along the RSA coastline is the regular cold fronts with their associated low pressure systems that pass west to east just to the south of the continent. These fronts together with two permanent high-pressure systems, that is, the South Atlantic high off the west coast and the Indian Ocean high off the east coast, totally dominate the wave-generating forces in the oceans surrounding the southern tip of the continent. A typical example of the passage of such a low-pressure system is shown in Figure 4 (Weather Bureau, 1979). These low-pressure systems normally shift towards the south in summer and towards the north in winter so that high waves occur more frequently in winter. They

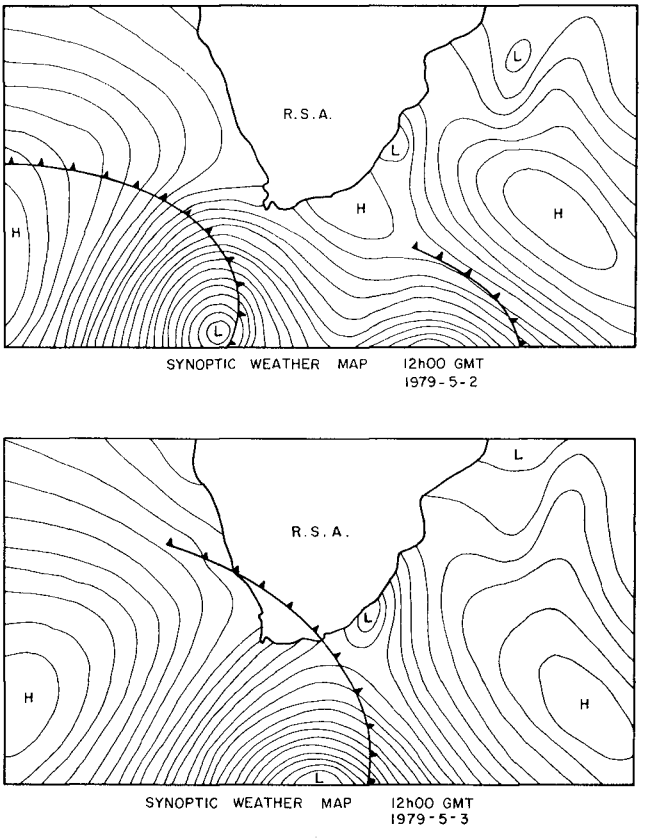

FIG. 4 PASSAGE OF A COLD FRONT CAUSING HIGH WAVES ALONG THE R.S.A. SOUTHERN COAST

do, however, on occasion move far enough north in summer to cause large waves but the occurrence of these high waves is less frequent in summer than in winter.

4.3 Wave Height Distribution

The 0,01 per cent wave height (H_S) obtained from the extrapolation of Waverider data for all the open-coast wave stations is shown in Figure 5. The 0,01 per cent wave height obtained from a shipborne wave recorder on a weathership stationed at 40°S, 10°E is also shown in this figure.

Comparing the wave heights along the west coast from Slangkop in the south to Walvis Bay in the north, it can be seen that a steady decrease in wave height occurs towards the north. This is very much in accordance with the weather patterns described earlier, that is, the wave height decrease with increase in distance from the storm centre.

From Figure 5 it can also be seen that the wave heights at Mossel Bay, Durban and Richards Bay along the east coast are very similar. The 0,01 per cent wave height at these stations vary from 5,5 to 6,0 m. At Gans Bay this wave height is 8,1 m which lies between the values at Mossel Bay and Slangkop.

An interesting wave station is the Waverider off SEDCO-K, a drill rig operating in the area offshore off Mossel Bay. As can be seen from Figure 5 the 0,01 per cent wave height at SEDCO-K is 9,7 m as compared with the 6,0 m at Mossel Bay closer inshore. The reason for this difference is thought to be the protection afforded by the land mass to the Mossel Bay station against the fronts approaching from the west. Another very interesting aspect of the SEDCO-K station is the similarity in wave conditions there with the station at Slangkop, 300 km to the west. Figure 6 illustrates this similarity.

In Figure 5 the 0,01 per cent wave heights obtained from VOS data are summarized for a few areas around the coast. Although these data are considered to be of lower quality with respect to wave height and period than the Waverider data, a few interesting points emerge. Firstly, the decrease in wave height towards the north up the west coast is also apparent from these data. The decrease in wave height is, however, much less pronounced than in the Waverider data and the wave heights are also considerably higher than those obtained from Waverider data. It is also interesting to note that the VOS data show the highest wave heights off East London. The reason for the higher wave heights by VOS in comparison to Waverider along the west coast is explained by wave directions and will be discussed

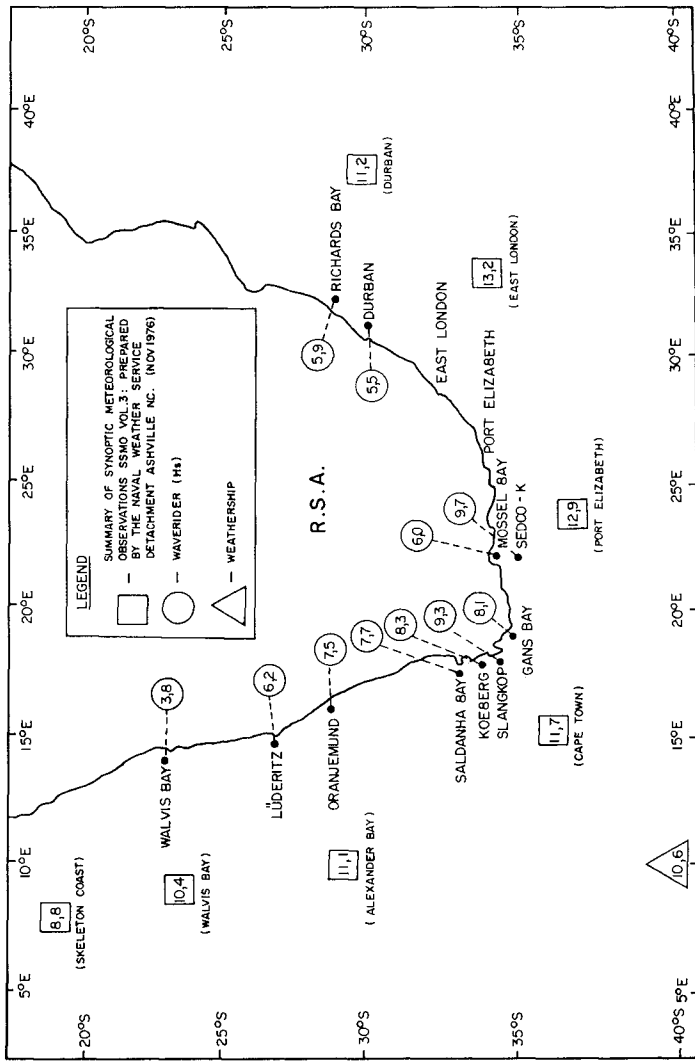

FIG. 5. DISTRIBUTION OF 0,01 PERCENT WAVE HEIGHT FROM WAVERIDERS, VOS AND WEATHERSHIP

in the next section. The reason for the higher waves off the east coast is explained by the presence of the very strong Agulhas current which flows from a NE'ly direction along this coast, directly opposing the dominant SW'ly waves. Energy transfer occurs from current to wave, resulting in so-called "freak" waves along this coast (Schumann, 1976).

4.4 Wave Direction Distribution

The wave direction distribution for four clinometer stations refracted to deepsea are shown in Figure 8 (Ashby, Harper and Van Schaik, 1973). Data from these four clinometer stations fully reflect the general wave direction pattern obtained for all the clinometer stations around the coast. The wave direction distribution for the weathership (Weather Ship Action Committee, 1973) as well as from VOS data (Hogben and Lumb, 1967) are also indicated on this figure.

The direction data obtained from clinometers show good agreement with the known weather patterns. It is clear that the main source of wave data are from the fronts to the south of the continent causing the waves along both the west and the east coast to have a resultant energy component towards the north. This is also in agreement with the known sediment transport pattern along the RSA coastline whereby sediment is transported towards the north on the west and east coasts and towards the east on the south coast.

A few interesting aspects also appear from the VOS data. Along the west coast the wave direction is very dominantly from the south-east, that is, either parallel to shore or in an offshore direction. These SE'ly waves, therefore, never reach the shore, which explains the large difference in wave height between the nearshore Waverider data and the VOS data recorded further offshore.

The wave direction at the weathership is very dominantly from the W'ly directions as can be expected in these latitudes.

Along the south and east coasts the agreement between the clinometer and VOS directional data is good.

4.5 Wave Period Distribution

Researchers normally find poor correlations between wave periods recorded by various means or analysed by different methods. The reason for this is that it is impossible to describe the periodicity of the waves by a single variable such as T_z, T_p, T_c, etc. For the purpose of this paper only the distribution of T_p as recorded at a number

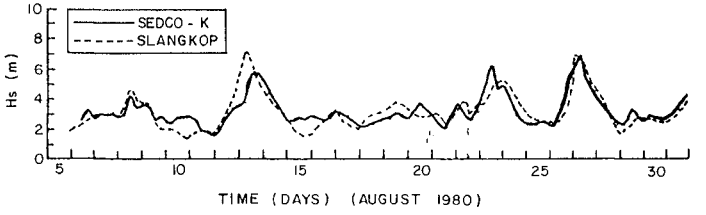

FIG. 6. COMPARISON OF WAVE HEIGHTS (Hs) RECORDED AT SEDCO-K AND SLANGKOP

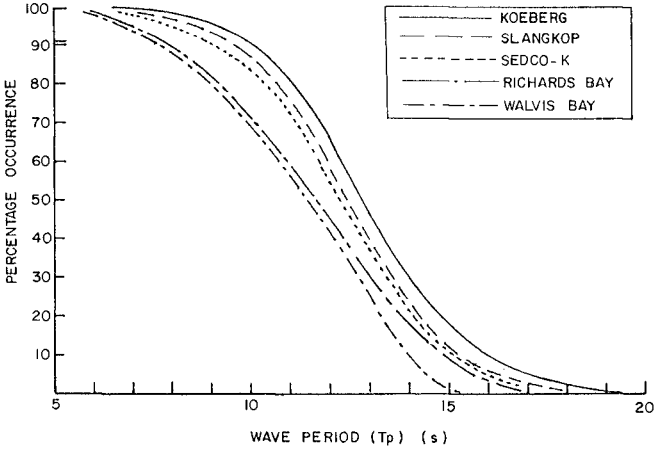

FIG. 7. DISTRIBUTION OF PEAK ENERGY PERIOD (Tp)

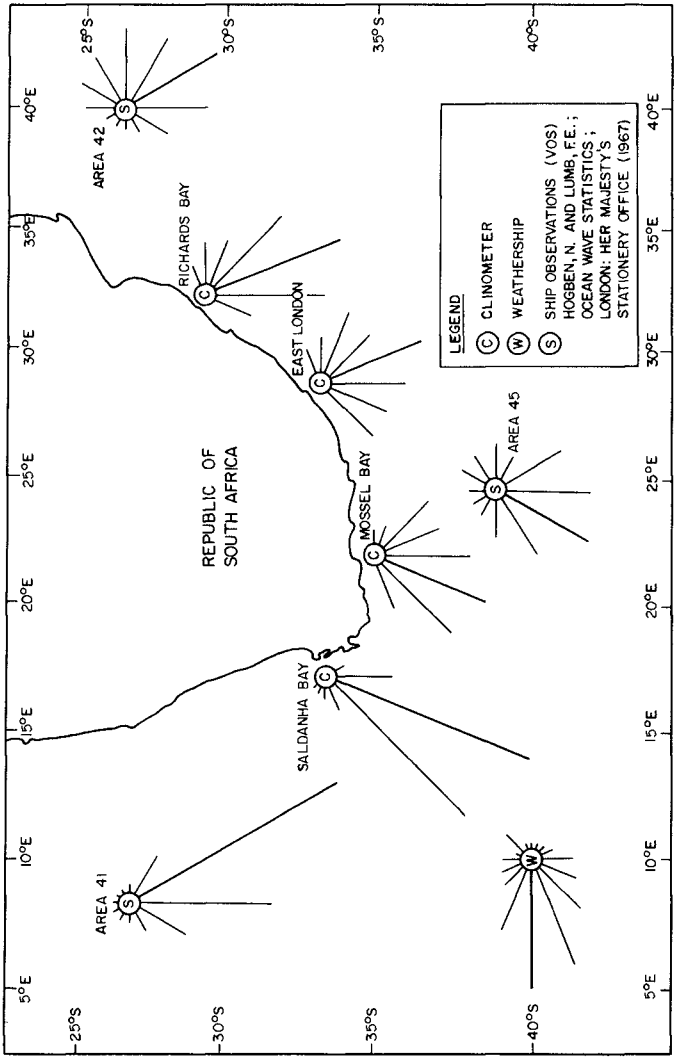

FIG. 8. WAVE DIRECTION DISTRIBUTIONS

of Waverider stations will be discussed, although it is fully realised that discussion and comparison of wave energy density spectra will be more satisfactory. A large quantity of spectral data is available but a lack of space prohibits it being discussed in this paper.

The peak energy period (T_p) distribution for a few Waverider stations is shown in Figure 7. From this figure it is obvious that the wave period distribution is very similar along the entire coastline with the wave periods along the southernmost parts of the country slightly longer than on the more northerly coasts. The period (T_p) exceeded for 50 per cent of the time varies from approximately 12,5 s in the south to 11,5 s in the north along both the east and west coasts.

Comparison between wave period data obtained from VOS and T_p obtained by Waverider shows very poor correlation with the VOS recording wave periods very much lower than the Waverider.

5. CONCLUSIONS

(i) A standard wave analysis program with special emphasis on data qualification routines has been developed for digital wave data.

(ii) The data qualification routines proved invaluable in the analysis of large quantities of data and help to detect hidden faults in the wave recording system.

(iii) A very clear wave pattern emerges from the available Waverider data and this is in accordance with the pattern to be expected from the known weather patterns around the coast.

(iv) Waverider data indicate considerable lower wave heights than those from VOS. The reason for this is thought to be that SE'ly winds generate waves parallel or offshore along the west coast which will lead to increasing wave height with increasing distance offshore. The difference in wave height along the east coast can be explained by energy transfer from the Agulhas current to the opposing SW'ly waves.

6. REFERENCES

ASHBY, D J, HARPER, A and VAN SCHAIK, C (1973). Deep sea wave clinometer data from 1967 to 1972. CSIR, Pretoria, Report ME1263.

HOGBEN, N and LUMB, F E (1967). Ocean wave statistics. Ministry of Technology, National Physical Laboratory, Teddington, Middlesex.

HOLROYD, S G (1982). NRIO microcomputer system. CSIR, Stellenbosch, Technical Report T/SEA 8134.

SCHUMANN, E H (1976). Changes in energy of surface gravity waves in the Agulhas current. Deep-Sea Research, 23(6): 509-518.

VISSER, C J, ENNIS, M and ROSSOUW, J (1980). Data qualification and spectral analyis of sea wave data. IMT, Simonstown, Technical Note TN-014-80.

VISSER, C J, ENNIS, M and ROSSOUW (not yet published). Computer program for data qualification and spectral analysis of sea wave data. IMT, Simonstown.

Weather Bureau (1979). Daily weather bulletin for the month of May, 1979. South African Weather Bureau, Department of Transport.

Weather Ship Action Committee (1973). South African Weather Ship. The Weather Ship Action Committee, WSAC TR No 2.

APPENDIX A

The "WAVES" Program Printout

The program is designed to print all the information of one record on a single printer page. From the top down, the page is divided into five areas. The areas are described, in order, in points 1 to 5:

1. The header area

   The first three lines of the printout contain the information necessary to identify the record (for example, degrees latitude and longitude) and information about how the sampling took place. The header area also gives the category assigned to the record.

2. Time domain parameter area

   The values of all the time domain parameters calculated are given in this area. As on the whole printout, the values are given separately for the two halves that the record is divided into.

3. Frequency domain parameter area

   The values of the frequency domain parametes calculated are given in this area.

4. Data qualification area

   The severity codes for the tests performed on the record are given in this area. A severity code of 0 means that all the requirements of the test were met. A code of 3 means that the record badly fails the test.

5. The spectral information area

   In this area, the last on the page, the power spectral density is given per frequency for each half of the record. The mean values for the two halves are also given. To facilitate interpreting the values, a small printer plot is provided.

```
WAVE ANALYSIS OF : SLANGKOP          (1ST:GOOD 2ND:GOOD) CATEGORY: GOOD
DATE: 1978 10   5. TIME: 1200.                                  PROGRAMME REVISION: 1
RECORDER:WAVE RIDER  ;DEPTH:   0M; 34DEG  3.1MIN S 18DEG  3.5MIN E;WATER DEPTH: 197M;SAMPLING INTERVAL:0.50S;SAMPLES/HALF:1024
```

TIME DOMAIN	HALF	P2	P3	P4	>P4	ERR	CON	G(MAX)	CORR	MEAN	VARIANCE	NS	N1	TZ	SKEWNESS	KURTOSIS
PARAMETERS:	1.	10	0	0	0	0	0	2.067	0.002	10.199	0.524	2.896	4.260	6.649	-0.062	2.722
	2.	8	0	0	0	0	0	2.094	-0.010	10.203	0.554	2.976	4.280	5.333	0.053	2.945

FREQ DOMAIN	NALF	TP	HM0	TM02	TM24	TM01	E	OP	LF.DET	NF.DET
PARAMETERS:	1.	11.907	2.809	5.608	2.455	6.864	0.899	2.168	0.023	0.004
	2.	10.667	2.910	5.369	2.616	6.332	0.873	1.680	0.032	0.003

DATA QUALIFICATION:	NALF	FLATHEAD	ERRATICS	CONSEC	MEAN#0	TREND	NON-NORM	LF.DET	CORR1#CORR2	MEAN1#MEAN2	VAR1#VAR2
	1.	0	0	0	1	0	0	0	0	0	0
	2.	0	0	0	1	0	0	0			

SPECTRUM	NO	FREQUENCY (HZ)	PERIOD (S)	SPECTRAL DENSITY(M*M/NZ) 1ST HALF	2ND HALF	MEAN	MEAN SPECTRAL DENSITY (% OF 8.964) 0 20 40 60 80 100
	1	0.006	170.667	0.003	0.003	0.003	|
	2	0.016	64.000	0.008	0.005	0.007	|
	3	0.025	39.385	0.005	0.007	0.006	|
	4	0.035	28.444	0.007	0.016	0.012	|
	5	0.045	22.261	0.005	0.008	0.007	|
	6	0.055	18.286	0.037	0.009	0.023	|
	7	0.064	15.515	0.283	0.254	0.269	|*
	8	0.074	13.474	2.147	1.897	1.622	|*********
	9	0.084	11.907	13.536	4.391	8.964	F|**********R**
	10	0.094	10.667	7.081	8.537	7.809	R|********E**********************************
	11	0.104	9.660	4.110	5.589	4.849	E|********Q********************
	12	0.113	8.828	2.460	4.435	3.448	Q|**************U*****************
	13	0.123	8.127	1.992	5.387	3.689	U|**************E******
	14	0.133	7.529	3.032	4.220	3.626	E|**************N*****
	15	0.143	7.014	1.549	1.783	1.666	N|*********
	16	0.152	6.564	1.353	2.411	1.882	C|**********
	17	0.162	6.169	0.826	0.538	0.682	Y|***
	18	0.172	5.818	1.346	0.929	1.137	|******
	19	0.182	5.505	0.559	0.903	0.731	|****
	20	0.191	5.224	0.315	1.591	0.953	|*****
	21	0.201	4.971	0.547	1.468	1.008	|*****
	22	0.211	4.741	0.986	0.874	0.930	|*****
	23	0.221	4.531	0.855	0.658	0.757	|****
	24	0.230	4.339	0.870	0.963	0.917	|*****
	25	0.240	4.163	0.378	0.857	0.617	|***
	26	0.250	4.000	0.518	0.711	0.615	|***
	27	0.260	3.850	1.071	0.838	0.955	|*****
	28	0.270	3.710	0.335	0.284	0.309	|*
	29	0.279	3.580	0.280	1.007	0.643	|***
	30	0.289	3.459	0.367	0.370	0.368	|**

RESOLUTION (DELTA F IN NZ): RAW = 0.00195 SMOOTHED OVER 5 LINES = 0.00977

FINAL SUMMARY (MEAN) : HS= 2.936 M HMO= 2.859 M TZ= 5.991 S TM02= 5.489 S TP= 11.907 S
```
```

APPENDIX B

Assigning severity counts to qualification parameters:

Parameter	Severity count	Test	Test values
FLATHEAD	0	"P2" ⩽ T1 and "P3" + "P4" + ">P4" = 0 or "P2" < T2 and "P4" ⩽ 1	T1=86-7,5"Hs" T2=46,2-3,45"Hs" + 5,24"P3"- 0,803"P3""P4"
	2	All other cases	
	3	">P4" > T3	T3=16,56-3,18"Hs"
ERRATICS	0	"ERR" < 5	
	1	5 ⩽ "ERR" ⩽ 10	
	3	"ERR" > 10	
CONSEC	0	"CON" = 0	
	3	"CON" > 0	
TREND	0	0,0 ⩽ |"CORR"| < 0,062	P = 0,01 and P=0,5 correlation test with 1 024 d.f.
	1	0,062 ⩽ |"CORR"| ⩽ 0,081	
	3	|"CORR"| > 0,081	
NON-NORM	0	0,0 ⩽ |"SKEWNESS"| ⩽ 0,26	
		2,3 ⩽ |"KURTOSIS"| ⩽ 3,85	
	1	0,26 < |"SKEWNESS"| ⩽ 0,3	
		2,0 ⩽ |"KURTOSIS"| < 2,3	
		or	
		3,85 < |"KURTOSIS"| ⩽ 5,0	
	2	0,3 < |"SKEWNESS"| ⩽ 0,4	
	3	|"SKEWNESS"| > 0,4	
		0,0 ⩽ |"KURTOSIS"| < 2,0	
		or	
		5,0 < |"KURTOSIS"| < ∞	
LF.DET	0	"LF.DET" < T14	T14=0,2+0,17"Hs"
	2	T14 ⩽ "LF.DET" ⩽ T15	
	3	"LF.DET" > T15	T15=0,4+0,2"Hs"

SYNTHESIS OF HURRICANE RESPONSE HYDROGRAPHS

by

Rodney J. Sobey,[1] M.ASCE

ABSTRACT: A hindcasting methodology is described for the total water level and wave hydrographs at a coastal site during a hurricane. It accommodates phasing of the separate components of the sustained water level (astronomical tide, storm tide, breaking wave setup), as well as storm variability and coastal bathymetry. Complete hindcast models are utilised, but an intermediate cost and precision is achieved by compromising the number of complete hindcast storms, rather than the precision of the hindcast model. A synthesis technique is developed to predict the response hydrographs of the remaining storms in the historical data set.

INTRODUCTION

Rational design in the coastal environment should be based on long term frequency estimates of extreme water level and wave conditions but the duration and quality of historical records of both water level and wave conditions during hurricanes are rarely adequate to provide the necessary information. However, suitable historical records of meteorological conditions are often available, which can be used in conjunction with suitable meteorological tide and wave prediction models to hindcast meteorological tide and wave conditions respectively.

---

1 Senior Lecturer, Department of Civil and Systems Engineering, James Cook University, Townsville, 4811, Australia.

In recent years, sophisticated numerical hindcast models have been developed to a respectable level of precision and acceptance. It is an inevitable consequence that they are computationally costly and this has inhibited their use in long term frequency studies where typically fifty storms would require hindcasting. Complete models, based on the long wave equations for storm tides or the radiative transfer equation for wind waves, hindcast the complete time history or hydrograph of the sea response to a storm, allowing consideration of the phasing of the peak storm tide, wave and breaking wave setup responses with the periodic astronomical tide as well as consideration of a number of topographical and shallow water influences. Less complete models rarely allow appropriate consideration of any of these points but they may nonetheless be used because of the frequently prohibitive cost of hindcasting a complete storm data set.

This paper describes a hindcasting methodology in a hurricane environment that provides an intermediate step between the above extremes. It is intermediate in both cost and precision. Site-specific experience is developed from a small number of complete storm hindcasts and this information is used to synthesise the response hydrographs for the remaining storms of the meteorological data set. The approach is broadly similar to the unit hydrograph procedure in surface water hydrology and it has been used successfully in a major hindcast study on Australia's North-West Shelf.

HISTORICAL RECORDS OF SEA RESPONSE

Under ideal circumstances, long term frequency estimates are based on long term records of the particular event. For storm tides, the relevant extreme value series would be drawn from long term records of total sustained water level at the particular site. For wind waves, it would be drawn from long term records of wind waves at the same site. Such ideal circumstances are rarely achieved in practice, for a variety of reasons.

If suitable records are available at all, they are rarely at the particular site in question. The data site may be sufficiently close that it is reasonable to ignore any difference in sea response at the two sites. In many cases however this may not be a reasonable assumption, especially in shallower nearshore areas where interest is frequently centred. Bathymetric and shoreline detail has a major impact on sea response and the storm tide in particular is very site sensitive. For a landfalling storm across a generally open coast, the peak surge level varies moderately rapidly along the coast and is particularly sensitive to the depth and width of the continential shelf, a wide shallow shelf inducing a much more intense surge. Coastal features such as bays and headlands control the

local flow patterns and can have a significant local influence, whose spatial extent is roughly the same order as the spatial scale of the coastal feature. Shallower water influences on wind waves are often more complicated. In addition to spatial and temporal variations in the forcing, the propagation characteristics of wind waves are modified by the continental shelf bathymetry. The waves are refracted, shoal and eventually dissipate on the shore. Refraction may concentrate wave energy around headlands or disperse wave energy within bays. Wave energy may be dissipated by bottom friction, bottom percolation interaction with a cohesionless bed material, bottom motion in a cohesive bed material and perhaps bottom scattering from irregularities in the bathymetry. Wave diffraction will also have a significant influence around major headlands and man-made breakwaters, dispersing wave energy into the geometric shadow of the feature.

Even where records are available at a suitable site, a number of significant problems remain. Storm tide records are rarely collected as such but can often be established from automatically-recording tide gauges which have been standard equipment at most established ports for many decades. The height of the astronomical tide has a major influence on shipping movements in and out of port and records are maintained for this purpose, even though little more than a year of records is necessary for traditional harmonic analysis on which published tide predictions are based. These gauges are sited at the convenience of the port authority and designed to record only the astronomical tide. Storm surge is also a long wave motion and will be recorded by conventional tide gauges, unless the storm surge is sufficiently extreme to damage the instrument or send it off scale. Harbour resonance may also be recorded on the gauge but this component should not be difficult to separately identify. Access to these records is perhaps the major problem. Historical records are mostly in analogue form on strip charts and this recording technique has generally continued to the present day. Consistent quality of such records is not assured. Port authorities naturally see little value in maintaining historical records but it has fortunately become a reasonably established practice, although record achival is often a rather haphazard process. Apart from the record sequences used for harmonic analysis (often a single twelve month period), there will have been little consistent interest in these records. Problems with local datum changes and possible reconstruction, relocation or replacement of the gauge are anticipated, together with the laborious task of separating the storm tide component from the analogue strip charts.

The systemic measurement of wave conditions has become a standard practice only in the last decade or so. Initially records were obtained on strip charts but present practice

records only a discrete record with a typical time spacing of 0.5 s. Good quality records are regularly obtained and an enormous amount of data is amassed in a relatively short time. However, the limitations of this data is estimating extreme events must be clearly recognised (Sobey, 1982), as each year of data contributes only one point to the extreme value series. The total duration of the data series must be considered in the light of potential meteorological trends and multiyear weather cycles, even natural or man-made changes in the local environment. Based on a study by Petrauskas and Aagaard (8), Borgman (2) has suggested that it is unwise to extrapolate beyond twice the duration of the record from the largest observation. Typical record lengths in many situations rarely exceed a few years, whereas design often relates to average recurrence intervals of 50 or 100 years. There is a large measure of uncertainty attached to record extrapolation to such extreme events, even following the adoption of an appropriate probability distribution.

HINDCASTING THE SEA RESPONSE

It is clear from the above discussion that historical data alone is often insufficient to develop satisfactory estimates of long term frequencies of sea response. The alternative is system modelling, in which advantage is taken of long term meteorological records of storm conditions to hindcast the sea response corresponding to the historical storm data.

The long wave response of a homogeneous sea to the meteorological forcing of a hurricane is adequately described by a two-dimensional vertically integrated form of the Reynolds' Equations - the Long Wave Equations. These equations represent the conservation of mass and the conservation of momentum in horizontal directions x and y and time t:

$$\frac{\partial \eta}{\partial t} + \frac{\partial U}{\partial x} + \frac{\partial V}{\partial y} = 0 \qquad (1)$$

$$\frac{\partial U}{\partial t} + \frac{\partial}{\partial x}\left(\frac{U^2}{\eta-d}\right) + \frac{\partial}{\partial y}\left(\frac{UV}{\eta-d}\right) - fV = -g(\eta-d)\frac{\partial \eta}{\partial x} - \left(\frac{\eta-d}{\rho_w}\right)\frac{\partial p_s}{\partial x} + \frac{1}{\rho_w}(\tau_{sx}-\tau_{bx}) \qquad (2)$$

$$\frac{\partial V}{\partial t} + \frac{\partial}{\partial x}\left(\frac{UV}{\eta-d}\right) + \frac{\partial}{\partial y}\left(\frac{V}{\eta-d}\right) + fU = -g(\eta-d)\frac{\partial \eta}{\partial y} - \left(\frac{\eta-d}{\rho_w}\right)\frac{\partial p_s}{\partial y} + \frac{1}{\rho_w}(\tau_{sy}-\tau_{by}) \qquad (3)$$

The x-y datum plane is located at the mean water level with the z axis directed vertically upwards. The water surface elevation with respect to datum is $\eta(x,y,t)$, the sea bed is $d(x,y)$ with respect to datum, U and V are depth-integrated flows per unit width, f is the Coriolis parameter and ρ_w is the mass density of sea water. The forcing influence of the hurricane is represented through the

surface wind shear stress vector $\underline{\tau}_s(x,y,t)$, resolved into components τ_{sx} and τ_{sy}, and the x and y gradients of the M.S.L. atmospheric pressure $p_s(x,y,t)$. The effect of bottom stress is represented through the seabed shear stress vector $\underline{\tau}_b(x,y,t)$, resolved into components τ_{bx} and τ_{by}. Numerical solutions of these equations are readily accomplished under quite general conditions of bathymetry, coastal detail and meteorological forcing. One such example is the numerical hydrodynamic model SURGE described by Sobey, Harper and Mitchell (14) and Sobey, Harper and Stark (13). This model has been used extensively in northern Australia at some fifteen different sites for some one hundred and fifty different storms. It can be applied to most coastal regions and includes the effects of undersea bathymetry, offshore islands, reefs and other coastal features, as well as the flooding of low lying land. Tropical cyclone size, intensity and track can be varied continuously throughout a simulation to produce water flow patterns, contours of water level, coastal surge profiles at any time and water level and flow velocity time histories anywhere within the model area. SURGE is a comprehensive software system, in which particular attention has been given to the quite considerable problems of input data format and especially output data selection and presentation.

A complex wind sea is described in terms of the variance spectral densty $E(f,\theta;x,y,t)$ in directional fequency (f,θ) space. In the absence of current, wave energy conservation may be written as

$$\frac{\partial}{\partial t}(C\,C_g E) + C_g \cos\theta \frac{\partial}{\partial x}(C\,C_g E) + C_g \sin\theta \frac{\partial}{\partial y}(C\,C_g E) + \frac{C_g}{C}\left(\sin\theta \frac{\partial C}{\partial x} - \cos\theta \frac{\partial C}{\partial y}\right)\frac{\partial}{\partial \theta}(C\,C_g E) = C\,C_g\,S \qquad (4)$$

where C is the phase speed and C_g the group velocity. The source function $S(f,\theta)$ on the right hand side represents the net transfer of energy to or from or within the spectrum. This equation, known as the Radiative Transfer Equation, formally summarises all the various physical processes that contribute to the evolution of the directional spectrum. In recent years considerable success has been reported in the representation of the source terms and in the numerical solution of the complete Radiative Transfer Equation. One such example is the numerical hydrodynamic model SPECT described by Sobey and Young (16) and Young and Sobey (21). This is a quite general model, applicable in both shallow and deep water. It has been used successfully in Australia for a twenty-eight storm hindcast study on the North-West Shelf, where good agreement with field data was obtained.

The aerodynamics of the hurricane and the hydrodynamics of the underlying water body are coupled by the atmospheric pressure p_s and wind shear stress τ_s at the air-sea

interface. Their estimation throughout the flow field during the passage of a tropical cyclone follows from the adoption of a suitable model of the near-surface meteorological structure of the storm. The model developed initially by Graham and Nunn (4) under the National Hurricane Research Project (NHRP) of the former U.S. Weather Bureau forms the basis of the storm sub-model in both cases. No claim is made that this model is entirely satisfactory; in fact our knowledge of tropical cyclone wind fields is far from complete. It was adopted in the absence of a more suitable alternative. More sophisticated models describing the dynamics of the atmospheric boundary layer in a moving hurricane could be used, but there is a significant computational penalty and the predictive capability of such models is not yet measurably superior for the NHRP model.

Many of the highly empirical aspects of the original NHRP model, such as rate of filling over land and the reduction of over-land wind speeds, have been omitted in favour of representing the major features of the tropical cyclone. In particular the radial wind and pressure profiles, the variation of the radial inflow angle and the asymmetry of the wind field are included and expressed in terms of the four parameters commonly assumed to characterise a hurricane: the central pressure p_o at M.S.L., the maximum sustained wind V_{10} at a height of 10 m above M.S.L., the radius of maximum winds R, the speed V_{FM} and direction θ_{FM} of storm forward movement. All four parameters are varied continuously to represent changes in storm intensity and track. Details may be found in Ref. 13. The over-water wind speed W_{10} at height 10 m above M.S.L. and the resulting shear stress τ_s on the water surface are assumed to be related as $\tau_s = C_{10} \rho_a W_{10}^2$, where C_{10} is a non-dimensional surface friction or drag coefficient and ρ_a is the mass density of air.

Now that sophisticated hindcast models have been developed to a respectiable level of precision and acceptance, hindcasting has many advantages in estimating the sea response to hurricanes. It permits an extreme value series to be esablished where no field records of sea response exist, the duration of which is the duration of the meteorological data and generally long enough to expect a satisfactory estimate of 50 and perhaps 100 year events. It also removes the temptation to use historical sea response data an another site whole characteristics are arguably different from the site in question. Where there is short term measured sea response data at the particular site, the hindcast data has a complementary role in confirming or defining the longer-term trends.

The major disadvantage of the complete hindcasting models (LWE and RTE) is their detail and hence computational and associated personnel costs. Hindcasting a complete data

set (typically of order 50 storms) is mostly well beyond the budget and also the time that is typically allocated to long term frequency estimates. Some compromise is often sought, usually the adoption of a less sophisticated hindcast model which compromises the detail as well as the cost of hindcasting the sea response. The consequences need to be fully recognised. In particular the use of historical data to its fullest potential gives direct consideration to the influence of storm track variability and storm intensification and decay, aspects that are difficult to consider in any less sophisticated approach. A related and perhaps more significant aspect is the phasing of astronomical tide, storm surge and wave conditions (17). Astronomical tides are often significantly variable. On Australia's North West Shelf, for example, the mean spring tide range is large (of order 3 to 4 m) but the mean neap tide range is small (of order 1 m). A peak storm surge of order 2 m would be a major event and its impact clearly depends on the timing and duration of its peak with respect to the astronomical tide. Its arrival at low tide would be little cause for concern and even at a typical high water neaps the total water level would not differ significantly from the highest astronomical tide (HAT). At a typical high water springs however its impact would be substantal. Similar arguments are valid regarding breaking wave setup, with the additional complication that peak wave and surge conditions will not necessarily correspond. Surge and wave response to hurricanes are related but physically distinct phenomena, in their generation and propagation and especially in their reaction to shoaling waters and coastal bathymetry. There is a considerable margin of safety available in the tidal characteristics and a realistic analysis of extreme water levels must give reasonable consideration also to this situation.

The often critical significance of coastal detail and shelf bathymetry has already been mentioned above, yet it is this detail that is first abandoned in less sophisticated hindcast models. For storm tides, the Bathystrophic Storm Tide model proposed by Freeman, Baer and Jung (3) considers only the steady-state momentum balance normal to the coast at the site in question. Mass and longshore momentum conservation is not considered, nor are the dynamics of the sea response. Coastal detail and shelf bathymetry is represented by the seabed profile at the site, other detail being ignored. For this approach to have any validity, it must be restricted to open-coast situations and slowly-moving, large-scale storm systems. An alternative approach to a less sophisticated hindcast model for storm tides is the nomograph method of Jelesnianski (5). This method is also restricted to open-coast situations but is based on computations utilising the complete Long Wave Equations. A standard continental shelf region was defined with a straight coastline and a uniform linear slope as the seabed

profile. A standard storm was defined and directed on a landfalling track normal to the coastline. These results are presented in terms of peak surge amplitude only, to which correction factors have been defined for different linear seabed profiles (the shoaling correction) and different forward speed and direction of the storm (the motion correction).

Less sophisticated hindcast models for wind waves differ in detail but not in spirit. The empirical models of Bretschneider (1), Ross (9), Lee (7) and Shemdin (10) have much in common. All neglect the dynamics of the sea response, assume exclusively deep water conditions and base their parameterisation of the sea response on the Sverdrup and Munk (18) or Kitaigorodskii (6) scaling relationships, which are identical. In quantifying the relationships, Bretschneider uses an integral interpretation of the Sverdrup-Munk fetch graphs, while Ross, Lee and Shemdin use field data from Gulf of Mexico hurricanes. Shemdin's model predicts the significant wave height and peak frequency of the dominant wave conditions ahead of a moving hurricane, giving specific consideration to the forward motion. The other three models predict the space and time variable wave field; the Bretschneider model is restricted to slowly-moving storms and the Ross and Lee models give no specific consideration to storm motion. None of these models predict dominant wave directions and quantitative agreement among the models is quite poor. In addition their is little consideration of storm variability in position and time and no consideration of important coastal detail and shelf bathymetry and associated shallow water effects.

AN ALTERNATIVE APPROACH

It is apparent from the above discussion that there are a range of influences on sea response to hurricanes that can be reasonably accommodated only by a complete hindcast model. The adopted methodology is a direct recognition of this situation. The separate steps are those of the complete approach: (i) hindcast the sea response (storm surge and/or wind waves) and the astronomical tide conditions during each hurricane of the historical storm data set, (ii) superimpose the storm surge, breaking wave setup and astronomical tide hydrographs to give the hindcast total water level hydrographs, and (iii) form extreme value series from total water level and wave hydrograph peaks during each of the historical storms for frequency analysis. The necessary compromise is in the number of storms that are hindcast by complete hindcast models. A limited number of project hurricanes (of order 5) are chosen as representative of the range of storm intensities and particularly storm tracks in the historical data set. Complete hindcasts of sea response for the project hurricanes together with the complete historical hurricane data set comprises the data

base for hindcasting the sea response to all storms in the historical data set. A hindcast model developed from this data base gives explicit consideration to the whole range of site specific and predominantly shallow water influences described above as collectively having a potentially major impact on the sea response at a nearshore site on the continental shelf.

The suggested methodology has been used in the estimation of long term frequencies of extreme wave height and total sustained water level at Mermaid Sound on Australia's North-West Shelf. The historical storm data set contained forty-three tropical cyclones, from which six were chosen as project storms. The specific examples described below have been taken from this study.

SYNTHESIS OF STORM RESPONSE

To synthesise the sea response hydrographs for all storms in the historical data set from the complete hindcasts for the small number of project hurricances, certain assumptions about generalised storm response must be made. The first major assumption of this analysis is that at each site, distinct hydrograph segments (e.g. rising limb, falling limb) can be represented in terms of a single amplitude scale H and a single time scale T, such that in general

$$h(t)/H = f(t/T) \tag{5}$$

h(t) being the response hydrograph at time t. For the rising limb of a hydrograph, H might be the peak height and T the half-life. Each separate hydrograph segment is representated as a two parameter curve, uniquely defined once H and T and the function f are specified.

The second major assumption involves the application of dimensional arguments to determine H and T for each storm. It is assumed that H and T are dependent only on the following variables: $\Delta p_o = p_\infty - p_o$, the central pressure deficit of the storm eye at closest approach; R, the radius of maximum winds at closest approach; V_{FM}, the forward speed of the storm at closest approach; S, the distance of the storm from the site at closest approach; ρ_w, the mass density of sea water and g, the gravitational acceleration. Consequently

$$H,T = f(\Delta p_o, R, V_{FM}, S, \rho_w, g) \tag{6}$$

The variation of Δp_o, R, V_{FM} and S during the passage of a hurricane can be quite considerable and it is an assumption of this analysis that the parameter values at closest approach are applicable. It could be argued that some time-averaged value for each parameter might be more appropriate, but resolution of this point would almost

require complete wave and surge hindcasts for each of the storms in the historical data set, just what the parametric approach is designed to avoid. A similar definition of the revelant storm parameters has been adopted by Ward, Borgman and Cardone (20) in extending hindcast wave data from twenty-six storms to a forty-eight storm historical data set.

Applying dimensional analysis to Equation 6 with R and V_{FM} as the recurring variables gives

$$\frac{H}{R} , \frac{T}{R/V_{FM}} = f(\frac{B_o}{R} , \frac{S}{R} , \frac{V^2_{FM}}{gR}) \quad (7)$$

where $B_o = \Delta p_o / \rho_w g$, the barometric head deficit of the storm eye at closest approach. It is generally recognised that R largely defines the horizontal or spatial scale of the sea response while B_o determines the intensity of the response, recognition of which leads to a reorgnaisation of Equation 7 as

$$\frac{H}{B_o} , \frac{T}{R/V_{FM}} = f(\frac{S}{R} , \frac{B_o}{R} , \frac{V^2_{FM}}{gR}) \quad (8)$$

The functions f are determined from the appropriate project storm hindcasts, as shown below. Intuitively one would anticipate a major dependence of the dimensionless amplitude at each site on S/R but perhaps only a minor dependence of the dimensionless time on B_o/R and S/R. No systematic dependence on the dimensionless Froude Number is anticipated.

SIGNIFICANT WAVE HYDROGRAPHS

Hindcast significant wave hydrographs typically have the same general shape, a rising limb to a single peak and a falling limb at a different and generally faster rate. An appropriate universal profile is sketched in Figure 1, both the rising and falling limbs being represented as Gaussian curves with different half-lives, T_1 and T_2 respectively:

$$h(t) = \begin{cases} H \exp [- c(\frac{t-T_p}{T_1})^2] & \text{for } t \leq T_p \\ H \exp [- c(\frac{t-T_p}{T_1})^2] & \text{for } t > T_p \end{cases} \quad (9)$$

where H is the peak amplitude, T_p is the time of the hydrograph peak and c = ln 2.

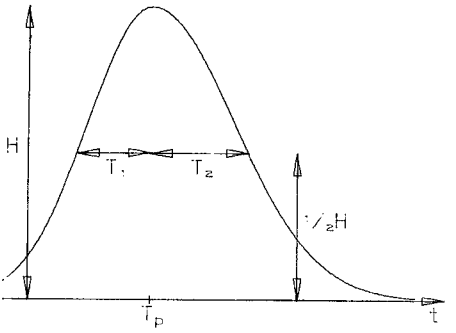

Figure 1. Parameterised Significant Wave Hydrograph

The complete hydrograph can be represented in terms of a single amplitude parameter H and three time parameters T_p - T_o, T_1 and T_2, T_o being the time of closest approach of each project storm. Each of these parameters have been extracted from the project storm hindcast hydrographs and non-dimensionalised and plotted in accordance with Equation 8. The final result for one site within Mermaid sound is shown in Figure 2. Several trial presentations were attempted before these plots were finalised. A major dependence on the direction of rotation of the track about Mermaid Sound was apparent and this was accommodated within the existing dimensional variables by afixing a sign to S, the distance at closest approach. A plus sign implied clockwise rotation and a negative sign anti-clockwise rotation.

The functional dependence indicated by Equation 8 was investigated in as much detail as the data allowed and no systematic dependence on either parameter was established. It seemed most appropriate to represent each dimensionless time as a constant value. The amplitude curve at the top of Figure 2 shows an anticipated intensification of significant wave height for storms passing anti-clockwise about Mermaid Sound. This H/B_o curve was used directly in estimating the peak amplitude for each of the forty-three storms. Each curve has been extrapolated outwards to its intersection with the S/R axis. Outside these intersection points, H/B_o is assumed zero, the storm passing sufficiently far from Mermaid Sound for this to be a reasonable assumption. It is of course possible that significant waves generated closer to the storm centre may propagate to and penetrate into Mermaid Sound. To the extent that such behaviour is not included among the six project storms it can not be accommodated within the present analysis.

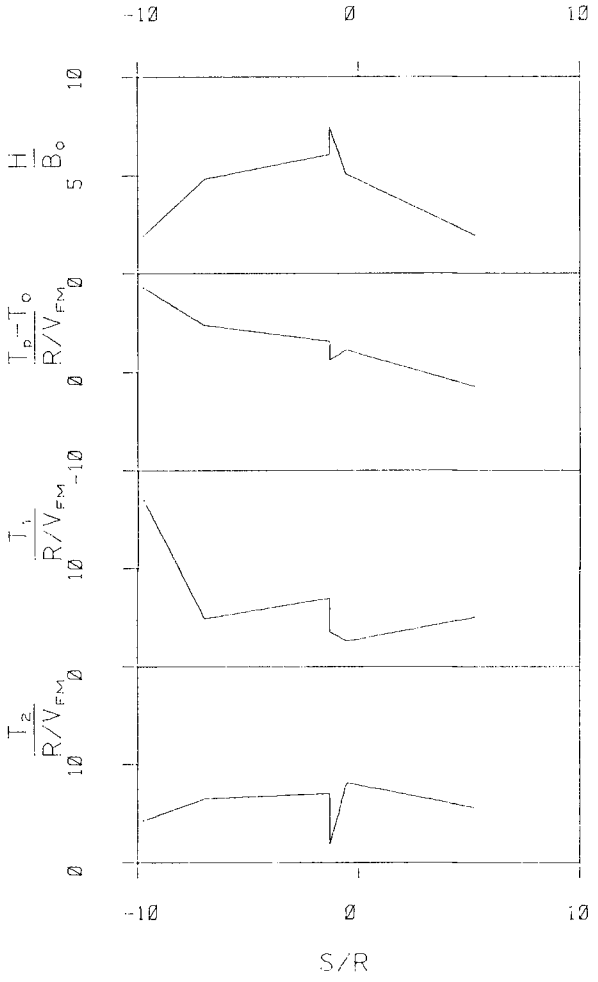

Figure 2. Dimensionless Parameters of Significant Wave Hydrographs

Breaking wave setup is a nearshore phenomenon related to the conversion of the kinetic energy of wave motion to quasi-steady potential energy for waves breaking on a beach slope. Where required, it was estimated from significant wave height in the manner recommended in the Shore Protection Manual (19).

STORM SURGE HYDROGRAPHS

A characteristic of the storm surge hindcasts for Mermaid Sound was the early and sustained response. In addition to the normal peak setup or setdown around the time of closest approach there is typically an initial peak setup or setdown several hours earlier, in response to the regional bathymetry and particularly the coastal topography. For landfalling storms passing to the east of (i.e. clockwise about) Mermaid Sound, an initial setdown is followed by a period of sustained setdown until a fairly rapid fall away after the second peak. For landfalling storms passing to the west of (i.e. anti-clockwise about) Mermaid Sound, an initial setup is followed by a period of sustained setup until the second peak around the time of storm landfall, after which there is again a fairly rapid fall away. For parallel moving storms tracking down the coast (i.e. anti-clockwise about Mermaid Sound), an initial setdown is followed by a somewhat more substantial setup. The reverse pattern of behaviour appears certain for parallel moving storms tracking up the coast although there is no such storm among the six project storms.

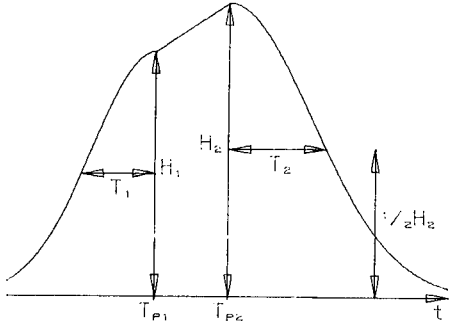

Figure 3. Parameterised Storm Surge Hydrograph

An appropriate universal profile to describe this complex hydrograph is sketched in Figure 3. The initial peak is at T_{p1} and the rising (falling) limb has a Gaussian profile with a half-life of T_1. The intermediate segment between T_{p1} and the major peak T_{p2} is assumed to follow a straight line, both peak water levels H_1 and H_2 being

potentially positive (setup) or negative (setdown). The falling limb from T_{p2} is again a Gaussian profile with half-life T_2.

$$h(t) = \begin{cases} H_1 \exp\left[-c\left(\frac{t-T_{p1}}{T_1}\right)^2\right] & \text{for } t \leq T_{p1} \\ H_1 + \frac{H_2 - H_1}{T_{p2} - T_{p1}}(t - T_{p1}) & \text{for } T_{p1} < t \leq T_{p2} \\ H_2 \exp\left[-c\left(\frac{t-T_{p2}}{T_2}\right)^2\right] & \text{for } t > T_{p2} \end{cases} \qquad (10)$$

The complete hydrograph can be represented in terms of two amplitude parameters H_1, H_2 and four time parameters $T_o - T_{p1}$, T_1, $T_{p2} - T_o$ and T_2. Each of these parameters has been extracted from the hindcast hydrographs, non-dimensionalised and plotted in accordance with Equation 8, in a similar manner to the previous section. The final result for one site within Mermaid Sound is shown in Figure 4.

Following the introductory discussion to this section it was necessary to distinguish between landfalling and parallel moving storms, in addition to the distinction based on direction of rotation about Mermaid Sound. This reduced the data set from six storms to two sets of three storms and required additional assumptions about the surge response to distant storms. This specific assumption has been that storms that do not approach closer than 10R to Mermaid Sound have no influence on water levels within the Sound and that response amplitude falls away towards the 10R position. The project hindcasts and experience elsewhere indicate that this is a reasonable assumption and it has been incorporated into Figure 4 as straight line segments.

Once again it seemed most appropriate to represent each dimensionless time as a constant value over all sites, with different values for landfalling and parallel moving storms. As also in the previous section, the H/B_o curves were used directly in estimating surge peaks for each of the forty-three storms. The shape of these curves follow the anticipated pattern, especially for landfalling storms which show the classic along-coast profile with setdown to the east and more substantial setup to the west.

ASTRONOMICAL TIDE HYDROGRAPHS

Hindcasts of astronomical tide hydrographs are generated from the classical harmonic series represetation of the vertical tide:

$$h(t) = H_o + \sum_{n=1}^{R} f_n H_n \cos(\omega_n t + V_n + u_n - g_n) \qquad (11)$$

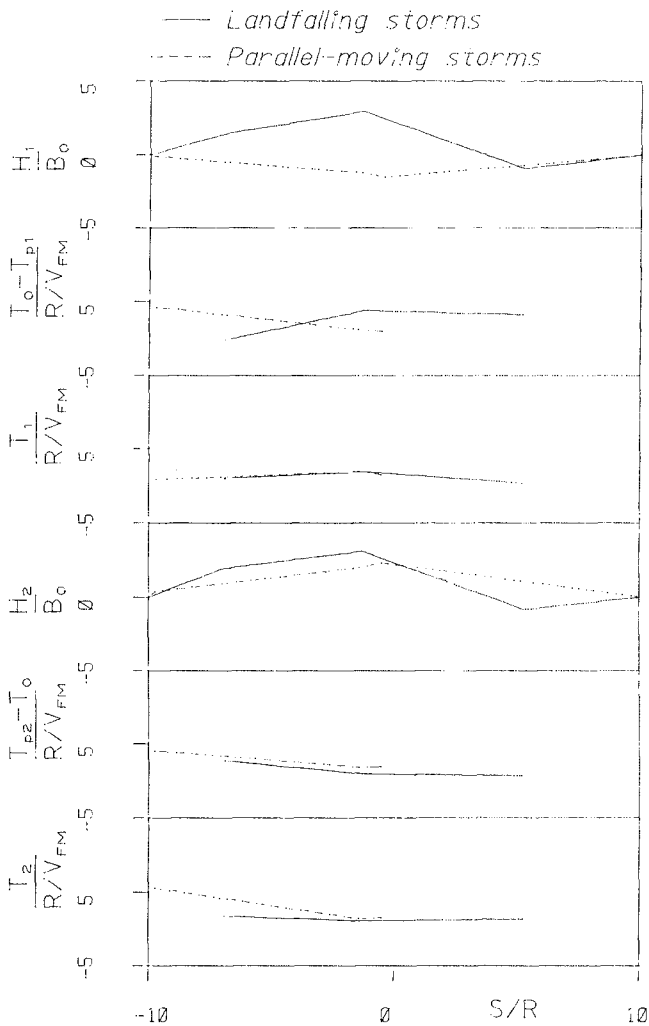

Figure 4. Dimensionless Parameters of Storm Surge Hydrographs

where H_o is the height of the M.W.L. above datum, n identifies a tidal constituent, R is the number of tidal constituents, f_n the node factor for the nth constituent, H_n the amplitude of the nth constituent, ω_n the angular speed of the nth constituent, t the local time, V_n the uniformly changing part of the phase of the nth constituent according to equilibrium theory, u_n the correction of V_n for regression of the lunar nodes, and g_n the phase of the nth constituent. The tidal constituent amplitudes and phases (H_n and g_n), determined originally by harmonic analysis from an historical data set normally of a year's duration, are appropriate for tidal prediction at both past and future time. The astronomical tide can be predicted with greater certainty than perhaps any other geophysical event in the coastal environment.

The hindcasts were completed using computer program HTIDE2 developed by the author, in which the definitions of the separate tidal constituents and the associated astronomical arguments f_n, V_u and u_n are those of Schureman (11). In a typical application the sixty-four major tidal constituents are used.

COMBINED WATER LEVEL HYDROGRAPHS

Hindcast sustained water level hydrographs have been determined from linear superposition of the hindcast astronomical tide hydrograph, the hindcast storm surge hydrograph and, where appropriate, the hindcast breaking wave setup hydrograph for a particular site. Breaking wave setup is only included for coastal sites. No attempt was made to consider any interaction among the separate components.

Figures 5 to 8 are typical results within Mermaid Sound, chosen to illustrate the scope of the technique and not the magnitude of especially extreme events. Figure 5, during Tropical Cyclone 194 (February 1948), is a good illustration of the influence of the diurnal inequality in the astronomical tide. A sustained peak surge of about 1.7 m (M.S.L. datum) coincides with an unusually low high water of +0.3 m and the total water level does not reach HAT. The immediately preceding high water reached +1.2 m and gives a good indication of the safety margin provided by the astronomical tide behaviour. Another characteristic of Figure 5 is the longer duration of the wave setup and its peaking at 0.5 m five hours or so after the peak storm surge.

Figure 6, during Tropical Cyclone 300 (March 1961), almost shows the combination of circumstances that is most dangerous, the coincidence of the peak surge, the peak wave setup and a higher high water (HHW) tide. Neither the storm

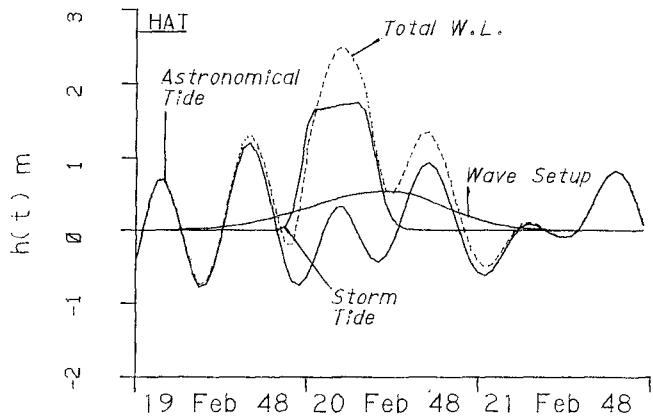

Figure 5. Hindcast Hydrographs during Tropical Cyclone 194

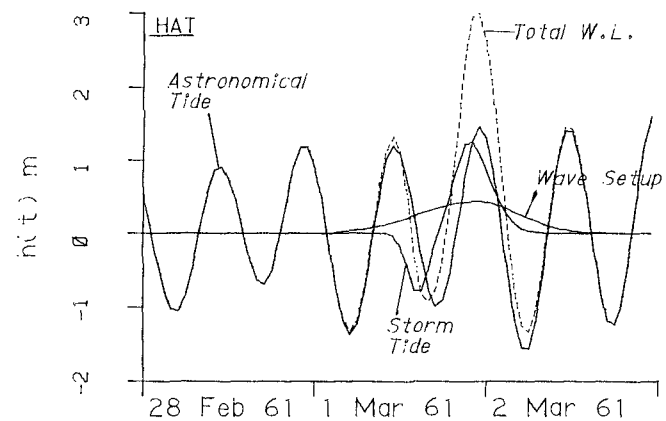

Figure 6. Hindcast Hydrographs during Tropical Cyclone 300

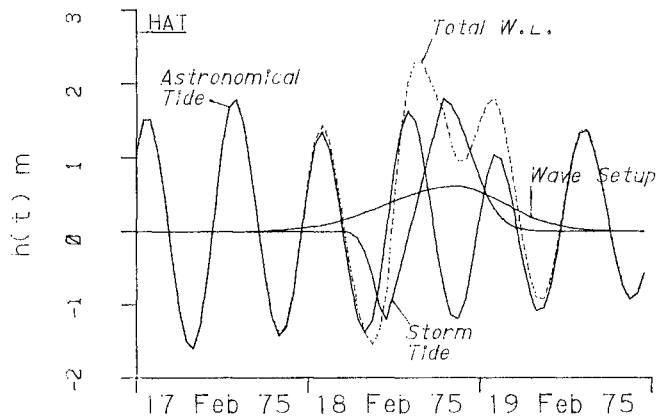

Figure 7. Hindcast Hydrographs during Tropical Cyclone TRIXIE

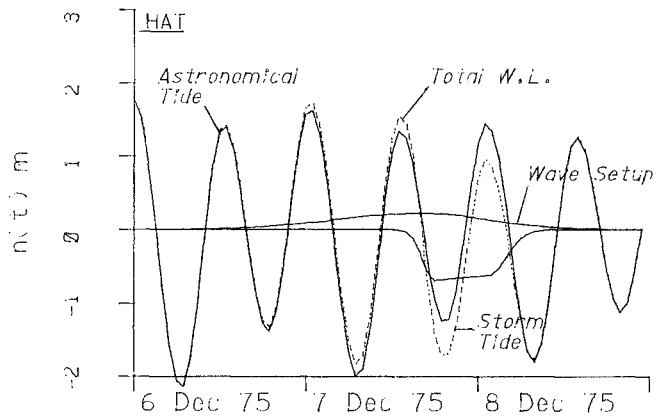

Figure 8. Hindcast Hydrographs during Tropical Cyclone JOAN

surge (+1.2 m) nor the high tide (+1.5 m) are extreme but the total water level nonetheless exceeded HAT by some 0.4 m. Another illustration of the potential safety margin inherent in the astronomical tide behaviour is provided in Figure 7, during Tropical Cyclone 448 TRIXIE (February 1975). The storm tide peaked at 1.8 m and wave setup at 0.6 m, but only an hour or two before the low tde. The maximum water level of +2.3 m is predicted some four to five hours earlier, just after a high tide of +1.6 m, and does not even reach HAT (+2.6 m, M.S.L. datum). Had the storm tide, breaking wave setup and the astronomical tide peaks all coincided a sustained water level of order +4.0 m might have been recorded, emphasising the importance of the phasing of the separate components.

The final example, Figure 8, illustrates the importance of storm track and coastal bathymetry on the storm tide and wave conditions. Tropical Cyclone 600 JOAN (December 1975) was a very significant storm whose central pressure fell to 920 mb but the storm track passed north of Mermaid Sound where predominantly offshore winds were experienced. A sustained storm setdown of order 0.7 m was hindcast in Mermaid Sound, coinciding with a low tide of -1.2 m and little wave setup. This however is perhaps a design constraint in its own right, as the drawdown level is potentially significant in the location of cooling water intakes for industrial plants, especially if the level falls below LAT (-2.6 m). The low water immediately before is -2.2 m and a major setdown at that time might have caused the total water level to fall below LAT.

CONCLUSIONS

A methodology has been demonstrated for hindcasting the total water level and wave hydrographs at a coastal site during a hurricane. It accommodates phasing of the separate components of the sustained water level hydrograph, as well as storm variability and coastal bathymetry. An intermediate cost and precision is achieved by compromising the number of complete hindcast storms, rather than the precision of the hindcast model. Dimensional analysis and the hindcast sea response from a few project storms is used to synthesise the response hydrographs for the remaining storms in the meteorological data set.

ACKNOWLEDGEMENT

Figures 5 to 8 are taken from a report prepared for Woodside Offshore Petroleum Pty. Ltd., Perth, and their permission to include this material is gratefully acknowledged.

REFERENCES

1. Bretschneider, C.L., 'A Non-Dimensional Stationary Hurricane Wave Model', Procs., 4th Offshore Technology Conference, Houston 1972, Vol. 1, pp. 51-68.
2. Borgman, L.E., 'Extremal Statistics in Ocean Engineering', Procs., Conf. Civil Engineering in the Oceans III, ASCE, 1975, pp. 117-133.
3. Freeman, J.C., Baer, L. and Jung, G.H., 'The Bathystrophic Storm Tide', Journal of Marine Research, Vol. 16, 1957, pp. 12-22.
4. Graham, H.E. and Nunn, D.E., 'Meteorological Considerations Pertinent to Standard Project Hurricane, Atlantic and Gulf Coasts of the United States', NHRP Report 33, U.S. Weather Bureau, 1959.
5. Jelesnianski, C.P., 'SPLASH (Special Program to List Amplitudes of Surges from Hurricanes) I. Landfall Storms', NOAA Tech. Mem. NWS TDL-46, 1972.
6. Kitaigorodskii, S.A., 'Physics of Air-Sea Interaction', Israel Program for Scientific Translations, Jerusalem, 1973.
7. Lee, Y.K., 'Hurricane Eloise Wave Spectra', Coastal Engineering, Vol. 4, 1980, pp. 151-156.
8. Petrauskas, C. and Aagaard, P., 'Extrapolation of Historical Storm Data for Estimating Design-Wave Heights', Journal of Society of Petroleum Engineers, Vol. 11, 1971, pp. 23-37.
9. Ross, D.B. and Cardone, V.J., 'A Comparison of Parametric and Spectral Hurricane Wave Prediction Products', Procs., NATO Symposium on Turbulent Fluxes through the Sea Surface, Wave Dynamics and Prediction, Marseille, 1978, Plenum Press, pp. 647-664.
10. Shemdin, O.H., 'Prediction of Dominant Wave Properties ahead of Hurricanes', Procs., 17th International Conference on Coastal Engineering, Sydney, 1980, ASCE, Vol. 1, pp. 600-609.
11. Schureman, P., 'Manual of Harmonic Analysis and Prediction of Tides', U.S. Coast and Geodetic Survey, Spec. Pub. 98, 1941.
12. Sobey, R.J., Discussion of Isaacson, M. de St.Q. and Mackenzie, N.G., 'Long-Term Distributions of Ocean Waves: A Review', Journal of Waterway, Port, Coastal and Ocean Division, ASCE, Vol. 108, 1982, pp. 234-235.
13. Sobey, R.J., Harper, B.A. and Stark, K.P., 'Numerical Simulation of Tropical Cyclone Storm Surge', Research Bulletin CS14, Department of Civil and Systems Engineering, James Cook University, May 1977, 311 p.
14. Sobey, R.J., Harper, B.A. and Mitchell, G.M., 'Numerical Modelling of Tropical Cyclone Storm Surge', Civil Engineering Transactions, Institution of Engineers, Australia, Vol. CE24, 1982, pp. 151-161.
15. Sobey, R.J., Mills, A.B. and Young, I.R., 'Mermaid Sound Extreme Water Level Study', Department of Civil and Systems Engineering, James Cook University, May 1979, 231 p. (unpublished report for Woodside Petroleum Development Pty. Ltd., Perth).

16. Sobey, R.J. and Young, I.R., 'A Spectral Model of Tropical Cyclone Wind Waves', sumbitted for publication July 1982.
17. Sobey, R.J., Young, I.R. and Mills, A.B., 'Hindcasting Total Water Level Hydrographs in a Tropical Cyclone Environment', Procs., 5th Australian Conference on Coastal and Ocean Engineering, Perth, 1981, Intitution of Engineers, Aust., pp. 258-262.
18. Sverdrup, H.U. and Munk, W.H., 'Wind, Sea and Swell: Theory of Relations for Forecasting', U.S. Navy Hydrographic Office, Pub. 601, 1947.
19. U.S. Army Coastal Engineering Research Center, 'Shore Protection Manual', 2nd Edition, 1975.
20. Ward, E.G., Borgman, L.E. and Cardone, V.J., 'Statistics of Hurricane Waves in the Gulf of Mexico', Procs., 10th Offshore Technology Conference, Houston, 1978, pp. 1523-1536.
21. Young, I.R. and Sobey, R.J., 'Numerical Prediction of Tropical Cyclone Wind Waves', Research Bulletin CS20, Department of Civil and Systems Engineering, James Cook University, July 1981, 378 p.

SECOND ORDER THEORY OF MANOMETER WAVE MEASUREMENT

F. BIESEL

ABSTRACT

The paper refers to pressure gage wave measurements . First order transformation of the pressure spectrum into a surface level spectrum leads to hitherto unexplained discrepancies with prototype simultaneous pressure and level measurements . Use of second order gravity wave theory allows to draw the following conclusions . Second order effects appear to give a reasonable explanation of the observed discrepancies . A complete check would require specially made wave measurements and analyses . Second order corrections do not significantly affect mean values, such as significant height, if the manometer depth is not unduly large .

1 INTRODUCTION

When measurements of irregular sea waves are carried out with an immersed pressure gage, standard procedures, based on random oscillations theory, allow to compute an estimate of the "pressure" power spectrum . With the further help of linear gravity wave theory, this spectrum can be transformed into a first approximation of the corresponding free surface spectrum .

Simultaneous measurements of pressure and surface levels have shown that this first approximation is not always satisfactory. For instance, CAVALERI (1980) found discrepancies as large as 20 % between wave spectra computed in this way and spectra computed from direct surface measurements . As a rule, wave attenuation with depth appeared to be larger than the theoretical value for the low frequency parts of the spectra and lower for the high frequency parts .

This poor agreement was rather surprising because laboratory tests, made with regular waves, have consistently shown that first order wave theory gives a very reliable estimate of the ratio between wave pressure and wave height . Non linear corrections are only necessary for large wave length to depth ratios or close to breaking wave heights .

The present paper results from an attempt to reconcile fact and theory, using second order wave formulae . This line of research may seem rather doomed beforehand as second order terms have no influence on the pressure to height ratio of "regular" waves . However, this proved not

1 General Manager of AMTEC 8,rue Jean Goujon 75008 PARIS FRANCE

to be the case for irregular waves and, actually, the second order theoretical value of these ratios may widely differ from their first order approximations .

2 NOTATIONS

The space coordinates are x,y and z . The origin is at the mean water level . The x and y axes are horizontal and the z axis is vertical upwards . The other notations are :

t time	g acceleration of gravity	Z surface elevation
H water depth	p_o atmospheric pressure	p water pressure
ρ water unit mass	$Q=(p-p_o)/(\rho \cdot g) + z$	

Random spectra are discretized into I "lines" (regular unidirectional component waves) . The ith line has the following parameters :

a_i amplitude ω_i angular frequency k_i wave number θ_i random phase

α_i angle of wave direction of propagation with positive x axis

For the theoretical outline and numerical examples, only unidirectional waves are considered (i.e. $\alpha_i=0$), moreover, spectral lines are equidistant (i.e. $\omega_i=i \cdot d\omega$, k_i being given by $\omega_i^2=g \cdot k_i \cdot \tanh[k_i \cdot H]$) .

Other parameters are defined to simplify the formulae in the text . Those relating to only one line are defined with the index "i" . Those relating to two lines are defined with indices "i,j" . These latter parameters are either what we shall call "add" type quantities, marked with a prime, or "subtract" type quantities, marked with a double prime . For both these quantities, the indices are not written except when they are different from i,j . "Add" terms exist for i=j but "subtract" terms are not used in this case .

$u_i=k_i \cdot (x \cdot \cos\alpha_i + y \cdot \sin\alpha_i) - \omega_i \cdot t + \theta_i$ $\quad u'=u_i + u_j$ $\quad u"=u_i - u_j$

$c_i= \cos u_i$	$c'= \cos u'$	$c"= \cos u"$
$s_i= \sin u_i$	$s'= \sin u'$	$s"= \sin u"$
	$k' = k_i + k_j$	$k"= k_i - k_j$
	$\omega' = \omega_i + \omega_j$	$\omega"= \omega_i - \omega_j$
		$\gamma"= \cos(\alpha_i-\alpha_j)$
$C_i= \cosh(k_i \cdot H)$	$C'= \cosh(k' \cdot H)$	$C"= \cosh(k" \cdot H)$
$S_i= \sinh(k_i \cdot H)$	$S'= \sinh(k' \cdot H)$	$S"= \sinh(k" \cdot H)$
$CZ_i= \cosh[k_i \cdot (H+z)]$	$CZ'= \cosh[k' \cdot (H+z)]$	$CZ"= \cosh[k" \cdot (H+z)]$
$SZ_i= \sinh[k_i \cdot (H+z)]$		

3 OUTLINE OF SECOND ORDER RANDOM WAVE THEORY

In this section, as mentioned above, we shall use a discretized form of random wave theory which allows numerical computations to be carried out for any spectral shape . We shall also only consider unidirectional waves, travelling in the direction of the positive x axis .

Surface elevation Z1 of such a discretized first order random wave is given by

$$Z1 = \sum_i a_i \cdot c_i$$

This means that we have replaced the continuous power spectrum by a line spectrum . We shall also assume that the spectrum lines are equidistant along the frequency axis . If the frequency step $d\omega$ tends to zero, with a proportional increase in the number of lines and decrease of the line intensities (a_i^2), the resulting motion tends to a truly random one with a spectrum density $S(\omega)$ such that

$$S(\omega_i) = a_i^2/(2 \cdot d\omega)$$

For each set of values given to the random phases θ_i we have different "realizations" of the random function Z1 but our real interest will be in the mean values, over the entire population of these realizations .

Wave elevation to the second order of approximation is given by

$$Z = \sum_i a_i \cdot c_i + \sum_i \sum_j a_i \cdot a_j \cdot B' \cdot c' + \sum_i \sum_j a_i \cdot a_j \cdot B'' \cdot c''$$

B' and B" are rather complex, therefore, their value is given in the appendix together with similar coefficients in the pressure formulae .

At any point (x,z),Z will be a sum of sine functions having frequencies of the form $n \cdot d\omega$. Each of these sine functions will itself be a sum of the nth first order term ($a_n \cdot c_n$) and of a number of second order components which will have one of the two following forms

$$a_i \cdot a_{n-i} \cdot B'_{i,n-i} \cdot c'_{i,n-i} \qquad \text{("add" terms)}$$

$$a_i \cdot a_{i-n} \cdot B''_{i,i-n} \cdot c''_{i,i-n} \qquad \text{("subtract" terms)}$$

Because of the random phase lags in these components, the average intensity A_n^2 of the nth line, in the second order power spectrum of Z, will be the sum of the squares of the components amplitudes

$$A_n^2 = a_n^2 + \sum_i (a_i \cdot a_{n-i} \cdot B'_{i,n-i})^2 + \sum_i (a_i \cdot a_{i-n} \cdot B''_{i,i-n})^2$$

Thus,starting from a "first order" power spectrum with line intensities a_n^2 , we can compute a second order spectrum with line intensities A_n^2 for the wave elevation Z .

We can do the same for the pressure variation at a depth -z . However, rather than the pressure p, we shall use the difference between p and the static pressure, divided by $\rho \cdot g$, i.e. expressed in height of water.

We shall call this quantity Q . We have a similar formula

$$Q = \sum_i q_i \cdot c_i + \sum_i \sum_j a_i \cdot a_j \cdot E' \cdot c' + \sum_i \sum_j a_i \cdot a_j \cdot E'' \cdot c''$$

where $q_i = a_i \cdot (CZ_i / C_i)$

(CZ_i/C_i) is the classical first order ratio between pressure and surface elevation for regular waves . As shown above for Z, these second order formulae allow us to compute the average intensity Q_n^2 of the nth line in the second order power spectrum of Q .

Finally, the apparent pressure reduction,for the frequency $i \cdot d\omega$,will be

$$Q_i / A_i \quad \text{instead of} \quad q_i / a_i = CZ_i / C_i$$

Following CAVALERI's example, we shall use the ratio α of these two ratios

$$\alpha = (Q_i / A_i) / (CZ_i / C_i)$$

to show the numerical results in a simple way .

4 NUMERICAL EXAMPLES

The numerical examples concern an unidirectional storm wave having a JONSWAP type first order spectrum . The peak period is 4 seconds, the peak enhancement coefficient is 5 and the significant height is 2.3 m . This spectrum is approximated by nineteen lines defined as follows

f(Hertz)	a^2 (m^2)	f(Hertz)	a^2 (m^2)
0.025	0	0.275	0.217
0.05	0	0.3	0.05
0.075	0	0.325	0.0286
0.1	0	0.35	0.0221
0.125	1.08 E-08	0.375	0.0169
0.15	0.00014	0.4	0.0129
0.175	0.0054	0.425	0.0099
0.2	0.0237	0.45	0.0077
0.225	0.083	0.475	0.006
0.25	0.235		

The water depth H is 12 meters for all examples .

Figure 1 shows the computed values of α for a manometer resting on the bottom . These values are very close to unity throughout the frequency range of the strong spectrum lines but they drop very steeply at the low frequency end . In such a case, there seems to be practically no significant error due to the neglect of second order terms .

The above spectrum was then slightly modified to incorporate some low frequency agitation such as may be due to surf beats or distant storms. For this purpose, the three first lines of the spectrum were given the

value 0.02 instead of zero . The effect on the values of α were quite significant as shown in figure 2 (thick lines) . This result was much more similar to CAVALERI's observations which are shown in thin lines on the same figure, as published in his paper, for manometer depth of the same order of magnitude . Values of α computed for manometer depth of 6 and 4 meters are shown on figures 3 and 4 together with CAVALERI's results for these depth ranges .

5 PHYSICAL EXPLANATION

A physical explanation can be briefly outlined here . We saw, in section 3, that there were two types of second order terms which we called "add" and "subtract" types . The first are chiefly higher frequency terms, because their frequency is the sum of two component frequencies. The corresponding pressure terms decrease less rapidly with depth than first order terms of the same frequency . This explains why decrease with depth is less for the higher frequencies . The reverse is true for the lower frequencies where subtract type terms decrease faster than their first order counterparts .

6 CONCLUSIONS

Second order theory of random waves appears to offer an explanation of observed discrepancies between attenuation of pressure fluctuations with depth and first order theory . More accurate checks would require to extend spectral analysis of wave records down to very low frequencies . Unfortunately, this raises difficult instrumentation problems .

Some computations were made with multi-directional waves, however, the results were not significantly different from those reported here . It would therefore seem that further investigations may be carried out with relatively "simple" unidirectional waves .

The second order formulae may be used to deduce the first order spectrum from the measured spectrum, neglecting terms of an order higher than two . Incidentally, this raises an interesting philosophical question : in which of the two surface spectra are we more interested, the first or the second order one ?

With moderate manometer depths, it would seem that, for most engineering purposes, second order corrections are not necessary because significant heights are practically unaffected . However, mean frequency of the first order spectrum may be over-estimated, chiefly when there is a sizable amount of low frequency agitation .

7 REFERENCES

CAVALERI, L. (1980) Wave Measurement Using Pressure Transducers - Oceanologica Acta Vol 3 No 3 July .
BIESEL, F. (1966) Les phénomènes du second ordre rayonnants dans les ondes de gravité - Houille Blanche No 4 .

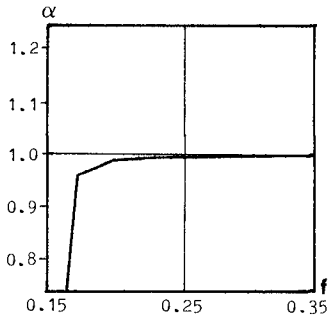

Figure 1

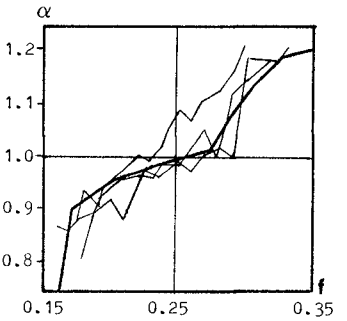

Figure 2

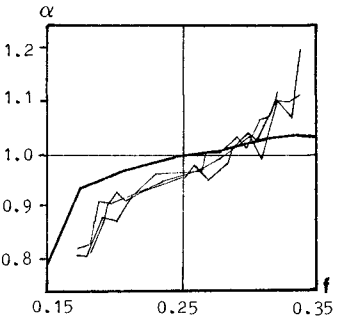

Figure 3

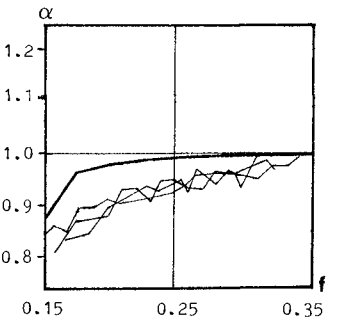

Figure 4

APPENDIX GENERAL SECOND ORDER THREE DIMENSIONAL FORMULAE

In sections 2 and 3,we restricted ourselves to unidirectional waves and to discretization with equidistant lines, but the formulae remain valid for multidirectional waves and for any other spectrum discretization . Thus, each line may represent a component wave having an amplitude, a random phase, a frequency and a direction of propagation independently defined, the sole restriction being that no two lines may have both the same frequency and the same direction . To write out the formulae, we still assume that the lines are identified by a single index varying from 1 to I .

The only information that is needed to use the formulae is the value of the second order coefficients, B' and B" for the water level Z , E' and E" for the pressure Q . We shall also define F' and F" for the velocity potential

$$\varphi = \sum_i F_i \cdot CZ_i \cdot s_i + \sum_i \sum_j a_i \cdot a_j \cdot F' \cdot CZ' \cdot s' + \sum_i \sum_j a_i \cdot a_j \cdot F'' \cdot CZ'' \cdot s''$$

where $F_i = a_i \cdot \omega_i / (k_i \cdot S_i)$

The formulae given for F' and F" are taken from BIESEL (1966), with a few changes in notation . Formulae for B',B",E' and E" may be deduced from the latter in a classical way .

$$F' = [\omega_i^3 \cdot S_j / S_i + \omega_j^3 \cdot S_i / S_j + 2 \cdot \omega_i \cdot \omega_j \cdot \omega' \cdot (C_i \cdot C_j \cdot \gamma - S_i \cdot S_j)] / D'$$

where $D' = 2 \cdot S_i \cdot S_j \cdot (\omega'^2 \cdot C' - g \cdot k' \cdot S')$

$$F'' = [\omega_i^3 \cdot S_j / S_i - \omega_j^3 \cdot S_i / S_j + 2 \cdot \omega_i \cdot \omega_j \cdot \omega'' \cdot (C_i \cdot C_j \cdot \gamma + S_i \cdot S_j)] / D''$$

where $D'' = 2 \cdot S_i \cdot S_j \cdot (\omega''^2 \cdot C'' - g \cdot k'' \cdot S'')$

$$B' = F' \cdot k' \cdot S' / \omega' + [k_i \cdot \omega_i \cdot C_i / S_i + k_j \cdot \omega_j \cdot C_j / S_j + (k_i \cdot \omega_j \cdot C_j / S_j + k_j \cdot \omega_i \cdot C_i / S_i) \cdot \gamma] / 2\omega'$$

$$B'' = F'' \cdot k'' \cdot S'' / \omega'' + [k_i \cdot \omega_i \cdot C_i / S_i - k_j \cdot \omega_j \cdot C_j / S_j + (k_i \cdot \omega_j \cdot C_j / S_j - k_j \cdot \omega_i \cdot C_i / S_i) \cdot \gamma] / 2\omega''$$

$$E' = F' \cdot \omega' \cdot CZ' / g - \omega_i \cdot \omega_j \cdot (CZ_i \cdot CZ_j \cdot \gamma - SZ_i \cdot SZ_j) / (2 \cdot g \cdot S_i \cdot S_j)$$

$$E'' = F'' \cdot \omega'' \cdot CZ'' / g - \omega_i \cdot \omega_j \cdot (CZ_i \cdot CZ_j \cdot \gamma + SZ_i \cdot SZ_j) / (2 \cdot g \cdot S_i \cdot S_j)$$

Note : In the double sums, the terms having indices i and j are equal to those having indices j and i . The above coefficients are doubled so that each pair of values i and j must be taken into account only once and, for "add" terms, when i=j, these coefficients must be divided by two .

HEIGHT DISTRIBUTION OF ESTUARINE WAVES

V. Barthel, Dr.-Ing.[1]

ABSTRACT

A field investigation program on waves was carried out in the Weser estuary, German Bight of the North Sea. Wave height and period distributions in this complicated wave climate can be approximated by a Rayleigh distribution. Empirical distributions of the wave heights characterise the different regions of the estuary. The presence of wave grouping as well as the group bounded long waves are shown in a few examples. The necessity of further investigations and analysis is highlighted.

1. INTRODUCTION

The necessity to gain more knowledge about the sea state has become increasingly important with growing demands, especially of the offshore industry, within the last few decades. Not only the needs for basic research work on wave dynamics but the necessity of field data and a fast evaluation of significant values derived even from fragmentary records or visual estimates is evident. This task seems to be simple when dealing ideally with straight shore lines and gradually decreasing water depths.

However, waves travelling from the open sea into shallow water areas of an estuary with a irregular topography and a pattern of deep channels, submerged bars, tidal flats and gullies are modified by shoaling, refraction, diffraction and even reflection processes. Combined with locally generated wind waves a very complex wave climate occurs, to which at a first glimpse hardly any of the existing theories or analysis procedures can be applied.

In 1975 a field investigation program was started in the Weser estuary which is part of the German Bight of the North Sea (Fig. 1). It was designed in order to gain information about the existing wave climate and therefore create a basis for the design of all coastal structures and the development of wave prediction methods.

The mouth of the river Weser opens into a V-shaped estuary with a width of approximately 2 km at its origin and more than 20 km at its transition to the open sea. The main channel divides into two branches in the inner wadden area where wave action is of minor importance for morphological stability. The first impact of waves is to be recognized

[1]Dr.-Ing., Federal Waterways Administration, F.R. Germany; present address: Hydraulics Lab., National Research Council Canada, Ottawa, Ontario K1A 0R6, Canada

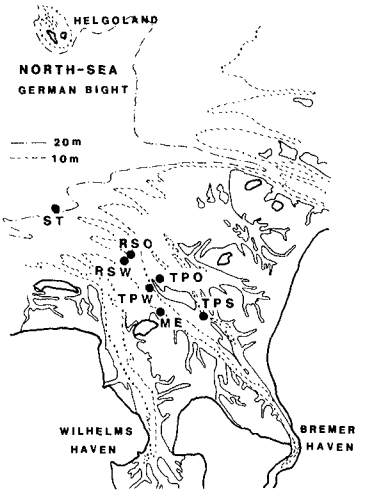

FIG. 1 WESER ESTUARY, GERMAN BIGHT, NORTH SEA
-LOCATIONS OF MEASUREMENTS-

at the edge of the wadden area. Then the major channel is again divided into two branches cutting through the reef region. In this area a strong littoral drift crosses the estuary and causes continuous shifting of bars and channels (1).

To be able to record conditions for typical regions of the estuary the wave recording stations were arranged in deep water (ST), in the reef region, at the edge of a deep channel (RSW), behind a submerged bar (RSO), in the wadden area in the main channel (TPW), in front of (TPO, ME) and behind (TPS) tidal flats.

The locations ST, RSW, RSO and TPW, the results of which are mostly being discussed in the following, were equipped with waverider buoys. Records of 20 min length of each station were stored on digital tape every 80 minutes. Wind measurements were taken on a centrally located lighthouse near RSW.

2. STATISTICAL ANALYSIS

The results of this investigation were to be used for different purposes, i.e. design of offshore and coastal structures and for wave prediction as a basis for the assignment of special ships (dredges, barges, etc.). Therefore, an extended analysis was performed on part of the data, which, among others, included spectral analysis, parameterization of multi-peak spectra and thereby separation of superimposed wave systems. Most of the results are presented in (2), (3) and (4). Since this procedure turned out to be very time-consuming and therefore costly, a simplified method was applied. By evaluating height and

period distributions significant values could be defined. Knowledge about ratios or distributions of different wave parameters allows estimating significant values from a fragmentary record or visual observations. Measured values from a reference station can be transferred to different regions of the estuary.

2.1 Wave Height Histograms

Subsequently the zero-up-crossing wave heights of every record were checked for their possible correspondence with one of the customary theoretical distributions:

a. the normal (Gaussian) distribution (N)
b. the log-normal distribution (NL), which is mostly applied for very long time series (16)
c. the Rayleigh distribution (R)

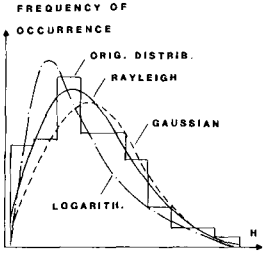

FIG. 2 WAVE HEIGHT DISTRIBUTION

The various possibilities in terms of histograms are shown in Fig. 2.

Fig. 3 shows the comparison for 20-min records of four stations. To find the best correspondence with a theoretical distribution the CHI^2 test, a stringent statistical method, was applied. To summarize the results of most of the 20-min time series obtained with wind coming from two prevailing sectors SW-NW and N-SE, Table 1 shows the percentage of records with a correspondence to the theoretical distributions (col. 2-4). The average probability of correspondence for the best fit (maximum percentage of records) is given in col. 5 whereas col. 6 shows the percentage of records without any theoretical fit. Finally, cols. 7 and 8 show the assignment of the records to periods of flood or ebb current. Percentages not adding up to 100% show that some of the records could not be assigned to either of the tidal phases. From this table it can be concluded that although there is some correspondence with the normal distribution the most likely theoretical one is the Rayleigh distribution. Others are negligible. Obviously the winds

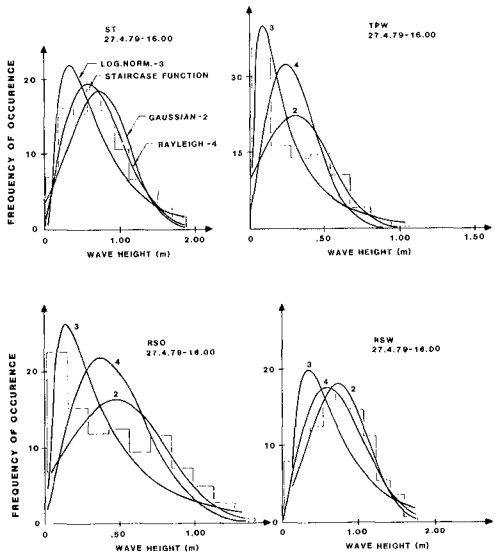

FIG. 3 HEIGHT DISTRIBUTION OF ESTUARINE WAVES

1	2	3	4	5	6	7	8
LOC.	PERC. OF REC. WITH CORRESPONDENCE TO (%)			PROBAB. OF BEST CORR. (%)	REC WITHOUT CORR. (%)	R (%)	
	N	NL	R			E	F
ST	11	-	48	14	61	28	62
	-	-	6	20	94	50	50
RSW	24	1	80	22	24	39	52
	42	1	82	29	15	42	58
RSO	22	1	64	23	37	50	50
	18	9	50	29	26	36	64
TPW	3	0	47	22	53	24	76
	7	2	37	33	61	27	73

TABLE 1 CORRESPONDENCE WITH THEORETICAL DISTRIBUTIONS
- WAVE HEIGHTS -

coming from the north-easterly sector show better results, but there is no evidence that deep water location-distributions (ST) have a better fit than those in shallower regions. It has to be mentioned that a percentage likelihood of 25% visually (Fig. 2) means a satisfactory correspondence of staircase function and theoretical function.

Tidal currents influence the height distributions especially at locations where tidal currents are concentrated in the main channel. The better correspondence can be found with currents and waves travelling in the same direction. The influence of currents on wave heights and periods has been discussed in (3).

3.2 Probability Distributions

Already in 1952 Longuet-Higgins (11) pointed out that for a narrow spectrum measured in deep water wave height distributions could be approximated by a Rayleigh distribution. In the meantime it has been mentioned by several authors that Rayleigh fits even broader spectra and is often valid for shallow water waves too. Since the Rayleigh distribution was derived on the basis of a narrow spectrum, it seems to be very likely that for a case of superposed wave systems this theoretical distribution must lie somewhere in between over- and underprediction due to the specific location of measurement. To evaluate this range, typical series of measurements taken either during flood or ebb tide were compared with the theoretical cumulative proportional probability

$$p(\eta) = 1 - e^{\frac{-\pi}{4}\eta\alpha} \qquad \text{with} \quad \eta = \frac{H}{\overline{H}}$$

where the wave height H is normalized with respect to the average wave height $\overline{H}$. In case of a Rayleigh distribution $\alpha=2$.

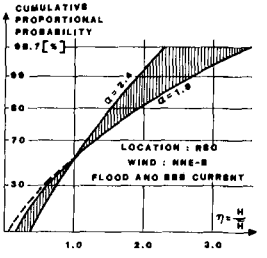

FIG. 4 WAVE HEIGHT DISTRIBUTION

$$p\left(\frac{H}{\overline{H}}\right) = 1 - e^{-\frac{\pi}{4}\left(\frac{H}{\overline{H}}\right)^{\alpha}}$$

It appeared that the cuves ranging in between the boundaries of Fig. 4 were not very smooth and intersected especially in times of changing tide (flood to ebb current and vice versa). However, typical values for the exponent α could be assigned to the various locations of the estuary. Table 2 summarizes the results.

CUMULATIVE PROPORTIONAL PROBABILITY:

$$p(\eta) = 1 - e^{-\frac{\pi}{4}\eta^{\alpha}} \qquad \eta = \frac{H}{\bar{H}} = \frac{H}{H_{AVE}}$$

OPEN SEA (LOC. ST):	$\alpha_F = 2.0$ $\alpha_E = 1.9$
REEF REGION (LOC. RSW):	$\alpha_F = 2.2$ $\alpha_E = 1.95$
REEF REGION (LOC. RSO): (SIT. LEE OF REEF)	$\alpha_F = 1.95$ $\alpha_E = 1.85$
TIDAL FLATS (LOC. TPW/TPO): (SIT. IN A TIDAL GULLY)	$\alpha_F = 1.8$ $\alpha_E = 1.7$

TABLE 2
PROBABILITY EXPONENTS α FOR DIFFERENT REGIONS OF THE WESER ESTUARY
F = FLOOD CURRENT E = EBB CURRENT

It appears that the exponents for flood currents (waves propagating with current) are bigger than the values for ebb conditions (waves propagating against currents). This was only different in a few cases with very strong southerly winds.

Based on these relationships and on the statistics which Longuet-Higgins (11) derived from the Rayleigh distribution or on an approximation of that given by Schüttrumpf (20), relationships between various wave height parameters like H_{MAX}, $H_{1/10}$, $H_{1/3}$ and H_{AVE} can be calculated using the number of waves in a record. According to this the following values were obtained as an average for the whole estuary:

$$H_{1/3}/H_{AVE} = 1.62$$
$$H_{MAX}/H_{1/3} = 1.88$$

2.3 Wave Periods

A comparable analysis was performed on the wave periods too.

1	2	3	4	5	6	7	8
LOC.	PERC. OF REC. WITH CORRESPONDENCE TO (%)			PROBAB. OF BEST CORR. (%)	REC WITHOUT CORR. (%)	R (%)	
	N	NL	R			E	F
ST	21	-	43	20	54	52	48
	8	-	28	13	70	73	27
RSW	45	9	66	26	20	45	55
	6	15	67	21	27	50	50
RSO	30	5	57	21	34	48	52
	18	13	51	22	33	45	55
TPW	10	23	46	21	36	39	61
	-	37	30	18	42	46	54
1	2	3	4	5	6	7	8

TABLE 3 CORRESPONDENCE WITH THEORETICAL DISTRIBUTIONS - WAVE PERIODS

Table 3 shows the comparison of the results of the same four locations in the estuary as given in Table 1. It appears again that the probability of the correspondence with a Rayleigh distribution is higher than others. Although the results seem to be comparable with those from height distributions, the scattering of cumulative probability curves did not allow an assignment of typical distributions to the different regions of the estuary which could lead to the calculation of maximum values of wave periods. During a storm tide in the inner estuary the significant wave period was measured to exceed

$$T_{1/3} > 15 \text{ s}$$

and the maximum value reached

$$T_{MAX} = 18.2 \text{ s}$$

These values were obtained by wave gauges and could not be verified by waverider recordings. The limitation of the waverider buoy for long period waves is a distinct disadvantage for respective investigations.

3. LONG WAVE ANALYSIS

3.1 Grouping of Waves

In recent years it has become more and more accepted that,especially in shallow water, waves tend to form groups which heights exceed a specified wave height, i.e. $H_{1/3}$ or H_{AVE}. The concentration of energy in wave groups could be critical for structures especially if the frequencies involved lie within the range of the characteristic or eigenfrequency of the structure. Ships or other floating structures can respond in a resonant rise. Investigations of grouping phenomena for the Weser estuary using the number of consecutive waves with a height $H_i > H_s$ have been performed by Barthel (2) and for other regions in the North Sea by Siefert (21) and Rye (17). All those seemed to match suggestions by Goda (10) based on theoretical considerations. Descriptions of wave grouping using the envelope of a time series of water surface elevations were given by Nolte and Hsu (14). This method, which simply connects peaks and troughs to indicate the presence of groups, seems to be a rather rough interpretation. Regarding the concentration of energy in a wave group, Funke and Mansard (8) presented the SIWEH-function (SIWEH = Smoothed Instantaneous Wave Energy History). This function

$$E(t) = \frac{1}{T_P} \int_{\tau=-T_P}^{T_P} \eta^2(t+\tau) \cdot Q_1(\tau) d\tau \quad \text{for } T_p \leq t \leq T_n - T_p$$

where T_n = length of the finite wave record
T_P = peak period of the spectrum
$Q_1(\tau)$ = smoothing window which acts as a low pass filter

describes the distribution of energy along the time axis with energy defined as the square of water surface elevations.

The description of the groupiness of a time series of the sea state is given by the dimensionless groupiness factor

$$GF = \frac{\sqrt{m_{0\varepsilon}}}{m_0}$$

where $m_{0\varepsilon}$ = zeroth moment of the SIWEH spectral density
m_0 = zeroth moment of the short wave spectrum.

This factor describes the standard deviation of the instantaneous wave energy about its mean. GF=.9 indicates a highly grouped sea state. GF-values up to 1.1 have been recorded. Typical values range between .5 and .8. Other important factors are the group repetition period, the length of the group and the variation of the group repetition period. A description of groupiness in terms of the SIWEH spectral density is given in Funke and Mansard (8).

In order to define grouping properties of estuarine waves a preliminary analysis using the SIWEH-function and calculating the groupiness factor was applied on a limited number of records. Fig. 5

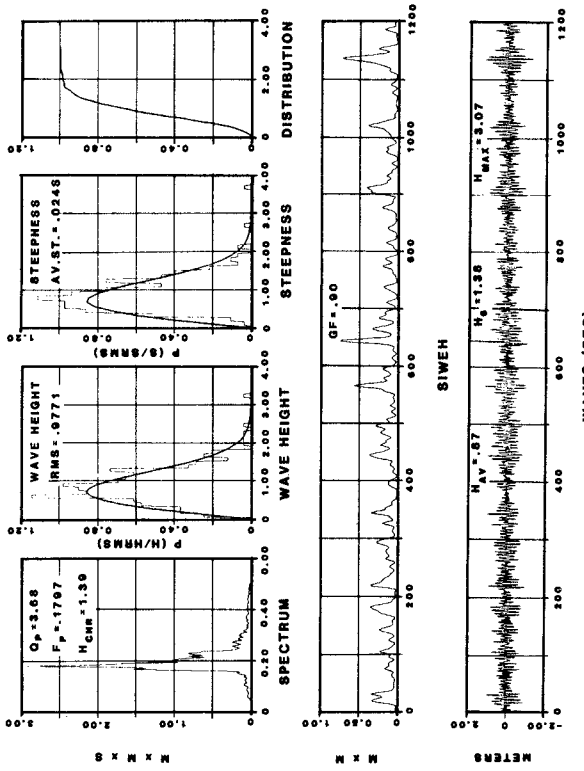

FIG.5 WESER DATA ANALYSIS - LOC. ST 23.4.80 - 17.40

shows an example of the results of the general analysis procedure. This time series recorded at location ST in relatively deep water at wind velocities of 12 m/s already shows distinct wave groups with a high groupiness factor of GF = .9. Wave heights as well as steepness fit visually quite well to the theoretical (Rayleigh) distribution. The variance spectral density shows a single peak spectrum with some energy contents in the low frequency region.

In Fig. 6 different wave parameters are plotted versus time for three locations in the estuary for one recorded long time series

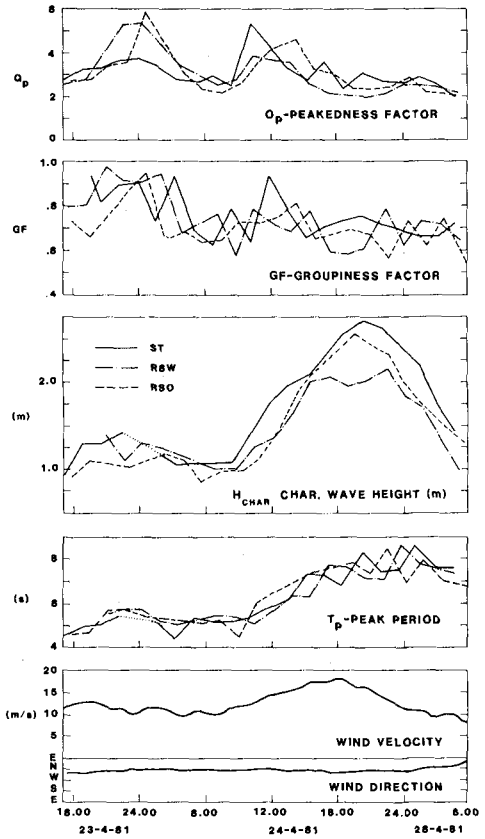

Fig. 6 WAVE PARAMETERS Q_p, GF, H_{CHAR} T_p WESER ESTUARY-ST-23.-25.4.81

available for this analysis. While characteristic wave heights and peak periods follow increasing and decreasing wind velocities nicely, it seems that the groupiness factor GF varies without any correlation to wind and other wave parameters. However, the time variations of the peakedness factor

$$Q_p = \frac{2}{m_0} \int_0^\infty f[S(f)]^2 \, df$$

which was introduced by Goda (9) seem to coincide somewhat with those of the groupiness factor GF. Both parameters grow with increasing wind up to a certain extent and then decrease again which agrees with observations of Rye (7) as far as the formation of groups is concerned. Though wave group formations were found to be more pronounced for a narrow, sharply peaked spectrum (Rye (18), Goda (10)), an interdependency of Q_p and GF could neither be detected in model studies (a synthesised spectrum can keep its shape for different groupiness factors) nor in the analysis of prototype data (13) so far. Spectral peakedness factors Q_p are plotted versus groupiness factors GF in Fig. 7 for the three locations under discussion. In spite of the scatter a distinct trend seems to indicate a relationship. The correlation coefficients are Rxy = 0.75-.78. However, this phenomenon has to be investigated for more records under different conditions.

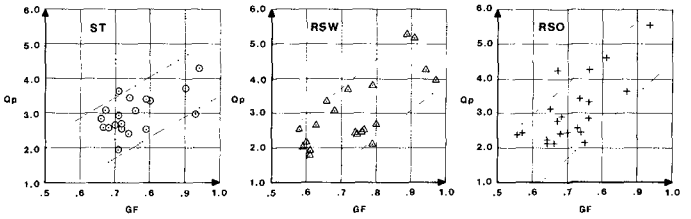

PEAKEDNESS Q_p VERSUS GROUPINESS GF
- WESER DATA -

GROUPINESS FACTOR (FUNKE & MANSARD , 1979) $GF = \sqrt{m_{0s}}/m_0$

PEAKEDNESS FACTOR (GODA , 1970) $Q_p = \frac{2}{m_0^2} \int_0^\infty f(S(f))^2 \, df$

Fig. 7 PEAKEDNESS Q_p VERSUS GROUPINESS GF
- WESER DATA -

4.2 Bounded Long Waves

Due to radiation stress, wave groups generate a group bounded long wave. This long wave typically appears as a setdown under the group and a setup in between the groups (Fig. 8) as shown by Longuet-Higgins and Steward (12) for groups of regular waves. As these long waves can

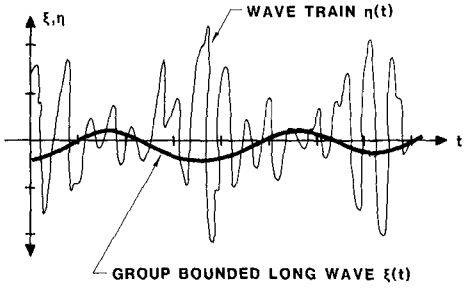

Fig. 8 GROUP BOUNDED LONG WAVES
- DIAGRAMMATIC SKETCH -

excite slow drift oscillations of moored structures and travelling ships or cause harbour resonance, their detection in a record, or rather in the spectrum, is of major importance. Unfortunately, many of the customary wave measuring devices are not capable of picking up these low frequency elevations among the short waves. The commonly used waverider buoy attenuates the output for frequencies below .1 Hz so that a compensation function has to be used. Somewhere between .06 and .05 Hz the instrument fails to record low frequencies. In order to estimate the amount of long wave energy present in prototype data recorded by similar instruments the long wave energy or long wave surface elevations have to be calculated. Bowers (6) and Dean and Sharma (7) used the Laplace-equation to define these second order waves. Another definition, based on the momentum equations, has been given by Ottesen-Hansen (15).

The various long wave components are computed using the Fourier coefficients of the primary wave train. Basically, each pair of frequencies resp. Fourier coefficients generates a long wave contribution. Hence the second order surface elevation becomes

$$\zeta_{nm}(t) = G_{nm}(f,\Delta f)[(a_n a_m+b_n b_m)\cos(\Delta\omega_{nm}t) + (a_m b_n-a_n b_m)\sin(\Delta\omega_{nm}t)]$$

with G_{nm} being the transfer function given by Ottesen-Hansen (15) and discussed by Sand (19).

4.3 Long Waves in Natural Wave Trains

As mentioned before, low frequency oscillations can be dangerous for floating structures. Especially vessels travelling in confined channels of an estuary with a limited water depth could be affected by groups of higher waves as well as by the group bounded long wave dependent on its height and repetition period. In order to get an idea about possible amplitudes and periods of these long waves, two 20-minute records were analysed with respect to long wave energy contents.

The following analysis procedure was used:

a. Fourier analysis is performed on the prototype wave train after application of a band pass filter.

b. All Fourier components for frequencies smaller than a given lower cut-off frequency and all components with an amplitude smaller than a given threshold are set equal to zero.

c. Fourier components of the bounded long wave are computed using the equations of Ottesen-Hansen (15) and Sand (19).

d. Inverse Fourier-transform is applied.

e. Superposition of short and bounded long wave train.

f. Spectral analysis.

g. Zero-crossing analysis on short and long wave train.

The program used for this purpose was developed in the Hydraulics Laboratory of the National Research Council Canada.

Fig. 9 shows the results of a record, obtained at location RSO (water depth = 8.0 m), with a groupiness factor GF = .90. The bounded long wave which is superimposed to the short wave train shows a distinct setdown under the wave groups. Spectral analysis was performed on the original wave train as well as on the superposed wave train (original + calculated bounded long wave). The encircled part in the spectrum on the right hand side was enlarged to show the difference in the low frequency part of the spectrum. From this it can be concluded that the energy contents in the low frequency part is considerably increased by taking the bounded long wave into account. This becomes more obvious by comparing the RMS-values, which were calculated separately for a certain low frequency range, where RMS_M refers to the measured and RMS_C to the superposed wave train. Zero-crossing analysis on both the measured wave train and the calculated bounded long wave yield the wave parameters $\overline{H} \triangleq H_{AVE}$, H_S and H_{MAX} as well as the mean period of the bounded long wave. Under the given conditions already a long wave with maximum height of .17 m and a mean period of 36 s can appear.

Since prototype records with more severe conditions were not at hand for this analysis, a wave train measured off the coast of Newfoundland, Canada, was applied to a water depth found at loc. ST in the Weser estuary. Wave heights and periods of comparable order of magnitude have been recorded at this location before.

Fig. 10 shows the results of the above mentioned analysis on this wave train with a groupiness factor of GF = .94. It appears again, that the superposition with the calculated bounded long wave adds a considerable amount of energy in the low frequency part of the spectrum indicated by the RMS-values which have been calculated only up to .05 Hz. A long wave with a mean wave height of .37 m and a maximum of .65 m

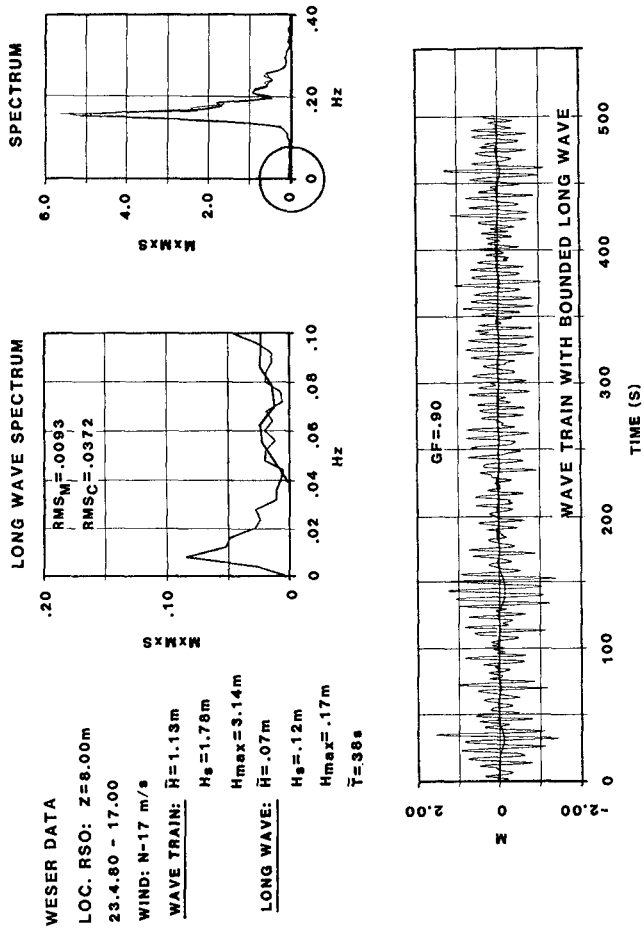

FIG.9 BOUNDED LONG WAVES IN NATURAL WAVE TRAINS

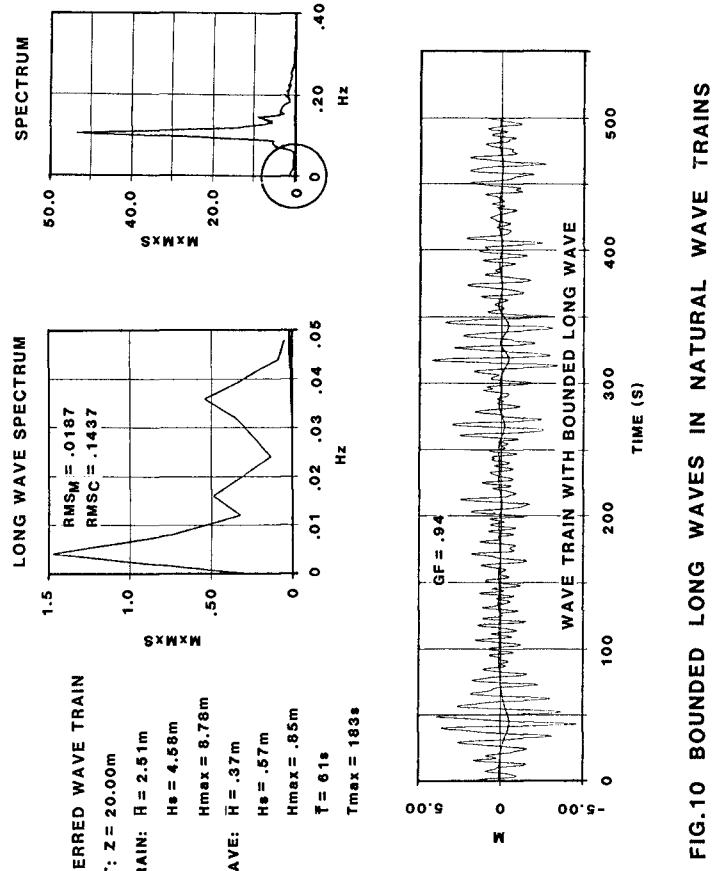

FIG.10 BOUNDED LONG WAVES IN NATURAL WAVE TRAINS

is present under these wave conditions. The mean period is 61 s whereas the maximum period goes up to 183 s. Typically these long waves tend to be stable and travel with the group velocity as long as the group is not attenuated, i.e. by breaking. According to model studies which have recently been done in the Hydraulics Laboratory of the National Research Council of Canada (5), it is very likely that these long waves are partly reflected on shoals. However, in deep channels they will propagate and penetrate into the inner estuary.

It is not yet known to what extent these long waves can affect the motion of travelling vessels. However, it has to be expected that, especially in confined shipping channels with a restricted water depth, a sudden increase of the draught or rather decrease of available water depth connected with grouped wave impact and in addition to squat, can lead to dangerous situations.

Analysis of all available records obtained in critical areas with respect to long wave activity is recommended.

5. CONCLUSIONS

Extended statistical analysis was performed on prototype data obtained in the Weser Estuary mostly with waverider buoys. Height and period distributions of 20-minute records were checked for their correspondence with theoretical distributions. The results permitted the following observations:

- Height and period distributions more likely follow a Rayleigh distribution than others.

- Modified empirical height distributions related to the Rayleigh distribution could be assigned to different regions of the estuary permitting the evaluation of different wave height parameters.

Further analysis using the SIWEH-function (8) and calculation of second order waves highlighted the presence of wave grouping in estuarine waves and the group bounded long waves. The findings suggest that

- in spite of a complex wave climate, grouping can be detected in this area,

- the spectral peakedness seems to be correlated to the groupiness factor,

- the group bounded long wave component, which has not been recorded, can be found and re-established by special analysis techniques.

Further research has to be performed on the long wave problem, including long wave statistics after analysis of all available data. In an additional project the influence of these long waves on travelling vessels ought to be investigated.

6. ACKNOWLEDGEMENTS

The field investigations were carried out during the author's employment with the German Federal Waterways Administration, Wasser-u. Schiffahrtsamt Bremerhaven, and supported by the German Ministry of Research and Technology (BMFT) via the German Coastal Engineering Board (KFKI). Further analysis was done in the Hydraulics Laboratory of the National Research Council Canada. The author would like to thank the management of all those institutions and the "Hafenbautechnische Gesellschaft, Hamburg" for support in presenting this paper at the 18th Conference on Coastal Engineering in Cape Town, South Africa.

7. REFERENCES

1. Barthel, V.: Stability of Tidal Channels Due to River Improvement Measures, Proc. 15th Conf. on Coast. Eng., Honolulu, Hawaii, 1976.

2. Barthel, V.: Analysis of Storm Tide Waves, Proc. 16th Conf. on Coast. Eng., Hamburg, 1978.

3. Barthel, V.: Seegang in einem Ästuar am Beispiel der Aussenweser, Dissertation, Die Küste, H. 35, 1980.

4. Barthel, V.: Wave Energy Distribution in an Estuary, Proc. 17th Conf. on Coast. Eng., Sydney, 1980.

5. Barthel, V. et al: Verification of Group Bounded Long Waves in Physical Models, submitted to Ocean Engineering, 1983.

6. Bowers, E.C.: Long Period Disturbances Due to Wave Groups, Proc. 17th Conf. on Coast. Eng., Sydney, Australia, 1980.

7. Dean, R.G. and Sharma, F.N.: Simulation of Wave Systems Due to Non-Linear Directional Spectra, Proc. Hydrodyn. in Ocean Eng., 2, Trondheim, Norway, 1981.

8. Funke, E.R. and Mansard, E.P.D.: On the Synthesis of Realistic Sea States in a Laboratory Flume, National Research Council Technical Report LTR-HY-66, Ottawa, Canada, 1979.

9. Goda, Y.: Numerical Experiments on Wave Statistics with Spectral Simulation, Report of the Port and Harbour Res. Inst., Vol. 9, No. 3, 1970.

10. Goda, Y.: On Wave Groups, Proc. Conf. Behaviour of Offshore Structures, Trondheim, Norway, 1976.

11. Longuet-Higgins, M.S.: On the Statistical Distribution of the Heights of Sea Waves, Journ. Marine Research, 11(3), 1952.

12. Longuet-Higgins, M.S. and Stewart, R.W.: Radiation Stresses in Water Waves, a Physical Discussion with Application, Deep Sea Res., No. 11, 1964.

13. Mogridge, G.R., Funke, E.R., Baird, W.F. and Mansard, E.P.D.: Analysis and Description of Wave Energy Resources, Proc. Hydrodyn. in Ocean Eng., Trondheim, Norway, 1982.

14. Nolte, K.G. and Hsu, F.H.: Statistics of Ocean Wave Groups, Proc. 4th Annual Offshore Technology Conference, Houston, OTC 1688, 2, 1972.

15. Ottesen-Hansen, N.E.: Long Period Waves in Natural Wave Trains, Prog. Report 46, Inst. for Hydrodyn. and Hydraulic Eng., Techn. Univ. Denmark, 1978.

16. Ploeg, J.: Wave Climate Study Great Lakes and Gulf of St. Lawrence, National Research Council Technical Report MH-107A, Ottawa, Canada, 1971.

17. Rye, H.: Wave Group Formation Among Storm Waves, Proc. 14th Conf. on Coast. Eng., Copenhagen, Denmark, 1974.

18. Rye, H.: The Stability of Some Currently Used Wave Parameters, Coast. Eng., 1, Amsterdam, 1977.

19. Sand, S.E.: Long Wave Problems in Laboratory Models, Journal of Waterways, Port, Coastal and Ocean Engineering, ASCE, Vol. 108, WW4, 1982.

20. Schüttrumpf, R.: Über die Bestimmung von Bemessungswellen für den Seebau am Beispiel der südlichen Nordsee, Mitt. Franzius-Institut d. Techn. Universität Hannover, H.39, 1973.

21. Siefert, W.: Consecutive High Waves in Coastal Waters, Proc. 15th Conf. on Coast. Eng., Honolulu, Hawaii, 1976.

ANALOGOUS DISPERSION PROPERTIES OF SURF ZONE AND ELECTROMAGNETIC WAVES

by
FRITZ BÜSCHING [1)]

ABSTRACT

Resonant interaction processes in the surf zone are marked by an anomalous dispersion property ($dc/df > 0$) as it is well known from resonance absorption processes of electromagnetic waves in dielectrics.

INTRODUCTION

At least since 1974 there has been an increasing number of publications dealing with so-called anomalous dispersion properties observed from deepwater wind waves (RAMAMONJIARISOA and COANTIC, 1976; LAKE and YUEN, 1978) as well as from waves in areas of transitional and shallow water depth (MASSEL and CHYBICKI, 1980; BÜSCHING, 1978). Most of the respective experiments are carried out by estimating the cross correlation or the cross spectral density functions from the signals of some wave gauges placed in the wave field appropriately.

From investigations in a large wind-water facility for deepwater wind waves for instance the most striking departure from theoretical values consists in the phenomenon of nondispersiveness $dc/df = 0$ especially at "phase-locked" higher frequency components with phase velocities close to the dominant wave celerity, see Fig. 1. There is, however, another deviation to be seen describing an anomalous dispersion $dc/df > 0$ in the low frequency range coincident with rather small energy

---

Lecturer and Chief Engineer, Dr.-Ing., Leichtweiss-Institute, Dept. Hydrodyn. and Offshore Eng., Techn. Univ. Braunschweig, Federal Republik Germany

densities. By contrast, the author's privious field investigations in the surf zone at heavy storm surge conditions have shown an anomalous dispersion property dc/df > 0 in the whole energy containing frequency range (BÜSCHING, 1978 a).

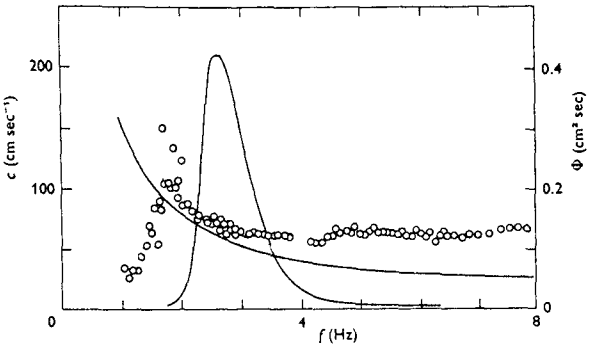

Fig. 1: The variation in phase speed of spectral components measured by RAMAMONJIARISOA (1974). The theoretical phase speed $c = g/2\pi f$ and the spectral shape are also shown.

The anomalous dispersion of low frequency components in "deepwater" wind wave spectra is often attributed to the presence of wave groups travelling with the appropriate group velocity (PHILLIPS, 1978). It is, however, doubted by the author whether the longer period frequency components can really be regarded as deepwater components even in a "large" wind-water facility, and moreover it is questionable whether it can be distinguished between phase velocities on the one hand and group velocities on the other hand both in the same plot based on spectral analysis. In the following it will be demonstrated that resonant interaction effects are responsible for an anomalous dispersion property to occur in the very shallow portion of the surf zone. The present contribution refers to measurements priviously evaluated in detail by the author, see BÜSCHING (1978 b).

ANOMALOUS DISPERSION OF SURF ZONE WAVES

Frequency Domain Data

In the upper parts of figures 2 and 3 two sets of synchronously measured energy spectra of water level deflexions are to be seen both characterizing different wind and water depth conditions at stations 100 m and 85 m distant from the shoreline respectively in a coast perpendicular measuring profile on the isle of SYLT/North Sea.

Although that measurements had been carried out at heavy storm surge conditions coherence $\overline{\gamma^2}$ is quite good at the energy containing frequency components (about $\overline{\gamma^2} = 0.8$ and $\overline{\gamma^2} = 0.7$ respectively). In this cases the phase velocity was calculated from the phase information of the transfer functions plotted below.

As to be seen from the graph at high coherence values the phase information can very well be approximated by a linear regression

$$\Phi(f) = \Phi_n + \alpha \cdot f \tag{1}$$

in which $\alpha \cdot f$ is due to the distance of the two measuring stations $\Delta x = 15$ m, and it can be shown from the conversion into phase velocity applying

$$c(f) = \frac{\Delta x \cdot 360^0}{\Phi(f)} \cdot f \tag{2}$$

that the magnitude of the positive portion of Φ_n decides on the degree of the anomalous dispersion property $dc/df > 0$.

As was found by the author in 1978 the anomalous dispersion gets more distinct with the water depth decreasing; hence, the magnitude of Φ_n in Fig. 3 is greater than in Fig. 2:

$$\Phi_2 > \Phi_1 \tag{3}$$

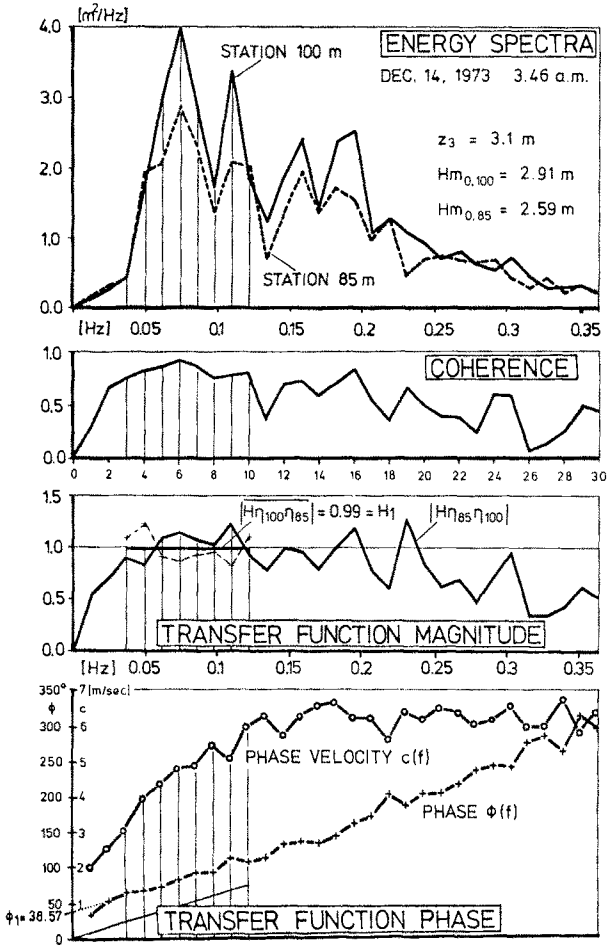

Fig. 2: Spectral functions of two wave gauge signals at a high tide water level.
Gauge distances from shore 100 m and 85 m respectively.

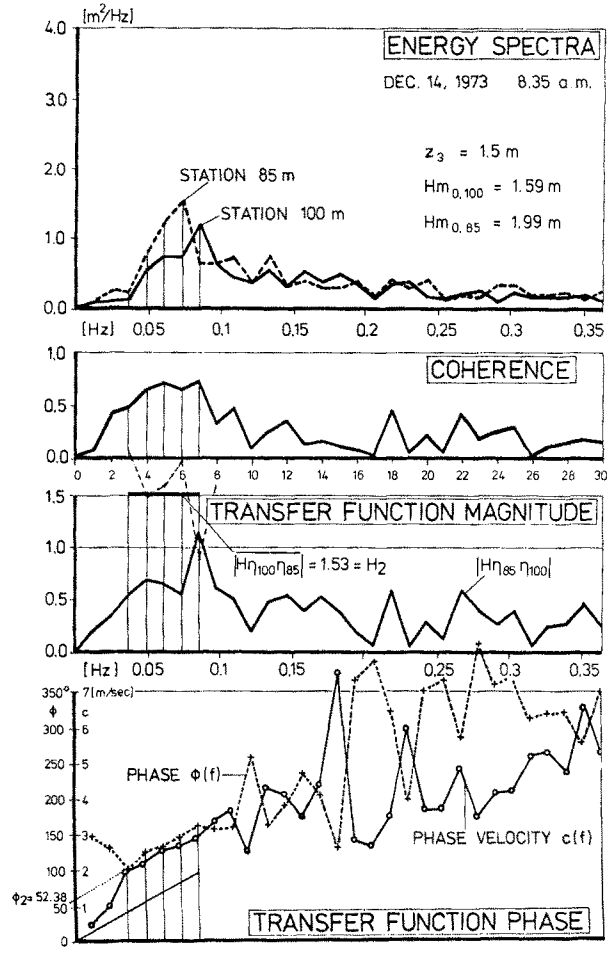

Fig. 3: Spectral functions of two wave gauge signals at a low tide water level.
Gauge distance from shore 100 m and 85 m respectively.

There is, however, another phenomenon to be seen from Fig. 3 representing a very shallow water depth condition. Obviously a peak shift to lower frequencies has happend on the rather short distance of $\Delta x = 15$ m in the upbeach direction, and additionally an increase in the maximum energy density can be watched. This fact also comes out clearly from the magnitude of the transfer function, if its inverse values are considered at high coherence only, resulting in an average value of

$$H_2 = |\overline{H\eta_{100}\eta_{85}}| = 1.53 \qquad (4)$$

Similar energy shifts to lower frequencies due to decreasing water depth are also to be seen from spectra published by SONU, PETTIGREW and FREDERICKS (1974) and GODA (1975). By contrast, at the condition of Fig. 2, marked by a greater water depth, energy density decreases from station 100 m to station 85 m accordingly resulting in an average value

$$H_1 = |\overline{H\eta_{100}\eta_{85}}| = 0.99 < 1 \qquad (5)$$

Time Domain Data

Increasing wave periods in the upbeach direction (in accordance with a peak shift to lower frequencies) could also be detected in the time domain from synchronously taken strip charts.

Figures 4 and 5 show the results of a zero crossing evaluation technique applied to the data of 6 and 5 measuring stations respectively still in operation in the same coast perpendicular measuring profile at normal weather conditions.

Besides the wave heights here the wave propagation velocity is plotted with reference to the water depth, the wave periods and the wave length respectively. Because of the lack of space here only two things shall be pointed out with respect to broken waves.

After breaking the wave deceleration is less than before breaking, and, as a consequence of an increasing "wave period", there is an anomalous

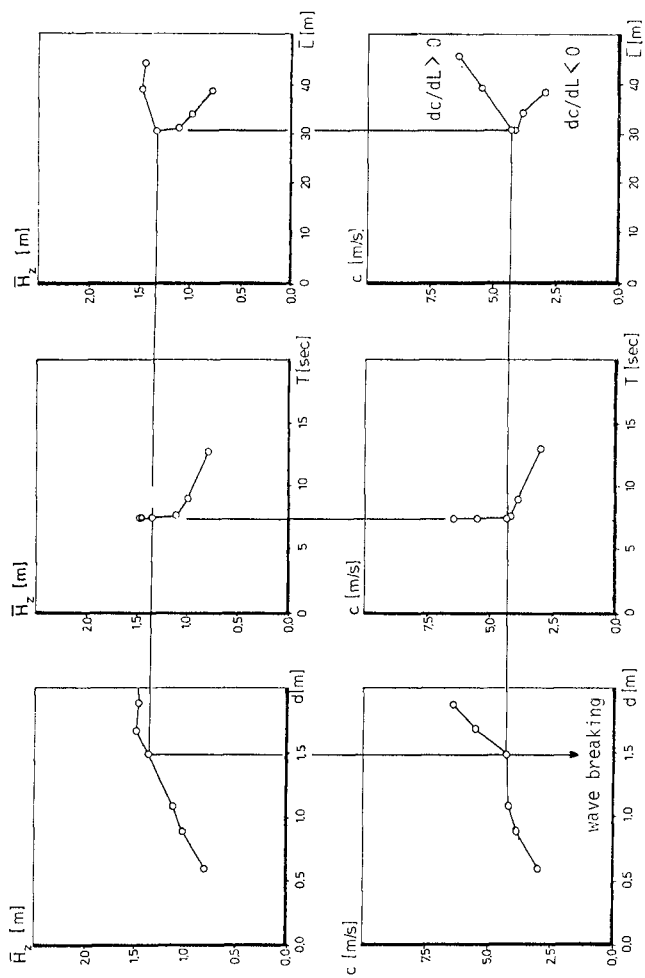

Fig. 4: Variation of mean wave heights $\bar{H}_z$ and propagation velocity c with water depth, wave period and wave length respectively in a coast perpendicular measuring profile on April 3rd, 1973

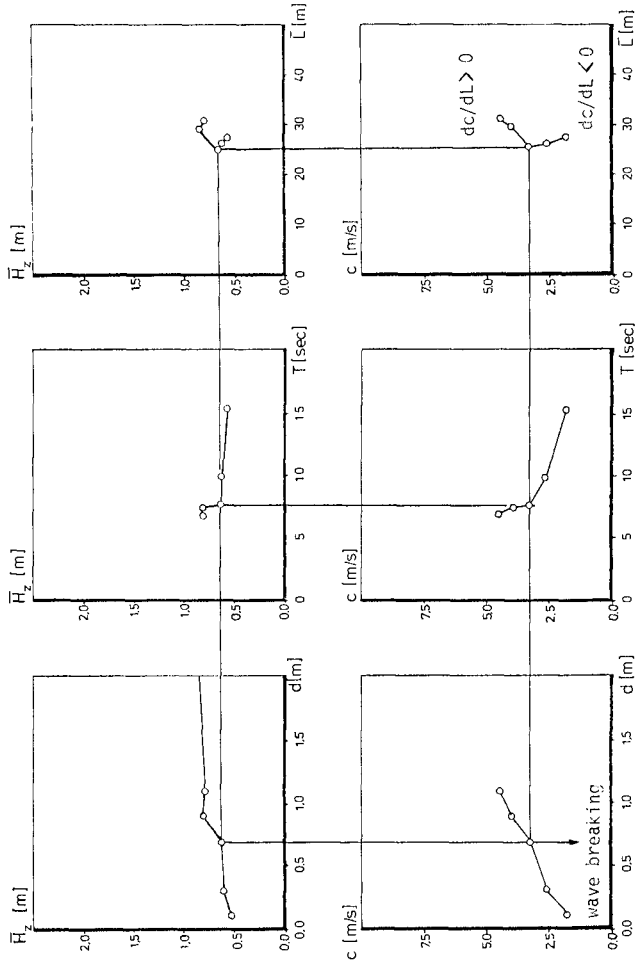

Fig. 5: Variation of mean wave heights $\bar{H}_z$ and propagation velocities c with water depth, wave period and wave length respectively in a coast perpendicular measuring profile on March 18th, 1973

dispersion characterized by $dc/dL < 0$. The details of that measurements are also given in BÖSCHING (1978 b).

ANOMALOUS DISPERSION OF ELECTROMAGNETIC WAVES

From electromagnetic waves it is well known that an anomalous dispersion of frequency components is due to a resonance phenomenon (resonance absorption in dielectrics). If one has an electromagnetic wave propagating through a medium made up of a number of oscillators (electrons or ions) per unit volume one gets a complex refractive index

$$n^* = n - ik \tag{6}$$

in which n is the real refractive index (also representing phase velocity) and $k = n \cdot \kappa$ is an absorption quantity (also representing the amplitude response near resonance).

As to be seen from Fig. 6 both components vary with wave length. By the equation (6) it is stated that resonance, absorption and anomalous dispersion are combined effects. If an incident component wave has nearly the same length or frequency as an oscillator of the medium resonance occurs. The oscillator absorbs the energy from the forcing incident wave. At resonance absorption represented here by k is a maximum, and in the vicinity of the spot of resonance always an anomalous dispersion $dn/dL > 0$ corresponding to $dc/df > 0$ (or $dc/dL < 0$ or $dn/df < 0$) appears. In a light spectrum this means that the sequence of spectral colours here is the inverse to the normal case: refraction of the red colour is a maximum instead of the violet colour. It is because of the coincident maximum of absorption that we are not as familiar with this kind of dispersion as we are with the normal dispersion property. In liquids and solids, due to molecular collisions and strong intermolecular forces, the absorption and dispersion curves become very much broadened, the broadening being very irregular owing to the varying molecular force field. Additionally damping is an essential quantity as it is true to all forced vibration processes.

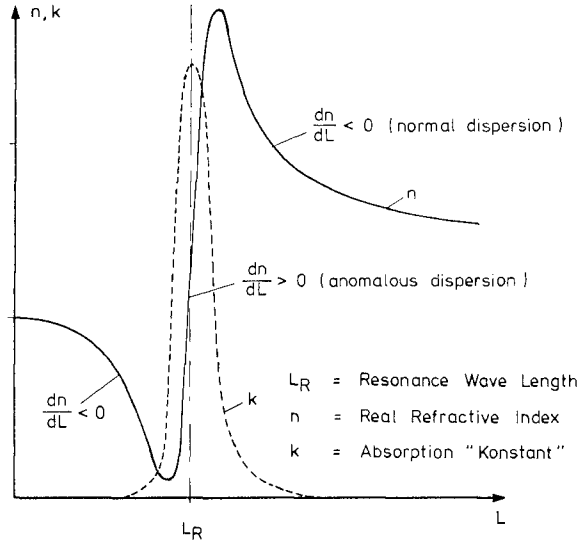

Fig. 6: Absorption above and below a region of anomalous dispersion centered about the resonance wave length

Moreover it is well known from thin film optics that dispersion properties depend on the actual film thickness, see for instance MAYER (1950).

With respect to the transmission of light through a gold film it can be seen from Fig. 7 that an anomalous dispersion property gets more distinct in the visible spectrum with the film thickness decreasing. At a rather thick film (solid line) the visible spectrum is dominated by a normal dispersion whereas at a very thin film there is an anomalous dispersion in the total visible spectrum.

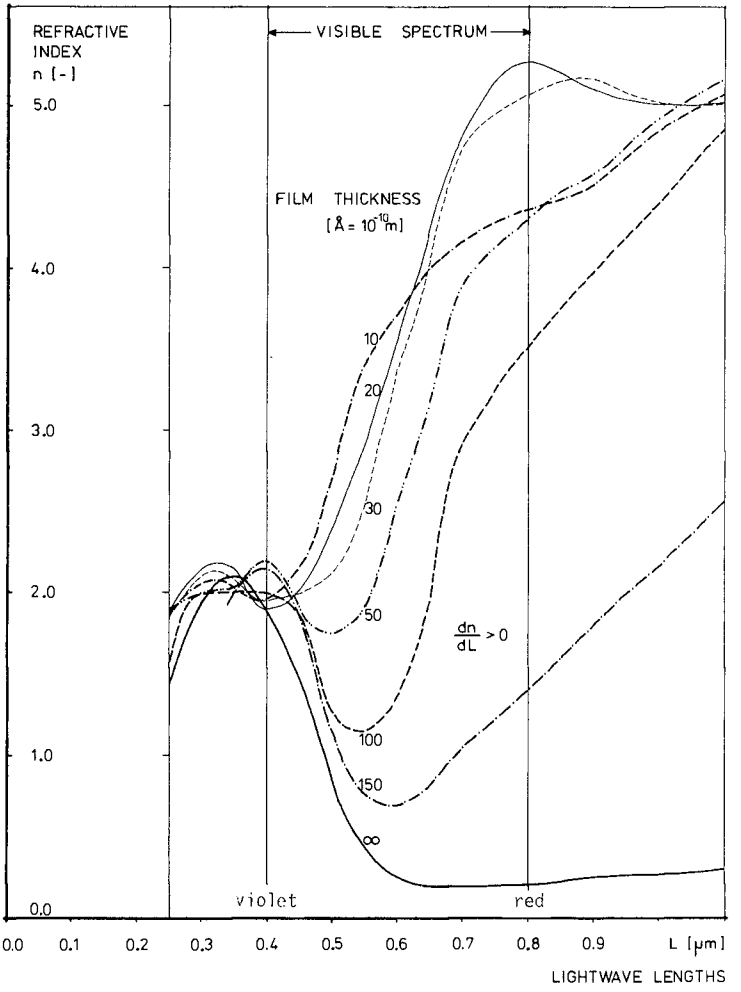

Fig. 7: Variation of dispersion properties at transmission of light through gold films with respect to decreasing film thicknesses

DISCUSSION AND CONCLUSIONS

Formerly the author was able to deduce an anomalous dispersion property combined with a peak shift Δf to lower frequencies from an equation

$$\Delta f = f_0 \cdot \frac{2 \cdot [c(x) - c_0]}{2 \cdot c_0 - c(x)} = f(x) - f_0 \qquad (7)$$

see BÖSCHING (1980) in which f_0 and c_0 are the component frequency and celerity respectively at a known position in the surf zone, and $c(x) < c_0$ and $f(x) < f_0$ are caused by a superimposed (accelerated) current at a certain position on the same wave beam nearer to the shore. Vice versa a positive frequency shift can be produced in applying $c(x) > c_0$. The author is still convinced that superimpored currents do have an important effect on wave deformation processes particularly taking place in the post breaking zone. For example in the lower part of Fig. 8 there are shown some additional spectra measured synchronously at stations 100 m and 85 m from the shore. If the respective sets of spectra are connected with the coast normal component of the mean residual velocities measured at station 85 m (see middle part of Fig. 8) actually different frequency shifts can be seen. In the present case there is

a) a negative frequency shift (red shift) combined with a seaward directed residual current (see first set of spectra),

b) almost no shift in correspondance with minimal residual currents (see second set of spectra) and

c) there is a positive shift (blue shift) coincident with a coastward directed residual current (see third set of spectra).

As, however, the additional phenomenon of an increasing energy density in the upbeach direction, especially at very low water depth conditions (first and third set of spectra), can not be explained in applying equation (7), in the following the question is considered whether the above demonstrated combined effects of resonance, absorption and anoma-

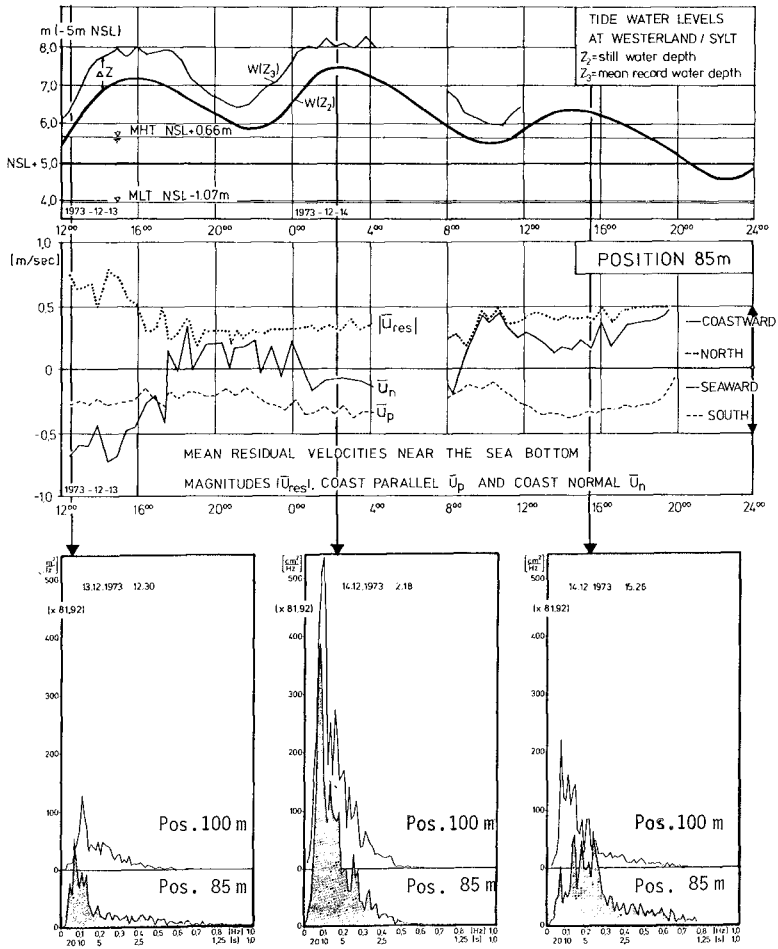

Fig. 8: Different frequency shifts by superimposed accelerated residual currents with respect to the onshore-offshore direction

lous dispersion, known from electromagnetic waves, also apply to surf zone characteristics.

In order to get a better understanding of that mechanism an inspection of the response characteristics of a single degree of freedom oscillator can be helpful, see Fig. 9.
As an analogue to the above shown transfer function this is also subdivided into magnitude and phase. The amplitude response characteristic as well as the phase characteristic both are plotted with reference to the frequency ratio

$$\eta = \frac{\text{forcing frequency}}{\text{natural frequency}} = \frac{f_f}{f_n} \tag{8}$$

instead of the frequency as it is used at the transfer functions.

Both components are significantly marked by the actual damping rate D which is well-defined by the respective families of curves.

Applying this model to the surf zone the forcing frequencies are those coming from offshore, and the volume of water present in the surf zone is characterized by some eigenfrequencies.

A similar concept is well known from edge wave investigations (GUZA and BOWEN, 1976; CHAPELL and WRIGHT, 1978).

In order to check its validity in the following it is tried to compare the response characteristics of Fig. 9 with the transfer function data of Fig. 2 and 3 respectively, both representing different wave conditions and different anomalous dispersion properties.

If the values H_1, Φ_1 and H_2, Φ_2 are transferred to Fig. 9 conditions (1) and (2) can be differentiated by suitable damping rates D and corresponding frequency ratios η.

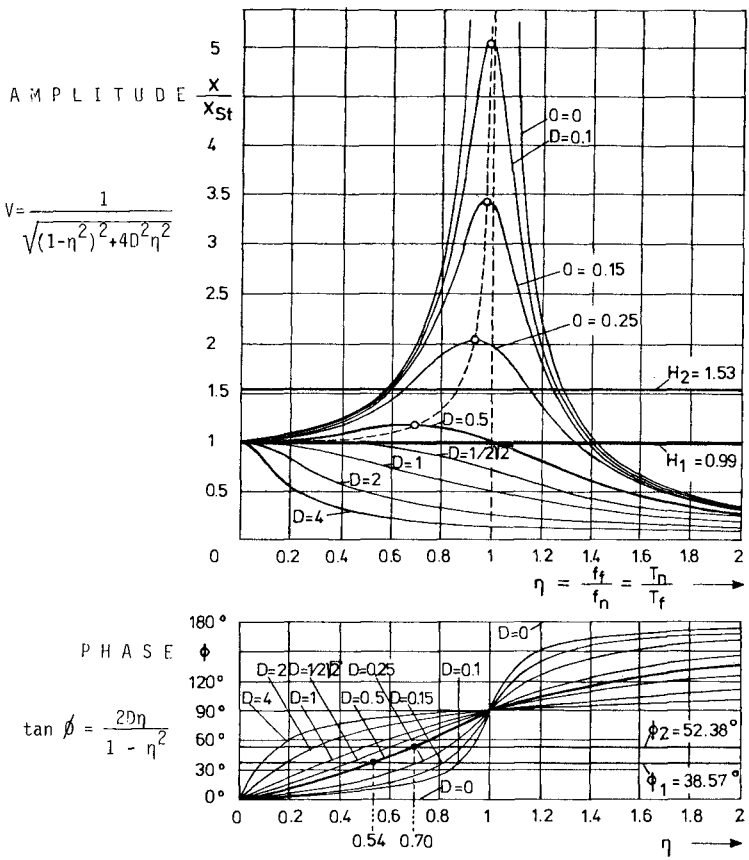

Fig. 9: Response characteristics of a single degree of freedom oscillator

At condition(1)a distinct amplitude and phase response can not be deduced because transfer function magnitude does not differ much from unity, and the phase angle is far from being $\Phi = 90^{o}$. Amplitude and phase characteristics ($H_1 = 0.99$ and $\Phi_1 = 38.5^{o}$) in this case get together at a frequency ratio

$$\eta_1 \simeq 0.46 < 0.54 \tag{9}$$

corresponding to a damping rate

$$0.5 < D_1 < \sqrt{2}/2 \tag{10}$$

Herewith it can be concluded that damping dominates in this case. By contrast, at condition(2)marked by a transfer function magnitude appreciably greater than unity ($H_2 = 1.53$) and a larger phase angle ($\Phi_2 = 52.38$) it is found a frequency ratio

$$\eta_2 \simeq 0.74 > 0.70 \tag{11}$$

and a corresponding damping rate

$$0.25 < D_2 < 0.5 \tag{12}$$

Hence, from this analysis there is an indication that resonant interactions including anomalous dispersion are more likely to occur in the surf zone at lower water depth.

This result, however, is infact in accordance with the above shown example from thin film optics, see Fig. 7. Moreover the analogous behaviour of electromagnetic waves at resonance absorption and surf zone waves is underlined by the fact that the ratio film thickness devided by light wave length is similar to the ratio water depth devided by wave length in the post breaking zone.

REFERENCES

RAMAMONJIARISOA, A., COANTIC, M., Loi expérimentale de dispersion des vagues produites sur une faible longueur d'action, C.R. Acad. Sci. 2B2 B, 111 - 114, 1976

LAKE, B.M., YUEN, H. C., A new model for nonlinear wind waves. Part 1, Physical model and experimental evidence. J. Fluid Mech. 88, 33 - 62, 197B

PHILLIPS, O. M., Strong interactions in wind-wave fields, Proc. NATO Conf. on Turbulent Fluxes through the Sea Surface, Wave Oynamics and Prediction, France, 1977

MASSEL, S. R., CHYBICKI, W., On the dispersion relation for wind waves in shallow water, Abstracts EUROMECH 114 Gdansk, 23 - 25 Sept. 19BO

BÜSCHING, F., Anomalous dispersion of Fourier components of surface gravity waves in the near shore area, Proc. 16th Int. Conf. Coastal Eng. Hamburg, 197B

BÜSCHING, F., Wave deformation due to decreasing water depth, Mitt. Leichtweiß-Institut, Techn. Univ. Braunschweig, H. 63, 197B

BÜSCHING, F., Ooppler aspects of near shore wave transformation, Abstracts EUROMECH 114 Gdansk, 23 - 25 Sept. 1980

SONU, C. J., PETTIGREW, N, FREOERICKS, R. G., Measurement of Swash Profile and Orbital Motion on the Beach, Proc. Int. Symp. Ocean Wave Measurement and Analysis, New Orleans, 1974

GOOA, Y., Irregular Wave Deformation in the Surf Zone, Coastal Engineering in Japan, Vol. 18, 1975

GUZA, R. G. and BOWEN, A. J., Resonant interactions for waves breaking on a beach. Proc. 15th Int. Conf. Coastal Eng., Hawaii, 1976

CHAPPELL, J. and WRIGHT, L. D., Surf zone resonance and coupled morphology. Proc. Int. Conf. Coastal Eng., Hamburg, 1978

MAYER, H., Physik dünner Schichten, Wissenschaftliche Verlagsgesellschaft M.B.H., Stuttgart, 1950

NUMERICAL CALCULATION OF SEICHE MOTIONS IN HARBOURS OF ARBITRARY SHAPE

P. Gaillard
Sogreah, Crenoble, France

ABSTRACT

A new method of calculation of wave diffraction around islands, offshore structures, and of long wave oscillations within offshore or shore-connected harbours is presented. The method is a combination of the finite element technique with an analytical representation of the wave pattern in the far field. Examples of application are given, and results are compared with other theoretical and experimental investigations.

lNTRODUCTION

The prediction of possible resonant response of harbours to long wave excitation may be an important factor at the design stage. Hydraulic scale models have the disadvantage of introducing some bias in the results due to wave reflection on the wave paddle and on the tank boundaries. Numerical methods on the other hand can avoid such spurious effects by an appropriate representation of the unbounded water medium outside the harbour.

Various numerical methods exist for calculating the seiche motions in harbours of arbitrary shape and water depth configuration. Among these, the hybrid-element methods, as described by Berkhoff [1] , Bettess and Zienkiewicz [2], Chen and Mei [3], Sakai and Tsukioka [8] use a combination of the finite element technique with other methods for representing the velocity potential within the harbour and in the offshore zone. This paper presents a new method based on the same general approach, with an analytical representation of the wave pattern in the far field. lt differs from the former methods in several aspects stressed hereafter.

We consider here two kinds of applications:

a) the first is the study of wave diffraction by islands or bottom seated obstacles in the open sea and the study of wave oscillations within and around an offshore harbour.

b) the second is the study of wave oscillations within a shore-connected harbour with a totally reflective coastline, which is assumed rectilinear beyond a certain distance.

BASIC EQUATIONS

The numerical calculation of long period water oscillations in harboursof arbitrary shape and bottom configuration is based on the linear shallow water wave equation for an inviscid fluid:

$$\nabla\cdot\left[h\nabla\zeta\right] - \frac{1}{g}\zeta_{tt} = 0 \qquad (1)$$

where $\zeta(x,y,t)$ is the water surface elevation above mean see level,
$h(x,y)$ is the water depth distribution,
g the acceleration due to gravity.

The numerical models based on the present method include two domains:

- in a bounded region D_1 including the harbour and the vicinity of the harbour entrance, the water depth is defined according to the bottom topography on the site studied, and a finite element technique is used for solving the above equation.

- In the outer region D_2 extending to infinity, and bounded by an unlimited rectilinear reflecting coastline in the case of a shore-connected harbour, the water depth is assumed constant, equal to h_0, and an analytical solution of (1) is used in the form of a finite series expansion.

The boundary C_{12} interconnecting both domains is either a full circle in the case of an island-type harbour or structure, or a half circle in the case of a shore-connected harbour, as shown in figure 1.

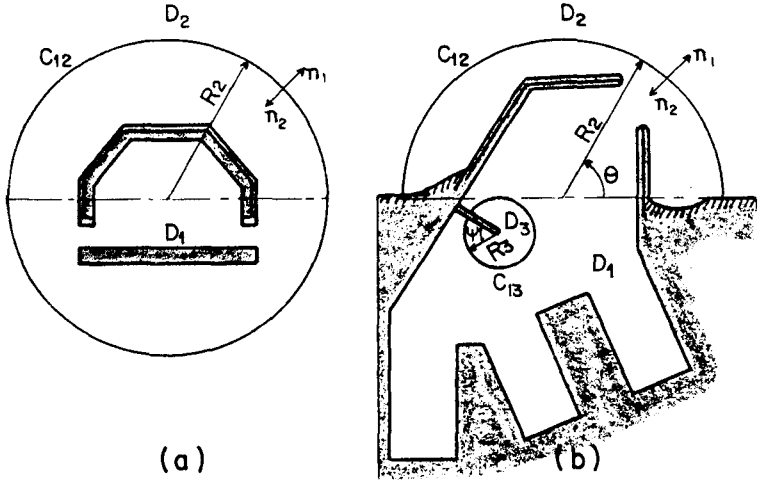

Fig.1 Definition sketch: (a) offshore case ; (b) nearshore case

A periodic excitation by a plane incident wave of arbitrary direction α, frequency f (or angular frequency ω) and height $2a_0$ is taken as input to the model at infinity and the steady-state dynamic response of the model is calculated. A variable frequency scanning technique is used to detect the resonant modes.

We thus reduce the problem to seeking, for a finite number of wave angular frequencies ω, a complex function of space $\bar{\zeta}(x,y)$ such that:

$$\zeta(x,y,t) = \mathrm{Re}\left\{\bar{\zeta}(x,y)\ \exp\ (-i\omega t)\right\} \tag{2}$$

This function is a solution of the Helmholtz equation:

$$\nabla.\left[h\,\nabla\bar{\zeta}\right] + \frac{\omega^2}{g}\,\bar{\zeta} = 0 \tag{3}$$

We shall refer to the solutions of (3) in D_1 and D_2 as $\bar{\zeta}_1$ and $\bar{\zeta}_2$ respectively. The boundary conditions imposed on these solutions are as follows:

$$\frac{\partial\bar{\zeta}}{\partial n} = 0 \qquad \text{on } C_{SB} \tag{4}$$

$$\bar{\zeta}_1 = \bar{\zeta}_2$$

$$\text{on } C_{12} \tag{5}$$

$$\frac{\partial\bar{\zeta}_1}{\partial n_1} = -\frac{\partial\bar{\zeta}_2}{\partial n_2} = G_{12}(\Theta)$$

$$\bar{\zeta}_2 \longrightarrow \bar{\zeta}_A \qquad \text{for } r\longrightarrow\infty \tag{6}$$

The first condition expresses that waves are totally reflected from all solid boundaries i.e. harbour structures and coastline. This assumption is generally valid as wave steepness is low for the periods considered.

The set of conditions (5) express the continuity of the water surface elevation and of the horizontal velocities at the common boundary C_{12}.

The last condition imposes the behaviour of the solution in the far field, behaviour which depends on the type of application considered.

In the case of an offshore harbour or structure $\bar{\zeta}_A$ is representative of the plane incident wave, which can be expressed, in polar coordinates (r,Θ) with the origin at the centre of C_{12}, as:

$$\bar{\zeta}_A = \bar{\zeta}_i = a_0 \sum_{n=0}^{\infty} \epsilon_n (i)^n J_n\,(kr)\,\cos\, n(\Theta-\alpha) \tag{7}$$

with: $i = \sqrt{-1}$

J_n = the Bessel function of order n

k = the wave number associated with frequency ω by:

$$k = \omega(gh_0)^{-1/2} \tag{8}$$

$$\epsilon_n = \begin{cases} 1 & n=0 \\ 2 & n \geqslant 1 \end{cases} \tag{9}$$

In the case of a shore-connected harbour, $\bar{\zeta}_A$ is representative of the superposition of the incident waves and of their reflection on the coastline, which is considered as totally reflective. Taking the origin of along the shoreline, $\bar{\zeta}_A$ is expressed as:

$$\bar{\zeta}_A = 2a_0 \sum_{n=0}^{\infty} \epsilon_n (i)^n J_n (kr) \cos n\alpha \cos n\theta \tag{10}$$

The solution in D_2 is consequently split into two components $\bar{\zeta}_A$ and $\bar{\zeta}_D$, where $\bar{\zeta}_D$ is representative of the diffracted waves due to the presence of the harbour or of the isolated structure under consideration. These waves radiate outward from the latter to infinity, and thus should satisfy Sommerfeld's radiation condition:

$$\lim_{r \to \infty} \left\{ \sqrt{r} \left[\frac{\partial \bar{\zeta}_D}{\partial r} - ik\bar{\zeta}_D \right] \right\} = 0 \tag{11}$$

VARIATIONAL FORMULATION

The solution of the problem is obtained through a variational approach, which is briefly described here. Considering first the two domains independently and the function $G_{12}(\Theta)$ in (5) as a given boundary condition, the solution in D_1 is ascribed to make stationary the functional:

$$F_1(\zeta) = \frac{1}{2} \iint_D \left[h(\nabla\zeta)^2 - \frac{\omega^2}{g} \zeta^2 \right] ds - \int_{C_{12}} h \zeta_1 C_{12} \, d\sigma \tag{12}$$

and the solution in D_2 is associated with the functional:

$$F(\zeta) = -\frac{1}{2} \iint_D \left[\nabla.(h\nabla\zeta) + \frac{\omega^2}{g} \zeta \right] \zeta \, ds + \int_{C_{12}} h \left[\frac{1}{2} \frac{\partial \zeta}{\partial n} + G_{12} \right] \zeta \, d\sigma \tag{13}$$

Since ζ_2 is represented in an analytical form which satisfies a priori equation (3), the first integral in (13) actually vanishes.

If we now consider G_{12} as an unknown function, our objective is to make stationary, for any first variation of ζ_1, ζ_2 and G_{12}, the functional resulting from the addition of (12) and (13), i.e.:

$$F(\zeta) = \frac{1}{2} \iint_{D_1} \left[h(\nabla\zeta)^2 - \frac{\omega^2}{g} \zeta^2 \right] ds + \frac{1}{2} \int_{C_{12}} h \frac{\partial \zeta_2}{\partial n_2} \zeta_2 \, d\sigma + \int_{C_{12}} h G_{12} (\zeta_2 - \zeta_1) d\sigma \tag{14}$$

G_{12} is a periodic function of Θ, which can be represented, in the case of an offshore structure, by a Fourier series expansion with unknown coefficients C_{1m}, C_{2m}. The requirement of stationarity of (14) for arbitrary first variations of these coefficients, leads to the following conditions:

$$\int_{C_{12}} (\zeta_2 - \zeta_1) \begin{Bmatrix} \cos m\Theta \\ \sin m\Theta \end{Bmatrix} d\Theta = 0 \qquad m = 0,1,2... \qquad (15)$$

When these conditions are satisfied, the last boundary integral of (14) vanishes.

In the case of a shore-connected harbour, $G_{12}(\Theta)$ is an even function of Θ. In this type of application, only those conditions in (15) involving cos $m\Theta$ are necessary.

The above functional can be represented in terms of the complex function $\bar{\zeta}$ by insertion of (2). It then appears as a function of time of the form:

$$F(\zeta) = \frac{1}{4} \mathrm{Re} \left\{ F_c(\bar{\zeta}) + F_v(\bar{\zeta}) \exp(2i\omega t) \right\} \qquad (16)$$

$$F_c(\bar{\zeta}) = \iint_{D_1} \left[h \nabla \bar{\zeta}_1 \cdot \nabla \bar{\zeta}_1^* - \frac{\omega^2}{g} \bar{\zeta}_1 \bar{\zeta}_1^* \right] ds + \int_{C_{12}} h \frac{\partial \bar{\zeta}_2}{\partial n_2} \bar{\zeta}_2^* \, d\sigma \qquad (17)$$

$$F_v(\bar{\zeta}) = \iint_{D_1} \left[h(\nabla \bar{\zeta}_1^*)^2 - \frac{\omega^2}{g} (\bar{\zeta}_1^*)^2 \right] ds + \int_{C_{12}} h \frac{\partial \bar{\zeta}_2^*}{\partial n_2} \bar{\zeta}_2^* \, d\sigma \qquad (18)$$

where $\bar{\zeta}^*$ is the complex conjugate of $\bar{\zeta}$.

The values of $\bar{\zeta}_2$ and of its normal derivative along C_{12} depend on the values of $\bar{\zeta}_1$ on this boundary, through the conditions (15). Consequently, the values of $\bar{\zeta}_1$ at N arbitrarily chosen nodes within D_1 and on its boundary constitute a complete set of independent degrees of freedom of the functionals F_c and F_v. By expressing F_c and F_v in terms of these variables, it can be shown that:

$$\frac{\partial F_v}{\partial \bar{\zeta}_1^*} = \left(\frac{\partial F_c}{\partial \bar{\zeta}_1^*} \right)^* \qquad (19)$$

In view of this property, the stationarity of $F(\zeta)$ is ensured at any time t when:

$$\frac{\partial F_c}{\partial \bar{\zeta}_{1n}^*} = 0 \qquad n = 1,2... N \qquad (20)$$

SOLUTION FOR AN OFFSHORE HARBOUR OR STRUCTURE

In the offshore case, in which C_{12} is a full circle, the solution in domain D_2 involves the following series expansion of $\bar{\zeta}_D$:

$$\bar{\zeta}_D\ (r,\theta) = \sum_{m=0}^{\infty} H_m^{(1)}\ (kr)\ \left[\varpi_{1m} \cos m\theta + \varpi_{2m} \sin m\theta\right] \qquad (21)$$

where $H_m^{(1)}$ is the Hankel function of the first kind and of order m.

The insertion of (21) into (15) leads to:

$$\begin{Bmatrix} \varpi_{1m} \\ \varpi_{2m} \end{Bmatrix} = \frac{\epsilon_m}{2\pi H_m} \int_0^{2\pi} (\bar{\zeta}_1 - \bar{\zeta}_A) \begin{Bmatrix} \cos m\theta \\ \sin m\theta \end{Bmatrix} d\theta \qquad m = 0,1,2 \ldots \qquad (22)$$

Where H_m stands for $H_m^{(1)}(kR_2)$, R_2 being the radius of C_{12}.

The integral in (22) which involves $\bar{\zeta}_A$ can be determined exactly for any value of the integer m, since the integrand is expressed in terms of trigonometric functions. On the other hand, the integral which involves $\bar{\zeta}_1$ can only be determined approximately, as the latter function of θ is calculated only at a discrete set of points along C_{12}. Assuming that $\bar{\zeta}_1$ is given at N_2 equally spaced nodes on this boundary, we obtain:

$$\begin{Bmatrix} \varpi_{1m} \\ \varpi_{2m} \end{Bmatrix} = \frac{\epsilon_m}{N_2 H_m} \sum_{p=1}^{N_2} \bar{\zeta}_{1p} \begin{Bmatrix} \cos \theta_{mp} \\ \sin \theta_{mp} \end{Bmatrix} - a_0 (i)^m \frac{\epsilon_m}{H_m} J_m\ (kR_2) \begin{Bmatrix} \cos m\alpha \\ \sin m\alpha \end{Bmatrix} \qquad (23)$$

$$\theta_n = 2\pi n/N_2$$

These expressions can also be derived by a direct identification of $\bar{\zeta}_2$ with $\bar{\zeta}_1$ at the N_2 points of the boundary C_{12}, and by applying a classical Fourier analysis.

It is known from the theory of spectral analysis that the sampling of the periodic function $\bar{\zeta}_1(\theta)$ at discrete points leads to a parasitic effect on the associated Fourier spectrum, so that it would be unrealistic to extend the application of (21) and (23) beyond a limiting value $m = N_2/2$. The order N_s of the finite series expansion used in practice is moreover dependent on the accuracy assigned in the numerical calculations. The latter criterion leads to a dependance of N_s on the value of the parameter kR_2.

It is seen from (23) that $\bar{\zeta}_2$ and its normal derivative along C_{12} are linearly dependent on the value of $\bar{\zeta}_1$ at the N_2 nodes located on this boundary:

$$\bar{\zeta}_2 = \sum_{p=1}^{N_2} \lambda_{2p}(\theta)\, \bar{\zeta}_{1p} \qquad M \in C_{12} \tag{24}$$

$$\frac{\partial \bar{\zeta}_2}{\partial n_2} = \sum_{p=1}^{N_2} \mu_{2p}(\theta)\, \bar{\zeta}_{1p} + \nu_2(\theta)$$

Calculations that will not be given in detail here, lead to the following expressions:

$$\lambda_{2p}(\theta) = \frac{1}{N_2} \sum_{m=0}^{N_s} \varepsilon_m \cos m\,(\theta - \theta_p)$$

$$\mu_{2p}(\theta) = -\frac{k}{N_2} \sum_{m=0}^{N_s} \varepsilon_m P_m(kR_2) \cos m\,(\theta - \theta_p) \tag{25}$$

$$\nu_2(\theta) = \frac{2a_0}{\pi R_2} \sum_{m=0}^{N_s} \frac{\varepsilon_m}{H_m} (i)^{m+1} \cos m(\theta - \alpha)$$

$$P_m(u) = \frac{H_m^{(1)\prime}(u)}{H_m^{(1)}(u)}$$

where the prime stands for the first derivative of the function considered.

Within the domain D_1, the problem is solved by a standard finite element technique. The solution and its spatial derivatives are represented by expressions of the form:

$$\bar{\zeta}_1(x,y) = \sum_n \gamma_n(x,y) \bar{\zeta}_{1n} \tag{26}$$

$$\frac{\partial \bar{\zeta}_1}{\partial x} = \sum_n \gamma_{xn}\, \bar{\zeta}_{1n} \qquad ; \frac{\partial \bar{\zeta}_1}{\partial y} = \sum_n \gamma_{yn}\, \bar{\zeta}_{1n}$$

where the summation extends over the whole set of finite elements, γ_n is an arbitrarily chosen interpolation function, depending on the type of discretisation and on the number of degrees of freedom within each element, and γ_{xn}, γ_{yn} are its spatial derivatives. Zero order continuity is generally sufficient for this class of partial differential equations.

By insertion of (24) and (26) into (17), we obtain:

$$F_c(\bar{\zeta}_1) = \sum_n \left[\sum_m A_{mn}\, \bar{\zeta}_{1m}\, \bar{\zeta}^*_{1n} + \sum_p B_{pn}\, \bar{\zeta}_{1p}\, \bar{\zeta}^*_{1n} + E_n\, \bar{\zeta}^*_{1n} \right] \tag{27}$$

$$A_{mn} = \iint_{D1} \left[h(\gamma_{xm}\,\gamma_{xn} + \gamma_{ym}\,\gamma_{yn}) - \frac{\omega^2}{g}\,\gamma_m\,\gamma_n \right] ds$$

$$B_{pn} = \int_{C_{12}} h\,\mu_{2p}\,\lambda_{2n}\, d\sigma \qquad ; \quad E_n = \int_{C_{12}} h\,\nu_2\,\lambda_{2n}\, d\sigma \tag{28}$$

The summation with index m includes all finite elements which involve node n, and the summation with index p includes all nodes located on the boundary C_{12}, whenever node n is itself located on this boundary. The term E_n, as well, is involved only in the latter situation.

From the previous results, we obtain for the coefficients B_{pn} and E_n:

$$B_{pn} = -\frac{2\pi k R_2 h_0}{N_2^2} \sum_{m=0}^{N_s} \varepsilon_m\, P_m(kR_2)\, \cos m\,(\Theta_p - \Theta_n)$$

$$E_n = \frac{4a_0 h_0}{N_2} \sum_{m=0}^{N_s} \frac{\varepsilon_m}{H_m}\, (i)^{m+1}\, \cos m\,(\alpha - \Theta n) \tag{29}$$

The conditions (20) then lead to the system of linear equations with N complex unknowns $\bar{\zeta}_{1n}$:

$$\sum_m A_{mn}\, \bar{\zeta}_{1m} + \sum_p B_{pn}\, \bar{\zeta}_{1p} = -E_n \qquad n = 1,2 \ldots N \tag{30}$$

The matrix of this system has a banded structure and symmetric coefficients, as can be seen from (28) for A_{mn} and (29) for B_{pn}. Moreover, all nodes which do not belong to the boundary C_{12} are associated with real coefficients. Substantial savings in core memory requirements and in computer time are obtained by taking account of these properties in the implementation of the method.

SOLUTION FOR A SHORE-CONNECTED HARBOUR

In the case of a shore-connected harbour, with a rectilinear coastline bounding D_2, $\bar{\zeta}_D$ is an even function of Θ, which can be represented by (21) with only cosine terms present. The same method then gives:

$$\varpi_{1m} = \frac{\varepsilon_m}{N_2 H_m} \sum_{p=0}^{N_2} \bar{\zeta}_{1p}\, \chi_p \cos \Theta_{mp} - 2a_0 (i)^m \frac{\varepsilon_m}{H_m} J_m(kR_2) \cos m\alpha \tag{31}$$

$$\Theta_n = \pi n / N_2 \qquad ; \quad \chi_p = \begin{cases} 0{,}5 & p = 0 \text{ or } N_2 \\ 1 & p = 1,2,\ldots N_2 - 1 \end{cases}$$

For the reason indicated above, the order N_s of the finite Fourier series should not exceed the value $m = N_2$, assuming that $\bar{\zeta}_1$ is defined at N_2+1 nodes C_{12}. The formula (31) leads to expressions of $\bar{\zeta}_2$ and of its normal derivative along C_{12} which are similar to (24), with the index p starting from zero.

We thus obtain a system of linear equations similar to (30), with the coefficients specified in (28). The expressions of B_{pn} and E_n derived from (31) are:

$$B_{pn} = -\chi_p \chi_n \frac{\pi k R_2 h_0}{N_2^2} \sum_{m=0}^{N_s} \varepsilon_m P_m(kR_2) \cos m\Theta_p \cos m\Theta_n$$

$$E_n = \frac{4a_0 h_0}{N_2} \chi_n \sum_{m=0}^{N_s} \frac{\varepsilon_m}{H_m} (i)^{m+1} \cos m\alpha \cos m\Theta_n \qquad (32)$$

The matrix of this system has the same general properties described for the preceding case.

FLOW AROUND THIN STRUCTURES

It is possible to account for the singularity of flow around the end of thin structures with the same method by introducing subdomains of circular shape D_3 at the tip, as shown in figure 1b. The functional F_c then involves additional integral expressions, in terms of N_3+1 unknown values of $\bar{\zeta}_1$ along the boundary C_{13} of these subdomains D_3:

$$F_c(\bar{\zeta}) = \iint_{D_1} \left[h \nabla \bar{\zeta}_1 \cdot \nabla \bar{\zeta}_1^* - \frac{\omega^2}{g} \bar{\zeta}_1 \bar{\zeta}_1^* \right] ds + \int_{C_{12}} h \frac{\partial \bar{\zeta}_2}{\partial n_2} \bar{\zeta}_2^* \, d\sigma$$

$$+ \int_{C_{13}} h \frac{\partial \bar{\zeta}_3}{\partial n_3} \bar{\zeta}_3^* \, d\sigma \qquad (33)$$

Since the solution of (3) within D_3 should have a finite value at the tip of the structure, its series expansion is of the form:

$$\bar{\zeta}_3(r,\psi) = \sum_{m=0}^{\infty} \rho_m J_{m/2}(kr) \cos \frac{m}{2} \psi \qquad (34)$$

where (r,ψ) is here a local polar coordinate system, with its origin at the tip, and its reference axis aligned with the structure centerline, and $J_{m/2}$ is the Bessel function of fractional order m/2.

Along C_{13}, $\bar{\zeta}_3$ and its normal derivative take a form similar to (24).

Insertion of this into the last integral of (33) provides additional terms in (27) and finally leads to the following system:

$$\sum_m A_{mn}\,\bar{\zeta}_{1m} + \sum_p B_{pn}\,\bar{\zeta}_{1p} + \sum_q D_{qn}\bar{\zeta}_{1q} = -E_n \qquad n = 1,2\ldots N \qquad (35)$$

with:

$$D_{qn} = \int_{C_{13}} h\mu_{3q}\,\lambda_{3n}\,d\sigma$$

$$D_{qn} = \chi_q \chi_n \frac{2\pi k R_3 h_3}{N_3^2} \sum_{m=0}^{N_s} \varepsilon_m\, Q_m\,(kR_3)\cos\frac{m}{2}\psi_q \cos\frac{m}{2}\psi_n \qquad (36)$$

$$Q_m(u) = J'_{m/2}(u)/J_{m/2}(u) \qquad ;\ \psi_n = 2\pi n/N_3$$

In (35), the summation with index q includes all nodes belonging to the boundary C_{13}, whenever node n is itself located on this boundary. The additional coefficients D_{qn} appearing in the matrix of the system are real and symmetric, as can be seen from (36). Thus, the inclusion of subdomains, such as D_3, within D_1 does not require any modification as concerns the numerical resolution of the system.

EXAMPLES OF APPLICATION

Several examples of application of the method will be given here. The first four cases are related to structures and harbours of simple geometry in constant water depth, for which results of other numerical methods and experimental investigations are available in the literature. The last example refers to an actual harbour project study, carried out by Sogreah, in which a complex harbour lay-out and a variable water depth are considered.

Wave diffraction by a circular cylinder

Figure 2a shows the finite element numerical model adopted for the analysis of the wave diffraction pattern around a cylindrical structure of circular shape, of radius R_0, subject to a plane incident wave.

The variation of the calculated relative wave height along the cylinder, for different values of the adimensional parameter kR_0, is shown in figure 3, where it is compared to the analytical solution of Mac Camy and Fuchs [7]. The agreement between both methods is satisfactory.

Figure 4a gives for $kR_0=1$, the spatial distribution of the relative wave height in the whole domain D_1, in the form of level curves.

Figure 4b gives the corresponding water surface level, at the instant of maximum elevation at the most exposed part of the cylinder. In the same

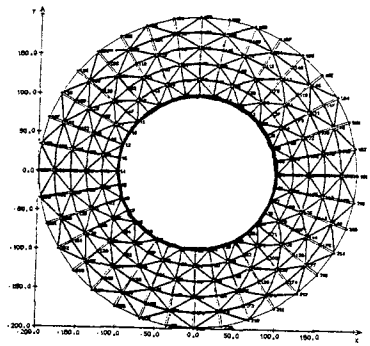

a

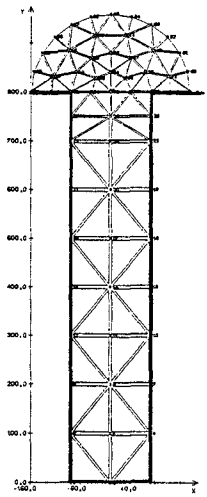

b

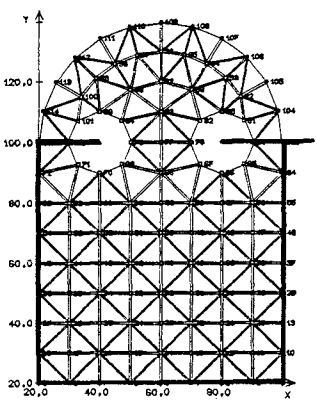

c

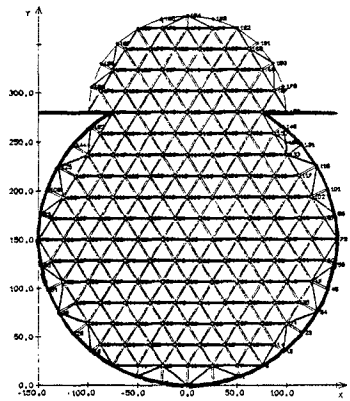

d

Fig. 2 Numerical models for : (a) a vertical circular cylinder, (b) a rectangular harbour b/L = 0.2, (c) a partially closed square harbour w/b = 0.5, (d) a circular harbour with 60° opening.

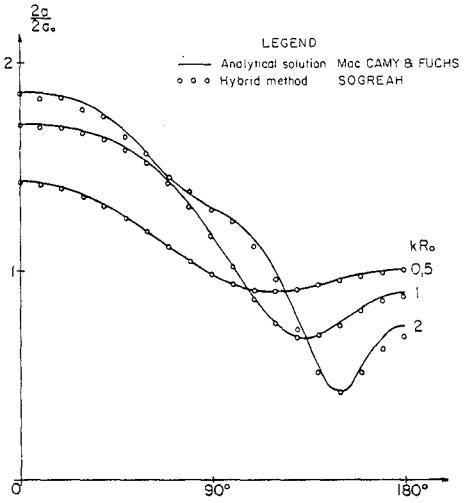

Fig. 3 Wave diffraction by a circular cylinder. Wave-height distribution along the structure for different values of kR_O.

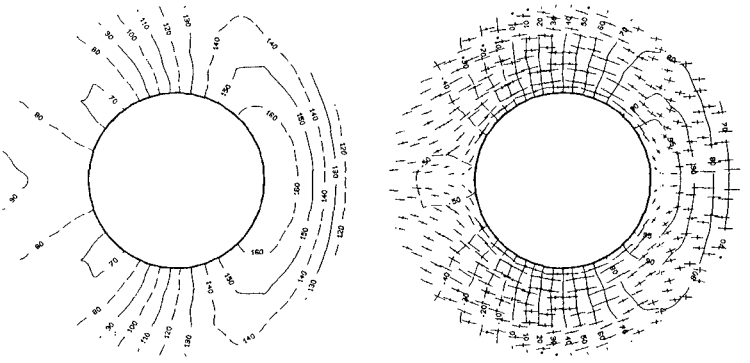

Fig. 4 Spatial distribution of the amplification coefficients (left), water surface elevation and horizontal displacements (right) for $kR_O = 1$.

Fig.5 CALCULATION OF SEICHE MOTIONS IN A RECTANGULAR HARBOUR WITH B/L=0.2

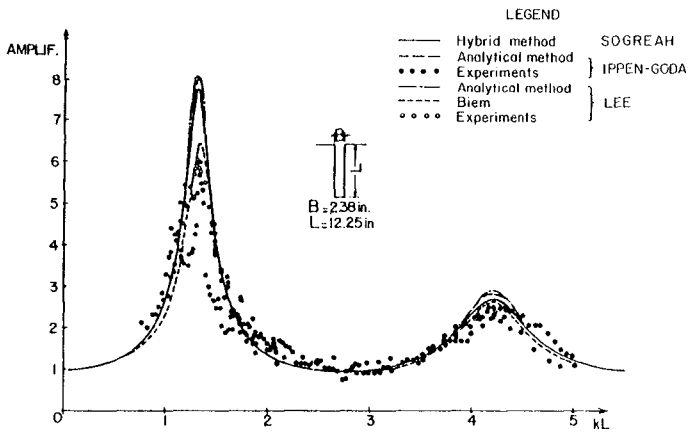

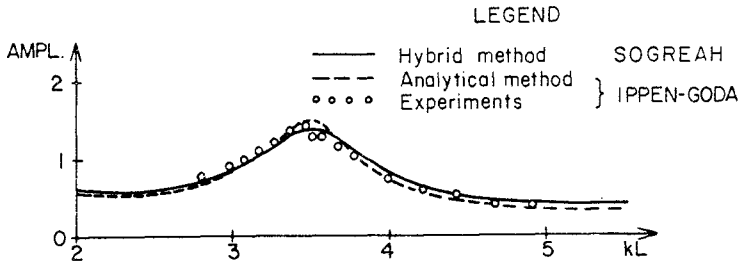

Fig. 6 Calculation of seiche motions in a partially closed square harbour with D/B = 0.5. Amplification at back wall.

figure are given the direction and length of the major and minor axes of the water particle horizontal displacements and hodographs, which are generally of elliptical form, as shown by the author in [4].

Seiche motions in a rectangular harbour

The second example is the study of resonant wave oscillations in a shore-connected rectangular harbour, with a width to length ratio W/L=0.2, and fully open on its narrow side, as shown in figure 2b. This situation was studied both experimentally and theoretically by Ippen and Goda [5], and by Lee [6], with a ratio W/L=0.193.

Figure 5 gives the frequency response obtained by these various approaches at the back wall of the harbour. The results obtained by the present method agree well with Ippen and Goda's and Lee's analytical solutions, which take explicitly account of the rectangular shape of the harbour. The results obtained by Bettess and Zienkiewicz [2] and by Chen and Mei [3], which are not shown here, also agree with the above results.

The experimental results and Lee's arbitrary shaped harbour theory, based on a boundary integral approach, agree with the other methods for the second mode of resonance, but give a noticeably lower amplification factor for the first mode. Ippen and Goda suggest that this could be due to energy dissipation, since experiments where actually performed with short waves of high steepness. It has not been investigated whether a refinement of the finite element network would improve the agreement with those experimental results.

Case of a partially closed square harbour

The case of a square harbour, partially closed by two thin aligned breakwaters, is given for illustrating the use of circular subdomains D_3 around the tip of harbour structures, as shown in figure 2c.

Figure 6 compares the numerical results obtained by the present method with Ippen and Goda's analytical solution and with their experimental results for an entrance width to harbour lehgth ratio W/L=0.5. The agreement between the different methods is very close.

Case of a circular harbour

The case of a shore-connected circular harbour with a 60° opening is an application involving more complex resonant nodes, which has been investigated both experimentally and theoretically by Lee [6].

Figure 7 gives the frequency response calculated at two different locations with the numerical model shown in figure 2d, together with the results of Lee's investigation.

Figure 8 shows the features of the first four resonant modes, which are obtained for kR_0=0.51, 2.21, 3.43 and 4.09 approximately, with the present method. The water surface elevation is indicated by means of level curves,

Fig. 7a CALCULATION OF SEICHE MOTIONS IN A CIRCULAR HARBOUR WITH A 60° OPENING

AMPLIFICATION COEFFICIENT AT POINT A ($r/R_o = 0.933 - \theta = 45°$)

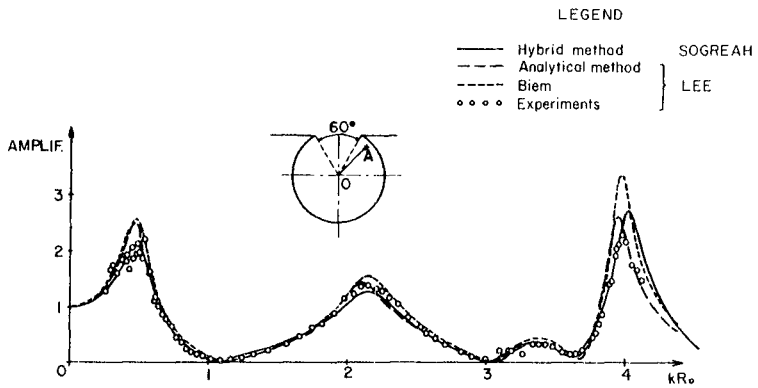

Fig. 7b CALCULATION OF SEICHE MOTIONS IN A CIRCULAR HARBOUR WITH A 60° OPENING

AMPLIFICATION COEFFICIENT AT CENTER O

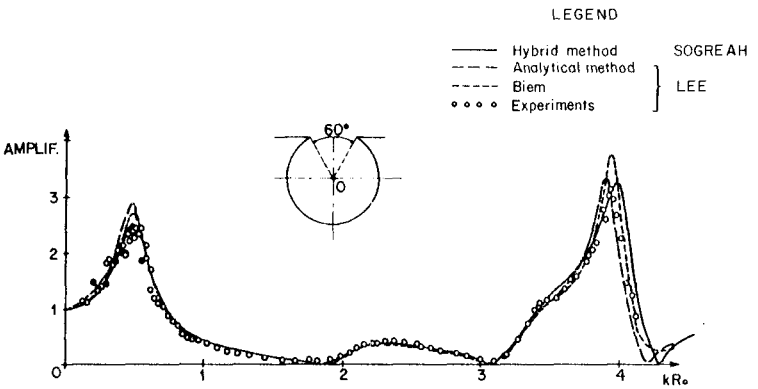

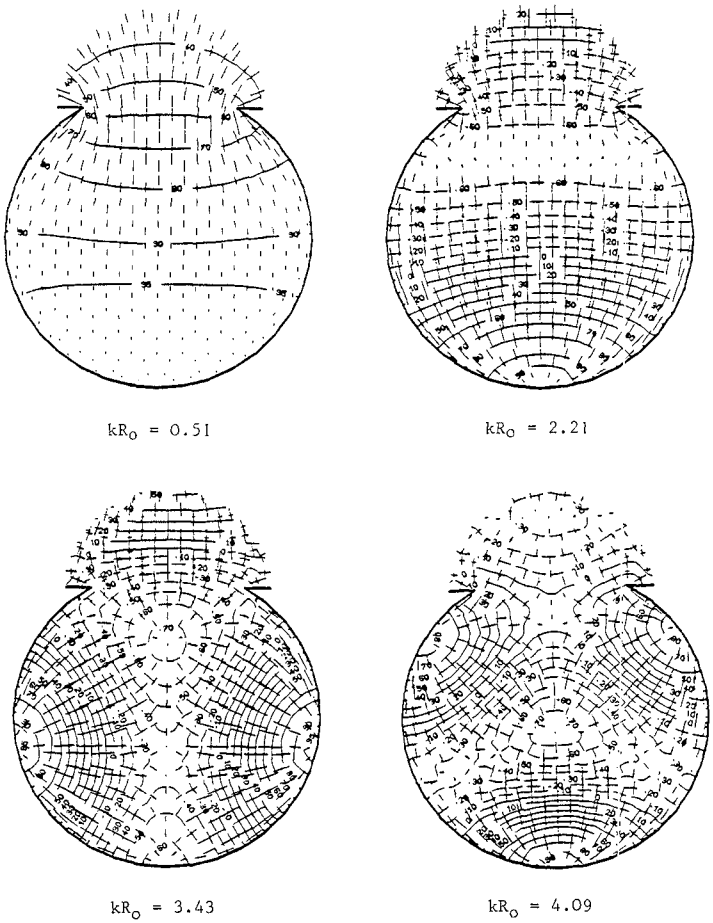

$kR_o = 0.51$ $kR_o = 2.21$

$kR_o = 3.43$ $kR_o = 4.09$

Fig. 8 Water surface elevation and horizontal displacements for the first resonant modes of a circular harbour with a 60° opening.

corresponding to given percentages of the maximum elevation. The instant taken as reference is that of maximum elevation at the point of highest amplification.

The direction and length of the major and minor axes of the horizontal water particle displacements and velocities are given on the same figure at the centroid of each finite element. The wave motion has essentially the character of purely standing waves in a great part of the harbour, and the water particles horizontal motion is practically rectilinear and oriented in the direction of the local amplitude gradient. This is not the case for particles located near the entrance, either within or outside the harbour, which have elliptical horizontal trajectories.

The resonant modes calculated by Lee are similar to the above. From the frequency response curve of the mean velocity at the harbour entrance, the values of kR_0 corresponding to resonance where found by Lee, to be 0.50, 2.18, 3.38 and 3.97. These figures agree to within 3% with these of the present model.

Case of a harbour of complex shape and variable water depth

Because of accuracy requirements, the maximum size of the finite elements should stay below a certain fraction of the local wave length, which depends on the type of spatial discretisation and interpolation functions used for $\bar{\zeta}$. With triangular elements and linear interpolation, for instance, this limit is of the order of 0.1. In the case of a harbour of variable water depth, the size of the finite elements will thus be dependent on the distribution of water depths to be considered.

Figure 9 is an example of application of the method to a harbour of complex shape and bottom topography (from 2 m to 15 m below MSL), with two main breakwaters extending offshore to protect the entrance channel. This model was set up for the study of the new Damietta Port Project in Egypt.

Figure 10 shows the frequency response curve obtained for one of the reference calculation points, which displays a great number of resonance frequencies. An in-depth investigation of each resonant mode was carried out on the basis of such results.

Figure 11 shows the features of one of the resonant modes of this harbour, in the form described for the circular harbour, i.e., level curves of water surface elevation and major and minor axis length and direction of horizontal water motion.

CONCLUSION

The present method leads to a system of linear equations, with symmetric coefficients, in which the only unknowns are the values of the complex function $\bar{\zeta}$ at nodes distributed within the bounded domain D_1, and along its boundary. In the other hybrid-element methods a larger system is obtained with additional unknowns, which are the Fourier coefficients ϖ_{1m}, ϖ_{2m} in Chen and Mei's method, the normal derivatives in Sakai and Tsukioka's method, the source strengths in Berkhoff's method, and the ζ_1, or velocity potential values, at nodes distributed along infinite elements in Bettess and Zienkiewicz's method.

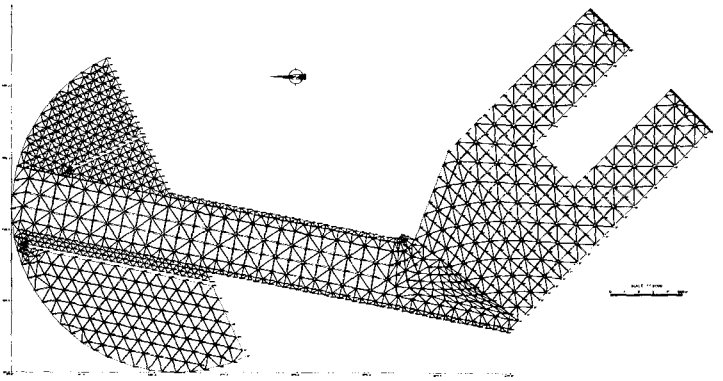

Fig. 9 - Numerical model set up for the study of seiche motions in the new Damietta industrial harbour (Egypt).

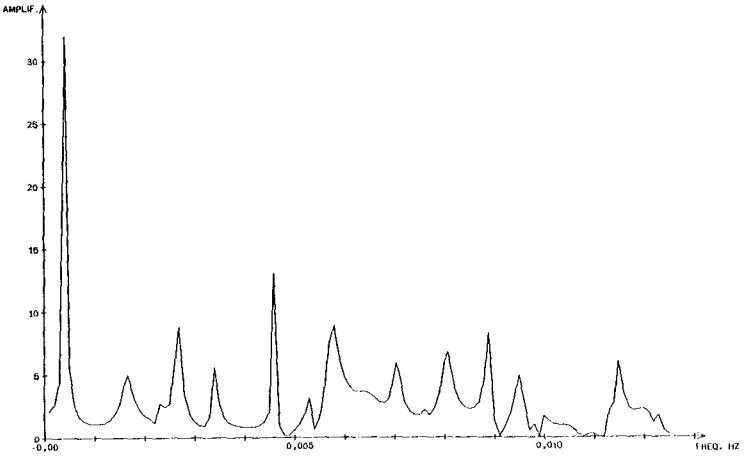

Fig. 10 - Frequency response curve at one of the reference nodes of the Damietta harbour model

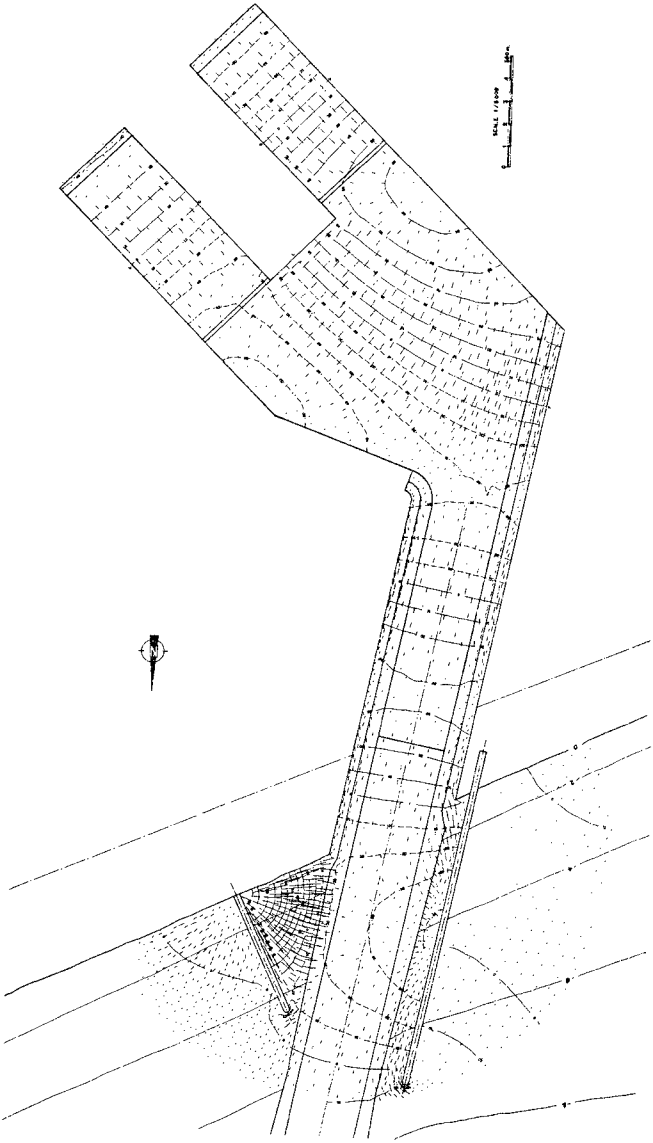

Fig. 11 - Water surface elevation and horizontal displacements for one of the resonant modes of the Damietta harbour model.

The present method is based on the same analytical representation of ζ in the outer domain D_2, as in Chen and Mei's approach. However, here an explicit formulation of ϖ_{1m}, ϖ_{2m} in terms of the incident wave characteristics and of the unknown values of $\bar{\zeta}_1$ along C_{12}, is given. This method is preferable to the matrix inversion technique used by the above authors. Another advantage of the method is the simplicity of form of the functional $F_c(\bar{\zeta})$ involved in (17) and (33), as compared to Chen and Mei's formulation.

The method, presented here in connection with studies of long wave oscillations in harbours, can be applied, with only minor changes as concerns the treatment of domain D_1, to the study of wave oscillations in the short and intermediate period range. It can also be extended to include energy dissipation and partial reflection along the shore and harbour structures.

The application of the present method to various situations for which other theoretical and experimental investigations have been carried out, has led to numerical results in good agreement with the above methods.

REFERENCES

[1] BERKHOFF J.C.W. (1972) "Computation of combined refraction-diffraction" Proc. 13th Int. Coastal Engineering Conf. Vol. 2, p. 471-490.

[2] BETTESS P & ZIENKIEWICZ O.C. (1977) "Diffraction and refraction of surface waves using finite and infinite elements" Int. journal for numerical methods in Engineering, vol. 11, p. 1271-1290.

[3] CHEN H.S. & MEI C.C. (1974) "Oscillations and wave forces in an offshore harbour. Application of hybrid finite element method to water wave scattering" M.I.T. Rep. No. 190, Ralph Parsons Lab. for Water Resources and Hydrodynamics.

[4] CAILLARD P. (1982) "Kinematic and dynamic properties of diffracted waves in constant water depth". In Engineering applications of Computational Hydraulics. Homage to Alexandre PREISSMANN, Vol. 1., Pitman Publ., p. 131-183.

[5] IPPEN A.T. & CODA Y. (1963) "Wave induced oscillations in harbours: The Solution for a rectangular harbour connected to the open-sea" Hydrodynamics Lab., Massasuchets Inst of Technology, Rep. No. 59.

[6] LEE J.J. (1969) "Wave induced oscillations in harbours of arbitrary shape" W.M. KECK Lab. of Hydraulics and Water Resources. California Inst. of Technology, No. KH-R-20.

[7] MAC CAMY R.C. & FUCHS R.A. (1952) "Wave forces on piles: a diffraction theory". Inst. Engineering Research. Waves Investigation Lab., Series 3, Issue 334, Berkeley, Calif.

[8] SAKAI F & TSUKIOKA K. (1976) "Finite element simulation of surface wave problems". Proc. 1rst Int. Conf. on Finite Elements in Water Resources. Princeton Univ., p. 4.3-4.17.

oOo

STATE OF THE ART IN TIDE PREDICTIONS

B. D. Zetler*

ABSTRACT

1. INTRODUCTION

By the end of the nineteenth century, scientists had succeeded in achieving the ability to make reasonably accurate tide predictions by the harmonic method (Schureman, 1941). Except for the building of larger and more sophisticated mechanical tide prediction machines using the harmonic technique, tidal mathematicians more or less rested on their laurels during the first half of the twentieth century; indeed, many scientists assumed there was no need for further tidal research. It is ironic that one of the very few geophysical sciences that already had acceptable methods of prediction should become the subject of significant improvement during the last half of this century. These improvements include: 1) least square analysis for all tidal constituents simultaneously, 2) response analysis and prediction, 3) extended harmonic analysis, 4) tidal measurements in deep water on the ocean floor, and 5) global numerical models of tides.

2. AIMS AND OBJECTIVES

The harmonic method of tide prediction is purely empirical, using predetermined tidal frequencies related to known astronomical and meteorological periods. It separates an observed time series of water level heights into a set of cosine curves, and then predicts by synthesizing the same curves for a future period. There is little geophysical enlightenment implicit in the procedure. Extended harmonic analysis increases the number of frequencies being considered; the previous limit was related to the use of a mechanical prediction machine, no longer a consideration since the advent of modern electronic computers. Although response analysis improves the accuracy of tidal predictions only slightly, it greatly enhances geophysical interpretation of the results, for the first time separating astronomical and radiational (meteorological) contributions. Pelagic (sea floor) tide data are necessary for global interpretations of tides, particularly for numerical modelers who combine sea-floor bathymetry with Laplace's tidal equations to produce cotidal and co-range charts for particular frequencies.

3. TECHNIQUES

To a large extent, most of the progress noted here has been made possible by the availability of fast electronic computers with large memory capacities.

3.1 Least square analysis.

Analysis of tidal data for n tidal frequencies requires a matrix solution of $(2n+1)$ normal equations, an impossible task 25 years ago, almost trivial today. This has become the usual harmonic method for a long series at many tidal institutions, (Zetler *et al.*, 1965).

3.2 Response analysis.

This uses as input functions the time-variable spherical harmonics of the gravitational potential and of radiant flux on the earth's surface; it computes complex weights for an observed series that are used for future predictions and for computing admittances, (Munk and Cartwright, 1966). At this time, it is primarily a research tool used to optimize geophysical interpretations.

* Scripps Institution of Oceanography, U.S.A.

3.3 Extended harmonic analysis.

This is an extension of (3.1) using many more tidal frequencies for extremely nonlinear tides, (Zetler and Cummings, 1967). If the matrices become too large, it is satisfactory to group constituents by species rather than solving for all simultaneously.

3.4 Pelagic tides.

The ability to accurately measure tides in deep water on the sea floor is a development of the last two decades. A recently published global compendium of tidal harmonic constants for pelagic stations contains information for more than a hundred places, (Cartwright *et al.*, 1979).

3.5 Numerical modeling of tides.

Solutions of Laplace's tidal equations now include energy dissipation, ocean shelf-attraction and the solid earth yielding to the weight of the oceanic tidal column. Some solutions for the principal tidal frequencies are reasonably accurate, (Hendershott, 1973).

4. RESULTS

The methods described in the previous section are to a large extent completed research and the application of these improvements depends largely on economic considerations.

5. RECOMMENDATIONS

The significant improvements described follow a half-century of depending on a methodology achieved by the end of the nineteenth century. Inasmuch as the various traditional tide manuals have not been updated to encompass these developments, this paper may be a useful interim guide to the changes.

INTRODUCTION

In populated areas where tides are important, local predictions have been published in newspapers for as long as living people remember; their availability is taken as much for granted as times of sunrise and sunset. For the most part, their accuracy is also unquestioned, although the public is aware that during storms and hurricanes "tides" much higher, and occasionally lower, than normal (i.e., predicted) may occur.

Although we know that tides result primarily from the tide-producing forces of the moon and sun acting upon the rotating earth, our knowledge of the dynamics of ocean and estuarine tides needs significant improvement; empirical procedures developed in the nineteenth century make it possible to prepare reasonably good tide predictions for any location provided that tide observations have obtained at that place in the past and the local sea-floor topography remains unchanged. It is a tribute to many scientists, in particular Sir William Thomson (later Lord Kelvin) and George Howard Darwin in England and William Ferrel and Rollin A. Harris in the United States, that the state of the art in tide predictions reached so high a plateau in the early twentieth century that significant improvements were not achieved for a half-century.

Although the Coast and Geodetic Survey (now called the National Ocean Survey) celebrated its centenary of published tide predictions in 1968, the Coast Survey had been supplying navigators with information from which they could prepare their own predictions as far back as 1844. This was done by including mean high-water lunitidal intervals (the interval between the moon's upper or lower transit over the local meridian and the following high water) and tidal ranges on the Survey's nautical charts. A published method for improving the crude predictions (presumably derived from John Lubbock's research in England in the 1830's) provided corrections for the effects of the phase of the moon and the declination and parallax of the moon and sun. However, the correlation between some tidal and lunar parameters were known and used long before the time of Newton.

Later in the nineteenth century, Thomson and Darwin developed the harmonic method of analyzing and predicting tides. The method uses sinusoids (tidal constituents) whose frequencies, derived from astronomic observations, are sums and differences of six basic frequencies in

the motions of the earth, moon, and sun: the day, month, year, 8.9 years (lunar perigee), 18.6 years (lunar nodes), and 21,000 years (solar perigee). The amplitude and phase lag behind a theoretical (equilibrium) tide for each constituent are obtained by analysis; a prediction synthesizes the same curves for same future period. The distortion of tides as they move into shallow water is simulated by analyzing for frequencies that are harmonics of the fundamental frequencies or combinations of these.

Sir William Thomson made the first tide-predicting machine in 1873 under the auspices of the British Association for the Advancement of Science; it summed 10 constituents and automatically traced a curve showing the predicted heights. This country's first mechanical tide prediction machine (19 constituents) was designed by William Ferrel of the Coast and Geodetic Survey. The machine, introduced in 1885, provided for times and heights of high and low tides to be read directly from the dial indicators but did not produce a plotted prediction. An improved mechanical predictor for 37 constituents was completed by R.A. Harris and E.G. Fischer of the Coast and Geodetic Survey in 1910. This machine was the first to compute simultaneously the height of the tide and the times of high and low waters, the machine automatically stopping to allow the information to be read from dials. It also produced a continuous plot with time marks for each hour, maximum and minimum. Although the 37 incommensurable curves summed by the machine range from one cycle per year to eight cycles per lunar day (24.8 h), no constituent accumulated a phase error greater than 2 degrees in a year's predictions, a remarkable achievement in designing and fabricating the gear system.

FIGURE 1. First U.S. tide-predicting machine, used 1885-1911.

FIGURE 2. Second U.S. tide-predicting machine, used 1912-1965.

For many North Sea locations, combinations of the customary shallow- water constituents cannot adequately reproduce the shape of the observed tides. Horn in Germany and Doodson in England developed nonharmonic procedures for empirically correcting predictions to improve the accuracy of published tables.

RECENT CHANGES

Rapid proliferation and improvements in electronic computers in the middle of this century finally ended the long status quo in the state of the art for tide predictions. Although the Coast and Geodetic Survey tide predictor withstood the first assault when predictions on an IBM 650 were found to take longer than on the half-century-old machine, its victory was short

lived, and by 1965 it had become a museum piece. A similar change took place at about the same time in England, but Kelvin mechanical tide-predictors may still be in use in some countries.

There were advantages other than speed and efficiency in shifting to electronic computers for tide prediction. As long as the fixed gearing of the mechanical predictor was limited to a finite set of particular constituents, research demonstrating the importance of other constituents had a low priority. Although there were sentimental regrets at replacing such a fine instrument, it was a distinct relief no longer to be dependent on the one machine; it was known to be wearing out, but, even worse, there was a fear of sabotage, particularly during war years.

In addition to the direct application of electronic computers to tide predictions, computer availability made possible more detailed analyses (for example, studies of 50 years of hourly heights, roughly a half million values) and digital recording (thus enhancing the state of the art for tide gauges as well as making possible more tide observations by reducing the manpower needs in data processing). Soon thereafter, dramatic advances were achieved in numerical modeling of tides, permitting for the first time research into the physics of tide generation in the world's oceans. Some of these advances have already contributed to improved predictions, and others will do so in the future.

It seems logical to group these recent improvements as follows:

A. *Data Analysis*

1. Change in harmonic analysis procedure. The traditional analysis in the Coast and Geodetic Survey (now the National Ocean Survey) solves for each constituent separately by a procedure that tries to emulate what would be achieved by cutting the marigram (tide record) into constituent periods (for example, every 25.82 h for O_1, a principal lunar diurnal constituent), piling the cut sections vertically and averaging a mean curve for the constituent period through the pile (Schureman, 1941). By means of stencil overlays, hourly heights (solar time) are identified as constituent hours (with errors not exceeding 0.5 h and algebraically averaging near zero), and then a Fourier analysis for the constituent frequency and possibly some harmonics is made of the constituent hourly means. An augmenting factor is applied to the amplitude to correct for a small reduction caused by using solar rather than constituent hours. Because it is impossible to have a finite length of observations that is commensurable for all tidal frequencies, the length of record chosen for Fourier analysis minimizes but does not completely remove the effect of interfering constituents. This effect is removed to a large extent by a further process called "elimination." In theory, repetitive elimination would refine the results even more, but this was not found necessary.

It is far more direct to solve for all constituents simultaneously, obtaining the complex amplitudes of cosine curves for each constituent that minimize the residuals in a least-square sense. For n constituents, we solve for $2n + 1$ coefficients (including the mean term) and then obtain the harmonic constants (amplitude and phase lag for each constituent) by simple trigonometry. For 37 constituents, a 75×75 matrix could not be solved without very large computers, and hence this approach was unthinkable until recent times. The procedure has been found to be more accurate for one-year analysis than the traditional methods, and it is now used in the National Ocean Survey (NOS) in this country and by the tidal authority in the United Kingdom, the Bidston Observatory of the Institute of Oceanographic Sciences. The process does not require equally spaced data (in the time sense) and will work with data in random time, although the software is more complicated as each data point must be identified in time (Zetler *et al.*, 1965). Comparative tests of the traditional and least-squares analysis procedures for 29-day series (approximate synodic period for phase, parallax, and declination of the moon) disclosed no advantage in the newer method; therefore the classical procedure has been retained in NOS, but the procedure has been modernized (in particular, stencil summing has been done away with). In 29-day analysis only K_1 and O_1 and M_2,S_2, and N_2 can ordinarily be resolved for species 1 and 2 (1 and 2 cycles per day, respectively).* Because the classical

*Principal tidal constituents: K_1 is lunisolar diurnal, O_1 is lunar diurnal, M_2 and N_2 are lunar semidiurnal, and S_2 is solar semidiurnal.

method infers the effect of other disturbing constituents in the elimination process, this probably gives it an advantage over the straightforward least-square analysis for the five constituents that offsets the improvements implicit in the latter process.

2. Extended harmonic analysis. Once tidal predictions were no longer constrained to a finite set of constituents, the door was opened to improving shallow-water predictions by adding additional compound tides (integral sums and differences of principal constituents). Two independent studies used 114 constituents with frequencies up to 12 cycles per day to improve predictions for Anchorage (Alaska) and for the Thames estuary (Zetler and Cummings, 1967; Rossiter and Lennon, 1968). Solving for 114 constituents simultaneously would involve a 229 × 229 matrix; fortunately this is not necessary as it has been demonstrated that sidebands are important only within each species (thus K_1 sidebands do not affect M_2), and therefore the solution may be simplified by requiring only that any particular matrix include all constituents within a species. A.S. Franco (Instituto de Pesquisas Tecnologicas, Sao Paulo, Brazil) has recently developed another approach using a matrix of the Fourier coefficients within a species to solve for constituent harmonic constants including numerous compound tides.

3. Determination of the continuum. On occasion, Walter Munk has used the expression, "Noise exists everywhere but in textbooks on tides." He was referring to the tendency to look only at the tidal lines in the spectrum, disregarding the level of the continuum between the lines. In a plot of energy (or amplitude) versus frequency, the extent to which the value at a tidal line protrudes above the continuum is a measure of reliability of the tidal constants for the constituent. Over a period of a few years, Munk and various associates made a determined effort to evaluate the level of the continuum for a wide band of frequencies. Very sharp filters discriminating against tidal lines were used to establish the continuum between tidal species (Munk and Bullard 1963). Then it was demonstrated that if the noise level is sufficiently low, two tidal constituents can be resolved in a record of length shorter than their synodic period (Munk and Hasselmann, 1964). An extremely fine-resolution analysis in the low frequencies (0 to 0.75 cycle per day) showed the continuum decreasing monotonically in energy for higher frequencies and no significant peaks other than previously determined tidal constituents (Groves and Zetler, 1964). Finally cusps of energy were found between tidal groups (separations of 1 cycle per month) and even between tidal lines within a group (Munk *et al.*, 1965). The knowledge derived in these studies was particularly important in the development of response analysis and prediction (see below) and serves to establish a limit on the accuracy to which one may aspire for barotropic tide predictions in the open ocean.

4. Response analysis and prediction. For any linear system, a input function $\chi_m(t)$ and an output function $\chi_n(t)$ are related according to

$$\chi_n(t) = \int_{-\infty}^{\infty} \chi_m(t-\tau)\omega_{mn}(\tau)d\tau + \text{noise } (t) ,$$

where $\omega_{mn}(\tau)$ is the "impulse response" of the system, and its Fourier transform

$$Z_{mn}(f) = \int_{-\infty}^{\infty} \omega_{mn}(\tau)e^{-2\pi if\tau}d\tau = R_{mn}(f)e^{i\Phi mn(f)}$$

is the system admittance (coherent output/input) at frequency f.

Response tidal analysis and prediction (Munk and Cartwright, 1966) uses as input functions the time-variable spherical harmonics of the gravitational potential and of radiant flux† on the earth's surface. In practice, the integrals are replaced by summations; χ_m, ω, and Z are complex. The discrete set of ω values are termed response weights.

This method is the first successful major departure from the traditional solutions in which the tide oscillations are described by the amplitudes and phase lags for a finite set of predeter-

†A function designed to vary with the radiant energy falling on a unit surface in a unit time; it is related to daily atmospheric pressure and wind variations and to seasonal changes in ocean temperature.

mined frequencies. Subsequently it was recommended that response analysis of short records (about one month) of pelagic tidal measurements use a response prediction at a nearby coastal station as the reference series (Cartwright *et al.*, 1969). The calculation of traditional harmonic constants from response admittances made results of the two methods compatible (Zetler *et al.*, 1969). The optimum number of weights in response analysis depends directly on the length of record and inversely on noise level in a tidal band; more weights degrade the prediction and generate an artificial wiggliness in the admittance (Zetler and Munk, 1975). This study showed for the first time that better results are obtained by centering the lags to a potential retarded by the age of the tide‡ rather than to a potential centered on the prediction time.

SCOR* Working Group 27, "Tides of the Open Sea," conducted an analysis workshop in conjunction with an intercomparison of open sea tidal pressure sensors. The report (Unesco, 1975) shows a clear superiority for response procedures as compared with classical methods used by various national tidal groups. In addition to this statistical advantage, response analysis is more intellectually pleasing in that one uses the entire tide-producing potential rather than having arbitrarily to choose a finite set of tidal frequencies.

The ability to separate gravitational and radiational contributions to the tide resolves an unsatisfactory aspect of results from classical analysis. If one plots the phase angles or the amplitude admittances (ratio of analyzed to equilibrium amplitudes) from traditional analysis against frequency, one usually finds a sharp bend or even a discontinuity at S_2 (30°/solar hour). It is not reasonable that the ocean oceans should exhibit such abrupt changes, particularly always at the same frequency. The smoothness of the plots obtained for the gravitational admittances in Figure 3 (Zetler and Munk, 1975) using response procedures is undoubtedly due to the separation of radiational from gravitational inputs, whereas classical analysis produces combinations of the two.

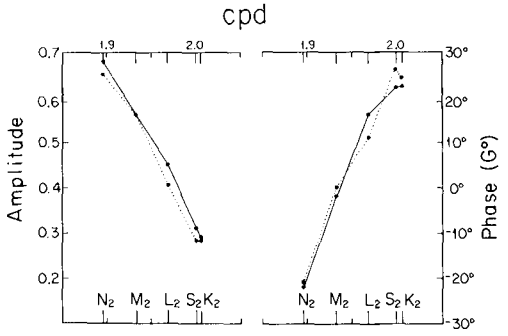

FIGURE 3. Amplitude and phase admittances for Bermuda referred to the gravitational potential. The solid lines are grav admittances from (grav and rad) response analysis; the dotted lines are admittances from traditional analysis. The response analysis was for three 355-day series over a 9-year period. The traditional analysis (1 year, 1934, IHB Spec. Pub. 26, #600) furnishes a lumped (vector) sum of grav and rad admittances.

‡The time interval between a maximum range in the equilibrium tide and a comparable range at a particular place. For example, equilibrium spring tides occur at new and full moon; in the ocean they occur 0.984 (S_2°−M_2°) hours later. There are comparable ages for maximum ranges related to perigee and to maximum declination of the moon.

*Scientific Committee on Ocean Research

B. *Numerical Modeling*

A cotidal chart is one showing an areal distribution of times of high tide for particular constituent relative to the equilibrium (theoretical) time of high tide for the same constituent. The cotidal lines, labeled in either solar or constituent hours, identify the locus of points at which high tide for the constituent occurs simultaneously. A feature of such maps is a system of nodal points, known as amphidromes, at which there is no vertical rise or fall. Some charts also include corange lines, contours of equal constituent amplitude. Near an amphidrome, corange lines tend to be concentric about the amphidrome with amplitudes increasing with distance from the zero amplitude point.

Historically, cotidal charts have been based on seaward extrapolation from coastal and island observations supplemented by general knowledge of how tides behave in mathematically described basins. Inasmuch as ocean tides are modified significantly in the continental coastal zones, use of coastal and, even worse, harbor and estuary observations make these ocean projections quite speculative. Nevertheless, until huge electronic computers became available, these empirical efforts were as good as could be done. In retrospect, some of the early cotidal charts have been found to be remarkably good and have served many useful purposes; those of Rollin Harris are outstanding examples of an advanced state of the art at the beginning of this century (Figure 4).

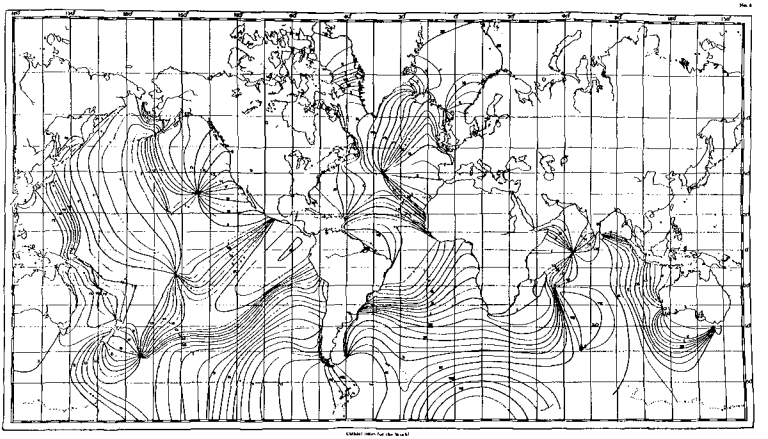

FIGURE 4. Harris cotidal chart for M_2.

In a parallel but quite different effort, hydrodynamicists have traditionally been concerned with solving the tidal equations developed by Laplace in 1775. Because of their complexities, various simplifying assumptions for hypothetical basins (such as flat bottom, boundaries, and stability) have been necessary (Hendershott and Munk, 1970). Although much has been learned in these earlier scientific efforts, the solutions have had little or nothing to do with tides in the real oceans. Realistic calculations require detailed bathymetry and boundaries, inconceivable before the advent of large electronic computers and marginal even today. When Pekeris presented a global solution for M_2 at an international meeting about 15 years ago, Joseph Proudman, a prominent tidal authority, commented that he had not anticipated seeing this degree of success in his lifetime.

A recent summary of the activities of SCOR Working Group 27, "Tides of the Open Sea" (Cartwright, 1975) noted various problems in numerical modeling of tides: "There are

numerous esoteric sub-problems concerning stability, mesh size, boundary and depth topography, friction, but the most important and difficult appear to be representation of energy losses at the boundaries of shallow seas and at places of steep topography where internal tides are generated, and the solution of the equations modified for a yielding Earth."

Hendershott's more recent numerical studies include energy dissipation, ocean self-attraction, and the solid earth yielding to the weight of the oceanic tidal column. Figure 5 is a recent M_2 cotidal chart by Hendershott and Parke. A description of other contemporary numerical tidal solutions (Hendershott, 1973) furnishes information on the tidal frequencies considered, boundary conditions, dissipation mechanisms (if any), and whether earth tides are considered

Thus, theoretical studies are now using real data in realistic ocean models. Solutions are improving; in particular, it appears that an amphidrome first identified in a numerical study is real. However, results indicate that many ocean areas are nearly resonant at semidiurnal

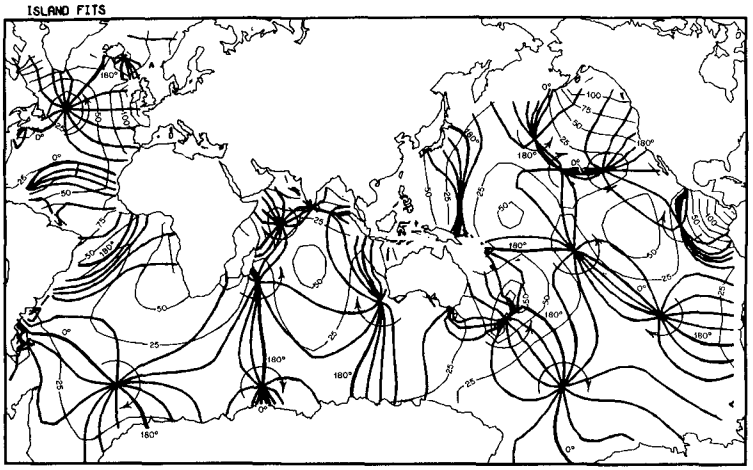

FIGURE 5. Hendershott and Parke cotidal and corange chart for M_2.

periods. As a result, a variation in mean depth of only several hundred meters may change the M_2 amplitude by a factor of 2 or 3. Furthermore, it has been found that changing the coastline slightly or refining the grid from a 2° to a 1° mesh changed the M_2 amplitude by as much as 3 m (Pekeris and Accad, 1969). This extreme sensitivity make it difficult to evaluate empirically the contribution of various parameters.

In the past, physical models of various estuaries have been built in order to determine the effect of proposed man-made structures on the tidal regime in the estuary. For example, the model of San Francisco Bay (built in Sausalito by the U. S. Army Corps of Engineers) has been used in studying the effect of proposed salinity barriers on the tide in the Bay. Garrett (1977) recently used a numerical model to study the effect of a proposed power-generating system in the Bay of Fundy, with the large ranges of tide as the energy source. Ordinarily one would expect such a utilization to diminish the tidal range and would need to consider the economic consequences of the anticipated change. However, Garrett found the resonant peak of the basin to be only slightly higher than the M_2 frequency (thus accounting for large tides) and that the proposed structure would reduce the resonant frequency, bringing it even closer to the M_2 frequency, and so would lead to very little, if any, reduction in amplitude.

C. *Recording*

Pelagic pressure sensors, capable of measuring the tide on the sea floor in the deep parts of the oceans are an important technological development in recent years (Unesco, 1975). Pioneered by Frank Snodgrass at Scripps Institution of Oceanography and Marc Eyries in France, the state of the art has rapidly advanced to the point that only financial considerations deter us from obtaining the global grid of tide observations needed for an optimum set of cotidal and corange charts. A recently published global compendium of tidal harmonic constant for pelagic stations contains information for more than a hundred places, (Cartwright *et al.*, 1979).

In the Unesco report on an international intercomparison of open-sea tidal-pressure sensors, five types of sensor were found to intercalibrate closely (Unesco, 1975). Among the several mooring techniques used in the experiment, the self-contained acoustic "pop-up" unit showed a clear superiority. In the MODE (Mid-Ocean Dynamics Experiment) exercise, tidal data were obtained for the first time from an array of pressure sensors on the sea floor. Figure 6 shows that the phase angles obtained for MODE stations match Dietrich's M_2 and K_1 cotidal charts well (Zetler *et al.*, 1975). The M_2 tidal currents inferred from the gradients of observed

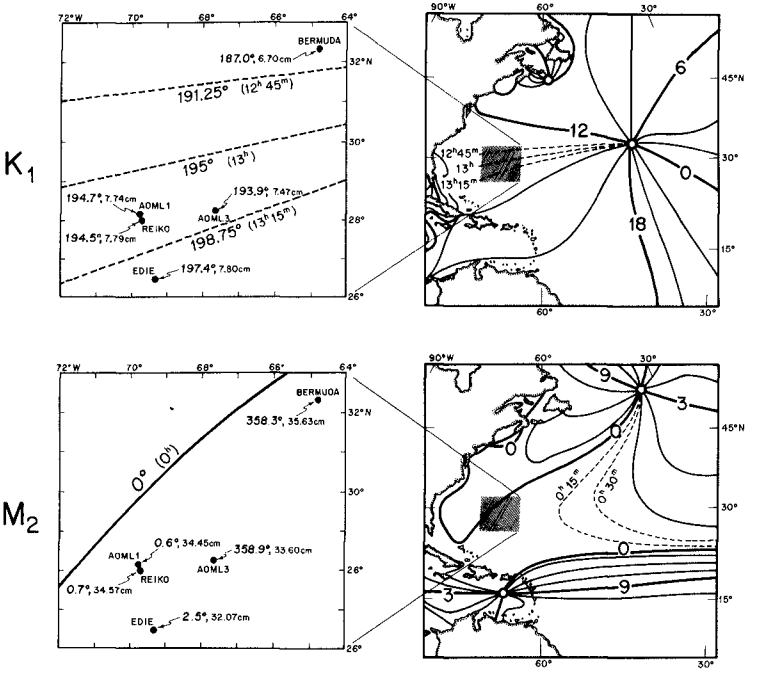

FIGURE 6. Right panels show Dietrich's (1944) cotidal lines in the North Atlantic for K_1 and M_2 tides, respectively. Values are in solar hours, with dashed curves designating interpolation by Zetler *et al.*, (1975). The MODE area falls within the shaded square, which is shown on an enlarged scale in the left panels, for comparison with the results at MODE stations (·).

pressures fit the barotropic component of the observed tidal currents reasonably well; the latter also contain large baroclinic components, whereas the small baroclinic contributions to the pressure gradients have been further reduced because the station spacings are roughly comparable to the baroclinic wavelength.

Numerical modelers have recommended observations at "antiamphidromes" (locations of maximum tidal amplitude) in order to calibrate their results. Furthermore, to work with intermediate scale models (portions of the world's oceans), because of the need for more dense topographic grids, they will need tidal observations at the boundaries of sections in the open ocean. The technology for this is now available, and some programs along these lines are already under way at the Institute of Oceanographic Sciences in England.

Time has passed by the 2000 or so conventional tide gauges used throughout the world; there have been few changes since Lord Kelvin argued the case for using a pencil before the Institution of Civil Engineers in 1882. The gauges continue to measure the height of a float in a stilling well (cylinder with a small orifice near the bottom to filter out wind waves). The only significant change has been the utilization of digital recording on magnetic and punched paper tape; these have significantly reduced tabulation and analysis costs, making it possible to obtain and process more observations with available resources.

CONCLUSION

Subsequent to the preparation of the abstract, a new publication (Zetler, 1982) describes modifications to the computing processes for tide analysis and prediction at the U.S. National Ocean Survey. This publication serves as a supplement to various National Ocean Survey manuals, in particular to Schureman (1941).

ACKNOWLEDGMENT

This study was supported by a grant from the National Ocean Survey, National Oceanic and Atmospheric Administration, Rockville, MD 20852, U.S.A.

REFERENCES

Cartwright, D.E. (1975). The future of oceanic tide research, Report of SCOR/IAPSO/Unesco Working Group 27, "Tides of the Open Sea" unpublished.

Cartwright, D., W. Munk, and B. Zetler (1969). Pelagic tidal measurements, a suggested procedure for analysis, *EOS 50*, 472.

Cartwright, D.E., B.D. Zetler, and B.V. Hamon, (1979). Pelagic tidal constants. IAPSO Publication Scientifique No. 30, IUGG, Paris. 65 pp.

Garrett, C. (1977). Predicting changes in tidal regime: the open boundary problem. *J. Phys. Oceanog. 7*, 171.

Groves, G.W., and B. D. Zetler (1964). The cross-spectrum of sea level at San Francisco and Honolulu, *J. Marine Res. 22*, 269.

Hendershott, M.C. (1973). Ocean tides, *EOS 54*, 76.

Hendershott, M., and W. Munk (1970). Tides, *Ann. Rev. Fluid Mech.2*, 205.

Munk, W.H., and E.C. Bullard (1963). Patching the long-wave spectrum across the tides, *J. Geophys. Res. 68*, 3627.

Munk, W.H. and D.E. Cartwright (1966). Tidal spectroscopy and prediction, *Phil. Trans. R. Soc. London A 259*, 533.

Munk, W.H., and K.F. Hasselmann (1964). Super-resolution of tides, Studies on Oceanography, Hidaka volume (Tokyo), pp. 339-344, reprinted U. of Washington Press, 1965.

Munk, W.H., B. Zetler, and G.W. Groves (1965). Tidal cusps. *Geophys. J. 10*, 211.

Pekeris, C.L., and Y. Accad (1969). Solution of Laplace's equation for the M_2 tide in the world oceans, *Phil. Trans. R. Soc. London A 265*, 413.

Rossiter, J.R., and G.W. Lennon (1968). An intensive analysis of shallow water tides, *Geophys. J. R. Astron. Soc. 16*, 275.

Schureman, P. (1941). *Manual of Harmonic Analysis and Prediction of Tides,* C&GS Spec. Publ. No. 98, U.S. Government Printing Office, Washington, D.C.

Unesco (1975). An intercomparison of open sea tidal pressure sensors, Report of SCOR Working Group 27, "Tides of the Open Sea," Unesco tech. papers in marine science, 21.

Zetler, B.D., M.D. Schuldt, R.W. Whipple and S.D. Hicks (1965). Harmonic analysis of tides from data randomly spaced in time. *J. Geophy. Res. 70 (12);* 2805-2811.

Zetler, B.D., and R.A. Cummings (1967). A harmonic method for predicting shallow-water tides, *J. Marine Res. 25,* 103.

Zetler, B., D. Cartwright, and W. Munk (1969). Tidal constants derived from response admittances, Sixth International Symposium on Earth Tides, Strasbourg. pp 175-178.

Zetler, B., and W. Munk (1975). The optimum wiggliness of tidal admittances, *J. Marine Res. Suppl. 33,* 1.

Zetler, B.D., W.H. Munk, H. Mofjeld, W.S. Brown, and F.O. Dormer (1975). MODE tides, *J. Phys. Oceanog. 5,* 430.

Zetler, B.D. (1982). Computer applications to tides in the National Ocean Survey, Supplement to Manual of harmonic analysis and prediction of tides (Special Publication No. 98). National Ocean Survey, Rockville, MD 20852, U.S.A. 85pp.

AUTOMATED DIGITAL SIMULATION OF TIDES & LONG WAVES

R.F. Henry*

Abstract

A system for indirect programming of shallow-water models is discussed, particular attention being given to facilitating successful operation by novice users. Pre-developed programs are used to check numerical coding of model layout, to execute the finite-difference computations required at each time step and to analyse the computed surface elevations and velocities. Many error-prone steps are thus eliminated and model development is speeded for modest increase in computation costs.

1. Introduction

This paper describes a method which simplifies development of numerical models of long-wave phenomena such as tides, tsunamis and storm surges. The irregular geometry of most coastal seas complicates the programming of numerical models severely, even for the simplest finite-difference representations of the governing shallow-water equations. The principal aim of the system of programs described here is to automate the detailed programming steps necessary to fit a finite-difference scheme to a particular coast. The availability of such programs permits even an inexperienced programmer to develop a working model quickly and, at the subsequent calibration and verification stages, allows experimental changes, such as relocation of boundaries, to be made rapidly without extensive debugging checks. The modeller is thus freed from programming difficulties and delays and is able to concentrate on scientific aspects of the work.

The basic concept used is that, after a suitable grid has been laid out to cover the coast in question, instead of programming the specific computational steps necessary for each variable on the grid, a numerical code is assigned to each variable to indicate the nature of that point and the type of calculation to be carried out there at each time step. In this way the task of programming the finite-difference calculations is split into two distinct stages,

a) numerical coding of coastline layout
b) development of a general time-stepping subroutine, which, given the corresponding code, performs the computation required at each grid-point under the particular finite-difference scheme adopted.

The advantage of this approach is that step b) has to be tackled

* Institute of Ocean Sciences, Sidney, B.C., Canada.

only once for a particular finite-difference scheme, and when the time-stepping subroutine has been fully checked out, a major source of programming errors is eliminated from all models employing it subsequently. Provided that the same governing equations hold, only stage a) has to be carried out when a new model is developed and as shown later, a graphical checking procedure can be used to ensure that no errors are made at that stage.

Leendertse (1967) used numerical coding to specify location of model boundaries but Heaps (1969) seems to have been first to perform all computations on the grid indirectly via numerical codes. Abbott, Damsgaard and Rodenhuis (1973) announced an extensive proprietary software package for indirect programming of shallow-water models, but limited information about this system and its later developments has appeared in the open literature. The work described in the present paper essentially extends Heaps' method, increasing the practicability by using a simpler grid, by breaking the coding process down into stages of which only the simplest has to be carried out by the user and by providing graphical means for checking the coding. The result is a set of programs, which can be used easily in 'black-box' fashion by inexperienced programmers but which are straightforward enough to be altered fairly readily by more experienced users to suit special requirements.

Unfortunately, the combination of grid and difference-scheme used by Heaps proves rather cumbersome for indirect programming. Because both components are defined at all velocity-points, 19 distinct types of velocity point are possible, even though only two types of boundary are permitted. This complexity makes it difficult to code the model geometry correctly. The Richardson grid (Figure 1) used here is better suited to indirect programming, as far fewer distinct configurations can occur at boundaries. This has facilitated development of a plotting program to permit visual checking of coded model layout. A plot of the model boundaries is produced from the allotted numerical codes. Comparison with the original grid diagram then quickly reveals any errors in coding. If the model boundaries are altered during development, the revised layout can be checked similarly. This graphical feedback makes indirect programming considerably more practicable.

To summarize the procedure, the modeller is required to choose a Cartesian grid of suitable orientation, size and spacing for the water body in question and to provide a corresponding array of mean water depths. The position and nature of the various boundaries are then coded numerically as described later and the coding is checked visually using a pre-developed graphical program. The numerical model is then programmed, all the necessary finite-difference calculations being handled by a pre-developed time-stepping subroutine. The modeller must supply a subroutine which provides values of any time-dependent forces or boundary conditions influencing the water body.

A model programmed using this technique takes roughly 20% more computing time than an equivalent model in which the finite-difference equations are programmed specifically for the particular grid in

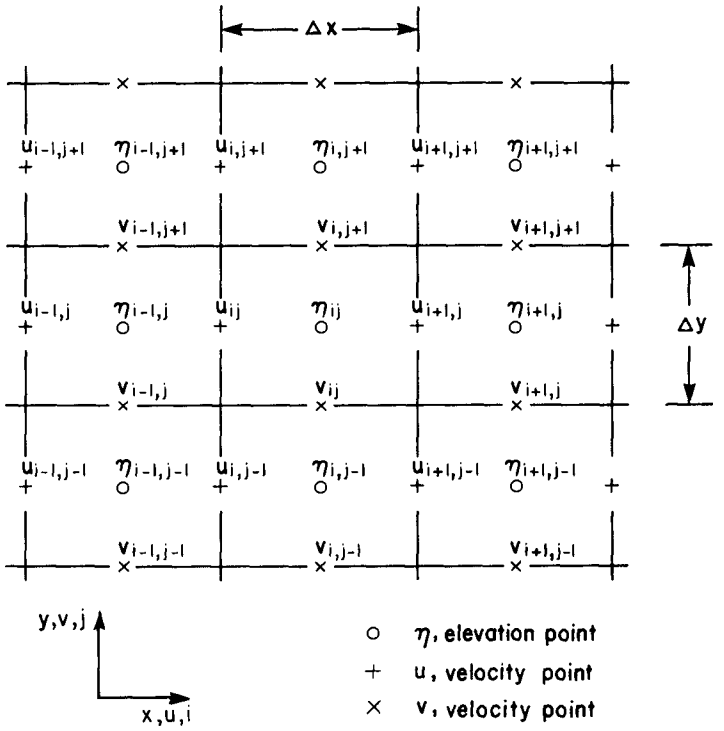

Fig. 1. The Richardson Grid

question, but the saving in initial programming effort and subsequent debugging time is substantial even for an inexperienced programmer. Memory requirements are increased by the need to store the code arrays required. Full details of the various programs which have been developed to implement the graphical and finite-difference operations discussed above are given in Henry (1982).

2. Governing Equations

The methods described in this paper apply to problems governed by the partly linearized shallow water equations

$$\eta_t = -(du)_x - (dv)_y \tag{1}$$

$$u_t = -g\eta_x + fv - F^{(u)} + G^{(u)} \tag{2}$$

$$v_t = -g\eta_y - fu - F^{(v)} + G^{(v)} \tag{3}$$

where

$\eta(x,y,t)$ = elevation of water surface above mean level
$u(x,y,t)$ = depth-averaged velocity in x-direction
$v(x,y,t)$ = depth-averaged velocity in y-direction
$d(x,y)$ = mean water depth
x,y = Cartesian coordinates in horizontal plane
f = Coriolis coefficient (assumed constant)
g = acceleration due to gravity
t = time

$F^{(u)}$ and $F^{(v)}$ represent bottom friction terms. One stepping subroutine makes provision for friction linearly proportional to velocity, i.e. $F^{(u)} = ru$, $F^{(v)} = rv$, while another uses the more commonly assumed quadratic friction forms:

$$F^{(u)} = \frac{ku(u^2+v^2)^{1/2}}{d} \quad ; \quad F^{(v)} = \frac{kv(u^2+v^2)^{1/2}}{d} \tag{4}$$

The respective friction coefficients r and k are currently taken to be uniform throughout the model, but later versions of the stepping subroutines will permit the friction coefficient to vary with position. Also it is intended to supply a version using $(d+\eta)$ in place of d in the denominators of (4), in order to simulate fluid behavior in very shallow water more accurately. By design, these stepping subroutines are readily interchangeable, so that variations on the underlying finite-difference scheme can be tried in the same model with negligible reprogramming. It would be possible to write a master stepping subroutine containing all options likely to be required, but this would be less economical in computing time.

The terms $G^{(u)}$ and $G^{(v)}$ in equations (1) - (3) represent relevant forcing effects due to external influences. In general these will be both time- and space-dependent. Appropriate values for these must be specified for the particular problem considered through a user-provided subroutine.

3. The Richardson-Sielecki Finite-Difference Scheme

The simple Richardson grid shown in Figure 1 was chosen as the basis for the finite-difference scheme because it minimizes storage requirements and permits particularly simple simulation of coastlines. At interior points of the grid, equations (1) to (3) are represented by Sielecki's (1968) scheme.

$$\frac{\eta'_{ij} - \eta_{ij}}{\Delta t} = -\frac{(d_{ij} + d_{i+1,j})u_{i+1,j} - (d_{i-1,j} + d_{ij})u_{ij}}{2.\Delta x} - \frac{(d_{ij} + d_{i,j+1})v_{i,j+1} - (d_{i,j-1} + d_{ij})v_{ij}}{2.\Delta y} \tag{5}$$

$$\frac{u'_{ij} - u_{ij}}{\Delta t} = -g\frac{\eta'_{ij} - \eta'_{i-1,j}}{\Delta x} + f\tilde{v}_{ij} - F^{(u)}_{ij} + G^{(u)}_{ij} \tag{6}$$

$$\frac{v'_{ij} - v_{ij}}{\Delta t} = -g\frac{\eta'_{ij} - \eta'_{i,j-1}}{\Delta y} - f\tilde{u}'_{ij} - F^{(v)}_{ij} + G^{(v)}_{ij} \tag{7}$$

where

Δt = time step
$\Delta x, \Delta y$ = grid interval sizes in in x,y directions respectively
d_{ij} = mean water depth at elevation point η_{ij}

$$\tilde{u}_{ij} = \frac{1}{4}\left[u_{i,j-1} + u_{1+1,j-1} + u_{ij} + u_{i+1,j}\right]$$

$$\tilde{v}_{ij} = \frac{1}{4}\left[v_{i-1,j} + v_{ij} + v_{i-1,j+1} + v_{i,j+1}\right]$$

Primes indicate variables updated during the current time step; unprimed variables are those evaluated at the previous step. The use of old (unprimed) values of v in the Coriolis term in (6) and new (primed) values of u in the corresponding term in (7) eliminates the need to store any but the most recently updated values of each variable, provided that the equations are applied in the order given, that is, at each time step, all η_{ij} are updated, then all of the u_{ij}, and finally all the v_{ij}. The same conclusion applies if

evaluated in the order η,v,u, using old values of u in the v-equation and new values of v in the u-equation. To reduce possible bias, the stepping subroutines provided evaluate the variables in the order η', u', v', on odd-numbered steps and η', v',u', on even-numbered steps.

Sielecki showed that the condition for stability of the above scheme, in the absence of boundaries, is

$$\Delta t \leq \frac{\Delta x \cdot \Delta y}{[g d_{max}(\Delta x^2 + \Delta y^2)]^{1/2}} \qquad (8)$$

4. Numerical Coding of Model Geometry

The choice of grid for a model is necessarily a compromise among many requirements. The location and orientation of the grid is influenced mainly by the accuracy with which the coastlines can be approximated by line segments of the grid. This fit can usually be improved by increasing the grid resolution, which implies using more variable points and taking shorter time steps to maintain numerical stability, thus raising computing costs. Once the grid has been chosen, as objectively as possible, all variable points on the grid are allotted appropriate (primary) integer codes. An elevation point η_{ij} is given the code number $(KE)_{ij} = 1$ if the point lies on a sea-boundary along which surface elevation is to be specified as a function of time; any other elevation point has the code $(KE)_{ij} = 0$.

Points on the grid where velocity components u_{ij} or v_{ij} are defined are each allotted a corresponding subscripted code $(KU)_{ij}$ or $(KV)_{ij}$ which can have the following values:

Primary codes KU,KV at Velocity Points	Location of Velocity Point
1	on line segment representing land boundary (coastline or island)
2	on line segment representing spit or causeway with water on both sides
3	at sea boundary where velocity is to be specified
4	on radiating sea boundary (discussed below)
0	elsewhere

The allocation of these codes will now be illustrated with the aid of the very simple example in Figure 2(a). Here, the velocities u_{11}, u_{12}, u_{13} on the sea-boundary at the left side and v_{41}, v_{51} at the bottom edge of the grid are specified functions of time derived from current meter observations. Elevations η_{72}, η_{73}, η_{74} at the right-hand sea boundary are also known functions of time, obtained from water level gauges.

The upper boundary on which points v_{46},v_{56} are located is a

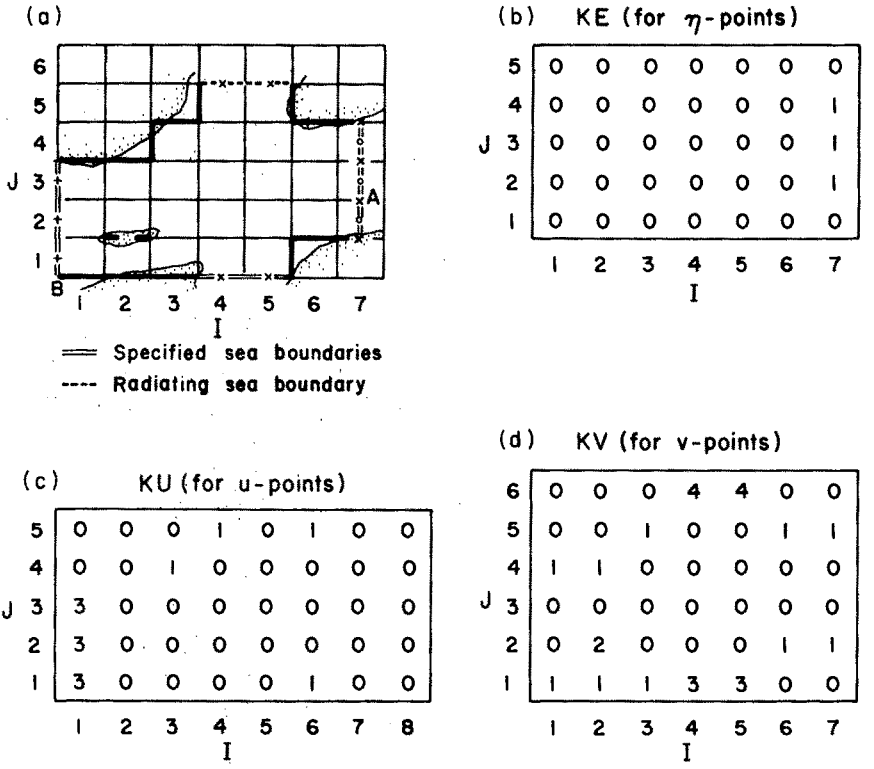

Fig. 2. Sample Water Body and Primary Codes

radiating sea boundary. Where there are good grounds for assuming that no waves enter the model area from an adjacent water body, it is appropriate to use a radiation condition on the sea boundary between the two. This permits waves reaching the sea boundary from the interior of the model to pass out of the model domain.

When choosing the model grid initially, radiating sea boundaries parallel to the x-axis of the model should be placed to run through v-points on the grid (as illustrated in Figure 2). Similarly, those parallel to the y-axis should run through u-points. It is assumed that the radiation problem can be treated one-dimensionally at each velocity point on the sea boundary and thus that the surface elevation and normal velocity at the boundary are related by

$$\text{outward normal velocity} = (g/d)^{1/2} \times \text{elevation}$$

Since there are no elevation points actually on the boundary, the nearest interior elevation value is taken instead, so that the formulas used in the stepping subroutines for u-points on radiating boundaries facing in the positive or negative x-direction are respectively:

$$u_{ij} = (g/d_{i-1,j})^{1/2} \cdot \eta_{i-1,j}$$

or

$$u_{ij} = -(g/d_{ij})^{1/2} \cdot \eta_{ij}$$

Similarly, at radiating sea boundaries facing in the positive or negative y-directions, the formulas used are respectively:

$$v_{ij} = (g/d_{i,j-1})^{1/2} \cdot \eta_{i,j-1}$$

or

$$v_{ij} = -(g/d_{ij})^{1/2} \cdot \eta_{ij}$$

For example, in the model shown in Figure 2, at each time step, the new velocity values v'_{46}, v'_{56}, on the radiating boundary are found from the newly-updated elevations η'_{45}, η'_{55} by putting

$$v'_{46} = (g/d_{45})^{1/2} \cdot \eta'_{45} \; ; \quad v'_{56} = (g/d_{55})^{1/2} \cdot \eta'_{55}$$

This simple but effective radiation condition was introduced by Heaps (1974). In practice, transmission across the boundary is nearly complete for waves impinging normally on the boundary, but there is considerable unwanted reflection when the angle of incidence exceeds 45°. Tests show that use of the radiation condition can reduce the permissible time step by as much as 50%. Equation (8) should therefore be amended to:

$$\Delta t \leq \frac{\Delta x . \Delta y}{2[\,gd_{\max}\,(\Delta x^2 + \Delta y^2)\,]^{1/2}}$$

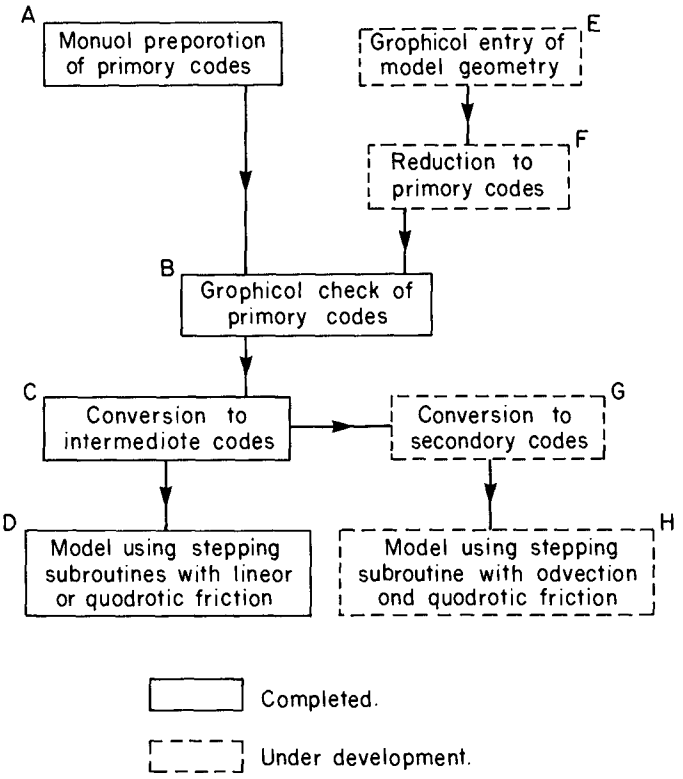

Fig. 3. Preparatory Steps

to ensure stability in models using the above type of radiating boundary.

There is to be no flow across any 'land' boundary in the model and consequently, all the corresponding velocity components, e.g. u_{34}, u_{61}, v_{11}, v_{24}, are to be set at zero. Also, v_{22} is zero, as there can be no transverse flow at the line segment representing the small island where v_{22} is situated.

The arrays of numerical codes which describe the geometry of this model, according to the list given above, are shown in Figures 2(b),(c) and (d). This coding stage of the procedure is represented by box A in Figure 3, which shows the sequence of preparatory steps required for a model. Currently, a file containing the numerical code arrays has to be prepared by the modeller, but work is in progress using interactive graphics (E in Figure 3) to replace manual entry. The coastlines and superposed grid are displayed and the grid segments which are to represent boundaries are then selected and designated using a cursor or light pen. The nature of each boundary is entered at the same time through the keyboard. However, manual entry of the primary codes, which will remain necessary in the absence of suitable graphics hardware, is very straightforward, due to the limited number of codes involved and the provision of a program for graphical checking. The latter requires only an off-line graphics facility.

5. Graphical Check of Primary Codes

Correct description of the location and types of the model boundaries is of such obvious importance that a program has been developed for plotting the model layout defined by the allocated primary codes. The plotting scale used can be set equal to that of the chart on which the model grid was set out, so that by overlaying the plot on the chart the correctness of the numerical coding can be checked very readily. It is also worthwhile repeating this graphical check (C in Figure 3) whenever changes are made to the primary codes, for whatever reason.

Figure 4 shows the plot thus produced from the primary codes given in Figures 2 (b), (c) and (d). The boundaries are distinguished by use of the following line codes:

———	closed boundaries
— —	spit or causeway
═══	sea boundary with specified variable
— — —	radiating sea boundary

The plotting program uses standard CALCOMP plotting subroutines.

6. Conversion from Primary to Intermediate Codes

Although the primary codes describe fully the location and type of every boundary, they do not contain certain information about relative locations required by the time-stepping finite-difference

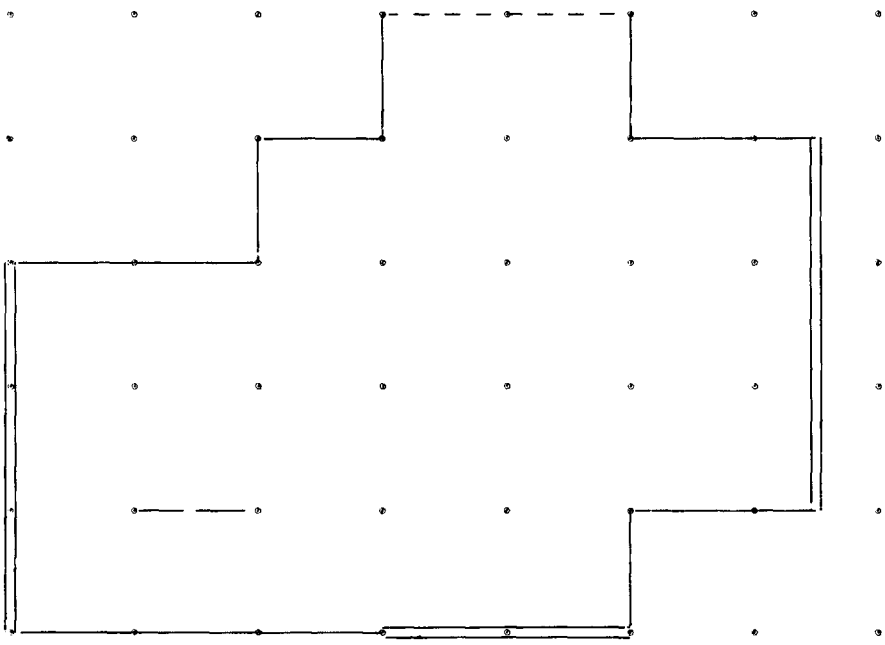

Fig. 4. Layout of Sample Model as Plotted from Primary Codes

subroutines. For this reason, another program is used (B in Figure 3) to convert the primary codes into a more numerous set of 'intermediate' codes. The latter distinguish, for example, between inactive variable points on land (or outside the model domain) and active points in the model interior. The primary to intermediate conversion program also works out the bounds of the area of grid containing active variable points, thus reducing the amount of computation required in the time-stepping subroutines at each time-step. Users generally need not concern themselves with details of the intermediate codes and scanning bounds.

Boxes G and H and Fig. 3 refer to programs being developed to permit substitution of a stepping subroutine based on the full non-linear shallow-water equations in place of the partly linearized versions presently available. An even fuller set of codes, here termed 'secondary', are required in that case to cope with the variety of special cases which occur in the vicinity of boundaries.

7. Programming a Model

After the above preparatory stages of coding, checking and code conversion have been carried out, one proceeds very much as in programming a model by the usual direct method, except that the intricate programming of the finite-difference calculations is replaced by a simple call to the appropriate time-stepping subroutine. The other major difference is that time-dependent forces and boundary values are supplied at each time-step by calling a subroutine which loads specific storage locations with this data, rather then by summoning values directly where required in the finite-difference coding.

It is useful to visualize the linear arrays used to store boundary values as lying parallel to the boundaries on which the values are used, as shown in Figure 5, which refers to the simple example of Figure 2. By having each array the same size as its respective side of the model grid, the same numbering can be used for both. Thus in the example, the values to be supplied at each step for u_{1j} are stored in $(BL)_j$, j=1,2,3; those for v_{i1}, in $(BB)_i$, i=4,5 and those for η_{7j} in $(BR)_j$, j=2,3,4. The storage arrays, which are a fixed feature of the time-stepping subroutines, can be used for holding elevation or velocity values as required for the model in question. Cases where this storage arrangement could lead to values for two different boundary points being allotted to the same storage location hardly ever seem to occur in practice and have not been catered for. Values supplied by the user at each time-step for the forcing terms $G^{(u)}$ and $G^{(v)}$ (equations 2 and 3) at every relevant variable point are stored in two-dimensional arrays where they are subsequently accessed by the stepping subroutine.

Some of the storage locations just discussed go unused in most models - for example, none of the boundary storage array BT pertaining to the upper boundary in Figure 5 is used - but this is a reasonable price to pay for other conveniences of the method.

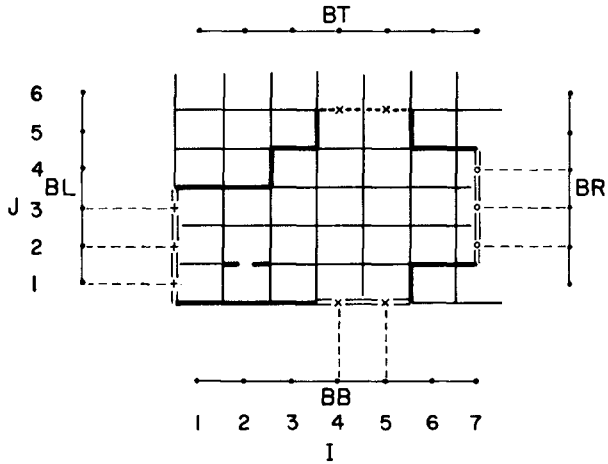

Fig. 5. Storage of Boundary Input Values for Sample Model

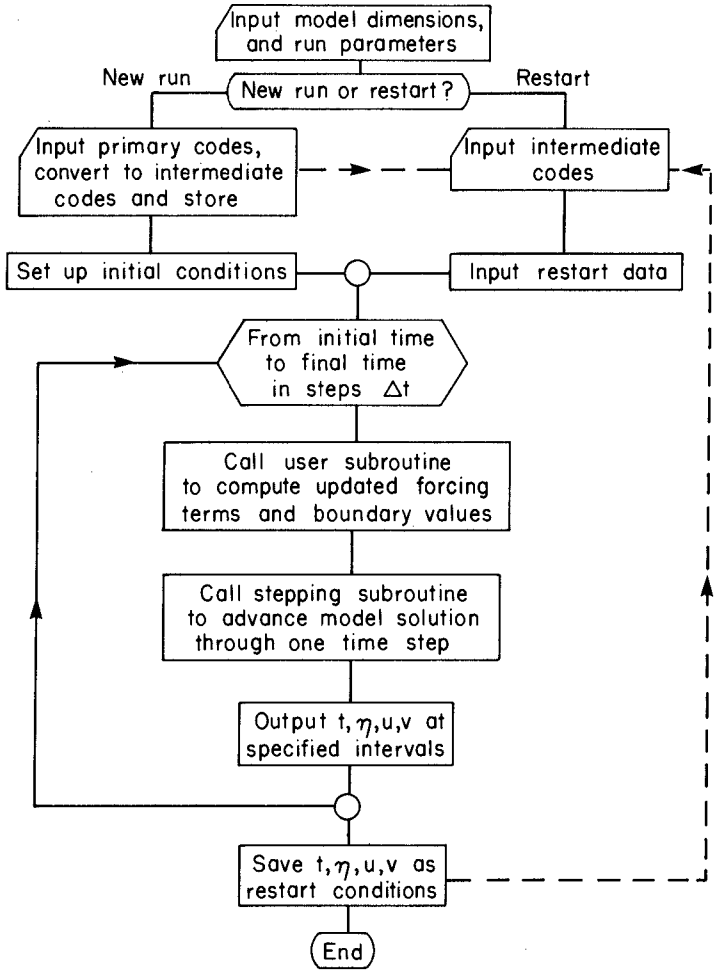

Fig. 6. Typical Model Flowchart

Figure 6 shows a simplified flowchart suitable for many models. The conversion from primary to intermediate code is shown included in the model program, since in many cases, modellers make numerous boundary changes during model development. Some further details are given in Henry (1982) and the results of an actual run with the model shown in Figure 2 are listed there for check-out purposes.

8. Further Developments

Besides extensions already mentioned, a number of auxiliary programs are being developed, mainly for performing standard analyses of results from production runs with the completed model. For tidal studies there is a program which carries out harmonic analysis of computed currents and surface elevations, while for storm surge models another program is being developed to log the maximum height reached at each elevation point during any specified period. Since the model shape is already expressed in the primary codes, the latter are used to confine the analysis computations to active variable points, to organize the layout of printed results of the analyses, and also to produce plots of the boundaries in subsequent graphical programs, such as one which can contour any designated scalar field computed during the analysis.

9. Conclusions

The method of programming shallow water models discussed in this paper is designed to answer a need for rapid, error-free application of well-known finite-difference methods to different coastal areas. The basic concept involved, indirect programming or selection of algorithms via numerical codes, has attracted interest for a number of years but has not come into widespread use. This paper proposes some improvements which should help to make indirect programming into a really practicable tool. These include:

a) the number of different numerical codes needed to describe the model layout is kept very small, the more numerous set of codes required to control the finite-difference computation being produced automatically by a pre-developed program;
b) the user's choice of codes to define the layout is checked graphically for errors;
c) the finite-difference scheme employed can be changed by replacing one subroutine by another.

References

Abbott, M.B., A. Damsgaard and G.S. Rodenhuis (1973), System 21, "Jupiter" (A Design System for Two-Dimensional Nearly Horizontal Flows), J. Hyd. Res., Vol 11, No.1, pp 1-28.

Heaps, N.S. (1969). A Two-Dimensional Numerical Sea Model, Phil. Trans. Roy. Soc., London, Ser. A, Vol. 265, pp. 93-137.

Heaps, N.S. (1974). Development of a Three-Dimensional Numerical Model of the Irish Sea. Rapp. P.-v. Réun. Cons. Int. Explor. Mer, Vol. 167, pp. 147-162.

Henry, R.F. (1982) Automated Programming of Explicit Shallow-Water Models. Part 1. Linearized Models with Linear or Quadratic Friction, Institute of Ocean Sciences, Sidney, B.C., Canada. Can. Tech. Rept. Hydrogr. Ocean Sci., No.3, 70 pp.

Leendertse, J.J. (1967). Aspects of a Computational Model for Long-Period Water-Wave Propagation. RAND Corp., Santa Monica. RM-5294-PR, 165 pp.

Sielecki, A. (1968). An Energy-Conserving Difference Scheme for the Storm Surge Equations. Mon. Weather Rev., Vol. 96, pp. 150-156.

LONG WAVES OVER THE GREAT BARRIER REEF

by

Eric Wolanski *

ABSTRACT

Low-frequency forcing of water currents over the continental shelf of Australia is quite strong and should be taken into account when the flow for durations greater than 1 day is important. In the case of the Queensland coast, the longshore wind generates barotropic continental shelf waves, raising or lowering the mean sea level by as much as 30 cm and generating longshore currents over the continental shelf, even very close to the coast, that are often larger than the tidal currents. These wind-driven currents can reverse sign, flowing alternately northward and southward, although the longshore wind stress, though fluctuating, does not change direction. To reproduce such phenomena in an analytical or computer model of wind-driven currents, it is necessary to extend the offshore boundaries of the model offshore from the continental shelf break.

1. INTRODUCTION

In 1966, Hamon digitized sea level observations at various ports around Australia, removed the tidal component from the time series and discovered that the "mean sea level" is not a constant. Shelf waves were thus discovered and have since been intensively studied by physical oceanographers (see a review by Allen (1980) and Winant (1980)). In their simplest mode, the continental shelf waves are disturbances of the sea level, highest near the coast and negligible in the deep ocean, with a longshore wave length often exceeding 1500 km, of duration typically one to two weeks, raising or lowering the mean sea level by as much as 50 cm.

Until recently, coastal engineers in Australia have often ignored these waves in many applications where currents were a design parameter, presumably because the sea level disturbance (say, 30 cm) is small compared to the tidal range (say, 2 m). Yet, as will be shown, the currents introduced by shelf waves can be stronger than the tidal currents. Further, the shelf-wave-driven currents can reverse sign, though the wind direction does not change, typically in one to two weeks, so that water current investigations of duration less than two weeks will likely lead to aliased data if the mean flow has to be determined, such as for estimating the dispersion of contaminants from outfalls.

2. FIELD STUDIES IN AUSTRALIA

As part of the research program in physical oceanography by the Australian Institute of Marine Science, I have run a long-term study of water currents over the continental shelf of the Great Barrier Reef.

* Principal Research Scientist, Australian Institute of Marine Science, P.M.B. No.3, Townsville, Q.4810, Australia.

The initial study site was the central region (16 to 20°S lat.) from 1980 to 1981, and more recently the northern region (9 to 15°S) from 1981 to 1982. The study in the central region, which is reviewed here, involved the deployment and maintenance for more than one year of self-recording current meters, water level recorders and weather stations. The location of some of the instruments is shown in Fig. 1.

Wind

It was found (Wolanski, 1982) that, in the trade wind season, the dominant wind direction changed from westward over the Coral Sea to northwestward over the continental shelf. The dominant wind component was found to be highly coherent over distances of at least 1500 km, with negligible time lags from site to site, so that the wind-field over the continental shelf can be treated as time-dependent but stationary. The wind is energetic at all periods greater than a few

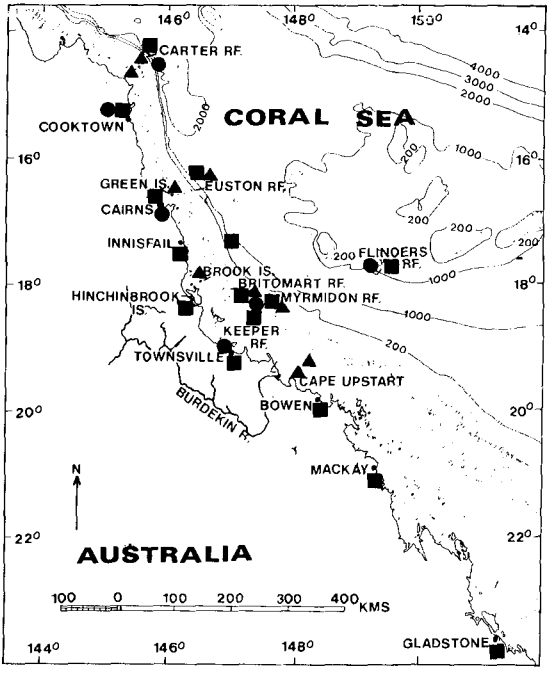

Figure 1 Location map, with depth in m, showing the mooring sites of some of the current meters (▲), water level recorders(■), and weather stations (●).

days, with a suggestion of a peak in the wind autospectrum at about 10 and 30 days duration.

Currents

Because the shelf is fairly flat (Fig. 2), the current meters were all in comparable depth. Baroclinic effects on the shelf are not very important, except near the shelf break (Wolanski and Pickard, 1983), because the shelf waters are well-mixed, the thermocline being located at 100 m depth or so, i.e. offshore from the continental shelf break. In Fig. 3 are shown the low-frequency (after removing the tidal signal) current time series at several locations, over roughly 4 months. At the Green Island mooring site, the tidal component of the currents is so weak that the longshore currents do not reverse sign with the tides, though a spring tidal range of about 3 m is experienced. Instead, as can be seen from Fig. 3, the currents are alternately northward and southward, reversing sign in typically one to two weeks. Such low-frequency forcing is apparent at all sites (Wolanski and Bennett, 1983). At Green Island and Euston Reef, the longshore currents are nearly equal and no residual 'mean flow' is found after several months, although, for practical purposes, the longshore wind component did not reverse sign (Fig. 3).

Sea levels

The variance of the sea level signal is primarily (90%) due to diurnal and semi-diurnal tides. The spring tidal range exceeds 3 m, the neap tide range is about 40 cm. The low-frequency signal is typically 30 cm from peak to trough (Fig. 3) and is found to be highly coherent at all stations

Propagation of the disturbances

Using lagged correlation techniques or coherence and phase calculations, it was shown (Wolanski and Bennett, 1983) that the low-frequency longshore current and sea level disturbances are travelling

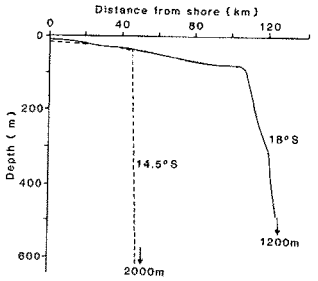

Figure 2 Offshore bathymetry at two locations.

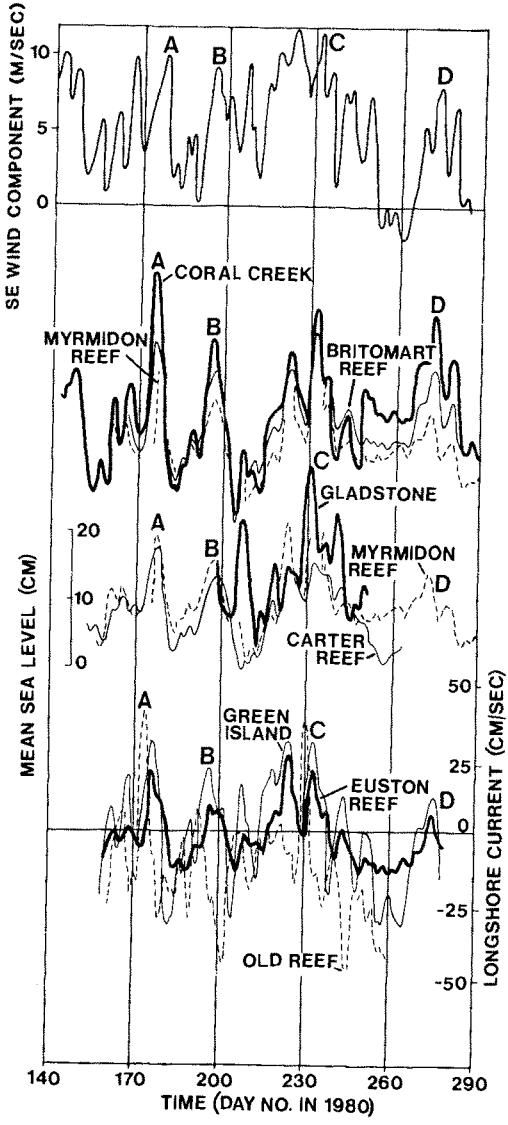

Figure 3

Time series of the low-frequency longshore wind component (positive if northward), of the low-frequency sea level and longshore currents (positive if northward) at various locations. The letters A to D identify some wind-driven events. Note that the longshore wind component is nearly always positive, but that the currents reverse sign.

longshore northward at a speed of roughly 450 km day^{-1}, although the wind field is stationary and the longshore wind component is highly correlated with both the low-frequency longshore currents and the low-frequency sea levels.

3. MATHEMATICAL FORMULATION

The f-plane shallow water wave equations are

$$u_t + uu_x + vu_y - fv = -gh_x + T^x/(H+h) - F^x/(H+h) \quad (1)$$

$$v_t + uv_x + vv_y + fu = -gh_y + T^y/(H+h) - F^y/(H+h) \quad (2)$$

$$h_t + ((H+h)u)_x + ((H+h)v)_y = 0 \quad (3)$$

where t is the time, x and y the horizontal Cartesian coordinates (x is oriented cross-shelf pointing offshore, y longshore poiting northward, the origin being at the coast), u and v the corresponding velocity components, T^x and T^y the wind stress components, and F^x and F^y the bottom friction components. A subscript indicates a partial derivative, g is the acceleration due to gravity, H is the undisturbed water depth, h the sea level disturbance, and f the Coriolis parameter.

Equations (1)-(3) are non-linear but can be greatly simplified without losing the important physical processes controlling the dynamics of water currents over the Great Barrier Reef continental shelf. Using the array of current meter and tide gauge data centered around Brook Island, it was possible (Wolanski and Bennett, 1983) to estimate a number of terms in equations (1)-(3). For example, as is shown in Fig. 4, the sea level vertical velocity, h_t, can be neglected in equation (3). This approximation is called the "rigid-lid assumption" (e.g., see Allen , 1980), and averages out the seiching which occurs during wind set-up. This seiching has a time scale appropriate to the time taken for a long surface gravity wave to traverse the shelf and that is about typically 1-2 hours. The cross-shelf momentum equation (1) is simplified in practice (Fig. 5) to a simple geostrophic balance between the longshore current, v, and the cross-shelf slope of the water surface, h_x. The non-linear terms can be neglected and the total depth (H+h) in equations (1) to (3) can be approximated by the undisturbed depth, H.

With these approximations, originating from the field data, the equations of motion become

$$-fv = -gh_x \quad (4)$$

$$v_t + fu = -gh_y + T^y/H - F^y/H \quad (5)$$

$$(Hu)_x + (Hv)_y = 0 \quad (6)$$

To model the wind-driven currents, we assume a simple topography, shown in Fig. 6 , namely a shelf of uniform depth H_s and extending

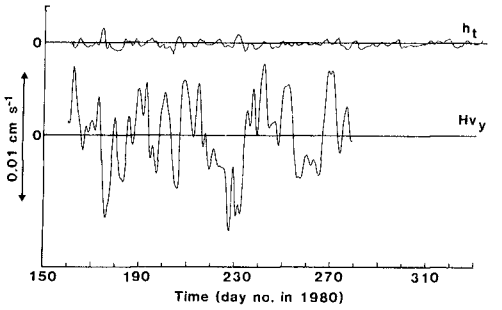

Figure 4 Term balance in the continuity equation (3)

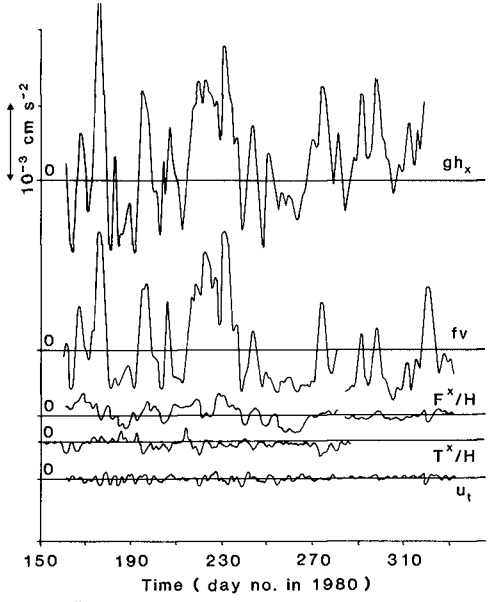

Figure 5 Time series of various terms in the cross-shelf momentum equation (1)

from the shore (x=0) to the shelf break (x=L), the ocean of depth H_o extending from x=L to infinity.

The boundary conditions are continuity of sea level h and of cross-shelf fluxes uH at x=L, the disturbance h vanishing as x goes to infinity (the data showing that the mean sea level perturbations are much smaller over the Coral Sea than over the shelf), and u=0 at x=0.

The forcing is provided by the longshore wind stress (from which the time-averaged mean wind has been substracted as the mean flow is very small)

$$T^y \begin{cases} =0, \text{ for } y < 0 \\ =T_o \exp(iwt), \text{ for } 0 < y < A \\ =0, \text{ for } y > A \end{cases} \qquad (7)$$

where T_o is a constant, w the frequency, A the size of the wind-field, and $i=(-1)^{\frac{1}{2}}$.

The solution, to order H_s/H_o, is

$$u = - xv_y \qquad (8)$$

$$h = (x-L)\, fv/g \qquad (9)$$

$$v = B \exp(iwt) \; (1 - \exp(-iwy/c) \exp(-by/c)) \qquad (10)$$

where

$$B = (T_o/H_s)/(i(w-ib)) \qquad (11)$$

$$b = r/H_s \qquad (12)$$

$$c = - fL \qquad (13)$$

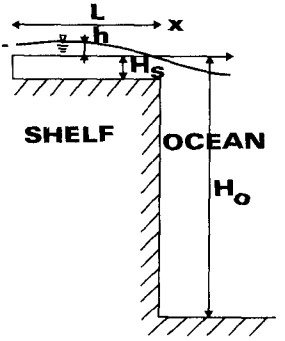

Figure 6 Sketch of the model geometry

where r is the friction coefficient, assuming a linear law

$$F^y = rv \qquad (14)$$

which turns out, from the field data, to be of the order of $2. \times 10^{-4}$ m s^{-1}. c is the phase speed of free shelf waves, about 200-230 km day^{-1} in this region.

A number of features of equations (8) to (10) are in good agreement with observations, namely that v is independent of x, that h is largest at the coast, and that v and h are in phase. Further, the correlation field of sea level and current disturbances propagate northward longshore at a phase speed of 2c, i.e. about 450 km day^{-1}, in good agreement with the observations. From equation (10), it is apparent also that the longshore current, v, can be alternately northward and southward, resulting in a net zero total displacement after one period (wind event).

Near the shelf break, the ocean stratification introduces important baroclinic effects. These are compounded by the effects of the Great Barrier Reef which, as it turns out, result in only a small enhancement of the friction over the shelf by damping the exchange of water between the continental shelf and the Coral Sea. The link between the shelf and the ocean effectively traps the disturbance over the shelf and implies that a mathematical or computer model of wind-driven currents over the shelf must cover an area extending offshore from the continental shelf break.

The low-frequency modulation of sea levels controls the frequency of inundation, hence the flushing of coastal wetlands in Queensland. This modulation of sea level can also be important in harbours where depth is limiting, and in shallow shipping lanes such as Torres Strait (Wolanski and Gardiner, 1981, Wolanski and Thomson, 1983).

4. REFERENCES

Allen, J.S. (1980), "Models of wind-driven currents on the continental shelf". Annual Review of Fluid Mechanics 12, 389-433.

Hamon, B.V. (1966), "Continental shelf waves and the effects of atmospheric pressure and wind stress on sea level". Journal of Geophysical Research 71, 2883-28893.

Winant, C.D. (1980), " Coastal circulation and wind-induced currents". Annual Review of Fluid Mechanics 12, 271-301.

Wolanski, E. and R. Gardiner (1981), "Flushing of salt from mangrove swamps". Australian Journal of Marine and Freshwater Research 32, 681-

Wolanski, E. (1982), " Low level trade winds over the western Coral Sea". Journal of Applied Meteorology 21, 881-882

Wolanski, E. and G.L. Pickard (1983), "Upwelling by internal tides and Kelvin waves at the continental shelf break on the Great Barrier Reef"

Special physical oceanography issue, Australian Journal of Marine and Freshwater Research (in press).

Wolanski, E. and A.F. Bennett (1983), "Continental shelf waves and their influence on the circulation around the Great Barrier Reef". Special physical oceanography issue, Australian Journal of Marine and Freshwater Research (in press).

Wolanski, E. and R.E. Thomson (1983), " Wind-driven circulation on the northern Great Barrier Reef continental shelf in summer", submitted for publication.

CYLINDRICAL LONG WAVE INTO A CYLINDRICAL SHELF

HENRY POWER*
UNIVERSIDAD CENTRAL DE VENEZUELA, VENEZUELA

ABSTRACT

Based on the linear non-dispersive theory, the reflection of a Converging Cylindrical long wave, of wave length L, onto a Cylindrical shelf, of radius r = a and positive or negative height Δ h relative to an otherwise flat bottom, is study analitically. It is found that these linear approximation agrees well with the existing non-linear numerical solution when the ratio a/L is large enough. It is also found that these two-dimensional reflection process is the contrary of the corresponding one-dimensional case, since the solution of these problem gives a negative reflected wave for a positive step and a positive reflected wave for a negative step.

1. INTRODUCTION

In this paper we will discuss the reflection of Cylindrical long waves by a submerged Cylindrical shelf of radius r = a. Solving, analitically the linear nondispersive Cylindrical wave equation.

It is known that for infinitesimal wave on constant depth, water motion in long waves is essentially horizontal, implying that the vertical variation is weak and the pressure is hydrostatic. If we consider a vertical fluid columm of base section $dr\, rd\theta$ and height $h + \eta$, where h is the water depth and η is the wave amplitude measured from the undisturbed water surface, the rate of change of fluid volume in the columm is $\partial\eta/\partial\tau\, rdrd\theta$. If, the vertical variation in the horizontal velocity is ignored as is suggested above, the net rate of volume flux into the columm is

$$-\nabla\cdot\bar{u}\,(h+\eta)\, rdrd\theta,$$

where ∇ denotes the horizontal gradient in polar coordinates

$\left(\frac{\partial}{\partial r}, \frac{1}{r}\frac{\partial}{\partial\theta}\right)$.

Mass conservation is satisfied, if the two rates are equal,(incompressible fluid) hence

$$\frac{\partial\eta}{\partial\tau} + \nabla\cdot\bar{u}(h+\eta) = 0 . \qquad (1)$$

*Profesor Agregado, Instituto de Mecánica de Fluidos, U.C.V.

For waves having a vertical axis of symmetry at all times, the above equation can be written as

$$n_t + \frac{1}{r}\,((h + n)\, r\, u)_r = 0\,, \tag{2}$$

where u is the radial velocity considered constant in the entire depth. In terms of the velocity potential, inviscid and irrotational flow, we have, that the linear version of equation (2) is

$$n_t + \frac{h}{r}\,(r\,\Phi_r)_r = 0\,. \tag{3}$$

In the momentum balance, we only consider horizontal components and neglect convective inertia (non-linear term), therefore

$$\vec{u}_t = -\frac{1}{\rho}\,\nabla p\,. \tag{4}$$

Assuming now, that the pressure is hydrostatic,

$$p = \rho\,(n-z)g\,,$$

The momentum equation becomes

$$\vec{u}_t = -\,g\,\nabla n\,. \tag{5}$$

Introducing the velocity potential into equation (5), we obtain

$$n = -\frac{1}{g}\,\frac{\partial \Phi}{\partial t}\,. \tag{6}$$

Substituting equation (6) into equation (3), we have

$$\frac{1}{C^2}\,\frac{\partial^2 \Phi}{\partial t^2} = \frac{\partial^2 \Phi}{\partial r^2} + \frac{1}{r}\,\frac{\partial \Phi}{\partial r}\,, \tag{7}$$

The above equation is the linear nondispersive Cylindrical wave equation, where $C = \sqrt{gh}$ is the shallow water phase velocity.

Chwang and Wu (1976) investigated the reflection and transmission of a converging cylindrical solitary wave due to a circular step of positive height Δh and radius $r = a$, based on a numerical solution of the three dimensional Boussinesq equation (non-linear theory). Their main conclusion was that after incident wave reaches the circular step, the leading reflected wave takes the form of a negative wave propagating in the positive "r" direction (see figure (1)). Wu (1979) presented a comparative numerical study of the above problem, using different theories of wave propagation. From Wu's work, it is possible to conclude that when a/L is large enough, where L is the wave length, the reflected waves predicted by the Boussinesq theory and the linear nondispersive long wave model are in good agreement (compare figure 2 with figure 1), just as the transmited waves predicted by the mentioned theories are differents, result that can be more appreciated when the waves approach the origin (focusing process). A non-linear analytic solution of this focusing process has been presented by Chwang and Power (1981), based on the inner-outer expansions technique to the Cylindrical Boussinesq equation.

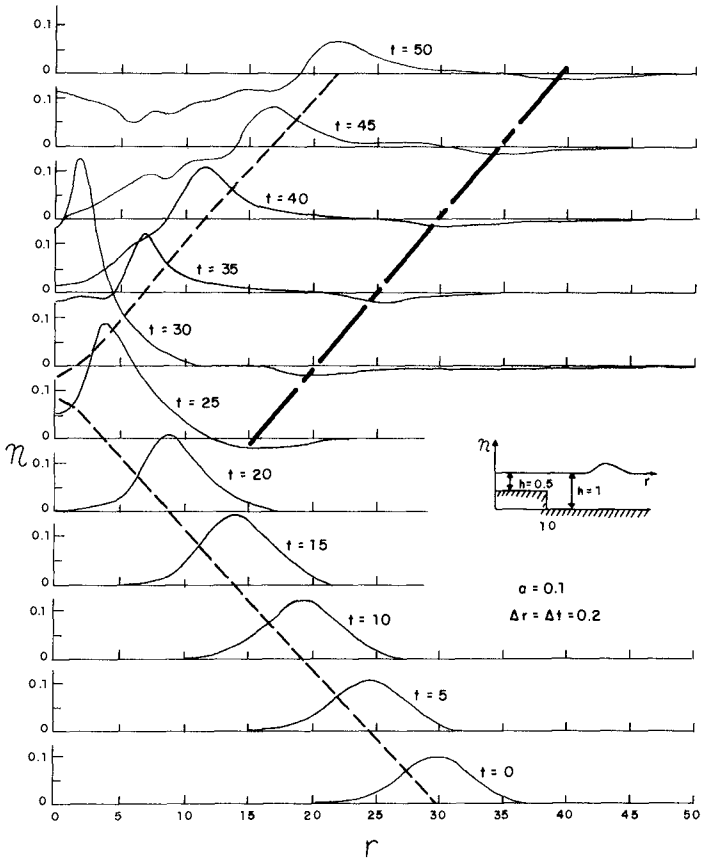

FIG. # 1

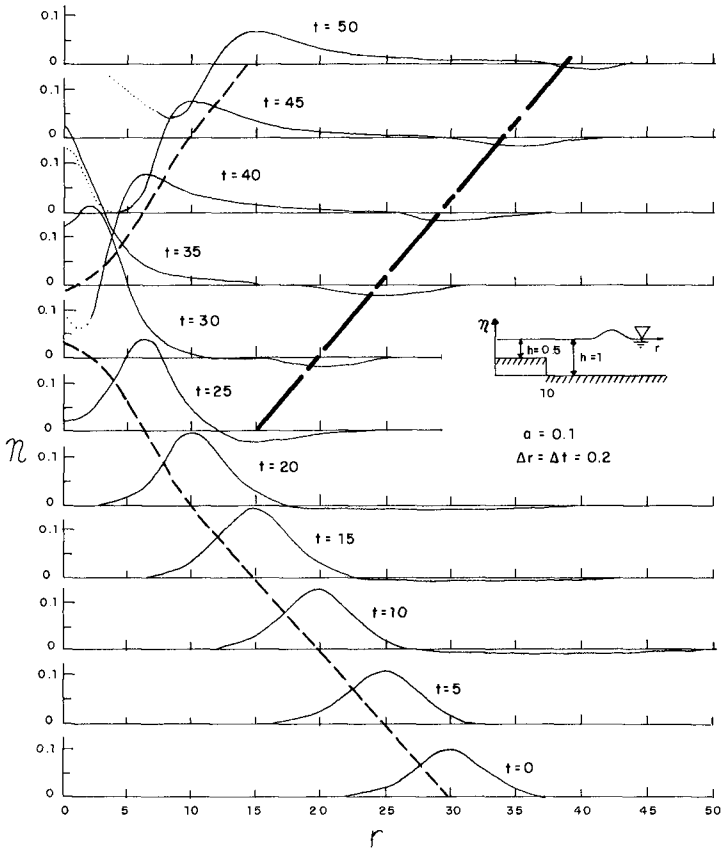
t = 50
t = 45
t = 40
t = 35
t = 30
t = 25
t = 20
t = 15
t = 10
t = 5
t = 0
0.1
0
η
r
h=0.5
h=1
10
a = 0.1
Δr = Δt = 0.2
0 5 10 15 20 25 30 35 40 45 50

FIG. # 2

The solution of such a problem in one dimension (reflexion of a planar wave due to abrupt change in the water depth) is extremely easy, owing to the simple general integral of the one-dimensional wave equation. As it is known in one dimension we have the deviations from the mean water level as

$$n_I = f(t + \frac{x - x_0}{c_1}) . \tag{8}$$

for the incident wave,

$$n_r = \frac{c_1 - c_2}{c_1 + c_2} f(t - \frac{x+x_0}{c_1}) \tag{9}$$

for the reflected wave, and

$$n_t = \frac{2 c_1}{c_1+c_2} f(t + \frac{x - \frac{c_2}{c_1} x_0}{c_2}) \tag{10}$$

for the transmitted wave, where the incident, transmitted and reflected waves have the same shapes, and for ($C_1 = \sqrt{gh_1}$) > ($C_2 = \sqrt{gh_2}$) the reflected wave takes the form of a positive wave propagating through infinity. The above conclusion for one dimensional wave is totally different from the one found by Chwang and Wu numerical solution for a two dimensional wave.

2. CYLINDRICAL LONG WAVES IN WATER OF CONSTANT DEPTH

In these section we are interested in studing the propagation of cylindrical incoming long waves in water of constant depth, whose maximum wave amplitude is located at $r = r_0$, sufficiently far from the origin when $t = 0$. To do it, we will follow Lamb(1902) original paper, "on wave propagation in two dimensions", and Whithan (1974).

To find a general solution for incoming waves of equation 7, we can use two different approaches, one consist on a Fourier superposition of the periodic incoming solution of equation 7 and the other technic consists on a uniform line distribution on the z axis, of three-dimensional point wave sources, the total disturbance from this line distribution is clearly a function only of the distance r from the z axis and the time t.

The wave equation in spherical coordinates reduces to

$$\frac{1}{c^2} \frac{\partial^2 \Phi}{\partial t^2} = \frac{\partial^2 \Phi}{\partial R^2} + \frac{2}{R} \frac{\partial \Phi}{\partial R} , \tag{11}$$

when $R = \sqrt{r^2+z^2}$. The source solution of the above equation producing incoming wave whose maximum wave amplitude is located at $R = r_0$, is

$$\Phi = - \frac{1}{4\pi R} f(t + \frac{R - r_0}{c}) . \tag{12}$$

The total potential produced by a line distribution of the above source is

$$\Phi\left(\frac{r-r_0}{c}, t\right) = -\frac{1}{4\pi}\int_{-\infty}^{\infty}\frac{1}{R} f\left(t+\frac{R-r_0}{c}\right) dz \ . \tag{13}$$

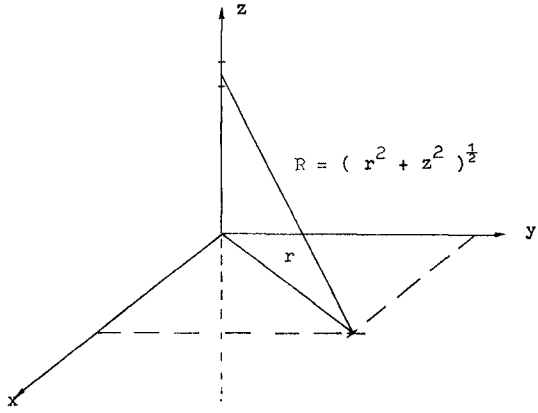

Let $z = r \ \text{senh}\ u$, therefore $R = r \cosh u$, and substituting this change of variable in equation (13), we obtain

$$\Phi = -\frac{1}{2\pi}\int_{o}^{\infty} f\left(t-\frac{r_0}{c}+\frac{r}{c}\cosh u\right) du. \tag{14}$$

To verify that the above equation is a solution of equation (7), subject to certain condition, let us substitute equation (14) into equation (7). Then

$$\begin{aligned} 2\pi\left(c^2\left(\Phi_{rr}+\frac{1}{r}\Phi_r\right)-\Phi_{tt}\right) &= \int_{o}^{\infty}\left(\cosh^2 u\, f''(\xi)+\frac{c}{r}\cosh u\, f'(\xi)\right. \\ &\quad \left. - f''(\xi)\right)du \\ &= \int_{o}^{\infty}\frac{c^2}{r^2}\frac{\partial^2}{\partial u^2} f(\xi)du \\ &= \frac{c}{r}\left(\text{senh}\, u\, f'(\xi)\right)_{u=o}^{u=\infty} \ , \end{aligned} \tag{15}$$

where $\xi = (t - r_0/c + (r/c)\cosh u)$. Equation (15) is identically equal to zero, therefore (14) is a solution of (7), if and only if f' tends to zero faster than senh u tends to infinit when u tends to infinite. Then under the above condition, equation (14) is a two-dimensional source of strength f (t - r_0/c), producing cylindrical incoming waves, whose maximum wave amplitude is located at r = r_0 when t = 0. Since

$$
\begin{aligned}
2\pi r\Phi_r &= -\frac{r}{c}\int_0^{\infty} f'(\xi)\cosh u\, du = -\frac{r}{c}\int_0^{\infty}(\operatorname{senh} u + e^{-u})f'(\xi)du \\
&= -\left(\int_0^{\infty}\frac{\partial}{\partial u} f(\xi)du + \frac{r}{c}\int_0^{\infty} e^{-u} f'(\xi)du\right) \\
&= f(t - r_0/c + r/c) - \frac{r}{c}\int_0^{\infty} e^{-u} f'(\xi)du ,
\end{aligned}
\qquad (16)
$$

Therefore, the following limit gives the source strength

$$
\lim_{r\to\infty} 2\pi r\Phi_r = f(t - r_0/c), \qquad (17)
$$

or in other words we have a two dimensional source of strength f(t'), where t' = t - r_0/c, whose initiation time is t' = - r_0/c.

The corresponding wave profile to the above two-dimensional potential is found by substituting equation (14) into equation (6). Then

$$
n\left(\frac{r-r_0}{c}, t\right) = \frac{1}{2\pi g}\int_0^{\infty} f'(t - r_0/c + \frac{r}{c}\cosh u)du, \qquad (18)
$$

Now at t = o we have

$$
n\left(\frac{r-r_0}{c}, o\right) = \frac{1}{2\pi g}\int_0^{\infty} f'\left(\frac{r}{c}\cosh u - \frac{r_0}{c}\right) du. \qquad (19)
$$

Therefore, the problem is reduced to solving the above integral equation of the first kind when the initial wave profile, $n((r - r_0)/c, o) = n_i((r-r_0)/c)$, is known.

The solution of equation (19) is

$$
f'\left(\frac{r}{c}\cosh u - \frac{r_0}{c}\right) = -4g\frac{r}{c}\cosh u\int_0^{\infty} n_i'\left(\frac{r}{c}\cosh u\cosh v - \frac{r_0}{c}\right)dv, \qquad (20)
$$

provided that $n_i(\infty) = 0$

To prove equation (20), let's substitute equation (20) into equation (19)

$$n_i\left(\frac{r-r_0}{c}\right) = -\frac{2}{\pi}\int_0^{\infty}\frac{r}{c}\cosh u \int_0^{\infty} n_i'\left(\frac{r}{c}\cosh u \cosh v - \frac{r_0}{c}\right)dv\,du \qquad (21)$$

Let $z = r/c \cosh u \cosh v$ and $y = r/c \cosh u \operatorname{senh} v$ so that $J(u, v) = (r/c)^2 \operatorname{senh} u \cosh u$ transforming the u and v independent variables in the double integral of equation (21) to z and y variables, then we have

$$n_i((r-r_0)/c) = -\frac{2}{\pi}\int_{r/c}^{\infty}\int_0^{(z^2-(r/c)^2)^{1/2}} \frac{n_i'(z-r_0/c)}{(z^2-y^2-r^2/c^2)^{1/2}}\,dy\,dz$$

$$= -\frac{2}{\pi}\int_{r/c}^{\infty} n_i'(z-r_0/c)\left(\operatorname{sen}^{-1}\left(\frac{y}{(z^2-r^2/c^2)^{1/2}}\right)\right)_0^{(z^2-r^2/c^2)^{1/2}} dz$$

$$= -\int_{r/c}^{\infty} n_i'(z-r_0/c)\,dz$$

$$= n_i\left(\frac{r-r_0}{c}\right), \qquad (22)$$

Since $n_i(\infty) = 0$, and equation (20) has being proved .

3. THE REFLECTION OF A SOLITARY WAVE

Consider a single cylindrical wave moving through the origin in water of constant depth h_1. Due to a discontinuous change in the depth by a Cylindrical shelf of depth h_2 and radius $r = a$, some of the inco - ming energy is transmitted beyond the step and the remaining part is re flected backwards. Let the incident wave be

$$n_I = \int_0^{\infty} g\left(t - \frac{r_0}{c_1} + \frac{r}{c_1}\cosh u\right) du \qquad (23)$$

with $C_1 = \sqrt{g h_1}$ the wave celerity in the region $r > a$, In this region, $r > a$, besides the incident wave there must be a reflected wave propa - gating through infinity that we may choose it to be

$$n_r = \int_0^{\infty} R\left(t + r_r/c_1 - \frac{r}{c_1}\cosh u\right) du . \qquad (24)$$

In a similar way, in the region $r \leq a$ we have a transmitted wave propa pating through the origin with wave celerity $C_2 = \sqrt{gh_2}$ that we may write it as

$$n_t = \int_0^\infty T(t - r_t/c_2 + \frac{r}{c_2} \cosh u\ )\, du. \tag{25}$$

The function g is known and R and T at $r = a$ are to be found from the matching of the pressure and volume flux at the edge of the cylinder $r = a$, as is usually done. Then, we have

$$\begin{aligned} & n_I + n_r = n_t \\ & h_1 \frac{\partial}{\partial r}(\Phi_I + \Phi_r) = h_2 \frac{\partial}{\partial r}\Phi_t \quad , \text{ a t } r = a \end{aligned} \tag{26}$$

In this way, we get

$$R(t + r_r/c_1 - \frac{a}{c_1} \cosh u\ ) = \frac{c_1 - c_2}{c_1 + c_2}\, g\,(t - r_0/c_1 + a/c_1 \cosh u\ ), \tag{27}$$

and

$$T(t - r_t/c_2 + a/c_2 \cosh u) = \frac{2c_1}{c_1 + c_2}\, g(t - \frac{r_0}{c_1} + \frac{a}{c_1} \cosh u\ ). \tag{28}$$

The prolongation of the relation (27) in the region $r > a$, can be given by

$$R\,(t + r_r/c_1 - \frac{r}{c_1} \cosh u\ ) = \frac{c_1 - c_2}{c_1 + c_2}\, g(t - \frac{r_0}{c_1} - \frac{(r - 2a)}{c_1} \cosh u\ ). \tag{29}$$

Substituting equation (19) into equation (24) for the reflected wave. We get

$$n_r = \frac{c_1 - c_2}{c_1 + c_2} \int_0^\infty g(t - \frac{r_0}{c_1} - \frac{(r - 2a)}{c_1} \cosh u\ )\, du\ , \tag{30}$$

The above relation is not a solution of the cylindrical wave equation, as can be seen by substituting the following potential

$$\Phi = \int_0^\infty f(t - \frac{(r - r')}{c} \cosh u)\, du \tag{31}$$

into the cylindrical wave operator. Since

$$(c^2 (\frac{\partial^2}{\partial r^2} + \frac{1}{r} \frac{\partial}{\partial r}) - \frac{\partial^2}{\partial t^2}) \int_0^\infty f\,(t - (\frac{r - r'}{c}) \cosh u)\, du =$$

$$\int_0^\infty (\frac{c}{r} f'\,(t - (\frac{r - r'}{c}) \cosh u) \cosh u - f''\,(t - (\frac{r - r'}{c}) \cosh u) \operatorname{senh}^2 u)$$

$$du = \frac{c^2}{(r - r')^2} \int_0^\infty (-\frac{\partial^2}{\partial u^2}\,(f\,(t - (\frac{r - r'}{c}) \cosh u)))\, du - \frac{c}{(r - r')}$$

$$\frac{r'}{r} \int_0^\infty f'\,(t - (\frac{r - r'}{c}) \cosh u) \cosh u\, du$$

$$= - \frac{c^2}{(r - r')} \frac{r'}{r} \int_0^\infty f' \left(t - \frac{r - r'}{c} \cosh u \right) \cosh u / c \, du$$

$$= - \frac{c^2}{(r - r')} \frac{r'}{r} \frac{\partial \Phi}{\partial r} \neq 0 \quad \text{for } 0 < r > \infty, \tag{32}$$

where we used the condition that f' tends to zero as u tends to infinite. Therefore, these standard technique does not bring a solution of the reflection of a general cylindrical long wave. The way around this difficulty is a Fourier superposition of the reflection of a cylindrical periodic wave , where the above technique gives the following solution for the reflection and transmition of the incident periodic waves

$$n_I = A_I H_0^{'} (k_1 r) e^{iwt} \tag{33}$$

propagating through the origin, as:

$$n_r = A_I R(w) H_0^2 (k_1 r) e^{iwt} \tag{34}$$

for the reflected wave and

$$n_t = A_I T(w) H_0^1 (k_2 r) e^{iwt} \tag{35}$$

for the transmitted wave. The function R(w) and T(w), reflection and transmission coefficient respectively, are determined by the matching condition at r = a, and are found to be

$$R(w) = \left(H_1^1(k_1 a) H_0^1(k_2 a) - \sqrt{\frac{h_2}{h_1}} H_0^1 (k_1 a) H_1^1(k_2 a)\right) / \left(H_0^2(K_1 a) H_1^1(K_2 a) \sqrt{\frac{h_2}{h_1}} - H_1^2(k_1 a) H_0^1(k_2 a)\right) \tag{36}$$

and

$$T(w) = \left(H_0^1(K_1 a) + R(w) H_0^2 (k_1 a)\right) / H_0^1(K_2 a), \tag{37}$$

where $K_1 = w/\sqrt{gh_1}$ and $k_2 = w/\sqrt{gh_2}$ and w is the wave frecuency. Therefore, the above equations give the dependency of the reflection and transmission coefficients with the wave frecuency.

By a Fourier superposition of the above problem, we have that an incident wave

$$n_I = \int_{-\infty}^{\infty} A_1(w) H_0^1(k_1 r) e^{iwt} \, dw. \tag{38}$$

will be reflected and transmitted as

$$n_r = \int_{-\infty}^{\infty} A_I(w)\, R(w)\, H_0^2\,(k_1 r) e^{iwt}\, dw \tag{39}$$

and

$$n_t = \int_{-\infty}^{\infty} A_I(w)\, T(w)\, H_0^1\,(k_2 r)\, e^{iwt}\, dw. \tag{40}$$

Then, the incident, reflect and transmitted waves have differents shapes. Because the Fourier coefficients of the above integrals are different functions of w, this is a new property characteristic of the three dimensional effect of the fluid motion (planar waves are reflected and transmitted with the same shape as the incident waves).

The above technique leads to integrals that must be solved numerically. For this reason in the remaing of the section we will present the following approximate asymptotic analysis of this problem. To do it we will look first for the reflection of a spherical wave due to the presence of a sphere of radius R = a of different density to that of the medium in which the incident wave is propagating.

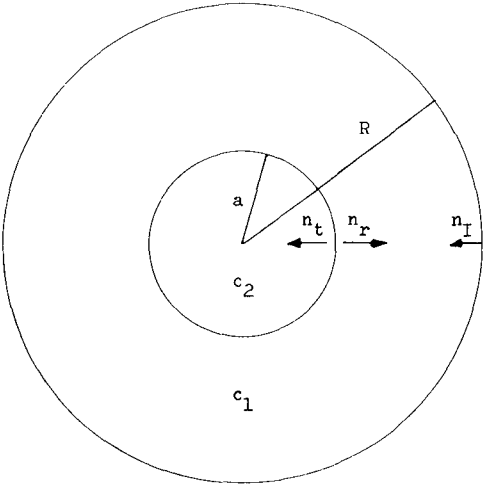

For an incident wave potential

$$\Phi_I = -\frac{1}{4\pi R}\, f\left(t + \frac{R - r_o}{c_1}\right), \tag{41}$$

Whose maximum is at $R = r_o$ when $t = o$, we will have a reflected wave potential

$$\Phi_r = -\frac{1}{4\pi R}\,Y\left(t-\frac{R-r_r}{c_1}\right), \tag{42}$$

whose maximum is at $R = r_r$ when $t = 0$, and a transmitted potential

$$\Phi_t = -\frac{1}{4\pi R}\,h\left(t+\frac{R-r_t}{c_2}\right), \tag{43}$$

whose maximum is at $R = r_t$ when $t = 0$. where r_r and r_t are to be found later.

The functions Y and h at $R = a$ are determined by the matching - condition at the surface of the sphere of radius $R = a$. From the flux condition, we have

$$\frac{\partial}{\partial R}\left(\Phi_I + \Phi_r\right) = \frac{\partial}{\partial R}\,\Phi_t \qquad \text{at} \quad R=a$$

or

$$\frac{1}{a}\left(f\left(t+\frac{a-r_0}{c_1}\right) - Y\left(t-\frac{a-r_r}{c_1}\right)\right) - \frac{1}{c_1}\left(f'\left(t+\frac{a-r_0}{c_1}\right) - Y'\left(t-\frac{a-r_r}{c_1}\right)\right)$$

$$= \frac{1}{a}\,h\left(t+\frac{a-r_t}{c_2}\right) - \frac{1}{c_2}\,h'\left(t+\frac{a-r_t}{c_2}\right), \tag{44}$$

If a is large enough, the above equation simplies to

$$\frac{1}{c_1}\left(f'\left(t+\frac{a-r_0}{c_1}\right) - Y'\left(t-\frac{a-r_r}{c_1}\right)\right) = \frac{1}{c_2}\,h'\left(t+\frac{a-r_t}{c_2}\right), \tag{45}$$

and from the pressure condition, we get

$$\frac{\partial}{\partial t}\left(\Phi_I + \Phi_r\right) = \frac{\partial}{\partial t}\,\Phi_t \qquad \text{at} \quad R=a$$

or

$$f'\left(t+\frac{a-r_0}{c_1}\right) + Y'\left(t-\frac{a-r_r}{c_1}\right) = h'\left(t+\frac{a-r_t}{c_2}\right), \tag{46}$$

by combination of equation (45) and (46), we obtain

$$h'\left(t+\frac{a-r_t}{c_2}\right) = \frac{2\,c_2}{c_1+c_2}\,f'\left(t+\frac{a-r_0}{c_1}\right) \tag{47}$$

and

$$Y'\left(t-\frac{a-r_r}{c_1}\right)= -\frac{(c_1 - c_2)}{c_1 + c_2} f'\left(t+\frac{a-r_o}{c_1}\right). \tag{48}$$

The prolongation of equation (47) and (48) in the region $R < a$ and $R > a$ respectively can be given by

$$h'\left(t+\frac{R-r_t}{c_2}\right) = \frac{2\,C_2}{c_1+c_2} f'\left(t+\frac{R}{c_2}+\frac{a}{c_1}-\frac{a}{c_2}-\frac{r_o}{c_1}\right). \tag{49}$$

Therefore $r_t = a + C_2 (r_o - a)/C_1$, and

$$Y'\left(t-\frac{R-r_r}{c_1}\right) = -\left(\frac{c_1 - c_2}{c_1 + c_2}\right) f'\left(t-\frac{R}{c_1}+\frac{2a}{c_1}-\frac{r_o}{c_1}\right), \tag{50}$$

Where $r_r = -(r_o - 2a)$, and a is sufficiently large compared to the wave lenght.

By a superposition of infinite sources on the z axis, line sources, as the ones given by equations (41) and (42), with the relation between y and f given by (50), we will have an outgoing wave

$$n_r = -\frac{1}{2\pi g}\left(\frac{c_1 - c_2}{c_1 + c_2}\right)\int_o^\infty f'\left(t-\frac{r_o-2a}{c_1}-\frac{r}{c_1}\cosh u\right)du \tag{51}$$

That will be the approximate reflected wave, from a cylinder of radius $r = a$, of the incident wave

$$n_i = \frac{1}{2\pi g}\int_o^\infty f'\left(t-\frac{r_o}{c_1}+\frac{r}{c_1}\cosh u\right)du. \tag{52}$$

Since in the integration that we have to do in order to get the reflected wave given by (51), the integrand is proportional to 1/R and therefore the mayor contribution comes from the sources near the origin, where the waves generated by that sources are the reflected waves by a surface almost cylindrical of radius $r = a$ of the corresponding spherical incoming waves, the above approximation tends to the exact solution when the radius r goes to infinite (see the definition sketch given below).

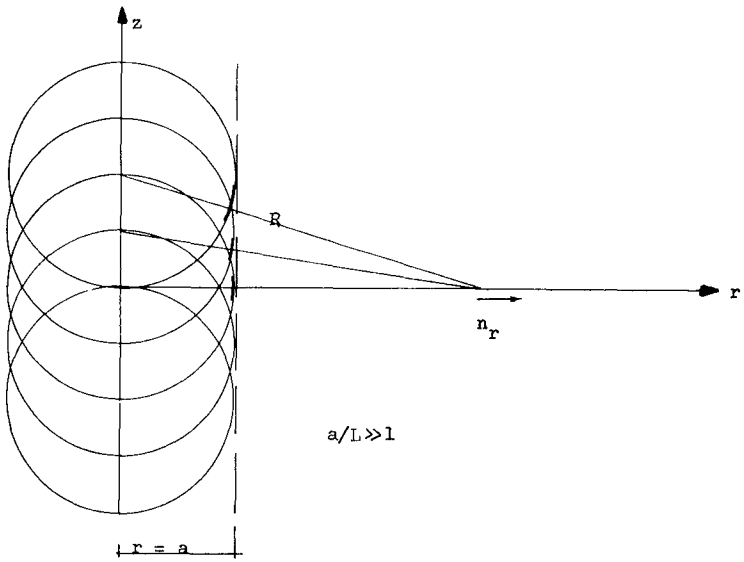

Using the equation(20) of section 2, we get that f' in the above equation is a function of the initial incoming wave profile, given by

$$f'\left(\frac{r}{c_1}\cosh u - \frac{r_0}{c_1}\right) = -4g\,\frac{r}{c_1}\cosh u \int_0^\infty n_i'\left(\frac{r}{c_1}\cosh u \cosh v - \frac{r_0}{c_1}\right)dv \tag{53}$$

or

$$f'\left(-\frac{r}{c_1}\cosh u - \left(\frac{r_0-2a}{c_1}\right)\right) = 4g\,\frac{r}{c_1}\cosh u \int_0^\infty n_i'\left(-\frac{r}{c_1}\cosh u \cosh v - \frac{(r_0-2a)}{c_1}\right)dv \quad . \tag{54}$$

Therefore, when we have an initial incoming wave profile $n_i(r - r_0)/C_1, t = 0)$, the reflected wave can be approximated, for a large r, by

$$n_r = \frac{2}{\pi}\,\frac{(c_1 - c_2)}{c_1 + c_2}\int_0^\infty \left(t - \frac{r}{c_1}\cosh u\right)\int_0^\infty n_i'\left(\left(t - \frac{r}{c_1}\cosh u\right)\cosh v - \left(\frac{r_0-2a}{c_1}\right)\right)dv\,du. \tag{55}$$

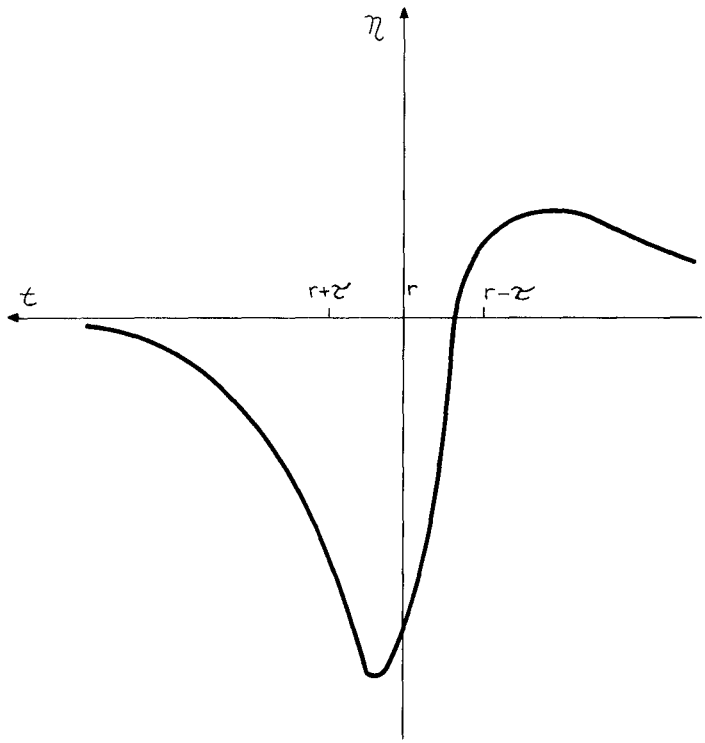

FIG. # 3

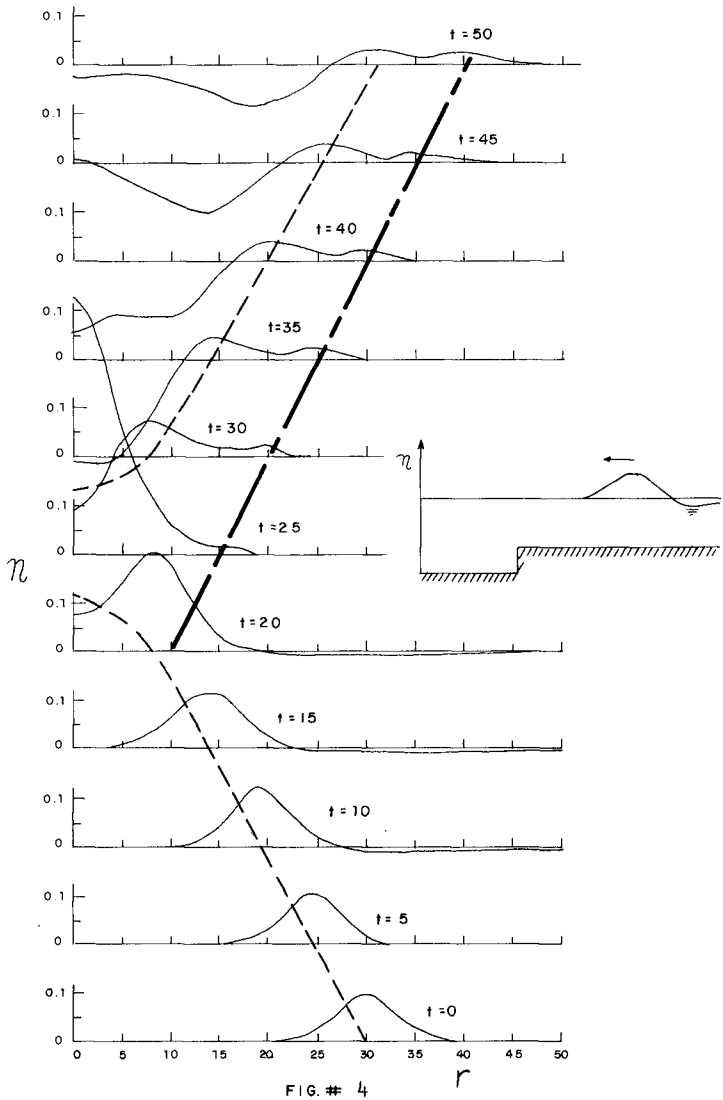
0.1
0
t = 50
t = 45
t = 40
t=35
t= 30
t=25
t=20
t=15
t=10
t= 5
t=0
η
0 5 10 15 20 25 30 35 40 45 50
r

FIG. # 4

In particular a solitary wave, free of discontinuities, can be obtained if Lamb's (1902) source strength is assumed as

$$f(t')= \tau/(t'^2+ \tau'^2) \text{ with } t'= t- \frac{(r_o-2a)}{c_1}, \tag{56}$$

where τ is a parameter, the function f (t') has no definite beginning or ending, but the range of time within which it is sensible can be made as small as we please by diminishing τ . With the above source strength, the asymptotic form of the reflected wave is

$$n_r= - \frac{1}{4\sqrt{2}} \left(\frac{c_1}{c_1} - \frac{c_2}{c_2} \right) \sqrt{\frac{\tau}{r}} \frac{1}{g\tau} \text{ sen } \left(\frac{\pi}{4} - \frac{S}{2} \right) \cos^{3/2} S,$$

where

$$S= \tan^{-1}\left(\frac{1}{\tau} \left(t- \frac{r_o-2a}{c_1} - \frac{r}{c_1} \right) \right). \tag{57}$$

Equation (57) is plotted in figure 3 for the case $C_1 > C_2$, consisting of a negative main wave followed by a longer positive small tail, and it is in agreement with the numerical solutions for both cases $C_1 \gtrless C_2$, where for a positive shelf, $C_1 > C_2$, the reflected wave is negative and for a negative shelf, $C_2 > C_1$, the reflected wave is positive (see figures 1, 2 and 4).

REFERENCE

- Chwang and Wu (1976): Unpublished

- Chwang and Power (1981): Focusing and reflection a Cylindrical solitary wave, International Tsunami Symposium, Japan.

- Lamb(1902): On wave propagation in two dimensions, Proc. Lond. Math. Soc. 35, 141-161.

- Whitham (1974): Linear and nonlinear wave, John Wiley and Sons, Inc.

- Wu (1979): On Tsunamis propagation evaluation of existing models Tsunamis, Proc. of National Science Foundation Workshop.

A PROPOSAL FOR WAVE ENERGY CONVERSION NEAR CAPE TOWN

G de F Retief[1], GK Prestedge[2], FPJ Müller[3]

ABSTRACT

The South African wave energy program has been underway for several years and has included an analysis of the temporal and spatial distribution of wave energy along the full coast-line, determination of energy attenuation perpendicular to the coast-line at a site on the south western coast, and the development of a wave energy converter which is most suited to local conditions and requirements.

The resource analysis has shown that the inshore power levels occurring along the south western coast are as promising as any elsewhere in the world. A bottom mounted, V-shaped wave energy conversion device driving an air turbine has been found to be most suited to prevailing conditions.

The conversion characteristics of the device are presented, based on 1:100 scale three dimensional and 1:50 scale two dimensional model studies. Preliminary design studies of the proposed conversion system have underlined its potential viability as a cost effective supplementary source of power.

1. INTROOUCTION

Over 93% of the electricity consumed in the Republic of South Africa is provided through the centralised distribution network of the Electricity Supply Commission (ESCOM) which derives almost all its power from coal-fired stations. ESCOM's presently installed generating capacity of over 19 000 MW will have to be expanded to nearly 70 000 MW by the turn of the century. About 10% of this requirement will probably be met by nuclear power, most of the remainder will be centered around the large coal fields situated to the north east of the country. Although this coal is relatively cheap (providing South Africa with the fifth cheapest electricity in the world) the long transmission distances involved and an awareness of the long term value of non-renewable resources have led to an investigation into the potential utilisation of ocean energy, and more specifically wave energy as a supplementary source of power.

---

1 Professor, Ocean Engineering, University of Stellenbosch
2 Principal Engineer, Watermeyer, Legge, Piesold and Uhlmann
3 Research Engineer, Ocean Engineering, University of Stellenbosch
South Africa

Wave energy has attracted interest throughout the world for many years. In a feasibility study of wave energy utilisation Leishman and Scobie (1975) listed some 340 United Kingdom patents, dating back to 1856, of devices which could apparently utilise ocean wave energy. The 1975 study showed that up until 1973 wave energy research had been a very low key activity, but that by 1974 a tremendous surge of interest was taking place, due mainly to the action of the OPEC countries, which had greatly affected the world's oil supplies. A great deal of work has since followed, mainly in the U.K. and Japan but with an increasing number of other countries also examining ways and means of utilising wave energy off their own shores.

Early assessments of the various ocean energy options in the coastal waters of South Africa identified the relative importance of wave energy for this region. Preliminary assessments of the resource were made by Van Wyk (1978) and Dutkiewicz and Nurick (1978), who identified relatively high energy levels to the south west of the country.

The present project which was initiated in 1979 included both a reassessment of the resource as well as the design of an energy conversion system. The resource analysis covered both a temporal and spatial distribution of wave energy using eight years of recorded wave data from a site near Cape Town (to determine long term variability), one year of synoptic wave data from representative sites for the coast-wise analyses and a three-gauge array off the Cape Peninsula to determine energy levels on a line perpendicular to the shore. Development of the wave power conversion system was based on the considerations listed in figure 1 and governed by the design philosophy which is presented in section 3.1.

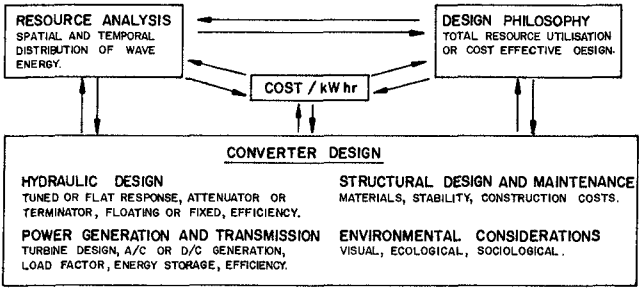

FIG I PROJECT COMPONENT DIAGRAM

2. WAVE POWER RESOURCE

2.1 Analysis procedures.

All the wave data used in this project were obtained by Datawell Waverider buoys recording digitally every six hours at a sample rate of 2 Hz for a record length of approximately 2048 data points. Records were then tested for quality control using the standard program of the National Research Institute for Oceanology (NRIO) which includes checks on successive equal values, wave steepness, low frequency energy, normality, stationarity and a number of other statistical improbabilities. After an FFT analysis the reduced data were stored in spectral density histogram form in a databank before further analysis.

Power computations were based on:

$$P = EnC \qquad (1)$$

using

$$H = H_{rms} = 2\,(2M_o)^{\frac{1}{2}} \qquad (2)$$

and

$$T = T_F = \Sigma\,(\frac{E_i}{F_i}) \;/\; \Sigma\, E_i \qquad (3)$$

All power figures were converted to representative "deep" water values except for the two shallow water stations in the wave gauge array off the Cape Peninsula.

2.2 Coast-wise distribution.

Waves formed in the major generating zone to the south west of Southern Africa undergo very little refraction before arriving at the tip of the sub-continent. A mean annual power level of approximately 45 kW per metre wave crest is typical off-shore of the Cape Peninsula. The remaining south western coastal belt (Danger Point to Saldanha Bay) has an annual average energy flux level of approximately 25 to 30 kW/m which diminishes northwards to levels of about 21 kW/m at Oranjemund and eastwards to constant levels of about 12 kW/m. Figure 2 shows the mean annual power levels at six coastal sites based on an analysis of one year's synoptic data for the period November 1978 to November 1979. The figures in brackets represent the wave power level in kW/m which is exceeded 90% of the year. A mean annual power level at a weather ship site 10^{o}S 400^{o}E is included merely for comparison purposes as the recording period did not coincide with that of the coastal analysis.

At an early stage of the project it was realised that in terms of power utilisation a wave power figure representing an average over a full year has very little value and can in fact be rather misleading. (Mean annual power levels are included in this paper for the sake of comparison with the many other wave energy studies which have limited their analyses to mean figures.)

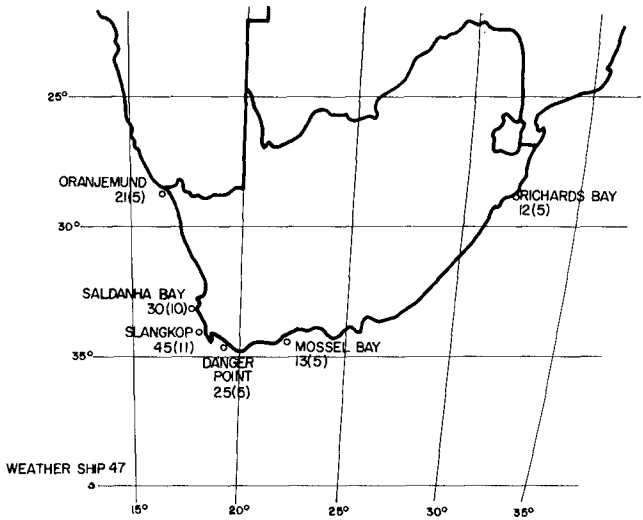

FIG 2 WAVE POWER DISTRIBUTION ALONG THE SOUTH AFRICAN COAST, POWER IN kW/m MEAN ANNUAL, (90% EXCEEDENCE)

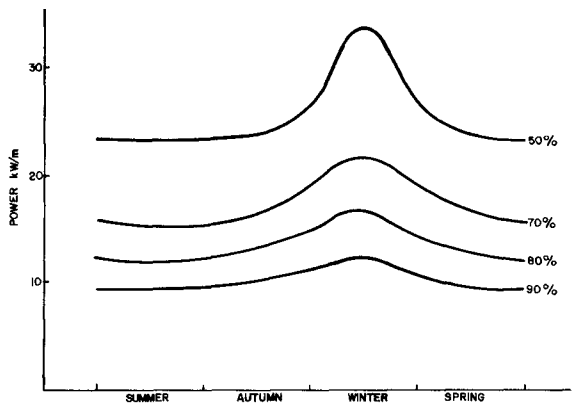

FIG 3 SEASONAL VARIATION OF POWER AT DIFFERENT EXCEEDENCE LEVELS : SALDANHA BAY

It will be noticed that 90% exceedence power levels of about 10 kW/m occur between Slangkop and Saldanha Bay, while the remainder of the coast-line displays a constant level of about 5 kW/m. These results can be very significant in terms of the level of optimum power conversion for which a wave power station is designed. For example, if a device were designed to produce an optimum cost benefit at a power level of 5 kW/m (which would provide power for 90% of the year) the potential application of this device along the coast would be totally different from some other device which was designed to convert all the wave energy it encountered at the highest hydraulic efficiency. Figure 3 shows the seasonal variation of power levels at 50%, 70%, 80% and 90% exceedence for Saldanha Bay.

The final analysis of the wave energy resource is thus of necessity dependent on the conversion characteristics of the proposed wave energy converter and the demand characteristics of the converted power. The interactions involved are shown in figure 1.

2.3 Wave power distribution at Slangkop.

In a joint project between the Universities of Stellenbosch and Cape Town, the Fisheries Development Corporation of SA Ltd and NRIO, three Waverider stations were maintained west of the Slangkop Light House on the Cape Peninsula for a period of over two years specifically to study shoaling effects on wave energy propagation. The dissipative mechanisms involved have been analysed by Shillington (1982).

The three stations were situated in 200 m, 24 m and 15 m water depths, and were backed up by a DOSO direction gauge (Retief and Vonk, 1974) at the 24 m station. A typical annual H-T scatter diagram with 10 kW isodynes for the 200 m station is shown in figure 4. Figure 5 shows the position of the three Slangkop stations with the mean annual and 90% exceedence wave power curves plotted against distance from shore. It can be seen that although there is a 30% reduction in mean annual power between off-shore and 0,8 km from shore (15 m deep station) the 90% exceedence curve displays a reduction of only 20%. The relatively high power levels occurring close inshore favour the use of fixed, shallow water energy converters which will avoid mooring problems and require minimum power transmission distances. Development of the energy converter was thus directed towards the inshore zone from the outset, as opposed to the initial deep-water approach of the United Kingdom researchers where the shallow-water power levels are relatively unfavourable (Crisp and Scott, 1981).

Although the Slangkop records displayed the highest mean levels of wave power measured around the coast this did not necessarily imply that Slangkop was most suited for wave power utilisation. In comparing the seasonal distribution of the 90% exceedence curves for Slangkop, Saldanha and Oranjemund (see figure 6) it was found that the more evenly distributed power at Saldanha suggested more favourable power generating characteristics than that at the higher energy Slangkop station.

Another form of analysis which assists in determining the design characteristics of the power converter is shown in figure 7 for Saldanha,

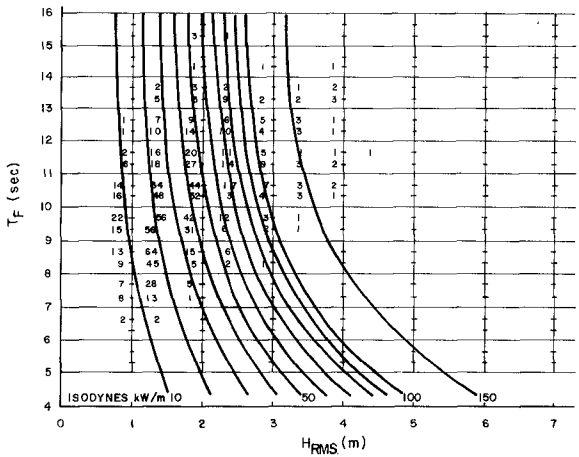

FIG 4 H-T SCATTER DIAGRAM FOR SLANGKOP (200m) VALUES IN PARTS PER THOUSAND

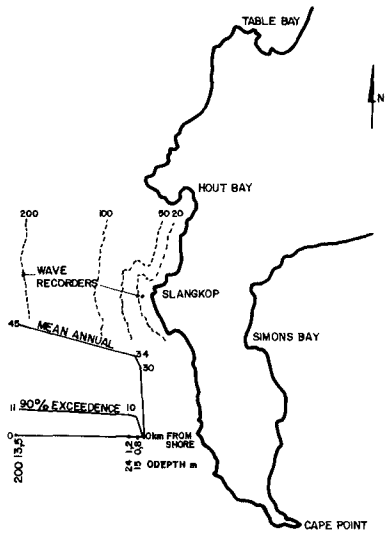

FIG 5 SLANGKOP WAVE POWER CHARACTERISTICS

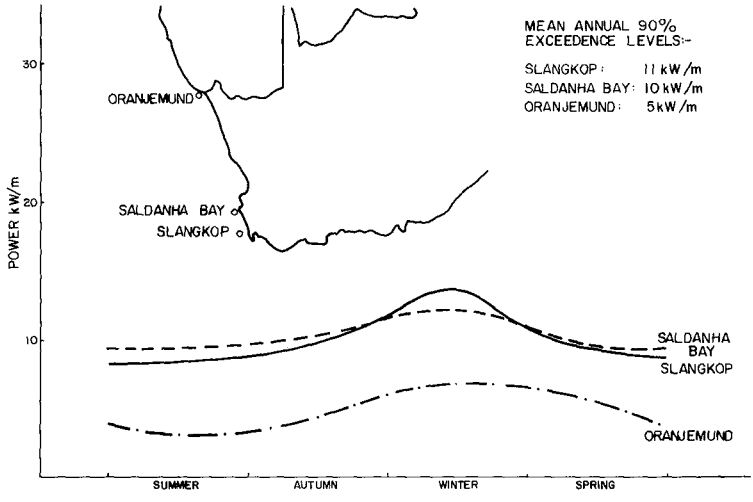

FIG 6 SEASONAL VARIATION OF POWER AT 90% EXCEEDENCE LEVEL FOR THREE STATIONS

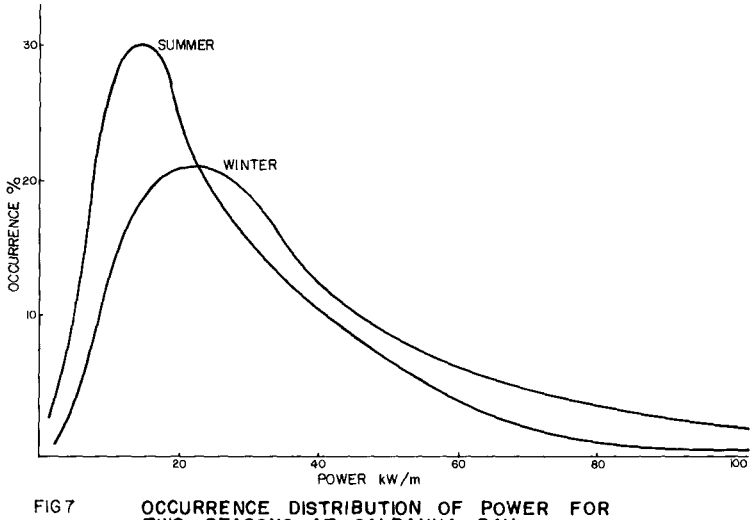

FIG 7 OCCURRENCE DISTRIBUTION OF POWER FOR TWO SEASONS AT SALDANHA BAY

where the occurrence distribution of power for various seasons or demand periods can prescribe optimum generating capability for the period under study.

In figure 7 the highest percentage of power in the summer occurs at about 14 kW/m while in the winter 22 kW/m appears to be most prevalent at this particular site.

Vimukta *et al* (1978) suggested that for a fairly large wave power program which is not combined with storage "there is little point in having a mechanical power cut-off greater than about 25 kW/m". For this project the larger converter described in section 3 was based on a 22 kW/m cut-off, the smaller on 13 kW/m.

3. ENERGY CONVERTER

3.1 Design philosophy.

In figure 1 the component interactions of the program are described and reference has subsequently been made to the concept of a design philosophy. In developing a new system in which a great number of variables interact it becomes essential to establish a well defined philosophy which will reduce the number of variables and qualify the project's stated objectives.

The following statements constituted this project's design philosophy:

- cost efficiency to be of prime importance (hydraulic conversion efficiency of secondary importance *per se*; total resource utilisation was not a specific objective if this should be in conflict with the cost objective).

- the system should not be dependent on energy storage (i.e. device to be optimised at a low power cut-off level).

- over design required for extreme storm events to be avoided.

- environmental impact and possible hazard to navigation to be minimised.

- design and construction of the device should fall within existing local technological capability.

- the apparent high levels of power occurring inshore along the south western coast of Southern Africa should be utilised if this could improve cost efficiency.

The decision to work independently of power storage was made mainly to reduce the number of variables and to produce a system which was more universal and versatile. (Where mountains occur close to the sea, wave power generators can naturally be employed to pump water to storage reservoirs. If sea-water is used and the reservoir is sited at least 600 m above sea-level the system can be used both as a pumped storage power scheme for the winter and a reversed osmosis fresh water

supply scheme for the summer.) The greater majority of previously proposed wave energy converters have been aimed at high hydraulic efficiency, requiring storage of the extreme levels of power generated during storms, contrary to the proposal by Vimukta *et al* (1978) that "the emphasis of research should be switched away from efficient extraction of the large amounts of power available in strong seas and towards cheapness and reliability of supply under ordinary and calm conditions".

3.2 Proposed converter.

The considerations listed under 3.1 led to the following preliminary conclusions:

- the converter should be a fixed structure thus producing an efficient reference frame, simple technology (no mooring or flexible transmission problems) and limited maintenance.

- the device should be submerged to minimise environmental impact and reduce storm loading.

- installation should be close inshore to reduce transmission distance and provide a limited wave direction spectrum and depth limited design wave height.

- the device should be non-tuned and relatively insensitive with robust and simple control requirements.

The simple, yet elegant oscillating water column concept, first developed in Japan and later researched by a number of wave energy groups, was judged as most suitable to meet the above requirements. However, instead of directly extracting power from the oscillating air flow, a manifold system similar to that proposed by French (1979) for the Lancaster Flexible Bag Device was used to provide a rectified air flow. To enhance capture efficiency and improve structural stability the converter is angled to the wave orthogonal. To improve generating cost efficiency a pair of collectors is coupled in a V-formation to a single air turbine and power generator mounted above water level in a tower at the apex of the V. Figure 8 illustrates the principles involved. Figure 9 shows an artist's proposal of a V-converter constructed on ring foot pillars along a sandy shore line in 15 m to 20 m water depth.

3.3 Model studies.

Model studies used in the development of the Stellenbosch Wave Energy Converter (SWEC) covered a variety of cross-sectional shapes and internal proportions for variable collector length, orientation angle and submergence depth. Two dimensional flume tests were carried out at a scale of 1:50 (figure 10), while three dimensional wide tank tests were performed at 1:100 (figure 11) in the hydraulics laboratory of the University of Stellenbosch.

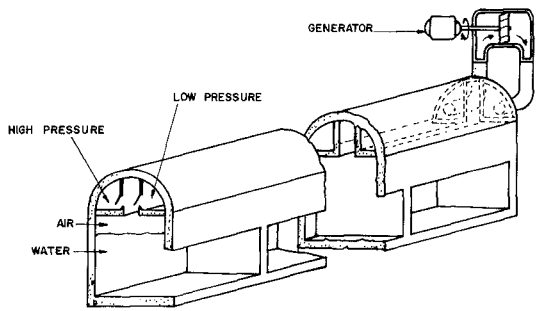

FIG 8 PRINCIPLES OF OPERATION OF THE SWEC

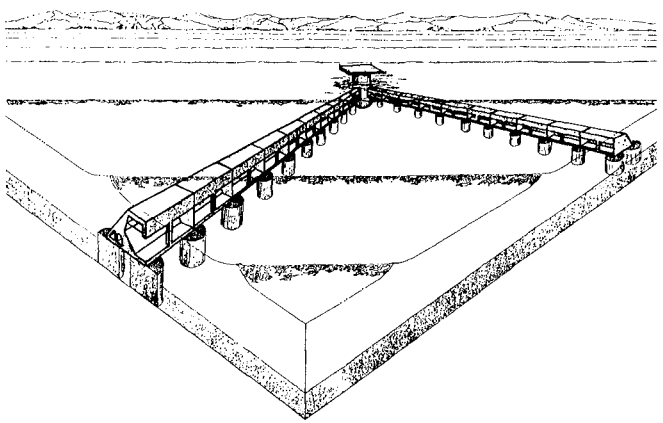

FIG 9 ARTISTS RENDERING OF THE SWEC

FIG 10 TWO DIMENSIONAL MODEL TESTS.

FIG 11 THREE DIMENSIONAL MODEL TESTS OF ONE COLLECTOR ARM.

The three dimensional models were built with the high and low pressure manifold ducts supported outside the model, above water level (see figure 11) so that Reynolds scale effects in the ducts could be minimised and observation and control facilitated. The compressibility of the air contained within the device cannot be scaled. To establish what effect this might have on the model studies a series of tests were carried out with compression chambers attached to the manifold ducts proportioned so that they would simulate the compressibility of air in the prototype. It was found that the compressibility of the contained air did not influence the device's power conversion capability but merely provided a damping effect on the higher frequency pressure fluctuations in the ducts.

Generated power in the model was measured by a sensitive volumetric gas flow gauge (fitted with a throttle control to simulate power loading) and pressure sensors monitoring the pressure gradient across the flow gauge. High frequency pressure fluctuations in the ducts (caused by valve slapping) were electronically filtered out to approximately simulate the prototype turbine response. Water level fluctuations inside the collector compartments were monitored by means of resistence probes. The two dimensional model was fitted with a constant head, variable volume air chamber to simulate the manifold system. Structural stability tests were carried out on a 20 m length of collector arm at a scale of 1:100 in a special test rig which measured horizontal shear and overturning forces simultaneously.

3.4 Converter characteristics.

Although the collector arms will normally be installed at an angle of about 30^{o} to the coast-line it can be seen from figure 12 that precise orientation is not critical in terms of conversion efficiency and can vary by up to $\pm 15^{o}$ of optimum.

Frequency response of the device (figure 13) displays a satisfactory band-width and allows a certain amount of freedom in fixing the length of the collector arm according to site conditions.

An important attribute of this device is that as long as the collector arm is maintained at some constant minimum length (sufficient to provide a smooth air flow through the turbine and dependent on the component of arm length normal to the wave crest) the cross-section of the collector arm can be scaled up or down and the cost efficiency of the system is maintained approximately constant. This implies that depending on the power cut-off level that is considered suitable for a specific site the device can be designed accordingly with no loss in cost efficiency.

The power cut-off is attained by throttling the air flow upstream of the turbine and the resulting conversion characteristics are shown in figure 14 for devices with cross-sectional height dimensions of 5,5 m and 9,0 m. Throttling of the air flow also limits vertical motion of the water surfaces within the collector arm and prevents slamming against the collector roof-slab.

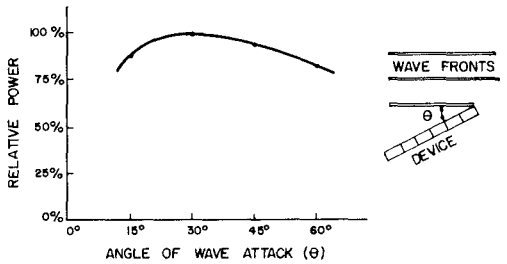

FIG 12 RELATIVE POWER GENERATED VS, ANGLE OF WAVE ATTACK FOR CONSTANT WAVE PERIOD (10 SEC.) AND ARM LENGTH (300 METERS)

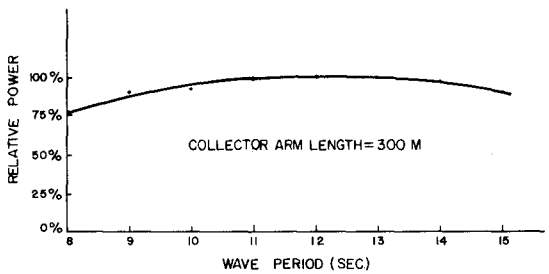

FIG 13 RELATIVE POWER GENERATED VS, WAVE PERIOD AT CONSTANT WAVE HEIGHT (2M)

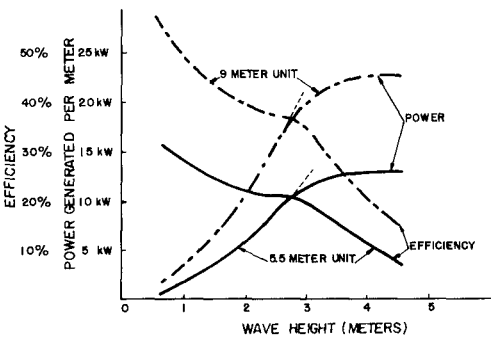

FIG 14 POWER GENERATED AND EFFICIENCY VS, WAVE HEIGHT FOR TWO CONVERTER SIZES

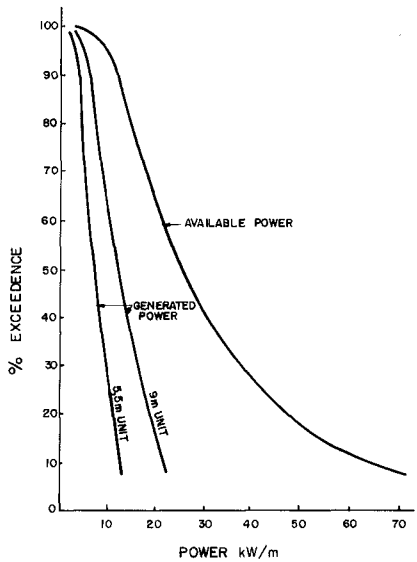

FIG 15 POWER EXCEEDENCE CURVES FOR SALDANHA: AVAILABLE AND GENERATED

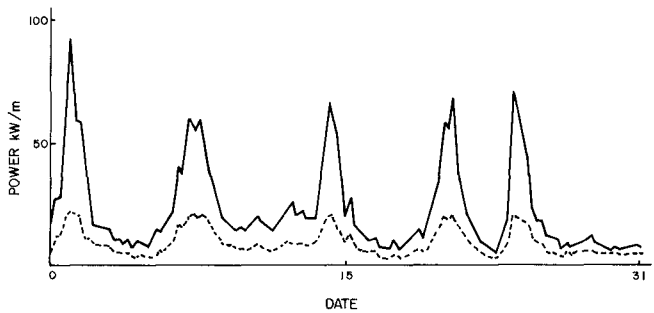

FIG 16 WAVE POWER AT SLANGKOP FOR JANUARY 1982
——— AVAILABLE
- - - - - GENERATED (9m UNIT)

Applying the curves shown in figure 14 to an actual site, the available and generated annual power exceedence curves for Saldanha Bay for the 9 m and 5,5 m units are shown in figure 15. The suppressed conversion characteristics of such a device can also be clearly seen in a time domain plot of available and generated power, as in figure 16 where the generation history of a 9 m unit installed at Slangkop is depicted for a period of one month in midsummer.

3.5 Prototype design.

For costing purposes engineering designs of a 9 m and a 5,5 m unit based on the format shown in figure 9 were drawn up. The design was based on a precast, 15 m long reinforced concrete module which is floated to site and cast into preplaced and ballasted ring foundations. Where installation is to take place on a rocky sea-bed the units will be laid on a prepared bed and fixed by means of rock anchors. The modules are intrinsicly very stable. In the flooded mode, used for placement, and before the units are anchored, they remain stable in waves of up to 3,5 m. This provides a useful weather window for fixing the units in place and coupling the air ducts (by means of flexible "subway" joints). The valves are durable, light-weight material offering low inertia and protected by buoyant "splash flaps". An airpump, housed in the access tower, will maintain the desired air volume in the system. The low pressure air turbine (Francis or axial flow) and coupled power generator will be housed above water level in the access tower so that flooding of the collector arms will not disturb the control and generating gear. Both A/C and D/C generating options have been considered and the rated output varies from 2,5 MW (mean annual) for a 5,5 m "V" collector to 4,4 MW for a 9 m unit. The final cost of A/C power delivered at the coast and based on a 100 MW grouping of "V" collectors along 9 km of coast, has been found to range from 4,5c to 5c per kWhr (RSA currency) which is considered competitive with existing power costs along large sections of the coast-line.

4. CONCLUSION

The Stellenbosch Wave Energy Converter has generally met all the original requirements described in section 3.1. The power produced appears to be cost competitive with existing power and the system relies solely on existing construction technology. Although further quantitative work is required on the potential disruption of littoral processes through the extraction of wave energy a preliminary assessment indicates that this should not be excessive. The device is robust and simple and will be virtually unaffected by marine growth with maintenance operations being largely limited to the access tower. At the end of its economic life the device can be flooded to become an artificial reef.

The primary aim of the above converter is to produce electricity at a viable present day cost. Consequently high hydraulic conversion efficiency was not a fundamental requirement. For an inshore device such as this, environmental considerations will in any case impose a limit on the extraction efficiency. The system is therefore not aimed at total resource utilisation but should offer a useful source of supplementary power for the future. Because of the ease with which the

device can be scaled, the step required to move from laboratory to pilot installation will not require the same level of risk capital as is the case in many previously proposed devices.

ACKNOWLEDGEMENTS

The authors gratefully acknowledge the financial and logistic support received from the CSIR and the many other individuals and organisations who assisted in this project.

REFERENCES

CRISP, GN and SCOTT, M. (1981). The spatial distribution of wave power on the Western U.K. Coast. Proc. 2nd BHRA Intl. Symp. on Wave and Tidal Energy, Cambridge, Sept. 1981.

DUTKIEWICZ, RK and NURICK, G. (1978). Wave Energy off the coast of Southern Africa. Proc. BHRA Intl. Symp. on Wave and Tidal Energy, Canterbury, Sept. 1978.

FRENCH, MJ. (1979). The search for low cost wave energy and the flexible bag device. Proc. First Symp. on Wave Energy Utilization, Gothenburg, Oct. 1979.

LEISHMAN, JM and SCOBIE G. (1975). The development of Wave power - a technoeconomic study. National Engineering Laboratory, Glasgow, Publication EAU M25. 116 pp.

RETIEF, G de F and VONK, APM. (1974). Low cost inshore wave direction indicator. Proc. 14th Intl. Conf. Coastal Eng., Copenhagen, 1, 212-204.

SHILLINGTON, FA. (1982). Wave energy variation of shoaling waves near Cape Town. Proc. 18th Intl. Conf. Coastal Eng., Cape Town, Nov. 1982.

VAN WYK, AC. (1978) Wave Power Study : An estimate of the wave power potential of the South West African and South African Coastal Waters. Council for Scientific and Industrial Research, Stellenbosch, Report No SEA IR 7808. 60 pp.

VIMUKTA, D, BAKER, TM and PLUMPTON, B. (1978). Integrating wave power into the electricity supply system. Proc. BHRA Intl. Symp. on Wave and Tidal Energy, Canterbury, Sept. 1978.

SOME PROPERTIES OF SWELL IN THE SOUTHERN OCEAN

by

Jon B. Hinwood[1],
Deane R. Blackman[2], and
Geoffrey T. Lleonart[3]

SUMMARY

Records of pressure from a bottom-resident instrument deployed near the western margin of Bass Strait have been analysed. Discrete wind-sea and swell spectra have been identified and have been related to meteorological events. The spectra fit a finite-depth form of the Wallops spectrum.

1. INTRODUCTION

Research in coastal and ocean engineering at Monash University has been planned to address topics of specific relevance to Australia. The Southern Ocean, effectively with an infinite fetch, is a source of strong swell to which the whole southern half of the continent is exposed. The present project involves the collection of wave data, particularly swell, and the numerical modelling of the generation, propagation and decay of waves in arbitrary bathymetry. An instrument and moorings suitable for a single point or a directional array were designed and made for this project.

The aim of the preliminary field experiment described here was both to test the instruments and to attempt some definition of the swell field impinging on the Strait to guide future experiments.

To the south of Tasmania the strong westerly winds of the Roaring Forties prevail. At the latitude of Bass Strait the weather patterns

---

[1] Associate Professor, Department of Mechanical Engineering, Monash University, Clayton, Victoria, Australia.
[2] Senior Lecturer, Department of Mechanical Engineering, Monash University, Clayton, Victoria, Australia.
[3] Research Associate, Department of Mechanical Engineering, Monash University, Clayton, Victoria, Australia, and Principal Lecturer, Footscray Institute of Technology, Footscray, Victoria, Australia.

are dominated by the eastward-moving succession of high and low pressure regions with its approximately four-day period. The lows are usually more strongly developed and give rise to stronger winds. The lows are often preceded by or merged with one or more cold fronts which are accompanied by strong winds but of short duration. The pattern of highs and lows moves north in winter making the northerly winds dominant from April to September, while southerlies are dominant from November to March. There is no "weather window" in Bass Strait and strong winds may be experienced in any month.

Owing to the dominant strong winds around latitude 40°S, the wave climate is particularly severe on the south-western coast of Tasmania, moderating with distance north —— towards the site of the present measurements. Strong wave and swell events reported here were generated by each of the wind systems: very large atmospheric systems south latitude 40°S, strong lows passing just south of or over Bass Strait and cold fronts passing over Bass Strait.

2. SOURCES OF DATA

Hourly wind speed and direction were obtained from the nearby Baseline Air Pollution Monitoring Station at Cape Grim with the cooperation of CSIRO. This observatory is 45 km south-east of the site of the experiment and stands on a cliff 90 m above the sea. Presently no corrections have been applied to the wind data.

The instrument used to measure the waves is a bottom-resident pressure-sensing recorder. The recorder is a micro-computer controlled digital cassette drive designed for minimum power consumption and capable of conditional sampling of the input. The instrument wakes every four hours and senses the sea state for a period determined by the firmware. If it decides there is sufficient surface activity it logs conditions as described and then enters an extended recording mode. In the present experiment this involved samples at 4 second intervals for a period of 30 minutes each.

The tape has a capacity of approximately 100 30-minute wave records. In the trial, the results of which are reported here, the instrument ran for 39 days. In this time six events reached the threshold value and resulted in wave records.

For this deployment the instrument was placed on the sea bed, though later deployments may use a taut-wire mooring system. Since the maximum depth for the instrument is 60 m, a station at the edge of the shelf was not attainable. The site selected, shown in Fig. 1, was 144° 20'E, 40° 28'S, 2.5 km north-west of Black Pyramid, a site which satisfied the above criteria although the sea bed was not as smooth as desired being a low rocky ridge rising 15 m above the general surroundings to a depth of 57 m below MWL.

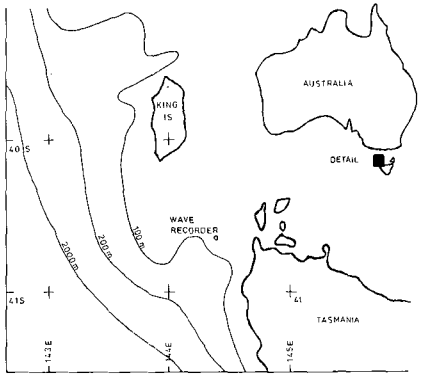

Fig. 1 Location map

3. SPECTRA

To reduce the records of bottom pressure to power spectra of the surface elevation the average of seven hanned periodograms was taken, and the correction for attenuation due to depth corresponding to each frequency component was applied to its spectral value to give the corrected spectrum at the surface. The magnitude of the depth correction factor reaches large values (~ 300) at the highest frequencies considered. For the spectra shown a filter has been applied attenuating components with periods less than 9 s.

The time history of the surface elevation was reconstructed by transforming the whole pressure record, making the depth correction in frequency space, and transforming inversely. The power spectrum of the surface elevation can also be obtained from this history; as expected the results are similar to those obtained from the pressure signal directly, as described above.

4. RESULTS AND DISCUSSION

Records of the hourly wind data from Cape Grim and the four-hourly wave data from Black Pyramid were combined as shown in Fig. 2 to represent a time history of wind and wave parameters during the 39-day period of the experiment. The wave height parameter used in the time history was based on the maximum crest-to-trough pressure difference observed during a 5-minute period. The units are metres of water. Because the wave recorder senses bottom pressure at a depth of 57 m, the description of the sea state obtained from it corresponds principally to swell conditions.

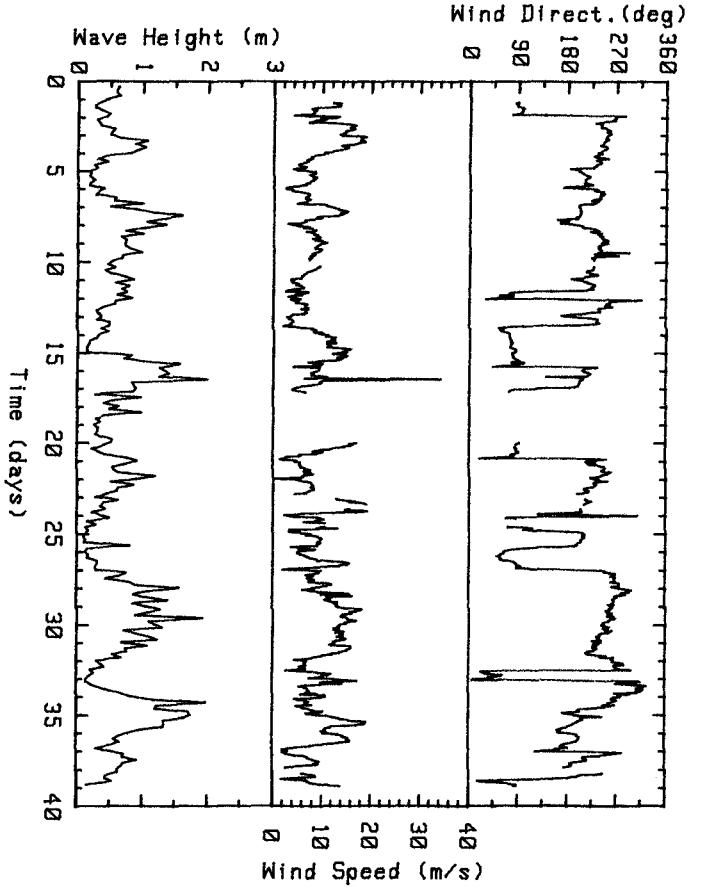

Fig. 2 Time series of measured sea state with wind speed and direction at Cape Grim

Some features of the time history are worthy of note. During the period of the experiment the wind blew mainly from the south-west and only on one occasion exceeded 20 m/s. The significant wave height varied between about 10 cm and 2 m and the periods of high and

low swell activity are clearly shown in Fig. 2. The first significant swell started to build up after day 6 (14 November 1982) and reached a peak between days 7 and 8, then gradually decayed until day 15 at which time it grew considerably. On day 16 (24 November 1982) of the experiment, between 0600Z and 1200Z wind from the SSW reached speeds of 34 m/s. This storm produced a wind sea, which in conjunction with the significant existing swell, was sufficient to trigger the instrument into the extended recording mode.

The first 30-minute wave record was taken during this intense but short-lived frontal storm. Analysis of the wave record obtained indicated a 14.2 s period swell peak in the surface elevation spectrum with an estimated significant wave height H_s of 2.1 m. The spectrum is shown in Fig. 3; clearly evident is a separate peak due to the wind sea.

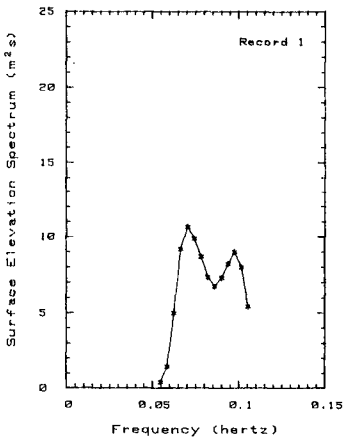

Fig. 3 Surface elevation spectrum showing separate swell and wind-sea peaks

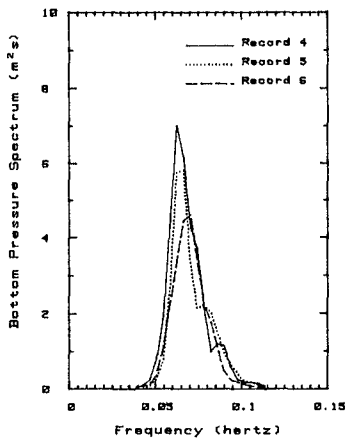

Fig. 4 Bottom pressure spectra showing evolution with time

A further 13 days passed before the second 30 minute record was taken. The swell level decreased from day 16 (24 November) until about day 20 (28 November); it increased slightly before falling to its lowest level on day 25 (2 December). Under the influence of strong west winds the wave activity then built up steadily; record 2, taken on day 30 (7 December), coincided with the passage of a storm of extended duration with winds up to 18 m/s from the west. The surface elevation spectrum corresponding to this record contained a single peak at a frequency of 0.1 Hz. Although the frequency range of the

data obtained from the pressure transducer is limited, an estimate of the H_s was found by fitting the experimental data to a Wallops spectrum modified to account for finite depth. This procedure yielded a H_s of 6.3 m. A Jonswap spectrum with a peak enhancement factor of 4.2 yielded essentially the same result.

Wave activity subsided after day 30 (7 December) to a new low level on day 33 (10 December), it then rose sharply and the swell reached a high level. Records 3, 4, 5 and 6 were taken during this period after which the swell again fell to a low level. The last three wave records obtained were taken successively at 4-hour intervals, commencing on day 35 (12 December) at 1600Z. An increase with time of the frequency associated with the peak in the swell spectrum is clearly evident in Fig. 4, where the bottom pressure spectra of records 4, 5 and 6 are presented. A distance of about 950 km to the source of the swell in these records was inferred from the frequency shift. Although limited in detail, the synoptic weather charts issued by the Australian Bureau of Meteorology indicate a likely storm source located some 1000 km SSW of the site of the experiment.

No swell peak was observed in the spectrum of the storm sea of record 2, but all the other spectra from the records obtained displayed prominent swell peaks, which, with the exception of record 6, were accompanied by locally generated wind-sea peaks.

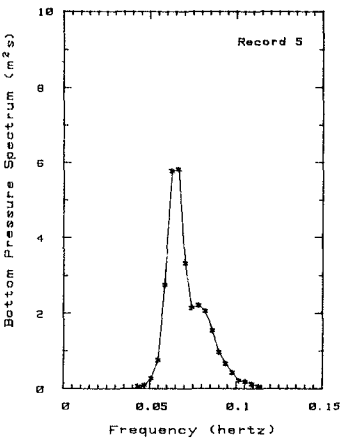

Fig. 5 Typical bottom pressure spectrum - Record 5

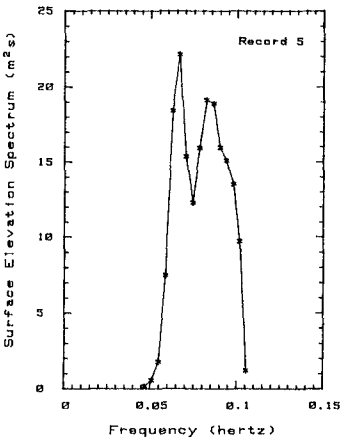

Fig. 6 Typical surface elevation spectrum - Record 5

The period of the swell peaks ranged from 14.2 to 15.3 s, and estimated values of H_s ranged from 2.1 to 3.1 m. Wave record 5 is typical and Figs. 5 and 6 represent respectively bottom pressure and surface elevation spectra for this record; in both representations swell and wind-sea peaks may be identified.

Record 6 was taken soon after the local wind sea had subsided and represents swell resulting from the events of 12 December. In an effort to describe theoretically swell we have modified the recently proposed Wallops spectrum to account for finite depth effects. The Wallops equation for the spectrum of surface elevation given by Huang et al (1981) is:

$$\Phi(f) = \frac{\beta g^2}{(2\pi)^4} \cdot \frac{f_p^{m-5}}{f^m} \cdot \exp\left\{-\frac{m}{4}\left(\frac{f_p}{f}\right)^4\right\} \qquad (1)$$

where f and the frequency of the spectral peak are now measured in Hertz.

As originally given the equation was suitable for deep water conditions. We have modified the functions β and m for intermediate depth water; the derivation of these forms is given in Lleonart, Blackman and Hinwood (1983).

$$\beta = \frac{\left\{2\pi S\left[\tanh\left(k_p d\right)\right]\right\}^2 \cdot m^{\frac{m-1}{4}}}{4^{\frac{m-5}{4}}\,\Gamma\left(\frac{m-1}{4}\right)} \qquad (2)$$

$$m = \left| \frac{\ell n\left(\sqrt{2}\pi S\right)^2 \left[\frac{\cosh\left(k_p d\right)}{\sinh^3\left(k_p d\right)}\left\{1 + \frac{1}{2}\cosh\left(2k_p d\right)\right\}\right]^2}{\ell n^2} \right| \qquad (3)$$

where

$$S \equiv \frac{\left(\bar{\eta}^2\right)^{1/2}}{\lambda_p}$$

$\bar{\eta}^2$ is the mean square surface elevation,
λ_p is the wave length corresponding to the spectral peak,
k_p is the corresponding wave number, and
d is the still-water depth.

These forms differ from those in Huang et al by the inclusion of the factors in square brackets.

Fig. 7 shows good agreement between the field data and the spectrum for surface elevation based on eqns (1) to (3). We have also developed a theoretical description of the spectrum of the swell in terms of bottom pressure, and a comparison of observations with the predictions is presented in Fig. 8. Further comparisons have been made with data from other sources as well as more recent data of our own. We have found agreement to be consistently good. Huang et al suggested it may be possible to apply the Wallops spectrum to cases where the spectrum contains multiple peaks and we have indeed found, for reasonably separated peaks, that two independent Wallops spectra may be combined to describe the full spectrum.

The derived time series of surface elevation were analysed to establish probability distributions and the extent of wave group formation among larger waves. Unlike the Pierson-Moskowitz spectrum, the Wallops spectrum has a variable bandwidth parameter and it should therefore be a valuable tool in characterising the statistics of wave groups.

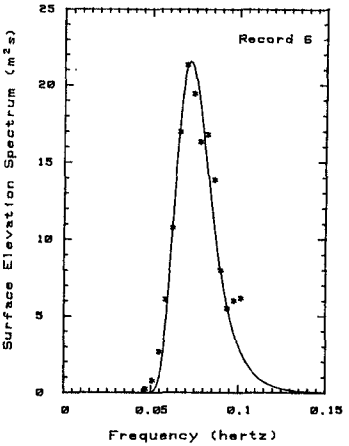

Fig. 7 Comparison of measured surface elevation spectrum with modified Wallops spectrum

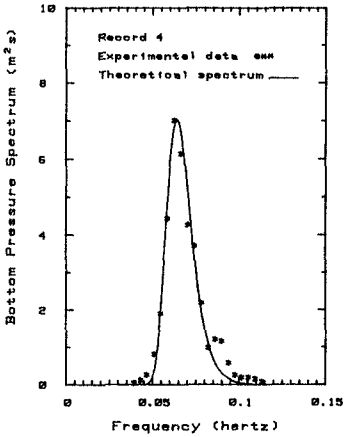

Fig. 8 Comparison of measured bottom pressure spectrum with modified Wallops type spectrum

5. CONCLUSIONS

The data obtained confirm that there is significant swell generated by identifiable meteorological events within the Southern

Ocean. The surface elevation spectra obtained fit a Wallops spectrum modified for the effects of shallow depth. Using the variable bandwidth property of the Wallops spectrum an analytical expression for the length of runs of high waves has been obtained and compared with field data.

6. REFERENCES

HUANG, N.E., LONG, S.R., TUNG, C.-C., YUEN, Y., and BLIVEN, L.F. (1981). A unified two-parameter wave spectral model for a general sea state. J. Fluid Mech., 112: 203-24.

LLEONART, G.T., BLACKMAN, D.R., and HINWOOD, J.B. (1983). Length of runs of high waves. In preparation.

UNUSUAL WAVES ON EUROPEAN COASTS, FEBRUARY 1979

by

Laurence Draper[1]

and

Lt. Cdr. T.M. Bownass RN[2] Ret'd

ABSTRACT

A depression in mid North Atlantic moved at a speed such that it generated high waves of unusually long period and large wavelength. These waves travelled in precisely the right direction to carry them into the English Channel, where they arrived during a time of spring tides and when low barometric pressure contributed to long waves impinging high on the foreshore, causing appreciable damage to sea defences and property.

OBSERVED EFFECTS

Unusually high wave activity, which caused considerable damage, occurred along the central and western coasts of The English Channel at about the time of high tide during the morning of Tuesday, 13 February 1979. Locations mentioned are shown on the map. Damage was particularly severe at Chiswell on the Isle of Portland, where waves over-topped Chesil Beach, the crest of which is about 12 metres above high tide level, causing extensive flooding and necessitating virtual rebuilding of parts of the Beach and settlement (Fig. 1). Eye witnesses described a considerable amount of water flooding through the beach, adding to the flooding due to overtopping. Chesil Beach is a narrow spit and is unusual in that the pebbles are graded in size over its ten-mile length, being smallest at the west and largest at the east.

The damage, on a south-westerly facing beach, took place at a time when the local wind was easterly of about 10 knots. This is in contrast to several times Chiswell has been flooded in the past, when

(1) Institute of Oceanographic Sciences, Wormley, Godalming, UK
(2) Foxbush School, Tonbridge, UK. The work was undertaken whilst this author was a postgraduate student at the University of Southampton.

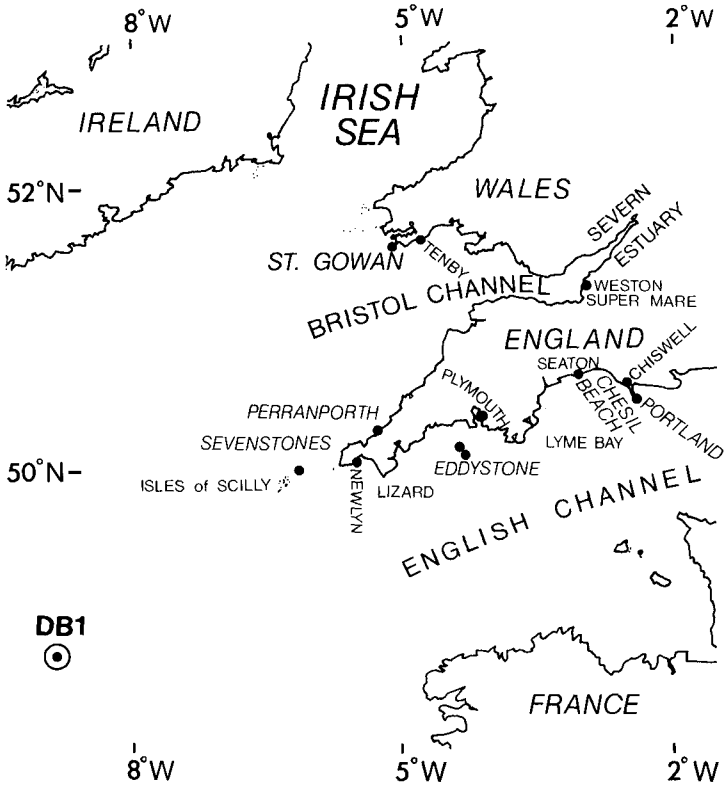

Location Map

Figure 1 Chesil Beach at Chiswell two days after the flooding. Much material had already been bull-dozed back up to the top of the bank. The sea is to the left.

PHOTOGRAPHIC SECTION HMS OSPREY CROWN COPYRIGHT PHOTOGRAPH

the damage was directly attributable to strong winds in the local area which resulted in overtopping of and percolation through the beach. (The most recent previous occasion of this was a strong southerly gale on 13 December 1978.)

In February 1979 there was damage all along the southern English coasts. In harbour in The Isles of Scilly the ship Scillonian tore her mooring bollard off the deck and ripped up her shore moorings. In Plymouth harbour the long waves arrived around 0500hr, high water was at 0700 and the peak activity occurred around 0800. When the dock gates were opened, craft broke moorings until the gates jammed shut. Spray from the waves broke over the breakwater light at the seaward side of Plymouth Sound at 19m. An RAF craft reported that sailing parallel to the crests was like having enormously long walls of sea either side, but that with such a great wavelength no difficulty was experienced.

At Seaton, further up-Channel, coastal structures were badly damaged, and even at Hayling Island, to the east and in the lee of the Isle of Wight, very long length swell waves caused flooding.

Elsewhere, in South Wales these waves caused damage, for example by breaking over the fore-shore at Tenby, and at Sines in Portugal the massive breakwater under construction, and already damaged by previous wave attack, again suffered considerably. Nearby, Leixoes also suffered damage.

An interesting observation of the contrast between effects of the storms of 13 December 1978 and 13 February 1979 was made by Lt. Cdr. J. Roberts, Meteorological Officer of HMS Osprey, Portland. In the former storm the seaward side of the remaining shingle was much too steep to climb up, the pebbles looking as though they had been shovelled out by the sea, leaving a cliff, whilst in the latter case the bank looked like a huge rounded whale-back. In the first case the damage was consistent with attack from short, steep waves, characteristic of locally-generated storm waves, or "sea", which destroy beaches and rip out sand and pebbles from a beach. In the second case, damage was consistent with attack from waves which are very long compared with their height, and are termed "swell", which carry sea-bed material towards the shore and build beaches.

OCEANOGRAPHIC ASPECTS

As the local wind could not have been responsible for generating any waves approaching from a westerly direction, the source of the wave energy must have lain in the Atlantic. Portland subtends only a small angle to the Atlantic, with an arc from perhaps 230 degrees to 260 degrees, so that any wind source must therefore lie within this "window". However, the "window" is not a simple "optical" one, because refraction, which itself will depend on wavelength and therefore ultimately on wind strength, and also on the direction of the original wind, will allow a displacement of the generating

zone into areas adjacent to those in the "optical window". There is, therefore, a range of conditions which could result in a wave orthogonal leading to Portland.

Probably the most important single parameter is the wave period; the periods of the waves at the time of the disaster lay outside the range of periods associated with substantial wave energy ever recorded in many years of wave recording in waters around the British Isles or of the North Atlantic.

WAVE DATA SOURCES

The Taunton laboratory of the Institute of Oceanographic Sciences maintains several wave recorders off the west coasts of the UK for climatological purposes. It has been possible to obtain and analyse data for the relevant times from a recorder on the Sevenstones Light Vessel off Land's End, one near Eddystone Lighthouse and another on the St. Gowan Light Vessel in the Bristol Channel south of Pembroke. The UK Data Buoy DB1 located 120 miles south west of The Isles of Scilly at 48°42'N, 8°58'W, was operated by the Departments of Energy and Industry and the United Kingdom Offshore Operators' Association, and measured meteorological and oceanographic parameters, including wave conditions, and transmitted the data by radio to EMI (Woking). A Waverider was maintained by the Hydraulics Research Station, Wallingford, off Perranporth, on the western Cornish coast south of Newquay; it was exposed to waves approaching from the west. Another was operating well up the Bristol Channel. Elsewhere, a Waverider was operating off the port of Sines in Portugal.

A SEARCH FOR THE GENERATING AREA

In order to find a possible generating area which could be the source of this wave energy and which lies within the "window", it is necessary to study the previous few days' North Atlantic synoptic weather charts. The chart for 1200 on 10 February 1979 shows a new depression (Low 992) south of Newfoundland. This depression deepened rapidly as it moved eastwards and by 0000hr GMT on 11 February it can be seen (Fig. 2) as low H, having deepened to 952 mb. The westerly winds on its southern flank were estimated to be of 50-60 knots. Such wind speeds are by no means uncommon in an Atlantic storm.

By 12 February the depression was incorporated as the southern part of a low pressure system having filled to 968 mb. Finally, by 0600 on 13 February the depression was centred approximately 120 nm south west of Land's End at 970 mb. In general, the longer-period waves generated by an Atlantic depression usually travel faster than the storm and so move out of the storm area, and the storms tend to move on a curved path. In this case the depression moved with roughly the same speed (30 knots) and in the same direction as that of the wave components of about 18-20 seconds which it had generated, and so

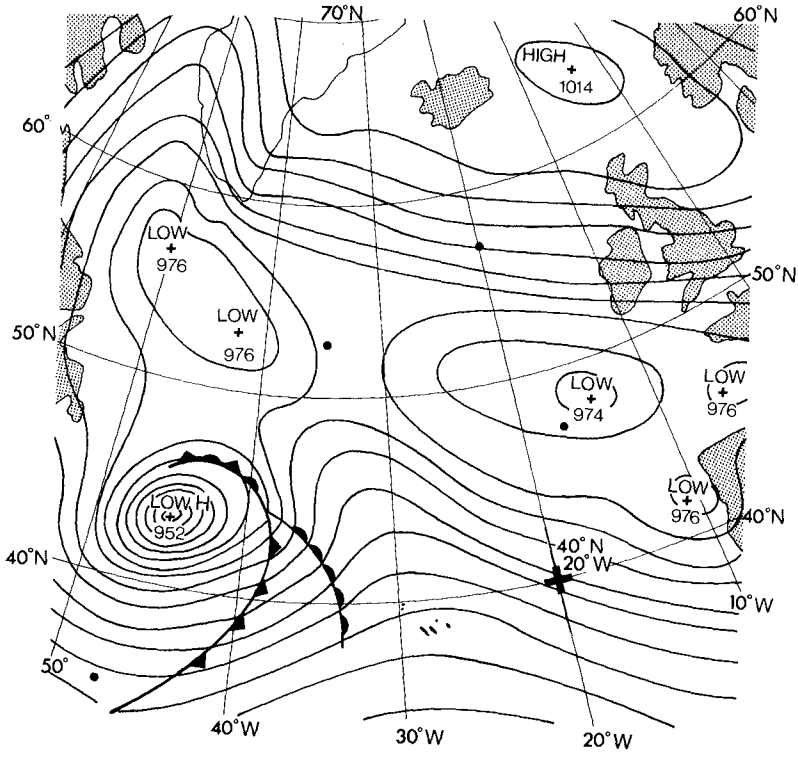

Figure 2 Meteorological Chart for 0000hr GMT 11 February 1979, showing the storm which generated the unusual wave conditions.

continued to input energy preferentially into this longer-period part of the wave spectrum for a considerable time, creating high and unusually long period sea waves. This is the primary cause of the problems at Portland.

A similar event occurred in the South Atlantic in July 1980, but the energy approaching the South African coast on that occasion, when the significant wave height was 3 metres, was only about a fifth of the energy present in the waves described in this paper. That event was described in a careful spectral study and interpretation by Shillington (1981).

THE WAVES ON EURDPEAN COASTS

The depression in mid-Atlantic filled rapidly, but the packet of wave energy it had produced continued eastwards as a swell at about 30 knots, and was detected at about 2400hr on 12 February by DB1 in the western Approaches to The Channel. During 12 February DB1 had consistently recorded waves with a zero-crossing period (T_Z) of around 12 seconds and a significant height (H_S) of about 4 metres, but by midnight the wave period had increased rapidly to nearly 17 seconds and by D100 13 February to over 18 seconds with a significant height of 7 metres. It continued to record these high values until about noon on 13 February. In Figure 3, parameters from DB1 for this storm are superimposed on a scatter diagram for Ocean Weather Station INDIA (59°N, 19°W), the most exposed IDS wave climatology station in one of the roughest oceans. This wave climatology is representative of conditions in the eastern Atlantic from about 45°N to 60°N. The 13 February 1979 conditions are outside the envelope of all data from over 40 previous instrument-years of measurements in all parts of UK waters; about 10 of these have been in locations well exposed to Atlantic conditions. According to the UK Meteorological Office ship routeing wave prediction model, these unusual wave conditions did not extend as far north as station LIMA (57°N 20°W), and this is confirmed by its measurements. (LIMA replaced INDIA in 1976.) (The wave period referred to in this report is the zero-up-crossing wave period, symbolized by T_Z. It is the average interval between successive crossings in the upward direction through the still-water level. The significant wave height, H_S, is the average value of the height of the highest one third of all the waves.) Captain Warren, Master of the oil rig Atlantic I working close to DB1, reported visual estimates of swells of up to 9 metres with periods of over 15 seconds, at times reported to be as high as 20-25 seconds.

Although there was no wave recorder operating at that time off The Isles of Scilly, the tide recorder at St. Mary's showed considerable disturbances starting at about 2200hr on 12 February and continuing until the early afternoon of 13 February. The period is difficult to determine due to heavy filtering by the tide recorder, but a period of about 10 minutes is detectable on the recorder. It seems probable that a local oscillation was induced by the storm waves.

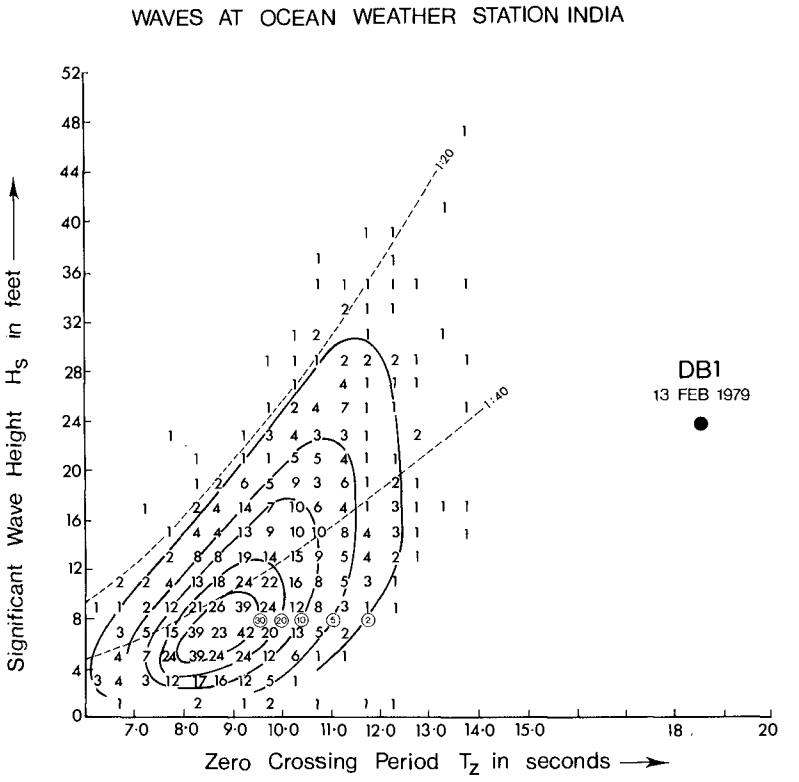

Figure 3 Wave Climatology for the eastern Atlantic as measured at Ocean Weather Station INDIA (59°N 19°W). These data are representative of the eastern Atlantic between about 45°N to 6D°N. The most severe of the parameters measured at DB1 on 13 February 1979 are plotted to show their unusual characteristics. (The wave climate at DB1 is still under confidentiality imposed by the UK Offshore Operators' Association and therefore not available for publication.) The 13 February 1979 conditions are outside the envelope of data from over 40 previous instrument-years of measurements in all parts of UK waters. According to the UK Meteorological Office ship-routeing wave prediction model, these unusual wave conditions did not extend as far north as station LIMA (57°N 20°W), and this is confirmed by its measurements (LIMA replaced INDIA in 1976).

A Shipborne Wave Recorder on the Sevenstones Light Vessel, between Land's End and The Isles of Scilly, measured waves with a significant height of around 3 metres and a zero-crossing period around 10 seconds during the evening of 12 February, but by 0600hr on 13 February the waves increased to over 5 metres in height and over 13 seconds in period. This Light Vessel is partially sheltered from such waves by The Isles of Scilly.

Off Perranporth, the significant height had been about 1 metre on 12 February, gradually increasing to about 1.5m by 2100hr, and then more than doubled by 0300hr on 13 February, staying around 3 metres until 0900 and then decreasing to somewhat over 2 metres by midnight. The direction of approach of these waves was such that they travelled almost parallel to the Perranporth coast, so that their height at the recorder would have been less than that further out at sea. The zero-crossing periods were around 8 or 9 seconds on the 12th until the arrival of the swell late in the day, and in the morning of the 13th reached 13.5 seconds, falling back by noon to 8 or 9 seconds again. Chart records show swell groups of 20 seconds period at Perranporth, and at the Severn Estuary site near Weston-super-Mare, also recorded by HRS.

At Eddystone, which is somewhat sheltered by The Lizard, the wave period had increased considerably by 0300hr on 13 February, and more so by 0600hr with an increase in wave height. The wave heights are lower than at OB1 because of the sheltering. The timing is consistent with the passage of the wave energy past the DB1 location. At St. Gowan in the Bristol Channel, a site well exposed to the source of this wave energy, records show that the wave period (T_z) there increased to 15-16 seconds by 0300hr on 13 February (a value in excess of anything recorded previously in over a year's measurements) and stayed high for at least six hours afterwards. Visual inspection of records from both these sites reveals considerable energy content at around 15 to 20 seconds period. At the NMI research tower in a relatively sheltered position in Christchurch Bay just northwest of the Isle of Wight, off the map to the east, these waves achieved a significant height of over 2 metres. At Hayling Island, to the north east of the Isle of Wight, the attenuated and refracted waves were still 1.5 metres in height at the coast.

The Waverider off Sines, south of Lisbon, experienced unusual conditions and recorded one wave with a height of 17.2 metres and a zero-crossing period of 20 seconds at 0340hr on 13 February. The significant height was 9.4 metres; these waves must have been generated by this same storm.

The ship-routeing wave prediction model run in real time by the UK Meteorological Office had forecast the heavy swell correctly for the morning of the 13th and again forecast heavy swell for mid-Channel for the evening, but apparently at the evening high tide the waves did not have a damaging effect at Chesil Beach. The correctness of the forecast is borne out by the measurements at DB1. However, the most likely explanation of the failure of the swell to arrive at Chesil on the evening tide of the 13th is that

the angle of approach had changed sufficiently (perhaps by only 10 degrees) to place Chesil in the shadow of the south western headlands.

THE APPROACH UP THE ENGLISH CHANNEL

A series of refraction diagrams has been constructed based on the approach of a broad front of waves travelling in directions appropriate to those generated in this storm, approximately towards the east north east. These show that waves of 20 seconds period can come to a focus in the middle of Lyme Bay, those of 18 seconds period focus almost directly onto the Isle of Portland and somewhat shorter period waves come to a real focus further east in The Channel or to a virtual focus inland. Clearly, Portland is particularly vulnerable to the approach of such long period swell coming up-Channel, and in the early hours of 13 February conditions were just right for the waves to make their land-fall in force.

SEA LEVELS

Although the incident occurred at the top of a spring tide predicted for 0740hr at Portland, it was not an unusually high astronomical tide; in fact in the first three months of that year at Portland over forty tides of the value expected for the morning of 13 February, or higher, were predicted, the highest being 0.6 metre higher. However, there was a surge in The Channel that morning, possibly connected with the low pressure centre over the western Channel at that time. At Newlyn, sea level was 0.85 metre above prediction, at Devonport (Plymouth) 0.6 metre and inside Portland harbour 0.52 metre.

The Bidston Laboratory of the Institute of Oceanographic Sciences has analysed surge levels at various ports in the UK and the highest value of surge recorded at Newlyn over an 18-year period was 0.88 metre. Such a surge as occurred on 13 February is unlikely to recur there, on average, more often than once in three years.

In addition to mean water level changes caused by tides and surges, on coasts exposed to wave action the ocean level can be lifted by wave set-up, a mechanism by which the momentum of subsequent waves holds the water carried up the beach by breaking waves and results in an even higher water level at the beach. This effect is not likely to have contributed to the surge levels measured in Newlyn or Portland harbours, but it has been estimated that with these extremely long waves it could perhaps have added about 1 metre to the near-beach water depth at places such as Chesil Beach.

RARITY OF THE EVENT

It seems possible that the situation on 13 February was near to the optimum for severity of effect at Portland. If the speed of the depression had been lower, waves of shorter period would have been enhanced, and focussing, if it occurred at all, would have given enhanced waves but probably further east and in mid-Channel. If the speed of the depression had been higher the enhancement would have taken place for waves of longer period with focussing further west, but the actual total energy at such periods, being even further down the tail of the energy distribution, would have been smaller than actually occurred on 13 February so that the effect at Chesil, and anywhere else in The Channel, would probably have been less.

Without a prolonged historical study of meteorological conditions over the whole Atlantic, it is virtually impossible to ascribe a number to the average return period of such an event. The occasional floodings of Chesil seem to be due to two causes: one, the most likely, occurs when there is a severe local southerly storm coincident with a high tide, and this seems to be the most common. The second, and the cause behind the 13 February 1979 flooding, appears to be a most unusual combination of events; its impact is very much greater because its real-time prediction is orders of magnitude more difficult and expensive, and so far its occurrence has come completely by surprise to the local population, almost literally "out of the blue".

CONCLUSIONS

It is obvious that the coastal damage came about as a result of the compounding of a number of improbable events. Although waves of these heights are likely to occur in the Western Approaches several times each year, it is the coupling with the long wave period which is the most destructive element in this phenomenon. This coupling, which would be directly responsible for wave set-up at an exposed coast, occurring together with a surge and a moderately high tide, is the basic cause of the destruction. At this time it is not possible, or possibly not even sensible, to attempt to quantify the probability of occurrence of such an event, but bearing in mind that the most likely cause of flooding is a local southerly storm, which is predictable, an unheralded flood caused by the factors which caused this one seems purely, on a hunch, to be of the order of a century or longer. This does not, however, mean that it cannot occur again next week; similar but not so severe events may well occur in most years.

The observations made by Lt. Cdr. J. Roberts, Meteorological Officer of HMS Osprey, Portland, of the shapes of the beach in the two floodings of December 1978 and February 1979 are consistent with the known wave conditions and their effects on beaches, and illustrate the completely different nature of the waves on the two occasions.

Needless to say, the effects on the local community were disastrously similar.

The most important engineering implication seems to be that, when an installation is being planned on or near an exposed eastern Atlantic coast, and probably other oceanic coasts as well, the susceptibility to heavy swells with wave periods of around 20 seconds and possibly longer must be considered, because the mechanism for their generation does seem to exist and, by rare chance, occur outside the envelope of all wave measurements covering over 40 instrument years in this part of the North East Atlantic. If inundation from such waves would be disastrous, then the possibility of their occurrence within the typical lifetime of many engineering structures must be considered.

ACKNOWLEOGEMENTS

The authors wish to express their appreciation of the considerable effort expended by many individuals and organizations in providing data and advice. In particular they would like to thank:- Mr. J.G. Berry, Bertlin & Partners; Mr. J.B. Boyle, Mr. J.R. Bishop, and Mr. G. Pearce, NMI; Or. B. Golding and Mr. J. Atkins, Meteorological Office, Bracknell; Mr. Norman Hornbrey, Meteorological Officer RAF Mountbatten; Mr. Howlett, AUWE; Mr. J. Read, G. Maunsell & Partners; Lt. Cdr. J. Roberts, Meteorological Officer HMS Osprey, Portland; Or. F.A. Shillington, University of Cape Town; Mr. R. Shuttler, Hydraulics Research Station, Wallingford; Mr. S. Waites, EMI Woking; Mr. B.O. Watkiss, Southampton Weather Centre; and several colleagues for providing data and advice, and for commenting on the draft.

REFERENCE

Shillington, F.A., 1981
Low frequency 0.045-H_z swell from the southern ocean.
Nature 290, No. 5802, pp 123-125, 12 March.

MEASUREMENTS OF TURBULENCE OVER VORTEX-RIPPLE

by
Masaki Sawamoto
Toshihiko Yamashita
and
Tadashi Kitamura

Tokyo Institute of Technology
Ookayama, Meguro, Tokyo 152, Japan

INTRODUCTION

When a wave propagates over a rippled bed, organized vortices are generated over the leeside slope of crest. They are shedded, collapse and finally supply energy to turbulence in the vicinity of bed. This process plays an important role in the sediment transportation and suspension due to waves. However, quantative measurements of this phenomena have been limited because of some difficulties.

Horikawa and Watanabe(1970) developed the electrolytic transducer and measured the turbulence over a rippled bed. Nakato, Locher, Glover and Kennedy(1977) used a hot-film anemometer controlled by a minicomputer and conducted a phase averaging sampling. One of the authors(1980) tried a phase averaging sampling of velocity field over an artificial ripple by a hot-film anemometer. Du Toit and Sleath(1981) used a He-Ne laser-Doppler anemometer to measure the velocity over artificial and selfformed ripples. Those are the principal contributions in this problem.

One of the difficulties depends on a velocity meter. A hot-film anemometer which is widely used to measure turbulence in an unidirectional flow has some weakness under the circumstances of sediment suspension. Another difficulty lies on a data processing. Because the oscillatory flow turbulence is unsteady process, we can not utilize an analogue data processing technique which is very useful for a steady flow and are forced to handle a large number of digital data.

In the experiments reported here, a laser-Doppler anemometer was introduced in order to overcome a first difficulty. The second one was solved by the combination of a wave-form-recorder-analyser and the desktop computer. The results show the good correlation of the turbulence variation and the movement of shedded vortices. Theoretical considerations on the time averaged turbulence are also presented.

EXPERIMENTAL EQUIPMENT AND CONDITIONS

The wave tank utilized is shown schematically in Fig.1; the test section was 0.4m wide, 0.6m high and 20m long. A 1.8 meter long sand pit was set at the central part of the tank. The same quartz sand, which has a diameter d=0.2mm and density *s=2640 Kg/m3, was used in all cases. An

CASE	WAVE PERID T	WAVE HEIGHT H	DEPTH h	RIPPLE LENGTH Ls	RIPPLE HEIGHT Hs
1	2.25 s	6.90 cm	30 cm	8.55 cm	1.57 cm
2	1.25	6.76	30	4.23	0.88
3	1.75	8.96	30	7.03	1.27
4	1.75	8.52	30	7.18	1.28
5	1.75	6.66	30	6.50	1.12
6	2.25	8.32	30	8.53	1.47
7	1.80	5.15	30	5.75	1.07
8	2.00	6.47	30	7.10	1.46
9	2.00	8.71	30	7.67	1.47
10	2.00	5.15	30	5.43	1.14
11	1.80	8.45	30	6.64	1.22
12	2.60	9.37	30	7.72	1.49
13	2.60	7.63	30	6.74	1.24
14	1.50	7.02	30	5.00	0.97
15	1.40	6.83	30	4.41	0.79

Table Experimental Conditions

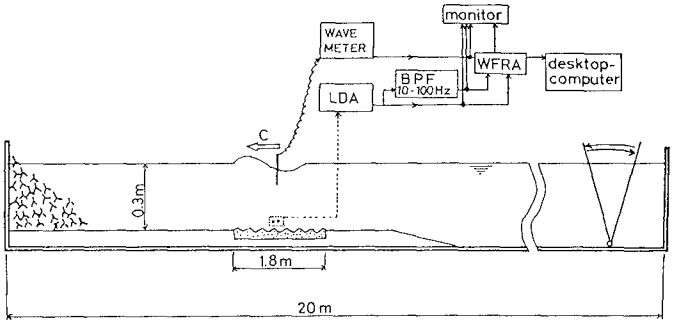

Fig. 1 Sketch of the wave tank.

artificial scratch on the flattened bed made easy to develop a two-dimensional ripple.

The experimental wave conditions and the developed ripples are summerized in Table. No asymmetrical ripple was observed in the experimental range listed here. Fig.2 shows the relation of ripple length Ls and the horizontal excursion length d_o of water particle. Cases 12 and 13 locate in the breakoff range and the others in the equilibrium one where the strong linear relationship are found.

It was confirmed that the length of the equilibrium ripples has a good agreement with the empirical equation reported by Homma and Horikawa (1977). The ripple height, however, was about 20% larger than Homma's results. Yalin and Karahan(1980) also reported the empirical relation of ripple geometry. Their relation gave a good agreement only when the propotional constant C, which they reported 1-1.37, was modified into 1.6.

The He-Ne laser-Doppler anemometer(LDA; Nihon Kagaku Kogyo Ltd.) was used to measure the horizontal velocity under the circumstances of sediment suspension. No seeding was need to pick up the frequency-shifted laser beam. Under the condition of the sediment concentration less than one thousand p.p.m., suspended sediment scarcely disturbed the velocity measurement. The disturbed signals could be easily detected and discarded.

Sampling of the output signal from LDA were synchronized with a wave-meter. Some phase averaged values were statistically online analysed and recorded by the wave-form-record-analyser(WFRA;Kikusui Electronics Co.). Recorded data were also stored on a magnetic casset tape and used for further analysis by the desktop computer(HP9835). The output signal of LDA were filtered by a electrical band-pass-filter in some cases as mensioned later.

DATA PROCESSING METHODS

Four methods were examined in advance.

i) Direct Phase Averaging Method

In an oscillatory turbulent flow, the mean velocity and turbulence should be defined by an ensemble average at a certain phase of wave as follows

$$\left.\begin{aligned} U &= \frac{1}{n}\sum_{i=1}^{n} u(\omega t+2\pi i) \\ \overline{u'^2} &= \frac{1}{n}\sum_{i=1}^{n} [\, u(\omega t+2\pi i) - U(\omega t)\,]^2 \end{aligned}\right\} \quad (1)$$

where u: instantaneous velocity, U: phase averaged velocity and u': turbulence. We refer this averaging PHASE AVERAGING. The phase averaging can be done by WFRA. This technique may give a good results in case of a purely oscillatory flow. In a wave field, however, turbulence evaluated by this method involves two kinds of error. One is due to wave randomness. In a random wave field this is not applicable at all. Furthermore, whatever good wave maker may be used in the experiment, a small amount of fluctuation of a wave period and height exist. The

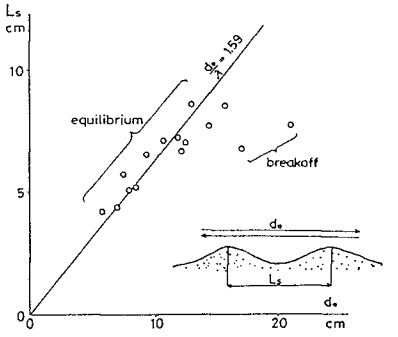

Fig. 2 Relation between the ripple length and the excursion length of water particle.

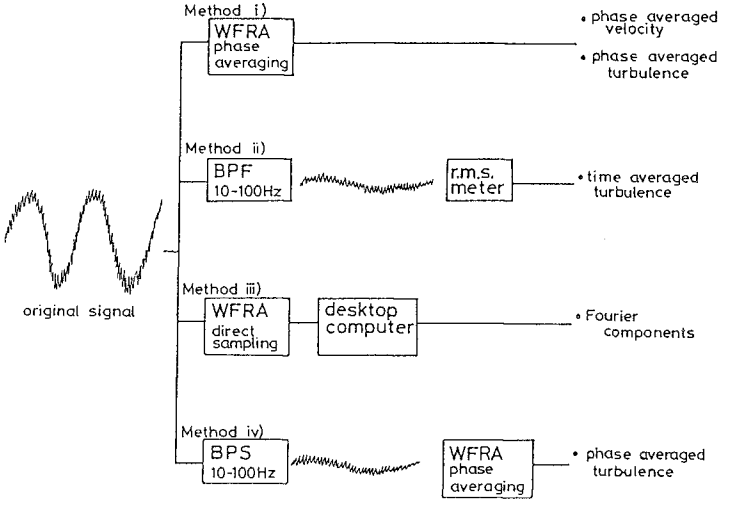

Fig. 3 Data processing methods.

other is due to the imperfect synchronization of sampling. Although the synchronizing signal must be free from any noise or fluctuation, such a situation can not be realized in the experiment. Since turbulence intensity is order of persents of main flow velocity, any fluctuation must be less than one hundredth percent if we want to get an accurate turbulence intensity. Finally, we used this method not to obtain a phase averaged turbulence but only phase averaged main flow velocity.

ii) Electrical Filtering Method

Since phase averaging method is useless in a random wave field, alternative definition of turbulence should be proposed. Turbulence has higher frequency fluctuation than a wave induced periodical velocty variation. So if output signal from LDA was processed by a high pass filter, turbulence velocity fluctuation may be separated. Reading it by a root mean square meter, we obtain long time averaged turbulence intensity as shown in Fig.3. The LDA has inherent noise at higher frequency range than hundreds Hertz, a low pass filter of one hundred Hertz was also used. Cutoff frequency of HPF was determined ten Hertz by trial and error method.

This method seems to be so simple and useful to obtain a set of data at many points. However, it contains a certain amount of error when a turbulence intensity level is low. Because no electrical filter has a sharp cutoff frequency, the high pass filtered signal still has a small fraction of low frequency main flow component which is almost same as or larger than the turbulence. This method was examined at a first stage but finally discarded.

iii) Fourier Expansion Method

The main flow velocity U, which variates in period T, can be expressed by some low frequency terms of the Fourier expansion. Subtracting it from the original variation u, we can obtain an instantaneous turbulent component u' as follows.

$$u' = u - \sum_{i=1}^{N} \left(a_i \cdot \cos(2i\omega t) + b_i \cdot \sin(2i\omega t) \right) \qquad (2)$$

where

$$a_i = \frac{2}{T} \int_0^T u \cdot \cos(2i\omega t)\, dt \qquad \text{and} \qquad b_i = \frac{2}{T} \int_0^T u \cdot \sin(2i\omega t)\, dt$$

If expansion was carried out in each cycle, this method is applicable to the random wave field. The number of expansion was selected by trial and error. Fig.4 shows the time averaged turbulence intensity calculated by this method. The abscissa is the number of expansion. It shows that the number of expansion should be larger than ten or more which coresponds the cutoff frequency higher than five Hertz.

Although this method make available further complicated analysis, it also forces us to process a large number of digitalized data. So it was used only when a detailed consideration was necessary.

iv) Combined Method of Band Pass Filtering and Phase Averaging

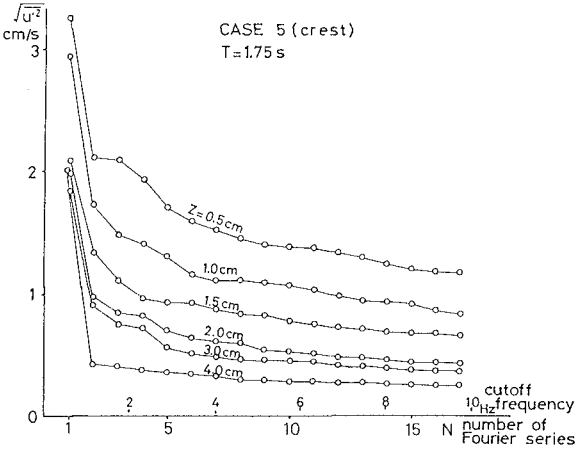

Fig. 4 Variation with N of the turbulence intensity evaluated by eq.(2)

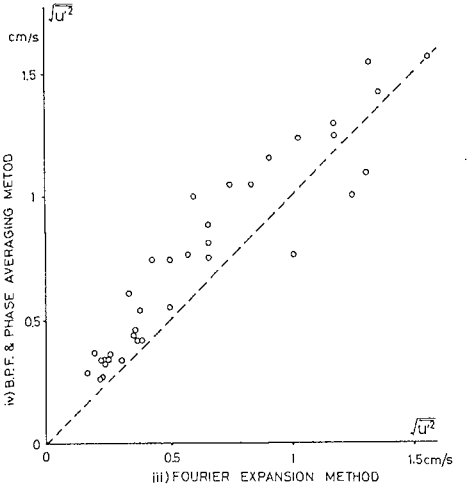

Fig. 5 Comparison of method iii) and iv).

In order to avoid the defects of methods i) and ii), the combined method of them was developed. The signal processed by the band-pass-filter was sampled by phase averaging technique. The low frequency component in the band-pass-filtered signal can be taken away in a sufficient degree by this method. Almost all turbulence data reported here were obtained by this method. The comparison of Method iii) and iv) is shown in Fig.5. The coordinate is the turbulence intensity evaluated by Method iii) and the abscissa is by Method iv) in which the expansion number is selected as 17 (cutoff frequency: 10 Hertz).

RESULTS AND CONSIDERATIONS

1) Turbulence Variation and Distribution

Fig.6-1 shows an example of the phase averaged velocity over a crest. In the figure, Z is a vertical distance from the crest. The variation at Z=6 cm , where the bed configuration has no effect on the velocity variation, is overrapped as a reference variation by broken lines. Fig.6-2 shows the variations of turbulence intensity and Fig.6-3 does velocity and turbulence distributions.

As shown in the figure, turbulence intensity becomes minimum at the phase $\omega t = (4/15)\pi$. At this phase, an organized vortex is growing over the leeside slope, any influence of which is detected at the measuring section. After a flow reversion($\omega t = (10/15)\pi$), the vortex moves over the crest, so the offshoreward velocity is intensified in the vicinity of bed. This phenomenon is noticed by a systematic deviation from the reference velocity variation in Fig.6-1. It is also remarked that the turbulence concentrates in the vicinity of bed. At $\omega t = (18/15)\pi$ another small systematic deviation from the reference velocity is observed. It associates the fact that another vortex developed at the neighbouring ripple passes the measuring section as shown in Fig.6-4 schematically. Because the vortex passes at higher position, the turbulence distributes more widely. Although the vortex passes across the measuring section again at $\omega t = (25/15)\pi$ as shown in Fig.6-4, any sign is not noticed on velocity or turbulence variation and distribution because its organized motion has collapsed by this phase. In another half cycle, almost same phenomenon repeats in the reverse direction.

2) Theoretical Considerations

A turbulence energy budget relation was examined. The turbulence budget equation is written as

$$\frac{D\,\overline{q^2}}{D\,t} = [\text{production}] + [\text{diffusion}] - [\text{dissipation}] \qquad (3)$$

Since the time variation is so complicated, only the time averaged turbulence intensity is considered. The experimental results including the visual observation show that the turbulence energy is supplied by the collapse of vortices in the vicinity of bed and diffused upward by its diffusivity and that the flow field is almost horizontally uniform except in the vicinity of bed. Those facts imply the possibility of two simplified models.

Because the production term does not play any important role except in the vicinity of bed, the diffusion term may balance with the

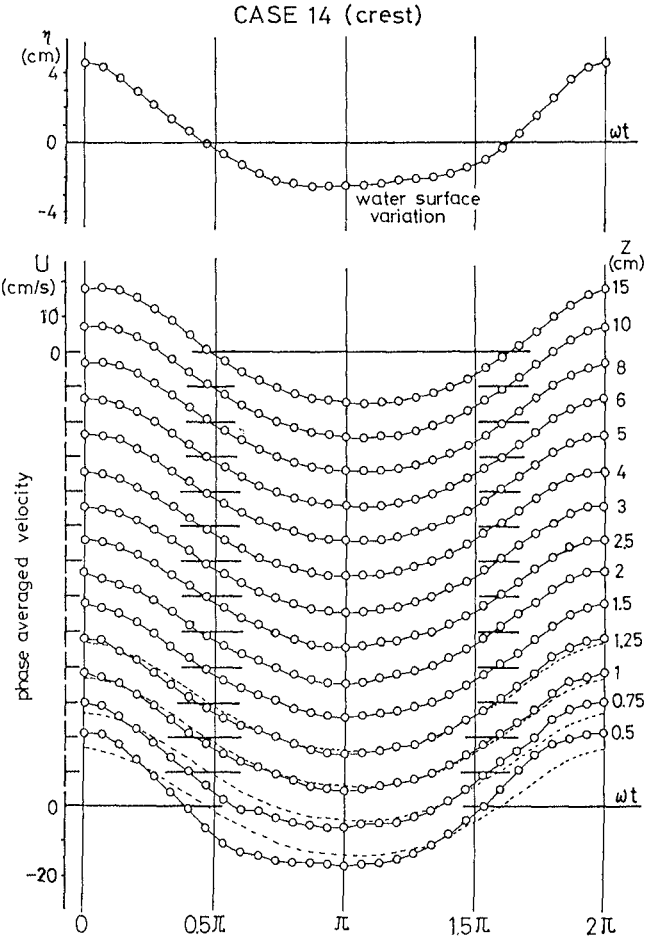

Fig. 6-1 Examples of the phase averaged velocity cycle.

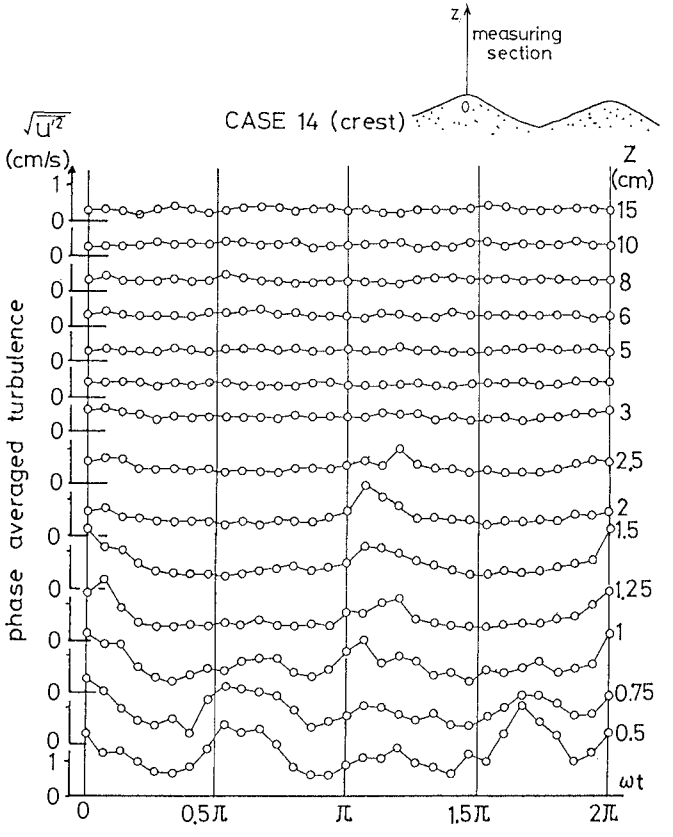

Fig. 6-2 Examples of the phase averaged turbulence variation.

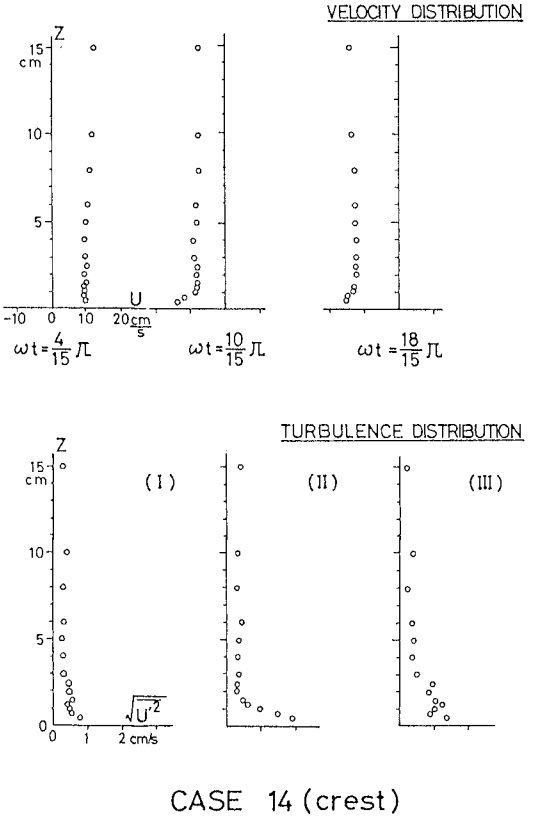

Fig. 6-3 Examples of the phase averaged velocity and turbulence distribution.

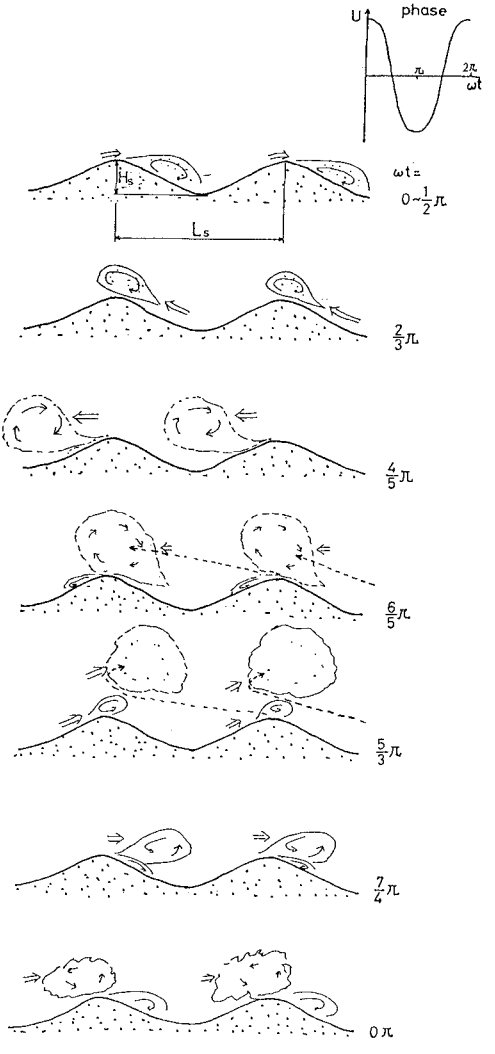

Fig. 6-4 Schematic view of the vortex movement.

dissipation term in the upper region shown in Fig.7. If we assume that Prandtl's mixing length hypothesis is also available in this case, we have

$$\underbrace{\frac{\partial}{\partial Z}\varepsilon_z \frac{\partial \overline{q^2}}{\partial Z}}_{\text{diffusion}} = \underbrace{\frac{A}{L}(\overline{q^2})^{\frac{3}{2}}}_{\text{dissipation}} \tag{4}$$

$$\varepsilon_z = B(\overline{q^2})^{0.5} L \tag{5}$$

where L is the mixing length, $\overline{q^2} = \overline{u'^2}+\overline{v'^2}+\overline{w'^2}$, ε_z is turbulence diffusion coefficient. The value of universal constants A and B are selected as 0.124 and 0.369 by the direct analogy of the unidirectional shear flow. Assuming the mixing length is constant, we obtain

$$\overline{q^2} = \overline{q_0^2}\cdot\exp\left(\frac{1}{L}\sqrt{\frac{2A}{3B}}(Zo - Z)\right)$$
$$\text{or} \tag{6}$$
$$\overline{u'^2} = \overline{u_0^2}\cdot\exp\left(\frac{1}{L}\sqrt{\frac{2A}{3B}}(Zo - Z)\right)$$

where qo is the reference turbulence intensity at the reference level Zo. Fig.8 shows the distribution of time averaged turbulence u'^2 which must be proposional to $\overline{q_0^2}$. The data fall on the curve predicted by eq.(6). In the theory, the mixing length was selected so that it give the best agreement with experiments, because we have no information about it. The values of mixing length L calculated by this criterion are plotted on Fig.9. It shows a good correlation between the mixing length and the geometrical length scale of ripple in the equilibrium range.

In order to determine the reference turbulence, let's consider the control volume shown in Fig.7. The energy production in a cycle must balance with the energy dissipation in it and the upward diffusion from it. The production may relate with the vortex strength Γ. Dimensional consideration concludes that the production during a cycle is proportional to the square of vortex strength; i.e.

$$[\text{production}] = \text{constant}\cdot\Gamma^2$$

The dissipation term is

$$[\text{dissipation}] = \frac{A}{L}(\overline{q_0^2})^{1.5}\cdot Ls\cdot T\cdot Z_0$$

The upward diffusion across Zo is

$$[\text{diffusion}] = -B(\overline{q_0^2})^{1.5}\sqrt{\frac{2A}{3B}}Ls\cdot T$$

Assuming Zo propotional to the ripple length Lo,

$$\frac{\Gamma^2}{LsT} = \text{constant}\cdot(\overline{q_0^2})^{1.5} \tag{7}$$

is concluded. Fig.10 shows the relation of reference turbulence intensity and the vortex strength, which was calculated from an

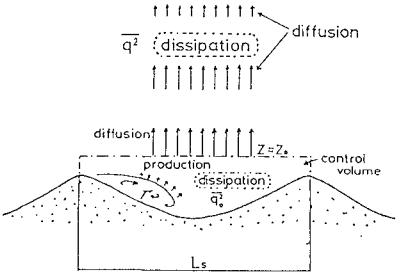

Fig. 7 Schematic relation of turbulence energy budget.

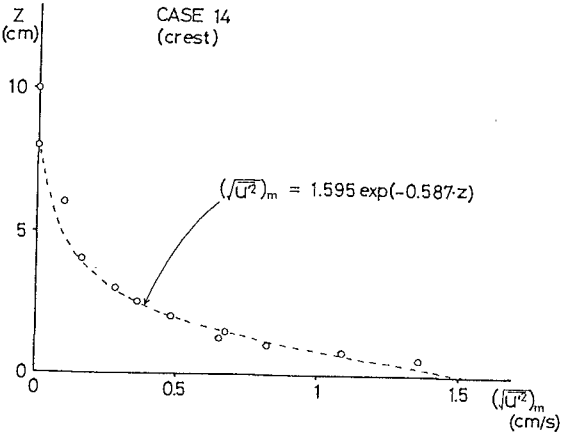

Fig. 8 Example of the time averaged turbulence distribution.

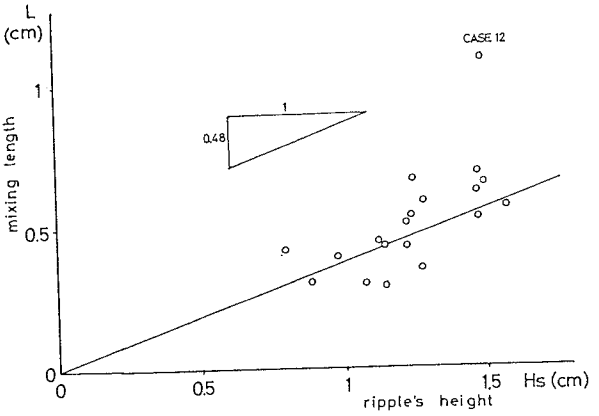

Fig. 9 Variation with the ripple height of the mixing length.

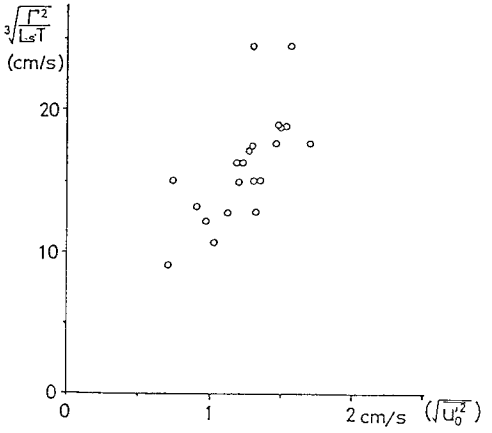

Fig. 10 Relation between the vortex strength and the turbulence intencity.

accumulation of vorticity flux across the section over the crest by the method proposed by the authors(1980). It shows a good correlation between them.

CONCLUSIONS

Turbulence over rippled beds was measured and the followings were concluded.

1. The variation and distribution of turbulence during a cycle closely relate to the movement of organized vortex shedded from the ripple.
2. The turbulence intensity averaged over a period can be explained through a simplified Prandtl's mixing length model
3. The linear relationship of mixing length and ripple's geometrical length is confirmed.
4. The maximum turbulence intencity which occurs near the bottom relates to the vortex strength.

ACKNOLEDGMENTS

The authors wish to express their gratitude to Professor M. Hino, Tokyo Institute of Technology, for his valuable suggestions. The support of the Grant in Aid for Scientific Research is also appreciated.

REFERENCES

Du Toit, C. G. and J. F. A. Sleath (1981); Velocity measurements close to rippled beds in oscillatory flow, Jour. of Fluid Mech., Vol.112, pp.71-96.

Homma, M. and K. Horikawa (1962); Suspended sediment due to wave action, Proc. 8th Conf. on Coastal Engg., pp.168-193.

Horikawa, K. and A. Watanabe (1970); Turbulence and sediment concentration due to waves, Proc. 12th Conf. on Coastal Engg., pp.751-765.

Nakato, T., F. A. Locher, J. R. G. Glover and J. F. Kennedy (1977); Wave entrainment of sediment from rippled beds, ASCE, WW1, Vol.103, pp. 83-99.

Sawamoto, M. (1980); Flow field over rippled beds induced by wave action, Proc. 3rd Int. Symp. on Stochastic Hydraulics, pp.621-630.

Sawamoto, M., T. Yamashita and T. Kurita (1980); Vortex formation over rippled bed under oscillatory flow, Tech. Rep. No.27, Dept. of Civil Engg., Tokyo Institute of Technology, pp.75-85.

Yalin, M. S. and E. Karahan (1980); On the geometry of ripples due to waves, Proc. 17th Conf. on Coastal Engg.

INVESTIGATIONS ON ORBITAL VELOCITIES AND PRESSURES IN IRREGULAR WAVES

by

K.-F. Daemrich[1], W.-D. Eggert[2], H. Cordes[3]

ABSTRACT

This paper deals with the results of hydraulic model investigations of orbital velocities and pressures in irregular waves. Different simulation methods in the time and frequency domain were checked or developed, and the theoretical results compared with measurements. Using simulation methods based on linear wave theory, results with good correlation are obtained. At locations near the water surface, however, a tendency towards over- or unterestimation exists.

1. INTRODUCTION

Orbital velocities and pressures are important input values for many dimensioning methods in coastal engineering. For regular waves, these values can be calculated using the various wave theories for given wave parameters. Although earlier test results confirm the theories only in a few cases, more recent results provide better agreement, due most probably to better equipment and an advanced control signal generation for the wave machines.

The aim of the investigations described in the following was to develop or check simulation methods which enable orbital velocities and pressures in irregular waves to be calculated theoretically from the wave time-series. The simulation methods were developed in accordance with analysis methods, and are so far based upon linear wave theory.

2. INSTRUMENTATION AND HYDRAULIC BOUNDARY CONDITIONS

The investigations were performed in the FRANZIUS-INSTITUT wave channel. The channel, which is equipped with a servo-controlled, hydraulically driven wave generator, is about

---

1) Dr.-Ing., Research Engineer, Franzius-Institut, University of Hannover, FRG
2) Dr.-Ing., Strom- und Hafenbau, Hamburg, FRG
3) Dipl.-Ing., Strabag Bau AG., ZN Wilhelmshaven, FRG

120 m long and 2.2 m wide. The water depth was 1.0 m in all tests. The control signals for the paddle movement of the wave machine are generated by a Wave Synthesizer (Wallingford type).

The wave spectra were JONSWAP spectra with significant wave heights in the range of 8 to 25 cm and with mean periods of 1.5 to 1.9 sec. The sequenth lengths of the wave time-series were typically about 4 to 5 minutes, depending upon the mean periods.

The velocity components and pressures were measured at 0.25m, 0.50 m and 0.85 m below the mean water level (submerged depth). For the orbital velocity measurements, a COLNBROOK inductive-type probe for two components (horizontal and vertical) was used; for the measurement of the wave trains, resistance wave probes (Delft GHM) were installed. The waves and the corresponding velocities and pressures were measured simultaneously in the same cross-section.

3. SIMULATION METHODS

Initial results of the velocity measurements have already been presented at the recent ICCE in Sydney (DAEMRICH, EGGERT, KOHLHASE (1980)), together with a discussion of three simulation methods. To avoide repetition only a brief description is given here. It should be pointed out that the major objective was to calculate and compare the maximum positive and negative velocity components or pressures in every individual wave of the wave train.

The first method, relating to the superposition method with theoretical TRANSFER FUNCTIONS, is based on frequency domain analysis. The FOURIER components of the wave train are calculated and each frequency component is multiplied by the pertinent value of the theoretical transfer function according to linear wave theory. Finally, using an inverse FOURIER-transformation, the theoretical time-series is recalculated or superposed. From this theoretical time-series, positive and negative amplitudes of the individual waves are determined and compared to the measured values.

The next simulation method is based upon time-series calculations. In this method, regular wave parameters must be defined for each individual irregular wave. Following the most common method, the ZERO-DOWNCROSSING parameters for wave height and period (according to IAHR definition) were used to calculate positive and negative maximum velocities and pressures by means of linear wave theory.

Owing to the fact that a comparison between the measured results and those obtained theoretically from the zero-downcrossing method showed very low correlations compared to the transfer function method, the COMPLEMENTARY method was developed. This method is very similar to the zero-downcross-

ing method, but makes use of other definitions for the wave parameters - typically half-waves and pertinent periods. Generally speaking the complementary method involves taking a more effective geometrical part of the wave in the physical sense and completing it, for the theoretical calculation, to a sine wave (or a higher order regular wave).

A definition sketch of the complementary parameters for velocity and pressure simulation is given in Fig. 1.

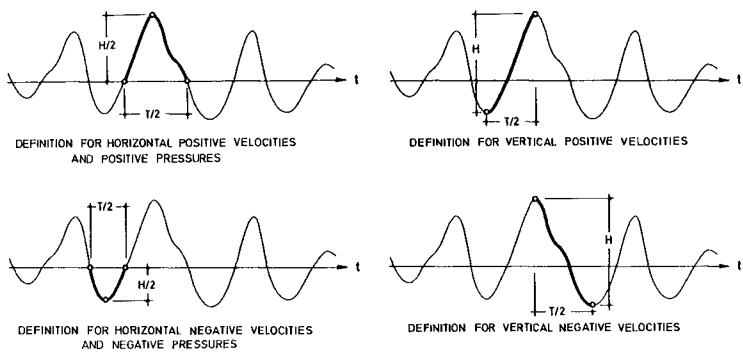

Fig. 1: Definiton sketch for determining wave parameters according to the complementary method

4. RESULTS OF THE ORBITAL VELOCITY INVESTIGATIONS

In Fig. 2, measured and theoretical horizontal velocity amplitudes (submerged depth of the velocity probe: 0.25 m) are compared using the three simulation methods. The results are devided into positive (upper part) and negative amplitudes (lower part of the figure).

The transfer function method and the complementary method both show a reasonable correlation, whilst the scatter in the results obtained from the zero-downcrossing method is markedly higher, and in most cases excludes the application for the calculation of single velocity events.

In the results from the transfer function method and the complementary method there is a general tendency that the measured horizontal velocities are lower than the theoretical ones under a wave crest, and higher than the theoretical ones under a wave trough. From Figs. 3 and 4, which show similar results from measurements for submerged depths of 0.50 and 0.85 m, it may be seen that this tendency decreases with increasing submergence and is no longer present near the bottom for this spectrum.

By comparing the results of calculations based upon higher

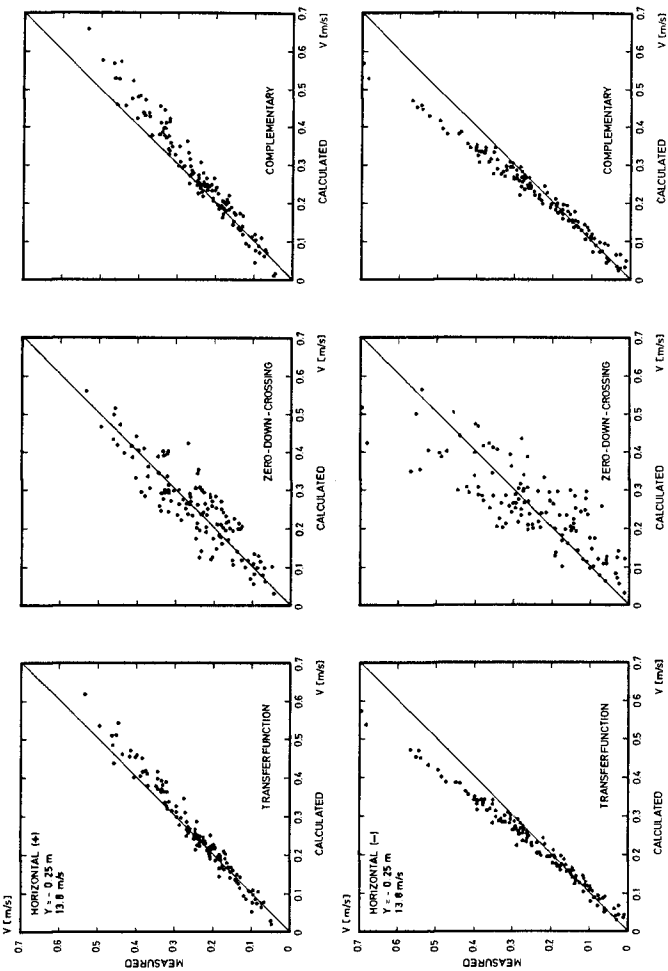

Fig. 2: Comparison between measured horizontal velocities and those calculated by different simulation methods (submerged depth 0.25 m)
(JONSWAP spectrum γ = 3.3, $\bar{U}$ = 13.8 m/sec., scale 1:20)

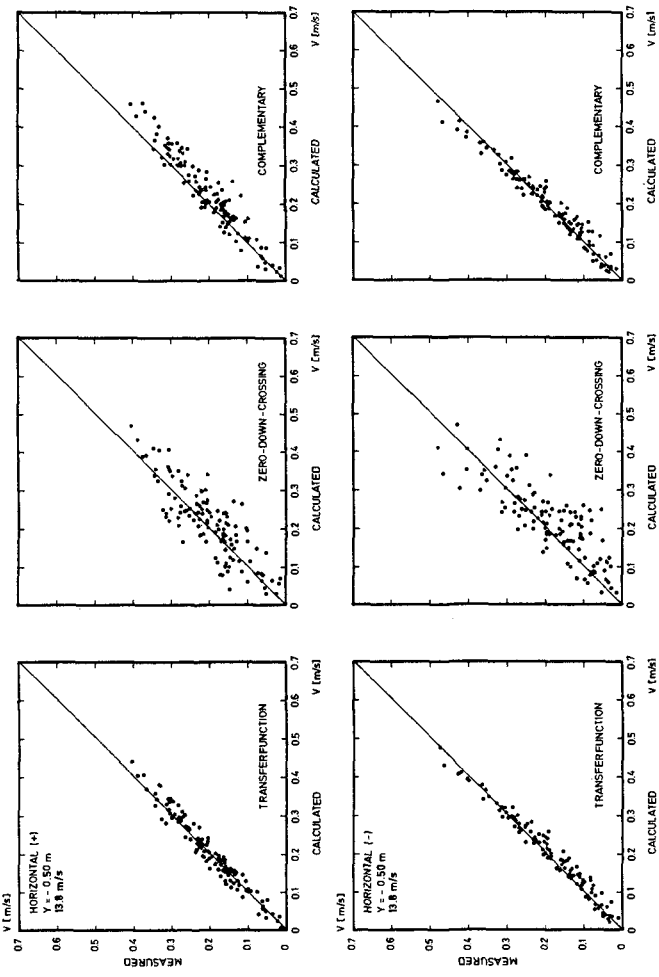

Fig. 3: Comparison between measured horizontal velocities and those calculated by different simulation methods (submerged depth 0.50 m)
(JONSWAP spectrum γ = 3.3, $\bar{U}$ = 13.8 m/sec., scale 1:20)

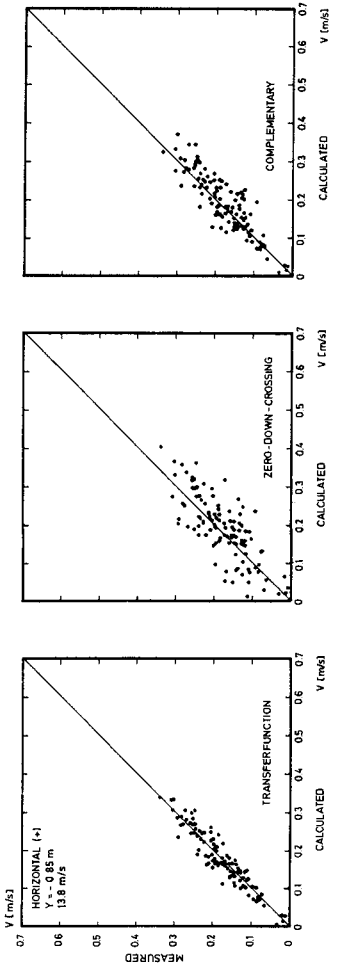

Fig. 4: Comparison between measured horizontal velocities and those calculated by different simulation methods (submerged depth 0,85 m)
(JONSWAP spectrum γ = 3.3, U = 13,8 m/sec., scale 1:20)

order wave theories and from the assumption of small amplitudes for the validity of the linear wave theory, it becomes evident that the latter tendency can be attributed to nonlinear effects.

For further details relating to the results of vertical velocity measurements, the reader is referred to the Proceedings of the ICCE, Sydney (DAEMRICH, EGGERT, KOHLHASE (1980)).

5. RESULTS OF THE PRESSURE INVESTIGATIONS

Corresponding results obtained from the simulation of pressure amplitudes in irregular waves are shown in Fig. 5, 6 and 7.

As before, the scatter in the results calculated by the transfer function method and the complementary method is distinctly smaller than that arising from the zero-downcrossing method. Compared to the velocity measurements, the scatter in pressure amplitudes obtained from the transfer function method is notably smaller.

The tendency to overpredict pressures under the wave crest and to underpredict pressures under the wave trough is similar to that obtained in the horizontal velocity measurements.

Considering the results obtained from the complementary method in more detail, it can be seen that the majority of the data points exhibit a very low scatter and a well-defined trend. A small number of points, however, are clearly overestimated. A visual inspection of the time-series at the relevant positions provides a seasonable explanation. This may be seen for example in Fig. 8, which shows a wave together with its pertinent pressure time-series (submerged depth 0.50 m).

The amplitude marked by an arrow is typical of an overestimated event. Clearly, the influence of the higher frequency component of about twice the basic frequency in this case cannot be neglected when estimating the maximum pressure amplitude. In other words, the actual half-wave form in this case is not properly represented by the complementary parameters, and a modification of the original parameters should be considered.

6. SIMULATION OF WAVE AMPLITUDES FROM PRESSURE MEASUREMENTS

For the recalculation of wave data from pressure measurements, the same simulation methods can be applied. Since, however, the value of the theoretical transfer function at the high frequency end of the spectrum can be exceedingly large, caution is necessary to avoid an upscaling of system noise.

In Fig. 9, a measured wave spectrum is compared with the wave spectrum calculated from the pressure spectrum using

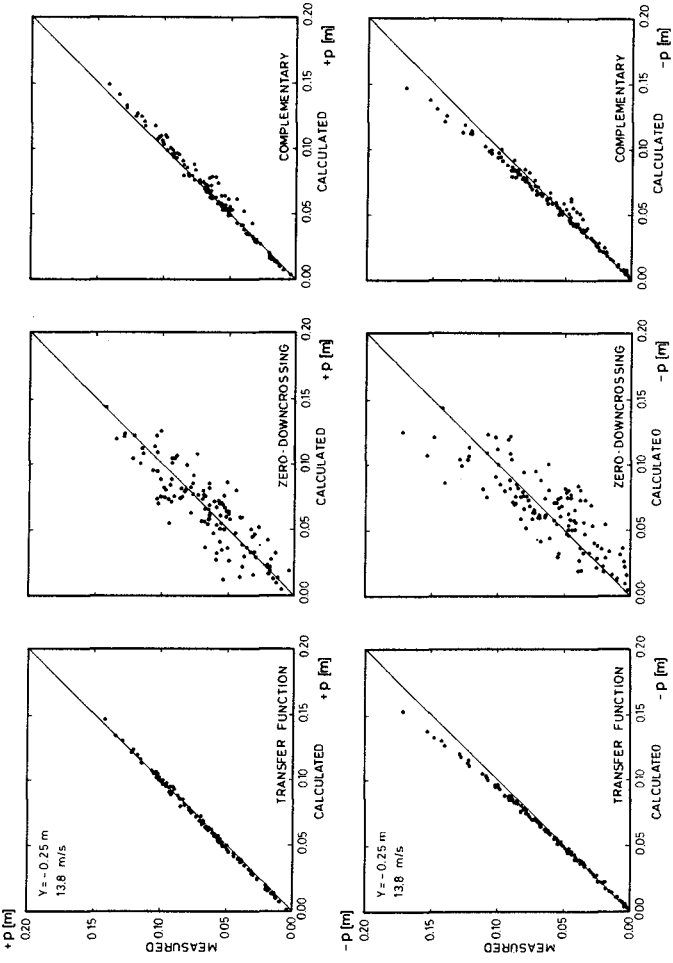

Fig. 5: Comparison between measured pressures and those calculated by different simulation methods (submerged depth 0.25 m)
(JONSWAP spectrum γ = 3.3, U = 13,8 m/sec., scale 1:20)

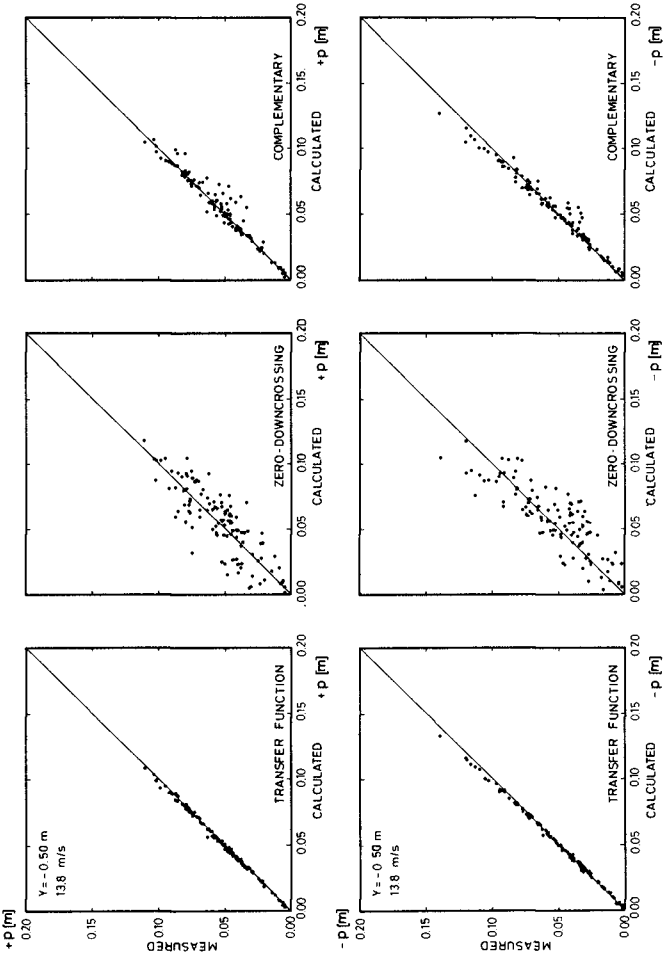

Fig. 6: Comparison between measured pressures and those calculated by different simulation methods (submerged depth 0.50 m)
(JONSWAP spectrum γ = 3.3, U = 13,8 m/sec., scale 1:20)

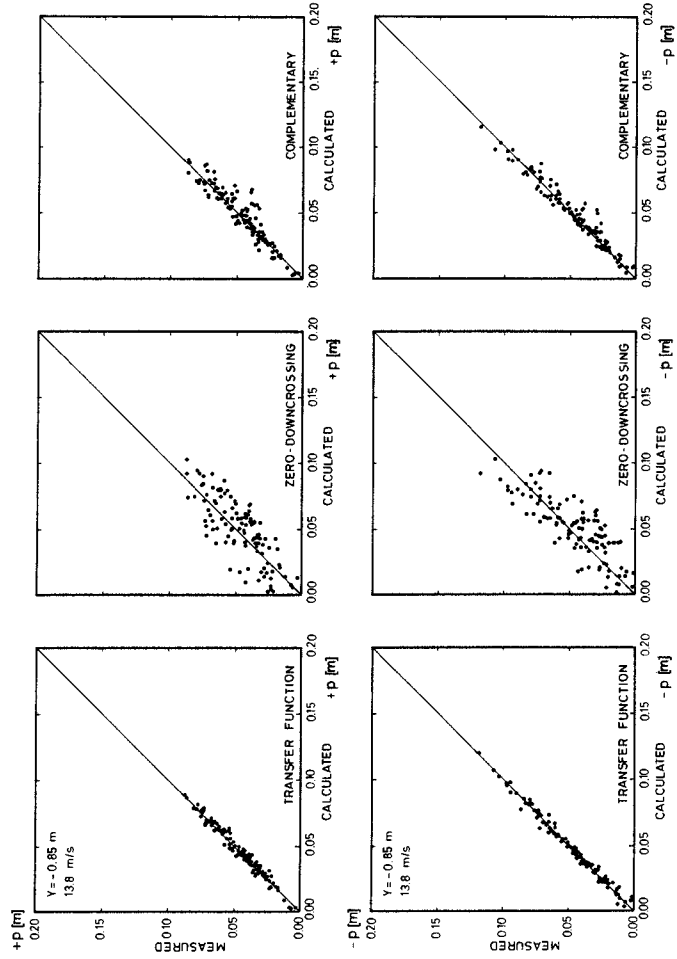

Fig. 7: Comparison between measured pressures and those calculated by different simulation methods (submerged depth 0.85 m) (JONSWAP spectrum $\gamma = 3.3$, $U = 13{,}8$ m/sec., scale 1:20)

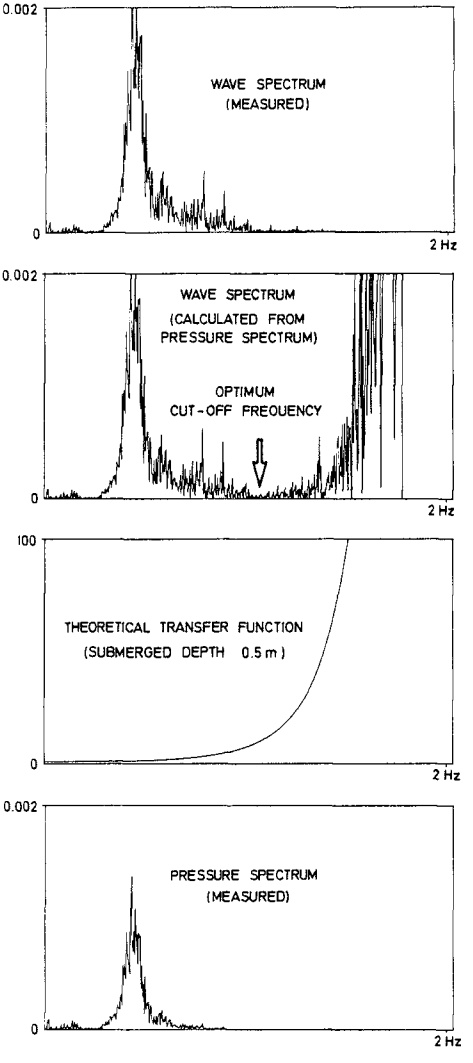

'ig. 9: Calculation of wave spectrum from pressure spectrum

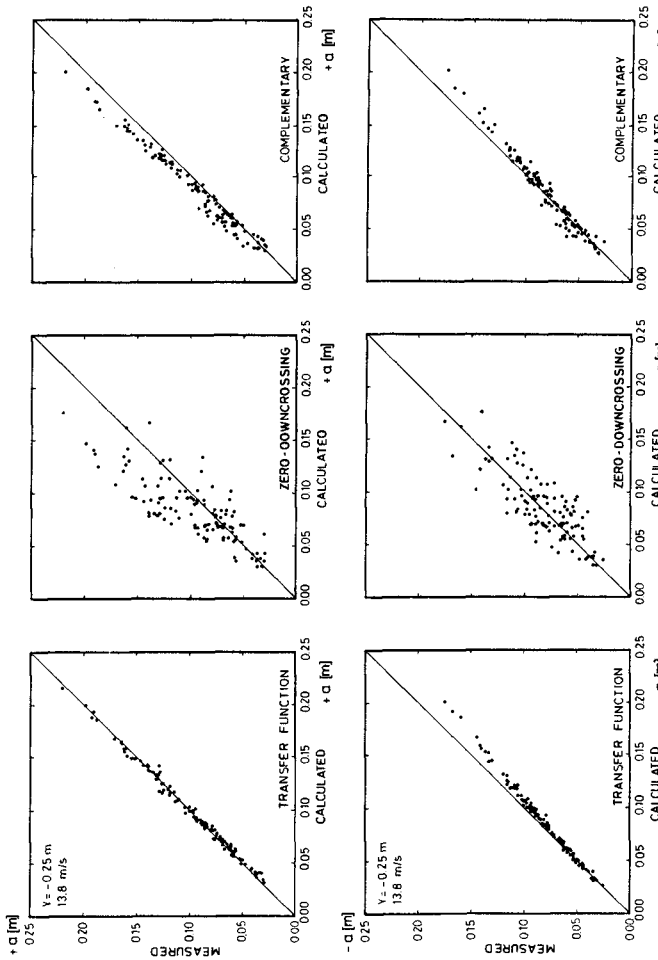

Fig. 10: Comparison between measured wave amplitudes and those calculated by different simulation methods (submerged depth 0.25 m)
(JONSWAP spectrum γ = 3.3, U = 13.8 m/sec., scale 1:20)

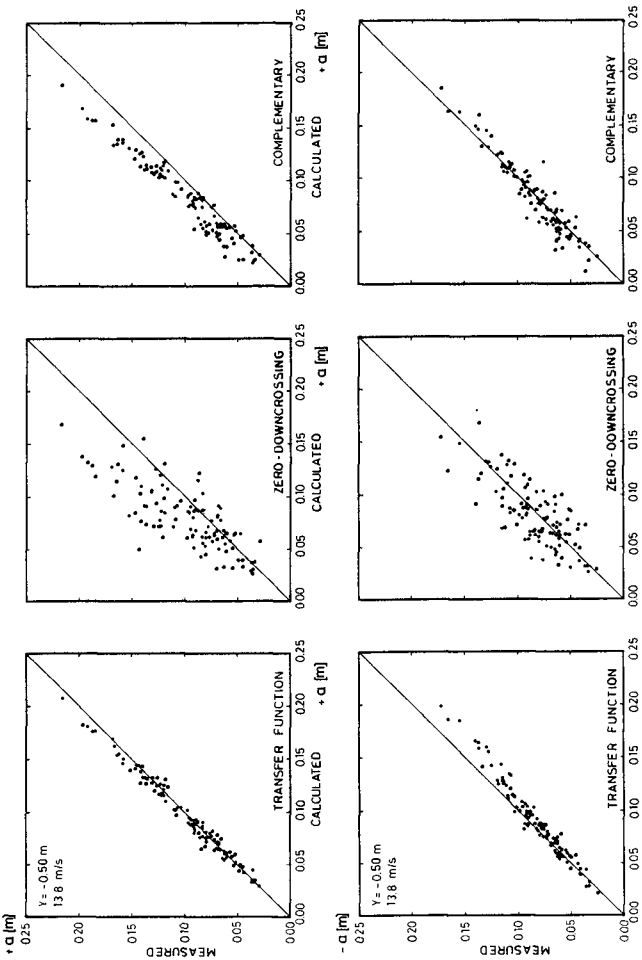

Fig. 11: Comparison between measured wave amplitudes and those calculated by different simulation methods (submerged depth 0.50 m)
(JONSWAP spectrum γ = 3.3, U = 13.8 m/sec., scale 1:20)

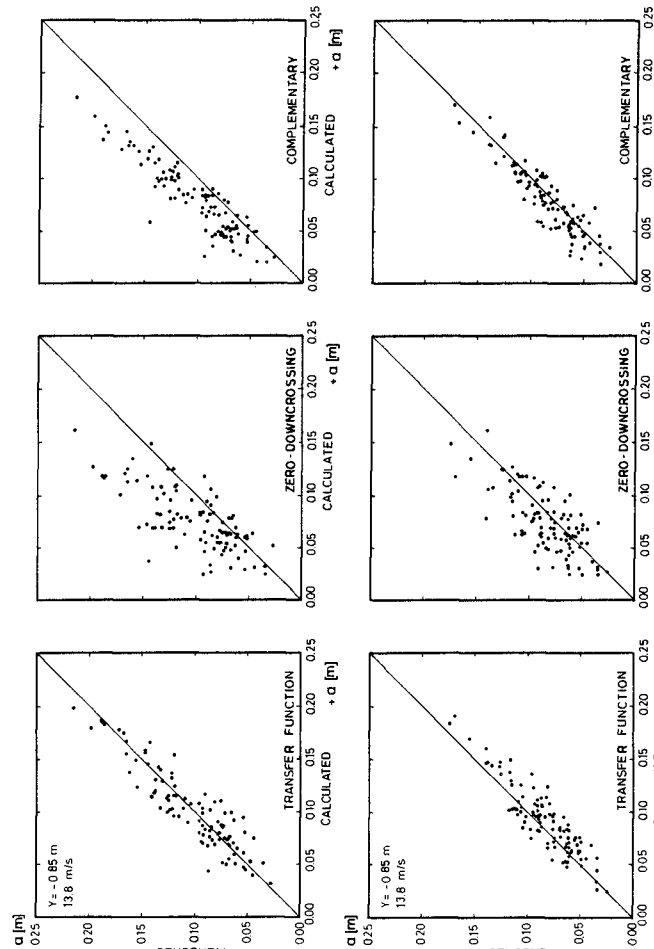

Fig. 12: Comparison between measured wave amplitudes and those calculated by different simulation methods (submerged depth 0.85 m) (JONSWAP spectrum γ = 3.3, U = 13.8 m/sec., scale 1:20)

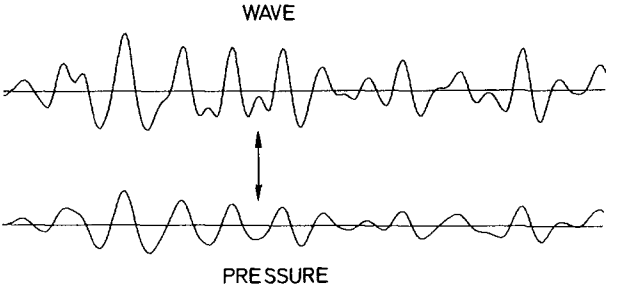

Fig. 8: Wave and pressure time-series
(location of pressure overestimation given by complementary method is marked by an arrow)

the theoretical transfer function. The increasing energy at the high frequency end of the calculated wave spectrum clearly indicates the point at which system noise starts to be dominant and from which point the frequency components should be suppressed (the location is marked by an arrow).

Figs. 10 and 11 show results based upon measurements with submerged depths of the pressure cell of 0.25 m and 0.50 m. Although best results are obtained when the pressure meter is situated near the mean water level, the results are also acceptable in a medium water depth for the spectrum considered. With the pressure meter located near the bottom, however, the scatter in the data was found to be relatively high (Fig. 12).

In deciding whether or not pressure meters may be used as wave gauges and at what depth they should be located, it is necessary to consider both the quality of the measuring and data aquisition systems and the desired accuracy of wave measurements.

7. ACKNOWLEDGEMENT

The investigation described in this paper was carried out as part of the research programme of the Sonderforschungsbereich 79 at the FRANZIUS-INSTITUT for Hydraulic Research and Coastal Engineering, University of Hannover. The authors gratefully acknowledge the Deutsche Forschungsgemeinschaft for their finanical support throughout the investigations.

8. REFERENCES

DAEMRICH, K.-F., EGGERT, W.-D. and KOHLHASE, S. (1980): Investigations on Irregular Waves in Hydraulic Models. Proc. 17th Conference on Coastal Engineering, Sydney

WAVE INDUCED VELOCITIES CLOSE TO A RIPPLED BED

by

C.G. du Toit*

The results are reported of velocity measurements in oscillatory flow over rippled beds. Velocities were measured with a laser-doppler anemometer in both an oscillating tray rig and an oscillatory flow U-tube. Both self-formed and artificial ripples were examined.

The results obtained in the two test rigs were compared and it was concluded that the flow fields obtained in the two cases were dynamically similar.

Measurements of the flow field clearly showed the formation, growth and ejection of vortices, as well as a strong surge of fluid over the ripples during and after flow reversal.

1 INTRODUCTION

A proper knowledge of the flow field in the boundary layer above the ripples on the sea bed is of considerable importance to the coastal engineer. It is essential to be able to fully understand the phenomena of sediment transport and energy dissipation.

A great deal of theoretical work has already been done on the subject and three different approaches can be distinguished. Firstly, it is assumed that the concepts used for turbulent boundary layers in steady flow over rough beds may be extended to oscillatory flow and that the vertical velocities may be neglected. Secondly, it is assumed that the mean velocity distribution may be well represented by a laminar solution if the exchange of momentum from one fluid layer to another is dominated by the mixing produced by the vortices rather than by the much smaller-scale turbulent eddies. Thirdly, a solution has been put forward, based on the "discrete vortex" method.

A number of experimental studies have also been made of the velocity distribution close to beds in oscillatory flow. However, in most cases the beds were essentially flat or the bed profiles did not closely resemble those of naturally occuring ripples. Horikawa & Watanabe (1970) and Nakato et al (1977) did measure velocities above natural sand ripples in oscillatory flow. They were, however, primarily interested in the turbulence

*Senior Lecturer, Department of Civil Engineering, University of Stellenbosch, Stellenbosch 7600, South Africa.

and suspended sediment distribution. A more detailed study of the flow field was made by Sawamoto et al (1980). They measured the velocities above a fixed ripple in an oscillatory flow wind tunnel.

The objective of this paper is to give a short account of measurements that were made of the flow fields above both artificial and natural sand ripples. A comparison of the various available theories with the data has already been made elsewhere by Du Toit & Sleath (1981).

2. EXPERIMENTAL EQUIPMENT

Experiments were carried out both in an oscillating tray rig and an oscillatory flow U-tube.

The oscillating tray rig is shown in Figure 1.
It consisted essentially of a flat tray 0.305 m wide which was oscillated in its own plane in a tank of still water. Simple harmonic motion was created by means of a variable speed motor with feed-back control driving a Scotch Yoke. Baffles, extending down to close to the bed, divided the tank into three sections. These baffles were to prevent vortices shed by the end of the tray from propagating into the central test section. Flow under these baffles were inhibited by compensating cylinders which had the same cross-sectional area as the tray.

Figure 2 shows a sketch of the oscillatory flow U-tube.
It consisted of a U-tube in which the water was caused to oscillate by a paddle driven, via a crank arm, by a variable speed motor with feed-back control. The central test section was 0.305 m wide and 0.45 m high. The arm containing the paddle was circular in section with an area 3.3 times that of the rest of the tube.

The oscillating tray rig could be operated over a wide range of strokes and periods of oscillation, whereas the oscillatory flow U-tube was restricted to periods close to its resonant period of 4.6 s.

The velocities were measured with a laser-doppler anemometer system. With the equipment available it was only possible to measure one component of velocity. The results given below are all for the horizontal component of velocity.

Phases were measured with the aid of a beam of light falling on a photo-electric cell for the oscillating tray rig. A flat plate, rigidly attached to the Scotch Yoke, interrupted the beam of light as the tray passed through the top dead-centre position. For the oscillatory flow U-tube the output from a resistance gauge in the open arm of the tube was used as a phase marker.

The outputs from the laser-doppler system and the phase marker were recorded on magnetic tape and subsequently fed through an analog-to-digital converter into a computor for analysis.

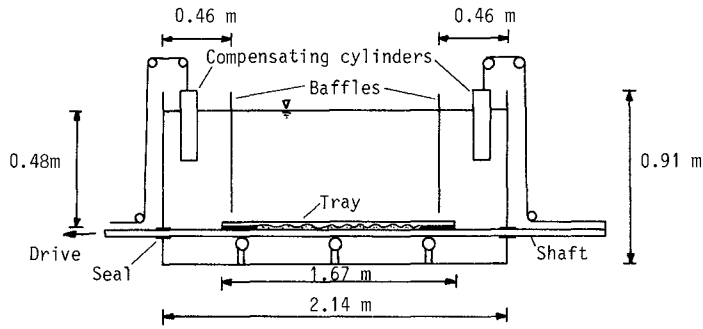

FIG. 1 Sketch of oscillating tray tank

Analog-to-digital conversion was carried out at a rate of between 600 and 720 samples per cycle.

All the tests with natural sand ripples were carried out with a sand of median diameter 0.41 mm, standard deviation 0.10 mm and specific gravity 2.65.

The artificial ripple bed was made out of wood and was machined on a numerically-controlled milling machine to the following profile.

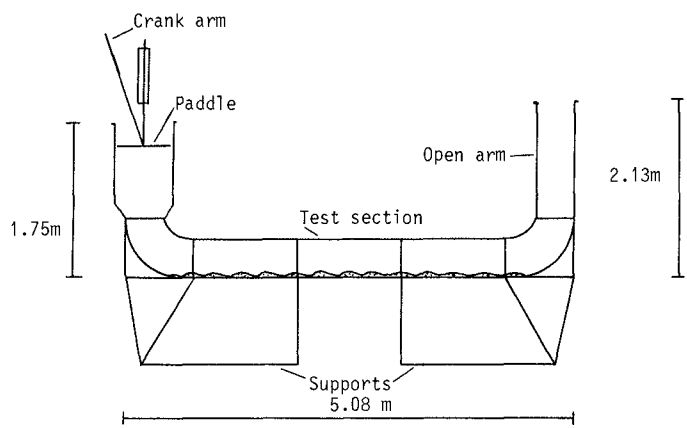

FIG. 2 Sketch of oscillatory flow U-tube

Test	a (m)	T (s)	$\frac{a}{L}$	$\frac{h}{L}$	β/k	$\frac{U_o L}{\nu}$
		(i) Artificial ripples				
32	0.06	3.29	0.6	0.17	15.02	10690.3
33	0.08	3.25	0.8	0.17	15.22	14637.0
34	0.10	3.36	1.0	0.17	15.05	17872.9
35	0.12	3.32	1.2	0.17	15.25	22039.2
36	0.04	3.47	0.4	0.17	14.94	7049.8
37	0.02	3.47	0.2	0.17	14.95	3528.1
38	0.02	1.86	0.2	0.17	19.92	6268.3
39	0.04	1.87	0.4	0.17	19.98	12603.5
40	0.06	1.90	0.6	0.17	19.98	18738.0
41	0.08	1.90	0.8	0.17	19.91	25036.1
42	0.10	1.89	1.0	0.17	20.03	31668.2
43	0.12	1.96	1.2	0.17	19.74	36937.0
44	0.02	5.45	0.2	0.17	12.05	2291.7
45	0.04	5.46	0.4	0.17	12.06	4593.0
46	0.06	5.47	0.6	0.17	11.99	6810.8
47	0.08	5.61	0.8	0.17	11.86	8888.8
48	0.10	5.66	1.0	0.17	11.86	11097.9
49	0.12	5.56	1.2	0.17	12.00	13644.6
		(ii) Self-formed ripples				
11	0.060	3.97	0.79	0.13	10.04	6280.7
84	0.065	3.91	0.72	0.18	12.08	8273.9
87	0.085	4.73	0.71	0.18	14.99	12570.8
90	0.110	4.98	0.67	0.17	19.89	20957.5
96	0.122	5.37	0.71	0.17	19.67	21617.5
97	0.096	4.22	0.83	0.19	15.05	14898.2
98	0.101	3.21	0.74	0.20	20.26	23884.0
99	0.195	4.87	0.77	0.17	30.27	55812.8
100	0.141	3.18	0.67	0.16	31.05	50935.9
101	0.081	5.75	0.75	0.19	12.10	8611.9
102	0.085	4.62	0.86	0.19	12.18	10001.4
103	0.166	4.65	0.68	0.18	30.54	49852.9
104	0.108	3.80	0.72	0.20	19.97	22676.9

TABLE 1. Test conditions

$$y = \tfrac{1}{2}h(\cos k\xi - 1), \quad x = \xi - \tfrac{1}{2}h \sin k\xi \qquad (1)$$

where the crest-to-trough height h of the ripple was 0.017 m and the wavelength $2\pi/k$ was 0.10 m. This profile was very similar to that of the ripples which form with the 0.41 mm sand.

Further details of the experimental equipment are given by Du Toit (1980).

3. TEST PROCEDURE AND RESULTS

At least one day prior to a test the tank was filled with tap water and left to de-aerate. Natural sand ripples were obtained by selecting the appropriate frequency and amplitude of oscillation and letting the rig run until the ripples reached their equilibrium profile. The rig was then stopped and the ripple geometry measured. On the day of the test the equipment was left on for at least an hour to warm up.

At least two vertical traverses were made during each test. For each traverse records of at least thirty cycles were made at various fixed heights above the bed. In all the tests traverses were made above a ripple crest and a ripple trough when the tray was in its central position. In some tests in the oscillatory flow U-tube two additional traverses were made a sixth and a third of a ripple length from the crest.

The water temperature and output from the various instruments were checked regularly during and the ripple geometry at the end of a test to ensure that no significant changes had taken place.

The conditions under which the various tests were carried out are summarized in Table 1. All the tests were in the fully-developed rough turbulent regime according to the criteria of Kajiura (1968), Sleath (1974a), Kamphuis (1975) and Jonsson (1980), except for a few tests with artificial ripples at the shorter amplitudes of oscillation.

3.1 Ripple and velocity similarity

It has been claimed, e.g. Brebner & Collins (1961), that flow fields simulated in the oscillating tray rig and the oscillatory flow U-tube are not dynamically similar. However, if the ripples are similar, Sleath (1974b) showed theoretically that the flow fields are dynamically similar.

A plot of ripple lengths against the corresponding amplitudes of oscillation for which the ripples had been obtained, is shown in Figure 3.

Added to the present data, are the experimental results of a large number of undergraduates, cf. Sleath & Ellis (1979), at the University of Cambridge in the same oscillating tray rig with the same 0.41 mm sand as the present study.

These are compared with the empirical predictions of Mogridge & Kamphuis (1972) and Sleath (1975), obtained from experiments conducted in wave flumes and oscillatory flow U-tubes.

The minimum and maximum Reynolds numbers $U_0/\sqrt{\omega\nu}$ obtained in the present experiments were respectively 42 and 207. The predictions of Sleath for these two values are shown in the figure.

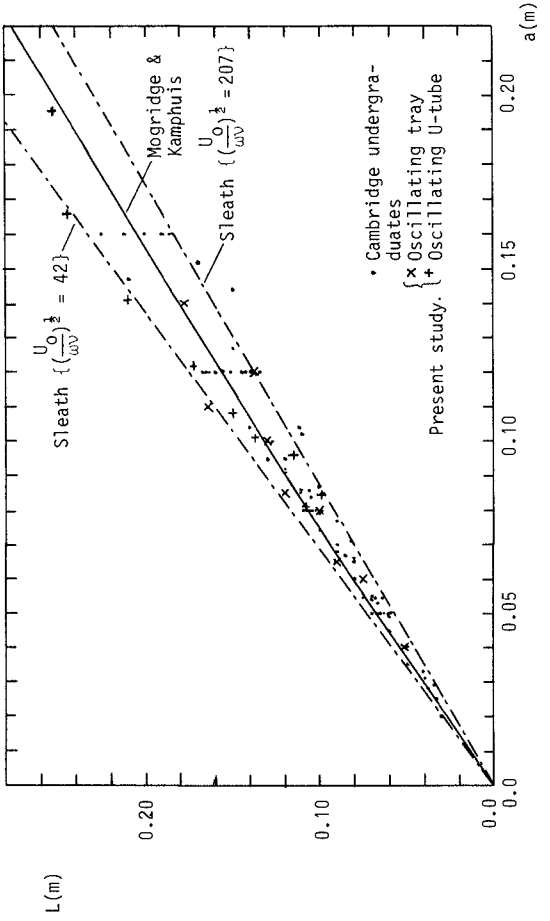

FIG. 3 Variation of ripple length with amplitude of motion

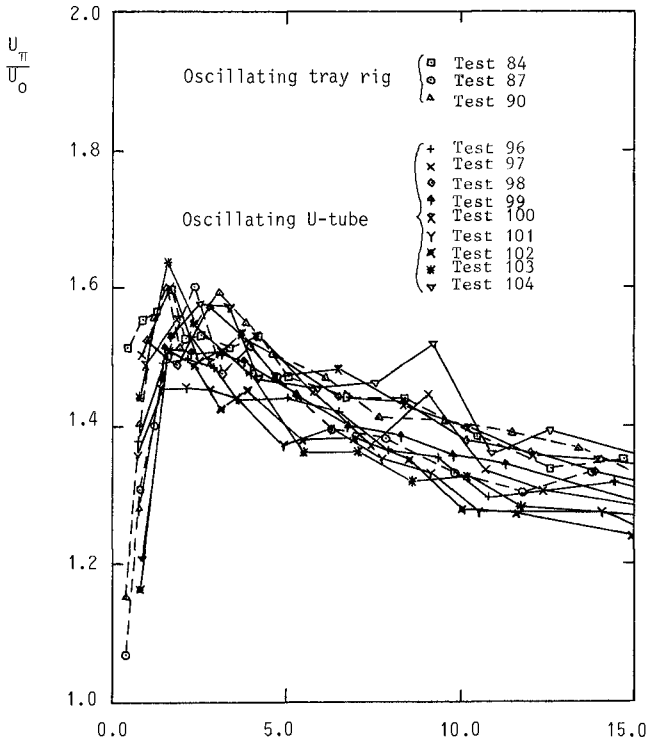

FIG. 4 Variation of $\frac{U_\pi}{U_o}$ with βy above ripple crest

The agreement between the various experiments and the predictions is quite close and there doesn't seem to be any consistent difference between the results obtained in the two different rigs. The ripple lengths obtained in the two cases are, therefore, similar.

In the case of the oscillating tray rig, the ripple is oscillating forwards and backwards past the measuring volume. The only instants, therefore, during the cycle when the velocities can be compared with those measured in the oscillatory flow U-tube for $\frac{a}{L} < 1.0$ and a vertical traverse above the crest, are when the measuring volume is directly above a crest. This occurs at $\omega t = 0$ and $\omega t = \pi$ and corresponds to maximum tray velocity for the

oscillating tray rig and maximum free stream velocity for the oscillatory flow U-tube.

Figure 4 shows how the non-dimensional velocities U_π/U_o change with distance βy above the ripple crest, where

$$\frac{U_\pi}{U_o} = \frac{1}{2U_o} \{U(\omega t = o) - U(\omega t = \pi)\} \quad (2)$$

and $\beta = \sqrt{\frac{\omega}{2\nu}}$. The oscillating flow U-tube velocities were converted to oscillating tray velocities by

$$\frac{U_\pi \text{ (tray)}}{U_o} = 1 - \frac{U_\pi \text{(U-tube)}}{U_o} \quad (3)$$

considering the variation in $\frac{\beta}{k}$, $\frac{h}{L}$ and $\frac{a}{L}$ for the various tests, the agreement is good and there seems to be not apparent difference between the velocity profiles obtained in the oscillating tray rig and the oscillatory flow U-tube. The velocities can, therefore, be taken as similar.

Due to the similarity in ripple lengths and velocity profiles it can, therefore, be concluded that the flow fields simulated in the two rigs are dynamically similar.

3.2 Velocities above an oscillating fixed ripple

The way in which $\frac{U}{U_o}$ changes with ωt for various positions above an oscillating fixed ripple is shown in Figure 5. Figures 5 (a) and (b) are for a crest traverse and Figures 5 (c) and (d) for a trough traverse. The instants when the measuring volume was directly above a crest are indicated in the figure with crosses. It should also be noted that the tray was travelling with the velocity $-U_o \cos \omega t$.

When a rippled bed is oscillated, the fluid in the viscous part of the boundary layer has to travel along with the ripple surface. However, in the outer layer the fluid moves over the crest in a direction opposite to that of the ripple surface, continuity then requires that the fluid over the trough should move in the same direction as the ripple surface. These features are clearly illustrated in Figure 5.

In Figure 5 (a) it can be seen that there is a sharp increase in the velocity in the direction opposite to that in which the ripple is travelling as the crest approaches the measuring volume. This corresponds to the fluid in the outer layer spilling over the ripple crest. As the viscous layer moves past the measuring volume there is a sudden switch in

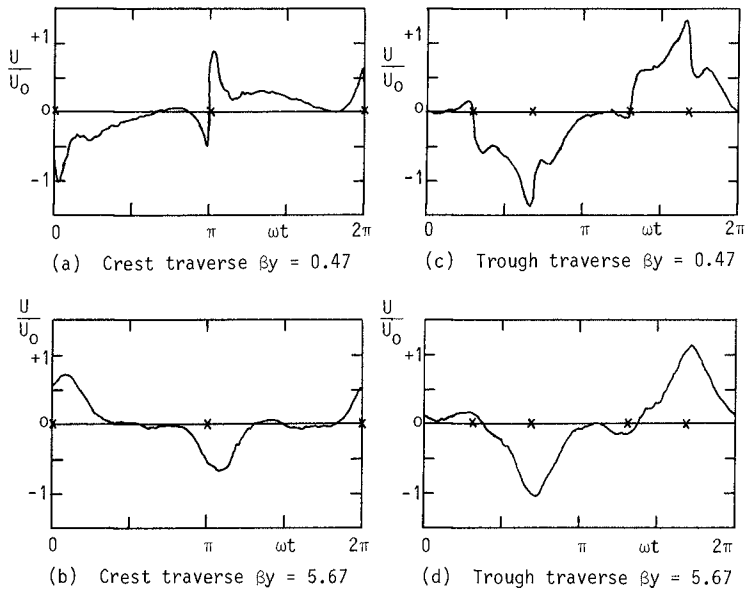

FIG. 5 TEST 32: Average velocity cycles for βy = 0.47 and 5.67 for crest and trough traverses

the velocity direction due to the viscous layer travelling with the ripple. This can be observed in Figure 5 (c) as well, though very much weaker. This viscous effect diminishes quickly and in Figure 5 (b) & 5 (d) it can not be observed any more. There the measuring volume is in the outer layer all the time.

An additional phenomenon can be observed in Figures 5 (c) & 5 (d). Very prominent peaks occur in the velocity cycles at $\omega t = 0.65\pi$ and 1.65π. These peaks occur just after flow reversal and correspond to the fluid surging over the ripple in the direction opposite to that in which the ripple is travelling. It is also associated with the ejection of the vortex which has been on the downstream side of ripple prior to flow reversal. This effect can be seen in the photographs published by Bagnold (1946).

3.3 Velocities above a stationary sand ripple

In contrast with the previous Figure, Figure 6 (a) shows the average velocity for βy = 1.44 above a ripple crest and Figure 6 (b) shows the average velocity cycle for βy = 1.18 above a ripple trough for stationary sand ripple in the

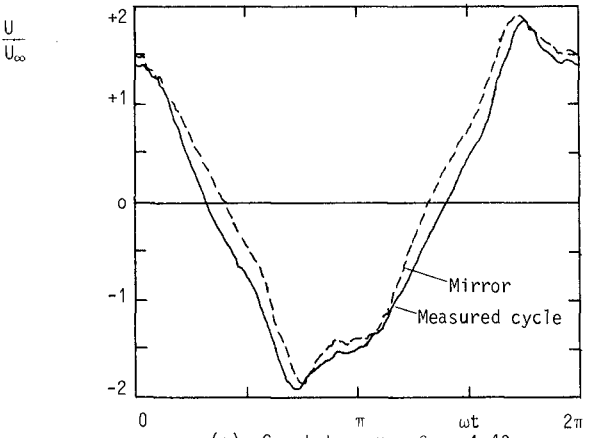

(a) Crest traverse $\beta y = 1.40$

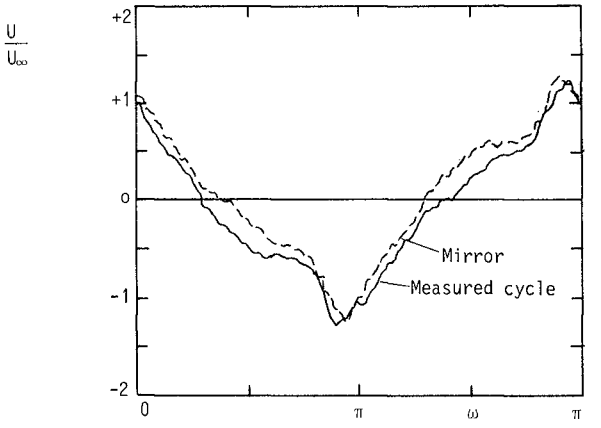

(b) Trough traverse $\beta y = 1.47$

FIG. 6 TEST 101: Average velocity cycles for $\beta y \approx 1.4$ for crest and trough traverses.

oscillatory flow U-tube. Also shown on the Figures are the "mirror" plots of the measured average velocity cycles. These were obtained by shifting the average velocity cycles by π radians and inverting them. Thus the difference between the two curves provides an indication of the magnitude of

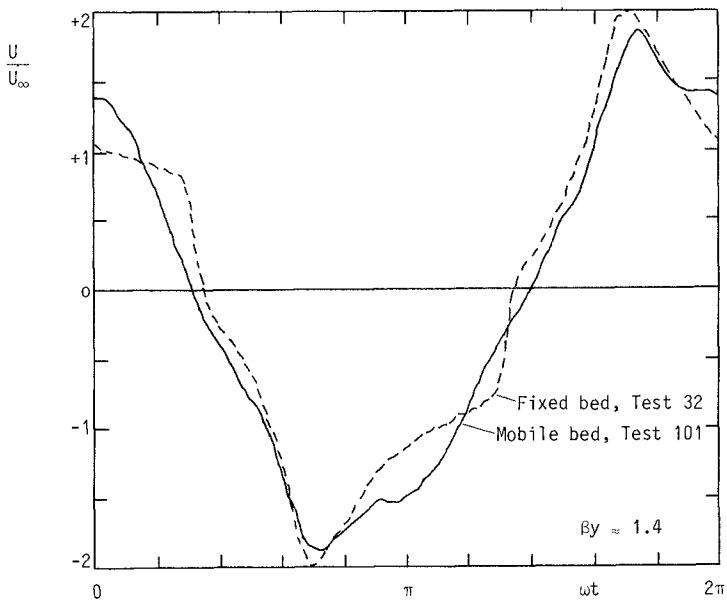

FIG. 7 Comparison between fixed bed and mobile bed velocity cycles.

experimental errors such as mean drift in the tank.

A prominent feature in both figures is the occurence of a peak in the velocity cycle at $\omega t = 0.9\pi$ and 1.9π for the trough plot. During the course of the experiments it was observed that the crest swayed from side to side, forming a small cusp of sand first on one side and then, as the flow reversed, on the other side. It was originally thought that the presence of the peak in the velocity cycles was due the swaying of the crest. However, comparison with results obtained for the fixed wooden bed in the oscillatory tray rig showed the same peak. This is illustrated in Figure 7, where the oscillatory tray velocities were converted to oscillating free stream results.

This peak corresponds to the strong surge of fluid going over the ripple crest and sweeping through the ripple trough, as illustrated in the photographs by Bagnold (1946). The surge occurs just after flow reversal and is associated with the ejection of the vortex which had been on the downstream side of the ripple prior to flow reversal.

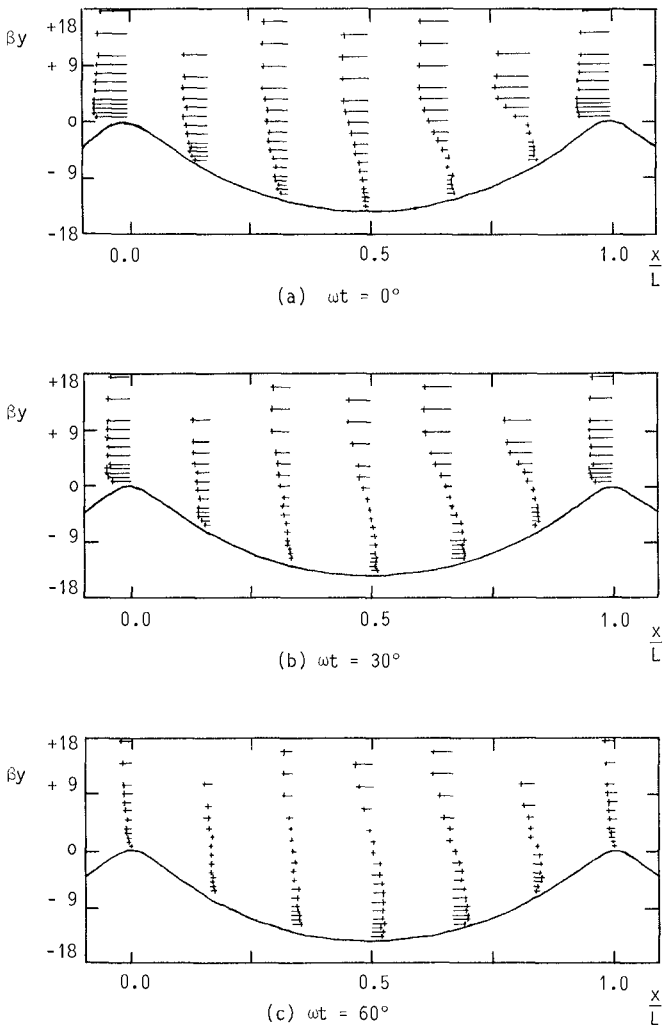

FIG. 8 Variation of the horizontal velocity component of the flow field above a rippled bed with time.

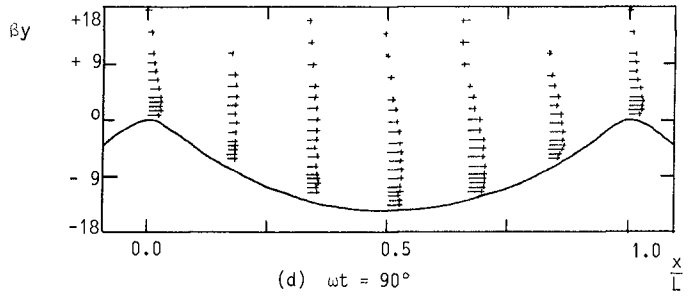

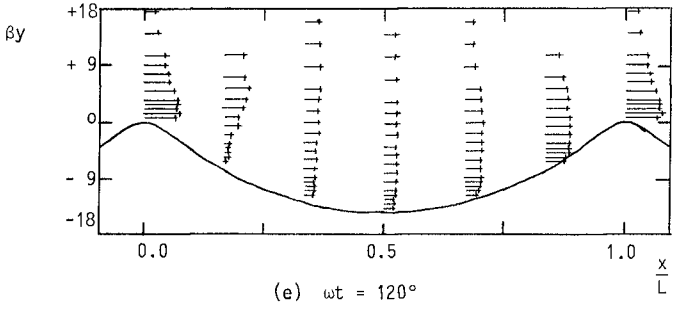

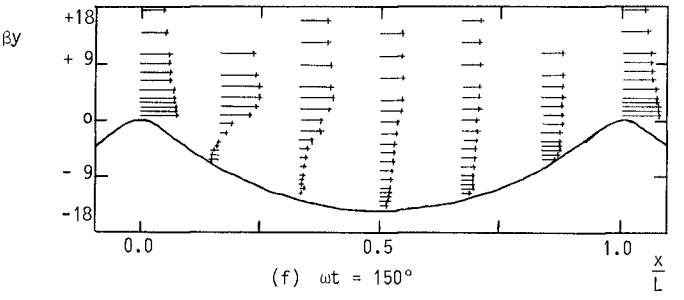

FIG. 8 Variation of the horizontal velocity component of the flow field above a rippled bed with time.

Thus although the change in position of the crest cusp is not the cause of the velocity peak, the velocity peak may be the cause of change in position.

The variation in the horizontal velocities in the flow field above a rippled bed during a half cycle is illustrated in Figure 8.

Only the instants $\omega t = 0$, $\pi/6$, $\pi/3$, $\pi/2$, $2\pi/3$ and $5\pi/6$ are shown.

In Figure 8 (a) the freestream is moving with maximum velocity from right to left and a well defined vortex fills almost half the ripple trough on the downstream side of the ripple. As the freestream decelerates, the vortex increases in size, Figure 8 (b), until it fills almost the whole trough, Figure 8 (c). Although the freestream has not reversed yet at this instant, $\omega t = 2\pi/3$, the flow near the ripple crest is on the brink of reversing. In Figure 8 (d) the freestream reverses. The vortex is being ejected over the crest and a strong surge of fluid sweeping through the ripple trough and spilling over the crest is building up. At $\omega t = 2\pi/3$, Figure 8 (e), the flow has already started separating at the crest and a new vortex starts to form. A jet, associated with the separation, shoots out over the trough and at $\omega t = 5\pi/6$ it has almost reached the trough.

The general flow features show good agreement with those photographed by Bagnold (1946), despite the differences in flow conditions and ripple geometry. Sawamoto et al (1980) used a ripple profile with a smaller steepness and a much more rounded crest and, therefore, the vortex was not as pronounced as in the present study.

4. CONCLUSIONS

The range of flow conditions covered during the present series of tests covers a wide spectrum of conditions encountered in practice. It is believed that the present results could help to improve our understanding of the boundary layer in oscillatory flow over rippled beds and lead to a better understanding of the associated phenomena.

The author would like to thank Dr. J F A Sleath of the University of Cambridge for his encouragement, as well as the South African CSIR, the British NERC and the Sir Henry Strakosch Memorial Trust for their financial support.

5. REFERENCES

BAGNOLD, R A (1946). Motion of waves in shallow water. Interaction of waves and sand bottoms. Proc. Roy. Soc., A 187, pp. 1-15.

BREBNER, A & COLLINS, J I (1961). The effect on mass transport of the onset of turbulence at the bed under periodic gravity waves. ASME Hydraulics Conf., Paper No. 61-EIC-8.

DU TOIT, C G (1980). Velocities close to a bed of sand in oscillatory flow. Ph.D. thesis, University of Cambridge.

DU TOIT, C G & SLEATH, J F A (1981). Velocity measurements close to rippled beds in oscillatory flow. J. Fluid Mech., 112, pp. 71-96.

HORIKAWA, K & WATANABE, A (1970). Turbulence and sediment concentration due to waves. Proc. 12th Conf. Coastal Engng., pp. 751-765.

JONSSON, I G (1980). A new approach to oscillatory rough turbulent boundary layer flow. Ocean Engng.,7, pp. 109-152.

KAJIURA, K (1968). A model of the bottom boundary in water waves. Bull. Earthquake Res. Inst., 46, pp. 75-123.

KAMPHUIS, J W (1975). Friction factor under oscillatory waves. J Waterways, Harbors & Coastal Engng. Div., 101 (WW2), pp. 135-144.

MOGRIDGE, G R & KAMPHUIS, J W (1972). Experiments on bed form generation by wave action. Proc. 13th Conf. Coastal Engng., pp. 1123-1142.

NAKATO, T, LOCHER, F A, GLOVER, J R & KENNEDY, J F (1977). Wave entrainment of sediment from rippled beds. J Waterways, Ports, Coastal & Ocean Div., 103 (WW1), pp. 83-99.

SAWAMOTO, M YAMASHITA, T & KURITA, T (1980). Vortex formation over rippled bed under oscillatory flow. Tech. Rep. No. 27, Dept. Civ. Engng. Tokyo Inst. Tech., pp. 75-85.

SLEATH, J F A (1974a). Stability of laminar flow at seabed. J Waterways, Harbors & Coastal Engng. Div., 100 (WW2), pp.105-123.

SLEATH, J F A (1974b). Velocities above a rough bed in oscillatory flow. J Waterways, Harbors & Coastal Div., 100 (WW4), pp. 287-304.

SLEATH, J F A (1975). A contribution to the study of vortex ripples. J Hyd. Res., 13 (3), pp. 315-328.

SLEATH, J F A & ELLIS, A C (1979). Ripple geometry in oscillatory flow. CUED/A - Hydraulics/TR2.

6. SYMBOLS

a = Amplitude of oscillation

h = ripple height

k = ripple frequency

= $2\pi/L$

L = ripple length

T = period of oscillation

t = time

U_o = maximum oscillating tray velocity

U_∞ = maximum freestream velocity

U_π = velocity at $\omega t = \pi$

β = measure of laminar boundary layer thickness

= $(\frac{\omega}{2\nu})^{\frac{1}{2}}$

ω = oscillation frequency

= $2\pi/T$

ν = kinematic viscosity of fluid

MASS TRANSPORT IN VOCOIDAL THEORY

by

J W Gonsalves and D H Swart*

ABSTRACT

The concept of mass transport is theoretically discussed within the framework provided by Vocoidal theory. The Lagrangian mass transport is divided into two parts; firstly treating the fluid as being inviscid and secondly, incorporating viscosity by means of the free surface and bottom boundaries. Eulerian mass transport is defined and is shown to correspond, in deep water, to the net flow predicted by Stokes and others.

INTRODUCTION

The Lagrangian mass transport is defined as the mean velocity of a marked particle and results from the fact that the trajectories of the fluid particles under finite amplitude waves are not closed. Since the original discussion by Stokes (1847), this concept remained theoretically untouched until 1953 when Longuet-Higgins treated it from the point of view of a viscous fluid. Since then many authors, of which Huang (1970) is the most notable, have written on this subject. Eulerian mass transport has only relatively recently been defined in papers by Dalrymple (1976) and Tsuchiya and Yasuda (1981).

Experimentally the effect was observed as early as 1878 by Caligny, the US Beach Erosion Board (1941) and Bagnold (1947). The most comprehensive observations were carried out by Russell and Osorio (1957), whose results confirmed the Longuet-Higgins model. In 1980 Tsuchiya, Yasuda and Yamashita observed drift profiles in a flume incorporating a natural water recirculation process. Results from these tests agreed with both their and the Stokes drift profiles, the net drift being forward throughout the fluid.

VOCOIDAL THEORY

Vocoidal theory was developed to predict the behaviour of non-breaking waves on a horizontal bed (Swart, 1978) and

* National Research Institute for Oceanology, CSIR, Stellenbosch, Republic of South Africa

applies to water of all depths. The theory is two-dimensional and is based on the equations of motion and continuity and adheres to the bed and free surface boundary conditions. The assumptions on which this theory is based can be summarised by the following three definitions.

Wave profile: $\eta/H = \{(\cos^2(\pi X))^P - \eta^*_t\}$ (1)

Wave celerity: $c^2/gd = \tanh(Nkd)/kd$ (2)

Horizontal orbital velocity:

$$u/c = \eta M(X) k \cosh[M(X)kz]/\sinh[M(X)k(d+\eta)] \quad (3)$$

where $X = (x-ct)/\lambda$; z = vertical coordinate (defined from the bed upwards); H = wave height; λ = wave length; k = wave number $(2\pi/\lambda)$; η^*_t is the dimensionless trough elevation and where P, N and $M(X)$ are parameters depending on the wave conditions (H/d, λ/d).

In deep water, when H/d and λ/d are small, Vocoidal theory reverts to Airy wave theory while in shallow water it becomes solitary wave-like. Curve-fitting techniques were used to allow the use of these numerically determined parameters in a predictive manner for an extensive range of H/d and λ/d values.

Because of an approximation to $M(X)$ during the curve-fitting process, a vorticity was introduced, that is, the theory is rotational whereas in principle it should have been irrotational. The vocoidal vorticity is defined by the equation $\omega = \nabla^2\phi$, where $\phi = -c\eta \sinh[M(X)kz]/\sinh[M(X)k(d+\eta)]$ is the vocoidal stream function.

In order to determine to what extent the theory is rotational the induced vorticity was compared with the vorticity generated by the straining in the irrotational motion (Phillips, 1966) and by the laminar bed boundary layer. The argument on which this comparison is based is that the dissipation of energy in a wave is accompanied by a decrease in wave momentum which, as Longuet-Higgins (1969) showed, is distributed throughout the fluid. This decrease in mean momentum must be accompanied by a mean stress across horizontal planes below the surface. A mean second order viscous stress is set up to balance this loss of momentum. Thus a mean second-order vorticity ω is generated below the free surface.

Comparisons of the average vorticity for various wave conditions are given in Table I, which shows that the average vorticity generated by Vocoidal theory is generally much less than that generated by the viscous and bed shear forces. Since the latter effects are regarded as

negligible in most wave theories Vocoidal theory can be regarded as essentially irrotational to second order.

MASS TRANSPORT

The treatment of mass transport by Vocoidal theory will be divided into three parts: the first dealing with the Lagrangian mass transport in an inviscid fluid, the second with the Lagrangian mass transport incorporating viscous and boundary layer effects, while the third part will deal with Eulerian mass transport.

(i) Lagrangian Mass Transport in an Inviscid Fluid

The mass transport in an inviscid fluid will be treated in a general manner.

The horizontal orbital excursion or displacement ξ_x is defined by $\frac{d\xi_x(t)}{dt} = U_\varepsilon(x,y,z,t)$, where $U_\varepsilon(x,y,z,t)$ is the horizontal velocity following the particle's path. Based on this definition the mass transport can be defined as:

$$U_m = \frac{1}{T}\int_0^T U_\varepsilon(x,y,z,t)dt \qquad (4)$$

For progressive waves of a permanent type the streamlines and particle paths coincide. Thus once the elevation of a specific streamline ψ^o is known, the particle Lagrangian velocity along this streamline can be obtained from $U_\varepsilon(x,t) = U(x,z_{ST})$, the Eulerian velocity at position (x,z_{ST}), where z_{ST}, the streamline elevation, is obtained by iteration of the expression:

$$z_{ST} = \frac{\psi^o}{c} + S(z_{ST}) \quad \text{and where the}$$

function S depends on the particular wave theory involved.

The mass transport is thus numerically obtained from the expression:

$$U_m(z_{ST}) = \sum_{i=1}^{n} U(x_i,z_{ST})\Delta t_i \Big/ \sum_{i=1}^{n} \Delta t_i, \qquad (5)$$

where the time interval Δt_i is defined as $\Delta t_i = \Delta x_i(u_i-c)$ and where n is such than $n.\Delta x_i = \lambda$. Results obtained by this method are similar to those of

Stokes, namely, forward at the free surface and backward near the bed.

TABLE I: THE RATIO OF THE VOCOIDAL VORTICITY TO VORTICITY GENERATED BY THE LAMINAR BED BOUNDARY LAYER AND FROM THE STRAINING IRROTATIONAL MOTION

T_c \ H/d	0.01	0.02	0.05	0.1	0.2	0.5	1.0
1.0	0.0071	0.0066					
2.0	0.0535	0.0482	0.0443				
5.0	0.0045	0.0035	0.0029	0.0027	0.0025	0.0015	
10.0	0.0006	0.0003	0.0003	0.0016	0.0012	0.0003	
20.0	0.0002	0.0032	0.0027	0.0027	0.0028	0.0019	0.0004
40.0	0.0034	0.0032	0.0029	0.0030	0.0033	0.0020	0.0006
60.0	0.0035	0.0032	0.0030	0.0030	0.0034	0.0025	0.0006

TABLE II: VALUES FOR THE NON-DIMENSIONALISED EULERIAN MASS FLOW $q_m/(H^2g/8c)$

T_c \ H/d	0.01	0.02	0.05	0.1	0.2	0.5	1.0
1.0	1.000	1.000					
2.0	1.000	1.000	0.999				
5.0	0.993	0.993	0.996	1.000	1.009	1.026	
10.0	1.031	1.033	1.040	1.074	1.093	1.039	
20.0	0.988	1.038	1.008	0.881	0.708	0.487	0.616
40.0	1.039	0.905	0.654	0.492	0.363	0.253	0.328
60.0	0.870	0.671	0.458	0.336	0.247	0.179	0.166

* Comment: $T_c = T\sqrt{g/d}$

(ii) Lagrangian Mass Transport in a Viscous Fluid

To incorporate the effects of viscosity within the framework of Vocoidal theory an approach similar to that given by Johns (1970) and Isaacson (1976) was used. The bottom boundary layer will be dealt with in some detail.

The horizontal flow velocity outside the bottom boundary is expanded in a Fourier series:

$$U = \sum_{n=-\infty}^{\infty} A_n e^{ik_n X} \tag{6}$$

where $A_o = 0$; $A^*_{-n} = A_n$; $k_n = 2\pi n/\lambda$ and $X = x - ct$. Applying the usual boundary layer approximations we have that the motion within the bottom boundary layer is described by:

$$u_t + uu_x + wu_z = U_t + UU_x + \nu[K(z)\, u_z]_z \tag{7}$$

where u is the boundary layer velocity, U is the velocity above the boundary layer and K(z), the eddy coefficient.

Expanding the boundary layer velocity u by the method of successive approximations (Schlichting, 1968) the equation above reduces to the following two equations:

$$\text{First-order:} \quad u_{1t} = U_t + \nu[K(z)u_{1z}]_z \tag{8}$$

$$\text{Second-order:} \quad u_{2t} + u_1 u_{1x} + w_1 u_{1z} = UU_x + \nu[K(z)u_{2z}]_z \tag{9}$$

Introduce a non-dimensional vertical coordinate η, where $\eta = \sqrt{(\sigma/2\nu)}z$ with $\sigma = 2\pi/T$; T = wave period; ν = kinematic viscosity coefficient and assume laminar flow, K(z) = 1. Further, assuming the first-order boundary layer velocity to be given by:

$$u_1 = \sum_{n=-\infty}^{\infty} A_n[1-F(\eta_n)]e^{ik_n X}, \tag{10}$$

it is found after substitution that the function $F(\eta)$ must satisfy the equation:

$$\frac{d^2F(\eta)}{d\eta^2} + 2iF(\eta) = 0 \tag{11}$$

with boundary conditions $F(0) = 1$ and $F(\infty) = 0$.

Substitution into the second approximation, where the vertical velocity component w_1 is obtained from the continuity equation, and extracting only the real time - independent second-order term, results in an expression for u_2, given by:

$$\bar{u}_2 = \sum_{n=1}^{\infty} \frac{A_n^2}{c} \mathrm{Im}(G(\eta_n)) \tag{12}$$

$\mathrm{Im}(G(\eta))$ is the imaginary part of $G(\eta)$, with $G(\eta)$ satisfying the equation:

$$\frac{d^2G(\eta)}{d\eta^2} = |F(\eta)|^2 - 2\mathrm{Re}(F(\eta)) + \frac{dF^*(\eta)}{d\eta} \int_0^{\eta} (1-F(\eta))d\eta$$

subject to the boundary condition $G(0) = 0$ and $G(\eta)$ finite as $\eta \to \infty$ (* implies the complex conjugate).

Substituting u_1 and $\bar{u}_2$ into second-order mass transport velocity, defined by Longuet-Higgins (1953), namely,

$$U_m = \bar{u}_2 + \overline{u_{1x} \int_0^t u_1 dt'} + \overline{u_{1y} \int_0^t w_1 dt'} \tag{13}$$

gives an equation for the transport above the bottom boundary layer as:

$$U_m = \sum_{n=1}^{\infty} \frac{A_n^2}{c} \mathrm{Im}(H(\infty)) \tag{14}$$

with

$$H(\eta) = G(\eta) + \frac{i}{2}\left[\frac{dF^*}{d\eta} \int_0^{\eta} (1-F(\eta))d\eta - 1 + 2\mathrm{Re}(F(\eta)) - |F(\eta)|^2\right]$$

Generalising the results of Huang (1970) to include both the free surface and interior regions, the mass transport throughout the fluid can be calculated. These results, however, depend on an important approximation, namely that the series solution be arbitrary but finite. If a zero net mass transport is assumed then the mass transport in the interior can be calculated from the expression:

$$U_m = \frac{1}{4} \sum_{n=1}^{m} \frac{A_n^2 \sigma_n k_n}{\sinh^2 k_n d} \left\{2 \cosh 2 k_n d\mu - \frac{3}{2}\left[1-(1-\mu)^2\right] \frac{\sinh 2k_n d}{k_n d} + \frac{9}{2}(1-\mu)^2 - \frac{3}{2}\right\} \tag{15}$$

with $\mu = z/d$ and the bed defined at $\mu = 0$ (that is, $z = 0$).

Calculations have shown that m need not exceed 50, even for the most highly non-linear case. Figures 1 to 4 show typical mass transport profiles for various values of T_c $(= T\sqrt{(g/d)})$ and H/d. For low values of T_c and H/d (Figure 1) we see that, with the exception of Longuet-Higgins, all profiles correspond to that given by Stokes. It should be noted that in order to distinguish between the

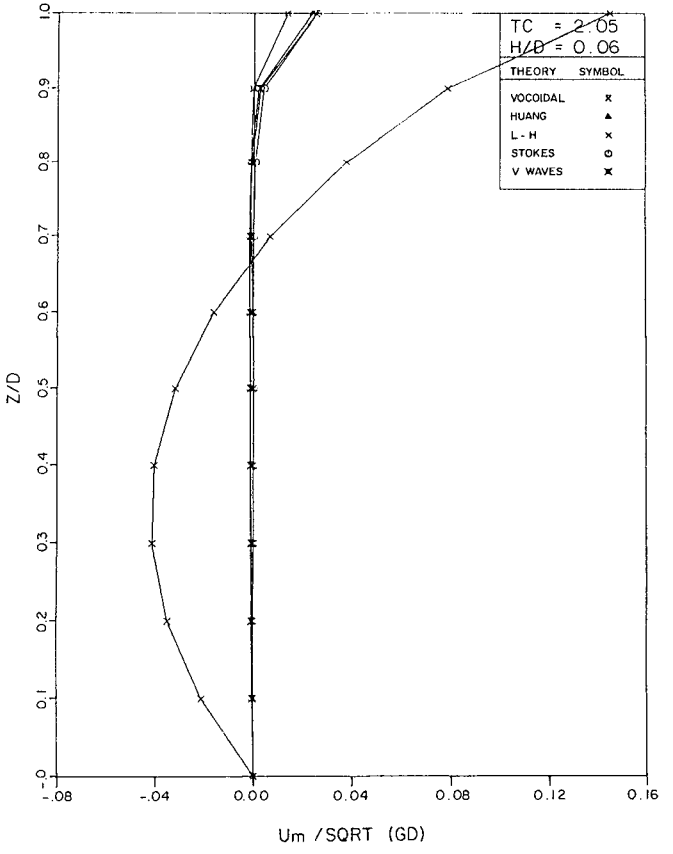

Figure 1 Comparison of the theoretical non-dimensional drift profiles for various wave theories

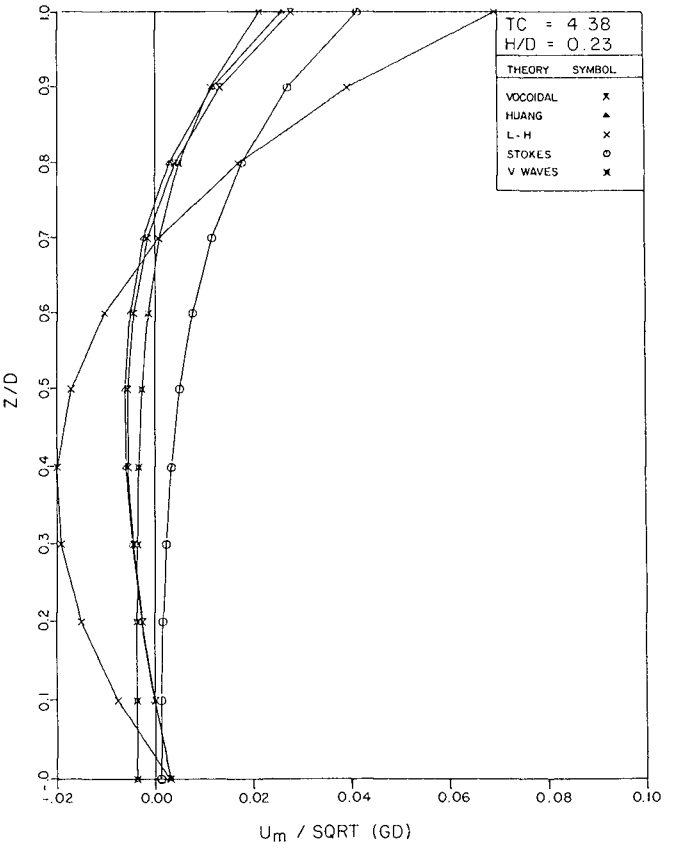

Figure 2 Comparison of the theoretical non-dimensional drift profiles for various wave theories

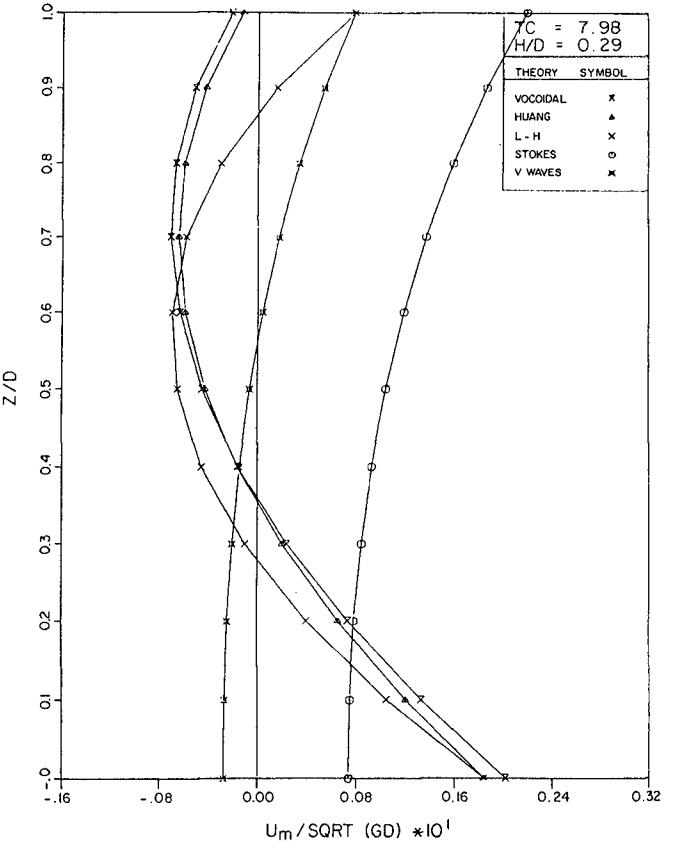

Figure 3 Comparison of the theoretical non-dimensional drift profiles for various wave theories

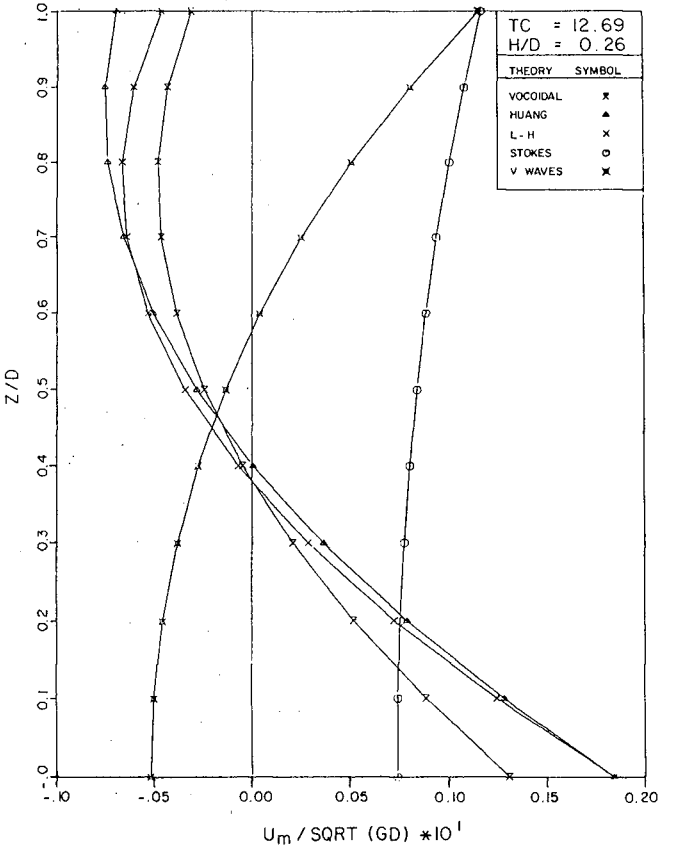

Figure 4 Comparison of the theoretical non-dimensional drift profiles for various wave theories

Stokes mass transport and the Vocoidal inviscid Lagrangian transport (V wave) the Stokes solution was not corrected for zero net mass transport. In order to do this a quantity $-H^2\sigma \coth kd/8d$ must be added to the Stokes results, thus shifting the profile to the left.

In the deep water region (Figures 1, 2 and 3) the mass transport velocity above the bottom boundary layer, as predicted by Vocoidal theory, is greater or equal to the values predicted by Longuet-Higgins and Huang. As the water becomes shallower the opposite is true (Figures 4 and 5). This latter result corresponds to the observations made by Brebner and Collins (1961). Figure 5 gives a comparison of the theoretical profiles with a data set observed by Russell and Osorio (1957).

(iii) Eulerian Mass Transport

The Eulerian mass transport will be determined using Dalrymple's (1976) approach and be defined as the net or average flow past any fixed point in the fluid:

$$M = \frac{\rho}{T} \int_0^T \int_0^{d+\eta} u(z,t)\,dz\,dt \tag{16}$$

Dalrymple obtained, for Airy theory, the well-known solution $M = \rho g H^2/8c$, while for Dean's stream theory he found that $M = -\rho\psi(x,\eta)$, the value of the stream function on the free surface.

Integrating the continuity equation over depth and applying the bed and free surface boundary conditions the net flux in Vocoidal theory is determined to within an integration constant:

$$\int_0^{d+\eta} u\,dz - c\eta = q_m \tag{17}$$

The choice $q_m = 0$ corresponds to a reference frame in which the net mass flux is zero (Tsuchiya and Yasuda, 1981). Assume $q_m \neq 0$, then in the light of Vocoidal theory's second order irrotationality the expression relating kinetic energy density to the momentum flux, namely,

$$\frac{\rho}{\lambda} \int_0^{\lambda} \int_0^{\eta+d} (u^2+w^2)\,dz\,dx = c\rho \int_0^{\lambda} \int_0^{\eta+d} u\,dz\,dx \tag{18}$$

(Starr, 1947; Longuet-Higgins, 1976) can be used to determine q_m. Since $q_m \neq 0$ the expressions for the orbital velocities change so as to include q_m. The resulting quadratic expression in q_m can be numerically

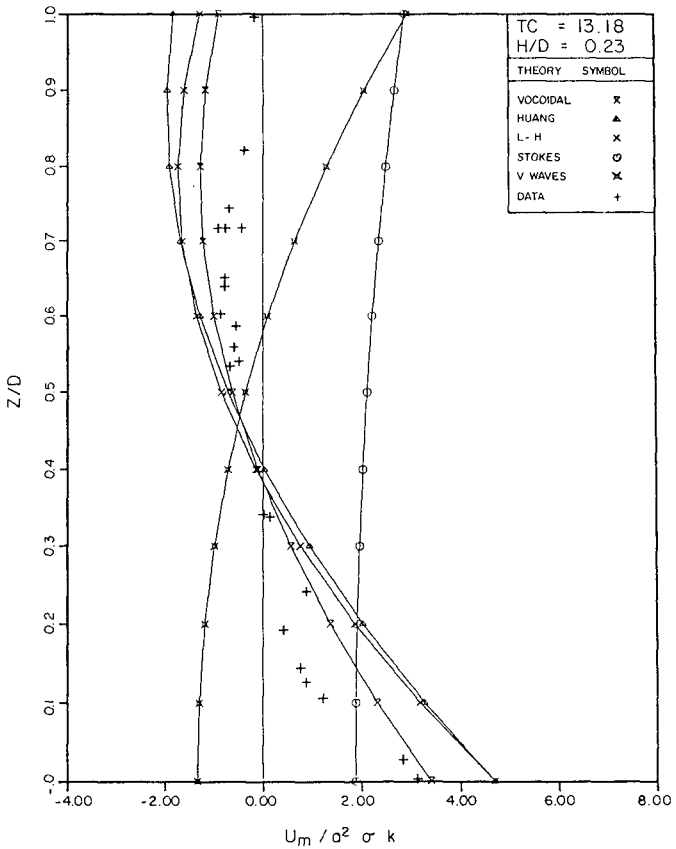

Figure 5 Comparison of the theoretical non-dimensional drift profiles and data observed by Russell and Osorio (1957, Figure 7)

solved, and values for various wave conditions can be seen in Table II. In the deep-water limit the expressions involving q_m reduces to:

$$q_m - q_m^2/cd = H^2g/8c.$$

CONCLUSIONS

(i) If viscosity is neglected the Lagrangian mass transport corresponds in profile to that given by Stokes.

(ii) Vocoidal mass transport including viscous effects is such that in deep water the velocities above the bed are generally greater than those predicted by Longuet-Higgins (1953) and Huang (1970) while for shallow water the reverse is true.

(iii) In deep water both the viscous and inviscid solutions coincide and reduce to the Stokes profile.

(iv) An Eulerian mass transport can be defined which approaches the Stokesian results in deep water but diverge as H/d and λ/d increase.

REFERENCES

BREBNER, A and COLLINS, J I (1961). Onset of turbulence at the bed under periodic gravity waves. Trans. Eng. Inst. Cam., 5 pp 55-62.

DALRYMPLE, R A (1976). Wave-induced mass transport in water waves. ASCE J. Waterways, Harbors Coastal Eng. Div., 102 (WW2) pp 255-264.

HUANG, N W (1970). Mass transport induced by wave motion. J. Mar. Res., 28 pp 35-50.

ISAACSON, M DE ST Q (1976). Mass transport in the bottom boundary layer of Cnoidal waves. J. Fluid Mech., 74 pp 401-413.

JOHNS, B (1970). On the mass transport induced by oscillatory flow in a turbulent boundary layer. J. Fluid Mech., 43 pp 177-185.

LONGUET-HIGGINS, M S (1953). Mass transport in water waves. Phil. Trans. Royal Soc., London, A 245 pp 535-581.

LONGUET-HIGGINS, M S (1969). On the transport of mass by time-varying ocean currents. Deep-Sea Res., 16 pp 431-447.

LONGUET-HIGGINS, M S (1975). Integral properties of periodic gravity waves of finite amplitude. Proc. Royal Soc., London, A 342 pp 157-174.

PHILLIPS, O M (1966). The dynamics of the upper ocean. Cambridge University Press.

RUSSELL, R C H and OSORIO, J D C (1957). An experimental investigation of drift profiles in a closed channel. Proc. 6th Conf. Coastal Eng., pp 171-193.

TSUCHIYA, Y, YASUDA, T and YAMASHITA (1980). Mass transport in progressive waves of permanent type. Proc. 17th Conf. Coastal Eng., pp 70-81.

TSUCHIYA, Y and YASUDA, T (1981). A new approach to Stokes wave theory. Bull. Disas. Prev. Res. Inst., Kyoto Univ., 31 pp 17-34.

SCHLICHTING, H (1968). Boundary layer theory. 6th edition (translated from German by J Kestin), McGraw-Hill.

STARR, V P (1947). A momentum integral for surface waves in deep water. J. Mar. Res., 6 pp 126-135.

SWART, D H (1978). Vocoidal water wave theory, Volume 1: derivation. CSIR Research Report 357, Stellenbosch, South Africa.

PROBABILITY DENSITY FUNCTION OF WAVE HEIGHTS OFF THE WESTERN COAST OF TAIWAN

by

Frederick L.W. Tang*

and

Jea-Tzyy Juang**

ABSTRACT

A new probability density function of wave heights off the western coast of Taiwan is submitted in this paper. According to the bathymetry of this area, waves from the central part of Taiwan Strait refract to the point of measurement and minor waves generated by local wind add the energy on the major ones; So an analytical solution is to be worked out by assuming that the wave energies are the linear sum of these two sources and convolution integral is adopted. The new model approaches reality better than Rayleigh's.

1. INTRODUCTION

Since 1952, The probability density function of wave heights is supposed to be Rayleigh's distribution. It will be physically sound if the water depth is infinitive, namely in the case of deep water wave. Another requirement is that the frequency band of wave spectrum should be as narrow as possible. In deep water waves, if the wave heights are defined to be the vertical distance

* Dr. Eng. Professor, Graduate School of Ocean Engineering, Researcher, Tainan Hydraulics Laboratory.

** M. Eng. Senior Graduate Student, Graduate School of Ocean Engineering, National Cheng Kung University, Tainan City 700 Taiwan, R.O.C.

between the tip of wave crest above mean sea water level and the bottom of wave trough below it. Such a restriction is fulfilled if we use zero-crossing method to read out the wave records. However, the probability density functions of wave heights in deep water are scarcely to be Rayleigh distribution exactly.

The authors measured and analyzed wave data off the western coast of Taiwan, and studied the wave height distributions. The curves can not said to be Rayleigh distributions. These curves have following characteristics:

(1) *The peak is higher than Rayleigh's curve and lower in two sides, namely the distribution is more concentrated.*

(2) *Two points of inflection can be found but there is only one in Rayleigh's curve.*

To explain such phenomena, we performed following two approaches.

(1) *Analyze the wave record directly to work out an empirical formula which can be adopted generally.*

(2) *According to the bathymetry off the western coast of Taiwan. The waves advanced to the point of measurement are refracted from the central part of Taiwan Strait and combined with local wind waves. A new statistical model can be worked out based on this situation. The analytical consideration of the wave height distribution caused by two wave spectra combination is described as follows.*

2. *STATISTICAL DISTRIBUTION OF WAVE HEIGHTS AFTER SPECTRA COMBINATION*

As mentioned above, the statistical features of waves in Taiwan Strait are not coincident with the theory. The reasons of such phenomenon are supposed to be as follows:

(1) *All wave records being analyzed are measured at shallow water area of western coast of Taiwan, where the waves are composed*

of two patterns. The larger one is transmitted from the central part of the strait by refraction, and the smaller one is directly generated by the prevailing NE-NNE wind along the coast as shown in Fig. 1.

(2)*Theoretical distribution of wave features are assuming that the water depth is infinite, i.e., the situation of deep water wave. Waves in Taiwan strait are shallow water waves in essence. According to the wave statistics in Taiwan strait as shown in Fig. 2, the Rayleigh distribution shows a lower estimated distribution. A new statistical model sounds necessary.*

Theoretical and practical approaches for explicating this problem are described as below.

Assuming that:

(1)*Wave energy E on a complicated random sea surface is the linear sum of the energies E_i transmitted from different sources with spectral functions $S_i(f)$, i.e.*

$$E = \frac{1}{8}\rho g H^2 = \sum_i E_i = \frac{1}{8}\rho g \sum_i H_i^2 \tag{1}$$

(2)*Wave height probability density function in each spectrum is Rayleigh distribution.*

$$\phi_{H_i}(H_i) = \frac{H_i}{4\sigma_i^2} \exp\left(-\frac{H_i^2}{8\sigma_i^2}\right), \quad 0 \le H_i < \infty \tag{2}$$

where $\sigma_i^2 = \int_0^\infty S_i(f)\,df$

(3)*Wave energies from different spectra are mutually independent random numbers.*

Probability density function of the wave height H of a random sea surface which is composed of two different wave spectra is to be derived as below:

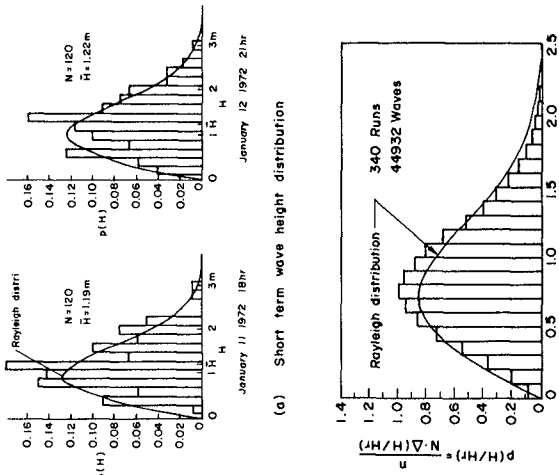

Fig. 2 Wave statistics in Taiwan Strait

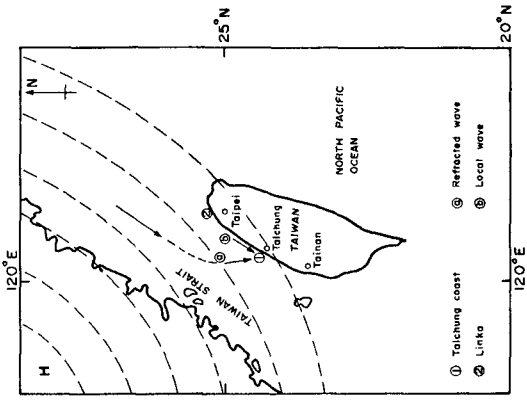

Fig. 1 Wind and wave situation in the winter and location of wave measurement

$$Let \qquad y_i = \frac{8E_i}{\rho g} = H_i^2 \qquad (i = 1, 2) \tag{3}$$

Density function of y can be found as follows

$$\phi_y(y) = \left|\frac{dH}{dy}\right| \phi_H\left(H = \sqrt{y}\right) = \frac{1}{2\sqrt{y}} \phi_H\left(\sqrt{y}\right)$$

$$\left.\begin{aligned} \phi_y(y_1) &= \frac{1}{2\alpha_1} exp\left(-\frac{y_1}{2\alpha_1}\right) \\ \phi_y(y_2) &= \frac{1}{2\alpha_2} exp\left(-\frac{y_2}{2\alpha_2}\right) \end{aligned}\right\} \tag{4}$$

where $\alpha_i = 4\sigma_i^2$

While two series of waves are mixing, their energies add together.

$$Let \qquad Z = y_1 + y_2 = H_1^2 + H_2^2 = H^2$$

$$\phi_z(Z) = \int_0^Z \phi_y(y_1)\, \phi_y(Z - y_1)\, dy_1$$

$$\phi_z(Z) = \frac{1}{2(\alpha_1 - \alpha_2)}\left[exp\left(-\frac{Z}{2\alpha_1}\right) - exp\left(-\frac{Z}{2\alpha_2}\right)\right], \qquad 0 \le Z < \infty \tag{5}$$

$$\phi_H(H) = \frac{H}{\alpha_1 - \alpha_2}\left[exp\left(-\frac{H^2}{2\alpha_1}\right) - exp\left(-\frac{H^2}{2\alpha_2}\right)\right], \qquad 0 \le H < \infty \tag{6}$$

Such a function has two points of inflexion at both sides of the peak whereas there is only one point locating to the right of maximum probability density in Rayleigh distribution.

Wave height distribution functions for the waves transmitted from 3 spectra are able to be calculated by similar way and the

result is as follows.

$$\phi(H) = \frac{\alpha_1 H}{(\alpha_1-\alpha_2)(\alpha_1-\alpha_3)}\left[exp\left(-\frac{H^2}{2\alpha_1}\right)-exp\left(-\frac{H^2}{2\alpha_3}\right)\right]$$

$$-\frac{\alpha_2 H}{(\alpha_1-\alpha_2)(\alpha_2-\alpha_3)}\left[exp\left(-\frac{H^2}{2\alpha_2}\right)-exp\left(-\frac{H^2}{2\alpha_3}\right)\right] \quad (7)$$

While the waves have multiple sources the wave height distribution function can be worked out by repeated convolution integration. A special case $H_1^2 = H_2^2 = \cdots = H_n^2$

let $$W = \sum_{i=1}^{n} H_i^2$$

$$\phi(W) = \frac{W^{n-1}}{(2\alpha)^n \Gamma(n)} exp\left(-\frac{W}{2\alpha}\right) \quad (8)$$

and $$\phi(H) = \frac{2H^{2n-1}}{(2\alpha)^n \Gamma(n)} exp\left(-\frac{H^2}{2\alpha}\right) \quad (9)$$

3. *CHARACTERISTICS OF THE NEW DISTRIBUTION*

From eq. (6), *for convenience, put* $\alpha_1 = a$, $\alpha_2 = b$, *the equation becomes*

$$\phi(H) = \frac{H}{a-b}\left[exp\left(-\frac{H^2}{2a}\right) - exp\left(-\frac{H^2}{2b}\right)\right] \quad (10)$$

$$\left.\begin{aligned} a &= 4m_{o,1} = 4\sigma_1^2 \\ b &= 4m_{o,2} = 4\sigma_2^2 \end{aligned}\right\} \quad (11)$$

The moments could be found as follows

$$m_o = \int_o^\infty \phi(H)\, dH = \int_o^\infty \frac{H}{a-b}\left[exp\left(-\frac{H^2}{2a}\right)-exp\left(-\frac{H^2}{2b}\right)\right]dH$$

$$= 1 \quad (12)$$

$$m_1 = \int_o^\infty H\phi(H)\, dH = \frac{1}{a-b}\left(\sqrt{\frac{\pi a^3}{2}} - \sqrt{\frac{\pi b^3}{2}}\right) \tag{13}$$

$$m_2 = \int_o^\infty H^2\phi(H)\, dH = 2\,(a+b) \tag{14}$$

$$m_3 = \int_o^\infty H^3\phi(H)\, dH = \frac{3}{a-b}\left(\sqrt{\frac{\pi a^5}{2}} - \sqrt{\frac{\pi b^5}{2}}\right) \tag{15}$$

$$m_4 = \int_o^\infty H^4\phi(H)\, dH = 8\,(a^2 + ab + b^2) \tag{16}$$

mean:

$$\mu = m_1 = \frac{\sqrt{\pi/2}}{a-b}\left(a^{3/2} - b^{3/2}\right) \tag{17}$$

variance:

$$\sigma_H^2 = M_2 = m_2 - m_1^2$$

$$= 2\,(a+b) - \frac{\pi}{(a-b)^2}\left(\frac{a^3+b^3}{2} - ab\sqrt{ab}\right) \tag{18}$$

skewness:

$$\sqrt{\beta_1} = \frac{M_3}{(M_2)^{3/2}} = \frac{M_3}{(\sigma_H^2)^{3/2}} \tag{19}$$

$$M_3 = m_3 - 3m_1m_2 + 2m_1^2$$

$$= \frac{3}{a-b}\left\{a^2\sqrt{\frac{\pi a}{2}} - b^2\sqrt{\frac{\pi b}{2}}\right\} - \frac{6\,(a+b)}{a-b}\left\{\sqrt{\frac{\pi a^3}{2}} - \sqrt{\frac{\pi b^3}{2}}\right\}$$

$$+ \frac{2}{(a-b)^3}\left\{\sqrt{\frac{\pi a^3}{2}} - \sqrt{\frac{\pi b^3}{2}}\right\}^3$$

kurtosis:

$$\gamma = \beta_2 - 3 = \frac{M_4}{M_2^2} - 3 \tag{20}$$

$$M_4 = m_4 - 4m_1m_3 + 6m_1^2m_2 - 3m_1^4$$

$$= 8(a^2+ab+b^2) - \frac{12}{(a-b)^2}\left\{\sqrt{\frac{\pi a^3}{2}} - \sqrt{\frac{\pi b^3}{2}}\right\}\left\{\sqrt{\frac{\pi a^5}{2}} - \sqrt{\frac{\pi b^5}{2}}\right\}$$

$$+ \frac{12(a+b)}{(a-b)^2}\left\{\sqrt{\frac{\pi a^3}{2}} - \sqrt{\frac{\pi b^3}{2}}\right\}^2 - \frac{3}{(a-b)^4}\left\{\sqrt{\frac{\pi a^3}{2}} - \sqrt{\frac{\pi b^3}{2}}\right\}^4$$

extreme value occurs at

$$H = \left\{\frac{2ab}{a-b}\, ln\left(\frac{ab - aH^2}{ab - bH^2}\right)\right\}^{1/2} \tag{21}$$

point of inflexion occurs at

$$H = \left\{\frac{2ab}{a-b}\, ln\left[\frac{a^2(H^3 - 3b)}{b^2(H^2 - 3a)}\right]\right\}^{1/2} \tag{22}$$

According to the above mentioned equations, we can found that all the characteristic values are influenced by a and b, i.e., influenced by wave energies of refracted and local wave.

4. *PROCEDURE OF DELINEATE PROBABILITY DENSITY CURVES FOR EXISTING RECORDS*

From eq. (17), *we have*

$$\overline{H} = \sqrt{\frac{\pi}{2}}\left(\frac{a^{3/2} - b^{3/2}}{a-b}\right) \tag{23}$$

let	$\sqrt{a} = x$	$\sqrt{b} = y$
then	$a = x^2$	$b = y^2$
	$a^{3/2} = x^3$	$b^{3/2} = y^3$

Eq. (23) *becomes*

$$\frac{\overline{H}}{\sqrt{\frac{\pi}{2}}} = P = \frac{x^3 - y^3}{x^2 - y^2} \tag{24}$$

The local wave energy b can not be equal to that of waves from the central part of Taiwan Strait.

$$a \neq b \quad , \quad i.e. \qquad x \neq y$$

then $$x^2 + xy + y^2 - Px - Py = 0 \tag{25}$$

This is the equation of an ellipse as shown in Fig. 3.

The total energy is the sum of local and refracted wave energies

$$a + b = 4\ (\ \sigma_1^2 + \sigma_2^2\ ) = 4\,\sigma^2 \tag{26}$$

Following relationship exists

$$\overline{H} = k\sigma \tag{27}$$

Eq. (26) *becomes*

$$x^2 + y^2 = (\ \frac{2\overline{H}}{k}\ )^2 = R^2 \tag{28}$$

This is the equation of a circle with radius R.

From equs. (25) *and* (28), *the energies* x, y, *i.e.*, a, b *can be worked out.*

For standardization

let $$X = \frac{\sqrt{2}}{2}x + \frac{\sqrt{2}}{2}y \qquad Y = -\frac{\sqrt{2}}{2}x + \frac{\sqrt{2}}{2}y$$

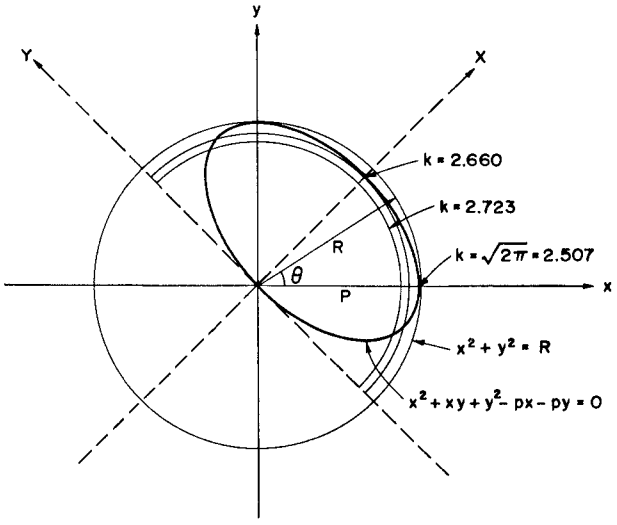

Fig. 3 Graphical solution of simultaneous equations

then $x = \frac{\sqrt{2}}{2}X - \frac{\sqrt{2}}{2}Y \qquad y = \frac{\sqrt{2}}{2}X + \frac{\sqrt{2}}{2}Y$

Eg.(25) *becomes*

$$3X^2 + Y^2 - 2\sqrt{2}PX = 0 \tag{29}$$

that is

$$\frac{(X - \frac{\sqrt{2}}{3}P)^2}{\frac{2}{9}P^2} + \frac{Y^2}{\frac{2}{3}P^2} = 1 \tag{30}$$

The shape of this ellipse was shown as Fig. 3. *Its Center at* $(\frac{\sqrt{2}}{3}P, 0)$, *long axis* $= \frac{2\sqrt{2}}{\sqrt{3}}P$, *short axis* $= \frac{2\sqrt{2}}{3}P$. *When* $Y = 0$, $X = 0$ *and* $\frac{2\sqrt{2}}{3}P$, *the ellipse curve passed at the original point. Besides, when* $y = 0$, $x = P$.

From Fig. 3, *we found that if we want to have solution of equs.*(25) *and*(28), *the condition is* $R \leq P$. *But from equs.*(24) *and*(28), *we have*

$$\frac{2\overline{H}}{k} = R \leq P = \frac{\overline{H}}{\sqrt{\frac{\pi}{2}}}$$

for $\overline{H} \neq 0$, *so* $k \geq \sqrt{2\pi}$ (31)

According to the field data measured at Taichung Harbor (① *in Fig.* 1) *in Taiwan Strait* (*Ou*, 1977), *the value of* $k = 2.723 > \sqrt{2\pi}$. *The new model can be used. But at Linko* (*north coast of Taiwan, as shown in Fig.* 1), $k = 2.461 < \sqrt{2\pi}$, *the new model is not adequate.*

For convenient computation, submit eq.(28) *into eq.*(25) *and*

change it into the polar coordinate

$$R^2 + R^2 (\sin\theta \cdot \cos\theta) - P \cdot R (\cos\theta + \sin\theta) = 0 \qquad (32)$$

$$\frac{1}{4} (\frac{R}{P})^2 \cdot \sin^2 2\theta + [(\frac{R}{P})^2 - 1] \sin 2\theta + [(\frac{R}{P})^2 - 1] = 0 \qquad (33)$$

let $\frac{R}{P} = A$, $\sin 2\theta = Z$

$$Z^2 + \frac{4 [A^2 - 1]}{A^2} Z + \frac{4 [A^2 - 1]}{A^2} = 0 \qquad (34)$$

again, let $\frac{4 [A^2 - 1]}{A^2} = B$

$$Z^2 + BZ + B = 0$$

The solution is

$$Z = \frac{-B \pm \sqrt{B (B - 4)}}{2} \qquad (35)$$

Use computer for computation, if we have k value (from the field data), then R, P, A, B can solved. Consequently, the values of Z, θ, x, y, a, b can fiud out. Therefore, the new distribution for combined wave spectrum is to be worked out.

5. *COMPARISON WITH TRADITIONAL DISTRIBUTION AND DISCUSSION*

Based on the wave statistical result of 21 *sets of field data in Taiwan Strait, the values of k are to be enumerated. They range from* 2.50 *to* 2.95. *After choicing k* = 2.600, 2.660 *and* 2.723. *The new distribution curves can be dipicted in figure* 4. *Also Rayleigh's curves of the same case are delineated.*

From these figures, it can be realized that the new distribution approaches reality much better than traditional Rayleigh's

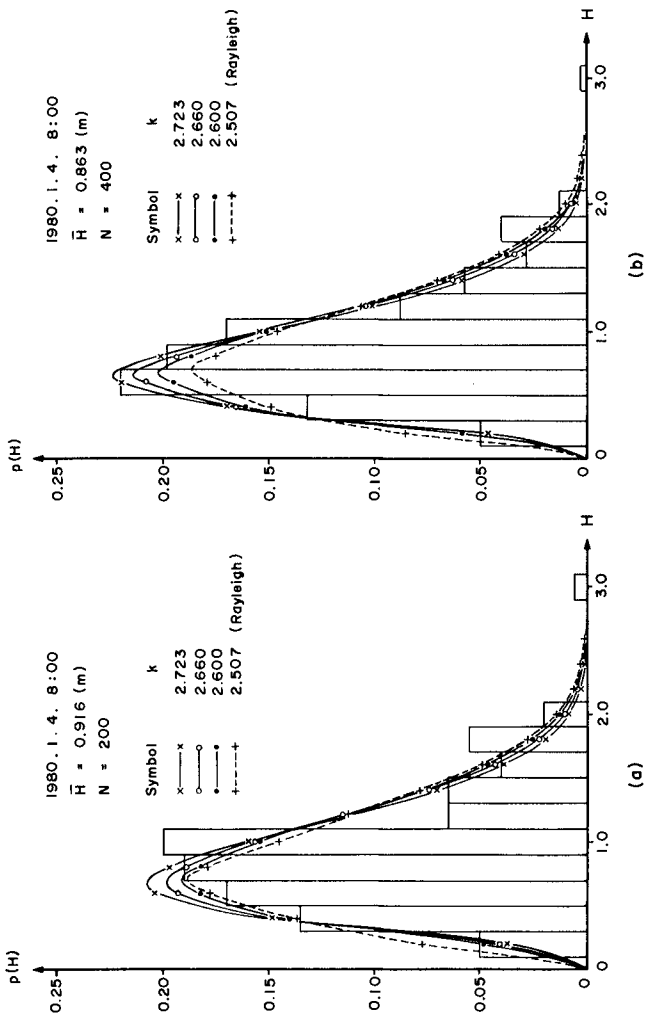

Fig.4 New probability density curve and measured data (1)

density function.

However, in the case of Linko, the winter monsoon attacks the seashore near vertically, the local wind waves are not able to be generated. The assumption of spectral combination is not suitable and the curve of new distribution can not be work out because the values of k is less than $\sqrt{2\pi}$.

In the summer of 1982, *the senior author was invited by Franzius Institute of The University of Hannover to be guest professor. He had the opportunity to analyze the wave records of Sylt. The k value is found to be* 2.46 *for the wind wave is moving depressions are almost approaching frontally to the coast. However, the waves in German Bight are similar to western coast of Taiwan. The wave height distributions over there are to be supposed to fit our new distribution.*

6. *CONCLUSIONS AND SUGGESTION*

1. *The new probability density function of the wave heights fits the reality better than Rayleigh's distribution.*
2. *The new model derived from the idea of the energies of local and refracted waves being combined together, especially conform to situation that the wind direction is parallel to the shoreline.*
3. *At the areas like Linko, local wave can't occur easily, the new model can not be used.*
4. *The forecasting of wave height distribution will be available, provided that the winds can be accurately predicted off the western coast of Taiwan and areas of similar condition.*
5. *Although the new density function approaches reality better than Rayleigh distribution. But the assumption of only two spectra combination will not too sound. Waves in the point of interest are come from every available direction and not able to be divided. However, from the clue used in this paper, it*

can be assumed to be that the wave energy is the linear sum of $S(f)\triangle f_i$, *and* $\triangle f_i$ *is so selected that every* $\triangle E_i = S(f)\triangle f_i$ *are equal, and eq.*(9) *will be a reasonable function to represent the distribution of wave heights if n is suitablely selected.*

ACKNOWLEDGEMENTS

The anthors are deeply indebted to the Gentlemens of Taichung Harbor Bureau and Chinese Petroleum Co. for offering wave data to be analyzed. Also, the authors would greatly appreciate Dr. Shan-Hwei Ou for quote his previous studies and receiving his useful suggestions.

REFERENCES

1. *Longuet-Higgins M.S.: On the statistical distribution of the heights of sea waves. J. Marine Research, Vol XI, No.* 3, 1952.
2. *Ou Shan-Hwei: Parametric determination of wave statistics and wave spectrum of gravity waves. Dissertation No.* 1. *Tainan Hydraulics Laboratory. Rep. of China*, 1977.
3. *Tang Frederick L.W., Ou Shan-Hwei and Juang Jea-Tzyy: Wave Forecasting and Wave Statistics in Taiwan Strait. A paper submitted to second Sino-Korean oceanography conference. Aug.* 1981.

STUDY OF HURRICANE WAVES AROUND THE TAIWAN COAST

By

Hou, Ho-Shong*

S.C. Kuo**

R.S. Tseng***

ABSTRACT

The objective of this research is to study the prediction method of hurricane waves around this island, especially in the Taiwan Strait. The paper describes the prediction of hurricane waves used by Bretchneider's (1976) Method and finds out the predicted waves are different from measured waves, therefore the Bretchneider predicted model is modified by the authors and then the modified model is applied to predict waves again. It is found out that predicted waves match well with the measured waves. The results of the modified Bretchneider model are compared with those of the Ijima tracing method and find out the former is better than the latter.

The second part is to apply the modified model to predict the extreme value of wave heights and compute the worse hurricane wave condition of the surrounding sea area around island, within recent score year (1959-1978). The calculated sites are Chu-Wei, Nan-Liaw, Ta-Shih, Cheng-Kung, Pu-Tai, Tung-Kang, Nan-Wan as shown in Fig.1 and Shiau Liu-Chieu totally 8 stations. Then use the Gumbel Distribution TYPE 1 to predict the extreme wave height of each returned period.

---

* Hou, Ho-Shong, Ph.D., M., ASCE, Deputy Director and Head of Harbor Planning and Design Section, Institute of Harbor and Marine Technology, Wuchi, Taichung, Taiwan, Republic of China.

** S.C. Kuo, Ocean Engineer, China Petroleum Corporation, Taipei, Republic of China.

*** R.S. Tseng, Assoc. Researcher, Energy Research Laboratory, ITRI, Taipei, Republic of China.

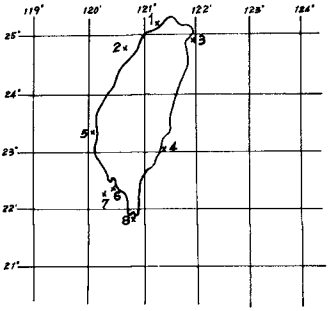

1 Chu-Wei
2 Nan-Liaw
3 Ta-Shih
4 Cheng-Kung
5 Pu-Tai
6 Tung-Kang
7 Nan-Wan

Fig.1 Location of Wave Calculation Sites

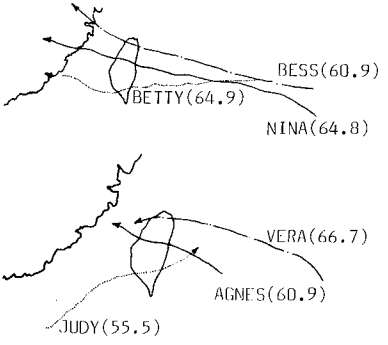

Fig.2a The pathes of six typhoons

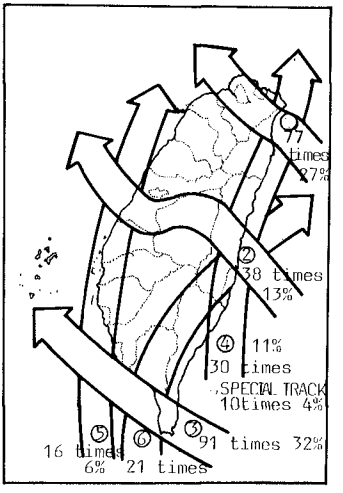

Fig.2b Statistics of Typhoon Track attacked this area

1. INTRODUCTION

"Typhoon" is the most severest atmosphere condition to natural damage when it is threatening the island of Taiwna, Republic of China. Because of the violent wind of typhoon, the induced wave height is stronger than that of the monsoon. Therefore, typhoon waves have to be considered as the design criteria of ocean and coastal engineering.

Usually there are several methods of typhoon wave prediction: (1) Tracing Method of Ijima (2) Graphic Method of Wilson (3) Numerical Calculation Method of Tang (4) Empirical Method of Bretschneider. The first three methods have good accuracy, but the calculation procedures are complicated. As for the Bretschneider empirical method, its calculation procedure and accuracy showed satisfactory results. In this paper, the authors calculated six typhoon waves in Kaohsiung, Taichung and other harbors of Taiwan by use of the empirical method. From the comparison of measured and calculated result, the empirical method have been added some modifications to fit for suitable use of the Taiwan areas.

The modified Bretschneider method is also applied to estimate the highest typhoon waves of Taiwan during the past 20 years. The statistical theory is used to get the possibly extreme waves of the recurrence interval of 100 years, 50 years,..., etc. This conclusion may provide a reference for the design of ocean structures.

2. BASIC THEORY

Typhoon Waves Calculation

The Bretschneider empirical method is modified from the practical application around Taiwan coastal areas. The procedures are as follow:

$$(1)\quad \frac{U_r}{U_R} = -\frac{1}{2}\frac{fR}{U_R}\frac{r}{R} + \sqrt{\left(1+\frac{fR}{U_R}\right)\frac{R}{r}e^{\left(1-\frac{R}{r}\right)} + \left(\frac{1}{2}\frac{fR}{U_R}\frac{r}{R}\right)^2}$$

$$(2)\quad U_R = K\sqrt{\Delta P} - 0.5fR \qquad \text{(Knots)}$$

$$(3)\quad U_{RS} = 0.865U_R$$

$$(4)\quad \Delta U = \frac{1}{2}V_F\cos(\theta+\beta)$$

$$(5)\quad U^*_{RS} = U_{RS} + \Delta U$$

$$(6)\quad H_R = K'\sqrt{R\Delta P}$$

$$(7)\quad H^*_R = H_R(1+\Delta U/U_{RS})^2$$

$$(8)\quad f_0^{-1}/U = 0.4\tanh[\ln(1+\frac{40H_s}{U^2} / 1-\frac{40H_s}{U^2})^{0.5}]^{0.6}$$

$$(9)\quad T_s = \sqrt[4]{\frac{4}{5}}\, f_0^{-1}$$

where U_r, U_R: wind speeds at distance r and R from the typhoon center

f : the Coriolis parameter

ΔP : $P_N - P_0$

P_N, P_0: normal pressure and central pressure, inches of H_g

R : radius of maximum wind, for U_R

K : 67, when latitudes = 20°N - 25°N

U_{RS}: average wind speeds at radius R for the 10m reference plane above mean sea level (Knots)

V_F: actual forward speed of typhoon (Knots)

θ : angle between wind direction and forward direction of typhoon

β= 25°, incurvature angle of wind to tangent of isobars

H_R: wave height at radius R (ft)

K': a coefficient which can be obtained from the following polynomial (Liang 1978)

$$K' = 7.59-41.21(\frac{fR}{U_R})+160.51(\frac{fR}{U_R})^2-219.32(\frac{fR}{U_R})^3$$

H_R^*: wave height at radius R for a hurricane moving at a constant forward speed

T_s: wave period (sec)

3. EXTREME WAVES ESTIMATION

There are a number of methods used in various engineering practices which can be applied to the problem for obtaining design wave height. This paper used a method called "Gumbel Distribution Method". The theory is briefly described as follows:

$$P = (\frac{S'}{S+1})\ 100 \qquad (\%)$$

where S : total number of occurrences on record

S': summation of occurrences, beginning with the highest value to any successive lower values until S'=S

the following equations are used

$$P = \exp(-\exp(-y))$$

$$y = -\ln(-\ln p)$$

Gumbel's theory of extreme values shows that the plot (on extreme-value paper) of a series of observed extreme values of wave heights X should approximate to a straight line.

$$X = X_0 + my$$

where X_0: the modal value of the distribution
m: slope of dx/dy

Gumbel has provided a method of calculating X_0 and m.

$$m = \pi/\sqrt{6}/\sigma_x$$

$$X_0 = \overline{X} - 0.5772/m$$

where σ_x: standard deviation of X_i
$\overline{X}$: average value of X_i

the recurrence interval can be found from

$$I = 100\ \frac{Y}{5P}$$

Y: number of years of record

4. PRACTICAL CALCULATION AND MODIFICATION

Six typhoons are chosen for the case study of wave calculation. Comparisons of the theoretical calculated and the measured waves are made, because of the information of winds and waves are very complete. These typhoons are (1) Judy (May 1966) (2) Agnes (Sep. 1971) (3) Bess (Sep. 1971) (4) Nina (Aug. 1975) (5) Betty (Sep. 1975) (6) Vera (July 1977). The pathes of these typhoons are shown in Fig.2.

There are a few parameters should be determined more carefully because of their significant influence on calculated result. They are discussed individually as follows:

(1) R

R can be determined from the empirical formula of Graham and Nunn (1959)

$$R=28.52\tanh[0.0873(|LAT|-28^{\circ})]+12.22\exp(-\Delta P/33.86)+0.2V_F+37.22$$

where R: radius of maximum wind (Km)
LAT: latitude of typhoon center
ΔP: $1013.2-P_0$ (mb)

(2) ΔP

ΔP can be determined from the formula of Wang (1978)

$$\Delta P = P_N - P_0 \approx 1000 + \frac{(1000-P_0)}{10} - P_0$$

(3) U_R

Bretschneider applies the equation $U_R=K\sqrt{\Delta P}-0.5fR$ in his method to calculate the maximum wind speed U_R. The result of calculation is not always coincident with typhoon record of the Central Weather Bureau. So we use the typhoon record instead of the equation of Bretschneider.

From the above procedures, the waves can be calculated and compared with measured data as shown in Table 1.

Table 1 Comparison of predicted and measured waves of six typhoons

day/hour(LMT)		$H_{1/3}$(m) prediction	measurement	$T_{1/3}$(sec) prediction	measurement
Typhoon: Betty		Sep. 1975		Site Oepth: 28m	
22	8	4.8	5.1	8.5	12.5
	10	5.3	5.5	9.0	12.0
	12	6.2	6.2	9.6	11.8
	14	6.7	6.0	10.1	11.9
	16	7.2	6.3	10.5	10.9
	18	6.6	7.0	10.0	11.6
	20	5.8	6.4	9.4	11.0
	22	5.0	5.0	8.8	10.1

day/hour(LMT)		$H_{1/3}$(m) prediction	$H_{1/3}$(m) measurement	$T_{1/3}$(sec) prediction	$T_{1/3}$(sec) measurement
Typhoon: Agnes		Sep. 1971		Site Depth: 19m	
18	16	3.4	4.4	7.1	8.3
	18	3.8	4.8	7.6	8.4
	20	4.3	4.6	8.1	10.1
	22	4.7	3.9	8.5	8.6
19	00	5.0	5.0	8.5	9.8
	02	3.8	4.0	7.5	9.2
	04	4.4	3.6	8.0	10.1
	06	4.5	2.8	8.2	8.6
Typhoon: Judy		May 1966		Site Depth: 12m	
30	08	3.8	2.8	7.7	9.6
	10	4.0	5.0	7.8	11.3
	12	4.1	5.4	7.9	10.8
	14	4.1	5.5	7.8	10.9
	16	5.1	5.9	8.5	9.7
	18	6.8	5.7	10.1	10.6
	20	6.4	4.9	9.8	9.5
	22	4.9	2.5	8.5	8.0
Typhoon: Nina		Aug. 1975		Site Depth: 28m	
3	06	5.3	5.3	8.8	12.3
	08	6.7	5.4	9.9	11.7
	10	7.8	6.1	10.7	11.8
	12	7.4	7.8	10.5	11.7
	14	5.0	5.8	8.6	9.3
	16	4.1	4.0	8.0	8.2
	18	3.4	3.2	7.7	9.2

day/hour(LMT)		$H_{1/3}$(m) prediction	$H_{1/3}$(m) measurement	$T_{1/3}$(sec) prediction	$T_{1/3}$(sec) measurement
Typhoon: Vera		July 1977		Site Depth: 38m	
31	06	12.9(ft)	11.4(ft)	7.4	9.3
	08	15.6	12.2	8.2	8.3
	10	19.9	12.6	9.4	8.0
	12	23.8	14.7	10.2	9.2
	14	28.1	22.1	11.1	10.4
	16	33.4	29.6	12.0	12.1
	17	36.0	40.9	12.3	14.0
	18	34.5	26.9	12.0	10.7
Typhoon: Bess		Sep. 1971		Site Depth: 19m	
22	16	3.8	3.0	7.5	6.4
	18	4.5	3.6	8.1	7.6
	20	5.1	3.8	8.7	8.1
	22	5.4	3.9	8.9	8.5
23	00	5.7	4.2	9.2	8.9
	02	5.8	4.6	9.3	9.1
	04	5.6	4.2	9.1	8.3
	06	5.3	3.7	9.0	7.8

The predicted wave height has good accuracy as shown in Table 1, but the predicted wave period is always greater than the measured data. So we use the wave period modification coefficient G

$$G = \text{average value of } \frac{\text{measured wave period}}{\text{predicted wave period}} = 1.2$$

Comparisons between two Wave Model with measured values are shown in Fig. 3.

5. ESTIMATION OF EXTREME WAVES

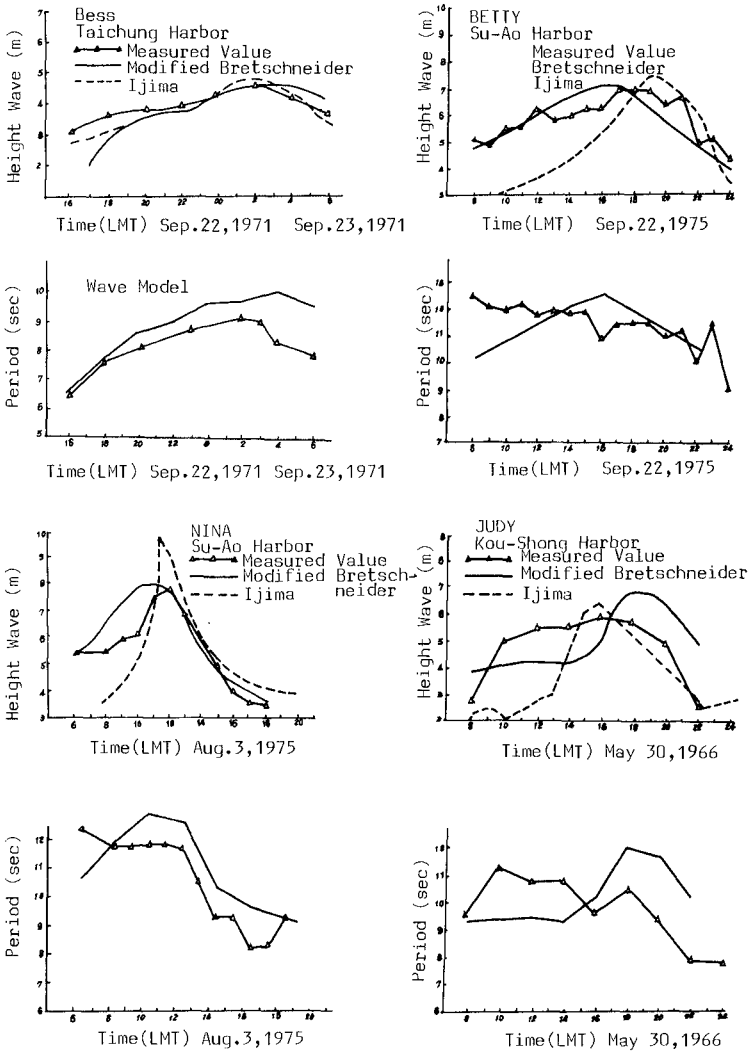

Fig.3 Comparison between Two Hurricane Wave Model

We select eight sites for the estimation of extreme waves. The sites are shown in Fig.1.

The calculation procedures are shown in the following:

(1) Select all typhoons from 1959 to 1978 (20 years) that influenced the coastal areas of Taiwan. Decide their best tracks and other information.

(2) Apply the modified Bretschneider method to calculate $H_{1/3}$ and H_{max} caused by these typhoons at the eight sites.

(3) If $H_{1/3} > 4m$, $H_{max} > 8m$, and typhoon passing within 3 degress of the estimation site, then it can be used to estimate the extreme waves.

(4) Apply the Gumbel distribution method to calculate the extreme waves.

From the above procedures, the extreme waves of eight sites can be obtained and enlisted in Table 2.

Table 2 Extreme Waves of Eight Sites

Site 1: Chu-Wei 25.1°N 121.2°E 30m depth					
$H_{1/3} = 1.600y + 5.928$ $H_{max} = 2.768y + 10.86$					
I(year)	100	50	30	20	10
$H_{1/3}$ (m)	14.3	13.2	12.3	11.7	10.5
H_{max}(m)	25.1	23.1	21.7	20.6	18.6

Site 2: Nan-Liaw 24.8°N 120.7°E 65m depth					
$H_{1/3} = 1.458y + 5.927$ $H_{max} = 2.548y + 10.713$					
I(year)	100	50	30	20	10
$H_{1/3}$ (m)	13.5	12.4	11.7	11.1	10.1
H_{max}(m)	23.8	22.0	20.7	19.7	17.9

Site 3: Ta-Shih 24.95°N 121.9°E 30m depth					
$H_{1/3}$ = 1.794y + 6.446 H_{max}= 3.104y + 11.674					
I(year)	100	50	30	20	10
$H_{1/3}$ (m)	15.8	14.5	13.6	12.9	11.6
H_{max}(m)	27.7	25.5	23.9	22.7	20.5

Site 4: Cheng-Kung 23.1°N 121.4°E 30m depth					
$H_{1/3}$ = 1.412y + 5.423 H_{max}= 2.381y + 10.369					
I(year)	100	50	30	20	10
$H_{1/3}$ (m)	12.9	11.9	11.2	10.6	9.6
H_{max}(m)	22.5	20.9	19.6	18.7	17.0

Site 5: Pu-Tai 23.4°N 120.1°E 30m depth					
$H_{1/3}$ = 1.329y + 5.126 H_{max}= 2.209y + 10.013					
I(year)	100	50	30	20	10
$H_{1/3}$ (m)	11.7	10.8	10.1	9.5	8.6
H_{max}(m)	20.4	18.8	17.7	16.8	15.2

Site 6: Tung-Kang 22.5°N 120.4°E 30m depth					
$H_{1/3}$ = 1.252y + 5.345 H_{max}= 2.174y + 9.878					
I(year)	100	50	30	20	10
$H_{1/3}$ (m)	11.5	10.7	10.0	9.5	8.6
H_{max}(m)	20.6	18.9	17.7	16.8	15.3

Site 7: Shiau Liu-Chieu 22.4°N 120.4°E 30m depth					
$H_{1/3}$ = 1.269y + 5.30 H_{max}= 2.2y + 9.696					
I(year)	100	50	30	20	10
$H_{1/3}$ (m)	11.7	10.8	10.1	9.6	8.7
H_{max}(m)	20.6	19.0	17.9	17.0	15.4

Site 8: Nan-Wan 21.9°N 120.8°E 30m depth					
$H_{1/3}$ = 1.172y + 5.386 H_{max}= 2.001Y + 9.939					
I(year)	100	50	30	20	10
$H_{1/3}$ (m)	11.3	10.5	9.9	9.4	8.6
H_{max}(m)	19.9	18.5	17.5	16.6	15.2

6. CONCLUSION

(1) The modified empirical method has pretty good accuracy in maximum hurricane wave height prediction. Therefore, it is very suitable for coastal areas of Taiwan.

(2) The extreme wave heights $H_{1/3}$ of 100 years recurrence interval at the eight sites are ranked by order: 15.8m, 14.3m, 13.5m, 12.9m, 11.7m, 11.7m, 11.5m, 11.3m. This result may be considered as design criterias of the ocean and coastal engineering at these sites.

(3) Bretschneider (1973) had used the ship observed data and typhoon information of past 10 years (1961-1970) to estimate the waves of Taiwan offshore areas. The result of his estimation was 16m ($H_{1/3}$ of 100 years recurrence interval), a little greater than the result of this paper. The reason of this small deviation may be the site depth - Bretschneider's estimation was in the deep sea, this paper's estimation was in the coastal sea.

7. REFERENCES

(1) Bretschneider, C.L. (1970) "Wave Forecasting Relations for Wave

Generation" Look Lab. Hawaii, Vol.1, No.3, June 1970.

(2) Bretschneider, C.L. (1972a) "A Non-Dimensional Stationary Hurricane Wave Model" Proceedings of 1972 Offshore Technology Conference, Houston, Texas, Paper No. OTC 1517, May 1972.

(3) Bretschneider, C.L. (1972b) "Revisions to Hurricane Design Wave Practices" Proceedings of the 13th Coastal Engineering Conference, ASCE, July, Vancouverm,Canada.

(4) Bretschneider, C.L. and E.E. Tamaye (1976) "Hurricane Wind and Wave Forecasting Techniques" Proc. 15th Conference on Coastal Eng. ch. 13, pp.202-237, Published by ASCE.

(5) Graham, H.E. and D.E. Nunn (1959) "Meteorological Conditions Pertinent to Standard Project Hurricane, Atlantic and Gulf Coasts of United States" National Hurricane Research Project, Report No.33, U.S. Weather Service.

(6) Griffith C.Y. WANG (9178) "Sea-Level Pressure Profile and Gusts within a Typhoon Circulation".

(7) Dennis J. Shea and William M. Gray (1973) "The Hurricane's Inner Core Region. I. Symmetric and Asymmetric Structure".

(8) Bretschneider, C.L. (1973) "A Tentative Analysis of Wave Data for Design Wave Criteria Around Taiwan" ACTA OCEANOGRAPHICA TAWANICA, No.3, December 1973.

(9) "ANNUAL TYPHOON REPORT" 1959-1978, Central Atmospheric Bureau, Taipei.

(10) Liang, N.K., Lin, W.C. (1978) "Comparison of the Measured and Calculated Waves of Vera Typhoon", Proc. of the 2nd Conference on Ocean Engrg., Taichung, R.O.C.

(11) Hou, Ho-Shong (1982) "Littoral Drift Model Investigation along the Taiwan Coast and Research of the Related Problems of Inlet Planning" Technical Research Reports, Institute of Harbor & Marine Technology, Wuchi, Taichung District, Taiwan, R.O.C.

WIND TURBULENCE OVER SEAS IN TROPICAL CYCLONES

W.H. Melbourne[1] and D.R. Blackman[2]

ABSTRACT

A study of wind data collected from the Waglan Island anemometer (Hong Kong) during 39 tropical cyclones indicates that turbulence intensity values in excess of 20% at a reference height of 50 m are likely during extreme wind conditions in a tropical cyclone. The implied surface drag coefficient of approximately 0.01 in these extreme wind conditions is consistent with wind flow over a land surface roughness of trees and suburban housing, but is much higher (by a factor of five) than that predicted by the currently accepted formulae from the reviews of Garratt and Wu for wind flow over a fully developed sea in neutral atmospheric conditions. For wind loading design calculations in extreme wind in tropical cyclone conditions it is recommended that mean wind and turbulence intensity profiles should be calculated with a roughness length z_0 = 0.20 m in the Deaves and Harris wind model.

1 INTRODUCTION

Major structures planned and being built in ocean environments are becoming increasingly wind sensitive as the frequency of their first mode becomes lower. The response of such structures to wind action is not only a function of wind speed but is significantly dependent on the turbulence structure of the wind flow, more explicitly on the turbulence intensity and spectral distribution. Similarly, wind loading on harbour and onshore structures are dependent on these same characteristics. It is important therefore to have estimates of the turbulence characteristics of wind flow over the sea surface in extreme wind conditions, such as might occur for return periods of 20 to 2000 years to cover limit state serviceability and collapse conditions.

Wind data collected in Hong Kong at several anemometer sites for 123 tropical cyclones causing persistent gales since 1884 have been corrected recently for anemometer position error and used to estimate design wind speeds for this area. In particular, model tests to correct wind data collected at a height of 75 m above sea level on Waglan Island, in a full ocean exposure, have given some access to wind turbulence data over the sea in tropical cyclone, extreme wind conditions. These results will be presented to provide some full scale information about wind structure over the sea in extreme wind conditions.

---

[1] Professor of Fluid Mechanics, Monash University, Australia
[2] Senior Lecturer, Monash University, Australia

2 WIND MODELS OVER SEA AND LAND

2.1 Over Land

The most recent review of data compiled to derive a wind model over land is that by Deaves and Harris (1978). The Deaves and Harris model of the structure of strong winds is a most thoroughly researched model and is in wide use in the wind engineering field. It is based on classic logarithmic law mean wind speed profiles and defines surface roughness in terms of the roughness length, z_o.

$$\text{i.e.} \quad \frac{\bar{V}_z}{u_*} = \frac{1}{\kappa} \ln\left(\frac{z}{z_o}\right) \qquad (1)$$

where u_* is the friction velocity $\left(= \sqrt{\frac{\tau}{\rho}} \right)$

$\bar{V}_z$ is the mean wind speed at height z

z is height above ground level

z_o is a roughness length

κ is the von Karman constant (=0.4)

ρ is air density

τ is surface wind shear stress

For the purposes of this study the central parameter is turbulence intensity, I_z, defined as,

$$I_z = \sigma_{v_z} / \bar{V}_z \qquad (2)$$

where σ_{v_z} is the standard deviation of wind speed at height z

A summary of the equations used in the Deaves and Haris wind model are given in Appendix 1. A study has been carried out (Melbourne 1980) using the Deaves and Harris wind model with a 50 ms^{-1} mean gradient wind speed (appropriate to strong wind, design conditions) and varying z_o, until a best fit with profiles for four defined surface roughness categories was obtained. A summary of the relevant turbulence intensity characteristics and roughness length values, with a little rounding, for four surface terrain roughness conditions is given in Table 1.

TABLE 1

TURBULENCE INTENSITY CHARACTERISTICS FOR THE DEAVES AND HARRIS MODEL OVER FOUR SURFACE TERRAIN ROUGHNESS CONDITIONS

Terrain Roughness	Height (m)	Turbulence Intensity I_z
1. Flat desert, snow, (z_o = 0.002 m) ($C_{D_{10}}$ = 0.0022)	5	0.165
	10	0.157
	50	0.128
	100	0.108
	200	0.085
2. Level grass plains, isolated trees, airfields (z_o = 0.02 m) ($C_{D_{10}}$ = 0.0041)	5	0.196
	10	0.183
	50	0.151
	100	0.131
	200	0.107
3. Trees, suburban housing (z_o = 0.2 m) ($C_{D_{10}}$ = 0.0104)	5	-
	10	0.239
	50	0.188
	100	0.166
	200	0.139
4. Forests, hilly terrain, city centres (z_o = 2.0 m) ($C_{D_{10}}$ = 0.061)	5	-
	10	0.448
	50	0.270
	100	0.233
	200	0.196

2.2 Over Sea

In spite of a bounteous literature, until very recently it has been a matter of contention whether the drag coefficient of the wind over the sea assumes a constant value for strong winds. The experimental difficulties probably account in large measure for this imprecision, but it will come as no surprise to find that measurements of strong wind parameters over the sea are very sparse, still less that adequate mathematical representations are wanting.

Garratt (1977) in his review of drag coefficients over oceans and continents concluded, that "observations are consistent with Charnock's (1955) relation,

$$z_o = \frac{\alpha u_*^2}{g} \qquad (3)$$

where α is a constant" (later to be given a value of 0.0185)

and that "for $4 < \bar{V}_{10} < 21$ ms^{-1} a neutral drag coeffficient (referred to 10 m) could be given by

$$\text{or} \quad \begin{aligned} C_{DN_{10}} \times 10^3 &= 0.51\ V_{10}^{0.46} \\ C_{DN_{10}} \times 10^3 &= 0.75 + 0.067\ V_{10} \end{aligned} \qquad (4)$$

which is similar to that proposed by Deacon and Webb (1962) and Wu (1969) for wind speeds less than 15 ms^{-1}, and that observations did not support a constant C_{DN} above 15 ms^{-1} as deduced by Wu (1969)" (p926).

Wu (1980) revisited the field and with more data further confirmed the relevance of Charnock's relation and suggested that the most appropriate value for the constant, α, was 0.0185 with $\kappa = 0.40$, and that

$$C_{10} = (0.8 + 0.065\ V_{10}) \times 10^{-3} \qquad (5)$$

which he also showed (Wu, 1983) is in close agreement for a reference height of 10 m to the generalised expression obtained from (1) and (3), i.e.

$$C_{D_z} = \frac{\tau}{\rho \bar{V}_z^2} = \left[\frac{u_*}{\bar{V}_z}\right]^2 = \left[\frac{\kappa}{\ln(1/a\ C_{D_z} F^2)}\right]^2 \qquad (6)$$

where F is a form of Froude number

$$\left(F = \bar{V}_z/\sqrt{g\ z}\right)$$

Wu (1983) also suggested on the basis of some new data that Charnock's relation and equation (5) appear to be applicable to much higher wind speeds than previously thought, even in hurricanes.

The conclusions of this recent work, in respect of values of drag coefficient and roughness length for wind flow over the sea surface as function of wind speed are summarised in Table 2. Values of the roughness length of the order 0.010 m, commensurate with a mean wind speed of 40 ms^{-1} at 10 m over the sea from Table 2, bear no relation to the physical scales apparent in a fully aroused sea. Of course, a reference height of 10 m is an obvious nonsense at such wind speeds when wave heights in excess of 20 m are likely to be present. It is not surprising that the applicability of current formulae for wind flow over land and sea is being challenged in respect of extreme (design) wind storm events over the sea.

TABLE 2

EVALUATION OF SURFACE DRAG COEFFICIENT, ROUGHNESS LENGTH AND FRICTION VELOCITY FROM EQUATIONS 5, 3 AND 6 RESPECTIVELY.

$\bar{V}_{10}$ ms^{-1}	$C_{D_{10}} \times 10^3$	z_o m	u_* ms^{-1}
10	1.45	0.0003	0.15
20	2.10	0.0016	0.84
30	2.75	0.0047	2.48
40	3.40	0.0103	5.44
50	4.05	0.0191	10.13

3 FULL SCALE MEASUREMENTS FROM WAGLAN ISLAND

The initial analysis of the Waglan Island data was based on the highest mean and three-second maximum gust wind speeds recorded by Dines anemometers for each tropical cyclone causing persistent gales in the Hong Kong region. These data were corrected for anemometer position error from wind tunnel topographical model studies of the anemometer sites. During the analysis of this data it was realised that the anemometer on Waglan Island, which is a small rock outcrop SE of Hong Kong Island, was ideally sited for the purpose of obtaining wind data over the sea in extreme wind conditions, because it is completely exposed to the open ocean for wind directions NE to SW and for the remainder the ocean fetch is mostly 5 km or more. The anemometer at Waglan Island is on a mast, approximately 20 m above ground level and 75 m above mean sea level. The anemometer position errors were initially measured to give freestream conditions at a reference height of 10 m. For extreme wind conditions and attendant wave heights this is obviously quite an artificial reference. Subsequent wind tunnel measurements have been made to correct these anemometer readings to the height of the freestream streamline passing through the anemometer.

3.1 Anemometer Position Error Corrections

A 1/600 scale model of Waglan Island, shown in Figure 1, was tested in two turbulent boundary layer wind models. The wind models were generated in a 2 x 2 x 15 m working section using triangular vorticity generators at the front followed by surface roughness blocks. The two wind models had the scaled characteristics of wind flow over open terrain and suburban/treed terrain, i.e. $z_o \approx 0.02$ and 0.2 respectively or in terms of power law profiles, for exponents $\alpha = 0.15$ and 0.24, where $\left(\bar{V}_z = \bar{V}_g (z/\bar{V}_g)^{\alpha} \right)$. The ratios of the parameters, mean and gust wind speed at the anemometer position and at a scaled height of 50 m in the freestream flow, was measured using hot wire anemometry. In fact, there have been four anemometer positions on Waglan Island since 1952. Between 1952 and 1963 the anemometer was placed on the Observatory Building with good exposure. From 1964 to July 1966 the anemometer was located 3 m above the Signal Tower roof, and being in

FIG. 1 1/600 scale wind tunnel model of Waglan Island used to determine anemometer position error corrections.

the wake of the building, these wind records are useless. In July 1966 the anemometer was raised to 19.5 m above ground level and was then shifted slightly again in December 1971 to its current position. An example of the position error corrections for mean wind speed, $\bar{V}$, and maximum gust wind speed, $\hat{V}$, are given in Figure 2 for the current anemometer position. Since these measurements were made, a set of mean velocity anemometer corrections was measured at the University of Western Ontario, Surry *et al.* 1981, for all anemometer positions and which compare well with the corrections shown in Figure 2.

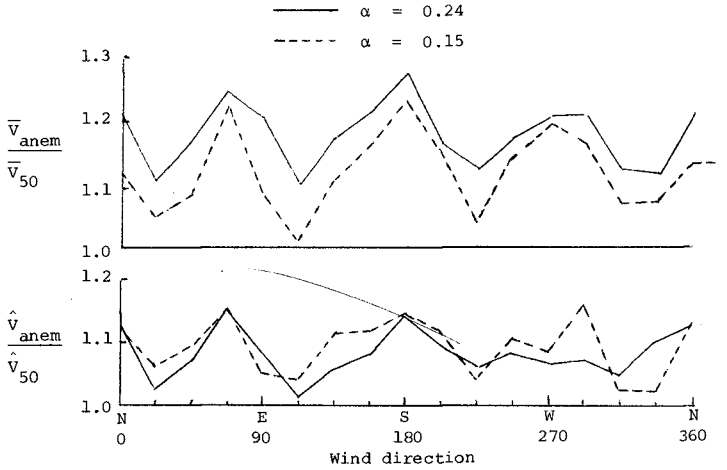

FIG. 2 Mean and gust wind speeds at the Waglan Island anemometer position (1971-) relative to freestream at 50 m above MSL as a function of wind direction for two surface roughness conditions (i.e. two boundary layer profiles)

Apart from the fact that a 10 m freestream reference height is physically meaningless there was another very important reason for correcting anemometer records to a greater height in the freestream flow: the sensitivity of the position error corrections to variations in the approach profile increases with reduction of the freestream reference height. It was therefore decided to use a reference height approximately the same as the freestream height of the streamline which passes through the anemometer on top of the buildings on the island (75 m). Accordingly a freestream reference height of 50 m above MSL was chosen. As can be seen in Figure 2 the correction ratios for the two approach profiles are almost the same for mean and gust wind speeds. The maximum mean and gust wind speeds from the Waglan Island anemometer for each tropical cyclone causing persistent gales in Hong Kong since 1982 (excluding records from January 1964 to June 1966), corrected to refer to a height of 50m above MSL in freestream flow, are given in Table 3.

3.2 Turbulence Intensity Measurements

In Table 3 values of the peak gust over mean wind speed ratio have been calculated. There have been a number of formulae offered in the literature which relate turbulence intensity to the ratio of the maximum gust over mean wind speed, most of which effectively state the number of standard deviations above the mean one might expect the maximum value to occur on average for a given short averaging period. This relationship depends on the response time of the anemometer as well as the averaging period. Deaves and Harris in reviewing

TABLE 3

MAXIMUM MEAN AND GUST WIND SPEEDS MEASURED AT WAGLAN ISLAND DURING TROPICAL CYCLONES CAUSING PERSISTENT GALES AT HONG KONG, CORRECTED TO REFER TO FREESTREAM CONDITIONS 50 m ABOVE MEAN SEA LEVEL

	Uncorrected anemometer data				Corrected to reference to 50 m above MSL in freestream approach flow			
	Max mean hourly wind speed		Max. gust wind speed					
	Direct.	$\bar{V}_{ms}$-1	Direct.	$\hat{V}_{ms}$-1	$\bar{V}_{ms}$-1	$\hat{V}_{ms}$-1	$\hat{V}/\bar{V}$	$\sigma_v/\bar{V}$
1953 Sept 18	NNE	30.9	ENE	47.9	28.6	41.7	1.46	0.12
1954 Aug 29	ENE	25.7	ENE	48.4	24.0	42.1	1.75	0.20
Nov 6	E	31.4	E	48.4	27.3	45.7	1.67	0.18
1957 July 16	S	22.6	S	36.5	19.7	32.0	1.62	0.17
Sept 22	E	31.4	ENE	51.5	27.3	44.8	1.64	0.17
1960 June 9	SSW	30.9	SSW	54.1	26.9	49.2	1.83	0.22
1961 May 19	ESE	25.2	SW	35.5	22.9	33.8	1.48	0.13
Sept 10	W	22.1	W	33.5	19.1	30.7	1.61	0.16
1962 Sept 1	NW	41.2	NNW	60.2	37.1	57.3	1.54	0.15
1966 July 13	ENE	25.7	E	36.5	22.4	34.4	1.54	0.14
1967 Aug 21	ENE	22.6	ENE	31.9	19.7	27.7	1.41	0.11
Oct 18	E	24.2	E	32.4	21.6	30.6	1.42	0.11
Nov 7	E	20.6	E	26.8	18.7	25.3	1.35	0.10
1968 Aug 21	NNE	34.5	NE	58.2	31.5	54.4	1.73	0.20
Sept 3	ENE	20.1	ENE	25.7	17.5	22.4	1.20	0.08
1969 July 28	SW	27.8	SW	38.1	25.3	36.3	1.43	0.12
1970 July 16	S	31.9	SW	42.7	25.7	40.7	1.58	0.16
Aug 2	SW	20.6	SW	30.4	19.6	29.0	1.48	0.13
Sept 14	NW	20.6	NW	28.3	19.3	27.5	1.42	0.11
1971 June 18	SSE	26.8	E	35.5	22.9	33.5	1.46	0.13
July 22	SW	28.3	WSW	41.2	25.7	39.2	1.53	0.14
Aug 16	ESE	39.1	ESE	52.5	35.6	52.0	1.46	0.12
1973 July 17	E	30.4	E	44.3	26.4	41.8	1.58	0.16
1974 Oct 12	E	23.2	E	29.9	20.7	28.2	1.36	0.10
Oct 19	E	25.2	E	36.5	22.5	34.4	1.53	0.14
Oct 30	ENE	22.6	ENE	28.3	19.7	24.6	1.25	0.07
1975 Oct 14	NNE	32.9	ENE	48.9	30.2	45.7	1.51	0.14
Oct 23	ENE	21.6	ENE	35.5	18.9	30.9	1.63	0.17
1976 Aug 24	SE	20.6	S	32.4	18.7	29.2	1.56	0.15
Sept 19	ENE	27.3	ENE	36.0	22.8	31.3	1.37	0.10
1977 Sept 24	ENE	23.7	ENE	33.5	20.6	29.1	1.41	0.11
1978 July 26	E	31.9	E	39.1	27.2	36.9	1.36	0.10
Aug 27	ENE	27.3	ENE	35.5	22.8	30.9	1.36	0.10
Oct 1	E	20.6	E	25.7	18.7	24.3	1.30	0.08
Oct 16	E	23.7	E	28.8	21.4	27.2	1.27	0.07
1979 Aug 2	SW	40.2	SW	55.1	35.3	52.5	1.49	0.13
Sept 23	E	34.0	E	41.2	28.3	38.9	1.37	0.10
1980 July 22	ENE	22.6	E	35.0	20.2	31.8	1.57	0.15
July 27	SW	22.6	SW	29.3	20.6	27.9	1.35	0.10

available data recommended the use of the following expression for a Dines anemometer, from which the maximum gust wind speed is estimated to be the maximum for a 3 second averaging period in an hour.

$$\frac{\hat{V}}{\overline{V}} = \left(1 + 3.7 \frac{\sigma_v}{\overline{V}}\right)$$

given turbulence intensity as

$$\frac{\sigma_z}{\overline{V}} = \left(\frac{\hat{V}}{\overline{V}} - 1\right)/3.7 \qquad (7)$$

Turbulence intensity for each storm has been evaluated in Table 3 and is given in Figure 3 as a function of wind speed.

4 TROPICAL CYCLONE DATA COMPARED WITH WIND DATA OVER THE SEA

The turbulence intensity of the wind in tropical cyclones as measured at Waglan Island imply a range of wind structure characteristics when fitted to, or compared with, the Deaves and Harris strong wind model. It is not suggested that the Deaves and Harris strong wind model is necessarily appropriate for wind flow over the sea surface in a tropical cyclone, but it is a wind model based on classical log profiles and in which there are well defined relationships between roughness length, friction velocity, drag coefficient, mean and gust wind speed and turbulence intensity profiles, all of which can be related to a surface roughness condition as characterised in Table 1. On Figure 3 three terrain roughness conditions from Table 1 are shown as a function of the turbulence intensity at a height of 50 m.

Inspection of the parameters implied by the Deaves and Harris strong wind model in Figure 3 indicates that as the wind speed increases the characteristics in the wind flow over the sea in a tropical cyclone take on progressively the characteristics of flow over (a) a flat desert at the lower wind speeds, (b) the flow over grass plains, and (c) the flow over trees and suburban housing at the higher wind speeds. In terms of the physical heights of the surface roughness (waves) this progression is not altogether unexpected.

These characteristics can now be compared with currently accepted characteristics of wind flow over the sea as described in §2.2. Possibly the most convenient parameter for comparison is the surface drag coefficient and this comparison is given in Figure 4. At the lower wind speeds the wind flow over the sea in a tropical cyclone is as predicted by Equation 4 from the reviews of Garratt and Wu. However that is where the similarity ends, because at progressively higher wind speeds the wind flow over the sea in a tropical cyclone shows a progressively higher surface drag coefficient, and hence implied higher surface roughness, than is predicted for wind flow over the sea by Equation 4.

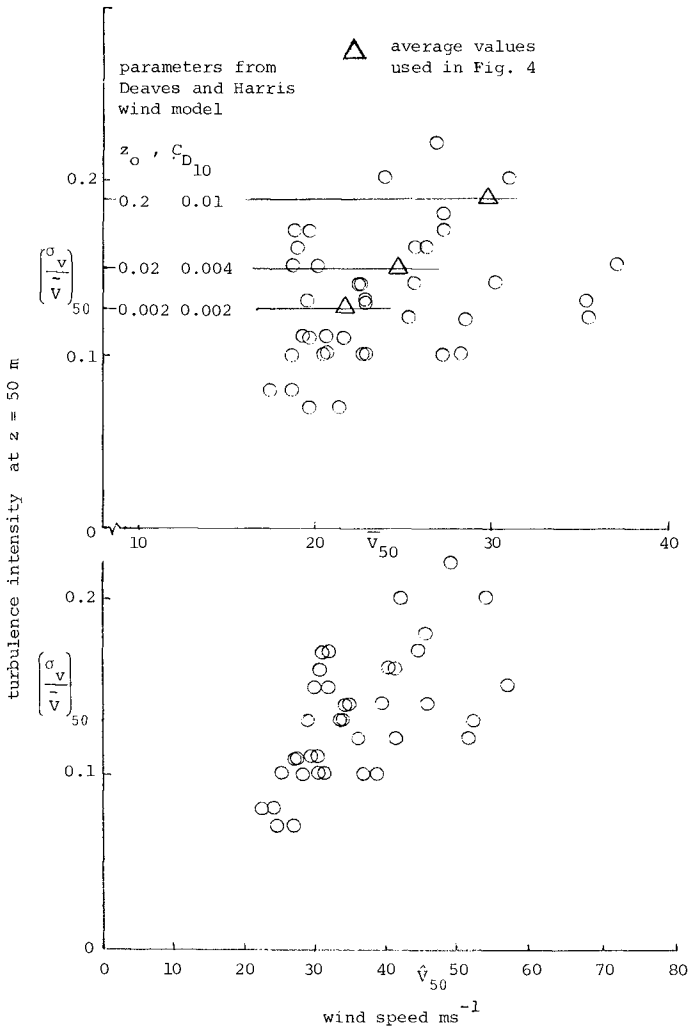

FIG. 3 Turbulence intensity at a height of 50 m above MSL from Waglan Island tropical cyclone data.

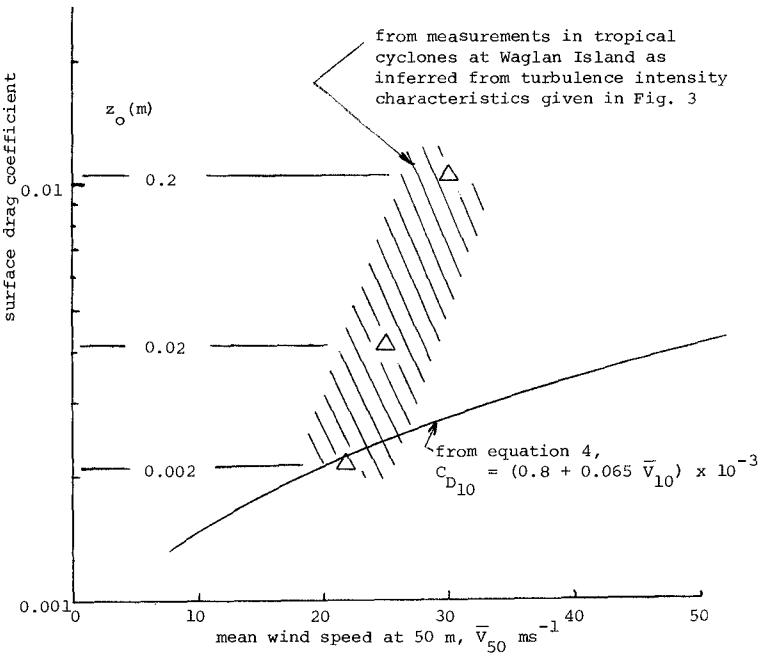

FIG. 4 Surface drag coefficients from Waglan Island tropical cyclone data and the reviews of Garratt (1977) and Wu (1980, 1983).

Further support for this observation is given by Choi (1978) who reported on the mean wind and turbulence characteristics of tropical cyclones in the lower 70 metres of the atmosphere. His work was based on anemometer measurements taken on a tower at Cape D'Aguilar, on a low lying headland stretching out from the southern tip of Hong Kong Island, close to Waglan Island, and with a similar exposure to the Pacific Ocean from where the typhoons approach. Choi fitted log law profiles to data from several tropical cyclones and the values of u_* and z_o are given in Table 4, along with typical values from a monsoon.

TABLE 4

PARAMETERS OF LOG-LINEAR PROFILE OF MEAN WIND SPEEDS IN TROPICAL CYCLONES, AFTER CHOI (1978)

Typhoon	$\bar{V}_{10}$ (ms^{-1})	u_* (ms^{-1})	z_o (m)
Freda	15.0	2.69	0.91
Freda	11.9	3.68	2.30
Rose	13.3	3.71	2.00
Rose	17.7	3.85	1.43
Rose	20.6	4.90	1.64
Dot	15.6	1.90	0.34
Dot	18.6	1.79	0.15
Dina	11.5	2.44	1.25
Monsoon	7.0	0.3	0.05

It can be seen, in comparison with monsoon winds, that u_* is an order of magnitude higher during tropical cyclones, even though wind speeds are only doubled. In the full scale situations the values of z_o reported cannot be taken too seriously because of the difficulty of establishing a zero plane for the site, however the values of u_* can be accurately estimated.

Obviously there are some aspects of the representation of the boundary layer over land and the boundary layer over the sea which do not apply in tropical cyclone or possibly other extreme wind conditions. Whether this is due to the convective conditions found in tropical cyclones, to the shorter wave length in the short fetch wave development, to a model which is simply not applicable to fully aroused sea states, or some other cause must await future investigation.

5 CONCLUSIONS

A study of wind data collected from the Waglan Island anemometer (Hong Kong) during 39 tropical cyclones indicates that turbulence intensity values in excess of 20% at a reference height of 50 m are likely during extreme wind conditions in a tropical cyclone. The implied surface drag coefficient of approximately 0.01 in these extreme wind conditions is consistent with flow over a land surface roughness of trees and suburban housing, but is much higher (by a factor of five) than that predicted by the currently accepted formulae from the reviews of Garratt and Wu for wind flow over a fully developed sea in neutral atmospheric conditions.

Whether these conditions of apparently greater effective surface roughness in tropical cyclones are due to convective conditions, the shorter wave length in the short fetch wave development or some deficiency in the wind model (when applied to wind flows in a tropical cyclone) is yet to be discovered. In the meantime it is concluded, for wind loading design calculations in extreme wind in tropical cyclone conditions, that the mean wind speed and turbulence intensity profiles should be taken as for a surface drag coefficient of 0.01, i.e. for a value of roughness length z_o = 0.20 m in the Deaves and Harris wind model.

6 REFERENCES

Charnock, J.R. (1955), Wind stress on a water surface. Quart. J. Roy. Met. Soc., Vol. 81, pp 639-640.

Choi, E.C. (1978), Characteristics of typhoons over the South China Sea. Jnl. of Indust. Aero., Vol. 3, pp 353-365.

Deacon, E.L. & Webb, E.K. (1962), Interchange of properties between sea and air. The Sea, Vol. 1, Interscience, pp 43-87.

Deaves, D.M. & Harris, R.I. (1978), A mathematical model of the structure of strong winds. CIRIA Report 76, England.

Garratt, J.R. (1977), Review of drag coefficients over oceans and continents. Mon. Wea. Rev., Vol. 105, pp 915-929.

Melbourne, W.H. (1980), Towards an engineering wind model. Monash University Course Notes on The Structural and Environmental Effects of Wind on Buildings and Structures, CH. 19.

Surry, D., Lythe, G., Horvath, G. & Davenport, A.G. (1981), A wind tunnel study of the influence of Waglan Island on readings from the Waglan Island anemometers. University of Western Ontario, Report BLWT-SS17-1981.

Wu, J. (1969), Wind stress and surface roughness at air-sea interface. J. Geophysc. Res., Vol. 74, pp 444-455.

Wu, J. (1980), Wind-stress coefficients over sea surface near neutral conditions - a revisit. Jnl Phys. Ocean, Vol. 10(5), pp 727-740.

Wu, J. (1983), Wind-stress coefficients over sea surface from breeze to hurricane. Private communication - to be published.

APPENDIX 1

Main equations from the Deaves and Harris (1978) Mathematical Model of the Structure of Strong Winds.

(1) Mean wind speed profile.

$$\bar{V}_z = \frac{u_*}{0.4}\left\{\ell n\left(\frac{z}{z_o}\right)+5.75\left(\frac{z}{z_g}\right)- 1.88\left(\frac{z}{z_g}\right)^2-1.33\left(\frac{z}{z_g}\right)^3+0.25\left(\frac{z}{z_g}\right)^4\right\} \quad \text{A1-1}$$

where z is height above ground level

z_o is the roughness length

u_* is the friction velocity, obtained from

$$\frac{V_g}{u_*} = \frac{1}{0.4}\left\{\ell n\frac{u_*}{z_o x 10^{-4}} + 1\right\} \quad \text{A1-2}$$

z_g is the gradient height, obtained from

$$z_g = \frac{u_*}{6x10^{-4}} \quad \text{A1-3}$$

V_z is the mean wind speed at height z (nominally hourly mean)

$\bar{V}_g$ is the mean gradient wind speed

(2) Turbulence intensity profile,

$$\frac{\sigma_{V_z}}{\bar{V}_z} = \frac{u_*}{\bar{V}_z}\, 2.63\eta\left\{0.538 + 0.09\ell n\left(\frac{z}{z_o}\right)\right\}^{\eta^{16}} \quad \text{A1-4}$$

where $\eta = 1-\left(\frac{z}{z_g}\right)$ A1-5

σ_{V_z} is the standard deviation of wind speed at height z

(3) Gust wind speed,

The 3 second maximum gust wind speed (which is defined as the maximum wind speed average over 3 seconds occurring in one hour) can, for a Dines anemometer, be expressed as

$$\hat{V} = \bar{V}\left\{1 + 3.7\left(\frac{\sigma_V}{\bar{V}}\right)\right\} \quad \text{A1-6}$$

A COMPUTER MODEL FOR THE REFRACTION OF NON-LINEAR WAVES

by

J B Crowley[1], C A Fleming[2] and C K Cooper[2]

ABSTRACT

A non-linear wave refraction model was developed which allows for the combined refraction and shoaling of Vocoidal waves over an arbitrary sea bed. The effects of bed friction and percolation are also catered for. The method is based on the cirular arc technique which is widely used for linear wave refraction. The method was extensively tested against Vocoidal wave refraction results obtained previously for a plane beach. A comparison of Vocoidal and linear wave refraction over an arbitrary sea bed indicated that Vocoidal waves refract less than linear theory, thereby yielding higher wave heights and angles of incidence at the breaker line. This result is in line with results of non-linear refraction over parallel bed contours quoted for other non-linear wave theories in literature. Further work is required before caustics can be adequately treated. Future research should include wave spectrum transfer and the re-evaluation of empirical relationships in use in the shallow water region and which will use this new higher-order refraction technique.

1. INTRODUCTION

The transformation of waves in shoaling water involves a change in wave height, length and velocity with depth. Wave refraction theory has been developed from solutions for light wave optics and its application is usually confined to the use of linear wave theory.

Wave ray methods are well suited to modelling of short waves. They solve the initial value problem so that there are few difficulties that can be encountered with boundary conditions as occurs with other methods. However, a number

---

1) National Research Institute for Oceanology, CSIR, Stellenbosch, RSA

2) Sir William Halcrow and Partners, Swindon, UK

of deficiencies have been identified. These are associated with the representation of topography, methods of computation and interprestation of wave refraction coefficients and the validity of using linear wave theory right up to the breaker line.

A number of theoretical investigations into wave refraction results with non-linear wave theories have been carried out. These have mostly been confined to the simplest cases of parallel contoured slopes, the only exception being a model developed in France for the refraction of third order Stokes waves over arbitrary contours (Gaillard, personal communication, 1982). Nevertheless, they have shown that the results obtained from non-linear theories can be significantly different to the linear counterparts.

One of the reasons in the past that non-linear wave refraction has not been rigorously persued for the case of arbitrary topography would seem to be the lack of non-linear wave theory that would allow wave speeds to be calculated with reasonable ease and economy. The Vocoidal wave theory combined with a circular arc solution provides an excellent basis for a fast and accurate numerical model.

2. MOTIVATION FOR USING VOCOIDAL THEORY

Depth refraction using first order cnoidal wave theory has been investigated for the simple case of straight parallel bottom contours (Skovgaard and Petersen, 1977). It was shown that the cnoidal wave would theoretically break at a greater water depth than linear waves due to greater amplification. Also the cnoidal wave orthogonal was found theoretically to refract less than the linear wave.

In fact it was concluded in all previous shoaling and refraction studies that linear wave theory progressively underpredicts both wave height and angle of incidence to a greater extent as the wave shoals towards the breaker line (see for example Sakai and Battjes (1980); Chaplin (1980); Skovgaard and Petersen (1977); Skovgaard et al. (1976); Dean (1973)). This is of fundamental importance to coastal engineers involved in nearshore modelling particularly in the surf zone where theory dictates a strong sensitivity to breaking wave conditions, particularly the angle of attack.

Figure 1 gives an example comparison between refraction for Vocoidal and linear wave theories over a plane beach with parallel contours. The same tendency as for the other well-known higher-order theories, such as Dean's stream function, cnoidal and Cokelet's theories is observed, with this exception that the wave height does not increase as sharply close to the breaker line as predicted by, for example, Cokelet.

Although the non-linear refraction results referred to above differ from those for linear wave refraction, it still remains to ascertain whether this difference is significant or not. Swart and Loubser (1979) made a comprehensive comparison of measured wave properties with predictions from 13 different theories. The results indicate that although linear theory provides an adequate description of wave profile, wave celerity and orbital motions in deep water, the comparison deteriorates as the relative water depth becomes less (see for example Figure 2). This is also apparent in the mean error in the prediction of wave length:

F_C range	Mean error in λ/d	
	Airy theory	Vocoidal theory
0 - 50	0,012	0,021
50 - 100	0,030	0,041
100 - 200	0,006	0,028
200 - 500	-0,041	0,010
500 - 1 000	-0,069	-0,018
1 000 - 60 000	-0,093	-0,017

Since refraction depends heavily on the wave celerity (or wave length) this result is significant for the application of linear theory in wave refraction where results are required near or at the breaker line.

Swart and Loubser (1979) finally concluded that Vocoidal theory is the only readily-applicable analytical wave theory with a good correspondence to measured data and a good adherence to the original wave boundary value problem in the whole range of non-breaking waves. This theory therefore not only provides a good correspondence to data but also a sound framework for the derivation of expressions for the prediction of secondary wave-induced phenomena, and as such also of refraction.

3. LINEAR WAVE REFRACTION

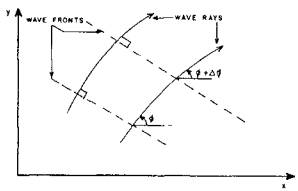

WAVE REFRACTION DIAGRAM

Wave refraction as a water-wave phenomenon has been realised for a long time. Early solutions used graphical techniques assisted with a template (Wiegel, 1963) and this still provides a useful means of obtaining a rapid overview for cases with simple topography. With the advent of the computer finite difference solutions were developed which used predictor-corrector techniques. A number of different schemes for representation of the bottom topography were proposed and included linear and quadratic surface fitting schemes. Topographic smoothing may also be recommended largely to reduce the number of caustics that may arise from small, but severe bottom irregularities. An interesting study was carried out by Poole (1975) who investigated a number of different interpolation functions for representation of sea bed topography. He found that for the cases tested there were broad similarities in the refraction patterns, but significant local variations occurred.

Abernethy and Gilbert (1975) investigated the anomalies than can arise when constructing conventional refraction diagrams, that is, a selected number of rays refracted from the offshore boundary towards the shoreline. They presented examples for which the method can result in large variations in refraction coefficients, depending on the density of rays used in the calculation. They concluded that there can be an inherent bias towards high wave heights, an excessive sensitivity to frequency, offshore direction and position which is greatest in region where refraction coefficients are large.

The curvature of a wave ray in still water expressed in cartesian coordinates is

$$\frac{d\theta}{ds} = -\frac{1}{c}\left(\frac{\partial c}{\partial x}\sin\theta - \frac{\partial c}{\partial y}\cos\theta\right) \qquad \ldots \quad (1)$$

where x and y are the coordinates, s the distance along the orthogonal and θ the angle between the orthogonal and the x-axis. This type of relationship or its equivalent can be solved most conveniently and accurately by using the 'circular arc' technique developed at the Hydraulics Research Station, Wallingford. Briefly the mehtod is based on the fact that, given linear variation of wave speed across a small triangular element, the ray path is described by a circular arc whose centre lies on the line of zero celerity and is tangential to corresponding arcs in adjacent elements. This provides a fast numerical solution which is not restricted to the use of linear wave theory.

The wave refraction coefficient reflects the change in wave height of a wave train purely due to convergence or divergence of the wave orthogonals. Over complex topography the ray separation factor may be evaluated from the

well-known expressions derived by Munk and Arthur (1952) whence:

$$\frac{d^2\beta}{ds^2} + p(s)\frac{d\beta}{ds} + q(s)\beta = 0 \quad \ldots (2)$$

where $$p(s) = -\frac{1}{c}\left(\frac{\partial c}{\partial x}\cos\theta + \frac{\partial c}{\partial y}\sin\theta\right) \quad \ldots (3)$$

$$q(s) = \frac{1}{c}\left(\frac{\partial^2 c}{\partial x^2}\sin^2\theta - \frac{\partial^2 c}{\partial x\,\partial y}\sin 2\theta + \frac{\partial^2 c}{\partial y^2}\cos^2\theta\right) \quad (4)$$

In the above β is the ray separation factor which is related to the wave refraction coefficient K_r by the square root of its inverse, that is,

$$K_r = \beta^{-0,5}.$$

Some of the deficiencies in forward tracking methods discussed above may be overcome by back tracking very closely spaced rays from a point of interest for a wide range of frequencies. This allows the computation of energy transfer from two-dimensional energy direction spectra and provides results that are usually consistent and stable. The two main disadvantages are that results can only be obtained for individual points of interest after quite a large computational effort and it is not possible to introduce wave decay due to bottom friction as the method relies on the independence of wave height in order to provide a complete family of results. The first problem may be overcome by applying statistical treatment to forward tracking results over discrete areas (Bouws and Battjes, 1982). The second requires the introduction of wave height into the calculation and is only really sensible for forward tracking methods (Skovgaard et al., 1976) until such time that bivariate distributions of wave height and frequency can be reasonably well-defined.

The following sections will show how the circular arc technique has been extensively extended to deal with wave refraction of non-linear waves using Vocoidal wave theory. It is shown that there can indeed be significant differences in comparative results, particularly when the sea bed topography is complex.

4. VOCOIDAL WAVE REFRACTION

The principle adopted was to use an existing refraction model using the circular arc technique and to adapt it in such a way as to cater for non-linear vocoidal waves. The specific model used is based on the Wallingford refraction program (Abernethy and Gilbert, 1975) and has the

capability of containing more than one grid up to a maximum of ten with a grid spacing that need not be the same for all grids. Each grid can contain up to 5 000 grid points. A more comprehensive review of the techniques used will be included in Swart and Crowley (1983b).

As stated previously, the application of the circular arc technique is not restricted to the linear wave theory, provided that wave celerities are available at the corner points of the grid element under consideration. This poses the first problem in the application of the circular arc method to predict refraction for higher-order waves, namely, **the celerity of higher-order waves is a function of the wave height, which is not known until after the wave refraction has been done.**

Furthermore, since the celerity is a function of wave height, which is determined in turn by refraction, shoaling, friction and percolation, it is not possible to separate the effects of these four processes as is customary for linear waves. In fact, the wave height change due to each of these processes in turn depends on the resultant of the others. A technique will therefore have to be found to solve for the wave height along the ray in an analogous way as was done for linear theory by using the ray separation equation (2) and which also includes the effect of percolation and bed friction.

This dependence of wave propagation on the wave height will make it difficult to deal with wave rays near caustics. Ways and means of overcoming this problem for the case of very irregular topographies should be investigated.

These three aspects will be discussed below. For the present only forward tracking is considered.

Wave celerity at grid points

Swart (1981) tabulated values of various wave properties in terms of H/d and $T\sqrt{g/d}$. From this tabulation one can observe the following typical variation in $c^2/(gd)$:

$T\sqrt{g/d}$	Values of $c^2/(gd)$					
	H/d=0,01	0,1	0,45	0,5	0,55	1,0
5	0,553	0,554	0,590	0,593	0,596	-
10	0,872	0,878	1,015	1,040	1,065	-
15	0,942	0,950	1,103	1,133	1,168	1,677
20	0,968	0,976	1,131	1,162	1,211	1,789
30	0,986	0,995	1,148	1,179	1,245	1,884
40	0,992	1,002	1,151	1,190	1,261	1,923

It is apparent that the value of c^2/gd is indeed strongly dependent on wave height.

An indication of the error introduced in $c/\sqrt{gd}$ as a result of using a wrong value of H/d, can be obtained by looking at the tabulated values for H/d = 0,45; 0,5 and 0,55.

$T\sqrt{g/d}$	5	10	15	20	30	40
[1] $E_{10\%}$ in %	0,25	1,20	1,43	1,71	2,04	2,30

$E_{10\%}$ is the error in $c/\sqrt{gd}$ for a 10 per cent deviation from the assumed mean value for H/d of 0,5.

It can thus be seen that the error in $c/\sqrt{gd}$ increases to about 20 per cent of the error in H/d for very high values of $T\sqrt{g/d}$. Since there is some correlation between the wave period and the wave height in the incident wave spectrum, one normally finds that the value of the parameter $T\sqrt{g/d}$ at wave breaking rarely exceeds 30. It can therefore be safely assumed that the error in $c/\sqrt{gd}$ will be restricted to 20 per cent of that in H/d.

On the other hand, if the celerities at H/d = 0,5 and 1,0 are compared with those at H/d = 0,01, it is found that the errors are appreciably more substantial.

$T\sqrt{g/d}$	5	10	15	20	30	40
[1] $E_{0,5}$ in %	3,43	8,43	8,88	8,73	8,55	8,70
[2] $H_{1,0}$ in %	-	-	25,05	26,44	27,66	28,18

1) $E_{0,5}$ is the relative difference in $c/\sqrt{gd}$ for H/d = 0,01 and 0,5, if the $c/\sqrt{gd}$ at H/d = 0,5 is assumed to be the correct value.

2) $E_{1,0}$ is the same as $E_{0,5}$ but with H/d = 1,0.

It is therefore quite clear that linear wave celerities, which are very close to those in Vocoidal theory for H/d = 0,01, should not be used for refraction of finite waves in shallow water.

The behaviour of Vocoidal wave celerity outlined above will form the basis of the discussion of a method for obtaining wave celerities at the corner points of grid elements.

Swart (1981) tabulated values of wave height H and angles of incidence θ for combined shoaling and refraction of Vocoidal waves on a plane beach with parallel depth contours, for deep water angles of incidence of 0°, 5°, 10°, 20°, 30°, 40°, 50° and 60°. The values of H/d and θ were tabulated for values of the ratio deepwater wave height H_o to water depth d between 0,01 and 1,30 and for values of the period parameter T_c ($= T\sqrt{g/d}$) between 1 and 60.

Results were obtained by simultaneously solving the energy flux equation, Snell's law and the Vocoidal wave length relationship.

The technique adopted for the computation of celerities at the corner points of the grid elements was based on these tabulated values of combined refraction and shoaling and consists of the following steps:

(i) It is assumed that the grid element is plane, that is, the contours across the element are parallel.

(ii) The entry conditions, that is, wave height, angle of incidence relative to grid element contours and water depth, at the point where the wave ray first enters the grid element, are used to refract the ray back to deepwater assuming contours parallel to those in the grid element. For this purpose the above-mentioned shoaling/refraction tables (Swart, 1981) were used to obtain curve-fitted equations for fictitious deepwater wave conditions, H_o and θ_o, which would have existed if the offshore bed topography had indeed consisted of a plane bed with contours parallel to those in the grid element under consideration.

(iii) These deepwater conditions are then used in the same curve-fitted equations to in turn obtain wave heights at the corner points of the grid element under consideration, again by assuming a plane bed seawards of the element. It should be emphasized that the wave heights computed in this manner do not form part of the output of the refraction computation, but are only used to obtain celerities at the corner points of the grid element which are in turn used as basis for the application of the circular arc method. A systematic comparison was made between values of wave height computed in this way and those obtained from the tables (Swart, 1981). It was concluded that the wave height is predicted to within acceptable limits. The extent of the difference between the tabulated (true) values of wave height and those computed in the manner described above depends on the variation in water depth over the grid element. Tests were done for

water depth variations of up to 100 per cent between the minimum and maximum depths in the element. Nevertheless, the difference in wave height was less than 10 per cent with a corresponding difference in predicted wave celerity which was always less than 2 per cent and mostly much less than 1 per cent. It will be shown later that this accuracy is sufficient to ensure an accuracy in the predicted wave heights and angles of incidence along the wave ray which are of the order of 0,1 per cent. The results also showed that the accuracy of predicted wave height can be significantly improved by reducing the grid size in the shallow water region, which can be easily done in the refraction program used.

(iv) The wave heights and celerities at the corner points of the grid element, computed in this manner, are then used to apply the circular arc method in exactly the same way as for linear wave theory.

(v) the accuracy of this procedure can be tested by comparing the angle of wave incidence along the wave ray for refraction over a plane beach against the tabulated results (Swart, 1981). An extensive comparison was made for a wide range of initial conditions and it was found that the true vocoidal angle of incidence at any relative water depth from deep water to the breaker line never differed from the computed angle by more than 0,01 degree. The method described is therefore considered to yield the correct result, even though the wave heights and celerities at the corner points of the grid elements did contain some inaccuracies.

Wave height along wave ray

The output of the circular arc method consists of the ray trajectory and thus also the ray orientation at the intersection points of the wave ray with the grid elements. The computations are continued until wave breaking occurs. The specific choice of the wave breaking criterion is left to the user of the program. Apart from the ray trajectory, however, wave heights are also required along the ray. In the linear wave theory the wave height along the ray is found by calculating the wave shoaling and refraction as well as the wave height reductions due to bed friction and percolation separately at each intersection point. The wave height H at that point is then simply the product of these four effects.

$$H = K_S K_r K_f K_p H_o \quad \text{(for linear theory)} \qquad \ldots \quad (5)$$

where K_s, K_r, K_f and K_p are coefficients of shoaling, refraction, friction and percolation relative to the starting point and H_o is the wave height at the starting point of the calculation.

This method does not hold for any higher-order theory, for the reasons given in the introduction to this section. Equation (2) which defines the ray separation factor β in linear wave theory, can however be used as the basis for the calculation of wave height by using the principle of energy flux conservation along the wave ray, namely,

$$\beta \, Enc = (Enc)_o \qquad \ldots (6)$$

where β is again the ray separation factor, E is the total wave energy per unit surface areas, c is the wave celerity and n is the ratio group velocity/wave celerity. Subscript "o" refers to the starting point of the wave ray. By putting $(Enc)_o = K_o$, where K_o is a parameter defined by the starting conditions, equation (6) can be rewritten as

$$\beta = K_o \zeta \qquad \ldots (7)$$

where $\zeta = (Enc)^{-1}$ $\qquad \ldots (8)$

Combination of equations (2) and (7) yields

$$K_o \frac{d^2\zeta}{ds^2} + p(s) \, K_o \frac{d\zeta}{ds} + q(s) \, K_o \, \zeta = 0$$

or

$$\frac{d^2\zeta}{ds^2} + p(s) \frac{d\zeta}{ds} + q(s) \, \zeta = 0 \qquad \ldots (9)$$

This equation can be solved numerically along the wave ray using Vocoidal wave properties in the same way as equation (2) was solved for linear wave theory. Values of wave height H along the ray are then found from equation (8) by using the Newton-Raphson iteration technique. This approach is necessary since E, n and c are all functions of wave height H (see Swart, 1978).

An extensive comparison was made between wave heights obtained in this way for refraction of a plane underwater topography and those tabulated by Swart (1981). In this comparison it was assumed that the effect of bed friction and percolation can be neglected. It was found that the difference between these two quantities was never more than 0,1 per cent of the "true" wave height, as interpolated from the tables. However, at least part of this already negligible difference can be attributed to rounding off

errors in interpolating from the tables. It is therefore considered that the method described herein for the computation of a total wave height along the wave ray yields reliable results of comparable accuracy to those obtained for linear wave refraction by using the ray separation technique.

Effect of dissipative forces

The effect of bed friction and percolation can be included in the technique described above by realising that the effect on wave height of these two phenomena can be assumed to be

$$H_{fp}/H_o = e^{-(\alpha_f+\alpha_p)t} \quad \ldots (10)$$

(Swart and Crowley, 1983a)

where H_{fp}/H_o is the additional wave height reduction due to bed friction and percolation, t is the time travelled by the wave and the parameters α_f and α_p are coefficients of friction and percolation respectively. These latter two parameters can be expressed in terms of vocoidal wave parameters. The effect of these two dissipative processes on the refraction is included by reducing the wave heights at the corner points of each grid element and the wave height along the ray trajectory in accordance with equation (10) before equation (8) is used with Newton-Raphson to solve for the wave height H. Since no test runs have as yet been done to test this part of the program, it will not be discussed further at the present.

5. DISCUSSION

The Vocoidal refraction program VOCREF developed along the lines outlined in Section 4 is at present being tested extensively for a number of prototype applications in parallel with a version of the program which used linear wave theory (LINREF). After completion of this sensitivity analysis and production testing it is intended to use this method (VOCREF) for routine analysis instead of LINREF. A number of interesting results have been obtained to date.

Since wave propagation is so strongly dependent on wave height in the case of non-linear waves and because of the fact that non-linear waves are not really defined for wave heights in excess of the cirtical breaker height, problems are encountered at or near caustics. Two ways of dealing with this problem have been investigated. By smoothing the bed in a linear manner in both directions along grid lines a sea bed topography is obtained which although smoother still exhibits the same overall tendencies as before smoothing. This process of two-way linear smoothing can be

repeatedly applied. With each application the contours are smoothed even more. Obviously there should be some optimal number of smooths beyond which the effect of the irregular topography becomes mushed. Kluger (CSIR, 1979) concluded that about eight smooths would be optimal in the case of very irregular topography for linear wave refraction although this would seem to be very high. See for example Figure 3 for the effect of three degrees of smoothing as compared to the unsmoothed case. Smoothing tends to reduce the number of caustics and allows for wave propagation across areas of possible caustic action. Figure 4 shows the results of refraction with various degrees of smoothing. The refraction diagrams are very similar except for the fact that a caustic at the right of the plot for the unsmoothed case is eliminated for three and eight smooths of the bed. The reason for the wave ray terminating at a caustic is that for higher-order theory it is not possible to calculate wave heights at the corner points of the grid elements in areas where the wave height would be higher than the critical breaker height.

At present the effect is being investigated of artificially putting the wave height equal to the critical breaker height in the vicinity of a caustic for as long as the wave height as obtained from the method given in Section 4 is higher than the critical height. In this manner the non-linear wave rays can be allowed to propagate through the region of the caustic.

It has proven useful to include in the standard output of the program a series of four plots containing the breaker line values of breaker depth, breaking wave height, angle of incidence at the breaker line relative to the local bed contours and the longshore energy flux factor $(0{,}5e_t H^2 nc \sin 2\theta$, where e_t is the total energy coefficient) (see Figure 5). Such plots clearly outline shore areas where caustic activity play a role. Overall tendencies in breaker line characteristics are also visible at a glance. At present the possibility is investigated of using the Monte Carlo technique as described by Bouws and Battjes to render the breaker line data even more useful. The effect of more smooths on the breaker line characteristics is to smooth out the variability and to enhance the clarity of the tendencies in these characteristics.

It appears that about three smooths of the contours would be optimal in defining all parameters sufficiently.

At a first glance the refraction diagrams produced by LINREF and VOCREF are very similar (see Figure 6). However, a comparison of breaker line characteristics shows up the differences remarkably (compare Figures 5 and 7; note that the scales in these figures are not all the same). In general the breaking wave height and the angle of incidence

relative to the local contours at the breaker line are higher for VOCREF than for LINREF. Correspondingly the longshore energy flux factor is also appreciably higher for the non-linear case. This has important consequences for sediment transport prediction and in fact for all design work in and near the breaker zone. The area affected by caustics is shifted laterally (alongshore) by going from linear to non-linear refraction, which is again of importance in interpreting refraction diagrams for design purposes.

Although comparisons between results of linear and vocoidal refraction over arbitrary contours is still in the early stages, it is already abundantly clear that it will be essential to preferentially use the non-linear refraction program VOCREF. However, it is quite clear that before the use of non-linear refraction programs such as the one described here can become standard practice a substantial re-evaluation of presently used empirical techniques will have to be carried out. While this is being done the present model should be extended to also include wave spectrum transfer. To allow this the problem of defining three-dimensional spectra or some relationship between the wave height distribution and frequency should be tackled.

6. SUMMARY AND CONCLUSIONS

The main conclusions of this study can be summarised as follows:

(i) A computer program was developed which allows for the computation of the combined shoaling and refraction of non-linear Vocoidal waves over an arbitrary sea-bed topography and which includes the dissipative effect of bed friction and percolation. The basis of the derivation is the circular arc method which is extensively used in linear wave refraction.

(ii) The computer program was verified by comparing its output for the case of combined refraction and shoaling over a plane bed with parallel bed contours with known results for this case.

(iii) Comparison of results obtained from the Vocoidal refraction model and its linear theory counterpart for the case of irregular topography indicates, in line with previous findings quoted in literature for non-linear wave refraction on a plane slope, that Vocoidal waves refract less than linear waves. Consequently the breaker-zone wave characteristics, that is, wave height and angle of incidence, are higher for Vocoidal than for linear refraction.

(iv) The influence area of caustics is shifted alongshore when Vocoidal refraction is done instead of linear refraction.

(v) Future reseach should be aimed first, at finding a workable solution for the problem of caustics (such as, for example, the Mote Carlo approach of Bouws and Battjes, 1982) and second, at the extension of the technique to include wave spectrum transfer.

(vi) In parallel to the research indicated under (v) all presently used empirical techniques for processes within the shallow-water area, such as longshore current prediction, should be re-evaluated to assess the effect of non-linearity of the waves on the values of the emprirical parameters.

7. REFERENCES

ABERNETHY, C L and GILBERT, G (1975). Refraction of wave spectra. Hydraulics Research Station, Report No 117.

BOUWS, E and BATTJES, J A (1982). A Monte Carlo approach to the computation of refraction of water waves. Journal of Geophysical Research, Vol 87, No C8, pp 5647-5662.

CHAPLIN, J R (1980). Developments of stream-function wave theory. Coastal Engineering, Vol 3, No 3.

CSIR (1979). Table Bay Harbour development Report No 4: Physical model calibration and wave refraction studies. National Research Institute for Oceanology, CSIR Report C/SEA 7926, Stellenbosch, RSA.

DEAN, R G (1974). Evaluation and development of water wave theories for engineering application. Special Report No 1, prepared for US Army Corps of Engineers, Coastal Engineering Research Center, Vol 1 and 2.

MUNK, W H and ARTHUR, R S (1952). Wave intensity along a refracted ray. US Natl Bur of Stds Circ 521: Gravity waves.

POOLE, L R (1975). Comparison of techniques for approximating topography in a wave refraction computer model. NASA Report No NASA TN D-8050.

SAKAI, T and BATTJES, J A (1980). Wave shoaling calculated from Cokelet's theory. Coastal Engineering, Vol 4, No 1.

SKOVGAARD, O, JONSSON, I G and BERTELSEN, J A (1976). Computation of wave heights due to refraction and friction. Proc ASCE, 101, WW1 (1975), 15-32, closure 102, WW1, 100-5.

SKOVGAARD, O and PETERSEN, M H (1977). Refraction of cnoidal waves. Coastal Engineering, 1, 43-61.

SWART, D H (1978). Vocoidal water wave theory, Volume I: Derivation. CSIR Research Report 357, 137 pp, CSIR, Stellenbosch.

SWART, D H (1981). Tables for the application of vocoidal water wave theory. CSIR Report T/SEA 8010, CSIR, Stellenbosch.

SWART, D H and LOUBSER, C C (1979). Vocoidal water wave theory, Volume II: Verification. CSIR Research Report 360, 130 pp, CSIR, Stellenbosch.

SWART, D H and CROWLEY, J B (1983a). Wave-generated water flow through a porous sea bed. Proceedings, First International Sandy Beaches Symposium, Port Elizabeth, South Africa, Published by JUNK.

SWART, D H and CROWLEY, J B (1983b). Vocoidal water wave theory: Refraction over arbitrary contours. CSIR Research Report, to be published, CSIR, Stellenbosch.

WIEGEL, R L (1963). Oceanographical Engineering. Prentice-Hill International Series in Theoretical and Applied Mechanics, Prentice-Hill Inc.

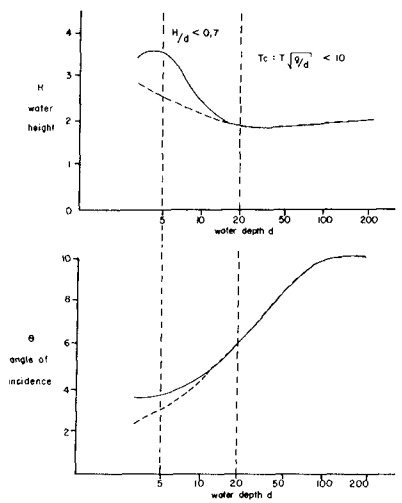

FIG. 1 REFRACTION OF VOCOIDAL AND LINEAR WAVES FOR PARALLEL CONTOURS $H_0 = 2m$; $\theta_0 = 10°$; $T = 14,35$

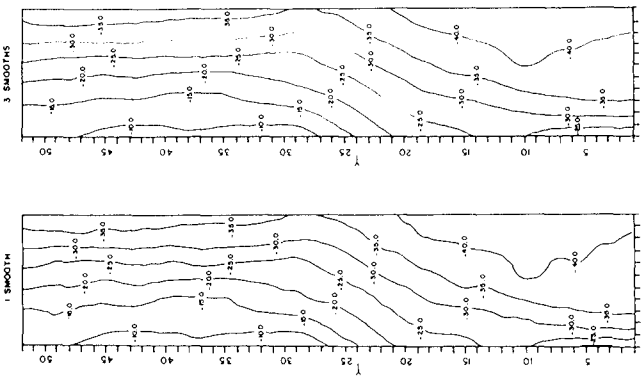

FIG. 3 RESULT OF VARIOUS DEGREES OF SMOOTHING ON SEABED CONTOURS

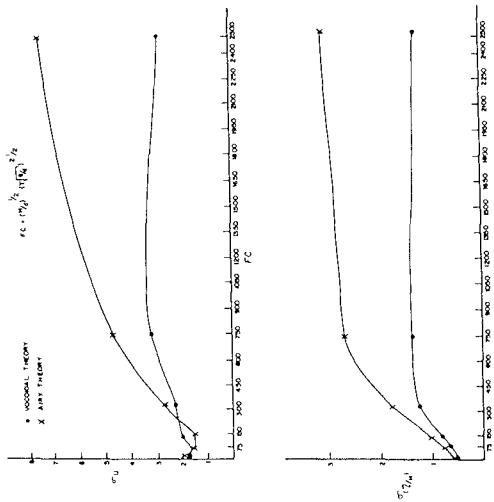

FIG. 2 STANDARD DEVIATION OF ERROR IN PREDICTION OF HORIZONTAL ORBITAL VELOCITY UNDER WAVE CREST (σ_u) AND WAVE PROFILE (σ_η)

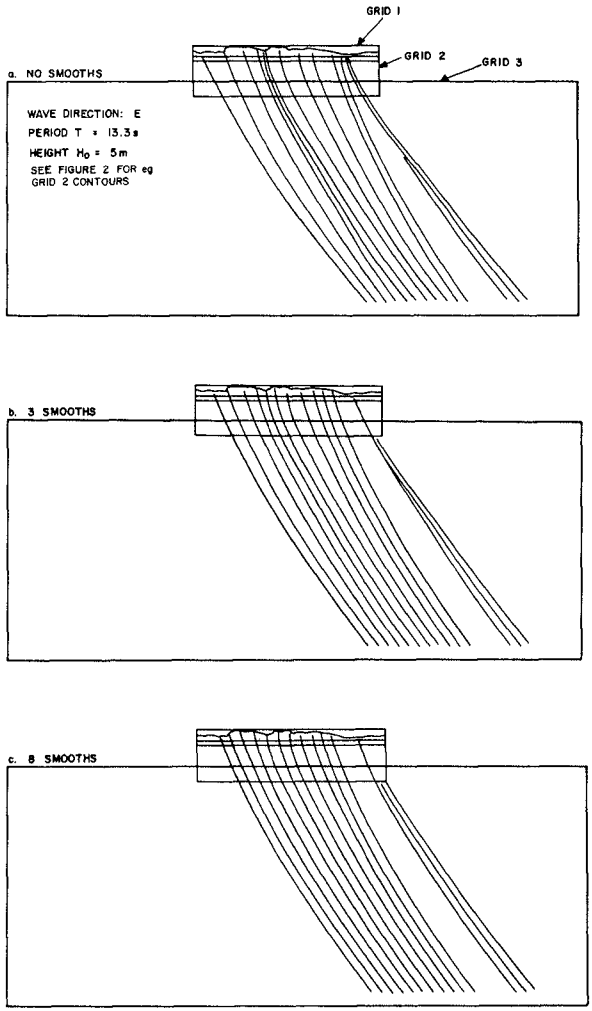

FIG. 4 RESULT OF VARIOUS DEGREES OF SMOOTHING ON REFRACTION PATTERN

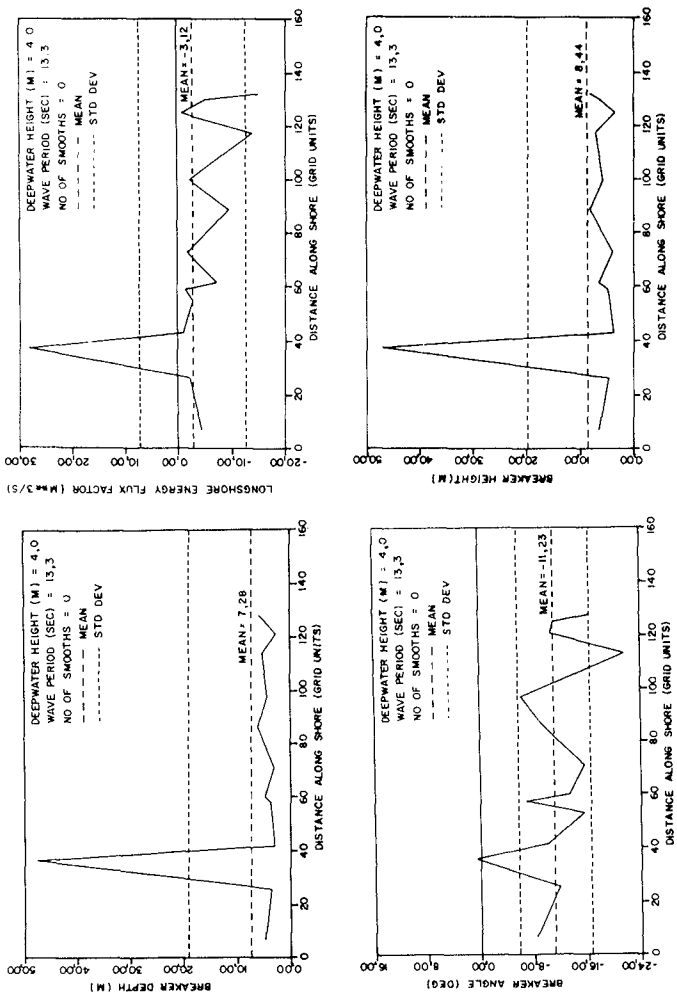

FIG.5 TYPICAL OUTPUT OF BREAKER ZONE CHARACTERISTICS FOR VOCOIDAL REFRACTION

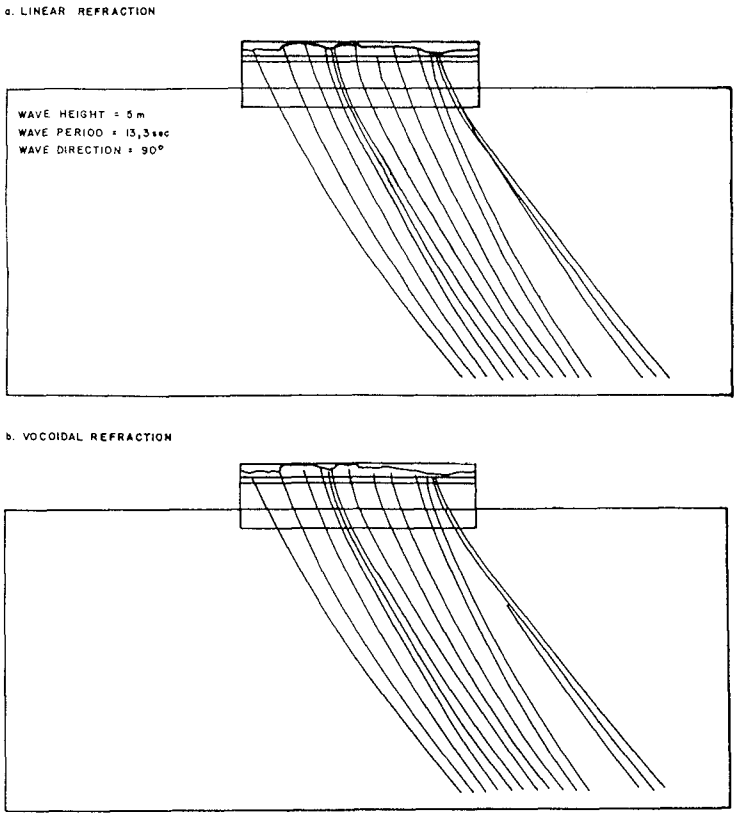

FIG. 6: COMPARISON BETWEEN REFRACTION DIAGRAMS WITH LINEAR AND VOCOIDAL THEORIES

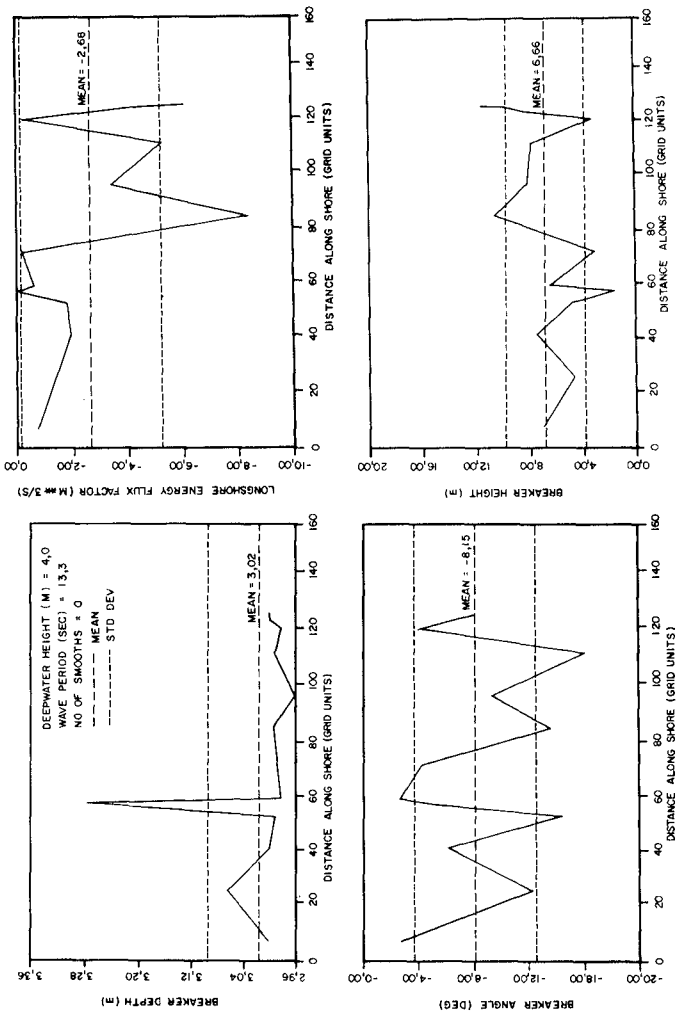

FIG. 7 TYPICAL OUTPUT OF BREAKER ZONE CHARACTERISTICS FOR LINEAR REFRACTION

WAVE AND CURRENT INTERACTION IN THE NEAR BED REGION.

Patrick H. Kemp and Richard R. Simons.

ABSTRACT.

The question of how waves and currents interact, especially in the near-bed region is of considerable importance in relation to sediment suspension and sediment transport. Whereas empirical relationships provide useful estimates and indications in relation to the data on which they are based, a more thorough understanding of the physical processes at work is necessary for interpreting sediment transport behaviour in a more generalized way. Clearly the conditions under which flow reversal occurs near the bed, and also the extent to which wave motion may modify the current induced turbulence in the boundary layer, are both of great interest, and these and other aspects have been included in the present study.

The research program was designed to look initially at the interaction between waves and currents in the absence of sediment, in order to define the mean velocity components, the structure of the turbulence, and the shear stresses. The study proceeded from experiments on waves alone, to waves propagating with the current and against the current. In all three cases the tests were carried out in the first instance with a smooth bed and subsequently with a rough bed consisting of two dimensional triangular slats. One of the main areas of interest was the height to which the water was disturbed above the bed when acted on by waves alone, and the comparable situation when a current was superimposed on the waves. Since the characteristics of the turbulent current were measured independently, it was possible to deduce whether there had been any interaction between the waves and the current, and also to infer what might happen to the distribution of the sediment which it was assumed would be put into suspension in the two cases. In the second stage of the research separate experiments were carried out in a standing wave channel and an oscillating water tunnel, using lightweight bed materials, in order to observe whether the inferences made from the clear water study were borne out by comparable changes in the distribution of the sediment in suspension.

Authors: Patrick H. Kemp, Reader in Fluid Mechanics, University College London, and Richard R. Simons, Research Engineer, University College London.

The results show that the sediment reflected the fluid motion characteristics, the sediment remaining in a band close to the bed under the action of waves alone, but rapidly dispersing when a turbulent current was introduced.

INTRODUCTION.

Comparatively little previous work has been carried out on the interaction between waves and currents, particularly near the bed. Grant & Madsen (1979) produced a theoretical analysis of combined wave and current flow over a rough boundary, predicting an increase in apparent bed roughness and shear stress when waves are superimposed on the current. A similar theory has been presented by Christoffersen (1980). Bakker & van Doorn (1978) also found an increased apparent bed roughness. George & Sleath (1979) described the cycle of vortex formation and ejection around spherical roughness elements in the presence of a weak current. The stronger downstream vortex was found to induce a weak reverse mean current just above the roughness elements.This is consistent with the observations of Inman & Bowen (1963) and Bijker, Hijum & Vellinger (1976), who both reported enhanced upstream sediment transport when a weak current was superimposed on waves. The present authors have carried out an extensive investigation on the subject of wave and current interaction, and a report of the main results may be found in Kemp & Simons (1982) and Kemp & Simons (1983). Since little information was available prior to these latter publications on the detailed flow structure under these condition, any inference between the flow characteristics and sediment in suspension has been tentative. Tunstall & Inman (1975) observed that in the case of waves alone, there was a limited thickness of the wave-induced vortex layer over a rippled bed, suggesting that sediment would be concentrated in this near bed layer. Bijker (1980), using first order wave theory and the assumption of a logarithmic profile, has formulated an expression for sediment concentration under waves and currents. The expression however contains a coefficient which is dependent on the wave motion and the bed roughness.

APPARATUS, INSTRUMENTATION AND ANALYSIS.

The investigation, and the apparatus used for the study of waves and currents in the absence of sediment, are described in the paper by Kemp & Simons (1982). This part of the work was carried out in a channel 14.5m long, 457mm wide and 690mm deep, with provision for flow in either direction and wave generation by a bottom-hinged paddle at one end. Two bed conditions were used in these tests. The first consisted of a smooth metal surface coated with gloss paint, and the second consisted of 5mm high triangular wooden strips stuck across the channel width and spaced at 18mm centres along the line of flow. The latter was chosen so as to generate a rough turbulent boundary layer both with the unidirectional current, and also with the larger waves in the absence of a current. It was also of similar geometrical form

to that used by Jonsson & Carlsen (1976) in their tests in an oscillating water tunnel. The height and spacing of the roughness elements also came within the range of possible ratios of height to length found in natural sand ripples. Fluid velocities were measured using a laser-Doppler anemometer, and the analysis of turbulent and wave-induced velocities was carried out by an on-line PDP8E minicomputer. The computer was programmed to produce ensemble average velocities, Reynolds stresses and wave elevation data. The cycle was sampled at 200 separate phase positions with up to 250 observations at each position. Measurements were made at up to 30 points in the vertical.

Measurements of wave attenuation and reflection were included in the program. In the case of waves opposing the current the current had to be introduced at the beach end of the channel. In order to avoid jetting and turbulence due to the presence of the beach, a wave absorbing device consisting of a slightly sloping metal plate submerged a short distance below the still water level, proved very effective. The device is referred to in Kemp & Simons (1983).

Observations of the behaviour of various lightweight sediments under the action of standing waves, and planar oscillatory motion, were carried out in a rocking channel which produced standing waves of comparable period to that in the water tunnel, which had a natural period of 2.3 seconds. The water tunnel could produce oscillations of different amplitudes, and in addition a current could be imposed in one direction, of variable strength. The materials investigated included various grades of pumice, anthracite, plumstone and polystyrene, with median diameters in the range 500 to 1000 micron, and fall velocities from 22mm/s to 52 mm/s. The polystyrene, however, was the one material which fell outside these ranges, with a median diameter distribution lying between 400 and 600 micron, and with a fall velocity in the region of 5 mm/s. These values were considered in relation to the r.m.s values of turbulence measured in the clear water tests, where for the case of the current alone the r.m.s. values in the lower half of the boundary layer lay between 13 mm/s and 15 mm/s, and for waves and currents combined the comparable figures were 18mm/s to 25 mm/s. As a result of these tests the polystyrene particles were used in the study of sediment concentrations under waves and currents in the water tunnel.

Measurements of sediment concentration were achieved by aiming a low-power laser through the water tunnel onto a photodetector whose voltage output, related to the blockage caused by the sediment, was recorded by the on-line computer. The photosensor was mounted in a blackened tube and protected by band-pass optical filters to minimise the effects of extraneous light. It was necessary to use neutral density filters to control the initial power of the laser beam to avoid the saturation of the photodetector when no particles were present.

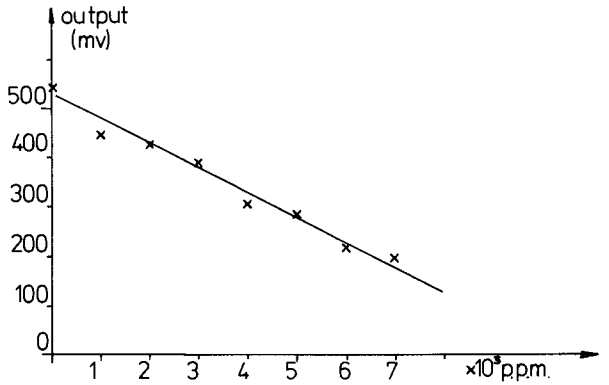

Fig. 1 Calibration curve for the laser sediment concentration meter using plumstone.

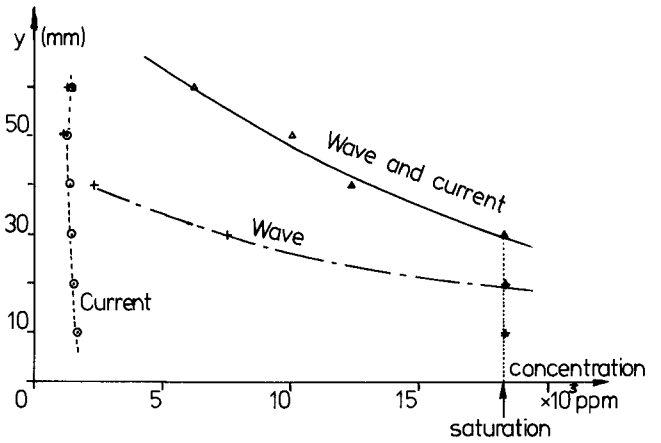

Fig. 2 Measurements of polystyrene concentration over a bed roughness apex, for combined wave and current, current alone and wave alone.

The system required calibration for the particular sediment in use, and this was done with the aid of a small perspex box of the same width as the water tunnel, placed between the laser and the photodetector. The box was filled with a mixture of glycerol and water, and a known volume of sediment added and shaken into suspension. The sediment was thus almost neutrally buoyant. For each concentration the box was oscillated across the beam, simulating the fluid motion anticipated in the tunnel, and the photodetector reading noted at regular intervals. The relationship between voltage and concentration was found to be closely linear for the plumstone (Figure 1), whereas for the polystyrene the curve was logarithmic. The glycerol mixture used maintained the sediment in suspension for long enough to give a reasonable sample length, while still allowing movement of the particles to produce an even distribution throughout the volume of the box.

RESULTS.

Waves and currents in the absence of sediment.

It was found that the unidirectional turbulent boundary layer is reduced in thickness by the superposition of waves propagating with the current over both rough and smooth beds. For all combined wave and current tests, flow reversal was experienced near the bed.

Waves propagating with the current over a rough boundary progressively reduce the mean velocities near the bed as the wave height is increased. For the smooth bed, however, waves with the current increase the velocity. Similar behaviour is experienced for waves on an opposing current.

In the outer flow the bed roughness effect becomes negligible. Here, for waves propagating with the current, mean velocities are reduced, whereas for the opposing current velocities are increased.

Figure 3 shows velocity profiles over a rough bed. The symbol WCR indicates waves and currents over a rough boundary. The mean centre-line velocity was 185mm/s. The wave heights in order were 22.7, 31.6, 40.4 and 46.6mm.

For the rough boundary tests the mean bed shear stress and roughness length scale were increased by the superposition of waves. Within two roughness heights of the rough bed the turbulence characteristics are dominated by the periodic formation of vortices. The overall increase in turbulence is limited to a region within six or seven roughness heights of the bed.

From these extensive initial tests and observations it was inferred that the combined stresses are likely to result in a considerable increase in sediment pick-up from a rippled bed.

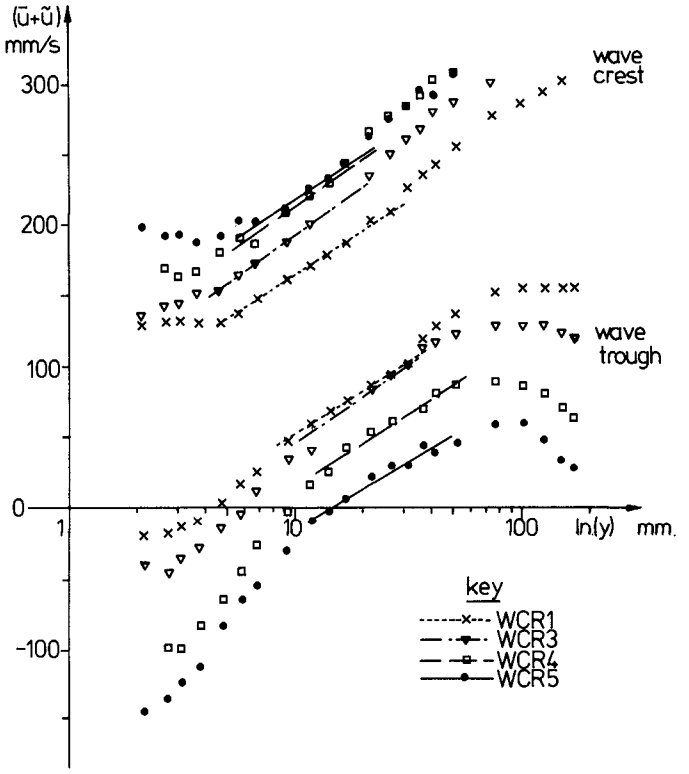

Fig. 3 Semi-logarithmic velocity profiles over a rough bed at phases corresponding to wave crest and wave trough; measured over the roughness apex.

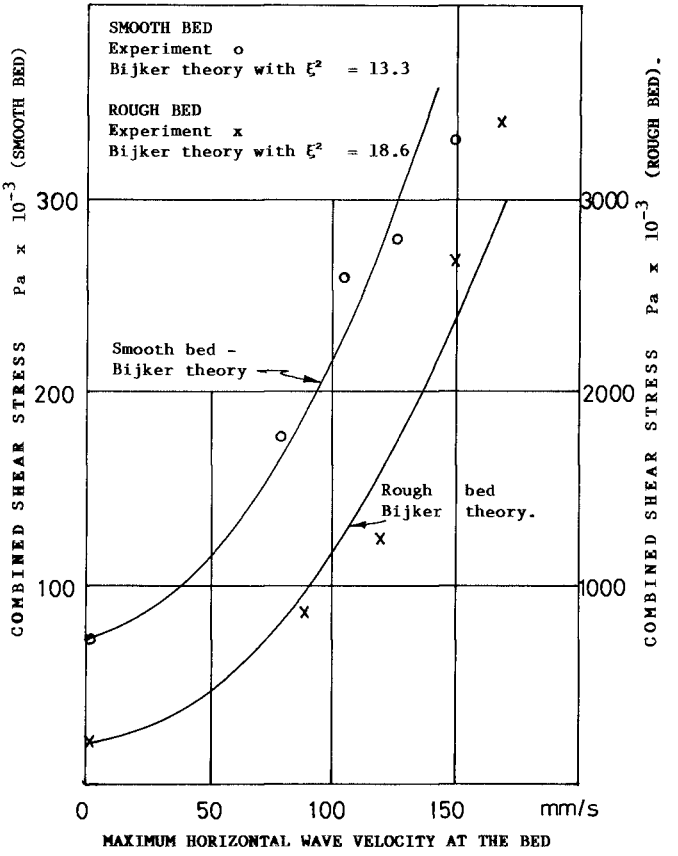

Fig. 4 Experimental values of combined wave & current shear stress, compared with the theory of Bijker (1980). See Appendix to this Paper.

Sediment response to the action of waves and currents.

Observations in both the standing wave rocking channel and in the small oscillating water tunnel showed that under the action of waves alone the sediment over the rough boundary, which consisted of triangular slats across the direction of motion, the sediment was put into suspension under the action of the vortices induced by the roughness elements. As predicted by the previous study in clear water reported above, the sediment layer was confined to a band only a few roughness heights in thickness. In the oscillating water tunnel the polystyrene particles under the action of the current alone produced only a very low concentration in the flow, and much of this consisted of the lighter particles which were maintained in suspension in the form of wash load. However, when this current was superimposed on the situation produced by the waves alone, the narrow band of vortex induced sediment in suspension rapidly expanded under the action of the turbulence. This is illustrated in Figure 2.

DISCUSSION AND CONCLUSIONS.

The main points arising from the clear water tests have already been set out under that heading above. However, from an experimental point of view and also in relation to the interpretation of the results and observations from other work in this area, the fact that the wave/current interaction reduces the boundary layer thickness both at the walls and the bed, means that the current is redistributed across the channel. All experiments of this nature should therefore take this into account.

So far as the sediment concentration is concerned when a current is superimposed on waves, it has been demonstrated that whereas the current alone might only produce slight movement of the bed particles, and the waves alone a dense concentration confined to a few roughness heights, the combination of the waves and currents produces a dramatic diffusion of the sediment layer.

Since the clear water tests provide data on shear stress under the action of waves and currents for both smooth and rough boundaries, it is of interest to substitute these in the expression proposed by Bijker (1980). This has been done in Figure 4 and the parameter ξ derived from these curves is shown on the diagram for the two cases.

REFERENCES.

Bakker, W.T. & van Doorn, Th. 1978 Near bottom velocities in waves with a current. 16th Conf. on Coastal Engng, Hamburg.

Bijker E.W. 1980 Sedimentation in channels & trenches. 17th Conf. Coastal Engng, Sydney.

Bijker E.W., Hijum,E.V. & Vellinger, P. 1976 Sand transport by waves. 15th Conf. Coastal Engng. Hawaii, vol 2 pp 1149-1167.

Christoffersen, J.B. 1980. A simple turbulence model for a three-dimensional current wave motion on a rough bed. Int. Rep No.1 Inst. Hydrodyn. Hydr. Engng. (ISVA), Tech Univ. Denmark.

George C.B. & Sleath J.F.A. 1979. Measurements of combined oscillatory and steady flow over a rough bed. J. Hydraul. Res. 17, 303-313

Grant W.D. & Madsen O.S. 1979. Combined wave and current interaction with a rough bottom. J.Geophys.Res. 84 pp 1797-1808.

Inman D.L. & Bowen A.J. 1963. Flume experiments on sand transport by waves and currents. 8th Conf. Coastal Engng. Mexico City. vol 2 ch.11, pp 137-150.

Jonsson I.G. & Carlsen N.A. 1976. Experimental and theoretical investigation in an oscillatory turbulent boundary layer. Jour. Hydraul.Res. 14, 45-60.

Kemp P.H. & Simons R.R. 1982. The interaction between waves and a turbulent current: waves propagating with the current. J. Fluid.Mech vol 116 pp 227-250.

Kemp P.H. & Simons R.R. 1983. The interaction between waves and a turbulent current: waves propagating against the current. J. Fluid. Mech. (In Press).

APPENDIX. Comparison of experimental values of combined wave and current shear stress with the theory of Bijker (1980)

According to Bijker : $V_{*cw} = V_{*c}\{ 1 + \tfrac{1}{2}(\xi\tilde{u}_o/\overline{V})^2 \}^{\frac{1}{2}}$

which can be written : $\tau_{cw} = \tau_c \{ 1 + \tfrac{1}{2}\xi^2\tilde{u}_o^2 /\overline{V}^2 \}$

The experimental results of Kemp & Simons in the present Paper have been used to evaluate the shear stresses as follows:-

SMOOTH BED: $\tau_{cw} = \{\nu.\frac{d}{dy}(\overline{u} + \tilde{u}_{max})\}_{bed}$

ROUGH BED : $\tau_{cw} = \{\rho(\widetilde{u'v'})_{max} + \tilde{u}_{max}\tilde{v}_{max}\}$

where τ_{cw} = wave + current shear stress; τ_c = current alone shear stress; ξ = wave and bed roughness factor; $\tilde{u}_o$ = max. orbital velocity at the bed; $\overline{V}$ = mean current velocity; ν = kinematic viscosity; $\overline{u}$ = local mean current velocity; $\tilde{u}_{max}$ = local orbital velocity; $\tilde{u}'$ and $\tilde{v}'$ = horizontal & vertical turbulent velocities.

EFFECT OF WAVE-CURRENT INTERACTION ON THE WAVE PARAMETER

Yu-Cheng Li[1] and John B. Herbich[2]

1. ABSTRACT

The interaction of a gravity wave with a steady uniform current is described in this paper. Numerical calculations of the wave length change by different non-linear wave theories show that errors in the results computed by the linear wave theory are less than 10 percent within the range of $0.15 \leq d/L_S \leq 0.40$, $0.01 \leq H_S/L_S \leq 0.07$ and $-0.15 \leq U/C_S \leq 0.30$. Numerical calculations of wave height change employing different wave theories show that errors in the results obtained by the linear wave theory in comparison with the non-linear theories are greater when the opposing relative current and wave steepness become larger. However, within range of the following currents such errors will not be significant. These results were verified by model tests. Nomograms for the modification of wave length and wave height by the linear wave theory and Stokes' third order theory are presented for a wide range of d/L_S, H_S/L_S and U/C. These nomograms provide the design engineer with a practical guide for estimating wave lengths and heights affected by currents.

2. INTROOUCTION

With increasing human activities in both the coastal and immediate offshore region, the problem of wave-current interaction has been evaluated by a number of researchers. From an engineering practice point of view, the effect of wave current interaction on the wave parameters must be known. Previous research involved different assumptions and considerations. Several researchers employed the linear wave theory combined with the idea of conservation of energy flux (5,12,13), or combined with the idea of conservation of wave action flux (8,9); others employed the non-linear wave theory (6,15). The problem concerning the interaction of waves and currents in an inlet has also been studied (3,7). Additional research (11,18) describes the change of velocity distribution due to the interaction of waves with currents.

One purpose of this study was to evaluate the difference between the change in wave parameters when employing either the equation of conservation of wave energy flux or the equation of conservation of wave

[1]Visiting Scholar, Ocean Engineering Program, Texas A&M University; Department of Hydraulic Engineering, Oalian Institute of Technology, Oalian, People's Republic of China, where the author is an Associate Professor.
[2]Professor and Head, Ocean Engineering Program, Texas A&M University, College Station, Texas 77843, U.S.A.

action flux. The results were evaluated with reference to practical engineering applications. Another purpose of this study was to determine the error in the calculated wave parameter by employing both the linear wave theory and non-linear wave theories (Stokes' third order wave theory was mainly considered). A two-dimensional case was considered and both the following and the opposing currents were analyzed.

3. THEORETICAL CONSIDERATIONS

Evaluation of change in the wave parameters may be obtained in two steps: a) evaluation of the change in wave length, and b) evaluation of the change in wave height. In both cases, the energy dissipation in wave propagation was neglected.

3.1 Change in Wave Length

The linear wave theory was considered first. The influence of non-linearity of waves is evaluated in the latter part of this section. The wave celerity in the current may be calculated as follows:

$$C_a = U + C_r \quad \ldots\ldots\ldots\ldots\ldots\ldots\ldots\ldots\ldots\ldots \quad (1)$$

where

$$C_r = \sqrt{g/k_r \, \mathrm{Th}\, k_r d} \quad \ldots\ldots\ldots\ldots\ldots\ldots\ldots\ldots\ldots\ldots \quad (2)$$

Equation 1 can be rewritten as

$$\frac{L}{T_a} = U + \frac{L}{T_r} \quad \ldots\ldots\ldots\ldots\ldots\ldots\ldots\ldots\ldots\ldots \quad (3)$$

From Equations 1, 2 and 3, the following equation can be obtained

$$\frac{L}{L_s} = \frac{C}{C_s} = \frac{1}{(1 - \frac{U}{C})^2} \frac{\mathrm{Th}\, k\, d}{\mathrm{Th}\, k_s d} \quad \ldots\ldots\ldots\ldots\ldots\ldots\ldots\ldots\ldots\ldots \quad (4)$$

and $L = L_a$, $C = C_a$.

In engineering applications, the value of $C = C_a$ is unknown, therefore, the ratio U/C is also unknown. Thus the following formula may be used

$$C_r/C_s = \sqrt{L/L_s \; \mathrm{Thkd}/\mathrm{Thk}_s d} = \frac{1}{1 - \frac{U}{C}} \frac{\mathrm{Thkd}}{\mathrm{Thk}_s d} \quad \ldots\ldots\ldots\ldots\ldots\ldots\ldots\ldots \quad (5)$$

Combining equations 6 and 7, the relationship between L/L_s with U/C_s and $k_s d$ can be obtained from

$$L/L_s = C/C_s = f(\frac{U}{C_s}, \frac{d}{L_s}) \quad \ldots\ldots\ldots\ldots\ldots\ldots\ldots\ldots\ldots\ldots \quad (6)$$

and

$$\frac{U}{C_s} = \frac{U}{C}\frac{C}{C_s}$$

3.2 Change of Wave Height

The process of the interaction of progressive waves with a steady uniform current (the following or the opposing current only) may be evaluated as follows: (a) in the first step only currents and waves propagate separately, (b) in the second step the combined current and waves interact and finally a steady motion of wave-current combination propagates as shown in Figure 1. If we neglect the change in the current profile because of the wave-current interaction, the current energy flux will remain the same before and after the interaction process.

To-date, two concepts, i.e. the conservation of wave energy flux (12,13) and the conservation of wave action flux (1,8) were employed. However, since there is no major difference between the two methods, the principle of conservation of wave action flux was selected for the analysis.

The idea of conservation of wave action flux was first suggested by Garrett and evaluated by Bretherton and Garrett (1). Jonsson (8) described a practical application for the case of interaction of waves with a steady uniform current. In the present case (as shown in Fig. 1) the following equation may be used

$$\frac{d}{dx}\left\{\frac{E}{\omega_r} C_{ga}\right\} = 0 \quad \ldots\ldots\ldots\ldots\ldots\ldots\ldots\ldots\ldots\ldots \quad (7)$$

Equation 7 indicates that the wave action flux before and after interaction must be the same, i.e.

$$\frac{E}{\omega_r} C_{ga} = \frac{E_s}{\omega_s} C_{gs} \quad \ldots\ldots\ldots\ldots\ldots\ldots\ldots\ldots\ldots\ldots \quad (8)$$

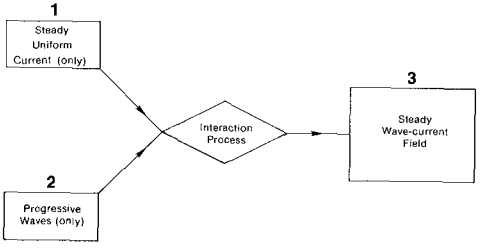

Fig. 1. Wave-current interaction

where

$$\omega_r = \omega_a - kU = \omega_s - kU \quad \ldots\ldots\ldots\ldots\ldots\ldots\ldots\ldots\ldots\ldots (9)$$

$$C_{gs} = \tfrac{1}{2} C_s A_s \quad \ldots\ldots\ldots\ldots\ldots\ldots\ldots\ldots\ldots\ldots (10)$$

$$C_{ga} = U + C_{gr} = U + \tfrac{1}{2} C_r A \quad \ldots\ldots\ldots\ldots\ldots\ldots\ldots\ldots (11)$$

$$C_{gr} = \tfrac{1}{2} C_r A \quad \ldots\ldots\ldots\ldots\ldots\ldots\ldots\ldots\ldots\ldots (12)$$

$$A = 1 + \frac{2kd}{\mathrm{Sh}2kd} \quad \ldots\ldots\ldots\ldots\ldots\ldots\ldots\ldots\ldots\ldots (13)$$

$$A = 1 + \frac{2k_s d}{\mathrm{Sh}2k_s d} \quad \ldots\ldots\ldots\ldots\ldots\ldots\ldots\ldots\ldots\ldots (14)$$

Thus Equation 8 can be rewritten as follows

$$\frac{E}{E_s} = \left(1 - \frac{U}{C}\right) \frac{L_s}{L} \frac{A_s}{A} \left(1 + \frac{U}{C} \frac{2-A}{A}\right)^{-1} \quad \ldots\ldots\ldots\ldots\ldots\ldots (15)$$

Accordingly, the wave height change can be determined by the following equations:

3.2.1 Linear wave theory

$$\frac{H}{H_s} = \left(1 - \frac{U}{C}\right)^{\frac{1}{2}} \left(\frac{L_s}{L}\right)^{\frac{1}{2}} \left(\frac{A_s}{A}\right)^{\frac{1}{2}} \left(1 + \frac{U}{C} \frac{2-A}{A}\right)^{-\frac{1}{2}} = R \quad \ldots\ldots\ldots\ldots (16)$$

When non-linear wave theory is employed, Equation 12 is no longer correct. Generally, the error in using this eouation instead of the correct one for non-linear waves will not be greater than 6 percent. Thus as a simplification for the non-linear wave analysis, Equations 12 and 15 may be used and will not produce a significant error. The results by Skjelbreia (14), Tsuchiya and Yasuda (17) were employed in calculating the wave energy.

3.2.2 Skjelbreia's Stokes' Third-Order Wave Theory (Old)

Wave energy E may be calculated by the following equation

$$E = \frac{\gamma H^2}{8} \left\{1 + \pi^2 \left(\frac{H}{L}\right)^2 \left[B + \frac{3}{(32)(256)} \pi^2 \left(\frac{H}{L}\right)^2 F\right]\right\} \quad \ldots\ldots\ldots\ldots (17)$$

where

$$B = \tfrac{1}{2} \left(\frac{1}{\mathrm{Th}\frac{2\pi d}{L}}\right)^2 \left(1 + \frac{3}{1+2\left(\mathrm{sh}\frac{2\pi d}{L}\right)^2}\right)^2 + \frac{9}{32} \frac{\mathrm{Ch}\frac{4\pi d}{L}}{\left(\mathrm{Sh}\frac{2\pi d}{L}\right)^6} \quad \ldots\ldots\ldots\ldots (18)$$

and

$$F = 3\left(\frac{1+8\left(Ch\frac{2\pi d}{L}\right)^6}{\left(Sh\frac{2\pi d}{L}\right)^6}\right) + \tfrac{1}{2}\frac{Th\frac{2\pi d}{L}\,Sh\frac{12\pi d}{L}\left(11-2Ch\frac{4\pi d}{L}\right)^2}{\left(Sh\frac{2\pi d}{L}\right)^{14}} \quad \ldots\ldots\ldots(19)$$

Accordingly, wave energy in still water, E_S, can be calculated similarly as

$$E_S = \frac{\gamma H_S^2}{8}\left\{1 + \pi^2\left(\frac{H_S}{L_S}\right)^2\left[B_S + \frac{3}{(32)(256)}\pi^2\left(\frac{H_S}{L_S}\right)^2 F_S\right]\right\} \quad \ldots\ldots\ldots(20)$$

where B_S and F_S may be obtained from a similar formula as B and F in Equations 18 and 19 (changing L to L_S only). The wave height change can then be calculated as follows

$$\frac{H}{H_S} = R\,\frac{\left\{1+\pi^2\left(\frac{H_S}{L_S}\right)^2\left[B_S + \frac{3}{(32)(256)}\pi^2\left(\frac{H_S}{L_S}\right)^2 F_S\right]\right\}^{\frac{1}{2}}}{\left\{1+\pi^2\left(\frac{H}{L}\right)^2\left[B + \frac{3}{(32)(256)}\pi^2\left(\frac{H}{L}\right)^2 F\right]\right\}^{\frac{1}{2}}} \quad \ldots\ldots\ldots(21)$$

where R is determined by Equation 16. This equation must be solved by iteration.

3.2.3 Tsuchiya's Stokes' Third-Order Wave Theory (New)

Energy flux, W, can be determined by the following equation

$$W = \frac{1}{8}\gamma H^2 C\left\{\tfrac{1}{2}A + \left(\frac{\pi H}{L}\right)^2 G\right\} \quad \ldots\ldots\ldots(22)$$

where A is defined by Equation 15, and G is

$$G = \frac{Ch^2 2kd + 3Ch2kd + 2}{16Sh^4 kd} + \frac{3}{4}Sh^2 kd + \frac{9(2kd + Sh2kd)}{64Sh^7 kdChkd}$$

$$+ \frac{3(Chkd + Ch3kd)}{8Sh^4 kdChkd} + \frac{kdThkd + Sh^2 kd}{2Sh^4 kd} \quad \ldots\ldots\ldots(23)$$

Since

$$W = \tfrac{1}{2}EC_r\left(1 + \frac{2kd}{1 + Sh^2 kd}\right) \quad \ldots\ldots\ldots(24)$$

Thus wave energy may be determined as follows

$$E = \frac{1}{8}\gamma H^2\left\{1 + 2\left(\frac{\pi H}{L}\right)^2\frac{G}{A}\right\} \quad \ldots\ldots\ldots(25)$$

and wave energy in still water E_S is

$$E_S = \frac{1}{8}\gamma H_S^2 \{1 + 2(\frac{\pi H_S}{L_S})^2 \frac{G_S}{A_S}\} \quad \ldots\ldots\ldots\ldots\ldots\ldots\ldots\ldots (26)$$

where G_S can be determined similarly as G from Equation 23, and the wave number k is changed to k_S in the case of still water. As a result, the wave height change can be calculated as follows

$$\frac{H}{H_S} = R \frac{\{1+2(\frac{\pi H_S}{L_S})^2 \frac{G_S}{A_S}\}^{\frac{1}{2}}}{\{1+2(\frac{\pi H}{L})^2 \frac{G}{A}\}^{\frac{1}{2}}} \quad \ldots\ldots\ldots\ldots\ldots\ldots\ldots\ldots (27)$$

where R is determined by Equation 16. Equation 28 must also be solved iteratively. When the non-linear wave theory is used, the wave celerity is determined not only by the parameter of kd, but also by the wave steepness H/L. Due to the interaction of wave and current, the wave steepness H/L can be changed, as the wave length determined by the non-linear wave theory L_N is not the same as that determined by the linear theory L, i.e., $L_N \neq L$. The value of L_N/L can be determined as follows

3.2.4 Employing Skjelbreia's Method

$$\text{Wave celerity } C_N = (\frac{g}{k}\text{Thkd})^{\frac{1}{2}} \{1 + (\frac{\pi H}{L})^2 \frac{14+4Ch^2 2kd}{16Sh^4 kd}\} \quad \ldots\ldots\ldots (28)$$

$$\text{and } L_N/L = 1 + \frac{1}{16}(\frac{\pi H}{L})^2 \frac{14+4Ch^2 2kd}{Sh^4 kd} = N_1 \quad \ldots\ldots\ldots\ldots (29)$$

where wave steepness H/L is the value under wave-current interaction.

$$\text{Thus, } L_N/L_S = \frac{L_N}{L} \cdot \frac{L}{L_S} = N_1 \frac{L}{L_S} \quad \ldots\ldots\ldots\ldots\ldots\ldots (30)$$

3.2.5 Employing Tsuchiya's Method

$$\text{Wave celerity } C_N = (\frac{g}{k}\text{Thkd})^{\frac{1}{2}} \{1 + \frac{1}{16}(\frac{\pi H}{L})^2 \frac{1}{Sh^4 kd}(8Ch^4 kd - 4Ch^2 kd + 5)\}$$

$$= (\frac{g}{k}\text{Thkd})^{\frac{1}{2}} N_2 \quad \ldots\ldots\ldots\ldots\ldots\ldots (31)$$

and

$$L_N/L = N_2 = \{1 + \frac{1}{16}(\frac{\pi H}{L})^2 \frac{1}{Sh^4 kd}(8Ch^4 kd - 4Ch^2 kd + 5)\} \quad \ldots\ldots\ldots (32)$$

Thus

$$L_N/L_S = \frac{L_N}{L} \cdot \frac{L}{L_S} = N_2 \frac{L}{L_S} \quad \ldots\ldots\ldots\ldots\ldots\ldots\ldots\ldots (33)$$

Coefficients N_1 and N_2 show the influence of non-linearity of waves.

4. DATA ANALYSIS AND RESULTS

4.1 The Results of Modification of Wave Length by the Linear Wave Theory Due to Wave-Current Interaction

Using Equations 4, 5 and 6 different combinations of dimensionless parameters U/C (or U/C_S), and d/L_S may be calculated. The results are shown in Figures 2 and 3. As shown in Figure 2, it is clear that the wave length change L/L_S with the relative current U/C is greater in deep water than in shallow water.

4.2 Modification of Wave Length by Non-Linear Wave Theory and Error Estimates Due to Linear Theory

Numerical calculations of the wave length were made employing Stokes' third order wave theory (14,17). The ratio of wave length computed by the non-linear wave theory with that computed by the linear wave theory is given in Table I. It can be seen that the wave length calculated by the non-linear wave theory is usually greater than that calculated by the linear theory. Within the range of $0.15 \leq 0.40$, $0.01 \leq H_S/L_S \leq 0.07$ and $-0.15 \leq U/C_S \leq 0.30$, the wave lengths computed by the linear wave theory are approximately 10 percent less than those computed by Stokes' third-order wave theory. Table II shows a comparison of the results obtained by the linear wave theory with data obtained by the non-linear wave theories and with model test data. It appears that the results obtained employing different methods are quite similar. Also a comparison of the wave length (obtained by the linear wave theory) with Hales' and Herbich's model tests data (2) are given in Table III; the agreement is considered quite good.

4.3 Modification of Wave Height

The results obtained with the linear wave theory (Equation 17) are shown in Figure 4.

The results given by Skjelbreia's Stokes' third-order wave theory for different wave steepnesses (i.e. $H_S/L_S = 0.01 \sim 0.07$) (Equation 26) are shown in Figures 5-8.

The results shown by Tsuchiya's modification of Stokes' third-order wave theory are presented in Figures 9-12 for wave steepness $H_S/L_S = 0.01 \sim 0.07$.

A comparison of the results employing the linear theory (Figure 4) with that of Skjelbreia's method (Figures 5 through 8) is shown in Table IV. The following observations were made:

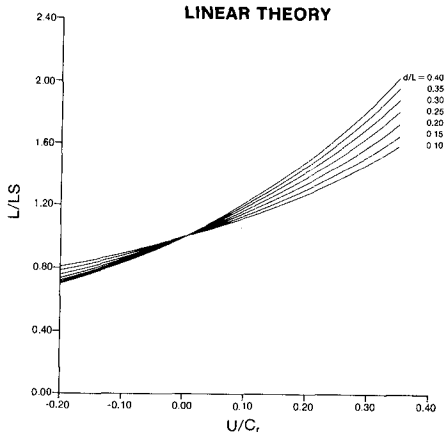

Fig. 2. Wave length change computed by linear wave theory (L/L_S versus U/C)

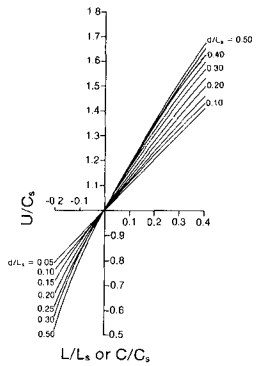

Fig. 3. The wave length change computed by linear wave theory (L/L_S versus U/C_S)

Table I. The Ratio of Wave Length L_N/L***

$\frac{d}{L_s}$	$\frac{H_s}{L_s}$	U/C_s = -0.15 (New*) Stokes III	-0.15 (Old**) Stokes III	-0.10 (New) St.III	-0.10 (Old) St.III	0.00 (New) St.III	0.00 (Old) St.III	0.10 (New) St.III	0.10 (Old) St.III	0.20 (New) St.III	0.20 (Old) St.III	0.30 (New) St.III	0.30 (Old) St.III
0.20	0.01	1.002	1.002	1.001	1.002	1.001	1.002	1.001	1.001	1.001	1.001	1.001	1.002
	0.03	1.010	1.019	1.008	1.016	1.008	1.014	1.007	1.013	1.008	1.013	1.010	1.017
	0.05	1.025	1.048	1.024	1.042	1.021	1.037	1.021	1.034	1.023	1.038	1.029	1.050
	0.06	1.034	1.064	1.032	1.057	1.031	1.054	1.031	1.049	1.035	1.056	1.044	1.077
	0.07	1.043	1.082	1.042	1.074	1.041	1.072	1.043	1.067	1.049	1.078	1.065	1.117
0.30	0.01	1.002	1.002	1.002	1.002	1.001	1.001	1.001	1.001	1.001	1.001	1.000	1.001
	0.03	1.007	1.018	1.006	1.014	1.005	1.010	1.004	1.007	1.004	1.006	1.004	1.006
	0.05	1.013	1.043	1.013	1.035	1.014	1.026	1.013	1.020	1.013	1.017	1.013	1.018
	0.06	1.017	1.058	1.018	1.047	1.020	1.037	1.020	1.028	1.020	1.025	1.021	1.026
	0.07	1.022	1.072	1.023	1.060	1.027	1.049	1.029	1.037	1.029	1.034	1.032	1.035
0.40	0.01	1.001	1.002	1.001	1.002	1.001	1.001	1.001	1.001	1.001	1.001	1.000	1.000
	0.03	1.004	1.018	1.004	1.014	1.005	1.009	1.004	1.006	1.004	1.005	1.004	1.004
	0.05	1.008	1.043	1.009	1.034	1.013	1.024	1.015	1.017	1.015	1.013	1.015	1.012
	0.06	1.010	1.057	1.013	1.045	1.018	1.034	1.023	1.024	1.018	1.019	1.025	1.017
	0.07	1.013	1.071	1.016	1.058	1.024	1.045	1.033	1.032	1.039	1.026	1.041	1.023

*Skjelbreia's result.
**Tsuchiya's result.
***L_N is the wave length calculated from nonlinear wave theory; L is the wave length obtained from linear wave theory.

Table II. A Comparison of Wave Length Computed Using Figure 2 With Test Oata and Computed Values From Non-Linear Wave Theories

d(m)	wave height H(m)	T (sec)	U (m/s)	$L_{exp.}$ (m)	d/L_s	U/C_s	$(L/L_s)_{cal}$	L_{cal}(m)	wave length error(%)$=\frac{L_{cal}-L_{exp}}{L_{exp}}\times 100$
0.587	0.021	1.25	-0.13	2.05	0.26	-0.067	0.88	1.98	-3.4
Note exp. by G.P. Thomas									
0.570	0.024	1.25	-0.20	1.82	0.26	-0.11	0.81	1.81	-0.5
Note exp. by G.P. Thomas									
30.5	15.2	10.0	+0.90	152.5	0.22	+0.07	1.10	151	-1.0
Cal. by Oalrymple									
10	2.5	12.0	+1.0	130	0.09	+0.11	1.09	126	-3.0
Cal. by T.S. Hedges*									

*T.S. Hedges used cnoidal wave theory.

Table III. A Comparison of the Wave Length Computed Using Figure 2 With the Model Test Oata of Hales and Herbich

d(m)	L_{mea}(m)	U(m/s)	d/L_s	U/C_s	$(L/L_s)_{cal}$ (from Fig. 2)	L_{cal}	wave length error (%) $= \frac{L_{cal}-L_{mea}}{L_{mea}} \times 100$
0.098	0.79	+0.277(flood	0.17	0.34	1.41	0.80	+1.2
	0.94	" current)	0.14	0.32	1.37	0.96	+2.0
	1.16	"	0.11	0.30	1.32	1.20	+3.4
	1.39	"	0.09	0.30	1.32	1.44	+3.6
	1.58	"	0.08	0.29	1.31	1.63	+3.2
	2.00	"	0.06	0.28	1.30	2.06	+3.0
	2.25	"	0.055	0.28	1.28	2.29	+1.8
0.098	0.69	+0.143(flood	0.17	0.17	1.21	0.69	0
	0.83	" current)	0.14	0.16	1.20	0.84	+1.2
	1.04	"	0.11	0.16	1.18	1.07	+2.9
	1.26	"	0.09	0.16	1.18	1.29	+2.3
	1.44	"	0.08	0.15	1.16	1.45	+0.7
	1.79	"	0.06	0.15	1.15	1.83	+2.2
	2.02	"	0.055	0.15	1.15	2.06	+2.0
0.098	0.50	-0.076(ebb	0.17	-0.09	0.88	0.50	0
	0.62	" current)	0.14	-0.09	0.88	0.62	0
	0.82	"	0.11	-0.08	0.91	0.82	-1.0
	1.00	"	0.09	-0.08	0.91	0.99	0
	1.14	"	0.08	-0.08	0.91	1.14	0
	1.49	"	0.06	-0.08	0.92	1.46	-2.0
	1.65	"	0.055	-0.08	0.92	1.65	0
0.098	0.42	-0.165(ebb	0.17	-0.20	0.70	0.40	-4.7
	0.53	" current)	0.14	-0.19	0.74	0.52	1.9
	0.71	"	0.11	-0.18	0.78	0.71	0
	0.88	"	0.09	-0.18	0.79	0.86	-2.3
	1.03	"	0.08	-0.17	0.80	0.99	-3.9
	1.32	"	0.06	-0.17	0.82	1.30	-1.4
	1.50	"	0.055	-0.17	0.82	1.47	-2.0

Table III. (continued)

d(m)	L_{mea}(m)	U(m/s)	d/L_s	U/C_s	$(L/L_s)_{cal}$ (from Fig. 2)	L_{cal}	wave length error (%) $= \frac{L_{cal}-L_{mea}}{L_{mea}} \times 100$
0.445	0.65	+0.265(flood	1.07	0.33	-	-	-
	1.22	" current)	0.47	0.22	1.39	1.31	+7.4
	1.72	"	0.32	0.19	1.29	1.77	+2.9
	2.41	"	0.22	0.16	1.20	2.46	+2.1
	3.04	"	0.17	0.15	1.18	3.06	+0.7
	4.07	"	0.12	0.14	1.16	4.15	+1.9
0.445	0.54	+0.134(flood	1.07	0.17	-	-	-
	1.10	" current)	0.47	0.11	1.20	1.13	+2.7
	1.57	"	0.32	0.09	1.14	1.56	-0.6
	2.23	"	0.22	0.08	1.11	2.26	+1.3
	2.84	"	0.17	0.08	1.09	2.83	-0.4
	3.81	"	0.12	0.07	1.08	3.86	+1.3
0.445	0.37	-0.055(ebb	1.07	-0.07	-	-	-
	0.92	" current)	0.47	-0.05	0.92	0.87	-5.4
	1.34	"	0.32	-0.04	0.94	1.29	-3.7
	1.95	"	0.22	-0.03	0.95	1.94	-0.5
	2.51	"	0.17	-0.03	0.97	2.51	0
	3.48	"	0.12	-0.03	0.97	3.47	-0.3
0.445	0.29	-0.168(ebb	1.07	-0.21	-	-	-
	0.76	" current)	0.47	-0.14	0.73	0.68	-10.5
	1.18	"	0.32	-0.12	0.80	1.09	-7.6
	1.80	"	0.22	-0.10	0.84	1.72	-4.4
	2.29	"	0.17	-0.09	9.88	2.29	0
	3.20	"	0.12	-0.09	0.89	3.18	-0.6

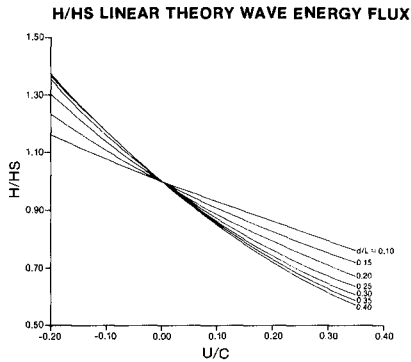

Fig. 4. The wave height change computed by linear wave theory

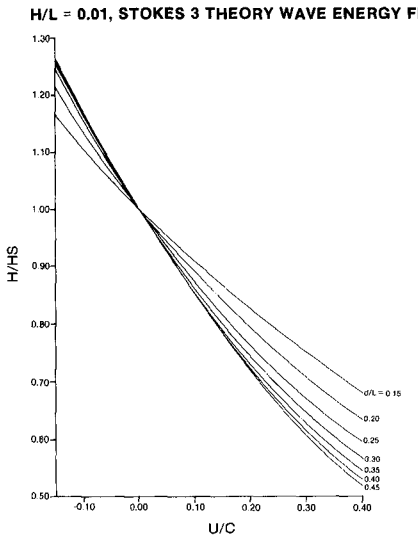

Fig. 5. The wave height change by Stokes (old) third-order wave theory for H_s/L_s=0.01

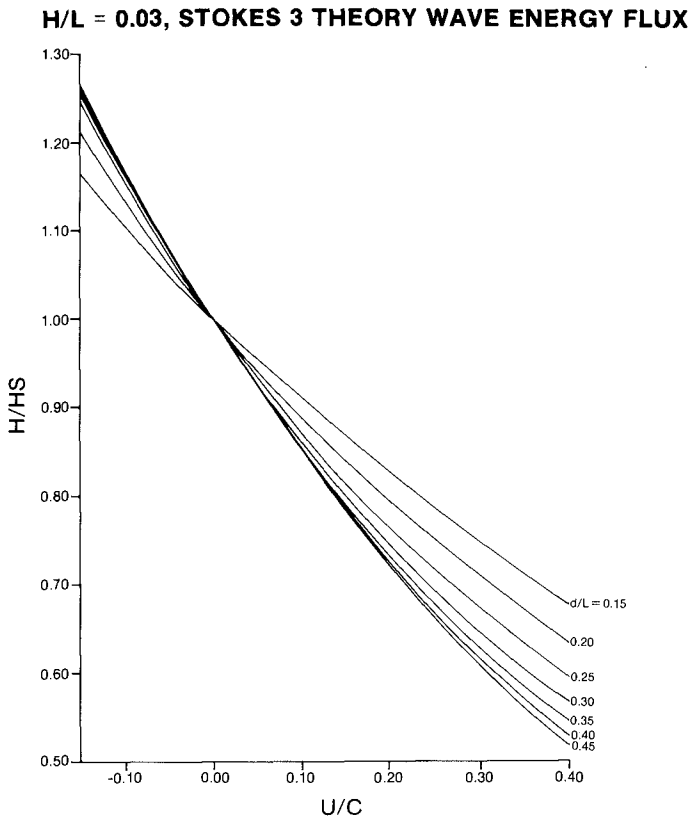

Fig. 6. The wave height change by Stokes (old) third-order wave theory for $H_s/L_s = 0.03$

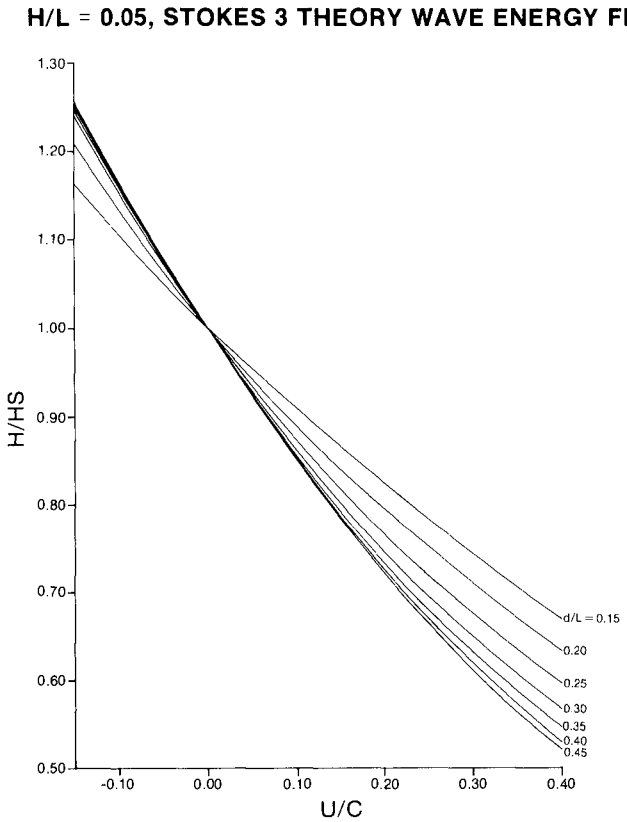

Fig. 7. The wave height change by Stokes (old) third-order wave theory for $H_s/L_s = 0.05$

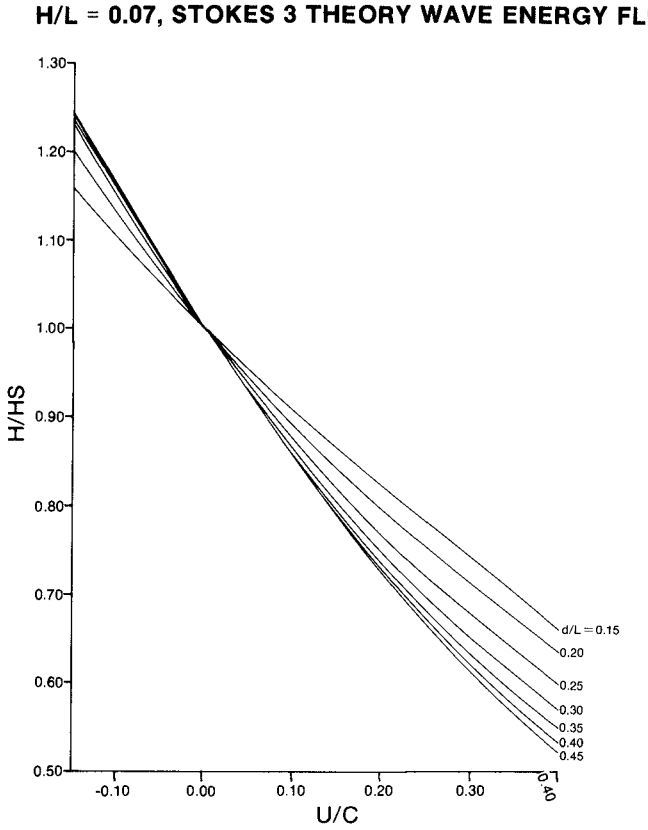

Fig. 8. The wave height change by Stokes (old) third order wave theory for H_s/L_s=0.07

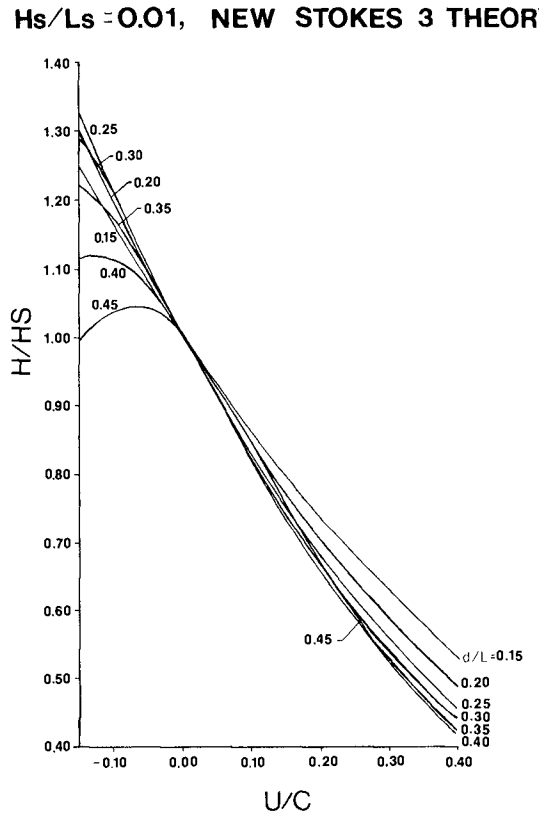

Fig. 9. The wave height change by Stokes (new) third-order wave theory for H_S/L_S=0.01

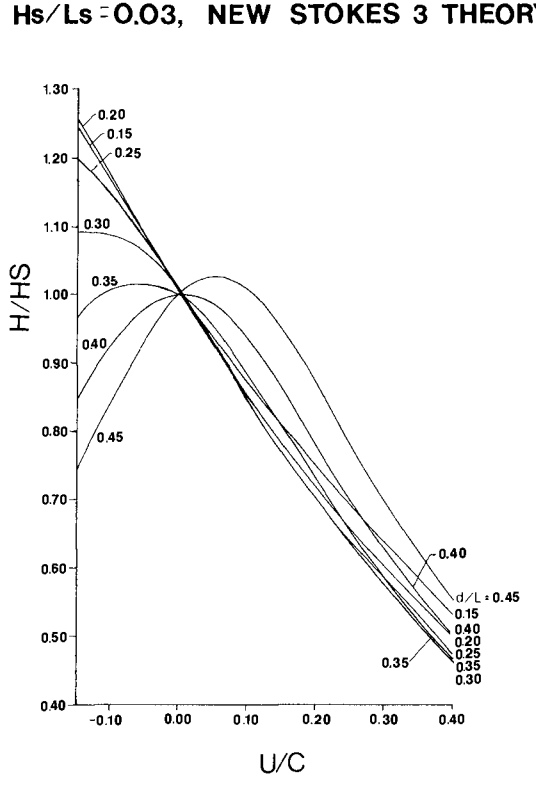

Fig. 10. The wave height change by Stokes (new) third order wave theory for H_s/L_s=0.03

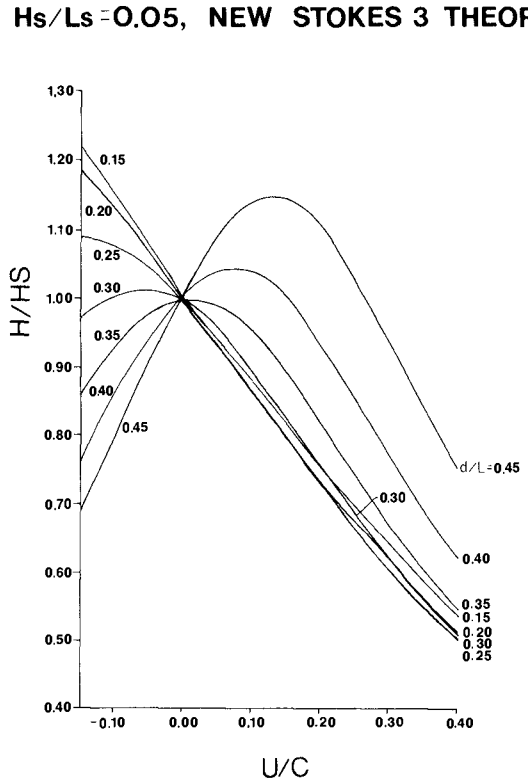

Fig. 11. The wave height change by Stokes (new) third order wave theory for H_s/L_s=0.05

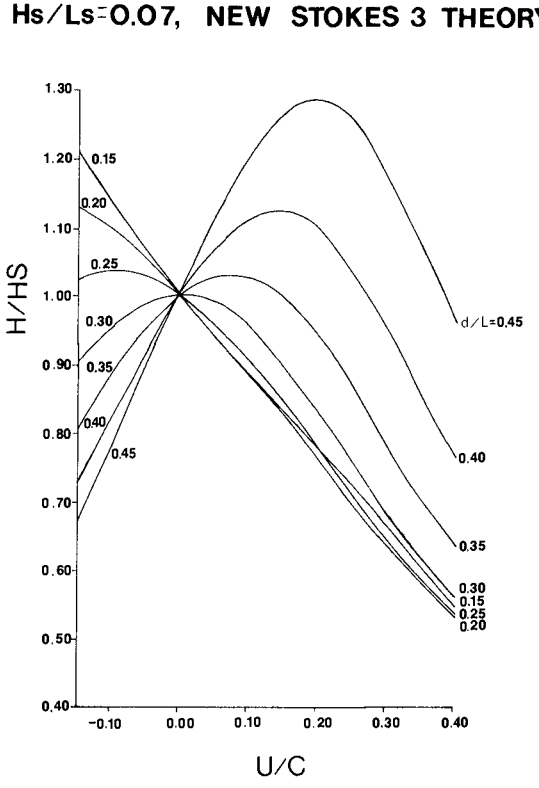

Fig. 12. The wave height change by Stokes (new) third order wave theory for H_s/L_s=0.07

Table IV. Wave Height Change H/H_s

$\frac{d}{L_s}$	$\frac{H_s}{L_s}$	U/C = -0.15		-0.10		0.00		0.10		0.20		0.30	
		Airy	(01d) Stokes 3	Airy	(01d) Stokes 3	Airy	(01d) Stokes 3	Airy	(01d) Stokes 3	Airy	(01d) Stokes 3	Airy	(01d) Stokes 3
0.20	0.01	1.305	1.300	1.193	1.190	1.000	1.000	0.841	0.841	0.708	0.708	0.593	0.593
	0.03		1.264		1.167		1.000		0.838		0.709		0.595
	0.05		1.210		1.129		1.000		0.834		0.709		0.597
	0.06		1.182		1.108		1.000		0.830		0.710		0.599
	0.07		1.154		1.086		1.000		0.827		0.710		0.601
0.30	0.01	1.359	1.353	1.228	1.224	1.000	1.000	0.815	0.815	0.664	0.664	0.541	0.541
	0.03		1.310		1.197		1.000		0.813		0.665		0.542
	0.05		1.245		1.154		1.000		0.810		0.666		0.545
	0.06		1.213		1.130		1.000		0.807		0.667		0.547
	0.07		1.182		1.106		1.000		0.805		0.669		0.550
0.40	0.01	1.357	1.351	1.229	1.225	1.000	1.000	0.806	0.806	0.646	0.646	0.515	0.515
	0.03		1.306		1.197		1.000		0.804		0.647		0.517
	0.05		1.240		1.153		1.000		0.802		0.649		0.520
	0.06		1.207		1.129		1.000		0.800		0.650		0.522
	0.07		1.174		1.104		1.000		0.798		0.652		0.524

(1) In the following current, errors in wave height change by the linear wave theory are minimal in comparison with the results obtained by the non-linear wave theories.

(2) When there is an opposing relative current and the wave steepness is sufficiently large, errors in wave height employing the linear theory will be greater than errors obtained employing the non-linear theories.

(3) When the relative current velocity U/C increases, the change of wave height by Tsuchiya's theory differs from the above results. Using his method, under deep water conditions the wave height change H/H_s increases with the increase of U/C and reaches a peak value, after which the value of H/H_s decreases with the increase of U/C.

4.4 Comparison of Numerical Solution Experimentally Obtained Results

Table V shows a comparison of the results of the wave height change by computation (Equation 21) with the experimental data. It can be seen that the computed values agree reasonably well with experimental data. The mean error is less than 8 percent.

Table V. Comparison of Calculated Values With Authors' Test Data

d/L_s	H_s/L_s	U/C	Experimental Data	H/H_s Calculated Value
0.093	0.048	0.083	0.97	0.89
0.093	0.048	0.161	0.87	0.85
0.054	0.012	0.075	0.87	0.91
0.092	0.030	0.151	0.86	0.85
0.067	0.017	0.157	0.90	0.80
0.244	0.075	0.078	0.89	0.84
0.244	0.075	0.177	0.64	0.71
0.250	0.043	0.080	0.73	0.84
0.134	0.013	0.069	0.88	0.88
0.141	0.035	0.070	0.92	0.88
0.271	0.073	0.136	0.77	0.71
0.094	0.019	0.122	0.88	0.81
0.183	0.021	0.148	0.85	0.73
0.159	0.063	0.145	0.70	0.81

Table VI shows a comparison of the results of the wave height change by numerical calculation (Equation 21) with the results of Hales' and Herbich's empirical formula (2). Their formulas are as follows:

Wave height change due to the following current:

$$\frac{H}{H_s} = 0.90760 - 0.98801 \frac{U}{C_s} + 0.21123 \left(\frac{U}{C_s}\right)^2 + 0.00164 \frac{L_s}{d} + 0.00006 \left(\frac{L_s}{d}\right)^2$$

$$+ 0.88017 \frac{H_s}{L_s} + 1.05971 \left(\frac{H_s}{L_s}\right)^2 - 0.00312 \frac{U}{C_s} \left(\frac{L_s}{d}\right) + 0.88371 \frac{U}{C_s} \left(\frac{H_s}{L_s}\right)$$

$$+ 0.24931 \frac{H_s}{L_s} \left(\frac{L_s}{d}\right) \quad \ldots\ldots\ldots\ldots\ldots\ldots\ldots\ldots\ldots\ldots (34)$$

Table VI. Comparison of Calculated Values With Hales' and Herbich's (H&H)

$\frac{d}{L_s}$	$\frac{H_s}{L_s}$	U/C_s = 0.10		0.20		0.30	
		H&H	Cal.	H&H	Cal.	H&H	Cal.
0.20	0.01	0.841	0.865	0.748	0.781	0.659	0.745
	0.03	0.886	0.862	0.795	0.780	0.689	0.743
	0.05	0.932	0.859	0.843	0.780	0.726	0.741
	0.07	0.979	0.853	0.891	0.779	0.764	0.737
0.30	0.01	0.834	0.848	0.742	0.765	0.653	0.736
	0.03	0.871	0.847	0.780	0.764	0.687	0.735
	0.05	0.929	0.844	0.820	0.763	0.724	0.732
	0.07	0.976	0.840	0.860	0.760	0.762	0.727
0.40	0.01	0.832	0.845	0.738	0.765	0.650	0.763
	0.03	0.865	0.843	0.773	0.764	0.686	0.734
	0.05	0.898	0.842	0.808	0.762	0.723	0.731
	0.07	0.933	0.838	0.844	0.759	0.761	0.727

Since Hales' and Herbich's model test data were discrete during the opposing current, a comparison of numerical calculations with their empirical equations was not made. From Table V it can be seen that the wave height change H/H_S decreases with the increase of relative depth d/L_S both by the theoretical method and by Hales' and Herbich's formula. It appears that the wave steepness variable has a greater influence in Hales' and Herbich's empirical formula than in the theoretical equation. On the average, the difference in the results given by these two methods is within a range of 5 to 7 percent.

5. CONCLUSIONS

1. There is no dominant difference in the results obtained for the change of wave length due to the wave-current interaction by using either the linear or the non-linear wave theories. Within the range of $0.15 \leq d/L_S \leq 0.40$, $0.01 \leq H_S/L_S \leq 0.07$ and $-0.15 \leq U/C_S \leq 0.30$, errors by the linear wave theory are less than 10 percent as compared with the results obtained employing the non-linear wave theories.

2. Numerical calculations of wave height change by different wave theories indicate that the errors resulting from the use of the linear wave theory in comparison with errors resulting from the non-linear theories are greater when the opposing relative current

and wave steepness both become larger. However, within the range of the following currents such errors will be minimal.

3. The important factors influencing the change of wave parameter are relative current velocity U/C (or U/C_s), relative water depth d/L_s and wave steepness H_s/L_s. The relative current velocity U/C is the most important parameter. In case of the wave-current interaction, not only the wave parameter is changed but also the velocity distribution of steady flow with depth is changed. In this paper the change of steady surface velocity due to wave-current interaction is neglected. This should be considered in further research.

4. For engineering purposes, the nomogram provided in this paper may be used to estimate the change of wave parameter due to wave-current interaction. Figure 3 and Figures 5 through 8 are recommended for the calculation of wave length and wave height changes, respectively.

APPENDIX I - REFERENCES

1. BRETHERTON, F.P. and GARRETT, C.J.R. (1969). Wavetrains in inhomogeneous moving media. Proc. Roy. Soc. A. 302, pp. 529-554.

2. CHRISTOFFERSEN, J.B. and JONSSON, I.G. (1980). A note on wave action conservation in a dissipative current wave motion. Applied Ocean Research.

3. DALRYMPLE, R.A. (1974). Models for nonlinear water waves in shear current. 6th Offshore Technology Conference, No. 2114.

4. HALES, L.Z. and HERBICH, J.B. (1974). Effects of a steady nonuniform current on the characteristics of surface gravity waves. Miscellaneous Paper H-74-11, Hydraulic Laboratory, U.S. Army Engineer Waterways Experiment Station.

5. HEDGES, T.S. (1979). Measurement and analysis of waves on currents. From "Mechanics of Wave-Induced Forces on Cylinders," editor: Shaw, T.L., Pitman Advanced Publishing Program, pp. 249-259.

6. HORIKAWA, K., MIZUGUCHI, M., KITAZAWA, O., and NAKAI, M. (1977). Hydrodynamic forces on a circular cylinder. Annual Report of the Engineering Research Institute, Faculty of Engineering, University of Tokyo, Vol. 36, pp. 37-48.

7. HUNT, N.J. (1955). Gravity waves in flowing water. Proceedings, Royal Society, London, A231, pp. 496-504.

8. ISMAIL, A.N. (1980). Wave-current interaction. Ph.D. Dissertation, Hydraulic Engineering Laboratory, College of Engineering, University of California, Berkeley.

9. JONSSON, I.G. (1979). Combinations of waves and currents. Institute of Hydrodynamics and Hydraulic Engineering, Technical University of Denmark.

10. JONSSON, I.G., SKOUGAARD, C., and WANG, J.D. (1970). Interaction between waves and currents. Proceedings, Twelfth Conference on Coastal Engineering.

11. LI, Y.C. (1981). A nomogram for the determination of wave length and wave celerity during the interaction of waves and currents. Technical Report No. COE-256, Ocean Engineering Program, Texas A&M University.

12. LIU, Y.B. (1965). The interaction of waves and currents: A study and experiment. Graduate thesis, Tienjin University (in Chinese).

13. LONGUET-HIGGINS, M.S. and STEWART, R.W. (1960). Changes in the form of short gravity waves on long waves and tidal currents. Journal, Fluid Mechanics, Vol. 8, Part 4, p. 565.

14. LONGUET-HIGGINS, M.S. and STEWART, R.W. (1964). Radiation stress in water waves: A physical discussion, with applications. Deep Sea Research, Vol. 11, p. 529.

15. SKJELBREIA, L. (1958). Gravity waves, Stokes third wave order. Council on Wave Research, The Engineering Foundation of the California Research Corporation.

16. SUN, C. (1959). Behavior of surface waves on a linearly-varying current. Moskov. Fiz-Tech. Inst. Issted. Meck. Priki. Mat., No. 3, pp. 66-84 (in Russian).

17. THOMAS, G.P. (1979). Wave-current interactions: an experimental and numerical study. From "Mechanics of Wave-Induced Forces on Cylinders," editor, Shaw, T.L., Pitman Advanced Publishing Program, pp. 260-271.

18. TSUCHIYA, Y. and YASUDA, T. (1981). A new approach to Stokes wave theory. Bulletin of the Disaster Prevention Research Institute, Kyoto University, Vol. 31, pp. 17-34.

19. VAN OFTEN, J.D.A. and KARAKI, S. (1976). Interaction of waves and a turbulent current. Proceedings, Fifteenth Conference on Coastal Engineering, Vol. 1, pp. 402-422.

APPENDIX II - NOTATION

The following symbols are used in this paper:

C = wave celerity;
Ch = hyperbolic cosine;
d = water depth;
E = wave energy;

H = wave height;
K = wave number;
L = wave length;
Sh = hyperbolic sine;
Th = hyperbolic tangent;
T = wave period;
U = surface current velocity;
ω = angular frequency.

Subscripts:

a = apparent value by the observer;
g = group velocity;
r = relative value of wave to current;
s = value in still water.

RESONANCE IN SOUTH AFRICAN HARBOURS

by

W A M Botes,* K S Russell* and P Huizinga*

1. INTRODUCTION

The geographic situation of Southern Africa, and the associated climate of the South Atlantic Ocean, cause the harbours on the west and south coasts of South Africa to be subjected to resonance or range action caused by long-period 50 s to 300 s waves.

Since the construction of Duncan Dock in Table Bay in 1940, Table Bay harbour has become a classical example of resonance. Range action in the harbour has been studied extensively in the past and extensive physical model studies were undertaken to optimise the layout of the Schoeman Dock, construction of which was completed in 1976.

In 1976 South African Railways and Harbours (now South African Transport Services) commissioned the Coastal Engineering and Hydraulics Division of the National Research Institute for Oceanology to optimise plans for future extensions to Table Bay harbour. As a preliminary study, the advantages and disadvantages of all existing methods of simulating resonance were reviewed. For this investigation it was decided to adapt an existing "finite-difference" numerical model developed by Leendertse (1967).

Prototype long-wave data were gathered in Table Bay and at a later stage at the cooling water intake basin of the Koeberg Nuclear Power Station. These data were used to calibrate the numerical model and an attempt was made to find a correlation between long waves and short wind waves in order to determine the frequency of occurrence of long waves.

A method was also developed to incorporate a range of frequencies in one model-run instead of single wave input conditions. This resulted in a considerable reduction of expense and time.

---

* Hydrodynamics Division of the National Research Institute for Oceanology, CSIR, Stellenbosch, Republic of South Africa

This resonance study method was used extensively in the Table Bay study and it has also been applied to investigations of alterations and proposed extensions on resonance in other South African harbours (ref. Section 5).

2. PROTOTYPE LONG-WAVE DATA ACQUISITION

2.1 Instruments

Pressure transducers housed in Teflon cannisters were used. The cannisters were attached to galvanized stands on the sea bottom or fixed to permanent harbour structures such as quay walls. Waterproof cables connected the transducers to the recorders which were installed in lockable containers accessible under all weather conditions. These instruments satisfied the following requirements:

(a) Record fluctuations of periods 30 s to 300 s at a sampling rate of 1,0 s.

(b) Automatic switch-on every 12 hours for a 50 min record.

(c) The recorders could be switched to a continuous mode during resonane conditions.

(d) The recorders were synchronised for the determination of the response beween different locations.

2.2 Sampling

It was necessary to obtain an entrance recording so as to be able to determine the response of the locations inside the harbour to that at the entrance. It was necessary that this recorder should be as far outside the harbour as practicable in order that a "clean" input record could be obtained without the influence of the harbour response and the reflections.

At both Table Bay and Koeberg harbour recorders were installed at the heads of the main breakwaters. In Table Bay six recorders were used inside the harbour and in Koeberg three recorders were used.

Records were obtained in Table Bay for a period of six months during 1978. Recording in Koeberg started in April 1981 and will continue until April 1983.

2.3 Analysis

Data analyses were done with the aid of Butterworth digital filters, computation of spectral densities by the auto-covariance method and the determination of responses with direct spectra-to-spectra relations and the cross-spectral

analysis method. Details of the analytical methods are described by Botes (1980).

A flow diagram of the data analysis exercise is schematized in Figure 2.

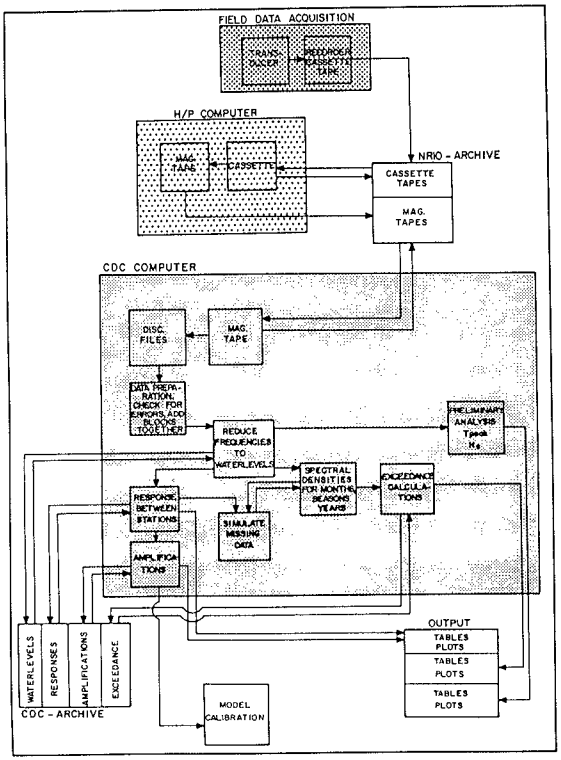

Figure 1 Flow diagram of the data analysis

2.2.1 Preliminary analysis

Raw data are expressed in frequencies and in blocks of 10 minutes each. These data are reduced to water-levels and five blocks joined together form 50 min data blocks. All data are filtered to obtain desired frequency bands and a preliminary spectral analysis is carried out for the qualification of the data and to obtain significant heights and peak periods.

2.2.2 Correlation with short waves

Until now long-wave data have been sampled for specific purposes such as for the calibration of a model. Occurrence figures for long waves in South Africa are virtually non-existent. This and a better knowledge of the origin and generation of long waves are becoming an urgent need.

A waverider is in operation ≈ 3 km from the entrance of Koeberg. An attempt was made to determine whether there is any correlation between increased short waves and long waves. The wave heights during a month were normalised by dividing the measured heights with the mean of the month for the short (1 to 30 s) and long waves (50 to 110 s). These waves were measured independently by means of a waverider and pressure transducer. The relationship between the short and long waves for April and September 1982 is illustrated in Figures 2 and 3.

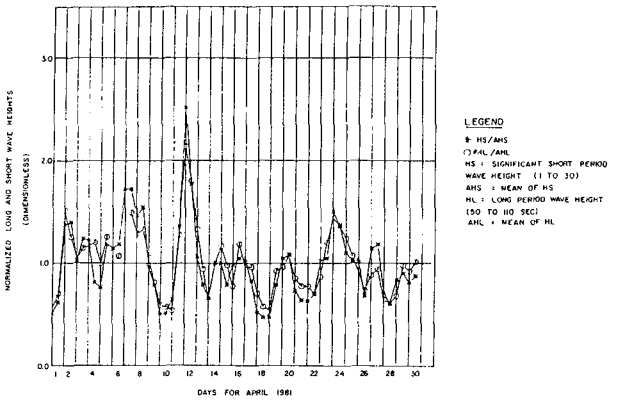

Figure 2 Normalised long and short period wave heights (April 1981)

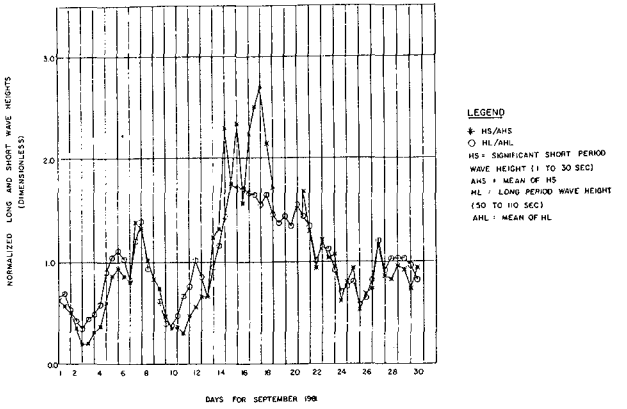

Figure 3 Normalised long and short period wave heights (September 1981)

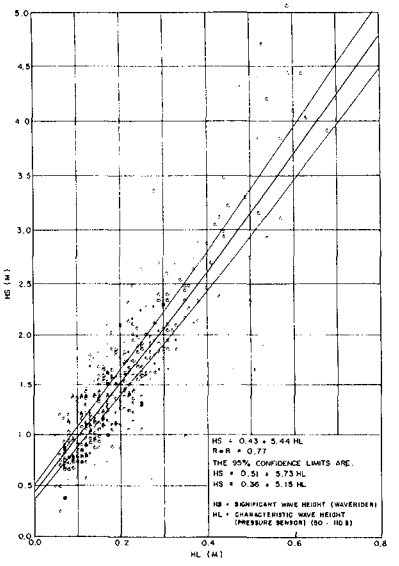

Figure 4 Correlation between long- and short-period wave heights

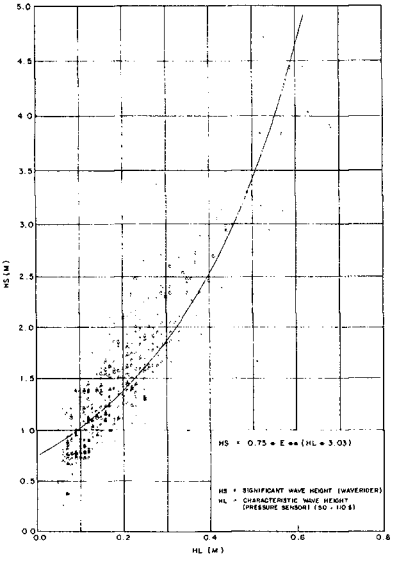

Figure 5 Correlation between long- and short-period wave heights

The height of short-period and long-period waves for 1981 were plotted and the following correlation was determined:

$$HS = 0,43 + 5,44\ HL \quad \text{(Figure 4)}$$
$$(R^2 = 0,77)$$

The 95% confidence limits are:

$$HS = 0,51 + 5,73\ HL$$
$$HS = 0,36 + 5,15\ HL$$

where HS = short period wave height (m) (1 to 30 s)
HL = long period wave height (m) (50 to 110 s).

An exponential fit is even more realistic as the long wave heights will not increase indefinitely (Figure 5).

$$HS = 0,75\ e^{3,03\ HL}$$

An attempt will now be made to find a correlation between the steepness of the short- and long-period waves.

The waverider data can then be used to determine a height and period occurrence of the long-period waves for several years.

2.2.3 Spectral density exceedance curves

In order to be able to obtain an idea of the magnitude of the wave spectra at Koeberg over a period, spectral density exceedance graphs were determined for all recording positions. From these figures it is also clear that each position in the harbour has its own characteristic spectrum as shown in Figures 6 and 7. Figure 8 indicates that the form of the spectra stay the same during calmer conditions.

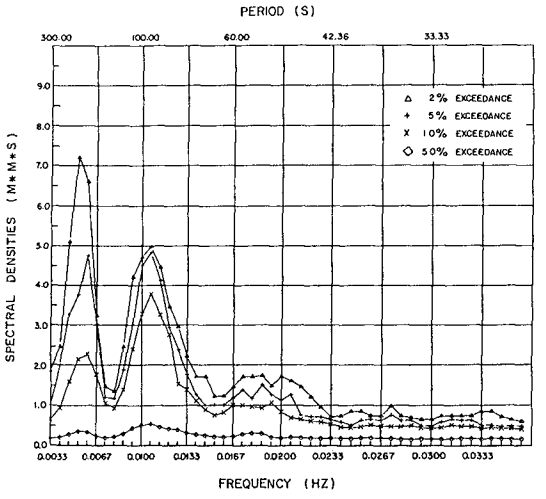

Figure 6 Spectral density exceedances for September 1981 at the entrance of the harbour

2.2.4 Response

The response between two stations is determined by means of a direct spectrum-to-spectrum relation or by means of a cross-spectral analysis technique. Examples of responses between different locations for Koeberg are illustrated in Figures 9 and 10.

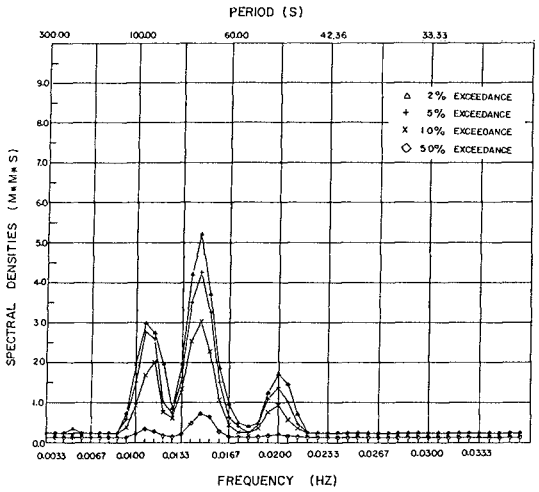

Figure 7 Spectral density exceedances for September 1981 inside the harbour

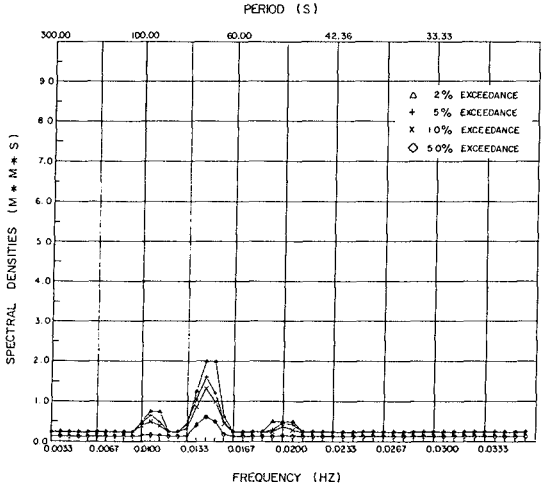

Figure 8 Spectral density exceedances for October 1981 inside the harbour

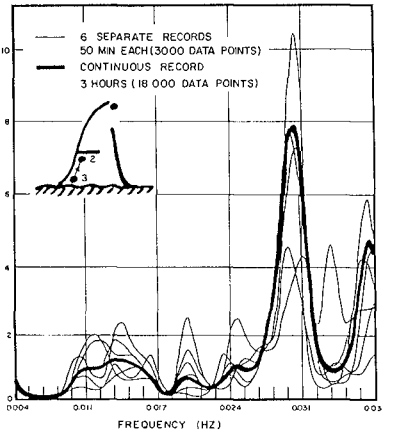

Figure 9 Response between positions 2 and 3

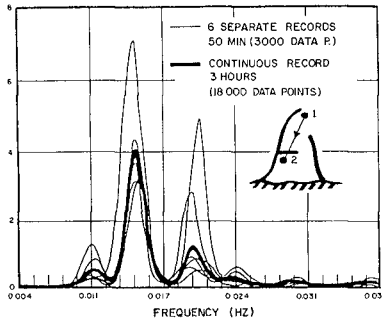

Figure 10 Response between positions 1 and 2

3. NUMERICAL MODEL

3.1 Description

The computations are based on the approximation of the hydrodynamic equations (conservation of mass and momentum

equations in terms of the water elevation and the depth average velocity) by using finite-difference techniques. The finite-difference model, originally developed by Leendertse (1967) was adapted to accommodate any harbour layout (Russell and Huizinga, 1978). The modifications include radiative open boundaries which can be applied to any of the model boundaries and permit the passage of reflected waves.

The model area is represented by a two-dimensional grid system; at each grid point the depth and bottom roughness are described and the water velocities and water levels are calculated.

3.2 Input Conditions and Calibration

An input open boundary is installed as the boundary of the model orientated to the dominant wave direction. Originally only single-period sine waves were used as input conditions. During the analysis of data sampled at Table Bay harbour it was found that the average spectrum at the entrance of the harbour was almost flat which could be simulated by the bandpass-filterng of a white noise spectrum as illustrated in Figure 11.

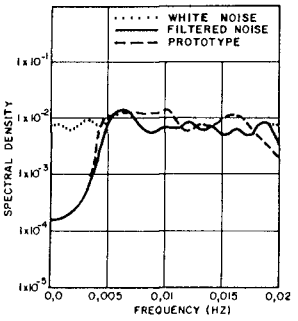

Figure 11 Simulated input spectrum for Table Bay Harbour

With the random noise as input condition, model spectra and model responses between the entrance position and other locations were obtained which were similar to those for the prototype (Figures 12 and 13).

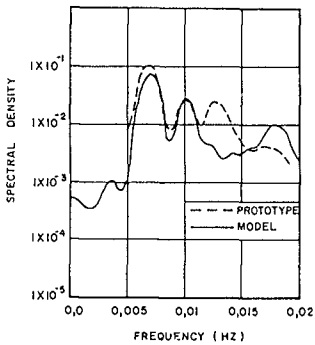

Figure 12 Model and prototype spectral density estimates

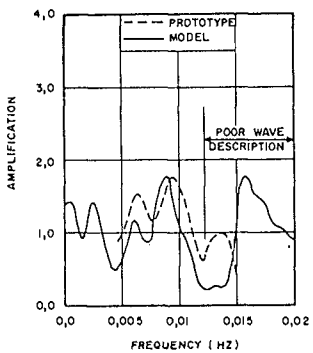

Figure 13 Model and prototype amplifications

This method of using a spectrum as input condition was a considerable improvement on previous studies as one model run accommodates a range of frequencies, instead of numerous expensive and time-consuming tests with single-period sine waves.

After a model run with a spectrum as input condition the frequencies which caused peak amplifications were selected and these were then used as input conditions in order to obtain amplification over the entire model area.

4. APPLICATIONS

4.1 Table Bay Harbour

The study was undertaken in 1976 on behalf of South African Railway and Harbours (South African Transport Services) to optimise plans for future extensions to the harbour. The results of a preliminary investigation have been given elsewhere (CSIR, 1978). Prototype data were recorded during 1978 (CSIR, 1979), after which the model calibration followed (CSIR, 1980a) and the investigations were made of the influence of future extensions (CSIR, 1980b). An example of the amplifications of one of the peak frequencies (93 s) is illustrated in Figure 14.

4.2 Mossel Bay Harbour

A preliminary study was carried out on behalf of the Fisheries Development Corporation of South Africa to determine whether proposed alterations in the harbour would

affect the long-wave response of the layout (CSIR, 1980c). The harbour layout and contours with the model grid superimposed on it is illustrated in Figure 15.

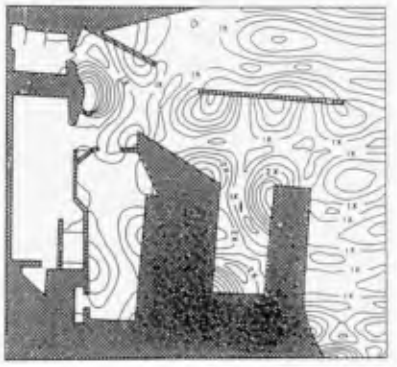

Figure 14 Maximum amplification for a wave period of 93 s (Table Bay Harbour)

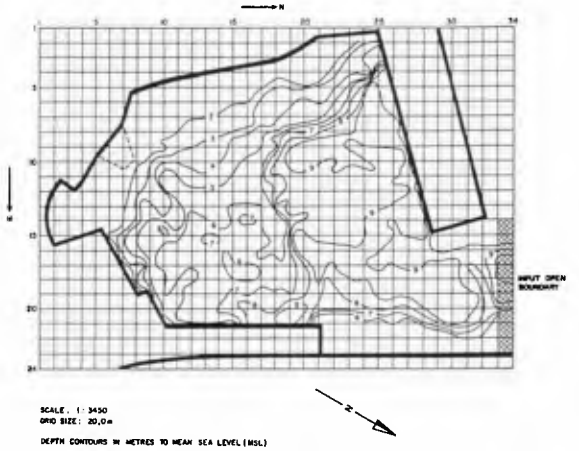

Figure 15 Mossel Bay Harbour layout with model grid superimposed on it

The amplifications of the original layout and a proposed layout for two positions are shown in Figure 16.

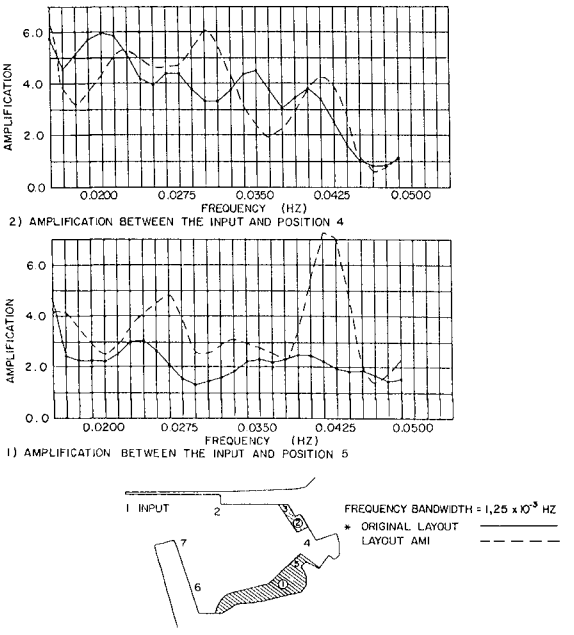

Figure 16 Amplifications for different layouts

4.3 Granger Bay Harbour

A proposed small-craft harbour at Granger Bay (situated next to Table Bay harbour) was tested to determine whether range action will be within the required design criteria for this type of harbour (CSIR, 1981).

Prototype conditions will be similar to Table Bay harbour. The harbour layout with the computational grid superimposed on it is illustrated in Figure 17.

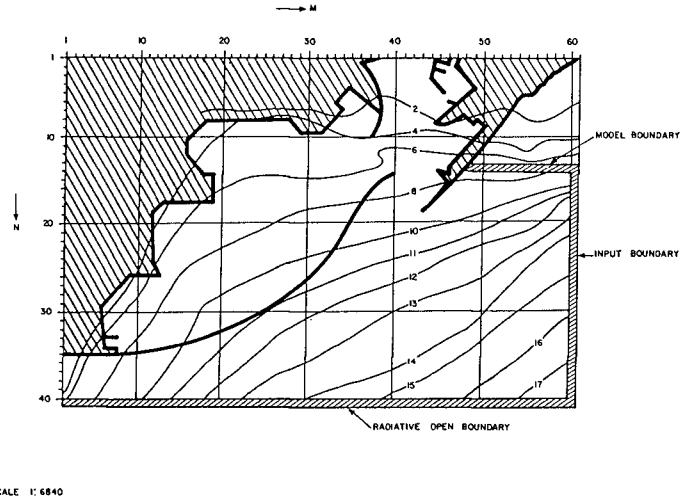

Figure 17 Granger Bay Harbour layout with the model grid superimposed on it

The maximum amplifications of a 60,0 s sine wave are shown in Figure 18.

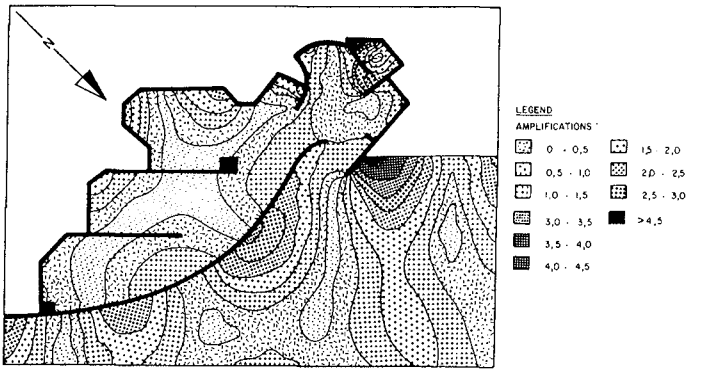

Figure 18 Maximum amplification for a period of 60,0 s

4.4 Koeberg

Prototype long-wave data were sampled at the cooling water intake basin of the Koeberg Nuclear Power Station as part of a post-construction monitoring program in order to determine the occurrence of long waves and the magnitude of the amplifications in the basin. The initial analyses of these data are described in Section 2. The data will also be used for the further verification and refinement of the model techniques and the investigation of the origin and generation of the long waves on the South African west and south coasts.

5. REFERENCES

BOTES, W A M (1980). Application of digital time series analysis to a resonance study at Table Bay harbour. CSIR Report SEA 8037, Stellenbosch.

CSIR (1978). Table Bay harbour development. Report No 2. Harbour resonance study: the numerical model. CSIR Report C/SEA 7815, Stellenbosch.

CSIR (1979). Table Bay harbour development. Report No 5. Harbour resonance study: recording and analysis of prototype long-wave data. CSIR Report C/SEA 7938, Stellenbosch.

CSIR (1980a). Table Bay harbour development. Report No 8. Harbour resonance study: calibration of the numerical model. CSIR Report C/SEA 8023, Stellenbosch.

CSIR (1980b). Table Bay harbour development. Report No 11. Harbour resonance study: application of the numerical model to the proposed harbour layout. CSIR Report C/SEA 8037, Stellenbosch.

CSIR (1980c). Mossel Bay harbour resonance. Numerical model study. CSIR Report C/SEA 8045, Stellenbosch.

CSIR (1981). Granger Bay harbour resonance. Numerical model study. CSIR Report C/SEA 8131, Stellenbosch.

LEENDERTSE, J J (1967). Aspects of a computational model for long-period water wave propagation. The Rand Corporation, RM-5894-PR.

RUSSELL, K S and HUIZINGA, P (1978). A two-dimensional finite-difference numerical model for the investigation of harbour resonance. CSIR Report IR 7804, Stellenbosch.

NUMERICAL MODEL STUDY OF TEMPERATURE DISTRIBUTIONS IN A HARBOUR

by

ROGER A. FALCONER[1]

ABSTRACT

The paper gives details of a study to predict numerically the background temperature rise in Poole Harbour and Holes Bay, in Dorset, England, caused by the siting of either a 700MW or a 350MW power station. The numerical model is based on the numerical integration of the flow equations which simulate the water movements of tides and upon numerical integration of the advective-diffusion equation representing the movement of heat.

The results of the study predominantly suggest that the temperature field is proportional to the station capacity, with the maximum and mean temperatures across the basin for the 700MW station capacity being almost exactly double the corresponding values predicted for the 350MW station capacity. Observations from the velocity fields and tidal prism ratios both tend to suggest that Poole Harbour and Holes Bay have poor flushing characteristics, which confirm the relatively high temperature predictions in that only a relatively small volumetric percentage of the heated water is flushed out of the basin during each flood tide.

INTRODUCTION

A two-dimensional numerical model has been developed to predict the depth average velocity fields and temperature distributions in narrow entranced harbours, within which a warm water outfall may be located. In a study for the Central Electricity Generating Board the model has been applied to Poole Harbour and Holes Bay, in Southern England, where the main objectives have been to determine the tide induced velocity fields and to make an assessment of the background temperature rise in the harbour as a result of a heated discharge from a power station having two possible capacities, i.e. either 700MW or 350MW. Water extracted from the entrance to Holes Bay, which is connected to the northern part of Poole Harbour and diametrically opposite the harbour entrance, flows through the condensers of the power station to be heated through 10K before being discharged back into

---

1 Lecturer in Civil Engineering, University of Birmingham, Birmingham, England

the middle of Poole Harbour through a diffuser located approximately 500m south of the northern shoreline of the Harbour, see Fig.1.

The numerical model is based on the depth integration of the governing hydrodynamic equations which define the tidal water movements within the basin, and upon integration of the advective-diffusion equation representing the movement of heat. The geometry of Poole Harbour is of particular interest to the numerical modeller since the narrow entrance illustrated in Fig.1, gives rise to relatively large advective accelerations. Also, the plan wetted surface area of the harbour changes considerably throughout the tidal cycle, with the surface area at low tide being appreciably smaller than the corresponding surface area at high tide.

Other difficulties encountered in the numerical model study were the treatment of the open boundary conditions, particularly for temperatures at the seaward boundary on the flood tide, and also the simulation of the temperature discontinuity at the point source outfall.

GOVERNING EQUATIONS

The governing equations used in the numerical model to determine the water elevations, the depth averaged velocity components and the horizontal temperature variations in Poole Harbour were the two momentum equations, describing the fluid motion in the horizontal plane, and the equations of mass and heat balance. For a constant density turbulent fluid flow on a rotating earth, the depth integrated momentum equation for flow in the x-direction can be expressed as, (see Falconer (1976) and Goldstein (1938):-

$$\frac{\partial q_x}{\partial t} + \beta\left[\frac{\partial Uq_x}{\partial x} + \frac{\partial Vq_x}{\partial y}\right] - fq_y + gH\frac{\partial \eta}{\partial x} + \frac{gq_x\sqrt{q_x^2+q_y^2}}{H^2C^2}$$

$$- \varepsilon\left[2\frac{\partial^2 q_x}{\partial x^2} + \frac{\partial^2 q_x}{\partial y^2} + \frac{\partial^2 q_y}{\partial x \partial y}\right] = 0 \qquad \ldots\ldots (1)$$

and similarly for momentum conservation in the y-direction:-

$$\frac{\partial q_y}{\partial t} + \beta\left[\frac{\partial Uq_y}{\partial x} + \frac{\partial Vq_y}{\partial y}\right] + fq_x + gH\frac{\partial \eta}{\partial y} + \frac{gq_y\sqrt{q_x^2+q_y^2}}{H^2C^2}$$

$$- \varepsilon\left[\frac{\partial^2 q_y}{\partial x^2} + 2\frac{\partial^2 q_y}{\partial y^2} + \frac{\partial^2 q_x}{\partial x \partial y}\right] = 0 \qquad \ldots\ldots (2)$$

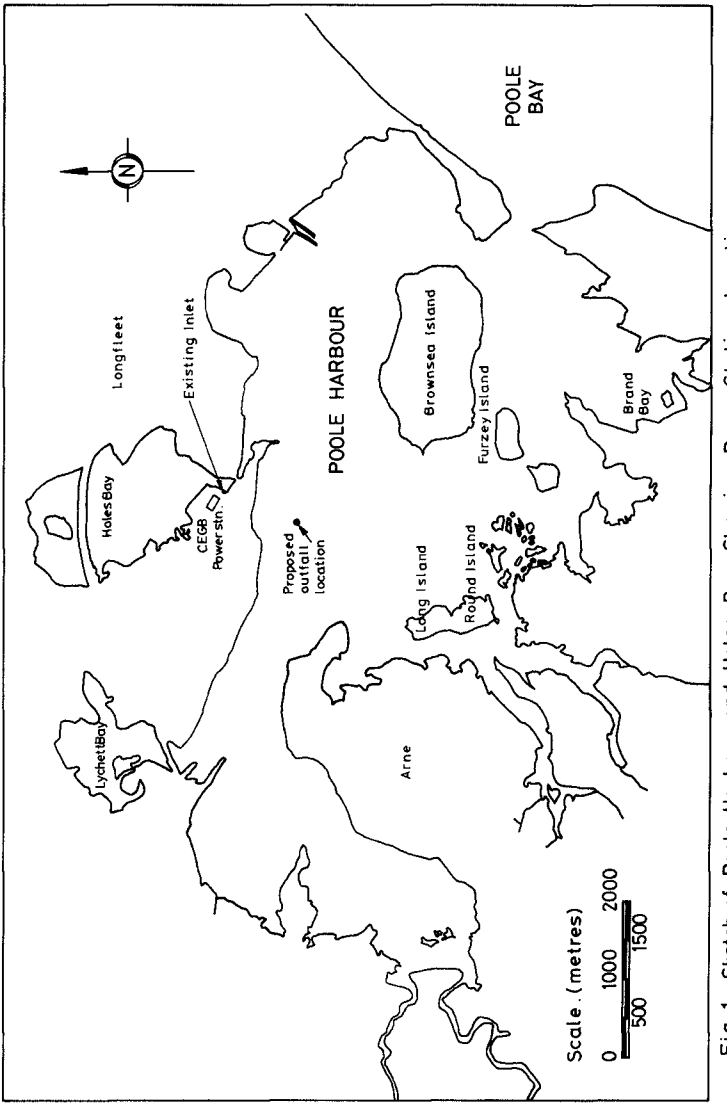

Fig. 1. Sketch of Poole Harbour and Holes Bay Showing Power Station Location.

where q_x and q_y = discharges per unit width in the x and y directions, with U and V being the corresponding depth averaged velocity components, β = a correction factor for the non-uniformity of the velocity distribution, H = total depth of flow, η = water surface elevation above chart datum, f = Coriolis parameter = $2\omega\sin\phi$ where ω is the angular velocity of the earth's rotation and ϕ the geographical latitude (assumed to be 50.012°), g = gravitational acceleration, C = Chezy's roughness coefficient = $H^{1/6}/n$ where n is Manning's roughness coefficient (assumed to be 0.035) and ε = depth mean eddy viscosity which, for an assumed logarithmic velocity profile in the vertical plane, becomes $0.07\sqrt{g(q_x^2+q_y^2)}/C$.

The depth integrated conservation equations for mass and heat transport can be expressed in a similar manner, giving for mass:-

$$\frac{\partial \eta}{\partial t} + \frac{\partial q_x}{\partial x} + \frac{\partial q_y}{\partial y} = 0 \qquad \ldots\ldots (3)$$

and for heat, see Fischer (1978):-

$$\underbrace{\frac{\partial TH}{\partial t}}_{(1)} + \underbrace{\left[\frac{\partial Tq_x}{\partial x} + \frac{\partial Tq_y}{\partial x}\right]}_{(2)} = \underbrace{-\frac{E(T-T_E)}{\rho Cp}}_{(3)}$$

$$+ \frac{(T_{IN}+\Delta T)Q_{OUT}}{A_{OUT}} + \underbrace{\frac{\partial}{\partial x}\left[HD_{xx}\frac{\partial T}{\partial x} + HD_{xy}\frac{\partial T}{\partial y}\right] + \frac{\partial}{\partial y}\left[HD_{xx}\frac{\partial T}{\partial x} + HD_{yy}\frac{\partial T}{\partial y}\right]}_{(5)} \qquad \ldots\ldots (4)$$

where T = depth averaged temperature, E = surface heat exchange coefficient (assumed to be $30W/m^2/K$), T_E = equilibrium temperature (assumed to be zero), ρCp = specific thermal capacity of fluid (assumed to be $4.2MJ/m^3/k$ for water), T_{IN} = temperature at power station inlet, ΔT = temperature rise across the condensers (assumed to be 10K), Q_{OUT} = discharge from the power station outlet (corresponding to $23.4m^3/s$ for a 700MW power station and $11.7m^3/s$ for a 350MW power station), A_{OUT} = plan cross-sectional area of outfall from power station and D_{xx}, D_{xy}, D_{yx} and D_{yy} = depth averaged dispersion coefficients in the x, y directions respectively, which have been shown by Preston (1981a) to be of the form:-

$$D_{xx} = \frac{(D_\ell q_x^2 + D_t q_y^2)\sqrt{g}}{\sqrt{q_x^2+q_y^2}\,C} \qquad D_{yy} = \frac{(D_\ell q_y^2 + D_t q_x^2)\sqrt{g}}{\sqrt{q_x^2+q_y^2}\,C}$$

$$D_{xy} = D_{yx} = \frac{(D_\ell + D_t)\, q_x q_y \sqrt{g}}{\sqrt{q_x^2 + q_y^2}\, C}$$

where D_ℓ and D_t are constants referring to the longitudinal dispersion and lateral diffusion components of the depth averaged dispersion coefficients and have assumed values of 5.93, after Elder (1959), and 0.15, after Fischer (1973), respectively for a logarithmic velocity profile. The numbered terms of the heat balance equation (4) refer to temperature variations within the domain as a result of : local effects (1), advective effects (2), net surface heat transfer (3), heat source such as an outfall (4) and turbulent diffusion and dispersion (5).

FINITE DIFFERENCE REPRESENTATION

The finite difference equations corresponding to the governing differential equations were expressed in an alternating direction implicit form with all terms being fully centred in both space and time, except for the pressure gradients in the momentum equations and the cross-product diffusion terms in the heat balance equation, see Falconer (1980 and 1981). The first order scheme, with accuracy $O(\Delta t, \Delta x^2)$, involved the discrete values of the variables being represented on a space staggered grid scheme in which water elevations and temperatures were described at different grid point locations to the discharges per unit width in the x and y directions.

The only terms requiring special mention are the advective accelerations expressing the lateral transport of momentum in the x and y directions of the momentum equation, e.g. the Vq_x product term in Eq.(1). These terms were represented in the finite difference scheme as for the Marker and Cell Technique so that their spatial locations were dependent upon the direction of the velocity components perpendicular to the axis direction being considered, see Williams and Holmes (1974).

The boundary conditions used for the hydrodynamic model of Poole Harbour included zero discharges per unit width perpendicular to the closed boundaries, with known uni-directional inflows being specified for the rivers and the power station throughflow. At the seaward boundary, just outside the harbour entrance, water elevation variations were assumed to vary in the same manner as for the mean spring and neap tidal curves given on the Admiralty Chart No.2611. The local discharge of heated water from the power station outlet was accounted for in the model by increasing the local water elevation in the mass conservation equation by an appropriate amount at the discrete point coinciding with the outfall.

For the heat balance equation the temperatures at the open boundaries also needed to be described as a function of time, together with the river inflow temperatures which were assumed to be zero at all times. At the outer seaward boundary, temperatures for the ebb tide were extrapolated linearly from values computed within the

computational field, as given by Leendertse and Gritton (1971). In this approximation only transport of heat by advection to the boundary was simulated, with dispersive heat transport assumed to be negligible. This method of determining the boundary temperature was also used to evaluate the temperature at the power station inlet, where flow was always in the outward direction across the boundary as for the ebb tide.

For the flood tide temperature variations at the open boundary PRESTON (1981b), in a study of the temperature variations at the mouth of Poole Harbour, suggested three possible methods for determining the governing temperatures. Of the possible representations given, the tidally averaged model was adopted due to its mathematical simplicity and relatively straightforward computational requirements. Based on a number of physical assumptions and assumed values for certain relevant data, Preston suggested that the boundary temperature could be expressed as:-

$$T(t) = \bar{\theta}\,\bar{\bar{T}} \qquad \ldots\ldots (5)$$

where $T(t)$ = tidal and spatially averaged input boundary temperature at time t, $\bar{\theta}$ = a tidally averaged integral function which, based on Preston's assumed data, had a value of 0.863, and $\bar{\bar{T}}$ = mean outflow temperature across the boundary, defined as:-

$$\bar{\bar{T}} = \frac{\int_{t_1}^{t_2} \left[\int_0^x q_x(t)T(t)dx + \int_0^y q_y(t)T(t)dy \right] dt}{\int_{t_1}^{t_2} \left[\int_0^x q_x(t)dx + \int_0^y q_y(t)dy \right] dt}$$

where, for any tidal cycle, t_1 and t_2 = the initial and final times of ebb flow across the boundary and x and y = the open boundary lengths in the x and y directions respectively. Once the mean outflow temperature $\bar{\bar{T}}$ had been determined for the ebb tide, the corresponding value was used in Eq.(5) to give the mean boundary temperature during the subsequent flood tide.

The local discharge of heat from the power station outfall gave rise to a local temperature discontinuity, in that the fluid flowing through the warm water outfall grid squares underwent an abrupt temperature rise. This discontinuity gave rise to a series of spurious wave-type temperature oscillations across the harbour, occurring as a consequence of the inability of the finite difference technique to represent rapidly varying variables in space, see Leendertse and Gritton (1971).

In order to overcome the problem of spurious temperature predictions, a number of different numerical schemes were studied for the heat balance equation. The first method considered was Lax's method, see Lax (1954), in which the temperature at the lower time-step for the time derivative in the heat balance equation was expressed as the average of the temperatures at the four surrounding

grid points. However, although this scheme eliminated the spurious solutions, the method introduced an effective artificial diffusion coefficient into the heat equation which, for this study, was found to be intolerably large, see Falconer (1981).

The second scheme considered involved using upstream differencing for the advective terms, with the addition of an anti-diffusion term to improve on the initial poor accuracy of the scheme, as used by Miles (1980). However, this method was found to be unsatisfactory for this particular study since the anti-diffusion term either had to be removed fully or reduced near to the outfall, thereby appearing to introduce small amplitude temperature waves.

The final scheme studied, and subsequently adopted, involved treating the temperature discontinuity as a shock front, and thereby introducing just sufficient artificial diffusion to counteract the disturbances caused by the temperature discontinuity at the outfall. The artificial diffusion term was chosen so that the required additional diffusive effect was obtained when adjacent temperature valves were widely different in the numerical model, but negligible when they were nearly equal, see Leendertse and Gritton (1971). Thus, added to the true diffusion terms in the heat balance Eq.(4) were two further diffusive terms of the form:-

$$D = \frac{\partial}{\partial x}\left[HD_x \frac{\partial T}{\partial x}\right] + \frac{\partial}{\partial y}\left[HD_y \frac{\partial T}{\partial y}\right] \qquad \ldots\ldots (6)$$

where the required diffusion coefficients are of the form:-

$$\left.\begin{aligned} D_{x_{j+\frac{1}{2},k}} &= \left[\frac{T_{j+1,k} - T_{j,k}}{T_{j+1,k} + T_{j,k} - 2T_b}\right]^2 \left[\frac{q_x \Delta x}{2}\right] \\ D_{y_{j,k+\frac{1}{2}}} &= \left[\frac{T_{j,k+1} - T_{j,k}}{T_{j,k+1} + T_{j,k} - 2T_b}\right]^2 \left[\frac{q_y \Delta x}{2}\right] \end{aligned}\right\} \qquad \ldots\ldots (7)$$

where j and k = grid point locations in the x and y directions respectively, and T_b = initial mean temperature, or base temperature, within the domain. Although the use of such an artificial diffusive term is by no means ideal in treating the temperature discontinuity arising at an outfall, the apparent advantage of this method is that the artificial diffusion falls off rapidly away from the outfall - where advection is often the dominant mode of heat transport.

In Poole Harbour large areas of shallow water exist such that marshes alternately dry and flood with each tidal cycle, and with much of the land-water boundary therefore being time dependent. In

simulating this moving boundary in the numerical model the procedure adopted was similar to that used by Leendertse and Gritton (1971), whereby the location of the land-water boundary was assumed to be a function of the current value of the depth. There were, however, two basic differences between Leendertse and Gritton's procedure and that used in this study. Firstly, the first and second checks in Leendertse and Gritton's method on whether or not a grid point should be dry were combined and carried out between the calculation for the new water elevation field and the temperature field. Also, only the two cross-sections in the implicit direction were considered rather than all four cross-sections for each grid square. Secondly, in the third check on a grid cell drying, the average water elevation was used in calculating each cross-section rather than just the water elevation at the grid point being considered. These changes allowed a reduction in the computational cost and appeared to reduce the influence of the instabilities generated in that the same cross-sections were used in these checks as in the finite difference equations themselves.

NUMERICAL MODEL APPLICATION AND RESULTS

The region of Poole Harbour and Holes Bay illustrated in Fig.1 was simulated in the numerical model using a finite difference mesh of 65 x 58 grid points, with an equal grid spacing of 150m. At the centre of each grid square a representative depth between chart Datum and the bed was determined by equating the corresponding cross-sections in the numerical model to those defined by the actual bed topography. The tidal data required at the open seaward boundary was obtained from the Admiralty Chart No.2611 and data provided by the Poole Harbour Commissioners.

The cold water inlet to the power station was approximated by a horizontal sink, which was represented by an open boundary grid square of length 150m. For the proposed outfall, which was coincident with the centre of four grid squares, it was assumed that the heated fluid was discharged vertically upwards and that complete mixing occurred equally among the four adjacent grid squares. The advantage of using four rather than one grid square for the outfall, was that in discharging the heated water over a larger plan cross-sectional area a more realistic localised temperature field was predicted in the vicinity of the source itself. However, since heat rather than temperature was being conserved in the model, it was not surprising to find that when comparisons were made between using one and four grid cells to represent the outfall, little difference occurred in the predicted temperatures across the domain - except in the region very close to the outfall.

The model was always started at high tide, with the assumption that the initial velocities and temperatures were zero everywhere and that the outfall temperature rise above the intake temperature was 10K. Each simulation was run for a maximum of fourteen repetitive tidal cycles, a restriction placed on the model by the relatively small grid spacing and the stability requirement given by Falconer (1976 and 1980), i.e. that the time step $\Delta t < \Delta x U$ - where U is the maximum depth averaged

velocity in the field and Δx the grid spacing (=150m). The resulting predicted water elevations, velocity components and temperatures were evaluated at each grid point, with the results being printed out in both numerical and graphical form at various phases of the tidal cycle.

In general, it is always preferable to be able to check the predicted results obtained from a numerical model with field measurements or otherwise before proceeding with any analysis of the numerical results; the same being true for a laboratory model investigation. For this particular study it was not possible to make any worthwhile comparisons between any measured and predicted velocities or temperatures, since no appropriate field data was available at the time. However, since the model has been applied to a number of rectangular harbours with different aspect (or length to breadth) ratios and has been shown to give good agreement with scaled physical model results, see Falconer (1980), then it was assumed that the results obtained for this study ought not to differ markedly from any similar laboratory model investigations.

The velocity and temperature fields were reproduced graphically for four main simulations. These simulations included predictions for both a 700MW and a 350MW power station and for fourteen consecutive spring and neap tidal cycles respectively. The results are documented and compared in some detail in Falconer (1981), with some typical velocity and temperature field predictions being given in Figs. 2-5 for the spring tide simulations with a 350MW power station. Comparison of Figs. 2 and 3 gives an indication of the variation in the plan cross-sectional wetted area during the tidal cycle, and with the advective effect of the tide on the thermal plume being clearly illustrated in Figs. 4 and 5. Similarly, low neap tide results are given in Figs. 6 and 7.

In comparing the temperature predictions obtained for the various simulations, see Falconer (1981), it appears that the mean temperature and the standard deviation across the harbour were almost exactly double for the 700MW station capacity as for the 350MW capacity. For the 700MW power station the mean temperature rise across the harbour for the spring tides was 0.8K and with a standard deviation of 1.2K, whereas the corresponding values for the 350MW capacity were 0.4K and 0.6K respectively. Similarly, the corresponding neap tide predictions for the mean and standard deviations were 1.1K and 2.1K respectively for the 700MW station, and 0.6K and 1.1K for the 350MW station. The build-up of the mean temperature in the harbour during the fourteen tides for both the spring and neap tidal cycles is shown in Fig.8 for the 350MW power station. More recent numerical model studies on Poole Harbour by the Author, however, indicate that the temperatures predicted in this study might well be on the pessimistic side for two reasons. Firstly, the simulation of conditions in the harbour for fourteen identical neap tides means that a pessimistically low sequence of tidal ranges has been assumed over the period modelled, giving rise to a lower degree of flushing than would occur in reality. Secondly, the assumption that 86% of the heat discharged out through the open seaward boundary returns on the next flood tide appears to be conservative in comparison with recent field data measurements recorded

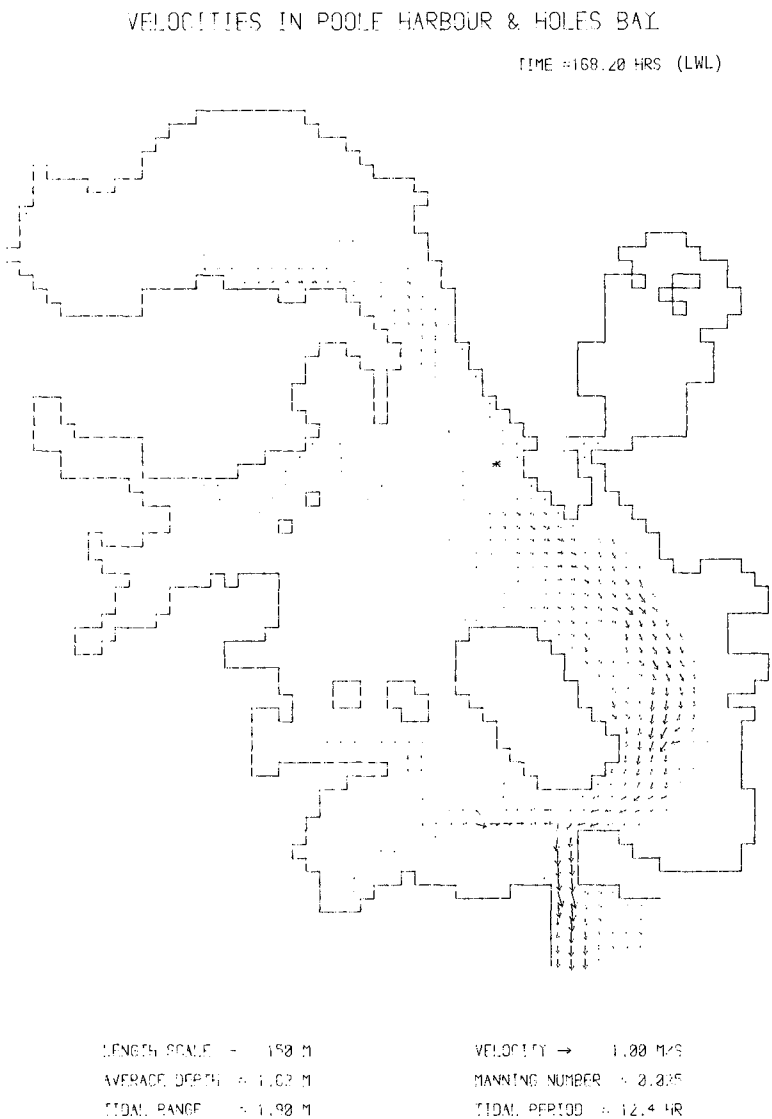

Fig.2. Velocities at low water spring tide for 350 MW power station

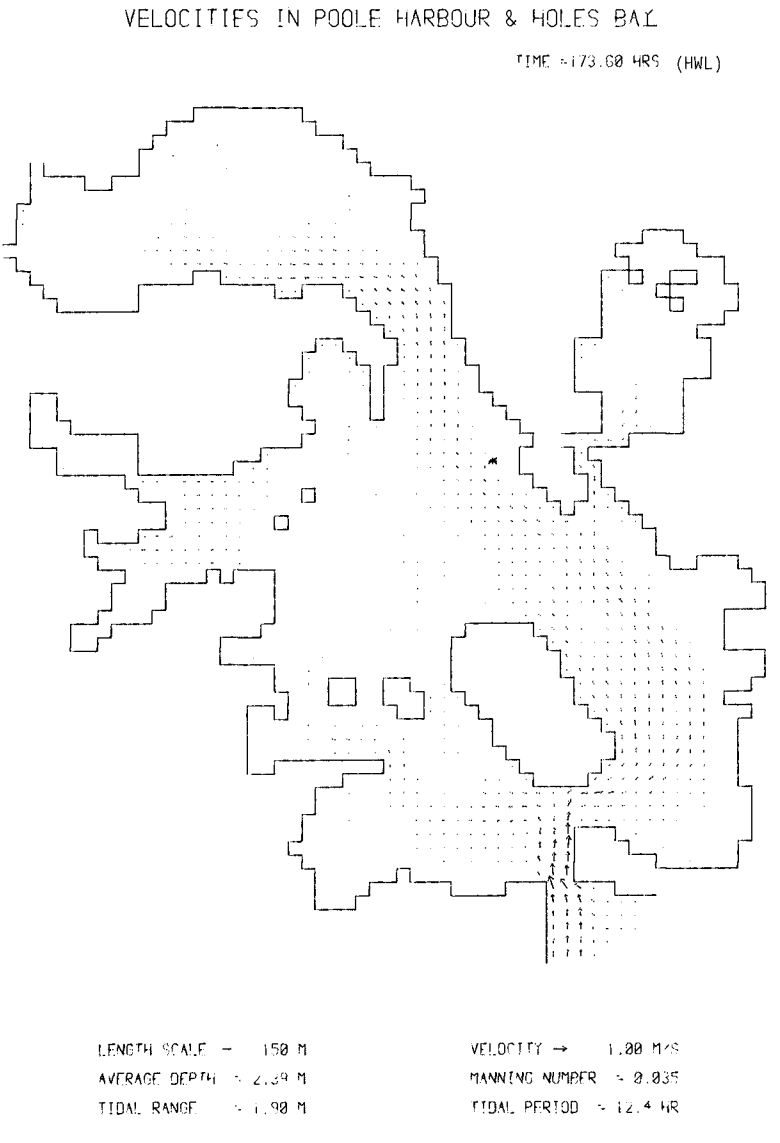

Fig.3. Velocities at high water spring tide for 350 MW power station

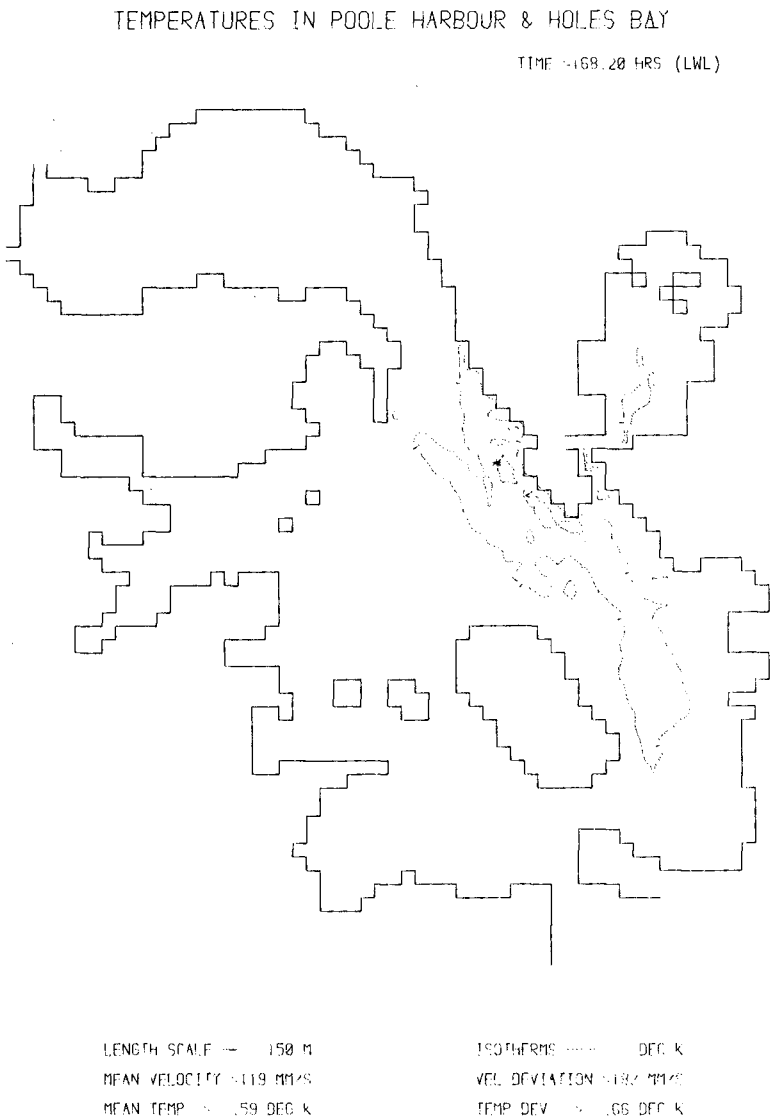

Fig.4. Temperatures at low water spring tide for 350 MW power station

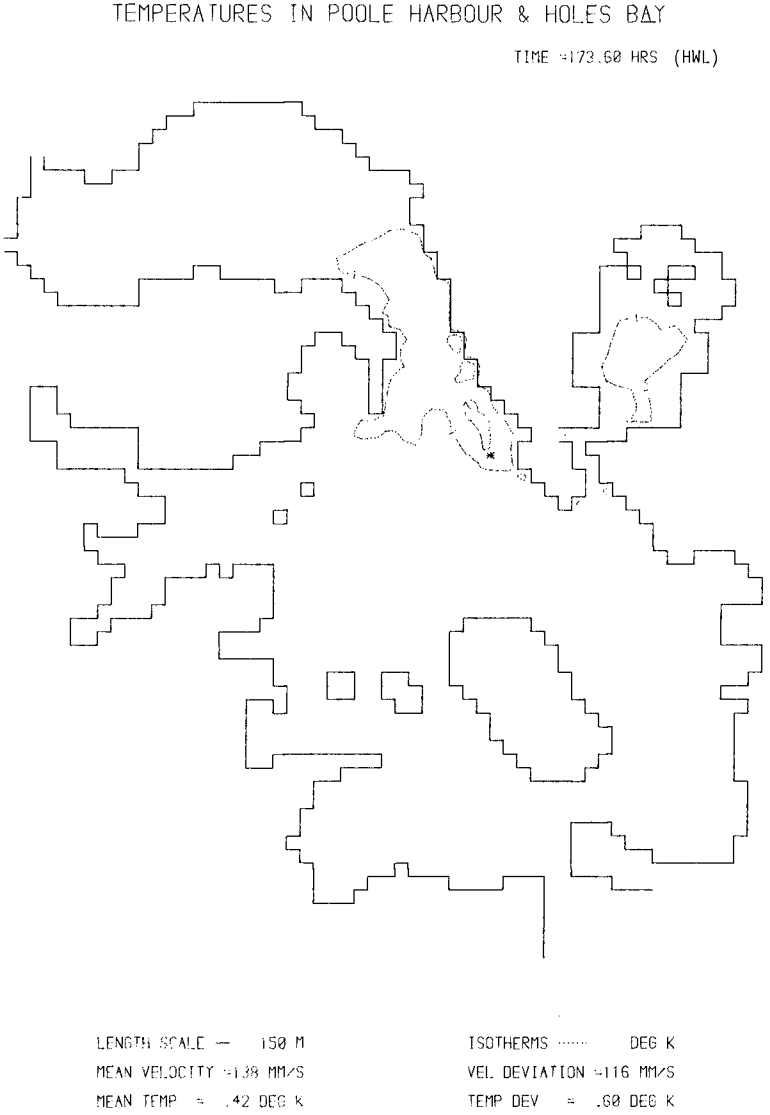

Fig.5. Temperatures at high water spring tide for 350 MW power station

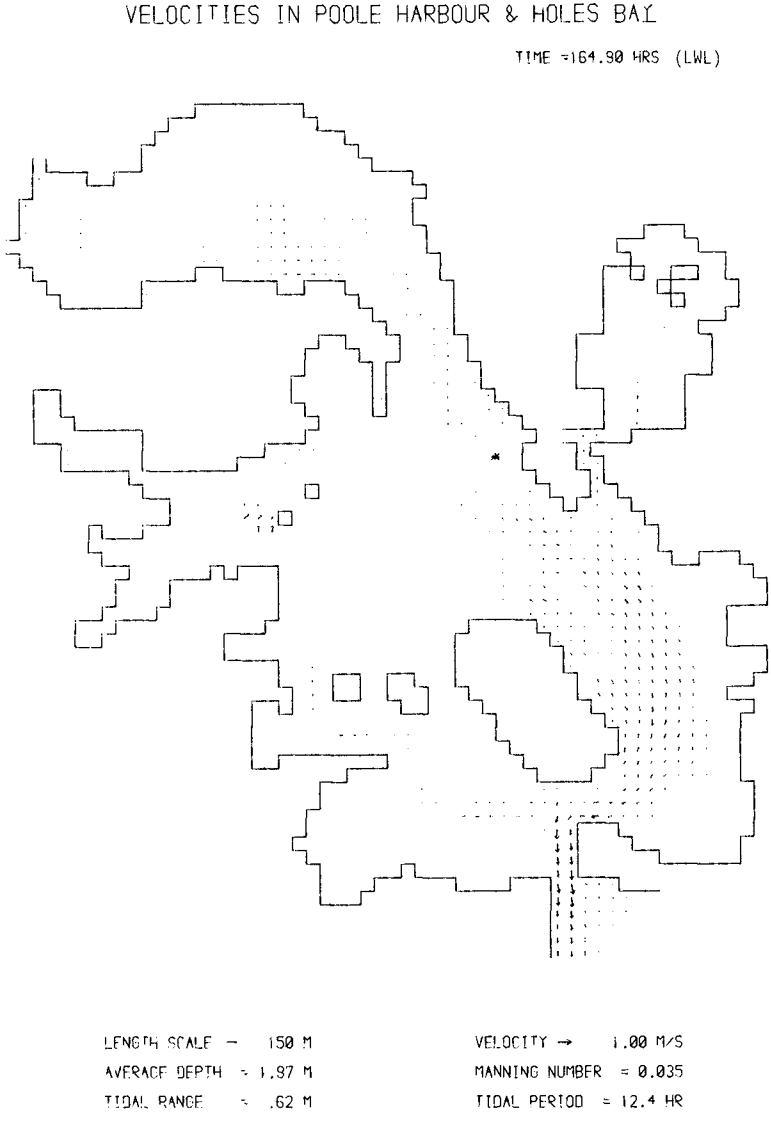

Fig.6. Velocities at low water neap tide for 350 MW power station

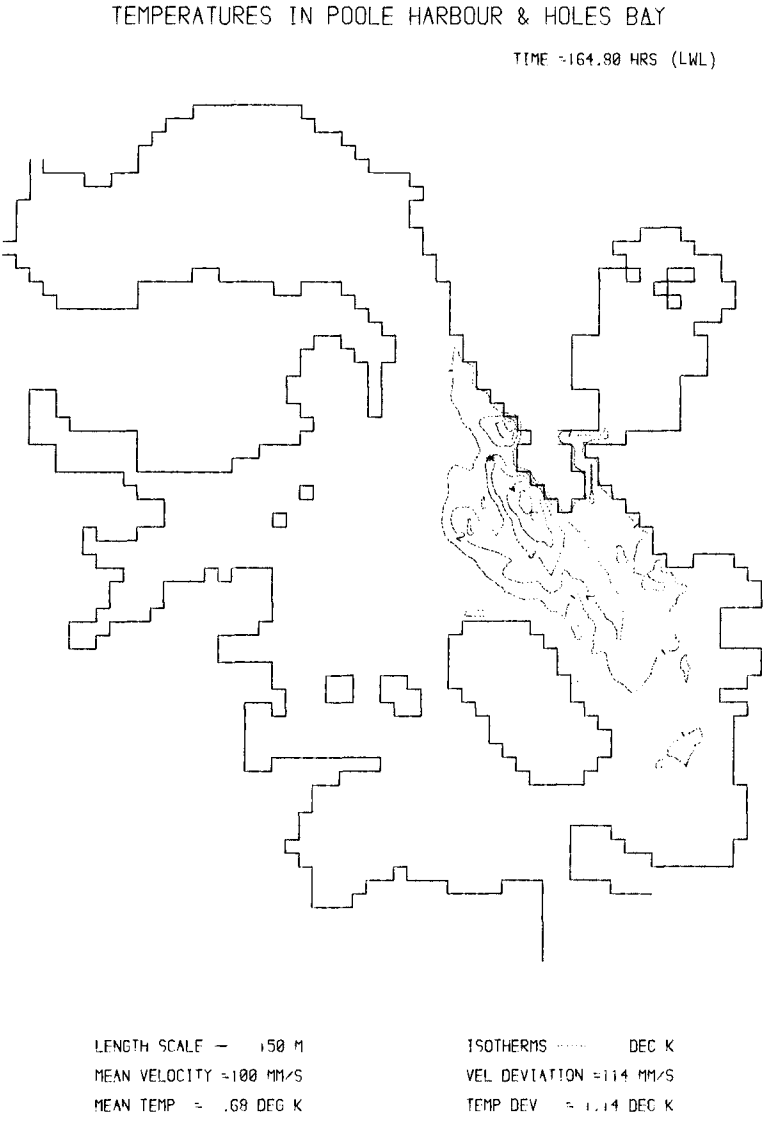

Fig.7. Temperatures at low water neap tide for 350 MW power station

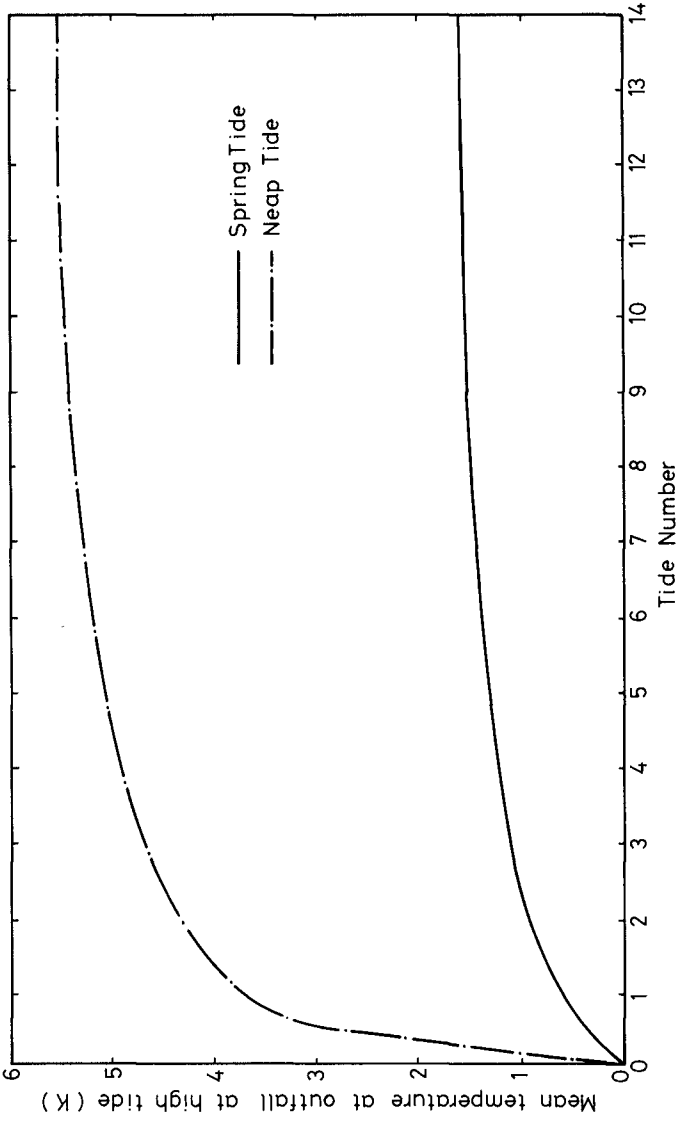

Fig. 8. Variation of high tide mean temperature at the outfall with tide number.

for other substances such as nitrates and phosphates.

Other indications from the numerical model study were that Poole Harbour and Holes Bay both appear to have poor flushing characteristics, particularly for neap tides where results showed that the net tidally averaged heat outflow across the entrance was extremely small.

CONCLUSIONS

A numerical model has been developed which is capable of predicting both the velocity and temperature distributions within a narrow entranced harbour, with a heated discharge being located within the basin. The results obtained have proved to be encouraging, with numerically stable predictions having been obtained for relatively large advective accelerations and appreciable changes in the plan-form wetted area during the tidal cycle.

The numerical difficulties associated with the finite difference representation of the temperature discontinuity arising at the outfall have been overcome by a weighted artificial diffusive term, where the weighting factor is proportional to the square of the temperature difference between adjacent grid cells.

The results of the study show that for the 350MW power station the mean temperature rise across the harbour is 0.4K for spring tides and 0.6K for neap tides, with the standard deviations for the tempertaure fields being 0.6K and 1.1K respectively. The corresponding predictions made for the 700MW power station were, in almost all cases, exactly double the temperatures predicted for the 350MW station. However, for the reasons given in the previous section these predictions are thought to be on the conservative side.

ACKNOWLEDGEMENTS

The study was funded by the Central Electricity Generating Board under the supervision of Mr. I. T. Hughes, Station Planning Engineer. The author is also grateful for the assistance provided by Mr. N. Ames and Mr. N. P. Baldwin of the Central Electricity Generating Board, Mr. R. W. Preston of the Central Electricity Research Laboraties and Miss G. Vaisey of the Department of Civil Engineering, University of Birmingham.

REFERENCES

ELDER, J.W. (1959). The Dispersion of Marked Fluid in Turbulent Shear Flow. Journal of Fluid Mechanics, Vol.5, part 4, pp.544-560.

FALCONER, R.A. (1976). Mathematical Modelling of Jet-Forced Circulation in Reservoirs and Harbours. Ph.D. Thesis, University of London, pp.237.

FALCONER, R.A. (1980). Modelling of Plan-Form Influence on Circulation in Harbours. Proceedings of the Seventeenth Coastal Engineering Conference, ASCE, Sydney, pp. 2726-2744.

FALCONER, R.A. (1981). Numerical Model Study of Temperature Distributions in Poole Harbour and Holes Bay. Report for the Central Electricity Generating Board, pp.63.

FISCHER, H.B. (1973). Longitudinal Dispersion and Turbulent Mixing in Open Channel Flow. Annual Review of Fluid Mechanics, Vol.5, pp. 59-78.

FISCHER, H.B. (1978). On the Tensor Form of the Bulk Dispersion Coefficient in a Bounded Skewed Shear Flow. Journal of Geophysical Research, Vol.83, No.C5, pp. 2573-2375.

GOLDSTEIN, S. (1938). Modern Developments in Fluid Dynamics. Oxford University Press, Vol.1, pp. 330.

LAX, P.D. (1954). Weak Solutions of Non-Linear Hyperbolic Equations and their Numerical Computation. Communications on Pure and Applied Mathematics, Vol.7, pp. 159-193.

LEENDERTSE, J.J. & Gritton, E.C. (1971). A Water-Quality Simulation Model for Well-Mixed Estuaries and Coastal Seas: Vol.11, Computation Procedures. The Rand Corporation, R-708-NYC, pp. 53.

MILES, G.V. (1980). A Numerical Model for Background Temperature Fields. Report No. EX806, Hydraulics Research Station, Wallingford, pp. 44.

PRESTON, R.W. (1981a). Representation of Dispersion in Turbulent Shear Flow. Private Communications, Central Electricity Research Laboratories, Leatherhead, Surrey, pp. 5.

PRESTON, R.W. (1981b). The Temperature Variation at the Mouth of Poole Harbour. Private Communications, Central Electricity Research Laboratories, Leatherhead, Surrey, pp.41.

WILLIAMS, J.W. & HOLMES, D.W. (1974). Marker-and-Cell Technique, a Computed Programme for Transient Stratified Flows with Free Surfaces. Report No.134, Hydraulics Research Station, Wallingford, pp. 54.

NOTATION

A_{OUT} = plan cross-sectional area of outfall from power station

C = Chezy coefficient

c_p = specific heat of fluid

$D_{xx}, D_{xy}, D_{yx}, D_{yy}$ = Combined depth averaged dispersion and diffusion coefficients in the two-dimensional plane

D_ℓ = longitudinal dispersion coefficient

D_t = lateral turbulent diffusion coefficient

E = surface heat exchange coefficient

f = Coriolis parameter

g = acceleration due to gravity

H = total depth of fluid

j,k = finite difference co-ordinates in x, y directions respectively

q_x, q_y = discharges per unit width in x,y directions respectively

Q_{OUT} = discharge from power station outlet

t = time

t_1, t_2 = initial and final times of ebb flow across boundary

T = depth averaged temperature at a grid point

T_b = base temperature, or temperature at start of simulation

T_E = equilibrium temperature for heat surface exchange

$\bar{T}$ = mean outflow temperature across the boundary

T_{IN} = temperature at power station inlet

U,V = depth averaged velocities in x,y directions respectively

x,y = longitudinal and lateral co-ordinates in the horizontal plane

X,Y = open seaward boundary length in the x,y directions

β = correction factor for non-uniformity of vertical velocity profile

Δt = time step

ΔT = temperature rise across condensers

Δx = grid spacing

ε = depth mean eddy viscosity

η = water surface elevation

$\bar{\theta}$ = tidally averaged integral function after Preston (1981b)

ρ = density of fluid

WAVE ENERGY VARIATION NEAR CAPE TOWN, SOUTH AFRICA

F.A. Shillington, Physical Oceanography,
University of Cape Town,
Rondebosch 7700, RSA.

ABSTRACT

A three month time series of wave height measurements taken every six hours for twenty minutes duration at two sites (one in 24 m deep water and the other in 15 m deep water) off the South African coast have been used to examine wave energy dissipation. The rocky nature of the bottom has ruled out the possibility of dissipation due to sediment motion and percolation and only dissipation due to bottom friction has been considered. The theoretical work of Hasselmann and Collins 1968 has provided the basic technique. Average friction factors obtained have been in the range 0.17 to 0.50 but have very large scatter. Such large friction factors were not considered possible until recently (Grant and Madsen 1982) when it has been shown that if the hydraulic roughness is of the same order as the bottom orbital excursion, the friction factor tends to a value of 0.23. An attempt will be made in future work to reduce the scatter of the results by careful selection from a longer subsection of the original time series.

INTRODUCTION

In 1980 a collaborative field measuring and analysis programme was set up with participants from the departments of Oceanography at the University of Cape Town, and Ocean Engineering at the University of Stellenbosch, and help from the National Research Institute for Oceanology (NRIO) Stellenbosch and Fisheries Development Corporation (FISCOR) Cape Town, to measure wave parameters on a line perpendicular to the shore. The main objectives were:

(a) to examine processes involving wave energy dissipation in shoaling water
(b) to obtain a long term series of wave heights and wave energy spectra to establish suitable statistics for wave energy extraction design studies. (Retief et al 1982).

SITE

The site chosen for the study resulted partly from historical programmes of NRIO. A 200 m deep wave recording station near Cape Town was initiated and maintained by NRIO for a number of years as a prime

research station for S.A. waters (van Ieperen 1976). It was decided that this station should serve as the outer or deep station for this study. New stations in 24 m deep water and 15 m deep water were deployed by this project. Only records from the 24 m and 15 m deep stations are discussed in this preliminary report.

The bottom topography of the site region is displayed in figure 1. The location of the three Datawell waverider buoys is indicated. The topography is reasonably regular and both SCUBA diver inspection and a later side scan sonar survey indicated that the bottom is composed of large, smooth sandstone slabs. These rocky slabs are covered with biological growth and the kelp *Laminaria pallidae* which ranges from 1 - 2 m tall. There are relatively small patches of sand in some of the gullies.

In order to estimate the incoming wave direction, a bottom mounted OOSO direction guage (see Retief and Vonk 1974) was deployed at the 24 m deep site. This instrument was later removed when it became obvious that the tripod on which it was mounted shifted its orientation under storm conditions. An idea of the boundary roughness can be obtained from an echo sounding profile shown in figure 2.

INSTRUMENTATION ANO OATA ANALYSIS

Wave heights were measured with standard DATAWELL waverider buoys; the analogue signal being transmitted ashore to a nearby lighthouse at Kommetjie. Here the signal was received and stored simultaneously on an analogue strip chart and on cassette magnetic tape as a 17.1 minute (2048 datapoints) time series of digitised wave heights sampled once every 0.5 s. The height resolution of the digitally recorded wave heights is 4 cm. Records were taken every 6 hours at all stations. The digital data on the cassettes were then transferred to 9 track CCT at FISCOR and then put onto disc storage on the UNIVAC 1100/80 computer at UCT. Spectra were then calculated by using standard FFT algorithms together with a wave data qualification suite of programmes (Visser et al 1980) described elsewhere in these proceedings (Rossouw et at 1982). The spectra have a frequency resolution of 0.01 Hz, a Nyquist or folding frequency of 1 Herz, and 20 degrees of freedom leading to 80% confidence bands of 0.7 times the spectral estimate x and 1.6 times x where x is the expected spectral energy density value. The wave directions measured with the OOSO in the early stages of the field have not been used in this study.

WAVE OISSIPATION MECHANISMS

Shemdin et al 1980 have conveniently summarized the possible wave dissipation mechanisms into two groups:

(a) linear processes
Percolation; wave induced bottom sediment motion; bottom scattering.

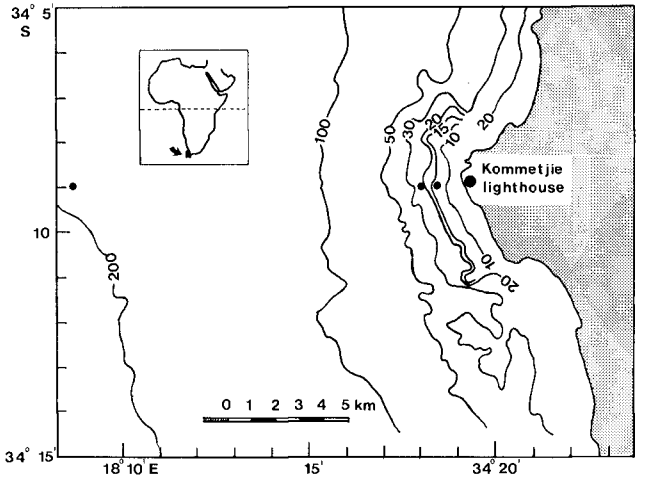

Figure 1. Site location of Datawell waverider buoys and bottom topography.

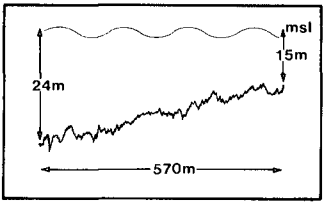

Figure 2. Typical bottom slope between shallow wave recorders from echo sounding profile.

(b) non linear processes
Bottom friction; weak non linear wave interactions in finite depth water.

In this experiment, due to the rocky bottom, it is assumed that the dominant dissipation mechanism would be bottom friction. Techniques for estimating the bottom friction coefficient have been derived by Hasselmann and Collins 1968 and Collins 1972, and have been subsequently used by various workers including van Ieperen 1975 in South African waters.

Hasselmann and Collins 1968 assume that the bottom shear stress is given by a quadratic law:

$$\tau_b = - \rho f_w \tilde{u}_b |\tilde{u}_b| \tag{1}$$

where f_w is the friction coefficient; $\tilde{u}_b$ is the bottom orbital velocity vector due to the waves passing overhead. Since it is difficult to measure $\tilde{u}_b$ directly in the field, we use linear theory to estimate $\tilde{u}_b$ from the surface wave height measurements. (This is justified for most wavelengths and moderate wave heights in this depth of water - see for example, Swart 1978).

$$\tilde{u}_b(k) = \frac{g\ k\ \eta(k)}{\sigma \cosh (kH)} \tag{2}$$

where $\eta(k) = A \cos (\tilde{k}.\tilde{x} - \sigma t)$, $2A$ is the surface wave height, σ the radian frequency, $\tilde{k}$ the wavenumber ($= \frac{2\pi}{L}$), H is the water depth.

We assume that there is no wind wave generation between the stations and that the wave field is steady, in which case we can write the radiative transfer equation as

$$Cg \frac{\partial E}{\partial x}(f,x) = - \Phi(f) \tag{3}$$

where Cg is the group velocity of component frequency f, and the sink function $\Phi(f)$, is given approximately by Collins 1972 as

$$\Phi(f) = \frac{f_w\ g\ k^2 E(f) < \tilde{u}_b >}{\sigma^2 \cosh^2 (kH)} \tag{4}$$

with

$$< \tilde{u}_b > = \left\{ \Sigma_f \frac{E(f)\ g^2 k^2\ \Delta f}{\sigma^2 \cosh^2 (kH)} \right\}^{\frac{1}{2}}$$

$E(f,x)$ is the wave energy density spectral function and $<\tilde{u}_b>$ gives the average steady bottom velocity as a linear superposition of exponentially depth decayed orbital velocities of the different wavenumbers present in the spectrum.

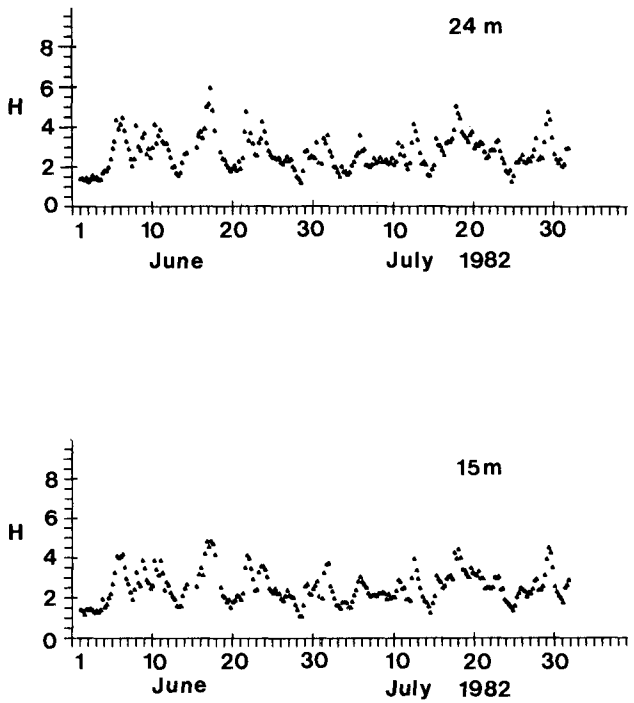

Figure 3. Time series of average significant wave height in 24 m and 15 m depth for June and July 1982.

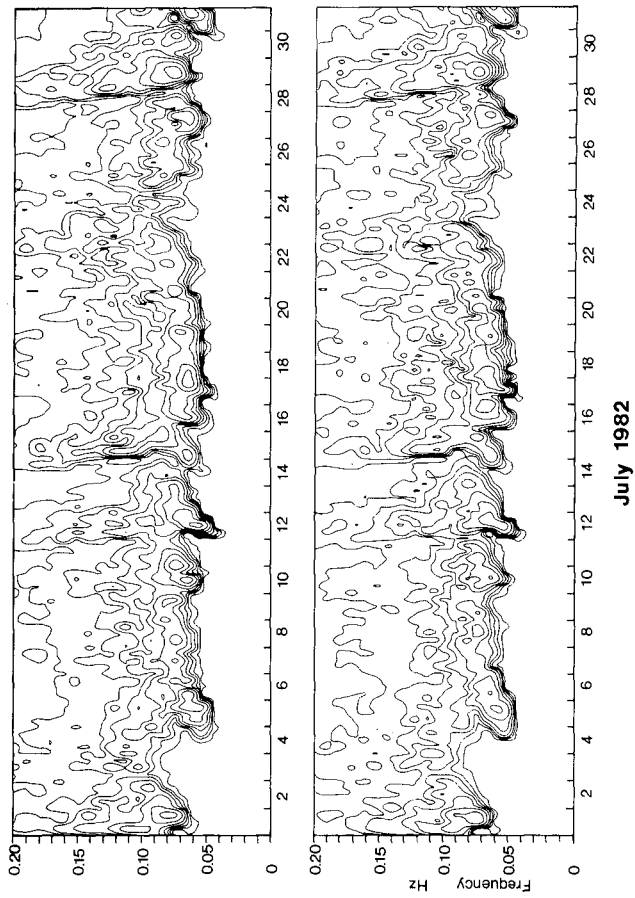

Figure 4. Energy, frequency, time diagram for 24 m (above) and 15 m (below) stations off Kommetjie, South Africa. Energy contours in decibels above 1 m^2sec with contour levels at -2.5, 0, 2.5, 5, 7.5 etc decibels.

RESULTS

As a preliminary analysis, a three month subset of the data for June, July, August 1982 has been used. Figures 3 and 4 show respectively the average significant wave height during June, July 1982 at the 24 m and 15 m depths and the energy-frequency time contour diagram for July 1982, also at both depths. The spectra were computed four times per day for both the 24 m and 15 m stations. Equation (4) was used to compute the friction factor f_w at each of the twenty frequencies

$$f(i) = (0.006 + \frac{5i}{1024}) \text{ Hz} \qquad \text{for } i = 0, 1, \ldots 19.$$

The friction factors for the entire data set (322 values at each frequency) were averaged in time and are shown in brackets in Table 1. The main data shown in Table 1 were selected using a criterion that H_s at the 24 metre deep station should be greater than H_s at 15 metres depth. As can be seen from the scatter diagram in figure 5, sometimes the shallower station experiences larger waves than the deeper one. This is considered to be due to convergent refraction of energy under southerly wave directions.

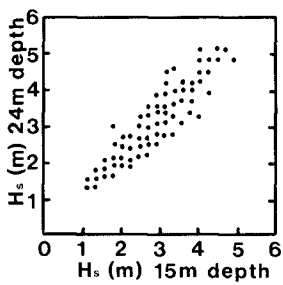

Figure 5. Plot of significant wave height in 24 m versus wave height in 15 m deep water.

Figure 6 shows a percentage occurrence diagram of friction factors f_w at selected frequencies. There is some tendency for the friction factor to increase in magnitude with increasing frequency, but the large scatter in the results makes it difficult to place confidence in such a conclusion.

DISCUSSION

Traditionally it is assumed that friction factors of order 10^{-2} are typical on sandy bottoms under waves. However, more recent work has

TABLE 1

f (Hz)	$\bar{f}_w$	σ	n	% of total records	
0,006 *	0,53 (,65)	1,8 (0,9)	81 (302)	95,3	(93,8)
0,016 *	0,32 (0,43)	1,3 (0,7)	85 (316)	100	(98,1)
0,025 *	0,24 (0,30)	1,2 (0,6)	85 (319)	100	(99,1)
0,035 *	0,83 (0,11)	0,9 (0,5)	85 (312)	100	(99,7)
0,045	0,17 (0,27)	1,3 (0,7)	85 (317)	100	(98,4)
0,055	0,27 (0,47)	1,8 (0,9)	83 (299)	97,6	(92,8)
0,064	0,28 (0,50)	2,0 (1,0)	80 (298)	94,1	(92,5)
0,074	0,24 (0,70)	1,9 (0,9)	85 (296)	100	(91,9)
0,084	0,31 (0,63)	1,8 (0,9)	84 (304)	98,8	(94,4)
0,094	0,32 (0,67)	1,8 (0,9)	84 (298)	98,8	(92,5)
0,104	0,45 (0,64)	1,8 (0,9)	82 (300)	96,5	(93,2)
0,113	0,27 (0,49)	1,8 (0,9)	84 (304)	98,8	(94,4)
0,123	0,28 (0,43)	1,7 (0,9)	84 (306)	98,8	(95,0)
0,133	0,21 (0,38)	1,7 (0,4)	84 (308)	98,8	(95,6)
0,143	0,33 (0,40)	1,9 (1,0)	82 (300)	96,5	(93,2)
0,152	0,33 (0,54)	2,0 (1,0)	81 (297)	95,3	(92,2)
0,162	0,35 (0,49)	2,3 (1,2)	81 (293)	95,3	(91,0)
0,172	0,37 (0,44)	2,8 (1,4)	77 (284)	90,6	(88,2)
0,182	0,17 (0,18)	3,4 (1,7)	78 (259)	91,8	(80,4)
0,191	0,50 (0,50)	4,1 (2,1)	65 (241)	76,5	(74,8)

* Waverider response at these frequencies does not allow a meaningful estimate to be made.

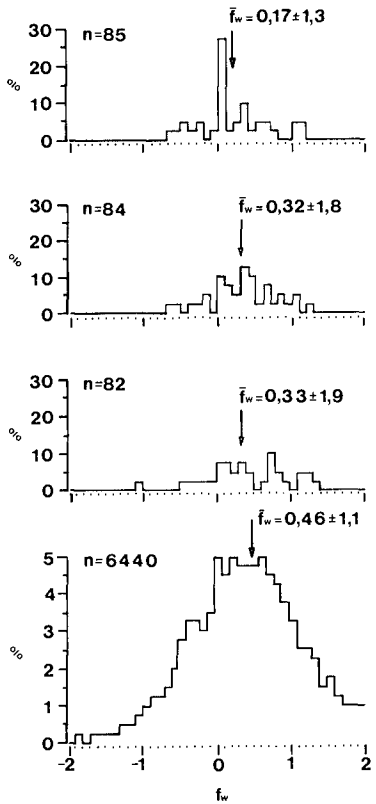

Figure 6. Percentage occurrence of friction factor f_w for frequencies from top: (a) 0.045 Hz, (b) 0.094 Hz, (c) 0.143 Hz and combined for all frequencies, bottom.

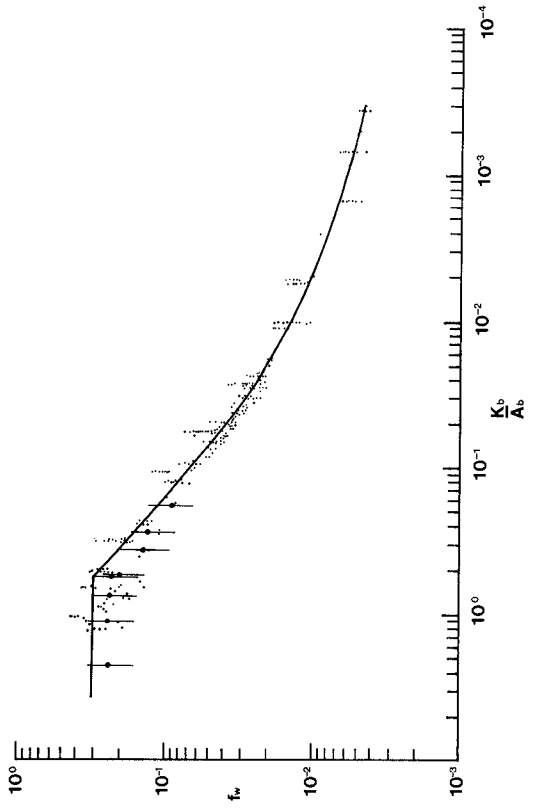

Figure 7. Friction factor f_w for wave tank observations at different hydraulic roughness lengths k_b as a function of $\frac{k_b}{A_b}$ where A_b is the bottom orbital excursion amplitude. (After Swart, unpublished, see also Grant and Madsen 1982).

shown that larger values of the friction factor are being obtained under various conditions. It appears from figure 7 (after Swart, pers comm.) that a limiting value for the friction factor is 0.3. This is also confirmed in recent work of Grant and Madsen 1982. In these instances the high friction factors result when the hydraulic roughness is of the same order as the bottom orbital excursion amplitude. Thus, in this experiment, it is assumed that the large values of the friction factor are due to a large hydraulic roughness. Grant and Madsen show that for values of $\frac{k_b}{A_b} > 1$ (where k_b is the hydraulic roughness length, A_b the bottom orbital excursion amplitude) that friction factor $f_w = 0.23$.

The main problem with the results is the large scatter. This scatter has been attributed to changes in wave direction as the storm pass to the south of the Cape, which then result in changes of energy due to refraction. It is anticipated that the scatter can be reduced by carefully selecting portions of the data set that might be expected to arrive from a particular direction.

No attempt has yet been made to model the effect of the large kelp on dissipating energy. Considering a boundary layer with a scale the same order of magnitude as the size of the kelp, one could consider the kelp in the sense of a percolation model. One would imagine that the kelp would be transparent to low frequency energy, but not so to high frequency energy.

ACKNOWLEDGEMENTS

The author would like to thank the SANCOR division of CSIR for the funding required by this project. The work would also not have been possible without the help of Mr R.C. Wyness in the maintenance and smooth operation of the wave recording equipment. Computer and diving assistance was obtained from the Fisheries Development Corporation.

REFERENCES

COLLINS, J.I. 1972. Prediction of shallow water spectra. *J.G.R.*, 77, 2693-2707.

GRANT, W.D. and O.S. MADSEN. 1982. Movable bed roughness in unsteady oscillatory flow. *J.G.R.*, 87, 469-481.

HASSELMANN, K. and J.I. COLLINS. 1968. Spectral dissipation of finite-depth gravity waves due to turbulent bottom friction. *J. Mar. Res.*, 26, 1-12.

RETIEF, G. DE F., G.K. PRESTEDGE and F.P.J. MULLER. 1982. A proposal for wave energy conversion near Cape Town. *18th ICCE* (ABSTRACTS).

RETIEF, G. DE F. and A.P.M. VONK. 1974. Low cost in shore wave direction indicator. *Proc. 14th Int. Coastal Engineering conference*, Copenhagen, 212-224.

ROSSOUW, J., L.W. COETZEE and C.J. VISSER 1982. A South African wave climate study. *18th ICCE* (ABSTRACTS).

SHEMDIN, O.H. et al 1980. Mechanisms of wave transformation in finite depth water. *J.G.R.*, 85, 5012-5018.

SWART, D.H. 1978. Vocoidal water wave theory. Volume 1: Derivation. *CSIR Research Report 357*, pp 137.

VAN IEPEREN, M.P. 1975. The bottom friction of the sea bed off Melkbosstrand, South Africa: A comparison of a quadractic with a linear friction model. *Deut. Hydrogr. Zeits.*, 28, 72-88.

VAN IEPEREN, M.P. 1976. Characteristics of wave fields recorded along the western coast of Southern Africa. *First Interdisciplinary Conf. on Mar. and Fresh Water Res. in S.A.*, Port Elizabeth, paper 45, pp 24.

VISSER, C.J., M. ENNIS and J. ROSSOUW 1980. Data qualification and spectral analysis of sea wave data. Paper 8 in: *Workshop on digital time series analysis with geophysical applications*, April 1980, Hermanus, South Africa.

INDIVIDUAL WAVE ANALYSIS OF IRREGULAR WAVE DEFORMATION IN THE NEARSHORE ZONE

by

Masaru Mizuguchi*

ABSTRACT

In a field observation, water surface fluctuations were measured at many points on line from the shoreline to just outside the surf zone. The data were analyzed by an individual wave method, where the concept of primary individual wave is introduced in order to investigate irregular wave deformation. Primary individual waves are defined by applying the zero-down crossing method with a suitable band width at the zero level to the high-pass filtered water surface fluctuation. It is shown that a wave thus defined behaves like a regular wave with a fixed period in the nearshore zone. A deterministic model based on wave height change of monochromatic waves on non-uniform beaches is then introduced. The model is found to describe the observed deformation process expressed by the primary individual waves.

1. INTRODUCTION

Shallow water wave deformation including wave breaking in the field is usually treated on the basis of representative waves such as the significant wave. A representative wave is a regular wave with a given period and deep-water wave height. However, use of one of the standard regular waves can give considerably different results in applications as compared with irregular waves. For example, a regular wave has a fixed breaking point with locally extreme phenomena at that point. In contrast, irregular waves have a broader wave breaking area and local extrema are largely non-existant.

The purpose of this study is to show how shallow water deformation, including wave breaking, can be described once a wave train is known outside the surf zone where the water depth is still not large.

There are two well-known methods to describe irregular waves; spectral analysis and individual wave analysis. Spectral analysis assumes that irregular wave trains consist of numerous small amplitude waves with random phases. In the nearshore region, however, nonlinearities in the existing finite amplitude waves are an essential feature, especially in the wave breaking process. The component waves in the frequency domain do not break, but real waves or individual waves in the time domain do break. Therefore, in treating shallow water wave deformation, including breaking, individual wave analysis appears more appropriate than spectral analysis.

* Department of Civil Engineering, Chuo University, Kasuga, Bunkyo-ku, Tokyo, 112 JAPAN

A few attempts have been made to model two (or one)-dimensional irregular wave deformation near the surf zone by using individual wave analysis. One approach is that of Goda (1975). He introduced the concept of selected wave breaking, which allows individual waves to break independently when they satisfy a breaking condition. Goda assumed that the wave height distribution changes due to the wave breaking in such a way that the broken wave heights are redistributed in proportion to the remaining distribution. This redistribution process is a probablistic one which can be doubted. Battjes and Janssen (1978) reported that the change of r.m.s. values of wave height in the surf zone could be well explained by their probabilistic model. They assumed a Rayleigh distribution with a cutoff at the maximum wave height for the wave height distribution in the surf zone. In the studies, mentioned above, the deformation process was treated from a probabilistic point of view, and the wave period distribution was ignored.

There have been reported in Japan several experimental studies on shallow water deformation of irregular waves (Iwagaki, Kimura and Kishida, 1977; Sawaragi, Iwata and Ishii, 1980; Isobe, Nishimura and Tsuka, 1980; Iwagaki, Mase and Tanaka, 1981). Most of these studies defined the individual waves automatically by applying a zero-cross method, and compared the behavior of the individual waves with that of a regular wave. Among them it is of worth pointing out that Isobe et al. (1980) demonstrated that an individual wave defined by the zero-down crossing method are not independent from the succeeding trough in the process of deformation.

Recently it has become possible to obtain field data of waves at many points in the nearshore zone by taking photos of the water surface elevation at poles with several sets of synchronized 16 mm memo-motion cameras. In the present paper, field data thus obtained are analyzed by an individual wave analysis, with emphasis on the question, "what is the best way to define the individual wave in the nearshore zone?". It will be shown that the individual waves as defined here behave like independent regular waves. A deterministic model is then developed and compared with the observed results. The model is found to predict the wave deformation process fairly well.

2. FIELD OBSERVATION

The field observation was conducted on December 14, 1978 at Ajigaura beach, Japan, facing east to the Pacific Ocean. In the field observation, the water surface elevation at many closely-spaced points was obtained by filming a large number of poles installed in the nearshore zone with twelve synchronized 16 mm memo-motion cameras. Forty-eight poles were set on a line directed on-offshore, extending from the shoreline to just outside of the surf zone. The distance between poles was about two meters. The techniques employed in the observation are described by Hotta and Mizuguchi (1980)

The observation period was 12 minutes 45.4 seconds and the sampling time was 0.2 s. In Fig. 1 are shown the bottom profile along the pole array and the mean water level. The bottom profile has a rather steep slope (about 1/12) near the shoreline, and an almost constant depth area

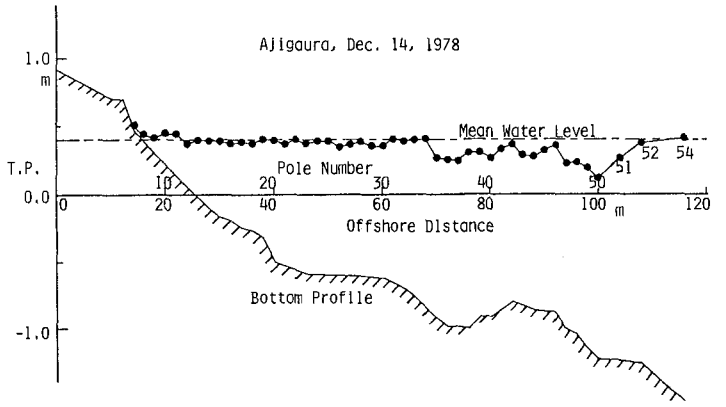

Fig. 1 Bottom profile, pole positions, and mean water level.

in the surf zone. As will be seen later, the average breaker zone was around Pole 43 at the offshoreward convex area. Outside the surf zone a uniformly sloping beach of about 1/40 is expected. The mean water level was obtained by averaging the water surface fluctuations over the observation period. One may consider the depression in the mean water level around the breaking point as wave set-down. However, the possible error in level surveying is too large to draw definite conclusions about the depression.

In this observation the horizontal current velocity near the bottom was measured at several points with electro-magnetic current meters including at Pole 23, the data of which will be used here. The current data gives some information about the wave directional properties (Nagata, 1964). The principal direction θ_p and modified long-crestedness γ^2 at Pole 23 were 2.3° and 0.112 respectively. Considering the error in directional alignment of the current meter placement, one can conclude that the waves were normally incident. The long-crestedness γ^2 is related to the n-th power of a $\cos^n\theta$ type directional spectra,

$$\gamma^2 = \frac{1}{n+1} \tag{1}$$

if the power is independent of the wave frequency. The calculated value of $\gamma^2 = 0.112$ corresponds to n = 8. The large value of n indicates that the incident waves were almost unidirectional.

3. INDIVIDUAL WAVE ANALYSIS AND PRIMARY INDIVIDUAL WAVE

We now apply an individual wave analysis to the obtained data. In the analysis, there are three points to be addressed.

3.1 Methods to Define Individual Waves

The first point in the wave analysis is to determine a method suitable to describe wave transformation in the nearshore zone. The choices are the zero-up crossing method, the zero-down crossing method, the trough to trough method, and the peak to peak method. Among these, the trough to trough method may give the most reasonable definition of an individual wave, since the dominant features of waves are largely determined by their peak configuration. However, technically it is difficult to determine trough points for shallow water waves with a long flat trough. Furthermore, theoretical treatments of irregular wave trains are based on the zero-cross methods (For example, Longuet-Higgins, 1975). Therefore, here we compare the two zero-cross methods.

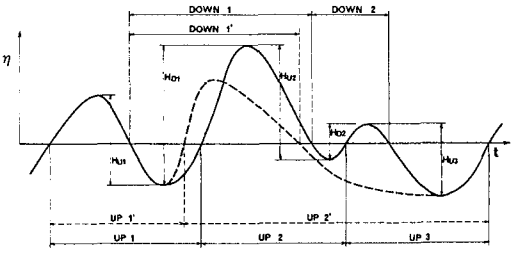

Fig. 2 Schematic illustrating the difference between zero-down crossing method and zero-up crossing method (after Hotta and Mizuguchi, 1980).

In Fig. 2 a clear difference is seen between the two zero-crossing methods when applied to waves with secondary waves, denoted by the solid line. The up method fails to define the small secondary waves by giving two almost equivalent waves denoted by UP 2 and UP 3, in contrast to the success of the down-method, which gives two waves denoted by DOWN 1 and DOWN 2. In this respect, the down method is superior to the up method in clearly reproducing one of the characteristic features of shallow water wave deformation, that is, development of secondary water surface fluctuations. In addition, the front rise of the wave peak is more important than its tail-down in the process of wave deformation in the surf zone. Therefore, the zero-down crossing method should be employed when treating shallow water deformation of individual waves.

Figure 3 shows the wave height and wave period distributions given by the zero-down crossing method and zero-up crossing methods at three representative locations. The two methods were applied to high-pass filtered data. A reading error of E_R = 1 cm (minimum value expected) was used, which gives a band width at zero level, and will be discussed later. At pole 54 in Fig. 3 (outside the surf zone), no appreciable

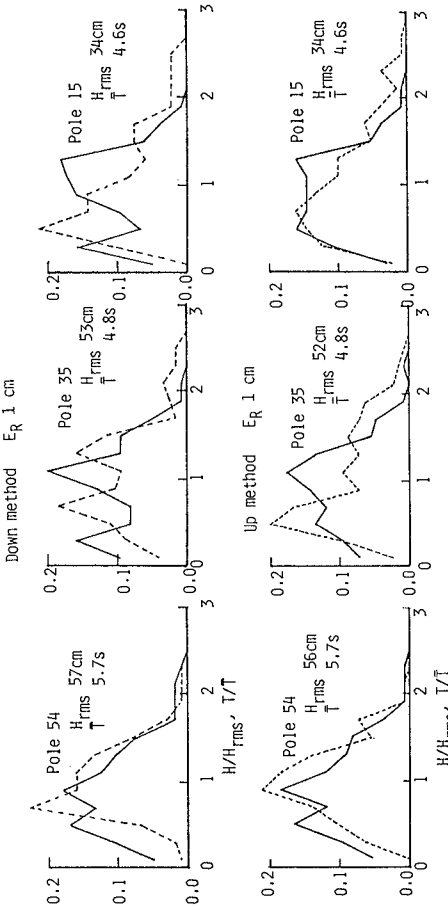

Fig. 3 Wave height (solid lines) and period (dotted lines) distributions both outside and in the surf zone.

difference is observed between the results at the two methods. The two methods thus give the same result when the irregular wave train consists of a summation of infinitesimal waves with random phases. This means that the two methods are equivalent as long as secondary fluctuations do not exist. However, at poles 35 and 15 in Fig. 3, the wave height distribution by the down method exhibits a double peak, contrary to the mono-peaked distribution given by the up method. This is expected from the previous discussion concerning Fig. 2, and confirms the superiority of the down method for use in the shallow water region.

It should be mentioned that statistical quantities, such as the significant wave height, $H_{1/3}$, and significant wave period, $T_{1/3}$, also differ according to the method used when secondary fluctuations exist. Generally, the down method gives larger values than the up method for quantities which are calculated by taking an average only over waves of height greater than a certain value. The smaller the quantity E_R employed, the larger is the difference. Figure 4 gives an example of the difference between the two methods with $E_R = 0$.

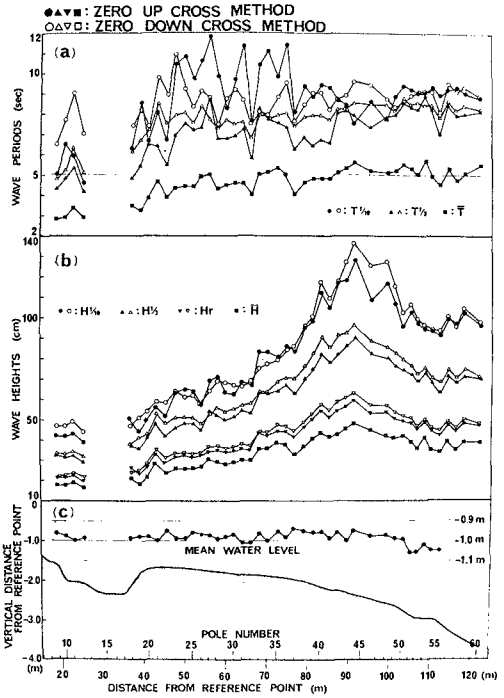

Fig. 4 Change of statistical quantities in shallow water transformation (after Hotta and Mizuguchi, 1979).

3.2 Long Period Fluctuations

The second point to be discuseed concerning the problem of defining waves is the well-known one that low frequency fluctuations have non-negligible power in the nearshore zone. These fluctuations affect the zero level for progressive individual waves, which is of concern here.

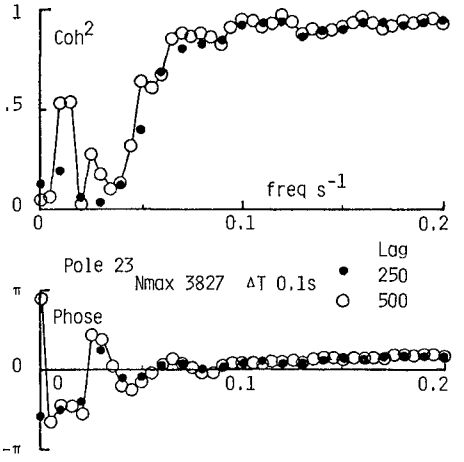

Fig. 5 Cross spectra between water surface fluctuation and onshore velocity at Pole 23.

Figure 5 gives an example of the cross spectra, coherence squared, and phase function between the water surface fluctuation and onshore velocity at Pole 23, about 20 m offshore at a depth of about 1.0 m. The cross spectra were calculated by the Blackman - Tukey method with the two lag numbers of 250 and 500 on 3827 data points. Generally speaking, a smaller lag number gives a more statistically reliable result for the spectra. Application of a spectral window, used to decrease statistical deviation due to the finiteness of the data length, requires neighboring frequency components be in phase when they are correlated. However, as shown in Fig. 5, the smaller lag number gives a lower value of the coherence than the larger lag number, especially in the low frequency region. This means that the lag number of 250 or the equivalent bandwidth of 0.01 s^{-1} failed to detect the rapid sharp change of the phase function in the lower frequency region, possibly due to the existence of standing waves. Therefore, in calculating the cross spectra by applying a small lag number for reliability, the result may be more contaminated because of taking the average over a wider frequency range.

Here, we will focus on the result with the lag number of 500. One notices that in the frequency region lower than 0.05 Hz, the coherence shows sharp fluctuations between zero to rather high frequencies, and

that the phase function shows regular shifts between plus $\pi/2$ to $-\pi/2$. These two observations indicate that the lower frequency components arise from standing waves. A standing wave in the on-offshore direction has a phase difference of $\pm\pi/2$ between surface fluctuation and onshore velocity, in contrast to the in-phase relationship for progressive waves. Further discussion on long period fluctuations in the nearshore zone can be found in Hotta, Mizuguchi, and Isobe (1981), and in Mizuguchi (1982). It is a future problem to investigate the interaction between the longer period standing waves and the shorter period progressive waves. At present, neglecting this interaction, the long period fluctuations should be removed in order to obtain well-defined individual waves.

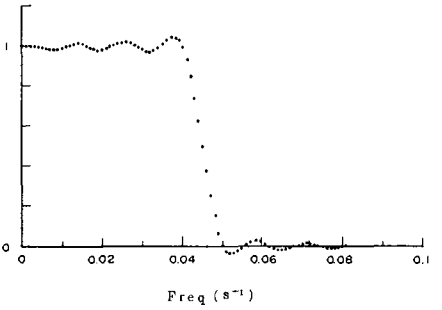

Fig. 6 Frequency response of applied numerical low-pass filter.

In the present analysis, we simply applied the low-pass filter shown in Fig. 6 to enhance the low frequency components. The cutoff frequency of 0.045 Hz was determined by the results shown in Fig. 5.

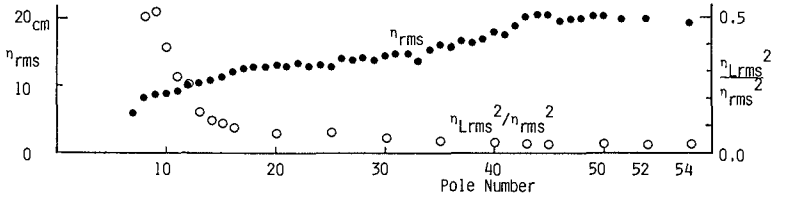

Fig. 7 Ratios of long period fluctuation and r.m.s. values of water surface fluctuation.

In Fig. 7 are shown the ratios of r.m.s. values between the long period fluctuation η_{Lrms} of the water surface fluctuation and the raw fluctuation η_{rms}. In this observation the long period fluctuation becomes significant near the shoreline. Standing waves are somewhat amplified near the shoreline and have a finite amplitude there, although progressive waves decay to disappear due to breaking. In Fig. 7 is also

shown the r.m.s. raw water surface fluctuation η_{rms}. The average breaking point was at Pole 43, at which point the r.m.s. values of η start to decrease. A wave reformation area, where the significant wave breakings ended and η_{rms} became constant, was visually observed to be between Poles 30 and 20. Secondary wave breaking was observed at Pole 18 where η_{rms} again started to decrease.

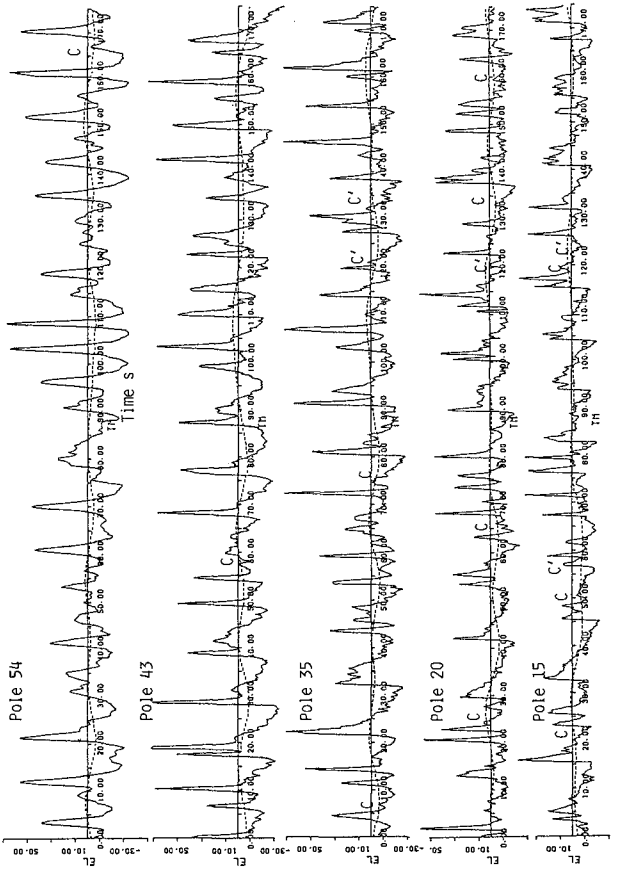

Fig. 8 Examples of observed water surface fluctuations (solid lines) and long period fluctuations (dotted lines).

The influence of the long period fluctuation on the individual wave analysis is shown in Fig. 8. Raw water surface fluctuations are plotted in solid lines, and long period fluctuations are plotted in broken lines at representative locations. When the long period fluctuations are significant, some zero-cross points will be missed. Those points are denoted by C, where the raw data is seen to miss crossing the mean water level but does intersect the level of the long period fluctuation. The points indicated by C' are opposite cases. Generally, the number of points C are greater than points C' in the surf zone, in particular near the shoreline. In the following, we will discuss the high-pass filtered data obtained by subtracting the long period fluctuation from the measured water surface fluctuation.

3.3 Reading Error and Secondary Fluctuations

Finally is discussed the reading error E_R as introduced previously. Reading errors are inevitable when the photographed surface elevation is digitized. The film was projected on a scale of 1/20 and the minimum scale reading was 1 mm. Therefore errors on the order of 2 cm are expected. This error may produce false zero-cross points, especially for waves with a mild slope tail-down. Therefore, a band width of magnitude E_R is introduced at the zero level. Then only the zero-down crossing points with successive peak and trough larger than E_R remain to define the individual wave.

Figure 9 shows examples of individual wave decompositions by the zero-down crossing method with E_R = 2 cm for high-pass filtered water surface fluctuations at representative locations. At Pole 54, the most offshoreward pole, no wave breaking was seen; Pole 43 was at the average breaking point; significant wave breaking terminated at Pole 35; Pole 20 was in the so-called reformed wave region; the secondary wave breaking zone was at Pole 15. The defined waves were numbered starting at Pole 54. The numbered waves were then traced as they propagated, as shown in the figure. Numbers joined by plus signs indicate that the waves united at that location; bracketed numbers denote wave separation. However, it should be noted that combination and separation is a matter of the defining process of the individual wave.

A characteristic feature observed in Fig. 9, and which should be emphasized, is that most of the primary wave peaks are easily identified throughout the observation area. This fact suggests introduction of the concept of "Primary Individual Wave", hereafter called PIW, characterized by an eminent peak, in order to describe irregular wave deformation in a deterministic way. In the nearshore zone, secondary waves are often observed, as already mentioned. Wave breaking also generates turbulent surface fluctuations. These problems are not easy to treat quantitatively at present. Here, as an expedient, the band width E_R, originally introduced to remove the effect of the error in reading, is adjusted to suppress these secondary fluctuations. Then the individual waves thus defined may have a one to one correspondence to the above-mentioned eminent peaks.

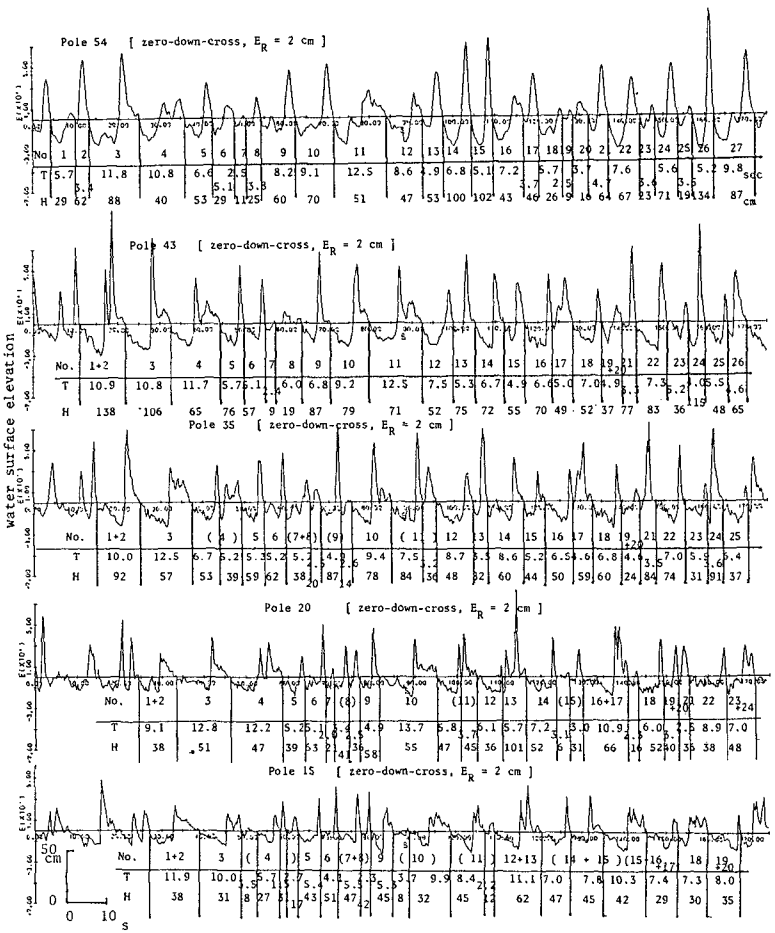

Fig. 9 Examples of individual wave decomposition by the zero-down crossing method with E_R = 2 cm.

What is an appropriate value of E_R for our purpose? As shown in Fig. 9, E_R = 2 cm is so small that some of the decomposed individual waves may correspond to secondary peaks. Figure 10 shows how wave height and period distributions change with increase of E_R at Pole 35, a location where secondary waves and turbulent surface fluctuations appear. The wave height destribution tends to be mono-peaked, neglecting small disturbances or secondary waves. The respective wave height and period distributions for E_R = 4 cm are almost the same, as for E_R = 5 cm. The representative wave height and wave period such as $H_{1/3}$, H_{rms}, and $T_{1/3}$, increase considerably with increase of E_R. A properly chosen value of E_R should give proper values for those quantities. Figure 11 shows the decrease in numbers of defined waves, N_w, at various locations with increase of E_R. The decrease in the surf zone is considerable, and the numbers of waves defined with E_R in the range from 3 to 5 cm are almost the same at all locations. Therefore there may be a suitable value of E_R which gives almost the same number of waves through the nearshore zone, and which also gives a stable joint probability distribution of wave height and period at each location.

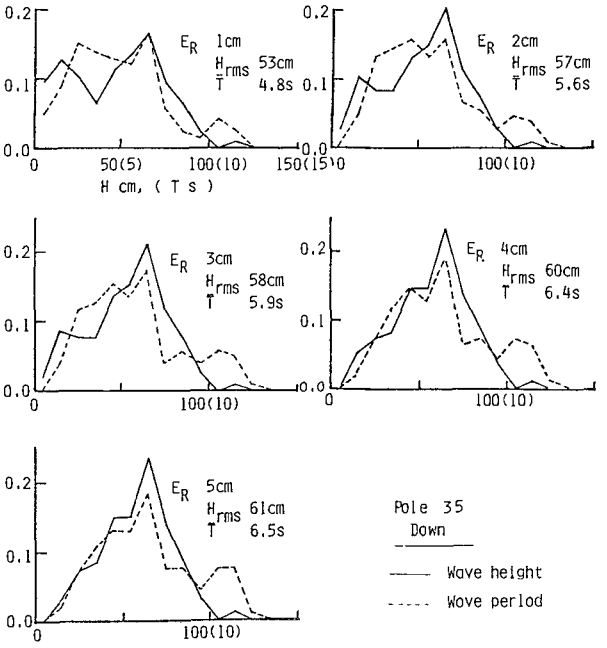

Fig. 10 Change of wave height and period distribution at Pole 35 by the down method with increase of E_R.

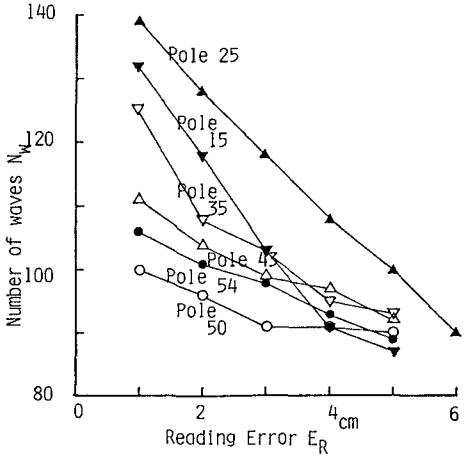

Fig. 11 Decrease in number of waves with increase in E_R.

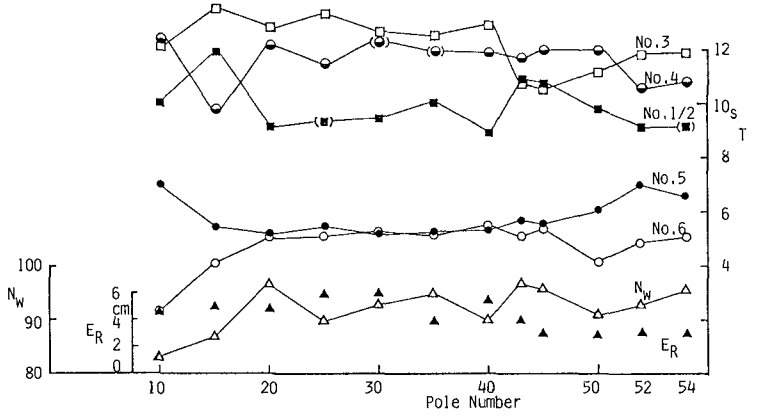

Fig. 12 Applied value E_R, numbers of waves defined with E_R, and changes in period of the first six observed waves.

3.4 Primary Individual Wave and its Deformation

The concept of PIW is now clear. A PIW can be defined by applying the zero-down cross method with a suitable value of E_R, a band width at the zero level, to the high-pass filtered water surface fluctuations. The suitable value of E_R may differ according to location. The proper value of E_R can be determined, as here, to give the same number of waves throughout the observation area as for the most offshore-ward region. It is conjectured that the ratio of E_R to wave height may depend on both the Ursell number and on the relative distance from the breaking point.

The deformation of the observed PIW in the nearshore zone will now be discussed. In Fig. 12 are shown the applied value of E_R, the resultant number of waves, and wave periods changes of the first six (or five) waves. The values of E_R were determined as mentioned above, with the magnitude of the observed secondary fluctuations taken into consideration. The number of waves is almost constant except very near the shoreline, where the PIW itself become small and can not be distinguished from the secondary fluctuations. Thus Fig. 12 demonstrates the fact that the wave period of the PIW does not change through the observation area.

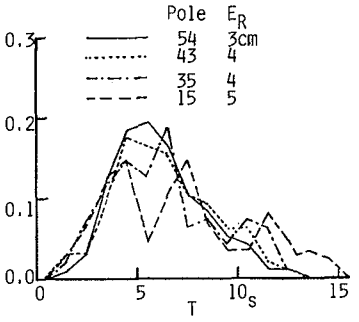

Fig. 13 Wave period distributions.

The corresponding wave period distributions shown in Fig. 13 are also seen to be essentially constant. Therefore, we can say that wave periods of the PIW are constant through the area of concern. This can be expected from the fact that wave celerity in the shallow water region can be well expressed by non-dispersive long wave theory. Therefore, each PIW can be treated as a regular wave. However, viewing the details of the distributions in Fig. 13, one can notice that they become flat near the shoreline. This suggests that near the shoreline, where the water depth is very shallow, secondary fluctuations are not negligible and should be included in modeling of the wave transformation. For the PIW, the wave height changes as it propagates, but the period does not.

4. MODELLING OF PIW DEFORMATION

We now attempt to model wave height change, and compare the calculation with the observed results. Outside the surf zone, the wave height is assumed to obey the relation

$$H^{5/2}[(gHT^2/d^2)^{1/2} - 2\sqrt{3}] = \text{const.} \tag{2}$$

where, H: wave height, d: water depth and, g: gravitational acceleration. Equation (2) was obtained by Shuto (1974), based on finite amplitude long wave (first order cnoidal wave) theory, and is valid only for large Ursell number.

The breaking criterion employed is that given by Sunamura and Horikawa (1974) for depth-controlled wave breaking.

$$H_b/H_o = s^{0.2} (H_o/L_o)^{-0.25} \tag{3}$$

Here, H_b: breaking wave height, H_o: deep-water wave height, s: slope of uniform beach, and L_o: deep-water wave length. This is an empirical formula for uniformly sloping beaches. Wave height change in two-dimensional laboratory experiments up to breaking has been found to be well described by Eq. (2) with Eq. (3) (e.g., Mizuguchi and Mori, 1981).

For the wave height change after breaking, a constant ratio of wave height to water depth has been used in many applications. However, it is clear that this ratio can not be constant on a real beach. Here an heuristic model developed by the author (Mizuguchi, 1980) is employed.

$$\frac{d}{dx}(Ec_g) = -\epsilon \tag{4}$$

$$\epsilon = \rho g \nu_e (kH)^2/2 \tag{5}$$

$$\nu_e = \nu_{eb}(H/\gamma d - c/\gamma)^{1/2} \tag{6}$$

where, c_g: group velocity, ϵ: energy dissipation ratio, ρ: fluid density, ν_e: eddy viscosity, k: wave number, ν_{eb}: eddy viscosity at the breaking point, γ: wave height to water depth ratio at the breaking point, and c: wave height to water depth ratio in the wave reforming zone. The critical point of this model is the form of the eddy viscosity in Eq. (6), which enables waves to recover under certain situations. The eddy viscosity ν_{eb} at the breaking point is determined by the wave conditions and the beach profile before breaking. This model was shown to well reproduce the experimental results of regular waves on various non-uniform beach profiles, except very near the shoreline (Mizuguchi, 1980)

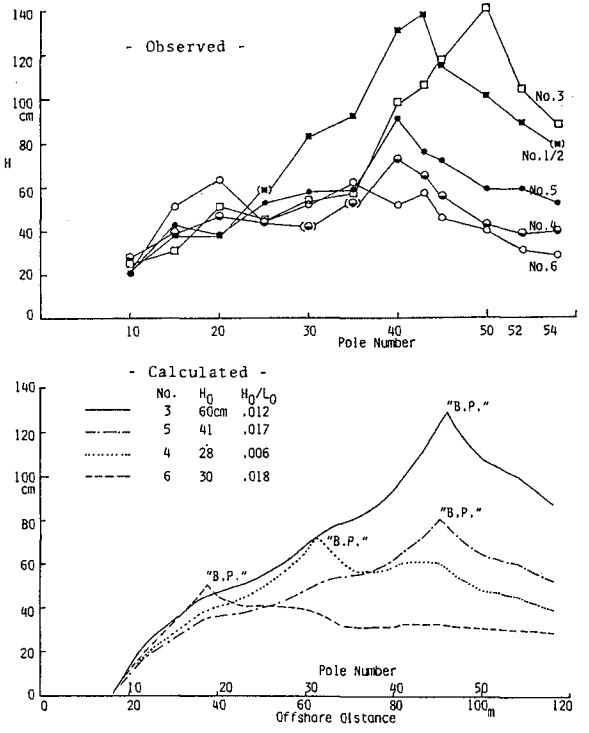

Fig. 14 Wave height changes of PIW, observed and calculated.

Figure 14 shows both the observed wave heights across the surf zone of the first five (or six) waves and the wave heights calculated by the model. Except for wave No. 4, the agreement is good, although decay after breaking is more rapid in the observation than in the calculation. An energy dissipation model of breaking waves based on the similarity to a hydraulic jump (Le Mehaute, 1962) gives a dissipation rate proportional to the third power of wave height. This model may better predict the observed rapid decay. For wave No. 4, the breaking position differs considerably. This is attributed to the fact that breaking condition in the calculation was not satisfied at the offshoreward slope; the continuing deeper area or trough in the bottom profile can not cause the wave to break in the present formulation. As previously stated, the zero-down crossing method has the defect that the succeeding tail-down of a peak is not fully included in the wave description. Isobe et al. (1980) found in laboratory experiments that the succeeding deeper trough

of a wave tends to delay the wave breaking. It has also been reported (Iwagaki et al., 1977) that individual waves defined by the zero-up crossing method tend to break, before satisfying the breaking criterion for regular waves on a uniformly sloping laboratory beach. The breaking criterion for PIW in a regular wave train on non-uniform beaches should be investigated further.

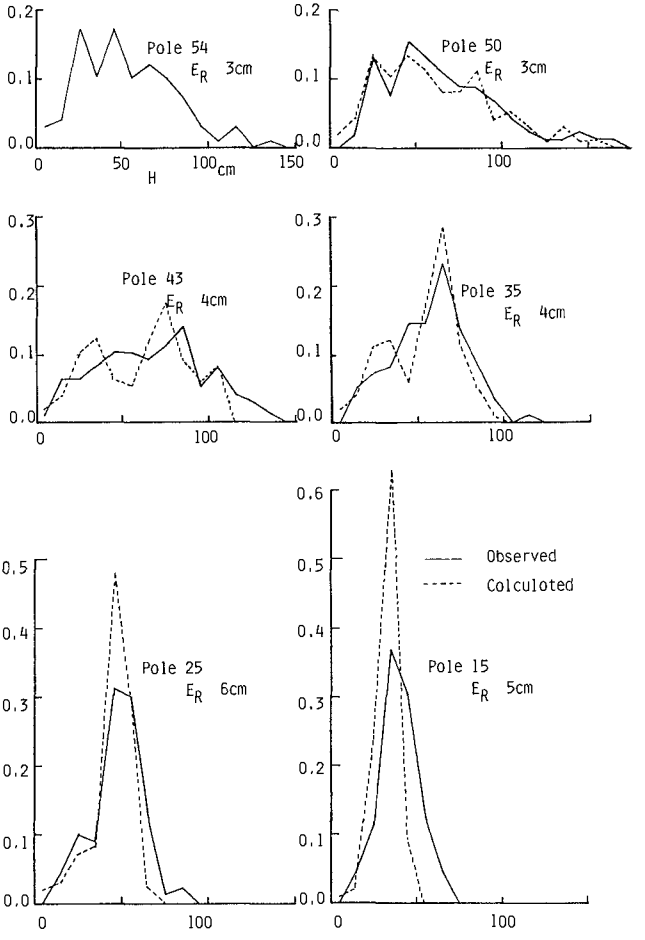

Fig. 15 Comparison of wave height distributions of PIW.

Near the shoreline, this model always predicts a smaller wave height than observed, since the wave height at the shoreline in the model is assumed to be zero, although in actuality there is always some run-up with finite wave amplitude at the shoreline. Wave set-up also has a little to do with the underestimation, as shown in Fig. 1.

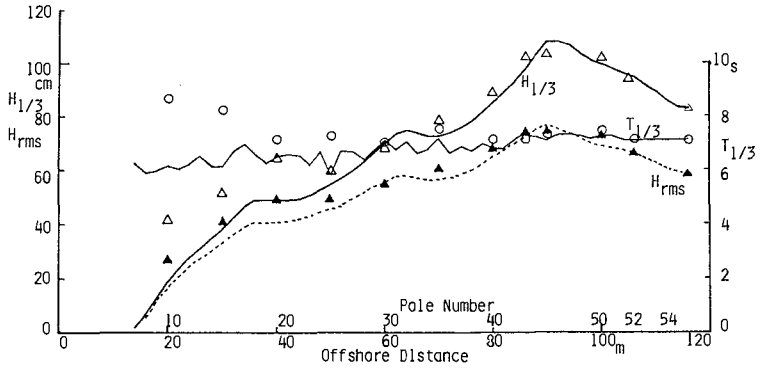

Fig. 16 Comparison of statistical quantities resulting from a PIW analysis. Symbols denote observed values and lines denote calculated ones.

Figure 15 gives comparisons between the observed wave height distributions of PIW and the calculated ones. The agreement is fair. The lack of agreement near the shoreline in the modelling is attributed to the two reasons given in the previous paragraph. Lack of agreement is also caused by the inapplicability of the concept of PIW near the shoreline as stated in the former section. The calculated statistical quantities are compared with the observed ones in Fig. 16. Again, agreement is good except near the shoreline. A local extreme, such as an unusually large wave height increase at the breaking point, expected in a representative wave approach, is not found either in the observation or in the calculation.

5. CONCLUSIONS

The following conclusions can be made:

First, a Primary Individual Wave can be defined by applying the zero-down crossing method to the high-pass filtered water surface fluctuation using a suitable band width E_R at the zero level. Second, the thus-defined PIW shows a regular wave-like behavior in the nearshore zone. Third, the shallow water wave deformation of an irregular wave train in and near the surf zone can be described with the PIW, except very near the shoreline, by applying a wave height change model as given here.

Finally, however, there are still some important topics remaining to be investigated in order to obtain full understanding of the shallow water deformation of field waves. These are mainly long period fluctuations, secondary fluctuations, and the effect of non-uniformity of the bottom profile.

ACKNOWLEDGEMENTS

This study was originally carried out in 1980 with assistance of Mr. C. Matsuda, who was an undergraduate student at Chuo University. The data used were obtained during a cooperative research project with Mr. S. Hotta, Tokyo Metropolitan University, in a joint field experiment under the supervision of Prof. K. Horikawa, University of Tokyo. The manuscript was proofread by Dr. N.C. Kraus, Nearshore Environment Research Center.

REFERENCES

Battjes, J.A. and J.P.F.M. Janssen (1978): Energy loss and set-up due to breaking of random waves, Proc. 16th Coastal Eng. Conf., Hamburg, pp. 569-587.

Goda, Y. (1975): Irregular wave deformation in the surf zone, Coastal Eng. in Japan, Vol. 18, pp. 13-26.

Hotta, S. and M. Mizuguchi (1979): Field observation of waves in the surf zone, Proc. 26th Japanese Conf. on Coastal Eng., pp. 152-156. (in Japanese)

Hotta, S. and M. Mizuguchi (1980): A field study of waves in the surf zone, Coastal Eng. in Japan, Vol. 23, pp. 59-80.

Hotta, S., M. Mizuguchi and M. Isobe (1981): Observations of long period waves in the nearshore zone, Coastal Eng. in Japan, Vol. 24, pp. 41-76.

Isobe, M., H. Nishimura and T. Tsuka (1980): Experimental study on the breaking of irregular waves, Proc. 27th Japanese Conf. on Coastal Eng., pp. 139-142. (in Japanese)

Iwagaki, Y., A. Kimura and N. Kishida (1977): An experimental study on the breaking of irregular waves on sloping beaches, Proc. 24th Japanese Conf. on Coastal Eng. pp. 102-106. (in Japanese)

Iwagaki, Y., H. Mase and G. Tanaka (1981): Modelling of irregular wave transformation in the surf zone, Proc. 28th Japanese Conf. on Coastal Eng., pp. 104-108. (in Japanese)

Le Mehaute, B. (1962): On non-saturated breakers and the wave run-up, Proc. 8th Conf. on Coastal Eng., pp. 77-92.

Longuet-Higgins M.S. (1975): On the joint distribution of the periods and amplitudes of sea waves, Jour. Geophys. Res., Vol. 85, No. 18, pp. 2688-2694.

Mizuguchi, M. (1980): An heuristic model of wave height distribution in surf zone, Proc. 17th Conf. on Coastal Eng., pp. 278-289.

Mizuguchi, M. (1982): A field observation of wave keinmatics in the surf zone, Coastal Eng. in Japan, Vol. 25, in press.

Mizuguchi, M. and M. Mori. (1981): Modelling of two-dimensional beach transformation due to waves, Coastal Eng. in Japan, Vol. 24, pp. 155-170.

Nagata, U. (1964): The statistical properties of orbital wave motions and their application for the measurement of directional wave spectra, Jour. Oceanogr. Soc. Japan, Vol. 19, No. 4, pp. 169-181.

Sawaragi, T., K. Iwata and T. Ishii (1980): Experimental study on Irregular wave deformation in surf zone, Proc. 27th Japanese Conf. on Coastal Eng., pp. 143-147. (in Japanese)

Shuto, N. (1974): Nonlinear long waves in a channel of variable section, Coastal Eng. in Japan, Vol. 17, pp. 1-12.

Sunamura, T. and K. Horikawa (1974): Two-dimensional beach transformation due to waves, Proc. 14th Conf. on Coastal Eng., pp. 920-938.

NEW EQUATION OF SURACE ELEVATION IN WAVE MOTION

by

Y. C. Ouyang* Y.Y. Chen** Frederick L.W. Tang***

ABSTRACT

A nonlinear solution of wave profile equation directly derived from stream function is submitted. In stead of expressing by trigonometric series to approach the real solution, implicit function is adopted. In the era of electronic computer, Such an expression will be convenient for practical utilization.

Equations in either deep water or in finite water depth are worked out. They are proved more reasonable in graphical shape of wave profile and consistant in the continuity of wave celerity in various depth in comparison with Stokes theory.

INTRODUCTION

For more than 100 *years, Stokes' wave theory has been applied to various engineering problems. However, the theory is an approximate solution strictly. Furthermore, we all have the experience that the* $(n+1)$ *th solution is not guaranteed to be better*

---

* *Senior Graduate Student, Civil Engineering Graduate School, National Cheng Kung University.*

** *Senior Graduate Student, Associate Researcher, Tainan Hydraulics Laboratory.*

*** *Professor,*
National Cheng Kung University
Tainan City 700 *Taiwan*
Republic of China

than nth. The only merit is that the equation is expressed explicitly. In the eva of electronic computer, implicit equation can be solved promptly. It is not necessary to be stuck on explicit equation. Reasonable solutions of wave profiles in deep and intermediate water area are worked out directly from stream function in following sections. Their validity and consistancy are examined closely.

FUNDAMENTAL EQUATIONS

(A) *Governing equations*

Water is supposed to be incompressible and irrotational, then the governing equations of wave motion are as follows :

$$\nabla^2\phi = 0 \quad , \quad \nabla^2\phi = 0 \tag{1}$$

$$\nabla^2 = \left(\frac{\partial^2}{\partial x^2} + \frac{\partial^2}{\partial y^2} \right)$$

x : *abscissa along the water surface, being positive toward the wave direction.*

y : *ordinate vertical to the water surface, being positive upward*

$\psi = \psi (x , y , t)$: *stream function*

$\phi = \phi (x , y , t)$: *velocity potential*

t : *time*

(B) *Boundary condition equations on free surface*

(a) *Dynamical equation*

$$\left(\frac{\partial \phi}{\partial t} \right)_{y=\eta} + g\eta + \frac{1}{2} \left[\left(\frac{\partial \psi}{\partial x} \right)^2 + \left(\frac{\partial \phi}{\partial y} \right)^2 \right]_{y=\eta} = Q(t) \tag{2}$$

g : *gravitational acceleration*

$\eta = \eta(x, t)$: *fluctuation of water surface elevation with respect to* $x-$*axis*

$$\frac{\partial \psi}{\partial x} = -\frac{\partial \phi}{\partial y} = v \ , \ \frac{\partial \psi}{\partial y} = \frac{\partial \phi}{\partial x} = -u$$

u , v : *horizontal and vertical velocity of water particle*

$Q(t)$: *Bernoulli's number varys with time only*

(b) *Kinematic equation*

$$\left(\frac{\partial \phi}{\partial y}\right)_{y=\eta} = \frac{\partial \eta}{\partial t} + \frac{\partial \eta}{\partial x}\left(\frac{\partial \phi}{\partial x}\right)_{y=\eta} \tag{3}$$

(C) *Boundary condition in bottom*

$$\left(\frac{\partial \phi}{\partial y}\right)_{y=-d} = \left(\frac{\partial \psi}{\partial x}\right)_{y=-d} = 0 \tag{4}$$

d : *vertical distance from* $x-$*axis to the bottom*

(D) *Assumptions of solution*

The solutions of above mentioned Laplace equation i.e. equation (1) *are to be assumed as follows* :

$$\psi(x, y, t) = \sum_{n=1}^{\infty} C_n e^{-nkd}\left\{e^{nk(d+y)} - e^{-nk(d+y)}\right\} cosnk(x - ct)$$

$$\phi(x, y, t) = \sum_{n=1}^{\infty} C_n e^{-nkd}\left\{e^{nk(d+y)} + e^{-nk(d+y)}\right\} sinnk(x - ct) \tag{5}$$

The stream function of free surface is :

$$\psi(x, \eta, t) = 0$$

So that

$$\eta(x,t)=\sum_{n=1}^{I}\frac{C_n}{c}e^{-nkd}\left[e^{nk(d+\eta)}-e^{-nk(d+\eta)}\right]\cos nk(x-ct)$$

C_n : *constants to be worked out*

n : 1 , 2 , 3 ……

e : *exponential*

k : *wave number*, $k=2\pi/L$

L : *wave length*

c : *wave celerity*

The motion is altered to be steady flow by adding an opposite velocity c, $(x-ct)$ *in above equations will be replaced by* x, *then*

$$\phi(x,y)=cy-\sum_{n=1}^{\infty}C_n e^{-nkd}\left[e^{nk(d+y)}-e^{-nk(d+y)}\right]\cos nkx$$

$$\phi(x,y)=cx+\sum_{n=1}^{\infty}C_n e^{-nkd}\left[e^{nk(d+y)}+e^{-nk(d+y)}\right]\sin nkx$$

$$\eta(x)=\sum_{n=1}^{\infty}\frac{C_n}{c}e^{-nkd}\left[e^{nk(d+\eta)}-e^{-nk(d+\eta)}\right]\cos nkx \tag{6}$$

NEW EQUATION IN DEEP WATER

In above equations , $d\to\infty$, $n=1$, *we get*

$$\phi(x,y)=cy-C_1e^{ky}\cos kx \tag{7}$$

$$\eta(x)=\frac{C_1}{c}e^{k\eta}\cos kx \tag{8}$$

η_{max} *and* η_{min} *are the elevation of crest and trough of wave profile.*

$$\eta_{max}=\eta_1=\frac{C_1}{c}e^{k\eta_1} \tag{9}$$

$$\eta_{min} = \eta_2 = \frac{C_1}{c} e^{k\eta_1} \tag{10}$$

Invoke a parameter ω *which is defined as the ratio of maximan particle velocity at the wave crest,* q_c*, to wave celerity,* c*, namely*

$$\omega = q_c / c = -\left(\frac{\partial \psi}{\partial y}\right)_{y=\eta_1} / c \tag{11}$$

ω *is to be* 0 *when wave is breaking, and will be* -1 *on calm water surface i.e.*

$$-1 \leq \omega \leq 0 \quad or \quad 0 \leq 1+\omega \leq 1$$

Substitute (7) *to* (11)

$$(1+\omega)/k = \frac{C_1}{c} e^{k\eta_1} \tag{12}$$

From equation (9)

$$(1+\omega)/k = \eta_1 = \frac{C_1}{c} e^{k\eta_1} \tag{13}$$

$$C_1 = \frac{c(1+\omega)}{k e^{(1+\omega)}} \tag{14}$$

is obtained.

Consequently:

$$\psi(x, y) = cy - \frac{c(1+\omega)}{k e^{(1+\omega)}} e^{ky} \cos kx \tag{15}$$

$$\eta(x) = \frac{1+\omega}{k e^{(1+\omega)}} e^{k\eta} \cos kx \tag{16}$$

From equations (9), (10) *and* (13)

$$-\frac{e^{k\eta_2}}{\eta_2}=\frac{e^{k\eta_1}}{\eta_1}=\frac{k e^{(1+\omega)}}{1+\omega} \tag{17}$$

H denotes the wave height $H=\eta_1-\eta_2$ 。

Accordingly

$$\frac{k e^{(1+\omega)}}{1+\omega}=\frac{e^{k(\eta_1-H)}}{H-\eta_1}=e^{(1+\omega)}e^{-kH}/\left(H-\frac{1+\omega}{k}\right)$$

i.e. $$kH=(1+\omega)(1+e^{-kH}) \tag{18}$$

Let $\delta=H/L$ *namely the wave steepness, equation* (18) *is altered to be*

$$1+\omega=\frac{2\pi\delta}{1+e^{-2\pi\delta}}=\theta \tag{19}$$

and

$$\psi(x,y)=cy-\frac{c\theta}{ke^{\theta}}e^{ky}\cos kx \tag{20}$$

$$\eta(x)=\frac{\theta}{ke^{\theta}}e^{k\eta}\cos kx \tag{21}$$

are oblained. Equation (21) *is an implicit equation, however, it is to be solved by Newton—Raphson's method promptly through computer.*

The curve is to be depicted for a critical case i.e. $\delta=0.142$ *and compared with Rayleigh's solution.*

Wave celerity c is worked out by following procedure.

In steady flow, $(\partial\phi/\partial t)$ *vanishes and* $Q(t)$ *becomes constant Q in dynamic boundary condition of free surface. Subslitute the new wave profile equation* (21) *to equation* (2)

$$\frac{\theta}{ke^{\theta}}e^{k\eta}\cos kx+\frac{1}{2g}\left\{c^2-2c^2\frac{\theta}{e^{\theta}}e^{k\eta}\cos kx+\frac{c^2\theta^2}{e^{2\theta}}e^{2k\eta}\right\}=\frac{Q}{g}=h$$

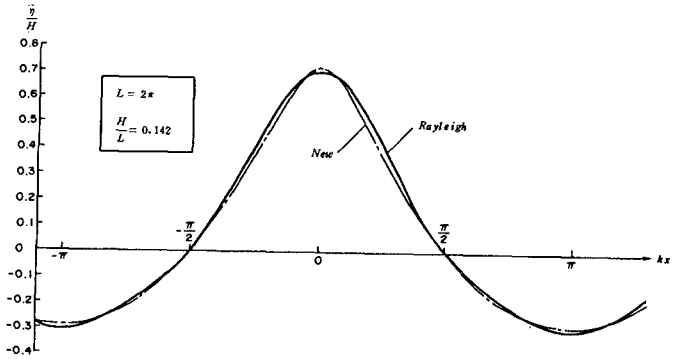

Wave profile in deep water

Put $e^{2k\eta} \doteqdot 1 + 2k\eta = 1 + \frac{2\theta}{e^{\theta}} e^{k\eta} \cos kx$, *this equation becomes*

$$\left(c^2 + \frac{c^2\theta^2}{e^{2\theta}} \right) + \frac{2\theta}{e^{\theta}} \left(\frac{g}{k} - c^2 + \frac{c^2\theta^2}{e^{2\theta}} \right) e^{k\eta} \cos kx = Q \qquad (22)$$

Q is a constant, the coefficient of variable term $e^{k\eta} \cos kx$ *must be zero. So we can get*

$$C^2 = \frac{g}{k} \left(1 - \frac{\theta^2}{e^{2\theta}} \right)^{-1} = \frac{g}{k} \left[1 - \left(\frac{2\pi\delta}{1 + e^{-2\pi\delta}} \right)^2 / exp \left(\frac{4\pi\delta}{1 + e^{-2\pi\delta}} \right) \right]^{-1} \qquad (23)$$

According to this equation, wave celerity increases with wave steepness exponentially in stead of linearly with the square of wave steepness in Rayleigh's theory, however, while δ *is small*

$$(c^2)_{\delta\to 0} = \frac{g}{k}\{\,1+(\frac{2\pi\delta}{1+e^{-2\pi\delta}})^2 / exp\,(\frac{4\pi\delta}{1+e^{-2\pi\delta}})\,\}$$

$$= \frac{g}{k}\{\,1+k^2\,(\frac{H}{2})^2\,\} \qquad (24)$$

Wave celerity calculated by the two theories are almost identical.

Following diagram shows the comparison of the wave celerities calculated by these two theories.

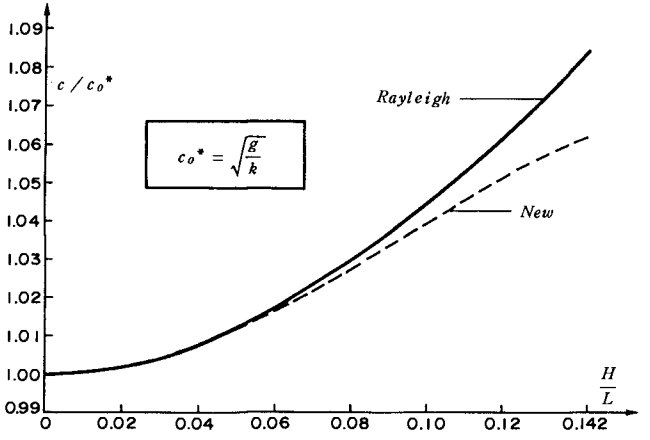

Comparison of wave celerity in deep water

The mean level of wave profile is worked out by the following equation

$$\xi = \frac{1}{L}\int_0^L \eta\,dx$$

Let $\eta \doteqdot \frac{\theta}{ke^{\theta}}(\,1+k\eta\,)\cos kx$

$$\eta = \frac{A\cos kx}{1-Ak\cos kx} \qquad A = \frac{\theta}{ke^{\theta}}$$

Substitute this expression to the integration

$$\xi = \frac{1}{k}\left[\frac{1}{\sqrt{1-A^2k^2}} - 1\right]$$

$$\xi = \frac{1}{k}\left[\frac{1}{\sqrt{1-\theta^2/e^{2\theta}}} - 1\right] \doteqdot \frac{1}{2k}\left[\frac{\left(\frac{2\pi\delta}{1+e^{-2\pi\delta}}\right)^2}{exp\left(\frac{4\pi\delta}{1+e^{-2\pi\delta}}\right)}\right] \qquad (25)$$

While the steepness is small i.e. $\delta \to 0$

$$\xi = \frac{4\pi^2\delta^2}{2k} = \frac{\pi H^2}{L}$$

coinciding to Rayleigh's theory.

To check the relative error, substitute the value of c i.e. equation (23) *to the following equation to calculate the difference of total water head due to adopting* $1+2k\eta$ *in stead of* $e^{2k\eta}$

$$\Delta h = \frac{1}{2g}\frac{e^2\theta^2}{e^{2\theta}}\left(e^{2k\eta} - 1 - 2k\eta\right) \qquad (26)$$

The result is shown in following figure, the relative error of total water head in the case of extreme heigh wave is about 10 %.

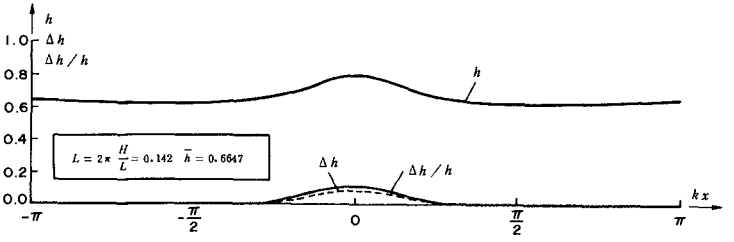

Relative accuracy in deep water wave

ENW EQUATION IN FINITE WATER DEPTH

Set $n = 1$ *in equations of number* (6)

$$\phi(x, y) = cy - C_1 e^{-kd}\left[e^{k(d+y)} - e^{-k(d+y)} \right] \cos kx \tag{27}$$

$$\eta(x) = \frac{C_1}{c} e^{-kd}\left[e^{k(d+\eta)} - e^{-k(d+\eta)} \right] \cos kx \tag{28}$$

$$\eta_1 = \eta_{max} = \frac{C_1}{c} e^{-kd}\left[e^{k(d+\eta_1)} - e^{-k(d+\eta_1)} \right] \tag{29}$$

$$\eta_2 = \eta_{min} = \frac{-C_1}{c} e^{-kd}\left[e^{k(d+\eta_2)} - e^{-k(d+\eta_2)} \right] \tag{30}$$

Parameter ω *is also invoked*

$$1 + \omega = \frac{C_1}{c} e^{-kd} \cdot k\left[e^{k(d+\eta_1)} + e^{-k(d+\eta_1)} \right] \tag{31}$$

$$0 \leq 1 + \omega \leq 1$$

From equation (29)

$$(1+\omega) / k\left[e^{k(d+\eta_1)} + e^{-k(d+\eta_1)} \right] = \frac{C_1}{c} e^{-kd}$$

$$= \eta_1 / \left[e^{k(d+\eta_1)} - e^{-k(d+\eta_1)} \right]$$

$$1 + \omega = k\eta_1 \coth(d + \eta_1) \tag{32}$$

is abtained.

From the following relationship and equation (31)

$$k(\eta_1 + d) = \tanh^{-1}\left(\frac{\eta_1}{1+\omega}\right) = \frac{1}{2} \ell n \frac{(1+\omega) + k\eta_1}{(1+\omega) - k\eta_1} \tag{33}$$

$$(1+\omega) c / k = C_1 e^{-kd}\left[\sqrt{\frac{1+\omega+k\eta_1}{1+\omega-k\eta_1}} + \sqrt{\frac{1+\omega-k\eta_1}{1+\omega+k\eta_1}} \right]$$

C_1 *is found to be*

$$C_1 = \frac{c}{k} e^{kd} \frac{\sqrt{(1+\omega)^2 - k^2\eta^2}}{2} \tag{34}$$

From equation (32)

$$1-(k^2\eta_1^2)/(1+\omega)^2=1-tanh^2k(d+\eta_1)=seeh^2k(d+\eta_1)$$

$$\sqrt{(1+\omega)^2-k^2\eta_1{}^2}=(1+\omega)\,sech\,k(d+\eta_1) \tag{35}$$

Conseqently

$$\phi(x,y)=cy-c\eta_1\frac{sinh\,k(d+y)}{sinh\,k(d+\eta_1)}\,cos\,kx \tag{36}$$

$$\eta(x)=\eta_1\frac{sinh\,k(d+\eta)}{sinh\,k(d+\eta_1)}\,cos\,kx \tag{37}$$

η_1 *should be expressed by wave height, length and water depth. From equations* (30) (34) *and* (35)

$$-\eta_2=H-\eta_1=\frac{\sqrt{(1+\omega)^2-k^2\eta_1{}^2}}{2k}\left[e^{k(d+\eta_1-H)}-e^{-k(d+\eta_1-H)}\right]$$

$$=\frac{(1+\omega)}{2k}\,sech\,k(d+\eta_1)\left[\frac{e^{k(d+\eta_1)}}{2e^{kH}}-\frac{e^{kH}\cdot e^{-k(d+\eta_1)}}{2}\right] \tag{38}$$

Substitute (33) *to* (38)

$$H-\eta_1=\frac{\sqrt{(1+\omega)^2-k^2\eta_1{}^2}}{2k}\left[\frac{\sqrt{(1+\omega)+k\eta_1}}{e^{kH}\sqrt{(1+\omega)-k\eta_1}}-\frac{e^{kH}\sqrt{(1+\omega)-k\eta_1}}{\sqrt{(1+\omega)+k\eta_1}}\right]$$

$$=\frac{1}{2k}\left[\frac{(1+\omega)(1-e^{2kH})+k\eta_1(1+e^{2kH})}{e^{kH}}\right]$$

$$=\frac{1}{k}\left[k\eta_1\cosh kH-(1+\omega)\sinh kH\right]$$

From equation (32)

$$kH=k\eta_1\left[(1+\cosh kH)-coth\,k(d+\eta_1)\sinh kH\right] \tag{39}$$

or

$$\delta = \frac{H}{L} = \frac{\eta_1}{L} \left[\left(1 + \cosh 2\pi\delta \right) - \coth k(d+\eta_1) \sinh 2\pi\delta \right] \qquad (40)$$

η_1 can also be computed by Newton – Raphson's method, then the stream function and wave profile are to be worked out, The curve of the new theory is shown in following figure, it is much reasonable in comparison with Stokes 3rd approximate curve.

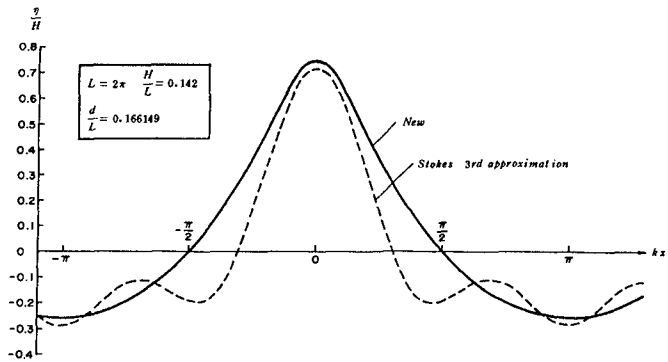

***Wave profile** in finite water depth*

The wave celerity can be calculated by adopting the same method in deep water. Substitute equation (37) to the dynamic boundary condition of free surface,

$$\frac{\eta_1 \sinh k(d+\eta)}{\sinh k(d+\eta_1)} \cos kx + \frac{1}{2g} \left\{ c^2 - 2c^2 k\eta_1 \frac{\cosh k(d+\eta)}{\sinh k(d+\eta_1)} \cos kx \right.$$
$$\left. + c^2 k^2 \eta_1{}^2 \frac{\sinh^2 k(d+\eta) + \cos^2 kx}{\sinh^2 k(d+\eta_1)} \right\} = \frac{Q}{g} = h \qquad (41)$$

Put the coefficient of variable term to be zero, the wave celerity is worked out to be

$$c^2 = \frac{g}{k} \tanh kd / \{ 1 - k^2\eta_1^2 \frac{\sinh^2 kd}{\sinh^2 k(d+\eta_1)} \} \tag{42}$$

For theoretical consistancy, wave celerity formulas in deep and shallow water must be continuous. Set $d \to \infty$ *in equation* (42)

$$(c^2)_{d\to\infty} = \frac{g}{k} [1 - (k^2\eta_1^2 / e^{2k\eta_1})]^{-1}$$

Substitute equations (13) *and* (19) *to this equation*

$$(c^2)_{d\to\infty} = \frac{g}{k} [1 - \frac{(\frac{2\pi\delta}{1+e^{-2\pi\delta}})^2}{exp(\frac{4\pi\delta}{1+e^{-2\pi\delta}})}]^{-1} \tag{43}$$

The reality shows that the new theory is superior to the Rayleigh's and Stokes.

The wave celerities in various relative depth are shown in following figure.

In this figure we also see lhat the new theory is better than Stokes which is unrcasonable that the wave celerities increase more rapidly in shallow water area.

The relative accuracy of water head is estimated as follows.

$$\Delta h = \frac{1}{2g} \{ -2c^2k\eta_1 \frac{\cosh k(d+\eta) - \cosh kd}{\sinh k(d+\eta_1)} \cos kx + c^2k^2\eta_1^2 \cdot \frac{\sinh^2 k(d+\eta) - \sinh^2 kd - k\eta \sinh 2kd + \cos^2 kx}{\sinh^2 k(d+\eta_1)} \}$$
$$+ \eta_1 \frac{\sinh k(d+\eta) - \sinh kd}{\sinh k(d+\eta_1)} \cos kx \tag{44}$$

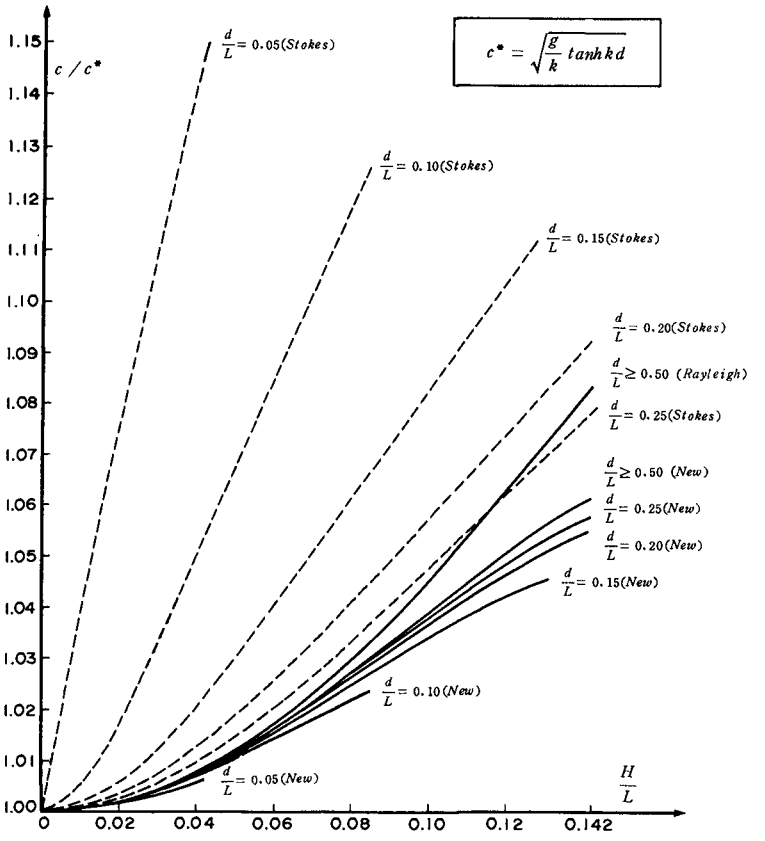

Comparison of wave celerity in finite water depth

The result of calculation is depicted in the following diagram, for very high waves, the relative errors are up to 20 %.

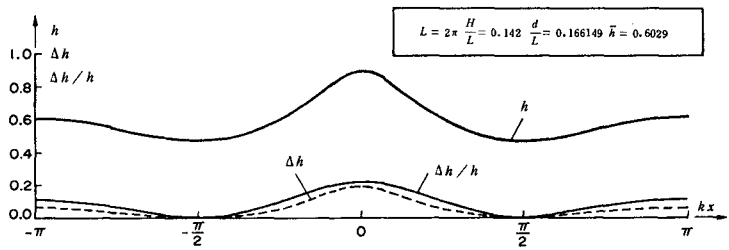

Relative accuracy in finite water depth

The mean level in the waves in this case is to be calculated as follows.

$$\xi = \frac{1}{L}\int_0^L \eta\, dx = \frac{2}{L}\int_0^{L/2} \eta\, dx$$

Equation (37) *can be expressed approximately by* :

$$\eta = \frac{\eta_1 \sinh k(d+\eta)}{\sinh k(d+\eta_1)} \cos kx$$

$$\doteqdot \frac{\eta_1 \sinh kd\, e^{k\eta}}{\sinh k(d+\eta_1)} \cos kx \doteqdot B(1 + k\eta)\cos kx$$

$$\eta \doteqdot \frac{B\cos kx}{1 - Bk\cos kx} \qquad B = \frac{\eta_1 \sinh kd}{\sinh k(d+\eta_1)}$$

$$\xi = \frac{2}{L}\int_0^{L/2} \frac{B\cos kx}{1 - Bk\cos kx}\, dx = \frac{1}{k}\left[\frac{1}{\sqrt{1 - B^2k^2}} - 1\right] \qquad (45)$$

It can be proved thad while $d \to \infty$, $B = A = \theta / ke^{\theta}$

Finally the significant range of this theory is shown in the next figure.

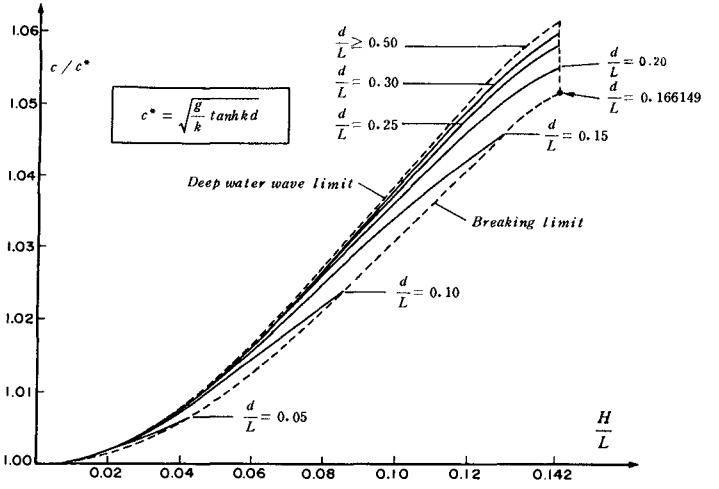

Significant range of the new wave theory

CONCLUSION

1. *The new wave profile equation describes the wave motion by an implicit function, can be seid to be an exact solution because no approximation approach is adopted.*
2. *In the procedure of calculating wave celerity, some approximate expressions are used, so that some errors will be acknowledged in total water head calculation. However, the wave celerity equation has been proved to be continuous, such a fact shows the new theory is superior to the Rayleigh's and Stoke's.*
3. *The relationship between wave celerity and relative depth d/L in Stokes theory is unreasonable. It is more consistant and*

will coincide with the reality in the new theory.

4. *In the era of electronic computer, the new wave profile equation is suggested to be adopted in practical use after some complement such as the exact position of x — axis is made.*

REFERENCE

1. *Stokes, G.G., " On the theory of oscillatory waves " Trans. Camb. phil. Soc,* 8. 441, (*Also in Mathematical and physical paper, Vol.I.Lond* : *Cambridge University Press, PP.* 197 — 229, 1880)
2. *Rayleigh. L., " On waves " Phill. Mag. Series* 5, 1. 257 — 279, 1876.
3. *Stokes, G.G., " Supplement to a paper on the theory of oscillatory waves " in Mathematical and physical paper, Vol.*1.*Lond* : *Cambridge University Press, PP.* 314 — 326, 1880.
4. *Burnside, W., " On periodic irrotational waves at the surface of deep water " Proc. Lond. Math. Soc., Series* 2, 14, *PP.*26 — 30, 1915.
5. *Levi — civita, T., " D'etermination rigoureuse des ondes permanentes d'ampleur finie " Mathematische Annalen, Vol.*93, *PP.* 264 — 314, 1925.
6. *Struik, D.J., " D'etermination rigoureuse des ondes irrotationnelles p'eriodiques dans uncanal a profondeur finie. " Mathematische Annalen, Vol.*95, *pp.*595 — 634, 1926.
7. *Schwartz, L.W., " Computer extension and analytic continuation of stokes' expansion for qravity waves " Jour. of Fluid Mech.* 62, 553 — 578, 1974.
8. *Cokelet, E.D., " Steep qravity waves in water of arbitrary uniform depth " phil. Trans. Roy. Soc. A.* 286, 183 — 239, 1977.
9. *Chen, Y.Y. and S.C.Lin, " Analyze on solitary wave theory by infinite series expansion of the oscillatory waves, Part* 1 : *On general derivation of theory " Proc, 6th conf. on Ocean Eng.*

R.O.C. (33) 1 – 12, 1982.

10. *Chen, Y.Y. and H.H. Hwung, " Analyze on solitary wave theory by infinite series expansion of the oscilltatory waves, part 2: The highest gravity wave of permanent type " Proc, 6th conf. on Ocean Eng. R.O.C.* (34)1 – 15, 1982.
11. *Chen, Y.Y. and Frederick, L.W.Tang, " Analyze on solitary wave theory by infinite series expansion of the oscilltatory waves, part 3: Supptement on the right angle of summit for highest wave of permanent type " 6th conf. on Ocean Eng. R.O.C.* (35) 1 – 9, 1982.
12. *Chen, Y.Y. and H.H.Hwung, " A note on the rotational water waves " Jour. of Oceanography, National Taiwan College of Marine Science and Technotogy,* 8.53 – 63, 1981.
13. *Rayleigh, L., " Hydrodynamicat Notes, " phil. Mag. Series* 6, 21, 177 – 195, 1911.
14. *Rayleigh, L., " On periodic irrotational waves at the surface of deep water " phil. Mag. Series* 6, 33, 381 – 389, 1917.
15. *Airy, G.B., " Tides and waves " Encyclopaedia metropotitana (London), Articte* 192, 1845.
16. *Ursell, F., " The tong – wave paradox in the theory of gravity waves " Proc. Camb. Phil. Soc.* 49, 685 – 694, 1953.
17. *Peregrine, D.H. " Long waves on a beach " , Jour. of Fluid Mech.* 27, 815 – 827, 1967.
18. *Lamb. H., " Hydrodynamics (6th ed), " London: Cambridge University Press,* 1932 *(New York : Reprinted by Dover Publications, Inc.,* 1945) 738*pp.*

Engineering Approach to Nonlinear Wave Shoaling

James Walker[1], Ph.D., P.E., M. ASCE
John Headland[2], AM. ASCE

ABSTRACT

Determination of a design wave height at a coastal structure requires calculation of a shoaling coefficient or determination of the maximum probable breaking wave height at the point of interest. In shallow water over a sloping bottom, low steepness waves are not accurately predicted by linear shoaling coefficients. Empirical breaking indices are inconsistent with both linear and nonlinear wave theories. Nevertheless, the coastal engineer must select a design wave in order to responsibly design the structure. A graphical procedure is presented herein to relate the equivalent deepwater wave to a breaking wave as it transitions into shoaling water. The procedure provides the coastal engineer with a more consistent understanding of the shoaling process. The results furthermore identify regions of relative depth and steepness where discrepancies arise when using linear shoaling coefficients that may significantly alter engineering design and laboratory studies.

INTRODUCTION

The purpose of this paper is to present a shoaling coefficient that can be used by coastal engineers to better describe the shoaling of finite height waves over sloping bottoms. The linear shoaling coefficient developed from Airy theory in conjunction with a $H_b = 0.78d$ breaking criterion predicts a wave height at the breaking point that is considerably lower than the breaker height predicted by empirical breaking indices commonly used in coastal engineering practice. Several investigators, cited later, have presented nonlinear shoaling curves to describe the phenomena, but they are not consistent with empirical breaker indices over sloping bottoms. These theories tend to predict greater wave heights at a given relative depth than suggested by empirical breaking coefficients. The coastal engineer requires a shoaling curve that is consistent with these commonly accepted breaking indices. This paper utilizes breaker indices as upper limits and the characteristics of theoretical and experimental nonlinear shoaling curves are used to develop a transition of wave height from deep to shallow water.

The problem is illustrated by the following example. Figure 1 shows a typical beach profile over which a long jetty is to be constructed. The design wave at various stations along the jetty is required to determine the armor unit size. For illustrative

---

[1] Chief Coastal Engineer, Moffatt & Nichol, Engineers, Long Beach, Calif.
[2] Coastal Engineer, Moffatt & Nichol, Engineers, Long Beach, Ca.

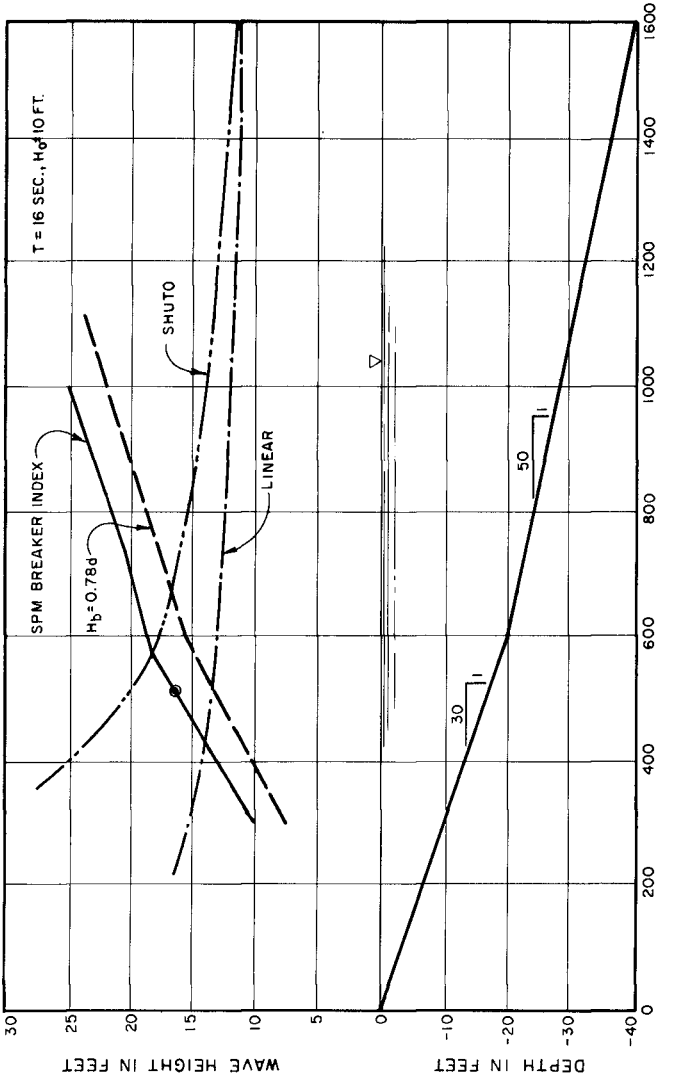

Figure 1. Example Problem for Nonlinear Shoaling.

purposes, a 16-second period is used with a 10-foot deepwater wave height. The dot-dash line represents the linear shoaling curve as determined by Airy theory. The circle represents the breaking height and depth as determined by empirical curves presented in Shore Protection Manual (1977). These data were developed by Goda (1970) and Weggel (1972).

The linear shoaling curve falls significantly below the empirically determined breaker point. Design wave heights shoreward of the breaker point can be determined by the limiting height criteria, but no consistent method exists to determine wave heights seaward of the breaker point. The linear shoaling curve is inconsistant with the breaker data. The theoretical nonlinear shoaling curve of Shuto (1974) is also plotted in figure 1. This curve predicts shoaling at a rate that exceeds the breaker point. While such a curve may be conservative, a shoaling curve more consistent with the breaker index is required for design applications.

EMPIRICAL BREAKER CURVES

Methods to determine breaker height and breaker depth over a given bottom slope for a given deepwater wave steepness are presented in Shore Protection Manual (1977). These procedures are widely used by coastal engineers. The work in this paper assumes these procedures to be representative of the best available data for use in engineering design.

Figure 2 is a graph for predicting breaking wave indices H_b/H'_o based on the work of Goda (1970). Goda reworked data of Iverson (1953) by correcting for side-wall friction and normalized this data using the nonlinear shoaling calculation of LeMehaute and Webb (1964) in deeper water and Iwagaki's (1968) procedure for more shallow regions. Figure 3 presents a graph which gives the ratio of breaker depth to height, d_b/H_b, based on the work of Weggel (1972). In his study Weggel consolidated breaking wave characteristics reported by a relatively large number of investigators.

The above two procedures account for the effects of bottom slope and implicitly include nonlinear shoaling effects. The procedures are widely accepted for use with monochromatic waves and are believed to provide reliable, conservative, estimates of breaking wave characteristics.

The empirical breaker data of figures 2 and 3 can be plotted as limit points in the form of a shoaling graph. The shoaling coefficient is defined as;

$$K_s = H/H'_o \qquad (1)$$

where H is the local wave height, and
H'_o is the equivalent deep water wave height.

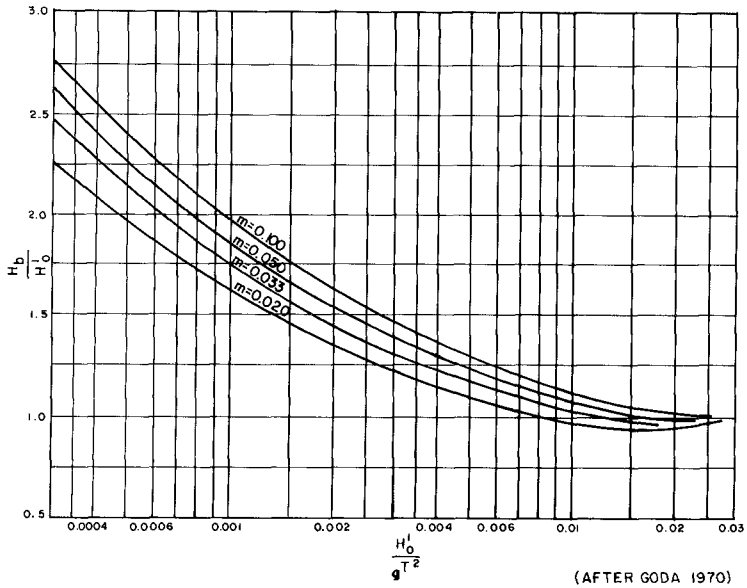

Figure 2. Breaker Height Index.

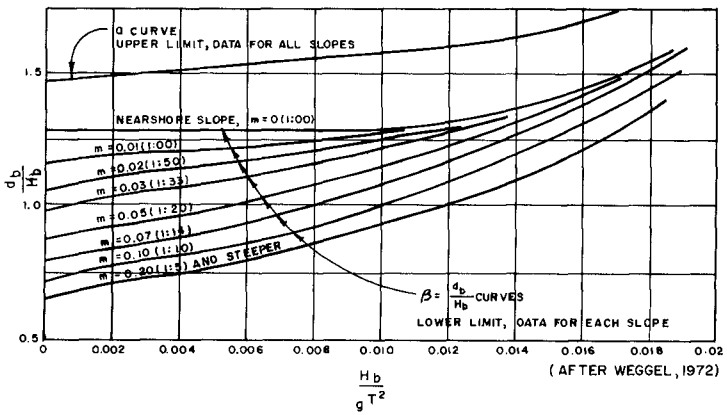

Figure 3. Relative Breaker Depth.

For linear theory, K_s, plotted in figure 4, is a function of relative depth, d/L_o, where d is the water depth, and L_o is the deep water wave length. For non-linear waves, K_s is also a function of bottom slope, m, and H'_o/L_o. The limiting breaker height, H_b/H'_o, determined from figure 2, can be used to find H_b/L_o for a given m and H'_o/L_o

$$H_b/L_o = (H_b/H'_o)(H'_o/L_o) \tag{2}$$

where H_b is the breaker height.

Finally, the relative depth can be determined using H_b/L_o found by equation (1) and d_b/H_b from figure 3.

$$d_b/L_o = (d_b/H_b)(H_b/L_o) \tag{3}$$

Results of these calculations are presented in Table 1.

H_b/H'_o is plotted in figure 4 as a function of d_b/L_o for $.001 \leq H'_o/L_o \leq .14$ and $.02 \leq m \leq .1$. Isolines of equal H'_o/L_o connect through the limit waves for the various slopes, m. Isolines of m were drawn through the data and these are shown in figure 5. It is noted that for the lowest value of wave steepness the m = .1 and m = .05 slopes tend to converge. The reason for this is not clear, but could be attributed to wave reflection, data reduction methods, or laboratory scale effects. The data points plotted in figure 4 represent the maximum value of a shoaled wave height over a sloping bottom, m, for a given H'_o/L_o.

THEORETICAL AND EMPIRICAL SHOALING CURVES

The purpose of this paper is to develop a shoaling curve that is consistent with the limit breaking points shown in figure 4. Several investigators have used various wave theories to develop nonlinear shoaling curves. LeMehaute and Wang (1980) present a discussion of nonlinear shoaling and determined that no single theory can accurately account for wave shoaling from deep to shallow water. Sakai and Battjes (1980) present an excellent comparative review of several theoretical studies and present a shoaling curve based on the work of of Cokelet (1977). The Cokelet shoaling curve is compared with the empirical breaking data in figure 6. The third order Stokes curve of LeMehaute and Webb (1964); the hyperbolic curve of Iwagaki (1968); cnoidal curve of Svendsen and Brink-Kjaer (1972), Shuto (1974), and Yamaguchi and Tsuchiya (1976) all have a slightly lower shoaling rate compared with Cokelet theory, but from a practical standpoint are in very close agreement. Figures 7 and 8 compare the nonlinear shoaling curves of Svendsen and Brink-Kjaer, and Shuto, respectively, to the empirical breaking data. The cnoidal shoaling theory of Svendsen and Brink-Kjaer (1972) is based on

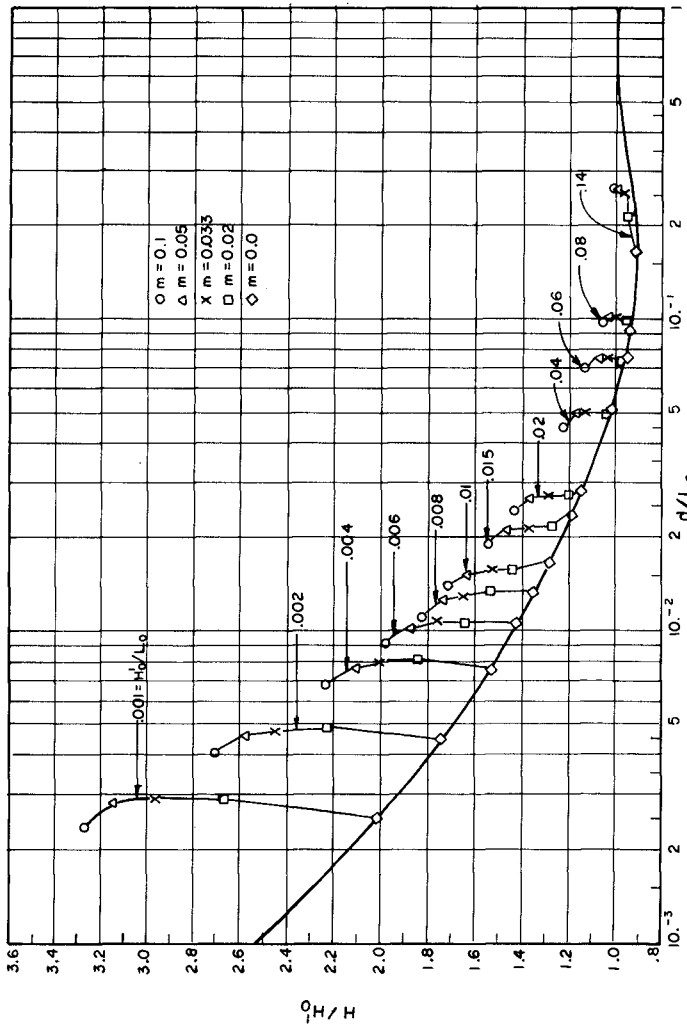

Figure 4. Breaker Points for Given Values of H'_o/L_o and m

Table 1. Breaker Points for Values of Wave Steepness and Beach Slope

m = .10				m = .033			
Ho/Lo	Hb/Ho	db/Hb	db/Lo	Ho/Lo	Hb/Ho	db/Hb	db/Lo
.001	3.275	0.74	.00242	.001	2.96	0.987	.00292
.002	2.70	0.75	.00405	.002	2.43	0.990	.00481
.004	2.24	0.76	.00683	.004	1.99	1.000	.00797
.006	1.98	0.77	.00914	.006	1.77	1.010	.01079
.008	1.83	0.78	.01137	.008	1.63	1.020	.01327
.010	1.72	0.79	.01360	.010	1.52	1.027	.01562
.015	1.54	0.81	.01870	.015	1.37	1.046	.02152
.020	1.44	0.84	.02410	.020	1.28	1.064	.02720
.040	1.23	0.93	.04580	.040	1.12	1.140	.05107
.060	1.13	1.04	.07040	.060	1.04	1.220	.07612
.080	1.06	1.16	.09823	.080	0.98	1.300	.10170
.140	1.00	1.87	.26200	.140	0.97	1.720	.23300
m = .05				m = .02			
Ho/Lo	Hb/Ho	db/Hb	db/Lo	Ho/Lo	Hb/Ho	db/Hb	db/Lo
.001	3.15	0.89	.00280	.001	2.66	1.082	.00288
.002	2.58	0.90	.00464	.002	2.22	1.086	.00482
.004	2.10	0.91	.00765	.004	1.84	1.094	.00806
.006	1.87	0.92	.01035	.006	1.64	1.100	.01085
.008	1.73	0.93	.01290	.008	1.52	1.106	.01340
.010	1.63	0.94	.01530	.010	1.42	1.112	.01580
.015	1.47	0.96	.02120	.015	1.27	1.126	.02147
.020	1.36	0.98	.02660	.020	1.20	1.140	.02740
.040	1.16	1.07	.04968	.040	1.04	1.190	.04950
.060	1.07	1.16	.07460	.060	0.97	1.247	.07260
.080	1.02	1.28	.10460	.080	0.95	1.310	.09960
.140	0.98	1.83	.25120	.14	0.96	1.577	.21200

Note: Values of H_o/L_o = .001 were extrapolated

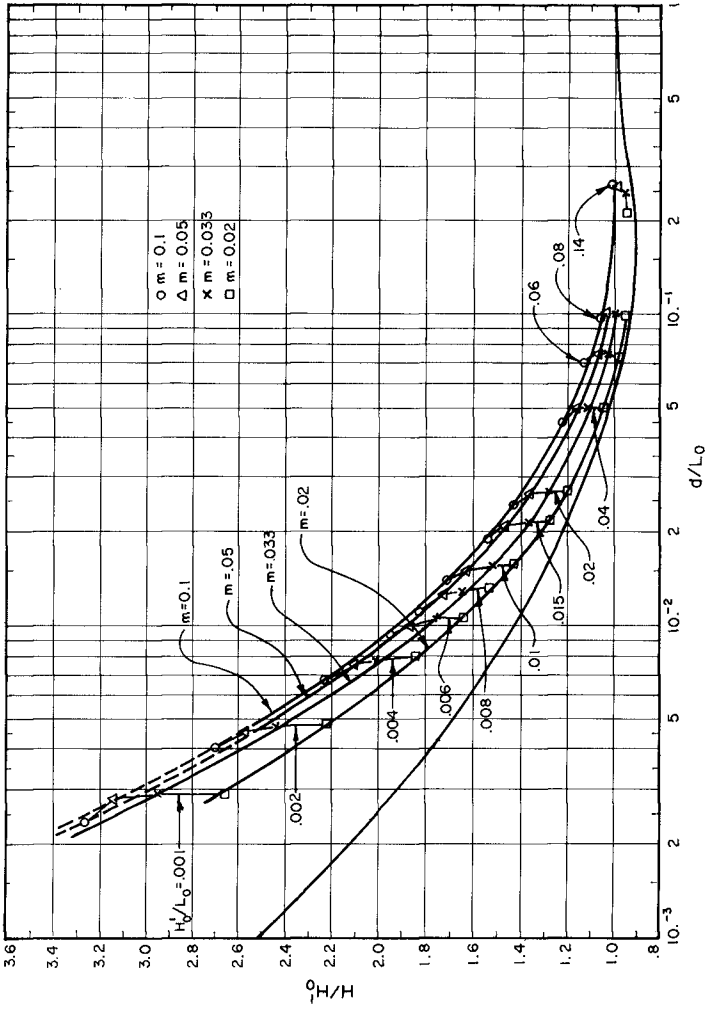

Figure 5. Isolines of Bottom Slope, m.

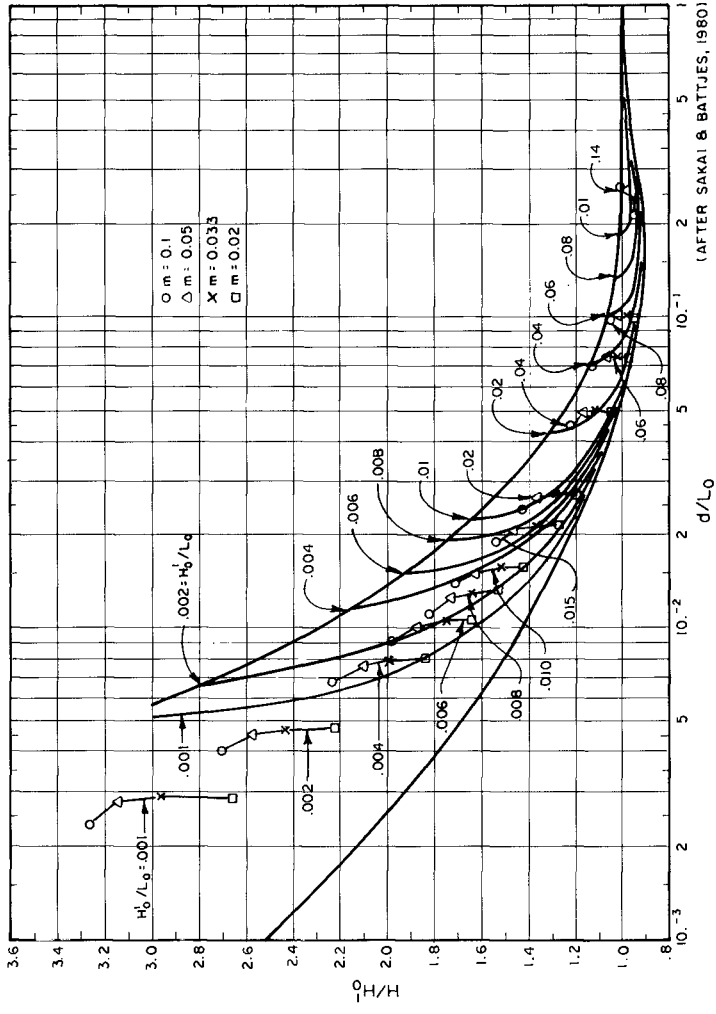

Figure 6. Nonlinear Wave Shoaling According to Cokelet's Theory.

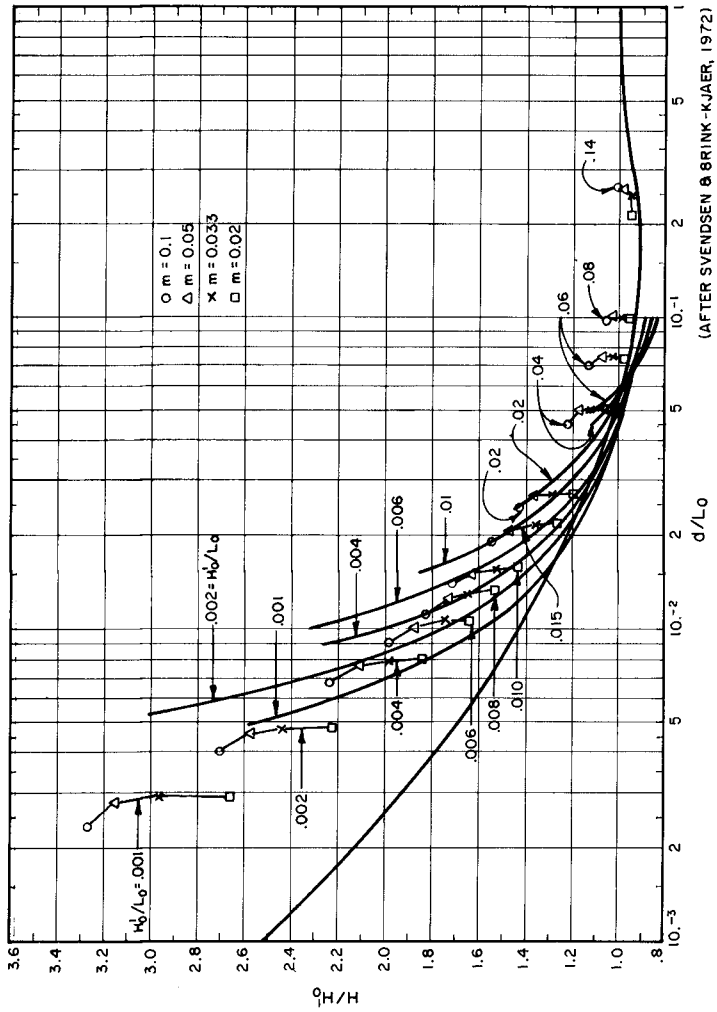

Figure 7. Nonlinear Wave Shoaling According to Cnoidal Theory.

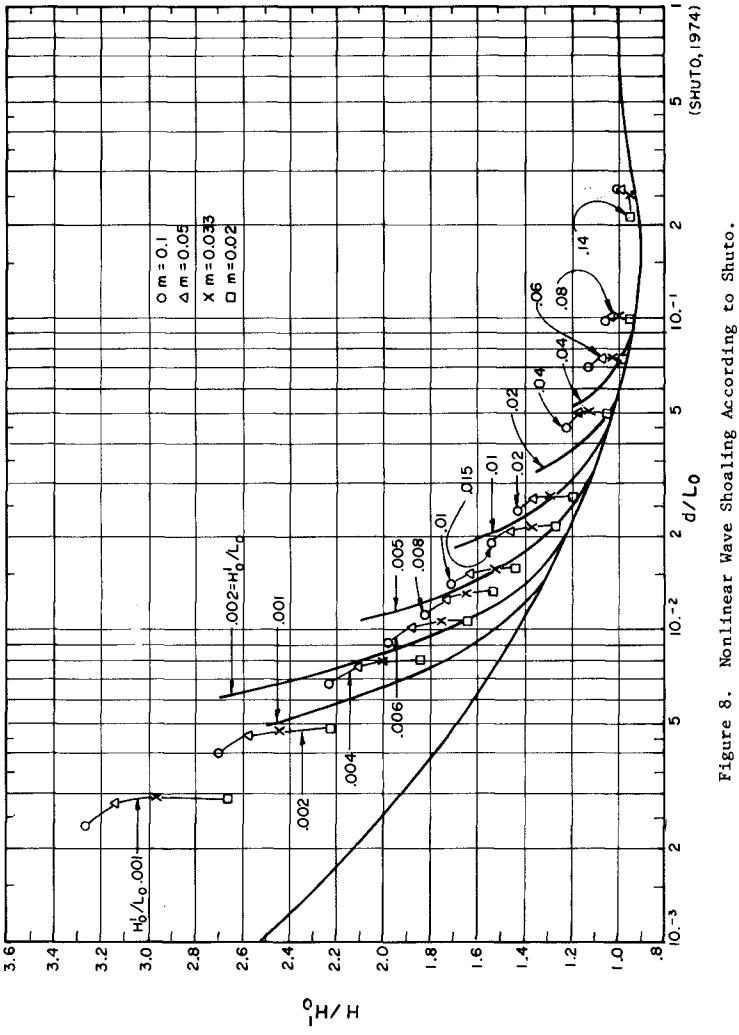

Figure 8. Nonlinear Wave Shoaling According to Shuto.

matching the wave energy flux according to cnoidal and sinusoidal wave theories at a relative depth $d/L_o = .1$. Experimental work done by Svendsen and Buhr-Hansen (1977) indicated that cnoidal wave theory more closely predicted their experimental results if wave height instead of wave energy is matched at $d/L_o = .1$. The effect of this change is to shift the cnoidal steepness curves, shown in figure 7, slightly to the right and upwards. Shifting the isolines of steepness towards the right moves them farther from the empirical breaker indices. Cnoidal wave theory predicts the data of Svendsen and Buhr-Hansen (1977) well but does not predict the breaker index data used to develop figures 2 and 3. This may be attributed to the free second harmonic waves generated by the sinusoidal motion of a piston-wave-generator, which were eliminated in Svendsen and Buhr-Hansen experiments. Sakai and Battjes found that the effect of finite height wave theory on deep water wave length has a relatively minor effect and that all of the above theories present shoaling curves that are in reasonably good agreement except near the breaking point.

Figures 6 through 8 clearly indicate that the above nonlinear approaches predict a significantly higher rate of shoaling than indicated by the experimental breaking limits. This indicate's that either a lower shoaling rate may exist or the emperical breaker indices are in error.

A theoretical nonlinear shoaling theory which accounts for beach slope was developed by Iwagaki and Sakai (1972). Iwagaki and Sakai presented theoretical nonlinear shoaling curves for several values of bottom slope, but limited these curves to values of $.006 \leq d/Lo \leq 0.0157$ and values of $H_o/L_o \leq 0.004$. Figures 9 and 10 compare the theoretical curves of Iwagaki and Sakai to the empirical breaker limits for values of $H_o/L_o = 0.001$ and 0.002 respectively. The qualitative agreement of these curves with the breaker limits is encouraging, however the limited range of conditions preclude their universal use.

Hydraulic model studies of wave shoaling have been conducted by Wiegel (1950), Iverson (1951), Ippen and Eagleson (1950), Eagleson (1956), Iwagaki (1968), Iwagaki and Sakai (1972), Walker (1974), Svendsen and Buhr-Hansen (1977), and Flick (1978). The more recent studies have been used primarily to verify various nonlinear shoaling curves cited in the previous section. The general result has been that the theories are comparable to the experimental data, except they tend to over predict shoaling near the breaker zone. The shoaling curve of Walker (1974) are compared with the limit breaking data in figure 11 for low values of wave steepness. This investigation shows a closer fit to the breaker limits than theory for low d/L_o.

SHOALING DIAGRAM

The form of the H_o/L_o curves suggests that a unique nonlinear shoaling curve exists for each beach slope. This is supported by the theoretical work of Iwagaki and Sakai (1972),

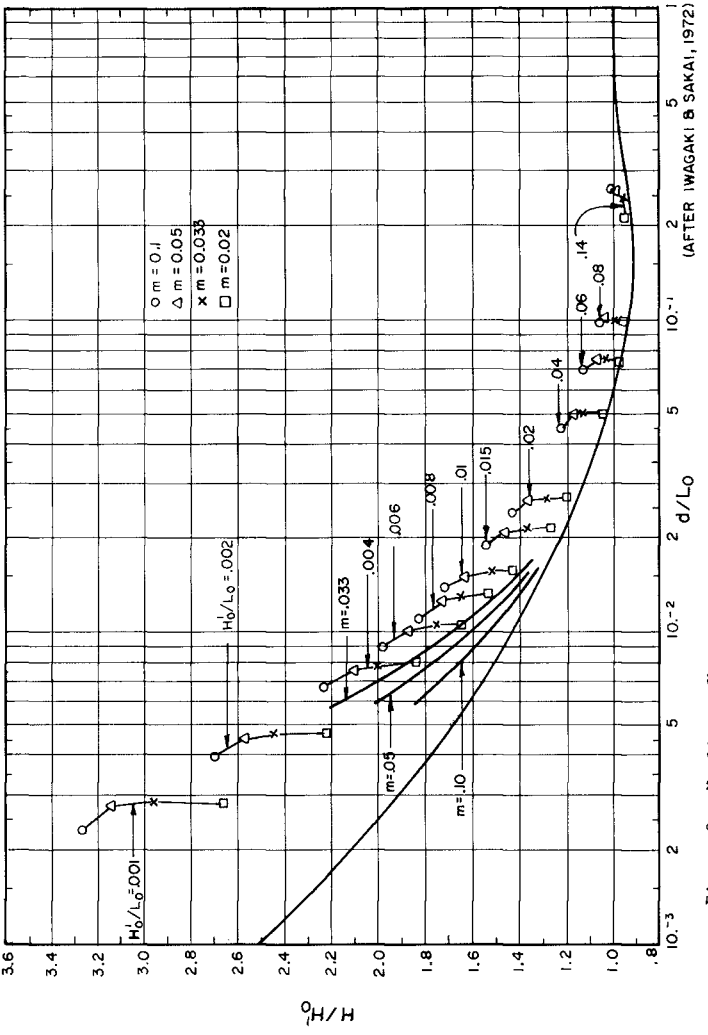

Figure 9. Nonlinear Shoaling According to Iwagaki and Sakai for H'_o/L_o = .001 and Several Values of Bottom Slope.

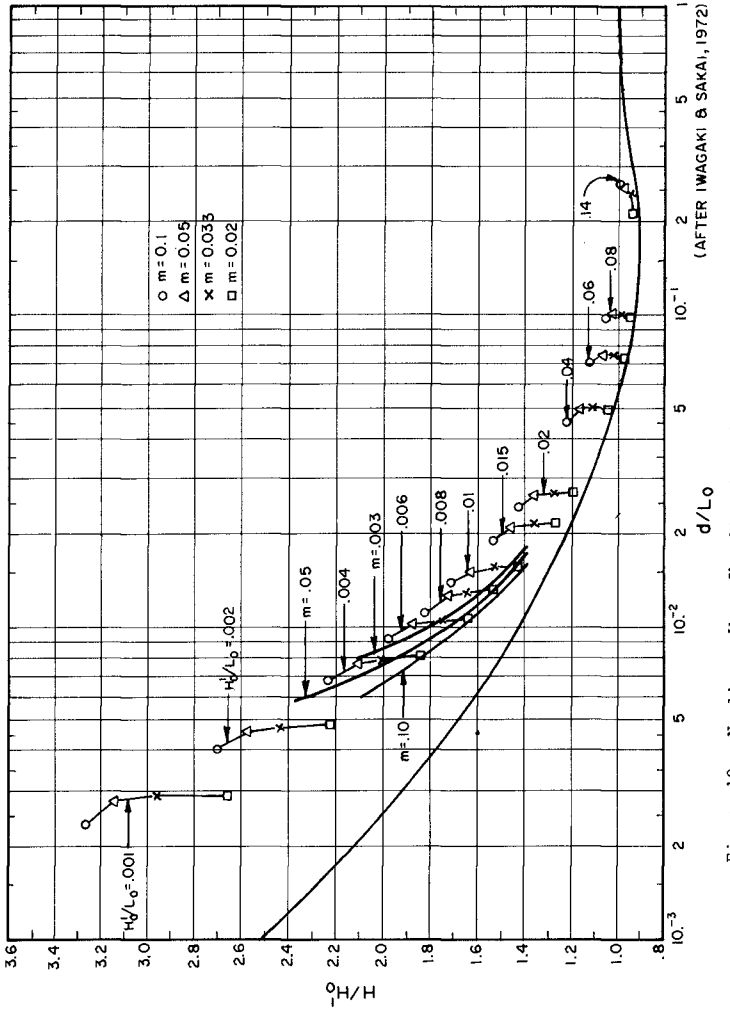

Figure 10. Nonlinear Wave Shoaling According to Iwagaki and Sakai for H_o'/L_o = .002 and Several Values of Bottom Slope.

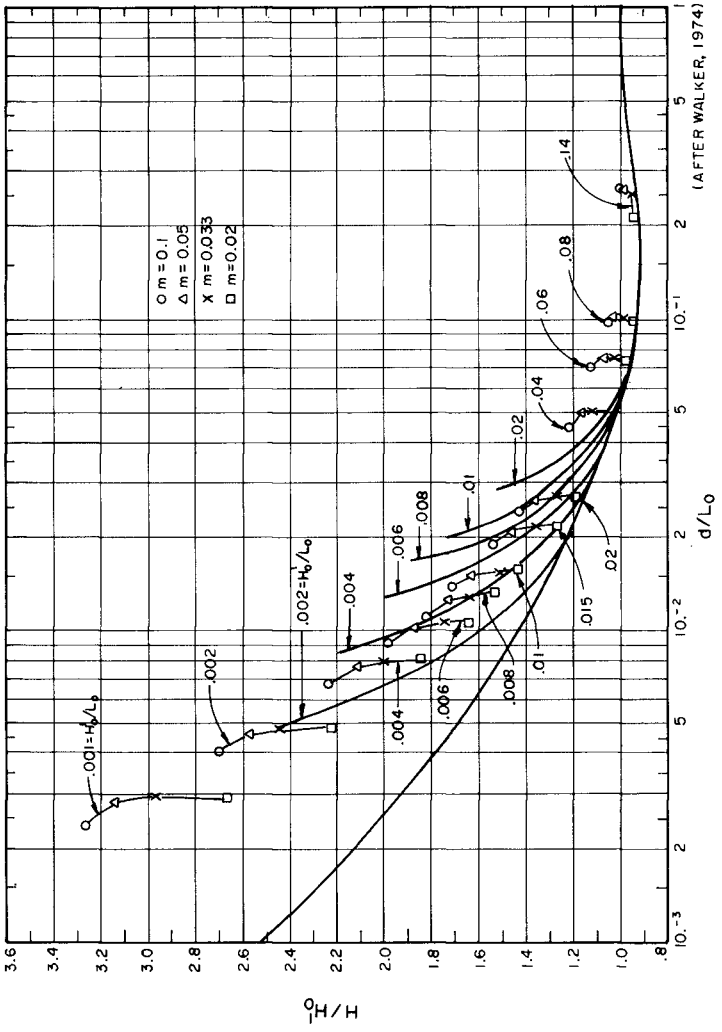

Figure 11. Nonlinear Wave Shoaling from Experimental Data.

but they only give curves for a limited range of values. The approach taken in this report was to draw isolines of steepness weighted towards m = .033 slope. This was done for several reasons. First m = .033 is found often in nature. Secondly, while the steepness curves were drawn to conform to the m = .033 slope, in most cases the curves also intersected, or nearly intersected, the m =.05 and m = .1 endpoints.

The isolines of wave steepness were drawn weighted towards the m = .033 endpoints starting from the linear curve at the point defined by Shuto (1974) were he found that linear shoaling no longer applies;

$$\frac{L_o H}{d^2} \sim \frac{30}{2\pi} \qquad (4)$$

The resulting curves are shown in figure 12. While constructing these isolines of wave steepness, each line was compared to the theoretical curves of Cokelet, Shuto and Svendsen and BrinkKjaer (cnoidal) and the experimental curve of Walker. The theoretical curves predict a faster rate of shoaling than the empirical curve. Furthermore, the H_o/L_o curves are shifted towards the right hand side of the diagram (higher d/L_o values). In general the nonlinear shoaling curve based on Cokelet's theory predicts the highest rate of shoaling and is farthest from the empirical data. The experimental isolines of H_o/L_o = .002, and .004 given by Walker are closest to the breaker data. The H_o/L_o = .006 line given by cnoidal theory is closest to the empirical curve although the cnoidal curve still lies to the right of the empirical curve. The empirical curve for H_o/L_o = .001 is shifted considerably towards the left from any of the curves. The empirical H_o/L_o = .02 curve is very well predicted by the cnoidal theory except in the region where they intersect the linear shoaling curve. The empirical H_o/L_o = .04 appears to be an average of the curves given by cnoidal theory and by Shuto. For higher values of H_o/L_o the only curves for comparison to the empirical curves are those given by Cokelet. All of these curves lie considerably to the right of the empirical curves and exhibit a different type of assymptotic behavior to the linear curve.

Theoretically, Iwagaki and Sakai (1972) found that the effect of beach slope on shoaling is that the rate of shoaling is lower on steeper slopes than flatter slopes. However the experimental data indicate that waves reach higher breaking values for steeper slopes. Therefore the effect of weighting the steepness lines towards the m = .033 endpoint is to overpredict wave shoaling for the m = .05, and m = .1 slopes and underpredict the wave shoaling for the m = .02 slope. There are insufficient theoretical and experimental results to estimate the error involved in quantitative terms. However, the error appears to decrease for higher wave steepness values. In terms of predicting peak shoaling values (i.e. shoaling coefficients at breaking)

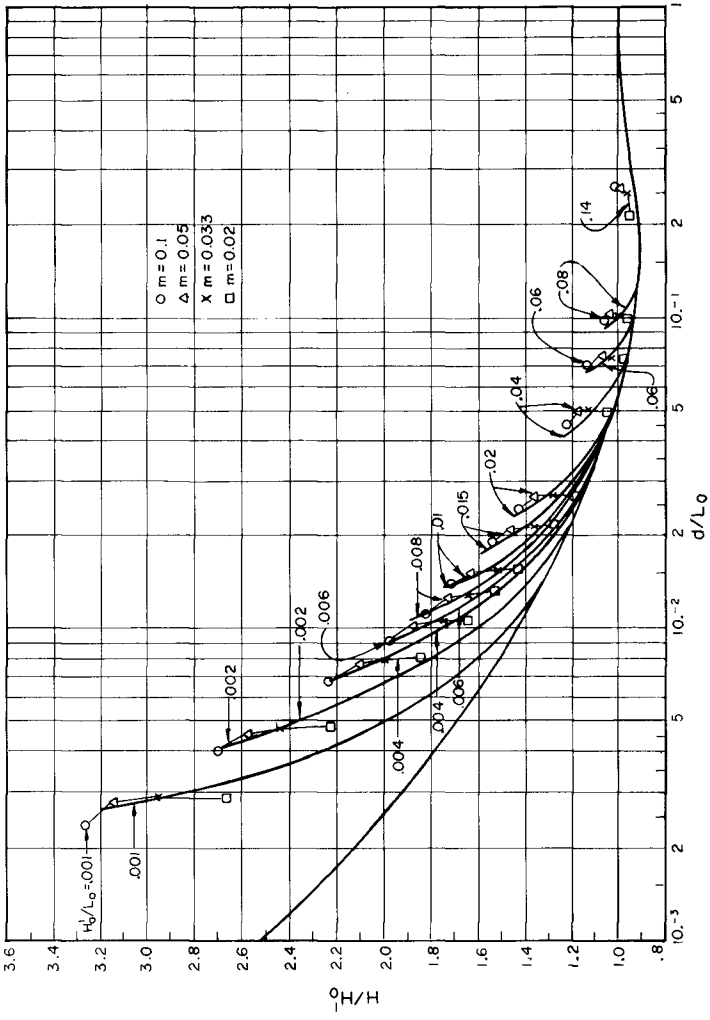

Figure 12. Isolines of H'_o/L_o.

weighting the curve towards m = .033 has the effect of underpredicting the breaker heights for the m =.02 slope, but predicts the breaker heights well for the other slopes. Again the largest error occurs for the lowest steepness values. Despite the fact that there is some error involved for the m = .02 it represents a better fit than linear theory. For more accurate estimates of breaker height and depth, one should use figures 2 and 3.

Superposing figures 5 and 12 results in a diagram for estimating nonlinear wave shoaling over a sloped beach. This curve is shown in figure 13. The linear curve is used for a flat beach (m = 0). This diagram is reasonably consistent with empirical breaking data now widely used for design purposes.

CONCLUSIONS

A nonlinear shoaling curve which provides the coastal engineer a reasonable means of determining wave heights over a sloped bottom seaward of breaking has been developed. The curve indicates that deviations from linear theory are relatively small for values of relative depth, $d/L_o > .05$. Deviations from linear theory reach a factor of 2 or more for $d/L_o > .003$. The curve indicates that wave shoaling is mildly dependent on beach slopes but insufficient data are available to quantify this effect.

The paper outlines the inconsistencies of various nonlinear wave theories compared with commonly used breaker indices. It is recommended that further experimental studies be conducted carefully to avoid adverse tank effects and that these studies be carried out over a range of beach slopes and wave steepnesses to verify nonlinear wave shoaling.

It is further recommended that design curves for wave runup, overtopping and similar phenonenom which use a linear shoaling coefficient to normalize wave height data be critically reviewed. As indicated in this paper use of the linear shoaling coefficient may lead to serious inconsistencies and unconservative designs.

Finally it is noted that the shoaling procedures in this paper apply to monochromatic waves.

ACKNOWLEDGEMENT

This work was conducted for the U.S. Navy under contract N00025-79-C-006 by Moffatt and Nichol, Engineers for preparation of the Design Manual DM26.2, "Coastal Protection."

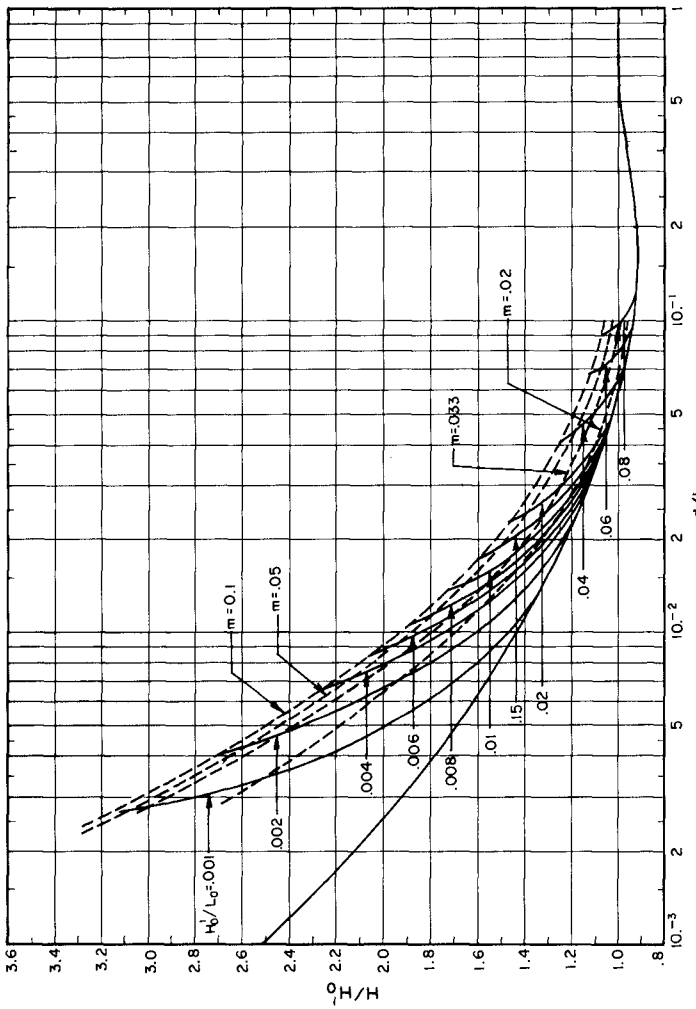

Figure 13. Nonlinear Shoaling Curve.

REFERENCES

Cokelet, E.D. (1977). Steep Cravity Waves in Water of Arbitrary Uniform Depth. Philos. Trans. R. Soc. London, 286, A1335. 183-230.

Eagleson, P.S. (1956). Properties of Shoaling Waves by Theory and Experiment. Trans. Am. Ceophys. Union, 37(5): 565-572.

Flick, R.E. (1978). Study of Shoaling Waves in the Laboratory, Ph.D. Thesis, University of California, San Diego, 159 pp.

Coda, Y. (1970). A Synthesis of Breaker Indices, Transactions of JSCE, Vol. 2, Part 2: 227-229.

Ippen, A.T. and Eagleson, P.B. (1955). A Study of Sediment Sorting by Waves Shoaling on a Plane Beach. BEB Tech, News, 63.

Iverson, H.W. (1953). Waves and Breakings in Shoaling Water, Proc. 3rd Conf. Coastal Eng. pp. 1-12.

Iwagaki, Y. (1968). Hyperbolic waves and their shoaling. Proc. 11th Conf. Coastal Eng., pp. 124-144.

Iwagaki Y. and Sakai T. (1972). Shoaling of Finite Amplitude Long Waves on a Beach of Constant Slope. Proc. 13th Conf. Coastal Eng. pp. 347-365.

LeMehaute, B. and Webb, L.M. (1964). Periodic Cravity Waves over a Gentle Slope at a Third Order Approximation. Proc. 9th Conf. Coastal Eng. pp. 23-40.

LeMehaute, B. and Wang, J.D. (1980). Transformation of Monochromatic Waves from Deep to Shallow Water. Tech. Rep. No 80-2, U.S. Army Corps of Engineers, Coastal Engineering Research Center. 43 pp.

Sakai, T. and Battjes, J.A. (1980). Wave Shoaling Calculated from Cokelet's Theory. Coastal Eng., 4: 65-84.

Shuto, N., (1974). Non-linear Long Waves in a channel of variable section. Coastal Eng. in Japan, 17: 1-12.

Svendsen, I.A. and Brink-Kjaer O. (1972). Shoaling of Cnoidal Waves Proc. 13th Conf. Coastal Eng. pp 365-383.

Svendsen, I.A. and Buhr-Hansen, J. (1977). The Wave Height Variation for Regular Waves in Shoaling Water. Coastal Eng. 1: pp 261-284.

U.S. Army Corps of Engineers (1977), Coastal Engineering Research Center, Shore Protection Manual, 3rd ed., Vols I, II and III, U.S. Covernment Printing Office, Washington, DC.

Walker, J.R. (1974). Wave Transformation Over a Sloping Bottom and Over a Three-Dimensional Shoal. James K.K., Look Lab of Oceanography Eng. Rep., 75-11. Dept. of Ocean Eng., Univ. Hawaii, 138 pp.

Weggel, J.R. (1972). Maximum Breaker Height For Design, Proc. 13th Conf. Coastal Eng. pp 419-431.

Wiegel, R.L., (1950). Experimental Study of Surface Waves in Shoaling Water. Trans. AM. Ceophys. Union, 31: 377-385.

Yamaguchi, M. and Tsuchiya Y. (1976). Wave Shoaling of Finite Amplitude Waves. Proc. 15th Conf. Coastal Eng. pp. 497-506.

WAVE REFLECTION FROM UNDULATING SEABED TOPOGRAPHY

by

A D HEATHERSHAW

Institute of Oceanographic Sciences, Crossway
Taunton, TA1 2DW, UK.

ABSTRACT

The results of experiments are described which show that surface waves may experience a resonant interaction with undulations on the seabed. This interaction manifests itself in a strong reflection of incident wave energy when the wavelength of the bottom undulation is about half that of the surface wave. It is shown that such a mechanism might enable a region of undulating seabed topography (eg sand bars or sand-waves) to extend in an up-wave direction, into a region of otherwise plane bed.

INTRODUCTION

The interaction of surface water waves with undulating seabed topography is a problem of fundamental importance to coastal engineers. While it has been shown, that, in the nearshore zone, quite complex patterns of wave motion (eg edge waves) may lead to beach cusps, shore parallel bars and even crescentic shore welded sand bars (Holman and Bowen, 1982), the problem that is considered in this study is how waves are likely to interact with a pre-existing pattern of regular undulations on the seabed. Such a pattern may consist of shore parallel bars formed by plane reflections of low amplitude swell waves from a beach, leading to standing waves of the type observed by Suhayda (1974). Alternatively, standing waves may occur seaward of the surf zone as a result of the time varying breakpoint forcing mechanism described by Symonds et al (1982). In this case a forced wave having incident wave group periodicity is radiated seaward from the breaker zone. Such a wave, interacting with incoming infragravity waves having periods in the range 30-300s, might lead to standing waves and consequently to bar formation. This latter mechanism seems to provide the most likely means of generating the multiple shore parallel bars which have been observed by Short (1975) and which would require wave periods of the order 100s.

A pre-existing pattern of bottom undulations might also be formed by tidally generated features such as sand waves (eg Langhorne, 1982) or sand ridges lying transverse to the general direction of wave propa-

gation and, as such, may occur well offshore away from the coastline.

In general, surface wave/seabed interactions may occur in any depth of water where the waves are able to "feel the bottom". It follows that such interactions may occur for a wide range of surface water wavelengths and bedform length scales.

Recent theoretical work Davies, 1980, 1982, has shown that large amounts of wave energy may be reflected as a result of resonant interactions between surface water waves and bottom undulations, the wavelengths of which lie in the ratio 2:1 approximately.

Davies (1980, 1982) has used linear perturbation theory to show that, to a first approximation, wave reflection from a finite number of submerged sinusoidal bars, having small amplitude and on an otherwise plane bed, is given by the wave reflection coefficient

$$K_r = \frac{a_r}{a_i} = \frac{2bk}{\{2kh + \sinh(2kh)\}} \cdot \left[\left(\frac{2k}{\ell}\right) \left| \frac{\sin\left(\frac{2k}{\ell}.m\pi\right)}{\left(\frac{2k}{\ell}\right)^2 - 1} \right| \right] \qquad (1)$$

where a_r and a_i are the reflected and incident wave amplitudes respectively, well away from the region of bedforms, b is the bar amplitude, h is the water depth, m is the number of bars and k and ℓ are the free surface and bar wavenumbers. Here $k = 2\pi/L$ and $\ell = \frac{2\pi}{L_b}$, where L and L_b are surface and bar wavelengths respectively. It should be noted that, strictly speaking, this is a two-dimensional formulation of the problem requiring long crested surface waves collinear with the bottom undulations.

Equation (1) illustrates that for a given number of bars (m), the wave reflection coefficient is oscillatory in $2k/\ell$, that is the quotient of twice the surface wavenumber and the bed wavenumber. The reflection coefficient is also resonant in the region $2k/\ell \cong 1$ and, at $2k/\ell = 1$ itself, is proportional to m which suggests that peak reflection coefficients are linearly dependent on the number of bars.

These results were without any detailed experimental proof and this paper describes experiments carried out in a wave tank to examine the nature of resonant interactions between surface waves and simple sinusoidally varying topography. Preliminary aspects of this study have already been described by Heathershaw (1982).

EXPERIMENTAL PROCEDURE

To test Davies' (1980, 1982) theoretical predictions, and in particular Equation (1), detailed measurements of wave reflection from submerged bars were carried out using the 45.72 x .91 x .91 m wave tank facility at the US Army Coastal Engineering Research Center, Fort Belvoir, Virginia, USA. Test sections of 10, 4, 2 and 1 x 1 m wavelength, .05 m amplitude sinusoidal bars were constructed in the tank and set in a false bottom. The barred test sections were

situated approximately mid-way between a hydraulically driven piston type wave generator, at one end of the tank, and a 1:10 slope wave absorbing beach at the other. Water surface elevations were measured using standard parallel-wire resistance type wave gauges and wave reflection coefficients determined using the method of Goda and Suzuki (1976).

Two pairs of gauges and a single gauge were used to make two types of measurement; first, incident and transmitted wave conditions were measured with one gauge pair 5 m on the up-wave side of the bars and the second gauge pair 5 m on the down-wave side. The remaining gauge was positioned midway along the test section. The up-wave gauge pair thus gave information on wave reflection from the bars while the second gauge pair provided data on the transmitted wave heights and the amount of wave energy reflected from the beach. In the second type of measurement two pairs of gauges were moved along the tank in such a way as to give surface elevation data every 0.25 m and to determine how wave reflection varied throughout the tank, first from the barred test section and finally from the beach. The remaining gauge was positioned at the end of the tank at the foot of the beach. These experimental arrangements are illustrated in Fig 1, with further details given in Davies and Heathershaw (1983).

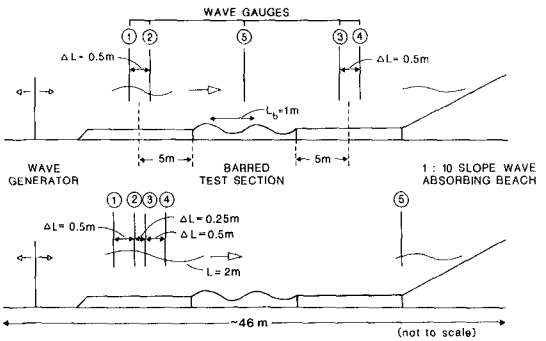

Figure 1 Position of gauges, in relation to barred test section (2 bars only), and wave absorbing beach, for two main types of measurements. Typical values of the wave gauge spacing ΔL are also shown.

With the bar wavelength, L_b, fixed at 1 m, incident surface wavelengths were varied over a range giving $.5<2k/\ell<2.5$, by varying the wave period in steps of .01 s. Thus, good resolution in non-dimensional wavenumber space $2k/\ell$, of the order of .01, enabled detailed investigations to be made of the oscillatory nature of the wave reflection coefficient and of the main resonant interaction peak. These tests were carried out using small amplitude monochromatic waves only. For the results shown here, water depths were varied to give bar amplitude - water depth ratios, b/h, in the range $.08<b/h<.40$.

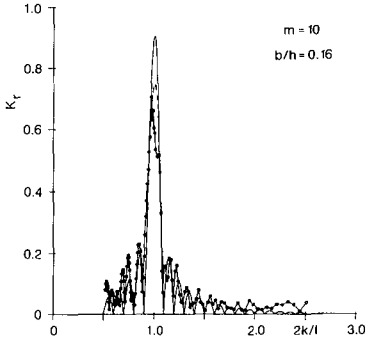

Figure 2a The variation of wave reflection coefficient K_r with the ratio $2k/\ell$ for m = 10 bars and for b/h = .16 (h = 31.3 cm). The broken and solid curves represent corrected and uncorrected theoretical predictions respectively; corrected theoretical predictions assume a linear attenuation of incident wave amplitude across the bar patch and uncorrected predictions assume no attenuation.

RESULTS

For surface water wavelengths approximately twice the bar wavelength, strong resonant interactions were observed leading to large reflection coefficients (in some cases as large as $K_r = .8$) and to dramatic partially standing wave patterns on the up-wave side of the bars. On the down-wave side of the bars the standing wave pattern gives way to progressive waves leaving the test section and travelling towards the wave absorbing beach.

Figure 2 shows the variation of wave reflection coefficient, K_r, with the wavenumber ratio $2k/\ell$ for 10, 4 and 2 bars and bar amplitude/water depth quotients of b/h = .16 and .32, corresponding to depths of h = 31.3 cm and h = 15.6 cm respectively. Also shown are the first order predictions from Davies (1980, 1982) both corrected and uncorrected for the effects of wave attenuation as the incident waves propagate over and are reflected by the bars. A striking feature of

these results is the large resonant interaction peak at $2k/\ell = 1$, and the oscillatory nature of K_r in respect of $2k/\ell$. Figure 2a, for m = 10 bars, shows that the measured reflection coefficients follow the

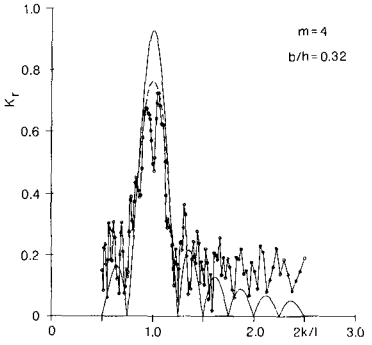

Figure 2b The variation of wave reflection coefficient K_r with the ratio $2k/\ell$ for m = 4 bars and for b/h = .32 (h = 15.6 cm). The broken and solid curves represent corrected and uncorrected theoretical predictions respectively (see Fig 2a).

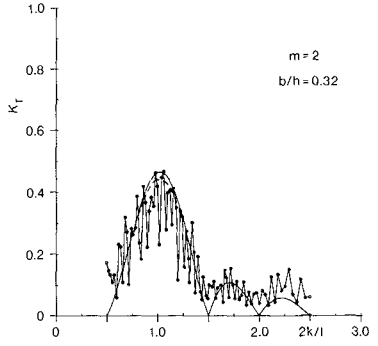

Figure 2c Variation of the wave reflection coefficient K_r with the ratio $2k/\ell$ for m = 2 bars and b/h = .32 (h = 15.6 cm). The broken and solid curves represent corrected and uncorrected theoretical predictions respectively (see Fig 2a).

trend of the theoretical curves closely throughout the resonant peak and on either side of it. Similarly in Figures 2b and 2c for m = 4 and 2 bars the central resonant peaks are well reproduced. However, in these cases the level of the measured reflection coefficient is in general above that predicted by the theory. Davies and Heathershaw (1983) have shown that this is probably due to a small, though non-negligible, amount of wave energy (less than ∿4%) being reflected from the wave absorbing beach at the far end of the tank.

The solid curves in Figure 2 represent theoretical values calculated assuming no attenuation of the incident waves across the bar patch and, consequently, no proper energy balance. The broken curves represent theoretical values calculated assuming a linear attenuation of the incident wave across the bars and giving the required energy balance. Details of the energy balance procedure may be found in Davies (1980).

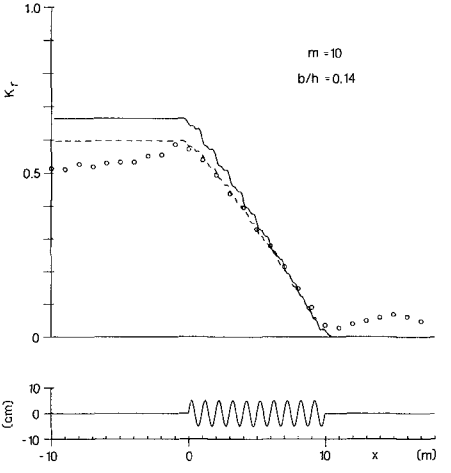

Figure 3a The variation of measured reflection coefficient K_r over the barred test section and on either side of it for m = 10 bars and for b/h = .14 (h = 35.7 cm). Broken and solid curves represent corrected and uncorrected theoretical predictions respectively. The corrected theory assumes a linear decrease in incident wave amplitude across the bar patch.

Figure 3 shows the results from 10 and 4 bars, of measurements of the reflection coefficient, K_r, at resonance, at different positions, x, along the tank and throughout the barred test section. In particular it should be noted that K_r is a value calculated by the method of Goda and Suzuki (1976) and that this may only be expected to agree with

the K_r given by (1) well away from the bars on the up-wave side of the bar patch. Measurements are shown for bar amplitude-water depth quotients b/h = .14 and .32, corresponding to water depths of 35.7 cm and 15.6 cm respectively. The resonant wave period settings for these measurements were 1.28 s and 1.73 s.

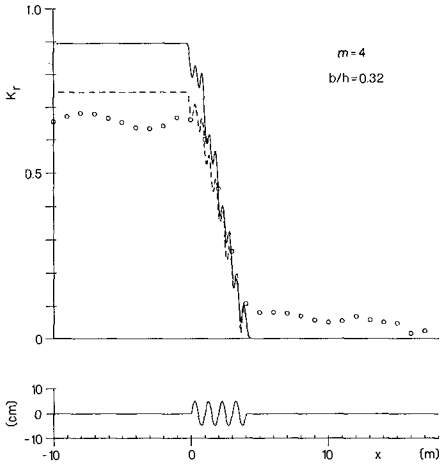

Figure 3b The variation of measured reflection coefficient K_r over the barred test section, and on either side of it for m = 4 bars and for b/h = .32 (h = 15.6 cm). Broken and solid curves represent corrected and uncorrected theoretical predictions respectively. The corrected theory assumes a linear decrease in incident wave amplitude across the bar patch.

The measurements show good agreement with theoretical predictions throughout the barred test section although in general they underestimate the theory on the up-wave side of the bars and overestimate it on the down-wave side. The results in Figure 3 show that on the up-wave side of the bars the measured reflection coefficient is more or less constant and rises to a peak value within a few water depths of the bars before falling, linearly throughout the test section, to a value of the order of .05 or less, which is the reflection from the beach alone. The increase in K_r towards the patch is believed to be due to viscous dissipation in the tank (see Davies and Heathershaw, 1983).

Figures 4a and 4b represent corresponding measurements of the amplitude of surface elevation throughout the barred test section and on either side of it for the conditions described above. These wave envelope observations confirm the presence of a standing or partial standing wave between the bars and the wave generator and show how

this gives way to progressive waves leaving the test section and propagating towards the beach. The results in Figures 4a and 4b show good agreement with the corrected theoretical curve (b), supporting the use of linear attenuation of incident wave amplitude across the bar patch. Details of the theoretical predictions of surface elevation amplitudes, in the vicinity of the bar patch, are given in Davies and Heathershaw (1983).

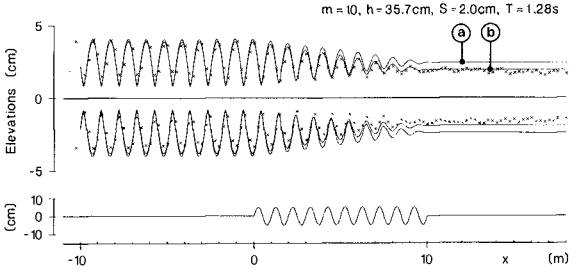

Figure 4a Surface elevation amplitudes measured throughout the barred test section and on either side of it for m = 10 bars and b/h = .14 (h = 35.7 cm). Curves (a) and (b) represent uncorrected and corrected theoretical predictions respectively. The corrected theory assumes a linear decrease in incident wave amplitude across the bar patch.

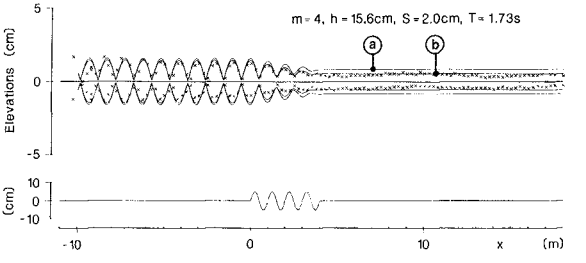

Figure 4b Surface elevation amplitudes measured throughout the barred test section and on either side of it for m = 4 bars and b/h = .32 (h = 15.6 cm). Curves (a) and (b) represent uncorrected and corrected theoretical predictions respectively. The corrected theory assumes a linear decrease in incident wave amplitude across the bar patch.

Results illustrating the variation of the maximum possible value of K_r with the number of bars (m) and the bar amplitude-water depth quotient (b/h) are shown in Figure 5. For each case, measurements of K_r were made over a range of $2k/\ell$ values at or near resonance and the reflection coefficient values averaged. Further details of these measurements and the averaging procedure are given in Davies and Heathershaw (1983). It should be noted that the number of measurements of K_r at or near a resonant peak may not have been representative of the true variation in K_r and for this reason values of K_r in Figure 5 are shown as means with standard deviation error bars.

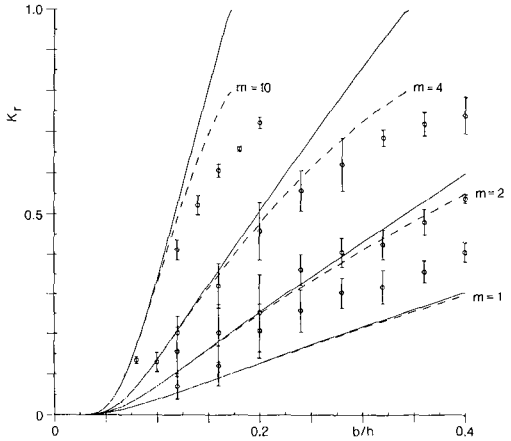

Figure 5 Measured peak reflection coefficients for m = 1, 2, 4 and 10 bars and for different values of b/h.

Results are shown in Figure 5 for m = 10, 4, 2 and 1 bars. For 10 and 4 bars (m = 10 and 4) measured reflection coefficients in general underestimate the theory which is shown uncorrected (solid curve) and corrected (broken curve) for the effects of wave attenuation across the bars. For 2 and 1 bars (m = 2 and 1) the measurements tend to overestimate the theory and, as shown by Davies and Heathershaw (1983), since the measured bar reflection coefficient is equal to the actual bar reflection coefficient plus or minus the value for the beach (dependent upon phase) this result most probably indicates the increasing importance of beach reflections as the predicted value of the bar reflection coefficient decreases with a smaller number of bars. Despite these shortcomings the measurements are generally supportive of the main theoretical conclusion that the peak wave reflection coefficient increases linearly with the number of bars (m) and as the water depth is decreased (b/h increased). However, it should be noted

that strictly speaking, K_r is only expected to increase linearly with m at $2k/\ell = 1$ and that in most cases the peak values shown in Figure 5 correspond to mean $2k/\ell$ values which are not exactly equal to 1 but which are in the range .9647 - 1.0171 with standard deviations of .0077 - .0538. Further details of these results may be found in Davies and Heathershaw (1983).

Following a suggestion of Davies (1980, 1982) some observations of sediment movement were also carried out in the wave tank. Davies suggested that as a result of the partial standing wave which forms up-wave from a reflecting bar systems, the pattern of wave orbital motions near the bed may lead to areas of preferential erosion and deposition of sediment. Potentially, at least, this provides a mechanism for bars to grow in the up-wave direction.

To confirm this result, fine sand of about 235μm mean diameter was sprinkled in a thin uniform layer throughout the barred test section (with 2 bars only) and for about 2-3 m on either side of it. Small amplitude waves were started and the wave amplitude increased until sediment motion was initiated. Sediment movement was then observed for a resonant wave reflection condition ($K_r = .34$) and the evolution of ripple patches recorded. On the up-wave side, ripple patches with a 1 m spacing were observed while down-wave a more or less continuous sheet of ripples developed. Erosion, and ripple formation, was observed to occur beneath the nodes of surface elevation of the partially standing wave. With increasing time, ripple heights were observed to grow on the up-wave side of each patch in such a way as to bring about an accumulation of material approximately mid-way between node and antinode and roughly in the position where bar crest formation would be expected to occur. These results confirm that a potential bar-growth mechanism exists up-wave of the bars but not on the down-wave side.

An example of the observed sediment distribution is shown in Figure 6. It should be noted that sediment accumulation at an antinode would not be expected in this case since the horizontal component of the wave induced current at this location is minimal and usually below the threshold of movement of all but the finest sediment. As was observed in this study, sediment accumulation and the cessation of sediment transport, would be expected to occur at a point intermediate between the high velocities at the nodes and the low velocities at the antinodes. This result may be contrasted with that of Nielsen (1979) who found that for fine sand ($d_{50} = 80\mu m$), sediment accumulation did occur beneath the antinode of a partially standing wave. In this case sediment movement was principally as suspended load whereas in this study material moved mainly as bedload or in a thin suspension layer due to vortex shedding from ripple crests.

CONCLUSION

In conclusion the results of these experiments have shown that significant and large amounts of wave energy may be reflected from submerged bar like structures and that these reflections are brought about by

resonant interactions between surface water waves and the bedforms. In particular, at resonance, incident surface water wavelengths are approximately twice the bedform wavelengths. The results have implications not only in terms of wave reflection from naturally occurring bedforms, say bars on beaches, but also for sediment transport processes in general.

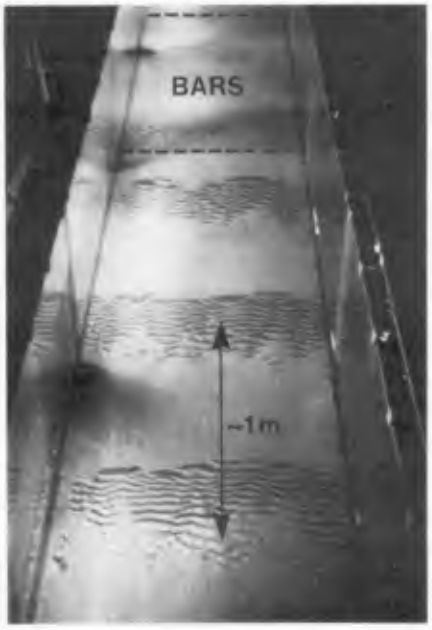

Figure 6 Ripple patches with a 1 m spacing formed beneath a partial standing wave on the up-wave side of 2 x 1 m wavelength bars. The bar amplitude is 5 cm and for these observations the water depth was h = 15.6 cm and the wave reflection coefficient was $K_r \cong .34$. Maximum ripple heights and wavelengths, in the ripple patches, were of the order 1.5 cm and 5.5 cm respectively.

ACKNOWLEDCEMENTS

I am grateful to the Commander and Director of the US Army Corps of Engineers, Coastal Engineering Research Center, Fort Belvoir, Virginia, USA for experimental facilities and to Dr A C Davies for much valuable discussion.

REFERENCES

DAVIES A C (1980) Some interactions between surface water waves and ripples and dunes on the seabed. Institute of Oceanographic Sciences Report No 108. 134 pp

DAVIES A G (1982) The reflection of wave energy by undulations on the seabed. Dynamics of Atmospheres and Oceans, 6 : 207-232

DAVIES A C and HEATHERSHAW A D (1983) Surface wave propagation over a patch of bottom ripples - theory and laboratory experiments. Institute of Oceanographic Sciences Report (in press)

GODA Y and SUZUKI Y (1976) Estimation of incident and reflected waves in random wave experiments. Proc 15th Conf Coastal Eng American Society of Civil Engineers, Honolulu, 828-845

HEATHERSHAW A D (1982) Seabed-wave resonance and sand bar growth. Nature, 296 : 343-345

HOLMAN R A and BOWEN A J (1982) Bars, bumps, and holes : Models for the generation of complex beach topography. Journal of Geophysical Research, 87 : 457-468

LANGHORNE D N L (1982) A study of the dynamics of a marine sandwave. Sedimentology, 29 : 571-594

NIELSEN P (1979) Some basic concepts of wave sediment transport Technical University of Denmark. Institute of Hydrodynamics and Hydraulic Engineering. Series Paper No 20, 160 pp

SHORT A D (1975) Multiple offshore bars and standing waves. Journal of Geophysical Research, 80 : 3838-3840

SUHAYDA J N (1974) Standing waves on beaches. Journal of Geophysical Research, 79 : 3065-3071

SYMONDS C, HUNTLEY D A and BOWEN A J (1982) Two-dimensional surf beat : Long wave generation by a time varying breakpoint. Journal of Geophysical Research, 87 : 492-498

THE EFFECT OF BED SLOPE ON WAVE CHARACTERISTICS

by
R.C. Nelson, Department of Transport and Construction, Australia

1. INTRODUCTION

In all wave theories used in engineering applications it is assumed that the profile of the bed is horizontal which results in a symmetrical wave shape and velocity field, so that, strictly speaking, they can be applied only to this condition. Nearshore bottom profiles are, however, seldom horizontal, and a wave moving over a shoaling slope has an asymmetrical profile which is associated with an asymmetrical velocity field within the wave which, in turn, directly influences the movement of bed sediment. As a matter of necessity, but within reason, engineers have ignored the influence of bed slope on the wave theory used. This course of action was justifiable on many counts, not the least of which was that inaccuracies associated with the theories used were far greater than any inaccuracies introduced by ignoring bed slope parameters. However, wave theories developed in recent years have become increasingly accurate and reliable so that it may now be necessary to take account of bed slope parameters in applying these wave theories before further improvements can be made in the techniques used to predict wave-induced sediment transport.

2. AIMS AND OBJECTIVES

This paper describes an experimental programme which assessed and quantified the influence of bed slope on the characteristics of non-breaking waves. The objective was to determine, for individual wave characteristics, the maximum slope up to which insignificant effects are induced and, for steeper slopes, to describe quantitatively the divergence from those results for a horizontal bed. The specific wave characteristics measured and compared for various slopes were:

(i) wave profile (n versus t);
(ii) wave celerity (and hence, by definition, wavelength);
(iii) potential energy;
(iv) ratio of crest time to wave period;
(v) ratio of trough time to wave period:
(vi) ratio of crest height to wave height;
(vii) ratio of trough depth to wave height;
(viii) crest skewness;
(ix) trough skewness; and
(x) ratio of asymmetrical wave slope to bed slope.

The definitions of these characteristics are given in Figure 1.

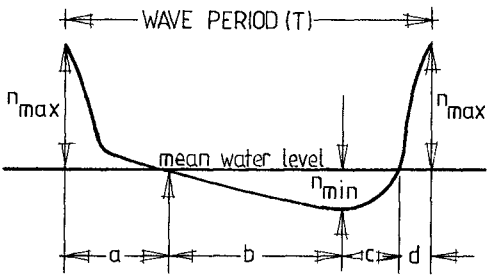

WAVE PROFILE (n versus t)	
WAVE CELERITY (and hence, by definition, wave length)	
POTENTIAL ENERGY	
RATIO OF CREST TIME TO WAVE PERIOD	$(a+d)/T$
RATIO OF TROUGH TIME TO WAVE PERIOD	$(b+c)/T$
RATIO OF CREST HEIGHT TO WAVE HEIGHT	$\eta_{max}/(\eta_{max}+\eta_{min})$
RATIO OF TROUGH DEPTH TO WAVE HEIGHT	$\eta_{min}/(\eta_{max}+\eta_{min})$
CREST SKEWNESS	$d/(a+d)$
TROUGH SKEWNESS	$b/(b+c)$
RATIO OF WAVE SLOPE TO BED SLOPE	$\lvert\eta_{min}\rvert/b \tan\theta$

Figure 1 : Definition Sketch

3. PREVIOUS WORK

Adeyemo (1968) investigated experimentally, for six bed slopes ranging from 1:4 to 1:18, the effects of bed slope on the ratio of crest height to wave height and various measures of crest skewness. The work covered a wide range of wave non- linearity using values of d/λ between 0.08 to 0.26. Adeyemo demonstrated that crest skewness was greater on steeper bed slopes and that it increased as the wave moved into shallower water, being a maximum at the breaker point. He also found that for small values of d/λ the ratio of crest height to wave height became progressively less on steeper slopes. Unfortunately, Adeyemo did not give any observed values of H/d at the points of measurement which limited severely the comparisons that can be made with other experimental studies and prevented the incorporation of the results into such studies. The work described in this report demonstrates, for example, that the ratio of crest height to wave height is also a function of the ratio of wave height to water depth.

Adeyemo (1970) investigated experimentally the relationship between wave shape asymmentry and wave-induced velocities near the breaker zone. From the results of experiments using a fixed wave period of 0.8 seconds, bed slopes of 1:9 and 1:18 and values of d/λ between 0.0800 and 0.1245, he concluded that there are qualitative and quantitative relationships between the asymmetry of wave shape, caused by bed slope, and the asymmetry of the resulting velocity field. Indeed, his observed velocity profiles shown in his Figures 3 and 4 for the two slopes tested demonstrate all the characteristics and trends shown on the observed wave shape profiles of Figure 4 in this paper.

4. EXPERIMENTAL EQUIPMENT AND TECHNIQUE

The basic apparatus used for the experimental programme was a glass-walled tilting flume with a test section 30m long, 0.99m deep and 0.75m wide. Tilting was effected by means of electrical drives about a central pivot point. The flume had a tilting slope range of between horizontal and 1:67. Other slope ranges could be obtained by building in fixed slopes with respect to the flume, and tilting these. The flume was fitted with a pneumatic, uniform wave generator. A mobile instrument carriage located on rails along the top of the flume was fitted with two parallel-wire, resistance wave transducers located centrally in the flume and 0.22m apart along the flume axis.

The carriage also carried the associated electrical equipment together with a water level follower and two analogue chart recorders. The carriage instrumentation was in turn connected to a Hewlett Packard System 1000, model 31 computer with a 21MXE central processing unit, an RTE II operating system and a 2240A measuring and control processor.

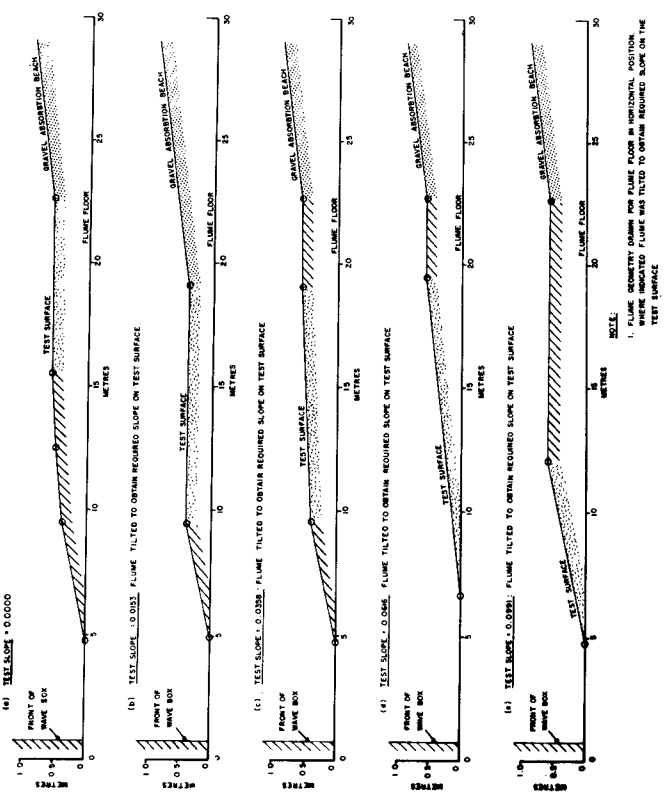

FIGURE 2 : Flume Profiles Used in Test Programme

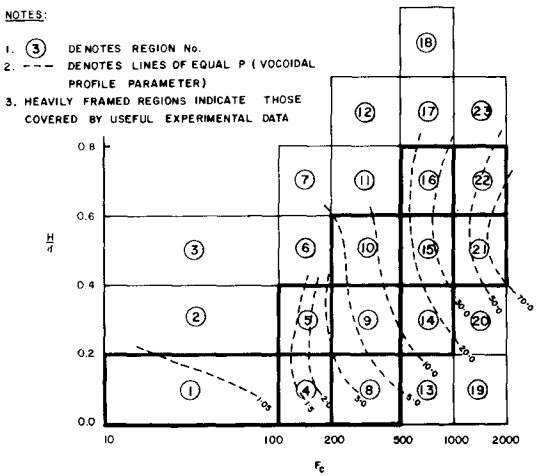

FIGURE 3 : Adopted Regions on H/d, Fc Field

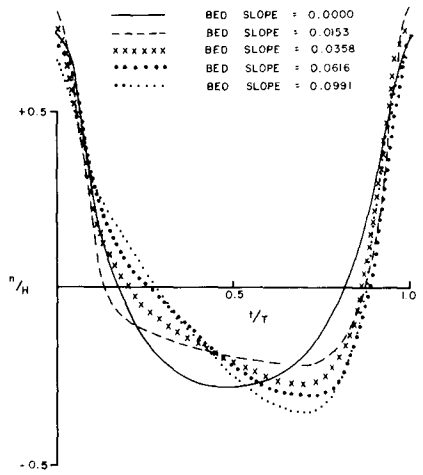

FIGURE 4 : Typical Observed Wave Profiles

All instrument calibration and data acquisition were performed on-line to the computer, the data being analysed immediately and then stored on disc file as well as printed out as a hard copy. Water level readings from each probe were logged every 30 milliseconds. A sample comprised of a number of consecutive, individual readings acquired simultaneously at each probe during a time period of at least two wave periods. A test run comprised of a specified number of samples acquired simultaneously at each probe, the wave height, water depth and wave period being the same for each sample.

It was possible to acquire any number of samples for any given test run but three was determined to be the optimum. This number was based on the results of pilot experiments in which no definite improvement in the standard deviation of the measured characteristics could be discerned for greater numbers of samples.

The occurrence of any water level set-down or set-up at the wave transducers was automatically accounted for in the data acquisition system.

Five slopes were used during the experimental programme, namely, 0.0000, 0.0153, 0.0358, 0.0616 and 0.0991. The flume profiles are shown in Figure 2. The slopes were not tested in this order. The testing order was 0.0153, 0.0358, 0.0000, 0.0991 and 0.0616. The order was determined as the programme proceeded but was governed mainly by two factors:

(i) the ease with which the flume could be adapted to another slope, and

(ii) the desire to test extremes so that the intermediate slopes that should be tested could be determined.

It was found that the experimental technique used precluded experimentation on slopes steeper than 0.100 because:

(i) wave reflection created significant secondary effects,

(ii) random ripples caused by wave-breaking and downrush created significant secondary effects, and

(iii) differences in depth between probes became significant.

5. EXPERIMENTAL DESIGN

Any dimensionless numbers used in the basic classification or grouping of data had to be free of theory-dependent parameters and preferably contain only those which could be measured directly. The only parameters capable of direct measurement at a point over a sloping bed, with a high degree of precision, are wave period (T), water depth (d) and wave height (H). Hence, use was made of the non-linearity parameter, Fc, after Swart (1978) and Swart and Loubser (1979). This is defined as;

$$Fc = (H/d)0.5 \quad (Tc)2.5$$

$$Tc = T\ (g/d)0.5$$

One helpful property of Fc is that waves of equal Fc have approximately the same relative wave shape. It was decided, therefore, to establish a system of comparison based on the measured experimental values of H/d and Fc.

Another problem to be solved was that a combination of test values T, d and H used on one slope would be physically impossible to reproduce exactly on each of the other slopes tested. The solution lay in the division of the H/d versus Fc plane into regions so that groups of resuts from identical regions could be compared. For this to be done two criteria would have to be satisfied. One of these was that the range of relative profile shape covered by each region should not be too large. The second, and more important criterion, was that the standard deviation of results obtained over any one region should not be too large, otherwise no significance could be attributed to differences between mean values obtained from various regions on different slopes. To determine the boundaries and size of these regions a pilot experiment was undertaken and the results investigated statistically. Regions were adopted which required between 4 and 6 test runs per region. The regions adopted are shown in Figure 3 together with the relationship between H/d, Fc and P the vocoidal wave profile parameter, which is a measure of relative wave shape after Swart (1978) and Swart and Loubser (1979).

It will be noted later that in Tables 1, 2 and 3 experimental values of celerity have not been used on their own, but rather the ratio of observed celerity to that predicted by vocoidal theory. This is called the celerity ratio and is simply a device to reduce the standard deviation of celerity measurement over any one region. The experimental values of celerity on their own showed too great a variation. This device in no way makes the final objective (the influence of slope on wave celerity) dependent on any wave theory. Any wave theory could have been used providing its celerity estimates varied with respect to T, d and H in a manner similar to that in real situations on horizontal beds. Obviously the greater this similarity, the less would be the standard deviation. It is emphasized that it is this similarity of variation with T, d and H that is important here and not the accuracy of the absolute value of celerity predicted by the theory. However, if there was similarity in this respect also, the ratio should be close to 1.0 in each region for a horizontal bed. This was in fact so when vocoidal theory was used.

TABLE 1

PERCENT VARIATION OF REGIONAL MEANS FROM HORIZONTAL BED RESULT WHERE A STATISTICALLY SIGNIFICANT VARIATION OCCURRED

(a) Celerity Ratio

Slope	0,0153	0,0358	0,0616	0,0991
Region 1				-3
Region 4				
Region 5	-3	-4		
Region 9			+4	
Region 10				
Region 15				

(b) Potential Energy Coefficient

Slope	0,0153	0,0358	0,0616	0,0991
Region 1	-2			
Region 4				
Region 5				
Region 9		-5	-5	
Region 10				
Region 15				

(c) Ratio of Crest Time to Wave Period

Slope	0,0153	0,0358	0,0616	0,0991
Region 1				
Region 4				
Region 5				
Region 9				+13
Region 10			+12	+23
Region 15			+13	+21

(d) Ratio of Trough Time to Wave Period

Slope	0,0153	0,0358	0,0616	0,0991
Region 1				
Region 4				
Region 5				
Region 9				-8
Region 10			-6	-11
Region 15			-7	-11

TABLE 1 (Cont'd)

PERCENT VARIATION OF REGIONAL MEANS FROM HORIZONTAL BED RESULT WHERE A STATISTICALLY SIGNIFICANT VARIATION OCCURRED

(e) Ratio of Crest Height to Wave Height

Slope	0,0153	0,0358	0,0616	0,0991
Region 1				
Region 4				
Region 5				-6
Region 9			-5	-11
Region 10			-7	-13
Region 15			-7	-12

(f) Ratio of Trough Depth to Wave Height

Slope	0,0153	0,0358	0,0616	0,0991
Region 1				
Region 4				
Region 5				+11
Region 9			+9	+21
Region 10			+19	+34
Region 15			+21	+33

(g) Crest Skewness

Slope	0,0153	0,0358	0,0616	0,0991
Region 1				
Region 4			-10	-10
Region 5				-7
Region 9	-7	-14	-18	-25
Region 10	-10	-18	-27	-32
Region 15	-21	-37	-47	-49

(h) Trough Skewness

Slope	0,0153	0,0358	0,0616	0,0991
Region 1				
Region 4				
Region 5				
Region 9		+33	+32	+24
Region 10		+46	+43	+41
Region 15	+63	+82	+80	+77

TABLE 2

RANKING OF WAVE CHARACTERISTICS IN RISING ORDER OF SLOPE INFLUENCE

Rank	Wave Characteristic	Fc range affected	Slope range affected	Greatest observed regional variation
(i)	Potential energy coefficient and celerity ratio	No consistent trend	No consistent trend	5%
(ii)	Ratios of crest time to wave period and trough time to wave period	>200	⩾0,062	23%
(iii)	Ratios of crest height to wave height and trough depth to wave height	>100	⩾0,062	34%
(iv)	Crest and trough skewness	>100	⩾0,015	82%

TABLE 3

RECOMMENDED FUNCTIONAL RELATIONSHIPS

Note: * denotes applicable to all tan $\theta < 0,100$

+ denotes that values may be in error by an amount approaching 10% for tan $\theta \to 0,100$ when Fc>500. With this proviso the value shown is applicable to all tan $\theta \leq 0,100$

# denotes that functional relationships should not be used for values of H/d <0,05 when Fc>200. In general all values applicable to all tan $\theta \leq 0,100$

Fc range	$^{+}$Celerity ratio
All Fc	1,00

Fc range	* tan α_w
All Fc	0,4 C tan θ

Fc range	* Potential energy coefficient
Fc < 10	0,062
10 < Fc < 100	0,061
100 < Fc < 200	0,059
200 < Fc < 500	$0,062 - 0,019(\frac{H}{d})^{0,56}$
500 < Fc < 1 000	$0,062 - 0,028(\frac{H}{d})^{0,56}$
Fc > 1 000	$0,062 - 0,036(\frac{H}{d})^{0,40}$

TABLE 3 (Cont'd)

RECOMMENDED FUNCTIONAL RELATIONSHIPS

Fc range	# $\frac{\text{Crest time}}{T}$
Fc < 10	0,50
10 < Fc < 100	0,46
100 < Fc < 200	$0,47 - 0,17(\frac{H}{d})$
200 < Fc < 500	$0,42 - 0,20(\frac{H}{d}) + 0,70 \tan\theta$
500 < Fc < 1 000	$0,42 - 0,20(\frac{H}{d}) + 0,90 \tan\theta$
Fc > 1 000	$0,38 - 0,20(\frac{H}{d}) + 2,70 \tan\theta$

Fc range	# $\frac{\text{Trough time}}{T}$
Fc < 10	0,50
10 < Fc < 100	0,54
100 < Fc < 200	$0,53 + 0,17(\frac{H}{d})$
200 < Fc < 500	$0,58 + 0,20(\frac{H}{d}) - 0,70 \tan\theta$
500 < Fc < 1 000	$0,58 + 0,20(\frac{H}{d}) - 0,90 \tan\theta$
Fc > 1 000	$0,62 + 0,20(\frac{H}{d}) - 2,70 \tan\theta$

Fc range	# $\frac{\text{Crest height}}{H}$
Fc < 10	0,50
10 < Fc < 100	0,54
100 < Fc < 200	$0,53 + 0,26(\frac{H}{d})$
200 < Fc < 500	$0,60 + 0,27(\frac{H}{d}) - 0,90 \tan\theta$
500 < Fc < 1 000	$0,63 + 0,25(\frac{H}{d}) - \tan\theta$
Fc > 1 000	$0,67 + 0,20(\frac{H}{d}) - 1,3 \tan\theta$

TABLE 3 (Cont'd)

RECOMMENDED FUNCTIONAL RELATIONSHIPS

Fc range	#$\frac{\text{Trough depth}}{H}$
Fc < 10	0,50
10 < Fc < 100	0,46
100 < Fc < 200	$0,47 - 0,26(\frac{H}{d})$
200 < Fc < 500	$0,40 - 0,27(\frac{H}{d}) + 0,90 \tan\theta$
500 < Fc < 1 000	$0,37 - 0,25(\frac{H}{d}) + \tan\theta$
Fc > 1 000	$0,33 - 0,20(\frac{H}{d}) + 1,3 \tan\theta$

Fc range	*Crest skewness
Fc < 10	0,50
10 < Fc < 100	0,50
100 < Fc < 200	$0,50 - 0,40 \tan\theta$
200 < Fc < 500	$0,50 - 0,71 (\tan\theta)^{0,85}$
500 < Fc < 1 000	$0,50 - 0,83 (\tan\theta)^{0,56}$
Fc > 1 000	$0,50 - 1,06 (\tan\theta)^{0,45}$

Fc range	*Trough skewness
Fc < 10	0,50
10 < Fc < 100	$0,50 + \frac{\tan\theta}{0,07 + 30 \tan\theta}$
100 < Fc < 200	$0,50 + \frac{\tan\theta}{0,06 + 14 \tan\theta}$
200 < Fc < 500	$0,50 + \frac{\tan\theta}{0,02 + 6,5 \tan\theta}$
500 < Fc < 1 000	$0,50 + \frac{\tan\theta}{0,015 + 4,3 \tan\theta}$
Fc > 1 000	$0,50 + \frac{\tan\theta}{0,01 + 4,0 \tan\theta}$

6. EXPERIMENTAL RESULTS

6.1 Coverage of Fc, H/d Field

It was not possible to acquire useful data in all the regions shown in Figure 3. The regions for which useful data were acquired, and their relation to other regions, are shown in Figure 3. In general, the extent of the coverage achieved was limited by the following factors.

(i) Secondary wave effects (solitons) became significant at values of Fc greater than 2 000

(ii) The occurrence of solitons and/or random ripple effects became significant in regions 13, 19 and 20

(iii) Test runs in regions 11, 12, 17, 18 and 23 could not be obtained because of wave breaking

(iv) Test runs in regions 2, 3 6 and 7 were precluded because the necessary wave heights could not be achieved by the wave generator at smaller wave periods.

The coverage obtained on the two extreme test slopes (0.0000 and 0.0991) requires some additional discussion. Testing beyond Fc = 1 000 was not possible on the 0.0991 slope, because of secondary effects caused by wave reflection and random ripples created by wave breaking and down-rush. Testing beyond Fc = 1 000 on the horizontal slope was also precluded because of the presence of solitons in the wave form. This was partly because when tests were done at small depths on the test surface, water depths at generation were less than those for other test slopes for which the flume was tilted to maximise the depth at the generator. Earlier preliminary testing had shown that solitons were less evident for greater depths at generation (see also Hulsbergen (1972) and Van Wyk (1975)).

However, of greater importance was the fact that values of H/d greater than 0.55 could not be obtained over a horizontal bed due to wave instability and wave breaking. This was confirmed by using three different arrangements of the experimental equipment. Initially, testing on the horizontal slope was attempted using the test surface shown in Figure 2b with the flume in the horizontal position, but this failed to produce ratios of H/d greater than 0.50 because of wave instability and wave breaking. This was conceivably due to the sharp change in bed slope at the top of the shoaling slope. Further testing on the horizontal bed was postponed until the arrangement of Figure 2a could be constructed with a smooth transition between the initial shoaling slope and the horizontal test surface. This arrangement had the added advantage of increasing the depth at generation. However, the same limitation on values of H/d remained but experimentation was continued and as large a coverage as possible was achieved.

When testing had been completed on all five test slopes a third attempt was made to achieve values of H/d greater than 0.55 over a horizontal bed using a modification of the flume profile shown in Figure 2d. A horizontal, symmetrical contraction to half the flume width was constructed over the top 5m of the shoaling slope, so that a horizontal bed, half the flume width, was available prior to the absorption beach. This increased the number of available combinations of T, d and H but the same phenomena of wave instability and wave breakup were observed.

The value of H/d of 0.5 at which breaking of waves occurred over a horizontal bed was well below the values of 0.8 and greater obtained on beds with slopes as low as 0.0153. The experience of other researchers (see Nelson, 1980) tend to confirm this limiting value of H/d for horizontal beds, and leads to the conclusion that unbroken, regular waves with values of H/d exceeding 0.55 cannot exist on a horizontal bed.

6.2 Statistical Significance and Magnitude of Slope Influence

One objective of the project was to determine those slopes on which wave characteristics became significantly different from those of waves moving over horizontal beds. Unfortunately, for five of the eleven regions tested no data were obtainable for the horizontal bed. For three of these regions (8, 14 and 21) this was due to secondary wave effects. The limiting value of H/d of 0.55 accounted for the other two (16 and 22). The fact that values of H/d of 0.8 were possible for these two regions on slopes as small as 0.0153, in itself indicates a significant slope effect.

For the six remaining regions (1, 4, 5, 9, 10 and 15) a direct comparison of all four finite slope results with the horizontal bed results, was possible for all measured wave characteristics. A statistical test of significance at the 5 per cent level was made to determine which slopes produced results which varied significantly from those obtained on the horizontal bed. Table 1 shows the percentage variations of regional means from the horizontal-bed result where a statistically significant variation occurred. All tables show that with respect to the combined considerations of magnitude of variation, range of slopes responsible and Fc range affected, the ranking in Table 2, in rising order of slope influence, applies.

The only parameter which was treated differently was the ratio of asymmetrical wave slope to bed slope. The reason for a different treatment is that it was difficult to read off (define) the asymmetrical wave slope when (i) the wave height to water depth ratio H/d was less than 0.2, and (ii) the non-linearity parameter Fc was less than 200. Sometimes the asymmetrical slope could be interpreted in more than one way. Such results were also neglected. Therefore the regional mean data were lumped together in two different ways rather than interpreting them separately, namely,

(i) by grouping the wave profile data for all regions together for any slope; and

(ii) by grouping all wave profile data for the same region (all slopes) together.

These results indicate that the overall mean of ($C \tan\theta/\tan\alpha_\omega$) has a value of about 2.50 with a standard deviation of 0.25. This implies that the 95 per cent confidence band would extend from about 2.0 to 3.0 with a best estimate of 2.50. No subgroup (population comprising the results of a given slope or region) had a mean result which differed significantly at the 95 per cent level from this overall mean result.

6.3 Recommended Values of Wave Characteristics

For the range of slopes tested, all the experimental data were used to derive empirical relationships for wave characteristics. These are shown in Table 3. Oue cognizance must be given to the remarks shown in the table when using these relationships.

The tables apply to bed slopes of less than 0.100. They show that wave characteristics can be functions of Fc, H/d and tan θ. This is so for the ratios of crest time to wave period, trough time to wave period, crest height to wave height and trough depth to wave height. The observation that for shallower water, the ratio of crest height to wave height becomes progressively less on steeper slopes agrees with the findings of Adeyemo (1970).

Crest and trough skewness are shown to depend only on Fc and tan θ. The results indicate that there may be some dependence on H/d but that it is either very small, or the data are inconclusive and conflicting.

For all practical purposes the potential energy coefficient is a function of only Fc and H/d on slopes less than 0.100, and the celerity ratio is independent of all three parameters. Since the celerity ratio used was that of experimentally measured values to those predicted by the vocoidal wave theory, the results tend to enhance the practicability of applying the vocoidal theory to a wide range of slopes for the purpose of celerity and wave length determinations.

The asymmetrical wave slope depends on the bed slope and the wave celerity and can be used in conjunction with the skewness parameters to reconstruct the wave profile schematically.

6.4 Typical Observed Wave Profiles

To assist the reader to appreciate the progressive influence of bed slope on wave profile some typical observed profiles are shown for region 15 in Figure 4.

7. CONCLUSIONS AND RECOMMENDATIONS

Experiments on the influence of bed slope on some parameters associated with unbroken regular waves lead to the following findings:

(i) It is doubtful whether unbroken, regular waves on a horizontal bed with wave height-to-water depth ratios exceeding 0.55, can ever exist. Bed slopes as low as 0.015 influence the wave mechanics sufficiently to increase this ratio to greater than 0.80. Therefore, the characteristics of waves near breaking on a gentle slope cannot be assumed to be the same as those on a horizontal bed.

(ii) The effect of bed slopes of less than, or equal to, 0.100 on potential energy and wave celerity is minimal and, for all practical purposes, can be ignored.

(iii) Bed slopes greater than or equal to 0.062 can significantly influence the ratios of crest height to wave height, trough depth to wave height, crest time to wave period and trough time to wave period. These modifications of profile shape will create a redistribution of potential bed particle transport because of consequent changes in the positive and negative wave-induced bed velocities.

(iv) The greatest influence of bed slope is on crest and trough skewness and the asymmetrical wave slope and becomes significant on bed slopes as low as 0.015. These resulting asymmetries of wave profile will result in an asymmetry of the velocity field within the wave, which will have a direct influence on potential bed-particle transport.

(v) Functional relationships relate bed slope and wave characteristics and these are as shown in Table 3.

8. REFERENCES

ADEYEMO, M.D. (1968). Effect of beach slope and shoaling on wave asymmetry. Proceedings of the 11th Coastal Engineering Conference, Vol. 1, 1968.

ADEYEMO, M.D. (1970). Velocity fields in the wave breaker zone. Proceedings of the 12th Coastal Engineering Conference, Vol. 1, 1970.

HULSBERGEN, C.H. (1972). Golfopwekking in relatief ondiep water. Delft, Waterloopkundige Laboratorium, Report S 55-111.

NELSON, R.C. (1979). The effect of bed slope on wave characteristics. National Research Institute for Oceanology, Council for Scientific and Industrial Research, CSIR Research Report No. 372.

NELSON, R.C. (1980). Limiting wave height anomalies in shallow water. Deakin University, School of Engineering and Architecture, Research Report No. CE4/80.

SWART, D.H. (1978). Vocoidal wave theory. Volume 1, derivation. National Research Institute for Oceanology, Council for Scientific and Industrial Research, CSIR Report SEA IR 7805.

SWART, D.H. and C.C. LOUBSER (1979). Vocoidal wave theory. Volume 2, verification. National Research Institute for Oceanology, Council for Scientific and Industrial Research, CSIR Report SEA IR 7905.

VAN WYK, A.C. (1975). An investigation into the occurrence of secondary waves during the generation of regular waves by means of the pneumatic wave generator. National Research Institute for Oceanology, Council for Scientific and Industrial Research, CSIR Report 1975.

SENSITIVITY OF PARAMETERS AND APPROXIMATIONS IN MODELS OF TIDAL PROPAGATION AND CIRCULATION

by
Jan J. Leendertse* and Shiao-Kung Liu*

Introduction

In the last ten years a system has been designed for the two-dimensional simulation of the hydrodynamics and water quality in well-mixed estuaries, coastal seas, harbors, and inland waters. The system called SIMSYS2D or WAQUA, can simulate the hydrodynamics in complicated geographical areas, and the model can determine the land/water boundary during simulation [1]. The system accounts for the sources of discharges, tidal flats, islands or dams, and time-varying or time-invarying flow restrictions such as generated by openings in dams, sluices, or storm-surge barriers. In the SIMSYS2D system numerous finite difference approximations of the vertically integrated hydrodynamic equations and their boundary conditions are available to the investigator.

A large number of models and model experiments with two-dimensional models have been described in the literature. In many instances, authors have emphasized the advantages of the particular approximations they were using in their model and sometimes made comparisons with other approximations by use of hypothetical geographical areas. Generally, no comparisons are given of different computation methods applied to actual estuaries.

Currently, no comprehensive overview of the comparative importance of the approximations of the terms of the hydrodynamic equations based on experiments of typical estuaries, is available. Nor has a practical assessment been made on the comparative importance of timestep size, grid size, depth accuracy, roughness estimates, and approximation of the closure term by viscosity or other expressions.

To obtain an insight into the relative importance of computational and systems parameters, a large number of experiments were made with models of the Eastern Scheldt using the SIMSYS2D system in many of its modes. Some of the more important results of this extensive analysis will be presented in this paper.

Method of Analysis

The Eastern Scheldt model, used for most of the experiments, had a grid size of 800 m. For a few experiments a model with a grid size of 400 m was used (Fig. 1).

A periodic tide was taken at the boundary of the model. The amplitude and phase relation of the boundary points to a fixed observation station near the location of the boundary was determined by means of cross-spectral analysis from a 5½ day simulation of a model with a grid size of 800 m, which included the coastal region outside the estuary and the estuary itself [2].

* The Rand Corporation, Santa Monica, California

After determination of a yearly averaged tide from observations at the fixed station, amplitudes and phases of every boundary point could be calculated from the amplitude and phase relations for the M_2, M_4, and M_8 tidal component.

Simulations, as long as 15 tidal cycles, indicated that a quasi-steady state condition was never obtained. The tidal residual currents computed as low-passed filtered Eulerian transports did slowly fluctuate. Mean water levels computed by the same low-pass filter (tidal eliminator) also showed some fluctuation. In addition, the computation appears to contain noise in a few areas due to the large grid size and the discrete changes in area's size when tidal flats and sandbars become dry or flood.

Consequently, comparisons of tidal wave propagation and amplification by means of a Fourier analysis of the computed records at stations along the periphery of the estuary were difficult to make. A much better approach appeared to be optimal estimation of amplitude and phase relationships between pairs of stations by cross-spectral analysis. In addition to the amplitude and phase relations, data about the confidence of the linear estimate could be computed.

Simulations of 5½ days were made and as at least one day is required for dissipation of the starting transient, 100 hours of the simulation was available for analysis. The 100 hours is a short series for cross-spectral analysis as only eight cycles of the primary tide are available, nevertheless, a very high coherency was always obtained for this frequency. This was not the case for the quarter- and sixth-diurnal tides. These appeared to be influenced by leakage from the very strong semi-diurnal tidal component.

To alleviate that problem, band pass filters, as described by Godin [3], were applied to the computed time series which eliminated the semi-diurnal tide but retained the quarter-diurnal or the sixth-diurnal tide. Subsequently, cross-spectral analyses were made on pairs of the resulting time series. The analyses were made of the records of adjacent stations on a line along the estuary as shown in Fig. 1.

To investigate the effect of the method of approximation of the finite difference equations or the sensitivity of certain parameters on residual circulation, (Eulerian residual transport) the mass transport rates through certain cross-sections were filtered with a low pass filter. Also, the mass transport rate at each section with a dimension of the grid size of Δx was computed and filtered with a boxcar filter with the length of the tidal period. Alternately, the filtering was done with a low pass filter which completely eliminated components in the tidal frequencies. Subsequently, the vector plots of the residual transport fields could be prepared.

Effects of the Main System Parameters

In this study an alternating direction implicit scheme is used to solve the set of partial differential equations which represent the two-dimensional equations representing the two-dimensional flow [4]. For the analyses of the effects of modifications of the main system parameters a higher order finite difference approximation in space was used as the base case. This representation was first used by Arakawa and

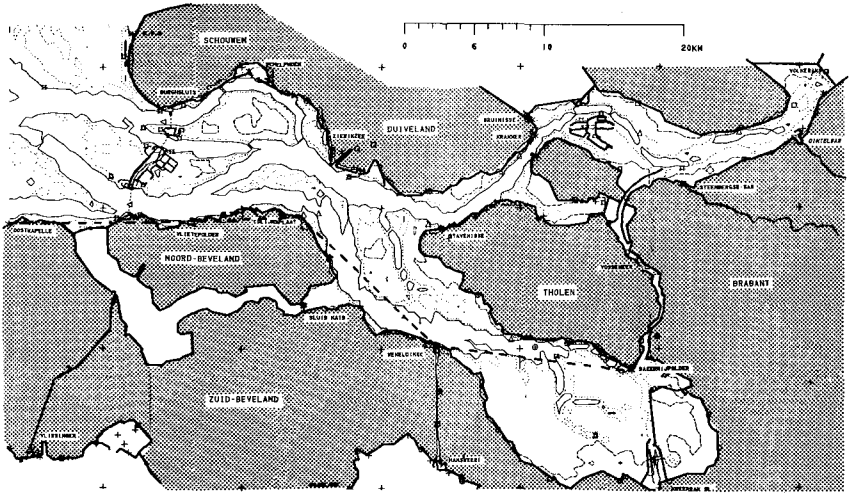

Fig. 1--Model area used for the experiments (dashed line indicates line of stations used for determination of amplification and phase lags)

has a second order accuracy in time [4]. The bottom stress terms in the semi-momentum equations were computed in a conventional manner using a Chezy value. The Chezy values were computed every half-hour from the transport depth from the bottom roughness expressed with a Manning's n coefficient.

In an earlier study it was indicated that the finite difference methods cause dispersion and amplification of a propagating tidal wave compared to solutions of the differential equations. These effects can be expressed with the complex amplification factor [5]. The dispersion and amplification is a function of the timestep, the grid size, and of the period of the wave. The base case was a simulation with the model which was already adjusted.

For the study of the effects of the main system parameters, five simulations were made, each one was a variation of the base case. We investigated a 10% decrease in Manning's n, a 5% increase in depth, a 50% increase in the multiplier (α) of the advection term, a doubling of the momentum diffusion and a reduction of 50% of the timestep (Fig. 2).

In the base case, we used for the momentum diffusion a value of 15 m^2/sec, $\alpha = 1$ and a timestep of 2.5 min. To show the effect of the parameter modifications the time lag between a boundary station (Oostkapelle) and an inland station (Razernijpolder) was computed for several components. The confidence intervals shown in this figure are for the analysis of the last two stations on the line. It will be noted that the confidence interval for the sixth-diurnal tide is much larger than for the semidiurnal tide. In the figure the results of an analysis of

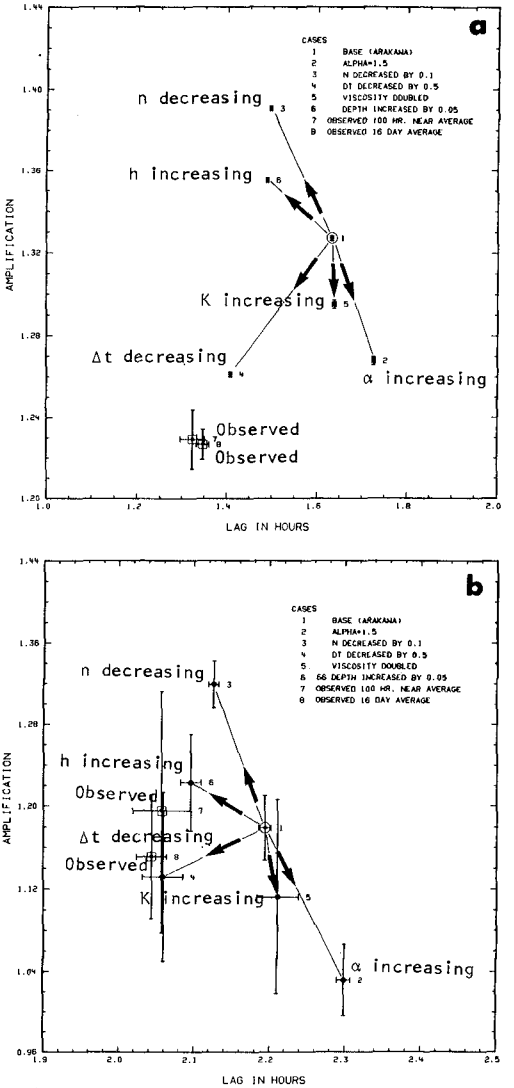

Fig. 2--Amplification versus phase lag for the relation between a station near the boundary (Oostkapelle) and an inland station (Razernijpolder): (a) semidiurnal tide (b) sixth-diurnal tide

field data is also shown. The spectral densities of the observed records in the main tidal frequency bands was nearly the same as for the boundary conditions used in the experiments.

Even though the use of a multiplier for the advection is commonly used in one-dimensional computations to account for the non-linear velocity distributions over the vertical, this multiplier is not used much for two-dimensional models.

From the results shown here it can be inferred that use of this coefficient does not seem effective as increasing n will give similar effects as increasing α.

Adjustment of parameters other than the timestep appears to be ineffective in obtaining better results. This conclusion can also be reached by a careful analysis of the behavior of the complex propagation factor. Only when the timestep is reduced does the amplification and phase lag approach the observed amplification in lag. A good agreement of all tidal components including the overtides could be obtained by reducing the grid size from 800 m to 400 m. Figure 3 shows the comparison between the observed and the computed tide at the inland station for 4 September 1975.

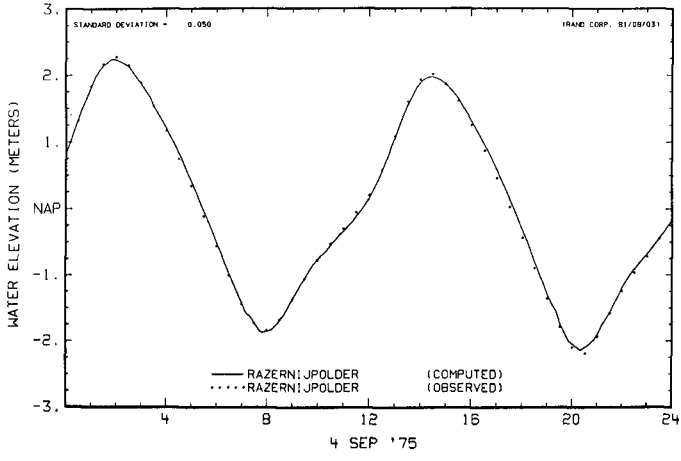

Fig. 3--Comparison of computed and observed water levels at an inland station (400 m grid model)

Choice of Advection Approximation

The approximation used for the advection terms in the momentum equations influences the tidal amplification and the transfer of energy of the primary tides to overtides.

Simulations were made with different advection terms. It appeared that the most simple advection term was the most effective in transferring energy from the semidiurnal tides to other tidal frequencies as can be seen from the amplification and phase lag plot (Fig. 4). The amplification and phase of other tidal components was not influenced much by the choice of the approximation. The choice of the approximation influences the residual circulations to a certain extent, but it did not change the general pattern. Omission of the advection terms reduces the computed residual circulations and one can conclude that advection is the primary mechanism generating residual circulations. A comparison of the computed residual circulation with and without the advection term is presented in Fig. 5.

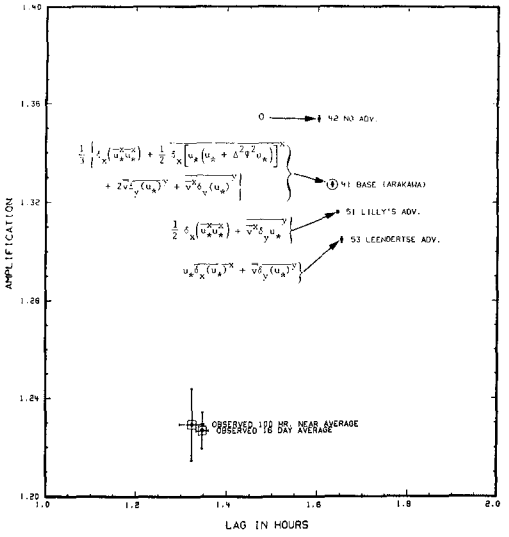

Fig. 4--Amplification versus phase lag of the semidiurnal tide for the relation between a station near the boundary (Oostkapelle) and an inland station (Razernijpolder) for computations with different advection term approximations

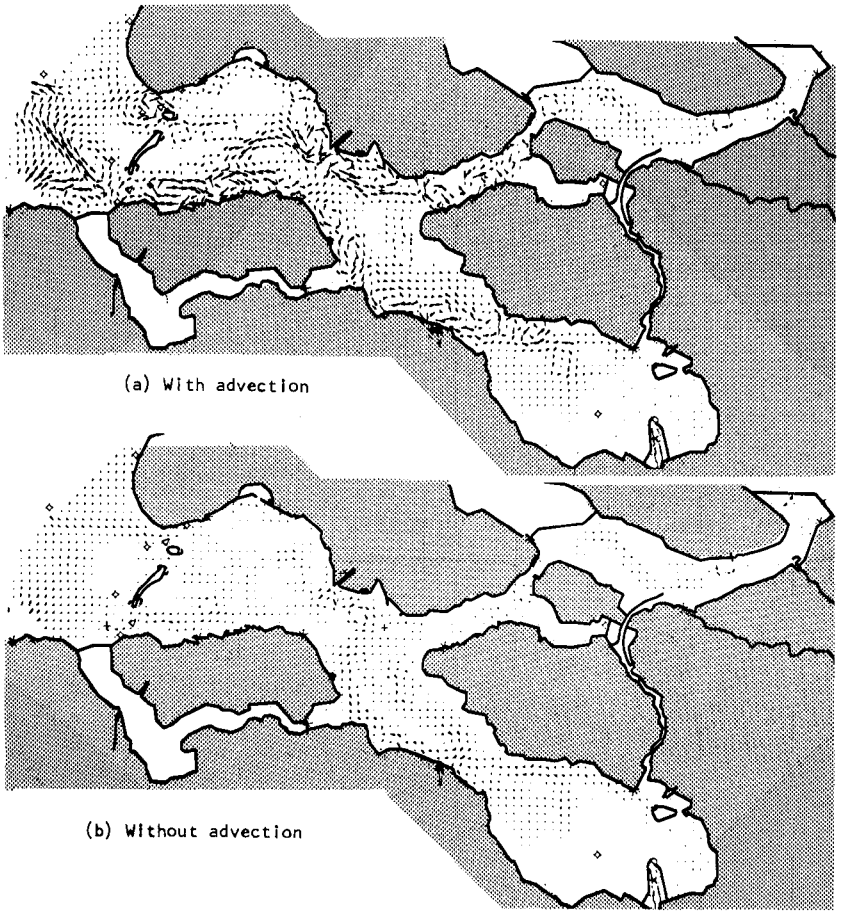

Fig. 5--Computed Eulerian residual transports for a computation with and without the advection terms

Bottom Stress Approximation

In tidal computations the bottom stress is generally taken as a function of the squared velocity and of the inverse of the depth and the squared Chezy coefficient.

In the design of a finite difference model the modeler has the option to compute the bottom stress term on the lower time level or make an expression which is central in time. Comparison of simulations with these options indicated that for practical purposes the same results are obtained. Nevertheless, the expression which is central in time is to be preferred when tidal flats and wind effects are simulated. Otherwise, a strong wind will accelerate water with a very limited depth which has just started to participate in the computational field due to flooding, to unrealistic high velocities because the bottom friction is zero.

The bottom stress can also be expressed as a function of the root of the local subgrid scale energy, the local velocity and a length scale. The local subgrid scale energy is computed as a constituent in the mass transport model. The energy is generated by the bottom stress and this generation is taken exactly the energy loss in the momentum equations. Its decay is taken as a function of the 3/2 power of the local energy intensity. The mixing length was assumed to be a fraction of the depth. By making these computations one has a two-dimensional model with a simple turbulence closure. Comparison of a simulation made with this closure model and a simulation with the bottom stress computed directly from the velocities reveal only minor differences as shown in Fig. 6.

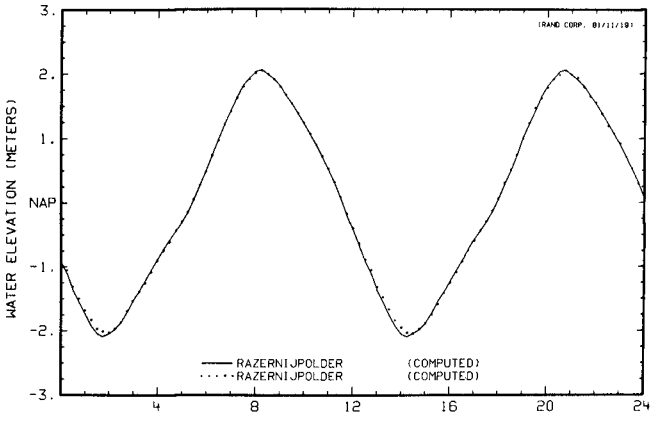

Fig. 6--Comparison of water levels at an inland station computed with a simple turbulence closure model (····) and computed by use of a stress term which is a function of the squared velocity (——)

Conclusions

From the experiments with an estuary model and from analytical considerations it can be concluded that a high resolution in time and space is required to obtain a good agreement between model and prototype. Adjustments of depth, viscosity or bottom roughness cannot compensate for insufficient resolution.

The advection terms cannot be omitted from the model as otherwise the tidal residual circulations are not properly computed. A simple expression for the advection terms appears to be the most effective in transferring tidal energy from the main tidal frequency to the overtides.

The use of a simple turbulence closure model appears to give virtually the same results as a computation with the bottom stress computed in a conventional manner.

References

1. Leendertse, Jan J., *SIMSYS2D: A Two-Dimensional Flow and Water Quality Simulation System*, Proc. Seminar on Two-Dimensional Flow Modeling, Hydrological Engineering Center, Davis, California, July 1981. Also, P-6646, The Rand Corporation, Santa Monica, California 90406.

2. Van der Ree, W. J., J. Voogt and J. J. Leendertse, *A Tidal Survey for a Model of an Offshore Area*, Proc. of the Sixteenth Coastal Engineering Conference, ASCE, New York, 1978.

3. Godin, Gabriel, *The Analysis of Tides*, University of Toronto Press, Toronto, Canada, 1972.

4. Leendertse, Jan J., A. Langerak and M. A. M. de Ras, *Two-Dimensional Tidal Models for the Delta Works*, in Transport Models for Inland and Coastal Waters, Academic Press, New York, 1981.

5. Leendertse, Jan J., *Aspects of a Computational Model for Long-Period Water-Wave Propagation*, RM-5294-PR, The Rand Corporation, Santa Monica, California 90406, 1967.

A NEW TWO DIMENSIONAL TIDAL MODELLINC SYSTEM

J.P. BENQUE[1], M.I. CHENIN[2], A. HAUCUEL[3],
S. SCHWARTZ[2], A.M. ASCE

ABSTRACT

A new method for numerical simulation of tidal currents is presented. Based on a technique involving the splitting of operators, it allows an accurate calculation of momentum advection, and wave propagation for large Courant numbers. It also provides a satisfactory treatment of tidal flat uncovering and flooding, and permits the use of a curvilinear computational grid. The generation method for such grids is presented here, followed by an engineering application on cartesian grid.

1. INTRODUCTION

Mathematical modelling of coastal shallow water areas where currents are influenced by tide and wind became a common engineering practice during the 1970's. Corresponding techniques are still developing and improving not only because faster and bigger computers are available, but, more importantly, because greater emphasis is being given to the environmental aspects of engineering works. To design the facilities themselves free surface elevation and global discharges are usually sufficient, and a fairly coarse modelling is satisfactory. However, the study of the impact that such works have on the environment asks for more refined models, in particular for a reliable simulation of currents.

(1) Head of the LNH-EDF, Chatou, France.
(2) Engineer, Dept. of Applied Mathematics, Sogreah, Crenoble, France.
(3) Head of the Research Division, LNH-EDF, Chatou, France.

In order to satisfy these requirements the Laboratoire National d'Hydraulique (LNH-Electricité de France), Chatou, and Sogreah, Crenoble, France developed jointly a new method of numerical simulation of tidal currents and a new modelling system called CYTHERE ES 1. A schematic diagram of the system, as used at Sogreah, is shown in Fig. 1.

This system was evolved for simulation of currents and consequently great care was taken to avoid three main drawbacks inherent in many programs developed in the 1970's, namely: numerical spurious damping and dispersion, inaccuracies and "polarisation" of velocity fields in ADI (alternating direction implicit method) for greater computational time steps, and inadequate simulation of uncovering tidal flats during ebb flow. Another difficulty is the choice between finite difference and finite element algorithms, the former being more economical, the latter representing the topography more accurately; an intermediate solution was chosen.

2. EQUATIONS

Nearly all industrially applied modelling systems use finite difference (FDM) discretisation of equations. Although finite elements (FEM) are often mentioned in technical literature, their application to the tidal flow equations is not common because it is expensive.

Indeed, they are no more suitable than FDM where hyperbolic equations are concerned and they lead to much higher computational costs. Their advantage as compared to FDM is that they give a much better fit with topographically complicated boundaries which are represented by stair-like steps in FDM. In order to minimise this disadvantage while using the more economical finite difference method, CYTHERE ES 1 can use an orthogonal curvilinear computational grid which improves boundary and current simulation in narrow estuaries and bays. The choice of an arbitrary (non-orthogonal) curvilinear system of coordinates was discarded because of the inaccuracies which such a transformation of equations would have introduced. Equations of tidal flow are written for an orthogonal curvilinear coordinate system by including projection parameters and metric coefficients. This allows the use of CYTHERE ES 1 in Cartesian coordinates as a special case of orthogonal curvilinear coordinates. In order to render the system efficient a preprocessor which generates a boundary fitted orthogonal curvilinear grid was developed. Its main principles are described later in this paper.

Figure 1

DIAGRAM OF CYTHERE ES1 SYSTEM USED BY SOGREAH

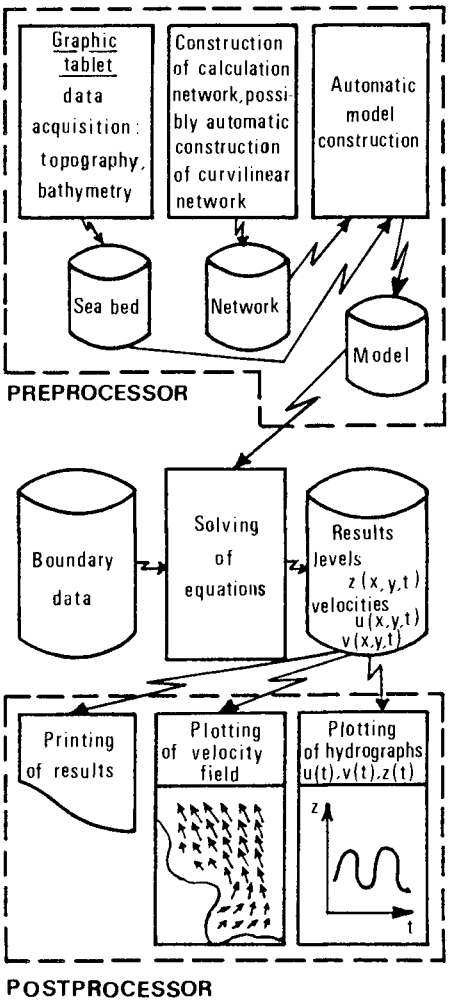

The two-dimensional tidal flow equations written for an orthogonal system of curvilinear coordinates (α,β) are:

$$\underbrace{\frac{\partial \vec{U}}{\partial t}}_{I} + \underbrace{\vec{U}\,\overrightarrow{\text{grad}}\,\frac{\vec{U}}{h} + \frac{\vec{U}}{h}\,\text{div}\vec{U}}_{II} + \underbrace{gh\,\overrightarrow{\text{grad}}Z}_{III} + \underbrace{\frac{\vec{\tau}_B - \vec{\tau}_S}{\rho}}_{IV} \underbrace{-2\vec{\Omega}\wedge\vec{U}}_{V} \underbrace{-\text{div}(K\overrightarrow{\text{grad}}\vec{U})}_{VI} = 0 \quad (1)$$

$$\underbrace{\frac{\partial Z}{\partial t} + \text{div}\vec{U}}_{III} = 0 \quad (2)$$

Where:

$\vec{U}$ = (U,V) = unit width discharge vector through depth h;
Z = free surface elevation;
$\vec{\tau}_B, \vec{\tau}_S$ = bottom friction and wind stresses, respectively;
$2\vec{\Omega}\wedge\vec{U}$ = Coriolis term, $\vec{\Omega}$ being the earth's rotation speed;
K, ρ = horizontal momentum diffusivity, water density.

As mentioned in previous publication [1], it is useful to give a physical interpretation to the six groups of terms of Eqs. (1) and (2) as follows:

I. Local flow acceleration,

II. Momentum transport by advection,

III. Mass conservation and momentum transfer by propagation,

IV,V. Momentum sources or sinks due to Coriolis force, surface wind stress and bed friction,

VI. Horizontal diffusion of momentum.

The three dependent variables of Eqs. (1),(2) are:
$U(\alpha,\beta,t)$, $V(\alpha,\beta,t)$ and $Z(\alpha,\beta,t)$.

3. FRACTIONAL STEP ALGORITHM

A qualitative examination of Eqs. (1) and (2) shows that they represent three physical processes with distinctive features and for which numerical approximations present different kinds of difficulties:

(i) momentum advection, groups I and II,
(ii) momentum diffusion, groups I, V and VI,
(iii) propagation, groups I,III and IV.

The algorithm used in CYTHERE ES 1 is based on the recognition of three physical phenomena and proceeds as follows. Suppose that the state of the model is known at time $n\Delta t$ (Z^n, U^n, V^n known at all points), the new state at time $(n+1)\Delta t$ is computed by the successive resolutions of the advection, diffusion and propagation operators. Each step is solved by a different numerical method so as to increase the accuracy and economy of the solution.

3.1 First step - Advection

The finite difference discretisation of advective terms in flow equations is the most important source of spurious damping and dispersion, both due to discretisation errors. To avoid this, space-centered finite differences are used such as:

$$\frac{\partial u}{\partial x} \simeq \frac{u_{i+1,j} - u_{i-1,j}}{2\Delta x} \quad ; \quad \frac{\partial u}{\partial y} \simeq \frac{u_{i,j+1} - u_{i,j-1}}{2\Delta y} \tag{3}$$

Where:

(x,y) = horizontal coordinate axes,

$u(x,y,t)$ = flow velocity in x-direction,

(i,j) = indices of computational points in x- and y- directions respectively,

$(\Delta x, \Delta y)$ = space computational steps in x- and y- directions respectively.

Approximation equation (3) is of 2^{nd} order if Δx = const, Δy = const. Numerical damping due to this approximation is negligible but dispersion is important and hampers the results so much that higher order approximations (4th order) are sought. The results are apparently more satisfactory, but this approach was not followed by the authors, who think that the high accuracy may often be misleading. Indeed, if the computational grid is not uniform ($\Delta x, \Delta y$ variable) the order of approximation decreases. More importantly a higher order of approximation is theoretically better when assuming that $\Delta x, \Delta y$ are small. Typically these intervals vary between 100 m and 1000 m. For a computational grid with Δx = 200 m Eq. (3) approximates the derivative with a difference of two velocities at points which are 400 meters apart! Fourth order approximation would involve 5 points distributed over a distance of 1000 m. In such a situation, the higher order approximation has the effect of smoothing and spreading out the differences through interpolation polynomials and local variations of advective currents cannot be accurately computed.

For the above reasons advective terms in the modelling system presented here were treated by the method of characteristics based on the principle derived by Holly and Preissmann [4]. During the advection step the following system of equations is solved between the time n Δt and an intermediate time notation n+1/3:

$$\frac{u^{n+1/3} - u^{n}}{\Delta t} + \frac{u_\alpha}{e_\alpha}\frac{\partial u}{\partial \alpha} + \frac{u_\beta}{e_\beta}\frac{\partial u}{\partial \beta} = 0 \; ; \quad \frac{v^{n+1/3} - v^{n}}{\Delta t} + \frac{u_\alpha}{e_\alpha}\frac{\partial v}{\partial \alpha} + \frac{u_\beta}{e_\beta}\frac{\partial v}{\partial \beta} = 0 \qquad (4)$$

Where:

(u,v) = velocity components along x- and y- axes of cartesian coordinate system,

u_α , u_β = projections of the velocity vector on the α- and β- axes of curvilinear coordinate system,

e_α, e_β = metric coefficients such that:

$$e_\alpha = \left[\left(\frac{\partial x}{\partial \alpha}\right)^2 + \left(\frac{\partial y}{\partial \alpha}\right)^2\right]^{1/2} \qquad e_\beta = \left[\left(\frac{\partial x}{\partial \beta}\right)^2 + \left(\frac{\partial y}{\partial \beta}\right)^2\right]^{1/2} \qquad (5)$$

The solution $u^{n+1/3}$, $v^{n+1/3}$ of Eq(4) is obtained by the method of characteristics in two dimensions as described in [1]. Although the computations are made at specified intervals, the method described in [4] enables numerical damping and dispersion to be almost completely avoided. Once intermediate velocities $u^{n+1/3}$, $v^{n+1/3}$ are found for all computational points, unit discharges $U^{n+1/3} = h^n u^{n+1/3}$, $V^{n+1/3} = h^n v^{n+1/3}$ can be computed.

3.2 Second step - Diffusion

Diffusion step equations are solved between two intermediate time notations n+1/3 and n+2/3 in terms of unit discharges.

$$\frac{U^{n+2/3} - U^{n+1/3}}{\Delta t} = \frac{1}{e_\alpha e_\beta}\left[\frac{\partial}{\partial \alpha}\left(K\frac{\partial U}{\partial \alpha}\frac{e_\beta}{e_\alpha}\right) + \frac{\partial}{\partial \beta}\left(K\frac{\partial U}{\partial \beta}\frac{e_\alpha}{e_\beta}\right)\right] + FV \qquad (6)$$

$$\frac{V^{n+2/3} - V^{n+1/3}}{\Delta t} = \frac{1}{e_\alpha e_\beta}\left[\frac{\partial}{\partial \alpha}\left(K\frac{\partial V}{\partial \alpha}\frac{e_\beta}{e_\alpha}\right) + \frac{\partial}{\partial \beta}\left(K\frac{\partial V}{\partial \beta}\frac{e_\alpha}{e_\beta}\right)\right] - FU \qquad (7)$$

Where F is the Coriolis acceleration parameter. Eqs.(6) and (7) are well-known parabolic equations. Their numerical solutions are accurate even with crude methods, so an ADI approach based on a fully implicit finite difference scheme is used for this step in CYTHERE ES 1. It gives new values $(U,V)^{n+2/3}$ at all computational points.

3.3 Third step - Propagation

This step is a crucial one because of the computer time it requires and also because of the numerical inaccuracies generated when economy in computer time is sought by using inadequate methods. "Polarisation" of velocity fields when using Alternating Directions (ADI) methods was described firstly in [3] then in [1]. Let us define Courant number Cr as:

$$Cr = \Delta t \sqrt{gh} \sqrt{\frac{1}{\Delta x^2} + \frac{1}{\Delta y^2}} \tag{8}$$

where:

Δt = computational time step,
h = local flow depth,
g = acceleration due to gravity.

Nearly all industrial programs use implicit finite difference schemes which enable Cr values of greater than 1 to be used, whereas explicit schemes are numerically unstable in these conditions. Since the fully implicit methods lead to excessive computational times, the ADI implicit methods are widely used. These methods, however, may give completely wrong results for Courant numbers greater than 5 to 10. Indeed the velocity fields become "polarized" along either x- and y- axes when the time step Δt corresponds to Cr greater than 5. This phenomenon is described in reference [1] and examples of obviously absurd results obtained with the ADI method for higher Cr values are given. Moreover the ADI method cannot correctly compute velocity fields along and across channels which are not parallel to the x- or y- axis, as has been shown in [6]. For these reasons a more efficient and accurate algorithm was used by the authors.

Working equations for the propagation step are:

$$\frac{Z^{n+1} - Z^n}{\Delta t} = - \frac{1}{e_\alpha e_\beta} \left[\frac{\partial}{\partial \alpha} (U_\alpha e_\beta) + \frac{\partial}{\partial \beta} (U_\beta e_\alpha) \right] \tag{9}$$

$$\frac{U_\alpha^{n+1} - U_\alpha^{n+2/3}}{\Delta t} = - gh \frac{1}{e_\alpha} \frac{\partial Z}{\partial \alpha} + \frac{U_\alpha}{h} \frac{\partial Z}{\partial t} - g \frac{U_\alpha \left\| \vec{U} \right\|}{C^2 h^2} + \frac{1}{\rho} \tau_{S\alpha} \tag{10}$$

$$\frac{U_\beta^{n+1} - U_\beta^{n+2/3}}{\Delta t} = - gh \frac{1}{e_\beta} \frac{\partial Z}{\partial \beta} + \frac{U_\beta}{h} \frac{\partial Z}{\partial t} - g \frac{U_\beta \left\| \vec{U} \right\|}{C^2 h^2} + \frac{1}{\rho} \tau_{S\beta} \tag{11}$$

Where:

C = Chezy coefficient,
$\left\| \vec{U} \right\| = (U_\alpha^2 + U_\beta^2)^{1/2}$.

Lack of space does not allow the authors to give details of the discretisation, the main principles of which can be found in [1]. Essentially, right hand terms of Eqs (9) to (11) are written under implicit formulation such as:

$$\frac{gh}{e_\alpha}\frac{\partial Z}{\partial \alpha} = \frac{g}{e_\alpha}\left[\theta h^{n+1}\left(\frac{\partial Z}{\partial \alpha}\right)^{n+1} + (1-\theta)h^{n}\left(\frac{\partial Z}{\partial \alpha}\right)^{n}\right] \qquad (12)$$

Then, from Eqs. (10) and (11) expressions for increments ΔU, ΔV during one time step Δt, as functions of known values and Z^{n+1} are extracted, (Note: $\Delta U = U^{n+1} - U^{n+2/3}$, etc). These increments are substituted into Eq (9) which, discretised, becomes an algebraic system of equations for the Z_k^{n+1}, ($k = 1, 2, \ldots, m$), where m is the number of computational points in the model.

This final system of equations is solved by an iterative method which is based upon the conjugate gradient method and is, with the method of characteristics used for the advection step, of crucial importance in the algorithm. Indeed, nowadays models of tidal areas can contain anywhere between 2000 and 8000 computational points; this effectively prohibits matrix inversion. Explicit formulation would lead to excessively small time steps. The ADI methods may give, as mentioned above, misleading results even when the time step is physically reasonable, hence the use of a special development of the conjugate gradient method (iteration through alternating direction operator with coordinator) described in [5].

The iteration procedure permits the use of high Courant numbers (20 and more) without loss of accuracy even when simulating channels angled at 45° to the coordinate axes. It should be stressed that with efficient programming one iteration needs less computer time than resolution of the propagation step by the explicit method.

4. ORTHOGONAL CURVILINEAR GRID GENERATION

The generation of curvilinear computational grid is semi-automatic in the CYTHERE ES 1 system at the preprocessor level (see Fig. 1). The details of the method, developed by Sogreah, are given elsewhere [2], only the main features are followed here.

The mathematical tool used to generate the orthogonal curvilinear grid is the conformal transformation. It is assumed that for a given domain D, D being a coastal zone or an estuary for example, which satisfies a number of conditions, there is a conformal transformation f which associates a rectilinear domain D' to D (a rectilinear domain is defined as a domain bounded by straight lines intersecting at right angles).

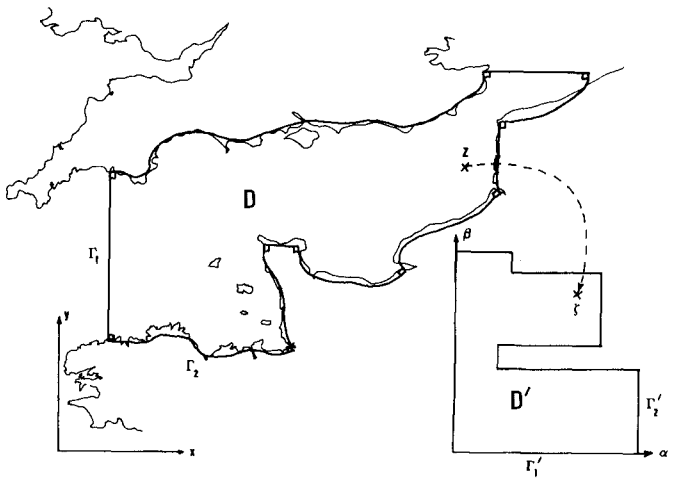

Fig. 2a Simplified domain D for the English Channel

Fig. 2b A priori shape of domain D'

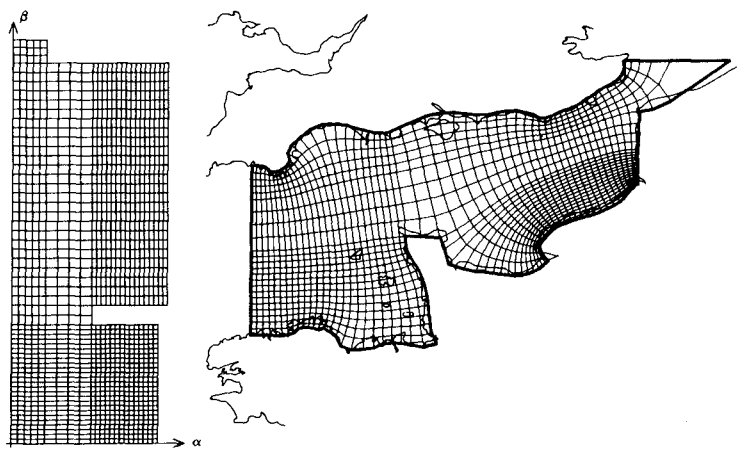

Fig. 3a Final shape of D' with cartesian grid

Fig. 3b Orthogonal Curvilinear grid in D

Using complex notations, to any point $Z = x + iy$ in D, f associates a point $\zeta = f(Z) = \alpha + i\beta$ in D'. The function f is analytic, hence α and β form a conjugate harmonic pair $\Delta\alpha = 0, \Delta\beta = 0$ and they satisfy the Cauchy-Riemann equations:

$$\frac{\partial \alpha}{\partial x} = \frac{\partial \beta}{\partial y} \qquad \frac{\partial \alpha}{\partial y} = - \frac{\partial \beta}{\partial x} \tag{13}$$

which implies that lines of constant α are orthogonal to lines of constant β . These conditions must hold true on the boundaries which are formed of segments on which either α or β is constant.

This method is applied to jagged coastlines or estuaries. In a first approach, the real topography of the domain is approximated by a simplified contour which represents only the most characteristic features. The size of the features to be taken into account for the model depends, of course, on the scale of the phenomenon to be modelled. The physical domain is thereby schematised into a simplified domain D (e.g. Fig. 2a).

The domain D must satisfy a number of conditions. It must be simply connected in the (x,y) plane, i.e. its boundary is a continuous line and D does not contain holes. Next, its boundary Γ has to be composed of an even number of curved segments Γ_i intersecting at right angles, $\Gamma = \cup \Gamma_i$. Hence, the transformed domain D' will be delimited by a contour $\Gamma' = \cup \Gamma'_i$, Γ'_i being the image of Γ_i, so that all straight segments Γ'_i and Γ'_{i+1} intersect at right angles, since the conformal transformation keeps the values of angles. Using this property, the contour Γ' can be drawn a priori, simply by turning at the end of each Γ'_i of an angle equal to the angle between Γ_i and Γ_{i+1}.

Thus, the domain D' is defined in a (α,β) plane where the α- axis is parallel to horizontal segments and the β- axis parallel to vertical ones. The direction of axes is chosen according to the contour orientation (see Fig. 2b).

The conformal mapping f is then computed numerically, with the help of a finite element method by solving a Laplacian equation with a Neumann boundary condition given on the contour Γ, and the final shape of D', i.e. the length of each Γ'_i is determined, as explained in [2].

In the second stage a Cartesian grid is built inside the transformed rectilinear domain D' parallel to the α and β axes, the spacing between vertical and horizontal lines need not to be constant (Fig. 3a). Using the inverse conformal transformation f^{-1}, this Cartesian grid will be mapped into an orthogonal curvilinear grid inside D (see Fig. 3b) since the property of orthogonality is conserved.

Numerical computation of f^{-1} uses the same finite element program as for f, for the simultanous resolution of four Laplacian equations with Dirichlet boundary conditions. Finally projection parameters and metric coefficients e_α, e_β of Eq. (5) are computed automatically.

The spacing between Cartesian grid lines in D' has been chosen to suit the desired spacing in the curvilinear grid, however the packing of the curvilinear grid lines obtained may be slightly different from that expected. It is not possible to add lines after the resolution of the second stage computations unless the process is reiterated from a new Cartesian grid inside D'. On the other hand, some of the lines can be eliminated provided that the new spacing satisfies a regular increase or decrease acceptable by the finite difference program. According to user's choice, one final program "erases" lines of the curvilinear grid, checks the regularity of the spacing and establishes a correspondence between the lines that have been kept and integer numbering of the finite difference grid (I = 1, 2,... ; J = 1, 2,...). The example of the orthogonal grid generated by the preprocessor shown in Fig. 3b illustrates the method. All points are determined by the intersection of two orthogonal lines, but since they are joined on the drawing by straight segments which do not exactly coïncide with the lines, some drafted angles are different from 90°, as in the top-right corner.

5. EXAMPLE OF AN APPLICATION TO AN ENGINEERING STUDY

The CYTHERE ES 1 modelling system has recently been used by Sogreah for a complex engineering study of development in South Korea: Kwang Yang Bay. The project consists of reclaiming a vast area in the bay located on river delta soils, and of dredging from a nearby area. A steel mill will be built on the reclaimed site together with a harbour for raw materials and finished products, for up to 250,000 dwt ships. The study involved:

- in-situ measurements;
- two-dimensional mathematical modelling of tidal currents in the bay with the projected steel mill, two options of river discharge: average or flood, and three tide conditions;
- one-dimensional mathematical modelling of the tide influenced section of the major river flowing into the bay;
- mathematical modelling of large ship navigation in the entrance channel in the bay, based on currents predicted for the new conditions (reclaimed and dredged area);

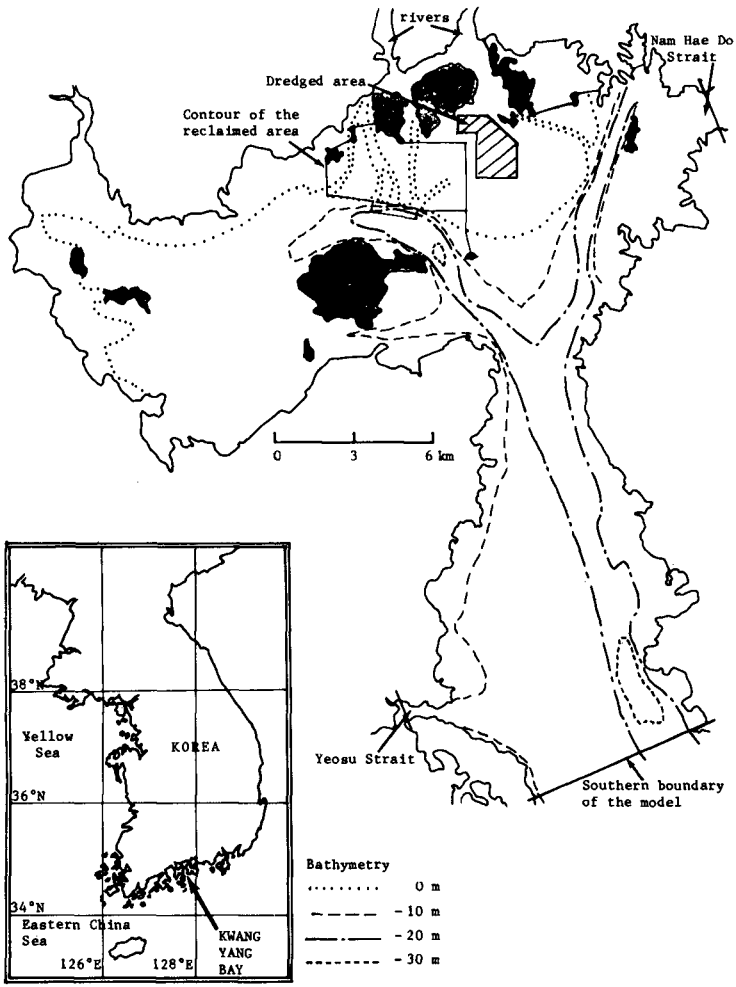

Fig. 4 Map of Kwang Yang Bay (islands in dark)

- scale model tests (1:25), in a specially equipped lake, of ship manoeuvres in the harbour, conducted by ship's pilots. The lake dimensions are 255 m by 190 m and the test crafts were scaled to represent up to 250,000 dwt ships;

- sediment transport evaluation.

Figure 4 shows a map of the bay, which has five open boundaries; two rivers to the north with given constant discharge, and three boundaries with time dependent water conditions obtained from in-situ measurements: the southern boundary directly connected to the Eastern China Sea, the Nam Hae Do Strait to the north east and Yeosu Strait to the south west, both connected to adjacent bays.

The grid was cartesian with irregular intervals in the x and y directions, and varying Strickler friction coefficients were used to account for sea weed culture on the tidal flats.

A most important feature of the model was its rapidly varying bathymetry: within a distance of less than 600 meters (three computational points) the bottom depth goes from a positive value (above lowest low water datum) to -20 meters. The original tidal flat computation procedure used in the propagation step (see [1]) and its link with deep water computation proved to be the critical point of the simulation.

Once the calibration of the model was completed, computed levels and currents compared very well with measured values (fig. 5). The current phase agreement was quite remarkable, and of particular importance as currents computed with the proposed facilities were to be analysed to define the time period of ship entry into the harbour. Current fields were drawn at different times during the tidal cycles. Figure 6 shows the currents in the vicinity of the steel mill, they are parts of the current charts drawn for spring tide at high water and at 4 hours before high water.

6. CONCLUSION

The original mathematical method used in the CYTHERE ES 1 method enables very good accuracy to be obtained at a reasonable computer cost. It has been applied to many engineering studies including modelling of the thermal impact of 30 coastal nuclear power plants in France by the LNH [7], investigation of ocean eroding action (river Canche estuary, France, LNH), a pollution study (bay of Saint-Brieuc, France, Sogreah), ... New developments include modelling of wind-induced currents and this is being applied to the study of a lake.

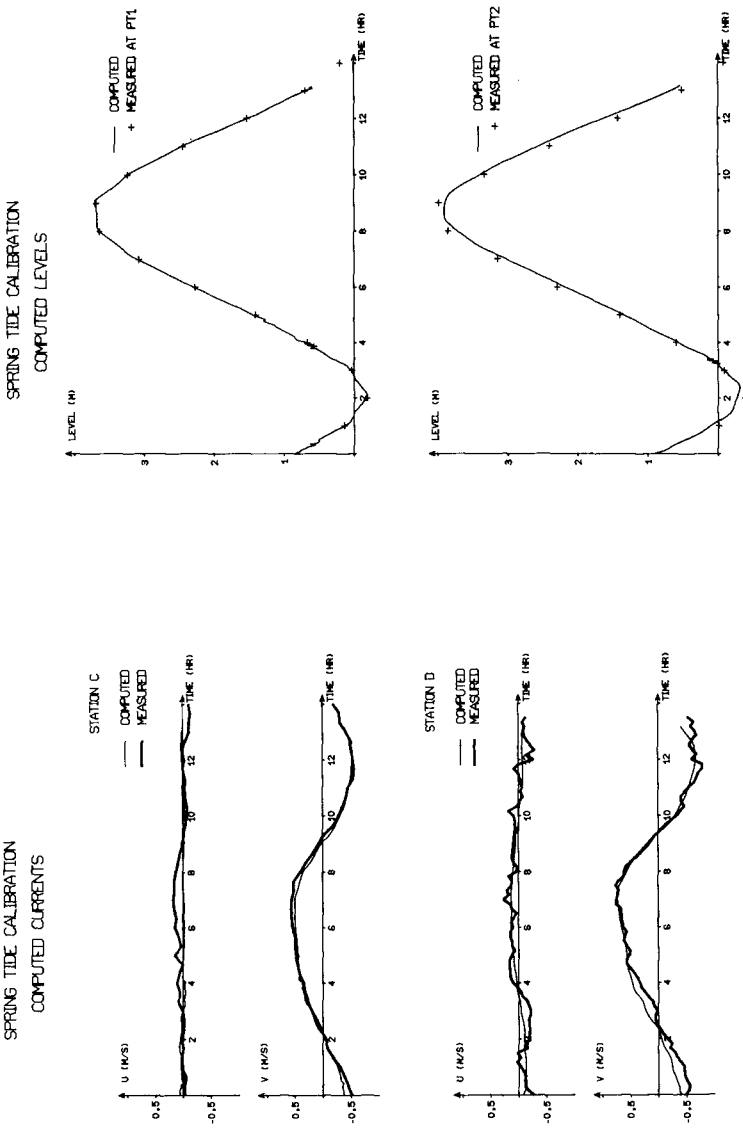

Fig. 5 Comparison of currents and levels for calibration of the model

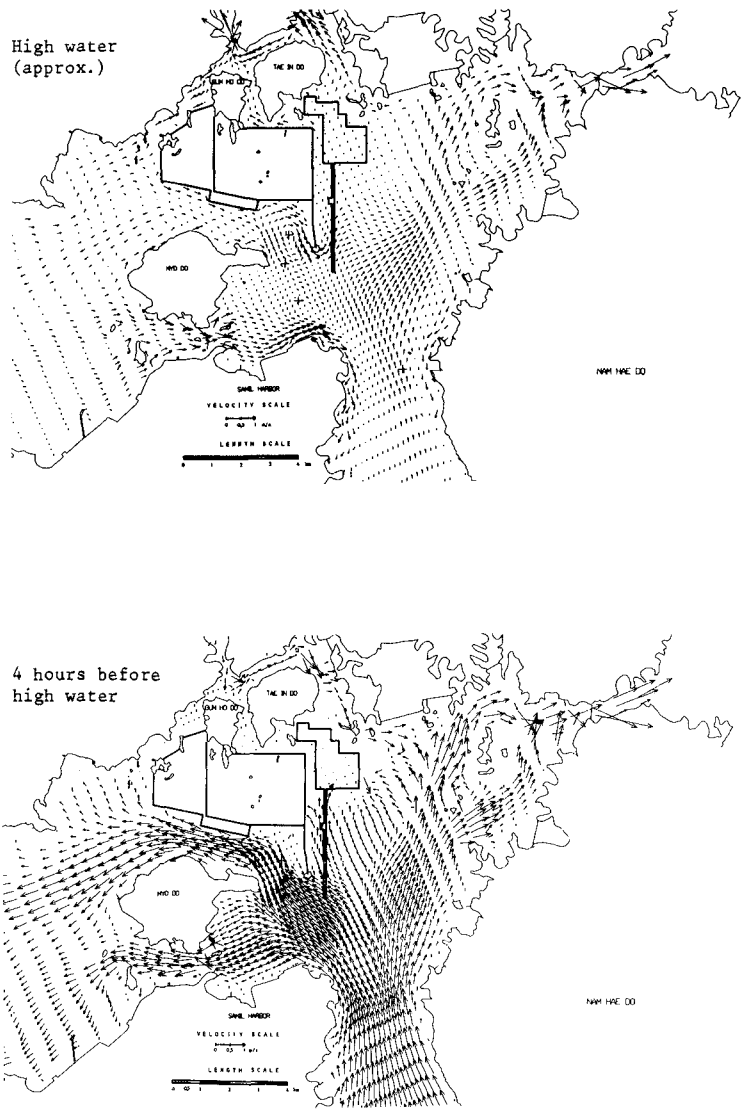

Fig. 6 Current fields for spring tide with simulated reclaimed and dredged areas

REFERENCES

[1] Benqué J.P., Cunge J.A., Feuillet J., Hauguel A., Holly F.M., (1982), "New method for tidal current computation", ASCE, J. of the Waterway, Port, Coastal and Ocean Division, vol 108, WW 3, pp 396-417.

[2] Chenin M.I., Schwartz S., (1982), "Generation of an orthogonal curvilinear computational grid for a finite difference method", International Symposium on Refined Modelling of Flows, sponsored by IARH, Paris, France.

[3] Cunge J.A., (1977), Special presentation during the exhibition on mathematical modelling at the 17th IAHR Congress, Baden-Baden, Germany.

[4] Holly F.M. and Preissmann A., (1977), "Accurate calculation of transport in two dimensions", ASCE, J. of the Hydraulic Division vol 103, HY11, pp 1259-1277

[5] Hauguel A., (1979), "Quelques mots sur la méthode d'éclatement d'opérateur avec coordination", Report E42/79.39, Laboratoire National d'Hydraulique, Electricité de France, 78400 Chatou, France.

[6] Weare T.J., (1979),"Errors arising from irregular boundaries in ADI solutions of the shallow-water equations", International Journal for Numerical Methods in Engineering, Vol 14, pp 921-931.

[7] Benqué J.P., Hauguel A., Viollet P.L., "Engineering Applications of Computational Hydraulics", vol. II, Pitman Books Ltd, London, UK, 1982, Part I.

oOo

A THREE-DIMENSIONAL MODEL OF BERING AND CHUKCHI SEA

by
Shiao-Kung Liu* and Jan J. Leendertse*

Introduction

A part of the continental shelf area of the Bering and Chukchi Sea are now being opened up for oil exploration. For engineering and ecological risk analyses, extensive field data collection efforts are being carried out by various United States agencies and petroleum corporations to understand the hydrodynamic behavior of this vast offshore area.

In addition, modeling studies are being made for which a three-dimensional model of the area, outlined in Fig. 1, has been developed. This model is dynamically coupled to a two-dimensional stochastic weather model. This weather model contains a Markov synoptic component and a storm track component. The parameters of this model are derived from a 20-year data base.

This paper presents a description of the three-dimensional model and the results of a series of simulations using the model to compute tidal propagation and circulations induced by tides and wind. The results of a simulation of a moving storm through the eastern Bering Sea are also presented.

The Three-Dimensional Modeling System

The modeling system used for the study is formulated according to the equations of motion for water and ice, continuity, state, the balance of heat, salt, pollutant and turbulent energy densities, on a three-dimensional finite difference grid. The vertical momentum, mass, heat and turbulent energy exchange coefficients are computed from the turbulent energy, thus the model contains a turbulence closure computation. Turbulent energy dissipation due to mixing of heavier water with lighter water is accounted for in the turbulence closure.

The horizontal grid conforms with the earth's ellipsoidal coordinates while the arbitrary vertical grid spacing approximates the bottom topography of the modeled area. The results are subsequently transformed on the Universal Mercator projection for graphical representation. For simplicity, the system of modeling equations is presented here by use of the standard finite difference notation on a regular spatial grid network in the horizontal direction, and on an irregular grid in the vertical (Fig. 2). The coordinates i, j, k, n, are used to denote discrete points on the x, y, z, t, domain. The finite difference formulation adapted for the computation takes the following form:

*The Rand Corporation, Santa Monica, California

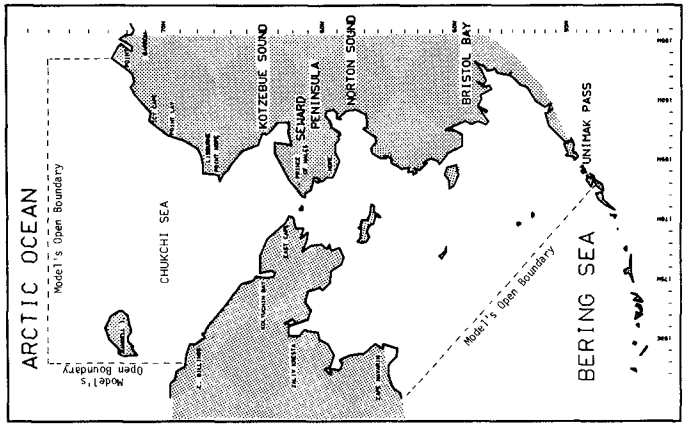

Location map showing eastern Bering Sea and Chukchi Sea modeling area.

Fig. 1

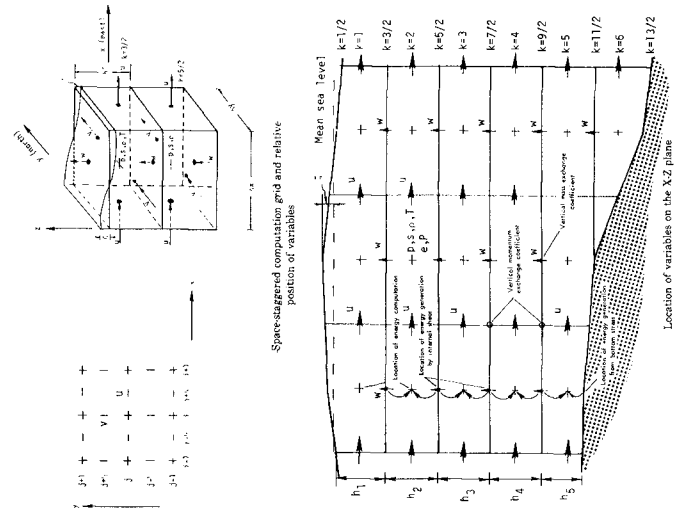

Fig. 2

$$\overline{\delta_t \zeta} = - \sum_k \left[\delta_x (\overline{h}^x u) + \delta_y (\overline{h}^y v) \right] \qquad \text{at } i, j, n \qquad (1)$$

where the variation of the water level ζ is derived from the continuity equation by vertical integration, and h is the layer thickness.

The momentum equation in the x-direction

$$\overline{\delta_t (\overline{h}^x u)}^t = - \delta_x (\overline{\overline{h}^x u}^x \overline{u}^x) - \delta_y (\overline{\overline{h}^y v}^x \overline{u}^y) - \overline{h}^x \delta_z (\overline{u}^z \overline{w}^x) + f \overline{h}^x \overline{v}^{xy} - \frac{1}{\overline{\rho}^x} \overline{h}^x \delta_x p$$

$$+ \frac{1}{\overline{\rho}^x} \left[h \delta_z \left(E_x \delta_z \overline{u}^{2t} \right) + \delta_x \left(h A_x \delta_x u \right)_- + \delta_y \left(\overline{\overline{h}^x A_y}^y \delta_y u \right)_- \right] \qquad (2)$$

$$\text{at } i + \tfrac{1}{2}, j, k, n$$

where E_x is the vertical momentum exchange coefficient, and A_x, A_y are horizontal exchange coefficients in x-direction and y-direction, respectively.

The momentum equation in the y-direction,

$$\overline{\delta_t (\overline{h}^y v)}^t = - \delta_x (\overline{\overline{h}^x u}^y \overline{v}^x) - \delta_y (\overline{\overline{h}^y v}^y \overline{v}^y) - \overline{h}^y \delta_z (\overline{v}^z \overline{w}^y) - f \overline{h}^y \overline{u}^{xy} - \frac{1}{\overline{\rho}^y} \overline{h}^y \delta_y p$$

$$+ \frac{1}{\overline{\rho}^y} \left[h \delta_z \left(E_y \delta_z \overline{v}^{2t} \right) + \delta_x \left(\overline{\overline{h}^y A_x}^x \delta_x v \right)_- + \delta_y \left(h A_y \delta_y v \right)_- \right] \qquad (3)$$

$$\text{at } i, j + \tfrac{1}{2}, k, n$$

The mass-balance equation for salt,

$$\overline{\delta_t (hs)}^t = - \delta_x (\overline{h}^x u \overline{s}^x) - \delta_y (\overline{h}^y v \overline{s}^y) - h \delta_z (w \overline{s}^z)$$

$$+ \delta_x \left(\overline{h}^x D_x \delta_x s \right)_- + \delta_y \left(\overline{h}^y D_y \delta_y s \right)_- - h \delta_z \left(\kappa \delta_z \overline{s}^{2t} \right) \qquad (4)$$

$$\text{at } i, j, k, n$$

where D_x and D_y are the horizontal diffusion coefficients and k is the vertical mass exchange coefficient. For temperature

$$\overline{\delta_t(h\bar{T})}^t = -\delta_x(\bar{h}^x u\bar{T}^x) - \delta_y(\bar{h}^y v\bar{T}^y) - h\delta_z(w\bar{T}^z)$$

$$+ \delta_x\left(\bar{h}^x D_x \delta_x T\right)_- + \delta_y\left(\bar{h}^y D_y \delta_y T\right)_- + h\delta_z\left(\kappa'\delta_z \bar{T}^{2t}\right) \qquad (5)$$

at i, j, k, n

where κ' is the vertical thermodiffusion coefficient.
For the SGS energy density in the system,

$$\overline{\delta_t(he)}^t = -\delta_x(\bar{h}^x u\bar{e}^x) - \delta_y(\bar{h}^y v\bar{e}^y) - h\delta_z(w\bar{e}^z)$$

$$+ \delta_x\left(\bar{h}^x D_x \delta_x e\right)_- + \delta_y\left(\bar{h}^y D_y \delta_y e\right)_- + h\delta_z\left(E_e \delta_z \bar{e}^{2t}\right) \qquad (6)$$

$$+ h\bar{S}_e^z - D_e h \qquad \text{at i, j, k, n}$$

where E_e is the vertical momentum exchange coefficient. For the pollutant constituent concentration,

$$\overline{\delta_t(hP)}^t = -\delta_x(\bar{h}^x u\bar{P}^x) - \delta_y(\bar{h}^y v\bar{P}^y) - h\delta_z(w\bar{P}^z)$$

$$+ \delta_x\left(\bar{h}^x D_x \delta_x P\right)_- + \delta_y\left(\bar{h}^y D_y \delta_y P\right)_- + h\delta_z\left(\kappa\delta_z \bar{P}^{2t}\right) \qquad (7)$$

$$+ hS_p - D_p h \qquad \text{at i, j, k, n}$$

The equation of state is approximated by

$$\rho = \left[5890 + 38T - 0.375T^2 + 3s\right] \Big/ \left[\left(1779.5 + 11.25T - 0.0745T^2\right) - \left(3.8 + 0.01T\right)s + 0.698\left(5890 + 38T - 0.375T^2 + 3s\right)\right] \qquad (8)$$

at i, j, k, n + 1

The continuity equation is used to compute the vertical velocity:

$$\delta_z w = -\delta_x\left(\bar{h}^x u\right) - \delta_y\left(\bar{h}^y v\right) \qquad \text{at i, j, k, n + 1} \qquad (9)$$

Similar equations for velocity components u and v can be written for the top and bottom layers, but now the effects of wind and bottom friction must be considered. We have at the surface:

$$\overline{\delta_t(\overline{h}^x u)}^t = -\delta_x(\overline{\overline{h}^x u}^x \overline{u}^x) - \delta_y(\overline{\overline{h}^y v}^x \overline{u}^y) - \overline{h}^x \delta_z(\overline{u}^z \overline{w}^x) + f\overline{h}^x \overline{v}^{xy} - \frac{1}{\overline{\rho}^x}\overline{h}^x \delta_x p$$

$$+ \frac{1}{\overline{\rho}^x}\left[\theta \rho_a w_a^2 \sin\psi - \left(E_x \delta_z \overline{u}^{2t}\right)_{k=3/2} + \delta_x\left(hA_x \delta_x u\right)_- + \delta_y\left(\overline{\overline{h}^x A_y}^y \delta_y u\right)_-\right]$$

$$\text{at } i + \tfrac{1}{2},\ j,\ 1,\ n \qquad (10)$$

where ψ is the clockwise angle between the model's y-axis and the direction toward which the wind is blowing. In the y-direction, the momentum equation becomes

$$\overline{\delta_t(\overline{h}^y v)}^t = -\delta_x(\overline{\overline{h}^x u}^y \overline{v}^x) - \delta_y(\overline{\overline{h}^y v}^y \overline{v}^y) - \overline{h}^y \delta_z(\overline{v}^z \overline{w}^y) - f\overline{h}^y \overline{u}^{xy} - \frac{1}{\overline{\rho}^y}\overline{h}^y \delta_y p$$

$$+ \frac{1}{\overline{\rho}^y}\left[\theta \rho_a w_a^2 \cos\psi - \left(E_y \delta_z \overline{v}^{2t}\right)_{k=3/2} + \delta_x\left(\overline{\overline{h}^y A_x}^x \delta_x v\right)_- + \delta_y\left(hA_y \delta_y v\right)_-\right]$$

$$\text{at } i,\ j + \tfrac{1}{2},\ 1,\ n \qquad (11)$$

where θ represents the wind-stress coefficient, w_a is wind speed, and ρ_a represents the density of air. At the bottom layer, the momentum equation becomes

$$\overline{\delta_t(\overline{h}^x u)}^t = -\delta_x(\overline{\overline{h}^x u}^x \overline{u}^x) - \delta_y(\overline{\overline{h}^y v}^x \overline{u}^y) - \overline{h}^x \delta_z(\overline{u}^z \overline{w}^x) + f\overline{h}^x \overline{v}^{xy} - \frac{1}{\overline{\rho}^x}\overline{h}^x \delta_x p$$

$$+ \frac{1}{\overline{\rho}^x}\left\{\left(E_x \delta_z \overline{u}^{2t}\right)_{k=K-\frac{1}{2}} - \overline{\rho}^x g u_- \left[u_-^2 + \left(\overline{v}_-^{xy}\right)^2\right]^{\frac{1}{2}} \Big/ \left(\overline{C}^x\right)^2\right.$$

$$\left. + \delta_x\left(hA_x \delta_x u\right)_- + \delta_y\left(\overline{\overline{h}^x A_y}^y \delta_y u\right)_-\right\} \qquad \text{at } i + \tfrac{1}{2},\ j,\ K,\ n \qquad (12)$$

$$\overline{\delta_t(\overline{h^y}v)}^t = -\delta_x(\overline{\overline{h^x u}^y \overline{v}^x}) - \delta_y(\overline{\overline{h^y v}^y \overline{v}^y}) - \overline{h^y}\delta_z(\overline{v^z w^y}) - f\overline{h^y u}^{xy} - \frac{1}{\overline{\rho^y}}\overline{h^y}\delta_y p$$

$$+ \frac{1}{\overline{\rho^x}}\left\{\left(E_y \delta_z \overline{v}^{2t}\right)_{k=K-\frac{1}{2}} - \overline{\rho^y} g v_- \left[\left(\overline{u_-}^{xy}\right)^2 + v_-^2\right]^{\frac{1}{2}} \Big/ \left(\overline{C}^y\right)^2\right.$$

$$\left. + \delta_x\left(\overline{\overline{h^y A_x}^y}\delta_x v\right)_- + \delta_y\left(hA_y\delta_y v\right)_-\right\} \quad \text{at } i,\ j+\tfrac{1}{2},\ K,\ n \qquad (13)$$

where C is Chezy coefficient.

In the modeled area, each vertical motion of water mass has to work against buoyancy forces induced by the density gradient. If the available kinetic energy of the turbulent motion is insufficient to overcome this stabilizing effect, turbulence is inhibited and suppressed. As a consequence, the process of momentum and mass-heat exchange will be lower than the neutral stability condition. The criteria for the onset of this turbulence-suppressing process in the system can be obtained by the local density gradient and turbulent energy level. Therefore, the variability of the vertical exchange coefficients in the model is computed by a turbulence closure technique using local turbulence intensity e.

$$E_y = \overline{\rho}^{yz} L\overline{\sqrt{e_-}}^{xz} \qquad (14) \qquad E_x = \overline{\rho}^{xz} L\overline{\sqrt{e_-}}^{xz} \qquad (15)$$

$$E_e = a_1 L\overline{\sqrt{e_-}}^{z} \qquad (16) \qquad \kappa = a_4 L\overline{\sqrt{e_-}}^{z} \qquad (17)$$

where a_1, a_4 are turbulence closure constants and L denotes the length scale, which can be approximated by an additional transport equation or by a parametric expression such as

$$L = k'z(1 - z/d)^{\frac{1}{2}} \qquad (18)$$

κ' is the von Karman constant, z represents the vertical distance from the bottom to the point considered, and d is the vertical distance from the surface to the bottom.

In the horizontal direction, the exchange coefficient is computed in two parts as a function of the local vorticity gradient and the local grid dimension. The first part is

$$A = \gamma \left| (\delta_x \overline{\omega}^y + \delta_y \overline{\omega}^x) \right| (\Delta \ell)^3 \tag{19}$$

where ω is the vorticity, γ is a coefficient, and $\Delta\ell$ is the local grid size. This part represents the exchange for a wave number lower than the spatial Nyquist frequency. The second part represents the contribution from the homogeneous subgrid scale turbulence above the spatial Nyquist frequency, which can be computed according to Kolmogorov's turbulence spectrum theory. The gross horizontal exchange coefficient is therefore

$$D_x = \bar{A}^x + a_5 \Delta \ell^{4/3} \qquad D_y = \bar{A}^y + a_5 \Delta \ell^{4/3} \tag{20} \quad (21)$$

where a_5 is a function of the energy dissipation rate. In the model, the amount of reduction in the vertical exchange due to stratification is based on the direct computation of the local gain in potential energy induced by vertical mixing. The exact amount is then taken out of the local turbulent (kinetic) energy budget. In the equation of energy (Eq. 6), the generation and dissipation terms become

$$\bar{S}_e^z - D_e = \underbrace{a_3 \overline{L\sqrt{e}}^z \left[(\delta_z \overline{u}^x)^2 + (\delta_z \overline{v}^y)^2 \right]}_{(1)} + \underbrace{a_3 \overline{L\sqrt{e}}^z \frac{g}{\bar{h}^z \rho} (\delta_z \overline{\rho}^z)}_{(2)} \underbrace{- a_2 e^{3/2}/L}_{(3)} \tag{22}$$

where the first term denotes production, the second term represents the portion supplied that is used in potential energy increase, and the third term is dissipation.

Modeling of Tides and Currents

Tide enters the Bering Sea through the central and western Aleutian, and enters the Chukchi Sea from the East Siberian Sea. The largest tidal amplitudes are found over the Bering shelf region and in these regions substantial tidal velocities can be observed. The tidal velocities in the Chukchi Sea are much smaller except in areas north of the Bering Strait where two tidal systems interact.

To study the tidal dynamics of the coastal system, the deep water tides at the model's open boundaries are generated using astronomical tidal prediction coefficients obtained from field measurements. A period in the beginning of August 1976 was selected for simulation as current data was available for this period which could be used for comparison of model results with field data. The simulations indicated that the propagation of tide in the study area is dominated by the bathymetry (Fig. 3), and to a certain extent, also influenced by the vertical density structure. The latter was known to cause the shifting of the location of amphidromic points during summer when strong pycnocline exist. Figure 4 shows an instantaneous distribution of computed tidal currents and water level in the modeled area projected on the Mercator plotting scale. As the figure indicates, at 0600 hours (GMT) on August 2, 1976, ebb tide occurred over the shelf break in the eastern Bering Sea. At the same time, water levels were rising in the Bristol Bay, Norton Sound, and over most of the Chukchi Sea.

To represent the tidal propagation in an efficient way co-tidal and co-range charts were prepared. The computed co-tidal chart for the semi-diurnal tidal component (Fig. 5) indicates that there are six major amphidromic systems in the modeled area. Over the eastern shelf area, the computed amplitude and phase, as well as the locations of the amphidromic points, agree extremely well with the observed values (Fig. 6) compiled by the National Oceanic and Atmospheric Administration. The computed co-tidal chart for the diurnal tidal components (Fig. 7) also agrees extremely well with the chart derived using observed data (Fig. 8).

Tidal currents in the study area have also been compared to the field data. Using a more detailed sub-model of the Bristol Bay, the computed tidal currents agree extremely well to the observed current data (Figs. 9, 10).

Tide-induced and Baroclinic Circulation

Circulation and transport associated with tidal propagation constitute one of the most important and everlasting driving mechanisms in coastal waters. The non-linear mechanisms generate net circulation over the shallow water in addition to the tidal excursion. This net "residual" transport is usually responsible for carrying constituents to areas much beyond the extent of tidal excursion over the time span of weeks or months. Therefore, one of the major functions of the three-dimensional model has been the determination of the tidal residual circulations.

When a long wave (e.g., the tide) propagates from the deep water through the shallow areas, the non-linear advection terms in the equation of motion, along with non-linear transport terms, generate higher harmonics of the fundamental frequency. In particular, the second harmonic increases in amplitude with the distance of propagation. Bottom friction generates odd harmonics. The varying depth and complicated boundaries

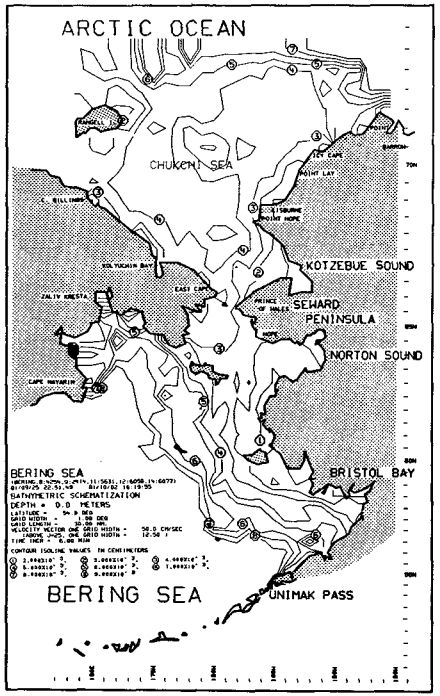

Bathymetric schematization of the three-dimensional model of Bering and Chukchi Sea.

Fig. 3

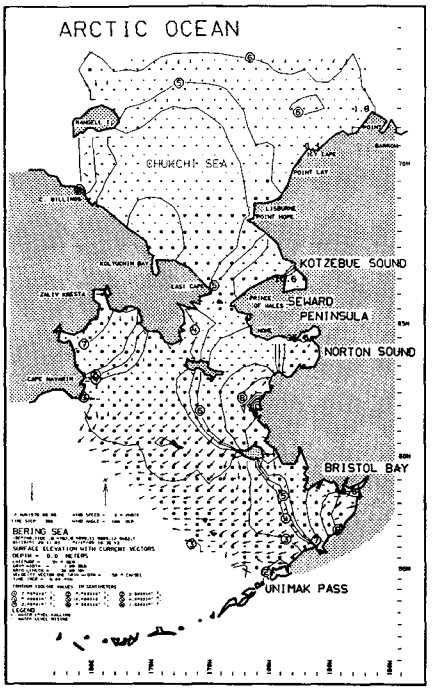

Computed instantaneous tidal currents and water level distributions in the Bering/Chukchi Sea system. A plus (+) sign denotes water level rise while a square (□) indicates falling of local water surface.

Fig. 4

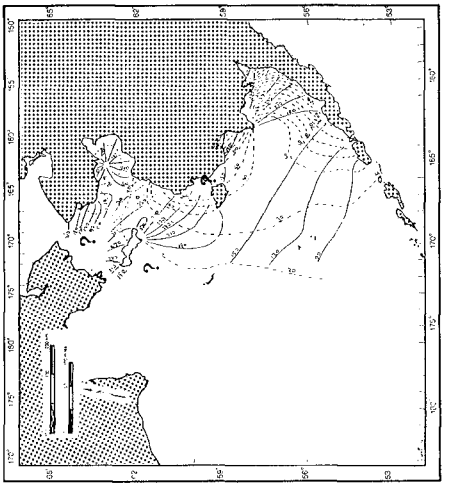

Co-tidal chart for the semidiurnal tidal component M_2 compiled by NOAA according to existing data.

Fig. 6

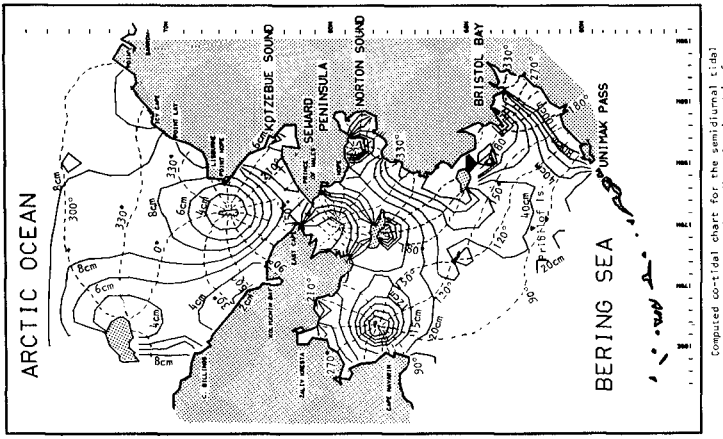

Computed co-tidal chart for the semidiurnal tidal component using the three-dimensional model of Bering/Chukchi Sea.

Fig. 5

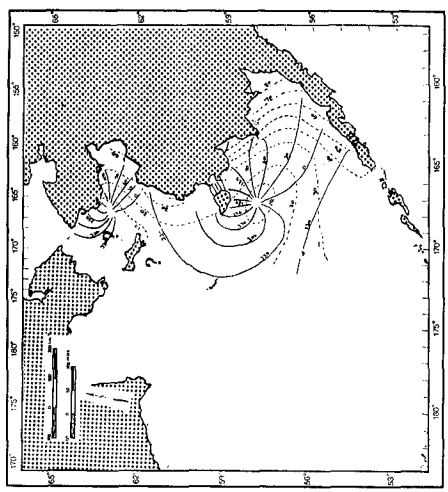

Fig. 8

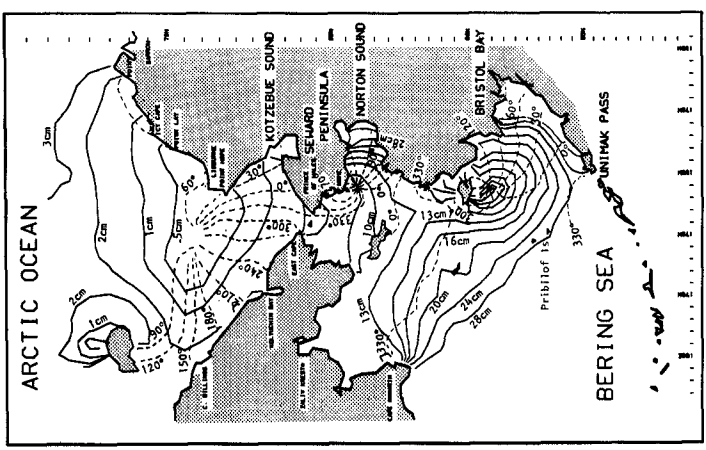

Fig. 7 Computed co-tidal chart for the diurnal tidal component using the three-dimensional model of Bering/Chukchi Sea.

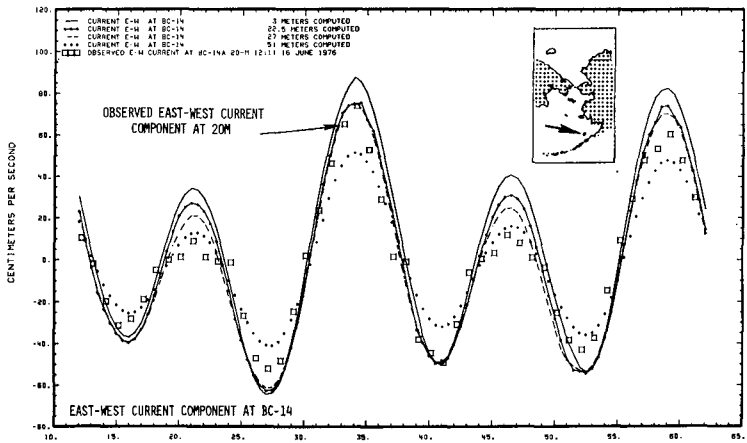

Fig. 9 Observed east-west current component at station BC-14 and the computed values at the nearby gridpoint

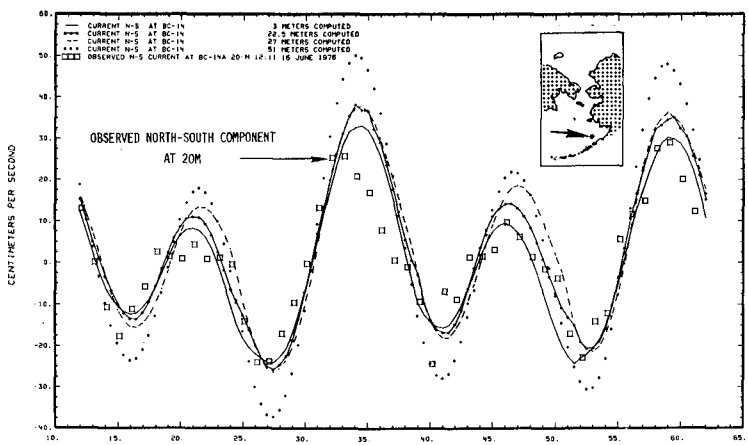

Fig. 10 Observed north-south current component at station BC-14 and the computed values at the nearby gridpoint

generate dispersion of energy by a combined effect described above and by the generation of local circulation through advection. Due to the non-homogeneity of the density in the vertical, the velocities over any vertical are generally not uniform in magnitude and direction. Since advection is the main mechanism by which the tidal residual is generated, a three-dimensional model is required to compute this non-linear circulation at various levels in the water column. The tidal residual circulation pattern is extremely difficult to establish by measurement as only a limited number of current meters can be employed in these vast area's. In addition, these residual currents are difficult to measure accurately because its magnitude is usually below the sensitivity of most current meters. Even with drogues, the wind effects are difficult to separate from the tidal residual components.

The seasonal changes of the density field in the horizontal direction contributes also to the residual circulation through the mechanisms in the baroclinic modes. Consequently, the residual circulation of a coastal area should be studied by considering both barotropic (tides, etc.) and baroclinic modes. In most cases, residual circulations derived from models using field data for adjustments, is extremely difficult to separate the contributions from these two different modes.

Field data collected over the past decades seems to indicate that the residual transport is from the Pacific Ocean to the Arctic Ocean through the Bering Strait. However, because of the vast area involved, it is rather difficult to obtain a set of records free from the weather's (wind) influence on the residual transport. In order to determine the net circulation pattern, simulations were made using the model with only tides and density field as its inputs. The computed tidal ellipses and residual circulation pattern in the surface layer for the summer season are shown in Figs. 12 and 13. It is derived by a numerical filtering process using a tidal eliminator. Again, the residual transport contains contributions both from tide and from the density field. One of the significant features is the northward transport along the shelf break (depth = 300 m) and along the 50-m isobath. Along this isobath is a transition from a well-mixed system in the shallower area to a two layer system. The general direction of the transport at this transition agrees with the basic theory of coastal residual circulations of non-homogeneous waters. It also agrees with the general drift of satellite-tracked drogues released in various locations in the Bering Sea.

Residual transport through the Bering Strait have been the subject of significant interest in the oceanography of the Pacific Ocean and the Arctic Ocean. The computed residual transport through the Bering Strait is about 0.5 Sv. in the absence of the north-south atmospheric gradient. This agrees with the value observed by Tripp, et al (Ref 1). Another large scale field monitoring program is presently being conducted to further confirm this.

Figure 14 shows the components of the tidal velocities at six different depths of a station in the Bering Strait. The east-west component of the velocities are predominately eastward and only during a short period in the tidal cycle the flow reverses.

The north-south components of the velocities are nearly always directed toward the north. The maximum velocity is in the surface layer and is 22 cm/sec. The magnitude of the current at that time is about 23 cm/sec and the direction is about 17° from the North. Higher modes (overtides)

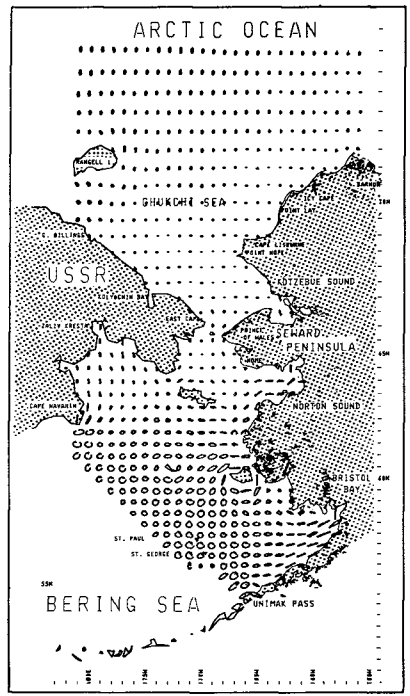

Computed 12.5-hour tidal ellipses in the second layer using a plotting scale of 86 cm/sec per horizontal grid-spacing

Fig. 11

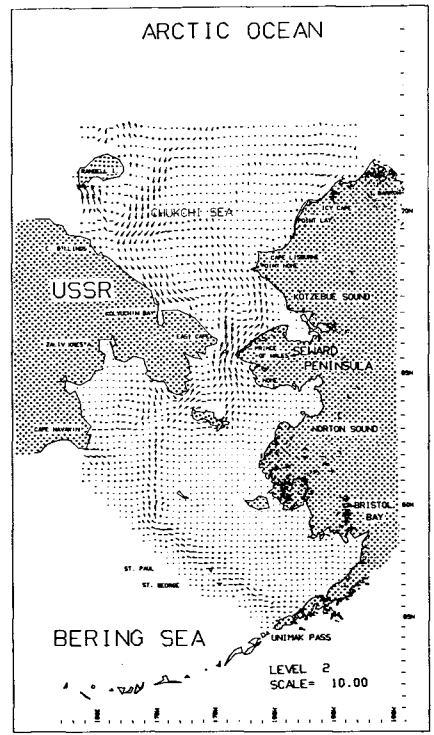

Computed residual current in the second layer using a plotting scale of 10 cm/sec per horizontal grid-spacing

Fig. 12

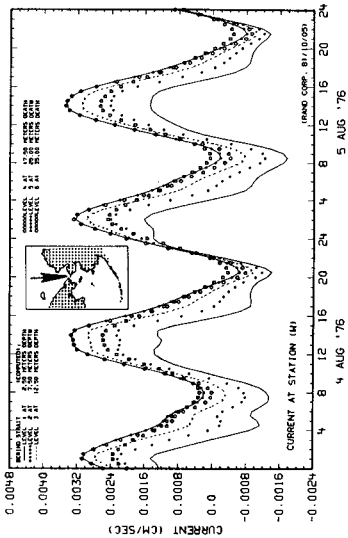

Fig. 13 Computed tidal velocities (U = E-W, V = N-S components) in six representative layers at a station in the Bering Strait.

Fig. 14 Computed vertical velocity (W) and the turbulent energy intensities in six representative layers at a station in the Bering Strait.

can be noticed in the computed currents. They appear mainly in the lower layers where frictional effects are strong and the velocities lag behind those in the upper layers. These characteristics are more obvious in the computed vertical velocity components (top graph, Fig. 14).

The turbulence variation in the bottom layer leads the variation on the upper layers as the transfer is inefficient by the vertical pycnostructure as shown in the bottom graph of Fig. 14. Note that the greatest turbulence intensity exist in the bottom layer. The intensities in this layer are indicated by small squares.

The vertical variation of velocities, energy densities and their phase differences are due mainly to the density variation (Fig. 15). The depth of thermocline in this area are generally deeper than the pycnocline associated with the salinity. This may be due to the more efficient heat diffusion process than the vertical mass exchange.

Residual circulation and stratification-related turbulence field also influence the diffusion process. The amount of diffusion and the net displacement varys throughout a water column. As illustrated in Fig. 16, for a case without surface wind stress particle group releases in the top layer experiences different amounts of advection, turbulent diffusion and net transport than the group release in a lower layer over a 24-hour period.

Storm-Induced Responses

The modeled area is situated within the climatological zone of "Aleutian Lows" which is one of the two major storm areas in the northern hemisphere (the other, Icelandic Lows). The average occurrence of a storm is approximately 3.5 per month with an average duration of 1.5 days.

Many simulations with a moving storm have been made. The weather inputs were derived from a simulation of the weather model. A typical wind and pressure field generated by the stochastic weather model (Ref. 2) is shown in Fig. 17. This particular storm is moving with a speed of 5.1 m/sec.

The computed flow field in the surface layer of the three-dimensional model are shown in Fig. 18, together with the contour lines of the water levels.

At the time of the graph a storm setup occurs in Bristol Bay and in the area northeast of Cape Navarin while low water levels are present in Norton Sound.

Model Use

The three-dimensional model and the stochastic weather are used together with a wind variability model to make simulations of the movements of spilled oil in case accidents would occur during oil exploration or exploitation. The movements are simulated for periods of one to two months originating from selected hypothetical spill sites. The movements can be traced either on the water surface, in or under the ice cover or dispersed in the water column

Results of many simulations are subsequently used to define the risk that certain sensitive areas are exposed to accidentally discharged oil.

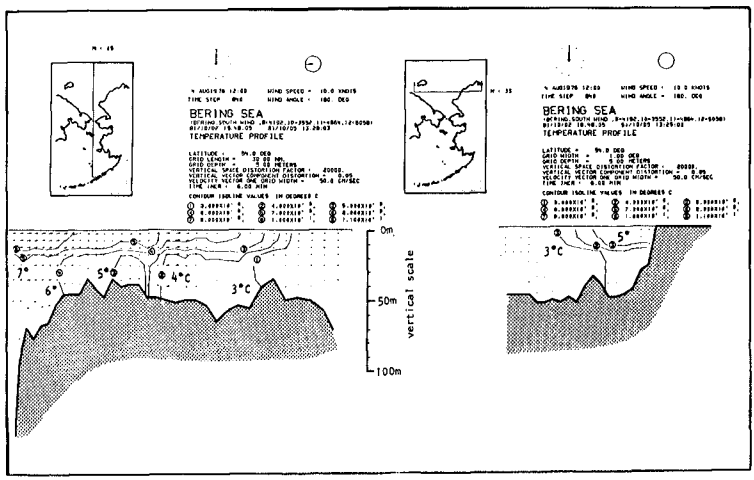

Fig. 15 Vertical temperature distributions through two cross-sections of the model.

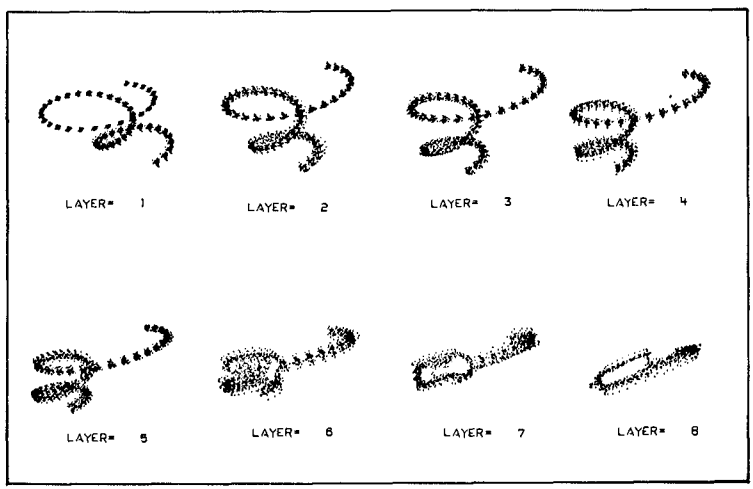

Fig. 16 Partially insulated by the pycnocline, 24-hour trajectories of particle groups released in the upper five layers experience less turbulent diffusion than the lower layers when the system is forced only with tidal energies

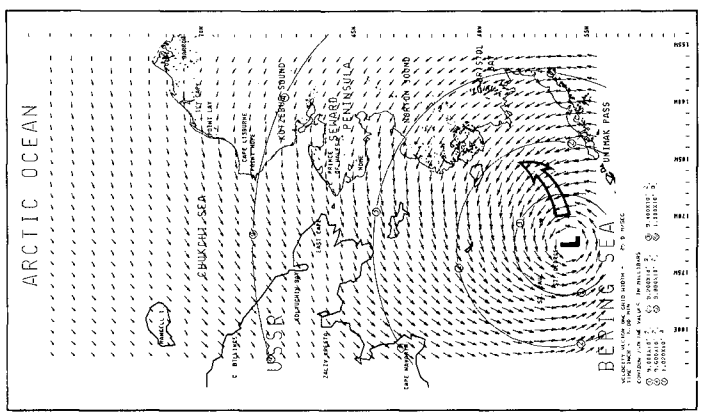

Synoptic wind field as generated by a moving low pressure system. The maximum 10-meter wind speed is approximately 30 meters per second

Fig. 17

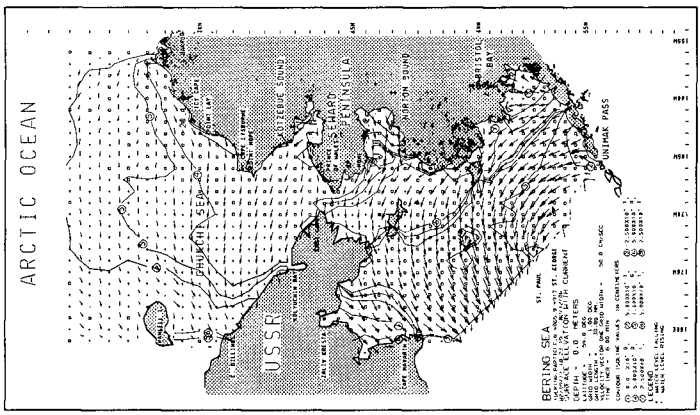

Water surface elevation and surface current distribution induced by the moving low pressure center shown in Fig. 17.

Fig. 18

ACKNOWLEDGMENTS

This study was supported by the U.S. Bureau of Land Management through interagency agreement with the National Oceanic and Atmospheric Administration (NOAA), under which a multi-year program responding to needs of petroleum development of the Alaskan Continental Shelf is managed by the Outer Continental Shelf Environmental Assessment Program (OCSEAP) Office.

The authors would like to express their appreciation to Drs. R. Overstreet, M. Pelto, J. Schumacher, H. Mofjeld, C. Pearson, C. Pease, J. Overland, M. Reynolds, and G. Hufford (all from NOAA); S. Martin, K. Agaard, and R. Tripp (from the University of Washington); W. Stringer and G. Weller (from the University of Alaska); D. Amstutz, R. Emerson, and B. Morris (from the Bureau of Land Management); and K. Lanfer, W. Samuels, and Robert LaBelle (from the U.S. Geological Survey) for providing data and valuable discussion during the course of our investigation. The authors obtained much support from the Technical Project Officer, M. Pelto, in arranging the field data survey for the model study and in coordinating their work with the efforts of other study groups.

Thanks also go to our Rand colleagues, A. B. Nelson and Ms. C. Johnson who modified various graphical programs for displaying simulation results on the Mercator projection and G. Coughlan for her efforts in paper preparation.

REFERENCES

1. Tripp, R. B., L. K. Coachman, K. Aagaard and J. D. Schumacher, *Low Frequency Components of Flow in the Bering Strait System,* American Geophysical Union Meeting, pp. 0-4, September 1978.

2. Liu, S. K., *Stochastic Analyses and Control of Estuarine-Coastal Water Quality Systems: Vol. II. A Stochastic Weather Model for Oil-Spill Analysis.* The Rand Corporation, (in preparation).

A FINITE ELEMENT METHOD FOR THE SHALLOW WATER EQUATIONS

by

A. HAUGUEL (1), G. LABADIE (2) and B. LATTEUX (3)

ABSTRACT

The paper reports the current progress in developing a finite element method for the shallow water equations. The main feature of the method is the special care given to the advective and diffusive parts of the equations, so that it can be of interest to use it when dealing with flows strongly influenced by convective and boundary layer effects. The solution procedure has been chosen so as to allow a calculation with a big number of nodes.

Section 3 of the paper outlines the method. In section 4, is detailed the procedure for the advective terms, involving the determination of the characteristic curves. Section 5 is devoted to the diffusion and propagation terms. Finally numerical results are presented in section 6.

1. INTRODUCTION

Environmental hydraulics often requires the calculation of flows in complex domains. Moreover, one often wishes a finer description for some zones of particular interest, while most of the domain can be approximated by a rather coarse grid. The finite element method provides such a flexibility and a growing interest is taken in its potential.

However the size of the resulting discrete system restricts the possibilities of using it. An interesting approach, presented here, leads to consider separate problems on each of the scalar variables (water level and flow discharge components) and hence allows to reduce the storage requirement.

(1) Head of the Research Hydraulic Division, Laboratoire National d'Hydraulique, E.D.F., Chatou, France.
(2) Research Engineer, Laboratoire National d'Hydraulique, E.D.F., Chatou, France.
(3) Research Engineer, Laboratoire National d'Hydraulique, E.D.F., Chatou, France.

2. NOTATION

$\underset{\sim}{F}$ = Coriolis and friction forces (components F_i)
$\underset{\sim}{g}$ = acceleration due to gravity
h = depth of water
h_m = average of h in time
K = momentum diffusion coefficient
$\underset{\sim}{Q}$ = uh flow rate per unit length (components Q_i)
$\underset{\sim}{u}$ = velocity field (components u_i)
z = free surface elevation.

3. EQUATIONS

The shallow water equations consist of the mass conservation equation and two momentum equations :

$$\frac{\partial z}{\partial t} + \nabla . \underset{\sim}{Q} = 0$$

(1)

$$\frac{\partial Q_i}{\partial t} + \nabla . (Q_i \underset{\sim}{u}) + gh \frac{\partial z}{\partial x_i} - K \Delta Q_i = F_i$$

A fractional step algorithm is used to decompose the equations into a pure convection system and the remainder.

$\underset{\sim}{Q}^n$, Z^n being given at time t^n, the unknowns at time t^{n+1}, $\underset{\sim}{Q}^{n+1}$, Z^{n+1} are computed by the two following successive steps :

- Determination of auxiliary unknown $\underset{\sim}{Q}^{n+\frac{1}{2}}$ solution of the convection equations :

(2) $$\frac{\partial Q_i}{\partial t} + \nabla . (Q_i \underset{\sim}{u}^n) = 0$$

- Resolution of the diffusion and propagation problem :

$$\frac{\partial z}{\partial t} + \nabla . Q = 0$$

(3)

$$\frac{\partial Q_i}{\partial t} - K \Delta Q_i + gh \frac{\partial z}{\partial x_i} = F_i$$

with initial conditions Z^n, $\underset{\sim}{Q}^{n+\frac{1}{2}}$

4. ADVECTION STEP

It involves the resolution of equations (2), which can be transformed into equations on velocity, by use of the continuity equation :

$$(4)\quad \frac{\partial u_i}{\partial t} + \underset{\sim}{u}^n : \nabla u_i = 0$$

This form has been prefered to the original form (2) as explained in section 6.

A characteristics method has been used to solve those equations (4). It requires two steps :

- computation of the characteristic curves passing through the nodal points ;
- interpolation at the foot of those curves.

The method is unconditionally stable and the time step has just to be small enough to catch the time variation of the velocity field $\underset{\sim}{u}$.

Moreover the amount of computation needed is very reasonable. In particular, there is no non-symmetric system to assemble and solve at each time step, as would appear in a standard implicit method.

As for accuracy, it is quite satisfactory, although somewhat depending on the time-step ; the only significant error being made when performing the interpolation at the foot P_j of the characteristic, the accuracy decreases when P_j is far from a mesh-point, particularly when using a linear interpolation. Finally, conservativity is not ensured by the scheme ; this is probably the main drawback of the method.

This technique has been applied for a long time in the solution of the Navier Stokes equations and is described in more detail in [1]. Some more research is done on the subject [2].

5. DIFFUSION AND PROPAGATION STEP

An implicit discretization has been chosen for system (3) except for the non linear term $gh\nabla Z$ which is partly explicited. There is no need for a second order scheme in time for such long waves as the tide.

If we drop, for sake of simplicity, the superscripts n+1, the system to solve in this step is of the form :

$$(5)\quad \alpha z + \nabla . \underset{\sim}{Q} = R$$

$$(6)\ \alpha \underset{\sim}{Q} - K\Delta \underset{\sim}{Q} + g h_m \nabla z = \underset{\sim}{T}$$

$$\text{with : } \alpha = \frac{1}{DT} \ ; \ R = \frac{1}{DT} z^n \ , \text{ and } \underset{\sim}{T} = \frac{1}{DT} \underset{\sim}{Q} + \underset{\sim}{F}^n - g(h^n - h_m)\nabla z^n$$

(h_m being the average in time of h, that is a function of space coordinates only).

The discretization of equations (5), (6) with their boundary conditions (Q given) yields to a large size linear system. A natural idea to reduce this size, is to eliminate Q between equations (5) and (6). This is achieved by applying the divergence operator to (6) and plugging (5) into the result. The equation obtained is :

$$(7)\ \alpha^2 z - \nabla . (K\alpha + g\, h_m)\nabla z = W$$

$$\text{with : } W = \alpha R - K\Delta R - \nabla . \underset{\sim}{T}.$$

Equation (7) is an elliptic equation, giving by discretization a symmetric matrix. It can easily be solved if a boundary condition is provided for z. If so, Q can be straight forwardly computed from equation (6) where the term $g h_m \nabla z$ is now a known function and can be rejected into the right hand side. With Dirichlet boundary conditions, equation (6) decomposes into two decoupled equations, one for each component Q_i of Q leading to the same symmetric matrix for the discrete system.

The problem then amounts to the determination of the trace of z on the boundary. The procedure used for this purpose is an extension of the technique proposed by Glowinski-Pironneau [3] for the Stokes problem. It is described in detail in [5].

This technique is advantageous on the point of view of computational efficiency. Two "domain" matrices have to be stored, one for the variable z, another for each component of Q (it is the same matrix for the two components). They are symmetric and sparse and small enough to be processed by an in-core solver such as an incomplete Choleski preconditioned conjugate gradient. In addition, the matrix of the boundary operator has to be factorized and stored.

6. NUMERICAL RESULTS

Several applications have been performed, from a very schematic case, in order to have a first view on the possible problems, to a realistic complex one, to give a more comprehensive test of the method.

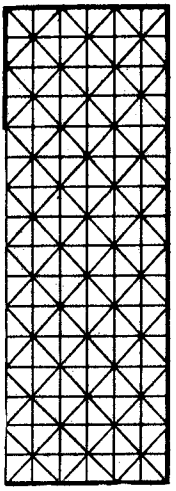

Fig.1_Finite elements discretization

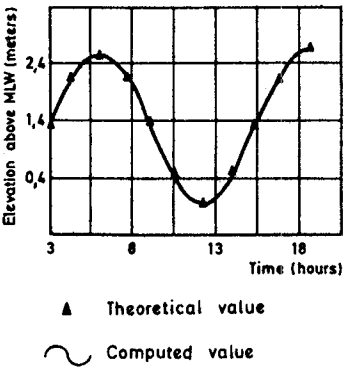

Fig.2_Average surface elevation

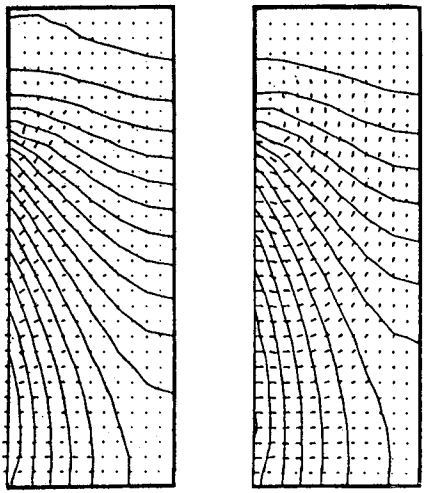

Fig.3
Velocity fields and
free surface
elevation lines

SCHEMATIZED MASSACHUSSETS BAY

6.1. Schematized Massachussets Bay

In this first experiment, emphasis has been laid on the general behaviour of the method rather than the comparison with actual data. Thus neither the friction and Coriolis force, nor the varying bottom topography were simulated. The domain was coarsely approximated by a rectangle (fig.1) divided into 192 triangular elements with respectively 119 and 429 nodes for piecewise linear and quadratic approximations. Both components of the flow discharge were prescribed on the boundaries ; this discharge was taken to be zero on the land limits, and was schematized on the ocean limit by a sinusoidal uniform flow.

Results as regards current fields and free surface elevation (fig. 2 and 3) were found to be quite satisfactory ; in particular global mass conversation has been insured at less than 1% of the total mass flux over a whole tide.

Teachings of this first application are as follows :

- linear and quadratic approximations for the water height, together with quadratic approximation for the flow discharge, have given closely the same results ;

- there exists some stability condition for the diffusion step ; the nondimensional number $(K.DT/DX^2)$ has to be more than about 10^{-4} to avoid oscillations of the computed solution (probably because of the conflict arising between a nearly hyperbolic system to solve and boundary conditions related to the diffusion, i.e. prescribed velocity on the limits) ;

- some kind of "overshoot" can appear in the advection step near the boundary when the flow gets out, due to a bad property of the quadratic interpolation on the flow discharge.

6.2. Dunkirk outer harbour

The second application, which is less schematic, concerns the computation of the tidal flow pattern in the vicinity of the new outer harbour of Dunkirk, located on the french coast of the North Sea.

This example has been chosen for two main reasons :

- the shape of the domain and the complexity of the laying out of the limits give the typical case where a finite element method turns out to be specially suitable (good boundary representation and local refinement facilities) and provide a rather severe test of the model ;

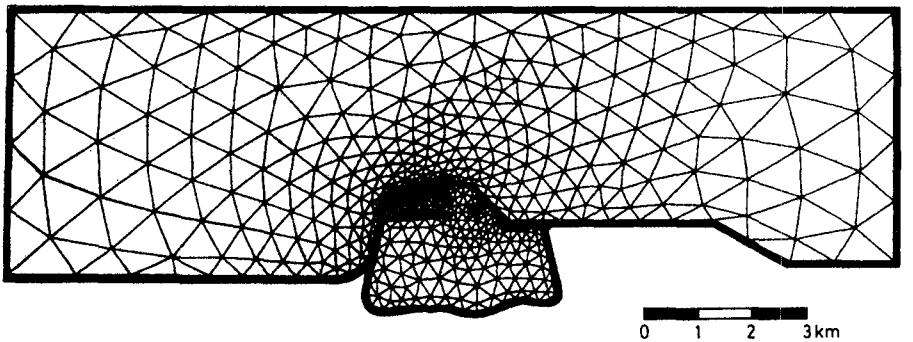

a. Mesh of the whole area

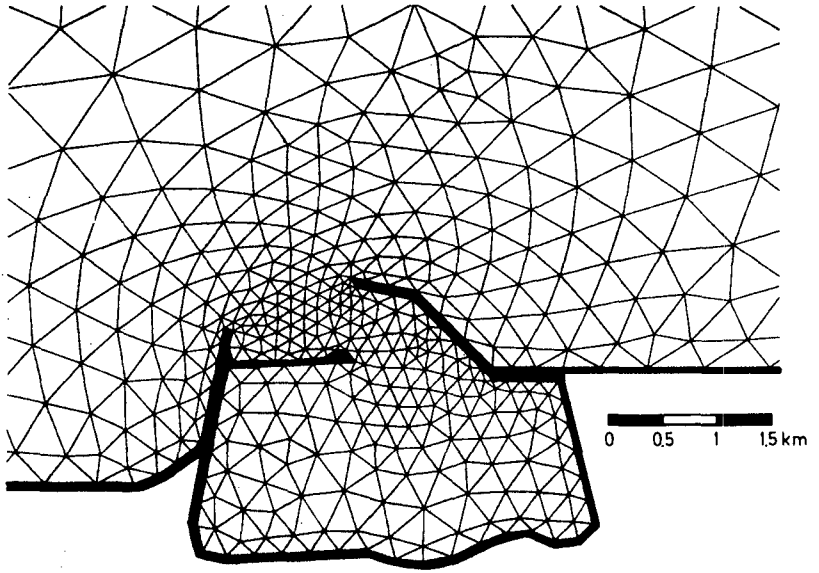

b. Detail of the harbour

Fig. 4 - FINITE ELEMENTS MODEL OF DUNKIRK OUTER HARBOUR

this case has been previously studied by means of a scale model and of a finite difference model ; so there exist references to which compare the results of the finite element model.

The finite element grid (fig.4) has been generated automatically by a program developed in our laboratory. As it can be noticed from this illustration, a special mesh refinement has been introduced near the limits, in order to obtain a better consideration of the boundary conditions (which is particularly useful for the land boundaries).

In this experiment a piecewise quadratic approximation has been used for each variable ; there are about nine hundred triangular elements and two thousand calculation nodes.

The characteristics of the computation are as follows :

. tide range is about five meters ;
. maximum velocity is about 1,5 m/s ;
. tide and current are in phase (that is to say that the tide wave is here quite purely progressive) ;
. eddy viscosity coefficient is equal to 5 m^2/s ;
. time step is sixty seconds and Courant number for propagation varies locally from 1 to 5.

Finally both components of the flow discharge are prescribed on the boundaries.

In fact two computations have been carried out successively in this case of Dunkirk : the first one under schematic conditions and the second one in a more realistic way.

6.2.1. Schematic computation

In the first trial the flow discharge is assumed to be sinusoidal and parallel to the upper limit ; the bottom is flat and bed friction is not considered, just as in the example of Massachussets Bay.

Some instabilities appeared in the current field during the computation ; the problem turned out to come from the advection step, solved at first on the flow discbarge Q :

$$\frac{\partial Q_i}{\partial t} + \underset{\sim}{u}^n \cdot \nabla Q_i = - Q_i \nabla \cdot \underset{\sim}{u}^n$$

The discontinuity of the term in the right hand side was found to he responsible for the instabilities. When using the formulation on velocity only, those instabilities actually disappeared.

Fig. 5 shows the evolution of the flow pattern in the vicinity of the harbour at the beginning of the flood current (slack occurs about three hours before high tide) : the flow deflection in front of the harbour and the formation of two eddies can be noticed :

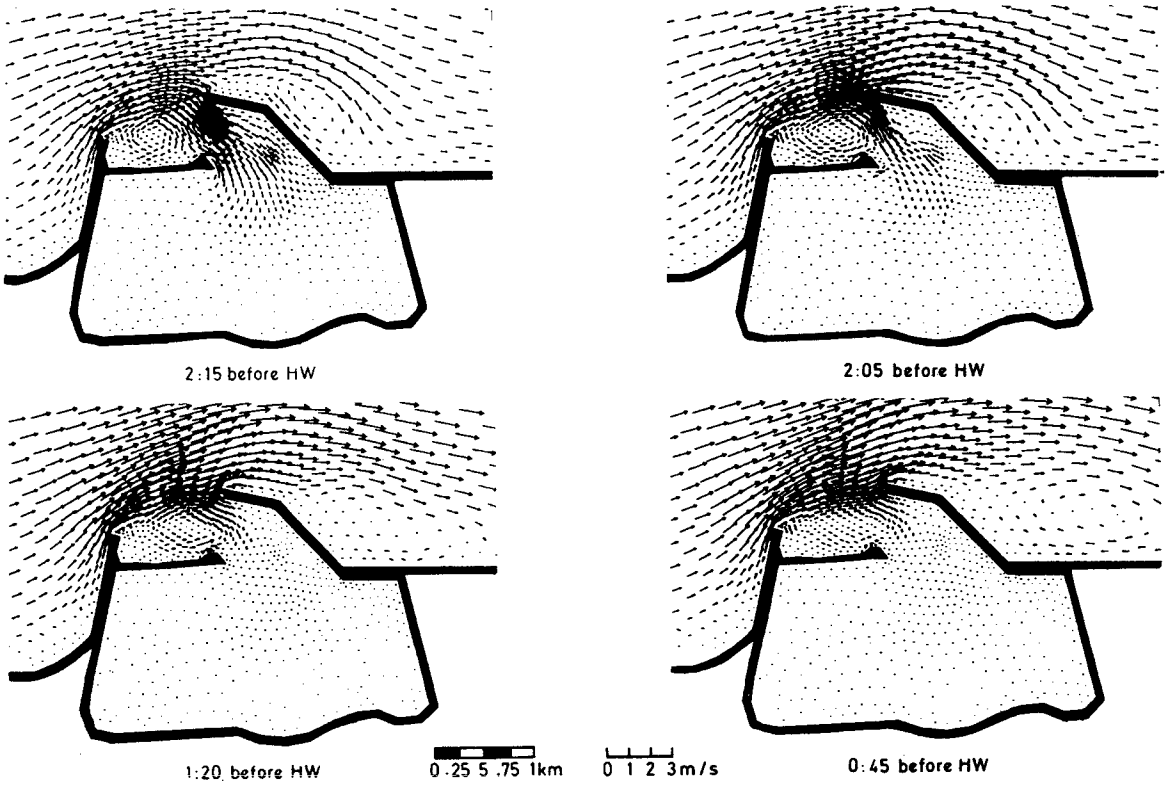

Fig.5_ SCHEMATIC MODELISATION OF DUNKIRK OUTER HARBOUR
Detail of the current fields

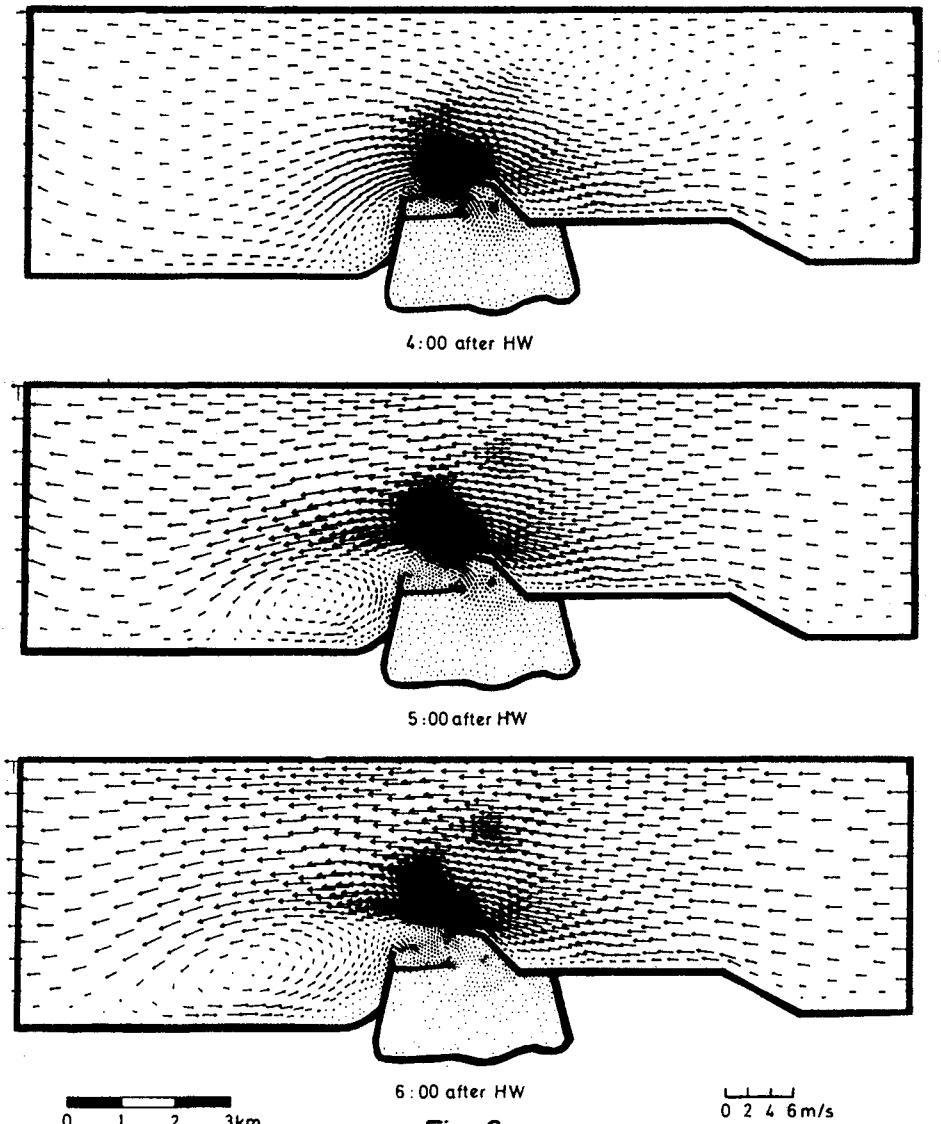

Fig. 6

SCHEMATIC MODELISATION OF DUNKIRK OUTER HARBOUR
COMPUTED CURRENTS IN THE WHOLE DOMAIN

. The first one in the harbour entrance ; it becomes weaker and weaker as the harbour fills in.

. The second eddy downstream the east jetty expands gradually eastwards and in fact it will fill at the end of the flood the whole eastern part of the domain because of the absence of bed friction and because the boundary conditions don't allow it to get out.

Fig. 6 points out in the whole domain the same phenomenon during the ebb ; an eddy appears at the beginning of the ebb on the left of the west jetty and expands progressively till the end of the ebb.

Finally mass conservation was found to be as satisfying as for the first example ; here also the global error regarding the free surface elevation over one tide is less than 1 % of the tide range.

6.2.2. Realistic computation

A second computation has been carried out after the insertion in the model of the bed friction and of the variability of the bed topography.

Fig. 7 exhibits the bathymetry in the vicinity of the harbour ; the depths are quite variable, especially because of the navigation channel for oil tankers ; the steepness of the edges of the channel (about 1:10) is in fact a severe condition for the shallow water equations.

Boundary conditions are now deduced from the results of a previous computation made with a finite difference method on a larger domain.

The computation has been worked out during more than one tide, and the results have been compared to the data obtained by photographs of surface floats on the scale model, built about twelve years ago for the study of the new outer harbour.

Fig. 8 to 10 display this comparison during the most interesting period, from the beginning of the flood till high water.

On fig. 8, at the beginning of the flood, an eddy appears in a similar way on both models, just behind the end of the west jetty, while the harbour fills in ; half an hour later, both eddies have shifted and spread out likewise.

Afterwards (fig. 9) the eddy expands gradually till it covers the whole entrance in both models, with perhaps a slight difference in the shape. The flow deflection due to the harbour can be noticed farther than one kilometer away from the entrance in both cases.

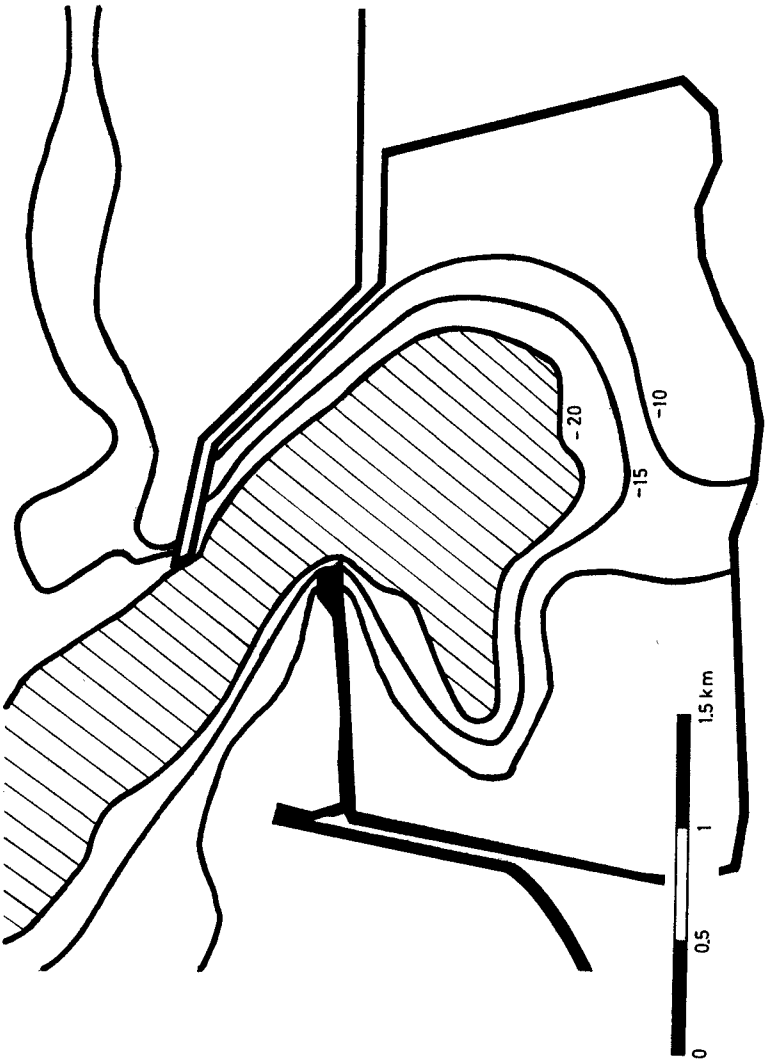

Fig. 7_DUNKIRK OUTER HARBOUR REAL BED TOPOGRAPHY

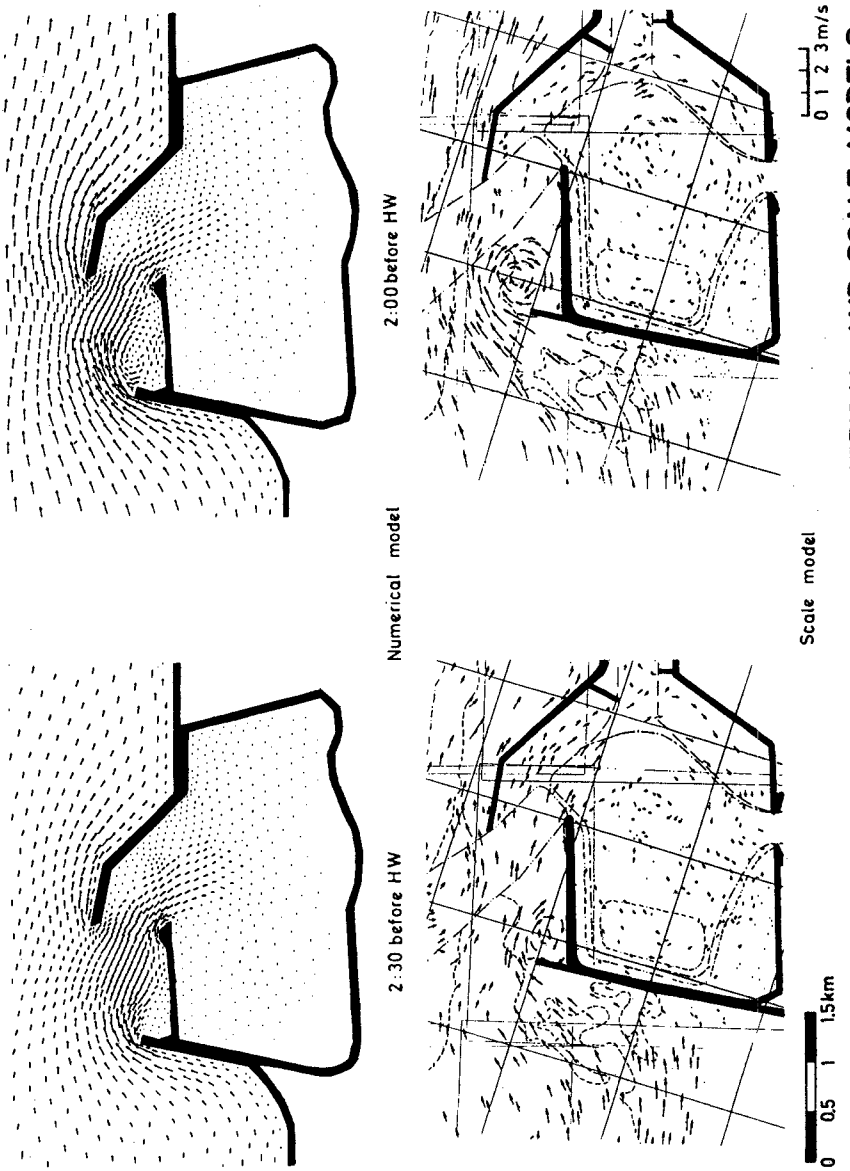

Fig. 8_COMPARISON OF THE RESULTS OF NUMERICAL AND SCALE MODELS

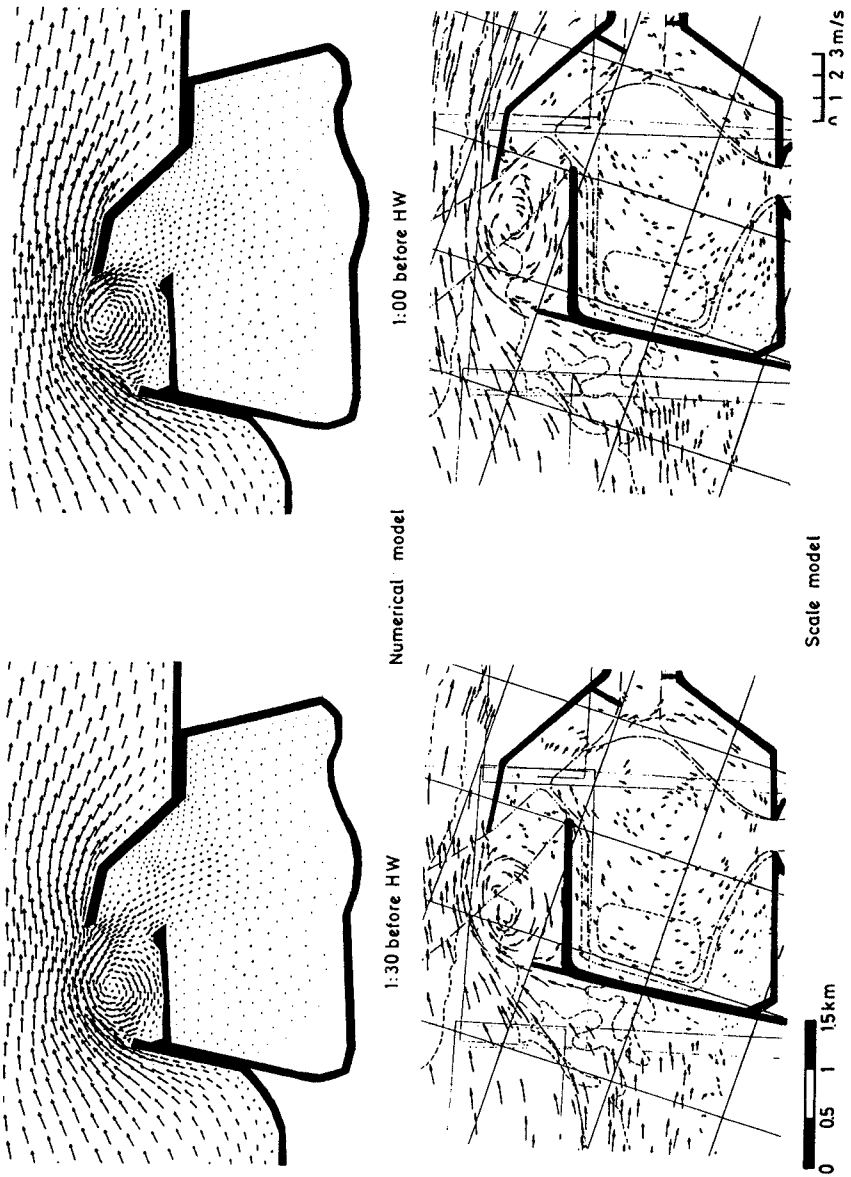

Fig. 9 COMPARISON OF THE RESULTS OF NUMERICAL AND SCALE MODELS

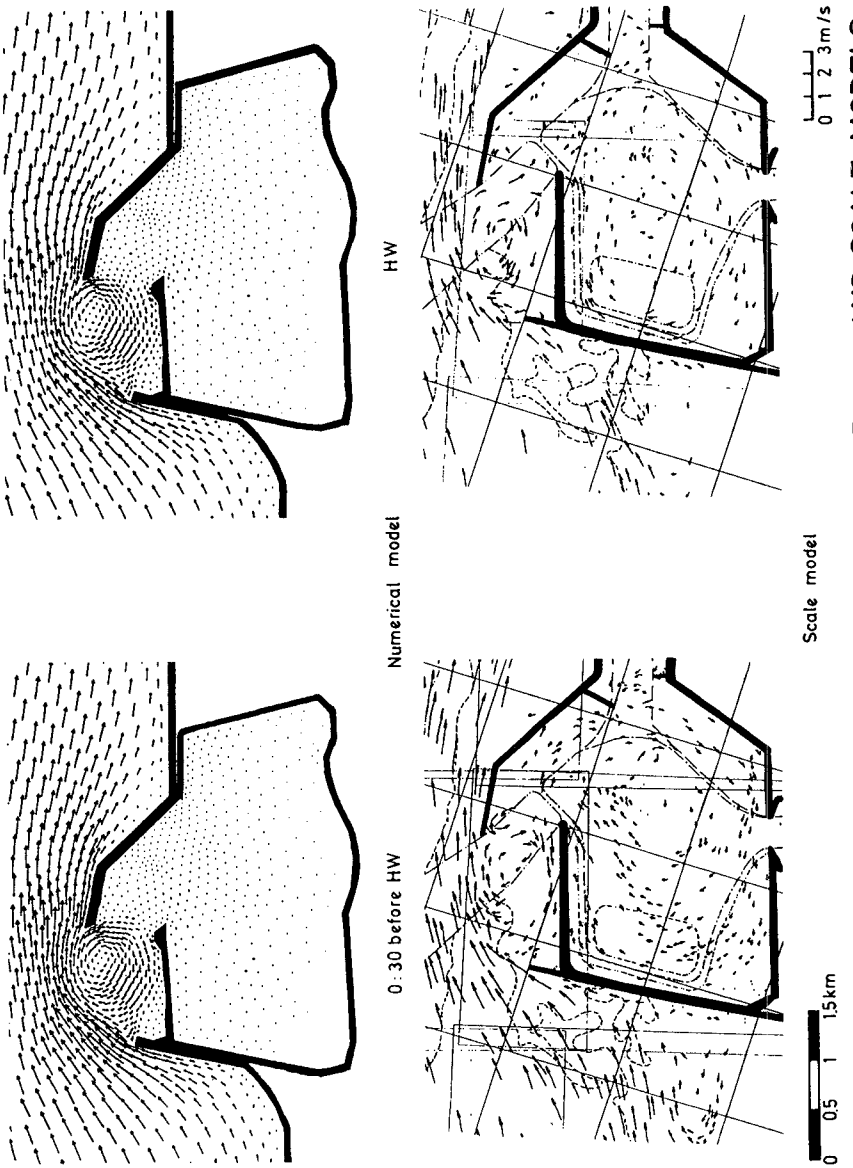

Fig.10_COMPARISON OF THE RESULTS OF NUMERICAL AND SCALE MODELS

From one hour before high water till high water (fig. 10) the eddy remains stable ; downstream the harbour, a slight flow separation can be noticed, but the computation does not develop a big eddy as in the case of the first computation (fig. 5).

The mass conservation is less accurately obtained than in the previous experiments : the global level error over one tide is about 3 % of the tide range ; this seems to be due to the steepness of the sea bed near the breakwaters ; the problem can probably be overcome by taking a more severe threshold of convergence in the numerical resolution of the linear systems.

7. CONCLUSION

Compared to the classical finite difference method, which is now currently used to solve the shallow water equations, this finite element method presents many advantages, such as a better description of the boundaries and a greater flexibility of the grid ; on the other hand, the implementation of the model is rather longer and more complex, and involves a bigger consumption of processing time ; nevertheless, due to the special care given to reduce the size of the systems to be solved, the in-core memory requirements are quite reasonable. As an example computation over one tide (12 h 24 mn) using nearly 2 000 nodes of discretization and a time step of sixty seconds has required about 2 hours of CRAY 1 processing time and 1 000 K bytes of in-core memory.

Numerical experiments have clearly shown that even under rather severe conditions the model has a nice behaviour and exhibits a fair comparison with experimental data .

At present, improvements are in progress, with the implementation of an incident wave condition and the consideration of the influence of wind stress and atmospheric pressure field. The model will soon be used on a domain covering the whole English Channel up to the edge of the continental shelf (fig. 11), with two purposes :

- firstly to examine the impact of a possible tidal power plant on the tidal pattern in this area ;

- secondly to study the generation and propagation of storm surges in the English Channel.

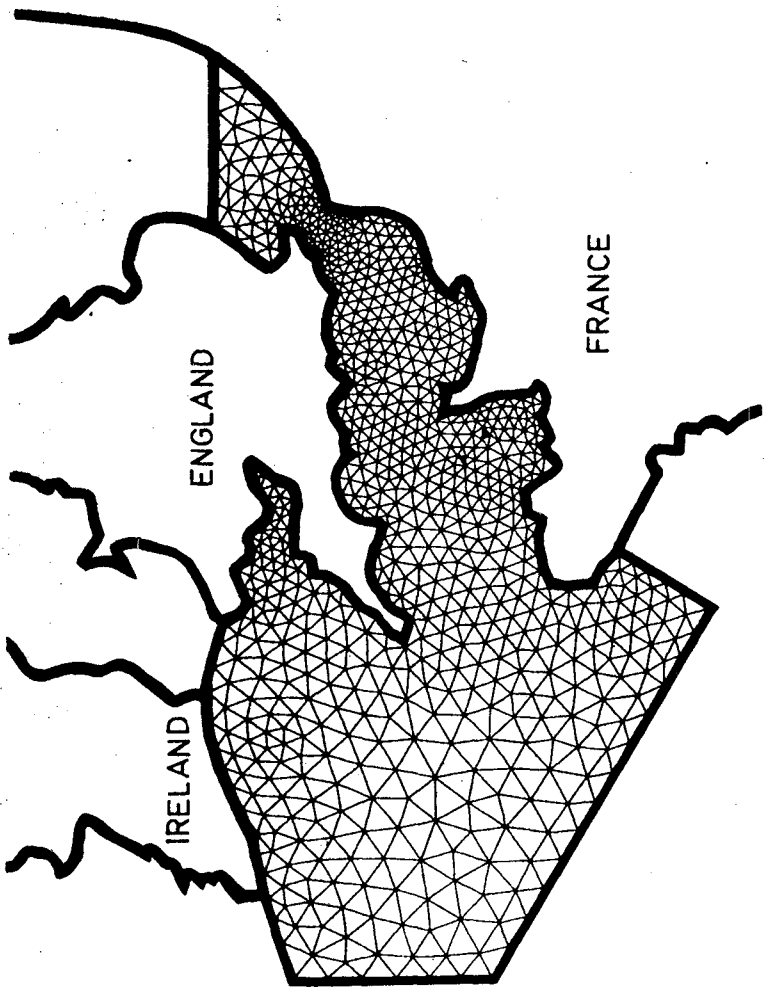

Fig. 11 - FINITE ELEMENTS MODEL OF THE ENGLISH CHANNEL

8. REFERENCES

1. J.P. Benqué, G. Labadie, B. Ibler

A finite element method for Navier-Stokes equations - First International Conference on numerical methods for non linear equations - Swansea, U.K., sept. 2nd - 5th 1980.

2. J.P. Benqué, J. Ronat

Quelques difficultés des modèles numériques en hydraulique - Fifth International Symposium on computing methods in applied sciences and engineering - INRIA, December 1981, Versailles, France.

3. M.O. Bristeau, R. Glowinski, J. Périaux, P. Perrier, O. Pironneau and G. Poirier

Application of optimal control and finite element methods to the calculation of transonic flows and incompressible viscous flows - Rapport de recherche 78-294, IRIA LABORIA, 78150 Le Chesnay, France.

5. G. Labadie, J.P. Benqué, B. Latteux

A finite element method for the shallow water equations - 2nd International Conference on numerical methods for laminar and turbulent flow, Venice, Italy, July 13-16 1981.

6. G. Labadie, B. Latteux

Résolution des équations de Saint-Venant par une méthode d'éléments finis - Rapports E.D.F. HE/41/82.15 et HE/42/82.34.

TRIDIMENSIONAL NUMERICAL MODEL FOR TIDAL AND WIND GENERATED FLOW

M.C. BURG* A. WARLUZEL** Y. COEFFE***

Abstract :

This report presents a three-dimensional numerical model, which calculates by a finite-difference method the vertical profile of horizontal velocities. The unsteady three-dimensional Navier-Stokes equations with a free surface are governing this flow. We assume a hydrostatic pressure, and simulate the turbulent effects by the Prandtl's mixing-length hypothesis. The model is validated by experiments carried out in a laboratory flume with a prismatic channel inclined 45° over the flow. Then, the model is applied successfully in Gironde estuary and coastal areas in France for the computation of tidal and wind generated currents.

I. INTRODUCTION

Very little information is presently available about currents induced by tides and wind in their time and space variations. In the particular case where the bathymetry is very irregular, the two-dimensionnal models cannot be used, considering the important three-dimensional aspect of this flow.

The purpose of this paper is to describe a numerical model dealing with this kind of flow and to present different applications.

II. ASSUMPTIONS AND EQUATIONS

The unsteady three-dimensional Navier-Stokes equations with a free surface are governing this flow. In the case of tidal or wind induced flows and if the slope of the bottom does not exceed 10 %, the flow pattern is almost horizontal. It is then possible to simplify these equations. The vertical acceleration can be assumed small compared with gravity. The pressure is thus directly related to the movement of the surface by a hydrostatic relationship.

* Engineer of the Research Division, Laboratoire National d'Hydraulique EDF Chatou. France.

** Engineer of the Research Division, Laboratoire National d'Hydraulique EDF Chatou. France.

*** Head of the Maritime Division, Laboratoire National d'Hydraulique EDF Chatou. France.

The second assumption is related to turbulent effects. The vertical mixing is modelled with the Prandtl's mixing-length hypothesis : the turbulent fluxes of momentum are simulated by vertical and horizontal eddy viscosities ν_z and ν_h. ν_z is expressed by

$$\nu_z = \ell^2 \left| \frac{\partial \vec{V}}{\partial z} \right|$$

where ℓ, mixing-length is assumed to be constant in the fluid except near the bottom and the sea-surface where it linearly varies with the distance from boundary. Horizontally, the velocity gradients are generally small and the convection transfers are predominant compared with the diffusion effects. Then it is possible to choose a constant horizontal diffusion coefficient with a reasonnable value.

In order to represent the bottom topography and the free surface, a curvilinear coordinate z* is used to get a flat and independant of time domain of integration. A rectilinear irregular finite difference will be used on this transformed domain (fig. 1).

z* is expressed as

$$z^* = \bar{S} \frac{(z - zf)}{(S - zf)} \qquad (1)$$

Where $\bar{S}$ is a horizontal reference level, i.e. water surface level at initial time

z_f (x,y) bed level

S (x,y,t) water surface level

z (x,y) vertical coordinate at any point.

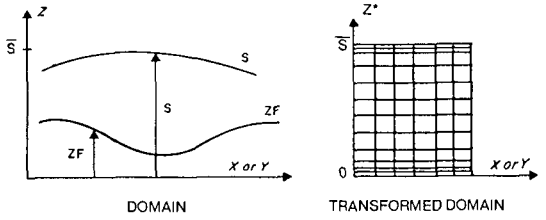

Fig. 1 - Vertical transformation.

The equations written with this new coordinate are of the same form, if a vertical velocity w* is introduced (see [1], [2], [4]).

$$w^* = \frac{\partial z^*}{\partial t} + u \frac{\partial z^*}{\partial x} + v \frac{\partial z^*}{\partial y} + w \frac{\partial z^*}{\partial z} \qquad (2)$$

Then the modified equations must be solved with appropriate boundary conditions.

A) Boundary conditions

Generally on open sea boundary, mass-currents integrated over the depth are known through field measurements or by mean of a two-dimensional computation of tide at a larger scale.
In order to obtain a velocity profile on the boundaries an Ekman type relation is used. In that case, it is necessary that around the boundaries the bathymetry is regular, in order to neglect horizontal gradients.

The Ekman type integration is done by solving the following relations.

$$\frac{\partial u}{\partial t} = \frac{\partial}{\partial z}\left(\nu z \frac{\partial u}{\partial z}\right) + fv - \frac{1}{\rho}\frac{\partial P}{\partial x} \qquad (3)$$

$$\frac{\partial v}{\partial t} = \frac{\partial}{\partial z}\left(\nu z \frac{\partial v}{\partial z}\right) - fu - \frac{1}{\rho}\frac{\partial P}{\partial y} \qquad (4)$$

where the pressure gradient is expressed in terms of mean currents (u, v) over the depth through depth averaged long wave equations Tox, Toy being shear stresses at sea bed, and f Coriolis parameter.
Integration over the depth gives :

$$\left.\begin{aligned} -\frac{1}{\rho}\frac{\partial P}{\partial x} &= \frac{1}{H}\frac{\partial \bar{u}H}{\partial t} + \frac{Tox}{H} - f\bar{v} \\ -\frac{1}{\rho}\frac{\partial P}{\partial y} &= \frac{1}{H}\frac{\partial \bar{v}H}{\partial t} + \frac{Toy}{H} + f\bar{u} \end{aligned}\right\} \quad (5)$$

B) Coastal boundary

Velocity components are taken to be zero.

C) Free surface

- Without wind we assume

$$\frac{\partial u}{\partial z} = 0 \qquad \frac{\partial v}{\partial z} = 0 \qquad w = 0$$

- With wind, it is assumed that wind action produces only a surface shear stress which is expressed in term of the wind speed at some standard height above the sea surface : $Tow = 1{,}3 \times CD \times |v_w| \times v_w$, where CD is a frictional coefficient evaluated by experimentations.

The shear stress can be related to the fluid flow field by the equations

$$\frac{\partial u}{\partial z} = \frac{1}{\rho}\frac{Towx}{\nu z} \qquad (6)$$

$$\frac{\partial v}{\partial z} = \frac{1}{\rho}\frac{Towy}{\nu z} \qquad (7)$$

the eddy viscosity being : $\nu_z = \ell^2 \sqrt{(\frac{\partial u}{\partial z})^2 + (\frac{\partial v}{\partial z})^2}$ (8)

In this condition, at the sea surface, the viscosity is related only to shear stress by a relation independant of time

$$\nu_z = \ell\sqrt{\frac{Tow}{\rho}} \qquad (9)$$

where ℓ is the mixing length.

D) Sea bed

Two types of condition have been tested :

- the velocity is zero. This first type of condition imposes to have a very small discretization near the bottom, in order to have a good description of the gradient. Therefore another solution was tested.

- Condition of slip on the sea bed.

A slip velocity condition has been imposed by assuming that shear stress is a quadratic function of the bed velocity. Introducing a constant c, the imposed relation can be written in the following form :

$$\nu z \frac{\partial u}{\partial z} = \frac{u\sqrt{u^2 + v^2}}{c^2} \qquad \nu z \frac{\partial v}{\partial z} = \frac{v\sqrt{u^2 + v^2}}{c^2}$$

with $\nu_z = (0,41)^2 \Delta z^2 \sqrt{(\frac{\partial u}{\partial z})^2 + (\frac{\partial v}{\partial z})^2}$

Where Δz (distance between the point where the condition is applied and the bottom) is chosen in order to stay in the logarithmic boundary layer.

It is possible, in the hypothesis of unidimensional flow, to calculate this new constant c in function of the mean diameter of the roughness, or if prefered in function of the mean water depth and the Chezy coefficient.

III. NUMERICAL SCHEME

The numerical discretization uses finite differences on an irregular rectilinear grid in three directions x, y, z*. In fact, the introduction of the vertical coordinate z* instead of z (real coordinate) leads to a curvilinear grid in the vertical direction, which fits very well the bottom topography and the sea surface.

Due to the large number of unknowns and computation points in the area, a complete implicit solution of all equations leads to an excessive storage requirement, and prohibitive computation time. On the other hand, a completly explicit solution would induced severe restrictions upon the time-step for the different parts of the resolution. These restrictions are mentionned below :

Surface-wave stability along the two horizontal directions.

$$t \leqslant \min \left(\frac{\Delta x}{\sqrt{g(S - zf)}}, \frac{\Delta y}{\sqrt{g(S - zf)}}\right)$$

Stability for horizontal and vertical diffusion.

$$\Delta t \leqslant \min \left(\frac{\Delta x^2}{2 \nu h}, \frac{\Delta y^2}{2 \nu h}\right) \text{ and } \Delta t < \left(\frac{\Delta z^2}{2 \nu z}\right)$$

Stability for horizontal and vertical advection.

$$\Delta t \leqslant \min \left(\frac{\Delta x}{u}, \frac{\Delta y}{v}, \frac{\Delta z}{w}\right)$$

For a channel in a not very deep sea, the order of magnitude of the unknowns are

$\Delta x = \Delta y = 100$ m

νh from 1 to 10^{-3} m^2/s

u from 0,5 to 1 m/s.

νz 5 10^{-2} m^2/s.

(S - zf) depth 20 m

i.e. for a time-step.

$\frac{\Delta x}{\sqrt{g(S - zf)}}$	$\frac{\Delta x}{\sqrt{g(S - zf)}}$	$\frac{\Delta x^2}{2 \nu h}$	$\frac{\Delta z^2}{2 \nu z}$	$\frac{\Delta x}{u}, \frac{\Delta y}{v}, \frac{\Delta z}{w}$
7 s	7 s	10 s	10 s	100 s

Among all these restrictions upon time-step, the most inconvenient are those of the free surface wave and the vertical diffusion. For solving these equations we have then been led to use the so-called fractionary step method, where the stages are treated by the best fitted method (implicit or explicit).

- Horizontal diffusion and advection.

This stage is entirely solved by explicit method and the time-step must respect the restrictions relative to this operator. The advection is treated with the help of characteristic method.

- Vertical diffusion.

The system is solved by a double sweep algorithm, the discretization used is implicit.

- Continuity and pressure or sea surface gradient.

The last left terms plus the continuity operation are solved together. The average over the depth of the remaining equations gives 2D equations relating sea surface elevation and the two components of the fluxes. These are solved first by a 2D implicit method in the same way than in our shallow water wave model. (see ref. [1]).

Then the horizontal velocity profiles are modified with the new sea surface gradient and the vertical velocity is calculated by integration of the local continuity equation.

IV. APPLICATIONS

To validate the model and evaluate the eddy viscosity, some measurements were carried out in a schematic physical model. A prismatic channel was set in a flume and a steady current was run with an incidence of 45° with the channel (fig. 2 and 3).

Different horizontal velocities profiles were obtained in the channel by micro-current meter of 0,01 m diameter. They showed an important deviation of the velocity near the bottom although there is a small deviation near water surface.

The numerical model includes the central part of the flume over 5,5 m length and 2,50 m width. The horizontal grid size is 0,212 m. The model includes 27 x 13 horizontal points and 24 points over the depth. The horizontal grid is regular, but the vertical discretization is very irregular ; the grid size is smaller near the bottom. The flow characteristics are the following :

- depth in the channel 0,125 m
- depth out of the channel 0,080 m
- mean up-stream velocity 0,17 m/s
- Reynolds number $2{,}5\ 10^4$
- Froude number $5\ 10^{-2}$.

Up-stream, the velocities being quite stable, we can adjust the constants of the turbulence model in order to obtain, at point 2, a velocity profile as close as possible of the measured one. This calibration has led to adopt the following values :

$\alpha = 0{,}2 \qquad k = 0{,}12.$

α is the fraction of the depth on which length scale is linear, k is the Karman constant.

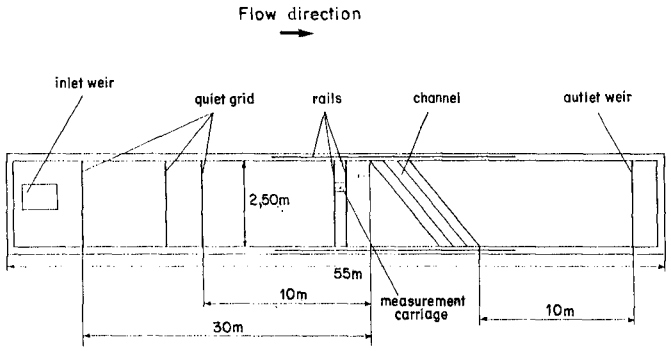

Fig. 2 - Physical model.

Experimental set up.
Velocity measurements : module velocity micro current-meter 0,01 m in diameter.

head whool thread.

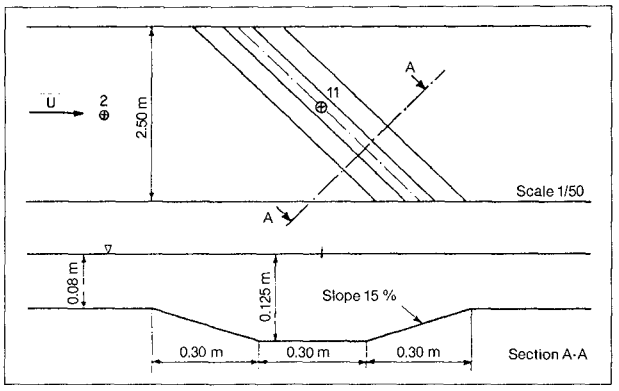

Fig. 3 - Prismatic channel.

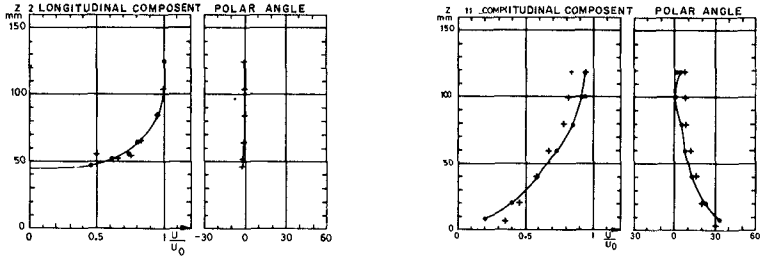

Fig. 4 - Vertical velocity profiles.

The value of constant k is small (k = 0,12) compared with value (k = 0,41) generally adopted. That probably comes from a low level of the turbulence in the flume (see [2], [4]).

With this tested value, the measured and predicted velocity profiles are rather similar as illustrated for point 11 situated in the center of the channel (fig. 4).

An important error appears between measured and predicted velocities at points near vertical wall along the flume. In fact near the walls, the numerical model does not take into account the effects of boundary layer.

With a non slip condition at the bed, the bottom stresses are not accurate enough to calculate the resulting sediment transport. Another computation was done with a condition of slip on bottom but with a Karman constant k = 0,41, a first mesh of 0,75 mm and a roughness of 0,3 mm. In that case the bed shear stress pattern obtained is more satisfying (see fig. 5). The knowledge of bed shear stresses permits to estimate bed transport using Meyer-Peter and Müller relation.

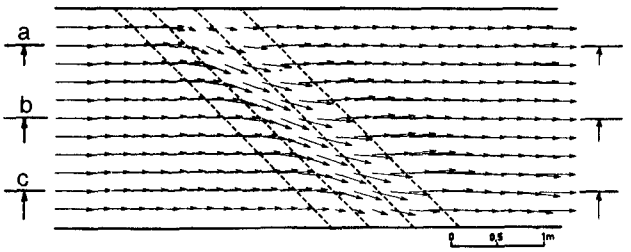

Fig. 5 - Bottom stresses before evolution.

Then, the bottom evolution is computed from the equation of conservation of sediment. The two computations are coupled. A bottom evolution changes the current pattern and the bottom stresses, which induce new bottom evolution. In order to take into account the difference of time scales between bottom and current evolutions, the current pattern is not re-computed at each time step of bottom evolution but after a time inducing significant changements (currently 900 time steps).

The predicted channel evolution is qualitatively quite satisfying. The accretion is greater on left upstream side, which is normal because the right side is more supplied by the cross flow from the channel. On the other hand the erosion is more important on the right side (fig. 6 et 7.).

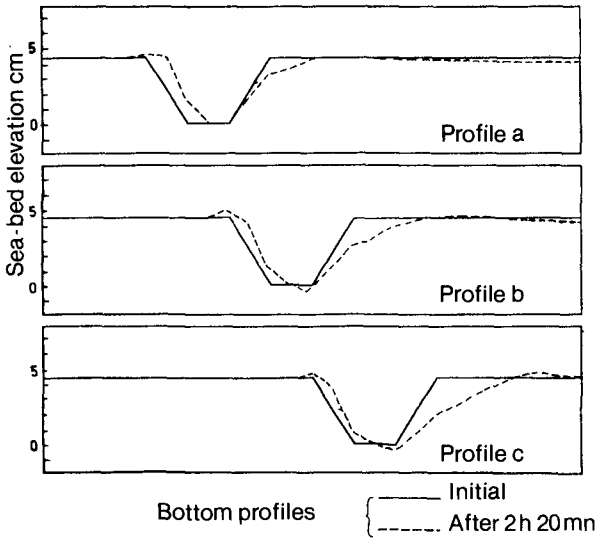

fig. 6 - Bottom profiles.

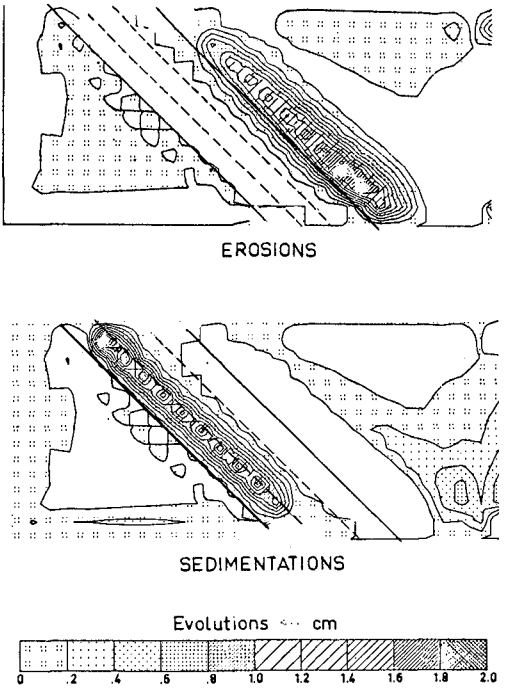

Fig. 7 - Evolutions (cm) after 2h 20 mn.

Tidal current computations

The model was successfully applied in estuaries and coastal areas in France for the computation of tidal and wind generated currents (fig. 8). At first, a study of tidal flow pattern in navigation channel of Verdon Harbour in Gironde was realized (model 1 of fig. 8). On the boundaries, the mass currents were obtained through a two-dimensional computation. In order to correctly represent the bathymetry, the grid size was fixed equal to 300 m. The area is included in a rectangle of 10 x 15 km, and is discretized by 36 x 51 horizontal points, and 15 points over the depth, the depth varies from 5 to 30 m. The time step is 120 s. One tide requires 40 mn of computer time on the CRAY ONE computer. The chosen tide is a mean spring tide (coefficient 95). The flow pattern was established after one tide and the results of the 2nd tide are compared to those obtained by a bidimensional model and measurement.Generally, a good agreement is obtained between predicted and measured velocities (see ref. [3]).

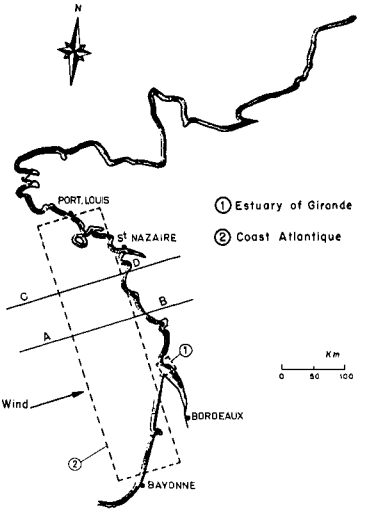

Fig. 8 - Coastal area model.

During flood tide and ebb-tide the flow is in the direction of channel axis and the bathymetry has no influence upon direction of flow near sea bed. At the end of the ebb-tide (low tide fig. 9) we observe a difference of head between sea bed and surface water, specially in the northern part of the channel submitted to a cross flow, at this moment of the tide. Likewise at the end of flood (high tide fig. 10), it is in the Northern and Central part that the differences are most important.

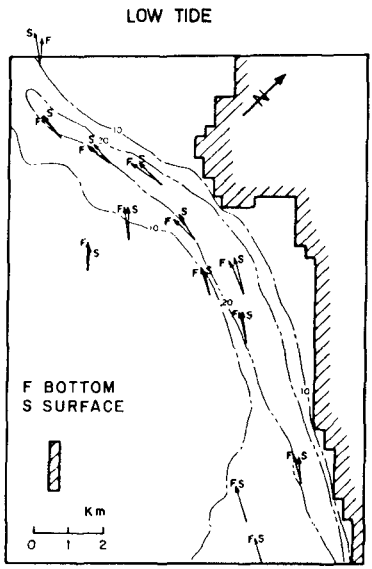

Fig. 9 - Currents at sea bed and free surface.

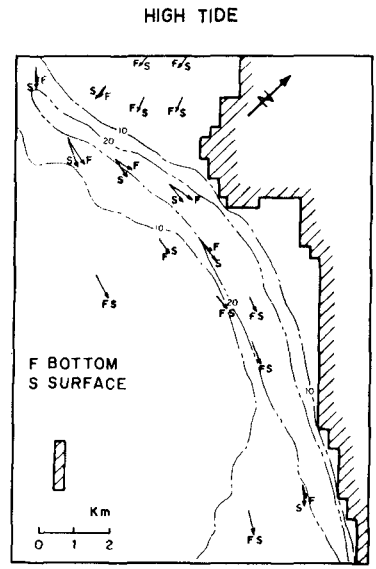

Fig. 10 - Currents at sea bed and free surface.

The present model has also been used to study wind induced circulation patterns on Atlantic French coast (model 2 on fig. 8). On the boundaries, the mass currents has been obtained through a two-dimensional computation of larger scale. At sea bed we have a no-slip condition with zero velocities. In order to simplify the 3D problem, the Atlantic has been schematically represented by a rectangle of 110 x 460 km. (see fig. 11). The bathymetry used is presented in fig. 12. In the in-coast areas, a schematic regular bottom shape has been introduced. The depth varies from 140 m to 10 m near coasts. There is a very deep region (500 m) in open sea in front of Gironde estuary. On the vertical axis the depth was divided into 23 elements of different length. The smallest are near bed and near free surface. The first grid size near the bed is 0,3 % of the depth and the last near free surface is 0,1 %.

The horizontal grid size is 10 km. On the whole area, there are 13500 points.

The time step is 120 s. A tide requires 1200 s of computer time on the Cray 1 computer. The computations of tide were made without or with a wind of 22 m/s parallel to Ox direction.

The shear stress induced at sea surface by wind is calculated with a coefficient CD = 0,9 10^{-3} if wind speed is smaller than 10 m/s, and CD = 2,9 10^{-3} if wind speed is greater than 10 m/s. The sudden change of value of CD is subjected by different behaviour of wind suddenly transformed at this speed of 10 m/s.

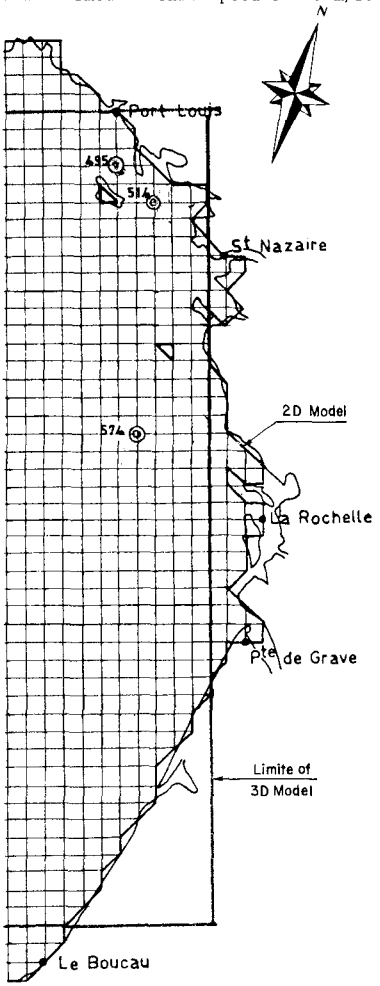

Fig. 11 - Area of coast Atlantic.

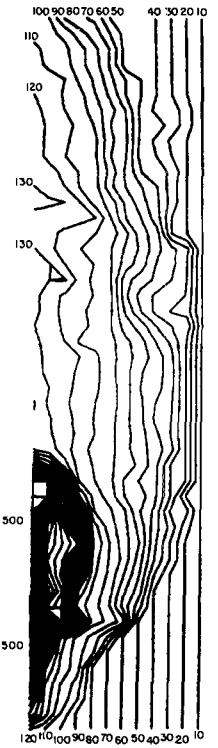

Fig. 12 - Bathymetry of 3D model

Without wind the results are in good agreement with field measurements and with two-dimensional computations particularly on tide level.
The circulation pattern is very modified by a prevailing western wind.
The flow pattern is influenced not only near surface where a large velocity is established but also near the bed. The velocity induced at surface is about 3,5 % of wind speed. The different directions between surface and bottom create a vertical circulation of water.
It is important at the ebb tide when wind is in reverse direction.
The depth of the reverse points is a function of depth flow (fig. 13).
Preliminary studies on only one vertical axis (solution of Ekman's equation in one point) seem to show that it is possible to discouple in that case the calculation of a tidal action from the one of wind, since the predicted velocities induced by coupled tide and wind are nearly equal to the addition of separate action of wind and tide. In the whole area, the results showed that the velocities induced near surface can also be computed separately. The error is 3 % of surface velocity.
However in the average mass currents calculated for a tide of period T by

$$\bar{u}_m = \frac{1}{T} \int_{t = to}^{t = to + T} u\,dt$$

are a few differences between coupled or separated action of wind and tide. In fact the velocities induced into the depth are different even if the surface velocities are the same. (fig. 14)

CONCLUSION

We have presented in this paper a numerical three-dimensional hydrostatic model and different applications. The turbulent effects are simply taken into account by an eddy viscosity. This model was successfully tested against laboratory flume data, then was applied in studies where three-dimensional effects were very important : navigation channel and wind-induced currents. This numerical model which gives velocity profiles over the depth and induced bottom stresses for tidal and wind generated flows is an important tool for a large range of studies : sea-surface, pollution transport, dispersion of a polluant in the water column (where vertical velocity profiles are fundamental), transport of sediment near the bottom, etc...

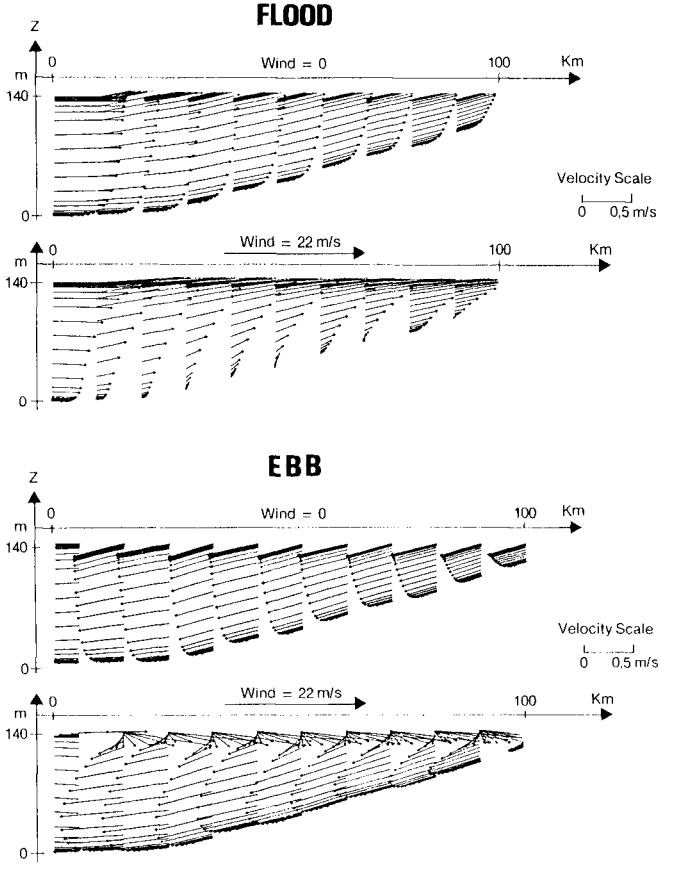

Fig. 13 - Vertical flow pattern in section CD.

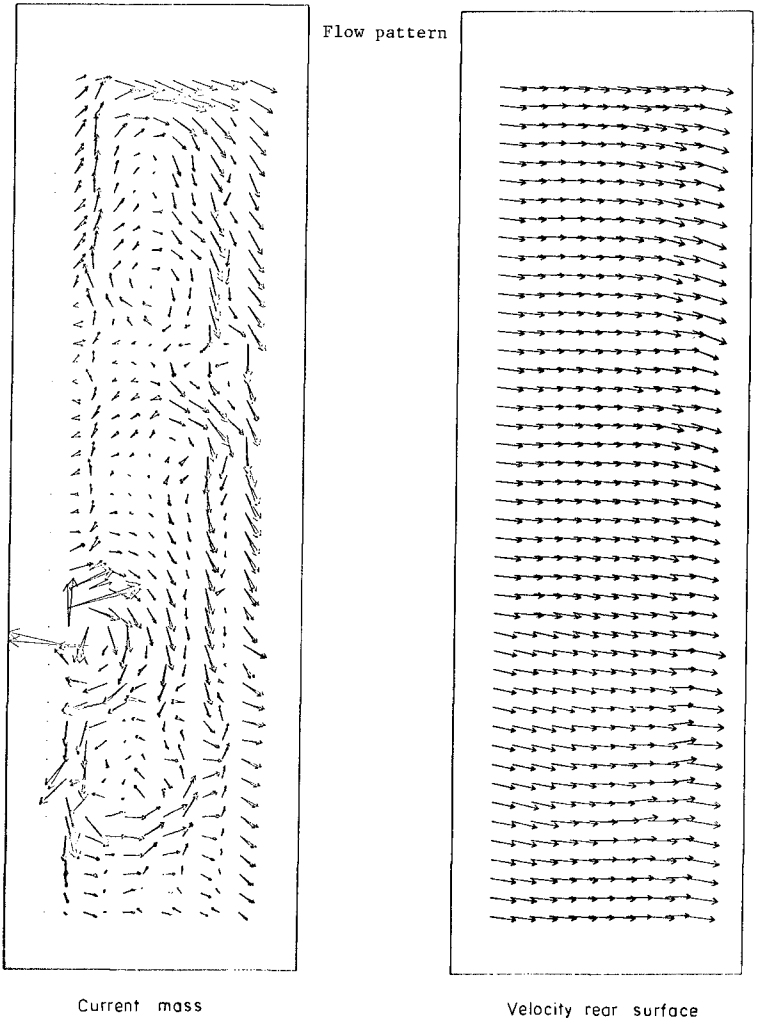

Fig. 14 - Comparison flow pattern.

REFERENCES

[1] J.P. Benqué, A. Hauguel, P.L. Viollet.
Engineering applications of computational hydraulics - volume II
Pitman

[2] M.C. Burg, Ph. Dewagenaere.
Courantologie dans les chenaux de navigation.
Rapport EDF HE041.78.15.

[3] M.C. Burg, A. Warluzel.
Extension du code chenaux à un cas général : application à
l'estuaire de la Gironde.
Rapport EDF HE041/80/19.

[4] A. Warluzel, M.C. Burg.
Chenaux de navigation.
Rapport EDF HE041/79/22.

COMPUTATION OF PARTICLE PATHS USING THE LAGRANGIAN LONG WAVE EQUATIONS

M. A. Savoie[1] and J. van de Kreeke[2]

0. ABSTRACT

The Lagrangian long wave equations and the Lagrangian expressions for stress and strain are derived. Retaining the dominant terms the long wave equations are solved using an explicit finite difference method.

Using the numerical solution, particle paths are computed for the tidal motion in a basin connected to the ocean by a single inlet. At the open boundary particle displacements are described. Computations are carried out with snd without the Coriolis force and for linear and nonlinear bottom friction.

1. INTRODUCTION

With regard to the physical oceanography of estuaries and lagoons, the coastal engineer's interest traditionally has been with current velocities and tide levels. Only recently as a result of the development of water quality models knowledge of water particle trajectories have become important. The current method of computing particle trajectories is to first solve for the Eulerian velocity field and then to calculate the successive particle positions by numerical integration and interpolation.

This paper illustrates the calculation of particle paths by integrating the Lagrangian form of the long wave equations. The Lagrangian long wave equations describe the particle position as a function of its original particle position and time, whereas the Eulerian equations describe the velocity (flow) at a fixed position in space. In addition to the particle trajectories, the Lagrangian long wave equations yield the water level and depth associated with a traveling parcel of water.

The Lagrangian equations are often overlooked because of the severe nonlinearity of some of the terms, the difficulty in calibrating and verifying the results and the lack of appropriate boundary conditions. Nevertheless the technique has been successfully applied to 2-D vertical fluid flow problems.

---

[1] Oceanographer, Kinnetic Laboratories, 519 W. 8th Ave., Anchorage, Alaska 99501

[2] Professor, Dept. of Ocean Engineering, RSMAS, University of Mimai, 4600 Rickenbacker Causeway, Miami, Fla. 33149

The general three-dimensional Lagrangian form of the Navier-Stokes equations can be found in various text books, e.g. Lamb [1932]. Neumann and Pierson [1966], Defant [1961] etc. Because a literature search revealed no previous studies aimed at specifically developing the Lagrangian form of the two-dimensional horizontal long wave equations a rather detailed derivation of these equations together with a derivation of the expressions for strain and stress is presented. Wherever possible, equations are derived starting from physical principles rather than applying a straight transformation from Eulerian to Lagrangian variables.

Past work utilizing the Lagrangian form of the fluid flow equations has been mainly in the area of surface gravity waves. Miche [1944] uses a perturbation technique to solve the Lagrangian equations for first and second order surface gravity waves. To a first order of approximation his results yield a wave profile similar to Gerstner's trochoidal wave, whereas in the Eulerian system this isn't possible until the third order of approximation. Goto [1979] and Shuto and Goto [1978] numerically computed tsunami run-up using the nonlinear 1-D long wave equations. In the equations bottom friction and viscosity was neglected. Brennen [1970] and Brennen and Whitney [1970] present a numerical solution to the problem of unsteady free surface gravity waves using the 2-D vertical Lagrangian equations.

Other studies of interest utilizing the Lagrangian equations are mainly in the field of turbulence, Pierson [1962], and the related problems of stirring, mixing and dispersion.

2. THE MOTION OF A FLUID ELEMENT; STRESS AND STRAIN

2.1 Coordinate System

Considered is a fixed Cartesian coordinate system x, y, z. The position of a particle is designated $s(a,b,c,t)$, $p(a,b,c,t)$ and $r(a,b,c,t)$ where s, p and r, and a, b and c are measured in respectively the x, y and z direction. $(a,b,c,0)$ represents the original position of the particle. In some instances it is convenient to use the particle positions $s'(a,b,c,t)$, $p'(a,b,c,t)$ and $r'(a,b,c,t)$ where $s' = s-a$, $p' = p-b$ and $r' = r-c$. The original position of the particle is then $s' = 0$, $p' = 0$ and $r' = 0$.

In the following only planar motion in the x, y plane will be considered.

2.2 Fluid Deformation

A fluid element subject to stresses undergoes deformation. For a rectangular element the deformation after a time Δt is shown in Fig. 1. In general the deformation is a combination of normal strains, shear strains and rotation.

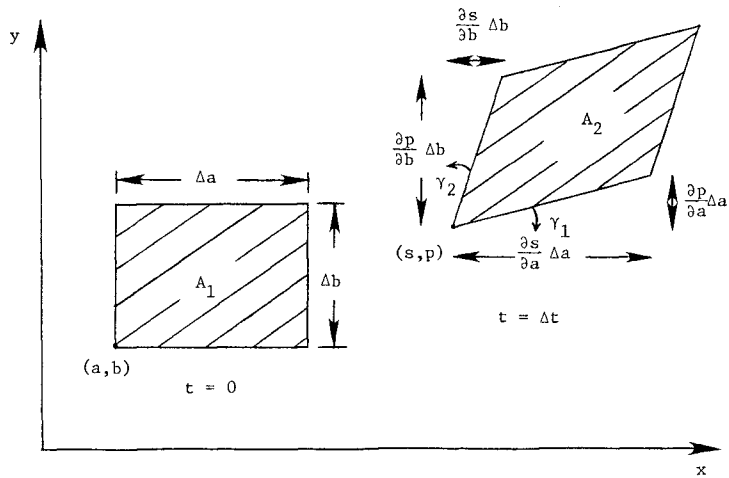

Figure 1. Deformation of a Fluid Element

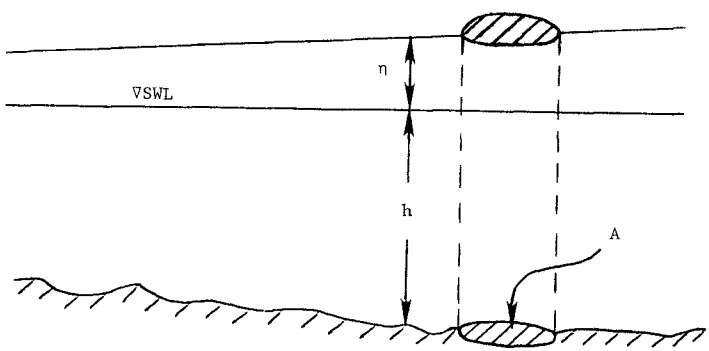

Figure 2. Cylinder of Fluid Extending from Free Surface η to the Bottom -h.

The position of the lower left hand corner of the element is designated s(a,b,t) and p(a,b,t).

2.3 Normal Strain

Normal Strain is defined as the change in length of a fluid element divided by its initial length. Accordingly, normal strain in the x direction is given by

$$\varepsilon_x\,(a,b,t) = \lim_{\substack{\Delta t \to o \\ \Delta a \to o}} \frac{\left.\frac{\partial s}{\partial a}\right|^{t+\Delta t} \Delta a \;-\; \Delta a}{\Delta a}$$

and thus

$$\varepsilon_x = \frac{\partial s}{\partial a} - 1 \tag{2.1}$$

similarly

$$\varepsilon_y = \frac{\partial p}{\partial b} - 1 \tag{2.2}$$

By convention an increase in length corresponds to a positive normal strain.

2.4 Shear Strain

Shear Strain is defined as the change in angle between two originally perpendicular lines as the element deforms. Referring to Fig. 1, for small deformations

$$\gamma_1 = \frac{\dfrac{\partial p}{\partial a}}{\dfrac{\partial s}{\partial a}} \simeq \frac{\partial p}{\partial a} \quad \text{since} \quad \frac{\partial s}{\partial a} = 1 + \varepsilon_x \simeq 1$$

similarly

$$\gamma_2 = \frac{\dfrac{\partial s}{\partial b}}{\dfrac{\partial p}{\partial b}} \simeq \frac{\partial s}{\partial b}$$

and thus the shear strain is

$$\gamma_{xy} = \gamma_1 + \gamma_2 = \frac{\partial p}{\partial a} + \frac{\partial s}{\partial b} \tag{2.3}$$

Shear strain is positive for a decrease in the angle between two originally perpendicular line elements.

2.5 Rotation

Rotation is defined as $\gamma_1 - \gamma_2$. Counter-clockwise rotation is taken as positive. Accordingly for small deformations the rotation in the x-y plane may be written as

$$\Theta_{xy} = \gamma_1 - \gamma_2 = \frac{\partial p}{\partial a} - \frac{\partial s}{\partial b} \tag{2.4}$$

2.6 Normal Stress

Water can be considered a Newtonian fluid where the stresses are linearly related to the time rate of strain, rather than to the strain itself as in elastic solids. Assuming an incompressible fluid, the normal stresses in the x direction are given by

$$\sigma_x = \bar{\sigma} + 2\mu \frac{\partial \epsilon_x}{\partial t} \tag{2.5}$$

where $\bar{\sigma}$ is the mean normal stress and μ is the dynamic viscosity coefficient. Based on experiments with incompressible fluids Daily and Harleman [1966], the mean normal stress $\bar{\sigma}$ is just the pressure as given below.

$$\bar{\sigma} = \frac{1}{3}(\sigma_x + \sigma_y + \sigma_z) = -p \tag{2.6}$$

Substituting for the mean normal stress in Eq. (2.5) and makinhg use of Eq. (2.1)

$$\sigma_x = -p + 2\mu \frac{\partial}{\partial a}\left(\frac{\partial s}{\partial t}\right) \tag{2.7}$$

similarly

$$\sigma_y = -p + 2\mu \frac{\partial}{\partial b}\left(\frac{\partial p}{\partial t}\right) \tag{2.8}$$

2.7 Shear Stress

The shear stress is linearly related to the time rate of change of the shear strain in the fluid.

$$\tau_{xz} = \tau_{yx} = \mu \frac{\partial}{\partial t}(\gamma_{xy}) \tag{2.9}$$

Substituting for the shear strain in Eq. (2.9) yields the shear stress

$$\tau_{xy} = \mu \frac{\partial}{\partial t}\left(\frac{\partial p}{\partial a} + \frac{\partial s}{\partial b}\right) \tag{2.10}$$

2.8 Vorticity

Vorticity is related to the time rate of change of rotation as follows.

$$\zeta = \frac{1}{2} \frac{\partial}{\partial t} (\Theta_{xy}) \tag{2.11}$$

Substituting the expression for rotation, the vorticity is

$$\zeta = \frac{1}{2} \frac{\partial}{\partial t} \left(\frac{\partial p}{\partial a} - \frac{\partial s}{\partial b}\right) \tag{2.12}$$

which is one half times the curl of the Lagrangian velocity vector.

3. CONSERVATION EQUATIONS

3.1 General Mathematical Relations

When mapping a region A_2 in the sp-plane into a region A_1 in the ab-plane (see Fig. 1), the Jacobian operator is

$$J = \frac{\partial(s,p)}{\partial(a,b)} = \begin{vmatrix} \frac{\partial s}{\partial a} & \frac{\partial p}{\partial a} \\ \frac{\partial s}{\partial b} & \frac{\partial p}{\partial b} \end{vmatrix} \tag{3.1}$$

The Jacobian operator is used when transforming double integrals from one coordinate system to another. Referring to Fig. 1,

$$\int_{A_2} F(s,p)dsdp = \int_{A_1} F[s(a,b,t), p(a,b,t)]\, J\, dadb \tag{3.2}$$

where F is an arbitrary function. For a geometric interpretation of the Jacobian set F = 1. The left hand side of Eq. (3.2) represents the area A_2, which can be expressed as the magnitude of the cross product of the vectors representing two adjoining sides.

$$A_2 = \left| \left(\frac{\partial s}{\partial a} \Delta a \hat{i} + \frac{\partial p}{\partial a} \Delta a \hat{j}\right) \times \left(\frac{\partial s}{\partial b} \Delta b \hat{i} + \frac{\partial p}{\partial b} \Delta b \hat{j}\right) \right|$$

which reduces to

$$A_2 = J\, A_1 \tag{3.3}$$

Other mathematical relations that will be used in the derivation of the conservation equations are the Lagrangina Del operator (∇_h) and the Lagrangian Laplacian (∇_h^2). The subscript h designates a 2-D horizontal operation. In the s-p system the Del operator is written as

$$\nabla_h = \frac{\partial}{\partial s}\hat{i} + \frac{\partial}{\partial p}\hat{j} \tag{3.4}$$

A direct transformation from the s-p space to the a-b space will be employed to find the Del operator in Lagrangian coordinates. The partial derivatives $\partial/\partial a$ and $\partial/\partial b$ are

$$\frac{\partial}{\partial a} = \frac{\partial}{\partial s}\frac{\partial}{\partial a} + \frac{\partial p}{\partial a}\frac{\partial}{\partial p} \tag{3.5}$$

$$\frac{\partial}{\partial b} = \frac{\partial s}{\partial b}\frac{\partial}{\partial s} + \frac{\partial p}{\partial b}\frac{\partial}{\partial p} \tag{3.6}$$

Equations (3.5) and (3.6) are solved for the partials $\partial/\partial s$ and $\partial/\partial p$

$$\frac{\partial}{\partial s} = \frac{\begin{vmatrix} \frac{\partial}{\partial a} & \frac{\partial p}{\partial a} \\ \frac{\partial}{\partial b} & \frac{\partial p}{\partial b} \end{vmatrix}}{\begin{vmatrix} \frac{\partial s}{\partial a} & \frac{\partial p}{\partial a} \\ \frac{\partial s}{\partial b} & \frac{\partial p}{\partial b} \end{vmatrix}} = \frac{\partial(\ ,p)}{\partial(a,b)}\ \frac{1}{J} \tag{3.7}$$

similarly

$$\frac{\partial}{\partial p} = \frac{\partial(s,\ )}{\partial(a,b)}\ \frac{1}{J} \tag{3.8}$$

Substituting Eqs. (3.7) and (3.8) into Eq. (3.4), the Lagrangian Del operator is obtained

$$\nabla_h = \left[\frac{\partial(\ ,p)}{\partial(a,b,)}\hat{i} + \frac{\partial(s,\ )}{\partial(a,b)}\hat{j}\right]\frac{1}{J} \tag{3.9}$$

The derivation of the Lagrangian Laplacian operator follows along the same lines as the Del operator and yields

$$\nabla_h^2 = \frac{\partial[\frac{\partial(\ ,p)}{\partial(a,b)}\frac{1}{J},\ p]}{\partial(a,b)} + \frac{\partial[s,\ \frac{\partial(s,\ )}{\partial(a,b)}\frac{1}{J}]}{\partial(a,b)}\ \frac{1}{J} \tag{3.10}$$

The Laplacian becomes highly nonlinear when converted to Lagrangian coordinates. A similar 3-D expression for the Lagrangian Laplacian operator is presented in Pierson [1962].

In deriving the conservation equations use will be made of the Reynolds' or Kinematic transport theorem. This theorem expresses the rate of change of a property moving with a body of fluid.

Let s(a,b,c,t), p(a,b,c,t) and r(a,b,c,t) be the coordinates of a fluid particle, where a, b and c are the coordinates of the original position. V is the volume of the fluid body under consideration. Take F(s,p,r,t) to be any function representing for example momentum or constituent concentration, and introduce the volume integral G(s,p,r,t).

$$G(s,p,r,t) = \iiint_V F(s,p,r,t)\, dsdpdr \tag{3.11}$$

The Reynolds' transport theorem is used in order to find the change in G with time, that is the total derivative dG/dt.

$$\frac{dG}{dt} = \frac{d}{dt} \iiint_V F(s,p,r,t)dsdpdr \tag{3.12}$$

Since the volume is deforming with time, the order of integration and differentiation cannot be interchanged. Making use of the 3-D equivalent of Eq. (3.1), it follows from Eq. (3.12)

$$\frac{dG}{dt} = \frac{d}{dt} \iiint_{V_o} F[s(a,b,c,t),p(a,b,c,t),r(a,b,c,t),t]\, Jdadbdc \tag{3.13}$$

V_o is the volume at t = 0. Because V_o is constant, the order of integration and differentiation can be interchanged.

$$\frac{dG}{dt} = \iiint_{V_o} \frac{d}{dt} (FJ)dadbdc = \iiint_{V_o} (\frac{dF}{dt} J + F \frac{dJ}{dt})dadbdc \tag{3.14}$$

It can be shown, Aris [1962] pp. 84, that

$$\frac{dJ}{dt} = [\nabla.(\frac{\partial s}{\partial t} \hat{i} + \frac{\partial p}{\partial t} \hat{j} + \frac{\partial r}{\partial t} \hat{k})]J \tag{3.15}$$

where the Del operator is the 3-D equivalent of ∇_h in Eq. (3.9). Substituting Eq. (3.15) in Eq. (3.14) yields the Reynolds' transport theorem.

$$\frac{dG}{dt} = \frac{d}{dt} \iiint_V F dsdpdr = \iiint_{V_o} [\frac{dF}{dt} + F\nabla.(\frac{\partial s}{\partial t} \hat{i} + \frac{\partial p}{\partial t} \hat{j} + \frac{\partial r}{\partial t} \hat{k})]Jdadbdc \tag{3.16}$$

where $\partial s/\partial t$, $\partial p/\partial t$ and $\partial r/\partial t$ are the particle velocities in respectively the x, y and z directions. This result will be used repeatedly in the derivation of the conservation equations. For further reference on the Reynolds' transport theorem see Aris [1962].

3.2 Basic Assumptions

In deriving the Lagrangian form of the long wave equations the

following basic assumptions will be employed.

1) Incompressible homogeneous fluid

2) Hydrostatic pressure, i.e. $\partial^2 r/\partial t^2 << g$

3) Vertical variations in horizontal velocity are negligible, i.e. planar motion

3.3 Conservation of Mass; Continuity

Consider a cylinder with volume V moving with the fluid and consisting of the same fluid particles. The surface and bottom of the cylinder are respectively $\eta(s,p,t)$ and $h(s,p)$. η and h are measured from the Still Water Level. From the assumption of planar motion it follows that the cylinder remains a cylinder even though the horizontal cross-section is allowed to deform; see Fig. 2.

Continuity implies that when moving with the fluid the volume of the cylinder remains the same.

$$V = \iint_A (h+\eta)dsdp = \text{constant} \tag{3.17}$$

where A is the cross-sectional area of the cylinder. The change in volume with time is zero. Making use of the 2-dimensional form of the Reynolds' transport theorem, Eq. (3.16), with $F = h+\eta$.

$$\frac{dV}{dt} = \iint_{A_0} \left\{ \frac{d(h+\eta)}{dt} + (h+\eta)\left[\nabla_h \cdot \left(\frac{\partial s}{\partial t}\hat{i} + \frac{\partial p}{\partial p}\hat{j}\right)\right] \right\} Jdadb = 0 \tag{3.18}$$

Because A_0 is an arbitrary area the integrand must be equal to zero. From this and Eq. (3.15) it follows

$$\frac{d}{dt}\left[(h+\eta)J\right] = 0 \tag{3.19}$$

When integraing Eq.(3.19) with respect to time from t = 0 to some later time t, the condition of continuity can be written in the form.

$$[h(a,b,t) + \eta(a,b,t)]\, J = h(a,b,0) + \eta(a,b,0) \tag{3.20}$$

It is noted that for 3-D and 2-D vertical incompressible fluid motion the continuity equation is simply J = 1, Lamb [1932], Neuman and Pierson [1966], Defant [1961], Miche [1944], Goto [1979] and Shuto and Goto [1978], where J is respectively the 3-D and 2-D equivalent of Eq. (3.1).

3.4 Conservation of Momentum; Equations of Motion

The rate of change of momentum within a material volume (cylinder) moving with the fluid equals the sum of the external forces. For the

momentum equation in the x-direction.

$$\frac{d}{dt} \iint_A \rho \frac{\partial s}{\partial t} (h+\eta) ds dp = \Sigma F_x \tag{3.21}$$

Using the 2-dimensional form of the Reynolds' transport theorem, Eq. (3.16), with F replaced by $\rho(h+\eta)\ \partial s/\partial t$.

$$\frac{d}{dt} \iint_A \rho \frac{\partial s}{\partial t} (h+\eta) ds dp = \iint_{A_o} \rho(h+\eta) \frac{\partial^2 s}{\partial t^2} J da db \tag{3.22}$$

The external forces acting on the cylinder consist of the surface forces (F_s) i.e. pressure and internal stresses, bottom shear stress (F_b) and Coriolis Force (F_C). Shear stress and horizontal gradients of the normal stress at the free surface, i.e. wind stress and atmospheric pressure respectively are assumed to be zero. In the following each of the external forcing terms will be discussed separately.

The total force associated with the pressure and internal stresses in the x-direction is given by the line integral

$$F_s = \oint [\sigma_x^* dp - \tau_{xy}^* ds] \tag{3.23}$$

in which

$$\sigma_x^* = \int_{-h}^{\eta} \sigma_x dr \text{ and } \tau_{xy}^* = \int_{-h}^{\eta} \tau_{xy} dr$$

The line integral is along the intersection of the cylinder and a horizontal plane. Green's theorem in the plane may be applied to Eq. (3.23) to transform the line integral into a double integral

$$F_s = \iint_A [\frac{\partial \sigma_x^*}{\partial s} + \frac{\partial \tau_{xy}^*}{\partial p}] ds dp \tag{3.24}$$

where as before A is the cross-sectional area of the cylinder. Substituting the expressions for σ_x^* and τ_{xy}^*

$$F_s = \iint_A [\frac{\partial \int_{-h}^{\eta} \sigma_x dr}{\partial s} + \frac{\partial \int_{-h}^{\eta} \tau_{xy} dr}{\partial p}] ds dp \tag{3.25}$$

The normal stress σ_x is composed of pressure and normal stresses associated with deformations. Considering the contribution of the

pressure only, Eq. (3.25) reduces to

$$F_{s1} = \iint_A \frac{\partial \int_{-h}^{\eta} -p \, dr}{\partial s} \, dsdp \tag{3.26}$$

(note the difference between the notation p for pressure and p for particle displacement in the y direction). The subscript 1 refers to the contribution of pressure to the surface force term in the x-direction. Transforming to the a-b space and making use of Eq. (3.7)

$$F_{s1} = \iint_{A_o} \left[\frac{\partial \int_{-h}^{\eta} p \, dr}{\partial a} \frac{\partial p}{\partial b} - \frac{\partial \int_{-h}^{\eta} p \, dr}{\partial b} \frac{\partial p}{\partial a}\right] dadb \tag{3.27}$$

From the assumption of hydrostatic pressure $p = \rho g r + \rho g \eta$, the pressure may be vertically integrated to yield

$$\int_{-h}^{\eta} p \, dr = \frac{1}{2} \rho g \, (h+\eta)^2 \tag{3.28}$$

Substituting in the expression for F_{s1}, the pressure force is obtained

$$F_{s1} = - \iint_{A_o} \rho g (h+\eta) \left[\frac{\partial(h+\eta)}{\partial a} \frac{\partial p}{\partial b} - \frac{\partial(h+\eta)}{\partial b} \frac{\partial p}{\partial a}\right] dadb$$

$$= \iint_{A_o} \rho g (h+\eta) \frac{\partial(h+\eta, p)}{\partial(a,b)} \, dadb \tag{3.29}$$

An attempt was made to evaluate the contribution of the viscous stresses, F_{s2}, by substituting in Eq. (3.14) the Lagrangian formulation for the normal stress σ_* and shear stress τ_{xy} respectively Eqs. (2.7) and (2.10). This resulted in a long and cumbersome expression. In order to arrive at a simpler and manageable result a direct transformation from Eulerian to Lagrangian variables is applied. Noting that f(s,p,t) is equivalent to f(x,y,t), the Eulerian expressions for the normal and shear stresses (Daily and Harleman [1966] pp. 102-104) can be written as

$$\sigma_* = 2\mu \frac{\partial(\frac{\partial s}{\partial t})}{\partial s} - p$$

$$\tau_{xy} = \mu[\frac{\partial(\frac{\partial s}{\partial t})}{\partial p} + \frac{\partial(\frac{\partial p}{\partial t})}{\partial s}]$$

Neglecting the pressure part of the normal stress term since it has already been accounted for, and substituting the expressions for the stresses in Eq. (3.25) yields

$$F_{s2} = \iint_A \left\{ 2\mu \frac{\partial[(h+\eta)\frac{\partial(\frac{\partial s}{\partial t})}{\partial s}]}{\partial s} + \mu \frac{\partial[(h+\eta)\frac{\partial(\frac{\partial s}{\partial t})}{\partial p}]}{\partial p} \right.$$

$$\left. + \mu \frac{\partial[(h+\eta)\frac{\partial(\frac{\partial p}{\partial t})}{\partial s}]}{\partial p} \right\} dsdp \qquad (3.30)$$

or, when rearranging

$$F_{s2} = \iint_A \left\{ \mu(h+\eta)\left[\frac{\partial^2(\frac{\partial s}{\partial t})}{\partial s^2} + \frac{\partial^2(\frac{\partial s}{\partial t})}{\partial p^2}\right] + 2\mu \frac{\partial(h+\eta)}{\partial s}\frac{\partial(\frac{\partial s}{\partial t})}{\partial s} \right.$$

(small)

$$+ \mu \frac{\partial(h+\eta)}{\partial p}\frac{\partial(\frac{\partial s}{\partial t})}{\partial p} + \mu \frac{\partial(h+\eta)}{\partial p}\frac{\partial(\frac{\partial p}{\partial t})}{\partial s}$$

(small) (small)

$$\left. + \mu(h+\mu)\frac{\partial}{\partial s}\left[\frac{\partial(\frac{\partial s}{\partial t})}{\partial s} + \frac{\partial(\frac{\partial p}{\partial t})}{\partial p}\right] \right\} dsdp \qquad (3.31)$$

$= 0$ (continuity)

If typical values are taken for the particle velocities in long waves $[\partial s/\partial t = \eta\sqrt{g/h}\sin(k_x s + k_y p - \omega t)]$, it can be shown that the first term on the righthand side of Eq. (3.31) is the dominant term.

Thus,

$$F_{s2} = \iint_A \mu(h+\eta)\,\nabla_h^2(\frac{\partial s}{\partial t})\,dsdp \qquad (3.32)$$

Transforming to the a-b space

$$F_{s2} = \iint_{A_o} \mu(h+\eta) \nabla_h^2 \left(\frac{\partial s}{\partial t}\right) \mathrm{J}\,da\,db \tag{3.33}$$

In the case of turbulent motion the coefficient of dynamic viscosity, μ, is replaced by the eddy viscosity or momentum transfer coefficient A_h.

In addition to stresses on the cylinder wall, the bottom of the cylinder is subjected to a shear stress. In general, the horizontal components of this stress are taken proportional to the square of the velocity. E.g. in the x-direction

$$\tau_{xz} = \rho F \frac{\partial s}{\partial t} \sqrt{\left(\frac{\partial s}{\partial t}\right)^2 + \left(\frac{\partial p}{\partial t}\right)^2}$$

where F is the friction coefficient. Integrating over the cross-section of the control volume, the bottom frictional force is

$$F_b = - \iint_{A_o} \rho F \frac{\partial s}{\partial t} \sqrt{\left(\frac{\partial s}{\partial t}\right)^2 + \left(\frac{\partial p}{\partial t}\right)^2}\ \mathrm{J}\,da\,db \tag{3.34}$$

Sometimes the bottom stress is taken proportional to the velocity. In that case, the expression corresponding to Eq. (3.34) is

$$F_b = - \iint_{A_o} \rho F_\ell \frac{\partial s}{\partial t}\ \mathrm{J}\,da\,db \tag{3.35}$$

where F_ℓ is the linear bottom friction coefficient.

Assuming the vertical velocities to be small compared to horizontal velocities the Coriolis force per unit volume can be written as

$$\rho f \frac{\partial p}{\partial t} \qquad \text{x-direction}$$

$$-\ \rho f \frac{\partial s}{\partial t} \qquad \text{y-direction}$$

where $f = 2\Omega \sin \phi$

Ω = angular velocity of earth

ϕ = latitude

Integrating the Coriolis force over the volume of the cylinder, the force acting on the control volume in the x-direction is

$$F_{cx} = \iint_{A_o} \rho(h+\eta)\ f \frac{\partial p}{\partial t}\ \mathrm{J}\,da\,db \tag{3.36}$$

Similarly for the Coriolis force in the y-direction

$$F_{cy} = - \iint_{A_o} \rho(h+\eta)\, f\, \frac{\partial s}{\partial t}\, J\,da\,db \tag{3.37}$$

Equating the rate of change of momentum and the external forces for the x-direction, omitting the integral signs (this is justified because the integration is over an arbitrary area) and dividing by $\rho(h+\eta)$ yields

$$\left[\frac{\partial^2 s}{\partial t^2} + \frac{F}{h+\eta}\,\frac{\partial s}{\partial t}\sqrt{\left(\frac{\partial s}{\partial t}\right)^2 + \left(\frac{\partial p}{\partial t}\right)^2} - f\,\frac{\partial p}{\partial t} - \frac{A_h}{\rho}\,\nabla_h^2\left(\frac{\partial s}{\partial t}\right)\right] J = - g\,\frac{\partial(h+\eta,\ p)}{\partial(a,b)} \tag{3.38}$$

This is the Lagrangian conservation of momentum equation for long waves in the x-direction. Similarly for the y-direction

$$\left[\frac{\partial^2 p}{\partial t^2} + \frac{F}{h+\eta}\,\frac{\partial p}{\partial t}\sqrt{\left(\frac{\partial s}{\partial t}\right)^2 + \left(\frac{\partial p}{\partial t}\right)^2} + f\,\frac{\partial s}{\partial t} - \frac{A_h}{\rho}\,\nabla_h^2\left(\frac{\partial p}{\partial t}\right)\right] J = - g\,\frac{\partial(s,\ h+\eta)}{\partial(a,b)} \tag{3.39}$$

An alternate form of the Lagrangian equation of motion is obtained by multiplying Eq. (3.38) by $\partial s/\partial a$ and Eq. (3.39) by $\partial p/\partial a$. This yields

$$\left[\frac{\partial^2 s}{\partial t^2} + \frac{F}{h+\eta}\,\frac{\partial s}{\partial t}\sqrt{\left(\frac{\partial s}{\partial t}\right)^2 + \left(\frac{\partial p}{\partial t}\right)^2} - f\,\frac{\partial p}{\partial t} - \frac{A_h}{\rho}\,\nabla_h^2\left(\frac{\partial s}{\partial t}\right)\right]\frac{\partial s}{\partial a} \tag{3.40}$$

$$+ \left[\frac{\partial^2 p}{\partial t^2} + \frac{F}{h+\eta}\,\frac{\partial p}{\partial t}\sqrt{\left(\frac{\partial s}{\partial t}\right)^2 + \left(\frac{\partial p}{\partial t}\right)^2} + f\,\frac{\partial s}{\partial t} - \frac{A_h}{\rho}\,\nabla_h^2\left(\frac{\partial p}{\partial t}\right)\right]\frac{\partial p}{\partial a} = - g\,\frac{\partial(h+\eta)}{\partial a}$$

Similarly multiplying Eq. (3.38) and (3.39) by $\partial s/\partial b$ and $\partial p/\partial b$ respectively and adding

$$\left[\frac{\partial^2 s}{\partial t^2} + \frac{F}{h+\eta}\,\frac{\partial s}{\partial t}\sqrt{\left(\frac{\partial s}{\partial t}\right)^2 + \left(\frac{\partial p}{\partial t}\right)^2} - f\,\frac{\partial p}{\partial t} - \frac{A_h}{\rho}\,\nabla_h^2\left(\frac{\partial s}{\partial t}\right)\right]\frac{\partial s}{\partial b} \tag{3.41}$$

$$+ \left[\frac{\partial^2 p}{\partial t^2} + \frac{F}{h+\eta}\frac{\partial p}{\partial t}\sqrt{\left(\frac{\partial s}{\partial t}\right)^2 + \left(\frac{\partial p}{\partial t}\right)^2} + f\frac{\partial s}{\partial t} - \frac{A_h}{\rho}\nabla_h^2\left(\frac{\partial p}{\partial t}\right)\right]\frac{\partial p}{\partial b} = -g\frac{\partial(h+\eta)}{\partial b}$$

3.5 Boundary and Initial Conditions

In order to solve the Lagrangian long wave equations, boundary conditions have to be specified. The type and number of boundary conditions that are necessary are given below.

for inviscid flow ($A_h = 0$)

at closed boundaries: normal particle displacement is zero

at open boundaries: particle path or water level along path is prescribed.

for viscous flow ($A_h \neq 0$)

at closed boundaries: normal and parallel particle displacement's are zero

at open boundaries: particle path or water level along path is prescribed

Initially the system is assumed to be at rest, i.e. the water level is at the Still Water Level and all particle displacements are taken to be zero.

4. NUMERICAL SOLUTION OF THE 2-D LONG WAVE EQUATIONS

For small deformations the non-linear terms in Eqs. (3.20), (3.40) and (3.41) can be neglected. Introducing the variables s' and p' (see section 2.1). Equations (3.20), (3.40) and (3.41) reduce to respectively

$$h\frac{\partial s'}{\partial a} + h\frac{\partial h'}{\partial b} = \eta + [h-h(a,b,0)] = 0 \qquad (4.1)$$

$$\frac{\partial^2 s'}{\partial t^2} - f\frac{\partial p'}{\partial t} + g\frac{\partial(h+\eta)}{\partial a} = -\frac{F}{h+\eta}\frac{\partial s'}{\partial t}\sqrt{\left(\frac{\partial s'}{\partial t}\right)^2 + \left(\frac{\partial p'}{\partial t}\right)^2} \qquad (4.2)$$

$$\frac{\partial^2 p'}{\partial t^2} + f\frac{\partial s'}{\partial t} + g\frac{\partial(h+\eta)}{\partial b} = -\frac{F}{h+\eta}\frac{\partial p'}{\partial t}\sqrt{\left(\frac{\partial s'}{\partial t}\right)^2 + \left(\frac{\partial p'}{\partial t}\right)^2} \qquad (4.3)$$

When assuming linear bottom friction the righthand sides of Eqs. (4.2) and (4.3) are respectively $-F_\ell\, \partial s'/\partial t/h+\eta$ and $-F_\ell\, \partial p'/\partial t/h+\eta$

The employed difference equations are

$$\eta^n_{i,j}+h^n_{i,j}[(s^n_{i,j}-s^n_{i-1,j})/\Delta a + (p^n_{i,j}-p^n_{i,j-1})/\Delta b]+h^n_{ij} = h^0_{i,j} \qquad (4.4)$$

$$\frac{1}{\Delta t^2}(s^{n+1}_{i,j} - 2s^n_{i,j}+s^{n-1}_{i,j}) - \frac{f}{4\Delta t}(p^n_{i,j}+p^n_{i+1,j}+p^n_{i,j}+p^n_{i+1,j-1}-p^{n-1}_{i,j}$$

$$- p^{n-1}_{i+1,j}-p^{n-1}_{i,j-1}-p^{n-1}_{i+1,j-1}) + \frac{F_\ell}{2^{x_{(\overline{h+\eta})}}\Delta t}(s^{n+1}_{i,j}-s^{n-1}_{i,j})$$

$$= -\frac{g}{\Delta a}[(h+\eta)^n_{i+1,j} -(h+\eta)^n_{i,j}] \qquad (4.5)$$

$$\frac{1}{\Delta t^2}(p^{n+1}_{i,j} -2p^n_{i,j}+p^{n-1}_{i,j}) + \frac{f}{4\Delta t}(s^n_{i,j}+s^n_{i-1,j}+s^n_{i,j+1}+s^n_{i-1,j+1}-s^{n-1}_{i,j}$$

$$-s^{n-1}_{i-1,j}-s^{n-1}_{i,j+1}-s^{n-1}_{i-1,j+1}) + \frac{F_\ell}{2^{y_{(\overline{h+\eta})}}\Delta t}(p^n_{i,j}-p^{n-1}_{i,j})$$

$$= -\frac{g}{\Delta b}[(h+\eta)^n_{i,j+1}-(h+\eta)^n_{i,j}]$$

with

$$x_{(\overline{h+\eta})} = \frac{(h+\eta)^n_{i,j} + (h+\eta)^n_{i+1,j}}{2}$$

$$x_{(\overline{h+\eta})} = \frac{(h+\eta)^n_{i,j} + (h+\eta)^n_{i,j+1}}{2}$$

$$h^n_{i,j} = \text{function}\left[\frac{s^n_{i,j} + s^n_{i-1,j}}{2}, \frac{p^n_{i,j} + p^n_{i,j-1}}{2}\right]$$

These equations operate over a finite number of points on a spatial and temporal grid. For a nonlinear bottom stress, the difference form of the friction term in the x momentum equation is written as

$$\frac{F}{h+\eta}\frac{\partial s'}{\partial t}\sqrt{\left(\frac{\partial s'}{\partial t}\right)^2 + \left(\frac{\partial p'}{\partial t}\right)^2} = \frac{F}{2^{x_{(\overline{h+\eta})}}\Delta t}(s^{n+1}_{i,j}-s^{n-1}_{i,j})\left[\frac{1}{\Delta t^2}(s^n_{i,j}-s^{n-1}_{i,j})^2\right.$$

$$\left. + \frac{1}{16\Delta t^2}(p^n_{i,j}+p^n_{i+1,j}+p^n_{i,j-1}+p^n_{i+1,j-1}-p^{n-1}_{i,j}-p^{n-1}_{i+1,j}-p^{n-1}_{i,j-1}-p^{n-1}_{i+1,j-1})^2\right]^{1/2}$$

Given the bottom topography the depth can be found as a function of the particle position.

Computations are started from rest. First $h^n_{i,j}$ is computed using the known bathymetry and particle positions at $n\Delta t$. Then $\eta^n_{i,j}$ values are computed from the continuity equation, Eq. (4.4). Last the particle positions, $s^{n+1}_{i,j}$ and $p^{n+1}_{i,j}$ at the next time step are computed from the momentum equations, Eqs. (4.5) and (4.6). For an analysis of the stability of the scheme the reader is referred to Savoie and van de Kreeke [1981].

5. NUMERICALLY COMPUTED WATER PARTICLE TRAJECTORIES IN A SEMI-ENCLOSED BASIN

Considered is a semi-enclosed basin of constant depth connected to the ocean by an inlet; see Fig. 3. The values used in the computations for the length of the basin, depth of the basin, and the tidal period are respectively L = 6,400 m, h = 3 m, T = 43,300 sec. The length and width of the inlet are equal to L/2.

Assuming nonlinear bottom friction, the water motion is described by Eqs. (4.1) - (4.3). For linear bottom friction the appropriate expressions for the friction terms are substituted. The friction terms are further simplified by assuming $h+\eta \approx$ = constant.

The boundary conditions at the open boundary are given by the particle trajectory p = 2000 sin $(2\pi t/T)$ m. This results in a tidal range of approximately 0.7 m when assuming the water level in the basin to fluctuate uniformly. The boundary conditions at the closed boundary require that a particle initially at the wall stays at the wall, that is the particle is allowed to slip but no flow is permitted through the wall.

The trajectories of the particles originally located at the position of the water levels (+ in Fig. 3), are computed for different values of the linear friction factor, the nonlinear friction factor, and the Coriolis coefficient.

The equations are solved using the explicit finite difference scheme presented in section 4, where the time step Δt = 90 sec and the space step $\Delta a = \Delta b$ = 800 m, see also Fig. 3.

Examples of computed particle paths are presented in Figs. 4, 5 and 6. In these figures the particle paths starting from t = 0 (designated by the symbol x) to t = 2T are shown. For linear friction and zero Coriolis acceleration the computed particle paths are presented in Fig. 4. The particle paths are virtually straight lines.

The straight line paths can be explained as follows. When neglecting the Coriolis term and assuming linear bottom friction and $h+\eta = h \approx$ constant in Eqs. (4.2) and (4.3), the corresponding vorticity equation is

$$\frac{\partial \zeta}{\partial t} + \frac{F_\ell \zeta}{h} = 0 \qquad (5.1)$$

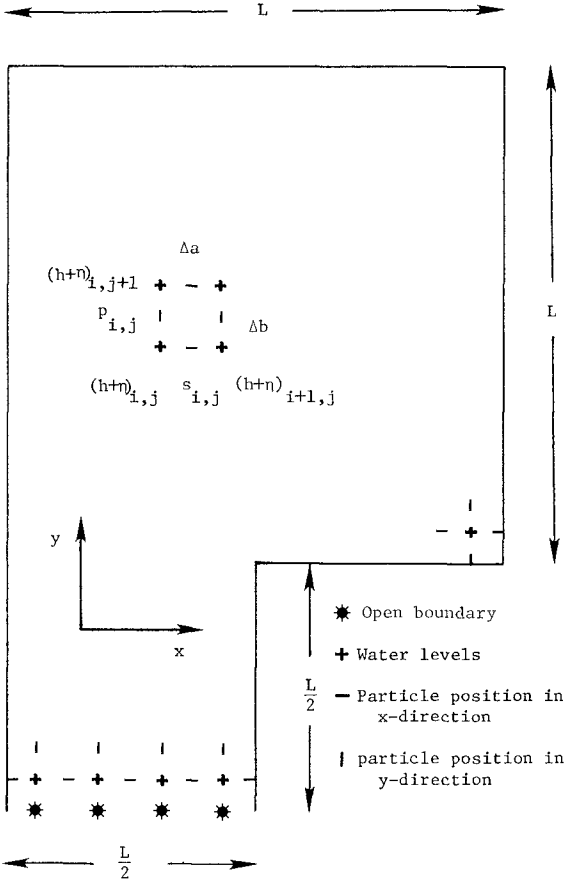

Figure 3. Configuration of Semi-enclosed Basin

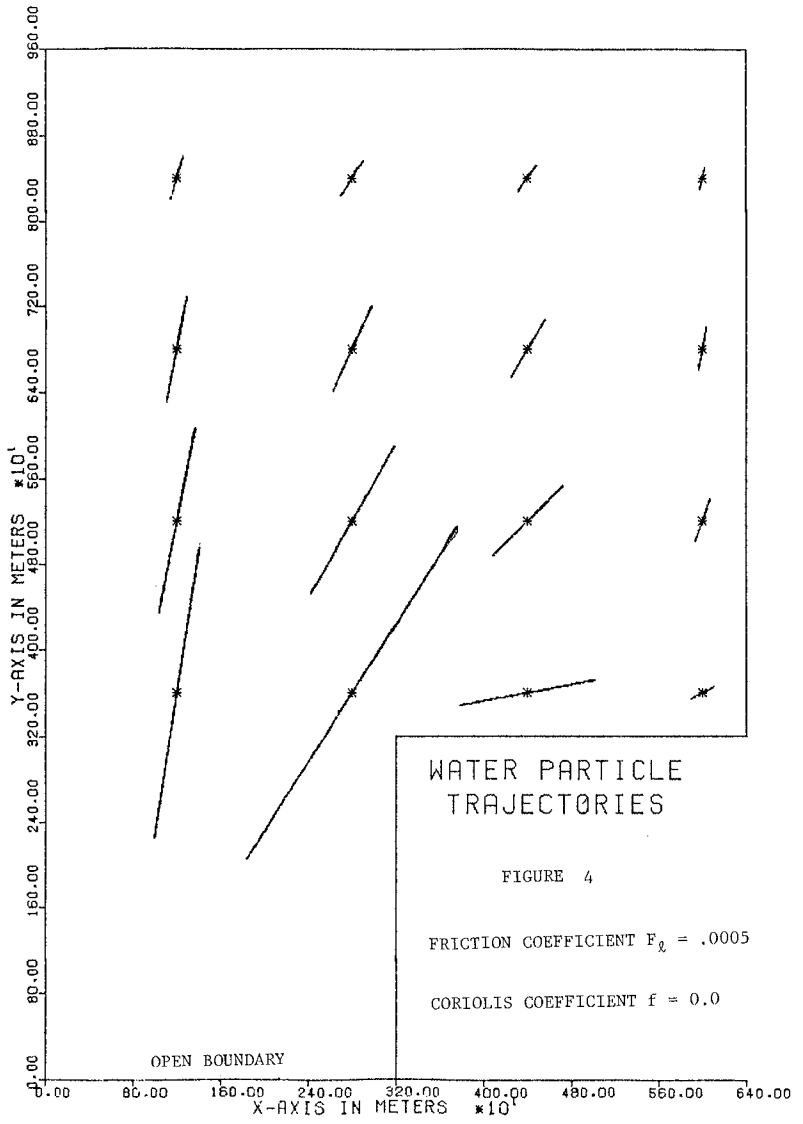
960.00
880.00
800.00
720.00
640.00
560.00
480.00
400.00
320.00
240.00
160.00
80.00
0.00
Y-AXIS IN METERS *10¹
0.00
80.00
160.00
240.00
320.00
400.00
480.00
560.00
640.00
X-AXIS IN METERS *10¹
OPEN BOUNDARY
WATER PARTICLE TRAJECTORIES
FIGURE 4
FRICTION COEFFICIENT F_ℓ = .0005
CORIOLIS COEFFICIENT f = 0.0

Because the basin is initially at rest, it follows from Eq. (5.1) $\zeta(t) = 0$. Thus the fluid motion is irrotational which allows introducing a (Lagrangian) velocity potential $\phi(a,b,t)$. Substituting in Eq. (4.1) yields

$$\nabla^2\phi = -\frac{1}{h}\frac{\partial \eta}{\partial t} \tag{5.2}$$

For a basin with dimensions much smaller than the wavelength

$$\frac{\partial \eta}{\partial t} \approx \frac{\omega A_c}{h A_b}\ \hat{\ell}\ \cos\omega t \tag{5.3}$$

where A_c is the cross-sectional area of the inlet, A_b is the surface area of the basin and $\hat{\ell}\sin\omega t$ represents the motion of the plunger. Combining Eqs. (5.2) and (5.3)

$$\nabla^2\phi = -\frac{\omega A_c}{h A_b}\ \hat{\ell}\ \cos\omega t \tag{5.4}$$

The solution to Eq. (5.4) is of the form

$$\phi(a,b,t) = \phi(a,b)\cos\omega t \tag{5.5}$$

It follows that the particle velocities

$$\frac{\partial s}{\partial t} = \frac{\partial \phi}{\partial a} \text{ and } \frac{\partial p}{\partial t} = \frac{\partial \phi}{\partial b}$$

are in phase and thus the path of a particle is a straight line.

The results when the Coriolis force is added to the linear equations is presented in Fig. 5. The Coriolis acceleration causes moving particles to follow elliptical trajectories in the direction of the indicated arrows.

Nonlinear bottom friction is employed to compute the particle paths presented in Fig. 6. Particle paths are elliptical as opposed to the straight lines in the case of linear friction. When using linear friction particles in the basin are found to oscillate about their initial locations. For nonlinear friction particles encounter an initial displacement when the computation is first started and then oscillate about the new equilibrium position. The initial displacement can be explained by means of the equations for the mean particle displacement and mean water level.

To derive these equations the Lagrangian long wave equations, Eqs. (3.38) and (3.39) are written in the form

$$\frac{\partial^2 s'}{\partial t^2} - f\frac{\partial p'}{\partial t} + g\frac{\partial \eta}{\partial a} + \frac{F_\ell}{h}\frac{\partial s'}{\partial t} = NL_1 \tag{5.6}$$

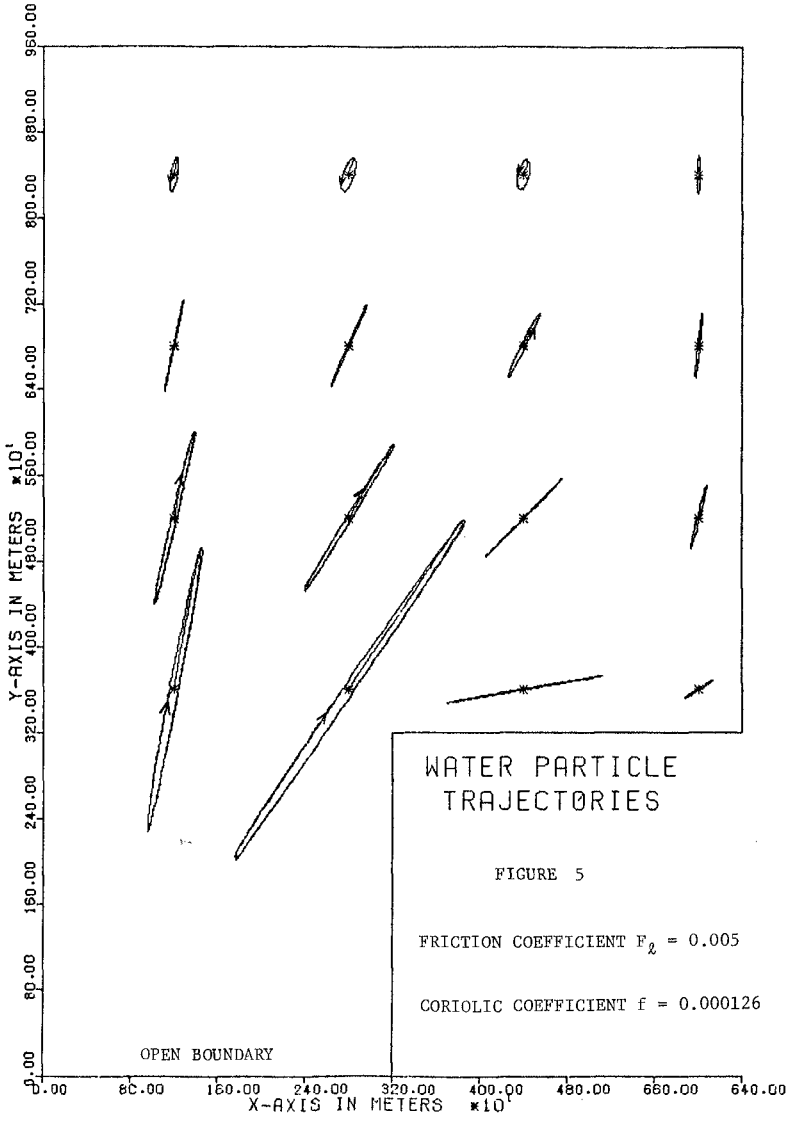
Y-AXIS IN METERS *10¹
0.00
80.00
160.00
240.00
320.00
400.00
480.00
560.00
640.00
720.00
800.00
880.00
960.00
X-AXIS IN METERS *10¹
0.00
80.00
160.00
240.00
320.00
400.00
480.00
560.00
640.00
OPEN BOUNDARY
WATER PARTICLE TRAJECTORIES
FIGURE 5
FRICTION COEFFICIENT F_2 = 0.005
CORIOLIC COEFFICIENT f = 0.000126

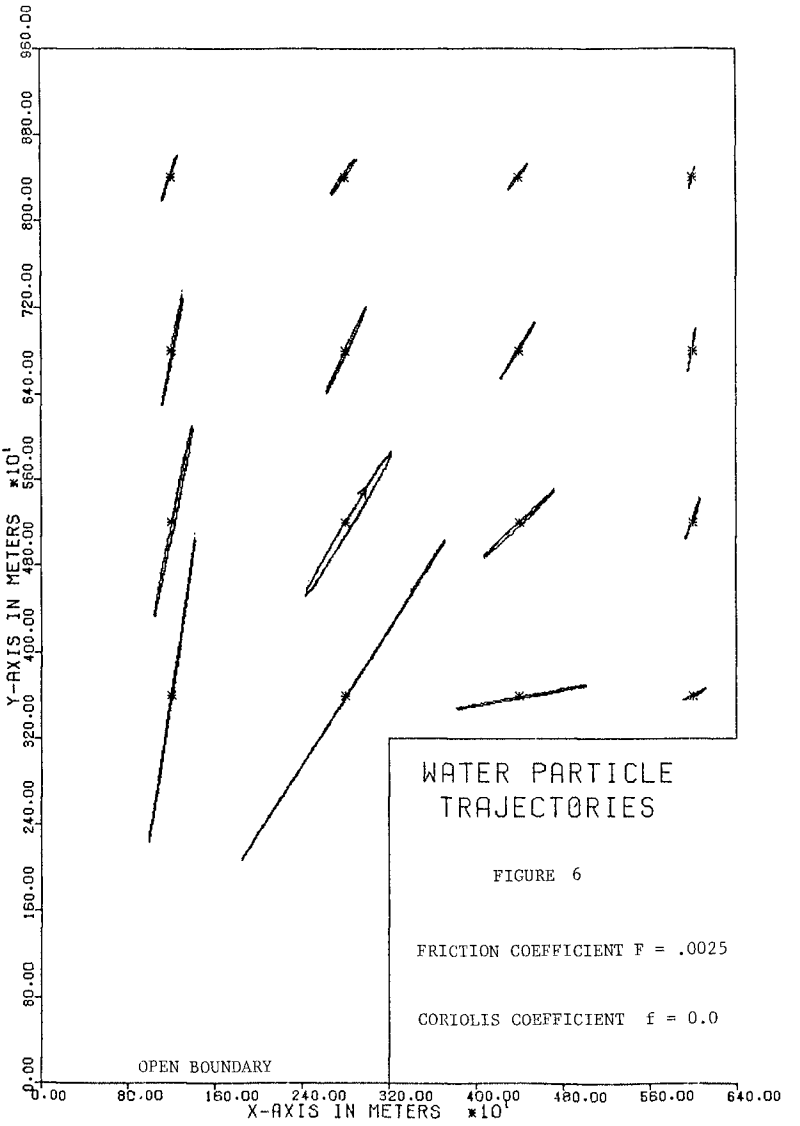
WATER PARTICLE
TRAJECTORIES
FIGURE 6
FRICTION COEFFICIENT F = .0025
CORIOLIS COEFFICIENT f = 0.0
OPEN BOUNDARY
Y-AXIS IN METERS *10¹
X-AXIS IN METERS *10¹
0.00
80.00
160.00
240.00
320.00
400.00
480.00
560.00
640.00
720.00
800.00
880.00
960.00

$$\frac{\partial^2 p'}{\partial t^2} - f\frac{\partial s'}{\partial t} + g\frac{\partial \eta}{\partial a} + \frac{F_\ell}{h}\frac{\partial p'}{\partial t} = NL_2 \tag{5.7}$$

$$h\left[\frac{\partial s'}{\partial a} + \frac{\partial p'}{\partial b}\right] + \eta = NL_3 \tag{5.8}$$

NL_1, NL_2 and NL_3, constitute the (higher order) nonlinear terms. It is assumed that the bay bottom is horizontal, i.e. $h(a,b,y) = h$. The nonlinear friction is approximated by a linear friction; the difference is contained in the terms NL_1 and NL_2.

Assuming a periodic forcing at the open boundaries in terms of s', p' or η, the solution to the Eqs. (5.6) - (5.8) can be written as

$$s'(a,b,t) = \langle s'\rangle(a,b) + s'_p(a,b,t) \tag{5.9}$$

$$p'(a,b,t) = \langle p'\rangle(a,b) + p'_p(a,b,t) \tag{5.10}$$

$$\eta(a,b,t) = \langle\eta\rangle(a,b) + \eta_p(a.b,t) \tag{5.11}$$

s'_p, p'_p and η_p are periodic in t with a period equal to the tidal period. $\langle\ \rangle$ denotes averaging over the tidal period. Substituting in Eqs. (5.6) - (5.8) and averaging the equations over the tidal period yields the equations for the mean particle displacement $\langle s'\rangle$, $\langle p'\rangle$ and the mean water level $\langle\eta\rangle$.

$$g\frac{\partial\langle\eta\rangle}{\partial a} = \langle NL_1\rangle \tag{5.12}$$

$$g\frac{\partial\langle\eta\rangle}{\partial b} = \langle NL_2\rangle \tag{5.13}$$

$$h\left[\frac{\partial\langle s'\rangle}{\partial a} + \frac{\partial\langle p'\rangle}{\partial b}\right] + \langle\eta\rangle = \langle NL_3\rangle \tag{5.14}$$

For the semi-enclosed basin, when using the linear equations, i.e., NL_1, $NL_2 = NL_3 = 0$, it follows from Eqs. (5.12) - (5.14) and the boundary condition that $\langle s\rangle = \langle p\rangle = \langle\eta\rangle = 0$ everywhere. Particles thus oscillate about their original position. When the values of NL_1, NL_2 abd NL_3 are not all zero, e.g., when using nonlinear friction, particles encounter a net displacement $\langle s'\rangle$ (a,b), $\langle p'\rangle$ (a,b) and will oscillate about this position.

6. SUMMARY AND CONCLUSIONS

A rigorous derivation of the Lagrangian long wave equations, and expressions for the deformation of a fluid parcel is presented. In the derivation no use is made of the corresponding Eulerian form of these equations and expressions. The purpose of this is to preserve a true Lagrangian approach to the problem even though in some instances

it would have been easier to transform directly from the Eulerian equations.

The equations of motion and continuity are highly nonlinear in Lagrangian form. The nonlinearities are associated with the deformation of the horizontal cross-section of a traveling water column. The Lagrangian expressions for stress, strain, rotation, and vorticity remain relatively simple.

An explicit finite difference solution is presented for the simplified set of equations i.e. neglecting the nonlinear terms except for the bottom friction. The technique is applied to a square bay of constant depth connected to the ocean by a single inlet. Particle trajectories in the basin are computed for different values of the friction coefficient and Coriolis parameter. The boundary condition i.e. the particle displacement in the inlet is described by a simple harmonic function of time. For nonlinear friction the particles tend to follow clockwise elliptical trajectories, whereas for linear friction the trajectories become straight lines. The Coriolis acceleration also induces an elliptical motion. In the case of linear friction the particles in the basin oscillate about their original locations. For nonlinear friction there is an initial displacement when the computations are started, but after the first tidal cycle the particle trajectories become virtually identical.

In summary it can be stated that

1) The numerical solution to the Lagrangian long wave equations when neglecting the nonlinear terms is not more involved than the numerical solution to the Eulerian equations.

2) Aside from the difficulties in prescribing the open boundary conditions, the method of computing particle trajectories using the Lagrangian equations rather than the Eulerian equations has a clear advantage in that it bypasses the computation of the velocity field.

REFERENCES

1. Aris, R., 1962. "Vectors, Tensors, and the Baaic Equations of Fluid Dynamics," Prentice-Hall, Inc.

2. Brennen, C., 1970. "Some Numerical Solutions of Unsteady Free Surface Wave Problems Using the Lagrangian Deacription of the Flow," in Holt (editor) Proceedings of the 2nd International Conference on Numerical Methods, pp. 403-409.

3. Brennen, C. and A. K. Whitney, 1970. "Unsteady, Free Surface Flows; Solutions Employing the Lagrangian Description of the Motion," Proceedings of the 8th O.N.R. Symposium on Naval Hydrodynamica, Pasadena, California.

4. Daily, J. W. and D. R. F. Harleman, 1966. Fluid Dynamics," Addison-Wesley Publ. Co.

5. Defant, A., 1961. "Physical Oceanography," Vol. I, Pergamon Press, London.

6. Goto, T., 1979. "Nonlinear Equation of Long Wave in the Lagrangian Description," Coastal Engineering in Japan, Vol. 22, pp. 1-9.

7. Lamb, H., 1932. "Hydrodynamics," 6th Edition, Cambridge University Press, New York.

8. Miche, R., 1944. "Mouvements Ondulatoires de la Mer en Profondeur Constante ou Decroissante," Annales des Ponts et Chausaee, Paris, France.

9. Neuman, G. and W. J. Pierson, 1966. "Principles of Physical Oceanograp;hy," Prentice-Hall, Inc., Englewood Cliffs, N.J.

10. Pierson, W. J., 1962. "Perturbation Analysis of the Navier-Stokes Equations in Lagrangian Form with Selected Linear Solutions," Journal of Geophysical Research, Vol. 67, No. 8.

11. Savoie, M. A. and J. van de Kreeke, 1982. "The 2-D Lagrangian Conservation Equations; Application to Tidal Hydraulics," University of Miami, RSMAS. TR 82-3, p 70.

12. Shuto, N. and Goto, T., 1978. "Numerical Simulation of Tsunami Run-up", Coastal Engineering in Japan, Vol. 21, pp. 13-20.

2- AND 3-DIMENSIONAL DETERMINISTIC FREAK WAVES

by

SØREN PETER KJELDSEN
Senior Research Engineer[1)]

1. ABSTRACT

The present paper deals with a new non-linear technique for generation of violent breaking freak waves (plunging breakers) at specified positions and times in wave basins. First, results concerning generation of non-linear wave trains, Stokes-waves and wave solitons in deep water are given. Then the technique for generation of non-linear wave transients are given with specified non-linear dispersion properties. Finally, the new techniques are used to obtain collisions between non-linear solitons coming both from the same direction (2-dimensional case), and from different directions (3-dimensional case) leading to generation of steep and violent plunging breakers.

2. INTRODUCTION

The amount of high violent breaking waves that is contained in a sea, is a most important factor to consider for design of both offshore structures, coastal structures and ships. Some critical events might happen just in certain kinds of steep extreme waves, but the same events do not happen in a normal sea state described and simulated in the laboratory by the use of the traditional wave spectrum. Stochastic simulations contain normally a low amount of breaking waves, and in most cases they do not contain extreme wave events, such as very high waves breaking as plunging breakers in deep waters. Further, the wave spectra might be identical for two wave simulations, one containing a very violent and dangerous freak wave leading to a critical event, the other not containing such a wave. Thus, use of a wave spectrum is not a complete and adequate description of a sea state and the effect it might have on structures. Finally, in stochastic simulations of irregular seas in the laboratory it is very often observed that the ratio between the maximum observed wave height and the significant wave height is too low. (The required ratio is 2 in most cases.)

An alternative technique for a fast, efficient and accurate determination of extreme responses and critical events that might occur at sea, is a new non-linear technique for generation of solitons that interact and break as very violent freak waves at a predetermined position and time in deep waters. The critical events that are under consideration here, are shown in Fig. 1.

1) NORWEGIAN HYDRODYNAMIC LABORATORIES
Division: Ship and Ocean Laboratory
P.O. Box 4118 - Valentinlyst
N-7001 Trondheim / Norway

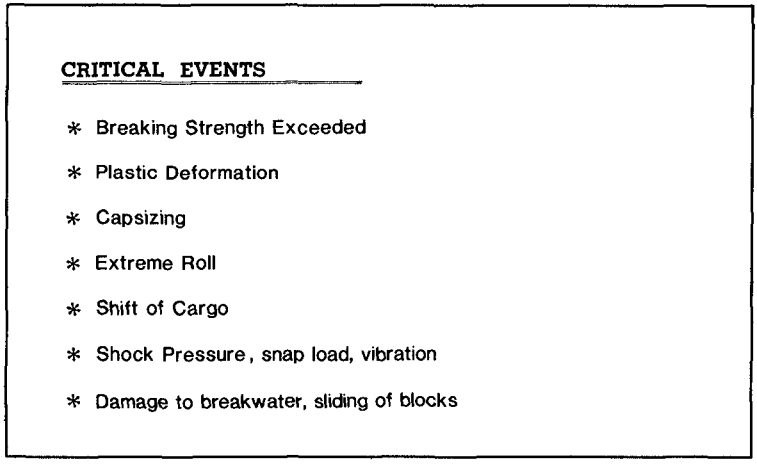

Fig. 1 Critical events.

Very often the designer has to investigate if such a critical event might happen or not. If the answer is yes, the designer then has to decide if such an event is acceptable or not. Very often he will then raise the question: "What is the probability for such an event?" If the probability is very low, he might then find that the conditions are acceptable. However, if the probability is high, he will often find that the conditions are not acceptable and he will develop a new design. Therefore, at the Norwegian Hydrodynamic Laboratories a new design philosophy is derived as follows:

1. Generate an extreme breaking freak wave in the laboratory.
2. Determine from wave statistics the statistical probability for occurrence of such a wave.
3. Measure the extreme response in an experiment.
4. Observe if a critical event occurs and repeat the experiment.
5. Give the probability for failure of the structure.

The procedure is shown graphically in Fig. 2.

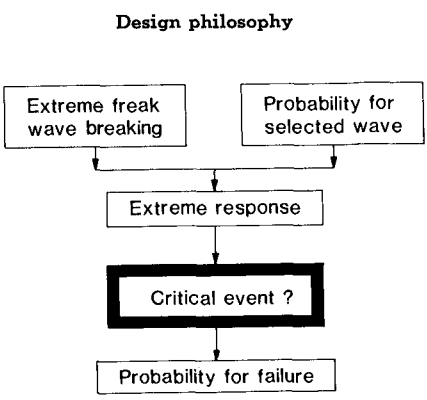

Fig. 2 Design philosophy.

This philosophy was first derived in a research programme "Ships in Rough Seas" (see publication from NSFI/RINA (1982)), but has now obtained much more international attention, and have recently been used in two projects performed for the offshore industry with experimental simulations performed at the Norwegian Hydrodynamic Laboratories. The same kind of philosophy might very well be applied to coastal structures. The present paper will only deal with the generation of extreme breaking freak waves in deep waters. Selection of design waves and probability calculations is given by Kjeldsen (1981).

3. STATE-OF-THE-ART IN WAVE GENERATION TECHNIQUES

In the following a brief summary of available wave generation techniques shall be given. Perfection of generation techniques for steady state longcrested, regular gravity waves (Stokes waves, cnoidal waves and sinusoidal waves) may be regarded as a first step in state-of-the-art of wave generation in hydrodynamic laboratories. The most interesting here is the non-linear generation techniques for Stokes waves in deep waters and cnoidal waves in shallow waters. However, it is also very well known that a sinusoidal command signal applied to a wave generator will not lead to generation of a sinusoidal wave train. Instead irregular waves are observed in the wave flume with the basic frequency superposed with freely travelling higher harmonics. Thus, the simple demand to reproduce a "clean" sinusoidal wave train in a wave flume without parasitic disturbances demands a laborous phase-compensating tehcnique, in which higher harmonics is supplied artificially in anti-phase with the unwanted parasitic noise. This technique is well known and described by Buhr Hansen, Schiolten & Svendsen (1975). The present paper will deal with the more complicated non-linear generation technique for generation of Stokes waves in deep waters.

The second step in state-of-the-art of wave generation techniques in laboratories is then the generation of a steady state stochastic sea containing irregular wave fields in 2- or 3-dimensions. The available techniques for generation of stochastic seas are all linear and are based on the use of Fourier analysis and one-dimensional or directional wave spectra. However, both the directional spectra for the 3-dimensional wave field, and the common frequency spectra for the 2-dimensional longcrested wave field must necessarily be truncated, due to the physical limitations in the frequency range that is present when a prescribed spectrum is simulated artificially with mechanical wave generators. In simulations of a directional spectrum the selection of the truncation parameter affects the magnitude of the spectral moments m_0, m_2 and m_4, and also the obtained crest lengths that

are achieved in the experiment (Kjeldsen & Price (1982)). Further, it is well documented that the frequency spacing in the spectral simulation is essential for correct reproduction of slow-drift phenomena. However, even the two-dimensional directional sea spectrum appears to be insufficient, for a proper description of sea states containing extreme waves, wave trains with sequences of breaking waves and wave groups. Several radically different time series have been found -some containing violent breaking freak waves or wave groups - others not, and all have the same wave spectrum (Johnson, Ploeg, Mansard (1978)). A quite high frequency both of damages to coastal and marine structures and of capsizings of smaller vessels that recently have been experienced in different parts of the world, suggest that state-of-the-art in selection of proper design waves or design spectra for various kinds of maritime structures is just not good enough (Baird et al. (1980), Bruun (1979), Nedrelid (1978), Stephens et al. (1981)).

With this background a third and more advanced step in wave generation techniques is under rapid development (Kjeldsen (1978), Funke & Mansard (1979), Takezawa (1981), Kjeldsen & Myrhaug (1980), Kjeldsen, Vinje, Myrhaug, Brevig (1980), Mansard, Funke, Barthel (1982)). These new techniques contain sequences of deterministic transient waves leading either to violent breaking freak waves or to formation of wave groups with specified characteristics, and these sequences might be included in a stochastic time series in such a way that a certain specified wave spectrum is matched. The present paper will deal with the following 2 subjects:

1) Description of development of a new non-linear experimental technique for deterministic generation of freak waves both in 2 dimensions (longcrested freak waves) and in a directional 3-dimensional shortcrested wave field.
2) Discuss various possible combinations of superposition of deterministic sequences containing wave transients, with stochastic time series as obtained in a 3-dimensional wave field.

Fig. 3 gives a summary of all available combinations.

Development of wave generation techniques for case no. 4, 8, 10 and 12 will be dealt with in the present paper and is therefore circled. Thus, in the following we shall concentrate on

case 4) Generation of non-linear steady-state wave trains.

case 8 & 10) Interaction and collisions between non-linear solitons in 2- and 3-dimensions.

case 12) A combination of the steady state stochastic simulation with the transient state deterministic simulation. This last case is linear because the stochastic directional sea is simulated using linear assumptions.

All the experiments and developments referred to in this study are performed at the Norwegian Hydrodynamic Laboratories in Trondheim, Norway.

Art of wave generation - steady state

1	Regular Sinusoidal Waves	Linear	Deep and shallow water
2	One-dimensional Spectrum	—	—
3	Directional Spectrum	—	—
(4)	Stokes Waves	Non-linear	Deep water
5	Cnoidal Waves	—	Shallow water

Art of wave generation - transient state

6	2-Dimensional Freak Wave	Linear	Shallow water
7	2-Dimensional Freak Wave	—	Deep water
(8)	2-Dimensional Freak Wave	Non-linear	—
9	3-Dimensional Freak Wave	Linear	—
(10)	3-Dimensional Freak Wave	Non-linear	—

Combined steady state/transient state

11	One-dimensional Spectrum with superposed Freak Wave	Linear	Deep Water
(12)	Directional Spectrum with superposed Freak Wave	—	—

Fig. 3 State-of-the-art in wave generation techniques.

4. GENERATION OF SOLITONS

The familiar non-linear Schrödinger equation (4.1) as first derived by Zakharov (1968) describes a wide variety of physical situations. Here, we shall limit the description of the theory to gravity water waves in deep water. The equation is:

$$i\left(\frac{\delta A}{\delta t} + \frac{\omega_o}{2k_o}\frac{\delta A}{\delta x}\right) - \frac{\omega_o}{8k_o^2}\cdot\frac{\delta^2 A}{\delta x^2}$$

$$- \frac{1}{2}\,\omega_o k_o^2 \cdot |A|^2 A = 0 \qquad (4.1)$$

Here, A is the complex envelope:

$$A = a \cdot e^{i\theta} \qquad (4.2)$$

and a is the physical amplitude.

According to the theory there exists a carrier wave number k_o and a corresponding cyclic frequency ω_o which remains constant throughout the evolution. Thus, variations in k can be described as deviations from the carrier wave number:

$$k = k_o + \Delta k \qquad (4.3)$$

The mathematical solution of eq. (4.1) relevant to deep water waves is given by Zakharov & Shabat (1972). Their main results are:

1) An initial wave envelope pulse of arbitrary shape will eventually disintegrate into a number of solitons and an oscillatory tail. The number and structure of these solitons and the structure of the tail are completely determined by the initial conditions.

2) Each soliton is defined as a permanent progressive wave solution to eq. (4.1) and has the form:

$$S_n = a_n \cdot \sec\sqrt{2}\,k_o^2 a_n \cdot \left[(x - \chi_n)\right.$$

$$\left. - \left(\frac{\omega_o}{2k_o} + V_n\right)t\right] + \exp\left\{-\frac{i}{4}k_o^2 a_n^2 \omega_o t\right.$$

$$\left. - \frac{4ik_o^2}{\omega_o}\cdot V_n\left[(x - \chi_n) - \left(\frac{\omega_o}{2k_o} + V_n\right)t + \theta_n\right]\right\} \qquad (4.4)$$

(Here, n is an index that refers to the n^{th} soliton. a_n is its amplitude and V_n is its velocity relative to the group velocity $\omega_o/2k_o$. χ_n and θ_n is its position and phase.)

3) Provided that wave breaking does not occur, the solitons are stable in the sense that they can survive collisions and interactions with each other with no permanent change except a possible shift in position and phase.

4) The remaining tail is relatively small and unimportant for a pulse initial condition. It disperses linearly resulting in a $1/\sqrt{t}$ decay of the amplitude.

Experiments with monochromatic steep non-linear wave trains were carried out in a 78 m long wind-wave flume at the Norwegian Hydrodynamic Laboratories. It was found that it was possible to use a sinusoidal command signal and a wave flap hinged at the bottom to produce highly non-linear solitons that dispersed in well controlled transient experiments with phase velocities and group velocities that exceeded predictions made from linear theory. Also a tail was observed behind the solitons that dispersed linearly. Further, it was found that the dispersion velocities for the obtained solitons agreed very well with numerical results given by Cokelet (1977) for high order Stokes waves.

With this knowledge a series of very well controlled experiments were then carried out in which two monochromatic steep non-linear wave trains with different frequencies were generated at different times. This was performed in such a way that two solitons were brought into interaction with each other at a position 60 m from the wave generator. This resulted in the generation of a violent plunging breaker in deep water obtained as a result of a collision between only two solitons.

An example of such an experiment is given by Kjeldsen, Vinje, Myrhaug & Brevig (1980) (Fig. 5, page 323 and Fig. 9, page 325). A large summary report containing all performed experiments will also be available Kjeldsen (1983).

5. THEORETICAL STORM MODEL

In the following a new theoretical model for travelling of wave transients with non-linear dispersion properties shall be derived. We introduce the operator:

$$\Lambda(\omega) = e^{-j\omega / \omega \sqrt{\frac{x}{g}} \frac{1}{\kappa}} \tag{5.1}$$

Λ is a frequency response function for non-linear waves that relates wave heights measured at two points separated by a distance x in the direction of travel. ω is the cyclic frequency, g is the gravity acceleration, while κ is a non-linear dispersion factor depending on wave steepness. As shown in section 6 the produced waves are solitons with a synoptic shape that shows a high degree of coherence with Stokes waves as calculated by Cokelet (1977) (using Padé approximants with series expansions to the order ε^{110}). Thus, for the non-linear wave transients under consideration here Cokelet's results are very good approximations. Fig. 4 shows κ as a function of wave steepness.

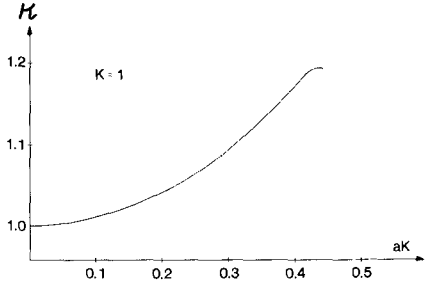

Fig. 4 Wave dispersion factor as a function of wave steepness $\left(a \cdot K = \frac{H}{L} \cdot \pi\right)$ (From Cokelet (1977)).

For non-linear waves we now introduce a "unit impulse response function" λ defined by the transformation:

$$\lambda(\tau) = \frac{1}{2\pi}\int_{-\infty}^{\infty} \Lambda(\omega) \cdot e^{j\omega\tau} \cdot \frac{1}{\kappa}\, d\omega \tag{5.2}$$

The unit impulse response function λ represents a convenient method of determining the response $q(t)$ to an input of any form $Q(t)$ through the method of Duhamel's convolution integral:

$$q(t) = \int_{-\infty}^{\infty} \lambda(\tau) \cdot Q(t-\tau)\, d\tau \tag{5.3}$$

Substituting eq. (5.1) into eq. (5.2) gives:

$$\lambda(\tau) = \frac{1}{2\pi}\int_{-\infty}^{\infty} e^{-j\omega/\omega/\frac{x}{g}\cdot\frac{1}{\kappa}} \cdot e^{j\omega\tau}\,\frac{1}{\kappa}\, d\omega \tag{5.4}$$

introducing trigonometric terms we obtain:

$$\lambda(\tau) = \frac{1}{2\pi}\int_{-\infty}^{\infty} \cos\left(\omega^2 \frac{x}{g}\frac{1}{\kappa} - \omega\tau\right) d\omega$$

$$+ \frac{i}{2\pi}\int_{-\infty}^{\infty} \sin\left(\omega\tau - \frac{\omega^2 x}{g}\frac{1}{\kappa}\right) d\omega \tag{5.5}$$

By use of the symmetry relations we finally obtain:

$$\lambda(\tau) = \frac{1}{\pi}\int_{0}^{\infty} \cos\left(\omega^2 \frac{x}{g}\frac{1}{\kappa} - \omega\tau\right) d\omega \tag{5.6}$$

We now consider non-linear waves of constant steepness κ.

We introduce the substitutions:

$$\xi = \frac{x^{1/2}}{g^{1/2}} \cdot \frac{1}{\kappa^{1/2}} \left(\omega - \frac{g\tau}{2x}\right) \tag{5.7}$$

$$\frac{d\xi}{d\omega} = \frac{x^{1/2}}{g^{1/2}}\,\frac{1}{\kappa^{1/2}} \tag{5.8}$$

and:

$$\sigma = \frac{g^{1/2}\cdot\tau}{2x^{1/2}\cdot\kappa^{1/2}} \tag{5.9}$$

We then obtain:

$$\lambda(\tau) = \frac{1}{\pi}\frac{\kappa^{1/2}\cdot g^{1/2}}{x^{1/2}}\int_{-\sigma}^{\infty} \cos(\xi^2 - \sigma^2)\, d\xi \tag{5.10}$$

and:

$$\lambda(\tau) = \frac{1}{\pi}\,\frac{g^{1/2}\cdot\kappa^{1/2}}{x^{1/2}}\left\{\cos\sigma^2\left[\int_{-\sigma}^{0}\cos\xi^2\,d\xi + \int_{0}^{\infty}\cos\xi^2\,d\xi\right] + \sin\sigma^2\left[\int_{-\sigma}^{0}\sin\xi^2\,d\xi + \int_{0}^{\infty}\sin\xi^2\,d\xi\right]\right\} \tag{5.11}$$

We can now recognise the well known relations for Fresnel's integrals:

$$\int_0^\infty \sin\xi^2\,d\xi = \int_0^\infty \cos\xi^2\,d\xi = \frac{1}{2}\sqrt{\frac{\pi}{2}} \tag{5.12}$$

and:

$$C(\mu) = \int_0^\mu \cos\left(\tfrac{1}{2}\pi\mu^2\right)d\mu \tag{5.13}$$

$$S(\mu) = \int_0^\mu \sin\left(\tfrac{1}{2}\pi\mu^2\right)d\mu \tag{5.14}$$

Substitution then gives:

$$\lambda(\tau) = \left(\frac{g\kappa}{2\pi x}\right)^{1/2}\left\{\left[\cos\sigma^2\right]\cdot\left[\frac{1}{2}+\frac{\sigma}{|\sigma|}\cdot C\left(\sqrt{\frac{2}{\pi}}\sigma\right)\right] + \left[\sin\sigma^2\right]\cdot\left[\frac{1}{2}+\frac{\sigma}{|\sigma|}\,S\left(\sqrt{\frac{2}{\pi}}\sigma\right)\right]\right\} \tag{5.15}$$

We now introduce a new parameter:

$$b = \left(\frac{\kappa\cdot g}{2\pi x}\right)^{1/2} \tag{5.16}$$

Eq. (5.9) then gives:

$$\sigma = \sqrt{\frac{\pi}{2}}\cdot\frac{b\tau}{\kappa} \tag{5.17}$$

and we finally obtain:

$$\lambda\left(\frac{b\tau}{\kappa}\right) = b\left\{\left[\cos\frac{\pi}{2}\frac{b^2\tau^2}{\kappa^2}\right]\cdot\left[\frac{1}{2}+\frac{\tau}{|\tau|}\,C\left(\frac{b\tau}{\kappa}\right)\right] + \left[\sin\frac{\pi}{2}\frac{b^2\tau^2}{\kappa^2}\right]\cdot\left[\frac{1}{2}+\frac{\tau}{|\tau|}\,S\left(\frac{b\tau}{\kappa}\right)\right]\right\} \tag{5.18}$$

This is thus the final expression for the "unit impulse response function" λ, expressed with Fresnel's integrals which are functions of the dimensionless time parameter $b \cdot \tau / \kappa$ that governs the non-linear interactions.

The freak wave is now approximated with the Dirac-function defined by:

$$\delta(t) = \frac{1}{2\pi} \int_{-\infty}^{\infty} e^{i\omega t} \, d\omega \tag{5.19}$$

This function has the properties:

$$\delta(t) = 0 \quad \text{if } t \neq 0 \tag{5.20}$$

$$\int_{-\infty}^{\infty} \delta(t) \, dt = 1 \tag{5.21}$$

$$\int_{t_1}^{t_2} q(t) \quad \delta(t-t_o) \, dt = \begin{cases} q(t_o) & \text{if } t_1 < t_o \leq t_2 \\ o & \text{otherwise} \end{cases} \tag{5.22}$$

(Eq.(5.22) is valid if q(t) is continuous at t_o and t_1, t_2 are constants with $t_2 > t_1$) If index 1 refers to the position of wave generation and index 2 refers to the position of the freak wave, then the time history at position 1 is given by Duhamel's integral eq. (5.3) as:

$$\eta(x_1, t) = \int_{-\infty}^{\infty} \lambda(\tau) \cdot \eta(x_2, t - \tau) \, d\tau \tag{5.23}$$

This can also be expressed as:

$$\eta(x_1, t) = \Lambda(\omega) \cdot \eta(x_2, t) \tag{5.24}$$

Eqs. (5.23) and (5.24) are the time domain equivalents of:

$$N(x_2, \omega) = \Lambda(\omega) \cdot N(x_1, \omega) \tag{5.25}$$

where N is the transform of the time histories obtained as:

$$N(x, \omega) = \frac{1}{2\pi} \int_{-\infty}^{\infty} \eta(x, t) \cdot e^{-i\omega t \frac{1}{\kappa}} \, dt \tag{5.26}$$

The freak wave at position 2 is now approximated with a Dirac-function and we have:

$$\eta(x_2, t) = \delta(t) \tag{5.27}$$

Then

$$N(x_2, \omega) = \frac{1}{2\pi} \int_{-\infty}^{\infty} \eta(x_2, t) \, e^{-i\omega t \frac{1}{\kappa}} \, dt = \frac{1}{2\pi} \tag{5.28}$$

and

$$N(x_1, \omega) = \frac{1}{2\pi} \Lambda^{-1}(\omega) \tag{5.29}$$

The inverse transform is then obtained as:

$$\eta(x_1, t) = \int_{-\infty}^{\infty} N(x_1, \omega)\, e^{i\omega t \frac{1}{\kappa}}\, d\omega \tag{5.30}$$

or:

$$\eta(x_1, t) = \frac{1}{2\pi} \int_{-\infty}^{\infty} e^{-i\{\omega^2 \frac{x}{g} \frac{1}{\kappa}) - \omega t\}}\, d\omega \tag{5.31}$$

or:

$$\eta(x_1, t) = \frac{1}{\pi} \int_{0}^{\infty} \cos(\frac{\omega^2 x}{g} \frac{1}{\kappa} - \omega t)\, d\omega \tag{5.32}$$

Eq. (5.32) is identical with eq. (5.6) and it is thus shown that the unit impulse response function λ represents the time series $\eta(x_1, t)$ at position 1. Eq. (5.18) can then be used directly to produce a command signal for the wave generator. For large values of σ, we obtain the simplification:

$$C(\mu) = S(\mu) \simeq \frac{1}{2} \tag{5.33}$$

and

$$\lambda(\tau) = \sqrt{2}\, b \cos(\frac{\pi}{2} \frac{b^2 \tau^2}{\kappa^2} - \frac{\pi}{4}) \tag{5.34}$$

Thus, we have obtained an extension and non-linear modification of a technique for linear transient waves described by Davis & Zarnick (1964).

6. DEVELOPMENT OF COMMAND SIGNALS FOR 2-DIMENSIONAL FREAK WAVES

The theoretical storm model given in section 5 can now be directly used to develop command signals for wave generators. Thus, eq. (5.18) or eq. (5.34) can be directly used to prepare analog signals for wave generators. Since 1977 experiments of this kind have been performed at the Norwegian Hydrodynamic Laboratories in 3 different wave flumes, first one 33 m long, 1 m wide and 1.6 m deep, second one 78 m long, 4 m wide and 1.6 m deep, and the third one 280 m long, 10 m wide and 10 m deep, all equipped with flap-type wave generators. Fig. 5 gives an example of such an experiment performed in the third wave flume. A large plunging breaker with a wave height 0.74 m is generated 41 m from the wave generator and 66 seconds after the start of the transient signal.

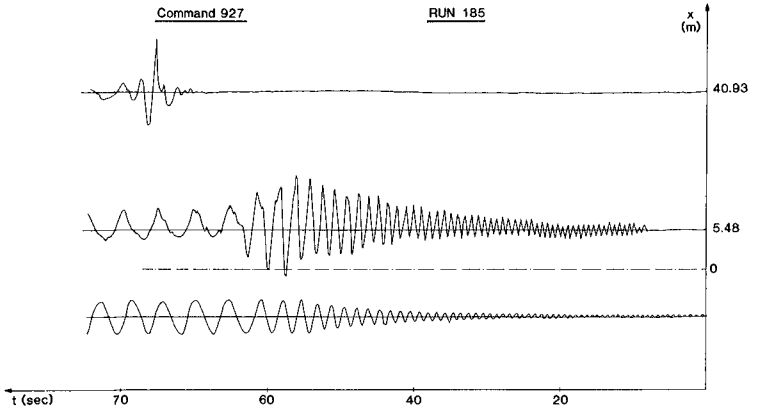

Fig. 5 Deep water plunging breaker generated from an interaction of 43 single wave components. The command signal to the wave generator is shown at the bottom.

It is most important to consider the fact that the analytical model developed in section 5 for dispersion of storm waves makes the assumption that all generated wave components have the same steepness. Thus, κ becomes a constant. To achieve this eq. (5.18) or eq. (5.34) has to be multiplied by a correction factor, that is an increasing function of time. With such a correction analog signals were prepared for the wave maker. At the wave maker waves were generated with a constant initial steepness 0.10, starting at a frequency 2 Hz. In this way the final plunging breaker obtained as a result of the collision of the 43 wave components was very close to the maximum that might be achieved. Fig. 6 shows results from 11 repeated experiments of this kind. Measured parameters are trough-to-crest wave height H_{zd}, zero-downcross wave period T_{zd}, horizontal asymmetry factor μ defined as the ratio between crest height and wave height, and finally crest front steepness ε_t (defined in Kjeldsen & Myrhaug (1980)). For each parameter both the mean value and the standard deviation σ are shown. From this result compared to 16 mm high speed film recordings of the plunging breaker, we conclude that the repetition in the generated freak waves is very high. Fig. 7 shows a non-dimensional plot of synoptic wave shape where experimental obtained values were compared with Cokelet's results for high order Stokes waves with the same steepness. $\varepsilon^2 = 0.70$ is Cokelet's expansion parameter.

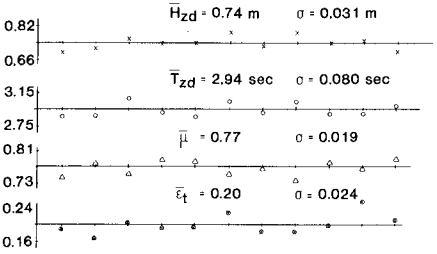

Fig. 6 Control of repetition in experiments.

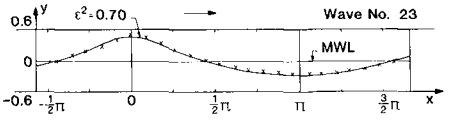

Fig. 7 Non-dimensional synoptic comparison of experimental wave component No. 23 at x = 5.5 m and Cokelet's results for high order Stokes waves.

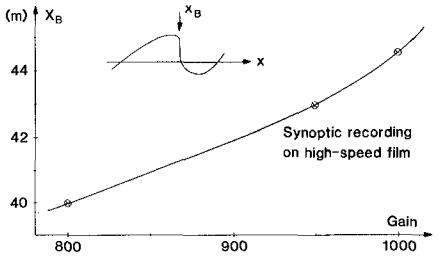

Fig. 8 Non-linear transfer of breaking point as a result of increase in gain on analog signal to wave generator.

The experimental wave component (No. 23) shown in Fig. 5 and measured at 5.5 m is converted from time domain to synoptic domain using equations given by Cokelet (1977, page 210). A coherence between experimental values and Cokelet's results is observed with steep wave crests and flat troughs. This is remarkable because Cokelet's results refer to a steady state condition, while the experiment is a highly transient condition. Thus, we take the observed coherence as a confirmation of the soliton theory used here. Finally, Fig. 8 shows a comparison between 3 identical transient tests with the same analog command signal but with a different gain on the wave maker. The positions x_B where the wave fronts become vertical are recorded and measured on high speed film and shown on the figure. Thus, when the gain is changed from 800 to 1000 the plunging breaker is shifted downwards in the wave flume from x_B = 40 m to x_B = 44.3 m. This is a true non-linear behaviour. Dispersion velocities of all wave components increase with increasing amplitude, and the experimental technique and control are advanced enough to keep the wave focusing properties. Thus, this new non-linear experimental technique can be used to finally adjust a violent plunging breaker to give a very direct strike on a test structure placed for instance 42 m from the point of wave generation.

7. DEVELOPMENT OF COMMAND SIGNALS FOR 3-DIMENSIONAL FREAK WAVES

The same technique was also extended to 3-dimensions. Experiments were carried out in the new ocean basin at the Norwegian Hydrodynamic Laboratories. The basin is 80 m long, 50 m wide and 10 m deep. At the 80 m long side 144 individually controlled single flap type wave generators are installed in an array. Each flap is a "Belofram" sealed membrane hinged 1.02 m below mean water level. At the other sides are efficient energy absorbing parabolic beaches. 144 different command signals of the same type as described in section 5 were prepared for these wave generators in such a way that focusing of wave energy would take place from many directions simultaneously resulting in a large pyramidal breaking wave close to the far end of the basin 40 m from the wave generators. Fig. 9 shows a very steep shortcrested breaking wave (pyramidal breaker) obtained at sea, while Fig. 10 shows a reproduction of the same situation in the ocean basin. The general conclusion from these tests is that non-linear effects in steep waves changed directional propagation and amplified energy focusing. Further, the small flap generators produced linear waves from linear command signals. Thus, it was not possible to generate non-linear solitons as described in section 5. (The wave maker used for the experiments shown in Fig. 5 is a large flap hinged 2.6 m below mean water level.) However, extreme non-linear waves were obtained in the end in the ocean basin as a result of the wave focusing, as can be seen in Fig. 10, but this was first obtained after a non-linear adjustment of wave phases. Finally, some experiments were carried out in which large freak waves were superposed at a certain time on a given directional spectrum using linear theory. However, this leads in all cases to spilling breakers and no plunging breakers were obtained in this way. A 16 mm film showing 3-dimensional experiments were shown at the conference. Further details on these experiments are given by Kjeldsen (1983).

Fig. 9 A dangerous wave captured at sea by Fukumi Kuriyama, Nikkor Club, Nippon, Kogaku, K.K. Japan.

Fig. 10 Reproduction of a pyramidal breaker at the ocean basin.

8. CONCLUSIONS

1) Linear wave theory failed to predict the experiments. Instead an analytical theory is developed that takes into account the observed non-linear dispersion of wave solitons. Command signals for generation of freak waves can thus be obtained as modified versions of equations (5.18) and (5.34).
2) Close to breaking individual wave components can no longer be regarded as travelling independently of each other. Instead, wave-wave interactions take place leading directly to generation of violent plunging breakers in deep waters.
3) The final amplitude of the obtained freak waves cannot be found as a sum of individual wave components measured close to the point of wave generation. A more complicated physical process determines the maximum amplitude where onset of wave breaking is the upper frame.
4) Transient non-breaking wave shapes can be generated with steepnesses that significantly exceed the theoretical value 0.14 for limiting steepness of steady state non-linear waves.
5) Application of this new non-linear transient wave generation technique showed the following advantages:

a) In most conventional tests performed with various structures in deep water plunging breakers are absent. In many conventional tests the total amount of breaking waves (spilling breakers, plunging breakers and bores) is too low. If a plunging breaker occasionally occurs in a simulated stochastic sea "by chance", it is nearly always out of the test section and far away from the structure under investigation. The transient test technique, however, can locate a most violent plunging breaker at a predetermined time and space that strikes exactly at the structure and repeats with great accuracy.

b) Both the total amount of breaking waves and the different types of breaking waves are main factors to consider in simulated seas. The amount of plunging breakers in simulated seas might determine if a critical event takes place or not (i.e. exceeding of breaking strength, capsizing of vessel). The transient deterministic test technique has been developed far enough to excitate resonance and amplify certain dangerous frequencies in a non-linear coupling. After establishment of a resonance a violent plunging breaker strikes the structure as the last wave in a long wave train.

c) The obtained 3-dimensional extreme waves represent a close approximation of the maximum wave height that might be obtained in a given directional wave spectrum with the physical restrictions and all the non-linear effects from wave interaction present. Thus, it represents an alternative choice, to the 100-year design wave obtained from an often uncertain mathematical extrapolation of limited field data from a short period of years.

d) Scale effects can be reduced because higher wave amplitudes and higher Keulegan-Carpenter numbers can be achieved. Conventional use of wave makers leads to lower wave amplitudes and larger scale effects.

e) Transient tests are more accurate than conventional test techniques. The deterministic transient tests can be programmed and planned in such a way that unwanted noise and parasitic disturbances on the responses can be avoided. The parasitic disturbances considered here are unwanted higher harmonics generated by the mechanical wave generators and unwanted reflections from beaches and flume walls. For this reason the transient test technique is a most efficient method to obtain the frequency transfer functions for responses of various structures in waves.

f) Application of transient deterministic test technique for mapping of extreme responses, means much more efficiency in the laboratory and lower costs, due to the fact that the extreme situation can be repeated with great accuracy many times in a single day of testing. On the other hand, conventional test programs for structures in deep waters very often have a long test period and in many cases not a single strike is obtained directly on the structure from a plunging breaker.

6) It was found that traditional stochastic experiments using wave spectra can be directly misleading in some cases. Stochastic experiments and transient experiments were performed on the same structure and the same maximum wave height was expected. However, the trough to crest oscillation in a measured mooring force became twice as high in the transient experiment compared to the stochastic experiment. Thus, conventional test methods give results that are on the non-conservative side in some cases and might lead to a severe underestimation of the wave forces the oceans are able to create.

9. ACKNOWLEDGEMENT

Norwegian Hydrodynamic Laboratories gratefully acknowledge a grant from the Continental Shelf Committee of the Royal Norwegian Council for Scientific and Industrial Research (NTNF).

10. REFERENCES

BAIRD et al. 1980: "Report on the Damages to the Sines Breakwater, Portugal" Proc. 17th Coast. Eng. Conf. Sydney, Australia.
BRUUN 1979: "Practical View on the Design of Mound Breakwaters". Rep. No. 7 Institute of Marine Civil Engineering, The Norwegian Institute of Technology, Trondheim, Norway.
BUHR HANSEN, SCHIOLTEN, SVENDSEN 1975: "Laboratory Generation of Waves of Constant Form" Series Paper No. 9. Institute of Hydrodynamics and Hydraulic Engineering, Technical University of Denmark, Copenhagen, Denmark.
COKELET 1977: "Steep Gravity Waves in Water of Arbitrary Uniform Depth" Philosophical Transactions of the Royal Society of London. No. 1335. Vol. 286, pp. 183-230.
DAVIS & ZARNICK 1964: "Testing Ship Models in Transient Waves" Proc. 5th Symposium on Naval Hydrodynamics, Ship Motions and Drag Reduction. Bergen, Norway.
FUNKE & MANSARD 1979: "SPLSH, A Program for the Syntesis of Episodic Waves" Report LTR-HY-65. Hydraulics Laboratory. National Research Council of Canada, Ottawa, Canada.
JOHNSON, PLOEG, MANSARD 1978: "Effects of Wave Grouping on Breakwater Stability". Proc. 16th Coast. Eng. Conf. Hamburg, Germany.
KJELDSEN 1978: "Breaking Waves in Deep Water". Paper and 16 mm Film presented at Euromech Colloquim No. 102. Bristol University, England.
KJELDSEN, VINJE, MYRHAUG, BREVIG 1980: "Kinematics of Deep Water Breaking Waves" Paper No. 3714. Proc. 12th Offshore Technology Conference, Houston, Texas, USA.
KJELDSEN & MYRHAUG 1980: "Wave-Wave Interactions, Current-Wave Interactions and Resulting Extreme Waves and Breaking Waves". Proc. 17th Conf. on Coast. Eng., Sydney, Australia.
KJELDSEN 1981: "Design Waves" Report No. 1 81008. Norwegian Hydrodynamic Laboratories, Trondheim, Norway.
KJELDSEN & PRICE 1982: "Wave Lengths and Average Crest Lengths in Tank Generated 3-Dimensional Irregular Seaways" Report No. 1 82112. Norwegian Hydrodynamic Laboratories, Trondheim, Norway.
KJELDSEN 1983: "Freak Wave Hydrodynamics - and some of the Engineering Applications" Summary Report prepared for the Continental Shelf Committee of the Royal Norwegian Council for Scientific and Industrial Research (NTNF) by Norwegian Hydrodynamic Laboratories, Trondheim, Norway. (in press)
MANSARD, FUNKE, BARTHEL 1982: "A New Approach to Transient Wave Generation" Proc. 18th Intern. Conf. on Coastal Engineering, Cape Town, South Africa.
NEDRELID 1978: "An Analysis of Earlier Capsizing Accidents". Report project "SHIPS IN ROUGH SEAS". Norwegian Hydrodynamic Laboratories, Trondheim, Norway. (in Norwegian)
NSFI/RINA 1982: "Seminar on the Norwegian "Ships in Rough Seas" (SIS) Project". Held at RINA 5th February, 1982. Occasional Publication No. 5. The Royal Institution of Naval Architects, London, England.
STEPHENS et al. 1981: "Sailing Yacht Capsizing". Chesapeak Sailing Yacht Symposium, Annapolis, Maryland, USA.
TAKEZAWA 1981: "New Wave Generation Techniques for Seakeeping Tests". Proc. 16th International Towing Tank Conference, Leningrad, USSR.

ZAKHAROV 1968: "Stability of Periodic Waves of Finite Amplitude on the Surface of a Deep Fluid" Journal of Applied Mechanics and Technical Physics. Vol. 2, pp. 190-194.
ZAKHAROV & SHABAT 1972: "Exact Theory of Two-Dimensional Self-Focusing and One-Dimensional Self-Modulating Waves in Nonlinear Media". Sovjet Journal of Experimental and Theoretical Physics. Vol. 34, No. 1. January 1972, pp. 62-69.

LABORATORY PHOTOGRAMMETRIC WAVE HEIGHT MEASUREMENT

J.D. POS[1] and F.A. KILNER[2]

ABSTRACT

The paper describes the experimental procedure used to produce a computor contour plot of the wave height distributions and wave directions in a model basin, using photogrammetric techniques. Only monochromatic waves are analysed. A technique is outlined to simulate and measure waves entering a basin of infinite extent, in other words to photograph the penetration of a wave train into a harbour basin before the pattern has been contaminated by reflections. Proof is offered that this infinite basin technique is a valid representation of the steady state situation of a continuous wave train entering an infinite basin.

INTRODUCTION

Model harbours are used by coastal engineers as an aid in the optimization of harbour designs. The models predict wave heights in full scale harbours, the results being used to reduce these wave heights to a minimum in order to prevent damage to moored ships, to the wharf structure and to the mooring systems. Two main limitations in experimental procedures are encountered, however, when attempting to measure accurately the wave height distributions within model harbours; these are:-

(1) Wave heights in model harbours are commonly measured using parallel wire resistance or capacitance wave probes. A number of these probes are usually mounted on a moveable instrument carriage which can traverse the wave basin to measure the wave heights. Such a configuration was used by Harms [3]. The disadvantage of this system is that the wave height at only a limited number of discrete locations can be measured at any one time. The system is also time consuming, since the instrument carriage has to be moved within the wave basin until the entire water surface has been measured. Furthermore, excessive spacing of these wave probes may result in points of maximum wave heights being overlooked.

---

[1] Ph.D. candidate, Civil Engineering Dept., University of Cape Town, South Africa.

[2] Associate Professor, Civil Engineering Dept., University of Cape Town, South Africa

(2) Wave measurements using the above system necessitate (in most cases) that the wave paddle must run continuously. This enables secondary effects, (such as wave reflections, basin oscillations, cross waves, etc.) to develop and distort the generated wave, thus causing marked anomalous wave height variations along the generated incident wave crests. These problems are discussed in depth by Harms [3].

The two abovementioned problems effectively prevent the achievement of accurate wave height and pattern measurement in model harbours. This paper describes research at U.C.T. directed towards solving these problems by using stereophotogrammetry. A photogrammetric technique is described which enables an instantaneous, synoptic and permanent three dimensional record to be obtained of the deformed water surface in a model harbour. A procedure is also described to achieve a computer generated contour plot of the experimental wave height distributions in a wave basin.

DEVELOPMENT OF THE TECHNIQUES USED

In some early attempts at using stereo-photography for the measurement of a deformed water surface, it was appreciated that in clear water it is difficult to distinguish surface features from bed details, thus some method was needed for making the water surface opaque. The substance used must not significantly affect the wave process under investigation, ideally it should also be cheap and non-contaminating with regard to laboratory installations. Surface applications such as aluminium powder and confetti were first tried and were found to be very inconvenient, then various solutions such as P.V.A. in water were tried but were found to settle out quite quickly. Eventually it was found that a low concentration of cutting oil in water, about 0,7 per cent, gave a suitably milky fluid which satisfied the above requirements.

It was found necessary to arrange for special illumination for the water surface and this was achieved by employing 4 conventional lecture room type overhead projectors placed 4m above the water surface in the plan positions shown in Fig. 1. However, when faced with the viewing and interpretation of stereopairs, it was found impossible to identify corresponding points in the photographs without introducing some optical contrast onto the water surface, and this was effected by placing transparencies in the projectors containing black geometrical shapes alternating with translucent areas. Initially, pattern geometry was used, for example concentric black rings, but this was abandoned because it was found that the pattern interfered with the viewer's three dimensional perception. Subsequently random assemblies of black stars and arrows were used, and this is now our standard practice. With regard to photography, two Zeiss Jena metric cameras were used at an elevation of about 5m above water surface and 1.9m apart. At first, the cameras, coupled to their synchronization device, were relied upon to give synchronized exposures of identical duration, but detailed examination of the camera performance showed that this was not reliable, and therefore the projectors were converted into flash units

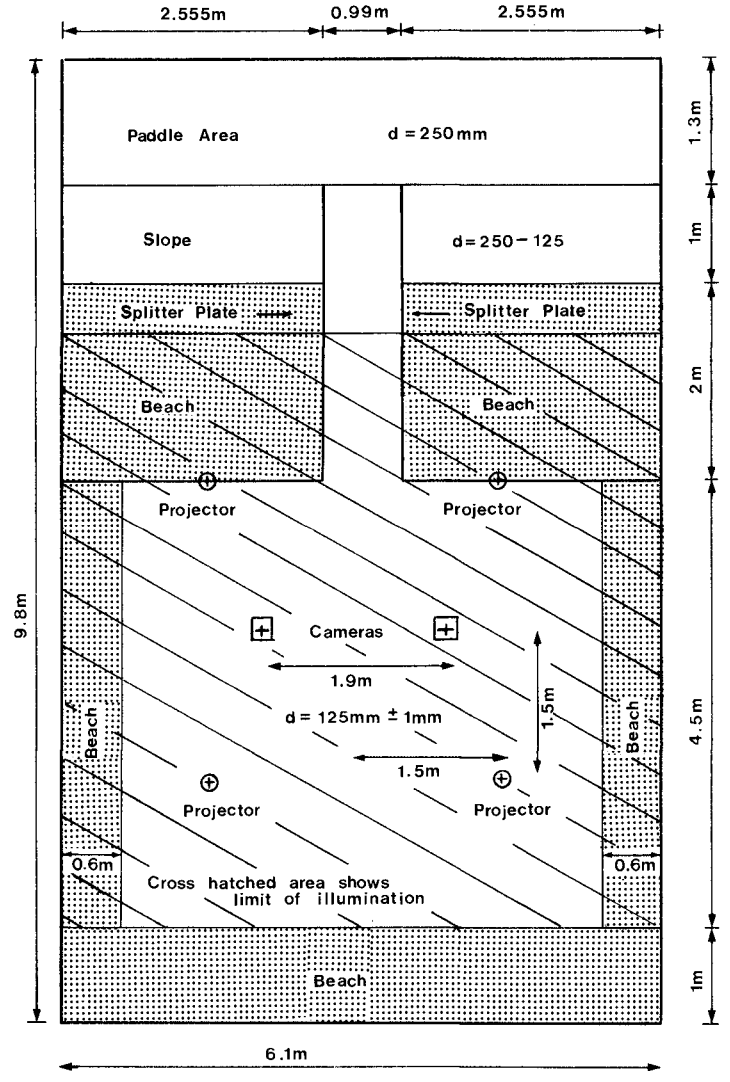

Fig. 1 TYPICAL HARBOUR CONFIGURATION

by replacing the conventional bulbs with flash bulbs, placed at the focal points of the focusing lenses, and fired by a common capacitance. A shutter speed setting of 1/30 second was used, to allow both shutters to be open a sufficient time to encompass the flash duration (allowing for the variation in shutter speeds between the cameras and their lack of synchronisation) and to ensure that the illuminated control points were adequately exposed. All photography took place at night. Due to the very short flash duration, of less than a millisecond, the water surface detail was effectively "frozen" (i.e. very little image movement) in the stereopairs.

The next concern is to consider how the photographs are to be interpreted to yield information about wave heights at points in the field of view. Bearing in mind that a wave height is the vertical distance between a crest at a selected point and a subsequent (or preceding) trough at that point, it is clear that two stereopairs are needed, and these were arranged to be taken such that the waves imaged in the 2nd stereopair are 180° out of phase relative to the waves imaged in the 1st stereopair, making use of two electronic microswitches triggered by the wave paddle mechanism. Algebraic subtraction of the two resulting deformed water surfaces gave the wave heights at all points where a crest or trough appeared in either stereopair. In the earlier stages of the investigation a Zeiss (Jena) Topocart stereoplotter was used to analyse the photographic plates, and was found capable of measuring the wave heights with an average error of 2 mm. This method, however, requires the use of very expensive metric survey cameras in addition to the very expensive stereoplotter (plus a specially trained operator), and therefore a cheaper and slightly more accurate alternative approach was adopted. These earlier stages of the investigation are described in full by Adams and Pos [2].

It was decided that the water surface elevations would be measured using projective transformations. A brief description of the theory of projective transformations is given by Adams [1]. The advantages of this method are that the plates can be viewed by a relatively inexperienced operator using a less expensive Zeiss (Jena) stereocomparator, (i.e. less expensive than a stereoplotter). The water surface elevations are determined by microcomputer using the theory of projective transformations. This method is inherently more accurate than the previous one since the human error involved in the relative and absolute orientation of the stereoplotter is eliminated. Also the projective transformation calculations enable the inner orientation elements (principal distance and principal point) of the cameras to be determined for each stereopair. (Thus far cheaper non metric cameras can be used).

PROJECTIVE TRANSFORMATION THEORY

The theory and mathematical techniques employed are described by Adams [1] and Welham [4]. For ease of reference the appropriate formulae and their solutions are summarised below.

Calculation of Transformation Parameters

$$X_i b_{11} + Y_i b_{12} + Z_i b_{13} + b_{14} - x_i X_i b_{31} - x_i Y_i b_{32} - x_i Z_i b_{33} = x_i, \quad (1)$$

$$X_i b_{21} + Y_i b_{22} + Z_i b_{23} + b_{24} - y_i Y_i b_{31} - y_i Y_i b_{32} - y_i Z_i b_{33} = y_i, \quad (2)$$

where

X_i, Y_i, Z_i are free net space co-ordinates of point P_i ,

x_i, y_i are comparator image co-ordinates of point P_i referred to an aribtrary origin,

b_{ij} are transformation parameters.

In the solution of the transformation parameters, both the image and object co-ordinates are assumed to be error free and the best mean b_{ij} terms are determined using normal equations formed from quasi-observation equations as follows:

b_{11}	b_{12}	b_{13}	b_{14}	b_{21}	b_{22}	b_{23}	b_{24}	b_{31}	b_{32}	b_{33}	= l
X_1	Y_1	Z_1	1	0	0	0	0	$-x_1X_1$	$-x_1Y_1$	$-x_1Z_1$	x_1
X_2	Y_2	Z_2	1	0	0	0	0	$-z_2X_2$	$-x_2Y_2$	$-x_2Z_2$	x_2
.	.	.	.	.	.	.	.	.	.	.	.
.	.	.	.	.	.	.	.	.	.	.	.
X_n	Y_n	Z_n	1	0	0	0	0	$-x_nX_n$	$-x_nY_n$	$-x_nZ_n$	x_n
0	0	0	0	X_1	Y_1	Z_1	1	$-y_1X_1$	$-y_1Y_1$	$-y_1Z_1$	y_1
0	0	0	0	X_2	Y_2	Z_2	1	$-y_2X_2$	$-y_2Y_2$	$-y_2Z_2$	y_2
.	.	.	.	.	.	.	.	.	.	.	.
.	.	.	.	.	.	.	.	.	.	.	.
0	0	0	0	X_n	Y_n	Z_n	1	$-y_nX_n$	$-y_nY_n$	$-y_nZ_n$	y_n

A matrix — L matrix

From these quasi-observation equations, the 'B' matrix can be solved as usual from $B = (A^TA)^{-1} A^TL$.

Most modern desk top or microcomputers can deal with a matrix inversion of this size (11 x 11) and the solution equations adopted take into account any redundant control points imaged and used for calculating the most likely b_{ij} values.

Calculation of Space Co-ordinates using Stereopair

$$\left.\begin{aligned}
(x_i b_{31} - b_{11})X_i + (x_i b_{32} - b_{12})Y_i + (x_i b_{33} - b_{13})Z_i &= b_{14} - x_i \\
(y_i b_{31} - b_{21})X_i + (y_i b_{32} - b_{22})Y_i + (y_i b_{33} - b_{23})Z_i &= b_{24} - y_i \\
(\bar{x}_i \bar{b}_{31} - \bar{b}_{11})X_i + (\bar{x}_i \bar{b}_{32} - \bar{b}_{12})Y_i + (\bar{x}_i \bar{b}_{33} - \bar{b}_{13})Z_i &= \bar{b}_{14} - \bar{x}_i \\
(\bar{y}_i \bar{b}_{31} - \bar{b}_{21})X_i + (\bar{y}_i \bar{b}_{32} - \bar{b}_{22})Y_i + (\bar{y}_i \bar{b}_{33} - \bar{b}_{23})Z_i &= \bar{b}_{24} \quad \bar{y}_i
\end{aligned}\right| \qquad (3)$$

where the unbarred elements refer to the left hand picture and the barred elements to the right hand picture. Let 'C' be the matrix of the left hand coefficients and 'L' the matrix of the right hand terms. The space co-ordinates of an image point (X, Y, Z) can be found from

$$\begin{pmatrix} x \\ y \\ x \end{pmatrix} = (C^T C)^{-1} C^T L.$$

It will be noted that the traditional elements of inner and relative orientation are not apparent, but these can be obtained from a knowledge of the b_{ij} elements if so desired.

Summarised, the appropriate inner orientation equations are:

Non-zero scalar λ:

$$\lambda^{-2} = b_{31}^2 + b_{32}^2 + b_{33}^2 \qquad (4)$$

Principal point co-ordinates (comparator system):

$$x_p = (b_{11}b_{31} + b_{12}b_{32} + b_{13}b_{33})\lambda^2 \quad , \qquad (5)$$

$$y_p = (b_{21}b_{31} + b_{22}b_{32} + b_{23}b_{33})\lambda^2 \quad , \qquad (6)$$

Equivalent principal distance:

$$c_x^2 = (b_{11}^2 + b_{12}^2 + b_{13}^2)\lambda^2 - x^2 p \quad , \qquad (7)$$

$$c_y^2 = (b_{21}^2 + b_{22}^2 + b_{23}^2)\lambda^2 - y^2 p \quad , \qquad (8)$$

Use average of c_x and c_y.

Unless it is intended to plot from the stereopair using a stereoplotter, the inner orientation elements are of academic interest only and therefore only equations (1), (2) and (3) are relevant.

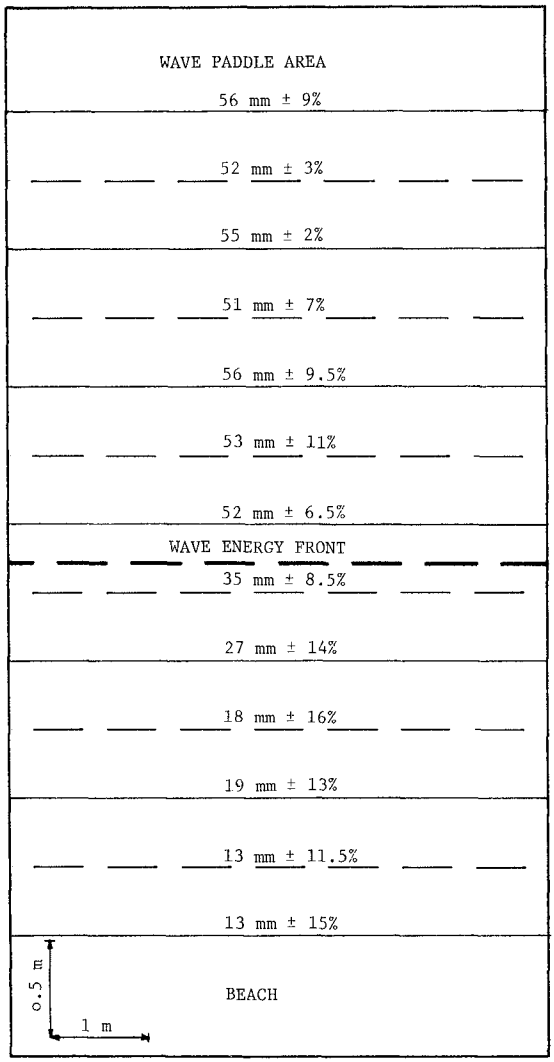

Fig.2 WAVE ENERGY FRONT

CONTROL POINT CONFIGURATION

Initially 12 control points were used (a minimum of 6 control points imaged in the overlap area of the stereopairs are required), 8 at levels above the water surface and 4 at levels below the wave surface (in open canisters). This was done since it was postulated that more accurate results would be obtained if the surface to be measured was straddled by control points, i.e. interpolation, rather than extrapolation as was the case for the first configuration (as described in [2]) which had 4 control points above the water surface. Stereopairs, using the infinite basin technique, were taken of the energy front of a plane long crested wave train entering an area of still water. On analysing the stereopairs it became obvious that the 280 mm maximum vertical distance between the two planes of control points was inadequate to determine the projective transformation parameters with sufficient accuracy. This problem was subsequently overcome by constructing an additional plane of 4 control points approximately 540 mm above the original upper control points.

To determine the XYZ positions of the 16 control points they were first levelled and then 48 inter control points measurements were taken using a steel tape. The corrected data was analysed using a least square adjustment program written for the Tektronix 4051 by Dr. H. Rüther of the Survey Department, U.C.T., and an accuracy in X, Y of better than 1 mm was achieved. Research work done by Welham [4] indicates that the control configuration used was more than adequate for the accurate determination of the projective transformation parameters. Since photography took place at night each control point was individually illuminated.

THE INFINITE BASIN TECHNIQUE

An analysis of the steady state results coupled with visual observations of the deterioration of the wave field in the basin after a very short period of wave paddle action lead to the development and adoption of the infinite basin technique. It was observed that when the wave paddle was subsequently stopped and the main wave train had traversed the basin, a marked reflection and resonsance mode was evident in the basin, which took a few minutes to dissipate. This reflection and resonance mode was obviously superimposed upon the wave field in the basin under steady state conditions.

It was hypothesized that it would be possible to simulate the steady state situation of a continuous wave train entering an infinite basin by sending a wave train into a model basin of still water and taking a stereopair of the water surface just as the wave energy front reached the peripheral beaches. To test this hypothesis, two stereopairs were taken of the wave energy front region of a typical wave train entering an open basin of initially still water. On analysis it was found that the wave heights of the crests immediately behind the wave energy front were closely equal to the mean wave height between the front and the generator. The experimental configuration analysed and the results obtained is shown in fig. 2 . A wave train of period T=0,74 seconds was propagated in a water depth d=138 mm. The crestlines observed in the 1st stereopair are shown as solid lines, while the trough lines

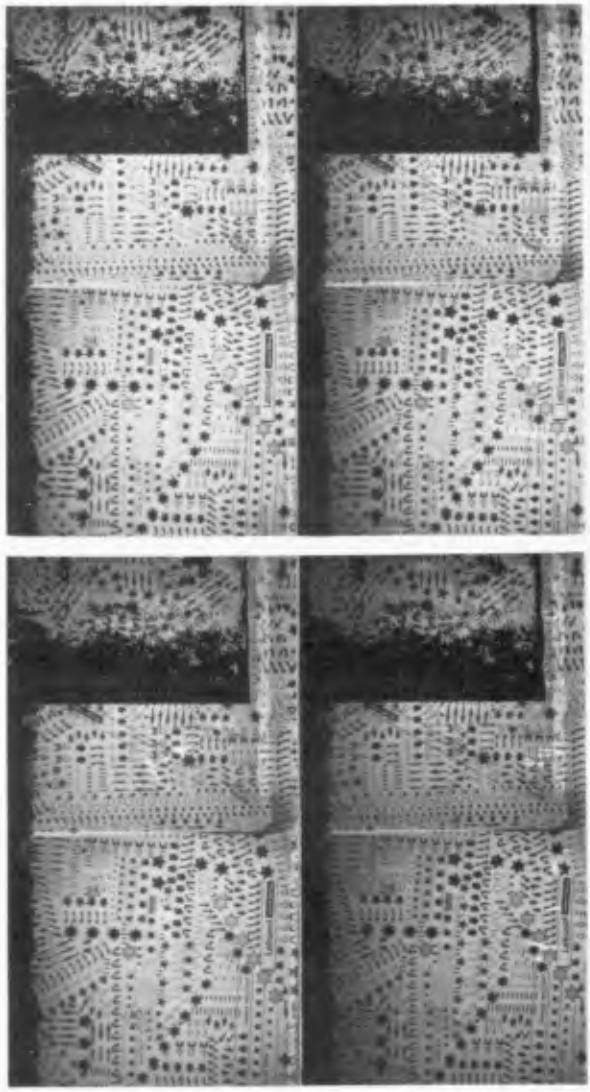

FIG. 3 STEREO PAIRS TAKEN OF MODEL HARBOUR CONFIGURATION

observed in the 1st stereopair are shown as dashed lines. The calculated position of the wave energy front is shown as a thick dashed line. The mean wave heights plus the observed percentage variation from the mean is shown for each crest and trough line. Note the trough lines observed in the 1st stereopair are coincident with the crest lines observed in the 2nd stereopair and vice versa.

MODEL HARBOUR CONFICURATION ANALYSED USING INFINITE BASIN TECHNIQUE

The stereopairs in fig. 3 show waves entering the model harbour basin shown in fig. 1. The basin is 4,5 m long and 4,8 m wide. (These dimensions do not include the crushed stone beaches along the side and back walls of the basin.) The incident wave train has the following characteristics: wave period 0,67 seconds, wave height approx. 55 mm, and wave length (calculated using Airy wave theory) 604 mm. The gap to wavelength ratio (i.e. B/L ratio) is 1,64 The water depth is 125 mm ±1 mm. The stereopairs shown were taken 14,5 seconds after starting the wave paddly at which stage the wave energy front was at the toe of the back wall beach. The second stereopair was taken with the waves in the basin 180° out of phase relative to the waves imaged in the first stereopair. This means that the troughs imaged in the second stereopair occupy the positions of the crests imaged in the first stereopair. If one substracts the crest and trough elevations of the first stereopair from their corresponding elevations in the second stereopair, one will achieve a plot of wave height distribution within the basin. Since the harbour configuration is symmetrical about the centre line, only the left hand side of the basin is shown in fig. 3.

WAVE HEIGHT MEASUREMENT PROCEDURE

The process of achieving a plot of wave height distributions within the model basin is briefly summarised in fig. 4. The stereopairs are analysed using a Zeiss (Jena) stereocomparator which is interfaced via an analog to digital converter and a data communications interface with a Tektronix 4051 microcomputer. The microcomputer, under program control, stores the X, Y and PX, PY data obtained from the stereocomparator for each point observed. The stereopairs can also be analysed on a digitiser tablet using a modified stereoscope and a special double cursor (as described by Welham [4]). Using this alternative technique the wave heights can be measured with an accuracy of 5 to 6 mm. Once a set of points has been observed, the raw data is edited, prepared for transfer to flexible disc, and then stored on tape. The tape is then transferred to a second Tektronix 4051 which has a flexible disc file manager, and the data transferred from tape to disc, under program control. All subsequent analysis is performed on the second Tektronix 4051.

The analysis procedure which is outlined by the procedural flowchart in fig. 5 is as follows: the control points and crests imaged in the first stereopair and the control points imaged in the second stereopair are observed using the stereocomparator. The observed data is then analysed using the program "Waveheight", written by the first author, to yield:- the inner orientation elements and projective transformation parameters for the 1st and 2nd stereopairs, the crest elevation data

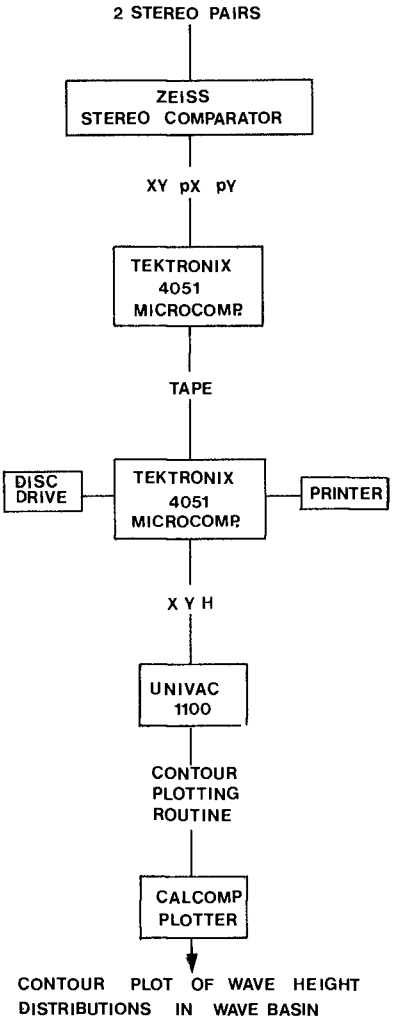

Fig.4 SEQUENCE OF ANALYSIS

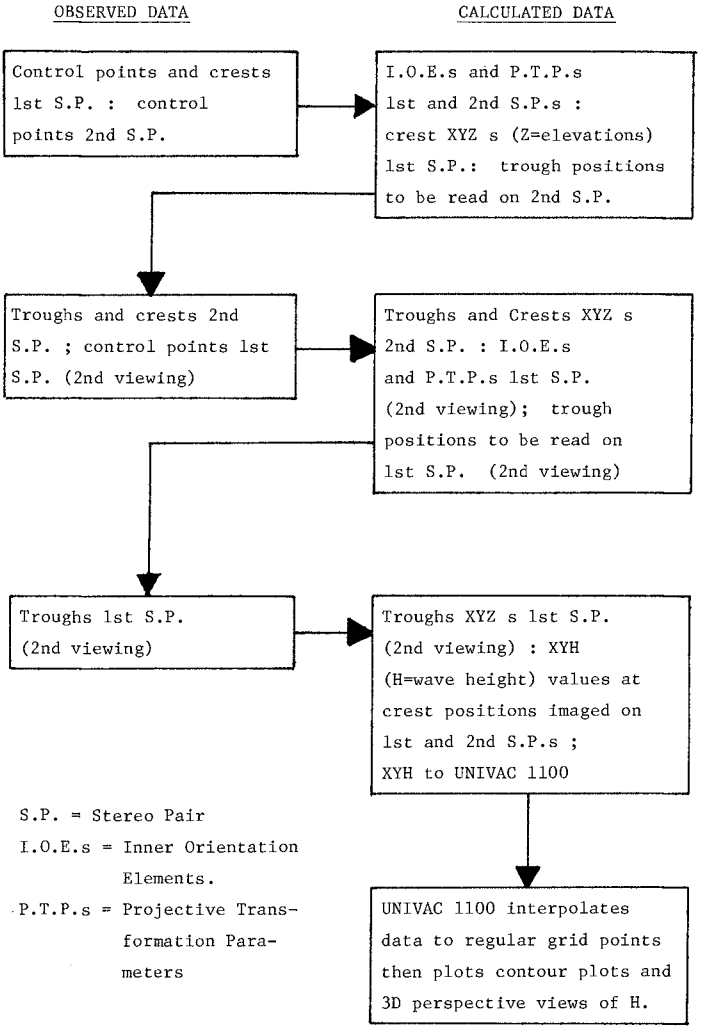

Fig.5 PROCEDURAL FLOWCHART

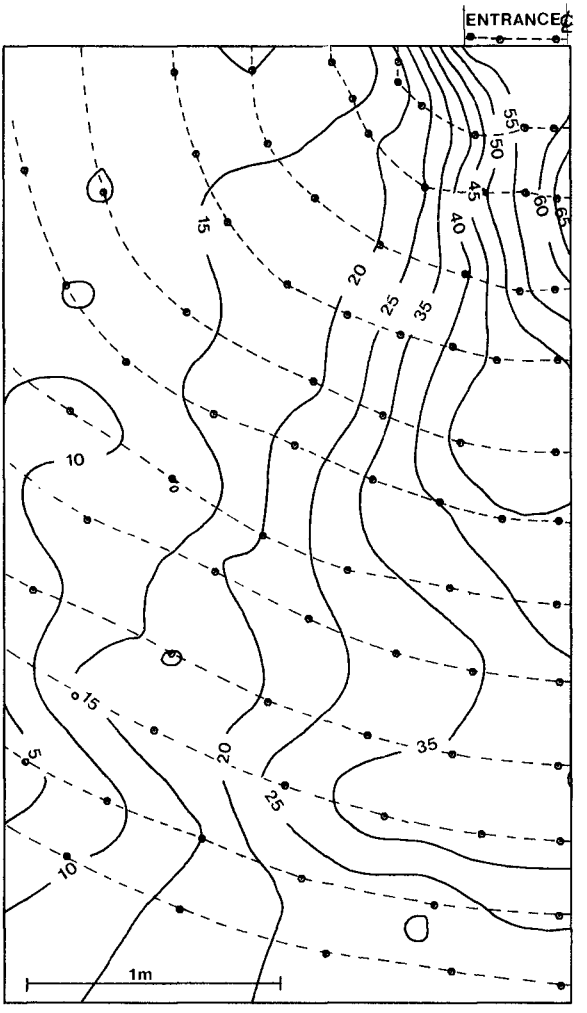

Fig.6 COMPUTER CONTOUR PLOT OF WAVE HEIGHTS IN A MODEL HARBOUR (HEIGHTS IN MM)

(crest XYZ data) for the 1st stereopair, and the positions at which the troughs must be observed on the 2nd stereopair. The troughs imaged in the 2nd stereopair are then observed at the predetermined points, while the crests are observed at arbitrary points selected by the observer. The 1st stereopair is again placed in the stereocomparator and the imaged control points are observed. This observed data is analysed using the programme "Waveheight" to yield: trough and crest XYZ data for the 2nd stereopair, inner orientation elements and projective transformation parameters for the 1st stereopair (2nd viewing), and the trough positions to be observed in the 1st stereopair (2nd viewing). The troughs imaged in the 1st stereopair are then observed. The observed data is then analysed using the program "Wave height" which yields: The trough XYZ data for the 1st stereopair and the XYH values along the crest lines imaged in the 1st and 2nd stereopairs, H is the wave height at a point within the basin. From the results obtained it is estimated that the wave heights can be measured with an accuracy of better than 2 mm.

The XYH data is then transfered to a file on the UNIVAC 1100 at U.C.T. The Saclant Graphics Package installed on the UNIVAC is then used to interpolate the raw data onto a rectangular equidistant grid. The interpolated data can then be used to plot a contour plot or a 3 dimensional perspective picture of the wave height distributions within the model harbour basin. The stereopairs, shown in fig. 3, were analysed using the procedure described above to yield the contour plot of wave heights within the basin, shown in fig. 6. Since the harbour configuration is symmetrical about the centre line, only the left hand side of the basin is shown. The dashed lines indicate the crest lines plotted from both stereopairs. The black dots indicate the crest line sampling points plotted from both stereopairs.

CONCLUSIONS

The two major problems which prevent the accurate measurement of wave heights in model harbours using conventional techniques (as described in the introduction) have been successfully solved using the photogrammetric technique. Problem (1) is solved since the two stereopairs of photographs can be taken in a much shorter period than is required for a scan using wave probes, and the information contained on the plates is permanent, synoptic and detailed. Furthermore, there is no instrumental interference in wave processes being observed. Problem (2) can be overcome by using the infinite basin technique, that is by photographing before the wave energy is reflected from internal walls, thus eliminating the distorting effects of wave reflections within a model basin. The infinite basin technique effectively enables the researcher to accurately model the situation of a continuous wave train entering a basin of infinite extent.

Three areas of utilisation for the photogrammetric wave height and pattern recording technique appear possible, the first is the routine use in applied investigations where refraction or diffraction effects are important, for example, the analysis of model harbour configurations. The second is to make use of the procedures as a check on the validity of various existing wave theories, where the information obtained (instantaneous and high accuracy) should be decisive. The third area of utilisation is to apply the technique in close conjunction with

mathematical modelling (such as finite element modelling) in order possibly to calibrate the models and thus improve their predictions.

ACKNOWLEDGEMENTS

The authors would like to thank Professor L.P. Adams, Dr. H. Rüther and Mr. L.G. Welham of the Department of Surveying, University of Cape Town, South Africa, for their assistance in the development of the photogrammetric technique.

REFERENCES

1. Adams, L.P., "An Experiment with Analytical Shadow Stereophotogrammetry", The Photogrammetric Record, Vol. 9, No. 54, October 1979.

2. Adams, L.P. and Pos, J.D., "Model Harbour Wave Form Studies by Short Range Photogrammetry", The Photogrammetric Record, Vol. 10, No. 58, October 1981.

3. Harms, W.W., "Diffraction of Waves by a Shore Connected Breakwater", Journal of the Hydraulic Division, Proc. of the ASCE, Vol. 105, December 1979.

4. Welham, L.G., Underwater Stereometrology for Scientists and Engineers using non-metric Cameras M.Sc thesis, Dept. of Surveying, University of Cape Town, South Africa, December 1982.

A NEW APPROACH TO TRANSIENT WAVE GENERATION

E.P.D. Mansard[1] and E.R. Funke[2]

ABSTRACT

An analytical model of an "episodic" wave as a function of time is given. The linear dispersion theory is applied to the transient to hindcast the wave train at a wave board which is a specified distance up-wave from a test site. First order wave board theory and linear system theory is used to convert the wave train at the wave board into a control signal. Conversion of the time discrete control signal into a smooth analog voltage signal by means of a real time digital program is described. Examples of numerical simulations and physical measurements are given.

INTRODUCTION

Testing of coastal structures in hydraulic laboratories is generally performed by wave attack with either regular or irregular waves. Occasionally it is desirable to study fixed or floating structures by exposing them either to extremely large waves or to particular successions of large waves as may be encountered in wave groups.

Whereas many researchers believe that the use of long sequences of random waves for testing purposes offers a high probability that all extreme test conditions will be encountered sooner or later, experience at NRC has indicated that this is not generally the case. During a capsize test of a communication buoy, irregular waves for a fully developed sea failed to capsize the buoy whereas a particular transient wave, designed to break at the buoy location, achieved a capsize every time (Photographs 1 and 2). Other examples for the application of transient wave conditions are overtopping tests and the measurement of pressure and forces due to extreme waves. Purely from the point of view of being able to exercise more precise control of wave profiles at the test site as well as the greater testing efficiency and resulting time saving, the deterministic approach to wave generation has an appeal to the experimental scientist.

Episodic waves have been generated successfully by various laboratories using a "sweep frequency" technique. The span and the

[1]Dr.-Ing., Associate Research Officer, Hydraulics Laboratory, National Research Council Canada, Ottawa, Ontario K1A 0R6, Canada.
[2]B.Sc., M.Sc., Senior Research Officer, Hydraulics Laboratory, National Research council Canada, Ottawa, Ontario K1A 0R6, Canada.

PHOTO 1

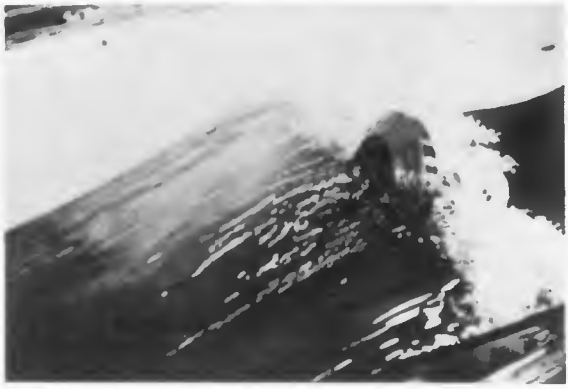

PHOTO 2

SEA KEEPING TEST OF A COMMUNICATION BUOY

sweep rate were determined experimentally to achieve a breaker at a certain distance from the wave board. A variation of this method was described by Funke and Mansard (1979) which determines the sweep rate by calculating the periods of successive wave singlets in a wave train which is being assembled to achieve breaking at a predefined distance from the wave board. This technique is described in Figure 1 which illustrates the principle that the singlet of period $1/F_a$ requires T_a seconds to travel a required distance D at group velocity. Therefore, if a second singlet is to be generated, which can catch up and overtake the first singlet within distance D, then it must do so in $T_a - 1/F_a$ seconds. Because there is now less time available, the second singlet must, of necessity, be of a longer period than the first because longer period waves travel faster.

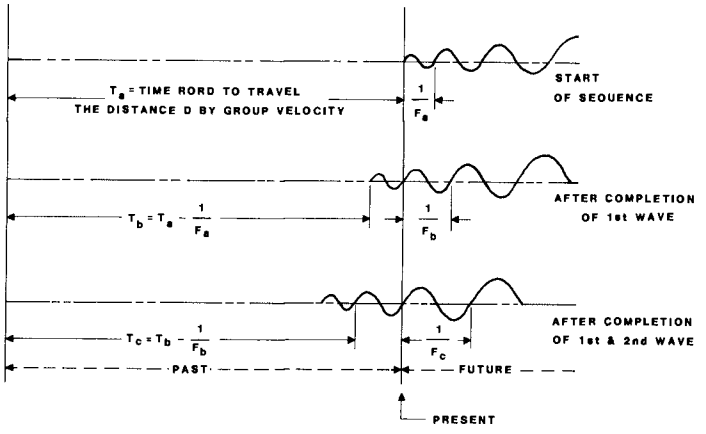

FIG.1 TRANSIENT WAVE GENERATION BY SWEEP FREQUENCY METHOD

Although the "sweep frequency" methods have proven that control over the wave breaker location is possible, they do not permit any control over the profile of the wave transient. The method by Funke and Mansard (1979) assumed that every singlet should have an amplitude of 1/10 of the associated wave length. As a result, the actual breaking occurs when the wave becomes critically steep due to the superposition of waves and not necessarily when all wave singlets have achieved phase coincidence.

The new method described here is based on a description of the desired wave transient at the test site and on the principle that, through the application of linear dispersion theory, the corresponding wave sequence at the location of the wave board can be hindcasted. It should therefore be possible to generate wave groups with an arbitrary number of waves per group and with arbitrary steepness. Limitations are, of course, imposed by physical realizability.

DEFINING THE WAVE TRANSIENT

To illustrate the method, the generation of a wave group with a finite number of waves is being described. In the absence of an analytical description of such a wave or wave train as a function of time, a mathematical function has been composed which gives the water surface elevation $\eta(t)$ as may be observed at a single point at the test site in a wave flume or basin. This function is given as:

$$\eta(i\cdot\Delta t) = \sum_{n=1}^{n_{max}} \frac{H\cdot T\cdot e^{-(\gamma\cdot t)^2}\cdot \sin(n\pi\rho/T}{\pi^2\cdot n^2\cdot\rho\cdot(1-\rho/T)} \cdot \sin(2\pi n\cdot i\Delta t/T) \qquad (1)$$

where n_{max} = is the maximum number of participating harmonics

H = is the wave height of an unmodulated saw tooth wave form

T = is the period of the saw tooth

γ = $\sqrt{3}/(\beta\cdot T)$

β = is the half amplitude width of the Gaussian envelope function

ρ = is a steepness parameter.

Equation (1) may best be understood with reference to Figure 2. See also Moskowitz and Racker (1951). The term

$$\frac{H\cdot T\cdot \sin(n\pi\rho/T)}{\pi^2\cdot n^2\cdot\rho\cdot(1-\rho/T)}$$

gives the nth Fourier coefficient for a saw tooth wave form with steepness parameter ρ. If ρ=0.5, the saw tooth is symmetrical with front and back steepness being equal. If ρ=1.0, then the wave front is infinitely steep. In practice, ρ=0.75 appears to be satisfactory. The

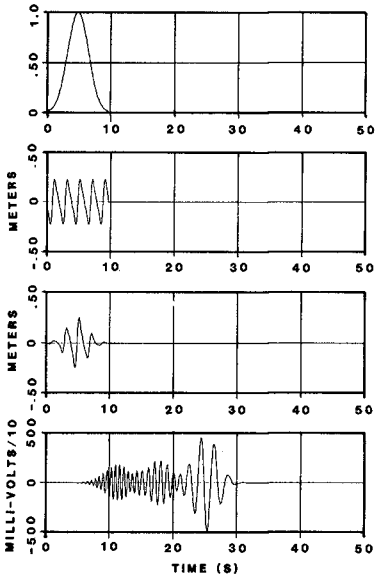

BELL SHAPE MODULATOR

WITH: $\beta = 2$

SAW-TOOTH WAVE WITH:
$H = 0.5M$
$\rho = 0.75$
$T = 2$ SEC
$n_{max} = 4$

RESULTANT TRANSIENT WITH:

TN = 50 SEC

CONTROL SIGNAL FOR WAVEMAKER WITH:

-PISTON MODE
-0.9M DEPTH OF WATER
-10M DISTANCE FROM TEST SITE

FIG.2 SYNTHESIS OF AN EPISODIC WAVE

second graph in Figure 2 illustrates five cycles of a saw tooth wave for H=0.5 m, ρ=0.75, T=2 seconds and n_{max}=4. This trace results from evaluating $\sin(2\pi \cdot n \cdot i\Delta t/T)$ for $0<i\Delta t<10$ seconds.

n_{max}, in the summation of equation 1, may be limited in order to avoid very sharp, non-realizable crests and troughs in the saw tooth. Alternatively, n_{max} may be used to limit the maximum frequency in the wave machine control signal.

The term $e^{-(\gamma \cdot t)^2}$ in equation (1) gives an amplitude modulator which is applied to the saw tooth. $\gamma=\sqrt{3}/(\beta \cdot T)$ may be used to control the width of this bell shaped function. In the example, β=2, which implies that the half amplitude width is $\beta \cdot T=4$ seconds, the bell function is centred at $t=1.21 \cdot \beta \cdot T$.

The result of modulating the saw tooth is given as the third trace in Figure 2. This is the theoretical wave transient as a function of time and represents the wave which is to be generated at a test site some distance from the wave board.

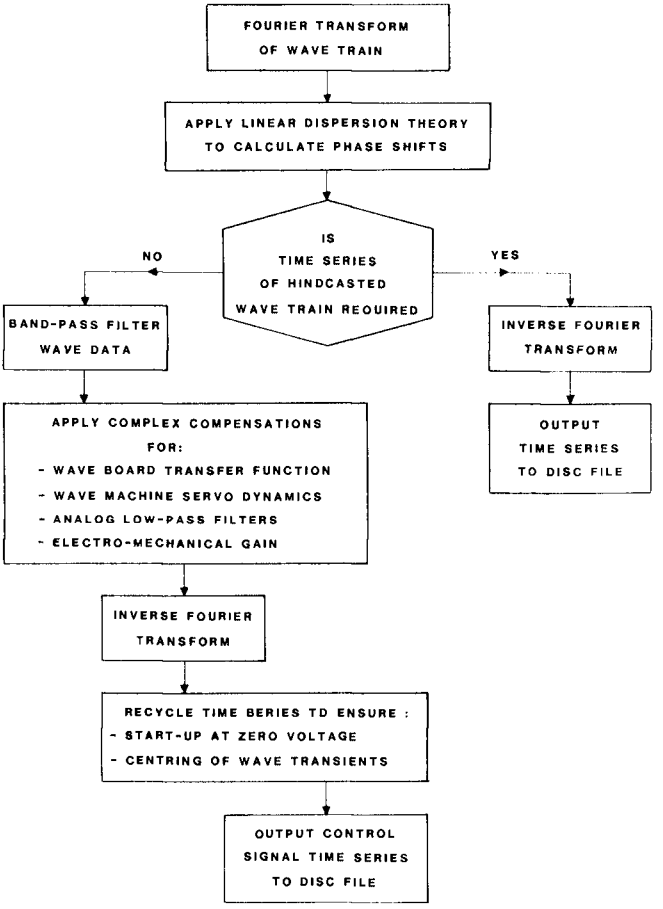

FIG.3 SUMMARY OF OPERATIONS REQUIRED FOR CONVERTING A WAVE TRAIN TO A WAVE MACHINE CONTROL SIGNAL

Discrete Fourier transform considerations require that a recycling period is specified. Also, for purposes of conducting a test, it is preferable to introduce a quiescent period between successive wave transients in order to permit disturbances in the flume to settle down after each transient has traversed the length of the flume. For this reason a recycling period T_n is introduced which was set to 50 seconds for the example of Figure 2.

COMPUTATION OF THE WAVE GENERATOR CONTROL SIGNAL

The conversion of the wave train, defined in Equation (1) and Figure 2, to a wave generator control signal is accomplished by first submitting the time series to a program known as RWREP which is described by Funke and Mansard (1983). This computer program performs a variety of operations which are summarized in Figures 3 and 4.

All these operations are being implemented in the frequency domain and therefore the desired wave train is first Fourier transformed.

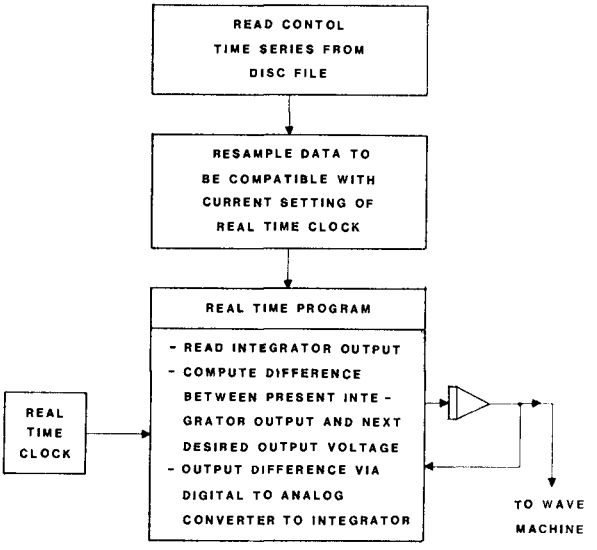

FIG.4 CONVERTING A CONTROL TIME SERIES TO A VOLTAGE SIGNAL

Linear dispersion theory states that all individual frequency components, which are constituent parts of a progressive wave train, propagate at their own phase velocity. This is, however, a function of both period and water depth. Under shallow water depth conditions, the phase velocities are all the same. But, under intermediate and deep water conditions, the low frequency waves propagate faster than the high frequency waves.

Experiments have indicated that the linear dispersion theory is a reasonable assumption under non-breaking wave conditions. Figure 5 illustrates the results of one experiment carried out in a wave flume with 0.92 m depth of water. A "random" wave train with a Pierson-Moskowitz spectrum with f_p=1 Hz was generated. Ten wave probes were placed along the wave flume at various intervals from 2 to 19 meters from the wave board. The signals monitored by each of the probes were Fourier analysed and the phase lags, relative to the first wave probe, were computed for 5 frequencies from 0.9 to 1.3 hz. Figure 5 gives the results and compares these with the phase shift based on linear dispersion theory. From this it was concluded that linear dispersion relations represent a reasonable approximation in calculating phase shifts for frequency components in complex wave trains and this is being applied by the program RWREP to hindcast the wave train in terms of its Fourier transform at the wave board.

The next step in Figure 3 gives the option to inverse Fourier transform the hindcasted data in order to provide a time series describing the wave train which will be generated at the wave board. The fourth trace on Figure 2 provides an interesting example of the wave train which must be generated at the wave board in order to produce the wave transient shown in the third trace. Although the sweep of frequencies from high to low frequencies are reminiscent of previously used techniques, the groupy modulation of amplitudes are a surprising result.

Following the computation of the hindcasted wave train, the data is optionally band pass filtered and then compensated for a variety of dynamic transfer functions which are in the path of a computer generated control voltage. The wave board transfer function described by Gilbert, Thompson and Brewer (1970) was expressed as a complex function to allow for the $\pi/2$ phase advance between the wave board position and the water surface elevations. To convert the time series for water surface elevation at the wave board to a time series of wave board position, the Fourier transform of the former is divided by this wave machine transfer function.

The electro-hydraulic servo transfer function of the wave machine can be obtained from measurements. Depending on the depth of water and the particular settings of the control loop parameters, this transfer function may vary somewhat. For most machines currently in use at the National Research Council this transfer function was found to be:

$$G(j\omega) = \frac{1}{(j\omega+1)^3}$$

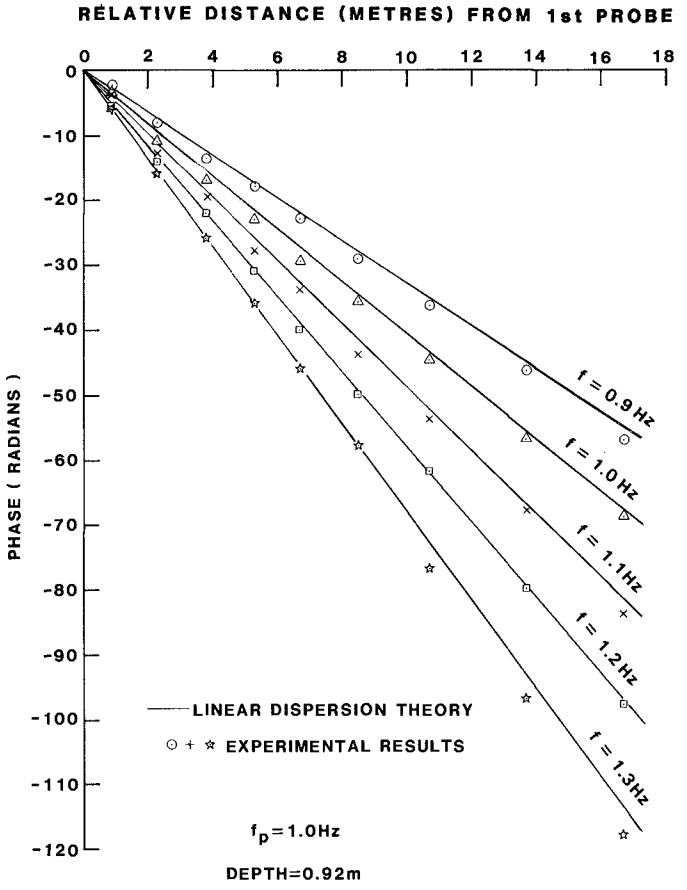

FIG.5 PHASE PROPAGATION OF INDIVIDUAL FREQUENCY COMPONENTS IN A PIERSON MOSKOWITZ SPECTRUM

Consequently, the Fourier transform of the wave board position signal is divided by $G(j\omega)$.

A low pass filter is frequently introduced at the output of a digital to analog converter in order to remove the sharp corners of the converter's output or to protect the machine from dynamic shock. A correction for such a filter should also be included.

At this stage all dynamic effects have been allowed for. However, in order to convert a wave board position signal to a voltage signal, a known wave machine calibration factor in terms of meters of board displacement per voltage input to the servo must be applied as a scale factor. It is also important to ensure that a positive value in a digital control signal leads to forward displacement of the wave board.

Application of the inverse Fourier transform supplies then the time series for the wave generator control signal. Some adjustments are then made to avoid severe start-up discontinuities or, as is the case for the generation of wave transients with long quiescent periods following the transients, the control signal is cycled around the vector length to ensure that the signal starts during the quiescent stage and not in the middle of the transient.

SIGNAL GENERATION

Whereas the above computations are all carried out in a digital computer resulting in a time series of the desired control signal, the ultimate step is the conversion of the time series into a smooth analog voltage signal. This is performed by a real time computer program operating in the "foreground" under control of the computer's real time clock as shown in Figure 4.

The real time clock is usually preset to be compatible with the highest frequencies which may have to be generated. Experience at the National Research Council over a period of ten years has indicated that a real time clock rate of 10 steps per second is more than adequate. However, during the digital wave synthesis process, such as described by equation (1), the intersample spacing, Δt, may not necessarily be 0.1 seconds. Therefore, an operation of re-sampling may be required to preserve the temporal integrity of the control signal. Under the GEDAP operating system described by Funke, Crookshank and Wingham (1980) this operation is transparent.

The actual operation of generating a smooth analog signal is performed by a digital to analog converter in conjunction with an integrator. The real time program monitors the output of the integrator by means of an analog to digital converter and computes the difference between the present integrator output and the desired integrator output one time step later and transmits this value to the digital to analog converter. This results in a straight line interpolation of analog voltages between successive discrete digital values as described in Funke, Crookshank and Wiegert (1981).

EXPERIMENTAL RESULTS

An example similar to Figure 2 has been tested in a flume and the results are shown in Figure 6 for various distances from 1.8 m to 22.8 m. This test was carried out at a depth of water of 0.60 meters. The transient was synthesized for a focal distance of 20 meters. It may be noticed from Figure 6 how the wave transient converges as it propagates towards its cataclysmic destiny. It should be noted that the actual breaking took place at about 23.4 meters. Photograph 3 shows the resultant appearance of the plunger.

Further experimental results are illustrated in Figure 7. The first three traces 'a' to 'c' show the degree of success with which a variety of wave groups can be generated. There are notable differences between the desired and the measured transients which may be explained by the fact that the formulation of a wave group in terms of equation (1) is not physically realizable for the water depth to wave length conditions of the test. The desired vertical asymmetry in Figures 7b and 7c did not reproduce and, instead, a severe horizontal asymmetry resulted.

PHOTO 3

PLUNGING WAVE ON A CONICAL STRUCTURE

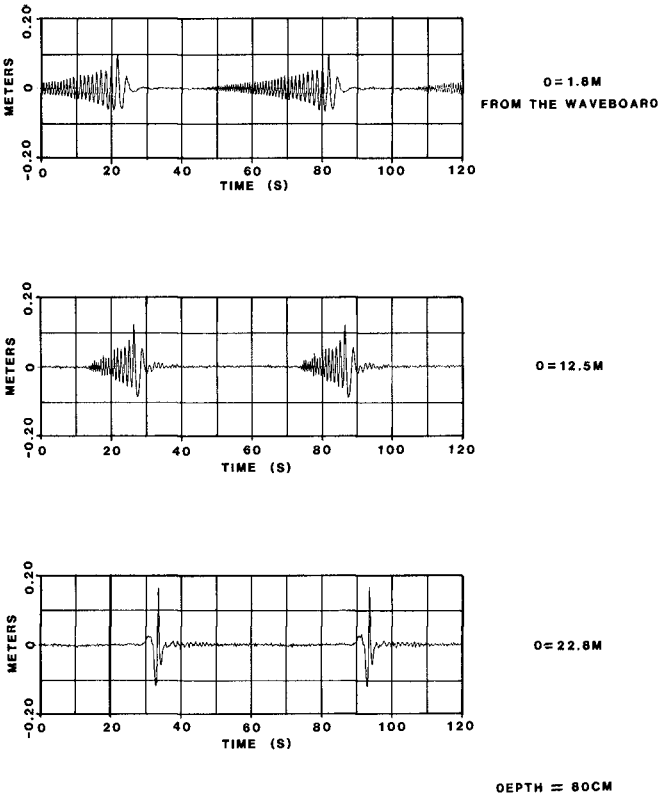

FIG.6 EPISODIC WAVE AS OBSERVED ALONG THE FLUME

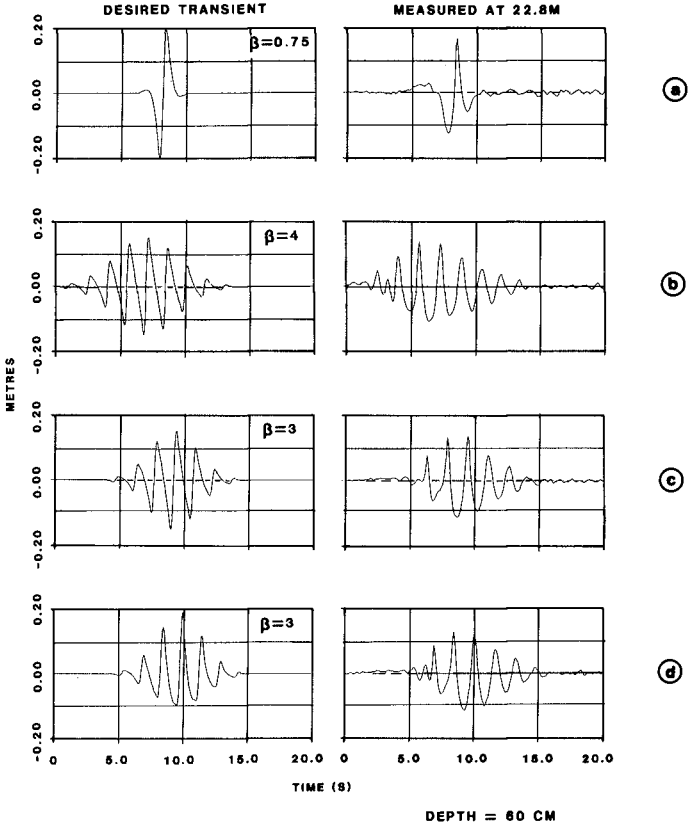

FIG.7 GENERATION OF WAVE TRANSIENTS IN THE FLUME

In order to improve on the formulation of equation (1), a new technique was introduced which was to lead to a more realistic definition of the wave transient. This technique is described by Funke and Mansard (1982). It involves a variety of non-linear distortions designed to increase crest heights while reducing the size of troughs and to shorten crest durations while lengthening trough durations without altering wave periods.

Figure 7d is an example of such a non-linear transformation applied to the group of Figure 7c. The resultant measured wave shows some improved reproduction which suggests that, through trial and error, further improvements may be realizable.

CONCLUSIONS

It has been demonstrated that transient wave forms can be generated in a flume or basin. Episodic waves could be generated with larger amplitudes than has previously been possible. The fidelity of reproduction is reasonable but can probably be improved by the application of non-linear dispersion theory and second order wave generator theory. The definition of the desired transient is, at this time, restricted to an amplitude modulated saw tooth with controlled front steepness. It is hoped that improved theoretical models of extreme wave transients as a function of time may also contribute in realizing more accurate generation of extreme wave conditions in the laboratory environment.

REFERENCES

Funke, E.R.R. and Mansard, E.P.D. (1979): "SPLSH A Program for the Synthesis of Episodic Waves". Hydraulics Laboratory Technical Report LTR-HY-65, National Research Council, Ottawa, Canada, April.

Funke, E.R.R., Crookshank, N.L. and Wingham, M. (1980): "An Introduction to GEDAP - An Integrated Software System for Experimental Control, Data Acquisition and Data Analysis". Hydraulics Laboratory Technical report LTR-HY-75, National Research Council, Ottawa, Canada.

Funke, E.R.R., Crookshank, N.L. and Wiegert, A.N. (1981): "Digital to Analog Converter with Straight Line Smoothing". Hydraulics Laboratory Technical report LTR-HY-80, National Research Council, Ottawa, Canada.

Funke, E.R.R. and Mansard, E.P.D. (1982): "Generation of "Random" Waves with Wave Asymmetries". Proc. 18th Conf. on Coast. Eng., Cape Town, South Africa.

Funke, E.R.R. and Mansard, E.P.D. (1983): "The Reproduction of Prototype Wave Trains in a Laboratory Flume". Hydraulics Laboratory Technical Report LTR-HY-64, National Research Council, Ottawa, Canada, April.

Gilbert, G., Thompson, D.M. and Brewer, A.J. (1970): "Design Curves for Regular and Random Wave Generators". Hydraulic Research Station Internal Report, Wallingford, U.K., June.

Moskowitz, S. and Racker J. (1951): "Pulse Techniques", Prentice-Hall, Electrical Engineering Series, 12 pp.

THE CONTROL OF WAVE ASYMMETRIES IN RANDOM WAVES

E.R. Funke[1] and E.P.D. Mansard[2]

ABSTRACT

The concept of wave asymmetry is reviewed and a prototype wave record is analysed. A three stage non-linear transformation, together with a Fourier transform substitution technique, is described. The method is tested by numerical simulation using statistical analysis procedures. Physical realizations are compared graphically.

1.0 INTRODUCTION

Nearly all techniques for the synthetic generation of "random" waves in laboratory flumes or basins assume that wind generated waves can be adequately described by a Gaussian stochastic process. This assumption has simplified both the process of wave generation and wave data analysis. However, many wave parameters are known to depart from the Gaussian hypothesis. Although these deviations are usually small in a statistical sense, they can represent significant factors in the study of structural responses to wave attack. Some of these non-Gaussian wave parameters deal with wave asymmetries which have recently been parameterized by Kjeldsen and Myrhaug (1979).

In this regard it is interesting to reminisce that, during the 1950 and 1960 period, one of the justifications in the defence for the construction of costly wind-wave flumes was based on the argument that the wind was essential to "steepen-up" the waves. This appears to be a correct observation because, as many experimenters in coastal engineering know, a random wave simulation based on a Pierson-Moskowitz spectrum for a fully developed sea, but without the use of wind, does not contain a significant number of breakers; a condition which does not correspond to Nature.

Such simulations are typically produced either from filtered white noise or by inverse Fourier transformations of amplitude spectra in association with randomly selected phases. Either of the two methods lead to functions of time which have Gaussian amplitude distributions. Such Gaussian stochastic processes are, on the average, perfectly symmetrical, that is to say that the average crest height equals the average trough height and that the crest front steepnesses are, on the average, equal to the crest rear steepnesses. However, the presence of

[1]B.Sc., M.Sc., Senior Research Officer, Hydraulics Laboratory, National Research council Canada, Ottawa, Ontario K1A 0R6, Canada.
[2]Dr.-Ing., Associate Research Officer, Hydraulics Laboratory, National Research Council Canada, Ottawa, Ontario K1A 0R6, Canada.

wave breakers implies that there is a strong preference for crest fronts to be steeper. This is a condition which must be considered a departure from the Gaussian hypothesis. In terms of spectral concepts, wave asymmetries imply a correlation of phases of harmonically related frequencies; a concept still requiring proof.

Wave profiles, however, do change when a wave propagates from deep into shallow water and begins to feel the bottom. The crest becomes larger and shorter while the trough becomes flatter and longer. Whereas it may not be unreasonable in deep water and in the absence of wind and currents to approximate "random" waves by Gaussian stochastic processes, this may not necessarily be so under other conditions. It is not uncommon to place a wave generator in "deep" water and then let the natural shoaling process transform the wave profiles. This can, at the expense of floor space, overcome the limitations of the generation technique. On the other hand, if possible, one should attempt to control the wave machinery to realize, at the boundary, all wave properties which are measurable in Nature. This approach to "random" wave generation has been referred to as a deterministic approach and has led to a number of innovations such as the generation of specific wave transients (Mansard and Funke 1982, S.P. Kjeldsen 1982), the control of the distribution of energy in the time domain (H. Lundgren and S.E. Sand 1978, Funke and Mansard 1980), and the generation of the correct group bound long wave components (Barthel et al 1983, and Sand 1982). This paper describes a method which imposes non-linear transformations in the time domain to a Gaussian function of time for the purpose of controlling wave asymmetries. These distorted functions of time are then used to create wave generator control signals which can produce the desired wave characteristics at the test site some distance away from the wave board.

2.0 WAVE ASYMMETRIES

Kjeldsen and Myrhaug (1979) have parameterized wave asymmetries as given in Figure 1. According to this, the horizontal asymmetry factor is $\mu = \eta'/H$ where η' is the crest height and H is the zero down crossing wave height. The horizontal asymmetry factor gives, therefore, the asymmetry about the horizontal axis at the mean water level. For Gaussian processes this should, on the average, be 0.5.

The vertical asymmetry factor, on the other hand, gives the asymmetry about the vertical axis at the point of the wave crest. This is given as $\lambda = L''/L'$ where L" is the crest rear length and L' is the crest front length, both measured along the horizontal axis. Intuition suggests that, for Gaussian processes, this ratio should be near one as the number of crests with steep fronts is expected to be equal to the number of crests with steep backs. However, as shown in Appendix A1, even if the waves are symmetrical, the expected value of this ratio is always greater than one. This ratio is therefore not a very useful measure for the detection of preferential asymmetries in crest steepnesses.

Two other parameters are the crest front steepness which is given by $\varepsilon = \eta'/L'$ and correspondingly the crest rear steepness which is

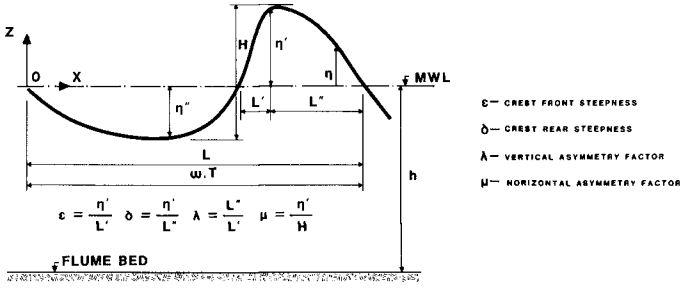

FIG.1 DEFINITION SKETCH OF WAVE ASYMMETRIES

$\delta = \eta'/L"$. These two prove more sensitive for the determination of departure from Gaussian behaviour.

A more traditional concept of steepness is the ratio of H/L where H is the zero down crossing wave height and L the associated wave length. Whereas this parameter provides some useful information about the development stage of the sea, it has nothing to do with asymmetrical distortions of the waves.

The measurement of wave asymmetry parameters at sea is not a simple matter. There are a number of difficulties which limit the accuracy of such measurements. Foremost of these is the fact that the greatest majority of wave records were obtained by means of Waverider buoys which are presumed stationary at a single point in space. Their output is derived from a double integration of a band limited acceleration signal. This results in a water surface elevation as a function of time. Wave length measurements are therefore not directly available and must be computed by relating individual zero crossing wave periods to wave lengths. Because an individual zero crossing wave period is a consequence of the superposition of several free running frequencies, it is not likely that the simple use of this individual period will lead to a correct calculation of the actual wave length. Nevertheless, there is little else one can do at the moment and one may be consoled by the fact that, whatever mistakes are being made, are also made under laboratory conditions. Therefore, comparative results are still valid.

Another, more serious, problem deals with the mooring system of a wave recording buoy. Figure 2 gives a highly simplified version of a buoy mooring system which assumes that the compliant mooring line

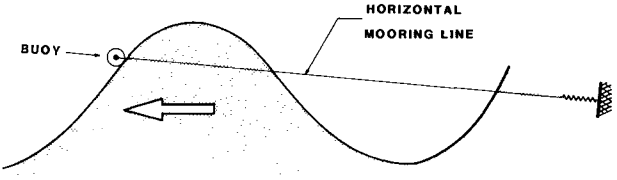

BUOY WITH HORIZONTAL MOORING
INTERACTING WITH A SINUSOIDAL PROGRESSIVE WAVE

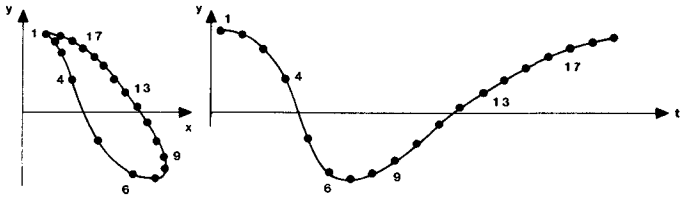

STROBO GRAPH OF BUOY

TIME HISTORY OF BUOY'S VERTICAL POSITION

FIG.2 NON-LINEAR DISTORTIONS DUE TO BUOY

exerts a nearly horizontal restraining force on the buoy. As a wave progresses from right to left, the buoy climbs up along the wave front. The additional uplift force, due to acceleration and friction, results in a stretch of the compliant line. When the buoy reaches the wave crest, it starts to slide down the rear of the crest, propelled by both the gravitational force as well as the spring force of the mooring line. This results in a rapid descent from the crest.

To illustrate this motion a hypothetical strobo-graph is shown in Figure 2 in which points represent buoy positions at constant time intervals. Points 1 to 7 represent the rapid descent whereas 8 to 19 correspond to the rise of the buoy to the crest. The corresponding time history, which is shown to the right of the strobo-graph, gives the same information except that all points are placed at constant time intervals along a time axis. From this it can clearly be seen how the mooring system causes a distortion of the water surface elevation measurement. This results in a crest rear steepness η'/L'' which is larger than the crest front steepness η'/L'.

Evidently, the examples in Figure 2 have been exaggerated to make a point. Nevertheless it must be expected that prototype wave recordings obtained from Waverider buoys do not supply reliable vertical asymmetry factors or crest steepnesses.

To overcome this problem, one may wish to investigate wave recordings obtained from staff gauges mounted on stable platforms. However, it should be remembered that these records do contain a set-down which depresses the mean water level under wave groups. In order to be strictly correct, such wave data should be high pass filtered prior to zero crossing analysis or else the wave asymmetry parameters may not be calculated correctly.

Figure 3 gives an example of a statistical analysis of wave asymmetry parameters for wave data recorded in the Hibernia field area off the east coast of Newfoundland using a Waverider buoy. It is noteworthy that the average crest rear steepness is 5% larger than the crest front steepness; a condition which is opposite to what one would expect in a severe storm. This indicates that the mooring system probably distorted the wave record. The horizontal asymmetry indicates a minor deviation from 0.5, which suggests that wave crests are slightly higher than wave troughs.

3.0 THE NON-LINEAR TRANSFORMATION

The non-linear transformation assumes the existence of a time series from a Gaussian stochastic process; in other words, a time series which is known to be symmetrical on the average.

The transformation takes place in three distinct steps; - the amplitude distortion, - the time distortion, and - the crest distortion.

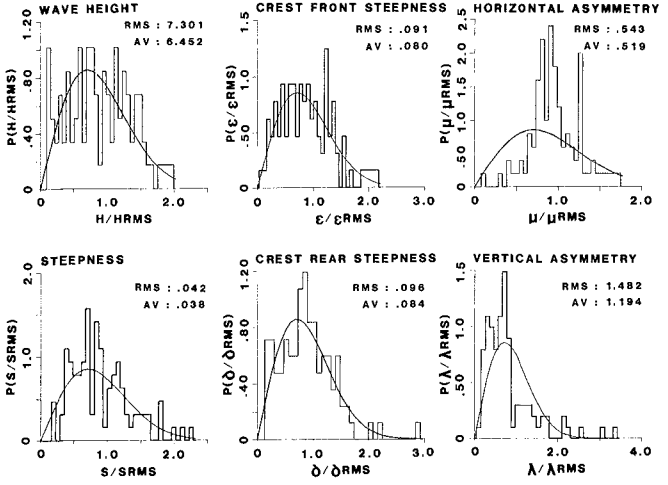

FIG.3 ZERO CROSSING ANALYSIS OF WAVE DATA RECORDED EAST OFF NEWFOUNDLAND IN 95M OF WATER

3.1 The Amplitude Distortion

The non-linear amplitude transformation is given as:

$$\eta 1_i = \eta_i + C_p \cdot \eta_i^2/\sigma_\eta \quad \text{for} \quad \eta_i > 0 \tag{1}$$

$$\eta 1_i = \eta_i + C_n \cdot \eta_i^2/\sigma_\eta \quad \text{for} \quad \eta_i < 0 \tag{2}$$

$$\eta 1_i = \eta_i \quad \text{for} \quad \eta_i = 0 \tag{3}$$

where:

η_i is the ith sample of the symmetrical time series

C_p and C_n are the non-linear transformation coefficients, and

σ_η is the standard deviation of the time series η_i and is introduced to permit the use of a normalized, non-dimensional transformation coefficient. By convention, the standard deviation σ_η is evaluated over the total length of the time series which is to be transformed. As an exception, when this transformation is applied to a wave transient, the evaluation of σ is limited to the duration of the transient only.

Naturally, a non-linear distortion of the type described in equations (1) to (3) must have an effect on the spectrum of the primary input signal. If this distortion were to be imposed on a pure sinusoid, one would notice that the spectrum of the distorted signal contains energy at frequencies which are second and higher harmonics to the fundamental.

The intent of this transformation is, however, not to modify the primary input spectrum and it is therefore a necessary condition for the transformation to succeed, that the primary input spectrum contains enough energy in those bands of frequencies which may serve as second or third harmonics to the lower frequency band of the same spectrum. In other words, narrow band spectra without a high frequency tail are not suitable for the generation of asymmetrical waves.

A corollary to this observation is that asymmetrical waves must have a broad spectrum.

In order to preserve the primary input spectrum, a technique is being used which makes a substitution of the Fourier amplitude spectrum and is therefore referred to as the Fourier transform substitution method. A similar technique has been used by Funke and Mansard (1980) and it works as follows. After the non-linear transformation of the primary input time series has been completed, a Fourier transform of the distorted time series is undertaken. This transform is resolved in terms of its amplitude and its phase spectrum. The amplitude spectrum is then discarded and replaced by the primary input spectrum after which an inverse Fourier transform is performed. Evidently, the resultant time series may not be as severely distorted as was initially intended but, if the spectrum is broad enough, the differences are hardly noticeable.

It is worthwhile to make two comments on this Fourier transform substitution. The fact that the input and the output amplitude spectra are identical, while their two respective time series exhibit different wave form distortions, means that the non-linear transformation described here only causes a realignment of the phase spectrum. Secondly, if the input time series had been a pure sinusoid, a violation of the broad spectrum condition, then the Fourier transform substitution would have restored the distorted sine wave back to its original pure sinusoidal shape.

Figure 4.1 illustrates a symmetrical time function with Gaussian amplitude distribution, referred to as the reference wave. Superimposed on this is a time series after the first non-linear transformation

and Fourier transform substitution. C_n and C_p values used in this example were 0.71 with σ = 0.048 m. To enhance comparison, a section from 45 to 60 is shown enlarged in Figure 5.1. This figure shows also the two variance spectral densities of the reference and the distorted wave train.

As an option, Appendix A2 gives a method for calculating C_n and C_p as a function of the parameter α defined in Section 3.2.

3.2 The Time Distortion

Whereas the time series was, up to this point, a series of regularly spaced samples $\eta 1_i$, it is now necessary to convert the data to a two-dimensional series of $(t_i, \eta 1_i)$ values. Then, for each zero down crossing interval, i.e. for an interval embracing a trough and the following crest, the time coordinates are transformed in two stages; first for the jth trough period according to:

$$t_i'' = (1 + \alpha) \cdot t_i' \tag{4}$$

where:

t_i' is measured from the instance of the relevant zero down crossing, and

α is a scaling parameter which is greater than zero,

and then for the jth crest period according to

$$t_i'' = (1 + \alpha) \cdot t_i' - \alpha' \cdot (t_i' - TNZ_j) \tag{5}$$

where:

α' is a scaling parameter greater than zero and is given by: $TZ_j \cdot \alpha / (TZ_j - TNZ_j)$

TNZ_j is the length of the jth trough period, and

TZ_j is the length of the jth zero down crossing period.

This transformation will expand the trough period and contract the crest period but not change the length of the total zero down crossing period. As a result, the transformation will affect the vertical asymmetry as well as the crest wave steepnesses. However, the symmetry of the crest steepness will not be affected.

A factor of α = 0.2 was applied to the reference wave train. Referring to Figure 4.2, the transformed wave train may be compared to this reference. The enlarged section between 45 and 60 seconds is presented in Figure 5.2 which shows quite clearly how the time scale distortion has been realized. It should also be noticed from this figure that the variance spectrum has not been affected to any significant extent. This suggests again that the only difference is in the realignment of the phase spectrum.

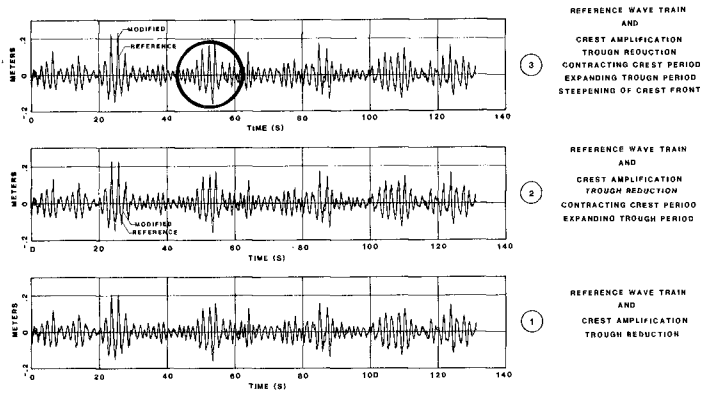

FIG.4

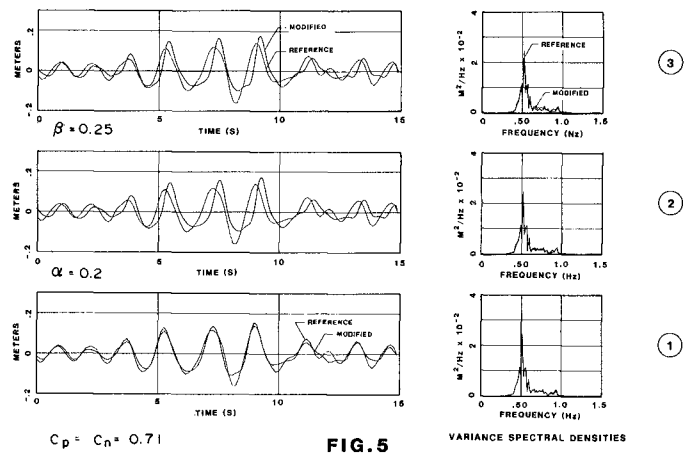

FIG.5 VARIANCE SPECTRAL DENSITIES

NUMERICAL SIMULATION OF WAVE ASYMMETRIES

It must also be pointed out that the compression of the crest duration and the associated expansion of the trough duration leads to an unavoidable shift in the mean value which must be removed subsequently. This adjustment in mean value has an effect on the horizontal asymmetry as is evident from Table I.

3.3 The Crest Distortion

The third transformation has the purpose of moving the location of the wave crest maximum forward, thereby increasing the crest front steepness and decreasing the crest rear steepness. First, the crest periods are identified by zero up crossings and following zero down crossings. Then, for each crest period, the time coordinates are transformed according to:

$$\tau_i'' = (1 - \beta)\cdot\tau_i' + \beta\cdot(\tau_i')^2/TZC_j \qquad (6)$$

where:

τ_i' is measured from the instance of a zero up crossing

TZC_j is the jth crest period, and

β is a scaling parameter greater than zero.

A factor $\beta = 0.25$ was applied to the reference wave train and Figure 5.3 illustrates the result of this last transformation which is only minor and therefore requires very close inspection to be noticed.

4.0 STATISTICAL ANALYSIS OF RESULTS

A statistical analysis was carried out on the four numerical simulations shown in Figure 4, the first of which is the reference wave and the other three represent the three stages in the non-linear transformations. Table I gives the results of this analysis.

Table I provides both the mean and the root-mean-square value (RMS) for each of the wave asymmetry parameters. These are given in diagonally opposite corners of each box. Inspection of the table reveals the following:

a) The average wave height has not changed significantly as a result of the transformations.

b) The average steepness has decreased by 10% after the first transformation but thereafter remained constant. It is not clear why this should be, in view of the fact that the average wave height remained unchanged and wave periods have not been altered in any way. The Fourier transform substitution, which takes place after the first transformation, will have some uncontrolled consequences which may be the reason for this phenomenon.

	WAVE HEIGHT	AVERAGE STEEPNESS	CREST FRONT STEEPNESS	CREST REAR STEEPNESS	HORIZONTAL ASYMMETRY	VERTICAL ASYMMETRY
REFERENCE WAVE TRAIN	0.114	0.034	0.088	0.088	0.487	1.09
	0.132	0.038	0.078	0.078	0.505	1.21
CREST AMPLIFICATION AND TROUGH REDUCTION	0.113	0.031	0.078	0.074	0.535	1.15
	0.132	0.034	0.090	0.088	0.550	1.31
CREST AMPLIFICATION TROUGH REDUCTION CONTRACTING CREST PERIOD AND EXPANDING TROUGH PERIOD	0.114	0.031	0.090	0.089	0.581	1.12
	0.134	0.034	0.108	0.107	0.597	1.25
CREST AMPLIFICATION TROUGH REDUCTION CONTRACTING CREST PERIOD EXPANDING TROUGH PERIOD AND STEEPENING OF CREST FRONT	0.114	0.031	0.098	0.085	0.580	1.25
	0.134	0.034	0.115	0.103	0.595	1.40

AVERAGE
RMS

WAVE ASYMMETRY PARAMETERS
BY NUMERICAL SIMULATION

TABLE 1

c) The crest front and crest rear steepnesses must be considered as pairs because as one increases, the other must, of necessity, decrease. Because the reference wave train has a Gaussian amplitude distribution, it could be expected that the crest is symmetrical and therefore the crest front steepness should be nearly equal to the crest rear steepness. According to Table I, this symmetry is preserved until the last transformation at which point the crest front becomes steeper than the rear. On the other hand, as the crest is being amplified, both crest steepnesses increase. Also, as the crest period is being decreased, crest steepnesses increase as well.

d) The vertical asymmetry of the reference wave is larger than one as can be expected according to Appendix A1. It is not clear why the crest amplification increases the average vertical asymmetry. It is suspected that the Fourier transform substitution is the cause of this. Reducing the crest period means that the scatter of crest front and rear steepnesses is reduced and therefore the average of the ratio of these steepnesses, namely the average vertical asymmetry is also reduced. Finally, the last non-linear transformation causes the vertical asymmetry to increase significantly.

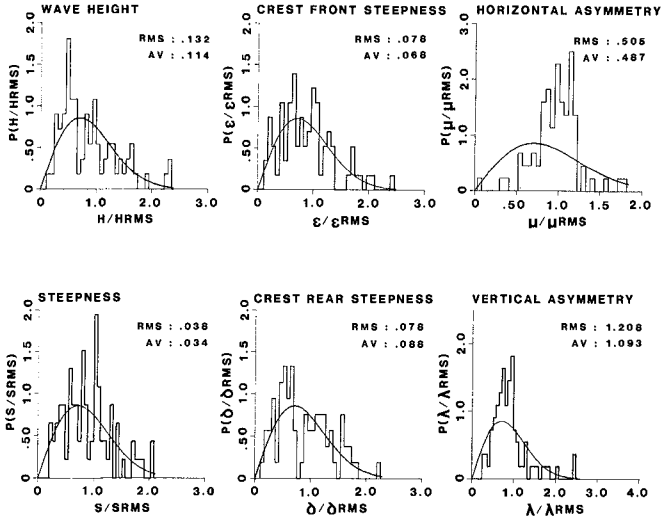

FIG.6 PROBABILITY DISTRIBUTION OF WAVE ASYMMETRIES

(NO DISTORTIONS)

A more detailed description of this statistical analysis is provided in Figures 6 and 7 together with Rayleigh distribution functions which were matched to the first and second moments. From these it may be noticed how the distribution of crest steepnesses changes as a result of the non-linear transformation. The vertical asymmetry distribution also demonstrates a change, leading to a reduced scatter of values.

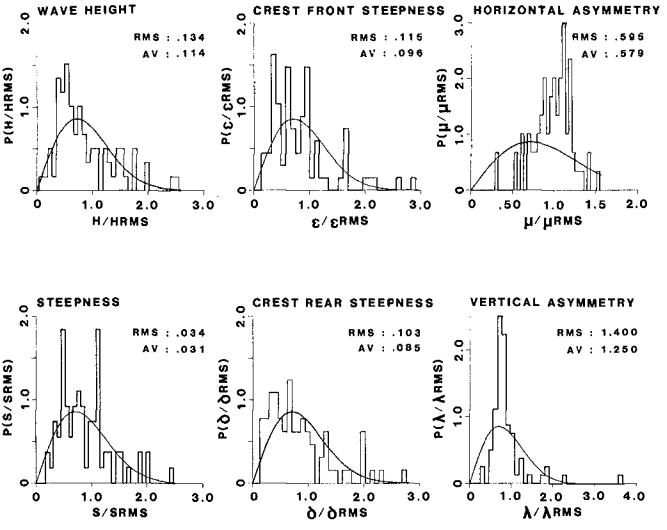

FIG.7 PROBABILITY DISTRIBUTION OF WAVE ASYMMETRIES

(WITH DISTORTIONS)

5.0 PHYSICAL REALIZATION OF ASYMMETRICAL WAVES

A prerequisite for the generation of asymmetrical waves in a wave flume or basin is the ability to reproduce a symmetrical wave train with reasonable fidelity. This is accomplished by a method described by Funke and Mansard (1983) which is based on linear dispersion theory and linear wave board theory. Figure 8 gives an example of such a reproduction from which one may clearly recognize and compare the various wave groups in the two wave records. Whereas wave grouping reproduces quite well, the accuracy of reproduction of individual waves is not perfect. However, this is, more or less, what is possible with present day technology.

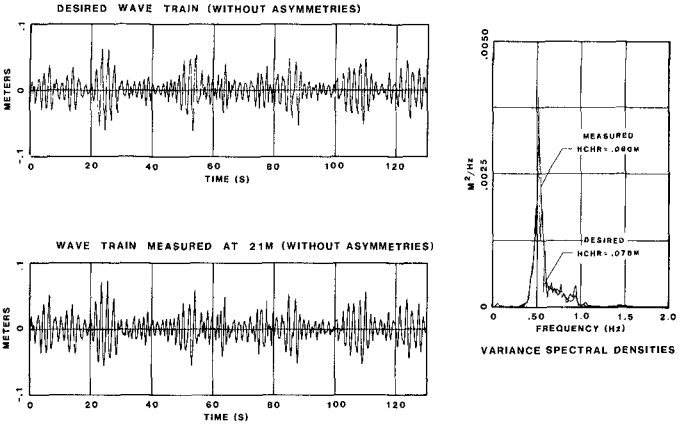

FIG.8 REPRODUCTION OF WAVE TRAIN IN THE FLUME (WITHOUT ASYMMETRIES)

Figure 9, on the other hand, compares the measured wave train without asymmetries to a wave train with asymmetries. Figure 10 shows a section from 40 to 120 seconds of the same waves at an amplified scale. Several of these waves show the effect of wave asymmetry transformations.

All operations for the synthesis, generation, data acquisition, analysis and graphic output were realized through the GEDAP software system operating on a HP 1000 computer (Funke et al 1980).

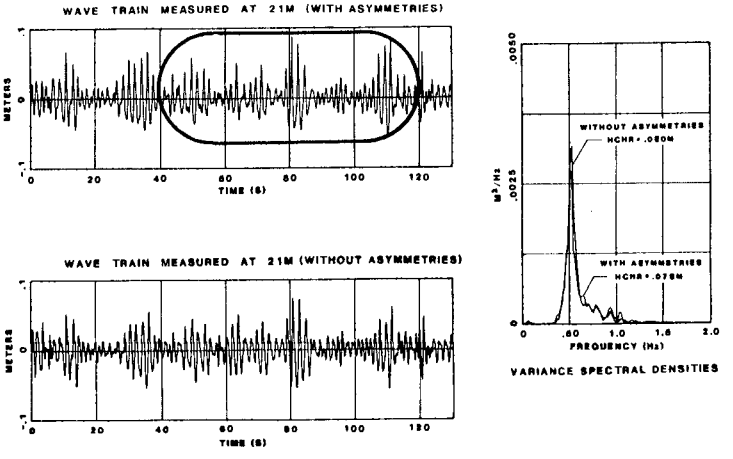

FIG.9

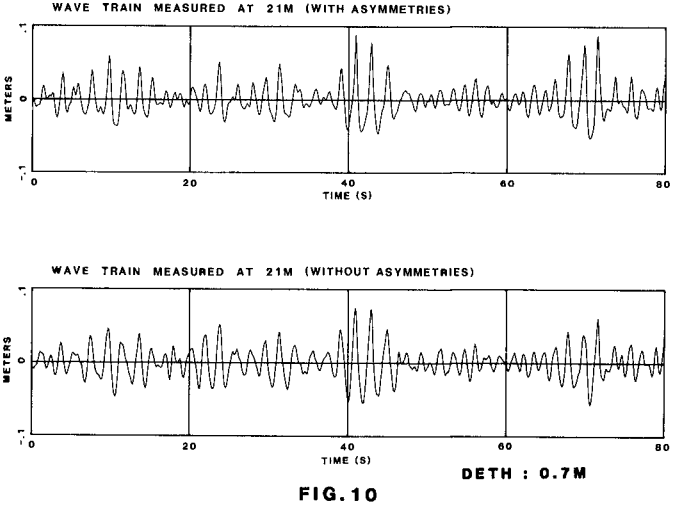

FIG.10

COMPARISON OF WAVE TRAINS MEASURED WITH AND WITHOUT ASYMMETRIES

6.0 CONCLUSIONS

A technique was described for the transformation of Gaussian stochastic functions into wave trains with various degree of wave asymmetry using two, three of four transformation parameters. The technique was tested by numerical simulation which indicated that the technique achieved the expected results. Physical reproduction of asymmetrical waves was shown to be possible although with reduced fidelity.

Insight, which resulted from the application of the non-linear transformation, suggests that waves with significant asymmetries must have broad spectra, that wave trains with and without asymmetries may have identical variance spectral densities and therefore, that the difference between the two must be contained in their respective phase spectra.

The ability to make a meaningful analysis of wave asymmetries on the basis of Waverider recorded wave data is limited because of distortions introduced by their mooring system.

Future research must explore the extent of physical realizability of wave asymmetry in wave flumes and basins, and match the distortion parameters to c, α and β to conditions observed in Nature. The sensitivity of experimental measurements for structural response to wave asymmetry simulations must also be determined. It is hoped that a non-linear transform can be developed for the compensation of Waverider records for their mooring effects.

7.0 REFERENCES

Barthel et al (1983): Group Bounded Long Waves in Physical Models. Joint Research Project by the Danish Hydraulic Institute, the Delft Hydraulics Laboratory and National Research Council Canada. Paper to be submitted to Ocean Engineering.

Funke, E.R.R. and Mansard, E.P.D. (1980): On the Synthesis of Realistic Sea States. Proceedings 17th International Conference on Coastal Engineering, Sydney, Australia. (See also NRC Report LTR-HY-66.)

Funke, E.R.R. and Mansard, E.P.D. (1983): The Reproduction of Prototype Wave Trains in a Laboratory Flume. Laboratory Technical Report LTR-HY-64, National Research Council Canada, April.

Funke, E.R.R., Crookshank, N.L. and Wingham, M. (1980): An Introduction to GEDAP - An Integrated Software System for Experiment Control, Data Acquisition and Data Analysis. Laboratory Technical Report LTR-HY-75, National Research Council Canada, March.

Kjeldsen, S.P. and Myrhaug, D. (1979): Formation of Wave Groups and Distribution of Parameters for Wave Asymmetry. VHL report No. STF 60 A79044, River and Harbour Laboratory, Trondheim, Norway.

Kjeldsen, S.P. (1982): Two and Three Dimensional Deterministic Waves in a Sea. Proceedings 18th International Conference on Coastal Engineering, Cape Town, South Africa.

Lundgren, H. and Sand, S.E. (1978): Natural Wave Trains: Description and Reproduction. Proceedings 16th International Conference on Coastal Engineering, Hamburg, Germany.

Mansard, E.P.D. and Funke, E.R.R. (1982): A New Approach to Transient Wave Generation. Proceedings 18th International Conference on Coastal Engineering, Cape Town, South Africa.

Sand, S.E. (1982): Long Wave Problems in Laboratory Models. Journal of the Waterway, Port Harbour and Ocean Engineering, ASCE, Vol. 108.

APPENDIX A1

Expected Value of a Ratio of Two Random Variables

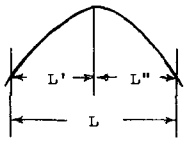

Suppose there are two random variables L' and L" such that:

$$L = L' + L'' \qquad \text{(A1)}$$

Assume also that:

$$L' = L/2 + \delta \qquad \text{(A2)}$$

where L is assumed constant, and

δ is a random variable with zero mean, i.e.

$$E\{\delta\} = 0$$

In order to estimate the expected value of L'/L" equations (A1) and (A2) are arranged as follows:

$$L'' = L/2 - \delta$$

and

$$\begin{aligned} L'/L'' &= (L/2 + \delta) \,/\, (L/2 - \delta) \\ &= (1 + 2\delta/L) \cdot (1 - 2\delta/L)^{-1} \\ &= (1 + 2\delta/L) \cdot (1 + 2\delta/L + (2\delta/L)^2 + (2\delta/L)^3 + +) \\ &= 1 + 2 \cdot (2\delta/L) + 2(2\delta/L)^2 + 2(2\delta/L)^3 + + \end{aligned}$$

Because the expected value $E\{2\delta/L\} = 0$, we have, as a first approximation for the assumptions given above, that:

$$E\{L'/L''\} = 1 + 2E\{(2\delta/L)^2\} > 1$$

This proves that even for symmetrical crests, i.e. $E\{\delta\} = 0$, the expected value of the vertical asymmetry is always greater than 1.

APPENDIX A2

Derivation of C-Coefficients as a Function of α

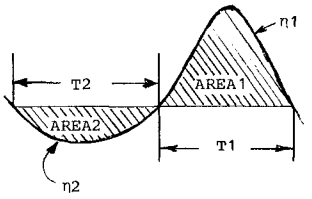

Let $\eta 1 = \eta(t) + C_p \cdot \eta^2(t)/\sigma$ for $\eta(t) > 0$
and $\eta 2 = \eta(t) + C_n \cdot \eta^2(t)/\sigma$ for $\eta(t) < 0$
Also let $T1 + T2 = T$
and $T1 = T/2(1 - \alpha)$
and $T2 = T/2(1 + \alpha)$

Object: To find C_n and C_p as a function of α.

Solution:

Assume $\eta(t) = A \cdot \sin(\pi t/T1) + (C_p/\sigma) \cdot A^2 \cdot \sin^2(\pi t/T1)$ for $\eta(t) > 0$
and $\eta(t) = A \cdot \sin(\pi t/T2) + (C_n/\sigma) \cdot A^2 \cdot \sin^2(\pi t/T2)$ for $\eta(t) < 0$

then

$$AREA1 = (C_p/\sigma) \cdot A^2/2 \cdot T1 + 2A \cdot T1/\pi$$
and
$$AREA2 = (C_n/\sigma) \cdot A^2/2 \cdot T2 - 2A \cdot T2/\pi$$

For the mean value to be zero, set

AREA1 = AREA2 or

$$(C_p/\sigma) \cdot A^2/2 \cdot T1 + 2A \cdot T1/\pi = (C_n/\sigma) \cdot A^2/2 \cdot T2 - 2A \cdot T2/\pi$$

Substituting for T1 and T2,

$$\frac{T}{2}(1-\alpha) \cdot \left[(C_p/\sigma) \cdot A/2 + 2/\pi\right] = \frac{T}{2}(1+\alpha) \cdot \left[(C_n/\sigma) \cdot A/2 - 2/\pi\right]$$

Hence

$$\alpha\left[\frac{A}{2\sigma}(C_n+C_p)\right] = \frac{A}{2\sigma}(C_p-C_n) + 4/\pi$$

If $C_n = C_p = C$

$$C = 4\sigma/(\pi \cdot \alpha \cdot A)$$

If the undistorted wave is a sinusoid, then

$$\sigma = A/\sqrt{2}$$

and

$$C = 2 \cdot \sqrt{2}/(\pi \cdot \alpha) \text{ for a sinusoid}$$

If the undistorted wave is a Gaussian stochastic function, then one may wish to set "A" corresponding to the wave crest of a wave with significant wave height, i.e.

$$\sigma = A/2$$

and

$$C = 2/(\pi \cdot \alpha)$$

THREE-DIMENSIONAL MARINE MODELS FOR IMPACT STUDIES

Jacques C.J. NIHOUL* and François C. RONDAY**

Abstract.

A three-dimensional non-linear hydrodynamic model is developed for the determination of the mesoscale (tides, storm surges, ...) and macroscale (residuals, gyre, ...) circulations in the North Sea. The model consists of a hierarchy of submodels of different grid sizes, with interactive coupling at boundaries.

The model is used to study the impact of coastal engineering projects along the Belgian coast and in the Scheldt estuary.

Introduction.

Considerable attention is now being paid to the possible environmental impact of coastal engineering works.

The consequences on surface elevations, currents and sediment transport of such large scale projects as the building of an important new harbor on the Belgian coast, — with the subsequent deployment of industrial activities —, and the modification of passes in the coastal zone and in the Scheldt estuary, have been investigated by means of a mathematical model, working in close cooperation with a reduced-scale hydraulic model of the area.

In the following, the mathematical model is described and tested on a series of in situ observations. Examples of application are given in illustration.

Mesoscale and macroscale models.

The general circulation of the North Sea can be, conveniently, divided into a macroscale or "residual" component, a mesoscale, "long wave", component and microscale turbulence. The reference is here made to the time-scales of the phenomena which range from a few minutes or less for microscale turbulence, a few hours to a few days for mesoscales processes like tides and storm-induced motions and to a few weeks or more for macroscale residual currents.

The mesoscale processes, tides, storm surges, ... are the most intense hydrodynamic phenomena with current speeds exceeding sometime $1\ m\ s^{-1}$. Marine chemists and marine biologists, however, are more interested in the much weaker residual circulation (a few $cm\ s^{-1}$), the characteristic times of which are comparable with typical ecological time scales (e.g. Nihoul, 1981).

* Professor of Geophysical Fluid Dynamics. University of Liège and University of Louvain, Belgium.

** Lecturer in Physics and Meteorology, University of Liège, Belgium.

Depth-integrated hydrodynamic models of the mesoscale circulation in the North Sea have been developed in several countries from the early "long wave" models applied to the computation of tidal currents and elevations (e.g. Hansen, 1956, 1966; Fisher, 1959; Leendertse, 1967).

The models of the present generation are highly accurate and appropriate to routine forecasting (e.g. Davies, 1976; Nihoul, 1976, 1982; Nihoul and Ronday, 1976; Ronday, 1976, 1979; Prandle and Wolf, 1978; Flather, 1979; Pingree and Griffiths, 1981a,b).

Three-dimensional models, on the other hand, are still at an early stage of development (e.g. Heaps, 1976; Nihoul, 1977, 1982; Backaus, 1979).

The macroscale ("residual") circulation is much more difficult to apprehend.

It is convenient to define the residual circulation as the mean circulation over a time T sufficiently large for mesoscale processes to roughly cancel out in the mean but sufficiently small to leave macroscale processes almost untouched in the averaging (e.g. Nihoul, 1975, 1982; Nihoul and Ronday, 1975; Maier-Reimer, 1977; Prandle, 1978).

The equations governing the residual circulation are then obtained, from the general hydrodynamic equations, by averaging over T *. Averaging the non-linear terms gives two contributions; the first of which is related to the product of the means while the second contains the mean products of mesoscale fluctuations.

This second contribution appears as an additional forcing on the residual flow and can be viewed as the action of mesoscale Reynolds stresses — analogous to the turbulent Reynolds stresses of microscale turbulence — on the mean flow.

If one excepts limited areas like the Norwegian Trench, the North Sea is shallow and the water column is always fairly well-mixed. The stratification which may occur in the summer is restricted to the Northern part.

Being essentially concerned by the Belgian coastal zone and the Southern Bight and mainly interested in winter situations when the most dramatic hydrodynamic events occur, one may assume vertical homogeneity (zero buoyancy) and write the basic equations in the form (e.g. Nihoul, 1982)**

$$\nabla . \mathbf{v} = 0 \tag{1}$$

$$\frac{\partial \mathbf{v}}{\partial t} + \nabla . (\mathbf{v}\mathbf{v}) + 2\,\boldsymbol{\Omega} \wedge \mathbf{v} = -\nabla q + \nabla . \mathbf{R} \tag{2}$$

where $\boldsymbol{\Omega}$ is the Earth's rotation vector,

---

* One of the characteristics of the North Sea is the distinct predominance of mesoscale motions. As a result, the solution of the time-dependent hydrodynamic equations (where only microscale turbulence has been parameterized) represents essentially the mesoscale circulation. The macroscale circulation is included but it is of the same order of magnitude as the error (e.g. Nihoul and Ronday, 1976; Nihoul, 1980; Nihoul and Runfola, 1981).

As a result, the direct determination of the residual circulation, by solving these equations and later averaging the solution over T, is often vitiated by an error which can be as high as a hundred percent as non-linear errors do not cancel in the averaging process.

On the other hand, this solution can be used to compute with satisfactory accuracy the mesoscale Reynolds stresses and these can be substituted in the average equations to give the residual circulation with great precision (Nihoul and Ronday, 1976; Nihoul and Runfola, 1981).

** The model has been extended to deeper, stratified seas (Nihoul, 1982) and is now being applied to the Adriatic.

$$q = \frac{p}{\rho} + g x_3 \ ,$$

p is the pressure, ρ the specific mass of sea water, x_3 the vertical coordinate and $\mathbf{R}$ the turbulent Reynolds stress tensor (the stress is here per unit mass of sea water) resulting from the non-linear interactions of three-dimensional microscale turbulent fluctuations.

The turbulent Reynolds stress tensor can be parameterized in terms of eddy viscosity coefficients. In microscale three-dimensional turbulence, these coefficients are of the same order of magnitude in the horizontal and vertical directions. Then, horizontal length scales being much larger than the depth, the last term in the right-side of eq. (2) can be written simply, with a very good approximation

$$(3) \qquad \nabla . \mathbf{R} = \frac{\partial \boldsymbol{\tau}}{\partial x_3} = \frac{\partial}{\partial x_3} (\tilde{\nu} \frac{\partial \mathbf{v}}{\partial x_3})$$

where $\tilde{\nu}$ is the vertical eddy viscosity and $\boldsymbol{\tau}$ the turbulent Reynolds stress (vector).

The residual flow is defined as the mean flow over a time T sufficiently large for mesoscale processes to roughly cancel out in the mean but sufficiently small to leave macroscale processes almost untouched in the averaging. If the subscript $_0$ denotes such an average, one may write, neglecting small terms (e.g. Nihoul, 1982),

$$(4) \qquad \mathbf{v} = \mathbf{v}_0 + \mathbf{v}_1$$

with

$$(5) \qquad (\mathbf{v})_0 = \mathbf{v}_0$$

$$(6) \qquad (\mathbf{v}_1) = \mathbf{0}$$

and

$$(7) \qquad 2\ \boldsymbol{\Omega} \wedge \mathbf{v}_0 = - \nabla q_0 + \frac{\partial \boldsymbol{\tau}_0}{\partial x_3} + \nabla . \mathbf{N}$$

where

$$(8) \qquad \mathbf{N} = (- \mathbf{v}_1 \mathbf{v}_1)_0$$

$$(9) \qquad \frac{\partial \mathbf{v}_1}{\partial t} + \nabla . (\mathbf{v}_1 \mathbf{v}_1) + 2\ \boldsymbol{\Omega} \wedge \mathbf{v}_1 = - \nabla q_1 + \frac{\partial \boldsymbol{\tau}_1}{\partial x_3}$$

with

$$(10,11) \qquad \nabla . \mathbf{v}_0 = \nabla . \mathbf{v}_1 = 0$$

One can see that the equation for $\mathbf{v}_1$ is essentially the same as the equation for $\mathbf{v}$ (they only differ by terms which are orders of magnitude smaller). It is the reason why, one can, with the appropriate boundary conditions, determine the mesoscale velocity $\mathbf{v}_1$, in a first step, and the residual velocity $\mathbf{v}_0$, in a second step, taking the coupling between the two types of motion into account in the calculation of $\mathbf{v}_0$ only. [$\mathbf{N}$ is explicitly computed from the results of the mesoscale model (eq. 9) and substituted in the macroscale model (eq. 7) which is then solved for the residual flow $\mathbf{v}_0$].

The tensor $\mathbf{N}$ plays, for mesoscale motions a role similar to that of the turbulent Reynolds stress tensor $\mathbf{R}$ in eq. (2) and may be called the "mesoscale Reynolds stress tensor". The last term in the right-hand side of eq. (7) represents an additional force acting on the residual flow and resulting from the non-linear interactions of mesoscale motions (tides, storm surges, ...).

The importance of this force was discovered, first, by depth-integrated numerical models of the residual circulation in the North Sea (Nihoul, 1975; Nihoul and Ronday, 1975) and the associated stress was initially referred to as the "tidal stress" to emphasize the omnipresent contribution of tidal motions.

In the absence of stratification, the vertical eddy viscosity* is parameterized in the form

$$\tilde{\nu} = L\, u_* \tag{12}$$

where u_* is the bottom friction velocity and L a length scale, evaluated as a function of the distance to the bottom and the free surface by a quadratic law of which the coefficients are adjusted to the local conditions (Nihoul, 1977, 1982)**. A similar parameterization has been proposed by Leendertse and Liu (1978).

In essence, the three-dimensional model can be described as the superposition of a two-dimensional model and a one-dimensional model (Nihoul, 1977, 1982).

The two-dimensional model is obtained by integration of the equations over depth. In this process, the bottom stress is introduced into the equations and it must be parameterized in terms of the depth-averaged velocity.

The one-dimensional model is obtained by solving eq. (2) locally, regarding the non-linear advection term as a given forcing, computed from the results of the two models at neighbouring grid points and previous time steps. As boundary conditions (at the surface and at the bottom), the wind stress and the bottom stress are imposed. The no-slip condition ($\mathbf{v} = \mathbf{0}$) at the bottom provides the extra equation needed to relate the bottom stress, the wind stress and the depth-averaged velocity.

The two-dimensional model and the one-dimensional model proceed thus "hand-in-hand" with a continuous double iteration on the bottom stress and the non-linear terms. The details of the procedure and its numerical implimentation are given in (Nihoul, 1982).

In the North Sea, the equation relating the bottom stress and the depth-averaged velocity can be shown to reduce, with a very good approximation, to the classical algebraic, quadratic bottom friction law (e.g. Nihoul, 1975) except during limited periods of weak currents (at tide reversal, in the absence of significant wind). Then, the direction of the bottom stress with respect to the mean flow is modified by a non-negligible Ekman veering and its magnitude is no longer directly related to the (evanescent) mean velocity but depends essentially on sustained turbulence in the bottom current (Nihoul, 1977, 1982).

However, when the currents are small, the advection terms are negligible. The one-dimensional model can be linearized and solved analytically by series expansions in the eigenfunctions of the vertical turbulent diffusion operator (Nihoul, 1977). It can be shown, then, that the bottom stress can be written in the simple form

---

* One emphasizes that the horizontal eddy diffusion of momentum is found negligible and that no artificial horizontal diffusion is introduced in the *numerical* model where advection terms are discretized by decentred forward finite differences.

** The model has been extended to include the effect of stratification. In this more elaborate version, u_* is replaced by the rootsquare of the mean turbulent kinetic energy which is a function of depth. An additional equation is included in the model for the mean turbulent kinetic energy.

$$(13) \qquad \boldsymbol{\tau}_b = D^{1/2} \|\boldsymbol{\tau}_b\|^{1/2} \bar{\mathbf{u}} - m \boldsymbol{\tau}_s + \gamma H \left(\frac{\partial \bar{\mathbf{u}}}{\partial t} + f \mathbf{e}_3 \wedge \bar{\mathbf{u}}\right)$$

where $\boldsymbol{\tau}_b$ and $\boldsymbol{\tau}_s$ are respectively the bottom stress and the wind stress (per unit mass), $\bar{\mathbf{u}}$ is the depth-averaged horizontal velocity, D is the drag coefficient, m and γ two numerical factors.

Eq. (13) can be used to determine $\boldsymbol{\tau}_b$ at time t in terms of simultaneous values of $\bar{\mathbf{u}}$ and $\boldsymbol{\tau}_s$ and the immediate past history of $\bar{\mathbf{u}}$ [$\bar{\mathbf{u}}(t - \Delta t)$]. One can thus run the 2D-model alone in regions where one doesn't need the highest accuracy or the details of the vertical structures. Large scale 2D-models provide then boundary conditions for the coastal 2D-models which are coupled with local 1D-models operated on a par with the former.

Depth-integrated models of the North Sea and the Southern Bight.

Fig. 1 shows the characteristics of the numerical grids used in modelling the North Sea (NS Model) and the Southern Bight (SB Model). The flow normal to the coasts is taken as zero. (The coast is a single streamline from one estuary to the next, in the model of the residual circulation, and the streamfunction increases at estuaries by amounts equal to the rivers' inflows.) Along open-sea boundaries, different types of boundary conditions, surface elevations*, velocities, velocity gradients and more or less sophisticated radiation conditions (e.g. Orlanski, 1976) have been tested for the mesoscale models (Ronday, 1976; Ronday and Nihoul, 1978, 1979; Clément et al., 1981).

Taking into account the data available on open-sea boundaries, the following boundary conditions were chosen for routine applications of the model (e.g. Daubert and Graffe, 1967; $\mathbf{n}$ is the unit vector normal to the boundary surface pointing outwards) :

(i) $\mathbf{v}.\mathbf{n} > 0$: surface elevation ζ ;

(ii) $\mathbf{v}.\mathbf{n} < 0$: surface elevation ζ , zero gradient of the normal velocity $\mathbf{v}.\mathbf{n}$ **.

In the macroscale models, the residual inflow is given at the open-sea boundaries (Ronday, 1976; Nihoul, 1982).

The open-sea boundary conditions for the SB-Model are determined by interpolation of the results of the NS-Model.

Fig. 2 shows a more sophisticated version of the models. The NS-Model (divided in two parts covering respectively the Western Channel and the Northern North Sea) and the SB-Model are now interactively coupled each of them providing boundary conditions for the others.

Comparison of the model's predictions with observations shows a fairly good agreement (slightly better with the NB-Model than with the NS- and SB-Models). Fig. 3 shows for instance a comparison between predicted and observed amplitude and phase of the current at the point 51°47'20 N 2°20'20 E of the Jonsdap 76 experimental network (Riepma, 1980).

---

* Surface elevations are determined by interpolation between Morlaix and Plymouth for the Western boundary and between the field observations along the line B.M for the Northern boundary (fig. 1).

** This additional condition is needed because the equations are non-linear (Daubert and Graffe, 1967).

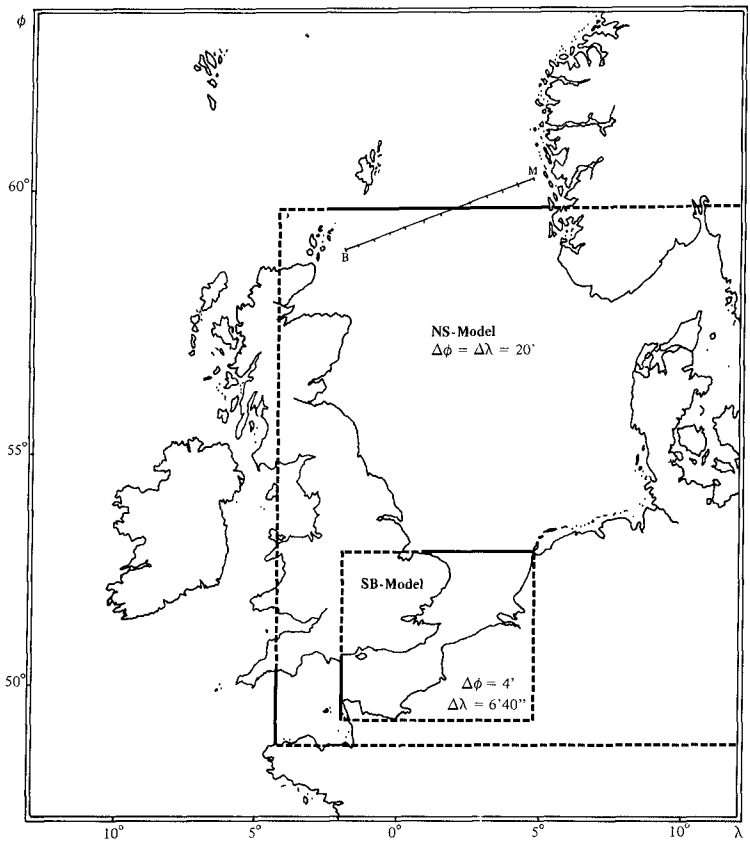

fig. 1.

Models of the North Sea and the Southern Bight
(Δt = 162.6 s)

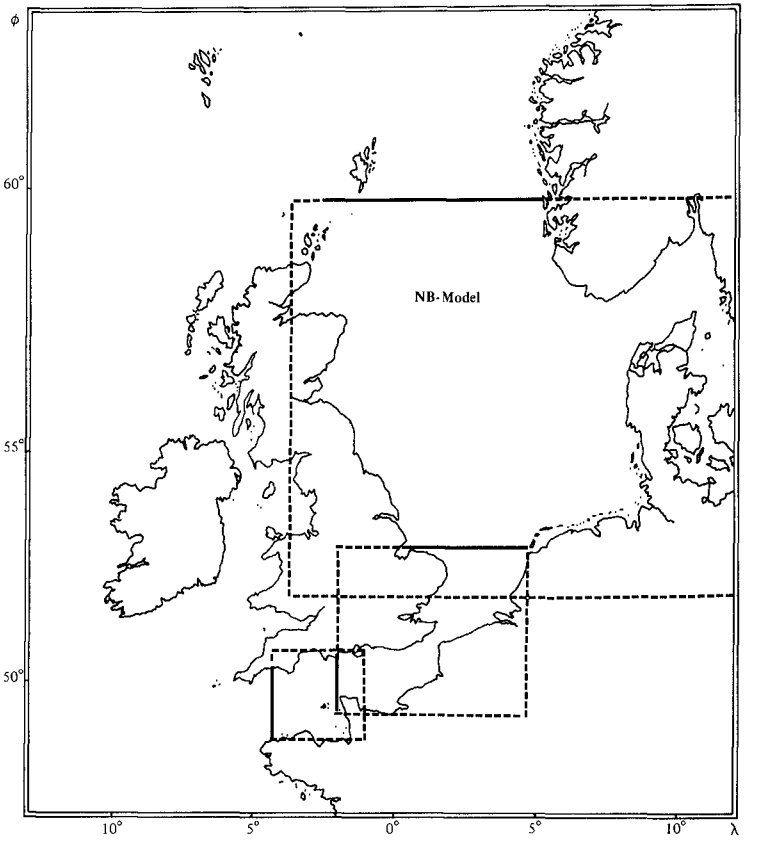

fig. 2.

Interactive, coupled models of the North Sea and the Southern Bight
($\Delta\phi$, $\Delta\lambda$, Δt, see fig. 1)

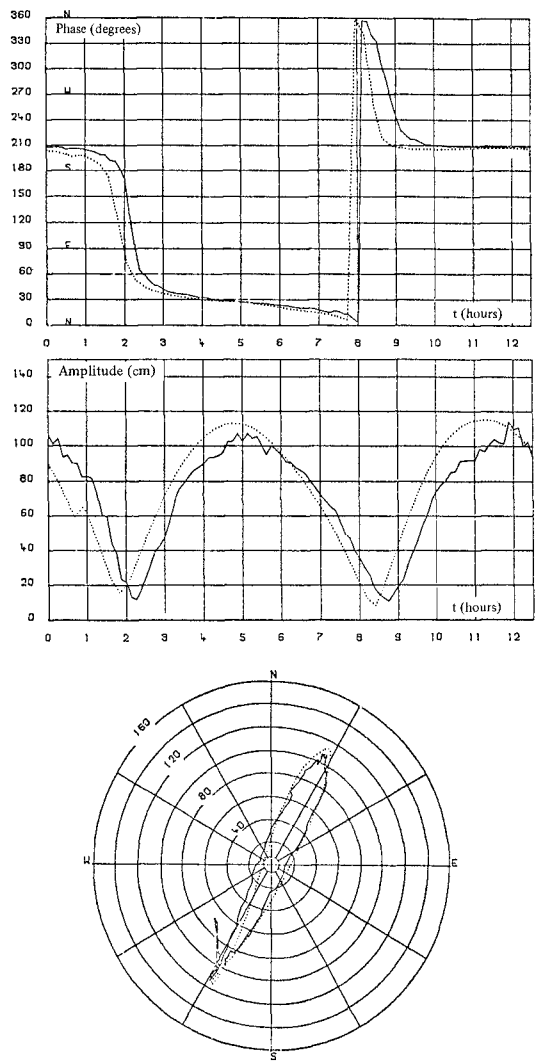

fig. 3.

Comparison between predicted (.....) and observed (——) amplitude and phase of the current at the point 51°47'20 N 2°20'20 E of the Jonsdap 76 network.

Three-dimensional models of the coastal zone and the Scheldt estuary.

Fig. 4 shows the characteristics of the numerical grids used in modelling the coastal zone (CZ-Model), the region of Zeebrugge (ZZ-Model) and the Scheldt estuary (SE-Model). The SE-Model is interactively coupled with a one-dimensional model of the Scheldt river from Doel to Gentbrugge (SR-Model).

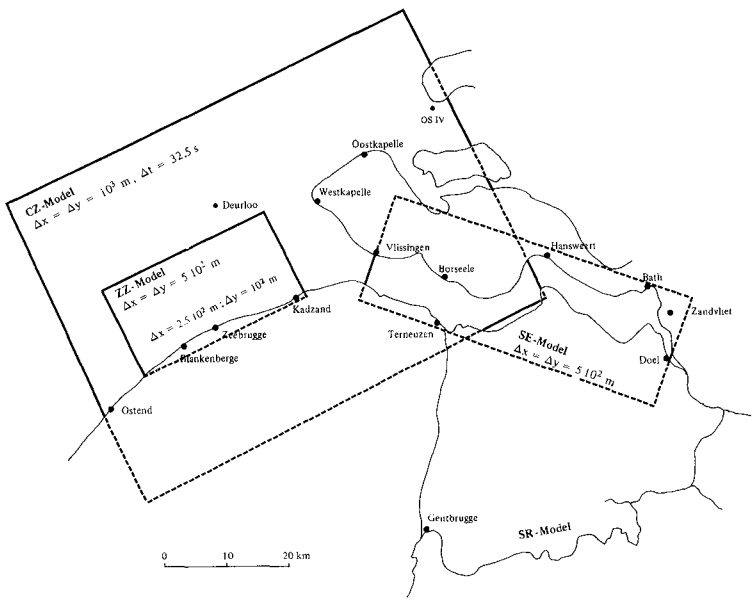

fig. 4.
Models of the coastal zone and the Scheldt

Open-sea boundary conditions are determined for each grid by the results of the larger scale model completed by the available field observations. Open-sea boundary conditions for the CZ-Model are provided by the NB-Model of the North Sea. The conditions at the coastal boundary points of the NB-Model can be computed by the coastal models – which have a more detailed resolution of the coastline and the sand banks' topography – and fed back in the NB-Model to improve the overall computation.

Figs 5, 6 and 7 show a very good agreement between the models' predictions and the observations*.

* Note that both observed and computed values are the actual values for that particular day (with the appropriate atmospheric and boundary conditions). No smoothing, filtering or harmonic analysis has been performed.

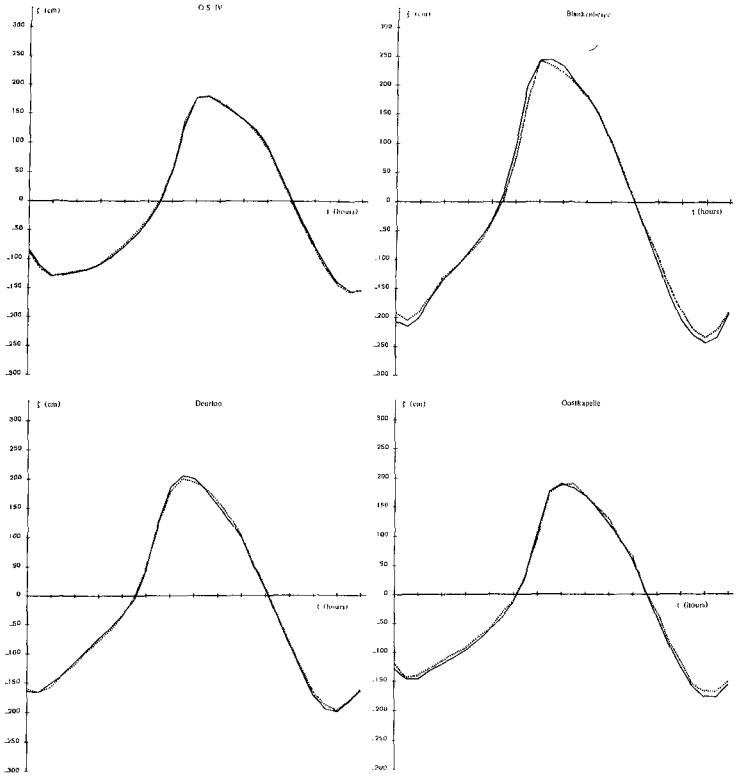

fig. 5.

Comparison between computed (·····) and observed (——) values of the surface elevation at four points of the coastal zone (fig. 4), Sept. 6, 1975.

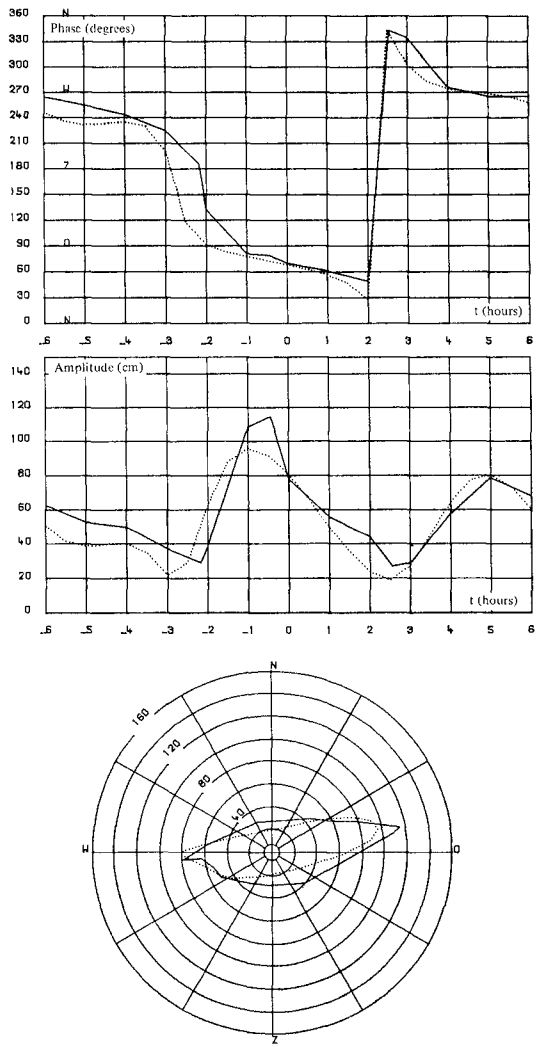

fig. 6.

Comparison between computed (·····) and observed (——) values of the amplitude and phase of the depth averaged current at Zeebrugge (~ 10^3 m offshore) for Sept. 6, 1975.

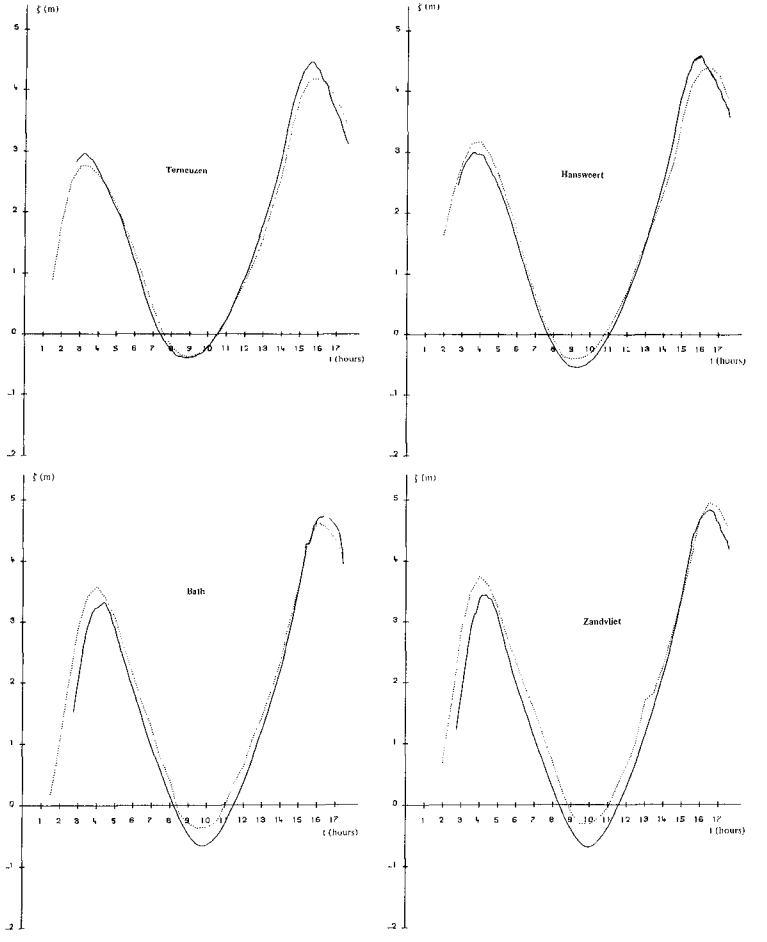

fig. 7.

Comparison between computed (——) and observed (·····) values of the surface elevation at four points of the Scheldt estuary during the storm of Jan. 3, 1976.

Applications.

The model has been applied to the routine forecasting of currents and water levels along the coast and in the Scheldt, to the prediction of the action of the sea on harbors, passes, dykes, ... and to the evaluation of the environmental impact of coastal engineering projects.

The influence of meteorological conditions on tidal elevations and velocities was determined for mean, spring and neat tides and for different wind conditions (mean wind, most frequent wind lasting at least three days, ...). The vertical profile of the horizontal velocity was calculated at several points of interest (dumping, sedimentation, bottom erosion, ...). Fig. 8 shows for instance the evolution of the velocity profile at a point near the coast under typical wind conditions. The veering of the velocity vector with height which one can see at tide reversal requires a more elaborate parameterization of the bottom stress as explained in section 1.

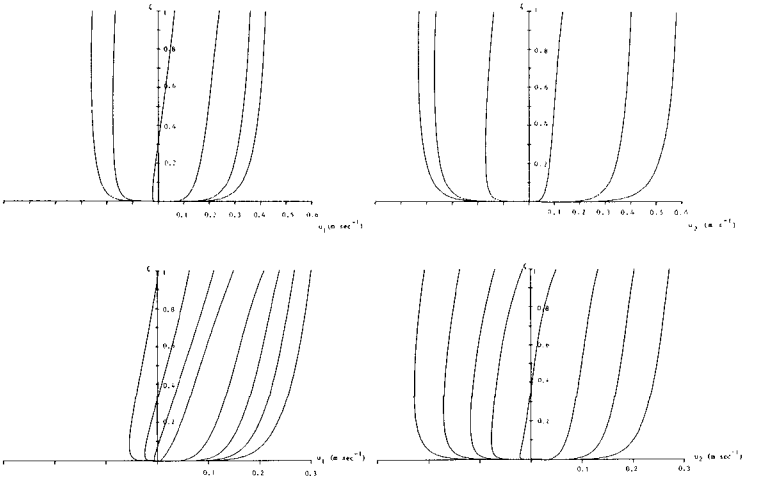

fig. 8.

Evolution with time of the vertical profile of the horizontal velocity vector **u** (left : eastern component; right : northern component) at the point 52°30'N 3°5'E.
Above : evolution over one half tidal period (the curves from right to left are vertical profile computed at 54' interval).
Below : evolution at tide reversal (the curves from right to left are vertical profile computed at 18' interval).
$\xi = (x_3 + h)/H$, $h \sim 22$ m, wind stress oriented to the North-East and equal to $2\ 10^{-4}\ m^2\ s^{-2}$ (per unit mass).

The impact of Zeebrugge's harbour on tidal and residual currents and elevations was studied for the existing and several proposed configurations as well as related dredging activities and industrial development on the coast. Fig. 9 shows, for instance, the predicted evolution, over a tidal period, of a patch of cold water produced by regasification at a planned gaz terminal on the new harbour's precinct.

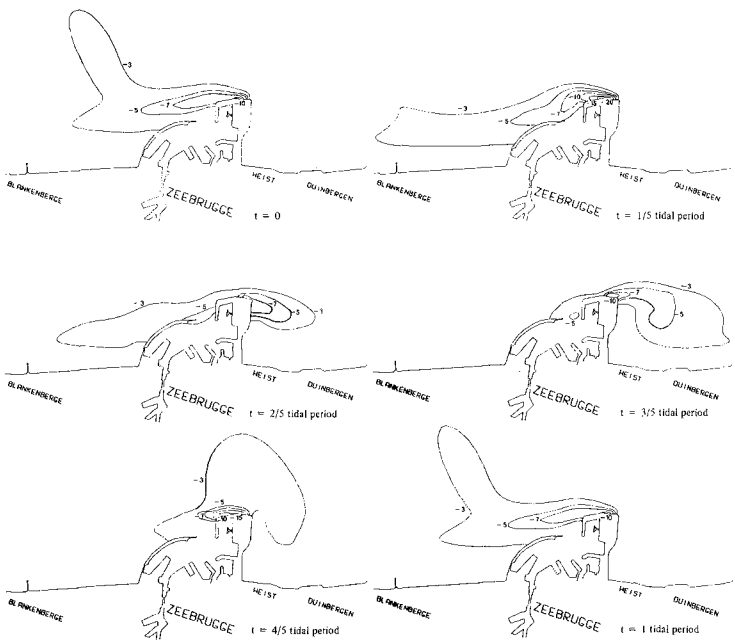

fig. 9.

Evolution over a tidal period of a patch of cold water released by a 110 MW source on the jetty of the new harbour at Zeebrugge (gasification process at a liquid-gaz terminal). The curves are graduated in 10^{-2} K (temperature degrees).

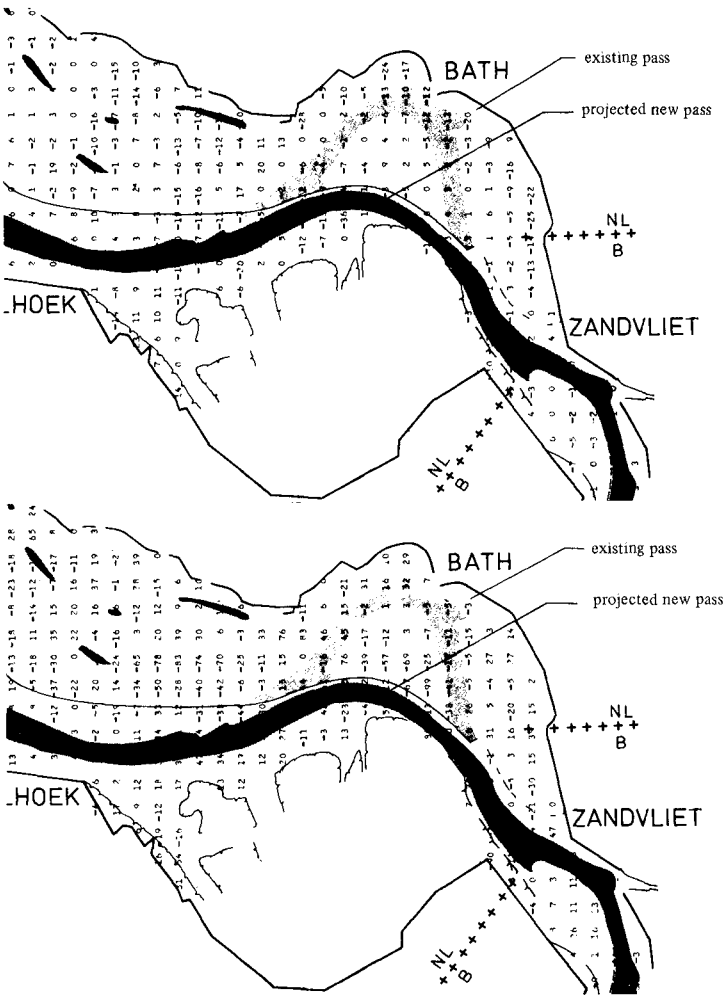

fig. 10.

Effect on the modification of a pass in the Scheldt estuary on maximum water level (above) and maximum velocity at flood-tide (below) during the storm of Jan. 3, 1976. (The numbers represent the differences between the predicted results for the new and the existing bottom topography.)

The effect of modifying passes in the Scheldt estuary was investigated in different tidal and wind conditions by hindcasting known situations with existing and proposed bottom topographies. Fig. 10 shows, for instance, the differences in water level and flood-velocities that would have been produced in the region of Bath, by a rectification of the pass.

The difficulty of "measuring" the residual currents* motivated an extended study of the macroscale circulation. Fig. 11 shows the residual streamlines in the North Sea in a typical situation.

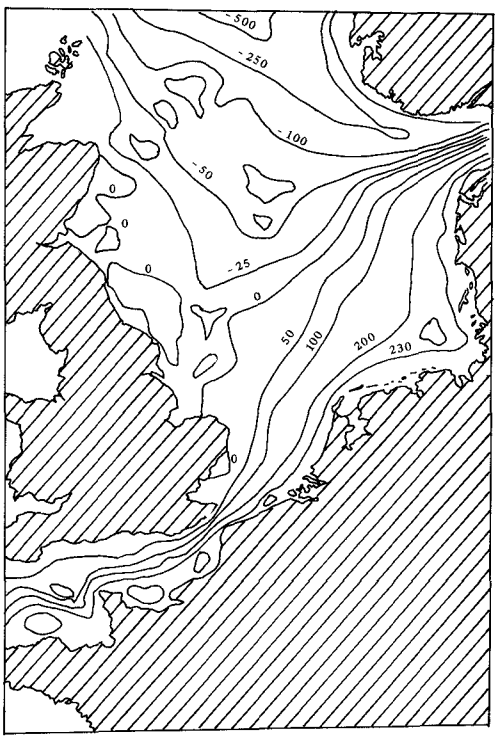

fig. 11.

Residual depth-averaged circulation in the North Sea. Streamlines ψ = const in 10^3 m^3 s^{-1}. [Real 1973 wind situation, boundary inflows according to Ronday (1976), residual bottom friction coefficient function of depth, mesoscale velocity and rugosity length (Ronday, 1976).]

* The residual currents constitute a very small part of the current meters' signal, of the order, in fact, of the instrumental error. Because of the non-linearities of the instruments (averaged speed, instantaneous direction) errors do not cancel with time averaging and experimental values can often be wrong by as much as 100 %.

The presence of a gyre off the Northern Belgian coast, confirmed by the results of the coastal models (fig. 12) and by observations (e.g. Beckers et al., 1976) is responsible for a south-bound coastal current which entrains the highly turbid Scheldt waters to the South.

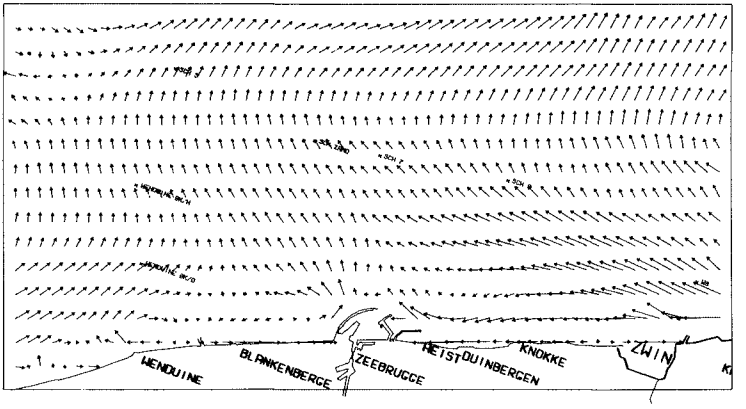

fig. 12.

Residual (depth-averaged) currents in the region of Zeebrugge, showing a south-bound coastal current along the Northern Belgian coast, in relation with the coastal gyre shown in fig. 11.

The predicted accumulation of silt along the Northern coast is confirmed by the observations (fig. 13).

Acknowledgements.

The present work was carried out under several private and official contracts. The authors are indebted to Distrigaz, Electrobel and TVZ 2 and to the Departments of Health, National Education, Public Works and Science Policy for their help, financial support and kind permission to use some of the results.

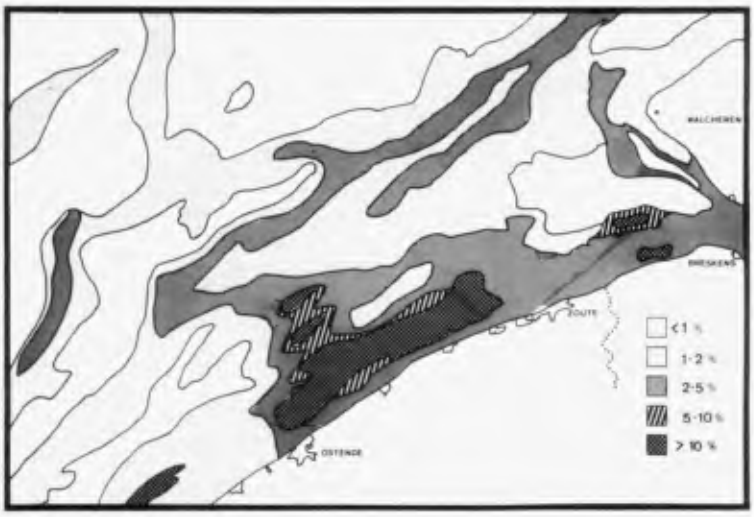

fig. 13.
Accumulation of silt along the Northern Belgian coast according to observations (Beckers at al., 1976)

References.

BACKAUS, J., (1979). *First results of a three-dimensional model on the dynamics in the German Bight*, in *Marine Forecasting*, J.C.J. Nihoul (Ed.), Elsevier Publ. Co, Amsterdam, 333-349.

CLÉMENT, F., RUNFOLA, Y., RONDAY, F.C. and NIHOUL, J.C.J., (1981). Modèle mathématique de la baie sud de la mer du Nord, Unité de Gestion de la mer du Nord et de l'estuaire de l'Escaut, CDN 120978, 422 pp.

DAUBERT, A. and GRAFFE, O., (1967). Quelques aspects des écoulements presque horizontaux à deux dimensions en plan et non permanents, *La Houille blanche*, **8**, 847-860.

DAVIES, A.M., (1976). A Numerical Model of the North Sea and its Use in Choosing Locations for the Deployment of Off-Shore Tide Gauges in the JONSDAP '76 Oceanographic Experiment, *Deutsche Hydrographische Zeitschrift*, **29**, 11-24.

DURANCE, J.A., (1976). A three-dimensional numerical model of tidal motion in a shallow sea, *Mém. Soc. Roy. Sc. Lg.*, **10**, 125-132.

FISHER, G., (1959). Ein numerisches Verfahrens zur Errechnung von Windstau und Gezeiten in Randmeeren, *Tellus*, **9**, 60-76.

FLATHER, R.A., (1979). *Recent results from a storm surge prediction scheme for the North Sea*, in *Marine Forecasting*, J.C.J. Nihoul (Ed.), Elsevier Publ. Co, Amsterdam, 385-409.

HANSEN, W., (1956). Theorie zur Errechnung des Wasserstandes und der Strömungen in Randmeeren nebst Anwendungen, *Tellus*, **8**, 287-300.

HANSEN, W., (1966). The reproduction of the motion in the sea by means of hydrodynamical-numerical methods, NATO Subcommittee on Oceanographic Research, 25, 57 pp.

HEAPS, N.S., (1976). *On formulating a non-linear numerical model in three dimensions for tides and storm surges*, in *Computing Methods in Applied Sciences*, R. Glowinski and J.L. Lions (Eds.), Springer, Heidelberg, 368-387.

LEENDERTSE, J.J., (1967). *Aspects of computational model for long-period water-wave propagation*, Ph. D. Dissertation Technische Hogeschool Delft, Rand Corporation, R.M. 5294-PR, 165 pp.

LEENDERTSE, J.J. and LIU, S.K., (1978). *A three-dimensional turbulent energy model for non-homogeneous estuaries and coastal systems*, in *Hydrodynamics of Estuaries and Fjords*, J.G.J. Nihoul (Ed.), Elsevier Publ. Co, Amsterdam, 387-405.

NIHOUL, J.C.J., (1975). *Modelling of marine systems*, Elsevier, Amsterdam, 272 pp.

NIHOUL, J.C.J., (1976). *Mathematical hydrodynamic models for the study of marine circulation and dispersion of pollutants in a shallow sea*, in *Computing Methods in Applied Sciences*, R. Glowinski and J.L. Lions (Eds), Springer, Heidelberg, 447-472.

NIHOUL, J.C.J., (1977). Three-dimensional model of tides and storm surges in a shallow well-mixed continental sea, *Dynamics of Atmospheres and Oceans*, 2, 29-47.

NIHOUL, J.C.J., (1980). Residual circulation, long waves and mesoscale eddies in the North Sea, *Oceanologica Acta*, **3**, 309-316.

NIHOUL, J.C.J., (1981). *Marine Hydrodynamics at ecological scale*, in *Ecohydrodynamics*, J.G.J. Nihoul (Ed.), Elsevier Publ. Co, Amsterdam, 1-12.

NIHOUL, J.C.J., (1982). *Hydrodynamic Models of Shallow Continental Seas*, Etienne Riga, éditeur, Liège, 198 pp.

NIHOUL, J.C.J. and RONDAY, F.C., (1975). The influence of the tidal stress on the residual circulation, *Tellus*, **29**, 484-490.

NIHOUL, J.G.J. and RONDAY, F.C., (1976). Hydrodynamic models of the North Sea, *Mém. Soc. Roy. Sc. Lg.*, **10**, 61-96.

NIHOUL, J.C.J. and RUNFOLA, Y., (1981). *The residual circulation in the North Sea*, in *Ecohydrodynamics*, J.G.J. Nihoul (Ed.), Elsevier Publ. Co, Amsterdam, 219-271.

ORLANSKI, I., (1976). A simple boundary condition for unbounded hyperbolic flows, *Journal of computational Physics*, **3**, 251-269.

PINGREE, R.D. and GRIFFITHS, D.K., (1981a). S_2 tidal simulation on the north-west European shelf, *J. Mar. Biol. Ass. U.K.*, **61**, 609-616.

PINGREE, R.D. and GRIFFITHS, D.K., (1981b). The N_2 tide and semidiurnal amphidromes around the British Isles, *J. Mar. Biol. Ass. U.K.*, **61**, 617-625.

PRANDLE, D., (1978). Residual flows and elevations in the southern North Sea, *Proc. Roy. Soc. London*, **A359**, 189-228.

PRANDLE, D. and WOLF, J., (1978). *Surge-Tide interaction in the southern North Sea*, in *Hydrodynamics of Estuaries and Fjords*, J.C.J. Nihoul (Ed.), Elsevier Publ. Co, Amsterdam, 161-185.

RAMMING, H.G., (1976). A nested North-Sea model with fine resolution in shallow coastal areas, *Mém. Soc. Roy. Sc. Lg.*, **10**, 9-26.

RIEPMA, H.W., (1980). Residual currents in the North Sea during the INOUT phase of JONSDAP '76, *"Meteor" Forsch.-Ergebnisse*, **32**, 19-32.

RONDAY, F.C., (1976). *Modèles hydrodynamiques*, in *Modélisation des systèmes marins. Projet Mer. Rapport final*, J.G.J. Nihoul (Ed.), Ser-

vices du Premier Ministre, Programmation de la Politique scientifique, Bruxelles, 1976, vol. 3, 270 pp.

RONDAY, F.C., (1979). *Tidal and residual circulation in the English Channel*, in *Marine Forecasting*, J.C.J. Nihoul (Ed.), Elsevier Publ. Co, Amsterdam, 351-384.

RONDAY, F.C. and NIHOUL, J.C.J., (1978). Mathematisch model van de zeewaartse uitbouw van de haven van Zeebrugge, Deelkontrakt 3, Department for Public Works, Brussels, Mod. 382 1, 262 pp.

RONDAY, F.C. and NIHOUL, J.C.J., (1979). Mathematisch model van de zeewaartse uitbouw van de haven van Zeebrugge, Deelkontrakt 3, Department for Public Works, Brussels, Mod. 382 2, 397 pp.; Mod. 382 3, 147 pp.

ANALYSIS OF TIDAL RECORDS OF THE 1964 ALASKAN TSUNAMI

Basil W. Wilson*, F.ASCE

abstract

The 8.5 magnitude Alaskan earthquake of March 27, 1964, generated a great tsunami in the Pacific Ocean. This paper presents results of energy spectrum analyses conducted on a sampling of 24 of the marigrams from some 105 tide-stations which recorded the waves. In the numerical digital procedure used, two important properties of the evolving energy spectra are invoked; the frequency resolution and statistical confidence. High confidence is obtainable only at the expense of poor resolution, and *vice versa*. Excessive resolution may give rise to physically unreal spectral peaks, just as excessive restrictions for confidence may cause blunting of the spectrum and possible loss of physically real spectral components. A trial-and-error compromise between these properties was sought by testing the effects on the energy spectra, for Hilo, Hawaii, of the parameters that control the digital process. An optimum selection of spectrum parameters was finally made so that the primary and secondary wave forms of components, identified by the analysis for the marigram of San Francisco, Calif., most closely agree with the corresponding wave forms obtained by use of Chrystal's (1904) graphical method of *residuation* analysis. Using the parameters so determined, and by application of band-pass filters in the digital analysis, the most prominent peaks of spectral energy in the marigrams of the 24 stations are isolated and their wave-forms computer-plotted. In all cases a recognizable long-period wave component is found having a frequency between 0.50 and 0.65 cy/hr (average period 1.73 hrs). General similarity of these primary wave forms as to period and shape of beats suggests their common origin at the source of the earthquake disturbance. The secondary wave forms of higher frequency (periods generally less than 40 mins) are ascribed to local free oscillations forced by the primary wave trains at the receiving stations. In some, but not all of the marigrams there is evidence of wave systems averaging 3.2 hrs in period. These are thought to be an independent wave-train originating at source.

1. INTRODUCTION

On March 27, 1964, a great earthquake in Prince William Sound, Alaska, (magnitude ≈ 8.5, Richter scale), generated a tsunami which swept the entire Pacific Ocean. Its coastal effects were recorded by some 105 tide-gauges at mainland and island stations throughout the area[1]. This paper reports on energy-spectrum analyses of the marigrams from a sampling of 24 represent-

* Consulting Oceanographic Engineer, Pasadena, California, U.S.A.

ative stations distributed along the periphery of the Pacific Ocean and on islands within its circumference. Fig. 1, which is derived from the arrival times of the tsunami at coastlines and islands, and allows for the refraction of the wave-fronts in accord with the ocean depths, shows the advance of the front at hourly intervals and the locations of the tide-stations selected for marigram-analysis.

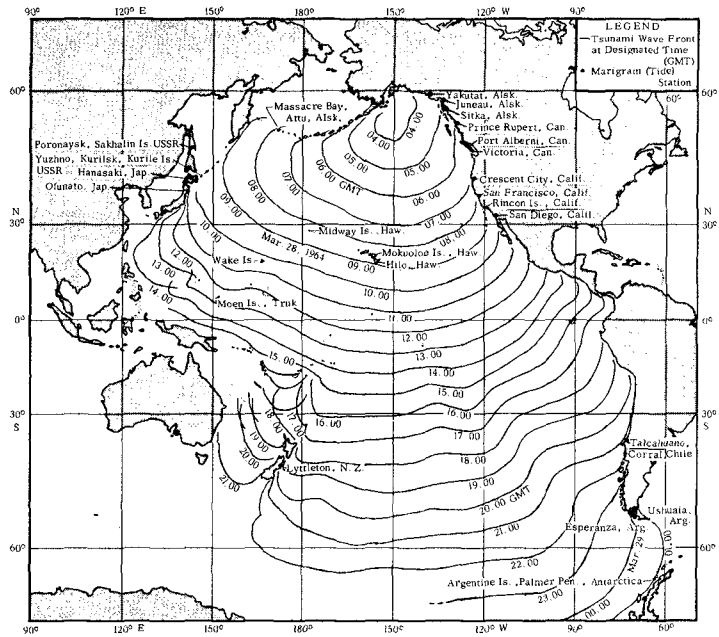

FIG. 1 - APPROXIMATE HOURLY (GMT) WAVE-FRONTS OF THE ALASKAN TSUNAMI OF MARCH 28-29, 1964. (Mercator projection).

A primary purpose of this investigation was to confirm of negate earlier analyses [2], undertaken during report preparation, (of necessity, hurriedly and at minimal cost), by use of Chrystal's graphical method of *residuation* [3]; thereby to verify the existence in the marigrams of exceptionally long-period wave systems, identified by those analyses, but hitherto unsuspected in tsunami occurrences (cf. Cox [4]). This paper summarizes a report of 1971 [5].

2. RESIDUATION VERSUS POWER-SPECTRUM ANALYSIS

Before numerical power-spectrum analysis had become one of the standard tools of oceanographic science in the 1950's [6,7,8], and preceded only by periodogram analysis [e.g. 9], (which in days before high-speed electronic computers was clumsy and time-consuming), Chrystal's method of *residuation*

offered a relatively quick and easy way of interpreting the composition of wave or seiche records. The method follows sound theoretical principles on the precept that a wave record can be approximated by a discrete spectrum of sinusoidal wave components. The writer made extensive and effective use of the method in the period 1940-'67 [e.g., 10], and is not ashamed that this period was overlapped by the ascendancy of the modern method of continuous power-spectrum analysis. In referring to the Residuation method, the writer, at various times, has named it "subjective", in the sense that, initially, it relies on the personal judgements of an analyst as to the periods of the discrete components supposed to exist in a wave record. In point of fact, however, as Chrystal showed, the method can be as objective as the analyst will allow, simply by use of a process of successive approximations. In the writer's experience, it has seldom been necessary to invoke closer approximations than first estimates, because one or more shorter-period components in a wave record can usually be detected unambiguously as to periodicity. The very process of "residuating", or eliminating, a suspected sinusoidal component, tends to reveal lower-order components more distinctly, so that they too, in succession, can be subtracted out from the residual record by the graphical method.

While the Residuation method of wave analysis is hardly to be recommend- for modern usage, it seems pertinent to point out that the now popular power-spectrum analysis, by use of the Fourier Double Integral Theorem and auto-correlation techniques, of itself yields only an estimate of the composition of a wave record, and is thereby subject to varying degrees of reliability. This aspect has been fully discussed elsewhere [5, 11], and will therefore be only briefly alluded to here. The method, it turns out, is quite sensitive to certain parameters which enter into the mathematical systems used, and, of necessity, have to be selected by the wave analyst. These parameters are:

(a) the number of digitized data-points, N, in the length of a wave record, T;
(b) the time increment, Δt, between adjacent data-points
(c) the number of lags, M, used for auto-correlation purposes
(d) the number of points, P, assigned to a numerical filter

Three important derivative parameters depend on the choice of (a), (b) and (c), namely:
(e) the frequency increment, or measure of *resolution*:

$$\left.\begin{array}{lll} \text{(i)} & \Delta\sigma = 2\pi(2\,\Delta t\,M)^{-1} & \text{radians-(time)}^{-1} \\ \text{or} \quad \text{(ii)} & \Delta f = (2\,\Delta t\,M)^{-1} & \text{cycles-(time)}^{-1} \end{array}\right\} \quad (1)$$

(f) the frequency range, or Nyquist cut-off frequency:

$$\left.\begin{array}{lll} \text{(i)} & \sigma_n = 2\pi(2\,\Delta t)^{-1} & \text{radians-(time)}^{-1} \\ \text{or} \quad \text{(ii)} & f_n = (2\,\Delta t)^{-1} & \text{cycles-(time)}^{-1} \end{array}\right\} \quad (2)$$

(g) the number of degrees of freedom, ν, or measure of *confidence*:

$$\nu = [\,N - M/4\,](M/2)^{-1} \approx 2N\,M^{-1} \qquad \text{when } M \ll N \qquad (3)$$

It is anomalistic that in seeking high confidence of results in auto-correlat-

ion, the number of lags M in Eq.(3) should be chosen as small as possible, although, thereby, the frequency increment, $\Delta\sigma$ or Δf, in Eq.(1) is also rendered large, and the resolution of the power spectrum therefore low. Confidence and resolution, unfortunately, are two mutually antagonistic properties. Poor resolution of the spectral density estimates results in excessive blunting of spectral peaks in the spectrum. Too high resolution, on the other hand, inevitably lowers the confidence that spectral peaks of energy are real. The tendency in spectrum analysis seems to have been to lean towards high confidence rather than strong resolution, with the result that wave energy spectra often appear to be devoid of sharp peaks. A question of importance for this study was to know the best common meeting ground for good resolution and reasonable confidence in the estimates of spectral energy density of the tsunami records.

3. SPECTRUM PARAMETERS FOR THE MARIGRAMS OF HILO, HAWAII, AND SAN FRANCISCO, CALIFORNIA

To test the effects of different values of spectrum parameters on resulting spectra, two cases, Hilo, Hawaii, and San Francisco, California, were selected initially for analysis. Hilo was chosen as being one station for which it was contended by Van Dorn and Cox [12], on the basis of spectrum analyses made by Loomis [13], that the marigram showed no evidence of the presence of waves as long in period as 1.8 hrs. The writer on the other hand, using the Residuation process, had found them to be present [2], and desired verification.

The tide records were digitized on a trace follower and read directly on to magnetic tape, from which co-ordinates of points were then transferred to decks of punched cards. Counts were recorded at time intervals of 0.02 hr over record lengths of 36 hrs. Fig. 2(a) is a computer-plot of the original marigram

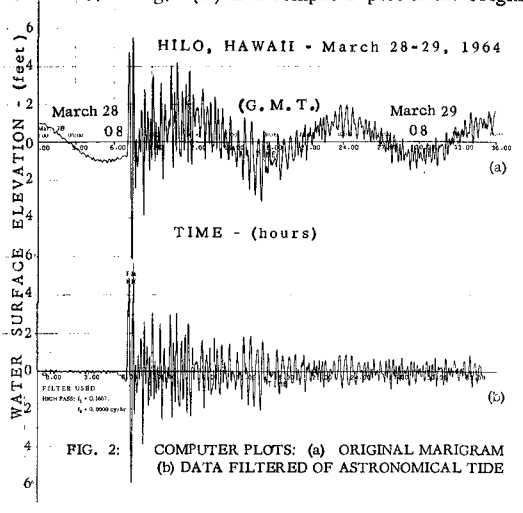

FIG. 2: COMPUTER PLOTS: (a) ORIGINAL MARIGRAM (b) DATA FILTERED OF ASTRONOMICAL TIDE

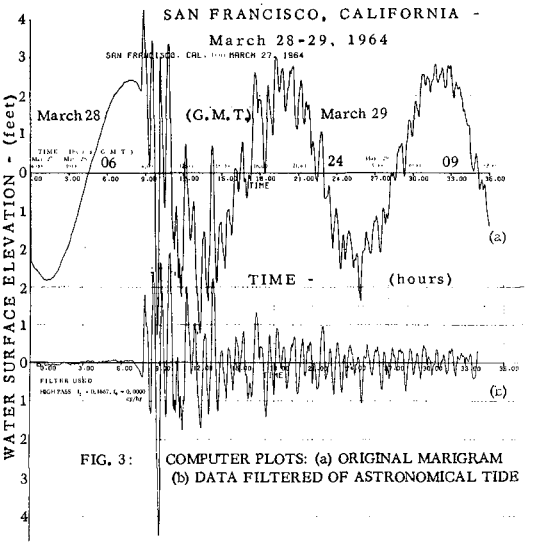

FIG. 3: COMPUTER PLOTS: (a) ORIGINAL MARIGRAM (b) DATA FILTERED OF ASTRONOMICAL TIDE

for Hilo, Hawaii, obtained in this fashion. Fig. 3(a) is the corresponding marigram for San Francisco, California. The digitized data were pre-filtered through a high-pass (2P + 1 =) 51-point filter for elimination of tides and other long wave effects in the frequency range 0 to 0.167 cy/hr (T > 6 hrs) with the results shown in Figs. 2(b) and 3(b). The filtered data were then analyzed to yield the energy spectra, substantially in accord with the principles detailed in references [5,11], and utilizing the spectrum parameter sets B to F given in Table I.

Loomis' spectra of 1966 [14], using the set A_1 in Table I, failed ro show any indication of an energy density peak at or near the frequency f = 0.555 cy/hr, (period 1.8 hrs). The resolution of A_1 is seen to be rather poor and the confidence only moderately good. In his later work of 1972 [13], Loomis' parameters A_2 yield somewhat better resolution at high confidence. Examination of his spectrum in this case does suggest the presence of somewhat low energy long waves at about 0.54 cy/hr (period T ≈ 1.85 hrs). This was apparently overlooked, or otherwise dismissed as noise, by Van Dorn and Cox [12].

The important effects of resolution, found by use of the parameter-sets C, D, E and F of Table I on the marigram for Hilo, Hawaii, are shown in the spectra of Figs. 4(a) to (d). Fig. 4(a), with low resolution and good confidence, fails to show any evidence of an energy peak at 0.55 cy/hr frequency (T≈1.8 hr). Fig. 4(b) reveals the emergence of several minor peaks as resolution improves and confidence recedes. The use of 51-point filters with parameters C and D led to difficulties in the plot-out of wave forms. Parameter set E was made

TABLE 1: SETS OF SPECTRUM PARAMETERS USED OR TESTED

Parameter Set	Investigator & Reference	SPECTRUM PARAMETERS ADOPTED							
		Record Length T_r (hrs)	No. of Points N	Time Interval Δt (hr)	Nyquist Frequency f_n (cy/hr)	No. of Lags M	Degrees of Freedom (Confidence) ν	Frequency Increment (Resolution) Δf (cy/hr)	No. of Filter Points 2P+1
A_1	Loomis (14)	8	249	0.03	15	41	12	0.372	?
A_2	Loomis (13)	34	1024	0.03	15	60	34	0.250	?
B	Wilson (5)	30	300	0.10	5	160	4	0.031	51
C	" (5)	36	1800	0.02	25	200	18	0.125	51
D	" (5)	36	1800	0.02	25	300	12	0.083	51
E	" (5)	36	1800	0.02	25	300	12	0.083	255
F	" (5)	36	1800	0.02	25	400	9	0.063	153

identical to D in all respects save for the adoption of 255-point filters. The more finely tuned filters had the influence of reducing energy losses in the high-pass filtering process, and as Fig. 4(c) shows, allowed emergence of more prominent spectrum peaks, compared to Fig. 4(b), including a small one at 0.56 cy/hr frequency ($T \approx 1.79$ hrs). In the case of Fig. 4(d) the number of lags was increased further (M = 400) and filter points reduced to 153 (P = 75). Resolution was hereby increased still further and confidence somewhat reduced ($\nu = 9$). The smaller value of P was a concession to reduction of computing time and reduction of terminal losses of output record-lengths resulting from application of filters. Fig. 4(d) further enhances the spectral energy peaks, including some residual tidal energy (unshaded) not completely removed by the initial high-pass filter.

In the case of the marigram for San Francisco (Fig. 3), application was made of the spectrum parameters B, E and F, with results shown in the spectra of Figs. 5(a), (b) and (c). It is very evident from Fig. 5 that the tsunami at San Francisco was composed primarily of two almost discrete wave systems with periods approximating 1.8 hrs and 40 mins. The high resolution of parameter-set B elicits some minor peaks in the equivalent spectrum Fig. 5(a). These are virtually smoothed away by the use of the parameter-set F [Fig. 5(c)], and are non-existent in Fig. 5(b), obtained from use of parameter-set E.

4. COMPARISON OF THE WAVE-FORMS FROM SPECTRUM AND RESIDUATION ANALYSIS

In Fig. 6 the primary (P) and secondary (S) wave systems of periods, respectively, $T_1 \approx 1.8$ hrs and $T_2 \approx 40$ mins, have been separated out from the San Francisco marigram by use of appropriate filters, for comparison with the results of the Residuation analysis, P(d) and (S). The computer results from

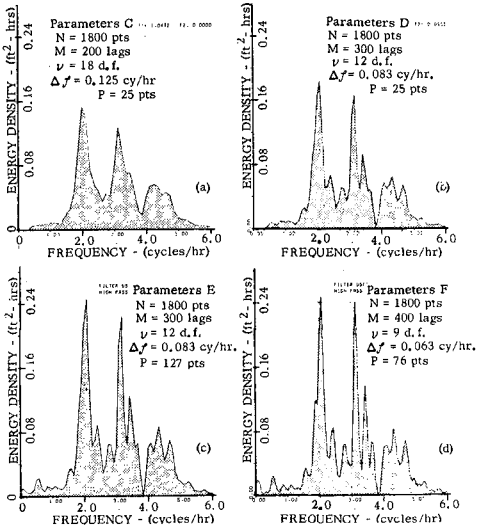

FIG. 4 - COMPARATIVE WAVE-ENERGY SPECTRA FROM HILO, HAWAII, MARIGRAM OF MAR. 28-29, 1964. T_r = 36 hrs; Δt = 0.02 hr.

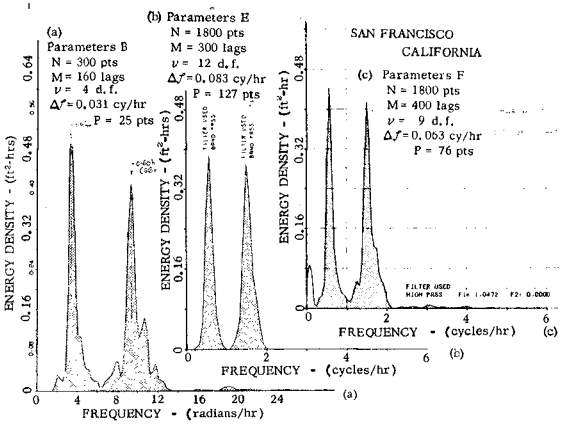

FIG. 5 - COMPARATIVE WAVE-ENERGY SPECTRA FROM SAN FRANCISCO MARIGRAM OF MAR. 28-29, 1964. T_r = 36 hrs; Δt = 0.02 hr.

use of the spectrum parameters E appear to accord most closely with the Residuation wave forms in period, amplitude and beat-shapes.

In the case of the Hilo, Hawaii, record, the wave form of the small peak of low frequency energy, centered at 0.56 cy/hr in Fig. 4(d), was obtained by passing the digitized wave data through a numerical band-pass filter having cut-off frequencies at $f_1 = 0.30$, $f_2 = 0.80$ cy/hr. The plot-out is shown as P(a) in Fig.7, and it is to be compared with P(b), obtained by the Residuation method [2]. The long-wave system P(a) in Fig. 7, obtained by use of a band-pass

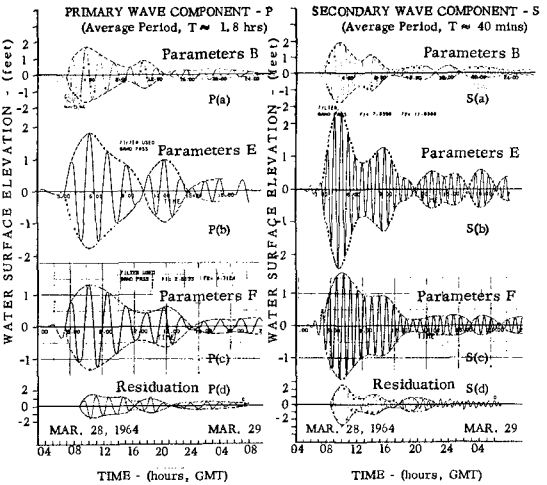

FIG. 6 - WAVE FORMS OF PRIMARY (P) AND SECONDARY (S) COMPONENTS OF MARIGRAM OF MAR. 28, 1964, SAN FRANCISCO, CALIFORNIA. Spectrum analyses a, b and c are derived from parameters B, E, F respectively (Table I); Residuation analyses d are graphical.

filter with cut-off frequencies $f_1 = 0.30$, $f_2 = 0.80$ cy/hr, retains some high-frequency contamination, but its envelope shape and maximum amplitude are generally similar to P(b). The remaining residual wave forms, after elimination of P(a) and P(b) are shown in Fig.7 as S(a) and S(b). There is again general similarity of shape and amplitude.

On the basis of this experimental probing, it was decided to adopt the spectrum parameter-set F as capable of yielding reliable results for spectrum analysis of the sampling of 24 marigrams. The parameter-set F was adopted in preference to E, the more desirable set, in the interests of economy, research funds being limited.

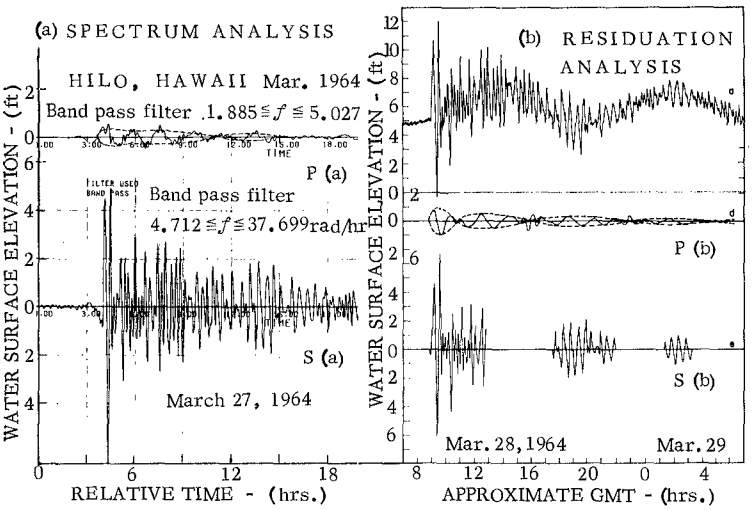

FIG. 7 - WAVE FORMS OF LOW-FREQUENCY COMPONENTS (P) AND SECONDARY COMPONENTS (S) IN MARIGRAM OF MAR. 28, 1964, FOR HILO, HAWAII. Spectrum analyses (a) used parameters F (Table I); Residuation analyses (b) are graphical.

5. SPECTRUM ANALYSIS RESULTS

As an example of the procedure followed in the spectrum analyses of the 24 marigrams, we give here briefly, the main elements of the analysis of the record for Hilo, Hawaii, being a case already cited, and one of the more complicated of all those analysed.

Use of the parameters F of Table I was shown to yield the spectrum given already in Fig. 4(d). The next step, typically followed, was to inspect the power spectrum for any peak in the frequency range 0.30 to 0.80 cy/hr. Within this band Residuation analysis had shown, in all cases, that a definitive wave component was to be expected [2]. In the case of Hilo, Hawaii, as already discussed, use of a band-pass filter with these frequency limits isolated the minor peak of energy shown in Fig. 8(a). The residual spectrum from S(a) in Fig. 7 is shown in Fig. 8(f). By using successive band-pass filters applied to the data, (in all cases, pre-filtered of tides), the important peaks of wave energy were isolated in succession, as in (b), (c), (d) and (e) in Fig. 8. The wave-form associated with each such peak or group of peaks was next computer-plotted to yield the wave components reproduced in Fig. 9. Fig. 9(a) and (b) are the same, respectively, as P and S in Fig. 7. Fig. 9(c) is the wave-form corresponding to the energy group of Fig. 8(b); 9(d), that of 8(c); 9(e),

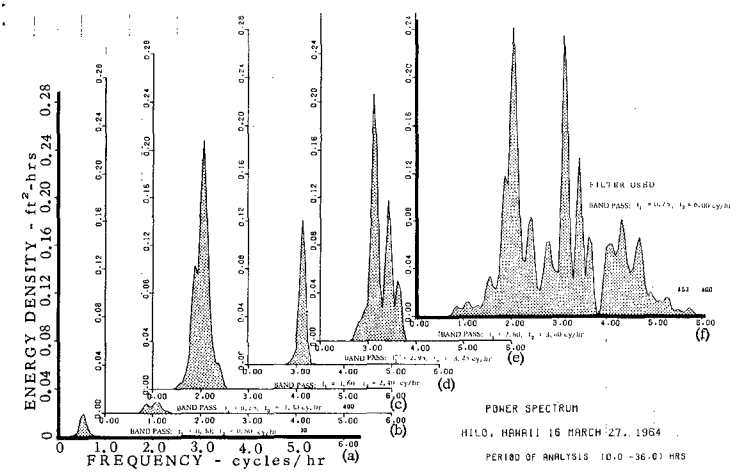

FIG. 8 - WAVE-ENERGY SPECTRA FROM DATA S(a) IN FIG. 7, AS FILTERED THROUGH BAND-PASS FILTERS (a) TO (f), HILO, HAWAII.

that of 8(e), and 9(f), that of 8(d).

Fig. 9 thus shows that the most dominant low-frequency components of the Hilo marigram were oscillations of periods 1.82 hrs, 1.0 hr, 29.1 mins and 19.2 mins. The latter, as revealed by Fig. 9(f), is a remarkably steady oscillation of long duration, (about 9 ins amplitude over 9 hours), before dying away. It is modulated, however, as apparent in Fig. 9(e), by the two wave components of periods 17.5 and 16.5 mins.

6. "PRIMARY" WAVES OF THE SPECTRUM ANALYSES

It is not possible in this short paper to reproduce results of all the spectrum analyses, as conducted in the form of Figs. 8 and 9. They are given, however, in full detail in Reference [5]. We limit ourselves here to presenting results for the lower frequency components of the tsunami at the different stations. Fig. 10 thus gives comparative evidence for the presence in all 24 marigrams studied, of a long wave component at a frequency between 0.50 and 0.65 cy/hr (average period 1.75 hrs). In all cases a definable peak of energy exists at or near this period, being very pronounced at stations close to the tsunami source, and at a few stations far afield. The relative heights of the energy peaks in the spectra are given along the top of the composite diagram as percentages in relation to 100% for Yakutat, Alaska. The spectrum peaks in Fig. 10, of necessity, have different ordinate scales. It will be seen that response at Port Alberni, Canada, was 10 times that of Yakutat. At Talcahuano, Chile, and at Lyttelton, New Zealand, about two thirds the distance across the Pacific Ocean from the source, in a north-south direction, the responses were 43% and 63%, .

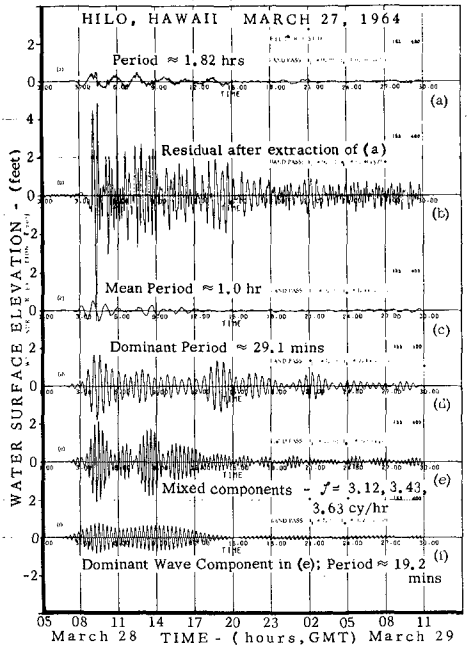

FIG. 9 - NUMERICALLY FILTERED AND PLOTTED WAVE-FORMS OF COMPONENTS OF THE ALASKAN TSUNAMI AT HILO, HAWAII, MARCH, 1964

respectively, virtual proof that this long-wave component was exciting some degree of resonance in the embayments at these locations.

The wave-forms corresponding to the spectrum peaks of Fig. 10 are computer plotted in Figs. 11 and 12; the vertical scales, be it noted, are not uniform. Considerable interest attaches to the beat-shapes of the envelopes of the wave-forms, which are often quite similar, as between stations fairly close together; even over great distances they still retain a general similarity. It appears that the number of waves in the first beat increases with distance in the north-south direction along the eastern boundary of the Pacific, from 5 near the source, to 6 at Prince Rupert, Canada, 7 at San Francisco, 8 at Talcahuano, Chile, and to semi-uniform wave-train formation near Antarctica. In the east-west and central north-south directions across the Pacific, the beat-shapes of the long waves, shown in Fig. 12, are quite markedly different from those of Fig. 11. Except in the cases of Hilo and Mokuoloe Is., Hawaii, the beats are all extremely long and phase changes apparently did not occur.

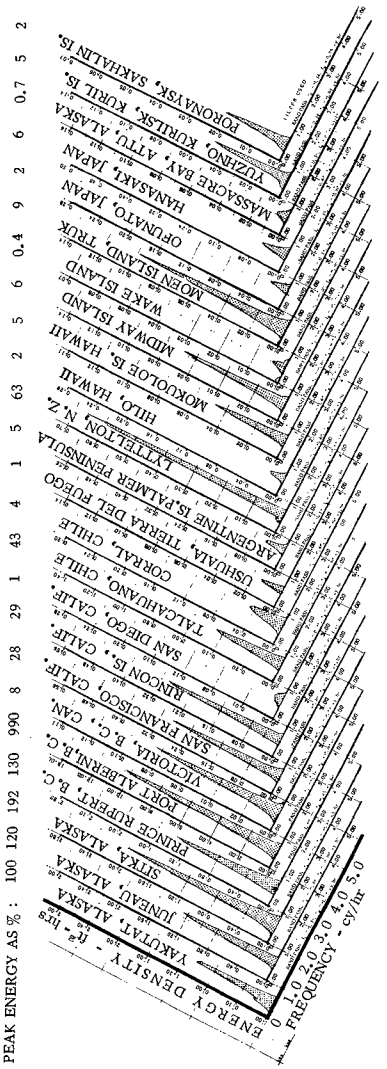

FIG. 10 - COMPARATIVE POWER-SPECTRA FROM BAND-PASS FILTERED DATA, ESTABLISHING THE PRESENCE IN ALL 24 MARIGRAMS OF PACIFIC OCEAN TIDE-STATIONS OF A DISTINCTIVE TSUNAMI COMPONENT-WAVE-FREQUENCY BETWEEN 0.50 AND 0.65 CY/HR (AVERAGE PERIOD 1.75 HRS). Note that ordinate scales are not all uniform.

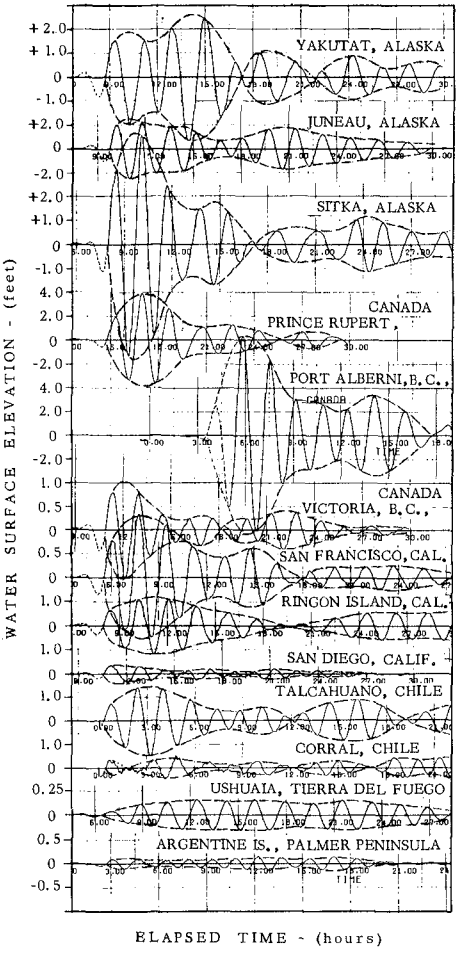

FIG. 11 - COMPUTER-PLOTTED WAVE-FORMS OF LONG-PERIOD COMPONENT (AVERAGE PERIOD 1.73 HRS) OF THE MARCH, 1964, ALASKAN TSUNAMI, NUMERICALLY DETERMINED FROM MARIGRAMS OF PACIFIC OCEAN TIDE-STATIONS.
Note: ordinate scales are not all uniform; dash-line envelopes are hand-drawn.
The plot for Port Alberni is intentionally set back to avoid confusion with adjacent plots.

It is of interest at this point to compare some samples of the Residuation analyses [2, 5], (as discussed earlier in Sections 2 and 4), with those obtain-in Figs. 11 and 12. Thus, Fig. 13 gives a selection of "primary" wave-trains *residuated* graphically from the marigrams of seven tide-stations. It is evident at once that the Residuation method succeeded in isolating the correct forms of the primary waves, both as to beat-shapes and number of waves in

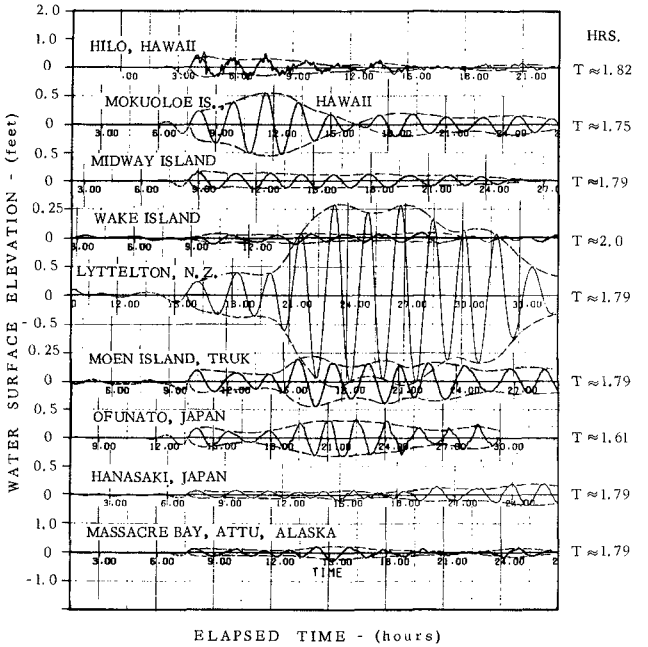

FIG. 12 - COMPUTER-PLOTTED WAVE-FORMS OF LONG-PERIOD COMPONENT (AVERAGE PERIOD 1.77 HRS) OF THE MARCH, 1964, ALASKAN TSUNAMI, NUMERICALLY DETERMINED FROM MARIGRAMS OF PACIFIC OCEAN TIDE-STATIONS: (ordinate scales not uniform; envelopes hand-drawn).

beats. Agreement on amplitudes is somewhat less satisfactory, but values are well within "ball-park" range of each other. The degree of concurrence of results from the two analysis methods is sufficient to validate the general reliability of the Residuation process used in Reference [2].

When the average period of the first three waves occurring in each wave-train of Figs. 11 and 12 are plotted as histograms of their relative frequency of occurrence, as in Fig. 14(a) and (b), the inference seems to be that along the west coast of the Americas, the predominant wave period of what we have called the *primary* waves was about 1.73 hrs, within a range from 1.55 to 1.95 hrs. In the west Pacific Ocean the dominant wave period was about 1.77 hrs within a tighter range of about 1.70 to 1.90 hrs.

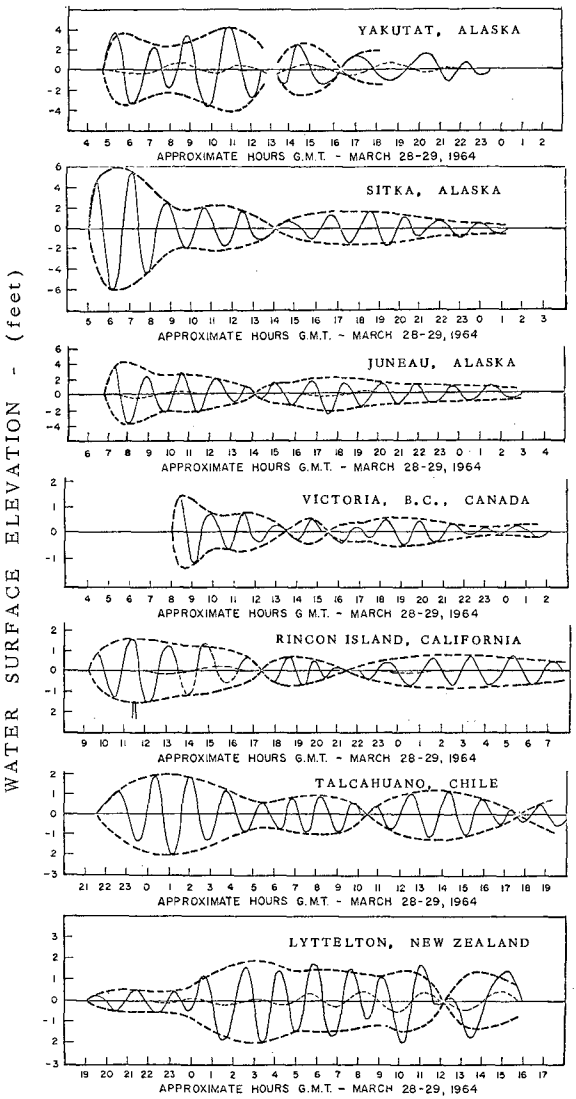

FIG. 13 - SAMPLES OF 'PRIMARY' WAVE TRAINS AS DETERMINED BY GRAPHICAL RESIDUATION OF THE MARIGRAMS FOR THE SEVEN TIDE-STATIONS; AVERAGE PERIOD 1.75 HRS: (Compare with computer-plots of 'Primary' waves obtained from Numerical Energy Spectrum Analyses in Figs. 11 and 12).

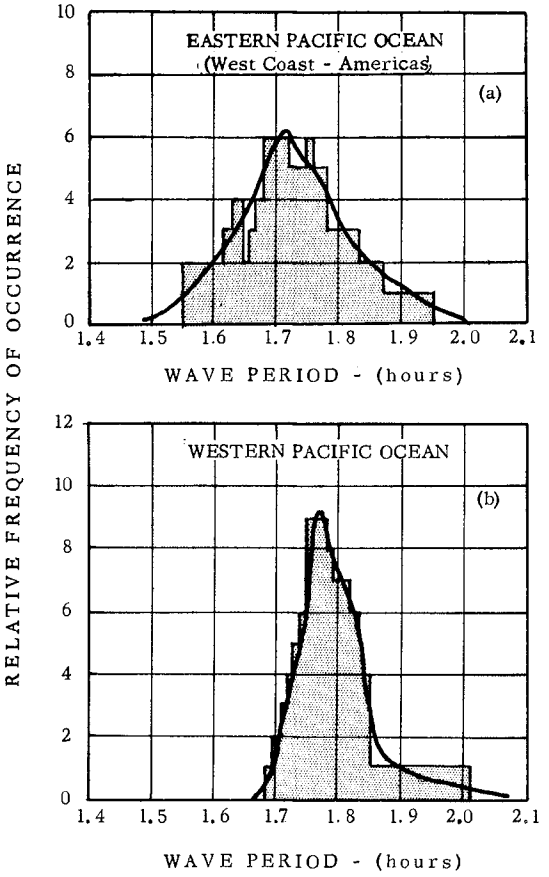

FIG. 14 - HISTOGRAMS OF WAVE PERIODS FOR "PRIMARY" LONG WAVE COMPONENT OF MARCH, 1964, ALASKAN TSUNAMI: (a) EASTERN PACIFIC OCEAN; (b) WESTERN PACIFIC OCEAN; (based on first three waves in Figs. 11 and 12)

On the supposition that the beats of long waves resulted from the interference of just two trains of periods T_1 and T_2 (frequencies f_1 and f_2), thereby yielding beat frequencies f_b and apparent wave frequencies f_a, it is readily shown that:

$$\left.\begin{array}{ll} \text{(i)} & T_1 = 1/f_1 = [\, f_a + f_b \,]^{-1} = [\, 1/T_a + 1/T_b \,]^{-1} \\ \text{(ii)} & T_2 = 1/f_2 = [\, f_a - f_b \,]^{-1} = [\, 1/T_a - 1/T_b \,]^{-1} \\ \text{(iii)} & T_b = 2(n-1)\,T_a \end{array}\right\} \quad (4)$$

where T_a and T_b, respectively, are the periods of the waves apparent in the beat and of the beat itself, n being the number of waves occurring in the beat. Adopting $T_a = 1.72$ hrs for the Eastern Pacific, the values of T_1 and T_2 for particular values of T_b and n are found in Table II. For the Western Pacific Ocean they are given in Table III, for the apparent wave period $T_a = 1.77$ hrs.

Table II shows that the periods T_1 and T_2 in the last columns, are contained quite easily in the period-spread of the histogram, Fig. 14(a). Table III, likewise, shows similar containment in the histogram spead of Fig. 14(b). The idea gains support, therefore, that the envelope shapes of the long wave systems are the result of interfering frequency components with periods of the

TABLE II - RANGE OF INTERFERING FREQUENCIES TO ACCOUNT FOR BEATS OF LONG WAVES (NOMINAL PERIOD 1.72 HRS)

(Eastern Pacific Ocean; west coast - Americas)

No. of Waves in beat	Beat Period [Eq. (7)]	Beat Frequency	Wave Frequency	Component Wave Frequencies		Component Wave Periods	
n	T_b (hrs)	f_b (cy/hr.)	f_w (cy/hr.)	f_1 (cy/hr.)	f_2 (cy/hr.)	T_1 (hrs)	T_2 (hrs)
5	13.76	0.0727	0.5814	0.6541	0.5087	1.53	1.96
6	17.20	0.0581	0.5814	0.6395	0.5233	1.56	1.91
7	20.64	0.0484	0.5814	0.6298	0.5330	1.59	1.88
8	24.08	0.0415	0.5814	0.6229	0.5399	1.61	1.85
10	30.96	0.0323	0.5814	0.6137	0.5491	1.63	1.82

TABLE III - RANGE OF INTERFERING FREQUENCIES TO ACCOUNT FOR BEATS OF LONG WAVES (NOMINAL PERIOD 1.77 HRS)

(Western Pacific Ocean)

No. of Waves in beat	Beat Period [Eq. (7)]	Beat Frequency	Wave Frequency	Component Wave Frequencies		Component Wave Periods	
n	T_b (hrs)	f_b (cy/hr.)	f_w (cy/hr.)	f_1 (cy/hr.)	f_2 (cy/hr.)	T_1 (hrs)	T_2 (hrs)
7	21.24	0.0471	0.5650	0.6121	0.5189	1.63	1.93
8	24.78	0.0404	0.5650	0.6054	0.5246	1.65	1.90
10	28.32	0.0353	0.5650	0.6003	0.5297	1.67	1.89
12	31.86	0.0314	0.5650	0.5964	0.5336	1.68	1.87

order given by T_1 and T_2 in Tables II and III. The seemingly consistent trends of change with distance, suggested by the increasing number of waves in a beat, and the varying periods given in Tables II and III are interesting, but as yet unexplained. It may be that this simplified an interpretation of the beat phenomena cannot be justified, because the declining component period T_2 with distance runs counter to an expected increase of period over distance and time for expanding waves. Despite this difficulty, the overall consistencies of change with distance from the origin suggest that the wave formations of Figs. 11 and 12 must have originated at the source and not as mere local excitations.

7. EXISTENCE OF ULTRA-LONG PERIOD WAVE-TRAINS

Both the Residuation and the Numerical Spectrum analyses have revealed that, for about half of the marigrams studied, there is evidence of still longer period wave-trains in the composition of the tsunami than those already discussed. They are found to lie within a frequency range of about 0.30 to 0.35 cy/hr, (average period 3.2 hrs). The strongest such wave-train of period 3.0 hrs occurred at Yakutat, Alaska, close to the tsunami source (Fig. 1). Its height (Fig. 15) was comparable to the height of the 1.85 hr period waves shown in Fig. 11 for Yakutat. For the marigrams in which these extremely long waves were detectable, as in Fig. 15, the largest effects besides those of Yakutat, occurred at Victoria, Canada, at the Palmer Peninsula, Argentine Island, Antarctica, and at Lyttelton, New Zealand. Some of the wave-trains in Fig. 15 overlie residual astronomical tide-waves, not completely eliminated in the numerical filtering for the 3.2 hr period waves.

At Yakutat, near the mouth of triangular-shaped Yakutat Bay (natural period of oscillation about 41 mins), the marine topography is not favorable to any resonance of incident waves with periods as large as 3.0 or 1.8 hrs. The much smaller triangular Monti Bay, at the head of which Yakutat harbor actually lies, is an offshoot of Yakutat Bay at its mouth, and therefore in a nodal position with respect to any oscillations of Yakutat Bay. Because of this and the fact that Monti Bay has a fundamental period of free oscillation of about 17 mins only, there could have been no possibility of resonant amplification of 1.8 and 3.0 hr tsunami wave components. The waves of these periods, shown in Figs. 11 and 15, would therefore have been incident waves enhanced only by the shoaling and funnelling effect of the small Monti Bay, to the extent perhaps of 6 times their deep-water height (in accord with Green's Law). The inference from this is that the nominal 1.8 and 3.2 hr component long waves of the tsunami originated from the source and propagated across the Pacific Ocean.

At Victoria, Canada, the natural periods of oscillation of the Juan de Fuca Strait (fundamental, about 4.3 hrs; second mode, about 1.8 hrs), would have been conducive to some enhancement of the long wave-trains, as Figs. 11 and 15 suggest. A pseudo-resonance effect would also have occurred at Lyttelton, N.Z., where the period of free oscillation for Port Lyttelton Channel and Pegasus Bay is about 2,6 hrs. The marigram for Lyttelton harbor, in fact, recorded 2.6 hr oscillations prior to the arrival of the tsunami waves; they were probably locally generated by barometric fluctuations or other causes. The

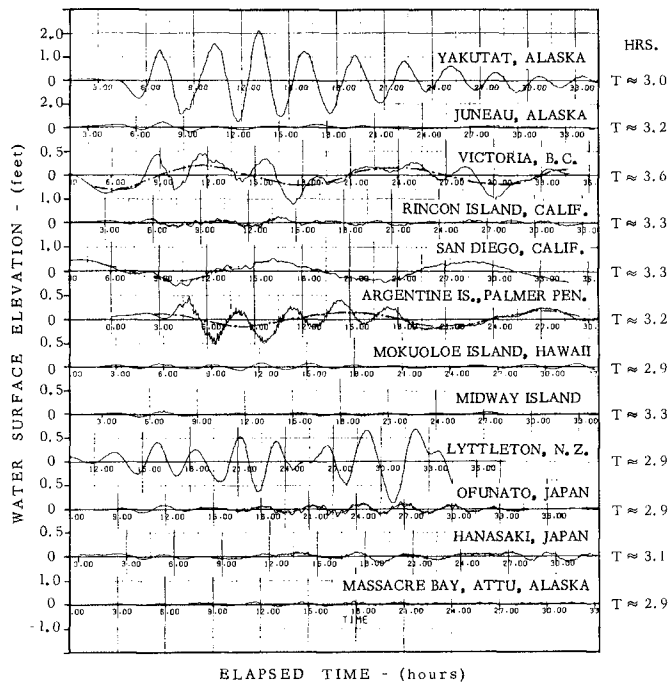

FIG. 15 - COMPUTER-PLOTTED WAVE-FORMS OF ULTRA-LONG PERIOD (AV. 3.2 HRS) OF THE MARCH, 1964, ALASKAN TSUNAMI.

enhancement of the 3.2 hr waves at Palmer Peninsula, Antarctica, probably relates to the shoaling and restrictive effect of the Antarctic Sound. As to why these ultra-long period waves drew no strong responses at other stations where the 1.8 hr period waves recorded well, as in Figs. 11 and 12, cannot be known without a detailed wave-refraction study and examination of the oscillating characteristics of the areas.

8. CONCLUSIONS

Numerical power-spectrum and graphical Residuation analyses have been shown to be mutually supportive of the existence in the records of the Alaskan tsunami of March, 1964, of very long wave-trains with periods approximating 1.75 and 3,2 hrs, originating at the source and propagating across the Pacific Ocean. In the north-south direction encompassing the eastern half of the Pacific Ocean, the 1.75 hr (nominal) period waves occurred in beats, their numbers per beat increasing with time and distance.

REFERENCES

1 Spaeth, M.C. and Berkman, S.C.: "The Tsunami of March 28, 1964, as Recorded at Tide Stations"; U.S. Coast and Ceodetic Survey, Dept. of Commerce, Rockville, Maryland, April 1965, 59 pp.

2 Wilson, B.W. and Tørum, A.: "The Tsunami of the Alaskan Earthquake, 1964; Engineering Evaluation"; Tech. Memo. No.25, Coastal Engineering Research Center, U.S.Army Corps of Engineers, Washington, D.C. May, 1968.

3 Chrystal, G.: "Investigation of the Seiches of Loch Earn by the Scottish Loch Survey"; (Parts I and II); Trans. Royal Soc. Edinb., v.45(2), 1906, pp. 361-396.

4 Cox, D.C.: "Status of Tsunami Knowledge"; Proc. of Tsunami Meetings, 10th. Pacific Science Congr., Monograph No. 24, Internatl. Union of Ceodesy and Ceophysics, Paris, July 1963, pp. 1-6.

5 Wilson, B.W.: "Tsunami Characteristics at Representative Tide Stations along the Pacific Seaboard"; Contract Report to Coastal Engineering Research Center, U.S.Army Corps of Engineers, Washington, D.C., May, 1971, 184 pp.

6 Pierson, W.J. and Marks, W.: "The Power Spectrum Analysis of Ocean Wave Records"; Trans. Amer. Geophys. Union, v.33(6), Dec. 1952, pp. 834-844.

7 Blackman, R.B. and Tukey, J.W.: "The Measurement of Power Spectra"; Dover Publications, New York, 1958, 190 pp.

8 Munk, W.H., Snodgrass, F.E. and Tucker, M.J.: "Spectra of Low Frequency Ocean Waves"; Bulln. Scripps Inst. Oceany., La Jolla, Calif., v. 7(4), 1959, Univ. Calif. Press, pp. 283-362.

9 Eagle, A.: "A Practical Treatise on Fourier's Theorem and Harmonic Analysis"; Longmans, Creen & Co., London, 1925, 178pp.

10 Wilson, B.W.: "Research and Model Studies on Range Action in Table Bay Harbour, Cape Town"; Trans. So. Afr. Inst. C.E., v.1(6), 1959, pp. 131-148; v.1(7), pp. 153-177

11 Wilson, B.W., Chakrabarti, S.K. and Snider, R.H.: "Spectrum Analysis of Ocean Wave Records"; Internatl. Sympos. on Ocean Wave Measurement and Analysis, New Orleans, LA, USA, Sept. 1974, ASCE, v.1, pp. 87-106.

12 Van Dorn, W.C. and Cox, D.C.: "Oceanic Character, Propagation and Coastal Modification of the 1964 Alaskan Tsunami"; The Great Alaska Earthquake of 1964; Oceanography and Coastal Engineering, Natl.Acad. Sci., Washington, D.C., 1972, pp. 147-157.

13 Loomis, H.C.: "The Major Tsunami in the Hawaiian Islands"; The Creat Alaska Earthquake of 1964; Oceanography and Coastal Engineering, Natl. Acad. Sci., Washington, D.C., 1972, pp. 181-190.

14 Loomis, H.C.: "Spectral Analysis of Tsunami Records from Stations in the Hawaiian Islands"; Bulln. Seis. Soc.Am., v.56(3), 1966, pp. 697-713.

Wave run-up caused by natural storm surge waves

by

Joachim Grüne *)

Abstract

This paper describes results of field measurements on wave run-up caused by storm surge waves. The measurements have been done with newly developed run-up probes at two locations at the German Bight with different dyke profiles. It was found from the results that the wave run-up, measured under real sea state conditions, have greater values than predicted by commonly used formulae. Furthermore the wave climate and the breaker type seem to have an influence on the magnitudes of wave run-up.

Introduction

For the design of seadykes the rising of the stillwater level due to wind stress during storm surges may be calculated with an exactness of some decimeters, whereas the appertaining wave run-up often has to be estimated in a range of up to meters. This results not only from the fact, that the wave climate on the nearshore of the dykes mostly is unknown, but also from the multitude of excisting formulae, which create different values (FÜHRBÖTER, Ref. 5).

There has been done a lot of investigations on wave run-up carried out in small-scale models with regular waves, some with wave spectra. But only a few results from field investigations are known (in respect of investigations at the german coast see COLDEWEY (Ref. 2), ERCHINGER (Ref. 3) and NIEMEYER (Ref.10)).

Due to unsolved problems with scale effects, which occur in breaker processes in small scale models and due to random characteristics of the waves in shallow water, there is still a great need to verify formulae, developed by model tests, under real sea state conditions.

*) Dipl.-Ing., research engineer, deputy operation manager of LARGE WAVE CHANNEL (University Hannover and Technical University Braunschweig), LEICHTWEISS-Institut (Div. of hydromechanics and coastal engineering) - Technical University Braunschweig, Germany

Field Measuring Equipment

For measuring the wave run-up in situ a probe was newly developed (GRÜNE, PIECHACZEK, Ref. 6), which should accomplish the following requirements:

1. Linearity over a total length up to 30 meters
2. One analog output signal for the actual run-up
3. Insensitive to the loads caused by waves and floats

This has been achieved by a 60-step-probe (Fig. 1). Each step consists of two electrodes, which are,electrically isolated,fixed in a small frame box and casted with synthetic epoxy resin. These steps are fixed on 2 meter long support frames in an optional distance,depending on the slope and the wanted accuracy (Fig. 2). The electronic circuit scheme is shown in Fig. 3. When the water of the run-up passes the electrodes of a step, an electric impuls will be released by closing an electronic circuit due to the conductivity of the water. This impulse actuate a awitch relay, which gives a defined voltage to an adder. The defined voltage of each individual step can be adjusted to the vertical range of each step (vertical distance to the preceding step). Therewith one gets an output aignal, which is linear to the vertical run-up, independent of the actual distance between the steps or of variations of the slope. The analog output signal, which gives the actual wave run-up, is formed by adding all defined voltages. To be recorded, the signal optional can be filtered by a low pass filter and attenuated.

Fig. 4 ahows the front of the electronic device with the LED-visual displays of each step. An example of a synchronous record of wave run-up and waves is given in Fig. 5.

Fig. 1: Wave run-up probe

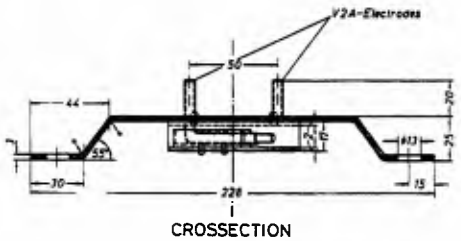

Fig. 2: Construction of steps and support frames

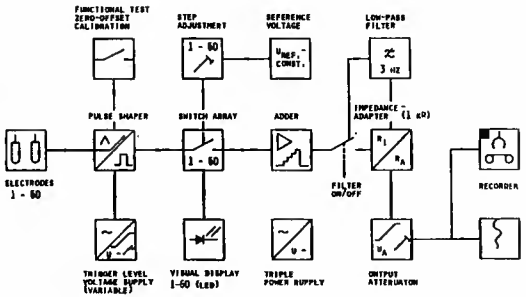

Fig. 3: Electronic circuit scheme

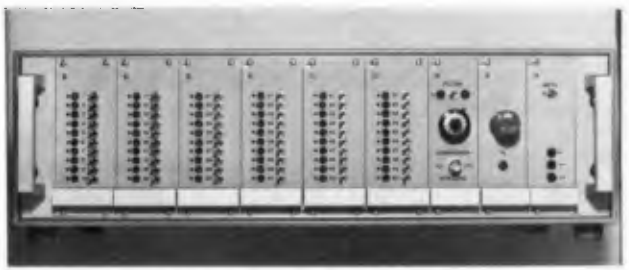

Fig. 4: Front view of electronic device

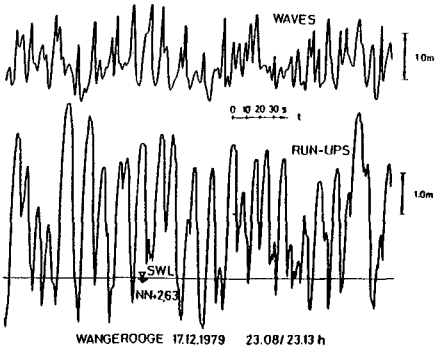

Fig. 5: Synchronous record of waves and run-ups

Such wave run-up probes as described above have been installed at two locations at the coast of the German Bight: WANGEROOGE and EIDERDAMM (Fig. 6).

At the location WANGEROOGE (an east frisian island) a heavy revetment with slope 1 : 4 was used (Fig. 7), which has a sand core and a cover layer made from asphalt concrete. In the upper part artificial roughness elements (prism concrete blocks - type Beverkoppen) are pasted on the asphalt layer. The run-up probe extend over 27 meters on the slope up to 6.2 m above Mean High Tide Level (MThw) with a vertical distance between the steps from 9 cm at the lower part up to 12 cm at the upper part of the probe. Fig. 1 shows the installed wave run-up probe on the revetment. Waves have been measured with a pressure transducer, which is situated 15 m in front of the revetment on the level NN + 0.15 m. The pressure data have been transfered to surface elevation by means of correction factors for wave heigths and wave periods as described later on.

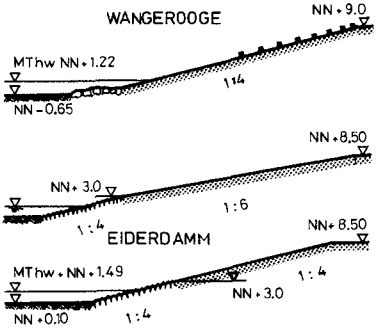

Fig. 7: Dyke profiles with run-up probes

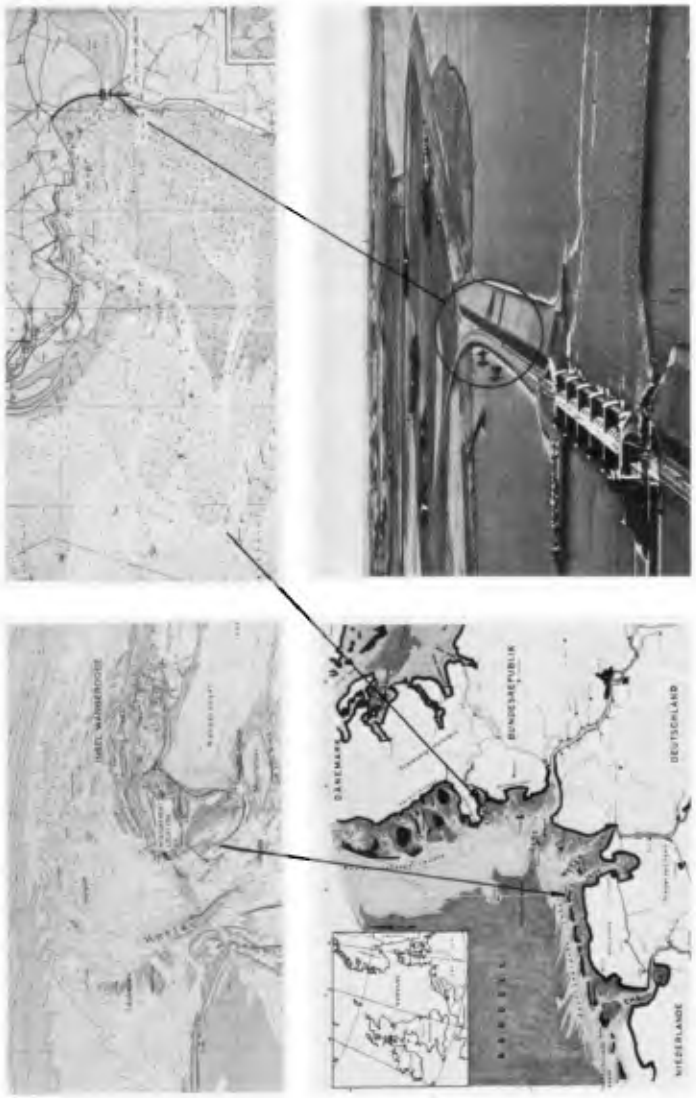

Fig. 6: German bight with measuring locations

Fig. 8: Air view of EIDERDAMM with measuring sections

The other location is the adjacent dam at the south side of the EIDER-river storm surge barrier. This dam has a sand core with bended slopes of 1 : 4 and 1 : 6. Thelower part with a slope 1 : 4 up to 1.5 meters above Mean High Tide is covered with a concrete-jointed natural stone revetment, whereas the subjequent slope 1 : 6 is covered with asphalt concrete (Fig. 7). Additionally there is a test section with a constant slope of 1 : 4, also with sand core and covered with asphalt concrete above the level NN + 3.0 m (Fig. 7). On both sections run-up probes have been installed on the asphalt layer (above the level NN + 3.0 m). The vertical distances between the steps vary from 8 cm to 12 cm on slope 1 : 4 and from 7 cm to 11 cm on slope 1 : 6 (smaller values at the lower part). In Figure 8 this two sections with run-up probes are markes with a circle. A pressure transducer on the lower part of the slope 1 : 4 was used to measure waves. Transferring pressure data to surface elevations will be described later on.

Measurements and data analysis

Waves and wave run-ups were recorded synchronously during several storm surges with a rise of the still water level up to 1.4 m above Mean High Tide Level (MThw) at WANGEROOGE and upto 2.3 m above MThw at EIDERDAMM location. An example of a record is shown in Fig. 5.

Due to some failures of analog magnetic tape recording system at EIDER-DAM location first all measurements were analysed in the time domain, the data presentation in this paper will be restricted to this analysis. The direct paper records were used to digitize the run-ups and the crests and troughs as shown in Fig. 9 with a semi-automatical device. Further data processing was then done with computer. It was defined that each run-up must have an substantial trough, "double-peaks" and "ondulations" have been ignored. The time interval between the troughs was defined as run-up period. Waveheights were defined as zero-down cros-

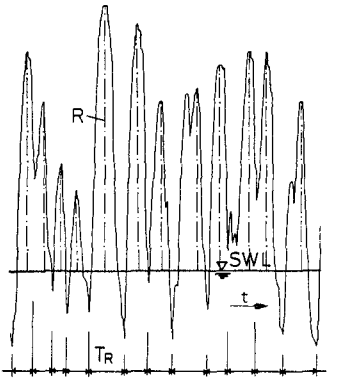

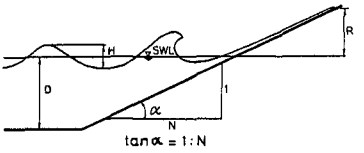

Fig. 10: Definitions of run-ups

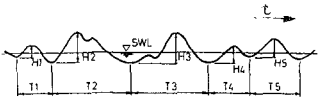

Fig. 9: Definitions of recorded run-ups and waves

sings heights, whereas for the periods(the same manner as for run-ups) the time intervals between the troughs were used.

Because the waves were measured with pressure cells, these data had to be transfered to surface elevations in means of two-dimensional progressive waves. It was found,existing formulas for wave pressure attenuation of previous investigations were not suitable for the measured wave climate conditions. This leads to do some calibration tests in a small-scale wave flume (scale appr. 1 : 5) with random sea state conditions with respect to the depth-, period- and windvelocity-conditions of the field measurements. An example of the results is shown in Fig. 11 for constant depth. The wellknown formula of pressure attenuation for linear wave theory was found useful by extending it with a Correctionfaktor KH, which is function of the relative depth Z/d of the pressure transducer. For the periods Correctionfactors were found also as a function of relative depth. Similar Correctionfactors were derived from the results of calibration tests for pressure transducers on a slope 1 : 4 (EIDERDAMM location). To compare wave data of both locations, the data from EIDERDAM, which were measured on the slope 1 : 4 closed to the breaker-zone and consequently affected by shoaling, furthermore are transfered to those in front of the dyke by means of a shoaling factor $KAS = H_B/H_I$, calculated by a formula,derived by LE MEHAUTE et al. (Ref. 9). Comparing the results of field measurements,done with pressure transducers 12 meters in front of the dyke and on the slope synchronously, this formula was modified by using the measured wave height and lenght on the slope near the breaker point:

$$KAS = 0.76 \cdot s^{1/7} \cdot (H_B/L_B)^{-1/4}$$

In the manner described above all wave data for both locations were transfered to those 15 m in front of the dyke profiles. The records were devided in consecutive time intervals, which are 15 to 20 minutes for WANGEROOGE location and 10 to 15 minutes long for EIDERDAMM location. For each time interval the mean still water level(SWL) as a constant value was determined from records of tidal gauges, which are at EIDERDAMM approx. 500 meters and at WANGEROOGE approx. 3000 m far from the field measuring devices.

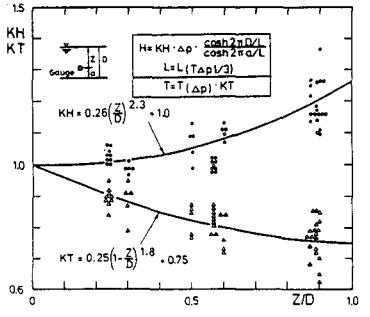

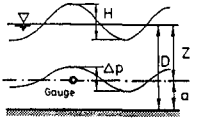

Fig. 11: Results of tests on wave pressure attenuation

Results

As mentioned before, results in this paper will be restricted to time domain analysis. Waves and run-ups first have been analysed statistical for each time interval. As an example the log-normal distributions of waves and run-ups are plotted in Fig. 12 for one time interval. In Fig. 13 the statistical values of the wave run-up R MAX, R 1/10 and R 98 are plotted against the mean values RM (WANGEROOGE). All ratios found with regression lines through zero, are listed in Table 1 for all dyke profiles at both locations:

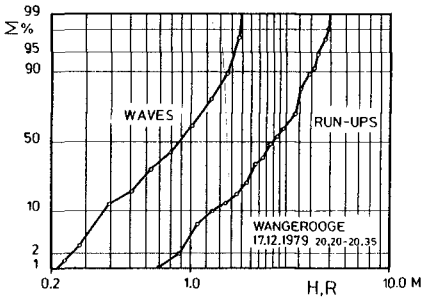

Fig. 12: Log-normal distribution of waves and run-ups for one record

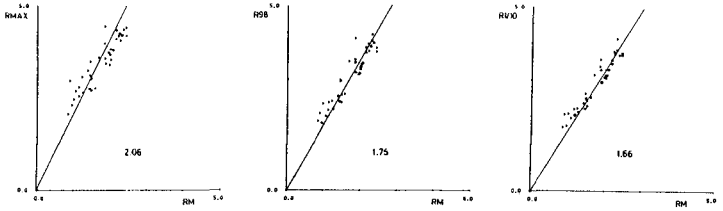

Fig. 13: Statistical values measured at WANGEROOGE

Table 1: Ratios of statistical values of wave run-up

Location	R MAX / RM	R 1/100 / RM	R 1/10 / RM	R 1/3 / RM	R 98 / RM	R 95 / RM	R 90 / RM
WANGEROOGE N = 4	2.06	1.90	1.66	1.39	1.75	1.60	1.46
EIDERDAMM N = 4	1.97	1.97	1.63	1.38	1.69	1.60	1.43
N = 6	1.90	1.86	1.58	1.34	1.69	1.57	1.40

There are no essential differences in this ratios apart from scattering and slightly smaller values for slope 1 : 6. Similar values are found by COLDEWEY (Ref. 2).

The statistical wave run-up value R 98, mainly used for practical engineering purposes, has been applied for comparing the measured wave run-ups with the calculated ones. Two well-known traditional formulae were used for calculation:

1. The formula $R_{98} = K \cdot H_S \cdot 1/N$ with K = 8, known as DELFT-formula and derived by WASSING (Ref. 14), which takes the significant wave-height and the slope into account.
2. The formula $R\ 98 = C \cdot T_m \cdot H_S \cdot g \cdot 1/N$ with C = 0.5, derived by HUNT (Ref. 8) and extended to irregular waves by VINJE (Ref. 13), which takes supplementary the period into account.

Comparisons of measured data with data calculated by these formulae are given in Fig. 14 to Fig. 16. It must be remarked, that the plots in Fig. 14 include only those data, which are not affected by the roughness elements on the upper part of the revetment. It was found that the regression line does not give smaller values for the empirical factors K or C, unless the maximum wave run-up does not pass over the third row of roughness elements (the effect of the roughness elements will be commented in the following). It must be considered that the data of the two slopes in Fig. 15 can't be compared directly, because the slope 1 : 6 is a bended slope (Fig. 7). Fig. 16 contains additionally data with significant waveheights, which had to be hindcasted from results of previous wave measurements at the same location, due to wave gauge defect. In all plots there is a certain amount of scatter, which always occur in wave related data, particularly from field measurements in surf zones. A conclusion of the plots in Fig. 14 to Fig. 16 indicate two main facts:

1. Wave run-up data, measured under real sea state conditions, normally have greater values than predicted by the common used formulae.
2. There are substantial differences between the data of both locations.

The empirical factors K and C for slope 1 : 4 are listed in Table 2. The measured run-up at EIDERDAMM compared to that of WANGEROOGE are 17 % higher, using the DELFT formula and 30 % higher, using the HUNT-VINJE-formula. A certain part of the differences might be caused to the manner of wave data transferring at EIDERDAMM location, described as above, but nevertheless this does not explain the total amount of differences.

Table 2: Comparison of empirical factors C and K for slope 1 : 4

	C			K		
	regression line through zero	max	min	regression line through zero	max	min
WANGEROOGE	0.71	0.92	0.53	11.32	13.80	7.52
EIDERDAMM	0.92	1.14	0.62	13.30	15.76	12.00

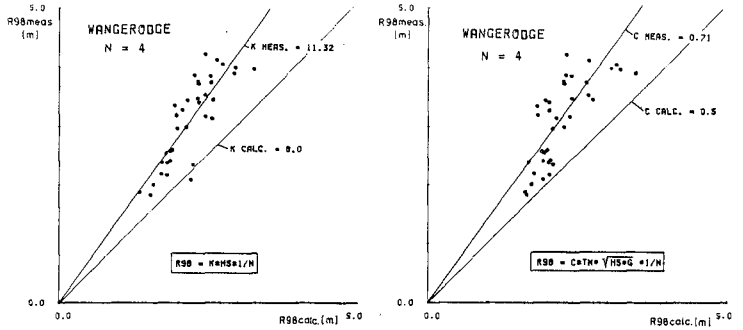

Fig. 14: Comparison of measured to calculated wave run-up

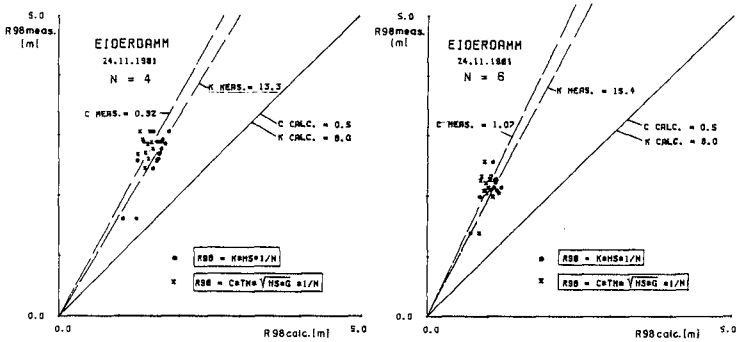

Fig. 15: Comparison of measured to calculated wave run-up

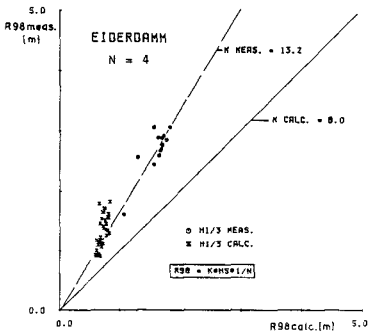

Fig. 16: Comparison of measured to calculated wave run-up

Previous investigations of VAN OORSCHOT and D'ANGREMOND (Ref. 12) showed considerable variation of the empirical factor C (C_n in Ref. 12, using the maximum energy density period $\hat{T}$ instead of statistic mean value T_m) in dependence on the shape of the wave energy spectrum (in means of spectral width parameter ε). Unfortunately this could not be checked due to the fact that there was no possibility to analyse the data in the frequency domain for both locations yet as mentioned above. On the other hand, comparisons of joint distributions of wave heights and periods for some time intevals let assume, that there is no significant variation of the wave energy spectrum shape, which may explain the differences of emperical factors C and K completely. As an example the joint distributions of two time intervals with approx. the same value C are shown in Fig. 17.

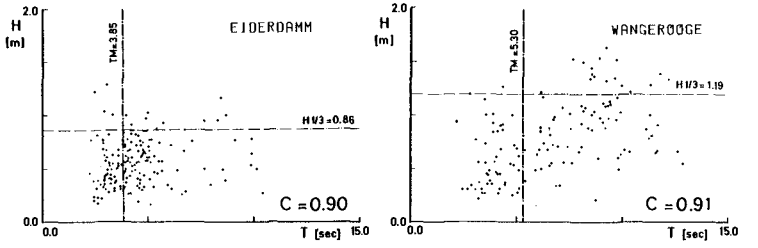

Fig. 17: Joint distributions of two measured time intervals

Furthermore the analysed data were used to find out the influences of environmental and wave parameters:

In Fig. 18 the ratio of measured to calculate run-up is plotted versus the windvelocity U_{oh} during the measurement, which gives a slightly increasing of the empirical factor with increasing windvelocity. The influence of the winddirection (the wave approach direction has not been measured) seems to be negligible as shown in Fig. 19, where β is the angle between winddirection during the measurement and the line of full dip of the slopes (positive β turns to north). This confirms, that the wave approach essentially is determined by the topography in such shallow water areas. Visual observations resulted in values for wave approach angle related to perpendicular direction, of $\pm$ 10° at WANGEROOGE location and of $\pm$ 20° at EIDERDAMM location.

From Fig. 20 follows that the influence of wave steepnees has the same trend for both locations, but there are different orders of magnitude. It can be stated that the empirical factor C increase with increasing Period and / or increasing wave height comparativly. The dependence on relative waterdepth D/H_s is shown in Fig. 21 for the factors C and K and for the ratio number of run-ups to number of waves NR/NW. Whereas the ratio NR/NW decreases with increasing relative waterdepth, the empirical factors C and K are increasing with increasing relative water-

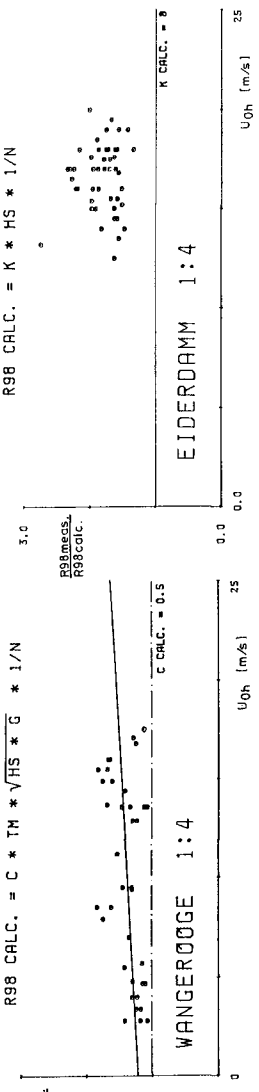

Fig. 18: Measured to calculated run-up versus windvelocity

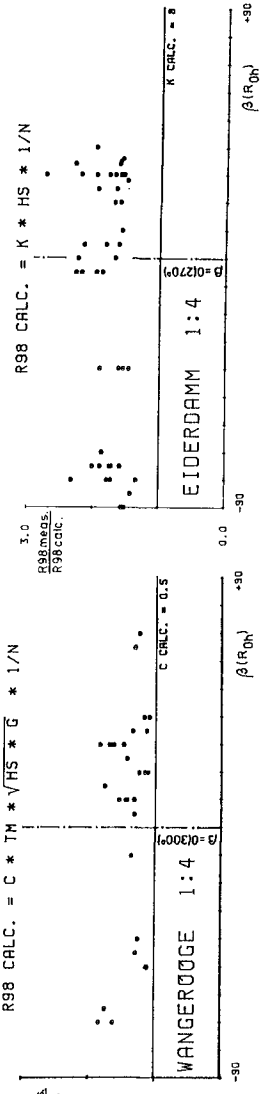

Fig. 19: Measured to calculated run-up versus winddirection

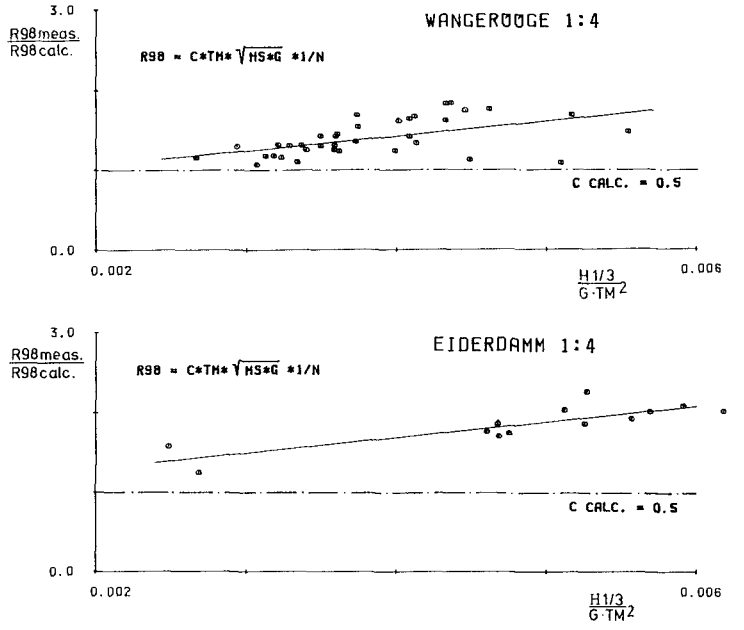

Fig. 20: Measured to calculated run-up versus wave-steepness

depth. From the influence of the relative waterdepth and the wave steepness one can suppose, that there might be a dependence on the breakertype for the empirical factors in the used formulae. An impression of the typical wave climate conditions at both locations is given in Fig. 22. At WANGERROGE the breaking waves are of the spilling and plunging type, whereas at EIDERDAMM only occur plunging type waves. This observations are in agreement with breakertypes, calculated with the BATTJES-Parameter $f_b = 1 : N / \sqrt{H_b/L_o}$. (Ref. 1). To determine, whether the waves break on the nearshore or on the dyke slope, the breakerdepth stated by HENSEN (Ref. 7) was used. He found by investigations on waves on tidal flats with nearly constant depth that waves begin to break with relative waterdepth smaller than 2.3. The values of relative waterdepths D/H and breaker parameter f_b are listed in Table 3:

Table 3: Wave parameters related to the wave run-up data

Location	$H_{1/3}$[m]	T_M [s]	$D/H_{1/3}$	D/H_{MAX}	$f_{b(H1/3)}$	breaker type
WANGEROOGE	0.6 to 1.6	4.5 to 7.3	1.9 to 3.2	2.3 to 2.2	0.10 to 0.15 (nearshore) 1.4 to 2.0 (dyke)	spilling / plunging
EIDERDAMM	0.5 to 0.9 (0.35)	3.7 to 5.2	4.1 to 5.2	2.7 to 4.0	1.3 to 2.0 (dyke)	plunging

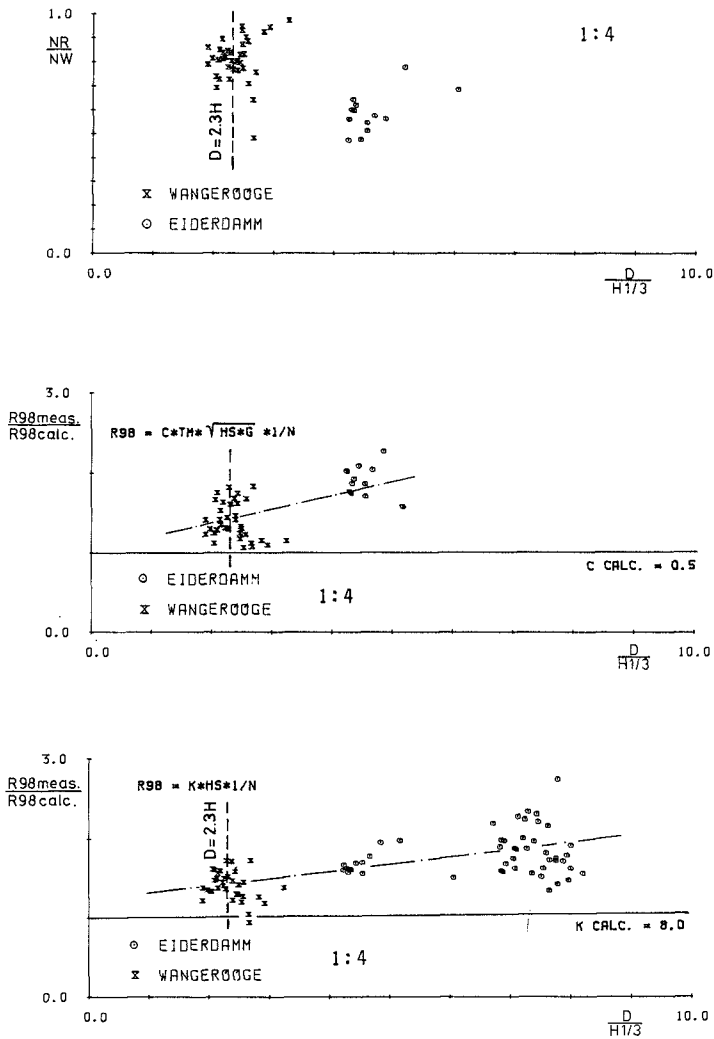

Fig. 21: Measured to calculated run-up versus relative waterdepth

WANGEROOGE 1:4

EIDERDAMM 1:4

Fig. 22: Typical wave climate at WANGEROOGE and EIDERDAMM

From Fig. 21 and Table 3 it is obvious, that at location WANGEROOGE at least the higher waves break on the nearshore and hence there must be a mixture of spilling and plunging breakers, which is in agreement with visual observations. From this results it can be supposed, that in general the wave run-up is relatively higher for plunging breakers than for spilling breakers. These investigations have to be continued to get more and detailed informations on criterions, which lead to a breaking on the nearshore or on the dyke slope or on both sections and to relate this criterions to the wave run-up data.

As mentioned before, the effectiveness of artificial roughness elements was found to be poor, if the elements only extend in the upper part of the run-up (Fig. 23). The solid line refers to experimental data of FRANZIUS (Ref. 4 and 12). For a comparison it must considered, that FRANZIUS used cubes with a constant distance to each other, whereas at WANGEROOGE prismn with triangle crossection were placed in rows. The distances between the rows decrease to the top of the dyke and the rows itself contains 2 single rows of prismn in the lower part and 3 single rows in the upper part.

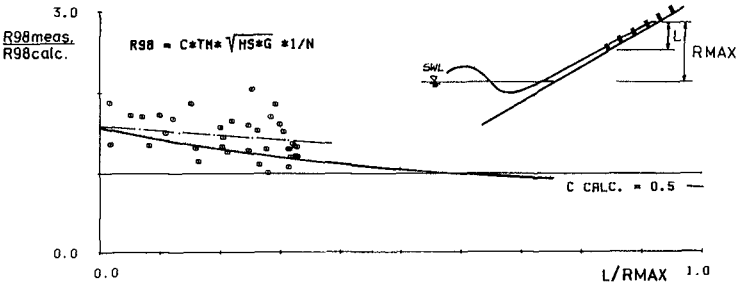

Fig. 23: Effectiveness of roughness elements (WANGEROOGE)

It may be stated , that a higher effectiveness in small scale models is created from the relatively higher amount of turbulence caused by such elements compared to real sea state conditions.

Results for a convex bended profile (Fig. 7) are shown in Fig. 24. The ratios of measured run-up for both dyke profiles are plotted versus the relative distance of the still water level to bending point $\Delta D/H_s$. There is no significant difference between both profiles, if the still water level is below the bending point. Further the influence of the lower slope seems to be neglectible small, if the still water level is more than two times the significant wave height higher above the bending point.

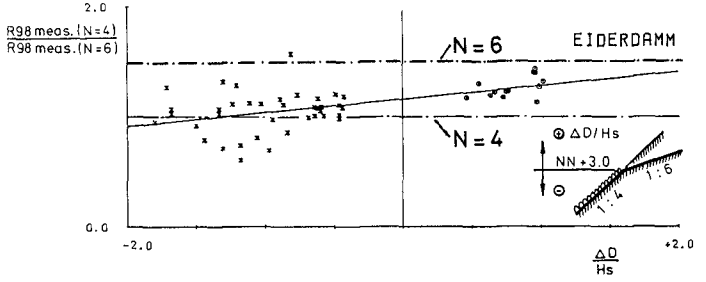

Fig. 24: Comparison of results for constant and bended slope (EIDERDAMM)

Conclusion

Wave run-up data, measured under real sea state conditions at two locations at the coast of the German Bight, in general are found to have greater values then predicted by common used formulae. Based on the formula

$$R\ 98 = C \cdot T_m \cdot \sqrt{H_s \cdot g} \cdot 1/N$$

a comparison for the empirical factor C with results of some previous investigations with irregular waves in model tests is given in Table 4:

Table 4: Comparison of empirical factors C:

		C	
VAN OORSCHOT / D'ANGREMOND	(Ref. 12)	0.60 to 0.77	$\hat{T}/T_m$ =1.05
BATTJES	(Ref. 1)	0.59 to 0.74	analytical model based on RAYLEIGH-distribution
TAUTENHAIN	(Ref. 11)	0.70 to 0.86	not comparable directly, based on wave distribution
AUTHOR		0.53 to 1.14	2 different locations

Data of field measurements, reported by ERCHINGER (ref. 3) and COLDEWEY (Ref. 2) cannot be compared directly with those of the author, due to different dyke profiles (bended profile with 3 different slopes in Ref. 3), but those data show the same trend in respect to higher measured run-up compared to calculated one.

It must be mentioned, that the breaker type has an influence on the order of magnitude of the empirical factor C.

The ratio number of run-ups to number of waves decreases with increasing relative waterdepth in the range of 0.95 to 0.50.

The effectiveness of artificial roughness elements is found to be poor, if the elements only extend in the upper part of the run-up.

Acknowledgements

The research work was done by the SONDERFORSCHUNGSBEREICH 79 / C 4 (supervision Prof. Dr.-Ing. FÜHRBÖTER) and has been supported by the GERMAN RESEARCH FOUNDATION (DFG).

References

1. BATTJES — Computation of set-up, longshore currents, run-up and overtopping due to wind-generated waves, Dept. of Civil Engineering, Delft University of Technology, Report Nr. 74-2, 1974

2. COLDEWEY — Naturmessungen zur Erfassung des Wattseegangs und des Wellenauflaufs auf Seedeiche, Berichtswerk INTERMARITEC '82, Hamburg, 1982 (in german)

3. ERCHINGER — Wave run-up in field measurements with newly developed instruments, Proceedings of 15th Coastal Engineering Conference 1976

4. FRANZIUS — Wirkung und Wirtschaftlichkeit von Rauhdeckwerken im Hinblick auf den Wellenauflauf, Mitt. des FRANZIUS-INSTITUTS, Heft 25, 1965 (in german)

5. FÜHRBÖTER — Äußere Belastung von Seedeichen, in: Seedeichbau, Theorie und Praxis (Hrsgb. Brößkamp), 1976 (in german)

6. GRÜNE, PIECHACZEK — Ein neues Meßgerät zur Erfassung des Wellenauflaufs auf Deiche und Deckwerke, Technischer Bericht, SFB 79 / C 4 (in german)

7. HENSEN — Modellversuche über den Wellenauflauf an Seedeichen im Wattengebiet, Mitt. der Hannoverschen Versuchsanstalt für Grundbau und Wasserbau, Heft 5, 1954 (in german)

8. HUNT — Design of seawalls and breakwaters, Proc. ASCE, Vol. 85, WW 3, 1959

9. LE MÉHAUTÉ, KOH — On the breaking of waves arriving at an angle to the slope, Journal of Hydraulic Research, 1967, Nr. 1

10. NIEMEYER — Wave climate study in the region of the east frisian islands and coast, Proceedings 16th Coastal Engineering Conference 1978

11. TAUTENHAIN — Der Wellenüberlauf an Seedeichen unter Berücksichtigung des Wellenauflaufs, Mitt. des FRANZIUS-INSTITUTS, Heft 53, 1981 (in german)

12. TECHNICAL ADVISORY COMMITTEE ON PROTECTION AGAINST INUNDATION — Wave run-up and overtopping, Government publishing office, DEN HAAG, 1974

13. VINJÉ — Investigation for coastal protection with concrete mats, North Sea Coastal Engineering Group, 1972 (given in Ref. 5)

14. WASSING — Model investigation on wave run-up carried out in the netherlands during the part twenty years, Proceeding of 6th Coastal Engineering Conference 1957

WAVE RUN-UP AT SEA DIKES UNDER OBLIQUE WAVE APPROACH

by

E. TAUTENHAIN[1], S. KOHLHASE[2], H.W. PARTENSCKY[3]

1. INTRODUCTION

Besides wave impact forces, erosion of the inner side of a sea dike is a serious cause of destruction. Therefore, wave run-up and overtopping effects have to be considered with respect to the safety of a dike. Strong relations were found between both these influences (TAUTENHAIN et.al., 1980, 1981, 1982), based on experiments in a wave flume and using an energy conservation concept. However, under natural conditions, an oblique wave approach has to be considered. This paper deals with the influence of wave direction on wave run-up on a smooth dike slope in order to provide a basis for calculating the overtopping rates for both regular and irregular waves.

2. PERFORMANCE OF EXPERIMENTS

The experiments were performed in a wave basin of 18 x 45 m, equipped with a servo-hydraulic wave generator. A dike with a uniform smooth slope of 1:6 was installed (Fig. 1).

The direction of the dike relative to the wave direction was varied stepwise in the range of $\beta = 0$ (normal wave approach) and $\beta = 60^{o}$. The wave heights and periods were varied between H = approx. 5 to 15 cm and T = 1 to 3 sec., respectively. The water depth was d = 35 cm for all test runs.

For the measurements of wave run-up and down-rush effects, a video-system was used. Wave absorbing elements were installed besides the dike structure to suppress model-induced reflections.

The notations and measured quantities are shown in Fig. 2.

---

[1]) Dr.-Ing., Operation Manager, Large Wave Channel, University of Hannover, FRG

[2]) Dr.-Ing., Chief Engineer, Franzius-Institut, University of Hannover, FRG

[3]) Prof. Dr.-Ing. Dr.phys., Franzius-Institut, University of Hannover, FRG

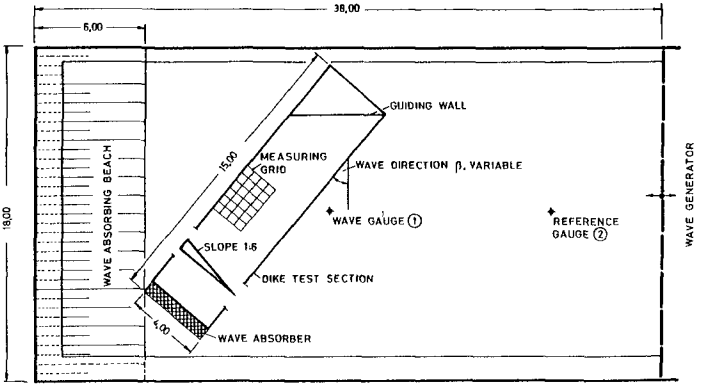

Fig. 1: General test arrangement

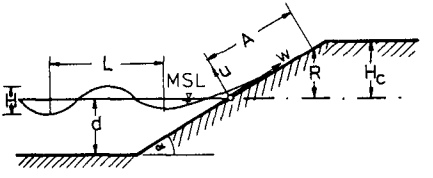

Fig. 2: Notations

3. EVALUATION OF TESTS

As already mentioned, the theoretical background is based on an energy conservation concept which combines the wave parameter in front of the dike and the actual energy of the uprushing wave, and includes the influence of the respective pre-wave of a given time series of incident waves as schematically drawn in Fig. 3.

Assuming that the energy of a monochromatic wave $\tilde{E}$ available for the wave run-up can be equated with the energy E of an equivalent wave of the spectrum, the following equation results (TAUTENHAIN and KOHLHASE, 1980)

$$E_{pot_{A_n}} = 2 \cdot \psi \cdot \tilde{E}_{pot_{A_n}} - E_{pot_{A_{n-1}}} \qquad (1)$$

where A_n = wave run-up of the wave n of a time series and
A_{n-1} = run-up of the pertinent pre-wave
ψ = form parameter

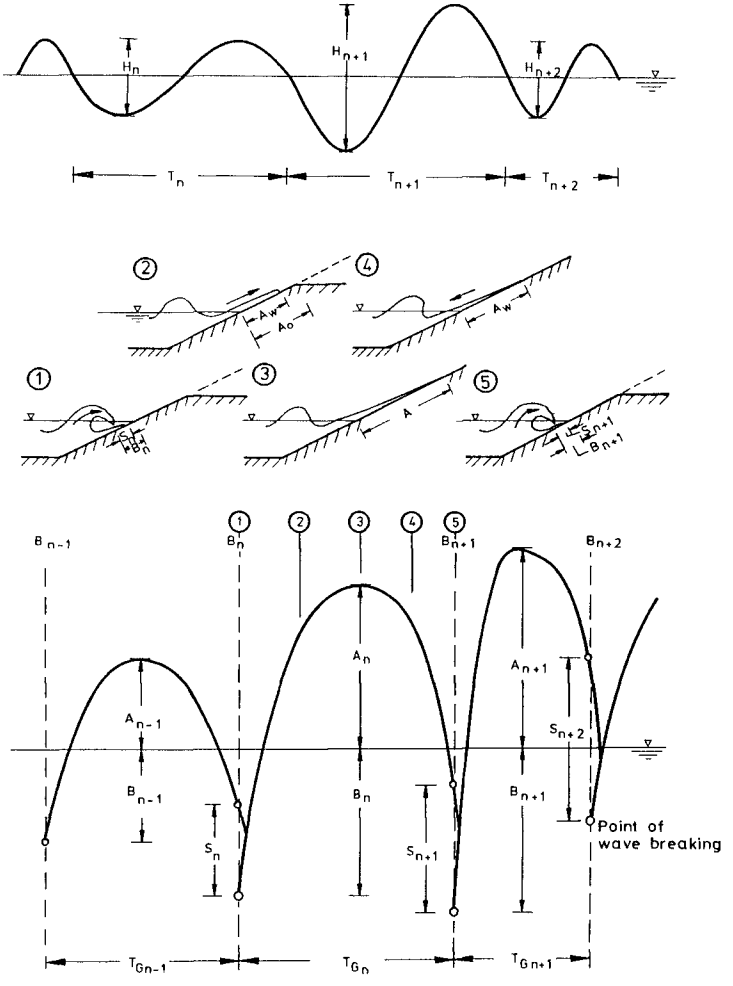

Fig. 3: Phases of wave run-up and down rush and intersections

The wave run-up A_n is given as follows

$$A_n = \tilde{A}_n \cdot \sqrt[3]{2 \cdot \psi - (\tilde{A}_{n-1}/A_n)^3} \qquad (2)$$

From two-dimensional experiments, the form parameter ψ was found (correlation coefficient, r = 0.96) to vary between $\psi = 0.63$ and $\psi = 0.73$ (average $\psi = 0.7$).

The wave run-up $\tilde{A}_n$ is given by

$$\tilde{A}_n = 1.29 \sqrt{H \cdot L_o}\ (1 - \kappa_R')/\cos\alpha \qquad (3)$$

in which κ_R' is the reflection coefficient related to the wave parameter H and L_o in front of the dike.

Equations (1) to (3) have been derived for normal wave approach and must be extended when applied to oblique wave directions.

Considering regular waves, the wave run-up $\tilde{A}_\beta$ was derived as follows

$$\tilde{A}_\beta = \tilde{A}_n \cdot \bar{k}_\beta \qquad (4)$$

where

$$k_\beta = \frac{\tilde{A}_\beta}{\tilde{A}_n} = \cos\beta \cdot \sqrt[3]{2 - \cos^3 2\beta} \qquad (5)$$

is an averaged parameter which includes both refraction and friction effects (wave breaking) as well as the angle of the down-rushing wave in relation to the up-rushing wave.

The parameter $\bar{k}_\beta$ was determined by means of comparative investigations for normal and oblique wave directions, as outlined in the following section.

4. EXPERIMENTAL VERIFICATION

The experiments were performed in two stages. In the first stage, two-dimensional tests were run because of slightly different boundary conditions and the reduced scale of the wave basin compared with previous investigations in a wave flume. The results of these experiments are plotted in Fig.4.

As may be seen in Fig. 4, the experimental results were found to comply well with the wave run-up equation (3). The observed differences of 2.6 % only were not thought to be due to model scale effects but rather to the limited number of tests.

The test results for an oblique wave approach are plotted in Fig. 5 for the measured wave directions $\beta \neq 0^\circ$. It can be readily seen that the basic equation (3) is also generally fulfilled for an oblique wave direction as indicated by the rather high correlation coefficients between the measured

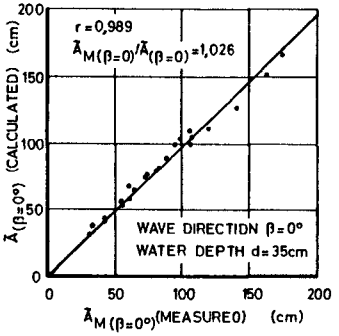

Fig. 4: Verification of equation (3) (ß = 0°)

wave run-up $\tilde{A}_M$ for ß = 0° and ß ≠ 0°, respectively. Therefore, it may be concluded that the influence of the wave direction can be generally summarized by the wave direction parameter k_β, as already illustrated. The effects of wave height and period are of lower order.

The results for all measured wave directions (regular waves) are summarized in Fig. 6.

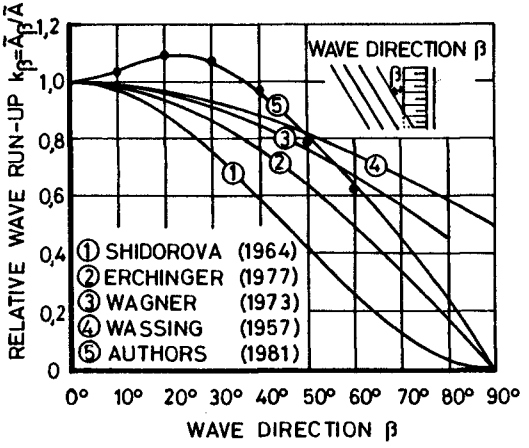

Fig. 6: Relative wave run-up. Summation of results ß ≠ 0.

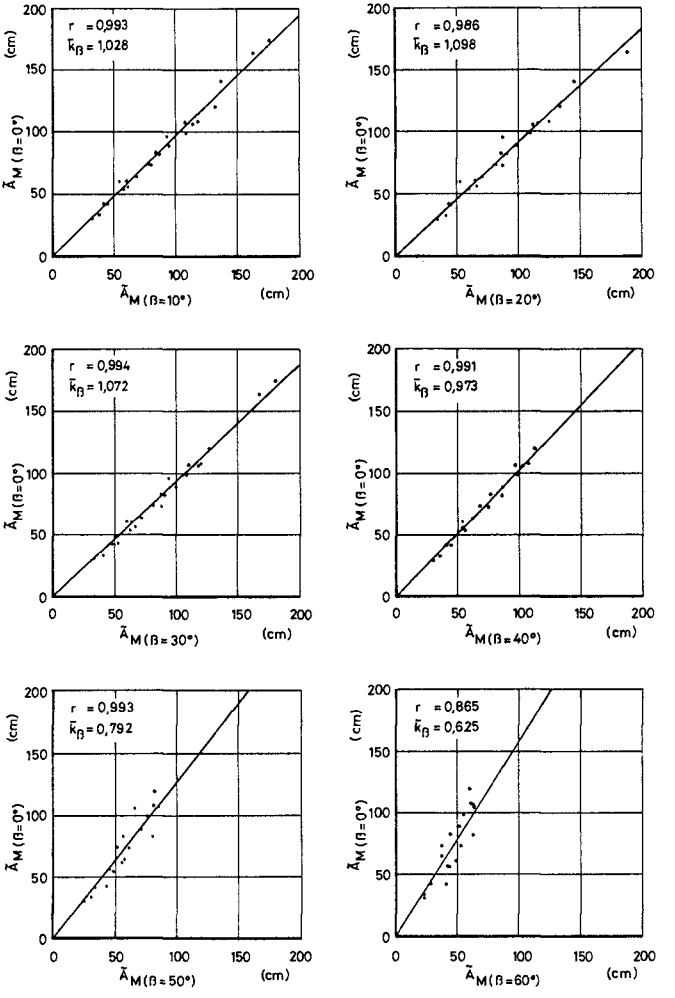

Fig. 5: Influence of wave direction on wave run-up

For the purpose of comparison, the results of a number of authors are also plotted in Fig. 6. The differences between the calculated (equ. 4) and mean measured relative run-up heights are in the order of ± 2 %, which may be neglected.

5. CONCLUSION

With respect to wave run-up at sea dikes, comparative investigations have been carried out for different angles of wave approach. The investigation has clearly shown that, in contrast to previous investigations by other authors, a remarkable increase of run-up heights compared to normal wave approach will occur for wave directions in the range of approx. $0 < \beta \leq 35^{o}$.

Since the maximum increase in comparison to normal wave approach conditions is of the order of 10 %, it is important that this effect should be considered in practice.

6. REFERENCES

TAUTENHAIN, E. and KOHLHASE, S.: Investigations on wave run-up and overtopping at seadikes. Int. Conf. on Water Resources Development, Taipei, 1980.

TAUTENHAIN, E.: Der Wellenüberlauf an Seedeichen unter Berücksichtigung des Wellenüberlaufs. Mitt. des FRANZIUS-INSTITUTS für Wasserbau und Küsteningenieurwesen der Universität Hannover, Heft 53, 1981.

TAUTENHAIN, E., KOHLHASE, S. and PARTENSCKY, H.W.: Relation between wave run-up and overtopping at seadikes caused by irregular waves. Int. Conf. on Water Resources Development, Bandung, 1982.

Water Waves Propagating on Beaches of Arbitrary Slope

by

*Y·Y. Chen** *Dr. H. H. Hwung***

ABSTRACT

When a small amplitude wave climbing along an arbitrary sloping beach from deep water toward the shore, the variation of characteristics in the process of wave motion has been described in this paper. From the results of theoretical derivation, it is found out that the variation of water surface and amplitude are function of beach slope(α) and dimensionless distance (kx) from the shore. And under the condition of the beach slope is $\alpha = 0$ and $\alpha = \infty$ that the solution will become a progressive wave and a standing wave respectively.

1. *INTRODUCTION*

Concerning the problems of water waves propagating on beaches of arbitrary slope, E.T. Hanson (1926) *assumed the angle of bottom with still water surface to be of the form $\pi/2q$ with integral q, and constructed a progressive wave derived from two standing waves. Lewy, H.* (1946) *gave a contour integral representation for a progressive wave for all angles between bottom and surface. Then, Stoker* (1947) *derived the exact linear theory and obtained approximate solution for surface waves in variable water depth. Biesel* (1952) *expressed the first-order approximation of the free surface equations and the trajectory of surface*

* *Associate Researcher of Tainan Hydraulics Laboratory National Cheng Kung University. Taiwan. R.O.C*

** *Director of Tainan Hydraulics Laboratory & Associate Professor of Hydraulic and Ocean Engineering Graduate School, National Cheng Kung University. Taiwan. R.O.C*

particle by Lagrangian form. Carrier & Greenspan (1957) *presented the explict solutions based on the non-linear shallow water theory.*

All the above investigations concentrated on the behavior of wave motion in the region near the coast, however, they didn't include the entire process of wave motion. Therefore, in this paper, the authors pay attention to the theoretical analysis on the variation of the water surface and amplitude when the water waves propagating on beaches of arbitrary slope under the condition without breaking.

2. *THEORETICAL CONSIDERATION*

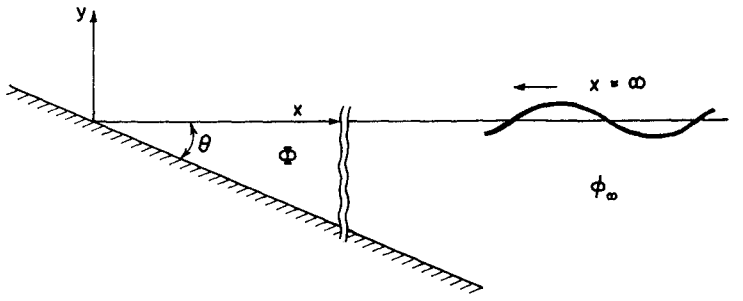

Fig. - 1

From the sketch diagram of water wave propagating from deep water toward shallow water area as shown in Fig. 1, *the governing equations of wave motion in two dimensional incompressible fluid are given by the follows:*

$$\Phi_{xx} + \Phi_{yy} = 0 \qquad \eta(x,t) \geq y \geq -h(x) \quad (1)$$

$$\Phi_t + g\eta + \frac{1}{2}(\Phi_x{}^2 + \Phi_y{}^2) = C \qquad y = \eta(x,t) \quad (2)$$

$$\Phi_y = \eta_t + \Phi_x \eta_x \qquad y = \eta(x, t) \tag{3}$$

$$\Phi_y = -h_x \Phi_x \qquad y = -h(x) \tag{4}$$

The subscripts of the above equations denote partial differentiation, and Φ *is velocity potential,* η *is water surface variation,* $h(x)$ *is water depth which can be expressed as* $h(x) = x \cdot \tan\theta = \alpha x$, *and C is Bernoulli's constant, g is gravity acceleration.*

From Cauchy's integral theorem, there is a constant M existence in the process of wave motion under the conditions without breaking. that

$$|\Phi| + |\Phi^{(n)}| < M \quad \text{for } 0 \le x \le \infty,\ \eta(x,t) \ge y \ge -h(x) \tag{5}$$

where $\Phi^{(n)}$ *denotes the* n^{th} *order's partial derivatives of* Φ *with respect to x, y or t. Furthermore, since the original source of wave motion comes from deep water, so that*

$$\lim_{x \to \infty} \Phi = \phi_\infty \tag{6}$$

According to the above consideration that seems reasonable to coincide with physical grounds and there is not any singularity taken place in the entire process of wave motion from deep water toward the shore. In the following derivation, it is convenient to express the quantities evaluated for $y = \eta(x, y)$ *by a bar, "—", over the quantity, and for* $y = -h(x)$ *by a bar under the quantity. Thus we have*

$$\int_{-h(x)}^{\eta(x,t)} \Phi_{yy}\, dy = \overline{\Phi_y} - \underline{\Phi_y} = \overline{\Phi_y} + h_x \underline{\Phi_x} \tag{7}$$

and

$$\int_{-h(x)}^{\eta(x,t)} \Phi_{yy}\, dy = -\int_{-h(x)}^{\eta(x,t)} \Phi_{xx}\, dy = -\frac{\partial}{\partial x} \int_{-h(x)}^{\eta(x,t)} \Phi_x\, dy + \overline{\Phi_x}\, \eta_x + \underline{\Phi_x}\, h_x \tag{8}$$

From eq. (7) and eq. (8), we get

$$\overline{\Phi}_y = -\frac{\partial}{\partial x}\int_{-h(x)}^{\eta(x,t)} \Phi_x dy + \overline{\Phi}_x \eta_x \tag{9}$$

Then the integral term of eq. (9) will be the following relation through integration by parts

$$\int_{-h(x)}^{\eta(x,t)} \Phi_x dy = \eta \overline{\Phi}_x + h \underline{\Phi}_x - \int_{-h(x)}^{\eta(x,t)} y \Phi_{xy} dy \tag{10}$$

and also the relation will be as

$$\int_{-h(x)}^{\eta(x,t)} h(x)\Phi_{xy}\, dy = h(x)\overline{\Phi}_x - h(x)\underline{\Phi}_x \tag{11}$$

Eliminating $\underline{\Phi}_x$ from eq. (10) and eq. (11), and this in turn lead through use of eq. (9) to

$$\begin{aligned}\overline{\Phi}_y &= -\frac{\partial}{\partial x}\left[h(x)\overline{\Phi}_x - \int_{-h(x)}^{\eta(x,t)} (y+h)\Phi_{xy} dy \right] + \eta_x \Phi_x - \frac{\partial}{\partial x}(\eta \overline{\Phi}_x) \\ &= -(h\overline{\Phi}_x)_x + \frac{\partial}{\partial x}\int_{-h(x)}^{\eta(x,t)} (y+h)\Phi_{xy} dy - \eta \overline{\Phi}_{xx}\end{aligned} \tag{12}$$

From the kinematic condition at free surface of eq. (2), taking the partial derivative with respect to t, so that

$$\eta_t = -\frac{1}{g}\left[\overline{\Phi}_{tt} + \left(\overline{\Phi}_x \overline{\Phi}_{xt} + \overline{\Phi}_y \overline{\Phi}_{yt} \right) \right] \tag{13}$$

Then substituting eq. (13) into eq. (3), we get

$$\overline{\Phi}_y = -\frac{1}{g}\left[\overline{\Phi}_{tt} + \left(\overline{\Phi}_x \overline{\Phi}_{xt} + \overline{\Phi}_y \overline{\Phi}_{yt} \right) \right] + \overline{\Phi}_x \eta_x \tag{14}$$

Thus, from eq. (12) and eq. (14), we have

$$\overline{\Phi}_{tt} = (gh\overline{\Phi}_x)_x - (\overline{\Phi}_x\overline{\Phi}_{xt} + \overline{\Phi}_y\overline{\Phi}_{yt}) - g\left\{\frac{\partial}{\partial x}\int_{-h(x)}^{\eta(x,t)} (y+h)\Phi_{xy}dy\right\} + g(\eta\Phi_x)_x \tag{15}$$

Up to now we have made no assumptions in addition to those made in deriving the non — linear theory. In other words, water waves propagating along an arbitrary sloping beach will be described completely in eq. (15). *Unfortunately, since eq.* (15) *is a high order non — linear partial differential equation, so that analytical solution is not able to be obtained and the approximate solution will be presented in this paper.*

From eq. (6), *we know that wave motion propagating along an arbitrary sloping beach comes from deep water. Accordingly, it is reasonable to imagine that the velocity potential in deep water,* ϕ_∞, *is part of wave motion in the propagating process. In this case, the velocity potential would be proposed by the following form,*

$$\Phi = \phi + \phi_\infty \tag{16}$$

The above equation makes a brief statement that the velocity potential, Φ, *existed in the propagating process is consisted of the velocity potential in deep water,* ϕ_∞, *and the velocity potential due to shoaling and reflection,* ϕ, .

After susbstituting ϕ_∞ *into the last three terms of the right side of eq.* (15), *then the first — order approximation of wave motion will be given as*

$$\overline{\Phi}_{tt} = (gh\overline{\Phi}_x)_x - \left[(\overline{\phi}_\infty)_x(\overline{\phi}_\infty)_{xt} + (\overline{\phi}_\infty)_y(\overline{\phi}_\infty)_{yt}\right] - g\left\{\frac{\partial}{\partial x}\int_{-h(x)}^{\eta(x,t)} (y+h)(\phi_\infty)_{xy}dy\right\} + g\left[\eta(\overline{\phi}_\infty)_x\right]_x \tag{17}$$

Furthermore, expanding the integral term of eq. (17) *and from the*

condition that ϕ_∞ substituted in eq. (14), we have

$$\overline{\Phi}_{tt} = (g h \overline{\Phi}_x)_x - [g h (\overline{\phi}_\infty)_x]_x + (\overline{\phi}_\infty)_{tt} \tag{18}$$

Because ϕ_∞ is part of Φ, we know that ϕ_∞ is a particular integral of wave motion. In other wordes, eq. (18) involves a particular solution and a complementary function which will satisfy the following homogeneous equation.

$$\overline{\Phi}_{tt} = (g h \overline{\Phi}_x)_x \tag{19}$$

Since the complementary function is due to shoaling and reflection of sloping bottom boundary, that the velocity potential at water surface is well to be proposed as the following form.

$$\phi = e^{i(kx-\sigma t+\epsilon)} Z(x) \tag{20}$$

where the exponential in eq. (20) represents the factor due to reflection, k and σ are wave number and angular frequency in deep water respectively, ϵ is the change in phasse as wave climbing along beach. $Z(x)$ is the function of water surface elevation resulted from shoaling and reflection.

After substituting eq. (20) into eq. (19), and taking real part, that it is easy to transform the result into zero order of Bessel function. And the solution will be given as

$$Z(x) = A J_0 \left(2 \sqrt{\frac{k x}{\alpha}} \right) \tag{21}$$

where J_0 is the Bessel function of the first kind of order zero, and A is a function of α, which has to be determined by an appropriate condition. Therefore, the velocity potential due to shoaling and reflection will be

$$\overline{\phi} = A J_0 \left(2 \sqrt{\frac{k x}{\alpha}} \right) \cos (kx - \sigma t + \epsilon) \tag{22}$$

Then the solution of wave motion can be expressed as

$$\overline{\Phi}=\overline{\phi}+\overline{\phi}_{\infty}=-\frac{gA_0}{\sigma}J_0\left(2\sqrt{\frac{kx}{\sigma}}\right)\cos(kx-\sigma t+\epsilon)+\frac{ag}{\sigma}\cos(kx+\sigma t) \tag{23}$$

The last term of the above equation is the solution of progressive small amplitude wave at water surface, and a is the amplitude, A is to be of $A_0=-\frac{\sigma}{g}A$ 。

From the theory of reflection as light—wave, the change of phase, ϵ *, is function of bottom slope,* α *, will be found out, as*

$$\epsilon=\epsilon(\alpha)=2\tan^{-1}\alpha \tag{24}$$

Combining eq. (23) *and eq.* (24) *then substituting in eq.*(2)*, and take the first — order approximation that we have the water surface elevation*

$$\eta(x,t)=A_0J_0\left(2\sqrt{\frac{kx}{\sigma}}\right)\sin(kx-\sigma t+2\tan^{-1}\alpha)+a\sin(kx+\sigma t) \tag{25}$$

Based on the energy conservation at the intersecting point of mean water level and bottom boundary, where the potential energy exists only, that we find

$$A_0(\alpha)=a\left[\cos(2\tan^{-1}\alpha)+\sqrt{\cos^2(2\tan^{-1}\alpha)+3}\right] \tag{26}$$

The relationship between A_0 *and* α *has been shown in Fig.* — 2 *From this figure, it illustrates that* A_0 *decreases with* α *increases, and as* $\alpha=\infty$ *, it becomes standing wave,* $\alpha=0$ *that it will be a progressive wave.*

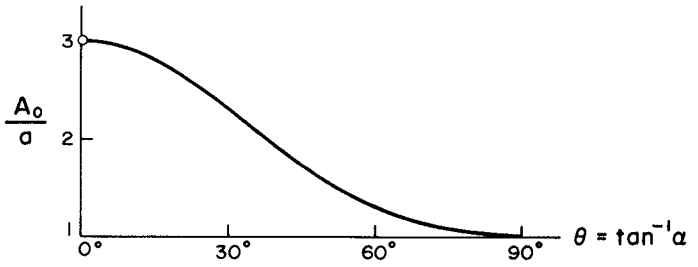

Fig. – 2

After substituting eq. (26) into eq. (25), the water surface elevation, $\eta(x, t)$, will be obtained. There are three examples presented through Fig. – 3 to Fig. – 5

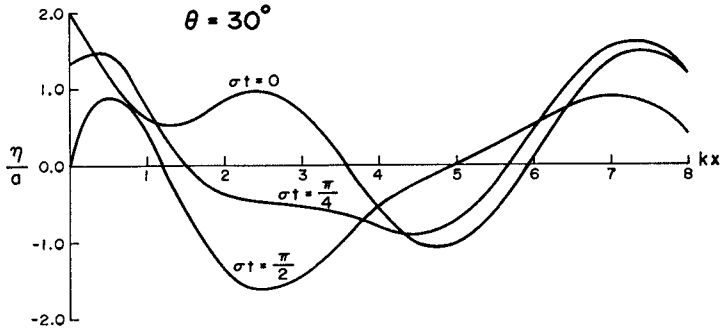

Fig. – 3

Furthermore, arrange the result of the expansion of eq. (25), that the relationship among water surface elevation, wave amplitude, wave number, bottom slope and dimensionless distance can also be expressed as the following forms,

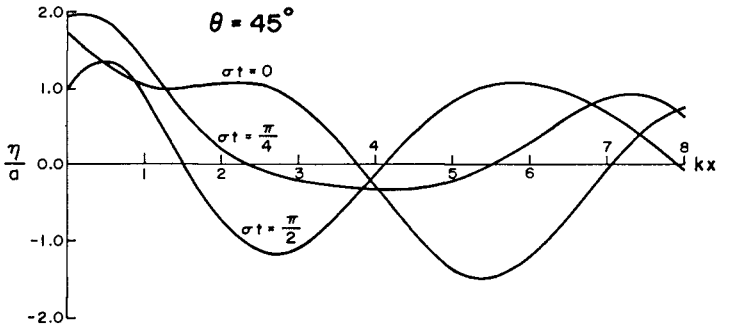

Fig. – 4

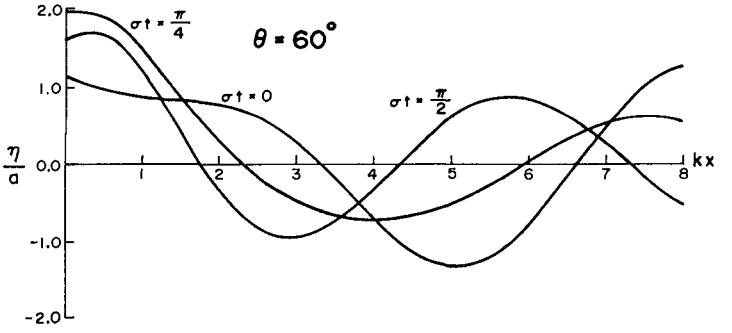

Fig. – 5

$$\eta(x,t)=\left[A_0J_0\left(2\sqrt{\frac{kx}{\alpha}}\right)\sin(kx+\epsilon)+a\sin kx\right]\cos\sigma t$$

$$+\left[a\cos kx-A_0J_0\left(2\sqrt{\frac{kx}{\alpha}}\right)\cos(kx+\epsilon)\right]\sin\sigma t$$

$$=B(x,\alpha)\sin\left[m(x,\alpha)\cdot x+\sigma t\right] \tag{27}$$

and

$$B(x,\alpha)=\left\{\left[a\sin kx+A_0J_0\left(2\sqrt{\frac{kx}{\alpha}}\right)\sin(kx+\epsilon)\right]^2\right.$$

$$+\left\{ a\cos kx - A_0 J_0\left(2\sqrt{\frac{kx}{\alpha}}\right)\cos(kx+\epsilon)\right\}^2\Big\}^{1/2} \tag{28}$$

$$m(x,\alpha) = \left[\tan^{-1}\left\{\frac{a\sin kx + A_0 J_0\left(2\sqrt{\frac{kx}{\alpha}}\right)\sin(kx+\epsilon)}{a\cos kx - A_0 J_0\left(2\sqrt{\frac{kx}{\alpha}}\right)\cos(kx+\epsilon)}\right\} + n\pi\right]/x \tag{29}$$

where n is a positive integer.

From the expression of eq. (27), the amplitude of wave motion climbing along an arbitrary sloping beach has been abtained as eq. (28) and it is function of the dimensionless distance kx and bottom slope α. That is to say, the amplitude varies along the horizontal distance due to shoaling and reflection as water waves propagate from deep water toward the shore. Several illustrations have been presented in Fig. – 6 for $\alpha = 0$, $1/\sqrt{3}$, 1 , $\sqrt{3}$ *and* ∞

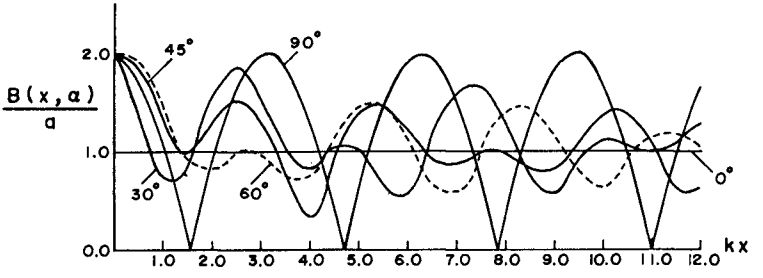

Fig. – 6

Figure – 6 illustrates the solutions for the bottom slope 0° , 30° , 45° , 60° *and* 90° *according to eq. (28). And we can see that all the variation of water surface will gradually decrease and become small amplitude wave in deep water except for the case of,* $\theta = 90°$ *, under that condition , it becomes a standing*

wave.

3. *DINCUSSION AND CONCLUSION*

From the theoretical results as above metioned that the variation of water surface and amplitute are function of beach slope and dimensionless distance from the shore. And the results will be more reasonable than Stokers' (1947) *which is expressed in eq.* (30)

$$\bar{\Phi}(x,t) = A_1\left[\cos(\sigma t-\epsilon_1)Y_0\left(2\sqrt{\frac{kx}{\alpha}}\right) + \sin(\sigma t-\epsilon_1)J_0\left(2\sqrt{\frac{kx}{\alpha}}\right)\right] \tag{30}$$

where A_1 , ϵ_1 *are the same significance as in this paper. But Stoker's solution, because contains only the linear terms so that the solution for the deep water becomes a straight line. Our solution, on the other hand, give a more reasonable solution which is a small amplitude wave when we include the potential function in deep water.*

4. *REFERENCE*

1 *Hanson, E.T., The theory of ship waves. Proc. Roy. Soc. Lond. A.* 111, 1926, 491-529.

2 *Lewy, H., Water waves on sloping beaches. Bulletin of the American Mathematical Society,* 52, 1946. 737-775

3 *Stoker, J.J., Surface waves in water of variable depth. Quarterly of Applied Mathematics,* 5, 1947, 1-54

4 *Stoker, J.J. Water waves. Institute of Mathematical Sciences New York University, New York,* 1968.

5 *Biesel, F., Study of wave propagation in water of gradually varying depth. U.S. National Bureau of Standards. Gravity wave NBS Circular* 521, 1952

6 *Carrier, G.F. and Greenspan, H.P., Water waves of finite amplitude on a sloping beach.J. Fluid Mech.*4, 1958. 97-109.

7 *Greenspan, H.P., On the breaking of water waves of finite amplitude on a sloping beach. J.Fluid Mech.* 4,1958. 330-334.

8 *Stokes, G.G., On the theory of oscillating waves Trans. Camb. Phil. Soc. Vol.*8,1847, *and Supplement. Scientific Paper, Vol.*1

9 *Chen Y.Y., Waves reflection and diffraction in Kaohsiung Harbor, Oceanogrophy,*6. *National Taiwan College of Marine Science and Technology,* 1978.

10 *Chen, Y.Y., Extension – poisson's Integral Formula, (in preparation*), 1981.

EXAMPLES OF STORM SURCE PREDICTION MODELS

by
P. Lencioni[1] - J.P. Benqué[2] - Y. Coëffé[3]

ABSTRACT

For a given site, deterministic models may be applied to predict the tide level with a rather good accuracy. However, a difference is observed between the observed and predicted tide level under storm condition. This difference is called storm surge. Two different storm surges prediction models are presented for the site of Le Havre : an autoregressive model ; a model using wind and pressure local data.

The autoregressive model can be used for a prediction 5 hours in advance. The availability of accurate wind and pressure predictions by the Meteorological Service of Le Havre within 36 hours in advance makes the use of the second model of great interest because it provides the possibility of predictions within 39 hours in advance.

1. INTRODUCTION

For a given site, deterministic models based on harmonic analysis may be applied to predict the tide levels with a rather good accuracy. However, differences are observed between the real and predicted tide levels under storm conditions. These differences are called storm surges (fig. 1).

In many cases, prevision of theoretical tide levels is not sufficient and it is very useful to know the possible storm surges. For instance, in coastal projects, the design of structures is often influenced by the largest storm surges possible. In that case, exceptionnal storm surges associated with a prescribed risk level are needed. On another side it is also useful to predict storm surges a few hours in advance, either for navigation aid, or to protect coastal work in progress.

1 REP-EDF, Principal engineer, Nuclear Safety Service, France
2 LNH-EDF Chatou, Head of Department "Laboratoire National d'Hydraulique, France
3 LNH-EDF Chatou, Head of Maritime Hydraulic Division, France.

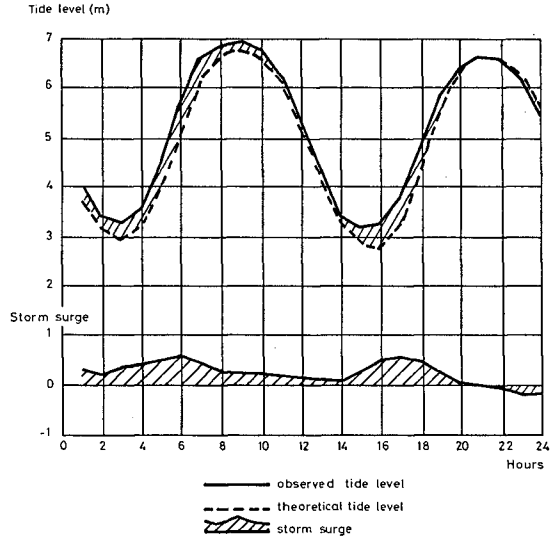

Fig. 1. DEFINITION OF A STORM SURGE

The present study is specially devoted to this second kind of prediction models, applied to the site of Le Havre (harbour of the Seine Estuary), but results obtained may be also used to predict exceptionnal storm surges by the mean of simulation.

The following steps of the study are described :

- analysis of storm surges, from the tide levels observed every hour on the site of Le Havre, from January 1976 to June 1978,
- elaboration of two storm surges prediction models :
  . an autoregressive model, where the storm surge at the time $t + k$ t is estimated knowing storm surges until the time t,
  . a model using wind and pressure local data, these variables being available from Meteorological Services with 36 hours prediction.

2. ANALYSIS OF STORM SURGES RECORDED AT LE HAVRE

Storm surge is the algebraic difference between the real and predicted tide levels. The analyzed data set of storm surges resulted from tide levels recorded, every one hour, at Le Havre harbour from the 1/1/1976 to the 30/6/1978 and tide levels predicted by the S.H.O.M. (Marine Hydrological and Oceanographical Service), giving 21 888 values.

Graphic examination of storm surges and corresponding wind and pressure data, give the main tendancies of the phenomenon (fig. 2).

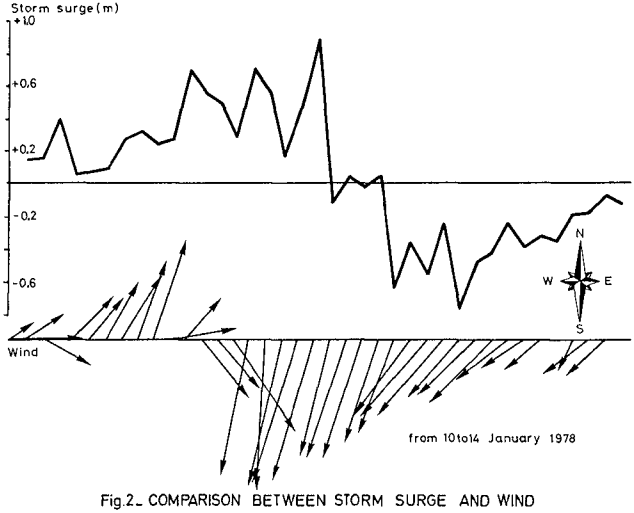

Fig.2_ COMPARISON BETWEEN STORM SURGE AND WIND

A quiet meteorological situation induces low storm surges. A low pressure and a strong intensity of wind raises high positive storm surges, with a 12 hours period (tide cycle). The maximum of the storm surge is generally situated around mean water level showing that the effect on tide may be seen as an increase (or decrease of mean water level) and a phase shift of the theoretical tide. To a high pressure corresponds negative storm surge.

Spectral analysis and autocorrelation functions of these storm surges (fig. 3 & 4) confirm the 12 hours period. Moreover three scales of time appear from the spectral analysis (6 hours, 12 hours and period greater than 24 hours). Autocorrelation functions show the high correlation between two values of storm surges separated by a short interval of time ; this is at origin of autoregressive model.

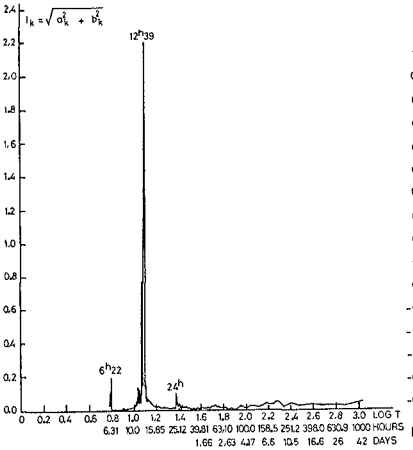

Fig.3_ SPECTRAL ANALYSIS OF STORM SURGES

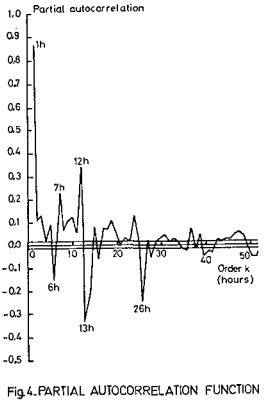

Fig.4_PARTIAL AUTOCORRELATION FUNCTION

3. AUTORECRESSIVE MODELS

In autoregressive models the storm surge at the time t + k Δt is estimated knowing storm surges until the time t. The examination of autocorrelation function and partial autocorrelation allowed to retain the following regressive models :

$$\hat{S}\ (t + k\Delta t) = C_o\ (k\Delta t) + C_1\ (k\Delta t)\ S\ (t + k\Delta t - 12) + C_2\ (k\Delta t)\ S\ (t) \qquad (1)$$

where

$\hat{S}$ predicted storm surge

S observed storm surge

kΔt prediction time (1 to 12 hours)

C_i model coefficient, function of kΔt, estimated from the totality of available observations (January 1976 to June 1978, 21 900 values), by least square method.

The multi correlation coefficient decreases when kΔt increases. Four values of kΔt were tried, respectively 1, 3, 6 and 12 hours. Multi correlation coefficients range between 0,89 with a 1 hour prediction and 0,68 with a 12 hours prediction.

The introduction of a Kalman filter was tried in this autoregressive model but did not give any better short term prediction.

Interest of Kalman filter is to use the last available observation to put model parameters straight. But autoregressive models also take into account this information and this can explain that for a short-range forecast model, Kalman filter does not improve results.

With or without Kalman filter multi correlation coefficient with a 1 hour prediction is 0,89. In 95 cases on 100, prediction error is ± 0,15 m. Figure 5 give a comparison between observed storm surges and predicted storm surges obtained by the autoregressive model with a 1 hour prediction.

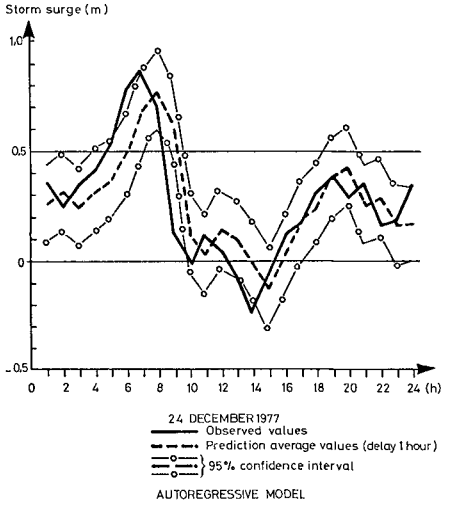

Fig.5- COMPARISON BETWEN OBSERVED AND PREDICTED STORM SURGES

4. MODEL USING WIND AND PRESSURE LOCAL DATA

Previous models cannot be really used with a prediction period greater than 12 hours.

A data analysis has shown that wind and local pressure data are able to explain the storm surges. The main interest to predict storm surges using these meteorological factors is that these variables can be given by Meteorological Services with a 36 hours prediction. Models based on wind and pressure data were then developped.

Spectral analysis of storm surges, pressure and wind at Le Havre was made. We considered the two components of wind, projected on rectangular axis ; E-W - 30° and N-S - 30°, these directions allowing the best correlation between wind and storm surge.

In this prediction model, the storm surge S has been splitted in 3 parts, according to spectral analysis and graphic examination of storm surges and concomitant meteorological data

$$S = S_1 + S_2 + S_3$$

S storm surge
S_1 storm surge corresponding to periods greater than 24 hours highly depending on recent meteorological events (wind, pressure)
S_2 storm surge corresponding to periods between 6 and 24 hours corresponding to tide periodicity. This cycle comes from a phase shift on tide theoretical cycle induced under some meteorological conditions (low pressure)
S_3 storm surge corresponding to periods smaller than 6 hours.

Standard deviations are respectively :
$\sigma(S) = 0,17$ m
$\sigma(S_1) = 0,14$ m $\quad \sigma(S_2) = 0,08$ m and $\sigma(S_3) = 0,05$ m

the most important part comes from S_1.

Each component is separatedly examined.

4.1. Component S_1 (period greater than 24 hours)

For a given class of wind direction, S_1 is computed from wind intensity and pressure by the following regression model :

$$\hat{S}_1(t) = a_o(\alpha) + a_1(\alpha)\, V(t-3) + a_2(\alpha)\, V^2(t-3) + a^3(\alpha)\, P(t-3) \qquad (2)$$

where :

α wind direction (18 classes of 20°)
$V(t-3)$ wind mean intensity at the time $t - 3$ hours
$P(t-3)$ pressure at the time $t - 3$ hours, zero pressure level corresponding to 1 013 mbars
a_i model coefficients, functions of wind direction.

The mean wind is determinated on 12 hours ; the two mean components EW and NS are computed as :

$$\bar{V}_{EW} = \frac{1}{5} \sum_{j=-2}^{2} V_{i-j} \cos \alpha_{i-j}$$

$$\bar{V}_{NS} = \frac{1}{5} \sum_{j=-2}^{2} V_{i-j} \sin \alpha_{i-j}$$

and the wind mean intensity

$$V(t) = \sqrt{\bar{V}^2_{EW} + \bar{V}^2_{NS}}$$

and its direction

$$\alpha(t) = \text{arc tg} \frac{\bar{V}_{NS}}{\bar{V}_{EW}}$$

Correlation coefficients between S_1 and P are highly significant and negative (this means S_1 increases while pressure decreases). Wind introduction allows increasing of multiple correlation coefficients.

Residue values, difference between real and estimated values of S_1 are biassed so that the model overvalues S_1 if S_1 is small and undervalues S_1 if S_1 is great. This is corrected by an empirical factor C

$$S = \hat{S}_1 + C$$

where :

$\hat{S}_1$ is given by regression model (2)

$C = 0,1\ (\sqrt{1 + 5\ \hat{S}_1} - 1)$ if $\hat{S}_1 > - 0,2$ m

$C = 0,1$ if $\hat{S}_1 < - 0,2$ m

In 95 cases on 100, the real value S_1 appears to be in the range of predicted $S_1 \pm 0,18$ m.

4.2. Component S_2 (periods between 6 and 24 hours)

Modelisation of S_2 is based on the time phase shift observed between real and predicted tide levels which can be detected from the presence in storm surges evolution of the tide periodicity. That induced cycle has zero value at high and low tide, extremum occuring during increasing or decreasing tide level.

This shape of the cycle of S_2 is confirmed if we consider the average of S_2 during a tide cycle in function of the pressure level (see fig. 6).

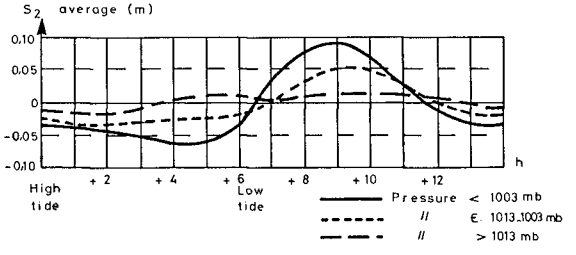

Fig.6. AVERAGE CYCLE OF S_2 FUNCTION OF THE PRESSURE LEVEL

Cycle is especially important for low pressures ; in opposite when pressure is greater than 1 013 mb, average of S_2 has pratically zero values.

The amplitude A of this cycle is computed in function of the pressure level, according to 3 classes, by the following relations :

. Low pressure $P < 1\ 003$ mb
the amplitude A is function of mean wind (V_M, α_M), as previously defined

$$A = 0,153 + 0,014\ V_M \cos \alpha_M$$

however if $A < 0,15$ m $\quad A = 0,15$ m

. Mean pressure $1\ 003 < P < 1\ 013$ mb
the amplitude A is constant $\quad A = 0,14$ m

. High pressure $\quad P > 1\ 013$ mb
in this case $S_2 = 0$

4.3. Component S_3 (periods smaller than 6 hours)

S_3 represents a white noise which is difficult to explain from wind and pressure, though its variability must be function of wind.

S_3 has been neglected in prediction.

4.4. Results

From comparison between real and predicted storm surges at the same time we can say, in 95 cases on 100, prediction error is :

$\pm$ 0,20 m if storm surge value is smaller than 0,20 m
$\pm$ 0,30 m if " " " " greater " "

Storm surges range being included between - 0,50 m and 1 m, this error can appear important, but evolution in the course of time is well reproduced (fig. 7).

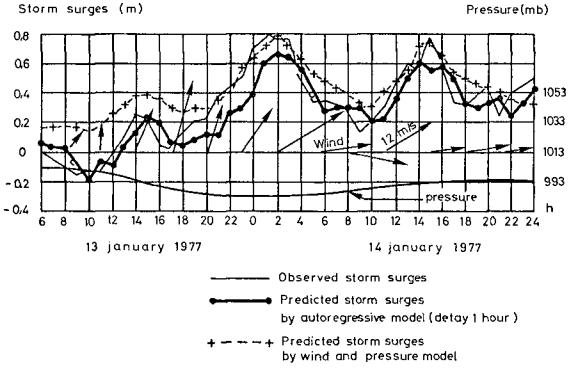

Fig.7. COMPARISON BETWEEN OBSERVED AND PREDICTED STORM SURGES

This model predict storm surges at the instant t, knowing pressure and wind (intensity and direction computed over 12 hours) at the instant t - 3 h. Correlation coefficient between observation and the 3 hours prediction is 0,75, slightly smaller than the value obtained by autoregressive model.

For the case where only storm surge prediction corresponding to high or low tide is needed, component S_1 gives directly the prediction of storm surge. In that case prediction error is limited to $\pm$ 0,18 m for 95 cases over 100.

It must be noticed that knowing a large sample of wind and pressures, it is possible, using this kind of model, to generate storm surges values which allow to predict exceptionnal storm surges of low probability.

5. CONCLUSION

The present study has shown that in the case of Le Havre an autoregressive model can be used for a prediction up to 5 hours in advance with a reasonable accuracy. For a more extended forecast, it is better to use models based on meteorology. The availability of accurate wind and pressure predictions by Meteorological Services of Le Havre within 36 hours in advance makes the use of the second model of great interest as it provides the possibility of prediction within 39 hours in advance.

When the interest is restricted to storm surges predictions high and low tides, the model based on meteorology appears to be especially easy to handle and reasonably accurate.

However, it is clear that local wind and pressure data are not enough to explain the totality of some storm surges. Such occurences cannot be predicted without knowing more on the interaction between large scale meteorological patterns and the tide propagation over the domain of interest.

This problem will be investigated by using a tide propagation deterministic model of the whole English channel, based on Saint-Venant equations. The results of interaction between typical meteorological patterns and the tide propagation should lead to a deeper understanding of the physical phenomena involved and allow the choice of adequate parameters for future prediction models.

WATERWAVES CALCULATION BY NAVIER-STOKES EQUATIONS

by O. DAUBERT*, A. HAUGUEL** and J. CAHOUET***

Abstract : N.S.L. program is a finite-difference code for two-dimensionnal flows with a free surface in a vertical plane. Basic equations are Navier-Stokes équations with a simple simulation of turbulent effects by an eddy viscosity coefficient related to the mixing length and the mean velocity gradient. Theses equations are solved in a variable domain in time. The main features of the numerical method are presented. Some comparisons with theoretical solutions give a good validation of the code both in linear and non linear cases. Other examples of application are given.

1. INTRODUCTION

Large computational programs, solving time-dependant Navier-Stokes equations, in two and even three space dimensions, are now well developped for industrial design. Their adaptation to waves problems should be a new and powerful mean of investigation in theoretical and practical studies, because non linear and viscous effects are taken into account.

The N.S.L. program "Navier-Stokes à Surface Libre" presented here, is a first step to this ambitious objective. It solves numerically N.S. equations in a vertical plane - i.e. only for two-dimensionnal flows - with a free surface. The free surface is a moving boundary for the computational domain, and is also an unknown of the problem. Time-varying pressure and velocity fields are the other results of this program for suitable initial and boundary conditions, and any given bottom shape. In order to give a more pratical background to the study, N.S.L. program can be considered as a "numerical wave flume". It allows simulation of all sorts of waves, in deep or in shallow water, with small or large amplitude, except perhaps breaking ones.

* Engineer of the Research Division, Laboratoire National d'Hydraulique. EDF. Chatou. France.

** Head of the Research Division, Laboratoire National d'Hydraulique, France.

*** Assistant Engineer, Research Division, Laboratoire National d'Hydraulique, France.

2. MATHEMATICAL FORMULATION

2.1. General equations :

In the fluid, velocities and pressure are related by dynamical and continuity equations :

$$(1)\quad \frac{DV}{Dt} + \frac{1}{\rho}\nabla p^* = \mathrm{Div}\ (\nu_T \nabla V)$$

$$(2)\quad \mathrm{Div}\ V = 0 \qquad\qquad (p^* = p + gz)$$

The turbulent viscosity coefficient, is given empirically by :

$$(3)\quad \nu_T = \nu + K^2 \ell^2\ (2\ \mathrm{Dij.Dij})^{1/2}$$

with $\mathrm{Dij} = \frac{1}{2}\ (V_{i,\,j} + V_{j,\,i})$

The mixing length l is constant in the fluid except near the bottom, where l is proportionnal to the distance from the bottom.

2.2. Computational domain and boundary conditions

They are summarized on figure 1.

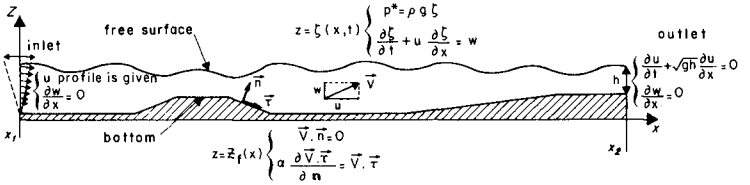

Figure 1 - Boundary conditions - Left b.c. simulates a wave- machine (e.g. $U = U_0(z)\ \sin \omega t$) - Right b.c. is absorbing if h is small enough to eliminate dispersive phenomena. On the bottom, the second b.c. simulates a tangential stress in a boundary layer.

2.2.1. Sea surface boundary conditions :

The second relation, shown in figure 1, is a partial differential equation which can be used for the free surface determination. It must be solved along the whole ζ -line, with its own boundary conditions. These ζ -boundary conditions, in $x = x_1$ and $x = x_2$, can be deduced from the u-ones, by using the horizontal projection of eq. (1), and the surface relation : $p^* = \rho g \zeta$.

$$(4)\quad \frac{\partial \zeta}{\partial x} = \frac{1}{\rho g}\frac{\partial p^*}{\partial x} = -\frac{1}{g}\left(\frac{Du}{Dt} - \mathrm{Div}\ (\nu_T \nabla u)\right) \simeq -\frac{1}{g}\frac{Du}{Dt}$$

Theoretically, another boundary condition is required, along the free surface, in order to well pose the problem - a zero tangential stress, for instance-. But this point is ignored in the present, because viscous terms are almost vanishing near the free surface, as long as wind effects are not studied.

2.2.2. Bottom boundary conditions :

The first one traduces the impermeability of a fixed bottom. The second one comes from the idea that the tangential stress

$$(5)\quad \rho \nu_T \frac{\partial(\vec{V}.\vec{\tau})}{\partial n} = \rho u_*^2$$

is prescribed. Its value is calculated by doing the hypothesis that the velocity profile, near the bottom, follows a logarithmic law, for instance :

$$(6)\quad \vec{V}.\vec{\tau} = u_* \left(\frac{1}{K} \text{Log} \frac{y}{d} + 8.5\right)$$

where y is the distance from the bottom.

As ν_T, near the bottom, reduces to

$$(7)\quad \nu_T \simeq K^2 y^2 \frac{\partial \vec{V}.\vec{\tau}}{\partial n}$$

one has, by elimination of u_*, a relation of the form

$$(8)\quad \alpha \frac{\partial \vec{V}.\vec{\tau}}{\partial n} = \vec{V}.\vec{\tau}$$

2.2.3. Lateral boundary conditions :

These conditions are fitted to wave flume simulation : the left one simulates a wave machine and the right one, allows the waves to get out without reflection. The absorbing boundary condition :

$$(9)\quad \frac{\partial u}{\partial t} + c \frac{\partial u}{\partial x} = 0$$

must be used in a shallow water situation. In dispersive waves, the celerity c depends on the wave length. It is thus necessary, for irregular waves, to reduce the depth with a mild slope, in order to have only shallow water waves at the boundary, and then a unique celerity $c = \sqrt{gh}$.

3. NUMERICAL METHOD

3.1 Coordinate transformation

Before solving numerically the system (1) (2) and its boundary conditions, a coordinate transformation is done :

$$(10) \qquad \begin{cases} \xi = x \\ \eta = H\ (z - Z_f(x))/(\zeta\ (x,t) - Z_f(x)) \end{cases}$$

This transformation maps the physical variable domain in a fixed one, with boundaries parallel to the coordinate-axis (figure 2).

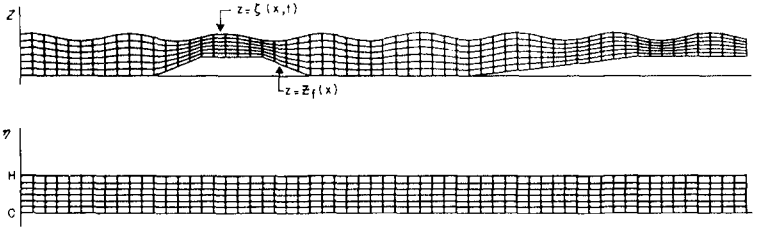

Figure 2 - The semi-curvilinear grid, transformed in a rectilinear one by the transformation : $\eta = H(z-Z_f/(\zeta - Z_f)$.

Equations and boundary conditions are expressed in the new independant variables (ξ, η, t).
Calculations are performed on the transformed domain, by solving a finite difference approximation of the transformed equations. These involve, in each derivative, one of the following factors :

$$(11) \qquad \eta_x = -\ (H\ Zf_x + \ (\zeta_x - Zf_x))/(\zeta - Z_f)$$

$$(12) \qquad \eta_z = H/(\zeta - Z_f)$$

$$(13) \qquad \eta_t = -\eta\zeta_t/(\zeta - Z_f)$$

which vary in time (due to the free surface motion) and are evaluated at each time step.

3.2. Algorithm of a time step

A fractionary step method is used [1]. This method is illustrated by the following scheme :

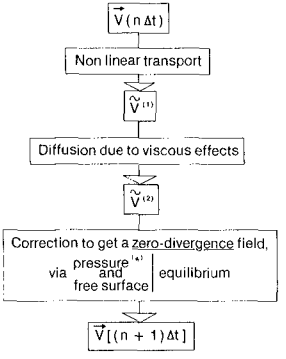

Each time step is splitted in three parts which are solved successively ; the velocity field $V^n = V(n\,\Delta t)$, being known at time $n\,\Delta t$, intermediate fields $\tilde{V}(1)$ and $\tilde{V}(2)$ are computed verifying respectively :
- a transport equation solved by the Characteristics method.

$$(14) \qquad \frac{\tilde{V}(1) - V^n}{\Delta t} + V^n \otimes \nabla V^n = 0$$

- and a diffusion equation solved by an explicit method

$$(15) \qquad \frac{\tilde{V}(2) - \tilde{V}(1)}{\Delta t} - \mathrm{Div}\,(\nu_T \nabla \tilde{V}^{(1)}) = 0$$

The definitive, zero-divergence velocity field, at time $(n+1)\,\Delta t$, V^{n+1}, is calculated via a pressure and free surface equilibrium, which is expressed by the following system of equations :

$$(16) \qquad \frac{V^{n+1} - \tilde{V}(2)}{\Delta t} + \frac{1}{\rho} \nabla p^* = 0$$

$$(17) \qquad \mathrm{Div}\, V^{n+1} = 0$$

in the domain

$$(18) \qquad p^* = \rho g \zeta$$

$$(19) \qquad \frac{\partial \zeta}{\partial t} + u^{n+1} \frac{\partial \zeta}{\partial x} = w^{n+1}$$

on the free surface

Elimination of V^{n+1} between (16) and (17), give a Poisson equation for pressure

$$(20) \qquad \Delta p^* = \frac{\rho}{\Delta t} \mathrm{Div}\, \tilde{V}^{(2)}$$

This equation is solved with Neumann boundary conditions, derived from the normal projection of equation (16), in which V(n+1).n is known, on the bottom and on lateral boundaries. On the free surface, p* verify the Dirichlet boundary condition (18). As ζ is related to V(n+1) by eq. (19), the system (16) to (19) is solved iteratively.
Discretisations, in space and time which are not specified in the formulas (14) to (19), are performed in a staggered grid, as shown in figure 3.

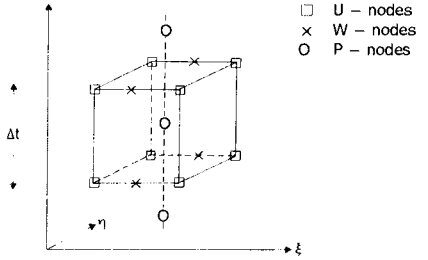

Figure 3 - Numerical staggered grid, in space and time.

Pressure nodes, on this figure, are drawn on three time levels to indicate that, in equation (16), the pressure gradient is splitted on three time steps ; let us write p^* without star :

$$(21) \quad \nabla p \simeq \alpha \nabla p^{n+\frac{3}{2}} + \beta \nabla p^{n+\frac{1}{2}} + \gamma \nabla p^{n-\frac{1}{2}}$$

$$\alpha + \beta + \gamma = 1$$

Wheighting coefficients α, β, γ are choosen as close as possible to 1/4, 1/2, 1/4 respectively ; nevertheless, α must be slightly greater than γ, in order to insure the stability of the numerical scheme(*). Of course, equation (20) is modified in consequence :

$$(22) \quad \Delta p^{n+\frac{3}{2}} = \frac{1}{\alpha} \text{Div} \left[\frac{\rho}{\Delta t} \tilde{V}^{(2)} - \beta \nabla p^{n+\frac{1}{2}} - \gamma \nabla p^{n-\frac{1}{2}} \right]$$

Pressure fields at $(n+\frac{1}{2})\Delta t$ and $(n-\frac{1}{2})\Delta t$ are assumed to be already calculated, and $p^{n+\frac{3}{2}}$ is the unknown of this equation.

It is thus necessary to prescribe, as initial conditions, not only velocities, but also pressures at two consecutive time levels. Equation (19), involving $\zeta^{n+\frac{3}{2}}$, and $\zeta^{n+\frac{1}{2}}$, is approximated with a centered discretisation.

Simpler methods have been studied, but they have shown a very poor accuracy in the tests presented hereafter.

4. COMPARISONS BETWEEN COMPUTED AND THEORETICAL RESULTS

N.S.L. program has been tested through numerous comparisons between computed and theoretical results, specially in two cases :

- the Stokes linear wave solution for small amplitude waves,
- the solitary wave's solution.

For these comparisons, viscous effects have been neglected.

4.1. Tests for small amplitude waves.

Figure 4 shows the waves calculated in the numerical wave flume, when the left boundary condition simulates a piston-wave-machine with period 4.5 s, and maximum velocity 0.2 m/s ; the right boundary condition is a radiative condition.

Water is at rest, at t = 0 ; then waves begin to propagate from left to right with a celerity about 5 m/s. At t = 50 s, five waves have gone out by the right boundary ; the movement is considered established ; celerity, wave lenght and wave amplitudes can be compared to the theoretical values given by the linear first order solution for irrotationnal waves of small amplitude.

(*) This method is a generalization of the one used by HAUGUEL in the numerical model of storm waves in shallow water [2] and [3].

Other tests have been done with a pivot-wave-machine, and with different depths. Comparisons with theoretical values are summarized in table I : the last case presented in this table, corresponds to figure 4 ;

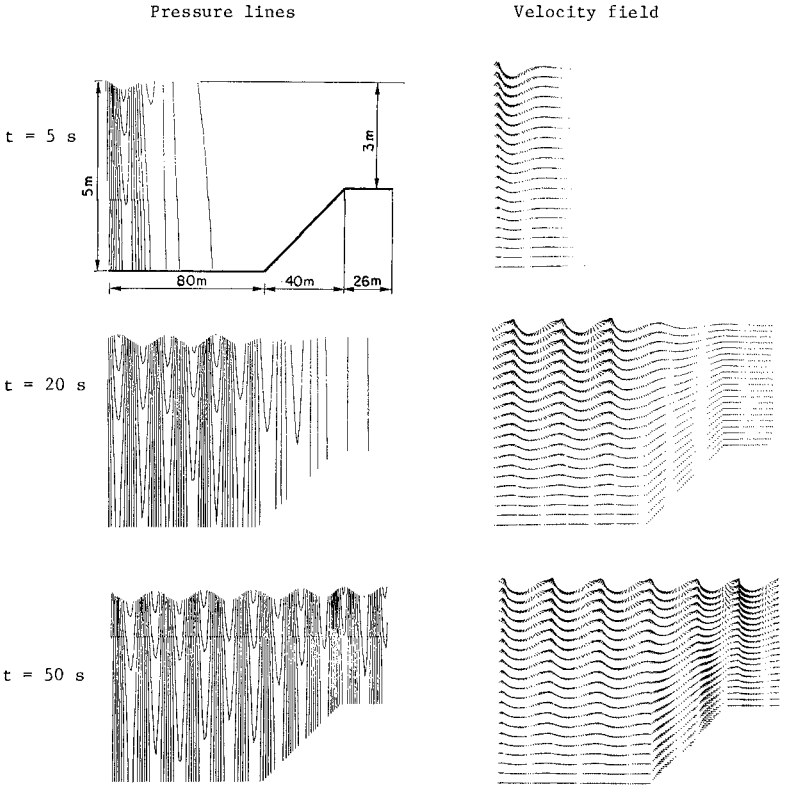

Figure 4 - Waves calculated in the numerical wave flume.
The left b.c. simulates a piston wave-machine (period = 4.5 s, maximum velocity = 0.2 m/s). The right b.c. is a radiative condition. (Δx = 1 m ; Δt = 0.15 s ; Δz = 0.25 m in the deep part of the flume)

Table 1 : Comparisons between computed and theoretical results for linear waves.

Flume characteristics		Wave-machine characteristics			Computed results and theoretical values(*)				
Depth	length		Period	Velocity maximum	wave length	celerity	wave height	top velocity	$\frac{\text{top } V^{ty}}{\text{bottom } V^{ty}}$
15 m	250 m		4.5 s	0.3 m/s	31.7 m (31.6)	7.05 m/s (7.02)	0.78 m (0.82)	0.58 m/s (0.56)	14 (10)
		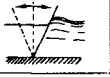	4.5 s	0.3 m/s (on surface)	31.5 m (31.6)	7.0 m/s (7.02)	0.57 m (0.60)	0.45 m/s (0.42)	10 (10)
5 m	250 m		4.5 s	0.2 m/s	26.1 m (26.3)	5.8 m/s (5.84)	0.30 m (0.31)	0.26 m/s (0.26)	1.8 (1.8)
variable 5 m slope 5 % 3 m	80 m 40 m 26 m		4.5 s	0.2 m/s	26.0 m (26.3) 21.5 m (22.1)	5.78 m/s (5.84) 4.78 m/s (4.91)	0.29 m (0.31) 0.27 m (0.32)		

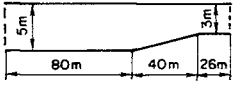

(*) Theoretical values are in parenthesis.

The others are performed in a longer horizontal wave flume ; in these cases, results are analyzed before the occurence of perturbations comming from reflection on the right boundary. Computed values are very similar to theoretical ones, indicated in parenthesis.

In these tests, the computing time is about 200 s of CPU for 50 s of physical time, on a CRAY 1.

4.2. Solitary wave tests

One is shown on figure 5 : on the left boundary (x = 0 m), the analytical value of the time-varying u-component is imposed ; w-component and free-surface level are computed results. The wave appears progressively in the domain of calculation, and propagates without deformation, like the theoretical solution [3] drawn on the same figure. The good quality of this result, insure that non linearities are well calculated.

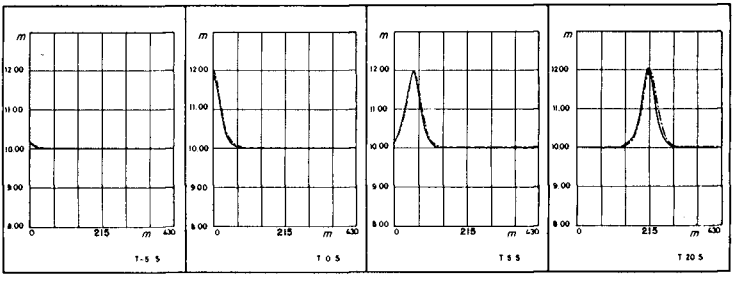

Figure 5 - Free surface of a solitary wave at t = -5 s, 0 s, 5 s, 20 s.
——— Theoretical solution -·-·- Computed solution by NSL program.

5. PRESENTATION OF SOME APPLICATIONS

As an example of the program possibilities, figure 6 shows how the solitary wave is transformed when it propagates on a rise. A similar case will be studied both numerically and experimentally. The numerical model is then able to give informations on the waves deformation by the bathymetry and then to test the validity of different integrated wave theories.

Another application, presented on figure 7, is specially devoted to the simulation of viscous effects ; it is the calculation of a permanent flow over a dredged trench. Drawings show the beginning of the flow : free surface remains nearly horizontal, and transient recirculations can be seen near the bottom. This flow has been studied experimentally in the Delft Hydraulic Laboratory [4], and it will be possible to use velocity measurements, in order to fit the parameters occuring in the turbulence simulation of the mathematical model : mixing length and bottom roughness. In the next future, the model will allow the study of viscous effects on propagating waves.

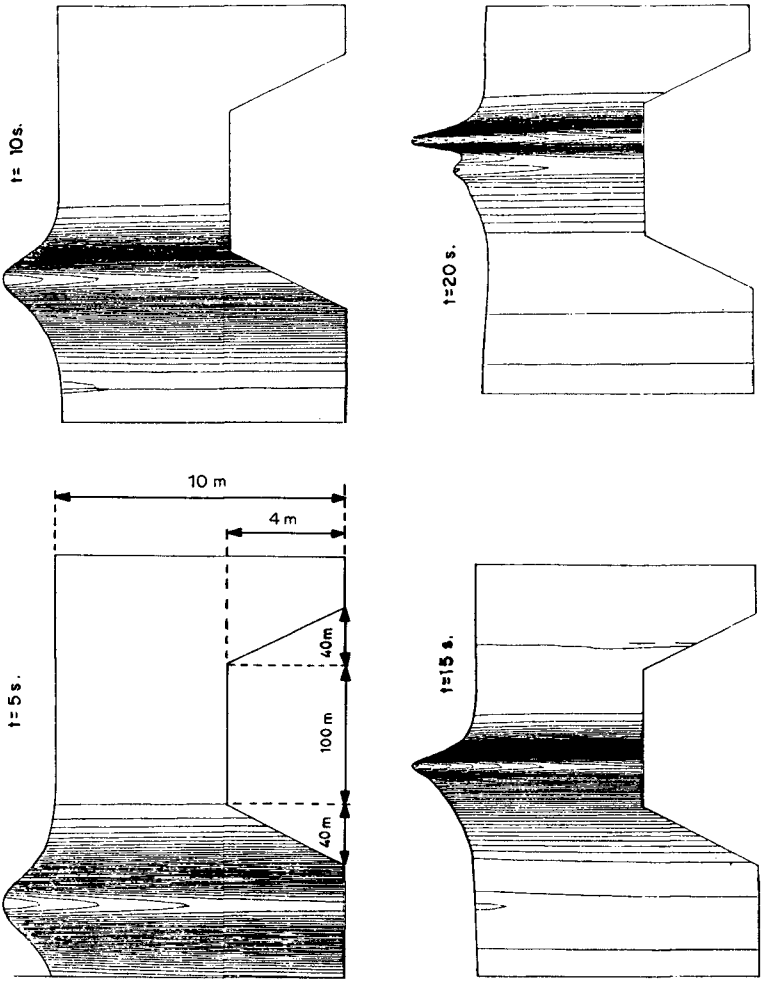

Figure 6 - Solitary wave propagating on a rise
Pressure field p^* (step = 0.05 m of water).

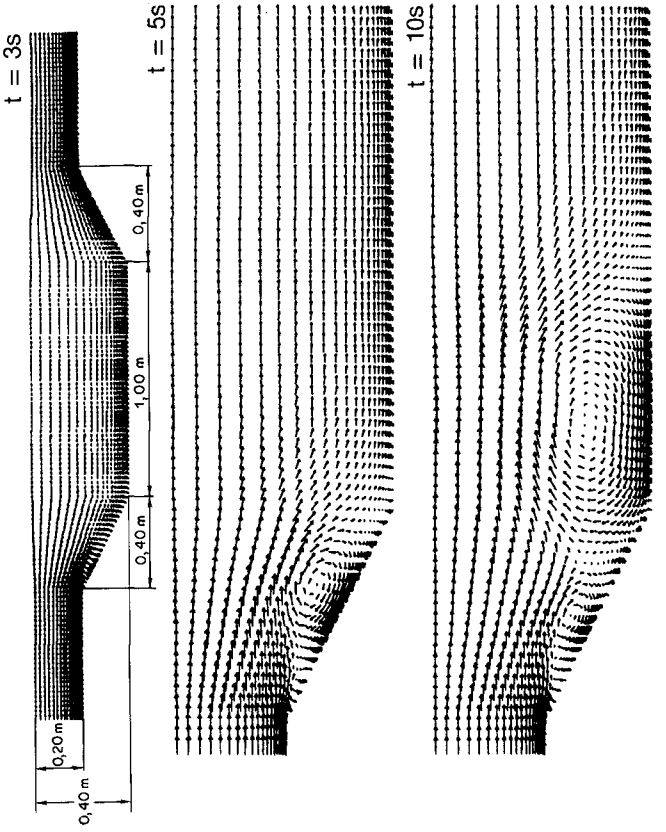

Figure 7 - Flow computation over a dredged trench. Velocity field.

N.S.L. program has also been stated to the study of irregular waves. On figure 8, the calculated heights in three points of a "numerical wave flume" are given. These level variations result from the superposition, at the left boundary of velocity profiles corresponding to three sinusoïdal waves, whose periods are 5 s, 8 s, and 13 s, and height 0.5 m, respectively. The evolution of the sea surface is quite comparable to what is expected in that case, and then, non-linear interactions taken into account in the numerical model, seem to be properly reproduced.

As the space and time steps, in this case, are chosen small enough to get a good precision for shortest wave (Δt = 0.15 s, Δx = 1 m, Δz = 0.75 m in the deep part of the flume), calculations need more computing time than the previous ones : about 800 s of CPU time in the CRAY 1, for 100 s of physical time. But this first test demonstrate the possibility to use the model on irregular conditions with a single simulation.

All these applications have ensured us that the idea of "numerical non linear wave flume" is viable. Further developments and applications will be made to demonstrate this possibility.

6. CONCLUSION

The main difficulty to tide over, for a numerical simulation of waves, was to get a good accuracy in propagation phenomena. Numerical models are often affected by excessive damping or phase-shift errors. The cases which have been choosen to test NSL program : - linear cases, as the first-order Stokes wave, and non-linear ones, as the solitary wave, - have lead to an efficient and accurate numerical method.

The other aspect to be tested now, are the turbulence and bottom boundary layer simulation in wave conditions.

N.S.L. program appears already to be an interesting tool for various fundamental studies, as velocities and pressure distributions in random waves, or in waves over immerged obstacles.

Developments of the code are projected to adapt its possibilities to stresses calculations on sharp obstacles and eventually on floating bodies in waves.

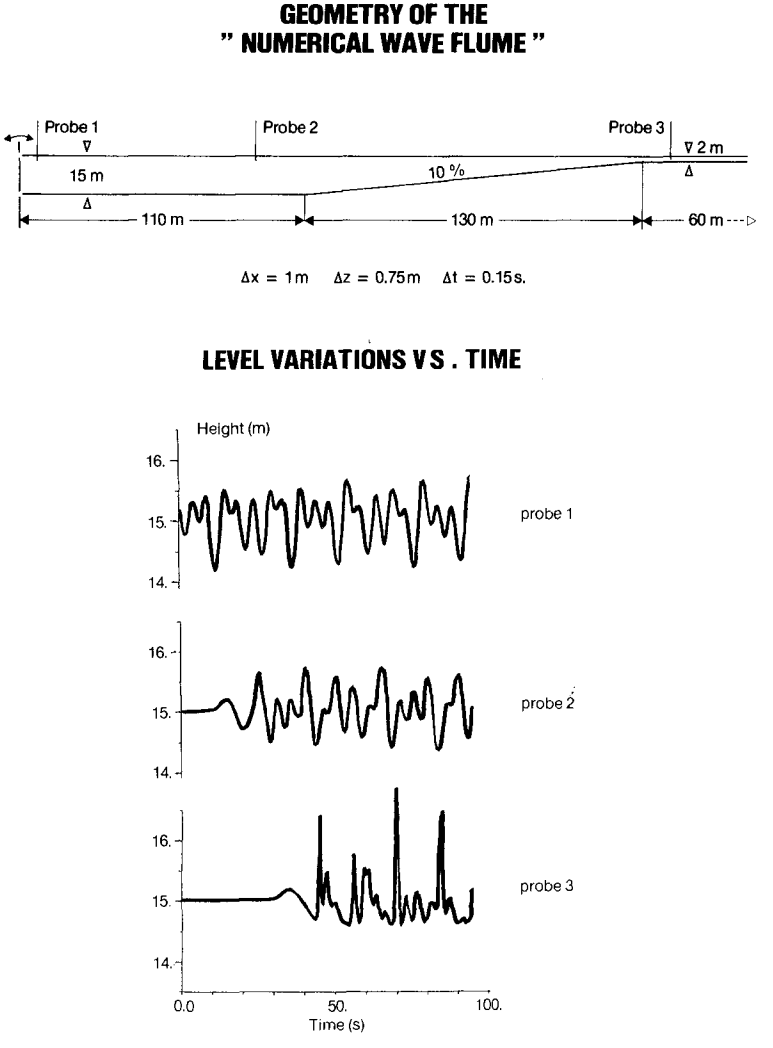

Figure 8 - Calculation of irregular waves.

7. REFERENCES

[1] YANENKO N.N. Méthode à pas fractionnaires. Résolution de problèmes polydimensionnels de physique mathématique. Translated by NEPOMIASTCHY P.A. Collection Intersciences A. COLIN - Paris 1962 -

[2] HAUGUEL A. A numerical model of storm waves in shallow water. Proc. of the 17th Conf. of Coastal Engineering - 1980 -

[3] HAUGUEL A. Calcul des houles de tempête en eau peu profonde. E.D.F. Rapport E42/79.41 - 1979 -

[4] ALFRINK B.J. The computation of turbulent recirculating flow using curvilinear finite differences. Application of the k - $\mathcal{E}$ model to the flow in dredged trenches. E.D.F. report HE/41/81.22 - 1981 -

8. NOTATIONS

x	horizontal coordinate
z	vertical coordinate
t	time
$\vec{V} = (u,w)$	velocity vector
p	pressure ($p^* = p + \rho gz$)
Z_f	bottom level
ζ	free surface level
ν	cinematic viscosity
ν_T	turbulent viscosity
K	Karman's constant (= 0.41)
ℓ	mixing length
ρ	volumic mass
g	gravity constant
y	distance along the normal to the bottom
$\vec{n}, \vec{\tau}$	normal and tangential unit vectors

Div=Divergence = $\frac{\partial}{\partial x} + \frac{\partial}{\partial z}$

∇ Gradient = $(\frac{\partial}{\partial x}, \frac{\partial}{\partial z})$

Δ Laplacian = $\frac{\partial^2}{\partial x^2} + \frac{\partial^2}{\partial z^2}$

Δt time step.
$\Delta x, \Delta z$ space steps

APPLICATIONS OF A NUMERICAL SHALLOW WATER WAVES MODEL

by

A. HAUCUEL (1), and PH. PECHON (2)

ABSTRACT

This paper relates three applications of a numerical model of storm waves in shallow waters developed in LNH. The equations are recalled at first and then the applications performed are presented.

The numerical model has been used in the case of the port of Fecamp, on the English Channel coast, on which the results of a scale model were available. The computed results compare well with the scale model measurements.

The second case is the simulation of a tsumami induced by a submarine landslide which appeared in 1979 near Nice ; the model has permitted the simulation of the rising of the wave.

The last applications consisted in simulating breaking waves by introducing a dispersion term in the equations. This simulation has been tested with a one-dimensional model at first. The results show that the numerical model reproduces the elevation of the mean sea surface due to the loss of energy in breakings. Then the longshore current induced by breaking waves coming obliquely over a rectilinear sloping shore has been reproduced with a two dimensional model.

The results show that the model is able to compute with a good accuracy refraction, diffraction and reflection, and that it appears to be very interesting for longshore currents simulation.

(1) Head of the Research Division, Laboratoire National d'Hydraulique, E.D.F., Chatou, France.
(2) Research Engineer, Laboratoire National d'Hydraulique, E.D.F., Chatou, France.

1. INTRODUCTION

This paper follows a previous one presented in the 17th conference, on the numerical model of storm waves in shallow waters developed in LNH. In this previous paper, the different assumption required and the governing equations (more complete than the Boussinesq type equations) were presented. Several indications were also given and the importance of non linear effects in storm waves problems was pointed out.

During the last two years, practical applications have been performed, and new possibilities have been introduced in the model. The applications presented are the computation in the port of Fecamp (English Channel coast) on which the results of a scale model were available, the simulation of a mini-tsunami which appeared near the works of the new airport of Nice in 1979, and the simulation of wave set-up and longshore currents induced by wave breaking over a rectilinear sloped shore.

2. EQUATIONS

By assuming that the vertical velocity linearly increases from the bottom to the surface, instead of assuming a hydrostatic pressure distribution, it is possible to average the Navier - Stokes equations to obtain the Serre type equations :

$$\frac{\partial h}{\partial t} + \frac{\partial U}{\partial x} + \frac{\partial V}{\partial y} = 0$$

$$\frac{\partial U}{\partial t} + \frac{\partial}{\partial x}\left(\frac{UV}{h}\right) + \frac{\partial}{\partial y}\left(\frac{UV}{h}\right) + \frac{\partial}{\partial x}\left(\frac{g+ß}{2} + \frac{\alpha}{3}\right)h\Big) = -(g+ß+\frac{\alpha}{2})h\,\frac{\partial z}{\partial x} - g\,\frac{U\sqrt{U^2+V^2}}{C^2 h^2}$$

$$\frac{\partial V}{\partial t} + \frac{\partial}{\partial x}\left(\frac{UV}{h}\right) + \frac{\partial}{\partial y}\left(\frac{V^2}{h}\right) + \frac{\partial}{\partial y}\left(\left(\frac{g+ß}{2} + \frac{\alpha}{3}\right)h\right) = -(g+ß+\frac{\alpha}{2})h\,\frac{\partial z}{\partial x} - g\,\frac{V\sqrt{U^2+V^2}}{C^2 h^2}$$

Where h is the water depth, U and V are x - and y - volume fluxes, z is the bed elevation, g the gravitational acceleration.

The new terms α and ß come from the new assumption, and characterize the vertical accelerations raised by the steepness of the waves and the slope of the bed :

$$\alpha = \frac{d^2h}{dt^2}\,,\quad ß = \frac{d^2z}{dt^2}\quad \left(\text{with } \frac{d}{dt} = \frac{\partial}{\partial t} + \frac{U}{h}\frac{\partial}{\partial x} + \frac{V}{h}\frac{\partial}{\partial y}\right)$$

A condition at the seaward boundary which simulates entering waves in the model at the seaward boundary and allows outgoing waves, is introduced in the following form :

$$-\vec{V}.\vec{n} + C\,(h + z) = (1 - \vec{u}.\vec{n})\,C\,Wi$$

where $\vec{V}$ is the volume flux
$\vec{n}$ is the outgoing unit-vector, perpendicular to the boundary side.
$\vec{u}$ is the unit - vector of propagation direction
Wi is the sea surface elevation of the incident wave
C is the wave celerity

The same sort of condition has been imposed on inside boundaries to model partial reflections :

$$-\vec{V}.\vec{n} + C\,(1 - r)\,(h + z) = 0$$

Where r is a coefficient of reflection (if r = 1 : total reflection, if r = 0 : no reflection).

3. AGITATION IN THE PORT OF FECAMP

The calculation is fitted to computations of non-linear agitation (periodic or not) in harbours of any bathymetry, including partial reflections. It has been used in the case of the port of Fecamp on the English Channel coast.

In 1970, a scale model was done in order to study the agitation in this port. The comparison between computed and scale model results has been performed to check the numerical model.

The figure 1 presents the port shape. Break-waters are situated along the sides of the access channel and the other boundaries are vertical quays. The wave characteristics at the entrance were very severe (height = 6m, period = 7s).

The available results of the physical model (fig. 2) display a great agitation in the center of the outer-harbour.

The characteristics of the calculation used are :

mesh dimension : DX = 3,5 m
time step : DT = 0,35 s

The free surface and the agitation contours are shown in figure 3 for a coefficient of reflection equal to 0,90 at the place of the break-waters. Considering the way of measuring agitation which smooths the agitation pattern, the computed results and the scale model results compare well since the computed agitation pattern displays the areas of great agitation in front of the "Grand Quai" and in the centre of the outer-harbour which appears in scale model.

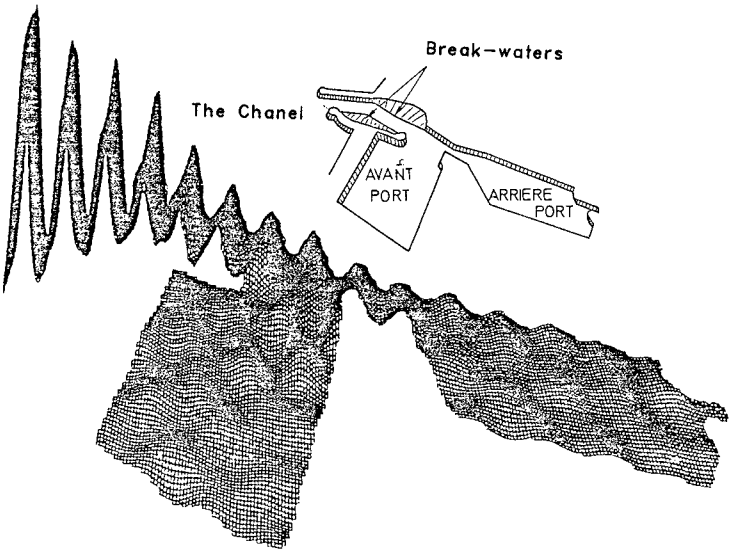

Fig.1 Computed Agitation Pattern

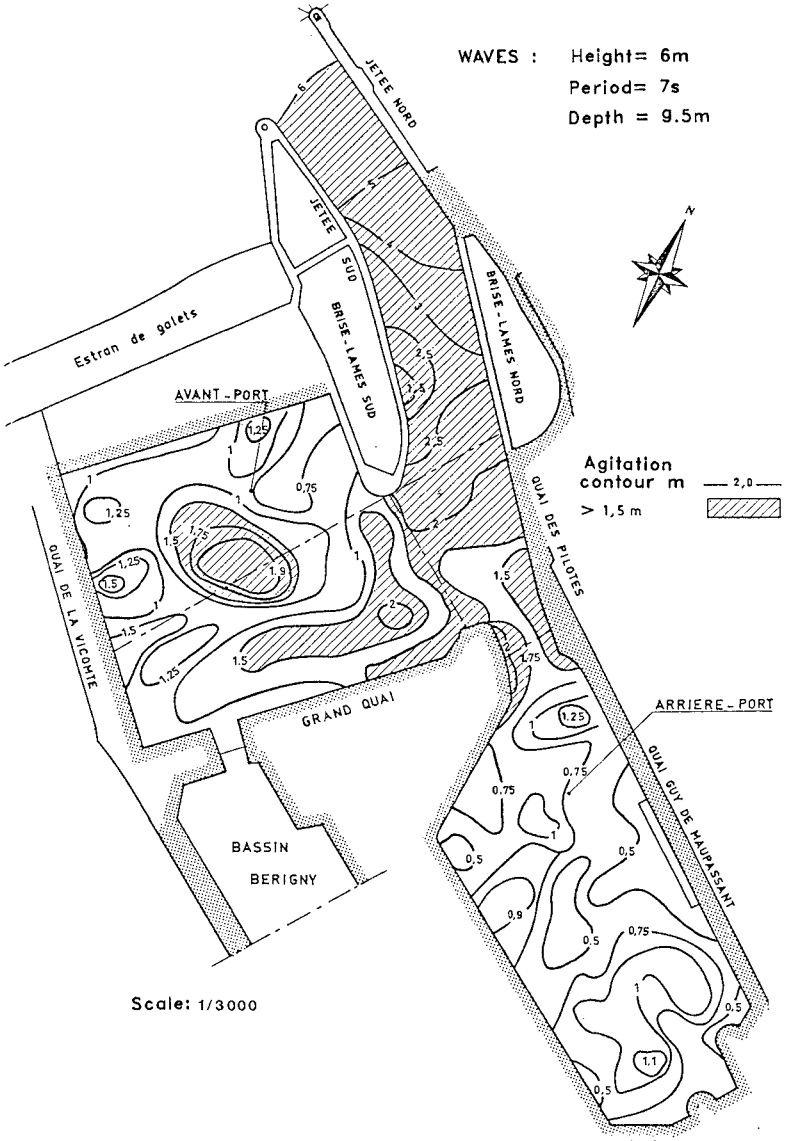

Fig.2 Agitation Contours of the Scale Model

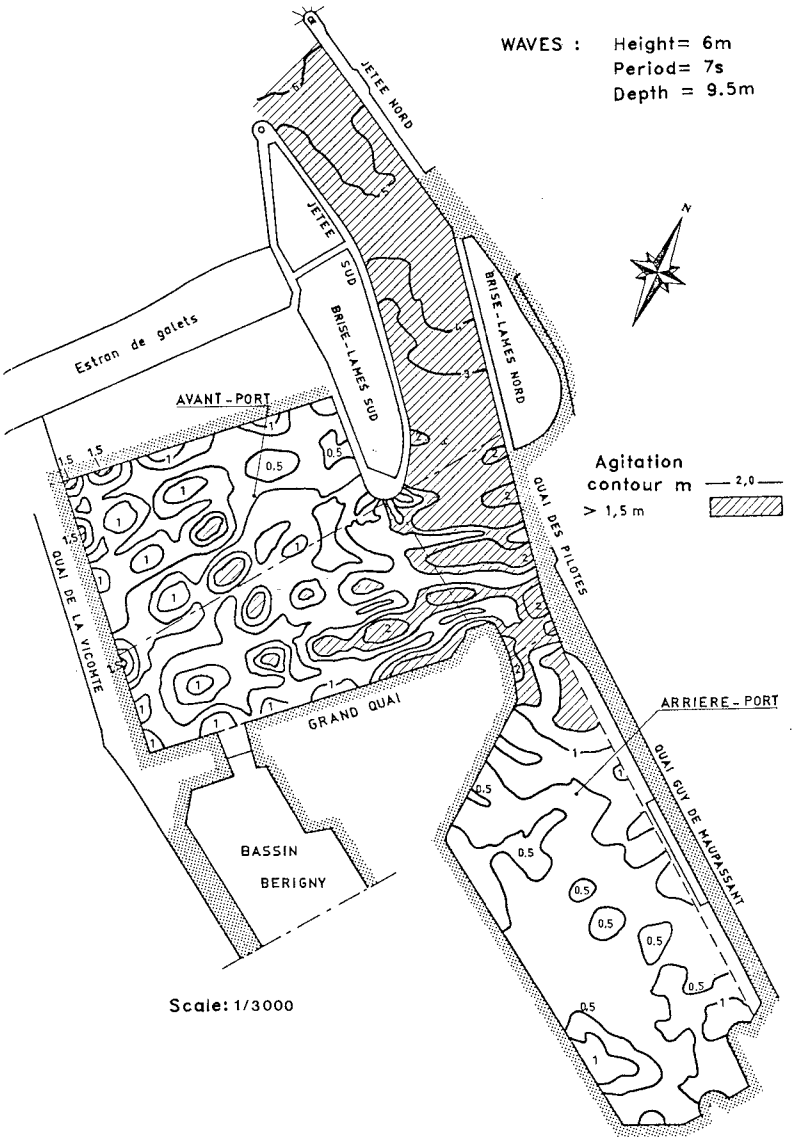

Fig.3 Agitation Contours of the Numerical Model

4. SUBMARINE LANDSLIDE NEAR NICE AIRPORT

As the model takes into account vertical accelerations resulting from the bottom shape, it allows the modelling of tsunamis. In october 1979, a mini-tsunami induced by a submarine landslide near the works of the new airport of Nice, damaged a part of the coast of "La Baie des Anges" in Mediterranean sea.

The introduction of sea-bottom changes, from the bathymetry before the tsunani to the bathymetry after it, has induced the rising of the wave (figure 4).

The model has been able to reproduce the first waves which occurred at the beginning of the landslide but secondary waves of great height which appeared 3 minutes after the first ones were not reproduced in the numerical model. This results shows that the secondary waves did not come from reflection effects but that they could be induced by turbidity currents or a second landslide.

5. SIMULATION OF BREAKING WAVES

Description

A simulation of breaking waves has been added in the numerical model. Taking into account the fluctuation of velocity (u', v') over the depth, the following terms appear in the governing equations :

$$\bar{\bar{T}} = \frac{1}{h} \begin{bmatrix} \int_0^h u'^2 \, dz & \int_0^h u' v' \, dz \\ \int_0^h u' v' \, dz & \int_0^h v'^2 \, dz \end{bmatrix}$$

Assuming an analogy with Fick's law for turbulent momentum fluxes, the tensor T is written :

$$\bar{\bar{T}} = - R \, \mathrm{grad} \, \vec{V}$$

Where $\vec{V}$ is the average of horizontal velocity over the depth.

Before breaking, the dispersion coefficient R is equal to zero, whereas it is high in the breaking zone so that the large variations of velocity over the depth in the breaking zone are simulated.

Wave breaking is assumed to occur at the location where the wave height H exceeds the Weggel's criterion :

$$H = (b(m) - a(m) \frac{H}{T^2}) \quad d$$

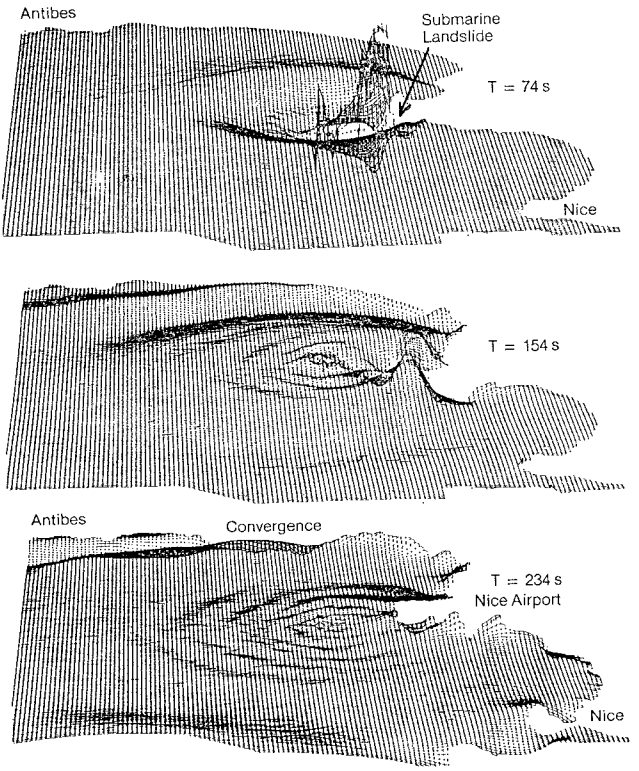

Fig.4 Simulation of a Submarine Landslide Near Nice Airport

Where m = bottom slope
T = period
d = still water depth (wave set-up is neglected).
$a(m) = 4,46\ (1 - e^{-19m})$
$b(m) = 1 / 0,64 \cdot (1 + e^{-19,5m})$.

The simulation of breaking waves has been tested over two cases :

- in a flume with a constant sloped bottom, using a one dimensional model

- in a rectilinear beach, limited by two groynes, under the action of waves with an offshore incidence of 30°.

One - dimensional model

The propagation and the breaking of waves over a constant sloped bottom has been tested in a flume geometry with various wave conditions and slope values.

When the wave height is smaller than Weggel's criterion, the dispersion coefficient is equal to zero.

When this criterion is reached, the dispersion coefficient is high from the breaking line to the coast. This value is chosen so that the ratio of wave height over still water depth is constant in this domain.

The bottom friction is assumed to be proportional to the squared velocity :

$$\vec{\pi} = - \frac{\rho g}{C^2} \vec{V} ||\vec{V}||$$

Considering Naher's studies, the coefficient of Chezy is equal to 25 $m^{1/2}/s$.

The obtained propagation in the flume is presented in fig. 5, with the following characteristics.

Off-shore wave conditions: period 9 s, wave height 2 m

Bottom slope 1,3 °/₀

Dispersion coefficient in the surf zone : 5 m^2/s
out the surf zone : 0 m^2/s

At first the wave is refracted and its height increases. When the height exceeds Weggel's criterion, the wave breaks, the height decreases from the breaking line to the coast. The wave surge coming from the wave energy loss has been obtained in the surf zone. In this case, the set-up is of 0,47 m.

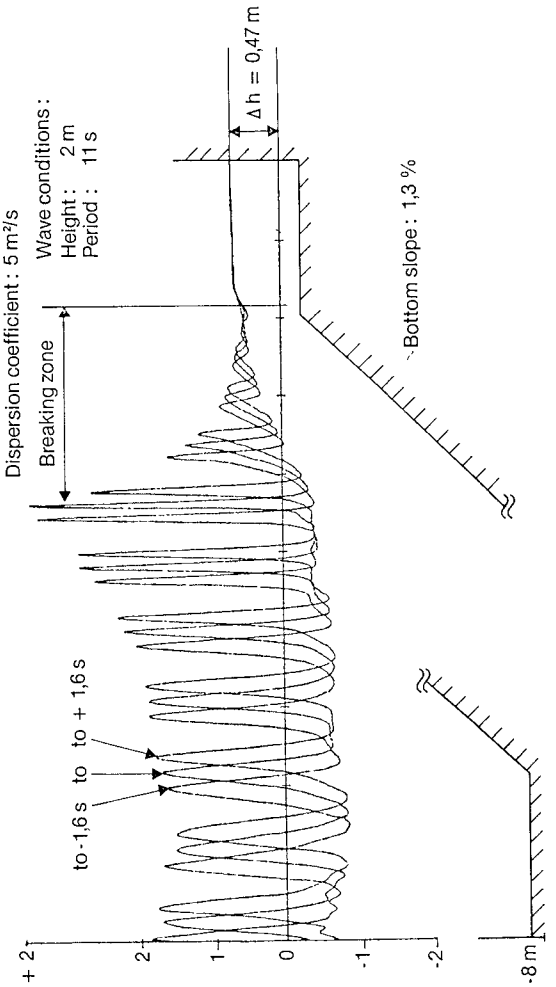

Fig.5 Wave Breaking Test with a One-dimensional Model

The dispersion coefficient has been estimated for various values of the slope and of the ratio of the wave-height over the wave length (fig. 6)

The one-dimensional tests have shown that the numerical model is able to simulate wave breaking and to predict wave surge.

A two-dimensional case has been computed to simulate longshore currents.

Two - dimensional model

The current induced by breaking waves has been studied in a 700 meters length rectilinear shore, limited by two groynes under the action of waves generated at the seaward boundary (fig. 7)

The off-shore wave conditions are : height 3 m
period 12 s
angle of incidence 30°

The mean level set-up at the coast is equal to 0,21 m (fig. 8)

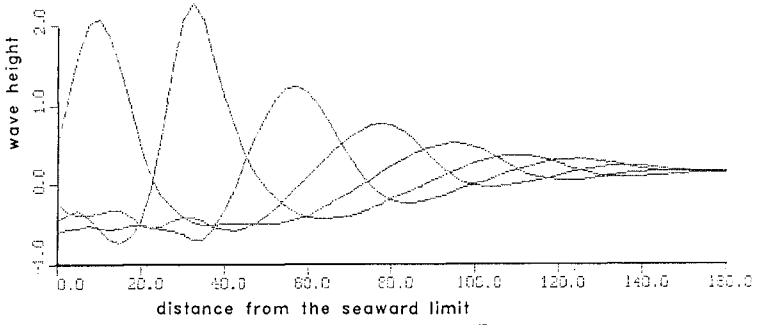

Fig.8 Wave Propagation along Section A-A

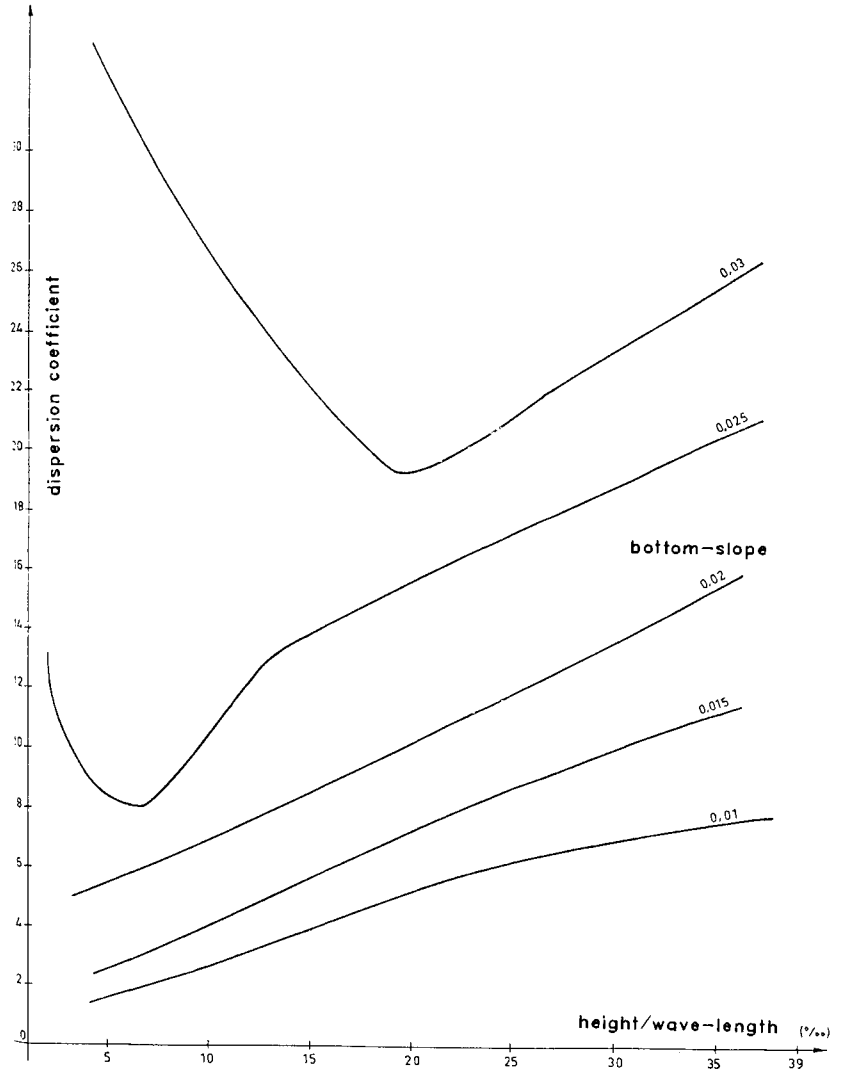

Fig.6 Dispersion coefficient R

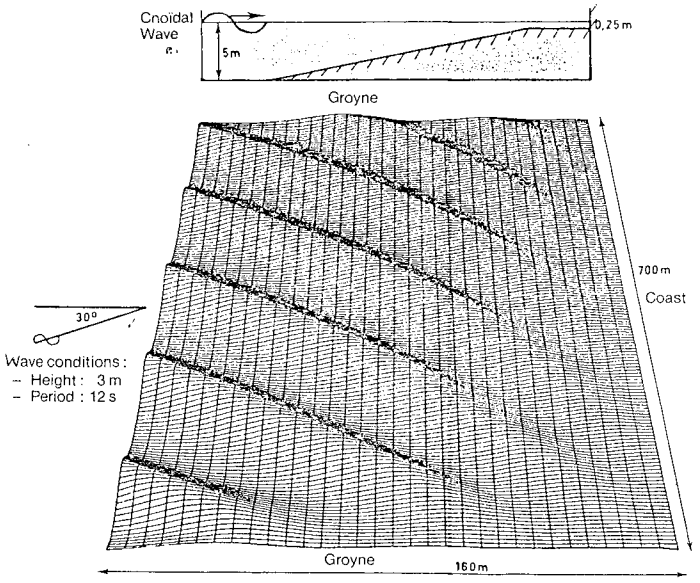

Fig.7 Simulation of Longshore Currents

The fig. 9 shows the instantaneous fluxes and the longshore current obtained by averaging fluxes over a period. A mean current parallel to the coast appears ; this is in good agreement with natural phenomenon. But a current takes place in the domain between the off-shore limit and the breaking line, in the opposite direction. Vortices appear between these two zones. This last current is due to the boundary condition which permits the waves to go out of the domain but prevents mean currents to go out.

The velocity distribution in a section perpendicular to the coast is shown on fig 10. The maximum value does not reach 0,3 m/s. This value seems rather small compared to measurements in scaled models or in nature. The reason of this difference could be imputed to the back current.

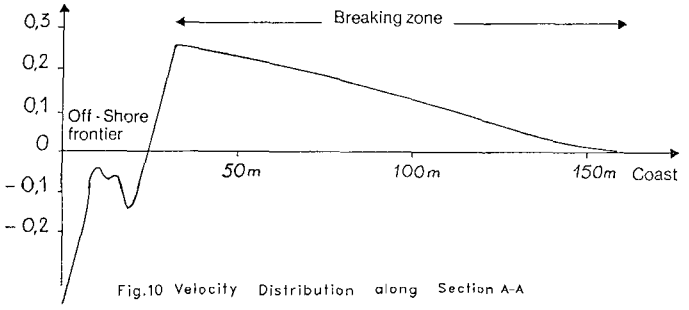

Fig.10 Velocity Distribution along Section A-A

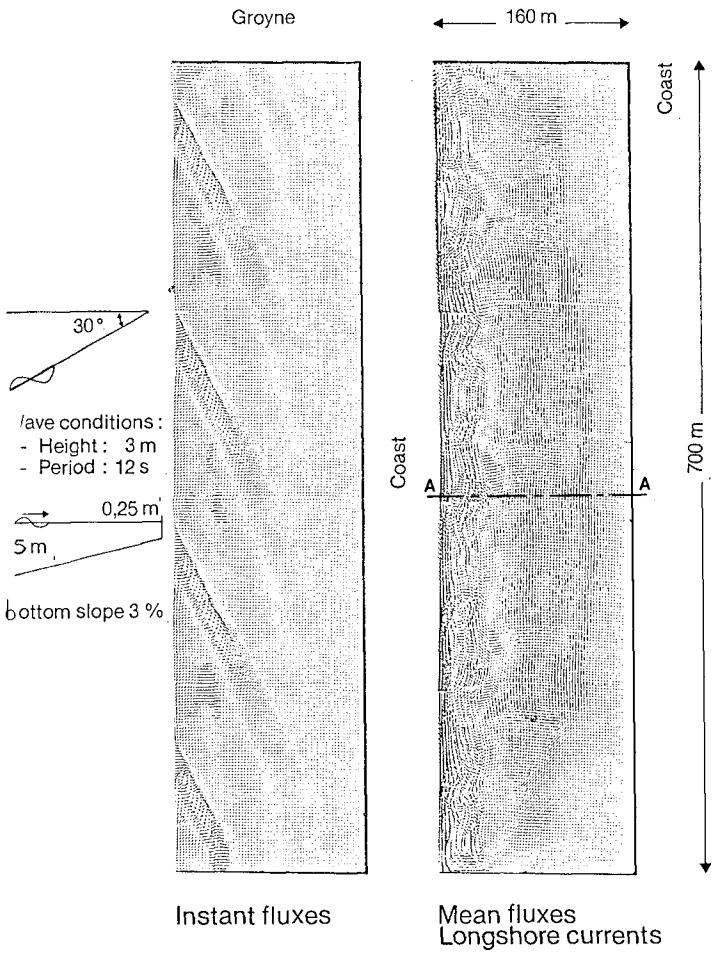

Fig.9 Fluxes Pattern in a Reactilinear Shore

6. CONCLUSION

The results of the numerical model applied to the agitation in the port of Fecamp and the submarine landslide near Nice airport show that the model is able to compute refraction, diffraction and reflection for non linear waves over any given bathymetry with a good accuracy.

The model appears to be very useful for breaking waves studies applied to longshore currents predictions. In the near future such results could give interesting informations for sedimentological studies concerning sea-bottom evolutions under waves action.

As the cost of numerical models is moderate in front of physical models, it is thought that the use of such numerical models in studies will increase substantially.

7. ACKNOWLEDCEMENT

This study was supported in part by the French "MINISTERE DE LA MER".

8. REFERENCES

HAUGUEL, A. (1980). Adaptation of tidal numerical models to shallow water waves problems. 17th I.C.C.E. Sydney pp 277-278.

LEPETIT, J.P., CLIQUE, P.M. and HERVOUET, J.M. (1981). Courants de houle après déferlement.
Modélisation unidimensionnelle du déferlement.
Rapport Electricité de France, HE/42/81.16.

NAHER, E. (1978) The damping of solitary waves. J. Fluid Mechanics vol. 76 past 1 p 177-185.

On the Variation of Characteristics of Two Wave Trains Crossing in Intermediate Depth

by

*Dr. H. H. Hwung** *C. P. Tsai***

ABSTRACT

In this paper , the authors paid attention to the non-linear interaction of two free wave trains crossing in intermediate water depth. From theoretical approaches , the velocity potential and water surface elevation have been expanded to the second-order by perturbation method. And wave height , velocity of fluid particles , pressure distribution , wave thrust and energy density of the common wave are also investigated. In order to verify the theoretical results , elaborated and numerous experiments have been performed. Some of the remarkable coincidence are obtained and the conclusions have been presented in this paper.

1. *INTRODUCTION* :

Concerning the non-linear interaction of the shortcrested waves has been obtained by Fuchs (1952) *for a second-order solution. Chappelear* (1961) *extended this to third-order in the same manner using a formal power expansion. Hsu & Silve-*

* *Associate Professor of Hydraulics and Ocean Eng. Graduate School , National Cheng-Kung University , Tainan , Taiwan , Rep , of China.*
Director of Tainan Hydraulics Laboratory.
** *Graduate Student of Institute of Oceangraph , National Taiwan University , Taipei , Rep. of China.*

ster (1979) have also presented the third-order solution which encompass all angles of incidence and can be extended to the limits for both standing and stokes waves. Further , the second-order Eulerian water particle velocities throughout the bottom boundary layer , mass transport of the first approximation and the limiting cases of progressive and standing waves have been obtained by Hsu , Silvester and Tsuchiya (1980). A comparision is also made with their available experimental data.

The above comprehensive program of research on short-crested waves are only applicable for the same period and height of the two component waves. However , for the non-linear interaction between pairs of intersecting gravity wave trains of arbitrary wavelength and direction on the surface in deep water has been developed by O. M. Phillips (1960). And the conclusion was made that the second-order terms give rise to Fourier components with wave numbers and frequencies formed by the sums and differences of those of primary components , and the amplitudes of these secondary components is always bounded in time and small in magnitude. But the third-order terms can give rise to tertiary components whose amplitude grows linearly with time in a resonant manner as the interactions are satisfied to the resonance loop. Furthermore , Longuet-Higgins (1962) has found that the rate of growth of the tertiary wave with time is a maximum when $\theta \doteqdot 17°$; the rate of growth with horizontal distance is a maximum when $\theta \doteqdot 24°$, where θ denotes the angle between the two primary wave components.

Based on the approaching method of Longuet-Higgins (1962) , *the paper presents the second-order solutions of*

velocity potential and wave profile after two wave trains crossing in intermediate water depth. Then the water particle velocity , pressure distribution , wave thrust and energy desity are also investigated. Moreover , the verification of the experiments has been performed in the laboratory.

2. *THEORETICAL APPROACH*

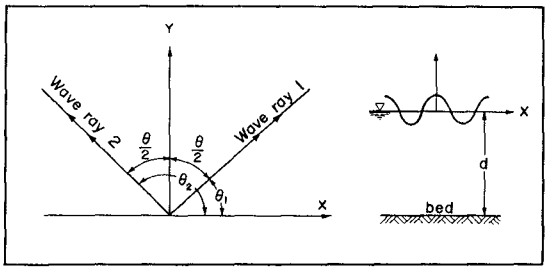

Fig. 1

Let us suppose that two free wave trains are crossing in the uniform , impervious intermediate water depth as shown in Fig. 1. *Since the presence of vorticity is very small , so that it is permissible to assume the existence of a potential function ϕ for the velocity U in an imcompressible non-viscous flow : thus*

$$U = \nabla \phi \quad , \quad \nabla^2 \phi = 0 \qquad \cdots\cdots\cdots(1)$$

And let Z be the vertical coordinate , then we have the dynamic condition at the free surface , as

$$g\eta+\phi_t+\frac{1}{2}U^2=F(t) \qquad at\ Z=\eta \qquad \cdots\cdots\cdots(2)$$

where $F(t)$ is Bernoulli's constant for linear case , but the nonlinear which can be expressed by Longuet-Higgins (1953)

$$F(t)=\left(\frac{1}{2}\overline{\eta^2}\right)_{tt}+\frac{1}{2}\left(\overline{(\nabla_h\phi)^2}-\overline{w^2}\right) \qquad \cdots\cdots\cdots(3)$$

Here " — " denotes the average for wave period and

$$\nabla_h=\left(\frac{\partial}{\partial x},\frac{\partial}{\partial y}\right)$$

The kinematic condition at the free surface is

$$\eta_t-\phi_z+\phi_x\eta_x+\phi_y\eta_y=0 \qquad at\ Z=\eta \qquad \cdots\cdots\cdots(4)$$

For notational simplicity that it is better to denote the partial differentiation by the subscript , $\phi_x=\partial\phi/\partial x$ $\phi_{tz}=\partial^2\phi/\partial t\,\partial z$ etc. Then taking the material derivative , D/Dt , of eq (2) *and subtracting g times eq* . (4) *, we obtain*

$$\phi_{tt}+g\phi_z+(U^2)_t+U\cdot\nabla\left(\frac{1}{2}U^2\right)=0 \qquad at\ Z=\eta \qquad \cdots\cdots\cdots(5)$$

Now let eq . (2) *and eq* . (5) *be expanded in Taylor's series about $Z=0$ to give*

$$g\eta+\left[\phi_t+\eta\phi_{tz}+\frac{1}{2}\eta^2\phi_{tzz}+\cdots\right]+\left[\frac{1}{2}U^2+\eta\left(\frac{1}{2}U^2\right)_z+\cdots\right]=Q$$

$$at\ Z=0 \qquad \cdots\cdots\cdots(6)$$

$$\{(\phi_{tt}+g\phi_z)+\eta(\phi_{tt}+g\phi_z)_z+\cdots\}+\{(U^2)_t+\eta(U^2)_{tz}+\cdots\}$$

$$+\{U\cdot\nabla(\frac{1}{2}U^2)+\cdots\}=0 \qquad at\ Z=0 \qquad \cdots\cdots(7)$$

Suppose that we define ϕ_{ij} , η_{ij} , U_{ij} *and* Q_{ij} *by the formal expressions* :

$$\left.\begin{aligned}
\phi &= (\alpha\phi_{10}+\beta\phi_{01})+(\alpha^2\phi_{20}+\alpha\beta\phi_{11}+\beta^2\phi_{02})+\cdots\cdots\\
\eta &= (\alpha\eta_{10}+\beta\eta_{01})+(\alpha^2\eta_{20}+\alpha\beta\eta_{11}+\beta^2\eta_{02})+\cdots\cdots\\
U &= (\alpha U_{10}+\beta U_{01})+(\alpha^2 U_{20}+\alpha\beta U_{11}+\beta^2 U_{02})+\cdots\cdots\\
Q &= (\alpha Q_{10}+\beta Q_{01})+(\alpha^2 Q_{20}+\alpha\beta Q_{11}+\beta^2 Q_{02})+\cdots\cdots
\end{aligned}\right\}\ \cdots\cdots(8)$$

where α , β *are to be small , independent and proportional to the surface slopes ,* $\alpha\phi_{10}$ *and* $\beta\phi_{01}$ *represent the first approximation of two crossing wave trains. The remaining terms represent wave interaction. Then substitute eq.* (8) *in eq.* (1) , (6) , (7) , *that we obtain* :

$0(\alpha)$:

$$\nabla^2\phi_{10}=0 \qquad \cdots\cdots(9)$$

$$g\eta_{10}+\phi_{10t}=Q_{10} \qquad at\ Z=0 \qquad \cdots\cdots(10)$$

$$\phi_{10tt}+g\phi_{10z}=0 \qquad at\ Z=0 \qquad \cdots\cdots(11)$$

$$\phi_{10z}=0 \qquad at\ Z=-d \qquad \cdots\cdots(12)$$

$0(\alpha^2)$:

$$\nabla^2 \phi_{20} = 0 \qquad \cdots\cdots(13)$$

$$g\eta_{20} + \phi_{20t} + \eta_{10}\phi_{10tz} + \frac{1}{2}U_{10}^2 = Q_{20} \quad at\ Z = 0 \qquad \cdots\cdots(14)$$

$$\phi_{20tt} + g\phi_{20z} + \eta_{10}(\phi_{10tt} + g\phi_{10z})_z + (U_{10}^2)_t = 0 \quad at\ Z = 0 \cdots\cdots(15)$$

$$\phi_{20z} = 0 \qquad at\ Z = -d \qquad \cdots\cdots(16)$$

$0(\alpha\beta)$:

$$\nabla^2 \phi_{11} = 0 \qquad \cdots\cdots(17)$$

$$g\eta_{11} + \phi_{11t} + \eta_{10}\phi_{01tz} + \eta_{01}\phi_{10tz} + U_{10} \cdot U_{01} = Q_{11} \quad at\ Z = 0 \qquad \cdots\cdots(18)$$

$$\phi_{11tt} + g\phi_{11z} + \eta_{10}(\phi_{01tt} + g\phi_{01z})_z + \eta_{01}(\phi_{10tt} + g\phi_{10z})_z + 2(U_{10} \cdot U_{01})_t = 0 \qquad at\ Z = 0 \qquad \cdots\cdots(19)$$

$$\phi_{11z} = 0 \qquad at\ Z = -d \qquad \cdots\cdots(20)$$

And the terms of $0(\beta)$, $0(\beta^2)$ *are the same expressions as* $0(\alpha)$, $0(\alpha^2)$ *but the subscript of* 10, 20 *from eq.* (9) *through eq.* (16) *will be changed by* o1, o2. *If we assume that the water is intermediate for the first-and second-order waves that the solutions will be obtained as* :

$$\phi_{10} = A_1 \cosh k_1(z+d) \sin\varphi_1 \qquad \cdots\cdots(21)$$

$$\eta_{10} = \frac{\sigma_1 A_1}{g} \cosh k_1 d \cos\varphi_1 \qquad \cdots\cdots(22)$$

$$\sigma_1^2 = g k_1 \tanh k_1 d \qquad \cdots\cdots(23)$$

$$\phi_{20} = \frac{3}{8} \frac{k_1^2 A_1^2}{\sigma_1 \sinh^2 k_1 d} \cosh 2 k_1 (z + d) \sin 2\varphi_1 \qquad \cdots\cdots(24)$$

$$\eta_{20} = \frac{k_1^2 A_1^2}{4 g} \frac{\cosh^2 k_1 d (\cosh 2 k_1 d + 2)}{\sinh^2 k_1 d} \cos 2\varphi_1 \qquad \cdots\cdots(25)$$

and

$$\phi_{01} = B_1 \cosh k_2 (z + d) \sin\varphi_2 \qquad \cdots\cdots(26)$$

$$\eta_{01} = \frac{\sigma_2 B_1}{g} \cosh k_2 d \cos \varphi_2 \qquad \cdots\cdots(27)$$

$$\sigma_2^2 = g k_2 \tanh k_2 d \qquad \cdots\cdots(28)$$

$$\phi_{02} = \frac{3}{8} \frac{k_2^2 B_1^2}{\sigma_2 \sinh^2 k_2 d} \cosh 2 k_2 (z + d) \sin 2\varphi_2 \qquad \cdots\cdots(29)$$

$$\eta_{02} = \frac{k_1^2 B_1^2}{4 g} \frac{\cosh^2 k_2 d (\cosh^2 k_2 d + 2)}{\sinh^2 k_2 d} \cos 2\varphi_2 \qquad \cdots\cdots(30)$$

for convenience , where

$$\varphi_1 = k_1 x - \sigma_1 t \quad \textit{and} \quad \varphi_2 = k_2 x - \sigma_2 t$$

Combining the solutions of the first-order from eq. (17) *through eq.* (20) *, then* ϕ_{11} *and* η_{11} *of the nonlinear term will also be found out.*

$$\phi_{11} = A_1 B_1 k_1 k_2 \left[\frac{F_1}{F_3} \cosh k' (z+d) \sin (\varphi_1 + \varphi_2) \right.$$

$$\left. + \frac{F_2}{F_4} \cosh k'' (z+d) \sin (\varphi_1 - \varphi_2) \right] \quad \cdots\cdots(31)$$

$$\eta_{11} = \frac{1}{g} A_1 B_1 k_1 k_2 \left\{ \left[(\sigma_1 + \sigma_2) \frac{F_1}{F_3} \cosh k' d + \frac{1}{4} G \right.\right.$$

$$\left. \cdot \cosh (k_1 + k_2) d - \frac{1}{4} H \cosh (k_1 - k_2) d \right] \cos (\varphi_1 + \varphi_2)$$

$$+ \left[(\sigma_1 - \sigma_2) \frac{F_2}{F_4} \cosh k'' d - \frac{1}{4} H \cosh (k_1 - k_2) d \right.$$

$$\left.\left. + \frac{1}{4} G \cosh (k_1 + k_2) d \right] \cos (\varphi_1 - \varphi_2) \right\} \quad \cdots\cdots(32)$$

where

$$F_1 = \frac{1}{2} \left(\frac{\sigma_1^2}{\sigma_2} \frac{\sinh k_2 d}{\sinh k_1 d} + \frac{\sigma_2^2}{\sigma_1} \frac{\sinh k_1 d}{\sinh k_2 d} \right) + 2 (\sigma_1 + \sigma_2)$$

$$\left(\frac{\cos \theta}{2} \cosh k_1 d \cosh k_2 d - \frac{1}{2} \sinh k_1 d \sinh k_2 d \right)$$

$$F_2 = \frac{1}{2} \left(\frac{\sigma_1^2}{\sigma_2} \frac{\sinh k_2 d}{\sinh k_1 d} - \frac{\sigma_2^2}{\sigma_1} \frac{\sinh k_1 d}{\sinh k_2 d} \right) + 2 (\sigma_1 - \sigma_2)$$

$$\left(\frac{\cos \theta}{2} \cosh k_1 d \cosh k_2 d + \frac{1}{2} \sinh k_1 d \sinh k_2 d \right)$$

$$F_3 = (\sigma_1 + \sigma_2)^2 \cosh k' d - g k' \sinh k' d$$

$$F_4 = (\sigma_1 - \sigma_2)^2 \cosh k'' d - g k'' \sinh k'' d$$

$$G = \frac{(\sigma_1 + \sigma_2)^2}{\sigma_1 \sigma_2} - 2\cos^2 \frac{\theta}{2}$$

$$H = \frac{(\sigma_1 + \sigma_2)^2}{\sigma_1 \sigma_2} - 2\sin^2 \frac{\theta}{2}$$

$$k' = |K_1 + K_2|, \quad k'' = |K_1 - K_2|$$

$$\theta = |\theta_1 - \theta_2|$$

If a_1, a_2 denotes the amplitude of two primary wave components respectively. Then both of the velocity potential and water surface elevation function of the second-order solution of the common wave will be given by

$$\phi = \frac{a_1 g}{\sigma_1} \frac{\cosh k_1 (z+d)}{\cosh k_1 d} \sin\varphi_1 + \frac{a_2 g}{\sigma_2} \frac{\cosh k_2 (z+d)}{\cosh k_2 d} \sin\varphi_2$$

$$+ \frac{3}{8} a_1^2 \sigma_1 \frac{\cosh 2k_1 (z+d)}{\sinh^4 k_1 d} \sin 2\varphi_1 +$$

$$+ \frac{3}{8} a_2^2 \sigma_2 \frac{\cosh 2k_2 (z+d)}{\sinh^4 k_2 d} \sin 2\varphi_2 + \frac{a_1 a_2 \sigma_1 \sigma_2}{\sinh k_1 d \sinh k_2 d}$$

$$\cdot \left[\frac{F_1}{F_3} \cosh k' (z+d) \cdot \sin(\varphi_1 + \varphi_2) \right.$$

$$\left. + \frac{F_2}{F_4} \cosh k'' (z+d) \sin(\varphi_1 - \varphi_2) \right] \qquad \cdots\cdots (33)$$

$$\eta = a_1 \cos\varphi_1 + a_2 \cos\varphi_2 + \frac{a_1^2 k_1}{4} \frac{\cosh k_1 d}{\sinh^3 k_1 d} (\cosh 2k_1 d + 2) \cos 2\varphi_1 + \frac{a_2^2 k_2}{4} \frac{\cosh k_2 d}{\sinh^3 k_2 d} (\cosh 2k_2 d + 2) \cos 2\varphi_2$$

$$+ \frac{a_1 a_2 \sigma_1 \sigma_2}{\sinh k_1 d \sinh k_2 d} \cdot \{ [(\sigma_1 + \sigma_2) \frac{F_1}{F_3} \cosh k' d +$$

$$+ \frac{1}{4} G \cosh (k_1 + k_2) d - \frac{1}{4} H \cosh (k_1 - k_2) d]$$

$$\cdot \cos (\varphi_1 + \varphi_2) + [(\sigma_1 - \sigma_2) \frac{F_2}{F_4} \cosh k'' d$$

$$- \frac{1}{4} H \cosh (k_1 - k_2) d + \frac{1}{4} G \cosh (k_1 + k_2) d] \cos (\varphi_1 - \varphi_2) \} \quad \cdots\cdots (34)$$

From above two equations , examples of water surface elevation after two wave trains crossing are graphed in Fig. 2. and Fig. 3. In Fig. 2, curve A is the first-order solution of common wave , curve B is the solution of Stokes wave which obtained from the front of four terms on the left side of eq. (34) , and curve C is the solutiom of eq. (34) , also representing the condition of short-crested wave , as noted by Hsu et al (1979). In Fig. 3 , the dash-line and solid-line denotes the solution of first-order and second-order respectively , and it is evident that the period of the common wave is equal to the least common multiple of the two primary wave components.

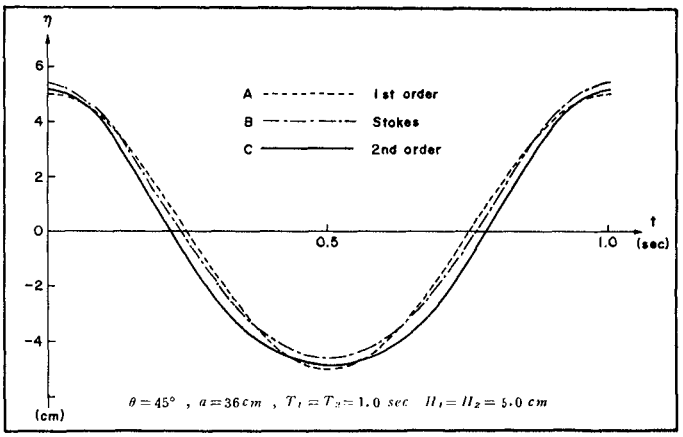
η
6
4
2
0
-2
-4
(cm)
A ---------- 1st order
B ——·——·—— Stokes
C ———— 2nd order
0.5
1.0
t
(sec)
θ=45° , a=36cm , T1=T2=1.0 sec H1=H2=5.0 cm

Fig. 2

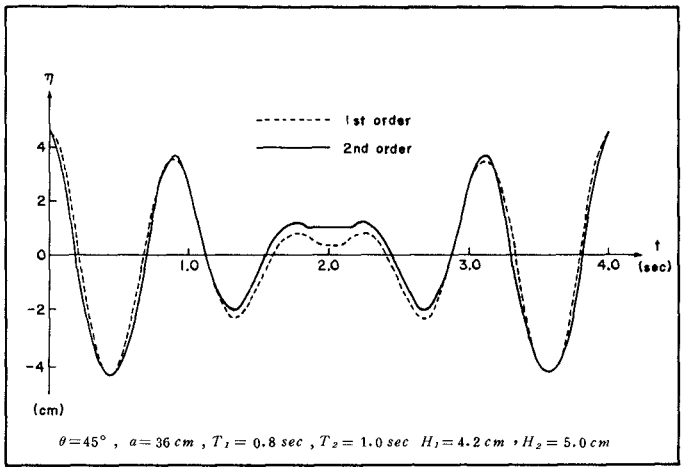
η
4
2
0
-2
-4
(cm)
--------- 1st order
———— 2nd order
1.0
2.0
3.0
4.0
t
(sec)
θ=45° , a=36 cm , T1=0.8 sec , T2=1.0 sec H1=4.2 cm , H2=5.0 cm

Fig. 3

Based on the velocity potential and water surface elevation funtion , the water particle velocity , pressure distribution , wave thrust and energy density can also be investigated as the following form :

(1) *water particle velocity :*

After two wave trains crossing , the components of water particle velocity (u , v , w) for the second-order can be expressed as

$$u = u_1 \cos\varphi_1 + u_2 \cos\varphi_2 + u_3 \cos 2\varphi_1 + u_4 \cos 2\varphi_2 + + u_5 \cos(\varphi_1 + \varphi_2) + u_6 \cos(\varphi_1 - \varphi_2) \quad \cdots\cdots(35)$$

$$v = v_1 \cos\varphi_1 + v_2 \cos\varphi_2 + v_3 \cos 2\varphi_1 + v_4 \cos 2\varphi_2 + + v_5 \cos(\varphi_1 + \varphi_2) + v_6 \cos(\varphi_1 - \varphi_2) \quad \cdots\cdots(36)$$

$$w = w_1 \cos\varphi_1 + w_2 \cos\varphi_2 + w_3 \cos 2\varphi_1 + w_4 \cos 2\varphi_2 + + w_5 \cos(\varphi_1 + \varphi_2) + w_6 \cos(\varphi_1 - \varphi_2) \quad \cdots\cdots(37)$$

from the above three equations , we have

$$(u_1, v_1, w_1) = \frac{a_1\sigma_1}{\sinh k_1 d}(\cos\theta_1 \cosh k_1(z+d), \sin\theta_1 \cosh k_1(z+d), \sinh k_1(z+d))$$

$$(u_2, v_2, w_2) = \frac{a_2\sigma_2}{\sinh k_2 d}(\cos\theta_2 \cosh k_2(z+d), \sin\theta_2 \cosh k_2(z+d), \sinh k_2(z+d))$$

$$(u_3, v_3, w_3) = \frac{3a_1^2\sigma_1 k_1}{4\sinh k_1 d}(\cos\theta_1 \cosh 2k_1(z+d),\ \sin\theta_1 \cosh 2k_1(z+d),\ \sinh 2k_1(z+d))$$

$$(u_4, v_4, w_4) = \frac{3a_2^2\sigma_2 k_2}{4\sinh^4 k_2 d}\{\cos\theta_2 \cosh 2k_2(z+d),\ \sin\theta_2 \cosh 2k_2(z+d),\ \sinh 2k_2(z+d)\}$$

$$(u_5, v_5, w_5) = \frac{a_1 a_2 \sigma_1 \sigma_2}{\sinh k_1 d \sinh k_2 d}\frac{F_1}{F_3} k'\{\cos\alpha_1 \cosh k_1(z+d),\ \sin\alpha_1 \cosh k'(z+d),\ \sinh k'(z+d)\}$$

$$(u_6, v_6, w_6) = \frac{a_1 a_2 \sigma_1 \sigma_2}{\sinh k_1 d \sinh k_2 d}\frac{F_2}{F_4} k''\{\cos\alpha_2 \cosh k''(z+d),\ \sin\alpha_2 \cosh k''(z+d),\ \sinh k''(z+d)\}$$

where , α_1 *is the angle between the vector of* (k_1+k_2) *and x axis* , α_2 *is the angle between* (k_1-k_2) *and x axis.*

$$\alpha_1 = \arctan\left(\frac{k_1\sin\theta_1 + k_2\sin\theta_2}{k_1\cos\theta_1 + k_2\sin\theta_2}\right)$$

$$\alpha_2 = \arctan\left(\frac{k_1\sin\theta_1 - k_2\sin\theta_2}{k_1\cos\theta_1 - k_2\cos\theta_2}\right)$$

(2) *pressure distribution* :

From Bernoulli's equation , the pressure can be expressured by the following form :

$$\frac{P}{\rho}=-gz-\phi_t-\frac{1}{2}u^2+F(t) \qquad \cdots\cdots(38)$$

from the perturbation method , and assume that

$$\frac{P}{\rho}+gz=(\alpha P_{10}+\beta P_{01})+(\alpha^2 P_{20}+\alpha\beta P_{11}+\beta^2 P_{02}+)\cdots \qquad \cdots\cdots(39)$$

$$F(t)=(\alpha F_{10}+\beta F_{01})+(\alpha^2 F_{20}+\alpha\beta F_{11}+\beta^2 F_{02})+\cdots \qquad \cdots\cdots(40)$$

then substitute eq (39) , (40) *and eq* (8) *in eq* (38) , *that we have* :

$$O(\alpha) \quad : P_{10}=-\phi_{10t}+F_{10} \qquad \cdots\cdots(41)$$

$$O(\alpha^2) : P_{20}=-\phi_{20t}-\frac{1}{2}\boldsymbol{u}_{10}^2+F_{20} \qquad \cdots\cdots(42)$$

$$O(\alpha\beta) : P_{11}=-\phi_{11t}-\boldsymbol{u}_{10}\cdot\boldsymbol{u}_{01}+F_{11} \qquad \cdots\cdots(43)$$

As for $O(\beta)$, $O(\beta^2)$ *which corresponds to* $O(\alpha)$, $O(\alpha^2)$ *but the subcripts* 10 , 20 , *will be changed into* 01 , 02 *respectively. Since* $F_{10}=F_{01}=0$, $F_{20}=\frac{1}{4}A_1^2k_1^2$, $F_{02}=\frac{1}{4}B_1^2k_1^2$ *and* $F_{11}=0$, *that the pressure after two wave trains crossing will be given by* :

$$\frac{P}{\rho}=-gz+a_1 g\,\frac{\cosh k_1(z+d)}{\cosh k_1 d}\cos\varphi_1+a_2 g\,\frac{\cosh k_2(z+d)}{\cosh k_2 d}\cos\varphi_2$$

$$+\frac{a_1^2 g k_1}{2\sinh 2k_1 d}\left\{\left[\frac{3\cosh 2k_1(z+d)}{\sinh^2 k_1 d}-1\right]\cos 2\varphi_1+\right.$$

$$+\left[1-\cosh 2k_1(z+d)\right]\}$$

$$+\frac{a_2^2 g k_2}{2\sinh 2k_2 d}\left\{\left[\frac{3\cosh 2k_2(z+d)}{\sinh^2 k_2 d}-1\right]\cos 2\varphi_2\right.$$

$$\left.+\left[1-\cosh 2k_2(z+d)\right]\right\}$$

$$+\frac{a_1 a_2 \sigma_1 \sigma_2}{\sinh k_1 d \sinh k_2 d}\left\{\left[(\sigma_1+\sigma_2)\frac{F_1}{F_3}\cosh k'(z+d)\right.\right.$$

$$-\frac{\cos\theta}{2}\cosh k_1(z+d)\cosh k_2(z+d)$$

$$\left.+\frac{1}{2}\sinh k_1(z+d)\sinh k_2(z+d)\right]\cos(\varphi_1+\varphi_2)$$

$$+\left[(\sigma_1-\sigma_2)\frac{F_2}{F_4}\cosh k''(z+d)-\frac{\cos\theta}{2}\cosh k_1(z+d)\right.$$

$$\left.\cdot\cosh k_2(z+d)-\frac{1}{2}\sinh k_1(z+d)\sinh k_2(z+d)\right]$$

$$\left.\cdot\cos(\varphi_1-\varphi_2)\right\} \qquad \cdots\cdots(44)$$

(3) *wave thrust*

From Longuet-Higgins & Stewart (1964) , *wave thrust will be written as the following form*

$$S_{ij}=\int_{-d}^{\eta}(P\delta_{ij}+\rho\mu_i\mu_j)\,dz+\int_{-d}^{0}\rho g z\,dz \qquad \cdots\cdots(45)$$

where " — " denotes the average of common wave period , and δ_{ij} *is Kronecker's delta. For the second-order approximation , then the above equation can be simplified as*

$$S_{ij} = \frac{1}{2}\rho g\overline{\eta^2}\delta_{ij} + \rho\int_{-d}^{0}\left(\overline{\mu_i\mu_j} - \overline{w^2}\delta_{ij}\right)dz \qquad \cdots\cdots(46)$$

thus :

$$S_{xx} = \frac{1}{2}\rho g\overline{\eta^2} + \rho\int_{-d}^{0}\left(\overline{u^2} - \overline{w^2}\right)dz \qquad \cdots\cdots(47)$$

$$S_{yy} = \frac{1}{2}\rho g\overline{\eta^2} + \rho\int_{-d}^{0}\left(\overline{v^2} - \overline{w^2}\right)dz \qquad \cdots\cdots(48)$$

$$S_{xy} = S_{yx} = \rho\int_{-d}^{0}\overline{uv}\,dz \qquad \cdots\cdots(49)$$

where S_{xx} , S_{yy} *represents the flux of horizontal momentum parallel to the* x , y *axis and* S_{xy} , S_{yx} *represents the flux of* $x-$, $y-$ *momentum across the plane* $y =$ *constant and* $x =$ *constant respectively. Then suppose* $E_1 = \frac{1}{2}\rho g a_1^2$, $E_2 =$ $E_2 = \frac{1}{2}\rho g a_2^2$, *that the components of wave thrust of the common wave will be given by*

$$S_{xx} = E_1\left\{\cos^2\theta_1\left(\frac{1}{2} + \frac{k_1 d}{\sinh 2k_1 d}\right) + \frac{k_1 d}{\sinh 2k_1 d}\right\}$$

$$+E_2\left\{\cos^2\theta_2\left(\frac{1}{2} + \frac{k_2 d}{\sinh 2k_2 d}\right) + \frac{k_2 d}{\sinh 2k_2 d}\right\}$$

$$+\frac{8E_1E_2k_1k_2}{\rho\sinh 2k_1 d\sinh 2k_2 d}\left\{\frac{F_1^2}{F_3^2}k'^2\left[\cos^2\alpha_1\left(\frac{\sinh 2k'd}{4k'} + \frac{d}{2}\right)\right.\right.$$

$$-\left(\frac{sinh2k'd}{4k'}-\frac{d}{2}\right)\Big]+\frac{F_2^2}{F_4^2}k''^2\Big[cos^2\alpha_2\left(\frac{sinh2k''d}{4k''}+\frac{d}{2}\right)$$

$$-\left(\frac{sinh2k''d}{4k''}-\frac{d}{2}\right)\Big]+\frac{1}{2g}\Big[\left(\sigma_1+\sigma_2\right)\frac{F_1}{F_3}\,cosk'd$$

$$+\frac{1}{4}Gcosh\left(k_1+k_2\right)d-\frac{1}{4}Hcosh\left(k_1-k_2\right)d\Big]^2$$

$$+\frac{1}{2g}\Big[\left(\sigma_1-\sigma_2\right)\frac{F_2}{F_4}\,coshk''d-\frac{1}{4}Hcosh\left(k_1-k_2\right)d$$

$$+\frac{1}{4}Gcosh\left(k_1+k_2\right)d\Big]^2\Big\} \qquad \cdots\cdots(50)$$

$$S_{yy}=E_1\left\{sin^2\theta_1\left(\frac{1}{2}+\frac{k_1d}{sinh2k_1d}\right)+\frac{k_1d}{sinh2k_1d}\right\}$$

$$+E_2\left\{sin^2\theta_2\left(\frac{1}{2}+\frac{k_2d}{sinh2k_2d}\right)+\frac{k_2d}{sinh2k_2d}\right\}$$

$$+\frac{8E_1E_2k_1k_2}{\rho sinh2k_1dsinh2k_2d}\Big\{\frac{F_1^2}{F_3^2}k'^2\Big[sin^2\alpha_1\left(\frac{sinh2k'd}{4k'}+\frac{d}{2}\right)$$

$$-\left(\frac{sinh2k'd}{4k'}-\frac{d}{2}\right)\Big]+\frac{F_2^2}{F_4^2}k''^2\Big[sin^2\alpha_2\left(\frac{sinh2k''d}{4k''}+\frac{d}{2}\right)$$

$$-\left(\frac{sinh2k''d}{4k''}-\frac{d}{2}\right)\Big]+\frac{1}{2g}\Big[\left(\sigma_1+\sigma_2\right)\frac{F_1}{F_3}\,coshk'd$$

$$+\frac{1}{4}Gcosh\left(k_1+k_2\right)d-\frac{1}{4}Hcosh\left(k_1-k_2\right)d\Big]^2$$

$$+\frac{1}{2g}\Big[\left(\sigma_1-\sigma_2\right)\frac{F_2}{F_4}\,coshk''d-\frac{1}{4}Hcosh\left(k_1-k_2\right)d$$

$$+\frac{1}{4}Gcosh\left(k_1+k_2\right)d\Big]^2\Big\} \qquad \cdots\cdots(51)$$

$$S_{xy}=S_{yx}=E_1\{\sin 2\theta_1\left(\frac{k_1 d}{2\sinh 2k_1 d}+\frac{1}{4}\right)\}$$

$$+E_2\{\sin 2\theta_2\left(\frac{k_2 d}{2\sinh 2k_2 d}+\frac{1}{4}\right)\}+\frac{8E_1E_2k_1k_2}{\rho\sinh 2k_1 d\sinh 2k_2 d}$$

$$\cdot\{\frac{F_1^2}{F_3^2}k'^2\left[\sin 2\alpha_1\left(\frac{d}{2}+\frac{\sinh 2k' d}{4k'}\right)\right]$$

$$+\frac{F_2^2}{F_4^2}k''^2\left[\sin 2\alpha_2\left(\frac{d}{2}+\frac{\sinh 2k'' d}{4k''}\right)\right]\} \qquad \cdots\cdots(52)$$

(4) *average energy density* :

The total average energy density is the sum of the kinetic and potential energy density , thus

$$\overline{E}=\overline{E}_p+\overline{E}_k \qquad \cdots\cdots(53)$$

according to the definition that

$$\overline{E}_p=\overline{\int_{-d}^{\eta}\rho g z\,dz}-\int_{-d}^{0}\rho g z\,dz=\frac{1}{2}\rho g\overline{\eta^2} \qquad \cdots\cdots(54)$$

$$\overline{E}_k=\frac{1}{2}\rho\overline{\int_{-d}^{\eta}u^2 dz} \qquad \cdots\cdots(55)$$

Then substitute the solutions of η *and* U *in the eq.* (54) , (55) , *the second-order solution of average energy density will be given by*

$$\overline{E}=(E_1+E_2)+\frac{2E_1E_2k_1k_2}{\rho\sinh 2k_1 d\sinh 2k_2 d}\{\frac{F_1^2}{F_3^2}k'^2\sinh 2k' d$$

$$+\frac{F_2^2}{F_4^2}k''sinh2k''d+\frac{2}{g}\left[\left(\sigma_1+\sigma_2\right)\frac{F_1}{F_3}coshk'd\right.$$

$$+\frac{1}{4}Gcosh\left(k_1+k_2\right)d-\frac{1}{4}Hcosh\left(k_1-k_2\right)d\Big]^2$$

$$+\frac{2}{g}\left[\left(\sigma_1-\sigma_2\right)\frac{F_2}{F_4}coshk''d+\frac{1}{4}Gcosh\left(k_1+k_2\right)d\right.$$

$$\left.-\frac{1}{4}Hcosh\left(k_1-k_2\right)d\Big]^2\right\} \qquad \cdots\cdots(56)$$

3. *EXPERIMENTAL RESULTS*

The experiments of two wave trains crossing in intermediate depth have been performed at Tainan Hydraulics Laboratory. A number of different testing runs are listed in Table. 1 , *and the comparison of the theoretical and experimental results are shown through Fig.* 4 *to Fig.* 10.

Table. 1

Run	θ	d (*cm*)	T_1 (*sec*)	T_2 (*sec*)	H_1 (*cm*)	H_2 (*cm*)	H_1/L_1	H_2/L_2	d/L_1	d/L_2
1	45°	36	1.0	1.0	4.0	4.0	0.028	0.028	0.252	0.252
2	45°	36	0.8	0.8	4.8	4.8	0.049	0.049	0.367	0.367
3	45°	36	0.8	0.8	3.2	6.4	0.032	0.064	0.367	0.367
4	45°	32	0.9	0.9	4.0	4.0	0.034	0.034	0.271	0.271
5	45°	36	0.8	1.0	4.8	4.0	0.049	0.028	0.367	0.252
6	45°	30	0.7	0.8	5.2	4.0	0.069	0.047	0.400	0.313
7	45°	32	0.7	0.9	4.4	4.0	0.058	0.034	0.421	0.271

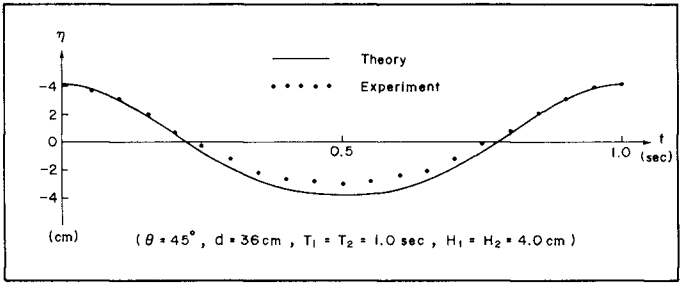

Fig. 4

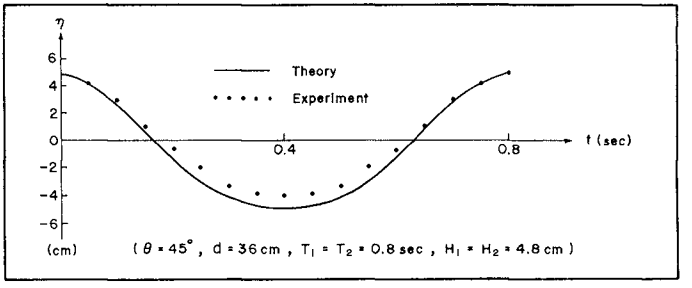

Fig. 5

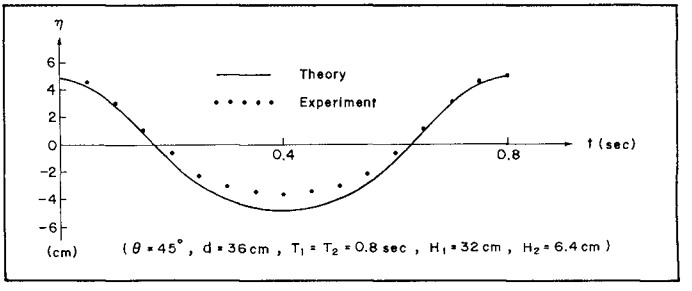

Fig. 6

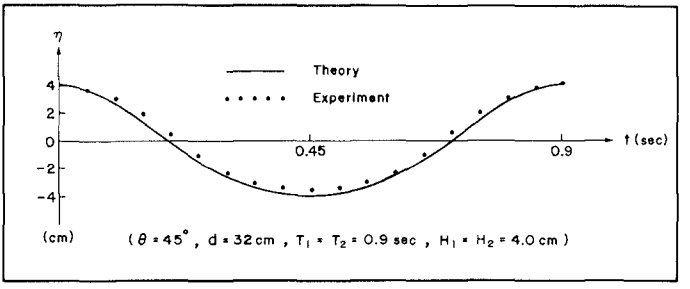

Fig. 7

The variation of water surface elevation for the same wave period and height or the same period but different wave height of two primary wave components crossing are illustrated from Fig. 4 to Fig. 7. It is obvious from these figures that the profiles of common wave are sinusoidal curves and the theoretical values of common wave height are just equal to the sum of two primary waves. Although , those of the experimental values are less than theoretical values but they are coincident very well. The above mentioned results are in agreement with Hsu (1979).

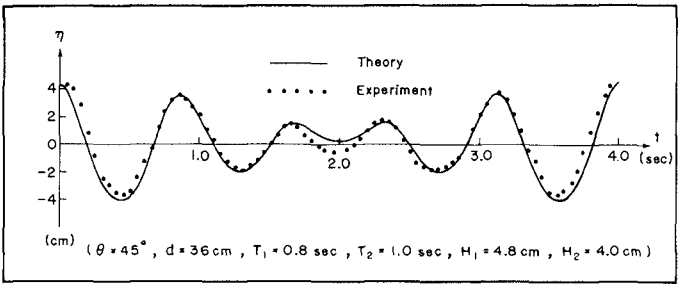

Fig. 8

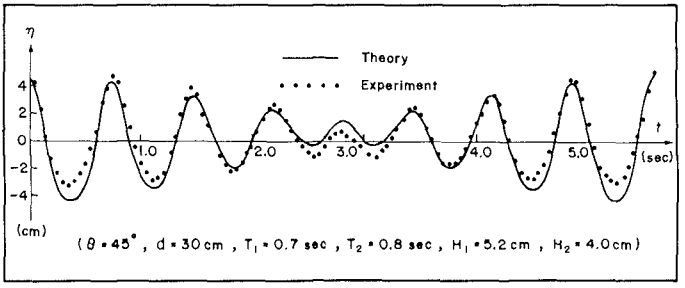

Fig. 9

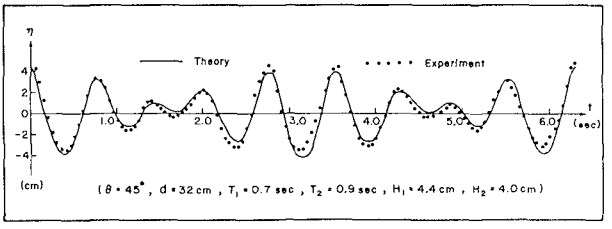

Fig. 10

Moreover, for the cases of different wave period and height, the variation of water surface elevation are shown from Fig. 8 *to Fig.* 10. *It is interested to find that the period of common wave are equal to the least common multiple of two primary wave components exactly and wave profiles of common wave are more complicated but the available experimental data are also coincident with theoretical curves. The comparative values of the theoretical and experimental results are presented in Table.* 2.

Table. 2

Run	T_1 (sec)	T_2 (sec)	H_1 (cm)	H_2 (cm)	H_t^* (cm)	H_p^* (cm)	H_1+H_2 (cm)	$\sqrt{H_1^2+H_2^2}$ (cm)	$\frac{H_t}{\sqrt{H_1^2+H_2^2}}$	$\frac{H_p}{\sqrt{H_1^2+H_2^2}}$
1	1.0	1.0	4.0	4.0	8.0	7.2	8.0	5.66	1.414	1.272
2	0.8	0.8	4.8	4.8	9.6	8.8	9.6	6.79	1.414	1.296
3	0.8	0.8	3.2	6.4	9.6	8.7	9.6	7.16	1.341	1.215
4	0.9	0.9	4.0	4.0	8.0	7.5	8.0	5.66	1.414	1.325
5	0.8	1.0	4.8	4.0	8.6	8.2	8.8	6.25	1.376	1.312
6	0.7	0.8	5.2	4.0	9.0	9.0	9.2	6.56	1.372	1.372
7	0.7	0.9	4.4	4.0	8.0	8.2	8.4	5.95	1.345	1.378

$*H_t$ *is the theoretical value ,* H_p *is the experimental value.*

4. *CONCLUSIONS*

In this paper , the authors pay attentiom to the non-linear interaction of two free wave trains crossing in intermediate water depth. From theoretical approaches , the velocity potential and water surface elevation have been expanded to the second order by perturbation method. And wave height , velocity of fluid particles , pressure distribution , wave thrust and energy density of the common wave are also investigated. In order to verify the theoretical results , elaborated and numerous experiments have also been performed in our laboratory. Some of the remarkable conclusions can be submitted as follows :

(1) *After the interaction of two free wave trains , the common wave period is just equal to the least common multiple (L.C.M.) of the period of two primary component waves.*

(2) *From the theoretical calculation and experimental verification of the non-linear wave interactions , the maximum common waves height are higher about* 20 % *to* 41.4 % *than those derived from energy superposition.*

(3) *It is well simplified from the theoretical results developed by the authors : as* $k_1 = k_2$, $a_1 = a_2$, *that it becomes short-crest waves ; as* $k_1 = -k_2$, $a_1 = a_2$, *it becomes standing wave and as* $k_1 = k_2$, $a_1 = a_2$ *it becomes stokes progressive wave. Here* $k_1 = |K_1|$, $k_2 = |K_2|$. K_1 , K_2 *and* a_1 , a_2 *are wave numbers vector and wave amplitude of the two primary wave components respectively.*

The tertiary interactions are proceeding continuously in our series researches and will be presented later.

REFERENCES

1. *Benney , D.J.* (1962) : " *Non-linear gravity wave interactions.* " *J. Fluid Mech.* 14 , *pp.* 577 - 584.
2. *Bretherton , F.P.* (1964) : " *Resonant interactions between waves.* " *J. Fluid Mech.* 20 , *pp.* 457 - 480 .
3. *Chappelear , J.E.* (1961) : " *On the descriptiom of short-crested waves.* " *Beach Erosion Bd , U.S. Army , Corps Engrs , Tech. Memo. No.* 125
4. *Fuchs , R.A.* (1952) : " *On the theory of short-crested oscillatory waves.* " *Gravity waves , U.S. Nat. Bur. Stand. Circular No.* 521 , *pp.* 187 - 200
5. *Hasselmann , K.* (1962) : " *On the non-linear energy transfer in a gravity wave spectrum.* " *part* 1 , *J. Fluid Mech.* 12 , *pp.* 481 - 500
6. *Hasselmann , K.* (1963) : " *On the non-linear energy transfer in a gravity wave spectrum.* " *part* 2 , *J. Fluid*

Mech. 15 , *pp* , 273 - 481

7. *Hsu , J. R. C.* (1979) : " *Short-crested water waves.* " *The thesis is prepared for his degree of Philosophy at the Univ. of Western Australia , Advised by Silvester , R., Dep. of Civil Eng.*
8. *Jeffreys , H.* (1924) : " *On the formation of water waves by wind ,* " *Proc. Roy. Soc. A* , 107. *pp.* 189 - 206.
9. *Kinsman , B.* (1965) : " *Wind waves* " *Englewood cliffs , N.J. : Prentice-Hall Inc*
10. *Longuet-Higgins , M.S.* (1953) : " *On the decrease of velocity with depth in an irrotaional water waves.* " *Proc. Camb. Phil. Soc.* 49 (3) , *pp.* 552 - 560
11. *Longuet-Higgins , M.S.* (1962) : " *Resonant between two trains of gravity waves.* " *J. Fluid Mech.* 12 , *pp.* 321 - 332
12. *Longuet-Higgins , M. S. and Phillips , O.M.* (1962) : " *Phase velocity effects in tertiary wave interactions.* " *J. Fluid Mech.* 12 , *pp.* 333 - 336
13. *Longuet-Higgins , M. S. and Stewart , R.W.* (1964) : " *Radiation stress in water waves ; a physical discussion with applications* " *Deep-Sea Res. Vol.* 11. *pp.* 529 ~ 562
14. *Phillips , O.M.* (1960) : " *On the dynamics of unsteady gravity waves of finite amplitude.* " *part.* 1 , *J. Fluid Mech.* 9 , *pp.* 193 - 217

INTEGRAL PROPERTIES FOR VOCOIDAL THEORY AND APPLICATIONS

G.P. Bleach

ABSTRACT

A comparison is made between two reference frames that can each be used to define "still water" for finite amplitude waves on water of finite depth. The reference frame characterized by zero mass flux due to the waves is used to find some exact relations between the wave integral properties. The averaged Lagranian (wave action) approach and the energy/momentum approach to the interaction of finite amplitude waves with slowly-varying currents are also derived in this reference frame. Results in many cases are simpler than those in the more commonly chosen reference frame characterized by zero mean horizontal velocity under the waves.

An application of the integral properties is made to Vocoidal wave theory, which is defined in the zero mass flux frame. It is shown that the rotation present in the orbital velocity field of Vocoidal waves is not always negligible.

INTRODUCTION

In the study of periodic surface gravity waves of finite amplitude on water of finite depth, Stokes (1847) considered two reference frames that can be used to define "still water". These are:

(i) reference frame R1, characterized by zero mean horizontal velocity beneath the wave trough;

(ii) reference frame R2, which has zero mass flux associated with the waves.

Stokes showed that these two reference frames are not equivalent (see section 2, equation (2.7); also Peregrine (1976)) and a choice must be made between them. Most surface gravity wave theories have used R1 to define still water; Stokes (1847) and Cokelet (1977) are examples. An exception in this respect is Vocoidal theory, defined in R2. (Swart and Loubser 1978, 1979a, b). Despite the predominance of R1, there has been recent interest in the use of R2. Reinecker and Fenton (1981) note that wave tank measurements often have zero mass flux, which makes comparison with wave theories defined in R1 more difficult. Whitham (1974) and Jonsson (1978) consider R2 to be valuable in the

Department of Physical Oceanography, University of Cape Town, S.A.

analysis of wavetrains on slowly-varying currents in water of slowly-varying depth. Stiassnie and Peregrine (1979) also speculate on the possible benefits of R2 for such wave/current work.

In view of this interest in R2 and prompted by the availability of the Vocoidal wave theory defined in R2, it was decided to investigate in R2 both the wave integral properties of Longuet Higgins (1975) and the equations governing wave/current interactions as given by Crapper (1979) and Stiassnie and Peregrine (1979). Results are presented for the transformations of wave integral properties between R1 and R2, for exact relations between the integral properties in R2 and for the governing equations for finite amplitude waves interacting with currents varying slowly along the stream. In numerous cases the relative simplicity of the results in R2 compared to those in R1 is evident, particularly in the wave/current interaction equations. This is true for both the momentum/energy interaction equations (Phillips (1966)) and for the averaged Lagranian approach to wave/current interaction (Whitham (1974)).

An application of the integral properties is made in R2 to Vocoidal theory in order to ascertain the amount of rotation present in the only orbital velocity field. It is found that the rotation is negligible only for deep water waves of small amplitude (approximating Airy waves) and for shallow water waves of large amplitude (nearly solitary waves).

REFERENCE FRAMES FOR PERIODIC GRAVITY WAVES ON STILL WATER

In this section the reference frames R1 and R2 are defined and compared. Two dimensional inviscid irrotational motion is assumed and periodic surface gravity waves are considered. The waves propagate in the positive x direction with the z axis vertical, positive upwards, and y is reserved for (later) use as the remaining horizontal coordinate. The bottom is flat and located at $z = -h$.

The most general form of the velocity potential for a periodic surface gravity wave is (Peregrine 1976)

$$\phi = \Phi(\chi,z) + \bar{u}x - \gamma t, \tag{2.1}$$

where the phase χ is related to the wavenumber k and frequency ω (relative to a fixed observer) by

$$\chi \equiv kx - \omega t. \tag{2.2}$$

Φ is the periodic part of ϕ and the constants $\bar{u}$ and γ are determined by the choice of horizontal and vertical reference frames respectively. $\bar{u}$ represents a depth independent current and γ is related to the mean water level. Here, t is taken as zero for convenience and γ is dispensed with (although it can always be found from the Bernoulli equation) until later.

Vertical reference frame

The choice made here is that z = o at the mean water level, i.e.

$$\overline{\overline{\eta}} \equiv o \tag{2.3}$$

where $$\overline{\eta} \equiv \frac{1}{\lambda}\int_o^\lambda \eta dx \tag{2.4}$$

and $\eta(\chi)$ is the wave elevation.

Horizontal reference frame

The reference frame is to be chosen so that there is no background current. There are two obvious choices, firstly to choose the mean horizontal velocity beneath the wave trough to be zero (reference frame R1) and secondly to choose the mass flux associated with the wave (reference frame R2) to be zero.

zero mean horizontal velocity (R1): $\overline{u} \equiv \frac{1}{\lambda}\int_o^\lambda u dx = o$ (2.5)

zero mass flux (R2): $$\overline{u}_m \equiv \frac{1}{\lambda h}\int_o^\lambda \int_{-h}^{\eta} = o \tag{2.6}$$

$\overline{u}$ is the mean horizontal velocity from the velocity potential ϕ and $\overline{u}_m$ is the (Eulerian) mass flux velocity.

Stokes (1847) showed that $\overline{u}$ and $\overline{u}_m$ are not equivalent, since $\overline{u}_m$ can be rewritten as follows, using ϕ from (2.1).

$$\overline{u}_m \equiv \frac{1}{\lambda h}\int_o^\lambda\int_{-h}^{\eta} \frac{\partial\phi}{\partial x}\, dzdx$$

$$= \frac{1}{\lambda h}\int_o^\lambda \int_{-h}^{\eta} \left(\frac{\partial\Phi}{\partial x} + \overline{u}\right) dzdx$$

Since $\overline{\eta} \equiv o$, $$\overline{u}_m = \frac{1}{\lambda h}\int_o^\lambda \int_{-h}^{\eta} \frac{\partial\Phi}{\partial x}\, dzdx + \overline{u} \tag{2.7}$$

The remaining integral for Φ is the average mass flux velocity due to the periodic wave motion and turns out to be positive, so $\overline{u}_m > \overline{u}$.

A choice must therefore be made between R1 and R2. The latter is not often used, despite the advantages mentioned earlier. These advantages are now explored below with the definition in R2 of wave integral properties and the relations they satisfy (following Longuet-Higgins' (1975) work in R1), followed by the analysis of wave/current interaction in the following section.

INTEGRAL PROPERTIES AND THE EXACT RELATIONS BETWEEN THEM

Integral properties for periodic surface gravity waves involve wave properties that have been averaged over the phase χ. If the averaging is done at a particular time t, this is equivalent to an average over the wavelength λ. Longuet-Higgins (1975) defined gravity wave

integral properties and derived relations between them, working in R1 in almost all cases. (See also Crapper 1979).

Here the transformations between R1 and R2 are given, followed by definition of the integral properties in R2 and the derivation of the relations they satisfy.

Notation: (i) printed quantities are those defined in R2

(ii) an overbar $\overline{(\ )}$ denotes $\frac{1}{\lambda}\int_0^\lambda (\ )dx$ throughout

Let U_r be defined as the velocity of translation of R2 with respect to R1. The velocities u and $\overline{u}$ and the velocity potential ϕ transform as follows:

$$u' = u - U_r \tag{3.1}$$

$$\overline{u}' \equiv \frac{1}{\lambda}\int_0^\lambda u'dx = \frac{1}{\lambda}\int_0^\lambda udx - U_r$$

$$\therefore \quad \overline{u}' = -U_r \text{ using (2.5)} \tag{3.2}$$

$$\phi' = \phi - U_r x \tag{3.3}$$

Integral properties for periodic surface gravity waves

The following definitions of the wave integral properties are essentially of Longuet-Higgins with the density ρ inserted. They are not yet specific to any reference frame. All definitions are per unit horizontal surface area.

Mean mass flux $$I \equiv \frac{\rho}{\lambda}\int_0^\lambda\int_{-h}^{\eta} u\, dzdx \tag{3.4}$$

$$= \rho h\, \overline{u}_m \qquad \text{by (2.6)}$$

Mean kinetic energy $$T \equiv \frac{\rho}{2\lambda}\int_0^\lambda\int_{-h}^{\eta} (u^2+w^2)dzdx \tag{3.5}$$

Mean potential energy $$V \equiv \frac{\rho}{\lambda}\int_0^\lambda\int_0^{\eta} gz\, dzdx \tag{3.6}$$

Radiation stress component $$S_{xx} \equiv \frac{\rho}{\lambda}\int_0^\lambda\int_{-h}^{\eta} [\frac{p}{\rho} + u^2]dzdx - \tfrac{1}{2}\rho g h^2 \tag{3.7}$$

Mean energy flux $$F \equiv \frac{\rho}{\lambda}\int_0^\lambda\int_{-h}^{\eta} [\frac{p}{\rho} + \tfrac{1}{2}(u^2+w^2)+gz]u\, dzdx \tag{3.8}$$

Additional quantities used by Longuet Higgins are as follows:

Mass flux in the steady flow relative to an observer moving with the phase velocity c

$$-Q \equiv \rho \int_{-h}^{\eta} (u-c)dz \tag{3.9}$$

Bernoulli constant $$B \equiv p + \frac{\rho}{2}[u^2 - 2uc+w^2] + \rho gz \tag{3.10}$$

Total head $$R \equiv p + \frac{\rho}{2}[(u-c)^2 + w^2] + \rho g(z+h) \tag{3.11}$$

$$= B + \rho gh + \frac{\rho c^2}{2}$$

Transformations of the integral properties between R1 and R2

The quantities defined in (3.4-11) are transformed from R1 to R2 by using (3.1-3). The relations (2.5, 2.6) that define R1, R2 are then used to simplify the results.

eg. mass flux $$I' \equiv \frac{\rho}{\lambda}\int_0^{\lambda}\int_{-h}^{\eta} u'dzdx \quad \text{by (3.4)}$$

$$= \frac{\rho}{\lambda}\int_0^{\lambda}\int_{-h}^{\eta} (u-U_r)dzdx$$

$$= I - \rho hU_r$$

Since $I' \equiv 0$, $$I = \rho hU_r \tag{3.12}$$

$$T' = T - \frac{\rho hU_r^2}{2} \tag{3.13}$$

$$S' = S_{xx} - \rho hU_r^2 \tag{3.14}$$

$$F' = F - U_r[3T-2V + \rho h\overline{(u_b)^2}] \tag{3.15}$$

where u_b is the u velocity component at the bottom (z = -h), the pressure p' = p and the vertical velocity w' = w.

The constants Q', B', R' are found to be:

$$Q' = Q \tag{3.16}$$

$$B' = B + \rho U_r[c-U_r] \tag{3.17}$$

$$R' = R \tag{3.18}$$

Exact relations between the integral properties in R2

A number of exact relations between the integral properties are given by Longuet-Higgins (1975). All except his relation (2.4) are in R1 and here his approach is followed to derive the equivalent relations in R2, making use of the fact that $I' \equiv o$ and using some of the above transformations for confirmation of the results. The results of L.H. are given for comparison, with ρ inserted and referenced by his equation numbers (or letters).

$$Q' = \rho c' h \qquad (3.19)$$

$$Q = \rho c h - I \qquad \text{L.H.(A)}$$

$$2T' = \rho c' h U_r \qquad (3.20)$$

$$= Q' U_r \qquad \text{essentially L.H.(2.4)}$$

$$2T = c\, I \qquad \text{L.H.(B)}$$

$$2T' = \left(\frac{c'}{\lambda}\right) \int_o^\lambda \eta \{c' - [1+(\frac{\partial \eta}{\partial x})]^{\frac{1}{2}}[2R' - 2\rho g(h+\eta)]^{\frac{1}{2}}\}dx \qquad (3.21)$$

The corresponding expression for 2T is identical in form (L.H.(E)). (A typographical error in L.H.(E) is the omission of the first η symbol). Note that the choice $\overline{\eta} \equiv o$ (2.3) removes the $\eta c'$ term after integration.

$$S_{xx}' = 4\,T' - 3V' + \rho h\overline{(u_b')^2} \qquad (3.22)$$

where

$$\overline{(u_b')^2} = \overline{(u_b^2)} + U_r^2 \qquad (3.23)$$

The corresponding Sxx expression (L.H.(c)) is again identical in form to the R2 expression.

$$F' = [3\,T' - 2\,V' + \tfrac{1}{2}\rho h\overline{(u_b')^2}]c' \qquad (3.24)$$

$$F = [3\,T - 2\,V]c + \tfrac{1}{2}[\rho h c + I]\overline{u_b^2} \qquad \text{L.H.(3.10)}$$

Note that the energy flux relation is simpler in R2 since the I' term is zero. This type of simplification occurs frequently in the conservation equations to be derived below and is a primary advantage of working in R2.

CONSERVATION EQUATIONS FOR WAVES ON SLOWLY-VARYING CURRENTS OVER SLOWLY-VARYING TOPOGRAPHY

Phillips (1966) derived a set of conservation equations for waves interacting with depth-independent currents that vary slowly along or

across the stream. These equations are mass, momentum and energy equations that have been vertically integrated and then horizontally averaged. Whitham (1974) derived an alternative set via a variational approach and the two sets were made fully compatible by Stiassnie and Peregrine (1979). A general review of wave/current interactions is given by Peregrine (1976).

All the above work is effectively in R1; the mean horizontal velocity at a fixed point below the wave trough is the current velocity. Stiassnie and Peregrine speculate that it may be better to work in a reference frame in which the total mass flux divided by ρd (where d is the water depth) is the current; i.e. the wave mass flux is zero, which is the defining property of R2.

The present work follows Phillips' approach in R2 and confirmed that the governing equations take a simpler form than in R1. The alternative approach of Whitham is also investigated in R2 and expressions are found for Luke's Lagrangian (Luke 1967), the Bernoulli term γ' (2.1) and Whitham's averaged Lagrangian. Once a suitable wave theory has been chosen, the wave action equation can be derived from the averaged Lagrangian given here.

Notation and definitions

Motion is now in three dimensions and Greek subscripts refer to components in the horizontal ($x_1 = x$, $x_2 = y$) plane. Since slowly varying waves and currents may change the water level from its undisturbed value at $z = o$, the water depth is denoted by $d(x_\alpha t)$. The slowly varying bottom is at $z = -h(x_\alpha)$, and $\partial_{\alpha\beta} \equiv 1$ if $\alpha = \beta$, else $\partial_{\alpha\beta} \equiv o$.

$$d = \frac{1}{\lambda}\int_o^\lambda (\eta+h)dx \tag{4.1}$$

The integral properties (3.4-3.8) are easily generalised for motion in the (x,y) plane with mean water level at $z = d-h$; the overbar represents (as before) the average over the wavelength.

$$I'_\alpha \equiv \overline{\rho\int_{-h}^{\eta} u'_\alpha dz} \equiv o \tag{4.2}$$

$$T' \equiv \overline{\frac{\rho}{2}\int_{-h}^{\eta}(u'_\alpha u'_\alpha + w^2)dz} \tag{4.3}$$

$$V' \equiv \frac{\rho g}{2}[\overline{\eta^2} - (d-h)^2] \tag{4.4}$$

$$S'_{\alpha\beta} \equiv \overline{\rho\int_{-h}^{\eta}(u'_\alpha u'_\beta + \frac{p}{\rho}\partial_{\alpha\beta})dz} - \tfrac{1}{2}\rho g d^2\partial_{\alpha\beta} \tag{4.5}$$

$$F'_\alpha \equiv \rho\int_{-h}^{\eta} u'_\alpha[\tfrac{1}{2}(u'_\beta u'_\beta + w^2) + \frac{p}{\rho} + g(z+h-d)]dz \tag{4.6}$$

Averaged mass, momentum and energy conservation equations.

The kinematic conservation equation is common to both approaches and is (Peregrine (1976)):

$$\omega' = \sigma' + k'_\alpha U'_\alpha \tag{4.7}$$

where ω is (as before) the wave frequency relative to a fixed observer, σ' is the frequency relative to the current and U'_α are the components of the depth independent current.

The mass, momentum and energy conservation equations in R2 are derived following Crapper (1979) - essentially Phillips' approach. In each case, the flow velocity is split into $U'_\alpha + u'_\alpha$ in the local conservation equation and the equation is then integrated over depth and averaged over a wavelength, which introduces the integral properties (4.2-4.6). Boundary conditions and the zero mass flux condition (4.2) are used finally to simplify the results. The method is sketched below for the mass conservation equation and the results for mass, momentum and energy conservation are compared with the corresponding results in R1 obtained by Stiassnie and Peregrine.

Mass conservation.

Local continuity equation: $$\frac{\partial}{\partial x_\alpha}(U'_\alpha + u'_\alpha) + \frac{\partial w}{\partial z} = 0 \tag{4.8}$$

Now $$\frac{\partial}{\partial x_\alpha}\int_{-h}^{\eta}(U'_\alpha + u'_\alpha)dz - (U'_\alpha + u'_\alpha)_{z=\eta}\cdot\frac{\partial \eta}{\partial x_\alpha} - (U'_\alpha + u'_\alpha)_{z=-h}\frac{\partial h}{\partial x_\alpha}$$

$$+ w|_{z=\eta} - w|_{z=-h} = 0 \tag{4.9},$$

where Leibnitz' rule has been used to reverse the order of differentiation and integration.

The kinematic surface boundary condition is

$$\frac{\partial \eta}{\partial t} + (U'_\alpha + u'_\alpha)\frac{\partial \eta}{\partial x_\alpha} = w \qquad \text{at } z = \eta \tag{4.10}$$

and the corresponding bottom condition is

$$-(U'_\alpha + u'_\alpha)\frac{\partial h}{\partial x_\alpha} = w \qquad \text{at } z = -h \tag{4.11}$$

The mass conservation equation is obtained after inserting (4.10) and (4.11) into (4.9), averaging over a wavelength and using $I_\alpha \equiv 0$.

$$\rho\frac{\partial d}{\partial t} + \frac{\partial}{\partial x_\alpha}[\rho d U'_\alpha] = 0 \tag{4.12}$$

Compare the result (in R1) of Stiassnie and Peregrine:

$$\rho\frac{\partial d}{\partial t} + \frac{\partial}{\partial x_\alpha}[\rho d U_\alpha + I_\alpha] = 0 \tag{4.13}$$

(The mass conservation equation also appears in the averaged Lagrangian approach described later.)

Momentum conservation.

The momentum conservation equation is found similarly, and is:

$$\frac{\partial}{\partial t}(\rho d U'_\alpha) + \frac{\partial}{\partial x_\beta}[\rho d U'_\alpha U'_\beta + S'_{\alpha\beta} + \tfrac{1}{2}\rho g d^2 \partial_{\alpha\beta}] - \rho g d \frac{\partial h}{\partial x_\alpha} = 0 \tag{4.14}$$

Compare the R1 expression:

$$\frac{\partial}{\partial t}(\rho d U_\alpha + I_\alpha) + \frac{\partial}{\partial x_\beta}[(\rho d U_\alpha + I_\alpha)(\frac{I_\beta}{\rho d} + U_\beta) + S_{\alpha\beta} + \tfrac{1}{2}\rho g d^2 \partial_{\alpha\beta} - \frac{I_\alpha I_\beta}{\rho d}]$$

$$- \rho g d \frac{\partial h}{\partial x_\alpha} = 0 \tag{4.15}$$

Energy conservation.

Energy conservation in R2:

$$\frac{\partial}{\partial t}[\tfrac{1}{2}\rho d(U')^2 + \tfrac{1}{2}\rho g(d-h)^2 + T' + V']$$

$$+ \frac{\partial}{\partial x_\alpha}[U'_\alpha\{\frac{\rho d}{2}(U')^2 + \rho g d(d-h) + T' + V'\} + F'_\alpha + S'_{\alpha\beta} U_\beta] = 0 \tag{4.16}$$

Corresponding equation in R1:

$$\frac{\partial}{\partial t}[\tfrac{1}{2}\rho d U^2 + \tfrac{1}{2}\rho g(d-h)^2 + T + V + U_\alpha I_\alpha]$$

$$+\frac{\partial}{\partial x_\alpha}[U_\alpha\{\tfrac{1}{2}\rho d U^2 + \rho g d(d-h) + T + V + U_\beta I_\beta\} + F_\alpha + I_\alpha[g(d-h)+\tfrac{1}{2}U^2]$$

$$+ S_{\alpha\beta}U_\beta = 0 \tag{4.17}$$

The relative simplicity of the equations in R2 is clear, since all terms involving I_α' are eliminated.

Averaged Lagrangian approach to wave/current interactions

Whitham's method (Whitham (1974), Peregrine (1976), Crapper (1979)) requires a Lagrangian to be chosen and an averaged Lagrangian to be obtained for the system. Here, Luke's (1967) lagrangian is used in R2.

Luke's Lagrangian: $$L' \equiv -\rho\int_{-h}^{\eta}\left[\frac{\partial\phi'}{\partial t} + \tfrac{1}{2}\left(\frac{\partial\phi'}{\partial x_\alpha}\cdot\frac{\partial\phi'}{\partial x_\alpha} + \left(\frac{\partial\phi}{\partial z}\right)^2 + gz\right]dz \quad (4.18)$$

where $$\phi' \equiv U_\alpha' x_\alpha - \alpha' t + \Phi(\chi', z), \quad (4.19)$$

and $$\chi' \equiv k_\alpha' x_\alpha - \omega t \quad (4.20)$$

The averaged Lagrangian $\mathcal{L}'$ is defined as

$$\mathcal{L}' \equiv \frac{1}{2\pi}\int_0^{2\pi} L'\,d\chi' \quad (4.21)$$

Use of L' from (4.18) and choosing a particular value of t to make the phase integral equivalent to an integral over the wavelength, one obtains:

$$\mathcal{L}' = \rho d(\gamma' - \tfrac{1}{2}U_\alpha' U_\alpha') - T' - V' - \tfrac{1}{2}\rho g[(d-h)^2 - h^2] \quad (4.22)$$

Compare $$\mathcal{L} = \rho d(\gamma - \tfrac{1}{2}U_\alpha U_\alpha) + T - V - \tfrac{1}{2}\rho g[(d-h)^2 - h^2], \quad (4.23)$$

obtained by Crapper (1979) in R1. The discrepancy in sign of the kinetic energy term is removed if expressions for γ, γ' are found. The Bernoulli equation for the whole flow is evaluated at z = - h, averaged and then (3.20) is used in the R2 expression to obtain:

$$\gamma' = g(d-h) + \frac{U_\alpha' U_\alpha'}{2} + \frac{u_\alpha' u_\alpha'}{2}\Big|_{z=-h} + \frac{2T'}{\rho d} \quad (4.24)$$

$$\gamma = g(d-h) + \frac{U_\alpha U_\alpha}{2} + \frac{u_\alpha u_\alpha}{2}\Big|_{z=-h} \quad (4.25)$$

On inserting these expressions into (4.22) and (4.23) respectively, the form of the averaged Lagrangians $\mathcal{L}'$ and $\mathcal{L}$ is identical:

$$\mathcal{L}' = \rho d\left(\frac{u'_\alpha u'_\alpha}{2}\Big|_{z=-h} + \frac{gd}{2} + \frac{T'}{\rho} - \frac{V'}{\rho}\right) \qquad (4.26)$$

The averaged Lagrangian can be used to obtain a set of conservation equations for the wave/current interaction. These are the mass conservation equation (identical to (4.12)), consistency conditions replacing the momentum equations and the wave action equation which replaces the energy equation. (See Peregrine (1976)). This completes the analysis of the conservation equations in R2 and shows their relative simplicity compared to the more commonly used equations derived in R1.

APPLICATIONS OF THE INTEGRAL PROPERTIES TO VOCOIDAL WAVE THEORY

Swart and Loubser (1978, 1979a,b) developed the Vocoidal gravity wave theory in an attempt to provide a theory that was relatively simple to use yet accurate. Swart et al (1979) found that Vocoidal theory matched 600 experimental data sets better than twelve other commonly used wave theories. (Cokelet's theory was not considered due to its complexity). Two rather unusual features of Vocoidal theory are that it is defined in R2 and that the orbital velocity field contains a small amount of rotation. The integral properties (3.4) - (3.8) have been defined for Vocoidal theory, but not the exact relations between them and the wave/current results above. These relations and results are valid only for irrotational wave motion. In this section, the amount of rotation in Vocoidal theory is checked by investigating the vertical dependence of $\overline{u'}$ since $\overline{u'}$ is independent of depth for an irrotational motion. This is shown by considering $\frac{\partial u'}{\partial z}$.

$$\frac{\partial u'}{\partial z} = \frac{\partial}{\partial z}\left[\frac{1}{\lambda}\int_0^\lambda u'\,dx\right]$$

$$= \frac{1}{\lambda}\int_0^\lambda \frac{\partial u'}{\partial z}\,dx$$

Irrotationality $\Rightarrow$ $\frac{\partial u'}{\partial z} = \frac{\partial w'}{\partial x}$

$$\therefore \frac{\partial u'}{\partial z} = w'(\lambda) - w'(0)$$

$$= 0 \quad \text{by periodicity of } w' \qquad (5.1)$$

Numerical integration of u' at various depths below the wave trough for Vocoidal waves of various steepnesses in a variety of water depths indicates that the theory is virtually irrotational both for low waves in deep water, where Vocoidal theory tends to Airy theory, and for high waves in shallow water, where the Vocoidal wave is virtually a

solitary wave. For situations in between these extremes, the rotation causes $\overline{u^r}(z)$ to vary considerably with z. Two typical results are shown below in Table 1 for a wave of period 4,0 seconds in 1.0 m water depth. (The low wave/deep water equivalence of Vocoidal and Airy waves is not shown). The parameter Z_r shows the relative depth under the wave trough at which $\overline{u^r}(z)$ has been calculated; Z_r = o at the bottom and Z_r = 1 at the trough. H is the wave height (crest to trough).

Table 1: Mean horizontal velocity $\overline{u^r}(z)$ at various depths

H(m)	Z_r	$\overline{u'(z)}$ (m/s)
0,20	1,0	- 0,006
	0,9	- 0,009
	0,8	- 0,012
	0,7	- 0,014
	0,6	- 0,016
	0,5	- 0,018
	0,4	- 0,020
	0,3	- 0,021
	0.2	- 0,022
	0,1	- 0,022
	0,0	- 0,022
1,40	1,0	- 0,522
	0,9	- 0,530
	0,8	- 0,536
	0,7	- 0,542
	0,6	- 0,547
	0,5	- 0,551
	0,4	- 0,554
	0,3	- 0,557
	0,2	- 0,559
	0,1	- 0,560
	0,0	- 0,560

Because of the rotation present in the theory, the exact relations (3.21), (3,22), (3.24) are unlikely to be obeyed accurately.

Numerical integration of the appropriate Vocoidal expressions on the right hand side of (3.21,2,4) and comparison with the Vocoidal values for $2T'$, S'_{xx}, F' respectively shows that there is good agreement in deep water but divergences of up to 50% elsewhere.

CONCLUSIONS

Although the existence of the two reference frames R1 and R2 have long been known, (see Stokes 1847) there has been little use made of R2. In this paper, some advantages of R2 are demonstrated, namely that the exact relations between the integral properties are as simple or simpler in form than those in R1 and that the equations for the interaction of finite amplitude waves with slowly varying currents in water of slowly varying depth are considerably simplified. Transformations from R1 to R2 are also given to facilitate the use in R2 of a wave theory originally defined in R1.

Vocoidal theory is defined in R2 from the outset and could easily be used in the wave/current interaction equations presented here if it were not for the presence of a small amount of rotation. This rotation is investigated via the mass horizontal velocity below the trough and it is found that the rotation is small for deep water waves of small height and for steep shallow water waves.

The presence of rotation is also reflected in the inaccuracies found when the exact relations (3.21, 2, 4) are tested for Vocoidal theory.

A further test for rotation that would be of interest would be that proposed by Truesdell (see Serrin, 1959 - section 27) who defines the following parameter Ω as a measure of rotation:

$$\Omega \equiv \frac{\omega_r}{\sqrt{2\, D_{ij}\, D_{ij}}} \tag{6.1}$$

where ω_r is the magnitude of the angular velocity. Dij are the components (xz plane) of the deformation tensor

$$Dij \equiv \tfrac{1}{2}\left(\frac{\partial u_i}{\partial x_j} + \frac{\partial u_j}{\partial x_i}\right) \tag{6.2}$$

For irrotational motion, $\Omega = 0$ and for rigid rotation $\Omega = \infty$. Serrin uses $\Omega < 10\%$ as an indicator of the presence of significant rotation.

REFERENCES

COKELET, E.D. 1977: Steep gravity waves in water of arbitrary uniform depth. Phil. Trans. Roy. Soc. A286, 183-260.

CRAPPER, G.D. 1979: Energy and momentum integrals for progressive capillary-gravity waves. J. Fluid Mech. 94, 13-24.

JONSSON, I.G. 1978: Energy flux and wave action in gravity waves propagating on a current. J. Hydraulic Res. 16, 223-234.

LONGUET-HIGGINS, M.S. 1975: Integral properties of periodic gravity waves of finite amplitude. Proc. Roy. Soc. A342, 157-174.

LUKE, J.C. 1967: A variational principle for a fluid with a free surface. J. Fluid Mech. 27, 395-397.

PEREGRINE, D.H. 1976: Interactions of water waves and currents. Advances in Applied Mechanics 16, 9-117.

PHILLIPS, O.M. 1966: "The Dynamics of the Upper Ocean", Cambridge University Press.

REINECKER, M.M. and FENTON, J.D. 1981: A Fourier approximation method for steady water waves. J. Fluid Mech. 104, 119-137.

SERRIN, J. 1959: "Encyclopaedia of Physics, Volume VIII/I: Fluid Dynamics I". p 125-263.

STIASSNIE, M. and PEREGRINE, D.H. 1979: On averaged equations for finite-amplitude water waves. J. Fluid Mech. 94, 401-407.

STOKES, G.G. 1847: On the theory of oscillatory waves. Trans. Camb. Phil. Soc. 8, 441-455 (or: Math. Phys. Paper 1, 197-229 (1880)).

SWART D.H. et al. 1979: Vocoidal water wave theory. Data report 1. Documentation of computer program for evaluation of experimental and analytical validity of 13 wave theories. NRIO (CSIR) Memorandum 7917.

SWART, D.H. and LOUBSER, C.C. 1978: Vocoidal theory for all non-breaking waves. Proc. 16th Int. Conf. Coastal Eng.

SWART, D.H. and LOUBSER, C.C. 1979a: Vocoidal water wave theory. Volume 1. Derivation. CSIR Research Report 357.

SWART, D.H. and Loubser, C.C. 1979b: Vocoidal water wave theory. Volume 2. Verification. CSIR Research Report 360.

WHITHAM, G.B. 1974: "Linear and Non-Linear Waves". Wiley Interscience.

Struisbaai, near Cape Agulhas

PART II
COASTAL SEDIMENT PROBLEMS

Wilderness Cape Province

ARTIFICIAL MANIPULATION OF BEACH PROFILES

Timothy W. Kana[1] and Michael Svetlichny[2]

ABSTRACT

A field study was conducted at Myrtle Beach, South Carolina (U.S.A.), to determine the response of natural beaches to artificial manipulation by sand scraping. Between March 1981 and May 1982, a total of 100,000 m^3 of sand was shifted from the lower beach to the backbeach on three occasions over a 14-km length of shoreline. Fifty-four profile stations were surveyed to the -1.0 meter contour as many as ten times during the study to determine the effect of scraping and fill along a stable-to-slightly erosional beach. The purpose of the scraping and fill was to provide temporary erosion relief, protect existing dunes and structures, and provide a wider recreational beach at high tide. It was found that scraping and fill had little adverse effect on the beach cycle in the northern zone of the project area, which is fronted by a natural dune system. Fill placed at a gentle slope along the seaward margin of the dunes remained in place for up to ten months before eroding to the prefill surface. In contrast, similar quantities of fill along shore protection structures in the southern zone eroded in several weeks to four months. The study found significant differences in the response of armored versus unarmored shorelines with higher erosion rates and slower recovery of the beach at armored stations.

INTRODUCTION

A field study was conducted at Myrtle Beach, South Carolina (U.S.A.) to determine the response of a natural beach to artificial manipulation by sand scraping. One purpose of the study was to establish limiting criteria for the degree of berm or dune maintenance feasible on moderate energy sand beaches, without adverse impact to the natural beach cycle.

Several U.S. east coast beach communities including Ocean City, Maryland (Kerhin and Halka, 1981), and Hilton Head Island (South Carolina) have made a practice for a number of years of borrowing sand from the lower beach and backfilling the berm or dune area. In the case of Myrtle Beach, the purpose of the artificial beach manipulation has been to widen the recreational, high tide beach and reduce the erosion rate of dune scarps. This practice has been controversial

[1]Coastal Dynamics Division, Research Planning Institute, Inc., 925 Cervais Street, Columbia, South Carolina, U.S.A. 29201

[2]Marathon Oil Company, Post Office 120, Casper, Wyoming, U.S.A. 82602

since it does not add sediment to the littoral system but merely shifts it around. The simplistic view holds that scraping adversely steepens the beach profile, making subsequent erosion more likely and severe. To our knowledge, this notion has not been tested.

GEOMORPHIC SETTING AND DEVELOPMENT PRACTICES

Myrtle Beach, located along the northern coast of South Carolina on the U.S. east coast (Fig. 1), is a mainland, strand shoreline. It consists of a broad, 16-km arcuate section of coastline backed by Pleistocene beach ridges. No major tidal inlets or marshes occur at that locality. In recent historic times, the shoreline has been slightly erosional experiencing dune recession rates averaging approximately one-third to one-half meter per year over the last century (Hubbard et al., 1977). Although erosion is slow, it has progressed to a point where the quality and character of the beach, on which much of the tourist economy depends, is becoming degraded. Rapid and sometimes haphazard development practices combined with steady recession of the shoreline have forced construction of retaining walls, bulkheads, and rock revetments to protect existing development.

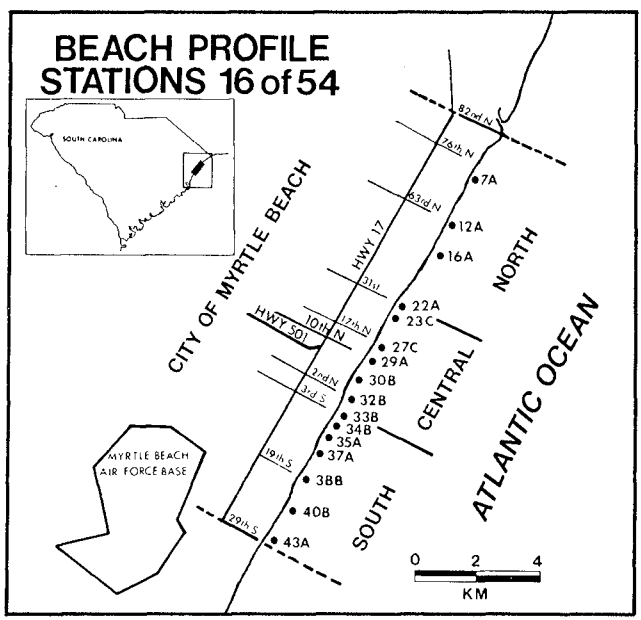

FIGURE 1. Location of Myrtle Beach (South Carolina) along the U.S. east coast. Selected beach profile stations along the northern-central and southern portion of the City are shown.

The shoreline along the City of Myrtle Beach is dominated by private residences in the northern half and hotels in the southern half (Fig. 2). Several piers and minor swashes (tidal channels emptying along the beach) interrupt an otherwise broad, arcuate shoreline. Isolated outcrops of Pleistocene-age mud or marsh clay deposits occur near the low watermark. Nearest navigable inlets are Little River (27 km to the northeast) and Murrells (21 km to the southwest). As Figure 2 shows, a narrow dune remains seaward of most residences in the northern portion of the city. The central area of the city shoreline has an increasing concentration of hotels. Natural dunes are rare; however, the shoreline edge is generally "soft" with landscaping or artificial fill along the seaward property boundaries. The southern third of the shoreline (Fig. 2c) is dominated by hard structures along the backbeach, with little or no setback of developed property.

NEARSHORE PROCESSES

The study area lies in a broad, wave-dominated embayment that forms an arc between Cape Fear (North Carolina) and Winyah Bay (South Carolina). A mean tidal range of 1.6 m (5.1 ft) and a spring tidal range of 1.8 m (6.0 ft) places Myrtle Beach in the high end of the microtidal (<2.0 m) class.

Nearshore bathymetry from the shoreline to 400 m offshore is characteristically concave upward and steep, with an average slope of 14 m/km. From 400 m to 4 km offshore, the rate is only 0.8 m/km and from 4 km to 12 km, the rate is 0.4 m/km (Brown, 1977).

Without the influence of inlet-associated tidal currents, the major mechanism affecting sediment transport is wave action. At Myrtle Beach, both longshore and onshore/offshore transport are significant in the surf zone. The observed cyclic changes of the beach profile are largely a result of the onshore/offshore component. Short-period storm waves erode beach sediment and transport it offshore where it commonly deposits as a bar. During fair-weather conditions, lower-energy waves move sediment back onshore. The longshore component is highly correlated with the prevailing seasonal winds that determine the direction and angle of wave approach and the resulting longshore current direction. On an annual basis, the net longshore sediment transport in South Carolina is to the south (Hubbard et al., 1977).

PREVIOUS WORK

There have been few studies dealing with beach scraping as a soft approach to beach restoration. Among the nonstructural means of restoring shorelines, artificial nourishment from offshore, inlet, and inland sources (Strock and Noble, 1975; Walton and Purpura, 1977; CERC, 1977) has been widely preferred and employed over the cannibalization of sand from portions of the beach. Beach scraping has generally been performed on a small scale, mainly to protect one or a few properties from wave attack.

FIGURE 2A) Northern Zone: Predominantly residential with existing low, natural foredune. Few shore protection structures.

FIGURE 2B) Central Zone: Transition from residential to predominantly hotels. Note encroachment of development up to dune line. Shore protection structures are generally fronted by landscaped, soft edges along the backbeach.

FIGURE 2C) Southern Zone: Dominated by hotels and hard structures along the backbeach. Natural dunes essentially nonexistent.

FIGURE 2. Representative oblique aerial photographs of the northern (2A), central (2B), and southern (2C) portions of the project area at Myrtle Beach, South Carolina. All photos taken at low tide on 3 February 1981.

Documentation on the effects of beach scraping projects have dealt with the comparison of beach volumes and morphologic changes along the manipulated profile; however, statistical applications for significance testing have not been performed. In a study of beach scraping conducted at Ocean City (Maryland), Kerhin and Halka (1981) report accelerated erosion in the backshore due to artificial disruption of the natural beach profile. Their project, however, preceded a winter season that proved to be one of the stormiest in recent history. Conclusions made from sweep-zone profile plots indicated that bulldozing of the lower foreshore oversteepened an already steep beach slope and interfered with the seasonal readjustment to an equilibrium profile, allowing erosion at a greater rate.

Tye (in press) presents a comparison of morphologic changes between scraped and nonscraped profile stations at Folly Beach (South Carolina) shortly after the passage of Hurricane DAVID (1979). Analyses of sequential profile plots had indicated an interrupted natural recovery cycle along scraped portions of the beach due to mechanical steepening of the lower foreshore, allowing a transformation in breaker type from spilling to plunging and inducing a net offshore movement of sediment. His emphasis from this study was placed on the importance of a quantitative assessment of the initial erosion and subsequent recovery as a baseline for implementing a more prudent beach scraping program.

Another concept of placing sand on the beach, practiced during the 1960s at Jupiter Island (Florida), is that of the Sauerman drag scraper (Department of Coastal and Oceanographic Engineering, University of Florida, 1969). In this project, borrow zones were located offshore, seaward of the normal surf zone, ranging frem 50 to 240 m from the shoreline. Approximately one year after scraping, a survey revealed a much steeper backshore and beach face, largely attributed to a coarser grain size transported from the offshore borrow area. The total volume of sand comprising the supratidal beach, however, was greater at the end of the study than before scraping. The beach fill had a positive effect in preventing any large-scale erosion, although it probably did not stop overall erosion along the profile.

Foredune construction through various sand-fencing materials and methods has been practiced at Cape Cod (Massachusetts), Core Banks (North Carolina), and Padre Island (Texas) (CERC, 1977). Recently, the townships of Ortley Beach and Lavalette (New Jersey) have experimented with erecting closely spaced sand fencing along the backshore, angled normal to the predominant northeast winds (S. Halsey, N.J. Environmental Protection Agency, pers. comm.). During fall and winter, sand is trapped by the fence, building up the backshore. Prior to the summer season, the fence is removed and the accumulated sand is mechanically redistributed both landward and seaward, creating an artificial berm and simultaneously decreasing the beach slope. These beach scraping and nourishment programs have all been conducted along highly developed, critically eroding barrier islands on the Atlantic coast, often in sediment-starved beaches. At Myrtle Beach, the erosion rate is considerably lower, and sediment supply is apparently more readily available from the eroding Pleistocene ridges and updrift sources.

DESIGN

Low cost attracted the City of Myrtle Beach to implement a beach-scraping maintenance program to enhance the backshore and provide temporary protection from shoreline recession, at least until longer-term solutions could be financed and implemented. This soft-engineering approach, though temporary, was considered cost-effective and aesthetically preferable to hard structures in 1981.

The plan for backbeach restoration followed the design shown in Figure 3 (Kana and Dinnel, 1981). Borrow areas were generally located along broad, low-relief intertidal ridges with higher volumes removed at localized accretion fillets around piers. Fill zones were graded to a gentle slope (approximately 1:10) as illustrated in Figure 4. Typical unit width volumes of borrow and fill were 6-8 m^3/linear meter of beach. Construction was by means of pan earth movers and bulldozers. The design of borrow zones attempted to distribute any adverse effects of scraping by identifying broad sections of the low-tide beach where relatively more sand was available, and by limiting the depth of scraping to within 0.3 to 0.5 m. This was determined by comparison of the total unit width volumes from 54 reference cross-sections.

DATA BASE

NETWORK OF STATIONS

The data base for design and evaluation of the Myrtle Beach scraping program consists of 54 beach profile stations (Fig. 1) measured up to ten times each between February 1981 and May 1982 (300 data sets total). Stations were spaced approximately 250 m apart and surveyed from the backshore to the -1.0 m mean sea level (MSL) contour.

The stations represent a variety of beach conditions and backbeach configurations ranging from natural dune/beach areas to armored shorelines. Erosional scarps of semilithified Pleistocene mud are also common along the central third of the project area. The most common armoring of the backbeach is by means of vertical concrete bulkheads; timber and sheetpile bulkheads are next common; riprap of 50-500 pound stone (typical) occurs at several stations.

These data offer a detailed comparison of short-term beach response due to artificial manipulation as well as natural changes along armored and unarmored beaches.

STANDARDIZED BEACH SEGMENTS

The basis for spatial and temporal comparison of profiles were standard unit width cross-sections of the intertidal beach from the base of scarps or armoring to the -1.0 m MSL contour (Fig. 5). These sections included backbeach, mid-beach, and low-tide ridge areas for evaluating the effect of scraping and fill on particular parts of the profile. Segments were normalized against mean beach section for statistical comparison and significance testing.

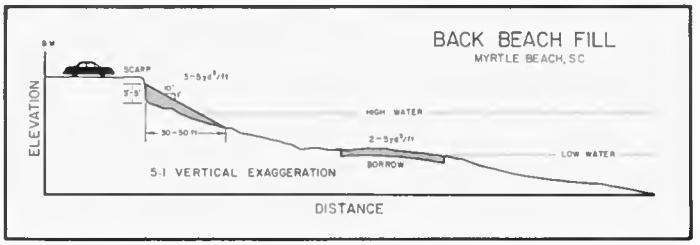

FIGURE 3. (Above) General design for beach scraping and backbeach fill at Mrytle Beach.

FIGURE 4. (A-C) Construction sequence showing pan earthmovers scraping near the low watermark on an intertidal ridge (4A); grading to a gentle 1:10 slope along the backbeach (4B); and the final condition after raking (4C). In general, mean high water was shifted seaward 10-15 m to the base of the fill zone.

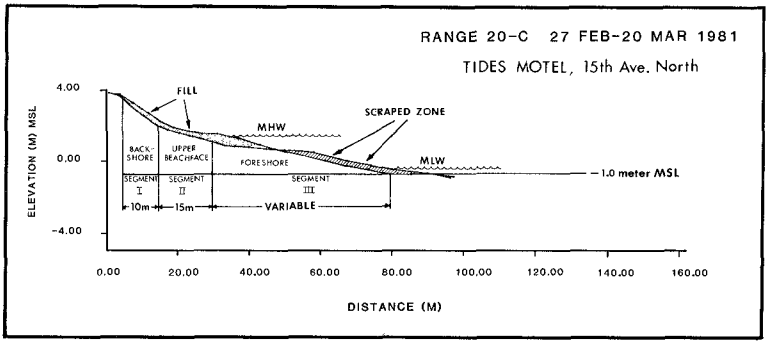

FIGURE 5. Representative reference beach cross-section in the central zone of Myrtle Beach. Principal borrow zones were along Segment III (foreshore) on intertidal ridges. Fill zones were located along Segment I (backshore) at or above the high watermark up to existing dune scarps or shore protection structures.

The backshore (Segment I) consists of a 10-m-wide section of the beach from the base of dunes or shore-protection structures and coincides with the zone of fill near high water. The upper beach face (Segment II) is designated as an arbitrary 15-m-wide zone which generally was undisturbed by scraping or fill. The lowermost segment (III) included the entire low-tide terrace and ridge system extending to the -1.0 m MSL contour. Width of Segment III varied from approximately 60 to 100 m, becoming narrower in the southern portion of the city, and incorporated all borrow zones. Table 1 is a summary of backshore station types over the project area. Note that the northern portion of the shoreline is dominated by dunes or sand fill, whereas the southern district is more commonly armored.

TABLE 1. Distribution of stations (%).

Region	Shoreline Length	No.	Armored	Natural Erosional Scarps	Dunes/ Old Fill
North	6.6 km	17	6%	12%	82%
Central	3.9 km	22	9	37	54
South	4.2 km	15	68	13	19
Overall	14.7 km	54	26%	21%	53%

Mean unit width beach volume from the dune line to the approximate -1.0 m MSL contour is given in Figure 6 for each zone of the project area. Also indicated are the proportion of armored versus natural stations and number of stations for each zone. Note the general decrease in unit beach volume from north to south. There was an average of 20 percent less sand in the reference sections along the more heavily armored southern zone than along the northern zone. All profiles were ohtained over a 3-day period in November 1981.

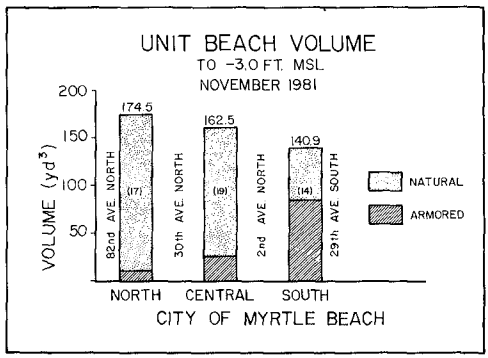

FIGURE 6. Mean unit-width beach volume for reference sections between the base of the dunes or the shoreline structures to the -3.0 ft (approx. -1.0 m) MSL contour. Relative proportion of armored versus unarmored stations and number of stations are indicated on each bar. Note the 20 percent decrease in unit volume from north to south correlating with increase in proportion of armored stations.

ARTIFICIAL BEACH CHANGES

Between March 1981 and May 1982, portions of Myrtle Beach were scraped along the lower beach and backfilled along the upper beach on three occasions. Approximately 25-50 percent of the project shoreline was directly affected by scraping or filling on the first two occasions. In some cases, borrow sections did not correspond to fill sections. This allowed evaluation of stations which were borrowed but not filled and vice versa. Total volume moved was approximately 29,000 m^3 during operations in March and June 1981. During a second-phase plan beginning January 1981, over 80 percent of the shoreline was scraped and filled (estimated volume 75,000 m^3).

PERFORMANCE EVALUATION

PHASE I CHANGES

Soon after the first sections of shoreline were scraped and backfilled, a minor northeast storm on 22 March impacted the Myrtle Beach area. The storm was sufficiently large enough to destroy a section of an ocean pier in the central zone of the project area. Beach measurements before and after the storm allowed evaluation of the effect of scraping and backbeach fill on selected portions of the shoreline. Figure 7 shows pre- and poststorm changes to the reference beach section (Segments I, II, and III, combined) for eight representative stations. All profiles were obtained between 21 and 24 March 1981. Figure 7 shows a trend of increasing erosion from north to south and somewhat higher erosion at armored stations (on average).

During the ensuing months, considerable natural recovery occurred. To illustrate how several representative stations responded, backbeach (Segment I) unit volume changes are given in Figure 8 for the period February-November 1981. The data represent short-term

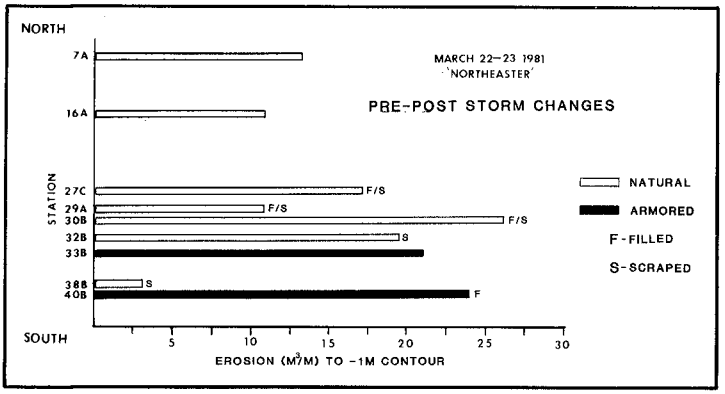

FIGURE 7. Pre- and poststorm beach changes at Myrtle Beach for 8 representative stations. Erosion is measured as the unit-width volume change (m^3/m) for a reference cross-section from the base of dunes or armor walls to the -1.0 m MSL contour.

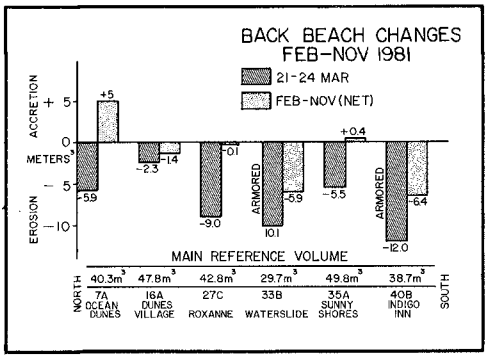

FIGURE 8. Representative poststorm (21-24 March) and six-month (February-November) backbeach volumetric changes for six variously armored, scraped, or filled stations along the project area. See Table 2 for status of each station.

erosion after the minor NE storm on 22 March 1981, and the net backbeach volumetric change along the landwardmost 15 m of beach. Profile data indicated were obtained on 27 February, 21 March, 24 March, and 8 November 1981. Table 2 gives the status of each station.

The zone that is compared in Figure 8 is the recreational backbeach area (Segment 1). The response at each station varied, but several trends were obvious. All stations eroded along the backbeach between 21-24 March; losses being greatest at the two armored stations (33B and 40B). At Station 7A, the fill placed in June accounts for much of the observed recovery after the storm. But at the other

TABLE 2. Status of each station given in Figure 8.

STATION) LOCALITY:	NOTES
7A) Ocean Dunes Hotel:	Scraped and backfilled with 8.5 m^3/m in June 1981; natural beach and dune system.
16A) Dunes Village:	Not scraped or filled; natural beach and dune.
27C) Roxanne Motel:	Filled with 8.5 m^3/m on 13 March before storm, but not scraped; Pleistocene scarp.
33B) Waterslide:	Not scraped or filled; vertical concrete bulkhead.
35A) Sunnyshores Motel:	Scraped and filled on 12 March before storm; natural scarp, no armoring.
40B) Indigo Inn:	Filled with 10 m^3/m on 20 March, but not scraped; vertical concrete bulkhead.

five stations, no fill was placed after the storm of 22 March. The response of these stations varied in large part as a function of the backshore armoring. Armored stations, 33B and 40B, eroded more during the storm (21-24 March volume change) and recovered less between March and November. On the other hand, unarmored stations generally eroded less and recovered to approximately their prestorm volumes. These trends were generally consistent for the entire data set of 54 profiles.

CHANGES THROUGH MAY 1982

Beach surveys were completed on ten occasions between February 1981 and May 1982 before, during, and after the three scraping and beach fill projects. Figure 9 summarizes the results, giving mean unit volume changes by zone (north, south, and entire shoreline); by beach segment (backbeach, upper heach face, and foreshore as defined in Figure 5); and by shoreline type (armored vs unarmored). Mean unit volumes were computed for each category for a particular survey and compared with the preceding survey to give the average change. Major trends of this data set include:

1) Erosion from February to April 1981 (pre- and poststorm of 22 March).

2) Accretion for the period May through October 1981.

3) Erosion between October 1981 and February 1982.

4) Net erosion for the entire period for armored stations.

5) Little net change for the period along unarmored stations.

6) Greater net change in the southern zone compared with the northern zone.

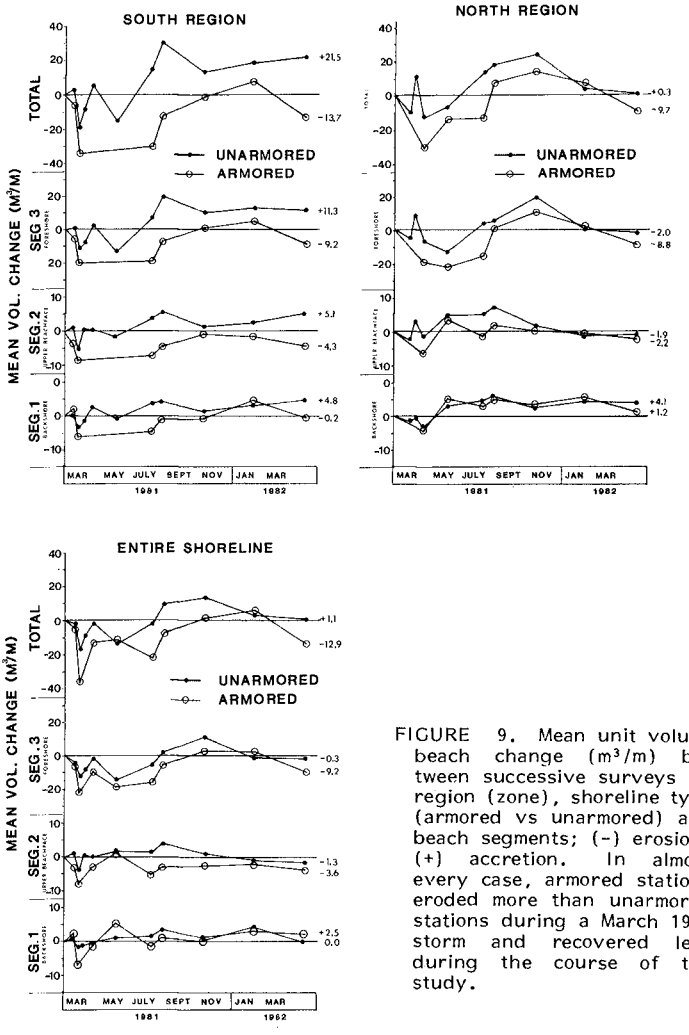

FIGURE 9. Mean unit volume beach change (m^3/m) between successive surveys by region (zone), shoreline type (armored vs unarmored) and beach segments; (-) erosion; (+) accretion. In almost every case, armored stations eroded more than unarmored stations during a March 1981 storm and recovered less during the course of the study.

Note that in almost every division of the data, armored shorelines showed greater losses, although erosion/deposition patterns were similar in form between successive time periods.

Comparative profile plots in Figures 10 and 11 illustrate two extremes between a northern station (16A) backed by a natural dune field and a southern station (40B) backed by a vertical bulkhead. In the case of Station 16A, fill placed along the backbeach was aided by buildup of a low-tide ridge (June-November 1981) which provided additional sand to the profile and reduced the threat of erosion at high tide. This station had a higher-than-average beach cross-section. Station 40B, however, had a lower-than-average beach cross-section to begin with and a poorly developed, low-tide ridge. Despite the addition of fill on two occasions from an updrift source (i.e., the lower beach at that station was not scraped), the station continued to erode at a high rate. Empirical evidence suggests the higher erosion rate was at least partly due to the presence of a vertical wall at the station which was exposed to wave action at high tide.

There was considerable deviation from the mean in net volumetric beach change from one station to another for the period. Figure 12 gives the variation in unit beach volume change proportioned about the mean by zone for the entire data set. Banded areas indicate stations which were armored or responded like armor stations [such as cohesive mud scarps (Station 12A)]. In general, there is a correlation between net erosion and the presence of vertical walls or scarps. The greatest variation occurs between Stations 32A and 35A which are affected by a minor swash inlet and an exposed rock outcrop along the lower beach.

SIGNIFICANCE TESTING AND DISCUSSION

Numerous comparisons were made between portions of the data set by Svetlichny (1982) to determine the significance of the observed changes in profile volume. Various combinations of station types and scrape/fill status were tested using standard statistical procedures to evaluate difference of the means (Ostle and Mensing, 1975). Figures 13 and 14 give two results.

Figure 13 shows overall means by beach segment for armored versus unarmored stations. For the indicated time period, the backshore and foreshore segments were significantly different at the 90 percent confidence level applied to a t-test supporting the notion that erosion was greater along armored stations.

Figure 14 provides a comparison between scraped, filled, and unaltered stations for the generally accretional period, March-November 1981. Combining means for armored and unarmored stations by each division of the data, it was found that there was no significant difference (at the 90 percent confidence level) between scraped and filled stations compared with unaltered stations. However, stations scraped but not filled eroded significantly more than unaltered stations or stations which were scraped and filled. The data of Figure 14 compare changes during an overall accretionary period and indicate the backbeach (Segment I) changes were dwarfed by natural changes along the

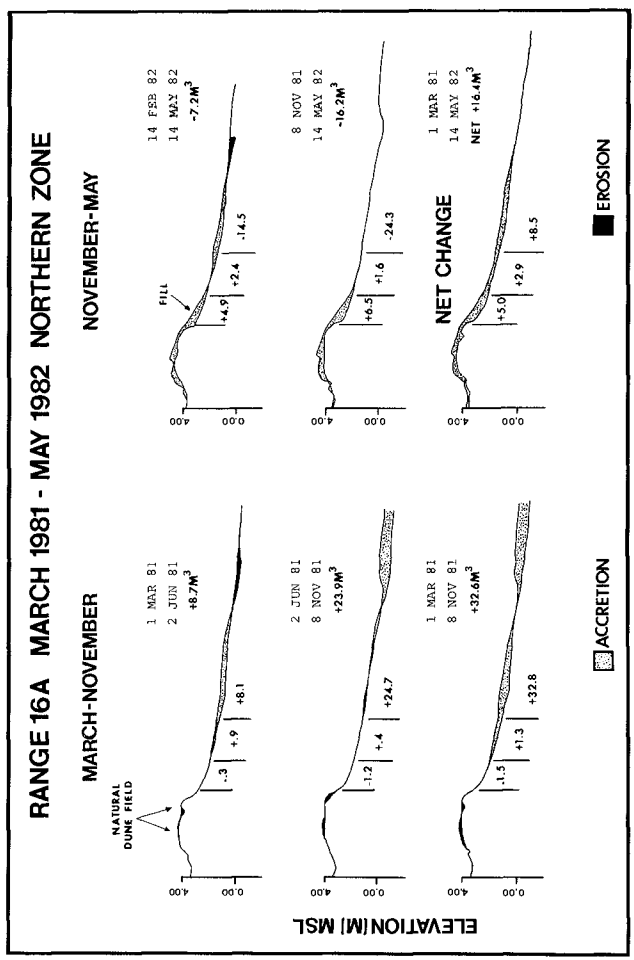

FIGURE 10. Comparative profiles for station 16A in the northern zone between 1 March 1981 and 14 May 1982. This station was backed by a natural dune field and developed a sizable, low-tide ridge during summer and early fall 1981. The lower beach was scraped and the backbeach filled with approximately 8 m^3/m in March 1981. Net accretion for the study period was double this amount.

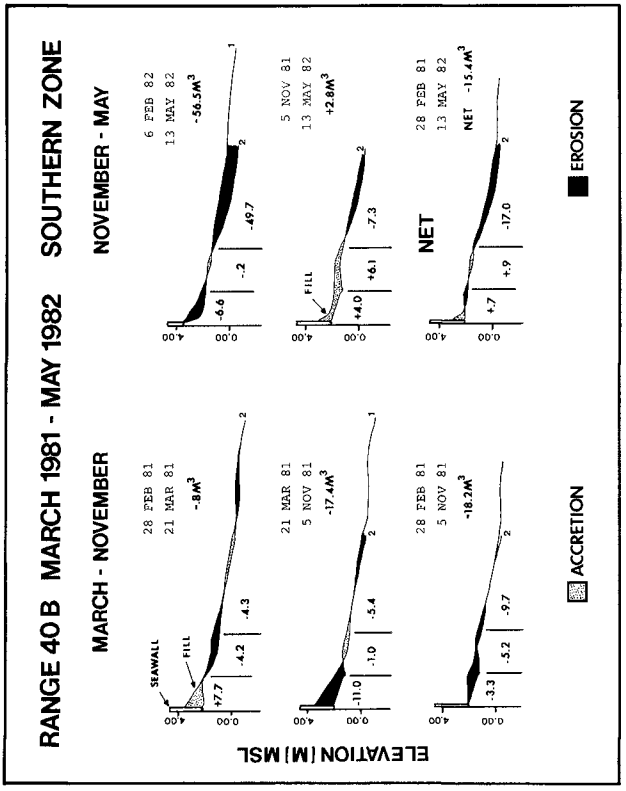

FIGURE 11. Comparative profiles for an armored station (40E) in the southern zone. This station was filled, but not scraped on two occasions, in March 1981 and February 1982. Note erosion of fill as well as the lower beach. Despite the addition of over 10 m^3/m from updrift sources, the station lost 15 m^3/m during the study period.

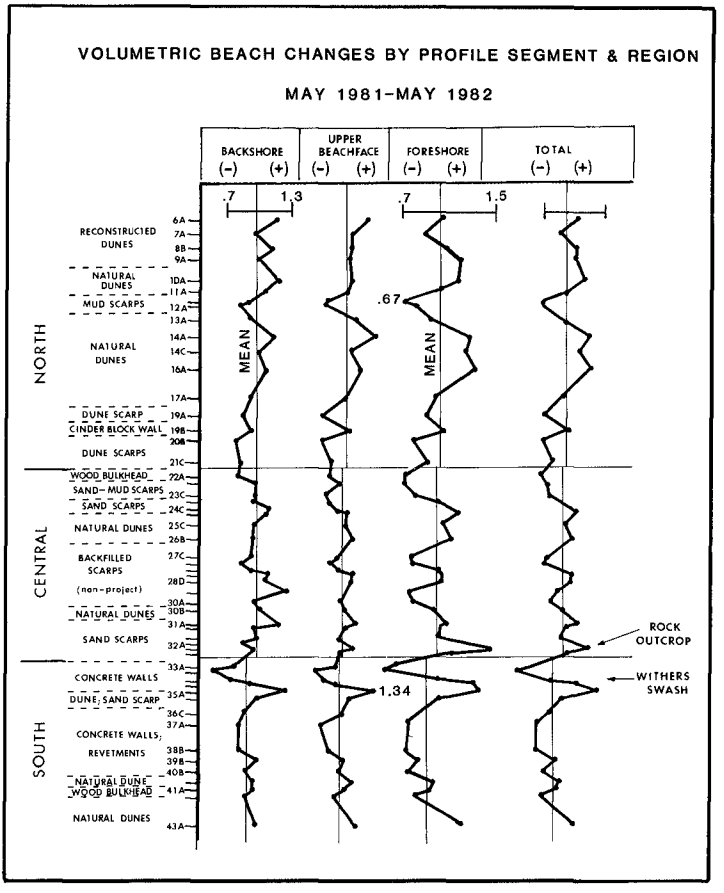

FIGURE 12. Mean unit volumes for 54 stations plotted as a ratio about the mean regional volumes for the northern, central, and southern zone. The left column describes the backshore configuration. Note that positive values generally occur where dune systems exist. Negative values generally correspond to shore protection structures or cohesive mud scarps.

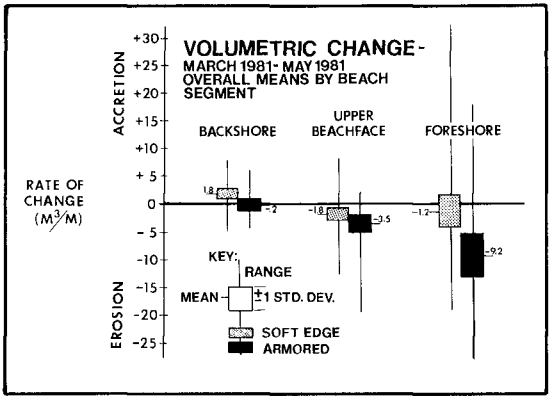

FIGURE 13. Bar graphs depicting the average rate of unit volume beach change between armored and unarmored stations for the study period. The differences are significant at the 90 percent confidence level for backshore (Segment I) and foreshore (Segment III).

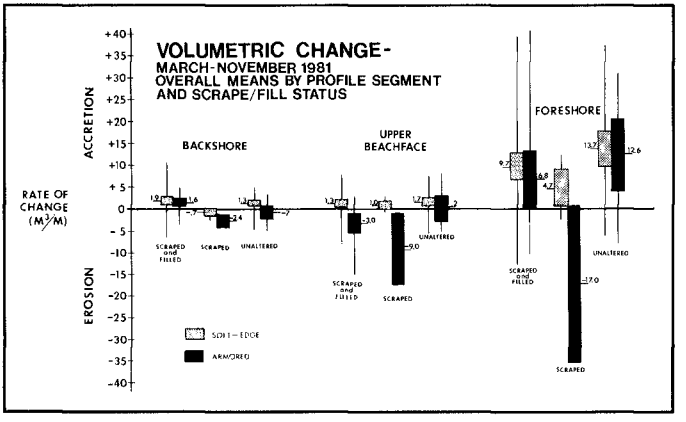

FIGURE 14. The average rate of changed by scrape-and-fill status. See text for explanation.

lower beach. (Note: There was an insufficient number of unaltered control stations for testing after November 1981.)

These results suggest that there were conditions under which beach scraping had no adverse effect on the profile, namely, along unarmored stations which had average or greater unit-width beach volumes; or during time periods when the shoreline tended to be naturally accretional. The data also indicate that scraping without concomitant beach fill adversely affected the profile [although areas where this was practiced generally had more sand at the time of the redistribution as per design (Kana and Svetlichny, 1981)].

In general, unarmored stations readjusted more rapidly to scraping than armored stations. It was found that the lower beach (Segment III) along natural profiles accreted twice as much as the lower heach fronting armored stations (10.7 m^3/m vs 4.9 m^3/m) between March and November 1981.

Tests for the 15-month study period revealed a distinct contrast in the response of armored and unarmored heaches to beach scraping. The foreshore at armored sections did not recover following the February 1981 scraping and yielded a net erosion of 9.2 m^3/m over the 15-month study. During the winter and spring, the foreshore at unarmored beaches eroded by 11.9 m^3/m, but recovered sufficiently so that the net change between March 1981 and May 1982 was only -1.2 m^3/m. The upper beach face (Segment II) eroded at an approximately uniform rate along the entire shoreline. Fill at armored backshores (Segment I) was completely eroded (net change was -0.2 m^3/m). Fill at soft-edge backshores was only partially eroded and had resulted in an average of 1.8 m^3/m more sediment than the initial (March 1981) prefill unit volume.

SEDIMENT BUDGET

A sediment budget was estimated for the study period March 1981 to May 1982 extrapolating from the reference profile cross-sections. As shown in Table 3 in units of m^3/km, the positive effect of beach scraping and backbeach fill was greatest in the northern zone where the backbeach had a net gain of over 2.2 m^3/m. The northern zone gained more recreational, high-tide beach as a result of scraping with virtually no overall loss of volume in the overall beach section. In addition, the fill in this area tended to remain in place for an entire year, protecting previously erosional dune scarps. Fill in the central and southern zones added little volume overall to the recreational backbeach due to the continuous erosion of the lower beach. Fill lasted several weeks to four months at most locations along the southern zone before erosional scarps or seawalls were reexposed. While it certainly provided some temporary recreational benefit (more high-tide beach) and some protection to the existing edge, it may have created a somewhat false sense of security, judging from the sediment losses along the lower beach (3-6 m^3/m). Although the backbeach fill held the shoreline stable near the high watermark in the central and southern zones, the potential remains for accelerated erosion due to losses along the lower beach.

TABLE 3. Sediment budget. Annualized by zones (March 1981-May 1982).

ZONE	VOLUMES (m^3/km)			
	Backshore	Upper Beach	Foreshore	Net Change
North	+2240	-1840	- 430	- 80
Central	+ 160	-2240	-5600	-7680
South	+ 480	- 400	-2960	-2880

CONCLUSIONS

There are a number of perspectives from which to judge the success or benefit of sand scraping and backbeach fill at Myrtle Beach. From the recreational standpoint, it provided a wider high-tide beach for a period of several weeks to almost one year at different localities. The benefit decreased from north to south and was least where most needed, in front of vertical walls. From a dune protection standpoint, the project delayed the time before reactivation of erosional scarps and further retreat of the strandline. Similarly, the buffer of gently sloping fill in front of shore protection structures reduced wave impact forces and potential damage to seawalls for the limited time it remained in place.

From a geological standpoint, the degree of profile manipulation by man was generally dwarfed by the natural cycle of beach changes, although there is some evidence that scraping in the northern zone promoted onshore movement of sand. In this latter case, the borrow zones tended to be narrower than existing low-tide ridges, leaving intact an effective breakpoint bar.

Finally, from a cost standpoint, the project was a relatively inexpensive experiment. Unit costs were approximately US$1.50-2.00 per linear foot of shoreline fill during each project. This compares with US$200 per foot for a typical bulkhead along the South Carolina coast.

Along stable or accretional shorelines, small-scale beach scraping should be highly preferred over armoring. Along slightly erosional shorelines such as the southern portion of Myrtle Beach, the scheme is at best temporary, but may be a suitable interim measure until long-term beach restoration can be implemented. In our opinion, this is preferable from an aesthetic as well as cost standpoint and should be considered as another shore protection option. Along highly erosional shorelines, scraping will obviously produce little benefit and may, in fact, accelerate erosion of the backbeach much like armoring appears to do.

ACKNOWLEDGMENTS

This research was supported by funds from the City of Myrtle Beach, the South Carolina Coastal Council, Research Planning Institute, Inc., and the University of South Carolina. Any views in this paper are those of the authors and do not necessarily reflect the opinions of these agencies or institutes.

REFERENCES

Brown, P. J., 1977, Variations in South Carolina coastal geomorphology: Southeastern Geology, Vol. 18(4), pp. 249-264.

CERC (Coastal Engineering Research Center), 1977, Shore protection manual, U.S. Army Corps of Engineers, Supt. of Documents, Wash., D.C., 3 vols.

Coastal and Oceanographic Engineering Laboratory, 1969, Cooperative study at Jupiter Island, Florida: Tech. Rept., Univ. Flor., Gainesville, 17 pp. + appendix.

Hubbard, D. K., M. O. Hayes, and P. J. Brown, 1977, Beach erosion trends along South Carolina coast: Coastal Sediments '77, ASCE, New York, N.Y., pp. 797-814.

Kana, T. W. and S. P. Dinnel, 1981, Beach scraping and backbeach fill plan, City of Myrtle Beach: RPI Summary Rept. to City of Myrtle Beach, Research Planning Inst., Inc., Columbia, S.C., 27 pp. + appendices + plates.

Kana, T. W. and M. Svetlichny, 1981, Design memorandum; beach scraping and backbeach fill plan, Phase II, City of Myrtle Beach: RPI Summary Rept. to City of Myrtle Beach, Research Planning Inst., Inc., Columbia, S.C., 12 pp. + appendices + plates.

Kerhin, R. T. and H. P. Halka, 1981, Beach changes associated with bulldozing of the lower foreshore: Maryland Geological Survey, Baltimore, Md., Open File Rept. No. 7., 28 pp.

Ostle, B. and R. W. Mensing, 1975, Statistics in research: Iowa State Univ. Press, Ames, Iowa, pp. 73-89.

Strock, A. V. and A. D. Noble, 1975, Artificial nourishment projects in southeast Florida: Marine Tech. Soc. Jour., Vol. 9(3), pp. 43-49.

Tye, R. S. (in press), Impact of Hurricane DAVID and mechanical restoration on Folly Beach, South Carolina: Shore and Beach.

Walton, T. L., and J. S. Papura, 1977, Beach nourishment along the southeast Atlantic and Gulf coasts: Shore and Beach, Vol. 45(3), pp. 10-18.

FIELD STUDY ON ONSHORE-OFFSHORE SEDIMENT TRANSPORT

by

Masataro Hattori*

ABSTRACT

The mechanism of onshore-offshore sediment transport and the process of beach profile evolution were studied through field investigations performed at Oarai Beach, Japan. The principal data set consists of twenty-four profile surveys taken at hourly intervals on each of two parallel lines spaced 10 m apart and of length 150 m. The lines extended from the backshore of the beach to a point on the sea bottom at a depth where no sand movement occurred. Simultaneous measurements of the waves and wave-induced currents were also made; the essential requirement of two-dimensionality was found to hold during the experiment. The profiles were used to calculate the net sediment transport rate on-offshore, and for an empirical eigenfunction analysis. A negative correlation was found between the transport direction (and resultant bottom change) and the mean sea level change. The sediment transport rate in the foreshore region was found to be proportional to the wave power, whereas outside the surf zone and near the breaker position it was proportional to the tractive force.

1. INTRODUCTION

Many laboratory studies have been undertaken to investigate the mechanism of onshore-offshore sediment transport on wave-formed beaches. However, there are several problems involved in transferring laboratory results to the prototype, such as the similarity law of movable bed models, scale effects, and so on. On real beaches, onshore-offshore sediment transport produced by waves and wave-induced currents occurs under very complicated conditions. It depends not only on the characteristics of the incident waves and bed material, but also on the specific location and bed form in the nearshore zone.

To understand the phenomena of sediment transport, more knowledge of the spatial and temporal dependence of the net rate and direction of transport is necessary. If adequate prototype data are available, onshore-offshore sediment transport as well as beach profile evolution can be inferred quantitatively with the aid of laboratory results. However, no analogous field studies have been performed because it is difficult to find sites where two-dimensionality in coastal processes is dominant. This paper reports such a field study made on onshore-offshore sediment transport processes.

---

* Professor, Department of Civil Engineering, Chuo University, Kasuga, Bunkyo-ku, Tokyo 112 JAPAN

The principal aims of this study are as follows:

(1) To relate the sediment transport rate to the onshore-offshore current velocity near the bottom.

(2) To clarify processes of sediment transport and beach profile evolution about the mean sea level due to the tide.

(3) To give a physical interpretation of the results by analysis of the beach profile.

Since this study aimed to investigate the onshore-offshore sediment transport in relation to beach profile change, it was necessary to measure accurately the bottom level changes along one or more lines running offshore. Many field studies have been made of the change in beach profile under waves in order to study the mechanism of sediment transport and the process of seasonal beach change. In only a few studies (e.g., Inman and Ruwnak, 1956; Nordstrom and Inman, 1975) were accurate measurements of the beach profile change performed. In most of the other studies, the profile data were usually contaminated by inaccuracies in the measurements. This resulted in difficulties in interpretating the phenomena of interest.

In laboratory experiments using two-dimensional wave flumes, the net rate and direction of the onshore-offshore sediment transport are usually calculated from a time series of bottom profile data by use of the continuity equation for bottom material (e.g., Watanabe, Riho and Horikawa 1982; Hattori and Kawamata 1982),

$$\frac{\partial h}{\partial t} = \frac{1}{(1-\lambda)} \frac{\partial q_x}{\partial x} \tag{1}$$

in which $h(x,t)$ is the water depth, q_x is the sediment transport rate on-offshore (along the x-axis), λ is the porosity of the bottom sediment, and t is the time. The coordinate system and notation are shown in Fig. 1.

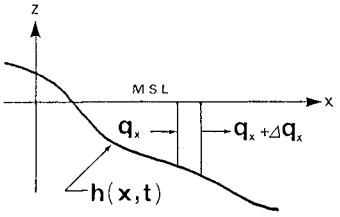

Fig. 1 Coordinate system and notation.

A preliminary experiment (Hattori and Komatsu, 1980) made in 1979 at the same study site (described below) indicated that the method of calculating the sediment transport rate in laboratory experiments could be applied to the field, if accurate measurements of the bottom change could be made. Based on this conclusion, a linear pole array technique was employed to measure the bottom level at fixed points on the beach.

2. EXPERIMENTAL PROCEDURE

2.1 Study Site

The field experiment was performed in August 1980 at Oarai Beach, Ibaragi Prefecture. The study area is a sandy beach with uncomplicated bathymetry, and is located adjacent to Oarai Harbor facing the Pacific Ocean (Fig. 2). The local beach material is quartz sand of median diameter 0.18 mm. Nearshore bottom profiles were measured by means of two linear pole arrays (labelled A and B in Fig. 2). The site selected for placement of the pole arrays was located 200 m north of the jetty. Diffraction at the breakwater 1400 m seaward produces relatively calm wave conditions of exceptional two-dimensionality. The pole arrays were of sufficient length to extend beyond the critical depth of sand movement during the experiment.

The spacing between the poles was 2 m and the total length of the pole arrays was 150 m. A reference point was defined, located on the backshore and landward of the maximum runup of swash. The pole array consisted of steel pipes 6.4 cm in diameter and 2 m to 5 m long. The pipes were driven into the sand bottom to a depth of about 1 m by means of a jet water pump.

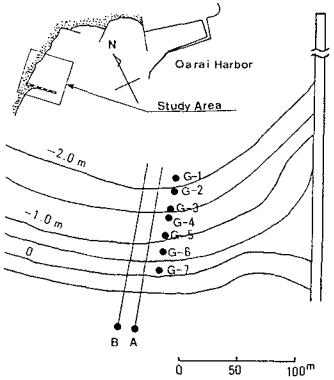

Fig. 2 Map of the study site.

Simultaneous measurements of the waves and wave-induced currents were made with capacitance-type wave gages and two-component electromagnetic current meters at seven locations indicated by G-1 to G-7 in Fig. 2. The seven wave gage stations were alined 10 m east of pole array A.

2.2 Profile survey

Surveys along the pole arrays were made every hour to yield a time series of the profile data over the 24-hr experiment period. Positions of the poles and absolute elevations of the pole tops were measured by using standard survey techniques and a bench mark on the backshore, which was derived from a permanent bench mark. Two supplemental reference points for measuring bottom level elevation were marked on each pole at distances of 1 m and 2 m. The height of the reference point from the bottom was measured by reading the scale of a survey rod, specially designed to avoid scouring around the pole and rod. From the survey result for the elevation of the tops of the poles, the bottom depth could be determined. The estimated accuracy of the absolute elevation of the bottom level was about 0.5 cm. The beach profile surveys were completed within about 15 min.

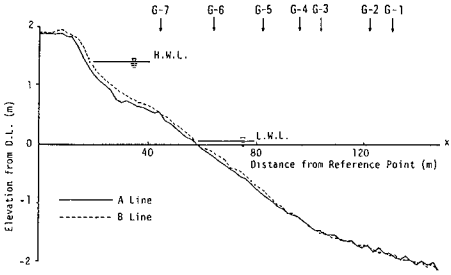

Fig. 3 Mean beach profiles at the study site.

Figure 3 illustrates mean beach profiles along the pole arrays, which were obtained by averaging the 24 sets of profile data taken over the experimental period. Arrows at the top of the figure indicate the positions of wave gage stations, G-1 to G-7. Figure 4 shows the positioning survey results of the pole arrays and wave gage stations. Pole positions are indicated by solid and open circles. The two pole arrays formed almost straight lines.

2.3 Instrumentation

Simultaneous measurements of the waves and wave-induced currents on the study beach are essential to understand the processes of sediment transport, and to confirm two-dimensionality of the various phenomena. Each wave gage station consisted of a capacitance-type wave gage and a two-component electromagnetic current meter. The wave gage, developed by Sato et al. (1980), has a superior frequency response than other conventional field wave gages, but has the shortcoming that the output signal level sometimes is reduced due to adherence of polluted sea water film to the capacitance line.

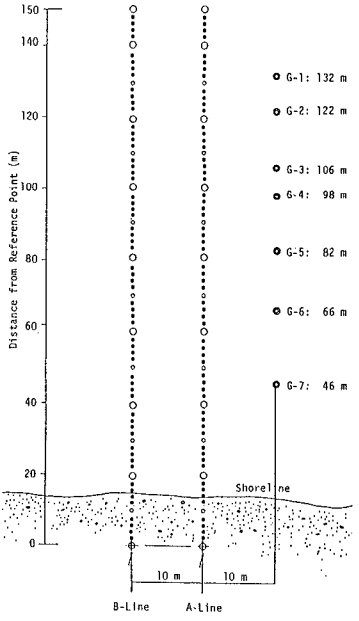

Fig. 4 Positioning survey results of the pole arrays and wave gage stations.

The current meters, used for measurements of the wave-induced current velocity, were fixed to steel frames at a height of 20 cm from the bottom of the frame. They were set on the sea bottom so that one of the two transducer axes was directed on-offshore. To supplement the measurements of the local wave characteristics on the beach, additional wave measurements were made about 200 m seaward of the tip to the jetty by means of a linear array of three pressure sensors (Fig. 5).

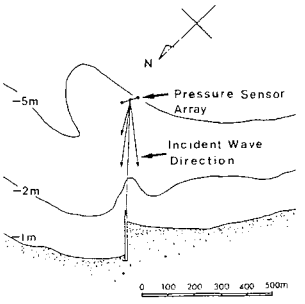

Fig. 5 Location of the pressure sensor array and the directional distribution of incident waves.

2.4 Data analysis

The survey data of the bottom level for each pole array were punched on cards for computer input and then stored on a magnetic disk for plotting profiles and for calculating the transport rate of sediment transport. Output of the wave gages and electromagnetic current meters was recorded on open-reel digital data recorders with a sampling interval of 0.2 s. Statistical characteristics of the waves and current velocities were calculated for each 16 min. of the collected data. In these calculations, wave components longer than 25 s entering in the free surface and in current velocity variations were cut off by using a high pass filter. The mean sea level variation on the study beach was not measured. Instead, the tide gage record at Oarai Harbor was used.

3. WAVE AND CURRENT VELOCITY

3.1 Characteristics of incident waves in the offshore

Figure 6 shows time histories of significant wave height and period measured at the pressure sensor array (Fig. 5), and the tide gage record at Oarai Harbor. This figure indicates that wave height and period in the offshore zone were almost constant over the duration of the experiment, 0.35 m and 7.3 s, respectively. The distribution of the incident wave direction obtained at the pressure sensor array is also given in Fig. 5. It is noticed from this figure that waves were incident normal to the study beach.

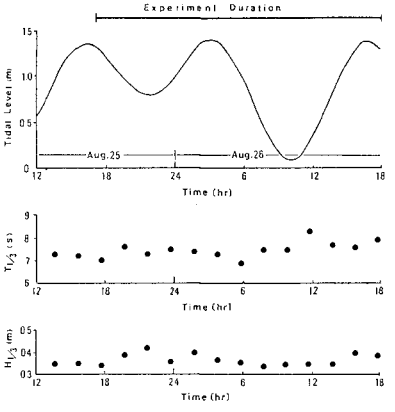

Fig. 6 Time histories of incident wave height and period at the pressure sensor array (Fig. 5) and tide gage record at Oarai Harbor.

Figure 7 gives examples of the record monitors of the free surface variations, η , at wave gage stations G-3 to G-7. It is seen that the waves proceeded to Station G-5 without wave breaking and that the breaking position was located near Station G-6. Solid lines on this figure indicate the propagation process of the marked wave.

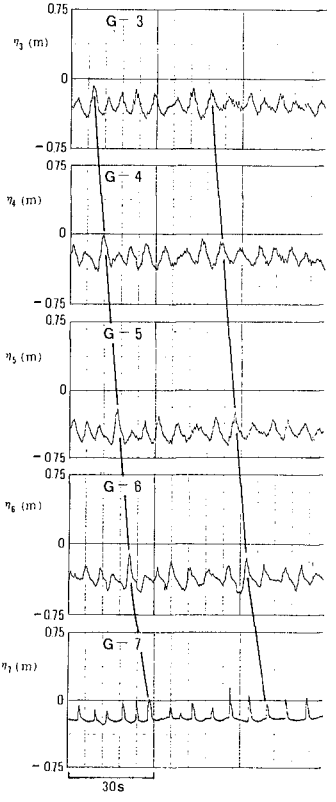

Fig. 7 Comparisons of the records of the free surface variation at Stations G-3 to G-7.
G-3 to 5: outside the surf zone,
G-6: near the breaker position,
G-7: inside the surf zone.

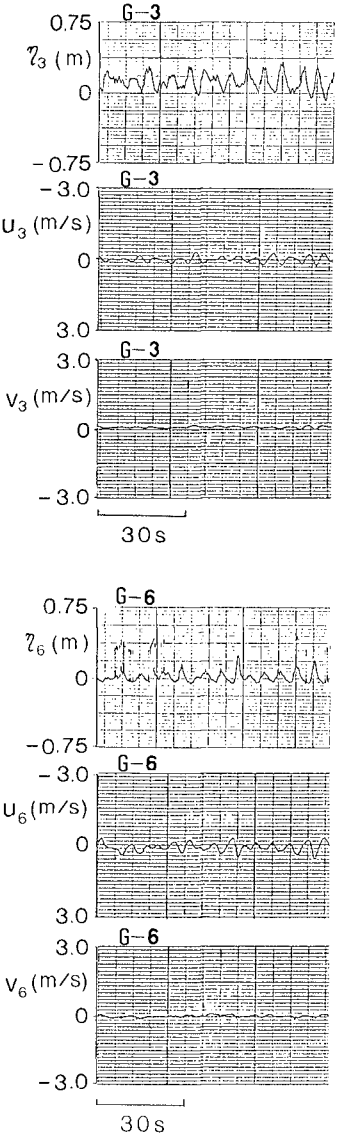

Fig. 8 Comparison of records of the free surface variation and of the on-offshore and longshore current velocities at Stations G-3 and G-6.

Figure 8 gives comparisons of monitor records of the free surface variation and of the on-offshore and longshore components of current velocity, U and V, respectively, at the wave gage stations G-3 and G-6. This figure clearly shows that the on-offshore current velocity fluctuated in phase with the free surface variation, and that the longshore component was very weak. Similar tendencies were observed at various locations on the beach over the entire duration of the experiment.

Based on the measured wave direction and current velocity, it is concluded that the coastal processes of interest on the beach maintained two-dimensionality, an essential requirement for this study.

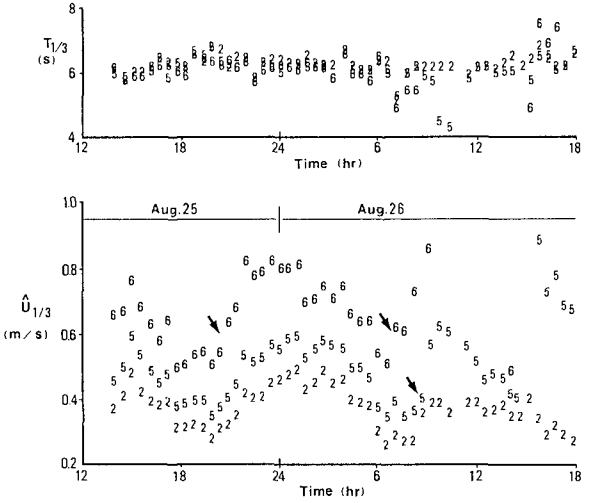

Fig. 9 Time histories of $\hat{U}_{1/3}$ and $T_{1/3}$ of the on-offshore current velocity at Stations G-2, G-5, and G-6.

Figure 9 illustrates time histories of the significant full amplitude and period of the on-offshore current velocity, $U_{1/3}$ and $T_{1/3}$. Plotted numbers represent the wave gage station where the data were taken. The velocity amplitude varies with the variation of the mean sea level due to the tide, but the period is almost constant (about 6.3 s).

According to Fig. 5, the mean period of the incident waves at the pressure sensor array is about 7.3 s, which is longer than the period derived from the on-offshore current velocity. Two factors may be pointed out as reasons why this difference in measured period occurred: (1) The frequency response of the electromagnetic current meter, 10 Hz, is higher than that of the pressure sensor. (2) In analysis of the on-offshore current velocity, the long period components were removed by a high-pass filter. The mean period of the incident waves was therefore taken to be 6.3 s for the experiment period.

Interesting behavior of the time histories of $\hat{U}_{1/3}$ can be noted. Rapid increase of $U_{1/3}$, indicated by thick arrows, indicates that the breaker position, in a statistical sense, was located near or at the wave gage station where the current velocity data were taken.

Since the longshore component of the current velocity was very weak, its mean with respect to time was negligibly small. On the other hand, a steady component of the on-offshore current velocity, $\bar{U}$, was observed at various locations of the beach. Figure 10 illustrates time histories of $\bar{U}$ at the wave gage stations G-2, 5, and 6. From this figure, it was found that, except during the rising period of sea level, from 14 hr to 17 hr Aug. 26, the steady current velocity was much lower than the maximum water particle velocity due to wave motion and was directed offshoreward. It is considered that this current did not have any significant influence on the onshore-offshore sediment transport.

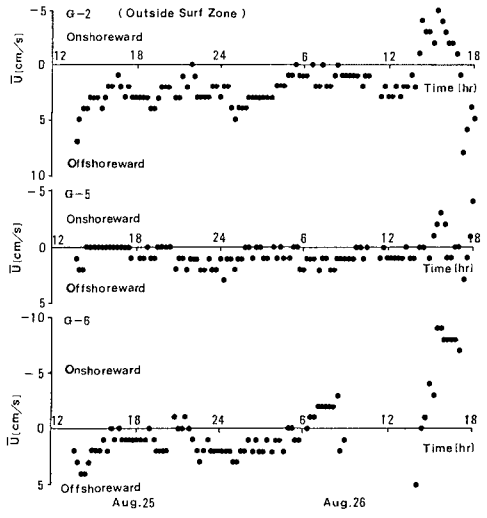

Fig. 10 Time histories of the steady on-offshore current velocity.

The breaking waves were mainly of the plunging type. The position of wave breaking was estimated by 1) visual observation facilitated by the pole arrays, 2) comparisons between time histories of the variations of the free surface and on-offshore current velocity (Huntley and Bowen, 1975), 3) rapid increase of the significant full amplitude of on-offshore current velocity (Fig. 9), and 4) spatial variation of the statistical characteristics of the waves and wave-induced currents.

4. RESULTS AND DISCUSSION ON THE SEDIMENT TRANSPORT

4.1 Net transport rate

The net rate of onshore-offshore sediment transport, q_x, was calculated from the time series of the profile measurements taken every two hours. Figure 11 shows the on-offshore distributions of q_x. In these calculations, the profile used was that given by the mean obtained from the two arrays. The numerals in the figure give the month, day, and time when the profile measurements were made. Locations of wave gage stations are indicated by arrows.

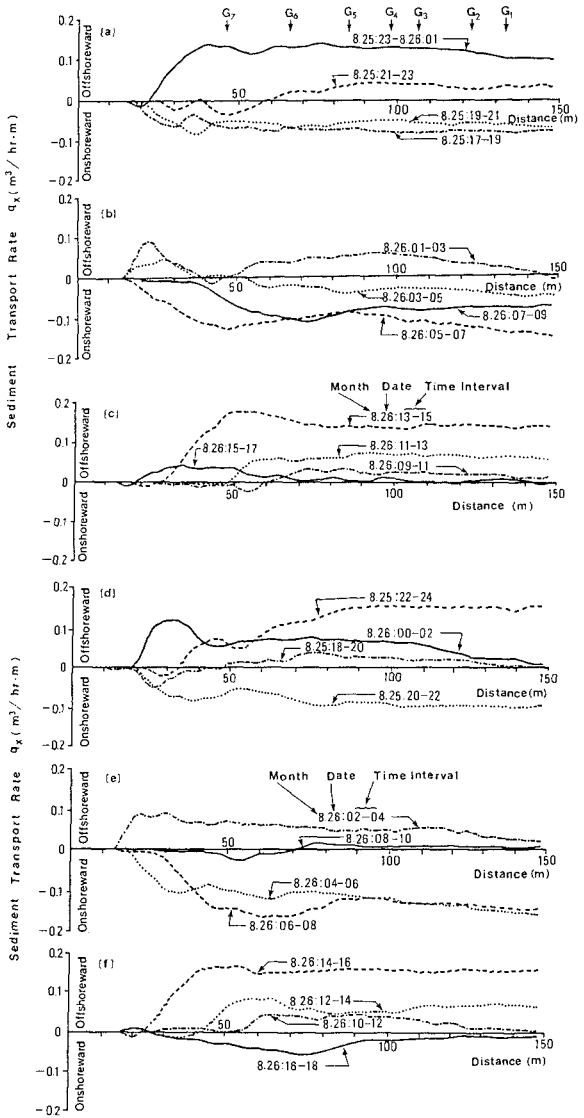

Fig. 11 Calculated results of the net rate of sediment transport.

It was found from the distributions of q_x that about half of the results did not satisfy the condition for the sediment budget. The distributions were calculated with the boundary condition $q_x = 0$ at the reference point on the backshore. Under calm sea conditions, sediment movement due to waves in the offshore zone is not active and bottom level changes are very small. When the change in sand level fell below 0.5 cm, inaccuracy in the profile measurements in the offshore led to a cumulative error in the calculation of q_x.

It was originally intended to express $|q_x|$ in terms of the significant full amplitude of the on-offshore current velocity, $\hat{U}_{1/3}$; however, no meaningful correlation could be found. This suggests the interesting possibility that sediment transport under irregular waves is mainly determined by the statistically averaged curreent velocity. It is therefore believed that the beach profile does not respond quickly to variations in current velocity caused by different incident wave forms. Instead of U_{max}, the maximum velocity of the on-offshore current velocity, for convenience the mean velocity $\hat{U}_{1/2}$ was used.

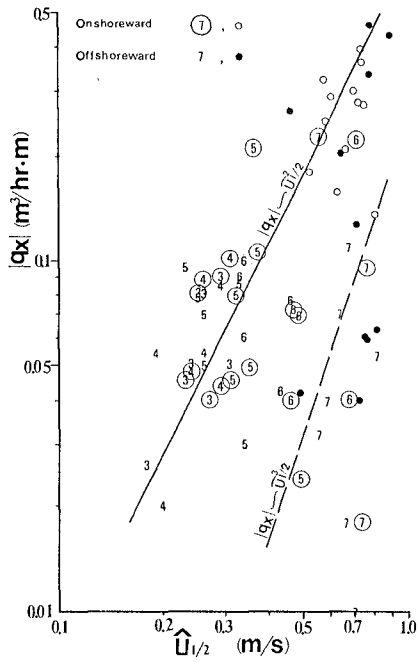

Fig. 12 Relationship between $|q_x|$ and $\hat{U}_{1/2}$.

The calculated absolute values of the net transport rates, $|q_x|$, at various locations were plotted against the mean full amplitude of the onshore-offshore current velocity, $\hat{U}_{1/2}$ as shown in Fig. 12. Numbers in the figure indicate the wave gage station. Filled and open circles denote data obtained in the preliminary experiment of 1979. Open circles and numbers in circles denote onshore transport, and filled circles and numbers without circles denote offshore transport.

Two distinct relationships between $|q_x|$ and $\hat{U}_{1/2}$ are apparent in Fig. 12. The solid line passes through the data obtained outside the surf zone and near the wave breaking position. The dashed line passes through the data obtained inside the surf zone. The slopes of the fitted lines are approximately 2.0 and 3.0 respectively. The standard expression for the shear stress acting on the bottom, τ_b, is given by

$$\tau_b = \frac{1}{2} \rho f_w u_{max}^2 \tag{2}$$

in which f_w is the wave friction coefficient, u_{max} is the maximum velocity near the bottom, and ρ is the density of the fluid. Although waves exhibit nonlinearities both inside and outside the surf zone, u_{max} will be replaced by $\hat{U}_{1/2}$. Thus Eq. (2) can be rewritten as

$$\tau_b = k \rho f_w \hat{U}_{1/2}^2 \tag{3}$$

where k is a coefficient representing the nonlinearity of the wave motion. Using Eq. (3), the two relationships in Fig. 12 can be written

$$|q_x| \sim \hat{U}_{1/2}^2 \sim \tau_b \qquad \text{(outside the surf zone and near breaking position)} \tag{4}$$

and

$$|q_x| \sim \hat{U}_{1/2}^3 \sim \tau_b \hat{U}_{1/2} \qquad \text{(inside the surf zone)} \tag{5}$$

The two empirically-based relationships between q_x and $\hat{U}_{1/2}$ expressed by Eqs. (4) and (5) indicate that two different processes of onshore-offshore transport can exist in the nearshore zone. In the present study, outside the surf zone and near the breaker position, the net transport rate was proportional to the tractive force acting on the bottom surface. Therefore, the dominant process of sediment transport was that of bed load. On the other hand, inside the surf zone, the net transport rate was proportional to the wave power, so that the dominant process was that of suspended load.

As seen in Fig. 11, the net transport rate varies with the distance offshore as measured from the reference point on the backshore. Figure 13 gives the time histories of the breaker position and location where the net transport rate takes a maximum value. From this figure, it can be noted that the maximum transport rate occurs near the breaker position.

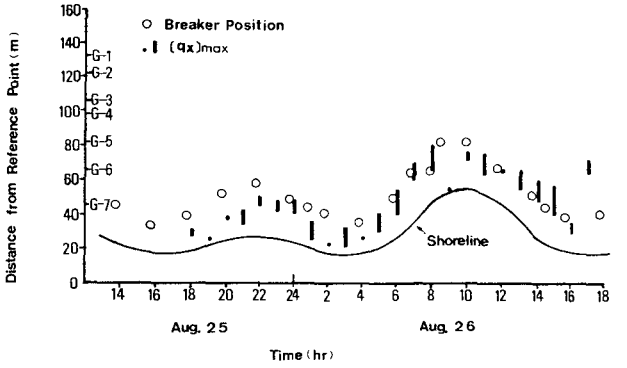

Fig. 13 Time histories of breaker position and location of $q_{x,max}$.

4.2 Direction of the Sediment Transport

To investigate effects of the mean sea level change due to the tide, temporal changes in the distributions of q_x were drawn schematically in Fig. 14, which gives the tidal record at Oarai Harbor. This figure clearly indicates that during ebb tide q_x was directed predominantly onshore, while during flood tide it was directed offshore. This suggests that the predominant direction of the net sediment transport on-offshore was governed significantly by the tide.

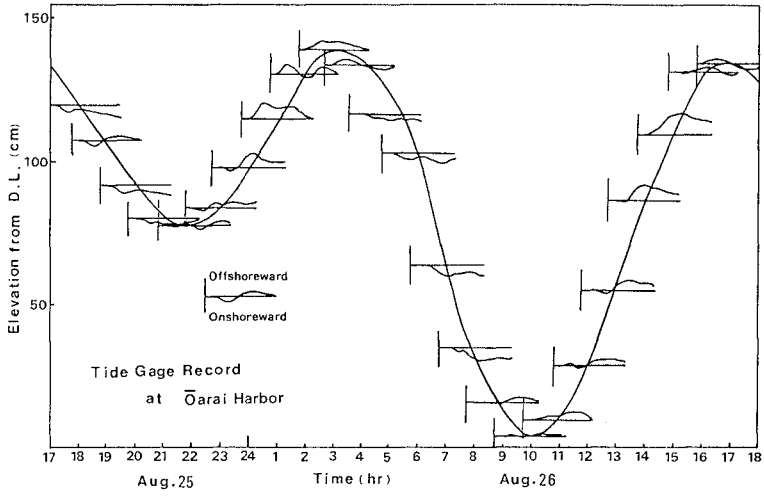

Fig. 14 Tide gage record and q_x distribution (Fig. 11).

As seen in Fig. 13, the range of the wave breaking position over the duration of the experiment covered a distance between 25 m to 80 m from the reference point. As the tide rose, the location of wave breaking advanced shoreward and the width of the surf zone became narrower, whereas when the tide fell, the surf zone became wider. From the mean beach profile in Fig. 3, the mean beach slope inside the surf zone during the high water period is estimated to be 1/20, and that during the low water period 1/32. Due to the beach cut pattern, the morphodynamic state of the surf zone and beach over a tidal cycle appeared to change from a reflective mode during the flood tide to a dissipative one during the ebb tide (Wright, 1982).

Hattori and Kawamata (1982) proposed a criteria for predicting the predominant direction of sediment transport on-offshore,

$$\frac{(H_o/L_o)\tan\beta}{(w_s/gT)} = C \begin{cases} > \\ 0.5 \\ < \end{cases} \begin{matrix} \text{(offshore transport)} \\ \\ \text{(onshore transport)} \end{matrix} \qquad (6)$$

in which H_o/L_o is the deepwater wave steepness, w_s is the fall velocity of the sediment, T is the incident wave period, $\tan\beta$ is the mean beach slope inside the surf zone, and g is the acceleration of gravity. The value of C during the high and low water periods are 0.76 and 0.47 respectively (H_o = 0.35 m, T = 6.3 s, d_{50} = 0.18 mm, and w_s = 2.3 cm/s). It is thus concluded from Eq. (6) that the direction of sediment transport during the flood tide was offshoreward whereas during the ebb tide it was onshoreward.

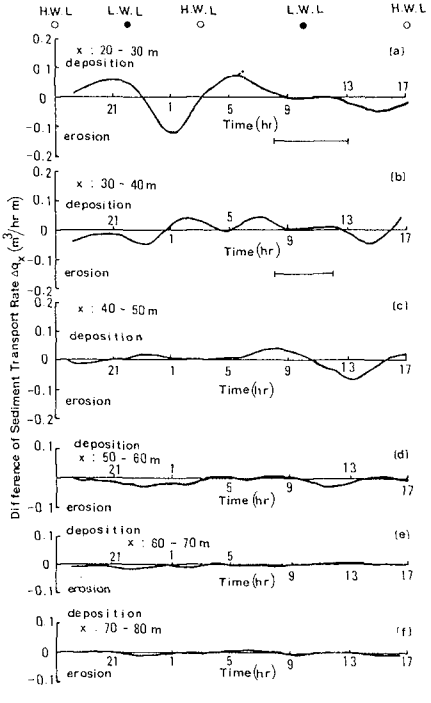

Fig. 15 Time histories of the rate of beach profile change inside the surf zone.

Figure 15 shows time histories of the difference of net transport rate, Δq_x, between adjacent locations inside the surf zone. This figure was obtained by using the q_x distribution curves given in Fig. 11. Horizontal solid lines indicate the duration the bed was dry during the ebb tide. At the top of the figure, the times of occurrence of H. W. L. and L. W. L. are indicated by open and filled circles. Since Δq_x expresses the rate of bottom change, comparison of these time histories indicates the trend of the beach profile evolution. During the flood tide, erosion on the upper beach was accompanied by sand accretion near the breaker position. During the ebb tide sand removed immediately from outside the surf zone was deposited on the low water terrace and foreshore. These trends of beach evolution support the hypothesis that the direction of net sediment transport is closely related to the change in the morphodynamic state of the beach over a tidal cycle.

5. DATA ANALYSIS BY EMPIRICAL EIGENFUNCTIONS

Seasonal patterns of onshore-offshore sediment movement and seasonal beach changes can be well described by means of the empirical eigenfunction technique. The application of this statistical technique promises to give further progress in our understanding of the process of beach profile evolution (Winant, Inman, and Nordstrom, 1975; Aubrey, 1979). The empirical eigenfunction technique was employed to analyze the profile data in order to get a more definite physical interpretation of the experimental results (Hashimoto and Uda, 1979).

The analysis was made taking into account the mean sea level due to the tide for the time series data of deviations from the arithmetic mean profile, as shown in Fig. 3 (Katoh, Tanaka, and Nadaoka, 1981). Since, in general, the data sets involve physical quantities with different units, each quantity was normalized so that its mean value was zero and its variance unity. The normalizing procedure is given in Eqs. (7) to (9).

$$F_{i,t} = (F_{i,t} - \bar{F}_i)/S \tag{7}$$

$F_{1,t} \sim F_{75,t}$: Bottom elevation

$F_{76,t}$: Sea level

$$\bar{F}_i = \frac{1}{n_t} \sum_{t=1}^{n_t} F_{i,t} \quad (n_t = 24) \tag{8}$$

$$S = \frac{1}{n_t - 1} \sum_{t=1}^{n_t} (F_{i,t} - \bar{F}_i)^2 \tag{9}$$

In these equations, $F_{i,t}$ is the physical quantity, (elevations of the bottom, and the sea level), $F'_{i,t}$ is the deviation of $F_{i,t}$ from the mean, $\bar{F}_i$ and S are the mean and variance of $F_{i,t}$. The subscript i is an index ranging between 1 and 76. The range from 1 to 75 covers the total number of points along the profile and the index 76 denotes the sea level. The subscript t is an index ranging between 1 and n_t, the total number of times the measurements were made (24).

The set of deviations from the mean value at time t, Φ_t, is given by Eq. (10),

$$\Phi_t = (F'_{1,t}, F'_{2,t}, \cdots\cdots, F'_{76,t})^T \tag{10}$$

where the superscript T is the matrix transpose operator. Then, Φ_t is expressed in terms of spatial and temporal eigenfunctions, e^*_n and $c^*_{n,t}$,

$$\Phi_t = \sum_{n=1}^{n_t} c^*_{n,t}\, e^*_n \tag{11}$$

where the subscript n denotes the order of the eigenfunction. Equation (11) means that the temporal characteristics of Φ_t is expressed by $c^*_{n,t}$. The correlation coefficient, $R_{n,i}$, between $c^*_{n,t}$ and $F^*_{i,t}$ is given by Eq. (12),

$$R_{n,i} = \sqrt{\lambda_n}\, e^*_{n,i} \tag{12}$$

in which λ_n is the n-th eigenvalue.

Since the index i indicates the location of the i-th pole from the reference point of the pole array, the relation between $R_{n,i}$ and i can be easily converted into a spatial dependence of R_n, which is equivalent to the spatial dependence of the eigenfunction e^*_n as shown by Fig. 16. The solid and broken lines in Fig. 16 represent the first and second eigenfunctions, respectively. The horizontal line at the top of the figure indicates the range of the breaking position.

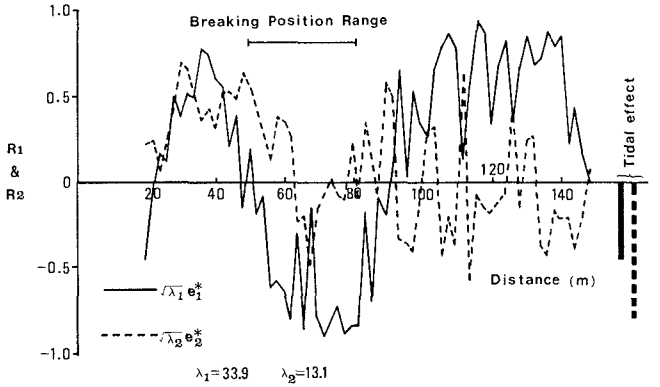

Fig. 16 Spatial dependence of the eigenfunctions, e^*_1 and e^*_2.

The first eigenfunction, e^*_1, exhibits a maximum near the foreshore, a broad maximum in the offshore, and a broad minimum over the range of the breaker position. In addition, e^*_1 indicates that a negative correlation exists between the effect of the tide and profile changes both in the foreshore and offshore, while a positive correlation exists over the range of breaker position. These results mean that as the tide fell, sand removed from the wave breaking zone was transported both shoreward and seaward, and was deposited on the foreshore and offshore.

The second eigenfunction, e_2^*, shows a broad maximum on the foreshore, but it does not exhibit any distinct dependence in the offshore. Since the correlation between the profile change and the tidal effect for e_2^* is stronger than that for e_1^*, e_2^* appears to represent the accretion of the foreshore caused by onshore sediment transport inside the surf zone due to seaward dislocation of the breaker position during the ebb tide. These interpretations of the spatial structures of e_1^* and e_2^* are supported by the time histories of beach profile change which are given in Fig. 15.

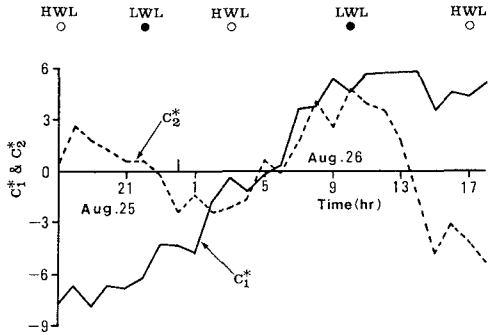

Fig. 17 Temporal dependence of the eigenfunctions c_1^* and c_2^*.

Figure 17 shows temporal variations of the eigenfunctions, c_1^* and c_2^*, denoted by solid and broken lines respectively. At the top of the figure, the times of occurence of H.W.L. and L.W.L. are indicated by open and filled circles. c_1^* shows a trend of gradual increase with time. This means that the study beach was accretive over the duration of the experiment (24 hr). On the other hand, the time dependence of c_2^* exhibits a strong periodicity indentical to that of the tide. During the ebb tide, the beach profile shows a tendency to accrete, while during the flood tide it shows an erosive tendency. Based on these temporal trends, the second temporal eigenfunction appears to adequately represent the profile change in the foreshore. It is thus substantiated by empirical eigenfunction anaysis that beach profile evolution as well as onshore-offshore sediment transport over a tidal cycle are greatly influenced by the mean sea level change caused by the tide.

6. CONCLUSIONS

The main conclusions from the present field study are now summarized.

(1) Two distinct relationships for the onshore-offshore sediment transport rate were found in the present experiment; i) the net transport rate was proportional to the tractive force acting on the bottom outside the surf zone and near the breaker position, and ii)

inside the surf zone the net rate was proportional to the wave power. The maximum transport rate occurred near the breaker position.

(2) The predominant direction of sediment transport during the flood tide was offshoreward, while during the ebb tide it was onshoreward. The effect of the tide on the direction of sediment transport was produced by the change in the morphodynamic state of the beach, as being either reflective or dissipative. The migration of the breaker position plays an important role in the change of beach characteristics.

(4) Analysis by the empirical eigenfunction method also indicated a negative correlation between the beach profile changes in the foreshore and offshore zones and tidal variation, while a positive correlation existed between the profile change and tide in the area of the breaker position.

(5) The first and second temporal eigenfunctions, respectively, were found to describe the evolutionary trend of the study beach and the trend of profile change in the foreshore, and were found to have the same periodicity as that of the tide.

ACKNOWLEDGEMENTS

The field work in this study was carried out through the sincere cooperation of many people, and I would like to thank all of them. In particular, I would like to express my appreciation to Mr. S. Hotta, Tokyo Metropolitan University, who suggested the idea of measuring beach profiles by means of a linear pole array system. I would also like to thank Dr. N. C. Kraus of the Nearshore Environment Research Center for proofreading the manuscript.

REFERENCES

Aubrey, D.G. (1979): Seasonal patterns of onshore/offshore sediment movement, J. Geophys. Res., Vol. 84, No. C10, pp. 6347-6354.

Hashimoto, H. and T. Uda (1979): Analysis of beach profile changes at Ajigaura by empirical eigenfunction, Coastal Eng. in Japan, JSCE, Vol. 22, pp. 47-57.

Hattori, M. and R. Kawamata (1982): Onshore-offshore transport and beach profile change, Proc. 17th Conf. on Coastal Eng. ASCE, pp. 1175-1194.

Hattori, M. and N. Komatsu (1980): Field experiments on on-offshore sediment transport and beach profile changes, Proc. 27th Japanese Conf. on Coastal Eng., JSCE, pp. 187-191. (in Japanese)

Huntley, D.A. and A.J. Bowen (1975): Comparison of the hydrodynamics of steep and shallow beaches, Chapter 4, Nearshore Sediment Dynamics and Sedimentation, Ed. by J. Hails and A. Carr, John Wiley & Sons, pp. 69-109.

Inman, D.L. and G.A. Ruwnak (1956): Changes in sand on the beach and shelf at La Jolla, California, B.E.B. TM-82, 30 pp.

Katoh, K., N. Tanaka, and K. Nadaoka (1981): Effects of tidal level and waves on two-dimensional deformation of foreshore, Proc. 28th Japanese Conf. on Coastal Eng., JSCE, pp. 207-211. (in Japanese)

Nordstrom, C.E. and D.L. Inman (1975): Sand level changes on Torrey Pines Beach, California, CERC, MP11-75.

Sato, M., K. Nakamura, and T. Tamura (1980): Field measurements of surf waves, Proc. 27th Japanese Conf. on Costal Eng., JSCE, pp. 124-128. (in Japanese)

Watanabe, A., Y. Riho, and K. Horikawa (1982): Beach profiles and on-offshore sediment transport, Proc. 17th Conf. on Coastal Eng., ASCE, pp. 1106-1121.

Winant, C.D., D.L. Inman, and C.E. Nordstrom (1975): Description of seasonal changes using empirical eigenfunctions, J. Geophys. Res., Vol. 80, No. 15, pp. 1979-1986.

MORPHOLOGY AND DYNAMICS OF CRESCENTIC BAR SYSTEMS

by

V. Goldsmith[1], D. Bowman[2], K. Kiley[3], B. Burdick[3], Y. Mart[4] & S. Sofer[4]

ABSTRACT : Aerial photograph and field studies in the southeastern Mediterranean, involving bathymetric mapping, and concurrent and antecedent wave measurements, have been used to delineate the sequential development of crescentic bars and associated dynamics. The bar sequence includes multiple parallel or wavy bars, ridge and runnels, oblique/transverse bars, single crescentic and double crescentic bars, and occurs during a calming down of wave activity from 2.5 to 0.5 m waves. The concomitant wave data, including wave directions, energy spectrum, significant wave height, and length of the calm period, showed strong correlation with the bar stages.

An increase in total bar occurrence during summer is related to a major wave energy decrease in the spring, when significant wave heights (H_s) $\leq$ 1 m sharply increase to 70-85% in April-May. Inner single crescentic and initial double-crescentic bars are largely restricted to the calmest wave months of May/April to October/November, which reflects their sensitivity to wave energy. The aseasonal occurrence is best shown by the mature double crescentic type, which apparently is the final stage in the crescentic bar development sequence.

Two bar developmental sequences were delineated: one shore-normal and the other initially oblique, but gradually rotating to shore-normal in the mature stage. Out of phase relationships between inner and outer bar systems resulted from the lag in response of the outer bars behind changes in wave direction. Among the inner crescentic bars and shore rhythms, phase-correlation was the rule.

Crescentic bars are well developed on this coast because of the dissipative conditions and the distinct wave climate. High waves in the winter remove the existing bars, and extended calms allow the full development of the crescentic bar sequence. Similar bar types occur on different coasts in different sequences and in different proportions of time. Thus, it is suggested that these differences are attributable to global differences in the occurrences of threshold wave height conditions.

---

[1]Israel National Oceanographic Institute, Haifa, Israel and
[2]University of South Carolina, Columbia, S.C.
[3]Ben-Gurion University of the Negev, Beersheva, Israel.
[4]Virginia Institute of Marine Science, Gloucester Point, Va.
[4]Israel National Oceanographic Institute, Haifa, Israel.

INTRODUCTION : During the past 15 years, several studies have attempted to define the specific dynamic conditions promoting the development of crescentic bars (e.g. Bowen & Inman, 1971; Greenwood & Davidson-Arnott, 1975; Owens, 1977). A global bar classification was proposed (Greenwood & Davidson-Arnott, 1979) including ridge and runnel, cusp, multiple parallel, transverse and straight bars, as well as sinuous to crescentic bars.

Recently it was shown that crescentic bars occur within a bar developmental sequence on both high wave energy macrotidal coasts (Short, 1979; Wright et al., 1979) and moderate wave energy microtidal coasts (Goldsmith et al., 1982). On the high wave energy Australian coast, Short (1979) observed that as wave heights decreased from 3 m to 1 m, the accretional bar stage sequence went from a parallel bar and channel to crescentic bars, megacusps, welded bar, and terminated in cusps and berm. Similarly, on the dissipative, moderate wave energy Israeli coast, Goldsmith et al. (1982) observed that as wave heights decreased from 2.5 m to 0.5 m, the accretional bar sequence went from multiple parallel bars to ridge and runnel, transverse/oblique bars, single and then to double crescentic bars. The first concern of this study is to further delineate the wide range of nearshore bars and shoal patterns along the southeastern Mediterranean microtidal coastline, and to widen our knowledge of environmental conditions of the different bar types. The second aim is to delineate the sequential stage developments of meandering-crescentic bar systems at HaHoterim coast, northern Israel (Fig. 1), and to relate this to specific wave parameters.

METHOD : The study includes all available air photos of the southeast Mediterranean taken in the period 1949-1980. Accordingly, 123 flights showing 150 clear coastal segments were available for bar pattern recognition. Also, a series of eight consecutive maps of the nearshore zone and beach at HaHoterim were made for depicting the bathymetry, rhythmic topography, and sequential bar development. Twenty-two repetitive overflights were conducted, twelve of which were taken at regular weekly intervals.

The air photos were compared to concomitant wave data, up to 60 days prior to each air photo date. The energy spectrum was computed for each digitized wave record, twice a day for one year, using a Fast Fourier Transform algorithm described in Clairbout (1976). The equations from Goda (1974) were used for height and period statistics.

THE SOUTHEASTERN MEDITERRANEAN : The 270 km long study area (Fig. 1) is a relatively smooth coast, with beaches generally narrowing to the north (Goldsmith, in press). Submerged and eroded eolianite remnants occasionally compose rocky outcrops in the inshore and along the water line. Haifa Bay is the northern border of the quartz sedimentary province of the Nile delta (Goldsmith & Golik, 1980). Well-sorted medium beach sand decreases in size from Egypt northwards to Tel-Aviv (Emery & Neev, 1960). Calcium carbonate is 6-8% in southern Israel, and is 65% of the sediment at HaHoterim, south of Haifa. At HaHoterim the beach sand is medium size (1.82 ϕ), moderately to well-sorted (S.D. = 0.45 ϕ), slightly negatively skewed and mesokurtic (Gwirz, 1982).

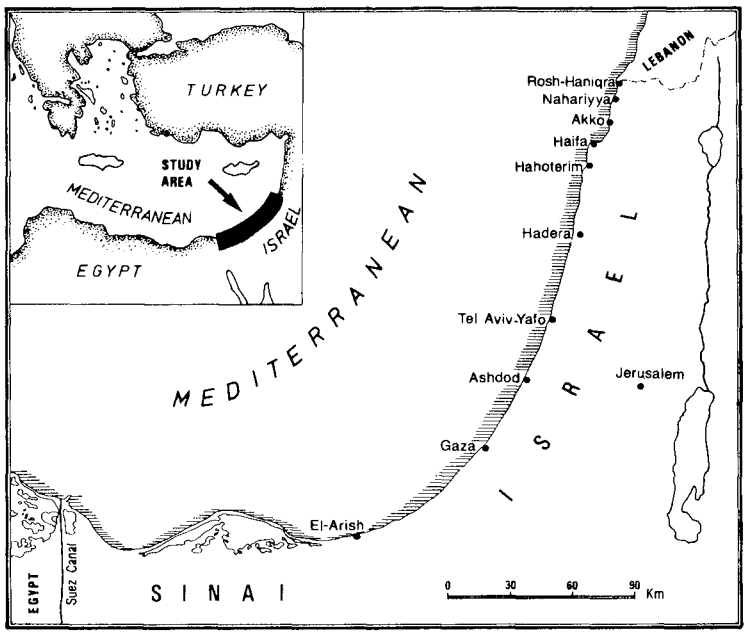

Figure 1. Location of study area in the southeastern Mediterranean.

The wave climate consists of three wave seasons (Goldsmith & Sofer, 1983): the highest wave months are December-March ($\bar{H}_s$ = 1.0 to 1.5 m); the lowest wave months are May, September-October ($\bar{H}_s$ = 0.6 to 0.8 m); and the intermediate wave months are June-August. The winter wave months are dominated by storm fronts passing at an average of 5-7 day intervals. Maximum winter significant waves reach 5 m and 13 sec, although only about 10% of H_s are $\geq$ 2 m high.

The same nearshore slope gradient of 0°20' to 1° dominates the nearshore. However, the slopes of the offshore facing bar flanks are considerably steeper, ranging from 1° to 5°. The Israeli coast, in spite of its low to medium wave height, and because of its high wave steepness and low mean beach gradient, falls mainly within the dissipative regime with $\varepsilon >> 33$ (Bowman & Goldsmith, in press). Field evidence for the extremely dissipative character is provided by the relatively wide (100-300 m) barred inshore, segmented into longshore sub-regions of troughs and shoals, and by the rhythmic beaches, abundant bar-types and dominant spilling breakers.

BAR MORPHOLOGY : The bars observed along this coast may be grouped within three distinct "families" (Bowman & Goldsmith, in press).

1. Non-rhythmic parallel bars. During severe storms (i.e., $H_s \geq 2.5$ m), it appears that the crescentic and other bars are destroyed. As the storm waves decrease, multiple parallel bars are discerned first by the multiple breaker lines, and then they are observed directly. These bars may be straight or meandering. Since during severe wave conditions the whole nearshore zone is filled with breaking waves, it is very difficult to determine the bar patterns. Nevertheless, it is clear that pre-existing bar patterns are completely removed. Observations made by helicopter appear to indicate that the multiple parallel bars form and migrate shoreward only when waves decrease to $H_s \leq 2$ m and when the strong rip current systems ameliorate. The rip current systems were observed to migrate in the longshore direction. During less severe storms ($2 > H_s \geq 1$ m), pre-existing crescentic bars are modified, but not totally removed.

As the waves decrease, the bars migrate shoreward. As the most landward bar approaches shore, it tends to migrate onshore non-uniformly in the form of a ridge and runnel, and portions of the ridge weld onto the beach, resulting in non-uniform widening of the beach.

2. Single crescentic bars. Initially oblique and transverse bars form, resulting from the non-uniform widening of the beach. Within a few days, and with wave heights $H_s < 1$ m, the seaward ends of the bars connect to form crescentic bars, while simultaneously, the landward ends of the oblique/transverse bars become detached from the shore (Fig. 2). The beach is usually in phase with bar cyclicity, forming a dominantly cuspoidal shoreline.

3. Double crescentic bars. Double crescentic bars form when low wave heights persist for several weeks after the single crescentic bars are formed (Fig. 2). The inner system consists of embryonic crescents

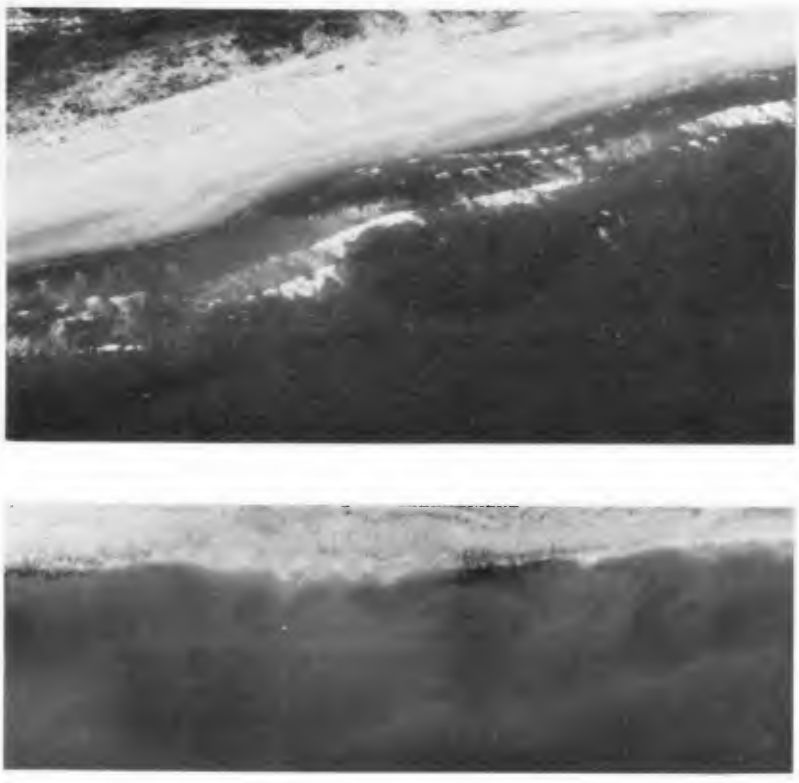

Figure 2. Single crescentic (top) and double crescentic (bottom) bar systems along the Israeli coast.

extending across the seaward end of recurring small rip channels. Wave data indicate that the formation of these inner double crescentic bars is preceded by a short energy pulse of $1.0 > H_s > 0.5$ m of a few hours to a day duration. In the mature stage they extend more than half way across the inshore width (i.e., between the shore and the initial single crescentic bars).

Phase correlation between the inner and outer bar systems is usually not evident. Since the inner crescentic bars form at a different time and under different wave conditions than the outer crescentic bars, one set may be either skewed or symmetric, differently than the other set. Groins and other coastal structures interfere mainly with the inner bar systems, whereas the outer bars often remain continuous and undisturbed.

BAR SEQUENCES : The sequence of bar developments, which was observed by mapping, overflights, and study of the historical aerial photographs, is summarized in Figure 3. The sequence includes, in order: multiple bars, ridge and runnels, transverse/oblique bars, outer crescentic and nested inner crescentic bars. The detailed sequence is discussed in Goldsmith et al. (1982).

In the storm stage, the shoreline is irregular, and the rip heads extend 200-300 m from shore. In the post-storm stage, the outer and inner meandering bars block the former rips and feeders, indicating circulation atrophy (Fig. 3, Seq. B). Three main levels of inshore bathymetry are discerned: 1) the deepest, which are the entrenched, stagnant rip channels; 2) shoals, which are the shallowest; and 3) the main accumulative bodies, which are the meandering and oblique bars.

The early stages of crescentic bar development are documented in a box core obtained in a shore-attached oblique bar at a distance of 80 m from shore, at a water depth of 1 m (Fig. 4). Five distinct units are shown. The lowest unit (A) represents an onshore-migrating bar. Unit B displays offshore-dipping foresets, indicating a rip current. Unit C, the thickest and largest unit, displays approximately one-half of a mega-trough, which may indicate a longshore channel or wave orbital scouring. The upper unit (E) again indicates onshore bar migration. The wave history shows that a severe storm ($H_s = 3$ m) occurred three weeks prior to obtaining the box core. Such storms tend to destroy all bars. This suggests that this entire core was formed during a post-storm sequence, although the depth of activity was not documented. The top unit, landward-dipping planar bedding, reflects the asymmetrical shoaling waves, which may correlate with the low waves prior to sampling.

During the extended calm, the sediment fill "blurs" the stagnant rip channel (Fig. 3, post-storm, Seq. B). Nested "micro" transverse bars and cusps, in phase with embryonic rips, dominate the foreshore and the shallow inshore. Also during extended-calm, a new, shore-normal inner microsystem grows out of the former shoals and embryonic rips. The inner system shows discontinuous crescents that match the shoreline microembayments. The inner system becomes less complex, and both bar systems, separated by a trough, are in phase with the shoreline and the trans-

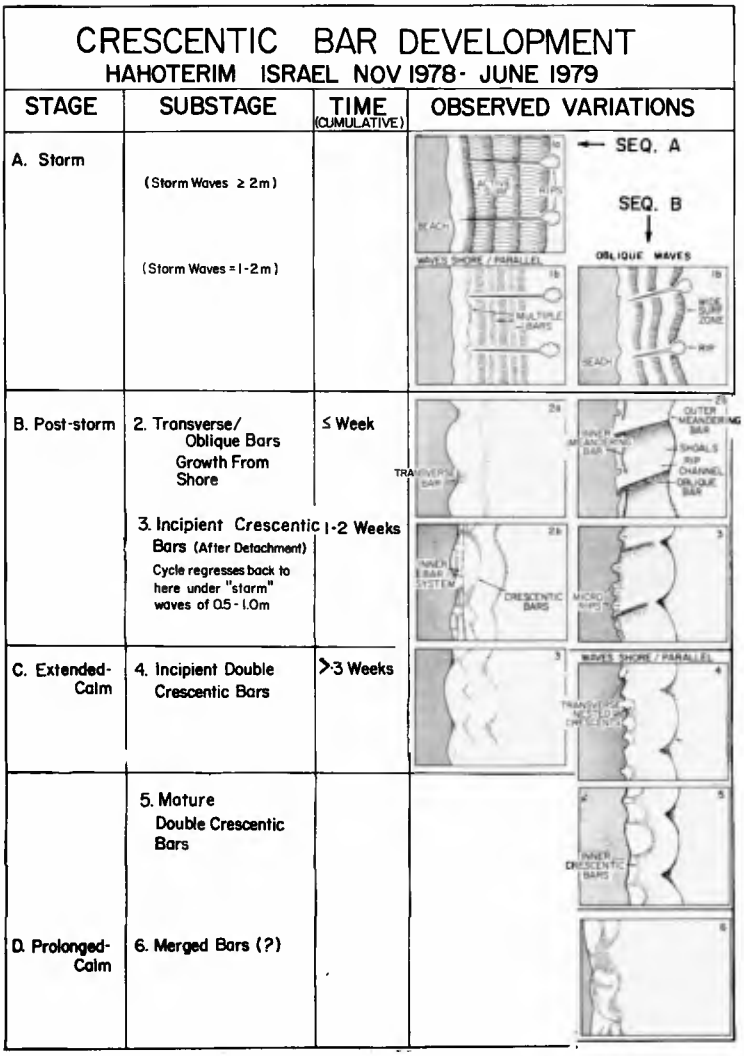

Figure 3. Crescentic bar development and concomitant waves in the south-eastern Mediterranean.

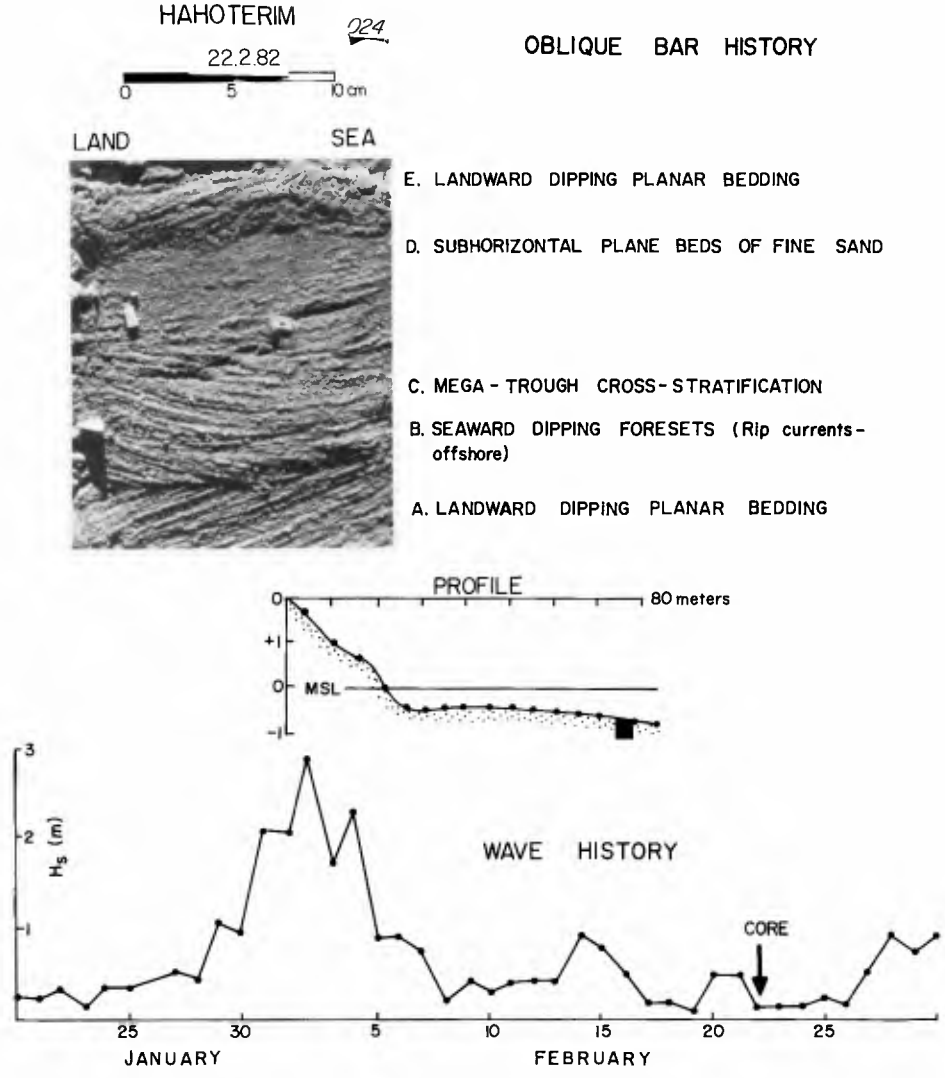

Figure 4. Sedimentation and wave history on an oblique bar, HaHoterim.

verse bars. The outer bars did not evolve during the inner crescentic low energy regime, but persisted from the moderate storms, and should be regarded as inherited. Their "memory" results in out-of-phase relationships between the outer and inner crescentic systems, i.e., the center of the outer crescentic bar corresponded to an inshore shoal, and the outer horns pointed toward an inshore rip channel. Sequence B (extended calm, Fig. 3) indicates the complete removal of the antecedent morphology under the influence of low waves. Phase correlation between the inner bars and the cuspate shore rhythms usually dominates this mature double crescentic stage.

The following wave characteristics were defined coincident with bar stages:

1) Storm, above threshold conditions for bar formation; spilling-plunging breakers, $H_s > 1.0$ m, main range of spectral density $> 10^{-1}$ m^2/Hz. These conditions typify stage A.

2) Wave energy conditions decrease below threshold; collapsing-surging breakers, $H_s < 0.5$ m, main range of spectral density 10^{-2} to 10^{0} m^2/Hz. These conditions indicate the start of crescentic development.

3) Calm, $H_s < 0.3$ m, main range of spectral density $< 10^{-2}$ m^2/Hz indicating the double crescentic bar stage. Minor storms in the range of 10^{-2} to 10^{-1} m^2/Hz did not modify the double crescentic bar pattern.

BAR AND WAVE SEASONALITY : Although the 150 observations of bars during the 1948-1980 period were spread throughout all months of the year, there is a definite tendency for more bars to occur during the six lowest wave months, June through November (62%), than the remaining six months (Fig. 5A). This tendency is explained by the monthly frequency of low waves ($H_s \leq 1$ m) during the 1948-1978 period (Fig. 5B). The parallelism between months of low waves and the annual distributions of bars is quite striking. Most notable is the increase in bars related to a major wave energy threshold in the spring, when the frequency of $H_s \leq 1$ m sharply increases from 58% in the winter months to 70% frequency in April and 85% in May. The calmer and barred summer composes an uninterrupted period of lower waves, explaining the observed seasonal stability of some of the bar types. Summer shows two peaks of low wave activity (Fig. 5B). May to June composes one low wave peak which, when one allows for the lag time needed for bar formation, is clearly related to the high occurrence of bars in June. July is stormier, and therefore both July and August have fewer occurrences of bars. August and September compose a second summer low wave peak, and this is mainly related to the bar-richest month of September. Thus peaks of bar occurrence and wave energy do not match perfectly, but rather indicate a lag in the adjustment of bars to wave power, also observed by Short (1979).

The mature double crescentic bars occur throughout the year, lacking seasonality (Fig. 6). The single crescentic and the initial double crescentic bars are the most energy-sensitive types, being non-existent during winter but abundant from May to November. Non-rhythmic morphologies also seem to occur most of the year (Fig. 6). The major excep-

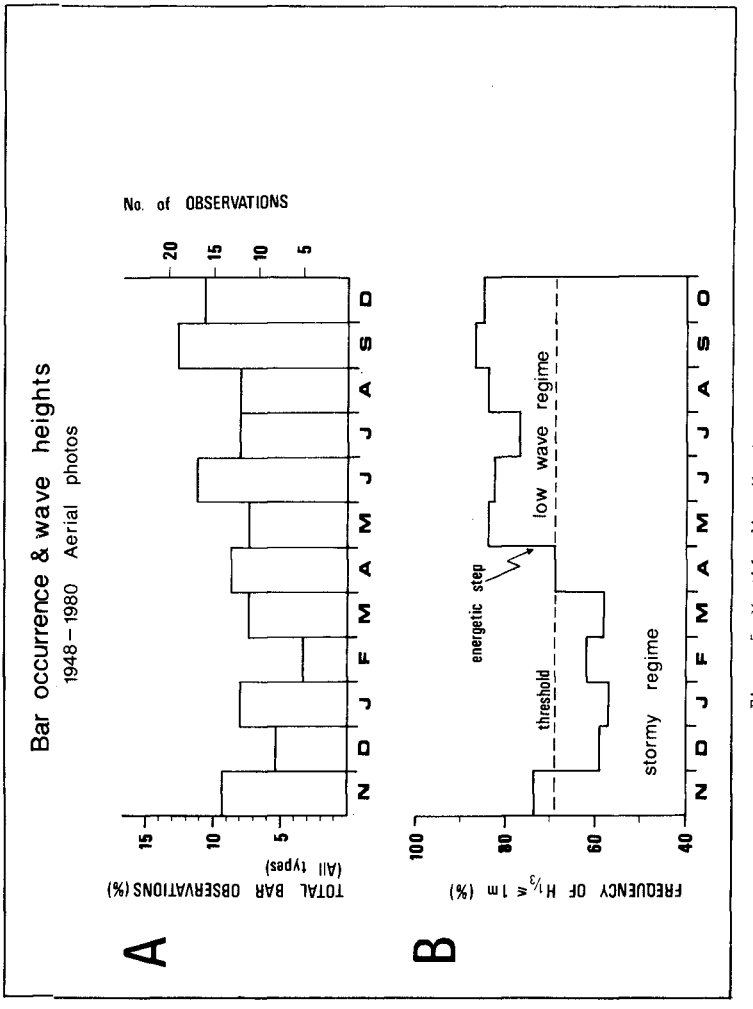

Figure 5. Monthly distribution of (A) bar frequency and (B) wave heights (H_s), 1948-1980.

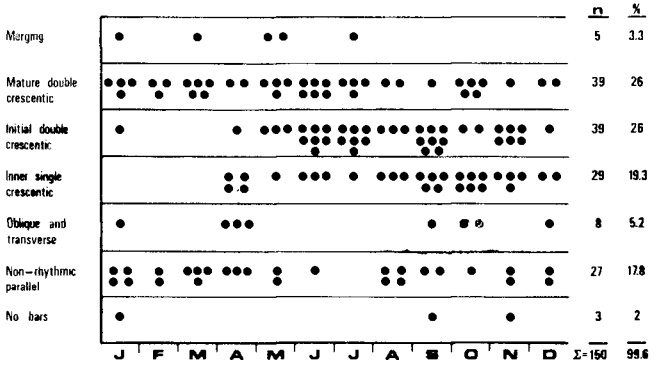

Figure 6. Seasonal distribution of bar types in the southeastern Mediterranean, 1949-1980.

tions are the months of May to July, when the crescentic families dominate. Because July has higher waves, August shows the reappearance of noncyclic systems. This antiphase relationship between non-rhythmic and crescentic bar families continues in September/October.

DISCUSSION : The coast of Israel is highly dissipative, and is dominated by single and double crescentic bar families, which compose 71% of the bars. Because of the cyclicity of storm waves followed by extended times of low waves, the sequence of bar types recurs several times per year. Therefore this may well be one of the best places to study bar sequences.

Thus, this coast is different from the Australian coast (Short, 1979; Wright et al., 1979), where the inner single crescentic bars, defined as megacusps and welded bars, dominated. This may be related to the higher Australian wave energy. This, in turn, differs from the observations of Greenwood and Davidson-Arnott (1979), who reported a lack of seasonal bar changes and continuous dominance of crescentic bars.

Similar bar types occur on most coasts, despite large differences in wave climate, tidal conditions, nearshore slopes and grain size. Most importantly, bars occur successively within definite sequences. However, on different coasts the bar types tend to occur in different sequences and in different proportions of time. It is suggested that these differences are directly attributable to global differences in the occurrences of threshold wave conditions. This, in turn, may be partly due to differences in sediment size and inner continental shelf slopes, as well as to the differences in wave climate.

ACKNOWLEDGEMENTS : This study emanated from a project on nearshore bar systems supported by the Geography Programs, Office of Naval Research, Contract No. N00014-78-C-0645, NP 388-148, V. Goldsmith, Principal Investigator. Additional support was furnished by the Israel Ministry of Energy and Infrastructure.

REFERENCES

Bowen, A.J. & Inman, D.L. 1971. Edge waves and crescentic bars. J. Geophys. Res. 76: 8662-8671.

Bowman, D. & Goldsmith, V. In press. Bar morphology and wave energy - an empirical model for moderate energy dissipative beaches. Mar. Geol.

Clairbout, J.F. 1976. Fundamentals of geophysical data processing with applications to petroleum prospecting. New York, McGraw-Hill, 274 pp.

Emery, K.O. & Neev, D. 1960. Mediterranean beaches of Israel. Bull. Geol. Surv. Israel 26: 1-24.

Goda, Y. 1974. Estimation of wave statistics from spectral information, in Ocean Wave Measurement and Analysis, Vol. 1. Edge, W. (ed.), New York, A.S.C.E., pp. 320-337.

Goldsmith, V. In press. Dynamic geomorphology of the Israeli coast: a brief review, in Goastal Problems in the Mediterranean. Fabbri, P. & Bird, E.G.F. (eds.), Gommission on the Goastal Environment, International Geographic Union, 14 pp.

Goldsmith, V. & Golik, A. 1980. Sediment transport model of the southeastern Mediterranean coast. Mar. Geol. 37: 147-175.

Goldsmith, V. & Sofer, S. 1983. Wave climatology of the southeastern Mediterranean: an integrated approach. Israel J. Earth Sci. 32(1).

Goldsmith, V., Bowman, D. & Kiley, K. 1982. Sequential stage development of crescentic bars: HaHoterim beach, southeastern Mediterranean. J. Sedim. Petrol. 52: 233-249.

Greenwood, B. & Davidson-Arnott, R.G.D. 1975. Marine bars and nearshore sedimentary processes, Kouchibougnac Bay, New Brunswick, Ganada, in Nearshore Sediment Dynamics and Sedimentation. Hails, J.R. & Carr, A. (eds.), New York, Wiley, pp. 123-150.

Greenwood, B. & Davidson-Arnott, R.G.D. 1979. Sedimentation and equilibrium in wave formed bars: a review and case study. Can. J. Earth Sci. 16: 312-332.

Gwirz, B. 1982. A sediment transport model based on granulometric analysis of the northern Carmel beaches. Unpubl. Manuscript, Geography Dept., Haifa Univ., 47 pp.

Owens, E.H. 1977. Temporal variations in beach and nearshore dynamics. J. Sedim. Petrol. 47: 168-190.

Short, A.D. 1979. Three dimensional beach-stage model. J. Geol. 87: 553-572.

Wright, L.D., Chappell, J., Thom, B.G., Bradshaw, M.P. & Gowell, P. 1979. Morphodynamics of reflective and dissipative beach and inshore systems, southeastern Australia. Mar. Geol. 32: 105-140.

LONGSHORE TRANSPORT DETERMINED BY AN EFFICIENT TRAP

by

R. G. Dean[1], M. ASCE, E. P. Berek[2], A.M. ASCE, C. G. Gable[3], and R. J. Seymour[4], M. ASCE

ABSTRACT

The Nearshore Sediment Transport Study (NSTS), sponsored by the National Sea Grant Office included a field component to quantify the total longshore sediment transport relationship. This component was conducted at Santa Barbara, California and encompassed a period of eighteen months during which ten surveys were conducted. To date, eight of these surveys have been analyzed, yielding seven intersurvey periods. A total of 288,600 m^3 of net sediment transport was documented by these eight surveys. The wave characteristics are based on one of two S_{xy} gages located in a water depth of 7 m. The most widely used correlation constant, K, in the relationship $I_\ell = KP_{\ell s}$ is 0.77. The values found from the data were 0.93 and 1.23 for linear and log best-fit values, respectively. The corresponding values of K_* relating I_ℓ and S_{xy} are 2.60 and 2.63 m/s, respectively.

INTRODUCTION

Many coastal engineering projects and interpretation of nearshore phenomena depend on an accurate quantitative relationship between total longshore sediment transport and the wave (and other) characteristics which cause the transport. Although a number of field studies have been carried out, the characteristics of most studies are such that considerable uncertainty exists in either the characterization of the forcing function (i.e. waves) or of the sedimentary response. In particular most of the early data sets

---

[1]Graduate Research Professor, Coastal and Oceanographic Engineering Oepartment, University of Florida, Gainesville, FL 32611, Formerly, Professor, Department of Civil Engineering and College of Marine Studies, University of Delaware, Newark, DE 19711.

[2]Research Engineer, Amoco Production Co., Tulsa, OK 74102, Formerly Graduate Assistant, Oepartment of Civil Engineering, University of Delaware, Newark, DE 19711.

[3]Associate Development Engineer, Scripps Institute of Oceanography, University of California, La Jolla, CA 92093.

[4]Associate in Oceanography, Scripps Institute of Oceanography, University of California, La Jolla, CA 92093.

relied on visual observations or hindcasts for wave direction. Additionally a number of the programs were based on tracer studies for determination of sediment transport quantities. In studies of this type, substantial uncertanties exist due to the approximations required to determine the effective vertical and lateral limits of transport.

The present paper describes a field measurement program carried out at Santa 8arbara, California. The wave characteristics were determined by an "S_{xy} gage" comprised of four pressure sensors positioned on the bottom at the corners of a 6 m square array in 7 m of water depth. These wave conditions were transformed to the breaker line where both P_{ls} and S_{xy} were established for correlation with the sediment transport. The net longshore sediment transport reported herein was established by means of eight surveys, each consisting of 67 beach profiles and 63 survey lines. The "near total" trap is the spit of sand which is attached to the eastern end of the Santa 8arbara breakwater and portions of the updrift beaches. The surveys encompassed a period of 13 months during which a total of 288,600 m^3 of net sediment transport was documented. Correlations are presented of the net longshore sediment transport with P_{ls}, the longshore component of energy flux at breaking and S_{xy}, the flux in the onshore direction of the longshore component of momentum.

PREVIOUS RELATED INVESTIGATIONS

The number of field investigations of longshore transport is very limited. Greer and Madsen (1979) undertook an evaluation of the field data sets available in 1978. These included a sediment trap at South Lake Worth Inlet, Florida, reported by Watts (1953), a study of erosion downdrift of a jetty at Surfside, California, reported by Caldwell (1956), and sand tracer experiments at El Moreno Beach, Mexico, and Silver Strand 8each, California, by Komar (1969). Greer and Madsen find convincing reasons for rejecting all but the Komar results and find that these, at best, are only order of magnitude estimates.

Subsequent to the Greer and Madsen review, three more data sets were reported at the Seventeenth Coastal Engineering Conference that overcame many of their objections to the first three. Seymour et al (1981) describe a sediment trap experiment at Santa Cruz, California, with an adjacent directional wave measurement array. Bruno, Dean and Gable (1981) report a series of experiments with a trap at Channel Islands Harbor, California, with a pair of wave gages nearby providing low resolution wave directional information. Inman et al (1981) describe tracer experiments at Torrey Pines Beach, California, employing a linear wave measurement array. In addition, Kraus et al (1981) report a series of tracer experiments at Ajigaura and Oarai Beaches in Japan.

The most widely used relationship to predict longshore sediment transport was formulated by Bagnold, Inman and Komar and is often referred to as the SPM method because of broad exposure through the Shore Protection Manual, U.S. Army Engineers (1977). The longshore transport rate is given by

$$I_{\ell} = K P_{\ell s} \quad (1)$$

where I_{ℓ} = immersed weight longshore sediment transport rate
$P_{\ell s}$ = longshore component of wave energy flux at breaking
K = proportionality factor

Values of the coefficient, K, have been established for each of the data sets noted above. The range of these values is shown in Table I. It can be seen that the values of K span over two decades. However, the two trap experiments with direct wave measurements (Seymour et al and Bruno et al) encompass a range of less than a factor of two.

TABLE I

LONGSHORE TRANSPORT COEFFICIENT, K
FOR VARIOUS FIELD DATA SETS

REFERENCE	RANGE OF K VALUES
Watts (1953)	1.0 - 1.2
Caldwell (1956)	0.1 - 2.2
Komar (1969)	0.5 - 1.3
Seymour et al (19B1)	0.5
Bruno et al (19B1)	0.7 - 0.9
Inman et al (19B1)	0.3 - 1.3
Kraus et al (19B1)	0.1 - 0.3

SITE OESCRIPTION

Santa Barbara is located on a sandy lowland on the coast of Southern California approximately 150 km northwest of Los Angeles. It is located on the Santa Barbara Channel which is an elongate marine feature bounded on the north and east by the mainland shoreline of Santa Barbara and Ventura Counties, in the south by the Channel Islands (San Miguel, Santa Rosa, Santa Cruz, and Anacapa) and bordered on the West by the open waters of the Pacific Ocean, Figure 1. The coast in the vicinity of Santa Barbara lies in an east-west direction and is generally rugged. It is characterized by projecting headlands of rock and boulders with intervening coves having cobble covered shores or sandy pocket beaches backed by high bluffs. There are no large rivers, but numerous steep streams, with torrential flow during rainy seasons, that run through arroyos and discharge onto the shore. Santa Barbara is located approximately in the middle of the Santa Barbara littoral cell which extends from Point Conception to Point Mugu. The shoreline between Point Conception and Santa Barbara trends east-west and is composed of sedimentary rocks and shale bluffs

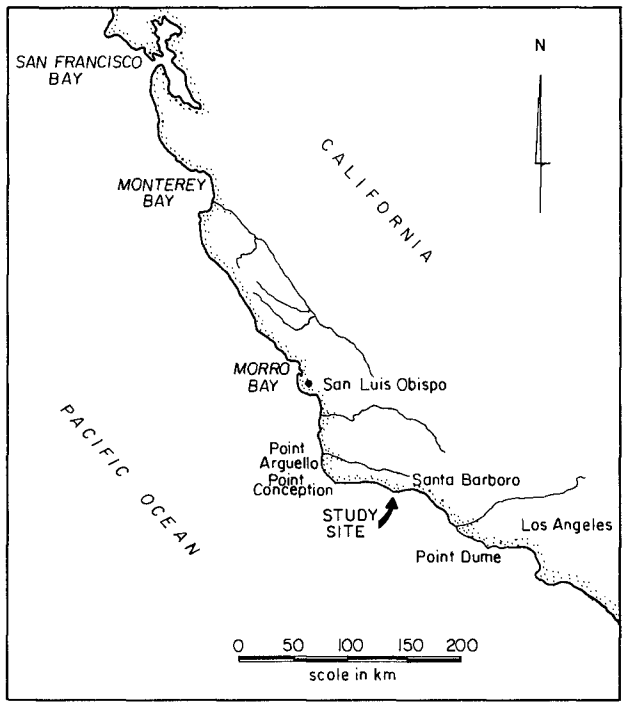

Figure 1 Geographic Location of Santa Barbara (from Trask, 1955).

fronted by sand and cobble beaches. The climate in Santa Barbara is Mediterranean and is controlled primarily by the position and intensity of the semi-permanent Pacific high pressure system over the ocean to the west. During the summer this high pressure feature covers the eastern North Pacific Ocean and deflects eastwardly moving storms to the north. During the winter months this Pacific high migrates southward and weakens, allowing occasional frontal systems that originate in the Aleutians to move through southern California. The most intense extratropical storms are those that develop between Hawaii and the California coast. These storms, because of their southerly position and intensity, often produce large westerly ocean swells which propagate into the Santa Barbara Channel between Point Conception and San Miguel Island.

Before the construction of the Santa Barbara Harbor breakwater the flow of sand was uninterrupted and was transported naturally to the beaches to the east within the Santa Barbara littoral cell. In

early 1930 when the harbor breakwater was completed, sand began accumulating west of the shore arm of the breakwater creating what is now known as Leadbetter Beach. Eventually, sand migrated along the breakwater and deposited in the lee or shadow of the structure forming a sand spit in the channel as shown in Figure 2. As a result, the sand spit created a navigation problem as well as stored the sand that was naturally previously transported to the downcoast beaches. Therefore, a dredging program was initiated in 1935 for placing obstructing material within the harbor on the starved downcoast beaches to prevent further erosion. This annual harbor maintenance and beach nourishment program is still in progress. There were two dredging episodes within the time frame of this experiment.

The wave climate at Santa Barbara is generated either between the Channel Islands and the coast (local wind waves) or generated in the ocean seaward of the Islands. The local wind waves from the south are usually insignificant with only choppy seas and small waves. Wiegel (1959) reports that local storms from the southeast have a fetch of 145 km and generate waves toward the Santa Barbara coast with significant wave heights ranging from 244 to 488 cm. The predominant waves are from the southwest and west that enter the Santa Barbara Channel between San Miguel Island and Point Conception. Leadbetter Beach is protected by the Channel Islands and Point Conception from swells generated by distant storms from all other active sectors. Wiegel (1959) reports that waves from the southwest and west range from 30 to 500 cm but average about 91 cm. The average wave period is 12 seconds, but ranges between 8 and 16 seconds. Leadbetter Beach is a feeder beach for the sandspit formed in the shadow of the breakwater. It is characterized by a steep beach slope, narrow surf zone, unique wave climate with a narrow window of approach and high angle of incidence, unique wave refraction effects, and a unidirectional longshore current of high magnitude. The sand is well sorted with a median size of approximately 0.22 mm. Gable (1980) provides a detailed description of the experiment site.

DESCRIPTION OF SURVEYS AND TECHNIQUES

The accumulation of sediment was measured at approximately 6-8 week intervals with profiles extending from the dry beach to a depth of about 10 meters. A total of ten beach and nearshore surveys of the sediment trap at Santa Barbara Harbor and the adjacent updrift "Leadbetter Beach" were completed between 18 October, 1979 and 26 February, 1981. Surveys were scheduled to coincide with days of large tidal ranges. The schedule was modified occasionally according to weather and dredge operations. Each survey required 4-5 days to complete. The starting dates for each survey were: (1979): 18 October, 30 November, (1980): 20 January, 25 February, 10 April, 3 June, 25 August, 22 October, 17 December, (1981): 26 February. The survey plan is shown schematically in Figure 3. A total of 63 nearshore profile lines was surveyed using an Automated Bathymetry System (ABS) on-board a small survey boat provided under contract by Ocean Surveys, Inc. (OSI). Each of these profile lines was surveyed with ABS three times to enable the averaging out of long period ocean swells. The beach surveys were carried out to wading depths, used conventional rod and level techniques and consisted of 67 profile

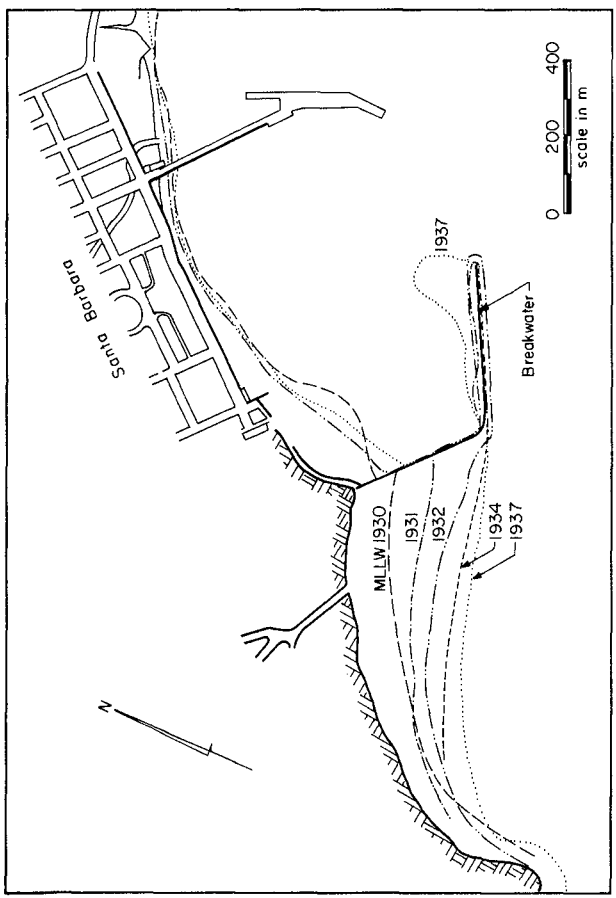

Figure 2 Shoreline Changes Upcoast of the Santa Barbara Breakwater (after Johnson, 1957).

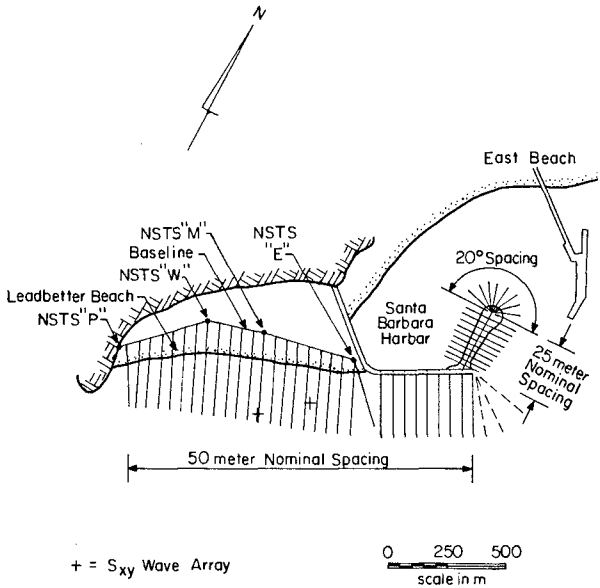

Figure 3 Plan of Sediment Impoundment Study and Location of Directional Wave Gages

lines. The nearshore and beach profiling were conducted over the maxima and minima of large tidal ranges, respectively, to achieve as much overlap as possible. Tide data necessary to reduce depth readings to the MSL datum were collected using a tide staff and a NOAA recording tide station. Range lines were defined by two survey points marked by flags, which a rodman aligned before each survey reading. Rod locations were established rapidly using a specially constructed plastic coated stainless steel survey line marked at 5 meter intervals seaward of the benchmark except where pronounced changes in slope occurred. An engineer's level and rod provided vertical control. Measurements were made out into the water by the tapeman paying out the tape in 5 meter increments from a fixed point on the baseline. The profile was terminated when the water became too deep for the rodman to wade or the breaking waves made it impossible to plumb the rod.

The nearshore bathymetry was measured using an ABS onboard a small survey boat. The "boat" surveys usually took three full days to profile all 63 lines (each three times) and required one boat operator, one field electronics engineer, and a minimum of two experienced surveyors. To assure that the boat remained on the given range azimuth and to assure accurate replication of the survey lines

from survey to survey, a transit and Cubic Autotape positioning responder were set up over each of the profile bench marks. The transit operator would turn the proper azimuth from a known backsight and give course corrections to the boat operator via FM radio. Two orange survey cones on-range were placed on the beach to provide the boat operator a visual line. Distance offshore measured from the responder located over the benchmark was continually monitored by the electronics operator on board the boat. This technique ensured that the proper cut-off distance offshore was met. The second responder of the Autotape positioning system was installed over a bench mark a sufficient distance up or down the beach to provide an accurate measure of the distance off-line at each position fix. The ABS consists of the following equipment: a Raytheon DE-719B Fathometer, Innerspace Model 412 Digitizer, Cubic DM-40A Autotape Range-Range Positioning Navigation System, Hewlett Packard Model 5150A Thermal Printer, and a Sea Data Model 1250 Data Logger and Cassette Recorder, see Figure 4. This equipment was secured into a 6.7 meter survey boat

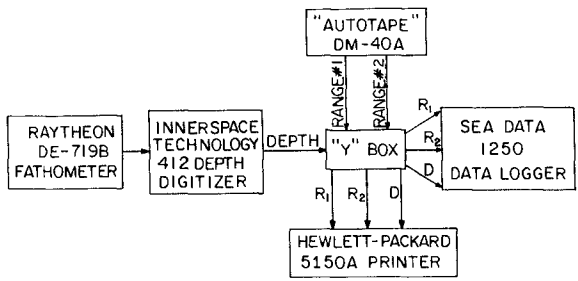

Figure 4 Block Diagram of OSI's Data Acquisition System

(Boston Whaler). The survey boat was conned along each transect by a transit operator on shore. However, boat position was fixed by logging two ranges of the Cubic Autotape positioning system. As the range determinations of the Autotape are updated at approximately one second intervals, the Autotape is designated the master for the automated system. At each update, a print command is sent to a Hewlett Packard Model 5150A thermal printer and a scan command is sent to the Sea Data Model 1250 digital cassette magnetic tape data logger. The range-range data, in parallel binary coded decimal (BCD), is thus recorded on both printed paper tape (hard copy backup and visual presentation of digital data for field data quality control) and magnetic tape. On command from the Autotape, both the printer and the data logger also record the current depth reading. Depth data are available from the Innerspace Model 412 depth digitizer. The digitizer accepts "start-stop" pulses from the Raytheon Fathometer. The interval of time between the start and stop pulses is directly proportional to depth. The fathometer records on strip chart and

provides depth readings to the digitizer nine times per second. Accordingly, the depth data are virtually instantaneously available at each Autotape command. Communication between all components of the system is provided to assure that position and depth data are not being updated at the instant of recording. An automatic "event" is also recorded at every 16th Autotape command on the cassette tape, printer paper tape, and fathometer strip chart. This event mark allows data processors to correlate the three recording media to check accuracy. As a "bookkeeping" function, each sequential event is numbered on the cassette tape. The cassette tape data logger also records times in the "header" for each data record as well as a manually entered run number, set by the operator at the beginning of each run. A "Y" box receives the BCD depth and range data and splits these signals for separate transmission to the printer and data logger allowing continued operation of the system should a failure occur in either of the recording media. A block diagram of the data acquisition system has been presented as Figure 4. The depth sounder and digitizer establish the elapsed time interval between transmission of an acoustic pulse and receipt of a return echo from the seafloor. To precisely relate this time interval to water depth, an adjustment is necessary on both instruments for the speed of sound in the water at the site. This was accomplished by conducting "bar checks", a process of lowering a target "bar" on a calibrated line to known depths below the depth sounder transducer. Both the depth sounder and digitizer are then adjusted to display this depth precisely. Bar checks were performed at nominally three hour intervals and at the beginning and end of each recording period. A more detailed description of the survey system and techniques is provided by Gable (1980).

WAVE ANALYSIS

The incident wave climate was measured using two slope arrays at a depth of approximately 7 m. A description of the hardware and the data retrieval and recording methods for a similar installation is contained in Seymour et al (1981). The location of these arrays is shown in Figure 3. Each array consists of four pressure sensors at the corners of a 6 m square frame. Pressures were sampled at 1 hz and 1024 samples (17+ minutes of data) were obtained at nominal six hour intervals for the duration of the experiment.

Two different approaches were used in analyzing the wave data to allow estimation of the longshore transport. The first method provides input for Equation (1). In this approach, the pressure signal from one of the sensors in each array was Fourier transformed, corrected to surface elevations by application of linear wave theory, and converted to an energy spectrum. A weighted characteristic frequency for this spectrum was then calculated. Using the cospectra of the surface elevation with the sea surface slope components, a characteristic wave approach direction was calculated. Employing the total energy in the spectrum, a singular wave was constructed having the characteristic frequency and direction. This wave was then refracted to the break point using linear shoaling theory. Finally, P_{ls} was calculated for this breaking wave.

In the second approach, the longshore component of shoreward directed radiation stress, S_{xy}, was calculated for each array. The slope array facilitates this calculation since, as shown in Higgins, Seymour and Pawka (1981), S_{xy} is proportional to the cross-spectra of the sea surface slopes.

Since the nearshore bathymetry is marked by non-parallel contours, the two arrays produce somewhat different values for either of the two parameters. In this work the data from the east array were employed.

RESULTS

The principal results are the correlations between the immersed weight longshore sediment transport rates, I_ℓ, and measures of the wave forcing as characterized by $P_{\ell s}$ and S_{xy}. For purposes of establishing, I_ℓ, the volume changes were based on the following areas: the spit in the lee of the breakwater, the area fronting the breakwater and the portion of Leadbetter Beach encompassed by the survey lines to the east of the easterly S_{xy} gage, see Figure 3.

Table II presents the characteristics of and results from the seven intersurvey periods. It is seen that there was much more sediment transported during some of the intersurvey periods than during others. For example, during the third intersurvey period the average immersed weight transport rate was almost 300 N/S whereas during the following intersurvey period, the rate was less by more than an order of magnitude. The seventh column of Table II presents the K value calculated from each individual data set and it is seen that these values range from 0.32 to 1.63, a range of approximately five. However the smallest value which exhibits the greatest deviation from the norm is associated with the fourth intersurvey period which is characterized by a very small value of I_ℓ. If this one point is not included, the ratio of the largest to smallest of the remaining individual K values is less than two, which appears reasonable for this type of measurement. Unless stated otherwise, the results presented herein will exclude this one "outlier" value. The I_ℓ vs $P_{\ell s}$ data are plotted in Figure 5 on a log-log scale. Values of K were determined that provided best least squares fits between I_ℓ and $KP_{\ell s}$ and between log I_ℓ and log $KP_{\ell s}$. The corresponding K values were 0.93 and 1.23, respectively. It is noted that a previous study for Santa Barbara by Galvin (1969) had combined sediment accumulation values developed by J. W. Johnson with wave characteristics deduced by Galvin based on wave hindcasts and a wave direction which yielded the maximum $P_{\ell s}$, (i.e. minimum K); Galvin's mean value of K was 1.60. The K value of 1.23 determined from the present study is smaller than that determined by Galvin and larger than the values (0.77) referenced in the Shore Protection Manual (1977) and most often employed. As shown in Figure 6 the value determined herein is in approximate agreement with an earlier correlation of K with sand size developed by Dean (1978), where the characteristics of the other data points presented in Figure 6 are described.

It seems plausible that I_ℓ should correlate reasonably well with the total longshore force, S_{xy}, acting on the surf zone, in the form

TABLE II

SUMMARY OF FIELD RESULTS BY INTERSURVEY PERIOD

Intersurvey Period	No. of Days	Dredging Event	Total Volume Change(m^3)	Immersed Weight Transport Rate I_ℓ(N/S)	Net Longshore Component of Wave Energy Flux at Breaking, $P_{\ell s}$(N/S)	$K = I_\ell / P_{\ell s}$	Net Onshore Flux of Longshore Component of Momentum S_{xy}(N/m)	$K_* = I_\ell / S_{xy}$ (m/s)
10/13/79-11/30/79	48	No	32,820	85.3	52.2	1.63	27.8	3.06
12/1/79-1/20/80	51	Yes,Major	65,070	159.1	101.4	1.57	46.4	3.50
1/21/80-2/25/80	35	Yes,Minor	82,810	295.0	352.4	0.84	119.6	2.47
4/11/80-6/3/80	53	No	10,290	24.2	76.6	0.32	37.9	0.64
6/4/80-8/25/80	82	No	22,220	33.8	31.7	1.07	17.6	1.91
8/26/80-10/23/80	57	No	38,760	84.8	63.8	1.33	32.6	2.60
10/24/80-12/17/80	54	Yes,Major	35,640	84.6	64.4	1.31	34.2	2.47

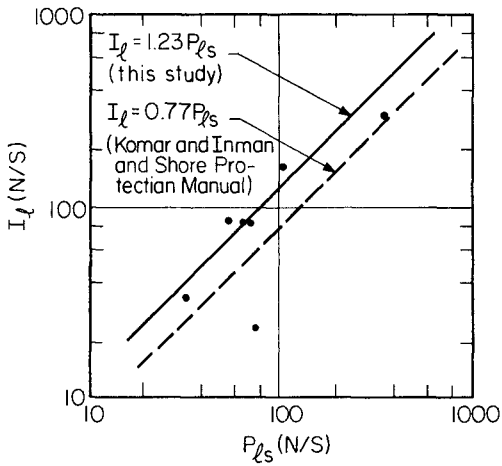

Figure 5 Data From Santa Barbara Field Experiment. I_ℓ vs $P_{\ell s}$, Present and Past Correlations.

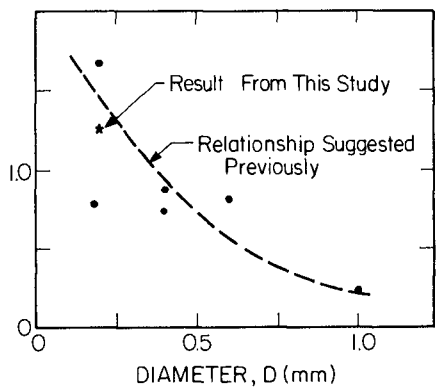

Figure 6 Plot of K vs D. Results of Present and Previous Studies (Modified from Dean, 1978).

$$I_{\ell} = K_{*} S_{xy} \quad .$$

One disadvantage of this form is that K_{*} is dimensional, whereas K (Eq. 1) is dimensionless. The S_{xy} and K_{*} values for each of the intersurvey periods are presented in Table II where it is seen that if the one "outlier" (small value) is not considered, the ratio of the maximum to minimum values of K_{*} is 1.83, only slightly less than the corresponding ratio for K. The I_{ℓ} vs S_{xy} values are plotted in Figure 7. Best fit linear and logarithmic values of K_{*} are 2.60 and 2.63 m/s, respectively.

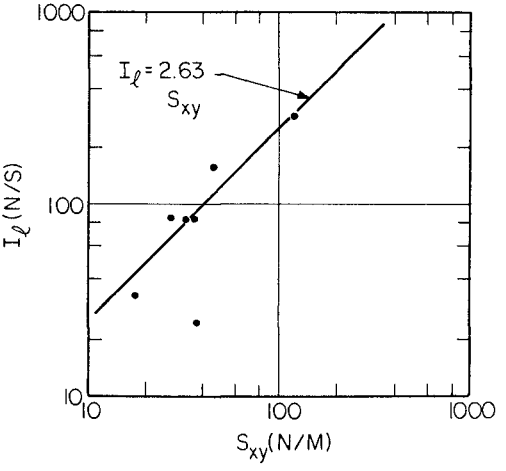

Figure 7 Data From Santa Barbara Field Experiment. I_{ℓ} vs S_{xy} and Best Least Squares Fit.

The values of K and K_{*} based on the cumulative I_{ℓ}, $P_{\ell s}$ and S_{xy} over all seven intersurvey periods are 1.07 and 2.40 m/s. Excluding the one "outlier", the values are 1.17 and 2.67 m/s.

SUMMARY AND CONCLUSIONS

Summary

A field experiment has been carried out with high-quality measurements of directional wave characteristics and the associated sediment transport. The results, documented herein, span approximately 13 months and include surveyed volumes of 288,600 cubic meters of sediment transport. The analysis, based on six intersurvey periods, yield best-fit linear and logarithmic values of K of 0.93 and 1.23, respectively. The corresponding values of K_{*} relating the immersed weight sediment transport rate, I_{ℓ}, and S_{xy}, the flux in the

onshore direction of the longshore component of momentum, are 2.60 and 2.63 m/s, respectively. While the value of K is somewhat larger than the most-often referenced value of 0.77, it is reasonably consistent with the value (1.6D) determined in an earlier study of Santa Barbara by Galvin and also is consistent with an earlier trend established by Dean of K with sediment diameter, D.

Conclusions

1. The results developed here are supportive of a variation of the sediment transport coefficient, K, with diameter, D. It is likely that K varies with other parameters: beach slope and morphology, wave characteristics, etc. Well documented (waves and sediment transport) field programs at locations with widely different conditions would be valuable in further defining the variation of K with other parameters of importance.

2. Although the two variables P_{gs} and S_{xy} are related and appear to provide approximately equally good fits to the longshore sediment transport, investigation should be continued of the relative merits of these two as correlating parameters.

ACKNOWLEDGEMENTS

The financial support provided by the Sea Grant Program to this component of the Nearshore Sediment Transport Program is greatly appreciated. The encouragement and guidance of Dr. David Duane as Technical Monitor of that program was especially valuable. The dedicated and professional efforts of Ocean Surveys, Inc. in the field surveys contributed significantly to the quality of the field data. Finally, the University of California at Santa Barbara was very helpful by providing vessels and highly competent personnel to assist in the field efforts.

REFERENCES

Bruno, R. O., R. G. Dean, and C. G. Gable, "Longshore Transport Evaluations at a Detached Breakwater," Proceedings, Seventeenth Coastal Engineering Conference, ASCE, Sydney, Australia, 1980, p. 1453-1475.

Caldwell, J. M., "Wave Action and Sand Movement Near Anaheim Bay, California," U.S. Army Corps of Engineers, Beach Erosion Board, Technical Memorandum No. 68, Washington, D. C., 1956.

Dean, R. G., "Review of Sediment Transport Relationships and the Data Base," Proceedings, Workshop on Coastal Sediment Transport, University of Delaware Sea Grant Program, 197B, p. 25-39.

Gable, C. G., Ed., "Report on Data from the Nearshore Sediment Transport Study Experiment at Leadbetter Beach, Santa Barbara, California, January-February 19BD." University of California, Institute of Marine Resources, IMR Ref. No. BD-5, 1981.

Galvin, C. J., "Comparison of Johnson's Littoral Drift Data for Santa 8arbara with the Empirical Relation of CERC TR 4", Memorandum for Record, Coastal Engineering Research Center, February, 1969.

Greer, M. N. and O. S. Madsen, "Longshore Sediment Transport Data: A Review," Proceedings, Sixteenth Coastal Engineering Conference, ASCE, Honolulu, Hawaii, 1978, p. 1563-1576.

Higgins, A. L., R. J. Seymour and S. S. Pawka, "A Compact Representation of Ocean Wave Directionality," Applied Ocean Research, Vol. 3, No. 3, 1981, p. 105-112.

Inman, D. L., J. A. Zampol, T. E. White, D. M. Hanes, 8. W. Waldorf, and K. A. Kastens, "Field Measurements of Sand Motion in the Surf Zone," Proceedings, Seventeenth Coastal Engineering Conference, ASCE, Sydney, Australia, 1980, p. 1215-1234.

Johnson, J. W., "The Littoral Drift Problem at Shoreline Harbors", ASCE Journal Waterways and Harbors Division, Vol. 83, Paper 1211, April, 1957.

Komar, P. D., "The Longshore Transport of Sand on Beaches," Thesis presented to the University of California, at San Diego, California, in 1969, in partial fulfillment of the requirements for the degree of Doctor of Philosophy, 1969.

Kraus, N. C., R. S. Farinato and K. Horikawa, "Field Experiments on Longshore Sand Transport in the Surf Zone," Coastal Engineering in Japan, Vol. 24, 1981, p. 171-194.

Trask, P. D., "Movement of Sand Around Southern California Promontories," U.S. Army Corps of Engineers, Beach Erosion 8oard, Technical Memorandum No. 76, 1955.

U.S. Army Coastal Engineering Research Center, Shore Protection Manual, U.S. Army Corps of Engineers, Washington, D.C., 1977.

Watts, G. M., "A Study of Sand Movement at Lake Worth Inlet, Florida." U.S. Army Corps of Engineers, Beach Erosion Board, Technical Memorandum No. 42, 1958.

Wiegel, R. L., "Sand 8ypassing at Santa Barbara, California, ASCE Journal Waterways and Harbors Division, Proc. ASCE, 85, WW2, 1959, p. 1-30.

FIELD EXPERIMENTS ON LONGSHORE SAND TRANSPORT IN THE SURF ZONE

by

Nicholas C. Kraus[1], Masahiko Isobe[2], Hajime Igarashi[3]
Tamio O. Sasaki[4] and Kiyoshi Horikawa[5]

ABSTRACT

Eight fluorescent sand tracer experiments were performed in energetic surf zones on natural beaches and on beaches near structures to measure the short-term longshore sand transport rate. Tracer of up to four distinct colors was injected on a line crossing the surf zone to investigate the on-offshore distributions of the longshore sand advection velocity and transport rate. The tracer advection velocity, v_a, and the depth of mixing into the bed, b, were determined from large numbers of cores taken in situ throughout the sampling area. The sand advection velocity and mixing depth were not constant across the surf zone, but usually exhibited a maximum either toward the shoreline or toward the breaker line, or in both regions. The local breaking wave height, H_b, and horizontal current velocity in the surf zone (yielding an average longshore current velocity $\bar{V}$) were also measured. The data were interpreted with simple dimensional arguments to give the following results: $b = 0.027\ H_b$, $v_a = 0.014\ \bar{V}$, and the volumetric transport rate $Q = 0.024\ H_b^2 \bar{V}$. Agreement was also found between the measured total longshore sand transport rate and a predictive expression due to Bagnold involving the breaking wave power and average longshore current velocity. Although the results appear reasonable and consistent, a problem remains concerning the apparent decrease in tracer advection speed alongshore recorded in most experiments at the longer sampling times.

1. INTRODUCTION

The longshore sand transport rate is usually the principal factor determining erosion or accretion along a coast. If the longshore sand transport rate can be estimated, a qualitative picture may be formed of the general evolution of the coastline, including changes of the shoreline around structures. This picture can be brought to a

1. M. ASCE, Senior Engineer, Nearshore Environment Research Center, 1202 Famille Hongo Bldg., 1-20-6 Mukohgaoka, Tokyo, 113 Japan
2. Associate Professor, Dept. of Civil Eng., Yokohama National University, 156 Tokiwadai, Hodogaya-ku, Yokohama, 240 Japan
3. Senior Engineer, INA Civil Engineering Consulting Co., Ltd., 22-1 Suido-cho, Shinjuku-ku, Tokyo, 162 Japan
4. M. ASCE, Chief Engineer, Nearshore Environment Research Center, 1-20-6 Mukohgaoka, Bunkyo-ku, Tokyo, 113 Japan
5. M. ASCE, Professor, Dept. of Civil Eng., University of Tokyo, 7-3-1 Hongo, Bunkyo-ku, Tokyo, 113 Japan

quantitative level with numerical models of shoreline change. Such models require a predictive formula for the total longshore transport rate in terms of the average wave and current conditions. Because structures extend across the nearshore zone, a predictive expression for not only the total transport rate, but also the distribution of the longshore transport rate, is required to accurately describe changes which occur in the sea bottom and shoreline in the vicinity of such structures.

Only a limited number of field measurements of the longshore sand transport rate have been attempted. For example, Bruno et al. (1980) discuss 56 field data points. Most of these measurements may be rejected for violating certain criteria or because of experimental uncertainties (Greer and Madsen, 1978; Bruno et al., ibid).

The goals of our sand tracer field experiment program were 1) to obtain data for evaluating predictive expressions for the short-term (order of hours) total longshore sand transport rate, 2) to obtain some knowledge of the distribution of the transport across the surf zone, and 3) to determine the applicability and limitations of tracer techniques applied to real surf zones. Five of the experiments were part of a comprehensive multi-institutional cooperative field investigation conducted in Japan from 1978 to 1982.

2. BACKGROUND OF EXPERIMENTS

2.1 Study Sites

Fig. 1 Location of experiment sites.

The experiments were performed on four beaches: Ajigaura, Oarai, Hirono and Shimokita, facing the Pacific Ocean on the east coast of Japan (Fig. 1). The experiments are referred to by the beach name, and year, if necessary, except for the two experiments at Hirono performed on consecutive days in 1980, termed Hirono-1 and Hirono-2. The experiments at Oarai were performed to investigate the influence of structures on the waves, current, and sediment transport. Table 1 gives the basic characteristics and brief descriptions of the sites.

The tidal range on these beaches is rather small, about 1 m. As much as possible, the experiments were performed during or near an inflection point in the tide to minimize its effect. The tide is considered to have had negligible influence except possibly for a rising tide occurring near the end of Oarai 81.

TABLE 1 Characteristics of beach experiment sites.

Experiment	Median grain size d_{50} (mm)	Sorting coef. $(d_{75}/d_{25})^{1/2}$	Specific gravity	Composition	Nearshore beach slope	Comments
AJIGAURA 78	0.23	1.1 (estimated)	2.65	quartz	1/50 to 1/70	Coast is 9 km long with no significant structures; Ajigaura 78 performed near south headland, Ajigaura 79 performed near middle of coast
AJIGAURA 79	0.27	1.1 (estimated)	2.65	quartz	1/50 to 1/70	
SHIMOKITA	0.18	1.06	3.13	quartz heavy minerals	1/40 to 1/60	Long coast (38 km) with uniform contours
HIRONO - 1	0.59	1.69	2.67	quartz sand & pebbles	1/10	Pocket beach
HIRONO - 2	0.59	1.69	2.67	quartz sand & pebbles	1/10	Same location as Hirono 1
OARAI 80	0.25	1.09	2.79	quartz	1/50 to 1/70	Near large groin and behind harbor breakwater
OARAI 81	0.24	1.16	2.79	quartz	1/50 to 1/70	Same location as Oarai 80
OARAI 82	0.25	1.05	2.79	quartz	1/30 to 1/40	Behind harbor breakwater and 2 km south of Oarai 80; beach slope steep due to erosion

TABLE 2 Summary of experiment arrangements.

ITEM	AJIGAURA 1978	AJIGAURA 1979	SHIMOKITA 1979	HIRONO 1980 13 Nov	HIRONO 1980 14 Nov	OARAI 1980	OARAI 1981	OARAI 1982
Longshore stations	12	13	17	18	18	18	18	20
Grid length alongshore (m)	130; 210	130	255	300	200	130	175	100
Offshore stations	6	7 & 9	8	5	5	7	9	12
Offshore spacing (m)	10	7.5	10	4	4	8	10	3
Width of surf zone (m)	60	52.5	80	20	20	56	90	36
Spatial Samplings	4	2	3	3	3	2	2	2
Start of sampling after injection (min)	15, 30 70, 120	30, 120	30 120, 180	45 105, 165	60 120, 180	90, 180	90, 180	60, 180
Temporal Samplings	-	13	12	-	16	19	30	-
Sampling interval (min)	-	15	15	-	15	15	10	-
Number of lines	-	2	2	-	1	1	1	-
Distance from injec. line to sampling line (m)	-	10, 20	10, 20	-	8	15	15	-
Number of tracer colors	2	3	2	1	1	3	3	4
Colors Outer	green	orange	green	-	-	orange	orange	orange
Colors Mid	-	red	-	red	green	red	red	blue, red
Colors Inner	red	green	red	-	-	green	green	green
Amount of tracer inj'd for each color (kgf)	100,100	100,100,100	150,150	50	60	50, 40, 40	27,27,27	1.5 per color
Wave measurement*	stereo photos direct sighting	PWG 16mm	16mm	16mm	16mm	16 mm PWG;CWG	CWG;PWG 16mm	16 mm
Current measurement*	floats	EMCM (5) floats	EMCM (3) floats	EMCM (2) floats	EMCM (3) floats	EMCM (3) floats	EMCM (2) floats	EMCM (3) floats

*) PWG (CWG) = pressure (capacitance) wave gage; 16mm = 16mm memo-motion camera;
EMCM = electromagnetic current meter (numbers in parenthesis give number of meters used)

2.2 Experiment Design

A schematic of the general experimental arrangement is shown in Fig. 2. A summary of the arrangements and sampling schedules of all eight experiments is given in Table 2. Four features distinguish these experiments from previously reported ones. These are:

i) Multicolor tracer injections were often applied to measure the distribution of the longshore transport rate, and to separate longshore and on-offshore effects.

ii) Core samples were taken in situ at all times and at all locations. Before 1980, hand-held wedge-shaped PVC tubes were used for sampling. From 1980, a special coring device was used (Kraus et al., 1981).

iii) Two to four samplings by the spatial integration method were made in all experiments. In addition, sampling by the time integration method was made in four of those experiments.

iv) Three experiments were performed near structures.

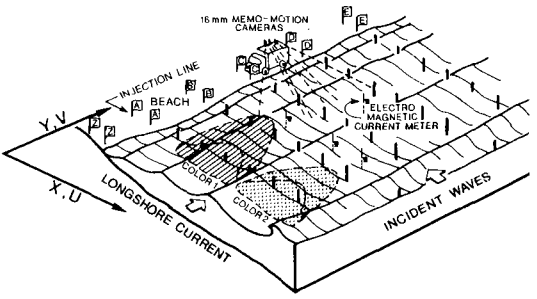

Fig. 2 Schematic of multicolor tracer experiments, and axes convention.

Two sampling methods were used. The spatial integration method (SIM) involves near-simultaneous sampling on a two-dimensional grid to determine the location of the tracer center of mass. The time integration method (TIM) involves frequent sampling on a line crossing the surf zone and down-current from the injection line to record passage of the tracer. Komar (1969) extensively used the SIM. Inman et al. (1980) performed the SIM and TIM in combination as we did in four experiments. In our experiments a one-time injection of tracer was used. Duane and James (1980) used a continuous injection method. These and other sampling methods have been described by Lean and Crickmore (1963) for tracer techniques applied to transport in rivers.

Sand from the area of the beach face and tagged with one of four fluorscent colors was presoaked in a solution of water and detergent and injected as a line source. We have found that injections in amounts of 1 kgf/m on-offshore yield acceptable results. If the amount is too large, the counting time increases due to high concentrations; if too little tracer is injected, statistically significant amounts will not be recovered. Normally, injection was made by carefully cutting open small bags of tracer held on the surf zone bottom. In Oarai 82 the tracer was injected to a depth of 5 cm by operating the core samplers "in reverse": no appreciable difference was noted.

The samples were segmented to a certain nominal depth, typically 6, 10 or 14 cm, depending on the results of a preliminary analysis of the mixing depth. In three experiments (Ajigaura 78, Ajigaura 79, and Oarai 82), all samples were processed as core samples (yielding on the order of a thousand segments of thickness 1 or 2 cm per experiment). In the other experiments, only samples on certain longshore and on-offshore lines were finely segmented in 1- or 2-cm lengths. The remainder were processed in 4- or 6-cm segments and treated as grab samples in the analysis. These data sets of several hundred to a few thousand segments per experiment provide a detailed picture of the horizontal and vertical movement of the tracer over a wide area of the surf zone.

The tracer was counted by hand under ultraviolet light. Concentrations were expressed as a number per unit volume of sample, in effect the number of grains per centimeter in the bed for a fixed sampler surface area. A spectrofluoroscopic counting method was devised for high concentrations (Farinato and Kraus, 1981). However, the method was not implemented because of the necessity for a chemical technician.

It was decided to make local wave measurements to avoid introducing uncertainties such as might arise from refracting waves from deep water, use of a breaking criterion, complications of diffraction from structures, etc. The wave field was measured by capacitance wave gages and by filming the water surface elevation at poles with 16mm cameras from a high elevation on the beach (Fig. 2; Table 2). The camera system is very reliable and has provided otherwise unobtainable data on wave characteristics in the nearshore zone (Hotta and Mizuguchi, 1980).

Except for Ajigaura 78, the current was measured with electromagnetic current meters, usually at three points on a line crossing the surf zone and near the injection line. Ideally, measurements should be made in the swash zone, in the midsurf zone, and just inside the breaker line. However, it is difficult to record in shallow water because the meter sensor is often exposed. Therefore the instruments usually had to be placed in the mid- and outer surf zone. The sensors of these two-component current meters were positioned 10 to 50 cm from the bottom.

3. METHOD OF ANALYSIS

3.1 General

Experiments based on a one-time injection of tracer require measurement of two quantities: 1) the sand advection velocity in the longshore direction, v_a, determined from the movement of the center of mass of the tracer and 2) the depth of mixing, b, determined from cores of material removed from the bed. The total volumetric rate of sand transport in the longshore direction, Q, is calculated by forming the product of these quantities with the width through which the transport takes place, usually the width of the surf zone, x_b:

$$Q = v_a \, b \, x_b \tag{1}$$

A conceptual model with the conditions and time scales for which Eq. 1 is expected to hold is given in Kraus et al. (1981).

Both the advection velocity and depth of mixing may vary across the surf zone. It is therefore appropriate to consider the volumetric transport rate per unit width of the surf zone, q, given by

$$q = v_a\, b \tag{2}$$

This quantity depends only on the sediment response. In multicolor tracer experiments, if the tracer remains localized on-offshore as it moves alongshore, q gives an estimate of the distribution of the transport rate on-offshore.

3.2 Tracer Center of Mass and Advection Velocity (SIM)

An element of the grand concentration array containing the number of recovered tracer grains per unit volume (or per centimeter in the bed) is represented by N(c,i,j,k,n), where the index c denotes the tracer color, i denotes the offshore grid coordinate, j denotes the longshore grid coordinate, k denotes the segment coordinate and n denotes the sampling time. In some experiments there were sufficient numbers of divers to sample the grid rapidly. Then the samples were taken semi-randomly proceeding from the injection line. In other experiments two teams of divers sampled simultaneously on their respective lines on-offshore. In this case a sampling took about 20 to 30 min, depending on the size of the grid and the wave conditions.

Formulae for calculating the tracer advection velocity are derived in the Appendix. In application, the notation is simplified by the following conventions: the offshore limit is assumed to be the station at the breaker line, the symbol $N_{i,j}$ represents a sum over k of all segments at the location (i, j), and the symbol c for color and summations over color are suppressed.

The longshore position of the tracer center of mass is given by

$$Y = t_o \sum_{i,j} \frac{y_j}{t_j} N_{i,j} \left(1 - \frac{y_j}{t_j} \frac{\Delta t_j}{\Delta y_j}\right) \Delta y_j \Big/ \sum_{i,j} N_{i,j} \left(1 - \frac{y_j}{t_j} \frac{\Delta t_j}{\Delta y_j}\right) \Delta y_j \tag{3}$$

The advection velocity is simply $v_a = Y/t_o$, where t_o is taken to be the time of sampling on the injection line. The position of the tracer center of mass on-offshore was calculated by the simple approximation

$$X = \sum_{i,j} x_i\, N_{i,j}\, \Delta y_j \Big/ \sum_{i,j} N_{i,j}\, \Delta y_j \tag{4}$$

3.3 Depth of Mixing

The depth of tracer mixing is a matter of definition. It has been variously defined as the depth of greatest burial (Komar, 1969; Gaughan, 1978) or as one of several kinds of concentration- or depth-weighted averages (Crickmore, 1967; Gaughan, 1978; Inman et al., 1980). In our experiments, most of the tagged sand in the cores was typically contained in the upper 6 cm, but frequently some grains were found as deep as 20 cm. This makes a maximum depth or depth-weighted definition of b either unrealistic or highly subjective.

Under steady waves and currents, a developing core concentration profile should have a maximum in the surface layer and decrease monotonically with depth. At equilibrium, the tracer should be uniformly distributed from the surface to some maximum depth. In reality, conditions are not steady and samples often exhibit one or more positive concentration gradients with depth, indicating the occurrence of two or more high energy turbulence events, or that local erosion or accretion took place.

We developed a definition of the depth of mixing with a variable parameter, the percentage of tracer contained in a core to a certain depth, in order to investigate the effect produced by the various irregular concentration profiles (Kraus et al., 1980, 1981). Within any core segment (typically of thickness 1 or 2 cm), the tagged grain concentration is assumed to be uniformly distributed. Then for each core, a local mixing depth is calculated which includes a specified percentage of the total tagged grains of a particular color. The mixing depth, b, is then defined as a simple average of a particular subset of local mixing depths. In previous work we used a concentration-weighted average but, because recovered numbers of tagged grains in a core can vary over two or three orders of magnitude, a simple average was later adopted. This procedure was strengthened with a criterion requiring that at least one segment contain more than a specified number of grains. After examining thousands of core profiles from several experiments, the minimum cutoff was set at 5 grain/cm. Assuming that this criterion eliminates statistically unreliable cores having a high "noise" content, the cores accepted for analysis can then be considered of equal weight.

An additional criterion was imposed in an attempt to remove cores suspected of being contaminated by erosional or accretionary events. Cores were rejected if a segment with no tagged grains appeared between segments containing 50% of the tracer in the upper part of the core. This criterion reduced values of b by approximately 25% from those calculated previously.

The effect of the cutoff percentage on the average mixing depth was examined. It was found that a linear relation is maintained to a certain cutoff percentage, after which the relation deviates significantly from linearity. An example is shown in Fig. 3 for Oarai 82. This result indicates that uniformity in mixing exists to a certain depth, after which the amount of tracer rapidly tails off. We found that a cutoff percentage of 80% was suitable for all the experiments, similarly to Kraus et al. (1980, 1981). A complete description of the experimental results and analysis of the depth of mixing is in preparation (Kraus and Isobe, in prep.)

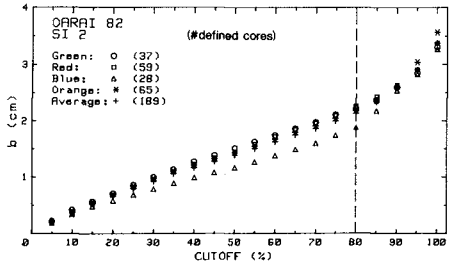

Fig. 3 Depth of mixing vs cutoff percentage.

4. RESULTS

4.1 Budget of Tracer

An estimate of the total number of tracer grains transported over the sampling grid can be made by assuming that the number of grains recovered at a site is representative of the surrounding area. Since the tracer grains in the samples were counted to their point of extinction, the calculation can be made without reference to the depth of mixing. Knowledge of the number of tracer grains per unit weight of the injected tracer allows comparison between the number of grains injected and the number accounted for by the sampling.

Although this procedure is straightforward in principle, in practice one cannot be certain of the absolute value of the calculated recovered amount because of the difficulty in counting the number of tagged grains in, say, 1 gf of tracer. Therefore, the acceptability of the measurements was judged by comparing the relative amounts recovered at the different (SIM) samplings. If a significantly smaller amount of tracer was recovered compared to other samplings, that sampling was considered unreliable. Most of the rejected measurements were from the earlier sampling times. This is attributed to the fact that the grid was relatively coarse with respect to movement of the tracer at the earlier times. Results associated with the earlier samplings were therefore not included in correlations employing waves and current.

4.2 Sediment Response

The principal results of the sediment response for the SIM experiments are summarized in Table 3. Background data on the average wave and current conditions are summarized in Table 4. In what follows, $(H_b)_{1/3}$ will be written as H_b. Values for the current in Table 4 are averages over the elapsed time of the final spatial sampling.

(1) Position of tracer center of mass (X, Y)

In Table 3, the notation "outer, mid, inner" refers to the relative positions of the different colors of tracer. It is seen from the X-entries that the tracer remained localized on-offshore (with the exception of Hirono-1 discussed in Subsection (4) below), even though the shore-normal component of the current was usually directed offshore (Table 4). An explanation for this might be that the transport produced by the steady offshore current in the surf zone, which we and co-workers have found to exist in the great majority of our field experiments, is balanced by the transport resulting from the large onshore component of wave orbital velocity due to wave asymmetry.

The purpose of performing two or more spatial samplings was to eliminate start-up or equilibration effects. We wished to check the reproducibility of the results by reference back to a previous position of the center of mass, not necessarily the injection line. Unfortunately, as can be seen from the Y-values in Table 3, for most experiments a large translation of the tracer alongshore was recorded at the earliest sampling and then very little movement took place in the later samplings. This result may also be attributed to the relative grid coarseness at the early samplings.

TABLE 3 Sediment response: Space integration experiments.

Experiment	AJIGAURA				AJIGAURA		SHIMOKITA			HIRONO-1			HIRONO-2			OARAI		OARAI		OARAI	
Sampling	1978				1979		1979			11/13/80			11/14/80			1980		1981		1982	
time (min)	15	30	70	120	30	120	30	120	180	45	105	165	60	120	180	90	180	90	180	60	180
X/x_b																					
outer	-	0.49	0.50	0.42	0.74	0.82	0.69	0.72	0.75	-	-	-	-	-	-	0.54	0.61	0.79	0.64	0.61	0.64
mid	-	-	-	-	0.66	0.77	-	-	-	0.72	0.32	0.23	0.56	0.39	0.45	0.36	0.41	0.42	0.50	0.57	0.58
mid	-	-	-	-	-	-	-	-	-	-	-	-	-	-	-	-	-	-	-	0.32	0.31
inner	-	0.36	0.32	0.35	0.30	0.44	0.44	0.43	0.45	-	-	-	-	-	-	0.31	0.29	0.21	0.24	0.28	0.20
Y (m)																					
outer	-	31.3*	21.9	33.6	42.0*	39.3	18.9*	20.9	15.3	-	-	-	-	-	-	11.5*	12.7	32.8*	39.7	23.3	25.0*
mid	-	-	-	-	12.5	18.8	-	-	-	17.1	2.2*	26.7	12.4	19.6	40.1	24.7*	19.4	15.0*	17.4	31.6	24.5*
mid	-	-	-	-	-	-	-	-	-	-	-	-	-	-	-	-	-	-	-	22.2	32.8
inner	-	26.3	16.4	27.6	34.7	47.6	32.6*	22.0	38.6	-	-	-	-	-	-	25.3	29.9	3.4	12.6	28.1	31.9
b (cm)																					
outer	3.7	3.7	4.2	5.1	2.2	2.9	1.4	2.5	3.5	-	-	-	-	-	3.8	2.2	2.0	2.5	3.2	1.6	2.0
mid	3.1	3.5	3.5	3.8	2.9	2.9	2.0	2.2	2.9	-	-	2.7	2.5	3.4	3.1	2.4	2.2	2.5	2.3	1.5	2.3
mid	-	-	-	-	-	-	-	-	-	-	-	-	-	-	-	-	-	-	-	1.5	1.7
inner	3.4	3.3	3.8	4.0	2.7	3.9	1.1	1.2	2.2	3.7	4.5	3.4	1.6	2.3	2.0	3.1	3.2	2.0	2.1	1.7	2.4
average	3.4	3.5	3.8	4.3	2.6	3.2	1.5	2.0	2.9	3.7	4.5	3.0	2.1	2.9	3.0	2.6	2.5	2.3	2.5	1.6	2.1
exp't avg.		3.8			2.9			2.1			3.7			2.7		2.5		2.4		1.9	
v_s (mm/s)																					
outer	-	17.4	5.2	4.7	23.3	5.5	10.5	2.9	1.4	-	-	-	-	-	-	2.1	1.2	6.1	3.7	6.5	2.3
mid	-	-	-	-	7.0	2.6	-	-	-	6.3	0.4	2.7	3.5	2.7	3.7	4.6	1.8	2.8	1.6	8.8	2.3
mid	-	-	-	-	-	-	-	-	-	-	-	-	-	-	-	-	-	-	-	6.2	3.0
inner	-	14.6	3.9	3.8	19.3	6.6	18.1	3.1	3.6	-	-	-	-	-	-	4.7	2.8	0.6	1.2	7.8	3.0
average	-	16.0	4.6	4.3	16.5	4.9	14.3	3.0	2.5	6.3	0.4	2.7	3.5	2.7	3.7	3.8	1.9	3.2	2.2	7.3	2.7
q (10^{-5} $m^3/s/m$)																					
outer	-	62.3	20.0	20.6	51.8	15.8	18.0	6.9	4.5	-	-	-	-	-	-	4.7	2.4	15.4	11.6	10.7	4.7
mid	-	-	-	-	20.4	7.5	-	-	-	23.2	1.6	8.2	7.1	7.8	11.0	10.7	3.9	6.9	3.7	12.8	5.2
mid	-	-	-	-	-	-	-	-	-	-	-	-	-	-	-	-	-	-	-	9.1	5.3
inner	-	49.2	14.1	14.8	51.6	25.7	28.4	5.1	9.2	-	-	-	-	-	-	14.6	8.8	1.2	2.5	13.2	7.1
Q (10^{-3} m^3/s)	-	33.5	10.2	10.6	21.7	8.6	18.5	4.8	5.5	4.6	0.3	1.7	1.4	1.6	2.2	5.6	2.8	7.0	5.3	4.1	2.0

* Per cent recovered low in relative sense

TABLE 4 Average wave and current conditions during experiments.

ITEM			AJIGAURA 1978	AJIGAURA 1979	SHIMOKITA 1979	HIRONO (1980) 11/13	HIRONO (1980) 11/14	OARAI 1980	OARAI 1981	OARAI 1982
Breaking Waves										
depth	h_b	(cm)	90	130	110	190	120	100	140	100
height	$(H_b)_{1/3}$	(cm)	98	110	63	161	100	100	111	80
surf. elev.	$(\eta_b)_{rms}$	(cm)	20	28	17	37	24	24	26	21
period	$(T_b)_{1/3}$	(s)	9.0	6.5	4.9	8.7	8.4	10.2	6.1	7.5
angle	θ_b	(deg)	6	2	6	2	3	~8	6	4
Longshore Current										
	$\bar{v}$ (cm/s)									
meter	1 outer		53*	31	18	22	14	6	27	1
	2 mid		52*	34	28	19	17	26	7	0
	3 inner		45*	37	25	**	15	**	**	5
	4 inner		**	28	**	**	**	**	**	**
	6 mid		**	34	**	**	**	**	**	**
Offshore Current										
	$\bar{u}$ (cm/s)									
meter	1 outer		**	8	25	15	5	~2	3	4
	2 mid		**	11	25	26	24	~6	1	15
	3 inner		**	13	23	**	5	**	**	13
	4 inner		**	9	**	**	**	**	**	**
	6 mid		**	24	**	**	**	**	**	**

* Current measured by floats.

(2) Depth of mixing (b)

The depth of mixing was calculated for each color of tracer according to the procedure discussed in the previous section. In Table 3, it is observed that the depth of mixing tended to increase slightly with time. In some experiments a bimodal distribution in b is noted whereas in other experiments a maximum is found either near the shoreline or near the breaker line. An unambiguous maximum was not found in the midsurf zone. Mechanical stirring of the bottom, which would result in large concentrations of suspended sediment and greater mixing depths, is expected under certain breaking waves and in the swash zone. There is normally no similar stirring process in the middle of the surf zone.

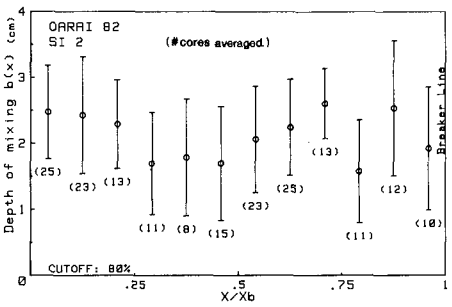

Fig. 4 On-offshore distribution of the depth of mixing (Oarai 82).

Figure 4 plots the on-offshore distribution of the mixing depth for the second spatial sampling at Oarai 82. The bars are two standard deviations. This representative result shows that there is great variability in the mixing depth at any one location. An average mixing depth calculated from a small number of cores would therefore be unreliable. It is seen that the mixing depth had maxima in the swash zone and near the breaker line in this experiment.

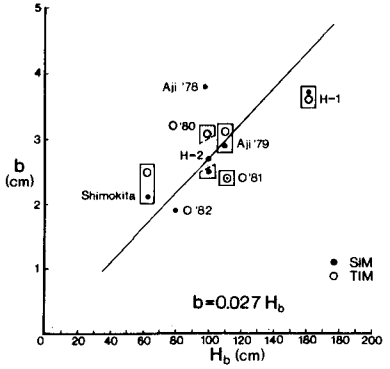

Fig. 5 Depth of mixing.

It is reasonable to assume that the mixing depth is proportional to the breaking wave height. The experiment-average values of b have been plotted against the significant breaking wave height in Fig. 5. It should be emphasized that these values are each the average of many cores. A best-fit straight line through the origin gives

$$b = 0.027\ H_b \qquad (5)$$

Equation 5 pertains to mixing depths resulting from steady waves, with minimal influence of the tide.

(3) Tracer advection velocity (v_a)

If the transport is fully developed, we expect the sand advection velocity to be proportional to the mean longshore current. Advection velocities for elapsed times greater than 60 min (SIM) are plotted against the average current over that time in Fig. 6. Although there is considerable scatter, by fitting a line through the origin, we get

$$v_a = 0.014\ \bar{V} \qquad (6)$$

The advection velocity determined by the TIM was always greater than that from the SIM. For the two experiments in which the TIM was performed on two distinct lines (Ajigaura 79 and Shimokita 79), the calculated advection velocity was essentially proportional to the distance from the injection line to the sampling line.

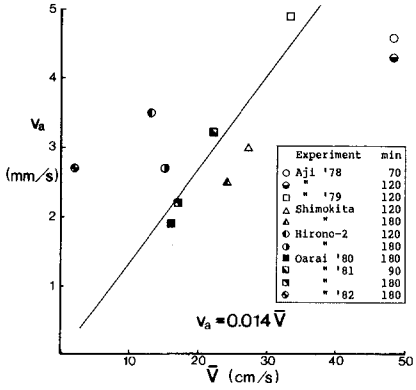

Fig. 6 Sand advection velocity.

To understand these results, the numbers of tagged grains found on the temporal sampling lines were plotted as a function of time. The numbers did not systematically increase and then decrease through the duration of the sampling as one would expect, but rather remained almost constant. Large numbers of grains were thus recovered both at the earlier and later samplings. The appearance of large numbers of grains at the early samplings produces a high transport rate because the TIM gives more weight to early times (Eq. A-5). The fact that large numbers were recovered at later

sampling times indicates that the tracer center of mass did not pass the sampling line, a result in contradiction to values computed with the SIM. Inman et al. (1980) also report higher advection velocities for the TIM. It appears that the TIM sampling line should have been located closer to the injection line (say, 5m), but in view of the SIM results this requirement is puzzling.

(4) On-offshore distribution of the transport rate (q)

The entries for q in Table 3 show that the distribution of the transport rate in the field does not take a universal form. The multicolor tracer experiments gave a constant distribution for Shimokita, a distribution with a maximum toward the breaker line for Oarai 81 and Ajigaura 78, a definite bimodal distribution for Ajigaura 79, and a distribution with a maximum toward the inner surf zone for Oarai 80 and Oarai 82. The diversity in distributions can be explained by considering the combined effects of the current and the mode of transport (bed load or suspended load).

It is the authors' experience that the typical longshore current profile in the field is rather flat across most of the surf zone, unlike the velocity distribution observed and predicted for a uniformly sloping (laboratory) beach, which is well peaked in the midsurf region. A flat profile was found in Ajigaura 79 and Shimokita (Table 4). Another such field example was reported by Kraus and Sasaki (1979). A broad flat longshore current profile may be explained to be a result of the step-type bottom which is usually found on gently sloping beaches (Mizuguchi and Horikawa, 1978). That is, waves can break, reform, and break again on nonplanar beaches. In the vicinity of structures, the longshore variation in wave height due to diffraction may also considerably alter the current distribution. For the beach at Oarai, the variation in breaking wave height produced by the harbor breakwater has been measured, calculated, and related to the sediment transport and shoreline change using a numerical model of shoreline evolution (Kraus and Harikai, 1983). Other three-dimensional processes on a real beach will also alter the idealized longshore current distribution (Sasaki, 1980).

Therefore, there is no reason to expect a well-defined peak in the longshore transport in the field on the basis of theoretical considerations of the longshore current on a plane beach (Komar, 1977), or as measured in laboratory experiments (Sawaragi and Deguchi, 1978; Tsuchiya, 1982). It does seem reasonable that the longshore transport would exhibit a peak, however, in regions where suspended load transport is high (swash zone and breaker zone under certain conditions). This approach must be refined by considering the criteria for the existence of a swash zone, and the breaker type (e.g., as done by Kamphuis and Readshaw, 1978).

The surf zones encountered for Hirono-1 and Oarai 82 illustrate this point. During Hirono-1, high waves arrived on this steep beach as collapsing breakers and continued to run up as a turbulent bore. The entire surf zone consisted of intense swash which moved up the beach in

expanding circular "wavelets". Near the shoreline the tracer was observed to move either in the direction of the mean longshore current or opposite to it, depending on the direction of the expanding circular wavelet of the bore at a given location. Under these conditions sand moved rapidly onshore with very little net longshore movement despite the strong current recorded in the deeper region near the breaker line.

In Oarai 82, waves broke mainly as spilling breakers. Little wave energy was expended at the breaker line. The surf zone was unusually turbulent and clouds of suspended sediment were seen at all locations. Table 3 shows that the advection velocity and transport were essentially constant in this four-color experiment, except near the shoreline, where the longshore current was relatively stronger. The slowly rising tide moved the most landward-injected tracer onshore.

(5) Total transport rate (Q; I)

The total transport rates are given in the last row of Table 3. They were calculated by averaging over the products of v_a and b for the respective regions and then multiplying by the width of the surf zone. In order to relate the transport rate to the wave and current conditions, Eqs. 5 and 6 were substituted into Eq. 1, and a planar beach slope was assumed, for which $x_b = h_b/\tan\beta = H_b/(\gamma_b \tan\beta)$, where $\tan\beta$ is the beach slope and γ_b is the ratio of wave height to water depth at the breaking point. An empirical formula is thus obtained,

$$Q = \frac{3.8\ 10^{-4}}{\gamma_b \tan\beta} H_b^2 \bar{V} \qquad (7)$$

which is dimensionally correct. For a given wave height and average longshore current, Eq. 7 states that the transport should be greater on a more gently sloping (wider) beach. The data are plotted in Fig. 7. The dependence of Q on the beach slope is given some support by comparing results for Shimokita (gentle slope) and Hirono (steep slope).

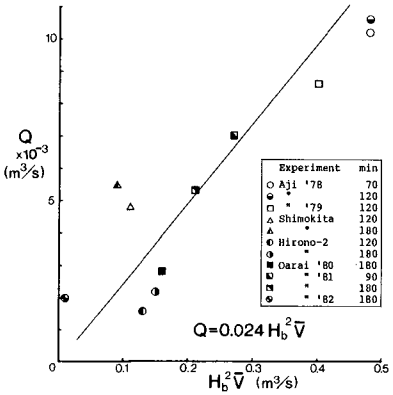

Fig. 7 Volumetric transport rate.

A popular theoretical expression for the longshore current generated by obliquely incident waves (Longuet-Higgins, 1970) contains the beach slope in the numerator and a friction coefficient in the denominator. Substitution of the theoretical average current into Eq. 7 would show Q to be inversely proportional to the friction coefficient, a physically reasonable result. Assuming an average beach slope of 1/50 and a breaking index of 0.8, Eq. 7 becomes

$$Q = 0.024\ H_b^2 \bar{V} \qquad (8)$$

The experimental results for the mixing depth and advection velocity have thus indicated that the combination $H_b^2 \bar{V}$ is a natural quantity on which the total volumetric transport rate should depend. In Fig. 7, the straight line is given by Eq. 8, which also gives the best-fit line through the origin. The data scatter in Fig. 7 is less than that in Figs. 5 and 6. This is because v_a and b are, roughly speaking, inversely related: the sand should move faster when the moving layer is thinner, and conversely, implying more complicated relationships than the simple intuititive functional dependencies given by Eqs. 5 and 6. However, since Q is formed as a product of v_a and b, it should be approximately invariant to the inverse relationship between v_a and b.

It is customary to consider the immersed weight transport rate, I, when correlating measured transport rates with the forcing functions of waves and current. The measured immersed weight transport rate, I_m is related to Q by

$$I_m = (\rho_s - \rho_w)\, g\, (1 - a')\, Q \tag{9}$$

in which ρ_s (ρ_w) is the density of sand (water), g is the acceleration of gravity and a' is the sand porosity.

Bagnold (1963) derived a predictive expression for the immersed weight transport rate in terms of the wave power at the breaker line (breaking wave height) and current velocity, namely,

$$I_p = K' (EC_g)_b \bar{V}/u_m \tag{10}$$

in which E is the wave energy density, C_g is the group velocity, u_m is the maximum orbital velocity and K' is a coefficient which must be empirically determined and which is not expected to be constant.

The well-known Bagnold/Inman/Komar, or CERC, formula is a special case of Eq. 10 in which the transport is due solely to oblique wave incidence (Komar and Inman, 1970). In the case of the Oarai series of experiments, the longshore current was produced by a combination of oblique wave incidence and systematic variation in breaking wave height as a result of diffraction at the harbor breakwater. In fact, in Oarai 80, the direction of the longshore current was opposite to that expected from oblique wave incidence. Due to the complexity of the origin of the longshore current in several of our experiments, and due to the potentially high uncertainty in determining the breaking wave angle, Eq. 10 was used because of its generality. In applications, such as numerical modeling of shoreline change, the burden of the calculation falls on computing the mean longshore current and breaking wave height.

Komar and Inman (1970) found K' = 0.28 on the basis of their fluorescent tracer experiments. The results of the present experiments are plotted in Fig. 8 together with the data of Komar and Inman. A best-fit line through the origin gives K' = 0.21 for the present experiments. In linear wave theory, $u_m = 0.5\, \gamma_b\, C_g$, and therefore Eq. 10 has the same basic dependence on the waves and current as given in Eqs. 7 and 8. It should be noted that the significant wave height was used in obtaining Eqs. 7 and 8, whereas the root mean square wave

height was used in the comparison of I_m and I_p, in order to be compatible with the results of Komar and Inman.

Our results give a lower value of the empirical coefficient K' in Eq. 10 than found by Komar and Inman (1970). This may be due to the strict procedure used in defining the depth of mixing. In contrast, based on results of a trapping experiment, Bruno et al. (1980), in a comparison using the CERC formula, report transport coefficients larger than those of Komar and Inman. We believe that a higher value is at least partially explained by the fact that sand caught by the trap includes a contribution from the longshore transport occurring outside the breaker line, and possible entrapment of onshore transport by the detached breakwater (Sasaki, 1975).

In Ajigaura 79, the two temporal sampling lines extended past the average breaker line. The (orange) tracer for the outer portion of the surf zone was also injected outside the breaker line. Significant quantities of orange tracer were recovered at the two stations outside the breaker line. Thus we can conclude that significant longshore transport of sand can occur immediately outside the breaker line. Interestingly, no tracer of the other two colors injected in the surf zone was recovered outside the breaker line.

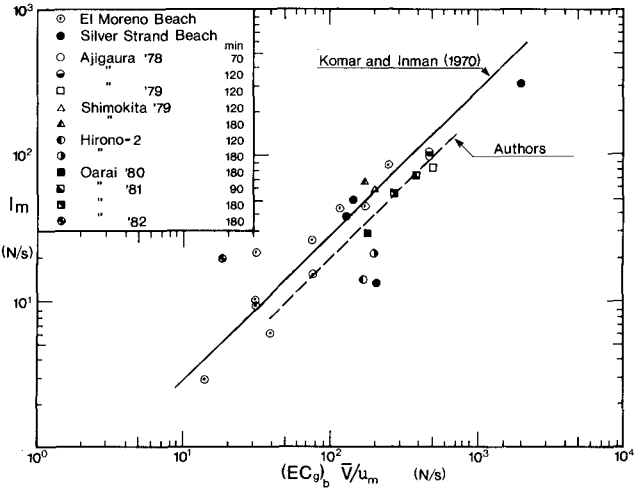

Fig. 8 Measured immersed transport rate plotted against Bagnold's predictive expression.

5. CONCLUDING DISCUSSION

Multicolor tracer experiments were found to be a practical method for obtaining information on the distribution of the sand transport rate across the surf zone. At least three colors are necessary to probe the often distinct transport regions of the swash zone, midsurf zone, and outer surf zone. As a result of these experiments, simple empirical expressions were obtained relating the sediment response (depth of mixing, advection velocity, and transport rate) to the average wave and current conditions. In particular, it was found that Eq. (7) for the total volumetric sand transport rate,

$$Q = (\text{factor})\ H_b^2\ \bar{V} / \tan\beta$$

is consistent with and offers an alternative to presently accepted predictive formulae.

At an increase in expense, refined versions of these experiments should be capable of revealing dependencies of the longshore transport rate on such factors as the beach slope, wave type (wave asymmetry), size and specific gravity of the sand, etc. A fundamental theoretical study of the vertical and horizontal movement of the tracer center of mass should also be made to better interpret such experiments.

ACKNOWLEDGEMENTS

The field work and sample processing in experiments of this size cannot be done without the assistance of many people, both known and anonymous. We would like to thank all of them including Mr. S. Hotta, who kept the 16mm cameras rolling in rain and shine; Messrs. S. Kubota, S. Harikai and S. Katori, who at various times assisted in all aspects of the field work, sample processing, and experiment administration; Dr. R. S. Farinato, who was an early collaborator, and Mr. J. Romeu for assistance with the figures and programming.

The experiments at Shimokita and Hirono were performed to predict beach evolution at the specific sites. The support of the Tohoku Electric Power Co., Ltd., and the Tokyo Electric Power Co., Ltd., is greatly appreciated.

APPENDIX: Governing Equations of Tracer Movement

The derivation is based on considerations of the tracer velocity distribution. It is assumed that the advection velocity of an individual tagged grain is constant during an experiment. The total population of tagged grains will have a continuous velocity distribution, such as sketched in Fig. A1.

For the SIM, the longshore position of the tracer center of mass, Y, at time t_o is given by

$$Y = \frac{\int_{-\infty}^{\infty} y\, N(y, t_o)dy}{\int_{-\infty}^{\infty} N(y, t_o)dy} \qquad (A\text{-}1)$$

$N(y, t_o)$ denotes the number of tracer particles integrated in the vertical and on-offshore directions, and y is the distance alongshore from the injection line (Fig. 2). The path of the line integral in Eq. A-1 is shown as the dashed line in Fig. A2. In order to calculate Y using Eq. A-1, all samples must be taken at the same time.

Instantaneous sampling at all points on a two-dimensional grid is not possible and, in practice, sampling is accomplished by moving systematically alongshore and taking samples simultaneously on each on-offshore line. In such a case, only the number $N(y, t)$ along the solid line in Fig. A-2 is known, where t is the time of sampling on a given line. Therefore, the path of the integral must be converted from the dashed line to the solid line. Then the number of tracer grains in the small interval AB is the same as in A'B' or A'B". Denoting the coordinates of A and A' by (y, t_o) and (y', t), and the differences along the y axis of AB, A'B', and A'B" as dy, dy', and dy", respectively, the following equations can be easily obtained:

$$y = y' \frac{t_o}{t} \qquad (A\text{-}2)$$

$$N(y, t_o)dy = N(y', t)\, dy"$$

$$= N(y', t)(1 - \frac{y'}{t}\frac{dt}{dy'})dy' \qquad (A\text{-}3)$$

Substitution of Eqs. A-2 and A-3 into Eq. A-1 yields

$$Y = \frac{\int_{-\infty}^{\infty} \frac{y't_o}{t} N(y', t)(1 - \frac{y'}{t}\frac{dt}{dy'})\, dy'}{\int_{-\infty}^{\infty} N(y', t)(1 - \frac{y'}{t}\frac{dt}{dy'})\, dy'} \qquad (A\text{-}4)$$

The advection velocity is given by $v_a = Y/t_o$, and it can be seen that v_a is independent of t_o.

The governing equation for the TIM can be obtained as a special case of Eq. A-4 by taking the path of integration from $(y_o, -\infty)$ to (y_o, ∞), where y_o is the fixed location of the sampling line. In this case, as dt/dy' goes to infinity, the term of unity on the right side of Eq. A-4 can be neglected: then by the chain rule, (dt/dy')dy' reduces to dt. This gives

$$Y = \frac{\int_{-\infty}^{t_o} \left(\frac{y_o}{t}\right)^2 N(y_o, t)\, dt}{\int_{-\infty}^{t_o} \left(\frac{y_o}{t}\right) N(y_o, t)\, dt} \qquad \text{(A-5)}$$

The advection velocity is $v_a = Y/t_o$ which is also independent of t_o. Note that the weighting functions of $(y_o/t)^2$ and (y_o/t) in the numerator and denominator differ from expressions found in other work (for example, Lean and Crickmore, 1963; Inman et al., 1980).

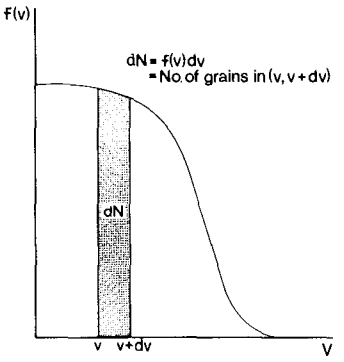

Fig. A1 Hypothetical tracer velocity distribution.

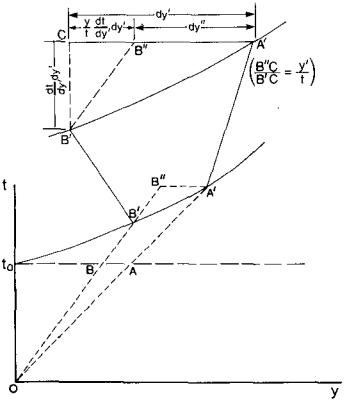

Fig. A2 Definition sketch for tracer movement.

REFERENCES

Bagnold, R.A. (1963): Mechanics of marine sedimentation, in "The Sea," ed. M.N. Hill, 3, Interscience, pp. 507-528.

Bruno, R.O., R.G. Dean and C.G. Gable (1980): Longshore transport evaluations at a detached breakwater, Proc. 17th Coastal Eng. Conf., ASCE, pp. 1453-1475.

Crickmore, M.J. (1967): Measurement of sand transport in rivers with special reference to tracer methods, Sedimentology, 8, pp. 175-228.

Duane, D.B. and H.R. James (1980): Littoral transport in the surf zone elucidated by an Eulerian sediment tracer experiment, J. Sed. Pet., 50, 3, pp. 929-942.

Farinato, R.S. and N.C. Kraus (1981): Spectrofluorometric determination of sand tracer concentrations, J. Sed. Pet., 51, 2, pp. 663-665.

Gaughan, M.K. (1978): Depth of disturbance of sand in surf zones, Proc. 16th Coastal Eng. Conf., ASCE, pp. 1513-1530.

Greer, M.N. and O.S. Madson (1978): Longshore sediment transport data: a review, Proc. 16th Coastal Eng. Conf., ASCE, pp. 1563-1576.

Hotta, S. and M. Mizuguchi (1980): A field study of waves in the surf zone, Coastal Eng. in Japan, 23, JSCE, pp. 59-79.

Inman, D.L., J.A. Zampol, T.E. White, D.M. Hanes, B.W. Waldorf and K.A. Kastens (1980): Field measurements of sand motion in the surf zone, Proc. 17th Coastal Eng. Conf., ASCE, pp. 1215-1234.

Kamphuis, J.W. and J.S. Readshaw (1978): A model study of alongshore sediment transport rate, Proc. 16th Coastal Eng. Conf., ASCE, pp. 1656-1674.

Komar, P.D. (1969): The longshore transport of sand on beaches, Ph.D. thesis, University of California, San Diego, 143pp.

Komar, P.D. and D.L. Inman (1970): Longshore sand transport on beaches, J. Geophys. Res., 75, pp. 5914-5927.

Komar, P.D. (1977): Beach sand transport: distribution and total drift, Proc. ASCE, 103, WW2, pp. 225-239.

Kraus, N.C. and S. Harikai (1983): Numerical model of the shoreline change at Oarai beach, Coastal Eng., 7, (in press).

Kraus, N.C. and T.O. Sasaki (1979): Effects of wave angle and lateral mixing on the longshore current, Coastal Eng. in Japan, 22, JSCE, pp. 59-74.

Kraus, N.C., R.S. Farinato and K. Horikawa (1980): Field experiments on longshore sand transport rate: on-offshore distribution and time-dependent effects, Proc. 27th Japanese Conf. on Coastal Eng., JSCE, pp. 245-249. (in Japanese)

Kraus, N.C., R.S. Farinato and K. Horikawa (1981): Field experiments on longshore sand transport in the surf zone: time dependent motion, on-offshore distribution and total transport rate, Coastal Eng. in Japan, 24, JSCE, pp. 171-194.

Lean, G.H. and M.J. Crickmore (1963): Method for measuring sand transport using radioactive tracers, in "Radioisotopes in Hydrology," International Atomic Energy Agency, Vienna, pp. 111-132.

Longuet-Higgins, M.S. (1970): Longshore currents generated by obliquely incident sea waves, J. Geophys. Res., 75, pp. 6778-6801.

Mizuguchi, M. and K. Horikawa (1978): Experimental study on longshore current velocity distribution, Bull. Fac. Sci. and Eng., Chuo Univ., 21, pp. 123-150.

Sasaki, T.O. (1975): Simulation on shoreline and nearshore current, Proc. Civil Eng. in the Ocean / III, ASCE, pp. 179-196.

Sasaki, T.O. (1980): A heuristic model of the nearshore zone, Proc. Coastal Zone '80, ASCE, pp. 3197-3213.

Sawaragi, T. and I. Deguchi (1978): Distribution of sand transport rate across the surf zone, Proc. 16th Coastal Eng. Conf., ASCE, pp. 1596-1613.

Tsuchiya, Y. (1982): The rate of longshore sediment transport and beach erosion control, Abstracts 18th Coastal Eng. Conf., ASCE, pp. 258-259.

LITTORAL PROCESSES IN CAMPELLO COASTS

J.J. DIEZ (*)

M. ARENILLAS (**)

ABSTRACT

The coasts of Campello (fig. 1), just at the North of Alicante, have undergone important erosions in the last few years. A study has been developped for over one year to separate seasonal and permanent variations of the shoreline. The geomorphology and the recent generation of these coasts have been established and the study and wind wave regimes have been defined to evaluate the littoral transports, particularly the longshore ones. The seasonal transversal profiling may show the seasonal changes in the littoral zone and the sieve and mineralogical analysis of the different samples of the beaches have completed the data for the discussion.

Taking into account other studies of the authors in other parts of the East and Southeast coasts of Spain, an hypothesis on the littoral processes has been established, separating the seasonal and the permanent and degradative consequences. Some recommendations to keep at least the present situation of the beaches and to protect the other stretches of the shore are presented as final conclusions.

1 INTRODUCTION

The especial quality of Mediterranean Coasts in Spain has suffered lately somehow because of the concurrence of several circumstances, as the reduction of solid materials apported by the rivers or the inadequate use of the littoral and coastal zones, without the necessary suitable shore protection implementations (COPEIRO, E. 1978; DIEZ, 1982, a). It obeys to a common worldwide phenomenon related to actions badly planned, which ignores the littoral dynamic and its role in the beach formation an evolution.

---

* Prof. Dr. Ingeniero de Caminos, Canales y Puertos. Director Departamento Puertos. Univ. Politécnica de Valencia. Spain.

** Prof. Dr. Ingeniero de Caminos, Canales y Puertos. Director Departamento Geología Aplicada. Univ. Politécnica de Valencia. Spain.

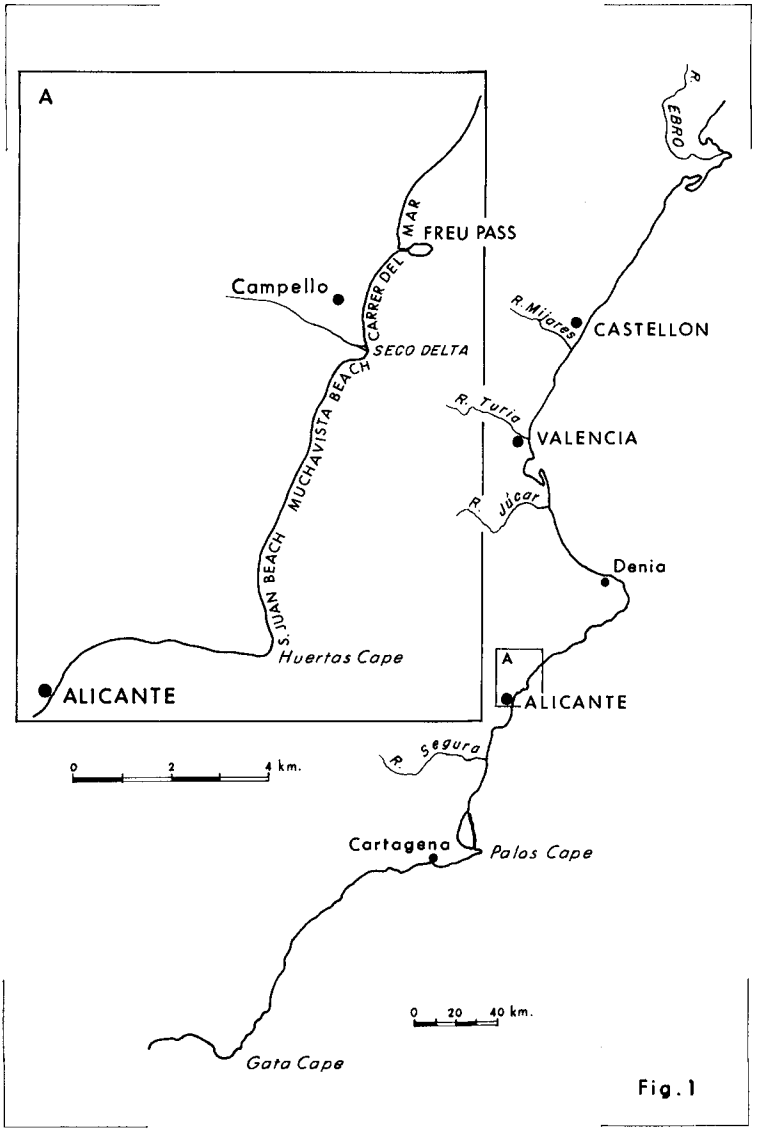
A
R. EBRO
FREU PASS
MAR
CARRER DEL
Campello
SECO DELTA
R. Millares
CASTELLON
MUCHAVISTA BEACH
R. Turia
VALENCIA
R. Júcar
S. JUAN BEACH
Denia
Huertas Cape
A
ALICANTE
ALICANTE
0 2 4 km.
R. Segura
Cartagena
Palos Cape
0 20 40 km.
Gata Cape

Fig. 1

Particularly, some parts of the coasts of Campello have suffered some apparently critical erosion in recent years. Since 1970 several shore protection systems have been tried without adequate results and, for that reason, a complete study has been developed along 1980-82. Even during the period of this study, while several perpendicular groins were being built, important damages in the village of Campello were produced by winter storms.

This study has been developed following two basic lines of research: a) Analysis of the littoral dynamic to define the littoral processes, and b) Identification of the forms existing in the coastal stretch.

The former has required the knowledge of the maritime winds to establish the accurate wind wave regimes (DIEZ, 1982, b) because sufficient wave register data are not available for this area. Advances in the methods for waves and storms forecasting (SUAREZ BORES, 1970; C.E.R.C., 1975), and the improvement in statistics data (HOGREN and LUMB, 1967; BRITISH ADMIRALTY, 1968) have been regarded.

The latter has been based on the present knowledge of the Geology of the area (MINISTERIO DE INDUSTRIA Y ENERGIA; ALONSO and PEREZ MATEOS, 1959) and on the results of the analysis of the samples obtained from the beaches of this coasts, placed at the South of La Nao cape, in the North end of the Southeastern Spanish littoral. Contributions for understanding the genesis and classification of the coastal formes (SUAREZ BORES, 1974) have been considered.

2 LITTORAL DYNAMIC

The principal and nearly exclusive factor involving the littoral processes in Spanish Mediterranean coasts is the wind wave regime. Winds affect somehow the formation and evolution of dunes and the filling of lagoons, and both surges and tides only modify the level of the wave action. Although changes of mean sea level caused by winds and/or pressure variations must be taken into account because of their incidence in the analysis of both observational data and changes of shoreline and transversal profiles. However this stretch is one of the least affected by them in all the Spanish coasts. The tide is extraordinary lessened here and the storm-surges do not seem to have produced elevations of the mean-sea level over 40 cm.

As in other coasts studied (DIEZ & ARENILLAS, 1982, a and b) no appropriate and sufficient registered or observed data of the sea exist to define the wind wave regime for this coast. Thus a forecasting method arising from wind regimes has been adopted, taking into consideration the criteria developed (DIEZ, 1982, b) which require establishing a wind regime first of all.

In accordance with those criteria the wind regime adopted for these coasts is the one adopted for Santa Pola bay by the authors. Other alternative based on the linnear interpolation is neither too different nor more accurate here because of the position and the general orientation of the coasts of Campello. The dominant sea winds are from E and SE, nearly facing the general shoreline direction. The abundant breezes and other local winds are superfluous with this method because their influence on the littoral processes is weak here.

In the Appendix the wind wave regime is obtained in accordance with all these considerations and an evaluation of the longshore littoral transport is reached by applying the C.E.R.C. formule. The directional wave regime shows clearly the importance of the fetch configuration effect on waves reaching the coast, particularly on the ones from the first quadrant (N, NE, E). The reduction is specially important for N and, in a minor degree, for NE waves. On the other hand the S and SE wind waves are practically saturated when reaching the coast. The seasonal analysis shows that the strongest waves occur in winter -and less frequently at the beginning of springtime-, when the waves from the first quadrant are more dominant.

The evaluation of the longshore littoral transport -also in the Appendix- show a clear dominance of the Southward transport, perfectely noticeable in the direction of the annual average resultant. Independently of the accuracy of the C.E.R.C. formule for these coasts, the method followed in the Appendix may be accepted because its inaccuracy will affect all directions in a similar proportion. The aim of the evaluation method is not to define an accurate annual longshore transport rate, but to establish an average wave incidence direction in relationship with the capacity of the waves to generate the littoral drift. Nevertheless the relative importance of the total transport respect to the net southward transport must be taken into account, especially to understand the genesis of the present San Juan bay.

3 DESCRIPTION AND GEOMORPHOLOGY

This sector of Campello littoral corresponds to a stretch of plain coast placed between two other cliff-stretches: Huertas Cape at the South and an alternating system of cliffs and "calas" at the North, from the Freu pass. From a point of view based on the longshore transport, this stretch cannot be considered as an isolated one, that is, as a physiographic unit because not even the Cape is a total barrier for the littoral drift. Nevertheless it constitutes a particular subunit, a little appart off the littoral transport and fundamentally fed by a singular source of materials; therefore it admits an individualized study.

From "San Antonio" and "La Nao" Capes southward, Spanish coast shapes in accordance with the general geological system of the

Betic chaines, which direct their aligrements from the Peninsular South to the capes and farther under the sea, emerging again in Pitiusas and Mallorca Isles. Prebetic and Subbetic chaines, at the North, and the actual Betic ones, at the South, close a wide Oval framing the coastal area between "La Nao" and "Palos" capes. The different chaines reach the sea transversally to the Coast in a wide and high montainous arc and in other minor sierras and spurs. They structure a series of bays and coves opened to the second quadrant and filled with Neogenic and Quaternary sediments forming the present coastal plains. Within this frame, the Campello coastal area is placed between the Paleogenic sierras of Bonalba and Ballestera, at the North, and the Miocene of Huertas Cape, at the South, and constitutes an important Quaternary deposit between the mountains and the sea.

The Prebetic formations of the interior area may be easily characterized as Mesozoic or Low-Tertiary ones; but the characterization of the carborated Jurassic and Cretaceous Subbetic formations offer many difficulties because of their strong tectonic in nappes and scales. The dominant materials in the plain are carbonates and detritus from the Prebetic and Subbetic Mesozoic, which, removed in different stages, have constituted most of the Tertiary and Quaternary sediments. Minor quantitative importance have the numerous Triasic and Jurassic outcrops from volcanic or subvolcanic origin (however some of their constituent mineral anpear in the beaches). The river Seco of Campello and its tributaries have principally canalized those materials towards the shore since the Pliocene. But other minor streams have colaborated in the drain of the generally intermitent run-off generating numerous aluviar cones and glacis between the mountains and the shoreline. So, three geological ensambles define this area: Betic chaines, the other minor Neogenic formations and the Quaternary fillings. These elements and the littoral dynamic have imposed the posterior evolution of the shore.

There are enough indicators of a progression of the shore in most of the points of this Spanish littoral since the final Tertiary in relationship with the variations in the Quaternary climatology and the tectonic factor afecting this zone; and the generation and posterior evolution of the lagoons of this area supports that hypothesis. Presently the human factor has introduced some incidences in the process.

The littoral of Campello may be considered divided in two stretches by the delta of the Seco river, but, initially, its shoreline should have been one only cordon-stretch, double-supported on the cliffs at the North, and on the Huertas Cape, at the South, and with an important massive singularity constituted by the river materials; its importance has led to the formation of an actual geometric singularity dividing the stretch. The evaluations of the average volume of materials dragged by the river entablish it in $2 \cdot 10^6$ ton/year. At present, however, this volume

must be reduced because of the industrial use of the materials as aggregates and the reduction and control of the water streams.

Southward from the delta a cordon-beach has closed an old lagoon up to the cape. Behind the beach and the berm, all along the cordon, one or several chaines of dunes advance towards the plain which once before was the lagoon. The more towards the south the wider and flatter the beach is, the less pebbles appear and the thicker the dunes are, though different buildings bumper that observation at present. At the North of Muchavista all the beach is constituted by pebbles which desappear in the middle of San Juan beach. All together it looks like a double-supported, though somehow onen beach, due to its length.

At the North of Seco river, along of "Carrer del Mar" the shore deposits look different. They are at the foot of a "rasa" of a gradually increasing level to reach the cliffs which shows both deltaic and littoral influence. All the up-beach shows a thick layer of large gravels, even cobbles, in spite of the sandy bottoms of the onshore zone.

4 STUDY OF THE SHORE MODIFICATIONS

The erosion of the beaches of Campello is noticeable for several years now, after their inhabitants observations, though no accurate documentation permits to define it. Inversely to other places like Denia, neither historical nor recent chartography has been available as a suitable reference. At the North of the old pass of the Freu, the sandy little beaches seem to show some regression for about 30 years now. Between the Freu and the delta ("Carrer del Mar") the erosion seems to have been obvious since the pass was closed, after some inhabitants, though others say that it began after the construction of the first groin (Fig. 2).

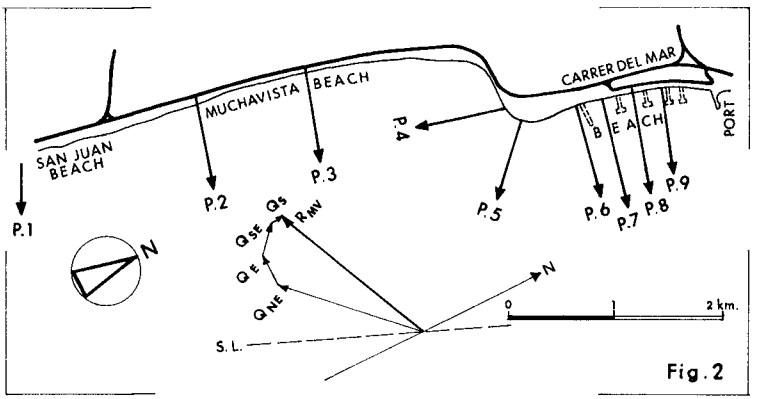

Fig. 2

Actually the seawall must not have had a good performance as a protector and afterwards the beginning of other T-groins has accelerated the erosive process destroying the revetment in both 1979-80 and 1980-81 winters.

In the San Juan bay, Muchavista beach is undergoing a slow but continuous process of regression which affects the promenade every winter for some years now; (it probably has begun just after the last Seco's flood and subsequent advance of the delta, about 20 years ago). The erosion has been spreading southwards and, in the two last winters, has reached even most of San Juan beach.

Nine transversal profiles (P.1 - P.9) have been determined twice a year, considering the experience in other studies of this area, which show not more than two different seasonal profiles. The profiles P.4 - P.5 - P.6, and even P.7, show their deltaic nature. The mean slopes are smaller at the South (P.1 - P.3). In general, the variations of the different profiles between February and October correspond to typical transformation from bar (storm) to berm profiles (Fig. 3). P.1 shows, besides, a loosing of sands and some retreat of the shoreline, increasing its mean slope. P.2 and P.3, on the contrary, show some accretion and an advance of the shoreline, decreasing their mean-slope. Their pebbles were practically covered by sands. The deltaic front (P.4 - P.6) shows some erosion. The accretion in P.7 seems to show a dominant southward transport during spring and summer times. P.8 and P.9 do not show any recovery after the winter erosions.

As a whole the erosions seem to dominate in spite of the seasonal quietness. During winter the products of the erosion in both the delta and Muchavista beach may reach San Juan beach (P.1); during summer the materials of the delta reach Muchavista beach, because of a more perpendicular incidence of the waves. Also during summer eolic action takes the sands upwards to the berms and dunes in San Juan. The eolic circulation of the sands is easily noticeable in the bay all the year round though at present it is almost totally interrupted because of the wall of buildings, which border all San Juan beach. The orientation of the shoreline in P.1 and the incidence of the summer waves may permit also some transport towards P.2.

In the very nine profiles several sand samples have been taken from the beach and from several points of the bottom surface of nearshore zone, principally from onshore zone. All the "Carrer del Mar" and nearly all the Muchavista beach have a cap of pebbles which the nearer the delta the thicker and wider is, showing its deltaic origine. The visual survey of the sections of beaches in depth did not show variability but in the distribution of grain sizes. The samples were analyzed in their size distribution (after eliminating the organic material) and in their mineralogical nature. These latter analysis have only looked for the rate of the most abundant fractions and, in case, the roundness degree of the grains.

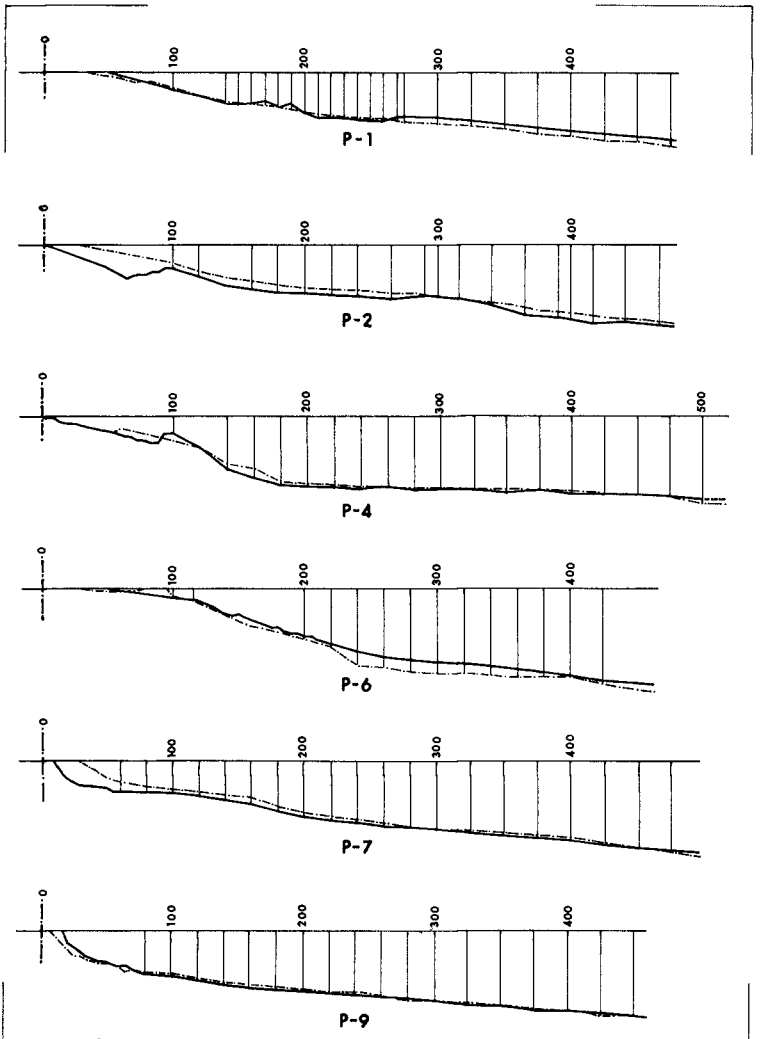
0
100
200
300
400
500
P-1
P-2
P-4
P-6
P-7
P-9
26-28 FEBRUARY 1981
22-27 OCTOBER 1981

Fig. 3

The rarer weight minerales had been studied (ALONSO & PEREZ MATEOS, 1959) and in this work it has been searched quartzs -white, grey and red-, tourmaline, circon, micas, lime organic rest and some meaning opaque one (particularly illmenita which is brought by Seco river from an ophitic outcrop).

Apart from the meaning of the mineralogical data, the influence of the deltaic materials in the formation of these beaches is well shown in the grain size distribution (Fig. 4) of some samples (change of concavity in P.4 - 150 m.; or variation of the slope around the nº 70 A.S.T.M. sieve size, in P.1, P.3 - 100 m. or P.7 - 200 m.). (Samples are named after the corresponding profile. If it is followed by a distance in meters it means that the sample has been taken at this distance from the shoreline; otherwise, the sample was taken at the beach).

The influence of the cap of pebbles in the formation of the beaches is shown, in turn, in the noticeable inflexion shown by several samples (P.9 - 100 m., P.8 - 50 m. and 100 m., P.2 - 100 m, P.3 - 300 m. and P.2 - 400 m.) about the nº 100 A.S.T.M. sieve size.

The uniformity of the size distributions of other samples must be due to the role of the littoral dynamic, and it is also noticeable that silts are more abundant at the North, and the farther from the shoreline the samples have been taken.

On the other hand, comparing the size distributions of all these samples to the ones of Santa Pola and Denia it seems that they are coarser here, the proportion of silts being minor.

The results obtained from the nature analysis are outlined in Fig. 5 in which the variation of the components along the shoreline is shown. The grey quartzs have abundant inclusions, which are not frequent in the other varieties of the quartz; this circumstance has not been found in the other areas studied in this littoral (Denia, Santa Pola). All but particularly the red quartzs show generally the crystalline faces of their grains, even the rounded ones, indicating a relatively short transport length. Tourmaline is especially angular. Carbonates are dominant in all fractions, constituting about 80% of the sands and the small grains show their shell nature; their source is here principally the cap of pebbles, which are rounded fragments of limestones.

The contains of organic material is minor than in other areas, being minima in the beaches (except in the beach of "Rincón", probably because some organic pollution), and maxima on the bottom of the deltaic front.

The lime fraction of sands varies very little either along shoreline or transversally. Quartzs are rather constant also: a) The roundness degree is higher at the South than at the North of the delta and in the nearshore than in the beach; b) the red quartz

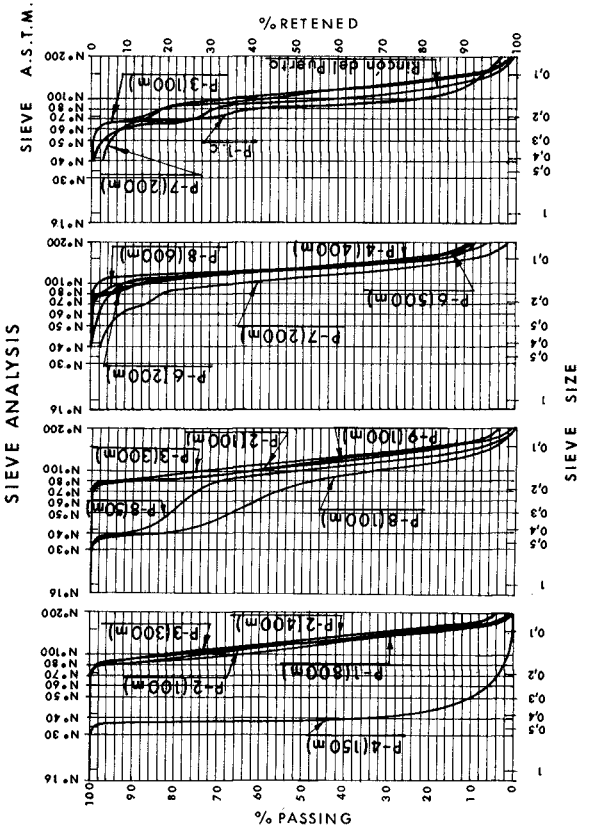
% RETENED
SIEVE A.S.T.M.
SIEVE ANALYSIS
SIEVE SIZE
% PASSING
Rinoçon dei Puerto
P-1 c
P-3 (100m)
P-7 (200m)
P-8 (600m)
P-4 (400m)
P-6 (500m)
P-6 (200m)
P-9 (100m)
P-2 (100m)
P-8 (50m)
P-8 (100m)
P-3 (300m)
P-1 (500m)
P-4 (150m)

Fig. 4

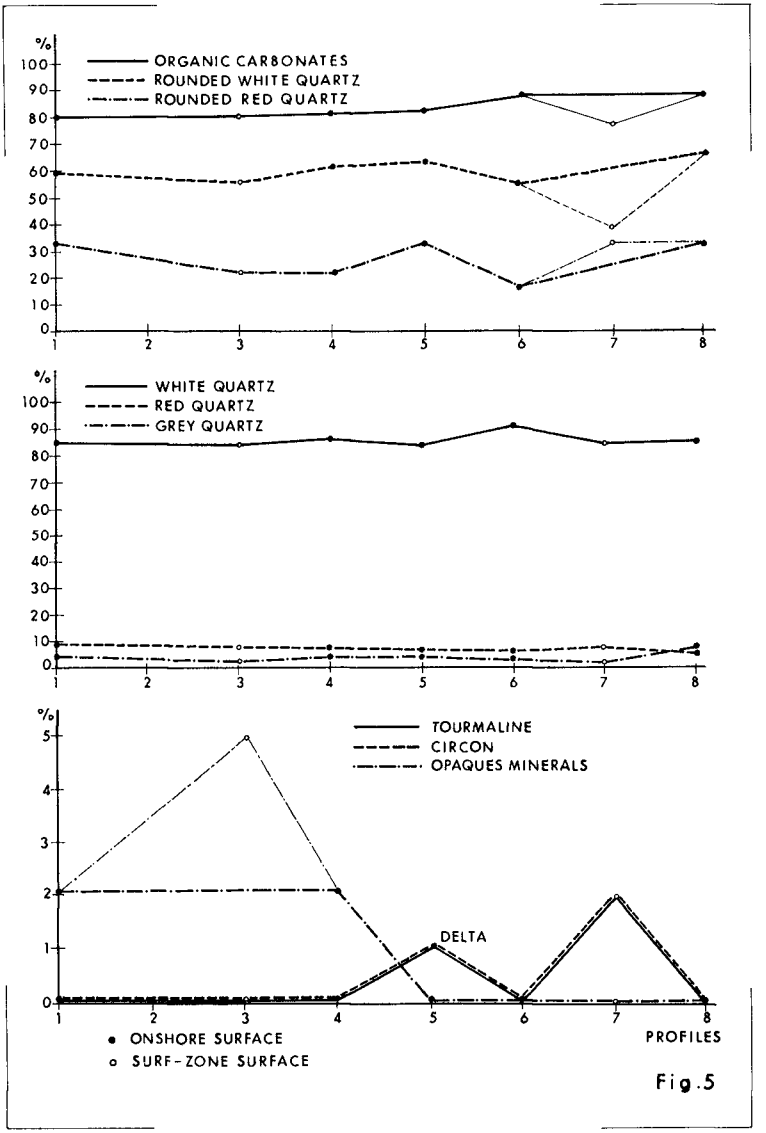
%
ORGANIC CARBONATES
ROUNDED WHITE QUARTZ
ROUNDED RED QUARTZ
WHITE QUARTZ
RED QUARTZ
GREY QUARTZ
TOURMALINE
CIRCON
OPAQUES MINERALS
DELTA
ONSHORE SURFACE
SURF-ZONE SURFACE
PROFILES

Fig.5

outnumbers the grey one, unlike in other areas of this littoral (Denia, Santa Pola), but it diminishes in front of the delta. There are grains (rather sharp) of illmenita only at the South of the delta (but for a small quantity in P.6), probably in relation ship with the dominant longshore transport. There are circon and tourmaline in San Juan beach (P.1) but not in Muchavista (P.2 and P.3); they seem to be in relationship with the quarrystones of the groins, in accordance with the studies of Denia and Santa Pola.

CONCLUSION

The study of the littoral dynamic shows a more or less pronounced dominance of the southward longshore transport. The results of the mineralogical analysis keep the same hypothesis. Nevertheless it is not possible to ignore the relevance of the longshore transport in both directions and the importance of the transversal dynamic. On the other hand a certain reduction of the available materials in the littoral zone is obvious and even the Seco river has diminished its activity lately. The present erosion of the deltaic front is therefore normal and, shomehow, does not present any cause of worry. The situation is different, however, in the beaches.

In the "Carrer del Mar", at the North of the delta, the reduction of materials has become practically total because of the clossure of the Almadraba pass, first of all, and of the construction of the first long groin, sometime later. The resultant physiographical pattern practically hampers any part of the littoral drift to reach the beach all along this stretch. Therefore the other shore protection messures adopted up to now could not be succesful. But, on the contrary, the weak vertical sea wall firstly constructed as shoreline revetment should only accelerate the process, by recycling itselt (The erosion takes the sandy materials off; consecquently the slopes grow up, particularly in the surf zone; the breaking waves become higher also and their action increases over the pebbles and, usinig them, over the wall). At present the process have led to a mean slope of the surf-zone between 6-8%, which is rather significant though it has not reached the extraordinary values of some other coasts like almazora's (up to 25% in several stretches).

The posterior construction of three T-groins was badly developped, being simoultaneously constructed their perpendicular branches and postponing too long the construction of their parallel ones which should constitute the actual and efficient protection. The pressence of perpendicular elements of the groins have accelerated the erosion even more.

In San Juan bay the erosion had begun in Muchavista beach but have reached now the very San Juan beach. The data of previous chapter seem to show an easier natural nourishment of the South of the bay from the nearshore, receiving directly the materials

from both the deltaic front and the littoral drift from the NE. The nourishment of the North of it, from the South, is humper by the asymetric bottom structure of the deltaic front (P.4), which is due to the dominance of the southward littoral dynamic. This funtional scheme must be completed with the eolian activity which permits sand to move in a cycle and to nourish the North of the bay (Muchavista beach) from the land. This hypothesis is perfec tly compatible with all the results of the observation and analy sis. The sands accumulated nearshore of San Juan beach during the winter, due to the NE and E waves, may reach the shore and backshore during the summer under the action of the winds perpen dicular to the coastline. During the autumn the dunes move northwards and the sands spread on the plain in the same way they have filled the lagoon; part of them reach the extreme North of the bay and renourish Muchavista beach, closing the cycle: Sands move southward in the bay and northward along the backshore. The latter parts of the cycle is obstructed at pre-sent by the presence of an inadequated wall of constructions, which have destroyed and substituted the dunes. Therefore the erosion appears rather advanced in Muchavista and only seems to begin in San Juan, but an increasing of the regression of the latter beach is foreseable.

As conclusions it is possible to establish the following state-ments:

1.- This stretch cannot be considered a physiographical unit since not even Huertas cape is a total barrier to the longshore transport. Nevertheless its most important source of material is interior to the very stretch (Seco river), being more diffi-cult for the general littoral drift to reach its beaches, parti-cularly that one of "Carrer del Mar" after closing the Freu pass. This difficulty is increased by the very presence of the delta which as counterweight is undergoing an appreciable regressive process, such as it has been noticed even during calm weather season.

2.- The littoral dynamic has an important transversal component. Its longshore component is alternating and significant in both directions though the southward transport is dominant along the mean year. This general consideration must be in accordance with the particular orientation of the shoreline in each point which may modify the direction of transport. So are the cases of the south end of San Juan bay and the north bord of the delta: south ward of a certain point in each of them only northward transport occurs in the surf-zone.

3.- The importance of the total longshore transport and the del-ta activity all along has permited the development of the presen-te plain through the formation of one or several successive ba-rriers and the posterior filling of the littoral lagoons. This evolution of the shore has been favoured besides by the progre-

ssion of the point delta, which acted as support of the barrier, and by the eolian activity, which accelerated the filling. During this period all this stretch, between Huertas cape and the cliffs of the North, behaved as a sink for total longshore drift in both directions.

4.- At present, however, the relative position of the deltaic front respect to the cliffs and the clossure of the Freu pass avoids practically any nourishment of the "Carrer del Mar" beach from the littoral drift. The erosion has begun to dominate and afterwards, to increase by the inadequacy of the succesive works for shore protection.

5.- The present dimensions of the San Juan bay, between the delta and Huertas cape, would be adequate, however to permit a sufficient nourishment, if the eolian migration of sandy cycle were not cut. Therefore the erosion has begun in the North of the bay as it always hapens leeward of a geometric singularity (the delta itself), but it is spreading riskibly southward and will reach the very San Juan beach.

6.- In order to implement some important harbour facilities for pleasure or a marina, within the district of Campello the very deltaic cone would be the best place since it would be planned without producing negative changes in the littoral processes. The port should be interior and especial cares should be taken to permit the evacuation of the floods and to avoid the entering of the sands.

RECOMMENDATIONS TO ACT

Considering the conclussions above some recomendations may be proposed. Apart from the delta, which would admit an interior port of pleasure, two sub-stretches will be distinguished:

a) The "Carrer del Mar" is very undernourished now from both directions and the transversal dynamic acts efficiently over it. Only some offshore system of protection, preferably complemented by an artificial replenishment might be suitable. The designed T-groins would likely have been succesful if the parallel breakwaters had been constructed quickly after beginning each T-groin; it had obliged to construct one after the other instead of simultaneously. Besides, some other breakwater will be necessary northward of the last one and related to the little haven. In any case, an important artificial replenishment will be necessary to get a suitable beach, but a reduction of the amount of sands would be possible employing material from the delta in the deep and back layers.

b) In Muchavista the undernourishment is more endemic but it would be less severe if the eolian feeding were not so diminished now. Any construction in this bay would affect its present aes-

thetic quality. Only the artificial nourishment in the north end of the bay might be effective. Nevertheless a suitable revetment with a soft slope will be necessary immediately to protect the promenade.

APPENDIX: LITTORAL DYNAMIC EVALUATIONS

The sectorial definition of the Fetch for a point placed in front of the Seco delta and in deep waters is shown in Fig. 6. The number of sectors is enough and the limits between each couple are placed so as to adequate it to the real Fetch.

The parameters of the sectors are shown in TABLE A.1. The directional wind wave regime obtained is shown in Fig. 7. From these regimes a valuation of the longshore littoral transport has been obtained by applying the C.E.R.C. longshore transport rate formule (in decimal units):

$$Q\ (m3/year) = 2.045 \cdot 10^3 \cdot f \cdot H_o^{5/2}\ (m) \cdot F\ (\alpha_o)$$

and following the method developped in other previous woks to obtain an annual average resultant wave.

In it, $f = (1-F_x) \cdot K_o \cdot K_f$, with

$$K_o = \frac{\text{nº of observations in the octant (sector)}}{\text{total nº of observations} = 1072}$$

TABLE A.1.

SECTOR (Nº)	AMPLITUDE (º)	(θ_i/θ_{i+1})*	LENGTH (km.)
1	2	(56-58)	872
2	4	(58-62)	270
3	10	(62-72)	151
4	8	(72-80)	154
5	2	(80-82)	781
6	11	(82-93)	1155
7	15	(93-108)	709
8	15	(108-123)	393
9	15	(123-138)	300
10	15	(138-153)	544
11	15	(153-168)	248
12	15	(168-183)	278
13	15	(183-198)	308
14	5	(198-203)	371
15	7	(203-210)	82

*The angles (θ_i) are refered to an origin defined by the general direction of the shoreline.

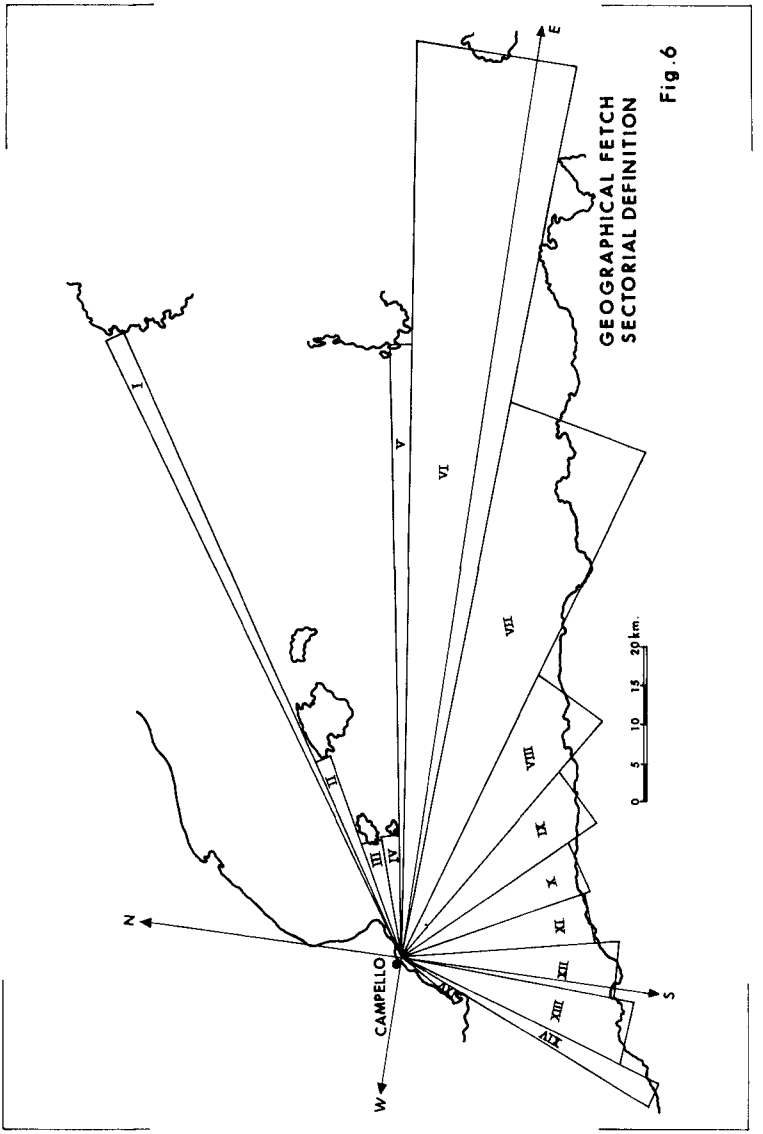
GEOGRAPHICAL FETCH
SECTORIAL DEFINITION
Fig.6
CAMPELLO
N
S
E
W
I
II
III
IV
V
VI
VII
VIII
IX
X
XI
XII
XIII
XIV
XV
0 5 10 15 20 km.

K_f = 1 for all directions (sectors) because the general direction of the shoreline coincides, in this case, with the N.NE - S.SW direction.

F_x may be obtained from the Fig. 7, where the regime of each direction must be considered shortened by the $(H_o)_{max}$ corresponding to the rerpective top wind speed observed.

The α_o value of each direction is the average of the two extreme α_o of the correspondent sector (octant).

The values of these variables for the four established directions are as follows:

a) NE direction: α_o = av (90º, 45º) = 67,5º
K_o = 162:1072 = 0,1511 ; $(H_o)_{max}$ = 3,51 m.

b) E direction: α_o = av (45º, 0º) = 22,5º
K_o = 222:1072 = 0,2071 ; $(H_o)_{max}$ = 5,56 m.

c) SE direction: α_o = av (0º, -45º) = -22,5º
K_o = 56:1072 = 0,0522 ; $(H_o)_{max}$ = 5,04 m.

d) S direction: α_o = av (-45º, -90º) = -67,5º
K_o = 81:1072 = 0,0737 ; $(H_o)_{max}$ = 3,72 m.

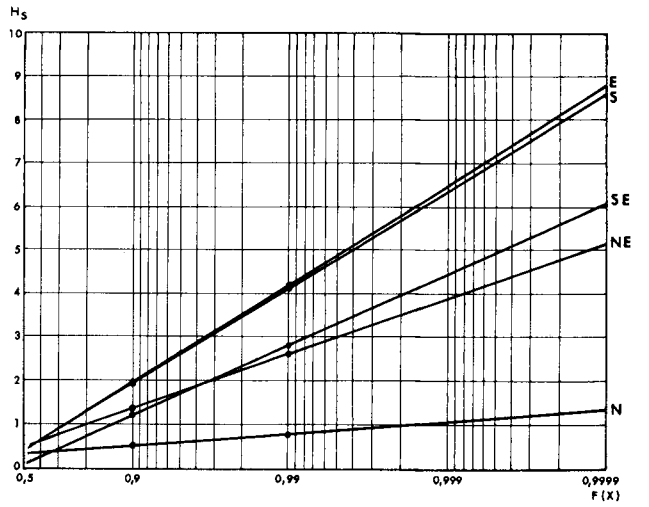

Fig.7

where sign (+) means southward longshore dynamic and sign (-) means northward longshore dynamic.

With these data the respective longshore transport rate induced are obtained in TABLE A.2.

The results show a clearly dominant southward transport though both the resultant total (Q_T = 1.071.404 m3/year) and net (Q_N = 593.158 m3/year) annual longshore transport rates are not to be considered as accurate ones.

Adscribing to each direction a vector defined by de α_o value and the particular Q value obtained from TABLE A.2. an average (equivalent) annual wave direction (A.V.) may be established (Fig. 2).

TABLE A.2.

H	$Q_{(NE)_i}$	H	$Q_{(E)_i}$	H	$Q_{(SE)_i}$	H	$Q_{(S)_i}$
0		0		0		0	
	2.738		2.833		- 582		- 876
0,5		0,5		0,5		0,5	
	18.467		26.350		- 4.629		- 7.920
1		1		1		1	
	28.656		56.388		- 8.470		- 16.470
1,5		1,5		1,5		1,5	
	28.757		78.037		- 10.024		- 22.149
2		2		2		2	
	23.325		87.287		- 9.588		- 24.073
2,5		2,5		2,5		2,5	
	16.669		86.023		- 8.080		- 23.053
3		3		3		3	
	10.952		77.944		- 6.261		- 20.297
3,5		3,5		3,5		3,5	
			66.519		- 4.569		- 16.832
		4		4		4	
			54.278		- 3.188		
		4,5		4,5			
			42.774		- 2.148		
		5		5			
			32.782				
		5,5					

$Q_{(NE)}$ = 129.564 $Q_{(E)}$ = 610.214 $Q_{(SE)}$ = -57.540 $Q_{(S)}$ = -131.772

Q_B = 929.090 Q_N = 550.466 α_i = 16°

REFERENCES

ALONSO, J.J. & PEREZ MATEOS, J.: Los arenales costeros del Levante español. III. La costa de Alicante. C.S.I.C. Instituto Lucas Mallada. Madrid. 1959.

BRITISH ADMIRALTY: ROUTEING CHARTS. North Atlantic Ocean. London. 1968.

COPEIRO, E.: "Los ritmos naturales de nuestras playas". Rev. Obras Públicas, nº 3157. Madrid, mayo 1978. Pág. 361-377.

DIEZ, J.J.: La ordenación de las costas y la dinámica litoral. Referencias al País Valenciano. Opening lesson. 1981-82 Academic course. Politechnical University of Valencia. 1982, a.

DIEZ, J.J.: "Bases para el análisis de la Dinámica Litoral del País Valenciano". Rev. Obras Públicas. Madrid. 1982, b.

DIEZ, J.J. & ARENILLAS, M.: Littoral processes in Denia coasts. S.E.M.E. Brugge. 1982, a.

DIEZ, J.J. & ARENILLAS, M.: Shore Management in Santa Pola Bay (Alicante, Spain). IV International Congress, IAEG. India, N. Delhi. 1982, b.

HOGBEN, N. & LUMB, F.: "Ocean Waves Statistics". Nat. Phis. Lab. V.K. 1967.

MINISTERIO DE INDUSTRIA Y ENERGIA: Mapa Geológico Nacional de España. E. 1:50.000. 2ª Serie. Num. 871-872.

SUAREZ BORES, P.: "Earth dam wave Protection". Comission Internationale des Grandes Barrages Q 36, R 50. Montreal 1970. Pág. 869-902.

SUAREZ BORES, P.: "Formas Costeras Estables". 2º Curso de Análisis y Gestión del Medio Litoral. Colegio Ing. Caminos, Canales y Puertos. Madrid. 1974.

U.S. ARMY. C.E.R.C.: Shore Protection Manual. 1975 Vol. I.

BARRIER BEACH FEATURES OF CALIFORNIA

Hugh Converse 1/

INTRODUCTION

Remarkable near-continuous examples of barrier beach features are found in many coastal areas, worldwide. The most notable North American examples are the margins of North America along the Atlantic and Gulf of Mexico, where barrier islands are found along more than 60 percent of the coastline. There are, in fact, 280 large-scale individual barrier features, 70 of which are highly developed and 100 more are being developed (Hobson, et al, 1980). These barriers have been built out of the enormous volumes of sediment available from the extensive watersheds of eastern and central North America and, through the ages, appear to have migrated long distances across a wide continental shelf in response to the interplay of waves and tidal currents, eustatic sea level fluctuations and sand supply.

Barrier features are less in evidence on the west coast of North America though they are by no means absent. For example, along a 60-mile reach of the Oregon-Washington coast adjacent to the Columbia River mouth, impressive barrier spits have straightened the coast by blocking the bays and headlands. These are black-sand beaches, formed from the large sediment supply of the extensive inland basin of the Columbia (Bascom, 1980; Cooper, 1967), which has the 29th-largest discharge of the world's rivers (Inman and Nordstrom, 1971). The longest spit in this reach is about 19 miles long. The North Pacific coast is a high-energy wave environment, and these spits are continually shifting. Indeed, one of the most outstanding examples of continuing shore movement in North America is found at Cape Shoalwater at the north side of Willapa Bay, Washington where the inlet has migrated about 2.5 miles northward in the last 95 years across homesites, a cemetery and a lighthouse (Terich and Schwartz, 1981; US Corps of Engineers, 1971a).

CALIFORNIA BARRIER BEACH FEATURES

The barrier beach features of California, which are principally composed of quartz and feldspar sands, are proportionally less extensive, but are more common than is generally recognized. Out of an open mainland coastline of 1,073 miles, approximately 210 miles, or about 20 percent may be termed barriers. (By comparison, all sand beaches on the coastline total about 550 miles - U.S. Corps of Engineers 1971b; these figures exclude offshore islands.) This figure is based on barrier features identified during a reconnaissance-level review of existing base maps, aerial photography, historical reports, narrative coastal inventories, and limited on-site inspections. (Especially valuable were U.S. Geological Survey quadrangles, and the file of low-level 35mm photography of the entire California coastline maintained by the State of California Department of Boating and Waterways.)

1/ Civil Engineer, USAE Div., South Pacific, San Francisco, Calif.

In all (see Figure 1), 181 separate barrier beach features were identified in California. Of these, 29 are highly developed with works of man, and 42 are partially developed. Of the total number, about 16 may be considered as major geological features with a length greater than three miles: these are commonly bay-mouth barriers and spits. The distribution of barrier length is shown in Table 1. The other features are generally small creek or bay-mouth barriers: some of which are to be found as an uncommon and analomous features on an otherwise rocky and precipitous coast and without sufficient drainage area to produce more than a relative modicum of sand. Barrier identification generally follows definitions by Shepard and others (Shepard, 1973; Putnam, et al, 1960) with a specific primary criterion that a coastal lagoon or inlet, marsh or permanent or semi-permanent wetland or water-body exists (or historically existed) behind part of the barrier; the barrier may be closed seasonally or permanently - as in the case of certain freshwater or brackish lagoons and lakes which have long been separated from the ocean. (The sheltered coastline of San Francisco Bay is excluded from this analysis.)

Table 1

Range of Lengths of California Barriers

Range	No. of Barriers In Each Range
0-1 miles	127
1-2	20
2-3	19
3-4	5
4-5	3
5-6	1
6-7	2
7-8	1
8 and up	3
	181 total

From north to south in California, a partial list of notable coastal barrier features include Big Lagoon; Humboldt Bay - the largest lagoon on the California coast (Shepard, 1973); Bodega Harbor; portions of Monterey Bay; Morro Bay; Los Angeles-Long Beach Harbor to Newport Bay; the Oceanside area, and San Diego Bay. Several of these are discussed below as case histories, with San Diego Bay being treated in more detail. Cenerally, it is true that these features owe their existence to plentiful present, or past, supplies of sediment and that extensive coastal wetlands and marshes with important wetland values are, or were, present in association with them. With the notable exception of the Los Angeles Harbor to Newport barriers which have been greatly modified, most California barriers still approximate their natural state insofar as coastal processes are concerned. However, the associated coastal marshes and wetlands have been greatly reduced by dredging, filling, and other urban activities, and many are also severely threatened by natural and man-induced sedimentation from upland runoff.

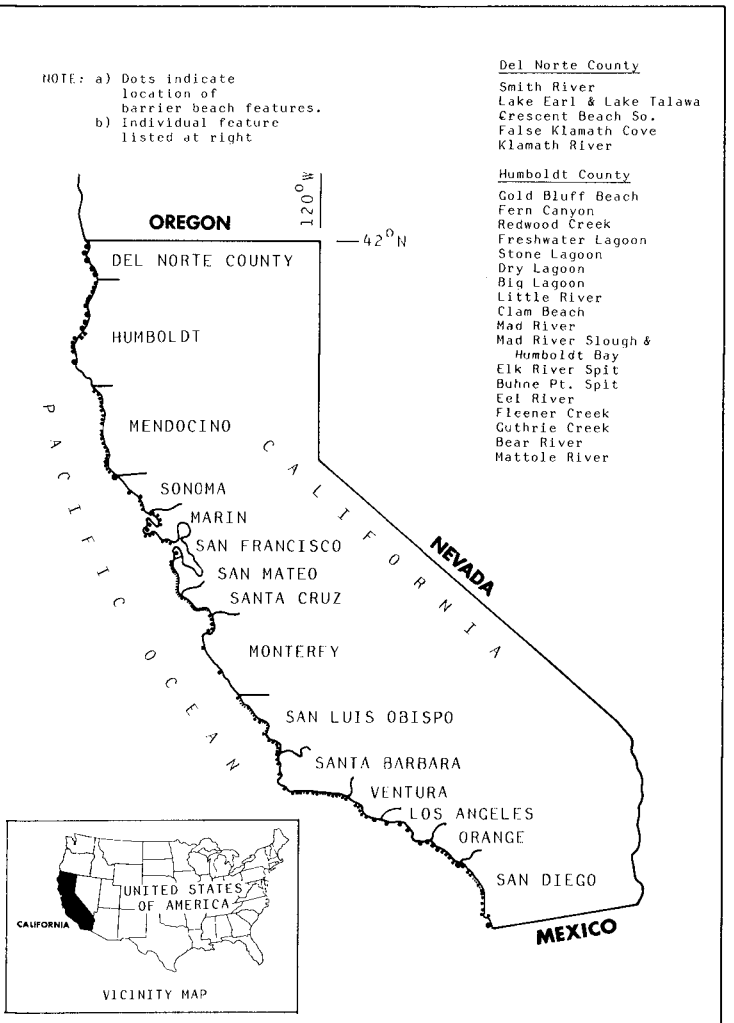

FIG. 1: BARRIER FEATURES OF CALIFORNIA BY COUNTIES

Mendocino County

Jackass Creek
Usal Creek
Cottaneva Creek
Hardy Creek
Juan Creek
Wages Creek
Ten Mile River
Inglenook to Lake Cleone
Virgin Creek
Pudding Creek
Noyo River
Caspar Creek
Big River
Little River
Albion
Big Salmon Creek
Navarro River
Greenwood Creek
Elk Creek
Alder Creek
Manchester Beach & Garcia River

Sonoma County

Gualala River
Russian River
Scotty Creek
Salmon Creek
Salmon Creek Beach So.
Bodega Spit
Estero Americano

Marin County

Estero de San Antonio
Sand Point
Tom's Point
Kehoe Beach
Abbots Lagoon
Drakes Beach
"D" Ranch
Drakes Estero
Bolinas
Muir Beach
Tennessee Cove
Rodeo Lagoon

San Francisco City/County

Lake Merced

San Mateo County

Laguna Salada
Montara Beach
Princeton Marsh
Elnar Beach
Tunitas
San Gregorio
Pomponio Creek
Pomponio Beach
Pescadero Creek
Arroyo de los Frijoles
Mile Forty-three
Yankee Jim Gulch
Gazos Creek
Cascade Creek

Santa Cruz County

Waddell Creek
Scott Creek
Laguna Creek
Majors Creek
Baldwin Creek
Mile Seventeen
Dairy Gulch
Wilder Creek
Terrace Point
Younger Lagoon
Nearys Lagoon & San Lorenzo River
Woods Lagoon/Santa Cruz Harbor
Schwans Lagoon
Corcoran Lagoon
Moran Lake
Capitola
Aptos

Santa Cruz & Monterey Counties

Pajaro River

Monterey County

McCluskey/Salinas Slough
Salinas River
City Lands
Seaside-Monterey
Carmel River & San Jose Creek
Little Sur River
Big Sur River

San Luis Obispo County

San Carpoforo Creek
Arroyo de la Cruz
Arroyo del Oso
Arroyo del Corral
Oak Knoll Creek
Mile Sixteen
Arroyo del Puerco
Little Pico Creek
Pico Creek
San Simeon Creek
Santa Rosa Creek
Villa Creek
Cayucos Creek
Whale Rock
Willow Creek
Toro Creek
Morro Bay
San Luis Obispo Creek
Pismo Creek
Oceano Lagoon
Dune Lakes
Oso Flaco Creek

San Luis Obispo & Santa Barbara Counties

Santa Maria River

Santa Barbara County

Shuman Creek and Ponds
San Antonio Creek
Santa Ynez River
Jalama Creek
Cañada del Cojo
Cañada de Santa Anita
Cañada Del Sacate
Gaviota Creek
Refugio
Dos Pueblos Creek
Tecolote/Winchester
Devereaux Lagoon
Goleta Lagoon
Goleta Slough
Arroyo del Burro
Mission Creek
Andrew Clark Lagoon
Carpinteria - El Estero

Ventura County

Rincon
Ventura River
Pierpont
Santa Clara River
McGrath Lake
Ormond Beach
Mugu Lagoon

Los Angeles County

Topanga
Malibu Creek
Ballona Creek
Rattlesnake/Terminal Island
Alamitos Bay & New River Slough

Orange County

Anaheim Bay
Bolsa Chica Beach
Santa Ana River
Newport Beach
Aliso Creek
San Juan Creek

San Diego County

San Mateo Creek
San Onofre
Las Flores Creek
French & Aliso Canyons
Cocklebur Canyon
Santa Margarita River
San Luis Rey River
Loma Alta Creek
Buena Vista
Agua Hedionda
Batiquitos
San Elijo
San Dieguito
Las Peñasquitos
La Jolla Shores
San Diego River & Mission Bay
Ballast Point
North Island to Tijuana River

FIG. 1 (Cont)

Most of the major barriers have remained essentially stable in shape and location during their recorded history, although some structures built on barrier beaches have been damaged during cyclic winter storms, and significant amounts of sand have artificially been placed on certain southern California barriers.

COASTAL ZONE MANACEMENT

Today, further building and development on California barriers, and beaches in general, is now constrained by strict State coastal zone management policies, which include regulations to protect recreational beaches and environmentally-sensitive habitat areas - such as barrier-associated coastal wetlands and marshes; and coastal hazard regulations which generally require that coastal structures be set back sufficiently from the shore so as not to be endangered by cyclical erosion (State of California, 1976).

The California Coastal Act of 1976, though of Statewide application, calls for the separate development and administration of Local Coastal Programs (LCP's) by local entities, consisting of land use plans and zoning regulations for upland areas (above mean high water). These programs are currently in process; to date about one-quarter of them have been approved by the State Coastal Commission (California Coastal Commission, 1979 and 1982), which still retains control of tidal and submerged lands below mean high water, including coastal wetlands and lagoons. In all, the 181 barriers identified in this review are variously located in many different jurisdictions. Within California there are a total of about 120 LCP's divided between 67 counties and cities, one university, and four ports.

Despite local differences in application, the net effect of these regulations will be to strictly limit development along California beaches, including the coastal barriers. Although it is yet too early to be completely sure, it appears that, under Coastal Commission and other State policies, major coastal structures are precluded except in port areas, or where an evident, water-dependent, public need, without a feasible alternative, can be demonstrated (California Resources Agency, 1978).

CASE HISTORIES

Long reaches of the California coastline are bordered by cliffs: either the steep faces of elevated marine terraces or the precipitous slopes of coastal hills or mountains. The open ocean coastline is, as indicated previously, fronted by sand beaches for about half of its length; many of these beaches are little more than a narrow strand along a steep or rocky backshore; wide, extensive sand beaches are generally only to be found where sizable streams or intermontane valleys come to the shore. Small barrier features may be found blocking small streams in many areas of the coastline, but longer, larger barriers are, of necessity, associated with more plentiful sand supplies from larger watercourses and drainage basins. Many barriers are also associated with hook-shaped bays which are an important and recurring feature of the California coast. These latter features occur in many areas of the world where a particular

wave direction acts obliquely on the coastline over eons, resulting in indented hooked or crenulate-shaped bays in the lee of prominent headlands (Silvester 1974).

The following case histories (see Figure 3 - Note: Figure 2 deleted) include Humbolt Bay where protective barrier beaches occur along a long straight reach of sandy coastline. By way of contrast, barrier spits at Bodega Harbor, Bolinas Lagoon and the elongated barrier at San Diego Bay have been built by wave-induced currents acting in the lee of prominent headlands; these features follow the hooked form.

Humboldt Bay

This brief review of case histories of selected California barriers begins with Humboldt Bay, a shallow tidal estuary 230 miles north of San Francisco. The bay, with a high tide area of about 25 square miles, is separated from the ocean by two long barrier spits which in turn are separated from each other by a jettied entrance channel with a maintained 40-foot depth. A treacherous, shoaling submerged bar at the entrance requires large volumes of regular dredging. Both spits, especially the north, have active dunes. The north spit is about 8 miles long, and averages about 3,000-4,000 feet in width. Although largely open space, there are industrial and residential areas along the bayward side, as well as numerous roads. The south spit is about 4 miles long and narrow, ranging from 600-1,500 feet in width; it is maintained as undeveloped open space. The likely sources of material for these features are modern and prehistoric sands from the nearby Mad and Eel Rivers: the latter stream being a prodigious sediment carrier during flood periods (Welday, 1970). Overall, since the entrance was fixed by jetty construction in 1890, the north and south spits have advanced seaward (Noble, 1971; Kieslich, 1981; Shapiro, 1979); at present, the spits are in a state of dynamic equilibrium. Fixing of the jetties and subsequent deepening of the entrance channel concentrated wave energy on an elevated bluff area bordering the bay inside and opposite the entrance. As an apparent result, the area has retreated up to 1,600 feet since 1854, almost obliterating the bluff area, and lengthy stretches of the shoreline have been armored (Tuttle, 1982; Shapiro, 1979). Also, two relatively small laterally-moving spits have been created inside the bay, one to the north and one to the south, continually extended by materials moved by wave energy coming through the entrance.

The applicable Local Coastal Program of Humboldt County emphasizes protection of the spits as valuable open space and habitat area. This fact, coupled with their essential stability, indicates that the barriers will remain relatively unchanged over the next several years.

Bodega Harbor

Bodega Harbor is a small triangular-shaped coastal lagoon 55 miles northwest of San Francisco. The water area at high tide is about 1.3 square miles. The lagoon is located directly on the San Andreas fault zone and is separated from the Pacific on the west by a wide (2,500' wide and greater) tombolo-like sand barrier which links the

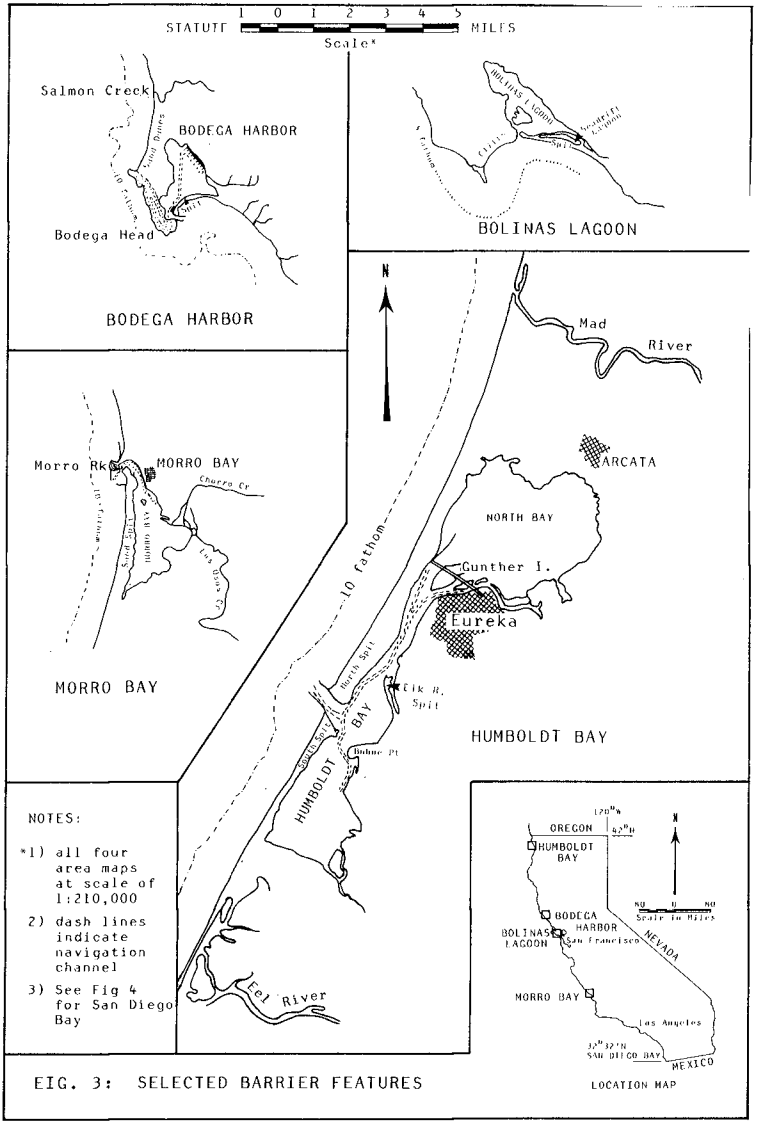

EIG. 3: SELECTED BARRIER FEATURES

mainland with Bodega Head, a rocky promontory to the west. To the south, the harbor is separated from the ocean by a much narrower curved barrier spit (600 feet or more in width), 1.6 miles long, with a jetty-protected entrance at the west end. The principle sources of the barrier sands are Salmon Creek and the Russian River, both to the north (Zeller, 1962). The entrance requires very little maintenance as the tidal prism balances the effects of wave attack. Past overgrazing had denuded the north barrier, resulting in movement of sand dunes and large volumes of sand blowing into the interior channels. In recent years, replanting of vegetation has stabilized the dunes resulting in lessened maintenance dredging. Filling of the harbor by landfills has also been halted.

The harbor area is an important recreational and commercial fishing center but developmental pressure is relatively low. The Local Coastal Program of Sonoma County provides for continuance of the barrier area as protected open space. The northern dune area is part of a State park and the curved barrier spit adjacent to the entrance is a County Park. Since both barriers are essentially stable, important physical changes are not expected in the foreseeable future.

Bolinas Lagoon

Like Bodega Harbor, Bolinas Lagoon is a triangular-shaped coastal inlet and is similarly located directly on the San Andreas fault zone, 15 miles northwest of San Francisco. The lagoon area is about 2.2 square miles. The lagoon is about 3.5 miles long by 1.5 miles wide and is separated from the ocean by a curving sand spit 700 to 1,500 feet wide and 2 miles long. An uncontrolled entrance to the lagoon is at the west end of the spit and is naturally maintained by the tidal prism of the inlet, though at a shoal depth. The tidal prism of the lagoon has been greatly diminished over the last century as agricultural and urban land use have resulted in accelerated sedimentation. Without watershed control of sediment loads, and possibly remedial dredging, the inlet will close and the lagoon will eventually become a meadow (Johnson, 1974). (As noted earlier, this is a general problem facing many lagoons in California.)

The primary source of material for the spit is northwest drift of material from the submerged bar (San Francisco Bar) offshore the Colden Cate and the cliffs to the west of the inlet entrance which are actively eroding (Wilde and Yancey, 1970). Most of the spit is privately owned above the mean high tide line and has been almost completely developed during the last 20 years with expensive single family dwellings. The spit has also been extensively reshaped on the inlet side and a sizable artificial lagoon has been created entirely within the spit.

Like most California beaches exposed to open ocean influence, the beach width on the Bolinas spit varies seasonally, narrowing in the winter due to storm erosion and widening again in the summer. The average seasonal variation is about 100 feet (Johnson, 1970). Unfortunately, however, since this figure is an average, extreme storm conditions can threaten the private homes, many of which are close to the beach. In 1977-78, nine homes were nearly undermined by erosion of the beach and adjacent low dunes during a combination of

high wave conditions superimposed on high tides. Temporary sandbagging and placement of a Longard tube was undertaken and some rock revetment was later placed (Domurat, 1978: Moore, 1978).

Despite a proper concern for the houses, there is no particular threat to the barrier spit as a geological feature while it remains in state of dynamic equilibrium. No significant amount of new construction nor intensification of use is likely under the applicable governmental policies.

Morro Bay

Morro Bay is a shallow natural harbor located about 200 miles south of San Francisco. The lagoon, which has an area at high tide of about 3.2 square miles, is separated from the open ocean by a barrier spit about 4 miles long and 1,700 feet wide, and is ridged with both active modern dunes and heavily vegetated dunes of intermediate and ancient age. The primary sources of sand are sediments from the Chorro Creek and Los Osos Creek drainages which continue to slowly fill the inlet (Shepard and Wanless, 1971; Cooper, 1967).

The natural entrance to the lagoon has been greatly modified for small craft navigation. The entrance, which is at the north end of the harbor and skirts the north end of the spit, is in the lee of Morro Rock, a large granitic monolith which is connected to the mainland by a tombolo-like formation. Formerly, the rock was an island with a sand bar in its lee dividing two separate shallow channel entrances into the bay - around the north the south side of the rock, respectively.

Harbor improvements constructed in the early 1930's cut off the north channel. Because of continuing shoaling, two converging breakwater - jetties were constructed to protect the entrance, one from the south side of Morro Rock and another from the barrier spit. Shoaling of the entrance remains a problem, however; and an average of about 120,000 cubic yards per year of material must be removed to keep the channels at a depth of 16 feet. Sand moves both ways but the net drift appears to be to the north; most of the shoaling is due to littoral movement though some material does blow off the spit into the interior channels. Spoil disposal has generally been on adjacent beaches. The harbor improvements have resulted in an accretion north of Morro Rock and readjustment of the position of the tip of the barrier spit; however, in general, the barrier is in a state of dynamic equilibrium. The most notable natural change in recent times would appear to be continued dune building and advance of dunes into the tidal flats and shallow water behind the spit (Cooper, 1967). The tip of the spit adjacent to the entrance is open space which will be protected by the City of Morro Bay's Local Coastal Program; the balance of the spit is a protected State park. The entire spit is without road access and is otherwise undeveloped. Its continued preservation seems assured.

San Diego Bay

San Diego Bay (Figure 4) is an elongated, crescent-shaped embayment of variable width with a high tide area of about 16.6 square miles. It is separated from the Pacific by a narrow sand barrier which

FIG. 4: SAN DIEGO BAY

connects with Coronado Island and North Island adjacent to the bay entrance at the north end of the bay. The bay entrance, which is partly protected by the sheltering headland of Point Loma to the west, is self-scouring to a natural controlling depth of about 25 feet; but is maintained at a much greater depth (up to 42 feet) to allow deep draft access to the bay, which is one of the finest natural harbors in the world. Tidal scour has been assisted by construction of a training jetty, on the barrier side of the channel, completed in 1904. Dredging maintenance requirements are low.

The bay appears to be a drowned, possible faulted valley, and the barrier grew by northerly currents moving sand from the Tijuana River and Otay River deltas (Shepard and Wanless, 1971) to the south (continued supply has been from the Tijuana in recent times). The narrow part of the barrier, or strand, is about 7 miles long and in its natural state had a variable width of about 500-700 feet. The beach was backed by low-active dunes averaging about 10 feet high which tend to encroach into the bay locally widening the strand considerably (Inman, et al, 1974). Although occasionally breached during high wave conditions, the barrier has always been continuous in historic times (Hertlein and Grant, 1944; Herron, 1980). North Island and Coronado Island were joined into one in 1944 by hydraulic filling with dredge material; the combined "island" feature is about 3 miles long and 2 miles wide. Hydraulic filling continued apace in the area from about 1910 to the 1970's; the northern and eastern margins of the bay were greatly reshaped and the barrier was widened at several places. The period of greatest activity was in war years of the 1940's when the bay was deepened extensively for the Navy, generating large volumes of spoil; over 28 million cubic yards of excess sand was placed on the seaward side of the barrier between 1940-46 (with smaller fills since), greatly widening the beach (Inman, et al, 1974). Despite slope readjustments, beach recession, and littoral movement, some of this sand remains in the area.

The barrier (or Silver Strand as the narrow portion is known) is remarkable for the diversity of the land uses - both military and civilian. At the north is the North Island Naval Air Station, while Coronado is an incorporated city with residential, commercial structures, and a wide recreation beach; further south, a four-lane highway backs a wide beach and continues south along the barrier; naval housing areas behind the highway contrast with a reach with several multi-story condominiums on the seaward side of the highway, some close to the beach and protected with a rubble seawall; near the south end, a former widened dune area has been dredged and reshaped on the bay side to create a residential marina community. About two miles on the beach serve as popular State beach recreation area; several more miles are reserved for the Navy as an amphibious training area. Further to the south where the barrier widens to join the Tijuana and Otay floodplain, is a large Naval radio station. In the past, a railroad spur extended for the length of the barrier but has now been abandoned. Detailed engineering studies of a second bay entrance crossing the barrier have also been made but are presently inactive.

A sandy beach fronts the floodplain for several miles further south to the Mexican frontier, bordering the residential community

of Imperial Beach, and is breached by the mouth of the Tijuana River. At the river mouth the beach consists of two narrow spits backed by a lagoon and marsh with an area of about 1.7 square miles, managed as a wildlife refuge.

In recent years, concern has grown about the maintenance of sand supply to the sand barrier primarily because the 1,730 square mile drainage of the Tijuana River, most of which is in Mexico, is now 72 percent controlled by dam construction (Phillips, et al, 1979). Previous to control, which was essentially completed at its current level about 1940, periodic floods supplied an annual average of about 700,000 cubic yards to Silver Strand beaches (Inman et al, 1974).

Littoral movements in the vicinity of the Tijuana River mouth are divided between north along the strand and south into Mexico. Physical evidence (movement of past fills, etc.) strongly supports a net northward movement along the strand. (Longshore transport calculations are not fully consistent in this matter although they indicate large transport to the north in the winter and to the south in summer.) It is known, however, that sand is moving along the barrier to the tip of North Island. Some of the material is accreting at the Zuniga Schoal area adjacent to the jetty along the east side of the entrance. Large amounts, however, are also moving into the entrance channel and are flushed offshore to a depositional area in depth of 50 to 110 feet. This latter volume is estimated at 2 million cubic yards per year, based on comparative bathymetric surveys (Inman, et al, 1974), but the estimate may need further investigation.

Therefore, since the natural sand source of the Tijuana River has been cut off, a continuing sand supply to balance losses at the northern end of barrier is no longer available and long-term recession of the beach can be expected without artificial protection or nourishment.

As might be expected, this problem should first become evident nearest the former source area. This hypothesis appears to be confirmed at Imperial Beach, just north of the Tijuana mouth, where erosion of the beach and damage to structures have occurred (U.S. Corps of Engineers, 1975). Due to the presence of a remnant delta of the Tijuana River, this area is a zone of wave energy convergence, which would tend toward increased erosion. The erosion has been countered by groin construction (which proved ineffective) and periodic beach nourishment; more permanent solutions such as an offshore submerged breakwater and fill are under consideration by the Corps of Engineers and the State of California.

Overall, the cutoff of sand from the Tijuana basin has resulted in a narrowing of the southern part of the barrier; however, at the north, the strand and North Island remain considerably widened over natural conditions due to past fills despite continued losses of material to Zuniga Shoal and the offshore sediment-deposition zone. Typical long-term changes, through the mid-1950's are as follows: Tijuana River and U.S. Naval Radio Station; average rate of change -2.3 feet per year (period of record 1889-1954); Silver Strand and North Island; average rate of change: +8.2 feet per year (period of record: 1856-1956). (May, et al, 1982)

Long-term stability of the barrier will require remedial human intervention and management. Artificial nourishment is a preferred

solution as long as sources of fill can be readily obtained. A recent (1978) Corps of Engineers channel deepening in the bay provided an additional 6 million cubic yards of sand for Imperial Beach and the Silver Strand; although disposal of such dredging cannot be regarded as a permanent solution, significant amounts of suitable beach can be obtained in this way. Possible long-term solutions might involve, for example, recycling of sand now transported north to Zuniga Shoal and/or the adjacent offshore sediment sink (possibly with added structures in the area to accrete sand in the shoal for recycling before it is lost to the sediment sink). Alternatively, extensive "hard" structures - such as an artificial headland or series of headlands - might be considered for all or part of the entire littoral cell between the Tijuana River and the harbor entrance. However, this would be expensive and require a great deal of planning and investigation to minimize adverse effects on adjacent areas. In any case, improved monitoring of the wave climate and beach changes will be necessary so that future engineering decisions will be based on accurate knowledge of coastal processes. (Monitoring measures now being considered are discussed subsequently.)

Management jurisdiction for the barrier is divided between the Local Coastal Programs of San Diego County and the cities of San Diego, Coronado and Imperial Beach, as well as the Navy - whose upland jurisdiction is generally exempt from the California Coastal Plan. The application of current Coastal Act guidelines and Navy policy will prevent further encroachments on the beach side of the barrier. (For example, construction of additional large multi-story condominiums, similar to those noted above at Coronado, would probably not be allowed.) Preservation of the barrier spits which front the Tijuana River Marsh is also indicated under the applicable governmental policies.

In summary, human activities to date have greatly modified the barrier between the Tijuana River and the San Diego Bay entrance with considerable enlargements at the north, by dredged fills and beach nourishment, counterbalanced by upstream control of the Tijuana River, the likely principal sand supply to the strand. Recognizing the high level of development of the barrier, continued and intensified management will be necessary to protect its physical form and the multiple uses it sustains.

OTHER BARRIERS

Los Angeles Basin

A notable series of barrier features (Figure 5) exist along about 22 miles of the 30-mile long segment of coastline bordering the southern side of the Los Angeles Basin. The basin is essentially a large alluvial plain formed by deposits of sediment carried by the San Gabriel, Santa Ana and Los Angeles Rivers which, even in historical times, frequently changed location during flood periods and inundated vast areas (Shepard and Wanless, 1971). Until this century, six well-developed bay-mouth barriers breached by tidal inlets or associated with river mouths, and backed by about 25 square miles of marshlands, existed in this area (Speth, et al, 1976; Cooper, 1967).

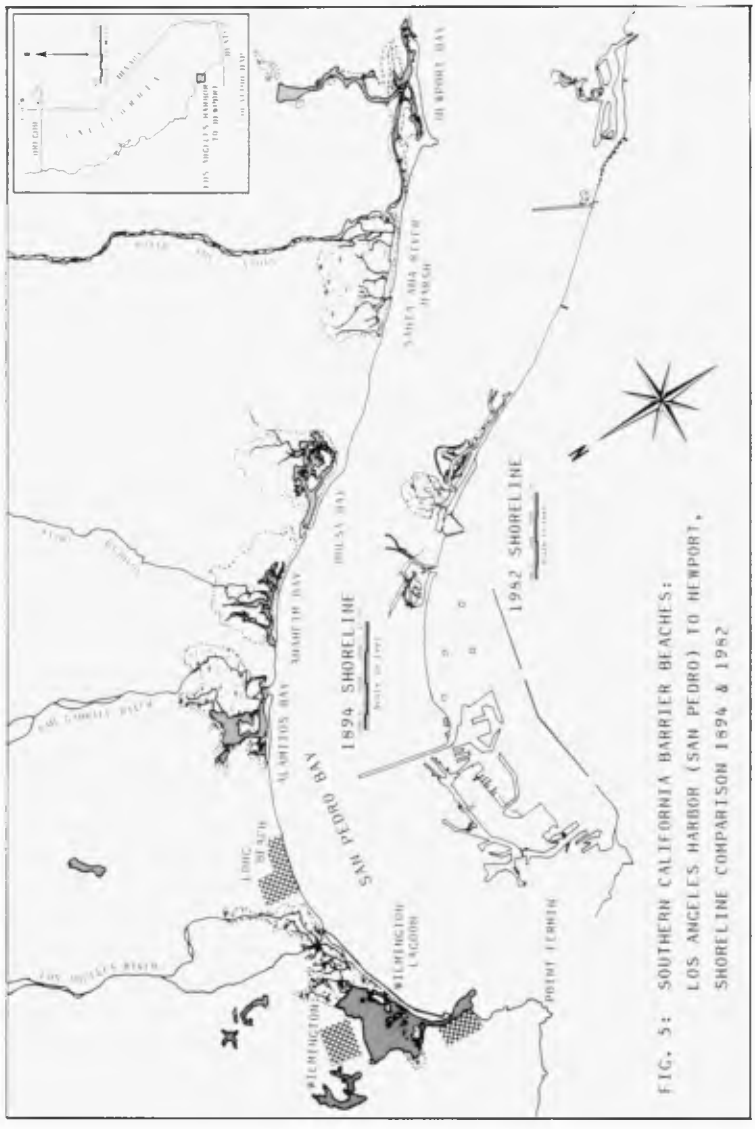

FIG. 5: SOUTHERN CALIFORNIA BARRIER BEACHES: LOS ANGELES HARBOR (SAN PEDRO) TO NEWPORT, SHORELINE COMPARISON 1894 & 1962

Today most of the area and the entire region has been utterly transformed by industrial and urban development. The Rattlesnake Island (or Terminal Island) barrier adjacent to the mouth of the Los Angeles River has become the center of a great port complex, almost totally reshaped and enlarged by dredging and filling, backed by intensive industrial, commercial and residential facilities, separated by the river by channelization and from the open ocean by three segments of Federal breakwater, with a total length of 8 miles (Parker, 1971)

Enlarged by fills, armored and bulkheaded, and in the wave shadow of the breakwater, the stability of the former natural barrier is no longer dependent on the usual coastal processes. The nearby barrier at Los Alamitos Bay adjacent to the mouth of the San Gabriel River lies just at the edge of the wave shadow of the breakwater; further downcoast are bay and river mouth barriers at Anaheim Bay, Bolsa Chica, Santa Ana River and Newport Bay. All of these areas (and intervening reaches) have suffered to some degree from beach erosion due to diminution of the sand supplied to the beach, notably at Surfside-Sunset (Anaheim Bay barrier) and at Newport which have residential areas close to the beach. Many factors have been advanced as contributing causes (Habel and Armstrong, 1977): diminished supply of sand from upland sources due to construction of dam and debris basins; sand and gravel mining from river channels; prolonged drought conditions in Southern California which act to limit supplies of sediment to the coast; jetty construction at Anaheim Bay; and losses to the submarine canyon at Newport Beach. In any event, it has been necessary to nourish most of the entire reach periodically with sands trucked from river beds or other inland sources, and more recently, dredged from an offshore borrow site. In addition, nine groins have been built along the west portion of the Newport barrier to retain beach fill.

Most of this coastline consists of sandy beaches, intensively used for public recreation and backed by a four-lane highway; the largest beach protection investments have been made in areas where residences and park facilities are on or close to the beach, in front of the highway or other roads. Under the Local Coastal Program policies of Orange County, and the cities of Seal Beach, Huntington Beach, and Newport Beach, the land uses should remain largely unchanged. Continued beach nourishment will probably be required.

Oceanside and Vicinity

A twenty-five mile segment of the coast southward from the vicinity of Oceanside, 65 miles south of Los Angeles Harbor, is of especial interest because of persistent beach and cliff erosion. The shoreline is bordered by elevated marine terraces fronted by generally narrow sandy beaches. At intervals, the terraces are interrupted by stream valleys containing brackish or saltwater lagoons and marshes which are separated from the ocean by narrow sand barriers. In all, nine such lagoon-marsh-barrier complexes are present in this reach.

Several communities lie along the marine terraces and border the lagoons. A particularly complicated situation exists at the town of Oceanside where breakwater-protected military and civilian small

craft harbors, with a common entrance and landfills, have been constructed (1940's-1970's) in marshy areas behind barriers adjacent to the San Luis Rey and Santa Margarita Rivers. With seasonal reversals in littoral drift, shoaling problems have been severe in the entrance, which tends to act as a sand trap. Concurrently, severe erosion has occurred on the 2.2-mile reach of beach immediately south of the harbor in front of the city of Oceanside, stripping off sand, leaving cobbles on the beach and threatening roads and homes. This reach has required repeated nourishment with sand dredged from the small-craft harbor and truck-hauled from inland sources. Numerous studies and remedial actions have been undertaken by the U.S. Corps of Engineers regarding this problem.

There are also concerns about the effects of the harbor interrupting sand supplies to the beach. However, the entire 25-mile reach, which - as noted - is primarily bordered by cliffs (marine terraces), appears to be retreating. Primary causes cited include diminution of sand supply to the coast by upstream controls and due to the prolonged drought period (1948-1978): these causes being preparatory to episodic erosion of the cliffs during high wave conditions. Cliff erosion is also worsened by changes in groundwater and drainage of the bluffs due to urban development (Kuhn and Shepard, 1980).

The problems of most concern to the affected communities do not involve critical erosion on the barrier beaches which front the lagoons (barriers occupy about 8 miles of the 25-mile reach and several are protected by revetments, seawalls and periodic nourishment, Habel and Armstrong, 1977); but, the general problem has prompted initiation of a major coastal processes monitoring and investigative effort by the Corps of Engineers which emphasize this particular area. The study will be expanded to include the Orange County and San Diego coastlines between Dana Point near San Juan Capistrano, and the Mexican border. (This Congressionally-authorized study known as the CCSTA: Coast of California Storm & Tidal Action study, will ultimately include additional areas of California.) Monitoring and investigation of barrier features, though not separately distinguished as such, will be contained within the CCSTA, as part of studies of the larger coastline.

THE COAST OF CALIFORNIA STORM AND TIDAL ACTION STUDY (CCSTA)

Before concluding this paper it might be useful to discuss the CCSTA. The study plan is still being formulated by the Corps of Engineers, Los Angeles District; a multi-year program is envisioned initially emphasizing gathering of basic data, including expansion of an existing state-of-the-art wave gaging network, and recurring beach profiling and sediment sampling. Study planners are considering inclusion of field and office studies of wave hindcasting; quantification of sediment sources (streams, cliffs, coastal longshore drift, fills) and sediment sinks (submarine canyons and offshore deposition zones); historical shoreline changes; sea level fluctuations; and, climatic changes.

Data gathered would be analyzed in order to evaluate present conditions, predict impacts of proposed changes and aid in formulation of local and regional solutions.

Although, as noted, this overall plan is still being developed, data collection for the CCSTA and related program has already begun; the existing Corps of Engineers wave gaging network (Domurat and Pirie, 1980) is being expanded to include directional wave gages at additional locations in the San Diego region, and beach profiles which will ultimately cover 100 ranges over the 85-mile reach from Dana Point to Mexico.

One directional gage (Seymour and Higgins, 1978) is being planned for installation at Imperial Beach at the south end of the Silver Strand, and at least one other gage further north along the barrier is under consideration. If carried out, this would be an important step toward better quantification of coastal processes between the Mexican border and Zuniga shoal.

SUMMARY OBSERVATIONS AND CONCLUSIONS

In summary, though of secondary importance, barrier beach features are widespread in California. As indicated in the above case histories, most California barriers have been essentially stable in historic times. Those subject to erosion have been maintained in place by artificial beach nourishment or other protection. Although present management practices will probably continue to be satisfactory, human intervention with beach nourishment and structures may be necessary in some areas. However, such intensified solutions will have to be based on more complete data on coastal processes, in order to respond to tightened State and local coastal management policies.

As recognized by various observers, the coast of California is readily characterized as one of cliffs and bluffs; the cliffs commonly being elevated marine terraces (Kaufman and Pilkey, 1979; Shepard and Wanless, 1971). Barriers are less extensive in California than in many other areas due in part to lesser sediment supplies from restricted drainage areas. Still, as noted, a sizable portion of the California shore is bordered by barriers; and as case studies indicate, their protective functions can be quite important. Some of the barriers are small-scale features occurring at the mouths of streams which breach long reaches of coastal cliffs or mountains. Others are sizable features, often associated with larger geologic elements such as intermontane valleys or alluvial plains - the Los Angeles Basin is an example - which adjoin the coast. Of the barrier beaches examined: Humboldt, Bodega, Bolinas, Morro Bay (and the large majority of smaller barriers identified) have remained essentially stable throughout historic times, despite varying degrees of human activity. Southern California barriers between Los Angeles and Newport and at San Diego have generally been subjected to erosion by interruptions to sand supplies - in part because of urban development. However, the barriers - some of which are no longer recognizable, have either been stabilized by protective works or artificial sand nourishment. In the Oceanside area, erosion problems at the several barriers have been dealt with by localized protection; however, a more general condition of beach and episodic cliff retreat continues along a 25-mile reach.

The latter case, and that of the San Diego Bay barrier (whose sediment supply is now dependent on a dam-truncated watershed), give

evidence that barriers are part of larger systems which should be better understood if intelligent coastal management is to be carried out. Regional studies of wave regimes, shoreline changes and related coastal and watershed processes are desirable to understand what is happening to the shore and to evaluate any prescribed actions, which might range from continuing current practices of incremental protection, through large-scale beach nourishment and engineered coastal stuctures.

Ultimately, some beaches and coastal barriers - especially in southern California - will need protection. Although artificial nourishment remains the favored technique, economic considerations may necessitate combining nourishment with structures to reduce losses of beach material. Certain barrier-associated coastal lagoons could also benefit from limited dredging to remove excessive sedimentation which threatens their continued existence. (This is, however, a controversial issue.)

This observer believes that State and local coastal plans, although strict, will prove flexible enough to allow necessary improvements, provided they are presented and justified on a rational and technically-sound basis. In this regard, expanded study, monitoring and evaluation of the impacts of coastal and related processes on barriers and other shoreline features such as those planned for the CSSTA study should prove useful.

ACKNOWLEDGEMENTS

The aid of personnel from the San Francisco and Los Angeles Districts of the U.S. Army Corps of Engineers is gratefully appreciated. Also, special thanks is due Ceorge A. Armstrong for aid in reviewing the remarkable file of aerial coastline photographs which he has taken for the California Department of Boating and Waterways.

The views of the author do not purport to reflect the position of the Corps of Engineers or the Department of Defense.

REFERENCES

BASCOM, W. (1980) Waves and beaches, Revised edition, Garden City, New York: Anchor Press, Doubleday. 366 pp.

CALIFORNIA, STATE OF (1976). California coastal act of 1976 as amended; Public Resources Code. Sect. 3000 et. seq.

CALIFORNIA COASTAL COMMISSION (1979). Revised, local coastal program manual, California Coastal Commission, San Francsco. 131 pp., appxs.

CALIFORNIA COASTAL COMMISSION (1982). Local coastal program, April, status summary. California Coastal Commission, San Francisco, 6 pp.

CALIFORNIA RESOURCES AGENCY (1978). Shoreline erosion protection policy. Resources Agency Memorandum, Sacramento, California, 7 pp.

COOPER, W.S. (1967). Coastal dunes of California, Ceological Society of America, Boulder, Colorado, Memoir 104, 131 pp.

DOMURAT, G. W. (1978). California coast storm damage, winter 1977-78. U.S. Army Engineer Districts, San Francisco and Los Angeles, 10 pp., appx.

DOMURAT, G. W. and D. PIRIE (1980). California coastal data collection program: data collection, analysis and dissemination. Proceedings of Coastal Zone 80. Am Soc of Civil Engrs. New York: 2171-2179.

HABEL, J. S. and ARMSTRONC, C. A. (1978). Assessment and atlas of shoreline erosion along the California coast. California Department of Navigation and Ocean Development, Sacramento, 277 pp. appx.

HERRON, W. J. (1980). Artificial beaches in southern California. Shore and Beach, 48 (1): 3-12.

HERTLEIN, L. G. and GRANT, U. S. IV (1944). Geology and paleontology of the marine Pliocene of San Diego, California, Memoirs of the San Diego Society of Natural History: 1-68.

HOBSON, R. et al. Recent geologic history of a barrier island. Proceedings of Coastal Zone 80, Am Soc of Civil Engrs, New York: 850-862.

INMAN, D. L. and NORDSTROM, C. E. (1971). On the tectonic and morphologic classification of coasts. Journal of Ceology, 79 (1): 1-21.

INMAN, D. L. et al (1974). Nearshore processes along the Silver Strand. La Jolla, Intersea Research Corp., Contract Report DACW09-74-0062 to U.S. Army Engineer District, Los Angeles, 67 pp.

JOHNSON, J. S. (1970). Seasonal bottom changes, Bolinas Bay, Calif. Proceedings of the 12th International Conference on Coastal Engineering, American Society of Civil Engineers, New York, 1383-1395.

JOHNSON, J. W. (1974). Bolinas Lagoon Inlet, California, U.S. Army Corps of Engineering Coastal Engineering Research Center, Fort Belvoir, Virginia. Miscellaneous Paper No. 3-74.

KAUFMAN, W. and PILKEY, O. H. (1979). The beaches are moving. Garden City, N.Y. Anchor Press/Doubleday, 326 pp.

KIESLICH, J. M. (1981). Tidal inlet response to jetty construction. General Investigation of Tidal Inlet, Coastal Engineering Research Center, Fort Belvoir, Virginia. GITI Report 19, 63 pp.

KUHN, G. AND F. P. SHEPARD (1980). Coastal Erosion in San Diego County, Calif. Proceedings of Coastal Zone 80, Am Soc of Civil Engrs, New York: 1899-1918.

MAY, S. K., et al (1982). CEIS: the Coastal Erosion Information System, Shore aud Beach, 50(1): 19-25.

MOORE, J. T. (1978). Emergency protection of eroding shores. Proceedings of Coastal Zone 76. Am Soc of Civil Engrs, New York, 2897-2910.

NOBLE, R. M. (1971). Shoreline changes: Humboldt Bay, California. University of California, Berkeley, Hydraulic Engineering Laboratory, Report HEL 24-2. 17 pp.

PARKER, N. E. (1970). Role of the Corps of Engineers in planning and developing ports in southern California. Shore and Beach, 38(1): 14-21.

PHILLIPS, R. P. et al (1979). Field trip guide to geology of northern Baja Calif., Mexico, Baja California Geology, (Abbot, P. L. and Gastel, R. C., Eds.) San Diego, S.D. State Univ., Fidelity Printing, 228 pp.

PUTNAM, W. C. et al (1960). Natural coastal environments of the world. University of California, Los Angeles, report to Office of Naval Research, Contract Report NR 388-013, 138 pp.

SEYMOUR, R. J. and HIGGINS, A. L. (1978). Continuous estimation of longshore sand transport. Proceedings of Coastal Zone 78, Am Soc of Civil Engrs, New York: 2308-2318.

SHAPIRO, J. et al (1979). Humboldt Bay wetlands review and baylands analysis. U.S. Army Engineer District, San Francisco. Shapiro & Assoc. Contract Report No. DACW07-78-C-0082 3 vol., 612 pp. apprxs.

SHEPARD, F. P. (1973). Submarine geology. Third edition. New York, Harper & Row, 577 pp.

SILVESTER, F. P. and WANLESS, H. R. (1971). Our changing coastlines. New York, McGraw-Hill, 579 pp.

SILVESTER, R. (1974). Coastal Engineering, 2, vol. 4B. Amsterdam, Elsevier Scientific Publishing, 338 pp.

SPETH, J. W. et al (1976). The natural resources of Anaheim Bay - Huntington Harbour, California Dept. of Fish and Game, Sacramento, CA, Coastal Wetlands Series Report No. 18. 183 pp, appxs.

TERICH, T. AND SCHWARTZ, M. (1981). A geomorphic classification of Washington State's Pacific coast. Shore and Beach, 49(3): 21-27.

TUTTLE, D. (1982). Personal communication. Humboldt Co Public Wks Department.

U.S. ARMY CORPS OF ENGINEERS (1971a). National shoreline study: inventory report, Columbia-North Pacific Region, Washington and Oregon. U.S. Army Engineer Division, North Pacific, Portland, Oregon 46 pp, appxs.

U.S. ARMY CORPS OF ENGINEERS (1971b). National shoreline study: California Regional Inventory, U.S. Army Engineer Division, South Pacific, San Francisco, California. 106 pp, appxs.

U.S. ARMY CORPS OF ENGINEERS (1975). Final environmental statement, San Diego Harbor, California, U.S. Army Engineer District. 84 pp., appxs.

WELDAY, E. (1970). Surficial geology of the California shoreline. unpublished report, 42 pp.

WILDE, P. and YANCEY, T. (1970). Sediment distribution and its relation to circulation patterns in Bolinas Bay, Calif. Proceedings of 12th International Conference on Coastal Engineering, Am Soc of Civil Engrs, New York: 1397-1413.

ZELLER, R. P. (1962). A general reconnaissance of coastal dunes of Calif. Beach Erosion Board, Washington, D.C. Misc. Paper 1-62. 37 pp.

CHANGES IN THE COASTAL MORPHOLOGY OF VRACHATI, GREECE

by
C.I. Moutzouris*
A.J. Rogan**, M. ASCE

ABSTRACT

The coastal morphology of Vrachati, which lays on the southeastern coast of the Corinthiakos Gulf, has considerably changed since the construction of two successive coastal structures. The present paper describes these changes and attempts to estimate the rate of longshore drifting sediment load. The description of the changes and the estimation of the rate are based on observations of aerial photographs of the area and on extensive bottom sediment sampling.

1. INTRODUCTION

The Corinthiakos Gulf lays between Peloponnesos and the mainland of Greece (see Fig. 1). According to Piper et al., 1980, it is a major late Cenozoic graben with maximum depth of 860m in its eastern part. It communicates with the Patraikos Gulf through the Rion Straits and with the Saronikos Gulf through the Canal of Corinthos. Beaches are coarsest and steepest where exposed to the prevailing winds.

Vrachati lays on the southern coast of the southeastern part of the Corinthiakos Gulf (see Fig. 2). The coast there has a mild slope mostly due to prodelta platforms from torrents draining into the sea and to accumulation of sediments. Cir-

* Senior Lecturer, ** Professor,
National Technical University of Athens, Civil Engineering Department, Patission 42, Athens, Greece.

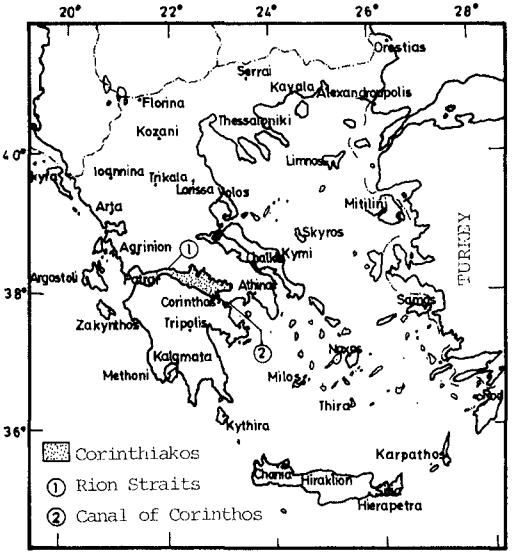

Fig. 1. -Map of Greece and the Corinthiakos Gulf

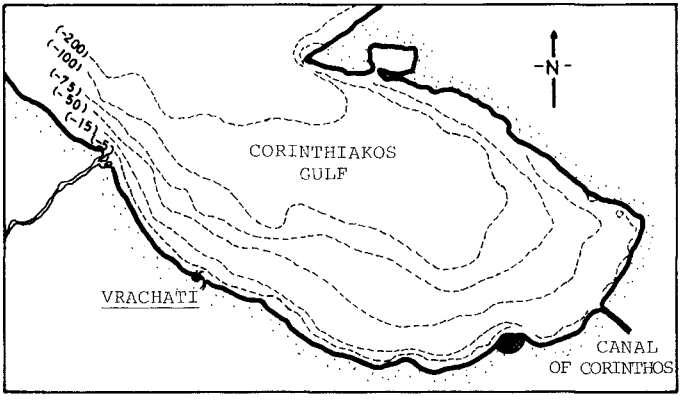

Fig. 2. -Southeastern part of the Corinthiakos Gulf

culation is mostly wind-driven. The tidal current through the Canal of Corinthos is rather weak and does not really affect the circulation in the Vrachati coast. Mean tidal range in the area is very small, locally less than 20 cm. There is an almost bimodal wind pattern from eastern and western directions, but longshore circulation is dominated by waves and wind-driven currents mostly from the W, due to their higher frequencies of occurrence.

A breakwater was built at Vrachati in 1939 in order to provide protection to small fishing vessels. The presence of the breakwater disturbed the nearshore circulation pattern and resulted in intense modifications of the coastal morphology. For this reason, a groin was built in 1967 upstreams of the breakwater. The groin only decreased the rate of coastal modifications. Even today considerable quantities of sediments are locally deposited, as it can be seen in Fig.3.

Fig. 3. -The coast of Vrachati

The effort at the Civil Engineering Department (CED) of the National Technical University of Athens (NTUA) has focused on the nearshore processes at the southern coast of the Corinthiakos Gulf, and more specifically at the Vrachati coast, for three main reasons :

- This coast suffers from extensive erosion and accretion. Efforts are being made now to deal with this problem : the latest one is a comprehensive study which is about to be assigned by the Ministry of Public Works.
- The existence at Vrachati of the breakwater and the parallel groin combined with the simultaneous existence of ae-

rial photographs taken regularly during the same period permit the study of the evolution of the shoreline. The system of the two structures acts as a trap and allows the study of longshore drifting small-sized sediments.

The first part of the present paper describes the evolution of the shoreline at Vrachati due to the construction of the two coastal structures. Then an estimation of the rate of longshore drifting sediments is made.

2. EVOLUTION OF THE SHORELINE

The shoreline of Vrachati was straight before the construction of the breakwater, which was built in 1939 perpendicular to the shoreline (see Fig. 4). Its total length is 189 m. Intense accretion to its left and right occurred after the construction of the breakwater. The zone of accretion to the left had a length of approximately 750m. Longshore drifting sediments were deposited there, due mainly to the presence of the breakwater which was a form of littoral barrier. The zone of accretion to the right was extending up to a torrent draining to the sea and had a length of approximately 330 m. Sediments were accumulating there mainly from the torrent. A part of the load deposited there is believed to have its origins also from the longshore drifting load. The general shape of accretion around the breakwater indicates that the main direction of drift of longshore sediments past the Vrachati coast is from left to right.

In order to protect the coast from the aforementioned accretion, a groin of 135m was built in 1967 perpendicular to the shoreline at a distance of 158m to the left of the breakwater. As a result, further accretion occurred to the left of the groin, because the longshore drifting sediments were now obstructed by the new littoral barrier. The shoreline started to retreat in the zone between the two structures. This is due to the decreased quantities of longshore drifting sediments by-passing the groin and being deposited in the zone. The evolution of the shoreline to the right of the breakwater has not shown any clear tendencies. A remarkable difference between the two beaches upstreams and downstreams of the two structures is noted here : the upstream beach is made of pebbles, while the downstream beach is made of fine sand.

Long observations in-situ under wave attack conditions led the writers to the conclusion that the longshore drift of sediments is partially interrupted by the groin. The groin is a classical partial littoral barrier. Most of the suspended load by-pass the groin and are partially deposited in the zone between the groin and the breakwater and in the zone protected by the breakwater. If there were only the

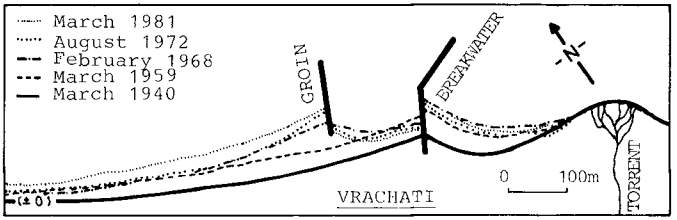

Fig. 4. -Evolution of the shoreline at Vrachati

groin, an erosion would have occurred downstream of the groin. Because of the presence of two successive structures (groin, breakwater), part of the suspended load is trapped in-between. The above qualitative observations are confirmed also by the grain-size analysis of the sediments, as it is analysed later.

3. MODEL APPLIED

It is commonplace to state that the second best method for estimating the rate of longshore drifting sediments, in cases where no data exist, is to study in detail the shoreline evolution as well as the sediments accumulated in the area. Following the above statement and according to the visual observations reported previously, the model chosen to apply for the estimation of the total rate of longshore drifting sediments was based partially on the shoreline evolution and partially on the sediment sizes (see Fig. 5). This model is somehow consistent with the Baker "two line theory" on partial transport blockage. The net total longshore drifting load S is composed of two components :

(1) $S=S_b+S_s$

S_b is the net bedload and S_s is the net suspended load. By definition, the grains of S_s are finer than those of S_b.

The bedload is estimated according to the shoreline evolution on the upstream sides of the two structures, because the structures act as littoral barriers and the accreted shoreline has not yet reached their heads. In order to apply the Pelnard-Considère method, as presented by Bijker, 1972, two time periods have been selected :

- period_a (1939-58), when only the breakwater existed.
- period_b (1967-81), when both structures existed.

The suspended load is estimated according to the size of sand sediments, which are deposited in the zone between the two structures. This zone is a natural trap for fine grains, because of decreased current action.

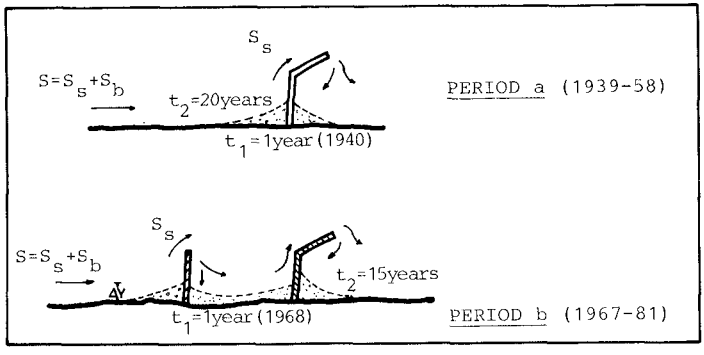

Fig. 5.- Model applied for the estimation of S

4. TECHNIQUES USED

The following techniques have been used for the application of the model : analysis of successive aerial photographs, sediment sampling and analysis and wave hindcasting.

4.1. Aerial photographs

Many sequences of aerial photographs were examined. They had been taken in successive years by the Directorate of Aerial Photographing, Ministry of Regional Planning, Housing and Environment. The examination permitted to follow the shoreline evolution as function of time and presence of coastal structures.

It was found that the shoreline progressed as follows (see Fig. 5) :

ΔY=35m during period a (upstreams of the breakwater)
ΔY=27m during period b (upstreams of the groin)

4.2. Sediment sampling and analysis

Many spot samples have been collected from various locations in the surf zone along the coast, because spot samples are

usually representative of one sedimentation unit (see Fig. 6). For comparison reasons, some of the samples have been collected from on-shore. In order to check the influence of the changing wave climate, samples have also been collected in summer and autumn times.

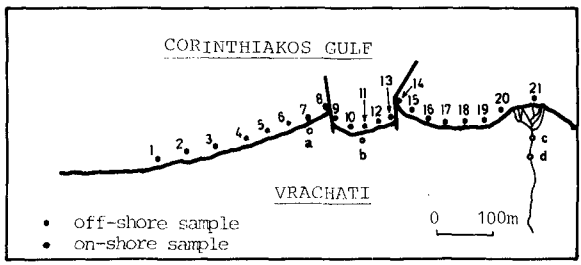

Fig. 6.- Sites of sampling along the coast

The samples were prepared for grain-size analysis and then analysed in the laboratory of the Chair of Foundations, CED/NTUA. Size distribution was determined by standard sieve analysis techniques. The size analysis data were plotted as cumulative curves with arithmetic ordinate, which is a commonly used method of graphic presentation (see Constantinidis and Mavromatos, 1982, and Markoulidis and Zissis, 1983). The material was found to range mainly from fine sand to gravel. The particle sizes and statistical parameters of the samples were found to change along the coast. The grain-size cumulative curves may be classified into 5 families :

Samples 1, 2, 3, 4, 5, 6, 7 (see Fig. 7)

They are coarse grained because they come from the exposed coast upstreams of the structures. Large quantities of the material existed there even before the erection of the structures : particles with diametres as big as 40mm cannot be transported by wave-induced currents. The population of these samples characterises most of the exposed beaches of Corinthiakos : it is a poorly sorted beach with strongly fine-skewed and mesokurtic population.

Samples 8, a, b (see Fig. 7)

They are characteristically bi-modal, because fine grains were trapped by the groin. Curve 8 is met in almost every samples from the zone upstreams of a littoral barrier.

Samples 9, 10, 11, 12, 13 (see Fig. 7)

They are fine grained because of extensive accretion in this area of reduced wave and current action. They characterize a moderately sorted beach with coarse-skewed and leptokurtic population.

Samples 14, 15, 16, 17, 18, 19, 20 (see Fig. 8)

They range from fine-grained (in the protected zone) to median-grained (in the zone of restored current action). Samples 14 and 15 are well sorted with coarse-skewed and platykurtic population.

Samples 21, c, d (see Fig. 8)

They are very coarse-grained, due to the contribution of the torrent.

No significant seasonal change has been detected in the size distribution curves of the samples, especially in the protected zones (see Fig. 9).

4.3. Wave hindcasting

Wave data do not exist in the area under examination. For this reason wave characteristics in deep sea were computed according to the SMB method. Wind data are regularly taken in the area by the National Meteorological Service (EMY). Annual frequencies of occurrence of winds, which generate waves in the Vrachati area, are shown in Table 1. The effective fetch F_{ef} from these directions and the corresponding wave heights H_o and periods T are given in Table 2.

Refraction diagrams for the most frequent waves from E, NE, N and NW were computed according to a numerical method used at the Chatou Research Center-CREC (see Lepetit, 1964). According to this method the refraction coefficient is analysed in two partial coefficients. The first is related to the variation of distance between the orthogonals. The second depends on the modification of the phase velocity. The data introduced for the numerical analysis of the differential equation were the bottom topography, the deep sea characteristics of the monochromatic waves and the phase velocity of the waves. The equation was solved numerically by computer (see Petridis, 1982). Resulting refraction diagrams for waves from E and NE are shown in Fig. 10.

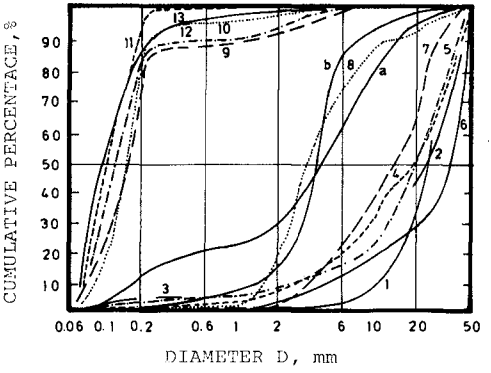

Fig. 7.- Grain-size cumulative curves

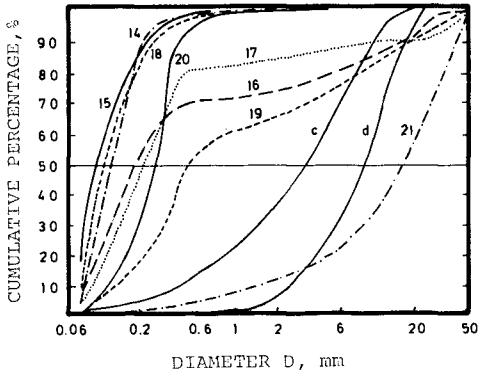

Fig. 8.- Grain-size cumulative curves

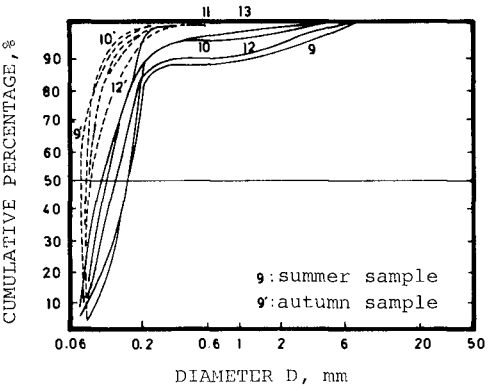

Fig. 9.- Grain-size cumulative curves as function of seasons

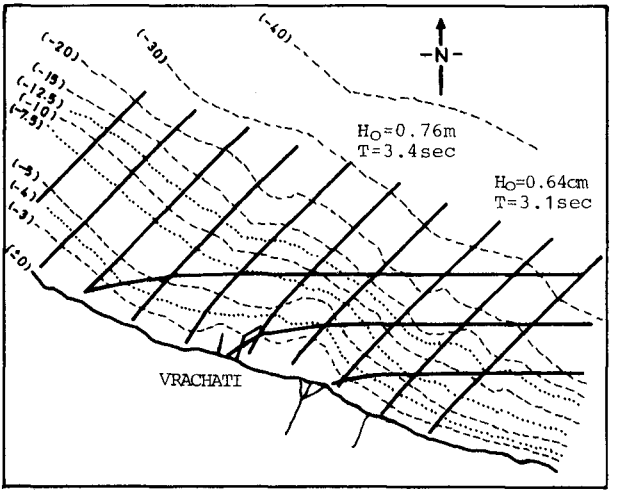

Fig. 10.- Refraction diagrams for waves E and NE

WIND Beaufort	NW	N	NE	N
4	3.2	1.9	0.5	0.4
5	1.4	1.2	0.4	0.7
6	0.4	0.4	0.3	-
7	0.02	0.04	0.03	-
8	-	-	0.01	-
TOTAL	5.02	3.54	1.24	1.1

Table 1.- Annual frequency (%) of occurrence of offshore winds (data from EMY)

WIND		NW			N		
Beaufort	(knots)	F_{ef} (n.m.)	H_o (m)	T (sec)	F_{ef} (n.m.)	H_o (m)	T (sec)
4	13	9.8	0.51	2.8	14.82	0.58	2.1
5	19		0.82	3.5		0.91	3.4
6	24		1.06	4.0		1.25	3.8
7	30		1.4	4.5		1.65	4.4
8	37		-	-		-	-
WIND		NE			E		
Beaufort	(knots)	F_{ef} (n.m.)	H_o (m)	T (sec)	F_{ef} (n.m.)	H_o (m)	T (sec)
4	13	7.98	0.46	2.7	4.62	0.41	2.5
5	19		0.76	3.4		0.64	3.1
6	24		0.98	3.8		0.85	3.5
7	30		1.28	4.4		1.13	4.0
8	37		1.65	4.9		-	-

Table 2.- Wave characteristics in deep sea at the Vrachati area

5. RESULTS

5.1. Bedload

The net load S_b was evaluated from the measured progression ΔY of the shoreline during a certain number of years. According to results reported earlier, the shoreline progressed 35m in 19 years (period a) and 27m in 14 years (period b). Surveys made in-situ indicated that the depth of active

sediment transport h is of the order of only 3m.

The angle of incidence α of each monochromatic wave is defined as the angle between the wavecrests and the shoreline. α_o is the value of α in deep sea. The average angles $\bar{\alpha}_d$ of wave incidence from each direction at the depth contour of -3m were evaluated from the refraction computations and are presented in Table 3. Positive (negative) values of a indicate incidence from the left (right) to the right (left) of Fig. 4. The average angle $\bar{\alpha}$ of wave incidence from all directions at the depth contour of -3m was evaluated according to the frequencies of occurrence of Table 1. $\bar{\alpha}$ was found equal to +1.21°.

DIRECTION	FREQUENCY	$\bar{\alpha}_o$ (°)	$\bar{\alpha}_d$ (°)
NW	0.0502	+67.5°	+33.50
N	0.0354	+22.5°	+12.92
NE	0.0124	-22.5°	-21.38
E	0.0110	-67.5°	-60.00

Table 3.- Average angles of wave incidence at -3m

After introducing the above values to the equations of Pelnard-Considère, it was found that :

$S_b = 36.5 \times 10^3 m^3/year$ during period a

$S_b = 31.8 \times 10^3 m^3/year$ during period b

As it can be seen S_b was higher in period a than in period b, due to the obstruction from the groin.

The above method of estimation of S_b has several weak points. But it is undeniable that most existing data of longshore drifting sediments quantities have been gathered from surveys of the accumulated material in littoral barriers (Bruun, 1976).

For comparison reasons, S_b was next computed according to a second method. In a very recent paper Hallermeier, 1982, proposed a method of computation of bedload, which accounts for the sediment sizes, the bottom slope and configuration, the wave diffraction, etc. According to this approach, S_b depends upon some characteristic parameters : the wave height H_e, length L_e and angle α_e at the seaward limit to littoral zone, the water depth d_e at the same limit, the parameter Θ ($=d_e/H_e$), the median sediment grain diameter M_D, the wave reflexion and the bottom angle. Table 4 presents the analytical computations of S_b according to Hallermeier for each monochromatic wave given in Table 2. Local surveys indicated that the average bottom angle in the area is of

WIND	f	T (sec)	d_e (m)	H_e (m)	L_e (m)	Θ	α_e (°)	Q (m^3/yr)
NW	0.032	2.8	0.92	0.490	7.76	0.533	29.34	14668.7
	0.014	3.5	1.48	0.786	12.28	0.531	30.46	17641.6
	0.004	4.0	1.91	1.018	15.92	0.533	31.32	8535.4
	0.0002	4.5	2.50	1.339	20.44	0.535	32.50	768.6
N	0.019	2.1	1.21	0.538	8.28	0.445	10.956	6449.8
	0.012	3.4	1.57	0.861	12.12	0.548	11.352	5531.3
	0.004	3.8	2.11	1.173	15.55	0.556	11.946	3540.1
	0.0004	4.4	2.80	1.550	20.80	0.554	12.705	668.9
NE	0.005	2.7	0.84	0.443	7.14	0.528	-20.025	1237.7
	0.004	3.4	1.37	0.73	11.46	0.533	-20.356	2688.6
	0.003	3.8	1.76	0.938	14.50	0.533	-20.6	3423.3
	0.0003	4.4	2.31	1.228	19.25	0.532	-20.944	595.7
	0.0001	4.9	2.94	1.50	24.10	0.537	-21.338	289.9
E	0.004	2.5	0.74	0.394	6.19	0.532	-50.583	1449.0
	0.007	3.1	1.15	0.614	9.54	0.534	-52.292	5793.6

Table 4.- Computation of bedload according to the Hallermeier equation

the order of 2°. The corresponding average wave reflexion coefficient is of the order of 3%. For the evaluation of the median diameter it was considered that the samples 18, 19 and 20 are the most representative : their grain-size cumulative curves agree well with the corresponding curves of samples from undisturbed areas. For this reason, M_D was taken equal to 0.3mm.

According to the computations in Table 4 the gross loads are as follows :

$S_b' = 57.8 \times 10^3 m^3/year$ from left to right

$S_b'' = 15.5 \times 10^3 m^3/year$ from right to left

The net bedload is :

$S_b = 42.3 \times 10^3 m^3/year$ from left to right

The load according to Hallermeier apparently represents the net bedload during the last years, because the estimation was based on recent field data.

5.2. Suspended load

For the computation of the net suspended load S_s which is transported along the coast, information was needed on the

grains trapped between the two structures. Finally it was assumed that the graphic mean diameter M_z, as defined by Folk, 1974, is representative of the diameters ensemble :

$$(4) \quad M_z = \frac{\phi_{16} + \phi_{50} + \phi_{84}}{3}$$

ϕ is the grains diameter expressed in the phi-scale. The average M_z for the samples 9, 10, 11, 12 and 13 is computed from equ. (4) and Fig. 7 :

$$(5) \quad M_z = 0.14\text{mm}$$

An equation proposed by the Laboratoire Central d' Hydraulique de France-LCHF was the computation of S_s (see Leclerc et al., 1976) :

$$(6) \quad S_s = KgHLTf(\alpha)$$

g is the gravitational acceleration, H and L are the wave height and length at a water depth of 15m, α_{15} is the angle of incidence at the same depth, $f(\alpha)$ is a function of the angle α_{15}. The coefficient K is given by equ. (7) :

$$(7) \quad K = 0.18 \times 10^{-5} \; D^{-05}$$

D is the grain diameter ($\leq$1mm). In the present study it is considered that the average graphic mean diameter of the samples corresponds with D.

The computations of suspended loads for each monochromatic wave given in Table 2 are shown in Table 5. The gross loads are as follows :

$S_s' = 2.2 \times 10^3 m^3/year$ from left to right

$S_s'' = 0.7 \times 10^3 m^3/year$ from right to left

The net suspended load is :

$S_s = 1.5 \times 10^3 m^3/year$ from left to right

5.3. Total load

The net total sediment load drifts from left to right past Vrachati and is equal to :

$S = 38.0 \times 10^3 m^3/year$ during period a

$S = 33.3 \times 10^3 m^3/year$ during period b

The computation of S was based on a wide range of data : wind, sediment, bottom and shoreline progression data.The difference between period a and b is due to the different

WIND	f	H_o (m)	T (sec)	L_o (m)	f(α)	Q (m^3/yr)
NW	0.032	0.51	2.8	12.25	0.36	298.7
	0.014	0.82	3.5	19.14	"	410.3
	0.004	1.06	4.0	24.99	"	226.1
	0.0002	1.4	4.5	31.63	"	21.3
N	0.019	0.58	2.1	11.30	0.6	233.0
	0.012	0.91	3.4	18.06	"	596.3
	0.004	1.25	3.8	22.56	"	381.2
	0.0004	1.65	4.4	30.24	"	78.1
NE	0.005	0.46	2.7	11.39	0.6	62.9
	0.004	0.76	3.4	18.06	"	166.0
	0.003	0.98	3.8	22.56	"	224.1
	0.0003	1.28	4.4	30.24	"	45.4
	0.0001	1.65	4.9	37.51	"	26.9
E	0.004	0.41	2.5	9.82	0.36	21.5
	0.007	0.64	3.1	15.11	"	111.9

Table 5.- Computation of suspended load

rates of shoreline progression during these periods.

For comparison reasons S was then computed according to the well known method of the Coastal Engineering Research Center CERC, as it is presented in the Coastal Protection Manual, 1976. This method ignores the sizes of the transported sediments and the bottom slope. The rate of longshore transport is proportional to the longshore wave energy flux. In other terms, the transport depends exclusively upon the wave climate in the area. The computation of S according to this method is shown analytically in Table 6. The gross loads are as follows.

$S' = 51.7 \times 10^3 m^3$/year from left to right

$S'' = 12.3 \times 10^3 m^3$/year from right to left

The net load S is :

$S = 39.4 \times 10^3 m^3$/year from left to right

The above value refers to time periods a and b, because it was computed from wind data covering both periods.

WIND	f	H_o (m)	Q (m^3/yr)
NW	0.032	0.51	6756.7
	0.014	0.82	6990.0
	0.004	1.06	5260.0
	0.0002	1.40	527.2
N	0.019	0.58	6897.5
	0.012	0.91	13432.4
	0.004	1.25	9901.6
	0.0004	1.65	1982.2
NE	0.005	0.46	1016.8
	0.004	0.76	2854.1
	0.003	0.98	4041.6
	0.0003	1.28	788.0
	0.0001	1.65	495.5
E	0.004	0.41	489.3
	0.007	0.64	2607.4

Table 6.- Computation of total load according to the CERC equation

The above computed values of net longshore drifting loads are shown in Fig. 11.

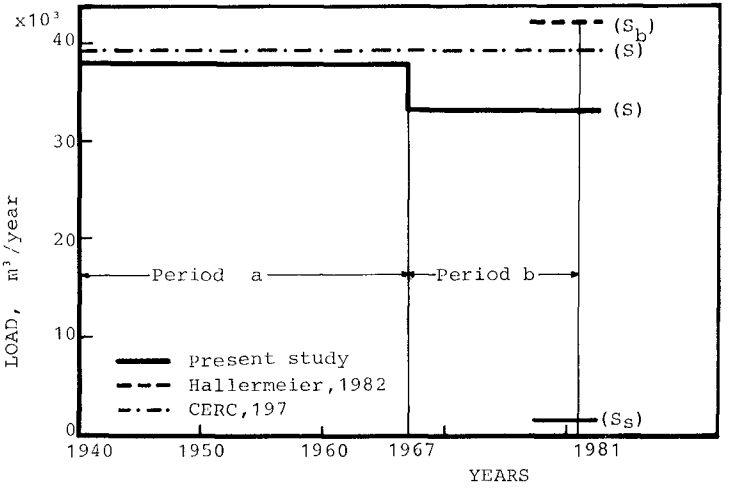

Fig.11.- Net longshore drifting load

6. CONCLUSIONS

The adopted method of estimation of the net longshore drifting load is the second best to direct measuring the load, because it is based on a wide range of data:wind, sediment, bottom, shoreline progression data. It can be applied when time presses, although many parameters are neglected. This method gives results averaged in time, while measurements of only one year or less may give very erroneous results.

The research described in the present paper will be continued with load measurements, in order to check the accuracy of the results.

7. ACKNOWLEDGMENTS

Acknowledgments are expressed to Miss Theodora Yantsi, Civil Engineer, for her assistance in the computations.

8. REFERENCES

Bijker, E.W., 1972, "Lecture notes for topics in Coastal Engineering", Delft University of Technology, pp. 79-99.

Bruun, P., 1976, "Port Engineering" 2nd edition,Gulf Publ. Co,Austin

CERC, 1976, "Shore Protection Manual" U.S.Army, Corps of Engineers

Constantinidis, D. and Mavromatos, N., 1981, "Erosion of the Corinthiakos Gulf:from Corinthos to Kiato", Diploma Thesis, Nat. Techn. Univ. of Athens, pp.2.69-2.77 (in Greek)

Folk, R. L., 1974, "Petrology of Sedimentary Rocks", Hemphill Publ. Co, Austin

Hallermeier, R.J.,1982, "Bedload and wave thrust computations of alongshore sand transport", Journal of Geophysical Research, Vol. 87, No C8, July 20, pp. 5741-5751

Leclerc, J.P., Bellessort, B. et Mignot, C., 1976, "Action de la houle sur les sediments", Laboratoire Central d' Hydraulique de France (LCHF), pp.143-144

Lepetit, J.P., 1964, "Etude de la réfraction de la houle monochromatique par le calcul numérique", Bulletin du CREC, No 9

Markoulidis, P. and Zissis, J., 1983, "Investigation of sediments flow and creation of a harbour in the area of Vrachati" , Diploma Thesis, National University of Athens (to

appear, in Greek)

Petridis , P., 1982, "Refraction of sea waves", Diploma Thesis , National Technical University of Athens, pp. 161-162 (in Greek)

Piper, D.J.W., Kontopoulos, N., and Panagos, A.G., 1980,"Deltaic coastal and shallow marine sediments of the western Gulf of Corinth", Thalassographica, Vol. 2, No 3, pp.5-14

Rogan, A.J. and Moutzouris, C.I., 1981, "Erosion and accretion of Greek coasts caused by harbour and coastal works", Proceedings of the 25th Congress of PIANC, Vol. 5, Edinburgh, pp. 799-806

COMPUTATIONAL ALGORITHM FOR LONGSHORE ENERGY FLUX INCORPORATING FRICTION

by

T.L. Walton, Jr.[1], M. ASCE
J.R. Weggel[2], M. ASCE

Introduction

The calculation of longshore sand transport on beaches is a significant coastal engineering problem with application to various areas of coastal structure design (i.e., jetties, groins, and offshore breakwaters), and inlet navigation channel design (i.e., studies of required maintenance dredging). Longshore sand transport as a first approximation is linearly related to longshore energy flux (see Bruno, et al. (1981)), hence, this paper simply presents a method for computing longshore energy flux as a means of determining longshore sand transport.

The approach used herein for calculating longshore energy flux includes an analytical method for incorporating frictional wave energy dissipation. The method is simple enough to program on a hand-held programmable calculator. It therefore provides a method by which rapid calculations can be made for a site at which offshore wave data exist. If offshore directional random wave data are available (i.e. directional wave spectra) then more advanced techniques should be used (see Walton and Dean (1981)).

Computation of the longshore energy flux factor P_{ls} is in accordance with the Shore Protection Manual (1977) equation (4-28)

$$P_{ls} = \frac{\rho g}{16} H_b^2 C_{gb} \sin 2\alpha_b \qquad (1)$$

[1]Hydraulic Engineer, U.S. Army Coastal Engineering Research Center, Fort Belvoir, VA 22060

[2]Chief, Evaluation Branch, U.S. Army Coastal Engineering Research Center, Fort Belvoir, VA 22060

in which P_{ls} is the longshore energy flux, ρ is the mass density of the fluid, g is the acceleration of gravity, H_b is the breaking wave height, C_{gb} is the wave group velocity at the point of wave breaking, and α_b is the angle the breaking wave crest makes with the shoreline, where the subscript "b" denotes breaking wave conditions. The quantity P_{ls} is not truly a longshore energy flux as Longuet-Higgins (1972) has noted, but since this terminology has been widely used (see Shore Protection Manual (1977)), this paper will not deviate from this usage.

Equation 1 can also be written as

$$P_{ls} = E_b C_{gb} \cos \alpha_b \sin \alpha_b \tag{2}$$

where E_b is the wave energy density at breaking given by,

$$E_b = \frac{\rho g}{8} H_b^2 \tag{3}$$

From conservation of energy considerations, for waves approaching shore over straight and parallel bottom contours,

$$E_i C_{gi} \cos \alpha_i = E_b C_{gb} \cos \alpha_b \tag{4}$$

if no energy dissipation has occurred from a given offshore site (represented by the subscript "i") to the breaker location (See Ippen (1966)). If energy dissipation is included, equation (4) must be modified to the following

$$K_e^2 E_i C_{gi} \cos \alpha_i = E_b C_{gb} \cos \alpha_b \tag{5}$$

where the factor K_e^2 accounts for energy reduction due to dissipation by bottom friction, percolation, or other dissipative mechanisms between the offshore site and the breaker location.

Equation (1) with frictional dissipation included can be rewritten as,

$$P_{ls} = K_e^2 \, (EC_g \cos \alpha)_i \sin \alpha_b \qquad (6)$$

where offshore wave data can be used directly to evaluate the term in brackets.

The values of K_e and $\sin \alpha_b$ can be found from linear wave theory transformation processes and a breaking wave height to water depth ratio which is dependent on bottom slope and offshore (deep water) wave steepness.

In this paper the energy dissipation is assumed to be due only to bottom friction; percolation is neglected. From a practical standpoint, the importance of percolation in wave energy dissipation is questionable since in many offshore areas sand is underlain by mud and/or rock. Also, the top layer of sand often has mixed within it organic material and very fine silts that reduce the permeability of this layer.

Bretschneider and Reid (1954) developed equations for the friction coefficient K_f (where $K_f = K_e$ in the case of no percolation) for both constant bottom slope and constant depth cases. Their method of estimating wave height decay requires numerical integration for the case of a constant bottom slope. In the absence of refraction, a chart with solutions has been presented for various values of parameters T^2/d and $\frac{fH_o}{md}$; where T is the wave period, d is the water depth, m is the offshore slope, H_o is the deepwater wave height, and f is a friction factor.

The present approach simplifies the constant slope equation by invoking the shallow water assumption and provides an analytical solution. Over much of the range of the parameters T^2/d and $\frac{fH_o}{md}$, the analytical solution provides answers that are within 5% of the more involved numerical integration solution. The analytical solution of the friction coefficient K_f allows computation of

K_f and P_{ls} on most hand-held programmable calculators. This simplified solution of K_f assumes straight and parallel offshore bottom contours.

The analytical solution for the friction coefficient, K_f, integrated from deep water to a shallow water depth d is:

$$K_f = \left(1 + \left(\frac{fH_o}{md}\right)(\cos \alpha_o)^{\frac{1}{2}}\, 0.12(k_o d)^{-\frac{1}{4}}\right)^{-1} \tag{7}$$

The derivation of equation 7 is given in Appendix A. For values of $\frac{L_o}{d} \geq 15$, and $\frac{fH_o}{md} \leq 1.0$, equation 7 estimates K_f with less than 5% error. Since in most practical applications the friction coefficient f is rarely known with any accuracy, this approximate K_f is believed satisfactory for most engineering purposes.

The method for solving sin α_b is as follows: (1) determine explicitly the breaking wave height using linear wave theory, and the ratio of breaker wave height to water depth (dependent on bottom slope m and deepwater wave steepness) by assuming breaking occurs in shallow water; (2) determine the breaking wave depth from breaker height to water depth ratio; and (3) solve for α_b, the breaking wave angle, using Snell's Law of Refraction. This approach is detailed in Appendix B. The equation used to find the breaking wave height is

$$H_b = \left[\left(\frac{\kappa}{g}\right)^{\frac{1}{2}} K_f^2\, H_i^2\, C_{gi} \cos \alpha_i\right]^{0.4} \tag{8}$$

where K_f represents a spatial average friction coefficient between the site where the wave data observations are available and the breaker site. The breaker depth is given by

$$d_b = H_b/\kappa \tag{9}$$

where

$$\kappa = 1.16\left[m(H_o/L_o)^{-\frac{1}{5}}\right] 0.22 \qquad (10)$$

Equation 10 is from the work of Singamsetti and Wind (1980) who reviewed various equations for the breaking wave height to breaker depth ratio using Battjes (1974) data.

As the friction coefficient K_f of equation 7 depends on the ratio of deep-water wave height to breaking depth $\frac{H_o}{d_b}$, the solution technique used assumes that $H_o \simeq H_b$ to a first approximation for directly computing K_f in equation 7.

The friction factor used is that defined by Bretschneider and Reid (1954) in which the bottom shear stress is defined by a shear stress equation given by

$$\tau_b = \rho f |U_b| U_b \qquad (11)$$

where U_b is the bottom orbital velocity given by linear wave theory. Values of the friction factor f for oscillatory flow have been given by Kamphuis (1975) and Vitale (1979), where f is defined as a function of the relative roughness parameter $\frac{k_e}{\zeta_b}$ and an oscillatory Reynolds number $\frac{U_b \zeta_b}{\nu}$, with k_e = the equivalent sand grain size on the bed, ζ_b = the total horizontal excursion of the water particle motion at the bottom in the absence of a boundary layer, and ν = the kinematic viscosity of sea water.

Kamphuis (1975) notes that k_e can be related to the size distribution of the sand on the bottom by

$$k_e = 2d_{90}$$

where d_{90} is the sand grain diameter such that 90% is finer. Using a Moody-Stanton-type diagram (as is used to present pipe friction factors), Kamphuis (1975) has presented his friction factor, f_k, as a function of Reynolds number

and relative roughness. Since Kamphuis used an alternative definition for his friction factor, the relationship between the friction factor used in this paper and Kamphuis' f_k is $f = \frac{f_k}{2}$.

Comparison of Measured and Predicted Breaking Wave Angles

The major error in calculating longshore energy flux involves predicting the breaking wave angle. The present algorithm for calculating breaking wave angle was compared to three sets of breaking wave data taken in three-dimensional laboratory wave basins. Two of these data sets (Shay and Johnson (1951), and Vitale (1981)) were obtained with movable bed models. The objective of their studies was to measure longshore sand transport and correlate transport rates with wave properties. The movable bed model tests had a large variation in breaking wave angle due to shoreline adjustment during the testing. Also, in the movable bed models, the breaking wave angle (defined to be the angle between the breaking wave and the shoreline) is more difficult to measure since the shoreline position is dynamic and difficult to define. The third set of data (Galvin (1965)) were from a fixed bed model. Observations of breaking wave angles had minimal variation and were averaged for each test to provide a good measure of the breaking wave angle. The friction factor used in the calculations (for all data) was assumed to be $f = 0.1$. This value appeared reasonable for the range of wave heights, periods, water depths, and bottom roughness for the laboratory tests. Results of the calculations were not sensitive to friction. Values of f ranging from 0 (no friction) to 0.1 did not change the correlation coefficients relating the calculations to the data by more than 5%, suggesting that frictional effects in the data are negligable relative to the overall scatter of the measurements and other difficulties inherent in measuring breaking wave angle.

In all laboratory tests the wave generators were in transitional water depths ($1/20 \leq d/L \leq 1/2$) and wave parameters in deep water were calculated using linear wave theory to provide input to the calculations.

The comparison between calculated and observed breaking wave angles is shown in Figure 1, along with the range of the variables and the correlation coefficient for each of the three data sets.

The best data for comparison (i.e., the least scatter for individual tests) was Galvin's (1965). This data set gave a correlation coefficient of $r = 0.97$.

Summary and Conclusions

A technique has been presented for calculating longshore wave energy flux which can be used in areas where offshore wave data are available and the offshore bottom contours are nearly straight and parallel. This method incorporates a simplified analytical technique for computing wave energy dissipation by bottom friction and can be applied with minimal computational effort using a hand-held programmable calculator.

Results for computation of breaking wave angles have been compared to existing laboratory data and found to provide good correlation in one set of tests and reasonable correlation (in view of laboratory data scatter) in two other sets of tests. It is felt that this method of computing longshore energy flux will find many useful applications in view of the simplicity of the algorithm developed.

Acknowledgements

The tests described and the resulting data presented herein, unless otherwise noted, were obtained from research conducted under the Littoral Data

Collection Methods and their Engineering Applications Work Unit, Shore Protection and Restoration Program, Coastal Engineering Area of Civil Works Research and Developmemt, U.S. Army Corps of Engineers. Permission was granted by the Chief of Engineers to publish this information.

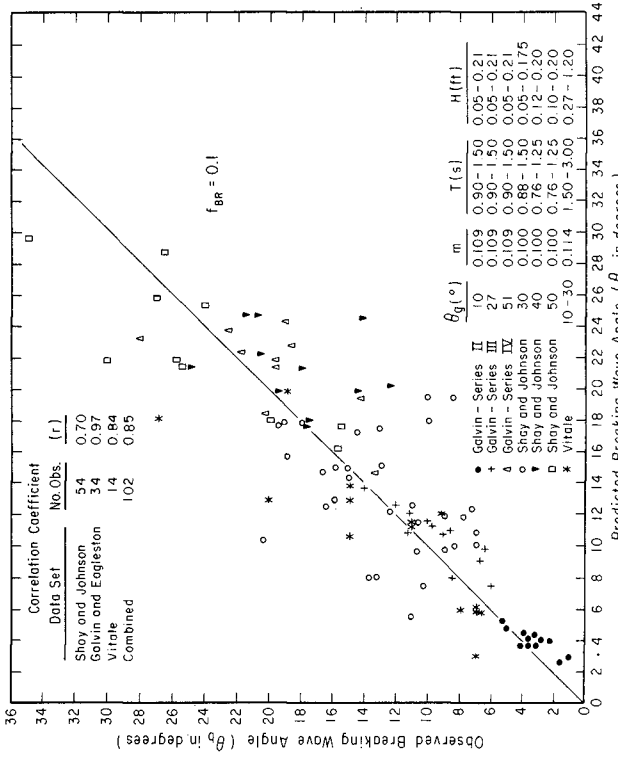

FIGURE 1 - Comparison of Observed and Predicted Breaking Wave Angles

APPENDIX A

Simplified Solution of Friction Coefficient K_f for Constant Bottom Slopes

Bretschneider and Reid (1954) have provided a numerical integration type solution for the friction coefficient K_f as given in equation (B-4a) of BEB TM 45. This solution is as follows:

$$K_f = \left(1 + \left| \frac{fH_o}{mT^2} \int_{\infty}^{d/T^2} \phi_f K_r \, \delta(d/T^2) \right| \right) \qquad (A\text{-}1)$$

where

$$\phi_f = \left(\frac{64\pi^3}{3g^2}\right)\left(\frac{K_s}{\sinh kd}\right)^3$$

and

K_r = refraction coefficient

K_s = shoaling coefficient

as normally defined in linear wave theory (see Ippen (1966)).

Equation A-1 can be nondimensionalized in terms of the deep water dimensionless wave number $k_o d$ and the site dimensionless wave number kd to be

$$K_f = \left(1 + \left| \frac{fH_o}{md}\left(\frac{4}{3\pi}\right) \int_{\infty}^{k_o d} \left(\frac{K_s}{\sinh kd}\right)^3 K_r \, \delta(k_o d) \right| \right)^{-1} \qquad (A\text{-}2)$$

Assuming that offshore bottom contours are straight and parallel, Snell's Law of Refraction can be applied from deep water to the site of interest where

$$K_r = (\cos \alpha_o / \cos \alpha)^{0.5} \qquad (A\text{-}3)$$

which can be reduced to the following for shallow water depth d to

$$K_r = (\cos \alpha_o)^{0.5} \left[(1 - (\sin^2 \alpha_o) k_o d\right]^{-0.25} \qquad (A\text{-}4)$$

As $(\sin\alpha_o)^2 k_o d$ is small over most of the wave transformation zone, Equation A-4 is simplified to

$$K_r \simeq (\cos\alpha_o)^{0.5} \tag{A-5}$$

Again assuming depth d is in shallow water

$$K_s \simeq (2kd)^{-0.5} \tag{A-6}$$

Upon applying the above assumptions to the integral term of equation A-2 the integral becomes

$$I_1 = \int_{\infty}^{k_o d} \frac{X^{-9/4}}{2^{3/2}}\, dX = \frac{1}{2^{3/2}} \left(-\frac{4}{5} X^{-5/4} \right) \Bigg|_{\infty}^{k_o d}$$

$$\simeq \frac{\sqrt{2}}{5} (k_o d)^{-5/4} \quad (1 - (k_o d/\infty)^{5/4}) \tag{A-7}$$

$$\simeq \frac{\sqrt{2}}{5} (k_o d)^{-5/4}$$

Applying the above integration to equation A-2 the simplified friction coefficient (from deep water to shallow water depth d) becomes

$$K_f = \left[1 + \left(\frac{4\sqrt{2}}{15\pi} \right) \left(\frac{fH_o}{md} \right) (\cos\alpha_o)^{0.5} (k_o d)^{-0.25} \right]^{-1} \tag{A-8}$$

For the case of no refraction ($\alpha_o = 0^o$ or $K_r = 1.0$) the equation becomes

$$K_f = \left[1 + 0.12 \left(\frac{fH_o}{md} \right) (k_o d)^{-0.25} \right]^{-1} \tag{A-9}$$

which can be compared to the values given by the Bretschneider and Reid (1954) complete solution, Equation A-2. The present solution and the percent error between the present solution and that of Bretschneider and Reid are given in Table A-1 and presented in Figure A-1 where the error E is defined as

$$E = \frac{K_f \text{ (Bretschneider-Reid)} - K_f \text{ (eq. A-9)}}{K_f \text{(Bretschneider-Reid)}} \qquad \text{(A-10)}$$

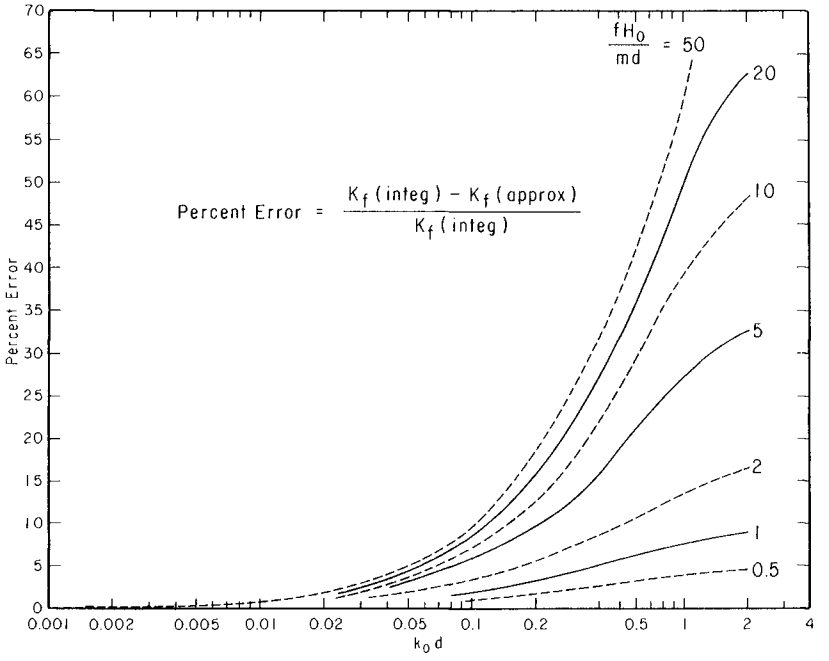

FIGURE A-1 - Percent Error in Approximate Solution

Table A-1

Comparison of Simplified Approximate Wave Height Attenuation by Friction to Asympototic Numerical Solution.

$k_o d$	$fH_{o/md}$	$K_{f(approx)}$	$K_{f(integ)}$	Error(%)
0.00200	0.05000	0.97241	0.97233	0.00869
0.00200	0.10000	0.94630	0.94614	0.01690
0.00200	0.20000	0.89808	0.89779	0.03208
0.00200	0.50000	0.77898	0.77844	0.06956
0.00200	1.00000	0.63798	0.63725	0.11391
0.00200	2.00000	0.46841	0.46763	0.16728
0.00200	5.00000	0.26061	0.26000	0.23268
0.00200	10.00000	0.14983	0.14943	0.26754
0.00200	20.00000	0.08098	0.08075	0.28920
0.00200	50.00000	0.03405	0.03394	0.30396
0.00500	0.05000	0.97793	0.97797	0.00335
0.00500	0.10000	0.95682	0.95688	0.00657
0.00500	0.20000	0.91722	0.91733	0.01259
0.00500	0.50000	0.81590	0.81613	0.02799
0.00500	1.00000	0.68905	0.68938	0.04726
0.00500	2.00000	0.52561	0.52599	0.07212
0.00500	5.00000	0.30709	0.30742	0.10533
0.00500	10.00000	0.18140	0.18162	0.12444
0.00500	20.00000	0.09975	0.09988	0.13686
0.00500	50.00000	0.04244	0.04250	0.14557
0.01000	0.05000	0.98138	0.98153	0.01487
0.01000	0.10000	0.96344	0.96372	0.02917
0.01000	0.20000	0.92946	0.92998	0.05630
0.01000	0.50000	0.84052	0.84159	0.12728
0.01000	1.00000	0.72491	0.72651	0.21955
0.01000	2.00000	0.56852	0.57049	0.34435
0.01000	5.00000	0.34514	0.34695	0.52264
0.01000	10.00000	0.20856	0.20989	0.63165
0.01000	20.00000	0.11642	0.11725	0.70518
0.01000	50.00000	0.05007	0.05045	0.75814
0.02000	0.05000	0.98430	0.98460	0.03101
0.02000	0.10000	0.96908	0.96967	0.06108
0.02000	0.20000	0.94001	0.94112	0.11848
0.02000	0.50000	0.86240	0.86475	0.27176
0.02000	1.00000	0.75809	0.76173	0.47777
0.02000	2.00000	0.61043	0.61516	0.76943
0.02000	5.00000	0.38528	0.39002	1.21412
0.02000	10.00000	0.23861	0.24225	1.50381
0.02000	20.00000	0.13547	0.13782	1.70752
0.02000	50.00000	0.05898	0.06010	1.85859
0.05000	0.05000	0.98747	0.98812	0.06576
0.05000	0.10000	0.97525	0.97652	0.12989

TABLE A-1 (Continued)

$k_o d$	fH_o/md	$K_{f(approx)}$	$K_{f(integ)}$	Error(%)
0.05000	0.20000	0.95170	0.95412	0.25351
0.05000	0.50000	0.88740	0.89268	0.59096
0.05000	1.00000	0.79760	0.80616	1.06232
0.05000	2.00000	0.66333	0.67526	1.76698
0.05000	5.00000	0.44075	0.45408	2.93519
0.05000	10.00000	0.28267	0.29373	3.76489
0.05000	20.00000	0.16460	0.17215	4.38458
0.05000	50.00000	0.07305	0.07679	4.86504
0.10000	0.05000	0.98944	0.99053	0.10929
0.10000	0.10000	0.97911	0.98123	0.21629
0.10000	0.20000	0.95907	0.96315	0.42375
0.10000	0.50000	0.90359	0.91270	0.99807
0.10000	1.00000	0.82413	0.83942	1.82061
0.10000	2.00000	0.70088	0.72327	3.09663
0.10000	5.00000	0.48380	0.51111	5.34385
0.10000	10.00000	0.31909	0.34329	7.04901
0.10000	20.00000	0.18983	0.20721	8.38713
0.10000	50.00000	0.08569	0.09465	9.46519
0.20000	0.05000	0.99111	0.99285	0.17595
0.20000	0.10000	0.98237	0.98581	0.34880
0.20000	0.20000	0.96535	0.97202	0.68551
0.20000	0.50000	0.91767	0.93286	1.62912
0.20000	1.00000	0.84786	0.87417	3.01039
0.20000	2.00000	0.73590	0.77647	5.22572
0.20000	5.00000	0.52709	0.58150	9.35737
0.20000	10.00000	0.35786	0.40994	12.70600
0.20000	20.00000	0.21792	0.25782	15.47490
0.20000	50.00000	0.10028	0.12200	17.80260
0.50000	0.05000	0.99292	0.99600	0.30947
0.50000	0.10000	0.98593	0.99203	0.61457
0.50000	0.20000	0.97225	0.98418	1.21210
0.50000	0.50000	0.93340	0.96137	2.90915
0.50000	1.00000	0.87512	0.92561	5.45497
0.50000	2.00000	0.77796	0.86152	9.69876
0.50000	5.00000	0.58359	0.71334	18.18890
0.50000	10.00000	0.41202	0.55441	25.68320
0.50000	20.00000	0.25946	0.38352	32.34710
0.50000	50.00000	0.12292	0.19926	38.31130
1.00000	0.05000	0.99404	0.99831	0.42771
1.00000	0.10000	0.98814	0.99662	0.85035
1.00000	0.20000	0.97656	0.99326	1.68076
1.00000	0.50000	0.94340	0.98331	4.05919
1.00000	1.00000	0.89286	0.96717	7.68345
1.00000	2.00000	0.80645	0.93643	13.87980
1.00000	5.00000	0.62500	0.85490	26.89210
1.00000	10.00000	0.45455	0.74657	39.11580
1.00000	20.00000	0.29412	0.59563	50.62040
1.00000	50.00000	0.14286	0.37075	61.46770
2.00000	0.05000	0.99498	0.99978	0.47994
2.00000	0.10000	0.99001	0.99956	0.95508

TABLE A-1 (Continued)

$k_o d$	fH_o/md	$K_{f(approx)}$	$K_{f(integ)}$	Error(%)
2.00000	0.20000	0.98022	0.99911	1.89126
2.00000	0.50000	0.95197	0.99779	4.59189
2.00000	1.00000	0.90834	0.99558	8.76290
2.00000	2.00000	0.83207	0.99121	16.05430
2.00000	5.00000	0.66466	0.97830	32.06020
2.00000	10.00000	0.49774	0.95752	48.01780
2.00000	20.00000	0.33133	0.91851	63.92750
2.00000	50.00000	0.16542	0.81846	79.78940

APPENDIX B

Development of Equation for Breaking Wave Angle

The conservation of energy equations from offshore to the breaker location for waves refracting over straight and parallel offshore bottom contours in the case of energy losses to bottom friction can be written as

$$\frac{\rho g}{8} H_i^2 C_{gi} \cos \alpha_i = \frac{\rho g}{8} H_b^2 C_{gb} \cos \alpha_b + \text{losses} \tag{B-1}$$

where the losses can be expressed in terms of a friction coefficient K_f as

$$\text{losses} = (1 - K_f^2) \frac{\rho g}{8} H_i^2 C_{gi} \cos \alpha_i \tag{B-2}$$

Upon combining equations B-1 and B-2, and canceling like terms it can be found that

$$H_b^2 C_{gb} \cos \alpha_b = K_f^2 H_i^2 C_{gi} \cos \alpha_i \tag{B-3}$$

Assuming breaking occurs in shallow water

$$C_{gb} = (g d_b)^{0.5} \tag{B-4}$$

Now assuming $\kappa = \frac{H_b}{d_b}$ is known (see equation 10 in text) equations B-3 and B-4 can be solved as

$$H_b = \left[\left(\frac{\kappa}{g} \right)^{1/2} K_f^2 H_i^2 C_{gi} \cos \alpha_i \right]^{0.4} \tag{B-5}$$

Using Snell's Law of Refraction and the shallow water assumption

$$\sin \alpha_b = \left(\frac{g H_b}{\kappa} \right)^{0.5} \left(\frac{\sin \alpha_i}{C_i} \right) \tag{B-6}$$

which can then be solved for α_b.

APPENDIX C - REFERENCES

BATTJES, J.A., Computation of Set-up, Longshore Currents, Run-up and Overtopping due to Wind-generated Waves; Dissertation, Delft University of Technology, 1978.

BRETSCHEIDER, C.L., and REID, R.L.; Beach Erosion Board, T.M. 45, U.S. Army, Corps of Engineers, Coastal Engineering Research Center, Fort Belvoir, VA October 1954.

BRUNO, R.O., DEAN, R.G., GABLE, C.G., WALTON, T.L., JR.; Longshore Sand Transport Study at Channel Islands Harbor, California, T.P. 81-2, U.S. Army, Corps of Engineers, Coastal Engineering Research Center, Fort Belvoir, VA, April, 1981.

GALVIN, C.J., and EAGLESON, P.S.; Experimental Study of Longshore Currents on a Plane Beach, T.M. 10, U.S. Army, Corps of Engineers, Coastal Engineering Research Center, Fort Belvoir, VA, Jan. 1965.

IPPEN, A.T. (editor); Estuary and Coastline Hydromechanics, McGraw-Hill, New York, 1966.

KAMPHUIS, J.W.; Friction Factor Under Oscillatory Waves, J. Waterways, Harbors, and Coastal Eng. Div., ASCE, Vol. 101, 135-144, 1975.

LONGUET-HIGGINS, M.S.; Recent Progress in the Study of Longshore Currents, In: R.E. Meyer (editor), Waves on Beaches and Resulting Sediment Transport, Academic Press, New York, pp. 203-248, 1972.

SHAW, E.A. and JOHNSON, J.W.; Model Studies on the Movement of Sand Transported by Wave Action Along a Straight Beach, Issue 7, Series 14, Institute of Engineering Research, University of California, Berkeley, 1951.

SINGAMSETTI, S.R. and WIND, H.G.; Breaking Waves Publication No. M1371, Waterstaat, Netherlands, July 1980.

VITALE, P., Movable-Bed Laboratory Experiments to Compare Radiation Stress and Energy Flux Factor as Predictors of Longshore Transport Rate, M.R. 81-4, U.S. Army, Corps of Engineers, Coastal Engineering Research Center, Fort Belvoir, VA, April 1981.

VITALE, P., Sand Bed Friction Factors for Oscillatory Flows, J. Waterway, Port Coastal and Ocean Division, ASCE, Vol. 105, WW3, pp. 229-245, August 1979.

WALTON, T.L., JR. and DEAN, R.G., Computer Algorithm to Calculate Longshore Energy Flux and Wave Direction from a Two-Pressure Sensor Array, (in preparation), U.S. Army, Corps of Engineers, Coastal Engineering Research Center, Fort Belvoir, VA 1982.

U.S. ARMY, CORPS OF ENGINEERS, Coastal Engineering Research Center, Shore Protection Manual, 3d ed., Vols. I, II, and III, Stock No. 008-022-00113-1, U.S. Government Printing Office, Washington, D.C., 1977.

BREACH/INLET INTERACTION AT MORICHES INLET

E.J. Schmeltz,[1] A.M.ASCE, R.M. Sorensen,[2] M.ASCE
M.J. McCarthy,[3] A.M.ASCE, G. Nersesian,[4] M.ASCE

ABSTRACT

Moriches Inlet is located on the south shore of Long Island, New York, approximately 45 miles (72 kilometers) west of Montauk Point and 80 miles (130 kilometers) east of New York City. The inlet forms the primary outlet through the barrier island between Moriches Bay and the Atlantic Ocean. The inlet is protected and stabilized by two stone jetties approximately 800 feet (245 meters) apart .

During January, 1980, a severe northeast storm resulted in the breaching of the barrier island immediately to the east of the existing Moriches Inlet. By the fall of 1980, the breach had expanded to nominally 2900 feet (885 meters) in width with a maximum depth of around 10 feet (3 meters) and the U.S. Army Corps of Engineers was requested to affect its closure. The method adopted by the Corps consisted of the placement of beach fill in the opening to develop a cross-section with a centerline elevation of +13.25 feet (4 meters) MLW and side slopes of 1V:25H. Initiated in October 1980, the closure operation was succesfully completed in February, 1981.

The formation of a significant breach immediately adjacent to the existing inlet and the artificial closure of the opening afforded a unique opportunity to study the dynamics of a tidal inlet under the influence of relatively rapid changes in tidal prism and cross sectional area. The purpose of this paper is to present the results of a field measurement program and subsequent analyses of the dynamics of the inlet/breach system. The analyses were based on data obtained before, during and after closure of the breach.

---

1. Manager Coastal Engineering, PRC Harris, 3003 New Hyde Park Road, Lake Success, New York
2. Professor of Civil Engineering, Lehigh University, Bethlehem, PA.
3. Principle Coastal Engineer, PRC Harris, 3003 New Hyde Park Road, Lake Success, New York
4. Chief, Coastal Engineering Branch, U.S. Army Corps of Engineers, New York District

DESCRIPTION OF THE STUDY AREA

The eastern 33 miles (53 kilometers) of the south shore of Long Island has eroding headlands that contribute sediment to the net littoral drift to the west along most of the south shore. Generally narrow beaches cut by six inlets (from east to west: Shinnecock, Moriches, Fire Island, Jones, East Rockaway and Rockaway) occupy the remaining 87 miles (140 kilometers) of the south shore. A vicinity map is shown in Figure 1.

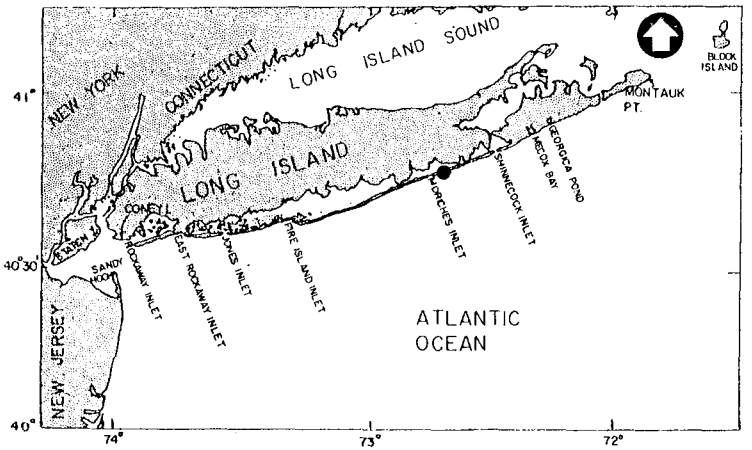

Figure 1 - Vicinity Map

Moriches Inlet, located about 80 miles (130 kilometers) from the western end of the island, connects Moriches Bay to the Atlantic Ocean. Moriches Bay extends about 13 miles (20 kilometers) along the coast and has a width of one to two miles in the vicinity of the inlet (Figure 2). The Bay, which is generally less than six feet (1.8 meters) deep, is open via narrow connections to Shinnecock Bay on the east and Great South Bay on the west. There is a small net flow through these connections into Moriches Bay which augments the ebb flow through Moriches Inlet. This system is crossed by the intercoastal waterway (ICWW) which is dredged to a depth of six feet (1.8 meters).

Inlet migration and offset patterns, sediment entrapment at groins and inlet structures, wave hindcasts, and grain size and trace mineral variations all indicate a strong net longshore transport to the west (Reference 1). Taney (Reference 2) estimated this drift in the vicinity of Moriches Inlet to be 300,000 cubic yards (230,000 m^3) per year; Panuzio (Reference 1) presents an estimated net rate of 350,000 cubic yards (269,000 m^3) per year. The longshore transport is consistently to the west except for the summer months when short term reversals can occur (Reference 3).

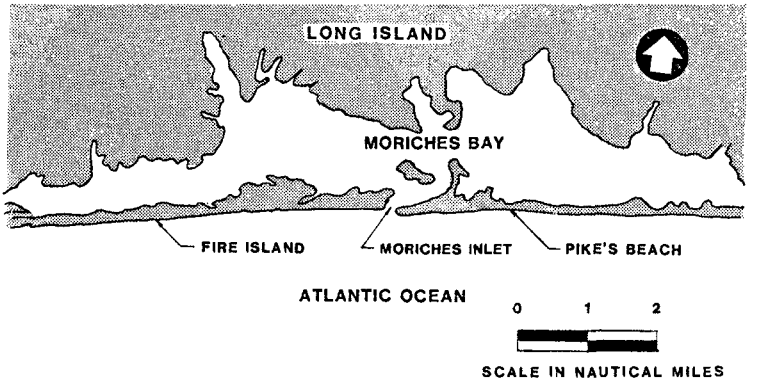

Figure 2 - Bay System (Local) Map

The history of Moriches Inlet has been treated by a number of investigators (Reference 4, 5, 6) and is summarized here only briefly. In 1828, there were two inlets to Moriches Bay, but both closed by 1838. The Bay remained landlocked for nearly a century until March, 1931, when a storm cut a new opening to the Atlantic Ocean. By 1949, this inlet had migrated 4000 feet (1220 meters) to the west and by May, 1951 it was again closed. In 1952-53, a pair of jetties was constructed in the dry at the location of the old inlet. Dredging was then initiated to cut a channel between the new jetties when a minor storm in September, 1953 completed the opening. Figure 3 shows the layout of the jetties and the pattern of adjacent channels in 1967. The jetties are spaced about 800 feet (245 meters) apart.

Further dredging was undertaken at Moriches Inlet in 1958, when a 10-foot (3 meter) deep, 200-foot (60 meter) wide channel,the Bay Channel, was cut from a point just inside the inlet to the northeast and then back to the ICCW (see Figure 3). This channel was widened to 300 feet (90 meters) in 1963. A second channel, the Northwest Channel, was dredged in the northwest direction back to the ICCW in 1966.

In 1956, just after the inlet was opened, the throat cross-sectional area was 6,500 square feet (600 m^2). The area increased to over 12,000 square feet (1,115 m^2) by 1975 as channel erosion assisted by the dredging caused the entrance cross sectional area to grow toward the estimated (Reference 4) stable value of about 18,000 square feet (1,675 m^2). The mean tide range in the bay increased from just under 0.5 feet (0.15 meters) in 1956 to about 2.0 feet (0.6 meters) in 1975. In the ocean, the mean range is 2.9 feet (0.9 meters) and the average spring tide range is 3.5 feet (1.06 meters). A photograph of Moriches Inlet as it appeared in 1973 is shown in Figure 4.

The ebb tidal flow through the Northwest Channel from the ICCW to the inlet is directed at Pikes Beach (see Figure 3). With increased flow, owing to increased inlet throat area, channel dredging and the ebb flow pattern in the main channel, the bay side of Pikes Beach adjacent to the east jetty underwent significant erosion from 1955 on. Czerniak (Reference 4) in a study of the inlet conducted for the U.S. Army Engineers, New York District identified the possibility of the formation of a breach in that area on the basis of existing flow patterns.

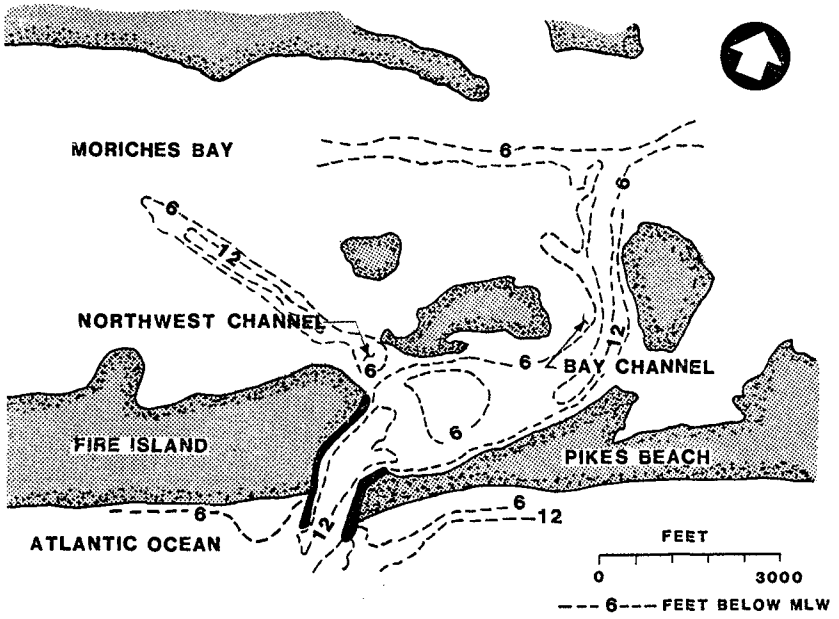

Figure 3 - Plan of Inlet and Adjacent Channels

The main (Bay) channel from the inlet to the ICCW developed a deep section adjacent to Pikes Beach (see Figure 3). Ebb flow concentrates in this section as it is deflected from a southerly to southwesterly direction. This, possibly assisted by the ebb flow from the Northwest Channel, was the likely cause of the severe erosion of the bay side of Pikes Beach adjacent to the inlet. The resulting necking of Pikes Beach is demonstrated by a photograph taken in January 1978, shown in Figure 5. Suffolk County had dredged sand from the bay to build up Pikes Beach to resist the necking of the beach but, as the photograph demonstrates, the reduction in beach width adjacent to the inlet was still quite significant.

Figure 4 - Moriches Inlet Viewed From the South (September 1973)

DEVELOPMENT OF THE BREACH

A severe Northeast storm on January 14-16, 1980 caused the formation of a breach through Pikes Beach, at the narrowest section about 1000 feet (305 meters) east of the east jetty. Figure 6 is a photograph taken soon after the breach occurred. Apparently, wave action and stronger ebb tidal currents in the bay resulting from the stronger winds and higher water levels during the storm caused excessive erosion on the bayside and washover of the barrier island from the ocean side.

The initial width of the breach when first observed on January 16 was estimated to be on the order of 300 feet (90 Meters) and the depth was estimated at about 2 feet (0.6 meters). A hydrographic survey on January 20 indicated the breach to be 700 feet (215 meters) wide and an average of 3.3 feet (1 meter) deep below Mean Low Water (Reference 7). By May 1980 the fillet between the breach and East Jetty was entirely removed and by October 1980 the breach was nominally 2900 feet (885 meters) wide. Figures 7 through 9 provide a photographic history of the development of the breach. Comparative shorelines indicating the necking of Pikes Beach and the subsequent breach development are shown on Figure 10.

Figure 5 - Pikes Beach Looking East(January 1978)

Figure 6 - Moriches Inlet and Breach Looking West (January 18, 1980)

FIGURE 7
Breach Development
April 1, 1980

FIGURE 8
Breach Development
July 12, 1980

Figure 9 - Breach Development - September 21, 1980

As a result of concerns expressed by local interests regarding increased exposure to storm induced flooding in the backbay areas and the impact of possible changes in bay salinity on the shellfish industry, the U.S. Army Corps of Engineers was requested to effect closure of the breach. It was intended that construction be completed prior to the winter storm season of 1980 - 1981 which essentially allowed for a six month construction period.

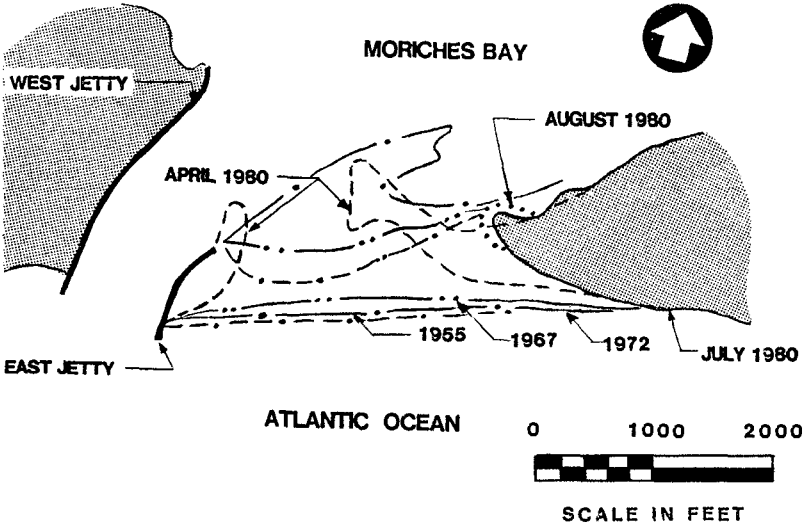

Figure 10 - Comparative Shorelines East of Moriches Inlet

The construction of the closure works and development of the methodology are treated by McCarthy, Schmeltz and Lehan (Reference 8). Briefly the design developed by the Corps of Engineers called for the placement of 1.2 million yds^3 (980,000 m^3) of beach fill in the opening to develop a cross-section with a centerline elevation of +13.25 feet (+4 meters) MLW and side slopes of 1V:25H.

For the construction, temporary steel sheetpiling was driven on the bayside of the breach essentially parallel to the original water line. The sheeting served to provide access for land based construction equipment and to "pinch off" flow in the newly formed channel. Construction proceeded from the easternmost point of the breach to the East Jetty of Moriches Inlet. Following placement of the fill the sheeting was removed and the material graded to the desired section.

Construction activities began in October 1980 and closure of the breach with the sheeting was effected in December 1980. The filling operation was completed to the final desired cross-section in February 1981. It is worthy of note that erosion of the bay side of Pikes Beach recurred after the closure. In order to stabilize this area 1600 feet (490 meters) of stone revetment was placed by Suffolk County (Reference 9) in April, 1982.

FIELD MEASUREMENTS

Prior to the startup of construction activities, a field measurement program was initiated in order to obtain data on the inlet/breach system. It was intended to collect information before, during and after closure of the breach. The program included the following measurements:

- Breach and Inlet cross-sections
- Velocity measurements as a function of breach closure and tides
- Tidal readings inside and offshore of the inlet

Data was obtained over a six month period. Systematic aerial photographs were also initiated by the Corps of Engineers in order to document the development of the breach from initial formation and continuing 15 months after closure.A chronology of activities related to the breach, closure operations and measurement program is presented in Table 1.

TABLE 1
MORICHES INLET/BREACH CHRONOLOGY

• Mid January, 1980	- Breach Opens Initially 300 Feet (90 meters)
• October 1, 1980	- Closure Operations Begun Breach 2900 Feet (885 meters)
• October 3, 1980	- Bay Tide Gauge Installed
• October 4, 1980	- 1st Current Profiling
• October 20, 1980	- Ocean Tide Gauge Installed
• October 21, 1980	- 2nd Current Profiling
• December 15, 1980(Apprrox.)	- Breach Closed
• December 19, 1980	- 3rd Current Profiling(Partial)
• January 19/20, 1981	- 4th Current Profiling
• January 31, 1981(Approx.)	- Construction Completed
• March 24/25, 1981	- 5th Current Profiling Removal of Tide Gauges
• April, 1982	- Stone Rip-Rap Protection Placed on Bay Shoreline

Cross sections of both Moriches Inlet and the breach were obtained at the locations shown on Figure 11 for each period of measurement. Depth measurements were made with a Raytheon DE 719 precision depth recorder. Profiles were obtained by piloting the vessel along a predetermined track at constant speed utilizing existing rangemarks and fixed objects to maintain alignment.

Results of the depth profiling were utilized at each measurement period to delineate segments of the inlet and breach for velocity profiling. The intent of the current measurements was to allow a volumetric analysis of flow through the respective channels. A representative sample of the segments utilized for one survey is shown in Figure 12.

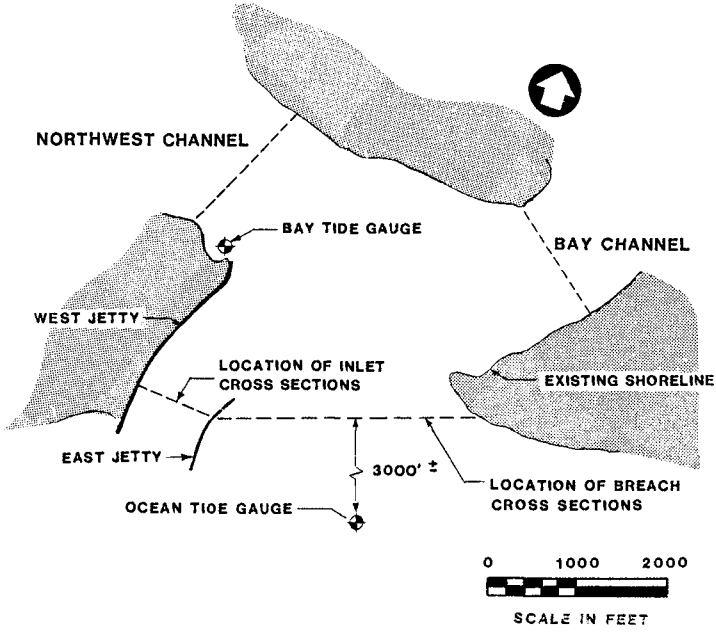

Figure 11 - Inlet Cross-Section and Tide Gauge Locations

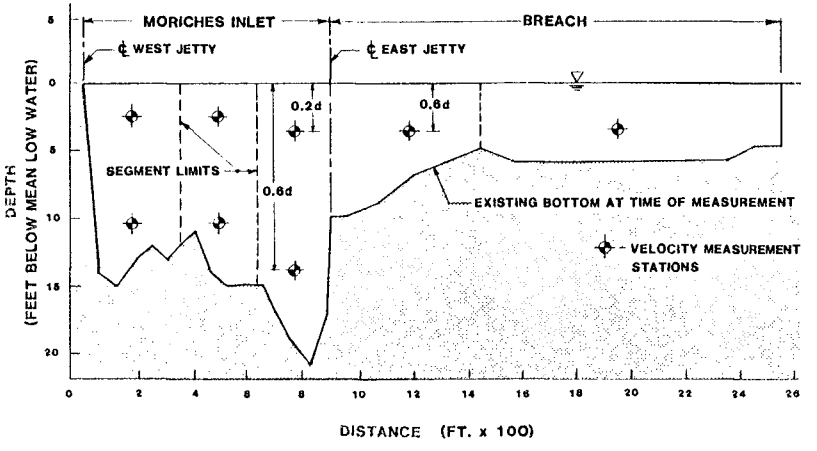

Figure 12 - Current Profiling Station Locations

Current measurements were obtained at each station at 0.2 and 0.8 of the average depth in the segment at the time of measurement. In cases where the depth was not sufficient to permit dual measurements, a single reading at 0.6 of the depth was obtained to reflect the average current in the segment. Measurements were made utilizing over the side current meters with directionality inferred from the surface currents. Readings were obtained atapproximately 1 hour intervals at each point of interest. Each monitoring period covered a minimum of 13 hours, sufficient to fully define a tidal cycle.

Cross-section data and velocity profiles were obtained on four occasions at approximately the following stages of construction of the breach closure:

- Profiling A - October 4, 1980 Prior to initiation of construction
- Profiling B - October 21, 1980 Breach half closed
- Profiling C - January 19 and 20, 1981 Closure complete
- Profiling D - March 25,1981 One month after completion of construction

Two recording tide gauges were installed on site, one inside and one outside of the inlet as shown on Figure 11. The inside or "bay" gauge was installed on October 3, 1980. This gauge was located at the base of a tide staff on the north end of the West Jetty. Initially it was intended that the "ocean" wave gauge be installed on a crib at the southern end of the West Jetty. However, due to hazardous conditions at this location the gauge was finally installed slightly east and offshore of the inlet as shown on Figure 11. This location was chosen in order to avoid the shoals offshore of the inlet and breach and to reduce the possibility of the gauge being buried by sediment transported away from the fill operations. The ocean gauge was installed on October 20, 1980.

Both of the tide gauges were bottom mounted pressure recording units set to record water levels at 10 minute intervals. Essentially concurrent readings were obtained both in the bay and in the ocean. During periods of current monitoring, tidal measurements were also obtained from tide staffs located adjacent to the north end of the inlet. Visual readings were obtained during on-site operations at 30 minute intervals.

DISCUSSION OF RESULTS

Breach and inlet cross sections obtained at various times prior to, during and after construction are shown in Figure 13 along with the relative locations of the temporary sheetpile closure structures. Cross section data is presented in tabular form in Table 2 for the breach, inlet and system total.

Initially, the inlet profile consisted of a relatively shallow channel on the west bank and a deep channel near the East Jetty. The breach was relatively flat and shallow until just east of the jetty where a small channel is apparent. As can be seen in the figure, both the inlet and breach began to deepen as closure was carried out. Examination of aerial photos also indicate significant shoaling in the ebb and flood tidal deltas. Overall the pinching off of the breach by the sheet pile retaining structure, however, resulted in a shift in tidal flow from the breach to the inlet with a commensurate increase in cross sectional area of the original channel.

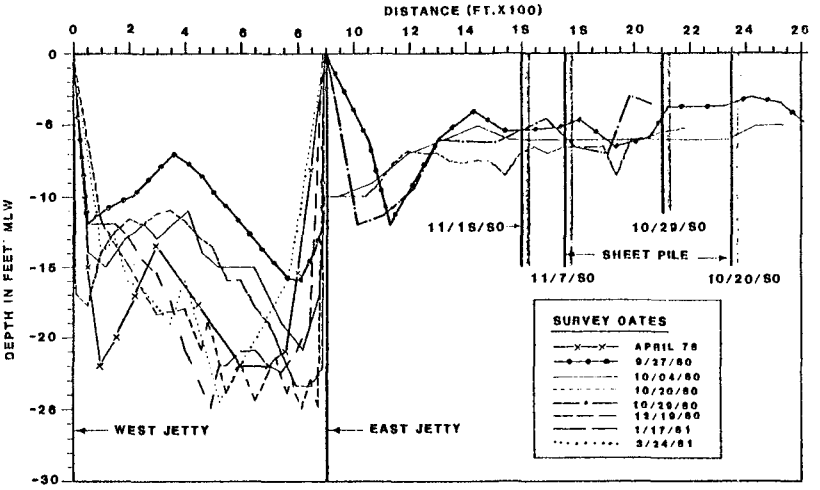

Figure 13 - Comparison of Cross-Sectional Areas

TABLE 2
TIDAL PRISMS AND CROSS-SECTIONS DURING BREACH CLOSURE

Date	Inlet			Breach			Total			A_{cs}
	Flood T.P. ($\times 10^8$ ft.^{3})	Ebb T.P. ($\times 10^8$ ft.^{3})	C.S. (ft.^{2})	Flood T.P. ($\times 10^8$ ft.^{3})	Ebb T.P. (ft.^{2})	C.S. ($\times 10^8$ ft.^{3})	Flood T.P. ($\times 10^8$ ft.^{3})	Ebb T.P. (ft.^{2})	C.S. (ft.^{2})	Per O'Brien (ft.^{2})
7/80	N.A.	N.A.	11,900	N.A.	N.A.	11,925	N.A.	N.A.	22,825	-
9/29/80	6.14	N.A.	9,975	N.A. (Breakers)	N.A. (Breakers)	N.A.	N.A.	N.A.	N.A.	-
10/6/80	3.95	4.3	12,975	2.83	3.02	10,570	6.8	7.32	23,475	14,075
10/20/80	3.3	3.3	13,797	2.1	2.2	9,589	5.4	5.4	23,381	10,800
12/19/80	N.A.	N.A.	16,273	←	Closed	→	N.A.	N.A.	16,273	-
1/20/81	11.5	10.9	15,663	←	Closed	→	11.5	10.9	15,663	22,800
3/25/81	5.9	5.7	14,765	←	Closed	→	5.9	5.7	14,765	11,620

NOTES:

1. Construction initiated approximately 10/9/80, sheet pile closure effected 12/80.
2. Breach approximately 1/2 closed as of 10/20/80.
3. N.A. indicates data not available.

Measurements obtained in July and September 1980, both prior to construction indicate that the cross sectional area of the inlet was decreasing, implying a possible instability towards closure of the inlet. It is, however, interesting to note that the gross cross-sectional area of the inlet and breach from the first available data in July 1980 through late October, 1980 (shortly after construction began) remained relatively constant near 23,000 ft^2 (2100 m^2). From the July measurements the gross area was divided roughly equally between the breach and inlet. As a result of the apparent consistancy of the gross cross-sectional area of the inlet/breach during this period, the cross-sectional areas of the Bay and Northwest channels were evaluated from the July 1980 data. The location of the lines is shown on Figure 11. These computations indicate a combined cross-section in these channels of approximately 22,500 ft^2 (2040 m^2). The inference, than, is that a secondary control may have existed in the form of these channels.

As closure progressed, the channel in the breach adjacent to the East Jetty initially deepened in response to the decrease in width, but eventually closed. Concurrently, the inlet cross section enlarged. After closure, the inlet became deeper and began to change to a single channel more centrally located between the jetties.

The cross-section of the inlet decreased from July to late October. Subsequently the inlet cross-sectional area shows a persistant increase reaching a maximum in December shortly after closure was completed with the sheet pile walls. Subsequent measurements indicate a slight decrease in the inlet cross section which may correspond to an increase in hydraulic efficiency as the inlet moved towards its more stable, prebreach condition. Data on variations in inlet and breach cross section as a function of time are plotted in Figure 14. Data prior to the breach were obtained from reference 4.

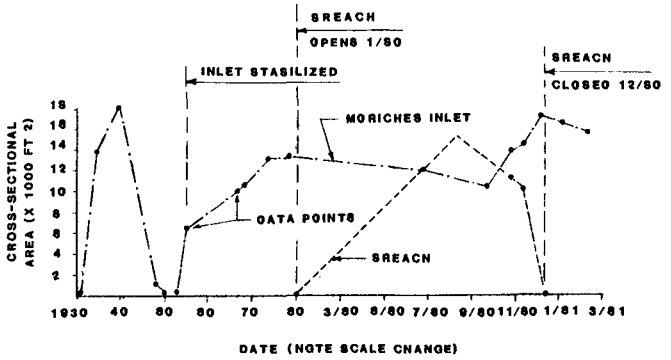

Figure 14 - Inlet/Breach Cross-Sectional Area Changes

It is interesting to note that earlier estimates by other investigators (References 4, 5) indicate a stable cross section of the inlet ranging from 16,000 ft^2 (1500 m^2) to 20000 ft^2 (2100 m^2). The latest available measurements of the cross section of Moriches Inlet prior to the breach, obtained in April, 1978, indicated an area of approximately 12500 ft^2 (1860 m^2). It appears, then, that the inlet was probably moving towards its prebreach condition at the time of the final measurements in this program.

Velocity measurements in the inlet and breach were utilized to assess variations in tidal prism at the time of measurements. Peak measured velocities, provided as an indication of the relative flow, during each measurement period are presented in Table 3. Tide ranges based on measured data from the "ocean" and "bay" as well as predicted tides in the ocean at the time of measurement (Reference 10) are also provided .Tidal prisms computed on the basis of field measurements are shown in Table 2.

TABLE 3
TIDE RANGES AND CURRENT VELOCITIES

DATE	TIDE TABLES (ft)	MEASURED TIDES (ft)		MAX. CURRENTS (ft/sec)	
		OCEAN	BAY	BREACH	INLET
10/4/80	3.3	n.a.	2.2	2.0	3.5
10/20/80	3.7	3.7	2.8	1.5	2.5
1/20/81	4.0	4.4	3.3	CLOSED	6.8
3/25/81	3.0	3.3	1.8	CLOSED	4.2

As shown in Table 3, measured ocean tide ranges varied during the measurements from 4.4 feet (1.3 meters) to a low of 3.3 feet (1 meter) and compare favorably with the predicted tide ranges. Tidal differentials and maximum current velocities in the inlet, show a marked increase as the closure was effected.

Considering the variations in the ocean tides experienced during the measurement periods, it appears that the tidal prism decreased slightly after closure was completed. However, considering that the cross section with the breach was nearly twice as large as the pre and post breach inlet sections, the change in flow quantity is relatively minor varying from a maximum of 7.3×10^8 ft^3 (2.07×10^7 m^3) with the breach open to 5.9×10^8 ft^3 (1.67×10^7 m^3) after closure. The maximum values are also substantially below the "potential" tidal prism determined by Mehta and Hou (Reference 5) of 1.5×10^9 ft^3. Note that both measurements sets were obtained with an ocean tide range of 3.3 feet (1 meter). Bay tide ranges, also decreased from 2.2 feet (0.67 meters) to 1.8 feet (0.55 meters) on the bay side of the inlet. These results should, however, be viewed with caution due to the limited nature of the available data and the effect of

secondary controls of the Bay and Northwest Channels on tide readings obtained immediately adjacent to the northern limit of the inlet.

In any case, the level of change in the tidal prisms with and without the breach seems to provide further substantiation of the secondary control of the Bay and Northwest Channels while the breach was open.

As a gross indicator of the overall stability of the system, O'Brien's Area/Tidal Prism relationship (Reference 11) was utilized with the measured tidal prisms to determine "stable" areas. The values determined in this evaluation are provided in Table 2. As seen in the table the values vary, as a function of the measured prism, from 10,800 ft^2 (1000m^2) to a high of 22,800 ft^2 (2120 m^2). Based on the measured prisms after construction, O'Brien's method yields a stable cross-sectional area of the inlet of nominally 12,000 ft^2 (1115 m^2) , close to the measured values in April 1978.

Overall the comparisons indicate that measured cross sections prior to closure were larger than could be sustained given the available tidal prism. Measurements after closure, in March 1981, show a closer agreement with computed values although it appears that a further reduction in area of the inlet is possible.

CONCLUSIONS

Prior to closure of the breach, the tidal prism determined from velocity measurements appears to have been inadequate to maintain the cross sectional area of the inlet/breach system, i.e. the system was probably unstable towards closure. However, the inlet was undergoing migration beyond its control structures which may have resulted in closure of the original inlet replaced by an uncontrolled, migratory channel. Based on previous experience with inlets at this location, the ultimate result may have been complete closure of the connection between Moriches Bay and the Atlantic Ocean.

The gross cross sectional area of the inlet/breach system, prior to the beginning of the closure operations, was on the order of 23,000 ft^2 (2140 m^2) divided roughly equally between the original inlet and the breach. During construction the cross-sectional area of the original inlet increased by nominally 25% relative to the pre construction condition to approximately 15,000 ft^2 (1390 m^2). The post construction cross section of nominally 12,000 ft^2 (1115 m^2) correlates well with measurements obtained before the breach. This seems to indicate that the channel was returning to its prebreach configuration as of the conclusion of the measurement program.

Both observations and measurements indicate that as the breach was "pinched off" by the temporary sheet pile structures, flow was shifted from the breach to Moriches Inlet. Both currents and tidal differentials showed a marked increase as construction progressed. Although the data are limited, tidal prisms appear to have decreased slightly after the closure was completed.

The magnitude of change in tidal prism, however, appears somewhat smaller than might have been expected. The Bay and Northwest channels which exist behind

the inlet may have exerted a secondary control on the system. The result of the influence of these channels could have been to minimize, at least temporarily, further increases in both the cross sectional area and flow through the inlet/breach system.

ACKNOWLEDGEMENTS

Some of the data described in this document were collected under the Civil Works Research and Development Program of the U.S. Army Corps of Engineers. Permission to publish this paper is appreciated. The findings of this paper are not to be construed as official Department of the Army position unless so designated by other authorizing documents.

The authors would also like to express their appreciation to Lizza Industries, Roslyn, NY and Ocean Surveys, Inc, Old Saybrook, CN for their invaluable assistance in the collection of the data utilized in these investigations; and to the Coastal Engineering Research Center for access to the aerial photographs of the site.

REFERENCES

1. Panuzio, F.L., "The Atlantic Coast of Long Island", Proceedings, Eleventh Conference on Coastal Engineering, Chapter 77, London, 1968.
2. Taney, N.E., "Geomorphology of the South Shore of Long Island, New York", Beach Erosion Board Technical Memorandum 128, September 1961.
3. DeWall, A.E., "Beach changes at Westhampton Beach, New York, 1962-73", MR 79-5 Coastal Engineering Research Center, August 1979.
4. Czerniak, M.T., "Engineering Concepts and Environmental Assessment for the Stabilization and Sand Bypassing of Moriches Inlet, New York", Tetra Tech, Inc., January 1976.
5. Mehta, A.J. and Hou, H.S., "Hydraulic Constants of Tidal Entrances II:Stability of Long Island Inlets", Technical Report No. 23, Coastal and Oceanographic Engineering Laboratory, University of Florida, Gainesville, FL, November 1974.
6. U.S. Army Corps of Engineers, "Moriches and Shinnecock Inlets, Long Island, New York: Survey Report.", September, 1957.
7. U.S. Army Corps of Engineers, New York District, "Specifications for Emergency Breach Closure Project, Moriches Inlet, Suffolk County, New York.", 1980.
8. McCarthy, M.J., Schmeltz, E.J. and Lehan, G.L., "Construction of a Breach Closure in a Barrier Island", Proceedings, Eighteenth Conference on Coastal Engineering, Capetown, November 1982.
9. Kasner, J. and Black, J.A., "Efforts to Stabilize a Coastal Inlet: A Case Study of Moriches Inlet, New York.", Shore and Beach, April, 1980.
10. U. S. Department of Commerce, National Oceanic and Atmospheric Administration, National Ocean Survey, "Tide Tables, East Coast of North and South America, 1980 and 1981".
11. Jarrett, J.T.,"Tidal Prism-Inlet Area Relationships", General Investigation of Tidal Inlets Report 3, Corps of Engineers, February 1976.
12. U.S. Army Corps of Engineers, New York District, "Reformulation Study and General Design Memorandum - Moriches Inlet", May 1982.

SHORE PROTECTION AT VENICE: A CASE STUDY

A. Muraca (*)

ABSTRACT

The lagoon of Venice (N. Adriatic) is the most important in Italy (Fig. 1). Between 1840 and 1933 the tidal entrances facing the lagoon were controlled by six large jetties, after the construction of which more evident erosion phenomena appeared in some tourist resort beaches near the inlets. Detailed historical, movable bed models, and field studies have recently been conducted with the aim of defining a proper defence system for these beaches. The results of these studies are reported here.

HISTORICAL REPORTS

The lagoon of Venice originated nearly 6,000 years ago as a result of slow invasion by rising sea-water over a wide alluvial zone, faced by a large dune system whose position has not significantly changed in time.

The first detailed historical reconstruction of the lagoon describes the site as it was about 1,000 years ago (Filiasi [2]). At that time the lagoon was connected to the sea by nine different mouths, called "ports", i.e. from NE to SW, Jesolo, Lio Maggiore, Treporti, S. Erasmo, S. Nicolò, Malamocco, Porto Secco, Chioggia and Brondolo (Fig. 2).

The following evolution of the northern lagoon area is shown in Fig. 3. In the 16th century five inlets were still present on this side, i.e. Jesolo, Lio Maggiore, Treporti, S. Erasmo and S. Nicolò. One century later, as a consequence of large deposits of river sediment, the port of Jesolo became a branch of the Piave river and that of Lio Maggiore an internal channel called "Pordelio". Sediment deposits continued in front of the Pordelio channel.

Finally, as a consequence of the construction of two big jetties between 1882 and 1910, Treporti, S. Erasmo and

---

(*) Assistant of Hydraulics, Institute of Applied Mechanics, University of Udine, Italy.

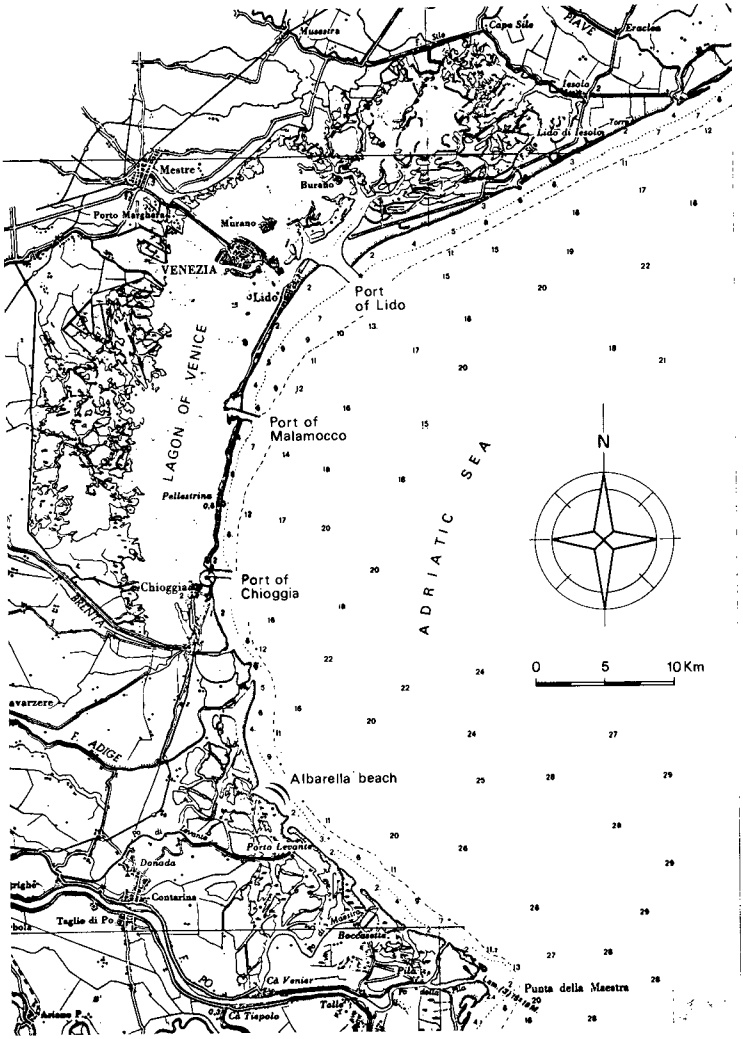

FIG. I : Study area

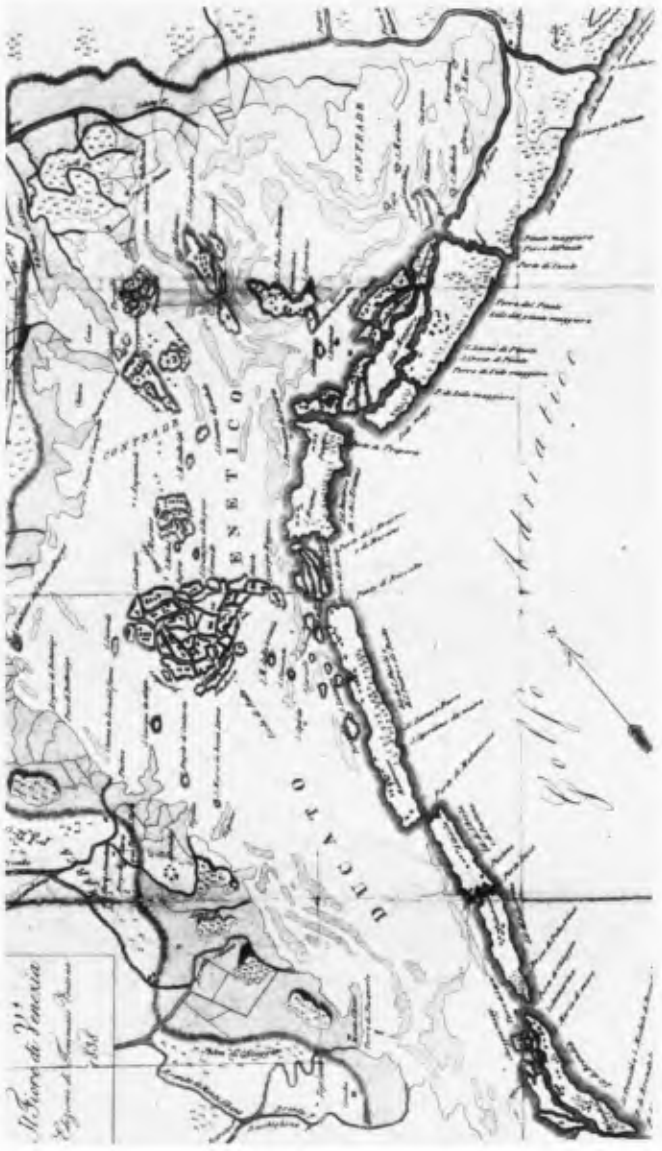

FIG. 2 : The lagoon of Venice one thousand years ago

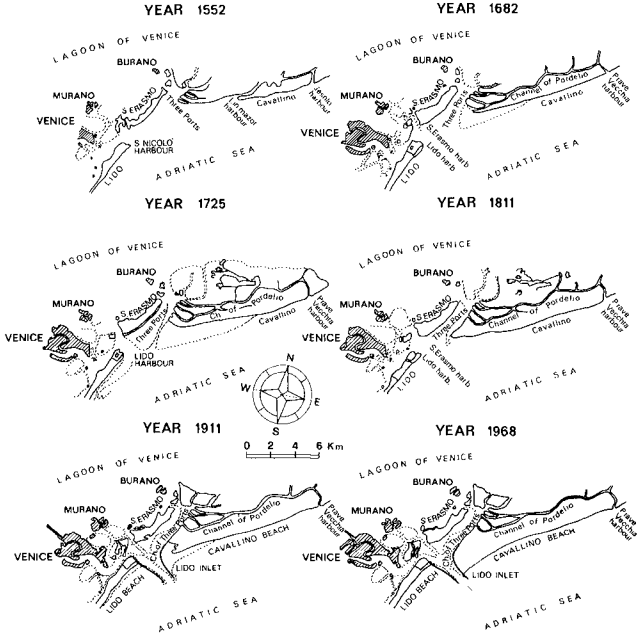

FIG. 3 : Topographic change of N-E lagoon area (after Miozzi [3])

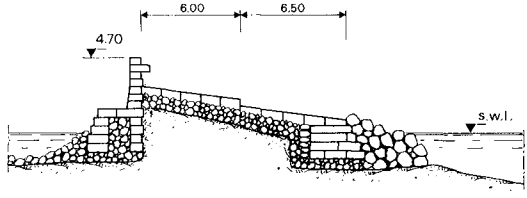

FIG. 4 : Seawall built between 1744 and 1782

the Lido (S. Nicolò) were united to form the Lido inlet. In the meanwhile, fewer modifications took place on the southern side of the lagoon, where the sediment supplied by river floodings had the effect first of closing the Porto Secco inlet and then of confining the Brondolo inlet to the border of the lagoon itself.

From the beginning of the 13th century, man's contribution became gradually more important. The Venetians generally followed three main directions while aiming at preserving the singular aspect of their lagoon:

1) they avoided large river sediment deposits inside the lagoon and preserved the activity of the inlets;
2) they favoured predominance of salt water over fresh in the lagoon;
3) they assured an efficient shore defence system to the islands composing the littoral belt.

To satisfy the first two needs (points 1 and 2), from the 14th century onwards, the main rivers formerly entering the lagoon were diverted outside it. Longshore sediment supply consequently increased at the borders of the lagoon.

Shore defence had been important since the 11th century, when the first artificial sand movements were performed, whereas the first structures were built around the 14th century. These consisted of groins and sea-walls, built of several lines of generally transversally connected wooden piles. Stones were also placed between the lines of the groins and at the foot of the sea-walls. The effect of these structures was, however, often unsatisfactory and the Venetian government was frequently obliged to remove or modify them. Between 1774 and 1886, about 20 km of large sea-walls were built. The first 5 km were built between 1774 and 1782 to protect positions between the Malamocco and Brondolo inlets, where beach extension was insufficient to avoid flooding during heavy storms. Although these structures, where concrete was used to increase the stability of the stones, represent an incredible technological level for those times (see Fig. 4), they underwent serious damage and the bottom erosion rate increased in front of the sea-walls. Parts of these structures were destroyed in November 1966, during a storm in which the sea rose approx. 2 m above normal levels. On that occasion, it was noticed that, two hundred years after their construction, damage to the sea-walls was mainly due to cavities which had formed under the stone covering, rather than to structural weaknesses.

EFFECTS OF JETTY CONSTRUCTION

Between 1840 and 1933, both to improve navigation facilities and to increase sea/lagoon water exchange, six large jetties were built, thus causing the present configuration of the lagoon. Fig. 5 shows this configuration: of the nine tidal inlets active 1,000 years ago, only three still remain. They are:

- the Lido, whose jetties were built between 1882 and 1910. The N jetty is 3,635 m long, the S one 3,155 m; the inlet channel is 900 m wide;
- Malamocco inlet, whose jetties were built between 1840 and 1872. The N jetty is 2,120 m long, the S one 930 m. This inlet is 470 m wide and separates the littoral of the Lido from that of Pellestrina;
- Chioggia inlet, whose jetties were built between 1911 and 1933. The N jetty is 1,800 m long, the S one 1,500 m; the inlet channel is 550 m wide.

To analyze the effects produced by the long jetties on the adjoining beaches, bathymetric charts up to 1810 have been collected and compared with the present situation.

As Figs. 6 and 7 show, large offshore bars were present in front of Malamocco and the Lido inlets before jetty construction: their orientation testifies to a net southward littoral drift. These bars were quickly eroded as a result of jetty construction and steady deepening of the bottom appeared in the central parts of Pellestrina and the Lido beaches.

Long-term profile changes (Fig. 8) show this behaviour (for location, see Fig. 5). The evolution of section 16 clearly reveals the process of bar destruction, while more gradual bottom erosion is seen in section 21. In profile 29, surveyed at the middle of Pellestrina beach, erosion actually increases at a slower rate, probably due to the presence of a steeper slope resulting from the construction of the sea-walls since the 18th century. However, the long-term trend of bottom evolution shows strongest erosion occurring between the 3- and 10-m depth contours in the central part of the Lido.

It is worthy of note that, while generally accretion or stability of the submerged beach has been noticed close to the jetties, clear-cut erosion has developed to the SE, close to the Malamocco inlet: this phenomenon may be partly ascribed to the limited extent of the jetty, which is the smallest of all.

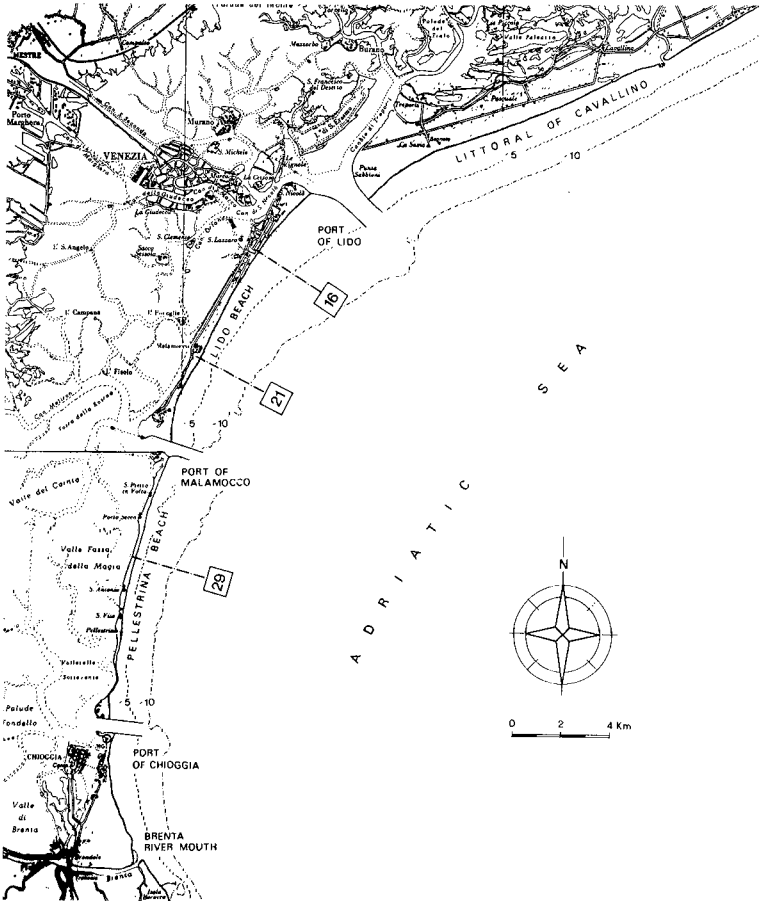

FIG. 5 : Venice coastline and profile location

FIG. 6 : Shoal orientation in front of Malamocco

FIG. 7 : Shoal orientation in front of Lido

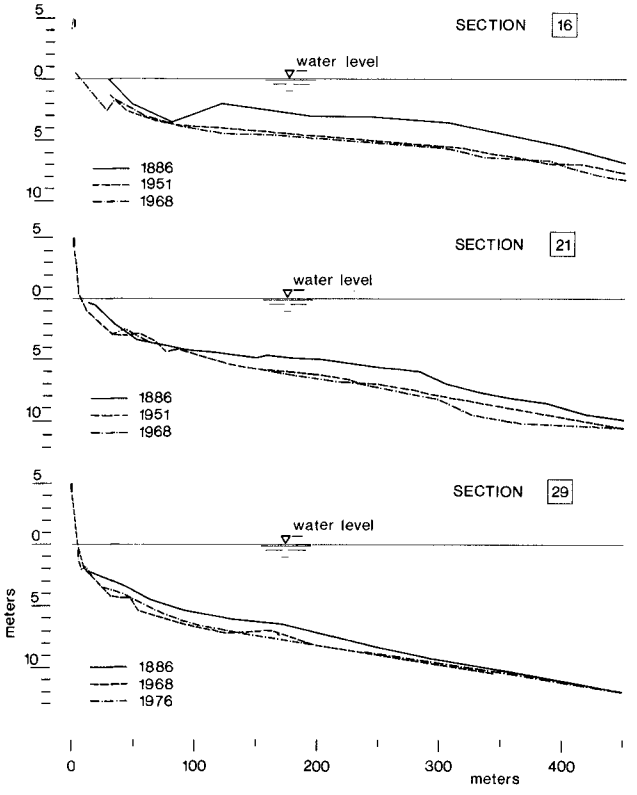

FIG. 8 : Beach profile changes in front of Lido and Pellestrina islands

Shoreline variations are shown in Fig. 9. Shoreline advance is evident close to the updrift jetty of the Lido inlet and reveals a southward net littoral drift. From the beginning of this century the average rate of shoreline advance (updrift side of jetty) was more than 10 m a year; the interrupted littoral drift has been evaluated between 350,000 and 400,000 cubic metres a year. Thus, this area represents a potential borrow site from which large quantities of sand could be dredged. Between the Malamocco and Lido inlets, net littoral drift was probably southward before jetty construction (see Figs. 3 and 6): shoreline variations show that sand tends to accumulate close to both updrift and downdrift jetties, while no variations are logically present in front of those stretches protected by sea-walls. Between Malamocco and Chioggia inlets, sand accumulates again close to both jetties, but this behaviour is less evident due to the great length of the sea-walls.

South of Chioggia inlet, both shoreline advance and orientation of the mouth of the Brenta river clearly show northward net littoral drift. The opposite net littoral drift direction existing at both extremities of Pellestrina leads to the hypothesis that an inversion of net longshore transport probably occurs along this shoreline. If this had also taken place in the past, due to the particular direction of the stretch of coast in question, the consequent sand transport deficit would explain the great "thinning" in time of this area compared with nearby stretches like the Lido.

SHORE DEFENCE PROJECT

In the last century, the Lido has become a very important tourist resort. In order both to arrest bottom erosion and to satisfy the need for improved tourist facilities, artificial beach nourishment represents the proper solution. As mentioned above, the area close to the updrift jetty of the Lido inlet represents a suitable borrow site, and a quantity of sand could be dredged from it sufficient to renourish the whole of the Lido. Moreover, the presence of the two jetties at the ends of the beach would assure good stability with respect to longshore transport: as a consequence, both in order to reduce the initial quantity of fill material and to increase its stability, a perched beach scheme was first considered.

Studies were conducted in a two-dimensional movable bed model to investigate the behaviour of different types of submerged structures (ref. [1]). Scale ratios for crushed

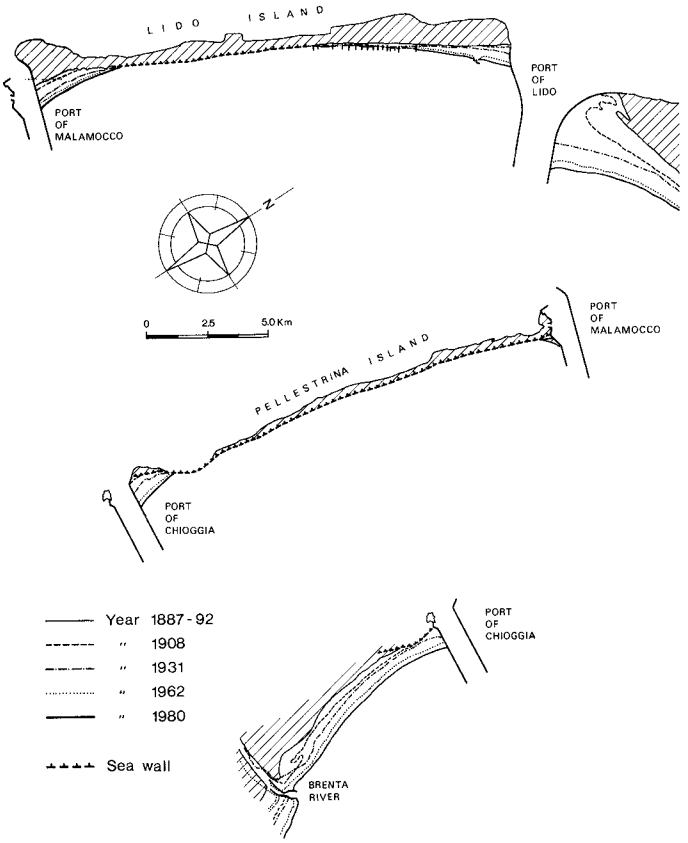

FIG. 9 : Shoreline changes (after Zunica [5])

bakelite as model material were first determined as reported by Noda [4] and applied as follows:

horizontal scale = 1:30
vertical scale = 1:20
median diameter of bakelite = 0.75 mm.

In order to calibrate the model, the initial nearshore slope was changed until an equilibrium profile similar to the natural one was experimentally achieved.

Different configurations of piled sandbags plus a concrete obstacle (see Fig. 10) were tested and summer and winter equilibrium beach profiles were reproduced in the laboratory. These experiments proved that piled sandbags were more stable and allowed less fill material to be transported offshore during winter wave attack. It was also found that the problem of scouring on the landward side of the obstacle could be successfully solved if one or two extra lines of bags were placed on the bottom (Fig. 10; configurations B and D). On a distorted scale, Fig. 11 shows the laboratory behaviour of the submerged structure with and without two extra lines of sandbags (Fig. 10; confs. C and D). The scouring phenomenon on the landward side of the obstacle clearly decreases if configuration D is applied.

Finally, the perched beach solution was tested in prototype conditions. Artificial nourishment stopped by a submerged obstacle was placed at Albarella, a partly eroding tourist beach close to Venice (Fig. 1).

One hundred cubic metres of fill material were placed along a 700-m segment of shoreline and a piled sandbag barrier was placed about 170 m offshore, at an average depth of 1.8 m. A groin of piled sandbags was also placed at the SE extremity to increase the stability of the fill material (Fig. 12). The size of typical filled bags was approx. 2.2 x 1.5 x 0.25 m. They were carefully placed on the bottom by a crane working from a pontoon; divers checked the crane's manoevers.

A comprehensive engineering analysis of the behaviour of the perched beach was carried out. Data evaluated include repetitive beach profiles, bathymetric surveys, visual observation of sea state, wave gage records, aerial photography, and refraction studies.

Unfortunately much of the fill material was removed, especially northwards, during the winter.

Analyses indicate that this behaviour was mainly due to the limited extent of the fill area: as a consequence, the

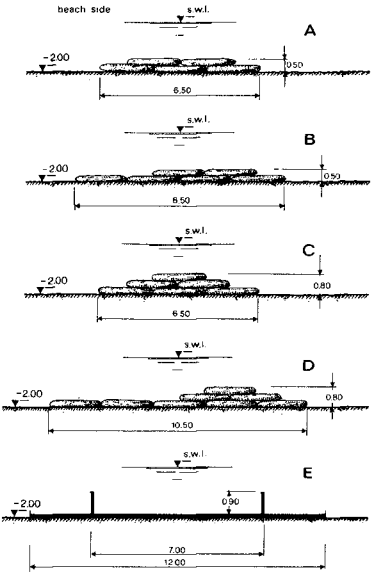

FIG. IO : Submerged structures tested in the model (prototype dimensions)

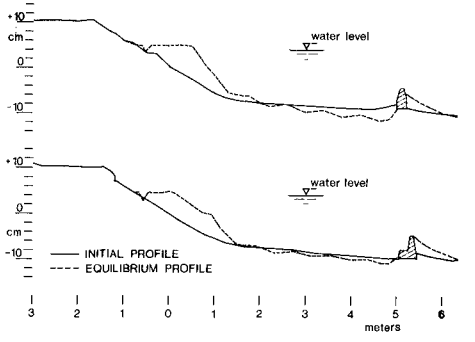

FIG. II : Comparison of equilibrium profiles (confs. C and D)

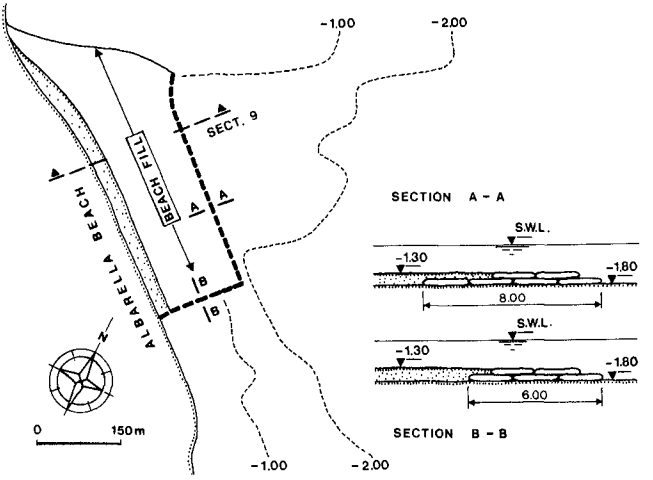

GENERAL MAP OF PROJECT LOCATION

SECTION 9

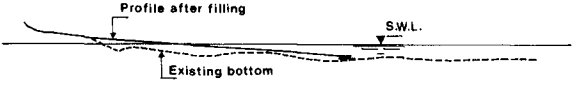

FIG. I2 : General features of perched beach construction

effect of both longshore littoral drift and lateral spreading of artificial sand prevailed, and the submerged obstacle did little to increase fill stability.

However, two years after construction of the artificial beach, the piled sandbags showed satisfactory behaviour: no sinking of the submerged structure was observed and no scouring occurred on the landward side, but sand tended to accumulate on the seaward side.

In any case, the above prototype experiment cannot be considered completely significant for the beaches of Venice: in fact, in front of the Lido, the fill area will be much larger and the long jetties bordering the shoreline will probably reduce the influence of longshore littoral drift. For these reasons, some doubts remain regarding the suitability of using submerged obstacles. Further three-dimensional laboratory studies will be conducted.

SUMMARY AND CONCLUSIONS

After jetty construction, the beaches situated between the three Venice tidal inlets have shown two main types of beach behaviour:

1) deposit of sand close to both updrift and downdrift jetties;
2) large-scale erosion of the bottom, with the rapid removal of offshore shoals.

Artificial beach nourishment is considered to be the proper solution both for the problems of bottom erosion and increased tourist facilities, and a perched beach scheme was tested both in the laboratory and in situ. Further research is still needed to evaluate the opportunity of complementary structures to increase the stability of the fill material.

If a submerged obstacle is to be used, a structure composed of piled sandbags has shown itself to be stable, both in the laboratory and in situ.

ACKNOWLEDGEMENTS

Part of the data presented in this paper was kindly supplied by the Genio Civile delle Opere Marittime of Venice and Albarella S.p.A. Permission to publish this information is appreciated. Acknowledgments is also due to Prof. Liberatore, University of Florence, for suggestions.

REFERENCES

|1| COLOMBO P., DE SANTIS M., MATTEOTTI G., MURACA A.: "Osservazioni sperimentali su alcuni tipi di difesa dei cordoni litoranei della Laguna". Università di Padova, May 1980.

|2| FILIASI J.:" Memorie storiche dei Veneti primi e secondi". Venezia 1794-1798.

|3| MIOZZI E.:"Venezia nei secoli". Casa editrice Libeccio, Venice, 1968.

|4| NODA E.K.: "Equilibrium beach profile scale model relationship". Tetra Tech Ref. no. TC-191, California, 1971.

|5| ZUNICA M.: "Le spiagge del Veneto", Tipografia Antoniana, Padova, 1971.

SEDIMENT BYPASSING AT MIXED ENERGY TIDAL INLETS

Duncan M. FitzGerald

ABSTRACT

Inlet sediment bypassing, through the previously recognized mechanisms of stable inlet processes and ebb-tidal delta breaching, has been documented at six mixed energy (tide-dominated) coasts around the world including the coasts of: central South Carolina, Virginia, southern New Jersey, New England, the East Friesian Islands, and the Copper River Delta in Alaska. Regardless of the mechanism, the end product of the bypassing process is the formation of a large bar complex that migrates onshore and attaches to the downdrift inlet shoreline. Thus sediment bypassing is a discontinuous process at mixed energy tidal inlets.

The morphology of the bar complexes is highly variable with widths ranging from 40-300m and lengths from 300 to over 1500m. Generally, the size of the bar complexes increases as inlet size increases and as the rate of longshore sediment transport increases. The frequency of bar welding events at mixed energy inlets varies from 3-7 years. The location where the bars attach to the downdrift beach and length of shoreline that is affected by the bar welding process is dependent on inlet size, orientation of the main ebb channel and wave versus tide dominance of the shoreline.

INTRODUCTION

Tidal inlets represent an interruption in the longshore sediment transport system. The manner in which inlets bypass sand on their ebb-tidal shoals controls the rate and location of sand nourishment to the downdrift barrier island. This paper will discuss how sediment moves past non-structured tidal inlets and the factors that influence this process along mixed energy (tide-dominated) depositional shorelines (Hayes, 1979; Nummedal and Fischer, 1978). Mixed energy coasts, as Hayes (1979) has described, are characterized by short stubby barrier islands, numerous tidal inlets with well developed ebb-tidal deltas, and a marsh and tidal creek system that separates the barriers from the mainland. The central South Carolina coast (Fig. 1) which has a 1.5m mean tidal range and 0.6m average wave height, is an example of such a coast. Other mixed energy (tide-dominated) shorelines that will be discussed in this paper are listed in Table 1. The wave and tidal energies of these coastlines are shown graphically in Figure 2.

[1]Department of Geology, Boston University, Boston, MA 02215

Figure 1. Mixed energy (tide-dominated) coast of central South Carolina coast showing Dewees Island in the foreground and Bull Island in the background.

Table 1. Mixed Energy (tide-dominated) Shorelines

1.	Central South Carolina Coast	FitzGerald et al, 1978; Nummedal et al, 1977; Hubbard et al, 1979
2.	Georgia Coast	Oertel, 1975; 1977; Oertel and Howard, 1972
3.	New Jersey and Virginia Coasts	Halsey, 1979; Rice et al, 1976; FitzGerald, 1981, 1982
4.	New England Coast	Hine, 1975; Hubbard, 1975; Magee and FitzGerald, 1980; FitzGerald and Fink, 1981
5.	Gulf of Alaska Coast	Hayes et al, 1976
6.	German Friesian Island Coast	Luck, 1976; Nummedal and Penland, 1981; FitzGerald et al, 1982
7.	Netherland Friesian Island Coast	Bruun and Gerritsen, 1959; Bruun, 1966

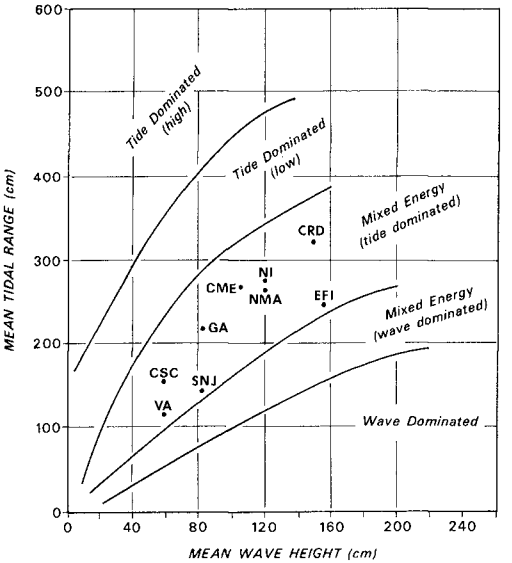

Figure 2. Coastal classification (after Hayes, 1979; Nummedal and Fischer, 1978). Mixed energy (tide-dominated) inlet shorelines where bar complexes weld to beach include: CRD - Copper River Delta, Alaska; EFI - East Friesian Islands, West Germany; NI - New Inlet, Massachusetts; NMA - northern Massachusetts, CME - central Maine; GA - Georgia (note that bar complexes do weld to these inlet shorelines as they do in other mixed energy coasts); CSC - central South Carolina; SNJ - southern New Jersey; VA - Virginia.

INLET SEDIMENT BYPASSING

Inlet sediment bypassing is defined as a process whereby sand is transported from the updrift side of the tidal inlet shoreline to the downdrift side. In a pioneering paper by Bruun and Gerritsen (1959) they described three methods by which sand moves past tidal inlets: 1) through wave induced sand transport along the periphery of the ebb delta (terminal lobe), 2) through the transport of sand in channels by tidal currents, and 3) by the migration of tidal channels and sand bars. They also showed that the type of bypassing process that occurs at an inlet could be determined using the following expression:

$$r = M_{mean}/Q_{max} \qquad (1)$$

where: (r) equals the ratio between the longshore sediment transport rate (M_{mean} in cubic yards per year) and the maximum discharge at the inlet under spring tidal conditions (Q_{max} in cubic yards per second). Inlets with high ratios (r>200-300) bypass sand by wave action along the terminal lobe and inlets with low values (r<10-20) bypass sand by the other two methods.

FitzGerald et al (1978) in a study of central South Carolina tidal inlet processes found that sediment bypassing occurs by the migration of tidal channels and/or sand bars (method #3). They presented two models which detailed the mechanics of sand bypassing at non-migrating inlets: bypassing by stable inlet processes and by ebb-tidal delta breaching (Fig. 3). The r values for these inlets range between 50 and 150 and thus it would seem that Bruun and Gerritsen's (1959) third method of inlet sediment bypassing may not be characteristic of tide-dominated inlets but rather a process that occurs at mixed energy inlets. In later papers by FitzGerald and Hayes (1980) and FitzGerald (1982) the models depicted in Figure 3 were shown to be applicable to other mixed energy tidal inlets (Table 1).

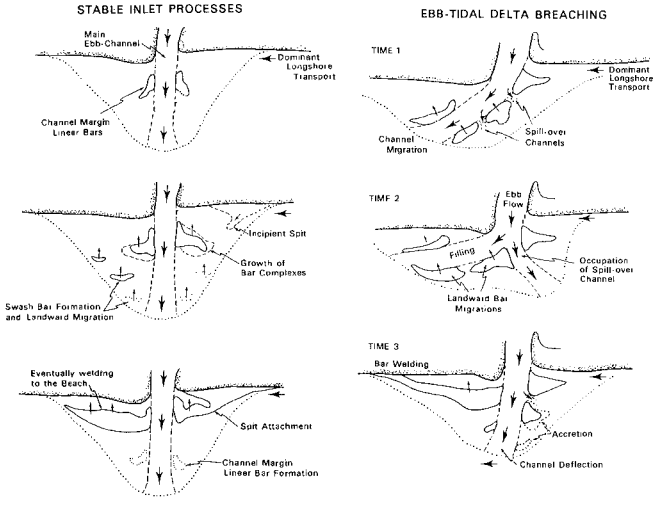

Figure 3. Models for inlet sediment bypassing at mixed energy (tide-dominated) coasts (from FitzGerald et al, 1978). Note that large bar complexes migrate onshore along the downdrift inlet shoreline in both cases.

Stable Inlet Processes

Stable inlets are defined as having a stable inlet throat (non-migrating) and a stable main ebb channel position through the ebb-tidal delta (Fig. 3). The pattern of sand circulation at mixed energy inlets has been described by a number of researchers including Oertel (1972), Hine (1975), FitzGerald et al (1976), Davis and Fox (1980) and Nummedal and Penland (1981).

The bypassing of sand at these inlets occurs through the formation, landward migration and attachment of large bar complexes to the downdrift inlet shoreline. The development of the bar complexes results from the stacking and coalescing of swash bars on the ebb tidal delta platform. Swash bars are wave built accumulations of sand (Hine, 1975) that form in the distal portion of the ebb delta from sand that is transported seaward in the main ebb channel. The swash bars move onshore due to the dominance of landward flow over the swash platform. As illustrated in Figure 4 waves breaking across the terminal lobe create bores of water that retard the ebb-tidal currents but that enhance the flood-tidal currents. Thus, there exists a net landward transport of sand on both sides of the main ebb channel. The net movement of sand onshore has also been attributed to increased wave suspension during the flood cycle than during the ebb cycle (Oertel, 1972; Hubbard et al, 1977; FitzGerald and Levin, 1981).

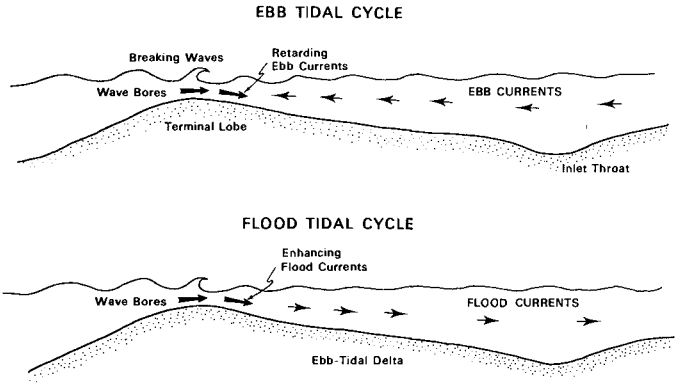

Figure 4. Wave swash model. Wave bores retard ebb tidal currents on the swash platform while they enhance the flood tidal currents. Net landward sediment transport results on both sides of the main ebb channel.

The stacking and coalescing of swash bars results from a decrease in the rate of their onshore migration. As swash bars migrate up the shoreface they gain a greater and greater intertidal exposure and thus wave swash, which causes their onshore movement, operates over an increasingly shorter period of the tidal cycle (Fig. 5). This developmental process is exemplified in the sequential sketches made of Price Inlet, South Carolina from aerial photographs taken between

1973 and 1977 (Fig 6). A photograph taken of the bar complex welding to the downdrift shoreline at Price Inlet in 1977 is shown in Figure 7.

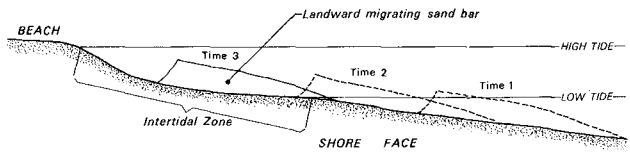

Figure 5. Model of bar migration up the shoreface. Note that the bar attains a greater intertidal exposure as it moves closer to shore. This will cause an increasingly shorter period of the tidal cycle in which wave swash operates. Thus onshore bar migration slows with time resulting in a stacking of swash bars.

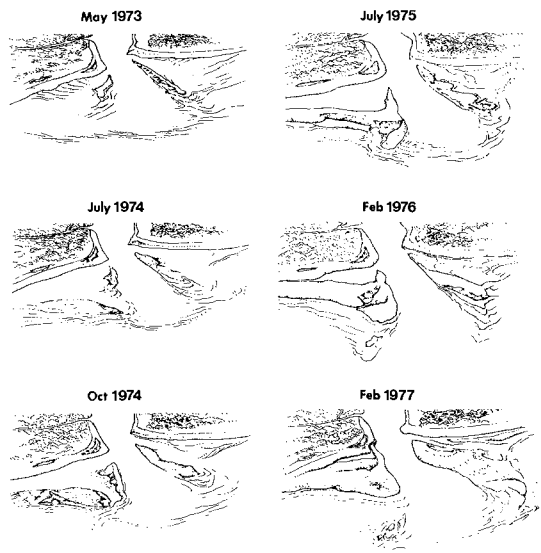

Figure 6. Sequential sketches of Price Inlet, South Carolina, drawn from aerial photographs. Note the bar complex development and its onshore migration.

Figure 7. Oblique aerial photograph of Price Inlet, South Carolina showing a bar welding event. Downdrift shoreline is in the foreground.

Ebb-Tidal Delta Breaching

Inlets that bypass sand through ebb-tidal delta breaching have stable inlet throat positions but their main ebb channels migrate (Fig. 3). The dominant direction of longshore sediment causes preferential deposition on the updrift side of the ebb-tidal delta. This results in a downdrift migration of the main ebb channel such that it will tend to parallel the downdrift inlet shoreline (Bruun and Gerritsen, 1959). This channel configuration produces a circuitous pathway for tidal exchange between the ocean and backbarrier area. Consequently, ebb flow in the main channel will breach a new channel through the ebb delta. This process may occur gradually during a six to twelve month period or it may happen catastropically during a single storm when tidal currents are stronger. A 1963 vertical aerial photograph of Breaches Inlet, South Carolina (Fig. 8) shows the breaching process in a stage of near completion. The old channel position is being abandoned.

Once the breaching process is completed, most of the water entering and leaving the inlet flows through the new channel. Because of the smaller volume of flow in the abandoned channel, scour by tidal currents decreases and the channel is gradually filled with sediment. The processes that cause this infilling include ebb and flood-tidal

currents, wave induced sediment transport on the swash platform and finally the landward migration of swash bars.

Ebb-tidal delta breaching results in the bypassing of a large proportion of the ebb delta sand. Some of this sand fills the abandoned channel while the rest forms a large bar complex similar to the bar complex described in the stable inlet processes section. These bars migrate onshore and attach to the landward beach. An example of a large bar complex that formed after delta breaching at Breaches Inlet, South Carolina is shown in Figure 9.

Figure 8. Vertical aerial photograph of Breaches Inlet, South Carolina showing that a new channel has recently been breached through the ebb-tidal delta. The abandoned channel is being filled with sediment at this time.

Figure 9. Oblique aerial photograph of the downdrift shoreline of Breaches Inlet, South Carolina. The large bar that has partially attached to the Isle of Palms formed after the ebb-tidal delta had been breached.

BAR MORPHOLOGY AND BEHAVIOR

Along mixed energy (tide-dominated) coastlines (Table 1) regardless of how sand bypasses the inlet, whether it be through stable inlet processes or ebb-tidal delta breaching, the end product is the formation of a large bar complex. These bars have been recognized and measured at many tidal inlets too numerous to mention. They are normally aligned parallel to shore and are cuspate in shape. Their lengths and widths are highly variable but an average range would be: length = 300-1500m and width = 40-300m. They are fronted by a .5 to 1.5m high slipface. Bar complexes associated with inlet sediment passing should not be confused with ridge and runnel systems that have been described by Hayes and Boothroyd (1969) and Davis and Fox (1972). They are normally much larger features and add a much greater volume of sand when they weld to the beach than do ridge and runnel systems.

As the bars migrate onshore they gain a larger and larger intertidal exposure. This is due to a combination of the bar's moving up the shore face and the continued welding of swash bars to its seaward side. The rate of landward migration of bar complexes is dependent on tidal range, wave energy and height of the bar with respect to mean low water. Bar migration rates have been measured at Price Inlet, South Carolina to be 110m/yr (FitzGerald, 1976) while in the East Friesian Islands, West Germany they migrate over 400m/yr (Nummedal and Penland, 1981). The greater migration rate in the Friesian Islands compared to that of Price Inlet is due to greater wave energy along the German coast (Fig. 2). Larger waves produce stronger wave swash and thus, a greater onshore sediment transport rate. Tidal range affects bar migration rates by controlling the period of time in which wave swash will be an active process.

When the bar welds to the intertidal beach its cuspate nature usually results in a small ponded water region being formed in front of the bar. The rate of migration of the bar up the beach is slow and highly dependent on the high tide level and wave energy. Migration is the greatest when spring tides coincide with large wave heights. The rate of migration also increases during moderate storms. During these events, although some of the lower bar sands may be eroded and move along shore or offshore, the large waves and storm surge cause increased wave swash and higher portions of the beach to be affected by this process. The final welding of the bar to the beach above mean high water occurs during a large spring tide with high wave activity. It could also happen during a storm.

OCCURRENCE OF BAR COMPLEXES

Remarkably similar shoreline morphologies found among mixed energy (tide-dominated) coasts throughout the world (Table 1), which presumeably is the result of similar ratios between wave and tidal energies (Fig. 2), would suggest that inlets along these shorelines should exhibit similar sand bypassing mechanisms. One indication that this is true is the documentation of landward migrating bar complexes along most of these coastlines. Examples from

five regions around the world will be used to corroborate this.

It has already been demonstrated that inlet sediment bypassing at central South Carolina inlets occurs through the attachment of large bar complexes to the downdrift beaches (Figs. 7 and 9) and therefore, further evidence will not be supplied. However, for a more detailed discussion of sand bypassing along this coast consult FitzGerald et al (1978) and Sexton and Hayes (1982).

On the New England coast, mixed energy barrier systems exist along parts of Cape Cod, Massachusetts, along a 30km stretch of shoreline between Boars Head, New Hampshire and Cape Ann, Massachusetts, and along sections of the central and southern coast of Maine. For the barriers north of Cape Ann northeast storms cause a net southerly longshore transport direction along the coast. Inlets of this region bypass sand by ebb-tidal delta breaching (Parker River Inlet, Fig. 10) and through stable inlet processes (Essex River Inlet, Fig. 11). In Figure 11A note that a bar has recently welded to the high beach and that another bar is developing on the swash platform. Nauset Inlet located on outer Cape Cod transfers sand to the south by both bypassing processes (Fig. 12).

Figure 10. Oblique aerial photograph of Parker River Inlet, Massachusetts. Note that the main ebb channel abuts the downdrift beach and that the bulge in the downdrift shoreline coincides with bar welding.

Along the central Maine coast most of the beaches occur in pockets between protective headlands or they are found at mouths of major river systems. The sand comprising the barriers in the latter setting are believed to have been derived from sediment that was discharging out of the rivers during deglaciation. The sand circulation pattern at one of these localities is illustrated in a diagram of the Popham Beach-Kennebec River system (Fig. 13). FitzGerald and Fink (1981) have described the exchange of sand between the beach and river as follows. Sand is transported seaward in the channel between Wood and Pond Islands by dominant ebb-tidal currents. It is deposited in the shallow water region between the

a

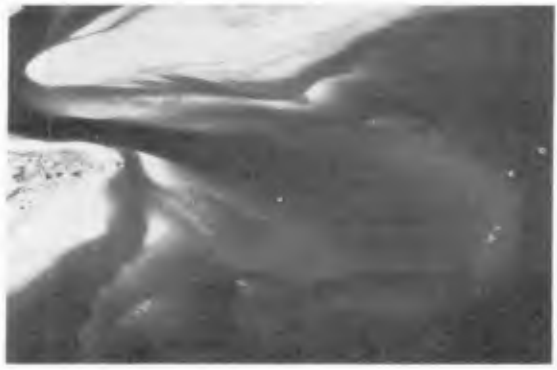

b

Figure 11a. 1978 Vertical aerial photograph of Essex River Inlet, Massachusetts.

11b. Oblique photograph showing bar development in 1980.

Figure 12. 1978 Oblique aerial photograph of Nauset Inlet, Massachusetts.

6 and 12 foot contours. Wave attack coming from a southeasterly direction drives the accumulating sand in an onshore direction toward Fox Island. Swash bars stack at this location, forming a large landward migrating bar complex over 1.5km in length. A bar complex welds to Popham Beach at a frequency of about once every five to seven years. An example of one of these bars is shown in Figure 14. As the bar migrates onshore it extends toward the Kennebec River and thus when it attaches to the shore a large portion of Popham Beach is affected. The sediment gyre is completed by flood and wave-generated currents that transport sand east along the beach and into the Kennebec River channel.

Along the southern New Jersey coast the transfer of sediment past inlets has been reported by Halsey et al (1981) and FitzGerald (1981; 1982). The dominant direction of longshore sediment transport on this coast is to the south. The updrift inlet shorelines are commonly formed by southerly accreting spits. The southerly downdrift inlet shorelines are sites of deposition. At Absecon Inlet and Great Egg Inlet on the New Jersey coast the dominant mechanism for inlet sediment bypassing is through ebb-tidal delta breaching. As a consequence of this process bars measuring between 500-1500m have moved onshore to the downdrift inlet shorelines of Atlantic City Beach and Ocean City Beach, respectively (FitzGerald, 1981; 1982). Two sequential U.S. Coast and Geodetic Survey bathymetric maps of Absecon Inlet illustrate the breaching process (Fig. 15). Note the deflection of the main ebb channel in 1864 and its straight seaward course in 1881. The sand that was bypassed during the delta breaching process moved onshore and had formed a large bar that had partially attached to the Atlantic City shoreline by 1881.

Inlet sediment bypassing on the Virginia coast has been discussed by Rice et al (1976) and FitzGerald (1982). Rice and others have described the historical migration of channels and the formation

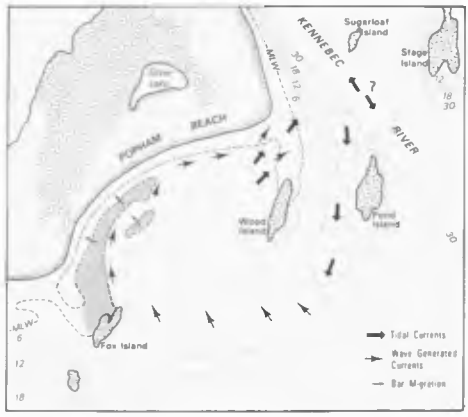

Figure 13. Sand circulation at Popham Beach, Maine (from FitzGerald and Fink, 1981). A sediment gyre is developed by: seaward transport by ebb-tidal currents, onshore transport by wave action, and northeast sand movement by flood-tidal and wave-generated currents. Bar complexes along this shore are over 1km long and weld to the beach every five to seven years.

Figure 14. Oblique aerial photograph of Popham Beach, Maine illustrating a bar welding event (photograph by Fink).

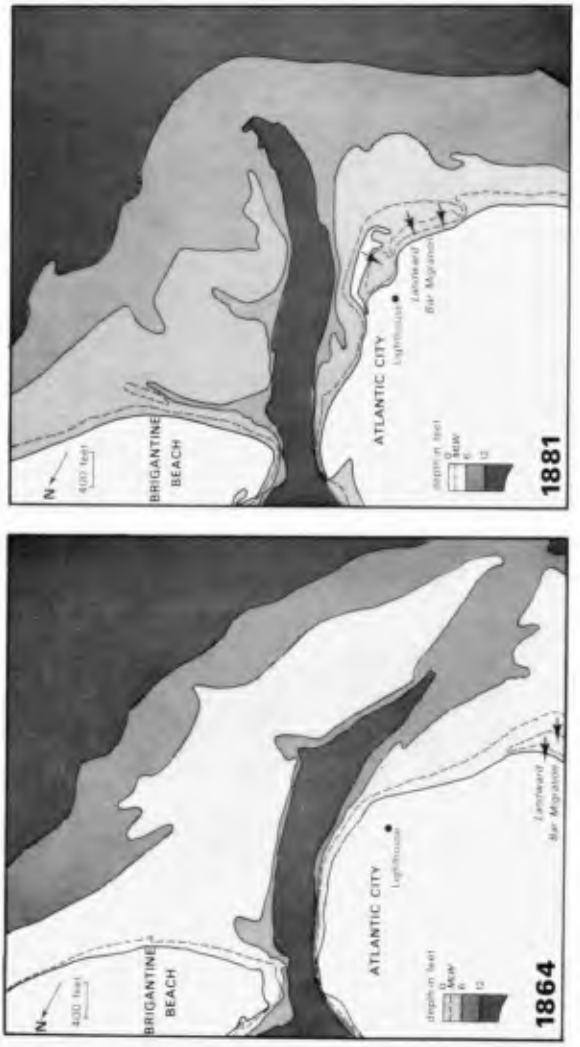

Figure 15. Bathymetric maps of Absecon Inlet, New Jersey redrawn from the 1864 U.S. Army Corps of Engineers survey and the 1881 U.S. Coast and Geodetic Survey coastal chart. The process of ebb-tidal breaching has been responsible for bar formation off northern Atlantic City Beach.

of bar complexes while FitzGerald has documented the landward migration and attachment of these bars to the downdrift inlet shoreline. Oblique aerial photographs (1971) of northern Parramore and Hog Islands illustrate different bar morphologies as they weld to the downdrift inlet shorelines of Wachapreaque and Quinby Inlets, respectively (Fig. 16).

Figure 16. Oblique aerial photographs of a. northern Parramore Island, Virginia and b. northern Hog Island, Virginia (photographs by Sue Halsey).

The East Friesian Islands are a chain of barriers located along the West German North Sea coast (Fig. 17). The pattern of inlet sediment bypassing along these islands has been studied by Nummedal and Penland (1981). Generally, sand is moving in an easterly direction along the coast due to the strong component of easterly wave energy flux. Sand bypassing occurs in the form of migrating swash bars (Nummedal and Penland, 1981). Tracks of bar movement at Norderneyer Seegat over a 31 year period of time are given in Figure 18. The tracks illustrate that bars migrate in a semi-circular pathway along the ebb delta periphery. As they move close to shore they tend to stack, forming large bar complexes which may

extend along the beach up to a 1km or more. Photographs of bar complexes migrating toward the updrift barrier shorelines of Langeoog and Spiekeroog are shown in Figure 19.

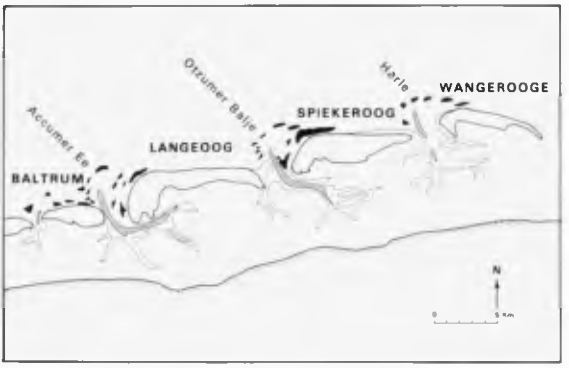

Figure 17. Map of the eastern two thirds of the Friesian Islands, West Germany. Note that the bulbous portion of these barriers coincides with the location where bars are attaching to the beach.

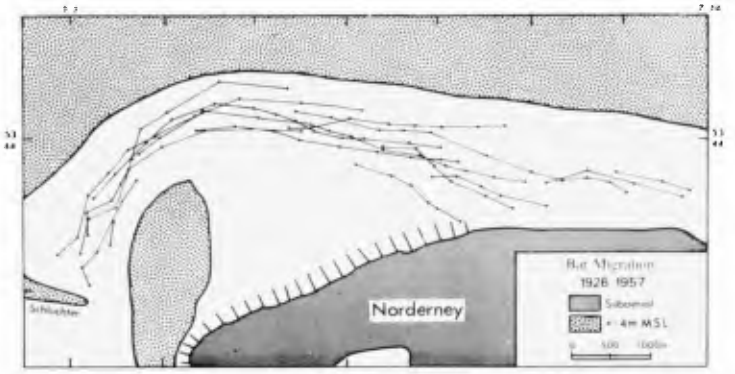

Figure 18. Map showing the pathway of easterly bar migration along the delta periphery. Each segment between adjacent dots indicates the amount of bar movement during a period of one year (from Homeier and Kramer, 1957).

a.

b.

Figure 19. Oblique aerial photographs of a. Langeoog and b. Speikeroog. These bars are over a kilometer in length.

The chain of barriers that fronts the Copper River Delta in the Gulf of Alaska is an unusual type of shoreline morphology to occur along a collision coast. Sediment discharged from the river has undoubtably been responsible for the existence of these islands. As Hayes et al (1976) have described, the barriers of this group have bulbous updrift ends (Fig. 20). They have attributed this barrier morphology to the uplift that occurred to this region in March 1964 and as a result of wave refraction around the ebb-tidal delta which produces a longshore transport reversal along the downdrift inlet shoreline. An oblique aerial of Egg Island, Alaska (Fig. 21) from Hayes et al (1976) reveals that progradation of the updrift end of the barrier may also be a product of the onshore migration of bar complexes.

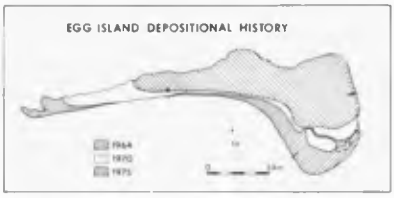

Figure 20. Depositional history of Egg Island, Alaska. The progradation of the eastern end of the island has, in part, resulted from the welding of bar complexes to the beach (from Hayes et al, 1976)

Figure 21. Oblique aerial photograph of Egg Island, Copper River Delta, Alaska. Note the bar (arrow) that is migrating onshore to the downdrift inlet shoreline. (from Hayes et al, 1976)

The Georgia coast fits well into the mixed energy (tide-dominated) coastline classification of Hayes (1979) and Nummedal and Fischer (1978) (Fig. 2). Although it has very similar coastal morphology, including inlet size and barrier island length, compared to that of the East Friesian Island coast, bar complex development does not appear to be an active process at the sounds along this coast. The reason for this is most likely related to the large tidal prisms (10^9-10^{10} m^3, Jarrett, 1976) and small wave energies (wave height = 80 cm, Thompson, 1977) of the Georgia coast. The

large ebb tidal deltas associated with these sounds extend 6-8km offshore where the depth is 5-6m. The low gradient slope (1:1200) created by the ebb deltas results in a gradual attenuation of the wave energy over the swash platform. Consequently, the formation of swash bars and their subsequent landward migration is not a large scale process on the ebb deltas. Oertel (1977) has shown that most of the transfer of sand from delta to the beach occurs very close to the inlet (200m) and affects a very small section of shoreline compared to the size of the inlet (width 1.5-6km) and the ebb tidal deltas. The presence of large landward migrating bar complexes along the East Friesian Island coast undoubtably is due to much greater wave energy of this shoreline compared to that of the Georgia coast.

LOCATION OF BAR WELDING

In the previous section it was shown that inlet sediment bypassing along mixed energy (tide-dominated) coasts occurs through the attachment of bar complexes to the downdrift inlet shoreline. From the time of bar's formation to the time that they weld to the beach can take anywhere from 3 to 7 years. The position where the bars come onshore has particularly important influence on the erosional-depositional patterns along the barrier island. A case has been made by FitzGerald et al (1982) that the location of bar attachment can significantly influence barrier island morphology. Notice in Figure 17 of the East Friesian Islands and Figure 20 of Egg Island that the bulbous portion of the barrier coincides with the site where bar complexes weld to the beach.

The location where the bar complexes move onshore and the length of barrier island shoreline that will be directly affected by the process is controlled by: 1) inlet size, 2) wave versus tide dominance, and 3) channel orientation (Fig. 22). There exists a fairly good correlation between inlet size and the size of the bar complexes that form on the ebb delta. Generally, larger inlets have larger bar complexes. The size of the bar complexes that are formed during the bypassing process is also strongly influenced by the net long shore sediment transport rate. The greater the rate of sand movement along the coast the greater is the volume of sand that must bypass the inlet. This would suggest that inlets that occur along coasts with high longshore sediment transport rates should have relatively large bar complexes. In support of this contention are the bar complexes that are found along the East Friesian Islands. Here the longshore transport rate is about 270,000m^3/yr and the bar complexes are over a kilometer in length (FitzGerald et al, 1982).

The dominance of wave action versus tidal currents at an inlet has been shown by Bruun and Gerritsen (1959) and Hubbard (1977) to control the manner in which sand bypasses the inlet. At wave dominated inlets sand is continuously transferred around the inlet by wave action on subtidal or intertidal bars (Fig. 22). At tide dominated inlets sand is bypassed in packets in the form of bar complexes welding to the beach.

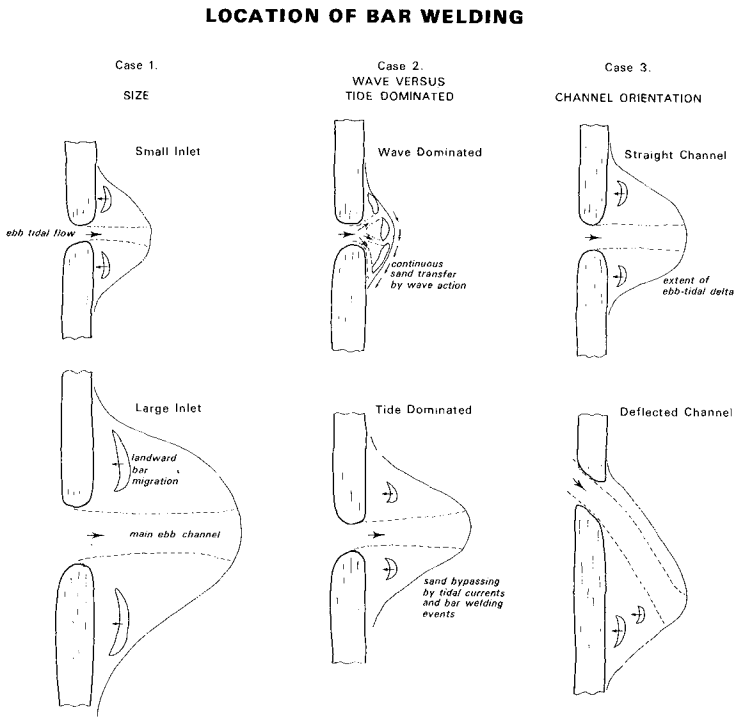

Figure 22. Model of the factors affecting the type of inlet sediment bypassing and where the bar complexes weld to the downdrift shoreline.

The orientation of the main ebb channel controls the distance away from the inlet that bar complexes attach to the shoreline (Fig. 22). If the channel has a straight seaward pathway out of the inlet then the bar complexes will attach to the beach relatively close to the inlet. A deflected channel position, downdrift deflection is most common, will result in bar complexes welding to the beach some distance away from the inlet. The deflected position of the main channel can be caused by preferential addition of sand to one side of the ebb-tidal delta or it may result from backbarrier tidal creeks approaching the inlet mouth at an angle. Prior to being jettied, Murrells Inlet on the South Carolina coast had a deflected main ebb channel due to both of these factors (Fig. 23). Parker River Inlet in Massachusetts (Fig. 10) is another example of an inlet that has a deflected main ebb channel. At this inlet

the dominant southerly longshore transport direction combined with northerly approach of the Parker River produce a main ebb channel that hugs the downdrift barrier. Along the downdrift barrier there is a distinct bulge in the shoreline where bar complexes weld to the beach.

Figure 23. Oblique aerial photograph of Murrels Inlet, South Carolina. Inlet sediment bypassing at this inlet occurred through ebb-tidal delta breaching prior to being jettied.

CONCLUSIONS

1. Two mechanisms, referred to as stable inlet processes and ebb-tidal delta breaching, account for most of the sand bypassing that occurs at mixed energy (tide-dominated) tidal inlets. These processes result in the formation of large bar complexes that migrate landward and attach to the beach. This means that along mixed energy (tide-dominated) coasts sand is not continuously transferred past inlets but rather it is added to the downdrift shoreline in discrete packets. This mode of inlet sediment bypassing comprises a separate class in Bruun and Gerritsen's (1959) scheme of sand bypassing with "r" values between their wave-dominate (r>200-300) and tide-dominated (r<20-30) classes.

2. Bar complexes are much larger features than the ridge and runnel systems of a constructional beach. Their morphology is highly variable with widths ranging from 40 to 300m and lengths from 300 to over 1500m. The size of the bar complexes appears to increase with increasing inlet size and volume of sand that is bypassing the inlet. An exception to this trend is the Georgia coast.

3. The location where the bar complexes move onshore and the length of coastline that experiences progradation directly from this bar welding process is dependent on: 1) inlet size, 2) wave versus tide dominance of the inlet and 3) orientation of the main ebb channel. The last factor is controlled by the configuration of the backbarrier tidal channels, dominant longshore sediment transport rate and direction, and bank stability of the main ebb channel.

ACKNOWLEDGEMENTS

The author's understanding of tidal inlet processes has benefitted greatly from discussions with Miles Hayes, Dag Nummedal, Dennis Hubbard and Shea Penland as well as from the pioneering work of Dr. Per Bruun. Drafting in this paper was done by Eliza McClennan, University Cartographer, Boston University Cartographic Services Laboratory. Some of the photographs and diagrams were supplied by Miles Hayes, Dag Nummedal, Sue Halsey and Ken Fink.

REFERENCES

Bruun, P., 1966, Tidal Inlets and Littoral Drift: v. 2, Universitelsforlaget, Oslo, 193 p.

Bruun, P., and Gerritsen, F., 1959, Natural bypassing of sand at coastal inlets: Jour. of the Waterways and Harbors Div., Amer. Assoc. of Civ. Eng., v. 85, p. 75-107.

Davis, R.A., and Fox, W.T.,1972, Coastal processes and nearshore sand bars: Jour. of Sed. Pet., v. 42, p. 401-412.

Davis, R.A., and Fox, W.T., 1980, Interaction between wave and tide generated processes at the mouth of a mesotidal estuary: Matanzas River, Florida: Marine Geol., v. 40. p. 49-68.

FitzGerald, D.M., 1976, Ebb-tidal delta of Price Inlet, South Carolina: geomorphology, physical processes and associated inlet shoreline changes: In: Terrigenous Clastic Depositional Environments (Hayes and Kana, eds.), Tech. Rpt. No II-CRD, Geology Dept., Univ. of South Carolina, Columbia, S.C., p. 158-171.

FitzGerald, 1981, Patterns of shoreline changes along Atlantic City Beach caused by Absecon Inlet processes: Tech. Rpt. No. 6, Coastal Environmental Research Group, Dept. of Geology, Boston University, Boston, MA. 60 p.

FitzGerald, D.M., 1982, Depositional processes along Ocean City Beach, New Jersey: Tech. Rpt. No. 7, Coastal Environmental Research Group, Dept of Geology, Boston University, Boston, MA, 53 p.

FitzGerald, D.M., and Fink, Jr., L.K., 1981, Sedimentation processes along Popham Beach, ME: 1981 SEPM Northeast Fieldtrip Guidebook, ed. by B. Timson (in press), p. 27.

FitzGerald, D.M., and Hayes, M.O., 1980, Tidal inlet effects on Barrier Island management: Proc. Coastal Zone 1980, American Soc. of Civil Engineers, p. 2355-2379.

_____, Hubbard, D.K., and Nummedal, D., 1978, Shoreline changes associated with tidal inlets along the South Carolina coast: Proc. Coastal Zone 1978, American Society of Civil Engineers, p. 1973-1994.

_____., and Levin, D., 1981, Hydraulics, morphology and sediment transport patterns at Pamet River Inlet: Truro, Massachusetts: Northeast Geol., v. 3, p. 216-224.

_____, Nummedal, D., and Kana, T., 1976, Sand circulation patterns at Price Inlet, South Carolina: Amer. Soc. of Civil Eng., Proc. 15th Coastal Eng. Conf., p. 1868-1880.

_____, Penland, S., and Nummedal, 1982, Tidal inlet control of East Friesian Island morphology: International Assoc. of Sedimentologist Conf., Abs. with Prog., Hamilton, Ontario, p. 163.

Halsey, S.D., 1979, Nexus: New model of Barrier Island development: In: Leatherman, S.P., ed., Barrier Islands: From the Gulf of St. Lawrence to the Gulf of Mexico: New York, Academic Press, p. 185-210.

Halsey, S.D., Ashley, G.M., and Farrell, S.C., 1981, Post-beach nourishment sediment dispersal patterns: Northern Long Beach Island, NS: Northeast section of Geol. Soc. of Amer., Abs. with Programs. v. 13, p. 136.

Hayes, M.O., 1979, Barrier island morphology as a function of tidal and wave regime: In Leatherman, S.P., ed., Barrier Islands: From the Gulf of St. Lawrence to the Gulf of Mexico: New York, Academic Press, p. 1-28.

Hayes, M.O., and Boothroyd, J.C., 1969, Storms as modifying agents in the coastal environment, In: Coastal Environments: NE Massachusetts, Hayes, M.O., ed., p. 290-315.

Hayes, M.O., Ruby, C.H., Stephen, M.F., and Wilson, S.J., 1976, Geomorphology of the Southern Coast of Alaska, Amer. Soc. of Civil Eng., Proc. 15th Coastal Eng. Conf., p. 1992-2008.

Hine., A.C., 1975, Bedform distribution and migration patterns on tidal deltas in Chatham Harbor Estuary, Cape Cod, Massachusetts: In Cronin, L.E., e., Estuarine Research: Academic Press, New York, v. 2, p. 235-252.

Homeier, H., and Kramer, J., 1957, Verlagerung der Platen im Riffbogen von Norderney und ihre Anlandung on den Strand, Uber, Forschungstelle Norderney, vol. 8, p. 37-60.

Hubbard, D.K., 1975, Morphology and Hydrodynamics of the Merrimack River Ebb-Tidal Delta, L.E., ed, Proc. 2nd International Estuarine Res. Fed. Conf., Myrtle Beach, SC, p. 253-266.

Hubbard, D.K., Barwis, J.H., and Nummedal, D., 1977, Sediment transport in four South Carolina inlets: Proc. Coastal Sediments 1977, American Society of Civil Engineers, p. 582-601.

Hubbard, D.K., Oertel, C., and Nummedal, D., 1979, Development of tidal inlet sand bodies: Jour. of Sed. Petrol., v. 49, no 4, p. 1073-1092.

Jarrett, J.T., 1976, Tidal prism-inlet area relationships. General Investigations of Tidal Inlets. Rep. no. 3., Coastal Eng. Research Center, Ft. Belvoir, VA, 32 pp.

Luck, C., 1976, Inlet changes of the East Friesian Islands, Amer. Soc., of Civil Eng., Proc. 15th Coastal Eng. Conf., p. 1938-1957.

Magee. A.D., and FitzGerald. D.M., 1980, Investigation of shoaling problems at Westport River Inlet and sedimentation processes at Horseneck and East Horseneck Beaches, Tech. Rpt. No. 3, Coastal Environmental Research Croup, Dept. of Geology, Boston University, Boston, MA. 118 p.

Nummedal, D., and Fischer, I.A., 1978, Process-response models for depositional shorelines: the German and the Georgia Bights. Proc. 16th Coastal Eng. Conf., Amer. Soc. of Civil Eng., p. 1215-1231.

Nummedal, Oertel, G.F., Hubbard, D.K., and Hine A.C., III, 1977, Tidal inlet variability--- Cape Hatteras to Cape Canaveral: Coastal Sediments 1977, American Society of Civil Engineers, p. 543-562.

Nummedal, D., and Penland, S., 1981, Sediment dispersal in Norderney Seegat, West Germany, Proc. of National Meeting on Holocene Marine Sedimentation in the North Sea Basin, International Assoc. of Sedimentologists Spec. Pub. 5, Texel, Netherlands, p. 187-210.

Oertel, C.F., 1972, Sediment transport of estuary entrance shoals and the formation of swash platforms: Jour. of Sed. Petrol., v. 42, p. 857-863.

Oertel, 1975, Ebb tidal deltas of Georgia estuaries: In Cronin, L.E., ed., Estuarine Research: New York, Academic Press, v. II, p. 587.

Oertel, C.F., 1977, Geormorphic cycles in ebb deltas and related patterns of shore erosion and accretion: Jour. of Sed. Petrol., v. 47, No. 3, p. 1121-1131.

Oertel, C.F., and Howard, J.D., 1972, Water Circulation and Sedimentation at Entrances on the Georgia Coast: IN: Swift, D.J.P., Duane, D.B., and Pilkey, D.H., eds, Shelf Sediment Transport: Process and Pattern, p. 411-428.

Rice, T., Niedoroda, A., and Pratt, A., 1976, Coastal processes and geology, Virginia barrier islands: in Virginia Coast Reserve Study: Ecosystem Description, The Nature Conservancy, Arlington, VA, p. 109-382.

Sexton, W.J., and Hayes, M.D., 1982, Natural Bar-Bypassing of sand at a tidal inlet, Amer. Soc. of Civil Eng., Proc. 18th Coastal Eng. Conf. (in press).

Thompson, E.F., 1977, Wave climate at selected locations along U.S. coasts: Washington, D.C., U.S. Army, Coastal Engineering Research Center, Tech. Rpt. No. 77-1, 364 p.

HARBOUR SEDIMENTATION - COMPARISON WITH MODEL

B.D. Pratte, D.H. Willis and J. Ploeg[1]

ABSTRACT

A mobile-bed model study of Pointe Sapin Harbour, in the Gulf of St. Lawrence, resulted in construction of a detached breakwater and sand trap to prevent harbour entrance infilling. The sand trap is filling in at a faster rate than predicted from the model. This is partly due to incomplete modelling of the wave climate; partly to incorrect modelling of distribution of alongshore sand transport; and partly to a complex sand supply at the site. Nevertheless, the sand trap solution is performing well.

POINTE SAPIN HARBOUR

Pointe Sapin Harbour is a small fishing harbour on the Gulf of St. Lawrence, see Figs. 1 and 2. Records show that the first wharf was built there in 1913 on a soft sandstone coast. The situation quickly changed however, for aerial photographs taken between the World Wars clearly show a sandy coast, and what is worse, sedimentation in the harbour berths. Then began the familiar extensions of the structures seaward in an attempt to block the transport of sand into the harbour.

By the mid-1970s it was time for another extension. During northeast storms, two or three times a year, the harbour entrance would completely fill in to above Low Water within 12 hours, see Fig. 3. The danger in this is obvious: vessels were caught in open water by the storm, with no refuge; and they were trapped in the harbour after the storm, unable to see to their traps and nets until the entrance could be dredged.

THE CAUSE

The cause appeared to be alongshore transport of beach sand by waves. As shown in Fig. 1, Pointe Sapin Harbour is sheltered by Prince Edward Island from waves from the southeast. To the northeast however, the available fetch is 225 km and from this direction come storms with significant wave height, H_s, of 3 m and peak period T_p, of 8 s. The result is an overwhelmingly predominant northeast-to-southwest transport of beach sand.

How much transport is a matter for debate. This is due to all the usual reasons, plus:

[1]Hydraulics Laboratory, Division of Mechanical Engineering, National Research Council Canada, Ottawa, Ontario K1A 0R6, Canada.

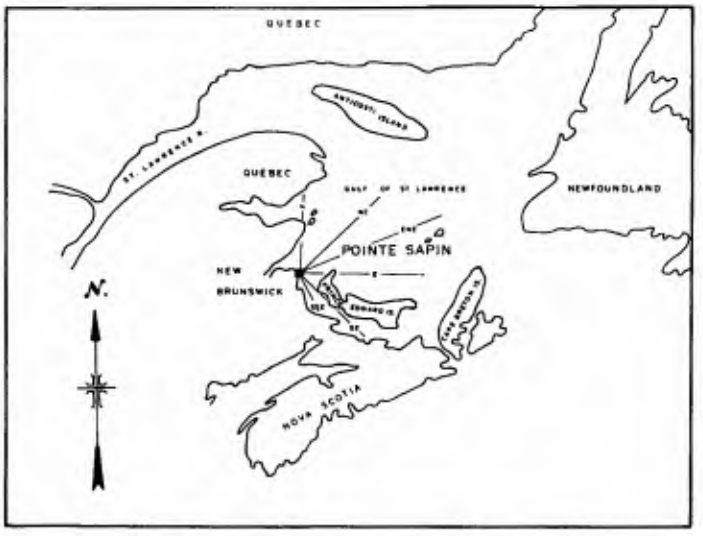

Fig. 1 Location of Pointe Sapin

Fig. 2 Harbour before sand trap construction

1. Sand supply is limited, there being a maximum of only a metre of sand overlying sandstone and till.

2. The profile is very shallow. The surf zone under the northeast storm waves can be as much as 1 km wide.

Estimates of the net northeast-to-southwest transport ranged from 120,000 m^3/yr (Pratte and Willis 1979) to 205,000 m^3/yr (Hydrotechnology Ltd. 1980). The only two fairly firm facts are: that 10,000 to 30,000 m^3 needed to be dredged annually from the harbour entrance; and that it took approximately 12 hours to fill in the entrance during storms.

THE MODEL

A physical model of Pointe Sapin Harbour was built in the Hydraulics Laboratory of the National Research Council Canada to seek engineering solutions to the infilling problem, see Fig. 4. The horizontal scale was 1:100 to fit into the available wave basin. Flume tests indicated a vertical scale of 1:30 (i.e. a distortion of 3:33) and a grain size of 260 μm would correctly model the beach slope under typical northeast storm conditions, wave height 3 m and period 8 s. An almost uniform silica sand of this size was used in a mobile bed 50 mm (1.5 m full scale) thick in the model.

Initial tests reproduced the observed infilling of the harbour entrance by running 90 minutes of the northeast storm waves. Assuming this corresponded to 12 hours full scale, an approximate sedimentological time scale of 8 was determined. However, since bedload transport

Fig. 3 Sand deposition in harbour entrance

Fig. 4 Sand deposition in model harbour entrance

on the model was being used to simulate suspended load transport in real life, it was recognized that the actual sedimentological time scale would be a function of the wave conditions and location in the model.

THE SOLUTION

The most obvious solution would have been to simply live with the existing entrance infilling and to make available a dredge on a permanent basis. This was not acceptable since Public Works' dredges were required to be mobile and serve many harbours. A second obvious solution, but one which we were determined to avoid, was buying a little more time for the harbour by extending into (temporarily) deeper water. Some such schemes were tested on the model of course, but so were more radical schemes attempting to achieve natural sand bypassing.

In the end, we proposed the solution shown in Fig. 5. This consists of a sand trap updrift of the entrance, protected by a detached breakwater. The breakwater not only provided calmer water to encourage settlement of the sand, but also created a sheltered area from which a dredger could clean out the trap and pump the sand across the entrance to the downdrift side of the harbour.

THE FULL-SIZE MODEL

At this point (1979) something rather unusual happened: the full-sized harbour was actually modified exactly as proposed by the model

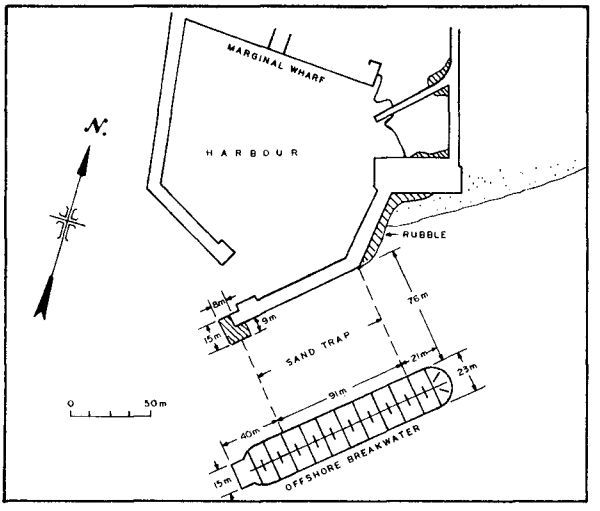

Fig. 5 Sand trap as built

study. This provided a rare opportunity to check the performance of a mobile-bed model.

Beginning in the spring of 1980 just before completion of the offshore breakwater, the National Research Council commissioned a time series of aerial photographs to be taken of the harbour. Five complete sets were obtained: May, August and November 1980, and May and November 1981. The similarities between model and nature are quite striking, as shown in Figs. 6 and 7.

However, the model considerably underestimated the rate at which the sand trap filled.

COMPARISON OF TRANSPORTS

To a certain extent, this underestimate could be explained by "model effect". For example, only the most severe annual storms were simulated on the model, whereas the real harbour was also exposed to every-day waves which contributed sand to the trap. We did attempt to compensate for this in analysing the model results, but perhaps that compensation was not enough.

Another model effect has already been mentioned: the representation of full-size suspended load by model bed load transport. As discussed above, our calculated sedimentological time scale of 8 could at

Fig. 6 Build-up in model sand trap

Fig. 7 Build-up in full-size sand trap

best be correct only within a narrow range of water depths close to the entrance. Expressed another way, the distribution across the beach profile of alongshore transport was incorrectly modelled.

In 1980, the opportunity presented itself to examine these two effects in greater detail. The Small Craft Harbours Directorate of Fisheries and Oceans Canada commissioned a 10-year hourly hindcast of breaking waves for several New Brunswick harbours (Hydrotechnology Ltd., 1980), one of which was Pointe Sapin. Palmer (1980) used this data to produce alongshore current statistics, including distribution, for Pointe Sapin from the method described in Willis (1978). These were converted to alongshore transport statistics, still including offshore distribution, following Willis (1979).

Fig. 8 presents the average annual transport rate distributions for the ten years of data. The approximate position of the breakwater is also shown. What is clear is that the major portion of the transport, 60%, is contained between the breakwater and the shore, in the sand trap in other words. By contrast, considerable transport had been noticed seaward of the breakwater in the model. Clearly, the use of only storm waves as well as the incorrect modelling of transport distribution were factors in the model underestimating trapping rates.

A third factor has come to light just this year, 1982: the complex distribution of sand sources at Pointe Sapin. The Canadian Coastal Sediment Study undertook two field surveys of the area as part of the process of choosing a site for a comprehensive investigation of

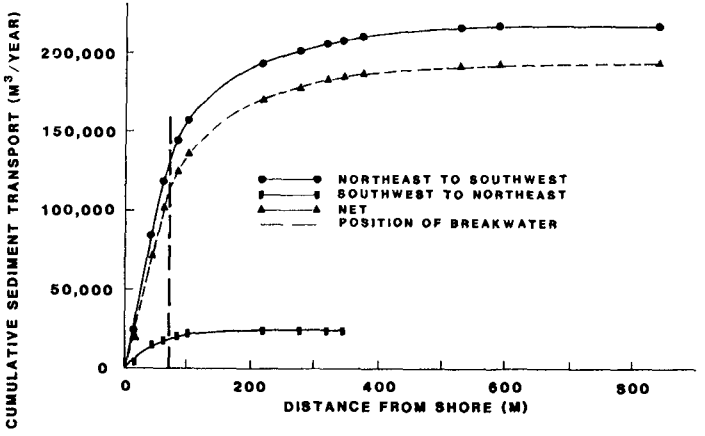

Fig. 8 Cumulative Sediment Transport

nearshore sand transport. These surveys found a predominantly soft sandstone nearshore seabed, with a thin sand layer only within 100 m from shore, see Forbes (1982). Forbes also found a second sand accumulation built up against a sandstone scarp farther offshore but still in relatively shallow water. It seems likely that some of this offshore material finds its way onshore and into the trap during storms.

CONCLUSIONS

Whatever the cause, the result remains that more sand than expected is accumulating in the Pointe Sapin trap, approximately 110,000 m^3/yr as compared to the previous dredging requirement of up to 30,000 m^3/yr. More dredging is required, and plans for a permanent dredging plant are being discussed. Nevertheless the main aim of the scheme has been attained, in that since the construction of the breakwater the harbour has remained open.

Meanwhile, the Canadian Coastal Sediment Study has chosen the Pointe Sapin site for its study of nearshore sand transport in the coming year. Pointe Sapin promises to be the most studied beach in Canada.

REFERENCES

Forbes, D.L. (1982): Sources of Sand Contributing to Harbour Shoaling at Pointe Sapin, New Brunswick. Proceedings Workshop on Atlantic Coastal Erosion and Sedimentation, Associate Committee for Research on Shoreline Erosion and Sedimentation, National Research Council Canada, November 1982, in press.

Hydrotechnology Ltd. (1980): The Design and Maintenance of Harbours in Northeast New Brunswick with Respect to the Alongshore Transport of Beach Sand. Ottawa, Ontario, March 1980.

Palmer, M.A. (1980): Sediment Transport Distribution at Pointe Sapin Harbour. National Research Council Canada, Hydraulics Laboratory Memorandum HY-206, September 1980.

Pratte, B.D. and Willis, D.H. (1979): Pointe Sapin Model Study. National Research Council Canada, Hydraulics Laboratory Technical Report LTR-HY-70, May 1979.

Willis, D.H. (1978): An Alongshore Current Beach Evolution Model. National Research Council Canada, Hydraulics Laboratory Memorandum HY-92, March 1978.

Willis, D.H. (1979): Sediment Load Under Waves and Currents. National Research Council Canada, Division of Mechanical Engineering, DME/NAE Quarterly Bulletin No. 1979(3), October 1979.

MODELING COASTAL CURRENTS AND SEDIMENT TRANSPORT

by

Y. Peter Sheng[1]
and
H. Lee Butler[2]

ABSTRACT

An efficient three-dimensional model of coastal currents and sediment transport has been developed. Simulations of tide- and wind-driven currents and sediment transport in the Mississippi Sound are presented. Results of a laboratory study on settling, resuspension, and deposition of sediment are briefly described. Wave effect on sediment resuspension is also addressed.

INTRODUCTION

Sediment transport in shallow coastal waters is an important coastal engineering problem. Many coastal waters, e.g. the Mississippi Sound, are receiving greater environmental concern due to increasing utilization of their resources, including dredging of shipping channels and disposal of dredged materials. To develop a regional plan of dredged material disposal alternatives, one should not only be concerned with the short-term fate of dredged material at specific sites, but more importantly the subsequent resuspension, transport, and deposition of sediment due to combined current and wave actions, particularly during the sporadic high-energy events.

The various physical processes that can affect the distribution of sediment in a coastal environment are shown in Figure 1. Definitive quantitative understanding of the various processes is crucial to the success of any large-scale model. Recent improvements in numerical estimation of currents and waves and the increased availability of field data and satellite imageries has made it feasible to carry out meaningful large-scale simulation studies of sediment transport events (e.g. Sheng and Lick, 1979; Sheng, 1980). In this paper, we highlight a systematic study of the sediment transport in the shallow coastal waters of the Mississippi Sound and adjacent continental shelf waters in the Gulf of Mexico.

---

[1]Aeronautical Research Associates of Princeton, Inc., P.O. Box 2229, Princeton, NJ 08540 U.S.A.
[2]Wave Dynamics Division, Hydraulics Laboratory, U.S. Army Engineer Waterways Experiment Station, P.O. Box 631, Vicksburg, MS 39180 U.S.A.

In the following, a three-dimensional hydrodynamic model will be presented first, followed by a realistic simulation of tide- and wind-driven currents in the Mississippi Sound and adjacent shelf waters. Transport, resuspension, and deposition of cohesive sediments are then discussed, followed by a discussion on the bottom boundary layer and wave effect.

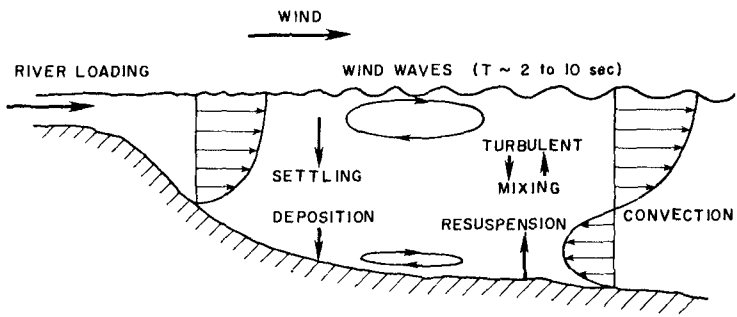

Figure 1. Schematics of Dominant Mechanisms Affecting Sediment Distribution in Shallow Coastal Waters.

A THREE-DIMENSIONAL NUMERICAL MODEL OF COASTAL CURRENTS

In order to study the dynamic response of coastal waters to tides, winds, and meteorological forcing, a three-dimensional, free-surface, time-dependent model is often desired. In addition, stratification and complex topography have to be properly resolved. For relatively long-term application, computational efficiency of the model is extremely important. Traditional three-dimensional, free-surface models (e.g., Leendertse and Liu, 1975) require an exceedingly small time step (associated with the propagation of gravity wave over the distance of a horizontal grid spacing), and hence require extraneous computational costs.

Special features of the present model include (1) a "mode-splitting" procedure which allows efficient computation of the vertical flow structures (internal mode), (2) an efficient ADI scheme for the computation of the vertically-integrated variables (external mode) (3) an implicit scheme for the vertical diffusion terms, (4) a vertically and horizontally stretched coordinate system, and (5) a turbulence parameterization which requires relatively little tuning.

Governing Equations and Boundary Conditions

The basic equations describing the large-scale motion in a large body of water consist of a continuity equation, momentum equations, conservation equations of heat and salinity, and an equation of state. For simplicity here, the last three equations have been combined into an equation for the density. Inherent assumptions are: (1) pressure

distribution is hydrostatic in the vertical direction, (2) Boussinesq approximation is valid, and (3) non-constant eddy viscosities and diffusivities are used to describe the turbulence. The resulting equations are as follows:

$$\frac{\partial u}{\partial x} + \frac{\partial v}{\partial y} + \frac{\partial w}{\partial z} = 0 \tag{1}$$

$$\frac{\partial u}{\partial t} = -\left(\frac{\partial u^2}{\partial x} + \frac{\partial uv}{\partial y} + \frac{\partial uw}{\partial z}\right) + fv - \frac{1}{\rho_o}\frac{\partial p}{\partial x} + \frac{\partial}{\partial z}\left(A_v \frac{\partial u}{\partial z}\right) + \nabla_H \cdot (A_H \nabla_H u) \tag{2}$$

$$\frac{\partial v}{\partial t} = -\left(\frac{\partial uv}{\partial x} + \frac{\partial v^2}{\partial y} + \frac{\partial vw}{\partial z}\right) - fu - \frac{1}{\rho_o}\frac{\partial p}{\partial y} + \frac{\partial}{\partial z}\left(A_v \frac{\partial v}{\partial z}\right) + \nabla_H \cdot (A_H \nabla_H v) \tag{3}$$

$$\frac{\partial p}{\partial z} = -\rho g \tag{4}$$

$$\frac{\partial \rho}{\partial t} = -\frac{\partial u\rho}{\partial x} + \frac{\partial v\rho}{\partial y} + \frac{\partial w\rho}{\partial z} + \frac{\partial}{\partial z}\left(K_v \frac{\partial \rho}{\partial z}\right) + \nabla_H \cdot (K_H \nabla_H \rho) \tag{5}$$

where x and y are the horizontal coordinates; z is the vertical coordinate pointing vertically upward to form a right-handed coordinate system with x and y; u, v, and w are the three-dimensional velocities in the x, y, and z directions; t is time; f is the Coriolis parameter; g is the gravitational acceleration; p is the pressure; ρ is the density; A_H, and K_H are the horizontal eddy coefficients; A_V and K_V are the vertical eddy coefficients; and

$$\nabla_H \cdot (A_H \nabla_H E) = \frac{\partial}{\partial x}\left(A_H \frac{\partial E}{\partial x}\right) + \frac{\partial}{\partial y}\left(A_H \frac{\partial E}{\partial y}\right) \tag{6}$$

At the free surface, the appropriate boundary conditions are: (a) the wind stress is specified,

$$\rho_o A_v \left(\frac{\partial u}{\partial z}, \frac{\partial v}{\partial z}\right) = (\tau_{sx}, \tau_{sy}) = \rho_a C_{da} (u_w^2 + v_w^2)^{1/2} (u_w, v_w) \tag{7}$$

where τ_{sx} and τ_{sy} are the wind stresses in the x and y directions respectively, ρ_a is the air density, C_{da} is the drag coefficient and (u_w, v_w) are the wind velocities at a certain height above the surface; (b) the kinematic condition is satisfied,

$$w = \frac{\partial \zeta}{\partial t} + u\frac{\partial \zeta}{\partial x} + v\frac{\partial \zeta}{\partial y} \tag{8}$$

where ζ is the elevation of the free surface; (c) the dynamic condition is satisfied, i.e., $p=p_a$, where p_a is the atmospheric pressure; and (d) the density flux, i.e., the heat flux and the salt flux, is specified.

At the bottom, the boundary conditions are: (a) a quadratic stress law is valid:

$$\rho_o A_v \left(\frac{\partial u}{\partial z}, \frac{\partial v}{\partial z}\right) = (\tau_{bx}, \tau_{by}) = \rho C_d \, (u_1^2 + v_1^2)^{1/2} \, (u_1, v_1) \tag{9}$$

where τ_{bx} and τ_{by} are the bottom shear stresses, C_d is the skin-friction coefficient, and (u_1, v_1) are the velocities at the first grid point above the bottom, and (b) heat flux (or temperature) and the salt flux are specified.

Grid Structure

Anticipating appreciable variation of bottom topography in the horizontal direction, the x,y,z coordinate system is vertically-stretched to a x,y,σ coordinate system, such that an equal number of grid points exist in the shallow coastal and the deep offshore areas (Figure 2a). The transformation takes the form:

$$\sigma = \frac{z - \zeta\,(x,y)}{h(x,y) + \zeta(x,y)} = \frac{z-\zeta}{H} \tag{10}$$

where h (x,y) is the local water depth and $\zeta(x,y)$ is the free-surface

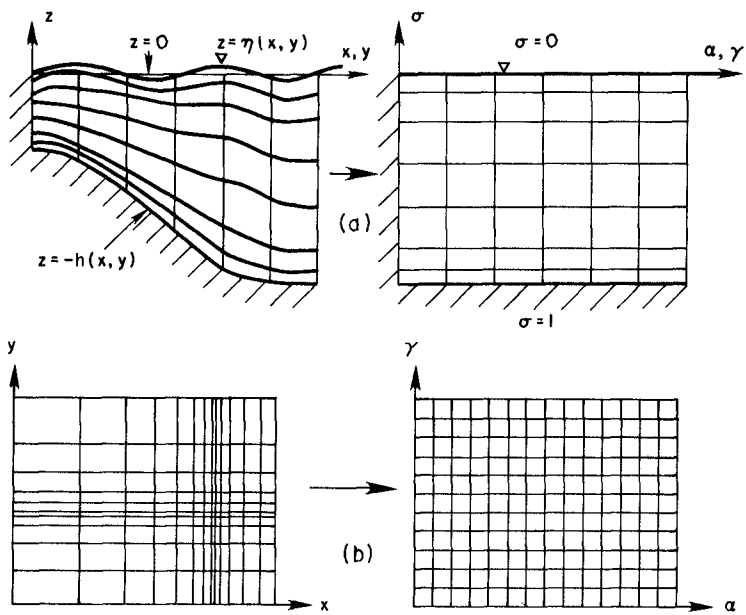

Figure 2(a). Vertical Stretching of the Coordinates,
(b). Horizontal Stretching of the Coordinates.

elevation. Such a transformation leads to (1) the same order of numerical accuracy in the vertical direction at all horizontal locations, and (2) a smooth representation of the bottom topography. Although additional terms are introduced by this transformation, the advantages warrant its application. Models using regular rectangular grid in the vertical direction cannot accurately resolve the shallow coastal area unless a large number of grid points is used in the deeper offshore area. In addition, if the bottom is approximated by a series of rectangular steps, estimate on bottom stress may be distorted and hence is not suitable for studying sediment transport problems.

To better resolve the complex shoreline geometries and bottom features, a non-uniform grid is often required in the x and y directions (Butler and Sheng, 1982). To allow ease in numerical analysis and as shown in Figure 2b, this non-uniform grid (x,y,z) is further mapped into a uniform grid (α,γ,σ):

$$x = a_x + b_x \alpha^{c_x} \quad ; \qquad y = a_y + b_y \gamma^{c_y} \tag{11}$$

The transformed three-dimensional equations of motion in α,γ,σ grid system are rather complex. Detailed equations and boundary conditions in non-dimensional form can be found elsewhere (Sheng, 1981). Staggered numerical grid is used in both the horizontal and vertical directions.

External Mode

In the present study, numerical computation of the vertical flow structures (internal mode), which are governed by slower dynamics, are separated from the computation of the vertically-integrated variables (external mode). This so-called "mode splitting" technique resulted in significant improvement of the numerical efficiency of a three-dimensional hydrodynamic model for Lake Erie (Sheng et al., 1978). It allows for computation of the three-dimensional flow structures with minimal additional cost over computation of the two-dimensional flow with a vertically-integrated model.

The external mode is described by the water level (ζ) and the vertically-integrated mass fluxes $(U,V) \equiv \int_{-1}^{0} (u,v)\, Hd\sigma$. Performing vertical integration of the transformed three-dimensional equations of motion, and rewriting (α,γ) as (x,y) for simplicity, we obtain:

$$\frac{\partial \zeta}{\partial t} + \frac{1}{\mu_x}\frac{\partial U}{\partial x} + \frac{1}{\mu_y}\frac{\partial V}{\partial y} = 0 \tag{12}$$

$$\frac{\partial U}{\partial t} = -\left[\frac{1}{\mu_x}\frac{\partial}{\partial x}\left(\frac{U^2}{H}\right) + \frac{1}{\mu_y}\frac{\partial}{\partial y}\left(\frac{UV}{H}\right) + H(u\omega)_{\sigma=0}\right] - fV - \frac{gH}{\mu_x}\frac{\partial \zeta}{\partial x} + \frac{1}{\rho_o}(\tau_{sx}-\tau_{bx})$$

$$- \frac{1}{\rho_o \mu_x}\int_{-1}^{0}\left[gH\int_{\sigma}^{0}\frac{\partial \rho}{\partial x}\,d\sigma + g\frac{\partial H}{\partial x}\left(\int_{\sigma}^{0}\rho\, d\sigma + \sigma\rho\right)\right]Hd\sigma + (H.D.)_x \tag{13}$$

$$\frac{\partial V}{\partial t} = -\left[\frac{1}{\mu_x}\frac{\partial}{\partial x}\left(\frac{UV}{H}\right) + \frac{1}{\mu_y}\frac{\partial}{\partial y}\left(\frac{V^2}{H}\right) + H(v\omega)_{\sigma=0}\right] + fU - \frac{gH}{\mu_y}\frac{\partial \zeta}{\partial y} + \frac{1}{\rho_o}(\tau_{sy}-\tau_{by})$$

$$-\frac{1}{\rho_o \mu_y}\int_{-1}^{0}\left[gH\int_{\sigma}^{0}\frac{\partial \rho}{\partial y}d\sigma + g\frac{\partial H}{\partial y}\left(\int_{\sigma}^{0}\rho d\sigma + \sigma\rho\right)\right]Hd\sigma + (H.D.)_y \tag{14}$$

where $\mu_x \equiv dx/d\alpha$ and $\mu_y \equiv dy/d\gamma$ are the stretching coefficients, $\omega \equiv d\sigma/dt$ is the vertical velocity in the stretched coordinate, and $(H.D.)_x$ and $(H.D.)_y$ are the horizontal diffusion terms. Notice that the bottom stresses (τ_{bx}, τ_{by}) are determined from the latest three-dimensional velocity profiles available from the internal mode computation, and hence are more accurate than the traditional vertically-integrated models which assume the bottom stress is proportional to the local vertically-integrated velocity or its square.

Treating implicitly all the terms in the continuity equation, while only the time derivatives and the surface slopes in the momentum equations, one can obtain the following finite-difference equations:

$$(1+\phi\lambda_x+\phi\lambda_y)W^{n+1} = [1+(1-\phi)\lambda_x+(1-\phi)\lambda_y]W^{n} + \Delta t D^{n} \tag{15}$$

where

$$\lambda_x = \frac{A\Delta t}{\mu_x \Delta x}\delta_x; \quad \lambda_y = \frac{B\Delta t}{\mu_y \Delta y}\delta_y;$$

$$A = \begin{pmatrix} 0 & 1 & 0 \\ gH & 0 & 0 \\ 0 & 0 & 0 \end{pmatrix}; \quad B = \begin{pmatrix} 0 & 0 & 1 \\ 0 & 0 & 0 \\ gH & 0 & 0 \end{pmatrix}; \quad D = \begin{pmatrix} 0 \\ D_x \\ D_y \end{pmatrix}; \quad W = \begin{pmatrix} \zeta \\ u \\ v \end{pmatrix} \tag{16}$$

where $(\Delta x, \Delta y)$ are the spatial grids, Δt is time step, D_x and D_y are terms in Eqs. (13) and (14) excluding the time derivatives and the surface slopes, superscripts n+1 and n indicate present and previous time step of integration, δ_x and δ_y are central difference spatial operators, and ϕ is a weighting factor, $0<\phi\leq 1$. If $\phi=0$, Eq. (15) reduces to a two-step explicit scheme. If $\phi>0$ the resulting schemes are implicit, with $\phi=1/2$ corresponding to the Crank-Nicholson scheme and $\phi=1$ corresponding to the fully implicit scheme. Eq. (15) can be factorized such that solution can be obtained by consecutive tridiagonal matrix inversions in the x-direction and y-direction. Further, we employ a method that solves only two variables during each sweep. This method allows very large time step to be used and has been found to be more stable than the traditional ADI method. Courant number based on the maximum propagation speed of surface gravity wave, $(gH_{max})^{1/2}\Delta t/\Delta x$, may now be as large as 100, compared to the limit of 1 for the explicit method. The maximum step is now governed by the CFL condition based on vertically-averaged advection speed in the system.

In the full three-dimensional model, the external mode computation

is carried out in conjunction with the internal mode computation. Depending on the problem of interest, the internal mode may be computed every so often with a time step equal to or greater than the external time step.

Internal Mode

The internal mode of the flow is described by the vertical flow structures and the density. Defining perturbation velocities as $u' \equiv u - U/H$ and $v' \equiv v - V/H$, the equations for the internal mode are obtained by subtracting the vertically-averaged momentum equations from the three-dimensional equations:

$$\frac{1}{H}\frac{\partial Hu'}{\partial t} = B_x - \frac{D_x}{H} + \frac{1}{H^2}\frac{\partial}{\partial \sigma}\left[A_v \frac{\partial}{\partial \sigma}\left(\frac{Hu'+U}{H}\right)\right] \tag{17}$$

$$\frac{1}{H}\frac{\partial Hv'}{\partial t} = B_y - \frac{D_y}{H} + \frac{1}{H^2}\frac{\partial}{\partial \sigma}\left[A_v \frac{\partial}{\partial \sigma}\left(\frac{Hv'+V}{H}\right)\right] \tag{18}$$

where B_x and B_y represent all terms in the transformed three-dimensional momentum equations except the surface slopes and the vertical diffusion terms, and D_x and D_y are defined in Eq. (16). Notice that the above equations retain the three-dimensionality and hence are different from the model of Nihoul and Ronday (1983) which is actually a superposition of a two-dimensional model and a vertical one-dimensional model.

The above equations do not contain the surface slope terms and hence a large time step may be used in the numerical computation. In the present model, a two-time-level or three-time-level scheme with a vertically implicit scheme is generally used. The bottom friction terms are also treated implicitly to ensure unconditional numerical stability in shallow waters. Care must be taken to ensure that the vertically-integrated perturbation velocities at each horizontal location (i,j) always equal to zero.

Once the equations for (u',v') are solved, and (u,v) obtained, vertical velocity ω and density ρ may be computed. As mentioned before, the internal mode may be computed as often as the external mode or as desired and as dictated by the problems of interest. The numerical time step for the internal mode is limited by the CFL condition based on the advection speed. In the present study, the drag coefficient C_d in the quadratic bottom stress law Eq. (9) is generally specified as a function of the bottom roughness (z_0), the distance above the bottom (z_1), at which (u_1,v_1) is computed, and the stability function of the bottom flow (ϕ_s):

$$C_d = k^2 \left(\ell n \frac{z_1}{z_0} + \phi_s\right)^{-2} \tag{19}$$

where k is the von Karman constant. It can be shown that the stability may increase (unstable case) or decrease (stable case) the drag

coefficient by as much as 40% (Sheng, 1980).

Turbulence Parameterization

A semi-empirical theory of vertical mixing is used in this study. The effect of stratification, as measured by the Richardson number, Ri, on the intensity of vertical turbulent mixing is parameterized by a number of empirical stability functions:

$$A_v = A_{vo}\,\phi_1(Ri);\quad K_v = K_{vo}\,\phi_2(Ri);\quad Ri = \frac{-g}{\rho}\frac{\partial \rho}{\partial z}\left[\left(\frac{\partial u}{\partial z}\right)^2 + \left(\frac{\partial v}{\partial z}\right)^2\right]^{-1/2} \qquad (20)$$

where A_{vo} and K_{vo}, are the eddy coefficients in the absence of any density stratification and ϕ_1 and ϕ_2 are stability functions. Traditionally, these stability functions have been determined empirically by comparing model output with measured data. As shown in Figure 3a, great discrepancy exists among the various empirical forms of the stability functions. In addition, the critical Richardson numbers, at which turbulence is completely damped by buoyancy, given by these formulas are much too high (10) compared to the measured value of 0.25 (Erikson, 1978). To unify this discrepancy, stability functions may be determined from a second-order closure model of turbulence. Assuming a balance between turbulence production and dissipation, i.e., the so-called "super-equilibrium" condition (Donaldson, 1973), we can obtain a simpler set of algebraic relationships between the turbulent correlations and mean flow gradients. As shown in Figure 3b, such a stability function leads to a

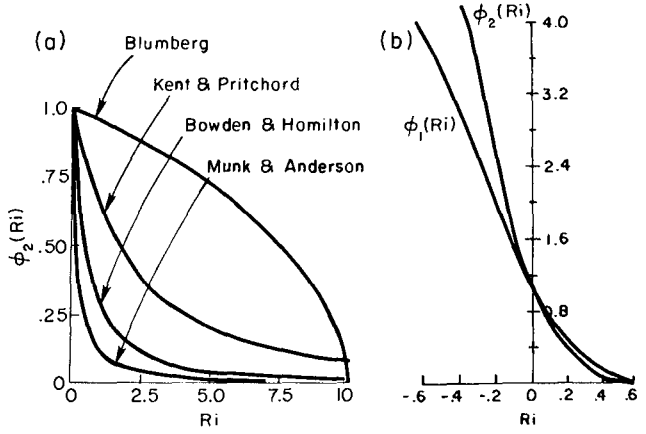

Figure 3. Stability Function vs. Richardson Number:
(a). Empirical Formulations,
(b). "Superequilibrium" Formulation Derived from Reynolds Stress Model.

critical Richardson number much closer to 0.25. In addition, such a formulation allows the definition of finite eddy coefficients in the unstable range (Ri < 0). In order to utilize these relationships, a turbulence length scale which varies with depth and Richardson number has to be prescribed empirically.

SIMULATION OF TIDE- AND WIND DRIVEN CURRENTS

The three-dimensional numerical model of coastal currents has been applied to simulate the tide- and wind-driven currents in the Mississippi Sound and adjacent continental shelf waters of the Gulf of Mexico. As shown in Figure 4, the horizontal grid is composed of 116 grid points in the y-direction and 60 grid points in the x-direction. The smallest grid spacing in the computational domain is on the order of 1 km. The water depth varies from only a few meters within the Mississippi Sound and the Mobile Bay to over 1000 m along the southern boundary.

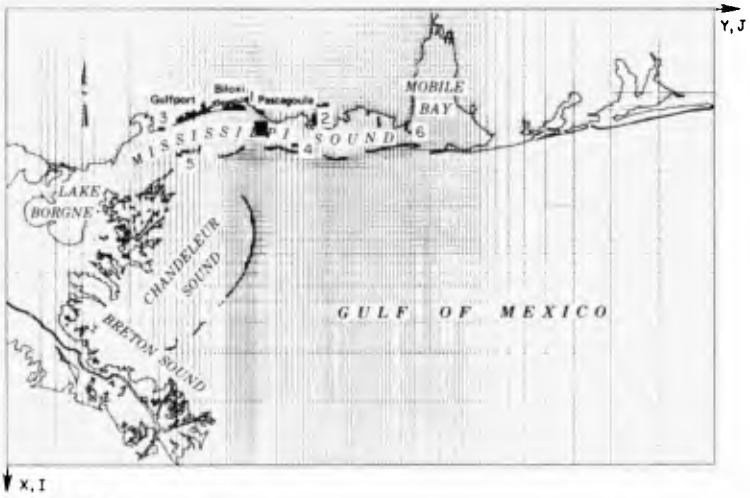

Figure 4. Computational Grid for Mississippi Sound Simulation.

Tides in the Gulf of Mexico

Gulf tides differ from tides in most other places in the world due to the dominance of the diurnal components K1, O1 and P1 collectively over the semi-diurnal components M2 and S2, except along the west Florida coast. Reid and Whitaker (1981) developed a numerical tide model for the Gulf based on the vertically-integrated, linearized tidal equations to portray the barotropic response of the Gulf to tidal forcing. Forcing at ports was also included with an impedance type condition. Detailed data from 20 tidal gages located in open coastal

waters of the Gulf were used for the fine tuning of their model. Their study confirmed that diurnal tide in the Gulf is primarily a co-oscillating tide driven by adjoining Atlantic Ocean and Caribbean Sea.

The water level response for a given tidal constituent is usually expressed in terms of the surface displacement ζ (Schureman, 1941):

$$\zeta = F(t)\, A(\lambda,\Phi) \cos [\, \omega_0 t + \chi - G\,(\lambda,\Phi)] \qquad (21)$$

where λ is the longitude, Φ is the latitude, A is the mean amplitude over 18.6 years and G the Greenwich phase or epoch at given position (λ,Φ), ω_0 is tidal frequency, χ is the astronomical argument, while F is the nodal factor, a slowly varying function of time. Tides at particular stations are characterized by A and G for individual constituents. In our study, A's and G's for 5 constituents (O1, K1, P1, S2 and M2) along the open boundaries of our grid are supplied from Reid and Whitaker's model. Surface displacements at the open boundary stations are determined from a linear combination of those due to the five tidal constituents.

Tidal Currents off the Mississippi Coast

As a first example, tides during 20 Sept. to 25 Sept. 1980 are computed with our three-dimensional model. The surface displacements at four stations (see Figure 4 for locations) within the Mississippi sound are compared with measured data in Figure 5. Notice that the measured data have been filtered such that variations due to short-period oscillations on the order of a few hours or less are not included. Initially, the diurnal tides are predominant. Towards the end of the five-day period, the diurnal tides become somewhat less predominant while the semi-diurnal tides became gradually more apparent. Good agreement is found at all stations.

In this simulation, a relatively large time step of 12 minutes was used for both the external and the internal modes. Seven grid points are used in the vertical direction. A relatively smooth bottom with a roughness length, z_0, of 0.1 cm was assumed. A parabolic length scale, Λ, was assumed in the vertical direction.

The tide-driven horizontal currents at mid-depth are shown in Figure 6 for two stations in the Mississippi Sound. Currents on the order of 30 cm/sec exist at both stations. Again, reasonable agreement is found between data and model results.

The horizontal velocity field at 1 m depth, after 3 days of simulation, is shown in Figure 7. Relatively large currents exist at the various tidal inlets and in the area between the Ship Island and the Chandelier Island. Except in these areas, at this instant of time, bottom shear stress generated by the tidal currents are generally less than 0.8 dyne/cm^2. Hence little sediment resuspension is expected. However, during strong spring tides, such as those during the period of 12 June to 16 June, 1980, relatively stronger currents and bottom shear stresses in excess of 0.8 dyne/cm^2 could prevail within the tidal

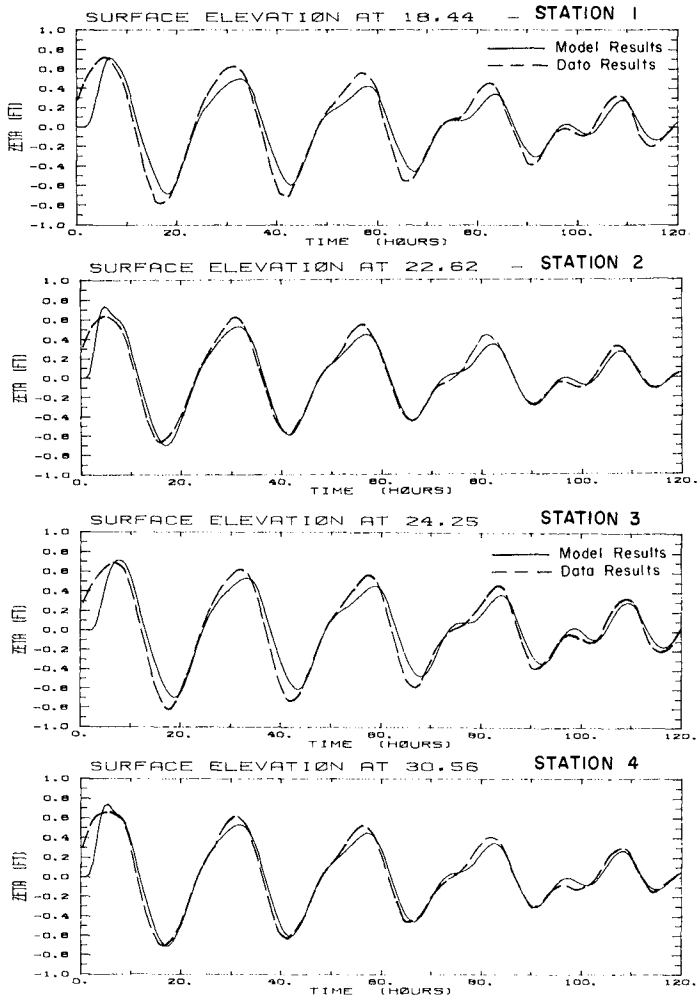

Figure 5. Surface Elevation at Four Locations (see Fig. 4) from 20 Sept. to 25 Sept., 1980.

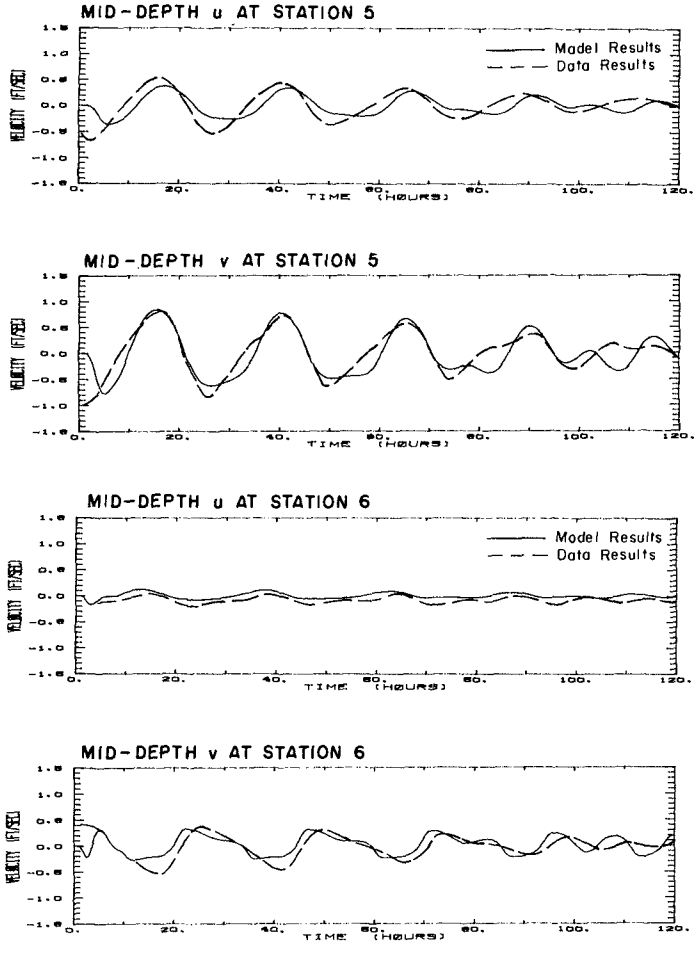

Figure 6. Mid-Depth Horizontal Velocities at Stations 5 and 6 from 20 Sept. to 25 Sept., 1980. Tide Forcing Only.

inlets and other shallow areas. Resuspension of cohesive sediment in these areas might occur and leave behind the coarser non-cohesive sediment.

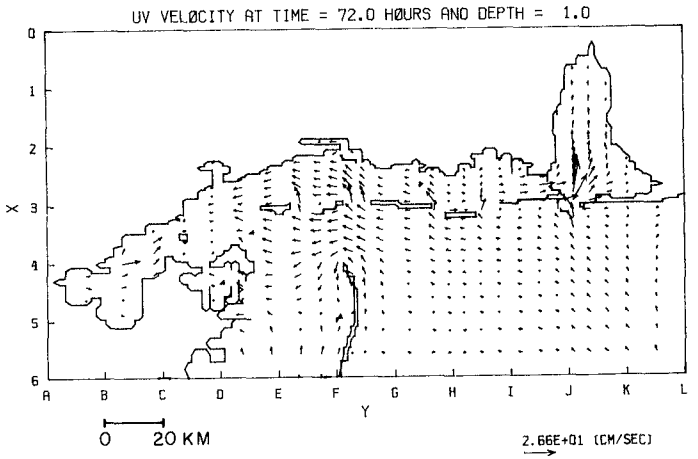

Figure 7. Tide-Driven Horizontal Velocities at 1 m Depth in the Vicinity of the Mississippi Sound at 0 hr, 23 Sept., 1980.

Wind-Driven Currents off the Mississippi Coast

The results presented in the above did not contain any wind-driven effect. During our study, wind data were collected at several meteorological stations surrounding the Mississippi Sound. The wind during the 5-day period was generally quite mild ($\lesssim$ 5 m/sec) from the Southeast. To examine the effect of wind on the currents, we carried out a three-day simulation from 20 Sept., using a uniform wind stress of 1 dyne/cm^2 from the Southeast. The southeasterly wind caused water to pile up within the Mississippi Sound, with a set-up on the order of 12 cm along the Northern shore, and only 6 cm behind the barrier islands.

The influence of wind on the current also depends on the location. Figure 8 shows the along-shore velocity at 2 locations over the 3-day period. At Station 5, off Cat Island, the presence of the wind did not have appreciable effect on the tidal current. At Station 6, within the pass between the Mississippi Sound and the Mobile Bay, the wind caused significant flow from the Mobil Bay into the Sound. This resulted in a significantly larger bottom shear stress which leads to the reduction in the amplitude of the tidal currents.

Wind-driven currents in the Mississippi Sound depend strongly on the wind direction. For example, assuming a uniform wind stress of 1 dyne/cm^2 from the West, our model results showed relatively stronger currents in the along-shore direction (Figure 9). Notice the near-surface and near-bottom velocities differ not only in magnitude but also in direction at some locations. This is partially associated

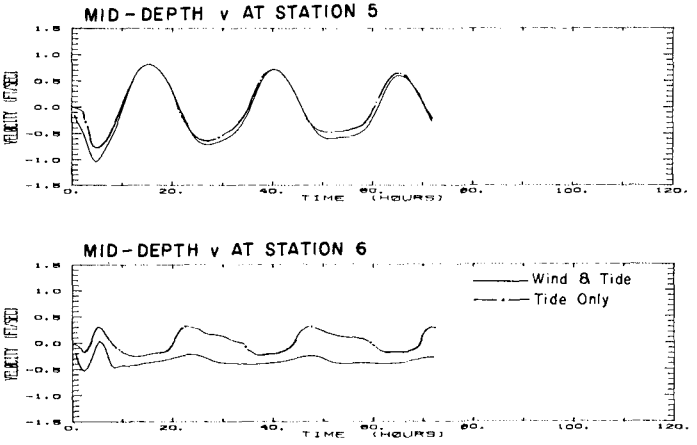

Figure 8. Mid-Depth Along-Shore Velocity at Stations 5 and 6 from 20 Sept. to 23 Sept., 1980. Tide and Wind Forcings.

with the pressure gradient caused by the wind set-up, which is on the order of 20 cm across the Mississippi Sound. According to a laboratory flume study on the erodibility of the Mississippi Sound sediments (Sheng, 1981), it is expected that the bottom shear stress generated by the strong Westerly wind in winter may cause significant resuspension of sediments.

TRANSPORT, RESUSPENSION, AND DEPOSITION OF COHESIVE SEDIMENTS

Transport Modes

The transport of cohesive sediment in the water column can be described by a conservation equation, similar to the heat or salinity equation, for the suspended sediment concentration. An equation similar to Eq. (5) can be written for the sediment concentration C. However, the vertical velocity in the sediment concentration equation should be composed of the sum of the fluid velocity (w) and a settling speed of the particles (w_s). In fresh water, the settling speed of cohesive sediment from a coastal environment shows a relatively flat spectral distribution. As the salinity increases, the sediment particles form aggregates and the spectral distribution becomes much sharper (Fig. 10). In this study, for simplicity, we assume the cohesive sediment in the Mississippi Sound can be described by one single settling speed. The settling speed of bottom sediment samples from the Sound was measured in laboratory, without adding dispersant to the samples, and a median settling speed determined.

The behavior of sediment in the water column depends on the

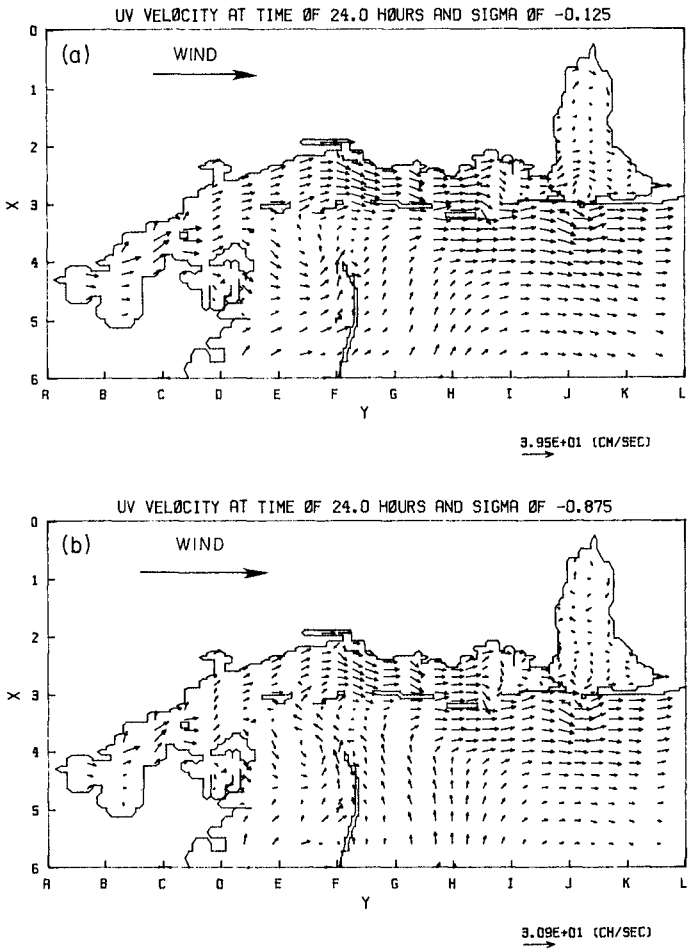

Figure 9. Horizontal Velocities in the Vicinity of the Mississippi Sound at 24 hrs after the Application of a Westerly Wind with τ_y = 1.0 dyne/cm^2.
(a). Near-Surface Currents, and
(b). Near-bottom Currents.

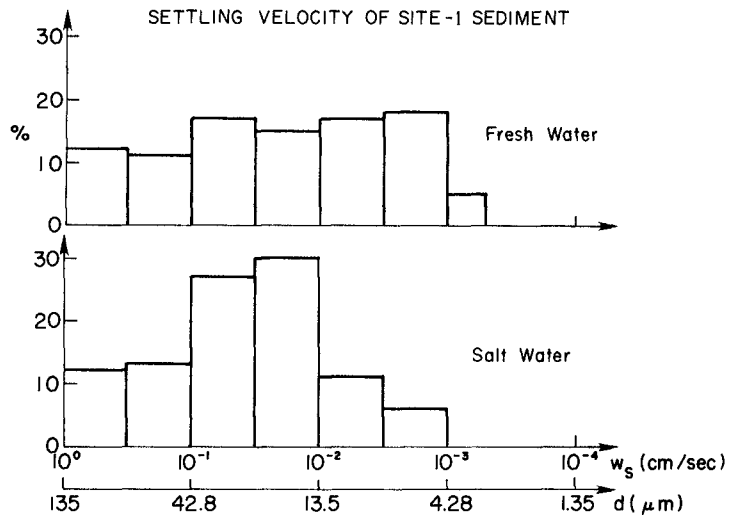

Figure 10. Settling speed of Mississippi Sound Sediments in Fresh and Salt Water.

cohesion and collision of sediment particles. Clay mineralogy and other chemical parameters determine the cohesion of sediment particles. However, in coastal waters where flow is generally turbulent, collision between particles play a more dominant role than cohesion in determining the state of flocculation. The frequency of collision between various groups of particles depends on the turbulent shearing rate on the dissipation scale and differential settling. Although our hydrodynamic model is capable of computing the small-scale turbulent shearing rate, there is insufficient data at this time to allow for precise determination of model coefficients for the flocculation model.

Resuspension and Deposition Modes

Resuspension and deposition of sediment at the sediment-water interface play important roles in the distribution of suspended sediment concentration. In general, resuspension and deposition depend on (1) the hydrodynamic forces generated at the bed within the turbulent bottom boundary layer; (2) bed properties such as sediment composition, water content, bed preparation (settling) time, and organic matter, bacteria, and benthos; and (3) fluid properties including salinity, temperature, and pH of pore water and overlying water.

Effects of dominant parameters (shear stress, water content, bed preparation time, and salinity) on resuspension and deposition were

investigated in a laboratory flume (Sheng 1981; Sheng et al. 1982). To prepare the bed, sediments are introduced into the flume, resuspended, and allowed to settle for a period of 1 to 10 days. A given bottom shear stress is then applied and the time history of sediment concentration recorded until an equilibrium concentration is reached, at which the resuspension balances the deposition. As shown in Figure 11, resuspension as indicated by the equilibrium concentration depends strongly on the applied shear stress. More than an order of magnitude increase in equilibrium concentration can be expected when the shear stress is increased by a factor of 5. Salinity affects the aggregation of particles and hence the erodability of the

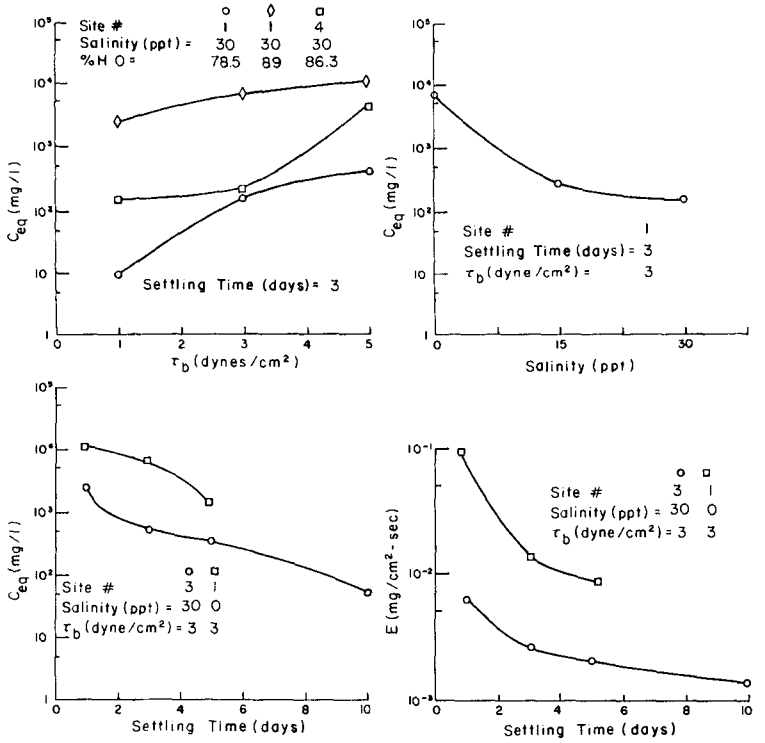

Figure 11(a). Equilibrium Suspended Sediment Concentration in Laboratory Flume as a Function of Applied Shear Stress,
(b). Effect of Salinity,
(c). Effect of Time History of the Bed, and
(d). Resuspension Rate as a Function of Time History of the Bed.

bottom sediments. The sediment becomes harder to erode at higher salinity, with most variation occurring between 0 and 15 $^{o}/_{oo}$. The sediment also becomes harder to erode as more time is allowed for the preparation of the bed. From the laboratory flume data, proper bottom boundary conditions for the sediment transport model can be derived in terms of the rate of resuspension (E) and deposition (V_dC) (Sheng, 1981). The bottom boundary condition for the sediment concentration (C) equation can be written as:

$$\text{Net Upward Flux} = w_sC - K_v \frac{\partial C}{\partial z} = E - V_dC \qquad (22)$$

where the deposition velocity $V_d > 0$ while the settling velocity $W_s < 0$.

Sediment Movement in the Mississippi Sound Due to a Westerly Wind

As an example to illustrate the important role of resuspension and deposition, we performed a 1-day simulation of sediment movement due to a Westerly wind.

Initially, the background concentration is assumed to be zero everywhere except within a square area (shown in Figure 12) where the concentration is 500 mg/l (newly introduced sediment). The sediment concentration is then computed with three different bottom boundary conditions: (1) zero net flux and zero settling speed, (2) with deposition and resuspension, but no resuspension of old sediment (vs. the newly introduced sediment) is allowed, and (3) deposition and resuspension allowed at all locations. For (2) and (3), a settling

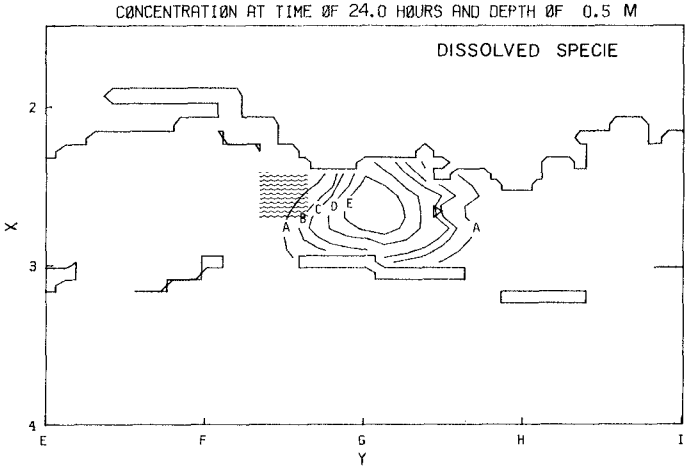

Figure 12. Suspended Sediment Concentration at 0.5 m Depth at the End of 1-day Simulation. Westerly Wind; No Settling; Zero Net Flux at Bottom.

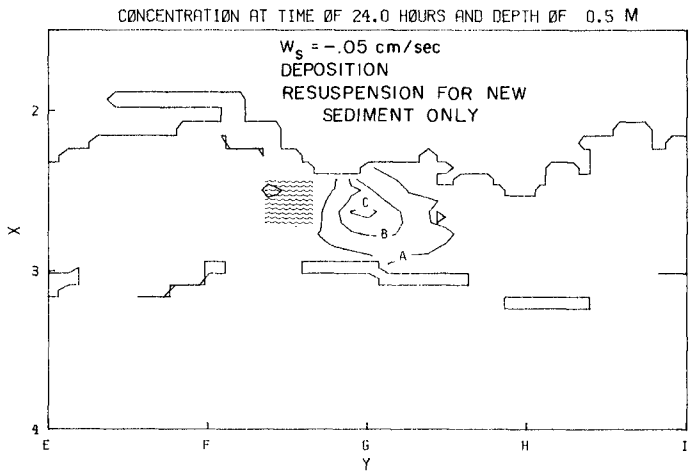

Figure 13. Same as Figure 12 except that w_s = -0.05 cm/sec; Deposition but no Resuspension for Old Sediment.

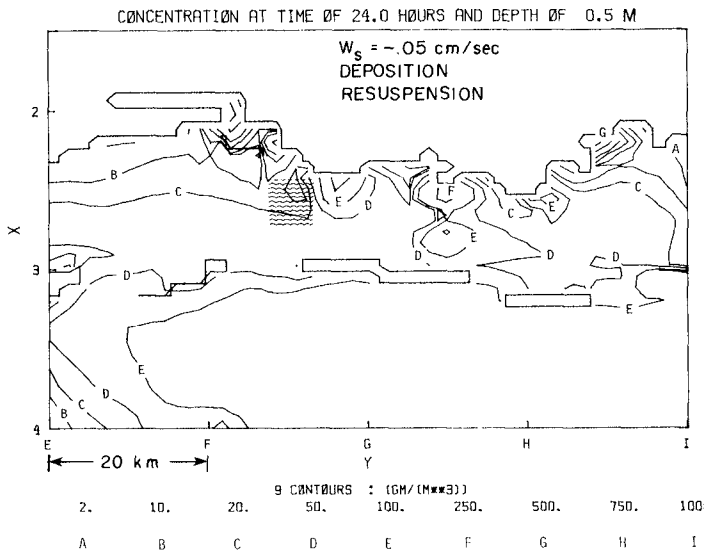

Figure 14. Same as Figure 12 except that w_s = -0.05 cm/sec; Deposition and Resuspension.

speed of 0.05 cm/sec was used. The results at 0.5 m depth at the end of one-day simulation are shown in Figures 12, 13 and 14. It is clear that resuspension of sediment plays a dominant role in redistributing sediment. The difference in results for (2) and (3) reflects the importance of quantifying the time history of bottom sediments, which strongly affects the erodability as shown in Fig. 11.

BOTTOM BOUNDARY LAYER AND WAVE EFFECT ON SEDIMENT RESUSPENSION

The wave climate during the September period of 1980 was studied by means of a spectral wave hindcasting model modified for shallow water. The blockage effect of the barrier islands allows us to assume that most of the wave energy in the Mississippi Sound was derived from the wind fetch within the Sound. From 20 to 25 Sept., wind was generally from the Southeast at about 5 m/sec. Results of the wave model indicate wave height generally under 30 cm and wave period under 3 sec. At a station off Gulfport (Station 17), the wave-induced bottom stress was the highest among all stations and on the order of 5 dyne/cm^2 during the first day (Fig. 15a). However, wave-induced stress over most of the sound was generally not very strong, as can be seen in Fig. 15b, the bottom stress at a station off the Biloxi channel (Station 10) was generally less than 1.3 dyne/cm^2. These findings are consistent with the sediment concentration data collected during this time period, which showed a slight initial increase in concentration followed by primarily depositional events. We also found that linear wave theory and empirical bottom stress formula tend to overestimate the wave-induced bottom stress within an oscillatory boundary layer.

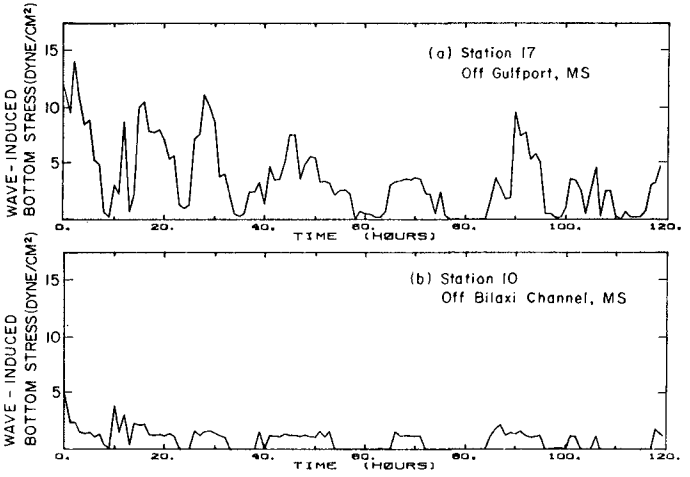

Figure 15. Wave-Induced Bottom Stress at two Locations in the Mississippi Sound from 20 to 25 Sept., 1980.
(a). Station 17 off Gulfport, MS.
(b). Station 10 off Biloxi Channel.

Oetailed turbulent dynamics of the bottom bounday layer under a pure wave (Sheng, 1982) and current-wave interaction (Sheng and Lewellen, 1982) have also been studied using a Reynolds stress model. Contrary to the general belief, the presence of the wave was found to not always enhance the current-induced stress.

CONCLUSIONS AND RECOMMENOATIONS

An efficient three-dimensional numerical model of coastal currents has been developed and is operational. The model is suitable for detailed short-term simulations as well as longer-term simulations. Currents in Mississippi Sound and adjacent offshore waters have been computed with the three-dimensional model. Results obtained during a five-day period in September 1980 agree very well with the measured data. Large spatial and temporal variation of bottom shear stresses exist within the area. Rate of resuspension of the Mississippi Sound sediments (primarily Smectite) has been determined experimentally and was found to increase with increasing shear stress, decreasing salinity, and shorter time-history of the bottom sediment. Studies are needed to elucidate the effect of turbulence on flocculation, the current-wave interaction within the bottom boundary layer, and the inclusion of sediment time-history as a parameter in the mathematical model.

ACKNOWLEDGEMENT

This work is supported by the U.S. Army Engineer Waterways Experiment Station under contract OACW 39-80-C-0087. Permission was granted by the Army Chief of Engineers to publish this information. Richard Schmalz and Bob Jensen provided valuable assistance in the study.

References

Blumberg, A.F., 1975: "A Numerical Investigation into the Oynamics of Estuarine Circulation," Chesapeake Bay Institute Report No. 91, Baltimore, MO.

Bowden, K.F. and P. Hamilton, 1975: "Some Experiments with a Numerical Model of Circulation and Mixing in a Tidal Estuary," Estuarine Coastal Marine Sci., 3, 281.

Butler, H.L. and Y.P. Sheng, 1982: "ADI Procedures for Solving the Shallow-Water Equations in Transformed Coordinates," Proc. 1982 Army Num. Anal. and Comp. Conf., Army Research Office, pp. 365-380.

Oonaldson, C.duP., 1973: "Atmospheric Turbulence and the Dispersal of Atmospheric Pollutants," in AMS Workshop on Micrometeorology (D.A. Haugen, ed.), Science Press, Boston, pp. 313-390.

Erikson, C.C., 1978: "Measurements and Models of Fine Structure, Internal Gravity Waves and Wave Breaking in the Deep Ocean," J. Geophys. Res., 83, pp. 2989-3009.

Kent, R.E., and D.W. Pritchard. 1959: "A Test of Mixing Length Theories in a Coastal Plain Estuary," J. Mar. Res., 18, pp. 62-72.

Leendertse, J.J., and S.K. Liu, 1975: "A Three-Dimensional Model for Estuaries and Coastal Seas, II: Aspects of Computation," Rand Report R-1764-OWRT.

Munk, W.H. and E.P. Anderson, 1948: "Notes on the Theory of the Thermocline," J. Mar. Res., 1, pp. 276-295.

Nihoul, J.C.J. and F.C. Ronday, 1983: "Three-Dimensional Marine Models for Impact Studies," Proc. 18th Int'l Conf. Coastal Eng., This Volume.

Reid, R.O. and R.E. Whitaker, 1976: "Wind-Driven Flow of Water Influenced By a Canopy," J. Waterways, Harbors and Coastal Eng. Div., Proc. ASCE, pp. 63-77.

Schureman, P. 1941: "Manual of Harmonic Analysis and Prediction of Tides," U.S. Department of Commerce Special Pub. No. 98, 317 pp.

Sheng, Y.P., 1980: "Modeling Sediment Transport in a Shallow Lake," in Estuaries and Wetland Processes (P. Hamilton, ed.), Springer-Verlag, Berlin, Heidelberg, pp. 299-337.

Sheng, Y.P., 1981: "Modeling the Hydrodynamics and Dispersion of Sediments in the Mississippi Sound," A.R.A.P. Report No. 455, 107 pp.

Sheng, Y.P., 1982: "Hydraulic Applications of a Second-Order Closure Model of Turbulent Transport," in Applying Research to Hydraulic Practice, (P. Smith, Ed.), ASCE, pp. 106-119.

Sheng, Y.P. and W.S. Lewellen, 1982: "Current and Wave Interaction within the Benthic Boundary Layer," EOS, 63, 3, pp. 72-73.

Sheng, Y.P. and W. Lick, 1979: "The Transport and Resuspension of Sediments in a Shallow Lake," J. Geophys. Res., 84, C4, 1809-1826.

Sheng, Y.P., W. Lick, R. Gedney, and F. Molls, 1978: "Numerical Computation of the Three-Dimensional Circulation in Lake Erie; A Comparison of a Free-Surface and a Rigid-Lid Model," J. Phys. Oceano., 8, pp. 713-727.

Sheng, Y.P., P.L. McCall, and J.B. Fisher, 1982: "Entrainment of Cohesive Sediments of the Gulf of Mexico," EOS, 63, 18, p. 358.

MODELLING OF SEA-BED EVOLUTION UNDER WAVES ACTION

by

Y. COEFFE (1) and PH. PECHON (2)

ABSTRACT

This paper presents a numerical model computing sea-bed evolution due to longshore currents, which has been developed at the Laboratoire National d'Hydraulique.

This model has been applied to a schematic semi-circular bay. The computation of sand sea-bed modifications reveals two main tendencies : a marked accretion in the "up-stream" zone of the bay and a marked erosion in the "down-stream" zone of the bay, as far as longshore currents are concerned.

1. INTRODUCTION

The action of waves is the predominant factor of sea-bed changes in the surf zone. The currents induced by breaking waves can be rather important, and their action is reinforced by the turbulent effects which appear in the breaking zone.

The model presented is able to predict longshore currents and sand transport field, and can deduce sea-bed evolutions under wave action for any bottom shape.

A mathematical model to compute longshore currents has been available at the Laboratoire National d'Hydraulique since 1977. In the numerical solution, energy transfers are simulated by introducing additional terms, derived from the Longuet-Higgins formulation, in the long wave equations.

(1) Head of the Maritime Hydraulics Division, Laboratoire National d'Hydraulique, E.D.F, Chatou, France.
(2) Research engineer, Laboratoire National d'Hydraulique, E.D.F, Chatou, France

This model has been applied to the simplified case of a semi-circular bay, the refraction of a monochromatic wave being computed with an other model, to estimate wave height, crest incidence and shoaling number in the domain. Recently, the introduction of a solid transport formula into the numerical model made it possible to estimate changes of the sea-bottom resulting from the longshore currents. Bijker formula has been selected because it takes into account the coupling of the average current over a vertical line and the wave orbital velocity. It is used to calculate bed and suspended load transport.

Once the quantities of transported materials are known, erosion and accretion can be calculated. The interaction between the modification of the sea-bed and wave induced currents is taken into account by adjusting the wave propagation after each significant change of the bathymetry and a new longshore current field is then deduced.

The modelling principles are summed up on figure 1. The numerical model includes at first a wave propagation model, then a current model and a bed evolution model ; this paper presents each part and the application to the schematic bay.

2. WAVES PROPAGATION MODEL

A classical pure refraction model is used, assuming linear wave theory, neglecting diffraction effects and using Snell's law.

The breaking of waves is considered. The method used here is to follow a wave orthogonal and to test in each point if breaking is occuring or not. The Battjes' criterion is used : the wave breaks at a place of depth d if the wave height H verifies

$$H \geqslant jd$$

where j is an experimental coefficient, function of bottom slope and local wave steepness, which determines the wave breaking evolution.

So, wave height incidence and shoaling number are estimated over the entire domain of interest.

This model has been applied to the schematic semi-circular bay, the characteristics of which being (fig 2) :

- radius of the bay = 260 m
- off-shore depth = 7,5 m

The off-shore wave conditions considered are :

- monochromatic wave
- height : 3 m
- period : 10s

The refraction diagram is shown on figure 3.

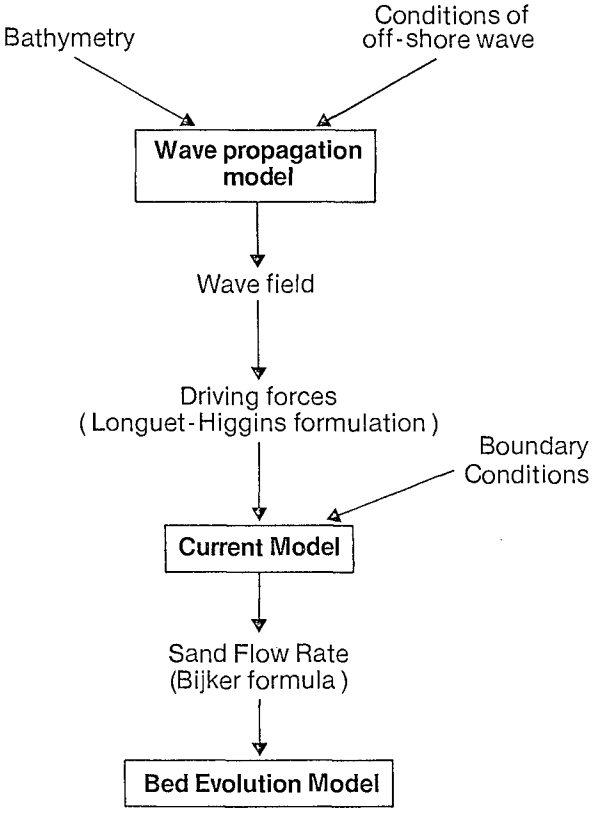

Fig.1 Modelling Principles

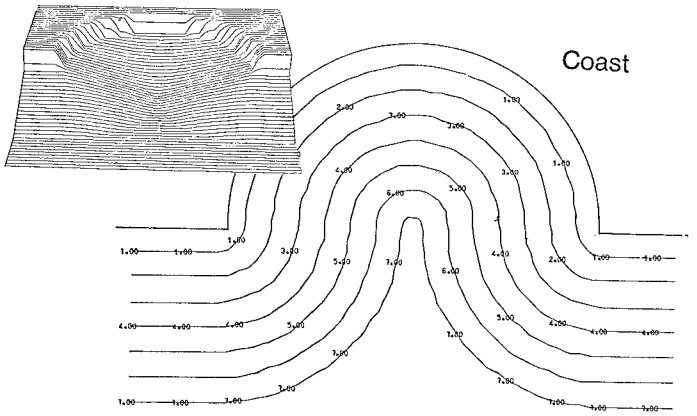

Fig.2 Initial Bathymetry of the Bay

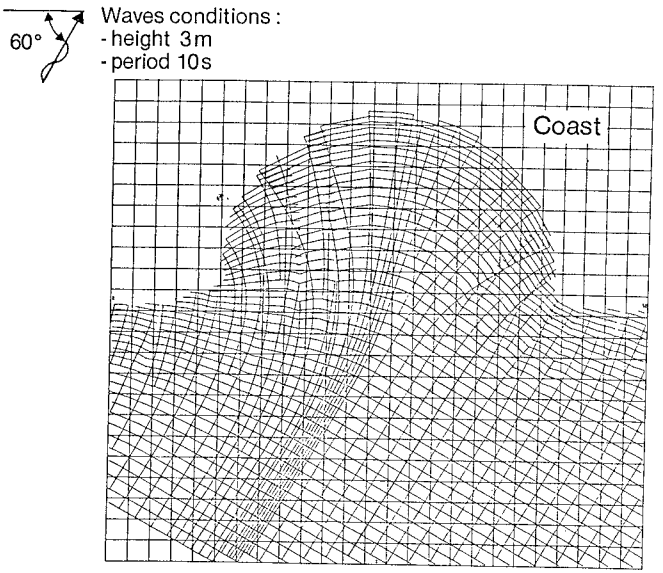

Fig.3 Refracted Waves Diagram

3. LONGSHORE CURRENT MODEL

3.1. Description

The assumptions of the longshore current model are :

- incompressible fluid
- linear Stokes waves
- the vertical component of the current is neglected
- for the calculation of waves currents, the variations of sea surface elevation are neglected compared to the total depth.
- the mass current is assumed to be constant over the depth
- wind action is neglected

With these assumptions, the Navier-Stokes equations can be integrated over the total depth and time averaged over a wave period. That leads to long waves equations in which appears a radiation stress tensor $\bar{S}$, representing the extra terms coming from averaging non linear terms involving velocities

The wave driving forces can be defined as follows :

$$\vec{\tau} = -\frac{1}{\rho} \operatorname{div} \bar{S}$$

Using Longuet-Higgins formulation, the tensor $\bar{S}$ is written :

$$\bar{S} = E \begin{bmatrix} (2n - \frac{1}{2}) \cos^2\alpha + (n - \frac{1}{2}) \sin^2\alpha & n \sin\alpha \cos\alpha \\ n \sin\alpha \cos\alpha & (2n - \frac{1}{2}) \sin^2\alpha + (n - \frac{1}{2}) \cos^2\alpha \end{bmatrix}$$

where $E = \frac{1}{8} \rho g H^2$ is the wave energy

n is he shoaling number

α is the wave incidence

The bottom friction has been assumed proportional to the squared velocity, taking into account the orbital velocity in the following form :

$$\vec{\tau}_b = -\frac{\rho g}{C_s^2} \vec{u} \, \| \vec{u} + \vec{u}_{orb} \|$$

where $\vec{u}$ = mean velocity

$$\vec{u}_{orb} = \frac{2H}{T} \frac{1}{\operatorname{sh}\left(2\pi \frac{d}{CT}\right)} \begin{bmatrix} \cos\alpha \\ \sin\alpha \end{bmatrix}$$

3.2. Application

The longshore current model has been applied to the semi-circular bay. Using the propagation model results, driving stresses are calculated. Then the wave height field is smoothed (fig. 4) to get a more regular radiation stress tensor. Then induced currents are computed.

The boundary conditions along the left side of the grid are coming from the application of the model to a rectilinear shore, with a bathymetry similar to the incoming part of the semi-circular bay. For this last case, the water flow obtained at the left boundary is transfered at the right one in order to get the stationary solution of an infinite shore.

At the right open boundary, a free exit of the current is imposed.

The obtained velocity pattern is shown on figure 5. Strong velocities appear in the breaking zone and an eddy takes place in the right part of the bay. The maximum velocities reach about 1,4 m/s, in the rectilinear part.

4. SEDIMENT TRANSPORT CALCULATION

4.1. Transport formula

A sediment transport formula was added to the current model. The chosen transport law is Bijker's formula which takes into account the coupling of the averaged current and the wave orbital velocity. The mean bed shear resulting of the combination of waves and longshore current is hold responsible for the stirring up of the material. Once the material is stirred up, it is transported by the normal current. For the bed load part this transport law is written as :

$$T_b = 5D\ (\mu\tau c/\rho)1/2\ \ e^{-0,27\ \frac{\Delta D\rho g}{\mu\ \tau_r}}$$

Δ : relative apparent density

D : grain size

μ : ripple coefficient

τ_c : bed shear due to mean current

τ_r : bed shear due to mean current and waves

Tb : bed load transport.

The suspended load is evaluated by assuming a logarithmic velocity distribution

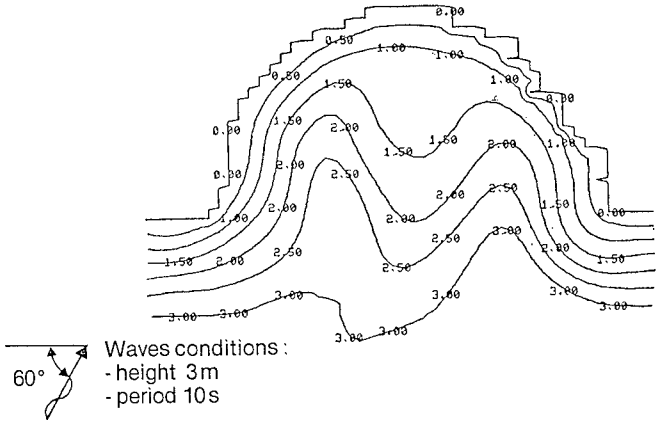

Fig.4 Contour-lines of Smoothed Wave Height

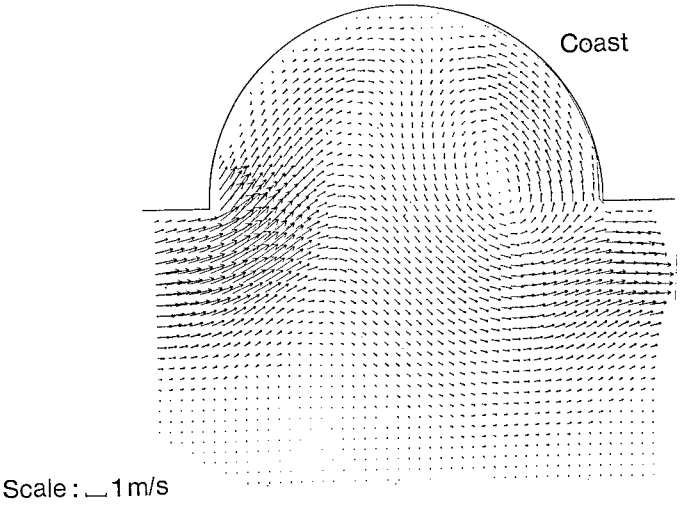

Fig.5 Velocity Field

The concentration c(z) is written as :

$$\frac{C(z)}{Ca} = \left[\frac{h - z}{z} \times \frac{a}{h - a}\right]^Z \quad \text{in which } Z = W/Kv*$$

Where W = fall velocity of the particles

K = Karman constant

v* = stress velocity due to wave and mean current

C_a = concentration of suspended load immediately above the bed

4.2. Application

The transport flow rate resulting from the velocity field in the bay is presented on figure 6, for a 0,5 mm grain size.

The total sand transport going through a section of the left rectilinear shore near the bay has been compared with the CERC formula and the formula of Larras and Bonnefille :

- formula of the CERC :

$$Q = 6{,}5\ 10^{-2}\ H^{5/2} \cos^{1/4} \alpha \sin 2\alpha$$

- formula of Larras et Bonnefille :

$$Q = K(H/L, D)\ \frac{H^3}{T} \sin \frac{7\alpha}{4}$$

where H is the wave height, α is the wave incidence, T is the period and D is the sand diameter.

The transport flow evaluated with the first formula is equal to 0,8 m^3/s whereas the second one gives 0,1 m^3/s. The difference between these two valuations comes from the difficuties of mesuring sand transport flow in the surf zone. The computation gives for this section (fig 7) Q = 0,3 m^3/s which is in the range of these formulae.

5. EVOLUTION OF THE SEA-BOTTOM

5.1. Description of the method

Continuity equation applied to the sediment transport gives the bed evolution :

$$\frac{\partial Z_F}{\partial t} + \text{div } \vec{T} = 0$$

where $\vec{T}$ is the sediment transport flow rate, and Z_F the bed level.

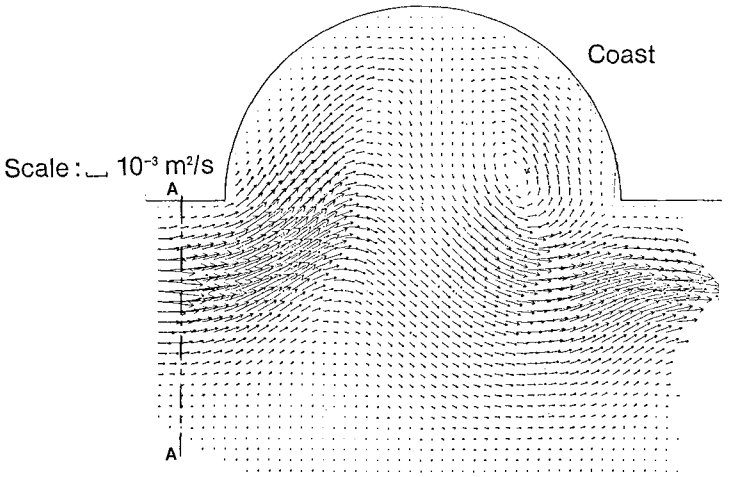

Fig.6 Sediment transport field

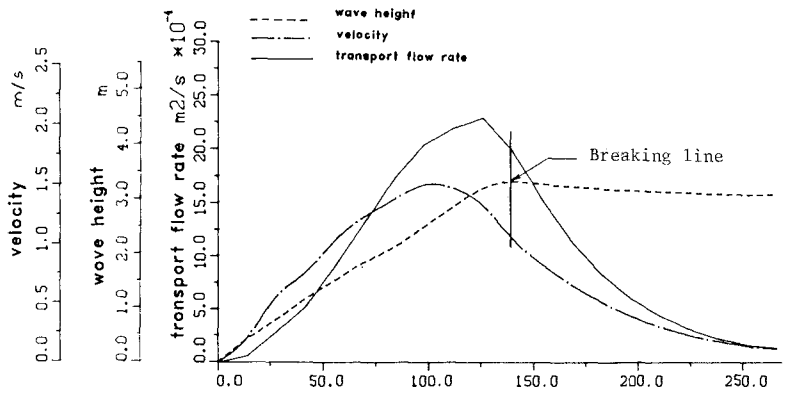

Fig.7 Velocity,wave height and transport distribution along A–A section

The bed evolution modifies progressively the waves propagation and the current field. It is very important to take this coupling into account, and to update the longshore currents according to new water depth. However the sedimentological time scale being much greater than the velocity time scale, the sea-bottom and water flow changes are calculated by doing two loops as shown on the following diagram :

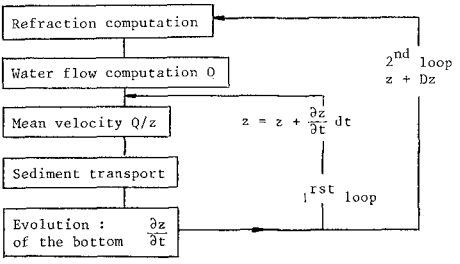

Fig.8 Modelling principles of bed evolution calculation

The first loop takes into account the interaction of the velocity field and the sea-bottom evolution for a constant water flow field, by the following way :

- sand transport calculation using Bijker's formula
- calculation of $\frac{\partial Z_F}{\partial t} = -\operatorname{div} \vec{T}$
- modification of sea-bottom $\frac{\partial Z_F}{\partial t}$ dt. The time step dt is chosen so that the water depth is changed of 5 % at most in the domain.
- adjustement of the velocity, considering a constant water flow rate and return to the first step.

When the modifications of the bathymetry are big enough, the waves characteristics in the domain are re-evaluated. The new driving forces and the induced longshore currents are computed again with the wave propagation model.

5.2. Results

In the case of the semi-circular bay, the comparison between the initial topography and the topography after 100 hours storms reveals the main following tendencies (fig 9) :

- large accretion in the left side of the bay due to incoming littoral transport
- large erosion of the beach in the right side of the bay due to reconstitution of littoral transport
- erosion of the area close to the left cape at the entrance of the bay and accretion just behind the cape
- general filling of the beach of the bay.

These changes agree with some natural tendencies but the obtained values need to be checked over real cases or physical model experiments.

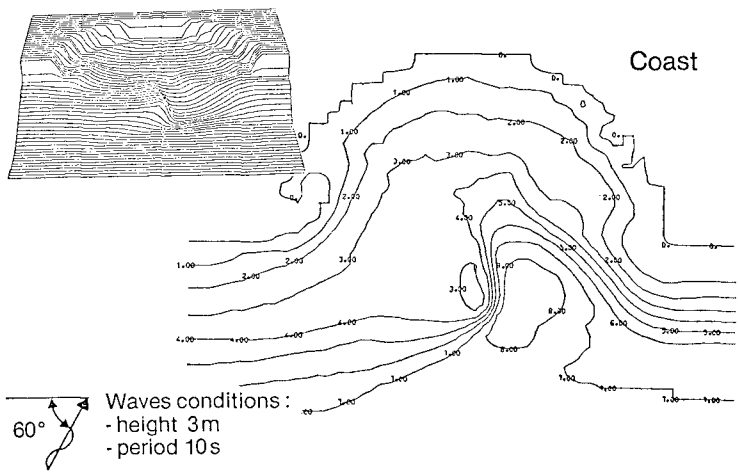

Fig.9 Bathymetry after 100 hours storm

6. CONCLUSION

The first results obtained by the mathematical model show that the modelling of sea bed evolution under the action of waves is no more a domain restricted to physical models.

The presented bidimensional model is able to compute longshore currents induced by breaking waves and to simulate bathymetry modifications, considering the interaction between sea-bed changes and velocity field. The application to a schematic semi-circular bay has given reasonnable results in agreement with known natural tendancies. However the developement of this model requires more accurate comparisons with scale model results or real cases. This work will be planned in the near future.

7. AKNOWLEDGEMENT

This study has been done as part of a joint research programm of EDF-LNH and the "Ministère de la mer".

8. REFERENCES

BIJKER, E.W. (1968). Littoral drift as function of waves and current. 11e Coastal Engineering Conference. London.

BIJKER, E.W. (1967). Some considerations about scales for coastal models with movable bed. Pub n° 50 of the Delft Hydraulic Laboratory.

FRIJLINK, H.C. (1952). Discussion des formules de débit solide de Kalinske, Einstein et Meyer-Peter et Muller. Deuxième journée de l'hydraulique. Transport hydraulique et décantation de matériaux solides. Grenoble.

SABATON, M, HAUGUEL, A. (1978). A numerical model of Longshore Currents. Rapport Electricité de France n° HE/42/78.34

DESIGN AND CALIBRATION OF FALSE BAY SEDIMENT MODEL

by

J S Schoonees* and J P Möller**

1. INTRODUCTION

False Bay is situated near Cape Town in the Republic of South Africa. The National Research Institute for Oceanology (NRIO) of the Council for Scientific and Industrial Research (CSIR) was commissioned to undertake studies on a recreational scheme in the Strandfontein area of False Bay. A tidal pool was built as phase 1 of this project. Phase 2 is a bathing improvement scheme (see Figures 1 and 2).

The aim of the bathing improvement scheme which consists of a number of structures, is to provide bathing facilities for the Mitchell's Plain community. At present the major part of the coast is rather unsafe for bathing mainly because of very steep beach profiles. Conditions were laid down to ensure safe bathing, e.g. a uniform flat beach slope and the absence of rock and rip currents. Further requirements were that a safe bathing beach must be formed soon after completion of the structures and that the adjacent coastline must not be adversely affected in the long term. This paper deals with the design and calibration of a sediment model which was chosen to evaluate and optimise the design of the proposed T-groyne and the system of detached breakwaters shown in Figure 3.

2. DESIGN OF THE MODEL

2.1 Design Philosophy

The basic prerequisite of a sediment model is to reproduce sediment motion correctly. This can be achieved by

* J S Schoonees, Sediment Dynamics Division, Coastal Engineering and Hydraulics, National Research Institute for Oceanology, South African Council for Scientific and Industrial Research, Stellenbosch.

** J P Möller, Sediment Dynamics Division, Coastal Engineering and Hydraulics, National Research Institute for Oceanology, South African Council for Scientific and Industrial Research, Stellenbosch.

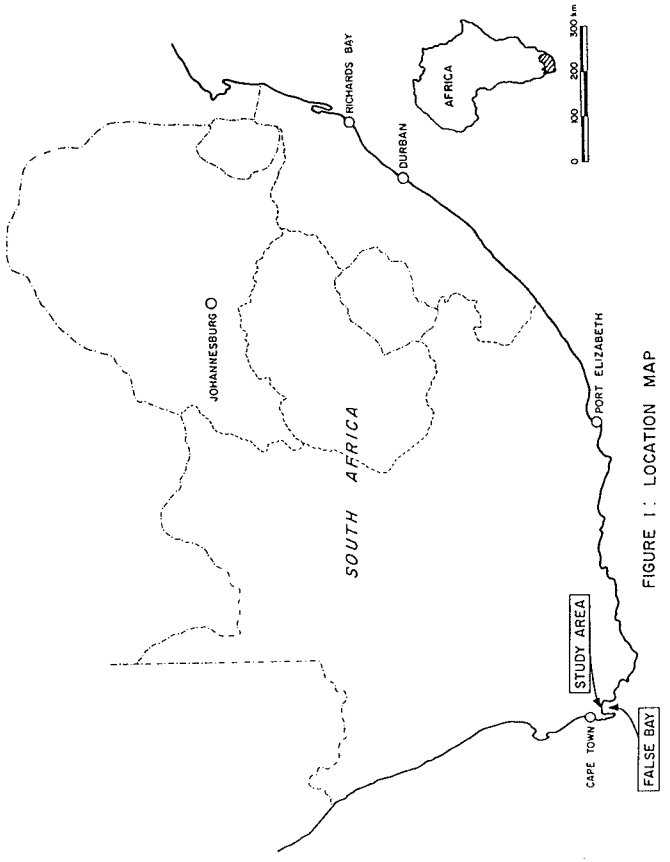

FIGURE 1: LOCATION MAP

FIGURE 2: STUDY AREA

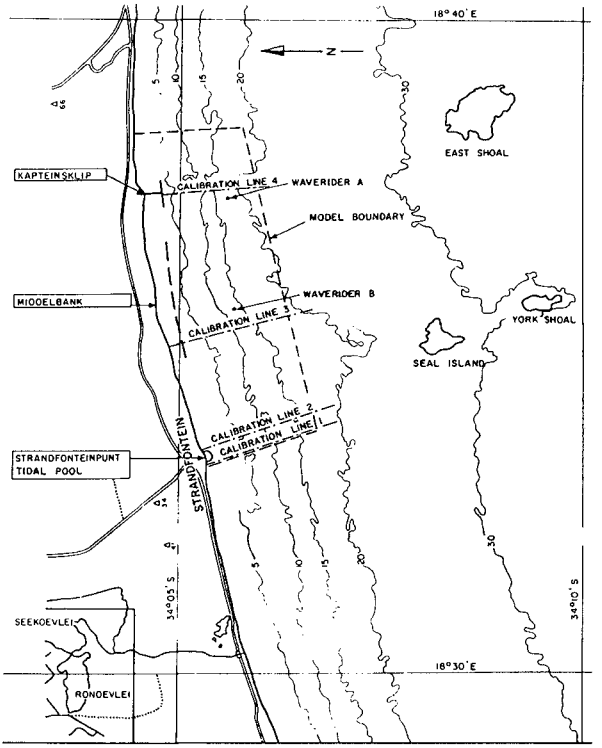

FIGURE 3: THE BATHING IMPROVEMENT SCHEME

modelling the on-offshore and longshore transport rates accurately. Inherent in this approach is the fact that the sedimentological time scale must not vary from place to place in the model. The time scale must also be constant in time, that is, as the experiment progresses. It will be shown that the selection of the bed material and the determination of the horizontal and vertical scales after model boundaries have been chosen, will ensure that sediment motion is correctly modelled and that a constant sedimentological time scale is obtained.

2.2 Choice of the Bed Material

Sand instead of lightweight material was chosen as the most suitable sediment for the model for the following reasons:

(a) To obtain the most accurate simulation of longshore transport the functional relationship between the transport and the driving forces should be examined. This relationship can, for most practical purposes, be approximated as:

$$S_x = a(v_* - v_{*c})^b \qquad (1)$$

where a, b = coefficients dependent on the grain size
v_* = shear velocity
v_{*c} = critical shear velocity at initiation of particle motion
S_x = longshore transport rate.

The best comparison between transport rates in model and prototype is obtained when v_{*c} and b are scaled 1 to 1. This can be done only by using sand for model material with approximately the same grain size as in prototype because v_{*c} and b are dependent on the grain size. The scale of v_* depends on the velocity scale and the hydraulic roughness scale. Bedforms are exaggerated in the model relative to prototype; this results in a roughness scale which is closer to unity than to the vertical scale. Consequently, more material is entrained on scale, due to higher turbulence close to the bed, than in prototype. The scaling process for longshore transport is completed by choosing a scale for the longshore current velocity which yields a velocity greater than that which would have been obtained from the Froude velocity scale in order to ensure a constant time scale. This is similar to the concept of an "ideal velocity scale" introduced earlier by Bijker (1967).

(b) It has been shown (Swart, 1974) that the geometric shape of the dynamic beach profile depends strongly on the grain size, wave height and wave steepness. Lightweight material, scaled according to the submerged weight, will be relatively too heavy out of the water, resulting in very steep (almost vertical) beach slopes near the water line. Therefore, to ensure the same breaker type in the model and

prototype and consequently also similar longshore current profiles, sand with the same grain size as the prototype material should be used.

The empirically derived relationship (Swart, 1974) for the equilibrium beach slope of sandy beaches is as follows:

$$m_r = 1{,}51 \times 10^{3}\left(\frac{H_o}{L_o}\right)^{-1}\left[H_o^{0{,}132}\, D_{50}^{-0{,}447}\left(\frac{H_o}{L_o}\right)^{-0{,}717}\right]^{-2{,}38} + 0{,}11 \times 10^{-3}\left(\frac{H_o}{L_o}\right)^{-1} \qquad (2)$$

where m_r = schematized equilibrium beach slope at the still water level
H_o = deep-water wave height
L_o = deep-water wave length
D_{50} = median sediment particle diameter.

(c) Porosity is normally greater at the grain sizes needed to model sedimentary processes with lightweight material than in prototype. Therefore substantial wave energy losses occur due to percolation. The correct modelling of the breaker characteristics and longshore water and sediment movement becomes extremely difficult to achieve in practice.

2.3 Selection of the Model Boundaries

The study area stretching from a slightly curved beach to the 22 m contour, is naturally bounded by two easily distinguishable features, namely, the tidal pool at Strandfonteinpunt and the rocks of Kapteinsklip - see Figure 3. Both of these form a partial obstruction to the longshore transport. The natural choice for the model boundaries is therefore as follows:

(a) From Strandfonteinpunt to approximately 1 km beyond Kapteinsklip. It was necessary to extend the model to the east of Kapteinsklip because the proposed scheme incorporates a groyne at Kapteinsklip.

(b) The depth at the offshore limit of the model is 22 m relative to mean sea level (MSL) but the movable bed terminates at the 16 m contour. This is safely beyond 8 m, the depth of significant sediment movement found in a theoretical analysis of longshore transport in a feasibility study.

2.4 Determination of the Horizontal and Vertical Scales of the Model

Swart (1974) devised a method to calculate the on-offshore transport that is based on the equilibrium beach profile concept. According to Swart (1974) the on-offshore trans-

port is directly proportional to the difference in configuration between the existing and equilibrium profiles. Therefore to model on-offshore transport correctly, the distortion of the model (ratio between the vertical and horizontal scales) must be equal to the ratio between the equilibrium beach slope in the model and that in prototype. This method was proposed by Bijker (1967) as well as Fan and Le Méhauté (1969). The Swart (1974) procedure for the calculation of the equilibrium beach slope was used. If the above-mentioned criterion is not met, additional on-offshore transport will take place in the model because of the incorrect distortion of the model - something that does not happen in prototype.

A horizontal scale of 1 in 120 was chosen to fit the model of the study area into the available model basin. From the results of the feasibility study the representative wave condition is: wave period = 10 s; deep-water significant wave height (H_S) = 2 m. The vertical scale was computed to satisfy the previously mentioned criterion as follows:

(a) Determine the prototype equilibrium beach slope:

From (2) $m_{r,p\infty} = 0{,}0240$ with $D_{50,p} = 450$ μm and $L_o = \frac{gT^2}{2\pi} = 156$ m (linear theory).
(g = gravitational acceleration; T = wave period; subscripts: m = model; p = prototype; ∞ = infinitely long time, that is, equilibrium conditions.)

(b) Select a vertical scale, say, 1 in 40.

(c) Calculate the equilibrium beach slope in the model with:

$H_{s,m} = \frac{1}{40} \times 2 = 0{,}05$ m

$L_{o,m} = \frac{1}{40} \times 156 = 3{,}90$ m (the wave length must be scaled with the vertical scale in order to model refraction correctly).

$D_{50,m} = 450$ μm (D_{50} must preferably be as close as possible to $D_{50,p}$, except for very coarse prototype material. For $D_{50,p}$ large, $D_{50,m}$ must be chosen such that $D_{50,m} < D_{50,p}$ or problems with the initiation of sediment movement will occur.

From (2): $m_{r,m\infty} = 0{,}0491$

(d) Check whether the slope ratio $(\frac{m_{r,m\infty}}{m_{r,p\infty}})$ is equal to the distortion factor (DF).

$$DF = \frac{1}{40} / \frac{1}{120} = 3,0$$

$$\frac{m_{r,m^\infty}}{m_{r,p^\infty}} = \frac{0,0491}{0,0240} = 2,04 \neq DF.$$

Choose a new vertical scale and repeat the procedure until $\frac{m_{r,m^\infty}}{m_{r,p^\infty}} = DF$. The result of this iteration process was a vertical scale of approximately 1 in 50. It must be added, because (2) is applicable only to sandy beaches, that the sediment in the model must be sand to permit the use of this method.

(f) Check that a realistic vertical scale is obtained by quantifying the internal friction and surface tension effects. If not, change the horizontal scale and repeat the iteration process.

Because it is a distorted model with the beach slope being steeper than in prototype, the breaker index will be influenced in such a manner that the breaker line will move inshore. To compensate for this effect, the wave height was increased to scale the width of the breaker zone correctly. This increase was, however, not significant enough to conflict with the requirements described in previous paragraphs.

3. DATA ACQUISITION AND CALIBRATION

3.1 Waves

Datawell Waveriders (accelerometer buoys) were deployed at the site to measure the wave heights and periods. Partly because of the complex bathymetry (see Figures 3 and 4) of the bay which caused unreliability of the theoretical refraction method used, and partly to obtain the best possible coverage in the limited recording period available (one year only - April 1980 to March 1981), recordings were made at two separate locations in a water depth to mean sea level (MSL) of approximately 20 m (see Figure 3 for the positions of the Waveriders). The results are summarized in Figures 5 and 6. Simultaneously a year-long exercise was undertaken during which aerial photographs were obtained of the study area approximately every second day. By orientating the individual photographs taken during each flight with the aid of a template, photographic strips of the coastline were obtained. The wave directions along the 6 m depth contour were then read off from these strips, thus acquiring a wave direction distribution along the coastline for every flight. The accuracy of this method, obtained from successive flights on two occasions (total number of repetitions: 48 flights) is 3,8°.

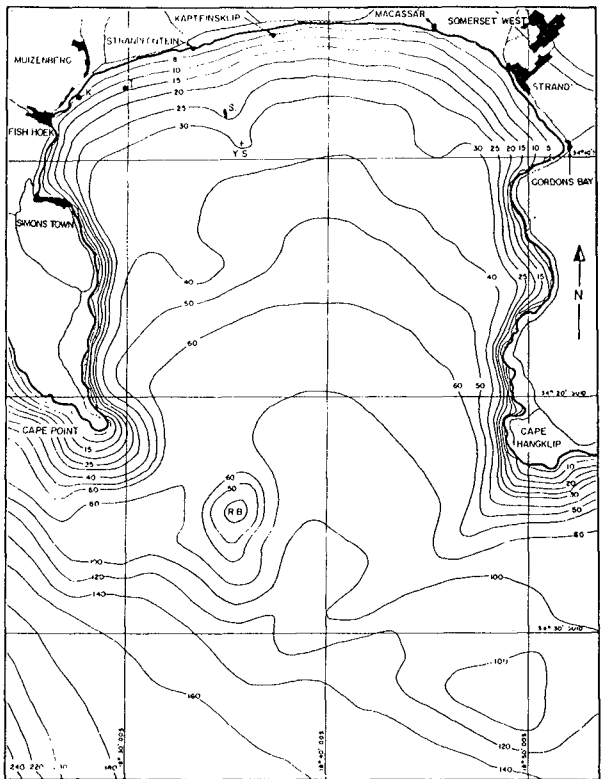

FIGURE 4: BATHYMETRY OF FALSE BAY

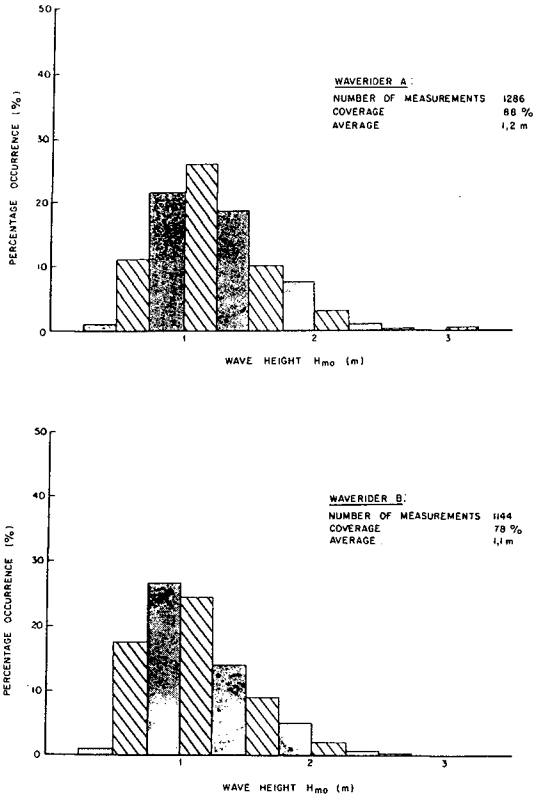

FIGURE 5: WAVE HEIGHT HISTOGRAMS

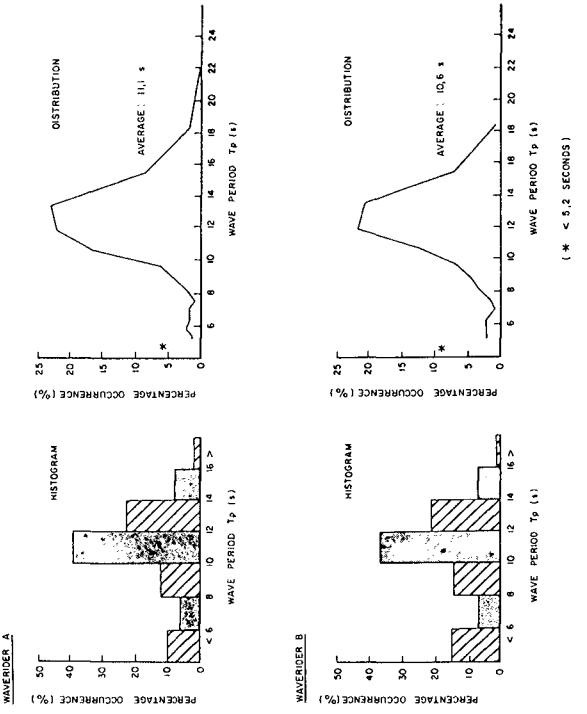

FIGURE 6: WAVE PERIOD OCCURRENCE

Deep-sea wave directions during the (Waverider) recording year (see Figure 7) were obtained from voluntary observing ships. The wave direction distribution along the 6 m depth contour was then compared with the distribution obtained from the theoretical wave refraction exercise. The measured wave patterns proved the theoretically-predicted tendencies.

Deep-sea ship observations also provided the wave climate over a period of 20 years (1960-1979). Equivalent deep-sea instrument (Waverider) data were computed for the 20-year period by using the relations (CSIR, to be published in 1982):

$$H_s \text{ (Waverider)} = 1{,}0 + 0{,}55\ H_s \text{ (ship)}$$

$$T_p \text{ (Waverider)} = 4{,}1\ T^{0\ 55} \text{ (ship)}.$$

By shoaling and refracting each of these observations the shallow water wave climate at the position of waverider A (see Figure 3) was determined, thus making it possible to see how representative the year's recorded data were. The wave height exceedance curves are shown in Figure 8, which indicates a relatively calm recording year.

The wave climate was divided into two parts, that is, westerly waves (causing eastbound longshore transport) and easterly waves (causing westbound longshore transport). For example, the westerly waves include waves from the WSW, SW, etc. As the wave energy is proportional to the product of the peak energy wave period (T_p) and the square of the significant wave height (H_s), it was possible to calculate $\overline{T_p}$ and $\overline{H_s^2 T_p}$ for easterly and westerly waves (the bar denotes mean values). Thus a representative wave that has the average wave energy is one with $H_s = (\overline{H_s^2 T_p}/(\overline{T_p}))^{1/2}$. This was done for both easterly and westerly waves, resulting in:

$$H_{s,east} = 1{,}0 \text{ m};\ T_{p,east} = 10{,}7 \text{ s}$$

$$H_{s,west} = 0{,}8 \text{ m};\ T_{p,west} = 12{,}2 \text{ s}.$$

The wave directions along the model boundary were measured from refraction diagrams for all possible wave directions and wave periods and weighted mean directions along the boundary obtained by using the deep-sea wave climate. However, irregular waves are preferred to regular waves due to the fact that in prototype the breaker line is continually shifting, as opposed to the stationary breaker line resulting from regular waves. Furthermore, irregular waves in the model will also reduce secondary wave generation effects. By using a period variator the periods were randomly altered around the calculated peak wave period according to a normal distribution with a standard devia-

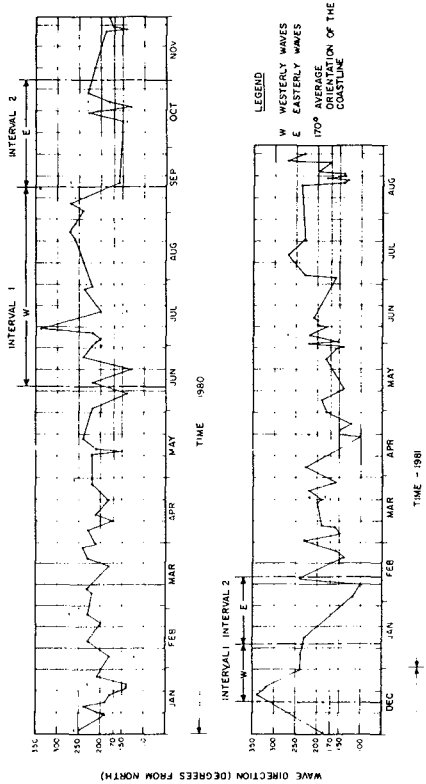

FIGURE 7: DEEP SEA WAVE DIRECTIONS (SHIP DATA)

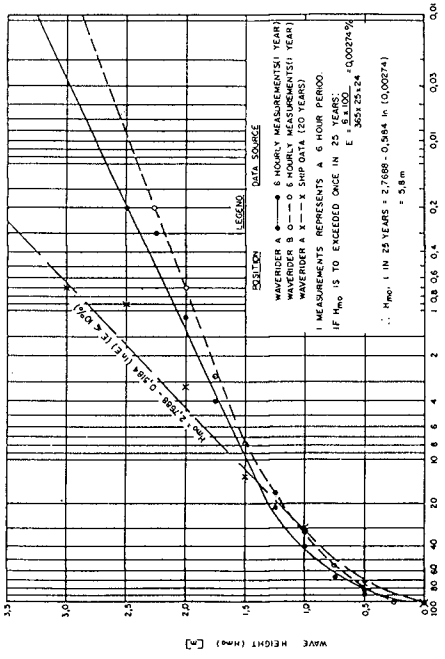

FIGURE 8 : WAVE HEIGHT EXCEEDANCE CURVES

tion of 0,2 s. At the same time the wave height was changed in a cyclic manner, resulting in quasi-irregular waves. A series of measurements were taken to ensure the correct reproduction of the input wave variables.

Because the calculated wave characteristics and the model sediment size differ from the original values, the vertical scale was recalculated. The discrepancy between these two vertical scales was insignificant.

3.2 Tides

The tides in the False Bay area are semi-diurnal with a mean range of about 1,6 m. Because tidal currents are negligible in this area (Atkins, 1970) the other tidal effects, that is, exposure of a steeper part of the beach profile to wave action, as well as causing the breaker line to change position, were modelled by testing 0,5 m above MSL and using quasi-irregular waves.

3.3 Sediment

Sediment samples were taken monthly at fixed positions along the beach. The particle size and distribution were determined in a settling tube. The median particle diameter for the 8 km stretch of coastline (upper and lower foreshore combined) from February 1980 to November 1981 was 450 μm. The beach between Strandfonteinpunt and Kapteinsklip is a moderately protected beach with little net sediment movement. Therefore it was difficult to acquire calibration data because quarterly hydrographic surveys showed beach and nearshore profile changes of less than 0,3 m (which approaches the measuring accuracy of the surveys). Figures 9 and 10 show typical beach and nearshore profiles. Daily aerial photographs used for determining the wave direction provided profile growth and recession rates at four places (see Figure 3 for the four calibration lines) along the coastline. After the scales of the photographs had been determined, the distances between the waterline and arbitrarily chosen beacons were measured. Tidal corrections, deduced from the beach profiles and the tidal heights at the time that the photographs were taken, were then applied to give the growth and recession of the waterline with time. Four distinct time intervals were identified from Figure 7, two for easterly and two for westerly waves. These, together with the corrected growth and recession rates are shown in Figures 11, 12 and 13. The rates of waterline movement were averaged for easterly and westerly waves at each of the calibration lines.

In order to model the prototype conditions, it was necessary to introduce and extract a longshore current as well as longshore sediment transport at the sides of the model.

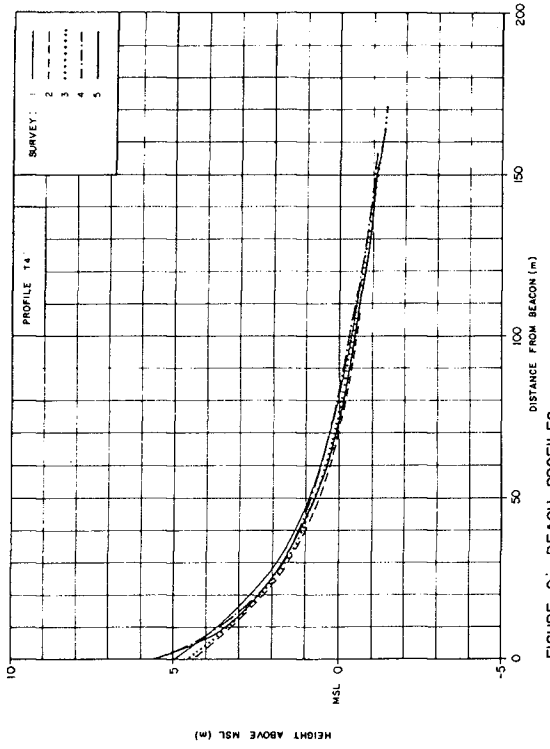

FIGURE 9: BEACH PROFILES

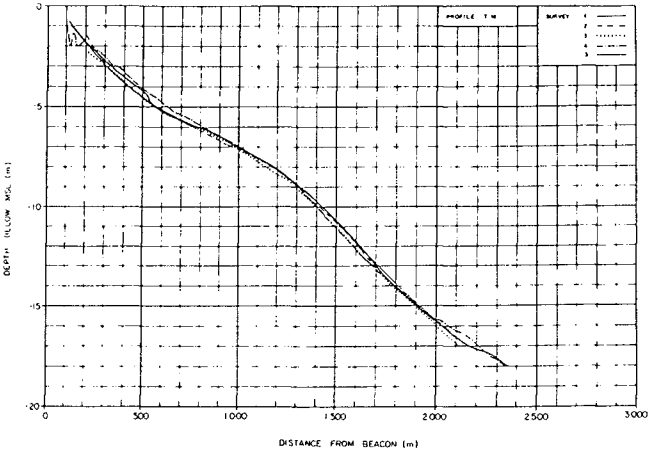

FIGURE 10: NEARSHORE PROFILES

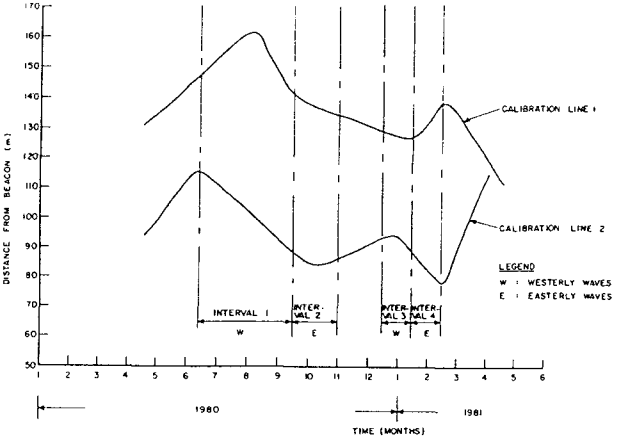

FIGURE 11: WATERLINE MOVEMENT AT STRANDFONTEINPUNT

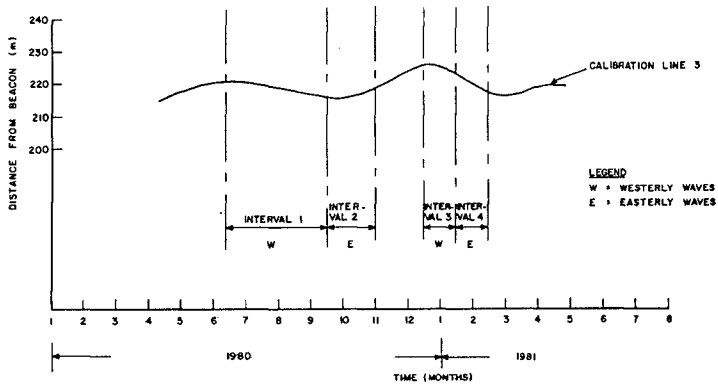

FIGURE 12: WATERLINE MOVEMENT AT MIDDELBANK

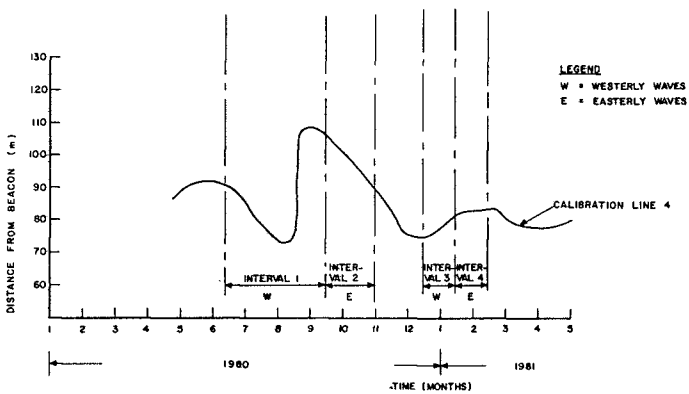

FIGURE 13: WATERLINE MOVEMENT AT KAPTEINSKLIP

Therefore the entrance/exit conditions had to be calibrated for both the easterly and westerly waves.

The overall water circulation pattern was monitored using a dye tracer to ensure the correct reproduction of the magnitude of the longshore current. The correct distribution of the longshore current (as predicted by Longuet-Higgins (1970)) relative to the average breaker line was obtained with a set of baffles. The sand feeding rate was determined by a trial and error process. It was found that because of the relatively slow longshore sediment movement, the feeding had to be intermittent. After these variables had been calibrated, verification tests were executed to determine the sedimentological time scale. The prototype tendencies of growth and recession were matched in the model except for calibration line 1. The proximity of this line to the edge of the model prevented its use during calibration procedure.

The distribution of the shallow-water wave climate according to wave direction, is as follows:

(i) westerly waves: 46,9%,

(ii) easterly waves: 13,2%,

(iii) calm periods (includes deep water waves moving away from the land): 36,5%, and

(iv) waves perpendicular to the coastline of the study area (for the 5° interval of 168° - 172°): 3,4%.

By taking this distribution into account, the following sedimentological time scale was obtained: 24 hours (model) ≡ 1 year (prototype). One year in prototype is therefore represented by five cycles, each comprising 3,75 h westerly and 1,05 h easterly waves.

4. CONCLUSIONS

A procedure is outlined for the design of movable bed coastal models, which uses the scales of the longshore and on-offshore transport instead of only longshore transport, as is common practice. This method indicates that sand is preferable to lightweight material for a movable-bed model.

Although the outlined iteration procedure results in large models, the verification is more easily accomplished.

In areas with low sediment transport, it is often possible to acquire good calibration data for a sediment model only if the model includes structures or coastal features that at least partially obstruct the longshore sediment movement. An alternative would be to undertake hydrographic

surveys before and after storms. This, however, can be very costly.

The use of aerial photography for the determination of wave direction provided useful additional coastline data. In this case the photographs were used to identify rocky areas and to obtain waterline growth and recession rates. The main disadvantage of this method is the impossibility of collecting data during stormy periods.

The utilisation of quasi-irregular waves nearly eliminated the formation of beach cusps due to secondary wave effects.

5. ACKNOWLEDGEMENT

The authors gratefully acknowledge the permission given by the consulting engineers, O'Connell, Manthé and Partners, to publish this paper.

6. REFERENCES

ATKINS, G R (1970). Winds and current patterns in False Bay. Transactions of the Royal Society of South Africa, Vol 39(2), pp 139-148.

BIJKER, E W (1967). Some considerations about scales for coastal models with movable bed. Delft Hydraulic Laboratory, Publ. No 50, 142 pp.

CSIR (to be published, 1982a). Valsbaai: velddataverslag (False Bay field data report). Contract Report C/SEA 8219, NRIO, Stellenbosch. (In Afrikaans.)

CSIR (to be published, 1982b). The effect on the Mvumase project on the Tugela estuary and the adjacent coastline. Contract Report, NRIO, Stellenbosch.

FAN, L and LE MéHAUTé, B (1969). Final Report. Coastal movable bed scale model technology. Tetra Tech No TC-131, Pasadena, California, 122 pp.

LONGUET-HIGGINS, M S (1970). Longshore currents generated by obliquely incident sea waves. J of Geophysical Research, Vol 75, No 3.

SWART, D H (1974). Offshore sediment transport and equilibrium beach profiles. Delft Hydraulic Laboratory, Publ No 131, 302 pp.

BLOWN SAND ON BEACHES

by

Susumu Kubota[1], Kiyoshi Horikawa[2]

and Shintaro Hotta[3]

ABSTRACT

The blown sand transport rate and the vertical and shore-normal distributions of the wind speed were measured simultaneously on a windy beach. The sand transport rate was measured with conventional total quantity-type traps and with a large trap in the form of a trench. The vertical distribution of the wind speed was measured using an ultrasonic anemometer array consisting of six meters. The distribution of wind speed at a height of 1 m in a section normal to the shoreline was measured with five ultrasonic anemometers. A logarithmic law for the vertical distribution of the wind speed was satisfied, and the wind speed in the section normal to the shoreline was almost constant. The Kawamura and Bagnold formulae were found to predict well the sand transport rate. The trench trap and conventional traps gave empirical coefficients of 1.5 and 1.0, respectively, for the sand transport rate averaged over a section normal to the shoreline. The lower value determined with the conventional traps (1.0) is attributed to their inefficiency compared with the trench trap. In order to obtain data at high shear velocities, a wind tunnel experiment was carried out. This experiment showed that both the Kawamura and Bagnold formulae were valid in the range between 60 to 300 cm/s in the wind shear velocity. The empirical coefficient in the laboratory experiments was 1.0: the difference between the field result with the trench trap and the wind tunnel experiment is attributed to the fluctuations in natural wind.

1. INTRODUCTION AND OBJECTIVES

From the viewpoint of coastal zone management in Japan, up to about 30 years ago the prevention of river mouth closure and the protection of cultivated land from intruding blown sand were important subjects for agricultural civil and coastal engineers. At that time there were rich sandy beaches. However, characteristics of the coast have changed in this country since then. Flood control systems for inland rivers brought about new serious problems of coastal erosion, and engineers

1. Research Engineer, Nearshore Environment Research Center, 1202 Famille Hongo Building, 1-20-6 Mukohgaoka, Bunkyo-ku, Tokyo 113, JAPAN
2. Professor, Department of Civil Engineering, University of Tokyo, Bunkyo-ku, Tokyo 113, JAPAN.
3. Research Associate, Department of Civil Engineering, Tokyo Metropolitan University, 2-1-1 Fukazawa, Setagaya-ku, Tokyo 158, JAPAN

have become intensely occupied with this challenge. As a result, it seems that the topic of blown sand was left behind as a field of engineering interest. However, blown sand can be an important factor affecting beach change where a strong seasonal wind is predominant. In such situations, sand transport by wind should be included in the sand budget. Therefore, the authors initiated comprehensive field investigations and laboratory studies to establish calculation methods for the transport of sand by wind on beaches. As a first stage of this study, the main effort was concentrated on calculating the total sand volume transported through a section normal to the shoreline (Horikawa, Hotta, Kubota, and Harikai, 1981; Horikawa, Hotta, and Kubota, 1982a).

Several formulae for predicting the total sand transport rate by wind have been presented (O'Brien and Rindlaub, 1936; Chepil, 1945; Kawamura, 1951; Bagnold, 1954; Zingg, 1952; Kadib, 1966; Hsu, 1974). A characteristic of the above formulae, with the exception of Kadib's, is that the total sand transport rate is proportional to the third power of the shear velocity (i.e., the wind speed) at a certain height. A number of detailed discussions of the above formulae have been given (e.g., Horikawa and Shen, 1960; Nakamura, 1971; Phillips and Willetts, 1978). These studies indicate that the various predictive expression can give relatively good results if the empirical coefficients in the formulae can be determined with reasonable accuracy. The two formulae most commonly employed for estimating the total transported sand volume by wind, and for comparison and discussion of experimental results, are those of Bagnold and of Kawamura. They are

$$q = B\sqrt{\frac{d}{D}}\,\frac{\rho}{g}\,u_*^3 \qquad \text{Bagnold (1954)} \qquad (1)$$

$$q = K\,\frac{\rho}{g}\,(u_* - u_{*c})\,(u_* + u_{*c})^2 \qquad \text{Kawamura (1951)} \qquad (2)$$

where q is the sand transport rate (unit weight/unit time/unit width), u_* is the shear velocity, u_{*c} is the critical shear velocity of sand grain movement, ρ is the density of air, g is the acceleration of gravity, D is the standard sand grain diameter (0.25 mm), d is the sand grain diameter forming the sand bed, and B and K are nondimensional empirical coefficients.

2. FIELD OBSERVATION

Two field observations were carried out. The first was conducted between January 7 and January 12, 1981, and the second between January 7 and 17, 1982. The observation site was Yonezu Beach on the west side of the Tenryu River in the middle part of the main island of Japan (Fig. 1). During winter, sand is continually in motion at this site due to the strong seasonal wind from the west, blowing parallel to the shoreline. The sand grain size on this beach ranges between 0.1 to 0.8 mm, and its median diameter is 0.4 mm. The sand is well sorted. During the experiments, dune configurations 20 to 50 cm high and 20 to 30 m long existed on the beach normal to the shoreline and normal to the predominant direction of the wind.

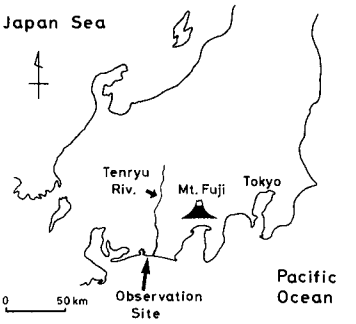

Fig. 1 Location map of the site.

2.1 Experiment Background

The wind speed was measured by an anemometer array consisting of six ultrasonic Doppler shift-type anemometers (Photo 1). An ultrasonic anemometer has the distinguishing merit that the wind speed can be measured precisely at high frequency, because the ultrasonic beam is emitted at 10 Hz. However, this instrument has a drawback for the present application. Data can be lost if a flying sand grain intersects a beam or hits the emitting probe. Therefore, this instrument is not suitable for measuring the wind speed near the beach surface where high concentrations of blown sand can appear. The lowest elevation used for the wind speed measurement was 10 cm. At this elevation noise sometimes appeared, but the frequency of occurrence was small and the noise could be excluded in the computer analysis.

Two kind of traps were used for measurement of the blown sand transport rate. One was a conventional total quantity-type trap and the other was a trench trap. The former was patterned after the traps used by Horikawa and Shen (1960), with some modifications based on field experience. Photo 2 shows a trap in operation. The mouth of the trap was 10 cm by 200 cm. In Photo 2, it is seen that local scour did not take place around the trap. Normally, local scour will appear around an object. Because of this, irregular trapping of the blown sand occurs during progress of the scour. To prevent the generation of scour, several procedures were attempted. We finally succeeded by spraying water around the trap during its setting. The sprayed surface resists erosion and no scour takes place. For the first few minutes, dried sand grains transported from upstream adhere to the wetted surface. Thereafter, a dry sand surface with no scour forms (as seen in Photo 2).

The other trap used for measurement of the blown sand transport rate is a trench-type trap. The idea of such a trap was suggested from previous studies. It is commonly known that the travel distance of a sand grain in saltation or in suspension is in the range of a few centimeters to a few meters. The experiment by Ishihara and Iwagaki (1952) showed that 97% of the total blown sand from upstream fell within 4 m of the waterline in the case of a pond or a stream. Iwagaki (1950) also reported that by utilizing the above information and constructing a

Photo 1 Ultrasonic anemometer array.

Photo 2 Total quantity type trap.

stream a few meters wide, cultivated land could be protected from intruding blown sand. This measure was implemented at Tottory beach in Japan. From the preceding results, the authors concluded that the entire quantity of blown sand could be trapped by a trench of width more than a few meters. A trench trap 8 m wide, 1 m deep, and 50 m long was therefore used.

Photo 3 shows the trench in the first observation: (a) at the beginning of the observation, and (b) at the same location after four days. The photo shows the upstream side slope, and indicates that the slope advanced while maintaining the rest angle of the dry sand. We can estimate the total amount of blown sand trapped by the trench given the width of the accumulated sand and the depth of the trench.

(a) Beginning of the observation. (b) End of the observation.

Photo 3 Trench trap.

2.2 Experiment Procedure

Figure 2 shows the beach profile and the arrangement of the instrumentation for the first observation. Symbols A to F indicate positions of the total quantity traps (arranged across a section normal to the shoreline). The open squares indicate locations where the vertical distribution of the wind speed was measured. Together with measurements of the vertical wind speed distribution at each position on the beach, blown sand was collected by the total quantity traps on January 8, 9 and 10, 1981. The sampling period for the transport rate was 10 minutes.

Survey poles with measurement scales were installed in the trench at 1-m intervals in the direction of the wind, and at 2-m intervals in the direction normal to the wind (See Photo 3). The change in the sand surface was measured from differences in distance from the tops of the poles to the sand surface. Measurement of the sand surface change in the trench was carried out around 9:00 am and 5:00 pm from January 8 to January 12.

Figure 3 shows the beach profile and the arrangement of the instruments for the second observation. Letters A to F give positions of the total quantity traps. Numbers 3 to 7 give the positions of the anemometers. While measuring the wind speed distribution continuously, the distribution of the sand transport by wind in a section normal to the shoreline was measured by total quantity traps on January 13 and 14, 1982. As in the first observation, the sampling period was ten minutes.

The trenches were dug as sbown in Fig. 3. The sand transport rate was measured at the most-upstream trench, TC. Tbe region S between the two downstream trenches TB and TA was used in an attempt to check the sand budget. The trench TB stops the blown sand from the upstream side, while the downstream trench TA collects the blown sand originating from region S. If we know the total sand volume which moved from region S, we can compare this amount with that collected in trench TA. To determine the total sand volume moved from region S, small steel pipes 12 mm in diameter and 1 m in length were hammered into the surface

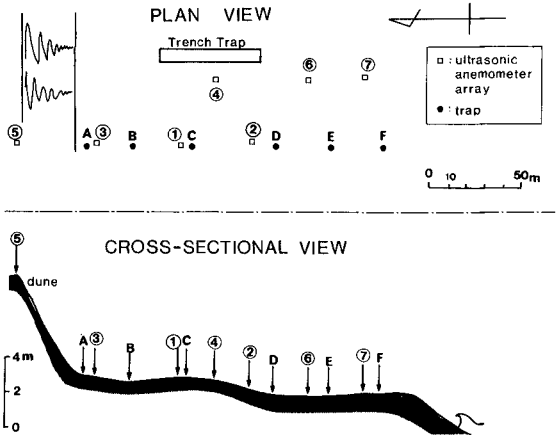

Fig. 2 Beach profile of the site and arrangement of instrumentation (first observation).

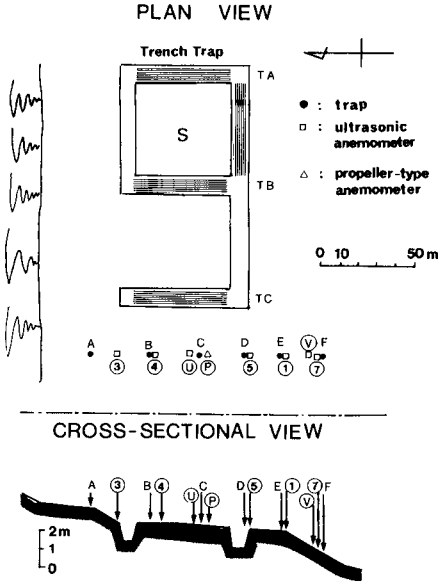

Fig. 3 Beach profile of the site and arrangement of instrumentation (second observation).

to form a grid with a 2 m by 2 m mesh. The distance between TB and TA was 50 m. A width of 50 m was choosen for the measurement. A total of 676 pipes were installed.

The region between TC and TB was used in an experiment of the drying process of the sand surface. Details of this experiment have been described elsewhere (Horikawa, Hotta, and Kubota, 1982b).

The circled letters U and V indicate the positions where the vertical distribution of the wind speed was measured on January 15 and 16, 1982. The ultrasonic anemometer has been rather recently developed. To discuss and compare results of our field observations relative to previous studies, one needs to know the characteristic difference, if any, between the ultrasonic anemometer and conventional anemometers such as the propeller-type, cap-type and so on. For this purpose, the wind speed at a height of 5 m was measured with a propeller-type anemometer at position P in Fig. 3. The statistical characteristics and 10-min averages of the two types of instruments were found to be essentially the same. The wind speed was recorded on an open-wheel recorder for both experiments, and the data were averaged in intervals of 10 minutes.

3. RESULTS

3.1 Sand Characteristics

The grain size distribution and the median diameter of the sand are important parameters governing the blown sand transport. Table 1 gives examples of the median diameter and the uniformity coefficient based on sieve tests of the sand trapped by the total quantity traps in the first observation. Here d_{50} is the median diameter, and the uniformity coefficient is $U_c = d_{60}/d_{10}$. In Table 1 is also given the median diameter (0.4 mm) and uniformity coefficient (1.75) of the surface layer sand to about 0.5 cm in depth, which was removed from the neighborhood of point C on January 10, 1981

Table 1 Median diameter of blown sand and uniformity coefficient.

Location (Fig. 2)	10 Jan 81		9 Jan 81		8 Jan 81	
	d_{50}	U_c	d_{50}	U_c	d_{50}	U_c
A	0.31	1.50	0.25	1.47	0.27	1.58
B	0.31	1.50	0.27	1.50	0.28	1.55
C	0.31	1.52	0.28	1.58	0.27	1.50
D	0.30	1.45	0.28	1.50	0.28	1.48
E	0.32	1.62	0.27	1.58	0.28	1.50
F	0.26	1.61	0.25	1.53	0.24	1.44
surface	0.4	1.75				
u_*	37.6 (cm/s)		39.5 (cm/s)		30.0 (cm/s)	

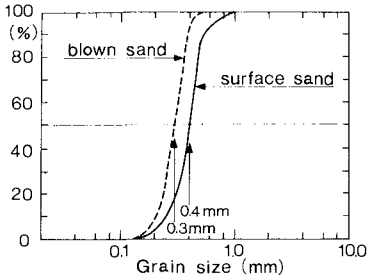

Fig. 4 Grain size accumulation curves of blown sand and surface sand.

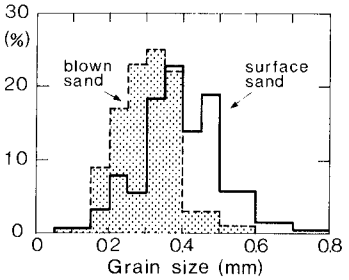

Fig. 5 Grain size distribution of blown sand and surface sand.

Figure 4 shows the particle size accumulation curves of the surface sand and a sample of the trapped sand at point C on January 10 (as listed in Table 1). Figure 5 shows the sand grain size distribution of both sand samples. The median diameter of the trapped blown sand is about 0.3 mm and the uniformity coefficient is around 1.5 (well sorted). Both the median diameter and the uniformity coefficient of the trapped sand are smaller than those of the surface sand. Larger grain sizes in the blown sand are seen to be limited in number (Fig. 4). It is therefore a difficult problem to determine the median diameter which represents the blown sand.

3.2 Wind Speed Distributions

To calculate the blown sand transport by Eqs. (1) and (2), the shear velocity u_* as an external force must be given. The shear velocity can be obtained as the gradient of a straight line on semilog paper, if the logarithmic law for the vertical distribution of wind speed is valid. That is,

$$u = 5.75\, u_* \log_{10} \frac{z}{z_o} \tag{3}$$

where u is the wind speed at a height z, the roughness of the sand surface is z_o, and u_* is the shear velocity. Equation (3) holds under the condition that the wind speed is not sufficiently large to move the sand grains. However, the distribution of the wind speed will be affected by the moving sand grains if the wind speed is greater than the critical wind speed and sand grains begin to move. Then Eq. (3) should be replaced by

$$u = 5.75\, u_* \log_{10} \frac{z}{z'} + u' \tag{4}$$

where (z', u') defines the "focal point" according to Bagnold (1954). Therefore, on semilog paper, all lines expressing the vertical distribution of wind speed converge to the focal point.

Figure 6(a) shows examples of the vertical distribution of wind speed observed on January 7 and 8 in the first observation. We can conclude that Eq. (4) is satisfied. Equation (4) was also satisfied at other observation points on the flat portion of the beach, except in the vicinity of a coastal dune located parallel to the shoreline.

The focal point observed in the first observation ranged between $u' = 130$ to 250 cm/s, and $z' = 0.11$ to 0.3 cm. Zingg (1952) suggested the following empirical equations for the focal point:

$$u' = 20\ d \quad \text{(mile/hr)} \tag{5}$$

$$z' = 10\ d \quad \text{(mm)} \tag{6}$$

Here d is the diameter of the sand in mm. We shall compare the observed results with Zingg's equations. If the diameter of the sand grains is taken as 0.4 mm (the median diameter of the sand bed), then

$$u' = 8.8 \cdot 10^2\ d = 358 \text{ cm/s} \quad \text{and} \quad z' = 10 \cdot 0.4 = 0.4 \text{ cm}$$

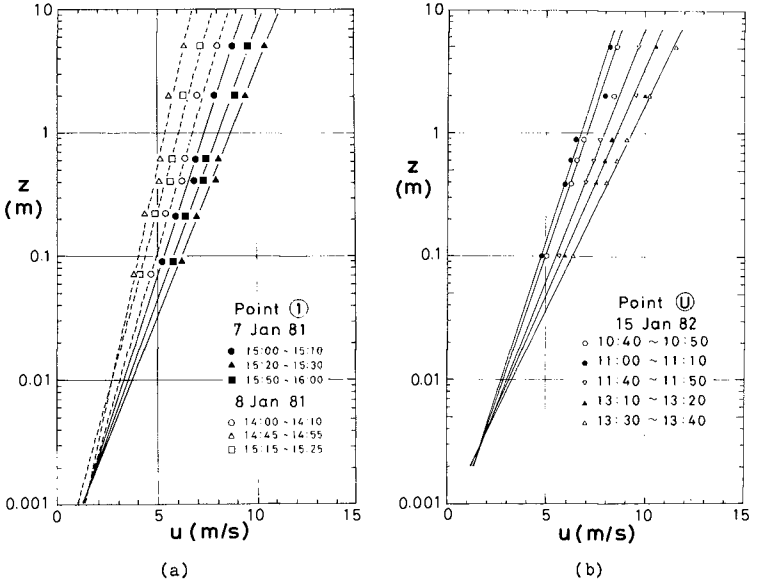

Fig. 6 Examples of vertical distribution of wind speed.

If d is 0.3 mm, the median diameter of the trapped blown sand, then

$u' = 264$ cm/s and $z' = 0.3$ cm.

For the first observation, Zingg's formulae agree with the upper limits from the field measurements.

In the second observation, the vertical distribution of wind speed was observed on January 14 and 15 (Fig 6(b)). Equation (4) was satisfied, but the focal point took on somewhat different values from the first observation. That is, u' was around 220 cm/s, and z' was around 0.6 cm, about twice that of the first observation. The value $z' = 0.6$ cm is somewhat larger than that predicted by Zingg's equation. To evaluate the utility of Zingg's equations, further observations are needed.

Another way to determine the shear velocity is to establish a relationship between the shear velocity and the wind speed at some specified elevation. Horikawa and Shen (1960) gave the following equations to calculate the shear velocity from the wind speed at heights of 1 m and 4.465 m. They are

$$u_* = 0.0690\, u_{100} - 18.4 \quad \text{(cm/s)} \tag{7}$$

$$u_* = 0.0548\, u_{446.5} - 14.7 \quad \text{(cm/s)} \tag{8}$$

Here u_{100} and $u_{446.5}$ are the wind speed at heights of 100 cm and 446.5 cm respectively. These equations are based on four assumptions; 1) Eq. (4), 2) Zingg's empirical formulae for the focal point, 3) the diameter of sand grain is 0.3 mm, and 4) the Karman constant is equal to 0.4. Assuming the same conditions, but directly inserting the measured average focal point ($u' = 200$ cm/s and $z' = 0.20$ cm), we obtain the following two equations:

$$u_* = 0.0644\, u_{100} - 12.9 \quad \text{(cm/s)} \tag{9}$$

$$u_* = 0.0511\, u_{500} - 10.2 \quad \text{(cm/s)} \tag{10}$$

Thus the shear velocity can be calculated from the wind speed at heights of 1 m and 5 m. Figure 7 shows a comparison of the shear velocity given by Eqs. (9) and (10) with the field data. The equations are seem to provide a good prediction.

Figure 8 shows an example of the ten-minute average wind speed at a height of 1 m across a section normal to the shoreline in the second observation. The data show that the wind speed was almost constant on the beach surface. Therefore, we can assume that the shear velocity acting on the sand surface was also constant.

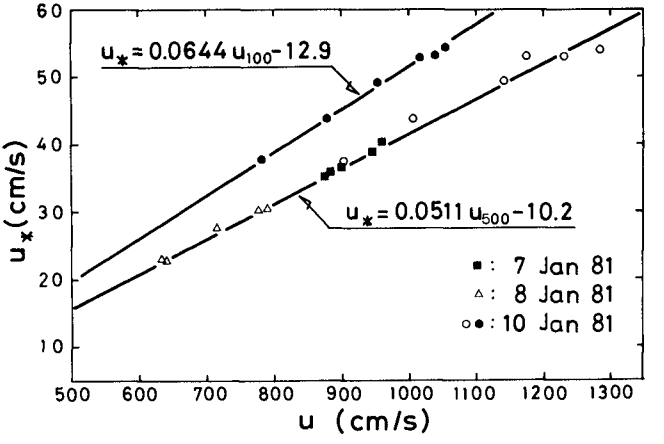

Fig. 7 Relationship between shear velocity and wind speed at heights of 1 m and 5 m.

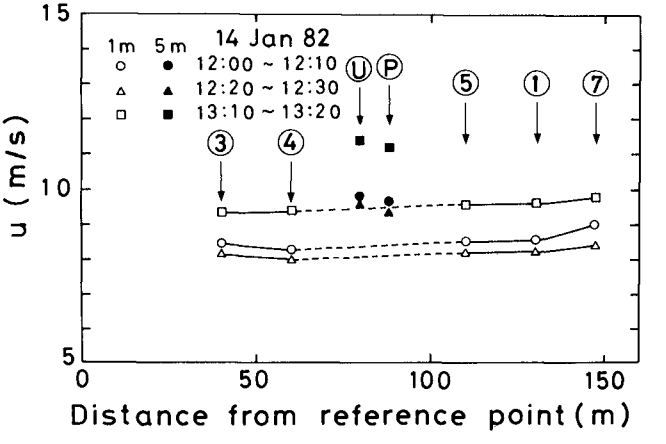

Fig. 8 Wind speed distribution at 1 m height in a section normal to the shoreline.

3.3 Sand Transport Rate

(1) Conventional trap

Figure 9 shows the distribution of the blown sand transport rate in a section normal to the shoreline on the first observation. Figure 10 shows a plot of the sand transport rate against the shear velocity at the measurement point C obtained from vertical distribution of wind speed measured simultaneously at the same point. In this figure, the curves calculated by the Bagnold and Kawamura formulae with empirical coefficients of 1.0 and 2.0 are also drawn. It is clear that both the Bagnold and Kawamura formulae agree well with the field data if the empirical coefficients are chosen to be about 1.0.

Figure 11 shows the sand transport rate distribution during the period in which the wind speed distribution was measured on the second observation. The sand transport rate was not constant in the section, although we had inferred that the shear velocity was constant on the beach (last paragraph of Subsection 3.2). We carefully observed the sand surface to resolve this problem. The surface consisted of a dune configuration about 30 to 50 cm high and about 15 to 20 m long. The dried sand layer was thick at the crest and thin at the trough. Sand was actively blown at the crest but not at the trough. We finally realized that the quantity of sand caught by the trap was dependent on the location of the trap. That is, a large amount of blown sand was trapped if a crest was located in front of the trap, whereas the amount collected was small behind a trough.

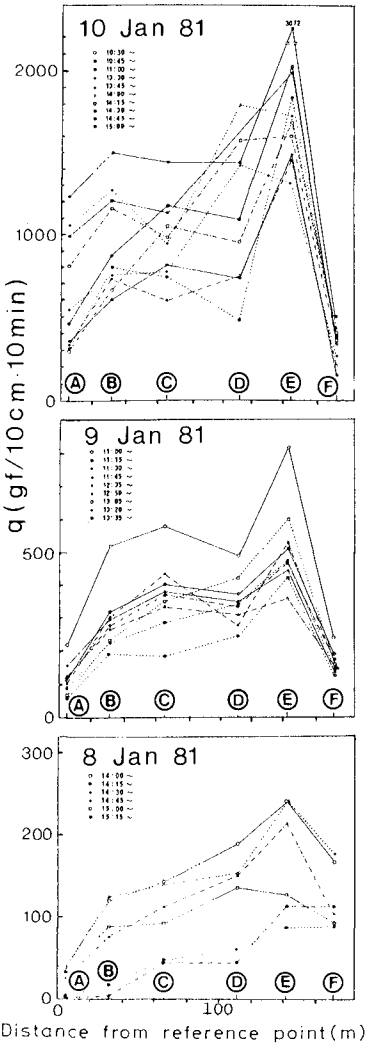

Fig. 9 Blown sand transport rate distribution in a section normal to the shoreline (first observation).

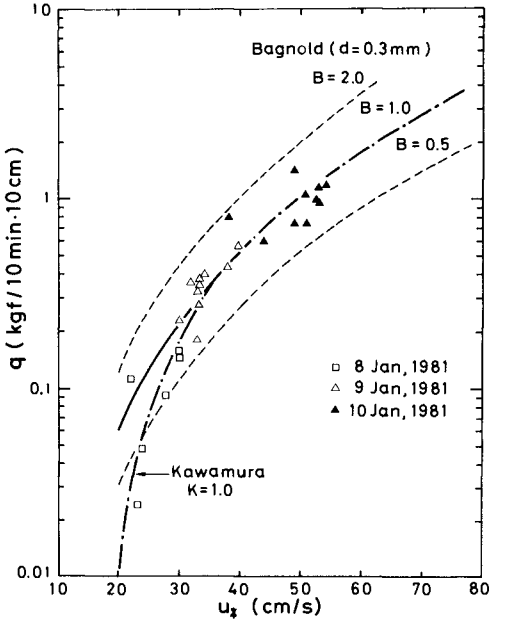

Fig. 10 Blown sand transport rate at point C (first observation).

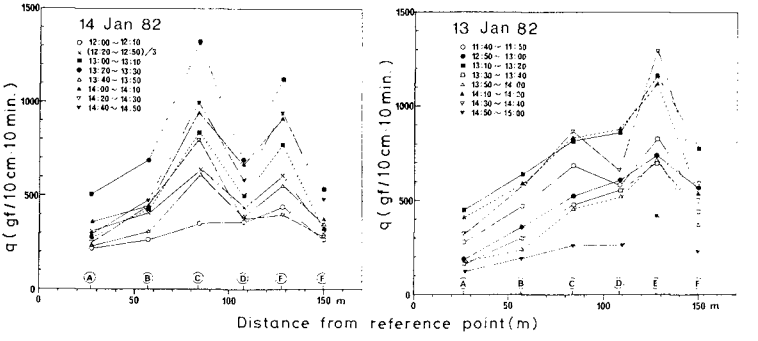

Fig. 11 Blown sand transport rate distribution in a section normal to the shoreline (second observation).

We found that the sand was not actively blown on the landward side of the beach which had been covered by dirt deposited by a storm. There was also very little sand blown in areas of dense coastal vegetation (e.g., measurement point A). We therefore can expect that a plot of the transport rate measured by point sampling against the shear velocity will show great scatter. However, for engineering purposes, it is more important to evaluate the average sand transport than to evaluate the local transport.

Figure 12 shows the average transport rate in the section A to F for the two observations. The shear velocity was calculated from the vertical distribution of wind speed for the first observation, and from Eq. (9) for the second observation. Both the Kawamura formula and the Bagnold formula agree well with the data when the empirical coefficient is 1.0. The Kawamura formula gives a particulary good result for the sand transport under shear velocities lower than 33 cm/s because it accounts for the critical shear, as was pointed out by Horikawa and Shen (1960).

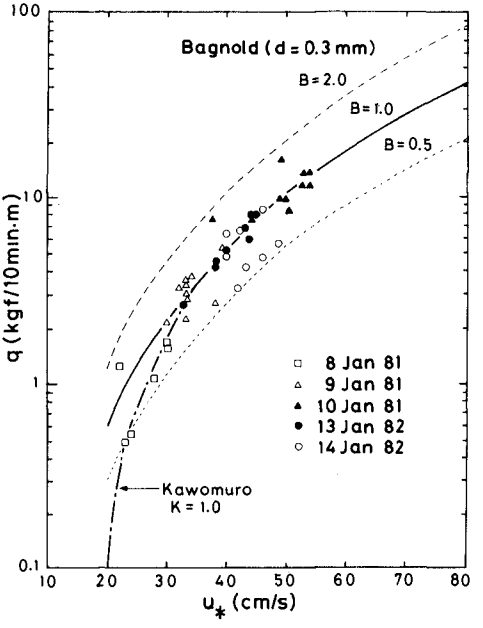

Fig. 12 Average sand transport rate (both observations).

(2) Trench trap

In Table 2, columns 1 to 3 list the times when sand was effectively blown, and the accumulated sand volume during the respective period. The measured sand volumes in the second observation were almost the same for trenches TC and TA (Fig. 3). The fourth column in Table 2 shows accumulated sand weights calculated assuming the dry sand has a weight density of 1650 kgf/m^3. The fifth and sixth columns indicate the estimated blown sand volume using Eqs. (1) and (2) for the transport rate, and (9) and (10) for the shear velocity. In the estimation, the following parameters were assumed: an empirical coefficient of 1.0 in the Bagnold and Kawamura formulae; a sand grain diameter of 0.3 mm in the Bagnold formula; u_{*c} of 20 cm/s in the Kawamura formula, and finally $\rho/g = 1.25 \cdot 10^{-6}$ (gf·s^2/cm^4).

The last two columns show the ratio of the measured blown sand volume to the estimated volume. The measured volume from the trench is greater than the estimated volume, about 1.25 (1.5) times the estimated amount for the first (second) observation. It is not clear why this difference appears, although it is reasonable to attribute it to experimental error. In Subsection 3.3 (1), it was found that the empirical coefficients for both formulae based on measurements by the conventional trap have a value of about 1.0. The difference in results most likely is due to the lower efficiency of the conventional traps. From this consideration, the efficiency of the conventionl trap is given by the reciprocal of the ratio of the measured sand volume to the estimated volume. The range in efficiency is about 0.65 to 0.8.

Accordingly, we conclude that the empirical coefficients for Eqs. (1) and (2) should be about 1.5.

Table 2 Blown sand measured by trench trap.

Date	Time	Observed sand volume		Estimated sond volume		Ratio of observed to estimated vol.	
		(m^3/m)	(Kgf/m)	Bagnold	Kawamura	Bagnold	Kawamura
1981							
Jan. 9	9:00 ~ 16:00	0.071	117	102	92	1.15	1.27
10	9:00 ~ 15:15	0.314	518	425	452	1.22	1.15
11	9:00 ~ 15:40	0.171	282	218	222	1.29	1.27
12	9:00 ~ 15:00	0.186	306	222	232	1.37	1.33
1982 Jan. 13, 9:00 ~ Jan. 14, 17:00		0.60	990	661	641	1.50	1.54

Now we will discuss the sand budget for region S and trench TA in the second observation. The sand volume blown off region S was about 1 m^3 per unit width in the period when effective blown sand took place, as listed in Table 2. If the weight density of the sand is 1650 kgf/m^3, the weight of sand blown off the region per unit width is 1650 kgf/m. This value is much larger than that caught in trench TA (or TC, Table 2). If this value is correct, it implies that trench TA did not stop the entire volume of blown sand from upstream. However, we observed

that only a very small volume of blown sand in suspension crossed over the trench. Therefore, it seems that the overestimation of the sand volume blown off region S was due to insufficient accuracy in the measurement of the sand surface change with the rods.

(3) Laboratory experiment

Measurements of the sand transport by wind obtained from this field study were limited to rather low shear velocities as seen in Fig. (11). The maximum shear velocity obtained in our field observations was around 60 cm/s. If we evaluate the wind strength at the height of 5 m, a shear velocity of 60 cm/s is equivalent to a wind speed of around 12 to 13 m/s for a ten-minute average, and around 18 to 20 m/s for a momentary maximum wind speed. It often happens that the wind speed is higher than the above values. It was, however, difficult for us to wait for such a condition to occur during the field investigation because of economic considerations. Therefore, we conducted a simple laboratory experiment on the sand transport rate by wind under a high wind speed. The results are now briefly described.

The experiments were carried out using a blowoff-type wind tunnel specially designed for studying blown sand. The wind tunnel is 1.1 m high, 1 m wide, and 20 m long. The bottom is tapered with a gradient of 1/10 at both ends. The cross section of the tunnel on which sand can be placed to a thickness of 10 cm is 1 m by 1 m. The wind speed can be varied from 3 to 30 m/s. The wind speed was measured by an array of four hot-film anemometers. The experimental facility is described by Horikawa, Hotta, and Kubota (1982b).

Sand from Yonezu beach (site of the field study) was used in the experiments. The vertical distribution of wind speed was measured, and the shear velocity was calculated from the distribution. The anemometers were placed 1, 5, 10, and 20 cm from the sand surface. Equation (4) was satisfied in this experiment, although the wind speed at the 1-cm height deviated somewhat from the straight line formed by the other measurement points (when the shear velocity was higher than around 180 cm/s). The sand passing the downstream end of the test section was considered to be the sand transported by wind. The time interval for applying the wind varied from two minutes to ten minutes, depending on the speed. Figure 13 shows that the Kawamura and Bagnold formulae agree well with the experimental results even at high shear velocities, with the empirical coefficient determined to be about 1.0.

4. DISCUSSION AND CONCLUSIONS

From results of the field study, we concluded that the empirical coefficient for the Bagnold and Kawamura formulae should be about 1.5. However, the laboratory experiments with high shear velocities indicate that the these coefficients should be about 1.0. Horikawa and Shen (1960) also found that the coefficient in the Kawamura formula is approximately 1.0 from their laboratory experiments using well-sorted sand of medium diameter 0.2 mm.

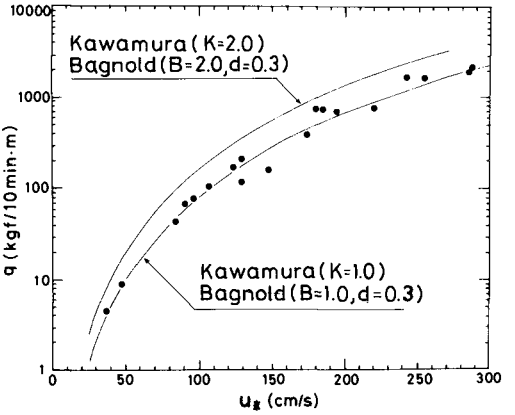

Fig. 13 Blown sand transport rate at high shear velocities.

The coefficients based on the field data are therefore larger than those obtained from the laboratory experiments. This may be due to a difference in characteristics between natural wind and latoratory wind. Usually a constant wind speed is maintained in laboratory experiments. However, the speed of natural wind varies, and a ten-minute average is ordinarily used in correlations. The blown sand transport rate is proportional to the third power of the wind speed, or of the shear velocity. A short interval of high speed wind is then efffectively equivalent to a longer interval of constant lower wind speed.

The value of 1.5 for the empirical coefficients in the Bagnold and Kawamura formulae found in the second field experiments fortuitously agrees with the result of Bagnold from laboratory experiments using well-sorted sand with median diameter of 0.25 mm. The reliability of the coefficient is increased by this field study. We consider both of the Bagnold and Kawamura formulae valid to estimate the total sand transport rate by wind. Both are equivalent at high shear velocities, but the Kawamura formula is recommended for low shear velocities.

Finally, we mention the fact that the total sand transport rate is strongly affected by the moisture in the sand layer. However, we have just begun to study this effect. An intense effort is necessary to clarify the role of moisture in the sand layer.

ACKNOWLEDGEMENT

The authors would like to express their appreciation to Mr. M. Nakura, head of the Management Department, Hamamatsu Construction Works Branch, Shizuoka Prefecture, for his considerable assistance. We also thank Dr. N. C. Kraus for proofreading, and Misses T. Kohno and K. Suzuki for typing the manuscript. The support of the Central Research Institute of Electric Power Industry over the course of this work is greatly appreciated.

REFERENCES

Bagnold, R.A. (1954): The physics of blown sand and desert dunes, Methuen & Co. Ltd., London, 265 pp.

Chepil, W.S. (1945): Dynamics of wind erosion, III, The transport capacity of the wind, Soil Science, vol. 60, no. 6, pp. 475-480.

Hsu, S.A. (1974): Computing aeolian sand transport from routine weather data, Proc. 14th Coastal Eng. Conf., pp. 1619-1626.

Horikawa, K. and H.W. Shen (1960): Sand movement by wind action (on the characteristics of sand traps), BEB, Tech. Memo. No. 119, 51 pp.

Horikawa, K. S. Hotta, S. Kubota and S. Harikai (1981): Blown sand on beaches, Proc. 28th Janapese Coastal Eng. Conf., pp. 574-578. (in Japanese)

Horikawa, K., S. Hotta and S. Kubota (1982a): Field observation of blown sand distribution across a beach, Proc. 29th Japanese Coastal Eng. Conf., pp. 269-273. (in Japanese)

Horikawa, K., S. Hotta and S. Kubota (1982b): Experimental study of blown sand on a wetted sand surface, Coastal Eng. in Japan, Vol. 25, JSCE, (in press).

Ishihara, T. and Y. Iwagaki (1952): On the effect of sand storm in controlling the mouth of the Kiku River, Bull. 2, Disaster Prevention Res. Inst., Kyoto Univ., pp. 1-32.

Iwagaki, T. (1950): On the effect of the sand-drift on the coast by wind for sand deposition in Ajiro Harbor, Journal of JSCE, Vol. 36(6), pp. 19-25. (in Japanese)

Kadib, A.L.A. (1966): Mechanics of sand movement on coastal dunes, Proc. ASCE,Vol. 92, WW Division, No. 2, pp. 27-44.

Kawamura, R;. (1951): Study on sand movement by wind, Rept. of the Inst. of Science and Technology, Univ. of Tokyo, Vol. 5, No. 3/4. pp. 95-112. (in Japanese)

Nakamura, H. (1971): Investigation on blown sand and its control, Report 71002, Civil Eng. Lab., Central Res. Inst. of Electric Power Industry, 125 pp. (in Japanese)

O'Brien, M.P. and B.D. Rindlaub (1936): The transportation of sand by wind, Civil Eng., Vol. 6, No. 5, pp. 325-327.

Phillips, C.J. and B.B. Willetts (1978): A review of selected literature of sand stabilization, Coastal Eng., 2(2), pp. 133-147.

Zingg, A.W. (1952): Wind tunnel studies of the movement of sedimentary material, Proc. 5th Hydraulics Conf., pp. 111-135.

CHANNEL SHOALING PREDICTION: A METHOD AND APPLICATION

R. B. Harley,[1] Member, ASCE and R. G. Dean,[2] Member, ASCE

ABSTRACT

Due to concerns of possible shoaling problems, an extensive field survey program was carried out at the site of the proposed Cerrejon coal port on the Caribbean coast of northeast Colombia. The program yielded considerable data on winds, waves, currents, and sediment factors. Techniques for the primary measurement of sedimentation-related tendency included dredged test pits, scour crosses, and suspended sediment samplers.

The port plan includes dredging a 4.6 kilometer long channel varying from 12 to 21 meters in depth. In order to assess the magnitude of maintenance dredging and related problems, a method was developed for incorporating the sediment response measurements into predictions of the areal and seasonal distributions of bed load and suspended sediment deposition.

Offshore test pits were monitored for rate of filling and character of the material being deposited. Suspended sediment samplers were similarly observed and also provided data on concentration versus depth.

The procedure which was developed for analysis and interpretation of the data included extrapolation of suspended sediment data to the seabed, investigation of correlations between wind activity and deposition rates, application of test pit data to a channel of larger dimensions, and testing of hypotheses regarding transport mechanisms. The procedure concluded that average annual shoaling would be approximately 300,000 m^3 and predicted areal and seasonal variation of deposition rates.

BACKGROUND

A 15 million ton per year coal export terminal is being

---

(1) Engineering Associate, Exxon Research and Engineering Company, Florham Park, New Jersey 07932.

(2) Graduate Research Professor, Department of Coastal and Oceanographic Engineering, University of Florida, Gainesville, Florida 32611

developed on the Caribbean coast in the northeast of Colombia (see Figure 1). The terminal is the outlet for coal received by rail from a mine being opened approximately 150 km inland. The mine, railroad, port and associated facilities are being developed by partnership of International Colombia Resources Corporation, an affiliate of Exxon Corporation, and Carbocol, a company owned by the government of Colombia.

The terminal is being designed to accommodate vessels up to 150,000 dwt. A site selection investigation identified Bahia Portete, a large natural bay near the tip of the Guajira Peninsula, as the optimum port site (see Figure 2). Further optimization studies resulted in a plan, shown in Figure 3, to dredge a 4.6 kilometer long channel extending from just within the mouth of the bay to the 21 meter contour. The channel varies in depth from 12 to 21 meters. The plan resulted from estimates of the relative cost for dredging versus trestle structures, assessment of wave conditions at the coast and further into the bay, and consideration of possibilities for future development of Bahia Portete.

Early site investigations noted the presence of a plume of turbid water flowing to the southwest along the coast of the peninsula and past Bahia Portete. Depending on the tide, the plume was periodically diverted into the bay. At the inside of the east headland of the bay entrance, a sand spit approximately 800 meters long extended into the bay. These conditions gave rise to concern over possible shoaling problems in the channel. As a result, a coordinated field survey program and analytical method were developed to provide predictions of shoaling in the proposed channel.

SITE CONDITIONS

Wind and Wave

The site is located in the tropical trade wind zone at approximately 12 degrees north latitude. As shown in Figure 2, the port will be situated near the northern tip on the leeward side of the Guajira Peninsula. Most wave activity in the area is generated by the easterly trade winds and passes the site farther offshore, north of the tip of the peninsula. Wave activity in the lee of the peninsula includes that which is diffracted around the peninsula and that which is generated by the northeasterly component of the wind regime (parallel to the coast). Little swell activity was observed or recorded during the field survey.

In addition to the protection afforded by the coastline orientation, waves approaching the site are further attenuated by refraction. Wave approach is primarily from the northeast and parallel to the coastal contours. While offshore waves exceed 2 meters 35 percent of the time, waves at the coast are rarely more than 1 meter (only 5 percent of the year). Between the end of the

FIGURE 1 - PROJECT LOCATION

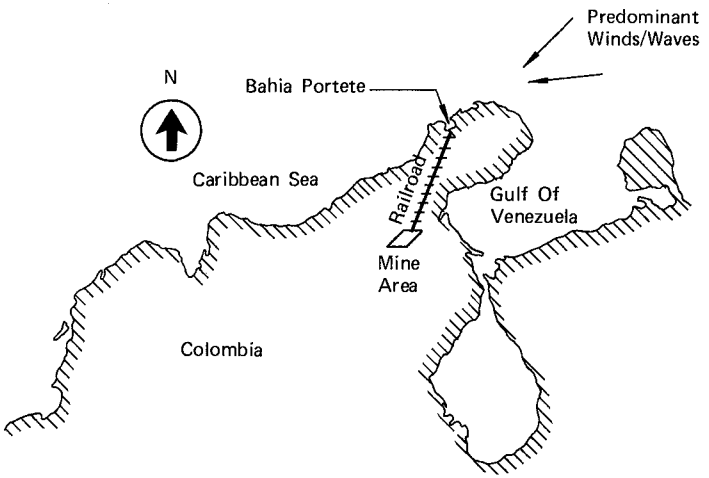

FIGURE 2 - PROJECT AREA

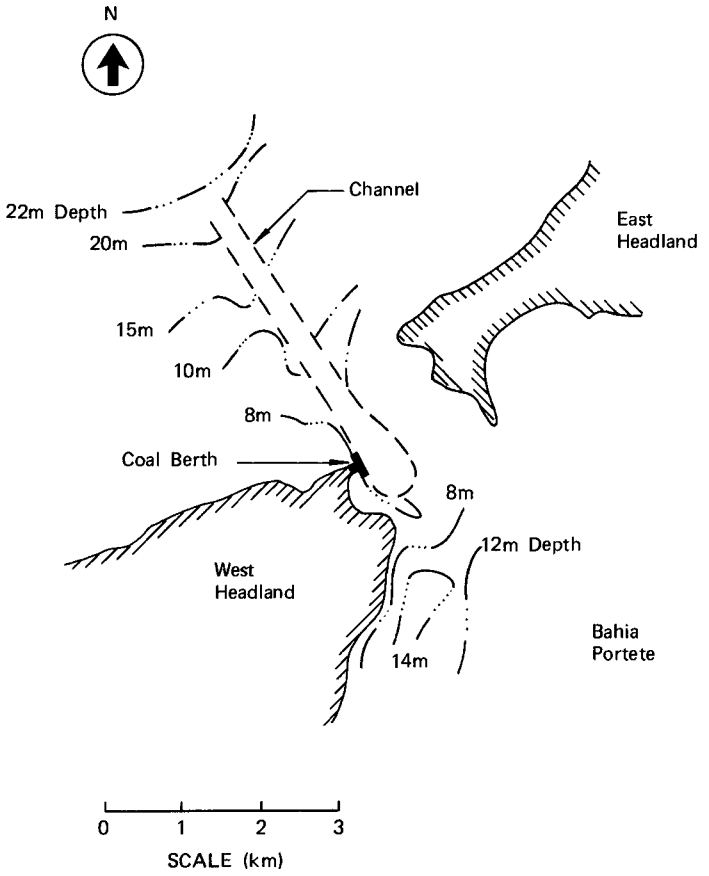

FIGURE 3 - PORT LAYOUT

channel (21 m depth) and the bay entrance, the prevailing waves change direction by up to 45 degrees.

Short wave activity (2-4 secs.) is also generated across the 10-15 kilometer fetch of the bay itself, primarily out of the east and southeast. Typically 0.3 - 0.5 meters in height, these waves can approach directly to the port area from across the bay.

Warm tropical winds persist at 20 to 30 knots for much of the year with June - August and January - April the more severe seasons. Field measurements of both winds and waves, and of sediment deposition rates, encompassed portions of both of these periods.

Climate and Topography

At the site, the Guajira Peninsula is predominantly dry, arid, and flat. There is little vegetation or runoff, and the area is sparsely populated. The shoreline is generally steep and rocky except in the inner reaches of the bay. At the headlands, the shoreline rises nearly vertically to elevations of 5 - 20 meters, except for a few pocket beaches. The face of the cliff-like shoreline is composed primarily of hard sandstone overlaying stiff clays. There is some evidence of shoreline erosion on the west headland, which is subjected to direct attack from offshore waves and those generated across the bay. Upcoast (windward) from the site, however, there is little sign of coastal erosion as the hard sandstone appears to resist the significantly attenuated waves. As such, the site appears to be sand starved, with pocket beaches that are not filled and no trace of an offshore deposit extending from the eastern headland of the bay entrance.

The seabed characteristics vary between the offshore and bay areas. Offshore and in the entrance, the seabed is largely a layer of silty sand up to 12 meters thick overlaying stiff clays and limestone. The entrance is only 3-8 meters deep but there is a natural trough in the entrance and a depression in the seabed offshore that indicate a lack of deposition, either through continued suspension by currents, or lack of a sediment source, or both. In the bay, the depth averages 10 meters and the seabed is very fine, mucky silt that is easily suspended.

There is a sand spit which extends into the bay from the inside of the east headland. The spit appears to be due to a relatively small sediment supply as compared to the transporting capacity of the waves. Thus, the sediment is driven into the bay where equilibrium is found between the Caribbean swell propagating into the bay and the short, locally-generated waves from the east within the bay.

Current and Tide

The tidal range is small, with a maximum range of only 0.5 meters. Runoff is negligible due to the arid nature of the

region. Nevertheless, the current regime is complex, consisting of alongshore coastal currents, tidal currents in the bay entrance, and density currents. Offshore of the entrance, currents vary from 0.3 to 0.6 knots, varying in direction with the tidal flow in and out, but generally running to the west. In the entrance, currents reach up to 1.5 knots in order to empty and fill the large area of the bay on spring tides. Also in the entrance, an outward flow exists near the bottom in the form of a warm, relatively dense turbid layer. This turbidity is interpreted to result from the densifying of water in Bahia Portete through evaporation, subsequent sinking, and outflow as a warm bottom layer with fine material in suspension. The material itself possibly results from suspension of fine sediments from the bottom of the bay, some erosion of the western headland, or diversion of alongshore drift into the bay by the incoming tide.

FIELD MEASUREMENT PROGRAM

Physical Factors

The site conditions were established through a nominal one year field survey program. The program included measurements of winds, waves, currents, tides, salinities, water temperatures, water density, and bathymetry.

The wave measurement program utilized both pressure gauges and waverider buoys. The instruments were situated at five different locations during the course of the survey, being moved to avoid repeated incidents of damage by vessels or vandalism, and to optimize the applicability of the data as site phenomena were established and the sediment monitoring progressed. One instrument remained in "deep water" at approximately the 21 meter depth contour for measurement of unmodified waves and correlation to deep water hindcast data. Wave direction was established by instrument aided observation in the offshore area and aerial observations.

The current measurement program included permanent installations of taut line moorings for varied periods at three locations. Two offshore locations, one closer to the entrance than the other, and a location at a proposed berth site in the bay, were monitored. Since the permanent installations included only one meter at a single elevation, vertical profiles were also established through measurements from a survey vessel at six different elevations through four daily tidal cycles in the bay entrance. Diver evaluation of current flows through observation and use of hand held meters were also included.

Bathymetric data were collected over an area including the bay entrance and areas extending 3 kilometers into the bay and 8 kilometers offshore. The data were taken by side-scan sonar and echo sounding on tracks sufficient to define seabed contours for estimates of dredging and more than sufficient for sediment study purposes.

Wind measurements were taken at the point of the west headland, which has good exposure to overwater conditions. Recordings were taken at one hour intervals for the duration of the field survey program.

Tidal data were continuously recorded for four months of the program and correlated to existing data at Cristobal, Panama for establishment of generalized relationships.

The salinity, temperature, and density measurements were concentrated in the entrance where the warm, turbid layer of density current was most evident. The data confirmed diver observations that a significant gradient exists at 1-2 meters above the seabed, below which the flow is warmer, denser, and more saline.

Sediment Monitoring

During the course of the survey of site conditions, suspended and bed load sediment activity were also monitored, primarily through the use of dredged test pits and time integrated sediment samplers (TIS's). Spot sampling of the seabed and suspended sediments; surf zone sampling and current measurements; aerial, coastline, and seabed reconnaissance; and motion pictures were also used to establish qualitative data described herein.

The test pits monitored the deposition of both suspended and bed load sediments at two locations along the proposed channel - one at the projection of the coast across the bay entrance (9 m depth), and a second at the mid-point between the first and the offshore end of the channel (14 m depth). The pits were 12 meters square with a nominal depth of 1 meter. Filling of the pits and scour around them were monitored over a period of 9 months, including the most severe weather periods, and the character of the deposited sediment was established. The intended purpose was primarily to establish the effects of sediments transported alongshore on potential channel filling, although all material being deposited was obviously included.

To facilitate measurement of the filling rates, a total of 21 metal rods were driven into the bottom, extending across and outside the pits (see Figure 4). At approximately monthly intervals, divers measured the distance from the top of each stake to the seafloor. In addition, underwater observations of bottom character and sediment motion were made and cores were taken and analyzed to document the character of material filling the pits.

All along the channel and especially through the bay entrance and adjacent to the test pits, the contribution of suspended sediments to deposition were monitored through collection of material falling through the water column in Time Integrated Samplers (TIS's). Vertically mounted sediment cups on a taut line mooring were open at the top to collect falling material. Six strings with cups located at 10, 20, 30 and 70 percent of the depth

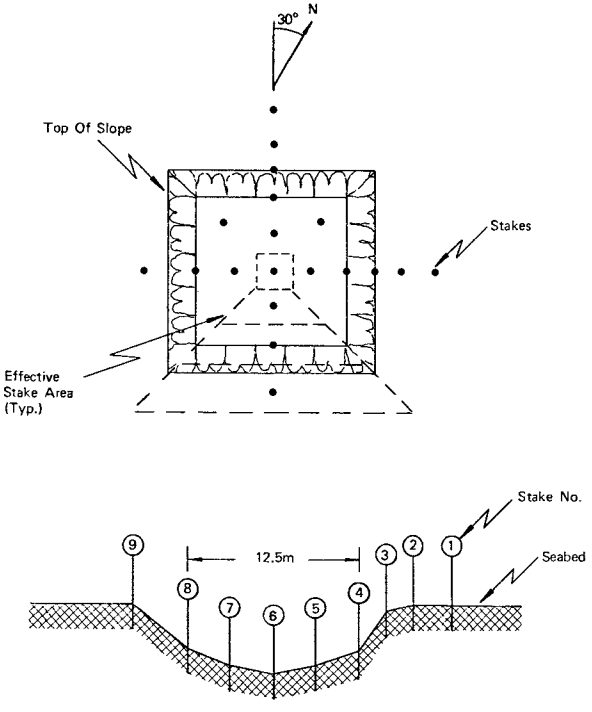

FIGURE 4 - DREDGED PITS PLAN AND PROFILE

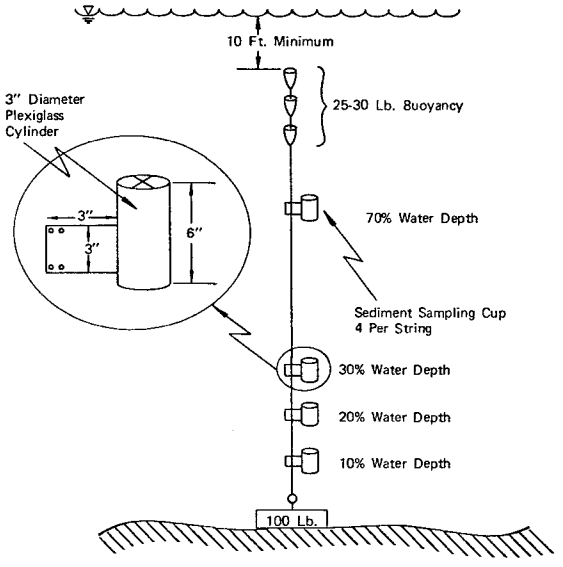

FIGURE 5 - TIS STRING

above the bottom were used (see Figure 5). Cross vanes inside the top of each cup served to reduce turbulence and any tendency for material deposited in the cup to be resuspended. The monthly servicing of these strings by a diver involved first capping each cup to avoid loss of sediment and then retrieving the entire string for fitting of clean collection cups. The dry weight of sediment in the cup was established later in the laboratory and, together with saturated density and porosity characteristics, used as a basis for calculating actual deposition rates in terms of centimeters per day of material added to the bottom.

FIELD DATA

Dredged Test Pits

Data reported from the monitoring of the offshore test pit is shown on Figure 6. The data shows that in spite of its narrow width relative to the proposed channel, the pit did not fill more than 0.5 meters in 27 weeks, and on the average much less than that. Most of the filling (up to 0.3 m) took place between the 18th and 21st week measurements - a period of only 3-4 weeks, but when the wind/wave environment was most severe.

As expected, the pit nearer shore filled somewhat more quickly than the offshore pit, becoming nearly full after 21 weeks. Again, the most rapid filling related only to the most severe wind/wave conditions, in an apparently non-linear manner. More than half of the filling occurred in a period of four of the 21 weeks. Practical assessment of the effect of rapid filling on actual channel shoaling predictions is discussed under "ANALYSIS OF SEDIMENTATION DATA."

In assessing the volume of material deposited in the pits, it was also necessary to consider the effective area of the pits and stake coverage as they bore relation to actual filling rates. Since slumping of the sides occurred and because the more fluid suspended load filled the deep center of the pits more rapidly, the average change in elevation was sensitive to the area considered. In general, the average decreased as greater area was considered. In order not to underestimate deposition, a reduced effective area was established based on analysis of the sensitivity and incorporating, for the most part, only the deeper and more rapidly filled portions of the pits.

Attention was also given to the fact that the deeper deposition at the stakes in the center of the pit represented a lesser area of the pit, due to the square plan of the pit and the pattern of stake placement (refer to Figure 4). Sub-dividing the pit into areas of individual stake coverage, the center stakes became less weighted in calculating the average rate of filling.

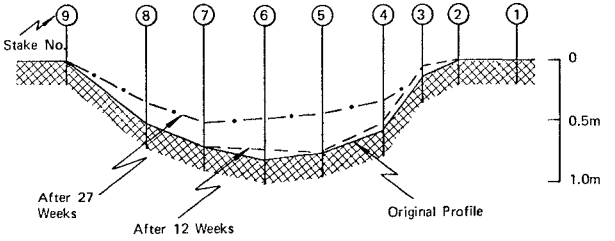

FIGURE 6 - DREDGED PIT DATA

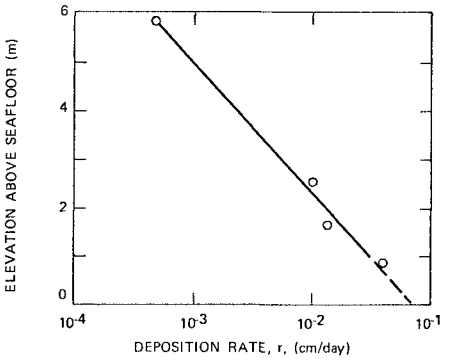

FIGURE 7 - TIS DATA

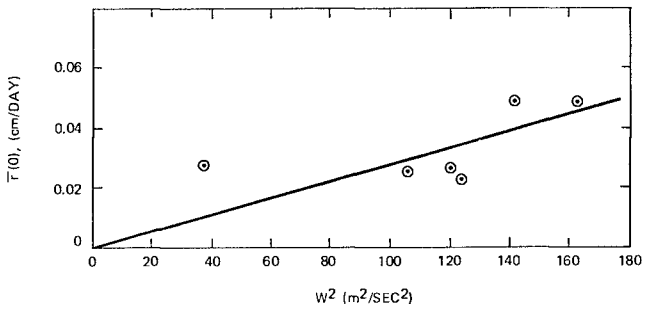

FIGURE 8 - CORRELATION OF SUSPENDED SEDIMENT DEPOSITION RATE, $\bar{r}(0)$, WITH MEAN WIND SPEED SQUARED, TIS 4

T1S Strings

A sample of data reported for one monitoring of a T1S string is shown on Figure 7. The graph shows the variation of material collection rate versus the elevation of the TIS cups above the seafloor. The collection rate was established from the laboratory measurements of the weight of material collected over the sampling interval. As shown, the graph is used to extrapolate collection rates to estimates of material deposited on the seafloor based on an exponential relationship.

Considering: (1) the material in suspension to be of uniform diameter and density and (2) the vertical eddy diffusivity, ε, to be uniform, the concentration, $C(z,t)$, of sediment is

$$C(z,t) = C_o(t)\, e^{-\frac{w}{\varepsilon(t)} z} \tag{1}$$

in which C_o is the concentration at the seafloor, and w is the fall velocity of the sediment. The seafloor concentration, $C_o(t)$, is related in an unknown way to the forcing factors (waves, winds, etc.). lt is noted that if there were N components of suspended sediment characteristics, Eq. (1) could be generalized to

$$C(z,t) = \sum_{n=1}^{N} C_{o_n}(t)\, e^{-\frac{w_n}{\varepsilon} z} \tag{2}$$

Returning now to the representation for a single sediment characteristic (Eq. (1)), the sedimentation cups are considered to result in a sheltered environment in which the sediment settles and is collected. ln this regard, it is noted that Gardner (1977) has conducted laboratory and field studies of the trapping efficiency of samplers of various geometries in steady currents. For cylinders of the aspect ratio used in this program, the "collection efficiency" is approximately unity. If the sedimentation cups perform as discussed above, the average depositional rate $\bar{r}(z)$ over a time, T, is

$$\bar{r}(z) = \frac{1}{T} \int_{t}^{t+T} wC(z,t)dt \tag{3}$$

and considering the average concentration to have the same form as Eq. (1), the average deposition rate can be expressed in the form

$$\bar{r}(z) = \bar{r}(0)e^{-Kz} \tag{4}$$

and taking the logarithm of both sides of Eq. (4)

$$\ln \bar{r}(z) = \ln \bar{r}(0) - Kz \qquad (5)$$

Thus, by plotting on semilogarithmic paper the average depositional rate at four elevations, it is possible to extrapolate to determine the deposition rate to be expected at the seafloor. Recalling the presence of the warm turbid layer of bottom water and the possible contributions from more than one sediment type component, it is important in cases where deviation from a straight line occurs to weigh the lower two measurements more heavily than the upper two in extrapolating to the seafloor.

Other Measurements

The observations and spot samples taken on site were used primarily to confirm the interpretation of the more quantitative data and to relate it to assessments of the overall seafloor processes. The lack of filled pocket beaches, for example, relates to the fact that the pits did not fill rapidly, attesting to the lack of a substantial sediment source. The presence of the seabed trough in the bay entrance is also indicative of either the sediment-starved nature of the area, or of the existence of a sufficient flushing mechanism (e.g. the density and tidal currents). The discovery of the density current at the seafloor supports a correlation of the sedimentation data to wind phenomena on the basis of evaporation (see the following section). The spot sediment samples indicated a generally exponential distribution of sediment concentration in the water column, confirming the TIS data shown in Figure 7.

ANALYSIS OF SEDIMENTATION DATA

An attempt was made to correlate the sedimentation data collected in the suspended sediment samplers and the test pits with relevant measured wind and wave characteristics. The final method developed includes a correlation between the seafloor extrapolated suspended sediment deposition and wind data. This relationship is then utilized to determine the portion of the trapped material in the test pits that is due to bed load transport (total deposition less suspended sediment deposition). These results are then applied to the prediction of shoaling in the navigation channel.

Correlation of Measured Suspended Sediment Deposition Rates With Winds and Waves

A reasonable index of the potential of the waves to cause suspended material sedimentation is the rate at which the waves dissipate energy on the bottom sediments. The average rate of wave energy dissipation is

$$\bar{\dot{e}} = \frac{1}{T} \int_{t}^{t+T} \tau_b U_b dt \quad \alpha \quad \frac{1}{T} \int_{t}^{t+T} |U_b|^3 dt \tag{6}$$

in which U_b is the magnitude of the wave-induced water particle velocity at the bottom. From linear wave theory

$$|U_b| = \frac{H}{2} \sigma \frac{1}{\sinh kh} \tag{7}$$

in which H is the wave height, h is the water depth, and σ and k are the wave angular frequency and wave number, respectively:

$$\sigma = \frac{2\pi}{T} \tag{8}$$

$$k = \frac{2\pi}{L} \tag{9}$$

with the wave length, L, and wave period, T, being related by the well-known dispersion equation

$$L = \frac{gT^2}{2\pi} \tanh kh \tag{10}$$

The values of $\bar{\dot{e}}$ were calculated and summed for all periods over which the TIS strings were emplaced. For this purpose, the local depth at the TIS string of interest was taken into account as was the transformation of wave height from the wave measurement location to each particular TIS location. For periods with less than 80% wave data return, the results were not included in the analysis.

The effect of the wind on shoaling rates at Bahia Portete is believed to be somewhat unusual due to the interrelationship between wind evaporation rates, densification and sinking of water in Bahia Portete, and the ultimate outflow of warm, dense and turbid water in the lower layers from Bahia Portete. The wind also contributes to shoaling through generation of local waves in Bahia Portete which then attack and erode the cliffs on the western side of the bay. The effect of the wind was characterized through the wind stress, or more simply, by the square of the wind speed, W^2. Since local monthly measurements of wind speed were available by percentages Δp_n in various class intervals, the monthly mean square wind speed was approximated by

$$\overline{W^2} = \sum_{n=1}^{N} \overline{W_n^2} \, \Delta p_n \tag{11}$$

where W_n is the magnitude of the wind speed associated with the n^{th} speed category. Table 1 summarizes values of extrapolated seafloor

TABLE 1

SUMMARY OF SEDIMENTATION RATES AND WAVE AND WIND DATA USED IN CORRELATION

TIS Location No.	Date Installed	Date Removed	No. of Days	$\overline{r}(0)$ (cm/day)	$\overline{\dot{e}} \times 10^3$ (m^3/sec^3)	$\overline{W}^2$ (m^2/sec^2)
1	1/13/79	2/28/79	46	0.038	7.48	122.0
1	2/27/79	3/26/79	28	0.013	2.69	37.6
2	7/23/78	9/30/78	69	0.072	7.76	138.1
2	8/12/78	9/12/78	31	0.082	4.34	140.5
2	11/13/78	12/13/78	30	0.062	5.20	119.2
2	12/13/78	1/14/79	32	0.052	24.06	105.9
2	2/27/79	3/27/79	29	0.028	9.44	37.4
3	11/13/78	12/12/78	29	0.022	7.55	119.3
3	2/27/79	3/27/79	29	0.041	14.47	38.0
4	7/13/78	8/12/78	30	0.049	8.06	163.3
4	8/12/78	9/12/78	31	0.049	1.67	140.5
4	11/13/78	12/12/78	29	0.026	2.07	119.3
4	12/12/78	1/15/79	34	0.026	11.90	105.7
4	1/15/79	3/1/79	45	0.023	13.21	124.0
4	2/27/79	3/27/79	29	0.028	4.48	37.4
5	7/16/78	8/12/78	27	0.065	29.42	163.0
5	8/12/78	9/12/78	31	0.018	6.80	140.5
5	11/13/78	12/13/78	30	0.062	7.91	119.2
5	1/15/79	2/28/79	46	0.049	45.03	123.5
5	2/27/79	3/27/79	29	0.041	13.57	37.4
6	2/27/79	3/27/79	29	0.121	13.57	37.4

deposition rates, the wave energy dissipation factor, $\overline{\dot{e}}$, and $\overline{W_j^2}$, for each TIS string and each intersurvey period.

The monthly mean seafloor deposition of suspended sediments was correlated with the monthly mean wave energy dissipation factor and the monthly mean square wind speed in the linear form

$$\overline{r}_j(0) = K_1 \overline{\dot{e}}_j + K_2 \overline{W_j^2} \tag{12}$$

using the method of least squares. In addition, the goodness-of-fit parameter, μ , was calculated for each TIS string, where

$$\mu \equiv \frac{\sqrt{\sum_j \delta_j^2}}{\sqrt{\sum_j [\overline{r}_j(0)]^2}} \tag{13}$$

in which

$$\delta_j \equiv \overline{r}_j(0) - (K_1 \overline{\dot{e}}_j + K_2 \overline{W_j^2}) \tag{14}$$

To provide insight into the interpretation of μ values, if Eq. (12) provided a perfect fit to the measured data, then μ would be zero. The maximum value of μ if no correlation existed would be unity as would be obtained by $K_1 = K_2 = 0$.

The results of the least squares procedure showed, somewhat surprisingly, that the sedimentation rates were very poorly correlated with the waves. However, there was quite good correlation with the wind. There are several possible explanations for wind appearing as an important causative factor. Wind is related to the local waves and, due to the predominant direction, the wind contributes to the westerly current which carries sediment from the shores located to the east of Bahia Portete. As noted previously, wind also causes evaporation of the water in Bahia Portete, thereby creating dense water which outflows as a turbid bottom current.

Because waves did not prove to be a strong correlative factor, the least squares procedure was again carried out with W^2 (which is proportional to wind stress) as the only correlation factor. The results are presented in Table 2 and an example given in Figure 8. Some of the fits are extremely good (TIS 1 and 2), whereas one is poor (TIS 3 - based on only two data points), and the others are reasonable and considered to provide a good basis for calculating the deposition rates due to suspended load.

Correlation of Bed Load

Deposition of material transported as bed load depends on the available energy to transport the material and the availability of such material to be transported. Since there were available

TABLE 2

SUMMARY OF BEST FIT COEFFICIENTS, K, AND NORMALIZED STANDARD DEVIATIONS, μ , FOR SUSPENDED SEDIMENT DEPOSITION RELATIONSHIP TO WIND STRESS

TIS No.	No. of Data Points	K $(cm\ sec^2)/(day\ m^2)$	μ
1	2	3.1×10^{-4}	0.03
2	5	5.4×10^{-4}	0.08
3	2	2.7×10^{-4}	0.70
4	6	2.8×10^{-4}	0.29
5	5	3.6×10^{-4}	0.42
6	1	Insufficient Data	

results from only two test pits, as compared to meaningful results from five TIS strings, and since the test pits are judged to remain effective in trapping over only eight months or so, the correlation for the pits is necessarily relatively less comprehensive. Fortunately, in the prediction results to be presented later, the bed load component constituted only 20% of the total deposition.

As noted previously, the bed load component in the test pit deposition was estimated from the total deposition as the complement of the suspended load as determined by extrapolation of the TIS data to the sea floor. (It is noted that a TIS string was located in proximity to each of the test pits.). The bedload was found to correlate best with the wave energy dissipation index (Eq. (6)) and that correlation was employed in the later predictions of shoaling rates in the navigational channel.

PREDICTION METHOD FOR CHANNEL SEDIMENTATION RATES

The two basic premises for prediction of deposition rates in the navigation channel are: (1) the test pits and TIS units accumulated representative measures per unit area of the suspended sediment that will occur in the channel and (2) per unit length, the test pits entrap the same bed load amount as would the channel.

The average daily total sedimentation rate, r_t, per unit area is expressed as the sum of the bed and suspended load components

$$r_t = r_B + r_S$$

which applies to both the test pits and to the navigation channel and in which the subscripts "t", "B" and "S" denote total, bed load and suspended load, respectively. Since the suspended sediment deposition rate is the same in the test pits and the navigation channel

$$(r_S)_{NC} = (r_S)_{TP} \tag{16}$$

where "NC" and "TP" denote "navigation channel" and "test pits," respectively. Since it is assumed that the bed load sediment deposition rate per unit channel length will be the same for both the navigation channel and test pit, it follows that

$$(r_B)_{NC} = (r_B)_{TP} \frac{W_{TP}}{W_{NC}} \tag{17}$$

in which W_{TP} and W_{NC} denote the respective widths of the test pit and navigational channel. The average daily total deposition rate for the navigational channel is then

$$(r_t)_{NC} = (r_t)_{TP} \frac{W_{TP}}{W_{NC}} + \left(1 - \frac{W_{TP}}{W_{NC}}\right) (r_s)_{TP} \qquad (18)$$

These concepts were applied using the correlation between wind and deposition rate to predict total seasonal deposition rates and annual deposition rates along the channel length.

RESULTS

The results of the correlation and prediction methods described in the previous section were applied to the estimation of: (1) total annual shoaling rate, (2) distribution of annual shoaling rate along the navigation channel, (3) seasonal distribution of total shoaling rates, and (4) shoaling due to extreme events.

The total annual shoaling rate was estimated at 306,000 m^3. The associated depositional distribution along the channel is presented in Figure 9. The monthly variation of shoaling is shown in Figure 10 and is reasonably constant due to the fairly steady winds which cause the dominant suspended sediment shoaling components.

SUMMARY AND CONCLUSIONS

A method has been developed and applied for predicting sedimentation in a reasonably deep dredged navigation channel. The procedure requires a substantial field component including measurement of suspended sediments and sedimentation in dredged test pits. Additionally, measurements and/or hindcasts are required of the potential causative factors: winds, waves, and currents.

In application of the method to a coal loading terminal at Bahia Portete, Colombia, which will require a 21 meter channel, the strongest correlation for suspended sedimentation rates occurred with wind speed squared rather than a measure of wave energy dissipation. The bed load deposition correlated best with the wave energy dissipation. Considering suspended and bed load deposition in the navigation channel to be plan area and perimeter dependent, respectively, predictions were made of seasonal, areal and total annual deposition rates.

The predictions are believed to slightly overpredict sedimentation due, in part, to the rather small size and equal plan dimensions of the test pits which results in the tendency to trap and weight equally the two orthogonal components of bed load whereas the navigational channel would entrap only that component perpendicular to the channel axis. The model does not account directly for density currents that result from high concentrations of suspended load near the bottom. This phenomenon would result in

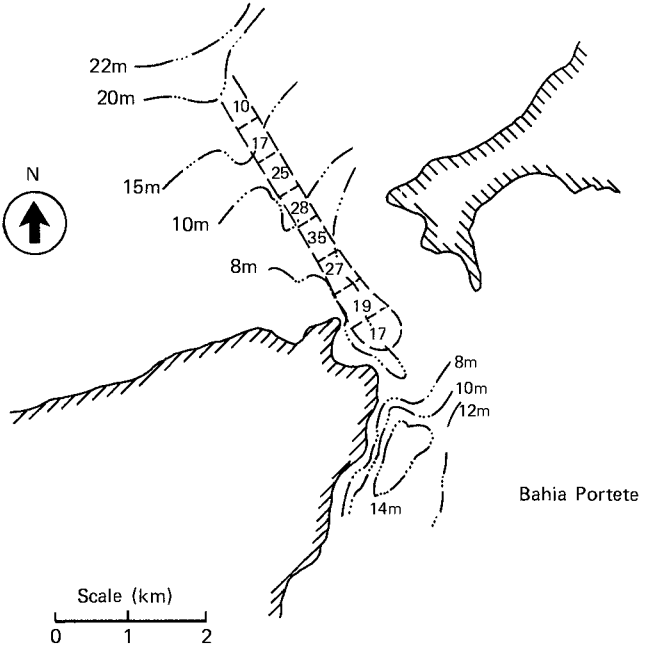

FIGURE 9 - ESTIMATED ANNUAL DEPOSITION RATES (IN cm/YR) FOR EACH ONE-HALF KILOMETER OF CHANNEL LENGTH

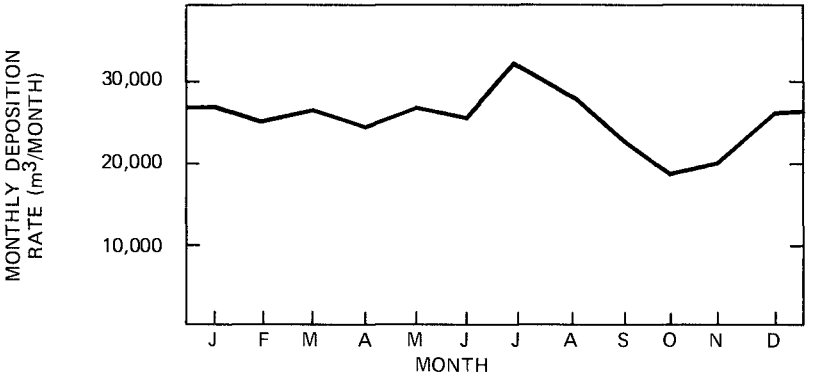

FIGURE 10 - AVERAGE MONTHLY DEPOSITIONAL RATES

greater deposition in deep channels than in shallow channels. Although this mode of transport (density currents) can dominate in some locations where very high turbidity exists, it is not believed to be a major factor at Bahia Portete.

As an overall summary statement, a qualitative assessment is that the uncertainties in the methodology and data are such that the shoaling predictions are somewhat excessive (say 10 - 15%). The coal exporting facility is now being constructed and it will be of interest to compare future maintenance dredging requirements with the predictions presented here.

ACKNOWLEDGEMENTS

Collection of the field data required for the shoaling analysis was accomplished by the combined efforts of Frederic R. Harris Engineering Corporation, Lake Success, New York; Hidrotec Ingenieros Consultores, Bogota, Colombia; Dames and Moore, Cranford, New Jersey; and T. L. Roscetti, Senior Staff Engineer, Exxon Research and Engineering Company.

REFERENCES

GARDNER, W. D., "Field Calibration of Sediment Traps", Woods Hole Oceanographic Institution, Undated and Unpublished Manuscript.

GARDNER, W.D., "A Laboratory Evaluation of Sediment Trap Dynamics", Woods Hole Oceanographic Institution, Unpublished Manuscript, March 1977.

CONSTRUCTION OF A BREACH CLOSURE IN A BARRIER ISLAND

M.J. McCarthy, A.M. ASCE[1], E.J. Schmeltz, A.M. ASCE[2],
G.R. Lehan, M.ASCE[3]

ABSTRACT

A breach was opened in the barrier beach along the south shore of Long Island, New York during a winter storm in January, 1980. Due to public safety and environmental concerns, a contract to close the breach using sand fill was awarded to a local contractor. This paper discusses the evolution of the construction procedures developed to allow the contractor to successfully complete the project on schedule and on budget.

1.0 INTRODUCTION

Moriches Inlet is located on the south shore of Long Island, approximately 130 kilometers (80 miles) east of New York City as shown on Figure 1. The inlet, which forms the primary outlet through the barrier island between Moriches Bay and the Atlantic Ocean, is stabilized by two stone jetties approximately 245 meters (800 feet) apart.

During January 1980, a severe northeast storm resulted in the breaching of the barrier island immediately to the east of the inlet. The breach, initially 90 meters (300 feet) in width, was probably the result of excessive erosion/washover from the bayside of the barrier island coupled with high waves and tides on the oceanside.

Tidal currents and wave action in the area resulted in the rapid growth of the breach until the fall of 1980 when, due to local concerns regarding exposure to storm induced flooding and effects on shellfish beds, construction was begun to effect it's closure. At that time, the breach, shown in Figure 2, had expanded to nominally 885 meters (2900 feet) in width with an average depth of 3 meters (10 feet). The plan selected for the closure consisted of the placement of 1.2 million cubic yards of beach fill with a final crest elevation of +4 meters (+13.25 feet) MLW and side slopes of 1:25.

---

1. Principal Coastal Engineer, PRC Harris, 3003 New Hyde Park Road, Lake Success, N.Y.
2. Manager, Coastal Engineering, PRC Harris, 3003 New Hyde Park Road, Lake Success, N.Y.
3. George R. Lehan, Consulting Engineer, 95 Claydon Road, Garden City, N.Y.

The purpose of this paper is to discuss the development and implementation of construction proceedures utilized to close the breach given the following criteria:

- minimize the loss of fill material placed in the breach
- minimize the time required to complete construction (maximum 6 months)
- allow construction to be accomplished primarily with land plant
- complete construction without creating any permanent structural modifications in the area

Monitoring of the inlet and breach area was conducted during construction activities to insure that these areas were reacting to the closure operations as expected. Several design modifications were instituted during construction as a result of these monitoring operations which contributed to the successful closure of the breach.

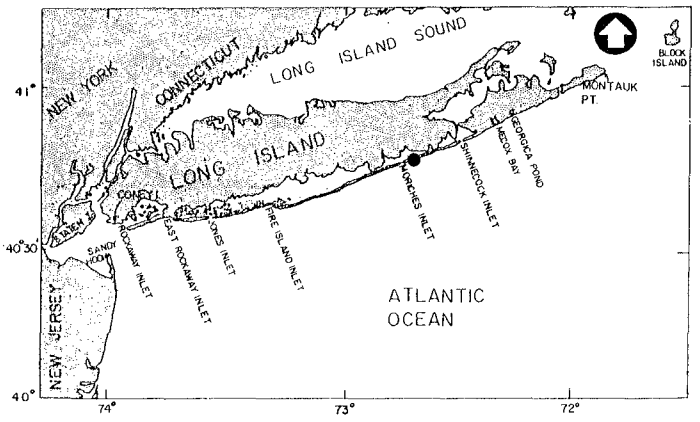

Figure 1 - Site Location

Figure 2 - Breach Immediately Prior to Closure (7/12/80)

2.0 SITE DESCRIPTION

Moriches Inlet is one of the five inlets through the barrier beach along the south shore of Long Island. Although the inlets and bays are interconnected, each inlet system functions relatively independently. Moriches Inlet primarily drains Moriches Bay from the Quantuck and Quogue Canals to the east to Narrow Bay to the west as shown on Figure 3.

Moriches Inlet has been opened and closed numerous times over the period in which records have been maintained (Reference 1). The present inlet was formed in 1931 as a result of a March storm. Between 1931 and 1947, the inlet migrated westward about 1220 meters (4,000 feet). A stone jetty was constructed along the west side of the inlet in 1947, in an attempt to stabilize it, however the inlet closed again during a storm in May, 1951.

The present stone jetties were constructed during 1952 and 1953, and extended in 1954. Despite the presence of the jetties, navigation through the inlet has been considered unsafe due primarily to the shifting shoals offshore of the inlet. The stabilized inlet has also experienced progressive erosion along the bay shoreline to the east of the jetties, as shown in Figure 4. This erosion was noted in a 1958 U.S. Army Corps of Engineers review of the inlet and has been described numerous times since then as the erosion became more pronounced, culminating in the breach during the January, 1980 storm.

Environmental conditions along the ocean shoreline in the vicinity of Moriches Inlet are typical of the entire south shore of Long Island. Nearshore wave heights average nearly 0.7 meters (2.3 feet) with maximum heights of approximately 4.1 meters (13.5 feet) (Reference 2). The lowest wave conditions occur during the months of May through September. Peak wave heights typically occur in February and March. Wave periods typically average between 4 and 7 seconds.

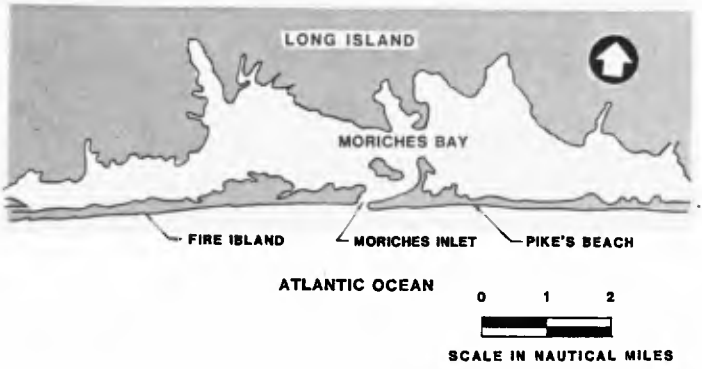

Figure 3 - Site Plan

Figure 4 - Erosion Along Pikes Beach (2/70)

Current velocities in the breach were estimated to be up to 5 feet per second prior to the start of closure operations. Current and bathymetric conditions were monitored during closure operations to assist in the development of the final closure procedures. The monitoring program and an analysis of inlet and tidal prism changes are the subject of a separate paper (Reference 3). Current velocities measured during closure operations ranged from zero during slack tide to over 1.7 meters (5.5 feet) per second at peak conditions.

Longshore transport in the inlet area is predominantly from east to west. The littoral transport rate averages over 300,000 cubic yards per year.

3.0 ALTERNATIVES CONSIDERED

A number of alternative procedures were considered to effect closure of the breach within the constraints identified above. Additional constraints considered in evaluating alternatives included:

- material sources were 600,000 cubic yards from bay dredging and 600,000 cubic yards from an upland source
- the contractor had a considerable quantity of PZ-27 steel sheet pile in varying lengths available for use

Preliminary options investigated included:

- placement of fill with no temporary retaining structures
- use of concrete pipe temporary retaining structures
- use of barges to retain the fill temporarily
- use of steel sheet pile temporary retaining structures

The initial option of placement of the sand fill with no temporary retaining structures included placement of the upland fill material along the ocean and bay sides of the breach to act as retention dikes for the dredged sand. The intent of this placement procedure was to provide protection for the dredged sand from severe erosion while it was in a slurry state. This option was discarded due to the expected high loss of fill even considering the special placement of materials proposed.

The second option evaluated for closure involved the use of scrap concrete pipe as a temporary retention dike for the sand fill. The concrete pipe was available in lengths ranging from 2.4 to 3.6 meters (8 to 12 feet) and diameters to 1.5 meters (60 inches). Several alternatives were developed to effect closure using the concrete pipes including placement in horizontal and vertical configurations to retain the sand fill. An additional alternative called for placement of the concrete pipes parallel to the currents and was intended to reduce the potential scour of the bottom as the breach was closed by providing culverts for the flow and scour protection. A controlled cutoff of the flow could then be effected by placing pipes to close off the culverts providing a quiet area to place fill. All alternatives involving the use of concrete pipes were ultimately discarded due primarily to the cost of transporting the pipes to and from the project site.

A third option evaluated consisted of sinking barges in the breach area to stop the current flow and allow placement of the sand fill. This option was discarded primarily due to the shallowness of the breach area which would require dredging to move the barges into position. In addition, due to the scouring of the bottom causing settlement of the barges as well as placement of fill along one side, it was felt that difficulties would be experienced in raising the barges at the conclusion of the project.

The fourth option investigated was the use of steel sheet piles driven to act as a retention wall for the fill during placement. Two basic alternative schemes utilizing the steel sheeting were developed and evaluated. The first, consisted of two single rows of sheet piles driven along the ocean and bay sides of the breach to effectively seal off the fill. Several potential problems were envisioned which caused this alternative to be discarded. These were:

- exposure of the sheet pile wall to ocean waves causing stability problems and scour at the toe
- scour of the sand fill placed between the widely separated walls due to currents moving around the ends of the sheet pile walls and by direct wave attack from the southwest

In response to these concerns, a second sheet pile alternative was developed. This alternative , shown in Figure 5, consisted of two parallel rows of sheet pile driven approximately 30 meters (100 feet) apart along the bay side of the breach. The advantages of this alternative were felt to include:

- control of tidal currents in the fill area
- potential for trapping a portion of the predominantly westward littoral drift
- protection for most of the retaining structure from wave attack
- protection against complete loss of the placed fill material in the event of a storm during construction

This alternate was eventually selected for use in the closure operation.

In an effort to further minimize fill loss it was decided to place the fill material from upland sources between the sheetpile dikes and along the ocean side of the breach. Dredge fill would then be placed between these two protective arms forming the center of the closure.

During final selection of the construction alternative, concerns over the stability of the cantilever sheet pile retaining walls under construction loads and the effects of scour along the bayside were addressed. Stability calculations were made to determine minimum setback distances for equipment operating within the sheet pile walls as well as the maximum tolerable scour along the bayside. In an effort to control this scour and enhance the stability of the retaining wall, short sheet pile "spurs", as shown on Figure 5, were proposed to be driven at right angles to the main wall on the bay side.

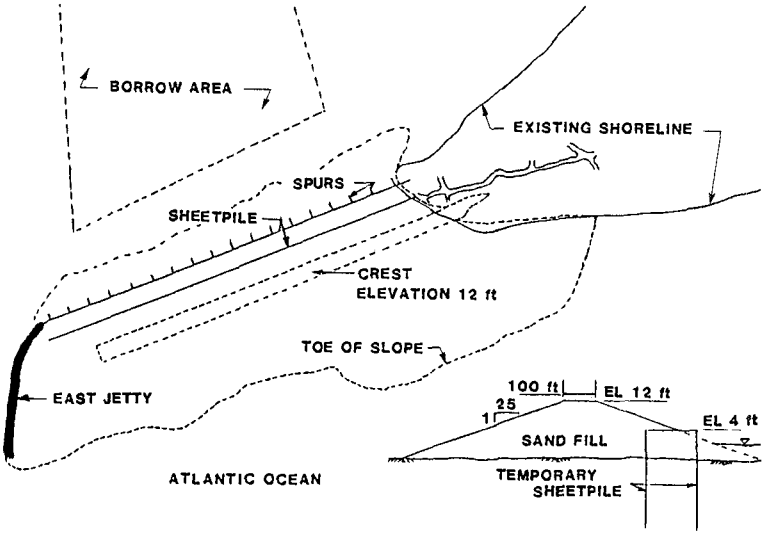

Figure 5 - Selected Construction Plan

4.0 CONSTRUCTION PROCEDURES/MONITORING

Construction operations began in early October ,1980. Initial operations consisted of cutting and stabilizing a haul road over the dunes leading to the construction site and moving in equipment and sheet piles. Placement of fill material from upland sources and driving of sheet pile walls commenced on October 10. Figure 6 is an aerial view of the construction site made on October 12, showing a short section of the sheet pile wall in place and the beginning of a sand bar along the ocean side of the closure. This bar was in evidence throughout the closure operations and seemed to be due to the entrapment of the westward littoral transport. In any event, the bar migrated westward as closure operations progressed and provided addtional protection from the ocean waves to both the fill material and the exposed portions of the sheet pile wall.

Placement of the sheet pile walls was accomplished using a Link Belt 138, 70 ton crane fitted with a vibratory hammer as shown on Figure 7. Construction operations were able to be continued during most weather and sea conditions although at several times the safety of the construction crew guiding the sheet piles into position required shutdown of these activities as shown on Figure 8.

Figure 6 - Initial Construction (10/12/80)
(note sheet pile retaining walls)

Figure 7 - Pile Driving Equipment

Figure 8 - Pile Driving Activities in Rough Conditions

Monitoring of the closure operations was conducted based on periodic field surveys as well as reports from construction foremen onsite. Of primary concern were the stability of the bayside sheet pile wall, reaction of the open portion of the breach as closure operations progressed and stability of the exposed east jetty. As shown on Figure 9, a deep channel began to form adjacent the east jetty as the closure was affected. Current measurements obtained during this period idicated that the primary flow was being shifted back to the original inlet, however significant currents were still being experienced in the breach. As discussed below, the changes in this section were closely monitored to attempt to prevent any further deterioration of the east jetty.

Additional concerns were identified during soundings made along the bayside of the sheet pile wall by the construction crew, indicating significant scour occurring along one section of the wall. A site visit by the engineers indicated that the sources of the problem were twofold involving both the spacing of the sheet pile spurs and the location of the sand bar on the bayside of the wall. As shown in Figure 10, the sand bar was causing flow from the Bay Channel to pass along the sheet pile wall. To alleviate this problem. the dredge was instructed to cut a channel through the sandbar to allow flow from the Bay Channel to move into the old inlet and spacing of the spurs was reduced in this area.

Final closure operations were begun in the beginning of December. As shown on Figure 11, the tidal currents were primarily moving in and out of the bay through the old inlet, due in part to the cut made by the dredge through the sand bar. To further channel the flow into the inlet a long spur was constructed to deflect the ebb tide away from the breach. These procedures worked as sand began to naturally accumulate in the remaining breach opening and closure operations were completed with no further difficulties on December 15.

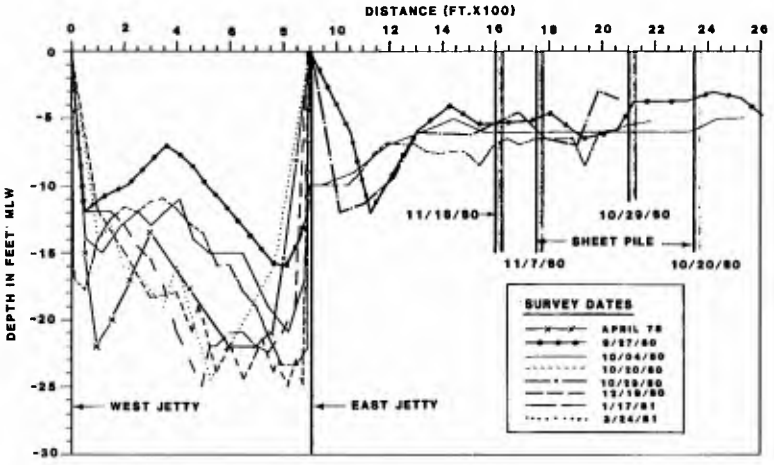

Figure 9 - Cross Section Changes During Construction

Figure 10 - Construction Progress (12/4/80)

Placement of sand from upland sources and by dredging continued until mid January, 1981. The sheet pile walls were also removed during this period and all construction activities were completed by the beginning of February 1981.

Figure 11 - Preperations For Final Closure (12/4/80)

5.0 CONCLUSIONS

As a result of the construction procedures developed in this study, the breach in the barrier island was closed utilizing primarily land based plant supported by dredging conducted in relatively protected areas. Despite working during a typically stormy portion of the year, constuction delays due to weather were minimal. The closure of the breach was effected nominally 2 months after startup of construction and the overall project was completed within 5 months of startup.

Losses of material were limited to approximately 15 percent of the gross volume of material placed at the site. These losses included those experienced during a storm which occurred several weeks after closure operations began. This storm had a return period of slightly over two years and caused some damages to the exposed sheet pile walls as well as loss of fill. Most observers agreed, however, that without the sheet piles, the majority of the fill placed would have been lost.

Close cooperation between the engineers and contractor allowed procedural and design changes to be made as site conditions changed. This cooperation contributed to the timely and succesful completion of the project within the constraints of the owner and the contractor.

6.0 ACKNOWLEDGEMENTS

Cooperation of the officials and field personnel of Lizza Industries during the conduct of these studies is gratefully acknowledged. In addition the authors would like to acknowledge the assistance of personnel from Ocean Surveys, Inc.in the conduct of field monitoring and the U.S. Army Corps of Engineers, New York District for their cooperation.

7.0 REFERENCES

1. Mehta, A.J. and Hou, H.S., "Hydraulic Constants of Tidal Entrances II: Stability of Long Island Inlets," Technical Report No. 23, University of Florida, November, 1974.

2. Jensen, R.E., "Wave Climatology Study for the South Shore of Long Island, Phase III, Station 47," U.S.A.E. Waterways Experiment Station, 1982.

3. Schmeltz, E.J., Sorensen, R.M., Nersesian, G. and McCarthy, M.J., "Breach/Inlet Interaction at Moriches Inlet," 18th International Conference on Coastal Engineering, 1982.

HYDROSEDIMENTOLOGICAL STUDIES IN BAHIA BLANCA

BY

Petroni R.V.[1], Serman D.D.[2] and Escalante R.S.[3]

1. INTRODUCTION AND SUMMARY

The increasing international grain trade make it necessary to have more deep facilities for large draught ships.

Within the areas of major agriculture developments, Bahía Blanca harbour complex, is one of the most important and consequently also its improvement. In order to achieve this improvement a deeper and wider navigation channel has to be designed.

The actual channel, 100 km. long is limited to bulk carriers up to 37 ft. draught. It is developed along a sandy and silty coast with large bars and islands. Bahía Blanca is located at the southwest of the Buenos Aires Province, within a Bay of trapezoidal shape, where the mean tidal range changes from 3,5 m in the inner part to 1,8 m in the outer part. Trying to improve a so long channel in a complex sedimentological area imply a rather difficult task, which requires a fully investigation programme to achieve an economical and technical solution. To this end, extensive field and desk studies were carried out covering all the influence area and testing different alternatives.

One of the major problems to solve is the sedimentological stability of the channel due to the action of currents and waves.

The use of mathematical models and of large and reliable field surveys, together with a pilot test dredging used as a one to one model for the calibration of the transport formulas, looks as the most suitable method to attack such problems.

The results of this study are part of the navigation channel project carried out by the firm NEDECO-ARCONSULT for the Argentine Government.

---

[1] Professor, President of EIH Estudio de Ingeniería Hidraúlica S. A. - Cerrito 1266 - Buenos Aires - Argentina

[2] Head of Hydraulics Department of EIH S. A.

[3] Vice-President of EIH S. A.

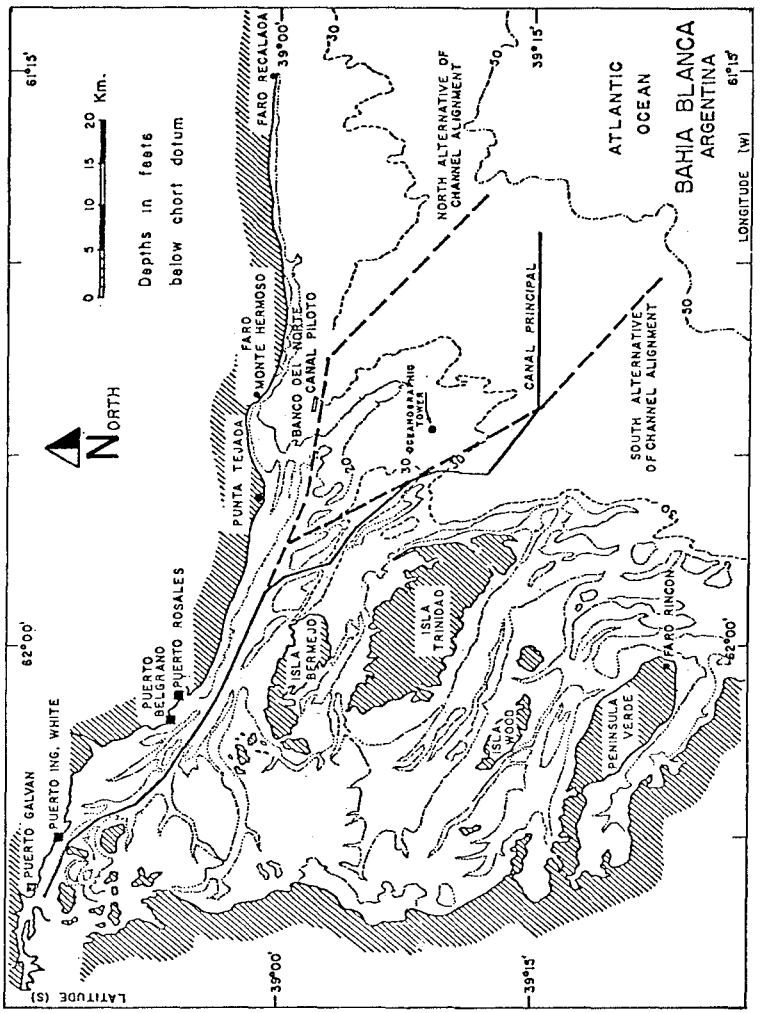

Fig. 1 Bahia Blanca, general view

2. SITE DESCRIPTION

PHISIOGRAPHIC CHARACTERISTICS

From the phisical point of view, Bahía Blanca is characterized by sandy and silty coasts with large bars and islands which show the result of a dentrictic shape. Fig. 1.

One of the most important physical factors of the area are the tides, which in the range up to 4 m. flood large part of those bars spreading the water surface from 745 Km2. in low water to aproximately 1.880 Km2 in high water; showing at this stage a unique water surface with a few islands.

This means that the difference between low water and high water is of about 1.135 Km2. of land, that is covered with water alternatively within 6 hours and a half.

This behavior has an important influence in the hydrosedimentological aspects of the area.

Other important picture of the area is that there is no fresh water supply, because only small creeks discharge on it.

It is a windy area with a dry climate. The reason of that is due to the fact that the most frequent winds are from the West and North, which induce a typical continental weather.

Eventhough, when this situation is reversed the winds from the South-East produce changes in the Bay behavior with wind set up and ocean waves conditions.

Due to the continental weather and the low depth, the water temperature is affected by the air temperature, making its variation from a maximum of 26°C and a minimum of 9°C.

HYDROOCEANOGRAPHIC CHARACTERISTICS

The Principal Channel has an extention of about 100 Km. long.

This is a natural channel, part of which has a depth of more than 60 feet. But there are other areas where the navegation is restricted by depth of about 30 feet, which imply a yearly mantainance dredging and also to make use of the tide to go in and out of the channel.

Those areas of shallowness are principally located on the outer zone, where, the sand bars movement are due to the combined action of currents and waves.

As a general feature of the channel, we can divide it in three different sections each of them with different geomorphological characteristics.

The inner part, is extended from Galvan Port to Belgrano Port

with aproximately 30 Km. Here we find soft rocks on the bed and therefore a very stable situation. On the other hand the flats are muddy convered, and due to the tidal action and wind induced turbulence we find in the water large amount of suspended sediment, getting from the tidal flats.

From Belgrano Port up to an extention of about 20 Km. the channel bed is of fine sand and silt. Here is where largest depth is found.

Out of this area, the channel becomes erratic and shallow. Rather than one defined channel we find several branches which also change in shape and depth due to storm conditions.

As it was said before, the tide characterizes the flow conditions in the area, generating reversible currents in the natural channels of about 0,3 to 1,3 m/s.

These currents induce the movement of large amount of sediment inward and outward the bay during flood and ebb. It can be said that the sediment transport induced by tidal currents has an almost zero net drift.

However under storm conditions, where wind driven currents and waves are present, the dynamic stability is broken.

Particulary in the outer area, the wave climate has a very important role in the sedimentation mechanisms.

Two wave systems are presented, the ocean waves coming from the S and SE and the localy generated wave by anshore winds.

The first one have waves up to 5 m. height and period of 12 seconds, which are strongly effected by the shoals and the second one goes up to 4 m. height but in the period of 7 to 8 seconds.

3. HYDROSEDIMENTOLOGICAL PROBLEM

As it was stated the outer part of the channel represent the major problem due to its sedimentological instability.

As we can see in Fig. 1 the existing channel turn to the south as it reach the end of the island area.

This behavior is somewhat unexpected because the tide and the current shows a symetric pattern in the angle formed by the norther shore and the West island shore.

Nevertheless, only after a good knowleged of the nature of the sediment of Banco del Norte, it will be possible to understand the problem. Previous works in the area, and spetially bottom sounding performed before, show us that this "Banco del Norte" remains identical along the time. The only possible reason for that, it would be that the surface of such a bank were harder than the original southen part.

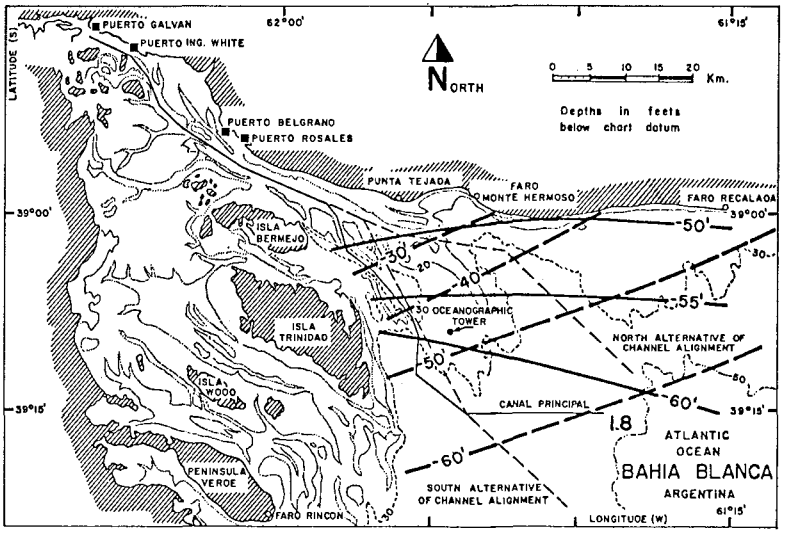

Fig. 2 Cotidal lines for high and low water

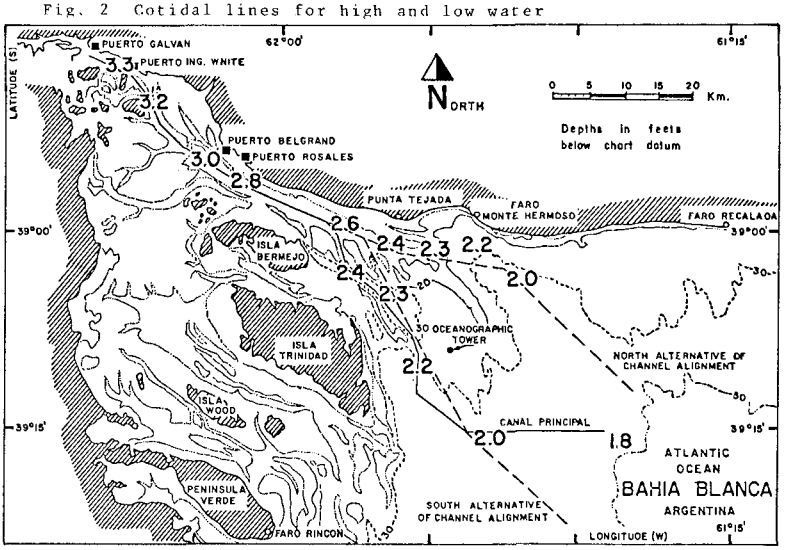

Fig. 3 Mean tidal amplitude

Moreover, if we consider in such alignment a new channel cutting Banco del Norte, it would be a good solution because the current will increase keeping the channel almost free of sedimentation.

For this reason we include the norther alignment in order to provide a new and shorter alternative for the access channel to the harbor complex.

The present paper deal with the hydrosedimentological studies carried out in this outer area.

What it was done and the resulting test carried out shows the difficulties with what we have to deal in order to estimate the sedimentation rate on a navegation channel dredged through a bank in an area with large waves and tidal currents.

4. FIELD SURVEY

The field survey was rather extensive and covered all the major aspect of the hydrosedimentological parameters.

The first work was a complet sounding of the area following the existing channel and the new alternative of alignments, previously selected from the existing data. The sounding extended over more than 1000 Km. was taken as a reference sea bottom level for all the future works.

Previously to the bottom sounding, 11 tidal gage station were installed adding to the two existing ones, which were recovered after the one mouth survey. The tidal data was first analized to get the chart datum level and to reduce the soundings.

Moreover determination of sea levels, tidal amplitudes, phase lags and harmonic analysis were carried out to provide information for navigation and hydrodinamic studies. Cotidal lines for high and low water are shown in Fig. 2 and the averaged tidal amplitudes in Fig. 3. As it can be seen the tidal flood go tinto the bay from south to north and the tidal ebb from NW to SF, also a large change in amplitude is recorded from the inner part to the outer part as a result of the funnel shape of the canal principal.

Current velocities and directions were measured at hourly intervals generally during 13 hours periods, at different points of the vertical at 22 stations, repeting most of them during both spring tide and neap tide conditions.

The variation of the current velocities in magnitude and direction under different tidal and meteorological conditions, were measured, generally during 14 days periods, using a non wave afected self-registered current meter, positioned at 10 stations.

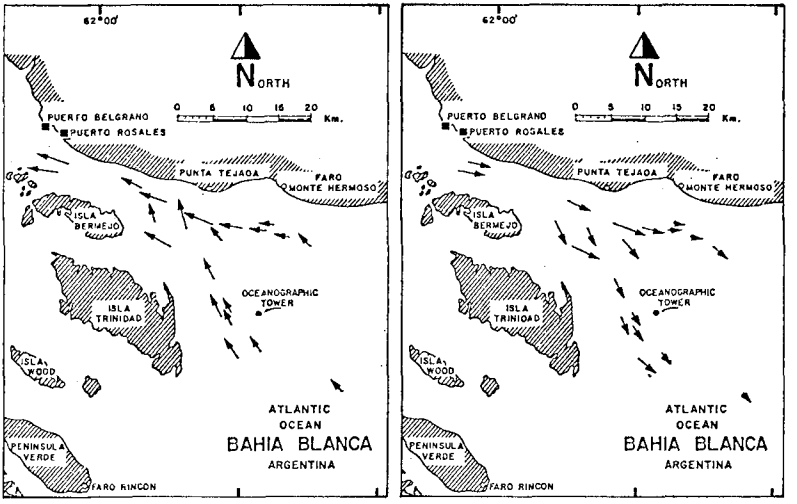

Fig. 4 Mean current pattern

The currents patterns, Fig. 4 shows in the inner part a larger velocity during ebb flow than during flood flow, ranger in the order of 0,7 - to 1,0 m/s. In the outer region the velocities decrease to the order of 0,3 m/s and the direction remains almost reverse within an angle of 10-15°. Further off shore the current directions rotate rather than reverse.

The climatological conditions at Bahía Blanca were obtained from the Servicio Meteorológico Nacional. Local winds statistic was obtained from Comandante Espora Station of the Navy.

A proper description of the wave climate in the estuary was required to design the navigation channel and for the hydrosedimentological computations. Since no wave measured data were available for the project, a Datawell waverider were first installed at the entrance of the bay for a six month period.

It was later moved to Banco del Norte, where is recording since more than one year. A wave staff was also installed on the measurement tower near buoy 8 (See Fig. 1)

Until the processing and analysis of the wave data of at least one year record has been completed other information had been used. For that the wave climate was divided in 2 categories: waves generated locally from onshore winds blowing from SW to NE directions and incoming ocean waves (swell) originating off shore from E-S directions.

The wave characteristics for onshore wind conditions were determined from the JONSWAP sepectrum (Ref. 1)

The ocean waves offshore Bahía Blanca were estimated by hindcasting on the basis of a mathematical model for the Argentina Sea developed by the Argentina Navy Meteorological Service.

On a 90 m. depth and for a period from May 1976 to January 1981, daily waves heights, periods and directions were computed, adding up a record of about 1700 data.

The ocean waves were refracted to get the shallow ocean waves climate for different points along the channels alternatives.

To this end, a mathematical model was used based on linear wave theory (Ref. 2)

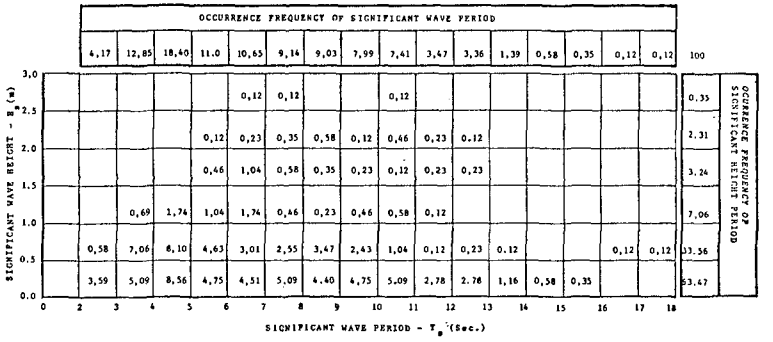

Fig. 5 Waves dispersion diagram

After the comparison with the one year measured data, a rather good correlation was verified, spetially in the local wind waves.

In Fig. 5 the dispersion diagram is illustrated which was prepared on the basic of the Draper analysis and wave spectrums.

Suspended sediment measurement were done by means of a turbidity meter and water samples at six points in each vertical, at the same locations of the current meter stations. Seabed samples were taken at several locations and at all current meter stations.

The grain diameter D50 varies from 30μ to 300μ showing three types of sediment in the full area. There are zones with full sand with D50 = 200μ , other areas with a mixture of sand and silt with D50 = 100μ and some small areas in which the sediment is composed basical by fine sand, silt and clay.

Other measurement related with the subbottom characteristics

were also done, like subbottom seismic profiles by uniboom and sparken technics, and vibrocoring in different location from which were obtained 6 m of samples and in some special points like the area of installing of the measurement tower a case drill hole up to 20 m. soil depth.

Most of this information, also usefull for sedimentation studies,was related with the dredgability of the soil in the channels alternatives.

5. THE PILOT DREDGE

After the analysis of the data collected from all the area along the existing channel and the alternatives was concluded, the pilot dredge was located. The selected area was the so called northern route because for the southern alignment other areas could be take as a control area, like channel sections between buoys 13-14 and 7-8.

Therefore a test channel of 2000 m long and 70 m wide, having a minimum depth of 13,5 m below datum, was dredged during December and January 1981-1982.

Fig. 1 shows the location of the pilot test dredge.

After the channel was completed, a bathymetric survey were done as well as current measurement both on the bank and on the channel by means of two self recording meter during 15 days.

The wave climate was controlled by the wave gage installed at Banco del Norte.

All this information together with a regular sounding each three mont, let us to check the sedimentation estimation rate providing a proper tool for the calibration of the sedimentation formula. An spetial measurement programm for the one year survey was carried out in January 1983, which includes measurements of currents, suspendend sediments and bed samples of 1 m core.

6. SEDIMENTATION ESTIMATES

A sedimentation estimates metodology was developed on the basis of the existing knowledge for areas were the combined action of currents and waves acts on the sea bottom sediment. With this metodology an estimation of the sedimentation rate were carried out for all the different sections of the channel, taking into account the different wave action and current patterns that are present in each of them.

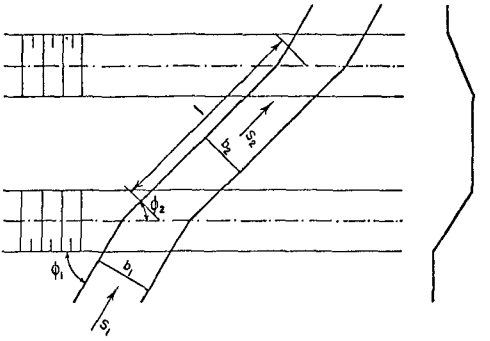

Fig. 6 Channel, definition sketch

Change in the current filled when the flow cross a dredged channel with a given angle, was estimulated on basis of the current refraction research conducted at HRS Wallingford (Ref. 3)

That approach was used for every section and for the pilot channel, where the previous estimation was obtained.

The sedimentation in a channel section can be determined by the difference in sediment transport entering and leaving this section.

Looking to the sedimentation mechanism it can be distinguished into the following three groups of processes.

1. Sedimentation due to the combined effect of waves and currents.

2. Sedimentation due to gravity infill at channel slope.

3. Sedimentation or erosion due to an extra inflow which results from changing hydraulic boundary conditions along the channel alignment.

From the three mechanism recalled, the first one is the most important, particulary in the outer area.

Therefore in the following only we will refer to this one.

The sediment transport by waves and currents approaching a channel under an angle ϕ in general decrease due to the decrease of turbulence in the channel.

The mathematical formulation for the adaptation of the suspendend sediment in the channel has been given by Fredsøe (1976) Ref. (4) and Bijker (1980) Ref. 5.

As a general approach, sediment transport can be classified in bed load and in suspended load. The suspended load could be of two origen: the fine sediment from the bed putted in suspension by the current and the wash load which is very fine sediment(fine silt and clay)already in suspension.

Looking to the channel scheme Fig. 6 the volume of sedimentation in the time Δt, can be estimated as:

$$V = (S_1 - S_2(\ell)\frac{b_2}{b_1} b_1)\,\Delta t \qquad (1)$$

where

S_1 = total load in the bank in equilibrium

$S_2(\ell)$ = total load at a distance ℓ along the streamline from the upstream side slope

in which assuming that the bed load adapts instantaneously to the hydraulics characteristics in the trench, we can write:

$$S_1 = S_{f_1} + S_{s_1} \qquad (2)$$

and

$$S_2(\ell) = S_{f_2} + S_{s_2}(\ell) \qquad (3)$$

where

$S_{f_{1\ 2}}$ = bed load in equilibrium in bed and trench

S_{s_1} = suspended load in equilibrium in the bank

$S_{s_2}(\ell)$ = suspended load at a distance ℓ along the streamline from the upstream side slope

Following Bijker, the suspended load in a trench due to currents and waves, can be written as:

$$S_s(\ell) = (S_{s_1}\frac{b_1}{b_2} - S_{s_2})\exp(-\frac{wE\ell}{V_2 h_2}) + S_{s_2} \qquad (4)$$

where

S_{s_2} = suspended load in equilibrium in the trench

$$E = \frac{h_{*1}(h_{*2} - h_{*1})}{h_{*2}(1 - \exp(-h_{*1})) - \beta h_{*1}(1-\exp(-h_{*2}))} \qquad (5)$$

and h_{*1}, h_{*2} = value of h_* outside and in the channel respectivily = $\frac{wh_1}{\varepsilon_1}$ and $\frac{wh_2}{\varepsilon_2}$

where

$$\varepsilon = 1/6\ V_{*cw} h \tag{6}$$

and

V_{*cw} = shear velocity under combined effect of wave and current according to Bijker (1967)

$$V_{*cw} = V_{*c}\left(1 + \frac{1}{2}\left(\xi \frac{U}{V}\right)^2\right)^{1/2} \tag{7}$$

$$V_{*c} = \text{shear velocity under current alone} = \frac{V g^{1/2}}{C} \tag{8}$$

w = fall velocity of sediment

h_1, h_2 = depth in the bank (1) and channel (2)

ℓ = distance from the channel boundary along the flow trajectory.

U' = maximum orbital wave velocity at the bottom

V = depth averaged current velocity

$$\xi = (fw/2g)^{1/2}\ C \tag{9}$$

fw = wave friction coefficient =

$$= \exp\left(-5{,}977 + 5{,}213\left(\frac{A}{r}\right)^{-0{,}194}\right) \tag{10}$$

(if $A/r \leq 1{,}47$, $fw = 0{,}32$)

A = orbital excursion at the bottom

$$\beta = \frac{Cb_1}{Cb_2} \tag{11}$$

Cb_2, Cb_1 = bottom concentration outside and in the channel respectively.

For the calculation of the suspended and bed load in equilibrium, on the bank and in the channel, we can use different formulae. The first approach used, was to estimate the total load by means of the Engelund-Hansen formulae and then divided the result in to bed and suspended transport by means of the so call Bijker-Einstein, so

$$S = \frac{0{,}05\ (V_{*cw})^4\ C}{g^{5/2}\Delta^2 D_{50}} \tag{12}$$

where

$$C = \text{Chezy coefficient} = 18 \log \left(\frac{12\,h}{r} \right) \qquad (13)$$

r = bed roughness

$$\Delta = \text{relative density of bed material} = \left(\frac{\rho s - \rho w}{\rho w} \right)$$

D_{50} = particle diameter (50% by weight)

and according to Einstein modified by Bijker since

$$S = S_f + S_s$$

$$S_s = 1{,}83\, S_f \left(I_1 \ln \frac{33h}{r} + I_2 \right) \qquad (14)$$

where I_1 and I_2 are the well known Einstein integral.

Following this approach it was estimated the sedimentation along the different alignment of the designed channel, taking into account the different wave and current influence for each section, so waves and current where schematized in group, with their associated percentage of occurrence. Therefore, the following formulae was applied

$$V_s = \sum_{w,c} V_{wc} p_w(H,T)\; p_c(V,\phi)$$

where

V_s = total yearly sedimentation

$p_w(H,T)$ = Wave percentage of height H and period T

$p_c(V,\Phi)$ = Current percentage of speed V and direction ϕ

V_{wc} = sedimentation volume due to waves and currents.

This approach was applied to the pilot dredge taking in to account, because their short lenght compared with the navegation channel, the sediment input from the both ends of the same and taking the field measurement current data for the bank and channel.

The result of this calculation, show an average value for the yearly sedimentation of about 0,80 m.

After seven month from the basic sounding of the pilot dredge, the sedimentation was higher. Fig. 7 and Fig. 8 shows some cross

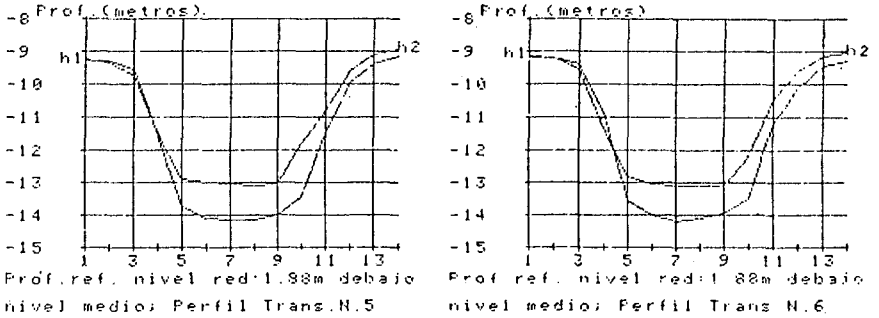

Fig. 7 Pilot dredge, comparison of cross sections after seven months.

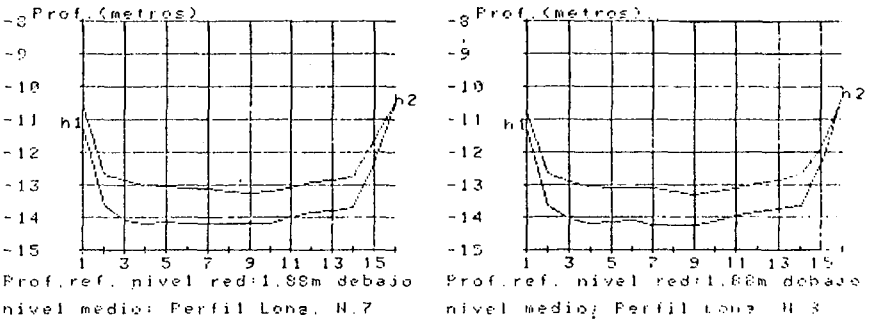

Fig. 8 Pilot dredge, comparison of longitudinal sections after seven month.

and longitudinal section of the channel. The averaged sedimentation observed in seven month is about 1 m.

After this dissapointment, we went back to ower estimation formulae and reanalized them.

First we found that the Engelund-Hansen formula it is very sensitive to the roughness of the bottom, parameter very difficult to estimate.

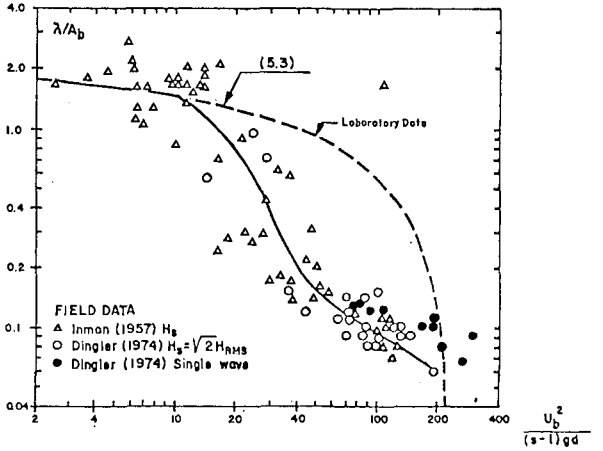

Fig. 9 Ripples height due to waves

Few data from the nature are obtained about the ripples height and wave length from the wave action.

Inman and Dingle data Fig. 9 shows that the prototipe result does not follow the laboratory test. Therefore the first thing to do was to change to another formulae, like the Bijker bed load for current and waves.

$$S_f = \frac{5\, D_{50} V \sqrt{g}}{C} \exp\left(-\frac{0,27 \Delta D_{50} g}{\mu V_{*wc}^2}\right) \qquad (16)$$

where

μ = ripple coefficient = $\left(\frac{C}{C'}\right)^{3/2}$

C' = Chezy coefficient for the grain size D_{90}

and taking, according with Einstein the suspended load, for which the bed concentration can be computed as:

$$Cb = \frac{S_f C}{6,34 V\, r\sqrt{g}} \qquad (17)$$

with a suspended vertical concentration distribution as follows:

$$C(z) = Cb \left(\frac{h-z}{z} \cdot \frac{r}{h-r}\right)^{z_*} \quad (18)$$

where

$$z_* = \frac{w}{kV_{*cw}} \quad (19)$$

k = Von Karman coefficient

The result of this calculation shows a less dependence with the bed roughness but now an overestimation of the sedimentation.

Looking to the results got from the Engelund-Hansen, and the Bijker approach, we come to the conclution, that the problem were located in the fact that in both methods the suspended load were overestimated.

The reason of that is because the calculation of the turbulent diffusion coefficient out of the wave boundary layer, is made as produced by the combined effect of the wave and current.

As it was shown by Kennedy experiments and by ISVA measurements, the sediment concentration due to waves decrease very fast as we go up from the bottom, confirmed that out of the wave boundary layer the turbulent diffusions is very small.

On the other hand, also the bed concentration could be overestimated if we consider that it came from the bed load by wave and current. Therefore, we also modified the bed concentration for the suspended load, taking it as due to the current alone. So the wave and current action only affect the bed load.

ROUGHNESS r (m)	BIJKER – EINSTEIN			FIELD DATA
	$\varepsilon = \varepsilon_{cw}$ $C_b = C_{b,cw}$	$\varepsilon = \varepsilon_c$ $C_b = C_{b,cw}$	$\varepsilon = \varepsilon_c$ $C_b = C_{b,c}$	
.012 $r = < \eta >$	7.5	2.6	0.9	1.00
.02	6.2	2.4	0.8	
.04 (Swart)	4.8	2.0	0.6	

Fig. 10 Sedimentation estimate in the pilot dredge, using different aproach, after seven months

In Fig. 10 we can see the result of these different approach, for different roughness criteria applied to 7 month for the pilot dredge from February to September 1982.

7. CONCLUTIONS

From the result got up to now, we can conclude, that for the estimation of the sedimentation in a channel in the open sea, it is still necessary to have a test channel.

It is also very important to have a complete picture of the hydrodynamic behaviour of the area, for which a simultaneous and complete field survey its neccesary.

We point out, also that in order to follow up in the knowledgement of the sedimentation by waves and currents an effort it has to be done in field measurements, like the ripple formations and suspended sediment concentration.

In such a way, we have planning to make careful measurement of concentration in the field, near the bottom, both on the banks and in the channel.

The formula currently applied has to be checked, but in the mean time we can conclude that the Bijker formula can be used but taking for the suspended load the turbulent diffusion coefficient as derived from the current alone.

REFERENCES

1.- Hasselman, K., et. al, "Measurements of wind-wave growth and swell decay during the joint north sea wave proyect (JONSWAP)", Deudsches Hydrographisches Institute, Hamburg, 1973.

2.- Dobson, R.S., "A programme to construct refraction diagram and compute wave heights for wave into shallowater" Civil Engineering Department, Stanford University, march 1967.

3.- HRS Wallingford, "Laboratory Studies of Flow across Dredged Channels". Report N° ex. 618, 1973.

4.- Fredsøe J. "Sedimentation Studies on the Niger River Delta" Proc. of N° 15th Coastal Engineering Conference, Chapter 126, Honolulu 1976.

5.- Bijker, E.W., "Sedimentation in channel and Trenches",Proc. of 17th Coastal Engineering Conference, Sydney, 1980.

SPENDING BEACH BREAKWATER AT SALDANHA BAY.

Ir. D. Zwemmer*, Ir. J. van 't Hoff**

1. ABSTRACT.

This paper describes the design and construction of a sand breakwater at Saldanha Bay exposed to the severe swell conditions of the south Atlantic.

The design of this spending beach breakwater was aimed to establish a seaward profile with sufficient "playroom" to incorporate profiles resulting from extreme wave conditions.
As far as the construction is concerned the emphasis is put on the sandlosses during execution of the works.
Finally the designed profile is compared with the actual established beach profile.

2. INTRODUCTION.

Saldanha Bay is situated some 110 km North West of Cape Town, South-Africa, on the Atlantic Coast. The bay has a wide entrance between protruding peninsulas which makes it one of the best natural harbours of the southern part of the African Continent. Through the centuries the bay has been used as a harbour of refuge by passing explorers and East Indiamen. Had it not been for the lack of fresh water, Saldanha Bay would have been developed as a major port long ago. Because of its proximity to deep water and the relatively few engineering works required, Saldanha Bay was chosen to be developed as harbour terminal of the iron ore export scheme, undertaken by the South African Iron & Steel Industrial Corporation Ltd. (Iscor).

* D. Zwemmer. Director Ingenieursbureau Ir. L.W. Lievense, Breda. The Netherlands.
** J. van 't Hoff. Head engineering department. Van Oord-Utrecht N.V. The Netherlands.

In order to enlarge the existing sheltered area of the inner bay, the northern peninsula Hoedjies Point was extended by a breakwater to Marcus Island situated in the middle of the entrance to Saldanha Bay (see illustration 1).
This breakwater was designed and constructed as an artificial sand beach on which the waves would spill and thus gradually dissipate their energy, hence the name "spending beach breakwater". This article describes the design and construction of the "spending beach".

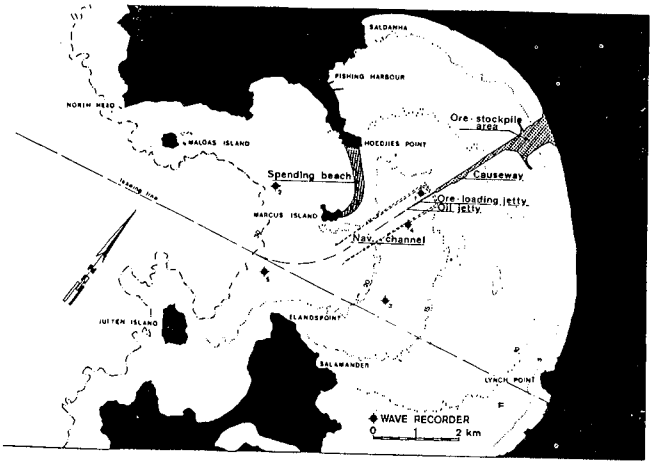

ill. 1. General lay out of harbour configuration at Saldanha Bay.

3. BASIC INFORMATION.

3.1. Waves.

During a period of two years, preceeding the design period, wave heights were measured at five different locations in the bay (ill. 1). Simultaneously "deep sea" wave heights, directions and periods were measured. The measurements were executed by the Council of Scientific and Industrial Research (C.S.I.R.).

At measuring station 2 situated just seaward of the proposed breakwater, at a depth of approximately 25,00 m below C.D. the results show the following:

Table nr. 1	Station 2			
Frequency exceeded %	H_s	$\bar{H}_s > H_s$	T_s	$\bar{T}_s$
	m	m	sec.	sec.
50	1,75	-	13,4	-
10	2,90	3,70		15,3
5	3,40	4,10		15,7
1	4,50	5,15		16,6

The maximum significant wave height recorded at station 2, was H_s = 4,90 m, corresponding with a deep sea wave height (significant) of H_s = 8,50 m. The wave height probability curves given in illustration 2 show the freguency of exceeding of H_s at station 2 and the centre part of the breakwater.

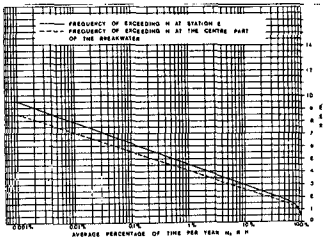

ill. 2. Wave height probability curves in station 2 and in the centre part of the breakwater.

The predominant deep sea wave directions are south-south-west and south-west. Measurements obtained by means of clinometer-readings show SSW 43,9 % of the time, SW 37,0 % and S 10,1 %.

Due to the configuration of the entrance of the outer bay, the combined effect of refraction and diffraction, forces the incoming deep sea swell to pass Marcus-Island with only a slight variation in wave direction.

A diffraction-refraction model built to acquire an insight into the wave reduction in the lee of the proposed breakwater, was also used to obtain photographs of the wave pattern of the area between Marcus Island and Hoedjies Point peninsula. Photographs were taken for different deep sea wave directions and periods. Aerial photographs taken of the actual wave crest patterns of know deep sea conditions, showed good correlation with the corresponding photographs of the model tests. An example hereof is given in illustration 3.

3.2. Wind.

Wind speed and direction were measured at Elandspoint, situated due south of Marcus Island, during the period March 1971 to February 1974.

The SSW-direction is the predominant wind direction with an average wind speed of 7 m/sec. The average windspeed during spring is 8,5 m/sec.

3.3. Tides.

The tides are as follows: MHWS : 1,76 / MHWN : 1,26 m / MLWN : 0,76 m / MLWS : 0,26 m ; all related to C.D.

3.4. Currents.

As only a few current measurements were made, only approximate values of currents could be established. Currents at a depth of 10 m in the north channel went up to 0,15 m/sec. during ebb-tide and to 0,24 m/sec. during flood-tide. The direction of the tidal currents was almost perpendicular to the line Hoedjies Point - Marcus Island. Wave induced currents could not be distinguished.

3.5. Geology of the sea-bed.

A seismic survey related to some borings in the area of the proposed breakwater showed that the bottom generally consists of compacted sands on top and in between layers of calcareous material varying in hardness. At the lee side (north-east) of Marcus Island some loose sand layers could be distinguished. At some places (Blinkklip Rock) granite outcrops stick through the bottom layers. The shoreline of both Hoedjies Point and Marcus Island consists of huge outcrops of solid granite and boulders.

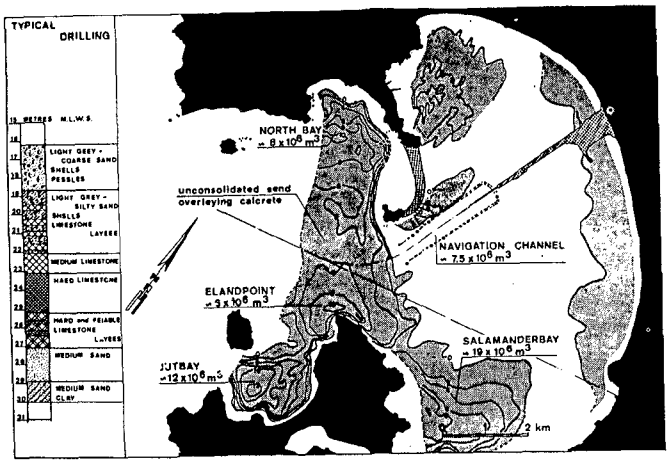

ill. 3. Loose sediments overlaying calcareous material, sandwinning areas.

3.6. Available building material.

As millions of m^3 of sand were required to build the spending beach breakwater, intensive soil investigations were carried out, comprising several sonar surveys, drilling/probing using a self elevating platform

and a shallow water structure placed on the bottom, also washborings were made using a floating platform.

In the Saldanha Bay area the basement is formed by the so called "Cape Granite". Drilling results showed that the buried granite surface is highly irregular. In this basement the valleys are filled in with recent and subrecent material, gently sloping down in the seaward direction. The infill material consists mainly of loose and compacted sands with layers of cemented, sand and calcrete, differing in hardness.

The areas where loose sediment is overlaying calcareous layers, are indicated on illustration 3, being the outcome of an extensive sonar survey. As main sandwinning areas could now be distinguished:
- Salamander bay area of which approximately 19 x 10^6 sand could be obtained and the
- navigation channel, with a total quantity of 7,5 x 10^6 m^3 including large quantities of cemented sands and calcareous materials.

A typical drilling of the area of the navigation channel is also given in illustration 3. The medium grain size diameter of the numereous samples varied considerably. The Salamander bay area showed some small areas of decomposed granite (600 μ) excellently suitable as building material for the breakwater.

4. DESIGN.

4.1. General.

In an early stage of the design, after discussion with the Delft Hydraulic Laboratory, it was decided not to execute an extensive model study as this could not give sufficient reliable results within the available time, but to establish a design based on the knowledge obtained from literature and on the measurements of comparable existing beaches. In the design two main items can be distinguished:
a. the horizontal alignement and
b. the seaward profile.

The horizontal alignement of a beach in general, must be designed in such a way that the predominant wave direction will always impinge perpendicular to the beach in order to prevent lateral transport of material.
It shall be clear from the geography of the bay that the location of Marcus Island in relation to Hoedjies Point offered a unigue possibility to build an artificial cove as a natural extension of North Bay beach (see illustration 1).
As other kidney-shaped beaches exist in the area, it was quite a challenge to try to design an artificial beach which could withstand the incoming ocean swell having its origin in the "roaring forties".

The seaward profile in general depends on the size of available sediment and the local wave conditions. Since wave conditions vary continuously, a single stable equilibrium profile cannot exist. The eguilibrium state will thus be of dynamic nature, continuously adapting itself to the momentary wave climate.

The design was aimed to establish a seaward profile, with sufficient "playroom" to incorporate profiles resulting from extreme wave conditions.

4.2. Horizontal alignment.

For different deep sea wave directions and wave periods, the wave crest patterns between Hoedjies Point and Marcus Island, as observed in the model test, are shown in illustration 4. The low-water line of the proposed breakwater was determined parallel to a fictive wave crest being the weighted average of the different wave directions and periods.
Taking into account the extended low water line of North Bay beach and the location of Marcus Island, the low water line of the proposed breakwater was now fixed, reflecting the kidney-shape like so many beaches in the area.
The width of the beach was determined by two factors. Firstly by the variation of the low water line being dependent on the wave direction and secondly by the variation of the seaward profile being dependent on the wave height.

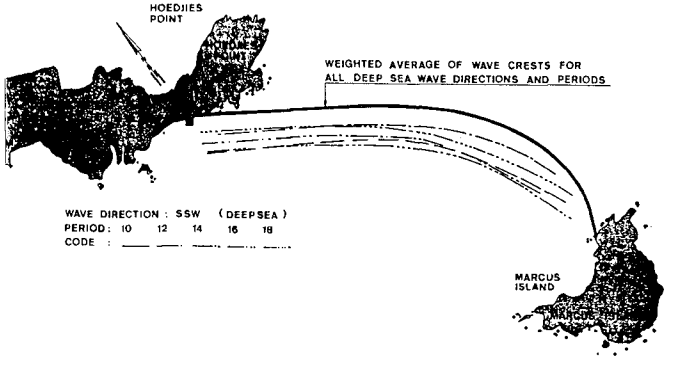

ill. 4. Wave crest patterns according to model studies.

When a wave approaches the beach at an angle a longshore transport is generated. This breaking wave and the movement of sediment is caused by the component of the wave in the longshore direction and the longshore current generated by the breaking wave. Tidal currents in the area of the proposed breakwater could be considered negligible.
The longshore transport, being dependent on the wave energy and the angle of wave approach, should gradually decrease and finally come to a stop as the shoreline is shaped into line with the incoming wave-crests. Studies of a.o. Bascom, Inman, Rusnak showed large variations in beach-profile and large areal movements of sand in relative short periods of time. It was therefore assumed that the horizontal alignment should adapt itself rather rapidly to a change in wave direction.

The width of the beach (shore) should thus be able to "accomodate" all the low water lines corresponding with the different deep sea wave directions. For other kidney shaped beaches in the area, although no beach measurements were taken over long periods, the verbal opinion of local fishermen indicated only minor changes in the low water line.

4.3. Seaward profile.

4.3.1. General.

The design problem was approached as being two-dimensional, i.e. the design of a cross-section which remains in equilibrium when subjected to local wave conditions, consistent with size and amount of available material.
This two-dimensional approach was considered acceptable due to the fact that tidal currents after the closure of the gap between Hoedjies Point and Marcus Island should be negligible, while generated longshore transport should always fade out the source of its origin, i.e. decrease the angle of wave approach by re-shaping the beach.

The main profile changes are limited to be inshore zone. A seaward profile is considered stable when in the long run the offshore transport equals the onshore transport of material. As the waves tend to change periodically, the profile adapts this change and in general a "summer" or step profile and a "winter" or bar profile can be distinguished. Under rough weather conditions a "winter" profile is formed with a shore line which may move landwards over a considerable distance. Large quantities of sand are then transported in the direction of the sea, where they are "stockpiled" in the form of one or more sand ridges or "bars". In calme weather the waves will gradually shift this sand back towards the shore.
There is accumulation of coarse sediment in zones of maximum wave energy dissipation and deposition of fine sediment in areas sheltered from wave action. This phenomenon is called sediment sorting.

4.3.2. The offshore region.

Waves travelling towards the projected breakwater, eventually reach a depth where the water motion near the bottom begins to effect the sediment on the bottom.
The water motion immediately above the sediment bed then exerts enough shear to move sand particles. This depth is called the incipient depth and is determined by the sediment size and wave characteristics. Initially only very fine material oscillates in the direction of the wave and as the water depth decreases coarser sand particles will be moved back and forth in ripples.

In order to determine the incipient depth it is necessary to calculate both the orbital velocity immediately above the seabed and the threshold velocity at which erosion of the bed material takes place. The orbital velocity is calculated as follows:

$$U_z = 0{,}7 \frac{\pi \times H}{T} \quad \frac{\cosh . \frac{2\pi (h - z)}{\lambda}}{\sinh . \frac{2\pi h}{\lambda}}$$

The threshold velocity at which movement of sand grains occurs, is computed as follows:

$$v_e = 4{,}5 \left[\log \frac{12\ h}{4\ d_{50}} \right] \sqrt{d_{50}} \quad \text{while} \quad \frac{v_e}{v_z} = \frac{\log 32 - \log d_{50}}{\log 8\ (h-z) - \log d_{50}}$$

Since no sudden major sand transport takes place in the offshore region (no "storm" and "summer" profiles), it is assumed that the bottom configuration is determined by median wave conditions. Table nr. II gives the median wave conditions for the different water depths, as well as the H_s 5 % wave conditions.

Table nr. II	H_s 50 % T, = 13,4 sec.		H_s 5 %, T = 15,7 sec.	
h in m	H_s in m	λ in m	H_s in m	λ in m
deep	1,84	280	3,47	384,5
30	1,73	202	3,35	246
25	1,75	188	3,40	236
20	1,79	171	3,56	207,5
17,5	1,82	160	3,64	192,3
15,0	1,87	148	3,73	180,7
12,5	1,93	140	3,89	165,3
10	2,01	126	4,08	146,3

It is assumed that transport of bottom material takes place above the "apparent" bottom in a band of approximately 0,75 x the height of the ripples. The ripple height is approximately 0,10 x the water depth. The graph of illustration 5 shows that for median wave conditions 200 μ sand starts to move at a depth of 26,25 m and 300 μ sand at a depth of 18,90 m.

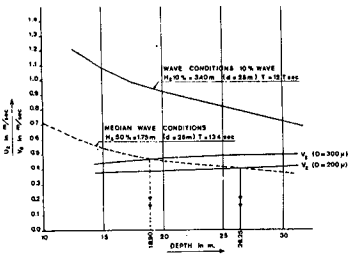

ill. 5. Critical velocity for D = 200 μ and D = 300 μ

The equilibrium slope developing in the offshore region can be estimated using the following equation:

$$\sin \alpha = \frac{k}{J} \cdot f_1 \left(\frac{h}{\lambda_0}\right), \text{ wherein } \frac{k}{J} = \frac{15{,}23\ H_0^2}{T \cdot \lambda_0 \cdot d_{50}^2} \cdot \left(\frac{d_{50}^2}{T}\right) \cdot 0{,}57 \text{ and}$$

$$f_1 \left(\frac{h}{\lambda_0}\right) = \frac{\cot gh^2 \left(\frac{2\pi h}{\lambda}\right)}{\sinh^2 \frac{2\pi h}{\lambda} + \frac{2\pi h}{\lambda_0}}$$

The results of the calculation are given in table III.

Table nr. III waterdepth	H_s . 50 % d_{50} = 300 μ	H_s . 50 % d_{50} = 200 μ	H_s . 5 % d_{50} = 300 μ
30 m			1 : 28
25 m	1 : 76	1 : 54	1 : 17
20 m	1 : 49	1 : 34	1 : 12
15 m	1 : 29	1 : 20	1 : 7
12,5 m	1 : 18,5	1 : 13	1 : 4

4.3.3. The breaking depth.

To estimate the depth at breaking, it is recommended by the Shore Protection Manual to use the empirical relationship between d_b/H_b and H_b/gT^2 as derived from various beach slopes.

Station 2:
$\bar{H}_s > H_s$ 1 % = 5,15 m
h = 25 m
T_s = 16,6 sec.

$\lambda_0 = 430$ m

$\frac{h}{\lambda_0} = \frac{25}{430} = 0{,}0581 \rightarrow \frac{H}{H_0^1} = 1{,}0 \rightarrow H_0^1 = 5{,}15$ m

$\frac{H_0^1}{\lambda_0} = \frac{5{,}15}{430} = 0{,}012$

slope 1 : 50	H_b = 7,11 m	d_b = 7,96 m
slope 1 : 30	H_b = 7,62 m	d_b = 8,08 m
slope 1 : 20	H_b = 8,14 m	d_b = 7,81 m

For $\bar{H}_s > H_s$ 50 % slope 1 : 50 d_b = 3,30 m

4.3.4. The inshore region.

At the time of the initial design, "inshore" eguilibrium profiles could not be calculated theoretically. A great number of underwater profiles of existing beaches in the Saldanha Bay area and at other locations were compared with regard to wave attack and median sand grain diametcr. This comparison indicated that an inshore profile slope of 1 : 35 with a sand of d_{50} = 300 μ should be a safe estimate. In illustration 6 the designed profile is compared with the actual profiles of North Bay beach. The so called "sorting effect" of the sand grains along the profile should result in steeper slopes and thus increased safety. In 1974 mr. D.H. Swart published a method of calculating the eguilibrium profile of the so called D-profile (developping profile). In illustration 7 the theoretically calculated D-profiles (part below still water level) are given for H_s 50 %, H_s 10 % and H_s 5 % wave conditions.

4.3.5. The foreshore (beach face).

Numerous field studies showed that there is a good correlation between median sand diameters and the slope of the foreshore. The foreshore (beach) slopes of the existing beaches around Saldanha Bay are corresponding closely with the data of these field studies. For an exposed beach and a medium grain size diameter of the sand of 300 μ, the slope of the foreshore shows 1 : 35.

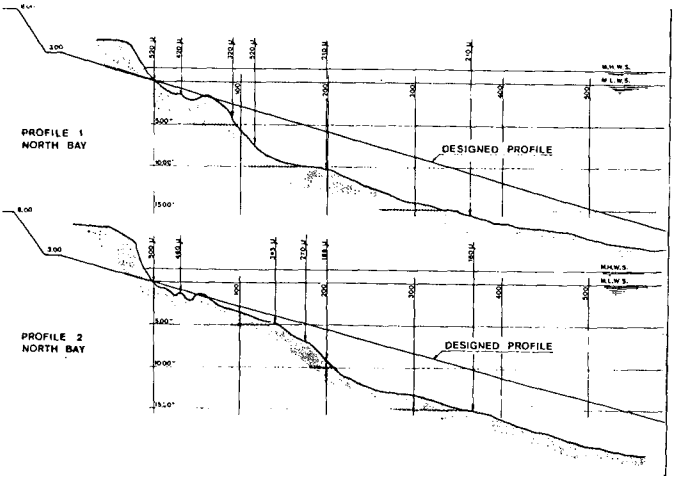

ill. 6. Comparison of designed profile with the actual profiles of North Bay beach.

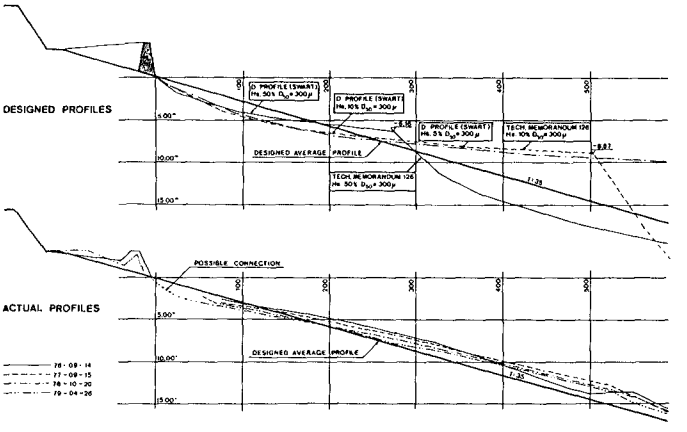

ill. 7. Theoretically calculated D-profiles, spending beach design and actual profiles.

4.3.6. The "set-up".

"Set-up" due to wave action is that phenomenon whereby the average water level along the beach rises above that encountered under so called still water conditions. According to Bowen the set-up "z" depends on the breaker height H_b and amounts to a maximum of $z = 0{,}25\ H_b$.

Assuming again the $\bar{H}_s > H_s$. 1 % wave conditions:
$\bar{H}_s > H_s$ 1 % : 5,15 m (at station 2), T_s = 16,6 sec, λ_0 = 430 m.
H_b = 7,62 m.

$$Z = 0{,}19 \left[1 - 2{,}82 \sqrt{\left(\frac{H_B}{gT^2}\right)} \right] . H_B = 1{,}23 \text{ m}$$

Since a "storm" profile could develop in a very short space of time the breaker depth d_b must be measured below C.D. ≙ M.L.W.S. The maximum height of the set-up "z" must be added to M.H.W.S. The maximum height of the wave run-up thus becomes 1,50 m (tide) + 1,23 m = 2,73 m$^+$ C.D. The design height of the berm crest was established at 3,00 m$^+$ C.D.

4.3.7. The back-shore.

Inland of the upper limit of wave set-up is called back-shore. The inland crest or berm crest could be overtopped by extremely high waves in which case the overtopping water flows down the so called deflation plane. Initially this plane was given a width of 20,00 m in order to take care of the changes in horizontal alignment. The final safety barrier (dike) was given a height of 8,00 m$^+$ C.D. (see ill. 8). As a result of the applied construction method, a stone wall was dumped at the proposed low water line up to a height of 4,00 m$^+$ C.D., the width at the crest being approximately 6,00 m. This relatively small stonewall consisted of quarry run 0-4000 kg. The stone crest was incorporated in the construction by filling the now 120 m wide plain between this stone crest and the root of the safety barrier up to a level of 3,10 m$^+$ C.D.

It shall be clear that this small stone wall prevented the foreshore (beach slope) to develop initially. It was assumed that the stone wall would finally disperse, due to wave action, below a level of M.H.W.S. with a seaward slope of approximately 1:4 - 1:6, thus offering an additional safety. The presence of this stone wall should also fix the horizontal alignment. Only the sand profile seaward of this wall could adapt itself to changes of incoming waves, resulting in varying depths just seaward of the wall. The final design profile is given on illustration 8.

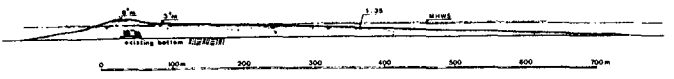

ill. 8. Designed cross-section of spending beach breakwater.

5. CONSTRUCTION.

5.1. General.

For the construction of the spending beach breakwater about 20 million m^3 of sandfill was required.

The main volume of sand was obtained from the winning area due east of Salamander Bay (see illustration 3) while an additional amount of approximately 7 million m^3 became available during the dredging of the navigation channel.
The initial programme showed the construction time of the breakwater to be one year. However, during the first months of construction it appeared that the estimated production quantities in the winning areas were far too optimistic. This was mainly due to the fact that the sand grains were more cemented than anticipated which lowered the concentration of the sand-water mixture flow towards the suction pipes of the trailhoppers. As a conseguence additional dredgers had to be mobilized in order to finalize the construction in time.

The breakwater was built in two stages. The first building stage comprized the dumping of sand in the profile by means of hopper dredgers up to a level of 6,6 m⁻ M.L.W.S. for which approximately 15 million m^3 of sand was required. The second building stage, being the closure of the upper part, was realized by the joint-effort of shallow draft hoppers and two big cutter-suction dredgers.

The closing started from Hoedjies Point in the lee of which the two cutter-suction dredgers operated initially. After the above water part protruded some 600 to 800 m from Hoedjies Point, one of the cutter-suction dredgers was moved in the lee of this above water part to recover sand from the underwater stockpile as well as the sand that was forced out of the profile due to wave action. It only took three months to close the "superstructure" of the spending beach breakwater, sometimes loosing some meters in the battle against a roaring Atlantic swell but always recovering guickly when the swell subsided.

5.2. The first building stage (see bottom up to 6,60 m⁻ M.L.W.S.)

The underwater mound was built of dredged material dumped into profile by hopper suction dredgers, the big hopper dredgers filling in the deeper parts and the smaller hoppers the shallower areas, always taking into account loaded draft and wave conditions. The local seabottom consisted of calcareous material interchanged with cemented sand layers and some loose sand. The original water depth varied from 16,00 m to 20,00 m below chart datum with steep granite slopes towards Marcus Island and Hoedjies Point. The dumping of sand by means of the different types of trailhoppers was carefully programmed and adjusted weekly in order to obtain a seaward under water profile closely approximating the designed profile.
On the 30th October 1975 the underwater mound was considered to be completed, having at that time an average height of 6,60 m⁻ M.L.W.S.
The guantities dumped into the underwater mound together with the spending beach stockpile, measured by shiploads, showed the following:

. "Humber River" (big trailhopper)	10,200,000 m^3
. "Willemstad" (med. trailhopper)	3,900,000 m^3
. "Volvox Zelandia" (transmundum type)	3,300,000 m^3
. "Geopotes 12" (transmundum type)	1,100,000 m^3
. "Queen of Holland" (cutter-suction) *)	1,900,000 m^3
Total	20,400,000 m^3

*) During the first vain attempt to close the spending beach, the cutter-suction dredger "Queen of Holland" pumped 1,900,000 m^3 into the spending beach, which quantity settled mainly below a level of 6,60 m minum M.L.W.S. and as such had to be added to the underwater mound.

The total quantity of 20,400,000 m^3 could be divided into 19,100,000 m^3 for the underwater mound and 1,300,000 m^3 for the spending beach underwater stockpile, situated at the lee side of the underwater mound along a distance of 800 m from Hoedjies Point.

The volumes of sand, including sandlosses, measured in situ as the difference of the initial soundings and the soundings at the day of completion of the underwater mound (30th October 1975) were as follows:

. underwater mound	15,200,000 m^3
. stockpile spending beach	1,100,000 m^3
. sandlosses (measured outside profile)	900,000 m^3
Total	17,200,000 m^3

In the cross section of illustration 9 the underwater mound, stockpile and sandlosses are indicated. The locations of the stockpile areas which were prepared during the first building stage and used for the closure of the upper part during.

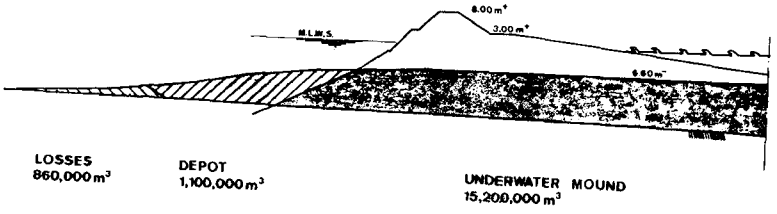

ill. 9. Cross section of spending beach after completion of stage I, including sand stockpile and sandlosses.

The difference between the so called shipload quantities and the actual in situ measured quantities, totalling up to 3,200,000 m^3, can be attributed to the following:

a. Settlement of the subsoil as a result of the sandweight. Taking into account the results of the drilling in this area an average settlement of 0,15 m over an area of 1,800 x 400 m was considered as reasonable: 1,800 x 400 x 0,15 ≈ 100,000 m^3.

b. Too high estimates of shipload quantities as a result of:
   1) sand remaining in the ship holds during discharging (dumping).
   2) ratio between solid and loosely packed sand.
   3) loss of very fine material during the dumping process. This very fine material settled in a large area outside the beach profile in a thin layer on top of the existing seafloor not noticeable by echosounding.

The experience gathered at Saldanha Bay justified a reduction of 18 % for the bigger trailhopper dredgers and 12 % for the "transmundum" type of trailhopper dredgers. These reduction applied to the given quantities, give:
0,18 (10,200,000 + 3,900,000) + 0,12 (3,300,000 + 1,100,000) = 3,100,000 m^3.
Total: (100,000 + 3,100,000) = 3,200,000 m^3.

Sandlosses underwater mound.

According to the in- and out surveys of the construction area the total volume of sand which eventually arrived outside the construction limits was 900,000 m^3 which is 5 % of the total measured quantity. A more complete insight in the distribution of the volume of sandlosses as found after stage I of the spending beach was completed, can be obtained from illustration 10. This illustration shows the quantities of sand leeward of the underwater mound including losses and stockpiled sand per section of 100 meter across the length of the breakwater. The outer boundary of the transported sediment is also indicated; as an average the sand was transported upto ca. 500 m behind the stockpile area.
The biggest quantities of sandlosses were found near Hoedjies Point. This is explained by the fact that the construction of the underwater mound started from Hoedjies Point and from there was gradually extended towards Marcus Island.
It is interesting to note that these sandlosses did not contribute to the volume of sand in the stockpile area. The total quantities dumped in this area as measured from the shiploads and reduced with the above mentioned reduction factors were as follows:

. "Humber River"	1,200,000 x 0,82 =	980,000	m^3
. "Willemstad"	100,000 x 0,82 =	80,000	m^3
. "Beachway"	35,000 x 0,88 =	30,000	m^3
. "Geopotes 12"	50,000 x 0,88 =	40,000	m^3
		1,000,000	m^3

which quantity approximately equals the measured quantity of 1,100,000 m^3 in the stockpile area.

5.3. The second building area stage (6,60 m^- C.D. up to 3,50 m^+ C.D.).

5.3.1. The temporary breakwater.

The first vain attempt to close the gap between Hoedjies Point and Marcus Island, resulted into a small beach around Hoedjies Point, shading off into part of the underwater mound.
This beach in conjunction with the depth contours of the underwater mound, existing during June-September 1974, caused a most unfavourable refraction-diffraction pattern, focusing the waves at the area of Smitwinkel Bay, in which the village of Saldanha and her different fish-factories are located. During the winter-period of 1974, storms caused therefore considerable damage to moored ships, guaywalls, small jetties etc. As the second building stage was scheduled for the period November 1974 - April 1976, a second winter-period had to be confronted. To secure the shelter of the existing fishing harbour area, it was therefore decided to build a so-called temporary breakwater. This breakwater, protruding from the lee side of Hoedjies Point, served at the same time as the outer limit of the sand stockpile nr. I behind Hoedjies Point (see illustrations 11 and 12).

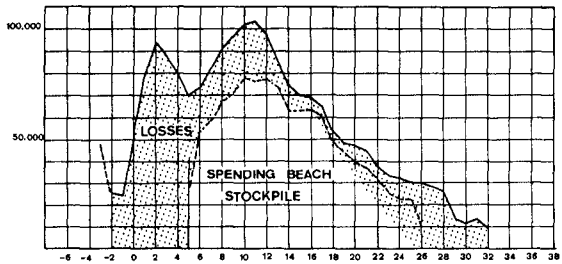

DISTRIBUTION OF SAND VOLUME LEEWARD OF UNDERWATERMOUND BEFORE START OF CONSTRUCTION STAGE II

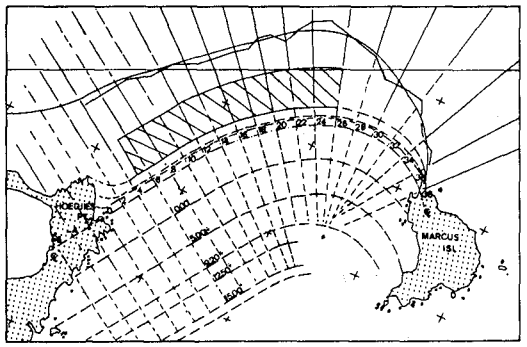

OUTERBOUNDARY OF TRANSPORTED SEDIMENT

ill. 10. Distribution of transported sediment.

ill. 11. Aerial photograph of Hoedjies Point at the beginning of the second building stage.

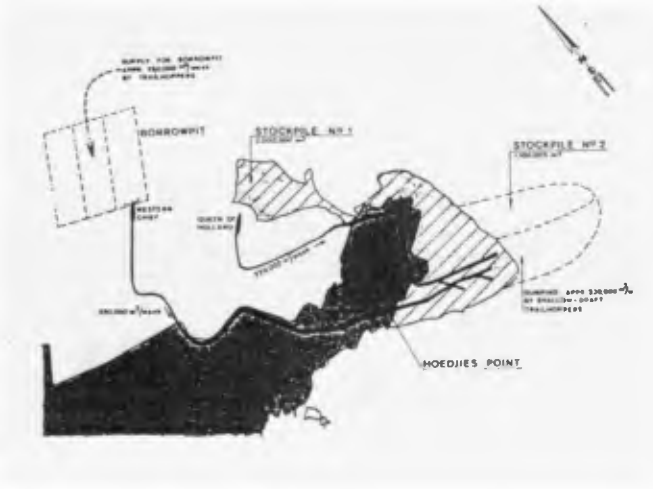

ill. 12. Operation of cutter suction dredgers at the beginning of the second building stage.

5.3.2. Working scheme and sand production.

The required amount of material for this second building stage comprized approximately 5,000,000 m^3.
To minimize the sandlosses a continuous high production was essential. For the "final attack", which started from Hoedjies Point two cutter-suction dredgers were used, having a joint production of approximately 500,000 m^3 per week, assisted by three transmundum type, shallow draft hoppers with a total weekly production of about 250,000 m^3.
Both cutter-suction dredgers operated initially in the lee of Hoedjies Point. One of these dredgers was operating in an earlier prepared stockpile (2 million m^3) while the other obtained his material from a borrowpit, continuously refilled by the bigger trailhopper dredgers. (See illustrations 11 and 12.) While the "above-water" part of the breakwater was striding along towards Marcus Island, the three transmundum type hoppers were used to dump immediately in front of the above-water part, taking full advantage of their horizontal sliding bottom doors.
A second underwater stockpile has been prepared behind the first 800 m to 900 m of the future breakwater, which stockpile was increased by the losses during the construction of the adjacent superstructure. As the construction of the superstructure progressed one of the cutter-suction dredgers, advanced from the stockpile no. 1 into the created shelter of the partly finalized breakwater. The complete sand transport scheme is given on illustration 12. The working scheme was adapted weekly in order to optimize the output of this expensive dredging fleet.

5.3.3. The superstructure.

The construction of the temporary breakwater in the lee of Hoedjies Point has learned that a stone wall located at the proposed low water line, with its crest at approximately 4,00 m^+, protruding seawards like a knife-edge, considerably restricted the amount of sand washed away from the head.
It proved that a relatively small stone wall (average 120 ton/m^1), combined with the pumping of sand at the seaside some 150 m distance behind this head, offered the best progress. The wave forces transported the sand along the seaward profile as well as longitudinally towards the "knife-edge" of the stone head.
Directly in the lee of the protruding stone-wall the sand settled and here bulldozers were used to push up the sand towards the backside of the wall. Sand accretion also took place in the deeper areas just in front of the head. As soon as the level here reached 0,00 m, stone was backtipped, shifting the spear head (knife-edge) forward again, as can be seen on illustration 13. This illustration also gives an impression of the enormous size of the breaking waves as compared to the size of the truck. Every 50 m a pipe branched off running through the small stone wall towards the seaside. It very quickly became clear that for the majority of the time, the seaward outlets had to be operated, making use of the waves to carry out the further transport of the spoil.
Hydraulic fill directly in the centre part of the spending beach was restricted to a distance of 150 m, backwards from the head in order to minimize sandlosses. The cutter production system was gradually improved during the course of the construction i.e. the lay out of the discharge pipelines and rubble mound dam and also the progress of the rubble mound.

The "safety barrier" with its crest up to 8,00 m^+ C.D. was made in the orthodox way by hydraulic fill in between aand walls.

ill. 13. Protruding stone wall shifted forward and acting as knife-edge. Note the size of the breaking waves.

The above described construction method made it possible to realize the closure in 14 weeks with a minimum loss of sand and two months ahead of schedule. The progress is made visible in illustration 14.

The maximum significant wave height encountered during construction was H_s = 3,30 m (7-12-1975). At station no. 2, some 1,500 m seaward of the crest line of the spending beach, the Datawell wave rider buoy measured a maximum wave of H_m = 5,05 m (T_s = 14,5 sec) at that day.

The amount of stone per m^1 increased during periods of heavy wave attack. It only happened once that an earlier reclaimed area had to be returned to the sea.

On December 17th 1975, while about 800 m of the 1,900 m gap between Hoedjies Point and Marcus Island was brought above water, current measurements were executed over the remaining part of the underwater mound (average depth 6,60 m^-). Wave conditions were moderate H_s = 1,75 m. Tide difference 1,30 m. Maximum current measured over a full tidal cyclus 0,30 m/sec.

Grain-size diameter.
During construction of the underwater mound a great number of bottom (grab) samples was taken mainly at depths between 7,00 m^- and 8,00 m^- C.D. The median grain-size diameter varied between 110 μ and 220 μ. The material of the superstructure however, proved to be much coarser. The average of six drillings made in the sand stockpile nr. 1 showed 53 % above 210 μ and 35 % above 420 μ. Samples taken from the cutter-suction dredger "Western Chief" gave an average of 370 μ for the median grain-size diameter. Unfortunately no bottom aamples on the seaward slope were taken after completion.

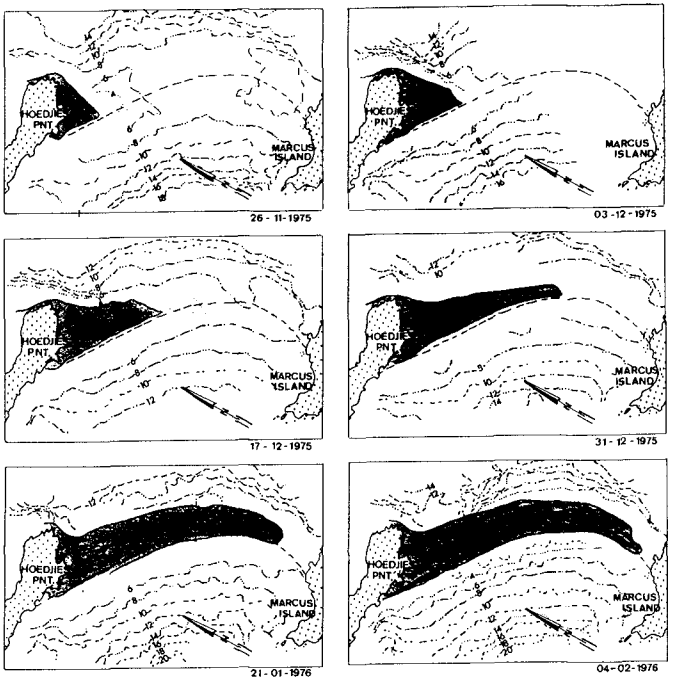

ill. 14. Progress of superstructure of spending beach breakwater.

As a result of the way of execution (pipe outlet on the seaside), the so called sorting effect started already during execution: the finer sand particles being washed away more easily by the waves and the bigger sand particles settling earlier. It can therefore be concluded that the median grain-size diameter of the seaward slope on average is in excess of 300 μ.

5.3.4. Sandlosses second building stage.

Sand losses of the superstructure were calculated up to 4-2-1976, being the data the connection with Marcus Island was realized. The quantities brought into the superstructure during the period from 30-10-1975 up to 4-2-1976 measured as follows:

. Transmundum type of trailhoppers 2,220,000 m^3	
Reduction factor to obtain solid m^3 x 0,88	~ 2,000,000 m^3
. Cutter-suction dredgers	~ 5,100,000 m^3
Calculated solid m^3	~ 7,100,000 m^3

The volumes of sand measured in situ as the difference between the depth soundings of 30-10-1975 and 4-2-1976 ~ 5.600.000 m^3

The total losses comprise 21,1 % of the total sand production during the second building stage.

The losses were defined as quantities shifted outside the reguired profile by wave action, currents etc. The majority of the losses of the first 900 meters of spending beach accumulated in the stockpile area number II and were recovered by the cutter suction dredger "Queen of Holland" in building the second half of the superstructure.
As the construction of the superstructure proceeded the dredging process improved. This can be illustrated by comparing the sandlosses which occurred during the construction of the first 900 meters with the sandlosses which occurred during the construction of the remaining second half of the superstructure. They were respectively 29,7 % and 11,8 % of the corresponding sand productions.
This reduction in losses can be ascribed to
- less wave action during the construction of the second half of the superstructure
- improvement of the fill distribution in the reclaim area.

6. CONCLUSION.

After the construction was finished, echo soundings were performed at regular intervals during the period 1976-1979 in order to establish the seaside slope of the spending beach breakwater. An example of these actual measured profiles is given in illustration 7.

1) Comparison between the designed profile and the actual measured profiles show a good correlation.

2) This seaward profile up to a depth of approximately 6.00 m^- is very simular to Swarts D-profiles. Correlation with Technical Memorandum 126 is poor, specifically in the shallower areas.

3) None of the numerous echo soundings show an underwater bar which could be explained by the fact that the wave seasons have only minor differences.

4) The relatively small stonewall - used during construction to minimize sandlosses - has shaped into a protective layer around the area of low water and as such fixes the low water line of the seaward profile.

- o - o - o -

SAND MOVEMENT INTO CARMEL SUBMARINE CANYON, CALIFORNIA

by

J.R. Dingler and R.J. Anima[1]

ABSTRACT

Carmel Submarine Canyon heads in shallow water near Monastery Beach at the southeast corner of Carmel Bay, California, U.S.A. Very coarse sand, shaped into large oscillation ripples, covers the narrow shelf between the beach and the canyon; when this sand enters the canyon head, it lies at angles as great as the angle of repose. In some areas, these sand slopes show evidence of active grain flows in the form of downslope-coarsening, inversely graded deposits.

The results of a dyed-sand tracer study adjacent to the canyon show that sand moved canyonward during the summer of 1979. Initially the dyed sand, which had been shaped into an oscillation ripple in the center of a 20-m by 60-m grid, moved offshore en masse. After a few days, though, the dyed sand dispersed with the center of mass moving canyonward.

As wave-transported sand accumulates along the canyon rim, the upper slopes oversteepen, thereby causing some of the sand to avalanche downslope. Systematic changes in sand levels along three lines of rods over 15 months document preferential deposition of sand along the upper slopes; the greatest change occurred at the top of the lines (12-15 m depth) and the least at the bottom (30-40 m). Greater accretion during the spring months than during the summer months probably reflects the more energetic springtime wave climate.

Between October 1981 and October 1982, 5.7 m^3 of sand was deposited per meter alongslope on the middle line, which gives a calculated depositional rate of approximately 500 m^3/yr in the study area. Although we have monitored this area for over a year, we have not yet documented any large-scale events capable of flushing sand out of the canyon head. The only erosive event we have observed was a small grain flow we generated while digging on the slope.

INTRODUCTION

Submarine canyons funnel sediment from the continental shelf

[1]U.S. Geological Survey, Menlo Park, California 94025

to deep water. Whenever a submarine canyon extends into shallow water, its head intercepts longshore-moving beach sand, removing it from the littoral zone. Inman and Frautschy (1966) described how such canyon heads terminate littoral cells along the southern California coast.

Instead of moving directly to deep water, most sand remains in the canyon head for an indefinite period of time probably ranging from months to years. Filling of the head continues until a combination of air, land, and sea conditions flushes sand into deeper water (Inman et al., 1976); investigators think that the sediment entrained by such an episodic event generates a turbidity current. Although no one has observed such a current, Inman et al. (1976) described strong, pulsating flows that finally produced a down-canyon flow strong enough to carry off their recording sensors. Divers who inspected the sensor mounts reported large sand losses from the canyon head.

Sand slowly accumulates in the canyon head, moving downslope from the canyon rim. Dill (1964) showed that slow gravity creep takes place in fine sand and decaying kelp in the head of Scripps Canyon. Dill (1966) attributed grain flows, seen in San Lucas Canyon, to steepening of sandy slopes beyond the angle of repose (33°). Dingler and Anima (1981) showed that grain flows down angle-of-repose slopes could produce the inversely graded, sandy deposits found in the head of Carmel Canyon.

After waves transport littoral sand to the canyon rim, gravity becomes the driving force. Gravity creep or sand avalanching redistribute sand within the canyon head, and sediment gravity flows remove sand to deeper water. This paper describes how sand moves into the head of Carmel Canyon from the littoral zone, and how small grain flows redistribute the sand onto slopes that dip at angles as great as the angle of repose.

SETTING

Carmel Submarine Canyon heads in shallow water in the southeast corner of Carmel Bay, California (Fig. 1). The canyon is one of several that cut into the continental shelf along central California; it enters the larger Monterey Canyon west of Monterey in a water depth of 2012 m (Shepard and Emery, 1941). Carmel Canyon is an extension of the adjacent land canyon that contains San Jose Creek (Shepard and Dill, 1966, p. 88). Shepard and Dill presumed that the sandy shelf between the beach and canyon rim is a filled part of the ancestral canyon.

Tributaries enter Carmel Canyon along its entire length; the shallow, nearshore ones lie close to a series of coarse-grained pocket beaches, collectively named the Carmel River State Beach. At its closest point, the canyon head lies less than 200 m from Monastery Beach, the southern most of the pocket beaches within the State Beach. Wave-generated ripples cover the narrow shelf

Figure 1: Section of a physiographic diagram of the head of Carmel Submarine Canyon and surrounding land (Alpha et al., 1981). Inserts show the location of the study area along the California coast.

between the beach and canyon (Hirschaut and Dingler, 1982). Water depth at the canyon rim, or shelf break, varies with location; it is less than 15 m at its shallowest point.

Although the wave climate at the canyon head is restricted by its location within Carmel Bay, storm waves from the northwest reach the area. Dingler (1981a) estimated from berm height that breaking waves higher than 3 m reached Monastery Beach too infrequently to produce a storm profile there commonly.

On land, Santa Lucia Granodiorite (Bowen 1965) is the principal rock type throughout the area. The conglomeratic Carmelo Formation (Bowen, 1965) crops out on both sides of Monastery Beach, and both the Carmel River and San Jose Creek drainage basins include other sedimentary rocks. Underwater, sand covers most of the bedrock, but granodiorite crops out in several localities around the canyon, and one sedimentary outcrop occurs along the east wall of the canyon head. Figure 2 shows the onshore distribution of rock types and the location of major underwater outcrops known to us.

Most of the sand on Monastery Beach, the adjacent shelf, and upper canyon slopes is very coarse to granular, but fine sand exists in some of the more quiescent areas. Along most shore-normal transects, grain size decreases from the beach to the rim and increases downslope to about 35 m (Fig. 3); below that depth grain size quickly drops below sand size.

A transect along the 15-m bathymetric contour from the rocks on the north passes through five zones with differing biota, texture, and surface expression before reaching the southern extent of the east wall (Fig. 4). Diopatra ornata tubes densely populate a substrate of fine sand in zone 1. The second zone has fine to coarse sand with clumps of red algae and partially exposed tubes of Platysereis bicanaliculata. This zone gradually merges into zone 3, which is different from the other zones in that it has no exposed biogenic sedimentary structures, though Platysereis exist within the sand. The shore-normal transect shown in Figure 3 passes through zone 3. When viewed from a distance, much of the sand appears to have slope-parallel stripes spaced 1 to 2 m apart. These, we believe, are the deposits of small avalanches. Zone 4 is similar to zone 2. Zone 5, which is offshore of a small kelp bed, contains both Diopatra and algae with a fine-sand substrate. Along the south wall, zone 5 terminates at granitic outcrops.

EXPERIMENTAL METHOD

Scuba divers conducted the experiments and made all the measurements and observations described herein. These included injecting dyed sand and sampling for it over time, emplacing aluminum rods and measuring them, and measuring dips on the sandy slopes. Figure 5 shows the location of the dyed sand sample area

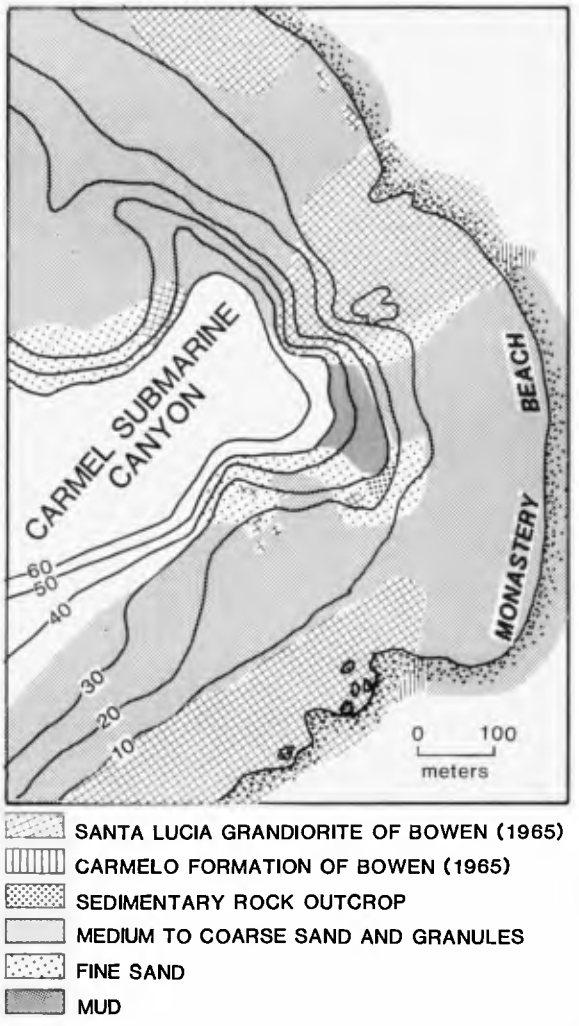

Figure 2: Distribution of rock types in the vicinity of Carmel Submarine Canyon.

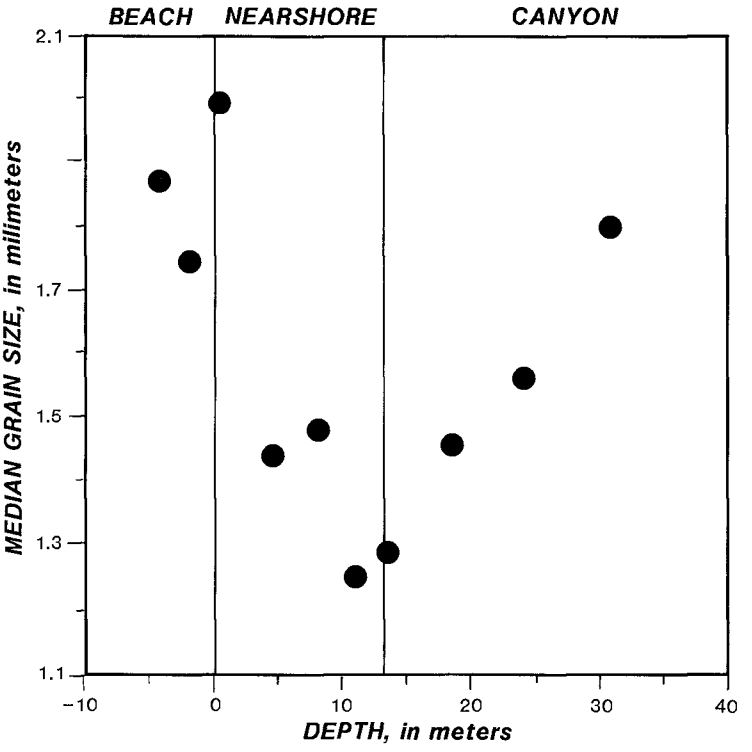

Figure 3: Grain-size distribution of sediment along a shore-normal transect that starts at Monastery Beach and ends within the canyon head. See Figure 5 for transect location.

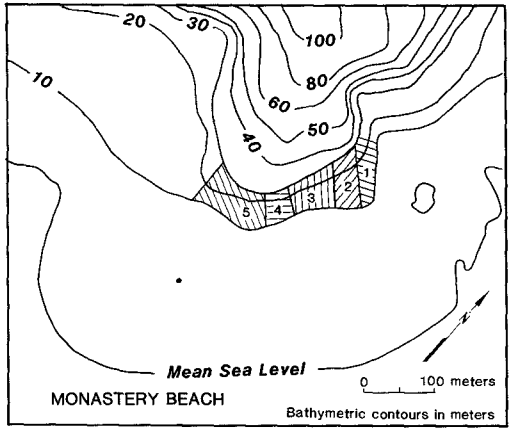

Figure 4: Bathymetric map of the head of Carmel Submarine Canyon and adjacent shelf. The east rim of the canyon is zoned on the basis of grain size and biota (lined areas). Because of this distribution we assume that active transport is greatest in zone 3 and negligible in zones 1 and 5. See text for further explanation.

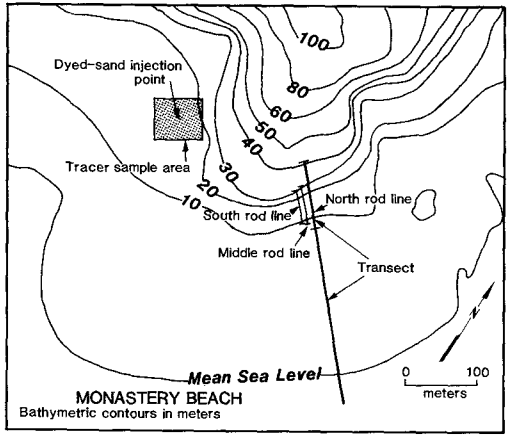

Figure 5: Location of dyed-sand tracer study adjacent to the south wall of Carmel Canyon and line of rods on the eastern slope. Line across shelf together with the north line represent the transect of Figure 3.

and the rod arrays. All measurements were made during fair weather.

To determine the transport direction of sand near the head of the canyon, we injected 161 kg of dyed sand on the shelf adjacent to the south rim prior to starting any experiments on the canyon slopes. We collected the sand from the center of a 70-m by 60-m grid, dried it, dyed it a fluorescent color, and returned it to the collection point. Injection consisted of replacing two meters of a ripple crest with the dyed sand. At irregular times, divers collected a surficial sample from each of 35 grid points; these samples were split and the dyed grains counted under an ultraviolet light.

Based on the biological and sedimentological patterns, we assumed that the most active part of the upper slope was in zone 3. To measure the rate of deposition there, divers drove aluminum rods into the sand on the slope, leaving part of each rod exposed. The rods formed lines that started on or near the shelf break and went downslope. In April 1981, we emplaced one line of 26 rods spaced 1 m apart at the site of one of our man-made avalanches (Dingler and Anima, 1981). Three months later we added a longer parallel, line about 5 m north of the first one. These two lines ended at a depth of 30.5 m. In May 1982 we added a third line about 15 m north of the second one. This last line had rods spaced 2 m apart, extending from the shelf to a depth of 36.6 m.

Two divers can measure the rods on two lines in one dive. Between the installation date and 15 October 1982, we measured the south line of rods 13 times, the middle line 12 times, and the north line 4 times. Once, the divers also measured slope angle using a dipmeter developed by Dingler (1981b). Accuracy of the rod measurements is roughly 1 centimeter and that of the dip measurements is 1 to 2 degrees. Because a dip error of 1° equals an error in elevation of 1.7 cm, we relied on the rod measurements in this study. Besides, the rod data can be used with one set of dip measurements to calculate dips at any time.

RESULTS

After injecting dyed sand on 30 April 1979, we inspected or sampled the grid on 3, 7, and 15 May, 7 June, 3 and 7 July, 3 and 16 August, and 26 September 1979. On the first two days most of the dyed sand remained in one ripple crest that had migrated about one wavelength (about 1 m) offshore. Some dyed sand also showed on the next offshore ripple and a few grains had dispersed toward the canyon. We saw no grains onshore of the injection point. The dyed-sand ripple crest had disappeared by 15 May, and dyed grains were scattered over the inner part of the grid with the greatest visible concentration being offshore and canyonward of the injection point. By 7 June, dyed grains had reached the boundaries of the study area with the highest concentration again

being offshore and canyonward (Fig. 6). This pattern continued through the study period.

The curves in Figure 7, which are based on dip measurements from 11 May 1982, are the slope profiles above 30.5 m of the three lines. The slopes parallel one another; the slight deviations near the top could reflect variations in location of large ripples that extend onto the upper part of the shelf break. Figure 8 contains selected data from the middle line; the rod-height data, which are representative of data from the other lines, have been converted into net deposition by subtracting the measured heights from the initial rod heights.

DISCUSSION

Determining depositional rates in the canyon head was the goal of this study. Although our coverage of the canyon head was limited, our three lines of data show how the sand that moves into the canyon head is distributed. Assuming that the depositional rates along the lines are representative of the east rim, an average volume is calculated and seasonal fluctuation noted.

Other investigators assumed that waves drove the sand from the beach to the canyon. Our dyed-sand experiment supports this assumption to the extent that sand near the canyon rim preferentially moves canyonward through a zone of wave-formed ripples. Wallin (1968) thought that the Carmel River was a major supplier of littoral sand to Monastery Beach, but Howell (1972) concluded, using wave refraction diagrams, that sand moved south from the Carmel River and north along Monastery Beach. As shown in Figure 9, these littoral sand streams turn seaward before reaching the large rock exposure just north of the canyon.

After not finding any through paths when diving amongst the rocks and analyzing sand samples from the midforeshore along Carmel River State Beach, we also conclude that little sand crosses the rocky area north of Monastery Beach. Along the northern part of Carmel River State Beach, south of the Carmel River, grain size increases to the south (Fig. 9). This trend is opposite to the downdrift distribution produced by littoral transport. However, the observed distribution would be produced by a southward increase in the granodiorite contribution relative to the littoral contribution.

At Monastery Beach, the mouth of San Jose Creek is usually deflected to the north, indicating a northward movement of littoral sand before it moves offshore. The sources of this sand are San Jose Creek and the local granodiorite, but we do not as yet know the proportions of each.

Once the sand reaches the canyon rim, it piles up until the upper slope oversteepens. Then a grain flow redistributes the sand downslope; the distance downslope varies from a few to tens

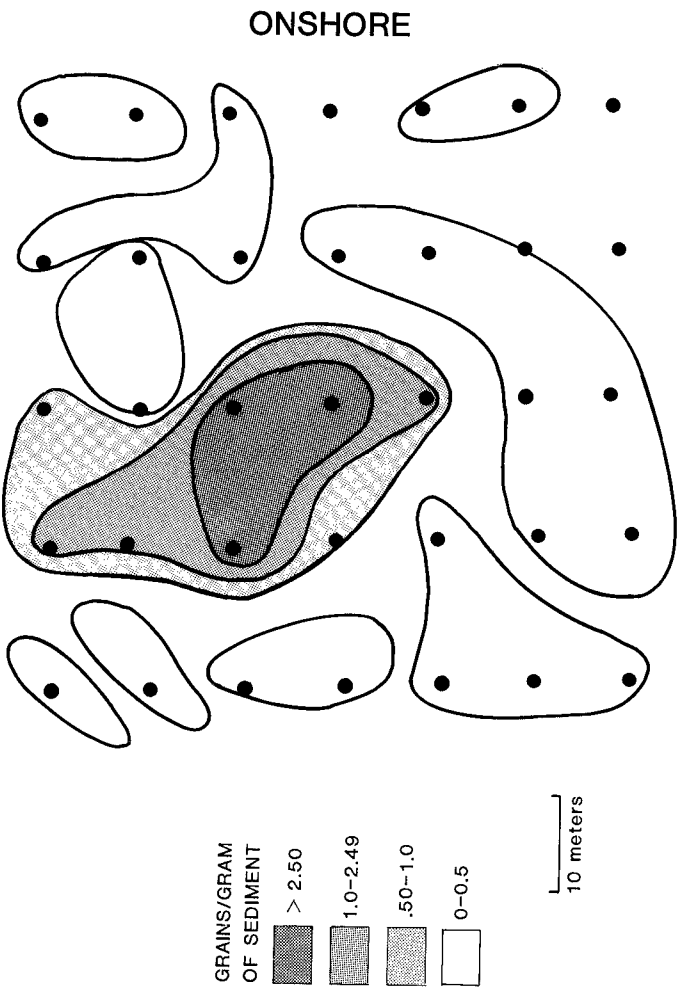

Figure 6: Distribution of dyed sand 38 days after injection on 30 April 1979. See Figure 5 for location of sampling grid.

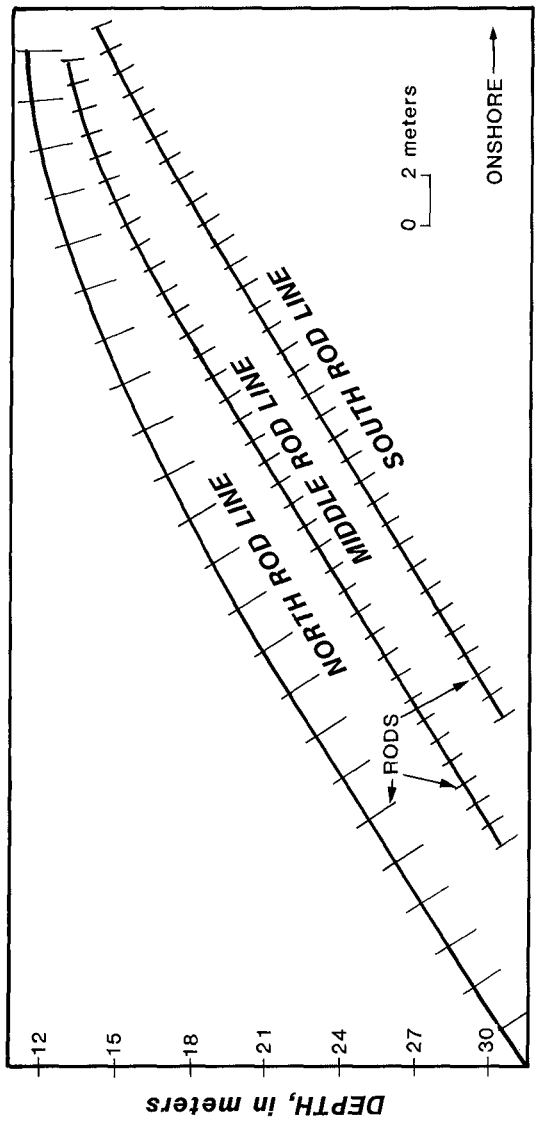

Figure 7: Bottom slopes along the three lines of rods located in Figure 5. Rods are not drawn to scale; those along the north line are 2 m apart and the others are 1 m apart.

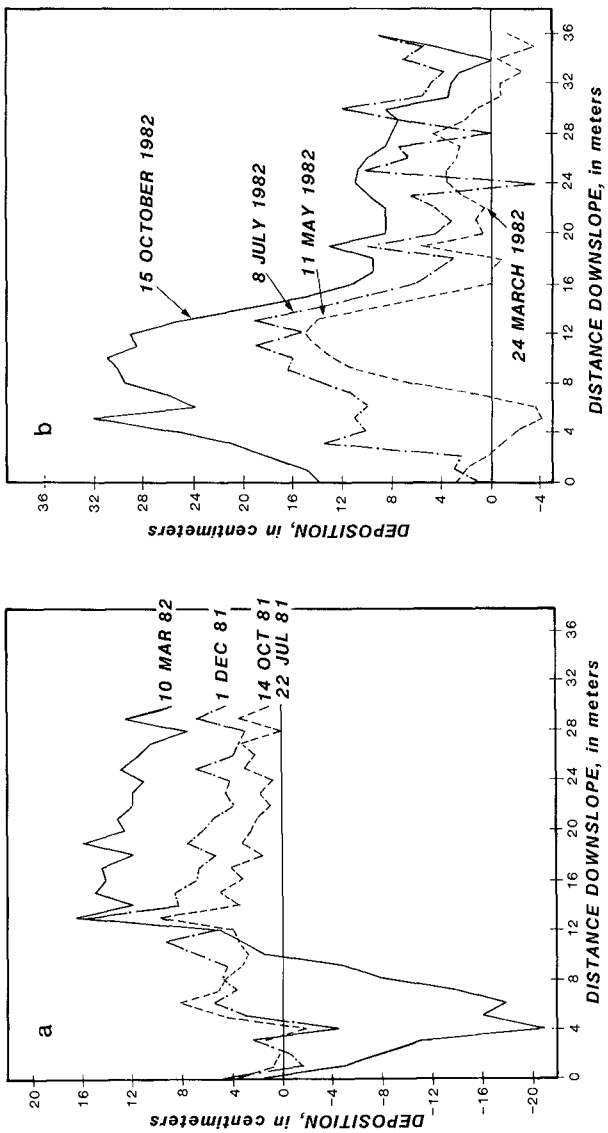

Figure 8: Net deposition at each rod on the middle line (a) from 22 July 1981 to 10 March 1982; (b) from 24 March 1982 to 15 October 1982. See Figure 5 for rod line location. Deposition between 10 and 24 March 1982 is unaccounted for because of accidentally generated grain flow on the latter data. See Figure 13 and text for more details.

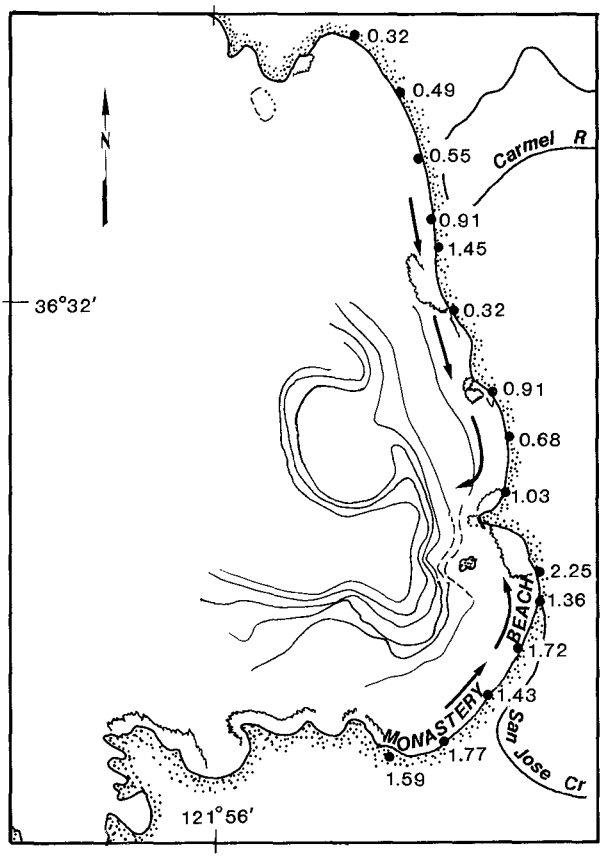

Figure 9: Littoral zone sand transport paths (arrows) into the head of Carmel Submarine Canyon (from Howell, 1972). Dots locate our textural samples, and the adjacent numbers give the mean grain size in millimeters.

of meters. We base this interpretation on systematic changes in deposition down the three lines of rods (Fig. 8). The greatest deposition takes place just over the rim (away from the ripples), and the least at the bottom. This process recurs at least on a monthly basis, and thus, the canyon rim slowly accretes.

Deposition Q_l, in units of volume per length alongslope, was calculated from the eguation:

$$Q_l = \Delta x(0.5z_1 + \sum_{i=2}^{n-1} z_i + 0.5z_n)$$

where Δx is the spacing between rods, n is the number of rods, and z_i is the amount of deposition at the ith rod. Figure 10 shows both the incremental and net deposition on the middle line, and Figure 11 recasts the incremental data in terms of average rates. These figures illustrate the seasonality of the canyon-head deposition: deposition was rapid in the late spring and early fall of 1982 and slow before and after the spring high. This trend appears on the south line, which also had relatively rapid deposition in the spring of 1981. This pattern probably mirrors the intensity of the wave climate, so fluctuations, such as hetween fall 1981 and fall 1982, would be expected because wave climate is variable.

Lateral variations also occur, even over the few meters between rod lines, as shown by the net deposition on the three lines between 11 May 1982 and 15 October 1982 (Fig. 12). During this time the most deposition took place on the south line, and the least on the north one. Using the data from the middle line, the depositional rate in the study area was 364 m^3/yr if all the sand moved through zone 3 (64 m wide), and 791 m^3/yr if it moved through zones 2-4 (139 m wide).

We have not found any evidence of large-scale slope erosion during our studies in Carmel Canyon. However, Shepard and Emery (1941, p. 101) speculated that erosive events must occur in the head of Carmel Canyon. They measured over 5 m of fill from 1934 to 1939, a rate that would fill the head within a few years unless there was an erosive event.

During one of our dives on 24 March 1982, we accidentally generated a grain flow along the southern line that redistributed much of the sand that had heen deposited during our study. While trying to dig out some buried rods near the middle of the line, we created a scarp-recession grain flow (Hunter, 1977). Sand fell into the upslope side of the hole and continued to flow downslope past us. Above the initiation point, previously buried rods appeared at a rate of more than one per minute; near the top of the rod array the height of the scarp had increased from a few centimeters to more than 30 cm. Figure 13 shows the approximate magnitude of erosion, assuming that a wedge of sand 25 cm thick at the top rod covered the rods hefore the grain flow. Although this grain flow only disturbed a small part of the slope, on a larger

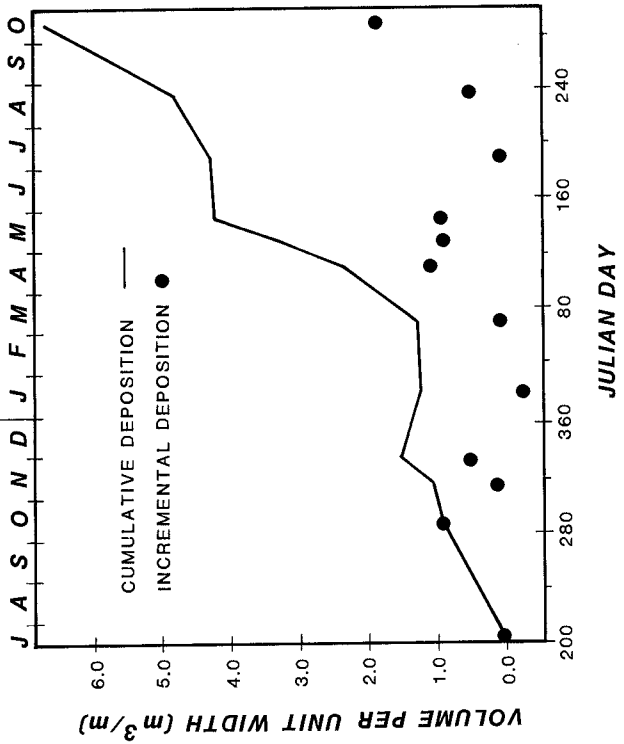

Figure 10: Net and incremental deposition along the middle rod line based on rod-height changes. See Figure 5 for rod line location.

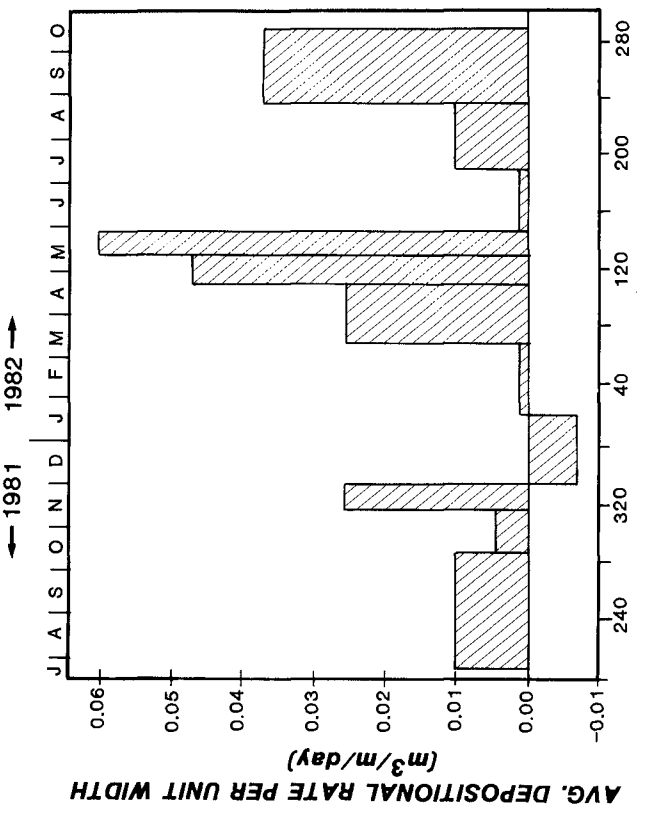

Figure 11: Average rate of deposition along the middle rod line, calculated by dividing the incremental values (Fig. 10) by the number of days between measurements. See Figure 5 for rod line location.

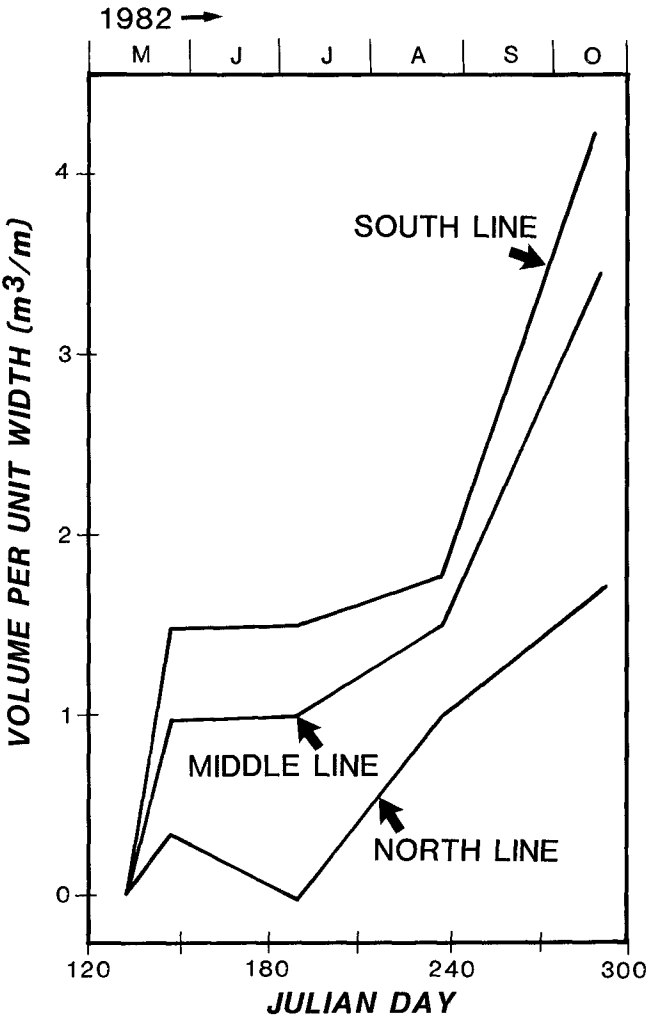

Figure 12: Net deposition on the three lines between 15 May 1982 and 15 October 1982.

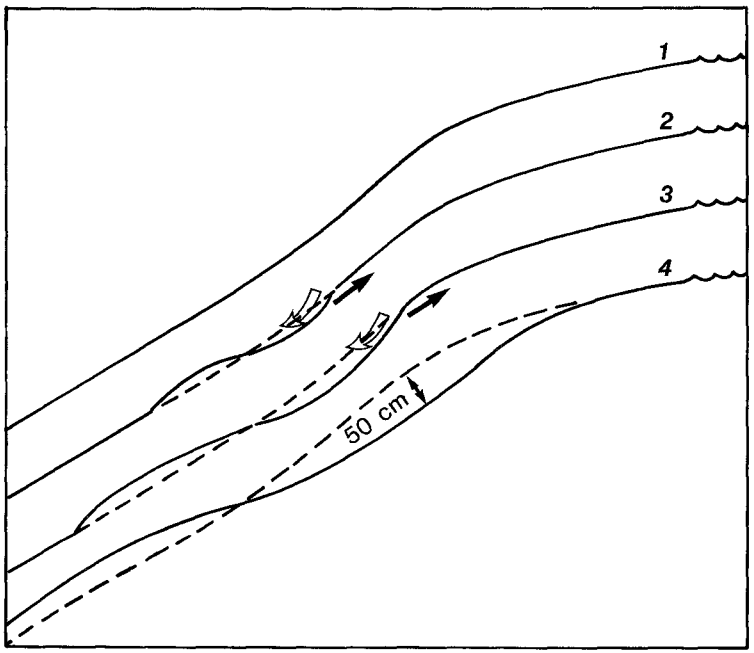

Figure 13: Changes in slope profile due to an accidentally generated scarp-recession grain flow on 24 March 1982. Maximum erosion was on the order of 50 cm. Profile 1 shows the slope before we disrupted it. Profile 2 shows sand falling into the hole we made and flowing downslope. Profile 3 shows the location of the scarp partway through the grain flow. Profile 4 shows the final profile. The dashed line in 2, 3, and 4 represents the original profile. Open arrows show the direction of sand flow; solid arrows show the direction of scarp recession. Scale is approximate.

scale this mechanism could easily initiate turbidity currents on angle-of-repose slopes.

CONCLUSIONS

1. Sand sporadically reaches the Carmel Submarine Canyon rim from the adjacent shelf. Sand entering the littoral zone comes from San Jose Creek and weathering of local granodiorite outcrops.

2. After reaching the Carmel Submarine Canyon rim, the sand collects until the slope becomes too steep. Then the sand avalanches, coming to rest farther downslope. Subsequent deposits may cause the slope below the rim to oversteepen, producing another avalanche. In this manner the slope slowly accretes seaward.

3. The depositional rate along the east rim of Carmel Submarine Canyon is on the order of 500 m^3/year.

ACKNOWLEDGMENTS

We thank the many people who dove with us during this study; Dave Molzan and Don Hirschaut were our principal aides. Gary Hill and Herman Karl reviewed this manuscript and made several relevant suggestions.

REFERENCES

Alpha, T.R., Dingler, J.R., Jones, D.R., Molzan, D.E., Peterson, C.P., and Morley, J.M., 1981, Physiographic diagram of the upper Carmel Canyon and Point Lobos, California: U.S. Geological Survey, Open-File Report 81-440, 1 map.

Bowen, O.E., 1965, Stratigraphy, structure, and oil possibilities in Monterey and Salinas quadrangles, California: American Assoc. Petroleum Geologists, Pacific Section Symposium, no. 40, p. 48-7.

Dill, R.F., 1964, Contemporary submarine erosion in Scripps Submarine Canyon [unpub. Ph.D. thesis]: Univ. of California, San Diego, 268 p.

_____, 1966, Sand flows and sand falls, in Fairbridge, R.W., ed., The Encyclopedia of Oceanography: Reinhold, New York, p. 763-765.

Dingler, J.R., 1981a, Stability of a very coarse-grained beach at Carmel, California: Marine Geology, v. 44, p. 241-252.

_____, 1981b, A dipmeter for underwater use: Jour. Sed. Petrology, v. 51, p. 662-663.

_____, and Anima, R.J., 1981, Field study of subaqueous avalanching (abs.); Bulletin, American Assoc. Petroleum Geologists, v. 65, no. 5, p. 918-919.

Hirschaut, D.W., and Dingler, J.R., 1982, A field study of large-scale oscillation ripples in a very coarse-grained, high-energy marine environment: U.S. Geological Survey, Open-File Report 82-733, 33 p.

Howell, B.F., 1972, Sand movement along Carmel River State Beach, Carmel, California [M.S. thesis]: Naval Postgraduate School, Monterey, CA., 71 p.

Hunter, R.E., 1977, Basic types of stratification in small eolian dunes: Sedimentology, v. 24, p. 361-387.

Inman, D.L., and Frautschy, J.D., 1966, Littoral processes and the development of shorelines: Am. Soc. Civil Engineers, Coastal Engineering Santa Barbara Speciality Conf. 1965, p. 511-536.

_____, Nordstrom, C.E., and Flick, R.E., 1976, Currents in submarine canyons: an air-sea-land interaction: Annual Review of Fluid Mechanics, v. 8, p. 275-310.

Shepard, F.P., and Dill, R.F., 1966, Submarine Canyons and Other Sea Valleys: Rand McNally, Chicago, 381 p.

_____, and Emery, K.O., 1941, Submarine topography off the California Coast: Canyons and tectonic interpretation: Geological Society America, Special Paper 31, 169 p.

Wallin, S.R., 1968, The sediments in the head of Carmel Submarine Canyon [M.S. thesis]: Naval Postgraduate School, Monterey, CA., 99 p.

Suspended Sediment Discharge on a Non-Tidal Coast

by J. P. Coakley[1] and M. G. Skafel [2]

Abstract

A field study was conducted on a non-tidal sand beach to measure the relationship between wave energy and the longshore transport of suspended sediment. The range of suspended sediment concentrations was similar to that reported elsewhere. The relation between longshore transport and longshore energy flux derived from this data set is about half that amount predicted by such widely quoted sources as Komar and Inman (1970).

Introduction

In recent times an increasing effort has been directed toward finding a universal mathematical expression for the rate of sand transport on beaches. Although the basic concepts of this phenomenon are well known, the problem still remains largely unsolved. For instance, it is well known that large volumes of sediment are displaced and transported along coasts through the action of currents which are induced when waves break in shallow water. It is also well known that the sand particles making up this longshore transport are moved either as bed load (i.e. material sliding or rolling while supported by, or in contact with, other grains on the bottom) or suspended load (i.e. material totally supported by the flow medium). Given these concepts as starting points, various relationships have been proposed to provide quantitative values for sand transport alongshore, based on variables related to the forces released when waves break on a beach (see, for example, Galvin and Vitale (1976)). However, for a variety of reasons, not the least of which is the complexity of the physical situation where turbulence and the variable nature of the bottom materials and geometry usually defy generalization, the goal of a generally-accepted universal relationship for longshore sediment transport has still not been achieved.

It is recognized, however, that, to be credible, such a relationship must be founded upon an adequate data base involving field measurements of those aspects of the physical situation that are most relevant, namely incident wave energy and the resulting longshore sediment transport. Because accurate measurement of the total transport (suspended and bed-load) still remains practically impossible on non-tidal beaches, it was decided that the longshore flux of suspended particles in the surf zone could serve as a reasonable estimate for the total transport in such cases. Furthermore, this is a parameter that is more amenable to direct measurement.

[1,2]Shore Processes Section, Hydraulics Division, National Water Research Inst., Canada Centre for Inland Waters, Burlington, Ontario, Canada.

The goal of this report is to describe the relationships obtained for a site in Lake Ontario between the suspended sediment flux under moderate to intense wave conditions and breaker zone wave energy calculated from concurrent wave measurements. It is also meant to provide a realistic indication of the scale of littoral processes on non-tidal coasts such as the Laurentian Great Lakes compared with that of marine and tidal areas.

Study Site Description

The site at which the measurements described here were taken is located at the extreme western end of Lake Ontario on a large bay-mouth bar separating Burlington Bay from the main body of the lake (Fig. 1). The shoreline is regular and trends approximately NNW, or perpendicular to the direction of maximum fetch (ENE, fetch - 400 km) for Lake Ontario. Waves reaching the site therefore can attain heights of more than 3 m and tend to approach the shore at close to right angles.

The local bottom topography in the inner nearshore zone (<3 m depth and <70 m from shore) is characterized by rhythmic sets of crescentic longshore bars (about 120 m long and 1 m high). Systematic monitoring of bathymetric profiles at the site since 1976 indicates that these structures are very sensitive to wave conditions, while, on the other hand, the bottom topography further offshore shows relatively minor changes during this period.

The nearshore bottom is composed of well-sorted sand, with grain sizes within the 5 m contour averaging 2.0ϕ (0.25 mm diameter). Coarser material (up to gravel size) often occurs in the vicinity of the beach step (<1 m depth) and on the subaerial beach face. Bottom slopes in the area range from 0.05 to 0.02 in the inner nearshore zone. The overall slope out to 300 m averages 0.017.

Methodology

The field measurement program was initiated in the fall of 1977. The methodology has been described in previous publications (Coakley and others, 1978, Coakley 1980). Briefly, the method entailed the collection at three vertical elevations (10, 30 and 100 cm above the bed) of 45 second averages of suspended sediment concentration, based on 2ℓ pumped samples of water/sediment suspensions; water depth values; and current velocity records (two orthogonal horizontal components) along a fixed nearshore transect, during periods of moderate to high wave activity. The transect extended approximately 100 m over water, terminating at a water depth of about 3.5 m. The instrument platform was a robust, open-work sled, equipped with a vertically-articulated boom protruding 1.5 m into the oncoming wave field, to which the suspended sediment sample intake, as well as the current sensors, were attached. The sled was manipulated from shore along the transect, stopping at up to ten regularly-spaced stations. A complete run took exactly 1 hour to complete, thus allowing replicate runs of the same storm to be carried out. A schematic illustration of the field layout is presented in Fig. 1.

Continuous records of wave parameters at the study site were also collected using a fixed, linear array of three surface-piercing wave gauges installed approximately 225 m from the shoreline in about 5 m of water (outside the breaker zone for all waves encountered). Wave measurements were made either immediately prior to, or during a sled experiment.

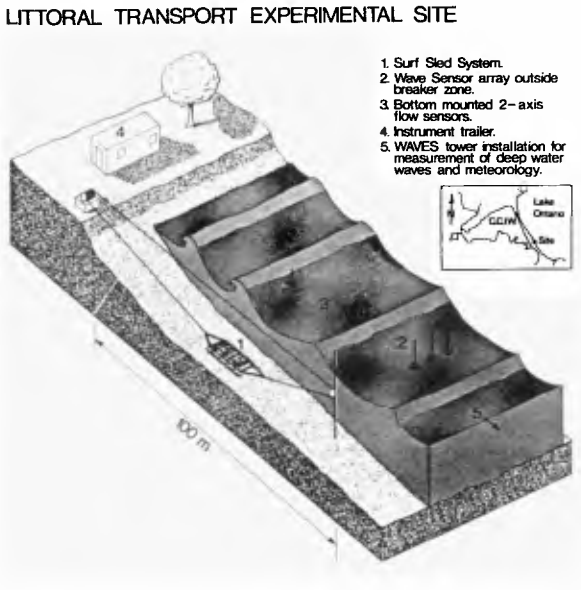

Figure 1 Perspective view of the experimental site, showing sled cableway, sled, wave sensor array and other instruments.

Description of the Data Set

1. Wave Data

The time series of instantaneous water elevations at the wave gauges were analyzed to obtain variance spectral densities, using the fast Fourier transform technique. Characteristic (significant) wave heights and peak periods were calculated for each experiment. Covariance spectral calculations allowed the determination of phase angle of the waves between wave gauge pairs as a function of frequency, and from this the direction of the peak of the spectrum was found. For each experiment, this latter value was used to characterize the wave direction at the location of the gauges.

The wave data at the gauges are summarized in Table 1. The characteristic or significant wave height is H_c, the period of the peak of the spectrum is T_p and the angle the waves make with the shore normal is α. (The wave parameters for experiment 7-1 were manually estimated from the time series.)

The bathymetric charts prepared from monitor surveys done after major storms at the experiment site were examined to determine the best way of transferring the wave information from the location of the gauges to the breaker zone. The nearshore bathymetry, as described previously, was irregular, with both small-and large-scale structures. Furthermore, the waves were "sea" as opposed to "swell" and, for this reason, a distinct breaker line was not always readily apparent.

Detailed wave ray calculations were done, but due to the irregular nearshore bathymetry, the resulting ray patterns did not give a consistent description of the waves inshore the wave gauge site. Several of the more common breaking criteria (such as the depth of breaking being equal to 1.28 times the breaking wave height) were tried in conjunction with the ray computations. These criteria were found to be ineffective in defining the surf zone as observed in the field. In the end, the method that gave the most consistent results and that was used here is as follows:

The bathymetry between the wave gauges and the shore was assumed to have straight contours parallel to the water's edge. The location and water depth of the breaker line was determined based on visual observations in combination with the position of normal breaker-line indicators, namely longshore bars. Snell's law was used to calculate the wave direction at the breaker line, and the shoaling and refraction coefficients were evaluated to get the breaking wave height.

The breaker line wave conditions, derived from the gauge data, are shown in Table 3. The depth at breaking is d_b, and the characteristic wave height at breaking is H_b; the other parameters have the same definitions as in Table 1, or as defined later.

2. Suspended Sediment Discharge

The data retrieved by the sled consisted of the following:

TABLE 1. Wave Conditions at the Wave Gauge Array
(approximately 225 m offshore)

Exp/Run	T_p s	H_c m	α degrees	Water Depth m
2-2	4.9	0.9	1.1	5.1
3-1	6.1	1.0	-3.5	5.2
3-2	6.1	0.9	-2.7	5.2
4-1	3.6	0.6	-19.4	5.1
4-2	4.1	0.6	-6.5	5.1
6-1	6.1	1.9	1.1	4.6
9-1	4.9	0.8	-1.8	4.3
9-2	4.9	0.7	0.0	4.3
10-1	6.1	1.0	-5.8	4.3
11-1	6.1	0.9	0.1	4.3
13-1	4.9	0.8	4.2	4.8
15-1	4.9	0.8	2.3	4.9
16-1	3.6	0.6	-2.0	4.8
2-1†	4.9	0.8	3.8	5.1
7-1†	5.6	2.1	-	4.3
16-2†	4.9	0.9	2.2	4.8
16-3†	4.9	0.8	1.0	4.8

* Negative angle implies northward currents (wave ray on south side of shore normal)

† Partial data set, not used for discharge calculations.

TABLE 2. Longshore Suspended Sediment Discharge per Unit Width of Surf-Zone Transect Measured at Each Transect Station (Discharge expressed in mg/s.cm)

Exp/Run	Inner Transect <35 m			Mid-Transect 35-70 m				Outer Transect 70-115 m			Total Longshore Discharge over Transect (kg/h)
	1	2	3	4	5	6	7	8	9	10	
2/2	58†	-70	-416	-1516	-276	-242	-134	-137	-190	42*	-10,265
3/1	30†	-165†	-541	-566	-395	-487	-651	-435	-191	-436	-12,734
3/2	15†	-54†	-3995	-1577	-1334†	-734	-213	-80	-111	-80	-29,106
4/1	-30†	-171	-363†	-146†	-347	-38	15	-32	-19	-10	-3,889
4/2	-21†	-17†	-307	-179	-194	3	-106	-58	-26	-16	-3,230
6/1	-108	-47†	-343†	-991	-3629	10,170	-4067	-2371*	-2059	-2909	-88,614
9/1	-46	-453	44	-405		-31	-184	-1	-41	0	-4,026
9/2	-59	-35	-95	-151		-217	-115	-54	-18	-12†	-2,351
10/1	-225	-725	-3291*	-7767†	-4489*	2,062	-908	-188†*	-274	-145†	-55,034
11/1	-492†	-371†	-235†	-53†	-422	-341	-1206	-148	-20	-181	-12,314
13/1	-417†*	-298†	-240	-97	-80	163	-110	170	45	99†	-1,838
15/1	743	349	348	-20	-63	-34	-15	-21	1	-9	+4,612
16/1	61	113	-174	-71	-104	-75	-39	-43	-27	-29†	-1,479

* Interpolation or extrapolation used to replace anomalously high value of concentration.

† Interpolation or extrpaolation used to replace missing value(s) of concentration or current.

Negative values indicate transport toward the north, positive toward the south.

TABLE 3. Summary of Breaking Wave and Suspended Sediment Transport Conditions at Van Wagners Beach, Lake Ontario (waves refracted into break-point)

Exp/ Run	H_b	T_p	α	Breaker Type	Breaker Depth d_b	Surf-Zone Width λ_b	ξ_b**	I_ℓ	P_ℓ
	m	s	degrees		m	m		N/s	N/s
2/2*	0.93	4.9	0.8	S	2.2	51	0.27	-17	+29
3/1	1.15	6.1	-2.4	S, P	2.2	51	0.31	-22	-139
3/2	0.99	6.1	-1.8	P	2.2	51	0.33	-49	-79
4/1†	0.60	3.6	-16.7†	S	1.9	43	0.26	-7	-194
4/2	0.63	4.1	-4.6	S	1.9	43	0.29	-9	-66
6/1*	1.98	6.1	0.9	P, S	3.7	200	0.10	-150	+181
9/1	0.96	4.9	-1.1	P, S	1.4	50	0.17	-7	-37
9/2*	0.85	4.9	0.0	P, S	1.4	50	0.19	+4	0
10/1	1.27	6.1	-3.5	S	1.4	50	0.19	-9.3	-206
11/1*	1.10	6.1	0.1	P, S	1.4	50	0.20	-21	+2
13/1*	0.85	4.9	3.1	S	1.9	65	0.19	-3	+93
15/1	0.90	4.9	1.6	(n.r.)	2.3	70	0.21	+8	+51
16/1	0.61	3.6	-1.5	S, P	2.1	60	0.20	-3	-18

* Sign of wave angle, α, indicates longshore current opposite in direction to measured by the surf-sled, or α=0. Confused breaker pattern noted in field.

† Wave angle anomalously high.

S: Spilling. P: Plunging. n.r.: not recorded.

** $\xi = \dfrac{d_b/\lambda_b}{(H_b/L_o)^{1/2}}$ the surf similarity parameter, where L_o is the deep water wavelength.

(i) Up to 30-2ℓ samples of suspension collected at 10 stations along the surf-zone transect; at three fixed elevations for each station.

(ii) Depth profiles along the transect measured by a recording pressure transducer mounted on the sled.

(iii) 45-second time-records of flow velocities collected for each of the three vertical sampling elevations measured at each station.

Mass/volume concentrations were later obtained gravimetrically from the samples. These concentration values were combined with the calculated time-averaged longshore component of flow to provide point discharge values at each of the three elevations comprising each station.

In Coakley (1980), an integration was done using 10 cm spaced point values which were interpolated through a computerized procedure in which the three measured points were fitted to a theoretical (exponential) distribution. Further appraisal of this technique in the light of the small number of points on the curve (3), as well as the frequent apparent deviation of the points from the expected theoretical curve, led us to abandon this technique. To obtain the results presented here, the water column was simply divided into four compartments with the time-averaged concentration/longshore current data points assumed to be representative of the space halfway to adjacent data points. Values for concentration above the top compartment (165 cm above the bed) were arbitrarily set to zero. This appeared reasonable as concentration values even at the top position sampled (100 cm) were almost always very low (< 100 mg/ℓ). The product of concentration and flow for each block was then summed to obtain total discharge for that station.

The values predictably are slightly different from those previously reported (Coakley, 1980) based on the curve-lifting procedure, but the differences are less than 20 percent in most cases. However, several cases (exp. 3-1, 9-1, 9-2, 13-1) where redigitizing and recalculation were necessary, show larger discrepancies, and differ from previously published figures by up to a factor of 3.

The vertically summed discharge values for each station were then summed horizontally over the transect length, using a simple half-interval product summation. The discharge values for each station and for the entire transect (expressed in kg/hr) are presented in Table 2, for each experiment run.

Data Screening

From the above, it is seen that a complete data set for each station should ideally contain a depth record, three 45-second averages of onshore-offshore and alongshore currents and three values for concentration at the three different sample elevations. In addition, such complete stations should occur, if not at all stations occupied, at least at enough stations to provide adequate coverage of the transect length.

This was, as could be expected, not achieved in a considerable number of experiment traverses. The data set was prone to missing values in any of the four measured variables. Such lapses were due mainly to mechanical failure in the hostile environment of the surf zone, where suspended sand and algal debris

tended to clog the moving parts of sensors, and occasional freezing of sample tubing made pumping impossible.

Data evaluation and screening was therefore a necessary step. Several entire runs or stations had to be left out of the present analysis due to large-scale absence of essential data components. Lesser gaps could be filled mainly by interpolation and extrapolation. Other experiment runs were virtually gap-free. Table 2, therefore, shows only the 13 experiment runs which survived the screening process. Only these will be considered in the calculation of suspended sediment discharge. Not shown on Table 2 are four other partial data sets which will be used in a later section only in examining the sediment suspension/wave energy relationship (Fig. 3). These data sets had no flow records, but wave and concentration data were recorded. The wave data for these four experiments are shown at the bottom of Table 1.

The Combined Data Set

In Table 3, the measured and derived parameters associated with the incident wave field and suspended sediment discharge are presented. The parameter, I_ℓ, is defined as the total immersed weight of suspended sediment discharge over the transect length, and is expressed in Newtons per second (Komar and Inman, 1970). It was obtained by converting the discharge figures shown in Table 2 to immersed weight quantities. P_ℓ is the value calculated for the lateral thrust times the phase speed (Longuet-Higgins, 1972), also called the longshore component of wave energy density flux, expressed in Newtons per second. The relationship used to calculate P_ℓ is:

$$P_\ell = \frac{gH^2_{rms} \cdot c_g \cdot \sin\alpha \cos\alpha}{8.0}$$

where $H_{rms} = H_b/1.416$, c_g = wave group celerity, and α =the angle between the wave orthogonal and the beach normal (all values at breaking). Also shown on the table are subjective breaker descriptions and a calculation of surf-zone width based on the position of the calculated break-point with respect to the strand-line on the day of the experiment.

Several of the experiments showed discrepancies between the transport direction of suspended sediment measured by the sled (as denoted by the sign of the discharge quantities in Table 2) and the expected direction as indicated by the sign of the wave angle, α (Table 3). The cases where this occurs are Exp. 2-2, 6-1, 9-2, 11-1, and 13-1. In addition, one experiment (4-1) showed a wave angle of 19.4° which is anomalously higher than the range of values measured. While most of these discrepancies could be explained in view of the spatially varying conditions in a surf-zone characterized by an irregular bathymetry and low wave angles, they nonetheless present problems for further analysis and interpretation of the data set. These problems will be addressed to some degree in the Discussion section.

Correlation Between Suspended Sediment Transport and Longshore Wave Energy

The values shown in Table 3 were plotted on log/log paper (Fig. 2), after the method of Komar and Inman (1970). Only the seven data points remaining after exclusion of those showing discrepancies have been plotted. Also

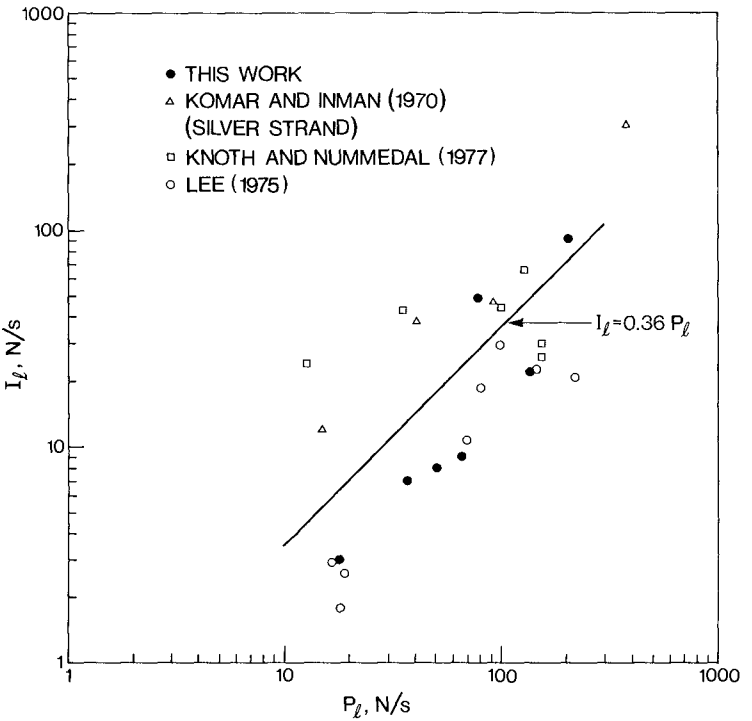

FIGURE 2. IMMERSED WEIGHT SUSPENDED SEDIMENT DISCHARGE vs LATERAL THRUST x PHASE SPEED.

shown for comparison are the data points for total transport listed in Komar and Inman (1970) for Silver Strand Beach, a beach of comparable slope to Van Wagners Beach, and those of Knoth and Nummedal (1977) for North Bull Island, South Carolina, and those of Lee (1975) for Lake Michigan.

The linear regression of I_ℓ against P_ℓ was calculated for the seven solid points, and was found to be:

$$I_\ell = 0.36\, P_\ell$$

and is plotted on Fig. 2.

This value of the coefficient of P_ℓ is therefore slightly less than one-half that calculated by Komar and Inman (1970) for the total transport of sand on marine beaches on the Pacific coast of North America (I_ℓ=0.77 P_ℓ). Our coefficient is, however, over twice the value of 0.15 that we obtained from the tabulated data of Lee (1975). The data of Knoth and Nummedal (1977) does not fit this type of model.

The correlation coefficient for the regression using the seven data points shown in the figure was calculated to be: r=0.84, compared to 0.99 (calculated by us) for the data tabulated by Komar and Inman (1970), p. 5921. The value of r=0.84 for the correlation coefficient is very significant, i.e. it exceeds the 99 percent confidence level (Fisher, 1970, p. 211).

Suspended Sediment Concentration vs. Wave Energy

The suspended sediment discharge figure calculated was based on the summed products of concentration and longshore velocity averaged over the sampling interval and integrated over the water depth and transect length. In view of the obvious difficulty in reconciling, with consistency, the calculated longshore flow direction with the measured flow especially in beaches with low wave angles and irregular bottom topography, it might be useful to examine the relationship between wave energy (total) and a non-directional parameter, such as mean concentration.

Figure 3 shows a plot on semi-log paper of total incident wave energy density (E) versus the vertically and horizontally averaged suspended sediment concentration termed the global concentration, or $\bar{C}^*$. This plot was based on a total of 17 data points, which included the four experimental runs referred to earlier where the flow components were not recorded, due to sensor malfunction.

The plot shows an obvious correlation between the two parameters, and the linear regression of $\bar{C}^*$ on ln E was calculated to be:

$$\bar{C}^* = -903 + 206 \ln E$$

where $\bar{C}^*$is in mg/ℓ and E in N/m. The correlation coefficient is 0.85. The value of the correlation coefficient is very significant at the 99 percent confidence level, and thus indicates concentration of suspended sediment can be well predicted using wave data alone. It should be kept in mind, however, that such a relationship is also dependent on the grain size of the beach in question, and care should be taken in extrapolating it to other beaches.

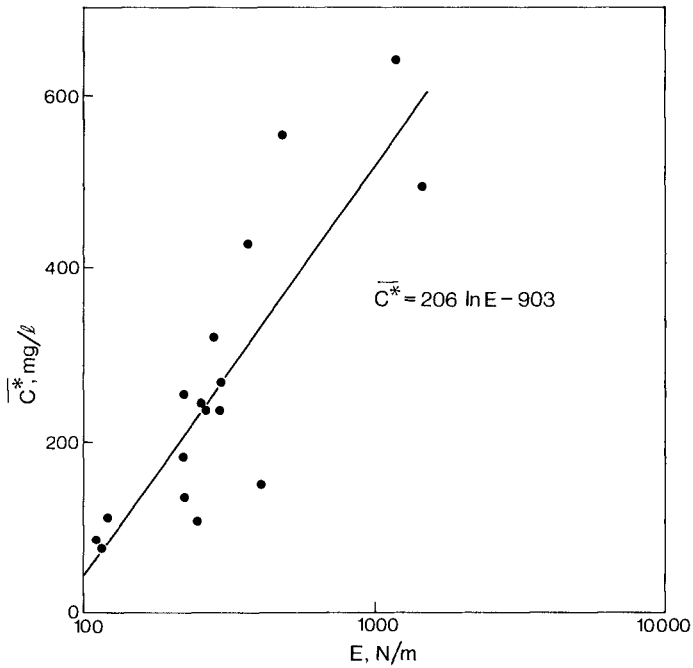

FIGURE 3. GLOBAL CONCENTRATION vs WAVE ENERGY DENSITY

Discussion

The results presented above were obtained using only screened data. Also, they were based on time-averaged point measurements of 45 s duration measured sequentially at three elevations (over a period of 3 min.), and were repeated at a series of stations across the surf-zone in succession; a process which took approximately one hour. There are several areas on which such an arrangement could be criticized, for instance:

- The discharge figures assume that the measurements are synoptic and that the transport has reached a steady-state condition, i.e. taking place at the same time across the entire zone and basically unchanging with time. The measurements covered a time-period of one hour while the vertical profile at each station took three minutes. From our knowledge of surf-zone dynamics, it is more likely that the process varies both in time and space even in a fully-developed storm and thus it should be sampled simultaneously over the zone for most accurate results.

- The time-duration of the sampling of sediment concentration and flow was only 45 s for operational reasons. The work of several researchers (Downing and others, 1981; Meadows, 1976, and Leonard and Brenninkmeyer 1978) indicated the presence of long-period events in surf-zone dynamics at time-scales ranging from fractions of the wave period to more than 120 s. This would imply that time series of 45 s, such as ours, might be subject to some inaccuracies.

These problems in experiment design, coupled with other complications introduced by irregular bottom topography, difficulty in defining accurately the wave angle at breaking, and in determining the width of the surf-zone with any accuracy, are probably all factors in the considerable variability which characterizes the data set. For this reason, the results presented above must be considered only as first-order approximations of a complicated and highly variable process, but which indicate, at least, the scale and overall trends in suspended sediment transport on beaches. Furthermore, the results must be considered as site-specific (to this particular Great Lakes beach) until more general insights into the influence of sediment grain-size, beach geometry and bottom topography can be included.

There appears to be no justification, therefore, for a more sophisticated treatment of the data than the conservative screening and empirical analysis featured in the previous section. Still, some pertinent and useful comments can be made on the results.

The data confirm that a statistically significant relationship exists between suspended sediment transport and the longshore component of wave energy density flux. We have also shown that a considerable quantity of sediment can be moved as suspended sediment (up to 88,600 kg/h (Table 2)) during intense Lake Ontario storms. We are, however, no closer to determining how large a proportion of the total littoral transport at the site this figure represents, since no reliable estimate of the bedload transport or the total drift at the site was possible. There is a danger in trying to obtain such a total drift estimate by applying empirical relationships, such as that of Komar and Inman (1970), since their base data were collected on marine coasts having no proven process-related affinity to beaches in the Great Lakes. Assuming that the total

transport is adequately represented by suspended transport (Kana, 1977), then the longshore sediment transport at Van Wagner's Beach is approximately half of the total transport on ocean beaches studied by Komar and Inman (1970). Furthermore, if the latter value is only regarded as an order of magnitude estimate, as suggested by Greer and Madsen (1978), then the results of this paper are in excellent agreement to that degree of accuracy.

Examination of the magnitude of the suspended sediment concentration and transport measurements reported by others (Kana, 1977 and 1978; Fairchild, 1977; Downing and others, 1981) provides an interesting comparison. Table 4 lists comparable statistics from these sources, along with values obtained in this study. In spite of the fact that procedures differed greatly, the statistics all include either average concentrations and/or suspended sediment discharge. The average concentrations are all of similar magnitude. Fairchild (1977) is larger because it is a measure of concentration very near the bed. The ranges of discharge measurements are all overlapping. The wave conditions reported by the various authors are quite different from the ones in this study. The wave heights in this study as a group form the high end of the range of all wave heights reported elsewhere. The waves are also relatively steep, because they were locally generated storm waves. The longshore energy flux values, on the other hand, are of the same order as those reported by Komar and Inman (1970). The difference is accounted for by the relatively small wave angles reported here.

Kana (1977) reported a marked difference in suspended sediment concentration depending on breaker type: "plunging waves entrain almost one order more sediment than spilling type breakers". Examination of Table 3 reveals that in our study there was only one case of clearly plunging breakers: the majority are a combination and a few are spilling only. Spilling waves entraining less sediment and the fact that waves reported here tended to be at least partly spilling would suggest that less transport is to be expected and thus is supportive of the lower value of the coefficient (0.36) found in this study. In a recent paper, Hallermeier (1982) points out that more effective transport apparently occurs for high values of ξ, the surf similarity parameter (Battjies, 1975). High ξ corresponds to swell conditions, and since the values of ξ were small for our experiments as shown in Table 3, correspondingly smaller measured transport rates are to be expected. It would appear, as more evidence is gathered, that the characterization of the beach and breaking conditions using the surf similarity parameter might lead to better prediction of transport rates. This approach is discussed in a paper in these Proceedings by Sayao and Kamphuis (1982).

Concluding Remarks

Suspended sediment, longshore current, and wave data have been collected during moderate to severe early winter storms at Van Wagner's Beach, Lake Ontario. This data set is distinguished from others in that the site is a non-tidal beach characterized by offshore bars; the wave heights were some of the largest encountered during experiments of this type; the angles of wave approach were relatively small.

The range of suspended sediment concentrations and the range of transport rates encountered are similar to those reported elsewhere. However, the relation between longshore transport and longshore energy flux derived from this data set suggests that about half the amount of sediment is moved in suspension for a comparable energy flux as was reported for total transport by

TABLE 4. Representative Suspended Sediment Transport Values from Several Published Sources

Researcher (s)	Beach Location	$\bar{C}$* (avg. concentration across surf-zone	Discharge
Downing, et al. 1981	Twin Harbours Beach Washington, U.S.A.	(not calculated)	76.5 m^3/h
Kana (1977) (examples given in Table 2, p. 378)	Price Inlet S. Carolina, U.S.A.	0.7 g/ℓ	1.3 - 130 m^3/h (49-4908 tonnes/day)
Kana (1978) (extracted from Fig. 5, p. 1734)	Price Inlet S. Carolina, U.S.A.	0.33 g/ℓ	
Fairchild (1972) (extracted from Fig. 3, p. 1086)	Ventnor, N. J.; Nags Head, S.C., and Mission Bay, California, U.S.A.	(not calculated)	15.3 - 350 m^3/h (4.8×10^2 - 1.1×10^4 yd^3/d)
Fairchild (1977) p. 46	Ventnor, N.J., Nags Head, N.C.	2.7 g/ℓ (typical within 0.4 ft (0.12 m) of bottom)	0.9-55 m^3/h based on maximum flux values 2700 kg/m^3 solids density 0.60 void ratio
Coakley and Skafel (this report)	Van Wagners Beach	0.27 g/ℓ	3.8 - 230 m^3/h

Komar and Inman (1970). This difference is not unreasonable given the complexity of shore processes and the difficulty of obtaining true measures of transport.

The controversy over the question of bed load versus suspended load has not been addressed. It is clear, however, that at our site substantial volumes of material are moved by suspended load.

References

Coakley, J. P., H. A. Savile, M. Pedrosa, and M. Larocque, 1978. Sled System for profiling suspended littoral drift. Proc. 16th Int. Conf. on Coastal Eng., ASCE, Hamburg, pp. 1764-1775.

Coakley, J. P., 1980. Field measurements of suspended sediment transport in the littoral zone of Lake Ontario. Proc. Cdn. Coastal Conf. 1980, Burlington, pp. 31-46.

Downing, J. P., R. W. Sternberg, and C.R.B. Lister, 1981. New instrumentation for the investigation of suspended sediment processes in the shallow marine environment. Marine Geol. 42 (in press).

Fairchild, J. C., 1972. Longshore transport of suspended sediment. Proc. 13th Int. Conf. on Coastal Eng., ASCE, pp. 1069-1087.

Fairchild, J. C., 1977. Suspended sediment in the littoral zone at Ventnor, New Jersey, and Nags Head, North Carolina. U.S. Army Corps of Engineers, CERC, Tech. Paper 77-5, 97 p.

Fisher, R. A., 1970. Statistical methods for research workers. 14th ed., Hafner Pubc. Co., Darien, Conn.

Galvin, C. J., and P. Vitale, 1976. Longshore transport prediction - SPM 1973 Revision. Proc. 15th Int. Conf. on Coastal Eng., Vol. 2, pp. 1133-1148.

Greer, M. N., and O. S. Madsen, 1978. Longshore sediment transport data: A Review. Proc. 16th Int. Conf. on Coastal Eng., Vol. 2, pp. 1563-1576.

Hallermeier, R. J., 1982. Bedload and wave thrust computations of alongshore sand transport. J. Geophys. Res. 87 (C8), pp. 5741-5751.

Kana,T. W., 1977. Suspended sediment transport at Price Inlet, S.C. Coastal Sediments '77, an ASCE Symposium, Charleston, S. C., pp. 366-382.

Kana,T. W., 1978. Surf zone measurements of suspended sediment. Proc. 16th Int. Conf. on Coastal Eng., ASCE, Vol. 2, pp. 1725-1743.

Komar, P. D., and D. L. Inman, 1970. Longshore sand transport on beaches. J. Geophys. Res., 75 (30), pp. 5914-5927.

Knoth, J. S., and D. Nummedal, 1977. Longshore sediment transport using fluorescent tracer. Coastal Sediments '77, an ASCE Symposium, Charleston, S. C., pp. 383-398.

Lee, K. K., 1975. Longshore currents and sediment transport in west shore of Lake Michigan. Water Resources Research 11 (6), pp. 1029-1032.

Leonard, J. E., and B. M. Brenninkmeyer, 1978. Periodicity of suspended sand movement during a storm. Proc. 16th Int. Conf. on Coastal Eng., ASCE.

Longuet-Higgins, M. S., 1972. Recent progress in the study of longshore currents. In "Waves on Beaches", Ed. by Meyer, Academic Press.

Meadows, G. A., 1976. Time-dependent fluctuations in longshore currents. Proc. 15th Int. Conf. on Coastal Eng., ASCE.

Sayao, O.S.F.J. and J. W. Kamphuis, 1982. Model tests on littoral sand transport rates. These Proceedings.

MODEL TESTS ON LITTORAL SAND TRANSPORT RATE

by

J.W. KAMPHUIS[1] and O.F.S.J. SAYAO[2]

ABSTRACT:

This paper is an analysis of two sets of experimental results on littoral sand transport. A littoral sand transport expression is proposed, relating littoral transport rate to surf similarity parameter and hence to wave energy dissipation rate. The expression indicates that the 'constant' in the CERC formula is dependent on the mobile bed beach slope and on the breaker index. The expression is also compared with some of the few published field measurements.

INTRODUCTION

One of the most important problems facing the engineer involved in coastal protection and harbour design is that of estimating the littoral sand transport along a shoreline. Usually, field measurement data are not available or not of sufficient accuracy and most empirical formulas do not take into account all the wave and sediment parameters in a satisfactory fashion.

Littoral sand transport tests were performed at Queen's University in a three-dimensional mobile bed coastal model with two different types of sand. Earlier tests by Readshaw (1979), and reported by Kamphuis and Readshaw (1978) used sand with a median diameter of 0.56 mm. The longshore sediment transport rate was found to be dependent on the beach profile characteristics and the rate of wave energy dissipation, as well as on the usual wave and sediment parameters.

---

[1] Professor of Civil Engineering, Queen's University, Kingston, Ontario, Canada.

[2] Associate Professor of Ocean Engineering, Universidade Federal do Rio de Janeiro, Brazil.

The present series of tests was performed in the same wave basin under similar test conditions. A finer sand of median diameter 0.18 mm was used. The results of these tests in combination with the earlier tests are the topic of this paper.

More details regarding both sets of experimental results may be found in Sayao (1982) and Sayao and Kamphuis (1983).

EXPERIMENTAL EQUIPMENT AND PROCEDURE

The three dimensional wave basin at the Coastal Engineering Research Laboratory, of Queen's University at Kingston is shown in Figure 1.

Monochromatic waves were produced with a piston type wave generator. Wave filters and splitters, were placed immediately in front of the wave generator to prevent formation of transverse standing waves and to filter out high frequency components. Wave guide walls were constructed and aligned along wave orthogonals calculated from refraction theory. Openings were cut in these training walls at several locations to facilitate filling and draining of the central test basin and the reservoir surrounding the central testing area. Three capacitance-type wave probes were used to measure the wave heights in the constant depth portion of the test basin, between the toe of the beach and the wave filters. Wave heights in the breaking zone and at any other location along the beach profile were measured with a fourth capacitance-type wave probe mounted on a transversely travelling trolley placed on the beach side of the travelling carriage. Beach profiles were measured with a blunt-ended point gauge mounted on a separate trolley also placed on the beach side of the travelling carriage. An initial model beach was shaped twice during the present test series by screeding and compacting sand to a thickness of 0.13 m. over a sloped concrete floor. The grain size distribution curves for the materials used for both sets of tests are shown in Figure 2.

The present experiments consisted of a total of 14 series of tests, each of several seasons of a predetermined duration varying from 15 to 110 minutes. The wave parameters were changed after every series and could be paired together to form a regular seasonal cycle as described in Kamphuis and Readshaw (1978). Although the beach initially had a uniform slope of 1:10, a beach profile was allowed to "develop" with time and each subsequent test was started on the beach profile remaining from the previous test. Slow, continuous recession of the shoreline was observed and at the end of series 5, after approximately 83 model hours of profile development, the initial slope of 1:10 was reshaped. Testing then resumed for another 87 model hours up to the end of test series 14.

During the experimental investigation the alongshore sediment transport rate was recorded continuously. Other data measured included breaker characteristics such as the breaker height H_b , the

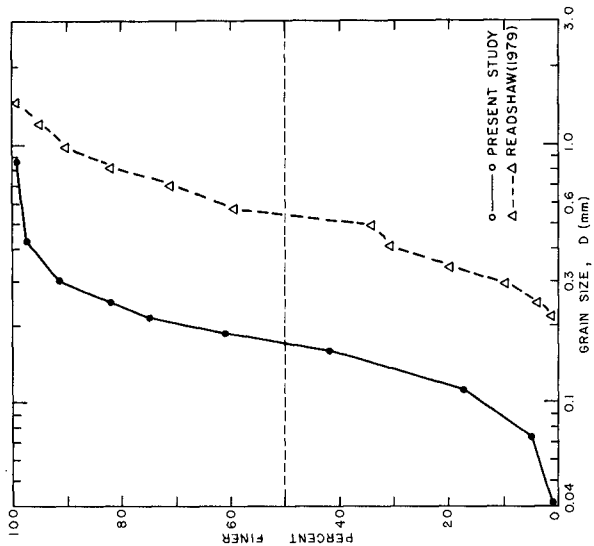

FIG. 2 GRAIN SIZE DISTRIBUTIONS

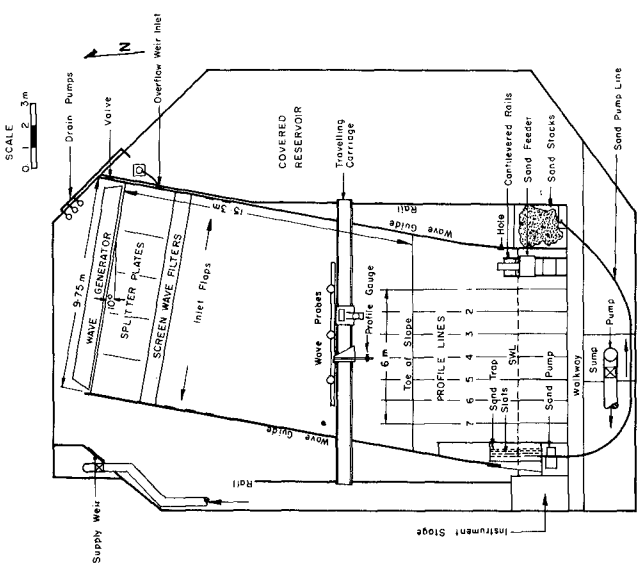

FIG. 1 PLAN VIEW OF THE WAVE BASIN

depth below still water level at the breaking point d_b, the breaker distance λ_b measured from the still water level shoreline, the velocity of wave propagation at the breaking point C_b and the incident angle of breaking α_b. Analysis of the measured breaker characteristics have been reported in detail in Sayao and Kamphuis (1982). It is to be noted that all these parameters have been evaluated for beach profiles rather than for plane beaches.

EXPERIMENTAL RESULTS

The experimental results are summarized in Table 1. A more detailed description of the present tests as well as Readshaw's (1979) data may be found in Sayao (1982) and Sayao and Kamphuis (1983).

Dimensional Analysis

Dimensional analysis for littoral transport rate yields:

$$\Pi_{Q_s} = \phi_{Q_s} \left(\frac{H_b}{L_o}, m, \frac{H_b}{D}, \frac{\rho_s}{\rho} \right) \quad (1)$$

where

$$\Pi_{Q_s} = \frac{Q_s}{\rho H_b^2 (H_b/T) \frac{1}{2} \sin 2\alpha_b} \quad (2)$$

Q_s is the dry mass littoral sediment transport rate, in kilograms per unit of time, ρ the water density, ρ_s the sediment density, H_b the wave height, L_o the deep water wave length, T the wave period, D the particle size and m the beach slope. The definition of beach slope m for mobile bed models has been the subject of considerable debate. From the present experiments - Sayao and Kamphuis (1983) - it was found that the most convenient form of beach slope definition,

$$m = \frac{d_b}{\lambda_b} \quad (3)$$

was also the definition which described surf zone phenomena, including littoral drift rate most accurately. This definition is called "mobile bed beach slope" throughout this paper.

Relationship between Beach Slope and Relative Grain Size

Figure 3 shows the mobile bed beach slope as a function of relative grain size parameter for the combined data set of the present tests and Readshaw's (1979) tests. Even though the data are scattered, a definite relationship between these two parameters is evident. From regression analysis the curve fitted through the data

TABLE 1

EXPERIMENTAL RESULTS (SAYAO, 1982)

Model Material: Sand of D_{50} = 0.18 mm

Wave Basin Depth of Water: 0.51 m

First Run: Test Series S1 to S5

Test Number	H_o (m)	H_b (m)	L_o (m)	d_b (m)	λ_b (m)	α_b (o)	$\bar{Q}_s$ (kg/hr)
S1L04	0.129	0.151	3.513	0.139	1.85	5.5	-
S1L08	0.120	0.135	3.513	0.128	1.788	5.5	-
S1L12	0.125	0.154	3.513	0.160	2.075	5.5	-
S2S04	0.044	0.060	2.137	0.074	0.75	4.0	17.4
S2S08	0.048	0.064	2.137	0.088	1.20	4.0	19.2
S2S12	0.047	0.058	2.137	0.088	1.163	4.0	16.2
S2L04	0.119	0.151	3.513	0.155	2.088	2.5	144.0
S2L08	0.131	0.150	3.513	0.143	2.038	2.5	132.0
S2L12	0.128	0.158	3.513	0.201	3.013	2.5	150.0
S2L14	0.127	0.147	3.513	0.202	3.038	2.5	150.0
S2L17	0.128	0.152	3.513	0.192	3.15	2.5	120.0
S2L20	0.128	0.162	3.513	0.184	3.138	2.5	120.0
S3S04	0.041	0.051	2.137	0.075	0.725	3.5	14.4
S3L06	0.119	0.144	3.513	0.170	2.963	2.5	150.0
S4L04	0.039	0.057	6.434	0.081	0.40	1.0	9.6
S4S07	0.043	0.064	2.137	0.078	0.738	2.5	14.4
S4L10	0.032	0.050	6.434	0.081	0.513	1.0	7.8
S4S13	0.040	0.049	2.137	0.089	0.80	2.5	15.0
S5L03	0.065	0.101	3.513	0.131	2.013	3.5	21.6
S5L06	0.074	0.103	3.513	0.130	1.963	3.5	21.0
S5S03	0.088	0.113	1.656	0.150	3.225	3.5	69.6
S5S06	0.084	0.110	1.656	0.152	3.35	3.5	46.8

TABLE 1 (continued)

Second Run: Test Series AS6 to S14

Test Number	H_o (m)	H_b (m)	L_o (m)	d_b (m)	λ_b (m)	α_b (o)	$\bar{Q}_s$ (kg/hr)
S6L05	0.092	0.108	2.845	0.087	1.25	6.5	120.0
S6L09	0.093	0.103	2.845	0.123	1.625	6.0	132.0
S6L15	0.093	0.106	2.845	0.128	1.788	7.0	114.0
S7S03	0.058	0.071	2.137	0.096	1.338	5.5	35.4
S7L04	0.045	0.063	2.845	0.063	0.975	6.5	13.2
S7S06	0.058	0.071	2.137	0.098	1.775	6.0	34.2
S7L07	0.047	0.064	2.845	0.077	1.425	7.0	6.6
S8S04	0.057	0.060	1.656	0.083	1.613	6.5	24.0
S8S08	0.055	0.074	1.656	0.104	2.40	6.5	21.0
S8S12	0.055	0.071	1.656	0.095	2.263	6.5	22.8
S8L04	0.093	0.113	3.560	0.160	2.825	7.5	60.0
S8L08	0.092	0.109	3.560	0.166	2.775	7.5	94.2
S8L12	0.096	0.111	3.560	0.129	2.288	7.5	75.0
S9S03	0.063	0.084	2.137	0.103	1.388	6.5	18.0
S9L04	0.077	0.095	2.845	0.118	1.80	6.5	38.4
S9S06	0.062	0.082	2.137	-	-	5.5	30.0
S9S07	0.063	0.083	2.137	0.079	0.838	5.5	19.8
S9L08	0.081	0.098	2.845	0.123	2.513	8.0	43.2
S9L09	0.078	0.098	2.845	0.126	2.425	8.0	42.6
S10L2	0.093	0.108	2.845	0.139	2.65	7.5	34.2
S10L6	0.096	0.107	2.845	0.143	2.60	7.5	37.8
S11L4	0.102	0.110	2.845	0.162	3.00	6.5	41.4
S11L8	0.102	0.112	2.845	0.155	2.963	8.0	39.6
S11S4	0.061	0.078	1.656	0.113	1.95	6.5	17.4
S11S7	0.061	0.078	1.656	0.112	2.075	6.0	20.4
S12L4	0.057	0.074	2.845	0.089	0.975	8.0	35.4
S12L8	0.054	0.073	2.845	0.102	1.575	7.5	34.8
S14L1	0.100	0.127	3.560	0.151	2.95	6.5	46.2
S14S2	0.073	0.093	2.137	0.132	2.675	5.5	48.6
S14L4	0.101	0.124	3.560	0.145	2.875	7.5	36.0
S14S4	0.071	0.078	2.137	0.098	1.213	25.5	61.2
S14S5	0.075	0.089	2.137	0.117	1.963	5.5	58.8

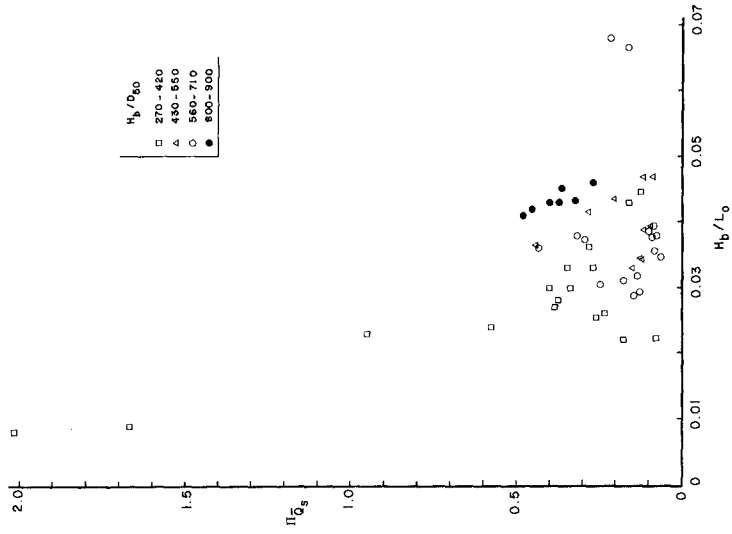

FIG. 4 AVERAGE DIMENSIONLESS TRANSPORT RATE AS A FUNCTION OF BREAKER STEEPNESS

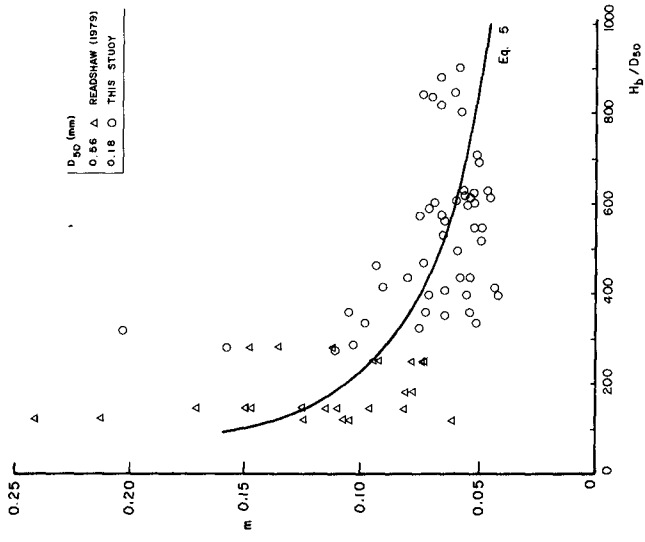

FIG. 3 MOBILE BED BEACH SLOPE AS A FUNCTION OF RELATIVE GRAIN SIZE

is:

$$m = 1.5 \left(\frac{H_b}{D_{50}} \right)^{-1/2} \qquad (4)$$

with $r^2 = 0.42$. The scatter of the data is further reduced if the wave steepness is included as a parameter, see Sayao (1982). It may be concluded that:

$$m \sim \sqrt{\left(\frac{D_{50}}{H_b} \right)} \qquad (5)$$

for medium and fine sands. This result agrees with earlier findings by other authors, reviewed in Sayao and Kamphuis (1982a) and with the well known fact that steeper beach slopes are formed by coarser sediments.

From the above analysis it may be concluded that the mobile bed beach slope m as a dimensionless variable for littoral transport includes much of the influence of relative grain size and hence the two are not completely independent as required by dimensional analysis. Thus, relative grain size and beach slope should not both be included in Equation 1. It was decided to retain beach slope in the relationship. Grain size can be re-introduced at a later stage to account for additional effect of grain size.

Since the model experiments were conducted using sand as the model material in order to avoid serious scale effects resulting from incorrect modelling of the density ratio (see Kamphuis 1975), Equation 1 may be rewritten in simplified form as:

$$\Pi_{Q_s} = \phi_{Q_s} \left(\frac{H_b}{L_o} , m \right) \qquad (6)$$

Figures 4 and 5 show the dimensionless average mass rate of littoral transport ($\Pi_{\bar{Q}_s}$) as a function of each of the dimensionless variables of Equation 6, the wave steepness and the mobile bed beach slope. "Average" refers to sediment transport rate averaged over a test with constant incident wave conditions. Both the present set of results as well as Readshaw's (1979) results are plotted.

For Readshaw's tests, the depth at the breaking point d_b and the breaker distance λ_b had not been measured directly and these quantities were determined by measurement from his published beach profiles. Figure 4 shows a decrease in $\Pi_{\bar{Q}_s}$ with breaker steepness. Also for the same value of the breaker steepness, Readshaw's coarser

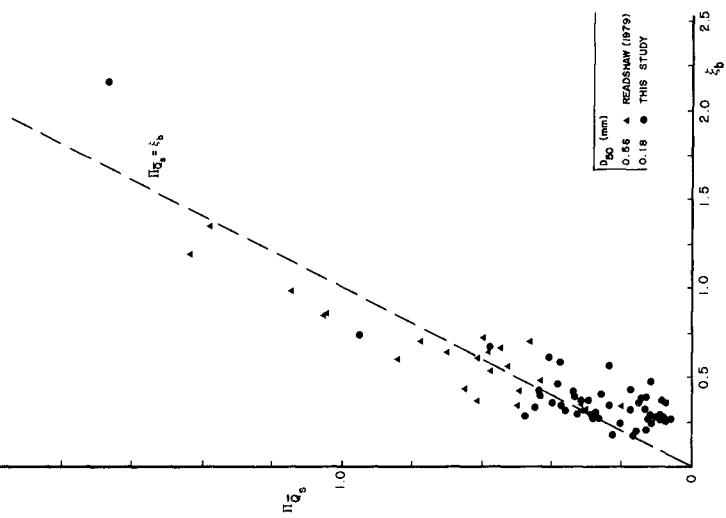

FIG. 6 AVERAGE DIMENSIONLESS TRANSPORT RATE VS SURF SIMILARITY PARAMETER, MEDIUM AND FINE SAND

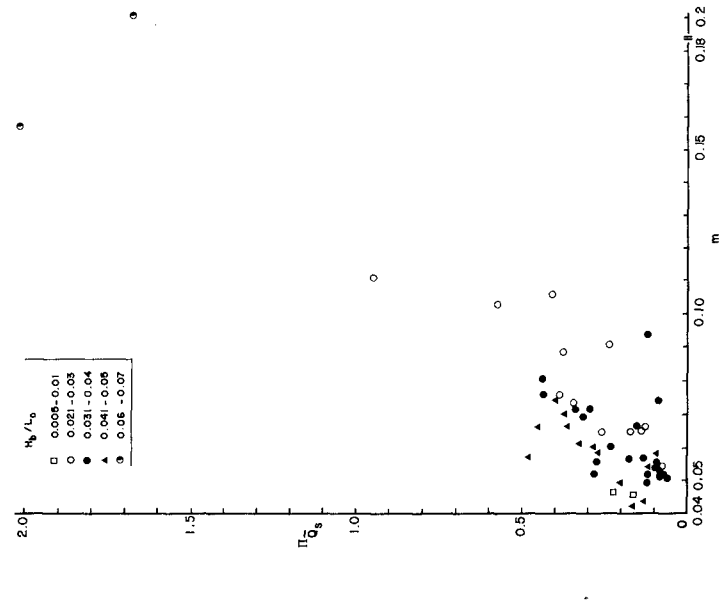

FIG. 5 AVERAGE DIMENSIONLESS TRANSPORT RATE AS A FUNCTION OF BEACH SLOPE

material produced higher dimensionless littoral transport rates, and two distinct curves for $\Pi_{\bar{Q}_s}$ versus H_b/L_o could be drawn. Figure 5 shows an increase of $\Pi_{\bar{Q}_s}$ with mobile bed beach slope.

Figures 4 and 5 indicate that some of the variation in $\Pi_{\bar{Q}_s}$ resulting from the breaker steepness may be compensated by the change in $\Pi_{\bar{Q}_s}$ resulting from the beach profile slope. The influence of the breaker steepness and beach slope on the dimensionless average mass rate of littoral transport might therefore well be expressed by:

$$\Pi_{\bar{Q}_s} \sim \frac{m}{\sqrt{(H_b/L_o)}} = \xi_b \qquad (7)$$

where ξ_b is the surf similarity parameter.

Kamphuis and Readshaw (1978) first proposed that dimensionless littoral transport rate is related to the rate of energy dissipation in the breaking zone and hence to the surf similarity parameter.

Littoral Transport Rate and the Surf Similarity Parameter

Figure 6 shows the dimensionless average mass rate of littoral transport as a function of surf similarity parameter, for the present results with fine sand and for Readshaw's (1979) results with the coarser material. The surf similarity parameter was defined from Equations 3 and 7 as:

$$\xi_b = \frac{m}{\sqrt{(H_b/L_o}} = \frac{d_b/\lambda_b}{\sqrt{(H_b/L_o)}} \qquad (8)$$

A strong straight line relationship between the dimensionless average mass rate of littoral transport and the surf similarity parameter may be seen and hence a good approximation of Equation 6 is:

$$\Pi_{\bar{Q}_s} = \kappa \cdot \xi_b \qquad (9)$$

where κ is a dimensionless constant. Numerical values for κ were found from regression analysis and are given in Table 2. Some variation in κ was noted possibly depending on grain size.

TABLE 2

VALUE OF κ

Experimental Data	Number of Points	Regression Analysis r^2	κ
Readshaw (1979)	24	0.83	1.09
Present results	50	0.83	0.84
Combined data set	74	0.81	0.94

Substitution of Equations 5 and 8 into Equation 9 yields:

$$\Pi_{\bar{Q}_s} = \kappa \cdot \xi_b \sim \frac{\sqrt{(D_{50}/H_b)}}{\sqrt{(H_b/L_o)}} \qquad (10)$$

This implies that the dimensionless littoral transport rate is proportional to the square root of the grain size, for medium and fine sands which agrees with Bajorunas (1970) and Castanho (1970). Laboratory tests conducted by Larras and Bonnefille (1965), reviewed in Sayao and Kamphuis (1982a) revealed that littoral transport rate goes through a maximum when related to the grain size, Lepetit (1972) and Bonnefille (1976). Thus for very coarse sands, Equation 10 will not be valid, and in the limit, for large rocks, the fluid is no longer capable of moving any material.

Equation 10 also shows that dimensionless average mass rate of littoral transport is inversely proportional to the square root of the breaker steepness. This inverse proportionality has been proposed earlier by Saint-Marc and Vincent (1954), Larras (1957) and Le Méhauté and Brebner (1961).

RELATIONSHIP BETWEEN LABORATORY AND FIELD DATA

Immersed Weight, Dry Mass and Alongshore Energy Flux Factor

An attempt to compare the present method and Equation 9 with field data is now presented. Unfortunately, at the present time, only few field data have been published and the quality of these few field data sets was questioned by Greer and Madsen (1978) and Bruno et al (1981). The relationship for dimensionless average mass rate of littoral transport (Equation 9) may be rewritten as:

$$\frac{g\,\bar{Q}_s}{\rho g\,H_b^{\,2}\,(H_b/T)\,\frac{1}{2}\,\sin 2\alpha_b} = \kappa \cdot \xi_b \qquad (11)$$

The average dry mass transport rate $\bar{Q}_s$ may be converted to immersed weight littoral transport rate I_ℓ by the following relation:

$$I_\ell = \frac{\rho_s - \rho}{\rho_s}\, g\, \bar{Q}_s \qquad (12)$$

For quartz sand with $\rho_s/\rho = 2.65$ and using the small amplitude expression for wave energy

$$I_\ell = \frac{8\kappa}{1.6}\,\frac{H_b\,\xi_b}{T}\,E_b\,\frac{1}{2}\,\sin 2\alpha_b \qquad (13)$$

Substitution of Equation 8 into Equation 13 yields

$$I_\ell = \frac{5\kappa}{\sqrt{2\pi}}\, m\, \sqrt{gH_b}\;\; E_b\,\frac{1}{2}\,\sin 2\alpha_b \qquad (14)$$

Longshore wave energy flux factor P_ℓ , is normally defined as follows:

$$P_\ell = \frac{1}{16}\,\rho g\,H_b^{\,2}\,n_b\,C_b\,\sin 2\alpha_b \qquad (15)$$

Using $n_b \approx 1$ for shallow water and C_b as given by small amplitude theory, shown to be correct in Sayao and Kamphuis (1982), P_ℓ becomes:

$$P_\ell = \sqrt{gd_b}\;\; E_b\,\frac{1}{2}\,\sin 2\alpha_b \qquad (16)$$

Now I_ℓ and P_ℓ may be related using Equations 14 and 16:

$$I_\ell = \frac{5\kappa}{\sqrt{2\pi}}\, m\, \sqrt{\gamma_b}\;\; P_\ell \qquad (17)$$

Equations 9, 14 and 17 are simply different expressions of the same relationship for littoral transport rate proposed in the light of the present findings. Equation 17 may be written in dimensionless form as:

$$K_p = \frac{I_\ell}{P_\ell} = \frac{5\kappa}{\sqrt{2\pi}}\, m\, \sqrt{\gamma_b} = 2\,\kappa \cdot m\,\sqrt{\gamma_b}\;. \qquad (18)$$

which shows that the value of K_p is not constant as expressed in the

CERC formula - U S Army Corps of Engineers (1977) - but varies as a function of the mobile bed beach slope and the breaker index. Figure 7 shows a plot of K_p versus $m\sqrt{\gamma_b}$ for the combined results of Readshaw (1979) and the present tests. Figure 7 is equivalent to Figure 6, but contains a little more scatter. Using a value for $\kappa \simeq 1$ (see Table 2), the curve fitted in terms of K_p becomes:

$$K_p = 2\, m \sqrt{\gamma_b} \qquad (19)$$

which was found valid for the model data, with $r^2 = 0.78$.

Preliminary Comparison of Experiments with Field Data

Existing field data on littoral drift have been compiled by Das (1971). The measurements were expressed in terms of immersed weight transport rate and longshore wave energy flux factor. Komar and Inman (1970) found

$$K_p = \frac{I_\ell}{P_{\ell r}} = 0.77 \qquad (20)$$

where $P_{\ell r}$ is P_ℓ evaluated using H_{rms}. The present CERC formula in which Komar's data as well as other available field data sets are used finds K_p equal to 0.78 (Bruno et al, 1981). If the significant wave height is used to calculate P_ℓ, then the comparable value for the CERC formula 'constant' becomes:

$$K_p = \frac{I_\ell}{P_{\ell s}} = 0.39 \qquad (21)$$

assuming the wave heights near breaking to be Rayleigh distributed. Equation 21 is also shown in Figure 7.

A comparison will be made between the present model results and the field data of Komar (1969), see also Komar and Inman (1970). For this comparison of field and model data it is assumed that the monochromatic model wave height H may be compared with the significant wave height H_s in the field. This has become a common assumption in the past for mobile bed model studies performed at Queen's University, as well as at other hydraulics laboratories.

Unfortunately, for Komar's field data, only typical beach profiles for each location were given (see Komar, 1969). For Silver Strand beach the wave data were collected at the same time as the

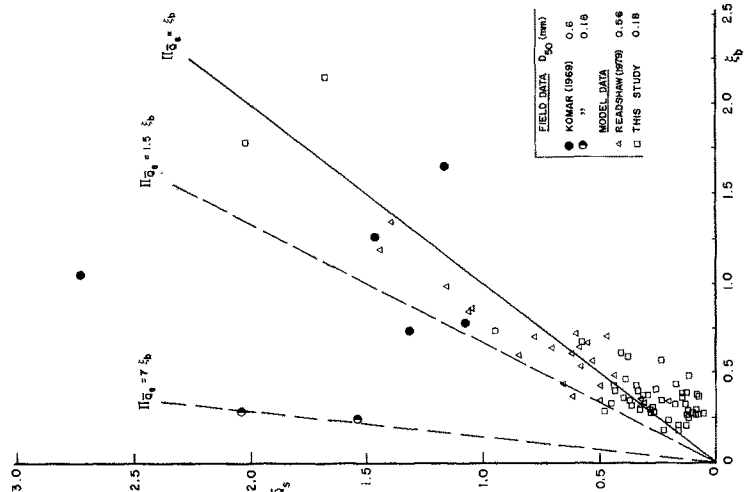

FIG. 8 COMPARISON OF FIELD AND MODEL DATA ON LITTORAL TRANSPORT RATE

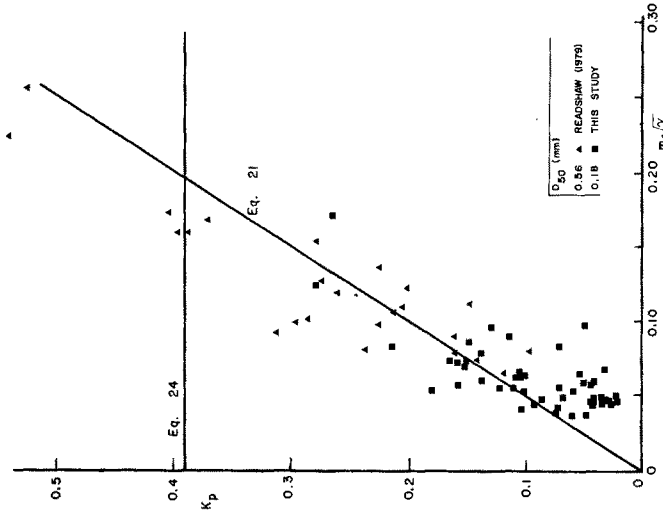

FIG. 7 VARIATION OF COEFFICIENT IN THE CERC FORMULA WITH BEACH SLOPE AND BREAKER INDEX

beach was surveyed. For El Moreno, the wave climate was considered for this study to vary on a seasonal basis, i.e. it was assumed that the profile surveyed in May 1968 was also valid for Komar's measurements of May 1966 and May 1967. Out of the 14 orginal data points only seven can be used in the present comparison. Table 3 shows the parameters used for calculating $\bar{\Pi}_{Q_s}$ based on Komar's (1969) own field measurements using

$$\bar{\Pi}_{Q_s} = \frac{1}{5} \frac{\sqrt{gd_b}}{H_b/T} \frac{I_\ell}{P_{\ell s}} \qquad (25)$$

TABLE 3

FIELD MEASUREMENTS FROM KOMAR (1969)

No	Site	Date	m		$(H_b)_{rms}$	α_b	I_ℓ	$(\xi_b)_s$	$(\bar{\Pi}_{Q_s})_s$	κ
				(s)	(m)	(°)	(N/s)			
	(1)		(2)	(3)	(4)	(3)	(5)	(6)	(6)	
1	SSB	4 Sep 68	1/55	11.10	0.528	5.8	47.1	0.29	2.04	7.03
2	SSB	5 Sep 68	1/55	9.50	0.565	4.3	37.9	0.24	1.54	6.42
3	EMB	4 May 66	1/7	2.72	0.316	10.0	45.1	0.73	1.31	1.79
4	EMB	5 May 66	1/7	3.28	0.398	14.0	84.4	0.78	1.08	1.38
5	EMB	22 May 67	1/7	4.72	0.317	9.8	28.7	1.25	1.46	1.17
6	EMB	23 May 67	1/7	5.88	0.287	5.3	7.5	1.65	1.17	.71
7	EMB	11 May 68	1/7	3.75	0.285	4.1	20.8	1.06	2.72	2.56

(1) SSB: Silver Strand beach, D_{50} = 0.18 mm
EMB: El Moreno beach, D_{50} = 0.6 mm
(2) From typical beach profiles given in Figure 9 of Komar (1969)
(3) Averaged daily values from data given in Appendix IV of Komar (1969)
(4) Averaged daily root mean square values from data given in Appendix IV of Komar (1969)
(5) Averaged daily values given in Table 1 of Komar (1969)
(6) Calculated using significant breaker height

The results were plotted in Figure 8 for which $\Pi_{\bar{Q}_s}$ was calculated using $(H_b)_s$ for the field data points (i.e. $(H_b)_{rms}$ was multiplied by $\sqrt{2}$). It may be seen from Figure 8 that Equation 9 is also valid for the field results, but that the value of κ based on the model results would underestimate the littoral transport rate by a factor of about 7 when compared with the Silver Strand field results and by a factor of about 1.5 when compared with the widely scattered El Moreno field results.

The fact that Equation 9 is valid for the field results is not surprising since there is no reason why field sediment transport rates should not be related to rate of energy dissipation. The fact that κ for the field results is higher than for the model is also reasonable. In the model (and on prototype beaches of large grain size), the sand is moved almost solely by bed load transport. For finer sands in the field, additional transport results from material suspension. In the model and the coarse material prototype, the driving force is related to shear stress. In the finer material prototype, additional consideration must be given to stirring of material into suspension by the turbulent breaker, to the settling mechanisms and fall velocity and to the effect of excess pore water pressures in the beach at the breaking zone, locally causing liquefaction of the sand mass and much higher rates of sediment transport.

The model results indicate that as D increases, m increases, ξ increases and hence Q_s increases. But the suspension and liquefaction mechanisms would indicate that as D increases, concentration of particles in suspension decreases and hence Q_s decreases. The first mechanism is taken into account with ξ, the second with κ. Further field comparisons are obviously necessary to prove the above preliminary hypothesis to be correct. No better comparisons can be made until more field measurements of littoral sand transport rate become readily available in which wave characteristics and beach profiles are simultaneously recorded.

For the sake of completeness a simple dimensional plot of I_ℓ versus $P_{\ell s}$, as suggested by the CERC formula (U S Army Corps of Engineers, 1977), is also produced in Figure 9. No strong relationship is evident.

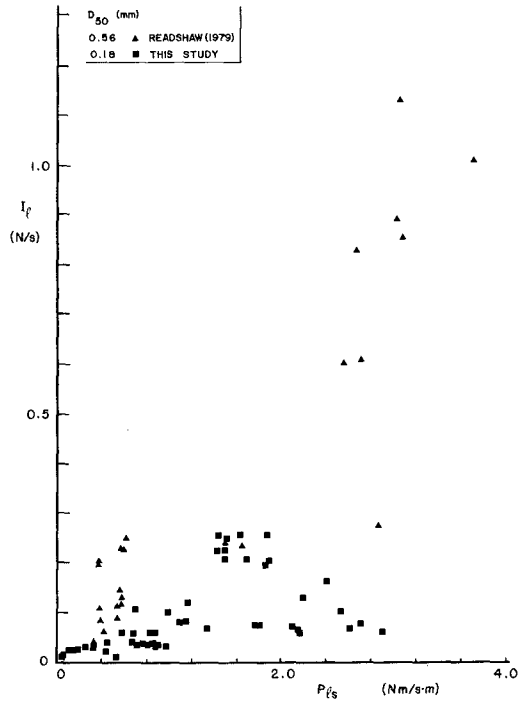

FIG. 9 I_ℓ VERSUS $P_{\ell S}$, FOR MODEL DATA OF MEDIUM AND FINE SAND

CONCLUSIONS

a. Littoral transport rate for medium and fine sand models may be expressed as

$$I_{\bar{Q}_s} = \kappa \xi_b \tag{9}$$

or

$$\frac{\bar{Q}_s}{\rho H_b^2 (H_b/T) \frac{1}{2} \sin 2\alpha_b} = \kappa \frac{m}{\sqrt{H_b/L_o}} \tag{26}$$

where κ was found to be approximately equal to one for the model studies.

b. The beach slope to be used for calculations of littoral transport rate in mobile bed models is

$$m = \frac{d_b}{\lambda_b} \tag{3}$$

which was found to be related to grain size

$$m \sim \sqrt{\frac{D_{50}}{H_b}} \tag{5}$$

c. Another form of Equation 26 is:

$$I_{\ell} = 2 \kappa m \sqrt{\gamma_b} P_{\ell_s} \tag{27}$$

which indicates that the "constant" in the CERC formula is not constant but varies with beach slope and breaker index.

d. Preliminary analysis of some field results indicates that Equation 9 is also valid for prototype beaches but that the value of sediment transport (and κ) for the field results is higher than for the model. This is hypothesised to be a result of additional transport in the field by material suspension.

REFERENCES

Bajorunas L (1970): "Littoral Transport and Energy Relationships"; Proc of the 12th Coastal Engineering Conference, Washington, U S A, ASCE, Vol II, pp 787-798.

Bijker E W (1967): "Some Considerations about Scales for Coastal Models with Movable Bed", Delft Hydraulics Laboratory, Publication No 50.

Bonnefille R (1976): "Cours d'Hydraulique Maritime"; Masson, Paris, 159 pp.

Bruno R O, R C Dean, C C Gable and T L Walton (1981): "Longshore Sand Transport Study at Channel islands Harbor, California"; Technical Paper No 81-2, CERC, U S Army Corps of Engineers.

Castanho J (1970): "Influence of Grain Size on Littoral Drift"; Proc. of the 12th Coastal Engineering Conference, Washington, U S A, ASCE, Vol II, pp 891-898.

Das M M (1971): "Longshore Sediment Transport Rates: A Compilation of Data"; Miscellaneous Paper No 1-71, CERC, U S Army Corps of Engineers.

Dean R G (1977): "Equilibrium Beach Profiles: U S Atlantic and Gulf Coasts"; Ocean Engineering Report No 12, Department of Civil Engineering, University of Delaware.

Creer M N and O S Madsen (1978): "Longshore Sediment Transport Data: A Review"; Proc of the 16 Coastal Engineering Conference, Hamburg, West Germany, ASCE, Vol II, pp 1563-1576.

Kamphuis J W (1975): "The Coastal Mobile Bed Model"; C E Research Report No 75, Department of Civil Engineering, Queen's University, Kingston, Canada.

Kamphuis J W and J S Readshaw (1978): "A Model Study of Alongshore Sediment Transport Rate"; Proc of the 16th Coastal Engineering Conference, Hamburg, West Germany, ASCE, Vol II, pp 1656-1674.

Komar P D (1969): "The Longshore Transport of Sand on Beaches"; Ph D Thesis, University of California, San Diego, 141pp.

Komar P D and D L Inman (1970): "Longshore Sand Transport on Beaches"; Journal of Geophysical Research, Vol 75, No 30, pp 5514-5527.

Larras J (1957): "PIages et Cotes de Sable"; Eyrolles, Paris. Le Méhauté B and A Brebner (1961): "An Introduction to Coastal Morphology and Littoral Processes"; C E Research Report No 14, Department of Civil Engineering, Queen's University, Kingston, Canada.

Lepetit J P (1972): "Transport Littoral: Essais et Calculs"; Proc of the 13th Coastal Engineering Conference, Vancouver, Canada, ASCE, Vol II, pp 971-984.

Readshaw J S (1979): "A Model Study of Alongshore Sediment Transport"; M Sc Thesis, Department of Civil Engineering, Queen's University, Kingston, Canada.

Saint-Marc M G S and M G Vincent (1954): "Transport Littoral Formation de Fleches et de Tombolos"; Proc of the 5th Coastal Engineering Conference, Grenoble, France, Council on Wave Research, pp 296-328.

Sayao O S F J (1982): "Beach profiles and Littoral Sand Transport"; Ph D Thesis, Department of Civil Engineering, Queen's University, Kingston, Canada.

Sayao O S F J and Kamphuis, J W (1982): "Wave Action on Beaches"; CE Research Report No 77, Department of Civil Engineering, Queen's University, Kingston, Canada.

Sayao, O S F J and Kamphuis, J W (1982a): "Littoral Sand Transport: Review of the State of the Art"; C E Research Report No 78, Department of Civil Engineering, Queen's University, Kingston, Canada.

Sayao O S F J and J W Kamphuis (1983): "Littoral Sand Transport: Model Tests 1977-1982"; CE Research Report No 79, Department of Civil Engineering, Queen's University, Kingston, Canada.

U S Army Corps of Engineers (1977): "Shore Protection Manual"; 3rd Edition, Coastal Engineering Research Center, Washington.

ACKNOWLEDGEMENTS

The financial support for the research project came from the Natural Sciences and Engineering Research Council of Canada. Dr. Sayao received financial support for his studies from the Conselho Nacional de Desenvolvimento Cientifico e Tecnologico of Brazil and was granted study leave from Universidade Federal do Rio de Janeiro. The authors wish to thank all three of these organizations for their interest and support. They also thank Mr. J. Readshaw for the very intense and fruitful discussions at the Capetown conference.

NOTATION

General

b	(as a subscript) at the breaker
C	velocity of wave propagation
C_b	velocity of wave propagation in the breaking zone
C_g	group velocity
D	sediment grain size
D_{50}	sediment grain size corresponding to sieve size retaining 50% of a sediment sample
d	local water depth, related to still water level
d_b	water depth at breaking, related to still water level
E	energy density in a wave (= 1/8 $\rho g H^2$)
E_b	energy density at time of breaking
g	acceleration due to gravity
H	wave height
H_b	breaker height
H_o	deep water wave height
H_{rms}	root mean square wave height
H_s	significant wave height
I_ℓ	immersed weight littoral sand transport rate
K_p	empirical dimensionless littoral transport coefficient
L	local wave length
L_b	wave length at point of breaking
L_o	deep water wave length
m	mobile bed beach slope (= d_b/λ_b)
m	(as a subscript) model

N	model distortion
n	energy propagation factor ($= C/C_g$)
n	model scale
p	(as a subscript) prototype
P_l	longshore wave energy flux factor
P_{l_r}	P_l evaluated using H_{rms}
P_{l_s}	P_l evaluated using H_s
Q_s	mass rate of littoral sediment transport
$\bar{Q}_s$	average mass rate littoral transport during one test
r	correlation coefficient
T	wave period
x	horizontal
y	vertical
α	angle of incidence between waves and shoreline
α_b	angle α measured at the breaking point
γ_b	breaker index ($= H_b/d_b$)
ξ_b	surf similarity parameter evaluated at the breaking point ($= m/\sqrt{(H_b/L_o)}$)
Π_A	dimensionless version of a property A
ϕ	dimensionless function
κ	empirical dimensionless constant
λ_b	breaker distance, measured between the breaking point and the shoreline, at still water level
ρ	density of water
ρ_s	sediment density

THE RATE OF LONGSHORE SEDIMENT TRANSPORT AND BEACH EROSION CONTROL

Yoshito Tsuchiya, M. ASCE*

ABSTRACT

The main purpose of this paper is to propose an ideal methodology for beach erosion control from the viewpoint of controlling the total rate of longshore sediment transport. For this, a new formulation of the rate of longshore sediment transport is made. The total rate is directly proportional to the longshore component of wave power in field coasts, but not in laboratory ones.

How to control the total rate of longshore sediment transport is considered. There are two ways applicable for practical purposes. The first is to decrease the breaker depth by changing the bottom topography, and the second to decrease the incident angle of breaking waves by changing either the bottom topography or the inclination of shoreline to the incidence of predominant waves. Two typical, but ideal examples are explained for beach erosion control by this methodology.

INTRODUCTION

Beach erosion has advanced actively in many countries of the world, especially in Japan(Tsuchiya, 1980) due to decrease in sediment input from rivers and by construction of coastal structures. Various works have been employed widely to prevent beaches from erosion, but few general concept of beach erosion control has been proposed.

The methodology of beach erosion control must be established by the knowledges of sand drift, as well as of beach processes. By wave power approach, formulations of the total rate of longshore sediment transport have been made by many authorities. Komer and Inman(1970) investigated the applicability of the Bagnold model(1963) for sand transport on beaches to find out some correlation between the model and empirical relation of the total rate of longshore sediment transport. Recently Kamphuis and Readshaw(1978) studied the total rate of longshore sediment transport in terms of the total thrust which is the longshore gradient of the alongshore component of radiation stress. More recently Seymour, Domurat and Pirie(1980) did the same approach which was compared with their observed results of longshore sediment transport and radiation stress.

A very simple model for the formulation of the rate of longshore sediment transport is first explained. Then, an ideal methodology for

* Professor, Disaster Prevention Research Institute, Kyoto University, Kyoto, JAPAN

beach erosion control is proposed from the viewpoints of controlling the total rate of longshore sediment transport and providing stable sandy beaches which have the lowest wave reflection coefficient to reduce the offshore sediment transport effectively.

THE RATE OF LONGSHORE SEDIMENT TRANSPORT

On the whole, movements of sediments are thought to be composed of alternating motion and these sediments are transported downstream by longshore currents even as they are undergoing sliding or saltation due to wave action. Thus, the mechanism of longshore sediment transport can be expressed as

$$q_x = \underset{\text{Wave motion}}{\overset{\uparrow}{\bar{c}_o}} \cdot d \cdot \underset{\text{Longshore currents}}{\overset{\uparrow}{u(y)}} \tag{1}$$

in which q_x is the rate of longshore sediment transport, u the velocity of longshore current in the x-direction, and $\bar{c}_o$ the averaged concentration of sediment. Einstein(1972) indicated that the motion of sediment transported by fluid can be expressed universally by a formula for sediment load. When the formula used to determine the rate of sediment transport by winds and currents(Tsuchiya and Kawata, 1971) is applied, the averaged concentration can be expressed as

$$\bar{c}_o = c_o \left(\frac{\rho}{\sigma}\right)\left(1 - \frac{\tau^*}{\tau_c^*}\right) \tag{2}$$

in which c_o is approximately equal to 0.2 although it varies slightly with the Shields parameter τ^*. τ_c^* in Eq.(2) is the value at the critical stage of sediment movement, and τ^* is given as

$$\tau^* = \frac{\tau/\rho}{(\sigma/\rho - 1)\, gD} \tag{3}$$

where

$$\tau/\rho = (1/2)\, f\bar{v}^2 \tag{4}$$

in which f is the coefficient of bottom friction, D the size of the sediment, σ/ρ the specific gravity of the sediment, g the acceleration of gravity, and $\bar{v}$ the maximum water particle velocity of waves on the sea bottom. The value for $\bar{v}$ can be expressed approximately by

$$\bar{v} = \begin{cases} \alpha\sqrt{gd}, \quad \alpha = \dfrac{1}{2}\left(\dfrac{L}{T\sqrt{gd}}\right)_B \left(\dfrac{H_B}{d_B}\right) & \text{for} \quad 0 \le Y \le 1 \\ \dfrac{1}{2}\left(\dfrac{H}{H_o}\right)\left(\dfrac{L}{L_o}\right)\left(\dfrac{H_o L_o}{Td}\right) & \text{for} \quad 1 \le Y < \infty \end{cases} \tag{5}$$

in which the subscript o refers to wave quantities at the deep-water limit and B to the breaker point, L is the wave-length, H the wave-height, T the wave-period, d the water depth, $Y = y/y_B$ the dimensionless variable, and y_B the width of surf-zone. Use of the equation for longshore currents of Longuet-Higgins(1970), allows us to rearrange the distribution of longshore sediment transport in the y-direction as

$$\frac{q}{\sqrt{gd_B}d} = \begin{cases} \dfrac{5\pi}{16} c_o \left(\dfrac{\alpha}{f}\right)\left(\dfrac{\rho}{\sigma}\right)\left(\dfrac{d_B}{D}\right)(\tan\beta \ \sin 2\vartheta_B)(1-R^2F_r^2Y^2)YU(Y) \\ \qquad\qquad \text{for} \quad 0 \le Y \le 1 \\ \dfrac{5\pi}{16} c_o\left(\dfrac{\alpha}{f}\right)\left(\dfrac{\rho}{\sigma}\right)\left(\dfrac{d_B}{D}\right)(\tan\beta \ \sin 2\vartheta_B \ (1-\dfrac{R^2F_r^2}{Y}) \\ \qquad\qquad \text{for} \quad 1 \le Y < \infty \end{cases} \tag{6}$$

in which $U(Y) = u/u_B$ where u_B is the velocity of longshore currents at the breaker line, tanβ is the average slope of the sea bottom, and R and F_r are

$$\left.\begin{aligned} R &= \frac{1}{2}\left(\frac{H_B}{H_o}\right)\left(\frac{L_B}{L_o}\right)\left(\frac{H_o}{H}\right)\left(\frac{L_o}{L}\right) \\ F_r^2 &= 16\pi\left(\frac{d_B}{H_B}\right)^2\left(\frac{L_o d_B}{L_B^2}\right)\frac{(\sigma/\rho-1)d}{fd_B}\tau_c^* \end{aligned}\right\} \tag{7}$$

The theoretical distribution of longshore sediment transport across the surf-zone in the dimensionless form given by Eq. (6) is shown as a

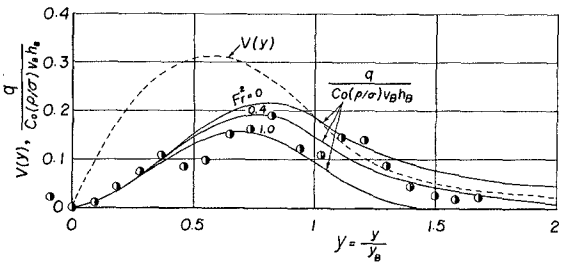

Fig. 1 Offshore distributions of the rate of longshore sediment transport and longshore current velocity

function of Y in Fig. 1 for a comparison with the experimental data obtained by the authors(1978), as well as with the velocity distribution of longshore currents. In the figure, the constant value of P is assumed to be 0.2 for the theory of longshore currents. Favorable agreement for the offshore distribution of longshore sediment transport is seen between the theoretical curves and experimental values. After integrating Eq. (6) with respect to Y over the domain of sand drift between the critical water depth for null sediment mevement and the shoreline(neglecting the so-called swash transport) the total rate of longshore sediment transport Q_x is given by

$$Q_x = C\left(\frac{\rho}{\sigma}\right) \ I(R, F_r) \ d_B^2 \sqrt{gd_B} \ \sin 2\vartheta_B \tag{8}$$

in which

$$\left.\begin{aligned} C &= \frac{5\pi}{16}\frac{c_o\alpha}{f} \\ I(R, F_r) &= a_o - b_o F_r^2 - d_0 (RF_r)^{\alpha_o} + e_o (RF_r)^2 \end{aligned}\right\} \tag{9}$$

Here $a_o = 0.298$, $b_o = 0.124$, $d_o = 0.373$, $e_o = 0.207$ and $\alpha_o = 1.11$ when $P =$

0.2.

The function of $I(R, F_r)$ is shown in Fig. 2. In field coasts, the value of F_r is normally very small, because the parameter F_r includes the ratio of sediment size to wave length. Therefore, the value of $I(R, F_r)$ becomes nearly constant, say 0.3. Then the total rate of long-

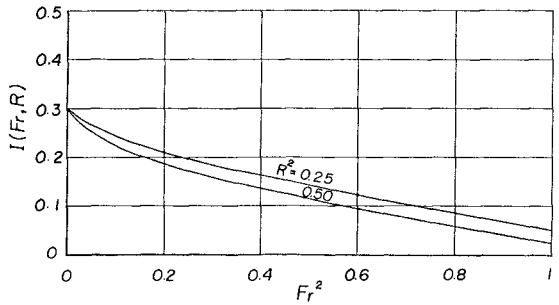

Fig. 2 Change in $I(R, F_r)$ with the parameter R and F_r

shore sediment transport is directly proportional to the longshore component of wave power. This is consistent with the usual empirical relationship for the total rate of longshore sediment transport which

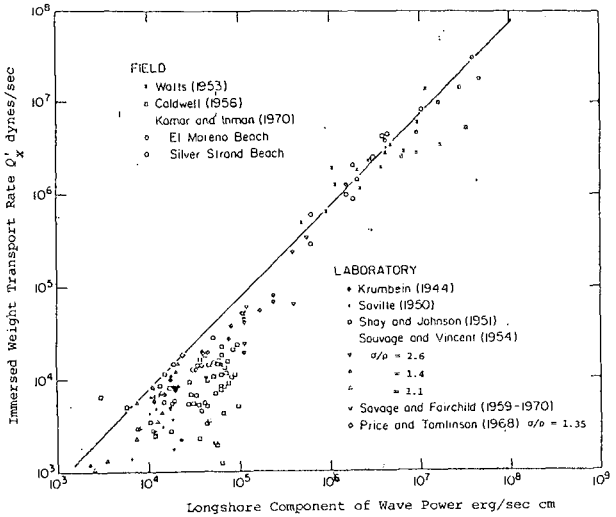

Fig. 3 Data on the immersed-weight sand transport rate as a function of the longshore component of wave power (Komer and Inman, 1970)

was derived by wave power approach. But, in laboratory experiment, the value of $I(R, F_r)$ is more smaller than that in field coasts. The value depends on characteristics of waves and sediment. It has been pointed out that the usual empirical relationship is not applicable for laboratory data of the total rate of longshore sediment transport, so that the data are plotted below the relationship. For example, Fig. 3 which was prepared by Komer and Inman(1970), shows a relationship between the immersed-weight sand transport rate and longshore component of wave power in which the laboratory data are shown below the relationship for the field data.

METHODOLOGY FOR BEACH EROSION CONTROL

Now, consider how to control beach erosion from the viewpoint of controlling the total rate of longshore sediment transport. As explained in Eq. (8), the total rate of longshore sediment transport is expressed by

$$Q_x = C' d_B^2 \sqrt{g d_B} \sin 2\theta_B \tag{10}$$

in which C' is a constant. The total rate of longshore sediment transport is expressed in terms of the breaker depth or breaker height, incident angle of the breaker and some other parameters included in the constant C' in Eq. (10). This formulation indicates that as already explained the total rate of longshore sediment transport is directly proportional to the longshore component of wave power.

An idea of controlling the total rate of longshore sediment transport can therefore be proposed for the conditions of changes in coastal sediment sources. For the conditions of decrease in coastal sediment sources the total rate of longshore sediment transport must be reduced in the given conditions. To reduce the total rate of longshore sediment transport the longshore component of wave power must be decreased effectively along the coast. To reduce the total rate of longshore sediment transport, in other words, two ways would be applicable from Eq. (10) for more practical purposes. The first is to reduce the breaker depth by changing the bottom topography to decrease the total rate of longshore sediment transport. And the second is to reduce the incident angle of breakers by changing either the bottom topography or the inclination of the shoreline to the incidence of predominant waves.

Table 1 A classification of beach erosion control

Method	Practical Works
To reduce the breaker height	To change the bottom topography Offshore beach nourishment Sand groin etc. To construct structures Submerged breakwater Floating breakwater Offshore breakwater etc.
To reduce the incident angle of breakers	Headland control Offshore breakwater etc.

A classification of beach erosion control is shown in Table 1. For controlling the breaker height or breaker depth, there are two ways such as to change the bottom topography and to construct structures. The former is offshore beach nourishment and sand groin, and the latter submerged, floating and offshore breakwaters. For controlling the incident angle of breakers, on the other hand, there are two ways such as headland control and offshore breakwater.

An example of wave reflection coefficients of wave absorbers and natural beaches is shown in Fig. 4, in which K_r is the reflection coef-

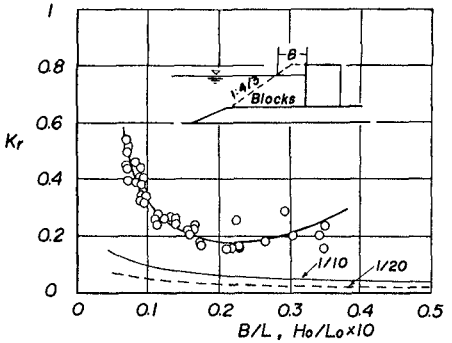

Fig. 4 Wave reflection coefficients of wave absorbers and natural beaches

ficient, B/L the ratio of the width of absorber to wave length, H_o/L_o the wave steepness at deep water limit, the thick solid curve indicates experimental values of reflection coefficient of wave absorbers with concrete blocks (Tanimoto, Kitatani and Osato, 1979), and the other two thin solid curves are those of sloping beaches of 1/10 and 1/20 respectively. It is well-known that the efficiency of natural sandy beaches in wave energy dissipation is very higher than other wave absorbers, and is nearly independent of wave periods. To reduce offshore sediment transport, emphasis is placed on the reduction of occurrence of reflected waves in considering how to control beach erosion.

From the viewpoint of controlling the total rate of longshore sediment transport, a possible method can be expected for application to practical beach erosion control. In this case, attention should be made in selecting suitable methods of beach erosion control by which be formed stable sandy beaches having the lowest coefficient of wave reflection to reduce the offshore sediment transport by reflected waves most effectively. From the viewpoint of applicability, the second one of the proposed methods would be more applicable for beach erosion control, because the inclination of shoreline can be changed easily by construction of artificial headlands or offshore breakwaters. Especially natural-like sandy beaches will be formed between headlands if necessary conditions for their formation are satisfied.

IDEAL EXAMPLES OF BEACH EROSION CONTROL

Two typical, but ideal examples can be explained for beach erosion by this methodology. The first is for beach erosion due to the decrease in sediment sources such as recent beach erosion near river mouths which has recently been remarkable in many countries of the world, especially in Japan(Tsuchiya, 1980). Surppose that a river is running into the sea as shown in Fig. 5, and the predominant waves are coming from the

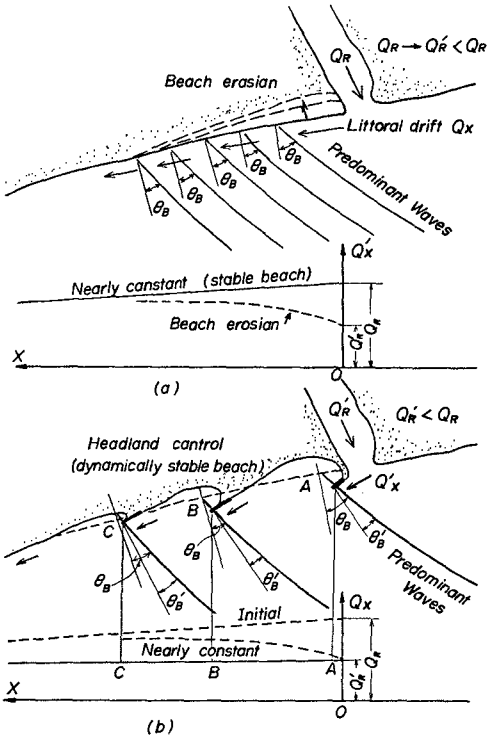

Fig. 5 Beach erosion control for the decrease in sediment input from a river

direction of which the incident angle is θ_B, producing the total rate of longshore sediment transport Q_x. The sediment input from the river was Q_R, but has recently been reduced Q_R'. Beach erosion has therefore advanced on the coast downstream of longshore sediment transport, the left-side coast of the river as shown in the figure.

The total rate of longshore sediment transport by the predominant waves can be assumed to be nearly constant so that the decrease in sediment input from the river takes place beach erosion. Consider how to control the beach erosion from the viewpoint of controlling the total rate of longshore sediment transport. For this the total sediment transport rate must be reduced along the left side coast, according to the decreased sediment input from the river.

There may be many ideas for this, but a possible solution of them is expected as shown in Fig. 5(b), in which a series of headlands is constructed at suitable angles and distances to make the total sediment transport rate decrease at the given total rates. This is to reduce the incident angle of the breakers from θ_B to θ_B' as shown in the figure. It may then be expected that a series of dynamically stable beaches(Silvester, Tsuchiya and Shibano, 1980) be finally formed, and they have the lowest coefficients of wave reflection to reduce the offshore sediment transport most effectively.

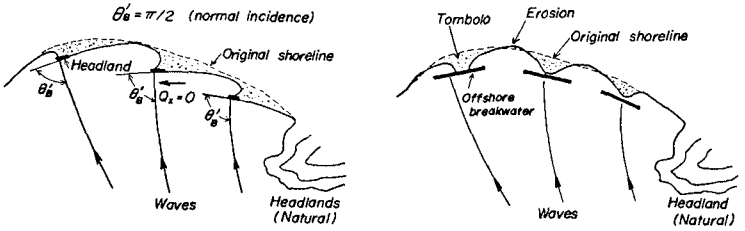

(a) Headlands (b) Offshore breakwaters

Fig. 6 Beach erosion control for the lack of sediment sources

The second example is for beach erosion due to the lack of sediment sources by reclamation of river mouth areas or by construction of large coastal structures. A solution for such beach erosion can be proposed by this methodology as shown in Fig. 6, in which a series of headlands (Silvester, 1976) or offshore breakwaters(Detached breakwaters, Toyoshima, 1974) is employed to make the total rate of longshore sediment transport vanish. By construction of such a series of headlands or offshore breakwaters, statically stable beaches(Silvester, Tsuchiya and Shibano, 1980) be finally formed between them.

CONCLUSION

Based on the formulation of the total rate of longshore sediment transport, an ideal methodology of beach erosion control has be proposed, and two typical, but ieal examples have been shown for controlling beach erosion due to the decrease or lack of sediment sources.

I must hereby remember the following two concepts;
"Water shall not be compelled by any fortse(force), or it will return that fortse onto you" which was introduced by Professor Per Brunn

(1972) in his theme lecture at the 13th Coastal Engineering Conference, and

"How to copy nature" which was emphasized by Professor Richard Silvester(1979) in his special lecture at the 1978-Annual Meeting of the Disaster Prevention Research Institute, Kyoto University.

The study reported in this paper was supported by Grant-in-Aids for Scientific Research, from the Ministry of Education, Science and Culture of Japan, under Grant Nos. 542044 and 57850167.

REFERENCES

Bagnold, R.A.: Mechanics of marine sedimentation, In The Sea, ed. M.N. Hill, Vol. 3, 1963, pp. 507-528.

Einstein, H.A.: Sediment transport by wave action, Proc. 13th Coastal Engineering Conference, ASCE, 1972, pp. 933-952.

Kamphuis, J.W. and J.S. Readshaw: A model study of alongshore sediment transport rate, Proc. 16th Coastal Engineering Conference, ASCE, 1978, pp. 1656-1674.

Komer, P.D. and D.L. Inman: Longshore sand transport on beaches, Jour. Geophys. Res., Vol. 75, No. 30, 1970, pp. 5914-5927.

Longuet-Higgins, M.S.: Longshore currents generated by obliquely incident sea waves, 1, Jour. Geophys. Res., Vol. 75, No. 33, 1970, pp. 6778-6789.

Longuet-Higgins, M.S.: Longshore currents generated by obliquely incident sea waves, 2, Jour. Geophys. Res., Vol. 75, No. 33, 1970, pp. 6790-6801.

Per Brunn: The history and philosophy of coastal protection, Proc. 13th Coastal Engineering Conference, ASCE, 1972, pp. 33-74.

Seymour, R.J., G.W. Domurat and D.M. Pirie: A sediment trapping experiment at Santa Cruz, Ca., Proc. 17th Coastal Engineering Conference, ASCE, 1980, pp. 1416-1435.

Silvester, R.: Headland defense of coasts, Proc. 15th Coastal Engineering Conference, ASCE, 1976, pp. 1394-1406.

Silvester, R.: A new look at beach erosion control, Annuals, Disas. Prev. Res. Inst., Kyoto Univ., No. 22A, 1979, pp. 19-31.

Silvester, R., Y. Tsuchiya and T. Shibano: Zeta bays, pocket beaches and headland control, Proc. 17th Coastal Engineering Conference, ASCE, 1980, pp. 1306-1319.

Tanimoto, K., T. Kitatani and M. Osato: A model experiment of irregular wave action on a caisson breakwater armored with wave dissipating concrete blocks, Technical Note, Port & Harbour Res. Inst., Ministry of Transport, Japan, No. 321, 1979, pp. 1-60(in Japanese).

Toyoshima, O.: Design of a detached breakwater system, Proc. 14th Coastal Engineering Conference, ASCE, 1974, pp. 1419-1431.

Tsuchiya, Y. and Y. Kawata: The rate of sediment transport by mechanics of saltation, Proc. 15th Japanese Conference on Hydraulics, JSCE, 1971, pp. 7-12(in Japanese).

Tsuchiya, Y. and T. Ysuda: A mathematical model of beach change, Proc. 25th Japanese Conference on Coastal Engineering, JSCE, 1978, pp. 189-193(in Japanese).

Tsuchiya, Y.: Principles and technical measures in shore protection, Jour. JSCE, Vol. 65, No. 2, 1980, pp. 2-8(in Japanese).

SEDIMENT TRANSPORT UNDER SHEET FLOW CONDITION

by

Kiyoshi Horikawa[1], Akira Watanabe[2] and Sadakazu Katori[3]

ABSTRACT

A series of laboratory experiments in an oscillatory tank was carried out to investigate the sheet flow of sediment. Objectives of the study were to determine the criterion for inception of sheet flow, and to evaluate the sediment transport rate under the sheet flow condition. In order to proceed with the investigation, it was necessary to develop devices appropriate for tracing the sediment particle movement, and for measuring the extremely dense sediment concentration in the moving layer of sheet flow. The chief results are: 1) the criteria for the inception of sheet flow given by Manohar (1955) and by Komar and Miller (1974) are both applicable to materials composed of spheroidal particles, and 2) the average rate of sediment transport for sheet flow is well described by an empirical relationship given by Madsen and Grant (1976) for the bed load transport rate on a plane bed in oscillatory flow.

INTRODUCTION

The prediction of beach profile change is, at present, one of the most important subjects in the field of coastal engineering. In order to proceed with the prediction of beach evolution, appropriate formulae must be developed for evaluating the sediment transport rate in the surf zone as well as in the offshore zone. The characteristics of waves, currents, and movement of sediment particles in these regions are evidently completely different depending upon the location. For example, Dingler and Inman (1976) presented diagrams of various types of bed configurations appearing in the shallow water region. These are the relict, rippled, transition, and sheet flow regimes. The rippled bed gives way to the sheet flow regime in the surf zone, in particular under storm conditions. Although studies on sediment transport in the sheet flow condition are necessary to understand beach profile change in the surf zone, very few investigations have been reported on this particular phenomenon.

---

1. Professor of Civil Engineering, Faculty of Engineering, University of Tokyo, Bunkyo-ku, Tokyo, 113, Japan
2. Associate Professor of Civil Engineering, Faculty of Engineering, University of Tokyo, Bunkyo-ku, Tokyo, 113, Japan
3. Research Engineer, Nearshore Environment Research Center, 1202 Famille Hongo Building, 1-20-6 Mukohgaoka, Tokyo, 113, Japan

The authors therefore initiated a series of laboratory investigations using an oscillatory flow tank to isolate the fundamental aspects of sheet flow. In this paper, the main results on the items listed below will be discussed. These are:

1) Criterion for inception of sheet flow,

2) Sediment concentration in the layer moving as sheet flow,

3) Advection speed of sand particles in the moving layer, and

4) Sediment transport rate under the sheet flow condition evaluated on the basis of items 2) and 3).

EXPERIMENT LAYOUT

The experiments were performed in an oscillatory flow tank. There are two reasons for using such an apparatus. First, sheet flow occurs in the surf zone where the environmental conditions are difficult to control, and where the fluid flow is complicated. Secondly, in order to produce sheet flow on a horizontal bed while at the same time avoiding the complication of wave breaking, a very large flume would be necessary. Therefore, it is convenient to use a tank such as ours in which the amplitude (max. 75 cm) and period (1 to 10 s) of the oscillatory flow can be varied over a wide range covering the scale of the prototype.

Figure 1 shows a schematic diagram of the oscillatory flow tank and the various measuring apparatus used. The oscillatory flow is produced by a piston. The flow section is 25 cm wide, 25 cm high and 200 cm long. Sediment materials were placed along the bottom plane of the test section as described in the next paragraph. The period, amplitude, and mean velocity of the oscillatory flow in the test section were evaluated from readings of a wave gage at the vertical riser of the oscillatory tank, as shown in Fig. 1. A motor-driven 35 mm camera was used to record the particle concentration in the upper layer of the flow, and to determine the particle advection speed throughout the flow. An electro-resistance sediment concentration detector was used to measure the concentration in the lower layer of the sheet flow. The instruments and techniques are discussed in detail as they appear below.

Figure 2 shows two types of setups in the test section. A vinyl chloride plate was introduced to reduce end effects. For the heavier materials, the test section was narrowed to obtain a higher flow velocity. Six kinds of bed material were used to study the inception criterion; three consisted of natural sands, and three of plastic particles. The characteristics of the test materials are given in Table 1. For studying the transport rate, only sand (1) in Table 1 was used (Toyo-ura standard sand, median grain size 0.2 mm).

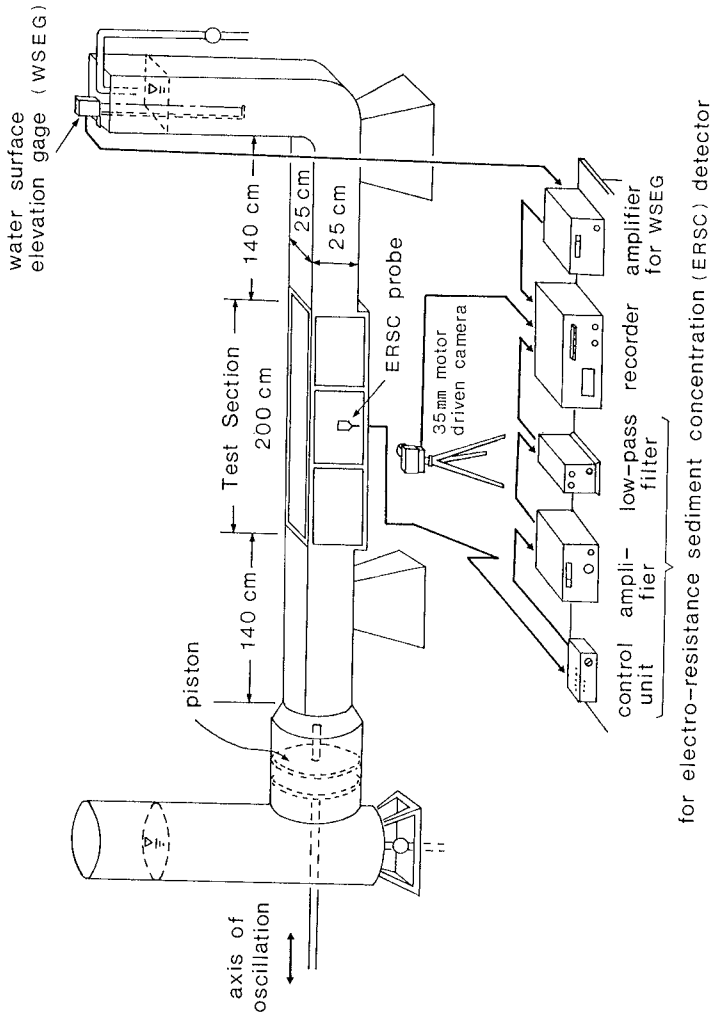

Fig. 1 Oscillatory flow tank and measuring apparatus.

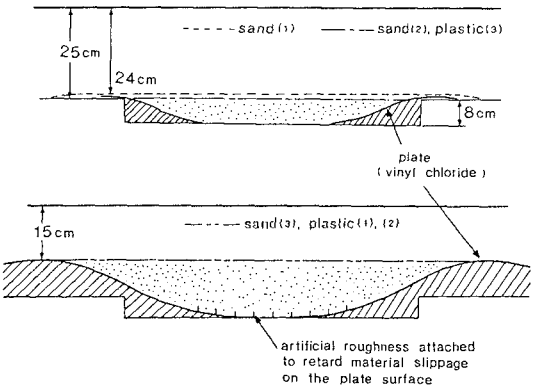

Fig. 2 Setting conditions of material.

TABLE 1 Characteristics of material used.

Material	d (cm)	ρ_s / ρ	α_1 (deg)	α_2 (deg)	w (cm/s)
Sand (1)	0.02	2.66	37.0	24.4	2.6
Sand (2)	0.05	2.66	35.9	26.2	6.5
Sand (3)	0.07	2.66	34.4	27.8	9.8
Plastic (1)*	0.2	1.42	36.9	24.4	11.8
Plastic (2)*	0.4	1.18	36.2	20.8	9.4
Plastic (3)	0.03	1.56	22.4	13.9	1.8

d : grain diameter, ρ_s / ρ : specific gravity
α_1 : angle of repose underwater (bed tilted from horizontal)
α_2 : angle of repose underwater (setting naturally)
w : fall velocity

* cylindrically shaped

CRITERION FOR INCEPTION OF SHEET FLOW

A series of runs was carried out under various flow conditions to determine the inception of sheet flow. The inception criterion was visually defined as the initiation of the plane-bed mode by two procedures. The first was to increase stepwise the amplitude of the flow velocity by reducing the period of oscillation while holding the horizontal amplitude of the piston constant. In this process, the generation, development, and disappearance of bed ripples were visually observed. The second procedure was to decrease the amplitude of the flow velocity from the already existing condition of sheet flow. During the latter process, the regeneration of bed ripples was observed. Figure 3 shows sample results. The horizontal and vertical axes in this diagram are the near-bottom orbital amplitude, and the period of oscillatory flow, respectively. It is seen that the two procedures give essentially the same inception criteria, and that, therefore, sheet flow can be detected fairly precisely.

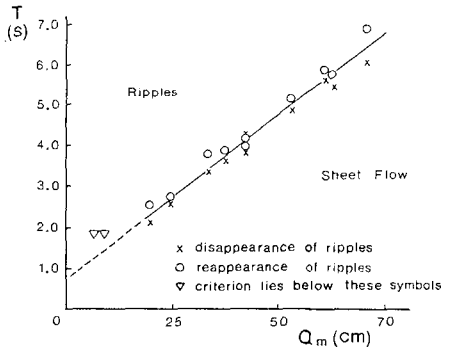

Fig. 3 Experimental results for criterion of sheet flow (sand (1)).

As far as the authors can determine, three criteria for the inception of sheet flow have been reported (Manohar, 1955; Komar and Miller 1974; Dingler and Inman, 1976). These are summarized in Table 2, for which the expression given for Manohar's criterion was derived by the authors on the basis of the original form. In Table 2, $\hat{U}$ is the maximum orbital velocity, $s = (\rho_s - \rho)/\rho$, ρ_s and ρ are the densities of the sand and fluid respectively, d is the grain diameter, ν is the kinematic viscosity of the fluid, g is the gravitational acceleration, and f_w is the wave friction coefficient of Jonsson (1966).

TABLE 2 Criteria for inception of sheet flow.

Manohar (1955)

$$\Theta \equiv \frac{\hat{U}^2}{sdg} = \frac{2 \times 10^3}{\sqrt{\hat{U}d/\nu}}$$

Komar · Miller (1974)

$$\Psi \equiv \frac{f_w \hat{U}^2}{2sdg} = \frac{4 \cdot 4}{(\hat{U}d/\nu)^{1/3}}$$

Dingler · Inman (1976)

$$\Theta = 240$$

Figure 4 gives a comparison of the criteria of Manohar (1955) and of Dingler and Inman (1976) with the present data and with Manohar's data obtained using an oscillatory plate. The vertical and horizontal axes are the non-dimensional parameters, Θ, and the Reynolds number based on the grain size, Re, respectively. From this figure it is seen that Dingler and Inman's criterion is likely to give a rough estimate of the criterion for inception of sheet flow. Manohar's criterion is seen to describe the data well except for those data pertaining to the cylindrically-shaped plastic particles (open triangles at upper right of Fig. 4; plastic (1) and (2), Table 1).

Figure 5 gives a comparison of Komar and Millers' (1974) criterion with the laboratory data, where the vertical and horizontal axes are, respectively, the Shields parameter Ψ and the Reynolds number based on the grain size, Re. In this diagram, Manohar's (1955) data were plotted together with the present data for reference. In general, Komar and Miller's criterion is seen to fairly well describe the trend of the experimental results. The data for sand (1) indicates a tendency for the inception criteria to level off at the lower Reynolds numbers, which is not reproduced by the expression of Komar and Miller. Although it appears from the present experimental results that the criterion of Manohar (1955) is somewhat superior to that of Komar and Miller, we must reserve judgement until more data are available.

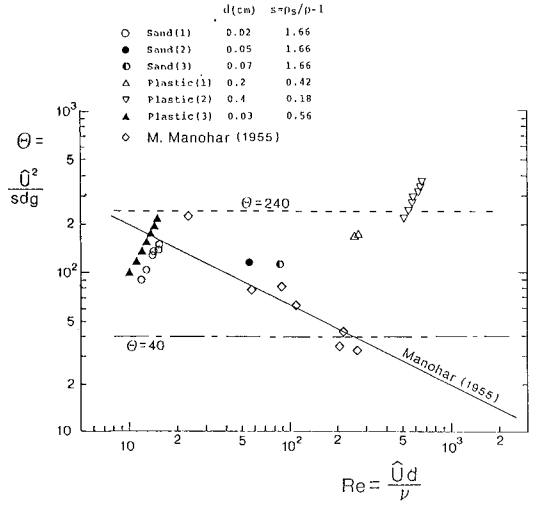

Fig. 4 Criterion for inception of sheet flow (Θ ~ Re).

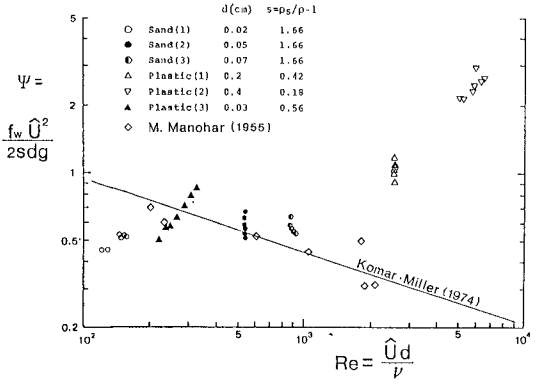

Fig. 5 Criterion for inception of sheet flow (Ψ ~ Re).

The main reason for the apparently anomalous results with the cylindrical plastic particles is that these particles did not move as easily as the other (spheroidal) particles. It can be concluded that the criterion for the inception of sheet flow is closely related to the shape of the sediment particles. More data are needed to determine an appropriate criterion for inception of sheet flow for odd-shaped particles.

SEDIMENT CONCENTRATION IN SHEET FLOW

Sediment Concentration Measuring Techniques

In order to measure the concentration of suspended sediment produced by wave action, photoelectric concentration meters are usually employed. However, this type of meter can not be applied to measure the sediment concentration in the sheet flow moving layer, because 1) the sediment concentration is too high to be measured by conventional apparatus, and 2) the meter itself disturbs the flow. Therefore, measurements were made employing a photographic technique and a newly developed electro-resistance type sediment concentration meter.

A photographic technique was used to measure the suspended sediment concentration in the upper layer. As shown in Fig. 6, a copper plate (0.1 mm thick, 1 cm wide and 20 cm long; painted black) was placed vertically and parallel to the flow direction, at a distance of 1 cm from the inside of the glass wall of the oscillatory tank. Successive pictures of sand particle movement during oscillatory flow were taken at certain intervals for 15 to 20 frames over the flow period using a motor-driven camera and a stroboscopic lamp. The sand particles passing through the 1 cm-wide section between the copper plate and glass wall were counted on the pictures.

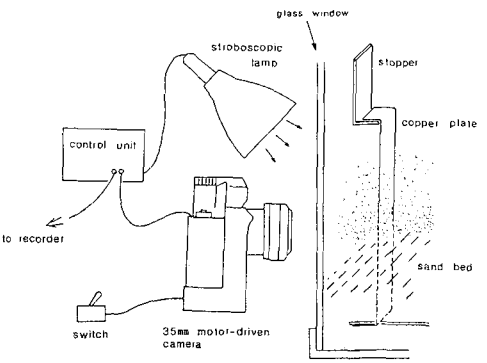

Fig. 6 Experimental arrangement for measuring grain movement in upper layer.

In the vicinity of, or inside the moving layer of sheet flow, the sediment concentration is extremely high and therefore a special measuring device was developed for the present investigations. The measurement principle is based on the fact that the electrical resistance of a water/sand mixture is a function of the concentration of sediment particles. A schematic of the measurement device is given in Fig. 7. In order to calibrate the instrument, a cylindrical tank (diagrammatically shown in Fig. 8) was used. This calibration tank is suitable for generating a uniform and constant suspended sediment concentration. The concentration can be varied over a wide range.

A typical calibration curve of the instrument is given in Fig. 9, where the horizontal axis C' is the relative volumetric concentration defined as C' = 0 for water only, and C' = 1.0 for sediment settled in still water. The vertical axis is the ratio between the output voltage V for a certain value of C', and the voltage V_o for C' = 1. The linearity of the calibration curve is adequate to measure the sediment concentration over a wide range of concentration. Another advantage of the device is the small size of the sensor, which minimizes disturbance of the flow field.

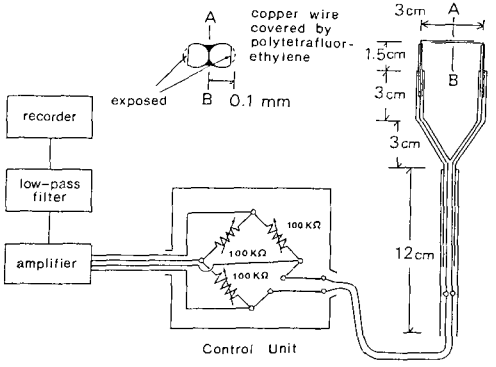

Fig. 7 Electro-resistance type sediment concentration meter.

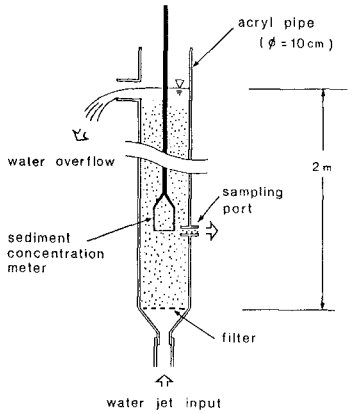

Fig. 8 Calibration apparatus for sediment concentration meter.

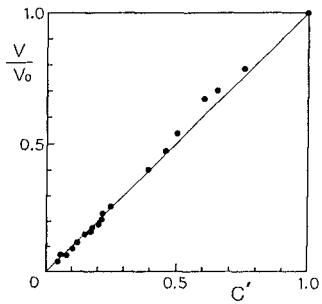

Fig. 9 Calibration curve for electro-resistance type sediment concentration meter.

Measured Concentration

Table 3 indicates the eight oscillatory flow conditions tested which produced the sheet flow regime in the bed material. The data obtained using the photographic technique will first be presented. This concerns the sediment concentration in the upper layer. Figures 10(a) and 10(b) exhibit some vertical distributions of sediment concentration under constant orbital amplitude and constant velocity amplitude, respectively. The vertical axis, y, is the elevation above the surface of the initial bed. The horizontal axis, $\bar{C}_N$, is the number of sand particles contained in a rectangular body of water with a horizontal cross section of 1cm by 1cm and a vertical length of 1 mm, averaged over one oscillatory cycle. Here the value $\bar{C}_N = 1.0$ corresponds to a mass concentration of 167 mg/liter.

From Fig. 10(a), it is seen that the suspended sediment concentration increases with increase in the velocity amplitude (that is, an increase of bottom shear stress) under the condition of constant orbital amplitude. Figure 10(b) indicates that the elevation which the sediment particle reaches above the bed decreases with a decrease in the oscillation period under the condition of constant velocity amplitude. This result is believed due to the fact that for shorter periods, the flow reverses direction before turbulence is fully generated along the bottom. The vertical distribution of the concentration of the sediment located higher than 7 mm above the bed is expressed well by an exponential function of distance from the bed.

TABLE 3 Experimental conditions.

Case	Half-excursion length, a_m (cm)	Period, T (s)	Maximum orbital velocity, $\hat{U}$ (cm/s)
1-1	72	3.6	127
1-2		4.2	108
1-3		4.8	95
1-4		5.4	87
1-5		6.0	76
2-2	58	3.4	108
3-2	44	2.6	
4-2	34	2.0	

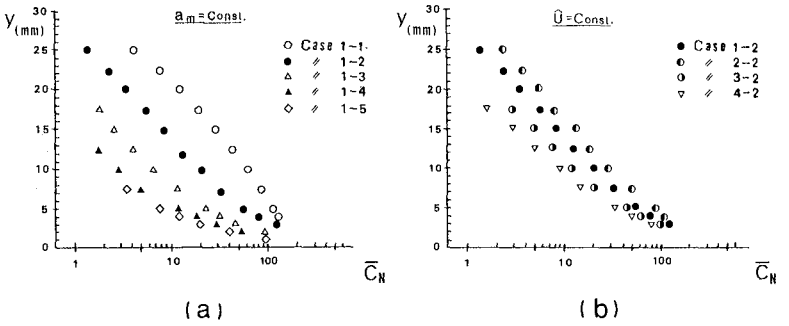

Fig. 10 Distribution of average concentration in upper layer.

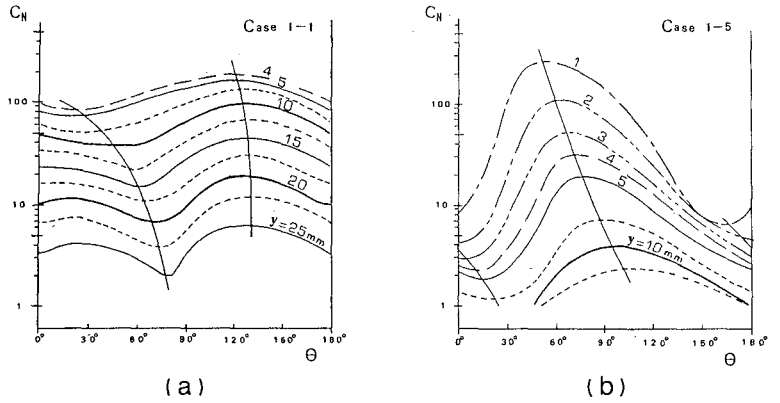

Fig. 11 Variation of concentration with phase angle.

Time variations of sediment concentration at selected elevations for two particular cases are shown in Figs. 11(a) and (b). Here the vertical axis, C_N, is the number of sediment particles in a certain volume of water, and the horizontal axis, θ, is the phase of oscillatory flow. The phase $\theta = 0^\circ$ corresponds to the time when the velocity changes direction, and $\theta = 90^\circ$ corresponds to the time when the velocity reaches a maximum. Figure 11(a) is a typical result, while Fig. 11(b) is atypical. The trends of the phases of maximum and minimum concentration are indicated by solid lines. On the basis of the data of all eight cases shown in Table 3, it can be concluded that the phase of the sediment concentration in the vicinity of the bed is almost equal to that of the oscillatory flow velocity, although the phase of concentration tends to move ahead as the flow period increases. The phase difference between the sediment concentration and the oscillatory flow velocity increases with increase in elevation.

Now, the sediment concentration in the moving layer of sheet flow will be considered. Figure 12(a) shows the vertical distributions of sediment concentration at various phases for Case 1-1, measured by the electro-resistance concentration meter. According to these plots, the sediment concentration changes considerably in the layer spanning 3 to 5 mm above and below the location of the initial bed surface. The minimum sediment concentration above the initial bed surface occurs a little after the phase of $\theta = 0^\circ$ (minimum flow velocity); the maximum concentration occurs at approximately $\theta = 90^\circ$ (maximum velocity).

The curves of sediment concentration at the phases of 90° and 120° have an inflection point in the layer just below the initial bed level. This phenomenon is presumably caused by strong vortices appearing near the bed. It can be observed from Fig. 12(a) that sand particles lifted up at the phase of high velocity fell to the bottom during the stages of velocity deceleration.

ADVECTION SPEED OF SAND PARTICLES

The advection speed of the sand particles was measured under the same conditions as those of the sediment concentration measurements. A number of pictures were taken at certain constant intervals with various shutter speeds by using a motor-driven 35mm camera. The advection speed of the moving particles was determined by tracing individual particles on successive frames.

In the upper layer, the camera was focused on interior particles to eliminate the influence of the glass wall. In the lower layer, because of the extremely high concentration, the advection velocity could not be obtained by direct observation of individual particles.

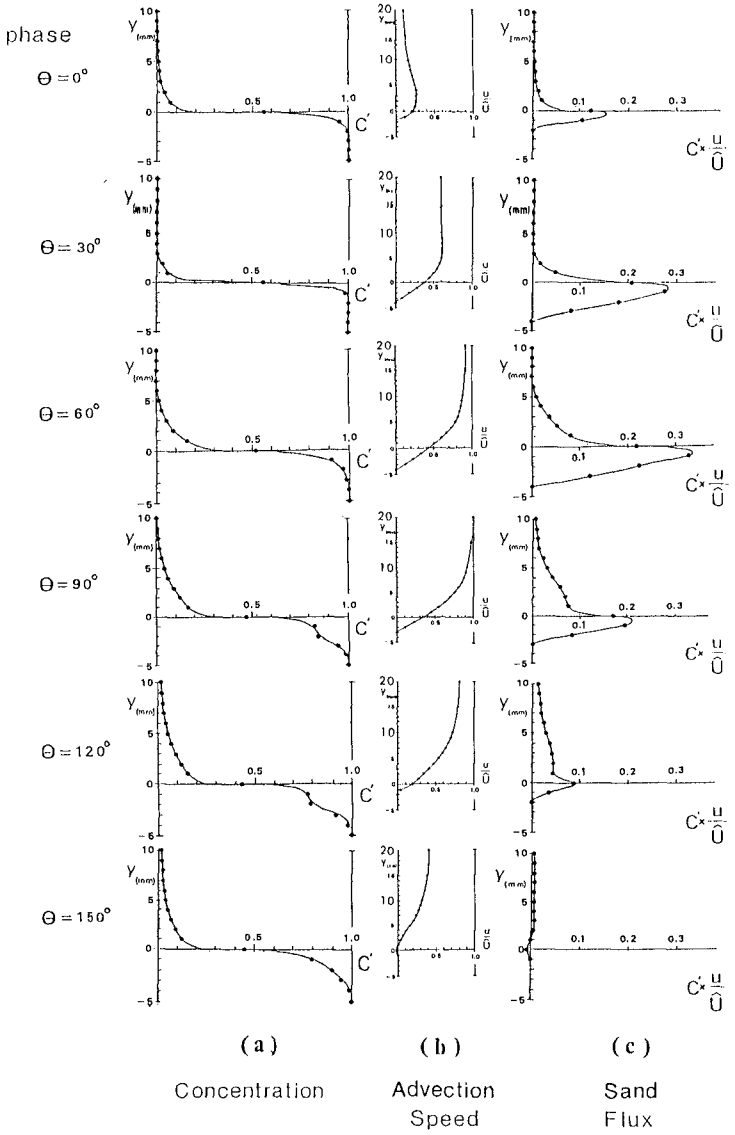

Fig. 12 Vertical distribution of concentration, advection speed, and sand flux.

Therefore, an extrapolation procedure was used as follows: 1) Amplitudes of motion down to an elevation of 2 mm from the initial bed were obtained by means of the normal camera technique. The depth at which the amplitude became zero was determined by measuring the position of the electro-resistance probe at maximum concentration (no sand dilation) for given flow conditions. The vertical distribution of amplitude in the lower layer not amenable to direct measurement was then estimated by curve fitting. 2) The phase of the motion during the time which the sand was assumed to move was determined by using the same photographic technique as described above, but using more readily visible plastic particles. 3) The advection velocity in the lower layer was then calculated using the amplitudes and phases derived by the above separate procedures.

Figure 12(b) shows curves of the vertical distribution of advection speed u normalized by the amplitude of the main flow velocity $\hat{U}$, at various phases in a half cycle of the oscillatory flow. It is seen that the vertical distributions of advection speed of sediment particles are quite similar to those of water particle velocity inside the oscillatory boundary layer flow: the sand advection speed in the upper layer ($y \geq 20$ mm) is almost always equal to the main flow velocity, whereas it decreases in amplitude and advances in phase with decrease in elevation. The gain in phase approaches about 45° at the lowest elevation of the moving layer, corresponding to that of the laminar boundary layer flow velocity. However, the advection speed in the lower layer does not vary sinusoidally in time, but changes intermittently, having significant magnitude only over a limited time duration at certain phases of the oscillatory cycle. This is due to the intense frictional forces between sediment particles.

SEDIMENT TRANSPORT RATE

The flux of sediment concentration is defined as the product of the concentration C' and the advection speed u at each elevation and each phase. Figure 12(c) gives the vertical distributions of the concentration flux (divided by the amplitude of main flow velocity, $\hat{U}$) thus obtained at the various phases for the present case. It is realized from this figure that the moving layer in the vicinity of the initial bed surface with a thickness of the order of 10 mm contributes significantly to the sediment transport rate.

The instantaneous sediment transport rate through a vertical cross-section was evaluated from the verical integration of concentration flux at each phase. Taking the average of the instantaneous transport rate over a half cycle of oscillatory flow yields the mean transport rate for each experimental case. In this way, a total of six data points for the mean sediment transport rate under the sheet flow condition were obtained.

Madsen and Grant (1976) treated bed load movement induced by oscillatory flow and proposed a formulae to relate the nondimensional transport rate Φ to the Shields parameter Ψ, based on a Brown-type formulae of bed load transport rate in a uni-directional flow. The relation is given by

$$\Phi = \frac{\bar{q}_s}{wd} = 12.5\ \Psi^3 \tag{1}$$

where $\bar{q}_s$ is the sediment transport rate averaged over a half wave cycle, w is the fall velocity of the sediment particles, and d is the grain size. The definition of the Shields parameter Ψ is given in Table 2. This relation was found to agree well the experimental data of Kalkanis (1964) and Abou-Seida (1965), obtained using an oscillatory plate moving horizontally in a sinusoidal manner in a still water basin.

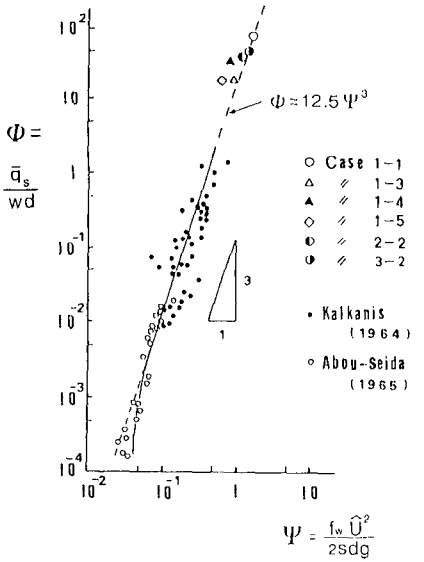

Fig. 13 Relation between non-dimensional transport rate and Shields parameter.

In Fig. 13, the present results, obtained under the sheet flow conditions, are plotted on a figure given by Madsen and Grant (1976). It is seen that the formula proposed by Madsen and Grant fits the present data quite well. However, since the amount of data obtained under the condition of high Shields parameter is scarce, further effort is needed to accumulate more data on the sediment transport rate of sheet flow.

It should be emphasized that the beach configuration is transformed due to the net rate of sediment transport, i.e., the difference between onshore and offshore transport rates. It is clear from Fig. 12 that the magnitudes of the instantaneous sediment flux are significantly different even for the same main flow velocity, depending on whether the flow is at the stage of acceleration or deceleration (compare $\theta = 30^{\circ}$ and 150°, or $\theta = 60^{\circ}$ and 120°). This implies that a more detailed examination of the sediment movement is required in order to establish a transport formula which can estimate the instantaneous or net rate of sediment transport under the asymmetrical variation of flow velocity such as occurs in the surf zone.

CONCLUSIONS

In order to elucidate the fundamental aspects of the sediment transport phenomena under the sheet flow condition, a series of laboratory experiments was performed in an oscillatory flow tank utilizing specially developed measuring devices and techniques. In particular, the electro-resistance type concentration detector was found capable of measuring exceptionally high concentrations which can not be measured by conventional photoelectric concentration meters.

From the experimental results, the following conclusions were obtained:

1) The criteria for the inception of sheet flow given by Manohar (1955), and by Komar and Miller (1974) agree favorably with the laboratory data (for spheroidal particles) in general. However, the shape of the sediment particles seems to exert significant influence on the criterion, as expected.

2) In the range of experimental conditions reported, the thickness of the moving layer of the sheet flow is of the order of 10 mm.

3) The data for the mean rates of sediment transport under the sheet flow condition agree with a bed load relation given by Madsen and Grant (1976). The upper limit of validity of this expression was thus extended.

4) Since the instantaneous transport rate differs between accelerating and decelerating phases of motion, further study is necessary to establish a formula for the net transport rate.

ACKNOWLEDGEMENTS

The authors appreciate the assistance of Dr. N. C. Kraus of the Nearshore Environment Research Center in the preparation of the manuscript. This work was partially supported by a grant in aid for scientific research by the Ministry of Education, Science and Culture, the Japanese Government.

REFERENCES

Abou-Seida, M.M.: Bed load function due to wave action, Univ. of Calif., Berkeley, Hyd. Eng. Lab, HEL-2-11. 78p., 1965.

Dingler, J.R. and Inman, D.L.: Wave-formed ripples in nearshore sands, Proc. 15th Coastal Eng. Conf., ASCE, pp. 2109-2126, 1976.

Jonsson, I.G.: Wave boundary layers and friction factors, Proc. 10th Coastal Eng. Conf., ASCE, pp. 127-148, 1966.

Kalkanis, G.: Transportation of bed material due to wave action, Coastal Eng. Res. Center, Tech. Memo. No. 2, 38p., 1964.

Komar, P.D. and Miller, M.C.: The initiation of oscillatory ripple marks and the development of plane-bed at high stresses under waves, Jour. Sed. Petrology, Vol. 45, No. 3, pp. 697-703, 1974.

Madsen, O.S. and Grant, W.D.: Quantitative description of sediment transport by waves, Proc. 12th Coastal Eng. Conf., ASCE, pp. 1093-1112, 1976.

Manohar, M.: Mechanics of bottom sediment movement due to wave action, Beach Erosion Board, Tech. Memo. No. 75, 121p., 1955.

MEASURED AND COMPUTED COASTAL OCEAN BEDLOAD TRANSPORT

Alan William Niedoroda[1], Chen-Mean Ma[2]
Peter A. Mangarella[3], Ralph H. Cross, III[4]
Scott R. Huntsman[5], and Donald D. Treadwell[6]

ABSTRACT

A comparison is made between the measured infilling of two test pits off the coastline of San Francisco and predictions using a coastal bedload transport model. The model, based on the work of Madsen and Grant (1967), relates the bedload transport to the bottom shear stress through an empirical relationship based on laboratory experiments. The bottom shear stress is estimated from the bottom currents created by waves and low frequency currents. The model applies beyond the breaker zone in contrast to littoral transport.

The test pits, dredged as part of the Southwest Ocean Outfall Project for San Francisco, were located 1.6 km (1 mi) and 3.2 km (2 mi) offshore in 13 m (42 ft) and 16 m (53 ft) of water. The depth of the pits relative to the natural seabed was about 8.4 m (25 ft). The comparison was conducted for a period up to 2 months in the fall of 1978.

The paper discussed the quality and scope of available data required as input to the model and shows how regional wave data were transformed to augment local measurements. Uncertainties in model results stemming from limitations in the input data are presented. With suitable adjustment of the scale of the gravitational term in the expression for the Shields parameter, overall agreement between computed and measured bedload was accomplished within the limits of accuracy of the bathymetric surveys. A sensitivity analysis of selected input conditions and coefficients was also conducted.

---

(1) Dames & Moore, Suite 200, 4321 Directors Row, Houston, Texas, 77092
(2) Woodward-Clyde Consultants, 7550 Westview Drive, Houston, Texas, 77055
(3) Woodward-Clyde Consultants, 100 Pringle Avenue, Walnut Creek, California, 94596 [Member ASCE]
(4) Woodward-Clyde Consultants, 5120 Bulter Pike, Plymouth Meeting, Pennsylvania, 19462 [Member ASCE]
(5) Department of Civil Engineering, University of California at Berkeley, Berkeley, California, 94720 [Assoc. Member ASCE]
(6) Woodward-Clyde Consultants, 100 Pringle Avenue, Walnut Creek, California, 94596 [Member ASCE]

INTRODUCTION

Over the past two decades there has been a marked increase in construction of facilities in the coastal zone and continental shelf. In engineering such facilities, the effects of marine bedload sediment transport on the facility or, conversely, the effects the facility will have on bedload transport are often important. For example, where trenching of the sea floor is needed for installation of large outfalls, cooling water intakes, or other structures, it is often necessary to estimate the amount of overdredging and the time frame for construction as determined by the local rate of bedload transport and siltation. In other cases, it is important to estimate the probable effects on local shoaling or scour caused by large offshore structures such as artificial islands and breakwaters. Where new navigation channels are planned, it is advantageous to examine various geometries of the channel and associated turning basins to minimize future maintenance dredging requirements. In light of these needs, various methods have evolved to evaluate marine bedload transport and siltation during the engineering phases of projects.

The purpose of this study to evaluate computed siltation rates, due to marine bedload transport, through comparison with measured data. The data available was typical of the quality available for engineering studies, and, as such, was not of optimum quality. Thus, this is a practical test of the present state-of-the-art for computing siltation rates.

The field data for this study was collected as part of the Southwest Ocean Outfall Project (hereafter SWOOP). The SWOOP project is part of a series of projects comprising the Clean Water Program of the City and County of San Francisco, California. The objective of the Program is to provide an efficient means for collecting and disposing both sanitary and storm wastewater flows resulting from the present and future needs of San Francisco. The Southwest Ocean Outfall will disperse these wastewaters at diffuser sections located well offshore in the Pacific Ocean. The outfall, a single conduit with an inside diameter of 3.7 m (12 ft), will be embedded throughout its length in a trench excavated as much as 8.4 m (25 ft) below the existing sea floor.

In order to evaluate some of the marine soil behavior, monitor marine siltation, and judge the effectiveness of floating marine equipment in the wave and current environment of the site, a Test Pit Program was conducted. Two test pits were excavated by a derrick barge to depths of approximately 8.4 m (25 ft) below the existing sea floor at locations 150 m (500 ft) south of the proposed outfall centerline. Test pit numbers 1 and 2 were located approximately 1.6 km (1 mi) and 3.2 km (2 mi) offshore in water depths of about 13 m (42 ft) and 16 m (53 ft) below mean lower low water (MLLW), respectively. Detailed bathymetric surveys were conducted on an approximately bi-weekly interval. Waves and near bottom currents were continuously measured in-situ. Figure 1 shows the location map of the project, and Figure 2 is a more detailed project map showing the test pits and oceanographic monitoring stations.

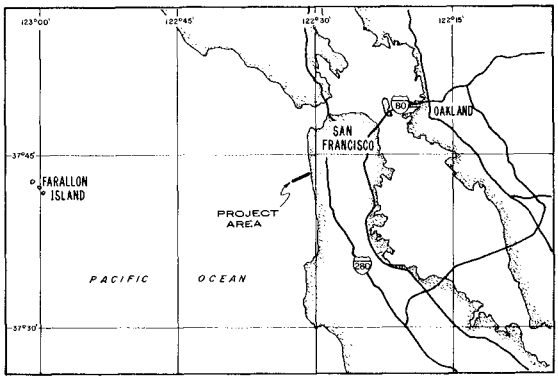

FIGURE 1

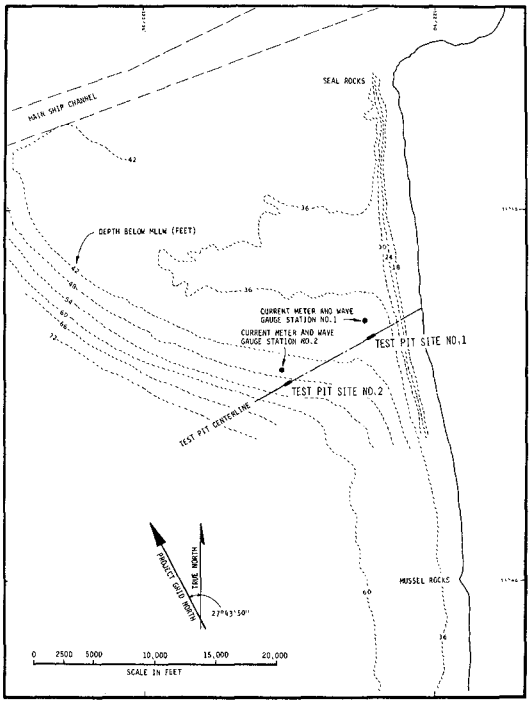

FIGURE 2

The original intent of the test pit program was to relate the measured siltation rates to the wave and current conditions in an empirical manner. However, the availability of this rather unique data set was an incentive to test a deterministic methodology to calculated siltation rates. The method developed by Madsen and Grant (1976) was selected as the basis for a computer program to calculate marine bedload transport and siltation within the test pits from the wave, current, and sediment data available from the SWOOP test pit program.

MEASUREMENTS

The measurements conducted during the SWOOP test pit program included waves, bottom currents, and sea floor sediment samples in addition to detailed bathymetric surveying. The methods, equipment, and techniques employed to make these measurements are discussed below.

Bathymetric surveying was conducted from the 20 m (60 ft) survey vessel POLARIS, using Raytheon Model DE719 survey fathometer with a hull-mounted, narrow-beam transducer. Horizontal positioning was accomplished with a Motorola Mini-Ranger III navigation system coupled to a data processor, terminal printer, and ship track plotter. Detailed surveys of the test pits were run using a grid with line spacing of about 24 m providing both primary and tie-lines. Tide height corrections were initially based on data collected visually from a shore station. Later, predicted tide levels for San Francisco was used as the two were well correlated. Considering all factors, such as position fixing, sea and swell, tides and variations in seawater sound velocity, the absolute accuracy in resolving depth was approximately ±0.3 m (±1.0 ft). Greater accuracy was obtained for differential depths between successive surveys, e.g., accuracy in resolving cut and fill at each test pit was approximately ±0.15 m (±0.5 ft) (Murphy, et al., 1979).

Bathymetric surveys were conducted at approximately two-week intervals from 4 September to 16 November 1978. The results of surveys conducted on 15 September, 4, 19 and 31 October and 16 November were used in the present study.

Seventy-seven sediment samples were obtained from the dredge clamshell, and 15 directly from within the test pits by SCUBA divers. SCUBA dives were made on September 5, September 20, and November 15, 1978. Thirty-nine of the 77 samples collected aboard the derrick barge and all of the diver-collected samples were seived to determine grain size distribution.

Two in-situ oceanographic instrument moorings were placed approximately 305 m (1,000 ft) north of the test pits at water depths of 13 m (41 ft) and 16 m (52 ft) below MLLW. An ENDECO Model 105 recording current meter was located 3 m (10 ft) above the sea floor on each mooring, and set to monitor at 30-minute intervals. Interocean Model WG/100 analog recording pressure transducers were incorporated in each mooring to measure waves. These operated only intermittently, and their data were of limited use to this study.

The current meters and wave gauges were initially installed on 15 August 1978, serviced on 20 September and 28 October and recovered on 15 November 1978, yielding a continuous record of currents for a period of 93 days. Due to numerous electrical and mechanical failures, only 21 days of data from one of the wave gauges was useful.

The lack of measured onsite wave data was partially offset by obtaining NOAA visual wave observations from Southeast Farallon Island, approximately 40 km (25 mi) offshore of the site (Figure 1). These observations consisted of swell height, period and direction, sea height and direction, and wind speed and direction, thrice daily. The steep offshore slopes around this island and its position well seaward of the project location made these visual observations reasonable estimates of the general sea and wind conditions.

DATA ANALYSIS

The data collected were analyzed both for engineering results and for the specific research aims of the present study, as discussed below.

The bathymetric records were reduced and corrected for tidal height by hand, and plotted according to the navigation data. In preparing successive bathymetric charts of each test pit, it was observed that the sea floor depths and morphologies beyond the edge of the test pits did not change significantly. Therefore, only changes in the shape and depth within the test pits were noted on subsequent charts. Examples of these charts are shown in Figures 3 and 4.

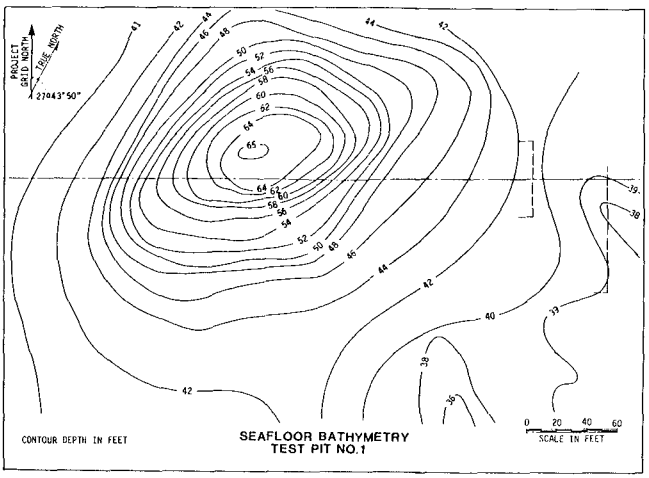

FIGURE 3

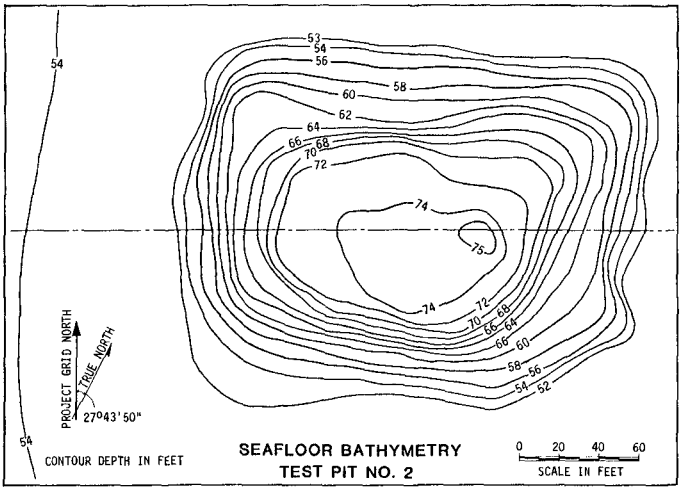

FIGURE 4

Sediment samples were analyzed using standard seiving procedures. The range of results are shown on Figure 5. Two shadings are used on this figure. One defines a band of gradation curves for the dredged sediments, and the other, gradation curves for sediments recovered by divers during the monitoring program, representing material recently deposited within the test pit. In general, both were very similar.

The film records from the current meters were processed to produce digital time series of speed and direction. Figure 6 shows a progressive vector diagram of currents at Test Pit No. 2 from the period 28 October through 15 November 1978. The figure shows net northeasterly drift with tidal oscillations.

As the field experiments were not planned to support a detailed sediment transport study, data on the vertical structure of the benthic boundary layer were not collected. For the purposes of the calculations, it was assumed that the current meters measured flow near the top of the benthic boundary layer. Data from other more detailed studies (Niedoroda, 1980; Niedoroda and Swift, 1981) suggest that 3 m is a reasonable estimate of the average boundary layer thickness at these distances from the shore. The method for computing marine bedload transport, described later, requires the depth averaged flow velocity over the thickness of the benthic boundary layer. In the absence of more detailed data, this was taken to be 80 percent of the measured values.

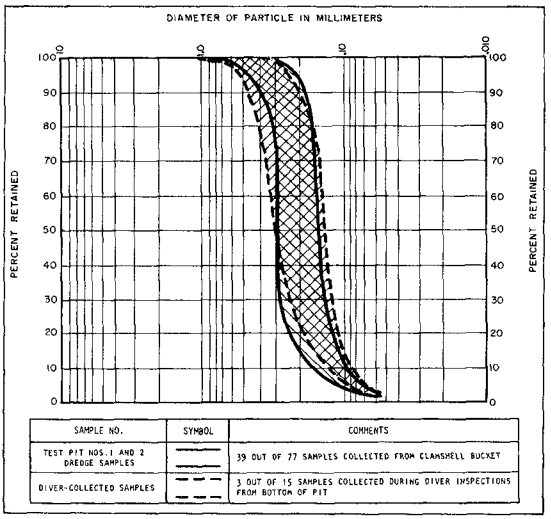

FIGURE 5

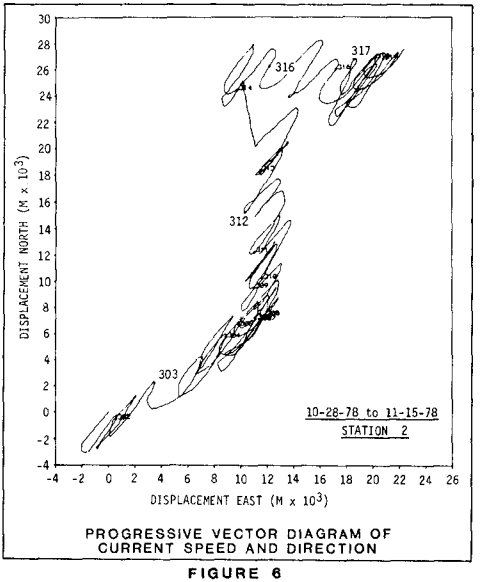

FIGURE 6

The primary wave data used in this study came from the NOAA visual observations recorded at Southeast Farallon Island, 31 km (19.5 mi) south of Pt. Reyes and 42 km (26 mi) west of San Francisco; near the edge of the continental shelf. Refraction drawings show essentially no modification of wave heights of open ocean waves arriving there. The other Farallon Islands to the NNW are too small and distant to affect the waves from that direction. With care, it should be possible to make valid incident wave observations from Southeast Farallon.

The data from South Farallon Island were transferred to the test pit sites by the following procedure. As part of the previous coastal engineering investigation, a series of refraction drawings using 10 and 12 second wave periods had been generated, and used to evaluate the propagation of directional components of waves from 10 severe storms to the outfall site. Because of the dominance of the partial sheltering influence of Pt. Reyes, the storm waves were divided into directional components. For each storm, the incident height and direction, and the refracted height and direction at the site were found, and the "response curves" of Figure 7 generated. For varying incident wave direction, these curves give both the reduction in wave height and the change in wave direction due to refraction.

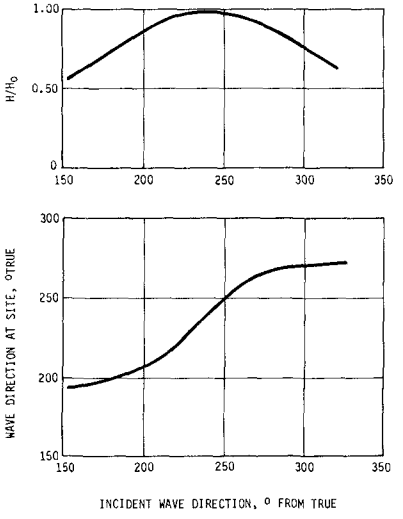

FIGURE 7

The actual location of the site referred to above is about 2.4 km (1.5 mi) west of the offshore test pit (No. 2); corresponding to the location of the outfall diffuser. Results of the wave spreading and refraction analysis at this site were considered representative

because wave heights and directions measured at pits 1 and 2 showed smaller differences than the uncertainty in both the raw data and the refraction analysis.

The response or transfer curves of Figure 7 were applied to both sea and swell. Strictly speaking, this is not correct for the swell, because the curves were generated using a directionally spread wave typical of sea, not the more narrowly spread swell. In this case it was believed important to include the effect of directional spreading, even if slightly overestimated for swell, due to the importance of Pt. Reyes in providing partial sheltering from the predominant NW and NNW sea and swell.

The sediment transport analysis considers the combined effect of currents and one wave train. As both sea and swell were generally present and recorded separately, it was necessary to combine the two. Adding wave energy densities gives the following relationship for the equivalent wave height (H_e).

$$H_e = (H_w^2 + H_s^2)^{1/2}$$

where H_w and H_s are the height of the sea and swell, respectively.

This relationship ignores the effect of wave and swell directional differences on the near-bottom kinematics, but most of the time, the waves and swell were nearly from the same direction (i.e., NNW and NW).

In summary, the quality of the raw wave data, although poor by some standards, was better than that often available for engineering projects. A comparison of the significant wave heights computed by this method from the Southeast Farallon data with data measured at Test Pit No. 1 is given in Figure 8. When the significant wave height

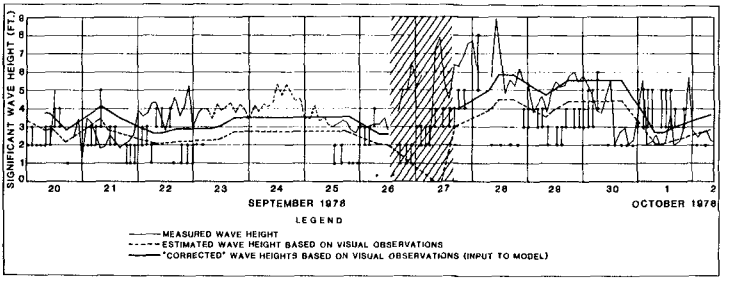

FIGURE 8

as measured (thin, irregular line) was compared to that from the corrected visual observations (heavy, dashed line), it was found that a 30 percent difference existed. This comparison excluded the period from the evening of 26 September to the evening of the 27 September, where the visual wave heights reported are suspect. The visual wave height estimates were thus corrected by a factor of 30 percent and are shown on this figure as a solid, heavy line.

MARINE BEDLOAD TRANSPORT CALCULATIONS

Several methods are available for computing marine bedload transport due to the combined effect of waves and current. The method selected for this study is given by Madsen and Grant (1976). This method was selected because: it incorporated the experimental work done by Jonsson (1966), Kalkanis (1964), Abou-Seida (1965), and several other researchers; the method is relatively straightforward to apply; and the input parameters were available from the field measurements.

The Madsen and Grant (1976) method uses the Einstein-Brown relationship to compute instantaneous bedload transport when the critical Shields parameter for sand entrainment is exceeded. The bottom shear stress formulation is the quadratic stress law where the instantaneous current is the vector sum of the near bottom wave orbital and the depth-mean benthic boundary layer velocities. The drag coefficient is in the form of Jonsson's combined wave-current friction factor.

A computer model was written to apply the method. The computer model used a two-dimensional 20 x 20 grid with 4.6 m (15 ft) spacing between grid points (the square defined by the grid points are referred to as elements) upon which the depths and local wave orbital velocities and near bottom depth-mean currents were specified. The orbital velocities were computed using Airy (linear) wave theory. The magnitude of the bottom boundary layer currents varied with depth to satisfy continuity. It was assumed that the structure of the near bottom flow is large in comparison to the size of the test pits and that no significant flow perturbations (e.g., large scale eddies) developed within the pits. A uniform mean sediment diameter of 0.22 mm was used throughout. A constant bedload flux boundary condition was imposed to eliminate erosion or deposition near the grid boundaries.

The bedload transport calculation was accomplished according to the following scheme. Wave and current data were entered at two-hour intervals. The instantaneous near bottom wave orbital and benthic boundary layer velocities were computed at each grid point for 17 sub-time intervals over a wave period (the near bottom current magnitude was also adjusted for the local depth). During each of the 17 sub-time intervals, the bottom stress (and in its nondimensional form, the Shields parameter) was computed from the resultant current. If the computed Shields parameter exceeded the critical Shields parameter, the instantaneous bedload transport was computed through the Einstein-Brown relationship. Otherwise the transport was set to zero for that sub-time interval.

Once the sediment transport flux at each grid point, for each of the individual sub-time intervals, was computed they were summed over the wave period, then divided by the wave period to determine the time-averaged rate of bedload transport. The calculation was done for all 400 grid points. The sediment continuity equation was then applied to each element to compute the net change in depth over the 2-hour time step. The program then read the wave and current data for the next two-hour interval and the above sequence was repeated.

It is important to note that gravitational effects were included in the Shields parameter in a bottom slope term (see Madsen and Grant, 1976, Appendix I). Madsen and Grant suggest a value of 0.07 for the coefficient in the term, while Fredsoe (1979) suggests a value of approximately 0.1 but points out that its actual value is poorly known. Evaluation of this coefficient was an important outcome of the present study.

In applying the results of the above-described program to the project data a problem arose with respect to defining an undisturbed seabed to serve as the datum for measuring siltation. The computer program showed small but significant erosion around the test pit lips; however, the data from the bathymetric surveys did not indicate any change in sea floor elevation outside of the pit. Therefore, computed erosion of the sea floor outside of the test pits was neglected when comparing the computed and measured values of siltation.

RESULTS

Prior to discussing results, it is important to review sources of error and uncertainty. The successive bathymetric surveys claimed accuracy in differential depth measurements of approximately ±0.3 m, corresponding to a volume difference over the area of siltation in the test pits of approximately 125 m^3 or a total error of approximately 250 m^3 (±) in estimating siltation from successive bathmetric surveys. The time history of infilling rates and associated error bars are shown in Figure 9. Inaccuracies in the wave data have been noted previously. The only complete time series of wave data is the transformed NOAA visual data. When these transformed data were used in raw form, they are identified as Wave Data 1. Where the wave heights have been increased by 30 percent (Figure 7) as previously discussed, they are referred to as Wave Data 2. Furthermore, in some numerical experiments the measured currents were used; whereas in others, depth mean bottom boundary layer current velocity was estimated as 0.8 times the measured current.

Measured and computed siltation rates for Test Pit No. 1 are shown on Figure 9 (the measured values with corresponding error bars). The dashed curve shows computed siltation rates using Wave Data Set 1 and the full value of the measured currents. The dash-and-single-dot curve shows the siltation rate computed using Wave Data Set 2 and the the measured currents. The dash-and-3-dot-curve shows the siltation rates using Wave Data Set 2 and the estimated depth mean value of the near bottom currents. In computing each of these curves, the value of the gravitational constant in the Shields parameter equation was 0.1. From the data shown on this figure it was concluded that Wave Data

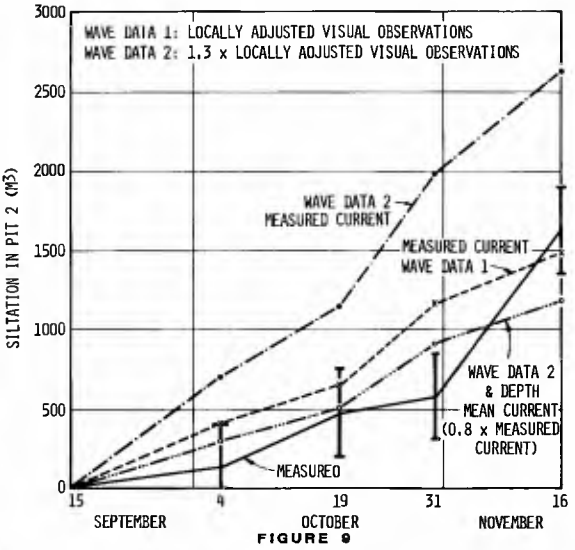

FIGURE 9

Set 2 and the depth mean value of the near bottom currents was most appropriate. Each of these curves could be adjusted by changing the value of the gravitational constant in the Shields parameter equation.

A series of numerical experiments were conducted to evaluate the gravitational constant (c_s) in the equation for the Shields parameter. Perfect overall agreement could be accomplished for measured and computed siltation at Test Pit No. 1 using the value of c_s of 0.123, as shown in Figure 10. It should be noted that computed

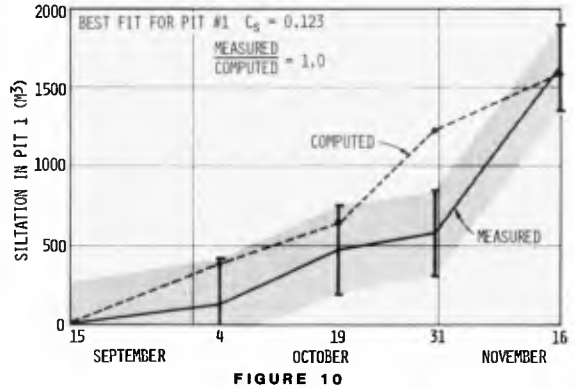

FIGURE 10

values of siltation are higher than those measured at the intermediate surveying dates. However, at two of these three points, the computed values lie within the range of error in the surveyed values. When this value of the gravitational constant in the Shields parameter equation is applied to data from Test Pit No. 2, the amount of siltation was underestimated (Figure 11). In order to accomplish perfect agreement in the overall measured and computed siltation for Test Pit No. 2 a value of c_s of 0.193 was required. In this case, the projected siltation for the intermediate survey data is less than the measured value. Nevertheless, the computed value is within the measurement error.

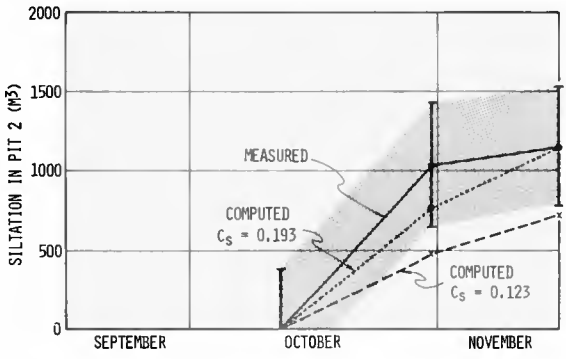

FIGURE 11

Figure 12 shows corresponding data for both Test Pit No. 1 and Test No. Pit 2. A value of c_s of 0.14 yields the best qualitative agreement for the data from both test pits. The difference between measured and computed siltation values is about 14 percent for Test Pit No. 1 and 28 percent for Test Pit No. 2. The value of the coefficient was selected to fit the data at Test Pit No. 1 better than that at Test Pit No. 2 because of the larger number of surveys and longer duration of measurements at Test No. Pit 1. Considering the rather large uncertainties in all of the measurements in this study, as well as those typical of marine engineering studies, the agreement between measured and computed siltation rates is reasonably good.

The computed siltation rates have been shown to depend on wave heights, wave periods, near bottom currents, and the gravitational constant in the equation for the Shields parameter (c_s). A series of numerical experiments were conducted to reveal the sensitivity of the computed siltation rates to variations in these parameters. Figures 13, 14, 15, and 16 show the sensitivity of siltation to variations in wave height, wave period, depth mean near bottom currents, and c_s, respectively. Figure 13 shows that siltation calculations are extremely sensitive to wave height and therefore errors in measurement of wave height significantly affect the reliability of projections. Figure 14 shows a more complex relationship to variations of wave period. If wave periods are higher than their true

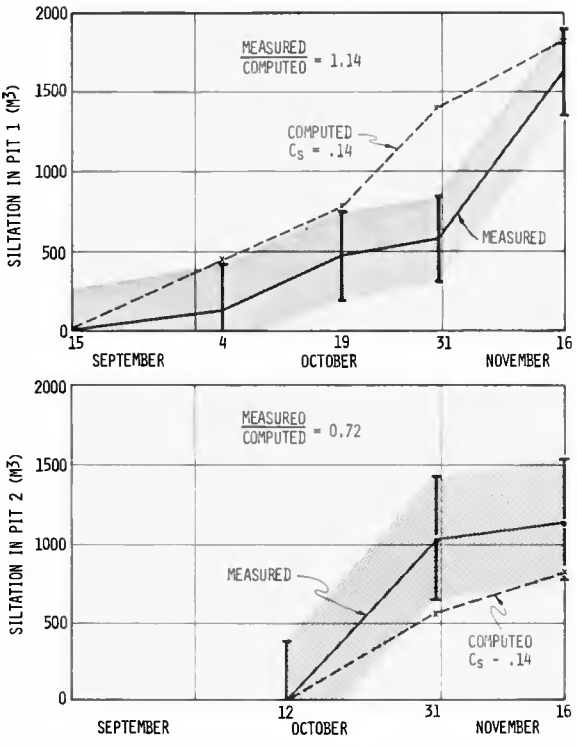

FIGURE 12

value the computed siltation rate decreases because the increase in wave period results in lower wave orbital velocities. If the wave period is decreased from its true value, the computed rate of siltation first increases and then dramatically decreases. This trend illustrates that given the depths of the test pits there is a narrow band of shorter wave periods for which near bottom orbital velocities are increased. Waves with even shorter periods produce lower near-bottom wave orbital velocities due to the depth-decay in orbital velocities. Figure 15 shows that computed siltation rates are less sensitive to variations in the magnitude of depth averaged near bottom currents than they are to waves. Figure 16 shows a linear relationship between the siltation rate and the constant in the gravitational term of the Shields parameter equation.

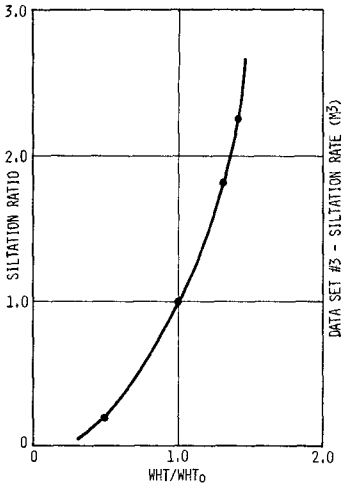

FIGURE 13

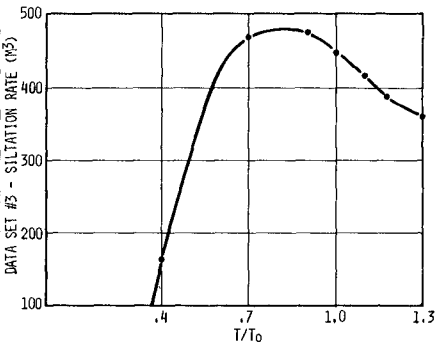

FIGURE 14

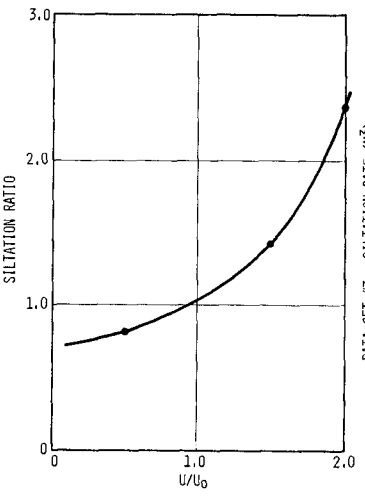

FIGURE 15

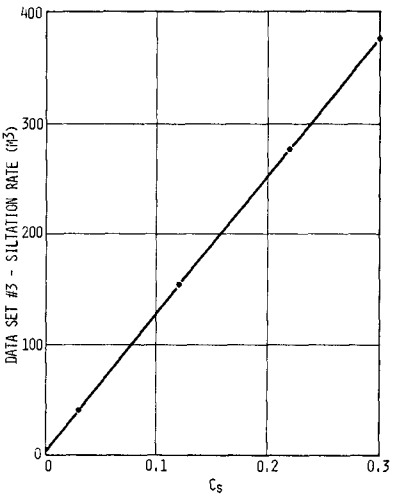

FIGURE 16

CONCLUSIONS

The Madsen and Grant analysis, based in part on laboratory experiments, appears to provide a sound basis for estimating bedload transport caused by the interaction of waves and currents beyond the breaker zone. Input data required of the analysis are commonly collected for coastal engineering projects or developed from other data sources as illustrated herein for the wave data.

The effect of bottom slope was important in this study and was varied (by varying the multiplicative coefficient in the term) to achieve better agreement between the predicted and measured siltation. The value of the coefficient for best fit for net sedimentation in each test pit was 0.12 for Test Pit No. 1 and 0.19 for Test Pit No. 2. The value of the coefficient for best fit for net sedimentation in both pits was 0.14. This value resulted in a maximum difficiency between measured and predicted sedimentation of about 25 percent.

The accuracy of predictions of marine bedload transport and corresponding erosion or siltation is controlled by the accuracy of input parameters in the following order: wave height, current speed and direction, bathymetry, sediment diameter, and wave period.

ACKNOWLEDGEMENTS

The authors wish to express their appreciation for the support provided by Dames & Moore, Woodward-Clyde Consultants, as well as the assistance provided by Ms. Janice Campbell, Mrs. Sandra Jackson, and Mrs. Jessica Knowles.

REFERENCES CITED

Abou-Seida, M.M., 1965, Bedload function due to wave action, Univ. Calif., Berkeley, Hydraulic Engr. Lab., HEL-2-11, 78 pps.

Fredsoe, J., 1979, Natural backfilling of pipeline trenches, J. of Petro. Techn. Oct., p. 1223-1230.

Jonsson, I.G., 1966, Wave boundary layers and friction factors, Proc. 10th Conf. Coastal Engr., A.S.C.E., V. 1, p. 127-148.

Kalkanis, C., 1964, Transport of bed material due to wave action, U.S. Army, C.E.R.C. Tech. Memo. No. 2, 38 pps.

Madsen, O.S. and W.D. Grant, 1976, Sediment transport in the coastal environment, R.M. Parsons Rept. No. 209, 104 pps.

Murphy, G.J., D.D. Treadwell, J.A. Belvedere and C.E. Hervert, 1979, Test pit program for San Francisco's ocean outfall, Proc. Civ. Engr. in the Oceans IV, A.S.C.E., V. II, p. 979-994.

Niedoroda, A.W., 1980, Shoreface-surf zone sediment exchange processes and shoreface dynamics, NOAA Tech. Memo. OMPA-1, 89 pps.

Niedoroda, A.W. and D.J.P. Swift, 1981, Maintenance of the shoreface by wave orbital currents and mean flow: observations from the Long Island coast, Geophys. Res. Letters, V. 8, N. 4, p. 337-340.

FIELD INVESTIGATION OF BEACH PROFILE CHANGES AND THE ANALYSIS USING EMPIRICAL EIGENFUNCTIONS

Hiroshi HASHIMOTO* and Takaaki UDA**

ABSTRACT

In order to investigate the response of beach profiles to incident waves, computations by the empirical eigenfunction analysis proposed by Winant et al. are performed. The analysis of the data obtained at Ajigaura Beach over three years from 1976 to 1979 indicates that beach profile changes due to longshore and onshore-offshore sediment transport are separable by the empirical eigenfunction method. The beach profile changes due to longshore sediment transport has a time lag of 12 weeks with respect to the change of wave direction at Ajigaura Beach. It was found theoretically that this time lag was due to the sand waves propagating in the longshore direction. Regarding as onshore-offshore sand transport, the second eigenfunction is associated with the beach changes due to onshore-offshore sand transport caused by the change of wave height.

I. INTRODUCTION

The movement of beach sand can be decomposed into two directional modes, namely, onshore-offshore movement and longshore movement. These modes respond to temporal changes of wave height, wave direction and longshore current. Accordingly, beach profiles should be analyzed as a time series in order to obtain a detailed understanding.

Winant et al.[1] studied beach changes at Torry Pines Beach by introducing an empirical eigenfunction method. The present authors[2),3),4)] are conducting an on-going study of beach processes at Ajigaura Beach. Field observations have been carried out over seven years at Ajigaura Beach, yielding data of the onshore-offshore profile, wave height and wave direction. In this paper the response of beach profiles to the wave characteristics is investigated using the empirical eigenfunction analysis.

II. METHOD OF FIELD INVESTIGATIONS

Field investigations were conducted at Ajigaura Beach, which lies on the southern part of 10 km long Tokaimura Coast, facing the Pacific Ocean in the central region of Japan, as shown in Fig.1. The sandy beach has a gentle slope of 1:40 and is blocked by a locky headland at the south end. The median grain size of the beach sand is about 0.24

* Chief, Coastal Engineering Division, Public Works Research Institute, Ministry of Construction, Tsukuba, Japan

** Chief Research Engineer, Coastal Engineering Division, Public Works Research Institute, Ministry of Construction, Tsukuba, Japan

mm. The prevailing winds in summer are from the south at Ajigaura Beach, causing southerly wave incidence, whereas the other seasons are characterized by northeasterly winds and the arrival of high waves.

A 100 m long pier was constructed on the beach in July, 1972 to furnish a fixed platform for measurements of waves, nearshore currents and bottom profiles in the surf zone. In February, 1976, the pier was extended to a length of 200 m to allow coverage of the full breaker zone as shown in Fig.2. Field measurements have been conducted at weekly intervals from June 25, 1975 to the present. Measurements were taken of the onshore-offshore profile, longshore profile, longshore current, wave height and wave direction. The onshore-offshore beach profile was measured at three meter intervals over a distance of 240 m as shown in Fig.2. Depth measurements along the pier were taken by sounding lead, while standard surveying method were used shoreward of the pier. Ground elevations along the shore over a distance of 100 m to both sides of the pier were also measured at 10 m intervals. Wave heights were measured at the head of the pier and at Kashima Port located 50 km to the south. The wave direction near the breaking point was observed at weekly intervals using an alidade positioned on top of a 30 m high dune located about 300 m from the shoreline. The longshore current in the surf zone was measured by tracking drifting floats released at three points along the pier.

III. METHOD OF ANALYSIS

The beach profile data are statistically analyzed using empirical eigenfunctions, which give a representation of the bed elevation h(y,t) as a linear combination of products of functions of the distance normal to the beach, y, and functions of time, t.

The data are represented as h_{yt}, where the subscript y is a distance index ranging from 1 to n_y, the total number of measuring points, and the subscript t is a time index from 1 to n_t, the total number of recording times. By the method, the set h_{yt} is expanded as

$$h_{yt} = \bar{h}_y + \sum_k C_{kt} e_{ky} \tag{1}$$

where $\bar{h}_y$ is the temporal mean of the beach profiles. Profile changes at the offshore end are considerably large because the spacial range of profile measurement is insufficient. Therefore, the variation of beach profile subtracted the mean beach profile from the original data is used in order to reduce the influence of end effects. In Eq.(1) the empirical eigenfunctions e_{ky} form an orthogonal set,

$$\sum e_{my} e_{ny} = \begin{cases} 1 & m=n \\ 0 & m \neq n \end{cases} \tag{2}$$

In order to generate these functions, a symmetric correlation matrix, A, is formed with the elements,

$$a_{ij} = \frac{1}{n_y n_t} \sum_{t=1}^{n_t} h_{it} h_{jt} \tag{3}$$

The matrix A possesses a set of eigenvalues λ_k and a corresponding

set of eigenfunctions e_{ky} which are defined by the matrix equation,

$$Ae_k = \lambda_k e_k \tag{4}$$

The time functions, C_{kt}, are then evaluated as

$$C_{kt} = \sum_y h_{yt} e_{ky} \tag{5}$$

IV. ANALYSIS OF ONSHORE-OFFSHORE BEACH PROFILES

The eigenfunction analysis was conducted by using the onshore-offshore data sets collected at Ajigaura Beach from February 5, 1976 to March 23, 1979. The total number of recording times is $n_t = 164$ and that of measuring points $n_y = 80$. The eigenvalues λ_k are given in Table 1. Here, the interpretation of the physical meaning will be given about the first and second eigenfunctions.

The first and second eigenfunctions are shown in Fig.3. The mean profile $\bar{h}_y$ is also shown in the figure. The mean beach profile has a gentle slope of 1:40 and shows scouring around the pier piles. The first eigenfunction e_1 has a positive value over almost the full region of the shore and takes a maximum at about y=160 m. The time function C_1 corresponding to the first eigenfunction and its average over five weeks are shown in Fig.4. Because the eigenfunction e_1 takes a positive value over a broad region of the shore, the increase of the time function C_1 indicates accretion on the beach and its decrease indicates erosion. The time function C_1 increased almost continuously for a year from February, 1976 to February, 1977. This means that the overall accretion occured on the beach during the period. Then, function C_1 decreased from February, 1977 to February, 1978 with the erosion of the beach.

Two causes of such beach changes are 1) longshore sand transport, and 2) onshore-offshore transport. In order to know the dominant cause, the relationship between the time function C_1 and the wave direction was investigated first. Figure 5 shows the temporal changes of wave direction measured counterclockwise from the east. A broken line shows the averaged value over 5 weeks. It should be mentioned that the mean shoreline is oriented at a direction of $8^\circ 54'$. Therefore, the wave direction with respect to the beach normal (β) is given by

$$\beta = \theta - 8^\circ 54' \tag{6}$$

The wave direction has a predominant annual change. In summer waves are from southern direction and northern waves are predominant in the other seasons. The time function C_1 increased almost continuously for a year from February, 1976 to February, 1977. This increase corresponds to the northern wave incidence from November, 1975 to November, 1976 with the time lag of about 3 months. Similarly the decrease of the function C_1 from February, 1977 to February, 1978 corresponds to the southern wave incidence with the time lag of some 3 months.

Oblique wave incidence generates longshore current. Measurements of longshore current were done at weekly intervals from June, 1975 to April, 1976 and from October, 1976 to March, 1979. Mean longshore current velocities averaged over the breaker zone are shown in Fig.6.

A positive velocity indicates a southward current. Northward current prevailed in summer and southward current in the other seasons. The changes of longshore current direction correspond fairy well to the changes of wave direction. It is thus concluded that the variation of the first eigenfunction is due to the longshore sand drift.

Since it is seen that the time function C_1 correlates the wave direction according to Fig.4 and Fig.5, a crosscovariance analysis is carried out between the average over five weeks of the time rate of the time function C_1, that is $\overline{dC_1/dt}$, and wave direction $\bar{\theta}$ in order to know the response of the beach profile to the change of wave direction. The cross-covariance function $R(\tau)$ is defined by

$$R(\tau) = C_{YX}(\tau) / (\sigma_X \cdot \sigma_Y) \tag{7}$$

$$C_{YX}(\tau) = \lim_{N\to\infty} \sum_{s=1}^{N} \{Y(s+\tau) - m_Y\}\{ X(s) - m_X\} \tag{8}$$

where σ_X and σ_Y are the variation of X and Y. m_X and m_Y are the average. The result of the cross-covariance analysis is shown in Fig.7. Here, $\bar{\theta}$ and $\overline{dC_1/dt}$ are substituted into X and Y in Eq.(8), respectively. The number of the total data is N = 163 weeks and the maximum lag τ_{max} = 20 weeks. The cross-correlation coefficient has a positive value when $\tau \geq 0$, and the maximum correlation is obtained at τ=12 weeks, though the coefficient is small because of large fluctuation of variables. Since wave direction has an one-year periodicity and does not have a definite periodic change of 12 weeks, the maximum correlation between $\bar{\theta}$ and $\overline{dC_1/dt}$ at 12 weeks is significant. This means that there is a time lag of 12 weeks between the change of wave direction and the beach profile change. Figure 8 shows the relationship between wave direction $\bar{\theta}$ and $\overline{dC_1/dt}$ with the time lag of 12 weeks. The following relation was obtained by the regression analysis,

$$\overline{dC_1(t)/dt} = -0.42 + 0.067\ \bar{\theta}(t-12) \tag{9}$$

Waves from the north generate the southward sand drift. This littoral drift accumulates over Ajigaura Beach because it is blocked by rocky cliffs at the end of the coast. It can be concluded that the increase of the time function C_1 corresponds to the accumulation caused by the longshore sand drift from the north, and that the eigenfunction e_1 represents the profile changes produced by the longshore sand transport.

The second time function C_2 corresponding to the second eigenfunction e_2 and its average over five weeks are shown in Fig.9. The second time function C_2 has a distinct periodicity. Since such periodic changes seem to correspond to onshore-offshore sand transport, the relationship between significant wave height and the time function C_2 was investigated. Figure 10 shows the weekly maximum value of the daily maximum significant wave height $\bar{H}_{max,max}$ at Kashima Port located about 50 km south of the beach. Broken line indicates averaged wave height over 5 weeks. It may be seen that the change of the function C_2 is correlated with significant wave height. In order to know the relation, a cross-correlation analysis was carried out between $\overline{dC_2/dt}$ and significant wave height $\bar{H}$. For the averaged significant wave height $\bar{H}$, wave heights defined by two different manner were used. One of them is the weekly mean value of the daily maximum significant wave height denoted by $\bar{H}_{mean,max}$ and the other is the weekly maximum of it denoted

by $\overline{H}_{max,max}$. The averaged significant wave height $\overline{H}$ and $\overline{dC_2/dt}$ are substituted into X and Y in Eq.(8), respectively. The obtained cross-covariance coeffecient is shown in Fig.7. Here, wave height data from May, 1977 to March, 1979 are used because of the lack of the measured wave height during March and April in 1977, and then N is equal to 100 weeks. In Fig.7 the maximum of the absolute value of the cross-covariance coefficient is obtained at $\tau = -1$ week when used the weekly mean of the daily maximum significant wave height, $\overline{H}_{mean,max}$, and $R(-1) = -0.47$. It is reasonable to consider that the time lag only becomes positive. Here, the time lag may be approximated to be zero, since the difference of the cross-covariance coefficient at $\tau = 1$ and $\tau = 0$ is small. The existence of the time lag may be attributed to the averaging of the time function C_2 two times. Figure 11 shows the relationship between $\overline{dC_2/dt}$ and $\overline{H}$ with no time lag. The following relation was obtained by the regression analysis,

$$\overline{dC_2/dt} = 1.13 - 0.55\overline{H}_{mean,max} \qquad (10)$$

where $\overline{H}_{mean,max}$ has an unit of meter. It is found that the critical wave height on onshore-offshore sand movement due to the component of the second eigenfunction is given by $\overline{H}_{mean,max} = 2.05$ m. Since the second eigenfunction e_2 takes on a positive value near the shoreline as shown in Fig.3, the increase and decrease of C_2 indicate accretion and erosion, respectively, near the shoreline. Consequently, it is concluded that the second eigenfunction is associated with beach changes due to onshore-offshore sand transport caused by the change of wave height.

Equation (10) expresses the relationship between significant wave height and the time rate of the time function C_2. It is possible to examine the same kind of relation by using wave steepness instead of wave height. Figure 12 shows the cross-covariance coefficient between wave steepness and the time rate of the time function C_2. The maximum of the absolute value of the cross-covariance coefficient is obtained at $\tau = 7$ weeks. This means that the change of beach profile occures seven weeks later compared with the change of wave steepness. However the physical meaning of the relation is not known at the present study.

V. THEORETICAL SOLUTION OF BEACH CHANGES DUE TO LONGSHORE SEDIMENT TRANSPORT

In the previous section it was found that the first time function C_1 had a time lag of 12 weeks compared with the change of wave direction. This time lag is considered to be due to the effect of longshore sediment transport because of the correlation between the first eigenfunction and wave direction. The rate of longshore sediment transport is mainly decided by wave height and wave direction. If the beach exists in an open coast without any obstructions, the beach does not change with the variation of wave direction. However at Ajigaura Beach it is blocked by a rocky headland in the south end. Therefore, it is suggested that large accretion or erosion, and time lag occured due to the movement of sand in the north-south direction.

It may be permissible to use the one-line model to analyze the problem, considering that the first eigenfunction e_1 has a positive value over almost full region of the shore.

The beach change due to the first eigenfunction, h'(y,t), is expressed as

$$h'(y,t) = \bar{C}_1(t)e_1(y) \tag{11}$$

Integrating Eq.(11) with respect to y, then the following relation is obtained,

$$A(t) = \int_0^\infty h'(y,t)dy = \bar{C}_1(t)\cdot\int_0^\infty e_1(y)dy \tag{12}$$

where A is the change of cross sectional area due to the beach change expressed by the first eigenfunction. In Eq.(12) the upper limit of integration is infinite, but it is impossible to integrate $e_1(y)$ from 0 to infinite, since the onshore-offshore profile of $e_1(y)$ is not known when $y \geq 240$ m. However, it may be possible to change the upper limit of the integration approximately from infinite to 240 m, because the function e_1 decreases zero uniformly near y = 240 m. Then, the integration of Eq.(12) gives 22.0 m.

On the other hand, the change of cross sectional area, A, has a linear relationship with the shoreline position as shown in Fig.13. The solid line in the figure is the relation :

$$A = 4.55y_s - 346 \tag{13}$$

where A has an unit of m , y_s is the shoreline position and has an unit of m. According to the above linear relationships given by Eq.(12) and Eq.(13) concerning $\bar{C}_1$, y_s and A, the shoreline position can be used for an independent variable instead of time function $\bar{C}_1$. The equations of one-line model of change of shoreline position is expressed by

$$\frac{\partial q}{\partial x} + h\frac{\partial y_s}{\partial t} = 0 \tag{14}$$

$$q = F\left(-\frac{\partial y_s}{\partial x} + \tan\theta\right) \tag{15}$$

where x is the longshore distance and the origin is at the south end of the coast, where the sediment transport rate is equal to zero, y_s the shoreline position, q the sediment transport rate, h the characteristic height of beach profile change, θ the wave direction.

F is the coefficient and is given by

$$F = \frac{w}{8}(H^2C_g)_0K_r^2\alpha \tag{16}$$

where w is the unit volume weight of sea water, $(H^2C_g)_0$ the energy flux in the deep water, K_r the refraction coefficient, α the Savage coefficient ($\alpha = 0.217$ m^3/t).

Since wave characteristics change temporally, the change of coefficient F should be analyzed first. Here, the data set taken at Kashima Port will be used, because wave measurement at Ajigaura Beach is not continuously taken. Figure 14 shows the temporal change of the coefficient F calculated from the daily mean value of significant wave height at Kashima Port. F is the order of 10^4 m^3/d. Though the change of F is considerably large, F may be assumed to be a constant in later analysis. Because wave angle changes its sign from positive to nega-

tive year by year and therefore it has an important effect on the erosion and accretion. On the contrary, F only affects the rate of beach profile changes.

Boundary conditions are given by

$$\frac{\partial y_s}{\partial x} = \theta \qquad \text{at } x = 0 \tag{17}$$

$$y_s \to 0 \qquad \text{at } x \to \infty \tag{18}$$

In Eq.(17) $\tan\theta$ is approximated by θ since the wave angle θ is small. In addition, we have such relation that

$$\theta(0,t) = \bar{\theta}(0) + \theta_o \cos\omega t \tag{19}$$

because wave angle has a periodic feature of one year as shown in Fig.5. Substituting Eq.(15) into Eq.(14) assuming that F is a constant, then we have the diffusion equation,

$$\frac{\partial y_s}{\partial t} = \frac{F}{h}\frac{\partial^2 y_s}{\partial x^2} \tag{20}$$

The solution of Eq.(20) subject to the boundary conditions given by Eq.(17) to Eq.(19) reduces Eq.(21), by the Laplace transform.

$$y_s(x,t) = -\theta_o\sqrt{\frac{F}{\omega h}}\exp\left(-\sqrt{\frac{\omega h}{2F}}x\right)\cos\left(\omega t - \sqrt{\frac{\omega h}{2F}}x - \frac{\pi}{4}\right) \tag{21}$$

Equation (21) is similar to Bakker's solution, who derived a solution of change of shoreline position near a groin during one storm period. It should be noted that the present problem has a much longer time scale than Bakker's one. The time lag between the change of shoreline position and the change of wave direction is given by

$$\delta = \sqrt{\frac{\omega h}{2F}}x + \frac{\pi}{4} \tag{22}$$

The phase velocity of the shoreline change has in the form

$$V = \sqrt{2F\omega/h} \tag{23}$$

The solution given by Eq.(21) shows that the amplitude of change of shoreline position decreases exponentially in the longshore direction and the change propagates with the phase velocity V.

Here, the time lag and the phase velocity will be estimated. The frequency ω is equal to 0.0171 (rad/d) since a periodic change of 1 year prevails in change of wave direction. The amplitude of wave direction may be assumed 0.13 rad from Fig.5. The characteristic height of beach profile is equal to $h = 4.55$ m from the relationship of Eq.(13), and F is 3.97×10^4 m^3/d, that is the averaged value estimated at Kashima Port. The estimated time lag at the location of the pier, which locates about 1 km north from the boundary, is $\delta = 14.7$ weeks, and this corresponds to the measured one of 12 weeks fairly well.

The amplitude of change of shoreline position becomes 92.5 m at $x = 0$ m and 34.3 m at the location of the pier. The shoreline changes at $x = 0$ m have not been measured so many times that it is impossible to

compare the predicted amplitude with measured one. However, it seems to be too large according to the survey data, which have been carried out once a year since 1975 at Ajigaura Beach. The cause may be due to the fact that wave diffraction around the headland located at south end of Ajigaura Beach was ignored in the theoretical analysis. On the other hand, at the location of the pier the measured amplitude of shoreline change is some 30 m and it corresponds with the predicted amplitude fairly well.

The phase velocity can be calculated from Eq.(23), and it becomes V = 17.3 m/d. The phase velocity can also be estimated from the results of longshore beach survey. Figure 15 is the x-t diagram, which shows the temporal change of longshore beach profile from December 8, 1977 to August 3, 1978. The abscissa is the measured date and the ordinate is the longshore distance from the pier, of which position is denoted by 0. The number in the figure shows the ground elevation. The dotted lines show the longshore propagations of sand waves and the propagation velocity is defined by the gradient of this line. There are four sand waves in the figure. It is found that the sand waves propagating from north to south correspond to the northern wave incidence with time lag of some 3 months, and vice versa for those propagating from south to north due to the comparison between Fig.5 and Fig.15. However, the solution given by Eq.(21) only predicts the sand waves propagating from south to north. Therefore the phase velocity is only derived from the second and fourth sand waves and they are given by 9.6 m/d and 11.4 m/d, respectively. The averaged velocity becomes 10.5 m/d. The phase velocity has a same order of predicted one. However, the cause of the existence of the sand waves propagating southward is not known in the present study and further study will be needed on the problem.

VI. CONCLUSIONS

Field measurement data of beach profiles taken over three years at Ajigaura Beach were analyzed by applying the empirical eigenfunction methods in order to understand the relation of beach profile with wave height, wave direction and longshore current. The results indicate that beach profile changes due to longshore and onshore-offshore sediment transport are separable by the empirical eigenfunction method. The beach profile changes due to longshore sediment transport has a time lag of 12 weeks with respect to the change of wave direction at Ajigaura Beach. It was found that this time lag was due to the sand waves propagating in the longshore direction. Regarding as onshore-offshore sand transport, the second eigenfunction is associated with the beach changes due to onshore-offshore sand transport caused by the change of wave height, and that the critical wave height is H ≈ 2.05 m.

REFERENCES

1) Winant, C.D., D.L. Inman and C.E. Nordstorm : Description of seasonal beach changes using empirical eigenfunctions, Jour. Geophys. Res., Vol.80, No.15, pp.1979-1986, 1975.
2) Hashimoto, H. and T. Uda : Analysis of beach profile changes at Ajigaura by empirical eigenfunctions, Coastal Eng. in Japan, Vol.22, pp.47-57, 1979.

3) Hashimoto, H. and T. Uda : An analysis of beach profile changes by empirical eigenfunction, Proc. JSCE, Vol.305, pp.59-71, 1981 (in Japanese).
4) Hashimoto, H. and T. Uda : On the dynamic response of shore profile to wave characteristics, Proc. JSCE, Vol.310, pp.77-88, 1981 (in Japanese).
5) Bakker, W.T., Klein Breteler, E.H.J., and Roos, A. : The dynamics of a coast with a groin system, Proc. 12th Conf. on Coastal Eng., pp.1001-1020, 1970.

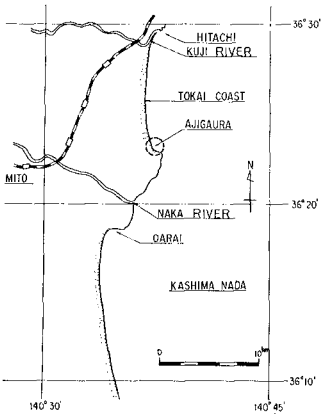

Figure 1 Location of Ajigaura Beach

Table 1 Eigenvalues (λ_k)

k	λ_k	$\lambda_k/Tr(A)$
1	0.0777	0.367
2	0.0464	0.219
3	0.0356	0.168

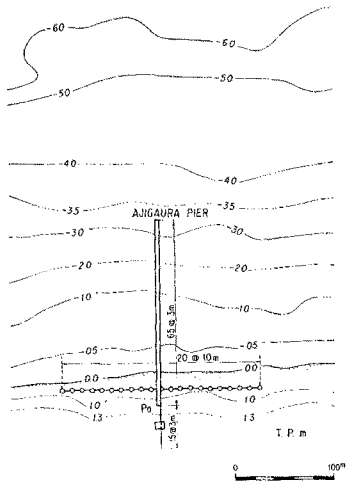

Figure 2 Alignment of the pier and measurement positions

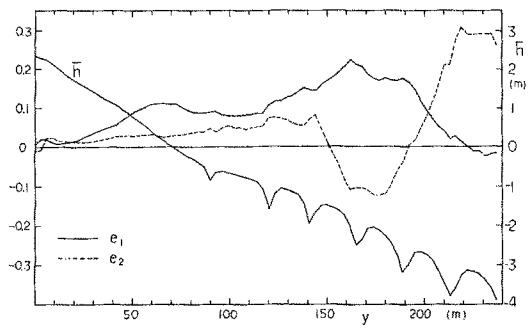

Figure 3 Mean beach profile $\bar{h}_y$ and onshore-offshore profiles of the first and second eigenfunctions, e_1 and e_2

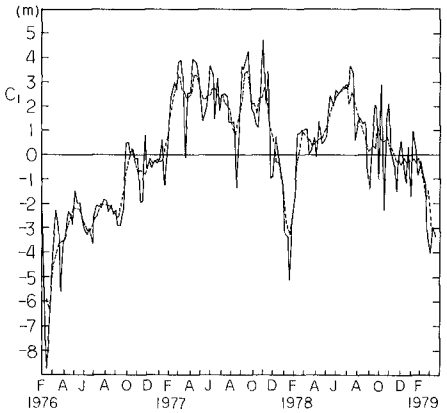

Figure 4 Time function C_1 corresponding to the first eigenfunction e_1 and time function $\bar{C}_1$ averaged over five weeks

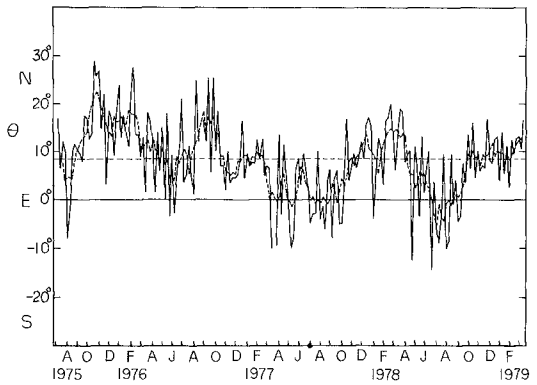

Figure 5 Temporal changes of wave direction

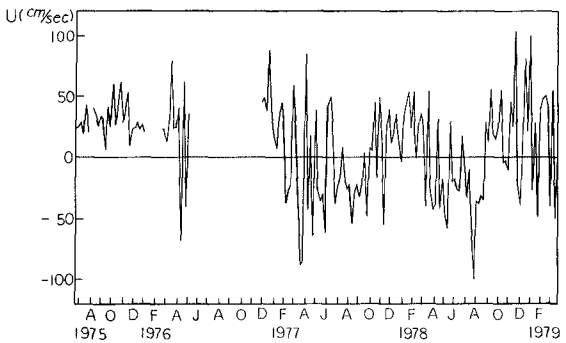

Figure 6 Longshore current velocity in the surf zone

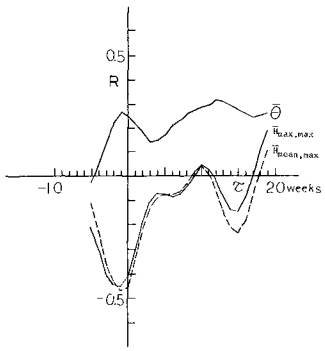

Figure 7 Cross-covariance coefficient

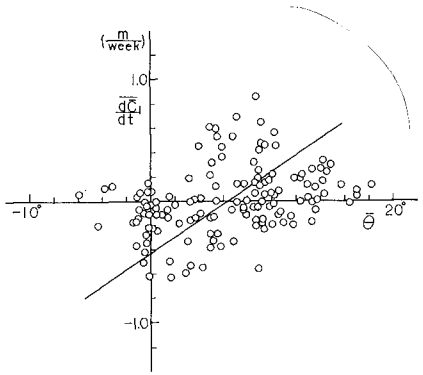

Figure 8 Relationship between the wave direction $\bar{\theta}$ and $\overline{dC_1/dt}$ with time lag of 12 weeks

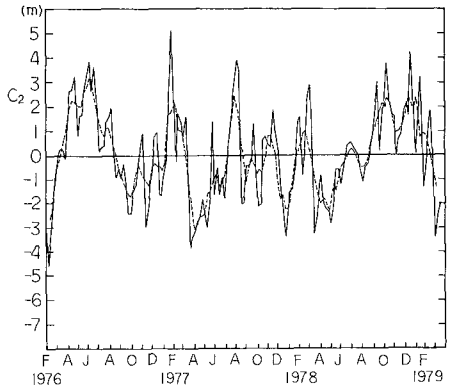

Figure 9 Time function C_2 corresponding to the second eigenfunction e_2 and time function $\bar{C}_2$ averaged over five weeks

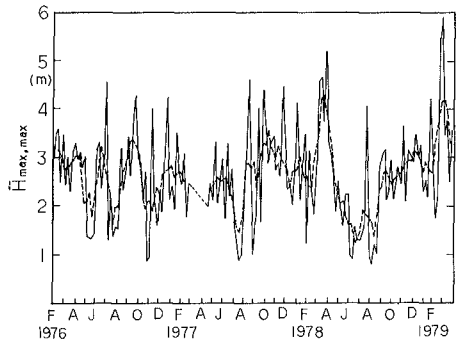

Figure 10 Weekly maximum value of the daily maximum significant wave height ($\bar{H}_{max,max}$) at Kashima Port

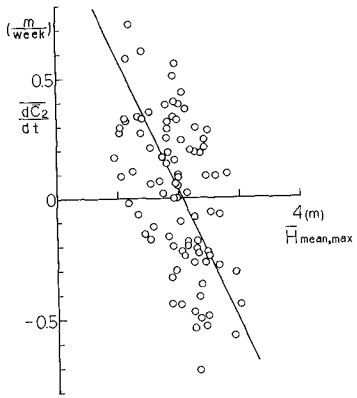

Figure 11 Relationship between $\overline{dC_2/dt}$ and $\bar{H}_{mean,max}$

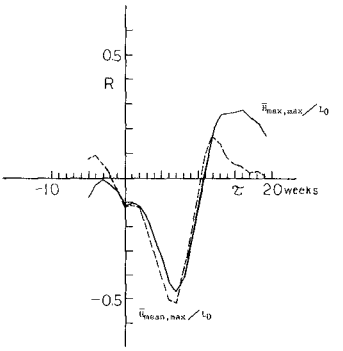

Figure 12 Cross-covariance coefficient between wave steepness and time rate of the time function C_2

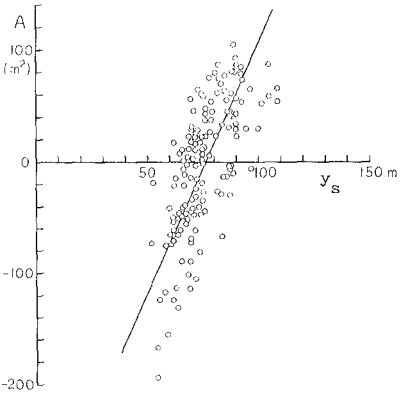

Figure 13 Relationship between cross sectional area,A, and shoreline position,y_s

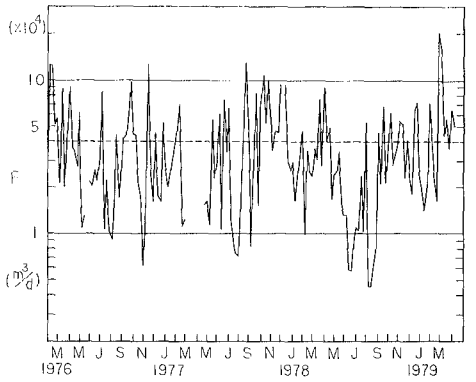

Figure 14 Temporal change of coefficient F

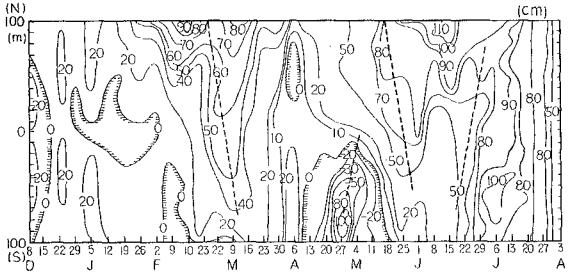

Figure 15 x-t diagram of change of longshore beach profile

EXPERIMENTS ON BEACH PROFILE CHANGE WITH A LARGE WAVE FLUME

By

Ryoichi Kajima*, Takao Shimizu**

Kohki Maruyama** and Shozo Saito***

ABSTRACT

Two-dimensional beach profile changes were investigated with a newly constructed prototype-scale wave flume. The flume is 205 m long, 3.4 m wide and 6 m deep. Sand of two grain sizes was used in the experiments. Analysis of the results was made through use of the parameter C, introduced by Sunamura and Horikawa (1974) to classify beaches as either erosional and accretionary. Beach profile changes obtained in the flume were similar to those in the prototype (field). Net sand transport rate distributions were classified into five types, two of which do not seem to have been observed in laboratory (small-scale) experiments. A simple model describing the five types was developed for evaluating two-dimensional beach profile changes.

INTRODUCTION

Construction of harbor and cooling water facilities of power stations can produce significant changes along the coast. Consequently, the development of coastal change prediction methods is very important to maintain the functions of these coastal structures and to preserve the coastal environment. In particular, studies on two-dimensional beach profile changes resulting from cross-shore sand transport occupy a very important position. However, most of the numerous investigations and results concerning two-dimensional beach changes have been based mainly on rather small-scale experiments. The consequences of unavoidable scale effects associated with these experiments are not easy to determine.

---

* Manager of Coastal Hydraulics Section, Civil Engineering Laboratory, Central Research Institute of Electric Power Industry (CRIEPI), 1646 Abiko, Abiko City, Chiba, 270-11 Japan.
** Research Engineer, CRIEPI.
*** Senior Research Engineer, CRIEPI.

This study is aimed at providing prototype-scale data for two-dimensional beach changes by means of a newly constructed large wave flume. The general similarities and differences between previous and the present experimental results will be discussed. It is shown that net sand transport rate distributions as determined from successive profile changes can be classified into five types, and that these distributions can be simulated by a simple model.

LARGE WAVE FLUME (CRIEPI FLUME)

Flume

The wave flume is shown in Fig. 1. It is made of reinforced concrete, and is 205 m long, 3.4 m wide, and 6 m deep in the 115 m-long generator-side flat section, which is joined to a shoreward section of 1/15 slope. The top of the flume is 1.5 m above ground level. Trucks for carrying or dumping bed materials can be driven in directly through the access slope adjacent to the end of the flume. The wave generator is of the piston type as shown in Fig. 2, with no water behind the blade. Seals for preventing water infiltration are installed along the side and bottom edges of the blade. The blade is driven by oil pressure supplied from two pumps, each driven by a 370 kw electric motor under the control of an electric-hydraulic servo mechanism. The system is capable of producing waves up to 2 m in height.

Because the blade and its supporting frame are fairly heavy (weighing a little over 10 ton), unusually rapid motion is dangerous. Therefore, an automatic, slow starter-stopper was installed. In the event that either an earthquake, water leakage, oil pressure drop, excess oil temperature rise or an overload is sensed, the blade automatically stops and the cause is indicated by lamps on the control board in the operation room. Usually the flume is run from the operation room near the center and at the side of the flume. In addition, the flume is equipped with a vehicle for measurement, and filtration equipment (maximum capacity: 120 m^3/hr).

Wave Generator

An example of waves generated in the flume is given in Fig. 3. The wave generator is designed to produce a maximum wave 2 m in height and 5 s in period in a water depth of 4.5 m, according to the wave generation theory of Biesel and Suquet (1951). Because a very large thrusting force is required, the hydrostatic force is compensated by two balancing actuators (each with maximum thrust force of 40 ton), and the dynamic force to produce waves is generated by a servo-actuator (maximum thrust force is 30 ton). The stroke length needed for the maximum wave is 2200 mm. The compensation of the volume change in the balancing cylinders and the oil pressure variation in the servo-valve is done by the accumulators. The maximum stroke length of the actuators is as 2400 mm including a $\pm$100 mm allowance. The displacement of the piston of the servo-actuator is detected through a rack and pinion gear, and counted by a rotary encoder.

For the surface contact of the water seals, a high-polymer tape 24 mm in width and possessing a very low friction coefficient is used. The tape is kept in contact with the slipping wall of the flume by air

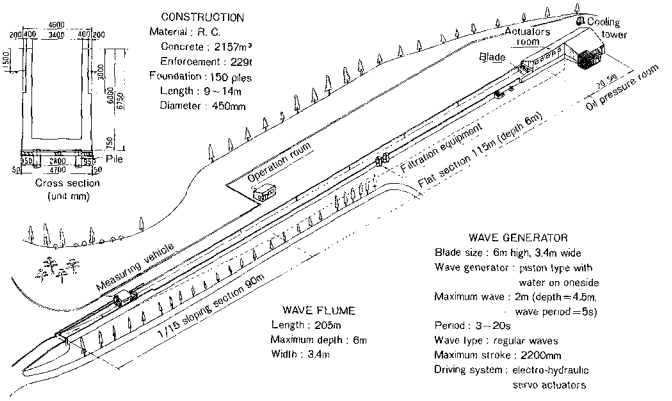

Fig. 1 Prototype wave flume for beach change experiment.

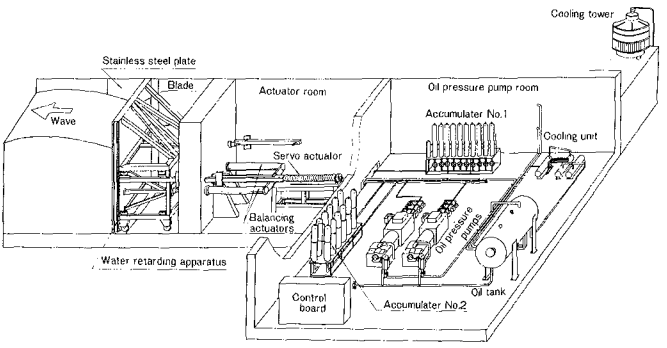

Fig. 2 Wave generator.

Fig. 3 Waves in the flume.

Table 1 Comparison of various types of wave gauges.

Wave gauge	Before breaking			After breaking		
	Error* (%)	Response	Operation	Error* (%)	Response	Operation
Ultrasonic type (under water)	4.2	A	D			D
Ultrasonic type (in the air)	−2.4	A	A	−5.9	C	A
Resistance type	−2.8	A	A	−8.0	D	C
Capacitance type-1	−7.0	B	A	−1.6	C	C
Capacitance type-2	4.5	A	A	−0.6	A	C
Buoy type	8.2	D	B			D
Pressure type (strain gauge)	6.8	D	B	−3.8	D	D

* : Relative error in wave height
A : Good
B : Acceptable
C : Marginally accaptable
D : Unacceptable

pressure (1.5 kg/cm^2) transmitted through waterproof urethane rubber. For reducing wear of the tape, the surface of the slipping wall of the flume is faced with stainless steel plates 5 mm thick.

Measuring System

The wave flume is equipped with a measuring vehicle (weight: 5 ton, maximum speed: 45 cm/s). Because measuring devices applicable to the field must be used, a thorough investigation of the accuracy and serviceability of the instrumentation was required. Seven types of wave gauges were tested to determine their suitability. The wave records from the various gauges were compared to the output of a video tape recorder. Characteristics of the gauges are shown in Table 1 (Shimizu et al., 1983). It was decided to use capacitance (type-2) wave gauges and an ultrasonic (in the air-type) wave gauge. For the measurement of water particle velocities, electromagnetic current meters were adopted. Ultrasonic depthmeters with secondary transmitter-receivers for calibration (calibration distance = 200 mm) were used for the subsurface bottom, and a sand surface detector of the surface contact type was also used for the profile above the water level.

The horizontal position of the vehicle and the vertical position of the post supporting the depthmeter are detected using rotary encoders. The depth was measured every 50 mm in the horizontal direction by raising or lowering a post according to the output of the depthmeter while moving the vehicle. For the measurement of the microscale topography such as sand ripples, the same system was utilized except that the sampling interval was reduced to 1 mm. The data acquisition system on the carrier is controlled by a 20 kB microcomputer. For data processing, mainframe computors (FACOM M200 and M160F) are used.

EXPERIMENTAL RESULTS

Procedure

Coarse sand (median diameter D_{50} = 0.47 mm) and fine sand (D_{50} = 0.27 mm) were used in the experiments. Material properties are summarized in Table 2. Initial profiles of all cases were formed as uniform slopes of $\tan\beta$ (= 5/100 or 3/100). Conditions of the test cases are summarized in Table 3. The water depth at the flat section of the flume was 3.5 m in CASES 2-1 to 2-3, while in the other cases this depth was 4.5m.

Measurements were made of the beach profile, wave height, water velocity and time-averaged concentration of suspended load. The breaking point, breaker type, run-up point, run-down point and number of waves in the surf zone were also observed. In general, measurements of the beach profile were made along the center line of the wave flume. In order to examine the two-dimensionality of the beach profiles, measurements of the beach profile in CASE 1-1 were made along three lines; one was the center line of the flume, and the others were 1.1 m to either side of the center line. It was found that the difference between measured profiles was within $\pm$5 cm. It was thereby confirmed that the measurement profile along the center line represents the two-dimensional beach profile in the wave flume.

Table 2 Properties of sand.

Material			coarse sand		fine sand	
Median diameter D_{50} (mm)			0.47		0.27	
Sorting coefficient $So=\sqrt{D_{75}/D_{25}}$			1.57		1.35	
Skewness parameter $Sk=\sqrt{D_{25}D_{75}}/D_{50}$			1.03		1.03	
Specific gravity			2.69		2.71	
Void ratio	wet sand	compacted	34 %	39 %	35 %	41 %
		not compacted	43 %		46 %	
	dry sand	compacted	34 %	37 %	39 %	41 %
		not compacted	39 %		43 %	
Angle of repose		underwater	33°		33°	
		in the air	33°		32°	

Table 3 Conditions and test cases.

CASE	Median diameter of sand D_{50} (mm)	Initial slope tan β	Wave period T (s)	Wave height* Ho (m)	Duration of wave action t (hr)
1-1	0.47	5/100	6.0	0.46	20.0
1-3			9.0	0.95	69.5
1-8			3.0	0.85	21.0
2-1		3/100	6.0	1.76	35.0
2-2			9.0	0.73	39.0
2-3			3.1	0.71	29.4
3-1	0.27	5/100	9.1	1.07	71.0
3-2			6.0	1.05	98.1
3-3			12.0	0.65	80.0
3-4			3.1	1.62	76.1

* Ho is estimated from the wave height at the uniform depth section.

Beach Profile Change

Figure 4 shows beach profiles at the final stages. Saville (1957) also conducted experiments using a prototype-scale wave flume, and published profiles of four cases. The profile of his case, T = 11.33 s, H = 1.8 ft, closely resembles the present CASE 3-1. In the other three cases, the beach profile changes reached the toe of the slope. In Fig. 4, it can be seen that profiles in most of our cases were not affected by the finite length of the slope. In laboratory experiments (e.g., Sunamura and Horikawa, 1974), accretion outside the surf zone is often observed under conditions of fine sand and steep slope. But in our cases corresponding to this situation (CASE 3-1 to CASE 3-3), erosion occurred outside the surf zone. In CASE 3-4, accretion occurred outside the surf zone, but the beach profile was considerably different from typical laboratory experimental results, especially near the bar.

In Fig. 4, locations of breaking points are indicated by triangles, an open triangle for the initial stage, and a solid triangle for the final stage. Plunging breakers were observed in almost all cases, except that plunging breakers with some characteristics of collapsing or spilling breakers were observed in CASE 1-3 and CASE 3-4, respectively. Battjes (1974) classified breaker types using the surf similarity parameter ξ_o,

$$\xi_o = \tan\beta \,/\sqrt{H_o/L_o} \tag{1}$$

where $\tan\beta$ is the beach slope, and H_o and L_o are the wave height and wave length in deep water, respectively. The critical value between spilling and plunging breakers was given as $\xi_o = 0.5$. However, in the present experiments, at the initial state of beach profile change the critical value was found to be $\xi_o = 0.15$. (A detailed discussion is given by Maruyama et al., 1983)

In CASES 2-1, 2-2, and 2-3, all with a gentle slope of $\tan\beta = 3/100$, secondary breaking was observed, particularly in CASE 2-1 shown in Fig. 5. Bars were formed in all cases and, in CASE 2-1 a smaller bar also formed near the secondary breaking point. In addition, a berm formed in all cases except for CASE 1-8 and CASE 3-4.

Sunamura and Horikawa (1974) found that shoreline changes could be classified by means of the nondimensional parameter C:

$$C = (H_o/L_o)\,(\tan\beta)^{0.27}\,(D_{50}/L_o)^{-0.67} \tag{2}$$

where, $\tan\beta$ is the average beach slope from the initial shoreline up to the critical water depth of sediment movement. In the present paper, $\tan\beta$ is equivalent to the uniform slope of the initial beach. The demarcation value of C between recession and advance of shoreline was 4 - 8 for laboratory measurements, and 9 - 18 for field measurements. Sunamura (1980a) eliminated noncredible data and added new data, and found that the demarcation value of C for field data was 18.

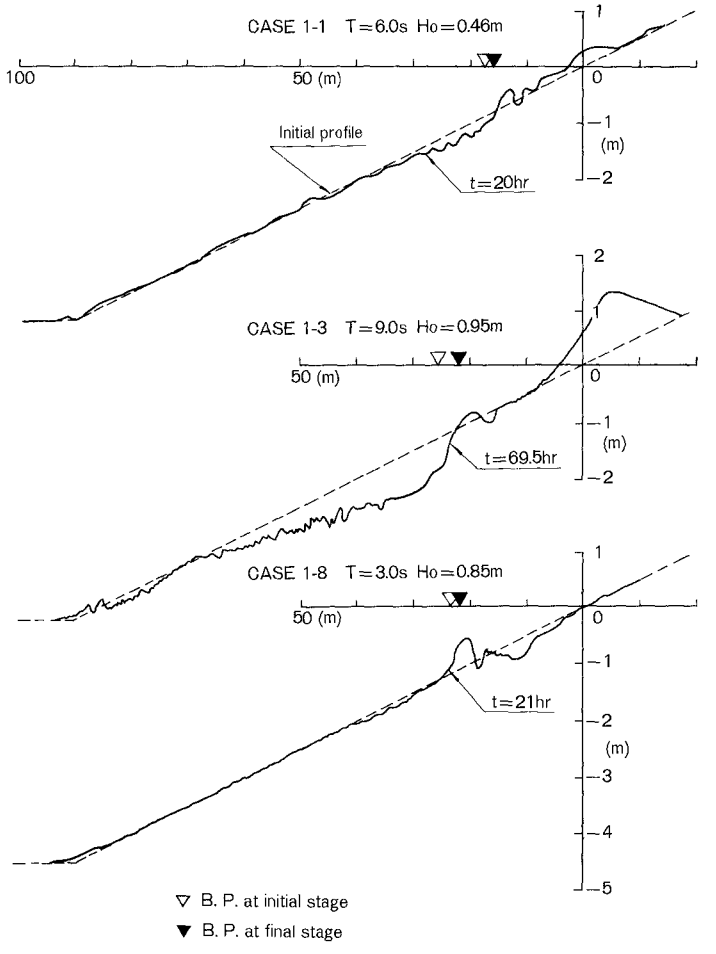

Fig. 4(a) Beach profile changes (steep beach with coarse sand).

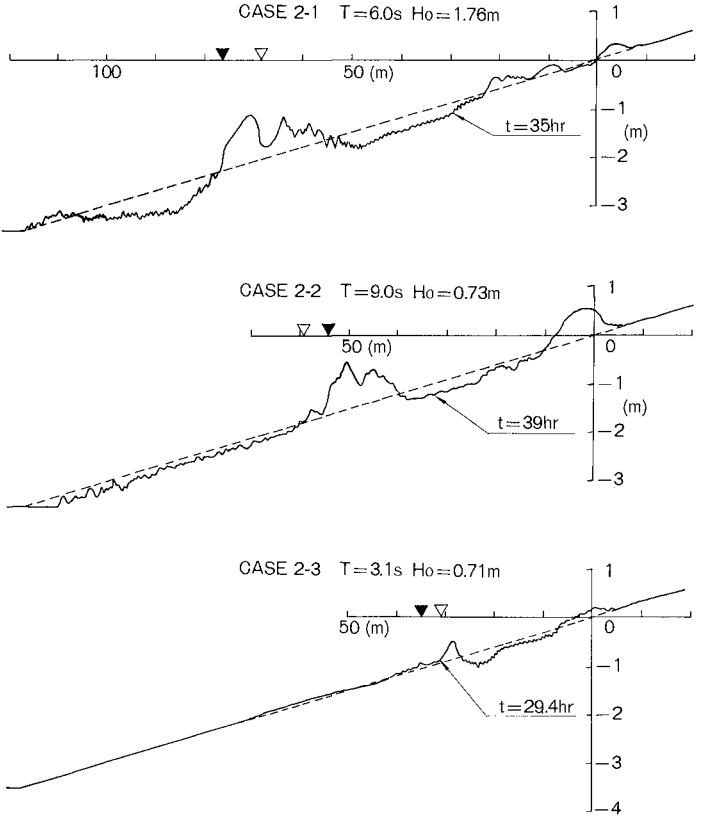

Fig. 4(b) Beach profile changes (gentle beach with coarse sand).

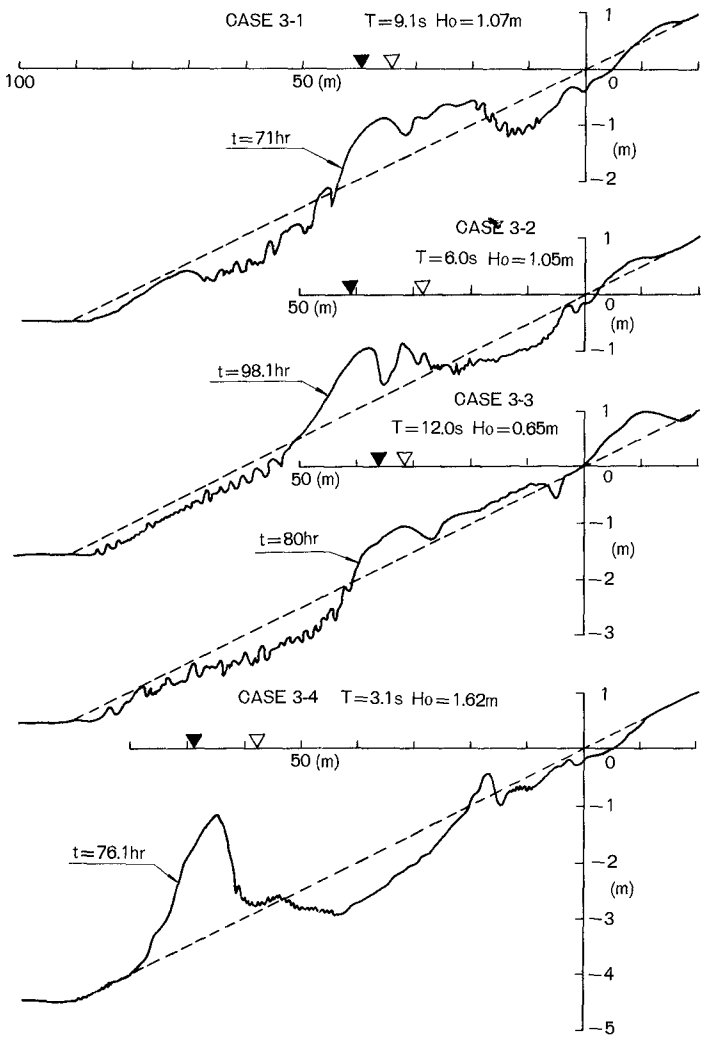

Fig. 4(c) Beach profile changes (steep beach with fine sand).

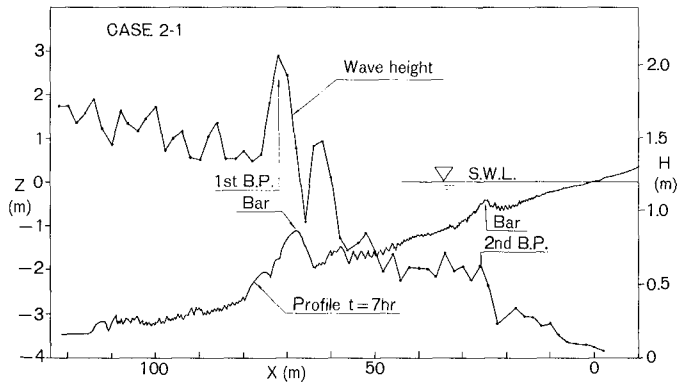

Fig. 5 Distribution of wave height in CASE 2-1.

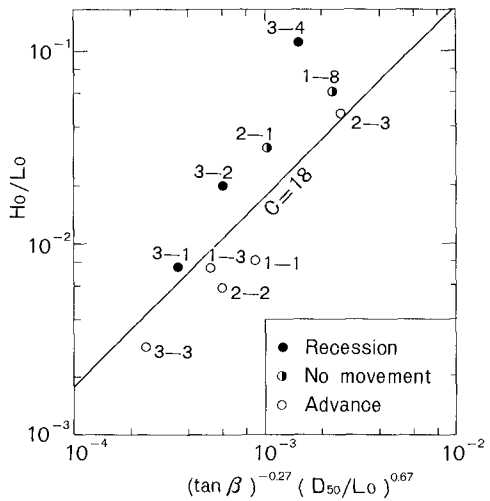

Fig. 6 Classification of shoreline change.

The results of applying this method to the present data are shown in Fig. 6. The transition from recession to advance of the shoreline is defined by C = 18, which is similar to the field data result. Consequently, the authors consider that processes of beach profile change in this wave flume are similar to those in the prototype. In CASES 1-8 and 2-1, by consideration of the parameter C, the shoreline was expected to recede. However, this situation did not occur (as shown in Fig. 6). It is believed that the shoreline change was produced by the waves near the shoreline rather than the deep water waves. In CASE 2-1, secondary breaking might also have influenced the shoreline change.

The critical water depths at which noticeable profile changes were observed are compared with the results of some previous studies described by Horikawa (1978) in Fig. 7. The results for CASE 2-2, CASE 3-2 and CASE 3-4 are excluded because in CASE 2-2 and CASE 3-2 the profile changes extended to the toe of the slope, and in CASE 3-4 the profile change did not reach the equilibrium state. It was found that the critical water depths for profile change agreed with the criterion of completely active movement given by Sato and Tanaka (1962), namely,

$$H_o/L_o = 1.35\,(D_{50}/L_o)^{1/3}\,(\sinh 2\pi h/L)\,(H_o/H) \tag{3}$$

where, h is the critical water depth of sediment movement and H and L are the wave height and wave length at the water depth h, respectively.

Net Sand Transport Rate

Net sand transport rate distributions for each case were calculated from successive beach profiles. Beach profiles and distributions were classified into three types as shown in Fig. 8. Type I (erosion type), Type II and Type III (accretion type) correspond to the beach profile classification of Sunamura and Horikawa (1974). In addition, the present experimental results for Type I and Type III were subdivided into Mono-crested and Bi-crested types. Bi-crested distributions of Type I and III tend to transform to Mono-crested distributions with time as the breaking point moves seaward or shoreward.

It was found that each type of net sand transport rate distribution could be classified according to the parameter C, as plotted in Fig. 9. The condition of transition from Type I to Type III occurs at C = 18. Furthermore, the Mono-crested and Bi-crested distributions could be classified by a newly proposed parameter P as follows:

$$\left.\begin{array}{ll} \text{Mono-crested distribution} & P > 10^{-3} \\ \text{Bi-crested distribution} & P < 10^{-3} \end{array}\right\} \tag{4}$$

$$P = (\tan\beta)^{-0.27}\,(D_{50}/L_o)^{0.67} \tag{5}$$

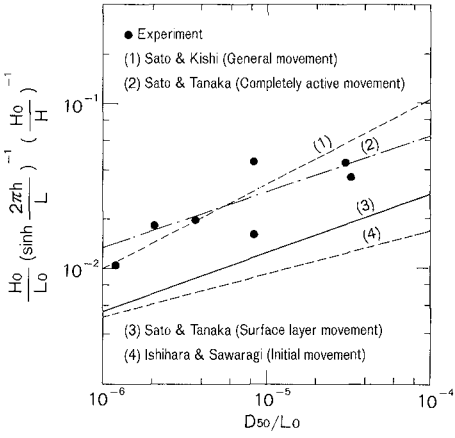

Fig. 7 Comparison between experimental results and various expression for sediment movement inception.

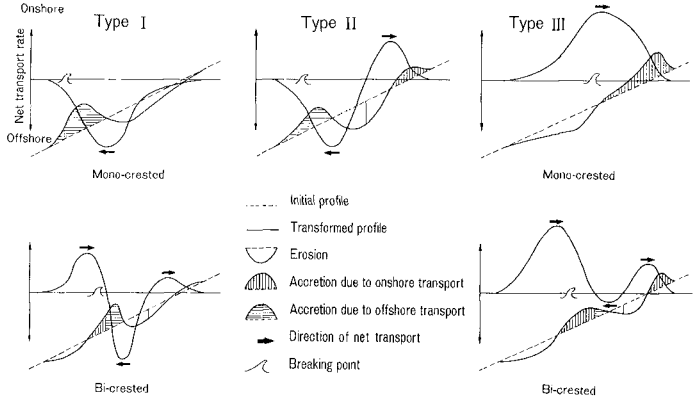

Fig. 8 Types of net transport rate distributions.

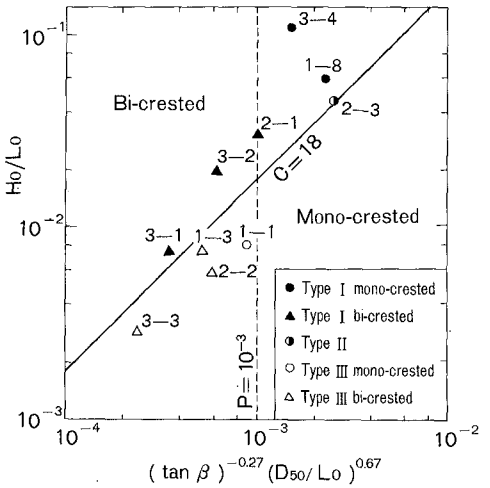

Fig. 9 Net transport rate distribution types classified by parameter C and P.

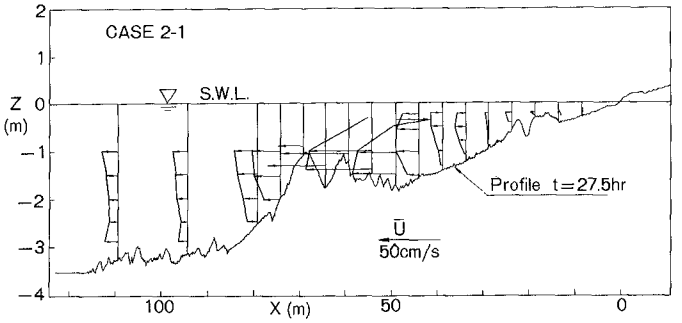

Fig. 10 Distribution of time averaged horizontal velocity of CASE 2-1.

Sawaragi and Deguchi (1980) classified into four types the net transport rate distributions obtained in rather small-scale experiments. Type II-2 of their classification corresponds to the Bi-crested distribution of our prototype-scale experiments. However, in laboratory experiments, Bi-crested types are rarely observed. One reason for this discrepancy may be that values of the parameter P in such laboratory experiments are different from those in prototype-scale experiments. For example, in almost all laboratory experiments conducted by Sunamura and Horikawa (1974), P was greater than 10^{-3}.

MODEL OF BEACH PROFILE CHANGE

At the present time, motions of the waves and fluid near and inside the surf zone have not been examined in sufficient detail to estimate the net sand transport rate directly from these quantities. Accordingly, as a first step in grasping the overall magnitude of sand transport in the present experiments, we constructed a rather simple model that directly relates the distribution of the net transport rate with the conditions of the waves and the beach, using the data corresponding to the cases with coarse sand (D_{50} = 0.47 mm). [Swart (1974) and Sunamura (1980b) proposed models based on the same basic ideas. However, application of their models is restricted only to erosional beaches, and consequently, their models can not express the growth of bars and berms.]

In the present model, it is assumed that the distribution of on-offshore sand transport rate Q (transport rate per unit width perpendicular to wave propagation) extending from the swash zone to outside the surf zone can be interpreted as the sum of relatively independent components of net sand transport (Q_1, Q_2 and Q_3) as follows,

$$Q = Q_1 - Q_2 + Q_3 \tag{6}$$

where

Q_1: net onshore transport outside the surf zone caused by nonlinearity of the fluid motion under waves

Q_2: net offshore transport inside the surf zone caused by time-averaged seaward-directed currents

Q_3: net onshore transport in the swash zone caused by wave run-up.

Figure 10 shows a typical distribution of time-averaged horizontal velocity for CASE 2-1. Strong seaward currents were observed throughout the surf zone, and the maximum velocity of these currents reached about 0.5 m/s. It is believed that these seaward currents have a great influence on the net sand transport rate Q_2.

The five types of net transport rate distributions shown in Fig. 8 then correspond to different relative magnitudes of the above components. According to the assumptions, the net transport rate distribution can be expressed as follows:

$$Q = Q_1 - Q_2 + Q_3$$

$$= A_1 \exp[-((x-x_1)/B_1x_b)^2] - A_2 \exp[-((x-x_2)/B_2x_b)^2] + A_3 \exp[-((x-x_3)/B_3x_b)^2] \quad (7)$$

Here x is the distance from the shoreline of the initial beach profile, and x_b denotes the breaking point. In Eq. (7), 1st term gives a peak A_1 near the breaking point ($x = x_1$); the 2nd term gives a peak A_2 near the center of the surf zone ($x = x_2$); and the 3rd term gives a peak A_3 near the shoreline ($x = x_3$). Each Gaussian distribution has a characteristic width of B_1, B_2, and B_3, respectively. For example, if either B_1, B_2 or B_3 is equal to 0.2, the width of the distribution is nearly equal to the width of the surf zone.

It is also assumed that the peaks A_1, A_2, and A_3 decrease exponentially with time from their initial values of A_{10}, A_{20} and A_{30},

$$A_1 = A_{10} \exp[-\alpha_1 t], \quad A_2 = A_{20} \exp[-\alpha_2 t], \quad A_3 = A_{30} \exp[-\alpha_3 t] \quad (8)$$

where t is the time, and α_1, α_2 and α_3 are decay coefficients. The tendency of the net transport rate distribution to transform from Bi-crested to Mono-crested types may be simulated by means of α_1, α_2 and α_3.

The continuity equation of two-dimensional beach profile change is

$$\frac{\partial h}{\partial t} = -\frac{\partial Q}{\partial x} \quad (9)$$

where h is water depth. Therefore, substituting Eq. (7) into Eq. (9) and integrating Eq. (9) over time starting from the initial beach profile, the beach profile at a given time can be obtained.

The initial distributions of net transport rate corresponding to the cases with coase sand were calculated from the difference between the initial profiles and those after three hours, and A_{10}, A_{20}, and A_{30} were determind by the least squares method. The results are shown in Table 4. In determination of these values, B_1, B_2 and B_B were assumed as shown in Table 4.

Table 4 Parameters of the model.

CASE	1—1	1—3	1—8	2—1	2—2
χ_b (m)	18.0	26.2	22.8	69.2	57.5
χ_1 (m)	24.8	32.7	27.8	78.4	57.5
χ_2 (m)	18.8	14.7	19.8	64.4	37.5
χ_3 (m)	0.8	−1.3	5.8	29.4	5.5
B_1	0.45	0.45	0.15	0.15	0.45
B_2	0.30	0.30	0.075	0.075	0.30
B_3	0.15	0.15	0.30	0.30	0.15
A_{10} (m^3/hr/m)	0.83	1.28	0.14	1.91	0.68
A_{20} (m^3/hr/m)	0.49	−0.26	1.11	2.65	0.22
A_{30} (m^3/hr/m)	0.11	1.18	−0.06	0.33	0.45

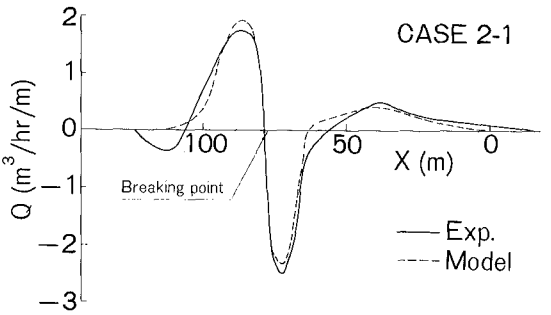

Fig. 11 Net transport rate distribution approximated by Eq. (7).

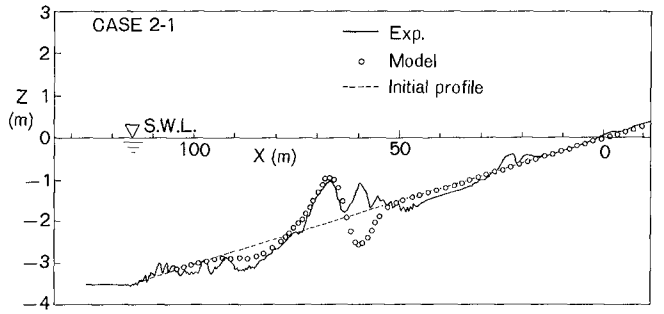

Fig. 12 Beach profile calculated by the model.

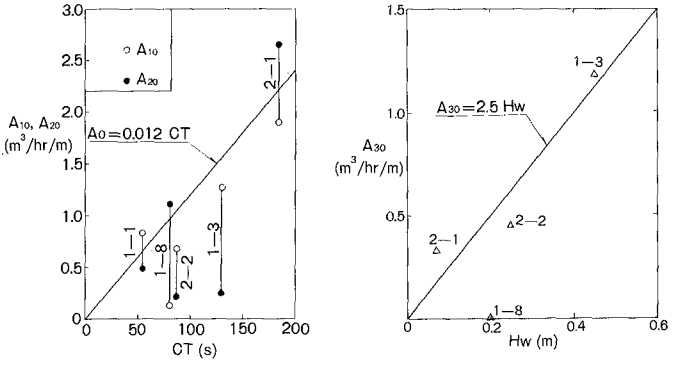

Fig. 13 Properties of the initial peak parameters A_{10} to A_{30}.

An example of the net transport rate distribution approximated by Eq. (7) is compared with the measured distribution in Fig. 11. It was found that the distributions of net transport rate in the other cases were also well approximated by Eq. (7).

Figure 12 is an example of the predicted from Eq. (9) and measured profiles for CASE 2-1 after 20 hours of wave action. The profile change outside the surf zone is well simulated by this model. On the other hand, the local profile change near the plunging point is not so well reproduced. In numerical calculation, the assumption was employed that the locations x_i, where each transport rate component Q_i has a peak, do not move when the bottom profile changes. To improve this model, therefore, it is necessary to take account the effect that the center of the Gaussian distribution of each component of Q can move with changes in the beach profile.

In order to generalize the present model, the dependence of the parameters A_{10}, A_{20} and A_{30} on the experimental conditions was investigated. The results are shown in Fig. 13. The parameter A_{10} in the accretionary cases and A_{20} in the erosional cases, which correspond to the most dominant components, appear to have a positive correlation with the product of the parameter C and the wave period T. The parameter A_{30}, which represents the onshore transport in the swash zone, appears to be related to the wave height at the shore-line H_w.

CONCLUSIONS

1) Shoreline change in these prototype-scale experiments was predicted by the parameter C (Eq. 2) of Sunamura and Horikawa (1974). The demarcation value of C separating recession and advance was confirmed to be 18 (Fig. 6).

2) The critical water depth of the beach profile change agreed well with the criterion of completely active movement (Eq. 3) given by Sato and Tanaka (1962).

3) The observed net transport rate distributions were classified into 5 types (Fig. 8). They could be identified by the parameters C and P (Fig. 9).

4) The net transport rate distributions were well approximated by the sum of three Gaussian distributions (Eq. 7). The parameters of this model were related to the wave and beach conditions (Fig. 13).

ACKNOWLEDGMENTS

We would like to extend our appreciation to Professor K. Horikawa, University of Tokyo, and Professor S. Hattori, Chuo University, for valuable discussions and advice. We are also grateful to Professor Nath, Oregon State University, for kindly supplying information about the wave flume at that institution. In addition, we would like to thank Dr. N. C. Kraus, Nearshore Environment Research Center, for critically reading the manuscript, and Miss T. Kohno for typing.

REFERENCES

1) Battjes, J.A.: Surf similarity, Proc. 14th Coastal Eng. Conf., ASCE, pp. 466-480, 1974.

2) Biesel, F. and F. Suquet: Les appareils générateurs de houle en laboratoire, La Houille Blanche, No. 2, pp. 147-165, 1951.

3) Horikawa, K.: Coastal Engineering, University of Tokyo Press, and Halsted Press, 402pp., 1978.

4) Maruyama, K., T. Sakakiyama, R. Kajima, S. Saito and T. Shimizu: Experimental study on wave height and water particle velocity near the surf zone using a large wave flume, Civil Eng. Lab. Rep. No. 382034, CRIEPI, 1983. (in Japanese)

5) Sato, S. and T. Tanaka, 1962. (see Ref. 3)

6) Saville, T. Jr.: Scale effects in two dimensional beach studies, Proc. 7th General Meeting, IAHR, pp. A3.1 - 8, 1957.

7) Sawaragi, T. and I. Deguchi: On-offshore sediment transport rate in the surf zone, Proc. 17th Coastal Eng. Conf., ASCE, pp. 1194-1214, 1980.

8) Shimizu, T., K. Maruyama, R. Kajima and S. Saito: Characteristics of field type measuring equipments tested in a large wave flume — wave gages, current meters, and depthmeters —, Civil Eng. Lab. Rep., CRIEPI, 1983. (in preparation, in Japanese)

9) Sunamura, T.: Predictive model for shoreline-position change on natural beaches, Proc. 27th Japanese Conf. on Coastal Eng., JSCE, pp. 255-259, 1980a. (in Japanese)

10) Sunamura, T.: A laboratory study of offshore transport of sediment and a model for eroding beaches, Proc. 17th Coastal Eng. Conf., ASCE, pp. 1051-1070, 1980b.

11) Sunamura, T. and K. Horikawa: Two dimensional shore transformation due to waves, Proc. 14th Coastal Eng. Conf., ASCE, pp. 920-038, 1974.

12) Swart, D.H.: A schematization of onshore-offshore transport, Proc. 14th Coastal Eng. Conf., ASCE, pp. 884-900, 1974.

DESCRIPTION OF BEACH CHANCES USINC AN EMPIRICAL PREDICTIVE MODEL OF BEACH PROFILE CHANGES

Takaaki UDA* and Hiroshi HASHIMOTO**

ABSTRACT

In order to analyze beach profile changes due to longshore and onshore-offshore sand transport, here is proposed a new model named the "empirical predictive model of beach profile change", which is an application of the empirical eigenfunction method. The analysis of the profile data obtained at the Misawa fishery port in Ogawarako Coast over five years from 1973 to 1977 indicates that profile changes due to longshore transport and to onshore-offshore transport can be separated. The model is shown to be effective in the analysis of profile changes near coastal structures.

I. INTRODUCTION

Recently many investigations about predictive models of beach profile changes due to littoral drift have been conducted. Pelnard-Considère[1] introduced an one-line theory and predicted the shoreline changes near a jetty, Bakker[2] developed a two-line theory and analyzed beach profile changes due to longshore and onshore-offshore sand transport near a jetty.

The present authors[3),4)] applied the one-line model for coastline changes to the Fuji Coast and to the planning of artificial beach nourishment at Kanazawa Beach. As a consequence of these analyses, it was concluded that if coefficients of the model are suitably selected, the shoreline change due to longshore sand transport can be predicted fairly well. However, the one-line theory cannot predict the profile variation when both longshore and onshore-offshore sand transport are significant.

In this paper, in order to consider such problems more closely, we analyzed shoreline changes near the breakwater of the Misawa fishery port with the one-line theory, and also applied the empirical eigenfunction method to the analysis of beach changes.

II. BEACH PROFILE CHANCES DUE TO THE CONSTRUCTION OF MISAWA FISHERY PORT

The Misawa fishery port lies on the southern part of the 100 km long Ogawarako Coast, facing the Pacific Ocean in Aomori Prefecture, as shown in Fig. 1. The construction of the port was started in November, 1973

* Chief Research Engineer, Coastal Engineering Division, Public Works Research Institute, Ministry of Construction, Tsukuba, Japan

** Chief, Coastal Engineering Division, Public Works Research Institute Ministry of Construction, Tsukuba, Japan

Construction Bureau, Ministry of Transport, 1976. (in Japanese)
7) Winant, C.D.,D.L. Inman, and C. E. Nordstrom: Description of seasonal beach changes using empirical eigenfunctions, Jour. Geophys. Res., Vol. 80, No. 15, pp. 1979-1986, 1975.
8) Hashimoto, H., and T. Uda: Analysis of beach profile changes at Ajigaura by empirical eigenfunction, Coastal Eng. in Japan, Vol. 22, pp. 47-57, 1979.

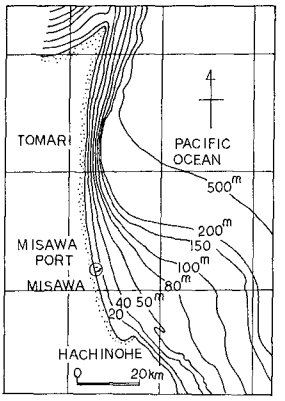

Fig. 1 location of Misawa fishery port

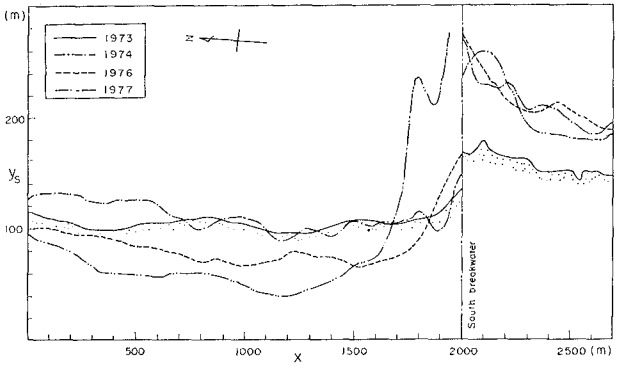

Fig. 2 Shoreline changes near Misawa port

and completed in December, 1977. Since the net sediment transport along this coast was toward the north,[5] accretion and erosion occurred, respectively, to the south and north of the breakwater of the port after its construction.

The beach profile near the port was measured once a year over five years from 1973 to 1977 at 50 meter intervals alongshore. Figure 2 shows the changes of the shoreline near the breakwater from 1973 to 1977. Over these five years, the shoreline advanced offshore by about 60 meters on the south coast of the breakwater, whereas it retreated landward by some 60 meters on the north coast. The shoreline near the north side of the breakwater advanced offshore more than 100m due to the diffraction of waves around the breakwater.

The detailed shoreline changes are shown in Fig. 3. The dates of construction stages are also summarized in Fig. 3. With the progress of the construction, the shoreline inside the port advanced offshore. Figure 4 shows typical examples of beach profiles along the P-P' section in Fig. 3. It is found that the accretion height amounted to approximately four meters in the port, and the profile changes extended from three meters above the mean sea level to eight meters below the sea level. The change of bottom elevation around the port was calculated from the measured profile data of 1973 and 1974, as shown in Fig. 5. Positive and negative values indicate accretion and erosion, respectively. According to Fig. 5, erosion occurred in the north and accretion in the south coast of the breakwater, respectively, implying sand movement from the south to the north at the head of the breakwater.

In addition, the relationship between the changes of the sectional area, A, of beach profile (such as the dotted area in Fig. 3) and the shoreline position, y_s , is shown in Fig. 6, and is approximated by

$$A = 11\ y_s \qquad (1)$$

This relation indicates that the characteristic height of the beach change is about 11 meters.

III. WAVE CLIMATE OF OGAWARAKO COAST

The wave climate of Ogawarako Coast has been measured at Takahoko by the Ministry of Transport[6], which is located about 24 km north of the Misawa port. The wave height was measured at the depth of 17.5 meters using an ultrasonic wave gauge, and the wave direction was measured by the deformation of a ball caused by the water particle velocity. The directional probability density of the wave height calculated from the measured data over seven years from 1971 to 1977 is shown in Table 1. The prevailing directions of the incoming waves are ENE, E and ESE. We calculated an effective directional sum of the wave energy flux to define characteristic wave heights which would give the same wave energy flux as the directional sum over one year. It was found that characteristic wave heights were 1.45, 1.34 and 1.17 meters in the ENE, E and ESE directions, respectively, and the corresponding predominant periods were 9.0 seconds in the ENE and E, and 7.5 seconds in the ESE.

Since the shoreline near the breakwater is oriented about 5° counterclockwise from the north, the northward component of the wave energy flux has the magnitude of the same order as the southward component, although the northward component is slightly larger.

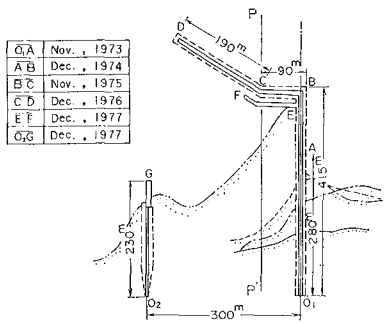

Fig. 3 Sketch of Misawa fishery port (refer to the legend in Fig. 2)

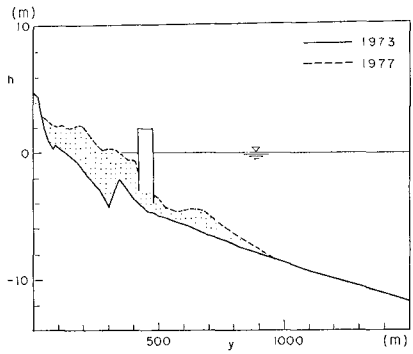

Fig. 4 Accretion near the port

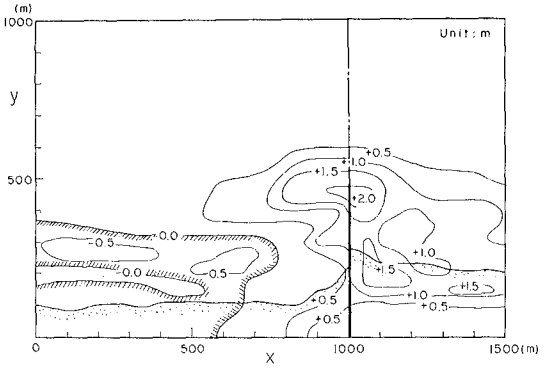

Fig. 5 Topographic changes around the port for one year from 1973 to 1974

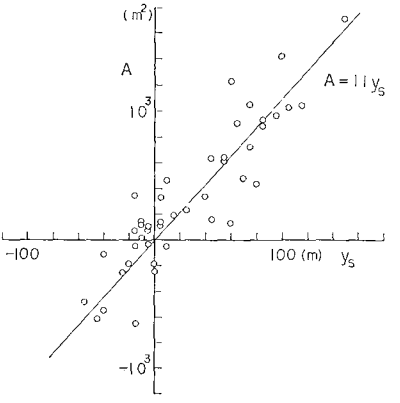

Fig. 6 Relationship between the changes of the beach section area, A, and the shoreline position, y_s

Table 1 Directional probability density of wave height calculated from the measured value from 1971 to 1977

wave height / direction	0.0 m ~ 05.	0.5 ~ 1.0	1.0 ~ 1.5	1.5 ~ 2.0	2.0 ~ 2.5	2.5 ~ 3.0	3.0 ~	Σ
NNE		0.001		0.001				0.002
NE	0.003	0.008	0.004	0.001		0.001		0.017
ENE	0.059	0.158	0.067	0.032	0.018	0.009	0.009	0.352
E	0.061	0.164	0.073	0.035	0.016	0.008	0.006	0.363
ESE	0.040	0.108	0.059	0.021	0.008	0.003	0.001	0.240
SE	0.005	0.012	0.006	0.002	0.001			0.026
Σ	0.168	0.451	0.209	0.092	0.043	0.021	0.016	1.000

IV. NUMERICAL SIMULATION OF SHORELINE CHANGES BY THE ONE-LINE THEORY

The one-line theory was applied to the shoreline changes near the Misawa port. The fundamental equations are,

$$\frac{\partial q}{\partial x}+h\frac{\partial y_s}{\partial t}=0 \tag{2}$$

$$q=F\left(-\frac{\partial y_s}{\partial x}-\tan\theta\right) \tag{3}$$

$$F=\frac{1}{8}\alpha w_0 K_r^2 H_i^2 C_{gi} \tag{4}$$

where q is the longshore sediment transport rate per unit length, h the characteristic height of beach change, y_S the position of shoreline, θ the wave direction, α the Savage coefficient, H_i the incoming wave height, and Cg_i the incoming wave group velocity.

First, the coefficient α was calculated from the volume changes and longshore component of wave energy flux at the site. The relation between volume changes per unit time, Q_z , and longshore component of wave energy flux, E_z , is expressed as follows:

$$Q_z=\alpha E_z \tag{5}$$

It was assumed to calculate the volume changes that northward sediment transport was fully blocked by the breakwater, and that shoreline changes outside of the survey area decreased exponentially with distance from the breakwater. The result is $Q_z = 1.56 \times 10^6$ m^3 for four years. Since the longshore component of wave energy flux of this coast is northerly, and given by $E_z = 1.93 \times 10^6$ ton.m/(m.year), we obtain $\alpha = 0.02$ using Eq. (5). This value corresponds fairly well to the traditional value of Savage coefficient, $\alpha = 0.217$.

The simulation of shoreline changes is carried out by solving implicit finite difference equations as follows,

$$\frac{1}{\Delta x}(q'_{i+1}-q'_i)+\frac{h}{\Delta t}(y'_{si}-y_{si})=0 \tag{6}$$

$$q'_i=F_i\left[-\frac{1}{\Delta x}(y'_{si}-y'_{si-1})-\tan\theta_i\right] \tag{7}$$

where the subscript i denotes a step of longshore distance, and the prime represents a time step. The boundary conditions, $q = 0$ at the breakwater and $y_S \to 0$ at $x = -2000$ meters were applied. The shoreline profile of the year 1973 was used as the initial condition. In this computation the time step was $\Delta t = 10$ days, the longshore width of the cell was $\Delta x = 50$ meters and the height of profile change was set $h = 11$ meters as discussed in the previous section.

For the seasonal changes of wave climate, the predominant wave height and wave direction for each month were given. The diffraction coefficient around the breakwater was once calculated for the initial topography to determine the longshore distribution of the coefficient, F, and this distribution was assumed unchanged.

Figure 7 shows the results of the shoreline simulation. Here, we set $\alpha = 0.18$ instead of 0.20, since $\alpha = 0.20$ resulted in overestimation of the shoreline changes. The calculated shoreline of 1976 agrees fairly well with the measured profile for $x < 1000$ meters although their difference increases near the breakwater. The measured and calculated shorelines of 1977 agree well for $x \leqq 1300$ meters, but the difference rapidly increases towards the breakwater.

Concerning the causes of the difference of measured and calculated shoreline changes, it should be mentioned that three-dimensional beach changes occurred in reality near the breakwater, since this south breakwater was extended in several stages and another breakwater was constructed 300 m north of it in 1977 as shown in Fig.3. The sand at the south of the breakwater moved along it and accumulated near its tip. Behind the breakwater, suspended sediment was also deposited in a relatively calm area. These phenomena are not considered in the calculation of coastline changes by the one-line theory, and it is necessary to use a three-dimensional model which takes into account the changes of wave, current and beach topography for the simulation in this region.

The shoreline change can be predicted to some extent, if suitable coefficient of the model are selected. However, the one-line theory does not have the capability for predicting changes of the onshore-offshore profile. Therefore, we apply the empirical eigenfunction method to the analysis of the beach profile changes in the next section.

V. EMPIRICAL PREDICTIVE MODEL OF BEACH PROFILE CHANGES

Winant et al.[7] studied beach changes at Torry Pine Beach by introducing an empirical eigenfunction method. They represented the bed elevation as a linear combination of products of functions of the offshore distance and of functions of time. The present authors[8] also applied this method to the analysis of data obtained at Ajigaura Beach. The results from the latter work indicates that the accretion caused by longshore movement of sand can be clearly separated from onshore-offshore movement.

The empirical eigenfunction method is essentially the same as the principal components analysis employed in the multivariate statistical

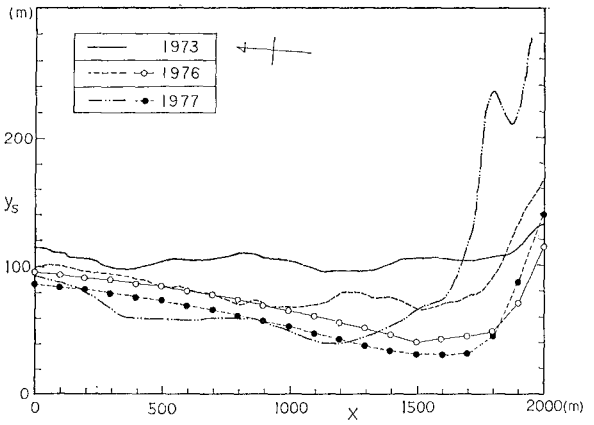

Fig. 7 Results of the shoreline simulation(The calculated shorelines of 1976 and 1977 are indicated by -○- and -●-,respectively. The measured profiles are shown by the solid, broken and chain lines.)

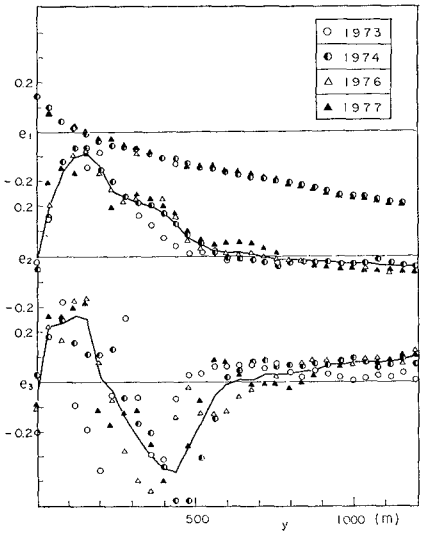

Fig. 8 Onshore-offshore profiles of the first, second and third eigenfunctions, e_1, e_2 and e_3

analysis. In the analysis of Winant et al., beach profile data at certain time intervals were used and the characteristic time changes were obtained. On the other hand, by analyzing beach profile data at certain longshore intervals, one can get the spatial characteristics of the profiles.

We now apply the empirical eigenfunction method to the bed elevation $h(x,y,t_0)$ which is a function of the offshore distance y, and longshore distance x at a certain time t_0. The expansion is expressed as follows,

$$h(x,y,t_0) = \sum_{k=1}^{n} e_k(y,t_0) \cdot C_k(x,t_0) \tag{8}$$

in which the empirical eigenfunctions e_k form an orthogonal set,

$$\sum_{y} e_m(y,t_0) \cdot e_n(y,t_0) = \begin{cases} 1, & m=n \\ 0, & m \neq n \end{cases} \tag{9}$$

In order to generate these functions, a symmetric matrix, A, is formed with the elements,

$$A_{ij} = \frac{1}{n_x n_y} \sum_{m=1}^{n_x} h(m\Delta x, i\Delta y, t_0) \cdot h(m\Delta x, j\Delta y, t_0) \tag{10}$$

where n_x and n_y are the total numbers of measuring points in the alongshore and offshore direction, respectively. The matrix A possesses a set of eigenvalues λ_k and a corresponding set of eigenfunctions $e_k(y,t_0)$, which are defined by the matrix equation,

$$Ae_k = \lambda_k e_k \tag{11}$$

The functions $C_k(x,t_0)$, which define the longshore changes of beach profile, are then evaluated as

$$C_k(x,t_0) = \sum_{y} h(x,y,t_0) \cdot e_k(y,t_0) \tag{12}$$

The method is useful to analyze spatial changes in beach profiles, such as the profiles around a breakwater or of a rhythmic topography. In some cases, it is desirable to use the data of changes of beach profile for the analysis of characteristic beach changes instead of the beach profile itself.

Although the functions e_k and C_k indicate beach characteristics at a certain time, they give the information of the characteristic beach changes. As far as accretion and errosion occur gradually, the functions e_k have approximately unchanged profiles and only the functions C_k change according to the time progress.

Figure 8 shows the onshore-offshore profiles of the first, second, and third eigenfunctions, e_1, e_2 and e_3. The solid line gives the average value over the four years indicated. The eigenfunction e_1 does not depend on the time. The eigenfunctions e_2 and e_3 show relatively larger time variations, but they can be reasonably approximated by the solid lines. Consequently, one can say that all the eigenfunctions e_k do not depend on the time for $k = 1$, 2 and 3.

The second eigenfunction e_2 has a positive value over a broad region of the shore and takes its positive maximum value near the shoreline as shown in Fig. 8.

The ratio of eigenvalues λ_k relative to the first eigenvalue λ_1 are $\lambda_2/\lambda_1 = 2.25 \times 10^{-2}$, $\lambda_3/\lambda_1 = 2.38 \times 10^{-3}$, and $\lambda_4/\lambda_1 = 7.38 \times 10^{-4}$. The contribution of each eigenfunction decreases by one order as compared to the preceeding eigenfunction.

Figure 9 shows the longshore changes of the function C_1 and C_2, which correspond to the first and second eigenfunctions, e_1 and e_2, respectively. The function C_1 shows almost no changes in 1973. However, the region having relatively small value expands gradually on the north coast of the breakwater year by year. This means that the beach slope of this region gradually became smaller. The function C_2, which indicates the longshore changes of the beach profile, is similar to the shoreline profile shown in Fig.2. The correlation between the function C_2 and the shoreline position y_s is drawn in Fig.10 and is given by

$$C_2 = \begin{cases} 0.065(y_s - 134), & y_s < 134m \\ 0.15(y_s - 134)^{0.75}, & y_s \geq 134m \end{cases} \qquad (13)$$

It is concluded from this that the second eigenfunction, e_2, corresponds to the profile changes due to the longshore sand transport.

We can calculate by the one-line theory the shoreline position, y_s, with a certain tolerance, which yields the value of the function C_2 through Eq. (13). Since the onshore-offshore profile is known at least approximately, we can then predict the three-dimensional beach changes due to the longshore sand transport from the products of the eigenfunction e_2 and the function C_2.

The function C_3 corresponding to the third eigenfunction e_3 is shown in Fig. 11. The absolute value of the function C_3 is smaller than that of the function C_2. As the third eigenfunction e_3 takes its positive value shoreward of the shoreline and a negative value in seaward, a positive value of the function C_3 implies accretion on the nearshore beach and erosion in the offshore zone as schematically shown in Fig. 12. On the south side of the breakwater, sand moved along the breakwater and accumulated at its offshore side. Accumulation also occurred near the shoreline but did not exceed that in the offshore. Therefore, the third eigenfunction is considered to correspond to the profile changes due to the sand movement along the breakwater.

The change of the function C_3 is supposed to be controlled by two factors which characterize respectively the profile changes near the shoreline and in the offshore zone. We selected the offshore distance y'' from the location of the four meter depth to the shoreline as shown in Fig. 12, and examined the relationship between y'' and the function C_3. The reason for the selection of this particular depth is that it approximately corresponds to the depth where the third eigenfunction e_3 takes its minimum value. As found in Fig. 13, we have the relation

$$C_3 = 0.0215(285 - y'') \qquad (14)$$

This indicates the possibility that the onshore-offshore profile changes might be represented by change of the offshore distance y'' between two characteristic lines. Since the function C_3 is determined by Eq. (14) if the offshore distance y'' is given, and the profile of the third eigenfunction e_3 is known, the three-dimensional beach changes around the breakwater can be evaluated.

As a typical example, we calculated the profile of the beach that lies 200 meters north of the south breakwater, using the measured shore-

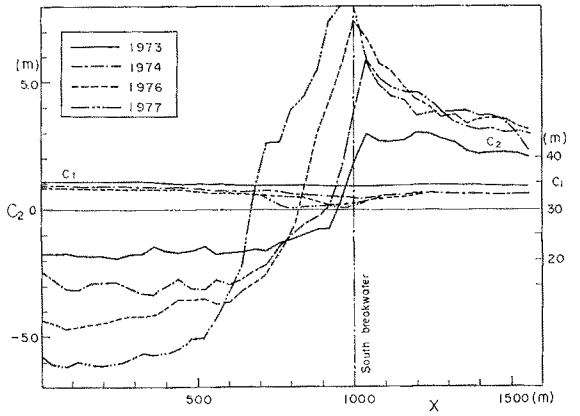

Fig. 9 Longshore changes of the functions C_1 and C_2 corresponding to the first and second empirical eigenfunctions

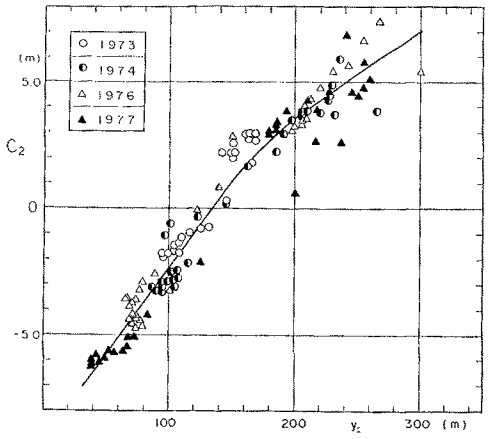

Fig. 10 Correlation between the function C_2 and shoreline position, y_s

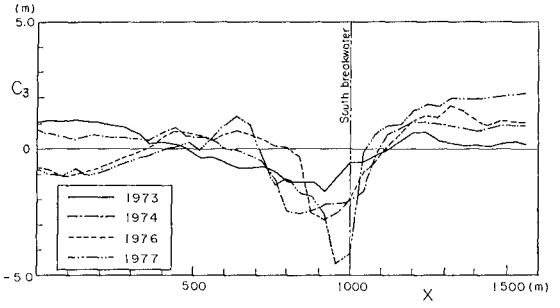

Fig. 11 Longshore changes of the function C_3 corresponding to the third eigenfunction

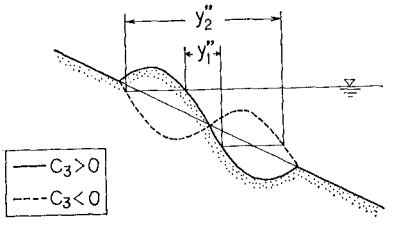

Fig. 12 A typical example of onshore-offshore profile changes

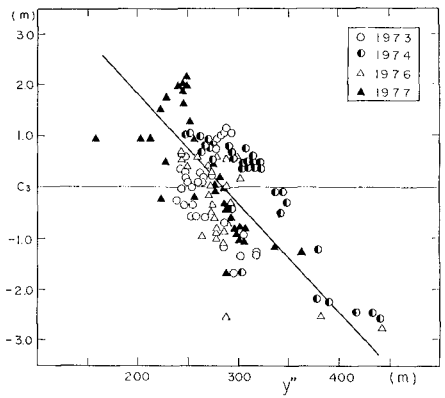

Fig. 13 Relationship between the distance y" and the function C_3

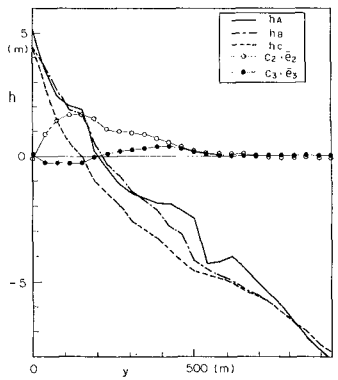

Fig. 14 Comparison of the measured beach profile and that calculated by the products of the eigenfunction e_k and the function C_k (h_A= measured beach profile, h_B= calculated beach profile, h_c= mean beach profile, C_2e_2, C_3e_3 = variation of beach profile corresponding to the second and third eigenfunctions)

line position. The shoreline position, y_s, and the offshore distance, y'', were given by 218 and 553 meters, respectively, at this location. By substituting these values into Eq. (13) and Eq. (14), C_2 and C_3 were found to be 4.16 and − 1.1 meters. In addition, C_1 is set to be 26.5 meters, which is the average taken over four years. Figure 14 shows the measured beach profile and the profile calculated by the products of the eigenfunctions e_k and C_k. The solid line, h_A, indicates the measured beach profile, the chain line, h_B, indicates the calculated beach profile, and the broken line, h_C, gives the mean beach profile. The calculated profile agrees fairly well with the measured one at the depth shallower than 2 meters, whereas thier disparity increases near the breakwater.

VI. CONCLUDING REMARKS

In order to discuss the beach profile change due to longshore and onshore-offshore sand transport, a new model was proposed, the empirical predictive model of beach profile change, by applying the empirical eigenfunction method. The model was applied to analyzing the data obtained at the Misawa fishery port.

As a consequence of this analysis, it was found that the first eigenfunction e_1 corresponded to the mean profile. The second eigenfunction e_2 turned out to correspond to the profile changes due to longshore sand transport, because its value was positive over a broad region of the shore, and the second time function C_2 corresponding to it, which gave longshore change of the beach profile, was correlated with the shoreline position, y_s. In addition, it was shown that the third eigenfunction e_3 corresponded to the profile changes due to the influence of the breakwater, because e_3 took positive values near the shoreline and negative values in the offshore zone, and the function C_3 was correlated with the offshore distance y'' of the four meter depth line from the shore.

Consequently, a basis of the two-line theory was substantiated, and the possibility of the development from a one-dimensional prediction model to a three-dimensional model of beach profile change was demonstrated.

REFERENCES

1) Pelnard-Considere, R.: Essai de theorie de lévolution des forms de rivage en plages de sable et de galets, Quatriemes Journées de l'Hydraulique, Paris, Les Energies de la Mer, Question III, rapport 1, Vol. 1, pp.289-298, 1956.
2) Bakker W. T.: The dynamics of a coast with a groyne system, Proc. 11th Conf. on Coastal Eng., pp.492-517, 1968.
3) Hashimoto, H.: Application of a prediction model for coastline changes to the Fuji Coast, Proc. 23th Conf. on Coastal Eng. in Japan, pp. 218-222, 1976. (in Japanese)
4) Tanaka, T., K. Noro, T. Suehiro, and T. Uda: An application of a prediction model for coastline changes to the planning of beach nourishment. Proc.25th Conf. on Coastal Eng. in Japan, pp. 213-217 1978. (in Japanese)
5) Sato, S., T. Kawanishi, N. Tanaka. and I. Irie: On the littoral drift of Ogawarako Coast, Proc. 19th Conf. on Coastal Eng. in Japan, pp. 7-11, 1972. (in Japanese)
6) Observation report of meteorology and wave climate in Ogawarako Province, Hachinohe Port Construction Office, Cecond District Port

MODELING ON-OFFSHORE SEDIMENT TRANSPORT IN THE SURFZONE

by James A. Bailard[1]

ABSTRACT

An energetics-based surfzone sediment transport model was evaluated in its ability to predict on-offshore sediment movements using current meter and beach volume measurements from the Nearshore Sediment Transport Study at Torrey Pines Beach, California. The magnitude of pertinent wave velocity moments were also evaluated from the same data set. These moments were found to be adequately represented by linear functions of the significant wave height. Because of the apparent noise in the beach volume measurements and the limited duration of the current meter records, the results of the model evaluation were inconclusive. However, a simplified version of the model, when coupled with estimated wave velocity moments, was found to mimic observed on-offshore sediment movements as a function of significant wave height.

INTRODUCTION

Waves breaking on a beach cause sediment to be transported both parallel to (longshore) and perpendicular to (on-offshore) a beach. Although on-offshore and longshore sediment transports are manifestations of the same process, past investigations have generally treated them separately for reasons of simplicity. Fortunately, this separate approach has been relatively successful, because wave refraction causes the waves to have near normal incidence to the beach at breaking, and the mean longshore and on-offshore currents are generally much weaker than the oscillatory velocity mangitude. As a result, the longshore transport has been found to be relatively well modeled (e.g., Inman and Bagnold, 1963; Komar, 1971) as the product of an oscillatory velocity-induced sediment load and a transport velocity proportional to the longshore current. Similarly, the on-offshore transport may be modeled as a balance between gravity, the asymmetry of the oscillatory velocity distribution, and the on-offshore steady current (e.g., Inman and Frautschy, 1966; Bowen, 1980; Bailard, 1981).

Although the above processes have been qualitatively understood for some time, relatively greater progress has been made in quantitatively predicting the longshore transport rate. Predicting the on-offshore transport rate has proven more difficult because: models predicting oscillatory velocity asymmetries and mean on-offshore currents inside the surfzone has been lacking; the effect of the downslope component of

[1]Naval Civil Engineering Laboratory, Port Hueneme, California 93043

the sediment load on the on-offshore sediment transport has generally not been adequately represented and the dynamic near-equilibrium of on-offshore transport on a stable beach tends to magnify the importance of second order effects such as the vertical velocity structure and the threshold criteria for sediment movement.

Because of these difficulties, most models have sought to correlate on-offshore sediment transport with incident wave properties. Some examples of this type of approach include: the wave steepness models by Dean (1973) and Hattori and Kawamoto (1981); the wave height models by Saville (1957), Aubrey (1978) and Short (1978); and the wave power model by Short (1978). A few models have considered a greater degree of detail in the fluid sediment motions, and include those by Inman and Frautschy (1966), Bowen (1980) and Bailard (1981). All three of the latter models are based on adaptations of Bagnold's (1963, 1966) sediment transport model for streams, with Bailard's (1981) model being the most complete in that nonnormal wave incident in the presence of longshore currents is considered.

A common aspect of Bowen's (1980) and Bailard's (1981) energetics-based models is the importance of several surfzone velocity moments in determining the direction and magnitude of the on-offshore sediment tranport. These moments are defined in terms of idealized monochromatic waves. However, they can be extended to spectral wave inputs as well (Guza and Thornton, in review). Using Stokes' second-order wave solution and Longuet-Higgins (1953) bottom streaming model to estimate the wave velocity asymmetry and mean on-offshore current, respectively, Bowen (1980) and Bailard (1981) were able to qualitatively describe the equilibrium beach profile as a funciton of the incident wave amplitude, the wave frequency, and the sediment fall velocity. Small amplitude, long period waves were found to produce a steep beach while large amplitude, short period waves were found to produce a flat beach. Large diameter sand grains with high fall velocities were also observed to produce steeper beaches than smaller diameter sand grains with lower fall velocities. These results qualitatively confirmed observed beach behavior, but neither the nonlinear wave solution nor the mean current solutions are considered valid inside the surfzone.

Because of the inability of existing wave shoaling models to accurately describe wave velocity asymmetry and mean on-offshore currents inside the surfzone, little is known about these quantities. Two recent studies describing limited field measurements of wave velocity moments (Huntley and Bowen, 1975; Guza and Thornton, in review) suggest that the magnitudes of these moments may be a function of the incident wave conditions, the beach slope, and the local water depth. Analysis of more comprehensive data sets are needed to test this hypothesis.

A lack of appropriate field data has also restricted the evaluation of existing on-offshore sediment transport models. Recently, however, a series of large-scale field experiments have been conducted as part of the Nearshore Sediment Transport Study (NSTS). The first of these experiments was conducted at Torrey Pines Beach, Calif., during November 1978. During this time, simultaneous measurements of deepwater wave characteristics, surfzone nearbottom velocity distributions, and beach profile changes were measured. Details of the experiment are described in Gable (1979).

The success of Bowen's (1980) and Bailard's (1981) total load surfzone models in qualitatively describing the variation of the equilibrium beach slope with wave and sediment characteristics suggested that Bagnold's energetics approach may be useful in quantitatively predicting the on-offshore sediment transport. Consequently, a study was initiated to test the ability of Bailard's (1981) total load sediment transport model to predict daily on-offshore sediment movements using data from the NSTS experiment at Torrey Pines Beach, Calif., in November 1978. The objectives of the study were threefold. First, the model was tested in its ability to predict daily beach volume changes using relatively short (1- to 2-hour) surfzone current meter records. Second, a relationship was sought between average values of surfzone velocity moments and incident wave characteristics. Lastly, a simplified on-offshore model was combined with the average surfzone velocity moments to predict the on-offshore sediment transport as a function of significant wave height.

SEDIMENT TRANSPORT MODEL

Bailard's (1981) total load sediment transport model is based on an adaptation of Bagnold's (1963, 1966) energetics-based total load sediment transport model for streams. The latter is generalized for time-varying flow over an arbitrarily sloping bottom, resulting in

$$\langle \vec{i}_t \rangle = \rho c_f \frac{\varepsilon_B}{\tan\phi} \left\langle \left|\vec{u}_t\right|^2 \vec{u}_t \right\rangle - \frac{\tan\beta}{\tan\phi} \left\langle \left|\vec{u}_t\right|^3 \right\rangle \hat{i}$$

$$+ \rho c_f \frac{\varepsilon_S}{W} \left\langle \left|\vec{u}_t\right|^3 \vec{u}_t \right\rangle - \frac{\varepsilon_S}{W} \tan\beta \left\langle \left|\vec{u}_t\right|^5 \right\rangle \hat{i} \qquad (1)$$

where $\vec{i}_t$ = instantaneous sediment transport rate vector

ρ = density of water

c_f = drag coefficient of the bed

ε_B = the bedload efficiency factor

ϕ = internal angle of friction of the sediment

$\tan\beta$ = the bed slope

ε_S = suspended load efficiency factor

W = is the fall velocity of the sediment

$\vec{u}_t$ = instantaneous nearbottom fluid velocity vector

$\hat{i}$ = unit vector directed upslope

$\langle\ \rangle$ = time-average

Note that both the bedload (first bracketed quantity) and the suspended load (second bracketed quantity), consist of a primary component directed parallel to the instantaneous fluid velocity vector and a secondary component directed downslope. The latter is associated with the downslope gravity component of the sediment load.

Equation 1 is assumed to be valid for any nearbottom velocity field and can be used with data from a two-axis (x and y) current meter to directly predict the time-averaged sediment transport rate vector at the current meter location.

Figure 1 depicts a plane contour beach with the x-axis directed shoreward and normal to the beach and the y-axis directed parallel to the beach. The slope of the beach is tan β. For modeling, it is convenient to use a monochromatic wave representation for the nearbottom water velocity field as a means of simplifying Equation 1. Bailard (1981) assumed a velocity field composed of an oscillatory velocity component $\tilde{u}$ oriented at an angle α to the x-axis and a steady velocity component $\bar{u}$ oriented at an angle θ to the x-axis. The total velocity vector $\vec{u}_t$ then becomes

$$\vec{u}_t = (\tilde{u} \cos \alpha + \bar{u} \cos \theta)\, \hat{i} + (\tilde{u} \sin \alpha + \bar{u} \sin \theta)\, \hat{j} \qquad (2)$$

In addition, the oscillatory velocity component is assumed to be asymmetrical being composed of a primary component u_m with frequency σ and a secondary harmonic u_{m2} with frequency 2σ so that

$$\tilde{u} \sim u_m \cos \sigma t + u_{m2} \cos 2\sigma t + \ldots \qquad (3)$$

An analysis of surfzone current meter records at Torrey Pines Beach showed that $\bar{u} \ll u_m$ and $\sin\alpha \ll 1$, thus substitution of Equations 3 and 4 into Equation 1, yields the idealized on-offshore transport equation

$$\langle i_x \rangle = \rho c_f u_m^3 \left\{ \frac{\varepsilon_\beta}{\tan \phi} \left[\Psi_1 + \frac{3}{2} \delta_u - \frac{\tan \beta}{\tan \phi} u_5^* \right] + \frac{u_m}{w} \varepsilon_s \left[\Psi_2 + \delta_u u_3^* - \frac{u_m}{w} \varepsilon_s \tan \beta\, u_5^* \right] \right\} \qquad (4)$$

where

$$\delta_u = \frac{\bar{u}}{u_m} \cos \theta \qquad (5)$$

$$\Psi_1 = \frac{\langle \tilde{u}^3 \rangle}{u_m^3} ; \qquad \Psi_2 = \frac{\langle |\vec{u}_t|^3 \tilde{u} \rangle}{u_m^4} \qquad (6a,b)$$

$$u_3^* = \frac{\langle |\vec{u}_t|^3 \rangle}{u_m^3} \; ; \qquad u_5^* = \frac{\langle |\vec{u}_t|^5 \rangle}{u_m^5} \tag{7a,b}$$

For weak mean currents, Snell's law and the spilling wave hypothesis can be used to estimate the magnitudes of α, u_m, u_3^*, and u_5^* throughout the surfzone as a function of incident wave conditions.† Unfortunately, the two skewness parameters Ψ_1 and Ψ_2, as well as the normalized mean onshore current δ_u, cannot be estimated from present surfzone wave shoaling models. One of the objectives of this study was to examine measured surfzone values of Ψ_1, Ψ_2, and δ_u using data from the NSTS Torrey Pines experiment (Gable, 1979). In this respect, the present study was a continuation of the study by Guza and Thornton (in review), who showed that the quantities defined in Equation 4 are meaningful only for monochromatic waves incident from a single direction α. On an actual beach the incident waves compose a spectrum with varying energy content at different frequencies and wave angles. As a result, Guza and Thornton (in review) defined equivalent quantities for Ψ_1, Ψ_2, u_m, u_3^* and u_5^*, which may be estimated from the measured current meter data as follows: Assuming that the current meter time series, $\vec{u}_t$ is composed of mean components $\bar{u}$ and $\bar{v}$, and oscillatory componets, $\tilde{u}$ and $\tilde{v}$, i.e.

$$\vec{u}_t = (\tilde{u} + \bar{u})\,\hat{i} + (\tilde{v} + \bar{v})\,\hat{j} \tag{8}$$

then

$$u_m^2 = 2\,(\langle \tilde{u}^2 \rangle + \langle \tilde{v}^2 \rangle) \tag{9}$$

$$u_m^3\,\Psi_1 = \langle \tilde{u}(\tilde{u}^2 + \tilde{v}^2) \rangle \tag{10}$$

$$u_m^4\,\Psi_2 = \langle |\vec{u}_t|^3\,\tilde{u} \rangle \tag{11}$$

$$u_m^3\,u_3^* = \langle |\vec{u}_t|^3 \rangle \tag{12}$$

$$u_m^5\,u_5^* = \langle |\vec{u}_t|^5 \rangle \tag{13}$$

†Note, however, that Guza and Thornton (in review) found that the commonly assumed spilling wave hypothesis did not lead to an accurate estimate of u_m.

DATA ANALYSIS

Data Set Description

In November 1978, a month-long field experiment was conducted at Torrey Pines Beach as part of the Nearshore Sediment Transport Study (NSTS). Torrey Pines Beach, Calif., is a plane-contoured beach with a concave profile. The slope of the beach face is approximately 0.05, decreasing to about 0.02 within the surfzone. The sand on the beach is moderately well sorted with a mean diameter of 0.17 mm. The beach exhibits little or no bar-trough features. The experiment consisted of the simultaneous measurement of incident wave conditions, nearbottom water velocities distributions, sand tracer movements, and beach profile changes. The incident wave climate was measured in 10 meters of water with a linear array of pressure sensors. Nearbottom water velocities were measured using dual-axis (x and y) electromagnetic current meters, while the beach profiles were measured with a rod and transit onshore and a fathometer offshore.

The current meters were placed in a cross-shaped pattern within the nearshore area. Referring to Figure 2, 7 current meters were placed in a line perpendicular to the beach, ranging in depth from 0.25 meters to 6 meters relative to mean sea level (MSL). Ten other current meters were placed in a line parallel to the beach at a depth of about 1 meter relative to MSL. The beach profiles were measured at five ranges along the beach. Further details of the experiment can be found in Gable (1979).

Model Evaluation

One of the objectives of the present study was to evaluate the ability of Equation 1 to predict daily beach volume changes using NSTS data. Following the approach used by Seymour and King (1982), daily beach volume changes were computed by integrating the beach profile changes across 100 meters of beach face. The seaward extremity of the integration interval roughly coincided with the location of the shore-parallel current meters so that a simple box model analysis could be used to estimate the beach volume changes. In the present study the flux of sand into or out of the seaward edge of the box was assumed to be predicted by Equation 1 using the measured current meter data from each shore parallel current meter. The measured beach volume changes used in the present study are those tabulated by Seymour and King (1982).

Equation 1 has 3 free parameters: the bed friction coefficient c_f, the bedload efficiency factor ε_B, and the suspended load efficiency factor ε_S. In the present study, a value of 0.005 was selected for c_f, based on an analysis of longshore current data at Silver Strand Beach, Calif., (Bailard, 1981). This beach has a bed slope similar to that found at Torrey Pines Beach (0.034) and is located 15 miles to the south. Thornton and Guza (1982) analyzed longshore current data at Torrey Pines Beach and concluded that $c_f = 0.01 \pm 0.01$. Thus because of the large uncertainty interval, the Torrey Pines data set could not be used to directly estimate the size of c_f.

The bedload and suspended load efficiency factors ε_B and ε_S are the remaining two free parameters in Equation 2. Rewriting Equation 1 to isolate these factors, we obtain

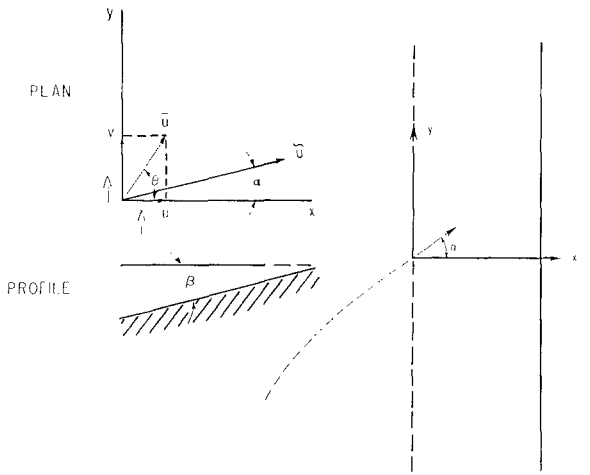

Figure 1. Schematic diagram showing the position of the beach (solid line), the breakpoint (dashed line), the wave angle α and the oscillatory and steady water velocities $\tilde{u}$ and $\bar{u}$ (from Bailard and Inman, 1980, with permission).

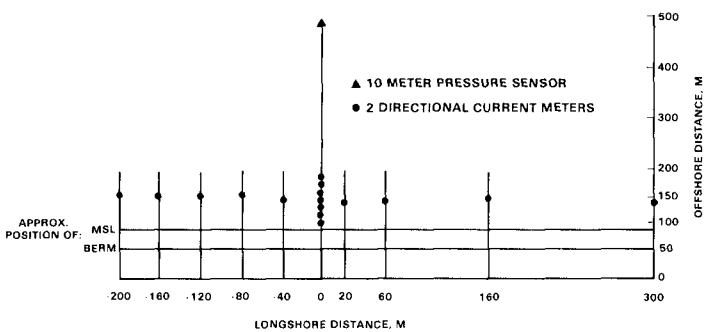

Figure 2. Relative current meter and pressure sensor positions for the NSTS Torrey Pines experiment (adapted from Seymour and King, 1982).

$$\langle i_x \rangle = \varepsilon_B I_A + \varepsilon_S I_B - \varepsilon_S^2 I_C \tag{14}$$

where

$$I_A = \frac{\rho c_f}{\tan \phi} \left\langle \left|\vec{u}_t\right|^2 \vec{u}_t \cdot \hat{i} \right\rangle - \frac{\tan \beta}{\tan \phi} \left\langle \left|\vec{u}_t\right|^3 \right\rangle \tag{15}$$

$$I_B = \frac{\rho c_f}{W} \left\langle \left|\vec{u}_t\right|^3 \vec{u}_t \cdot \hat{i} \right\rangle \tag{16}$$

$$I_C = \frac{\rho c_f}{W^2} \tan \beta \left\langle \left|\vec{u}_t\right|^5 \right\rangle \tag{17}$$

Equation 14 expresses the on-offshore transport rate in terms of the immersed weight transport. The volumetric transport rate Q_x may be related to the immersed weight transport rate $\langle i_x \rangle$ by the following equation

$$Q_x = \frac{\langle i_x \rangle}{(\rho_s - \rho) g N_o} \tag{18}$$

where ρ_s = density of the sand grains

g = gravity

N_o = "at rest" volume concentration of sediment assumed here to be 0.6

The procedure used to estimate the bedload and suspended load efficiencies ε_B and ε_S was as follows. First, daily estimates of I_A, I_B and I_C were obtained from 64-minute records for each of the 10 shore-parallel current meters. These estimates were averaged together to form a single daily estimate, assumed to be representative of the general experiment area. Table 1 contains a summary of the estimated values for I_A, I_B, and I_C. Next, a correlation analysis was conducted to determine the lag time between the predicted volume changes and the measured changes. Using previously estimated values of $\varepsilon_B = 0.21$ and $\varepsilon_S = 0.025$ (Bailard, 1981), Equation 14 was used to predict the beach volume changes which were then correlated with measured volume changes using lag times of zero and 1 day. The maximum correlation ($R^2 = 0.19$) occurred with a lag time of 1 day, as was found by Seymour and King (1982) for several other models using the same data set. The lag time result was insensitive to a range of values of ε_B and ε_S, although R^2 varied as would be expected.

A nonlinear least-squares estimation procedure (Draper and Smith, 1966), was used to estimate ε_B and ε_S from the lagged data in Table 1.

The estimation procedure required constructing a contour map of the mean square error S, defined as

$$S\ (\varepsilon_B\ \varepsilon_S) = \frac{1}{n-2} \sum_{i=1}^{n} (V_{meas} - V_{pred})^2 \qquad (19)$$

where n = number of data pairs (17)

V_{meas} = measured beach volume change with a 1-day lag time

V_{pred} = predicted beach volume change

Figure 3 shows a plot of S versus ε_B and ε_S. The minimum mean square error occurred at $\varepsilon_B = 0.10$ and $\varepsilon_S = 0.020$. These estimates are similar in size to those estimated by Bailard (1981) ($\varepsilon_B = 0.21$ and $\varepsilon_S = 0.025$) based on longshore transport data, however, the 95% confidence limits on ε_B and ε_S are much broader in the present study reflecting in part the low degree of correlation between the measured and predicted beach volume changes. In both cases, however, the predicted values of ε_B and ε_S fall within each other's areas of uncertainty.

Figure 4 shows a plot of the measured and predicted beach volume changes as a function of time. The figure also shows a plot of the signficant wave height as a funciton of time. The beach volume changes shown in Figure 4b were predicted from Equation 1 using the procedure described above. The beach volume changes shown in Figure 4a were predicted by the simplified Equiation 4 and will be discussed later.

Comparing the predicted and measured beach volume changes, Figures 4b and 4c respectively, it is clear that the measured volume changes are not well predicted by the model. Only the maximum erosional event on 12 November was predicted by the model and then at a reduced magnitude. The erosional and accretional events on November 6, 7 and 20 are clearly not predicted by the model.

The low degree of correlation between the measured and predicted beach volume changes raises questions about the ability of Bailard's (1981) sediment transport model to predict on-offshore sediment transports. It should be recognized, however, that predicting the on-offshore sediment transport rate is a severe test of a model because the net transport represents a small difference between two relatively large instantaneous on and offshore sediment transports. Small biases in either the onshore or offshore direction can significantly influence the predicted direction and magnitude of the net transport. Additional factors which may account for the lack of correlation include the temporal and spatial variability of the measured wave velocity moments and the apparent nosiness of the measured beach volume data.

Considering the wave velocity moments, a sensitivity analysis was performed whereby, for selected days, estimates of the on-offshore transport rate were calculated for consecutive 64-minute segments of time. For a day with moderate waves (November 4), the standard deviation of these estimates was 22% of the predicted mean for four consecutive segments. For a day with larger waves (November 12), this value

increased to 46% for three consecutive segments. In addition, individual current meters showed a much wider range of variation (up to 800%) between consecutive hours. These results suggest that although the beach may generally be in a state of near dynamic equilibrium, small changes in the incident wave conditions or the tide may significantly influence short-term local on-offshore movements. Moreover, for the data set studied, it appears that current meter records of 1 to 4 hours may not be of long enough duration to accurately estimate the daily beach volume changes.

Another factor which may account for a low correlation between predicted and measured beach volume changes are potential inaccuracies in the measured beach volume changes. These changes were calculated from the integrated difference between the daily beach profile measurements. Although the precision of these estimates is difficult to assess, daily variations as great as ± 10 m^3/m-day are seen in Figure 4c without a corresponding change in the significant wave height (4d). Seymour (in review) also noted the relative noisiness of the Torrey Pines data set compared with later NSTS data sets measured at Leadbetter Beach, CA, and Virginia Beach, VA.

Because of the above uncertainties, the evaluatuion of Bailard's (1981) sediment transport model was judged inconclusive. Other data sets with longer current meter records and more accurate beach profile measurements are needed before an accurate evaluation of the model can be made. It may also be that it is inherently difficult to predict macro-scale beach volume changes using a micro-scale sediment transport model.

Velocity Moment Magnitudes

The above discussion concerned the ability of Equation 1 to predict on-offshore sediment transports. Equation 4 is a greatly simplified version of Equation 1, and is potentially more useful for modeling on-offshore sediment transports. Unfortunately, this equation still contains a number of surfzone velocity moments, of which little is known. These moments include the wave velocity skewness parameters Ψ_1 and Ψ_2, the normalized onshore current δ_u, and the normalized velocity magnitudes u_3^* and u_5^*.

Of these quantities, only u_m, u_3^*, and u_5^* can be estimated from linear wave theory. For normally incident waves having a Gaussian distribution and weak mean currents, u_3^* and u_5^* can be shown to be equal to 0.562 and 1.13, respectively (Guza and Thornton, in review). Similarily, assuming wave saturation and spilling waves, linear wave theory predicts that

$$u_m = \frac{\gamma}{2}\sqrt{g\,h} \tag{20}$$

where $\gamma = H/h$

h = local water depth

H = local wave height

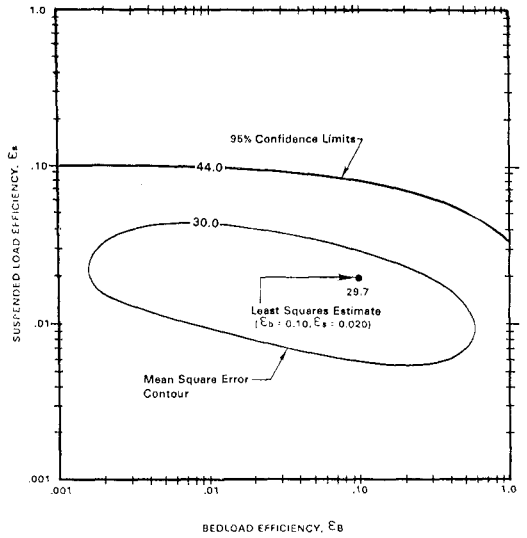

Figure 3. Least squares estimated bedload and suspended load efficiency factors, ϵ_B and ϵ_S.

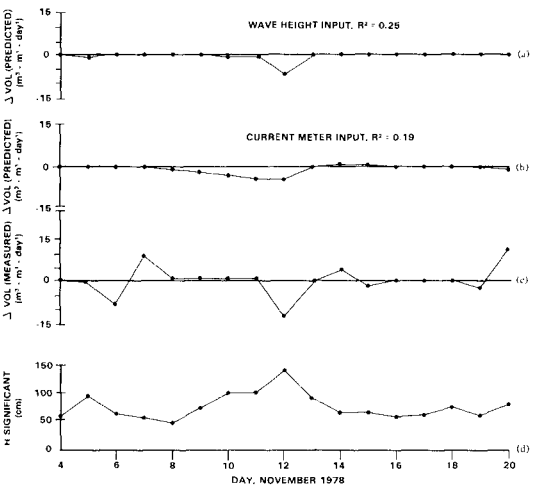

Figure 4. Comparison between predicted beach volume changes (a, b) and measured beach volume changes (c). The volume changes shown in (a) were predicted from Equation 4 using the measured wave heights (d), while the volume changes shown in (b) were predicted from Equation 1.

Equation 20 suggests that u_m should decrease from a maximum at the breakpoint to zero at the beach. In fact, field measurements at Torrey Pines Beach have shown that u_m is almost constant across the surfzone, due to the presence of low frequency surf beat motions within the inner part of the surfzone (Guza and Thornton, in review). The remaining parameters in Equation 4 (Ψ_1, Ψ_2, and δ_u) are zero for linear waves but nonzero for nonlinear waves. Measurements (Huntley and Bowen, 1975, Guza and Thornton, in review) bave shown that they are in fact nonzero under actual field conditions and may vary in magnitude and sign with varying incident wave conditions.

One of the objectives of the present study was to investigate these surfzone wave velocity moments using the NSTS Torrey Pines data set and determine whether their magnitudes can be estimated from incident wave conditions. Values for the parameters Ψ_1, Ψ_2, δ_u, u_3^* and u_5^* were estimated from 64-minute-long records for each of the seven shore perpendicular current meters closest to shore. Because of the temporal and spatial variability of these quantities, mean surfzone values were obtained by averaging the results of all seven current meters. Table 2 is a summary of these average surfzone velocity parameters and the incident wave characteristics for each of the 9 days investigated. The wave characteristics were obtained from Guza and Thornton (1980, 1982, in review) and Seymour and King (1982) who analyzed pressure sensor records measured in 10 meters of water.

Linear and second-order wave theories suggest that the even velocity moments u_m, u_3^*, and u_5^* should be related to the significant wave height, while the odd velocity moments Ψ_1, Ψ_2, and δ_u should also be related to the wave period and the average beach slope. It can be hypothesized that the odd velocity moments may be a function of a surf similarity parameter such as that introduced by Battjes (1974), Guza and Inman (1975), and others. This parameter, ε, can be defined as

$$\varepsilon = a\,\sigma^2 \Big/ g \tan^2\beta \qquad (21)$$

where a = half the breaking wave height

For small values of ε, less than 2.0 to 2.5, reflective conditions with surging breakers are observed, while for larger values of ε, dissipative conditions are observed.

For the conditions found at Torrey Pines Beach during the NSTS experiment, dissipative conditions prevailed, but it could not be determined whether the odd wave velocity moments were a function of ε. The range of significant wave heights varied from 55 to 140 cm; however the peak wave period varied much less, ranging from approximately 10 to 14 seconds. The variation in mean beach slope during the experiment was also very small, so that the slope was approximately a constant 0.02. As a result, the surf similarity parameter ε was primarily a function of the significant wave height H_s. This suggested that for the Torrey Pines data set, a relationship might be sought between all of the relevant surfzone velocity moments and the significant wave height H_s.

After plotting the mean surfzone values of Ψ_1, Ψ_2, δ_u, u_m, u_3^* and u_5^* versus H_s (Bailard, 1982), a linear relationship between variables

Table 1. Estimated and Measured Beach Volume Changes and Incident Wave Characteristics

Day (Nov 1978)	I_A (dyne cm^{-1} sec^{-1} x 10^{-6})	I_B (dyne cm^{-1} sec^{-1} x 10^{-4})	I_C (dyne cm^{-1} sec^{-1} x 10^{-4})	V_{pred} (m^3 m^{-1} day^{-1})	V_{meas} (lagged 1 day) (m^3 m^{-1} day^{-1})
4	9.87	3.76	4.00	0.72	0.21
5	-14.8	1.18	6.42	0.32	-0.28
6	-9.78	0.65	3.05	0.02	-8.2
7	10.2	2.54	1.78	0.52	9.3
8	-17.5	0.66	1.94	-0.27[a]	1.45
10	-61.5	-10.6	10.2	-2.41[a]	1.08
11	-115	-15.6	12.1	-3.74[a]	1.08
12	-121	-16.1	21.6	-3.9	-13.4
13	-5.53	2.47	6.62	0.36	0.05
14	15.7	5.05	5.72	1.0	3.9
15	12.1	6.00	4.92	1.12	-2.05
16	-4.32	0.86	1.99	0.10	1.05
17	11.3	4.10	4.20	0.79[a]	0.78
18	-1.36	3.21	5.50	0.52[a]	0.78
19	1.83	2.00	4.25	0.34	-1.99
20	-33.0	-2.84	5.00	-0.79	11.2

[a]Estimated as half the 2-day change.

Table 2. Average Surfzone Velocity Parameters and Incident Wave Characteristics

Date (Nov 1978)	H_s (cm)	S	Ψ_1	Ψ_2	δ_u	u_m (cm sec^{-1})	u^*_3	u^*_5
4	55	0.00126	0.206	0.204	-0.131	58.2	0.550	1.25
6	65	0.00148	0.197	0.240	-0.124	59.2	0.603	1.20
7	59	0.00117	0.234	0.362	-0.088	51.8	0.594	1.35
10	101	0.00163	0.097	-0.019	-0.160	69.8	0.731	1.26
11	99	0.00303	0.106	-0.152	-0.250	78.4	0.687	1.11
12	140	0.00341	0.134	-0.035	-0.210	87.2	0.574	0.940
13	91	0.00124	0.222	0.326	-0.100	69.3	0.587	1.27
17	62	0.00194	0.232	0.352	-0.081	56.9	0.574	1.24
19	73	0.00128	0.223	0.350	-0.070	56.1	0.574	1.28

was suggested. Using regression analysis, the following equations were obtained:

		Correlation Coefficient R^2	
$\Psi_1 = 0.303 - 0.00144\ H_s$		0.98	(22)
$\Psi_2 = 0.603 - 0.00510\ H_s$		0.83	(23)
$\delta_u = 0.458 - 0.00157\ H_s$		0.96	(24)
$u_m = 31.9 + 0.403\ H_s$		0.99	(25)
$u_3^* = 0.548 + 0.000733\ H_s$		0.99	(26)
$u_5^* = 1.50 + 0.00346\ H_s$		0.99	(27)

where u_m is measured in cm/sec and H_s in cm.

Equations 22 through 27 show that for the conditions found at Torrey Pines Beach, Ψ_1, Ψ_2 and δ_u decrease markedly with increasing wave height. This is in direct contrast to Stokes' second-order wave solution and Longuet-Higgins' (1953) bottom-streaming solutions, which predict increasing values of these variables with increasing wave height. The remaining parameters, u_m, u_3^*, and u_5^*, behave more as would be predicted by linear wave theory, with u_m increasing with increasing wave height and u_3^* and u_5^* being relatively constant. Typical observed values of u_3^* and u_5^* were 0.6 and 1.2, respectively (very close to the theoretical values based on a Gaussian wave distribution).

ON-OFFSHORE TRANSPORT SIMULATION

The simplified on-offshore sediment transport model Equation 4 contains the wave velocity skewness parameters Ψ_1 and Ψ_2, the mean on-offshore current δ_u, the orbital velocity magnitude $\tilde{u}_m$, and the normalized total velocity magnitudes u_3^* and u_5^*. Combining Equation 4 with Equations 22 to 27, the average surfzone on-offshore transport rate and direction can be predicted as a function of the significant wave height and the sediment fall velocity. The other free parameters in Equation 4 include the bed drag coefficient c_f, the bedload efficiency ε_B, and the suspended load efficiency ε_S. For the present study these variables were assumed to be equal to 0.005, 0.21, and 0.025, respectively, based on an analysis of field and laboratory data (Bailard (1981).

Figure 5 shows a plot of the predicted on-offshore sediment transport rate as a function of the significant wave height. The sediment fall velocity was assumed to be equal to 4 cm/sec, which is appropriate for the sand found at Torrey Pines Beach. The bedload-transport rate is depicted by the dashed line, the suspended load transport rate by the dotted line, and the total load transport rate by the solid line. Figure 5 suggests that, for conditions similar to those at Torrey Pines Beach during the NSTS experiment, sand is moved onshore when the significant wave height is less than approximately 90 cm and offshore when

it is greater. The maximum onshore transport rate (0.8 m^3m^{-1} day^{-1}) occurs when H_s is equal to approximately 59 cm. For waves with a significant wave height greater than approximately 150 cm, the transport rate is larger by a factor of 10 and directed offshore. Under most conditions, the predicted bedload and suspended load transports are both in the same direction. Near the null point (H_s ~ 90 cm), however, the bedload is directed offshore while the suspended load is directed onshore.

Qualitatively, Figure 5 confirms some aspects of observed beach behavior. During prolonged periods of small waves, a beach is seen to slowly accrete. With the appearance of the first large swell, however, the beach can cut back dramatically within a few days. Figure 5 also qualitatively supports Short's (1978) observations at several Australian beaches that the neutral point wave height separating accretion from erosion was equal to 120 cm. Although the present study suggests a neutral point wave height of 90 cm, the magnitudes are similar.

The simplified on-offshore transport model represented by Figure 5 can also be used to predict beach volume changes at Torrey Pines Beach from the measured signficant wave heights. Referring to Figure 4, the predicted beach volume changes (4a) can be compared with the measured changes (4c). As with the more complex model (Equation 1), only the erosion event on 12 November is predicted but at a decreased magnitude. The degree of correlation, R^2, between predicted and measured beach volume changes is 0.25 for the simple model versus 0.19 for the more complex model. The simple model is thus somewhat better in predicting the measured changes.

Neglecting for a moment the observed relationship between the beach slope and the sand size, the relative effect of different sediment fall velocities on the total load sediment transport rate may be predicted from Equations 4 and 22-27. Referring to Figure 6, increasing the fall velocity is seen to decrease the magnitude of the on-offshore transport rate. As a result, a beach with fine sand would be expected to experience more rapid beach volume than an equivalent beach with coarse sand.

DISCUSSION

The applicability of these results to other sites and to other wave conditions is unknown; however, it is hypothesized that the results are relatively site and time specific. For monochromatic waves and plane contour beaches, the surfzone hydrodynamics have been analytically shown to be a function of the incident wave height, direction, and period, as well as the beach slope. For random waves, the shapes of the energy and directional spectrums may also be important. During the NSTS Torrey Pines experiment, the waves were almost normally incident with a near uniform period. Moreover the beach slope changed little during the month. The only parameter that varied to any significant degree was the wave height, which varied by a factor of 3. As a result, Figure 5 cannot be easily extended to more general conditions.

Qualitatively, however, it can be hypothesized for that there may be a family of curves, similar in shape to those in Figure 5 but which vary with beach slope. Flat beaches typical of large waves and fine sand would be expected to have a neutral point corresponding to a larger

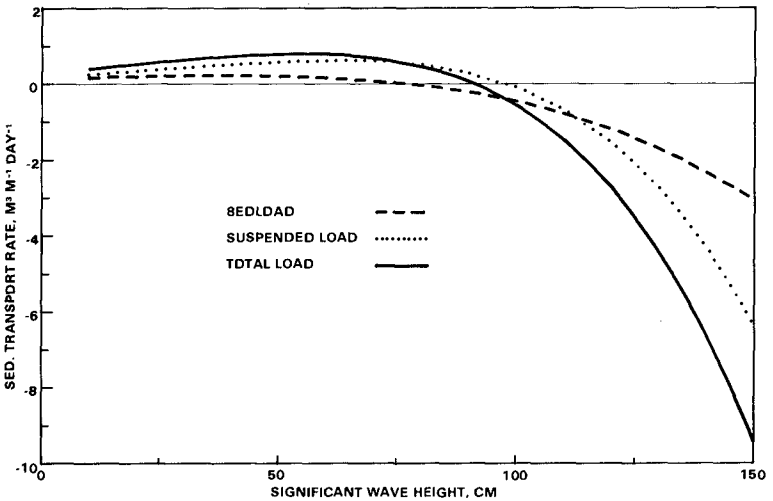

Figure 5. Predicted on-offshore sediment transport rate as a function of significant wave height. The individual contributions of the bedload and suspended load transports to the total transport are shown by the dashed and dotted lines, respectively. The point of neutral transport (equilibrium) occurs at a significant wave height of 90 cm.

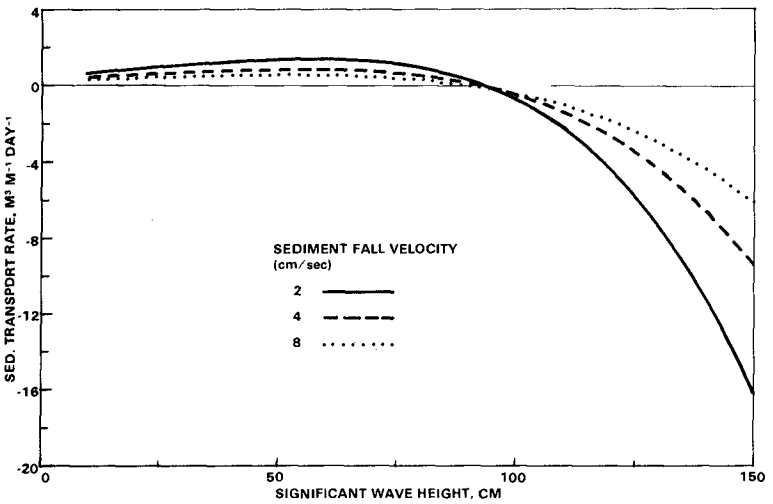

Figure 6. Predicted total load on-offshore sediment transport rate as function of significant wave height and sediment fall velocity. Greater rates of transport are found for smaller sized sediments.

wave height and would exhibit greater rates of change for a given wave height. Steep beaches typical of small waves and course sand would have smaller neutral point wave heights and would exhibit less rapid change for a given wave height. Figures 5 is believed to represent transition conditions. Partial support for the above hypothesis is provided in the study by Aubrey (1978), who found that future beach profiles at Torrey Pines Beach were best predicted when the existing beach profile shape and the incident wave height were known. Presumably, additional data sets having a wider range of beach slope and wave conditions are needed to develop a more complete beach profile predictive capability.

Further discussion is needed concerning possible errors in the estimated surfzone velocity moments. The odd moment quantities Ψ_1, Ψ_2, and δ_u, in effect, represent small differences between large numbers, so they are especially sensitive to small errors in the measured current meter data. Because of this sensitivity, considerable care was exercised in prescreening the data. The quantity u_*^3 was found to be particularly sensitive to data errors and was used as an indicator of bad sections of data. In spite of this care, the data itself could be subject to an inherent bias due to current meter inaccuracies.

One error in particular may be that the mean on-offshore currents are a manifestation of a current meter rectification process which has been hypothesized to occur in combined oscillatory and longshore currents.* Some evidence, however, suggests that rectification may not be too significant. Wright et al. (1978) reported measuring onshore currents in the upper part of the water column inside the surfzone and offshore currents near the bottom. These measurements were made with small ducted fan current meters unlike the electromagnetic current meters used in the NSTS experiments and, presumably, would not be subject to the same rectification characteristics. Nevertheless, until more exhaustive studies are done on the response of the electromagnetic current meters in combined oscillatory and steady flows, the magnitudes and directions of the mean on-offshore currents are open to question.

It is disappointing that the present sediment transport model is not more accurate at predicting the measured beach volume changes. The reason for its lack of accuracy is unknown. The variability in the estimated on-offshore transport rates between consecutive hourly data sets suggests, however, that the on-offshore transport rate may vary significantly on an hourly basis due to small changes in the incident wave field and the tide. The latter changes the position of the surfzone relative to the existing beach profile, which can significantly alter the breaking wave characteristics. As a result, it may be intrinsically difficult to test the capability of a micro-scale on-offshore sediment transport model to predict daily beach volume changes using current meter records of very limited duration.

In addition, some of the measured beach volume changes seem to be anomalous in light of our present limited knowledge. In particular, the large on-offshore rates of sand movements during periods of small waves

*From personal communication with R. T. Guza and D. G. Aubrey.

on November 6, 7, and 20 are difficult to understand. It would appear that wave energy should have been insufficient to generate this volume of sediment transport. One possible explanation may be a temporary local convergence or divergence of the longshore transport rate. Another explanation may be inaccuracies in the beach profile measurements.

CONCLUSIONS

Based on the results of this study, the following conclusions can be made:

1. An evaluation of the ability of Bailard's (1981) surfzone sediment transport model to predict daily beach volume changes was not possible due to inadequate surfzone current meter record lengths and to apparent noiseness in the beach volume estimates.

2. Average surfzone wave velocity moments were found to be well represented by linear functions of significant wave height. Additional data sets are needed to determine their relationships to wave period and average beach slope.

3. Predicting beach volume changes using a highly simplified form of Bailard's (1981) surfzone sediment transport model appears promising in that observed on-offshore transport is qualitatively supported. Analysis of additional surfzone current meter data sets having different wave and beach slope characteristics is necessary before a useful predictive capability can be developed.

REFERENCES

Aubrey, D. G. (1978). Statistical and dynamical prediction of changes in natural sand beaches, Ph. D. thesis, University of California at San Diego. San Diego, Calif., 1978.

Bagnold, R. A. (1963). "Mechanics of marine sedimentation," The Sea: Ideas and Observations, vol 3. New York, N.Y., Interscience Publishers, 1963, pp. 507-526.

Bagnold, R. A. (1966). "An approach to the sediment transport problem from general physics," U.S. Geological Survey Professional Paper, no. 422-I, 1966, 37 pp.

Bailard, J. A. (1981). "An energetics total load sediment transport model for a plane sloping beach," Journal of Geophysical Research, vol 86, no. C11, 1981, pp 10938-10954.

Bailard (1982) "A model for on-offshore sediment transport in the surfzone," Naval Civil Engineering Laboratory Technical Note N-1649, 44 pp.

Battjes, J. A. (1974). "Surf similarity," in Proceedings of the Fourteenth Coastal Engineering Conference, Copenhagen, Denmark, Jun 24-28, 1974. New York, American Society of Civil Engineers, 1975, pp 466-479.

Bowen, A. J. (1980). "Simple models of nearshore sedimentation; beach profiles and longshore bias," in Proceedings of the Conference on Coastline of Canada, Halifax, 1978. Geological Survey of Canada, 1980.

Dean, R. G. (1973). "Heuristic models of sand transport in the surf zone," in Proceedings of the Conference on Engineering Dynamics in the Surf Zone, Sydney, Australia. New York, American Society of Civil Engineers, 1973, 7 pp.

Draper, N. R., and H. Smith (1966). Applied regression analysis. New York, N.Y., John Wiley & Co., 1966, 407 pp.

Gable, C. G., Editor (1979). Report on data from the nearshore sediment transport study experiment at Torrey Pines Beach, California, November-December, 1978. University of California at San Diego, Institute of Marine Resources, IMR Reference No. 79-8. San Diego, Calif., 1979, 142 pp.

Guza, R. T., and D. L. Inman (1975). "Edge waves on beach cusps," Journal of Geophysical Research, vol 80, no. 21, pp 2997-3012.

Guza, R. T., and E. B. Thornton (1980). "Local and shoaled comparisons of sea surface elevations, pressures and velocities," Journal of Geophysical Research, vol 85, no. C3, 1980, pp 1524-1530.

Guza, R. T., and E. B. Thornton (1982). "Swash oscillations on a natural beach," Journal of Geophysical Research, vol 87, no. C1, pp 483-491.

Guza, R. T., and E. B. Thornton (in review). "Velocity moments in the surf zone," submitted to Journal of Waterway Port, Coastal and Ocean Engineering, American Society of Civil Engineers.

Hattori, M., and R. Kawamata (1981). "Onshore-offshore transport and beach profile change," in Proceedings of the Conference on Coastal Engineering, Sydney, Australia, Mar 23-28, 1980. New York, American Society of Civil Engineers, pp 1175-1194.

Huntley, D. A., and A. J. Bowen (1975). "Comparisons of the hydrodynamics of steep and shallow beaches," Nearshore Sediment Dynamics and Sedimentation. New York, N.Y., John Wiley & Co., 316 pp.

Inman, D. L., and R. A. Bagnold (1963). "Littoral processes," The Sea: Ideas and Observations, vol 3. New York, N.Y., Interscience Publishers, 1963, pp 529-533.

Inman, D. L., and J. D. Frautschy (1966). "Littoral processes and the development of shorelines," in Proceedings of Coastal Engineering, Santa Barbara, Calif. New York, American Society of Civil Engineers, Specialty Conference, pp 511-536.

Komar, P. D. (1971). "The mechanics of sand transport on beaches," Journal of Geophysical Research, vol 76, no. 3, 1971, pp 713-721.

Longuet-Higgins, M. S. (1953). "Mass transport in water waves," Philosophical Transactions of the Royal Society, London, England, Series A, vol 245, 1953, pp 535-581.

Saville, T., Jr. (1957). "Scale effects in two-dimensional beach studies," in Proceedings of International Association of Hydraulics Research, Lisbon, Portugal, 1957.

Seymour, R. J., and D. B. King (1982). "Field comparisons of cross-shore transport models," Journal of Waterway Port, Coastal and Ocean Engineering, American Society of Civil Engineers, vol 108, no. WW2, pp 163-179.

Seymour, R. J. (in review), "Estimating shoreline position changes under the action of waves and tides along straight beaches," Journal of Geophysical Research.

Short, A. D. (1978) "Wave power and beach stages: A global model," in Proceedings of the Sixteenth Coastal Engineering Conference, Hamburg, Germany, Aug 27-Sep 3, 1978, vol 11. New York, American Society of Civil Engineers, 1978, pp 1145-1162.

Thornton, E. B., and R. T. Guza (1982). "Longshore currents and bed shear stress," Directional Wave Spectra Applications, '81, Specialty Conference, Berkeley, Calif. New York, American Society of Civil Engineers, 1982, pp 67-385.

Wright, L. D., B. G. Thom, and J. Chappel (1978). "Morphodynamic variability of high-energy beaches," in Proceedings of the Sixteenth Conference Coastal Engineering, Hamburg, Germany, Aug 27-Sep 3, 1978. New York, American Society Civil Engineers, 1978, pp 1180-1194.

SEDIMENT TRANSPORT AND BEACH TRANSFORMATION

Tomoya Shibayama, A.M. ASCE *

and

Kiyoshi Horikawa, M. ASCE **

ABSTRACT

Laboratory and field investigations were performed in order to formulate a predictive model of two-dimensional beach profile change. The observed transport was classified into six types, and transport formulas were deduced for each type based on a microscale description of sediment movement caused by wave action. A numerical model of two-dimensional beach transformation was then developed. Beach profile changes calculated with the model were then compared with the laboratory results. The model was found to give reasonable results except in the vicinity of the wave plunging point. The sediment transport calculation is based on a sinusoidal velocity profile. The model appeares to give good results as long as the wave motion can be reasonably approximated by linear wave theory.

1. INTRODUCTION

Surface waves traveling in shallow water over a sandy bed produce back and forth sand movement. Various attempts have been made to establish quantitative relationships for the sand movement and fluid motion. For example, Madsen and Grant (1976) found a clear relationship between a nondimensional averaged transport rate and the Shields parameter by extending the results of unidirectional flow sediment transport. However, in order to achieve the goal of developing a practical calculation method for sediment formula due to wave action, more precise observations are required to understand the complex mechanism of sediment movement. If the spatial and temporal variations of net sediment transport can be predicted, then two-dimensional beach transformation can be estimated. Here we report results of a study of the theoretical and empirical relationships of wave sediment transport and of two-dimensional beach profile change. The study is based on laboratory and field

* Research Associate, Dept. of Civil Eng., University of Tokyo, Bunkyo-ku, Tokyo 113 JAPAN
** Professor, Dept. of Civil Eng., University of Tokyo, Bunkyo-ku, Tokyo 113 JAPAN

observations. The results are restricted to on-offshore sediment transport; longshore transport is left for future work.

The various topics of the investigation are presented in the following order. 1) A simple classification of sediment transport patterns based on the dominance of a bed load or a suspended load, and on the direction of the sediment transport is described; 2) A bed load formula is presented; 3) A formula for calculating the suspended load created by vortices in the vicinity of sand ripples is introduced; and 4) A simple quantitative model for predicting two-dimensional beach transformation is presented, and comparisons are made with laboratory results.

2. SEDIMENT TRANSPORT

2.1 Sediment transport types and classification

The bed configuration, in particular the presence of ripples, is considered to be one of the main factors necessary to suspend sand. The ripples also govern the sediment transport direction. Therefore, precise observations of sand movement and bed form patterns were made for a wide range of flow conditions in order to classify the sediment transport as a function of flow conditions.

The experiments were carried out both in a wave flume and in an oscillatory flow tunnel. The laboratory conditions are shown in Table 1. Well-sorted sands were used as bottom materials except for Cases 3 and 4 in the oscillatory tunnel, for which polystyrene particles were used. The sediment movement was recorded using either an 8-mm movie camera or a 16-mm high-speed motion analysis camera.

Field observations were carried out at Sabigahama Beach on Miyake Island, and at Ajigaura Beach and Oarai Beach, both in Ibaragi Prefecture, Japan. The field conditions are shown in Table 2. The transport mode was observed directly and recorded using an underwater 8-mm movie camera and an underwater 35-mm camera.

Based on both the laboratory and field observations, the sediment transport due to nearly sinusoidal wave action was classified according to predominance of bed load or suspended load, and according to the direction of sediment transport. We found it convenient to classify the sediment transport into six types as shown in Fig. 1.

1) Bed Load (BL): The bed is practically flat and no suspended sand clouds exist: sediment particles move along the bed surface. The direction of sediment transport is the same as the water flow.

2) Bed Load Suspended Load Transient (BST): Suspended sand clouds are formed above a rippled bed. Both bed load and suspended load exist.

Table 1: Laboratory conditions

WAVE FLUME

Case	Period (s)	Deep water wave height (cm)	Initial slope	Sand grain diameter (mm)
1	1.5	10.0	0.1	0.2
2	1.5	7.6	0.1	0.2
3	1.5	9.3	0.1	0.7
4	2.0	7.5	0.05	0.7
5	1.7	5.4	0.05	0.7
6	2.2	4.5	0.05	0.7
7	1.8	5.8	0.05	0.2

OSCILLATORY FLOW TUNNEL

Case	Period (s)	Orbital diameter(m)	Particle diameter (mm)	Specific gravity
1	2.1 - 8.7	0.26 - 1.20	0.2	2.7
2	3.5 - 4.2	0.24 - 1.10	0.7	2.7
3	1.8 - 3.8	0.24 - 1.20	2.0*	1.4
4	2.9 - 7.1	0.22 - 0.70	0.3*	1.2

* Polystyrene Particles

Table 2: Field conditions

Case	Deep water wave height (m)	Period (s)	Sediment diameter (mm)	Date	Site
1	0.35	5	2	3 Nov 79	Sabigahama
2	0.3 - 0.45	7 - 8	10	24 Mar 80	Sabigahama
3	0.25 - 0.75	6 - 10	0.4 - 0.5	4 - 5 Jul 78	Ajigaura
4	0.25 - 0.50	4 - 10	0.2 - 0.3	28 Aug - 1 Sep 81	Oarai

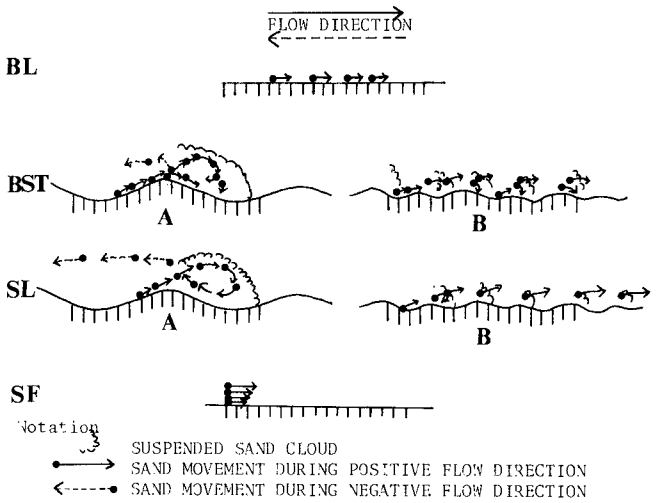

Figure 1: Sediment transport types

2-a) Ripple length and the water particle orbital diameter nearly equal (BST-A), sand particles suspended during the positively directed flow are first confined within a vortex, and then are transported towards the negative direction after the flow direction changes. We here use "positive" to indicate water flow direction in the first half wave period, and "negative" for the second half wave period. The transport of sediment which started moving during the first half wave period is either in the positive or negative direction depending on whether the bed load or suspended load is predominant.

2-b) Ripple length much smaller tban the water particle orbital diameter (BST-B), sand particles suspended during positively directed flow are not confined within a vortex, and are therefore transported in the positive direction. Both suspended sand and sand moving along the bed move in the positive direction.

3) Suspended Load (SL): Suspended sand transport is predominant.

3-a) Ripple length and water particle orbital diameter nearly equal with sediment suspended during the first half wave period being transported in the negative direction (SL-A).

3-b) Ripple length much smaller than water particle orbital diameter with transport in the positive direction (SL-B).

4) Sheet Flow (SF): Ripples disappear. Sand particles move as a layer. The sediment transport direction is the same as the water flow.

In the SL and BST modes, the sediment transport direction changes depending upon the ratio of ripple length to water particle orbital diameter. The laboratory and field observations suggest that when the ripple length and the orbital diameter are of the same order, i.e., the latter is less than about three to five times the former, suspended sand clouds which were formed on the down-flow flanks of ripples are first confined witbin strong vortices. Then the sand clouds are transported in the negative direction during the period of negative flow, and are deposited on the bed under gravitational force (type A). When the ripple length is smaller than the water orbital diameter (i.e., the latter greater than about three to five times the former) suspended sand clouds formed on down-flow flanks of ripples are not confined in vortices and are transported in the positive direction during the period of positive flow (type B). In the BST mode, a part of the bed load is suspended to form sand clouds and some particles are deposited on the bed immediately after suspension.

The above-described types were classified by means of three parameters as will now be described. In order to discuss the BL type, the initiation of sediment movement must be considered. Madsen and Grant (1976) analyzed laboratory data and found that the Shields parameter was an important descriptor. The Shields parameter is expressed in terms of the maximum value of the near bottom water velocity, and is defined as

$$\psi_m = \rho f_w u_b^2 \,/\, 2(s-1)\rho g d \qquad (1)$$

where f_w is Jonsson's (1966) wave friction factor, u_b the maximum value of near bottom velocity, s the sediment specific gravity, g the gravitational acceleration, ρ the fluid density and d the sediment diameter. Madsen and Grant showed that the critical value of Shields parameter corresponding to the initiation of sediment movement is a function of a quantity S. This quantity S depends only on the sediment and fluid properties, and is given by

$$S = d\left[(s-1)gd\right]^{0.5} / 4\nu$$

where ν is the kinematic viscosity of the fluid. For sediment particles of specific gravity 2.65 and diameter 0.2 to 2.0 mm , the critical value of Shields parameter is 0.03 to 0.05.

Komar and Miller (1975) analyzed laboratory data concerning initiation of ripple formation (under low shear stress) and the dissapearence of ripples (under high shear stress). They found that the limiting value of Shields parameter for the existance of ripples changes according to the sediment diameter. For sediment diameters 0.2 to 2.0 mm, the limiting value of Shields parameter for the disappearance of ripples varies from 0.4 to 0.8. However, in the present observation of the initiation of ripple formation, the critical condition was not sufficiently described by the Shields parameter and sediment diameter. The critical condition was also found to be a function of both time and the initial bottom configuration. The critical condition for the initiation of ripple formation is a very difficult problem.

The SL and BST transport types were further divided into two sub-types (A and B) depending upon the ratio of ripple length to water orbital diameter. Nielsen (1979) gave a functional relationship between this ratio and the nondimensional water velocity. According to his result, this ratio is nearly constant when the square of the dimensionless velocity, $u_b^2/(s-1)gd$, is less than 25. Thus, sub-types A and B can be classified by using the square of the dimensionless velocity.

The parameter u_b/w is the ratio of maximum fluid velocity near the bed to the sediment particle fall velocity. Laboratory observation suggests that suspended sediment particles move at almost the same speed as the water particles. This implies that the parameter u_b/w is an indicator of the distance that a sediment particle travels when suspended. Thus the parameter u_b/w is related to suspended sediment movement.

The parameter ψ_m is related to the bed shear stress. Figure 2 shows the resulting classification of the laboratory and field data. This figure shows that the transport modes are well described by the two parameters, u_b/w and ψ_m.

For the limiting boundary between no-movement and BL, and BL and BST, the bed form pattern is the key factor, with the Shields parameter determining the transition. For BST and SL types, both u_b/w and ψ_m determine the limiting boundaries.

For the critical value for sub-types A and B of SL, a value of the square of the dimensionless velocity equal to 25 roughly corresponds to a value of the Shields parameter ψ_m in the range 0.125 to 0.25, if the wave friction factor is 0.01 to 0.02. An example with the value $\psi_m = 0.19$, which corresponds to $f_w = 0.015$, is also indicated in Fig. 2 (labelled "Nielsen").

It should be noted that the transition from SL-A to SL-B cannot be clearly classified by the dimensionless velocity alone. The transition is also related to the water orbital diameter. When the orbital diameter increases, the mode SL-B appears at lower velocities. Due to the same reason, the BST-B type appears when the water orbital diameter becomes longer than the ripple wave length.

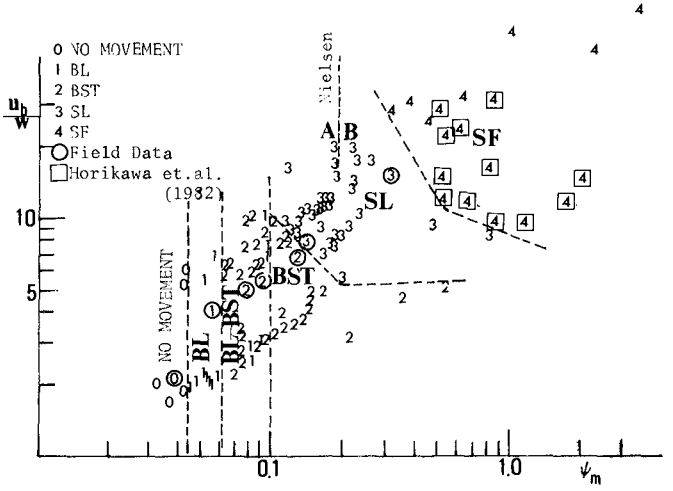

Figure 2: Transport type classification

2.2 Bed load

Vincent (1957) and Abou-Seida (1965) measured the bed load transport rate in a wave flume. Manohar (1955), Kalkanis (1962), and Abou-Seida (1965) performed experiments using an oscillatory plate in a tank of still water. In these experiments, the sediment was collected in a sampler which was set into the bed and the average transport rate over one wave period was evaluated. No consideration of transport direction was included. Sleath (1978) used an oscillatory plate and measured the quantities of bed material in motion at each instant of a cycle. Horikawa et al. (1977) measured the bed load using a sand trap which was buried in the bottom of a wave flume. They correlated the results with the beach profile change.

Madsen and Grant (1976) proposed an empirical relationship between a dimensionless time averaged rate of sediment transport and the Shields parameter, based on analyzing the laboratory data of Kalkanis (1962) and Abou-Seida (1965). They used a quasi-steady application of the Einstein-Brown sediment transport relationship and Jonsson's (1966) wave friction factor, and obtained an expression for the bed load transport rate due to sinusoidal wave motion. In the present work, experiments were performed to measure quantities of sand in motion and the water particle velocity at each instant of the wave cycle in a flume. The results were compared with a formula derived by modifying the Madsen-Grant transport formula. The Madsen-Grant formula, which was based on an analogy of quasi-steady undirectional bed load transport, was supported by the present experiments which measured the history of sand transport rate within one wave period.

Madsen and Grant (1976) used a quasi-steady assumption with Brown's formula and obtained a similar relationship for oscillatory flow, namely,

$$\Phi(t) = 40\,\psi^3(t) \tag{2}$$

$$\psi(t) = \tau(t) \,/\, (s-1)\rho g d \tag{3}$$

in which Φ is the dimensionless sediment transport rate, ψ is the Shields parameter, and τ is the bed shear stress.

Assuming a sinusoidal velocity change, they obtained a relationship between the time-averaged dimensionless transport rate and the Shields parameter as

$$\overline{\Phi} = 12.5\,\psi_m^3 \tag{4}$$

in which

$$\overline{\Phi} = \bar{q}_s \,/\, wd \tag{5}$$

$$\psi_m = \tau_m \,/\, (s-1)\rho g d \tag{6}$$

where $\bar{q}_s$ is the time-averaged volumetric rate of sediment transport and w is the sand particle fall velocity. The quantity τ_m is the maximum bed shear stress given by

$$\tau_m = f_w \rho u_b^2 / 2 \tag{7}$$

We now use the observation that a sand particle moving as bed load will not stop until the flow direction changes. When sand particles are accelerated, the transport rate is estimated with Eq. (2). Assuming a sinusoidal velocity change, we get

$$\Phi(t) = 40\,\psi_m^3 \sin^6 \sigma t \tag{8}$$

in which $\sigma = 2\pi/T$, where T is the wave period. For the time interval after the volume of moving sand attains a maximum, sand

particles once started in motion will not stop during the interval. We have

$$\Phi(t) = \Phi_m \, u(t) \, / \, u_b \tag{9}$$

in which Φ_m is the maximum value of transport rate. Assuming a sinusoidal velocity change,

$$\Phi(t) = 40 \, \psi_m^3 \sin\sigma t \tag{10}$$

The transport rate averaged over the first half wave period is thus estimated from

$$\overline{\Phi} = 2\left(\int_0^{T/4} 40 \, \psi_m^3 \sin^6\sigma \, t \, dt + \int_{T/4}^{T/2} 40 \, \psi_m^3 \sin\sigma \, t \, dt\right) / T \tag{11}$$
$$= 19 \, \psi_m^3$$

Experiment 1 was performed in a wave flume 11 m long, 0.2 m wide, and 0.3 m deep. In the middle of the flume, a volume of sand was placed 0.04 m deep and 0.8 m long over the full flume width. Sand samples were well sorted and their median grain size was 0.7 mm. The wave conditions were as follows: wave height in the inspection section was 7.1 to 10.7 cm, wave period 0.94 to 1.44 s, and water depth 15.4 to 16.7 cm.

During the experiment runs, no sand ripples formed and the sand was transported as bed load. Polystyrene particles of diameter 2 mm and specific gravity 1.02 were injected into the water to measure the water particle movement. In order to measure the number of moving sand particles, a flat plate 2 cm long with a skirt to prevent local erosion was installed on the sand surface. The movement of sand particles which crossed the plate, and the motion of the polystyrene particles over the section, were observed using a CANON 16-mm movie camera utilizing a film speed of 48 frames per second. The relation between the wave phase and the film was determined by using a timing light system with a wave gage. The number of sand particles which crossed the section and the polystyrene particle movement was obtained by analyzing the 16mm film. The near bottom velocity was then estimated from the movement of the polystyrene particles.

An example of the results obtained in Experiment 1 is compared with calculated values of the instantaneous transport rate in Fig. 3. The surface profile, the near bottom velocity and the number of the sand particles crossing the section at each instant of a wave period are shown in the figure. Sand particles did not start moving until the Shields parameter exceeded 0.05. When the transport rate was calculated from the velocity records, it was assumed to be zero when the motion was accelerated, and the instantaneous Shields parameter was less than 0.05. When the motion decelerated and the Shields parameter fell below 0.05, the transport rate was not taken to be zero because particles can continue in motion. Using Eqs. (2) and (9), a value of the sand flux was calculated.

As seen in Fig. 3, which is a representative result from thirteen runs, the agreement between the calculated and the measured values indicates the validity of the calculation scheme. The result also indicates that when the fluid decelerates, Eq. (9) gives a better approximation than Eq. (2) alone. However the real physical phenomena appears to be described by some intermediate combination of the two equations. From the laboratory observations, as the wave period becomes shorter, Eq. (9) becomes more applicable. The present model (Eqs. (2) and (9)) also seems to give a better estimate than Eq.(2) alone of the average transport rate integrated over the period of onshore flow direction.

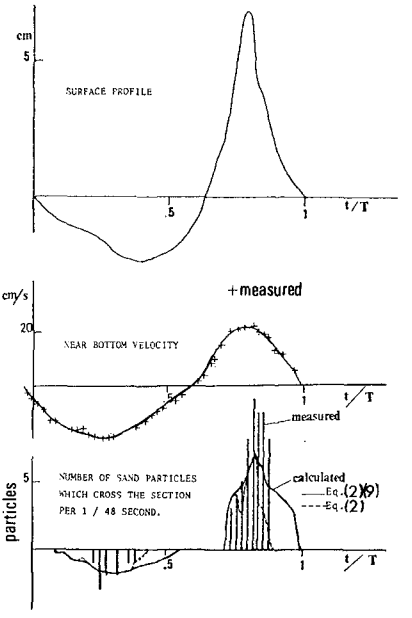

Figure 3: Result of Experiment 1

2.3 Suspended load

Hom-ma and Horikawa (1963) measured auspended sediment concentrations and interpreted the results with a diffusion equation approach. Nakato et al. (1977) studied sediment concentration and velocity fluctuations using an Iowa-type concentration meter and a hot-film anemometer. The above two experiments concern the concentration distribution. Nielsen (1979) attempted to calculate the suspended load using the product of concentration and velocity distributions, but the results were far from satisfactory.

Concerning sand movement above a rippled bed, Inman (1957) studied ripple formation and suggested that suspended sand cloud formation is an important factor in considering sediment transport due to waves. Inman and Bowen (1971) found that there exists an offshore sand transport as suapended load due to ripple asymmetry and resulting differences in intensity of the vortices. Sunamura, et al. (1978) observed sand movement over ripples and described precisely how the sand is confined within vortices formed behind sand ripples and moved by the wave oscillatory flow.

Here, the rate of sand suspension is estimated by application of the Madsen-Grant transport formula and is compared with laboratory data. When strong vortices are created on the onahore sides of ripples, suspended sand clouds form.

When the flow velocity is in the onshore direction, sand is transported along the offshore flanks of the ripples as bed load and then suspended at the crests of the ripples. The suspended sand forms a suspended sand cloud as shown in Fig. 4. Because of the ripple asymmetry, vortices created on the offshore sides of the ripples are weak. For our purposes, a strong vortex is taken as a circulation strong enough to produce suspended sand clouds. From here on, only strong vortices will be treated.

We now consider the time interval $t_i \leqq t \leqq t_e$ during which suspended sand clouds are formed. The time t_i indicates the time when clouds start to form and t_e indicates they stop increasing in size. The time average transport rate for a half wave period is estimated in the same manner as bed load to be

$$\bar{\Phi} = 80\psi_m^3 \left(\int_{t_i}^{T/4} \sin^6\sigma t \, dt + \int_{T/4}^{t_e} \sin\sigma t \, dt\right) / T$$
$$= C\psi_m^3 \qquad (13)$$

From the laboratory observation, suspended sand cloud formation starts at 0.05T to 0.15T and ends at 0.45T to 0.50T. Therefore the constant C varies from 16 to 19. We here set $t_i = 0$ and $t_e = 0.5T$ which gives the maximum value of C. Equation (13) then becomes

$$\bar{\Phi} = 19\psi_m^3 \qquad (14)$$

Experiment 2 was performed to study suspended load. The same flume was used as in Experiment 1 for bed load. In the middle of the flume, a volume of sand was placed which was 4 cm thick, 80 cm long and 20 cm wide. Sand samples were well sorted and their median grain size was 0.2 mm. The wave height was 5.8 to 8.3 cm, and the period 0.84 to 1.30 s.

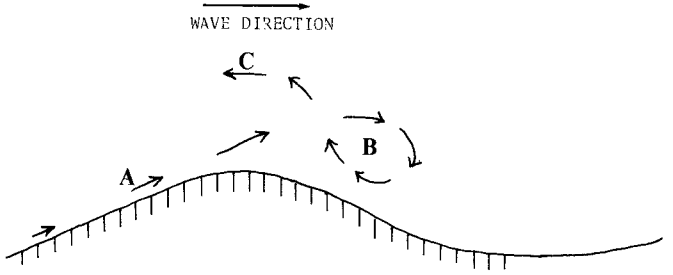

A: Sand is transported along the offshore flank of the ripples
B: Sand forms a suspended sand cloud
C: The cloud is transported in the offshore direction

Figure 4: Formation of suspended sand cloud

When waves were generated, sand ripples formed after 200 to 300 wave periods. The resultant ripple lengths were 3.0 to 5.7 cm and the height were 0.35 to 0.90 cm. The ripples were asymmetric and strong vortices were generated on the onshore sides of the ripples; vortices formed on the offshore sides were much weaker.

In order to obtain the rate of sand suspension at the crests of ripples, the distribution of suspended sediment concentration above the rippled bed must be measured. A concentration meter was installed close to the bed. It could measure the spatially averaged concentration of the suspended sand clouds. Here, the same assumption as Sunamura et al. (1979) was applied. They assumed that the concentration within the cloud is homogeneous. This assumption is reasonable because of the strong mixing effects of vortices. This condition was seen in precise observations of sand movement by Sunamura et al. and in the present experiment. The concentration was averaged over the time during which the suspended sand cloud was formed.

The concentration of the clouds was measured with a KENEK suspended sand concentration meter which optically measures the suspended sand concentration. The output of the meter was recorded on oscillograph paper together with the output of the wave gage. The cross-sectional area of the suspended sand cloud was obtained from 16-mm films. The amount of suspended sand in the cloud was estimated as the product of the concentration and the cross-sectional area of the cloud.

The results for the rate of sand suspension are shown in Fig. 5 together with the laboratory data of Sunamura, et al. (1979), and a more recent result, Sunamura (1982). Sunamura (1979, 1982) directly determined the net sediment transport rate by measuring the sand weight. The agreement between Eq. (14) and the laboratory data is good. This result implies that the suspended load can be estimated by Eq. (14) for the bed load moving along the ripple flanks.

2.3 Sediment tansport formulas

Simple formulas for the six types of sand transport are now given using the above results. The description of the suspended load requires the introduction of two quantities. The quantity α is the ratio of suspended load originating from the bed load to the bed load. The quantity β is the ratio of suspended sediment confined by a vortex to the suspended sediment. These two quantities are a function of sediment diameter, specific gravity, near bottom velocity, ripple geometry, vortex circulation, etc. Figure 6 shows a schematic diagram for the two parameters.

For type BL, Eq. (6) is used directly. For type SL-A, Eq. (14) is used taking into consideration the number of ripple lengths the suspended sand clouds travel in the second half wave period. Therefore the quantity N is introduced, which is the maximum integer not exceeding the quantity D/λ, where D is the orbital diameter of water particles and λ the ripple wave length. Thus N indicates how many ripple lengths the cloud travels during a half wave period. We then obtain the formula

$$\bar{\Phi} = -19N\psi_m^3 \qquad (15)$$

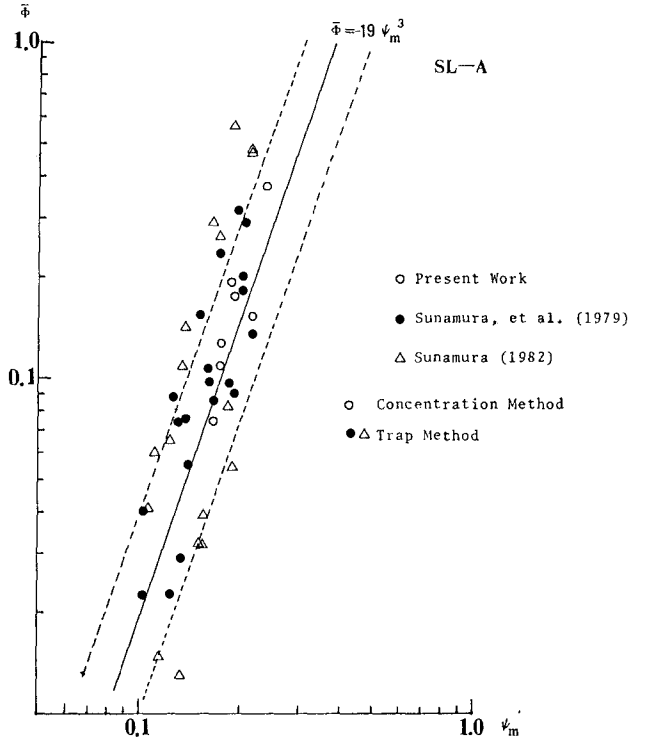

Figure 5: Rate of sediment suspension

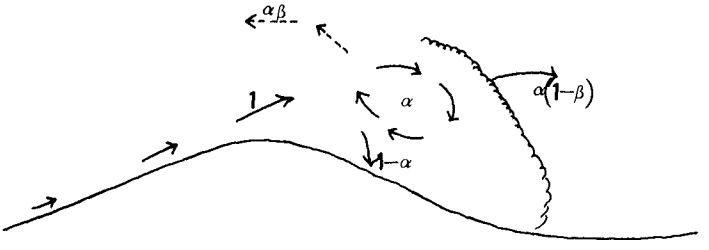

α : ratio of suspended sediment to bed load

β : ratio of suspended sediment confined by vortex to suspended sediment

Figure 6: Explanation of two parameters

Figure 7 shows a comparison between Eq. (15) and the laboratory results. Good agreement is seen. In type BST-A, a part of the bed load is suspended to form clouds and some of the sand particles are deposited on the bed immediately after suspension. We obtain

$$\bar{\Phi} = (1 - \alpha)19\psi_m^3 - 19\alpha N\psi_m^3 = (1 - \alpha - N\alpha)\ 19\psi_m^3 \qquad (16)$$

for type BST-A. Values of α must be determined empirically. For types SL-B and BST-B, the suspended sand clouds formed along the down-flow flanks of ripples are transported in the same direction as the water flow. The formula for type SL-B and BST-B is

$$\bar{\Phi} = 19\ \psi_m^3 \qquad (17)$$

For type SF, Horikawa et al. (1982) performed experiments to determine transport rate. As shown in Fig. 8, Eq. (11) fits their data.

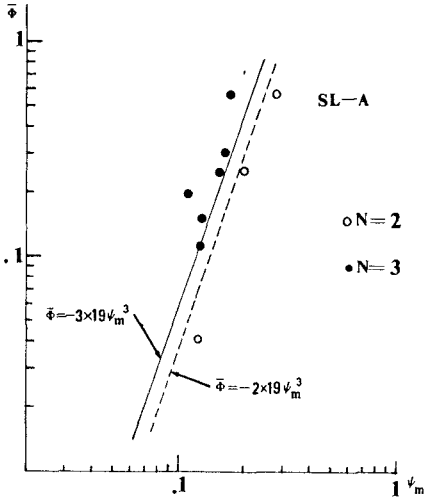

Figure 7 : Comparison with laboratory data, SL-A type

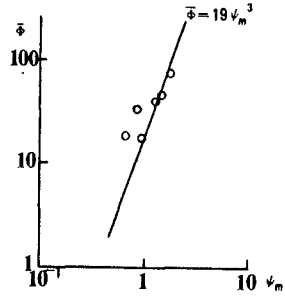

Figure 8: Transport rate for SF type

Figure 9 shows the six types of transport and their respective calculation. Although the results are too simple for general use at present, the approach of reducing the complex phenomena into simpler divisions as done here is considered to be promising.

3. TWO-DIMENSIONAL BEACH TRANSFORMATION

The transport formulas derived in the previous section are now applied to predicting beach profile change by comparing the calculation with laboratory results.

Many works had been done to analyze two-dimensional beach transformation. For example, Johnson (1949) classified beach profiles into bar and step types and first gave governing parameters by which beach type can be classified. Eagleson et al. (1963) were the first to attempt to calculate beach profile change, but the calculated results did not agree with the measured results. This is probably because they did not consider the effect of ripples. In this study, beach profile change will be discussed based on the sediment transport mechanism of ripples.

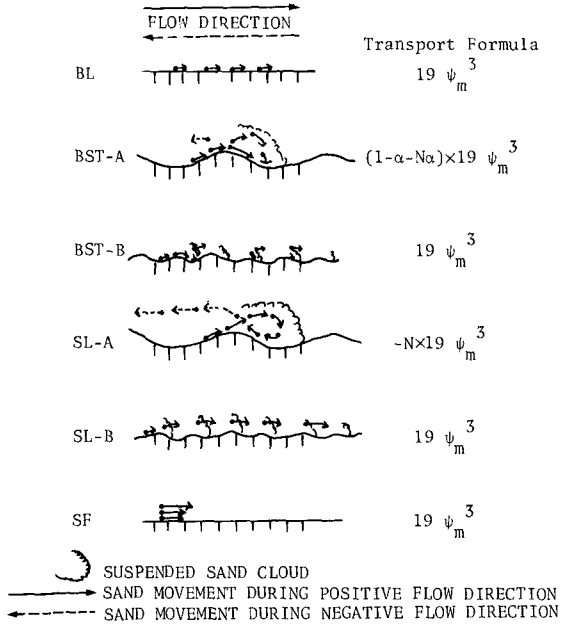

Figure 9: Sediment transport formula

In the present calculation, the above transport formulas were applied to the entire area of the beach because the same transport mechanism was observed in most areas (e.g., the transport in the breaking region was different and therefore an exception). Figure 10 shows the procedure of the computer simulation. The calculation can be started from an arbitrary initial beach profile. Wave transformation and velocity fields are calculated from the incident wave condition and bottom profile. Using the above results, the sediment transport rate can be calculated. Then the beach profile change can be calculated using the continuity equation for bed material.

In order to calculate, the following assumptions were made based on the laboratory and field investigations (see Fig. 11):

1) The wave transformation is given by linear wave theory using incident wave conditions and water depth in the offshore region. The wave breaking condition is given by Madsen (unpublished lecture notes) as

$$H_b/L_b = 0.142 \tanh\left[(0.8 + 5i)\, 2\pi h_b / L_b \right] \qquad (18)$$

where H_b is the breaking wave height, and L_b is the wave length at the breaking point. The wave height after breaking is assumed to decrease proportionate to the distance between the breaking point to the maximum run-up point. The run-up height, R, from the still water level is given by Hunt (1959) to be

$$R = 1.01\, i \sqrt{H_0 L_0} \qquad (19)$$

where i is the beach slope.

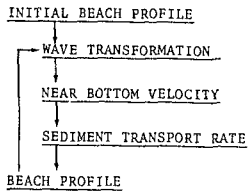

Figure 10: Procedure of computer simulation

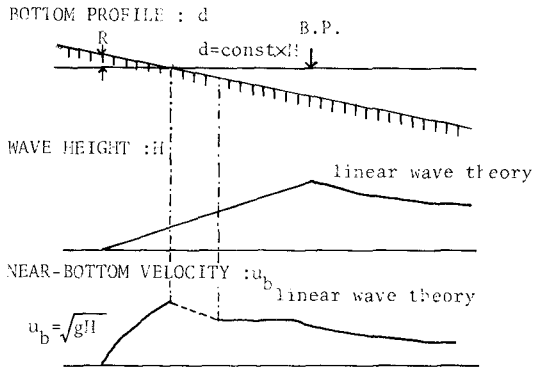

Figure 11: Assumptions for simulation

2) The maximum value of the near-bottom velocity is calculated from linear wave theory using the wave height and water depth where the wave height is less than the water depth (Region 1). In the swash zone, where beacb surface is situated above the still water level (Region 2),

$$u_b = \sqrt{gH} \tag{20}$$

is adopted as suggested by Ogawa and Shuto (1981). Here H is the local wave height. In the transition zone between Regions 1 and 2, the maximum velocity is assumed to change proportional to the distance from Region 1 to 2.

3) The sediment transport rate is calculated from the formulas in the previous section. Due to the non-linear effect of wave motion over gently sloping beaches, the maximum value of the water velocity in the onshore direction is greater than that in the offshore direction. From observation in the laboratory, the transport rate of sand which started moving during the onshore directed flow is much larger than the sand which stared moving during offshore directed flow. Therefore, we calculate only the sand which started moving during onshore directed flow. The value for BST type transport is calculated assuming a linear relationship with the Shields parameter. This means that the value changes from 0 to 1 proportionate to the Shields parameter in the area of BST transport type; i.e., $\alpha = (\psi_m - \psi_1)/(\psi_2 - \psi_1)$, where ψ_2 is the maximum Shields parameter which corresponds to BST transport type for specific u_b/w, and ψ_1 is taken as the minimum value in Fig. 2. In order to calculate the parameter N, the ripple wave length was obtained from an expression given by Nielsen (1979):

$$\lambda / D = 1.1 - 0.172 \left[u_b^2 / (s-1)gd \right]^{0.34} \tag{21}$$

The time step for the calculation is selected to be 6 s for a step-type and 1 min. for a bar-type beach. This was found acceptable for the present condition. When beach profile was calculated from transport rate, beach profile was smoothed if transport rate rapidly changed comparing with those of vicinity places.

Three sets of laboratory experiments were performed to examine the model. During the experiments, bottom profile change, suspended sediment concentration, near bottom velocity and surface profile were measured. In order to measure the near bottom velocity, polystyrene particles were injected and a 16-mm camera was used to record the movement of this tracer.

Figure 12 shows the laboratory results of beach profile change. Figure 13 shows the results of the simulation. The two results show reasonable agreement. Figures 14 and 15 give detailed comparisons of the wave height, near bottom velocity, transport rate and beach profile change.

The prediction with this model gave a good approximation to the profile change in the offshore region, but the estimate was not so good in the surf zone. This is mainly caused by the fact that in the surf zone, pure sinusoidal wave motion is no longer present, and the effect of wave breaking is very strong. The agitation due to breaking waves suspends the bed material, and the concentration of the suspended sediment in the vicinity of breaking point is high. In order to improve this model, the velocity field in the surf zone should be evaluated more precisely. A study based on this point of view was made by Shibayama and Horikawa (1982).

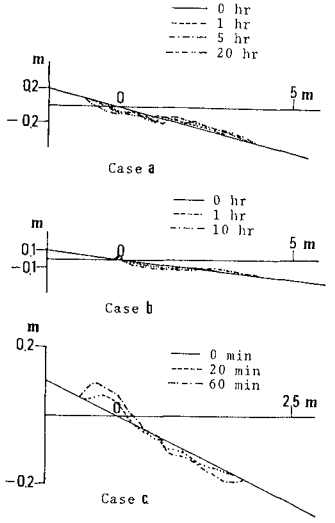

Figure 12: Laboratory results

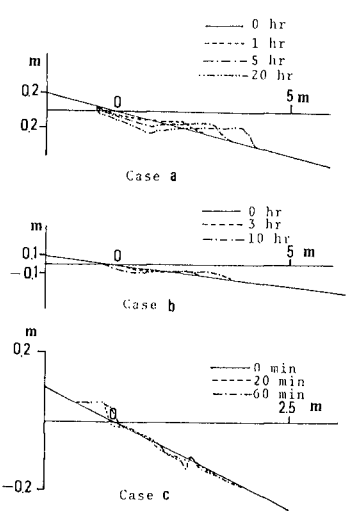

Figure 13: Simulation results

5. CONCLUSIONS

The main results of the present study are as follows:

1) Sediment transport can be classified into six types according to whether bed load or suspended load is predominant, and according to the sediment transport direction.

2) The transport type can be classified by three parameters, the Shields parameter, the ratio of maximum fluid velocity to sediment particle fall velocity, and the ratio of water particle orbital dismeter to ripple wave length.

3) By using certain assumptions and empirical information, bed load and suspended load under waves can be estimated by expressions originally derived for unidirectional bed load transport.

4) Net sediment transport formulas were developed. These expressions were applied to predict two-dimensional beach profile change in the laboratory. Reasonable agreement was obtained in regions where the wave motion can be reasonably approximated by linear wave theory.

ACKNOWLEDGEMENT

The authors thank Dr. N. C. Kraus of the Nearshore Environment Research Center for his advice in correcting an early version of the manuscript.

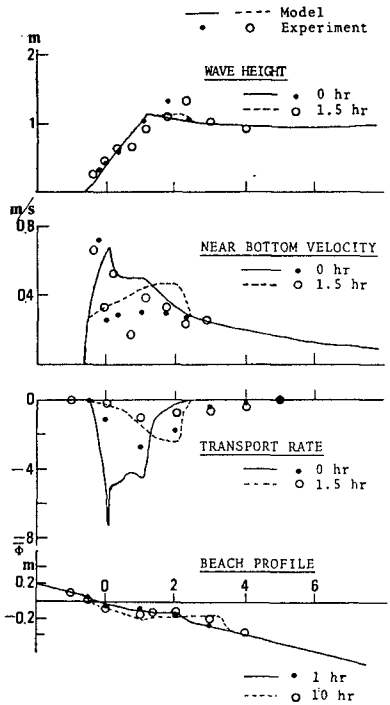

Figure 14: Comparison of model and measured value, Example a

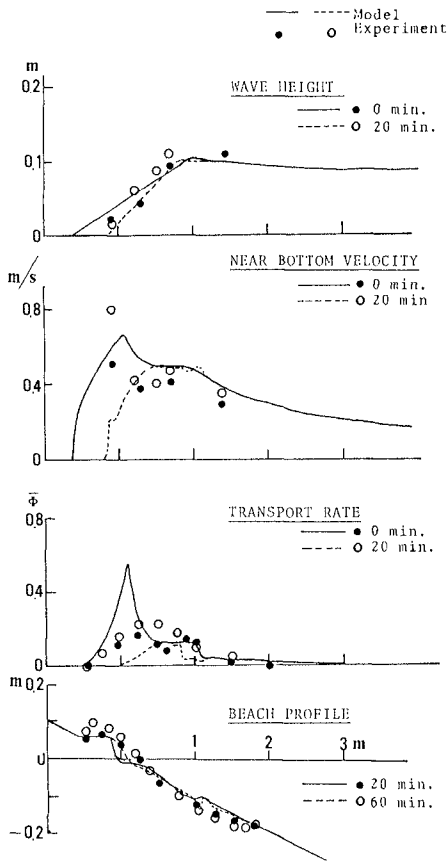

Figure 15: Comparison of model and measured value, Example b

REFERENCES

1) Abou-Seida, M. M. :"Bed load function due to wave action," Univ. of Cal., Berkeley, Hydraulic Eng. Lab., HEL-2-11, 78pp., 1965.

2) Dingler, J. R and Inman, D.L. :"Wave-formed ripples in nearshore sands," Proc. 15th Coastal Eng. Conf., pp. 2109-2126, 1976.

3) Eagleson, P.S., Glenne, B and Dracup, J.A. :" Equilibrium characteristics of sand beaches," Proc. ASCE, Vol. 89, No. HY1, pp. 35-37, 1963.

4) Hom-ma, M and Horikawa, K., :"Suspended sediment due to wave action," Proc. 8th Coastal Eng. Conf., pp. 108-193, 1963.

5) Horikawa, K., Sunamura, T. and Shibayama, T. :"Experimental study of two-dimensional shore transformation," Proc. 24th Japanese Conf. on Coastal Eng., pp. 170-174, 1977 (in Japanese).

6) Horikawa, K., Watanabe, A., and Katori, S., :"Sediment transport under sheet flow condition," Proc. 18th Conf. on Coastal Eng., 1982 (in press).

7) Inman, D. L. and Bowen, A. J., :"Flume experiments on sand transport by waves and currents," Proc. 8th Coastal Eng. Conf., pp. 137-150, 1963.

8) Johnson, J. W. :"Scale effects in hydraulic models involving wave action," Trans., A.G.U., Vol.30, pp. 517-525, 1949.

9) Jonsson, I. G. :"Wave boundary layers and friction factors," Proc. 10th Coastal Eng. Conf., Vol.1, pp. 127-148, 1964.

10) Kalkanis, G. :"Transport of bed materials due to wave action," CERC, Tech. Memo. No.2, 38 pp., 1964.

11) Komar, P. D. and Miller, M. C. :"The initiation of oscillatory ripple marks and the development of plane-bed at high shear stresses under waves," Jour. of Sedimentary Petrology, Vol.45, No.3, pp. 697-703, 1975.

12) Madsen, O.S. and Grant, W.D. :"Quantitative description of sediment transport by waves," Proc. 15th Coastal Eng. Conf., pp. 1093-1112, 1976.

13) Manohar, M. :"Mechanics of bottom sediment movement due to wave action," BEB Tech. Memo. No. 75, 121 pp., 1955.

14) Nakato, T., Locher, F. A., Glover, J.R. and Kennedy, J.F. :"Wave entrainment of sediment from rippled beds," Proc. ASCE, Vol. 103, No. WW1, pp. 83-99, 1977.

15) Nielsen, P. :"Some basic concepts of wave sediment transport," Series Paper No.20, Tech. Univ. of Denmark, 160 pp., 1979.

16) Ogawa, Y. and Shuto, N. :"On the dynamics in surf zone," Proc. of 29th Japanese Conf. on Coastal Eng., pp. 135-140, 1982 (in Japanese).

17) Shibayama, T. and Horikawa, K. :"Laboratory study on sediment transport mechanism due to Wave action," Proc. JSCE, No.296, pp. 131-142, 1980-a.

18) Shibayama, T. and Horikawa, K. :"Bed load measurment and prediction of two-dimensional beach transformation," Coastal Eng. in Japan, Vol. 23, pp. 179-190, 1980-b.

19) Shibayama, T. and Horikawa, K. :"Sediment suspension due to breaking waves," Coastal Eng., in Japan, Vol. 25, 1982 (in press).

20) Sleath, J.F.A. :"Measurement of bed load in oscillatory flow," Proc. ASCE, Vol. 104, No. WW4, pp. 291-307, 1978.

21) Sunamura, T., Bando, K. and Horikawa, K. :"Experimental study of sand movement and transport over asymmetrical ripples," Proc. 25th Japanese Conf. on Coastal Eng., pp. 250-254, 1978 (in Japanese).

22) Sunamura, T. :"On-offshore sediment transport in shallow water region," Proc. 29th Japanese Conf. on Coastal Eng., pp. 239-243, 1982 (in Japanese).

23) Vincent, G.E. :"Contribution to the study of sediment transport on a horizontal bed due to wave action," Proc. 6th Coastal Eng. Conf., pp. 326-354, 1958.

A PROCESS-RESPONSE MODEL FOR HURRICANE WASHOVERS

John R. Suter,[1] Dag Nummedal,[1] Amy K. Maynard,[1] and Paul Kemp[2]

ABSTRACT

The passage of Hurricane Allen over Padre Island in August 1980 presented an excellent opportunity to study the effects and controls of coastal morphology on hurricane deposits. In the Caribbean Sea, Hurricane Allen achieved a central pressure of 899 mb, making it the second strongest Atlantic hurricane ever recorded. Once in the Gulf of Mexico, the storm approached the Texas coast from the east-southeast, building a significant storm surge. Near Brownsville, the storm stalled, spending much of its energy offshore before making landfall early on August 10th near Brazos Santiago Pass at the southern tip of Padre Island.

Surge gauges show that peak recorded storm tides of about 3 m occurred at Port Mansfield, some 35 km north of landfall. Analysis of tide data indicates a time lag of some 14 hours on the rising storm tide between the Gulf and south Laguna Madre. This is due both to the limited tidal exchange across Padre Island and to set-down in the lagoon due to southward-directed cyclonic winds. By contrast, measurements taken in Corpus Christi Bay, some 180 km north of landfall, show that at that point Gulf and bay tides were in phase. The cross-barrier water level differential at South Padre Island (up to 1.5 m) greatly facilitated hurricane breaching of the island.

Oblique and vertical aerial photography show that Padre Island was breached in many places, with about 40 major hurricane channels still open several days after the storm. Surge heights were sufficient to inundate all of South Padre Island except for isolated "dune islands" resulting in broad and often coalescing washover deposits. The more continuous dune ridge on North Padre Island resulted in smaller, discrete washovers. Intensity, distribution, and morphology of washovers are functions of storm tide elevation, its phase relationships, island topography, and lagoonal water depth. The relationship is complex, yet precise enough to permit prediction of the island's response to the impact of a given storm.

---

[1]Department of Geology, Louisiana State University, Baton Rouge, Louisiana 70803

[2]Coastal Studies Institute, Louisiana State University, Baton Rouge, Louisiana 70803

Introduction

Normal, day-to-day physical processes along the northwestern shores of the Gulf of Mexico are relatively low energy. The area is micro-tidal (Hayes, 1979), and the broad, low gradient continental shelf serves to dissipate much of the incident wave energy. In this environment, storm related processes are usually dominant.

The barrier islands of the Texas coast are affected by two types of storms: extratropical cold fronts ("northers") and tropical storms and hurricanes. Both storm types have significant impact on coastal sedimentary environments, but along the Texas coast major effects on the barrier islands of the Gulf shoreline, such as breaching, overwashing, and dune planation are mostly the result of hurricanes.

The last such storm to impact the Texas coast was Hurricane Allen, which made landfall over Padre Island on August 10, 1980 (Figure 1). Oblique and vertical aerial photography showed that the island was breached in many places, and that a variety of washover deposits were laid down. Tide gauge data indicate a time lag of some 14 hours on the rising storm tide between the Gulf of Mexico and the south Laguna Madre. This time lag, or phase difference, set up a cross-barrier water level differential of up to 1.5 m. In this paper, we simulate the currents that could have resulted from storm surge, examine the regional variability in washover types, and discuss the interactions between the storm surge and island morphology.

Hurricanes as Geologic Agents

The importance of hurricanes as geologic agents has been recognized by many workers, and a number of excellent case studies exist in the literature (e.g., Hayes, 1967; Scott and others, 1969; McGowen and others, 1970; Nummedal and others, 1980). A general review of hurricane effects on the Texas coast was presented by McGowen and Scott (1975). Hurricanes are accompanied by torrential rains and high winds, but long term geologic effects are usually the result of the super elevated sea level known as storm surge. Surge height controls the extent of flooding, and permits higher breakers to be brought closer to shore, increasing the incident wave energy.

The sea level variation associated with hurricanes is governed by a number of independent factors, which can be broadly grouped as meteorologic, or those pertaining to a given storm, and geographic, or those relating to the area affected. Meteorologic parameters include the central pressure index (the ratio of pressure in the storm's center to that on its periphery), which causes the bulge-up of water called the "inverse barometer effect", and the frictional stress of the hurricane winds on the water surface, which results in a set-up at the coastline. These factors are functions of a storm's size, intensity, overwater duration, and angle of approach (Simpson and Riehl, 1981).

A given hurricane will produce greatly different surge heights depending upon where it makes landfall, primarily as a result of shoaling of the surge on the continental shelf, and local shoreline configuration. Embayed coastlines will experience a greater surge than open, straight coasts, and broader continental shelves produce greater surges in their corresponding land areas that narrower ones. Figure 2 shows the magnitude of this "shoaling factor" for the Northwestern Gulf of Mexico

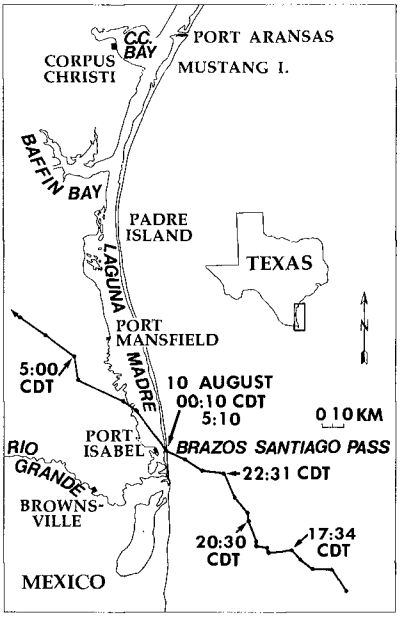

Figure 1. Plan view of Padre-Mustang Barrier Island System along the South Texas coast, northwest Gulf of Mexico. Also shown is the track of Hurricane Allen as it approached landfall (radar data from National Weather Service).

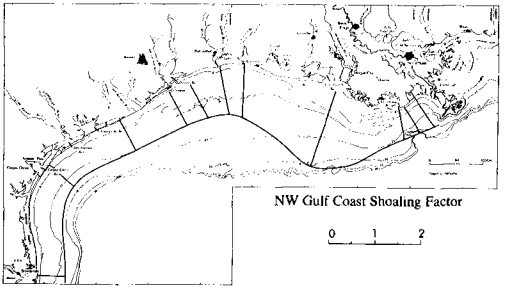

Figure 2. Distribution of the hurricane surge shoaling factor along the northwest coast of the Gulf of Mexico (after Jelesnianski, [1972]).

(Jelesnianski, 1972). From this, it can be seen that a landfalling hurricane will produce a considerably higher surge off the western Louisiana coast than at South Padre Island, Texas.

Superimposed on the storm surge are the effects of astronomical tides and wave set-up. Wave set-up is the nearshore water super elevation produced by the shoaling and breaking of a wave train. These factors combine to produce the actual storm tide (after Coastal Engineering Research Center, 1973). In some areas, wave set-up and/or astronomical tides can be of great significance, but in the northwestern Gulf of Mexico, storm surge is overwhelmingly dominant for large storms. Values given in this paper refer to actual storm tide levels.

Studies of hurricanes on the Gulf coast have led to a general geological effects model for storm impact, separating storm processes and coastal responses in chronological order (Hayes, 1967; McGowen and others, 1970; Nummedal and others, 1980). Storm approach is accompanied by rising waters, waves and wind, which attack the barrier islands, resulting in dune erosion, island breaching, and deposition of washovers on the surge flood. The counterclockwise circulation of the storm (Figure 3) causes the greatest energy to be concentrated in the right front quadrant. Thus, surge heights and storm effects are always greatest north of landfall. As the storm moves onshore, wind shifts produce changes in currents south of the eye, and modification of flood deposits begins. Storm aftermath is marked by the surge ebb, as well as high rains inland.

Storm Tide of Hurricane Allen

Hurricane Allen deviated somewhat from the generalized pattern discussed above. Allen became a hurricane in early August of 1980. While still in the Caribbean Sea, it achieved a central pressure of 899 mb, making it the second strongest Atlantic hurricane on record (an unnamed storm in 1935 attained a central pressure of 892 mb; U.S. Army Corps of Engineers, 1980). Once in the Gulf of Mexico, Allen headed more or less directly for the south Texas coast.

The U.S. Army Corps of Engineers maintains a network of continuously recording tide gauges, as well as surge and crest gauges, along the coast of Texas. Figure 4 shows the distribution of Hurricane Allen's storm tides, as measured by surge and crest gauges, which record peak water levels. Highest open coast storm tide for Allen was slightly less than 3 m at South Padre Island, while the highest bay tides were over 3 m near Corpus Christi. In most plots of this type, the highest storm tides occur in bays or lagoons, where local funneling and wind stress in restricted basins are pronounced (Simpson & Riehl, 1981). Possibly Allen's storm tides may have been higher in the area between South Padre Island and Baffin Bay, but no readings exist for that stretch of coast.

The relatively diffuse nature of Hurricane Allen's surge contrasts sharply with the more peaked asymmetric pattern of the storm tide of Hurricane Carla in 1961 (Figure 4). Carla was a large, intense storm and produced the highest storm tides ever measured on the Texas coast, almost 4 m. The more intense surge felt to the north of landfall is a pattern typical of a direct approach. The diffuse pattern of Allen's surge can be explained in terms of the offshore stallout and subsequent weakening of the storm, as well as the lower data density.

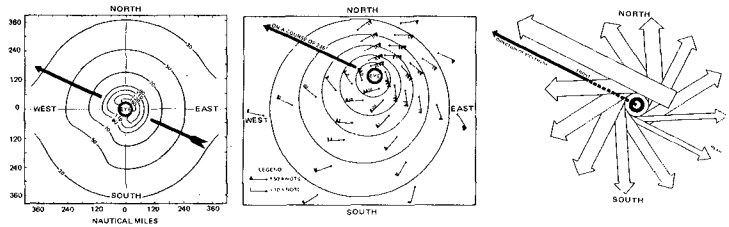

Figure 3. Distribution of pressure, surface winds, and waves within a typical northern hemisphere tropical storm (from Crutcher and Quayle [1974]).

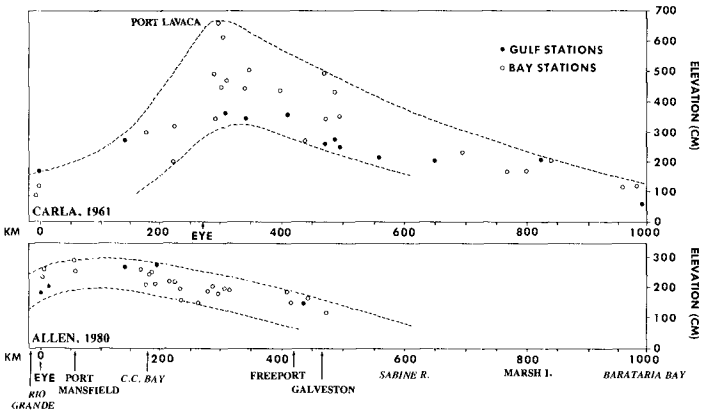

Figure 4. Distribution of observed maximum storm tides along Texas coast for Hurricanes Allen and Carla. Note the peaks occur to the north (or east) of landfall, and that bay tides are much higher than on the open Gulf. Data from Harris (1963) (Carla) and U.S. Army Corps of Engineers (1980) (Allen).

As the storm neared the Texas coast, it stalled offshore for over 24 hours before making landfall (Figure 5). During this time, the storm weakened considerably. Central pressure had risen to 945 mb just before landfall. As a result, the storm surge flood stage was considerably prolonged and diffused.

Early in the morning of August 10, Allen moved onshore just north of Brazos Santiago Pass on South Padre Island, thus spending most of its energy on the least populated stretch of the Texas coast. The major effects of the storm on Padre Island can be understood by a consideration of the regional and local geology.

Regional Geology of the Texas Coast

The southernmost links in the Texas barrier island chain are Mustang and Padre Islands (Figure 1). Taken as a whole, from Aransas Pass in the north of Brazos Santiago Pass in the south, over 200 km of unbroken barrier island faces the Gulf of Mexico. At one time, the two islands were separated by a series of inlets at the southern end of Corpus Christi Bay. Most stable tidal inlets on the Texas coast are located at the southeastern tip of the estuarine basin, where their positions are maintained by north winds during frontal passage. However, deepening of Aransas Pass in the 1920's to accomodate shipping to the Port of Corpus Christi diverted enough of the tidal flow to result in the choking off of the Packery Channel/Corpus Christi Pass inlets (Price and Parker, 1979). Presently, tidal exchange between the Gulf and estuaries in this area occurs only at the northern and southern extremes, and through two shallow artificial cuts, Mansfield Pass in Central Padre Island and Corpus Christi Fish Pass in Mustang Island.

The Padre-Mustang barrier system creates and maintains the extensive Corpus Christi Bay and Laguna Madre estuarine complex. Corpus Christi Bay occupies the valley of the Pleistocene Nueces River, while the linear Laguna Madre lies on a drainage divide. Both are actively infilling with sediment; the process being more apparent in the shallow lagoon, which averages less than one meter in depth and is in fact often emergent in its central reaches. This difference in back barrier basin morphology produces significant variations in hurricane responses.

The Padre-Mustang Barrier system itself displays a north-south morphologic dichotomy. Mustang, North, and Central Padre Islands are relatively broad, high-profile features with continuous foredune ridges of up to 10 m. In the vicinity of Mansfield Pass, island topography changes to a narrow, lower profile with poorly developed, discontinuous foredunes. Morton (1977, 1979 b) showed that regional variations in barrier island types could be correlated with positions relative to deltaic headlands. Near the deltas, thin, transgressive, low profile barriers occur; while within the interdeltaic embayments, thicker, broader, high profile barrier islands are formed (Figure 6). The regional distribution of erosional and stable landforms shown in Figure 7 can be explained by envisioning that wave refraction around deltaic headlands would produce cells of longshore drift convergence in the embayments. Throughout the Holocene, the decreased delivery of coarse sediments has combined with the wave energy concentration at the headlands and compactional subsidence of deltaic deposits to produce headland erosion. Longshore drift convergence concentrated sand in the embayments, producing the accretionary high profile islands. Today, the process has effectively straightened

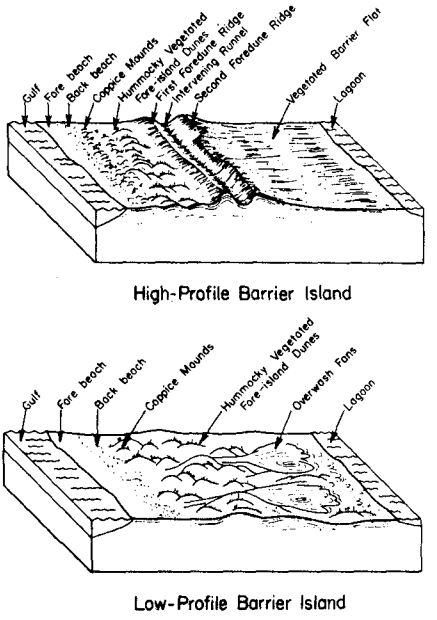

Figure 5. Diagram of high- and low-profile barrier island types. Mustang and North Padre Islands are high profile, while South Padre Island is low-profile, and thus more vulnerable to hurricane washover (from White and others, 1978).

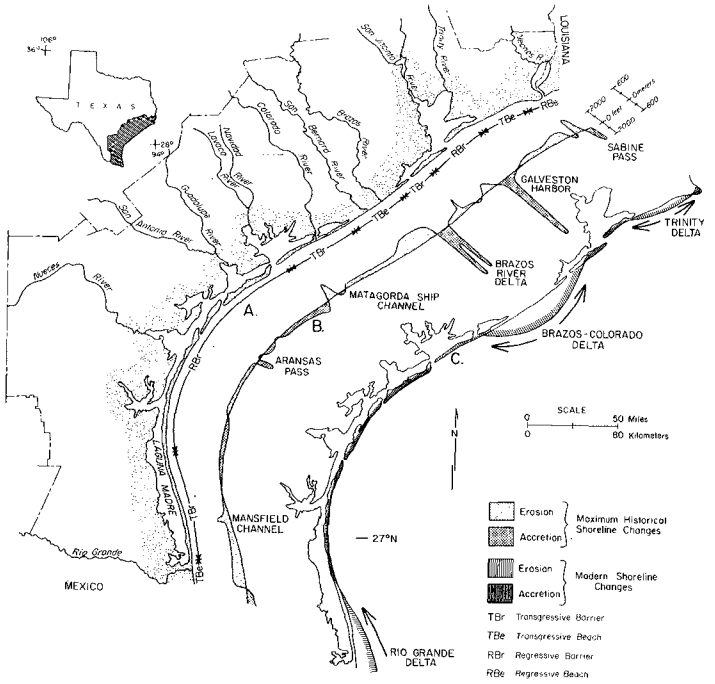

Figure 6. Maps showing (A) morphogenic provinces of the Texas coast, (B) maximum shoreline changes between 1850-83 and 1973-75, and (C) hypothesized late Holocene shoreline showing major promontories and long-shore drift cells. Maximum rates of erosion and low profile barriers occur near deltaic headlands, while accretion and high profile barriers occur in embayments. Long-shore drift convergence is now in the area of 27° N. From Morton (1979b).

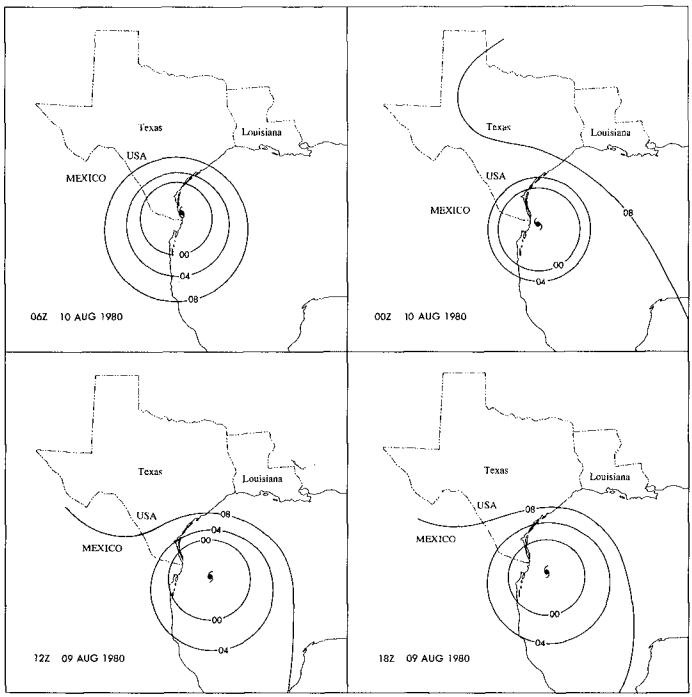

Figure 7. Series of simplified weather maps showing leisurely approach and weakening of Hurricane Allen offshore as it made landfall (data from National Weather Service).

out the Texas Gulf shoreline, and the pattern of drift has changed, converging now on Central Padre Island.

South Padre Island formed on an abandoned lobe of the Holocene Rio Grande Delta (Brown and others, 1980) while Central and North Padre and Mustang Islands formed in the embayment between the Rio Grande and Brazos-Colorado deltas (Brown and others 1976, 1977). South Padre is actively eroding (Morton, 1977) while the remainder of Padre and Mustang Islands are stable, owing to the current longshore drift convergence pattern. This contrast between the island types is well displayed by their response to Hurricane Allen.

Storm Surge Simulations

In the immediate vicinity of landfall, continuous recording tide gauges at Cameron Pier on the Gulf side and Gulf Intracoastal Waterway Marker 75 in Laguna Madre showed marked differences in water level response (Figure 8a). Significant and continuous rise in water levels began on late August 8th on the Gulf side, but lagoonal waters rose some 14 hours later. This time lag, or phase difference in the gulf and lagoon surges, is attributed to the southward directed cyclonic winds of the hurricane piling waters toward the southern outlet at Brazos Santiago Pass. Once Gulf water levels exceeded 1 m, washover of South Padre Island began, causing the lagoonal water levels to begin rising. Peak water in Laguna Madre exceeded 2.5 m before the shift in winds as the hurricane made landfall drove the waters back through hurricane channels.

Similar measurements taken at Brazos Santiago Pass to the south and at Aransas Pass to the north do not display this pattern (Figures 8b, c). There, Gulf and lagoonal surges are in phase. The set-up of water at the south end of Laguna Madre and the passage of surge waters through the inlet at Brazos Santiago combined to produce the in-phase measurements recorded there. Corpus Christi Bay has a considerably different morphology than Laguna Madre, and experienced lesser winds due to its distance from landfall.

The time lag between Gulf and lagoonal surges on the rising storm tide suggests that gravity-driven currents may have been quite strong once breaching of the island occurred. Figure 9 shows simple current velocity simulations derived from the surge level differentials using the Manning equation.

The roughness factor, n, is assumed to be 0.03, the value given by Chow (1959) for sandy streams, and also the average of that measured by Watson and Behrens (1976) during tidal current measurements in the newly dredged Corpus Christi Fish Pass. Barrier width is set at 900 m, we assume that the entire water level differential corresponds to the drop across the barrier, and lagoonal water levels are assumed to be horizontal.

Flow regime 1 simulates the currents for unconfined sheet overwash, with a flow depth of 30 cm. Velocities increase during the rising storm tide, peaking at 55 cm/sec at midnight August 8, and persisting for almost 24 hours. This period should represent the time of most active transfer of Gulf water into Laguna Madre. Due to the lesser elevation differentials, ebb velocities are generally slower, peaking at 46 cm/sec, and shorter lived.

Since a very large number of hurricane channels were cut across

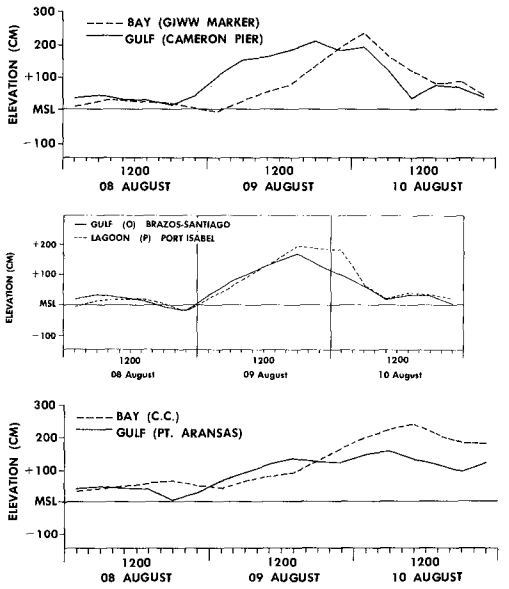

Figure 8. Time series of water surface elevations during impact of Hurricane Allen on south Texas coast, taken from continuous recording tide gauges. A) South Padre Island, B) Brazos Santiago Pass, C) Aransas Pass and Corpus Christi Bay. See Figure 1 for locations.

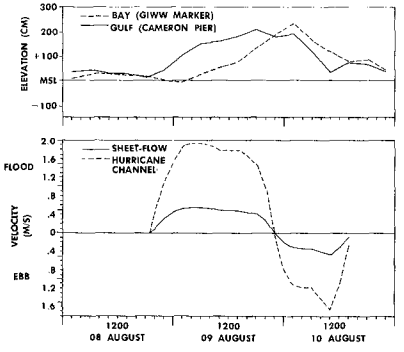

Figure 9. Current velocity simulations for flow across South Padre Island, based on Manning equation. Data from Figure 8A. Flow Regime 1 is for 30-cm deep sheet overwash; Flow Regime 2 refers to 2-m deep hurricane channel.

Padre Island, perhaps a more realistic picture is given by flow regime 2, which corresponds to flow in a confined hurricane channel of 2 m depth. Calculated velocities, as expected, are much higher. During surge flood, a strong lagoonward current of up to 1.92 m/sec persists for almost 24 hours. Maximum simulated ebb velocities reached 1.62 m/sec as surge waters returned to the Gulf.

These simulations represent the simplest case, and refer only to gravity driven currents. More sophisticated techniques should include consideration of wave pump (Bruun and Kjelstrup, 1979) and wind stress. Morton (1979 a) analyzed back barrier bedforms, and estimated wind driven currents in the range of 1.3 to 1.9 m/sec, very similar to those calculated here. The interaction of such intense currents produces the complex patterns of sediment dispersal seen on the back barrier flats.

Greater surge flood currents and the longer duration of the flood versus the ebb cast light on the timing of island breaching. The morphology of hurricane deposits on the back barrier clearly indicates that they are laid down on the surge flood, so it is likely that most of the breaches are initiated on the seaward side of barriers. However, breaches are also known to have occurred from the back side on surge ebb currents as shown by the opening of Pass Drury, Alabama after Hurricane Frederic in 1979 (Nummedal and others, 1980).

Another problem lies in the origin of widespread coarse grained deposits on continental shelves known to occur after major storms. Hayes (1967) suggested that these sediments were deposited by density currents in the ebb surge out of hurricane channels, while Morton (1981) contended that wind induced shoreface bottom return flow (Csanady, 1976; Swift, 1976) was responsible. The morphology of South Padre Island washovers indicate that there was a moderate amount of seaward sediment transport during the storm surge ebb. Current measurements during earlier storms (Forristal and others 1977; Murray, 1970) indicate that seaward shoreface currents peak before or during lamdfall. Therefore, we suggest that both mechanisms provide sediment for the inner shelf graded storm beds.

Washover Channels

The north-south dichotomy of form of the Padre-Mustang system is well illustrated by Figure 10, which shows the location and number of hurricane washover channels cut across the island by Hurricane Allen. Mapping of the channels was done primarily from high altitude photographs taken by NASA ten days after landfall.

Clearly, the vast majority of the breaches occurred along the southern portion of the barriers, due both to the proximity to the point of landfall and the low profile nature of South Padre Island. Surges of over 2 m were experienced all along the barrier system, but foredune height and ridge continuity prevented breaching in the higher profile segments further north.

The abrupt disappearance of washover channels on the northern section of the system is difficult to explain fully, but relates to a gradual transition to a continuous foredune ridge from south to north, and to the resolution of the 10 km sampling interval. Sudden reappearance of major channels at 170 km is due to re-opening of the old tidal inlets that once separated the two islands.

Spacing of the channels presents intriguing problems. Most workers

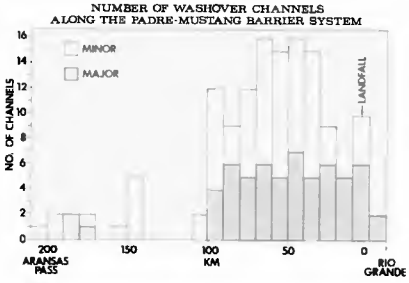

Figure 10. Locations of hurricane channels cut across Padre-Mustang Barrier System by Hurricane Allen. Major channels are those cut below mean sea level, minor channels are less deep.

Figure 11. Vertical aerial photograph showing irregular periodicity of washover channel spacing on Central Padre Island (photo taken 8/20/80).

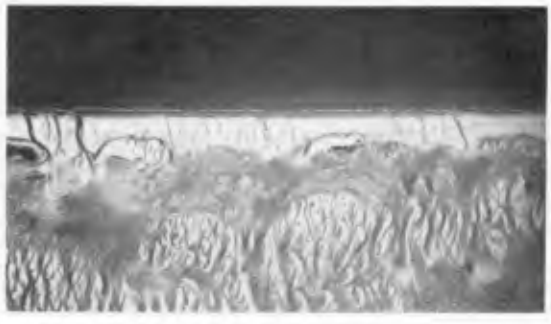

Figure 12. Vertical aerial photograph of washover terrace on South Padre Island, fed by multiple minor and major channels. Note regular channel spacing (photo taken 8/20/80).

attribute locations of washovers to island topography, but there is certain periodicity to the location of the channels within the heavily breached southern area. A series of major washover channels spaced approximately 2.5 km apart begins abruptly at 100 km, coinciding almost exactly with the beginning of the emergent portion of the Laguna Madre. Periodicity also exists in the spacing of minor washover channels in some areas (Figure 12).

This suggests the possibility that some surf zone phenomenon may be enhancing surge levels at regular intervals, and controlling or contributing to location of island breaching, as suggested by Dolan and Hayden (1981). This argument is complicated by the fact that the position of breaches is largely inherited from previous storms. Locations of Hurricane Allen channels coincide with those cut by Hurricane Beulah in 1967. It appears that periodic phenomena are operating, but that pre-existing topography also determines washover location.

Morphology of Washovers

Surge height elevation and barrier geometry not only control the number of hurricane breaches, but also the form of the resulting washover deposit. A variety of washover deposits were laid down by Hurrican Allen. Their type and location can be systematically related to geomorphologic characteristics of the barriers.

Along the higher profile portions of Mustang and Padre Islands, surge heights were insufficient to breach the foredune ridge. Minor discontinuities, such as aeolian blowouts, were attacked and relatively small, discrete interdune fans were deposited (Figure 13). Locally, interdune fans were laid down at two different levels as the storm surge rose, creating a double washover contained within the foredune ridge. Other examples of interdune fans occurred in areas of South Padre with extensive back island fields.

At the other end of the spectrum, washover terraces occurred in areas where the foredune ridge is discontinuous to absent (Figure 12). On south Padre Island, a continuous washover terrace is created by coalescing washover deposits fed by numerous hurricane channels. This contrasts with other examples of such deposits which are generally the result of sheet overwash, such as can be found along other low profile barriers of the Texas and Louisiana coasts (Morton, 1979 a; Boyd and Penland, 1981).

Where the foredunes are extant but discontinuous, channelization of surge resulted in the cutting of major hurricane channels which deposit the washover fan (Figure 14). These washovers are an order of magnitude larger than interdune fans, and are a major features. The form and thickness of the washover fan is determined by the relationship between surge strength and water depth within the back barrier basin. Those deposits laid down by Hurricane Allen have considerable variability in detail, but all are more or less heart shaped owing to flow onto the broad, low gradient back barrier flats of Central and South Padre Islands. Figure 14 approaches the ideal form of such features. Nowhere on Padre Island were any flame shaped washovers (Morton, 1979; Nummedal and others, 1980) seen. These have been reported from the Matagorda Peninsula of Texas (Morton, 1979 a) and Dauphin Island, Alabama (Figure 15; Nummedal and others, 1980). In both of these cases, there was considerable water depths in the back barrier basin at the time of breach-

Figure 13. Oblique aerial photograph of small interdune fan deposited within dune ridge on Mustang Island (photo taken 8/20/80).

Figure 14. Vertical aerial photograph of washover fan fed by major hurricane channel on South Padre Island. Dunes create channelization of flow (photo taken 8/20/80).

ing. As the surge waters crossed the barriers and encountered the deeper water, a hydraulic jump occurred, and the flame shaped washovers were deposited. Lack of these features on South Padre Island is attributed to much different morphology of the back barrier and the shallower Laguna Madre.

The last major washover type was of limited extent due to its specialized nature. The reactivated tidal delta occurred only in the area of juncture between Mustang and Padre Islands, where major breaks in the foredune ridge are located in the choked off tidal inlets (Figure 16). These deposits are the largest washovers laid down by Hurricane Allen, and actually represent modifications of pre-existing flood tidal delta deposits. As such, they would be very difficult to distinguish as washovers in ancient deposits. However, they are illustrative of the fact that interdune fans are not the only type of hurricane deposit that can be expected in high profile barrier islands. Indeed, deposits of this type may be the most significant stratigraphically. Examination of barriers along the Texas coast reveals an extensive series of large, arcuate forms on the back sides of barriers which probably represent washover modified flood tidal deltas (Andrews, 1970). Differences in older and younger deposits no doubt reflect variations through time in island morphology and storm intensity and numbers.

Summary and Conclusions

Hurricane Allen's impact on the south Texas coast confirmed many of the previous concepts of geologic effects of hurricanes on barrier islands. Aerial photography and ground observations revealed that four main types of washover deposits occurred: interdune fans in areas with continuous foredunes, washover terraces in areas with few foredunes, washover fans in areas where the foredune ridge is discontinuous, and reactivated tidal deltas in relict tidal inlets. A number of factors control the form and location of the washovers including storm surge height, barrier island topography and geometry, position relative to storm landfall, and water depth in the back barrier basin. Further analysis may reveal the existence of periodic phenomena interacting with these factors to control washover location. The relationships cannot be easily quantified, but can be easily understood conceptually and applied by coastal planners, engineers, and geologists.

In closing, it is worth mentioning that effects of hurricanes on barrier islands is a subject of increased importance in the years ahead. If there is indeed a secular warming trend caused by inceased CO_2 levels in the atmosphere (Hansen and others, 1981), it can be expected that hurricanes will increase in both number and intensity (Nummedal, 1982). Such increases, coupled with rising sea levels accompanying the global warming and the major population shift to coastal areas, would make the prospect of major hurricane problems in the future a gloomy one indeed.

Figure 15. Vertical aerial photograph of reactivated tidal deltas in Corpus Christi Pass-Packery Channel area between Mustang and Padre Islands (photo taken 8/20/80).

Figure 16. Vertical aerial photograph of flame shaped washovers, Dauphin Island, Alabama, formed during Hurricane Frederic in September, 1979.

Acknowledgements

The authors would like to acknowledge financial support from the Office of Naval Research, Coastal Sciences Program, through contract no. N00014-78-C-0612, and a grant to John R. Suter from the Gulf Coast Association of Geological Societies. Additionally, the U.S. Geological Survey Office of Marine Geology at Corpus Christi, Texas, furnished the vertical aerial photographs and provided work space and logistical support.

References cited

Andrews, P. B., 1970, Facies and genesis of a hurricane washover fan, St. Joseph (San Jose) Island, central Texas coast: Texas Bureau of Economic Geology, Report of Investigations 67, 147 p.

Boyd, R., and S. Penland, 1981, Washover of deltaic barriers on the Louisiana coast, Trans. Gulf Coast Assoc. of Geol. Soc., v. XXXI, p. 243-248.

Brown, L. F., J. L. Brewton, J. H. McGowen, T. J. Evans, W. L. Fisher, and C. G. Groat, 1976, Environmental Atlas of the Texas Coastal Zone - Corpus Christi Area, Texas Bureau of Economic Geology, 123 p.

Brown, L. F., J. H. McGowen, T. J. Evans, C. G. Groat, and W. L. Fisher, 1977, Environmental Atlas of the Texas Coastal Zone - Kingsville Area, Texas Bureau of Economic Geology, 140 p.

Brown, L. F., J. L. Brewton, T. J. Evans, J. H. McGowen, W. A. White, C. G. Groat, and W. L. Fisher, 1980, Environmental Geologic Atlas of the Texas Coastal Zone - Brownsville Harlingen Area, Texas Bureau of Economic Geology, 139 p.

Bruun, P., and S. Kjelstrup, 1979, The wave pump: Port and Ocean Engineering under Arctic conditions, Proc. 5th Conferences, v. I, p. 288-308.

Chow, V. T., 1959, Open Channel Hydraulics: McGraw-Hill Book Company, NY, 680 p.

Coastal Engineering Research Center, 1973, Shore Protection Manual, v. I.

Crutcher, H. L. and R.G. Quayle, 1974, Mariners Worldwide Cilmatic Guide to Tropical Storms at Sea; Naval Weather Service Command, Naval Weather Environmental Detachment, Asheville, NC, 114 p. + 312 charts.

Csanady, G. T., 1976, Wind driven and thermohaline circulation over continental shelves: in Manowitz, B., ed., Effects of Energy-Related Activities on the Atlantic Continental Shelf, BLM Report 50484, p. 31-47.

Dolan, R., and B. Hayden, 1981, Storms and shoreline configuration, Jour. Sed. Petrology, v. 51, p. 737-744.

Forristal, G. Z., R. C. Hamilton, and V. J. Cardone, 1977, Continental shelf currents in Tropical Storm Delia: observations and theory, Jour. Phys. Oceanography, v. 7, p. 532-546.

Hansen, J., D. Johnson, A. Lacias, S. Lebedeff, P. Lea, D. Rind, and G. Russell, 1981, Climatic impact of increasing atmospheric carbon dioxide, Science, v. 213, p. 957-66.

Harris, D. L., 1963, Characteristics of the hurricane storm surge, Technical Paper no. 48, U.S. Weather Bureau, Washington, D.C.
Hayes, M. O., 1967, Hurricanes as geologic agents: case studies of Hurricane Carla, 1961, and Cindy, 1963: Texas Bureau of Economic Geology Report of Investigations 61, 56 p.
Hayes, M. O., 1979, Barrier island morphology as a function of tidal and wave regime: in Leatherman, S. P., ed., Barrier Islands, Academic Press, NY, p. 1-28.
Jelesnianski, C. P., 1972, SPLASH - Special program to list amplitudes of surges from hurricanes; National Oceanic and Atmospheric Adm. Tech. Memo. NWS TDL-46, 52 p.
McGowen, J. H., C. G. Groat, L. F. Brown, W. L. Fisher, and A. J. Scott, 1970, Effects of Hurricane Celia - A focus on environmental geologic problems of the Texas Coastal Zone, Texas Bureau of Economic Geology, Geologic Circular 70-3, 35 p.
McGowen, J. H., and A. J. Scott, 1975, Hurricanes as geologic agents on the Texas coast, in Cronin, L. E., ed., Estuarine Research, v. II, Geology and Engineering: NY, Acad. Press, p. 23-46.
Morton, R. A., 1977, Historical shoreline changes and their causes: Texas Gulf Coast, Texas Bureau of Economic Geology, Geologic Circular 77-6, 8 p.
Morton, R. A., 1979a, Subaerial storm deposits formed on barrier flats by wind-driven currents, Sedimentary Geology, v. 24, p. 105-122.
Morton, R. A., 1979b, Temporal and spatial variations in shoreline changes and their implications: examples from the Texas Gulf Coast, Jour. Sed. Petrology, v. 49, p. 1101-12.
Morton, R. A., 1981, Formation of storm deposits by wind-forced currents in the Gulf of Mexico and the North Sea, International Assoc. Sedimentologists, Spec. Publ. 5, p. 385-396.
Murray, S. P., 1970, Bottom currents near the coast during Hurricane Camille, Jour. Geophysical Res., v. 75, p. 4579-4582.
Nummedal, D., S. Penland, R. Gerdes, W. Schramm, J. Kahn, and H. Roberts, 1980, Geologic response to hurricane impact on low-profile Gulf Coast barriers: Trans. Gulf Coast Assoc. Geol Soc., v. 30, p. 183-195.
Nummedal, D., 1982, Hurricane landfalls along the Northwestern Gulf coast, in D. Nummedal, ed., Sedimentary processes and environments along the Louisiana-Texas coast, Geol. Soc. America Guidebook, p. 63-78.
Price, W. A., and R. H. Parker, 1979, Origins of permanent inlets separating barrier islands and influence of drowned valleys on tidal records along the Gulf Coast of Texas, Trans. Gulf Coast Assoc. Geol. Soc., v. 29, p. 371-385.
Scott, A. J., R. Hoover, and J. H. McGowen, 1969, Effects of Hurricane Beulah, 1967, on Texas coastal lagoons and barriers, in A. A. Castanares and F. B. Phleger, eds., Lagunas Costeras, un simposio, p. 221-236.
Simpson, R. H., and H. Riehl, 1981, The hurricane and its impact: Louisiana State University Press, Baton Rouge, LA 398 p.
Swift, D. J. P., 1976, Continental shelf sedimentation, in Stanley, D. J., and Swift, D. J. P., eds., Marine Sediment Transport and Environmental Management: John Wiley & Sons, NY, p. 311-350.

U.S. Army Corps of Engineers, 1981, Report on Hurricane Allen, 3-10 August 1980: Galveston, TX, 62 p.

Watson, R. L., and E. W. Behrens, 1976, Hydraulics and dynamics of New Corpus Christi Pass, Texas: a case history, 1973-75, General Investigations of Tidal Inlets, report no. 9: U.S. Army, Coastal Engineering Research Center, Ft. Belvoir, VA, 175 p.

White, W. A., R. A. Morton, R. S. Kerr, W. D. Kramer, and W. B. Brogdon, 1978, Land and water resources, historical changes, and dune criticality: Mustang and North Padre Islands, Texas, Texas Bureau of Economic Geology, Report of Investigations 92, 46 p.

NATURAL BAR-BYPASSING OF SAND AT A TIDAL INLET

Walter J. Sexton[1] and Miles O. Hayes[1,2]

ABSTRACT

Captain Sam's Inlet, a shallow unstable inlet, periodically migrates up to three kilometers (km) alongshore over a 30- to 40-year period. As the inlet migrates, sediment accumulates at the seaward terminus of the tidal inlet to form a wave-modified ebb-tidal delta that trends downdrift. Continued sediment accumulation on the tidal-delta shoal and subsequent lengthening of the tidal channel in a downdrift direction results in an unstable channel configuration. The ebb delta is eventually breached on its updrift side, releasing a sediment package for inlet bypassing.

The sediment-bypassing process was initiated at Captain Sam's Inlet after the final landfall of Hurricane DAVID in September 1979. Initially, the newly formed updrift hurricane channel scoured 1.1 m, migrated updrift, and became the predominant tidal channel at the inlet with eventual abandonment of the prehurricane, main ebb channel. These two channels outlined a portion of the ebb-tidal delta that was freed for bypassing. The initial sediment volume contained in the bypassing shoal, above the -0.6 m (-2 ft) MSL contour, was 47,000m^3. The sediment volume of the bypassing shoal did not change significantly until final attachment to Seabrook Island. This channel dominance and the wave-induced migration of the bypassing sediment package aided the bypassing of sand at the inlet. Immediately after filling of the prehurricane, main ebb channel on the delta, the downdrift beaches began accreting. The accretion continued throughout the bypassing process. The tidal prism and cross-sectional area reflected little change during the bypass, showing evidence of the system's overall stability.

INTRODUCTION

Sediment bypassing at tidal inlets is an essential process in maintaining a balanced sediment budget along a barrier island chain. Since bar-bypassing was first identified (Bruun and Gerritsen, 1959), few field studies have been conducted documenting the process.

---

[1]Research Planning Institute, Inc., 925 Gervais Street, Columbia, South Carolina, U.S.A. 29201

[2]Department of Geology, University of South Carolina, Columbia, South Carolina, U.S.A. 29208

Captain Sam's Inlet, located on the central South Carolina coastline, is a small tidal inlet with a downdrift-trending ebb-tidal delta (Fig. 1). Previous studies of the inlet (Hubbard, 1977; FitzGerald, 1980) indicated that large volumes of sediment frequently migrate across the inlet. This sediment migrates in the form of a nearshore bar from the updrift side of the inlet to the downdrift side.

Continued sediment accumulation on the tidal delta and progressive extension of the main ebb channel in a downdrift direction results in an unstable channel configuration. The ebb delta is eventually breached on its updrift side, releasing a packet of sediment for inlet bypassing (Fig. 2).

Utilizing the previous material published on tidal inlet dynamics, work done by Bruun and Gerritsen (1959), who first identified tidal inlet sediment bypassing, and observations made by Hubbard (1977) and FitzGerald (1980) at Captain Sam's Inlet, a preliminary understanding of the sediment bypassing process was possible. Hubbard (1977) determined a simplified model of bar-bypassing from the observations made at Captain Sam's Inlet and other similar tidal inlets along the South Carolina coastline (Fig.2).

The objective of this study was to quantitatively study the actual process of bar-bypassing which occurred at Captain Sam's Inlet during the switch in channels due to Hurricane DAVID. Utilizing bathymetric maps, beach profiles, and current and tide data collected during the bypass, quantitative calculations of sediment volumes and tidal inlet hydraulics were possible.

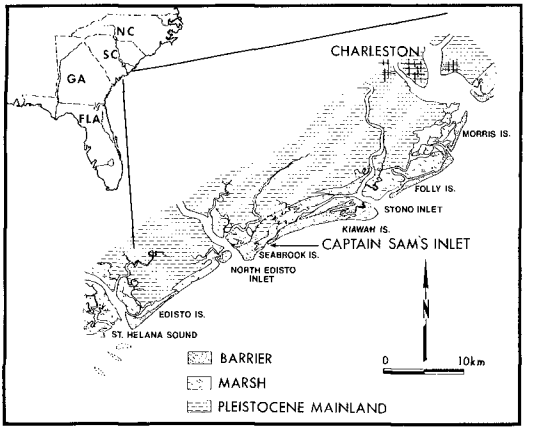

FIGURE 1. Location map of Captain Sam's Inlet, South Carolina. Captain Sam's Inlet is a small tidal inlet in comparison with its neighboring tidal inlets, Stono and North Edisto. The difference in inlet size is partially the result of the relationship between the cross-sectional geometry of the inlet and the back-barrier system.

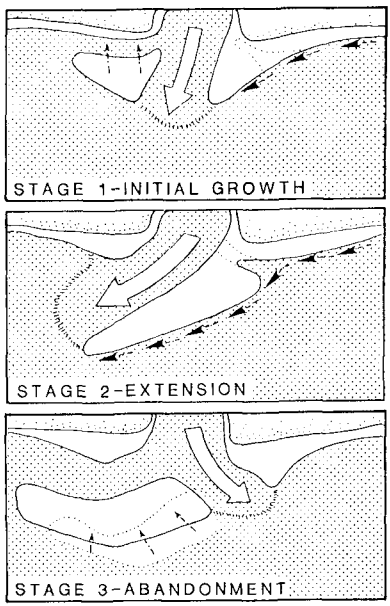

FIGURE 2.

A simplified three-stage model of bar-bypassing (after Hubbard, 1977):

1) Initial growth, sediments accumulating, forming a downdrift-trending delta.

2) Continued accretional growth, approaching an overextended configuration.

3) Breachment of the overextended delta, abandonment of the prebreachment main channel, followed by landward migration of the nearshore bar (swash bar).

PHYSICAL SETTING

The study area is influenced by prevailing winds from the south-southwest and storm winds generally from the northeast. Winds from the south-southwest occur 28 percent of the time. Even though northeast winds are less frequent than the prevailing south-southwest winds, their greater strength results in significant waves, energy flux, and longshore transport directed to the southeast in the study area (Finley, 1975).

Winds of hurricane strength [exceeding 75 miles per hour (mph)] have a frequency of occurrence along South Carolina of one event every 14 years (Myers, 1975). These winds are relatively rare at Captain Sam's Inlet, but can cause significant geomorphic changes on local beaches (Sexton and Moslow, 1981). Average wave heights on the South Carolina coastline are 50-60 centimeters (cm) (Finley, 1976; Kana, 1977). Tides at Captain Sam's Inlet range from 1.4 meters (m) (neap tide) to 2.2 m (spring tide) and are semidiurnal in nature. The tidal range is mesotidal (2-4 m), using Davies (1964) classification. These tides rarely reach heights above 2.2 m except during storm conditions.

Net longshore transport of sediment on the South Carolina coastline is predominantly from the northeast to the southwest (Finley, 1976; FitzGerald, 1977; Kana, 1977; Knoth and Nummedal, 1977). This

dominance of southerly transport is evidenced by numerous south-southwest-trending geomorphic features (e.g., recurved spits, tidal inlets) along the South Carolina shoreline. Transport rates are on the order of 75,000-300,000 m^3/yr. These values are based on measurements taken during several studies on the South Carolina coast, both on central portions of barrier islands and near tidal inlets (Finley, 1976; Kana, 1977; FitzGerald, 1977; Knoth and Nummedal, 1979).

Sediments are fine-grained quartz sand (mean grain size = 2.82 phi units or 137 microns) and are well sorted. Samples taken at dunes were very well sorted, and sorting of the sand in the intertidal area of the inlet improved when exposed to active wave swash (e.g., top of bypassing shoal, active beach face).

DATA BASE

BATHYMETRIC MAPPING

Three bathymetric maps were produced from surveys of Captain Sam's Inlet during September 1979, January 1980, and June 1980. The inlet was surveyed with a Hewlett-Packard 1038 total-station microwave transit. This instrument has a horizontal accuracy of six millimeters (mm) per km and a vertical accuracy of 0.3 mm/km. The precise nature of these surveys allowed quantitative comparisons of sediment volumes at the inlet.

BEACH PROFILES

A sampling grid of 11 beach profile stations was established at the beginning of the study. Profiles of the beach and inlet configuration for the 11 stations were taken six times throughout the 10-month study using the Emery (1961) method.

CURRENT MEASUREMENTS

Tidal currents were monitored six times during the 10-month field study. The first five current surveys were taken using a ducted impellar current meter, modified after a design presented by Byrne and Boon (1973), whereas the final tidal current survey was conducted using a Marsh-McBirney Model 201 electromagnetic flowmeter. Tidal currents were monitored for a minimum of 13 hours during each survey, beginning one hour before slack low water and running until the next slack low.

AERIAL PHOTOGRAPHS AND COASTAL CHARTS

Historical shoreline changes at Captain Sam's Inlet were determined using 12 historical charts dating from 1696 to 1924 and seven photo mosaics dating from 1939 to 1979. Also during the 10-month bypass, seven overflights were made for observation and oblique photography.

BAR-BYPASSING AT CAPTAIN SAM'S INLET, SEPTEMBER 1979 THROUGH JUNE 1980

On 4 September 1979, Hurricane DAVID made final landfall on the southern portion of the South Carolina coast. The storm was a moderate hurricane and maximum winds reached 90 mph (Sexton and Moslow, 1981). The associated storm tides (0.5-1.0 m above normal), and waves caused considerable damage to the southern and central coastline of South Carolina. At Captain Sam's Inlet, a new channel was scoured through the ebb delta to the north of the previous main tidal channel (Fig. 3). This newly formed channel was important because, as shown in previous studies of the area (Hubbard, 1977; Hayes et al., 1979), it initiated the bar-bypassing process.

Within two weeks of the landfall of Hurricane DAVID, a field study was initiated to monitor the bar-bypass process. On September 17 and 18, detailed bathymetric surveys of the inlet were made (Fig. 4) and 11 beach profile stations were established on the adjacent beaches as shown in Figure 4.

Utilizing the bathymetric map surveyed during the study, the volume of sediment contained in the bypassing shoal above the -0.6 m (-2 ft) mean sea level (MSL) contour area shown on Figure 3 was calculated using the prismoidal formula (Hodgman, 1947):

$$V = 1/6\ H(S_0 + 4S_1 + S_2)$$

where V = shoal's volume
H = height of shoal (difference between top and base contours)
S = plane variable.

The total volume for the shoal, released for bar-bypassing above the -0.6 m contour, was 47,510 m^3.

FIGURE 3. Photo mosaic of Captain Sam's Inlet and vicinity taken at low tide on 23 September 1979. The area mapped is bordered in black and the white arrow points to the hurricane channel.

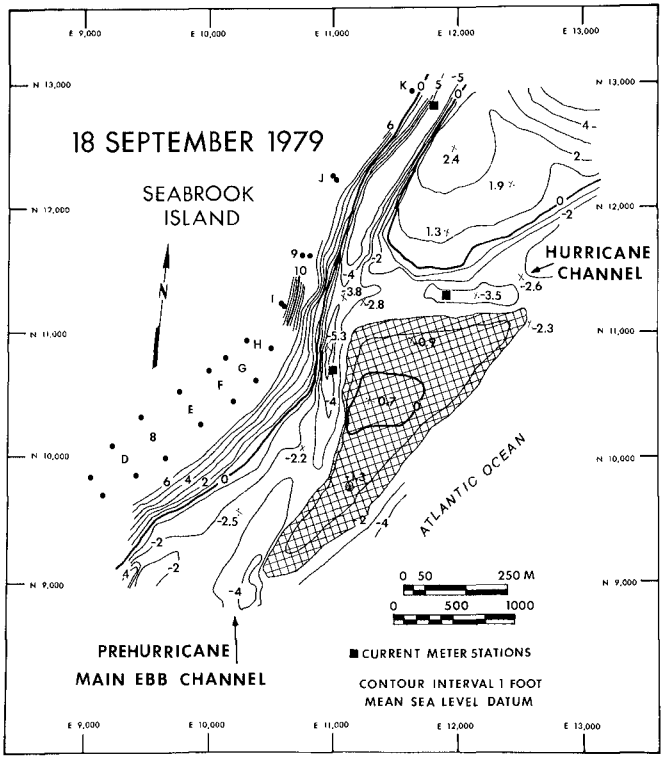

FIGURE 4. Bathymetric map of Captain Sam's Inlet, surveyed in September 1979, 14 days after hurricane landfall. Note the positions and depths of both the prehurricane, main ebb channel and hurricane channel. The hatched area on the delta was used for sediment-volume calculations and outlines the bypassing shoal.

Beach profiling across the ebb-tidal delta was quite unique and was possible only because of the shallow tidal channels at the inlet. Review of the beach profiles provides a cross-sectional view of the geomorphic form of the inlet whereas the bathymetric map is a plan view. From the beach profile data taken in September 1979, a variety of beach configurations were identified (Fig. 5).

The beach profile plot for Station E (Fig. 5) begins in a field of immature, prograding beach ridges and traverses a low-amplitude foredune ridge onto a steep beach face. Seaward of the active beach face lies a 110-m-wide bay that terminates at the toe of the southern

portion of the delta at the inlet. Beach profile Station J (Fig. 5) is positioned along the most unstable section of coastline at Captain Sam's Inlet. Previous studies (Hayes et al., 1976; Sexton and Hayes, 1980) measured erosion rates of 40-60 m/yr in this vicinity. At Station J there is a large (2.5 m) erosional scarp with a narrow beach face that slopes into the Kiawah River. Seaward of the river lies the broad intertidal recurved spit platform.

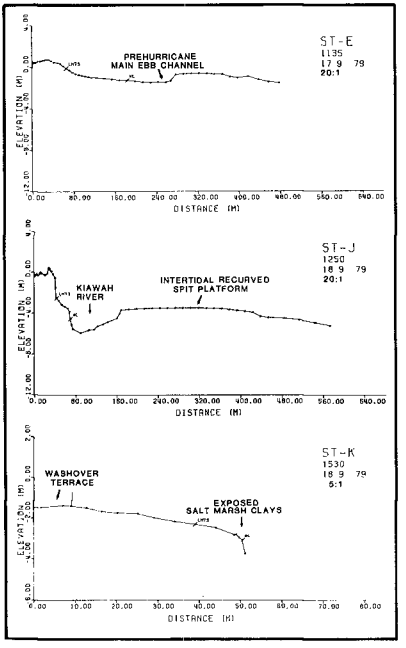

FIGURE 5.

Plots of beach profiles monitored in September 1979. Station locations are shown in Figure 4. The variety of beach configurations located in the small area indicate the high degree of variability in shoreline conditions. Also observe the total distance of each profile and the changes in vertical exaggeration (5:1; 2:1).

During the four months following the hurricane, the inlet was monitored closely to document the change that had occurred. In early January 1980, a second bathymetric map was constructed (Fig. 6). The morphology of the inlet area had changed significantly since September (Fig. 4). Some of the more outstanding changes were:

1) The hurricane channel had scoured 0.7 m deeper and had shifted 80 m to the north.

2) A new middle channel had formed, truncating the northern tip of the bypassing shoal.

3) The bypassing shoal had migrated 215 m landward and 164 m downdrift in a southwesterly direction.

4) The prehurricane, main ebb channel had been filled with as much as 1.3 m of sediment.

5) Sediment volumes contained in the bypassing shoal, the volume above the -0.6 m MSL contour, had not changed significantly since September remaining at approximately 50,000 m^3.

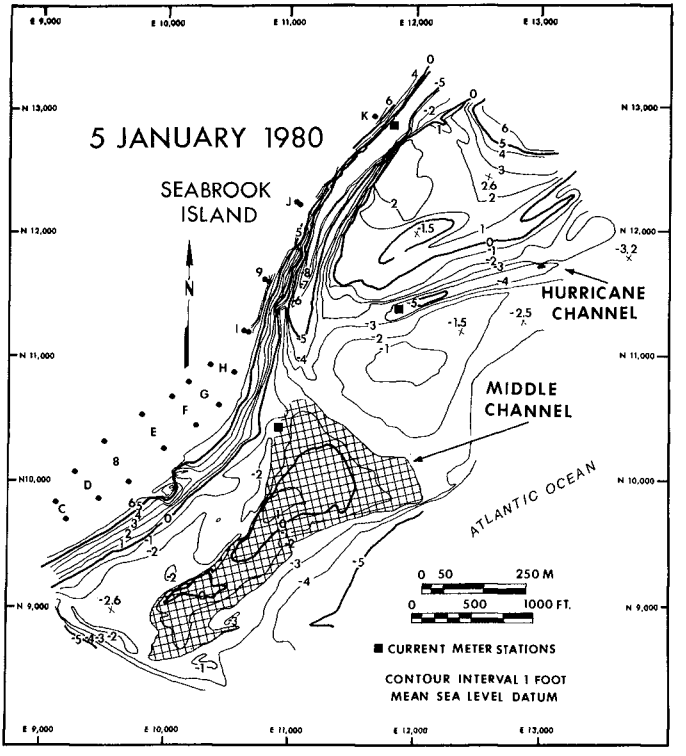

FIGURE 6. Bathymetric map of Captain Sam's Inlet surveyed in January 1980. The hatched area on the map was used for sediment-volume calculations for the bypassing shoal.

The tidal currents active in the tidal channels at the inlet had shown several distinct patterns. Shortly after the hurricane channel was formed, the current velocities in the channel were very erratic. Velocity changes of over 100 cm/sec were recorded in less than one hour while other channels were recording velocities of less than 50 cm/

sec during the same period. By December 1979, the current velocities in the hurricane channel were the same as those measured in the Kiawah River indicating that the hurricane channel was becoming the main channel for the inlet. The current velocities in the prehurricane, main ebb channel were flood dominant with low values when compared to the currents in the hurricane channel. This indicates that the prehurricane, main ebb channel was functioning as a marginal flood channel (Hayes, 1980). Also, during the first four months of the bypass, the cross-sectional area of the inlet's throat reduced slightly from 492.5 m^2 to 472m^2 or about four percent.

During the last six months of the monitoring program (January-June 1980), the bypass process was essentially completed. Results from the final bathymetric survey are shown in Figure 7. During the six month period since January 1980, the bypassing shoal had migrated onshore with little additional downdrift migration to the south. Previously (between September 1979 and early January 1980) shoal migration was dominantly in a downdrift direction. The bypassing shoal had attached to Seabrook Island on its northern end, and only a narrow trough separated the remaining portion of the shoal from the island. The newly formed middle channel was well formed, with the formation of an ebb-tidal delta seaward of the channel. The northern portion of the tidal delta, north of the middle channel, had accreted as evidenced by the filling of the hurricane channel. The volume of sediment contained in the bypassing shoal above the -0.6 m MSL contour was 34,817 m^3. The volume of sediment in the bypassing shoal had been reduced by 27 percent since January. The reduction of the total sediment volume in the ebb-tidal delta at the end of the process can be accounted for by accretion of the downdrift beaches where the shoal was attaching to the shoreline.

Results of the tidal currents monitored toward the end of the bar-bypassing process indicated that the tidal exchange measured in the inlet's throat closely resembled the currents monitored on the ebb delta in the middle channel. In conjunction with the current readings during the entire bypass, little change in the salinity of the seawater through the inlet was recorded, reading consistently around 32 parts per thousand.

The cross-sectional area of the tidal inlet throat had increased slightly by six percent to 503.5 m^2. The tidal inlet had once again regained a single channel configuration on its delta, similar to that prior to the landfall of Hurricane DAVID.

DISCUSSION AND SUMMARY

A review of the bar-bypassing process that occurred at Captain Sam's Inlet is shown in Figure 8. Prior to the bar-bypass process, the inlet had a single channel configuration on its delta (Fig. 8A). Through the process, the inlet had as many as three active channels on the delta (Fig. 8C). Toward the end of the bypass, the inlet once again regained a single channel configuration on its delta lobe (Fig. 8F).

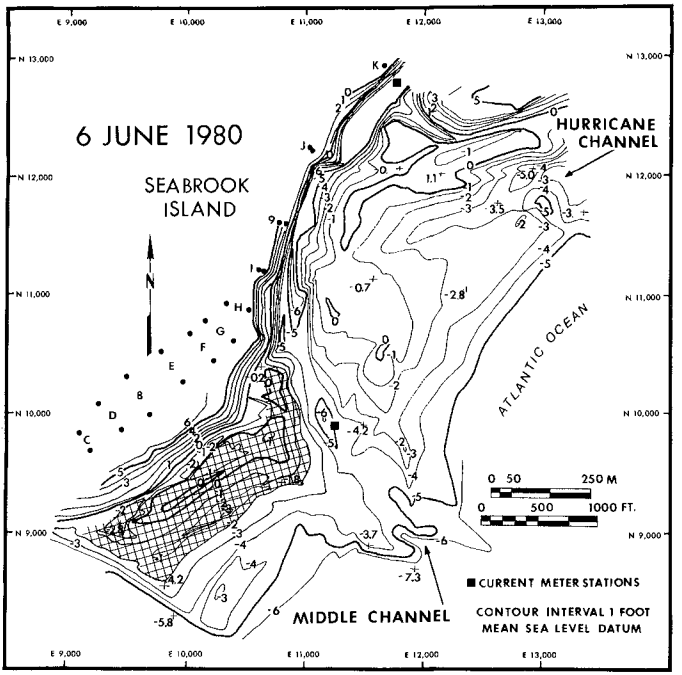

FIGURE 7. Bathymetric map of Captain Sam's Inlet in June 1980. The hatched area was used for sediment-volume calculations for the bypassing shoal. An ebb-tidal delta had formed seaward of the inlet at the location of the middle channel while the hurricane channel had been filling.

Sediment volumes calculated from the three bathymetric maps for the bypassing shoal is shown in Table 1. The volume of sediment contained in the bypassing shoal above the -0.6 MSL contour remained constant until the end of the bypass procedure. Stability in sediment volume was achieved even though the northern one-third of the bypass shoal was truncated from the main body of the shoal by the formation of the middle channel (Figs. 6 and 8C). Three possible explanations for the sediment volume stability are:

1) The addition of sediment to the bypassing shoal from longshore and onshore sand transport.

FIGURE 8A.

Low-tide photo of Captain Sam's Inlet taken on 7 December 1978. The inlet had only one channel active on the delta at this time.

FIGURE 8B.

Oblique low-tide photo taken on 6 September 1979, following Hurricane DAVID. The channel scoured by the storm is marked by the white arrow.

FIGURE 8C.

Aerial photo taken at low tide on 8 November 1979. The inlet had three channels active on the delta with the middle channel (marked by the white arrow) forming during the first two months of the bar-bypass.

FIGURE 8D.

Oblique aerial view of Captain Sam's Inlet taken on 21 December 1979. The prehurricane, main ebb channel was nearing abandonment.

FIGURE 8E.

Low-tide photo taken on 11 April 1980. The hurricane channel had filled with sediment and the middle channel was clearly the dominant channel active at the inlet.

FIGURE 8F.

Aerial photo taken at low tide on 29 May 1980 at Captain Sam's Inlet. Only a narrow trough separates the bypassing shoal from the mainland.

2) Movement of the bypassing shoal into shallow water, therefore exposing more of the shoal above the -0.6 m MSL contour.

3) The addition of sediment from the eroding scarp formed during the migration of the inlet system.

Of the three possible explanations, the third appears to be the most responsible for adding sediment to the system during the bypass. A total sediment volume of 43,152 m^3 (calculated from beach profile data) was eroded during the bypass due to the migration of the inlet system. This value would provide a substantial sediment supply to the bypassing shoal during the 10-month process.

TABLE 1. Sediment volume of the bypassing shoal, calculated above the -0.6 m ft) MSL contour at Captain Sam's Inlet.

MAP 1 September 1979	MAP 2 January 1980	MAP 3 June 1980
47,510 m^3	47,689 m^3	34,817 m^3

After the delta was breached during the hurricane, the shoal, freed for bar-bypassing at the inlet, migrated in a south-southwesterly direction for a total of 215 m (using the -0.6 m MSL contour), with the majority of the migration occurring during the first four months. Landward migration of the shoal caused 1.3 m of fill in the prehurricane, main ebb channel, but this tend was reversed toward the end of the study after the middle channel stabilized and scoured 1.2 m of sediment from the same general location at the inlet (Fig. 9).

Measurements made from the three bathymetric maps showed the hurricane channel initially scoured and migrated in a northerly direction. During the later stages of the bar-bypassing, the hurricane channel began to fill with sediment and migration continued to the north (a total of 175 m).

The currents monitored in the prehurricane, main ebb channel resembled that of an active marginal flood channel on an ebb-tidal delta (Hayes, 1980), which are dominated by flooding currents. The currents active in the marginal flood channel (prehurricane, main ebb channel) tended to lag in a flood direction, whereas currents in the main ebb channel were still flowing seaward. This flood dominance influenced the bar-bypassing procedure by assisting in the filling of the channel.

The cross-sectional area of the inlet below MSL showed little change throughout the study (Table 2). There was a slight overall enlargement of the inlet's throat toward the end of the study (31 m^2 or 6 percent). O'Brien (1969, 1972) found that, based on Pacific

Coast data, inlets tend to stabilize and balance by enlarging their cross-sections and varying the tidal prism and supply of sand to the inlet. This slight enlargement in the cross-section during the bypass may be the result of Captain Sam's Inlet regaining its single-channel, stable configuration. O'Brien and Dean (1972) also developed an index on the stability of tidal inlets to closure relative to deposition on filling with sediment. Essentially, they found that the stability or resistance of tidal inlet to closure depends on three main factors:

1) $\Delta L/L$ on the depositional length (L) of the inlet's channel.
2) The storage capacity of the inlet.
3) The inlets ability to transport sediment out of its channel.

These factors have a significant impact on Captain Sam's Inlet. When the inlet has a single channel on the tidal delta, the depositional length (total single channel length) of the channel is high; therefore, it would tend to be unstable. Also since the inlet is shallow and narrow, it would have a low storage capacity. When the length of the single channel on the delta is long, the frictional drag on the tide would reduce the efficiency of the tide to transport sediment out of the channel. These three principles are very important at Captain Sam's Inlet during the bar-bypass process.

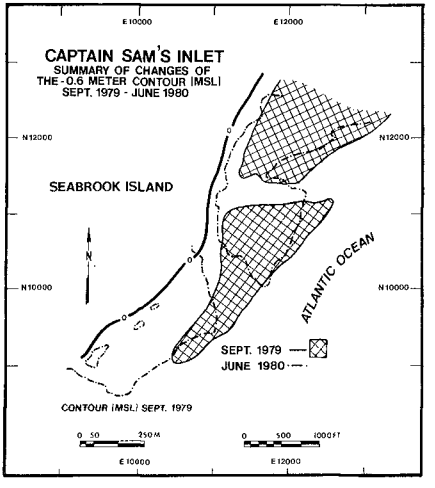

FIGURE 9.

Comparison map of the bathymetry of Captain Sam's Inlet showing changes in the -0.6 m (-2 ft) MSL contour, comparing maps surveyed in September 1979 with June 1980. Note the south-southwesterly migration of the bypassing shoal with eventual attachment to Seabrook Island.

TABLE 2. Values for the tidal prisms (in m^3) and cross-sectional areas (in m^2) for Current Station 3 (Fig. 4), the inlet's throat, at Captain Sam's Inlet.

Date	Tidal Prisms		Cross-Sectional Areas
	Ebb	Flood	
September '79	6,533,023 m^3	6,679,296 m^3	492.5 m^2
November '79	6,084,268 m^3	4,838,493 m^3	472.0 m^2
May '80	4,537,472 m^3	5,024,484 m^3	503.5 m^2

CONCLUSIONS

This paper documents sediment bypassing at a small, natural tidal inlet in South Carolina. The process of bar-bypassing occurs at Captain Sam's Inlet in conjunction with the continual migration of the entire inlet system.

The following conclusions are offered:

1) Periodically, Captain Sam's Inlet attains a long unstable, single-channel configuration that results in the formation of shorter, more efficient channels initiating bar-bypassing.

2) Channel formation and abandonment facilitate bar-bypassing at the inlet, as opposed to continuous channel migration.

3) In this study, the volume of sediment contained in the shoal that bypassed remained constant until final attachment to the mainland. This is partially due to the addition of sediment to the downdrift side of the inlet from erosion during overall inlet migration.

4) Major changes in the inlet tidal prisms or cross-sectional areas were not observed during the bar-bypass process, although a slight enlargement of the channel cross-section toward the end of the process could indicate inlet stability.

5) The bypassing of sand at the inlet did transfer significant amounts of sand (approximately 50,000 m^3) across the inlet to the downdrift barrier island, creating a zone of rapid accretion.

Although Captain Sam's Inlet exhibits many characteristics of a short-lived inlet (eventual closure), the stable nature of the inlet's throat indicates that the inlet attains a state of equilibrium despite the radical behavior of the delta portion of the system.

ACKNOWLEDGMENTS

Financial support for this work came from the National Sea Grant Program, Seabrook Island Company, and the Kiawah Island Company. We would like to thank Bill Ficken and the staff at Research Planning Institute for their assistance in both field work, data reduction, and report preparation.

REFERENCES CITED

Bruun, P. and F. Gerritsen, 1959, Natural bypassing sand at coastal inlets: in Proc. Jour. Waterways and Harbors Div., ASCE, Vol. 85(WW4), pp. 75-107.

Byrne, R. J. and J. D. Boon, III, 1973, An inexpensive, fast-response current speed indicator: Chesapeake Science, Vol. 14, pp. 217-219.

Davies, J. L., 1964, A morphogenic approach to world shorelines: Zeit. fur Geomorph., Vol. 8(Sp. No.), pp. 127-142.

Emery, K. O., 1961, A simple method of measuring beach profiles: Limnology and Oceanography, Vol. 6, pp. 90-93.

Finley, R. J., 1975, Hydrodynamics and tidal deltas of North Inlet, South Carolina: in L. E. Cronin (ed.), Estuarine Research, Vol. 2, Academic Press, New York, N.Y., pp. 227-292.

Finley, R. J., 1976, Hydraulics and dynamics of North Inlet, South Carolina, 1974-75: General Investigation of Tidal Inlets, Rept. No. 10, U.S. Army Corps of Eng., Coastal Eng. Res. Cent., Ft. Belvoir, Vir., 188 pp.

FitzGerald, D. M., 1977, Hydraulics, morphology, and sediment transport at Price Inlet, South Carolina: Ph.D. Dissert., Dept. Geol., Univ. South Carolina, Columbia, 84 pp.

FitzGerald, D. M. and M. O. Hayes, 1980, Tidal inlet effects on barrier island management: in Coastal Zone '80, Vol. III, ASCE, New York, N.Y., pp. 2355-2379.

Folk, R. L., 1974, Petrology of sedimentary rocks: Hemphill Publ. Co., Austin, Tex., 182 pp.

Hayes, M. O., 1980, General morphology and sediment patterns in tidal inlets: Sedimentary Geology, Vol. 26, pp. 139-156.

Hayes, M. O., et al., 1979, Assessment of shoreline changes, Seabrook Island, South Carolina: RPI Summary Rept. to Seabrook Island Co. (Charleston, S.C.), Research Planning Inst., Inc., Columbia, S.C., 82 pp.

Hodgman, C. D. (ed.), 1947, Handbook of chemistry and physics: The Chemical Rubber Publ. Co., Cleveland, Ohio, 30th Ed., 260 pp.

Hubbard, D. K., 1977, Tidal inlet variability in the Georgia embayment: Ph.D. Dissert., Dept. Geol., Univ. South Carolina, Columbia.

Kana, T. W., 1977, Suspended sediment transport at Price Inlet, South Carolina: in Proc. Coastal Sediments '77 Conf., ASCE, New York, N.Y., pp. 366-382.

Knoth, J. S. and D. Nummedal, 1977, Longshore sediment transport using fluorescent tracers: in Proc. Coastal Sediments '77 Conf., ASCE, New York, N.Y., pp. 383-398.

Myers, V., 1975, Storm-tide frequencies on the South Carolina coast: Natl. Weather Serv., Office of Hydrology, Silver Springs, Md., 79 pp.

O'Brien, M. P., 1969, Equilibrium flow areas of inlets on sand coasts: Jour. Waterways and Harbors Div., ASCE, New York, N.Y., Vol. 95, pp. 43-52.

O'Brien, M. P. and R. G. Dean, 1972, Hydraulics and sedimentary stability of coastal inlets: in Proc. 13th Coastal Eng. Conf., Vancouver, B.C., Canada, Vol. II, pp. 761-779.

Sexton, W. J. and M. O. Hayes, 1980, Beach erosion studies of Seabrook Island - December 1979 through October 1980: RPI Final Rept. to Seabrook Island Co. (Charleston, S.C.), Research Planning Inst., Inc., Columbia, S.C., 10 pp.

Sexton, W. J. and T. F. Moslow, 1981, Effects of Hurricane DAVID on the beaches of Seabrook Island: in Proc. NE Geol. Symp. on Barrier Islands, Philadelphia, Penn.

SHOALING WITH BYPASSING FOR CHANNELS AT TIDAL INLETS

Cyril Galvin, M. ASCE*

ABSTRACT

A channel dredged at the mouth of a tidal inlet is subject to rapid shoaling because of longshore transport, but this shoaling is slower than would be computed from simple trapping of all the moving littoral drift. The reduction in shoaling rate is due to the bypassing of littoral drift which occurs simultaneously with shoaling. This report presents a systematic method for computing the rate of shoaling in channels subject to shoaling with bypassing. The method also permits estimates of the effect of the dredged channel on the downdrift beaches.

INTRODUCTION

Stable Tidal Inlet. A **tidal inlet** is a waterway that connects a large body of water (usually the ocean) with a smaller body of water (Figure 1). The tidal inlet tends to shoal because ocean waves drive sand into the inlet channel, but a stable inlet channel is kept open because tidal currents prevent the wave-driven sand from depositing.

Waves bring sand to the inlet by the process of **longshore transport.** Longshore transport can occur from the ocean beaches on both sides of the inlet, but usually there is a dominant direction of longshore transport (say from left to right in Figure 1) that permits identification of an **updrift side** (the side from which sand is driven) and a **downdrift side** (the side toward which sand is driven). At a stable tidal inlet, the joint action of the waves and tidal currents results in natural **bypassing** of the sand across the inlet channel from the updrift side to the downdrift side, at a more or less steady rate, when averaged over a period of years.

The tidal currents which maintain an inlet are those which result from the daily rise and fall of tides in the ocean. As the tide rises in the ocean, water flows from the ocean to the bay; as the tide falls in the ocean, water drains from the bay to the ocean. The volume of water which enters the inlet from the time of low water slack to the time of highwater slack is the **tidal prism.** It has been known for a long time that the inlet cross section is proportional to the tidal

*Coastal Engineer, Box 623, Springfield, Virginia 22150, U.S.A.

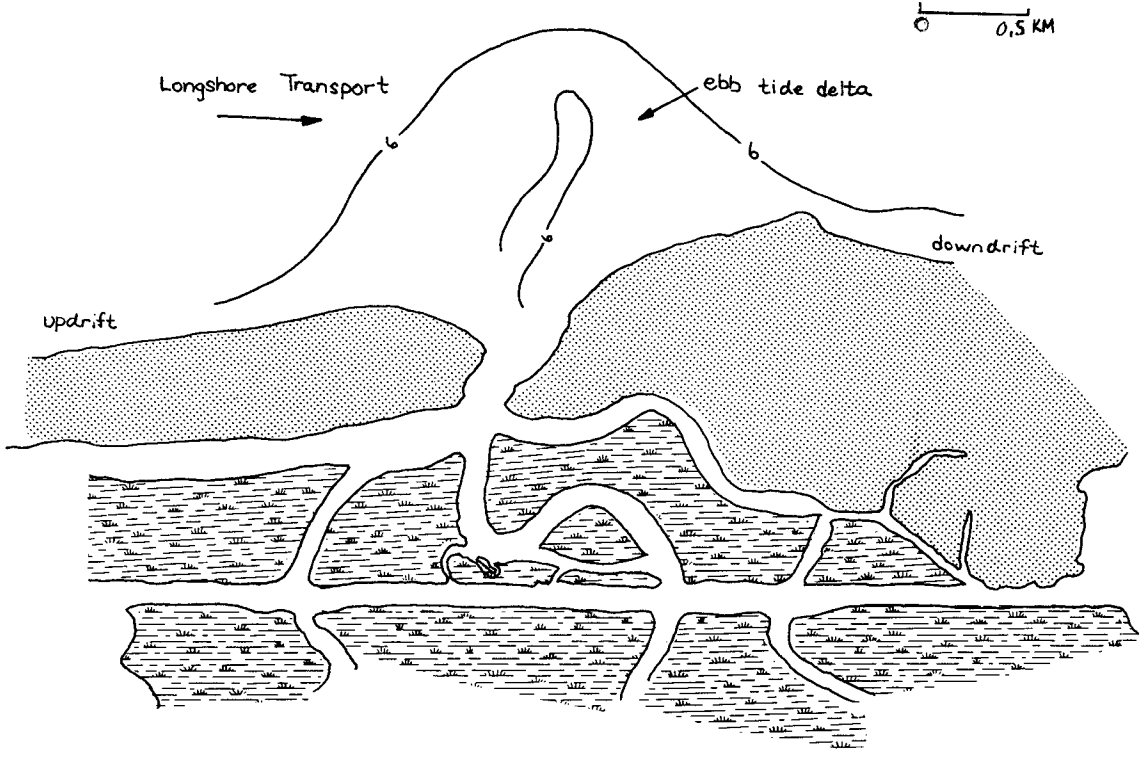

Figure 1. TYPICAL EBB TIDE DELTA AT TIDAL INLET (ADOPTED FROM BREACH INLET, FORT MOULTRIE, S.C. USGS QUAD.)

prism (LeConte, 1905; O'Brien, 1931; Jarrett, 1975). However, the maximum velocity through that section does not vary much with the size of the tidal prism, being on the order of 1 meter per second in naturally stable sandy inlets over a considerable range of tidal prisms.

There is a minimum size to the cross section of an inlet below which the channel will shoal and eventually seal off. This minimum cross section, or the corresponding minimum tidal prism, is proportional to the magnitude of the longshore transport; channels subject to larger longshore transport rates require greater tidal prisms to keep the channel open. Escoffier (1940), Keulegan (1967), O'Brien and Dean (1972) and others have examined the hydraulics of flow in tidal inlets in order to estimate the minimum stable cross section.

Tidal inlets are common on many coasts. For example, on the Atlantic coast of the United States, there are at least 37 permanent tidal inlets between Montauk Point, New York, and Miami, Florida, a shoreline distance of about 2050 kilometers. On many coasts, such as the east coast of India, shallow tidal inlets are the only waterways connecting the open sea with safe harbors along hundreds of kilometers of coast.

Definition of Depth. Seaward of these inlets, tides and waves create an **ebb tide delta.** Minimum depth for navigating through a tidal inlet is usually the sand bar at the crest of this delta. This minimum depth is the **controlling depth,** and the cross section of the channel which contains the minimum depth is the **controlling section.** Natural bypassing by waves and currents transports sand along the ebb tide delta in the downdrift direction (Figure 1). If the controlling section is deepened by dredging, the channel will begin to shoal, mostly from the updrift side. At the same time, because of the relatively shallow depth and flat side slopes of the dredged channel, some sand will be transported out of the channel, mostly to the downdrift side. The difference between the incoming and outgoing transport rates produces shoaling in the channel.

The initial rate of shoaling is a function of the natural controlling depth (d_1) and the initial dredged depth (d_2). At any time after dredging there will be an existing depth (d) such that (Figure 2)

$$d_1 < d < d_2 \tag{1}$$

In applying the analysis in this paper, all depths should be measured from Mean Sea Level (or Mean Tide Level) rather than chart datum, since chart datum is typically Mean Low Water or some lower elevation.

The design question is: how long will it take d to decrease from an initial overdredged value of d_2 to some project depth, d_p, where d_p is defined as the minimum depth for practical navigation by the design vessel. This time interval will be called the duration of project depth, and indicated by the symbol t_p. Time t has a value t = 0 on the day when dredging is completed.

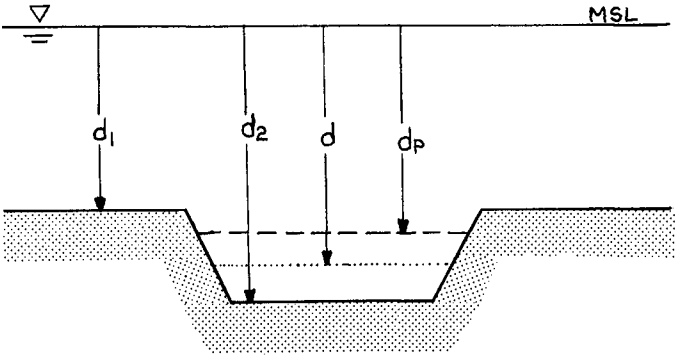

Figure 2. DEFINITION OF DEPTHS AT CONTROLLING SECTION

Purpose. The purpose of this paper is to present and illustrate by example a simple technique to obtain a rational estimate of t_p, the duration of project depth at the controlling section in the dredged channel.

The remaining text of this paper is organized into 4 principal sections. An analysis section derives the shoaling rate equation and presents Lent's solution of this equation. Lent's solution permits direct calculation of t_p. The justification for specific steps in the analysis section is presented in the following discussion section. An applications section follows the discussion to show by examples how to use the results in practical problems. Finally, the text ends with a summary section.

ANALYSIS

Bypassing Sediment Transport Ratio. As a starting point for this analysis, sediment transport rate is assumed to be proportional to the rate of energy expended by the flow:

$$\text{Transport} = \text{Coefficient} \times \text{Shear} \times \text{Velocity} \qquad (2)$$

This equation is assumed to describe sediment bypassing across the ebb tidal delta in the downdrift direction. After the channel has been dredged, the channel traps a greater percentage of the longshore transport due to the greater depth, and bypassing is reduced. The ratio

of the bypassing rate after dredging to the bypassing rate before dredging is defined as the **bypassing sediment transport ratio,** or the transport ratio for short.

$$\underset{\text{Ratio}}{\text{Transport}} = \underset{\text{Ratio}}{\text{Coefficient}} \times \underset{\text{Ratio}}{\text{Shear}} \times \underset{\text{Ratio}}{\text{Velocity}} \tag{3}$$

The flow is assumed to be well into the turbulent regime with low relative roughness both before and after dredging so that to a first approximation

$$\text{Coefficient Ratio} = 1 \tag{4}$$

This reduces the solution of (3) to the task of finding expressions for the shear ratio and the velocity ratio.

The shear in equation (2) is taken to be bottom shear induced by the wave orbital velocity on the ebb tidal delta. The general equation for such shear is

$$\text{Shear} = \text{coefficient} \times U^2 \tag{5}$$

where U is the amplitude of the wave-induced orbital velocity on the ebb tidal delta, and the coefficient incorporates a friction factor, density of seawater, and a dimensionless number depending on the definition of the friction factor. As in equation (4), it is assumed that the coefficient does not change significantly after dredging so that

$$\text{Shear Ratio} = U_{after}^2/U_{before}^2 \tag{6}$$

U is known from small amplitude shallow water theory, so that

$$\text{Shear Ratio} = (H_2^2 d_1)/(H_1^2 d_2) \tag{7}$$

The subscripts 1 and 2 refer to conditions before and after dredging, as on Figure 2. Equation (7) can be further simplified using the appropriate form of energy conservation in shallow water (Green's Law) to get

$$\text{Shear Ratio} = (d_1/d_2)^{3/2} \tag{8}$$

Equation (8) is one of the two ratios needed to solve equation (3). The required second ratio is the velocity ratio, which is derived as follows. Let the symbol, q, indicate the unit tidal discharge in the ebb channel at the controlling section. Thus,

$$\text{Velocity} = q/d \tag{9}$$

$$\text{Velocity Ratio} = (q_2 d_1)/(q_1 d_2) \tag{10}$$

The velocity ratio (10) depends on how the unit discharge in the ebb channel is affected by dredging. Two particular end conditions are possible. If the dredging merely increases the channel area, and the tidal prism remains the same, then the ratio q_s/q_1 remains unity and

$$\text{Velocity Ratio} = d_1/d_2 \text{ for constant discharge} \tag{11}$$

On the other hand, it is possible that the dredging may make the channel more efficient and increase the tidal prism. An upper limit to the velocity in this case is expected to be close to the predredging velocity, since scour by the ebb flow maintains the channel against longshore transport. In this case,

$$\text{Velocity Ratio} = 1 \text{ for constant velocity} \tag{12}$$

The transport ratio (3) can now be solved using equations (4), (8) and (10).

$$\text{Transport Ratio} = 1 \times (d_1/d_2)^{3/2} \times (q_2 d_1)/(q_1 d_2) \tag{13}$$

This may be simplified to

$$\text{Transport Ratio} = (d_1/d_2)^m \tag{14}$$

where $$3/2 \leq m \leq 5/2 \tag{15}$$

to account for the two possible end conditions for the velocity ratio given by equations (11) and (12).

Equation (14) is a specific expression for the bypassing sediment transport ratio immediately after the channel has been dredged to a depth d_2. Since the assumptions and reasoning which lead to (14) hold even better for any lesser depth, d, the symbol d_2 in (14) can be replaced by d to indicate the transport ratio for any post-dredging depth.

Shoaling Rate. The objective of this section is to derive an equation for shoaling rate. Shoaling rate will depend on the bottom area of the channel and the quantity of longshore transport reaching that channel bottom. To describe these factors, the following definitions are useful.

- Q longshore transport rate
- R fraction of Q which takes place above depth d_2
- C length of dredged channel (Figure 3)
- W width of dredged channel (Figure 3)

The amount of littoral drift carried into the dredged channel by longshore transport from the updrift side is RQ. Note that RQ is also the bypassing across the channel before dredging, or in other words, the denominator of equation (3).

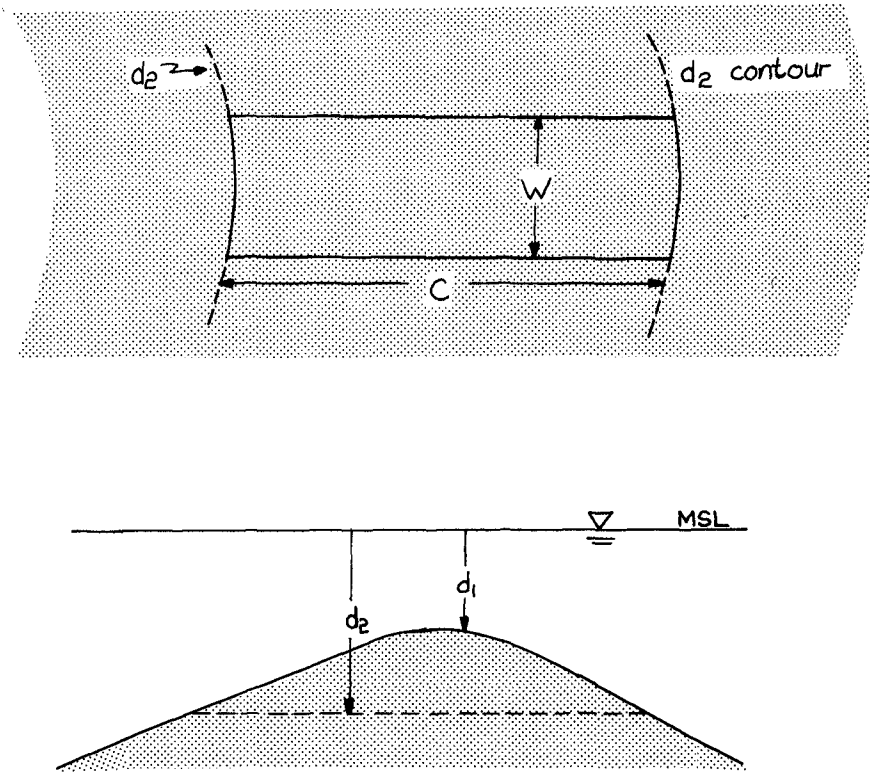

Figure 3. DEFINITION OF CHANNEL DIMENSIONS ACROSS EBB DELTA

The volume of sand trapped by the dredged channel per unit time is the trapping rate. From the above definitions,

$$\text{Trapping Rate} = RQ - \text{Bypassing after, above } d_2 \tag{16}$$

$$= RQ\ [1 - \text{Transport Ratio}] \tag{17}$$

The trapping rate given by (17) is a volume rate. To convert this volume rate to a shoaling rate, divide (17) by the bottom area of the channel, CW. For convenience, define K to be a characteristic shoaling rate.

$$K = RQ/CW \tag{18}$$

Thus, dividing equation (17) by CW and substituting equations (14) and (18) into the result gives

$$\text{Shoaling Rate} = K[1 - (d_1/d)^m] \tag{19}$$

Duration of Project Depth (Lent's Equation). The shoaling rate is mathematically equivalent to the time derivative of the depth

$$d(d)/dt \equiv \text{Shoaling Rate} \tag{20}$$

The duration of project depth, t_p, is obtained by integrating (20)

$$\int_0^{t_p} dt = t_p = \int_{d_2}^{d_p} \frac{d(d)}{\text{Shoaling Rate}} \tag{21}$$

An exact integral solution of (21) has not been found after some searching, but an approximate solution has been developed by Arnold H. Lent (personal communication, 30 Dec 1982). Lent's solution is as follows.

$$t_p \cong \frac{1}{K}\left[(d_2 - d_p) + \frac{d_1}{m}(\ell nA - \ell nB)\right] \tag{22}$$

where

$$A = (d_2 - d_1)/(d_p - d_1) \tag{23}$$

$$B = \frac{1 + \frac{m-1}{2}\left(\frac{d_2 - d_1}{d_1}\right)}{1 + \frac{m-1}{2}\left(\frac{d_p - d_1}{d_1}\right)} \tag{24}$$

Equation (22) approximates equation (21) with a degree of accuracy that exceeds the probable sounding accuracy of measured channel depths.

To find t_p by using equation (22), the values of K, m, d_1, d_2, and d_p must be obtained. The value of K is given by equation (18). The value of m depends on the likely effect of the proposed dredging on the velocity ratio, but is expected to be in the range given by equation

(15). The value of d_1 is the controlling depth obtained from soundings. The value of d_p is the requirement of the user, and the value of d_2 is the design choice to be tested.

DISCUSSION

Qualitative Evaluation. In order to obtain the principal results of the preceding section in minimum space, discussion of key assumptions necessary in the derivation was deferred to this section. But before examining the key assumptions, it is useful to observe that, however equations (21) and (19) were obtained, they agree qualitatively with intuition and experience.

The qualitative agreement is illustrated by the shape of the curves on Figure 4. Figure 4 plots depth on the vertical axis against time on the horizontal axis for three combinations of d_1 and d_2 (d_1 equals 4 feet, 6 feet, and 8 feet, each combined with the same d_2 value of 12 feet). The curves on Figure 4 are numerical solutions of equation (21) using equation (19) for the shoaling rate. Two values of the exponent, m, are used, corresponding to equations (11) and (12), i.e., the constant velocity case (m = 3/2) and the constant discharge case (m = 5/2). The curves on Figure 4 agree qualitatively with intuition and experience in at least 4 ways:

a. The maximum rate of shoaling occurs right after dredging (the curves are steepest at the deepest depth).

b. The channel shoals faster when post-dredging velocity is reduced (constant discharge, m = 5/2) than when the post-dredging velocity is not reduced (constant velocity, m = 3/2).

c. The channel shoals fastest when no bypassing occurs. This is equivalent to $m = \infty$ in equation (19) and plots as the dotted straight line on Figure 4.

d. Shoaling approaches d_1 more slowly when the depth of the dredged cut ($d_2 - d_1$) is smaller, d_2 being held constant.

Transport Equation. The starting point of the analysis is equation (2) which states that bypassing sediment transport rate is proportional to work done by the waves on the bottom. In the absence of an inlet, the bypassing rate is simply the longshore transport rate. The usual "energy flux" method of predicting longshore transport (Galvin and Schweppe, 1980) is, in effect, an assumption that sediment transport rate is proportional to the power supplied by waves to the surf zone. This is physically analogous to equation (2).

The form of equation (2) is also that used by Bagnold (1966) in his stream power hypothesis for sediment transport, which Bagnold assumes involves bed load transport. The proportionality between transport rate

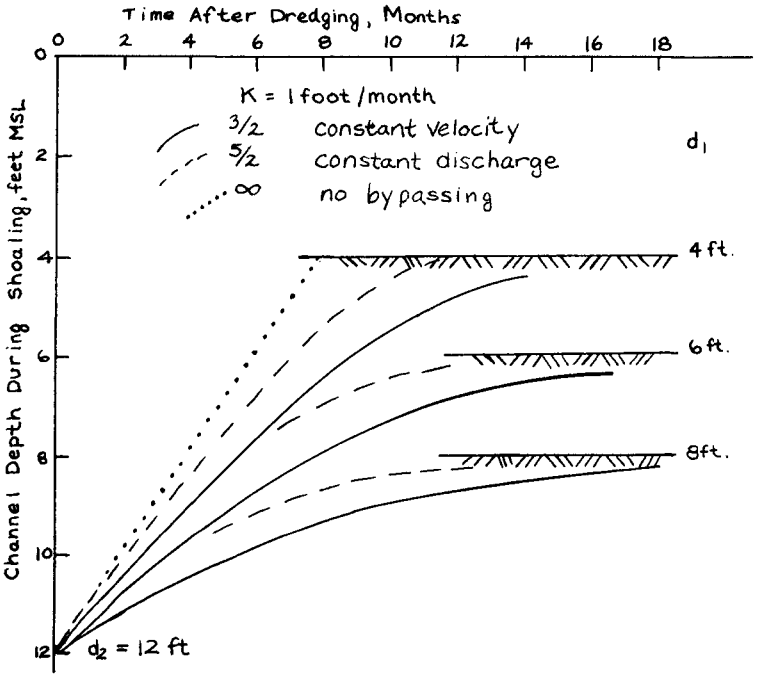

Figure 4. EFFECT OF BYPASSING ON CHANNEL SHOALING FOR THREE CHANNELS DREDGED TO 12 FEET MSL

and bottom shear required by equation (2) has been verified experimentally by Parsons (1972) for sediment grains in laminar flow.

Coefficient Ratios. The friction coefficients in equations (2) and (5) are assumed not to change after depth is increased by dredging. Increase in depth decreases the relative roughness of the flow on the typical friction factor diagram (shown in all hydraulics text books). For the moderate to high Reynolds numbers and small relative roughness expected in the navigation channel, such friction factor diagrams predict little change in f for large percentage changes in relative roughness. Thus, the assumption involved in equation (4) appears justified.

Velocities. There are three velocities to consider in the bypassing with shoaling process involved here. First, there is the ebb current velocity where it passes the controlling section of the navigation channel. This current has a characteristic maximum value of about 1 meter/second. (Flood currents are usually lower than ebb currents when they pass through the controlling section because flood flows are commonly more widely distributed over the ebb delta.)

Second, there is the bottom velocity due to the orbital motion of water particles under waves. The wave-induced bottom particle velocity on the ebb delta has a characteristic maximum amplitude, U, which approaches the magnitude of the maximum ebb current. The periodic reversal of the wave-induced velocity during the passage of each wave makes this velocity more effective in initiating sediment motion than tidal currents, but to first order, the wave-induced motion does not cause a net current.

Finally, there is the velocity of the longshore currents. The magnitude of longshore currents is only a fraction of U, with characteristic values on the order of 0.25 meters/second on open coast beaches. These velocities will be further diminished where they cross the controlling section of the navigation channel due to the deeper water there. Thus, the magnitude of the longshore current is distinctly less than the other two velocities involved in shoaling with bypassing.

The derivation assumes that wave-induced velocities stir up the sediment and that ebb currents distribute the sediment in the channel. The waves provide the shear component of equation (2) and the tides supply a convective velocity. This differs from the usual formulation of (2) in which the velocity that produces the shear is also the velocity causing the convection, but here the shear velocities are periodic and do not provide net transport. The longshore aspect of the motion is imposed on the shoaling equation (19) through the coefficient K which incorporates the longshore transport rate, Q, as given in equation (18).

Note that if U is used to obtain the velocity ratio, the velocity ratio will simply be the square root of the shear ratio (8). This results in a transport ratio exactly of the form given by equation (14) with the exponent m equal to 9/4, which is within the limits on m given by equation (15).

The use of linear shallow water wave theory to estimate U in equation (7) is technically not permissible because the waves on the ebb delta will have a height-to-depth ratio that is not negligible. However, linear theory has been used to describe such conditions many times before with adequate results (for example, Longuet-Higgins, 1970). Further, in the dredged cut, the height-to-depth ratio will be reduced, making linear theory more applicable.

Bypassing Mechanisms. During the meeting at which this paper was delivered (the 18th International Conference on Coastal Engineering), there were two descriptive papers on sediment bypassing at inlets (Sexton and Hayes, 1982; FitzGerald, 1982). Both these papers describe bypassing as the movement of discrete bars of sediment, usually initiated by a shift in the ebb channel from a downdrift location to an updrift location. This well-described process of discrete transport differs from the more continuous bypassing process of this paper, in which the longshore transport continually moves sand across the rim of the ebb delta and through the ebb channel. (This continuous longshore transport may in fact be accompanied by the motion of small bed forms.)

While bypassing undoubtedly occurs as described by Sexton and Hayes (1982) and FitzGerald (1982), it appears that the volume rate of this transport, when averaged over the time for the shifted ebb channel to complete one cycle, is only a fraction of the estimated annual longshore transport rates at the sites. Approximate estimates suggest that 10 to 30% of the longshore transport may be accounted for by the bar bypassing described in those papers.

Further, since dredging makes the ebb channel more efficient, it is less likely to shift in position. The deeper depths of the dredged channel are also expected to inhibit discrete bars moving across the channel. Therefore, in the dredged condition under investigation, most of the bypassing is expected to occur by relatively continuous longshore transport.

APPLICATIONS

Tabulation of t_p'. The following subsections show by example how to apply the analysis to practical problems. To aid in computing the duration of project depth, t_p, it is useful to rewrite equation (22) in dimensionless form.

$$t_p' = Kt_p/d_1 = d_2' - d_p' + \frac{1}{m}(\ell nA - \ell nB) \quad (25)$$

where $$d_p' = d_p/d_1 \quad (26)$$

$$d_2' = d_2/d_1 \quad (27)$$

and K, m, A, and B are defined by equations (18), (15), (23), and (24), respectively.

Equation (25) has been tabulated for m = 3/2 (Table 1) and m = 5/2 (Table 2) over a range of values of d_p' and d_2'. Ordinarily, in typical inland waterways, d_p' would be only slightly less than d_2', the difference due to the allowable overdredging which is rarely more than 2 or 3 feet. However, in dredging shallow tidal inlets in the active littoral zone, significantly more overdredging may be required to maintain floatation of the dredge and to reduce the frequency (and thus cost) of maintenance dredging.

Tables 1 and 2 list the values of t_p', defined by the right hand side of equation (25), as a function of d_p' and d_2', defined by equations (26) and (27). (The selection of m determines which of the two tables is used.) Any combination of d_1, d_p, and d_2 will give values of d_p' and d_2', and these give a value of t_p' either by direct reading of the table or by interpolation if necessary.

In the dimensionless form of equation (25), deep channels and shallow channels with variable amounts of overdredging can be conveniently covered by the same tables. The unit used for depth (feet, meters) does not matter as long as it is not changed during any single calculation, and as long as K is expressed in the same unit per time.

Example 1: Shoaling.

(a) Existing Condition: A permanent shallow draft tidal inlet is located in a relatively sheltered site on a large bay. The controlling depth is 1.5 meters chart datum, which corresponds to a mid tide depth of 2.5 meters. The longshore transport is estimated to be 50,000 cubic meters/year, with 80% of it occurring during the 4 month monsoon season. Characteristic storm waves have breaker heights of about 2.5 meters.

(b) Desired Improvements: A local company wishes to ship high value ore through the inlet during the non-monsoon season. The ore will be transported in barges needing a 4.0 meter project depth, measured from mid tide elevation. To get the barges through the inlet, the company plans to dredge a channel 30 meters wide and 150 meters long.

(c) Question: The shipper would like to dredge only once a year, right at the end of the monsoon season. How deep must he dredge (what is d_2?) in order to maintain a navigable depth for the 8 months until the start of the next monsoon?

Table 1. DIMENSIONLESS DURATION OF PROJECT DEPTH FOR m = 3/2 (Constant Velocity Condition)

Row Number	d_p'	d_2' =	t_p' = 1.10	1.20	1.33	1.50	1.75	2.00	2.25
1	1.05		0.50	1.05	1.49	1.91	2.40	2.81	3.17
2	1.10		x	0.55	0.99	1.41	1.90	2.30	2.67
3	1.20		x	x	0.44	0.86	1.35	1.76	2.12
4	1.30		x	x	0.09	0.51	0.99	1.40	1.77
5	1.40		x	x	x	0.23	0.72	1.13	1.49
6	1.50		x	x	x	x	0.48	0.89	1.26
7	1.75		x	x	x	x	x	0.41	0.77
8	2.00		x	x	x	x	x	x	0.37

Table 2. DIMENSIONLESS DURATION OF PROJECT DEPTH FOR m = 5/2 (Constant Discharge Condition)

Row Number	d_p'	d_2' =	t_p' = 1.10	1.20	1.33	1.50	1.75	2.00	2.25
1	1.05		0.31	0.66	0.96	1.26	1.62	1.94	2.24
2	1.10		x	0.35	0.65	0.95	1.31	1.63	1.92
3	1.20		x	x	0.30	0.60	0.96	1.28	1.57
4	1.30		x	x	0.06	0.36	0.72	1.04	1.34
5	1.40		x	x	x	0.17	0.53	0.85	1.15
6	1.50		x	x	x	x	0.36	0.68	0.98
7	1.75		x	x	x	x	x	0.32	0.62
8	2.00		x	x	x	x	x	x	0.30

(d) Solution: Based on the preceding description:

d_p = 4.0 m
d_1 = 2.5 m
C = 150 m
W = 30 m
t_p = 8 months

To use the table, it is necessary to find the dimensionless duration of project depth, t_p'. This term is defined by equation (25) as a function of K and d_1. Thus, K is needed. K is defined by equation (18) as a function of R, Q, C, and W. To estimate R, the fraction of longshore transport occurring above depth d_2, compare d_2 to the breaker depth of storm waves. The characteristic storm waves are given above as 2.5 meters, which will break in about 3.25 meters. Since this breaker depth is above d_2, assume R = 1.0. The value of Q during the nonmonsoon months is, from the data given above,

$$Q = 0.20 \times 50{,}000 \text{ cubic meters/8 months}$$

$$= 1250 \text{ cubic meters/month}$$

Thus from (18)

$$K = 1.0 \times 1250/(30 \times 150)$$

$$= 0.28 \text{ meters/month}$$

From equation (25)

$$t_p' = (K/d_1)t_p = (0.28/2.5)8$$

$$= 0.90$$

From equation (26)

$$d_p' = 4.0/2.5 = 1.6$$

This value of d_p' falls between rows 6 and 7 on the tables. Table 1 is the most favorable (gives the longest duration of project depth for a given d_2). Examination of Table 1 shows that t_p' = 0.90 between rows 6 and 7 is equivalent to d_2' somewhere between 2.00 and 2.25. Thus based on Table 1, the dredged depth d_2 must be at least twice the controlling depth (5.0 meters at least) in order for the channel to last the 8 months.

If a more exact solution is required, equation (25) can be solved by trial and error for t_p' = 0.90 and d_p' = 1.60. Such a solution for the favorable case of m = 3/2 yields d_2' = 2.14, which indicates d_2 = 5.35 meters.

Example 2: Bypassing

(a) Existing Conditions: Same as in Example 1.

(b) Desired Improvement: Same as in Example 1.

(c) Question: The property owner downdrift of the inlet in question is worried about the interruption in longshore transport due to the trapping of sand in the dredged channel. If d_2 = 5.1 meters, what will be the maximum reduction in bypassing rate?

(d) Solution: From equation (17), the maximum reduction in bypassing will equal the maximum trapping rate right after dredging for the case of m = 5/2 (constant discharge).

$$\text{Max Trapping Rate} = RQ\,[1 - (d_1/d_2)^{2.5}] \tag{28}$$

$$= 1250\,[1 - (2.5/5.1)^{2.5}]$$

$$= 1040 \text{ cubic meters/month}$$

This type of calculation can indicate the rate at which downdrift beaches need replenishment following dredging, if the dredged material cannot be placed directly on the downdrift shore.

SUMMARY

The basic contribution of this paper is to provide an organized method of computing the duration of project depth in a channel overdredged through a tidal inlet.

The duration of project depth, t_p, is predicted by equation (22). To solve this equation, the following data are required: the controlling depth before dredging, the project depth needed for navigation, the proposed depth of dredging, and the length and width of the channel. These parameters are defined in Figures 2 and 3 as d_1, d_p, d_2, C, and W, respectively. In addition, the longshore transport above the depth d_2 must be known, and the effect of dredging on the ebb velocity in the channel must be estimated (the value of m in equation (15)).

The analysis developed here can be used for the following practical problems:

a. computing the duration of project depth (use equation (22) or Tables 1 or 2).

b. testing whether a proposed depth of dredging will last a desired length of time (see example 1).

c. estimating the decreased rate of bypassing caused by a given channel (see example 2).

Based on the techniques used here, a typical shallow draft channel across the ebb tide delta has a lifetime measured in months, but due to bypassing the life of the channel is significantly longer than would be the case for complete trapping of longshore transport.

ACKNOWLEDGEMENTS

The problem implied by the title of this report was originally posed by Stanley Maisel, Chief, Planning Branch, New York District, Army Corps of Engineers. Dr. Arnold H. Lent, Technicare Corporation, Solon, Ohio 44139, provided the approximate solution given as equation (22). Mr. L. K. Ghosh, Central Water and Power Research Station, Pune, India, raised several questions which resulted in improvements to the present manuscript. Data shown in Figure 4 and Tables 1 and 2 were computed by S. J. Weinheimer, J. R. Hill, and D. J. Galvin, Jr. Figures were drawn by P. E. Politi and the manuscript typed by Sheila Zukor.

REFERENCES

BAGNOLD, R.A., "An Approach to the Sediment Transport Problem from General Physics," U.S. Ceological Survey, Prof. Paper 422-J, 1966.

ESCOFFIER, F.F., "The Stability of Tidal Inlets," Shore and Beach, Vol. 8, No. 4, 1940, pp. 114-115.

FITZGERALD, D.M., "Interactions Between the Ebb-Tidal Delta and Tidal Inlet Shoreline," Abstract from 18th International Conference on Coastal Engineering, Cape Town, South Africa, Paper No. 67, Nov. 1982, pp. 132-133.

CALVIN, C.J., and C.R. SCHWEPPE, "The SPM Energy Flux Method for Predicting Longshore Transport Rate," CERC TP No. 80-4, June 1980, 34 pp.

JARRETT, J.T., "Tidal Prism - Inlet Area Relationships," U.S. Army Corps of Engineers, GITI-3, Oct. 1975, 32 pp.

KEULEGAN, G.H., "Tidal Flow in Entrances: Water-Level Fluctuations of Basins in Communication with Seas," U.S. Army Committee on Tidal Hydraulics, Technical Bulletin No. 14, July 1967, 89 pp.

LECONTE, discussion of paper by Watt, D.A., "Notes on the Improvement of River and Harbor Outlets in the United States," Transactions ASCE, Vol. 55, Dec. 1905, pp. 288-321.

LONGUET-HIGGINS, M.S., "Longshore Currents Generated by Obliquely Incident Sea Waves, 1," Journal of Geophysical Research, Vol. 75, No. 33, Nov. 1970, pp. 6778-6789.

O'BRIEN, M.P., "Estuary Tidal Prisms Related to Entrance Areas," Civil Engineering, Vol. 1, No. 8, 1931, pp. 738-739.

O'BRIEN, M.P., R.G. DEAN, "Hydraulics and Sedimentary Stability of Coastal Inlets," Proceedings of the 13th Coastal Engineering Conference, Vancouver, Canada, Vol. II, Chapter 41, July 1972, pp. 761-780.

PARSONS, D.A., "The Speeds of Sand Grains in Laminar Flow Over a Smooth Bed," Sedimentation, edited by H.W. Shen, Chapter 1, 1972, pp. 1-25.

SEXTON, W.J., and M.O. HAYES, "Natural Bar-Bypassing of Sand at a Tidal Inlet," Abstract from 18th International Conference on Coastal Engineering, Cape Town, South Africa, Paper No. 190, Nov. 1982, pp. 374-375.

DREDGING TO MINIMIZE WAVE PENETRATION INTO A HARBOUR

BY

H.P.RIEDEL[1] & A.P.BYRNE[2]

ABSTRACT

Wave protection within a new harbour development has been achieved by shaped dredging in place of long breakwaters. The dredging shape was initially established through wave refraction calculations and then confirmed and optimized in a physical three dimensional model. The cost of additional dredging for the specified shape was A$100,000 compared to estimated breakwater costs of A$1,000,000.

1. INTRODUCTION

For the development of offshore gas reserves near Dampier, northern Western Australia, the developers, Woodside Offshore Petroleum, required a supply base harbour to be established. A harbour site was selected at the southern end of Mermaid Sound. See Figure 1. The site is protected from Indian Ocean swell and subjected to a relatively mild short period wave climate because of limited fetches. However, the area is subjected to cyclones with their associated winds, waves and storm surge.

The harbour site has natural protection from three sides and is only directly exposed to waves on the western side. Preliminary design had allowed for a breakwater to provide protection from the west. During detailed design, shaped dredging was investigated as an alternative to breakwater type protection.

As an aid to design of the facility, a three-dimensional physical model had been constructed to optimise the layout with respect to wave protection and to assist in the determination of design waves for seawall, revetment and breakwater design. In the modelling process it was found that a conventional channel approach as shown in Figure 2 tended to concentrate wave energy in the northeast corner of the basin. A breakwater length of approximately 200 metres was required to reduce waves to an acceptable height in the basin during cyclones.

---

[1] B.E., M.Sc., Ph.D., Riedel & Byrne Consulting Engineers Pty., Ltd., Melbourne, Australia.

[2] B.E. Riedel & Byrne Consulting Engineers Pty., Ltd., Perth, Australia.

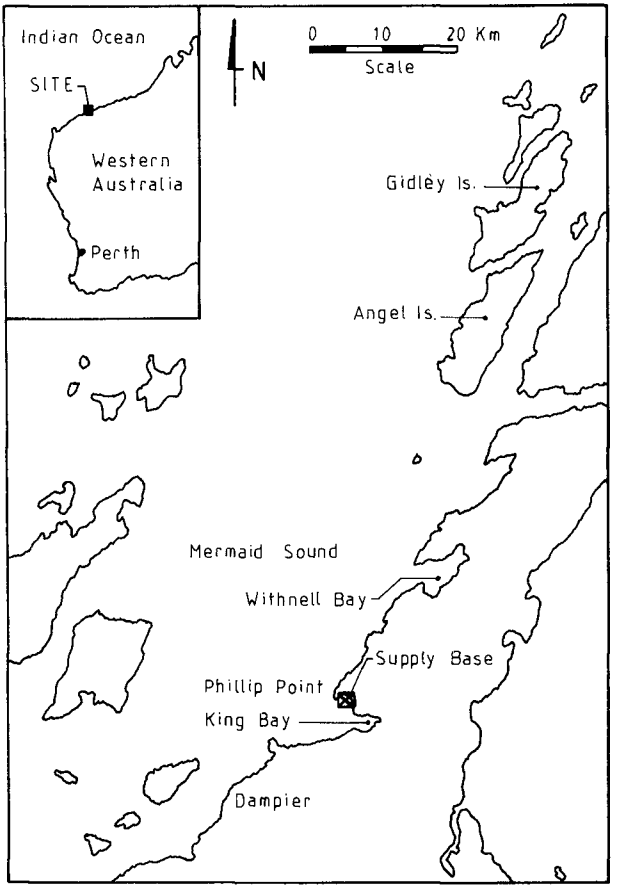

Figure 1. Location Diagram

It was therefore decided to investigate the possiblity of reducing wave heights by shaping the entrance channel so that it would act as a diverging lens. Initially, variations in channel shape and alignment were investigated by mathematical wave refraction calculations. These calculations indicated that shaped entrance channel dredging would reduce wave heights in the basin.

The calculations were confirmed in the physical model where both refraction and diffraction could be simulated.

2. CONCEPTUAL SUPPLY BASE LAYOUT

The layout shown in Figure 2 was chosen to utilise the natural wave protection in the lee of Phillip Point. The alignment and position of the basin was primarily controlled by geotechnical constraints so that rock dredging was minimised. The channel alignment and width were chosen to minimise the extent of dredging keeping in mind safe navigation for the vessels using the supply base.

Whilst the supply base design required that damage be negligible for a cyclone of 50 year return period intensity, it was not intended to provide a haven for vessels during a cyclone. There were therefore two sets of design criteria for wave activity in the harbour:

(i) that wave heights along the supply base wharf be less than 0.5 metre aligned with berthed vessels or less than 0.3 metres beam on for operational (non-cyclonic) conditions.

(ii) that wave heights be minimised to give the most economic, safe design of revetments and breakwaters for cyclonic conditions.

The design wave for operational conditions is generated from the western sector with H_{sig} = 0.9 m and a wave period of 3.5 seconds.

Cyclone generated waves can arrive at Phillip Point from any direction between west and north. The largest and longest period waves arrive from the north and are generated outside Mermaid Sound and propagated to the site. The supply base is well protected from these waves. Shorter period waves are generated within Mermaid Sound. For cyclone conditions these have a significant wave height of 2.5 metres and period of 5 to 6 seconds.

The conceptual layout provided satisfactory wave conditions for operational conditions. However, for cyclone generated waves approaching from the west, wave heights at the northeast corner of the basin were large and for some test conditions even amplified. Without a breakwater at Phillip Point, waves as high as 3 metres were recorded.

In order to reduce waves to a nominal 1 metre height, a 200 metres long breakwater would have been required. The 1980 cost estimate was A$1 million.

3. ALTERNATIVE CHANNEL DESIGNS

Since in the physical model it was apparent that the navigation channel was focusing wave energy into the basin, methods of altering the channel were investigated in the hope of reducing the breakwater length. Wave refraction calculations were carried out for several channel alignments and finally for a channel with a large hole dredged in its northern side. Figure 3 shows the range of channels used for wave refraction calculations. The refraction calculations indicated a significant improvement for both a straightened channel and a channel with the adjacent dredged hole. Figure 4, a typical forward ray refraction diagram, shows the diverging lens effect of the dredged hole.

The refraction calculations excluded the effects of diffraction and wave reflection which would be expected to have some influence.

These calculations were sufficient to show that wave heights could be reduced significantly in the harbour basin by redesigning the approach channel. Confirmation of these calculations was necessary in the physical model where the effects of diffraction and reflection were included.

4. MODEL TESTING

The dredged hole was modified to a shape shown in Figure 5 which could realistically be dredged. Extensive model tests were then conducted in the three dimensional physical model at an undistorted scale of 1:100. Both the straightened channel and the channel with the adjacent dredged hole were modelled. A total of 75 tests were completed to investigate the two channels and the improvements in wave conditions inside the harbour with a range of breakwater lengths. Earlier modelling had been conducted on the channel shown in Figure 2.

Figure 6 shows the 2 metre wave height contours in the harbour basin for the original channel and the two improved channel shapes identified by the refraction calculations for a typical test condition. The approach channel with the adjacent dredged hole gave consistently calmer wave conditions than a straightened channel to the harbour basin. This channel was chosen for detailed model testing and design and resulted in the design wave for the revetments being halved in height without the need of a costly breakwater.

Earlier model testing had shown that a 200 metre long breakwater was required to reduce the design wave heights to these levels with the original approach channel.

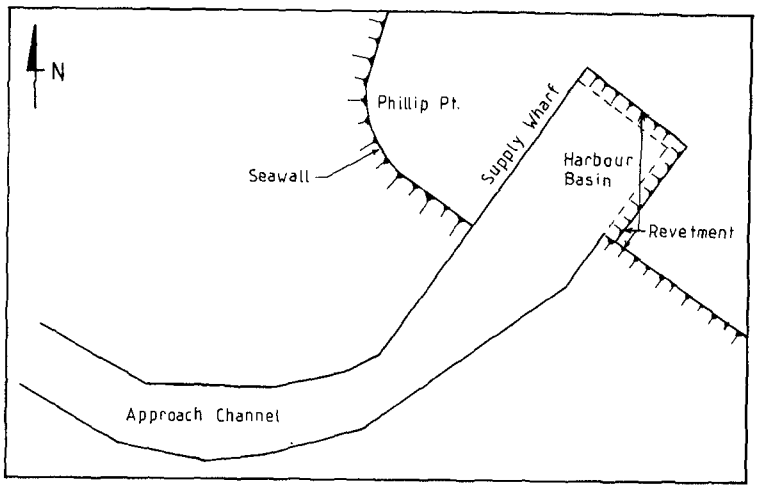

Figure 2. Initial Approach Channel

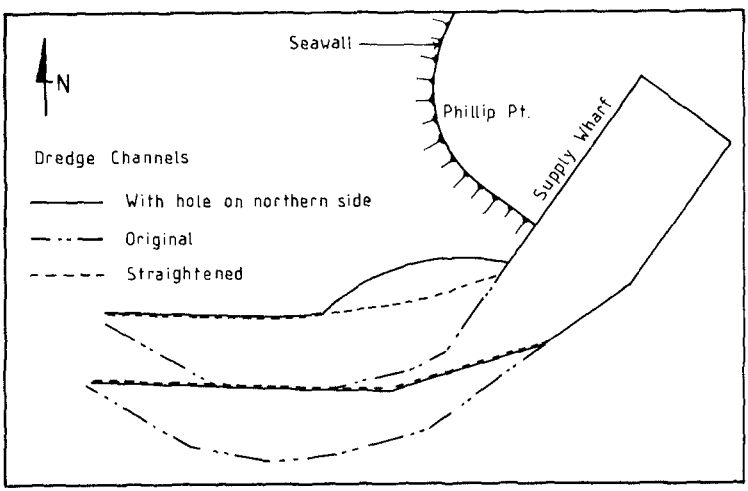

Figure 3. Channels Used in Wave Refraction Calculations

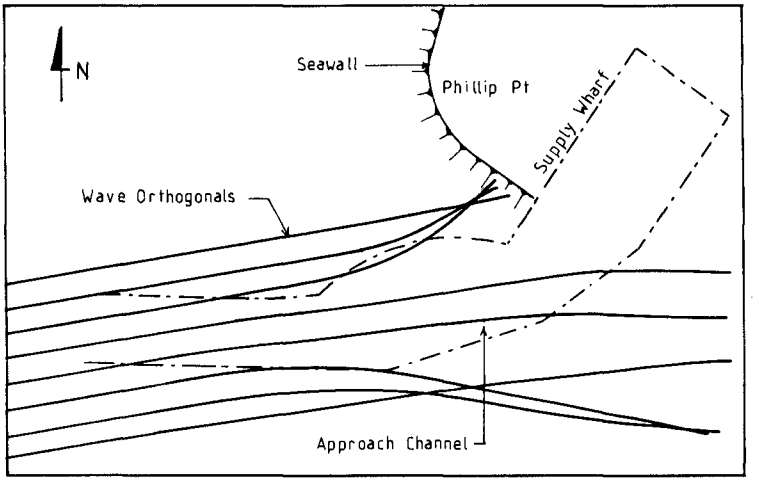

Figure 4. Typical Wave Refraction Diagram for Preferred Solution

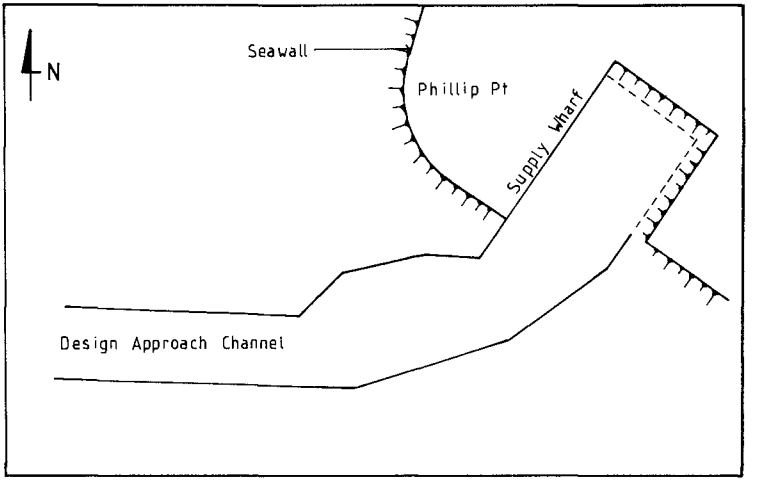

Figure 5. Design Approach Channel

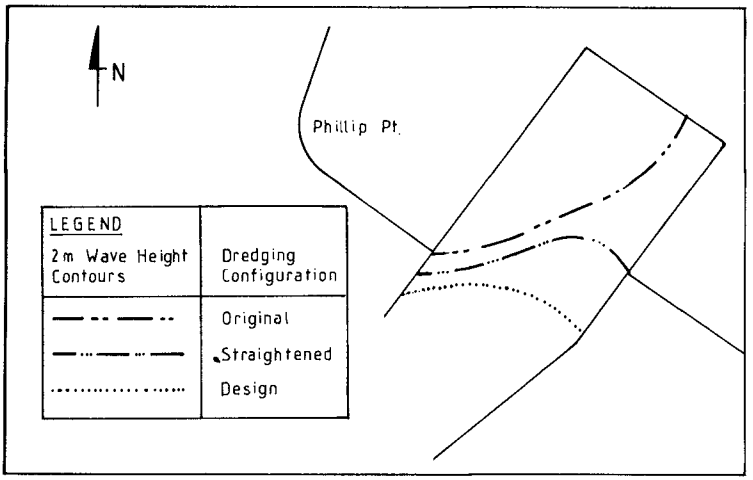

Figure 6. Comparison of Wave Height Contours for Typical Cyclone condition.

5. ECONOMIC CONSIDERATIONS

For the operation of the supply base there was no need for a breakwater under non cyclonic conditions with the original channel. However, during a cyclone if the breakwater were not present the revetments lining the harbour basin would have had to be constructed of much larger rock and to a higher crest elevation if damage during a cyclone were to be negligible. This would have required higher levels of reclamation so that the additional cost would have been in excess of A$0.5 million. Also any future extension of facilities to the eastern side of the basin would need to be designed for these high waves.

A 200 metre long breakwater would have cost about A$1 million in 1980.

By comparison, a dredge hole positioned so that all material to be removed was relatively soft and easily dredged with available plant, cost about A$100,000. The dredging of the hole was an extension of dredging that had to be carried out for the approach channel regardless of the final design.

6. CONCLUSIONS

Shaped dredging can be an effective method of changing wave conditions in the lee of the dredged area. For the North West Shelf project it was possible to effect substantial cost savings by the use of shaped dredging rather than a breakwater to provide wave protection for the Supply Base.

Caution must be applied to ensure that shaped dredging does not cause an unacceptable worsening of wave conditions adjacent to the site under investigation.

Dredged entrance channels and harbour basins may have a profound effect on waves propagated over them. The effects of wave concentration should always be checked in the design stage.

7. ACKNOWLEDGEMENTS

The permission of Woodside Offshore Petroleum Pty Ltd to use material developed on project work for this paper is gratefully acknowledged.

All model testing referred to was undertaken by the Water Research Laboratory of the University of New South Wales, Australia.

SCOUR BEHIND CIRCULAR CYLINDERS IN DEEP WATER

by

JORG IMBERGER
Centre for Environmental Fluid Dynamics
Department of Civil Engineering
University of Western Australia
Nedlands, Perth, WA 6009

DES ALACH
Kinhill Stearns
Engineers
111 St George's Terrace, Perth, WA 6000

JOHN SCHEPIS
Department of Civil Engineering
University of Western Australia
Nedlands, Perth, WA 6009

Abstract

Flume test data is presented for the depth of scour in deep water near a vertical cylinder placed in a uniform sand and a fine calcareous ocean sediment. The ratio of the depth of scour to the cylinder diameter at equilibrium is shown to depend only on the ratio of the shear velocity to the critical shear velocity at which bed motion is initiated.

Protection against scour by placing collars around the cylinder is shown to be of marginal value.

1 INTRODUCTION

Scour around cylindrical piles has long been of importance in the design of bridge piers and ocean jetties (Durant Claye 1873). In most cases investigators have emphasised the influence of the water surface effects and further, most tests have been carried out with sand as the foundation material. With the growth of the off-shore industry there is an increasing need to estimate scour around piles in water which is many pile diameters deep and where the foundation material is made of calcareous particles of a fine sandy consistency by the ocean. Further, scour tolerances on off-shore structures are such that attention must be focused on the range of shear velocities from the inception of scour to values at which bed load motion commences.

Such data do not appear to exist and this need has led to the above general investigation of scour around plain vertical circular cylinders and cylinders with protective collars. The sediment used is typical of that found along the whole of the Western Australian continental shelf in water between 50m and 200m (see H.A. Jones 1973). The photograph in Figure 1a shows that the particles are an approximate size of 0.1mm, are angular in nature and possess irregular shapes. A typical size fraction of these sediments is shown in Figure 1b and Figure 1c shows the size fraction of the fine river sand used in the control experiments.

Recent measurements of velocities very close to the ocean bottom (Caldwell and Chris 1979) have revealed that the bottom boundary layer possesses a "law of the wall" region above the viscous sublayer in which the familiar velocity scaling,

$$u = 2.5u_* \ln \frac{z}{z_o}$$

is applicable, where u is the velocity, u_* is the shear velocity, z is the vertical distance from the bed and z_o is the bottom roughness parameter. These measurements imply that a useful experiment of the scour depth may be carried out in a laboratory flume, provided the depth of water is kept large compared to the cylinder diameter.

The dominant feature responsible for scour around a pile is the large scale eddy system created by the pile itself. It is generally accepted that this eddy system causes the scour around the pile to commence at about half the critical threshold velocity. Shen, Schneider & Karaki (1966) reported that depending on the pile type and free stream

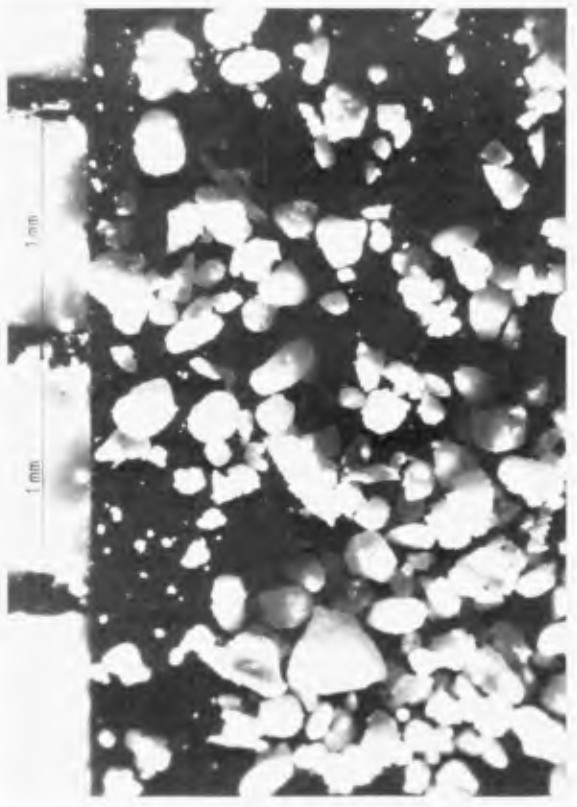

FIGURE 1a

Photograph of ocean sediment.

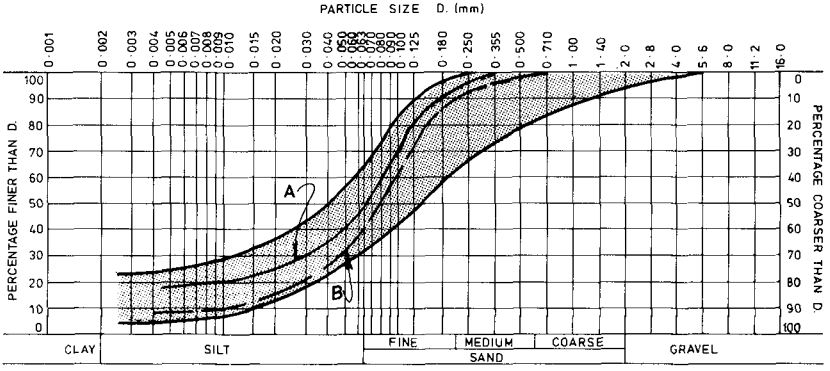

CALCAREOUS SEDIMENT FIGURE 1b

Dry sieve analysis of typical ocean sediment after separating coarse material used in experiments (A: +0.6mm; B: +1.2mm)
From Fugro Report K-1052/XVIII).

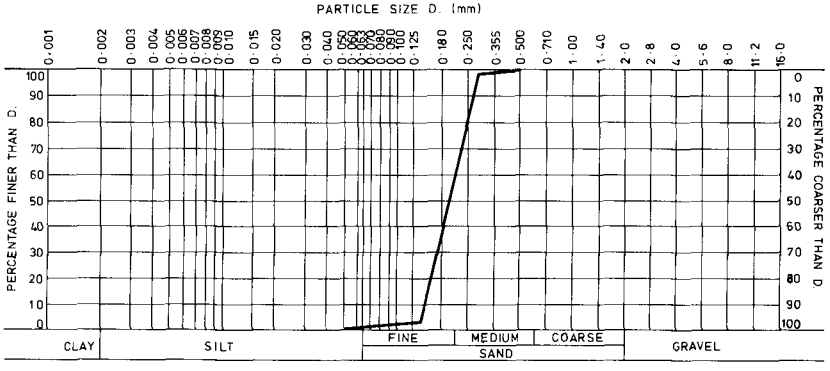

SAND FIGURE 1c

Sand sample particle distribution used as a control soil sample.

conditions, the eddy structure may be broken down into regions of a forward horseshoe vortex, a wake vortex amalgamation and a trailing vortex system.

The horseshoe vortex filament is the major influence on scour around a cylindrical pile. The variations in the intensity of the horseshoe vortex and in the strength of the downflow, and the interaction between them were examined qualitatively by Melville (1975) and reinterpreted by Jain & Fischer (1979).

The horseshoe vortex was reported to be initially small and comparatively weak. When the scour hole forms, however, the vortex rapidly grows in size and strength as additional fluid attains a downward component and the strength of the downflow increases. The expanding cross sectional area increases but, at a decreasing rate as the scour hole enlarges. The rate of increase in the cross sectional area is controlled by the quantity of fluid supplied to the vortex from the downflow ahead of the cylinder. This downflow is determined by the free stream velocity.

The scour resulting from this flow pattern leads to an increasing depth of scour with increasing flow velocity. However, as shown by Shen et al (1969), there is some doubt whether scour continues once the critical shear velocity is exceeded. Their results are at variance to those of Jain and Fischer (1980), but there is some evidence that once an active bed load has been established the rate of filling equals the rate of scouring and a type of scour equilibrium is reached. The reader is returned to the article by Breusers, Nicollet and Shen (1977) for a good comprehensive summary.

Thomas Zdenek (1967) examined the influence of protective collars and presented data for two collar sizes. The results showed that scour still occurred around the pile under the collar but of a lesser depth. With the collar directly on the bed at $u_* = u_{*_c}$ and $D_c/b = 3$, where u_{*_c} is the critical shear velocity, D_c is the diameter of the collar and b is the diameter of the cylindrical pile, the scour depth was reduced to 24.6% of the scour which was recorded when no collar was present.

A similar reduction was observed by Tanaka and Yano (1967).

Scour around deep ocean structures can thus not be determined from previous work. Little data exists for small surface Froude numbers, although an introductory discussion may be found in Carstens and Sharma (1975). Experiments on interlocking-type soils in flows with a small surface Froude number are thus required. Such an investigation was carried out and is described in this paper.

2 EXPERIMENTAL DESIGN

Scour behind a vertical cylinder depends on the sediment structure and composition, the mean velocity field, the turbulent velocity field in the water column and the shape of the structure. Defining the depth of scour as d_s and the diameter of the cylinder as b it is possible to write,

$$d_s/b = f(u_*, u_{*c}, u, g', d_{50}, h, \nu) \tag{1}$$

where u_* is the shear velocity, u_{*c} is the shear velocity at which bed motion is initiated over an unobstructed bed, u is the free stream velocity, g' (= $(\frac{\Delta\rho}{\rho})g$) is the effective acceleration due to gravity of the sediment particles, $\Delta\rho$ is the density difference between the sediment and the water, ρ is the density of the water, d_{50} is the median particle size, h is the depth of flow and ν is the kinematic viscosity.

In writing equation (1) it is assumed that the sediment structure and particle size distribution are characterised by the parameters u_{*c} and d_{50}. Cohesive soils are not considered in the present discussion. Further, the mean flow profile and the turbulent kinetic energy field are assumed to be that described by the "law of the wall" and so are completely characterised by the shear velocity u_*.

Invariance to a transformation of the dimensions requires that equation (1) may be written in the form:

$$d_s/b = f(u_*/u_{*c}, u_*^2/g'd_{50}, h/b, ub/\nu, d_{50}/h), \tag{2}$$

where the dimensional groups have been chosen to reflect the most likely force balances. In the order in which the groups appear in equation (2) the following interpretations are noteworthy:

a) u_*/u_{*c} is the ratio of the applied shear velocity to the value at which motion is initiated on a flat bed. This ratio captures the influence of the drag force exerted by the flow on the sediment bed as a fraction of the stress required to move the sediment without flow disturbances due to the structure. Scour usually commences at shear velocities well below the critical value because the cylinder induces a locally higher value immediately adjacent to the perimeter. The value of u_{*c} captures the erosion resistance characteristics of the sediment and so will not only depend on the sediment type and size, but also on its gradation and the final packing.

b) $u_*^2/g'd_{50}$ is the ratio of the inertia force on a sediment particle associated with the turbulent fluctuations of the flow to the effective weight of a sediment particle. The turbulent fluctation possesses velocities of the order of u_* and so the inertia term is merely a reflection of the form drag (pressure $0(\rho u_*^2)$ multiplied by the area presented by the particle) on the sediment particle.

c) h/b is the depth to cylinder diameter ratio. The importance of this parameter lies in the fact that as this boundary layer flow is intercepted by a vertical structure, the stagnation pressure at the leading edge of the structure will vary from ρu^2 in the core flow to 0 at the sediment base. This pressure difference is experienced by the flow over the velocity transition layers leading to a vertical pressure gradient at the leading edge of the structure of $0(\rho u^2)$. This pressure gradient induces a vortex motion of radius r_o which is swept around the pile forming a trailing vortex pair in the wake of the structure. The velocities associated with this trailing vortex pair combine with the mean flow causing a local increase of u_* in the immediate lee of the structure.

d) ub/ν is the cylinder Reynolds number. For Reynolds number larger than about 10^3 little effect may be expected until a value of 10^5 is reached. For values greater than 10^5, the separation is retarded by the turbulent boundary layer and the rear wake is somewhat narrower than that which would be expected from a laminar boundary layer. The pressure field in the wake arising from this separated flow combines with that from the trailing vortex pair to produce the observed total flow.

e) d_{50}/h is the relative roughness of the bed material. In coarse materials this parameter determines the turbulent structure in the bottom boundary layer. For the calcareous sediment and the sand under study the median diameter d_{50} ranges from 0.04 - 0.125mm and 0.25mm respectively implying that for smooth flat beds the flow is hydrodynamically smooth and the parameter d_{50}/h is of minor importance. For strongly roughened or pitted surfaces, however, a new parameter e/h must be added. The variable e is used to designate the roughness height of the undulations.

In the strictest sense the depth of scour will depend on all of the above parameters as well as possibly the sediment structure. However, interest here is centered around deep water structures for which h/b is large. Assuming experiments are not carried out at the critical Reynolds number, it may thus be expected that equation (2) reduces to the form:

$$d_s/b = f(u_*/u_{*c}, u_*^2/g'd_{50}) \tag{3}$$

and all other variables would be small scale effects. The experiments were designed to investigate the form of the function in equation (3).

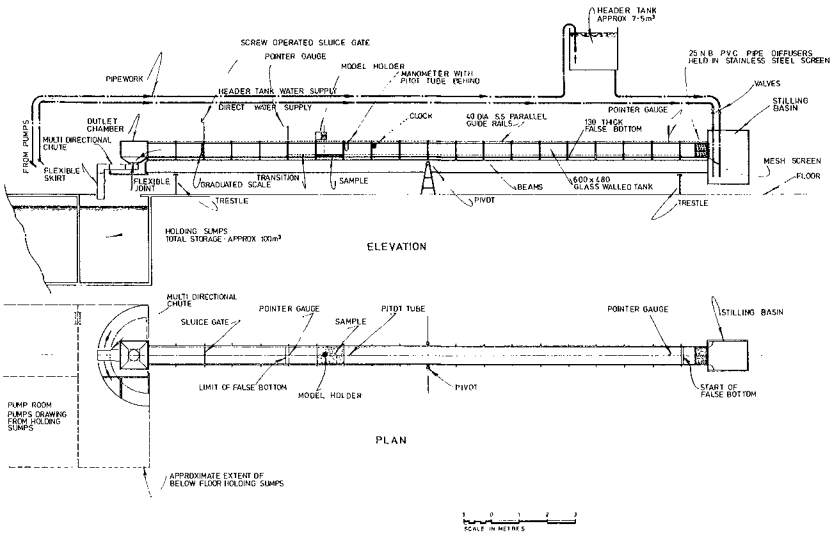

FIGURE 2 General arrangement of test flume.

3 EXPERIMENTAL PROCEDURE

The model tests were carried out in the Hydraulic Laboratory of the Department of Civil Engineering at The University of Western Australia. The experiments necessitated the construction of a 20m tiltable glass walled flume, the installation of a pitot-static tube and the design of sediment sample preparation techniques.

Experimental Flume and Apparatus

The general layout of the experimental test flume is shown in Figure 2. The flume consisted of a 20m long test section with a cross-section 600mm wide and 480mm deep. All tests were carried out with the flume in a horizontal position. The supply of water for the flume came from the laboratory storage tanks beneath the laboratory floor and was routed to the header tank of the flume via two pumps. Under normal operating conditions the system allowed the level in the flume to be kept constant to approximately $\pm$2mm. From the header tank the water moved through a converging entrance into the flume section through a multiple pipe diffuser installed in the first bay of the test section. The purpose of the pipe diffuser was to dissipate any wave action and uneven flow that may have arisen from the introduction of the water into the header tank.

The normal way of operating the flume was to set the downstream sluice gate at predetermined openings (15mm, 30mm, 50mm, 85mm, 100mm and 115mm) and then to adjust the two valves at the inflow to yield a full depth test. In this way it was possible to repeat experiments with almost identical flow conditions.

The flume was fitted with two surface rails accurately aligned allowing equipment to be positioned accurately within the flume. The pointer gauge, the pitot tube and the test section were all fitted in the flume from specially constructed trolleys running on the rails.

In order to be able to fit a 100mm deep sediment tray into the flume bed for the tests, it was necessary to construct a false bottom for most of the upstream part of the flume. This false bottom was constructed for 3m upstream and 1m downstream of reinforced P.V.C. sheeting. Upstream of this the flume bed was lined with bricks which were covered with a thin grout to yield constant depth of flow. The false bottom was painted and then while the paint was still wet, sprinkled with dry sediment. After drying, the surface remaining on the paint very closely resembled a smooth sediment surface with the same roughness properties as the sediment itself. Great care was taken to ensure that all the joints were smoothly aligned and that the sediment test section which fitted into the

false bottom through a cavity was accurately placed. The small gaps left were filled with plasticine to ensure a smooth, flat bed.

Sediment Tray

It was realised at the outset of the experiments that it would not be possihle to deposit sediment in the total length of the flume. Although this would have been advantageous in that it would have allowed tests to be carried out above the critical shear velocity, the logistics for obtaining such large quantities of deep ocean sediment and further of depositing the sediment in the flume made this impracticable. It was therefore decided to construct a test pan 100mm deep and 1m long which fitted across the flume. The material was sieved and redeposited into this test tray as described below after which time the tray was lifted with a small crane and positioned into the cavity of the false floor. The tray was constructed of reinforced fibreglass with a strong structural base to ensure no movement of the tray base occured during installation of the tray.

The Pitot Tube

The velocity in the flume was measured with a standard pitot-static tube with an outside diameter of 4mm. The pressure difference in the pitot tube was measured with a differential manometer. This manometer was filled with turpentine which had a specific gravity at room temperature of 0.808. The use of turpentine and water allowed accurate measurement of velocities even down close to the viscous sub-layer. The surface tension effect was minimised by choosing 10mm diameter tubes for the manometer. This meant that the instrument also had a large damping time allowing easy determination of the mean velocity profile.

Test Cylinders

The test cylinders were straight circular cylinders with diameters of 25mm, 50mm and 100mm with and without circular metal collar discs 3mm thick. The discs had diameters twice, three and four times the diameter of the cylinders and were made to allow for positioning at various heights above the upper surface of the sediment when the model structure was in position.

The leading edge of each of the model cylinders was fitted with a sharp V lip which was ground to a very fine edge in order that the whole circumference of the model would cut through the sediment with minimum disturbance during installation. A small hole was drilled through the upper flange of the model to allow the air to escape as the cylinder

was inserted into the sediment. This avoided possible compaction of the soil within the centre of the cylinder and the consequent disturbance of the soil adjacent to the cylinder wall by bearing capacity failure.

Sample Preparation

The 100mm thick calcareous sediment samples were prepared by a wet "sand rain" technique in an attempt to reproduce the natural method of in-situ deposition of the coastal sediments. This method is similar to the conventional dry "sand rain" technique used for uniform granular samples (Jewell et al (1980)).

A mass of 1.00kg of the sediment which had been packed wet and sealed after collection at sea was wet further to a moisture content of approximately 60% and moulded into a slurry. This slurry was spread uniformly onto a No. 14 mesh screen of exactly the same dimensions as the sample tray and then washed through the sieve with fine water jets into the tray below. After allowing at least 45 minutes for the finest particles to settle, all water more than approximately 5mm deep over the sample was siphoned off and the next layer was rained in until the prepared sample was at least 5mm above the top of the tray top lip. When the sample was required in the flume for testing, the excess water was siphoned off, the skirt removed from the tray and the soil above the top lip of the tray cut off. This was achieved by moving a vibrating cutter fitted with a vacuum system across the top of the tray producing a smooth surface without evidence of tearing or drag marks on the sample surface. The prepared sample tray was then weighed and lifted into the flume for testing. The average void ratio achieved by this method in the large sample trays was 1.73 which was somewhat higher than the understood typical field value of 1.35, with the layering and structure being reproduced rather well.

The control tests were carried out with clean, dry, uniform sand sieved to provide a d_{50} of 0.2mm. This was poured slowly into the sample tray which had previously been filled with water, vibrated vigorously on a vibrating platform normally used for preparing concrete test cubes, trimmed to height with a straight edge and then lifted into the flume for testing. The particle size distribution for this sand was almost linear between 0.125mm and 0.3mm.

Flume Performance

In order to verify the performance of the flume a number of tests were carried out to check the logarithmic profile above the smooth plastic false bed, the fixed sand sediment bed and the actual sediment tray. Table 1 summarises the results from this test and gives

TABLE 1 Flume performance data.

Code	Bottom			Flow Depth	Water Temp.	Flow Vel.	Shear Vel.	Measured roughness	$\frac{9z_o u_*}{\nu}$	Date of Test
	Material	d	d_{50}	H	T	$u_{0.1}$	u_*	z_o		
		m	m	m	^oC	$msec^{-1}$	$msec^{-1}$	m		
		10^{-3}	10^{-3}	10^{-3}		10^{-3}	10^{-3}	10^{-6}		
S3-a	P.V.C.			300	15.5	129	6.3	28.0	1.30	23.8.81
S3-b	P.V.C.			275	15.5	278	12.0	9.4	0.99	23.8.81
S3-c	P.V.C.			190	15.5	535	22.0	6.1	1.15	23.8.81
S7	Fixed Sed.			307	15.5	555	22.6	4.9	0.71	8.9.81
S17	Fixed Sed.			307	16.0	526	21.6	5.8	1.06	29.9.81
S5	Sed.	15	0.06	207	16.0	560	23.9	8.6	1.56	27.8.81
S6	Sed.	50	0.06	225	16.0	549	21.9	4.3	0.98	28.8.81

Test Result Summary: Flume Performance

the flow depth, the water temperature, the flow velocity at 100mm, the shear velocity as calculated from the slope of the velocity profile, the measured roughness as calculated from the intercept of the velocity profile with the velocity axis and the last column gives the ratio of the measured roughness length, z_o to that predicted for a smooth bed. The velocity profiles were logarithmic as shown in Figure 3, and in general the effective roughness was in good agreement with the theory (see Table 1).

Test Results

All together 22 scour tests were carried out with the following configurations:

a) Circular cylinders in uniform sand.
b) Circular cylinders in ocean sediment.
c) Circular cylinders with a circular collar disc at the level of the ocean sediment surface.
d) Circular cylinders with a circular collar disc at a given distance off the ocean sediment surface.

In each case the soil tray was placed into position and the flume carefully filled with water with the sluice gate closed. The model cylinder was then inserted into the sediment, care being taken not to unnecessarily disturb the sediment. The tests were started by setting the sluice gate to a 15mm opening and adjusting the depth of flow with the upstream valves. Normally, tests were carried out with sluice gate openings at 15, 30, 50, 85, 100 and 115mm. Each test was recorded on video tape for later reference. The velocity corresponding to each sluice gate setting was measured at a height of 100mm from the channel floor with the pitot tube attached to the manometer and the shear velocity was determined by assuming a logarithmic velocity profile. The scour contours were sketched as the experiment proceeded and the depth of the deepest scour hole was recorded for each equilibrium situation. The velocity was raised in the channel until either scour had reached the sediment tray bottom (100mm) or until the shear velocity was equal to or a little greater than the critical shear velocity. Tests for shear velocities above the critical value could not be carried out as the experimental apparatus had no provision for upstream sediment replenishment.

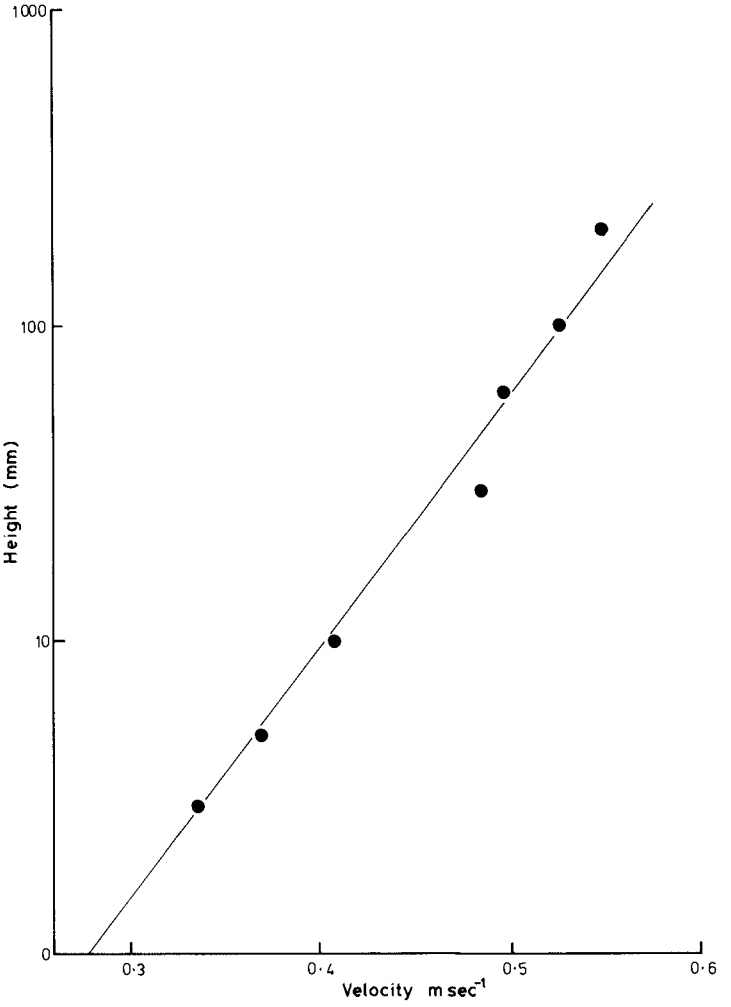

Velocity distribution over a fixed sediment bed.

4 RESULTS

The Critical Shear Velocity

The critical shear velocity is defined as that shear velocity at which the particles on the bed begin to consistently move. In the case of the sand bed the initiation of motion was well defined and little ambiguity existed regarding the determination of the critical value of the velocity. Two separate tests, specifically conducted to determine the critical shear velocity, yielded values of 13mmsec^{-1} and 15mmsec^{-1} respectively. These values may be compared with the prediction from the Shield's diagram (Vanoni, 1975) of 13mmsec^{-1} for a uniform sand of 0.2mm median diameter. A value of 13mmsec^{-1} was chosen for the data reduction of the sand scour tests.

The determination of the critical shear velocity for the calcareous sediment was made difficult by the very patchy nature of the initiation of the bed particle motion. Distinct from sand this material formed small scour depressions when close to the critical shear velocity. These depressions deepened to about 1mm and widened to an elongated ellipse with a size of about 300mm in length and 10mm wide. At this stage further movement stopped and the activity shifted to other parts of the bed. It was therefore difficult to judge the exact value of the critical shear velocity, but two test trays yielded critical shear velocities of 24mmsec^{-1} and 23mmsec^{-1} respectively. During the whole range of the other scour tests conducted these values were repeatedly confirmed and so a critical velocity of 23mmsec^{-1} was chosen for all the data reduction.

This value of the critical shear velocity for the calcareous sediment may be compared to the prediction of 12mmsec^{-1} from the Shield's diagram for a uniform sand with an equivalent diameter of 0.06mm. The calcareous sediment therefore derived from the interlocking of the particles an appreciably higher resistance to erosion than sand of equivalent size.

Scour Near A Circular Cylinder: Sand

Three sand scour tests were conducted mainly as control to enable comparisons with published data.

The scour patterns from all the tests were geometrically similar. The final depression for a test with the 50mm diameter cylinder is shown in Figures 4a and 4b where it is seen that the majority of the material which scoured out from near the cylinder was redeposited immediately to the rear of the scour depression.

FIGURE 4a Photograph of sand scour depression around 50mm cylinder at maximum u_*.

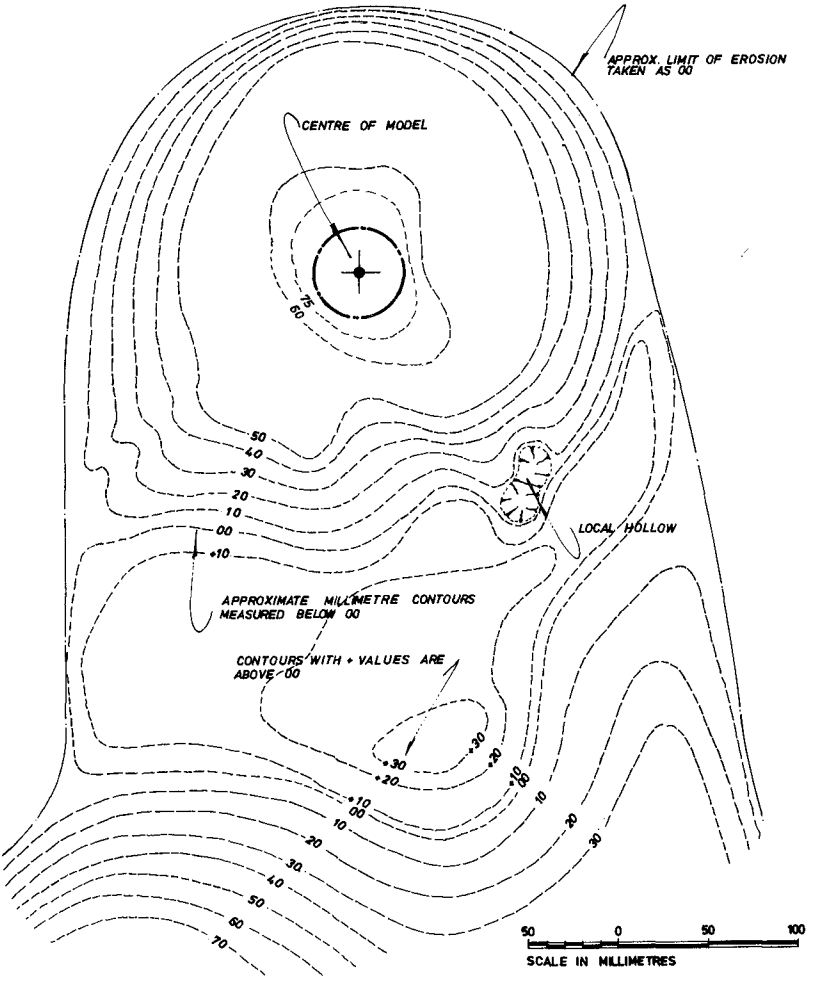

Sketch of sand scour depression contours around 50mm cylinder at maximum u_*.

The vortex motion and turbulence was seen to lift the sediment into suspension near the cylinder wall and the mean current carried the material out of the depression. This removal of material from the base of the depression always resulted in a slope adjustment further up the depression which replenished the areas where scour had taken material away. This process, as shown in Figure 4a, was symmetric and the scour depression was cone-shaped. Interesting radial depressions formed around the perimeter of the cone due to the presence of radial vorticity, but no detailed investigation of this mechanism was undertaken (see Figure 4b).

The equilibrium maximum scour depths are shown in Figure 5 for the tests with 25mm, 50mm and 100mm diameter cylinders. The data was plotted according to equation (3) and it is seen to display a linear trend with scour commencing at a value of $u_*/u_{*_c} = 0.5$.

Scour Near A Circular Cylinder: Sediment

The evolution of scour was characterised by a beginning of scour at the rear and either side of the cylinder. This happened at a u_*/u_{*_c} of approximately 0.3 to 0.4. As the velocity in the channel was raised the scour depression deepened at the rear and moved forward around the perimeter of the cylinder. The mode of deepening was similar in all cases. Small depressions would form locally, deepen up to 5mm and then broaden to the outer boundary of the depression. This led to sheet like striations at the edge of the scour depression as is seen in Figure 6a. This photograph also clearly shows a local depression next to the cylinder in the deepest part. The forward bank tended to be very steep and the spoils from this scour did not resettle in any of the experiments, but were swept downstream into the sump (see Figure 6b). This is further evidence that the particles interlock, giving the bed an erosion resistance far greater than the equivalent sand. The shear stress required to break this interlocking is considerably higher than that required to transport the particles once loose. This is in contrast to the sand case, in which the scoured sand was mostly deposited immediately in the lee of the scour depression indicating that the scour stress was only marginally higher than the transport stress.

The thickness of each scour layer evident in Figure 6a is many times greater than the individual layering introduced during sample preparation and it is not likely that the sample preparation formed the layers.

It is seen from Figure 7 that the data from the different tests form a linear correlation between d_s/b and u_*/u_{*_c} independent of the internal particle Froude number. The line of best fit is given by the equation:

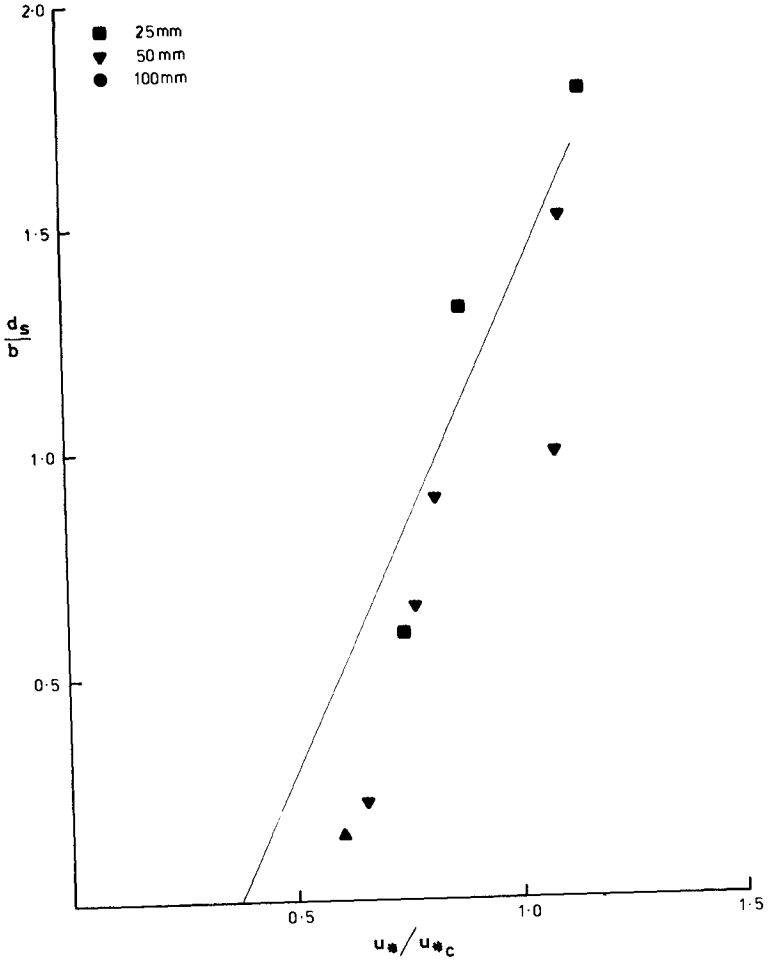

Dimensionless plot of scour depth against the shear velocity for a circular cylinder in 100mm deep sand.

FIGURE 5.

FIGURE 6a Photograph of ocean sediment scour depression around 50mm cylinder at maximum u_*.

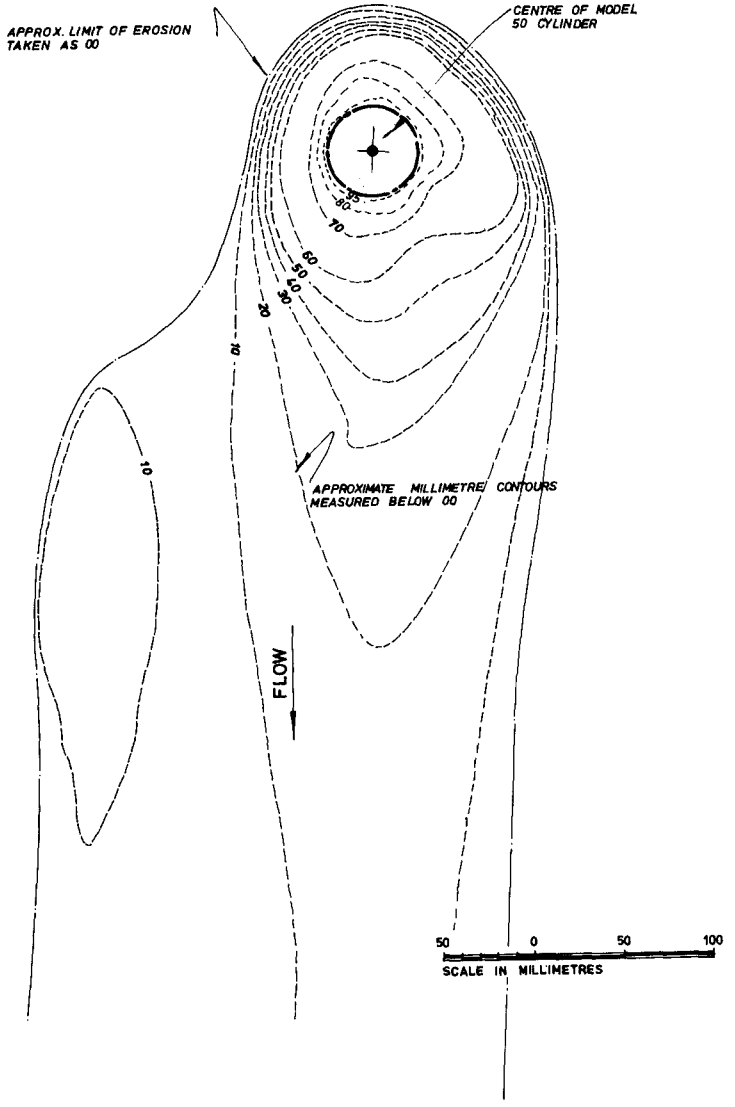

Sketch of ocean sediment depression contours around 50mm cylinder at maximum u_*.

FIGURE 6b

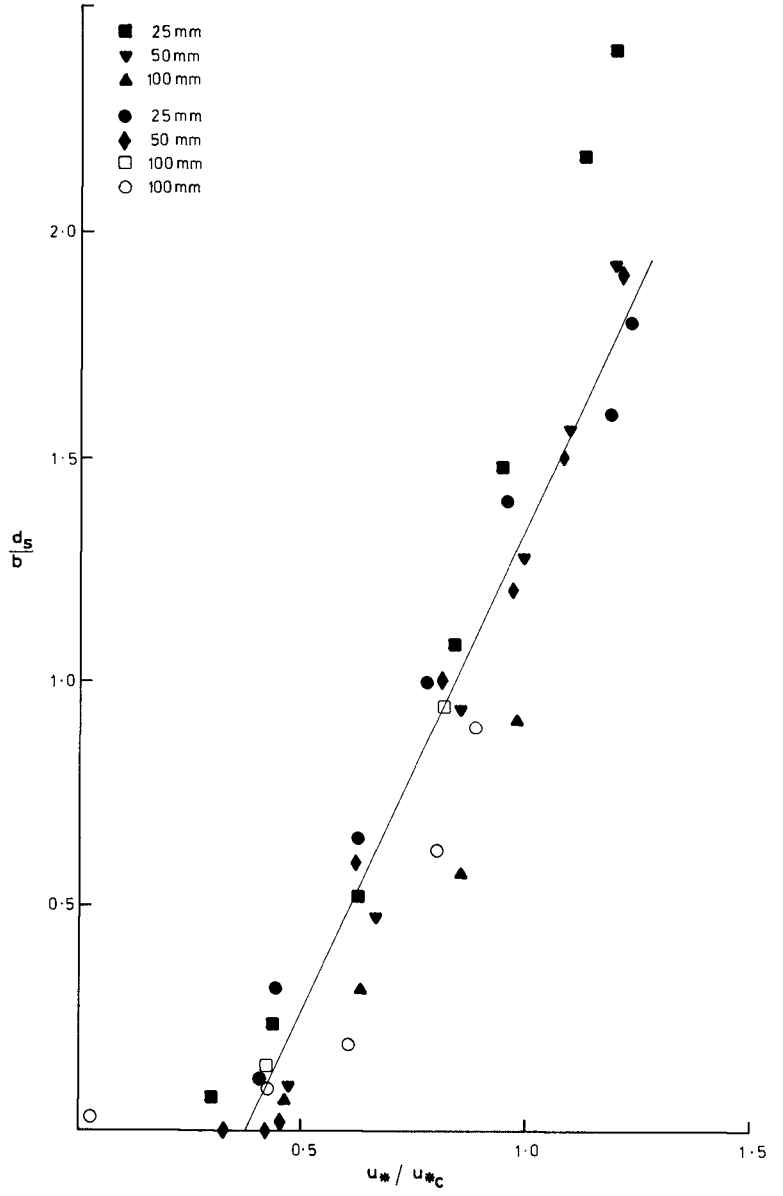

Dimensionless plot of scour depth against the shear velocity for a cylinder in 100mm deep ocean sediment.

FIGURE 7.

$$d_s/b = B(u_*/u_{*c} - 0.374) \quad (4)$$

where the constant B = 2.18.

Effects of Collars on Scour Depth

Visualisation of the flow with dye streaks clearly showed the formation of a horseshoe vortex around the front of the cylinders which was then swept around the perimeter of the cylinder. In the wake the vortex filaments combined to give a fairly confused wake with a peak outward flow at the bed of about half diameter in the lee of the cylinder and spaced approximately one third cylinder apart.

It was postulated that placing a metal collar around the cylinder should protect the bed from this increased flow intensity and so a series of experiments were conducted with differing collar to cylinder diameter ratios and at three levels; tests were carried out with the collar level with the bed, 20mm from the bed and one with the collar at 60mm from the bed.

Scouring for all collar ratios, with the collars at bed level, started at a u_*/u_{*c} of about 0.4 with this initial scour occuring downstream of the collar within the wake region. Initial scour did not occur as for the plain cylinder but rather resembled a surface scraping process in the wake region well away from the collar perimeter. As the flow was increased, the scour area widened and moved upstream up to the collar eventually undermining the downstream half of the collar area. For collar to cylinder diameter ratios of 3 and 4 the scour depression widened very considerably as seen in Figure 8, leading to a depression width of 2-3 times the diameter of the collar. Reduction of the diameter ratio led to progressive movement of the scour depression upstream under the collar into the cylinder. For the case of a ratio of 2 scour occured around nearly three quarters of the cylinder immediately below the collar.

The equilibrium depth for a particular shear velocity was always achieved by a central deepening and then a progressive widening. The final scour depths are shown in Figures 9a, b and c for the different collar to cylinder diameter ratios.

From these diagrams it is seen that scour commenced at much the same value of u_*/u_{*c} as with no collar, but the rate of scour was slower until d_s/b of about 1 where upon scour seemed to increase. Although it was not possible to attain in the present facility, the data indicate a trend back towards the cylinder without collar curve for ratios of d_s/b

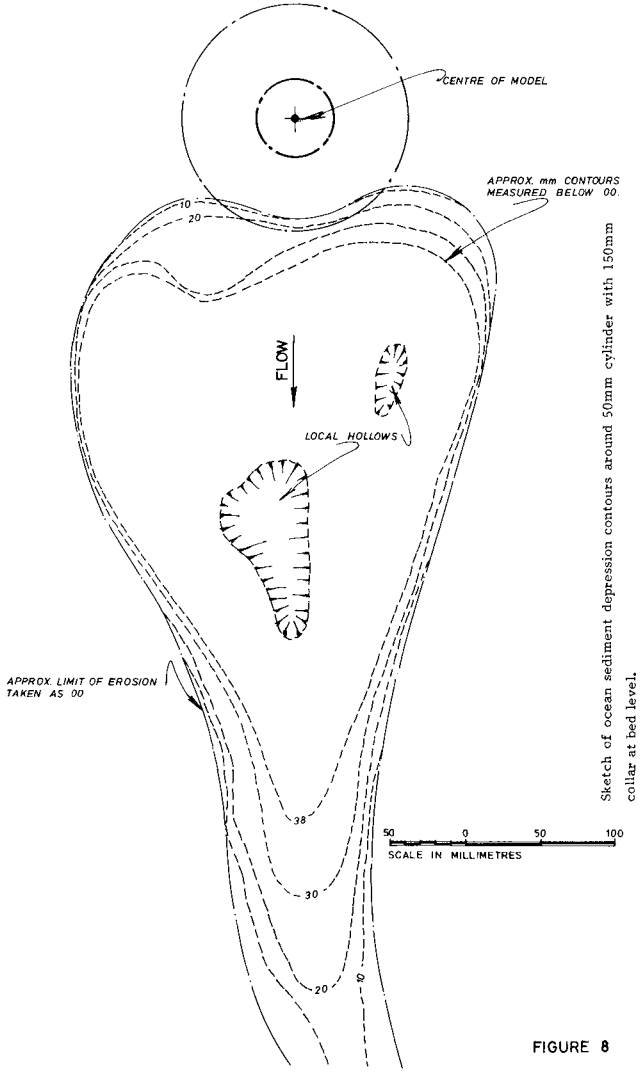

Sketch of ocean sediment depression contours around 50mm cylinder with 150mm collar at bed level.

FIGURE 8

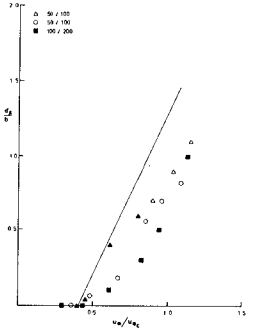

Dimensionless plot of wave depth to ocean sediment against the shear velocity for cylinders with rafting at bed level.
(a) $D_c/D = 2.0$ (b) $D_c/D = 3.00$ (c) $D_c/D = 4.0$

FIGURE 9a

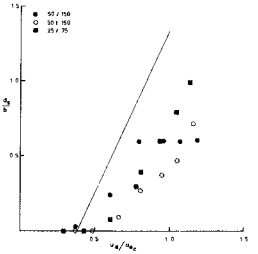

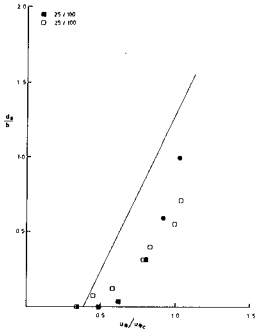

FIGURE 9c

larger than about 1. The scour retardation seemed to be more marked the larger the value of d_s/b.

To investigate the transition back to the plain cylinder case, the effective d_s was increased by raising the collar 20mm above the sediment bed. The results from these tests are shown in Figure 10. All ratios of d_s/b are included and it is seen that there is a general trend back to the plain cylinder line until at d_s/b of about 1.5 the scour depth is back to that found in the plain cylinder case. The scour process in the raised collar tests differed very little to that described above for the level collar tests. For the ratio d_s/b = 3 and 4 the scour developed at the perimeter of the cylinder after which it became localised in the region directly under the collar. For the ratio d_s/b = 2 the scour was very erratic, most probably due to the added turbulence caused by the edges of the collar.

The tests with the 50mm diameter cylinder indicated a disappearance of the effect of the collar at d_s = 75mm to 80mm. Subtracting the 20mm, would imply that a 50mm diameter cylinder with a collar at 60mm height would show no effect of the collar. The results shown in Figure 10 substantiate this conclusion, indicating that the horseshoe vortex is affected by plates or collars for a distance above the bed of about 1.5 times the cylinder diameter. This is considerably larger than the horseshoe vortex diameter ratio of 0.25 predicted by Qadar (1981).

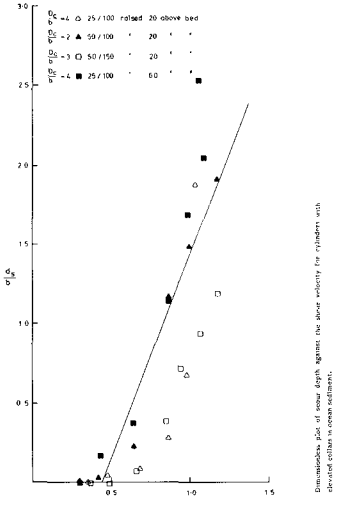

Dimensionless plot of scour depth against the above velocity for cylinders with elevated collars in ocean sediment.

FIGURE 10

5 DISCUSSION AND CONCLUSION

The work carried out in the present investigation has brought to light the importance of the parameter u_*/u_{*c} for the determination of the depth of scour. It appears that the other parameter, the internal sediment Froude number, plays only a minor role. In order to test this hypothesis further, all available data from the literature for circular cylinders in model tests were reduced onto the same graph. Figure 11 is the resulting variation, with the data plotted being obtained directly from the publications of Breusers (1977), Chabert and Engeldinger (1956), Jain and Fischer (1980), Qadar (1981), Shen et al (1966) and of course the present results. The experimental data plotted in Figure 11 is listed in Table 2 and is from tests the details of which are included in Table 5. The soil types range from the present calcareous sediment with a $d_{50} \simeq 0.06$mm through sands varying in diameter from 0.2mm up to a maximum diameter of 3mm (test of Chabert and Engeldinger (1956)). This means that the range of u_{*c} covered in Figure 11 is from about 12mmsec^{-1} to about 35mmsec^{-1}. Similarly the range of cylindrical pile diameters covered by the data is from 25mm to 200mm.

Only those data which represent ratios of flume depth to cylinder diameter of greater than 3 were included in the presentation. An exception to this case is some of the data from Shen et al (1966) which included ratios marginally smaller than three. However, these values were corrected for the smaller depth to diameter ratio by a formula suggested by Breusers et al (1977) who postulated the depth of scour to the depth to diameter ratio $d_s/b = 1.5 \tanh h/b$.

All the data show a very definite trend about the line of best fit derived from the sediment experiments (Figure 7). The scatter is not unusually severe for sediment transport or scour type experiments and it is believed that the most important correlation is captured in Figure 11. This means that the influence of different void ratios, soil structure and soil scour on the resistance is all provided for through the value of the critical shear velocity.

Unfortunately there is very little data available from larger laboratory experiments or from bridge pile monitoring of large depth to cylinder diameter ratios, and for values of u_*/u_{*c} less than unity. The work by Qadar (1981) would indicate that the horseshoe vortex diameter is determined by the diameter of the cylinder and to a much smaller degree by the height of the bottom shear region. This would suggest that the present results should scale to prototype situations. However, the present results suggest a considerably larger vortex diameter than predicted by Qadar (1981).

TABLE 2

Test	Diameter	25mm	Test	Diameter	50mm	Test	Diameter	100mm
	u_*msec^{-1}	d_s mm		u_*msec^{-1}	d_s mm		u_*	d_s
SS8	0.0067	2	SS9	0.0071	0	SS10	0.0073	0
	0.0098	6		0.0103	5		0.0102	7
	0.0138	13		0.0145	24		0.0140	32
	0.0183	27		0.0187	47		0.0188	58
	0.0208	37		0.0219	64		0.0215	97
	0.0248	54		0.0240	78			
	0.0264	60		0.0264	96			
S13	0.0093	3	S9	0.0096	0	S19	0.0054	3
	0.0102	8		0.0103	10		0.0096	10
	0.0142	15		0.0140	30		0.0139	20
	0.0176	26		0.0184	50		0.0184	63
	0.0218	35		0.0221	60		0.0202	90
	0.0271	40		0.0247	75			
	0.0280	45		0.0277	95			
						S11	0.0097	15
							0.0187	95

Scour depths for ocean sediment bed for plain cylinder $u_{*c} = 0.023$msec^{-1}; water depth h = 0.307m; water temperature = 17.0°C (Mean); Sediment bed depth = 0.10m.

Scour depths for ocean sediment bed for cylinder with a collar at bed level:
u_{*c} = 0.023msec^{-1}; water depth h = 0.307m; water temperature = 17.0°C (Mean);
Sediment bed depth = 0.10m.

TABLE 3

Test	Cylinder Diameter	25 mm	Test	Cylinder Diameter	50 mm	Test	Cylinder Diameter	100mm
	u_* ms^{-1}	d_s mm		u_* ms^{-1}	d_s mm		u_* ms^{-1}	d_s mm
S25 Collar D_c=75mm	0.0069	0	S21 Collar D_c=100mm	0.0091	0	S12 Collar D_c=200mm	0.0072	0
	0.0099	0		0.0105	2		0.0098	0
	0.0141	2		0.0141	20		0.0142	10
	0.0187	10		0.0184	30		0.0191	30
	0.0217	15		0.0209	35		0.0218	50
	0.0241	20		0.0237	45		0.0261	100
	0.0263	25		0.0265	55			
S24 Collar D_c=100mm	0.0078	0	SS12 Collar D_c=100mm	0.0080	0			
	0.0110	0		0.0107	3			
	0.0142	2		0.0148	9			
	0.0183	8		0.0188	28			
	0.0210	15		0.0212	35			
	0.0235	25		0.0241	41			
SS11 Collar D_c=100mm	0.0076	0	S10 Collar D_c=150mm	0.0093	2			
	0.0099	2		0.0135	10			
	0.0127	3		0.0180	30			
	0.0174	8		0.0222	30			
	0.0184	10		0.0247	30			
	0.0219	14		0.0278	30			
	0.0228	18						
			SS13 Collar D_c=150mm	0.0084	0			
				0.0109	0			
				0.0149	5			
				0.0180	14			
				0.0212	19			
				0.0234	24			
				0.0257	36			

TABLE 4

Test	Cylinder Diameter	25mm	Test	Cylinder Diameter	50mm
	u_*msec^{-1}	d_s mm		u_*msec^{-1}	d_s mm
SS14	0.0080	0	SS16	0.0069	0
Collar	0.0106	1	Collar	0.0092	2
D_c=100mm	0.0149	2	D_c=100mm	0.0141	12
Elevation	0.0193	7	Elevation	0.0180	58
20mm	0.0216	17	20mm	0.0218	75
	0.0231	45		0.0250	96
SS17	0.0069	0	SS15	0.0081	0
Collar	0.0097	4	Collar	0.0108	0
D_c=100mm	0.0141	9	D_c=150mm	0.0149	4
Elevation	0.0191	28	Elevation	0.0189	20
60mm	0.0218	42	20mm	0.0213	36
	0.0244	52		0.0237	47
	0.0264	63		0.0264	60

Scour depths for ocean sediment bed for cylinder with a raised collar:
u_{*_c} = 0.023msec^{-1}; water depth h = 0.307m; water temperature = 17.0°C (Mean);
Sediment bed depth = 0.10m.

TABLE 5

Author	Cylinder Diameter	Material	
	mm	Type	d_{50} mm
Breusers 1971	50 & 110	Sand	0.2
Chabert & Engelhinger 1956	50, 100 & 150	Sand Sand	0.52 1.5 3.0
Jain & Fischer 1980	516	Sand	0.29 0.50 0.63
Qadar 1981	25, 50 & 75	Sand	0.17 0.7 1.5
Shen, Schneider & Karaki 1966	150	Sand	0.24 0.46

Cylinder diameters and bed materials used by various other authors listed.

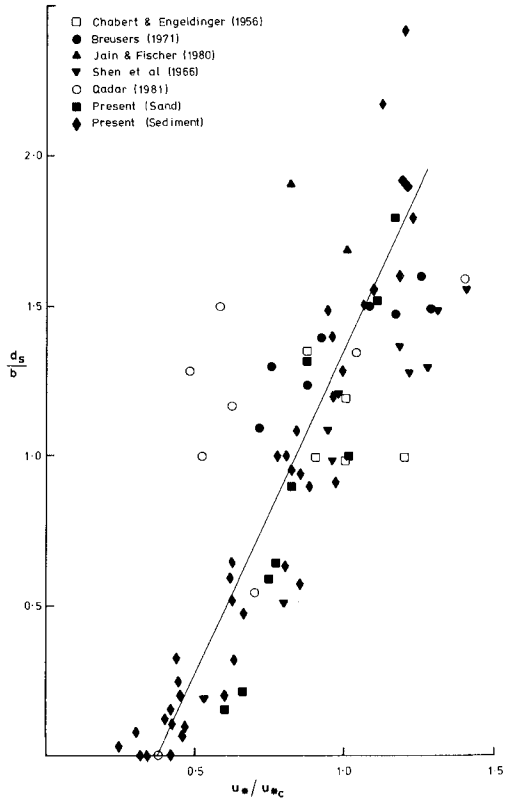

Dimensionless plot of scour depth against the shear velocity for cylinders without collars showing line of best fit from present results.

FIGURE 11.

The mechanisms for scour in the sediment and in the sand were discussed in section 4 where the very different nature of the two mechanisms was pointed out. In the case of sand, scour is achieved by the suspension of the material and subsequent slumping. By contrast, in the case of the sediment it appeared that the eddying in the horseshoe vortex caused local scour which deepened at first and then broadened to form a sheet like scour depression. The failure of the soil was much more hy lateral or horizontal scouring by the fluid as it swept past the near vertical sediment walls. There was very little evidence of the sediment slumping at any stage of the scour process. It is therefore quite remarkable that the sediment data and the sand data show the same correlation between d_s/b and u_*/u_{*_c}. This implies that, even though the mechanisms are different, it is the turbulent kinetic energy that is ultimately responsible for the scour. Similarly it is the single parameter u_{*_c} which determines the resistance of the soil to scour.

Installation of a protective collar hecame effective for collars at least twice the diameter of the cylinder. However, even for the large collars, scour holes formed and deepened to a depth comparahle to plain cylinders for u_*/u_{*_c} larger than unity, hut by the action of the wake rather than the horseshoe vortex. For collar diameters equal to twice the cylinder diameter the effect of the collar became negligible for d_s/b beyond a value of 1.5.

Acknowledgement

The authors would like to thank Woodside Offshore Petroleum Pty. Ltd. and the North-West Shelf Development Project Joint Venturers for funding and support of the research and Mr. R. Jewell for assisting in the design of the sample preparation technique.

BIBLIOGRAPHY

Breusers H.N.C., Nicollet G, & Shen H.W. 1977 — "Local Scour Around Cylindrical Piers". Journal of Hydraulic Research I.A.H.R. Vol 15 No. 3 1977

Breusers H.N.C. 1971 — "Local Scour Near Offshore Structures". Proc Symp on Offshore Hydrodynamics, Wageringen 1971 (also Delft Hydraulics Laboratory Publication No. 105).

Caldwell D.R. & Chris J.M. 1979 — "The Viscous Sublayer at the Seafloor" Science, 205, pp1131 to 1132.

Durand Claye, A.A. 1873 — Experiences sur les affouillements; Ann des Ponts et Chaussees, ler semestre, p467.

Carstens T & H.R. Sharma 1975 — "Local Scour Around Large Obstructions" Proc 16th I.A.H.R. Congress Sao Paulo, 2, pp251-262.

Chabert J & Engeldinger P 1956 — "Etude des affouillements autour des piles de ponts; Lab Nat D'Hydr Chatou Octobre.

Fugro 1981 — Report Nv: K-1052/XVIII

Jain S.C. & Fischer E.E. 1980 — "Scour Around Bridge Piers at High Flow Velocities" Proc A.S.C.E. HY11 November 1980, pp1827/1842.

Jain S.C. & Fischer E.E. 1979 — "Scour Around Bridge Piers at High Froude Number" Report No. FH-WA-RD-79-104. Federal Highway Administration Washington D.C. April 1979.

Jones H.A. 1973 — "Marine Geology of the Northwest Australian Continental Shelf" Bureau of Mineral Resources Bulletin 136.

Jewell R.J., Fahey, M. Wroth C.P. 1980 — "Laboratory Studies of the Pressure Meter Test in Sand". Geotechnique Vol XXX No. 5. December 1980.

Melville B.W. 1975 — "Local Scour at Bridge Sites" Rep No. 117 School of Engineering, University of Auckland, Auckland, N.Z.

Qadar A. 1981 — "The Vortex Scour Mechanism at Bridge Piers". Proc Inst'n Civil Engineers, Part 2, 1981, 71, September pp739-757.

Shen H.W., Schneider V.R. & Karaki S. 1966 — Mechanics of Local Scour; Supplement Methods of Reducing Scour, Colorado State Univeristy CER66 H.W.S. 36.

Tanaka S. & Yano M 1967 — "Local Scour Around a Circular Cylinder" Proc 12th I.A.H.R. Congress, Ft Collins 3 pp 193/201.

Vanoni V.A. ed 1975 — "Sedimentation Engineering" Manuals & Reports on Engineering Practice No. 54 A.S.C.E. 1975.

Zdenek T. 1967 — "An Interesting Hydraulic Effect Occuring at Local Scour. Proceedings I.A.H.R. Congres Vol. 3 Colorado September 1967.

INCIPIENT MOTION OF PARTICLES UNDER OSCILLATORY FLOW

by

L Lenhoff*

ABSTRACT

This paper is aimed at the establishment of a generally applicable criterion for the onset of grain motion under the influence of oscillatory flow. Data from previous studies are used in a dimensional analysis and an empirically derived relationship between the dimensionless parameters R* (shear Reynolds number) and D* (dimensionless grain parameter) is proposed as a criterion to be used in coastal engineering problems.

This study forms part of a larger programme by the Sediment Dynamics Division of the National Research Institute for Oceanology in Stellenbosch, RSA, which is aimed at the re-evaluation and updating of the input parameters and relationships for the predictive equations for coastal sediment transport.

1. INTRODUCTION

Coastal sediment transport formulae are based mainly on the transport formulae derived for uniform flow. In contrast with the initiation of sediment motion under wave action, the conditions for movement under unidirectional steady flow have been widely studied by numerous researchers during the past years and well established criteria for the beginning of movement exist. The applicability of the criteria for incipient motion under uniform flow to oscillatory motion is, however, questionable.

A number of excellent studies with respect to oscillatory flow have already been done. The problem, however, is a complex one, mainly due to the numerous variables involved. Therefore most authors preferred to base their criteria on experimental rather than purely theoretical analyses. Although each individual study was obviously well designed and the results were very convincing, the different criteria are not always compatible, mainly due to

---

* Sediment Dynamics Division, National Research Institute for Oceanology, CSIR, Stellenbosch, RSA.

differences in experimental set-up and initial conditions employed. The subsequent different ranges of applicability also make direct comparisons difficult. Different authors also presented their results in different ways and for comparative purposes all the criteria should be written in the same form. This was done by Silvester (1974) who calculated the critical near bed velocity at the onset of movement under specific boundary conditions, using the empirical formulae derived in a number of previous studies. He concluded that little correlation exists between the different criteria, mainly because some criteria were used outside their ranges of applicability.

Despite this apparent lack of correlation, it was nevertheless felt that the vast amount of data which are available may still yield satisfactory results if they are analysed within a general theoretical framework and the results brought together on a single curve.

All the relevant available studies were subsequently investigated with special emphasis on the quality of the data. Aspects which were carefully looked at were, for example, the experimental procedure, sediment characteristics, parameters directly measured during the experiment and the authors' definition of incipient motion.

2. EVALUATION OF AVAILABLE DATA

The data which were used in this study can be broadly subdivided into four groups based on the experimental set-up, namely, those tested with:

(i) The simple harmonic motion of sediment particles through still water.

(ii) Water oscillating in a U-tube over bed material.

(iii) Progressive waves over bed material in a conventional wave flume.

(iv) Direct measurement of water movement on the sea floor due to surface waves, that is, prototype data.

According to these four types of data, the different data sources which were used in this study can be grouped as follows:

Oscillating bed material	U-tube	Wave flume	Prototype
Bagnold (1946) Manohar (1955)	Ishihara and Sawaragi (1962) Carstens et al. (1967) Rance and Warren (1968)	Vincent (1959) Horikawa and Watanabe (1967)	Davies and Wilkinson (1978)

3. DEFINITION OF INCIPIENT MOTION

The determination of the actual onset of movement during an experiment is normally done by visual observation. Unfortunately the definition of incipient motion is not clear cut. Normally it relates to the proportion of moving grains on the bed surface. Manohar (1955), for instance, found that at a certain critical velocity a few particles were dislodged from their position of equilibrium and moved a short distance from their initial position. This movement of a few particles in the top layer was defined as initial movement.

Vincent (1959) considered the initial motion condition to be characterised by the displacement of the very first grains.

Carstens et al. (1967) defined incipient motion on a flat bed when approximately 10 per cent of the surface particles were rolling back and forth.

Rance and Warrent (1968) considered the dislodgement and small downstream movement of the first one or two grains to be the onset of motion.

This variation in definitions is a major handicap in any comparative study. Even when the onset of motion is properly defined within a single experiment, the assesment of the exact onset of motion is difficult and subjective. In addition, the particles in the sandy bed are not of uniform size, and consequently the onset of motion will be largely dependent on the grain size distribution of the bed material. This is clearly illustrated by the prototype data of Davies and Wilkinson (1978). Although the wave period stayed essentially constant during their observations, the measured horizontal orbital velocity at incipient motion varied by a factor two.

4. RE-ANALYSIS OF DATA

As it is the purpose of this paper to bring data from different sources together on one universal curve, a considerable scatter must therefore be expected. The question at this stage would be which parameters to use in the dimensional analysis to obtain the most acceptable results for application in coastal engineering studies. Various relationships have been used in the past to present the results of studies on incipient motion. A typical example is the critical sediment number (N_{SC}) as defined by Carstens et al. (1967), namely,

$$N_{SC} = \frac{U_{OC}}{(\Delta_S \, d \, D_{50})^{1/2}} = f(T, D_{50}, \rho_W, \rho_S) \quad \ldots \quad (1)$$

where U_{OC} = horizontal orbital velocity at bed at onset of movement

D_{50} = median grain diameter of bed material

ρ_W = density of fluid

ρ_S = density of material

Δ_S = relative buoyant sediment density = $(\rho_S - \rho_W)/\rho_W$.

The main disadvantage of this parameter in defining incipient motion lies in the fact that it does not contain the bed roughness in any way and can therefore not be used for a unique determination of the critical shear stress. Since the sea bottom is normally rippled in the areas of coastal engineering interest, the ultimate goal would be to extend any incipient motion criterion to ripple bed conditions. The sediment number can therefore hardly be unique for flat bed as well as rippled bed conditions.

The parameters which were chosen for the graphical presentation of the data in this study are the shear Reynolds number R* and a dimensionless grain diameter D* (by analogy with Bonnefille and Pernecker (1966) where

$$R_* = \frac{U_* \, D_{50}}{\nu} \quad \ldots \quad (2)$$

and

$$D_* = \left(\frac{\Delta_S g}{\nu}\right)^{1/3} D_{50} \quad \ldots \quad (3)$$

with U_* = shear velocity

ν = kinematic viscosity of fluid.

The choice of R* enables the inclusion of the bed roughness since

$$U* = \left(\frac{\bar{\tau}}{\rho_w}\right)^{1/2} \quad \ldots (4)$$

with $\bar{\tau}$ = mean shear stress = $^1/_4\ \rho\ f_w\ U_o^2$ ... (5)

and $f_w = f(a_o/r)$ where

a_o = maximum orbital excursion from mean position of the motion of water particles at the bed

r = bed roughness

f_w = wave friction factor

The procedure by which the data were re-analysed depended for each set on the parameters which were directly measured during the original experiment. In the case of oscillating bed material as well as the oscillating water tunnel, the angular velocity (ω) and the horizontal displacement (a_o) were usually directly measured at the onset of motion. The subsequent determination of R* and D* in such cases is straighforward, using the standard relationships for simple harmonic motion and equations (2) an (3).

In experiments which were done in conventional wave flumes the wave height (H), wave period (T) and the water depth (h) at the incipient motion condition were normally observed. It was felt that all the data which were obtained by means of progressive waves should be treated in the same manner and for this purpose the Vocoidal water wave theory of Swart (1978) was employed. A computer program which used the Vocoidal theory was written to calculate R* and D* for any combination of T, d, H, D_{50} and ρ_s.

The generalised procedure of analysis may therefore be summarised as follows:

(i) Computation of the wave properties U_o and a_o.

(ii) Computation of the bed roughness r using the following formulae:

$r = 2\ D_{90}$ (flat bed; Kamphuis, 1975)

$r = 25\ \Delta_r\ \left(\frac{\Delta_r}{\lambda_r}\right)$ (rippled bed; Swart, 1976)

where Δ_r = ripple height

λ_r = ripple length.

(iii) Computation of a_o/r.

(iv) Computation of orbital Reynolds number

$$R = \frac{U_o a_o}{\nu}$$

(v) Determination of the wave friction factor f_w using empirical relationships based on more than 600 data sets (Swart, in preparation, 1982).

(vi) Calculation of R* and D* using equations (2), (3), (4) and (5).

5. RESULTS

A total number of 643 data points consisting of combinations of R* and D* at the onset of movement were calculated in the above manner. Figure 1 shows a logarithmic plot of the results together with a best fit curve through the data points. This empirical curve was found to be very closely simulated by the following parabolic equation:

$$\log_{10} R* = 0{,}092(\log_{10} D*)^2 + 1{,}158 \log D* - 0{,}367 \quad .. \quad (6)$$

It is also possible to test the validity of equation (6) by making use of laboratory and field measurements of sediment load under waves in conjunction with appropriate predictive sediment load equations which include an incipient motion criterion. For this purpose the Ackers and White sediment load formula for steady flows, as modified for application in the coastal area (see Swart and Fleming, 1980) will be used.

The original formula for the prediction of sediment transport rates under steady-state conditions was (Ackers and White, 1973):

$$S = 1{,}45\, U\, D_{35}\, C \left(\frac{Pfg/\rho}{U^3_{fg}}\right)^n \left(\frac{Pcg/\rho}{U^2_{cg} U_r}\right)^{1-n} \left(\frac{Fgr}{(Fgr)crit} - 1\right)^m \quad ... \quad (7)$$

where C, n, m and $(F_{gr})_{crit}$ are grain size dependent parameters, for which empirical relationships are given by Ackers and White; F_{gr} is the sediment mobility = $(U^n_{*fg}\, U^{1-n}_{*cg})/(\Delta_s\, g\, D_{35})^{1/2}$;
P is the stream power; U_r the resultant velocity (= U for steady state) and U* is the shear velocity = $(\tau/\rho)^{1/2}$; subscripts "fg" and "cg" respectively denote the "fine grain" and "coarse grain" versions of the properties. The

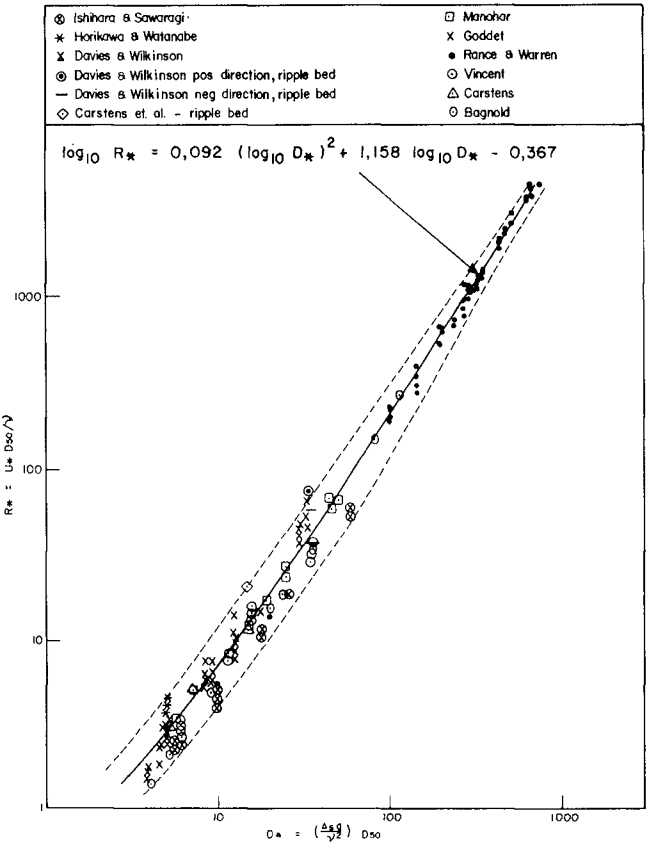

FIG. 1 INCIPIENT MOTION OF SEDIMENT PARTICLES UNDER OSCILLATORY FLOW - EXPERIMENTAL RESULTS

value for fine-grained sediment is obtained by using the actual bed roughness r, as described before, whereas the value for coarse-grained sediment is obtained by using the grain size D_{35} instead of r in the appropriate equations. For steady state conditions the efficiency term reduces to $(U/U*_{fg})^n$.

Various adapted versions of the original steady-state Ackers and White formula were in use in 1980, varying only in the way in which the effect of waves was included in the stream power and mobility terms (Swart, 1976; Willis, 1978; Van de Graaf and Van Overeem, 1979). Swart and Fleming (1980) discussed these versions and came to the conclusion that all three methods quoted above had shortcomings. They then suggested a fourth alternative which used the better aspects of each method and discarded the rest. The main points of improvement of this latter method as opposed to the earlier modifications were the following:

(1) The average effect of the inclusion of waves on the mean mobility number is calculated by integrating the instantaneous mobility number with respect to time, that is,

$$F_{wc} = \overline{F_{gr}(t)} = {}^1/_T \int_0^T F_{gr}(t)dt \quad \ldots \quad (8)$$

where F_{wc} is the mean sediment mobility for combined current and wave action.

(2) The instantaneous value $E_f(t)$ of the efficiency term, as given in equation (9) is averaged to obtain the mean value E_{fwc} of the efficiency term for combined current and wave action, namely,

$$E_{fwc} = \overline{E_f(t)} = {}^1/_T \int_0^T E_f(t)dt \quad \ldots \quad (9)$$

$$\text{where } E_f(t) = \left(\frac{P_{fg}(t)/\rho}{U*_{fg}(t)^3}\right)^n \left(\frac{P_{cg}(t)/\rho}{U*_{cg}(t)^2\, U_r(t)}\right)^{1-n} \quad \ldots \quad (10)$$

Values for the instantaneous resultant velocity at the bed $U_r(t)$ and the instantaneous shear stress at the bed $\tau(t)$ are found by vector addition of the contributions by the waves and the currents.

By equating measured sediment load data under known wave conditions to the right-hand side of this adapted version of equation (7), values for the critical sediment mobility $(F_{gr})_{crit}$ were calculated. Since $(F_{gr})_{crit}$ is simply related to R* by

$$(F_{gr})_{crit} = R_* D_*^{-3/2}, \quad \ldots (11)$$

corresponding values for R_* could be computed.

The results of this calibration technique for the threshold of motion can be seen in Figure 2. The threshold values calculated in the above manner agree very well with the threshold criterion proposed in terms of equation (6). The result is also extremely significant in the sense that it illustrates the efficiency of the adapted Ackers and White formula for the prediction of sediment load under waves, provided that equation (6) is used to define the critical sediment mobility.

Equation (6) can be rewritten in terms of a non-dimensional shear velocity V_*,

where $V_* = U_*/(g\Delta_S \nu)^{1/3}$ ... (12)

This implies that

$$R_* = U_* D_*/(\Delta_S g \nu)^{1/3} = V_* D_* \quad \ldots (13)$$

Equation (5) therefore reduces to

$$\log V_* = 0{,}092(\log D_*)^2 + 0{,}158 \log D_* - 0{,}367 \quad \ldots (14)$$

The relationship between V_* and D_* as obtained from equation (14), as well as the scatter observed in the data, is indicated in the following table where V_* represents the value obtained from equation (14), while V_{*max} and V_{*min} corresponds to the upper and lower envelopes of the experimental data:

D_*	V_*	V_{*max} [1]	V_{*min} [1]
4	0,51	1,00	0,31
10	0,63	1,35	0,40
20	0,83	1,75	0,55
50	1,22	2,70	0,86
100	1,75	3,20	1,50
200	2,75	3,75	2,50
500	4,60	6,00	4,00
700	5,71	6,43	4,86

Comment: 1) These numbers reflect the maximum variability in the data.

The scatter indicated by this table may look appreciable for low values of D_* but is in fact of the same order of magnitude as that observed in the Shields diagram for steady flow and may be attributed to experimental errors and the use of different definitions for incipient motion.

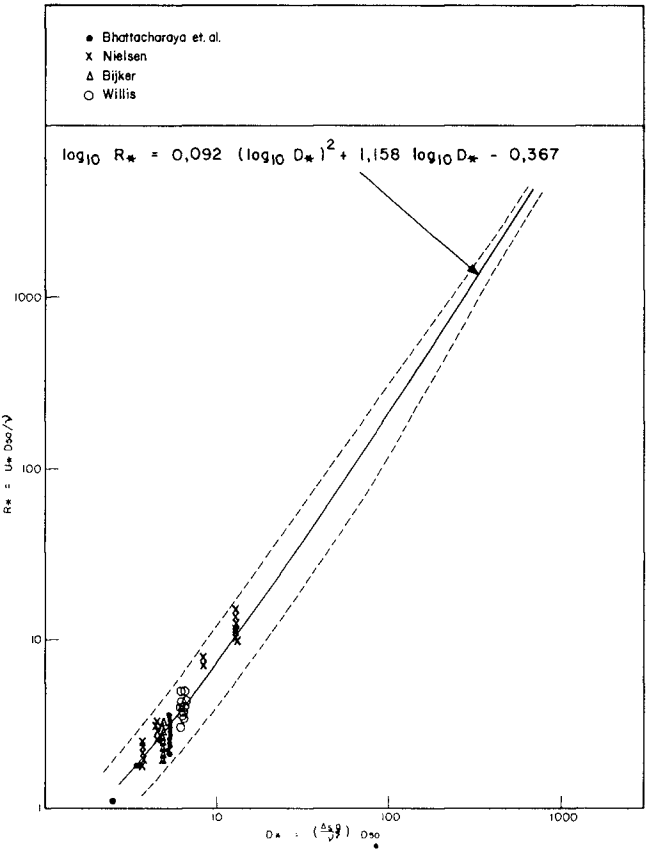

FIG. 2 COMPARISON WITH THRESHOLD VALUES COMPUTED FROM SEDIMENT LOAD DATA

6. COMPARISON WITH UNIDIRECTIONAL FLOW CRITERIA

The conditions for movement under unidirectional steady flow have been widely studied by numerous researchers and well established criteria for the beginning of movement exist. The work by Shields (1936) and Ackers and White (1973) are probably the most widely used and acknowledged in this respect. A direct comparison between these two criteria and the results of this study can now be made. Figure 3 shows the original Shields and Ackers and White data points together with the curve defined by equation (6). The envelope encompasses data scatter for oscillatory flow. The unidirectional data can be seen to fall well within the scatter of the oscillatory flow data points. It can therefore be concluded that there is no significant difference between the criteria for uniform flow and the criterion of oscillatory flow as derived in this study. A single criterion can be applied with the same degree of accuracy for both flow conditions. Consequently it is reasonable to assume that the criterion developed in this study can be applied for wave-generated flows, current-dominated flows and all combined flow modes in between, provided that the correct definition of the shear velocity is used in equations (6) and (14).

7. CONCLUSIONS

The main conclusions drawn from the present study are as follows:

(1) An empirical criterion, equation (6) or (14), was derived for the onset of grain motion on either a flat or a rippled bed under the influence of wave action.

(2) It was shown that the new criterion is not only valid for incipient motion due to waves but also does not differ from widely used incipient motion criteria for steady-state conditions (Shields, 1936; Ackers and White, 1973). In addition, provided that the correct definition of the bed shear is used, it also applies to the case of combined current and wave action. It can therefore be seen as a fairly universal criterion for the onset of grain movement.

(3) Comparison to sediment load data via the adapted Ackers and White sediment load formula given by Swart and Fleming (1980) yielded values of the incipient motion mobility number which would have been required to allow the sediment load formula to predict the measured sediment load. These indirectly calculated incipient motion data fall within the scatter of the original data used to derive equation (6). This serves as a very strong independent proof of the adapted Ackers and White sediment load formula given by Swart and Fleming (1980).

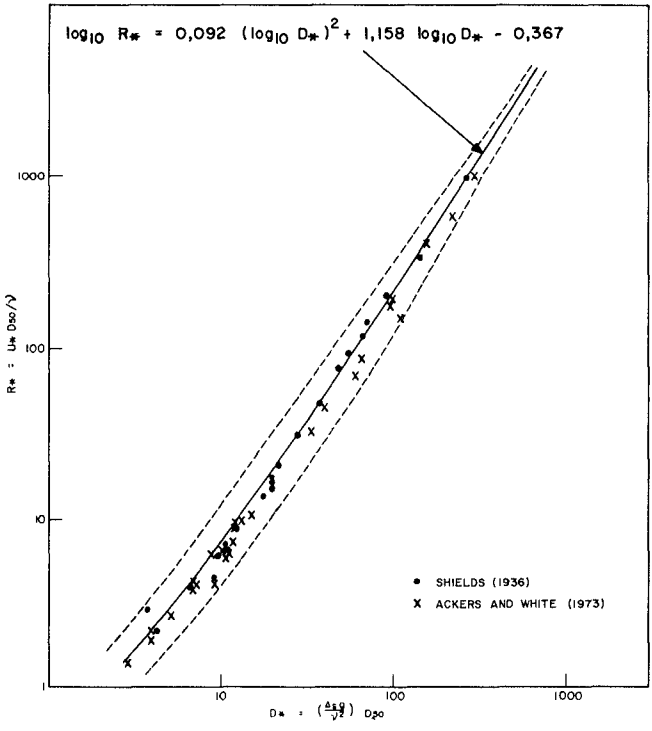

FIG. 3 COMPARISON WITH UNIDIRECTIONAL FLOW CRITERIA

8. REFERENCES

ACKERS, P and WHITE, W R (1973). Sediment transport: new approach and analysis. Proc. ASCE Journ. of the Hydr. Div., HY11.

BAGNOLD, R A (1946). Motion of waves in shallow water-interaction between waves and sand bottoms. Proc. R. Soc. A187, pp. 1-18.

BHATTACHARYA, P K (1971). Sediment suspension in shoaling waves. Ph.D. thesis, University of Iowa.

BIJKER, E W (1971). Longshore transport computations. Proc. ASCE, Journ. of the Waterways, Harbors and Coastal Engineering Division, WW4.

BONNEFILLE, R and PERNECKER, L (1966). Le début d'entrainement des sédiments sous l'action de la houle. Bulletin du CREL, No 15.

CARSTENS, M R, NEILSON, F M and ALTINBILEK, H D (1967). An analytical and experimental study of bed forms under water waves. Georgia Inst. Tech., Final Rep. Proj A-798.

DAVIES, A G and WILKINSON, R H (1978). Sediment motion caused by surface water waves. Proc. 16th International Conference on Coastal Engineering, Paper No 106.

GODDET, J (1960). Etude du début deutrainment des matériaux mobiles sous l'action de la houle. Houille Blanche 15, pp 122-135.

HORIKAWA, K and WATANABE, A (1967). A study on sand movement due to wave action. Coast. Eng. Japan, Vol X, pp 39-58.

ISHIHARA, T and SAWARAGI, T (1962). Fundamental studies of sand drifts. Coast. Eng. Japan 5, pp 59-65.

MANOHAR, M (1955). Mechanics of bottom sediment movement due to wave action. Beach Erosion Board Tech. Mem., 75.

NIELSEN, P (1979). Some basic concepts of wave sediment transport. Institute of Hydrodynamics and Hydraulic Engineering, Technical University of Denmark, Series Paper No 20.

RANCE, P J and WARREN, N F (1968). The threshold of movement of coarse material in oscillatory flow. Proc 11th Conf. Coast. Eng., 1; pp 487-49.

SHIELDS, A (1936). Amvendung der aehulichterts-mechanik und der turbulenz forschung auf die geschiebewegung. Mitterlungen der Preussischen Versuchsanstalt fur Wasserbau und schiffbau, Heft 26.

SILVESTER, R (1974). Coastal Engineering II. Elsevier Scientific Publishing Co., New York.

SWART, D H (1976). Coastal sediment transport, computation of longshore transport. Delft Hydraulics Laboratory. Report No R968, Part 1.

SWART, D H (1978). Vocoidal water wave theory Vol 1: derivation. Coastal Eng. and Hydr. Div., NRIO, Stellenbosch, CSIR Research Report 357.

SWART, D H and FLEMING, C A (1980). Longshore water and sediment movement. CSIR Technical Report SEA/8009, Stellenbosch, South Africa.

VINCENT, G E (1958). Contribution to the study of sediment transport on a horizontal bed due to wave action. Proc. 6th Conf. Coastal Eng., pp 326-355.

VAN DE GRAAF, J and VAN OVEREEM, J (1979). Evaluation of sediment transport formulae in coastal engineering practice. Coastal Eng., 3(1).

WILLIS, D H (1979). Sediment load under waves and currents. DME/NAE Quarterly Bulletin No 1979(3).

RESUSPENSION OF DEPOSITED COHESIVE SEDIMENT BEDS

By Ashish J. Mehta[1], M. ASCE and Emmanuel Partheniades[2], M. ASCE

ABSTRACT

Surficial layers of estuarial fine, cohesive sediment beds are deposited from flow and often are in a state of partial consolidation. A series of laboratory investigations were carried out to elucidate the erosional behavior of deposited cohesive sediment beds in flumes using kaolinite. A significant feature of such beds is that they are stratified with respect to the density and the cohesive shear stength. Under a given bed shear stress, erosion occurs at a continuously decreasing rate up to a depth at which the bed shear stress equals the shear strength. This bed shear stress is therefore also equal to the critical shear stress for erosion at that depth. An expression for the rate of erosion relating this rate to the difference between the bed shear stress and the critical shear stress has been obtained. The critical shear stress increases both with depth and with the bed consolidation time. The rate of erosion decreases with increasing consolidation time.

INTRODUCTION

The sediment at the bottom and in suspension in most estuaries is typically fine, cohesive in nature (14). Cohesive sediments are comprised primarily of particles in the clay and silt size-range plus organic matter and waste materials. Surficial layers of cohesive sediment beds in estuaries generally consist of partially consolidated material deposited from flow (9). Such layers have a high water content and very low cohesive shear strength which tends to exhibit a non-uniform variation with depth below the bed surface. The shear strength is however too low for it to be measured, for example, with such device as a penetrometer (13). The bed can exhibit two modes of failure. The first, known as surface erosion, involves floc-by-floc rupture and entrainment of the surficial sediment. The second, known as mass erosion, results from a dynamic shear loading of the bed. In this case the plane of failure lies deep in the bed, and failure results in an almost instantaneous entrainment of the sediment above the plane. Under typical estuarial environment, erosion occurs predominantly at the surface and is considered here. Until recently,

---

[1]Assoc. Prof., Dept. of Coastal and Oceanographic Engrg., Univ. of Florida, Gainesville, FL.

[2]Prof. of Hydr. Structures, Aristoteles Univ. of Thessaloniki, Greece; and Prof., Dept. of Engr. Sci., Univ. of Florida, Gainesville, FL.

the erosional behavior of deposited beds was not investigated adequately (9). Attempts to relate the rate of erosion with standard soil indices such as the Atterberg limits were unsuccessful because these indices do not properly account for the resistance to erosion which essentially depends upon the strength of the inter-particle electro-chemical bonds (12, 14). Resistance to erosion must be characterized by physico-chemical parameters, some of which have been identified more recently (8).

Laboratory investigations were carried out at the University of Florida in order to investigate the erosional behavior of deposited cohesive sediment beds. The main findings are summarized below. Details are given elsewhere (1, 7, 11, 16).

APPROACH

The rate of surface erosion, ε, expressed as the mass of sediment eroded per unit bed area per unit time, is related to the time-rate of change, dz/dt, of the depth of erosion, z, below the initial bed surface according to:

$$\varepsilon = h\frac{dC}{dt} \tag{1}$$

$$\frac{dC}{dt} = \frac{\rho(z)}{h}\frac{dz}{dt} \tag{2}$$

where h = depth of flow, dC/dt = time-rate of change of suspended sediment concentration, C, and $\rho(z)$ = depth-varying dry density of the bed. Several investigators measured the variation of dC/dt with time t for deposited beds in a closed system and observed that, under a constant bed shear stress, τ_b, dC/dt (and therefore ε) generally decreases continuously with t, beginning with a relatively high value when erosion commences (9). For a certain range of τ_b and "large" t ranging from a fraction of an hour to several hundred hours depending upon the type of fluid-sediment mixture and the magnitude of τ_b, the rate of erosion, ε, becomes equal to zero or approaches zero. In other words, C becomes constant or approaches a constant value asymptotically. Given the bed density distribution $\rho(z)$, the magnitude of the constant value of C and the rate of approach of C to this value depend upon τ_b (which defines the erosive force), and upon parameters which characterize the resistance to erosion. Important among the latter is the cohesive shear strength of the bed with respect to erosion.

In the reported studies, resistance to erosion was varied by two means: 1) by varying the conditions for bed preparation, and 2) by varying the salinity of the fluid. Time-concentration data obtained under a wide range of τ_b values have been used together with the bed density in order: 1) to elucidate the mechanics of the resuspension behavior of deposited beds, and 2) to obtain an expression for the rate of erosion in terms of the bed shear stress and parameter(s) characterizing resistance to erosion.

APPARATUS AND MATERIAL

The experiments were performed in two flumes: a rotating annular flume and a flow recirculating flume. The two main components of the annular flume (Fig. 1) are: an annular fibreglass channel (0.21 m wide, 0.46 m deep, and 1.5 m in mean diameter) containing the fluid-sediment mixture, and an annular ring of slightly smaller width positioned within the channel and in contact with the fluid surface. A simultaneous rotation of the two components in opposite directions generates a uniform turbulent flow field free from floc-disrupting elements such as pumps and diffusors in which very high shearing rates generally prevail. By a proper adjustment of the speeds of the two components the rotation-induced secondary currents are eliminated, and the distribution of the bed shear stress across the channel width is found to be uniform (5). The steel recirculating flume, open at the top (Fig. 2), is 18 m long, 0.6 m wide and 0.9 m deep, with an underflow-type control gate at the downstream end. The return pipe diameter is 0.2 m. One side of the flume is made of glass panels for visual observations (1).

A commercial kaolinite with a cation exchange capacity of approximately 12 milliequivalents per hundred grams was used in all tests. The median diameter of the deflocculated sediment was 1 micron, with a range of 0.2 to 40 microns. The fluids were: 1) distilled water as well as salt water of 35 ppt concentration using commercial grade sodium chloride in the annular flume, and 2) tap water with a very low total salt concentration of 0.28 ppt as well as salt water of 35 ppt concentration in the recirculating flume. Kaolinite readily flocculates even in distilled water. The sediment was equilibrated with the fluid for atleast two weeks prior to each test series. The depth of flow was maintained at 31 cm in the annular flume and 23 cm in the recirculating flume. Fluid temperature varied with the ambient. The mean was approximately 26°C.

EXPERIMENTS AND RESULTS

There were four experimental series. These are described in the order in which they were performed.

Series 1 Experiments

These experiments were carried out in the annular flume using kaolinite in distilled water (7). Two types of beds were used: the first was deposited gradually from suspension while the flume was in motion and the bed shear stress was kept slightly less than τ_{bmin}, i.e., the shear stress at which the entire amount of initially suspended sediment deposits eventually (6). The second was prepared outside the flume at a density close to that of the deposited sediment and subsequently placed and leveled into the flume. The main difference between these two beds was with respect to the vertical distribution of their cohesive shear strength. In the formation of the first bed there was a preferential deposition whereby larger and more cohesive flocs deposited first while the smaller, less cohesive flocs deposited later. For this reason the first bed may be referred

Fig. 1. A View of the Annular Rotating Flume.

Fig. 2. A View of the Open, Flow Recirculating Flume.

to as stratified, a situation commonly encountered in estuaries. In contrast, the second bed may be termed uniform, since it had practically constant properties in the vertical direction.

Figure 3 shows the time-concentration relationship for the case of a stratified bed eroded under a shear stress τ_b = 0.207 Nm^{-2}. The ordinate gives the suspended sediment concentration as a fraction of the total dry weight of the bed material. It is observed that the slope of the curve, i.e., the erosion rate, decreased with time and became nearly zero at the end of the test. This observation is in agreement with the erosion test results of Partheniades (13) with a bed composed of natural, flocculated, silty-clay from the San Francisco Bay and deposited in an open flume at low velocity. The predominant clay mineral of that sediment was montmorillonite with some illite.

Figure 4 shows an erosion test for a uniform bed under a shear stress of 0.413 Nm^{-2}. Two additional tests were carried out at shear stresses of 0.445 and 0.483 Nm^{-2}. The results were similar to those shown in Fig. 4. Inasmuch as four sample taps at four different elevations were used and since a vertical concentration gradient was generally present in the suspension, a spread of data is observed during certain times. The solid line represents the mean curve. After a relatively short period, the slope of the line, and, therefore, the rate of erosion, became constant. The same was true of the two other tests. The corresponding erosion rates, ε, were 2.03×10^{-6}, 2.64×10^{-6} and 2.92×10^{-6} g cm^{-2} min^{-1}. These rates, when appropriately non-dimensionalized and plotted against the corresponding bed shear stress also in the non-dimensional form, agreed with the earlier results of Partheniades (7, 13).

Two important observations may be made: 1) with reference to the results of the experiment with the uniform bed (Fig. 4), the observed constancy of the rate of erosion implies that the eroded material did not redeposit, since simultaneous erosion and deposition would ultimately result in a state of equilibrium in which the rates of erosion and deposition are equal, and the suspended sediment concentration attains a constant value (6, 13, 14). The absence of exchange of material between the fluid and the bed during erosion under a constant bed shear stress was noted previously by Partheniades (13). In this context it may be noted that flow turbulence varies in the vertical direction from the bed to the surface. Close to the bed a zone of high shear prevails. In the remainder of the flow the shear is relatively much lower. Depending upon the size and the strength of a settling floc at a given instant and the corresponding instantaneous value of the near-bed shear, the floc may deposit, i.e. stick to the bed, or may rupture, with the pieces re-entrained above the near-bed zone. Absence of exchange precludes deposition but not the process of settling and re-entrainment. 2) in the absence of exchange, the attainment of a constant value of the concentration in the case of the stratified bed may be explained by noting that constancy of the concentration occurs when bed erosion is arrested. This is the case because the shear strength increases with depth below the initial bed surface so that no erosion will occur below the depth at which the bed shear stress equals the shear strength.

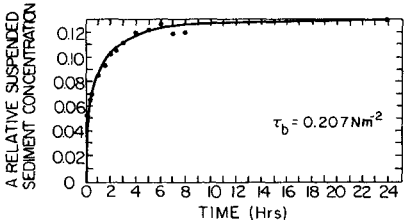

Fig. 3. Relative Suspended Sediment Concentration against Time, t, for a Stratified Bed using Kaolinite in Distilled Water at τ_b = 0.207 Nm^{-2}.

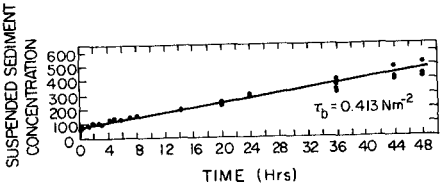

Fig. 4. Suspended Sediment Concentration, C, against Time, t, for a Uniform Bed using Kaolinite in Distilled Water at τ_b = 0.413 Nm^{-2}.

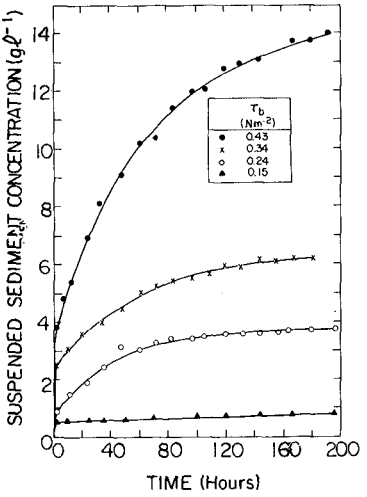

Fig. 5. Suspended Sediment Concentration, C, against Time, t, for a Deposited (Stratified) Bed using Kaolinite in Salt Water at Four Values of τ_b.

Series 2 Experiments

In these experiments, kaolinite in distilled water as well as in salt water was used in the annular flume (16). Stratified beds were prepared in a manner similar to that noted under Series 1 experiments. An example of the results from tests using distilled water is shown in Fig. 5. At the beginning of each test, an almost instantaneous and significant rise in the suspended sediment concentration was noted. It was concluded that this was partly due to mass erosion resulting from a sudden movement of the flume at start. In later experimental series, this problem was obviated by starting the flume more slowly. After nearly 200 hours, whether or not the suspended sediment concentration, C, attained a constant value is observed to have been dependent upon the magnitude of τ_b. In the test with τ_b = 0.15 Nm^{-2}, C became constant within the first few hours. In the test with τ_b = 0.24 Nm^{-2}, C became constant after approximately 140 hours. In the test with τ_b = 0.34 Nm^{-2}, C appears to have approached a constant value after 180 hours. Finally, in the test with τ_b = 0.43 Nm^{-2}, C was increasing with time at a slow rate even after 190 hours. In general, at any instant after test initiation both the magnitude of C and dC/dt (and therefore ε) are observed to vary with τ_b.

Selecting C_s as the asymptotic value of C which was close to the value of C extrapolated to 200 hours, it was found that most of the time-concentration data, after accounting approximately for the mass erosion effect, agreed with the following relationship:

$$C = C_s(1 - e^{-\beta t}) \tag{3}$$

where β is an empirical coefficient whose value was found to be within a relatively narrow range of 0.013 to 0.028 hr^{-1}, particularly for comparatively high values of τ_b. An example of the agreement between Eq. 3 and the experimental values is shown in Fig. 6 for the tests corresponding to Fig. 5. Tests using kaolinite in salt water confirmed these trends. Further tests using a natural mud in salt water also agreed with Eq. 3. The clay mineral constituents of this mud were kaolinite, montmorillonite and illite.

The observed variation of the asymptotic value of C with τ_b may be examined qualitatively with reference to the descriptive relationship between the shear strength, τ_s, and the depth z below the bed surface shown in Fig. 7. As confirmed by experimental evidence presented later, τ_s in a stratified bed increases with z, beginning with a small but finite value close to the surface. This increase is more significant in the top layer of perhaps a few millimeter thickness than in lower layers, where, infact, τ_s may approach a constant value or, atleast, the variation of τ_s with z becomes relatively small. For a given sediment-fluid mixture, the nature of the $\tau_s(z)$ distribution is determined by the flow conditions during deposition, the degree of consolidation of the bed and thixotropic rearrangement of the interparticle floc network (7). Given such a distribution of $\tau_s(z)$, under a bed shear stress τ_{bA} the bed will erode to a depth z_A at which point $\tau_{bA} = \tau_{sA}$. The rate of erosion therefore depends on the "excess" shear stress $\tau_b - \tau_s$. Similarly, if the shear stress is

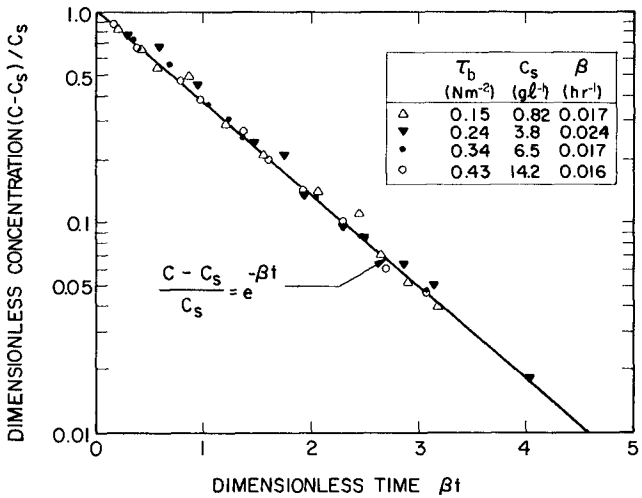

Fig. 6. Normalized Concentration, C_S-C(t)/C_S, against Normalized Time, βt. Equation 3 is Compared with Data from Tests Corresponding to Fig. 5.

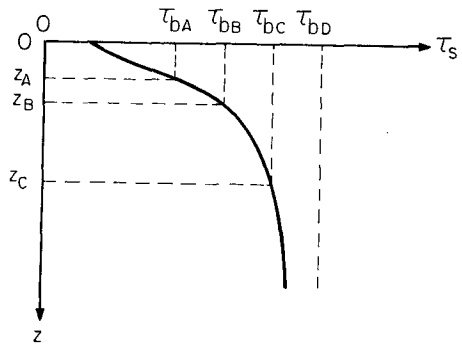

Fig. 7. Descriptive Relationship between Cohesive Bed Shear Strength with Respect to Erosion, τ_S, and Depth, z, below Bed Surface.

τ_{bB} or τ_{bC}, the corresponding depths of erosion will be z_B or z_C. Integrating Eq. 2 yields

$$C = \frac{1}{h} \int_0^z \rho(z)dz \qquad (4)$$

provided h is assumed to be constant. Since ρ also increases with z, the difference between C_C and C_B will be much greater than the difference between C_B and C_A. This aspect is further noted later. Finally, for a shear stress τ_{bD}, the bed will continue to erode indefinitely, atleast in principle, since the condition $\tau_{bD} = \tau_{sD}$ can not be attained. In a test conducted by Krone (4) using a silty-clay from San Francisco Bay, erosion continued even after 500 hours.

Series 3 Experiments

These experiments were conducted in the annular flume using kaolinite in salt water. A schematic description of the manner in which the bed shear stress was varied with time during the tests is shown in Fig. 8. Such a variation results in three phases of sediment transport. Phase I is a mixing stage in which a sediment of concentration C_0 is mixed at a shear stress τ_m for a period T_m. The shear stress τ_m must be large enough to prevent any deposition of the suspended material. In Phase II the flow is reduced to yield a comparatively lower shear stress τ_{d1}, which is maintained for a duration T_{d1}. Deposition will occur in this phase. Given a sufficient duration T_{d1} and shear stress $\tau_{d1} < \tau_{bmin}$, the entire amount of sediment will deposit and the flow will be clarified. On the other hand, if $\tau_{d1} > \tau_{bmin}$, a certain fraction C_{eq}^* of C_0 will remain in suspension indefinitely (6). In the latter case, a second lowering of the shear stress to $\tau_{d2} (< \tau_{bmin})$ for a period T_{d2} will clarify the suspension. The last sequence in Phase II is a period T_{dc} with no flow. During this period the remaining small fraction of the sediment in suspension will deposit rapidly and the bed will consolidate. Phases I and II together define the pre-erosion stress history of the bed, which is characterized by C_0, τ_m, τ_{d1}, τ_{d2}, T_m, T_{d1}, T_{d2} and T_{dc}. In order to investigate the influence of consolidation on the rate of erosion, T_{dc} was varied while maintaining all other parameters nearly constant.

Resuspension will occur in Phase III in which a series of shear stresses τ_{b1}, τ_{b2} etc., of increasing magnitudes are applied over corresponding durations (time-steps) T_1, T_2 and so on. In choosing the magnitudes of τ_{b1}, τ_{b2} etc., it is convenient to select the normalized differential shear stress $\Delta\hat{\tau}_{bi} = (\tau_{bi+1} - \tau_{bi})/\tau_{bi}$, where i = 1, 2, etc., as an experimental parameter. The selection of $\Delta\hat{\tau}_{bi}$ and the corresponding period T_i is an important factor in experimental design (11).

As an example of the results, the time-concentration relationship obtained during a test is shown in Fig. 9. Values of the various parameters selected for the test are given in the figure. The shear stress τ_{d1}, was less than τ_{bmin} (= 0.15 Nm^{-2}). During each time-step

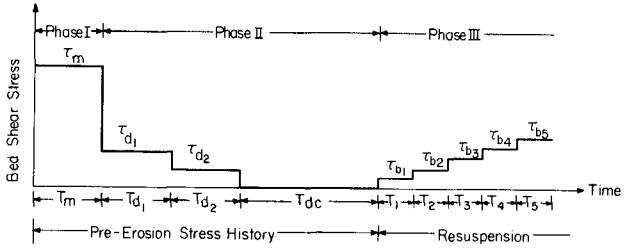

Fig. 8. Schematic Representation of the Variation of Bed Shear Stress, τ_b, during Bed Preparation and Resuspension Tests in Experimental Series 3 and 4.

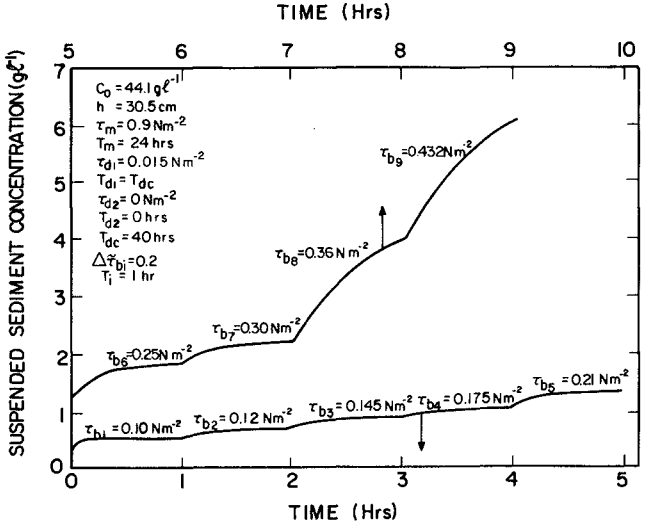

Fig. 9. Variation of Suspended Sediment Concentration, C, with Time, t, during a Test using Kaolinite in Salt Water Following the Approach Schematized in Fig. 8.

i, the rate of erosion decreased from an initially high value, as noted in the previous two experimental series. This trend was found to be qualitatively similar to that suggested by Eq. 3. An important difference between the profiles in steps i = 1 through 7 and steps i = 8, 9 is that in the former (which will be referred to as Type I), the concentration appears to have approached a constant magnitude, whereas in the latter (Type II), the concentration did not attain a constant value at the end of the time-step. This difference between Type I and Type II profiles is also apparent from Fig. 10, in which $C(T_i)$, the concentration at the end of the time-step, i, is plotted against τ_{bi}, for consolidation times T_{dc} = 24, 40 and 135 hrs. In general it appears to be possible to represent the $C(T_i)$ - τ_{bi} curve by two straight lines meeting at a point where $\tau_{bi} = \tau_{ch}$, a characteristic value of the bed shear stress (11). When $\tau_{bi} > \tau_{ch}$, $C(T_i)$ increases more rapidly with τ_{bi} than in the case when $\tau_{bi} < \tau_{ch}$. The value τ_{ch} also increases with T_{dc}. Similar trends can be discerned from the data presented in Fig. 5 as well as from the results of a number of previous investigations (2). The significance of these trends can be recognized with reference to Fig. 7. In qualitative terms, τ_{bA} and τ_{bB} are both less than τ_{ch}, while τ_{bC} and τ_{bD} are greater than τ_{ch}. The value τ_{ch} lies somewhere between τ_{bB} and τ_{bC}, and the corresponding depth of erosion is between z_B and z_C. Since the increase in the shear strength, τ_s, with z is more significant in the range of $\tau_b < \tau_{ch}$ in comparison with the range of $\tau_b > \tau_{ch}$, if erosion is allowed to proceed for a constant duration T_i under a given bed shear stress, the amount of bed scour will be much greater when $\tau_b > \tau_{ch}$ than when $\tau_b < \tau_{ch}$. Consequently, the rate of change of $C(T_i)$ with τ_b will be much more pronounced in the range of $\tau_b > \tau_{ch}$ in comparison with the range of $\tau_b < \tau_{ch}$.

The above explanation can be used to examine the difference between Type I and II time-concentration profiles in Fig. 9. As long as the condition represented by the shear stress τ_{b0} in Fig. 7 is not attained, i.e. as long as the shear strength $\tau_s < \tau_b$ at some depth z, it is possible to obtain Type I profiles. This may be achieved by increasing T_i, i.e. the time allowed for erosion under a constant bed shear stress. Type II profiles result because T_i is insufficient for the bed to scour to a depth where $\tau_b = \tau_s$.

For Type I profiles, since the condition $\tau_b = \tau_s$ is attained, the depth-variation of τ_s can be determined, provided the depth z of erosion at the end of each time-step i (when $\tau_b = \tau_s$ for that time-step) is known. This can be done using Eq. 2 if $\rho(z)$ is known. The variation of the bed density with depth at the end of Phase II, i.e. just prior to resuspension, was determined for various periods, T_{dc}, with the help of a specially designed 2.5 cm diameter metal tube in which the bed core samples were frozen in situ, using a mixture of alcohol and dry ice (11). These tests were carried out in a separate series in which conditions in Phases I and II were identical to those for the resuspension tests. Figs. 11a,b present the density profile and the corresponding variation of τ_s with depth for the test shown in Fig. 9. The $\tau_s(z)$ distribution is qualitatively similar to the description of Fig. 7. The value of τ_s at z = 0 corresponds to the minimum value of the bed shear stress required to initiate erosion in

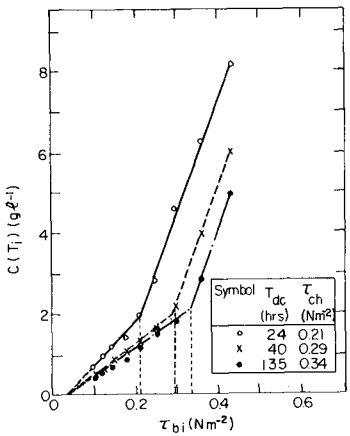

Fig. 10. Concentration, $C(T_j)$, against Corresponding Bed Shear Stress, τ_{bj}, for Three Tests using Kaolinite in Salt Water at Three Values of Consolidation Time, T_{dc} (9).

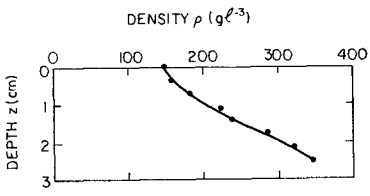

Fig. 11a). Variation of Bed Density, ρ, with Depth, z, in Test Corresponding to Fig. 9.

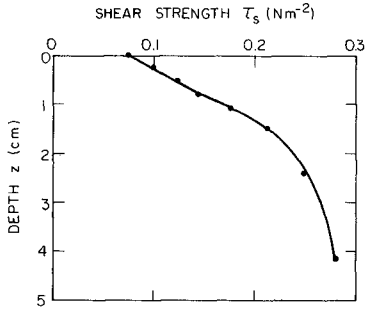

Fig. 11b). Variation of Bed Shear Strength, τ_s, with Depth, z, in Test Corresponding to Fig. 9.

the flume. Indeed as noted further in the following, τ_s obtained in this way is, in general, also equal to the critical shear stress for erosion at the corresponding depth.

Series 4 Experiments

These experiments were similar to those conducted under Series 3. Kaolinite in tap water was used in the recirculating flume (1). Test characterizing parameters were: C_o = 21.7-24.1 gl^{-1}, h = 23 cm, τ_m = 0.46 Nm^{-2}, T_m = 4 hr, τ_{d1} = 0.026 Nm^{-2} (which was less than τ_{bmin} = 0.18 Nm^{-2}), T_{d1} = 12 hr, τ_{d2} = 0 Nm^{-2}, T_{d2} = 1 hr, $\Delta\hat{\tau}_{bi}$ = 0.52 and T_i = 1 hr. Nine tests with values of T_{dc} = 2, 5, 11, 24, 48, 72, 96, 144 and 240 hr were conducted.

Figures 12a,b are normalized plots of bed density variation with depth. After T_{dc} = 48 hr, the variation seems to conform to the dimensionless relationship (1, 9):

$$\frac{\rho}{\bar{\rho}} = \zeta \left(\frac{z'}{H}\right)^{-\xi} \tag{5}$$

where z' = H-z, H = bed thickness, $\bar{\rho}$ = value of ρ averaged over H, ζ = 0.794 and ξ = 0.288. It is observed that H decreased and $\bar{\rho}$ increased with increasing T_{dc}. Equation 5 is in agreement with the reanalyzed data of Owen (10) and of Thorn and Parsons (15) for four natural muds which gave ζ = 0.660 and ξ = 0.347 (1).

The time-concentration data were found to exhibit a trend which was qualitatively similar to that shown in Fig. 9. These data were analyzed as follows: 1) it was assumed, as noted before, that at the end of time-step i of the Type I profile, the bed shear stress $\tau_b = \tau_c = \tau_s$, where τ_c is defined as the critical shear stress for erosion. 2) using this assumption the variation of τ_c with z was obtained as in Fig. 11b. 3) a relationship between the rate of erosion, ε, and the normalized excess shear stress $(\tau_b-\tau_c)/\tau_c$ was empirically derived from the time-concentration variation for each time-step of the Type I profiles. In obtaining this relationship, ε was calculated using Eq. 1 for each value of dC/dt. The corresponding value of τ_c was obtained using Eq. 2 together with the $\rho(z)$ distribution (Figs. 12a,b or Eq. 5 for T_{dc} > 48 hr) and $\tau_c(z)$ distribution (e.g. Fig. 11b). Finally, 4) it was assumed that the rate expression was applicable over the entire depth of erosion. The time-concentration data of Type II profiles were then used, together with representative depth-mean values of the coefficients (ε_o and α as noted below) of the rate expression based on Type I profiles, to determine the variation of τ_c with depth z below the depth where this information could not be obtained from Type I profiles. The erosion rate expression was found to be:

$$\frac{\varepsilon}{\varepsilon_o} = \exp\left[\alpha \frac{\tau_b-\tau_c}{\tau_c}\right] \tag{6}$$

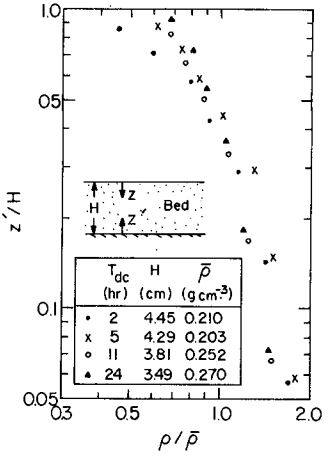

Fig. 12a). Normalized Bed Density, $\rho/\bar{\rho}$, against Normalized Depth, z'/H, for Kaolinite in Tap Water with T_{dc} < 48 hr (9).

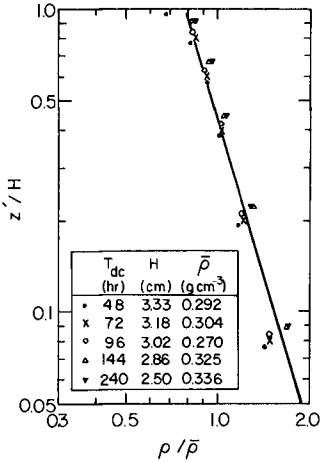

Fig. 12b). Normalized Bed Density, $\rho/\bar{\rho}$, against Normalized Depth, z'/H, for Kaolinite in Tap Water with $T_{dc} \geq 48$ hr (9).

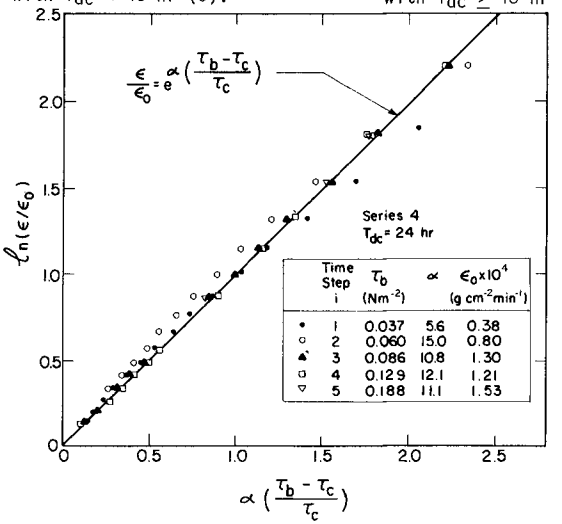

Fig. 13. ϵ/ϵ_0 against $\alpha(\tau_b-\tau_c)/\tau_c$ for a Test using Kaolinite in Tap Water with T_{dc} = 24 hr.

where ε_o and α are empirical coefficients. In Eq. 6, τ_c is a function z and, therefore varies with time t. With increasing time, τ_c increases and approaches τ_b in such a manner that the ratio $(\tau_b-\tau_c)/\tau_c$ decreases and, therefore, ε decreases. As an example, in Fig. 13 Eq. 6 has been compared with test results corresponding to T_{dc} = 24 hr. The value of α ranged from 5.6 to 15.0 and ε_o from 0.38×10^{-4} to 1.53×10^{-4} g cm^{-2} min^{-1}. Similar results from tests with T_{dc} = 48 and 240 hr are shown in Figs. 14 and 15. In Fig. 16, reanalyzed data from the test shown in Fig. 9 under Series 3 experiments are plotted in the same manner. In this case, α ranged from 5.5 to 8.4, and ε_o from 0.04×10^{-4} to 0.30×10^{-4} g cm^{-2} min^{-1}. It was, in general, found that in each test, ε_o and α appeared to vary somewhat with the time-step, and therefore with depth z below the bed surface, in a systematic manner. Further investigations are required for elucidating the precise nature of the dependence of ε_o and α on z. In general it was noted that ε_o and α became nearly independent of z for depths greater than a few millimeters. These two coefficients were also found to be independent of consolidation time, T_{dc}. In Fig. 17, the depth-average value $\bar{\varepsilon}_o$ of ε_o from each test is plotted against the corresponding T_{dc}. Results from Series 3 (kaolinite in salt water) as well as Series 4 (kaolinite in tap water) are included. In Fig. 18 a similar plot is given for α. Overall mean values of ε_o and α are: 7.9×10^{-5} g cm^{-2} min^{-1} and 9.3, respectively, for kaolinite in tap water (Series 4) and 4.0×10^{-5} g cm^{-2} min^{-1} and 5.9, respectively, for kaolinite in salt water (Series 3). The mean ε_o and α for kaolinite in tap water are higher than for kaolinite in salt water. These differences imply that kaolinite is resuspended with greater facility in tap water than in salt water. This trend appears to be consistent with the flocculation characteristics of kaolinite in the two fluids (5, 6, 9).

As an example of the variation of τ_c with depth z, Fig. 19 shows results from four tests with T_{dc} = 2, 11, 48 and 144 hr. In general, τ_c increased with T_{dc} for all $z > 0$. The value of τ_c remained practically invariant at the surface. This observation is in agreement with a similar observation made by Partheniades (13). As a result of the exponential form of Eq. 6, the significance of the variation of τ_c with T_{dc} is that the rate of erosion, ε, decreases measurably with increasing value of T_{dc}.

The form of Eq. 6 has been predicted previously from a reinterpretation of the rate process theory of chemical reactions (1, 3, 12). This theory involves the activation energy concept according to which a "threshold" energy barrier must be crossed for the conversion of reactants to products. As Paaswell (12) has noted, Eq. 6 makes possible the understanding of erosion as an internal energy/external energy system, where ε is a measure of the work done on the system (reflected in τ_b) and τ_c, α and ε_o represent measures of internal energy, and therefore the resistance to the erosion of the deposit.

CONCLUSIONS

1. The rate of surface erosion of stratified, deposited beds continuously decreases with time and can even become zero as the

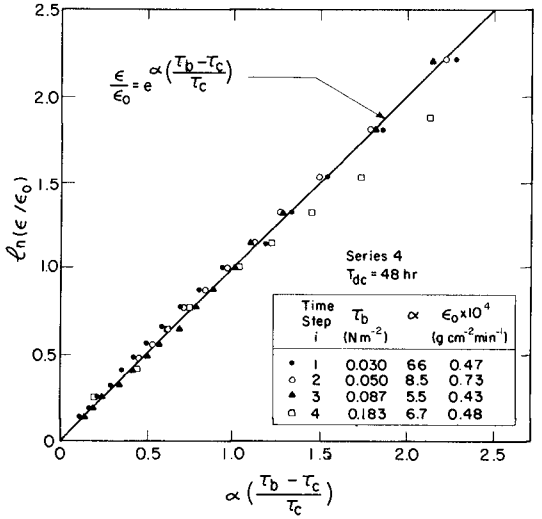

Fig. 14. ϵ/ϵ_0 against $\alpha(\tau_b-\tau_c)/\tau_c$ for a Test using Kaolinite in Tap Water with T_{dc} = 48 hr.

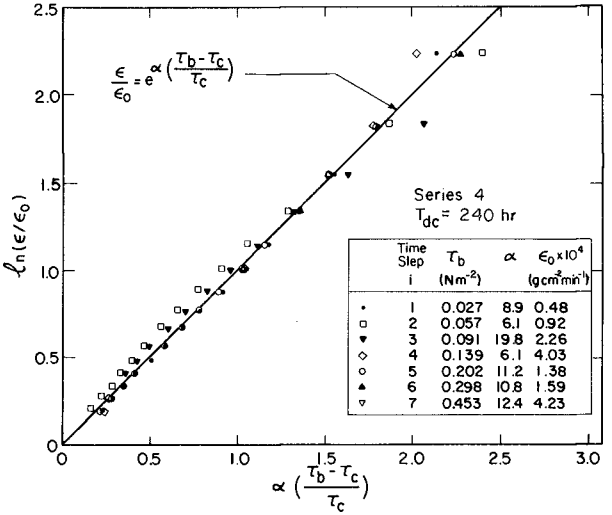

Fig. 15. ϵ/ϵ_0 against $\alpha(\tau_b-\tau_c)/\tau_c$ for a Test using Kaolinite in Tap Water with T_{dc} = 240 hr.

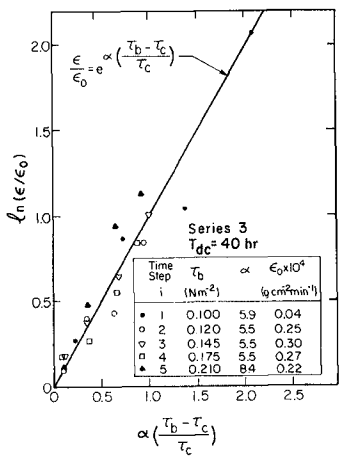

Fig. 16. $\varepsilon/\varepsilon_0$ against $\alpha(\tau_b-\tau_c)/\tau_c$ for a Test Corresponding to Fig. 9.

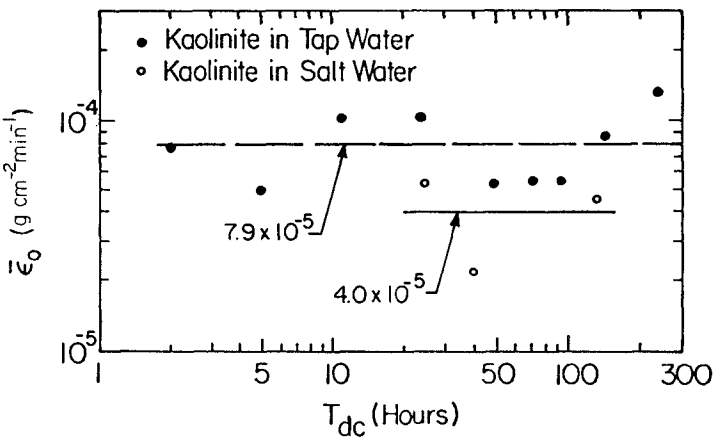

Fig. 17. $\bar{\varepsilon}_0$ against T_{dc} from Tests with Kaolinite in Salt Water and with Tap Water (9).

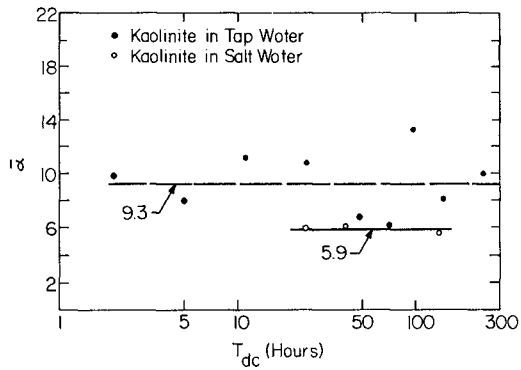

Fig. 18. $\bar{\alpha}$ against T_{dc} from Tests with Kaolinite in Salt Water and with Tap Water (9).

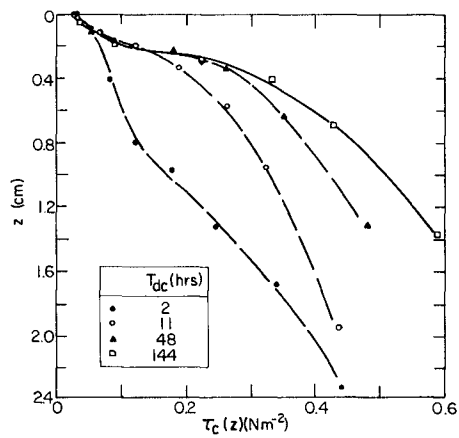

Fig. 19. Variation of τ_c with z from Tests using Kaolinite in Tap Water with T_{dc} = 2, 11, 48 and 144 hr.

depth of erosion increases. On the other hand, the erosion rate of uniform beds remains practically invariant.

2. The decrease in the erosion rate of stratified beds occurs because the cohesive shear strength with respect to erosion of the bed increases with depth. Ouring erosion flocs are detached from the bed and entrained, but redeposition of the entrained sediment does not occur. Erosion is arrested at a depth where the bed shear stress, τ_b, equals the bed shear strength. This value of τ_b is equal to the critical shear stress, τ_c, of the bed at that depth.

3. An expression for the rate of surface erosion is found. The rate varies exponentially with the normalized excess shear stress, $(\tau_b-\tau_c)/\tau_c$.

4. The critical shear stress in general increases with depth below the initial bed surface and also increases with bed consolidation time. As a result the rate of erosion decreases with increasing consolidation time.

ACKNOWLEDGEMENT

Support provided by the National Science Foundation (Grant No. GK-31259) and the Environmental Protection Agency (Grant No. R80668401D) is sincerely acknowledged.

REFERENCES

1. Dixit, J. G., "Resuspension Potential of Deposited Kaolinite Beds," M.S. Thesis, University of Florida, Gainesville, FL, 1982.

2. Hunt, S. D., "A Comparative Review of Laboratory Data on Erosion of Cohesive Sediment Beds," Report UFL/COEL-81/7, Coastal and Oceanographic Engineering Department, University of Florida, Gainesville, FL, 1981.

3. Kelly, W. E., and Gularte, R. C., "Erosion Resistance of Cohesive Soils," Journal of the Hydraulics Division, ASCE, Vol. 1D7, No. HY10, Oct., 1981, pp. 1211-1224.

4. Krone, R. B., "Flume Studies of the Transport of Sediment in Estuarial Processes," Final Report, Hydraulic Engineering Laboratory and Sanitary Engineering Research Laboratory, University of California, Berkeley, CA, June, 1962.

5. Mehta, A. J., "Depositional Behavior of Cohesive Sediments," Ph.D. Thesis, University of Florida, Gainesville, FL, 1973.

6. Mehta, A. J., and Partheniades, E., "An Investigation of the Depositional Properties of Flocculated Fine Sediments," Journal of Hydraulic Research, Vol. 12, No. 4, Dec., 1975, pp. 1037-1D57.

7. Mehta, A. J., and Partheniades, E., "Kaolinite Resuspension Properties," Journal of the Hydraulics Division, ASCE, Vol. 105, No. HY4, April, 1979, pp. 409-416.

8. Mehta, A. J., "Review of Erosion Function for Cohesive Sediment Beds," Proceedings of the First Indian Conference on Ocean Engineering, Vol. I, Indian Institute of Technology, Madras, India, Feb., 1981, pp. 122-130.

9. Mehta, A. J., Parchure, T. M., Dixit, J. G., and Ariathurai, R., "Resuspension Potential of Deposited Cohesive Sediment Beds," Estuarine Comparisons, V. S. Kennedy ed., Academic Press, New York, NY, 1982, pp. 591-609.

10. Owen, M. W., "Erosion of Avonmouth Mud," Report INT-150, Hydraulic Research Station, Wallingford, United Kingdom, Sept., 1975.

11. Parchure, T. M., "Effect of Bed Shear Stress on the Erosional Characteristics of Kaolinite," M.S. Thesis, University of Florida, Gainesville, FL, 1980.

12. Paaswell, R. E., "Causes and Mechanisms of Cohesive Soil Erosion: the State of the Art," Soil Erosion: Causes and Mechanisms, Prevention and Control, National Research Council ed., Highway Research Board, Special Report 135, Washington, D.C., Jan, 1973, pp. 52-74.

13. Partheniades, E., "Erosion and Deposition of Cohesive Soils," Journal of the Hydraulics Division, ASCE, Vol. 91, No. HY1, Jan., 1965, pp. 105-139.

14. Partheniades, E., "Erosion and Deposition of Cohesive Materials," River Mechanics, H. W. Shen ed., Vol. II, Ch. 25, H. W. Shen Publisher, Fort Collins, CO, 1971.

15. Thorn, M. F. C., and Parsons, J. G., "Erosion of Cohesive Sediments in Estuaries: An Engineering Guide," Proceedings of the Third International Symposium on Dredging Technology, BHRA, Paper F1, Bordeaux, France, March, 1980.

16. Yeh, H. Y., "Resuspension Properties of Flow Deposited Cohesive Sediment Beds," M.S. Thesis, University of Florida, Gainesville, FL, 1979.

BED LOAD TRANSPORT OF FINE SAND BY LAMINAR AND TURBULENT FLOW

by

Anthony J.Grass* and Ragaei N.M.Ayoub**

ABSTRACT

An experimental study is described in which the rate of transport of fine sand over a flat bed was measured as a function of the shear stress exerted on the bed by both laminar and turbulent flows, for a range of water temperatures. The results confirm the great sensitivity of the transport rate to changes in both shear stress and temperature over the test range. The hypothesis is propounded that in certain specified circumstances, the net rate of local bed load transport generated by an arbitrary unsteady flow, can be estimated by integration, using the measured steady laminar flow transport relationships in conjunction with the time history or probability distribution of the fluctuating bed shear stress. The concept has been tested using the measured data with encouraging results. It is suggested that this method of linking the characteristics of the near bed flow field to the local induced rates of sediment transport could be productively applied in a range of studies including the initiation and development of bed sand ripples by the action of various combinations of waves and steady currents.

1. INTRODUCTION

Over the past decade, considerable progress has been made in developing instrumentation such as the laser doppler anemometer for flow velocity measurement and also numerical mathematical modelling techniques for predicting flow behaviour. These advances coupled with significant improvements in digital data processing methods, have led to a rapidly expanding knowledge and understanding of the complex turbulence and other near bed flow charactertistics in both steady and unsteady boundary layers and separated flows. (See for example Grass(1971,1982), Kemp and Simons (1982), and Etheridge and Kemp (1979)).

As in the past, progress in sediment transport research has lagged very much behind due to the formidible theoretical and experimental difficulties. In order to fully exploit the new fluid mechanics information in the study of coastal and other sediment processes, including for example, the formation of bed ripples by

* Lecturer, Department of Civil and Municipal Engineering, University College London, England
** Senior Engineer, Ministry of Electricity and Water, Kuwait

waves and currents, it will be necessary to establish improved links between the measured or computed characteristics of the fluctuating driving flow and the corresponding response of the bed sediment.

A primary objective of the present investigation was to derive one such linking relationship for the case of bed load transport of fine grained sand.

2. BED LOAD SEDIMENT TRANSPORT

Consider an arbitrary, unsteady fluid flow inducing transport on a flat bed of non-cohesive sediment. Then, for a particular fluid viscosity, physical reasoning suggests that there will be a close correlation between the instantaneous flow velocity immediately adjacent to the bed and the simultaneous local shear stress acting on the bed and hence the induced instantaneous rate of local bed load sediment transport. Experimental evidence supporting this postulation has been previously presented and discussed by Grass (1970,1971) based on photographically recorded observations of the response of fine bed sand to the rapid fluctuations in bed shear stress generated by a turbulent boundary layer flow.

For fine grained sediment producing an hydraulically smooth boundary condition in typical water flows, the fluid forces are transferred to the bed sediment primarily by viscous shear. The hypothesis is advanced that under these conditions the instantaneous local bed load transport rate produced by a particular instantaneous value of viscous bed shear stress, τ, can be represented by the transport rate, $q_{s\ell}(\tau)$, induced by a steady laminar flow with the same bed shear stress and fluid viscosity.

In a situation where the fluctuating bed shear stress is a known function of time, t, as for example in the case of an oscillatory laminar boundary layer, then the net mean sediment transport rate, q_{st}, over a time interval T, can be calculated using the following equation:

$$q_{st} = \frac{1}{T}\int_{o}^{T} q_{s\ell}(t)dt \qquad (1)$$

If however, the fluctuating bed shear stress is random and unpredictable as in the case of turbulent boundary layer flows induced by a random wave spectrum, then the following alternative equation can be used to estimate the net be load transport rate:

$$q_{st} = \int_{\tau_{min}}^{\tau_{max}} q_{s\ell}(\tau)p(\tau)d\tau \qquad (2)$$

where $p(\tau)$ is the probability density function of the fluctuating bed shear stress τ.

The hypothesis expressed in equations (1) and (2) was tested in the present investigation by comparing the measured values of bed load sediment transport produced by a steady unidirectional turbulent boundary layer flow with the corresponding values calculated using equation (2) substituting $q_{s\ell}(\tau)$ values provided by corresponding measurements in a steady laminar flow. This procedure circumvents severe difficulties in attempting to measure the instantaneous fluctuations in bed load sediment transport rate directly.

3. EXPERIMENTAL TECHNIQUES

A fine 140 micron quartz sand from the Mersey Estuary was used in the present experiments as in the earlier study of initial movement of bed sand grains by Grass (1970). The bed load sediment transport rate was measured as a function of mean bed shear stress and water temperature ($4^0C, 17^0C, 30^0C$) under laminar and fluctuating turbulent flow conditions. Novel experimental apparatus and techniques were employed which have been described in detail by Ayoub (1977). These tests broke new ground in that they were designed to obtain strictly flat bed transport rates for bed shear stress values ranging up to 25 times the critical shear stress for initial sediment movement. This was achieved by measuring over short sample times prior to the formation of flow disturbing sand ripples.

The laminar flow experiments were carried out using the specially designed apparatus illustrated in Figure 1. A low Reynolds number, high bed shear stress laminar flow was produced between two closely spaced parallel plates 2 millimetres apart and 1 metre long and 0.4 metres wide. The carefully levelled flat sand bed was contained in a recessed pit 0.4 metres long and 0.25 metres wide located at the downstream end of the lower plate. Water was supplied to the test section from a constant head tank and the bed shear stress was determined by monitoring the streamwise pressure gradient. The sediment transport rate was measured by collecting and weighing sand samples over a know time interval using the sliding box arrangement shown in Figure 1. Very short and accurately measured sampling times were achieved using a sliding plate inlet valve and an automatic timing device attached to the sampling box. Sampling times were reduced with increasing bed shear stress down to periods as low as 1 second in the case of the higher bed stress values in order to avoidsignificant erosion of the sand bed surface. Repeated tests at the same bed shear stress indicated good reproducibility of the individual measured values of bed load sediment transport rate.

The turbulent flow was generated on a flat plate 1.5 metres long and 0.3 metres wide which was supported on a carriage and towed through still water as shown in figure 2. A sand bed 0.4 metres long and 0.2 metres wide was located at the downstream end of the plate.The plate boundary layer was tripped by means of a wire close to the leading edge and achieved a steady stable state very soon after the plate had been rapidly accelerated to its constant terminal velocity. Once again, the bed load sand transport rate was measured by weighing the sand collected in a specially partitioned box located under the downstream end of the sand bed.Differences in the weights of two sand samples collected from two experimental runs in which the bed plate

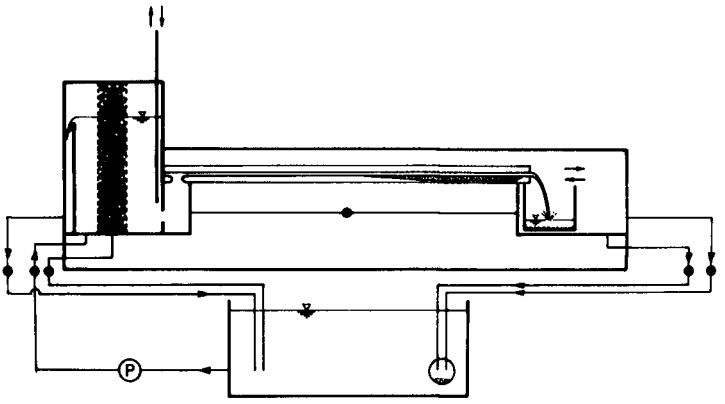

FIGURE 1. Laminar flow channel used to measure bed load sediment transport induced by a laminar boundary layer formed between closely spaced parallel plates.

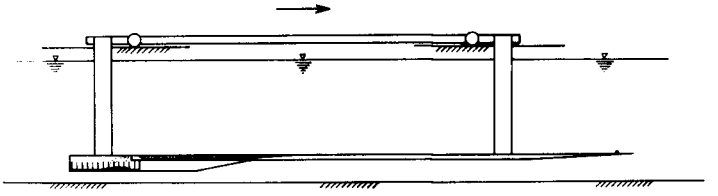

FIGURE 2. Apparatus used to measure bed load sediment transport induced by a turbulent boundary layer formed on a flat plate towed through still water.

underwent identical acceleration and deceleration phases but travelled different known intermediate distances at a common constant velocity, were used in these bed load calculations in order to eliminate end effects. Sampling times, which were simply and accurately determined from the travel distance and the known carriage velocity, were again kept very short (down to 1.5 seconds for the highest bed shear stress) in order to avoid bed erosion and also the formation of nascent sand ripples on the bed surface. Mean bed shear stresses were obtained from velocity profile measurements using a carefully calibrated hot film anemometer. This instrument was also used to record the velocity fluctuations in the viscous sublayer at the downstream end of the bed plate. The probability density functions of the fluctuating bed shear stress were calculated from these measurements. Tests were repeated four times for each of the lower values of mean bed shear stress and twice for the remainder in order to obtain closely reproducible values of the average bed load transport rates.

4. RESULTS AND DISCUSSION

The measured sediment transport rates are shown plotted in terms of the relevant non-dimensional variables in Figure 3 in which u_* is the bed shear velocity, d is the sand diameter, ρ_s and ρ are the sediment and fluid densities respectively. The slope of the fitted linear regression lines indicates that over the central experimental range the bed transport rate varies as approximately the fourth power of the bed shear stress for both the laminar and turbulent flows.

Consistent with the results obtained by Taylor and Vanoni (1972), the sediment transport rate also shows considerable sensitivity to changes in bed particle Reynolds number, R_*. Between 4^0C and 30^0C the water viscosity, ν, is halved which gives rise to a threefold increase in the bed load transport rate.

It is interesting to note that for a particular constant low value of bed transport rate, defining the initial movement stage of the bed particles, the optimized data correlation presented in Figure 3 indicates that Shields parameter, τ_{c*}, will be proportional to $R_*^{-0.64}$. This result is in good agreement with the criteria for initial motion of fine bed sand previously suggested by Grass(1970) for the same range of bed particle Reynolds numbers.

The use of equation (2) in calculating the net mean rate of bed load sediment transport from the laminar flow transport function and the probability density function of the fluctuating bed shear stress produced by a steady turbulent boundary layer flow, is illustrated in Figure 4. The particular probability distribution shown in Figure 4 and used throughout the present study, is a smoothed curve fitted to data measured in the present tests and in experiments reported by Grass (1970), Ecklemann and Reichardt (1972), and by Blinco and Simons (1974). When the various probability distributions which cover a wide range of flow Reynolds numbers and different types of steady unidirectional flow, are plotted in standard form in terms of the fluctuations in bed shear stress scaled by their standard deviation about the mean, it is found that they can be accurately summarised by a single unique curve. This takes the form of the positive skew

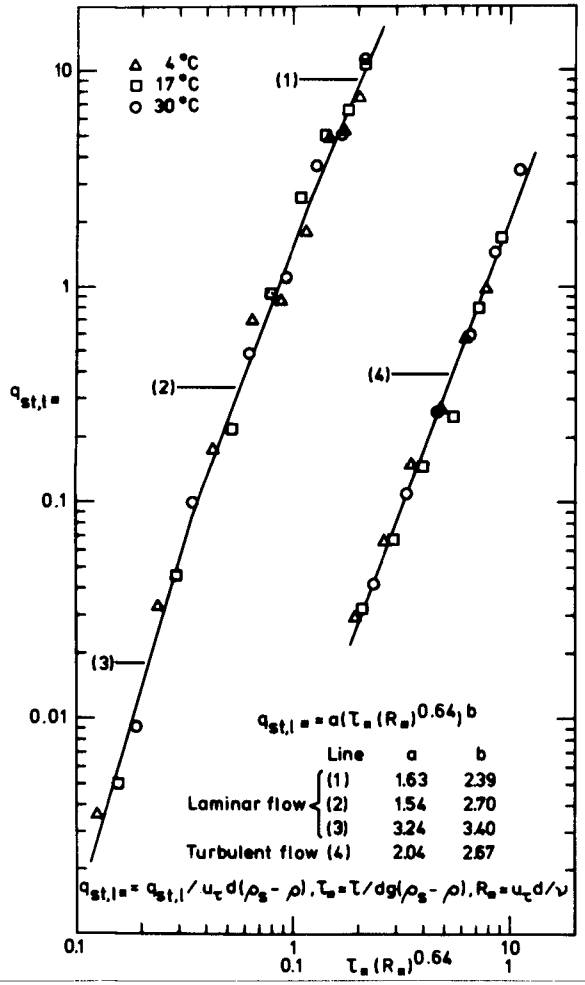

FIGURE 3. Optimized correlation of measured bed load sediment transport rates induced by laminar and turbulent flows.

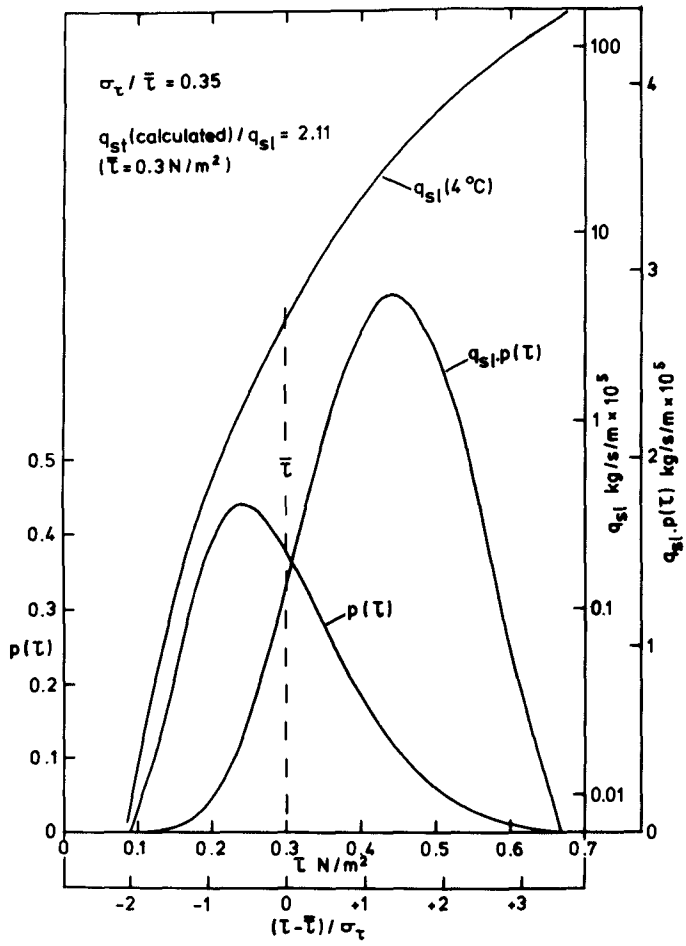

FIGURE 4. Sample illustration of the method of calculating bed load transport rate produced by a turbulent flow, q_{st}, at a particular mean bed shear stress $\bar{\tau}$ of 0.3N/m^2, from the laminar flow transport relationship, q_{sl}, and the probability distribution, $p(\tau)$, of the fluctuating bed shear stress, τ, induced by the turbulent flow.

distribution reproduced in Figure 4.

The calculation illustrated in Figure 4 is for a mean bed shear stress of $0.3N/m^2$. As can be seen, the fluctuations in instantaneous shear stress range between approximately $0.1N/m^2$ and $0.7N/m^2$. The corresponding induced rate of instantaneous bed load transport increases by four orders of magnitude over the shear stress range. For the lower instantaneous shear stresses there is negligible transport over the bed surface whilst the higher shear stress fluctuations produce very large instantaneous transport rates. This is in close accord with the evidence from direct observations of the fluctuating sand transport behaviour reported by Grass (1970).

The strong non-linearity in the sediment transport rate with increasing bed shear stress, produces maximum contributions to the next bed load transport rate at instantaneous shear stress values greatly in excess of the mean shear stress of $0.3N/m^2$, in spite ofthe rapid reduction in $p(\tau)$, as indicated by the location of the peak in the $q_{sl}.p(\tau)$ curve. In the particular example presented in figure 4, the calculated value of net mean sediment transport rate produced by the turbulent boundary layer flow with a mean applied bed shear of 0.3 N/m^2, is in excess of twice the corresponding laminar flow transport rate with the same bed shear stress.

A comparison between the experimental and calculated equation (2) values of the ratio between the turbulent and laminar flow transport rates is shown in figure 5. The experimental results are seen to lie satisfactorily in a zone bounded by the values calculated using bed shear stress standard deviation to mean bed shear stress ratios, $\sigma/\bar{\tau}$ of 0.25 and 0.35. These $\sigma/\bar{\tau}$, magnitudes correspond to the range of values measured in the present tests with both fixed and mobile beds and also to the measurements reported by Mitchell and Hanratty (1966) and by Eckelmann (1974).

The relatively rapid decreasing trend in the magnitude of the transport ratio from approximately 2 to 1.3 over the bed shear stress range from $0.3N/m^2$ to $0.9N/m^2$, the approximate observed the threshold shear stress for intial sediment suspension, suggests a possible decrease in the effective $\sigma/\bar{\tau}$ ratio with increaing flow Reynolds number. This is consistent with trends in data obtained in the present investigation and by Laufer (1951) and by Blinco and Simons (1974).

The rapid increase in the transport ratio at the lower end of the bed shear stress range indicated in Figure 5 is due to the fact that as the shear stress approaches the critical value for intial sand grain movement under laminar flow conditions, the laminar flow transport rate tends to zero. However, the corresponding transport rate, at thesame mean bed shear stress, under turbulent flow conditions remains finite and the transport ratio therefore increases asymptotically to infinity.

The detailed physics and charactistics of the two phase flow in the mobile sand layer and its interaction with the driving flow are in reality extremely complex. These effects are inevitably only partially allowed for in the proposed simple bed load transport model. Bearing

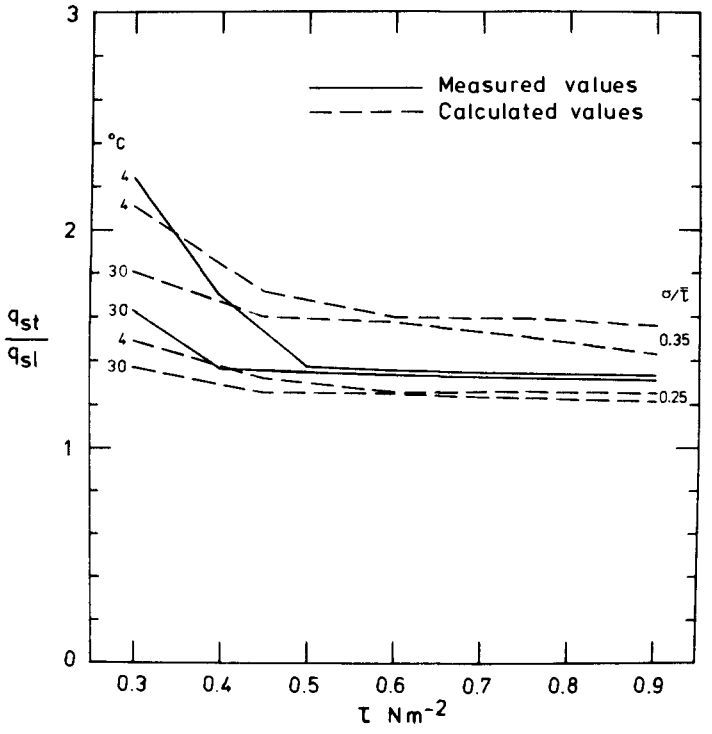

FIGURE 5. Comparison between the calculated and measured ratios of bed load transport rates, q_{st}, and q_{sl}, induced respectively by turbulent and laminar flows, as a function of mean bed shear stress.

these facts in mind, the levei of agreement between the experimentai and calcuiated results in Figure 5 is very encouraging.

5.CONCLUSIONS

a.The investigation was successful in providing completely new bed load sediment transport reiationships for strictly fiat bed conditions.
b. The test resuits confirmed the great sensitivity of the bed load sediment transport rate to changes in both bed shear stess and water temperature over the experimental range considered.
c. Under hydraulically smooth bed conditions with fine sands, the measured laminar flow transport relationship appears, on the evidence of the present results, to provide a satisfactory link function oetween instantaneous bed shear stress and the local simuitaneously induced bed load transport rate.
d. The general validity of the proposed method for caicuiating local net rates of bed load transport under arbitary unsteady flow conditions is thus confirmed as are the basic concepts on which the method is based.
e. There are several areas of study where the type of approach outiined might be productiveiy appiied in both steady and unsteady flow situations. These include quantitative mathematicai modeiling of the instability of the sand bed interface involving the initiai formation of ripples on fiat beds and their subsequent deveiopment and the prediction of their equilibrium height. The relevance in this context is demonstrated by the recent work of Sleath (1982) and Ruiter (1982). The proposed relationship between the iocal flow characteristics and the induced bed load transport can also be applied in modelling certain types of locai scour problems. Further tests will need to be carried out however in order to assess the infiuence of local bed siope on the laminar fiow transport function.

6. REFERENCES

AYOUB,R.N.M. (1977) Transport of fine bed sand by laminar and turbulent water flows. Ph.D.Thesis, London University.

BLINCO,P.H. and SIMONS,D.B.(1974) Characterstics of turbulent shear stress. J.Eng. Mech.Div.ASCE. EM2. pp.203-220.

ECKELMANN,H. and REICHARDT,H. (1972) An experimental investigation in a turbulent channel flow with a thick viscous sublayer. Proc. Symp on Turbulence in Liquids, University of Missouri-Rolla.

ECKELMANN,H.(1974).The structure of the viscous sublayer and the adjacent wall region in a turbulent channel fiow.J.Fiuid Mech.Voi.65, Part 3,pp.437-459.

ETHERIDCE,D.W. and KEMP,P.H.(1979). Velocity measurements downstream of re-award facing steps with reference to bed stability. J.Hyd. Res. Vol.17, No.2, pp.107-119

GRASS,A.J.(1970) Initial instability of fine bed sand.J.Hyd.Div. ASCE. HY3, pp.619-632.

GRASS,A.J.(1971) Structural features of turbulentflow over smooth and rough boundaries. J. Fluid Mech.Vol.50, Part 2, pp.233-255.

GRASS,A.J. (1982) The influence of boundary layer turbulence on the mechanics of sediment transport. Proc. Euromech 156 Colloquium: The Mechanics of Sediment Transport. Editors:B.Mutlu Sumer and A.Muller. Balkema Publications, Netherlands.

KEMP,P.H. and SIMONS,R.R.(1982) The interaction between waves and a turbulent current: waves propagating with the current. J.Fluid Mech. Vol 116, pp.227-250.

LAUFER,J.(1951) Investigation of turbulent flow in a two-dimensional channel NACA Report 1053.

MITCHELL,J.E. and HANRATTY,T.J.(1966). A study of the turbulence at a wall using an electro-chemical wall shear stress meter. J.Fluid Mech. Vol 26, Part 1, pp.199-221.

RUITER,J.C.C.de (1982) The mechanism of sediment transport on bed forms. Proc. Euromech 156 Colloquium: The Mechanics of Sediment Transport Editors: B.Mutlu Sumer and A.Muller. Balkema Publications, Netherlands.

SLEATH,J.F.A.(1982) The suspension of sand by waves. J.Hyd.Res. Vol.20, No.5, pp 439-452.

TAYLOR,B.D. and VANONI,V.A. (1972). Temperature effects in low-transport flat bed flows. J.Hyd.Div.ASCE. HY8, pp.1427-1445.

SURVEY TECHNIQUES/PROCEDURES AND DATA PROCESSING FOR MONITORING NEARSHORE SEDIMENT TRANSPORT

by

J ZACKS

1. INTRODUCTION

The cost of many coastal projects is often increased by the expensive beach repair and maintenance required to remedy the destabilising effects of structures on the adjoining coastline. Physical and/or mathematical models have been developed for use in planning these projects in order to *predict* and *quantify* the effects of marine sediment transport on the coastal topography.

Such models need to be calibrated against prototype data and one method of gauging volumetric sediment movement is by successive bathymetric/topographic *profiling surveys* which are performed seasonally and annually. Since large quantities of sediment are related to small changes in bed elevation it is clear that this profiling needs to be done with the utmost *precision*.

The areas most affected extend from the beach through the surf zone to water depths of about 25 metres. The surf zone in particular is a dynamic and hostile area which falls outside the traditional activities of both the hydrographic and land surveyors. Consequently innovative methods, deficient in sound survey principle and practice, have often been pursued in this area without any attempt being made to assess the tolerance on the data.

This paper attempts to show that it is possible to produce reliable and verifiable results to the required accuracy by using *conventional* survey equipment and techniques, also by taking the necessary precautions against the many possible sources of survey error. The procedures and techniques described have evolved from NRIO's involvement over the past decade in major projects at Richards Bay, Durban, Koeberg and in False Bay. The results of a recent verification investigation are fully reported in this paper.

2. METHODOLOGY

In principle the method is to survey a number of *parallel profiles* orthogonal to the coastline and extending across the beach, tidal and surf zones. Staff/polling methods are used from the beach to as far into the water as an operator can walk (or use a dinghy). A skiboat fitted with precision echosounder is used to work from behind the surf, and through the surf zone, towards the beach.

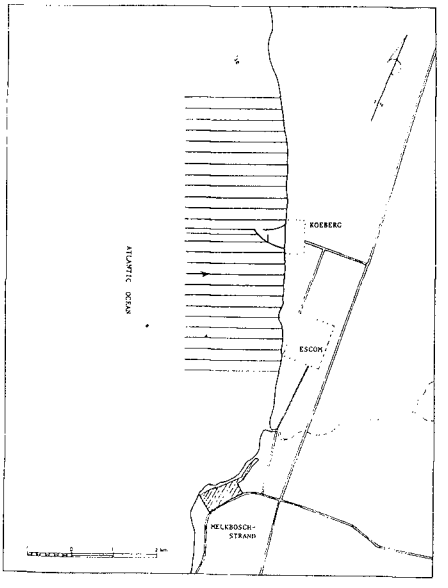

FIG. 1 KOEBERG SURVEY LOCATION

By regulating the work to span the low and high *spring tides*, a degree of overlap can be achieved between these two independent methods which permits verification of the data. By repeating certain profiles along the same lines (very exactly) further verification of the accuracy can be obtained.

The problem of precisely repeating the same echosounder footprint and the corrections required (for boat squat, wave profile, tides, etc) are dealt with in the following sections in which procedures are described for eliminating *random* errors and minimising *systematic* errors.

3. POSITION AND HEIGHTING

The profiling surveys are always preceded by a control survey to establish or replace substantial *reference beacons* erected along the coastline, based on the national trigonometrical co-ordinate and benchmark systems as datums for position and heighting. These beacons provide a reference for all measurements along a profile and for precise relocation of profiles during successive surveys. The location of the beacons should ensure unrestricted visibility, also security against erosion and wilful disturbance or removal.

3.1 Equipment

The use of electronic instrumentation is limited by the high initial cost, expensive maintenance (in the coastal environment) and the logistic requirements for recharging DC power supplies in the field. Optical/mechanical survey instrumentation is robust, portable, easily replaceable and is also required for the control survey. The close proximity of the survey area to the shore facilitates the use of conventional optical survey instrumentation with a resolution of 5 mm/km.

The basic instrumentation requirements are:

(a) Electronic distance measuring (EDM) equipment for control survey (and beacon replacement) measurements.

(b) Three precise (single-second) theodolites for accurate measurements over distances up to about 5 km.

(c) Two sounding poles consisting of aluminium tubing of 5 m length, 63 mm diameter, fitted with a flat base of 200 mm diameter and clearly marked in lengths of precisely 1 metre (painted white/black alternately).

(d) Four (plus back-up) radio transceivers (operating on VHF/HF frequencies) to synchronise observations and for general communication.

(e) Three measuring tapes to determine the elevations of theodolites above the beacons.

(f) One levelling staff.

(g) A lightweight dinghy (roof-top) powered by an outboard motor, for pole soundings in calm conditions (waves $\leq$ 0,5 m).

3.2 Procedure

The field party of *five* consists of three trained survey technicians, who undertake all optical measurements, and two others (boat/echo-sounder operators) who assist in the control survey and beach profiling (as pole carriers).

The reference beacons are linked by a closed traverse between two fixed survey stations (triangulated or Trig beacons) with orientation rays (full arc) being observed at each beacon. The levelling is connected to a benchmark at each end of the traverse, differences in elevation being determined from simultaneous reciprocal vertical observations (observed on both faces) between two theodolites and the measured heights of instruments above the beacons. The observers advance alternately (leap-frog) for successive measurements.

Position and heighting along a profile are both determined by indirect measurement from *synchronised* optical observations. Theodolite intersection techniques are used to determine accurately, relative to the survey beacons, the positions and corresponding elevations of targets (either stationary or moving) as they progress along the profile line at regularly incremented distances.

For beach profiling the traditional tachymetric survey method is discarded in favour of simultaneous observations by two (or three) theodolite observers to the *pole* which is held upright on the beach (at regular intervals) as the carrier progresses down the beach and as far as possible into the sea (to -2,00 MSL during 3 hours spanning low spring tide). The pole observations can be extended seaward to -6,00 MSL using the dinghy. The advantages of this method are:

(a) Economy of observations, three readings per pointing instead of five required for tachy, resulting in less pressure on the observer and more rapid progress. With good coordination a team of three observers and two carriers can complete nine beach profiles per hour.

(b) Greater length of beach profile can be covered since no fine staff graduations need be distinguished for the observation.

(c) Greater reliability and accuracy of the data (due to accurate distance, ± 5-10 cm) especially in the surf where the base of the staff is rapidly eroded during the observation.

For bathymetric profiling two theodolites are set up at suitable beacons, to fulfil the geometric requirements for accurate intersection, while the third instrument is set up at each intermediate beacon (in rotation) in order to position and continuously guide the boat by radio communication.

The boat traverses a fixed path (within two meters laterally), corresponding to the *exact bearing* of the profile sections, while theodolite observations are made at regular intervals of about 30 seconds. The boat operator assists in maintaining a straight track by visually aligning transit marks (topographic features) situated inland. For subsequent surveys the respective profiles are exactly relocated from the beacons.

The observations are made at regular intervals of about 30 seconds to a target mounted on the boat. These consist of *simultaneous* determinations of vertical and horizontal angle measurements, synchronised by the echosounder operator by radio, which are manually recorded, together with annotation of date, time, line and "fix" numbers.

3.3 Error Reductions

By maintaining a high degree of accuracy in the control survey (± 1 cm in elevation and position) it is possible to determine when beacons have been tampered with or replaced by unauthorised/unqualified persons. Affected or missing beacons are accurately replaced and verified by independent measurements from *both* the adjoining beacons.

Systematic errors in heighting, due to incorrect measurement of instrument elevation, are eliminated by *routinely* observing vertical angles to both the adjoining beacons (or instruments) prior to profiling. This also serves to verify the data of the control beacons which are used in further calculations.

Orientation errors in the intersection positions are eliminated by observing the known orientations to two distant beacons at the start and at the end of the observations for each profile.

The effects of random errors in observations of reciprocal vertical angles can be eliminated (and accuracy increased) by observing to both the instrument and the top of the beacon.

Instrumental error is eliminated by determining the corrections to be applied to the observations and by avoiding "creep" in the clamping/tracking mechanisms of the instrument. The index error (for correction to vertical observations) is determined by observations on both faces of the circle while the telescope is pointed at a distant object, correction = $\frac{1}{2}$ x index error (i.e. <360°>). The slow-motion tangent screws should always be turned against the spring to avoid creep.

Refraction and curvature corrections, to be applied to heighting over distances longer than 500 metres, can be verified by the index error observations if the distant object is a survey beacon.

Vertical accuracy in indirect heighting is increased by the accurate measurement of distance, from which the height is derived, or by reducing the elevation between the beacon and the target.

Observation and/or data processing errors are identified in the intersection method by comparison of the independently calculated elevations. A third observation enables an independent evaluation of accuracy to be made and allows the elimination of errors without loss of data. The conventional tachy method produces unchecked data.

The use of a theodolite for heighting, in preference to a level, enables the heighting error, due to the tilt of the staff, to be eliminated by sighting to a mark near to the base.

The accuracy of observations, when tracking a moving target, is dependent on the relative motion of the object. By maintaining a minimum distance of about 700-1000 metres from the boat, the movement can be followed accurately using the clamp and tangent screws of the theodolites.

The comparative accuracy attained in past surveys are 0,1 to 0,4 metres in position and 0,01 to 0,08 m in elevation for distances up to 3 km. Typical results for beach profiling are illustrated in Table 1. Similar pole soundings were previously made from a dinghy, to -3,0 MSL during neap tide, and a vertical accuracy of 2-3 cm (probable error) was obtained. It is estimated that a probable error of <0,10 m is possible for pole soundings at 5 m depths.

4. ECHO SOUNDING

The short period fluctuations in the elevation of the echosounder, resulting from waves or swells, are mirrored accurately in the continuous record of the depth profile provided that the sea bed is a flat sediment surface with regular changes of slope. For an irregular rocky

TABLE 1 - BEACH PROFILE DATA BY INTERSECTION METHODS

	Line OP.1		OP.1/ (MSL)	OP.2/
	Dist(a)	Dist (b)	Ht(a)	Ht(b)
1.	183,46	355,00	-0,93	-0,94
2.	160,60	354,40	-0,65	-0,70
3.	124,64	334,52	-0,19	-0,20
4.	85,03	318,48	+0,73	+0,68
5.	50,85	305,90	+1,64	+1,60
6.	27,39	300,24	+2,35	+2,30
7.	4,55	295,55	+3,10	+3,05
	Line OP.2		OP.2/	OP.1/
1.	5,43	294,68	+3,33	+3,26
2.	54,88	294,51	+1,36	+1,36
3.	87,04	296,48	+0,38	+0,37
4.	120,66	303,39	-0,33	-0,35
5.	143,61	310,72	-0,68	-0,66
6.	177,99	323,58	-1,19	-1,18
	Line OP.3		OP.3/	OP.2/
1.	184,97	282,03	-1,20	-1,21
2.	169,62	273,18	-0,92	-0,91
3.	139,34	259,44	-0,57	-0,56
4.	95,90	243,84	+0,23	+0,24
5.	64,11	236,78	+1,09	+1,11
6.	31,68	233,09	+2,10	+2,10
7.	8,44	234,03	+3,24	+3,22
	Line OP.4		OP.4/	OP.5/
1.	182,00	324,91	-1,28	-1,26
2.	152,12	303,02	-0,82	-0,82
3.	118,80	288,09	-0,35	-0,36
4.	79,01	270,26	+0,51	+0,52
5.	35,39	258,46	+1,88	+1,89
6.	5,54	254,57	+3,03	+3,04
OP.5	0,00	254,06	+0.05	+0,08(Instr/ Instr)
	Line OP.5		OP.5/	OP.4/
1.	7,32	253,58	+3,07	+3,12
2.	31,12	253,12	+1,88	+1,89
3.	81,16	259,62	+0,31	+0,34
4.	107,04	266,78	-0,28	-0,29
5.	129,93	276,07	-0,68	-0,64
6.	167,66	300,48	-1,39	-1,38

	Line OP.6		OP.6/	OP.5/
1.	7,5	-tache-	+3,25	-
2.	29,97	264,30	+2,08	+2,06
3.	67,62	268,92	+0,82	+0,82
4.	92,79	275,07	+0,12	+0,14
5.	129,76	286,27	-0,55	-0,56
6.	162,06	295,18	-0,99	-0,99
	Line OP.8		OP.8/	OP.9/ Corrn+0,02
1.	167,77	306,10	-1,24	-1,25
2.	140,51	284,54	-0,85	-0,86
3.	128,35	279,14	-0,74*	-1,02*
4.	102,84	269,97	-0,14	-0,14
5.	73,15	259,59	+0,82	+0,81
6.	43,93	254,97	+2,04	+2,01
7.	13,0	-tache-	+3,46	-
	Line OP.9		OP.9/ Corrn+0,02	OP.8/
1.	11.50	-tache-	+3,30	-
2.	30,39	255,88	+2,16	+2,17
3.	53,74	260,53	+1,14	+1,18
4.	82,70	268,53	+0,18	+0,19
5.	108,77	278,40	-0,36	-0,32
6.	125,26	285,86	-0,83	-0,77
7.	135,98	291,75	-1,50	-1,44
OP.10	242,52		+7,29	- (T/Pipe)s/b
OP.10	242,52		+8,09	+8,10(T/Instr)s/b
	Line OP.10		OP.10/	OP.9/ Corrn+0,02
1.	4,28	242,63	+4,63	+4,62
2.	37,11	244,97	+2,39	+2,38
3.	57,44	249,25	+1,39	+1,39
4.	82,00	256,03	+0,44	+0,44
5.	108,00	266,99	-0,37	-0,39
6.	125,17	274,59	-1,29	-1,31

bottom along the profile, the effects of water level fluctuations and topographic undulations are combined to produce a confusing echo trace which cannot be resolved with sufficient accuracy.

4.1 Equipment

A 5,6 m skiboat, powered by twin outboard motors to ensure high manoeuvrability and safety in the surf zone, is used as a platform for the echosounder. A cabin houses the essential electronic instrumentation and provides protection and shelter to the crew. A spherical target (120 mm diameter) is fitted, for theodolite observation, to a mast projecting above the cabin.

The survey echosounder can operate on single/dual frequencies of 30 kHz and 210 kHz, the latter for greater accuracy in profiling and calibration, and has facilities for recording analog and/or digital depth data. The analog facility has an expandable depth scale producing a maximum resolution of 5 m/200 mm chart width, providing a resolution of about 1 cm, for accuracy in the calibration of the instrument and recording depths in calm sea conditions. Both transducers are mounted *inboard* in a well which is moulded onto the centre of the hull, and operate effectively through the hull with little loss of power provided that the well is filled with water (no splashing) and that *no air* is entrapped in the laminations of the hull.

A calibration bar is used to physically calibrate the echosounder during the survey. The bar consists of a 1,8 m length of open galvanised steel pipe, 125 mm in diameter, with a 14-metre length of light chain welded to each end. Tags are attached to the short links of both chains at predetermined distances from the pipe and exactly 1 metre apart.

An accurate tide gauge must be installed to record the sea level continuously throughout the survey. The resulting tide data are used to relate the recorded depth profiles to the vertical datum of the benchmarks (and beacons).

Radio communications are used to coordinate the operation of the echosounder with the theodolite observations.

4.2 Survey Procedure

The marine operation is performed by two operators (the crew) who can interchange their respective duties. The surveyors complete the manpower requirements for launching/recovering the boat from the beach when necessary.

The following relationships must be determined accurately for each survey boat:

1 The elevation of the transducer face relative to the reference target which is mounted on the mast.

2 The elevation of the transducer face relative to the gunwales, to

the deck and also relative to the sea level while the boat is stationary in the water.

3 The squat (settling in the water) of the boat while it is moving at various survey speeds ranging from 4 to 7 ms^{-1}.

These specifications are determined in a sheltered harbour under calm sea conditions with the aid of a theodolite, used as a level, and a levelling staff. The theodolite is set up at a slipway, near to the water level and aimed at the staff to measure the elevation of the various parameters. The respective rev-counter readings are noted at the various constant speeds.

Calibrations of the echosounder are performed *twice daily* in the work area. Instrument controls (for adjustment), which are initially set by the echosounder operator, include switches for the channel (frequency) selection, chart calibration settings and the attenuation of signal strength and stylus voltage in order to produce an optimum trace of the seabed at the maximum profile depth.

The boat is *anchored* and the calibration bar is then suspended below the boat by both chains so that the pipe hangs horizontally in a vertical plane through the transducers and directly below, the corresponding tags of each chain being held exactly on the edges of the gunwales while the top surface of the pipe is precisely 12 metres (or more) below the transducer faces. Further settings of the recorder controls are made for vertical scale expansion (set to maximum), the transducer depth below sea level (set accurately below zero line) and the "sound velocity" is finally adjusted to correct the recorded depth of the bar to the exact value. The depth of the bar is now decreased, in stages of 2 m (or 1 metre) throughout the depth range, while the measured depths are recorded and checked (should be exact). The bar is taken aboard. No further adjustments are necessary (or permissible) other than depth phasing, scale expansion and paper speed.

On completion of the day's depth profiling, a second calibration is performed as before.

The bottom trace is recorded (at anchor) for three minutes, using the event marker, in order to measure the dominant wave period and wave height for determining the relationship between wave form and water depth.

The survey boat traverses the profile line continuously from a predetermined depth to a least depth of 1,5 metres, thereby obtaining bathymetric data (to about -0,70 MSL) during a period of 1½ hours spanning spring high tide, while position fixes are coordinated by the echosounder operator for the theodolite observations.

The boat speed is regulated so as to be overtaken by 5 to 6 swells per minute (confirmed by the echo trace), a requirement for accurately eliminating the wave action from the depth profile. A *constant* speed must be maintained between position fixes to permit interpolation of intermediate positions, speed changes should coincide with the fixes. The boat must also maintain its position between the breakers, hanging back while

avoiding aeration in the water which will strongly attenuate the transducer signal. Repeated runs may have to be made in the surf in order to obtain the required profile coverage. The decision, to terminate the profile, rests with the skiboat operator who is advised by the echo-sounder operator on the clearance beneath the boat.

The observed position fixes coincide with the manually activated event marks which are on the analog depth trace. These marks must be fully and correctly annotated for time, date, line and fix numbers.

All profile lines are run *inshore* only. Previous attempts at running the lines in alternate directions produced a consistent difference of about 0,2 metres in the respective depths recorded (in/out), presumably due to the greater vertical acceleration resulting from a higher frequency of wave-crossings on the outward track.

Twelve profile lines (length 1,5 to 3 km) are normally surveyed in 3 hours each day and the survey may extend over several days because of delays resulting from poor sea conditions. Selected control profile lines (2 or 3) are therefore surveyed repeatedly, once each day, in order to verify the consistency of the data by comparison of the profile sections.

The recorded bathymetric depth data, measured from sea level, are related to the benchmark level datum by *accurate* tide data which are recorded continuously for the duration of the survey. The tide data are regularly

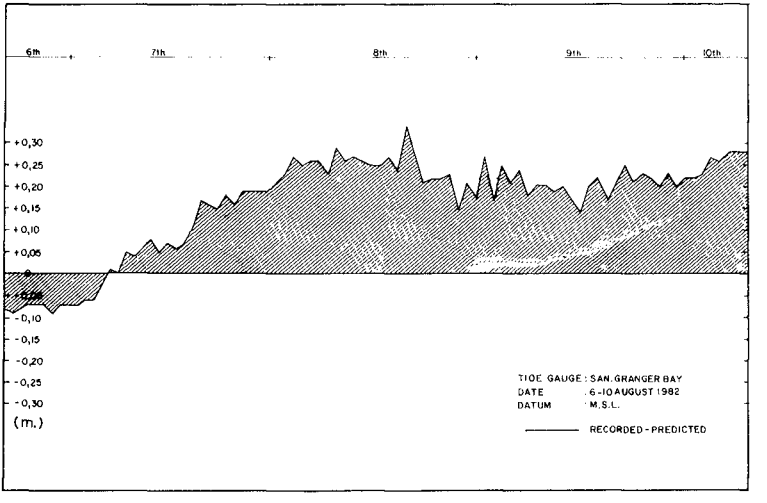

FIG.2 RECORDED VS. PREDICTED TIDE LEVELS

verified by direct observation and measurement, preferably with the aid of a stilling well or other sheltered and damped sea surface, or by comparison with similar data recorded independently nearby. The chart recordings must be meticulously *annotated* with reference to time, date and location.

Suitable tide-gauges, infrequently calibrated due to shortage of staff, are operated at various South African ports by the Hydrographer of the Navy and these data are freely available.

4.3 Error Reduction

Differences of about 300 mm (or more) often occur in elevation between recorded prototype tide data and predicted data, as prepared by the S A Navy and published in the TIDE PREDICTION TABLES, largely due to the effects of fluctuating meteorological parameters (see Figure 2) and therefore the *predicted data are totally unacceptable* for sediment profiling.

Inaccuracies in the time-scale of recorded tide data are a common cause of systematic error in the reduced bathymetric depth profile. By surveying only for a limited period spanning high tide, when the rate of change in elevation is small, the effects on individual profiles are reduced while the cumulative effect on the survey is eliminated.

Localised areas of rock outcrops along the profile *must* be identified and excluded from the comparisons. Large areas of rock may totally disqualify the location as being unsuitable for monitoring.

Temperature profiling should be carried out at random in the work area to ensure a consistent propagation (speed) of sound for all profiles.

The second calibration (each day) verifies the initial one and ensures that no "drift" in the electronics of the echosounder has taken place. The data are discarded and the profiles *resurveyed* if the calibrations differ.

When surveying in the vicinity of river estuaries during periods of flood or heavy run-off, the 30 kHz facility is used simultaneously with the 210 kHz as a precaution against the presence of dense layers of sediment (in the water column) which could mask the seabed and cause a false bottom to be recorded.

The boat speed is calculated between fixes to verify the squat correction (which is applied with the tide level correction). Squat varies in relation to the boat speed, from 10 - 11 cm at 4 ms^{-1} to 3 - 4 cm at 6 ms^{-1}. Care must also be taken to note changes in the buoyancy of the boat due to leakage of the hull and varying content of the 240 litre inboard fuel tanks.

The elevation of the boat is determined from theodolite observations to the target in order to verify the effects of wave set-down/set-up in shallow water. Observations beyond the breakers serve to further verify the tide data for gross errors.

The profile data is abstracted directly from the echo trace and tabulated together with the range distances for determining profile section and areas. The necessary precautions have been taken to ensure *direct profile comparisons* by the precise relocation of all profiles. In no circumstances need profile data be interpolated from contour plans.

5 DATA PROCESSING (GENERAL)

The processing of survey data requires a special awareness of the potential survey inaccuracies and the need to personally scrutinise the many outputs of comparative data at different stages of the work.

Independent checks are systematically applied during each phase of processing the data which is first validated before being further applied. Sufficient observations are made to verify and correct any errors which had been made in the measurements.

Much of the data is processed manually and this also requires specialised experience and a knowledge of local conditions. To increase consistency in reducing the data of successive surveys, the manual reductions are always undertaken by the same persons (to reduce the effects of personal error) in successive surveys and scrutinised by a second party.

5.1 Equipment

Portable calculators are used in the field for processing the essential control survey data while an on-line mainframe computer is available for the processing of the resultant statistical data (profile section areas, etc) at headquarters. Printers are used (with the calculators) to reduce the probability of transcription errors being made in the data.

5.2 Procedure

The processing of all survey data is performed, both in the field and at headquarters, by the survey technicians of the field party.

All data relating to the control survey are processed manually and fully validated before the profiling survey is commenced. During periods of unfavourable weather or sea conditions, the available time is utilised by processing the other survey observations. All calibration data are immediately validated by inspection and comparison. Independent checks are systematically applied to all the survey data.

A graphical comparison is made of the recorded and predicted tide data, and with independently recorded data, in order to check for anomalies (such as errors in the time-scale).

The effects of swell and waves on the analog recording of the profile are reduced graphically, prior to applying the tide corrections, by applying an established theory to relate wave form to water depth (see Figure 3). The reduction graph is based on the VOCOIDAL WAVE THEORY (Swart 1977) defining the relationship (Nc) of the mean water level (WL) to the crest and trough of a design wave relative to water depth. The parameters of

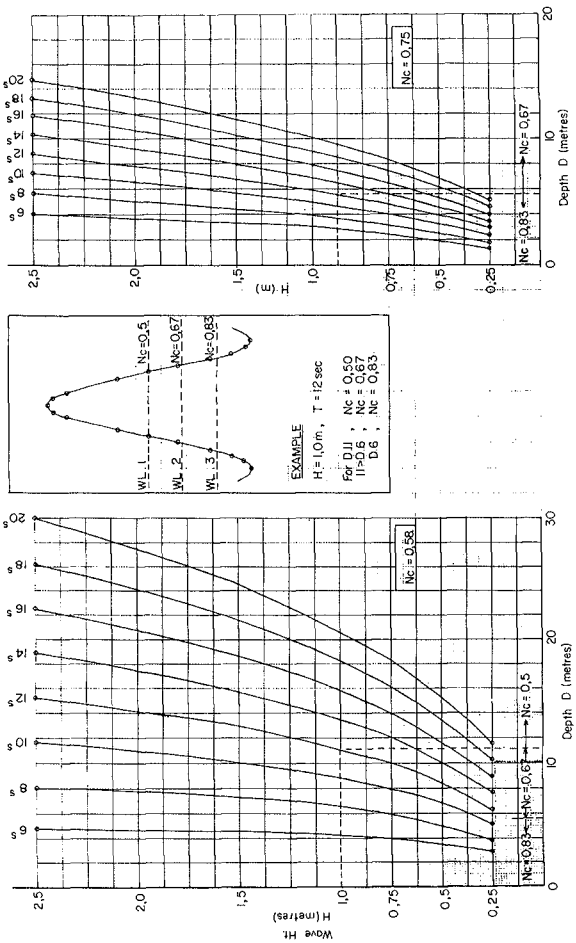

FIG. 3 WAVE REDUCTION GRAPH

wave height and wave period are derived from the initial calibration record of each day and critical depth values for Nc = 0,5 and Nc = 0,67 (also Nc = 0,83) are determined from the graph.

The inverted wave crests on the echo trace are all joined by straight lines, as are the inverted troughs. The corrected WL image is then reconstructed in accordance with the Nc/depth relationship and smoothed. This is regarded as the true image of the sediment bed. All intermediate changes in slope are annotated and their proportional range distances are derived from the calculated "fix" positions. Tide (and squat, etc) corrections are then applied to all the recorded depths of both the "fix" and annotated positions and the data are then abstracted for the determination of the profile sections.

Graphical comparisons are made of the overlap of profile data derived independently from the beach and sonic profiling.

6 RESULTS OF A VERIFICATION EXPERIMENT

During a regular profiling survey at Koeberg in September 1982, a number of additional profile sections were surveyed in order to evalulate the probable error in the depth soundings for various sectors along the profile.

Line 10 was chosen as the control profile and ten runs were made over the profile in a consistently calm/moderate sea state with swell height of about 0,5 to 0,7 metres. There were four runs on 16 September and six runs on 17 September. No overlap was obtained with the beach profile, neither were vertical intersection angles observed in this exercise. The abstracted profile data are listed in Table 2.

6.1 Sounding Error

The following methods were used to determine the values for the probable error of the soundings:

1 The *average* depth was determined for each range position at intervals of 50 metres along the profile, these values were adopted as the *correct* values and the respective errors were determined for each of the range positions throughout the profile length from range distance 300 metres to range distance 2 050 metres. These error values are plotted against the range distance, from the reference survey beacon, to indicate the error distribution (see Figure 4). The standard deviation was likewise calculated and also plotted against the range distances (see Figure 4).

The probable error of a single depth sounding in the surf zone varies from ±0,06 m to ±0,10 m while offshore the probable error of a depth sounding varies from ±0,02 m to ±0,04 m where

$$P.E. = 0,6745 \sqrt{\frac{[dd]}{(n-1)}}$$

TABLE 2 - SOUNDINGS TAKEN AT LINE 10, KOEBERG

DEPTH IN METRES (MSL DATUM)

RUN NO (m) DIST	1	2	3	4	5	6	7	8	9	10	AVE		7/9
250	-2,11	-1,77	-1,90	-1,91	-2,09	-1,94	-1,97	-2,09	-2,35	-2,10	-2,023		-1,87
300	2,55	2,16	2,49	2,44	2,52	2,43	2,34	2,57	2,60	2,62	2,472		2,42
350	3,00	2,77	2,89	3,06	3,00	2,94	2,77	3,07	2,85	3,13	2,948		3,02
400	3,55	3,49	3,45	3,64	3,55	3,57	3,70	3,66	3,65	3,80	3,606		3,70
450	4,38	4,37	4,27	4,46	4,70	4,50	4,72	4,76	4,71	4,60	4,547		4,34
500	5,14	4,88	4,86	5,23	5,03	4,91	4,95	5,11	4,82	5,30	5,023		5,07
550	4,88	4,80	4,90	4,74	4,93	5,06	4,81	4,80	4,91	5,00	4,883		4,47
600	5,15	4,87	4,94	4,96	5,30	5,16	5,07	5,08	5,08	4,92	5,053		5,12
650	5,67	5,59	5,60	5,66	5,76	5,67	5,60	5,74	5,53	5,63	5,645		5,98
700	6,27	6,40	6,36	6,34	6,35	6,37	6,42	6,41	6,23	6,34	6,349		6,64
750	7,02	7,13	7,09	7,01	6,96	7,02	7,10	7,04	6,96	7,05	7,038		7,17
800	7,64	7,66	7,70	7,70	7,67	7,65	7,67	7,64	7,69	7,69	7,671		7,74
850	8,16	8,17	8,20	8,18	8,08	8,19	8,17	8,13	8,08	8,21	8,157		8,20
900	8,54	8,49	8,52	8,54	8,64	8,61	8,55	8,59	8,47	8,59	8,554		8,55
950	8,89	8,82	8,83	8,89	9,02	8,91	8,88	9,00	8,87	8,92	8,903		8,89
1000	9,24	9,14	9,16	9,19	9,31	9,19	9,21	9,30	9,24	9,24	9,222		9,15
1050	9,57	9,45	9,48	9,47	9,60	9,48	9,52	9,61	9,60	9,57	9,535		9,48
1100	9,87	9,76	9,76	9,78	9,88	9,79	9,80	9,91	9,88	9,85	9,828		9,77
1150	10,20	10,07	10,10	10,10	10,18	10,10	10,08	10,20	10,17	10,13	10,133		10,03
1200	10,52	10,39	10,42	10,44	10,48	10,41	10,38	10,50	10,47	10,43	10,444		10,33
1250	10,81	10,72	10,73	10,79	10,77	10,73	10,73	10,80	10,77	10,73	10,758		10,67
1300	11,13	11,04	11,11	11,14	11,10	11,06	11,08	11,10	11,06	11,10	11,092		11,02
1350	11,48	11,37	11,50	11,49	11,46	11,40	11,42	11,43	11,42	11,47	11,444		11,39
1400	11,84	11,70	11,88	11,82	11,82	11,74	11,75	11,76	11,78	11,83	11,792		11,72
1450	12,18	12,03	12,18	12,17	12,18	12,08	12,07	12,09	12,14	12,19	12,131		12,10
1500	12,51	12,36	12,47	12,51	12,51	12,42	12,40	12,44	12,47	12,54	12,463		12,36
1550	12,84	12,70	12,76	12,85	12,84	12,76	12,76	12,78	12,79	12,90	12,798		12,66
1600	13,20	13,02	13,10	13,16	13,17	13,10	13,11	13,13	13,10	13,24	13,133		13,00
1650	13,54	13,41	13,42	13,45	13,49	13,40	13,46	13,43	13,38	13,52	13,450		13,33
1700	13,89	13,74	13,76	13,74	13,81	13,71	13,70	13,72	13,64	13,77	13,748		13,70
1750	14,12	14,00	14,08	14,01	14,13	14,01	13,93	13,99	13,89	14,02	14,018		13,97
1800	14,32	14,27	14,28	14,30	14,34	14,26	14,16	14,28	14,17	14,26	14,264		14,22
1850	14,52	14,53	14,48	14,56	14,50	14,47	14,40	14,48	14,44	14,50	14,488		14,46
1900	14,71	14,68	14,63		14,67	14,61	14,62	14,68	14,63	14,71	14,660		14,63
1950	14,89	14,78	14,76		14,81	14,72	14,73	14,82	14,75	14,83	14,788		14,71
2000	15,00	14,86	14,86		14,92	14,82	14,87	14,94	14,84	14,89	14,889		14,84
2050	15,14	14,95	14,97		15,02	14,91	15,02	15,03	14,94	14,97	14,994		14,96
2100	15,30	15,15	15,15		15,14	15,06	15,18	15,17	15,11	15,18	15,160		15,08
2150	15,49	15,38	15,32		15,36	15,33	15,32	15,37	15,34	15,46	15,374		15,22
2200	15,69	15,64	15,62		15,60	15,60	15,50	15,58	15,58	15,73	15,616		15,46
2250	16,02	15,95	15,91		15,85	15,90	15,91	15,89	15,82	16,00	15,917		15,80
2300	-16,38	-16,26	-16,20		-16,16	-16,24	-16,29	-16,22	-16,16	-16,27	-16,242		-16,13
$[\frac{d}{u}]$	-0,050	+0,052	+0,028	-0,004	-0,034	+0,022	+0,027	-0,026	+0,021	-0,047	0,000		+0,044
Speed m/s	4,27	3,70	3,81	4,20	4,51	4,62	4,06	4,60	4,25	4,74	4,28		
Date	16/9/82				17/9/82								

Surf Zone — Calibration Range — Nearshore

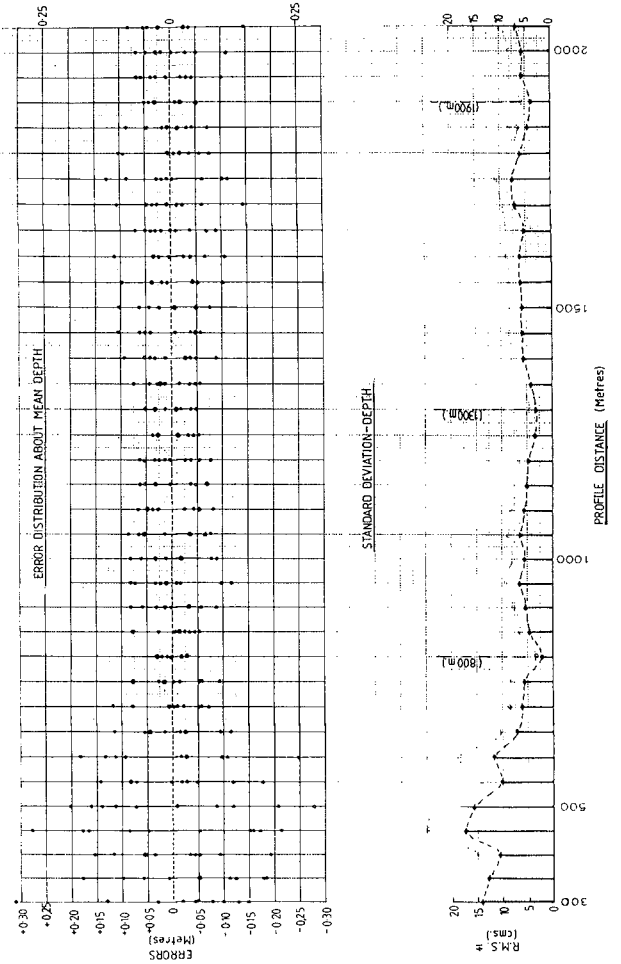

FIG. 4 EVALUATION OF ERRORS IN SONIC PROFILING

The error limits within the *95% confidence band* were found to be ±0,20 - 0,33 m in the surf zone and ±0,07 - 0,13 m offshore (for 9 degrees of freedom).

In comparing the *average* elevations of each run with the mean elevation (of all 10 runs), the differences are found to have a standard deviation of ±0,04 m.

Of special interest in Figure 4 are the apparent node points in the error distribution which recurs at regular intervals of 500-600 m apart and is apparent again at a range distance of about 2 500 m (for only three runs). These nodes indicate some tide level phenomenon, similar to a "standing wave" situation, which accounts for 50% of the probable sounding error beyond the surf zone.

The profile data listed in Table 2, under column 7/9, were recorded on 7 September during an earlier survey which was aborted because of deteriorating weather and sea conditions. A comparison of these data, with those which were acquired on 16-17 September, indicates the consistency of the profile data obtained during routine surveys.

2 No *correct* value is assumed for this analysis and the errors are derived on the basis of direct comparison between *any pair* of measurements taken, in all there are 45 possible combinations (from 10 measurements). Calculation of the probable errors of a depth sounding (as in the first method) yields values which are consistently 40% higher than previously. Within the 95% confidence limit, the errors are ±0,27 - 0,42 m in the surf zone and ±0,09 - 0,18 m in the offshore area.

Profile section *areas* were calculated for each of the 10 profile runs and the error values were determined from the mean values, a distinction being made between the surf zone, offshore and for the overall section. These results are shown in Figure 5 together with the probable error, indicated above (n = 10). For the 95% confidence band the magnitude of error value is increased by a factor of 3,35.

A second analysis was done of the section areas, as for the sounding error, and the probable errors are also indicated in Figure 5 (as n = 45) except for the overall chart where n = 36. For the 95% confidence band the magnitude of error is increased by a factor of 3.

6.2 Spacing Error

The effect of spacing error, due to the insufficient density in the profile spacing, was investigated by surveying an extra four profiles (marked A-D) which were fairly evenly spaced between the regular profiling lines 10 and 11. The section areas of profiles A-D were calculated and these values are tabulated in Table 4 and indicated graphically in Figure 6 (where comparative elevations are shown for volummetric calculations).

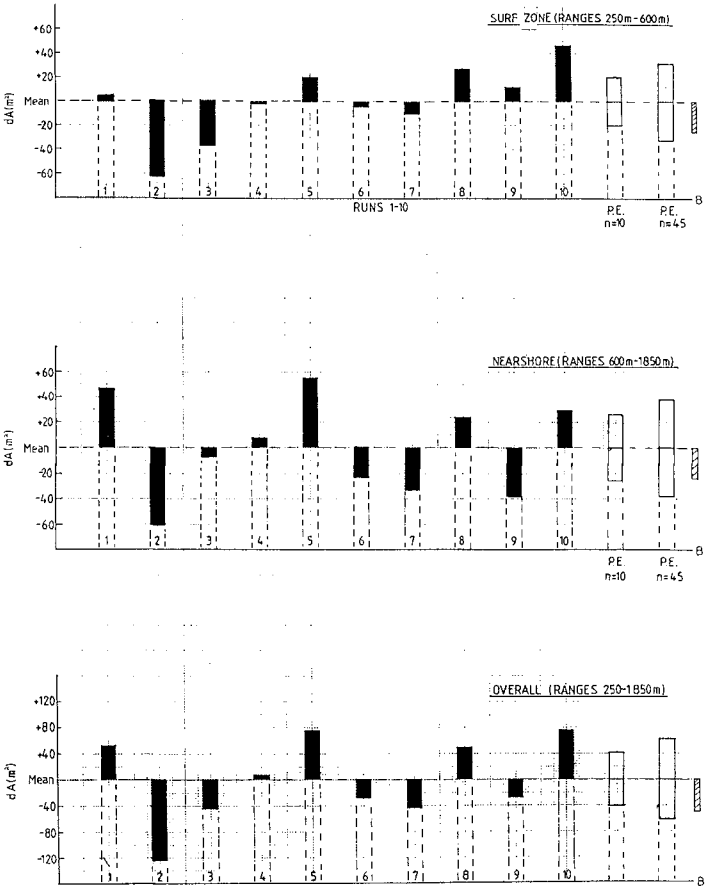

FIG. 5 ERROR DISTRIBUTION FOR PROFILE SECTION AREAS

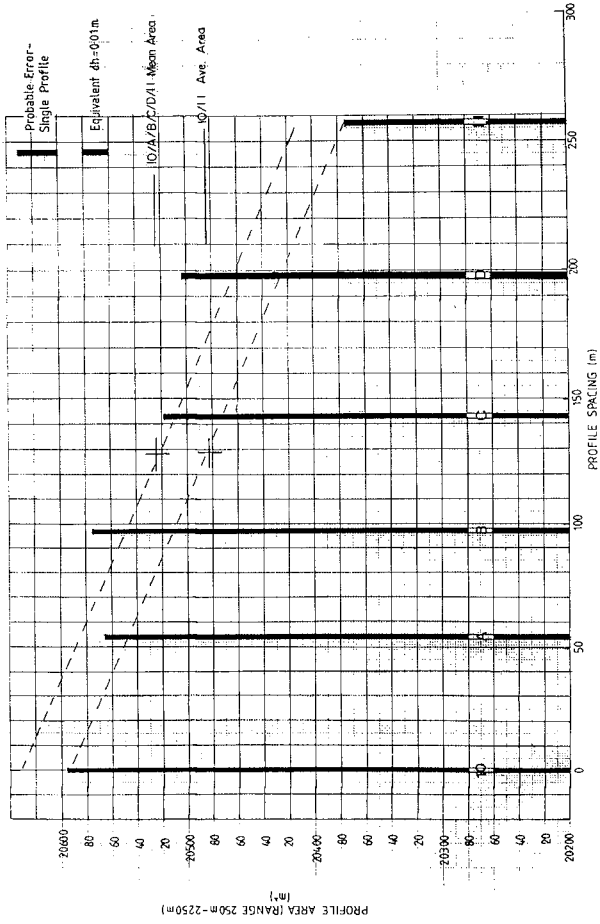

FIG. 6 SPACING ERROR FOR PROFILE DENSITY

TABLE 3 - COMPARISON OF SECTION AREAS WITH AVERAGE PROFILE

RANGE DISTANCE (m)	RUN										
	1	2	3	4	5	6	7	8	9	10	Average 1-10
250-600 Δa_1	1356 +5	1289 -62	1314 -37	1350 -1	1371 +20	1347 -4	1341 -10	1378 +27	1363 +12	1398 +47	1351 RMS ±31
600-1850 Δa_2	13164 +47	13056 -61	13110 -7	13125 +8	13172 +55	13094 -23	13084 -33	13140 +23	13078 -39	13146 +29	13117 RMS ±39
600-2250 Δa_3	19239 +89	19090 -60	19135 -15		19207 +57	19104 -46	19103 -47	19178 +28	19094 -56	19197 +47	19150 RMS ±56
250-1850 Δa_4	14520 +52	14345 -123	14424 -44	14475 +7	14543 +75	14441 -27	14425 -43	14518 +50	14441 -27	14544 +76	14468 RMS ±64
250-2250 Δa_5	20595 +95	20379 -121	20449 -51		20578 +78	20451 -49	20444 -56	20556 +56	20457 -43	20595 +95	20500 RMS ±81

Δa = Deviation from the average area (Profile OP.10)
RMS(250-600) = ±9m²/100m; RMS (600-2300) = ±3m²/100m; RMS (250-2300) = ±4m²/100m

TABLE 4 - COMPARISON OF INTERMEDIATE SECTION AREAS WITH PROPORTIONAL AREAS

PROFILE SECTION	10	A	B	C	D	11
Calculated area (m^2)	20595	20566	20574	20518	20504	20374
Proportional area (m^2)		20539	20504	20467	20422	
Δarea = (m^2)		+27	+70	+51	+82	
Profile spacing (m)	53,96	42,71	46,21	55,27	58,72	
	256,87					

The apparent result of spacing error in the volume, as calculated from the end section areas, is 10 143 m^2 which is equivalent to an average error in elevation of 0,02 m (which is well within the accuracy indicated for the probable error). From a visual comparison of the intermediate areas, A to D in Figure 6, with their assumed profile areas (indicated by the broken line from profile 10 to profile 11), it is obvious that here the disagreement is also within the limits of the sounding error.

The spacing of about 250 m between profile lines 10 and 11 is adequate for this particular section of the sea bed. Since the bathymetry of the area is very regular and the coastline is straight (see Figure 1), the profile intervals are assumed to be acceptable although further sampling of the spacing is required.

7 CONCLUSION

The results of the experiment indicate clearly that the required accuracy of measurement can be achieved under normal conditions by standard survey procedure and that the effects of systematic errors are significantly reduced. The spacing of profiles, about 250 m, is apparently acceptable in the case study.

The field operation is cost efficient in terms of capital outlay, reliability of instrumentation and optimum productivity of personnel. The required technical expertise is easily acquired without specialised training.

The survey procedure is highly efficient in the identification/elimination of random errors and the evaluation and reduction of systematic errors thereby increasing the degree of accuracy which is attained.

The precise relocation of profiles in successive surveys, together with the verification of the data, serves to confirm the validity of the resulting quantitative assessment of sediment transport.

FIELD INVESTIGATION OF LONGSHORE TRANSPORT OISTRIBUTION

by

E. P. Berek[1], A.M. ASCE and R. G. Oean[2], M. ASCE

ABSTRACT

Following a change in wave direction, the active contours in an idealized pocket beach respond by rotating such that they approach a perpendicular orientation relative to the incoming wave rays. Assuming that cross-shore sediment transport does not contribute to this contour rotation, and that the contours are in the early stages of this equilibration process, the amount of contour rotation can be interpreted as the cross-shore distribution of the longshore sediment transport.

As part of the Nearshore Sediment Transport Study, detailed nearshore profile measurements were conducted at Santa Barbara, California. Twenty-two of these profile lines were located on Leadbetter Beach, which is a quasi-pocket beach. To explore the concept described above, two of the nine intersurvey periods were selected due to their strong indications of wave direction change. Analysis of these data sets yielded two estimates of cross-shore distribution of longshore sediment transport which were compared with those presented by Komar, Fulford and Tsuchiya. Although these three distributions differ significantly, the effect of the tidal variations is to "smear" the differences in the inferred distributions as evident in the contour displacements. It was found that none of the relationships for longshore transport distribution predicted the amount of transport inferred in water depths greater than one meter. It is possible, especially for one of the intersurvey periods that the changes in contour locations were so extreme that substantial cross-shore sediment transport was induced and would be interpreted as longshore transport occurring in water depths greater than had actually occurred. The method introduced here should be useful in other field and laboratory programs to investigate the cross-shore distribution of longshore sediment transport.

---

[1]Research Engineer, Amoco Production Co., Tulsa, OK 74102; Formerly Graduate Assistant, Department of Civil Engineering, University of Delaware, Newark, DE 19711

[2]Graduate Research Professor, Coastal and Oceanographic Engineering Department, University of Florida, Gainesville, FL 32611; Formerly Professor, Oepartment of Civil Engineering and College of Marine Studies, University of Delaware, Newark, DE 19711

INTRODUCTION

Practically all coastal engineering projects require quantitative estimates of the longshore sediment transport at the project site. This information can be derived from a variety of sources including experience at nearby structures, channels which impound sediment and computations based on local wave characteristics. Generally, even if impoundment data are available, computations are employed, partly in the interest of developing confidence in the impoundment estimates, but also because of the uncertain quality of most impoundment documentation. For example, much of the initial nearshore accumulation at jetty structures can be the result of the onshore transport of a portion of the material which formerly resided in the ebb tidal shoal. In addition to the need for estimates of total longshore sediment transport, there are a number of project/problem types that require estimates of the distribution of longshore sediment transport across the surf zone. Examples include: design of the length and elevation of the weir section of a weir jetty system, design of the length of a groin or jetty, computation of the total longshore sediment transport in cases where a portion of the surf zone is paved by beach rock or particles too coarse to yield significant amounts of transport, etc.

The Nearshore Sediment Transport Study (NSTS) was sponsored by the National Sea Grant Office of the National Oceanic and Atmospheric Administration (NOAA); the objectives of this study included the enhancement of general knowledge and understanding of nearshore hydrodynamics and sediment transport processes with an emphasis on the improvement of the capability to compute longshore sediment transport for engineering purposes (Duane and Seymour, 1978). One component of the NSTS directed specifically at this latter objective was an eighteen month measurement program carried out at Santa Barbara, California. Through measurements of volume accumulations by the near-complete trap formed by the spit in the lee of the breakwater and portions of the updrift beaches, the net longshore transport could be documented with good accuracy. The wave characteristics were provided by two S_{xy} gages located in a water depth of approximately 7 m directly off Leadbetter Beach. The initial plan did not include an attempt to determine information relating to the cross-shore distribution of longshore sediment transport. However, as the data from a number of surveys accumulated, the "rotation" of the nearshore contours resulting from shifts in the dominant wave direction suggested that some of the available data sets were well-conditioned to address the problem of longshore sediment transport distribution.

REVIEW OF RELATED WORK

The difficulties of conducting field measurements of the cross-shore distribution of longshore sediment transport have prevented the determination of any well-accepted results. Methods attempted include bed load traps by Thornton (1973) and tracer studies. Thornton estimates the efficiency of the bed load traps to be between 40 and 100 percent. He also stated that the traps appeared to be more efficient under light wave conditions and tend to bury themselves under heavy wave conditions.

Thornton (1973), Komar (1977), and Tsuchiya (1982) have developed predictive equations for the cross-shore distribution of longshore sediment transport. Thornton utilized a Bagnold (1963) model and considerations of the role of the longshore current to develop a predictive relationship for $q_y(x)$, the distribution across the surf zone of the longshore sediment transport. Thornton's results expressed $q_y(x)$ as proportional to the product of the average energy dissipation per unit bed area and the longshore current. The proportionality factors were considered to be different inside and outside of the surf zone due to the different causes of energy dissipation. The field measurements conducted by Thornton included sediment transport as determined by the bed load traps and longshore currents based on surface float trajectories or current meters. The transport proportionality factor outside the surf zone exceeded that inside the surf zone by slightly more than an order of magnitude. There is substantial uncertainty regarding the efficiency of the bed load traps. Integrating Thornton's results across the surf zone results in a proportionality factor, K, for the total transport which is approximately two orders of magnitude less than the commonly accepted value of 0.77 (Das, 1972, Figure 6).

Komar combines the sediment transport concepts of Bagnold with longshore current distributions as developed by Longuet-Higgins (1970) and modified by Komar (1976). The resulting expression for $q_y(x)$ is proportional to the product of the bottom shear stress and the longshore velocity. Results are developed in which the bottom shear stress is based on the gradient of S_{xy} (the onshore flux of the longshore component of momentum) and this gradient augmented by the longshore current. Komar finds that the magnitude of $q_y(x)$ depends on the breaker height to depth proportionality factor, a mixing parameter which controls the form of the longshore current and the friction factor for the profile. The maximum of $q_y(x)$ is predicted to be at approximately $0.8\ x/x_b$, where x_b is the offshore breaking distance. Oue to the predicted abrupt discontinuity in bottom shear stress at the surf line, q_y is also discontinuous at this location. Additionally, Komar's distribution does not include any "swash" transport, i.e. landward of the mean water line. An example is presented in Figure 1.

Tsuchiya (1982) bases his predictive relationship on an equation which appears to be appropriate only for suspended sediment transport and which does not account for the correlation, over the vertical, of the suspended sediment distribution and the longshore current distribution. Tsuchiya combines the longshore current representation by Longuet-Higgins (1970) with earlier work conducted by Tsuchiya on sediment transport by currents. In the brief 1982 abstract, Tsuchiya does not present his method in detail; however, it appears that the basic form of the longshore sediment transport is approximately proportional to the product of the longshore current distribution and the depth. An example of Tsuchiya's results is presented in Figure 1, in which the continuity of sediment transport across the surf line and lack of swash transport are evident.

Fulford (1982) determined an empirical distribution of longshore sediment transport based on a wave basin study conducted by Savage

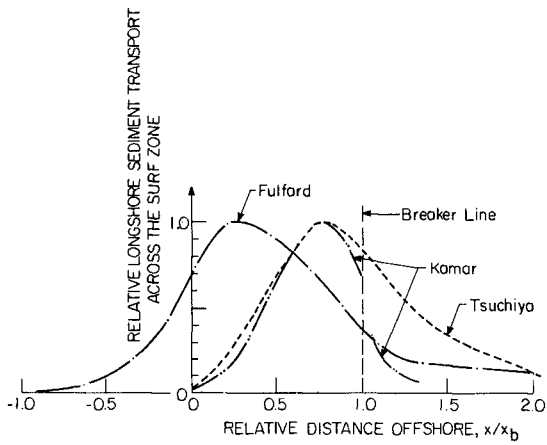

Figure 1. Illustration of Cross-Shore Distributions of Longshore Sediment Transport as Determined by Various Investigators.

(1959). In the tests utilized, Savage allowed the beach processes to equilibrate under the action of waves approaching at an angle. A long high impermeable groin was then introduced into the system. The analysis by Fulford was based on the two-dimensional equation of sand conservation

$$\frac{\partial q_x}{\partial x} + \frac{\partial q_y}{\partial y} - \frac{\partial h}{\partial t} = 0 \tag{1}$$

in which q_x and q_y represent the local sediment transport rates per unit width in the offshore and longshore directions, respectively and h represents the local water depth. To determine the distribution of $q_y(x)$, the above equation was integrated with respect to y

$$\int_0^y \frac{\partial q_x}{\partial x}\, dy + \int_0^y \frac{\partial q_y}{\partial y}\, dy = \int_0^y \frac{\partial h}{\partial t}\, dy \tag{2}$$

with the assumption that in the early stages of accumulation by the groin, the offshore sediment transport is zero, i.e. the first term is zero and the second term can be integrated directly to yield

$$q_y(x,y) - q_y(x,0) = \int_0^y \frac{\partial h}{\partial t}\, dy \qquad (3)$$

The second term is zero if the groin is impermeable. If the integration is carried out to a sufficient distance (y value), then the unaffected transport is determined. The distribution determined by Fulford is presented in Figure 1. Note that a considerable amount of transport is located in the "swash" zone and that the maximum of Fulford's distribution is considerably landward of those in the Komar and Tsuchiya distributions.

SITE CHARACTERISTICS

Santa Barbara is located on the Southern California coast, 150 km northwest of Los Angeles and 560 km southeast of San Francisco. The beaches lie on the Santa Barbara Channel which is separated from the Pacific Ocean by the Channel Islands. Because of the origin of the waves, the sheltering influence of the offshore islands, and the refraction of the waves (O'Brien, 1950), the wave pattern at Santa Barbara is nearly the same for most of the year, with the exception of infrequent waves from southeast storms.

During 1927-28 a detached rubble-mound breakwater with a concrete cap was constructed off Point Castillo to protect the Santa Barbara harbor. The breakwater was 1425 ft. in length roughly parallel to shore, with a 400 ft. arm directed towards shore. The resulting diffraction pattern in the lee of the breakwater caused the sand normally transported along the shore to be deposited in this area. Because of this undesirable effect, the breakwater arm was connected to shore in 1930 (Figure 2).

The now L-shaped breakwater was an effective trap of the longshore transport and the area west of the breakwater soon developed into a substantial beach (Leadbetter Beach) where the present experiment took place. Leadbetter Beach is therefore bordered on the east by the breakwater which, depending on beach contour planform, can act as an effective barrier to eastward sediment transport. The western end of Leadbetter Beach, approximately 1 km from the breakwater, is bordered by a high cliff, with many rocks at its base, extending oceanward to Santa Barbara Point. This western boundary essentially precludes any sediment transport out of Leadbetter Beach to the west. Wiegel (1964) has presented an excellent summary of the Santa Barbara breakwater construction history and resulting shoreline response.

After forming Leadbetter Beach, which represented a shoreline advancement of some 300 m, the sand moved along the breakwater and eventually began infilling the harbor area. By 1935 it was necessary to begin a program of periodic harbor dredging. From 1938 to 1953, maintenance dredging was done biennially, placing most of the dredged material on the beaches to the east, which had suffered substantial erosion after the breakwater construction. In 1954 it was decided to allow part of the continuously forming sand spit at the eastern end of

the breakwater to remain as protection to the harbor from southeast storms. A wooden structure has been constructed along the axis of the spit extending almost due north from a distance of about 20 meters to about 270 meters from the centerline of the breakwater. This spit area is believed to trap all the sand being transported alongshore at Santa Barbara and was used as the major site of NSTS Task 4-C (Dean, Berek, Gable and Seymour, 1982).

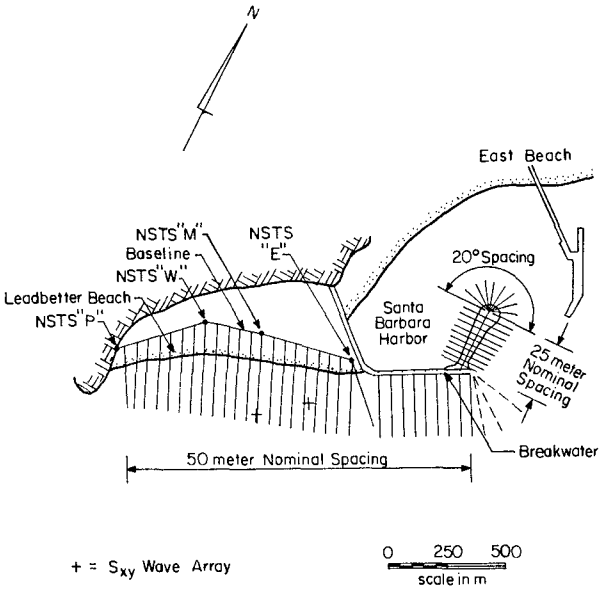

Fig. 2. Study Site, Survey Lines, and Location of the Two S_{xy} Wave Arrays

SURVEY PROCEDURES

Ten surveys were conducted at Santa Barbara from October 1979 to February 1981 (see Table I). Conventional land surveying techniques, overlapped by bathymetric surveys were utilized. Survey lines were run on the spit, on the seaward side of the breakwater and along Leadbetter Beach. A total of 22 lines were surveyed on Leadbetter Beach, two originating from the same point near the "elbow" of the breakwater, the others being at 50 m intervals along the beach, see Figure 2 for a survey plan and location of the S_{xy} gages.

The bathymetric survey was accomplished by a recording fathometer from a boat precisely located by a Cubic Autotape system. To eliminate the effects of waves, each line was surveyed three times and the depth and distance determined by averaging the values obtained over a five meter interval in the offshore direction.

Table I. Survey Oates

Survey Number	Survey Oates
1	10/18/79 to 10/22/79
2	11/30/79 to 12/04/79
3	01/20/80 to 01/25/80
4	02/25/80 to 03/01/80
5	04/10/80 to 04/13/80
6	06/03/80 to 06/09/80
7	08/25/80 to 08/28/80
8	10/22/80 to 10/25/80
9	12/16/80 to 12/20/80
10	02/26/81 to 02/28/81

Tide elevations in Santa 8arbara Harbor were documented during the bathymetric surveys to correct the fathometer data to Mean Sea Level. In addition, the surveys were checked at distances far offshore at water depths presumed sufficiently great to be outside the region of sediment transport. Fathometer calibrations were made frequently during bathymetric surveys.

In addition to the sediment data, wave information was obtained by an S_{xy} array consisting of four bottom-mounted pressure sensors as described by Seymour and Higgins (1978). In general, wave data were recorded at six-hour intervals.

8each profiling was performed during low tide periods, whereas the boat surveys took place during high tides to attempt to maximize overlap distance as much as possible. The profiles were taken with rod and level at five meter intervals, or pronounced changes in beach slope. In general, the overlap was satisfactory. The survey line locations are shown in Figure 2. A more complete description of site characteristics and survey procedures is provided by Oean, 8erek, Gable and Seymour (1982)

ANALYSIS METHOOS

Interpretation of Idealized Pocket Beach Response

The estimation of the longshore sediment transport distribution across the surf zone is based on the idealized response characteristics of a pocket beach to a change in wave direction. If no sediment flux into or out of a pocket beach can occur, and if a change in wave direction occurs, the pocket beach will respond such

that the contours will approach an orientation which is approximately perpendicular to the incident wave direction. Other contour modifications can occur due to a change in wave height and/or period. For example, it is well-known that an increase or decrease in wave steepness without a change in wave direction can cause the profile to flatten or steepen, respectively. Figure 3 summarizes the assumptions utilized in this study: that the even and odd portions of the contour displacements are due to cross-shore and alongshore sediment transport, respectively.

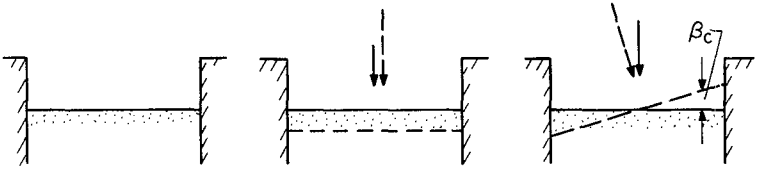

Figure 3. Representative Contour Displacement Signatures for an Idealized Pocket Beach Due to Cross-Shore (Sketch b) and Longshore (Sketch c) Sediment Transport.

The interpretation of the odd component of the beach contour displacements is as follows. Consider the contour changes shown in Figures 3b) and c) and the two dimensional equation of continuity.

$$\frac{\partial q_x}{\partial x} + \frac{\partial q_y}{\partial y} - \frac{\partial h}{\partial t} = 0 \tag{4}$$

If the depth change effect is separated into an even component $(\frac{\partial h}{\partial t})_e$ due to the cross-shore sediment transport and an odd component $(\frac{\partial h}{\partial t})_o$ due to alongshore sediment transport, then by assumption

$$\frac{\partial q_x}{\partial x} = (\frac{\partial h}{\partial t})_e \tag{5}$$

$$\frac{\partial q_y}{\partial y} = (\frac{\partial h}{\partial t})_o \tag{6}$$

It is the odd component which will be of primary concern here. Since contour displacements, rather than depth changes are required, the transformation is introduced relating the time rate of change in depth to the time rate of displacement of a particular contour h_c, i.e.

$$\left(\frac{\partial h}{\partial t}\right)_o = \frac{\partial h_c}{\partial x}\left(\frac{\partial x_c}{\partial t}\right)_o = \frac{\partial q_y}{\partial y} \tag{7}$$

and where $\left(\frac{\partial h_c}{\partial x}\right)$ is the slope, m_c, of the beach profile at the contour of interest. Integrating from an arbitrary location y to the end of the beach compartment, $y = \ell$, where the transport, q_y is zero,

$$q_y(h_c,y) = - m_c \int_y^{\ell} \left(\frac{\partial x_c}{\partial t}\right)_o dy \tag{8}$$

which relates the longshore transport along a particular contour, h_c, to the integral of the time rate of displacement of that contour. If the location y is taken as the centerline of the pocket beach and if the contour change is approximately linear as shown in Figure 3c, with slope, β_c, then the magnitude of the longshore sediment transport rate is

$$|q_y(h_c,y)| \propto m_c \tan\beta_c \tag{9}$$

Without discussing in detail the time response of a particular contour to a change in wave direction, it is relevant to note that the initial effects are manifested at the ends of the compartment and that an odd contour change that is linear is indicative of an adjustment that has nearly achieved equilibruim under the changed wave direction. The ideal data set for establishing the transport distribution is one in which all of the contours have rotated sufficiently to allow volumes transported to be measured accurately, but a sufficiently small transport such that offshore transport has not been induced nor has equilibrium been achieved. In the general case, it would be necessary to employ Eq. (8) rather than Eq. (9).

There are three main limitations to the method described for determining the distribution of longshore sediment transport from contour rotations in pocket beaches. The first and most obvious limitation is that the pocket beach should be "sand tight" such that any alongshore transport along a contour will be manifested by a rotation of that contour rather than by being transported out of the system. The second limitation is that the method assumes that sand transported along a contour will remain on that contour. It is clear that as a result of steepening or flattening of a profile, offshore and onshore sediment transport will occur, respectively. The final limitation relates to the duration between intersurvey periods relative to the time required for the system to achieve equilibrium under the altered wave conditions. Given sufficient time, all active contours would "rotate" into the incoming wave direction and therefore it would be impossible to determine any information relating to the cross-shore distribution of longshore sediment transport. Thus the response should be documented in the early stages of the equilibration process.

Determination of Odd and Even Contour Displacement Components

For each survey, the locations of various depth contours were determined from the data by interpolation. The computer program which determined these locations also established the changes in the contour positions between consecutive surveys. These contour displacement data were then smoothed and the number of lines along Leadbetter Beach reduced to ten, resulting in a spacing of one hundred meters between lines. This smoothing was accomplished by a simple moving average filter:

$$X_1 = x_1 \tag{10}$$

$$X_i = 0.25\, x_{2i-2} + 0.50\, x_{2i-1} + 0.25\, x_{2i} \; ; \; i = 2, 10$$

where: X_i = smoothed displacements
x_i = measured displacements

To separate the contour displacements into even and odd components, the following formulas were used:

$$(f_{odd})_i = \frac{X_i - X_{(N-i)}}{2} \tag{11}$$

$$(f_{even})_i = \frac{X_i + X_{(N-i)}}{2} \tag{12}$$

where: N = total number of points (i.e., 10)

The odd parts of the contour displacements are, by definition, antisymmetric about an axis through the center of the beach planform. This axis is therefore a pivot point about which contour rotations are measured.

Wave Analysis

Wave information was obtained throughout the period of study from an S_{xy} array consisting of four bottom mounted pressure sensors, as described by Seymour and Higgins (1978). Wave recordings were normally available every six hours and spectral information summarizing the wave characteristics of each recording period was provided by R. J. Seymour and D. Castel of the Scripps Institute of Oceanography.

For longshore transport calculations the wave quantities of particular importance are the root mean square breaking wave height, H_b, and the breaker angle, α_b. A value of $P_{\ell s}$, the longshore component of wave energy flux, was calculated as

$$P_{\ell s} = C_1 (H_b)^{5/2} \sin 2\alpha_b$$

where C_1 is a proportionality factor and H_b and α_b were obtained by refraction and shoaling computations which transformed the data from the gage location to the breaker line.

Prediction of Average Longshore Transport Along a Particular Contour Including the Effect of Tidal Variations

Consider the application of a particular predictive distribution for longshore sediment transport, $q_y'(x)$. In this relationship, the origin of x is at the mean water line and the application must account for the effect of the varying tide, $\eta_T(t)$. In the approach utilized herein, the distribution with distance $q_y'(x)$ was first transformed to a distribution with depth, $q_y''(h)$, by the relationship

$$q_y''(h) = \frac{1}{m_c} q_y'(x) \tag{13}$$

in which the beach slope, m_c, was determined from the representative beach profile presented in Figure 4.

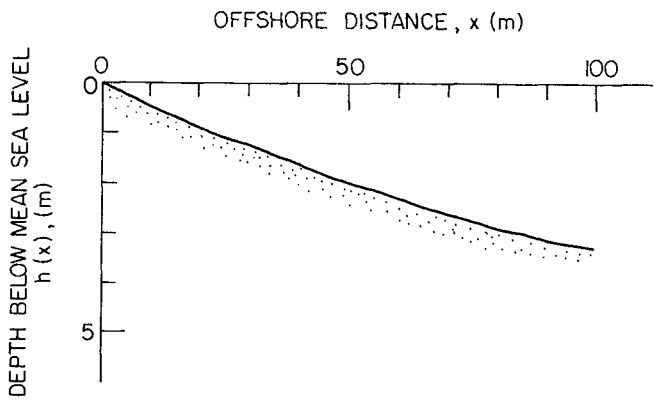

Figure 4. Representative Beach Profile.

The longshore sediment transport along a particular depth contour (h_c) then becomes

$$q_y(h_c,t) = P_{ls}(t)\, q_y''(h + \eta_T(t)) \tag{14}$$

where the distribution $q_y''(h)$ is normalized to unit area and is scaled at each time in accordance with the breaking depth $h_b(t)$ associated

with each $P_{ss}(t)$. This procedure is illustrated schematically in Figure 5. The values of $q_y(h_c,t)$ were calculated for the time-varying tide and wave characteristics at time increments of one hour. The average computed longshore transport values for each contour were determined by integrating Eq. (3) over the time interval of the intersurvey period. These computations were carried out for the distributions of Komar, Fulford and Tsuchiya as presented in Figure 1.

RESULTS

Two intersurvey periods showing significant planform rotations have been analyzed: June-August, 1980 and October-December, 1980. The character of the net beach response to the wave environment was fundamentally different in the two cases; this difference will be discussed briefly. Considering the schematic diagram of Leadbetter Beach in Figure 6, the beach contours during the June-August period rotated counterclockwise (Figure 6a), and during the October-December period the rotation was clockwise (Figure 6b). Because the breakwater does not extend sufficiently far seaward to prevent all the longshore transport, the system is "leaky" when the contours rotate clockwise. When the contours rotate counterclockwise the system is "sediment tight" or "not leaky".

Following the procedure described earlier for the determination of the odd components of the contour displacements, the survey data were analyzed and the results are presented in Figures 7a) and 7b). The odd components are of course antisymetric about the center-line of the beach compartment. Based on these figures, values for the slopes of the contour displacements, β_c, defined in Figure 1c were determined. The resulting transport is proportional to the product of tan β_c and the local beach slope, m_c,

$$q_y \propto m_c \tan \beta_c$$

It is of interest to note that for the October to December intersurvey period, the value of β_c decreases monotonically from the mean sea level contour to the deeper contours. The value of β_c for the June to August period changed in a more complex manner; first increasing slightly from the mean sea level contour to the 1.0 meter contour, followed by a decrease. This pattern leads to a very different expected profile for $q_y(x)/q_y(0)$ for the two intersurvey periods, as shown in Figure 8. The June-August period distribution shows the transport distributed over a much wider range of depths, with transport being greater than $q_y(0)$ to the 1.0 meter contour.

These two measured distributions have been compared with three predicted distributions, which are also shown in Figure 8, and are due to Komar (1977), Fulford (1982), and Tsuchiya (1982).

During the June to August intersurvey period and for depths greater than 0.5 m, all of the predicted transport distributions are less than that inferred from the measured contour displacements. Recalling the earlier discussion of the effect of large contour

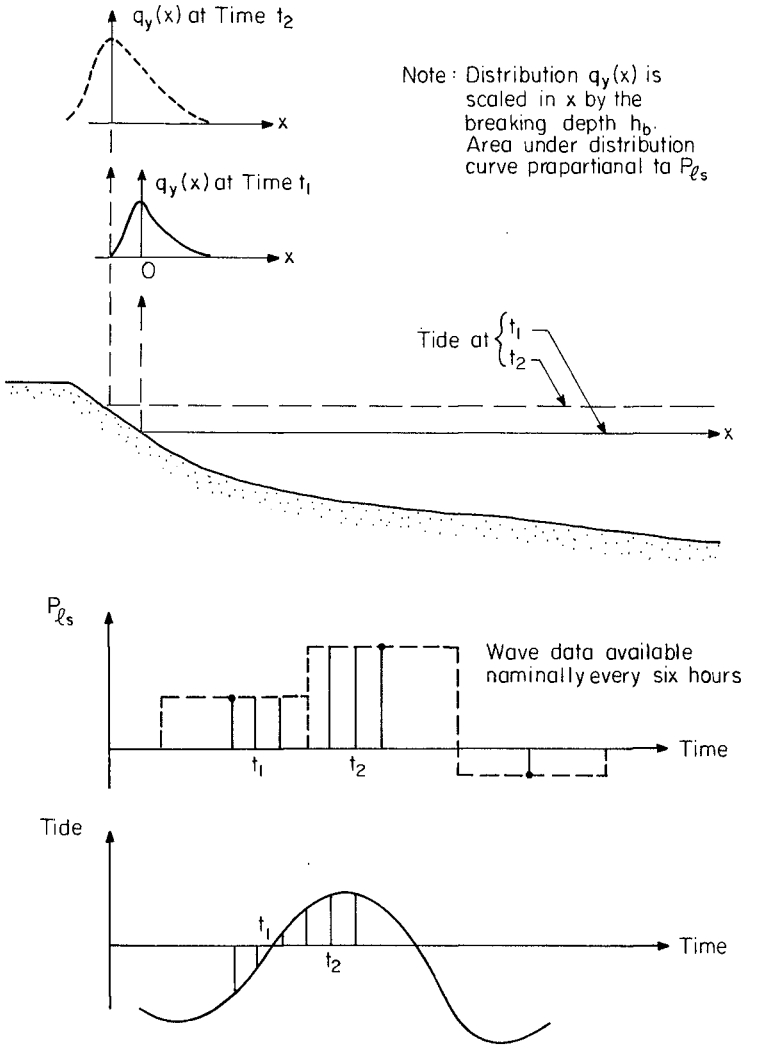

Figure 5. Illustration of Procedure for Predicting Longshore Transport Distribution for Varying Wave Conditions and Fluctuating Tides.

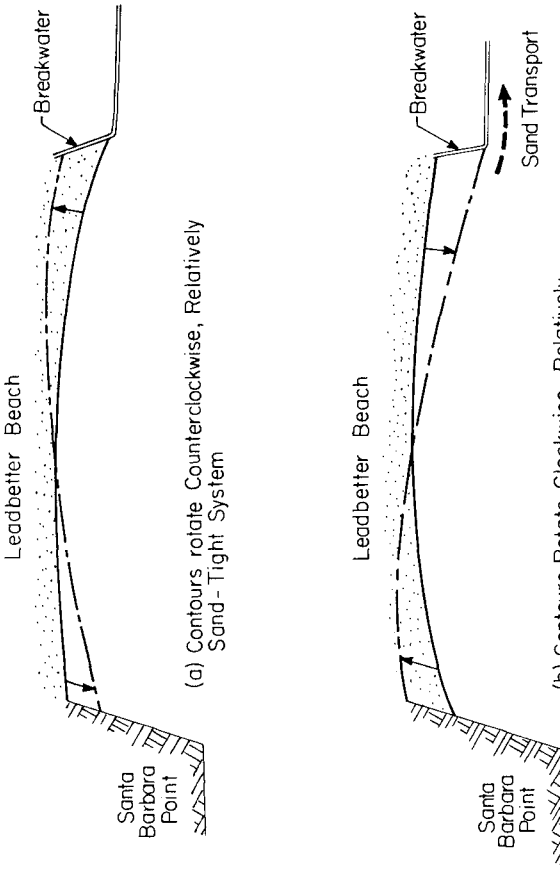

Figure 6. Illustration of Different Sand Retention Characteristics for Clockwise and Counterclockwise Rotation of Beach Contours

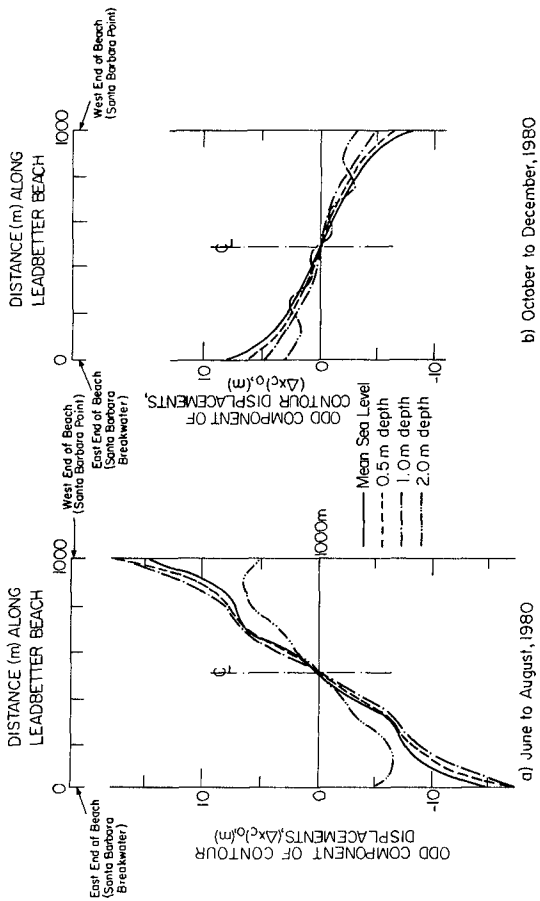

Figure 7. Odd Components of Contour Displacements for Two Different Intersurvey Periods

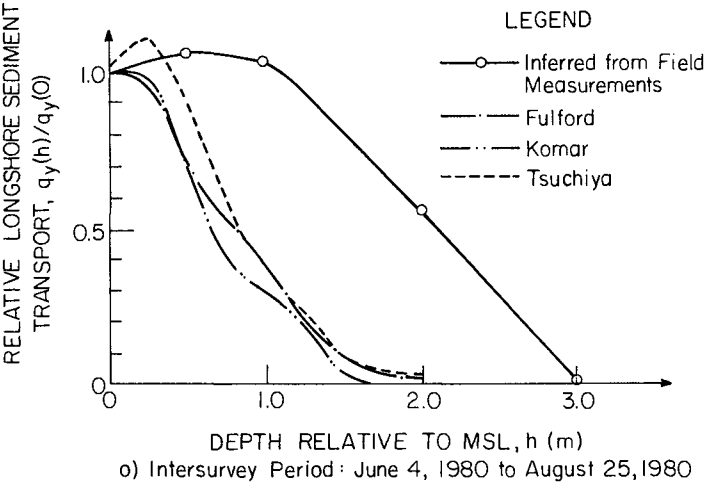

a) Intersurvey Period: June 4, 1980 to August 25, 1980

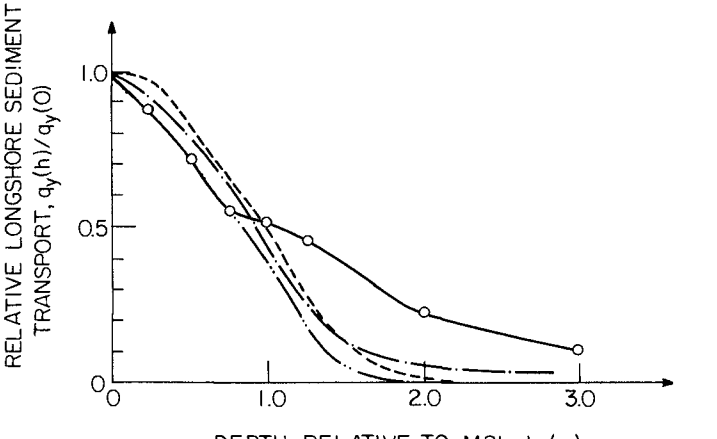

b) Intersurvey Period: October 23, 1980 to December 17, 1980

Figure 8. Comparison of Predicted Relative Longshore Sediment Transport Distributions with the Distributions Inferred from Field Measurements

displacements on the inferred distribution and referring to Figure 7a and Figure 4, it appears likely that the contour displacements of approximately 17 m at the ends of the pocket beach compartment may have caused cross-shore transport. As noted, under the assumptions employed herein, the deposition resulting from cross-shore sediment transport would be interpreted as longshore sediment transport in greater water depths than had actually occurred. Moreover, the triangular distributions of the contour displacements for this intersurvey period (Figure 7a) suggest that an equilibrium planform had been achieved, at least for depths of 1 m and shallower. Although the contour displacements were in a direction such that the compartment should be sand tight, the violations of the assumptions as noted above would appear to invalidate the results of this particular intersurvey period as a basis for evaluating the cross-shore distribution of the longshore sediment transport.

The contour displacements associated with the October to December intersurvey period are clockwise and thus the pocket beach would tend to be "leaky". However, examination of these displacements in Figure 7b indicates that the other two requirements are satisfied much better than for the earlier intersurvey period: (1) the contour displacements are much smaller, and (2) the form of the displacements suggests that the equilibration process may be in the early to intermediate stages. The comparison of the distribution inferred from measurements and those based on the predictions is presented for this intersurvey period in Figure 8b. In water depths less than approximately one meter, there is good general agreement, with the Komar distribution providing the best fit. In greater depths all predicted transport values are less than the measured with Fulford results being in slightly better agreement than the other two. It appears that in water depths greater than one meter, there may be some effect of cross-shore transport induced by the contour displacements.

SUMMARY AND CONCLUSIONS

Summary

Following a change in wave direction, the active contours in an idealized pocket beach will respond by rotating such that they approach a perpendicular orientation relative to the incoming wave rays. A method has been presented for interpreting the rotation of various contours to determine the cross-shore distribution of the longshore sediment transport. The requirements for the method to be applicable are: 1) the longshore and cross-shore transport gradients result in odd and even changes in the position of a contour, respectively, (2) the pocket beach compartment should be sand tight, (3) the contour displacements should be sufficiently small that only minimal cross-shore transport is induced as a result of the perturbation of the equilibrium beach profile, and (4) the contour displacements should be documented while the equilibration process is in its initial stages.

The method has been evaluated by analyzing the NSTS Leadbetter Beach profile data from two intersurvey periods. These results are

compared with predictions based on three proposed longshore transport distributions.

Conclusions

1. The two intersurvey periods analyzed herein were for June to August, 1980 and October to Oecember, 1980. Neither of these two data sets satisfy entirely the requirements identified for determining the longshore sediment transport distribution from contour displacements. For the first period, the contour rotation was counterclockwise such that the compartment would be sand tight; however, the amount of change and duration of transport prior to documentation appear to result in an indication of excessive transport in water depths greater than one meter. For the second period, the clockwise rotation of the contours tends to result in a somewhat "leaky" system. However the character of the contour displacement indicates that little cross-shore transport was induced and that the equilibration process was in the early stages. Thus, greater confidence is assigned to the second intersurvey period.

2. Although the forms of the three trial distributions differ substantially, the effect of "tidal smearing" is to reduce these differences as manifested in predicted contour displacements and inferred distributions.

3. Although the three distributions (after tidal smearing) are not markedly different, for the second intersurvey period, which is considered to satisfy more completely the requirements of the method, the distribution of Komar provides the best agreement in depths less than one meter and that of Fulford agrees best in water depths greater than one and one-half meters.

4. To better evaluate candidate distributions, it would be desirable to apply the procedure in locations where no tide is present, such as the Great Lakes if a beach segment with proper planform controls could be identified. If applied in areas with tides, the tide range should be small compared to the representative breaking wave height.

5. It is hoped that the method will be useful in further determinations of the cross-shore distribution of longshore sediment transport, both in laboratory and field studies.

ACKNOWLEDGEMENTS

The financial support provided by the Sea Grant Program to this component of the Nearshore Sediment Transport Program is greatly appreciated. The encouragement and guidance of Dr. David Duane as Technical Monitor of that program was especially valuable as was that of Or. R. J. Seymour as Program Manager. The dedicated and professional efforts of Mr. C. G. Gable of Scripps Institute of Oceanography and personnel of Ocean Surveys, Inc. in the field surveys contributed significantly to the quality of the field data. Finally, the University of California at Santa Barbara was very helpful by

providing vessels and highly competent personnel to assist in the field efforts.

REFERENCES

8agnold, R.A., "Mechanics of Marine Sedimentation," The Sea, M.N. Hill, ed., Interscience Publishers, John Wiley & Sons, New York, N.Y., Vol. 3, 1963. p. 507-528.

Das, M. M., "Suspended and Longshore Sediment Transport Oata Review," Proceedings, Thirteenth International Conference on Coastal Engineering, 1972, p. 1027-1048.

Oean, R. G., E. P. 8erek, C. G. Cable and R. J. Seymour, "Longshore Transport Oetermined by an Efficient Trap," Proceedings, Eighteenth International Conference on Coastal Engineering, 1982.

Ouane, O. B. and R. J. Seymour, "The Nearshore Sediment Transport Study," Proceedings, Sixteenth International Conference on Coastal Engineering, Chapter 92, 1978, p. 1555-1562.

Fulford, E., "Oistribution of Longshore Sediment Transport Across the Surf Zone," M.S. Thesis, Oepartment of Civil Engineering, University of Delaware, Newark, DE, September, 1982.

Gable, C. G., ed., "Report on Oata from the Nearshore Sediment Transport Study Experiment at Leadbetter Beach, Santa 8arbara, California, January-February, 1980," IMR Reference No. 80-5, University of California, Institute of Marine Resources, February, 1981.

Komar, P. D., "Longshore Currents and Sand Transport on 8eaches," Ocean Engineering III, ASCE 1976, p. 333-354.

Komar, P. D., "Beach Sand Transport: Distribution and Total Drift," Journal of the Waterway, Port, Coastal and Ocean Division, ASCE, 103 (WW2), 1977, p. 225-239.

Longuet-Higgins, M. S., "Longshore Currents Generated by Obliquely Incident Sea Waves, 1," Journal of Geophysical Research, Vol. 75, No. 33, 1970, pp. 6778-6789.

O'Brien, M.P., "Wave Refraction at Long 8each and Santa Barbara, California." Bulletin of the Beach Erosion Board, U.S. Army Corps of Engineers, January, 1950.

Savage, R. P., "Laboratory Study of the Effect of Groins on the Rate of Littoral Transport: Equipment Development and Initial Tests," U.S. Army Corps of Engineers, Beach Erosion Board, Technical Memorandum No. 114, 1959.

Seymour, R. J. and A. L. Higgins, "Continuous Estimation of Longshore Sand Transport," ASCE Proceedings, Coastal Zone '78, 1978, p. 2308-2318.

Thornton, E.B., "Distribution of Sediment Transport across the Surf Zone," Proceedings, Thirteenth International Conference on Coastal Engineering, 1973, p. 1049-1068.

Tsuchiya, Y., "The Rate of Longshore Sediment Transport and Beach Erosion Control," Paper No. 132, Abstracts, Eighteenth International Conference on Coastal Engineering, 1982, p. 258-259.

Wiegel, R.L., Oceanographical Engineering, Chapter 18, Prentice Hall, Inc., New York, N.Y., 1964, p. 472-486.

NEW FRAMEWORK FOR PREDICTION OF LONGSHORE CURRENTS

by

C A Fleming[1] and D H Swart[2]

ABSTRACT

The accuracy of prediction of longshore sediment transport depends largely on the accuracy with which the wave-driven longshore currents within the breaker zone can be predicted. Longuet-Higgins (1970) developed a formulation for longshore transport which is widely used today. In the present paper the basic theory of Longuet-Higgins is re-examined. The effect of bed roughness on the magnitude of the longshore current is quantified with the aid of over 350 individual data sets and the theory is theoretically extended to include the effect of random waves, in a similar way to Battjes (1974), and higher-order waves. For this latter purpose the Vocoidal water wave theory of Swart (1978) is used. It is shown that the use of Vocoidal theory leads to a velocity distribution which is in closer correspondence to measured data than that predicted by using linear wave theory.

1. MOTIVATION AND BACKGROUND

The magnitude and distribution of the wave-driven longshore current in the breaker zone depends on the momentum balance, which in turn depends on the underwater profile, the incident wave characteristics and the wave breaking mechanism. In 1970 Longuet-Higgins solved this momentum balance equation in the longshore direction in the shore area by making specific assumptions regarding three individual terms, namely, the driving force or radiation stress term, the bed shear and the lateral mixing, the latter two being dissipative terms.

The momentum balance in the longshore direction x as given by Longuet-Higgins is:

---

1) Sir William Halcrow and Partners, Swindon, UK

2) National Research Institute for Oceanology, CSIR, Stellenbosch, RSA

$$\frac{\partial R_{yx}}{\partial y} + B_x + \frac{\partial D_y}{\partial y} = 0 \quad \ldots \quad (1)$$

where $\frac{\partial R_{yx}}{\partial y}$ = variation in flux of x-momentum with distance y offshore;

B_x = bed shear in the direction of the longshore current; and

$\frac{\partial D_y}{\partial y}$ = exchange of momentum due to lateral mixing.

The type of solution obtained, or more specifically the variation of the current with distance offshore, depends on the assumptions made regarding these three terms.

Predicted longshore sediment transport rates are very sensitive to the **distribution** and **magnitude** of the longshore current. An error in prediction of the longshore current of 10 per cent could cause an error in the prediction of the longshore sediment transport of as high as 70 per cent.

In a laboratory study into current patterns in the vicinity of a proposed coastal structure it was observed that the longshore current velocities generated by regular waves on a very flat beach ($\approx$ 1 in 100) were between 2 and 5 times higher than predictions with the Longuet-Higgins model would tend to indicate (CSIR, 1978). This anomaly is seemingly coupled to the bed roughness.

In the shallow water region where sediment transport calculations are normally performed the waves are decidedly non-linear. Swart and Loubser (1979) have shown that linear theory does not allow for a proper representation of the time-dependent wave properties in this area. In a comparison of the applicability of 13 different wave theories they found that Vocoidal water wave theory, developed by Swart (1978), is the most applicable theory under all wave conditions tested in the shallow water region, and was significantly better than the linear theory. In addition, waves in prototype are not regular but random and do not always break as spilling breakers, as has to be assumed in order to obtain a solution for the longshore current profile.

Swart and Fleming (1980) already reported briefly on the effect of the bed roughness and the bed slope on the Longuet-Higgins solution without going into the background for the re-analysis. Subsequently more research was done into the effect of the non-linearity of the incident waves on the longshore current profile.

The objective of this paper is to report on progress made towards the understanding of the effect of the above-mentioned factors. It will deal mainly with

- the effect of bed roughness; and
- the effect of both higher-order and random waves on the type of solution obtained.

2. TREATMENT OF LINEAR, REGULAR WAVES

The theory of longshore current generation by linear, regular waves breaking, as spilling breakers, on a plane beach was covered authoritively by Longuet-Higgins (1970) and will not be repeated here. Only those points which are relevant to the present discussion will be highlighted.

Driving forces

The driving force for the longshore current is obtained by considering the variation in the flux of longshore momentum with distance y offshore.

$$\frac{\partial R_{yx}}{\partial y} = -\frac{5}{16}\gamma^2 \rho g d \tan\alpha \sin\Theta \cos\Theta \quad \ldots (2)$$

(Longuet-Higgins, 1970)

where γ = breaker index, that is, the ratio of breaking wave height H_b to corresponding water depth d_b; this index is assumed constant throughout the breaker zone;

ρ = mass density of water;

g = gravitational acceleration;

d = water depth;

α = beach slope;

Θ = angle of incidence of the waves, measured between the wave crest and the local bed contour.

Resistive forces: Bed shear

It was shown (CSIR, 1978) that the general expression for bed shear B_x in the longshore direction is:

$$B_x = \frac{2}{\pi}\rho\,(C_{LH1}\,u_o v + g v^2/C_n^2) \quad \ldots (3)$$

where C_{LH1} = a friction coefficient

$$= \left(\frac{f_w g}{2C_n^2}\right)^{0,5} \quad \text{(CSIR, 1978)} \quad \ldots \quad (4)$$

u_o = maximum value at the bed of the horizontal orbital velocity;

v = longshore current velocity at depth d;

C_n = Chezy roughness coefficient = 18 log (12d/r);

f_w = wave friction factor, as defined by Jonsson (1966).

Longuet-Higgins (1970) assumed that $v << u_o$ and obtained a simplified version of equation (3), namely,

$$B_x = \frac{2}{\pi} \rho C_{LH} u_o v \quad \ldots \quad (5)$$

In the present study the simplified equation (5) as used by Longuet-Higgins will be employed. Any approximations introduced in this manner for cases where v/u_o is not negligible, which is normally the case, will exhibit itself as a scatter in the empirical values of C_{LH}.

Resistive forces: Lateral mixing

Longuet-Higgins (1970) assumed that Dy is given by:

$$D_y = -\mu_e d \frac{\partial v}{\partial y} \quad \ldots \quad (6)$$

where μ_e = horizontal eddy viscosity

$$= N\rho y(gd)^{0,5} \text{ (Longuet-Higgins, 1970)}$$

N = dimensionless constant.

Although the eddy viscosity as defined by Longuet-Higgins increases indefinitely with distance from the shoreline, even outside the breaker zone where it would be expected to decrease markedly, the results obtained via this method are very realistic.

Solution

Using equations (2), (5) and (6) above, Longuet-Higgins obtained the longshore current profile:

$$v = v_{or} f(y,P) \quad \ldots \quad (7)$$

where v_{or} = scaling velocity at the breaker line

$$v_{or} = \frac{5\pi}{16} \frac{\gamma(gd_b)^{0,5}}{C_{LH}} \tan\alpha \sin\theta_b \cos\theta_b \quad \ldots (8)$$

P = dimensionless lateral mixing parameter; and subscript b refers to the initial breaker line.

After investigating all available data sets on longshore current, as summarised by Galvin and Nelson (1967), Longuet-Higgins (1970) found that if he neglected those data sets termed questionable by Galvin and Nelson the parameter C_{LH} varied between 0,0036 and 0,012 with a mean value of 0,0082. He therefore concluded that "C_{LH} is of order 0,01". This has subsequently been interpreted by researchers to mean that C_{LH} is a constant. Since C_{LH} is by definition a roughness coefficient this is obviously an erroneous conclusion.

Re-analysis of data

To settle this matter, the data as tabulated by Galvin and Nelson were re-analysed, along with some newer data, in an approach similar to the earlier analysis performed by Longuet-Higgins. Only the mean longshore current velocity was available for most of the data. Longuet-Higgins showed that the mean current velocity is given by:

$$\bar{v} = \frac{5\pi}{16} \beta_m \frac{\gamma^{0,5}(gH_b)^{0,5}}{C_{LH}} \tan\alpha \sin\theta_b \cos\theta_b \quad \ldots (9)$$

where β_m depends on the intensity of lateral mixing, and has a mean value of 0,33 with a possible variation of plus/minus 30 per cent.

Equation (9) can be rewritten to obtain C_{LH} in terms of a dimensionless parameter Φ_o, namely,

$$C_{LH} = \frac{5\pi}{16} \beta_m \gamma^{0,5} \Phi_o \quad \ldots (10)$$

where $$\Phi_o = \frac{(gH_b)^{0,5}}{\bar{v}} \tan\alpha \sin\theta_b \cos\theta_b \quad \ldots (11)$$

For each data set the parameter Φ_o is a function of the bed roughness and, perhaps surprisingly, of the bed slope. If one, however, keeps in mind that the bed slope influences the breaker type which in turn is strongly related to the extent of lateral mixing, it becomes apparent that Φ_o implicitly contains the effect of lateral mixing.

In this context lateral mixing is quantified by means of the lateral mixing coefficient P, which was found by Longuet-Higgins to have a theoretical upper limit of 0,4. By inspection of the available data on longshore current profiles Longuet-Higgins concluded that the data are adequately bracketed by theoretical profiles with values of P = 0,1 and P = 0,4. Furthermore, the mean value of P appeared to be P = 0,2. In the present analysis it was therefore assumed that P = 0,2 and that any effect of a different mixing coefficient would be rectified for by the value obtained for C_{LH} (or Φ_o in the present stage of the computation). Keeping the comment about β_m in mind it is then reasonable to expect that C_{LH} will also exhibit a variation of plus/minus 30 per cent, which was indeed later shown to be the case.

For a value of P = 0,2 the function f(y,P) in equation (7) becomes:

$$f(y,P) = \begin{cases} -1,74(y/y_b)^{1,61} + 2(y/y_b) & \text{for } 0 \leq y/y_b \leq 1 \\ 0,26(y/y_b)^{3,11} & \text{for } 1 < y/y_b \leq \infty \end{cases} \quad \ldots (12)$$

In analogy with the result in equation (4) it is assumed that the actual value of the roughness parameter C_{LH} is related to roughness by

$$C_{LH} = K\left(\frac{f_w g}{2C_n^2}\right)^{0,5} \quad \ldots (13)$$

Parameter K is a proportionality constant which according to Figure 1 should be a function of the bed slope.

With the aid of the data in Figure 1 and equation (10) it was found that

$$K = 25(\tan\alpha)^{0,85} \quad \ldots (14)$$

which means that

$$C_{LH} = 25\left(\frac{f_w g}{2C_n^2}\right)^{0,5} (\tan\alpha)^{0,85} \quad \ldots (15)$$

A comparison between measured and predicted values of C_{LH} is given in Figure 2.

It is interesting to note that Komar and Inman (1970) in an analysis of the same data found that

$$C_{LH} \approx 0,15 \tan\alpha \quad \ldots (16)$$

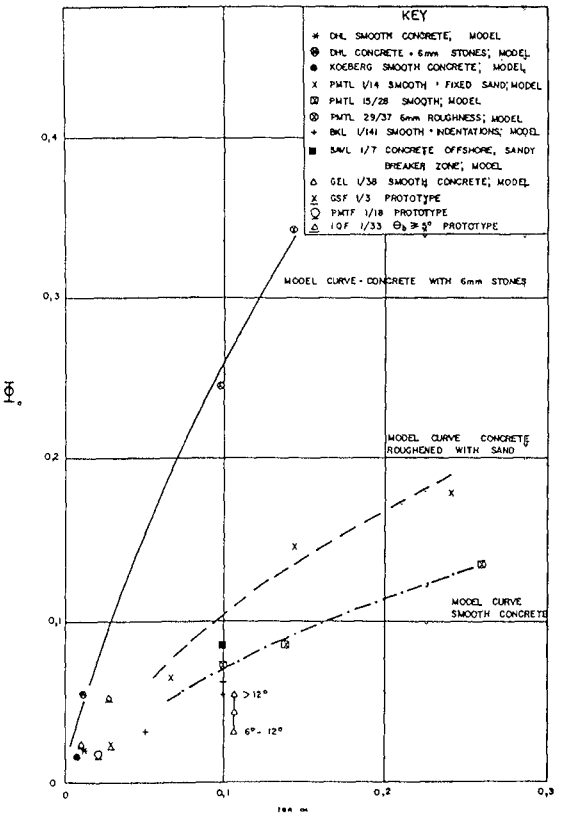

FIG. 1 RELATIONSHIP BETWEEN Φ_o, BEACH SLOPE AND BED ROUGHNESS

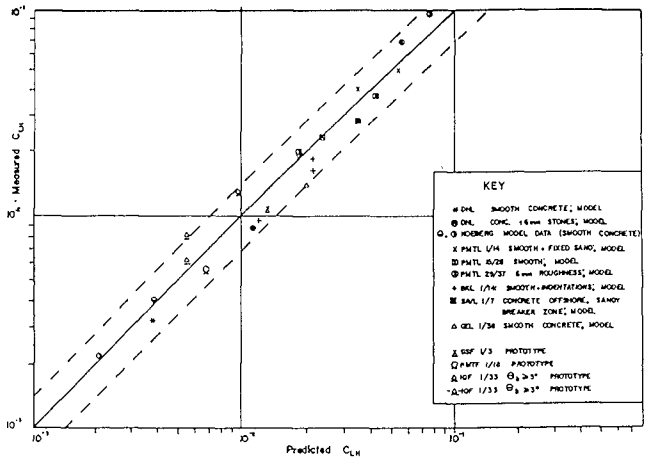

FIG. 2 RELATIONSHIP BETWEEN PREDICTED AND MEASURED C_{LH} VALUES FOR MODEL AND PROTOTYPE CONDITIONS

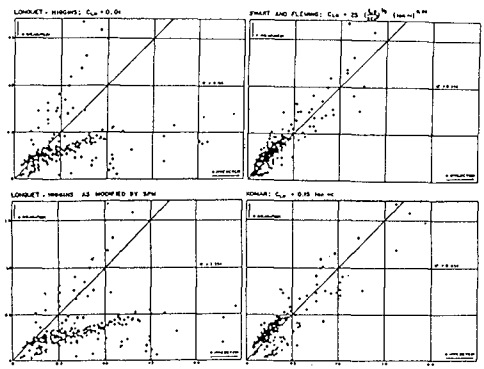

FIG. 3 PREDICTED VERSUS MEASURED LONGSHORE CURRENT VELOCITIES BY FOUR DIFFERENT METHODS

This would imply that the velocity is independent of bed slope.

Figure 3 gives a comparison of the "goodness of fit" to the data when using the present technique, Komar's method, the Longuet-Higgins method with the assumption of $C_{LH} \approx 0,01$ and a slight variation to this last approach, which also assumes a constant value for C_{LH} and which is the method recommended for use by the Shore Protection Manual (SPM, 1973). A root-mean-square error was computed for each of the four methods tested, based on the comparison between the theoretical/emprirical models tested and all 352 available data sets. The present method has a rms error of 0,248, which is only about 40 per cent of that found for the Komar method, and which is an order of magnitude better than the methods which assume a constant value for C_{LH}.

It is interesting to note that the two methods with the closest correspondence to the data, that is, the present method and Komar's method, suggest a very much lower dependence on bed slope than predicted by the classical theory. The explanation for this apparent anomaly lies in the fact, as was pointed out earlier, that the roughness coefficient contains, at least in part, the effect of the lateral mixing, which is a function of amongst other things the bed slope.

It should be borne in mind that although the method derived here is far superior to the method normally used, it is still not applicable to the case of waves breaking as plunging breakers or for waves breaking on a barred beach.

3. TREATMENT OF LINEAR, RANDOM WAVES

A theoretical framework for the prediction of longshore currents generated by random waves was developed by Battjes (1974) which yielded reliable results. It is comparable to the Longuet-Higgins approach for regular waves except that wave set-up was not neglected and for the obvious differences between regular and random waves. The method has to be applied numerically since no analytical solution was found. Battjes draws the very important conclusion that lateral mixing is not nearly as important in the determination of the velocity profile for random waves as it is in the case of regular waves.

In this section a derivation will be done for random waves at the same level of assumption as was done by Longuet-Higgins for regular waves.

Assumptions

(i) Linear wave theory is used;

(ii) Waves are random with a Rayleigh height distribution;

(iii) Waves break as spilling breakers with a constant breaker index $\gamma = H_b/d_b$ throughout the breaker zone;

(iv) The wave spectrum within the breaker zone is treated in the same way as done by Battjes (1974), that is, waves in excess of γ times the water depth are reduced to γ times the water depth;

(v) Wave set-up is initially neglected although its effect will be discussed later;

(vi) The bed slope α in the breaker zone is considered constant;

(vii) The bed roughness coefficient C_{LH} is constant over the breaker zone; and

(viii) Lateral mixing is neglected (Battjes, 1974).

Governing equations

The same momentum balance equation (equation (1)) applies as for regular waves. The assumptions outlined above lead to the following expression for the driving force term when shallow-water wave conditions are assumed:

$$\frac{\partial R_{yx}}{\partial y} = -\frac{5}{16}\rho\gamma^2(gd)\exp\left(-\frac{\gamma^2 d^2}{H_{frms}^2}\right)\sin\Theta\cos\Theta\tan\alpha \quad \ldots (17)$$

where H_{frms} = **fictitious rms wave height** at water depth d, which would have existed under the influence of shoaling, refraction and bed friction if **no wave breaking** had occurred.

When looking at the resistive forces, the bed shear is written in the simplified form of Longuet-Higgins (see equation (5)), which after substitution of shallow-water wave conditions reduces to

$$B_x = \frac{1}{\pi} C_{LH}\,\rho\left(\frac{\bar{H}}{d}\right) v(gd)^{0,5} \quad \ldots (18)$$

where $\bar{H}$ = mean wave height at depth d, after including the effect of wave breaking.

Solution

The combination of equations (17) and (18) yields an expression for the longshore current velocity at water depth d:

$$v = \frac{5\pi}{16} \frac{\gamma^2 (gd)^{0,5}}{C_{LH}} \left(\frac{d}{H}\right) \exp\left(-\frac{\gamma^2 d^2}{H^2_{frms}}\right) \tan\alpha \sin\theta \cos\theta \qquad (19)$$

If, in analogy with regular waves, one writes, with lateral mixing now being neglected

$$v = v_{oir} f(y) \qquad \ldots (20)$$

it follows that

$$v_{oir} = \frac{5\pi}{16} \frac{\gamma (g d_{bs})^{0,5}}{C_{LH}} \tan\alpha \sin\theta_{bs} \cos\theta_{bs} \qquad \ldots (21)$$

and $$f(y) = \left(\frac{d}{d_{bs}}\right) \left(\frac{d}{H}\right) \gamma \exp\left(-\frac{\gamma^2 d^2}{H^2_{frms}}\right) \qquad \ldots (22)$$

where subscript bs refers to the significant breaker line.

An example of the comparison between the velocity profiles as predicted for regular waves with lateral mixing and for random waves without lateral mixing is given in Figure 4.

In the above derivation the wave set-up was neglected. If, however, the depth d is taken to be the still-water depth plus the wave set-up, the slope $\tan\alpha$ should actually read $(\partial d/\partial y)$, then a very good first approximation of the actual effect of wave set-up is obtained. For the present equations (21) and (22) can be used together with the value of C_{LH}, as given by equation (15). However, it is deemed advisable to obtain more data on longshore currents generated by random waves, especially under controlled conditions.

Furthermore, in the case of longshore currents generated by random waves breaking as plunging breakers on a barred beach, the longshore current profile will not be as smooth as indicated by, for example, Figure 4. In this case one should for the present return to the Battjes approach. However, the effect of lateral mixing has to be included since the lateral velocity gradients, which according to equation (6) are not small any more, will lead to higher lateral mixing, especially near the breaker line.

4. TREATMENT OF REGULAR, VOCOIDAL WAVES

The only known case in the literature of a derivation for longshore currents based on a higher-order theory, is that of James (1974). James based his model on hyperbolic waves in the nearshore region and on Stokes waves further out to sea. Due to the disadvantage of coupling different wave theories at a given water depth, the limited range of applicability of the hyperbolic theory and the fact that

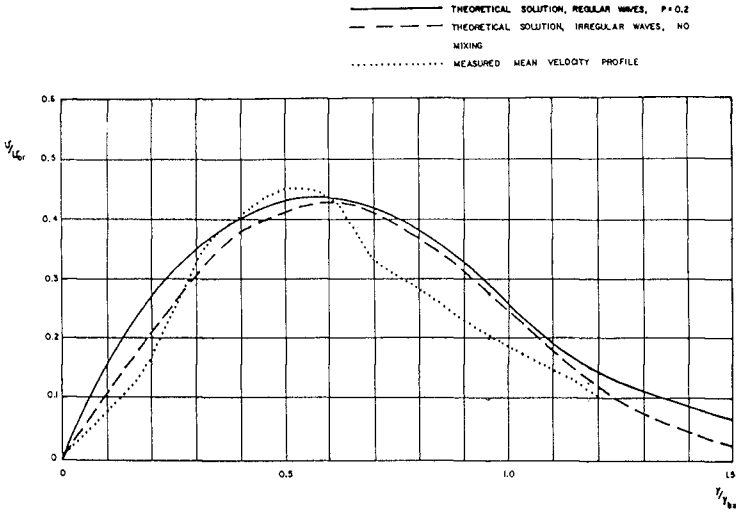

FIG. 4 COMPARISON BETWEEN THEORETICAL SOLUTION FOR REGULAR AND IRREGULAR WAVES RESPECTIVELY AND MEAN MEASURED PROFILE

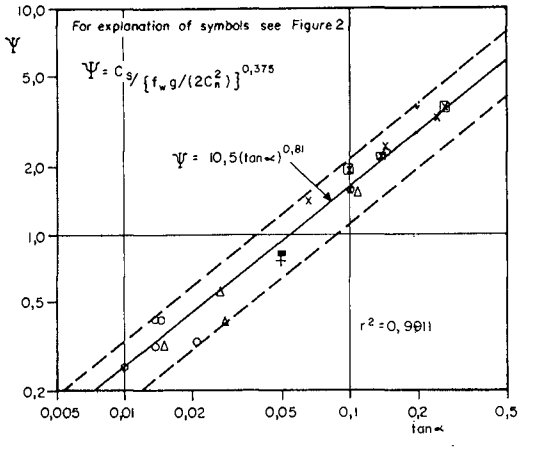

FIG. 5 RELATIONSHIP BETWEEN Ψ AND TANα

the longshore current model of James is numerical, this method is not considered further.

Swart and Loubser (1979) made a comprehensive comparison of measured wave properties with predictions from 13 different theories. The results indicate that although linear theory provides an adequate description of wave profile, wave celerity and orbital motions in deep water, the comparison deteriorates as the relative water depth becomes less. Swart and Loubser concluded that linear theory gives satisfactory results only for values of a non-linearity parameter $F_c \leq 200$ and should not be applied for $F_c > 200$. The parameter F_c is defined by

$$F = (H/d)^{0,5} \left(T(g/d)^{0,5}\right)^{2,5} \quad \ldots (23)$$

If one assumes breaking wave conditions with $H/d = 0,7$, the above restriction would imply that linear theory can only be applied for $T\sqrt{g/d}$ less than 8,9. The following table shows values of d, below which the theory should then not be applied, for different values of wave period T.

T (s)	d (m)	T (s)	d (m)
6	4,4	14	24,1
8	7,9	16	31,4
10	12,3	18	39,8
12	17,7	20	49,1

It is therefore clear that the use of the linear theory to predict breaker-line wave data is not advisable.

On the other hand, the same study by Swart and Loubser indicated that Vocoidal theory adheres well to data for all values of F_c covered by the data, which extended to $F_c = 60\ 000$. In fact, they finally concluded that Vocoidal theory is the only readily applicable analytical wave theory having a good correspondence to measured data and a good adherence to the original wave boundary value problem for the whole range of non-breaking waves. This theory therefore not only provides a good correspondence to data but also a sound framework for the derivation of expressions for the prediction of secondary wave-induced phenomena, including longshore currents.

In this section those aspects of the derivation of the longshore current as driven by Vocoidal theory will be highlighted which differ from the theory outlined in Section 2.

Driving forces

The radiation stress term R_{yx} for Vocoidal waves is given by

$$R_{yx} = 2E_{ku} \sin\theta \cos\theta \quad \ldots (24)$$

as compared to

$$R_{yx} = En \sin\theta \cos\theta \quad \ldots (25)$$

for linear waves.

In the above E_{ku} is the kinetic energy per unit surface area due to the horizontal orbital velocity, E is the total wave energy per unit surface area and n is the group velocity/celerity ratio.

In shallow water the ratio R_1 between R_{yx} as determined for the Vocoidal and linear theories respectively becomes, if one assumes for the moment that H and θ are equal for the two theories:

$$R_1 = (R_{yx})_{voc}/(R_{yx})_{lin} = 16e_{ku} \quad \ldots (26)$$

where e_{ku} is defined by $E_{ku} = e_{ku}\ \rho g H^2$.

As an example of the variation in R_1, consider the case of H/d at breaking = 0,8.

$T(g/d)^{0,5}$	R_1	$T(g/d)^{0,5}$	R_1
5	broken waves	25	0,36
10	0,74	30	0,31
15	0,56	35	0,27
20	0,44	40	0,23

It is thus apparent that the coefficient of the radiation stress term is appreciably lower for Vocoidal theory than for linear theory.

The driving force term in the momentum balance equation then becomes:

$$\frac{\partial R_{yx}}{\partial y} = -\frac{5r_{yx}}{2}\gamma^2 f_{yx}\ \rho(gd)\ \tan\alpha \sin\theta \cos\theta \quad \ldots (27a)$$

where $R_{yx} = r_{yx}\ \rho g H^2$ defines r_{yx}; and

$$f_{yx} = 1 + \frac{d}{r_{yx}} \frac{\partial r_{yx}}{\partial d} \quad \ldots (27b)$$

Resistive forces

Similarly, the bed shear as given by Vocoidal theory can be written as

$$B_x = \frac{2}{\pi} a_{voc} \rho C_s u_o v \quad \ldots (28)$$

as opposed to equation (5), where a_{voc} is the ratio between the bed shear in the longshore direction as predicted by Vocoidal and linear theory respectively and C_s is the roughness coefficient applicable to Vocoidal waves, as opposed to C_{LH} for linear waves.

Again using H/d = 0,8, one finds:

$T(g/d)^{0,5}$	10	15	20	25	30	40
a_{voc}	0,91	0,65	0,50	0,40	0,34	0,26

Solution

In setting up a momentum balance equation, the fact that the coefficient of R_{yx} is also a function of distance offshore should be kept in mind. When neglecting lateral mixing, one finds for the Vocoidal theory at the breaker line, that

$$v_{or} = \frac{5\pi}{16}(P_{reg}) \frac{\gamma(gd_b)^{0,5}}{C_s} \tan\alpha \sin\theta_b \cos\theta_b \quad \ldots (29)$$

where P_{reg} is a parameter containing the effect of the non-linearity (vocoidalness) of the waves.

The following table gives values for P_{reg} in terms of γ and T_c, where $T_c = T\sqrt{g/d}$.

T_c	Values of P_{reg}									
	γ=0,1	0,2	0,3	0,4	0,5	0,6	0,7	0,8	0,9	1,0
5	1,84	1,83	1,82	1,81	1,80	1,79	-	-	-	-
10	1,77	1,77	1,74	1,68	1,63	1,61	1,61	1,65	1,70	-
15	1,79	1,77	1,71	1,64	1,58	1,54	1,56	1,63	1,69	1,77
20	1,93	1,87	1,80	1,72	1,66	1,65	1,70	1,79	1,84	1,90
25	2,08	2,03	1,95	1,86	1,78	1,78	1,88	1,99	2,06	2,10
30	2,31	2,24	2,15	2,04	1,95	1,98	2,11	2,24	2,31	2,35
35	2,60	2,53	2,42	2,29	2,17	2,22	2,40	2,54	2,60	2,63
40	2,98	2,90	2,77	2,62	2,46	2,56	2,75	2,89	2,95	2,95

The above table shows that P_{reg} is a function of the deep-water wave steepness and the breaker index.

Equation (29) is identical to its linear theory counterpart (equation (8)) except for the inclusion in equation (29) of the parameter P_{reg}. As a first approximation to the effect of non-linear waves on the longshore current profile one can write

$$v = v_{or} \{(P_{reg})_d/(P_{reg})_{d_b}\} f(y,P) \quad \ldots (30)$$

where subscript d (or d_b) means that P_{reg} is computed at depth d (or d_b), v_{or} is given by equation (29) and $f(y,P)$ is the same function as before (equation (12)) with $P = 0,2$. The original longshore current data as compiled by Galvin and Nelson (1967) were re-analysed to obtain C_S in an analogous fashion to that described in Section 2 for the computation of C_{LH}. The equation of best fit is given by:

$$C_S = 10,5 \left(\frac{f_w g}{2C_h^2}\right)^{0,375} (\tan\alpha)^{0,81} \quad \ldots (31)$$

(see Figure 5)

A comparison of values of C_S obtained from equation (31) with those derived directly from the data resulted in a correlation coefficient $r^2 = 0,9911$. On the ohter hand, a comparison of values of C_{LH} as obtained from equation (15) with values of C_{LH} derived directly from the data yielded a correlation coefficient $r^2 = 0,9471$, that is, the correlation is not as good as that for C_S. Not only does the Vocoidal approach therefore yield a description of the current profile which is more in line with shallow-water waves than the linear theory approach, but it also yields a better estimate of the mean longshore current velocity.

More research is needed where the deep-water wave steepness is varied in a more systematic manner to improve this relationship. Nevertheless equation (31) constitutes the best estimate of C_S available at present and when used in conjunction with equation (30) it should yield better results than those predicted with the aid of the linear theory.

In the above it was implicitly assumed that the mean value of P remains 0,2 as was the case for linear waves. This assumption may not be correct, as pointed out by James (1974) and still needs to be carefully investigated with the aid of well-designed experiments.

5. TREATMENT OF RANDOM, VOCOIDAL WAVES

The same assumptions as those for the case of longshore currents generated by random, linear waves apply in the present study of random, vocoidal incident waves. The resulting shape of the longshore current profile after analogous deductions as in Sections 2 to 4 is:

$$v = \frac{5\pi}{16} P_{ran} \frac{\gamma^2}{C_s}(gd)^{0,5} \left(\frac{d}{H}\right) \exp\left(-\frac{\gamma^2 d^2}{H_{rms}^2}\right) \tan\alpha \sin\theta \cos\theta \quad \ldots (32)$$

where P_{ran} is a Vocoidal parameter known simply in terms of Vocoidal wave properties.

Equation (32) is identical to its linear, random theory couterpart, equation (19), except for the inclusion of P_{ran} in equation (32).

In the following table values of P_{ran} are given in terms of T_c and γ.

T_c	Values of P_{ran}									
	H/d=0,1	0,2	0,3	0,4	0,5	0,6	0,7	0,8	0,9	1,0
5	1,53	1,53	1,52	1,51	1,50	1,49	-	-	-	-
10	1,46	1,46	1,38	1,39	1,34	1,31	1,33	1,36	1,40	-
15	1,63	1,61	1,56	1,49	1,44	1,41	1,42	1,49	1,54	1,61
20	1,74	1,68	1,65	1,55	1,49	1,48	1,53	1,61	1,66	1,71
25	1,77	1,73	1,65	1,58	1,51	1,52	1,60	1,69	1,75	1,79
30	1,79	1,75	1,67	1,59	1,51	1,53	1,64	1,74	1,80	1,83
35	1,80	1,75	1,68	1,59	1,51	1,55	1,66	1,76	1,81	1,82
40	1,70	0,11	1,67	1,58	1,49	1,55	1,66	1,75	1,78	1,78

In analogy with linear waves a dimensionless scaling velocity v_{oir} is defined (see equation (21)):

$$v_{oir} = \frac{5\pi}{16} (P_{ran})_{bs} \frac{\gamma(gd_{bs})^{0,5}}{C_s} \tan\alpha \sin\theta_{bs} \cos\theta_{bs} \quad \ldots (33)$$

It follows that

$$v = v_{oir} f(\gamma) \quad \ldots (34)$$

where $$f(\gamma) = \left(\frac{d}{d_{bs}}\right) \left(\frac{d}{H}\right) \gamma\left[(P_{ran})_d / (P_{ran})_{d_{bs}}\right] \exp\left(-\frac{\gamma^2 d^2}{H_{rms}^2}\right) \quad \ldots (35)$$

The value of the roughness coefficient C_S for Vocoidal waves given by equation (31) applies. The same comments about wave set-up which were valid before are valid here, except that it has to be borne in mind that a new theory for the prediction of wave set-up due to random, vocoidal waves will have to be developed and tested.

6. SUMMARY AND CONCLUSIONS

The following is a summary of the main findings from the present study:

(1) The friction coefficient C_{LH} in the Longuet-Higgins model for longshore current prediction is not a constant, as was suggested previously, but varies with roughness and breaker zone beach slope. This supports earlier work by Komar and Inman.

(2) Using random incident waves a model was developed with the same approximations as for regular waves, except that lateral mixing is neglected, which gives very realistic profiles in close similarity with previous numerical work by Battjes.

(3) Using Vocoidal theory, explicit equations were derived for the longshore current profile under both regular and random wave attack. The friction coefficient is redefined and although it has a similar dependence on roughness and slope as in the linear case the actual values are higher.

(4) Although not discussed here, these four models, that is, for longshore current prediction under regular or random wave attack using linear or Vocoidal wave theory, have been extended to include the effect of mildly varying bed slope and mildly varying breaker index.

(5) Although the development of these models constitutes an appreciable advance, the models are only valid for the rare case of spilling breakers on a beach for which the water depth shows a monotonic decrease from breaker line to shore. Extensive research is still required on, for example, the non-steady nature of the longshore current, longshore currents on barred beaches and the effect of rip currents on longshore currents.

7. REFERENCES

BATTJES, J A (1974). Computation of set-up, longshore currents and overtopping due to wind-generated waves. Doctoral thesis, Technische Hogeschool, Delft.

CSIR (1978). Koeberg Nuclear Power Station, Report No 8, Sediment transport study current tests. CSIR Report C/SEA 7808, Stellenbosch, South Africa.

GALVIN, C J and NELSON, R A (1967). Compilation of longshore current data. US Army Coastal Engineering Research Center, Miscellaneous Paper 2-67.

JAMES, I D (1974). A non-linear theory of longshore currents. Estuarine and Coastal Marine Science, Vol 2, pp 235-249.

JONSSON, I G (1966). Wave boundary layers and friction factors. Proc. Tenth Coastal Engineering Conference, Tokyo.

KOMAR, P D and INMAN, D L (1970). Longshore sand transport on beaches. Journal of Geophysical Research, Vol 75, pp 5914-5927.

LONGUET-HIGGINS M S (1970). Longshore currents generated by obliquely incident sea waves, 1. Journal of Geophysical Research, Vol 75, No 33.

SPM (1975). Shore Protection Manual. US Army Coastal Engineering Research Center.

SWART, D H (1978). Vocoidal water wave theory, Volume 1: Derivation. National Research Institute for Oceanology, CSIR Research Report 357, 138 pp.

SWART, D H and LOUBSER, C C (1979). Vocoidal water wave theory, Volume 2: Verification. National Research Institute for Oceanology, CSIR Research Report 360, 130 pp.

SWART, D H and FLEMING, C A (1980). Longshore water and sediment movement. Proc. 17th Coastal Engineering Conference, Sydney.

MODELING LONGSHORE CURRENTS FOR FIELD SITUATIONS

by

Seetharama R. Vemulakonda[1], James R. Houston[2], and H. Lee Butler[3], Members ASCE

Abstract

There is a growing need for generalized numerical models for longshore currents and nearshore circulation that solve the complete equations of motion, are flexible in the formulations chosen for various terms, and can be applied to field situations at a reasonable cost. The development and application of one such model is described in this paper. The model was first tested by comparing its results to known analytic solutions and experimental data. There was good agreement. It was next applied to a field situation near Oregon Inlet, North Carolina. The results appeared to be reasonable and the computational costs were modest.

Introduction

Over the last two decades, a considerable amount of literature has been published on the computation of longshore currents and nearshore circulation due to the action of breaking waves. However, most of this literature (for example, 2, 6, 8, 10, 12) has been devoted to idealized situations such as plane beaches and periodic bathymetries. Often the analytical and numerical models used have been limited in scope. The limitations include assuming a steady state, using a linear friction, neglecting advection and/or eddy viscosity terms, etc. The development of generalized numerical models (5, 13) that can handle more complex situations is relatively recent. As of now (1982), very little work has been reported on the application of numerical current models to field situations at a reasonable cost. In view of the increasing tendency of the coastal engineering profession to employ numerical models for sediment transport in the nearshore region, there is a pressing need for generalized longshore current models. In this paper, the development and application of one such model is described.

[1]Research Division, Coastal Engineering Research Center, Fort Belvoir, Virginia 22060; formerly, Wave Dynamics Division, U. S. Army Engineer Waterways Experiment Station, Vicksburg, MS 39180.

[2,3]Wave Dynamics Division, U. S. Army Engineer Waterways Experiment Station, P. O. Box 631, Vicksburg, Mississippi 39180, U.S.A.

Equations of Motion

The governing equations for the problem under consideration are obtained from the general equations of conservation of mass and momentum, after averaging over time (one wave period) and depth. They are expressed in terms of the mean horizontal velocities U, V and the mean free surface displacement $\bar{\eta}$ as follows (refer to Fig. 1):

Momentum

$$\frac{\partial U}{\partial t} + U\frac{\partial U}{\partial x} + V\frac{\partial U}{\partial y} + g\frac{\partial \bar{\eta}}{\partial x} + \frac{1}{\rho d}\tau_{bx} + \frac{1}{\rho d}\left(\frac{\partial S_{xx}}{\partial x} + \frac{\partial S_{xy}}{\partial y}\right) - \frac{1}{\rho}\frac{\partial \tau_{xy}}{\partial y} = 0 \quad (1)$$

$$\frac{\partial V}{\partial t} + U\frac{\partial V}{\partial x} + V\frac{\partial V}{\partial y} + g\frac{\partial \bar{\eta}}{\partial y} + \frac{1}{\rho d}\tau_{by} + \frac{1}{\rho d}\left(\frac{\partial S_{xy}}{\partial x} + \frac{\partial S_{yy}}{\partial y}\right) - \frac{1}{\rho}\frac{\partial \tau_{xy}}{\partial x} = 0 \quad (2)$$

Continuity

$$\frac{\partial \bar{\eta}}{\partial t} + \frac{\partial}{\partial x}(Ud) + \frac{\partial}{\partial y}(Vd) = 0 \quad (3)$$

Here g is the acceleration due to gravity, ρ is the mass density of water, d is the total depth $= h + \bar{\eta}$, h being the local still water depth, τ_{bx} and τ_{by} are the bottom friction stresses in the x and y directions, respectively, S_{xx}, S_{xy}, and S_{yy} are radiation stresses (refer to Longuet-Higgins and Stewart (7) for their significance), and τ_{xy} is the lateral shear stress due to turbulence. For monochromatic waves, the radiation stresses are defined in terms of the local values of the wave height H, wave number k, and wave direction θ. For the numerical model under consideration, the latter variables are obtained by using a considerably modified form of the refraction program developed by Noda, et al. (9). This particular program has the advantage that H, k, and θ can be computed at the centers of the cells of a rectangular numerical grid, and wave breaking can be accounted for by a breaking index model for wave heights in the surf zone. Wave-current interactions may also be taken into account; however, this last feature was not used in the results that follow.

Bottom Friction. For the bottom friction, a linear formulation, similar to that of Longuet-Higgins (8), was used for the applications that are described here. Thus,

$$\tau_{bx} = \rho\, c\, \langle|u_{orb}|\rangle\, U \quad (4)$$

$$\tau_{by} = \rho\, c\, \langle|u_{orb}|\rangle\, V \quad (5)$$

where c is a drag coefficient (of the order of 0.01) and $\langle|u_{orb}|\rangle$ is the time average, over one wave period, of the absolute value of the wave orbital velocity. From linear wave theory,

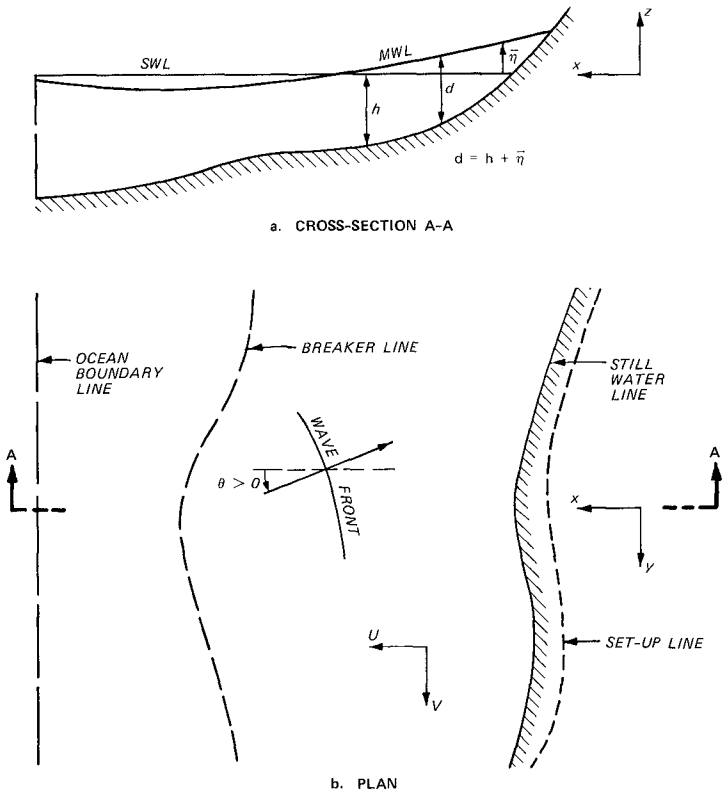

Figure 1. Definition sketch for an irregular beach

$$<|u_{orb}|> = \frac{2H}{T \sinh kh} \tag{6}$$

where T is the wave period. Eqs. 4 and 5 amount to a "weak current" assumption. The numerical model described here has the flexibility that other formulations such as a non-linear friction can be easily incorporated in the future.

Lateral Shear. In the numerical model, the coordinate scheme was chosen such that x was positive offshore and y was in the alongshore direction. An eddy viscosity formulation was chosen for the lateral shear, τ_{xy}. The eddy viscosity was assumed to be non-isotropic. Denoting ε_x and ε_y as the eddy viscosities in x and y directions, respectively, in general, ε_y was assumed to be a constant and ε_x a function of x and y. Accordingly,

$$\tau_{xy} = \rho \left(\varepsilon_y \frac{\partial U}{\partial y} + \varepsilon_x \frac{\partial V}{\partial x}\right) \tag{7}$$

For the plane beach application with lateral mixing, the eddy viscosity ε_x was assumed to vary within the surf zone in the manner suggested by Longuet-Higgins (8):

$$\varepsilon_x = N \times \sqrt{gh} \tag{8}$$

where x is the distance from the shoreline and N is an empirical coefficient. The eddy viscosity was kept constant beyond the breaker line.

For the field application, the eddy viscosity ε_x was chosen according to the relationship given by Jonsson, et al. (6). Thus,

$$\varepsilon_x = \frac{H^2 gT}{4\pi^2 h} \cos^2 \theta \tag{9}$$

This represents twice the value used by Thornton (12). It was felt that Eq. 9 represented the eddy viscosity values for the field situation more realistically than Eq. 8.

Numerical Model

Numerical Scheme. The numerical current model uses a three time level, alternating direction, implicit, finite difference scheme. The model is based on a long wave model known as WIFM (Waterways Experiment Station (WES) Implicit Flooding Model) (refer to Butler (3) for details). In view of the similarity between the equations for long waves and currents, WIFM was converted into a model for currents by the addition of radiation stress terms and modification of friction and eddy viscosity terms, etc. Because of the advection terms, a stabilizing correction

scheme was used. The numerical model has the capability that the size of the grid cells in both horizontal directions may be varied so that the grid may be made finer in regions of greater interest such as the surf zone, inlets, etc. For this purpose, a mapping function defining the mapping from real (X) space to the computational (α) space is used. The function is

$$X_i = a_i + b_i \alpha_i^{c_i} \qquad i = 1,2 \qquad (10)$$

where X_1 , X_2 correspond to x and y , respectively, and the coefficients a_i, b_i, and c_i are calculated for different regions of the grid by an interactive program. The mapping transforms the variable grid in real space to a uniform grid in computational space. Afterwards, the relevant equations are solved in the computational space.

Solution Technique. In order to apply the finite difference scheme, a rectangular grid is used to represent the region of interest. In real space, the cell dimensions in x and y directions are denoted by Δx and Δy . These dimensions may vary from cell to cell. This grid is mapped into a uniform grid with constant cell dimensions $\Delta\alpha_1$ and $\Delta\alpha_2$ in the computational space. Let m and n denote indices in the x and y directions corresponding to the center of an arbitrary cell (refer to Fig. 2). All the variables except the velocities U and V are defined at the cell centers. Velocities U and V are defined respectively at cell faces $m + 1/2$ and $n + 1/2$. The time level is indicated by a superscript k . The governing equations are written in a finite difference form. To advance the solution from a time level k to $k + 1$, an intermediate stage of the solution marked by a superscript * is introduced. The solution procedure is carried out in a two-step operation. In the first step, we sweep the grid in the x-direction. The x-momentum equation is centered about the cell face $m + 1/2$ and the continuity equation about the center of the cell (m,n) and the two equations are solved, using in the process the result $U^* = U^{k+1}$. At the end of this sweep, we know $\bar{\eta}^*$ and U^{k+1} . Next we sweep the grid in the y-direction. In this sweep, the y-momentum equation is centered about the cell face $n + 1/2$ and the continuity equation about the cell center (m,n) . Upon solving the two equations, the values $\bar{\eta}^{k+1}$ and V^{k+1} for each cell are obtained. Thus the two sweeps together complete the solution.

For each sweep, the governing equations for all the cells together with the boundary conditions can be arranged in the form of a matrix equation involving the unknown variables. Since the matrix is tri-diagonal, the solution is obtained by recursion. Finally, it should be emphasized that even though we have discussed the solution procedure in terms of (x, y) coordinates for convenience, actually the governing equations are first transformed into the (α_1, α_2) coordinate scheme and solved in the computational space.

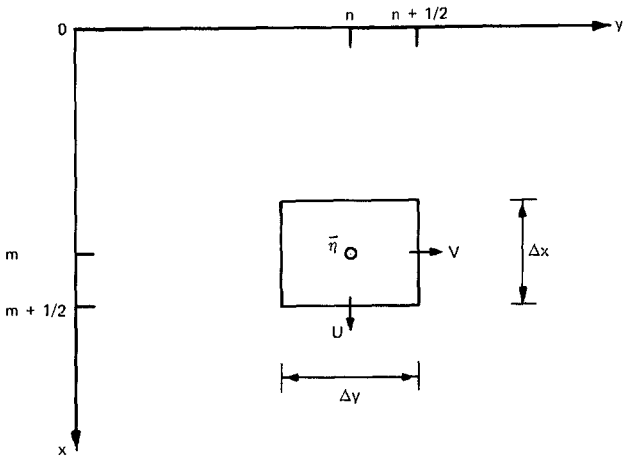

Figure 2. Notation for a cell

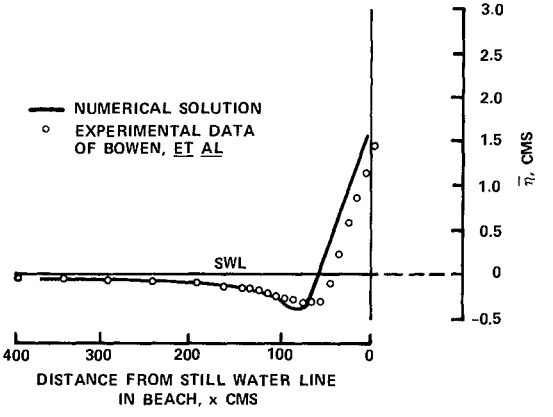

Figure 3. Comparison of the numerical solution for set-up with experimental data

Initial and Boundary Conditions. In order to solve the problem under consideration, appropriate initial and boundary conditions must be applied. For the examples reported here, an initial condition of rest was chosen so that $\bar{\eta}$, U and V are zero at the start of the calculations. To avoid shock, the radiation stress gradients were gradually built up to their full values over a number of time steps. The solution was stopped when a steady state was reached.

As for boundary conditions, along the shoreline a 'no flow' (wall) condition was assumed at the still water line. Thus, no flooding was permitted on the beach. For the lateral boundaries, a flux type boundary condition was often used. That is, the flux at a boundary cell was made equal to that at the next interior cell. It worked very well. For the offshore boundary, it is common practice to use conditions of either 'no flow' (wall) or constant elevation. However, both of these are highly reflective in nature and as a result the transients developed during the start-up of the numerical solution tend to bounce back and forth between the offshore and nearshore boundaries and take a long time to damp out. This is highly undesirable. In view of this, a radiation boundary condition of the type suggested by Orlanski (11) was selected for the offshore boundary and implemented in the numerical scheme. It worked quite well and permitted the transients to propagate out of the grid and allowed the set-down at the offshore boundary to assume an appropriate value.

Tests for Idealized Conditions

To develop confidence in the validity of the model and the accuracy of its results, several tests were run on the model and comparisons were made between model results and available laboratory data and analytic solutions. All of these tests were for plane beaches, for which the coordinate scheme is chosen such that the y-axis coincides with the still water line in beach and the x-coordinate is measured from the still water line. Note that for plane beaches, there is no variation in the alongshore (y) direction.

Plane Beach: Normal Incidence. The model was run for a case of normal incidence on a plane smooth laboratory beach, reported by Bowen, et al. (1). The conditions were as follows: T = 1.14 sec, deep water wave height H_o = 6.45 cm, and beach slope s = 1:12. To run this case on the model, a 50 x 3 variable rectangular grid with overall dimensions of approximately 40 m x 30 cm (the laboratory channel was 40 m long) was used with $\Delta\alpha_1 = \Delta\alpha_2$ = 10 cm and Δt = 0.05 sec. In this example, walls were used for the lateral boundaries as well as the offshore boundary to correspond to the laboratory situation. Since for normal incidence, the velocities U and V would be zero everywhere corresponding to the steady state, advection, eddy viscosity and friction terms were turned off in the model. The solution allowed for the effect of set-up on the wave heights in the surf zone. As the solution proceeded, since $\bar{\eta}$ changed, the wave heights for cells in the surf zone were computed afresh for each time step by using $H = \gamma(h + \bar{\eta})$, where γ is a breaking index and the radiation stresses were changed accordingly. As

suggested by Bowen, et al., a γ of 1.15 was used. A build-up time of 10 Δt was used at the start. A comparison of the steady-state set-up values from the model (after 150 Δt) with those observed by Bowen, et al. is shown in Fig. 3. As can be seen, there is excellent agreement in the offshore region. In the surf zone, the numerical model predicts higher set-ups than observed. This is not surprising since the model does not allow flooding and runup. It is to be noted that the slope of the mean water line in the surf zone is approximately the same in both cases.

Plane Beach: Oblique Incidence. For this case, a plane beach of constant bottom slope s = 1:30 was selected. A monochromatic wave with the following deep water characteristics was chosen: T = 12 sec, H_o = 10 ft, and angle of incidence in deep water, θ_∞ = 20 deg. A drag coefficient c of 0.01 and a breaking index γ of 0.82 were used in the model. A 100 x 6 uniform grid with $\Delta x = \Delta y$ = 60 ft was used for most of the runs. Uniform flux and radiation boundary conditions were used for the lateral and offshore boundaries, respectively. The build-up time varied from 15 Δt to 50 Δt, depending on the Δt used.

First the model was run without allowing for the effect of set-up on wave heights and radiation stresses. Mixing and advection were ignored. A time step Δt of 0.5 sec was used. The steady-state velocity distribution obtained (after 800 Δt) is compared to the triangular distribution of Longuet-Higgins in Fig. 4. There is good agreement. Note that for positive θ , V will be negative for our coordinate scheme. Later a finer grid ($\Delta x = \Delta y$ = 30 ft) with a Δt of 0.25 sec was used. As can be seen in Fig. 4, as the grid is made finer, the numerical solution tends to approach the analytic solution.

The effect of set-up was taken into account next. A time step Δt of 1.5 sec was used for this case. The velocity distribution from the model is compared to the corresponding analytic solution in Fig. 5. There is good agreement. Note that the numerical solution goes to zero at the still water line because a wall was assumed there. On the other hand, Longuet-Higgins' solution goes to zero at the set-up line. To plot his solution, the distance from the still water line to the set-up line was estimated by using a relation provided by Dalrymple, et al. (4).

The effect of lateral mixing was studied next, without taking the effect of set-up into account. A time step Δt of 5.0 sec was used for these runs. The mixing parameter P of Longuet-Higgins was varied between 0.01 and 0.4. Note that P is defined as

$$P = \frac{\pi}{\gamma} \frac{sN}{c} \tag{11}$$

Fig. 6 shows the effect of P on the numerical solution. As expected, the magnitude of the peak decreases, the peak moves closer to the shoreline and the velocities offshore of the breaker line increase as P increases.

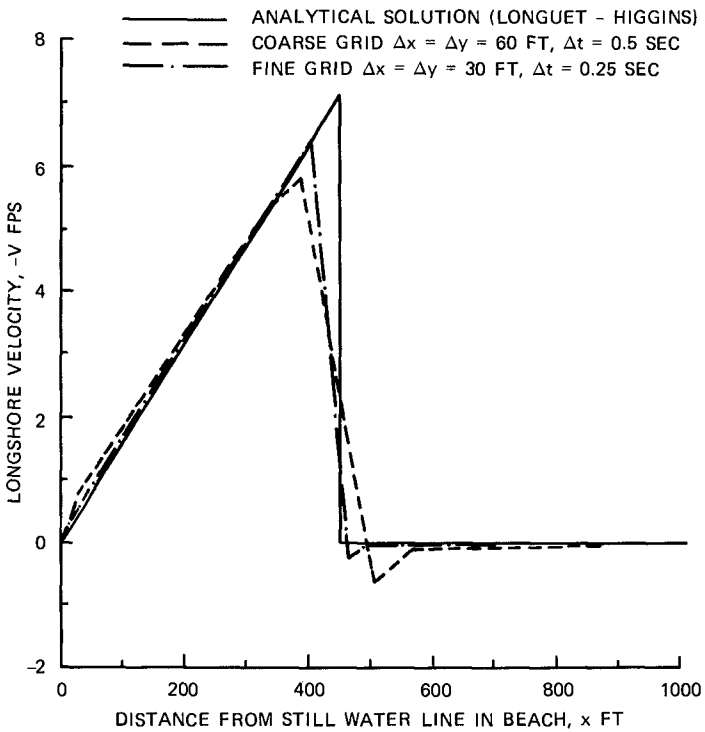

Figure 4. Plane Beach: Solution for longshore current without taking set-up into account

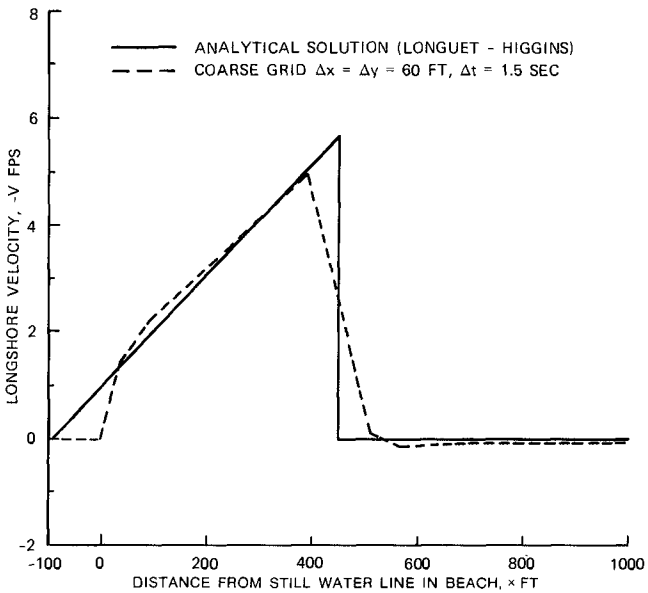

Figure 5. Plane Beach: Solution for longshore current taking set-up into account

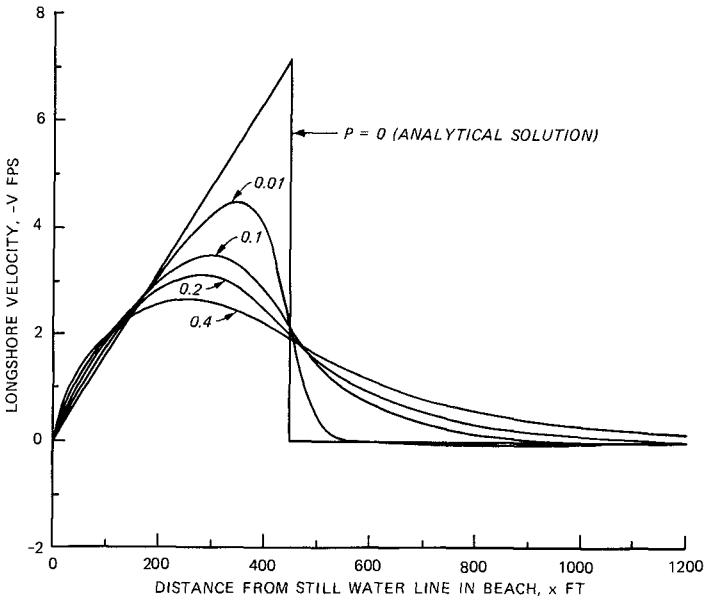

Figure 6. Plane Beach: Effect of mixing parameter P on the numerical solution (set-up is neglected)

Difficulties Involved in Applications to Field Situations

While it is relatively easy to apply a numerical current model to idealized cases, one must face several difficulties in applying the model to field situations. Among these is the highly irregular nature of the bathymetry, especially near inlets where channels and shoals exist. The topography must be smoothed to a certain extent in order for the wave climate and longshore current models to work properly. Yet, one must be careful not to completely change the basic features of the topography. The shoreline as well as the breaker line may be irregular and may be oblique to the grid axes. There may be more than one breaker line. There are problems connected with discretization of the shoreline and breaker line(s). Selection of appropriate values for empirical coefficients such as friction and eddy viscosity coefficients and breaking index is not easy. There are problems in connection with the wave climate model also, especially if wave-current interactions are to be taken into account.

A Particular Field Application

In order to demonstrate the applicability of the numerical model to field situations, the case of Oregon Inlet, North Carolina, was selected. Oregon Inlet is a tidal inlet in a barrier island system. Behind the inlet toward the main land is Pamlico Sound. Most of the problems mentioned in the previous paragraph had to be addressed and solved satisfactorily in this application. For purposes of the numerical simulation, a rectangular region approximately 62,400-ft long in the alongshore direction and 29,400-ft wide in the offshore direction was considered. It included a portion of Pamlico Sound. The variable grid used for the simulation is shown in Fig. 7. The grid was 77 cells wide in the alongshore direction and 54 cells wide in the offshore direction. It may be noted that the minimum cell widths in the alongshore and offshore directions were 400 and 100 ft, respectively. These widths were used near the inlet and surf zone, respectively. Note that $\Delta\alpha_1 = \Delta\alpha_2 = 100$ ft. The topography used in the simulation corresponding to this grid is shown in Fig. 8. The elevations are shown in feet and the datum is Mean Low Water (MLW). There are several points that must be mentioned about this three-dimensional perspective plot. First, the vertical dimensions are highly exaggerated compared with the horizontal. Secondly, the depths are plotted in the computational space and not the physical space. So the horizontal dimensions are distorted. The topography was somewhat modified compared to the actual topography, with respect to the depths near the offshore boundary and the land elevations on the islands. In spite of these factors, Fig. 8 helps one to visualize the irregular nature of the bathymetry. Also, the locations of the channels and shoals in the region of the inlet may be seen clearly in the figure.

A monochromatic wave with a height of 11.39 ft, period of 8.0 sec, and $\theta = 51.1$ deg in 60-ft depth of water was selected for the simulation (the depth of water at the offshore boundary of the numerical grid was 60 ft). This wave corresponded to the significant wave during a part of the Ash Wednesday storm of March 1962 at the inlet. In this case,

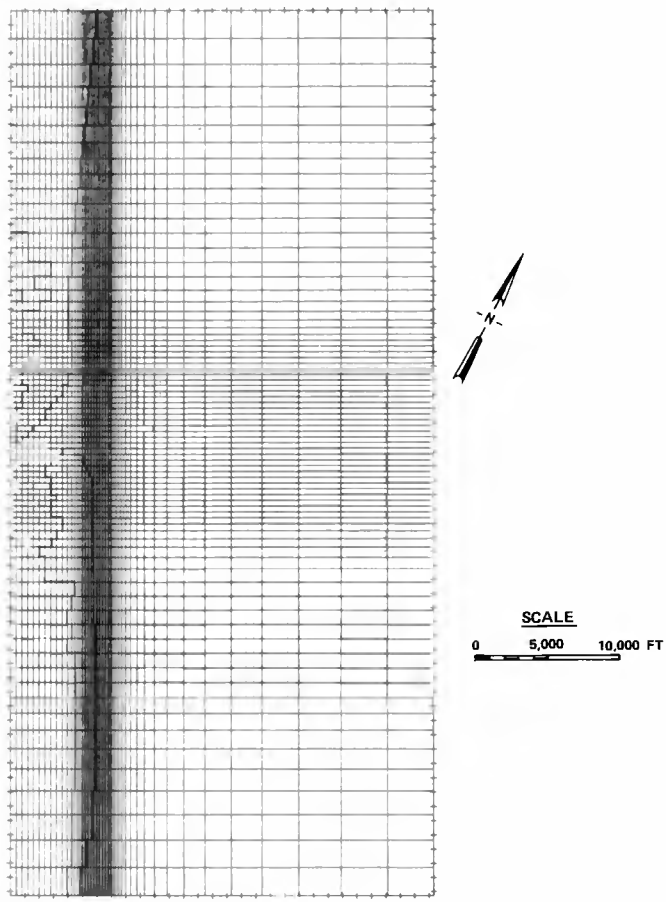

Figure 7. Numerical grid for Oregon Inlet, North Carolina

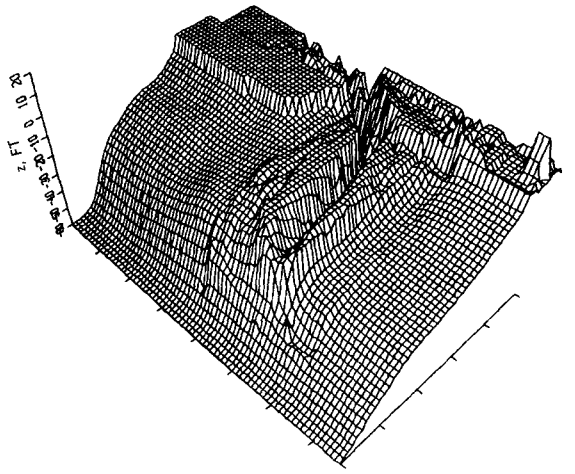

Figure 8. Topography for Oregon Inlet Numerical Model

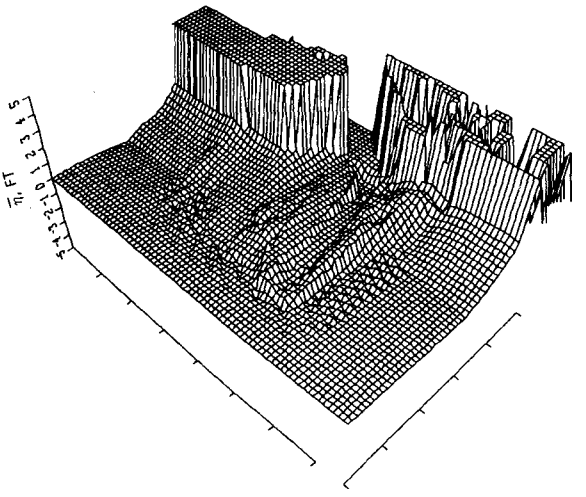

Figure 9. Surface elevation plot for Oregon Inlet

besides using 'no flow' conditions at the shoreline, a radiation boundary condition offshore and flux boundary conditions at the lateral boundaries, a flux boundary condition was used over a part of the inland side of the Sound, while the rest of the Sound was closed off. A time step Δt of 18.0 sec and a drag coefficient c of 0.01 were used in the numerical model. The breaking index γ was chosen according to the breaking criterion employed by Noda (10):

$$\frac{H_b}{L_b} \simeq 0.12 \tanh \left(\frac{2\pi d_b}{L_b}\right) \qquad (12)$$

where L corresponds to the wave length and the subscript b indicates values at breaking. A build-up time of 15 Δt was used at the start. The eddy vicosity ε_x was chosen according to Eq. 9 and the eddy viscosity ε_y was set equal to the value of ε_x at the offshore boundary. For the case under consideration, the complete equations (Eqs. 1, 2, and 3) were solved. An approximate steady-state was reached after 67 Δt. Figs. 9 and 10 represent the corresponding mean water levels and velocity vectors, plotted on the grid in the computational space. The velocity vectors are plotted for every other cell in each coordinate direction. To avoid confusion, the plotting of velocities with mangitudes less than 0.1 ft/sec is suppressed.

Referring to Figs. 8, 9, and 10, let us first consider the two portions of the beach away from the inlet. The shorelines in these regions are approximately straight and the contours are approximately straight and parallel. As we approach the shoreline from offshore, there is a small set-down followed by a set-up. The velocities are mainly alongshore and the velocity distribution is similar to that for a plane beach except that it exhibits two peaks at some locations.

The situation is more complicated in the region of the inlet (the central part of the grid). Here the breaker line is farther offshore. The depth in the main channel decreases first and increases later as we go toward the inlet. Because of these factors, the water sets up around the inlet and tends to create a flow into the inlet through the various channels, as one would naturally expect. A part of the main alongshore flow goes around the channels and shoals, to the other side.

Near the shoals, the patterns of mean water level and velocity are irregular. This is because of the fact that the waves refract around the shoals and break, creating locally set-ups and currents that do not necessarily conform to the general patterns. As the waves go toward the islands, they re-form because the depth increases.

Figs. 9 and 10 do not reflect the influence of tides and freshwater flows through the inlet. In nature, these phenomena tend to modify the patterns shown in these figures.

Computational Costs. For those interested in computational times, it should be noted that all the computations described in this paper were performed on a Cray-1 computer, which has vectorizing capabilities.

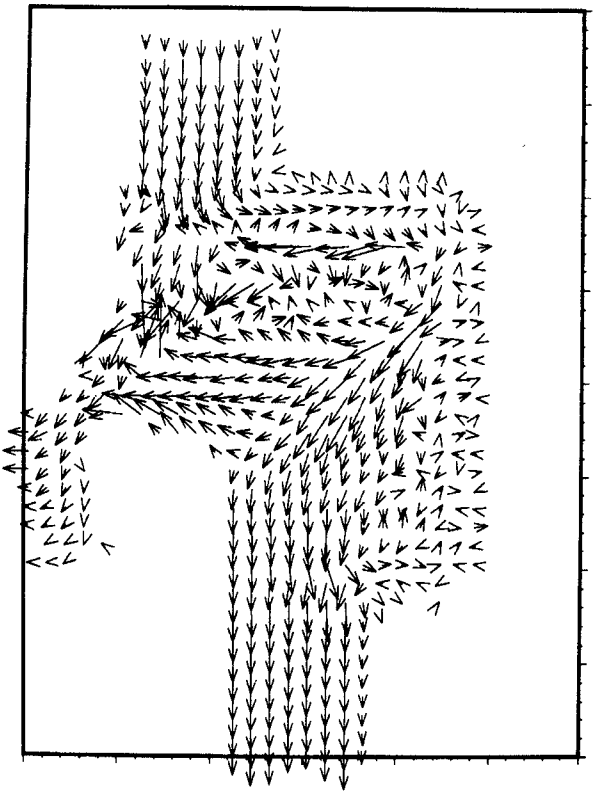

Figure 10. Velocity vector plot for Oregon Inlet

For the field application involving a 54 x 77 grid with 4,158 grid points, the Central Processor Unit (CPU) time for 67 time steps of simulation was approximately 15.5 seconds. The total cost for the job including program compilation, CPU time and data file manipulation, was approximately ten U. S. dollars. So the computational costs for the model may be considered reasonable.

Conclusions

A generalized longshore current model was developed. It retains the unsteady terms as well as advection and lateral mixing terms in the equations of motion and can be easily modified for different formulations of friction, eddy viscosity, etc.

A radiation boundary condition was successfully applied to the offshore boundary. It permits the transients due to start-up of the numerical scheme to be propagated out of the numerical grid.

Comparisons were made with known analytic solutions and experimental results. There was good agreement.

The model was applied to a complex field situation and the results obtained appeared to be reasonable. The computational costs were modest.

For the future, it is proposed to allow non-linear friction. Coordinate transformations will be used to transform the shoreline and breaker line(s) into lines parallel to the coordinate axes. It is proposed to simulate also the effect of structures such as jetties on the longshore currents and nearshore circulation.

Acknowledgements

The work reported herein was conducted in the Wave Dynamics Division, Hydraulics Laboratory, U. S. Army Engineer Waterways Experiment Station. The study was authorized by the U. S. Army Engineer District, Wilmington. The permissions given by the District as well as the Chief of Engineers to publish this paper are hereby acknowledged. The authors acknowledge also the assistance of Paul D. Farrar in furnishing results of the wave climate model for the Oregon Inlet Study. The findings of this paper are not to be construed as official Department of the Army position unless so designated by other authorized documents.

References

1. Bowen, A. J., Inman, D. L., and Simmons, V. P., "Wave 'Set-Down' and Set-Up," Journal of Ceophysical Research, Vol. 73, No. 8, 1968, pp. 2569-2577.

2. Bowen, A. J., "The Ceneration of Longshore Currents on a Plane Beach," Journal of Marine Research, Vol. 27, 1969, pp. 206-215.

3. Butler, H. L., "Evolution of a Numerical Model for Simulating Long Period Wave Behavior in Ocean-Estuarine Systems," Estuarine and Wetlands Processes with Emphasis on Modeling, Marine Science Series, Vol. 11, Plenum Press, New York, 1980.

4. Dalrymple, R. A., Eubanks, R. A., and Birkemeier, W. A., "Wave-Induced Circulation in Shallow Basins," Proceedings, Journal of the Waterway, Port, Coastal and Ocean Division, ASCE, Vol. 103, No. WW1, February 1977, pp. 117-135.

5. Ebersole, B. A., and Dalrymple, R. A., "Numerical Modelling of Nearshore Circulation," Proceedings, 17th Conference on Coastal Engineering, 1980, Vol. III, Chapter 163, pp. 2710-2725.

6. Jonsson, I. G., Skovgaard, O., and Jacobsen, T. S., "Computation of Longshore Currents," Proceedings, 14th Conference on Coastal Engineering, 1974, Vol. II, Chapter 40, pp. 699-714.

7. Longuet-Higgins, M. S., and Stewart, R. W., "Radiation Stresses in Water Waves; A Physical Discussion, with Applications," Deep-Sea Research, Vol. 11, 1964, pp. 529-562.

8. Longuet-Higgins, M. S., "Longshore Currents Cenerated by Obliquely Incident Sea Waves, 1 and 2," Journal of Geophysical Research, Vol. 75, No. 33, November 1970, pp. 6778-6789 and pp. 6790-6801.

9. Noda, E. K., Sonu, C. J., Rupert, V. C., and Collins, J. I., "Nearshore Circulations Under Sea Breeze Conditions and Wave-Current Interactions in the Surf Zone," Tetra Tech Report TC-149-4, February 1974.

10. Noda, E. K., "Wave-Induced Nearshore Circulation," Journal of Geophysical Research, Vol. 79, No. 27, September 1974, pp. 4097-4106.

11. Orlanski, I., "A Simple Boundary Condition for Unbounded Hyperbolic Flows," Journal of Computational Physics, Vol. 21, 1976, pp. 251-269.

12. Thornton, E. B., "Variation of Longshore Current Across the Surf Zone," Proceedings, 12th Conference on Coastal Engineering, 1970, Vol. I, Chapter 18, pp. 291-308.

13. Vreugdenhil, C. B., "A Method of Computation for Unsteady Wave-Driven Coastal Currents," Report R 1174, Part I, Waterloopkundig Laboratorium, Delft Hydraulics Laboratory, August 1980.

SHORE-PARALLEL FLOWS IN A BARRED NEARSHORE

By

Brian Greenwood[1] and Douglas J. Sherman[2]

ABSTRACT

A field experiment to measure the horizontal and vertical structure of shore-parallel, nearshore currents was conducted at Wendake Beach, Georgian Bay, Canada, in 198D. Waves and currents were measured with continuous resistance wire wave staffs and bi-directional, electromagnetic current meters, respectively. Substantial variations from theoretical horizontal velocity profiles were found as an influence of small amplitude nearshore bars. Data smoothing resulted in a Longuet-Higgins type mixing parameter estimate of P=D.1B. Vertical velocity profiles analysis suggests that an estimate of mean, surf zone roughness length is of the order of $1x10^{-3}$m.

INTRODUCTION

Since the seminal work of Longuet-Higgins and Stewart (1962) on the concept of radiation stress, a strong body of theory has emerged for the prediction of depth-integrated, mean, shore-parallel flows generated by non-normally incident progressive gravity waves breaking across a planar beach slope (Longuet-Higgins, 1970a b; Dstendorf and Madsen, 1979). However, intrinsic to the modelling of fluid motion using momentum flux across the surf zone are indices describing lateral mixing and bed shear. Unfortunately, prototype experiments of a sophistication necessary to test existing theory and also provide data for determining the coefficients involved in a stress balance model of longshore currents are limited. This limitation is extreme where topographic effects-nearshore bars- introduce a potentially important modifying effect on current generation. Sonu (1972) provided a qualitative description of a spatially variable nearshore current in the presence of a bar but only very recently have more quantitative studies been undertaken (Meadows, 1977, 1978; Symonds and Huntley, 1980; Allender et al., 1979; Allender and Ditmars, 1981). This paper presents

1 Professor, Departments of Geography & Geology, Scarborough College, University of Toronto, West Hill, Ontario, M1C 1A4.

2 Graduate Student, Department of Geography, Scarborough College, University of Toronto (currently: Dcean Engineering, Woods Hole Dceanographic Institution, Woods Hole, Mass., D2543.

the results of a field experiment designed specifically to examine the horizontal and vertical structure of the shore-parallel flow field across a non-tidal, barred nearshore under a wide range of incident wave conditions and to provide a dataset suitable for determining parameters describing the nearshore mixing and bed friction.

Location of Study Site

The experimental site was located at Wendake Beach, Ontario (Fig. 1): the area is a non-tidal, low-energy, storm-wave dominated coastal system with a maximum fetch of 84 km to the WNW but extremely restricted in width. Short period, steep waves that may exceed 2 m significant height with 5 to 6 second peak periods are generated during the passage of cyclonic disturbances. Wave approach angles frequently change even within a single storm in response to wind shifts in this fetch limited environment, and waves are subject to continuous forcing within the nearshore zone throughout most of the storm period.

The nearshore slope is gentle (approximately 0.015) and characterized by 3 bar-trough systems (Fig. 2); the outermost bar is highest (0.40 m) and essentially straight with a crest some 110 m offshore, while the inner two bars at distances of 65 m and 10 m from the shoreline have heights of only 0.15 m to 0.20 m and are sinuous to crescentic. The surf zone width is clearly constrained by these bars under many conditions but the general nearshore gradient is so low that breaking waves occur lakeward of the outermost bar, with a fully developed surf zone landwards, during much of the period of storm wave activity.

Experimental Design

Two types of instruments were used to monitor the fluid motions. Water surface elevation changes associated with waves were measured by surface piercing, continuous resistance wave staffs. Two or three meter long, helically wound steel wires (0.35 mm diameter) set in 18.8 mm PVC pipe (groove 0.75 mm, pitch 18.8 mm) were mounted by insulated brackets on 37.5 mm galvanized steel pipe. The latter was mounted on a two meter long base with fin to prevent rotation, and was jetted into the bed. The staffs were field calibrated individually to specific oscillator-detector circuits and were linear except for the lowermost 0.25 m. RG58A/U coaxial cable provide the shore-link. The oscillator circuit provides a 5 kHz square wave output and a simple half-wave rectifier and R-C Filter acts as a detector.

Shore-normal and shore-parallel flows were monitored using bi-axial, electromagnetic flow meters designed by Marsh-McBirney, Inc. (Model OEM 512). Based on the Faraday Principle of electromagnetic induction, they use a time constant of 0.2 s and measure flow up to 3 ms^{-1}. Considerable work on the accuracy of these meters has been undertaken (Cunningham et al., 1979; White, 1979; Huntley, 1979 etc.)

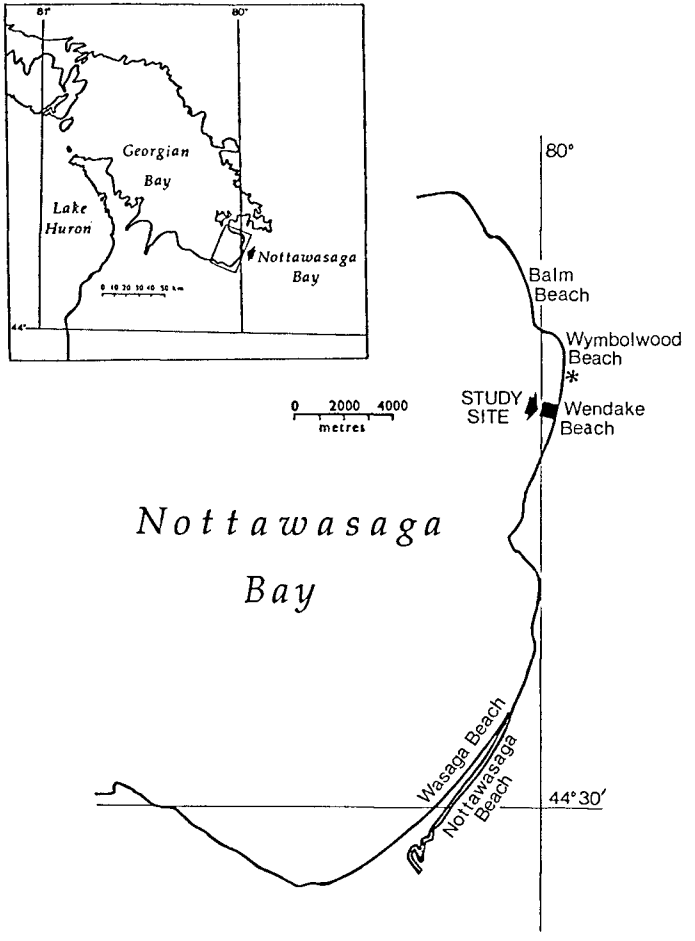

Figure 1: Location map of the study site, Wendake Beach, Ontario, Canada.

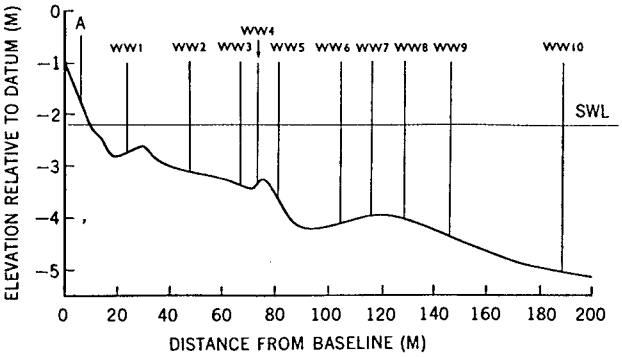

Figure 2a: Locations of instruments along the central profile, 1980:05:12 to 1980:06:05.

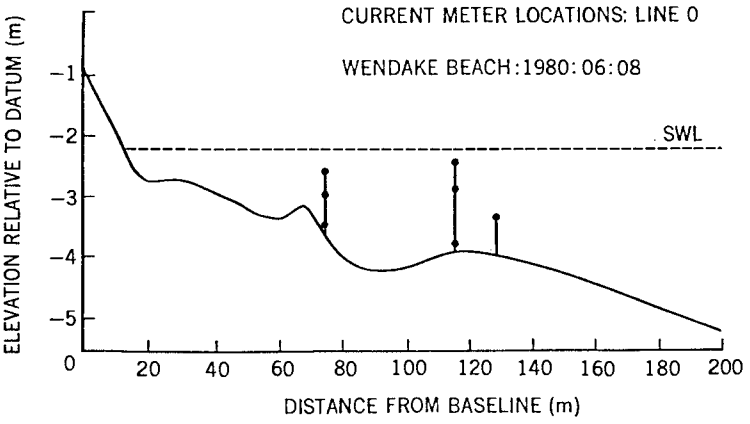

Figure 2b: Locations of current meters, 1980:06:06 to 1980:06:12.

and while some problems still exist the level of accuracy is better than 10%. The meters were mounted on a specially designed bracket (to allow rotation in both the vertical and horizontal planes), which itself was mounted on a stainless steel support. A galvanized steel pipe with fin to prevent rotation provide the base support and this again was jetted into the bed. The locations of the instruments are shown in Figures 2 and 3.

All sensors were hardwired to shore where a computer-controlled, data acquisition system (Fig. 4) provided instrument power, signal conditioning and detection, and data storage. A Hewlett-Packard 9835B mini computer with 125 K bytes of memory and real time clock controlled a high speed scanner-multiplexer (HP3495A) and digital voltmeter (HP3437A) allowing high density sampling of the current and wave sensors. Up to 40 channels could be monitored simultaneously. Record lengths varied between nine and twenty-five minutes with sampling at 2 Hz. Digital storage was on magnetic tape cartridges or flexible disc (HP9895).

Two specific plans were adopted for instrument deployment: a shore-normal array of ten wave staffs and seven flowmeters (Fig. 2a) allowed examination of the horizontal flow structure, while two sets of 3 flowmeters mounted vertically at the locations of wave wires 5 and 7 gave information on the vertical flow structure (Fig. 2b). At regular intervals during the experiments the system was activated to provide synchronous records of waves and currents at different positions across the surf zone thus giving a time series for evaluating the spatial and temporal variability of shore-parallel flows under a wide range of incident wave conditions. Specifically the datasets were used to evaluate: (i) the spectral characteristics of the incident waves; (ii) the spatial and temporal variability of shore-parallel flows; (iii) the parameters necessary to determine lateral mixing and eddy viscosity across the surf zone; (iv) the coefficients necessary to describe bed friction; (v) the influence of the non-planar slope on the above mentioned properties. Two storm events on May 30 - June 1, and June 8, 1980, will be described in this paper, with emphasis on lateral mixing and bed friction effects.

Nearshore Slope

An estimate of nearshore slope was obtained by fitting a least-squares regression line to measured profile data. R^2 values of better than 0.99 were obtained for a slope of 0.013 that intercepted the axis ($x = 0$) at -0.40 m. For a given value of water depth at the breaker line, h_b, the slope and intercept approximations were used to predict the width of the surf zone. Then an estimate of the actual slope was obtained using $s = h_b/x_b$. The process may be summarized:

$$s = 0.013\, h_b/(h_b - 0.40) \tag{1}$$

The resulting values of s ranged from 0.017 to 0.014.

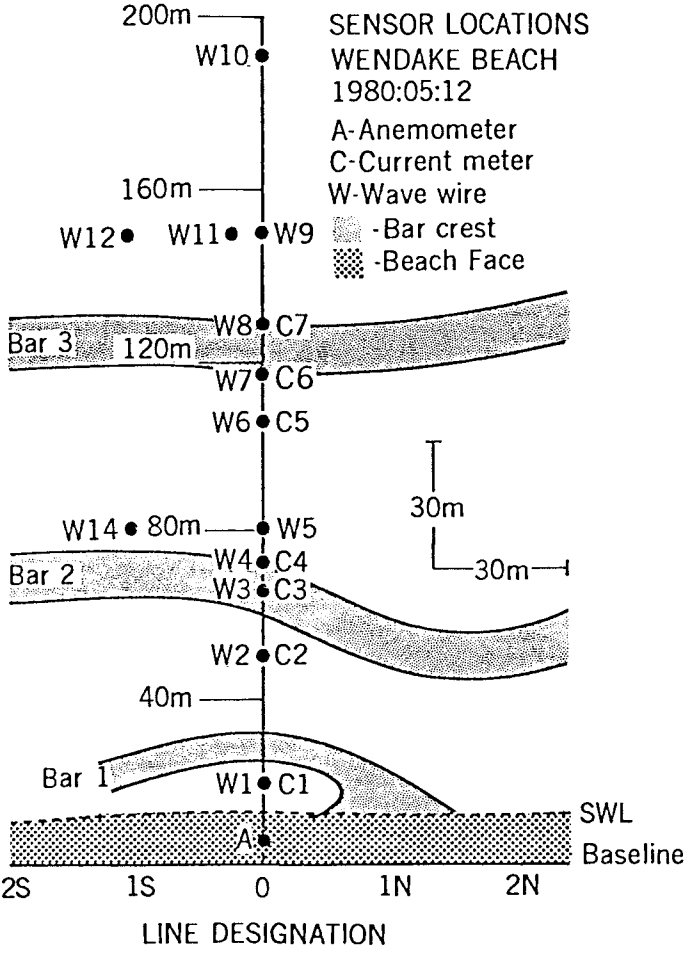

Figure 3: Map view of instrumentation locations utilized for monitoring the first storm: W indicates a wave staff, C, a current meter, and A, an anemometer and wind vane.

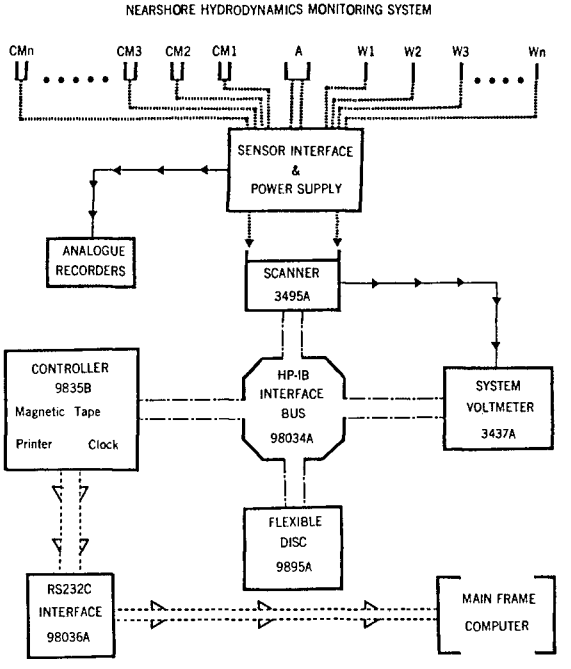

Figure 4: Schematic of the nearshore hydrodynamics monitoring system.

Storm Wave Characteristics

During the passage of depressions, waves in excess of 1.3 m mean amplitude and 5 s peak period provide the major local forcing for shore-parallel flows. Figures 5a and 5b illustrates the characteristic wave energy spectra incident to the surf zone during storms. A number of features are noteworthy:

(i) wave spectra in this continuous forcing environment exhibit large energy values over a wide range of frequencies below the peak frequency, which itself is marked by a very sharp truncation at the lower frequency end in all cases.

(ii) as expected, spectral growth (Fig. 5a) is accompanied by a consistent shift in the spectral peak to lower frequencies while there is an equally rapid increase in frequency during the decay phase (Fig. 5b). There is some evidence, however, for a dispersive effect during the decay period since at 0620 h the peak period (4.9 s) is greater than during the storm peak (4.6 s) and a broader peak at these longer periods is present.

(iii) during the most intense part of the storm, wave breaking produces a marked bimodal spectrum with the secondary peak at the frequency of the first harmonic.

(iv) in general there is very little evidence for structure in the spectra at frequencies lower than that of the incident spectrum. Some evidence is seen for a subharmonic during the early part of the storm (Fig. 5a & b) and for an oscillation at a frequency 1/4 times that of the incident wave; such structure is however, within the 95 percent confidence band for the spectra. The lack of low-frequency energy probably reflects the distance offshore of the wave staff, since under highly dissipative conditions many workers have noted the dominance of low frequency components (Huntley, 1976; Holman, 1981; Wright et al., 1982, etc.). Certainly storm conditions at Wendake Beach produce highly dissipative conditions, with the surf scaling parameter (Guza and Inman, 1975) ranging up to 192 x 10^2 (Greenwood and Sherman, 1983). Examination of the wave spectra nearer to the shoreline does indeed reveal an increase in this low frequency component.

Shore-Parallel Flows

HORIZONTAL STRUCTURE

During the storm event 1980:05:31 to 1980:06:01 fourteen records of the horizontal variability of longshore currents were obtained and Figure 6 illustrates six discrete records, from the periods of wave growth (Fig. 6a), the storm peak (Fig. 6b) and wave decay (Fig. 6c).

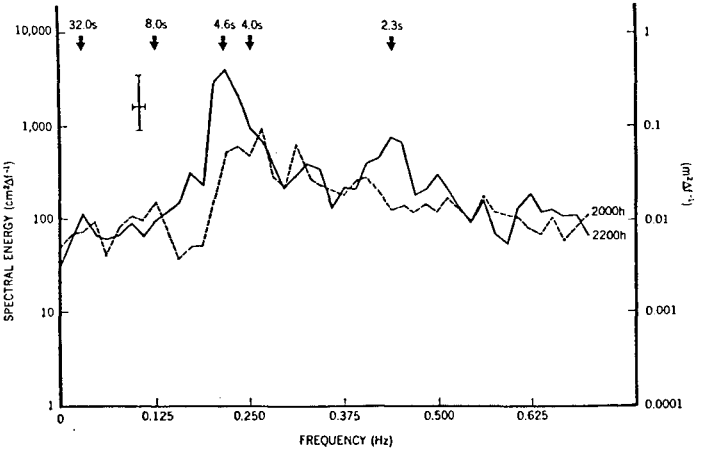

Figure 5a: Wave spectra from waxing limb of storm, WW9, 1980:05:30, 32 degrees of freedom. Vertical and horizontal crossbars indicate 95% confidence bar and unit bandwidth (0.016 Hz), respectively.

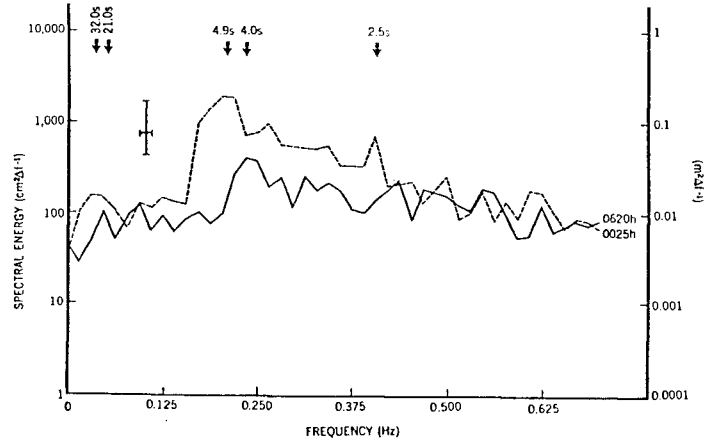

Figure 5b: Wave spectra from waning limb of storm, WW9, 1980:06:01, 32 degrees of freedom. Vertical and horizontal crossbars indicate 95% confidence bar and unit bandwidth (0.016 Hz), respectively.

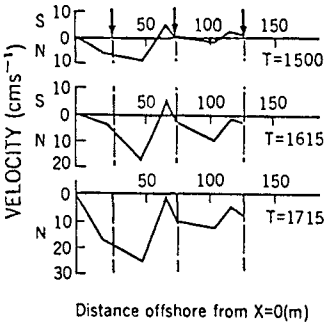

Figure 6a: Beginning of storm

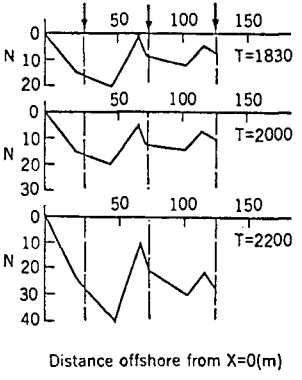

Figure 6b: Peak of storm

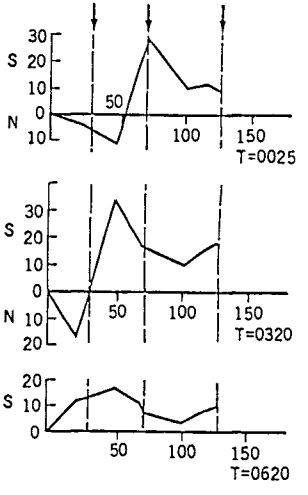

Figure 6c: End of storm

Figure 6: Time series of mean shore-parallel flows across a barred surf zone. Note the bars are located 20 m, 75 m, and 120 m, from the zero baseline.

As the storm grows flows accelerate with the increased wave driving and become more coherent up to the storm peak at 2200 h. At this time velocities reached a maximum of 40 cms^{-1}, with a maximum mean wave amplitude of 1.3 m at this time and peak period of 4.6 s.

Although bar heights are low and beach slope extremely flat in the nearshore, the topography exerts a marked influence on the horizontal structure of the flow field. Two distinct compartments of flow are associated with the outermost two bars. A marked reduction in velocity immediately landward of the bar crest should be noted with maximum flows in the trough on the landward side where water depth begins to decrease. Considerable variability in velocity is evident: excluding the zero velocity at the beach face a four-fold variation is present during the peak of the storm (2200 h). This contrasts markedly with the relative uniformity of surf zone flows across a bar-trough system claimed by Allender and Ditmars (1981). High velocities in the trough have been noted previously by Teleki et al., (1976) and ascribed to a longshore pressure gradient forcing due to wind setup.

A reversal in wind and wave direction around 2300 h produced a rapid response of the shore-parallel flows within the surf zone (Fig. 6c) in this fetch limited environment. However, an interesting feature of surf zone structure at this time was a horizontal stratification of flow reflecting a bi-directional disequilibrium response to the local wave forcing. This reversal persisted for more than 3 hours and may relate to the existence of a longshore pressure gradient (Komar, 1976, p. 196; Symonds and Huntley, 1980). However, it is important to note that between 2330 h and 0025 h the bulk of the surf zone flow was reversed and accelerated to a speed of 30 cms^{-1} in association with the change in direction of wave approach, thus implying dominance of the local forcing.

LATERAL MIXING

It is clear that a strong shore-normal variability in the average shore-parallel component of flow is evident on barred topography with the maximum velocities displaced landward of the initial break point which would occur on the bar crests. Such a pattern has long been recognized (Bowen, 1969; Longuet-Higgins, 1970 a & b) and although the shifting position of the breaker zone has been suggested as a significant control in a random wave field (Thornton, 1978) the primary control on a planar beach has been thought to be the lateral mixing associated with the horizontal Reynolds'stresses present under breaking waves. The latter tend to diffuse the local momentum flux and provide a smearing effect on the theoretical monotonic decay of currents across the surf zone (Longuet-Higgins, 1970 a & b). In an effort to compare the observations on a barred nearshore with the theory for a planar slope developed by Longuet-Higgins, estimates of his lateral mixing parameter, P, were attempted.

Dimensionless Velocity Profiles

Relative velocity values across the surf zone were calculated following Longuet-Higgins (1970b) by determining: (a) surf zone width based upon incident wave amplitudes, solitary wave breaking criterion and mean beach slope; (b) computed maximum velocity at breaking in the absence of lateral mixing, which involved a wave angle measure derived from a weighted orbital vector derived from the coherence between the surface elevation fluctuations and the measured orbital velocities; (c) a drag coefficient of the Darcy-Weisbach form assuming fully turbulent flow, a smooth boundary, and an equivalent grain roughness (following the experiments by Nikuradse).

Thus the longshore current at the breaker line, V_o (assuming no lateral mixing), is obtained from

$$V_o = \frac{5\pi}{8} \frac{\alpha S}{C} \sqrt{g h_b} \sin\theta_b \tag{2}$$

where α is a breaking criterion ($\alpha = 0.39$), C is the drag coefficient, and θ the angle of wave approach at the breaker line. Figure 7 illustrates the typical form of these profiles. Note praticularly the drop in velocity in the troughs immediately landward of the bars, and the increase to a maximum velocity in the mid trough. This shift in maximum velocities landward from the break point reflects the lateral mixing while the velocity differential from bar crest to the trough immediately landward reflects both differences in energy dissipation as a result of increasing water depths and differences in mass also as a result of increasing water depths.

Mixing Parameter P

Estimates of the Longuet-Higgins mixing parameter, P, were attempted by averaging and smoothing the relative velocities and then fitting the observed distribution to theoretical distributions based on differing mixing values (Fig. 8). The extreme values associated with non-coherent flow reversals and the local perturbations associated with the second bar have been eliminated in Figure 8 and the dimensionless velocity profiles have been averaged over the storm period and over a given interval of offshore relative distance (0.2X). It should be noted that in all cases at least six points were averaged in each interval, except for the lakeward most unit, represented by one value. The upward deflection of the curve at this location is thus less powerful an indicator of the nearshore flow.

Initial examination of the average velocity profile reveals a pattern for the whole surf zone which is very similar in its general shape to the predicted curves. The distribution is however, skewed landwards to a significant degree. To effect a best fit comparison with the Longuet-Higgins' curve the empirical-average, relative velocities were purposefully adjusted so that the measured maximum was

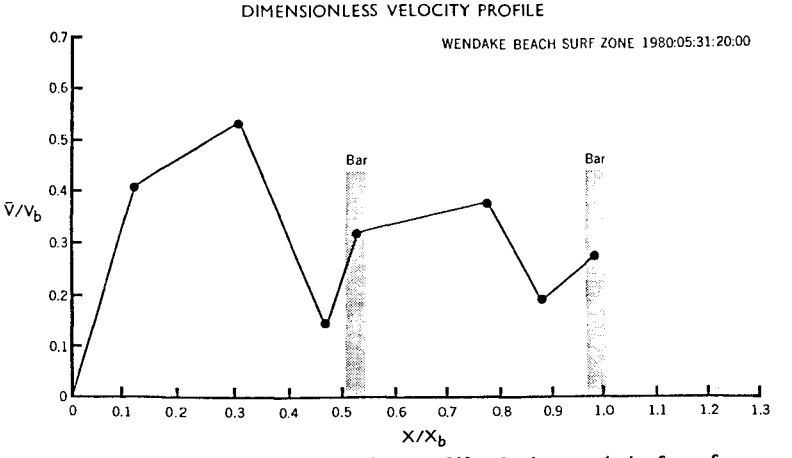

Figure 7: Dimensionless velocity profile during period of surf zone extension to outer bar.

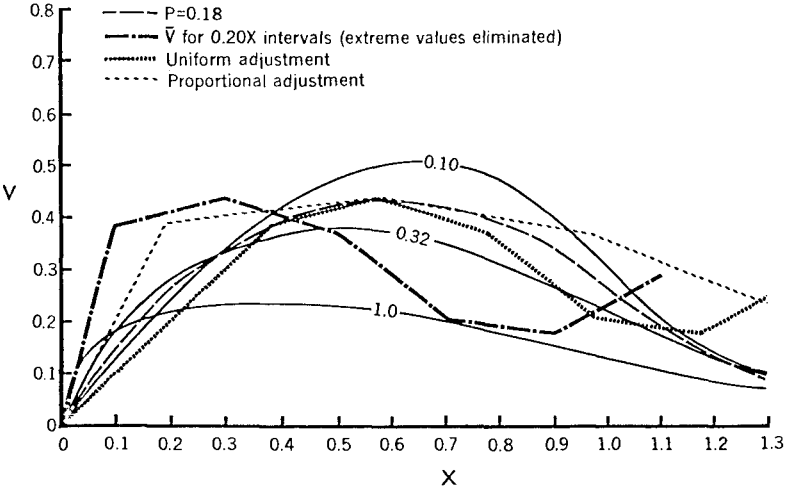

Figure 8: Theoretical and Empirical velocity profiles across the Wendake Beach surf zone.

coincident in position with the theoretical maximum. Both an absolute uniform adjustment and a proportional adjustment was applied to each value. In the former case each relative velocity is translated the same absolute distance as the maximum while in the latter case each velocity is translated a distance in the same proportion as the maximum velocity. Given the constraints of this adjustment, the best fit curve suggests a mixing parameter value of about 0.18, similar to other estimates that have been made (Longuet-Higgins, 1970b; Komar, 1975; Horikawa and Isobe, 1980; Symonds and Huntley, 1980).

VERTICAL STRUCTURE

Two sets of three current meters were used to measure the vertical structure of the longshore current (Fig. 2b). A depth-averaged, mean longshore current velocity was obtained for the storm of 1980:06:08, comprising a set of 27 observations. Mean values for specific elevations above the bed were also computed. The respective values are plotted with the overall mean as illustrated in Figure 10. For vertical arrays 1 and 2 (Fig. 9), the depth-averaged, mean velocities were 21 cms^{-1} and 28 cms^{-1}, respectively. The numbers associated with the current meter locations indicate the ratio of mean currents at that elevation to the overall mean. Note that the maximum mean variability is only about 10% of the depth-averaged flow. These findings are consistent with those of Meadows (1977), and the data suggests that the common practice of modeling longshore currents as depth-average or integrated values is not inappropriate.

Nevertheless, the form of these profiles also shows a consistent deformation of the velocity field strongly suggestive of the influence of bed friction. Assuming a logarithmic boundary layer velocity profile, and examining data from the lower two current meters in the lakeward array (VA2), estimates of boundary roughness may be obtained from

$$\ln Z_o = \frac{(V_b \cdot \ln Z_a) - (V_a \cdot \ln Z_b)}{V_b - V_a} \qquad (3)$$

where Z_o is the boundary roughness length, V is the longshore current velocity, Z is the elevation above the bed, and the subscripts $_a$ and $_b$ refer to values of the upper and lower current meters, respectively. Velocity measurements are obtained directly from the current records. Because the sand bed is moveable, however, estimates of instrument elevation must be made.

From direct measurement, the bed elevation before and after the storm is known. The maximum bed depression is also known from depth of activity rod and box core data (Greenwood et al., 1980). Other values for bed elevation are then interpolated between these three points by assuming that the magnitude of bed elevation change is directly proportional to V^2 and the total elevation changes through the storm. These estimates then provide the basis for solutions to

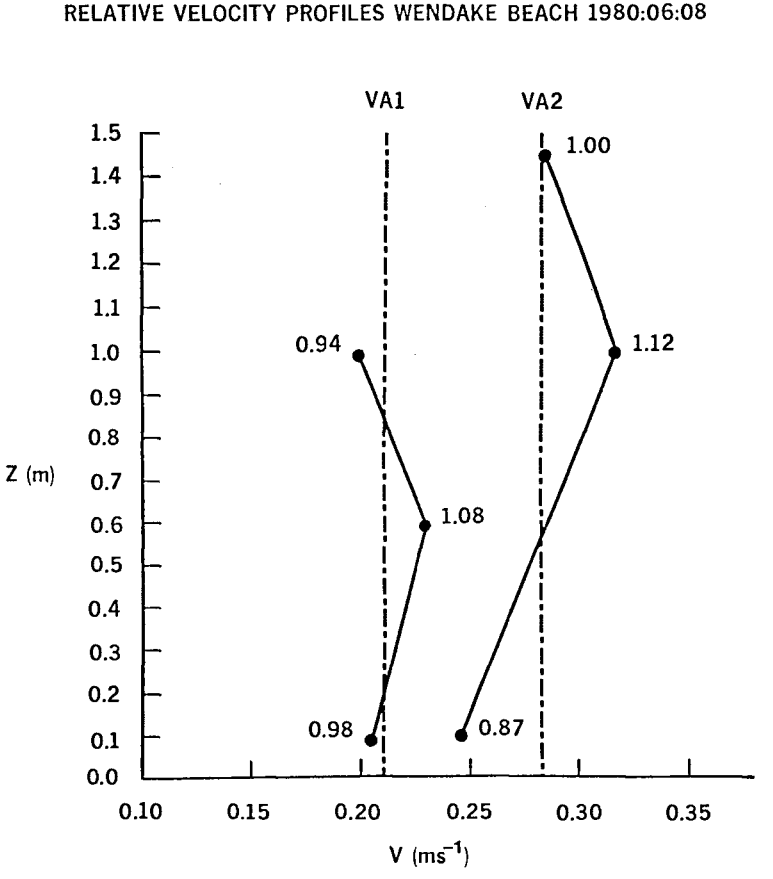

Figure 9: Mean velocity profiles from vertical current meter arrays, 1980:06:08.

equation (3). By plotting V_Z and lnZ, estimates of Z_0 may also be obtained graphically as the intercept of the line representing a logarithmic profile. Figure 10 illustrates these profiles. The dashed lines at ln 10 cm and 100 cm illustrate the values of Z that would have been used without the attempt at modeling bed elevation change. The lower dashed line represents a practical lower limit on expected values of Z_0, as determined from considerations of minimum roughness associated with skin friction on a plane bed. This relationship assumes that a Nikuradse equivalent sand grain roughness K_s, is approximated by $2D_{50}$, where D_{50} is mean grain size by weight-frequency distribution, and further, that $K_s/30 = Z_0$. It is reassuring that all of the estimates of Z_0 from the velocity profiles lie near or above this limit. This partially justifies the use of two points to determine the logarithmic profile. In terms of absolute values, the estimate of $2D_{50}/30$ obtained for the Wendake Beach data is about 0.013 mm, whereas the measured values range between about .01 mm and 3.28 mm. This variability in bed roughness over two orders of magnitude is believed to be mainly a reflection of changes in bedforms associated with wave orbital velocities, although the velocity profile measurements will also reflect changes in the wave boundary layer and internal stratification due to sediment transport. Further details concerning this analysis are presented in Sherman and Greenwood (1983).

For estimates of bed roughness effects on the deformation of the velocity field, a value for the friction (shear) velocity may be obtained from:

$$V_Z = \frac{V_*}{\kappa} \ln (Z/Z_0) \tag{4}$$

where V_* is the friction velocity and κ is Von Karman's constant (0.40). Values of V_* may further lead to estimates of boundary shear stress due to the mean current through solving

$$\tau_0 = \rho V_*^2 \tag{5}$$

where τ_0 is the boundary shear stress.

CONCLUSIONS

The data obtained during the Wendake Beach experiments allows a numerical approximation of key parameters controlling nearshore hydrodynamics. Qualitatively, the strong influences of minor nearshore relief upon the horizontal velocity structure have been demonstrated. Quantitatively, values for a lateral mixing parameter and a wave-current friction factor have been obtained for use in further modeling of the longshore flow. Specific conclusions may be summarized as follows:

1) On a "statistically" planar nearshore slope, bars of low amplitude (less than 0.4 m) exert strong control on longshore current development, particularly the horizontal structure .

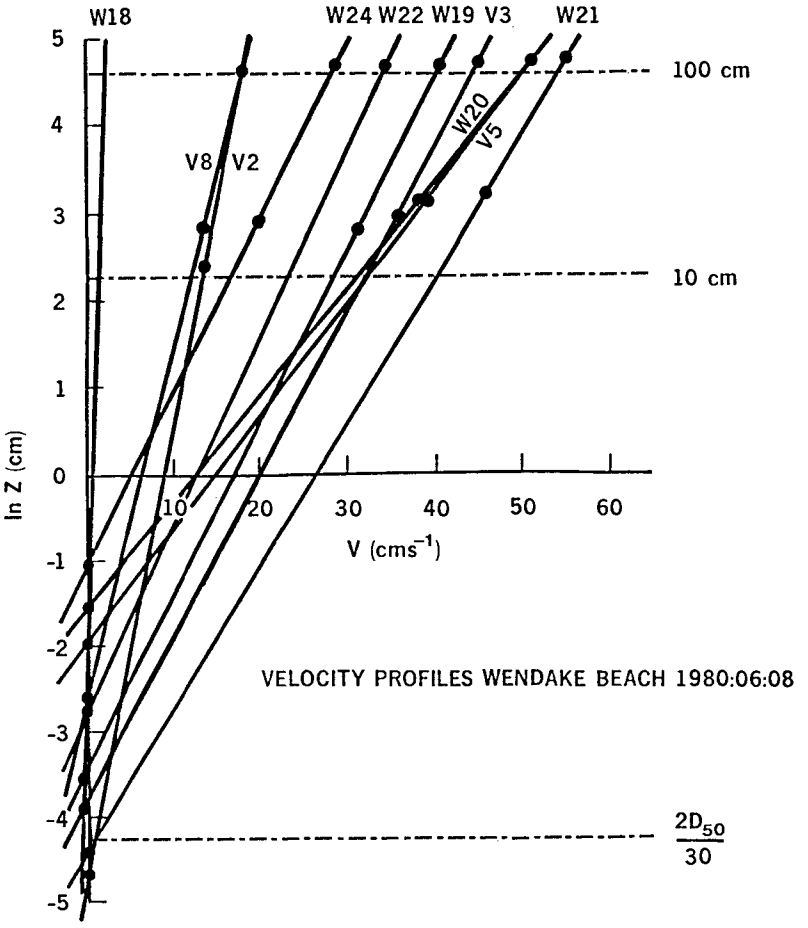

Figure 10: Graphical estimation of boundary roughness length from measurements of average longshore current velocity and estimated elevations above the bed. V and W are file designators here. V files are of 18-20 min. duration and W files of 9 minute length.

2) By discounting localized topographic effects, averaging methods yield an empirically derived, horizontal current structure in good agreement with the theoretical predictions of Longuet-Higgins (1970 b).

3) An estimate of the lateral mixing parameter, P, was found to be approximately 0.18 for the Wendake Beach nearshore.

4) Based upon assumptions of a logarithmic vertical velocity profile an average boundary roughness length of $Z_0 \simeq 1$ mm is obtained from this data set.

5) Estimates of Z_0 vary over two orders of magnitude, presumably reflecting changes in bedform configuration and sediment transport.

ACKNOWLEDGEMENTS

This study forms a part of a continuing research programme at Scarborough College in Nearshore Hydrodynamics and Sedimentation supported by both capital (E3921B, E6614) and operating grants (A7956) from the Natural Sciences and Engineering Research Council of Canada awarded to B.G. University of Toronto Open Fellowships and an Ontario Graduate Scholarship are acknowledged by D.J.S. Assistance with computer costs was given by both Scarborough College and the Department of Geography, University of Toronto. The Academic Workshops at Scarborough College assisted with instrument design and construction, while the Graphics and Photography Division of the College produced the illustrations. We gratefully acknowledge field and laboratory assistance from M. Rollingson, P. Christilaw and R. Sutherland, Scarborough College and R.G.D. Davidson-Arnott and D. Randall, Department of Geography, University of Guelph. Gretchen McManamin, Woods Hole Oceanographic Institution, typed the manuscript. The results and interpretations presented in this paper are, however, the sole responsibility of the authors.

REFERENCES

Allender, J.H., J.D. Ditmars, W. Harrison and R.A. Paddock (1979), "Comparison of Model and Observed Nearshore Circulation," Proceedings of the 16th Conference on Coastal Engineering. A.S.C.E., New York, pp. 810-827.

Allender, J.H. and J.D. Ditmars (1981), "Field Measurements of Longshore Currents on a Barred Beach," Coastal Engineering, Vol. 5, pp. 295-309.

Bowen, A.J. (1969), "The Generation of Longshore Currents on a Plane Beach," Journal of Marine Research, Vol. 37, pp. 206-213.

Cunningham, P.M., R.T. Guza, and R.L. Lowe (1979), "Dynamic Calibration of Electromagnetic Flow Meters," Proceedings, Oceans, '79, IEEE, Inc., New York, pp. 298-301.

Greenwood, B., P.B. Hale, P.R. Mittler (1980), "Sediment flux determination in the nearshore zone: prototype measurements," Proc. Workshop on Instrumentation for Currents and Sediments in the Nearshore Zone, pp. 99-102, NRC-Associate Committee for Coastal Erosion and Sedimentation, Ottawa.

Greenwood, B. and D.J. Sherman (1983), "Wave-Induced Currents, Sediment Flux and Morphological Response in a Barred Nearshore System," forthcoming in "Wave Dominated Coastal Environments," ed., Greenwood, B. and R.A. Davis, Jr., Sedimentary Geology, Special Issue Elsevier, Amsterdam.

Holman, R.H. (1981), "Infragravity energy in the surf zone," Journal of Geophysical Research, Vol. 86, pp. 6442-6450.

Horikawa, K. and M. Isobe (1981), "Dynamic Characteristics in the Nearshore Area," Proceedings of the 17th Conference on Coastal Engineering, A.S.C.E., New York, pp. 480-498.

Huntley, D.A. (1979), "Electromagnetic Flowmeters in Nearshore Field Studies," Proc. Workshop on Instrumentation for Currents and Sediments in the Nearshore Zone, Ottawa, National Research Council, Canada, pp. 47-60.

Huntley, D.A. (1976), "Long period waves on a natural beach," Journal of Geophysical Research, Vol. B1, pp. 6441-6449.

Komar, P.D. (1975), "Nearshore Currents: Generation by Obliquely Incident Waves and Longshore Variations in Breaker Height," In, Proceedings of the Symposium on Nearshore Sediment Dynamics, ed., Hails, J.R. and A. Carr, London, Wiley, pp. 17-45.

Komar, P.D. (1976), Beach Processes and Sedimentation, Englewood Cliffs, New Jersey, Prentice-Hall, pp. 429.

Longuet-Higgins, M.S. (1970a), "Longshore Currents Generated by Obliquely Incident Sea Waves, 1," Journal of Geophysical Research, Vol. 75, pp. 6778-6789.

Longuet-Higgins, M.S. (1970b), "Longshore Currents Generated by Obliquely Incident Sea Waves, 2," Journal of Geophysical Research, Vol. 75, pp. 6790-6801.

Longuet-Higgins, M.S. and R.W. Stewart (1962), "Radiation Stress and Mass Transport in Gravity Waves," Journal of Fluid Mechanics, Vol. 13, pp. 481-504.

Meadows, G.A. (1977), "Time Dependent Fluctuations in Longshore Currents," Proceedings of the 15th Conference on Coastal Engineering, A.S.C.E., New York, pp. 660-680.

Meadows, G.A. (1978), "A Field Investigation of the Spatial and Temporal Structure of Longshore Currents," Great Lakes Coastal Research Lab., Purdue University, Tech. Report No. 6.

Ostendorf, D.W. and O.S. Madsen (1979), An Analysis of Longshore Currents and Associated Sediment Transport in the Surf Zone, R.M. Parsons Laboratory for Water Resources and Hydrodynamics, Report No. MITSG 79-13, Cambridge, Mass., Massachusetts Institute of Technology, pp. 169.

Sherman, D.J. and B. Greenwood (1983), "Friction Coefficients and Bed Roughness in the Surf Zone," forthcoming in "Wave Dominated Coastal Environments," ed., Greenwood, B. and R.A. Davis, Jr., Sedimentary Geology, Special Issue, Elsevier, Amsterdam.

Sonu, C.J. (1972), "Field Observations of Nearshore Circulation and Meandering Currents," Journal of Geophysical Research, Vol. 77, pp. 3232-3247.

Symonds, G. and D.A. Huntley (1980), "Waves and Currents over Nearshore Bar Systems," Proceedings of the Canadian Coastal Conference, 1980, National Research Council of Canada, Ottawa, pp. 64-78.

Teleki, P.G., R.K. Schwartz, and F.R. Musialowski (1976), "Nearshore Waves, Currents, and Sediment Transport," Abstract, Proceedings of the 15th Conference on Coastal Engineering, A.S.C.E., pp. 569-572.

Thornton, E.B. (1978), "Review of Longshore current relationships and data base," In 'Proc. Workshop on Coastal Sediment Transport', University of Delaware, pp. 41-57.

White, B.F. (1979), "Engineering Aspects of a Littoral Drift Measurement Array," Workshop on Instrumentation for Currents and Sediments in the Nearshore Zone, Ottawa, National Research Council, Canada, pp. 29-46.

Wright, L.D., A.D. Short, and P. Nielsen (1982), "Morphodynamics of high energy beaches and surf zones: a brief synthesis," Coastal Studies Unit Tech. Rept. No. 82/5, 64 pp., Dept. of Geography, University of Sidney.

Richards Bay South breakwater

PART III
COASTAL STRUCTURES AND RELATED PROBLEMS

Waves breaking over Gans Bay breakwater

FORCES INDUCED BY BREAKERS ON PILES

by

Robert L. Wiegel, F. ASCE*

ABSTRACT

This paper consists of three parts. The first part presents a method for analyzing the forces exerted by breaking waves on a cirular pile. The force consists of two components, a slowly varying force and a much larger but very short duration quasi-impact force (probably of the order of 1/100 of a second). The second part is concerned with breaker characteristics, with emphasis being given to the few field data that have been measured. The third part consists of a presentation of some available data on surf zone bottom profile variations with time.

Information on all three of these parts is needed for the proper design of a pile supported structure in the surf zone. If the bottom along the site of a proposed pier is sand, an estimate of the variability with time of the profile must be made. The effect of bottom depth and configuration on the height of waves moving shoreward, and the effect of this, in turn, on the wave loading is important in the calculations of wave-induced moments about the bottom. The ability of the structure to withstand these horizontal loads depends in part upon the depth of penetration of the piles. If the bottom varies with time, then calculations of wave characteristics and wave-induced loads on the piles should be made for appropriate bottom configurations.

INTRODUCTION

A large number of pile-supported structures have been built that extend from a beach through the surf zone (Simison, Leslie and Noble, 1978), and many more will be built in the future. The forces exerted on the piles and the ability of the structure to withstand these forces depend upon a number of factors such as pile shape and material, structure configuration, breaker type, beach configuration, tides, currents, and wave climate. The beach configuration changes with changing wave conditions, which further complicates the problem, as there is a relatively strong interaction between breaker characteristics and bottom configuration. Much work has been done in regard to the "design wave," but almost no work is available to the practicing engineer on the "design bottom profile." Both are needed for a well designed structure. In addition, the effect of possible local scouring at the piles or along the entire pier, must also be considered (U.S.

*Professor of Civil Engineering, University of California, Berkeley, CA

Army, Corps of Engineers, Coastal Engineering Research Center, 1982).

BREAKER FORCES ON PILES

Only a few measurements are available of the forces exerted by breaking waves on piles located in the surf zone. These measurements show a slowly varying force similar to that exerted by a nonbreaking wave, together with a very short duration rather large force that occurs just as the wave breaks at the pile, Figure 1. Some field measurements of forces induced on a circular pile by breaking waves in the surf zone are given in papers by Snodgrass, Rice, and Hall, 1951; Morison, Johnson and O'Brien, 1953; Miller, Leverette, O'Sullivan, Tochko and Theriault, 1974. Results of laboratory studies have been given by Hall, 1957; Goda, Haranaka and Kitahata, 1966; Watanaba and Horikawa, 1974. It is difficult to measure this "impact" force reliably owing to its very short duration combined with the dynamic characteristics of the test system.

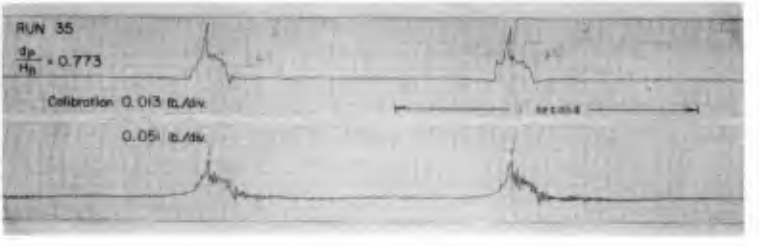

Figure 1. Force Record (From Hall, 1957)

The cause of the "impact" force can be understood by considering the analogy of the wave loading of a horizontal circular cylinder that is alternately in the air and then immersed by a passing wave crest (Kaplan and Silbert, 1976; Faltinsen, Kjaerland, Nottveit and Vinje, 1977; Sarpkaya, 1978). In this problem, one force term is $\dot{\eta}(\partial m_y/\partial t)$, where $\dot{\eta}$ is the time rate of change of the water surface in the vertical direction, and m_y is the vertical component of added mass. $\dot{\eta}(\partial m_y/\partial t$ can be given by

$$\dot{\eta}(\partial m_y/\partial t) = \dot{\eta}^2(\partial m_y/\partial y) \qquad (1)$$

Here, $\partial m_y/\partial_y$ is the change in the vertical component of added mass with with immersion by the wave of the horizontal structural member. This term has been calculated by Kaplan and Silbert (1976) and is shown in Fig. 2 as a function of the relative immersion z/r, where r is the radius of the circular cylinder and z is the immersion, and ρ is the mass density of the fluid. Note for z/r = 0, just as the circular cylinder is first immersed, the coefficient has the value of π and then decreases rapidly.

Additional papers of interest in regard to the problem described above are Attfield, 1975, Dalton and Nash, 1976, and Kjeldsen and Myrhaug, 1979.

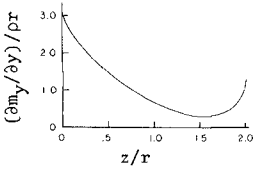

Fig. 2. $(\partial m_y/\partial y)/\rho r$ vs. z/r (From Kaplan and Silbert, 1976)

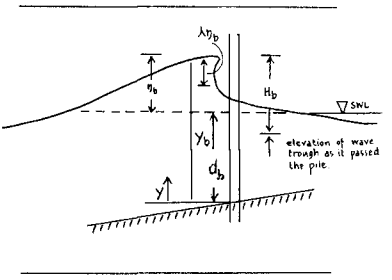

Fig. 3. Definition Sketch

The approach described above can be used to calculate the force due to a breaking wave acting on a vertical circular pile, using $\partial m_x/\partial x$ in place of $\partial m_y/\partial y$, where x is the horizontal coordinate and $\partial m_x/\partial x$ is the change in the horizontal component of added mass with immersion of the vertical pile by the breaking wave (Wiegel, 1979). One can calculate the horizontal component of the slowly varying wave-induced force using the Morison equation from y = 0 to $y = y_b - \lambda\eta_b$ (see Fig. 3). Then, one can compute the "impact" force on the section of the pile that is struck by the vertical or nearly vertical portion of the breaking wave (or, "foam" line or bore), $\lambda\eta_b$. (See the variation of dynamic pressure measurements with distance beneath the surface by Miller, et al., 1974 for the reason that this can be done).

$$F_s \approx \dot{\eta}^2(\partial m_x/\partial x) \approx \frac{1}{2}\rho C_s D C_b^2 \qquad (2a),(2b)$$

Here, the maximum value of $C_s = \pi$, D is the diameter of the pile, C_b is the velocity at which the breaking wave crest moves, and F_s is the "impact" force per unit length of the pile subject to this force, $\lambda\eta_b$. This equation is of the same form as the one developed by Goda, Haranaka and Kitahata, 1966. (See, also, Watanabe and Horikawa, 1974). λ is a function of the

type of breaker. For the range of wave steepnesses used in these tests and bottom slopes of 1/100 and 1/30, λ was less than 0.1. These were for spilling breakers. For plunging breakers on a steep slope(1/10), λ was as great as 0.5. These values of λ were obtained indirectly, and the original papers should be consulted for details. Analysis of some field data by the writer showed that η_b/H_b ranged from 0.55 to 0.95.

The interval of time during which C_s is about at its highest value is very short, with C_s decreasing from this value. Consider a design breaking wave height of 10 m, and a 1.0 m diameter pile. From other studies $C_b = 1.12\ (2g \times 10)^{\frac{1}{2}} = 15.7$ m/sec. The time it would take for the breaker to immerse completely the $\lambda\eta_b$ section of the pile would be 1/15.7 sec (about 0.06 sec). The value of C_s would be decreasing from the initial value of π during this time. Thus, the "impact" force would occur during a short time, substantially less than 0.06 sec., probably of the order of 1/100 sec. The more slowly varying wave-induced force and moment from y=0 to y=y_b calculated using the Morison equation would probably be used by most design engineers to control the design. However, the effect of the large loadings of short duration on the fatigue life of the pile must be taken into consideration (see Attfield, 1975 for a discussion of a similar problem).

It appears from the work of Snodgrass, et al, 1951; Hall, 1957, 1958; and Watababe and Horikawa, 1974, that the Morison equation is adequate for waves that have not yet broken, insofar as any individual pile is concerned. A wave breaking in the plunging manner at a pile induces a greater force in the $\lambda\eta_b$ portion of crest (see Miller et al, 1974). "Foam lines" (bores) resulting from plunging breakers exert a very large force on a pile in the same manner, Figure 4. Sketches are given in Fig. 5, which show the various types of breakers designated in Fig. 4. An example of breaking waves passing the test structure taken from the individual frames of a motion picture film is given in Fig. 6. Similar results were found in the field tests of Miller et al, 1974, for a vertical flat plate of small width and thickness.

BREAKER CHARACTERISTICS

Values of breaker characteristics are needed for the calculation of wave-induced forces on a pile. These are η_b, λ, H_b, d_b, and C_b (forward speed of the wave at time of breaking, or bore speed after breaking), together with the water particle velocities and accelerations within the wave.

One important parameter used in predicting breaker characteristics is the relationship between the type of breaker that occurs and the two primary factors; deep water wave steepness and the slope of the beach (Patrick and Wiegel). They observed this relationship during an extensive field study, followed by a hydraulic laboratory study. For later laboratory studies, see, for example, Galvin, 1968, Weggel, 1972, Battjes, 1974, Singamsetti and Wind, 1980. The most important factor has been found to be the ratio of beach slope to the deep water wave steepness:

$$\xi = \tan\theta/(H_o/L_o)^{1/2} \qquad (3)$$

where θ is the angle between a plane beach and the horizontal, H_o is the deep water wave height, and L_o is the deep water wave length. This ratio has been given the name "surf similarity parameter." It is sometimes

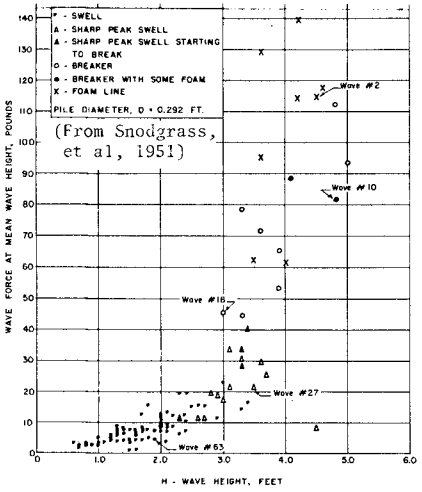

FIGURE 4. WAVE FORCE AT MEAN WAVE HEIGHT VS. WAVE HEIGHT

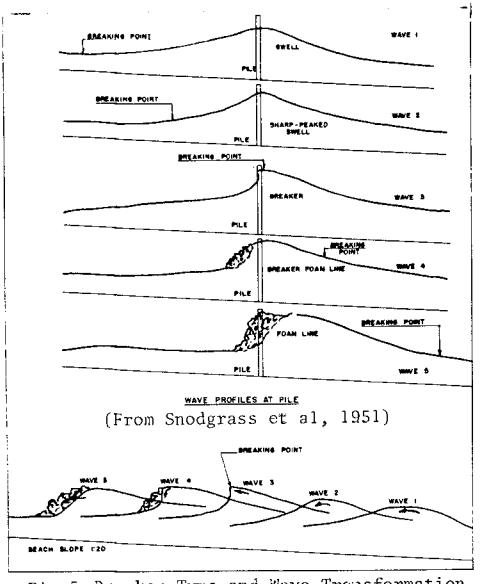

Fig.5. Breaker Type and Wave Transformation

FIGURE 6. – WAVE NO. 2 – FOAM LINE (From Chappelear et al.)

designated the "Irabarren Number," when used in regard to breaker types at a rubblemound breakwater. Numerical values of this ratio and their relationship to breaker type have been reported for plane rigid impervious beaches. A set of calculations has been made to show this relationship, and the results are presented in Table 1.

TABLE 1

Relationship Between Surf Similarity Parameter

(Irabarren Number)$(\tan\theta/\sqrt{H_0/L_0})$ and Breaker Type. *

Beach Slope tan θ		1/5	1/10	1/15	1/20	1/25	1/30	1/40	1/50	1/75	1/100
		0.2	0.1	0.0667	0.05	0.04	0.0333	0.025	0.02	0.0133	0.01
Wave steepness H_0/L_0											
1/10	0.1000	.64	.32	.21	.16	.13	.10	.08	.06	.04	.03
1/15	0.0667	.77	.39	.26	.19	.16	.13	.10	.08	.05	.04
1/20	0.0500	.90	.45	.30	.22	.18	.15	.11	.09	.06	.04
1/25	0.0400	1.00	.50	.33	.25	.20	.17	.13	.10	.07	.05
1/30	0.0333	1.09	.55	.36	.27	.22	.18	.14	.11	.07	.05
1/35	0.0286	1.18	.59	.39	.30	.24	.20	.15	.12	.08	.06
1/40	0.0250	1.26	.63	.42	.31	.25	.21	.16	.13	.08	.06
1/45	0.0222	1.34	.67	.45	.34	.27	.22	.17	.13	.09	.07
1/50	0.0200	1.42	.71	.47	.35	.28	.24	.18	.14	.09	.07
1/60	0.0167	1.55	.78	.52	.39	.31	.26	.19	.16	.10	.08
1/70	0.0143	1.67	.83	.56	.42	.33	.28	.21	.17	.11	.08
1/80	0.0125	1.79	.89	.60	.45	.36	.30	.22	.18	.12	.09
1/90	0.0111	1.90	.95	.64	.48	.38	.32	.24	.19	.13	.09
1/100	0.0100	2.00	1.00	.67	.50	.40	.33	.25	.20	.13	.09
1/125	0.0080	2.24	1.12	.75	.56	.45	.37	.28	.22	.15	.11
1/50	0.0067	2.45	1.23	.82	.61	.49	.41	.31	.25	.16	.12
1/175	0.0057	2.65	1.32	.88	.66	.53	.44	.33	.27	.17	.13
1/200	0.0050	2.83	1.41	.94	.71	.57	.47	.35	.28	.19	.14
1/225	0.0044	3.00	1.50	1.00	.75	.60	.50	.37	.30	.20	.15
1/250	0.0040	3.16	1.58	1.06	.79	.63	.53	.40	.32	.21	.16
		Surging Breakers	Plunging Breakers						Spilling Breakers		

*Breaker classes shown are based upon the following assumption.

Surging Breaker	$\tan\theta/\sqrt{H_0/L_0} > 2.0$
Plunging Breaker	0.4 to 2.0
Spilling Breaker	< 0.4

Many laboratory measurements have been made of breaker characteristics, nearly all for simple plane bottoms, rather than for the more complex bathymetry of natural beaches. The design engineer needs data on more realistic models of bottom configuration, with tests being made with wave spectra as the input. An even greater need, however, is for field data of the type obtained by Suhayda, 1974, Thornton, 1979, and Wright, et al, 1979, 1982.

In nature, sand beaches are not plane, nor are they impervious,

nor are they uniform in the direction along the beach; in addition, the bottom configuration changes with changing wave conditions and tide range. In general, the combination of steep beaches and relatively flat waves (swell) result in a relatively highly reflecting wave condition (called a surging breaker). The combination of steep waves (local storm waves) and a relatively flat beach result in spilling breakers. Plunging breakers occur for intermediate values of the parameter.

As mentioned above, for the combination of a very steep beach and waves of relatively small steepness, much of the wave energy is reflected. The surging type of breaker is of this type, and the runup of the waves on the beach is relatively great, and the drawdown is fast. Often, edge waves are formed under these conditions, and these appear to be associated with the formation of cusps along the beach. For flat beaches and steep waves, the waves spill over a wide surf zone. Most of the wave energy is dissipated in this process, and the wave runup on the beach is rather small. Through a complicated process there is a set-down at and just seaward of the region of breaking, and a setup of the water level within the surf zone, landward of the breakers (for example, see Saville, 1962; Longuet-Higgins, 1970; Komar and Guaghan, 1972; Battjes, 1974; Jonsson and Buhelt, 1978; van Dorn, 1978). On ocean beaches this serup varies with time, exhibiting long-period oscillations known os surf beat (most commonly in the 60 to 150 second period range). Rip currents exist, as a part of a complicated littoral current system created by the breaking waves. Between these two types of breakers are the plunging breakers, which occur for intermediate combinations of beach slopes and wave steepnesses. Strong rip currents are also observed under these conditions. Owing to the complexity of natural beaches with one or more bars present, breakers which have plunged often run as a bore in water which is somewhat deeper landward of the location at which the wave breaks, with the bore dissipating most of its energy before finally moving up a small amount onto the beach face.

Three equations sometimes used to calculate breaker speeds, C_b, needed in Eq. 2 are:

$$C_b = K_1(2g\eta_b)^{1/2}, \quad K_2(gy_b)^{1/2}, \quad \text{or } K_3(2gH_b)^{1/2} \qquad (4)$$

The writer analyzed the field measurements made by Snodgrass, et al, 1951. In these field tests a marker pole was set 6.04 m seaward of the test pile. The wave crest velocity was determined by counting the number of frames of the motion picture film for the wave crest to pass from the marker pole to the test pile (see Fig. 6). The film speed (in frames per second) was determined from a clock which appeared in the film. During the tests thirty-one waves broke at the test pile, or were foam lines (bores) or sharply peaked swell (these broke just landward of the test pile). The average value of the ratio of the measured wave crest velocity to $(2gH_b)^{1/2}$ was 1.12. The average value of the ratio of the measured wave crest velocity to $(gy_b)^{1/2}$ was 1.14. Here, both H_b and y_b were measured values at the test pile, obtained from the motion picture film. y_b may be calculated for some beaches using the equation

$$y_b = d_b + \eta_b \qquad (5)$$

where d_b is the water depth at breaking and η_b is the height of the

crest of the breaking wave above the still water level. η_b was found to be approximately equal to $0.8H_b$ from another set of field measurements, Figure 7. The average value of η_b/H_b is in agreement with the laboratory data of Wiegel and Beebe, 1956, and van Dorn, 1978. Values of η_b are needed in Eq. 5, in the first of Eqs. 4, and in the application of Eq. 2 (to calculate $\lambda\eta_b$).

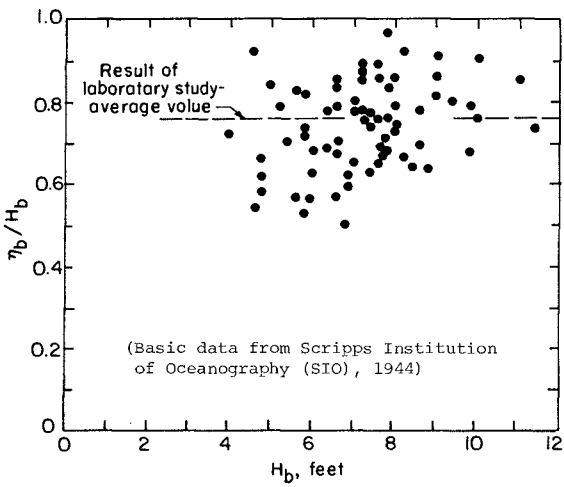

Fig. 7. η_b/H_b, Field Data, SIO Pier, CA.

The relationships among beach slopes, breaker heights, and the the water depths in which the waves break have been studied in the laboratory by a number of piople, each of whom has developed a slightly different semi-empirical equation. The general forms of the equations used to predict breaker heights and the depth of water in which waves break are

$$H_b/H_o = A(\tan\theta)^B(H_o/L_o)^C \qquad (6)$$

$$H_b/d_b = \gamma_b = D(\tan\theta)^E(H_o/L_o)^F \qquad (7)$$

Here, d_b is the mean water depth at breaking (including setdown) and A,B,C,D,E and F are empirically determined coefficients. These, and other formulae have been compared by Singamsetti and Wind, 1980, for several beach slopes. They suggest the use of

$$H_b/H_o = 0.575\ (\tan\theta)^{0.031}\ (H_o/L_o)^{-0.254} \qquad (8)$$

with the range of validity being $0.02<H_o/L_o<0.065$ and $1/40<\tan\theta<1/5$. This curve is the "best fit" curve by Singamsetti and Wind through the other suggested curves. Note the relatively insensitivity to beach slope, except for very steep beaches [$(\tan\theta)^{0.031}$ is 0.93 for $\tan\theta=1/10$, 0.91 for $\tan\theta=1/20$, 0.89 for $\tan\theta=1/40$, and 0.87 for $\tan\theta=1/100$].

The formula for H_b/d_b recommended by Singamsetti and Wind is

$$H_b/d_b = 0.937\ (\tan\theta)^{0.155}\ (H_o/L_o)^{-0.130} \qquad (9)$$

with the range of validity being $0.02< H_o/L_o<0.06$, and $1/40 \leq \tan\theta \leq 1/5$. They state that the results for the 1/5 slope differ considerably from this, and that the following formula is a better approximation for the flatter slopes

$$H_b/d_b = 0.568\ (\tan\theta)^{0.107}\ (H_o/L_o)^{-0.237} \qquad (10)$$

with the range of validity being $1/40 < \tan\theta < 1/10$. A formula similar to the one presented above (due to J.A. Battjes) is

$$H_b/d_b = 1.16\ [\tan\theta/(H_o/L_o)^{1/2}]^{0.22} \qquad (11)$$

Some measurements have been made of the breaker "bore heights as the bores (also called "foam lines") move shoreward over the bottom which has a rather flat slope. These measurements were made over the shoreward 150 meters of a wide surf zone (about 400 to 500 meters) at a beach just west of the entrance to The Coorong in South Australia (east of Adilaide). The beach is composed of fine sand (mean diameter of 0.13 mm), with the bottom slope of the 150 meter wide section where the studies were being made, of about 1/100. The beach is exposed to long high-energy southwesterly swell. During the experiment the significant breaker height was about 3 meters and the wave period in the range of 12-15 seconds (hence, ξ -see Eq. 3- in the range of 0.085 to 0.11). The average spring tide range is only 0.8 meter and the neap tide range is only 0.4 meter. No rip cells or beach cusps were present during the experiment. The measurements of the bore heights (i.e., "foam lines" after breaking) were made in the shoreside 150 meter wide portion the the surf zone. The relationship between significant bore heights and local water depth, d, was measured and the data presented in the report. The average value of γ (H_{bore}/d) was found to be only 0.42.

Van Dorn discovered a rather simple equation for the horizontal component of water particle velocity, u, along a vertical line directly under the crest of a wave just as it starts to break. It appears to be reasonably reliable for beaches flatter than 1/25. This equation is

$$u/C_b = 0.2 + \frac{0.10(y/y_b)}{1.125 - (y/y_b)} \qquad (12)$$

A reasonable approximation for calculating C_b is either

$$C_b = 1.12(2gH_b)^{\frac{1}{2}} \quad (13a) \quad \text{or} \quad C_b = 1.14(gy_b)^{\frac{1}{2}} \quad (13b)$$

where H_b is the breaker height. y_b nay be cakcukated fir sime beaches by Equation 5.

Much work has been done in the laboratory on the water particle velocity (see, for example, Hedges and Kirkgoz, 1981) and acceleration fields in breaking waves, while little field data are available (see, for example, Miller and Ziegler, 1964; Thornton, 1979; Stive, 1980). Space limitations prevent going into this problem in detail herein.

The main difficulty in applying the several equations presented above for breakers is that they have not been checked sufficiently by measurements of ocean waves with the variable bottom slopes that exist on ocean beaches. Furthermore, the laboratory studies have nearly all been for plane rigid impervious beaches, and these are not a good representation of natural beaches.

A very useful study is that of the field data measured at the Scripps Institution of Oceanography pier (Scripps Institution of Oceanography, May 1944 and October 1944; U.S. Navy Hydrographic Office, 1944). A number of characteristics of breakers (such as H_b/d_b, the ratio of the breaker height to the "still water depth" at the point of breaking) were found to depend upon the configuration of the bottom. In the report on field measurements it is stated that during the period that observations were made, two types of nearshore underwater slopes occurred: Type 1, which was a reasonably plane bottom with a slope of about 1/40; Type 2, which has an outer portion with a slope or about 1/25, then a bar, with a slight trough shoreward of this, called the middle portion. The breakers were classed into two groups: Group 1, those that broke over the outer portion, and Group 2, those that broke over the middle portion. Values of H_b/d_b were considerably smaller for the Group 2 waves breaking on the Type 2 bottom configuration than for the other three combinations.

BOTTOM CONFIGURATION

Sand is moved along a beach by the action of waves breaking at an angle to the beach, by the movement of water rushing up and down the beach in a zig-zag motion, and by the longshore currents generated in the surf zone by the breaking waves. The littoral currents are often three dimensional, with rip currents moving out to sea at intervals along a beach, with a number of "cells" existing along a beach (Shepard and Inman, 1952; Sonu, 1972; Sasaki, Horikawa and Hotta, 1976; Mei and Liu, 1977). Sand is moved up and down the beach, and in and out of the surf zone in an onshore-offshore direction by wave action (Wiegel, 1964) and by the currents generated gy winds blowing onshore, with return currents near the bottom flowing towards the offshore (King, 1959; Kraai, 1969; Sonu and van Beek, 1971; Sonu, 1972). Neglecting the wind generated currents, anc their effects, there is evidence that the parameters that describes the direction of the net motion of sand is (Hattori and Kawamata, 1980):

$$(H_o/L_o) \tan\theta / (w_s/gT) \begin{cases} < \\ = \\ > \end{cases} \begin{matrix} \text{(onshore transport, accretive)} \\ 0.5 \text{(neutral, equilibrium profile)} \\ \text{(offshore transport, erosive profile)} \end{matrix} \quad (14)$$

where w_s is the fall velocity of the median diameter sand grains. It can be seen from this, that it is difficult to apply this to actual beaches owing to the variation of sand size along a profile.

Relatively steep waves cause a net motion of sand off a beach face into the surf zone, often forming a bar. Waves of low steepness generally move sand from the bar and other portions of the surf zone onto the beach. These mass movements of sand onto and off the beach cause a modification in the characteristics of the breaking waves, the runup and rundown of the waves on the beach face, and the littoral currents, as mentioned previously. There is a strong relationship between the type of breakers and the beach slope (Patrick and Wiegel, 1955; Wiegel, 1964; Sonu, 1972; Wright, Chappell, Thom, Bradshaw and Cowell, 1979).

In planning the installation of a pier (or a pipeline) across a beach and through the surf zone, one must consider that the action of waves, currents, and winds continuously change the beach configuration, both on the shore and in the nearshore region. In calculating the bending moments exerted on piles by waves during the "design storm" one must consider the associated problem of the actual water depth along the section of a pier in the surf zone during the design storm (Wiegel, 1979), as well as the waves. An example of the variation of the bottom profile of a beach subject to heavy wave activity is shown in Figure 8. An extremely difficult problem is that of estimating where the bottom will be under various conditions (Wiegel, 1980). One must estimate the "design bottom profile."

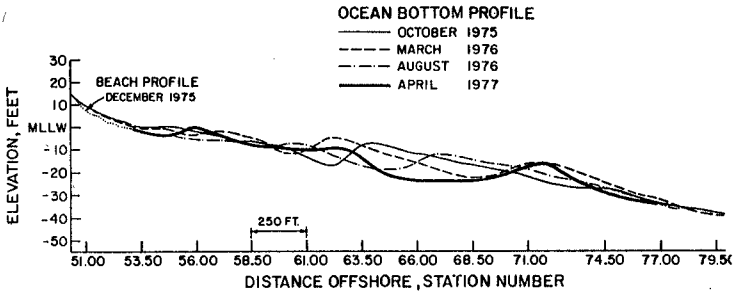

FIGURE 8. BEACH AND NEARSHORE PROFILES, SAMOA, CALIFORNIA, OCTOBER 1975-APRIL 1977 (FROM WINZLER & KELLY, 1976).

There is no simple answer to the question of how much change can be expected to occur as a result of a severe storm. It depends upon the recent past histories of the waves, tides (i.e., spring tide, neap tide, etc.) and beach profile of the particular site in question.

One of the longest set of records of beach and nearshore profiles is that obtained by Shepard,1950. He made measurements from a pier at La Jolla, California. His data are summarized in Fig. 9. This region is not as greatly exposed to waves as are many other regions, such as the northern California coast or the southeast coast of Australia.

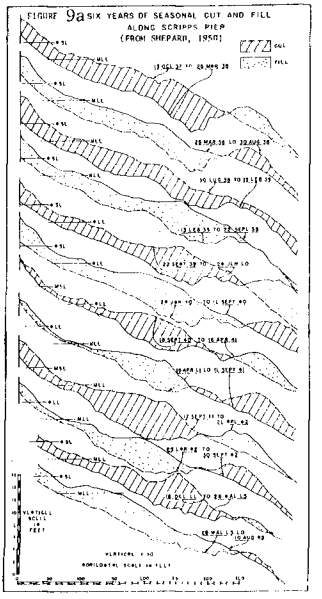

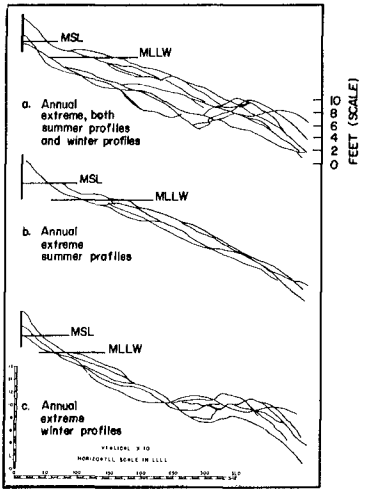

FIGURE 9b — ANNUAL EXTREME PROFILE CONDITIONS FOR 6 YEARS, DATA FROM SHEPARD (JULY, 1950) SCRIPPS PIER.

Shepard studied in detail the bar crest depths (bar depth) and bar trough depths (trough depths). It was found that the bar at the pier seemed to disappear on some occasions. Whether the bar did disappear, or was simply missing along the pier was not determined. Bars are not continuous along a beach, and there are gaps in them. That this is so can be seen by observing waves breaking on a beach where a bar is present offshore. A line of breakers (breaking over a bar) can be followed for some distance, separated by a gap, follow-by another line of breakers. The waves move in through the gap (where the water is deeper, likely about the same depth as the trough) and break closer to shore. In considering the data given by Shepard, note that the ratio of bar depth to trough depth for the large bars measured at very exposed locations along the Oregon and Washington coast is about 2 or so, rather than the smaller values at other locations, Figure 10.

Much additional work is needed on the variations of bars with wave conditions. These appear to be pertubations about some mean bottom profile on sand beaches. Dean, 1977, has found that a mean bottom profile curve can be approximated by the following formula, neg;ecting bars:

$$h = Ax^{0.67} \qquad (15)$$

Here, h is the vertical distance below the mean low water level, x is

the horizontal distance out from the origin (taken as the intersection of the beach with mean low water), and A is a coefficient to be determined empirically. As an example, consider one profile across Ninety-mile Beach, Victoria, Australia, Figure 11. Using the survey data, and an average value through the survey, it was found that $A = 0.235\ ft^{1/3}$. It is important to note that Dean found 70% of the values calculated for 502 beach profiles were between 0.1 and 0.2, and that another 18% were between 0.2 and 0.3.

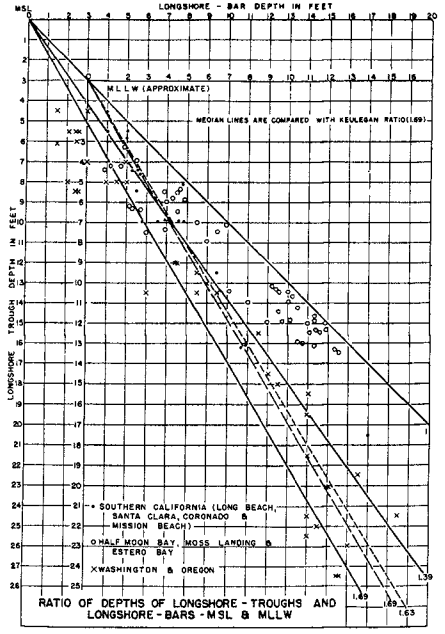

FIGURE 10. (FROM SHEPARD, 1950).

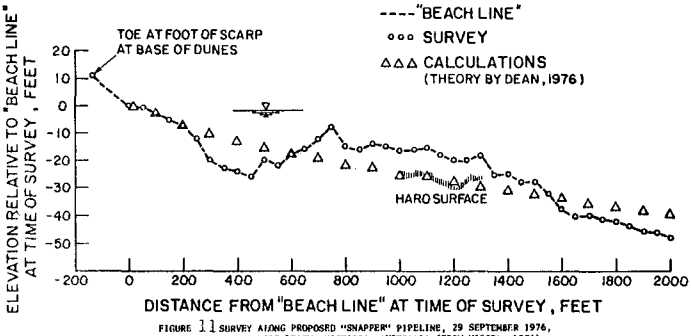

FIGURE 11 SURVEY ALONG PROPOSED "SNAPPER" PIPELINE, 29 SEPTEMBER 1976, NINETY-MILE BEACH, VICTORIA, AUSTRALIA (FROM WIEGEL, 1976).

REFERENCES

Attfield, Keith, "Gas Platforms-How Designers Underestimated North Sea," Offshore Technology, June 1975, pp 19-22.

Battjes, J.A., "Surf Similarity," Proc. 14th Coastal Engineering Conference, June 24-28, 1974, Copenhagen, Denmark, ASCE, Vol. 1, Ch. 26, pp 466-480.

Dalton, Charles and James N. Nash, "Wave Slam on Horizontal Members of an Offshore Platform," 1976 Offshore Technology Conference, May 3-6, Houston, Texas: Proceedings, Paper OTC 2500, pp 769-780.

Dean, Robert G., Equilibrium Beach Profiles: U.S. Atlantic and Gulf Coasts, unpublished manuscript, Ocean Eng. Rept. No. 12, Univ. of Delaware, October 1977.

Faltinsen, O., O. Kjaerland, A. Nøttreit and T. Vinje, "Water Impact Loads and Dynamic Response of Horizontal Circular Cylinders in Offshore Structures,"Preprints of the 1977 Offshore Technology Conference, Houston, Texas, OTC No. 2741, pp 119-124.

Galvin, C.J. Jr., "Breaker Type Classification in Three Laboratory Beaches," Jour. Geophys. Res., Vol. 73, No. 12, June 15, 1968.

Goda, Y., S. Haranaka, and M. Masahata, "Study of Impulsive Breaking Wave Forces on Piles, Rept. Port and Harbour Res. Inst., Ministry of Transport, Japan, Vol.5, No. 6, 1966, 20 pp (in Japanese).

Hall, M.A., Laboratory Study of Breaking Wave Forces, Tech. Rept.: Series 5, No. 2, Inst. Eng. Res., Univ. Calif., Berkeley, CA, Jan. 1957. Also, Tech. Memo. 106, BEB, U.S. Army, Corps. Eng.,1958.

Hattori, M. and R. Kawamata, "Onshore-Offshore Transport and Beach Profile Change," Proc. 17th Coastal Engineerinf Conference, March 23-28, 1980, Sydney, Australia,ASCE, Vol.II, Ch. 72, pp 1175-

Hedges, T.S. and M.S. Kirkgoz, "An Experimental Study of the Transformation Zone of Plunging Breakers" Coastal Engineering, Vol. 4, No. 4, April 1981, pp 319-333.

Hallermeir, R.J. , Calculating a Yearly Limit Depth to the Active Beach Profile, Tech. Paper 77-9, U.S. Army, Corps of Engineers, Coastal Engineering Research Center, Fort Belvoir, VA, 1977.

Hallermeier, Robert J., "A Profile Zonation for Seasonal Sand Beaches from Wave Climate, " Coastal Engineering, Vol. 4, 1981, pp 253-277.

Jonsson, Ivan G. and Nils P. Buhelt, "Calculation of Wave Set-up," Breaking Waves, Surf, and Run-up on Beaches, Bristol, 18-21 July 1978,EUROMECH Colloquim No. 102, 1978, 4pp.

Kaplan, Paul and Mark N. Silbert "Impact Forces of Platform Horizontal Members in the Splash Zone," Proceedings, 1976 Offshore Technology Conf., May 3-6, Houston, TX, Vol. 1, Paper OTC 2498, pp 749-758.

King, A.M. Beaches and Coasts, E. Arnold, London, U.K., 1959, 403 pp.

Kjeldsen, S.P., and D. Myrhaug, "Breaking Waves in Deep Water and Resulting Wave Forces," 1979 Offshore Technology Conf., April 30-May 3, Houston, TX: Proceedings, Paper OTC 3646, pp 155-162.

Komar, Paul D. and M.K. Guaghan, "Airy Wave Theory and Breaker Height Prediction," Proc. 13th Conf. Coastal Engineering, July 10-14, 1972, Vancouver, B.C., Canada, ASCE, Ch. 20, pp 405-418.

Komar, Paul D., "Beach Profiles Obtained whth an Amphibious DUKW on the Oregon and Washington Coasts," The Ore Bin, State of Oregon, Dept. of Geology and Minerial Industries, Vol. 39, No. 11, Nov. 1977.

Kraai, Peter T., "Comparison of Wind Wave and Uniform Wave Effects on a Beach, " Shore and Beach, Vol. 37, No. 2, October 1969, pp 60-71.

Longuet-Higgins, M.S. "Longshore Currents Generated by Obliquely Incident Sea Waves, " Jour. Geophysical Res., Vol. 75, No. 33, November 1970, pp 6778-6789.

Mei, C.C. and P.L.-F. Liu, "Effects of Topography on the Circulation in and near the Surf Zone - Linear Theory," Estuarine and Coastal Marine Science, Vol. 5, No. 1, January 1977, pp 25-37.

Miller, R.L., S. Leverette, J. O'Sullivan, J. Tochko and K. Theriault, "Field Measurements of Impact Pressures in Surf," Proc. 14th Coastal Eng. Conf., June 24-28, 1974, Copenhagen, Denmark,ASCE, pp 1761

Miller, R.L., and John Zeigler, "The Internal Velocity Field in Breaking Waves," Proc. Ninth Conf. Coastal Engineering, ASCE, 1964, Ch. 7, pp 103-122.

Morison, J.R., J.W. Johnson and M.P. O'Brien, "Experimental Studies of Forces on Piles," Proc. Fourth Conf. Coastal Engineering, Chicago, Ill., Oct. 1953, ed. by J.W. Johnson, Council on Wave Research, The Engineering Foundation, Ch. 25, 1954, pp 340-370.

Patrick, D.A. and R.L. Wiegel, "Amphibian Tractors in the Surf," Proc. First Conf. on Ships and Waves, Hoboken, New Jersey, Oct. 1954, The Engineering Foundation and the Society of Naval Architects and Marine Engineers, 1955, Ch. 29, pp 397-422.

Sarpkaya, Turgut, "Wave Impact Loads on Cylinders," Proc. 1978 Offshore Tech. Conf., Houston, Texas, OTC 3065, pp 169-176.

Sasaki, Tamio and Kiyoshi Horikawa, "Nearshore Current System on a Gently Sloping Bottom," Coastal Engineering in Japan, Vol. 18, 1975, pp 123-142.

Sasaki, T.,K. Horikawa, and S. Hotta, "Nearshore Current on a Gently Sloping Beach," Proc. 15th Conf. Coastal Engin.,July 11-17, 1976, Honolulu, Hawaii, ASCE, Ch. 36, pp 626-644.

Saville, Thorndike, Jr., "Experimental Determination of Wave Set-up," Proc. 2nd Tech. Conf. on Hurricanes, June 27-30, 1961, Miami Beach, Florida, ed. by M.A. Alaka, National Hurricane Research Project Report No. 50, Part 1, U.S. Dept.Commerce, Washington, D.C., 1 March 1962, pp 242-252.

Scripps Institution of Oceanography, Effect of Bottom Slope on Breaker Charactistics as Observed along the Scripps Institution Pier, S.I.O. Wave Project Report No. 24, (unpublished), 23 Oct 1944, 15p

Scripps Institution of Oceanogrhphy, Waves in Shallow Water, Report No. 1, Change in Wave Height along the Scripps Institution Pier with Special Enphasis on Breaker Characteristics, S.I.O. (unpublished), 11 May 1944, 9 pp. plus photographs, tables and figures.

Shepard, F.P., Beach Cycles in Southern California, Tech. Memo. No. 20, U.S. Army, Corps of Engineers, Beach Erosion Board, Washington, D.C., July 1950, 26 pp.

Shepard, F.P., Longshore Bars- and Longshore-Troughs, Tech. Memo. No. 15, U.S. Army, Corps of Engineers, Beach Erosion Board, Washington, D.C., January 1950, 32 pp

Shepard, .F.P. and D.L. Inman, "Nearshore Circulation," Proc. First Conf. on Coastal Engineering, Berkeley,California:The Engineering Foundation, Council on Wave Research, 1951, pp 50-59.

Singamsetti, S.R. and E. G. Wind, Characteristics of Shoaling and Breaking Periodic Waves Normally Incident to Plane Beaches of Constant Slope, Delft.Hyd. Lab.(DHL), Rept. No. M1371, July 1980.

Simison, E.J., K.C. Leslie and R.N. Noble, "Potential Shoreline Impacts from Proposed Structures at Point Conception, California," Coastal Zone '78: Symposium on Technical, Environmental, Socioeconomic and Regulatory Aspects of Coastal Zone Management, San Francisco, CA, March 14-16, 1978, ASCE,pp1639-

Snodgrass, F.E., E.K. Rice, and M. Hall, Wave Forces on Piling (Monterey Field Test), Tech. Rept. No. 35-4, Inst. Engr. Res., Univ. California, Berkeley, CA, June 1951, 9 pp plus 18 figures.

Sonu, Choule J., "Field Observations on Nearshore Circulation and Meandering Currents," Jour. Geophys Res., Vol. 77, No. 18, June 20, 1972, pp 3232-3247.

Sonu, Choule J. and J.L. Van Beek, "Systematic Beach Change on the Outer Banks, North Carolina," The Journal of Geology, Vol. 79, No. 4, July 1971, pp 416-425.

Stive, M.J.F., "Velocity and Pressure Field of Spilling Breakers," Proc 17th Coastal Engineering Conference, March 23 to 28, 1980, Sydney, Australia, ASCE, Vol. I, Ch. 34, pp 547-566.

Suhayda, J.N."Standing Waves on Beaches," Jour. Geophys. Res., Vol.79, No. 21, 20 July 1974, pp 3065-

Thornton, Edward B., "Energetics of Breaking Waves within the Surf Zone," Jour. Geophys. Res., Vol.84, No. C8, 20 August 1979, pp 4931-4938.

U.S. Army, Corps of Engineers, Coastal Engineering Research Center, Basic Environmental Data Summary, CERC Field Research Facility, Duck, North Carolina, October 1982, 33 pp.

U.S. Navy Hydrographic Office, Breakers and Surf, Principles in Forecasting, H.O. No. 234, Nov. 1944

van Dorn, W.G., "Breaking Invariants in Shoaling Waves," Jour. Geophys. Res., Vol. 83, No. C6 June 2D, 1978, pp 2981-2988.

Watanabe, Akira and Kiyoshi Horikawa, "Breaking Wave Forces on a Large Diameter Cell," Proc. 14th CoastalEnginr. Conf., Copenhagen, Denmark, June 1974, ASCE, Ch. 102, pp 1741-1760.

Weggel, J., "Maximum Breaker Height," Jour. Waterways, Harbors and Coastal Engineering Division,Proc. ASCE, Vol. 98, No. WW 4, November 1972, pp 529-548.

Wiegel, R.L. and K.E. Beebe, "The Design Wave in Shallow Water," Jour. Waterways Division, Proc. ASCE Vol. 82, No. WW1, March 1952, Paper 910, 21 pp.

Wiegel, Robert L., Oceanographical Engineering, Prentice-Hall,Inc, 1964, 532 pp.

Wiegel, R.L., Beach Erosion, Seadrift, California, Coastal Engineeeing Data and Analysis; Summary of Problem and Remedial Action, a report to Seadrift Property Owners Association, 8 Jan.1979.

Wiegel, R.L., Recommendations Concerning Waves and Wave-induced Forces, Trestle and Unloading Pier, Hadera Offshore Coal Unloading Terminal, a report to S. Yaron - J. Shimoni Consulting Engineers, Ltd. Tel Aviv, Israel, May 1979, 52 pp.

Wiegel, R.L. "Engineering Aspects of Beach and Nearshore Bottom Changes," Proc. 4th Conf. on Ocean Engineering in the Republic of China, September 1980, Chinese Inst. Civil and Hyd. Engrs., ROC, pp 1-

Winzler & Kelly, Consulting Engineers, Humboldt Bay Wastewater Authority Oceanographic Study, Third Period, Winzler & Kelly, Consulting Engineers, Eureka, CA, 30 June 1976.

Wright, L.D., J. Chappell, B.G. Thom, M.P. Bradshaw and P. Cowell, "Morphodynamics of Reflective and Dessepative Beach and Inshore Systems: Southeastern Australia," Marine Geol., V.32, 1979,pp 105-

Wright, L.D., R.T. Guza and A.D. Short, "Dynamics of a High-Energy Dissipative Surf Zone," Marine Geology, Vol. 45, 1982, pp 41-62.

GANSBAAI FISHING HARBOUR - THE DESIGN AND CONSTRUCTION OF A BREAKWATER ON A HOSTILE COAST

by

W S van Dijk * A P M Vonk ** G de F Retief ***

ABSTRACT

This paper describes the design and construction of a fishing harbour on a rocky coastline exposed to the prevailing south westerly swell of the South Atlantic and to severe westerly gales.

Because of economic pressure the first phase of the development was undertaken without adequate knowledge of the wave regime or the topography of the sea-bed in the area and resulted in a virtually unusable harbour.

The second phase of construction was therefore only embarked upon after extensive hydrographic surveys, wave recording and analyses, and probably the most exhaustive series of model tests ever undertaken for such a small project.

These investigations and the good co-operation between research staff, engineers and contractors resulted in the elimination of most of the initial problems and the creation of a functional fishing harbour.

INTRODUCTION

Gansbaai is a small fishing village situated 170 km south east of Cape Town as shown in figure 1, and only a few kilometres from Danger Point, scene of the tragic wreck of the Birkenhead in 1852. When this ship went aground more than 400 soldiers *en route* to the eastern frontier of the Cape Colony perished.

This coastline near the southern tip of the African Continent is exposed to the prevailing south westerly swell of the South Atlantic and the full force of westerly gales.

---

* Technical Manager, Fisheries Development Corporation of SA Ltd

** Senior Research Engineer, Fisheries Development Corporation of SA Ltd

*** Professor in Ocean Engineering, University of Stellenbosch, Stellenbosch, South Africa.

A landing place for fishing vessels developed at Gansbaai because a deep channel in line with the direction of the waves provided an approach route relatively free from breaking waves.

Although the fishing village has been in existence since the late 19th century, the first noteworthy harbour works were constructed in 1939-1942 when breakwaters were built from the northern and southern shores to enclose an area of approximately 4 hectares, of which less that 1 hectare was deeper than 3 metres at low water ordinary spring tide. Unfortunately the northern breakwater cuts across the deep entrance channel forcing boats entering the harbour to deviate from the channel towards the less safe shoaling bottom south of the channel (see figure 2).

Rapid expansion of the pelagic fishing industry in the late 1950's created a demand for improved facilities at Gansbaai as at other fishing harbours, particularly on the west coast of South Africa.

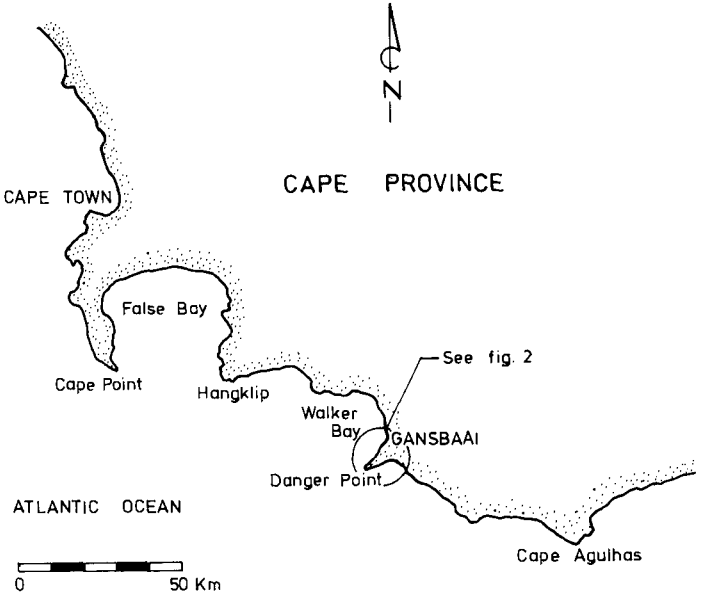

Fig 1. Location Plan

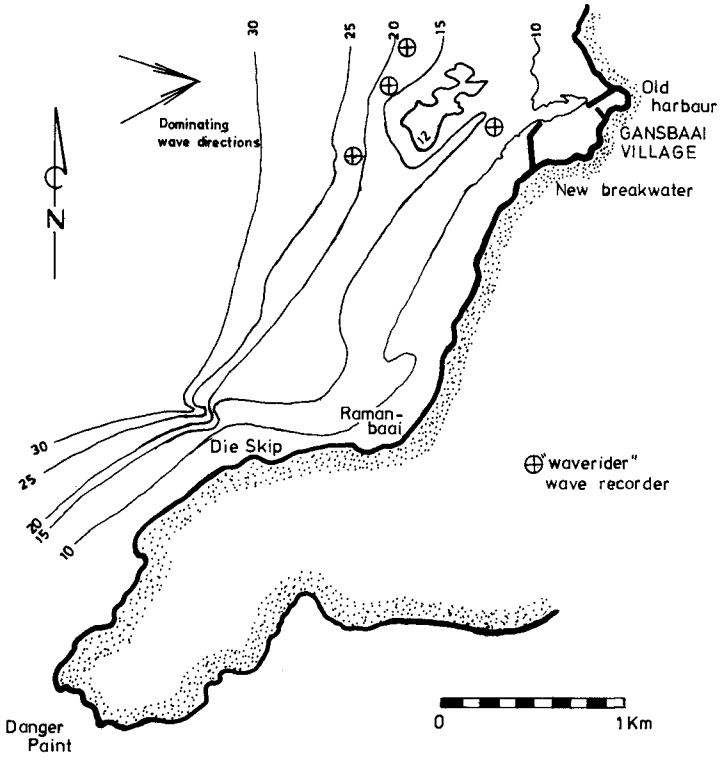

Fig 2. Coastline around Gansbaai

As no obvious solution for the improvement of the existing harbour presented itself, other sites in the vicinity notably Roman Bay and "The Ship" on the north western shore of the Danger Point Peninsula (see figure 2) were investigated. These options were discarded because of the high cost of breakwaters in the deep water at these two sites and the additional cost of a road from the existing village and it was decided to construct a new breakwater south west of the existing harbour at Gansbaai.

FIRST PHASE OF DEVELOPMENT

The new breakwater was to serve a two-fold purpose, viz to protect the entrance to the existing harbour and to provide additional mooring space which could be developed into a fully fledged fishing harbour at a later stage.

The alignment of a breakwater required to effectively protect the entrance to the old harbour, presented difficulties because it would have to extend into or across the deep channel, as shown in figure 3. Such a breakwater would be expensive and could create the same problem as that caused by the existing northern breakwater, i.e. forcing incoming boats into the shoaling water on the opposite site of the channel. Reflection of wave energy by the new breakwater could also create turbulent conditions in the entrance channel.

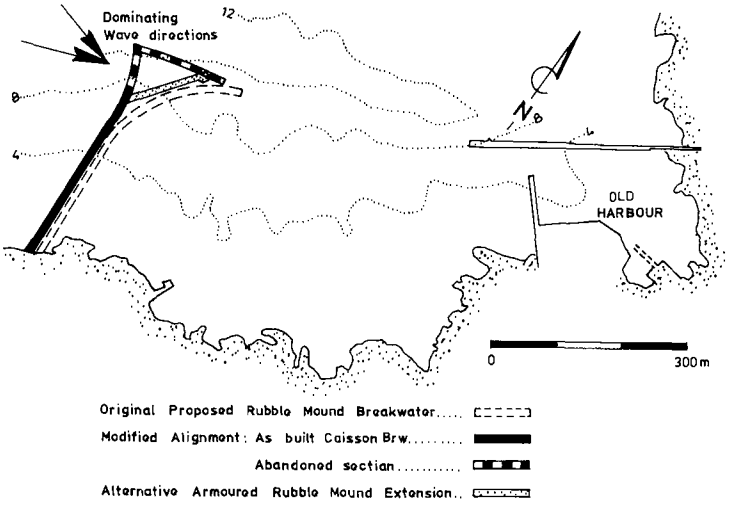

Fig 3. Layout of Breakwaters - Phase I

In 1964 the South African Council for Scientific and Industrial Research (CSIR) was requested to carry out a model study to determine the most suitable alignment for the new breakwater. A fixed bed model was constructed in an existing tank in Pretoria at a scale of 1 in 100.

The study was to be based on hydrographic and other information supplied by the Fisheries Development Corporation of SA Ltd. Unfortunately the urgency of the project precluded the collection of adequate wave data. From the deepsea wave recordings of the fisheries research vessel Africana II in 1962/63 (ref 1) it was concluded that wave heights of 6,1 m from the west and 5,5 m from the south west occurred in the area about 10 times a year for a duration of 6 hours.

Experienced fishermen in the area maintained that deepsea waves exceeding about 6 m in height would break on a series of reefs situated about 1 to 1,5 km west and south west of the harbour (see figure 2). Under storm conditions this break was continuous right across the bay making the harbour inaccessible. It was therefore concluded that even the highest waves, on reforming, would not exceed 6 m in height at or near the proposed breakwater. (Later wave recordings proved this assumption to be incorrect because of the focussing effect of the reefs.)

The hydrographic survey of the area was also inadequate. The original survey was carried out in a small dinghy with position fixing by theodolites on shore. The high swells and the distance from shore led to inaccuracies and an inadequate coverage of the area seaward of the proposed harbour. Consequently the modelling of the sea-bed was not sufficiently accurate and did not extend far enough out to sea to ensure correct reproduction of the waves in the vicinity of the proposed breakwater. It was not realised at the time that the outlying reefs resulted in marked focussing of waves at certain frequencies on to the line of the proposed new breakwater as shown in figure 6.

Before completion of the model study the pressure for the provision of additional harbour facilities became so great that a contract based on an armoured rubble mound breakwater was advertised on the assumption that minor deviations in the alignment of the breakwater indicated by the model study could be accommodated in the course of the work.

The lowest tender for the work was based on an alternative design by an international construction company for a vertical wall consisting of concrete caissons anchored to the sea-bed with post-tensioned cables. Although a vertical wall was not favoured and it was realised that the seaward face might ultimately require some form of energy absorber, it was argued that the cost of such absorber would be offset by the advantage of a quay on the inside face of the wall.

Considerable doubts had also arisen as to the practicability of obtaining suitable large rubble from the highly fractured quartzitic sandstone in the local quarry. The contract was therefore awarded in 1965 on the basis of the alternative design. Details of the original caisson structure are shown in figure 4 together with the modifications which later proved to be necessry.

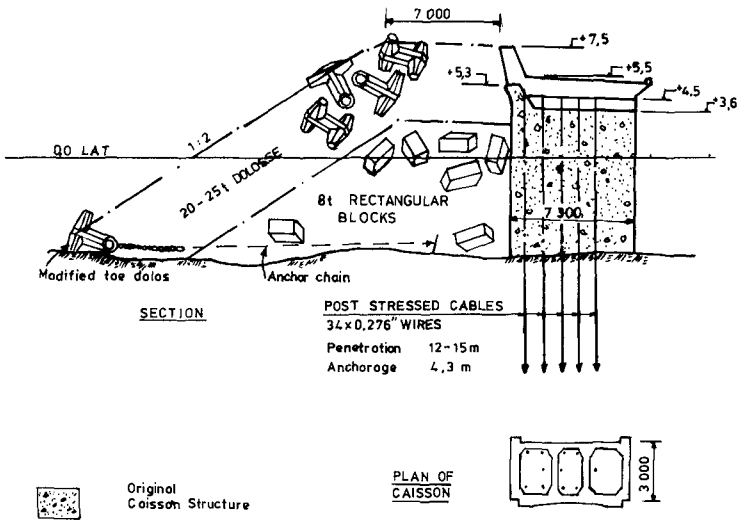

Fig 4. Caisson Breakwater (with armouring added later)

The wall, 6 m wide in shallow water and 7,3 m wide in deeper water, was constructed in open reinforced caissons 3 m long in the direction of the wall and divided into 3 cells with 300 to 400 mm thick walls. The units, approximately 3 m high, were stacked one on top of the other on a bed of broken stone and filled with concrete to within ± 400 mm of the top.

The deck was cast to a level of 3,6 m above low water and 90 mm diameter holes for the installation of the anchor cables drilled to a depth of 12 to 15 m below sea-bed level. The holes were pressure grouted to seal off fissures in the bedrock, interstices in the broken stone bed and construction joints in the concrete structure, and re-drilled. The wires were grouted in over a length of 4 to 5 m at the bottom of the hole, stressed and finally grouted in up to the level of the deck.

During construction of the wall, sea conditions were found to be more severe than anticipated. Placing of caissons was only possible when the wave height was less than about 1,5 metres. Overtopping hampered the work to such a degree that the level of the deck had to be raised from 3,6 m to 4,5 m above low water and the splash wall had to be re-designed at a very early stage of the work.

Fig 5. Wave attack on vertical breakwater

During storms the gantry crane which was specially built for the work and ran on rails concreted into the deck had to be moved back onto land. The crane was washed off the breakwater twice during the course of the work. It also became apparent that it would not be possible to use the wall as a quay and that boats would not even be able to moor near the wall because of the excessive overtopping.

The rock formation on the sea-bed proved to be highly fractured which made sealing of the holes for the stressing cables very difficult. The grouting and redrilling often had to be repeated several times before the hole could be considered watertight. (This method eventually proved to be ineffective in protecting the cables against corrosion. This was proved by ultrasonic tests on the stressed cables in 1977 and confirmed when a portion of the wall was demolished during a subsequent contract.)

When the caisson wall was incorporated in the model the excessive overtopping of the wall and the reflection of waves from the vertical face was clearly demonstrated. It was evident that the reflection of waves from west north west and north west off the last section of the breakwater would result in extremely rough conditions in the access channel to the old harbour. Various remedial measures were considered but eventually a revised alignment was proposed whereby the wall would initially curve westwards and then at chainage 360, bend sharply eastwards so that the first section would reflect waves to the south western shore and the second section would be almost parallel to the direction of the waves (see figure 3).

The adoption of this unusual alignment was unfortunate because it moved the breakwater towards deeper water and a concentration of wave energy near the proposed bend. Refraction diagrams based on more extensive hydrographic surveys carried out later confirmed this focussing effect. An example is shown in figure 6.

As the construction of the wall approached the proposed bend, sea conditions became more severe and the contractor became more and more concerned about the prospect of not being able to retrieve the crane during stormy weather via the sharp bend in the new alignment of the breakwater.

Doubts as to the efficacy of the stressing system increased as the water depth increased and the sea-bed became more highly fractured. Eventually it was decided to abandon the idea of a sharp bend in the breakwater at 360 metres, and to end the vertical wall at 300 metres. The remainder of the breakwater would be constructed as an armoured rubble mound as shown in figure 7 which would reflect less energy into the approach channel.

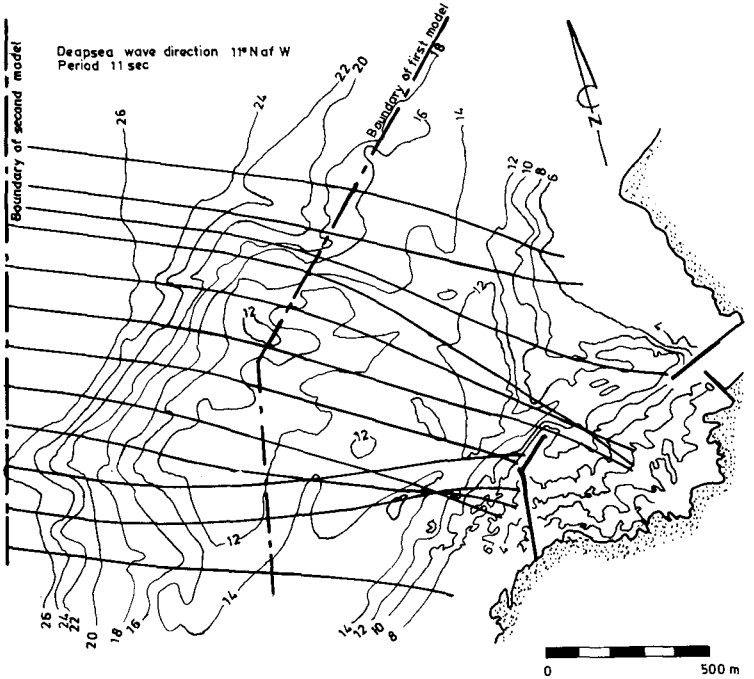

Fig 6. Wave Refraction

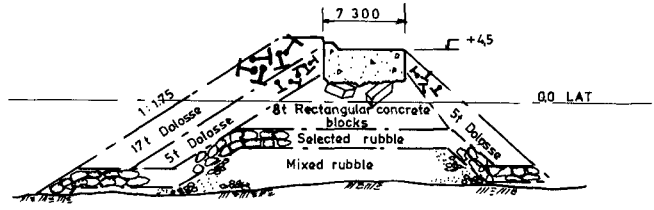

ORIGINAL PROFILE

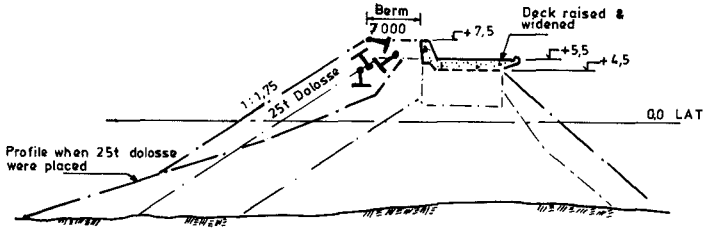

MODIFIED PROFILE

Fig 7. Armoured Rubble Mound Breakwater

Construction of this rubble mound extension of the breakwater proved to be no less difficult than construction of the caisson wall. The fractured quartzitic sandstone available for rubble in the core contained a high percentage of fines of which large quantities were washed away. Due to the shortage of the specified selected rubble a layer of 5 ton dolosse was initially placed over the rubble core. Later 8 ton rectangular blocks were used for this purpose. These units helped to prevent the immediate loss of core material but allowed considerable quantities of fine material to be leached out with the passage of time. This loss of core material combined with the structural weakness of the 5 ton dolosse, resulted in marked settlement of the deck over several sections. One section of the deck had to be demolished and rebuilt in order to fill the large cavity which had developed under the deck.

Wave recordings which had commenced in 1968 at a depth of 15 m on a position inside the reefs as shown in figure 2, had indicated that waves up to 8 metres could be expected at the breakwater. Further model tests had shown that the 17 ton dolosse used for the armouring might not be adequate. The contractor's plant, however, did not allow for the placing of heavier units at the distances required and the design could therefore not be altered without prohibitive additional costs.

The weakest section of the rubble mound breakwater was found to be at the interface with the vertical wall. This was probably due to the focussing of waves on to this section of breakwater and the lack of interlock between the vertical wall and the rubble mound breakwater. The deflection of wave energy off the flat end of the caisson wall could also have contributed to the damage which occurred repeatedly to the breakwater along this section. Several unsuccessful attempts were made to reproduce this damage in a wave flume and in a later 3 dimensional model study. The damage was probably aggravated by fracturing of the 5 ton dolosse between the core and the deck or the overlying 17 ton dolos layer and possibly by low packing density of the dolosse.

The leeward slope of the rubble mound breakwater which was protected with 5 ton and later 12 ton dolosse also suffered considerable damage in the first year after completion because of heavy overtopping and because of the penetration of wave energy through the highly permeable 5 ton dolos layers underlying the deck. Reasonably successful attempts were made to repair the erosion of the inner face by sealing the cavities with concrete pumped into filter cloth bags and providing a steeper leeward slope so that overtopping waves could expend their energy into the enclosed basin.

It was feared that the roundhead at the end of the breakwater would be particularly vulnerable but it suffered relatively little damage possibly because the armour units were chained together above the low water level.

Although at this stage the objectives of the scheme (i.e. to provide safe mooring space for additional and larger fishing vessels and to improve the entrance conditions at the old harbour where the factory was still situated) had not been achieved, the completion of the rubble mound breakwater in 1969 marked the end of the first phase of attempts to improve facilities at Gansbaai. The fishing industry had by this time entered into a period of decline and additional funds for further development were not readily available.

SECOND PHASE OF DEVELOPMENT

Although the urgency for further development of the harbour had abated, a number of questions regarding the durability of the completed portions of the work had to be resolved. The overall stability of the rubble mound breakwater was a matter for concern because of the quality of the rubble and the inadequate mass of the armouring of 17 ton dollosse. (This concern was proved to be justified when a section was destroyed in 1979 shortly before it could be reinforced with 25 ton dollosse.)

An even more serious problem was the uncertainty regarding the stability of the caisson wall. This wall which had originally been designed with a factor of safety against overturning of 1,5, had subsequently been raised from an effective height of 3,6 metres above low water to 4,5 metres above low water and was also being subjected to attack from waves higher than the original design wave height. New calculations had shown that the factor of safety was lower than originally intended. Factors such as the force taken up by the higher splash wall, an occasional higher still water level due to set up and transverse resonance (recorded locally and confirmed by a mathematical analysis by the Danish Hydraulic Institute) were taken into account. The higher SWL also accounted for higher overtopping than expected.

A series of two dimensional tests confirmed that the factor of safety was nearer 1,0 and in some sections of the wall probably less than 1,0. The 2 dimensional tests which were being conducted to investigate the caisson stability were extended to explore various ways of reducing the overtopping of the wall (such as different shapes of splash wall and a lower splash wall on the seaward side with a secondary splash wall on the leeward side).

Serious doubts had also arisen regarding the soundness of the stressing cables which supplied the major proportion of the moment of resistance against overturning. Ultrasonic tests conducted in 1977 (ref FDC report F92-2) revealed that these wires were in fact seriously corroded especially at the interfaces between the caissons and the sea-bed and the caissons and the deck slab. The continued stability of the wall could probably be ascribed to the angle of wave attack which resulted in the forces on the wall only reaching maximum values over very short sections of wall at any given instant and the transfer of these forces to adjacent caissons through the deck and the keys between the caissons.

In order to solve the many problems which had by now been identified, i.e. stability and excessive overtopping of the completed new breakwater, and also provide design guidelines for the completion of the harbour works preferably as one combined larger harbour, a second 3 dimensional model study was commissioned in 1975. Again the FDC would be responsible for the field work while the CSIR would carry out the model study.

An intensive study of the wave regime was carried out between July 1975 and September 1978. To obviate the mistakes which had occurred in the first model a series of three "Waverider" recorders were installed seaward of the reefs and one waverider nearer the breakwater. As the direction of wave attack on the breakwaters had proved to be critical, a wave direction recorder (DOSO) developed by the FDC was installed seaward of the reef close to the central waverider. The effect of the reefs on wave refraction could therefore be accurately determined. The positions of the recorders are shown in figure 2.

More detailed hydrographic surveys were also carried out (including side scan surveys to determine the shape and nature of the rock strata). Accurate refraction diagrams, verified by numerous aerial photographs under the complete spectrum of wave attack, as recorded by the 4 waveriders and DOSO were used to calibrate the wave reproduction in the model. The model was constructed on a scale of 1 in 80 over a much larger area than for the previous model in order to reproduce the wave regime as accurately as possible.

The result of the 2 dimensional tests on stability of the caisson wall were verified in the 3 dimensional model by constructing the caisson wall of 100 mm wide hinged box sections fitted with strain gauges at several elevations. The forces and overturning moments were determined and the results compared well with those of the previous 2 dimensional models.

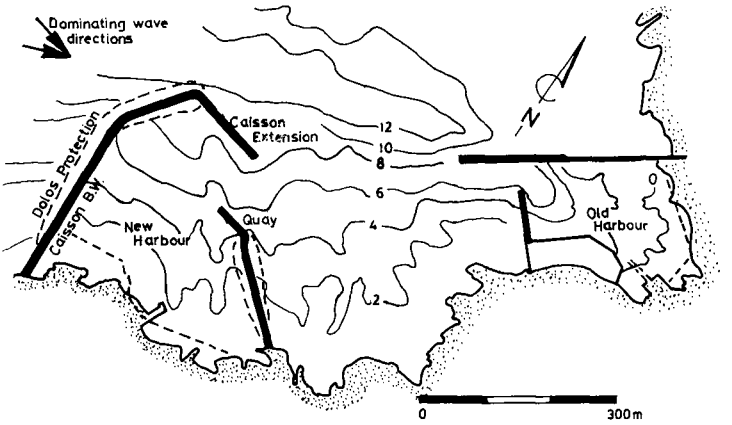

Fig 8. Revised layout of new harbour

Many different alignments, sections of breakwaters and absorbing structures seaward of the caisson wall were tested under all recorded wave directions, heights and periods, as small variations in these parameters affected the focussing of waves along the breakwaters considerably. A solution was found for the safeguarding of the existing new breakwater and an extension of this breakwater to create satisfactory entrance and mooring conditions in the "new" harbour was successfully tested. No really successfull solution was found for the combination of the old and new harbours because of the distance between the ends of the main breakwaters of the two harbours. One layout tested involved the construction of a T-breakwater halfway between the two harbours. The cost of this scheme, however, rendered it unacceptable. Even the most favoured scheme involving the extension of the north breakwater of the old harbour was not justifiable. The main part of the model study was completed in 1978 but additional tests involving mainly construction techniques continued up till 1981.

In 1978 it was decided to proceed with a scheme involving the safeguarding of the existing caisson and rubble mound breakwaters, the extensions of the rubble mound breakwater and the construction of a quay and approach mound from the southern shore. This would enclose a protected water area of approximately 7 hectares of which 3 hectares would have a water depth exceeding 4 metres at low tide.

The measures adopted to protect the existing caisson and rubble mound breakwaters took into account the variation in design wave height along the length of the wall in the design of deck and splash wall height, mass of armour units and width of berm at the top of the armoured layer. The final deck height was 5,5 m above low water and the top of the splash wall varied from 6,5 to 7,5 m.

20 and 25 t dolosse placed to a slope of 1:2 on a core of 8 t corrugated rectangular blocks were used on the outside of the caisson wall as shown in figure 4 and 25 t dolosse placed to a slope of approximately 1:1,75, were used to protect the rubble mound breakwater as shown in figure 7. A horizontal 7 m wide berm at splash wall level (7,5 m) was used for additional absorbtion of wave energy.

Specific attention had to be given to the stability of the toe of the dolos layers because of the relatively smooth sea-bed seawards of the caisson wall coupled with reflected wave energy from the wall. Model tests indicated that the toe line of dolosse would move out of position at relatively low wave heights (1,5 m). A special reinforced "toe dolos" was developed with a lowered centre of gravity to prevent overturning and with two projections on the ends of the lower fluke to prevent rocking (see figure 9). To prevent sliding these dolosse were tied back into the mound with heavy chain and a rudimentary anchor.

Fig 9. Reinforcing of toe dolos

Fig 10. Storm damage to rubble mound breakwater

The contract for the above work was awarded at the beginning of 1979, but in August of the same year, before any remedial work could be carried out, a major storm breached the existing rubble mound breakwater. Other storms followed and eventually almost 60 m of the breakwater was destroyed as shown in figure 10. Model studies were again carried out to determine the most effective way of repairing the breach, and a construction method using 8 t corrugated concrete blocks as a core with a double layer of 25 t dolosse as armouring was eventually successfully used. During the repairs to the breach the junction between the vertical wall and the rubble mound breakwater was reconstructed. The section of the vertical wall extending beyond the rubble mound breakwater was eliminated and a smooth curve introduced. Fortunately no severe storms occurred during these critical stages of the work.

The extension of the main breakwater by means of another vertical wall more or less parallel to the direction of the waves and the construction of a secondary breakwater with caisson quay from the eastern shore were also completed without serious problems.

CONCLUDING REMARKS

The construction of the extension to the Gansbaai fishing harbour has been successfully concluded but only after a disproportionate volume of model testing and other investigations. The project was carried out over a span of almost 20 years which coincided with a period of rapid development in the science of coastal engineering.

The initial mistakes were due to inadequate field data, a lack of appreciation of the effect of distant topographical features of the sea-bed on the wave regime, the adoption of an untried design without model testing and the commencement of construction before completion of the model tests.

The project has highlighted the need for closer co-operation between research personnel, designers and contractors.

ACKNOWLEDGEMENT

The authors wish to thank the Fisheries Development Corporation of South Africa Limited for permission to publish this paper.

REFERENCES

1. Hydraulics Research Unit (CSIR) -
Wave and Wind Conditions for the Natal and Western Cape Coastal Areas Ocean Wave Research - Report No 1

MEG 665/1 Pretoria, Republic of South Africa April 1968

2. Hydraulics Research Unit (CSIR)

MEG 396 Cansbaai Fishing Harbour Extension Model Investigation Oct. 1965

MEG 578 Navigability Studies for Gansbaai Fishing Harbour Extension June 1967

MEG 705 Model Tests Related to a New Harbour Layout and the Protection of the New Breakwater at Gansbaai Aug. 1968

MEG 779 Gansbaai Fishing Harbour Extension Model Investigation : Layout Tests with Rubble Breakwaters Feb. 1969

3. Fisheries Development Corporation of SA Ltd
Cape Town, Republic of South Africa

F 92 - 1 Twee-dimensionele modelondersoek van Westelike Caisson Breekwater te Gansbaai May 1974

F 92 - 2 Gansbaai Caisson Breakwater - Anchor Cable Report June 1977

F 92 - 3 Gansbaai Caisson Breakwater - Two Dimensional Model Investigation Oct. 1977

F 92 - 4 Gansbaai Caisson Breakwater - Two Dimensional Model Investigation Final Report Sept. 1978

F 92 - 5 Gansbaai - Wave Overtopping at Caisson Breakwater March 1979

F 92 - 6 Gansbaai - Slope Stability and Wave Overtopping at Caisson Breakwater May 1979

F 92 - 7 Gansbaai - Different Alignments of the Access Mound July 1979

F 92 - 8 Gansbaai - Comparative Model Tests on Revised Design of Caisson Breakwater End Nov. 1979

4.	R R Minikin	Wind, Waves and Maritime Structures 2nd Edition	1963
5.	S Nagai	Shock Pressures exerted by Breaking Waves on Breakwaters.	
		Waterways and Harbours Division Proceedings ASCE	June 1960
6.	Coastal Engineering and Hydraulics Division, National Research Institute for Oceanology (CSIR) Stellenbosch, Republic of South Africa		
	Gansbaai Model Study - Progress Reports No 1 - 11		
	C/sea/7801	Summary of 1st Phase of Study	Jan. 1978
	C/sea/7919	Summary of Field Data and 2nd Phase of Model Investigation	July 1979
	C/sea/7922	Final Summary Report	Aug. 1979
	C/sea/7931	Report on Additional Model Tests	Oct. 1979
	C/sea/8136	Construction Stage Tests. Report No 1, Volumes 1 & 2	
		Blocks and Dolos Protection to the Existing Caisson Breakwater and the Final Layout	June 1982
	C/sea/8137	Construction Stage Tests. Report No 1. Methods of Temporary Repair of Storm Damage	

REPAIR TO A DOLOS ARMOURED BREAKWATER

C.W. Glodowski, B.Eng., Marine Directorate, Public Works Canada
D.L. Lajoie, Ba.Sc., Marine Directorate, Public Works Canada
Y. Ropars, Ma.Sc., Quebec Region, Public Works Canada

1. Introduction

In recent international experience several breakwaters armoured with concrete units have failed shortly after or during construction of the structure. Although investigators have not necessarily agreed on the causes of these failures, it has been generally implied that there is a relationship to breakwater construction in deep water with large units and severe wave conditions (4,9). However, the damaged sections of the dolos armoured breakwater that is the subject of the paper, are in water depths of 6 to 8m with depth limited wave conditions.

The original design parameters for selecting the dolos weight appear to have been reasonably accurate by current estimates. The recent hydraulic model tests indicate that the breaking wave conditions and overtopping of the breakwater have combined with the breakage of dolosse in the resulting failure.

The recommended repair work which was the primary objective of the study, consisted of armouring the crest of the damaged section with large stone (20t) and leaving the damaged front layer of dolos below low water level. It was judged that the further use of concrete dolosse was not economically justifiable and that there did not exist a satisfactory procedure to design dolos armour within the scope of the study.

2. Site and Damage Descriptions

2.1 Location and Breakwater

Rivière-au-Renard is located on the eastern end of the Gaspé Peninsula on the Gulf of St. Lawrence in Québec, Canada. The main breakwater is about 785m in length and encloses a natural bay to protect a fishing harbour facility. The breakwater construction was completed in 1972 (see Figure 1).

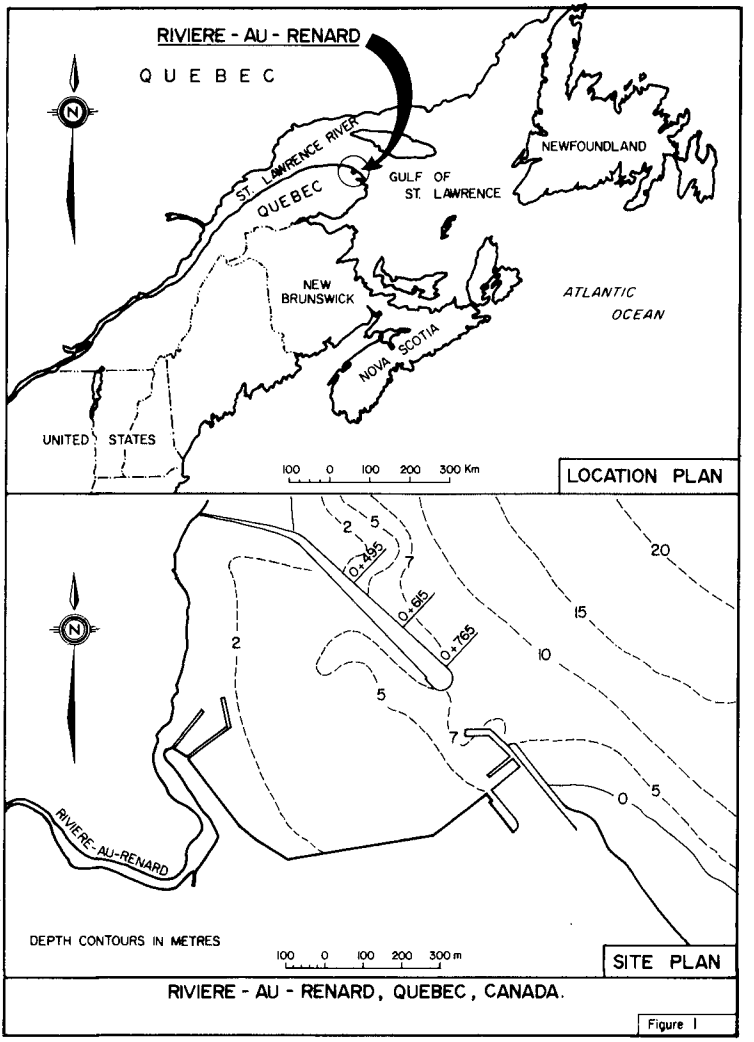

RIVIERE - AU - RENARD, QUEBEC, CANADA.

Figure 1

The outer portion of the structure of about 350m in length, was armoured with concrete dolos units of two sizes. Units at the head are 12.7t and extend back about 30m on both front and back slopes in water depths of 7 to 8m. Dolosse in the trunk are 4.5t and cover the crest and front slope only in depths of 4 to 7m. Typical cross-sections are shown in Figure 2. Unit placement was in double layer random in the densities estimated from the S.P.M. (1)

The design crest elevation of the breakwater varied from 5.3 to 8.0m over the concrete armoured section of the structure.

2.2 Construction

Some problems were encountered during construction which may have had a bearing on the subsequent damage.

Initially the contractor had some difficulties obtaining the required strength specification of 31 MPa at 28 days. An unspecified number of units near the time of the job completion were placed after a striking time of about 12 hours.

The contractor was also allowed to cover sections of the crest filter layer with quarry run material to permit equipment access. This finer material was not removed from the filter layer.

2.3 Damage Surveys and Inspections

Rivière-au-Renard has been cited in previous publications as an example of a successful dolos installation (7). It can no longer be considered as such.

In 1978 it was visually observed that the crest elevations in sections of the main trunk had decreased. Storms in the fall of 1980 eventually opened a major breach at one location and severely damaged another section, both in the 4.5t units.

Field inspections in 1981 revealed the following:

- There was a high percentage of broken dolosse along the full length of the structure including the 12.7t head section. Estimates for broken units on the front slopes above and below mean water level ranged from 10 to 50% not including the areas of the breaches.

- The major breach extended for a length of about 50m and a typical section is shown in Figure 3 (i.e. Section +615). Estimates of broken dolosse in the breach are about 30% on the front below low water, 90% on the crest and front above low water and 65% on the back.

- The secondary breach was in deeper water but extended only 10m in length and was not as extensively damaged. However, dolosse were also piled at the back side of the breakwater (section not shown).

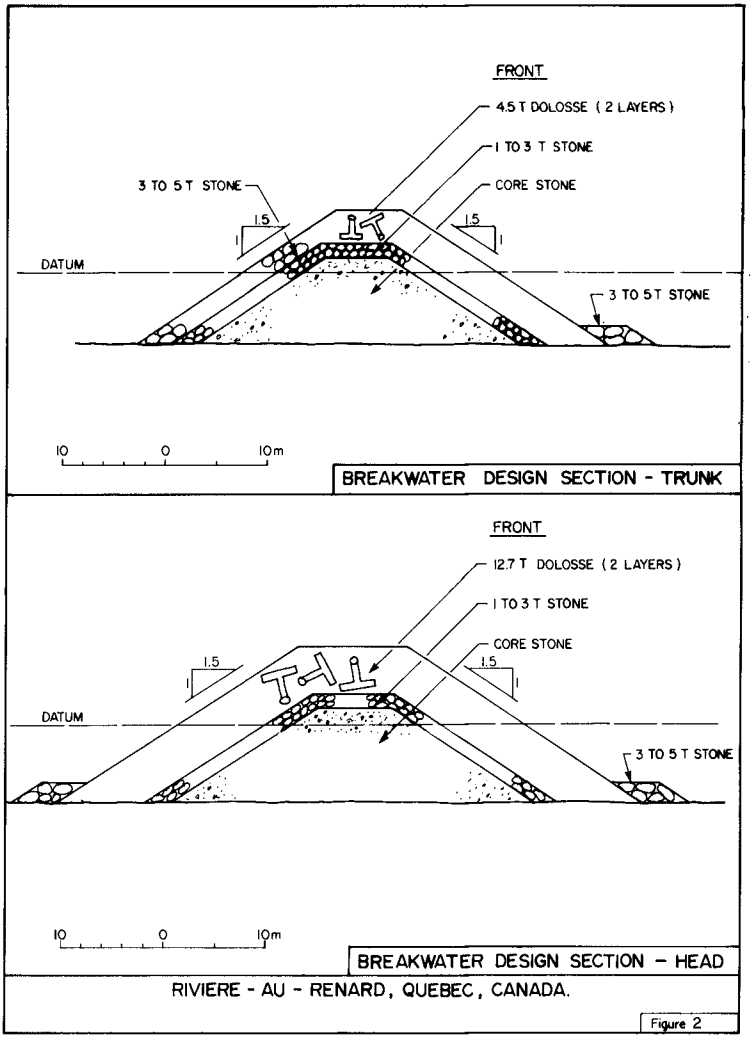
FRONT
4.5 T DOLOSSE (2 LAYERS)
1 TO 3 T STONE
CORE STONE
3 TO 5 T STONE
1.5
1.5
DATUM
3 TO 5 T STONE
10 0 10m
BREAKWATER DESIGN SECTION - TRUNK
FRONT
12.7 T DOLOSSE (2 LAYERS)
1 TO 3 T STONE
CORE STONE
1.5
1.5
DATUM
3 TO 5 T STONE
10 0 10m
BREAKWATER DESIGN SECTION - HEAD
RIVIERE - AU - RENARD, QUEBEC, CANADA.
Figure 2

- Overall the slopes were very steep on the landward side of the structure in the area above mean water level. It appeared as if the dolosse in the crest area had been pushed back en masse (see Figure 3 of Section +495), however it is not known whether the original placement met specifications. Seaward side slopes were varied and irregular but showed some tendency to form an 'S'-shape.

- The 12.7t dolosse at the breakwater head showed unusual and steep slopes that could not be accounted for without assuming significant deviations from the design specifications (see Figure 4 of Section +765).

- Over most of the breakwater crest the visible filter layer material appeared to be composed of or filled with much smaller core type stone.

- Most of the rock berm protecting the front toe was either damaged or missing and in areas where the structure resided on sand there was a small trough in place of the berm.

3. Original Design Parameters

Although details of the original design calculations are not available at the time, the Hudson stability formula was used with the K_D, or stability coefficient probably of the order of 15 to 22 for the breakwater head and trunk respectively in breaking waves on a 1 to 2 slope. Assuming a K_D of 22 for the trunk on Rivière-au-Renard, the 4.5t dolos were designed for a wave height H = 5.1m; similarly for the 12.7t dolos with K_D of 15 the H = 6.3m (Note: slope was 1 to 1.5 vertical to horizontal).

The design crest elevation of the dolos section ranges from 5.3 to 8.0m above datum and high water large tides are 2.44m. At the time of the design and even to date, there are very limited data available for estimating wave runup and overtopping and the effects on the breakwater stability (8). However, it would appear the breakwater was intended to be overtopped especially in the initial sections of the 4.5t units. In fact, economic considerations likely dictated minimizing material quantities.

To verify the original design data, wave conditions were hindcast from wind data over an 11 year period by a system of computer programs based on the S.M.B. technique (2). The system produces hourly values of significant wave height and peak period by deep water compass directions. Within this period of data, the largest significant wave heights are of the order of 6.5m with an associated peak period of 12 to 14s. The deep water wave directions for these conditions are almost perpendicular to the breakwater alignment. The wave climate in 1980 reaches similar levels to the previous 10 years, however, the occurrences of the high conditions are greater than the average year.

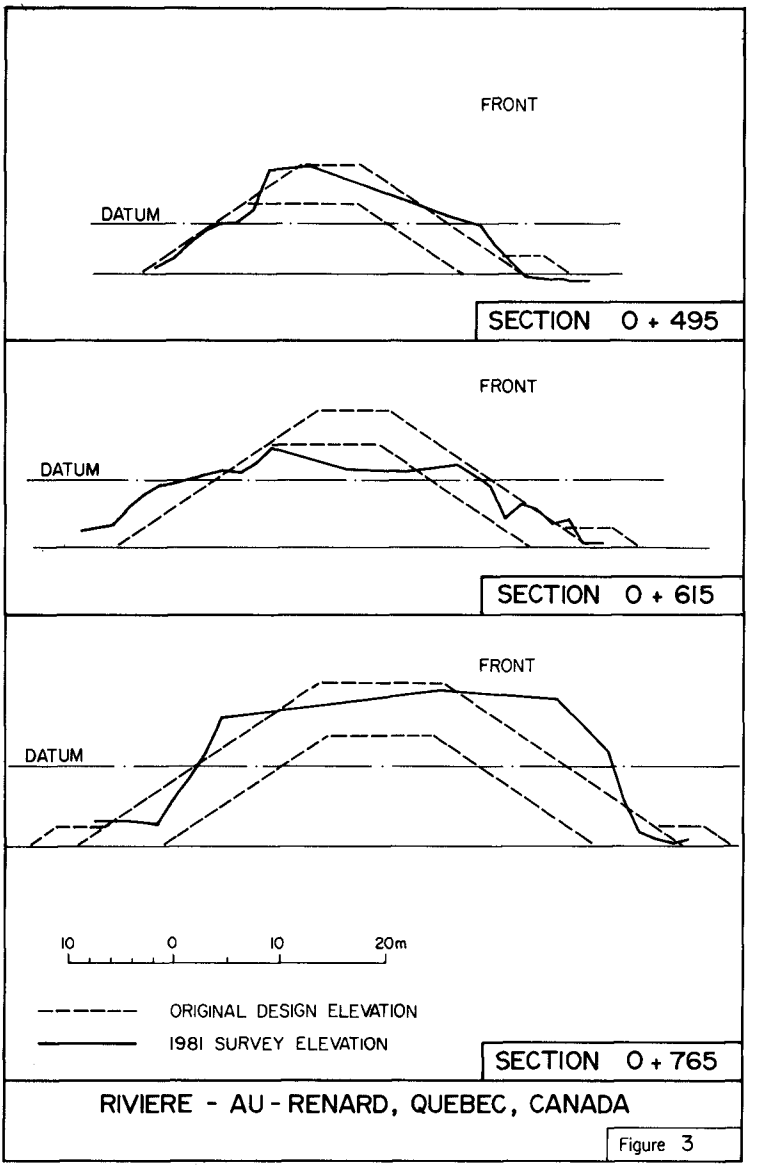
FRONT
DATUM
SECTION 0 + 495
FRONT
DATUM
SECTION 0 + 615
FRONT
DATUM
10 0 10 20m
ORIGINAL DESIGN ELEVATION
1981 SURVEY ELEVATION
SECTION 0 + 765
RIVIERE - AU - RENARD, QUEBEC, CANADA
Figure 3

No detailed refraction analyses were undertaken for this study. The bathymetric contours are reasonably uniform and parallel to the breakwater and the higher waves approach such that there would only be a slight reduction in height due to refraction. The depths and slopes in the approaches are such that larger waves are depth limited and break offshore and in front of the breakwater.

It appears that the original 'design wave' data used were of the correct order of magnitude with the possible exception being the selection of the height for the 4.5 t dolos. It is noted that significant damage has occurred in the larger units as well. The design is complicated by other factors such as overtopping and breaking of waves, however the resultant level of damage indicates that the analysis procedure for stability is not adequate for concrete dolosse.

4. Hydraulic Model Study

4.1 Background

The primary objective of the test program was to recommend remedial works to the breached sections of the breakwater with the 4.5t dolos. Consideration was given to replacing the lost armour material with concrete units of different types or sizes and with large armour stone.

The model test facility available at the time was the 1.8m wide wave flume at the National Research Council Canada in Ottawa. The flume is approximately 1.25m deep by 67m deep and has the capability of generating and measuring irregular waves. Model dolosse were available in two sizes in a sulphur concrete material that gives the units correct specific gravity and dimensions but does not scale concrete strength (i.e. units are not breakable in model loading conditions).

The model scale chosen was 1 to 35 linear such that weight and volume were proportional to the cube of the length scale. Preliminary calculations had indicated that much heavier armour material would be needed but it was also required to model the existing failure as well as possible in the 4.5t units. This presented a conflicting requirement as only one scale could be used within the time allotted. The result was that the smaller lab units were modelled as 12.8t in prototype and these units were in fact used in the 4.5t breached section. This did not represent a gross inaccuracy since the prototype dolosse in the breach were essentially all broken pieces and tests were not intended to totally recreate the whole failure process. The approach slopes in the flume were modelled out to a prototype distance of 800m and depth of about 30m and the modelled section was .9m in width.

Wave conditions generated by each test were for irregular sea states (6). The measurement system in the flume consisted of three wave probes at locations along its length. The wave conditions generated for the tests were selected combinations of deep water significant wave height and peak period, as listed in the following prototype parameters: 2.5m and 6s; 4.0m and 8s; 5.1m and 10s; 6.2m and 12s; 6.8m and 14s.

4.2 Test Series

In general, the wave conditions were run on a test section by starting at low levels and increasing to the maximum with a constant water level (usually at high tide). Each wave condition was run for 15 to 30 minutes in model time (note: time scale approximately 1 to 6 for model to prototype).

4.2.1 Damaged Section +615

Section +615 was chosen as the model section that was typical of the main breach. Two tests were run on this section before remedial works were undertaken. The section was constructed with deliberately broken dolos pieces in the percentages indicated from surveys and diving inspections. The purpose of testing this section was to observe the wave-structure interaction at this stage of damage and to devise repair work accordingly.

The following are observations of the hydraulic tests and describe the progression of the failure at this stage:

- Dolos pieces were rocking and displacing at low wave heights (i.e. 4.2m).
- Overtopping occurred for 4m waves or larger and was quite severe at higher levels.
- Units and pieces below low water on the front became packed after initial movements and remain stable.
- Dolos pieces at the leading edge (i.e. front at crest) were pushed across the top and piled up at the back of the crest.
- Dolos units and pieces were progressively pushed over and rolled down the back slope.
- The crest was eventually stripped level to the core.
- The core became dished out behind the leading edge of the armour allowing more pieces to move across the top.
- Continued wave attack piled a mixture of all the materials behind the back slope.

It was concluded that heavier armour material would be required on the crest to prevent units from being rolled down the back from wave overtopping. Given the excessive movements of modelled dolosse and the evidence of breakage even in the 12.7t prototype units, it was assumed that a small increase in dolos weight would not be an adequate remedial measure. However, a large increase would not be economical especially since there were no available methods to estimate the structural loadings and behaviour of dolosse.

4.2.2 20 t Armour Stone

Three remedial test series were undertaken using 20t stone to fill the breach of Section +615. These included a single layer of armour stone, a double layer and a double layer with additional filter stone added (i.e. each section elevation was progressively increased).

The single layer was built directly over a tested section and run through a complete wave series at mean water level. The section was severely overtopped but remained stable. One or two stones were displaced near the front.

The double layer section was constructed by placing more armour on the previous test section. The section was run at mean water level for the 6m wave conditions. Overtopping was still occurring, but the section remained stable with no armour stone displacements.

The third test was constructed on a rebuilt damaged section and included 1 to 5t filter stone beneath the double layer of armour such that the original design height was achieved. The section remained stable with no armour displacements though it was still overtopping at higher wave conditions.

4.2.3 15 to 11 t Armour Stone

A series of tests using a double layer of smaller armour stone to repair the breach were undertaken in response to initial indications that sufficient 20t stone might not be available. The two test series were constructed over the damaged section and included 1 to 5t filter stone. The heavier armour (15 to 13t) was placed at the front of the crest and the lighter (13 to 11t) to the back of the crest.

The first test section was constructed to the original breakwater height and run at mean then high water level. The armour on the front experienced some initial rocking with no displacement while several stones were displaced down the back at the 6m wave conditions. During the high water level conditions one stone was displaced at the front, two or three more at the back and the overtopping was severe. The section remained stable but sustained significant damage on the back of the crest.

The crest elevation was raised by about 1.5m in the second test section with the increase provided by adding core material in the centre of the breach. At mean water level the section initially resisted overtopping but the 13 to 11t stone began to be rolled down the back with 5m waves. After continued testing at higher wave conditions and high water level, the elevation of the front crest was decreased by 2m and the back by 3m. The severe overtopping eventually stripped the back of the crest down to the core material.

4.2.4 12.8 t Dolos

Two test series were undertaken using 12.8t dolosse in the cross-section configuration of the original trunk design to provide a limited assessment of the stability of the units and the causes of the failure.

The first test used all intact units and appropriate filter layers. These tests began at mean water level and indicated rocking of several dolossse on the front crest near still water level for 4m waves and greater. The rocking was quite severe at higher wave conditions and at high water level there was a major displacement of units down the back. Further testing could not properly simulate the failure at Rivière-au-Renard as the dolosse in the model were not breakable.

The test was repeated with broken pieces introduced in the front of the crest down to low water level (i.e. about 30% broken units). The section went through the stages of: units and pieces rocking at the front then displacing down the front; gaps opening in the front; several units being rolled over the back; units and pieces at front below low water stabilizing; the top of the crest being eaten down to core with material piled over the back. The results appeared to be similar to the damaged section at the site.

4.3 Summary Comments

Under the severest of wave and water level conditions, the 20 t armour stone remained stable. The 15t stone indicated adequate stability with only a minor displacement, however lighter units experienced significant displacement.

The tests with dolosse demonstrated the necessity to account for the breakage of units in hydraulic modelling though the techniques used here cannot readily be proposed for other applications.

5. Conclusions

5.1 Hydraulic Tests

Within the limitations of the test procedures, the model appeared to give a reasonably accurate scenario of the intermediate stages of the failure. Sections in the model were shaped in a similar manner to those in the breach and materials were damaged or displaced in the same areas.

The model did not account fully for the structural behaviour of the dolosse even with pieces artificially injected and it may be subsequently argued that their performance in all the test series is not valid.

The model was not used in a predictive manner to estimate number of storms vs degree of damage and it is not possible to accurately estimate the time frame for the survivability of the existing breakwater. However, it would appear that the remainder of the breakwater is susceptible to a similar mode of failure at any location (probably in 4.5t section first).

5.2 Causes of Failure

It is not clear that any one specific factor has resulted in the extensive damage to the breakwater at Riviere-au-Renard. It may be more broadly attributed to the design procedures recommended for concrete dolos units.

The breakage of the dolosse at the front and crest appears to precipitate an almost total destruction of the units in a particular area. The breakage appears to be related to the potential for rocking or displacement of individual dolos and the unit's inability to resist the resultant loadings (3). The model tests indicate that the breached sections would not have failed in the observed manner if the units had remained intact. However, this is not conclusive in that heavier units were used in the hydraulic testing compared to the prototype dolosse in the breached sections.

The hydraulic testing and prototype surveys (even for the heavier dolos) demonstrated a mode of failure due to overtopping that could not be accounted for in the original design procedure. The severity of the overtopping was capable of displacing units from the back of the crest and down the slope. This phenomenon is related to a number of factors such as the height of the breakwater, the breaking wave conditions at this particular site and the degree of absorptivity of the filter layers beneath the dolos armour.

5.3 Remedial Works

Based on the hydraulic studies and the performance of the existing dolosse, the recommended remedial work consisted of filling the breaches with a double layer of 20t armour stone (17t minimum) and filter material of 3 to 5t. Dolosse were not recommended as there was no satisfactory design process to ensure that an increased size or a reinforced unit could withstand the loadings in the breakwater. The selection of a heavier concrete dolos (i.e. above the 12.4t) would not have proved economical or have provided any guarantee of the unit's structural integrity.

It was assumed from observation of the model tests that the existing dolos armour on the front slope below low water would remain stable. However, it is recommended that regular inspections of this area are undertaken to assess this assumption.

The repair was undertaken in the fall of 1981 and the breakwater was inspected in the summer of 1982. The remedial work had remained stable though a new breach appears to be in the process of opening between the two rearmoured sections. It appears that a long term solution will be required to maintain the remainder of the breakwater.

6. Acknowledgements

Special thanks are due the staff of the National Research Council Canada under the direction of Mr. J. Ploeg for assistance in the construction and operation of the model at the hydraulic laboratory facility in Ottawa.

7. References

1. SHORE PROTECTION MANUAL. Second edition. U.S. Army Coastal Engineering Research Centre, Department of the Army Corps of Engineers. 1975.

2. BAIRD, W.F. and GLODOWSKI, C.W. "Estimation of wave energy using a wind wave hindcast model". International Symposium on Wave and Tidal Energy. Canterbury, 1978.

3. BAIRD, W.F., CALDWELL, J.M., EDGE, D.L., MAGOON, O.T., and TREADWELL, D.D. "Report on the damages to the Sines Breakwater, Portugal". Proc. of 17th Coastal Engineering Conference, ASCE. Sydney, Australia, 1980.

4. EDGE, B.L. and MAGOON, O.T. "A review of recent damages to coastal structures". Proc. of Coastal Structures '79, ASCE. Alexandria, 1979.

5. HUDSON, R.Y. "Laboratory investigation of rubble mound breakwaters". Proc. of ASCE Journal of Waterways and Harbors Division, Vol. 85. September 1959.

6. JOHNSON, R.R., MANSARD, E.P.D., PLOEG, J. "Effects of wave grouping on breakwater stability". Proc. of 16th Coastal Engineering Conference, ASCE. Hamburg. 1978.

7. LILLEVANG, O.J. and NICKOLA, W.E. "Experimental Studies in stresses within the breakwater armor piece-dolos". Proc. of 15th Coastal Engineering Conference, ASCE. Honolulu, 1976.

8. MERRIFIELD, E.M. "Dolos - a new breakwater and coastal protection block". The Dock and Harbour Authority, Vol. 50, No. 594. April 1970.

9. WHILLOCK, A.F. "An appraisal of rubble mound breakwaters". The Dock and harbour Authority, Vol. LXII, No. 732. November 1981.

ZEEBRUGGE'S MAIN BREAKWATERS

ir. L.V. Van Damme*

ABSTRACT

The design scheme of the Zeebrugge Outer Harbour, Belgium, consists mainly of two breakwaters protruding into the sea as far as 1,750 m beyond the existing môle or 3.000 m out from the coastline. The west outer breakwater is 4,450 m long, the east breakwater runs 4,300 m out from the seafront. The east outer harbour will accommodate terminals for liquid bulk products such as LNG. The west outer harbour will provide space to install two harbour bassins to suit general cargo, hazardous cargo, container and ferry traffic.

In the paper emphasis is put on the environmental design conditions (wave height, wave period, water depth), the development of preliminary designs and the final design. Some design features such as dimensions, wave breaking carpet, armour units, workable limits in respect to rock grade, etc ... are discussed.

By developing the design the rubble-mound breakwater has been judged to be the only viable alternative versus the caisson type breakwater, taking into account costs, technical risks, construction problems and flexibility under changing environmental conditions.

The main feature of the breakwaters is that a huge concrete parapet will have been avoided. A so called flat semi-cube armour unit has been developed. The main advantage lies in the substantial economic benefit whilst maintaining the same stability performance as a concrete cube armour unit.

* Principal Engineer, Ministry of Public Works, Ostend, Belgium

1. INTRODUCTION

The construction of the existing port of Zeebrugge has been a royal decision, pronounced by H.M. King Leopold II in 1881. A few years later the construction started and in 1907 the port has been inaugurated.

Almost a century later, in 1970, the Belgian Government decided to the extension of the port complex. Prior to this decision the port has been adapted to the prevailing traffic demands whilst remaining within the boundaries set by its initial development scheme of 1907. The annual throughput has been some 10 million tons in 1971 and 15 million tons in 1981.

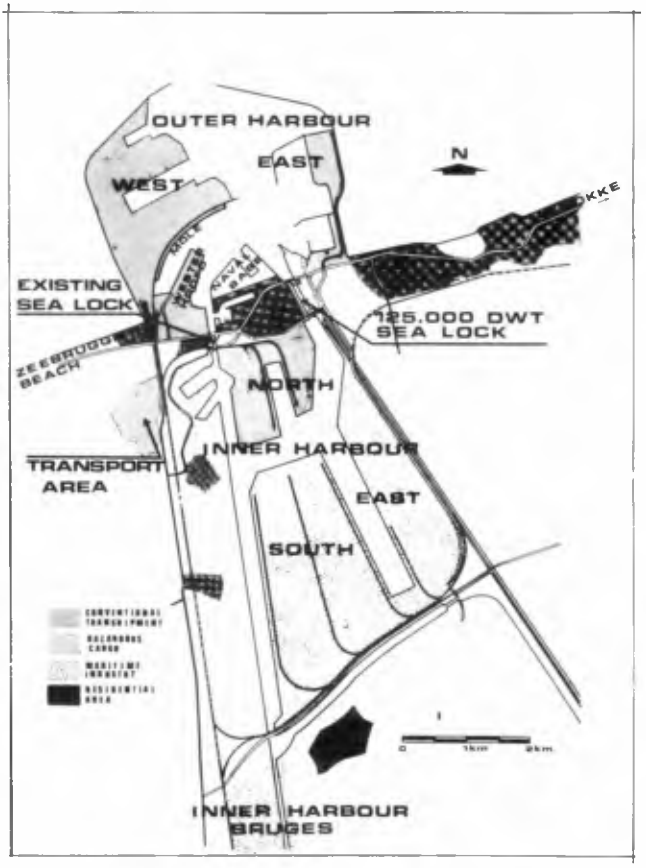

Fig. 1 : General layout of the Zeebrugge Port Extension Scheme

The master plan finally adopted provides 3,370 ha sub-divided (fig. 1) as follows :

- Outer harbour, including the existing outerport and naval base 1,165 ha
- Inner harbour 1,705 ha
- Port area of Bruges 450 ha
- Transport area 50 ha

The design scheme of the outer harbour consists mainly of two breakwaters protruding into the sea as far as 1,750 m beyond the existing môle. The west outer harbour breakwater is 4,450 m long. The east breakwater runs 4,300 m out from the seafront (fig. 2). The east outer harbour will accommodate terminals for liquid bulk product such as LNG. The west outer harbour will provide space to install two harbour basins to suit general cargo, hazardous cargo, container and ferry traffic.

2. PLANNING

The first phase of the east outer port sets up a newly built work harbour as the existing outer port is congested and no space is available to install the necessary harbour facilities and construction site yards.

Only the mound type has been retained for the service-port breakwaters. The sand-asphalt mound with open stone asphalt revetment has been selected against the rubble mound design by balancing construction costs, design and construction risks and practical construction aspects.

The southern east breakwater has been conceived as a sandfilled peninsula of ca. 36 ha. in order to install the land-based LNG-terminal facilities. The perimeter and sea defence of this peninsula are provided by rubble-mound breakwaters of ca. 1,360 m long to the west ca. 1,200 m long to the east and a north closure of ca. 500 m long.

The armour layers and inner slopes have been adapted to wave conditions and exposure time. The west slope (1:2) with 20 T cubic concrete blocks in single layer, the east slope (1:2) in quarry rock 3/6 ton grade and the north slope (1:1,5) in double layer 25 T cubic concrete blocks. The inner slopes vary from 2/300 kg quarry run to quarry rock 1/3 ton grade in double layers. Several design alternatives following different construction schemes and methods have been contemplated. Special attention has been paid to the filter construction between the rubble cores and the hydraulic sand-fill. (fig. 3)

The LNG-harbour proper will be completed by a semi-curved 975 m long, low crested rubble mound, the so called LNG-breakwater. The layout, planning and design of the LNG-terminal harbour works have been finally adopted to satisfy the stringent and draconic time schedule of the LNG-terminal project as a whole. (fig. 2)

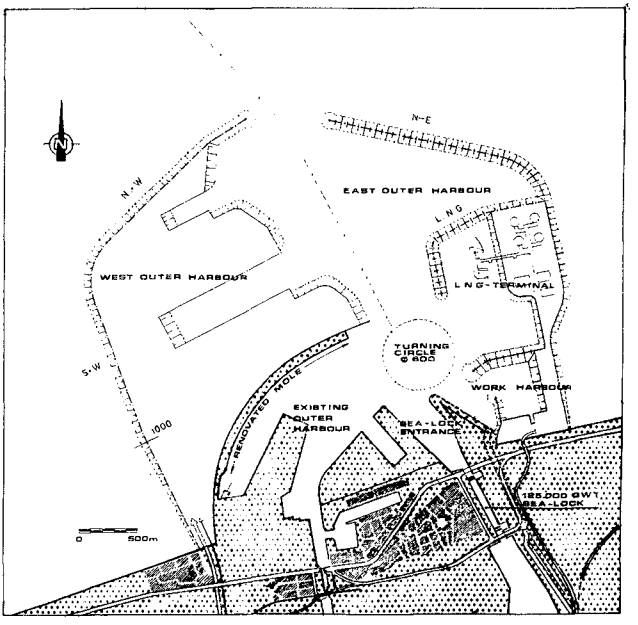

Fig. 2 : Layout Masterplan Zeebrugge Outer Harbour

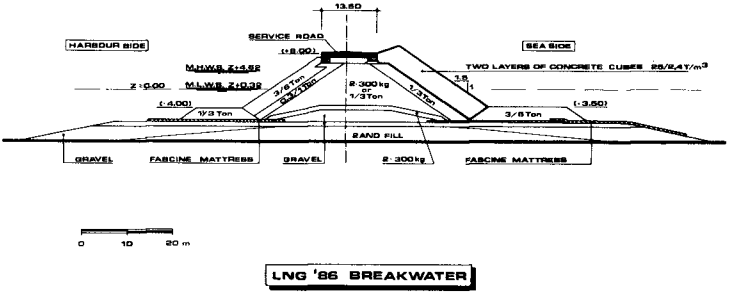

Fig. 3 : Typical cross section LNG '86 - breakwater

The northern section of the east breakwater is ca. 2,000 m in length. The west breakwater will be 4,400 m long. Up to 1,000 m out from the shore, the area between this breakwater root-section and the ancient môle has been hydraulically filled with seasand to create a secondary work and marshalling yard for the quarry rock to be worked up by truck dumper and crawler crane into the west breakwater. Because of the adjoining sandy beaches of the holiday resorts, this breakwater section has been conceived with due regard to the environmental visual impact.

In general the design up to the Z-4.00 bottom contour line (ca. 1,000 m out of the seafront) consists of a core built successively in sand, brick debris and quarry run with a concrete open pavement revetment on sublayers of crushed gravel and quarry rock of grade of 2/300 kg to 1/3 tons.

3. ENVIRONMENTAL DESIGN CONDITIONS

3.1. The **bottom** depth in the alignment of the outer harbour breakwaters ranges fairly between Z-5.00 and Z-7.00 (chart datum Z = mean low water spring + 0.08).

3.2. The **tide** is semi-diurnal with levels ranging from amplitudes of 4.40 m at mean spring tide to 2.80 m at mean neap tide. The **meteorological** set-up is up to 2.45 m in the defined design period and probability of exceedance.
The **tidal currents** at the final breakwater alignment will be (at surface) 1.2 m/s to 2.00 m/s at spring flood tide and 1.0 m/s to 1.6 m/s at spring ebb tide.

3.3. The **soil conditions** in the Zeebrugge area are rather difficult. A comprehensive geotechnical survey was undertaken with boreholes, static cone penetration tests and continuous seismic profiling.

The synthetically recorded geological profile is presented in fig. 4. The striking point is the rather pronounced accidental surface separating the tertiary sediments and the quaternary coverlayers. With as main feature the cuesta of the Bartonian clay formation with dips up to 30 % .

The less resistant bottom "sandwichlayers" consisting of alternate thin layers of soft clay and sand, mainly ca. 4 to 6 m in thickness, cover in the wester breakwater alignment, a considerable deposit of fairly dense to densely packed quaternary sand. In the eastern-alignment the deposit of quaternary sand is up to 15 m thick upon the tertiary Bartonian clay deposit. This tertiary layer rises towards the sandwich voverlayer at the head eastern breakwater.

4. DESIGN WAVE CONDITIONS

4.1. Design wave height

From 1958 to 1971 waves are systematically measured by shipborne wave recorders at the WESTHINDER lightship more than 40 km from Zeebrugge. Since 1977 wave riders record steadly at several locations in the vicinity of Zeebrugge. The measured data transmitted is analysed and synthesized by computer to statistical profiles of several relevant wave parameters.

The preliminary and final designs are based on the wave climate derived from the WESTHINDER data by refraction analyses. This analysis being carried out for different approaches, wave periods and waterlevels. The analysis showed that the existing seabed gives areas of wave concentration at the northern west and east breakwater with coefficients from 1.4 up to 1.9. The channel Pas van 't Zand / Ribzand dissipates wave energy, the coefficient at the planned harbourmouth can be 0.5.

The detailed designs are based on the more long-term wave data (1958-1971) compared and correlated with the more short-term measurements from the wave-rider buoys. In the graphs 5 and 6 the results of the comparison with the wave rider data of January '78 to December '80 is explained. Summarized :

- For the same probability of exceedance the originally established wave heights (H_S) are, compared with the wave rider values, over-estimated by :

  0.40 to 1.40 m at the N.E. - breakwater
  0.40 to 0.70 m at the W - breakwater
  0.10 to 0.50 m at the harbour entrance

- The design wave height of the outer harbour breakwater $H_S = 6{,}10$ m needs not to be changed as it is still defined by the limiting waterdepth.

- The design wave height of the LNG-breakwater and other breakwater sections defined by an average annual exceedance of 10 % (short-term risks of less than 5 years of exposure time) can be changed from $H_S = 5.75$ to 4.90 m.

- The workability defined on the $H_S = 1.00$ m and $H_S = 2.00$ m threshold values has been underestimated by roughly 7 to 8 % .

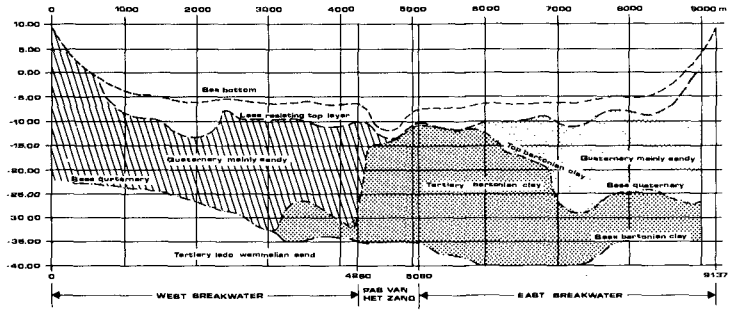

Fig. 4 : Geological profile outer harbour breakwater alignment

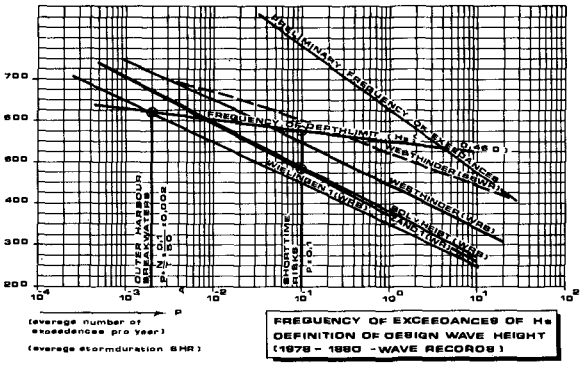

Fig. 5 : Wave height distribution - re-iteration and comparison procedure (wave rider measurements '78 - '80)

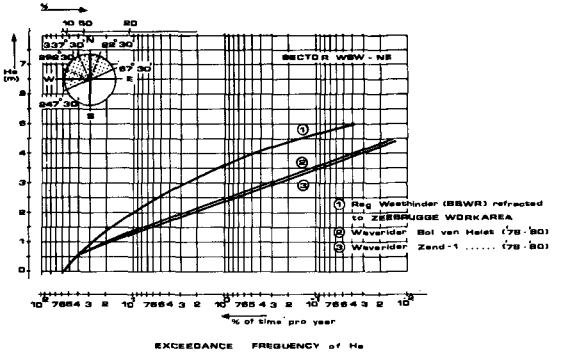

Fig. 6 : Wave climate at the Zeebrugge worksite

4.2. Design wave periods

From the Westhinder wave measurements and from the 1977 recorded wave-rider data the following conclusions can be made :

- the maximum mean period : 7 sec.
- the maximum mean peak period : 9 sec.
- the highest peak period measured : 10 to 11 sec.

As in the wave flume and wave tank studies performed by the LCHF at Maisons-Alfort, wave-trains are applied, the 9 sec. period is used finally for stability research and the 10 to 11 sec. period for research of phenomena during overtopping at maximum uprush.

4.3. Summary of design wave height conditions

The design wave height conditions, amended on the basis of the '78 - '80 wave records, are summarized in following table (fig. 7). By defining these conditions, the risk of exceedance of the design wave height has been fixed at 10 % in the design life or exposure time. For short wave risks (max. 3 to 5 years of exposure time) an average yearly frequency of 10 % has been taken. This results in the adopted design wave heights and risks levels reported in the table.

	Workharbour Northern breakwater	Southern East breakwater			LNG breakwater	Outer harbour breakwater		
		East	North	West		SW	NW/NE	Mouth
Design wave height H_s (m)	4.00	3.00	5.75	5.75	4.90	5 à 6	6.10	6.10
Design see level (m)	Z + 5.20	Z + 6.85	Z + 6.00	Z + 6.00	Z + 6.00	Z + 6.85	Z + 6.85	Z + 6.85
Accepted damage (%)	-	0-5	0-5	5-10	0-5	0-5	0-5	0-5
Probability of exceedance (%)	40	10	40	25	40	10	10	10
Lifetime or exposure time (year)	5	50	5	3	5	50	50	50

Chart datum Z = mean low low water spring + 0.08

Fig. 7 : Table : Summary of design wave height conditions

5. DEVELOPMENT OF DESIGN

5.1. For the LNG-breakwater and outer harbour breakwaters two main alternatives have been contemplated in the project definition and pre-project design stage :

- Rubble mound breakwaters
  designed according to different construction methods e.g.
  - mounds worked up over the constructed core by truck dumpers in combination with or without hydraulic dumped sand-fill. (fig. 8 and 9)
  - mounds with rubble cores and armour revetments worked up by purpose-built barges.

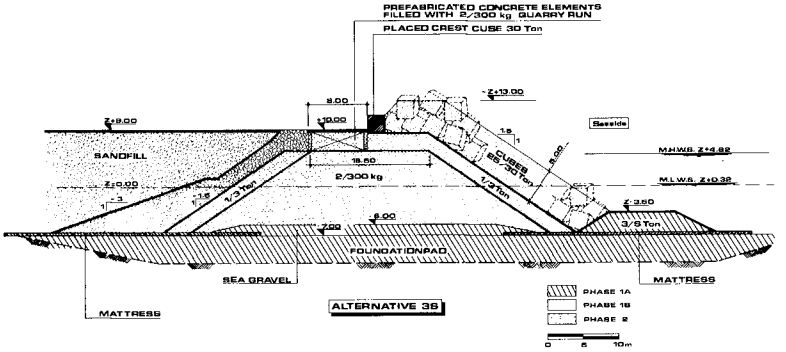

Fig. 8 : Development of design : rubble-mound breakwater alternative 3 b - core built by dumping over the head

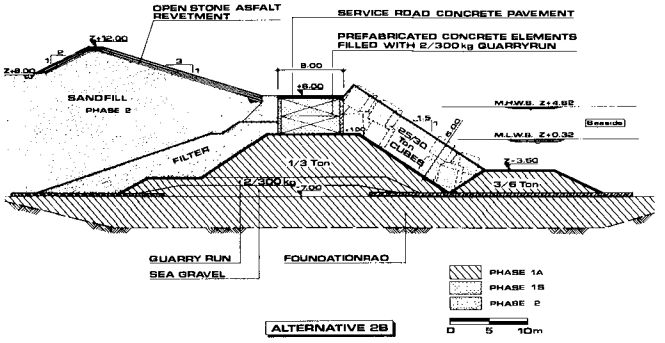

Fig. 9 : Development of design : rubble-mound breakwater alternative 2b - core built by dumping barges

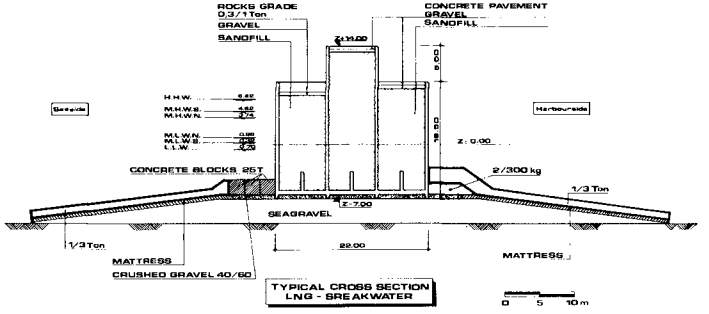

Fig. 10 : Development of design : caisson type breakwater (typical section at LNG-breakwater site)

Caisson breakwaters
prefabricated and floating caissons sunk on a prepaired foundation bed. Fig. 10 shows the conceptual design for the LNG-breakwaters.

After balancing the criteria of costs, risks, technical equivalence and construction aspects the hydraulic sandfill independent rubble breakwater type has been selected (3b).

The latter being amended for the southern west breakwater. As these sections are designed finally with an inner sand-beach, constructed simultaneously with the breakwater core.

5.2. The caisson type breakwater was judged to be unfeasible for the outer harbour breakwaters due to the unadequate soil conditions.

This initial conclusion should be amended. Indeed, the caisson type breakwater should be feasible as for almost all breakwater sections, now under construction, the detailed design specifies a foundation pad realized by a soil improvement by replacement of the soft layers with coarse dumped seasand.

As a matter of fact by the conceptual design of the breakwaters, in 1977/78, the seaworthy cutter-suction dredgers needed for such a foundation concept in unprotected waters, were not available. It was only later, during the construction of the northern service port breakwater and the LNG-terminal peninsula, that this soil improvement technique was successfully developped.

However the introduction and development of the soil improvement technique by replacement in open sea with dumped sand highlights once again the flexibility proper to the rubble mound design concept !

Indeed the soil amelioration technique has been assessed by evaluating the alternative of a mound laid directly on the existing seabed, where the overall stability is given by equilibrium embankments at both sides. Even in the instances of allmost equal costs, the soil improvement profile still offers a more controlled construction and a foundation bed with a higher quality level.

However, when choosing between rubble mound and caisson type breakwaters the other criteria are still valid.

- flexibility : the rubble mound offers more possibilities not only through adaption to local soil conditions, but also to the specific hydraulic conditions at the site (currents, waves, sedimentation, erosion, etc...).
- costs : compared with the rubble mound, the technical equivalent caisson type costs ca. 33 % more.
- construction risks : the construction problems on a site as Zeebrugge, exposed to waves, currents and siltation are of paramount importance by caisson type breakwaters.

6. FINAL DESIGN

The final design on the retained concept, the 3b-alternative, was finished in June '81. It consists mainly of (fig. 11) :

- *A foundation pad*

  A soil improvement by replacement with dumped sand is executed for all outer harbour breakwater sections. Seaworthy self propelled cutter suction dredgers with floating discharge hose remove the soft soil layers. The dumping of sea-sand is executed by trailing suction hopper dredgers. In general no extra densification has been revealed necessary after systematic controlling by static cone penetration tests of the performed works.

- *Bottom protections*

  Simultaneously with the sanddumping operations the sandlayers are covered by sea gravel layers of 0.60 m to 1.00 m thick placed by trailing suction hopper dredgers or splitbarges. Only a fortnight differ the sanddumping and sea-gravel carpet operations to avoid and excess of erosion of sand.

  Fascine mattresses, ballasted from 0.6 t/m² up to 1 t/m² by quarry run 2/80 kg and 80/300 kg grade by deck shovel barges, are covering the previous laid gravel layers.

  Where possible a 1.5 m thick core gravellayer is placed between the fascine mattresses.

  Gravel layers between fascine mattresses are covered by quarry rock 2/300 kg grade filterlayer.

  Erosion of sand and gravel between operations is detected by systematic surveys and echo-soundings. When necessary the eroded sand and gravel layers are refilled.

  To avoid an excess of materiallosses in the breakwater alignment these foundation works with bottom protection works have to be planned and executed well in advance of the core construction.

  A toe protection

  Provided by a large ca. 35.00 m wide wave breaking carpet on level Z-7.00 with fascine mattresses and quarry stone embankments of grade 3-6 ton up to a maximum level of Z-2,50 m with a gentle slope facing the seaside. The seaward 3/6 - ton and harbour side 1/3 - ton grade embankments are placed by dumpbarges or deck shovel barges.

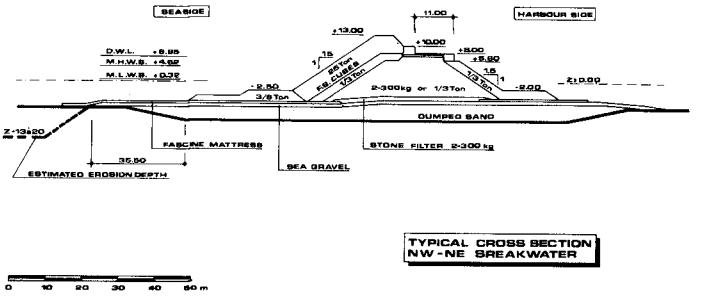

Fig. 11 : Typical cross-section NW-NE breakwater

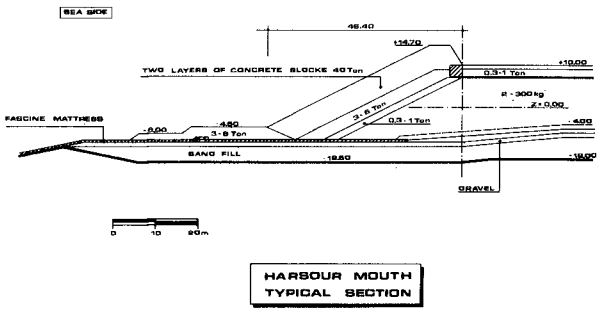

Fig. 12 : Typical cross-section (axis) at harbour mouth

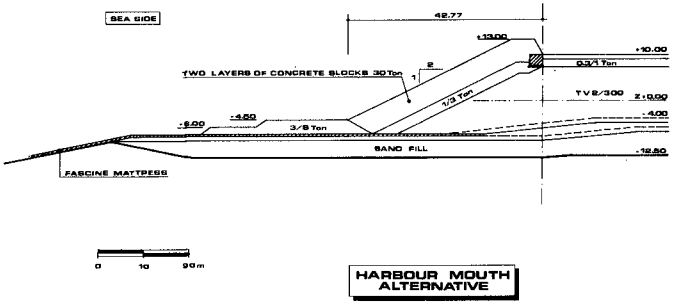

Fig. 13 : Typical cross-section (axis) - Design alternative harbour mouth (under construction)

- *A breakwater core*

  In quarry run 2/300 kg or 1/3 ton quarry rock with filterlayers 1/3 - ton grade. The armour revetment is realized by concrete cubes of 25 ton / 2,4 t/m³ density on a slope of 1:1,5 in the running profile. The head of the breakwaters (figs. 12, 13) at the harbour mouth dips 1:2 with concrete cube units of 40 T and 2,4 t/m³ on a 3/6 ton filter layer. The worklevel for the 40 ton grade truck dumpers, crawler crane, hydraulic cranes and bulldozers, working up the material, is Z + 6.80 m. This level guaranties in average a workability of minimum 90 % of the time.

- *A crest levelled to ca. Z + 13.00*

  As in the future the adjacent harbour area will be equipped with tidal basins and storage areas, no major overtopping will be allowed below the design wave conditions. The crest is finished by placing 30 t crest cubes outward and inward and a 1.00 m thick concrete pavement.

The southern west breakwater design differs slightly from the typical outer harbour design (fig. 14). The hydraulic sandfill of the protecting inner beach will progress simultaneously with the mound construction. The inner beach provides protection of the 1:1,5 innerslope in 1/3 - ton grade quarry rock against NW and N oblique wave attack as construction is running.

7. DESIGN FEATURES

7.1. Dimensions of breakwater

The width of the breakwater core is defined by following considerations (fig. 15):

- The structure is designed in such a way that the construction from core to finished crest goes continuous. The worklength e.g. the distance from the construction front to the finished crest is at maximum 200 to 300 m for the SW breakwater and 125 m up to 200 m for the NW/NE - sections.

- The serviceroad on level Z + 8.00 : min. 9.00 m wide, to assure maintenance works.

- The temporary workroads on levels Z + 6.80 to Z + 8.00 are 10.00 m wide : dubble track road for 40 - ton rockdumpers.

- The level of the construction front is defined on Z + 6.80 by 13.70 m wide (including the top of the 1/3 ton grade filterlayers. It assures a workability of min. 80 % and the manoevrability of crawler crane and one track for dumpers.

7.2. Crest of breakwater

To obtain a continuous progress in construction a parapet wall has been avoided (figs. 11, 14, 15). This has showed to be profitable both for the stability of the armour by better wave energy absorption and limited uprush. Force measurements in the wave flume concrete pavement with rather limited thickness, showed clairly that the overpressures in the core are limited and there is no risk for a resulting uplift force.

7.3. Wave breaking carpet

The sedimentological study conducted both on physical and mathematical models ascertain the possibility of huge erosion pits in front of the SW/NW - breakwater section (from Z - 13 up to Z - 20.00). The NW - breakwater (up to Z - 6.00) and the W harbour head section (Z - 14.00).

The aim of the designed carpet is to limit the wave action on the armour to the design wave height defined by the existing seabottom on Z - 7.00. Flume and wave tanks tests have demonstrated that a carpet of 35.00 m out of the 3/6 - ton grade toe protection on level Z - 7.00 will provide this limited wave action independent from the final erosion depth (Z - 13.00 and Z - 20.00 are tested). However the final erosion depth plays a significant part in the wave stability of the ballast of the fascine mattress. For the applied design conditions $H_S = 6.10$, $T = 9$ to 11 sec : an adequat ballast is found by :

Z - 13.00 : 1 T/m² 2/80 and 80/300 kg - grade
+ 0.75 T/m² 0.3 to 1 ton grade

Z - 20.00 : 1 T/m² 2/80 and 80/300 grade
+ 2,1 T/m² 1/3 ton grade

The performance of the 25 T/2.4 T/m³ - armour has been the same in both test series.

It should be noted that the judgment on damage of the mattresses ballast has been rather severe as the function of the carpet is essential to the breakwater safety and survey of damage detection and maintenance will be very difficult.

7.4. Armour units

For the main breakwater the groved concrete cubic block has been choosen as armour unit. However a rather interesting cost optimization was possible. The fig. 16 shows all different cubic and semi-cubic bloc types in use by the construction. All these cube types were cast in only three different forms (8,7; 10,42 and 12,5 m³) as for the harbour mouth the alternative 30,6 Ton will be choosen.

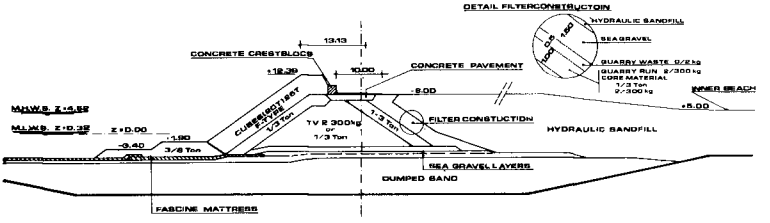

Fig. 14 : Typical cross-section - Design alternative at harbour mouth (Chainagepoints P1795 - P2150)

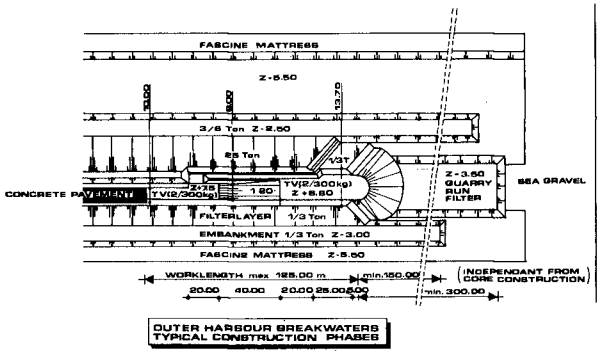

Fig. 15 : Breakwater construction in progress Worklength - typical construction phases

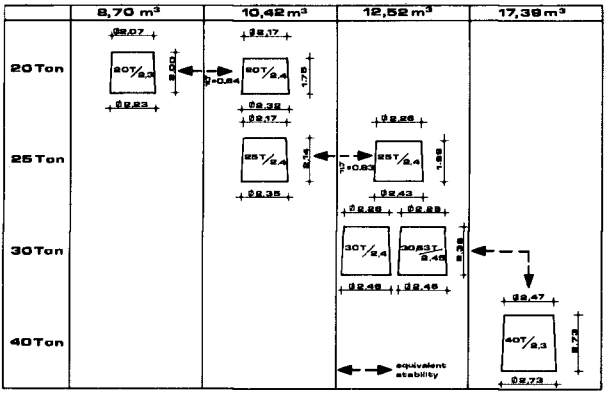

Fig. 16 : Summary of cubic or flat semi-cubic armour bloss applied or considered for the Zeebrugge breakwaters

Flume tests and wave tanks revealed that 25 T/2,3 t/m³ - cubes were necessary at the SW/NW bend section. However cost calculations show that armour layers of 25 T/2,3 t/m³, 25 T/2,4 t/m³ and 30 T/2,4 t/m³ differ only in marginal terms of max. 3% . In counterpart the safety margin for the 30 T layer yields up to 13 % of the significant design wave height.

By the same optimization process so called flat semi-cubes (F.S. - cube) were tested in the flume and wave tank. The maximum "flatness index" has been $h.r^{-1} \geqslant 0.8$ (h = height, r = bottom measure). The tests revealed no significant difference in stability between the cubic unit and the F.S. - cubic unit of equal weight. Costwise the difference is more substantial : 5 to 6 % of the armour cost in favour of the F.S. - cubes.

The choice of the groved cube for the armour is placed in evidence by comparing with a typical dolosse breakwater. The conceptual design is showed on fig. 17. By this concept two sizes of dolos-armour are compared with the cubes.

Type I : 12 T / 5,22 m³ : slight or no damage by design conditions but rocking could be considerable ($K_D \geqslant 15$).

Type II : 19,55 T / 8,5 m³ : beginning of movement (rocking) by design conditions $K_D = 10$. By 1,35 x H_{SO},slight damage can occur ($K_D > 23$).

Costwise the dolos armour revealed to be uneconomical compared with the cubes-armour-elements (tens of percent higher).

7.5. Core material

The core of the breakwater consists of rock material grade 2/300 kg or 1/3 ton. The stability of these quarry grade were tested with the construction phase of the breakwaters (fig. 15) both stationnary (static) and in progress (dynamic). The main results are (fig. 18) :

1) Construction in progress limits
   - upper threshold value for use of quarry rock grade 2/300 kg : $H_S = 1.00$ m
   - for 1.00 m > H_S > 2.00 to 2.50 m quarry rock grade 1/3 ton is to be used
   - by $H_S > 2.50$ m construction will be stopped and a provisional head with quarry rock grade 3-6 ton is to be constructed

2) Construction stopped at night and weekends

   by exceeding 0.80 m to 2.00 m significant wave height, a 1/3 ton provisional breakwater head is to be constructed. On the basis of this information the principal and contractor decided to stop every weekend from September to April with a provisional breakwater head in 1-3 ton grade quarry stone.

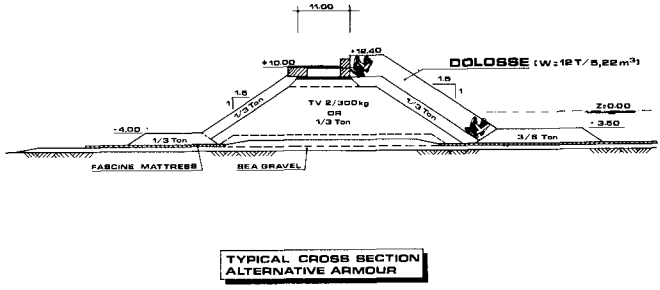

Fig. 17 : Typical cross-section NW/NE-breakwater with dolosse armour revetment

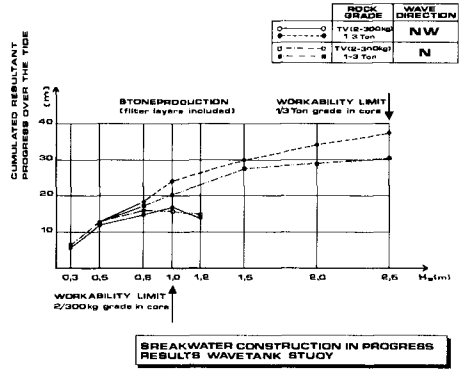

Fig. 18 : Breakwater construction in progress
Limits of 2/300 kg and 1/3 ton rubble grade

3) Detailed information has been becoming available concerning allowed protrusions of breakwater core versus armour revetment and damage to be accepted by special construction stages of breakwater e.g. by the inner slopes of the southern east peripherical breakwaters. This kind of study has been executed also for the west and east core of the LNG-terminal peninsula and the LNG'86 - breakwater. The results of all these studies differ only slightly despite the different locations and wave directions. A predominant factor is the average stone production into the core. In Zeebrugge the design production is 250 T/Hr.

7.6. Meteorological forecasting services

In order to maximise the exploitation of the information achieved by the flume tests, the principal of the works, the Ministry of Public Works - Coastal Service at Ostend - in cooperation with the Meteo Wing of the Belgian Air Force, has set up a special on site Meteorological Forecasting Service.

Twice a day a weather forecast is released with a correlated wave forecast. Directional windforce/wave-height correlation graphs have been established by the consultant on the basis of wave and wind data measured in prototype.

On this 24 hour-forecast the contractor's site managers and principal's site surveyors can judge work limitations in forthcoming shifts on breakwater constructions.

The meteo service is also equiped with an on-line wave analysis computer system, hard-ware programmed. This system is analysing on site wave data received from the wave rider buoy posted at the construction front. This is supplying sufficient information to forecasters and construction site managers about wave growth and height correlated to windforce and direction.

Besides the construction front wave-rider four to five other buoys are operational. The analysed wave data can become available if necessary within one week. In this way any damage can be correlated to the observed wave action.

These measures are only a part of a comprehensively established survey programme with analysis of data and evaluation of measures piloting the construction works.

7.7. Placement pattern of armour cubes

Once more this pattern is revealed of paramount importance. Two kinds of practical patterns are studied thoroughly. The first has been used on the LNG-terminal breakwaters,the second at the LNG '86 breakwater and outer harbour sections. The two differ only by the number of required positions of the crawler crane. By testing both patterns the first revealed a rather high risk to jam up by reaching the design conditions. The second pattern has better blocking properties.

8. STATE OF CONSTRUCTION BEGIN NOVEMBER '82

The present status of the Zeebrugge outer port extension scheme is summarized (fig. 2) :

- Project-planning and design : finalised July '81.
- Southern East-peninsula : commissioned to LNG - terminal operator at 1 September '81.
- Northern - East - breakwater : foundation works and gravellayers finished, fascine mattresses and quarry-run filter layers construction is still going but almost finished.
- Western - breakwater :
  - . breakwater construction : chainagepoint P 1750 is reached by the core up to Z + 6.80.
  - . the foundation works covered by gravellayers is finished to P 3900. The fascine mattresses with quarry-run gravellayer are finished up to ca. P 2200.

More than 50 % of the total deployed length of breakwater works is finished at present.

9. CONCLUSIONS

1. By developping the design, the rubble mound breakwater has been judged to be the only viable alternative taking in to account costs, technical risks, construction problems and flexibility by changing environmental conditions.

2. The wave breaking carpet has shown to be an adequate solution in order to limit wave action on the armour.

3. A huge concrete parapet wall can be avoided and is not necessary for an economical design of breakwaters in the Zeebrugge conditions.

4. It is of paramount importance to check and analyse both the geotechnical stability of the rubble mound on the foundation bed and the internal stability of the mound under wave action. In this connection outer and even inner slopes of 1:1,5 show marginal stability with an inadequate safety facts in some specific cases.

5. Concrete cubes as armour units have been revealed for this case to be more economical and justified. A security margin of a 13 % can be obtained and approximately no costs when upgrading up to 30 T the in the flume and wave tank tests found cube of 25 T. Semi cubes flattened to index $h/r \geqslant 0.80$ reveals to be 5 to 6 % more economical than the cube of the same weight. By tests no significant stability difference was observed.

6. A proper planned placement pattern is demonstrated, once again, necessary.

7. A meteorological forecasting service equipped with wave rider buoys gives adequate information in order to construct in a controlled manner a rubble mound structure and to avoid excessive damage during construction hardly to repair.

ACKNOWLEDGMENTS

The author is grateful to ir. D.J. VANDENBOSSCHE, Director of Haecon, Ghent, Belgium, the Consulting Engineers of the Zeebrugge Outer Port Extension Project. Indeed, his suggestions and support by preparing and editing the paper is highly appreciated.

The principal of the Zeebrugge Harbour Project is the Ministry of Public Works, Coastal Service, Ostend, Belgium.

The Contractor for the outer port extension is the joint venture Zeebouw-Zeezand, Knokke-Heist, Belgium.

CONSTRUCTION SEQUENCE MODELLING FOR HARBOUR BREAKWATER

ROGER W HENORY* Pr Eng BSc MICE MSAICE

Abstract

Gansbaai fishing and pleasure craft harbour is situated approximately 160km east of Cape Town. Modifications and extensions were required to the existing breakwater as well as construction of an internal access mound. An investigation was commissioned into alternative construction methods and construction sequences for the modifications and extensions.

The aim of the study forming the subject of the paper was to establish as accurately as possible the optimum sequence of construction for the various phases of the work and to establish the optimum construction methods to be adopted so that any damage to the work was minimised as construction proceeded. By means of a three dimensional hydraulic model, alternative construction methods and sequences were investigated under varying wave heights and sea conditions. Minimum wave heights and the sea direction causing damage or localised displacement of the elements of construction were studied.

1.0 INTROOUCTION

1.1 General

Gansbaai fishing and pleasure craft harbour is situated approximately 160km east of Cape Town. Modifications and extensions were required to the existing breakwater as well as construction of an internal access mound. The contractor awarded with the contract for the work to be carried out commissioned an investigation into alternative construction methods and construction sequences for the modifications and extensions. The investigation was to be undertaken by means of a three dimensional hydraulic model. Various construction methods and construction sequences were to be studied under certain wave heights and sea conditions for the modifications and extensions to the new harbour.

*Principal-in-Charge in Oames & Moore Consulting Engineers

Certain construction phases were to be modelled, varying the sequence of operations, during which time the minimum wave height parameters were to be established which would result in damage or localised displacement of the elements used in the construction. Simultaneously the extent of the damages would be assessed and possible protective measures to be taken would be studied.

1.2 Model Availability

The National Rsearch Institute for Oceanology (NRIO) at Stellenbosch was commissioned by the Fisheries Development Corporation to make available to Oames & Moore the model of the New Harbour at Gansbaai which had been used during the design stage model analysis (Ref 1). Personnel for the operation of the model and for building the additional model facets required for the tests were supplied by NRIO.

2.0 CONSTRUCTION SEQUENCE

Various methods of construction and possible construction phase sequences which were envisaged as being viable during prototype construction were considered during the planning of the construction sequence modelling. The various construction sequence alternatives would require to be analysed on the model under varying sea conditions. A diagrammatic representation of the harbour is shown in Figure 1.

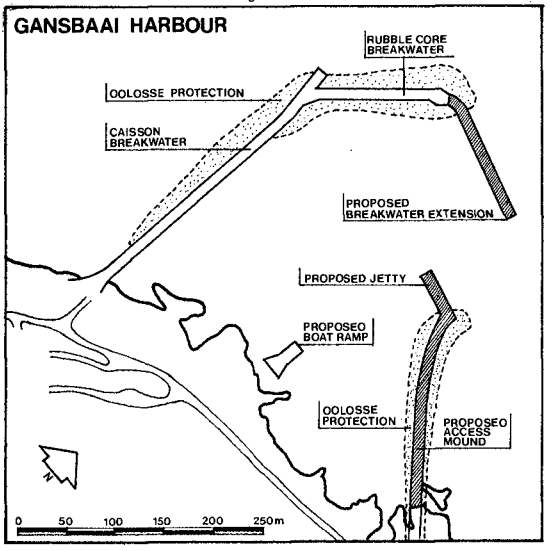

Fig. 1 Gansbaai Harbour

The information required from the model analysis may be summarised as follows:

2.1 Rubble Access Mound

It was required to establish sea and wave height parameters under which the construction of the rubble access mound could proceed.

The rubble access mound was to be modelled to two different lengths representing two stages of construction. At each of the two construction stages the access mound would be subjected to a range of wave height conditions from the direction 11° north of west.

During the test series the proposed caisson breakwater extension would be varied in length from its fully completed length to approximately 1/3 of its length.

2.2 Caisson Extension to Rubble Core Breakwater

It was required to examine the effect of various sea and wave height parameters on the construction of the caisson extension to the rubble core breakwater.

The hollow caissons to be used during construction were to be modelled to the appropriate mass and dimensions. Various placing sequences and stacking permutations were to be modelled with both hollow and concrete filled caissons. As the caissons were to be placed in various sequences, they were to be subjected to a wide range of sea and wave conditions.

2.3 Modifications to Existing Caisson Breakwater

It was required to examine the effect of varying wave heights, particularly storm conditions, on an advancing construction stage of the modifications to the existing caisson breakwater. It was assumed that 8t fluted concrete blocks would be used in the core underneath the dolosse armouring. The blocks were to be modelled and installed at a particular chainage. The advancing face of the blocks would be left exposed and the dolosse armouring would be completed to a distance of some 10 metres (in the prototype) behind the advancing face.

This construction stage was to be subjected to a range of wave height conditions.

3.0 MODEL FACILITIES

The scale of the model was 1:80. Wave height and period input to the model were based on records obtained from a prototype wave rider situated approximately 1,4km west of the harbour.

The two wave directions used during the model analysis were 11° north of west and due west. The period of the waves from both directions was 13 secs and the sea was considered to be at Mean Sea Level (MSL).

Apart from the basic model layout at NR10 the construction sequence modelling required certain additional features for incorporation in the model during testing. The main items which were to be used in the model testing programme and which were constructed for the model are as follows:

Dolosse	20t and 25t
Caissons	20t (approximately)
Rubble	50-500kg
	1, 2 and 3t
Concrete blocks (fluted)	8t
Concrete blocks (plain)	25t
	40t (for experimental purposes only)
Chain mesh	10t

4.0 MODEL TESTING

4.1 Test programme

For various reasons, some concerning the time required for the manufacture of certain items of construction to be incorporated in the model, it was decided that the order in which the major aspects of the contract would be studied, would be as indicated below.

1 Rubble Access Mound to the jetty
2 Caisson Extension to Rubble Core Breakwater
3 Modifications to Existing Caisson Breakwater

4.2 Model Testing Sequence

The following table, Table 1, contains the sequence of testing carried out during the study of the three aspects of the test programme.

TABLE 1 4.2.1 Rubble Access Mound

Rubble Access Mound	Caisson Extension	Sea Conditions
Full construction length (Ch190)	Full construction length (Ch125)	Wave spectrum 1-6,7m Wave direction 11° North of West
" " "	2/3 construction length (Ch93)	Wave spectrum 1-7,1m Wave direction 11° North of West
" " "	1/3 construction length (Ch40)	Wave spectrum 1-7,1m Wave direction 11° North of West

4.2.2 Caisson Extension to Rubble Core Breakwater

Caisson Placing System	Sea Conditions
Horizontal : 1 to 7 layers Caissons not concrete filled	Wave spectrum 1-4m Wave direction west
Stepped : 1 to 7 layers Caissons not concrete filled	Wave spectrum 1-3m Wave direction west
Vertical (single column) : 1 to 7 layers Caissons not concrete filled	Wave spectrum 1-2m Wave direction west
Vertical (single to multiple columns): 1 to 7 layers Caissons concrete filled	Wave spectrum 1-5m Wave direction west
Vertical and Stepped multiple columns Caissons concrete filled	Wave spectrum 1-6m Wave direction west

4.2.3 Modifications to Existing Caisson Breakwater

Exposed advancing face of 8t block core beneath dolosse	Sea Conditions
No protection	Wave spectrum 1-3m Wave direction 11° north of west
Protection : 4 strings of 3 blocks each fixed to breakwater	Wave spectrum 1-3m Wave direction 11° north of west

Exposed advancing face of 8t block core beneath dolosse	Sea Conditions
Protection : 40t blocks along toe of advancing face	Wave height 3m Wave direction 11° north of west
Protection : 25t blocks along toe of advancing face and chained to breakwater	Wave spectrum 3-7m Wave direction 11° north of west
Protection : Chain mesh approximately 10t	Wave height 4m Wave direction 11° north of west

5.0 RESULTS AND OBSERVATIONS OF MODEL TESTING

The model testing was carried out in the sequence shown in Section 4.2. Photographs were taken prior to the commencement of any test sequence and following each test performed.

5.1 Construction of Rubble Access Mound

The construction of the rubble access mound was modelled at two construction stages:

(i) Full construction length
(ii) Approximately 2/3 construction length

During the testing of the rubble access mound at both of these stages in construction, the caisson extension to the existing rubble mound breakwater was varied from a fully constructed length to 1/3 of the proposed construction length.

The layout of the breakwater model showing the rubble access mound and the caisson extension to full construction lengths is shown in Figure 2.

Each test was run for 10 minutes in the model representing a time of approximately 1½ hours in the prototype. The wave direction was set at 11° North of West at a period of 13 sec. The level of the sea was set at mean sea level (MSL) and the heights of the waves were varied, all waves being as measured at the prototype wave rider buoy west of the harbour.

The results of the testing at the various stages of construction of both rubble access mound and the caisson extension to the breakwater are summarised in Table 2.

Fig. 2 Model layout of Gansbaai Harbour

TABLE 2

Deep Sea Direction	Wave Height	Duration (prototype)	Observation
RUBBLE ACCESS MOUND FULL CONSTRUCTION LENGTH CAISSON BREAKWATER FULL CONSTRUCTION LENGTH			
11° N of W at 13 sec	1,0m - 2,0m	1½ hrs	No damage
"	3,2	1½ "	Slight movement of 2t rock on seaward slope
"	4,2	1½ "	Increased movement of 2t rock
"	5,4 - 6,0	1½ "	Appears calmer at entrance. No further damage
"	6,7	1½ "	No further damage

TABLE 2 (contd)

Deep Sea Direction	Wave Height	Duration (prototype)	Observation
RUBBLE ACCESS MOUND FULL CONSTRUCTION LENGTH CAISSON BREAKWATER 2/3 CONSTRUCTION LENGTH			
11° N of W at 13 sec	1,0m - 3,8m	1½ hrs	No damage
"	5,0	1½ "	50-500kg rubble movement. 1,2&3t rock movement. Damage becoming severe
"	5,9	1½ "	Severe damage
"	7,1	1½ "	" "
RUBBLE ACCESS MOUND FULL CONSTRUCTION LENGTH CAISSON BREAKWATER 1/3 CONSTRUCTION LENGTH			
11° N of W at 13 sec	1,0m - 1,5m	1½ "	No damage
"	1,8	1½ "	Slight rock movement
"	2,8	1½ "	Rock movement increasing
"	4,0	1½ "	Damage becoming severe
"	4,8 - 7,1	1½ "	Severe damage
RUBBLE ACCESS MOUND 2/3 COMPLETE CAISSON BREAKWATER 1/3 CONSTRUCTION LENGTH			
11° N of W at 13 sec	1,0	1½ "	Slight rock movement
"	2,0	1½ "	Severe damage. Advancing face destroyed
CONSTRUCTION OF ACCESS MOUND 2/3 COMPLETE CAISSON BREAKWATER AT 2/3 CONSTRUCTION LENGTH			
11° N of W at 13 sec	1,1m	1½ "	No damage
"	2,0	1½ "	Severe damage to advancing face

TABLE 2 (contd)

Deep Sea Direction	Wave Height	Duration (prototype)	Observation
CONSTRUCTION OF ACCESS MOUND 2/3 COMPLETE CAISSON BREAKWATER AT FULL CONSTRUCTION LENGTH			
110° N of W at 13 sec	1,0m	1½ "	No damage
"	2,0	1½ "	Fairly severe damage
"	3,0	1½ "	Severe damage advancing face demolished

The effect of a wave causing severe damage to the advancing face of the rubble access mound is illustrated in Figure 3. This shows a typical erosion and mixing of rubble to the leeward and seaward sides of the mound. Rubble is also tossed up onto the capping as the whole of the mound ahead of capping becomes eroded.

Fig. 3 Damage caused to advancing construction by 3m wave

5.2 Construction of the Caisson Extension to the Rubble Core Breakwater

The caissons to be used in the prototype construction are shown in Figure 4.

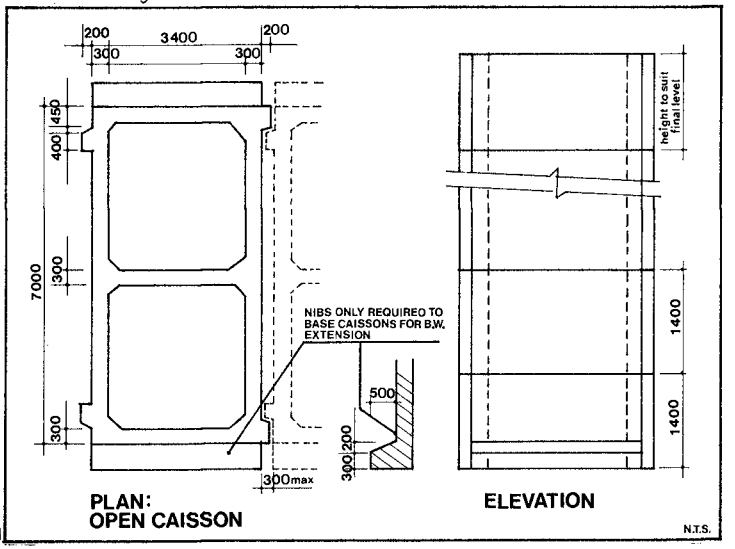

Fig. 4 Caisson design for extension to breakwater

These were modelled using polyester resin and barium sulphate.

In the prototype the caissons were to be placed in position singly and empty. Once in position, they were to be concrete-filled. During this phase of the model testing, an attempt was made to establish the optimum placing and concrete filling sequence, so that in the prototype under all likely sea conditions, the caissons would remain stable immediately after placing prior to and after concrete filling.

Filling the empty caissons in position in the model was simulated by pouring sand and a fine gravelly material into the caissons. This was found to be relatively successful although when the caissons reached the level of the surface of the water, the gravel tended to be washed out of the upper caissons by the wave action, and had to be continually topped up.

The proposed plant to be used during construction was also taken into account during the modelling. It was envisaged that a block/dolosse placing rig would be used on the breakwater with

a maximum load carrying capacity of 25t at a radius of 35m. Taking the parameters of this equipment into account and the dimensions of the caissons, it was assumed that the maximum number of caissons which could be placed on one level in line would be 7. On this basis the model analysis went ahead and within this range various placing sequences were modelled. The wave direction was adjusted from that used in the access mound testing described in Section 5.1, to try and simulate the most arduous conditions which might be experienced on the caisson extension. To give the worst conditions which might be expected at the harbour entrance the wave was therefore set at a direction west at a period of 13 sec. The duration of each test was approximately 10 minutes on the model simulating an hour and a half in the prototype. Occasionally the test run was shortened to approximately 1 hour in the prototype.

Figure 5 shows a typical layout of caissons in five horizontal layers and seven per layer.

Fig. 5 Typical layout 5 caissons high in 7 columns

Figure 6 illustrates the type of damage which could be expected after a particular wave had acted on the structure for a specific length of time.

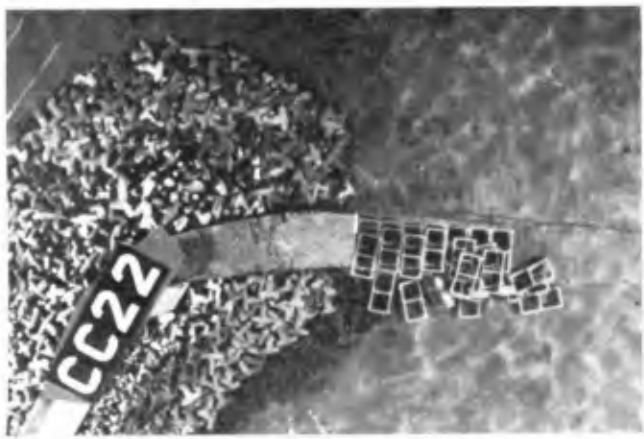

Fig. 6 Displacement by 2,0m wave of 6 layers, 7 columns placed empty

The results of the testing with various block placing combinations and sequences are summarised in Table 3.

TABLE 3

Deep Sea Direction	Observation
CAISSONS PLACED IN HORIZONTAL LAYERS	
1 LAYER (empty)	
West at 13 sec	Caissons displaced at 2,9m
2 LAYERS (empty)	
West at 13 sec	Caissons displaced at 4,0m
4 LAYERS (empty)	
West at 13 sec	Caissons displaced at 1,9m
6 LAYERS (empty)	
West at 13 sec	Caissons displaced at 2,0m
CAISSONS PLACED IN STEPPED CONSTRUCTION	
3 LAYERS STEPPED (empty)	
West at 13 sec	Caissons displaced at 2,0m

TABLE 3 (contd)

Oeep Sea Oirection	Observation
5 LAYERS STEPPEO (empty)	
West at 13 sec	Caissons displaced at 1,Om
7 LAYERS STEPPED (empty)	
West at 13 sec	Caissons displaced at 1,4m
CAISSONS PLACEO IN VERTICAL COLUMNS 1 VERTICAL (empty)	
West at 13 sec	Caissons slightly displaced at 2,Om
4 VERTICAL (empty)	
West at 13 sec	Caissons displaced at 1,Om
CAISSONS PLACEO IN VERTICAL/STEPPEO CONSTRUCTION AND CONCRETE FILLEO 5 VERTICAL CONCRETE FILLEO	
West at 13 sec	No damage up to 6m wave
7 VERTICAL CONCRETE FILLED	
West at 13 se	Caissons destroyed at 4,6m
7 VERTICAL - 3 COLUMNS - CONCRETE FILLEO	
West at 13 sec	Caissons displaced at 4,9m
CAISSONS PLACEO VERTICALLY ANO STRAPPEO TOGETHER 7 VERTICAL - 3 COLUMNS & 3 COLUMNS STEPPED - CONCRETE FILLED	
West at 13 sec	Caissons tend to become displaced at 5,Om wave but straps prevent further movement

Figure 7 shows a typical 3 column construction without strapping.

Fig. 7 Typical 7 layers placed in 3 columns unstrapped filled with gravel (simulating concrete)

In Figure 7 all caissons have been concreted to a level approximately 1,5m above MSL. The caissons are not strapped together. Figure 8 shows the same group of caissons after a 4,9m wave has impacted it for 45 minutes. After 35 minutes the outside column began to sway and move away from the second column. After 45 minutes the upper three caissons on the outside column toppled forwards.

Fig. 8 Model damage to structure in Figure 7 after prototype 4,9m wave impact

Figure 9 shows a typical layout of caissons in 7-stepped arrangement. All caissons are filled with concrete except for top caisson in each column. The arrangement represents 7 caissons recently placed in stepped construction on top of previously placed and concreted caissons.

Fig. 9 Stepped arrangement in 7 columns

5.3 Modifications to Existing Caisson Breakwater

The first phase of construction during the modifications and extensions to the Gansbaai Harbour will be the modifications to the existing Caisson Breakwater.

It was decided therefore, based on the previous model analysis by NRIO, that the area subjected to the worst sea conditions was in the vicinity of chainage 280 to 300 on the existing caisson breakwater. The modification to the existing caisson breakwater required a core consisting of 8t fluted concrete blocks placed along the outside of the breakwater to be protected by 20t dolosse which included toe dolosse held in position by means of connecting chains. The chains fixed to the toe dolosse were held in position by the core blocks. A typical section through the caisson breakwater is shown in Figure 10.

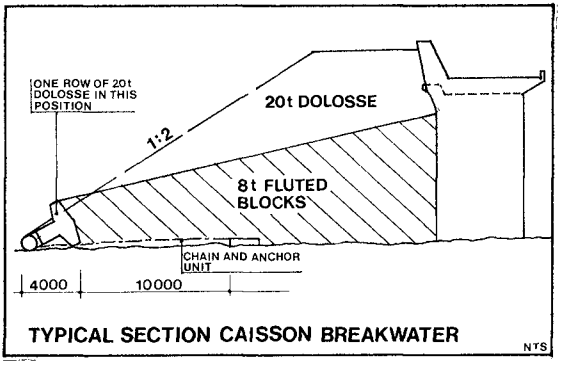

Fig. 10 Typical section of caisson breakwater as modelled

The model of the completed cross section of the modifications was constructed up to chainage 280. From Ch280 to Ch290 the density of dolosse was reduced and from Ch290 to Ch300 the 8t concrete blocks were exposed and constructed in a slope from a level of +1 GMSL to the sea bed. Toe dolosse anchored back underneath the concrete blocks over this section were also constructed. The advancing face of exposed construction is shown modelled in Figure 11.

Fig. 11 Advancing face of breakwater protection

During this series of tests the advancing face of the construction was protected in various ways and subjected to waves varying in height from 1m to 6,2m. The following methods of protection were studied:

(i) Protection by chaining exposed 8t blocks together
(ii) Protection to exposed toe of advancing construction using 25t blocks chained to breakwater
(iii) Protection to the 8t block core by means of a chain mesh

The test was also carried out with no protection at all to the advancing core and dolosse construction.

To prevent the advancing face of the core blocks from being displaced parallel to the breakwater and seaward and thus releasing the holding chains of the toe dolosse, the most effective method proved to be by means of 25t toe anchor blocks tied back across the advancing face and fixed to the breakwater. A recorded wave height of 6,2m at the wave rider failed to dislodge the 25t protective blocks. The importance of keeping the dolosse armouring as close as possible to the advancing face was clearly illustrated during the tests.

Figure 12 shows the damage resulting from a wave 11° N of W at an height of 2,8m lasting for 1½ hours. The unprotected 8t core blocks washed away from the core mass towards the sea. Others bunched up against the caisson wall. Toe dolosse broke free when the anchor chains became exposed.

Fig. 12 Damage to advancing face of breakwater protection by 2,8m wave

6.0 CONCLUSIONS

Some of the basic essentials for carrying out the contract under the sea conditions prevailing in the Gansbaai area were established. The model study indicated in specific areas the most advantageous sequences of prototype construction when adopting certain methods. Within the bounds of model error wave heights at the wave rider were established above which construction would not be possible without protective measures against damagement and displacement.

It was not possible to simulate meaningfully the actual placing of the caissons and dolosse through the waves and the tests were therefore directed at the stability of the elements once these had been lowered into position.

6.1 Rubble Access Mound

On completion of the above series of model tests, it was felt that within the bounds of experimental error and scale model limitations, a considerable amount of useful information was gathered regarding construction sequence and protection measures to be adopted.

From the tests carried out at the intermediate construction stage (approximately 2/3 of full length), it became clearly apparent that only in relatively calm seas, i.e. when the wave height as

recorded at the Waverider B registered less than 1m to 2m would construction of the rubble access mound be possible, without first considerably advancing the construction of the caisson extension to the rubble core breakwater. As continuous calm conditions do not exist, particularly in the vicinity of the proposed works, it was apparent that no construction could be commenced on the rubble access mound until construction of the caisson extension to the rubble core breakwater had been constructed at least ¾ of its length.

During prototype construction, this conclusion from the model testing was observed and only one small washaway was experienced with a wave height of 6m recorded at the wave rider buoy. Protection by means of 1, 2 and 3t rock was kept close to the advancing face.

6.2 Caisson Extension to Breakwater

Least damage to the caissons was experienced when these were advanced in stepped fashion (Figure 9). However caissons placed in this manner which had not been concreted became unstable when placed to within 2,5m of MSL when a wave height exceeding 1,5m was recorded. Nearer the surface the caissons became unstable in waves of 1m height. A form of fixing the caissons to each other using temporary tiebacks increased their resistance against sliding and toppling forwards. The stability of caissons filled with concrete is considerably higher than empty ones in the same position in the construction. For example, a filled caisson showed no tendency to slide laterally or forwards within 2,5m of MSL when the wave height was increased to 6,0m. An empty one became displaced in a wave height of 1,0m at this position. However there was a tendency for consecutive rows or columns of concreted caissons to open up under severe wave conditions. For example, caisson construction (concreted) to the level of the underside of the capping, i.e. above water level but not fixed together in any way, remained stable in wave heights up to about 4m. An increase over this wave height however caused the outside rows or columns to start moving apart. It was therefore concluded that when the construction height of the concreted caissons reached to within a metre or so of MSL, a form of linking the rows or columns of caissons together should be introduced. This would safeguard against the outer column moving away from the remainder as construction advanced. The tendency of the completed columns of caissons to part in high wave conditions decreased as construction moved further from the end of the rubble core breakwater.

During prototype construction placing of caissons commenced in steps as suggested by the model. However as with the model, the wave pattern parallel to the breakwater tended to suck out the concrete from the recently filled caissons. The method of placing caissons was therefore changed to a rapid placement of caissons in column formation. In addition, nibs were cast into the top of

each caisson which would fit into slots cast in the bottom of each succeeding caisson. Caissons were placed empty one at a time until the column had reached a height of one caisson above water level. The whole column was then cast. Protection against the removal of concrete through a sucking action of the passing wave was afforded by the top caisson which was approximately 1,5m above MSL. The tendency for the front column to move forwards as demonstrated by the model was pre-empted by strapping the exposed column to the previously cast columns until such time as the column was filled and the concrete set. The straps used for this purpose in the prototype were highly stressed by the wave action on the foremost column of caissons proving their absolute necessity.

6.3 Modifications to Existing Caisson Breakwater

It was established during the model study that either protection would be needed if construction was discontinued for a spell or a continuous operation and good luck would be required. Tests performed on this section of the construction proved conclusively that the advancing face of the 8t block core would require protection if left unattended in a storm. However there appeared little danger of the dolosse immediately behind the 8t concrete blocks becoming seriously displaced.

The most effective method established during the model testing of preventing movement and thus protecting the core block mass, was by means of 25t toe anchor blocks tied back across the advancing mass face and fixed to the breakwater. As the mass of blocks tends to shift the anchor blocks prevent forward movement and the chains holding back the blocks become very taut. These tieback chains fixed to the breakwater in turn assist in holding the mass of core blocks preventing them from vertical and lateral displacement. The chains and toe blocks are easily removed enabling further construction to continue. However during prototype construction the practicalities of constructing placing and anchoring 25t blocks were not considered feasible. Rather a continuous operation was carried out until the construction was past the critical area on the breakwater. The dolosse protection was kept close behind the core blocks and the toe dolosse were held back by chains on top of which the concrete blocks were placed. A wave height of 8m was experienced during one stage of construction and the concrete core blocks and toe dolosse behaved precisely as predicted by the model. There was a tendency for the blocks to move away from the breakwater and the toe dolosse to move seawards. Figure 12 illustrates this in the model.

7.0 ACKNOWLEDGEMENTS

The author is grateful to Marine Civil (Pty) Ltd for permission to publish this paper and to the Fisheries Development Corporation of SA Limited and the National Research Institute of Oceanology for the use of the hydraulic model and testing facilities.

8.0 REFERENCES

GANSBAAI MODEL STUDY. Progress Report No 11 CSIR Report c/sea 7817.

FISHERIES DEVELOPMENT CORPORATION OF S A LTD. Limited Contract F92 K243 Modifications and Extensions to Breakwater and the Construction of a Boat Ramp and a Jetty with Rubble Approach Mound.

Supplementary Information to Contract F92 K243 Climatic and Sea Conditions.

DESIGN AND CONSTRUCTION OF HAOERA OFFSHORE COAL UNLOADING TERMINAL

by

S.L. Yaron[1], J. Shimoni[1], C. Tzachar[2], D. Zwemmer[3]

INTRODUCTION

A new coal fired power plant constructed by the Israel Electric Corporation on the Mediterranean coast off Hadera, Israel, requires the import of 3.3 million tons of coal per year.

As there is no port on the Israeli Mediterranean coast capable of handling the 60,000 to 140,000 DWT bulk carriers required for transferring of coal, several studies were conducted in order to decide on the most feasible facility for mooring and unloading these boats.

Rather than expand existing ports or build a new protected port, a decision was finally taken to construct an unprotected offshore terminal at the power plant site.

The terminal was designed to accommodate bulk carriers of up to 140,000 DWT in the first stage, and up to 170,000 DWT with future expansion.

The design of the coal unloading terminal in an unprotected environment created the need to develop design criteria as well as operational and structural systems that will respond to problems arising from unloading bulk in the open sea. As there was no known precedent of an unprotected unloading terminal, the criteria was based on experience in existing offshore loading terminals, laboratory tests and engineering judgement.

The construction of an unprotected offshore terminal, at a cost of $60 million (excluding mechanical equipment), represents a considerable saving of time and money in comparison to the expansion of existing ports or construction of a new protected facility.

---

(1) Partners, Yaron-Shimoni & Partners Consulting Engineers Ltd., Israel
(2) Partner, Muller-Shnabel-Tzachar Consulting Engineers, Israel
(3) Partner, Ir.L.W. Lievense, Consulting Engineers, Breda, Holland

PRELIMINARY CONSIDERATIONS

Initial studies were conducted for development of the existing Haifa port. This port, situated 50 km north of the Hadera power plant is in the bay of Haifa, and can presently accommodate boats of up to 35,000 DWT. It is not suitable for handling bulk carriers of the designated size without a substantial investment in port expansion and land transportation systems.

This investment was estimated to be twice as high as the cost of building the unprotected facility in Hadera.

Other options for building a new protected port at the power plant site in Hadera were investigated as well. These options included several harbour layouts with breakwater protection. The various layouts and types of breakwaters (Fig. 1) were tested in a marine laboratory in order to find the feasibility and efficiency of the proposed harbours.

Laboratory tests showed that placing a breakwater in the open sea did not provide sufficient protection against heavy storms and did not provide sufficient berth availability for the ships. Capital investments in each of these solutions was also very substantial, as costs and risks of building breakwaters at water depths of 24 to 27 meters are very large.

In addition, soil investigations performed at that time showed that the soil does not provide a good foundation for the various types of breakwaters. The soil found at the site is characterized by a 5 meter top layer of loose sand, overlying a 5 meter layer of soft clay which can develop circular shear failure modes under breakwater loads. The soil in general was more suitable to pile foundations than other methods of load transfer.

These considerations led to the belief that a "finger" type, pile supported pier, connected to the shore by a pile trestle (Fig. 2), will provide the sufficient berth availability needed for unloading the required quantity of coal and at much lower costs.

Operational analyses were conducted in order to estimate the required berth occupancy for importing 3.3 million tons of coal annually. These analyses, which used as parameters various possibilities of unloading equipment and various sizes of bulk carrying boats, showed that a 50% berth occupancy when unloading operation is continuous, or 65% if no unloading is performed Saturdays and holidays, would be sufficient for unloading the necessary amount of coal.

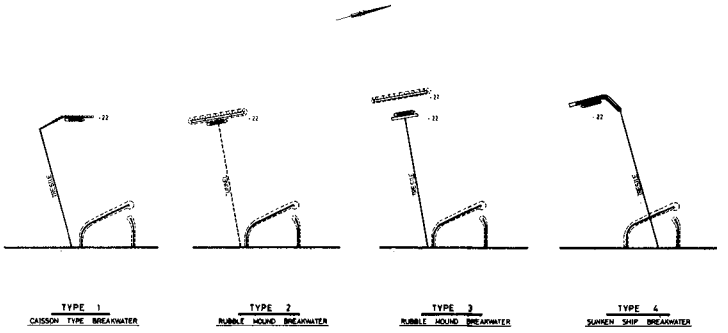

Fig. 1. Layout of Protected Harbours

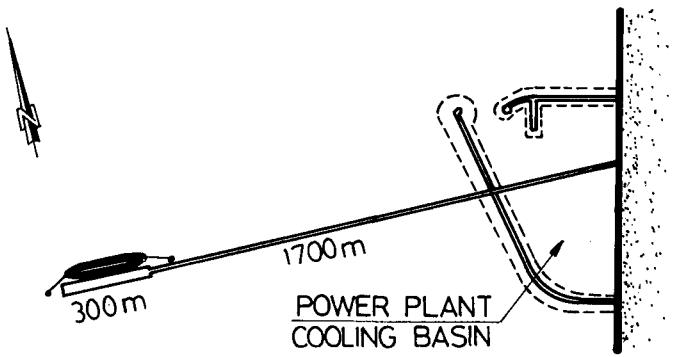

Fig. 2. Unprotected Pier

MODEL TESTS:

In order to test the berth availability of the "finger" pier, operational criteria had to be established. Limiting criteria were set for boat movements at the pier, for safe berthing and mooring and for maneuvering procedures at approach and departure of boats (see Ref. 1).

These criteria were established by consulting with ship captains and unloading equipment operators, as well as by comparing accelerations and velocities of ship movements with those of the unloader bucket movements.

Model tests were conducted on two ship models, a 60,000 DWT and 120,000 DWT. Each boat was tested in full load and in light ballast conditions.

The model tests indicated the optimum mooring fendering system that provides maximum berth availability and berth operability at the existing sea states in the location of the terminal.

These tests showed that the expected yearly unloading operability will be about 80% to 90%, depending on ship size and load. The expected yearly average berth availability will be 80% to 85%.

TERMINAL DESCRIPTION

The pier is a 300x24 meters structure, heading due west into the main direction of the waves. It is a pile supported open structure which absorbs very little impact from the waves and causes little or no reflection of waves between the pier and the boats moored along its side. The boats are moored against dolphins adjacent to the pier, bow heading into the main direction of the waves (Fig. 3). Mooring lines are connected to a quick release hook system placed on the mooring and breasting dolphins. Breastlines can be tied either to near breasting dolphins, or under the pier deck to far breasting dolphins (Figs. 3 & 4).

The pier is located at water depths of 20 to 40 meters and is connected to shore by a 1700 meters long 12 meters wide approach jetty. The approach jetty is built of 200 meters long sections.

The approach jetty deck is a composite construction of prefabricated concrete slabs on steel girders, supported on pile bents placed every 40 meters. Typical pile bents have two battered piles that provide the transverse stability. Longitudinal stability is provided by fixed points, with four battered piles, placed at the middle of the 200 meters trestle sections.

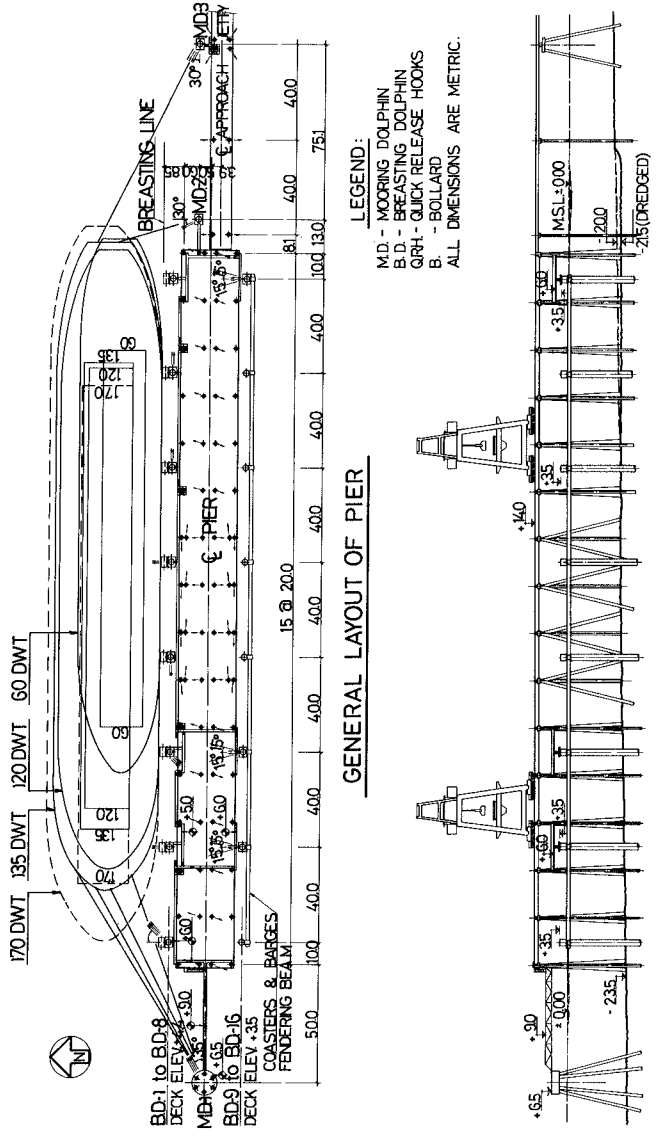

Fig. 3. General Layout of Pier

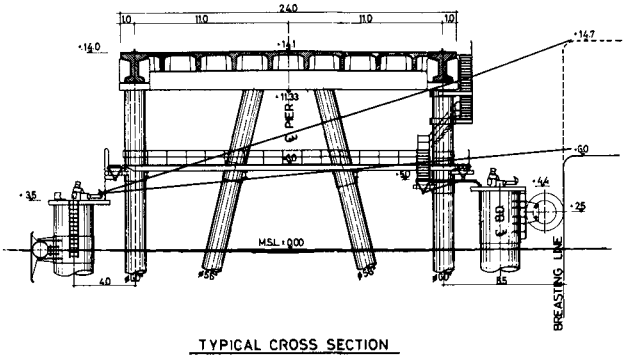

Fig. 4. Typical Cross Section

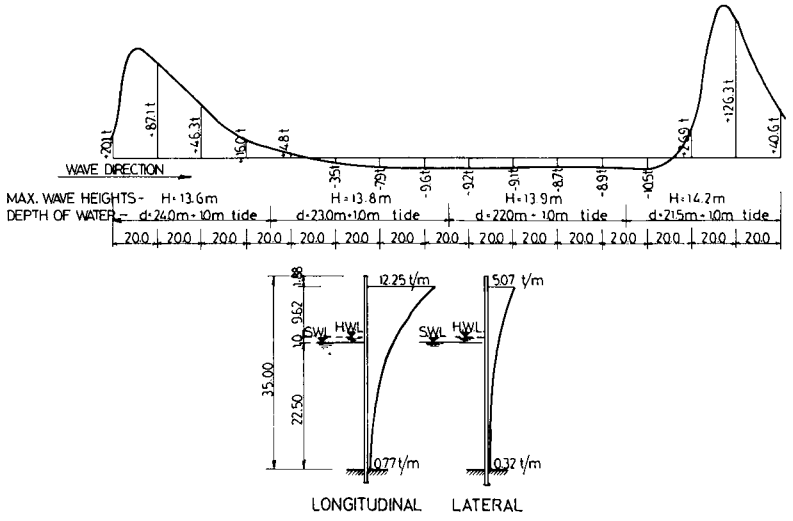

Fig. 5 Wave Shape and Forces on Pier Piles

Pier and approach jetty deck are at +14.0 meters above M.S.L.

SEA STATE AND DESIGN CONSIDERATIONS

Two groups of sea states are essentially considered in the design of the terminal. The lower sea state is the state at which the pier is operable. In this sea state the boats can be moored and unloaded, and the general layout is based on behaviour of the boats at this sea state.

Model tests, as well as the short experience accumulated to date, show that the pier is operable at wave heights of up to 4.0 to 4.5 meters max. (2.5 meters significant waves). These waves are generally 9 to 12 seconds waves, and as such are shorter than the design ship lengths, and cause ship movements that are smaller than those set by the limiting criteria.

This sea state exists over 300 days per year. The other sea state considered is the high, 1:100 year sea state, which governs the structural design and stability of the facility. At this state no boats are moored at the pier and the maximum design waves act on the structure. The 1:100 year deep water design wave at the pier is an 8.7 meters significant wave with a respective maximum wave of 14.5 meters. In general, these waves have return periods of approximately 15 seconds. The maximum wave height at the pier location (water depths of 20 to 24 meters) corresponding to the deep water design wave, is 13.7 meters. The shape of the wave at this location is cnoidal (Fig. 5) with a crest height of approximately 9.5 meters above H.W.L. or 10.5 meters above M.S.L. Pier deck elevation was set at +14.0 meters above M.S.L. so that the underside of the deck will be above the crest line.

The maximum waves breaking zone is located in the approach jetty region approximately 100 to 400 meters east of the pier (1300 m. to 1600 m.from shore) at water depths of approximately 18 meters. The maximum wave at the breaking zone is best represented by a Modified Solitary wave shape with a crest level of approximately 11.4 meters above H.W.L. This crest level is app. 1.0 meter higher than the bottom of the pile cap beams and acts with a slamming force on the structure (Fig. 6). Lenghts of approach jetty sections were set so that each section will absorb the impact of no more than one crest of the higher waves. Accordingly the sections of the approach jetty are 200 meters long with one or two fixed points for longitudinal stability. The fixed points at maximum waves breaking zone are also designed to absorb the slamming forces on the pile cap beams.

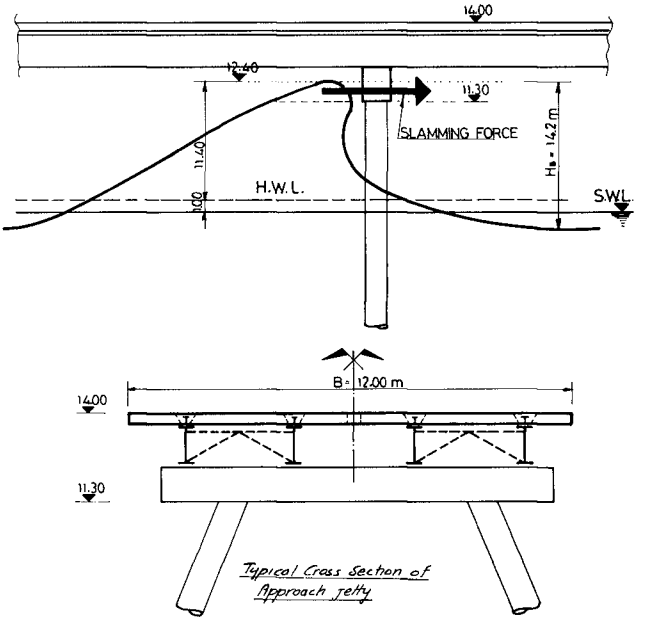

Fig. 6. Wave Forces on Approach Jetty Piles

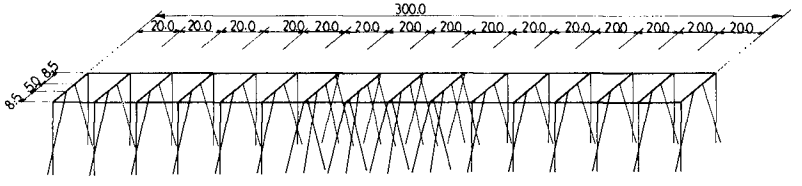

Fig. 7. Structural System of Pier

The design of the structural systems of the pier and approach jetty is based on a space frame analysis fully continuous in all directions with nonlinear soil-pile interaction (Fig. 7).

The structural design was based on a combination of the following codes - DNV (Det Norske Veritas), "Rules for Design Construction and Inspection of Offshore Structures", API-RP2A, "Recommended Practice for Design, Construction and Inspection of Fixed Offshore Structures", Israeli Codes for design of concrete and prestressed concrete structures and AISC specifications for steel design. Some of those codes are based on Ultimate Limit State (ULS) and some on serviceability Limit State (SLS). To enable the combined use of these codes, modifications had to be introduced.

All parts of the structure were designed for the 1:100 year wave loads with the exception of the walkway system under the pier deck. These walkways, at elevation +6.0, were designed for 25 year return period waves and are expected to be repaired periodically.

The supporting piles were designed for the following load combinations:

1.3P + 1.3L + 1.0D + 0.7E (ordinary)
1.0P + 1.0L + 1.0D + 1.3E (extreme)

where P - Permanent loads
L - Live loads
D - Deformation loads
E - Environmental loads

The piles were designed with a factor of safety of 1.5 for both the ordinary and extreme load combinations, which allowed for a total factor of safety of 2.0 for the "theoretical working" loads. A reduction of 20% of the factor of safety was permitted in a few piles at the approach jetty fixed points when loaded by the extreme slamming forces caused by the maximum breaking waves.

SOIL CONDITIONS AND FOUNDATIONS

Extensive soil investigations were performed at the site. Over 30 borings were performed in order to enable the preliminary studies of the various alternative layouts. Of these more than 20 were directly on the pier and trestle alignment. The borings were performed in water depths of up to 26 meters, and generally to 40 meters penetration in the soil. Several additional borings were performed during construction to penetration of up to 100 meters in the sea bed.

The soil formation at the site is characterized by three different layers, a top layer of fine sand, approximately 5.0 meters thick, overlying a second layer of very soft clay, app. 4.0 to 6.0 meters thick, overlying medium to dense sand alternating with calcareous sandstone layers. The bottom layer showed high S.P.T. values, ranging from 40 to 100. Based on these soil investigations, the piles selected for the pier were 56" diameter, 7/8" thick, steel pipe piles and the piles selected for the approach jetty were 48" diameter, 3/4" thick steel pipe piles. The required ultimate capacity of the 56" pier piles was 1000 tons, and for the 48" diameter approach jetty piles - 600 tons. The contractor proposed a change in the vertical pier piles, using a single, 60" diameter, 1 1/8" thick steel pipe pile, with ultimate capacity of 1800 tons, instead of two 56" diameter piles used in the basic design put out for tender.

A load test was performed on the 60" pile with 31 meters penetration. The test pile failed at approximately 1100 tons instead of the required 1800 tons.

As changes in the design were impractical at this stage of construction, the contractor proposed to drive the piles until the required resistance was met. This was achieved at a penetration of approximately 70 meters and at very great costs. Since the construction was delayed at that time due to heavy damages to the contractor's equipment caused by a storm, time was available to find alternative solutions for increasing the pile capacities.

Analysis of the 60" test pile failure has shown the pile has not formed a sufficient soil plug, and has cut through the sand and calcareous layers like a "cooky cutter" through batter. In order to avoid this the piles were driven to approximately 35 meters penetration, the soil inside the pile was removed by a rotary drill, and a concrete plug was cast inside the pile (Fig. 8). When concrete has reached sufficient strength, the pile was redriven to the required resistance. Redriving the piles has increased the resistance from 8 to 10 blows/10 cm to 50 to 90 blows/10 cm over an additional penetration length of 50 to 70 cms, much more than the required resistance, which was calculated to be 35 blows/10 cm when using a menck 2500 pile driving hammer (delivering 31 ton meters energy) (see Fig. 9).

The concrete plug and redrive method could not be adopted easily to the 56" diameter battered piles used in the pier. These piles with ultimate capacities of up to 1350 tons, had also to be driven to 70 meters penetration in order to develop the required resistance. In order to reduce the penetration to approximately 35 meters, a steel annulus ring was welded into the pipe approximately 15 meters from the bottom tip (see Fig. 8). The introduction of this annulus ring assisted in forming a better soil plug and develop additional bearing

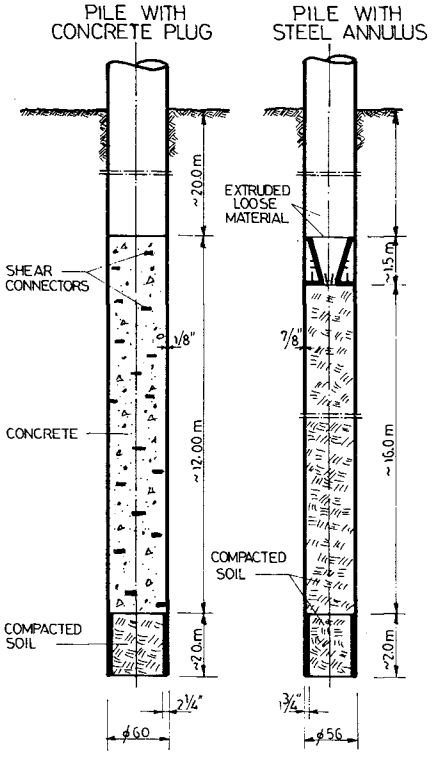

Fig. 8. Piles with Concrete and Steel Plugs

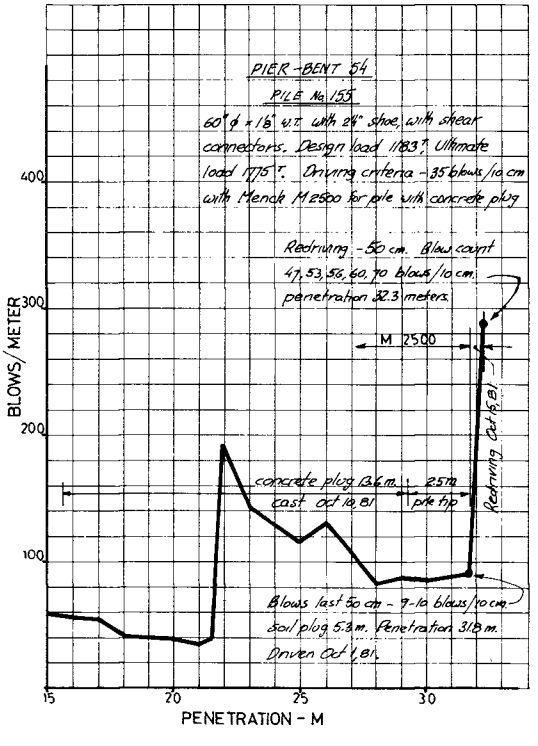

Fig. 9. Driving Record of a 60" Diameter Vertical Pile Before and After, Concrete Plug Installation

surface. The piles driven in that manner reached the required resistance at the expected penetration (Fig. 10).

These alternative solutions proved to be far less expensive than driving the piles to 70 meters penetration.

DOLPHINS

An important feature of the design is that the bulk carrying boats be berthed and moored to dolphins which are separated from the pier structure. These dolphins are designed to absorb the energy of the boats at approach and departure conditions, and take the forces of the mooring lines when the boats are moored.

For this purpose, the dolphins are designed as flexible cantilevered piles with large rubber fenders which help absorb the energy without developing large forces.

The tender documents called for a system of dolphin piles interconnected by hinged struts. The contractor has chosen to use single pile dolphins of 2600 mm. and 2800 mm. diameters with wall thickness ranging from 34 to 70 mm. The fenders used are "Vredestein" jumbo type fenders, 2700 mm outside dia., 1350 inside dia. and 4000 mm long.

The dolphins are designed to absorb the impact of 170,000 DWT boats approaching at a maximum docking speed of 20 cm/sec.

CONSTRUCTION

Construction of the terminal began in March 1980 and was scheduled for completion January 1982. The contractor was permitted to make certain changes in the design that were more adaptable to his equipment and experience, provided that they do not influence the basic concept and layout of the terminal. The contractor was also required to perform the detailed design of these changes according to the design criteria that was specified in the contract documents.

Damages that were caused to the contractor's equipment by the severe storm mentioned above as well as the problems encountered with the piles that were proposed by the contractor, delayed the final completion of the terminal. Construction of the pier and dolphins was completed in January 1982 and construction of the approach jetty was completed in August 1982.

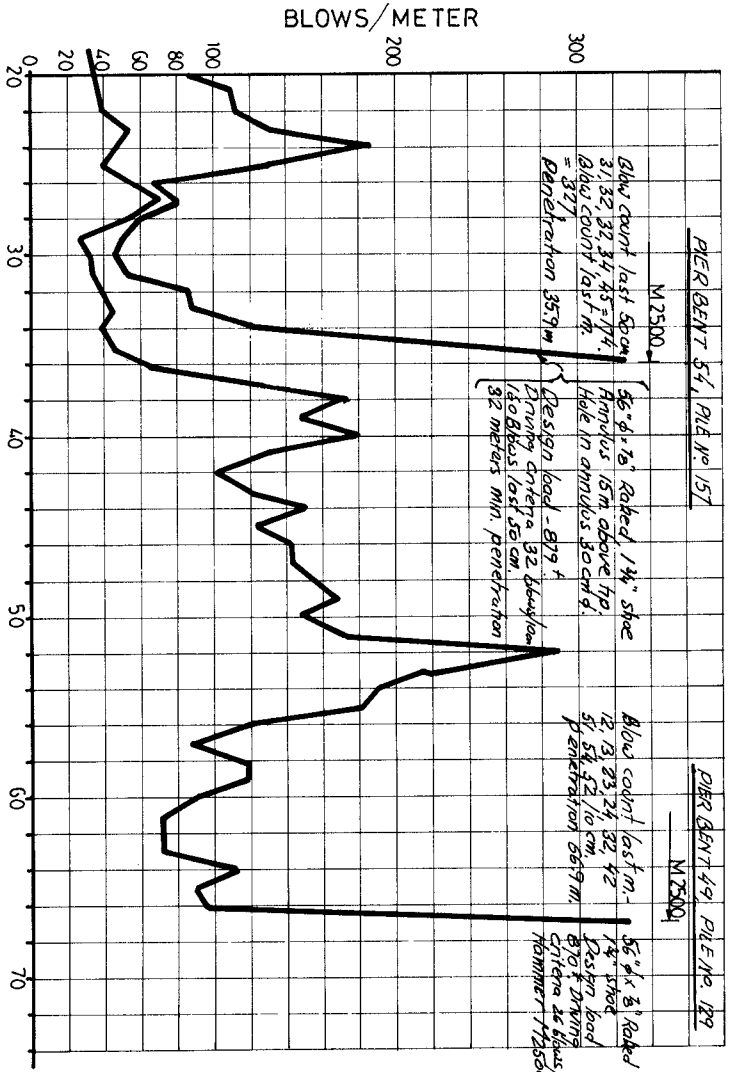

Fig. 10. Driving Records of Similarly Loaded 56" Diameter Piles With, and Without, Annulus

The first boat was unloaded at the pier in August 1982 into 500 DWT coasters that were moored at the opposite side of the pier and which delivered the coal to shore. With the completion of the approach jetty, the coal was temporarily unloaded to trucks running from the pier to shore. This will continue until the conveyor belt system is complete. To date, the behaviour of the boats at the pier was very much as expected from the model tests, with little interference from winter waves.

REFERENCES

1. Yaron S., Shimoni J., Tzachar C., Zwemmer D., "The Hadera Offshore Coal Unloading Terminal: A New Approach to Unloading of Bulk in the Open Sea" 14th Annual Offshore Technology Conference, paper OTC 4396, Houston, 1982.

2. Yaron S., "New Approach to Conceptual Design of the Hadera Coal Unloading Terminal", Proc. of 1st Israeli Conference of Civil Engineers, Nov. 1982 (In Hebrew)

3. Rosen D., and Vajda M., "Establishment of Basic Design Criteria and Testing of Models for the Hadera Coal Unloading Terminal", Proc. of 1st Israeli Conference of Civil Engineers, Nov. 1982.

4. Shimoni J., "Codes and the Analysis of Marine Structures", Ibid.

5. Tzachar C., "Design of Pier and Dolphins for large boats", Ibid.

6. Zeitlin J. G., Komornik A., Weisman G., "Design of Foundation for the Offshore Coal Unloading Terminal", Ibid.

7. Zander D., "Construction of the Offshore Coal Unloading Terminal at Hadera", Ibid.

Wave Forces on Piles of Variable Diameter

Bernard LeMehaute[1] Ph.D., M. ASCE
James Walker[2] Ph.D., P.E., M. ASCE
John Headland[3], A.M. ASCE
John Wang[4] Ph.D., M. ASCE

SUMMARY

A method of calculating nonlinear wave induced forces and moments on piles of variable diameter is presented. The method is based on the Morrison equation and the linear wave theory with correction parameters to account for convective inertial effects in the wave field. These corrections are based on the stream function wave theory by Dean (1974). The method permits one to take into account the added wave force due to marine growth in the intertidal zone or due to a protective jacket, and can also be used to calculate forces on braces and an array of piles.

INTRODUCTION

Design of coastal structures such as piers requires calculation of wave induced forces on piles. The basic methodology is based on the application of the Airy theory in the Morrison equation. This has been a very useful tool, but the Airy theory does not account for many of the nonlinear dynamic and kinematic effects which finite amplitude waves exhibit. Several investigators have used various nonlinear wave theories and corrections to linear theory. The stream function wave theory by Dean (1965) has been determined to be one of the most originally accurate theories (LeMehaute and Dean, 1970). It has been used by Dean (1974) to determine wave forces on piles. Dean has also used stream function theory to develop a number of simple graphs which give the total wave force and moment about the mudline on pile of uniform diameter (SPM, 1977).

Many coastal engineering applications require calculation of the wave loading distribution on the pile. On a pier, the top of the pile is in some cases fixed and therefore the moment about the mudline is not a useful parameter, the designer requires the load distribution. Furthermore, the geometry of many marine structures are complicated by

[1]Chairman, Dept. of Ocean Engineering, RSMAS, University of Miami, Fla.
[2]Chief Coastal Engineer, Moffatt & Nichol, Engineers, Long Beach, Ca.
[3]Coastal Engineer, Moffatt & Nichol, Engineers, Long Beach, Ca.
[4]Associate Prof., Dept. of Ocean Engineering, RSMAS, University of Miami, Fla.

Photograph 1. Pile of Variable Diameter.

the presence of marine fouling. Barnacles, mussels and other marine organisms can significantly increase the diameter of a pile in the intertidal zone as shown in Photograph 1. Wooden piles are often protected by, or their useful life extended by, a jacket wrapped around the pile. Both marine growth and protective jackets introduce a variable diameter pile near the water surface. Because the diameter is increased near the free surface, wave forces are increased for a given wave condition. Figure 1 schematically shows a pile of three diameters which could represent the situation of marine growth on a protective jacket on a pile.

The objective of this paper is to present a methodology for the coastal engineer to readily calculate the nonlinear, wave-induced loadings on piles of variable diameter. Considering the large number of parameters, it is not possible to present an exact solution to the problem in the form of a few graphs. Therefore an approximate method has been developed in which the velocity and acceleration fields, and forces and moments are initially obtained at the pile location from the linear wave theory. These parameters are integrated from the sea floor into an arbitrary elevation, z_i, which can be the free surface. The free surface is given by the nonlinear wave theory of Dean (1974). Then correction coefficients are introduced to account for the nonlinear convective inertial forces on the velocity and acceleration fields. By so doing the method is, with a few approximations, amenable to description by a limited number of graphs. The graphs reduce by an order of magnitude the interpolations required and permits the engineer to calculate the load distribution to a high degree of accuracy with a minimal effort. Furthermore, the pile can comprise multiple diameters.

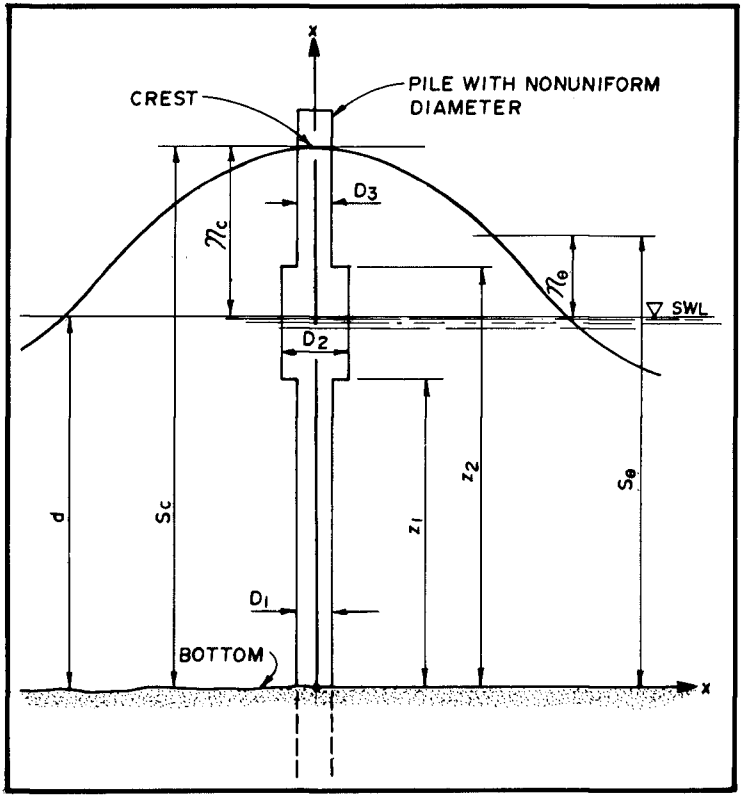

Figure 1. Definition Sketch for a Pile with Three Diameters.

The force on an array of piles can be determined by calculating the forces at various phase angles.

The methodology therefore permits the engineer to calculate wave forces on piles taking into account many of the physical properties of waves observed in nature and the laboratory as well as special circumstances which must be addressed in practical design problems. The force and moment correction factors are primarilly greater than unity and therefore will yield forces and moment which are greater than those calculated by linear theory. Where force and moment correction factors are less than unity, the correction was retained as unity for the sake of conservatism.

FORCES ON CYLINDRICAL PILES: BASIC FORMULATION

A cylindrical vertical pile subjected to a time dependent horizontal velocity, u(t), has a force, f, per unit length of cylinder which is the sum of a drag force, f_D, and an inertia force, f_I:

$$f = f_D + f_I = \tfrac{1}{2} \rho C_D u|u| + \rho C_m \frac{\pi D^2}{4} \frac{du}{dt} \qquad (1)$$

where ρ is the density of sea water, D is the pile diameter, u is the particle velocity, $\frac{du}{dt}$ is the particle acceleration, C_D is the drag coefficient, and C_m is the inertia coefficient.

When a cylindrical pile is subjected to a water wave, one considers that these equations hold true, provided u(t) is the horizontal component of the velocity field at the pile location as if the pile did not exist. The deformation of the velocity field by the pile, wave diffraction, the effect of the vertical velocity component, the vertical acceleration component and the elasticity of the pile are neglected. The equation is commonly called "Morrison's equation".

The total force, F_T, on the pile is determined by integrating the unit forces from the sea floor to the water surface, S_θ.

$$F_T = \int_0^{S_\theta} f \, dz \qquad (2)$$

where subscript θ refers to phase angle.

Forces due to nonlinear waves over piles of variable diameter, D_i, can be calculated using equations (1) and (2) using expressions for u and du/dt from the linear wave theory and adjusting them according to results obtained from the nonlinear wave theory. Nonlinear corrections are taken from the stream function theory as presented by Dean (1974). Two basic corrections are made: the asymmetric free surface correction and the nonlinear correction to the wave field.

Figure 1 shows a pile of three diameters, D_1, D_2 and D_3. The total force, F_T, acting from the sea bottom (z=0) to the elevation of the free surface ($z=S_\theta$) is given by:

$$F_T = \int_0^{z_1} f(D_1)\, dz + \int_{z_1}^{z_2} f(D_2)\, dz + \int_{z_2}^{S_\theta} f(D_3)\, dz \qquad (3)$$

where F_T = total force on the pile and $f(D_i)$ = total force per unit length acting on pile diameter D_i.

Graphs can be constructed which integrate unit force and moment from the sea floor to an elevation z_i. Then equation (3) can be written.

$$F_T = \int_0^{z_1} f(D_1)\, dz + \int_0^{z_2} f(D_2)\, dz - \int_0^{z_1} f(D_2)\, dz + \int_0^{S_\theta} f(D_3)\, dz - \int_0^{z_2} f(D_3)\, dz \qquad (4)$$

This expression can be written:

$$F_T = F(D_1)|_{z_1} + F(D_2)|_{z_2} - F(D_2)|_{z_1} + F(D_3)|_{S_\theta} - F(D_3)|_{z_2} \qquad (5)$$

where $F(D_i)|_{z_i}$ = wave force acting on a pile of diameter D_i from the sea bottom to a level z_i.

Use of equation (5) requires evaluation of the force $F(D_i)|_{z_i}$ on a pile of arbitrary diameter, D_i, and elevation above the bottom, z_i. This is done using the linear wave theory with the appropriate correction coefficients in order to account for the effects due to the nonlinear wave theory. This gives:

$$F(D_i) = \tfrac{1}{2}\, \rho\, C_D\, D_i\, \frac{H^2}{T^2}\, d\, K_D|_{z_i}\, \phi_D + \rho\, C_m\, \frac{\pi D_i^2}{4}\, d\, \frac{H}{T^2}\, K_I|_{z_i}\, \phi_I \qquad (6)$$

where H = wave height, T = wave period, and d = water depth. $K_D|_{z_i}$, and $K_I|_{z_i}$, are dimensionless drag and inertial coefficients respectively, obtained by integration from the mudline to an elevation z_i, and ϕ_D and ϕ_I are correction factors to the forces obtained by the linear theory. ϕ_D is the correction relating to u^2 and ϕ_I is the correction relating to du/dt.

According to linear theory:

$$K_D|_{z_i} = K_{DM}|_{z_i}\, \cos\theta|\cos\theta| \qquad (7)$$

$$K_I|_{z_i} = K_{IM}|_{z_i}\, \sin\theta \qquad (8)$$

The maximum values $K_{DM}|_{zi}$ and $K_{IM}|_{zi}$ integrated from the mudline to an elevation z_i are:

$$K_{DM}|_{z_i} = \frac{1}{8}\frac{gT^2}{d}\left[1 + \frac{2kz_i}{\sinh 2kz_i}\right]\frac{\sinh 2kz_i}{\sinh 2kd} \quad (9)$$

$$K_{IM}\, z_i = \tfrac{1}{2}\frac{gT^2}{d}\frac{\sinh 2kz_i}{\cosh kd} \quad (10)$$

where k = wave number = $2\pi/L$ and L = wavelength. $K_{DM}|_{z_i}$ and $K_{IM}|_{z_i}$ are given by figures 2 and 3, respectively, as a function of z/d and d/L_o.

NONLINEAR FREE SURFACE

$F(D_3)|_{z_i}$ at $z_i = S_\theta$ requires the knowledge of the free surface elevation S_θ as function of phase angle, θ. This is done by applying the free surface given by the stream function wave theory by Dean (1974). The results are presented in the form of S_θ/d as a function of H/H_b, d/L_o and θ, in figure 4. H_b is the limit wave height as defined by Dean (1974).

The use of figure 4 is illustrated by an example. Given d/L_o = .033, θ = 20° and H/H_b = .75 enter figure 4 vertically with a value of d/L_o = .033. As indicated by the arrow in the figure, one proceeds downward until the line of H/H_b = .75 is intersected. A line is then drawn horizontally towards the right until the θ = 20° line is intersected. Now move vertically downward to read S_θ/d = 1.256.

CORRECTIONS FOR NONLINEAR WAVE KINEMATICS

The second correction to linear theory is due to the nonlinear wave particle velocity and acceleration fields. The correction coefficients ϕ_D and ϕ_I incorporate a number of nonlinear effects, most notably due to the convective acceleration terms. These nonlinear effects are a complex function of relative depth, d/L_o, wave phase angle, θ, the ratio of the local height to breaking height, H/H_b, and the ratio of elevation to water depth, z/d. These are given by the ratio of the forces obtained by using the values obtained by a nonlinear wave theory to the corresponding value given by linear theory. To incorporate all of these variables at each z would require a large number of nomographs. Therefore a conservative approach was adopted where the nonlinear correction factors at the free surface were applied over the water column. While the nonlinear effects actually vary with z/d and θ, the most important corrections are near the free surface. Therefore only a global nonlinear correction is applied over the entire pile length, from the sea bottom to the nonlinear free surface. Also the phase variations given by $\cos\theta$ and $\sin\theta$ respectively, are retained in the general equation. The error resulting from this simplification is that forces are generally over-predicted by a few percent at levels below the free surface. Figures 5 and 6 present the nonlinear correction factors ϕ_D and ϕ_I as a function of phase angle, θ, H/H_b and d/L_o. Note that the corrections approach unity for θ = 30° and 50° for drag and inertia respectively. For greater θ, corrections are less than unity, but a conservative design procedure would be to use the correction at unity for $\theta > 30°$ for drag forces and $\theta > 50°$ for inertia forces.

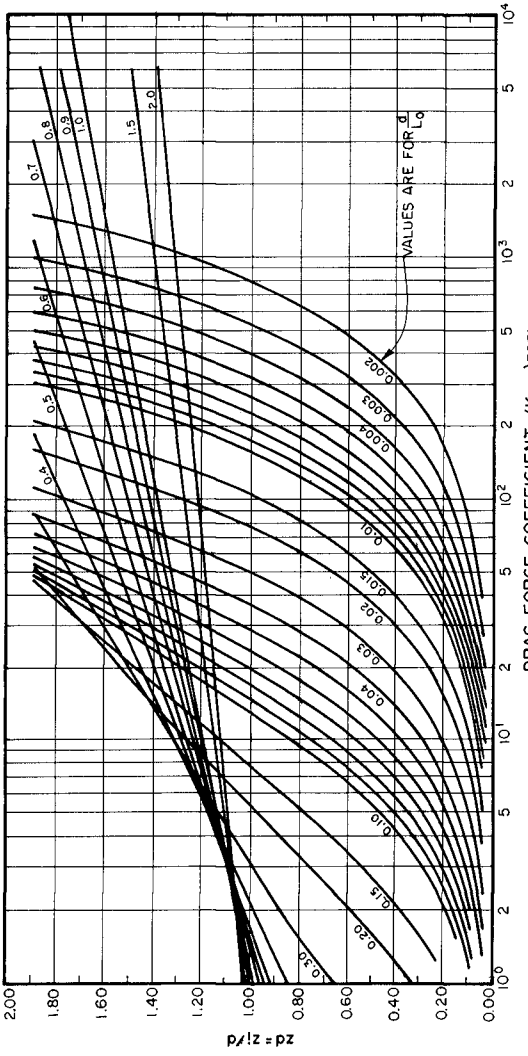

Figure 2. Drag Force Coefficient.

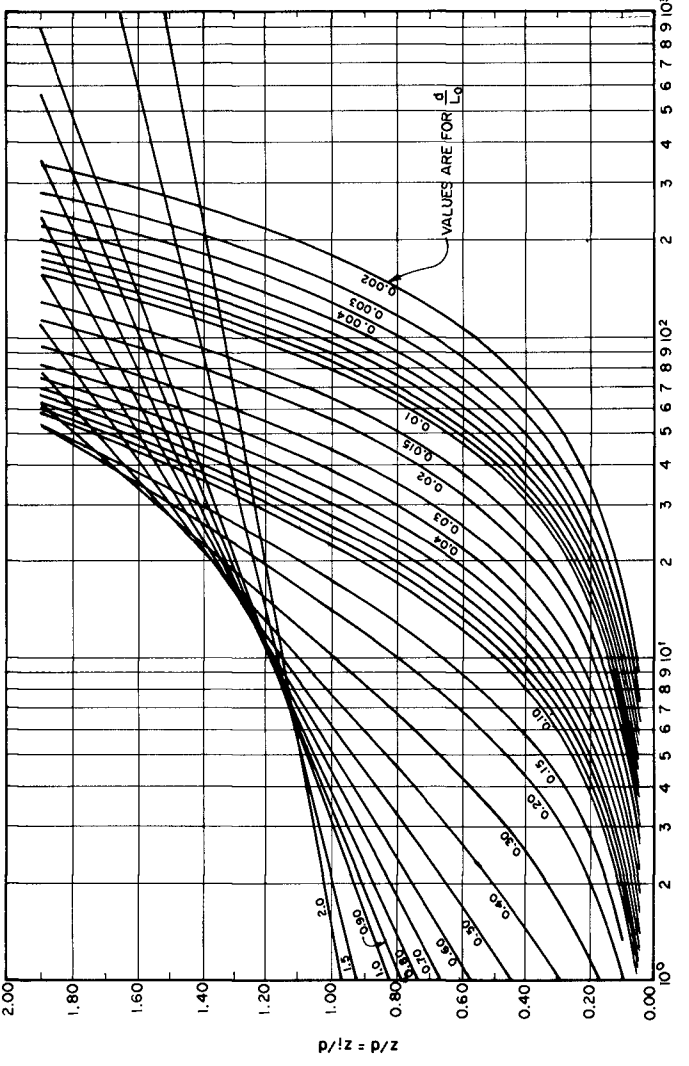

Figure 3. Inertial Force Coefficient.

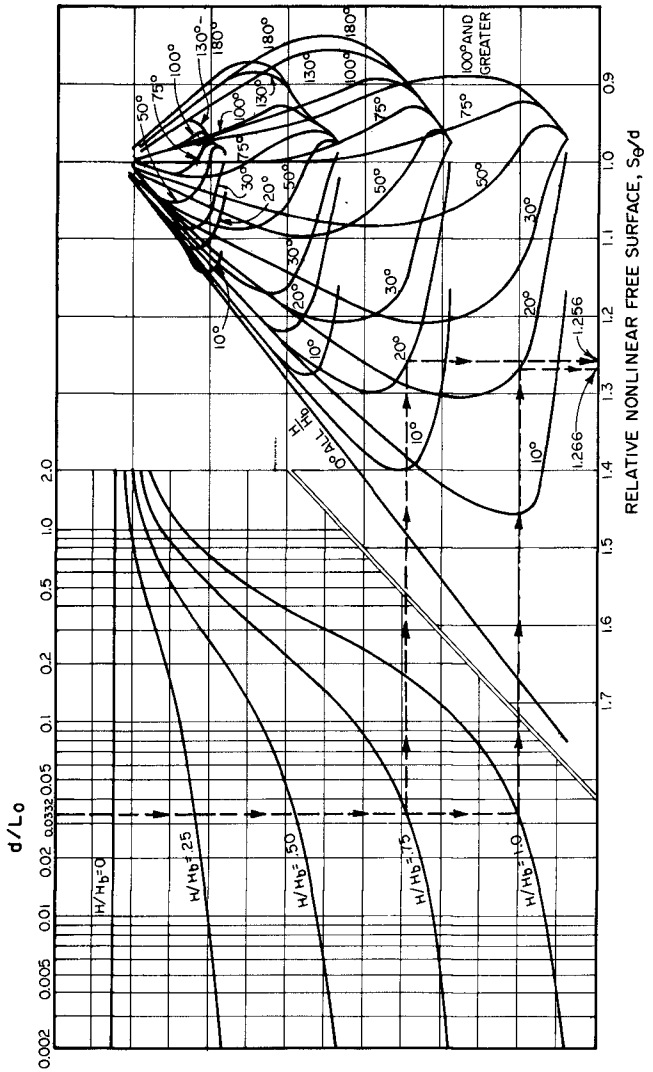

Figure 4. Nonlinear Free Surface.

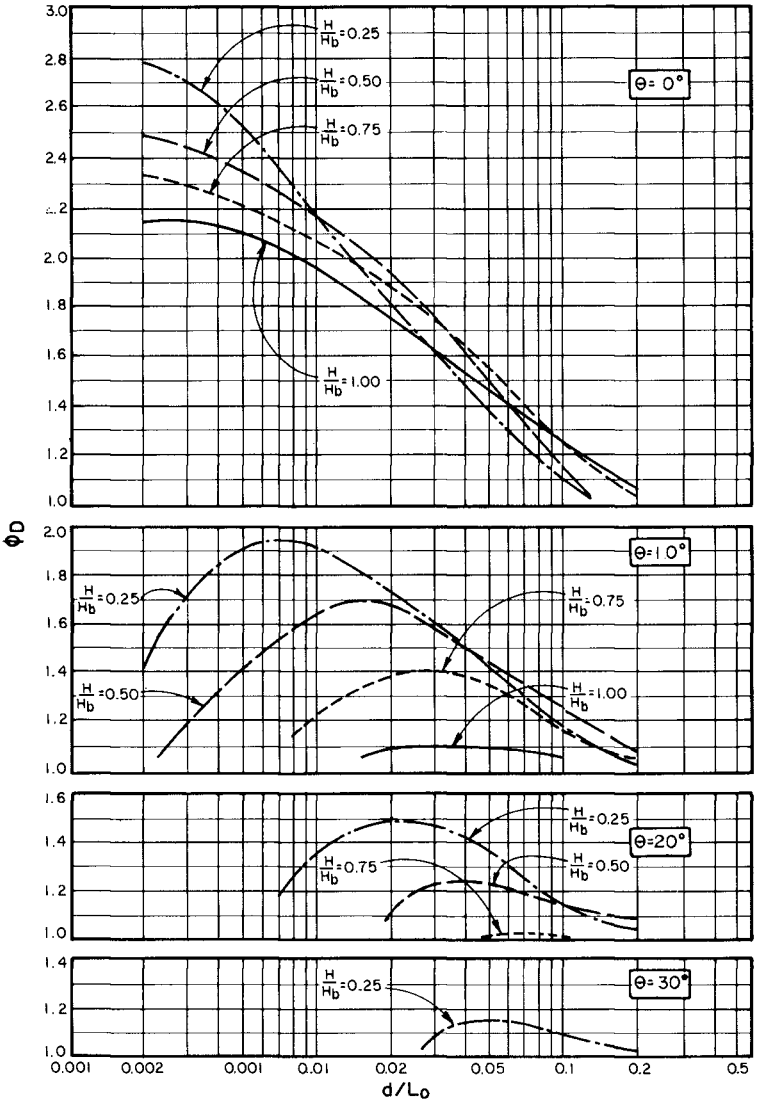

Figure 5. Nonlinear Drag Force Correction Factor.

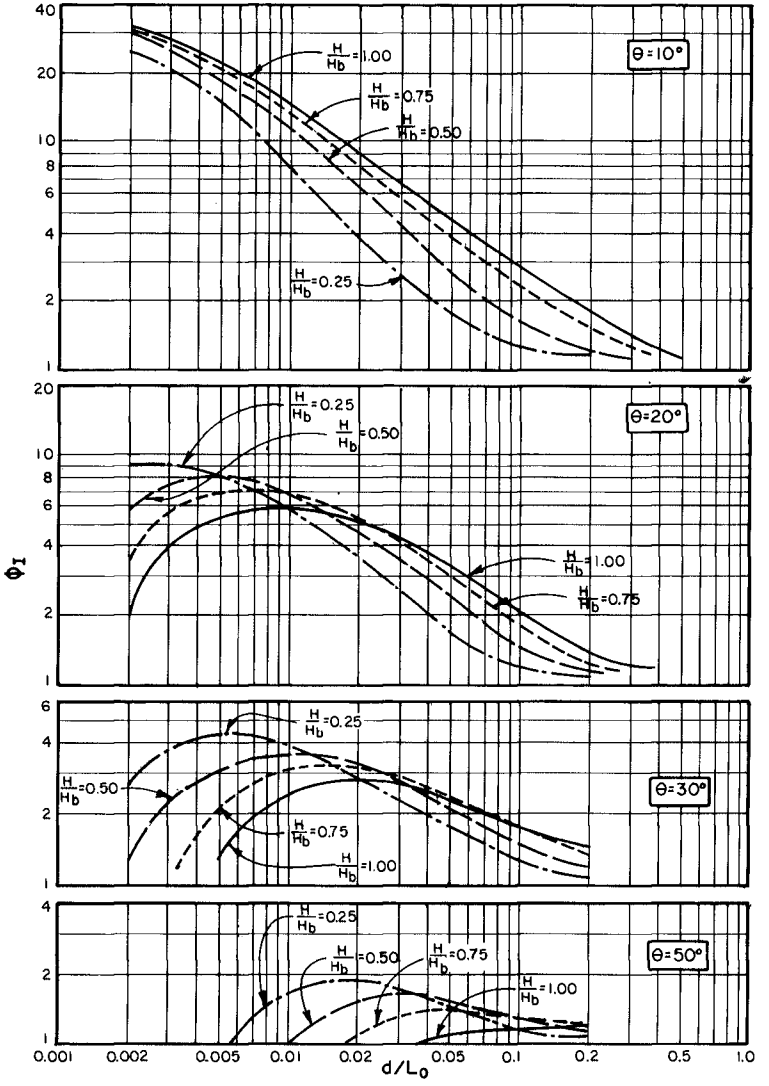

Figure 6. Nonlinear Inertial Force Correction Factor.

TOTAL FORCE ON PILE OF VARIABLE DIAMETER

Based on these assumptions the total force on a pile of three diameters can now be written:

$$F_T = F_D + F_I \tag{11}$$

$$F_D = \tfrac{1}{2}\,\rho\, C_D \frac{H^2}{T^2} d \left[K_{DM}\big|_{z_1} (D_1 - D_2) + K_{DM}\big|_{z_2} (D_2 - D_3) + K_{DM}\big|_{S_\theta} (D_3)\right] \phi_D \cos\theta|\cos\theta| \tag{12}$$

$$F_I = \rho\, C_M \frac{\pi d}{4} \frac{H}{T^2} \left[K_{IM}\big|_{z_1} (D_1^2 - D_2^2) + K_{IM}\big|_{z_2} (D_2^2 - D_3^2) + K_{IM}\big|_{S_\theta} (D_3^2)\right] \phi_I \sin\theta \tag{13}$$

MOMENT CALCULATIONS

Expressions analogous to the above force equations are presented for calculation of the wave moment on a pile of diameter, D_i, at an elevation acting about the sea bottom. The moment expression is:

$$M_T = \int_0^{S_\theta} f\, z\, dz \tag{14}$$

Referring to figure 1 and using a similar approach, the total moment, M_T, acting about the sea bottom can be written as:

$$M_T = M(D_1)\big|_{z_1} + M(D_2)\big|_{z_2} - M(D_2)\big|_{z_1} + M(D_3)\big|_{S_\theta} - M(D_3)\big|_{z_2} \tag{15}$$

where M_T = total moment acting about the sea bottom; $M(D_i)\big|_{z_i}$ = wave moment acting on a pile of diameter D_i about the sea bottom to a level z_i. Equations for $M(D_i)\big|_{z_i}$ are given:

$$M(D_i)\big|_{z_i} = \tfrac{1}{2}\,\rho\, C_D \frac{H^2}{T^2} d^2\, \Gamma_D(D_i)\big|_{z_i}\, \Psi_D + \rho\, C_M \frac{\pi D_i^2}{4} \frac{H}{T^2} d^2 \Gamma_I(D_i)\big|_{z_i}\, \Psi_I \tag{16}$$

where: $$\Gamma_D(D_i)\big|_{z_i} = \Gamma_{DM}(D_i)\big|_{z_i} \cos\theta|\cos\theta| \tag{17}$$

$$\Gamma_I(D_i)\big|_{z_i} = \Gamma_{IM}(D_i)\big|_{z_i} \sin\theta \tag{18}$$

$$\Gamma_{DM}(D_i)\Big|_{z_i} = \tfrac{1}{2}\frac{g^2T^4}{g^2}\frac{1}{(8\pi)^2}\frac{1}{\cosh^2 kd}\left[1 + 2(kz_i)^2 + 2kz_i \sinh 2kz_i - \cosh 2kz_i\right] \quad (19)$$

$$\Gamma_{IM}(D_i)\Big|_{z_i} = \frac{1}{8\pi^2}\frac{g^2T^4}{d^2}\frac{\sinh kd}{\cosh kd}\left[1 + kz_i \sinh kz_i - \cosh kz_i\right] \quad (20)$$

$\Gamma_{DM}(D_i)\Big|_{z_i}$ and $\Gamma_{IM}(D_i)\Big|_{z_i}$ are given as functions of z/d and d/L_o in figures 7 and 8 respectively and can be evaluated up to the free surface elevation given by figure 4. Ψ_D is the drag moment correction for the velocity field and Ψ_I is the inertial moment correction for the acceleration field. Other variables are as previously defined. The nonlinear moment correction factors, Ψ_D and Ψ_I, are given in figures 9 and 10, respectively, as functions of d/L_o, θ, and H/H_b.

MAXIMUM VALUES - EFFECT OF PHASE ANGLE

The total maximum force and total moment phase angle cannot be readily determined for a pile of variable diameter. The drag force is maximum at $\theta = 0$, and for small diameter piles, the maximum value is near $\theta = 0$; but as the diameter increases the inertial force becomes more prevalent and shifts the location of the maximum total force toward $\theta = 90°$. The maximum inertial force occurs at some unknown angle, but its maximum value can be determined as a function of H/H_b and d/L_o only by application of formula (13) in which one takes $z_3 = d$ and one replaces $\phi_I \sin\theta$ by ϕ_{IM} given by figure 11. A similar method applies to calculate the maximum moment due to inertia. The correction factor, Ψ_{IM}, is then given by figure 12.

CONCLUSION

The preceding outlines the methodology for determining nonlinear wave forces on piles of variable diameters. The methodology greatly simplifies the interpolation required in using stream function theory and permits one to estimate wave forces and force distribution over the pile column. The method presented is for a general case. The US Navy Manual DM26.2 (1982) describes other cases in more detail to simplify the wave force and moment calculation for special cases.

By considering θ as a variable, the time history of the total force and moments on piles of varying diameter can be determined. Therefore the method is amenable to determine the total wave forces on structures supported by a number of piles.

ACKNOWLEDGEMENT

This work was conducted for the U.S. Navy under Contract N00025-79-C-006 by Moffatt and Nichol, Engineers for preparation of the Design Manual DM26.2, "Coastal Protection."

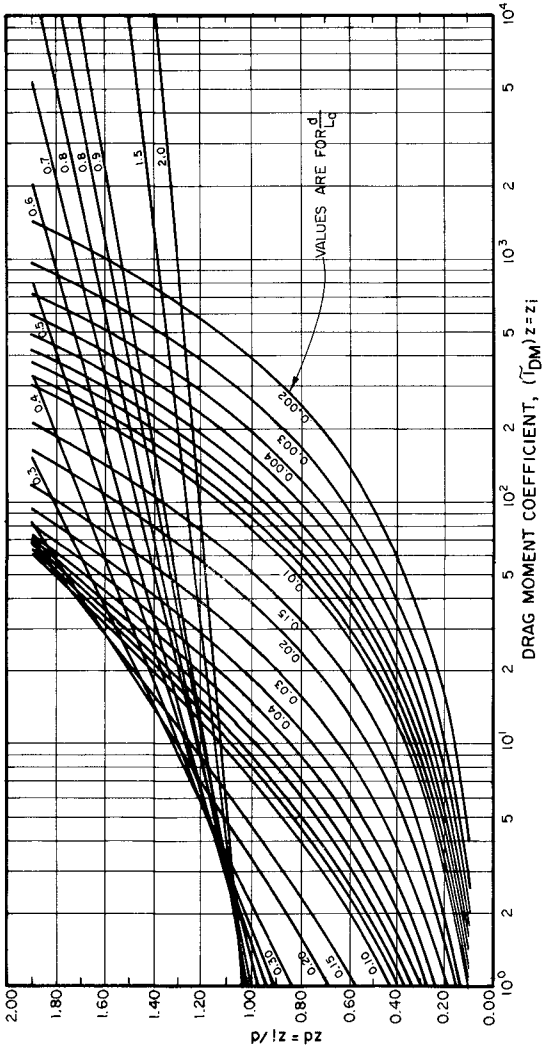

Figure 7. Drag Moment Coefficient.

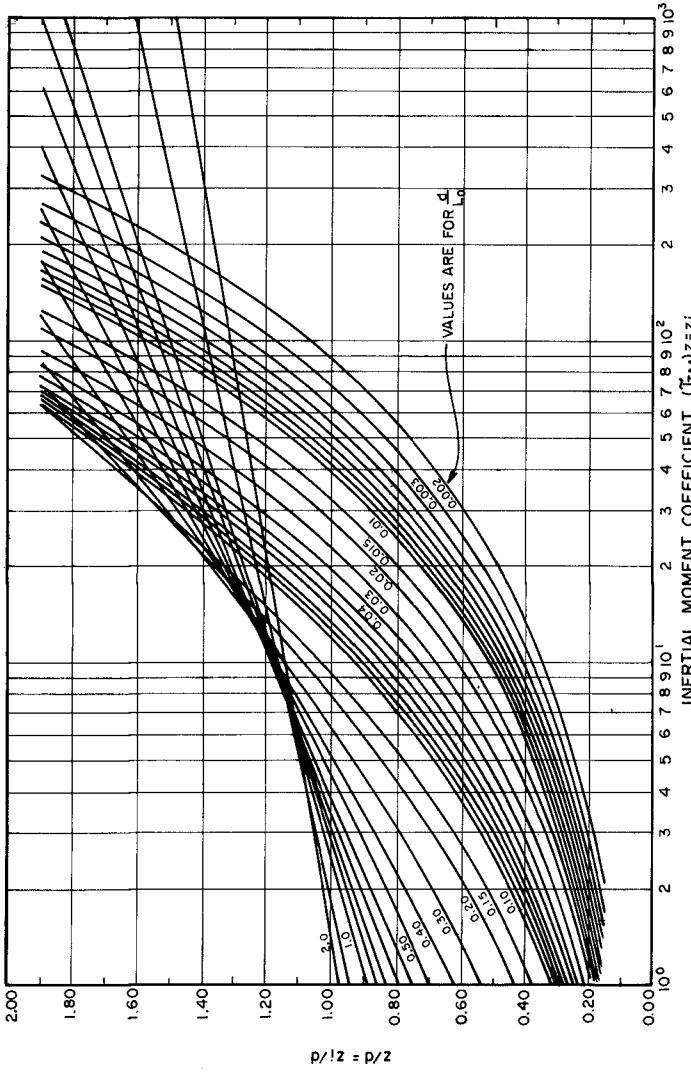

Figure 8. Inertial Moment Coefficient.

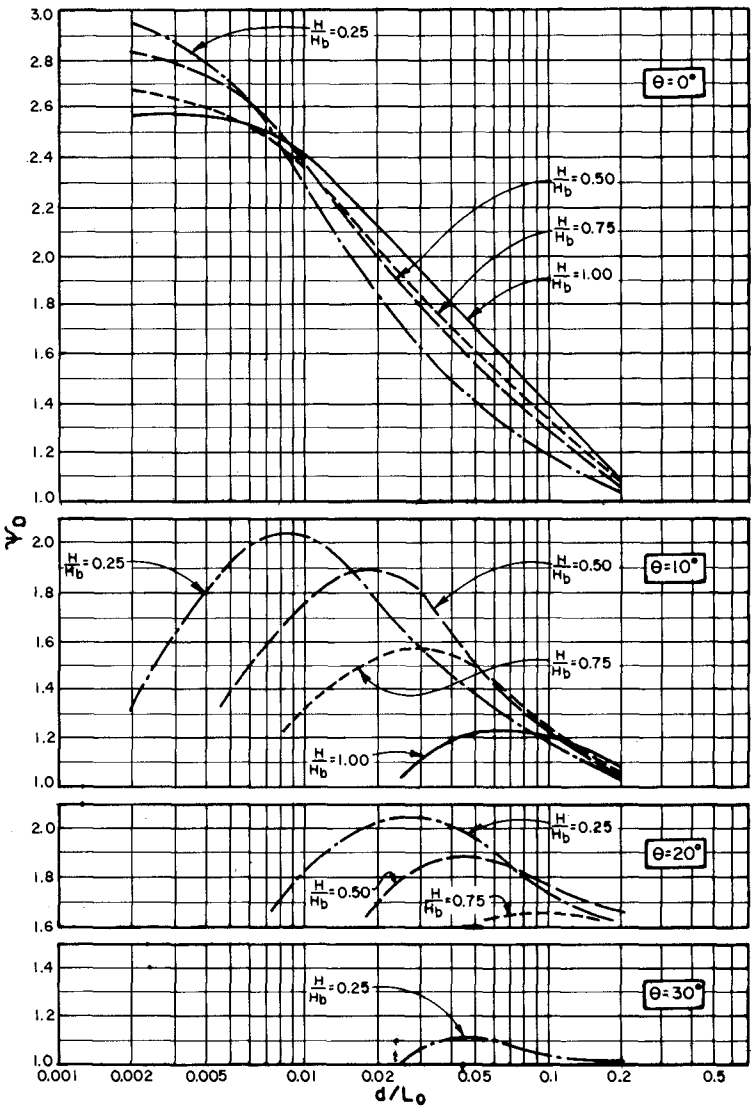

Figure 9. Nonlinear Drag Moment Correction Factor.

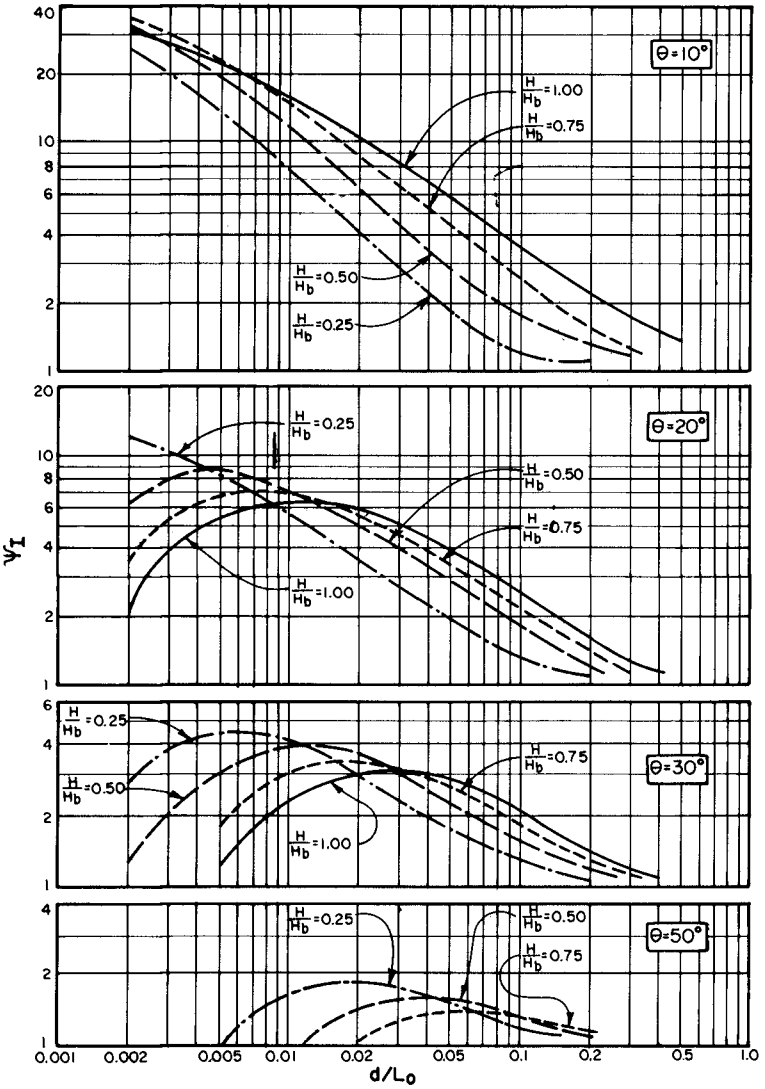

Figure 10. Nonlinear Inertial Moment Correction Factor.

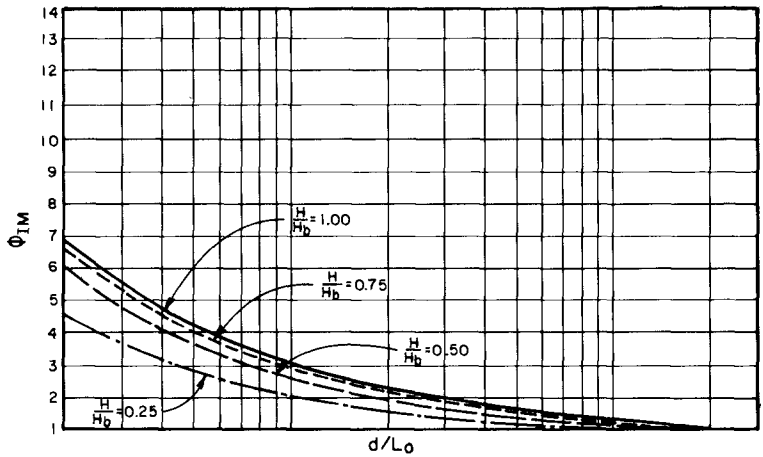

Figure 11. Maximum Nonlinear Inertial Force Correction.

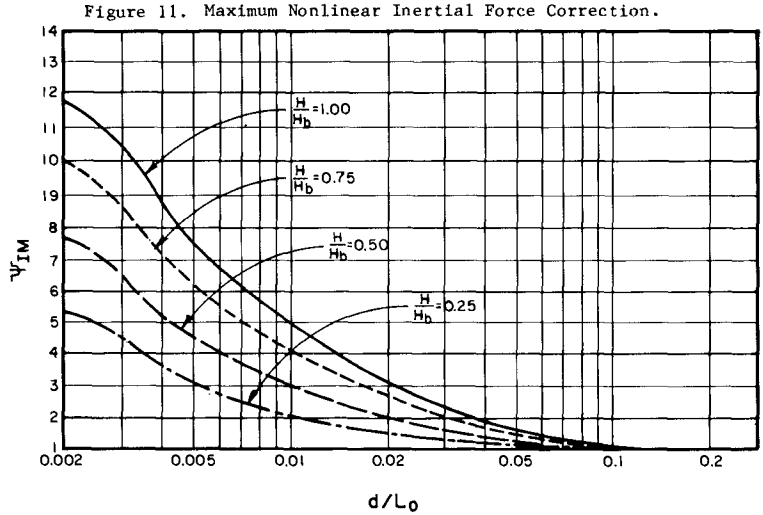

Figure 12. Maximum Nonlinear Inertial Moment Correction.

REFERENCES

Dean, R.G., "Stream Function Wave Theory; Validity and Applications", Santa Barbara Specialty Conference, Santa Barbara, California, October, 1965.

Dean, R.G., "Evaluation and Development of Water Wave Theories for Engineering Application", Special Report No. 1 Volumes I and II, U.S. Army Corps of Engineers Coastal Engineering Research Center, Fort Belvoir, Va., November, 1974.

Dean R.G. and LeMehaute B., "Experimental Validity of Water Wave Theories," Paper presented at the 1970 ASCE Structural Engineering Conference, Portland, Oregon, April 8, 1970.

U.S. Army Corps of Engineers, Coastal Engineering Research Center, Shore Protection Manual, 3d ed., Vols. I, II, and III, U.S. Government Printing Office, Washington, DC, 1977.

U.S. Navy, Design Manual DM26.2, "Coastal Protection," Naval Facilities Engineering Command, May 1982.

NOTATION

C_D = drag coefficient

C_m = inertia coefficient

d = water depth

D_i = pile diameter

$f(D_i)$ = wave force per unit length of pile of diameter D_i

$F(D_i)$ = wave force on a pile of diameter D_i

F_T = total wave force

g = 32.2

H = wave height

$k = 2\pi/L$

$K_D|_{z_i}$ = linear drag force coefficient evaluated at an elevation zi above the sea bottom

$K_{DM}|_{z_i}$ = maximum linear drag force coefficient evaluated at an elevation zi above the sea bottom

$K_I|_{z_i}$ = linear inertia force coefficient evaluated at an elevation zi above sea bottom

$K_{IM}|_{z_i}$ = maximum linear inertia force coefficient evaluated at an elevation z_i above the sea bottom

L = wavelength

$M(D_i)$ = wave moment on a pile of diameter D_i

S_θ = free surface elevation at arbitrary wave phase angle θ

T = wave period

z_i = elevation above the bottom

$\Gamma_D|_{z_i}$ = linear drag moment coefficient evaluated at an elevation zi above the sea bottom

$\Gamma_{DM}|_{z_i}$ = maximum linear drag moment coefficient evaluated at an elevation zi above the sea bottom

$\Gamma_I|_{z_i}$ = linear inertia moment coefficient evaluated at an elevation zi above the sea bottom

$\Gamma_{IM}|_{z_i}$ = maximum linear inertia moment coefficient evaluated at an elevation zi above the sea bottom

θ = wave phase angle

ρ = density of water

ϕ_D = nonlinear drag force correction factor

ϕ_I = nonlinear inertia force correction factor

Ψ_D = nonlinear drag moment correction factor

Ψ_I = nonlinear inertia moment correction factor

PROTOTYPE TESTS ON RIPRAP UNDER RANDOM WAVE ATTACK

J.D. Pitt and P. Ackers (Member ASCE)*

ABSTRACT

This paper describes the performance of test panels of riprap on an offshore island in the Wash estuary, UK, for the first 2½ years after their construction, by which time all but one had failed. It outlines the methods used in obtaining and analysing data on stone size, wind, tides and waves. The techniques used in surveying the test panels for damage and the reduction of the survey data to yield quantitative estimates of damage are described.

Comparisons are made between the damage to the riprap panels and what might have been estimated using laboratory data. Results do not support any scale effect causing riprap sized on laboratory data to be larger than necessary, and this conclusion is supported by the outcome of model tests carried out retrospectively by the Hydraulics Research Station (now HRS Ltd) at Wallingford, UK.

Slope protection is sensitive not only to wave height and stone size but also to construction methods and, bearing in mind possible departures from the desired specification, a cautious approach to the design of riprap protection is advisable.

1. INTRODUCTION

1.1 Use of Riprap for Slope Protection

In the context of this Report riprap is a graded quarry-stone layer on the sloping surface of an embankment protecting it from erosion by the action of wind generated waves. To prevent leaching of the embankment material through the riprap layer, one or more sub-layers (Filter layers) of smaller graded stone may be necessary. This method of slope protection is an alternative to continuous paving, interlocking slabs or precast concrete armour units. Because the cost of the slope protection can be a significant proportion of the total cost of a project, the reliability of available design information is important.

1.2 Limitations of Model Testing

Most design methods for riprap are based on results of hydraulic model tests, and their validity depends on the reproduction of all the characteristics of the prototype. It is seldom possible to meet this requirement fully, and errors arising from such limitations are referred to here as 'model effects'. The behaviour of riprap under wave attack depends on so many factors that some model effects are almost certain to be present (e.g. it is very difficult to ensure that the stone shape used in the prototype is reproduced in a model).

Even if the model accurately resembles the prototype, the forces are not necessarily reproduced exactly to scale, because all the

* Senior Engineer and Hydraulics Consultant, Binnie and Partners, London, ENGLAND.

requirements for dynamic similarity can not be met. Errors arising from this difficulty depend on the scale of the model, and are therefore known as 'scale effects'. Scale effects in laboratory tests of riprap were highlighted by work in the USA(1) which suggested that the use of small scale models could result in costly overdesign.

1.3 Background to the Study

Many of the early investigations into the behaviour of riprap and other forms of slope protection were based on model tests using regular waves. In that type of test, a significant 'model effect' is inevitable as real waves are irregular in height, frequency and direction. One of the first attempts to relate results of tests using regular waves to those using irregular waves is described in a U.K. Construction Industry Research and Information Association (CIRIA, formerly CERA) publication(2) on laboratory tests sponsored at the U.K. Hydraulics Research Station (HRS).

Research on the subject continued at HRS, in collaboration with CIRIA, with paddle-generated irregular waves, culminating in the publication of CIRIA Report 61 in 1976.(3). This comprehensive Report reviewed current practice under the headings of wave prediction, design procedure, design wave height, size, grade and shape of riprap, placing and thickness, filter design and run-up. Design curves and procedures based on these new measurements were presented.

1.4 The need for Field Tests

An important conclusion reached in CIRIA Report 61 was that, contrary to the American findings, no allowance for scale effects could be recommended when using these laboratory results with irregular waves for riprap design. The implication of this conclusion is demonstrated by reference to a possible Wash water storage Scheme(4) where riprap slope protection for bunded reservoirs in an intertidal zone was estimated to cost £38 m (1975 prices), about 65% of the total reservoir cost. Allowance for scale effects to reduce the size of riprap would have reduced the costs by about 30%.

With this in mind, field tests were proposed as the best method of establishing whether or not scale effects are indeed significant. An opportunity to carry out such tests arose during the construction of an offshore trial embankment in the Wash estuary, which formed part of the study of the feasibility of the water Storage Scheme.

2. OBJECTIVES AND SCOPE

The principal objective of the field trials was to compare observed behaviour at full scale with results predicted from small scale laboratory tests: hence to establish whether scale effects are significant and the scope, if any, for reducing costs of slope protection.

The field tests also provided a valuable opportunity to study practical aspects of handling and placing riprap, of checking the grading of both riprap and filter layers and of surveying the extent of the damage.

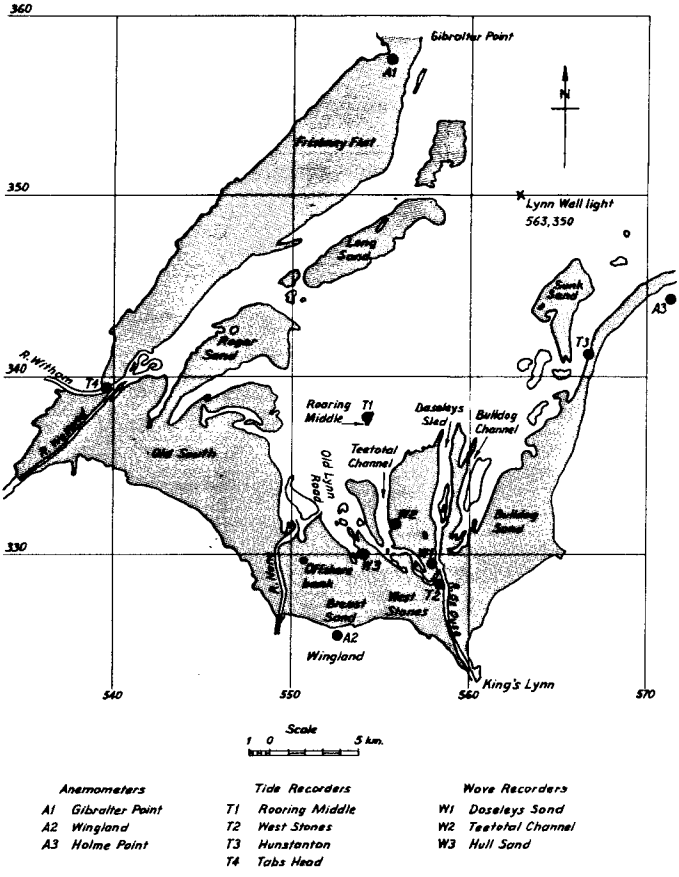

FIG. 1. LOCATION OF EXPERIMENTAL SITE AND DATA AQUISITION STATIONS.

The field study has since been rounded off by retrospective model tests, in which the test panels and wave and tide conditions that actually caused the main damage were reproduced at laboratory scale.

This paper concentrates on the field trials, but quotes the conclusions of the retrospective model tests. Details of these studies have recently been published[5],[6] and a further report[7] by CIRIA reviews both the laboratory and field tests.

3. DESCRIPTION OF THE FIELD TRIALS

3.1 Design of the Test Panels

The site in the Wash estuary is shown in Figure 1. The main trial embankment was circular in plan (Figure 2) and was constructed from hydraulically placed sand fill to a height of about 15 m above the sea bed. The large tidal range of the site (about 8 m at spring tides) was such that the foreshore was dry for about half the tidal cycle but some part of the lower half of the slopes was exposed to wave action for the other half of the cycle. The outside face of the main embankment was protected by heavy riprap (designated HRR) which was designed to withstand severe wave attack whether or not scale effects existed.

Four special riprap test panels were constructed, each 6 m wide and approximately 26.5 m long, on top of the main surface protection. Design of these panels was difficult because, for positive results, measurable damage (and perhaps failure) was desirable within a reasonable time scale. In view of the uncertainties over scale effects and in forecasting wave action, a range of sizes was selected so that the smallest riprap would almost certainly fail within a year or two with lesser damage (or none) expected to occur on the largest size. A fifth test section was selected from the adjacent permanent slope protection (HRR) which was also monitored.

3.2 Riprap grading

The specification called for riprap with the grading characteristics shown in Table 1, each size having a median diameter within a stated band, no stones exceeding a particular size, shape being such that the longest dimension was not more than three times the shortest dimension, and the small end of the grading defined by a minimum figure for the lower percentile (D_{15}).

TABLE 1 DIMENSIONS OF RIPRAP AND FILTER LAYERS

	Panel 1	Panel 2	Panel 3	Panel 4	Panel 5 (HRR)
RIPRAP					
Specified D_{100}	300–375	450–525	600–675	825–900	-
Specified D_{15}	155–190	225–270	310–355	425–460	-
Specified D_{50}	200–250	300–350	400–450	550–600	650–850
Measured D_{50}(mm)	230	400	500	560	660
Layer thickness, t (mm)	440	480	570	760	1320*
t/D_{50}	1.92	1.21	1.14	1.35	2.0*
FILTER LAYER					
D_{50}(mm)	40	40	40	40	40
Layer thickness (mm)	380	380	390	430	300*+

*design values
+also 200-mm layer of fine filter underneath.

It will be appreciated that checking the grading of riprap is not easy. Sieving is out of the question, yet, in most laboratory researches at small scale materials have been defined by sieve size. Samples in the field have to be treated as individual stones, most of which are so heavy that mechanical handling is needed. This not only poses problems on site, it also means that it is impracticable to expect a quarry to select and deliver riprap complying with a close specification.

After delivery of the material to the offshore bank site, a representative sample (about 15%) of the three smaller sizes was taken. Samples were also taken from Panels 4 and the HRR, although these samples were a smaller percentage of the total volume of stone delivered in these sizes. Every effort was made to ensure that the samples were representative of the bulk of material, but the procedure was necessarily subjective.

The material in each sample was graded by weighing on a spring balance while for every fifth stone in each sample three orthogonal dimensions were measured. The methods of weighing and measuring are described in reference 4.

The mass grading curves obtained were converted to dimensional grading curves (figure 3) using the relationship suggested in Reference 3:

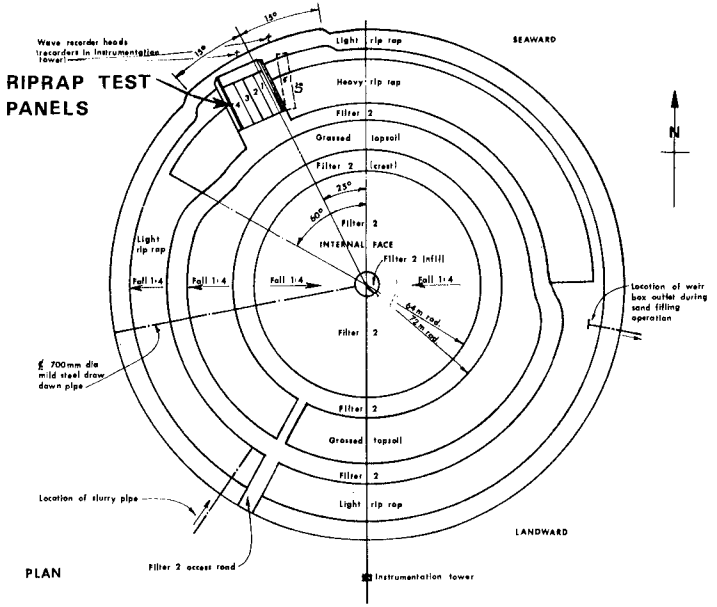

FIG. 2. LOCATION OF TEST PANELS ON OFFSHORE BANK.

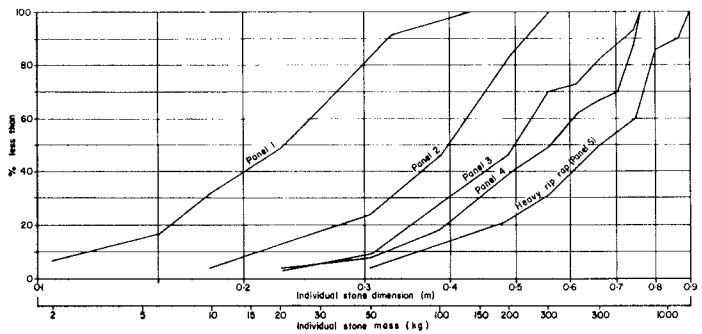

FIG. 3. GRADING CURVES FOR RIP RAP.

$$M = 0.65 \varrho D_S^3$$

which is based on conversion of sieve gradings, where D_S is sieve size, to individual stone mass, M. This relationship was implicit in the original specification of the riprap grading. The conversion showed that the materials for Panels 2 and 3 were outside the tolerance specified, being somewhat oversize.

3.3 Construction

The first stage of constructing the four test panels was to blind the selected area of main riprap protection with a layer of filter material to ensure that no settlement of the test panels would occur through the filling of voids beneath them. A fabric sandwich, consisting of two layers of a non-woven sand-tight fabric separated by a sheet of PVC, was placed on the blinded surface to make the test panel foundation impervious, in an attempt to match the previous laboratory arrangement. A layer of filter was placed over the fabric on which the stone forming the test panels was laid, with the panel containing the smallest stone (Panel 1) at the eastern edge of the test area, each panel being flanked on its western edge by the panel containing the next larger size of stone. The location and arrangement of the panels on the embankment is shown in Figure 2, and a longitudinal section through one of the panels is shown in Figure 4.

Proposals for strengthening the edges of the panels, so that if one panel failed completely the adjacent panel would not be weakened were considered. However, any method of edge strengthening would then form an upstanding edge, which could cause undesirable wave reflections interfering with the performance of the riprap or could itself be washed away. Bearing in mind the cost and uncertain performance of any such arrangement, no special edge treatment was incorporated.

The area of the main bank protection selected as Panel 5 lay immediately to the east of the special test section. No special provisions were made in placing this riprap or in placing the two filter layers separating the permanent riprap from the sandfill of the embankment.

The stone was imported by sea from quarries in Belgium. It was then brought from offshore stockpiles by barge and placed direct in position by floating crane using a 4 tonne cactus grab.

Segregation is a problem with riprap and is made worse by multiple handling, as necessarily occurred with the construction techniques employed offshore in the Wash. It also increases with widely graded stone. Despite efforts on site to control the work so as to minimise segregation generally, and particularly in the test panels, it was not practicable to correct segregation other than marginally once it occurred.

For the test panels, control of the placing operation was strict and the quality of the finished slope protection is probably better than would normally be found using this method of placing. Nevertheless,

visual inspection revealed that the riprap surface was rough and fairly open, with occasional holes through which the surface of the filter layer could be seen, this being particularly noticeable on Panel 4. The mean thicknesses of the riprap are listed in Table 1 which also shows that in all panels except Panel 1 the relative layer thickness ratio, t/D_{50}, was less than 2.0, the value recommended on the basis of laboratory research.

Three factors tended to reduce the relative layer thickness below the intended value:

1. Penetration of the riprap into the filter layer material.
2. Loss of material in transport and handling, which could not be made good at the time.
3. Because the stone tended to be oversized, the given coverage in terms of mass per unit area yielded a lower ratio of t/D_{50}.

The derivation of mean layer thickness is not always defined in earlier work but the problems of controlling this parameter are considered in Reference 5. Discrepancies must be expected in difficult field conditions.

3.4 Data Collection

There were two principle components of data collection: wave climate and damage to riprap. Measurement and analysis of wave action was a major task and only an outline of the methods adopted can be presented here (details are given in reference 5).

Waves were measured by two pressure transducer wave recorders mounted near the seabed in front of the trial panels, and data on wave heights and periods were obtained at approximately hourly intervals through the high tide period under control from a lunar clock. Water levels were measured continuously in order to identify the level at which wave attack was concentrated. The direction of wave attack was deduced from wind data obtained from an anemometer set up on the coast, about 1.5 km away.

Damage to the riprap panels was measured at regular intervals so that it could be related to the wave action. The method of surveying damage was based on the procedure used previously in the laboratory, and involved measuring profiles along the riprap surface in relation to a fixed framework.

Five survey lines for each panel were fixed by stretching piano wire tagged at the required intervals, from a frame at the toe of the panels to a pulley fixed to a second frame at the top of the panels. The level at each plan position was obtained by measuring down from the tags on the piano wire, using a vertical scale fitted with a spirit level and having a hemispherical foot. The diameter of the hemisphere was equal to half the average of the specified median stone size limits of the panel being surveyed, and thus a different foot was required for each panel.

In addition to the levelling survey, each panel was photographed from a fixed point whenever a survey visit was made.

A total of 17 surveys were carried out over the 2½ years period of study.

3.5 Damage Analysis

The survey data were analysed by computer to give a quantitative description of the damage sustained by each panel and a surface profile plot of each line surveyed.

The definition of damage was that used in the HRS laboratory studies reported by CIRIA(3) : the volume removed, expressed as an equivalent number of D_{50} - size spherical stones for a $9D_{50}$ width of panel, considering only downward movements of the surveyed profiles (reductions in thickness). In the laboratory tests, these movements occurred in a fairly well-defined area about the still-water level. Positive movements (accretion of displaced stone) generally occurring in the region below the eroded area were ignored, since these are not of interest when considering the ability of the riprap layer to withstand damage (Figure 5).

The volumes of material eroded from each panel since the beginning of the study, and also since the previous survey, were obtained by differencing the relevant profiles. The eroded volumes were then converted to the mass of stone removed and then to the equivalent number of D_{50} size spheres over a 9 D_{50} width.

Some statistical analysis of the individual survey measurements was made to give measures of the mean movement of the surface in each section, the roughness of the surface, and changes in individual measurements between surveys.

4. RESULTS

4.1 Wave events and General Damage History

It was unfortunate that large waves (H_S just over 1 m) occurred with high water levels very early in the project, during the gale lasting from 16 to 18 November 1975, within days of laying the test riprap. The main effect was the total failure of Panel 1 (Figure 6). The riprap and the underlying filter were completely washed away from the central section of the panel, part being deposited in the lower section of the panel and part being completely lost. The upper limit of damage, about 6 m from the top of the panel, was marked by a near vertical face exposing the riprap and filter layers. The failure of Panel 1 had been expected to occur during the course of the first winter, but the occurrence of a severe storm so early meant that no results on progressive damage were available for this panel.

Erosion damage on Panel 2 was also serious on this occasion, being assessed at 112 D_{50} stones. Damage was concentrated on the side

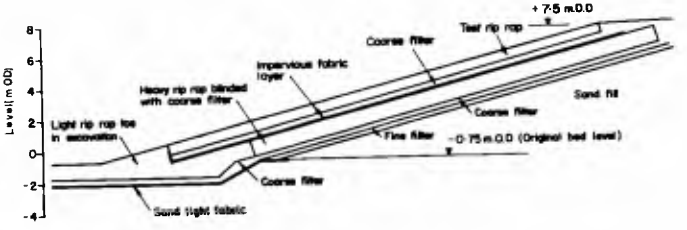

FIG. 4. SECTION THROUGH TEST PANEL.

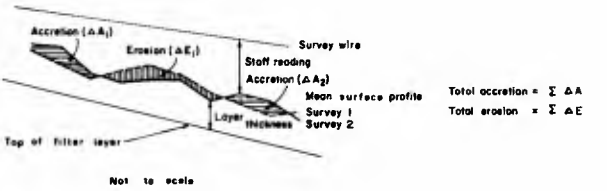

FIG. 5. ILLUSTRATION OF DAMAGE ANALYSIS.

FIG. 6. FAILURE OF PANEL 1, NOVEMBER 1975.

closest to Panel 1, and a considerable part was undoubtedly because of the loss of edge support resulting from the total loss of riprap and underlying filter from the central part of Panel 1. Table 2 lists the survey dates and the damage status.

During December 1975 three wave events were recorded, one of which included waves with H_S nearly 0.9 m. The two most severe events occurred with winds orthogonal to the panels, but tide levels were in general low at the time and so there was little additional damage to the panels. The next severe gale occurred on 3 January 1976, when winds of up to 40 m/s (90 mile/h) were recorded. Waves on this occasion were not very large, partly because the wind did not reach its peak until some time after high water and partly because it was blowing from the west with a very restricted fetch. Tide levels were high, however, and waves at high water were large enough to cause further erosion at the top of Panel 1, as filter material was washed out from the foot of the vertical cliff marking the upper limit of earlier damage. Over the next week, this caused the area of Panel 2 affected by loss of edge support to extend up the slope.

Three events with waves of about 0.75 m occurred between mid-January and mid-February 1976. Only the first event was with winds directly in line with the test panels, the second and third events being with winds from the east and northeast respectively. However, damage to Panel 3 and 4 as well as further damage to Panel 2 was noted.

The period to April 1977 covering the next winter, was relatively calm: the maximum significant wave height recorded was 0.83 m, but on this occasion the wind was further from the northeast (70° from orthogonal). Only minor drainage was observed, comparable to the probable maximum error in measuring damage, so was not significant.

Data collection in the Spring of 1977 was marred by the loss of wave records from 19 March to 8 May, a period when northerly and north-easterly winds were dominant. However, hindcasting of wave events demonstrated that particularly severe wave attacks (H_S = 1.4 m) occurred immediately after surveys on 5/6 April. Waves were directly orthogonal to the bank and, being the severest to date, some damage was to be expected to most of the panels, although no further survey was carried out until August 1977.

Immediately following the August survey there was further severe wave action (4 days with H_S up to 1 m at high tide). Winds were primarily from the north east, though they backed to north north west and resulted in the total failure of Panel 2 (see table 2, survey on 12.10.77) and further damage to Panels 3, 4 and 5.

One further event, with waves nearly 1.0 m high, was recorded in December 1977, but the wind was from the west and no damage was observed.

Waves recorded in the event of 11/12 January 1978, the third winter of observation, when winds were from the north, were far in

Table 2. Comparison of surveyed and calculated damage (No. of D_{50} stones.)

Panel No.	Survey Date	Since previous survey		Since initial survey	
		Surveyed damage	Calculated damage	Surveyed damage	Calculated damage (See note 1)
1	19.11.75	839	313	839	313
E=39 (See	14.5.76	329	241	1075	554
note 2)	12.10.77	108	F(See note 3)	1170	F
2	19.11.75	83	32	83	32
	3.12.75	10	5	73	37
(E=26)	18.12.75	17	12	74	49
	15.1.76	47	6	95	55
	17.2.76	29	8	103	63
	2.3.76	16	0	108	63
	18.3.76	38	0	93	63
	31.3.76	40	0	117	63
	13.5.76	5	9	92	72
	16.8.77	48	(71)	139	(143)
	12.10.77	121	37	231	(180)
	9.3.78		F		F
3	3.12.75	3	0	3	0
(E=21)	18.12.75	3	2	1	2
	15.1.76	9	0	2	2
	29.1.76	12	0	5	2
	17.2.76	24	0	18	2
	2.3.76	3	0	9	2
	18.3.76	2	0	7	2
	29.4.76	12	0	8	2
	14.5.76	3	0	4	2
	6.12.76	12	0	10	2
	5.4.77	4	3	5	5
	15.8.77	16	(23)	7	(28)
	11.10.77	16	11	18	(39)
	9.3.78	231	137	236	(176)
4	2.12.75	10	0	10	0
(E=17)	16.1.76	5	0	9	0
	17.2.76	18	0	33	0
	13.5.76	2	0	24	0
	6.12.76	19	0	32	0
	5.4.77	12	0	9	0
	15.8.77	18	(14)	20	(14)
	11.10.77	19	5	35	(19)
	9.3.78	162	63	188	(82)
5(HRR)	16.1.76	16	0	16	0
(E=12)	2.3.76	6	0	19	0
	13.5.76	6	0	14	0
	7.12.76	13	0	25	0
	6.4.77	4	0	20	0
	15.8.77	11	(4)	28	(4)
	11.10.77	8	1	27	(5)
	9.3.78	12	31	27	(36)

Notes:

1. Sum of calculated damage between surveys.
2. E is probable maximum error in calculated damage.
3. F indicates damage beyond range measured in the laboratory

Bracketed values derived from data which includes hindcast wave conditions.

excess of the previous maximum (H_S = 2 m) and resulted in the total failure of Panels 3 and 4 (Figure 7) (see Table 2, survey of 9.3.78). Panel 5, the permanent riprap, suffered very little damage. This was a very rare combination of wave attack and high tide: the tide level exceeded the calamitous 1953 storm surge in fact.

4.2 Damage calculated from Laboratory results

Results of the laboratory study[3] were used with the recorded wave data to hindcast the damage sustained by the test panels. The method used is a variation of that set out as Method 2 in CIRIA report 61(3), making the appropriate allowance for the different water densities in the laboratory and fieldwork. The data contained in that Report were used to prepare Figure 8, in which damage is related to number of waves incident on the panel and the ratio H_S/D_{50}. The total damage expected was obtained by summing the damage arising from waves of each height, i.e. as if they were attacking an undamaged surface.

The laboratory work showed that a damage level of about 115 stones removed corresponds to the level of failure at which the filter layer could be touched with the survey probe. However, the differences between field and laboratory conditions (Section 3.1) reduce the significance of this value. The lower ratio of thickness to stone size used on the test panels suggests that failure might occur with fewer stones being removed. On the other hand, varying water levels would cause damage over a larger area than in the laboratory tests, suggesting that a greater level of damage could be tolerated before local failure is reached.

4.3 Comparison between measured and hindcast damage

Table 2 summarises the comparison between damage to the test panels as measured by field surveys and that hindcast on the basis of laboratory tests. The general impression is that measured damage is rather greater than that calculated except in the case of panel 5, where measured and calculated damage are comparable (but small in absolute terms and only of the order of possible survey error).

In interpretting the results of this comparison, it should be remembered that the conditions of the field study inevitably differed from those in the previous generalised, somewhat idealised, laboratory research in the following respects:

1. The presence of tides causing the water level to vary continuously from below to about three quarters of the way up the test panels.

2. The variability of the wave events.

3. The sequential action of waves at different elevations and with differing heights.

4. The range of directions from which the waves approached the test panels.

FIG. 7. FAILURE OF PANELS 3 AND 4, JANUARY 1978.

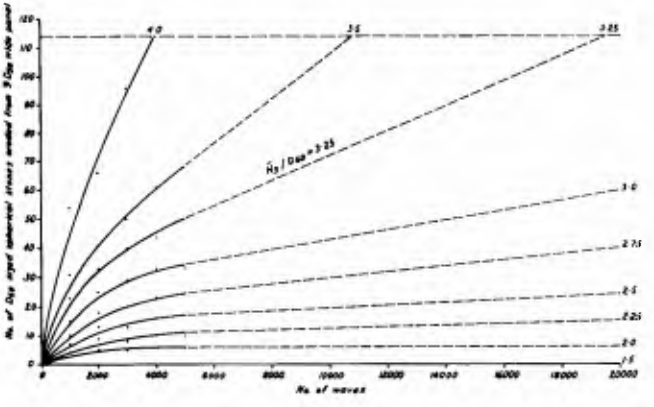

FIG. 8. DAMAGE FROM WAVE ATTACK, BASED ON HRS RESULTS (REF. 3)

5. The very large number of waves involved.

6. A different ratio of filter-size to riprap size.

7. The thickness of the panels ($2D_{50}$ in the laboratory work: but considerably less than that in Panels 2, 3 and 4 in the field trials).

8. Different methods of placing the riprap, involving some degree of segregation and differing bulk density of the finished layer.

9. Problems of measuring stone size and differences in the grading and shape of the riprap.

10. The very different sizes of the stone in the laboratory and site situation and the consequential scale effects.

Some or all of these differences between field and laboratory conditions undoubtedly account for discrepancy between observed and calculated damage, based on scaling up the laboratory work, and could perhaps obscure scale effects if they existed. Nevertheless, the clear conclusion is that using laboratory research results for riprap design, omitting any allowance for scale effects, does not result in an over-conservative design.

4.4 Retrospective Model Tests

The overall impression was that agreement between earlier laboratory tests and field trials was fair and that there was no evidence of major scale effects. Nevertheless, further evidence was sought from specific model tests in which the conditions actually observed during the field trials were reproduced as far as possible. These retrospective model tests were undertaken by HRS in 1981 and results have now been published(6). These small scale (1:17) laboratory tests satisfactorily reproduced the damage behaviour observed in the field tests, thus adding weight to the conclusion on the absence of significant scale effects.

5. CONCLUSIONS AND RECOMMENDATIONS

5.1 Evidence for Scale Effects

In general, the amount of damage sustained by the test panels was slightly greater than that calculated from laboratory research results. The exception was Panel 5 which, in the most severe event, suffered slightly less damage than predicted, though the difference is within the survey and other tolerances. The discrepancies between observed and hindcast damage can be explained by inevitable differences between laboratory and field conditions. Retrospective model tests in which the field conditions were more realistically represented than in previous basic research showed good agreement between model and full scale results.

This study has thus not confirmed the CERC findings(1) concerning scale effects, namely that small scale model results tend to overestimate the size of riprap needed to provide protection against waves of a particular height.

5.2 Practical Aspects of Riprap Design and Construction

The field trials, which were undertaken under close supervision, demonstrated the problems of laying riprap to meet specified gradings, mean size and layer thickness.

Procedures developed for monitoring and analysing progressive damage to riprap involved considerable effort but were successful and are recommended for any future full scale study.

Whilst the general guidelines for riprap design given in CIRIA report 61 have been validated by results of field tests, gaps remain in our knowledge of the behaviour of riprap. These include the effect of varying water level, the effect of oblique attack, the influence of non-uniformity arising from segregation of graded stone, the importance of layer thickness and grading of both filter layer and of the riprap itself, and the modes of progressive failure resulting from locally damaged areas.

5.3 Recommendation for Design

Results of small scale hydraulic model tests on riprap should be adopted without making allowance for "scale effects" which might justify smaller sizes. If model tests are not conducted specifically for the slope protection in question, then the design procedures given in CIRIA report 61 are recommended.

Designers should be aware of the practical difficulties in meeting specifications for riprap. If the consequences of damage to riprap are not acceptable than a cautious approach to design should be adopted.

6. ACKNOWLEDGEMENT

The field trials described in this paper were funded through the Construction Industry Research and Information Association, London (CIRIA). Their permission to publish the results obtained is gratefully acknowledged. The collaboration of R.M. Shuttler of the Hydraulics Research Station and many other authorities and individuals has been much appreciated.

REFERENCES

1. THOMSEN, A.L., WOHLT, P.E., and HARRISON, A.S. Riprap stability on earth embankments tested in large and small scale wave tanks. US Army Corps of Engineers, Coastal Engineering Research Centre, Technical Memorandum 37, June 1972.

2. BURGESS, J.S. and HICKS, P.H. Riprap protection for slopes under wave attack CERA (now CIRIA) Report 4, 1966.

3. THOMPSON, D.M. and SHUTTLER, R.M. Design of riprap slope protection against wind-wave attack CIRIA Report 61, 1976.

4. BINNIE & PARTNERS. The Wash water storage scheme. Private communication, February 1976.

5. YOUNG, R.M., PITT, J.D., ACKERS, P. and THOMPSON, D.M. Riprap design for windwave attack: long term observations on the offshore bank in the Wash. CIRIA Technical Note 101, July, 1980.

6. HYDRAULICS RESEARCH STATION. Riprap design for wind wave attack. Retrpsoective model tests of the measured damage to riprap panels on the offshore bank in the Wash. HRS Report IT213, December 1981 (Price £10).

7. PITT, J.D. and ACKERS, P. Review of field and laboratory tests on riprap CIRIA Report 94, 1982.

8. AHRENS, J.P. Large wave tank tests of riprap stability U.S. Army Corps of Engineers, Coastal Engineering Research Centre, Tech. Memo 51, May 1975.

OFFSHORE ARTIFICIAL STRUCTURES AND THEIR INFLUENCE ON THE ISRAEL AND SINAI MEDITERRANEAN BEACHES

by
Yaacov Nir
Geological Survey of Israel,
Marine Geology and Geomathematics Division,
30, Malkhei Israel St., Jerusalem 95501, ISRAEL.

INTRODUCTION

The Israel Mediterranean shore forms a gentle curve from an almost easterly direction in north Sinai to an almost northerly direction in Israel. This shore forms the southeastern corner of the Levantine Basin which itself forms the extreme eastern part of the Mediterranean Sea. The length of the Israel shoreline from Rosh Haniqra near the Lebanese border to northern Sinai in the south is about 230 km, while the Sinai coast from Rafah to Port Said (Fig. 1), is almost 200 km long. The coastline region consists largely of Quaternary carbonate cemented quartz sandstone, known by local name "kurkar". Recent faulting is responsible for the shape and, to a certain extent, for the morphology of large parts of the central coastline, which is characterized by kurkar cliffs (Neev et al., 1973 & 1978). Wide sandy beaches are found in the southern parts, while an abraded rocky platforms occur mainly in the central and northern parts, where the beaches are narrow having kurkar cliffs at their backshore side.

Four different morphological sections can be found in the Israel Mediterranean shore, (Nir, 1982). These differ in their beach and inland morphology on one hand, and in their sedimentological properties on the other. The four different sections from north to south are:

1) Rosh Haniqra to Akko. A sedimentologically isolated region, bounded on both the south and north. Beach sediments are mostly of local calcareous material of marine origin. Akko promontory is the most northern limit of Nile derived sands and plays as the recent edge of the Nile sedimentary cell (Nir, 1980). 2) Haifa Bay. Wide sandy beaches, bounded on the north by the Akko promontory, and by the Carmel "nose" on the south. 3) Mount Carmel coastal plain, is sedimentologically somewhat isolated region with relatively narrow beaches and small kurkar cliffs. Sediments consist of both local and imported components. 4) The kurkar cliffs and sandy beaches from Caesarea to Rafah. Beaches of differing width having quite uniform petrographic components, mostly quartz grains originating from the Nile river and transported along the Sinai beaches to the Israeli beaches. Some of the present beach components are derivated from the abraded kurkar cliff.

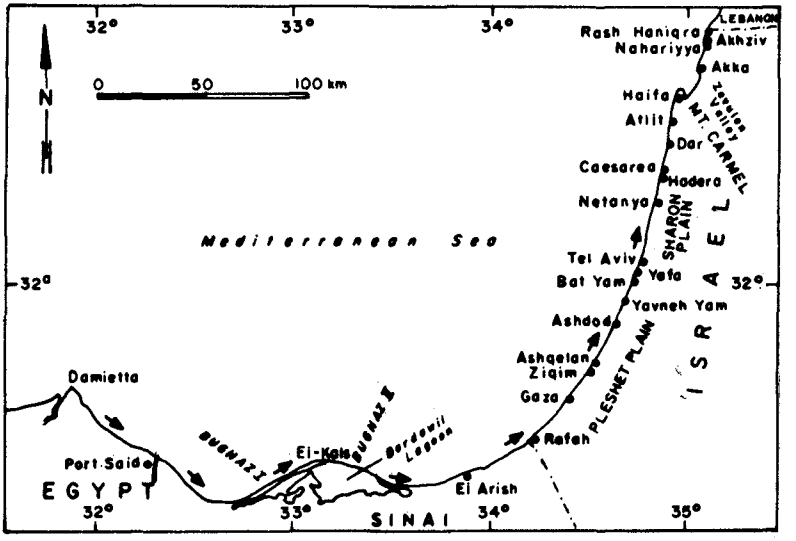

Fig. 1. Northern Sinai and Israel Mediterranean beaches, location map.

THE BEACHES

The Israel Mediterranean beaches are mostly sandy, with a few exceptions where local kurkar or limestone pebbles are found. The sands are light in colour, white to light yellow, and are mostly composed of quartz grains. The beaches between Rosh Haniqra and Akko and some parts of the Carmel Coastal Plain are exceptional in that the sands are of local origin and mostly composed of skeletal material, mostly algae and molluskal debris. Kurkar cliffs constitute a very distinct morphological feature along the shores. Most of the cliffs are 20–40 m high and are very strongly abraded by the sea at the foot of the cliff, and by rainwater along its slopes (Fig. 2).

The following scheme shows the qualitative budget of sand along the North Sinai and Israel Mediterranean beaches, showing both onshore and offshore sand sources and sinks: 1) Offshore Losses – by sand mining and dredging in harbours, accumulation of sand in and around harbours and artificial objects. 2) Seaside contribution – Nile sands transported along the beaches, destruction of beaches in the Nile delta and northern Sinai, and organic production mostly of pelecypod shells. 3) Onshore losses – sand mining (up to 1964), use of beach and artificial tombolo areas, wind blown sand and dune formation. 4) Landside contribution – erosion and abrasion of the kurkar cliffs, river alluvium, and sand dunes.

Quartz sand dunes cover relatively large areas of the nearshore regions of the Coastal Plain of Israel. The majority of the dunes are located in the southern part, connected with the north Sinai enormous sand dune sea. The origin of their quartz grains, which make up the primary component of the beach, has been investigated mineralogically (Shukri and Philip, 1960; Pomerancblum, 1966; and Nir, 1973 & 1982). Certain conclusions can be drawn: 1) Nile-derived sediments are transported along the beaches of the Nile Delta, Sinai and Israel by waves and wave generated longshore currents and the counterclockwise East Mediterranean current. 2) A relatively minor amount of sandy sediments are also introduced by local rivers (wadis), which are active only during winter floods.

Fig. 2b. Kurkar cliff near Hadera. Most of the cliff is composed of soft friable red loam ("Hamra") and sand. Landslides are typical on these cliffs, causing talus of huge blocks at their base.

Fig. 2a. Steep kurkar cliff south of Netanya. The beaches are narrow, but show maximum development in this photo.

In the cliff regions, beaches are very narrow, reaching a width of only 10-20 m and much less during winter time (Fig. 2a). The sandy beaches are relatively wide in regions where kurkar cliffs are absent, in some parts reaching widths of 60-80 meters.

Large quantities of beach-sand were quarried until 1964, at an estimated annual rate some 10 to 20 times larger than the naturally occuring annual sand replenishment. This quarrying produced a sand deficit along many beaches, causing an accelerated erosion of the beaches and nearby cliffs.

SEDIMENT TRANSPORT ALONG THE BEACHES

Artificial constructions such as groins, breakwaters, barges, etc. found along the Sinai and Israeli shores trap some of the longshore sand drift, causing damage downstream and sometimes enabling us to ascertain the qualitative and even quantitative net sand drift at a certain point.

These shores on a whole belong to the large sedimentary cell which starts at the two Nile Delta outlets at Rosetta and Damietta, and extends along the Sinai shores as far north as Akko in Israel (Nir, 1980). Zenkovich (1971) shows a very clear easterly directed sediment transport along most of the Nile Delta beaches.

Two channels ("Bughaz") were dug in the outer Bardawil bar in order to maintain its water connection with the open sea. Groins were constructed to keep the channels from silting up. As a result, sand accumulated on the western side of these groins and Inman and Harris (1970) estimated the yearly net easterly sand transport at the western outlet (Boughaz 1) to be on the order of 300-800,000 m3/year.

The El Kals temporary harbour and sand mining close and west of El Arish caused severe erosion to nearby dunes and summer houses respectivelly (Fig. 3).

Wadi El Arish drains practically all of northern and central Sinai. The beach near the outlet of this ephermal wadi is straight and usually conforms with the regular shoreline. In a very short period of time, at the end of February 1975, a voluminous flood transported several hundred million cubic meters of water and sediment to the sea. These clastic sediments formed a large new delta more than 400 m offshore with a large submarine extention. This new delta partially dammed the sand drift, resulting in a sediment accumulation on the delta's western flank, on the one hand and a very effective abrasion on the down-drift shores east of the outlet on the other (Fig. 4). The sediments of this delta were transported eastwards quite quickly and the delta changed shape, reaching an almost straight and regular shoreline (Fig. 5).

All the obstacles east of El Arish up to Rafah show a clear net easterly drift, while those northwards almost up to Tel Aviv show a northern drift. These obstacles are: a barge east of El Arish (Fig. 6), two groins and the wreck between them in Gaza Harbour (Fig. 7), a harbour with two groins on its southern and northern sides at Ziqim (Fig. 8), and the huge Ashdod Harbour, whose main breakwater reaches 18 m water depth. This last structure impedes sand transport and accumulates sand in large

quantities in the offshore at relatively great depths (Dornhelm, 1972; Kran, 1980; and Finkelstein, 1981).

Fig. 3. Summer houses at El Arish, N. Sinai. The collapse was a result of the sand deficit caused by quarrying of beach sand ("Zifzif") nearby.

Fig. 4. Roots of palm groves were exposed to wave action east of El Arish as a result of the provisional damming of the regular eastward sand transport by the delta of Wadi El Arish in Feb. 1975.

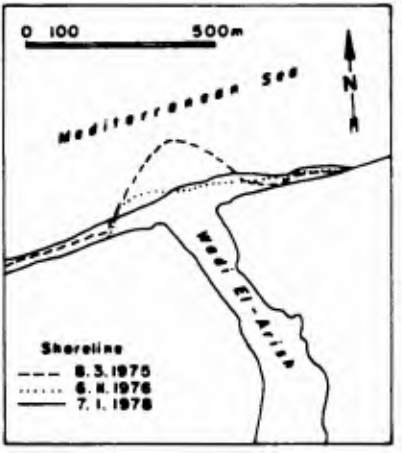

Fig. 6. A barge at N. Sinai beach east of El Arish accumulates sand on its western side, thus clearly illustrating the easterly sand transport.

Fig. 5. Schematic map of Wadi El-Arish Delta , drawn from aerial photographs, showing its different development and disapearing stages.

Dornhelm (1972), and Kran (1980) who reanalysed Dornhelm's charts show that the Ashdod Harbour's main breakwater interrupted about 80% of the annual northward transport of sand. Finkelstein (1981) also shows a

tremendous offshore sand accumulation during 13 years which reaches perhaps 4 million cubic meters at the main breakwater and westwards. Northwards he shows accumulation close to the lee breakwater and a large area of erosion farther north. By and large this agrees with the main trend of northerly drift. He also estimated the net annual northerly transport at Ashdod to be on the order of 560,000 m3, which is a very high value.

Fig. 7a. Aerial photo showing Gaza Harbour, which is made of two groins, about 120 m long and about 500 m apart.

Fig. 7b. The southern groin of Gaza Harbour, showing accumulation of a large volume of sand south of the groin, causing heavy damage to the beach structures further north.

Fig. 8. A map of Ziqim Harbour, drawn from an aerial photograph. Note the extreme widening of the beaches to the north. These are now almost totally exposed of their sand cover yearround. Prior to harbour construction beaches to the north had normal sand quantities and normal widths even during severe winter storms.

The old site of Yavneh Yam show northerly drift in the form of a large retreat of the seashore which has caused damage to the old site (Fig. 9).

Northwards from Tel Aviv the net transport decreases significantly, and at the Carmel Head transport is to the east and to the south, and the region between here and Atlit is to a certain extent isolated.

Fig. 9. The beach north of Tel Yavneh-Yam ("Minnet Rubin"), suffers from heavy abrasion due to the sand deficit and the protruding promontory of the Tel. Beaches here have withdrawn about 50 m during the last 50 years. In Early British Mandatory topographic maps almost no promontory was shown here.

Emery and Neev (1960), assumed a northerly sand transport for the southern Israel beaches and a southerly one for the central and northern beaches. A northerly directed offshore current and sediment transport of mostly fine grained sediments was also suggested. This transport is responsible for most of the present influx of fine sand to Haifa Bay.

On the basis of theoretical studies Migniot (1974), Sauzy et al., (1974) and Manoujian and Migniot (1975) show that the annual resultant sediment transport is always directed to the north and reaches about 400,000 m3 at Gaza, 215,000 m3 at Ashdod, 100-150,000 m3 at Hadera and only 80,000 m3 at Atlit.

Goldsmith and Golik (1978) summarized the Israel Mediterranean wave climate and constructed a longshore sediment transport model for these beaches. In general they support the conclusions of the earlier studies regarding sediment transport.

OFFSHORE STRUCTURES OF THE ISRAEL MEDITERRANEAN SHORELINE

Prior to 1960 with the exception of a few ancient harbour sites such as Akko, Haifa, Caesarea and Yafo (Jaffa), the Israel Mediterranean shore did not have any large offshore structures (Kravitsky, 1966).

The main stage of offshore construction for recreational purposes took place in the late sixties and the early seventies when 25 structures (15 breakwaters and 10 groins) were built along the beaches from Gaza in the south to Akhziv in the north (Fig. 1). The environmental impact of these structures were studied in the field, by succesive aerial photos, and by bathymetric and topographic maps of the sites and their vicinity. They were also studied with regard to their engineering characteristics (Fried, 1975 & 1976; Tauman, 1975 & 1976). Vajda (1975) investigated their sedimentological development in the laboratory in order to limit as much as possible their erosional effect. Nir (1976) gives a

detailed description of the different offshore structures with their sedimentological characteristics and their relationships to the nearby beaches. Spar (1976), and Sofer and Sass (1982) studied in detail the sedimentology of the Netanya twin breakwaters.

Most of the structures have developed a tombolo at their "shaded" landward side. These tombolos typically have a trapezoidal shape (Figs. 10 & 11). They reach a mature stage (at which significant size changes cease) about 5 years after the end of construction (Fig. 12). The sand accumulated in these tombolos comes mostly from the nearby beaches and shallow sea. In most cases these beaches have therefore suffered severe erosion during the first 3-4 years after the construction, while in some cases this erosion even continues beyond maturity.

Many of the detached breakwaters and groins were built in very populated areas in order to increase the amount of beachfront and to calm the relatively rough seas occuring during the bathing season in July and August. These problems were partially solved by the tombolo which was formed in the shaded area of the breakwater and by the attendent of areas of quiet water.

These breakwaters were mostly constructed about 200 m offshore of the original shoreline, mostly on a submarine exposed rocky strip in about 3-4 m water depth. This rocky strip (Fig. 13) was chosen for the practical economic purpose of reducing foundation costs. As their length almost equals their distance offshore, huge tombolos started to grow out from shore which later joined with the breakwater. Figure 12 and the following table show the aerial development with time of these tombolos, following their completion. Most of these tombolos reached almost one half of their final size within a period of one or two years. There is a sharp decrease in the rate of expasion of the sand area in the second year after the end of the construction.

Site	Time (years) for tombolo volume to go from 0-50%	50-100%	Total years
Carmel Beach	3.23	2.60	5.83
Netanya (south)	1.06	3.52	4.58
Netanya (north)	1.56	2.10	3.66
Tel Aviv 1	1.50	4.07	5.57
Tel Aviv 2	3.15	2.66	5.81

Table 1. Time needed (yrs)for tombolo volume to develop from 0-50% and from 50-100%. The averages show that the tombolo reaches its half volume in about two years and that it takes another 3 years to reach the mature stage.

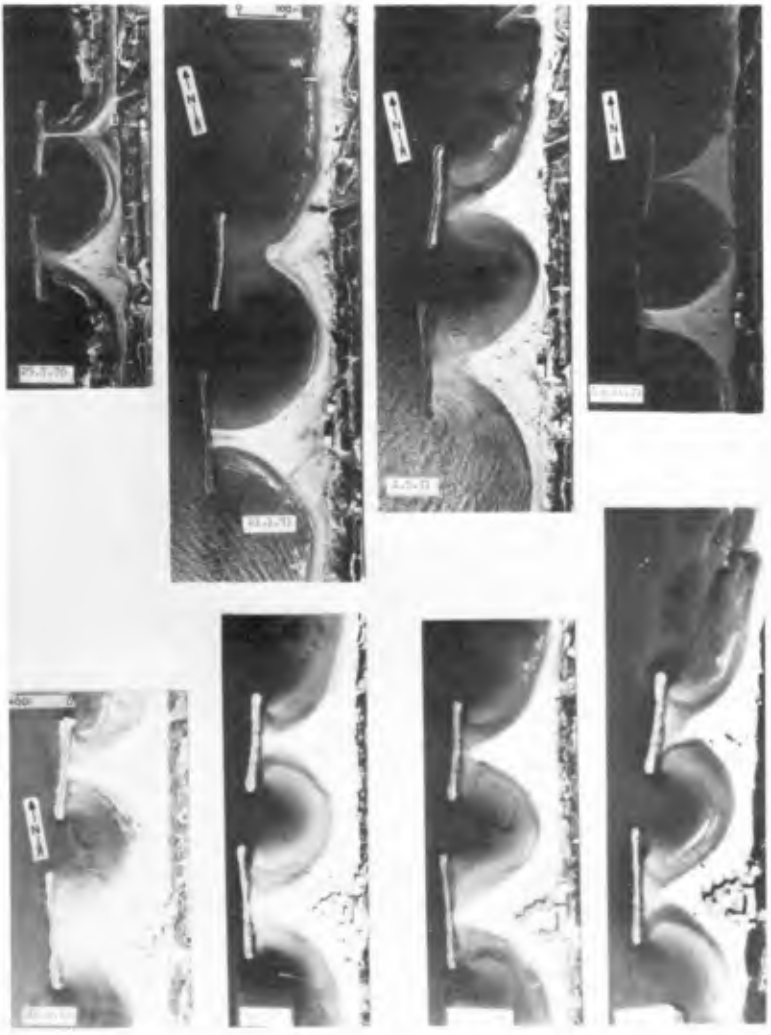

Fig. 10. The twelve year history of the twin tombolos off the Netanya beaches. The tombolos reached their first maximal stage at the end of 1973, and since then they show seasonal fluctuations. Winter storms usually open a channel between the tombolo and the breakwater.

This slowing in sand accumulation is primarily because the nearby beaches, which are the main suppliers of sand to the tombolos, have already suffered an enormous sand deficit due to sand capture by the newly built structure, and also because of the increase in water depth around the tombolo. In sites where two structures were built, the tombolo of the most recently built structure reached its 50% sand volume in a much longer time than the first structure. In Netanya, this time difference is about 50% while in Tel Aviv it required more than twice as long to reach the 50% sand volume stage, this probably due to the general deficit of sand in the Tel Aviv beaches. The Netanya case on the other hand, at the second stage of its development, shows faster accumulation at the northern structure which is the younger, with probably preferred southerly directed longshore transport.

Most tombolos reached their mature size between the 5th and the 6th year after construction. Thereafter the only changes are seasonal with maximum tombolo size at the end of summer, or more precisely just before the first storm at the end of autumn. Some decrease in size occurs during winter and early spring (Fig. 10). This fits very well with the regular winter to summer variations in beach width. In his study of the shallow Ma'agan Mikhael beach Eitam (1975) also found that the accretion period extends over the autumn.

Aerial photographs of the different sites where one or more detached breakwaters were constructed, taken before, during, and after construction, show the different stages of tombolo growth on the one hand and the fast erosion of the nearby beaches on the other (Fig. 15). At the Carmel Beach site the nearby beaches were almost totally stripped of their sands. A large beach area, just next to and south of the tombolo, disappeared 12 years ago and has not been rebuilt (Fig. 14). The Carmel Beach structure was chosen to represent a single breakwater tombolo while the Netanya structures typify twin tombolos. Fig. 10 illustrates the different stages of tombolo growth as they attain their mature stage in 4–5 years time.

In Netanya tombolos began to grow during the construction activities, and about 70,000 m3 of sand were attracted from the nearby beaches and shallow sea in 3–4 years time. Prior to construction, Netanya's beaches were already in very bad shape and waves were reaching the base of the steep kurkar cliffs. This was among other morphological and stratigraphic reasons due to the enormous quantities of sand being quarried all along Israel's Mediterranean beaches up to 1964; for example, Emery (1963) estimated that about 1/3 of the beach sand reserves had by that time already been quarried. Following formation of these tombolos, abrasion in the

nearby kurkar cliffs was accelerated, so that measures had to be taken to protect the cliff. Recently Ron (1982) has proved enormous cliff retreat in the region of Netanya during the last 35 years.

Table 2 summarizes the sand quantities that accumulated in the aerial parts of the seven first built tombolos at the different sites. These account for about 270,000 m3 of sand. It is assumed that about the same quantity or more of sand was deposited underwater in the vicinity of the tombolos. Therefore, altogether these offshore structures (with the exception of the huge quantity deposited near Ashdod Harbour), captured about 600,000 m3 of sand in a period of 4–5 years. This volume is much larger than the actual sand available from the annual import from the Sinai beaches. The volume of sand at each separate site was calculated using the following formula (derived by John K. Hall):

volume of sand $V = dc(2a+b)/3$; where:

2a – is the length (in m) of the tombolo's offshore edge (taken parallel to the shoreline).

b – is 1/2 of the length of the base of tombolo (in m).

c – is the distance between the base and the seaward edge of the tombolo(in m).

d – water depth (m) at the seaside edge of tombolo.

Site	Quantity of accumulated sand (in m3)
Nahariyya	20,000*
Shavey Zion	5,000–18,000
Carmel Beach	55,000
Netanya (north)	34,000
Netanya (south)	38,000
Tel Baruch	15,000
Tel Aviv 1	45,000
Tel Aviv 2	20,000
Bat Yam	26,000
Total	258,000–271,000 m3

Table 2. Sand quantities which were accumulated at the different offshore structures along the Mediterranean coasts of Israel (including only the subaerial sand bodies within the tombolos).
* Some sand was quarried from the tombolo.

Figures 10, 12 and 14 show the developments that occurred around the twin detached breakwaters in Netanya. The different shorelines were drawn from aerial photos of the site, taken at various time intervals. Comparison between the areas of the successive tombolos and the quantities of accumulated sand shows that one of the main

Fig. 11. The different stages of tombolo development for the Carmel beach structure, from the very early stages of construction(11a), to the formation of an enormous tombolo (11d) some 5 years later.

factors affecting the sand quantity is the ratio between the length of the breakwater and its distance from the original shoreline. The smaller the ratio – the smaller the tombolo that develops.

Empirical study shows that there is a direct relationship between a structure's distance from shore and its length (or its projection onto the shoreline): the larger this ratio the smaller the sand volume accumulated in the tombolo. Accretion is very little, or does not occur at all, if this ratio has a value of 2 or more (Fig. 16) This value is somewhat smaller than that of Inman and Frautschy (1966), who studied the Californian beaches showing that non-depositional conditions prevail only when this ratio reaches a value of 3: "pronounced accretion does not occur if the structure is situated offshore a distance equal to or greater than 3 to 6 times the length of the detached breakwater". Although there are no structures in Israel with these high ratios, it is apparent that no accretion occurs here if the ratio is smaller.

The area of the mature tombolo ranges between 40 and 75% of the rectangular area between the breakwater and the original shoreline. Beach area for that particular section of shoreline has been increased, but on the other hand the protected bathing area has been commensurately decreased; among other reasons are dead algae accumulations at the protected areas. The regions of turbulent water around the edges of the breakwater are dangerous for bathers and present another major problem resulting from the construction.

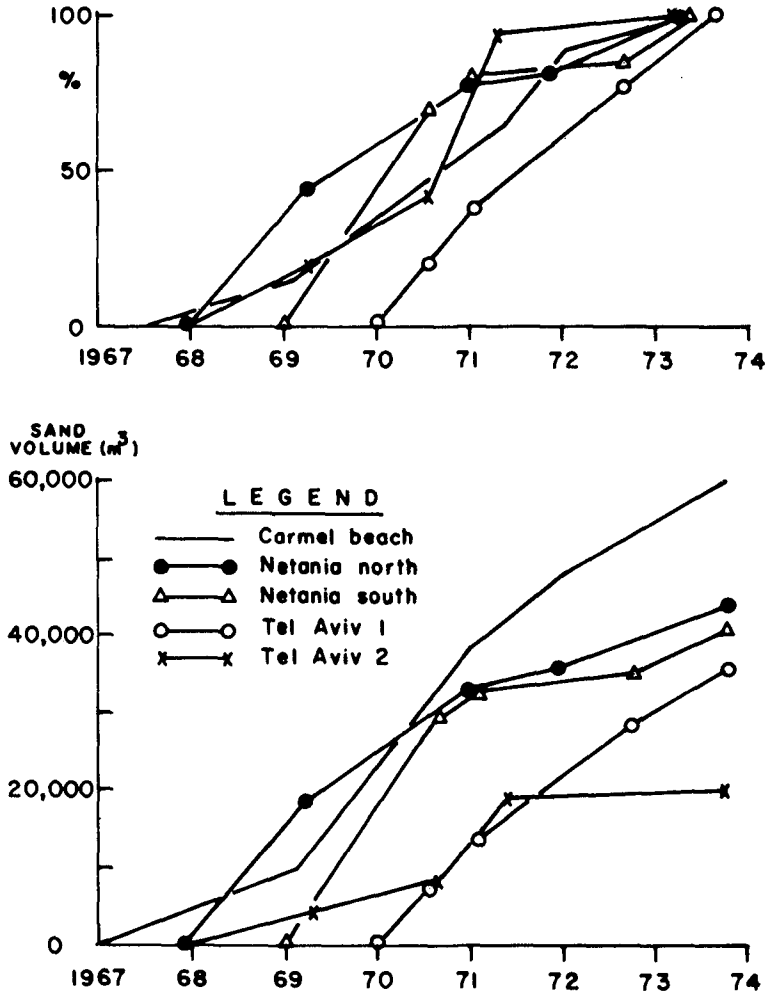

Fig. 12. Tombolo development at the different sites: Carmel beach, Netanya and Tel Aviv. The upper graph shows the cumulative percentage of the tombolo's area while the lower one shows cumulativesand volume both show the relatively quick sand accumulation at the early life stages of the structures.

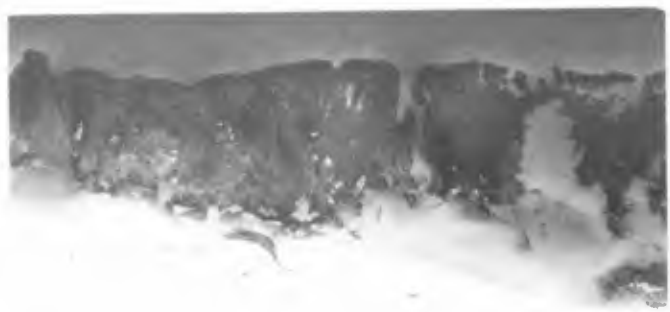

Fig. 13. Central Israel – underwater relicts of kurkar strata showing the clear outlines of two submerged ridges and a wadi (dry creek) between them.

Fig. 15. Severe beach erosion near offshore structures. Fig. 15a. Heavy destruction on the beaches south of Tel Baruch structure (16/6/80). Fig. 15b. Shore buildings north of the Gaza Harbour groins have suffered heavy damage. Small nearshore structures parallel to the beach were erected here to prevent further collapses. Fig. 15c. Exposed beach basement at Bat Yam, after a severe storm (19/4/71). Damage was greater here because marine construction on a half closed pool in shallow water caused buildup of water during storms. Fig. 15d. Small bay north of King Herod's ancient harbour in Caesarea. While in operation this now submerged harbour caused heavy damage to the Roman aquaduct and therefore measures should have been taken to protect the aquaduct whose broken remnants appear in the foreground.

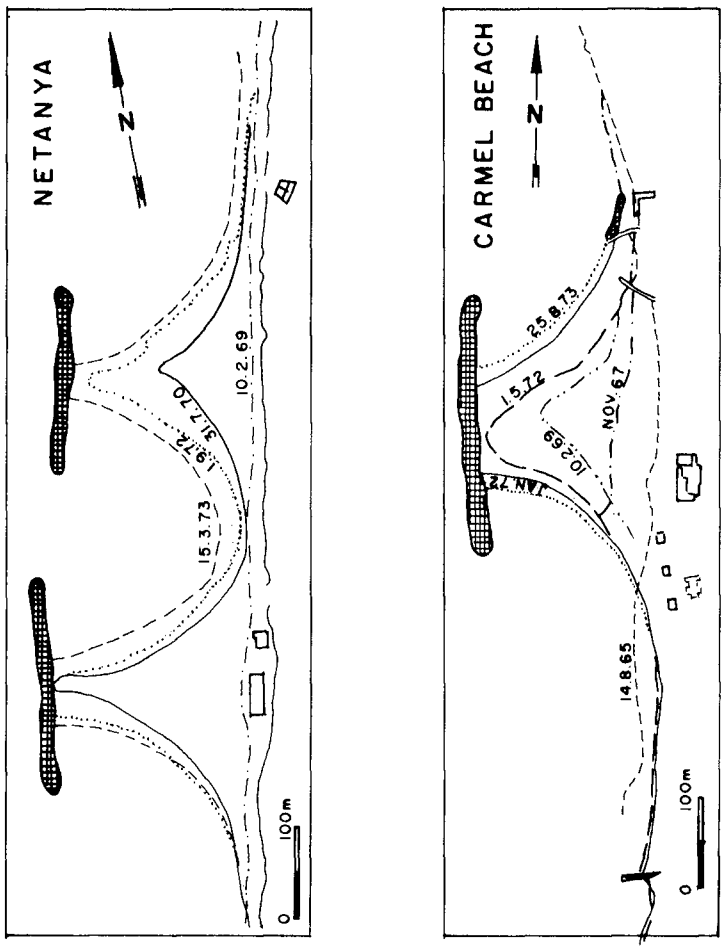

Fig. 14a. A map of Netanya's twin breakwaters and tombolos, showing the "step by step" growth of the twin tombolos and the formation in the internal of a new small bay between them. In the first few years the cliff at the backshore by the space between the tombolos suffered serious abrasion.

Fig. 14b. Map of Carmel Beach tombolo development from its early stages to mautrity. Note the original shoreline of August 1965, south of the tombolo, which shows the missing beach which has not since recovered.

Site	Distance from shore (m)	Length of breakwater (m)	Distance / Length
Nahariyya	70	180	0.38
Carmel Beach	200	280	0.71
Netanya (north)	200	207	0.97
Netanya (south)	216	240	0.90
Tel Baruch	100	200	0.50
Tel Aviv 1	200	310	0.64
Tel Aviv 2	200	240	0.83

Table 3. Dimensions, distance to length ratio, and the average sand layer thickness for the different sites.

The data given in Table 3 above was used to determine the relationship between the distance to the length ratio and the average tombolo sand layer thickness. The graph in Fig. 16 shows that the sand layer equals zero (i.e. that there is no sand accumulation at all) when the distance to length ratio is somewhat larger than 2.

The equation for the least squares straight line through the data in Fig. 16 is:

$$Y = 1.786 - 0.809\,x$$

where: Y is the average sand layer thickness of the tombolo (in m), and
X is the distance to length ratio.

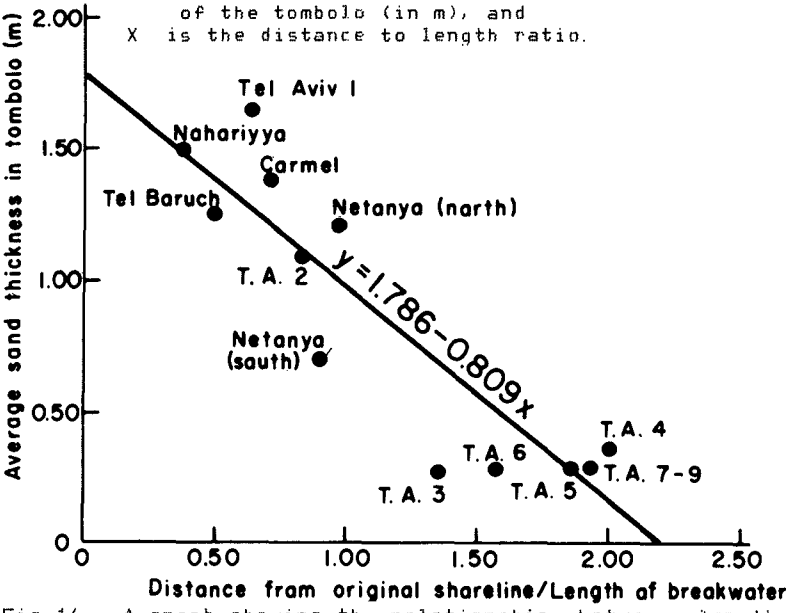

Fig. 16. A graph showing the relationship between length of the breakwater, its distance from the original shoreline and sand accumulation in the different tombolos.

This empirical formula is supported by the latest measurements of the size and quantity of sand accumulated in the tombolos developed in the more recently built breakwaters (Nos. 3-9) in Tel Aviv. These new breakwaters' dimenstions and distance offshore came from laboratory model studies by Vajda (1975). The ratio of distance from shore to breakwater length was enlarged to 1.85 and more, with the result that tombolo sizes were much smaller than the ones developed on the original structures (Fig. 17). Extrapolating the sand quantities accumulated in the modeled structures, excellent agreement was found with the above formula. It should be noted that the model studies hypothesized an unlimited sand supply to the sites, which perhaps is not the case at present in the Tel Aviv beaches.

Fig. 17. Offshore structures at the Tel Aviv beaches. The northern (right) are long and relatively close to the shoreline, so that huge tombolos developed. The chain of 7 breakwaters south of the marina (left) have shorter lengths than the northern ones, and are found at somewhat larger distances offshore so that the sand accumulation in their "shadows" is much smaller.

SUMMARY AND CONCLUSIONS

A very large number of detached breakwaters, groins, harbours and other marine structures were constructed along the Israeli Mediterranean shore during the late sixties and up to the mid-seventies.

Sand accumulated rapidly in the "shaded" areas and up-current, causing heavy damage to the nearby and downcurrent beaches. This erosional sand deficit was in addition to the large deficit caused by the heavy mining of sand for construction purposes up to 1964.

As most of the detached breakwaters were constructed relatively close to the shoreline, large tombolos have developed. It was found here that accretion is very small or negligible when the distance of the breakwater from the original shoreline is more than twice the breakwater length.

The southern beaches provide an excellent demonstration of downcurrent erosion; beaches north of structures were heavily damaged, with their sand cover almost totally removed and the backshore cliff starting to collapse (Fig. 8).

As there was almost no distinctive sand accumulation south of the main breakwater of Ashdod harbour, it appeared as if this gigantic structure did not interfere with the longshore sand transport. Recently Finkelstein (1981) showed that huge amounts of sand are being accumulated next to and off the deep parts of the main breakwater. This accumulation is equal to the transport of many years which is removed from the cycle, and the beaches north of Ashdod thereby suffer from increased erosion.

Due to the heavy damage and other environmental problems that these structures create, measures should be taken to minimize downcurrent erosion as much as possible, mainly by a continuing artificial replenishment to the affected beaches. On the other hand, if beach conditions are bad then offshore structures should be either improved or not permitted.

ACKNOWLEDGEMENTS

The author is very grateful to Dr. John K. Hall, Head of the Marine Geology and Geomathematics Division, for his thorough work in editing and reviewing the manuscript, and to Prof. D. L. Inman and Mr. I. Perath for reviewing the manuscript and last but not least to Mrs. Dina Ashkenazi of the Division for her careful typing of the text, and to the GSI Graphics Unit for preparing the artwork.

With just one exception, the aerial photographs were obtained by the Survey of Israel, Ministry of Labour, and are reproduced with their kind permission.

This work was carried out under Project No. 20677 with the Israel Ministry of Energy and Infrastructure.

REFERENCES

Dornhelm, R. B., 1972. Determination of the longshore sand transport rate in the vicinity of Ashdod Port. GSI Marine Geology Div. Rep., 45p. unpub.

Eitam, Y., 1974. Morphological and grain size seasonal changes in the Ma'agan Mikhael coast and shallow sea. M. Sc. thesis, Hebrew Univ. Jerusalem, 89 p. (in Hebrew).

Emery, K. O., 1963. Some remarks on the sediments of the Israel Mediterranean Beaches. "Zifzif Co." Rep. Appendix 2, 2 p.; Min. of Dev. Report (in Hebrew).

Emery, K. O. & D. Neev, 1960. Mediterranean beaches of Israel. Bull. GSI No. 26, 24 p.
Finkelstein, A., 1981. Sedimentological developments around Ashdod Harbour 2nd Symposium on Beach Problems, Tel Aviv, May 25, 1981, Unpub. Manus. 6p.
Fried, I., 1975. Foreshore and beach development of Tel Aviv and Natanya. Symposium on "Foreshore and beach development from the Coastal Engineering aspect". Assoc. of Eng. & Archit. in Israel, 9 p (in Hebrew).
Fried, I., 1976. Coastal protection by means of off- shore breakwaters, Proc. of the 15th Coastal Engineering Conference, Honolulu, Hawaii, 10 p.
Goldsmith, V. and A. Golik, 1978. The Israeli Wave Climate and Longshore sediment transport model. Israel Ocean. and Lim. Res. Rep. 78/1, 56 p.
Inman, D. L. and J. D. Frautschy, 1966. Littoral processes and the development of shorelines. Chap. 22 in Coastal Engineering. Am. Soc. Civ. Engrs., pp. 511-536.
Inman, D. L. and R. W. Harris, 1970. Preliminary report on the inlets of the Bardawil Lagoon. Report submitted to the Nat. Coun. for Res. and Development, Haifa, 13 p.
Kravitsky, A., 1966. Inventory of offshore structures in Israel shoreline. Min. of Transport, Haifa, 8 p. mim.
Kran, N., 1980. Analysis of bathymetric data and sedimentation near Ashdod Harbour (1964-1971). Marine Geol. Div., GSI, Rep. No. MG/6/80, 9 p.
Manoujian, S. and C. Migniot, 1975. Sedimentological study in three dimensional Model. Lab. Cent. Hydrol. France, Report, 57 p.
Migniot, C., 1974. Creation of a New Power Station north of Hadera cooling water basin, Natural Phenomena Study and Sediment Movement Study with radioactive and fluoroscent tracers. Int. Atomic Energy Agency, Report. 34 p. with appendix.
Neev, D., Y. Nir and M. Pomerancblum, 1963. Problems regarding sand quarrying along the Mediterranean beaches of Israel. GSI Unpub. Rep., 19 p. (in Hebrew).
Neev, D., N. Bakler, S. Moshkovitz, A. Kaufman, M. Magaritz and R. Gofna, 1973. Recent faulting along the Mediterranean coast of Israel. Nature, v. 245, pp. 254-256.
Neev, D., E. Schahnai, J. K. Hall, N. Bakler and Z. Ben-Avraham, 1978. The young (Post Lower Pliocene) Geological History of the Caesarea Structure. Israel Jour. Earth-Sci., v. 27, pp. 43-64.
Nir, Y., 1973. Geological History of the Recent and Subrecent sediments of the Israel Mediterranean shelf and slope. GSI, Unpub. Rep., 179 p.
Nir, Y., 1976. Detached breakwaters and groins and their influence on the Israel Mediterranean beaches. GSI, Unpub. Rep., 33 p., (in Hebrew).
Nir, Y., 1980. Recent sediments of Haifa Bay. Report Marine Geology Div. GSI, MG/11/80, 8 p.

Nir, Y., 1982. Israel and Sinai Coastal Morphology. in: The Encyclopedia of Beaches and Coastal Environments. M.L. Schwartz Ed., Hutchinson Ross Pub. Co., Stroudsburg, Pennsylvania, pp. 86-98.

Pomerancblum, M., 1966. The distribution of the heavy minerals and their hydraulic equivalents in sediments of the Mediterranean Continental Shelf of Israel. Jour. Sed. Pet., vol. 36, pp. 162-174

Ron, Z. Y. D., 1982. Destruction and withdrawal of Netanya's Sea Cliff. A. Shemueli and M. Braver eds., Netanya Book, Am Oved, pp. 45-67 (in Hebrew).

Sauzay, G., Ch. Gilat, M. Meltzer, G. Courtois, I. Frenkel, A. Levin and S. Blit, 1974. Study of sediment transport on the bed and on the beach at the site of the Hadera Power Plant Israel Atom. Energy Com. Rep., 40 p.

Shukri, N. M. and G. Philip, 1960. The mineralogy of some recent deposits in the El-Arish-Gaza area. Bull. Faculty of Sci., Cairo Univ. vol. 35, pp. 73-85.

Sofer (Spar), S. and E. Sass, 1982. Sedimentological and morphological characteristics of seashore sands at Netanya's twin breakwaters. Netanya Book, A. Shemueli and M. Braver, eds. Am Oved, pp. 69-79 (in Hebrew).

Spar, S. M., 1976. Sedimentological behavior of the beach sand in the vicinity of the Netanya Breakwaters. Unpub. M. Sc. thesis, Hebrew Univ., Jerusalem, pp. 56.

Tauman, J., 1975. Foreshore and Beach development of Bat-Yam (Bathing Beach Development with enclosing structure). Symp. on "Foreshore and Coastal Eng. Aspect". Assoc. Eng. & Archit. in Israel; 8p.

Tauman, J., 1976. Enclosing scheme for bathing beach development. Amer. Soc. Civ. Eng. 15 Coastal Eng. Conf. Honolulu, Hawaii, Chap. 84, pp 1425-1438.

Vajda, M., 1975. Tel Aviv Shore Development Model Study, Hydrodynamics and Hydraulic Eng. Lab., Technion Research and Development Foundation, Haifa.

Zenkovich, V. P., 1971. Dynamic elements of Nile Delta shoreline. in: New studies of shore processes; Akad. Nauk. SSSR, "Nauka", Moscow, pp. 35-49. (In Russian).

COASTAL PROTECTION DEVICES - A REVIEW**

D.N. Foster, M.I.E. Aust., M.A.S.C.E.*

ABSTRACT

Coastal protection devices include, but are not limited to, dune stabilization, seawalls, groynes, detached breakwaters, sand bypassing and beach nourishment. These are the "tools". The "rules" for their use comes from a knowledge of the beach processes which in many instances are site specific. Systems which work satisfactorily at one location may not necessarily work at another. A plan is made for authors to give more information on these processes when describing case histories.

The variability of the physical conditions and the non-linear nature of many of the coastal processes often dictates how coastal protection works will behave; a fact which is not always taken into account by the designer.

For coastal protection devices to be developed to their full potential requires improved instrumentation and data bases and a greater knowledge of the coastal processes than is available at the present time.

1. INTRODUCTION

This paper was prepared as an introduction to the poster session on coastal protection devices at which seven papers were presented. (Reference 1-7). These varied between the use of low cost protection measures such as car tyres, sandbags, oil drums and other devices in the U.S.A. to the use of sand filled Longard tubes as groynes and seawalls in N.W. Canada, massive boulder seawalls in Australia, groynes in Portugal, large scale sand nourishment and bypassing operations in South Africa and detached breakwaters in Japan and Israel. The common denominator in these and other studies is, I believe, in the functional design based on a knowledge of the coastal processes.

It is not uncommon to think of coastal protection in terms of dune stabilization, seawalls, groynes, detached breakwaters, sand bypassing, beach nourishment and so on. Whilst extensions to this array and an improved understanding of accepted techniques is most important, this does not represent today's "State of the Art" in coastal defense. These are simply the "tools" and not the "rules". The "rules" come from a

* Associate Professor of Civil Engineering and Officer-in-Charge Water Research Laboratory, The University of N.S.W., Australia.

**This paper is an overview of the papers discussed in the poster session on Shore Protection Devices. The papers discussed are presented in Chapters 112 - 118.

knowledge of the coastal processes. Today's art lies more with the capability to understand the relative significance of the various natural forces which make defense necessary and the ability of the engineer to use this understanding to determine the optimum defense strategy making the most appropriate use of all the devices available.

2. COASTAL PLANNING

The first coastal protection device that should always be considered is that of coastal planning. Within this context the question can be aptly asked as to why coastal protection is necessary at all? Inevitably the answer will be that man wants to use the land which nature wants to take away for purposes such as:

- Recreation
- Housing
- Industry
- Airports
- Harbours
- Reclamation

This more often than not, means that man is in conflict with nature right from the very beginning. In comparison to other forms of development the coastal region tends to be different in that the highest valued land is commonly in the area of highest risk (Plate 1).

This is in contrast to flood plain land for example which tends to have the opposite trend with property values decreasing with the increased risk of being flooded. However in some respects the two have much in common.

- A certain level of protection can be justified by the reduced damages that it will provide
- Reduction of risk encourages further development
- Further development results in increased damages which justifies a higher level of protection.

This type of development in the past has ended up with the need for massive expenditure of funds to fight a never ending battle against erosion. More careful planning by our forefathers in many instances would have avoided or reduced the problems and the associated cost.

It could be argued both then and even today that many of the mistakes have been made because of our lack of understanding of the coastal processes involved. However examples of poor engineering practice in the management of the coastal zone are still evident in almost all

PLATE 1: - HIGH VALUE DEVELOPMENT IN AREA OF HIGH RISK

PLATE 2: - DAMAGE FROM NATURAL LONG TERM EROSION

countries throughout the world and all too often it is a case of trying to provide coastal protection to a problem which could have been avoided by more careful initial planning. Much of the blame must be laid on the inability of the engineer to convince the public and the legislators of the need for such planning and the long term benefits which would eventuate.

3. THE DIFFERENTIAL LITTORAL DRIFT COASTLINE

One of the most difficult coastal erosion problems is that pertaining to the differential littoral drift coastline resulting from a change to the littoral supply (Reference 1,5) or because of the natural configuration of the coast as exemplified by the Byron Bay embayment in northern N.S.W., Australia (Reference 8). At Byron Bay the littoral input is 15,000 m^3/year whilst the output is 200,000 m^3/year. As a result the whole of the embayment is eroding at rates between 1 to 5 m/year, except where the coastline is held by retaining structures such as groynes, seawalls or training walls. The end result of a small village built in the path of the sea is shown in Plate 2. The long term fight against erosion has been lost with seawalls gradually being outflanked and finally succumbing to the forces of the sea.

The owners of these homes undoubtably agree with the second demand for coastal protection suggested by Per Bruun (Reference 9) "Thou shall protect it against the evils of erosion". However, on further thought is erosion all that evil? Most modern day coastal protection strategies start with a statement of the sediment budget relating sand supply to and sand losses from a coastal region; and are aimed at reducing losses (by the use of groynes, detached breakwaters, dune stabilization, or bypassing plants for example) or by increasing the supply (by beach nourishment and sand bypassing for example). When we look at the sediment budget on an eroding coast one of the major supply terms is the coastal erosion itself which implies that if an eroding section of the coastline is protected by any method other than beach nourishment accelerated downdrift erosion will result. It is for this reason that it is difficult to simultaneously satisfy Per Bruun's second demand for coastal protection as set out above with the seventh "Thou shalt not steal thy neighbour's property, neither shalt thou cause damage to his property by thy own protection".

How do you provide protection to a shoreline such as Byron Bay?

- By beach nourishment provided there is an unlimited quantity of sand available which there isn't
- By seawalls or dykes provided you are happy to convert a sandy recreational beach into an artificial rocky coast which you are not
- By use of structures such as groynes, detached breakwaters, artificial headlands designed to equalise the littoral drift over the entire physiographic unit provided you can afford the cost which you can't.

In practice the cost of any of these options is often prohibitive, except in very densely populated areas or where they are associated with major harbour and port development.

A lower cost solution (particularly for relatively undeveloped sections of the coast) would be to provide protection to some sections of the coastline and accept accelerated erosion at others. This requires the acceptance by government and the public to changes in the configuration of the coastline. Under present legislation and the land rights of private individuals this is not easy to achieve. This cause has not been helped by the tendency for engineers in describing coastal protection case histories to give so little detail of what has or will happen outside of the area of immediate protection.

4. NATURE AS A SCALE MODEL

Nature provides many examples of coastal protection and coastal erosion. It is common to use small scale hydraulic models to assess the effect of large scale engineering works (Reference 7). Sometimes it is forgotten that a model does not have to be smaller than the prototype as the powerful principals of similarity and dimensional analysis are completely reversible. For Froudian scaling the length scale is proportional to period squared and consequently laboratory and nature provides a wide range of examples which can be scaled both up or down. Consequently the model studies of detached breakwaters undertaken by Rosen and Vajda (Reference 7) have much in common with the studies undertaken by Edge (Reference 2) in bays and lakes and those of Toyoshima (Reference 1) for the Pacific Ocean.

Consider the tidal inlet. In Australia such inlets at coastal lagoons, creeks and river systems are often closed off by the longshore transport under wave action, only to later break out during high fresh water or flood flows. From the study of the effect of artificially opening of the entrance of a small tidal lagoon at Dee Why, (Reference 10), Gordon was able to identify and to quantify a rather unusual cause of beach erosion at a much larger scale which can be typified by the conditions at Tathra in southern N.S.W. (Reference 11) as shown schematically in Figure 1.

This beach is a relatively small pocket beach contained between two major headlands. The Bega river, which is known to supply sand to the coast, enters the system at the northern end. As for most Australian rivers, daily flows in the Bega River vary from zero to very high flood flows. During relatively low river flows a plug of sand is moved from the beach resulting in shoaling of the mouth. During major floods this plug of sand is flushed far out to sea to form a shoal of mixed marine and fluvial sand. In the post flood period much of this sand bypasses the Tathra system under the predominant southerly wave climate. During the same period beach sands are moved in to reform the shoals at the entrance. As a result rapid erosion of the beach results after each flood event which slows down as the shoals are re-established.

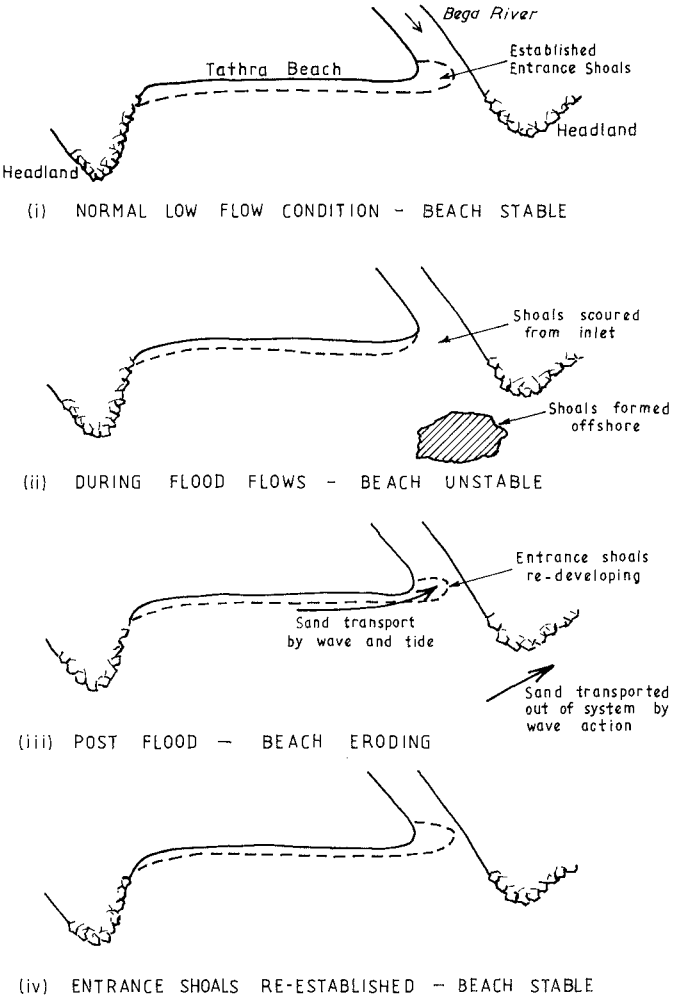

FIGURE 1: EROSION OF TATHRA BEACH AS A RESULT OF FLOOD FLOWS
(SCHEMATIC ONLY)

If it is accepted that nature provides us with many examples of both coastal erosion and protection it is surprising that not more use is made of this model, and to use conditions in bays and lakes to make quantitative predictions of what will occur in the ocean or vice versa. This technique was used by the author with some success to transfer the known behaviour of the sand bypassing system at Channel Island (Reference 12) to a less exposed region in Western Australia (Reference 13).

One of the reasons the technique is not used more often is, I believe, because many papers on case histories do not give sufficient detail of the physical parameters such as wave climate and its variability, local currents, tides, sediment characteristics to enable such scaling to be undertaken with confidence.

5. VARIABILITY OF COASTAL PROCESSES

The variability of the coastal processes often means that coastal protection is site specific. One form of protection which may work effectively at one location may be totally ineffective at another. Per Bruun (Reference 9) noted that when the techniques of the successful Dutch groynes were transferred to Denmark they did not work and large scale downdrift erosion resulted. It was suggested that this was because the Dutch groynes were supplied with sand by tidal currents whilst the Danish groynes were not.

This point can be further illustrated by the behaviour of the coastline adjacent to three natural detached breakwaters formed by offshore islands in Australia as shown schematically in Figures 2-4.

The first example is at Palm Beach near Sydney in N.S.W. (Reference 14). The coastline has a near zero net littoral drift. Because of the wave protection provided by an offshore island a shore connected tombola has developed. The tombola is of sufficient height and width not to be breached by even the largest storm and it forms a natural sand breakwater to a recreational harbour in its lee. Aside from normal changes in the beach profile resulting from rough and calm weather conditions the beach system is relatively stable.

The second example is on the Warilla-Perkins beach system to the south of Sydney (Reference 15). The total beach system is bounded by two major headlands which inhibit any significant movement of sediments into or out of the embayment. An offshore island within the embayment separates Warilla beach from Perkins beach. During calm weather sand is moved from both beaches into the lee of offshore island to form a tombola which eventually becomes connected to the island to form a groyne which inhibits further sand movement. During storms, which are dominantly from the south, the tombola is breached and the sand (some of which originated from Warilla) is transported northwards onto Perkins. The process then repeats itself. Consequently Warilla beach is suffering continuous erosion whilst Perkins is continuously accreting. The offshore island, which is acting as a detached breakwater, is obviously the cause of the erosion of Warilla beach.

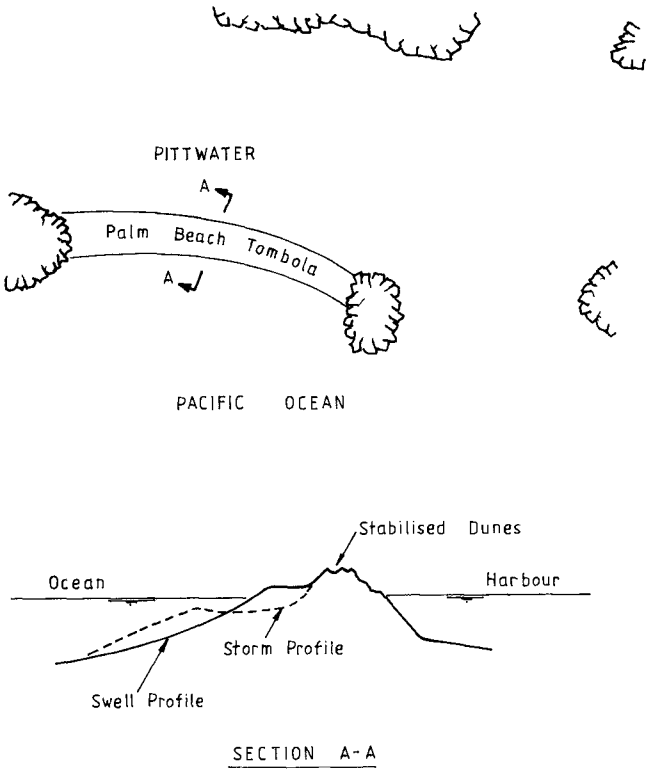

FIGURE 2: PALM BEACH N.S.W
(SCHEMATIC ONLY)

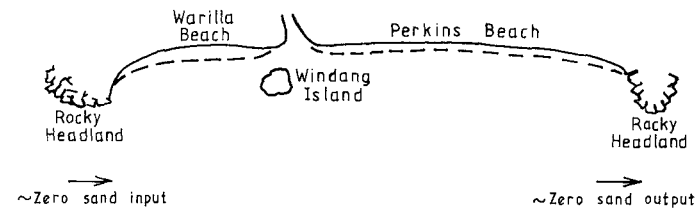

(i) INITIAL CONDITIONS IMMEDIATELY FOLLOWING A STORM

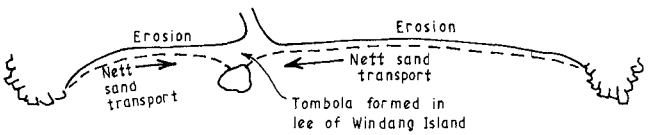

(ii) CONDITIONS UNDER CALM WEATHER FOLLOWING A MAJOR STORM

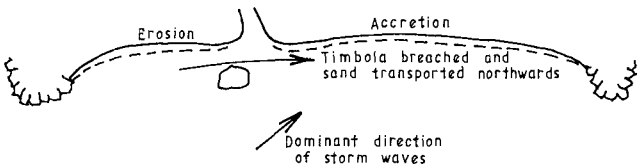

(iii) CONDITIONS DURING A MAJOR STORM

FIGURE 3: WARILLA/PERKINS BEACH SYSTEM
(SCHEMATIC ONLY)

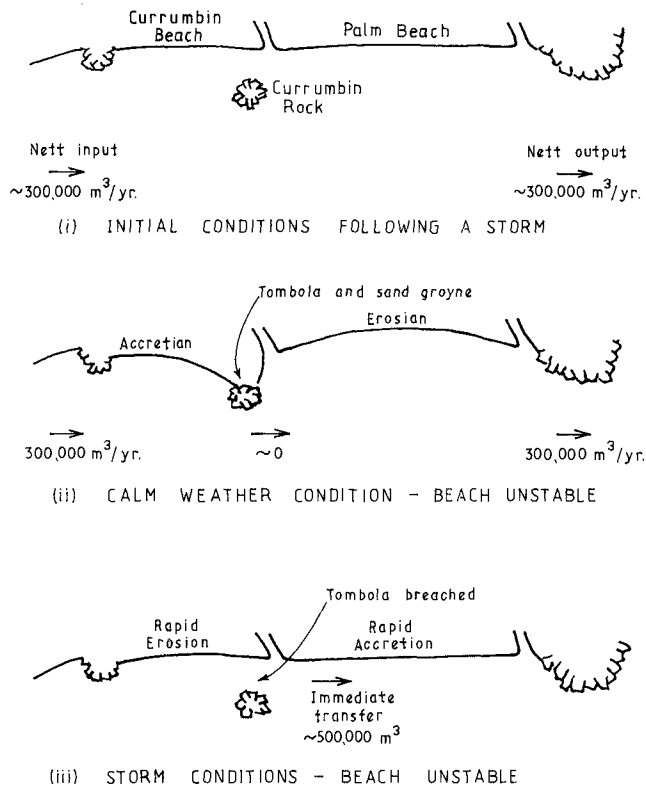

FIGURE 4: CURRUMBIN/PALM BEACH SYSTEM QUEENSLAND. (SCHEMATIC ONLY)

The third example is at Currumbin on the Queensland Gold Coast (Reference 17,18). The situation is similar to the previous example in that an offshore island which acts as a detached breakwater separates the beaches of Currumbin and Palm Beach (Queensland) and basically behaves in a similar way. During calm weather a tombola is formed in the lee of the breakwater eventually becoming connected to the island after which it acts as a groyne. During storms, which are again predominantly from the south, the tombola is breached and sand is transferred northwards. The basic difference between the Warilla/Perkins and Currumbin systems is that for the latter there is a net littoral drift of some 300,000 m^3/year (Reference 19). Surveys (Reference 17-18), have shown that during calmer weather practically the whole of the littoral drift over a period of years may be stored on the beaches to the south only to be transferred to the north within days during a storm. As a result the beaches to the north tend to erode during calm weather and build up during and following a storm, a paradox to that normally expected.

A further consequence of this action is that the sand is supplied to the coast in slugs. Tracer measurements by Chapman and Smith (Reference 20) indicate that these slugs maintain their identity over a substantial period of time and over long distances. Consequently at any given time some sections of the coastline tend to be under-nourished whilst others are over-nourished.

Plate 3 shows the end result of two houses at Wamberal on the N.S.W. central coast which were unlucky enough to be sited opposite a rip current on an under-nourished section of the coastline when a moderate storm occurred. Some weeks later the system had moved some 200 m to the north as indicated by the undermining of a flexible gabion mattress placed as toe protection in front of a Seabee seawall (Plate 4). The importance of toe protection, the desirability of flexibility of toe armour and the need to allow for the variability of the physical processes in seawall design (Reference 4) is obvious.

As coastal processes differ from site to site, no all embracing rules can be set down for the design and use of coastal protection devices. It is important that papers describing case histories of coastal protection give sufficient detail of the coastal processes to adequately assess their use in other areas.

6. NON-LINEARITY OF COASTAL PROCESSES

Closely related to the variability of coastal processes is the highly non-linear nature of these processes. The C.E.R.C. equation indicates that longshore transport is proportional to wave height squared. Einstein's equation indicates that bed load transport in rivers is proportional to discharge squared and velocity to the fourth power. In other formulae the power may differ but it is always substantially greater than unity. Consequently the larger events play a major role in the movement of sediment to and along the coast. For example a flood with a flow of 10 times the average can carry 100 times the sediment load of the average flow.

PLATE 3: - DAMAGE RESULTING FROM SHORT TERM CHANGES

PLATE 4: - SCOUR BLANKET PROTECTING SEAWALL AGAINST SHORT TERM VARIATIONS

Currents induced at coastal protection works will obviously have a very significant effect on how these protective works behave.

An exampie of using the non-iinearity of coastai processes to advantage is at Durban (Reference 21) where an artificial offshore sand bar was constructed to protect the beaches. The sand was obtained from dredging of the nearby harbour. Small to moderate waves pass over the bar with little change to the natural surfing and recreationai use of the beach. Under storm conditions the sand bar acts as a submerged breakwater forcing the waves to break and dissipate a proportion of their energy. As sediment transport is approximateiy proportionai to wave height squared there should be a rapid response to the reduced wave height.

The non-linear nature of many of the coastal processes and the variability that this produces is not always taken into sufficient account in the design or the description of coastal protective works.

7. THE FUTURE

More initiative and iaterai thinking is needed in the design of coastal protection works if the engineer is to be more successful than he has been in the past. Dune stabilization, seawalls, groynes, breakwaters and artificial nourishment will continue to be important toois. However this shouid not blind the engineer to other methods which might be equally or more effective.

If erosion is accepted as an aiiy as well as an enemy restructuring the shape of the coastline by providing sacraficial land has much to commend it.

At Port Botany (Reference 22) and Phiiip Point (Reference 23) configuration dredging has been used to change the wave refraction pattern and redistribute the wave climate to that more suitable for port operations. If configuration dredging has been successfuiiy used in these two exampies, it can obviousiy be considered in association with offshore beach nourishment programmes to defiect wave energy onto headlands or rocky sections of the coast whiist reducing wave energy or changing wave direction along the sandy beaches.

As the relationship between sediment transport and velocity is highly non-linear methods aimed at breaking up destructive currents whether they be rip, flood, tidal currents, or currents induced by coastal protection works must potentialiy be a very powerful tool.

Coastai protection devices need to be extended beneath the sea surface. At Coiiaroy in Sydney coastai process studies have indicated that a major cause of the beach erosion is the result of gaps in a natural offshore protective reef, (Reference 24) which if ciosed wouid go a long way towards eliminating the probiem.

Seawaiis do not have to be immobile. A sand breakwater has been constructed at Saiamander Bay South Africa (Reference 25) whilst a

breakwater of run of the quarry rock has been constructed at King Island Australia (Reference 26). Beach nourishment is a seawall of sand and shingle beaches serve the same purpose. There would appear to be a wide range of options within these limits awaiting future development.

It is now possible by the use of chemicals to turn sand into beach rock at relative low cost (Reference 27) which opens up many possibilities for the future.

These are but a few of the options which are or may become available in the future.

8. CONCLUSIONS

I would reiterate my introductory remarks. Coastal protection devices are simply the tools, the rules for the use of these tools came from a knowledge of the local coastal processes pertaining to each specific site. It is only when these processes are known will the engineer be able to develop coastal protection devices to their full potential. Much work and improved instrumentation and data bases are needed to refine the knowledge in this area.

9. ACKNOWLEDGEMENTS

Messrs. M. Geary and A.D. Gordon are co-authors of this paper. Both are engineers with the Coastal Branch of the Department of Public Works, New South Wales, Australia. Many of the examples referred to in the paper are taken directly from coastal process studies with which they have been associated. Their assistance and that of the Department of Public Works is gratefully acknowledged.

10. REFERENCES

[1] O. Toyoshima "Variation of foreshore due to detached breakwaters". Proc. 18th Int. Conf. Coastal Eng. Capetown, South Africa, 1982.

[2] B.L. Edge and J.G. Housley, "Results of shoreline erosion demonstration program". Proc. 18th Int. Conf. Coastal Eng. Capetown, South Africa, 1982.

[3] V.K. Shah, "Performance of sand filled tube shore protection, Tuktoyaktuk, N.W. Territories, Canada". Proc. 18th Int. Conf. Coastal Eng. Capetown, South Africa, 1982.

[4] A.W. Smith and D.M. Chapman, "The behaviour of prototype revetment walls". Proc. 18th Int. Conf. Coastal Eng. Capetown, South Africa, 1982.

[5] I.B.M. Oliveira, A.J.S.F. De Valla and J.C.C. Miranda, "Littoral problems in the Portuguese West Coast". Proc. 18th Int. Conf. Coastal Eng. Capetown, South Africa, 1982.

[6] K.A. Barnett "Durban beaches reclamation practical aspects". Proc. 18th Int. Conf. Coastal Eng. Capetown, South Africa, 1982.

[7] D.S. Rosen and M.L. Vajda, "Sedimentological influences of detached breakwaters". Proc. 18th Int. Conf. Coastal Eng. Capetown, South Africa, 1982.

[8] A.D. Gordon, D.B. Lord and M.W. Nolan, "Byron Bay - Hastings Point Erosion Study", Public Works Dept., N.S.W. Coastal Engineering Branch Report No. PWD 78026, Nov. 1978.

[9] Per Bruun, "The History and Philosophy of Coastal Protection", Proc. 13th Int. Conf. of Coastal Engineering, Vancouver, 1972.

[10] A.D. Gordon, "The Behaviour of Lagoon Inlets", Proc. 5th Aust. Conf. on Coastal & Ocean Engineering, Perth, 1981.

[11] A.D. Gordon, D.B. Lord and M.W. Nolan, "Tathra Erosion Study", Public Works Dept., N.S.W. Coastal Eng. Branch Report No. 79015, Feb. 1980.

[12] W.J. Herron and R.L. Harris, "Littoral Bypassing and Beach Restoration in the Vicinity of Port Hueneme, California". Proc. 10th Int. Conf. of Coastal Eng., Tokyo, 1966.

[13] D.N. Foster, C.A. Miller and B.C. Wallace, "Assessment of Sand Bypassing, Secret Harbour, Western Australia". University of N.S.W., Water Research Laboratory Tech. Report No. 82/07, April, 1982.

[14] J.G. Hoffman, "Palm Beach - Beach Erosion and Management Study". Public Works Dept., N.S.W., Coastal Branch, Report No. PWD 82027, Sept, 1982.

[15] Soros-Longworth and McKenzie, "Lake Illawarra Waterway Planning Study". Report to Dept. of Public Works, N.S.W., June, 1976.

[16] C.T. Brown, T.L. Piggott and D.N. Foster, "Stabilisation of Currumbin Creek". University of N.S.W., Water Research Laboratory, Tech. Report No. 79/01, April, 1979.

[17] D.N. Foster and K.B. Higgs, "Coastal Changes and Entrance Stabilisation at Currumbin Creek". University of N.S.W., Water Research Laboratory, Tech. Report No. 81/6, May, 1981.

[18] Delft Hydraulics Laboratory, "Gold Coast, Queensland, Australia - Coastal Erosion and Related Problems". Report to Government of Queensland, 1970.

[19] D.M. Chapman and A.W. Smith, "A Ten Year Review of Variability on an Ocean Beach". Proc. 5th Aust. on Coastal and Ocean Eng. Perth, 1981.

[20] Zwamborn, J.A., Fromme, G.A.W. and FitzPatrick, J.B., "Underwater Mound for the Protection of Durban Beaches". Proc. 12th Int. Conf. on Coastal Eng., Washington, D.C., 1970.

[21] J.M. Wallace, "Control of Wave Action by Configuration Dredging at the Entrance to Botany Bay, Sydney, Australia". 1977 P.I.A.N.C. Congress, Leningrad.

[22] H.P. Riedel and A.P. Byrne, "Dredging to Minimise Wave Penetration into a Harbour". Proc. 18th Int. Conf. on Coastal Engineering, Capetown, South Africa, 1982.

[23] N.S.W. Department of Public Works Coastal Engineering Branch, "Offshore Mapping of Bed Rock Sydney to Broken Bay", in preparation.

[24] D. Zwemmer and J. Van't Hoff, "Spending Beach Breakwater at Saldanna Bay". Proc. 18th Int. Conf. on Coastal Engineering, Capetown, South Africa, 1982.

[25] K.R. Burren, "Investigation Design and Construction of a Harbour on King Island Tasmania". Proc. The Institution of Engineers Australia.

[26] Pakenaka Aqua Reactive Chemical Soil Stabilisation System - P.A.C.S.S. Japan.

VARIATION OF FORESHORE DUE TO DETACHED BREAKWATERS

by

Osamu TOYOSHIMA

1. INTRODUCTION

As coastal areas are very valuable for mountainious Japan, many countermeasures against beach erosion have been taken. The length of seawalls for beach erosion amounts to 5,600 kilometers, which is much longer than the length of seadikes for flood tide, which is 2,900 kilometers. In addition, 10,000 groins and 2,300 detached breakwaters have already been constructed for beach erosion. Especially, we used many detached breakwaters for the last ten years.

Fig.1 showes the increase of total length of seawalls and seadikes for the last twenty years.

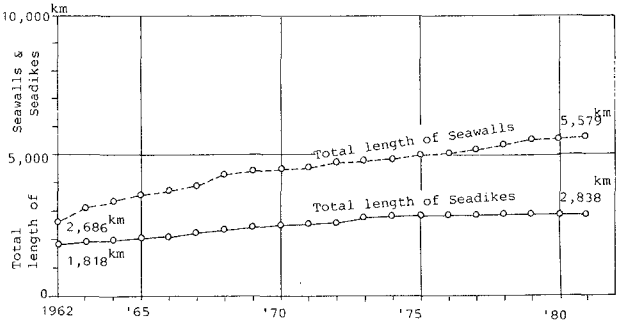

Fig.1 Increase of seawalls and seadikes in Japan.

The rate of the increase of seawalls and seadikes are as follows respectively.

seawalls : 5,579 km / 2,686 km = 2.08

seadikes : 2,838 km / 1,818 km = 1.56

Professor, Faculty of Marine Science and Technology, TOKAI University, 1000, Orido, Shimizu-shi 424 Japan

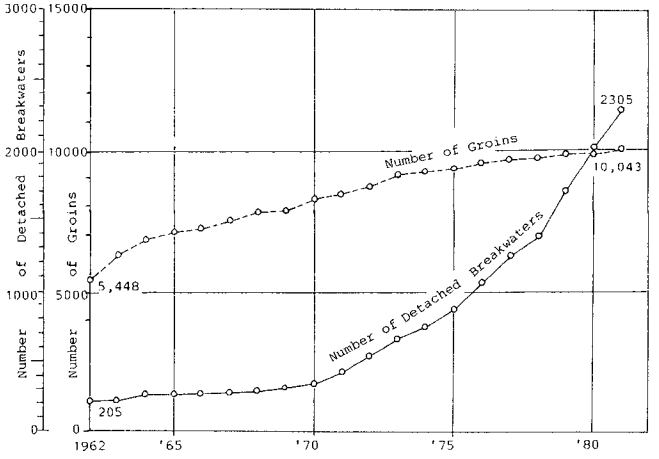

Fig. 2 Increase of groins and detached breakwaters.

Fig.2 showes the increase of number of groins and detached breakwaters for the last twenty years. The rate of the increase of groins and detached breakwaters are as followes respectively.

groins : 10,043 / 5,448 = 1.84

detached breakwaters : 2,305 / 205 =11.24

It was in the year 1966, that the author proposed a new detached breakwater system as a new countermeasure against beach erosion. After the year 1970, number of detached breakwaters showes sharp increase in contrast with that of groins in Fig.2.

Here, I take the Kaike coast as an example of the detached breakwater system, and show the variation of the tombolo and sea bed in the foreshore due to the detached breakwaters.

2.OUTLINE OF THE KAIKE COAST

Kaike coast locates on the root of the Yumiga-hama Peninsula which is believed to be a sand spit formed by sand deposition discharged from the Hino River that fed sand to this coast.

Huge waves from the east-northeast are refracted in Miho Bay as shown in Fig.3. These refracted waves give rise to the longshore current in the western direction along the Yumiga-hama Peninsula.

In the 1910's, the shoreline of the Kaike coast was advancing offshoreward year by year, and at that time, Kaike coast had sandy beach of width of more than 200 meters.

About 1920, iron sand collecting for Japanese traditional steel making was abondaned in the upper reaches of the Hino River. In addition to this, a number of Sabo dams and agricultural weirs were constructed

along the Hino River. These facts brought a remarkable reduction in sediment supply from the Hino River, and the advancing tendency of the Kaike coast turned into the receding one. The shoreline at Kaike has receded more than 200 meters during the last half century.

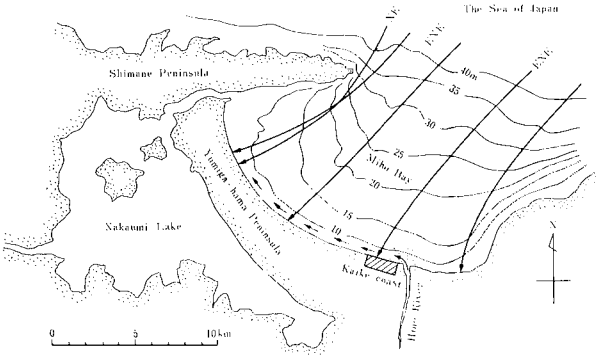

Fig. 3 Kaike coast and longshore current.

In 1947, after the War, the first experimental groin composed of rubble stones was constructed. Between 1949 and 1954, thirteen groins composed of large scale concrete blocks were constructed. As seen in Fig.4, the function of groin system gave satisfactory effect in 1954. In 1955, the Kaike coast was heavily eroded by giant waves caused by a typhoon and shoreline was in full retreat.

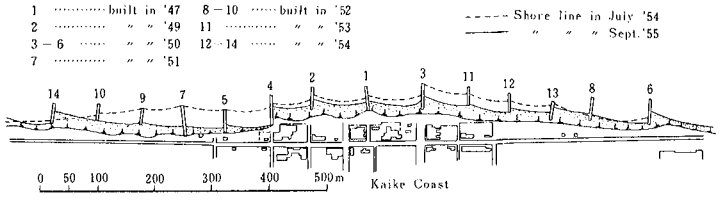

Fig. 4 After completion of groin system, Kaike was eroded.

After the heavy erosion due to a typhoon, seawalls along the shoreline were constructed. Based on the technical consideration in those days, concrete stepped face seawalls illustrated in Fig.5 have been adopted as suitable prevention structures against beach erosion in Japan. The construction of seawalls was made between 1955 and 1961. For several years after the completion of the seawalls, the Kaike coast looked like a stable beach, where very wide sandy beach extended in front of the seawalls.

Even when the Kaike coast seemed to be stable, a large amount of beach sediment was carried offshoreward with every attack of severe wind

waves in winter. After a lull in beach retrogression, Kaike coast began to retreat again in the early 1960's. Incident waves directly struck and overtopped seawalls. In order to reduce wave overtopping, wave defence works composed of artificial concrete blocks were constructed in front of the seawalls.

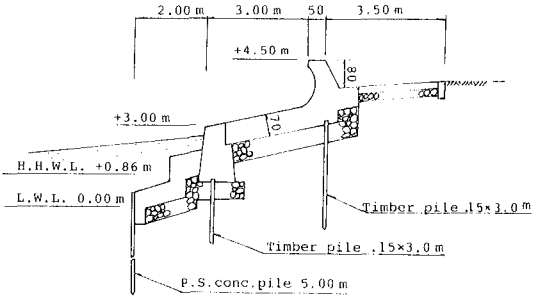

Fig. 5 Concrete stepped face seawalls was adopted.

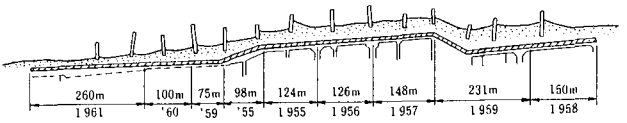

Fig. 6 Seawalls were constructed between 1955 and 1961.

As severe waves have repeatedly hit the Kaike coast, the combination system of groins and seawalls with wave defence works has shown its inadeqacy in the protection function against beach erosion. When incident waves approach normally to the shoreline, some portions of incident wave energy are reflected from the seawalls. This wave reflection results in considerable scour in front of seawalls and receding waves take away beach sediment offshoreward. Due to these unfavourable effects by the seawalls, groins and wave defence works settled and scattered. In the early 1970's, the Kaike coast was severely eroded again.

3. PROPOSAL OF A DETACHED BREAKWATER SYSTEM

Countermeasures against beach erosion in Japan was studied on a trial-and-error basis until the recent years. Many prevention works, such as seawalls and groins, have been constructed during the past thirty years. However, as the results of field investigations, it has become clear that, seawalls and groins have not been necessarily useful for beach erosion prevention, and adversely, in some cases they have promoted the beach erosion. Then, the author proposed a detached breakwater system as a new measure.

The first experimental work of this system was carried out on Isizaki coast, Hokkaido Prefecture, under the direction of the author in 1966. Soon after the completion of the work, the tombolo was formed behind the breakwater, and the system was effective in the restoration of shoreline. Generally, of cause, construction work of the detached breakwaters is not easy and maintenance cost is also high, when they are constructed on steep and deep sea bed.

The detached breakwater system at Kaike coast was proposed by the author as a new countermeasure against the beach erosion. However, the planning position of the breakwaters had considerably deeper depth than those where the previous experimental breakwaters were constructed. Therefore, the adoption and positioning were determined after long series of field surveys and researches.

4. CONSTRUCTION OF THE DETACHED BREAKWATER SYSTEM IN KAIKE COAST

In June 1971, the construction of the first breakwater in Kaike was commenced, and was completed in September of the same year. The breakwater with the length of 150 meters was constructed 110 meters offshoreward from the seawall where the water depth was about 5 meters. The breakwater as seen in Fig.7 was composed of rubble stones and armoured by tetrapods.

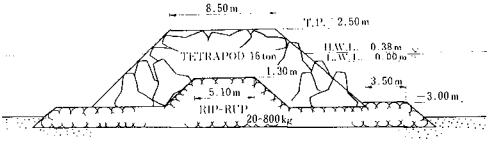

Fig. 7 Cross-section of the breakwater in Kaike

The breakwater has been quite effective in trapping sand transported from offshore zone and in forming a large scale tombolo behind it. The thickness of deposited sand was about 4 meters at the apex of the tombolo, and about 2 meters in front of the seawall.

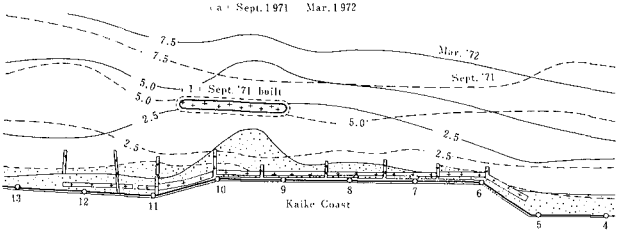

Fig. 8 The first breakwater was constructed in 1971.

Encouraged by the successful result of the first experimental detached breakwater, three more breakwaters were constructed as planned in the following three years.
The breakwaters, whose lengths were 150 meters, were positioned at equall space of 50 meters. The No.1 breakwater was constructed in downdrift zone of the longshore current along the Kaike coast, and the No.2 was constructed on the updrift side of the No.1 breakwater.
In progress of the No.2 breakwater construction, beach retrogression in the downdrift zone of the No.1 breakwater was observed.
To eliminate the undesirable effects by the Nos.1 and 2 breakwaters, the No.3 breakwater was sited on the downdrift side of the No.1 breakwater. The No.4 was in the updrift side of the No.2 in order to increase the covering area.

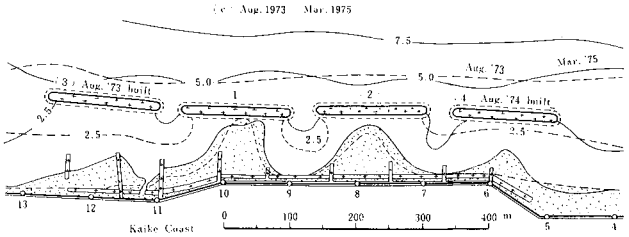

Fig.9 The No.4 breakwater was constructed in 1974.

During the later seven years, seven breakwaters were constructed annually, one breakwater every year respectively. In 1981, the detached breakwater system in the Kaike coast has completed with eleven breakwaters construction.

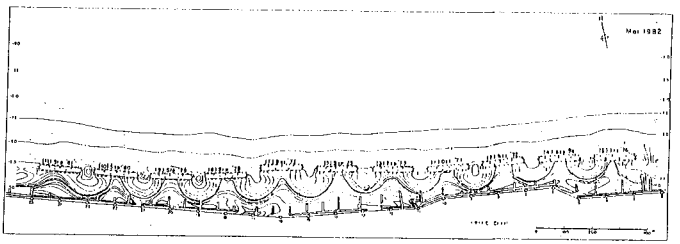

Fig. 10 The detached breakwater system has completed in 1981.

5. TRANSFORMATION OF SEA BED

Before the construction of the breakwaters, there were considerable transformation in the sea bed configuration. However, after the construction, the transformation of the sea bed have become very little. Fig.11 and Fig.12 are typical example of survey results for profile line No.8 which is located at the center of the No.2 breakwater.

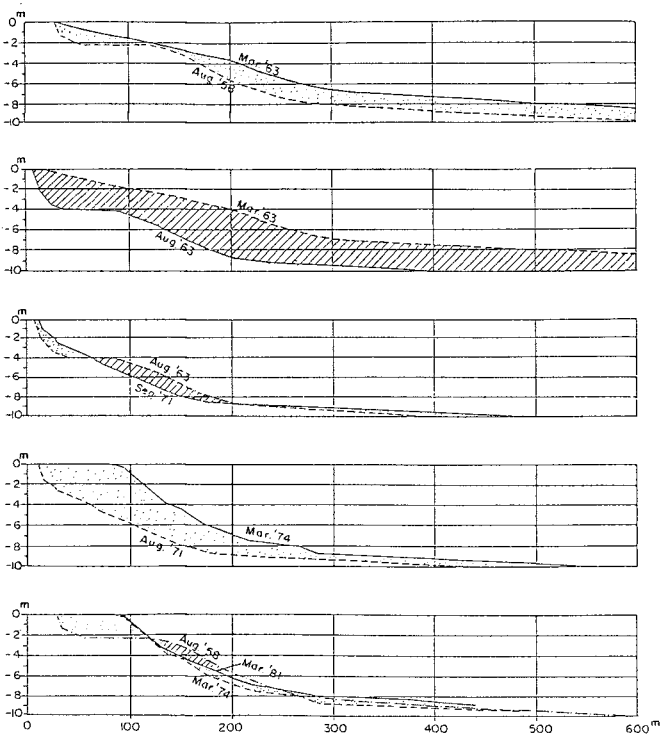

Fig. 11 Transformation of sea bed on the section No.8

The survey have been executed twice a year, spring and autumn. Fig.11 shows some striking transformations of the sea bed extracted from the annual survey results.

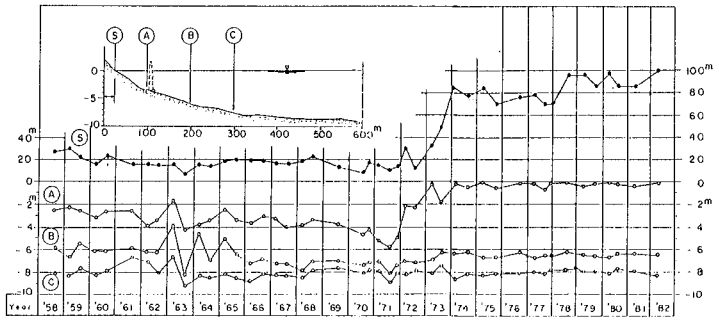

Fig. 12 Annual transformation of shoreline and sea bed on No.8

The greatest transformation of the sea bed configuration came about during March and Autumn in 1963. Maximum erosion of the sea bed amounts to about five meters in depth on the point 200 meters distant from the seawall.

In Fig.12, (S) represent the horizontal distance of shoreline from the seawall, and (A), (B) and (C) the water depth from the still sea water level at the points of 100, 200 and 300 meters distant from the seawall. The No.2 breakwater was constructed in front of the section No.8 in August 1972. Right after its construction, the sea bed at the point (A) indicated a remarkable shoaling, and the shoreline (S) greatly advanced. Since then the shoreline and sea bed have been very stable in contrast with that before the construction of the breakwater.

6. VARIATION OF SHORELINE AND EQUI-DEPTH LINE

Figs.13 to 20 show the variation of shoreline and equi-depth line before and after the construction of the detached breakwaters. Before the construction, there was considerable variation in the shore line and equi-depth line. However, since the construction, the variations of sea bed have become very little, and a lot of sand were transported from the offshore zone to the nearby areas of the breakwaters not only onshore side but also offshore side of the breakwaters.

Still more strange to say that, the equi-depth line at the offshore sea bed has become very smooth, uniform and paralleled to the line of the row of detached breakwaters.

We can not explain the reason of this flat and plane sea bed even now.

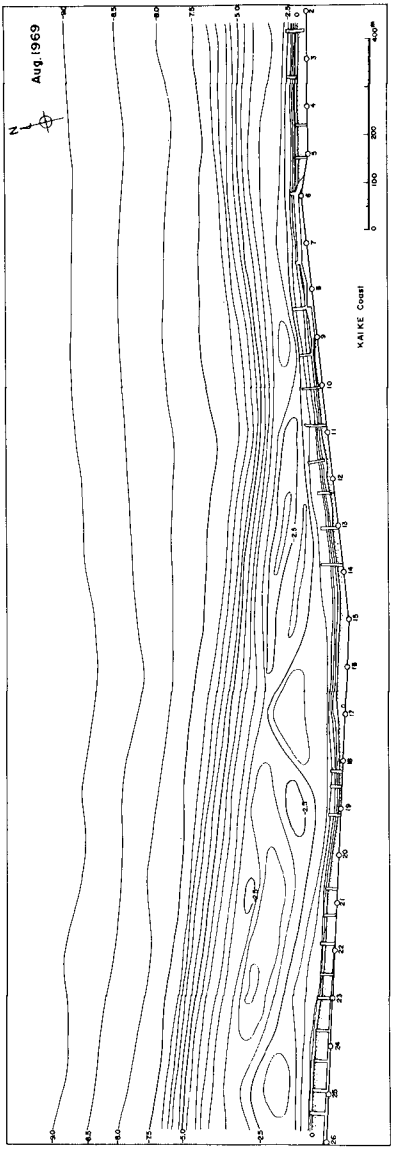

Fig. 13 Sea bed before the construction of the detached breakwater system in Kaike coast. There were many bars and troughs in the foreshore zone. These bars and troughs moved about every time the surveys had been executed.

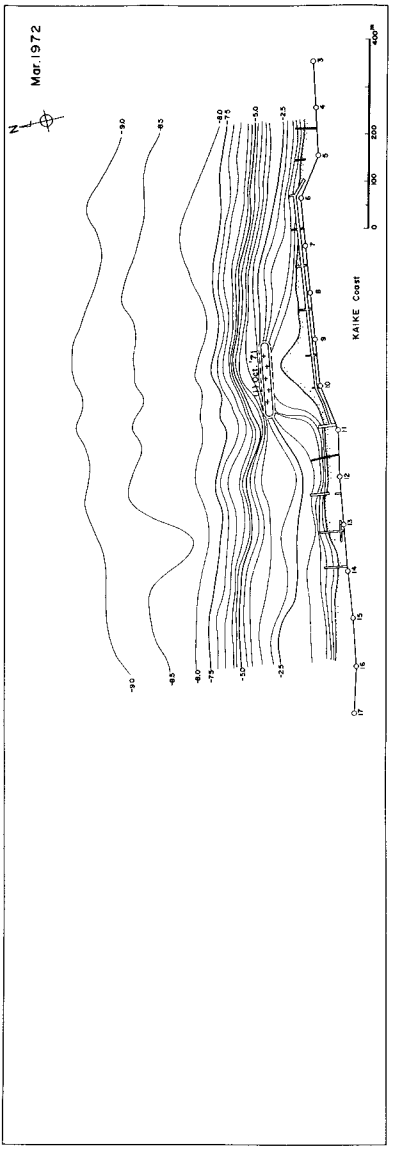

Fig. 14 The sea bed six months after the construction of the No.1 detached breakwater. A large tombolo developed behind the breakwater, and the shoreline in front of the station Nos.11 to 16 advanced offshoreward.

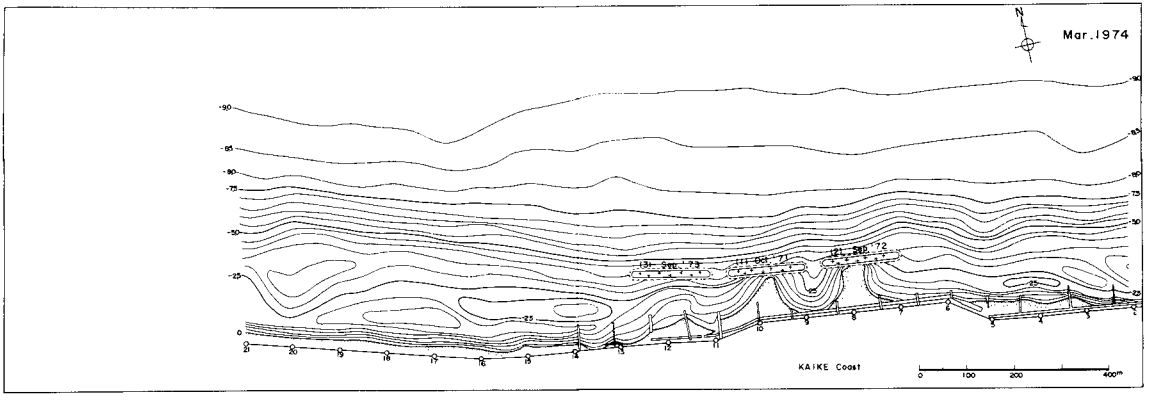

Fig. 15 Two years after the Fig.14. Three breakwaters are constructed, and there are three tombolos behind the each breakwaters. The left breakwater is the latest one, and the tombolo of it is still small in contrast with another two previous tombolos. The direction of the longshore current in Kaike coast is westward as previously stated, the rightmost tombolo is usually larger than the remaining left side tombolos.

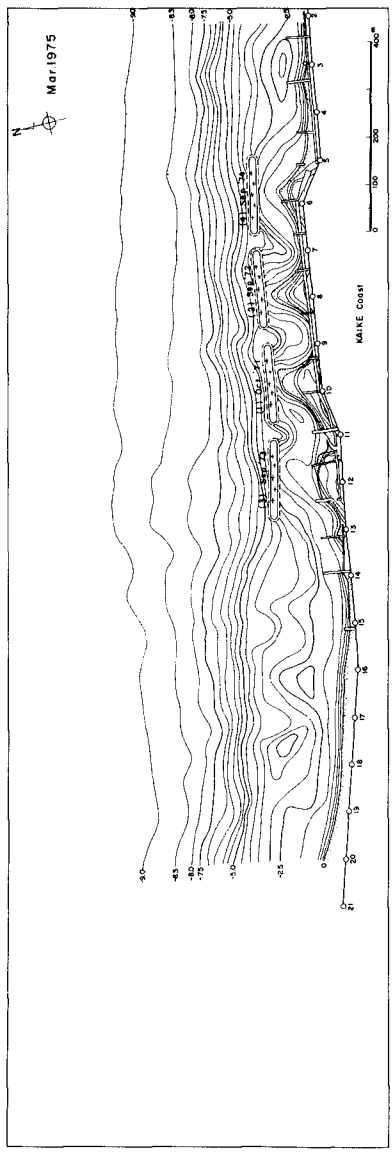

Fig. 16 One year after the former figure. No.4 breakwater was constructed six months before, and its tombolo is yet small though it is situated on the rightmost. The equi-depth line of -5 m advanced offshoreward a little in contrast with the Fig.13, before the construction of detached breakwaters.

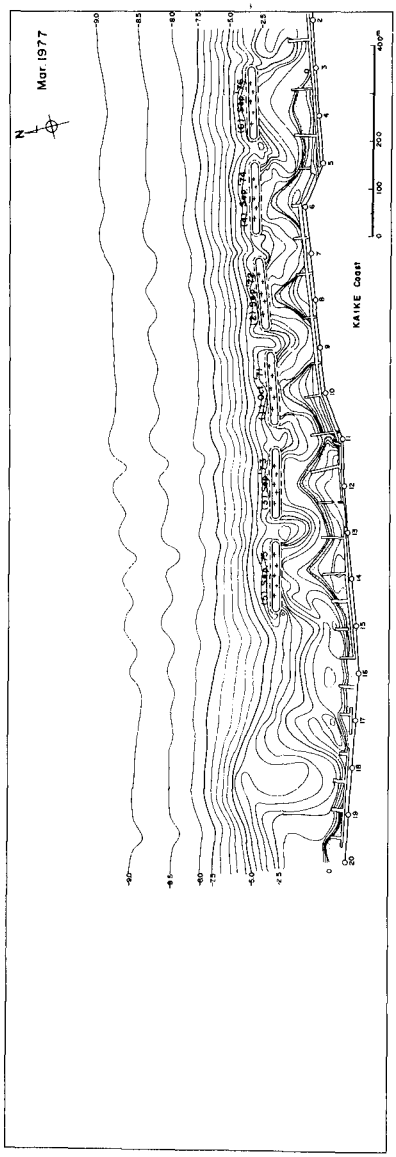

Fig. 17 Two years after the former figure, and the No.5 and No.6 breakwater were constructed during the two years. The tombolos developed respectively except the latest No.6's one. The equi-depth lines from -5m to -9m have become smooth and parallel gradually. However, the foreshore in front of station Nos.15 to 20 are left unstable.

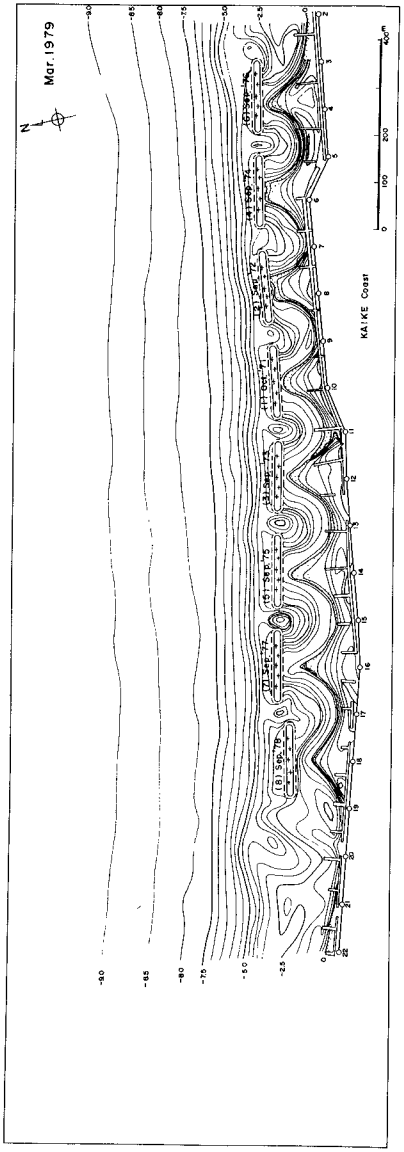

Fig. 18 Further two years after the former figure. Nos.7 and 8 breakwaters are constructed, and they have good-sized tombolos respectively. The equi-depth lines of the offshore zone have become smooth in succession.

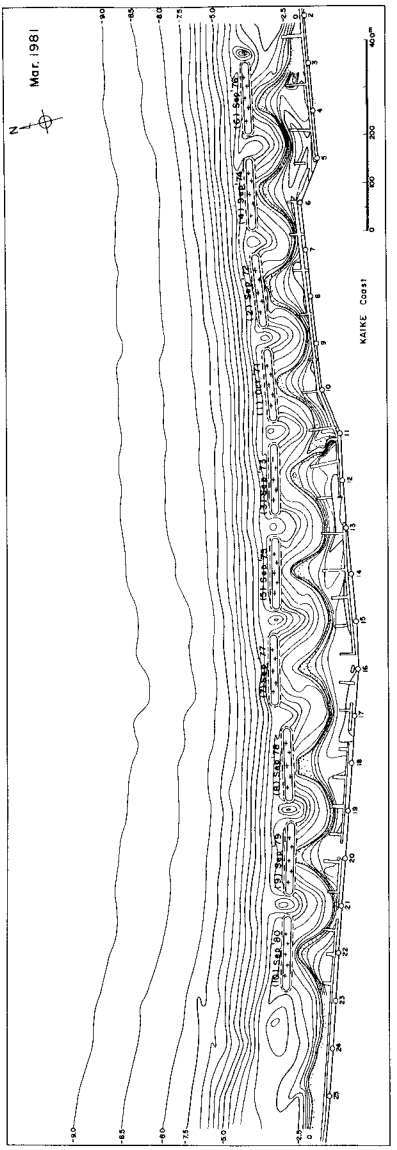

Fig.19 Ten breakwaters were constructed until 1980. Each breakwater has a good sized tombolo respectively, and the offshore sea bed has become stable and smooth.

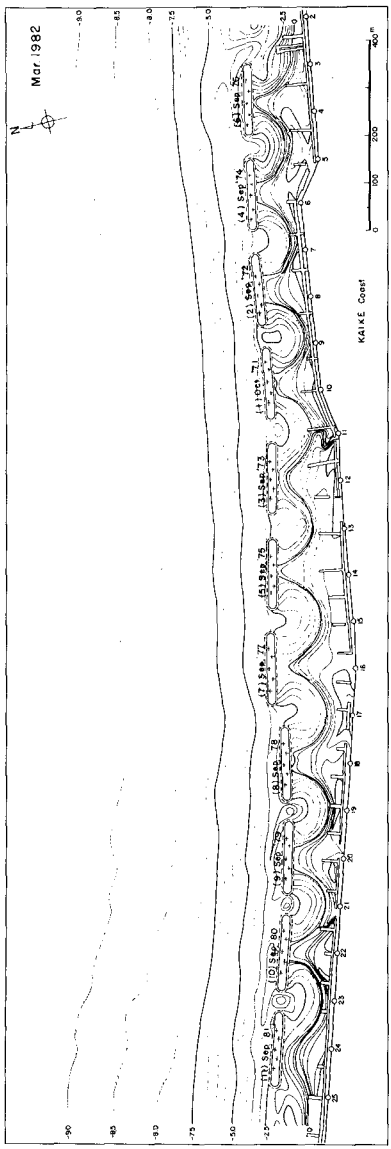

Fig.20 The Detached Breakwater System in Kaike Coast has completed in 1981. Eleven breakwaters are constructed, and all of them are successful. Each breakwater has a great tombolo behind it and all of these tombolos are very stable in spite of the every winter's huge waves. The equi-depth line in the offshore zone have become more smooth, uniform and paralleled to the line of row of detached breakwaters.

7. VOLUMETRIC CHANGES IN THE SEA BED

Table 1 shows volumetric changes in the beach profiles calculated from the survey results during the period from September 1971, before the construction, to March 1982, after the construction of the eleventh breakwater.

Table 1 Volumetric changes in the sea bed after the construction of the detached breakwaters.

Number of breakwater	Onshore side of breakwater	Offshore side of breakwater	Total volume
No. 1 breakwater zone	+ 35,800 m³	+ 86,100 m³	+121,900 m³
No. 2 breakwater zone	+ 48,800	+ 89,200	+138,000
No. 3 breakwater zone	+ 18,300	+ 49,200	+ 67,500
No. 4 breakwater zone	+ 45,000	+ 84,200	+129,200
No. 5 breakwater zone	+ 18,900	+ 21,800	+ 40,700
No. 6 breakwater zone	+ 28,900	+ 95,400	+124,300
No. 7 breakwater zone	+ 24,800	- 19,500	+ 5,300
No. 8 breakwater zone	+ 15,300	- 43,700	- 28,400
No. 9 breakwater zone	+ 13,400	- 31,600	- 18,200
No.10 breakwater zone	+ 28,300	- 41,100	- 12,800
No.11 breakwater zone	+ 7,400	- 68,700	- 61,300
Total	+284,900 m³	+221,300 m³	+506,200 m³

It is noticed from this table that a considerable volume of sand has been deposited on the sea bed in the onshore and offshore zones of the breakwaters since the construction schme of detached breakwaters commenced. However, there are some erosion in the offshore zone of station Nos.7 to 11. These areas correspond to down drift of the littoral transport in Kaike coast.

Now, Kaike coast has gained a stable sea bed and shoreline by virtue of this detached breakwater system.

Photo 1 The aerial view of the Kaike coast and four detached breakwaters on Octover 1974.

Photo 2 The detached breakwater system in Kaike Coast has completed in 1981. The photograph shows the Kaike coast just after the eleventh breakwater construction,on Octover 15th 1981.

8. OTHERS

Although the detached breakwaters are very effective in the shoreline protection, some problems involved in this system still remain to be solved. The most important problem is subsidence of the breakwaters. Up to now, the subsidence of the breakwaters in Kaike coast is fortunately considered to be moderate, but it is urgently needed to develop methods by which the speed of subsidence can be minimized.

Hereupon, our efforts must be continued without a break, so that the re-created beach may not be lost again.

(END)

RESULTS OF SHORELINE EROSION DEMONSTRATION PROGRAM

B. L. Edge[1] M. ASCE and J. G. Housley[2] M. ASCE

1. Introduction

Very little has been done in the United States to assist the private landowner when his property has been threatened by coastal erosion. Primarily, efforts have been concentrated on large scale shoreline protection efforts which cover municipalities or large regions. These efforts have been basically Federal or large state projects. Between 1974 and 1980, the United States government conducted a national program to fill this void by demonstrating a low cost technology for shoreline defense. The objective of this paper is to report on the program itself and its results.

2. The Section 54 Program

The United States Congress in 1974 authorized in Section 54 of Public Law 93-251, 93rd Congress, a program to develop and demonstrate low cost methods of shore protection. Further the Act specified that the Chief of the U.S. Army Corps of Engineers was to conduct this program and appoint a Shoreline Erosion Advisory Panel (SEAP) to advise him on its execution. Members of the Panel represented various geographic areas, professional disciplines, employers, and environmental groups. All of the members however, had knowledge and experience in some aspect of shoreline erosion and protection. The legislation specifically stated that the program would include a minimum of sixteen sites from around the shoreline of the United States. Six of these sites were to be in Delaware Bay, as mandated by the legislation, and the other ten sites were to be selected based upon the criteria provided by the SEAP. The selection of devices or systems of devices to be demonstrated at the specific sites was made by the Chief of Engineers, based on the recommendation of the Panel.

[1]President, Cubit Engineering Limited, P.O. Box 1271, Clemson SC 29631

[2]Office of the Chief of Engineers, HQ(DAEN-CWP-F), Washington DC 20314

Additionally the Act allowed that non-Federal lands could be used for demonstration sites as long as the non-Federal owner had a sponsor which was willing to pay at least 25% of the construction cost. Also as a part of the program, a number of low cost, shore protection systems, already installed at other sites, were included in the monitoring program. Including these additional sites allowed observation and evaluation of a greater number of devices and environmental conditions than would have been possible with only the sixteen mandated sites.

Another important feature of the legislation was that the effectiveness of vegetation was to be demonstrated wherever it could be employed. Often it was necessary to employ vegetation in conjunction with a protective structure until it was able to sustain itself under the environmental conditions. The Soil Conservation Service of the Department of Agriculture was involved in much of the vegetative work, selecting indigenous vegetative species, assisting to plant the materials, and in evaluating the response of the plants to the environmental conditions.

Each of the sites was monitored intensively by the Corps of Engineers. Monitoring included wind, wave and current data on a daily basis as well as bathymetric surveys, ground photographs and aerial photography flown at about three-month intervals. Sediment samples were collected from the beach and offshore. A Corps engineer would visit a site at least monthly to report on its status. A special monitoring program was used for the vegetative aspects of each site. The monitoring program was very comprehensive although few quantitative measurements were taken. The results of the monitoring were assimilated and analyzed by the Coastal Engineering Research Center.

3. Results

Originally the program was to have continued for five years, however, few projects were tested for more than two years. Thus interpretation of the performance of these structures is limited by the short life of the program. A summary, by generic system, of the performance of the devices that were installed and monitored under this program is included in Table I. Those that were "possibly successful" are devices which did not fully succeed at the particular installation that was monitored, but the devices could have succeeded if they were either in a more appropriate environmental location or had minor changes to the initially designed structure. Table II gives specific comments on the modifications which could be made to make some devices successful.

TABLE I

PERFORMANCE OF SYSTEMS INVESTIGATED

Type of System	Successful	Could be successful*	Failed
A. Bulkheads and Seawalls	Treated timber, Steel and timber, Concrete sheetpile	Rubber tire and piles, Longard tube, Earth-filled concrete pipe, Rubber tire stack, Untreated timber	Welded-wire fence and sand bags, Concrete and timber
B. Revetments	Stone riprap, Sand-cement bags	Concrete blocks, Gabions, Concrete rubble, Steel barrels	Concrete slabs, Sandfilled-bags, Fabric, Tires and fabric
C. Breakwaters and Sills	Stone riprap, Timber sheet piles, Rubber tires on piles, Sand-cement bags	Floating tire, Longard tube, Gabions, Concrete bags, Z-wall Surgebreaker, Sandgrabber	Sta-pods, Sand-filled bags, Brush dike
D. Groins	Timber, Timber and stone, Riprap, Concrete rubble, Sand-cement bags, Corrugated steel pipe, Rock with asphaltmastic	Longard tube, Gabions, Steel fuel barrels	Sandfilled bags
E. Nonstructural	Perched beach, Beach fill	Vegetation, Vegetation with protective structure	

*These could be made successful with minor changes or use in a more appropriate environment than used in the program

TABLE II

MODIFICATIONS REQUIRED FOR CERTAIN DEVICES

Type of System	Device	Comments
A. Bulkheads and Seawalls	Rubber tire and piles	Fair performance; needs good filter; tire fill material washed out; good way to dispose of used tires
	Longard tube	Tube must be away from bluff to prevent displacement by slides; sand-epoxy coating helps protect against vandal and debris damage
	Earthfilled concrete pipe	Fair performance; some pipes tipped over; needs stock pile of used pipe
	Rubber tire stack	Fair performance, but fasteners failed; system needs improvement; good way to dispose of used tires
	Untreated timber logs	System failed due to filter wash out; useful where logs are plentiful; boring insects could be a problem; needs good filter system
B. Revetments	Concrete blocks	Good performance when blocks are sized and shaped to match wave environment; easy to install, but subgrade must remain even; good small project system
	Gabions	Good performance, but broken basket wires may be a problem; needs proper sized stone fill; good substitute for stone riprap on small projects
	Concrete rubble	Good performance but failed where improperly designed; good way to dispose of large amounts of rubble

TABLE II (continued)

MODIFICATIONS REQUIRED FOR CERTAIN DEVICES

Type of System	Device	Comments
C. Breakwaters and Sills	Floating tires	Fair performance, but some systems pull apart; better interconnections needed; good way to dispose of used tires; use limited to short-period wave climate
	Longard tubes	Good performance if tubes are not damaged; requires special equipment; vandalism of tubes made demonstrations inconclusive
	Gabions	Good performance, but structural failure seemed imminent at demonstration site
	Concrete boxes	Fair performance, but requires special equipment; covers needed to keep sandfill in boxes
	Z-wall	Good performance, but structure deteriorated; system not recommended until hinging of modules is improved
	Sandgrabber	System locally effective but depletes downdrift beaches; structures deteriorated; probably could be improved, but other shore protection systems are available that perform better
D. Groins	Longard tubes	Good performance until structure failure; vandalism and debris damage is a problem
	Gabions	Good performance, but deterioration of outer ends exposed to high waves is a problem
	Steel fuel barrels	Good performance, but use is limited to Arctic regions

Of the materials tested in the program, it was found that quarry stone rubble performed well and survived longer than any other type of device. However, it was seldom one of the lowest cost devices employed. On the other hand, concrete rubble was only satisfactory when used with adequate filter material and shaped appropriately to eliminate flat and elongated pieces. In areas of the country where timber was an abundant material, it proved to be very successful because of its cost and the ease with which it could be shaped and fastened together. In the Alaskan environment, the steel drum proved to be one of the most effective and lowest cost devices available. Although these would ordinarily not be the first choice for shore protection, because of the abundance in that area, they have proved to be quite useful. Gorrosion was a problem however, whenever they were used south of the Arctic Circle.

Generally only those Gabion structures which were filled with stone larger than four inches in diameter proved useful in sites exposed to even moderate wave energy. The Gabion basket is a low cost device which is easy to install and will perform well functionally. Many baskets, however, were ripped open either from vandals, floating debris or movement of stone inside the baskets during wave action. Similarly Longard tubes were effective functionally as breakwaters, bulkheads, revetments and groins. However, at every site they were badly damaged by vandals or floating debris. When built in the dry, the Longard tubes could be coated with a sand-epoxy coating which would help to minimize damage. However, when the structures were installed in the water, no protective coating proved successful. Sand bags proved very effective functionally, but they were subject to the same damages by vandals and debris as the Longard tubes. Bags filled with a sand-cement mixture hardened into concrete modules that generally hold their shape together well after the fabric deteriorates.

In practically every demonstration project, a device was built with and without filter cloth to illustrate the importance of a filter. Although it is quite common knowledge among the coastal engineering community that a filter material is necessary, it was important that this should be emphasized.

Used rubber tires were successfully employed in several structures, although they were somewhat unsuccessful in others. In general they functioned very well as floating breakwaters, but did not function well as a revetment even when filled with concrete. Although the tires were never aesthetically pleasing, they tended to be both functionally and structurally successful on many occasions.

Vegetation was used primarily as a shore protection device only in very low wave energy environments when the underlying soil was adequate for their growth. Often the vegetation was employed in conjunction with another type of device which would provide appropriate shelter for the plant material to begin growth. Best results occurred when an underlying layer of loam or peat existed beneath a veneer of sand. Vegetation varied considerably around the country according to the locally available and adequate species. In all regions efforts were made to employ intertidal, supertidal and upland plant materials wherever appropriate.

4. Dissemination

One of the important aspects of the program was the dissemination of the results to the public. A dissemination program was planned by a team of SEAP members, Corps representatives and a private contractor. The basic document which summarized the entire project including all devices at each site was that prepared for the U.S. Congress (2). That publication has a history and compilation of all data at each site.

The basic components of the dissemination program which were prepared for the public are:

Low Cost Shore Protection: A Property Owners Guide - This report is intended for owners of property who face the decisions of dealing with their erosion problems. It contains information on the shoreline processes, explains available alternatives, reviews the decision process leading to a choice among solution options, and identifies sources of additional help.

Low Cost Shore Protection: A Guide for Engineers and Contractors - This report was prepared to familiarize engineers and contractors with established methods of low cost protection. It is written for those familiar with traditional civil engineering design and construction but who are not specialists in coastal engineering or shoreline protection.

Low Cost Shore Protection: A Guide for Local Government Officials - This report was prepared to assist and inform those government officials who have some involvement in shoreline erosion control through planning, permitting regulation or other function. The report includes a description of shoreline processes, devices available for use as solutions, guidance for selection from alternatives, permitting

requirements and a directory of information sources.

These three volumes provide the basic information for non-specialists to understand the erosion process, protection techniques and available devices. Although these references are oriented to low wave energy environments, the information is useful for all waterfront property owners. Each of these documents are available by contacting J. G. Housley, Office of the Chief of Engineers, HQ(DAEN-CWP-F), Washington DC 20314.

The program also developed brochures describing each demonstration site for those who could visit the area. At the conclusion of the program four regional workshops were held to acquaint the Corps district offices and state and local government officials with the results of the program. A 50-minute slide presentation is also available to present the results of the program to local groups. It presents a summary of coastal processes, available alternatives, and requirements for a successful project. The slide presentation can be obtained by contacting a Corps of Engineers district office or through the address given above.

5. Conclusions

Although low cost shore protection is amenable to only select sites, it certainly is a concept that has to be explored for the thousands of miles of eroding shoreline which are in the hands of private citizens. The results of this program will be helpful to the landowner in identifying the type of solution which he may employ and how to go about designing those solutions for his own particular problem.

6. References

1. Edge, B.L., J.G. Housley and G.M. Watts (1977). A Review of the National Shoreline Erosion Control Program, Journal of the Marine Technology Society, Vol. 11, No. 3.

2. U.S. Army Corps of Engineers (1981). Low Cost Shore Protection: Final Report of Shoreline Erosion Control Demonstration Program (Section 54). Office of the Chief of Engineers, Washington DC.

3. U.S. Army Corps of Engineers (1982). Low Cost Shore Protection: A Property Owners Guide. Office of the Chief of Engineers, Washington DC.

PERFORMANCE OF SAND-FILLED TUBE SHORE PROTECTION TUKTOYAKTUK, NORTH WEST TERRITORIES, CANADA

V.K. SHAH, M. Sc., C. Eng., M.I.C.E., P. Eng.
PUBLIC WORKS CANADA, OTTAWA, CANADA

1. INTRODUCTION

Seawalls, revetments and groynes designed to protect shorelines require normally timber, natural stone or concrete for their construction. In Tuktoyaktuk, none of these materials is available and to avoid excessive costs, an alternative form of construction, using long sausage shaped tubes filled with sand, was devised on an experimental basis.

Tuktoyaktuk is situated on the eastern side of Kugmallit Bay in the Western Arctic at north latitude of 69 deg. 27' and west longitude of 133 deg. 02'. It is approximately 90 miles north of Inuvik and 1450 miles northwest of Edmonton (figure 1). The area is mainly comprised of a long, narrow, boot-shaped peninsula oriented in approximately north-south direction, a complex lagoon, which has been developed as a harbour, east of the peninsula and an island straddling the mouth of the lagoon (figure 2). Certain dwellings exist at the southern and southeasterly shores of Tuktoyaktuk Harbour. A large majority of the inhabitants reside in settlements developed on the peninsula and the southern area linking the peninsula with the mainland. Tuktoyaktuk is used as a transfer point linking the Mackenzie River barge transport with coastwide shipping serving the western arctic seaboard and inland settlements and bases. As a result of this the TUK settlement has grown to be the largest of the western arctic coast settlements.

Tuktoyaktuk is receiving further prominence owing to the recent oil explorations in the Beaufort Sea and if oil is discovered in the area, Tuktoyaktuk will see considerably increased activity and prominence. Dome Petroleum and Gulf Canada have already committed large investments in administrative support facilities at Tuktoyaktuk and Exxon is moving its northern offices there. Tuktoyaktuk is thus likely to become the Beaufort Sea administrative support center for the oil and gas industry.

Tuktoyaktuk is generally flat. Its shoreline is demarcated by steep cliffs. The Tuktoyaktuk peninsula is approximately 4,400 feet long and 1,400 ft. to 300 feet wide. It is 5 to 25 feet above the sea level and covers an area of approximately 16 acres. The Tuktoyaktuk Island is approximately one mile long, and on an average 600 feet wide. The island is characterized by its flat top which is approximately 30 feet above the sea level and cliffs steeply plunging to the sea. The harbour runs inland in a southwesterly direction and is approximately 7 miles long. The terrain around the harbour is flat and contains numerous lakes.

The whole shoreline at Tuktoyaktuk has been receding at considerable rates. Reports indicate that similar erosion is occurring along much of the adjoining coastlines. The length of shoreline of immediate concern was the shoreline at the settlement peninsula where several buildings including a local school were under threat of being undermined. There were no precedents of shore protection works in the arctics where the erosion regimes are different from those in the south, and a decision was made to protect the school building as a prototype experiment to learn from and develop a design to protect the whole settlement peninsula.

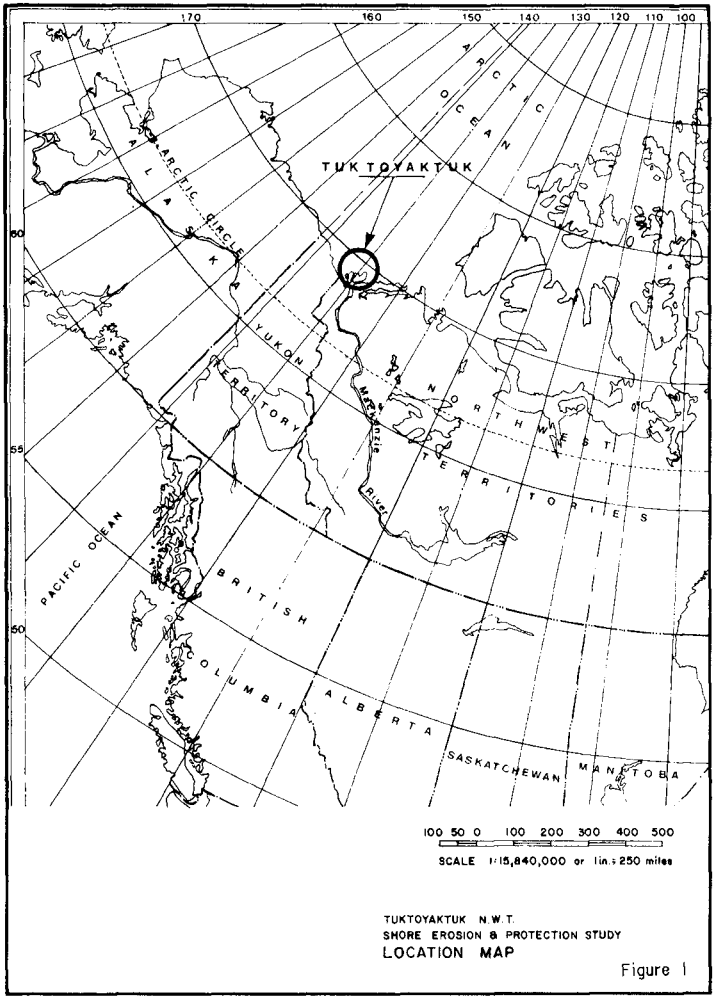
170
160
150
140
130
120
110
100
60
55
50
ARCTIC OCEAN
TUKTOYAKTUK
ALASKA
ARCTIC CIRCLE
YUKON TERRITORY
MACKENZIE RIVER
NORTHWEST TERRITORIES
PACIFIC OCEAN
BRITISH COLUMBIA
ALBERTA
SASKATCHEWAN
MANITOBA
100 50 0 100 200 300 400 500
SCALE 1:15,840,000 or 1in.= 250 miles
TUKTOYAKTUK N.W.T.
SHORE EROSION & PROTECTION STUDY
LOCATION MAP

Figure 1

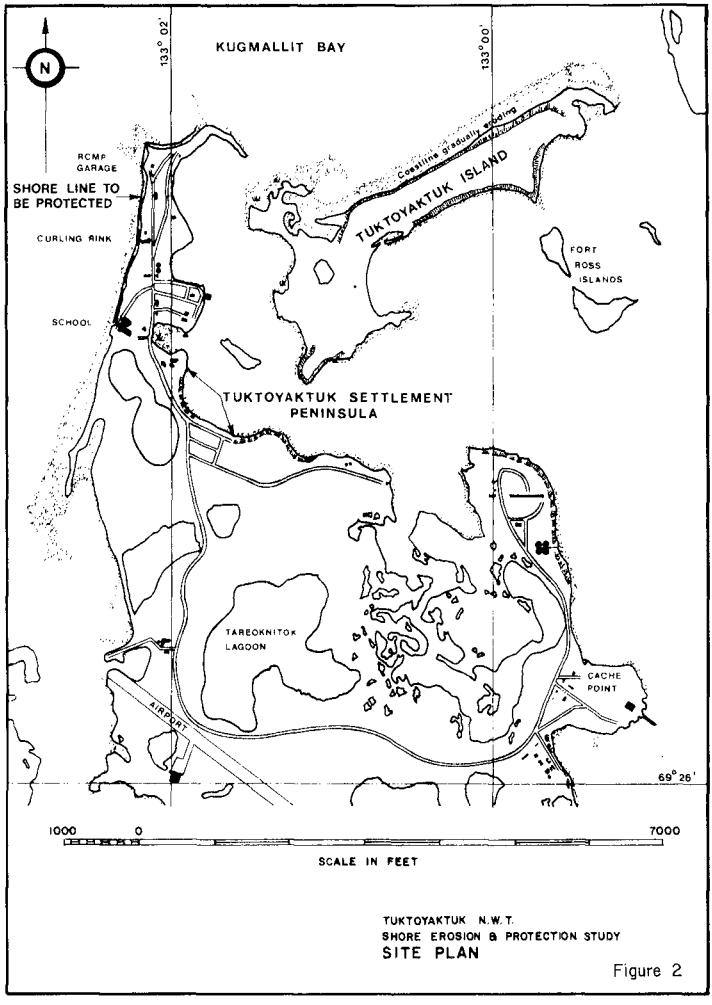

TUKTOYAKTUK N.W.T.
SHORE EROSION & PROTECTION STUDY
SITE PLAN

Figure 2

2. COASTAL GEOMORPHOLOGY

2.1 General

The coast of Tuktoyaktuk can be described as a shallow, embayed and receding coast. It is generally flat and contains narrow beaches and steep cliffs. The area is mostly underlain by fluvial sands and silts and fine grained deltaic sands. These deposits are capped by a thin layer of a mixture of sands, peat lacustrine deposits, gravel and clayey till like deposits. The subsurface includes permafrost and lenses and sheets of massive ice.

2.2. Subsurface

The analysis of test borehole samples and thermistor readings indicates that generally the subsurface can be divided into two zones. These zones are: (1) an active zone which is frozen in the winter and thaws out in the summer and (2) a permanently frozen zone below the active zone. The active zone consists of sands, silts and gravel, in places covered by peat or organic material. In areas where there is a cover of peat the thickness of the active zone as measured was small, varying from 1 to 2 feet. In the inorganic soils, the thicknesses of the active zones measured were relatively large, varying from 4 to 16 feet. The permanently frozen zone consists of layers of sands, silts and gravel together with ice crystals, lenses of ice and sheets of massive ice. The thickness of the permafrost zone was not determined. It is, however, known to extend from above to below the sea level, or in other words it straddles the sea level (figure 3).

3. EROSION REGIME

3.1 General

There are two major causes of the erosion occurring at Tuktoyaktuk. In the warm regions of the world the usual cause of erosion is the physical force of the waves. In the arctics, where ice rich soils and massive ice abound within the soil, thawing caused by the warmer temperatures in the summer and warmer sea water can be a major cause of shore recession and an accelerating factor in shore erosion. Both of these phenomena impinge on the Tuktoyaktuk coast.

3.2 Erosion by Waves

The erosion of Tuktoyaktuk shore, attributable to the physical forces of waves, can be seen to be taking place in two distinct ways depending upon the shore topography. In places where high cliffs exist, the cliffs are degraded by undermining and removal of slices from them. In areas where dunes occur, the dunes are shifted landward in varying alignments depending upon the direction of storms. The importance of these two shore erosion factors compared with the factors of thermal erosion discussed in the following section, cannot be precisely established.

The shore material transport rates calculated using a method known as the wave energy flux method do not reconcile with the large coastal recession rates of Tuktoyaktuk given by aerial photographs and surveys.

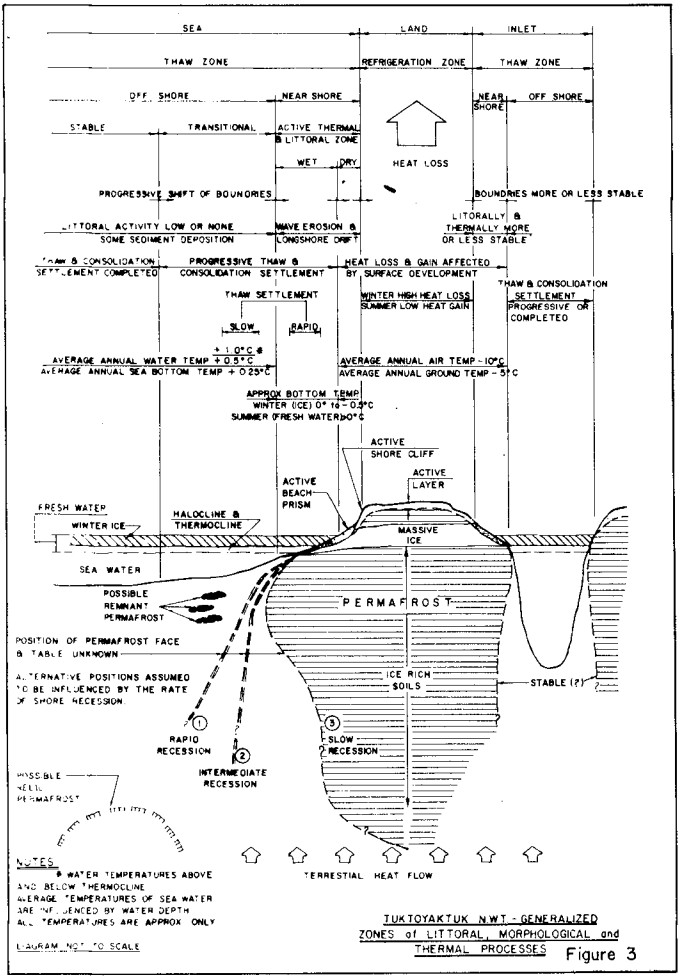

TUKTOYAKTUK N.W.T. - GENERALIZED ZONES of LITTORAL, MORPHOLOGICAL and THERMAL PROCESSES Figure 3

3.3 Thermal Erosion
Thermal erosion is considered to be the major contributory cause of the coastal recession occuring at Tuktoyaktuk. There are two ways in which the thermal action is affecting the Tuktoyaktuk coast. These are (1) the melting of the ice present in the coastal land by warm water waves at high storm water levels and (2) thawing of the permafrost and ice contained in the beach and underwater soils, by the warm summer environment (figure 4).

4. DESIGN
As discussed in the preceding section, the erosion occurring at Tuktoyaktuk is mainly as a result of an inadequate cover over the ice and permafrost present in the ground at the site. Direct solar heat and thermal action of warm water waves are the main agents that cause the erosion at Tuktoyaktuk. During normal weather conditions the water levels are low and the waves do not impinge upon the coast. In storm weather situations, high water levels occur and the beach and the coastal areas are rendered liable to direct thermal action of warm water and thermal and physical action of waves. To protect the beach and the coast from the thermal action, an insulating cover is required over the area. To abate the wave action a barrier is needed. The insulating cover and the barrier must be of flexible type to accommodate any initial and long term settlement.

The design wave length considered ranged from 60 feet to 100 feet. The design wave height (storm maximum wave height) adopted was 8 feet. The cover required to protect the permafrost and ice was estimated to be 7 feet.

Construction materials available locally are confined to sand and gravel. The materials ocur in offshore regions, along the coast and inland. While there are adequate supplies of sand and gravel within short distances from Tuktoyaktuk, there are no sites in the vicinity of the area for any rock. Experienced contractors and heavy construction equipment similarly do not exist in the area. To obtain the required materials other than sand and gravel, construction services and equipment, Inuvik and areas as far as Edmonton have to be relied upon. The logistics are further complicated by the inaccessibility of Tuktoyaktuk by land. Because of this, all the requisites must be either transported by water or flown by air.

Various alternative forms of construction were considered for the test installation, including a rock revetment, rubblemound bulkhead, steel sheet pile wall, timber crib wall, and certain patented steel wire gabions. A product known as the "Longard" tube was at that time being introduced into the North American market. The "Longard" tubes which are sausage shaped, merely require sand to fill them and had been found to be functioning well in Europe and in certain ice covered environments. The use of the "Longard" tubes as shore protection work units showed good possiblities and a decision was made to proceed with the test program using these.

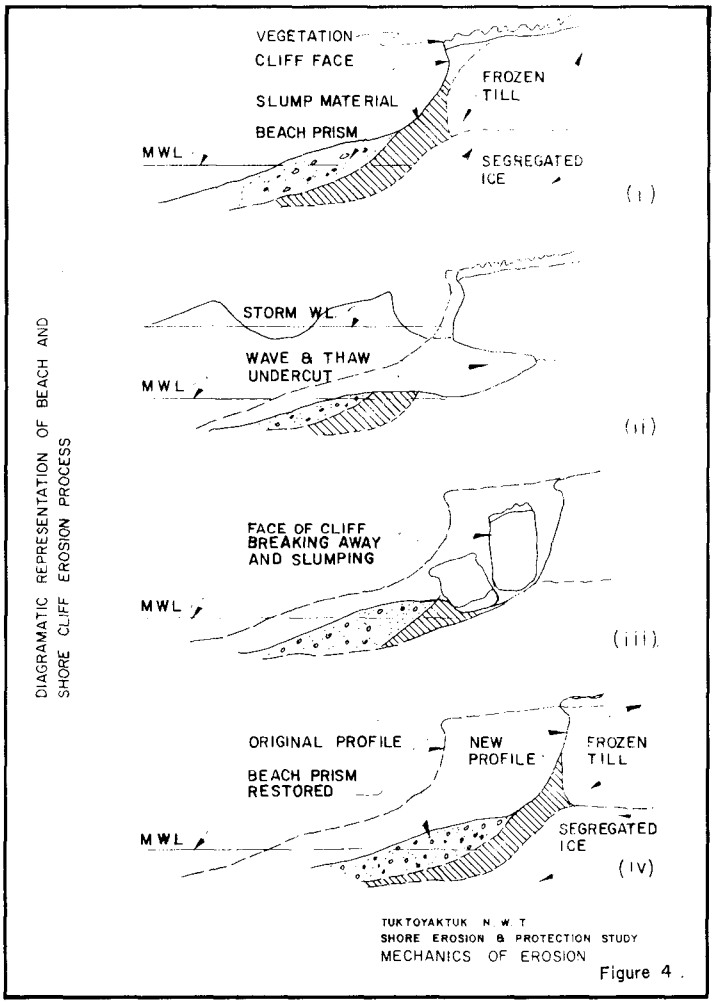
DIAGRAMATIC REPRESENTATION OF BEACH AND SHORE CLIFF EROSION PROCESS
VEGETATION
CLIFF FACE
SLUMP MATERIAL
BEACH PRISM
MWL
FROZEN TILL
SEGREGATED ICE
(i)
STORM WL
WAVE & THAW UNDERCUT
MWL
(ii)
FACE OF CLIFF BREAKING AWAY AND SLUMPING
MWL
(iii)
ORIGINAL PROFILE
BEACH PRISM RESTORED
NEW PROFILE
FROZEN TILL
MWL
SEGREGATED ICE
(IV)
TUKTOYAKTUK N.W.T.
SHORE EROSION & PROTECTION STUDY
MECHANICS OF EROSION

Figure 4.

The test design devised utilised one metre diameter Longard tubes, Longard and Terrafix filter mats and Dura bags as sand bags. Basically, the design consisted of a bulkhead at the bottom of the cliff, another bulkhead lower down on the beach and four main groynes separated by three shorter intermediate groynes, at right angles to the bulkheads. The cliffside bulkhead consisted of a double tube. The beachside bulkhead and the groynes were built with single tubes. The bulkhead tubes were laid on filter mats held down during construction by sand bags. Originally the compartments formed by the groynes and the bulkheads were to be filled with beach material. Owing to lack of funding the compartments between the groynes and the bulkhead were left unfilled. Due to construction difficulties also the groynes were constructed without the filter mats. The length of the installation was approximately 360 feet (figures 5 and 6).

5. PERFORMANCE

The principal objectives of the test were to provide protection to the local school which was under threat of being undermined by the sea and to gain experience to develop a full scale system to protect the whole settlement peninsula of Tuktoyaktuk. Imperative in these objectives was longevity of the test installation. While the test installaton has protected the school as envisaged and provided considerable information on how we may proceed with further shore protection works in Tuktoyaktuk, the installation has been subject to an incredible amount of willful damage. The Longard tubes can withstand heavy pressures required to fill them with sand under pressure and adequately resist the natural environment. In their exposed condition they cannot, however, withstand vandalism. The groynes have been practically slashed open by vandalism. The beachside bulkhead has also suffered from deliberate cuts. The cliffside bulkhead, which was backfilled and has been covered has, however, survived.

Technically, the installation has performed as envisaged. Erosion at the school has been completely halted. There has been, in actuality, accumulation of material between the bulkheads and between the groynes. There has been a greater accretion of material on the north end of the installation confirming littoral drift to be from north to south. Because of the lack of supply of material from the north, as would be anticipated, certain erosion has occurred of the southern end of the installation.

The performance of the test installation suggests that certain modifications can be made in the geometry of any full scale shore protection work in the area. The short intermediate groynes have been virtually ineffective in trapping material and can be eliminated. The long groynes have been allowing bypassing of material to occur and can be extended to deeper water. The cliffside bulkhead has remained virtually undisturbed and if an adequate bulkhead can be built at the beachside with backfill to the cliff, the cliffside bulkhead can be eliminated except at certain locations.

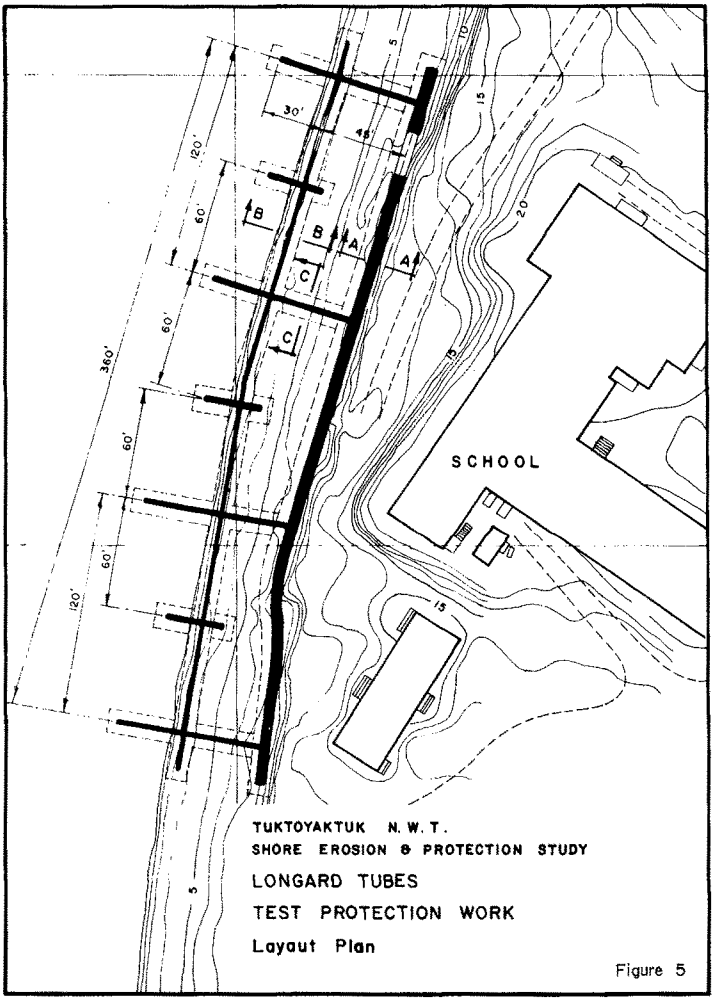
SCHOOL
TUKTOYAKTUK N. W. T.
SHORE EROSION & PROTECTION STUDY
LONGARD TUBES
TEST PROTECTION WORK
Layout Plan

Figure 5

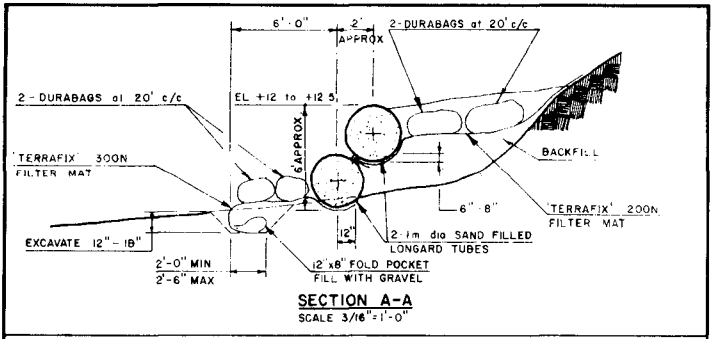

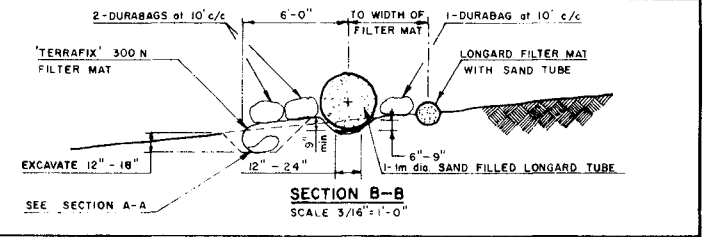

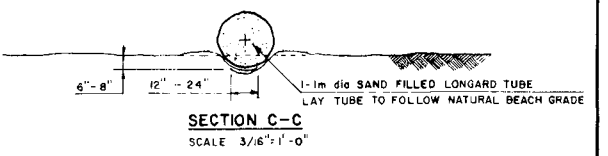

TUKTOYAKTUK N. W. T.
SHORE EROSION & PROTECTION STUDY
LONGARD TUBES
TEST PROTECTION WORK
Sections

Figure 6

Means are now available to protect the tubes against vandalism.

Basically, there are two steps that can be taken to make the design resistant to vandalism. These include coating the tubes with a hard shell and backfilling the installation with granular fill, covering the tubes to the top. The coating material available consists of an epoxy resin glue applied by painting rollers and sand which is either sprinkled manually or dumped onto the wet glue mechanically with dump trucks. The backfilling of the installation was a design requirement not accomplished in the test installation. Its purpose was to provide a blanket on the beach to protect the permafrost underneath from destabilization by the sea and the warm summer temperatures. In the final design the backfill will in addition protect the Longard tubes from damage from vandalism and from any sharp floating debris that can otherwise strike and damage the tubes with wave action.

To investigate the coating a length of one meter diameter Longard tube was obtained and assembled at the National Research Council of Canada for certain tests. Five different combinations of coating were applied to the tube. These were:

(1) uncoated
(2) one coat of epoxy glue, followed by sand
(3) two coats of epoxy glue followed by sand
(4) one coat of epoxy glue followed by sand and a second coat of epoxy glue followed by sand
(5) one coat of pre-mixed epoxy glue with sand

Several different types of tests were carried out on each section. These included resistance to slashing by hand, resistance to puncture by a knife with a proctor-needle assembly, flexure and bending tests at -40 deg.C and burning with a propane torch.

Hand slashing tests were carried out using a hunting knife. The uncoated tube offered very little resistance to hand slashing. Among the coated sections of the tube the double coating type 4 (glue - sand/glue - sand) offered the most resistance to slashing. Another advantage of coating observed during these tests was that the cuts made in the coated sections remained simply as closed cuts while the cuts made in the uncoated sections opened out allowing the sand-fill to run out.

PROTOTYPE TESTING OF SAND COATED TUBES USING A HUNTING KNIFE

PROTOTYPE TESTING OF SAND COATED TUBES FOR RESISTANCE AGAINST FIRES

Figure 7

The results of the penetration tests carried out using the hunting knife and Proctor Needle Assembly are tabulated below (figure 7).

Type of Coating	(1)	(2)	(3)	(4)	(5)
	65	69	48	90	63
	62	63	53	100	77
Pounds of Force for	50	56	58	93	77
Knife Penetration	43	57	63	120	
	62	62	59	96	
	45	61	64	89	
Average	55	61	58	98	72

The fire resistance tests with a propane torch showed the following results (figure 7).

Type of Coating	(1)	(2)	(3)	(4)	(5)
Time in seconds required to burn through coating	5	100	45	120	-

Flexure and blending tests were performed using samples from sections with type 2, 3 and 4 coating.

Relative comparisons of the results showed type (4) coating to be the most superior, both at room temperature as well as at -40deg.C.

The test results show the section with a double coating (one coat of glue followed by sand and a second coat of glue followed by sand) to be the most effective section and the final design for Tuktoyaktuk will include this double coating.

6. CONCLUSIONS

In remote areas of the Canadian north, sand filled tubes offer an attractive alternative compared with traditional materials in the design of flexible type shore protection works. The tubes in their uncoated form are vulnerable to vandalism. Techniques now exist to protect the tubes against damage and this feature should prove invaluable to guard against vandalism that can occur in remote areas.

THE BEHAVIOUR OF PROTOTYPE BOULDER REVETMENT WALLS

By A.W. Smith * & D.M. Chapman **

1. lntroduction

This paper reports the results of on-site observations of coastal revetment structures under extreme storm conditions on the Gold Coast of Australia. The Gold Coast is located at approximately Lat. 27° S on the East Coast of Australia facing the Tasman sea behind a narrow continental shelf and exposed to a relatively high energy wave climate as depicted in Fig 1. Tropical cyclones generate the highest storm activity on the Gold Coast with Ho values commonly exceeding 10m with the resultant onshore wave i.e. either the second or third wave reformed breaks within the range of 2.5 to 3.5m. Storm wave periods are usually between 8 to 18 seconds. The ocean beach on the Gold Coast, some 30km long has been receding since the early forties and this has resulted in the construction of nearly 20km of revetment walls to "protect" the rear beach. Whilst some walls in particularly erosion-prone areas were constructed in the 1920 decade, most have been constructed since 1967 which represented a particularly high cyclone prone year. Since the latter period the walls have been exposed to three further periods of high cyclone energy attack in 1972, 1974 and 1976. Nearly all revetment walls demonstrated at least some settlement and damage but over the three storm periods at least 0.8km of wall was completely destroyed. Most wall failures were monitored on site and whilst the construction of the walls varied in quality the observational results might well be classified as full scale prototype performance tests.

2. Boulder Walls

Over 90% of all Gold Coast revetments are boulder walls constructed from natural stone with a filter layer of well weathered quarry overburden material that effectively consists of a natural mixture of weathered gravel and clay.. All boulder revetments are founded at Mean Sea Level because below this the beach resists excavation by going "quick" and cofferdamming costs are prohibitive. Local philosophy has always been to found walls at M.S.L. and merely top them up in response to settlement and storm damage. The typical form of Gold Coast boulder walls is shown in Fig 2(a) and the official design standard in Fig 12(a).

The collapse mode of boulder walls is set out diagrammatically in Fig 2 starting with the as-built wall and finishing with the wall completely vanished and buried beneath the eroded beach profile. The initial failure has always been triggered by subsidence of the toe, this has then caused the face armour to rattle down until the wall's freeboard has been reduced enough to allow overtopping. As soon as the overtopping has become practically continuous the erosion of filter material became extremely rapid with the rump of the wall finally collapsing landwards into the

* Gold Coast, Queensland, Australia
** University of Sydney, Australia

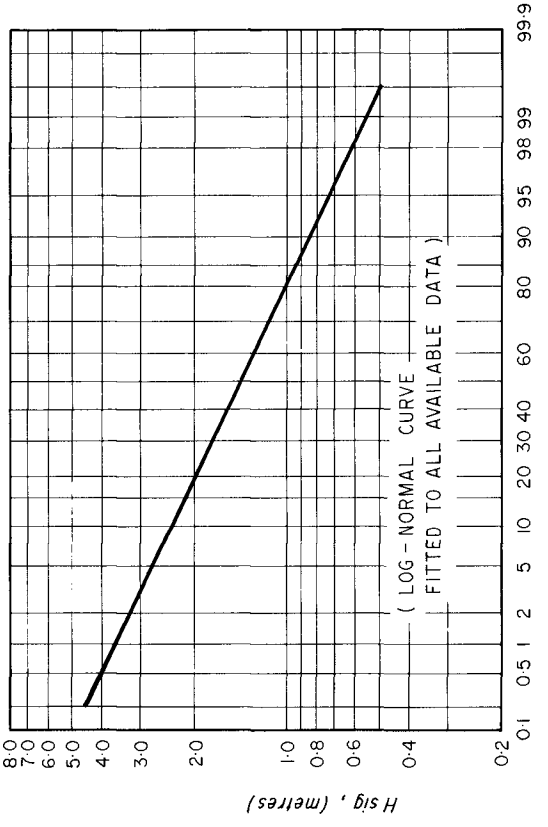

FIG. 1 WAVE HEIGHTS, GOLD COAST
PROBABILITY of EXCEEDANCE

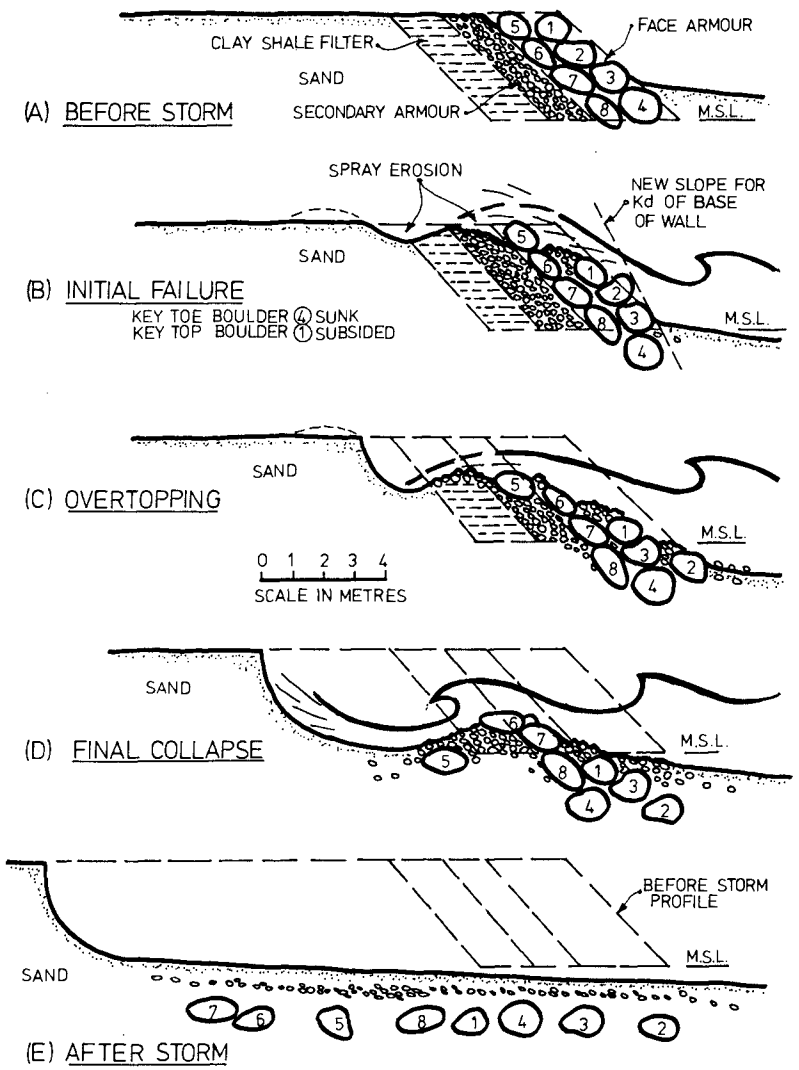

FIGURE 2:— COLLAPSE MODE OF BOULDER REVETMENT.

eroded space. The full sequence of events as shown has been observed to occur within less than 20 minutes for walls over 5m. high. The initial step by step and final positions of the numbered boulders shown in Fig 2 is typical of observed wall collapses, but it is naturally not universal, the shapes of boulders provide highly variable interlocking, some boulders bounce out of the wall during the rattle-down sequence, and small boulders (particularly in position 5) are readily plucked off the top of the wall and rolled landwards.

The initiation of toe failure has always followed the generation of semi-fluid or quicksand conditions in the beach under the toe as the lower end of the wave's trailing edge passes this zone. Once the sand becomes periodically fluidised the very low specific surface of the boulders ensures that they sink very rapidly step by step under each wave. Five tonne boulders have been observed to completely disappear in less than 150 seconds, or only 8 to 10 waves. Back-wash scour is not the mechanism of boulder settlement, as the filter layer erodes and the wall ruptures, overtopping generates a full work prism in the sand under the wall and the wall debris settles within the fluidised zone in proportion to the particle specific surface as shown in Fig 2(e) and confirmed by subsequent excavation of the beach. It might thus be observed that the practice of testing revetment walls of the class herein reported in "hard-bottom" flumes, i.e. without a sand underlay would be unlikely to reproduce the observed collapse mode of these prototypes.

From Fig 2(b) it may be noted that as the toe of the wall subsides the slope of the near toe boulders increases, thus the stability of the wall i.e. its Kd value decreases. Continued wave attack may then extend wall damage at an increasing rate, even with a constant or declining wave energy input.

3. The Role of Key Boulders

As can be seen from Fig 2 the two key elements of wall stability are the leading toe boulder (No. 4 in the diagram) and the top face boulder (No. 1 in the diagram). If neither of these boulders move the wall may maintain a capacity to resist in the short term very high hydraulic overloads.

Early efforts locally to increase the stability of the toe led to the use of the largest boulders as the key toe units. This approach was a complete failure, the bigger boulders had a lower specific surface and thus sank into the fluidised beach more easily and more quickly than standard boulders. Indeed some very large toe units sank into the beach during comparatively mild wave conditions and the walls supported by them had become dislocated before the arrival of the first storm. An alternative approach of bedding the toe boulders on secondary armour and filter material has to date also been only partially effective, since toe stability cannot be assured until the key toe unit is founded at the bottom of the work prism fluidised during a storm. Without the expedient of cofferdamming therefore it has had to be accepted that the full design capacity of the local walls cannot be attained until they have been "tempered" by one or several storm attacks and the walls topped up to accommodate the essential toe settlement.

The use of heavier boulders for the key top units has, however, proven rather more successful. In order for the key top unit to hold a Kd value equal to the other face units it should be larger in any case, the top boulder has no gravity surcharge and the least interlocking with its neighbours. It is thus the unit most susceptible to uprush and backwash forces. It is difficult however to place large top boulders flush with their surrounding armour, their size alone tends to result in them standing proud of their neighbours and leaving large gaps in between them. In this position they are very prone to rolling landwards under wave uprush and in one case a 15 tonne key unit was rolled 4 metres inland by an overtopping rush of white water only about a metre deep. The best solution seems to lie in using the largest high aspect boulders available laid flat in the top zone of the wall with their smallest face exposed to the sea and extend the top of the wall with extra top armour as shown in Fig 12(b).

An extremely effective expedient adopted on the Gold Coast for existing walls during high storm activity has been the provision of temporary top armour in the form of a single layer of sandbags laid flat and touching as shown in Fig 3. Such temporary armour however must be continually maintained by manual replacement and repair as it becomes damaged and as it distorts in response to settlement of the wall.

4. Timber Walls

At various times many segments of timber seawalls have existed on the Gold Coast with the earliest constructed circa 1920. All however have failed at one time or another and been replaced or faced seawards with boulder walls. The failure mode of a typical timber wall as shown in Fig. 4 is characterised by initial toe scour and undercutting accellerated by a lack of filter backing and the inability of the wall to settle. After a storm the partial skeleton of a timber wall may usually be seen well seaward of the erosion scarp it has failed to halt and the only reinforced masonry block wall constructed locally suffered the same fate in the same manner.

5. Grouted Walls

At one stage grouted walls became quite popular on the Gold Coast, these walls consisted of ordinary boulder walls where the Owner placed concrete in the voids between the rocks. The storm performance of these walls however has been very poor and they have always failed more rapidly than the standard walls. Ordinary face boulders absorb a great deal of wave energy by rocking and impacting on their neighbours; all boulder walls can be heard to "growl" under heavy wave attack and vibrations and movements within the armour can be felt by merely standing on top of them. Grouted armour cannot respond in this manner and the smoother more impervious face of grouted walls results in much larger uprush and overtopping volumes which lead to extensive early soil erosion behind them. It is practically impossible to effectively grout boulders in a semi submerged toe zone so once toe failure is initiated and the toe boulders settle the mass of the wall is left suspended until it collapses in a single shattering event as shown in Fig 5.

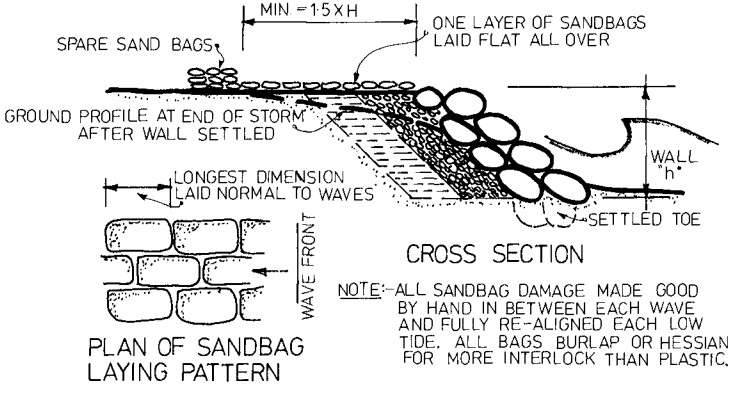

FIGURE 3:- GOLD COAST TEMPORARY TOP ARMOUR FOR REVETMENT WALLS.

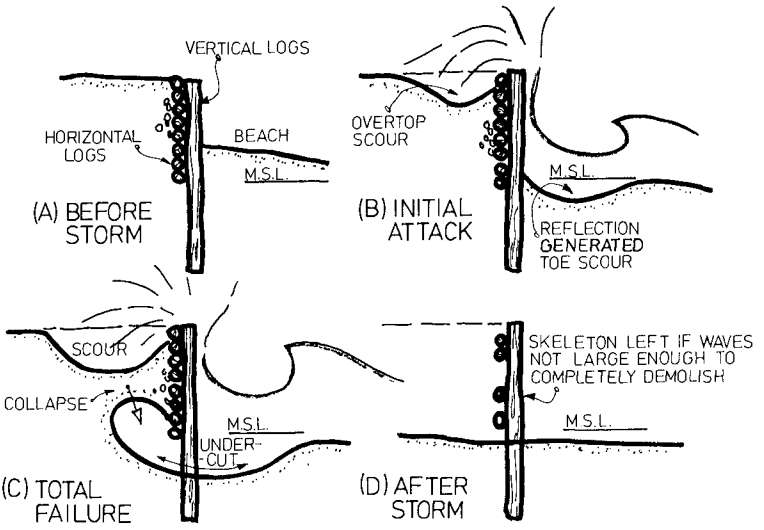

FIGURE 4:- FAILURE MODE OF LOG WALL

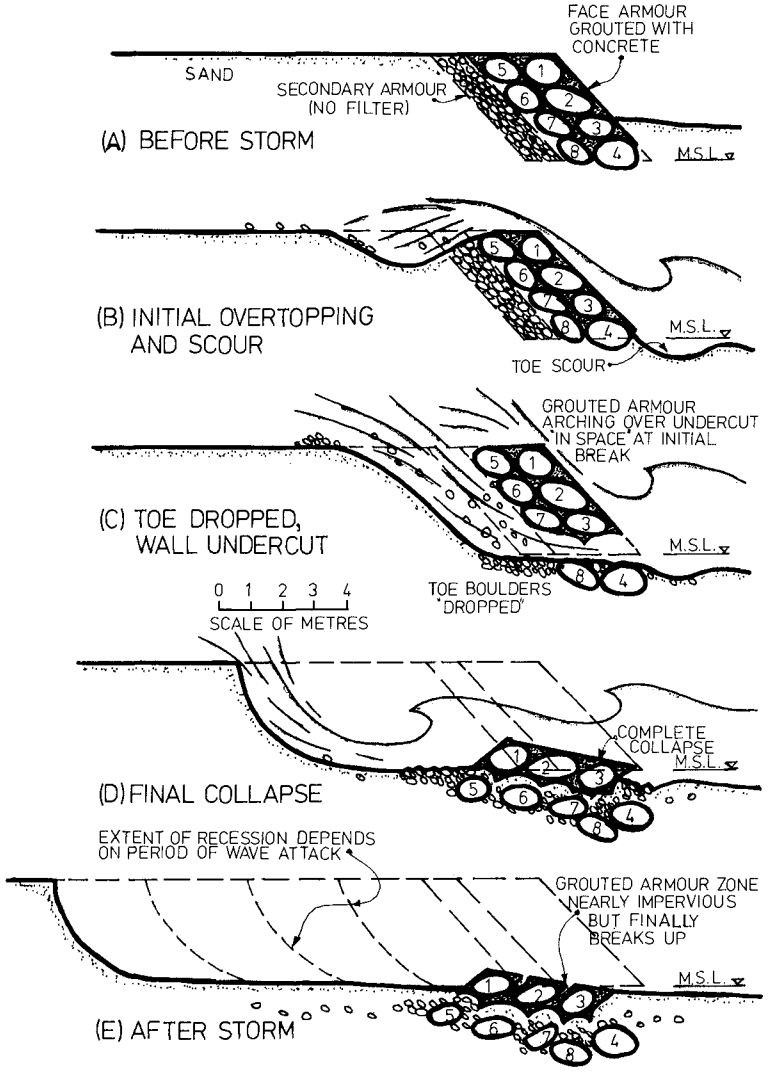

FIGURE 5:- COLLAPSE MODE OF GROUTED WALL

6. Double Waves

Of all the natural phenomena that may be included in a tropical cyclone event on the Gold Coast, the most frightening by far is the development of double waves. At least three times, in 1967, 1972 and 1974 during major storms this phenomenon has generated at least one short train of super waves, usually limited to four but sometimes reaching six in number. During a lull or low period in the incoming wave train the beach immediately in front of the revetment wall has been left nearly "dry", but this lull has been followed by a sequence of relatively large long period waves. The celerity of the first of these waves is retarded as it runs up the beach as a bore, usualy only some 2 metres deep; but the next waves celerity is not affected so it runs over the top to produce a double wave with a combined amplitude which may reach 5 metres and sometimes much more. Once the first double wave is generated the next three or four waves then also ride over the local high set-up which has been formed and the doubling phenomenon continues until the temporary set-up initiated by the first wave double drains away, and a normal wave train is re-established.

Such double waves however can do immense damage. On natural beaches such waves may overtop the highest dunes and as been observed, cause nearly seven metres recession of an erosion scarp for each double in a train. They also overtop local revetment walls with nearly two metres of green water, smashing into houses and washing away cars and other movable objects. On the Gold Coast their frequency to date has been about three major wave doubles on the beach per 8000 deep water peak storm waves per storm event but their probability remains unknown. Locally the phenomenon occurs often enough however to ensure that it will be inevitable that all revetment walls during their life-time must and will be exposed somewhere to very massive overtopping. Fortunately this process has always tended to be localised, the maximum length of beach observed affected has not exceeded a kilometer and has usually been only a third of this. Double waves can, and do, pop 5 tonne boulders out of revetment walls like champagne corks, a sight never to be forgotten once seen.

7. Gravity Forces

In the design of coastal structures it is easy to proportion the armour size and geometry for wave resistance properties alone. In addition to absorbing wave energy these structures must also maintain the capacity to hold themselves up; clearly any structure which is at its limit under body, or gravity forces alone, cannot be expected to hold any useful reserve to accept additional hydraulic forces. The local boulder revetments constructed at a slope of $1\frac{1}{2}$:1 have a factor of safety under gravity of only 1.06, a very sobering thought. It would not be surprising that for any sea wall near to its own self weight capacity, then the first element to fail should be the leading edge toe boulders, they are the most heavily stressed of all. Any seabed toe liquifaction can then only guarantee an initial failure and settlement.

8. Wave Set-Up Surge

Most coastal design texts e.g. the S.P.M. (C.E.R.C., 1977) provide ample tools for estimating surge levels due to barometric drop and wind set-up but the estimation of a realistic wave set-up appears to be a rather more

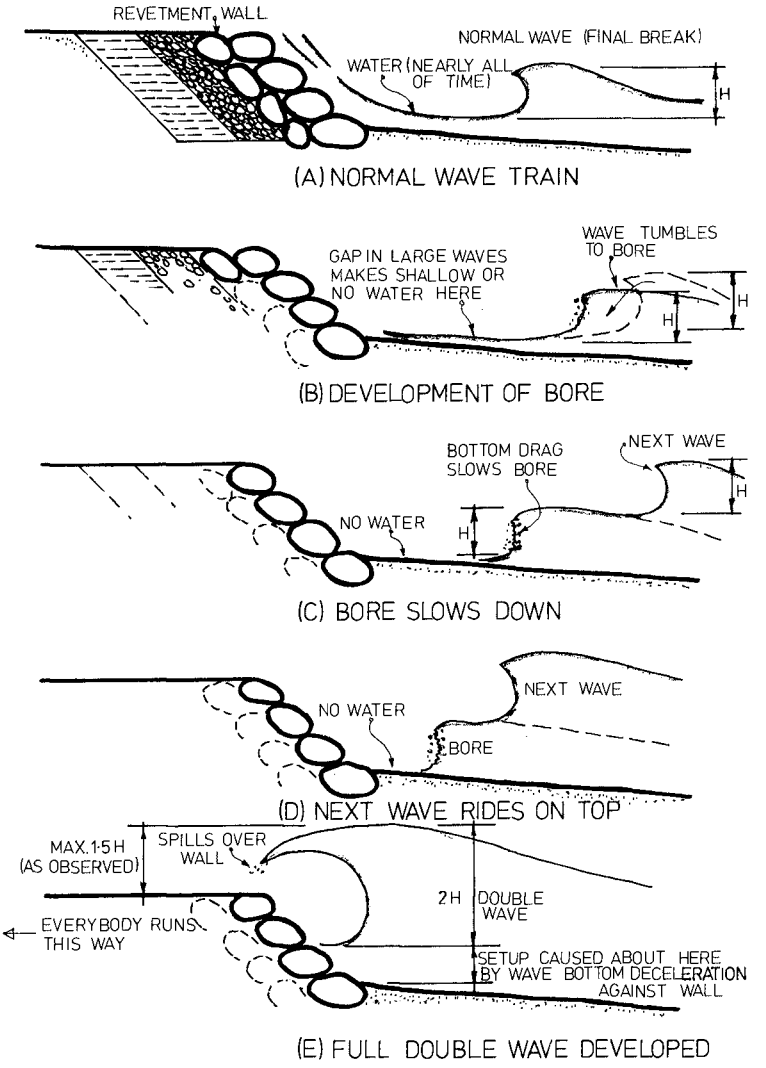

FIGURE 6:– DEVELOPMENT OF DOUBLE WAVES

intractable problem.

On the local coast during storm wave trains with Hsig exceeding 7 metre there are at least three main wave break zones with the waves reforming between each break and breaking again progressively as the water shallows up to the beach. For wave trains with Hsig generally 6 metres or less only two breaks are generated and for 3 metres or less there is usually only one significant breaking zone. Ten years observations of storms have indicated that each time a wave breaks it generates a wave set-up but that each set-up is localised to lie almost completely within the zone that the waves peak-up, break and then reform. As such for all offshore break zones each break set-up results in a local hump in the mean sea level that drains away on both sides of the breaking zone and it is only the final wave break on the beach itself that generates any set-up directly connected with the shore. The general resultant variations in mean sea level are shown diagrammatically in Fig. 7. Long term observations that the peak wave set-up within each breaking zone is approximately 25% of the breaking height seem to agree with Foster's estimates (pers. com.) but they do not support the assumption that any fixed percentage of Ho persists as a surge from the initial offshore break right onto the beach itself.

Elsewhere after great storms much evidence has been reported of apparantly unprecedented penetration by the sea to remarkable distances inland, and to such heights on dunes and local ground elevations that investigators have been led to postulate great surge levels to explain the evidence. It is quite likely however that much of this evidence has merely been the result of wave doubling. For example, eyewitness accounts record signs of wave attack levels over 13 metres above M.S.L. at Bathurst Bay in Australia in 1899 due to Cyclone "Mahina". Subsequent analyses by Silvester & Mitchell (1977) would predict a simple surge level of only 6.5 metres, but such a large cyclone must have generated many thousand waves much higher than 7 metres and it would require only one final shoaling wave of double height to reach the recorded water damage level on the shore itself, or indeed only one wave of 7 metres to ride over the beach surge, if it could penetrate that far, to attain the same result.

9. Revetment Wall Toe Exposure

The estimation of the likely water depth in front of a revetment wall at the time that it is likely to be exposed to a major storm is unfortunately rather a probabilistic exercise. A revetment wall is fixed in position but sandy ocean beaches are highly mobile with short term variations often completely masking long term recession or accretion, see for example Chapman and Smith (1981). The likely level of the beach in front of the wall, excluding localised toe scour will depend entirely upon where it is positioned within the overall swept prism of the beach (See Fig. 8). The swept prism represents the total mobile volume of the beach in response to all wave climates and sediment changes on the beach but the temporary response to great events, particularly in the offshore-onshore mode may be so large that long term trends are quite infinitesimal by comparison. Nevertheless some estimate of the probable limits of the swept prism must be made before the potential variations in shore level in front of the structure can be considered (See Fig. 9). Once a "hard" structure is constructed within the swept prism, that structure must be exposed to the same energy that would have been absorbed by the natural

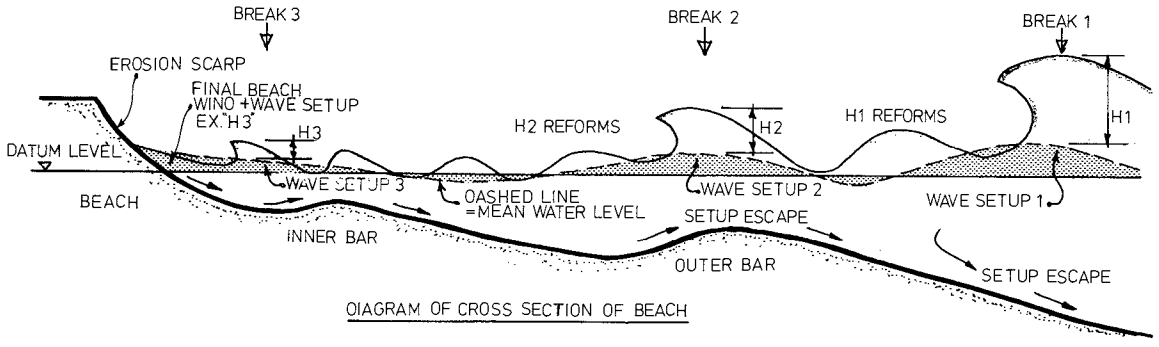

DIAGRAM OF CROSS SECTION OF BEACH

NOTES:— VISUAL OBSERVATIONS OF BEACHES INDICATE:—

(1) EACH WAVE BREAK REFORMS AND BREAKS AGAIN ABOUT HALF PREVIOUS "H"

(2) WAVE BREAK SETUP IS APPROX. 25% OF BREAKING WAVE HEIGHT AND IS LOCALISED WITHIN ACTUAL WAVE BREAK ZONE. WIND SETUP APPEARS CONCENTRATED MAINLY AT FINAL BEACH BREAK.

(3) GOLD COAST FINAL WAVE BREAK IS ALMOST NEVER ABOVE 3METRES SO THIRD OFFSHORE BREAK DOES NOT OCCUR UNTIL Ho EXCEEDS 7METRES.

(4) WAVE TROUGHS ARE NEARLY FLAT IN ALL WAVE BREAK ZONES BETWEEN INDIVIDUAL WAVES SO Ho SINE CURVE STRUCTURE BELOW LEVEL DATUM HAS BEEN SUPPRESSED AT OR BEFORE FIRST OFFSHORE BREAK.

FIGURE 7:- APPEARANCE OF SEA SURFACE AT GOLD COAST BEACHES DURING MAJOR CYCLONE/STORM EVENTS.

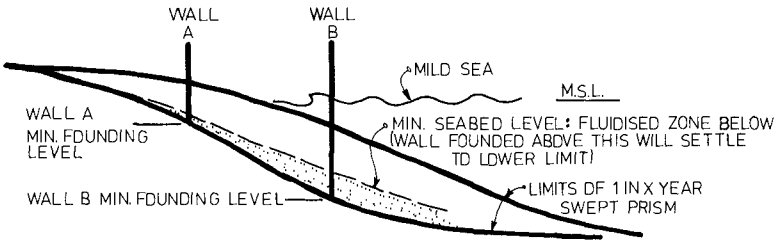

FIGURE 8:—EFFECT OF SEAWALL POSITION WITHIN SWEPT PRISM.

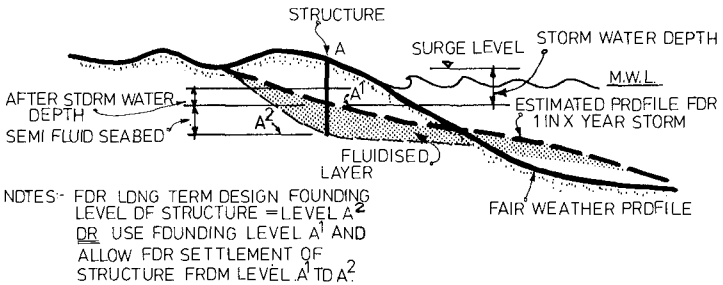

FIGURE 9:—DESIGN FOUNDING LEVELS FOR REVETMENT WALLS.

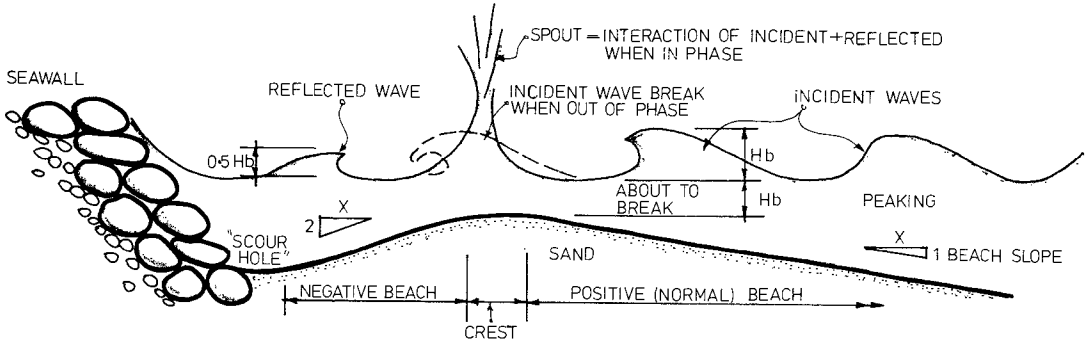

FIGURE 10:— REFLECTED WAVE PHENOMENON

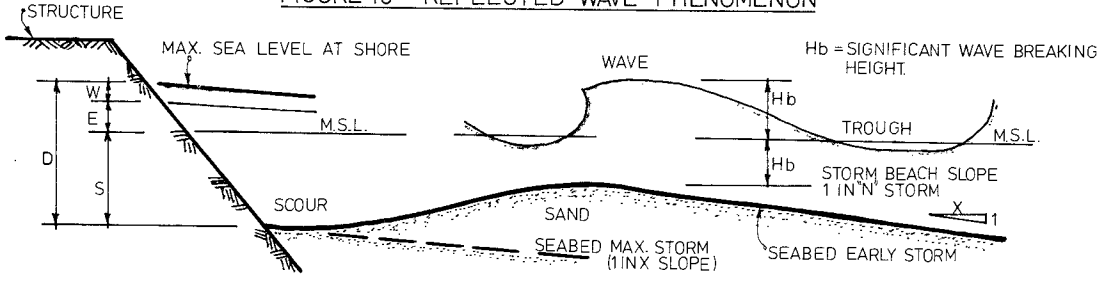

D = TOTAL MAX. WATER DEPTH EXPOSURE
W = WAVE SETUP = Hb/4 (THIS FLUCTUATES)
E = CALCUATED BAROMETRIC PLUS WIND SETUP
S = DESIGN SCOUR DEPTH = 2Hb + Hb/2 = 2·5Hb
NOTES:- MAX. POTENTIAL SINGLE WAVE ATTACKING STRUCTURE Hb(MAX.)= D.
DOUBLE WAVES WILL NOT OCCUR ONCE S > 0·75Hb AS A RULE OF THUMB.

FIGURE 11:— DESIGN HYDRAULIC EXPOSURE

beach volume now cut off from the waves by the structure itself. This it usually does in two ways - firstly by direct absorption of breaking energy by the face armour and secondly by reflecting the waves or part thereof again. Observations on the Gold Coast suggest that the reflected wave energy is then absorbed by two further concurrent processes; part of the outgoing wave energy is absorbed by the sediments themselves which adopt a "negative" beach slope in response, and the rest is absorbed by collision with the incoming waves. The total process is shown diagramatically in Fig. 10. The result is a sea-bed hollow in front of the revetment locally known as "toe scour".

Unfortunately little data have ever been collected on accurate toe scour depths but on the Gold Coast one section of boulder revetment wall during a short term beach starvation period was exposed to the ocean such that initially there was about 30 cm. of water at the toe at mean tide. Within two years the toe scour, depth "S" in Fig 11, reached 3m. at low tide and the wall had to be topped up twice, all during a calm period with the waves striking the wall seldom exceeding 1m. high. Many more observations have however been made of the magnitude of the waves reflected by boulder walls. With small waves striking rock walls reflection co-efficients of over 60% have been observed but during storms with well air entrained breaking waves (i.e. 2nd or 3rd storm breaks) the reflection co-efficient has varied between 25% and 50%. For design purposes locally the 50% factor is adopted for reasonable conservatism and the likely depths of water in front of a revetment at the beginning of a storm would be calculated as shown in Fig. 11, with depth "D" adopted for the maximum exposure at the peak of the storm.

10. Conclusions

On prototype revetment walls observations tend to suggest that many unexpected events occur in Nature that may seldom or never be detected in conventional flume tests on models. The most important results of local long term observations have been discussed and some of the resultant recommendations are set out below. Although the Gold Coast revetments represent only once class of such structures - that is a revetment sited with beach sediment all around it, i.e. in front, under and behind it; it is at least hoped that the "real time" observations may be of interest to some hydraulic structure designers.

11. Recommendations

For the design of boulder revetment walls of the simple class adopted on the Gold Coast similar to the details shown in Fig 12(a) it is recommended:-

(a) Special attention should be applied to extra toe scour delay features and additional top armour as shown in Fig. 12(b).

(b) Design wave set-up calculations should include consideration of Fig. 7.

(c) Design exposure water depths in front of revetments should include consideration of Figs. 8, 9 and 11.

(d) Wave testing of Gold Coast type revetments should be conducted in "soft bottom" tanks large enough to contain a compatible section of swept prism.

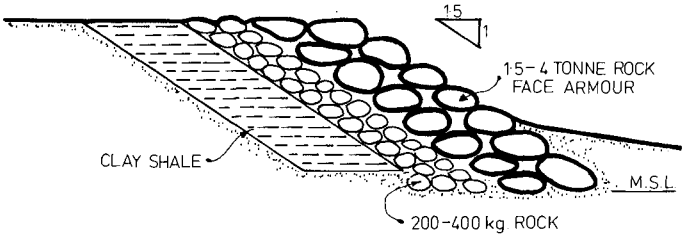

(A) GOLD COAST STANDARD

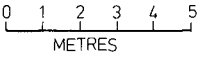

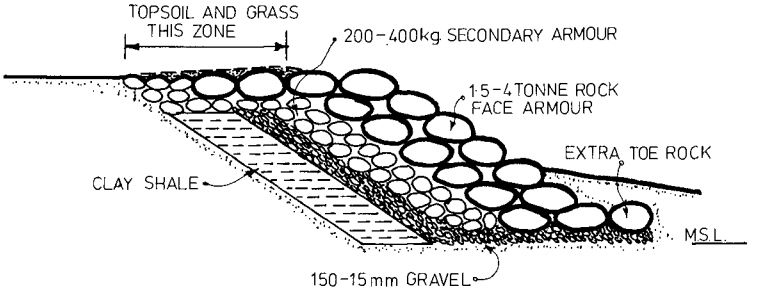

(B) RECOMMENDED REVISIONS

FIGURE 12:- BOULDER WALL DESIGNS

(e) There is nothing original in the concept of a "design storm" yet the basic armour and revetment stability factors might well merit the consideration of a "design event" say a cyclone or hurricane attacking the revetment for say 3 high tides of each 4 hours duration or say 3000 waves in total.

(f) Such a design wave climate might then well be simulated in the laboratory by a wave train of the form

(i) 1000 waves amplitude = 0.6D period = 10_s
(ii) 500 waves amplitude = D period = 15_s
(iii) 10 waves amplitude = 2D period = 20_s
(iv) 500 waves amplitude = D period = 15_s
(v) 1000 waves amplitude = 0.6 D period = 10_s

Such a design wave climate is highly arbitary but it does hold some resemblence to what at least local prototypes must be expected to withstand during a 1 in 50 and a 1 in 100 year event.

12. References

C.E.R.C. (1977) Shore Protection Manual. Washington, D.C., U.S. Army, Corps of Engineers, Coastal Engineering Research Center.

Chapman, D.M. and Smith, A.W. (1981)
A Ten Year Review of Variability on an Ocean Beach. 5th Aust. Conf. on Coastal & Ocean Eng. (1981) In Press.

Silvester, R. and Mitchell, H.L. (1977)
Storm Surges Around Australian Coasts. 3rd Aust. Conf. Coastal & Ocean Eng. Pub. 77/2. Inst. Eng. Aust. (1977).

SEDIMENTOLOGICAL INFLUENCES OF DETACHED BREAKWATERS

by
Dov Sergiu Rosen[1], M. ASCE and Michael Vajda[2], M.IAHR

ABSTRACT

Wave diffraction and refraction in the surroundings of a new detached breakwater induce currents strong enough to cause substantial local sediment transport and consequently morphologic changes, the main feature of which are sand spits or tombolos.

As shown by field studies the morphologic changes cause an equilibrium state with some minor fluctuations due to changing wave climate. Model studies have also proved the existance of such an equilibrium state for any given geometry and sea state

The present paper treats mainly this equilibrium state, but also attempts to explain the mechanism of sand transport characterizing the initial and transitional states. According to observations by the authors in small scale models, the transporting mechanism in the transitional state involves sea bottom erosion, especially near the breakwater heads outside the protected area, and transport of sand towards the shore of the sheltered area in the form of small migrating sand bars, which finally join the shore line and widen it. Results of experimental investigations conducted by the authors, for the particular case of high impervious breakwaters attacked by waves of normal incidence, as well as results of field and model studies given by others, are used to define relationships among the factors determining the equilibrium state and to base a new hypothesis regarding the equilibrium state. This hypothesis states that a morphologic and sedimentologic equilibrium is reached behind a detached breakwater, when the shape of the contour lines becomes such, that along the sheltered beach the diffracted waves have components of momentum opposed to the gradients of the mean sea level induced by radiation stress due to non uniform wave heights along the wave fronts approaching from both sides of the breakwater. The significant parameters characterizing the dimensions of the spit or tombolo in the equilibrium state are shown to be the relative length of the breakwater (compared to its distance from the original shore line), the relative distance from the original shore line (compared to the position of the breakers' line) and the relative height of the breakwater crest (above M.S.L, compared to the incident wave height).

INTRODUCTION

Offshore detached breakwaters are used worldwide for four engineering purposes; to shelter water bodies from waves, to protect beaches against erosion, to prevent silting of harbour entrances and to facilitate shore accretion for reclamation. The achievement of these goals

---

[1] Chief Engineer, M.Sc., Israel Coastal and Marine Engineering Research Institute, Technion City, Haifa 32000, Israel.

[2] Associate Professor, D.Sc. Faculty of Civil Engineering, Technion - Israel Institute of Technology; Scientific Advisor, Israel Coastal and Marine Engineering Research Institute, Technion City, Haifa 32000, Israel.

can be accomplished by diminishing the wave heights inside the area protected by the breakwater, mainly due to wave diffraction, and by trapping sand inside this area in the shape of a spit, which in certain circumstances becomes attached to the breakwater and then it is called tombolo.

In the past the construction of these breakwaters was based on field experience and on empirical rules. Lately, there have been certain attempts to treat the complex hydraulic and sedimentologic phenomena and processes related to the presence of such an artificial obstacle in a wavy sea by theoretical methods and by laboratory investigations on reduced scale models.

The hydraulic and morphologic processes induced by the construction of a detached breakwater may be characterized by three stages of development as follows:

a - initial state
b - transitional state
c - equilibrium

Following the construction of a detached breakwater the current pattern in its surroundings changes immediately. In this initial state a circulatory current cell develops on each side of the axis of symmetry in the sheltered area as observed in the field by Johnson (1919), viewed in small scale model by Sauvage et al. (1954) and proved theoretically by Liu et al. (1974). These currents are directed near the shore towards the sheltered area and are generated by lateral gradients in the mean sea level in the zone of diffraction, due to the effect of radiation stresses in a non uniform wave field, as explained best by Gourlay (1974, 1976).

In the transitional state, the above mentioned currents transport sand and deposit it in the sheltered area, building a new morphological land shape named spit, or if this becomes attached to the breakwater, tombolo.

In the field this state has been studied by a number of researchers by different methods. Ingle (1966), used granulometric analysis to check the change of the mean sand grain size on the foreshore apex of the sheltered area of the Santa Monica breakwater with time (1940-1962). He found that the mean grain size at the spit apex became thinner as time passed. The explanation brought by him was that while the spit apex progressed towards the breakwater due to continuous sand deposit, regions with less and less wave energy were reached, where only small grains could be transported. U.S. Engineer Office (1939), Johnson (1940, 1949), Handing et al (1950), Wiegel (1966), Nir (1976) and Toyoshima (1976) have used differential bathymetric maps or control profiles to study the transitional state. These indicated accretion of the shore line and decrease of water depths in all sheltered area. No one succeeded to confirm whether the origin of sand deposited in the sheltered area was from the neighbouring shore or mainly from the area opposite the breakwater heads or else. However, Nir indicates (for breakwaters built inside the dominant surf zone) that the sand trapped in the whole sheltered area in the first year reached about 50 percent of the total sand trapped in the final state. In the second year the sand accretion rate regressed significantly but increased again in the following one to three years by the end of which it stopped and

and morphologic equilibrium was achieved. To Nir's opinion, the regression in the second year was due to the temporary diminution of sand sources in the area surrounding the breakwater. Furthermore, according to his opinion the main sand source was sand from the neighbouring beaches, which consequently suffered erosion in the first years.

The transitional state was studied also by means of small scale models. Sauvage et al. (1954) applied on a shore parallel detached breakwater normal waves and also waves of equal oblicity from both sides of the breakwater, while continuously supplying sand (artificial) in the surf zone outside the sheltered area. In both cases they found that the shore line progressed parallel to its original shape towards the breakwater with only a small spit formation until the distance from the breakwater reached a critical value beyond which a tombolo developed. According to their opinion, sediment deposit was best facilitated along the axis of symmetry in the sheltered area because of two reasons: a) collision of the two opposite currents developed, b) turbulence decrease due to diminished wave height on the center line. However, in certain cases they found that the main sand deposit occurred as two spits which developed opposite each breakwater head. This phenomenon was explained by wave diffraction. Their main conclusion was that the process of tombolo formation depends on the wave characteristics and on the breakwater geometry. Additional information was brought by Shinohara et al. (1966) who studied in a small scale model with natural sand the process of sand deposit behind shore parallel detached breakwaters under the action of waves of normal incidence. Two wave steepnesses representing summer waves (H_o/L_o = 0.019) and winter waves (H_o/L_o = 0.046) were applied on a breakwater model of fixed length but located alternately at different distances from the original shore line such that the relative distance X_B/Y_B was 0.5; 1.0; 1.75; 2.5. They studied mainly the change of the water line with time, giving a few other contour lines only for the final state.
Currents were not measured. Regarding the development process the main fact which may be observed from the data brought by these authors is that in almost all the tests the spit development started with the formation of two small spits each one opposite one of the breakwater heads. Furthermore, the transitional state ended with the formation of a spit of stable morphologic state but tombolo formation never occurred. for these testing conditions.

Finally, numerical models have been developed which forecast the shore (water) line in the sheltered area of a detached breakwater, all being based on the differential equations developed originally by Pelnard-Considere (1956). Results of numerical models developed by Hashimoto (1974), Sasaki (1976) and Perlin (1979) show considerable progress in the representation of the transitional state, forecasting shore line accretion with one or two spits. However, when compared with small scale model results, it comes out that the numerical results are mainly of a qualitative nature and differ considerably in forecasting the quantitative values. The accuracy of the numerical model results is limited because of problems related to accurate solution of combined refraction, diffraction and reflection in water of changing depths, non-linear wave-wave effects, correct solution of two phase (water-sediment) flow, problems related to numerical modelling methods, etc.
The equilibrium state was studied by a number of researchers by field observations and in small scale models.

Many field observations indicated that the new land formed by sand deposit behind a detached breakwater reaches finally a relatively stable shape, which fluctuates around an average state due to changing wave climate (Johnson (1952), Spataru (1963), Inman et al. (1966), Silvester (1972), Toyoshima (1974), Nir (1976) and Noble et al. (1978)). The conclusion reached by Inman et al. (1966) was that tombolo formation would take place if the ratio X_B/Y_B is less than a third, but if this ratio is larger than six the size of the spit formed would be very small. Toyoshima (1974) observed that the final quantity of sand trapped by the detached breakwater is influenced by position of the breakwater relative to the position of the breakers line. (Nir (1976), found for detached breakwater built inside the predominant surf zone that the area of the new land reclaimed reached from 25 to 75 percent of the sheltered area (X_B/Y_B) and that the morphologic equilibrium state was achieved in three to five years from the construction. Dean (1978) found from field surveys of the shores of the Atlantic and those of the Gulf of Mexico that the shape of the shore line behind two headlands or two detached breakwaters (in equilibrium state of tombolo)could be approximated by an ellipse and that the change in the depths on the median between the two breakwaters is a function of the relative distance of the breakwaters from the initial shore line at the power 2/3. As one can see, the quantity of information gathered from field observations is quite limited.

Studies of the equilibrium state in small scale models brought further information regarding the equilibrium state. Sauvage et al. (1954) brought a most important evidence for the understanding of the equilibrium state. This is presented in a picture which showed the shape of the water line of a tombolo in equilibrium state. It may be observed that this shape is elliptical and not circular, as one might assume by analogy to the shape of diffracted wave fronts.

The results of a model study by Shinohara et al. (1966) proved again that a morphological equilibrium state is achieved behind a detached breakwater and from a limited number of tests in which the wave period and the breakwater length were kept equal and constant,concluded that the equilibrium state is influenced by the wave steepness and by the relative distance from the initial shore line. However, one could observe that the actual influence was due to the different wave heights and therefore the different relative positions of the breakwater with respect to the breakers' line. These results indicated that a maximum sand deposit occurs in the sheltered area for the case when $X_B/Y_B = 1$. Silvester (1970, 1974) studied the equilibrium state of the shore lines of tombolos formed between adjacent detached breakwaters or headlands. Using the findings of Yasso (1965) which showed that the natural water line between adjacent headlands is stable in nature and can be described by a section of a logarithmic spiral, Silvester described the equilibrium water line between two adjacent breakwaters as being formed by a section of a logarithmic spiral and a straight section tangent, to this spiral section. Furthermore, the hypothesis used by him to describe the equilibrium state was, that it occurs when no more sediment is moved in the sheltered area due to the development of contour lines parallel to the diffracted wave fronts. This, according to him would lead to zero oblicity of the wave fronts with the contour lines and hence to zero longshore sediment transport. Further information regarding the equilibrium state was brought by

Gourlay (1974, 1976). Though his study purpose was to prove other things, its results can be used to prove that the hypothesis brought by Silvester and generally accepted since then (Komar (1978)) is wrong. Gourlay (1976) measured the currents developing in the sheltered area of a detached breakwater model. The bottom's contourlines were casted in concrete so that outside the sheltered area they were straight and parallel to the breakwater but in the sheltered area they were made as concentric circular sections reproducing a tombolo shape and the breakwater was attacked by waves of normal incidence. Thus, the contour lines were parallel to the incident wave fronts both outside and inside the sheltered area. This however did not prevent the generation of currents in the surf zone of the sheltered area which had in this model speeds larger (0.4 m/sec) than the incipient natural sand transport velocity. The study showed that they were generated by a gradient in the mean sea level between the unsheltered area and the sheltered area due to non uniform wave heights (and hence different radiation stresses) in two regions. Therefore the general hypothesis used until now to describe the equilibrium state is erroneous.

PARAMETRIC DESCRIPTION OF THE EQUILIBRIUM STATE

The significant physical parameters influencing the morphologic equilibrium resulting by the implantation of a detached breakwater are as follows:

- Y_B - the length of the breakwater
- X_B - the breakwater's distance from the initial shoreline
- S - the elevation of the breakwater's crest above MSL.
- K - the porosity of the breakwater
- D_B - depth at centerline of the breakwater
- $\beta(x)$- local bottom slope
- H_o - deep water wave height
- T - wave period
- α - wave approach angle

In addition some parameters pertaining to the local sediment may be mentioned , like:

- ρ_s - the specific density of the sediment
- d_{50} - median grain diameter
- θ_r - repose angle
- σ_ϕ - skewness factor of grain size distribution
- S.F.- shape factor of the grains

However, all this features may be summarized by the most significant property of the sediment from the point of view of the transport process, it is the characteristic fall velocity (V_f).

In the particular case of tombolo or spit formation induced by a shore parallel, impermeable and high breakwater (not overtopped by waves) the following dimensionless relationships can be deduced from the list of the relevant significant physical parameters:

- When only a spit is formed then

$$(1)\quad \frac{X_A}{X_B} = \phi \left(\frac{Y_B}{X_B}, \frac{X_{br}}{X_B}, \frac{H_o}{V_f \cdot T}, \frac{H_o}{L_o}\right)$$

where the parameter X_A represents the distance from the land spit at its apex measured from the original (equilibrium)shore line,

- In the case of a complete tombolo, the characteristic dependent variables are Y_T, A_T and V_T. Consequently the dimensionless relationships may be written as:

$$(2)\quad \frac{Y_B - Y_T}{2X_B} = \phi_2 \left(\frac{Y_B}{X_B}, \frac{H_o}{V_f T}, \frac{H_o}{L_o}\right)$$

$$(3)\quad \frac{A_T}{X_B Y_B} = \phi_3 \left(\frac{Y_B}{X_B}, \frac{H_o}{V_f \cdot T}, \frac{H_o}{L_o}\right)$$

$$(4)\quad \frac{V_T}{Y_B X_B^2 \tan\beta} = \phi_4 \frac{Y_B}{X_B}, \frac{H_o}{V_f \cdot T}, \frac{H_o}{L_o}$$

where:

Y_T - the attachment width at the breakwater

A_T - the accreted sand area

V_T - the total volume of sand trapped in this protected area

The expressions indicate the dependence of the geometric parameters characterizing the sedimentologic development caused by a detached breakwater on the parameters of the waves, of the sediments and of the beach profile.

SMALL SCALE MODEL STUDY

A series of tests were carried out in a small scale moveable bed model with a high impervious detached breakwater parallel to the shore line attacked by waves of normal incidence. The model study was conducted in a wave tank. A beach was built of artificial sand (coarse bakelite, $\rho_s = 1.42$ gr/cm^3, $d_{50} = 0.64$ mm, $V_f = 2.9$ cm/sec)see slopes

in fig. 1. The beach was 7 m long, the depth near the wave generator was 40 cm and the water line was located at about 9 m from the wave generator.

Three groups of tests were performed for three deepwater wave steepnesses (H_o/L_o) of 0.015, 0.025 and 0.040. For each wave steepness only one wave height H and one wave period were used. For each group of tests the breakwater length Y_B and its distance from the original shore line (X_B) varied (see table 1) to cover different conditions.

For each group of wave steepness the beach was initially brought to a natural equilibrium state, taking care that the equilibrium state would not be influenced by the initial beach slope using Dalrymple et al. (1976) conclusions. Then for such an equilibrium beach a detached breakwater with the smallest length (Y_B = 0.5 m) was implanted at a distance X_B from the new equilibrium water line and attacked by the same waves.

When morphological equilibrium state was attained, the breakwater was lengthened to Y_B = 1.0 m attacked further with the same waves until a new equilibrium was attained and then the process was repeated with Y_B = 2.0 m. At the end of these tests the initial beach slope was rebuilt, brough again to equilibrium by the same waves and the small breakwater was then built at a new distance X_B from the natural(equilibrium) water line. Then the process of breakwater lengthening was carried out as explained above.

During each test the transitional state was monitored by eye observation, by pictures, by marking with small sticks the progressing water line and by measuring control profiles by means of a point gauge installed on a carriage moving above the model area.

Morphological equilibrium was indicated by the stability of the water line, and by the practical identity of three consequitive outcomes of control profile measurements which also served as a basis for the contour charts.

SEDIMENT TRANSPORT IN THE TRANSITIONAL STATE

The process of sand deposit in the sheltered area was continously observed during the development stage. Current patterns were visualized using fluorescent dye. The observed phenomena are described below:

a) After the implantation of the detached breakwater, two circulatory currents as described theoretically by Liu et al. (1971) were observed. In some cases the dye indicated currents returning to the unprotected side of the breakwater around the heads (kind of fluctuating rip current).

b) Sand was observed to be transported from area outside the sheltered zone towards the sheltered zone and towards the shore line. Inside the sheltered area the sand accumulated around the axis of symmetry (perpendicular to the shore line) in such a way, that the resulting bathymetry was saddle - like due to concentration of sand deposit near the original shore line and near the breakwater.

c) From time to time, the formation of submerged sand bars was observed in the inshore area, opposite each one of the breakwater heads.

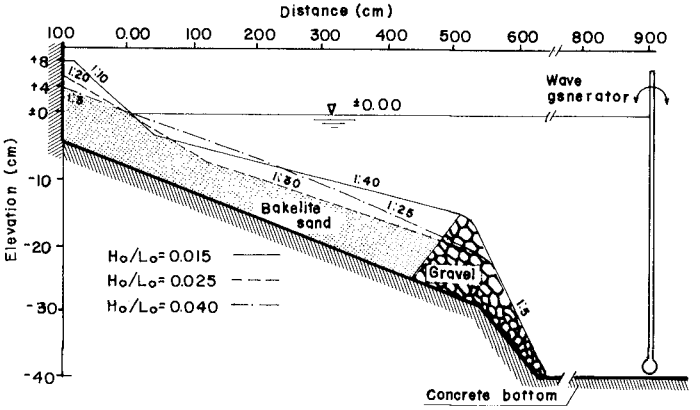

Fig.1- INITIAL BEACH SLOPES FOR THE THREE SERIES OF TESTS PERFORMED

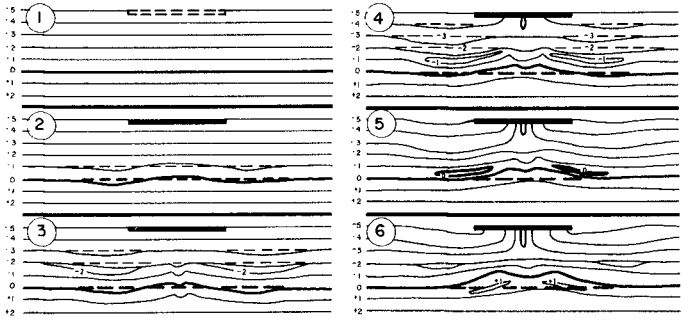

Fig. 2- TRANSITION STATE

DEVELOPMENT OF THE SAND SPIT BEHIND A DETACHED BREAKWATER

On these bars the sand moved with the waves and also with the circulatory current.

The slope of the bar was relatively moderate in the direction of wave progress but terminated with a steep slope (almost vertical) on its shoreward end (see fig. 2). The typical height of the sand bars was about 5 mm. The sand bars migrated towards the shore from both sides of the breakwater and towards each other. When they were close to the foreshore, they created with the shore line a kind of troughs. On the symmetry axis the two troughs joined and formed a channel near the water line. In the two troughs relatively high velocities were observed, but the sand was transported mainly near the edges of the troughs. The transporting speed was also high in the channel formed on the axis of symmetry of the sheltered area, but sand was transported mainly as bed load towards the ridge of the "saddle" area described previously, were most of the sand settled. The rest moved further towards the breakwater heads, parallel to the breakwater.

d) After some time, the migrating bars joined the shore creating two small spits. With time other sand bars joined them and also the area between the two spits filled with sand so finally in most cases a single spit was formed.

ANALYSIS OF THE TESTING RESULTS

The beach morphology in the equilibrium state was analyzed by comparing the change in the beach profile at control sections (fig.3), and by comparison of the final water lines obtained in each test (see figs. 4,5 and 6).

It was considered that the sand deposit in the sheltered area can be well represented by the value of X_A, i.e. the size of the sand spit at its apex measured from the initial (equilibrium) water line. Using the beach profiles the influence of the breakwater length (Y_B), its distance from the shore line (X_B), and of the wave steepness (H_o/L_o) on the size of the spit were studied. The main results of these analyses are presented in the following lines:

Influence of the breakwater length (Y_B)

The lengthening of the breakwater in a given wave regime lead usually to sand deposit in the sheltered area. The amount of sand deposited decreases from the axis of symmetry towards the unsheltered area.

Near the breakwater in the sheltered area a channel parallel to the breakwater is formed. Its dimensions grow with increasing breakwater length, especially when the breakwater was relatively far from the original water.

In the front of the breakwater, a series of sand bars develop with their length of the same approximate size like that of the breakwater. This is clearly due to wave reflection.

Influence of the distance of the breakwater from the shore line(X_B)

The closer the breakwater is placed to the shore line, the larger the sand deposit in the sheltered area and the bigger the chance that the spit would become a tombolo.

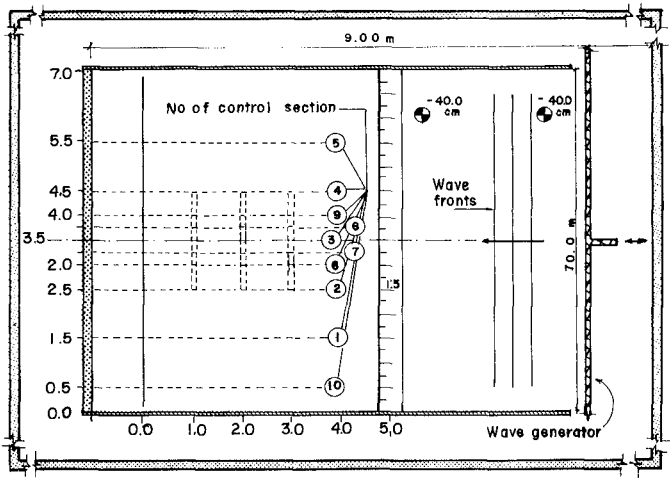

Fig. 3 - LAY OUT OF THE MODEL IN THE WAVE TANK AND LOCATION OF THE BREAKWATERS AND OF THE CONTROL PROFILES.

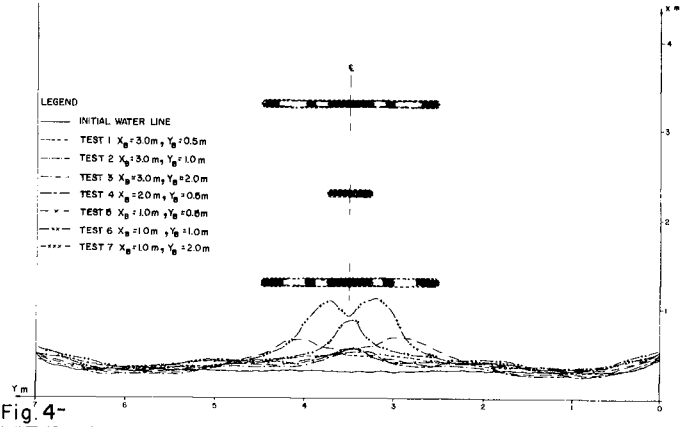

Fig. 4- WATER LINES IN EQUILIBRIUM STATE FOR TESTS SERIES H_o/L_o= 0.015

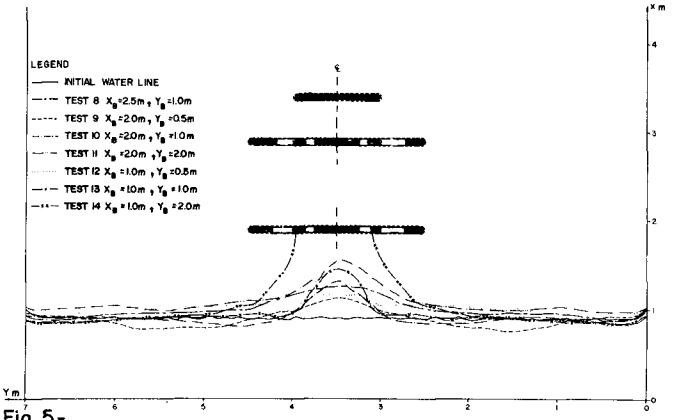

Fig. 5-
WATER LINES IN EQUILIBRIUM STATE FOR TESTS SERIES H_o/L_o=0.025

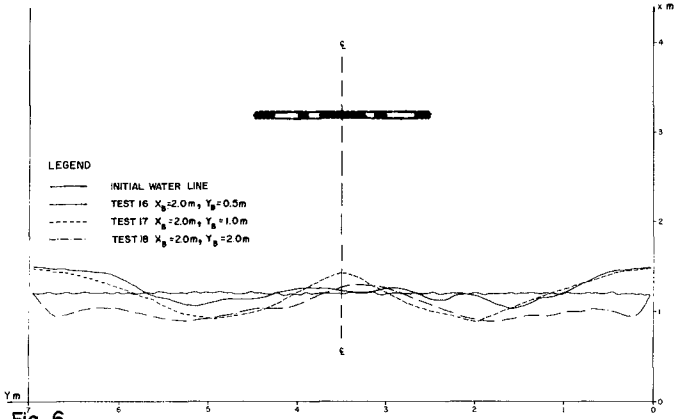

Fig. 6-
WATER LINES IN EQUILIBRIUM STATE FOR TESTS SERIES H_o/L_o=0.040

When the breakwater is placed close to the shore line the channel which develops near the breakwater, when it is far from the shore line, disappears.

Influence of the non dimensional parameter Y_B/X_B

Regarding the influence of both Y_B and X_B, and considering the outcome of the dimensional analysis it was concluded that the actual independent variable on which the geometry of the sand spit depends is the relative length of the breakwater Y_B/X_B. This served, as a matter of fact for the preparation of fig. 7, in which the dependence of the spit geometry on this factor is clearly demonstrated.

This analysis included also results from nature and from other model studies which are summarized in tables 2 and 3.

Further, for the cases when a tombolo was formed (X_A/X_B=1.0) another analysis was made and the outcome is presented in fig. 8.

For points in fig. 7, indicating tombolos formed in nature, the distance of the breakwater relative to the breaker line (X_B/X_{br}) is not specified because it is variable, usually including cases with $X_B/X_{br}<1$.

Influence of the wave steepness (H_o/L_o)

It was found that the general equilibrium beach profile differred considerably for wave steepness 0.015 which was of a "summer" type, relative to the general beach profile obtained for the other two steepnesses(0.025 and 0.040), which were of similar "winter" type. This result corresponds well to the ones obtained by Johnson (1952), but also to the ones of Dean (1973) which concluded that the fall velocity parameter $H_o/V_{f.T}$ determines the type of beach profile, the critical value for transition from summer profile to winter profile being 0.85 (see table 1).

ANALYSIS OF THE EQUILIBRIUM STATE

The existence of a morphologic equilibrium in the surroundings of a detached breakwater under the influence of a certain incoming wave was proved by the present study. Additional information obtained from actual observations in the nature shows, that this statement can be extended for the average morphology developing under the influence of a certain wave climate.

There are various hypothesis how this equilibrium state is reached and how can the stability of the new configuration be physically explained or characterized by the relevant mechanism of sediment transport.

The attempts to find such an explanation led to the following assumptions:

a) Due to bathymetric changes the longshore current in the sheltered area fades completely or becomes so weak that the longshore sediment transport stops.

b) The longshore transport does not stop in the sheltered zone (along the tombolo beach) but continuity is maintained by recirculation of sand.

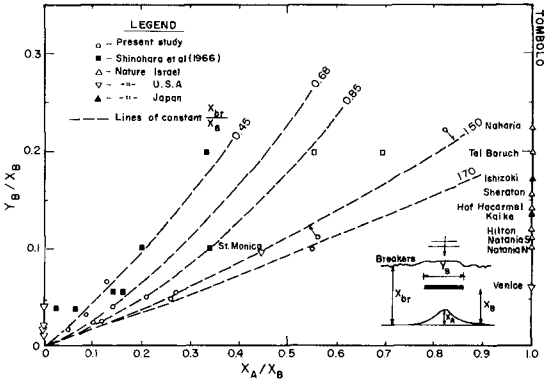

Fig. 7 -
RELATIONSHIPS AMONG PARAMETERS DETERMINING THE SPIT SIZE IN THE EQUILIBRIUM STATE

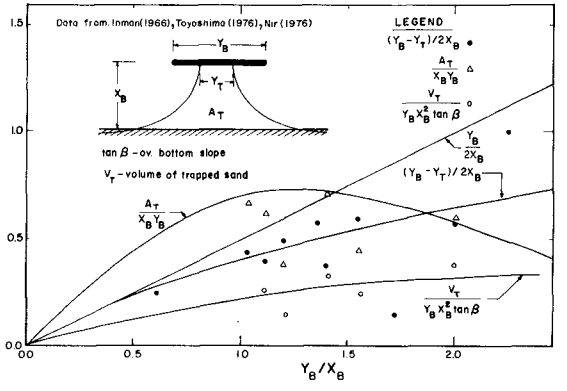

Fig. 8 -
RELATIONSHIPS AMONG PARAMETERS DETERMINING THE TOMBOLO SIZE IN THE EQUILIBRIUM STATE

$\frac{H_o}{L_o}$	Test No.	H_o (cm)	T (sec)	L_o (m)	X_B (m)	Y_B (m)	X_A (m)	X_{br} (m)	$\frac{Y_B}{X_B}$	$\frac{X_A}{X_B}$	Y_T (m)	$\frac{Y_B - Y_T}{2X_B Y_B}$	$\frac{H_o}{V_f . T}$
	1				3.0	0.5	0.16	1.36	0.167	0.053			
	2				3.0	1.0	0.26	1.36	0.333	0.087			
	3				3.0	2.0	0.38	1.36	0.667	0.127			
0.015	4	1.5	0.8	1.0	2.0	0.5	0.21	1.36	0.25	1.105			0.65
	5				1.0	0.5	0.24	1.36	0.56	0.24			
	6				1.0	1.0	0.56	1.36	1.11	0.56			
	7				1.0	2.0	0.82	1.36	2.22	0.82			
	8				2.5	1.0	0.35	1.70	0.40	0.14			
	9				2.0	0.5	0.23	1.70	0.25	0.115			
	10				2.0	1.0	0.42	1.70	0.50	0.21			
0.025	11	3.9	1.0	1.56	2.0	2.0	0.66	1.70	1.0	0.33			1.34
	12				1.0	0.5	0.26	1.70	0.50	0.26			
	13				1.0	1.0	0.55	1.70	1.0	0.55			
	14				1.0	2.0	1.0	1.70	2.0	1.0	0.86	0.57	
	15				1.0	0.5	0.25	1.70	0.5	0.25			
	16				2.0	0.5	0.05	1.0	0.25	0.025			
0.040	17	8.0	1.15	2.06	2.0	1.0	0.24	1.0	0.50	0.12			2.40
	18				2.0	2.0	0.23	1.0	1.0	0.115			

TABLE - 1: Experimental data conditions and results

Author	$\frac{H_o}{L_o}$	H_o (cm)	T (sec)	L_o (m)	X_B (m)	Y_B (m)	X_A (m)	X_{br} (m)	$\frac{Y_B}{X_B}$	$\frac{X_A}{X_B}$
					0.75	1.50	0.25		2.00	0.333
					1.50	1.50	0.30		1.00	0.20
Shinohara and	0.0192	2.55	0.922	1.33	2.625	1.50	0.375		0.57	0.14
					3.75	1.50	0.25		0.40	0.067
					0.75	1.50	0.52		2.00	0.693
Tsubaki (1966)	0.0461	6.12	0.922	1.33	1.50	1.50	0.50		1.00	0.333
					2.625	1.50	0.425		0.57	0.16
					3.75	1.50	0.10		0.40	0.027
Horikawa and Koizumi (1974)	0.020	8.7*	1.15	2.06	2.0	4.0	1.1		2.00	0.55
Sasaki (1976)	0.02*	8.7*	1.15	2.06	2.0	4.0	0.70		2.00	0.33
					100.	200.	26		2	0.26
					100.	300.	48		3	0.48
Perlin (1979)	0.0086*	86.0*	8.0	100.0	100.	400.	35		4	0.35
					100.	600.	28		6	0.28
					400.	800.	50		2	0.125
					200.	400.	96		2	0.24
					50.	100.	18		2	0.18
	0.0217	2170*	8.0	100.0	100.	200.	50		2	0.50
	0.030	30*	8.0	100.0	100.	200.	11		2	0.11
Sauvage et al (1956)			0.80	1.00	1.00	0.80	1.00		0.80	1.0

*Estimated by present authors from other data given by the author

TABLE 2: - Results obtained by other researchers by numerical and physical small scale models

Author	Location	Name of structure	h_B (m)	X_B (m)	Y_B (m)	X_A (m)	Y_T (m)	$\frac{Y_B}{X_B}$	$\frac{X_A}{X_B}$	$\frac{Y_B - Y_T}{2\ X_B}$	Remarks
Inman et al (1966)	*Venice*	*Venice breakwater*	*5.0*	*300*	*180*	*300*	*36*	*0.60*	*1.0*	*0.24*	*Groyne not removed*
Noble	*St. Monica*	*St. Monica brwtr.*	*7.2*	*555*	*540*	*~250*	*-*	*0.97*	*0.45*	*-*	
(1978)	*Thum's Island*	*Island B*	*9.0*	*780*	*325*	*~ 0*	*-*	*0.42*	*0*		
	- " -	*- " - C*	*9.0*	*1666*	*325*	*~10*	*-*	*0.20*	*0.006*	*-*	
	- " -	*- " - D*	*12.0*	*1985*	*260*	*~ 0*	*-*	*0.13*	*0*	*-*	
	Rincon Island	*Rincon Island*	*12.5*	*1650*	*160*	*~ 0*	*-*	*0.10*	*0*	*-*	
Bruno et al (1979)	*California*	*Channel Island Harbour brwtr*	*9.0*	*600*	*700*	*260*	*-*	*1.167*	*0.433*	*-*	
Toyoshima	*Ishizaki*		*-*	*35*	*60*	*35*	*50*	*1.714*	*1.0*	*0.143*	
(1974,1976)	*Kaike*		*5.0*	*110*	*150*	*110*	*25*	*1.364*	*1.0*	*0.568*	
Nir		*Naharia*									*Groynes in its*
(1976)	*Naharia*	*brwtr.*	*-*	*80*	*180*	*80*	*20*	*2.25*	*1.0*	*1.0**	*neighbourhood*
	Haifa	*Hof Hacarmel*	*3.0*	*200*	*280*	*200*	*130*	*1.40*	*1.0*	*0.375*	
	Netanya	*North brwtr.*	*-*	*200*	*207*	*200*	*35*	*1.035*	*1.0*	*0.43*	
		South brwtr.	*-*	*215*	*240*	*215*	*70*	*1.116*	*1.0*	*0.395*	
	Tel Aviv	*Tel Baruch*	*3.0*	*100*	*200*	*100*	*105*	*2.00*	*1.0*	*0.475*	
		Sheraton	*4.0*	*200*	*310*	*200*	*75*	*1.55*	*1.0*	*0.588*	
		Hilton	*4.0*	*200*	*240*	*200*	*45*	*1.20*	*1.0*	*0.488*	

TABLE 3: - Data regarding spits and tombolos in nature

Silvester (1970, 1974) explained hypothesis a) by assuming that the bottom contour lines become parallel to the diffracted wave fronts. Model tests carried out by Gourlay (1976) indicate, that this may not be the case, because such a morphology involves strong currents capable of causing intensive sediment transport along the sheltered beach. Consequently, hypothesis a) should be discarded. The condition for hypothesis b) clearly must be the existence of a circulatory current strong enough to maintain longshore transport along the equilibrium spit or tombolo beach. However, continuity considerations show, that such a strong current may not exist in the vicinity of a detached breakwater because the current at the breakwater heads would be much weaker than that at the shore, facilitating there sediment deposit which would mean that equilibrium was not reached. This was also indicated by the model tests of Gourlay (1976). Therefore, this conclusion leads back to hypothesis a) which had to be given another physical explanation.

DISCUSSION OF A NEW EQUILIBRIUM HYPOTHESIS

The authors observed in the model and then in nature that the morphological equilibrium was reached when the shape of the contour lines was not completely parallel to the diffracted and refracted wave fronts (see fig. 9 and 10). The present hypothesis states that a morphologic and sedimentologic equilibrium is reached when the shape of the contour lines is such that along the sheltered beach the diffracted waves have a component of momentum opposed to the gradient of the mean sea level induced by radiation stress due to non uniform wave height along the wave fronts. This explains the fading of the currents which caused sediment transport during the earlier stages of development.

Fading of the currents does not mean a complete absence of them, but rather indicates a state of lack of longshore sediment transport, due either to the weakness of the remaining currents, or to the combined influence of diffracted waves and weak currents, which cause only local oscillation of sediments.

As a matter of fact, weak currents may be observed along tombolo beaches in spite of their apparent state of equilibrium.

In model tests carried out in our laboratory involving detached breakwaters the weakening of the circulatory currents towards the end of the development process of tombolos was clearly observed.

In the same state sand movement along the tombolo beach could not be detected. This also confirms our hypothesis concerning the dynamic conditions required for the establishment of equilibrium in the process of tombolo development.

ACKNOWLEDGEMENTS

The present paper is based on a thesis prepared by the first author under the supervision of the second author for partial fulfillment of requirements for a M.Sc. degree in Civil Engineering, submitted to the Technion-Israel Institute of Technology.

The financial assistance of Israel Coastal and Marine Engineering Research Institute, Haifa, is acknowledged.

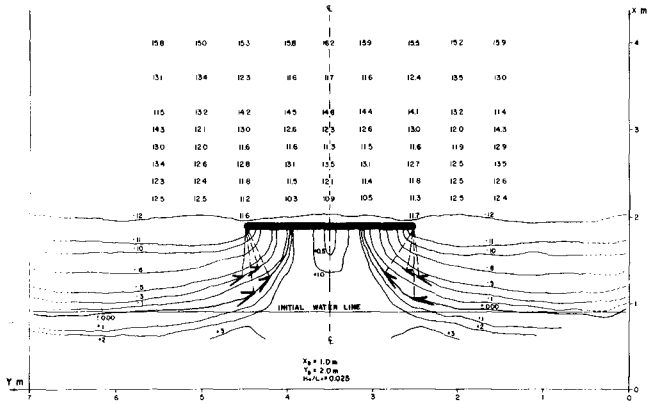

Fig. 9- TOMBOLO DEVELOPMENT-MODEL
(CONTOUR LINES NOT PARALLEL WITH DIFFRACTED WAVE FRONTS)

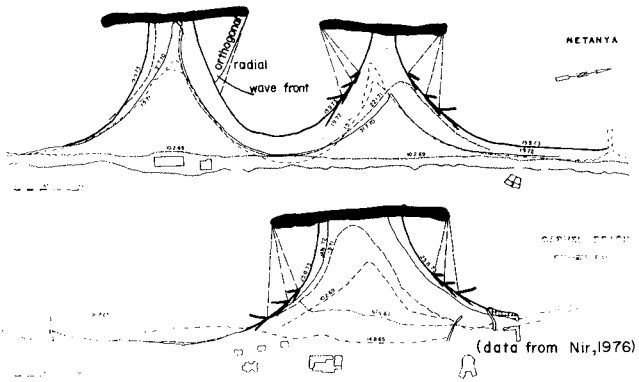

Fig. 10- TOMBOLO DEVELOPMENT-NATURE
(SHORE LINE NOT PARALLEL WITH DIFFRACTED WAVE FRONTS)

LIST OF REFERENCES

DALRYMPLE, R.A., THOMPSON, W.W., (1976), "Equilibrium Beach Profiles", 15th Coastal Eng. Conference, Vol. 2, pp. 1277-1296.
DEAN, R.G., (1965), "Stream Function Wave Theory; Validity and Application", Coastal Engineering, Santa Barbara Specialty Conference, ch. 12, Oct. 1965.
_____, (1973), "Heuristic Models of Sand Transport in the Surf Zone", Conference on Engineering Dynamics in the Coastal Zone.
_____, (1978), "Diffraction Calculation of Shoreline Planforms, Proc. 16th Coastal Eng. Conference, Vol. II, ch. 15, pp. 1903-1917.
GOURLAY, M.R. (1974), "Wave Set-up and Wave Generated Currents in the Lee of a Breakwater or Headland". Proc. 14th Conf. on Coastal Eng.
_____, (1976), "Non Uniform Alongshore Currents" 15th Conference on Coastal Engineering. ch. 40, pp. 701-720.
HANDING AND LUDWICK (1950) "Accretion of Beach Sand Behind a Detached Breakwater", Beach Erosion Board, Tech. Memo, No. 16, May 1950, 13 p.
HASHIMOTO, H., (1974), "A Model to Predict the Influence of Erosion to Neighboring Beaches with a Detached Breakwaters", Proc. 21st Conf. on Coastal Eng. in Japan (in Japanese).
INGLE, JR. JAMES C., (1966), "The Movement of Beach Sand", Developments in Sedimentology 5, Elsevier Publ, No. 60.
JOHNSON, D.W., (1919), "Shore Processes and Shoreline Development" Hafner Publ. Com. N.Y. & London 1965 (facsimile) of the first edition of 1919).
JOHNSON, A.G., (1940), "A Report on Protection and Development of the Beaches in the Westgate Addition and Santa Monica Additions", City of Los Angeles, Dept. of Public Works, Bureau of Engineering.
_____, (1949), "Scale Effects in Hydraulic Models Involving Wave Motion", Trans. A.G.U., Vol. 30, pp. 517-525.
_____, (1952),"Sand Transport by Littoral Currents". Proc, of the 5th Hydro. Conf. June 9/11/1952, Univ. of Iowa.
LIU, PHILIP L.F. and MEI CHIANG C., (1974), Effects of a Breakwater on Near Shore Currents, Due to Breaking Waves", MIT Report No. 192, Sept. 1974.
NIR, JACOB, (1976), "Detached Breakwaters, Groynes and Artificial Structures on the Mediterranean Shore and Their Influence on the Structure of the Israeli Shore", Rep. No. 3, 76/2, Jerusalem, March 1976 Ministry of Industry and Commerce, Geological Institute, Marine Geology Section, (in Hebrew).
NOBLE, R.M., (1978), "Coastal Structures' Effects on Shorelines" Proc. 16 Conf. on Coastal Eng, Vol. III, ch. 125, pp. 2069-2085.
PELNARD-CONSIDERE, R., (1956), "Essai de theorie de l'evolution des formes de rivage en plages de sable et de galets". Quatrieme Journees de L'Hydraulique, Paris, Vol. 1, Juin 1956, pp. 289-298.
PERLIN, M., (1979), "Predicting Beach Planforms in the Lee of Breakwater" Symp. on Coastal Structures 79, ASCE, vol. 2, pp. 792-808.
ROSEN D.S., (1981), Sedimentological Influences of Detached Breakwaters, M.Sc. Thesis Faculty of Civil Engineering, Technion, Israel Institute of Technology, Haifa, Israel. pp. 236, (in Hebrew with English abstract).
SASAKI, T. (1976), "Simulation of Shoreline and Nearshore Current", Proc. 15th C.E. vol. I, pp. 179-196.
SAUVAGE DE ST. MARC M.G.,et VINCENT, M.G., (1954), "Transport littoral, formation de fleches et de tombolo", Proc. of 5th Conf. on Coastal Eng.

in Sept. 1954, Councilon Wave Research, pp. 296-327.
SHINOHARA, K. TSUBAKI, T., (1966), "Model Study on the Change of Shoreline of Sandy Beach by Offshore Breakwater", Proc. of 10th Conf. on Coastal Eng., Tokyo, 1, pp. 550-564.
SILVESTER, R., (1970), "Growth of Crenulate-Shaped Bays to Equilibrium", Journal of the Waterway and Harbours Division, May 1970, WW2, pp. 275-287.
_____, and HO, S.K., (1972), "Use of Crenulate Shaped Bays to Stabilize Coasts", Proc. 13th Conf. on Coastal Eng., Vol 2, pp. 1347-1366.
_____, (1974), "Coastal Engineering", Vol. II, Elsevier Publ. Co.
SPATARU, A., (1966), "Lucrari de Protectia Coastelor", Studii de Hidraulica, Comitetul de Stat al Apelor, Inst. de studii si Cercetari Hidrotehnice, Bucuresti (in rumanian, with english and french summary).
TOYOSHIMA, OSAMU, (1974), "Design of a Detached Breakwater System", 14th Conf. on Coastal Engineering.
_____, (1976), "Changes of Sea Bed due to Detached Breakwaters", 15th Coastal Eng. Conference, 1976, vol. 2, pp. 1577-1589.
U.S. ENG. DEPT. (1939), "Los-Angeles Long Beach Detached Breakwater (on Cover: Design & Construction of Composite Type Detached Breakwater), Los Angeles, Cal. U.S, Eng. Office 132 p, Sept. 1939.
WIEGEL, R.L. (1966), "Experimental Study of Surface Waves in Shoaling Water, Trans. Amer. Geophys, Union, 31,3 (June 1950), pp. 377-385.

LITTORAL PROBLEMS IN THE PORTUGUESE WEST COAST

I.B. Mota Oliveira[1], A.J.S.F. Valle[2], F.C.C. Miranda[3]

ABSTRACT

This paper summarizes a study recently concluded of a sandy coastal reach, 110 km long, on the portuguese west coast. The final objective of that study was the design of a sea defense master plan covering all the stretch, to be built at a long term. That coastal reach has been under a strong erosion process for a long time. The history of the problem and its present situation were thoroughly analysed. Different techniques, related to different aspects of the general problem (wave climate, littoral transport, sand bypassing, long term evolution under accretion or erosion conditions, groin field, spiral beaches, etc.)were used. In what concerns littoral transport and sand bypassing the improvement of currently available methods was tried. The need of an accurately defined wave climate was felt; some rather disappointing results can surely be related to the lack of accurate wave data.

1 - INTRODUCTION

The study deals with a coastal stretch 110 km long on the Portuguese west coast, limited to the north by the Leixões harbor and to the south by the Cape Mondego - FIG. 1. The stretch faces the North Atlantic Ocean, withstanding a severe wave climate. The Douro river, joining the sea just south of the town of Oporto, and the Aveiro lagoon entrance are the main geographical features of this coast.

From a geological point of view the stretch can be divided in three zones. The northern zone, only 4 km long, between the Leixões harbor and the Douro river, has a predominantly rocky nature. The second,15km long, presents a series of rocky outcrops defining a series of sandy beaches of high recreational value due to their proximity to important urban areas. The third one, to the south of Espinho, is a long and almost straight sandy stretch of 90 km.

Some centuries ago this stretch suffered a period of alluvial over feeding. The lagoon of Aveiro was formed in that period, as a result of the southward growing of a sand spit - FIG 2. Concerning this subject , a very interesting paper (The History of a Tidal Lagoon Inlet and its

---

1 - Associate Professor, Instituto Superior Técnico, University of Lisbon. PORTUGAL
2 - Hidrotécnica Portuguesa, Consulting Engineers, Lisbon. PORTUGAL
3 - Assistant on Hydrology, Instituto Superior Técnico, University of Lisbon. PORTUGAL

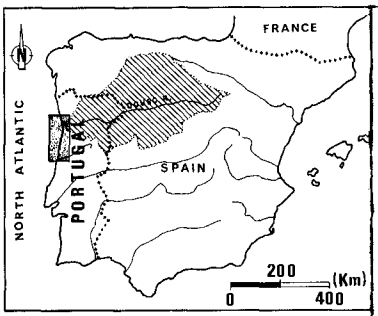

FIG 1 - Location map

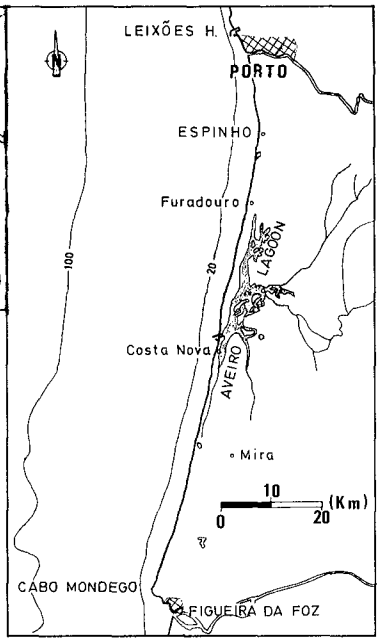

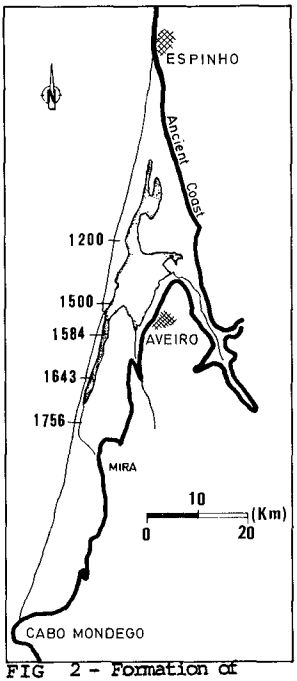

FIG 2 - Formation of the Aveiro Lagoon

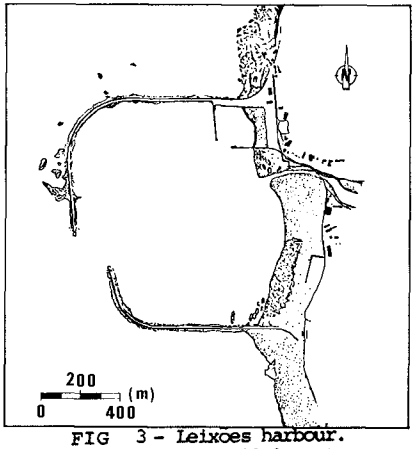

FIG 3 - Leixoes harbour. The 1892 layout

Improvement - the Case of Aveiro, Portugal) was presented by Abecasis , C.K. at the 5th Conference on Coastal Engineering, Grenoble, 1954.

In that paper a close relation between the above-mentioned phenomenon and the Douro river as an alluvial source is established. It has to be said that the phenomenon is not specific of this coastal stretch; in fact, one could refer to other cases of the same historical period around the Iberic Peninsula and even in the Portuguese coast, clearly demonstrating a situation of strong alluvial feeding. Although very interesting, the purpose of this paper is not the discussion of the causes which determined that situation.

The first records concerning the erosion process are 120 years old and concern Espinho and Furadouro which were, at that time, very small fishing villages in the northern area of the stretch - FIG 1. One is almost sure that the erosion process began earlier; however, human presence along the littoral area was almost null and the problem was not reported.

In 1892 the two long breakwaters of the Leixões harbor were completed - FIG 3. By those days the erosion process in Espinho had already begun at least 20 years ago. Even so, many people related and some people keep on relating the problems of Espinho with the construction of the port of Leixões.

The today town of Espinho has a long history of damages caused by the sea. Figure 4 registers the evolution of the water-line position (distance to a fixed point) in Espinho. We can see that from 1885 to 1910 (25 years) the coast receded 225 m (9 m/year). Even more striking is Figure 5, showing that the old village center was almost completely "swallowed" by the sea between 1880 and 1912. A historical photo taken on the 20th Dec. 1904 - FIG 6 - registers the falling down instant of the tower of Nª. Srª. da Ajuda church (see location on FIG 5).

From 1912 till 1929 the sandy coast recovered a lot, by reasons not clearly understood, although it had been related to the construction of three groins between 1911 and 1918, the first protection works ever built in the Portuguese west coast. Since then several improvements and extensions of the earlier protection scheme were performed: new groins, a sea-wall, etc. Although the town of Espinho had become really protected, the protection scheme couldn't avoid the withering of the sandy beach; by 1980 it had almost disappeared in front of the town.

A few other places along the stretch also have their historical evolution fairly well documented.

The zone just south of the Leixões harbor lost its only alluvial source, that is, the coast to the north, when the two breakwaters were built (1982). In fact, the retention effect upon the southward directed littoral transport and the dredging of the harbor entrance removed almost completely the sediment feeding of the stretch between the harbor and the Douro river mouth - FIG 1. The result has been the loss of some sandy beaches which, in the first decades of the century, were preferred by people of the northern area of the country.

The adjacent urban area remains naturally protected by the rocky coast; the landscape remains highly appreciated; but its recreational value is no longer the same as in the old days. At present, we begin

thinking on the possibility of establishing artificial beaches taking advantage of natural rocky outcrops to be improved as littoral barriers , and doing some artificial sand filling.

Taking into account the history of a disappeared little church in Furadouro - FIG 1 - it seems that the coast receded some hundred meters , between 300 and 400 m, since the last decades of the 18th century till 1930.

Quite recently (1959) the construction of two jetties in the Aveiro lagoon entrance has caused important changes on the local littoral regimen, with a strong accretion in the northern stretch and strong erosions in the southern stretch - FIG 7.

It can be said that, at present, only the last southern 30 kilometers of the whole stretch do not present any erosion problem. That is the result of the retention effect on the Cape Mondego, acting like a big natural groin. But one can be sure that the problems will "propagate" to the south as time goes by.

Erosion is particularly threatning just south of Espinho and south of the Aveiro lagoon entrance.

Until now protection works have been built separately, at different points of the coast, whenever the risk of destruction of a particular urban area occurs, without a rational plan. A study was undertaken with the final objective of establishing a long term sea defense master plan covering the whole stretch.

2 - RECENT EVOLUTION. PRESENT SITUATION

2.1 - General characterization

By "recent evolution" one means after 1950. What differentiates this period from the previous one is the existence of data, namely topo-hydrographical surveys and aerial photos adequate to a quantitative evaluation of the coastal evolution.

Topo-hydrographical surveys concern only some places or some limited coastal stretches where erosion problems are relevant on account of the patrimonial or social importance of the littoral areas; the greater this importance, the better the data of this type.

For the whole coastal stretch, the best data we could afford were aerial photos, at different times. It was possible to analyse data of this type at intervals of more or less one decade, since 1947.

Initial fears about the accuracy of this approach were not confirmed. Some difficulties had been antecipated: the correct identification of the water-line on the beach slope; the correct identification of fixed references in remote and densely wooded littoral areas; and mainly the inaccuracy resulting from a changing tidal level (one photo taken during high-water over a beach of normal slope can display an "erosion" of some 30-50 m or even more when compared with another one taken during low-water, if the tide is 3-4 m high).

Nevertheless, the result was very coherent and encouraging. Figure 8 displays the coastal evolution south of Espinho and the Aveiro lagoon

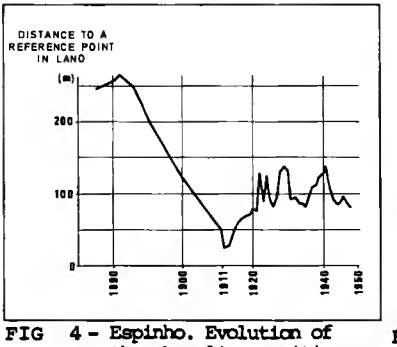

FIG 4 - Espinho. Evolution of the shoreline position

FIG 6 - Espinho, 1904. A church goes to ruins

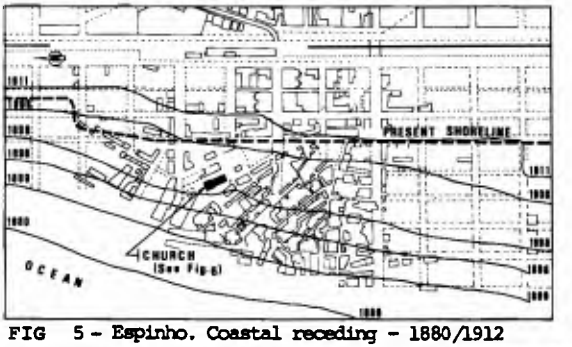

FIG 5 - Espinho. Coastal receding - 1880/1912

FIG 7 - The Aveiro lagoon inlet

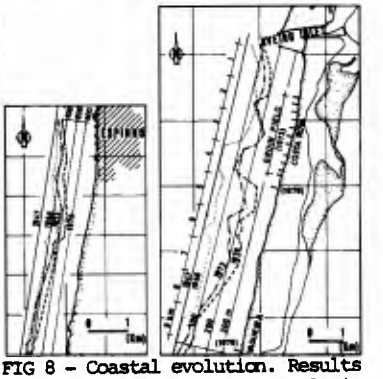

FIG 8 - Coastal evolution. Results from aerial photography analysis

inlet (FIG 1) between 1947 and 1978, as obtained from aerial photo analysis.

Both places present maximum erosion rates of 8 meters per year (temporal mean values) during that period of 30 years; erosion was particularly severe in the periods 1947/58, south of Espinho, and 1958/73, south of Aveiro (following the construction of the jetties), with local rates higher than 10 m/year.

The results of some analysis show the erosion "propagating" to the south with time; during the seventies erosion problems were present along a distance of some 20 km to the south, with mean erosion rates of several meters per year.

2.2 - Specific Cases

2.2.1 - Introduction

Some specific cases have been deserving special attention since a long time, owing to the urban value of littoral areas affected by the coastal receding phenomenon or by some other reasons (e.g. Espinho, Aveiro lagoon inlet). Therefore, data are relatively abundant, specially in what concerns hydrographical surveys, which allowed the quantitative (volumetric) evaluation of the erosion process.

Nevertheless, some difficulties were encountered as a result of data deficiencies. By far, the most important one is related to the lack of information below the zero hydrographical level. In fact, most hydrographical surveys cover the areas above that level only, in practice above low water level. So, the volumetric evaluation of the specific coastal erosion cases concerns only the zone of the beach above datum level.

The evaluation was accomplished according to the following approach:
- beach profiles, with a 200 m spacing, were drawn;
- the corresponding areas (A) above zero datum level were evaluated;
- curves A (s) for each available survey were drawn, s being the abscissa along the beach;
- areas under those curves, representing sand volumes above zero level [$V = \int A(s)ds$] were measured;
- a curve V (t) was drawn, t being the time variable (years).

The evolution of the Aveiro lagoon outer bar was evaluated by comparing the hypsometric curves characterizing the global morphology of the bar in each date.

Some comments on the results obtained in two exemplifying cases (Espinho and Aveiro lagoon bar and adjacent littoral stretches) are added.

2.2.2 - The beach of Espinho

The beach of Espinho was divided into three stretches: A (375 m), to the north of the sea defense scheme; B (1500 m), corresponding to the sea defense scheme, which comprised a sea-wall and several short groins; C (625 m) to the south (downdrift) of that scheme. Figure 9 shows the evolution curves of stretches B and C.

Curve B displays an almost regular erosion rate of 18,500 m^3/km.year above zero datum level. On the contrary, curve C displays two different

evolution periods: before and after middle sixties; the mean erosion rate raised from 19,500 m^3/km.year, in the first period, to 70,000m^3/km.year, in the second; in linear terms, coastal receding in this stretch raised from 2.3m/year to 9.2 m/year between the two periods; it should be noticed that in a period of 13 years (1964-1977) the coast receded 120 m in this stretch.

2.2.3 - Aveiro lagoon inlet area

The construction of the outer jetties of the Aveiro lagoon inlet (1950-58) determined important morphological changes in the surrounding areas: updrift and downdrift beaches and outer bar. Those changes were intensively analysed; we can only summarize here the most relevant results - FIG 10.

Nowadays, the accretion updrift zone is 8 km long. The weakening of the littoral transport and the intense extraction of sand for the construction industry led to the conclusion that the length of the above-mentioned zone may have stabilized.

The available hydrographical surveys cover a length of 3.5km and concern only the area above zero datum level. Therefore, for the evaluation of the accretion rates along the whole zone, some assumptions had to be considered.

Erosion problems in the downdrift (southward) beaches began even during the construction of the outer jetties. By the end of the sixties coastal receding had begun endangering the summer resorts of Barra and Costa Nova. From 1972 to 1973, a groin field (11 groins), protecting a beach length of 2,400 m, was built; of course, the erosion process continued very active to the south. In 1979, two long groins (250 m) were built, one just south of the village of Vagueira, the other as a complement of the previous groin field. Nowadays, erosion problems are felt south of Vagueira, in a coastal length of several kilometers.

The construction of the outer jetties also induced important changes, both on the outer bar and the lagoon channels.

Curves on Figure 10 characterize some of the main effects of the morphological evolution of those three zones: updrift and downdrift beaches and outer bar.

The accretion rate in the updrift zone above datum level displays strong interannual irregularities. Nevertheless , since the end of the sixties it shows a regular decreasing trend, which can be related to the position of the low-water line vis-à-vis the north jetty head. In the first three years the rate was particularly high: 800,000 m^3/year. Such a value led us to think, for the first time, that the mean annual littoral transport could overpass the value of 10^6 m^3, usually accepted for this coastal stretch.

Taking into account the storage under the zero datum level, a mean storage rate of 600,000 m^3/year, for the whole period (1950-1978) was found; if one also considers the sand extracted for the construction industry, it means that a volume of about 20 million m^3 has been subtracted form the natural littoral process, since the beginning of the construction of the jetties (1950). This event fully explains the erosion problems felt in the downdrift beaches.

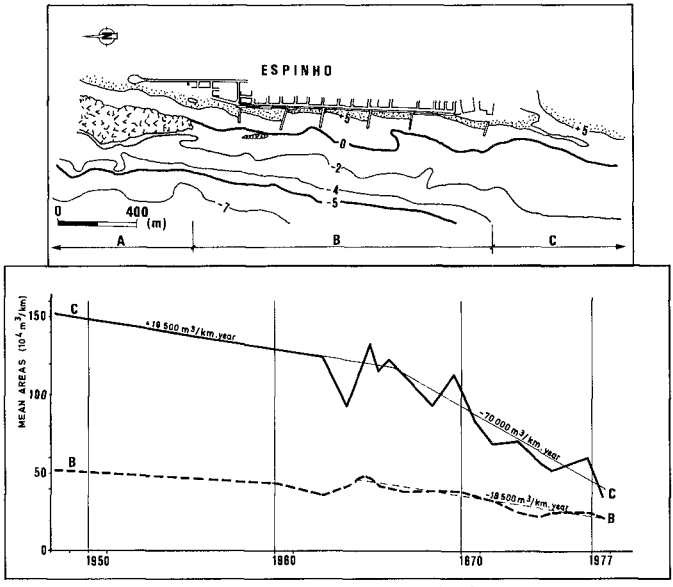

FIG 9 - Espinho beach. Evolution after 1950

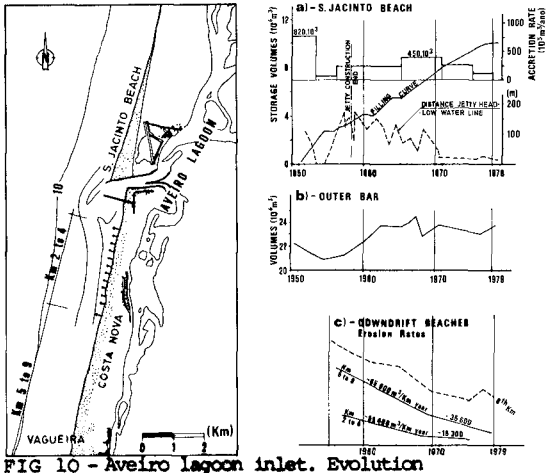

FIG 10 - Aveiro lagoon inlet. Evolution of the surrounding areas after 1950

The volumetric evolution of the outer bar displays a first withering phase (4 years) followed by recovering and stabilizing periods. This situation can be related to the advance of the northern jetty during the construction phase and to the rate of bypassing of this structure. Qualitatively, the stabilization of the outer bar and the decreasing of the accretion rate in the updrift zone can be correlated.

The erosion process in the downdrift beaches was analysed in detail, taking into account stretches 1 km long, afterwards combined into larger stretches with a particular physical meaning (e.g., stretch protected by the groin field, stretch influenced by the outer bar). The volumetric evolution presents irregularities throughout the years, as exemplified on Figure 10 with the 8th km curve. Nevertheless, one can clearly distinguish two periods concerning erosion rates above zero datum level. Curves on Figure 10 pertain to the stretch which is more directly influenced by the outer bar (from kms 2 up to 4), as well as to the downdrift stretch (from kms 5 up to 9). Erosion rates on the former has always been smaller than on the latter. That can be related to the known trap effect exerted by a big outer bar; nevertheless, any of them displays a clear reduction of the erosion rate in the last years. Again, one can correlate this erosion rate reduction, the stabilization of the outer bar and the decreasing of the accretion rate on the updrift zone.

Some other relevant results can be presented as follows:
- in the period from 1954 to 1978 (24 years), the mean coastal receding along the whole stretch (9 km) amounted to 150 m;
- during a period of two years after the construction of the groin field, the adjacent southward stretch (1750 m) receded 50 m;
- during a period of 15 years (1954-1969), the stretch south of the groin field (from kms 5 up to 9) lost 5 million m^3 of sand above the zero datum level.

3 - LITTORAL PROCESS

3.1 - Introduction

Several studies concerning the littoral process of the Portuguese west coast were carried out, namely the evaluation of the strength of alluvial sources, the evaluation of the littoral transport, the mathematical modelling of coastal morphological changes and the determination of the equilibrium beach line orientation.

3.2 - Alluvial sources

The almost exclusive alluvial sources of the coastal stretch between Leixões and Cape Mondego have been the coast north of Leixões and the Douro river. For a coast in a dynamic equilibrium state, the evaluation of the strength of those sources would be equivalent to the evaluation of the littoral transport.

The coast north of Leixões harbour is fed by several rivers. River Minho is the most important one. It constitutes border between Portugal and Spain (FIG 11). Surely the sediments carried by these rivers are transported to the south. Before the last decade of the 19th century, when the breakwaters of Leixões harbor were built, those sediments ente

red the stretch under analysis; since then they have been dredged at the entrance of that harbour.

Taking advantage of the long dredging record available, and discarding the fine fraction of the dredged material (normally absent from the littoral drift), it was possible to conclude that the littoral transport coming from the north coast would have been of the order of 150,000-180,000 m^3/year.

In what concerns the Douro river, two approaches were used. The first one took into account the above result and the areas of the catchment basins geologically suitable for the "production" of sand. A detailed survey of the available geological charts was made in order to identify those areas in the Douro river catchment and in the river basins tributaries of the coastal stretch north of Leixões. In this approach some assumptions were made: over the several basins, the mean rainfall regimen, the forest and agricultural occupation and the mean orographical (sloping) conditions are nearly the same.

Considering these assumptions, the strength of the updrift coast, as an alluvial source, would have been, previous to any human interference, of the order of 15 to 20% of that of the Douro river. Taking into account the littoral transport concerning the coast north of Leixões (150,000-180,000 m^3/year), it was concluded that the Douro river would have produced, in natural conditions, a mean annual volume of beach material of 0.75 to 1.2 million m^3. This means that a total mean annual volume of 0.9 to 1.4 million m^3 entered the stretch under analysis. This result fits quite well the currently accepted mean annual value of the littoral transport in this zone of the Portuguese west coast ($10^6 m^3$).

However, another approach for the evaluation of the Douro river strength as an alluvial source produced a much higher result. Four different theoretical bed load formulas (Dubois, Meyer Peter-Müller, Einstein-Brown and Engelund-Hansen) were used together with three different mean annual hydrological regimens: the natural, previous to the first important dams (before 1930), the present and the future one, when the plan for development of the Douro river basin will be fully implemented.

As usual, the scattering of the results is considerable. For instance, for the natural hydrological regimen the results were as follows:

	($10^6 m^3$/year)
Dubois	1.4
Meyer Peter-Müller	0.7
Einstein-Brown	3.5
Engelund-Hansen	1.8

In any case the Einstein-Brown value was much higher than the others. Besides, it exceeds largely the commonly accepted value for the littoral transport (10^6 m^3/year); therefore, it was discarded. Taking into account the average value of the remaining three formulas, the following results were obtained (10^6 m^3/year):

* natural regimen 1.8
* present situation 1.3
* after the conclusion of the Crestuma dam, under construction near the upstream limit of the Douro estuary 0.25

Considering the above natural regimen results and the littoral drift coming from the updrift coast, one gets a value of the order of 2×10^6 m^3/year. This rises the idea that the potential transport capacity of the wave climate is significantly higher than it is commonly accepted.

The coastal alluvial feeding is directly influenced by the extrac - tion of sand for the building industry; its importance is even higher than initially suspected. It's rather difficult to assess correctly the importance of this activity, owing to the more or less uncontrolled way under which it was exerted during a long period. Direct inquires along the lower reach of the Douro river were made and the scarce records were searched and analysed.

Since 1980, this activity is generally forbidden along the Portuguese coasts, with the exception of a few very specific places. One of these places is the accretion zone updrift of the jetties of the Aveiro lagoon inlet (S. Jacinto beach - FIG 10); in the last years the extraction rate increased considerably in this area, amounting to 400,000 m^3, in 1980.

Nowadays, along the lower 50 km reach of the Douro river, including its estuary, sand and gravel extraction seems to be of the order of 1.5×10^6 m^3/year.

3.3 - Littoral transport

3.3.1 - Sediment budget concept

For the evaluation of the littoral transport two approaches were used: the sediment budget concept in successive cells from north to south and the CERC littoral transport formula, using the available wave climate.

To apply the first approach, the coast between Espinho and Cape Mondego was divided into 5 cells. In this analysis the stretch Leixões--Espinho, with a predominantly rocky nature, and therefore in a sedimentary equilibrium state, was discarded.

A lot of work had to be done in order to evaluate the erosion (or accretion) inside each cell, since 1950. Some specific places have been morphologically surveyed quite regularly but, most of the time, above the zero datum level only. In those places assumptions for the relation between the erosion cross-section areas above and under datum level had to be made.

Nevertheless, for most of the stretch Espinho-Cape Mondego only the successive positions of the beach line, as registered by aerial photography, were known. At this point, an important step of the study was to establish an erosion profile. A mixed type profile was adopted: rectangular above, trianguler under the zero datum level - FIG 12. Site inspection and topographical data allowed the knowledge of the upper level of the erosion profile, i.e., the level of the littoral dunes under erosion (FIG 12, dimension A). On the other hand, taking into account some available hydrographical surveys extending to underwater areas, the lower level of the erosion profile could be established (FIG 12, dimension B). B values varying from 7.5 m up to 9.5 m between Espinho and Cabo Mondego were adopted.

Wind action is surely irrelevant in the littoral process of this particular case. Sand losses to deeper areas, due to transversal movements, were also discarded.

Boundary conditions concerning the littoral drift flowing through the cross-section of Espinho (X m^3/year) had to be established. Taking into account the results concerning the alluvial sources, the following values were assigned to the X variable

Period	X(m^3/year)
1950/59	800,000
1960/64	600,000
1965/69	400,000
1970/74	250,000
1975/78	100,000

Figure 12 presents the final result of this approach concerning two sections: one at the updrift limit of the accretion zone of the Aveiro lagoon inlet; the other at Cape Mondego. This figure warrants the conclusion that the potential littoral transport capacity of the wave climate seems to be of the order of 2×10^6 m^3/year. The littoral drift flowing through the section of Espinho being much smaller, the wave climate "nourishes" itself with the sand deposits (beaches) of the southward stretch; nevertheless, the stretch Espinho-Torreira doesn't seem big enough to saturate the potential transport capacity of the wave climate; in fact, the mean value of the littoral drift flowing through the cross-section of Torreira seems to be of the order of 1.5×10^6 m^3/year. Another interesting result of this approach concerns the natural bypassing of the Aveiro lagoon inlet. It seems that, nowadays, it remains of the order of several hundred thousand m^3/year, despite the storage on the updrift accretion zone, the extraction of sand in that zone and the weakening of the alluvial sources.

3.3.2 - Theoretical evaluation

The CERC littoral transport formula was used. Despite the amount of work developed in this analysis, the results were quite disappointing. In the next paragraphs the studies developed are summarized.

With some well-known assumptions concerning the breaking region, the CERC formula may be written as follows:

$$Q_s = 750\, H_b^{5/2} \sin 2\alpha_b \qquad (1)$$

Q_s being evaluated in m^3/hour and H_b being the root mean square breaking height.

The available wave climate data were recorded in a 6 year period (1954-60) in Figueira da Foz, a summer resort located just south of Cape Mondego. Based on this data, the mean annual deepwater wave conditions can be characterized in terms of frequence distributions of directions, periods and heights. Considering the results of some previous studies based on these data, some difficulties were expected since the beginning.

For the discretization of the wave climate, seven directions (from SSW to NNW), eleven heights (from 0.75 up to 10.5 m) and three periods (8, 11 and 14 s) were considered; that formed a set of 231 "waves" (7 x 11 x 3) characterizing the mean annual wave conditions. A computer program was prepared for the evaluation of the gross and net transport

capacities of these "waves".

Another computer program performed refraction diagrams between deep water and the (-5.00 m) contour line. Shoaling (K_S) and refraction (K_r) coefficients and directions (α) at the (-5.00 m) contour were assigned to each "wave" as input of the littoral transport program. To apply Equation (1) breaking values (H_b, α_b) area needed; however, only some particular "waves" will break at a (-5.00 m) position.

The smaller the wave height, the nearer to the beach it will break and, therefore, the greater the refraction effect. This means that the period (T) and the deep water wave direction (α_0) are not sufficient to define α_b, K_S and K_r at the breakers, the problem being of an implicit type: α_b and H_b depend on the refraction effects but, on the other hand, these effects also depend on the wave height.

To solve this problem, the following approach was used:

- Snell's law was considered valid between the (-5.00 m) contour line and the breaker line

$$\frac{\sin\alpha_b}{C_b} = \frac{\sin\alpha_5}{C_5} \quad (2); \qquad Kr_{5-b} = \sqrt{\frac{\cos\alpha_5}{\cos\alpha_b}} \quad (3)$$

- Phase velocity follows the solitary wave theory

$$C = \sqrt{g(d + H)} \quad (4)$$

- Breaking criterium: $H_b = d_b$ (5)

- Wave shoaling: as given by the linear wave theory for shallow water

$$Ks \simeq 0.5 \cdot \frac{\sqrt{T}}{\sqrt[4]{d}} \quad (6)$$

Applying Eq. (6) at the (-5.00 m) position and on the breakerline, the shoaling effect between them will be

$$Ks_{5-b} = \sqrt[4]{\frac{d_5}{H_b}} \quad (7)$$

Combining Equations (2), (3), (4), (5) and (7) we get

$$\alpha_b = \arcsin\left(\sqrt{\frac{2H_b}{d_5 + H_5}} \cdot \sin\alpha_5\right) \quad (8)$$

$$H_b = \sqrt{\frac{\cos\alpha_5}{\cos\alpha_b}} \cdot \sqrt[4]{\frac{d_5}{H_b}} \cdot H_5 \quad (9)$$

In these equations d_5 equals 5 m plus the tidal level. Equations (8) and (9) are solved iteratively. For the starting step, to obtain a first approximation of α_b and H_b, H_b takes the value of H_5.

Example: with a 2 m tidal level, d_5 = 7 m; let us consider three waves with $\alpha_5 = 10^o$ and H_5 = 5 m; 3 m; 1 m; according to this approach, breaking heights and directions would be

H_5 (m)	5	3	1
H_b (m)	5.36	3.56	1.49
α_b	9.4^o	8.4^o	6^o

The first results obtained with the littoral transport computer program were absolutely unacceptable. In fact, a northward net littoral drift of 1.1×10^6 m^3 was obtained, and it's known for sure that the net littoral drift is southward directed.

Such a result seems to mean that the available wave climate is southward biased, i.e., the true wave climate must be richer in waves coming from the north-west quadrant. Therefore, several tryings were made aiming to "construct" a more likely wave climate; this was accomplished by transferring occurence percentage values, for instance, from W to NNW.

Two measures of its likeliness were available:

- the wave climate has to produce a southward net littoral drift;
- the same wave climate, acting over a coastline making an angle of some degrees with the true coastline, would produce a zero net littoral drift (according to the studies presented in item 3.5, in the area of Aveiro this equilibrium angle would be of the order of 4^o to 6^o).

Eight wave climates were "constructed" this way; Figure 13 presents two wave roses, one concerning the original wave climate (Cl_0) and the other one related to the northmost biased wave climate (Cl_8). Four coastline directions were considered: the true coastline and three others making angles of 2^o, 4^o and 6^o with the real one (in these tryings the beach was "rotated" above the (-5.00 m) level, only). For each wave climate and for each coastline direction, the gross and the net littoral drift were evaluated.

Despite the amount of work developed, the results were inconclusive. For instance, for an intermediate wave climate, labeled Cl_4, one got (values in $10^6 m^3$/year):

	True coastline	Beach angle with the true coastline direction		
		2^o	4^o	6^o
Gross littoral drift	13.1	12.0	11.6	11.6
Net littoral drift	-4.4	-0.6	+3.2	+7.1

(minus signal means "southward directed").

We recall that the true wave climate would produce a zero net littoral drift for an angle of 4 to 6 degrees. According to the above results the Cl_4 vanishing angle would be 2.3^o only; nevertheless, the same Cl_4, acting over the true coastline, produced an unacceptable high value for the net littoral drift.

We notice that the "rotation" of the coastline produces a minor effect over the gross littoral drift; on the other hand, the net littoral drift displays a great sensitiveness to that "rotation".

It seems unquestionable that these difficulties result mainly of inaccuracies of the available wave climate data. But one also has to

keep in mind that "even with exact wave data, it is believed that the longshore transport can only be predicted within approximately -67% to +200%" (Dean, 1978).

3.4 - Mathematical modelling of morphological changes

A mathematical model was prepared with two main objectives: the study of the coastal evolution in the stretch south of Espinho and the foreseeing of the expected changes of S. Jacinto beach, as a result of another extension of the length of the north jetty of the Aveiro lagoon inlet; if the model had proved well, it would have been used in the planning of the sea defense scheme. However, the results were not satisfactory, mainly on account of inaccuracies of the wave data.

Basically, the mathematical model uses the approach of Willis and Price (1975). Two complementary devices were added: one takes into account the influence of the morphological changes on wave refraction effects; the other aims to simulate the bypassing process around a littoral sediment barrier.

One knows that a short term accretion or erosion will only affect the beach profile above a relatively high level in a shallow water region. Therefore, wave refraction effects will change only in a relatively narrow strip, adjacent to the shoreline; thus, it is not worthwhile to elaborate again all the refraction diagrams, specially when dealing with a more or less straight shoreline, in order to account for those changing effects.

The objective of the proposed approach is the evaluation of the breaking angle α_b at the modified shoreline. For that purpose, an equation of the following type is currently used

$$\alpha = \alpha_o - \arctan \frac{\partial y}{\partial x} \qquad (10)$$

α_o being the angle relative to the initial undisturbed shoreline.

The starting data for the proposed approach are the breaking wave height and the angle (H_b, α_b); they are available as output of the computer program described in item 3.3.2. In the region affected by the morphological changes the validity of equations (2), (4) and (5) is again assumed.

Knowing the breaking values of H and α, one goes back to an undisturbed depth, that is, a depth not affected by the short term morphological changes (for instance, d = 8 m under the reference level). Combining equations (2), (4) and (5) it is found

$$\alpha_{d.o} = \arcsin \left(\sqrt{\frac{d + H_b}{2H_b}} \cdot \sin\alpha_{b.o} \right) \qquad (11)$$

$\alpha_{b.o}$ being the breaking angle relative to the initial shoreline, and $\alpha_{d.o}$ the corresponding value at an undisturbed depth (d). In this approach the wave height variation was neglected.

"Rotating" the shoreline

$$\alpha_d = \alpha_{d.o} - \arctan \frac{\partial y}{\partial x} \qquad (12)$$

being α_d the wave angle relative to the "rotated" shoreline, at an undis-

turbed depth (d).

Reversing equation (11), the angle at breaking position can be found

$$\alpha_b = \text{arc sin} \left(\sqrt{\frac{2H_b}{d+H_b}} \cdot \sin \alpha_d \right) \qquad (13)$$

Summarizing, in the proposed approach equation (10) is replaced by equations (11), (12) and (13). Let us consider a breaking wave 2 m high, with $\alpha_{b.o} = 5^o$; if the shoreline rotates 2^o, as a consequence of an accretion process, equation (10) will give $\alpha_b = 3^o$ while the sequence of equations (11), (12) and (13) will give $\alpha_b = 3.67^o$ (considering d = 7 m as the undisturbed depth).

To simulate the bypassing process another device was used: it relates the bypassing rate with the position of the surf zone vis-à-vis the head of the littoral barrier - FIG 14.

For the distribution of the littoral transport capacity across the surf zone, a triangular type law was assumed, with its maximum value at the breaker line. Equation (5) was again adopted as the "breaking criterium". The width of the surf zone (B) for the used assumptions depends on the breaker depth (d_b) and on the bottom slope. Therefore, a bottom profile had to be assigned to the breaker region in each specific case; in the case of the Portuguese west coast one of the mixed type was adopted-FIG14.

When the wave breaks landward of the littoral barrier head, bypassing doesn't occur ($Q_{bp} = 0$); if it breaks seaward, the bypassing rate will be a fraction of the littoral drift arriving at the barrier (Q), that fraction corresponding to the part of the triangular transport diagram which is not intercepted by the littoral barrier. That is (FIG 14)

$$Q_{bp} = \left[1 - \left(\frac{X}{B}\right)^2\right] . Q \qquad (14)$$

X being the distance from the waterline to the head of the littoral barrier.

Some difficulties were encountered in defining a Q with a physical meaning (the littoral drift arriving at the barrier). For instance, if Q is related to the orientation of the shoreline in the adjacent stretch, and if this stretch is a fixed number of integration steps Δ s long, then the bypassing rate depends on the integration step Δs. Finally, Q was related to the orientation of an adjacent stretch with a fixed length exceeding the surf zone width of the highest waves (for instance, 400m).

Difficulties of another type were risen when the accretion-erosion effects reached the limits of the mathematical model stretch; boundary conditions such as Y = const or Q_s = const were no longer valid. Besides, in the present case accretion caused by an artificial barrier occurs over a shoreline under a general erosion process. It seems that, in such a case, the best approach would be, like in other fields, to obtain the boundary conditions as output of another far-field model, covering a much longer coastal stretch.

To test this model the accretion process of S. Jacinto beach (2.2.3) was simulated between 1950 and 1978. The results were not satisfactory.

One should be reminded of the presumed inaccuracies of the mean annual wave climate used in the whole study. However, the accretion process

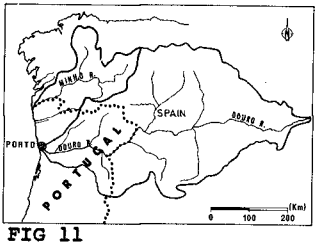

FIG 11
Stretch Leixões-Cabo Mondego
Alluvial sources

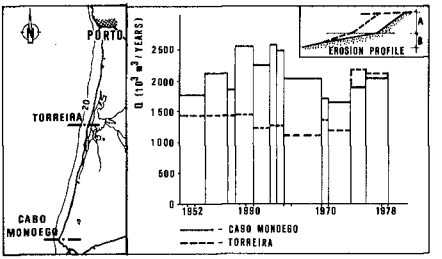

FIG 12 - Results of the "sedimentary budget" analysis

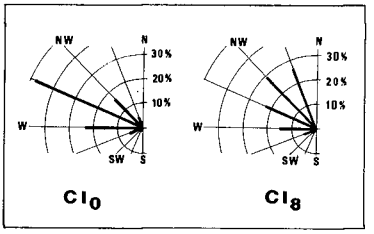

FIG 13 - Cl_0 and Cl_8 wave roses

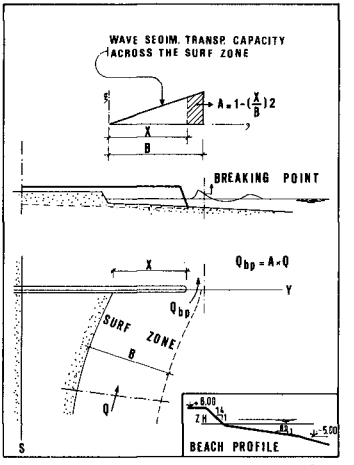

FIG 14 - Bypassing process of a littoral barrier

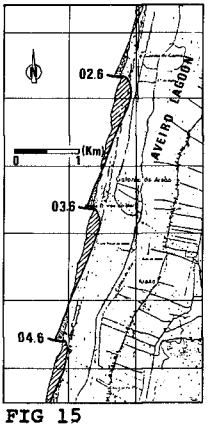

FIG 15
Sea defense plan.
Some typical structures

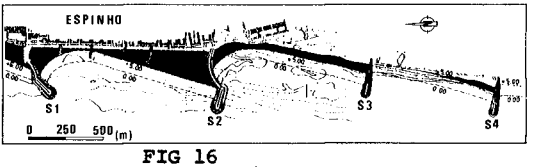

FIG 16
Beaches of Espinho.
Proposed protection plan

to be tested has been the result of wave conditions changing year after year. In fact, the true wave conditions that determined the accretion process of S. Jacinto beach are unknown. Besides, the accretion process reached the updrift model boundary much faster than in the prototype. These may be some of the reasons of the above-mentioned difficulties.

3.5 - Equilibrium beachline orientations

It will be seen further on that the sea defense master plan was designed for a zero net littoral drift condition. Therefore, the assumed beaches that will be formed between coastal protection works, will present shapes and positions corresponding to an equilibrium state. When foreseeing those beach forms, the evaluation of the equilibrium orientation of some existing beaches was very helpful. Such an approach assumes the existence of a dominant deep water wave direction characterizing the whole stretch. If that existed, one could determine the equilibrium orientation of any beach along the stretch.

Three beaches were selected for this study (FIG 1): Leça, just north of the breakwaters of Leixões, Espinho and S. Jacinto.

The first one can be considered almost in a equilibrium state, due to the relatively weak littoral drift arriving from the north. Taking into account two available hydrographic surveys, one determined a mean value $\theta_b \simeq 13.5^o$, θ_b being the beach angle with the north-south direction.

The beach of Espinho has not surely been in a equilibrium state. Surveys made at 14 different times were carefully analysed. Two particular stretches of the beach were considered, each one on the updrift side of old groins. Based on this analysis a value $\theta_b = 17.5^o$ was adopted.

Nowadays, the S. Jacinto beach is 8 km long and it is not in an equilibrium state for sure. For the evaluation of the equilibrium angle, only the 500 m long stretch, adjacent to the north jetty of the Aveiro lagoon inlet, was considered. Hydrographic surveys were analysed at 37 different times. A value $\theta_b \simeq 22^o$ was adopted.

Considering the results of the refraction diagrams, the following dominant deepwater wave directions θ_o were obtained (when wave periods of 10 to 12 s are considered):

Angles with N - S direction

	b	o
Leça	13.5^o	$37^o - 45^o$
Espinho	17.5^o	$38^o - 50^o$
S. Jacinto	22.0^o	$43^o - 50^o$

The results agree fairly well with one another, despite the fact that the stretch Leça-S.Jacinto is 60 km long. Therefore, a deepwater dominant direction $\theta = 50^o$, with a wave period T = 12 s, was adopted for the whole stretch. The corresponding θ_b equilibrium values along the stretch, necessary for the sea defense planning, were determined using the results of the refraction diagrams.

4 - SEA DEFENSE PLAN

The plan includes more than 60 structures, almost exclusively of the groin type.

In the northern zone, between Leixões and Espinho, the spacing and the length of the coastal structures are quite variable. This results from the occurence of many granitic outcrops that ought to be used to anchor the groins. In this northern zone the coastal structures will have an almost unique objective which consists of improving the existing beaches. In fact, the defense of the coast is insured by its rocky nature.

A sandy coast extends to the south of Espinho with long reaches of dunes, sometimes bordering pine forests, other times facing little towns and villages. Wherever the littoral areas have a low patrimonial value, the spacing between coastal structures is relatively large (2 km and even more). This means that some additional erosion, in some specific points of the coast, will have to be accepted; on the other hand, the number of coastal structures, always very expensive, becomes quite reduced. Figure 15 displays the proposed solution for a stretch of beach located between Aveiro and Mira. In such a case the plan took advantage of the spiral beach concept, studied by Silvester (1972) and others.

Wherever the coastal receding had to be stopped, on account of the high patrimonial value of the littoral areas, the plan used the groin field concept, in which the accretion zone of a groin reaches the updrift one. The results of experimental studies carried out at LNEC (Civil Engineering National Laboratory, Lisbon) were used. According to Barcelo' (1969) the ratio D/C varies with α as follows

α	D/C
20^{o}	2.5
15^{o}	3.5
5^{o}	4.0

D being the groin spacing, C its lenght and α the angle between the crest of the dominant wave and the shoreline.

In order to reduce the number of coastal structures a large spacing (D) was adopted; current values for D and C have been D = 875 m, C=250m.

Figure 16 presents four structures protecting a coastal length of 3 km. They have been the first sea defenses of the whole plan to be built; presently (summer, 1982) its construction is about to be concluded. The objectives of the structures labeled S1 and S2 are twofold: to defend the town of Espinho and to restore its old importance as a summer resort. This explains the length of the groins S1 and S2. They were planned to trap a "spiral beach" 1,200 m long. During the last year more than half a million m^3 of sand was naturally accumulated between S1 and S2.

5 - CONCLUSIONS

Coastal erosion became a major problem of almost every coast. The main reason for such a situation is the weakening of the alluvial sources, due to the improvement of the river basins. Human activity along the coasts often aggravates the situation by diverting the natural path of the littoral sediments. Therefore, in many instances, it seems advi-

sable to consider the long term vanishing of the littoral transport when planning a sea defense scheme.

Mathematical modelling of littoral evolution requires two main work bases: accurate wave data and a dependable littoral transport formula. If wave conditions are very variable in what concerns either heights, directions or periods, the difficulties faced when defining accurately a wave climate may be higher than those of elaborating a mathematical model. In such a case, a mathematical model seems to be a too sophisticated tool, leading to disappointing results. That has been the case on the studies undertaken concerning the littoral problems of the Portuguese west coast.

6 - REFERENCES

BARCELÕ, J.P.. Experimental study of the hydraulic behaviour of groin systems. LNEC, Lisboa, Memória nº 350, 1969.

C.E.R.C. - Shore Protection Manual. Vol. I. U.S. Army Corps of Engineers, 1977.

DEAN, R.G. - Review of Sediment Transport Relationships and the Data Base, in Workshop on Coastal Sediment Transport. University of Delaware, 1978.

KOMAR, P.D.. Beach Processes and Sedimentation. Prentice-Hall, 1976.

SILVESTER, R.. Headland Defense of Coasts. 15th Coastal Engineering Conference, Honolulu, Vol. II, p. 1394, 1972.

WILLIS, D.H. and PRICE, W.A.. Trends in the Application of Research to Solve Coastal Engineering Problems, in "Nearshore Sediment. Dynamics and Sedimentation". London, John Wiley and Sons, 1975.

DURBAN BEACHES RECLAMATION : PRACTICAL ASPECTS

K.A. Barnett, B.Sc (Eng.) *

1 INTRODUCTION

Much controversy has revolved around the stability of Durban's beaches over the years and in its concern for this valuable tourist asset, the Durban City Council commissioned several studies culminating in a commission in 1961, jointly with the South African Transport Services, with the Council for Scientific and Industrial Research in which they were required to investigate the possibilities of maintaining the harbour entrance channel at certain depths and to find some means to stabilise and improve the Durban beaches.

1.1 Early History

In the period 1851-1903 harbour entrance channel works initiated disturbance to the beach equilibruim, causing the beaches to progress generally seawards. It was thought that this was the result of greater protection against swells from the south.

However, increase in the harbour channel depth over the period 1903--1926 caused beach losses north of Vetch's Bight, whilst in that Bight itself further deposition took place. (See Fig. 1). From 1905 onwards sand has been dredged from a sand trap to the south of the harbour entrance (Cave Rock Bight) and since 1925 the dredging rate has been relatively constant at about 600 000 m^3 per annum. Subsequent to 1926 more deposition occurred in Vetch's Bight but the general beaches continued to erode and in 1935 the Council commissioned the first sand pumping scheme with a view to nourishing the South and Central Beaches.

Sand was delivered by the South African Transport Services (S.A.T.S.) dredgers from the mooring at the North Pier to the Vetch's Pier area from where it was re-dredged by the Council scheme and pumped northwards as far as the present day South Beach.

1.2 Post-War Period

Erosion of the northern beaches continued and in the period 1950-1953 sand was pumped directly to Vetch's Bight from an area to the south of the South Pier by means of a submarine pipeline across the harbour entrance. Owing to insufficient sand collection within reach of the dredging plant, the original system with the S.A.T.S. dredgers pumping sand from the North Pier was resumed.

* Principal Engineer, City Engineer's Department, Durban, Republic of South Africa.

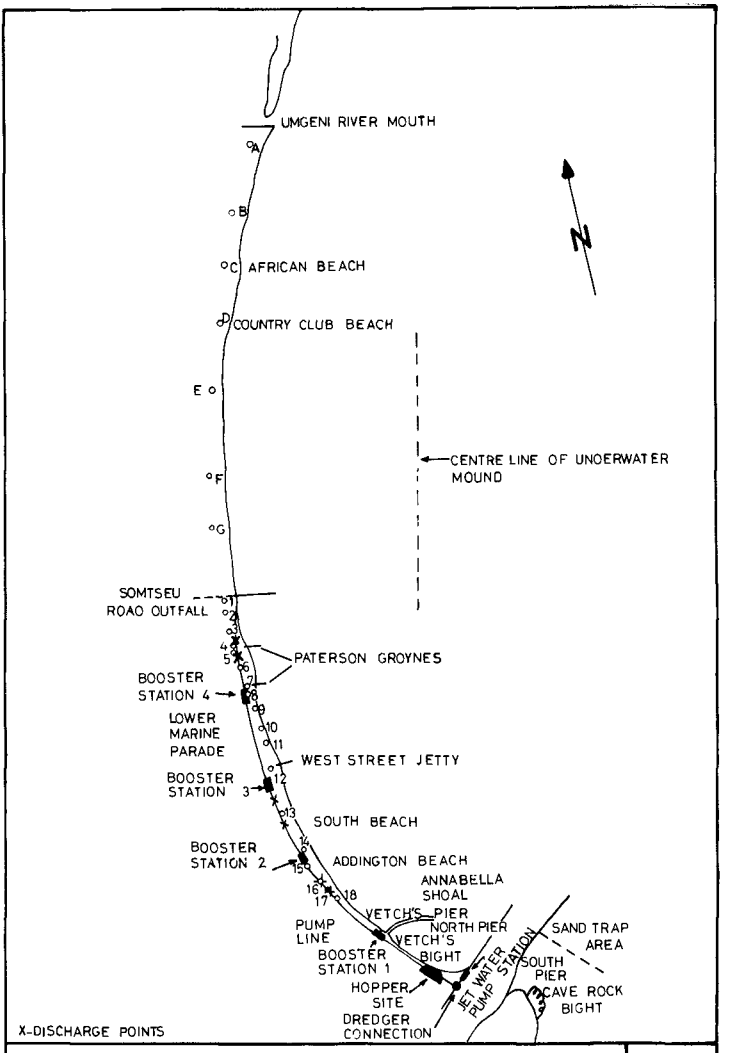

BEACH RENOURISHMENT IN THE SOUTHERN AREA — FIG 1

The two Paterson Groynes were built between 1954-1956 in the hopes of stabilising the Central Beaches but this was not realised.

Over ths yeare most of the material dredged by the S.A.T.S. has been dumped in a specific area at sea, called the "Dump" and it has besn found that this tends to focus wave energy, under certain conditions, near the Paterson Groynes.

1.3 Recent Developments

As was stated previously, the C.S.I.R. was commiesioned in 1961 to investigate, in depth, Durban's beach problems and several recommendations were made after extensive field and model studies. However, a further C.S.I.R. report was submitted to the Council in 1964 recommending that an underwater, offshore mound be constructed using S.A.T.S. dredgings. It was considered that the mound would offer good protection to the beaches by reducing incoming wave energy and it was thought that the beaches would improvs as a result of the presence of the mound. The mound was constructed between 1966 and 1974 but could not be raised to its full design height mainly because of the draught requirements of the dredgers.

However, further studies showed that the mound was not as effective as first thought and the littoral drift continued. The area to the eouth of Somtseu Road was subject to long term erosion at the rate of 70 000 m^3 per annum and the area to the north of Somtseu Road was in a long term state of equilibruim.

After correlation of the voluminous previous reports and findings, and of the considerable field data which had been collected as part of the monitoring programme, the C.S.I.R. submitted in 1977 a report outlining firm recommendations for a beach restoration scheme. Basically these were as follows:-

(i) The mound should not be completed to its design dimensions.

(ii) Establish a controlled zone covering the area 40 m landward of the 1977 highwater line throughout the Bight area; permit no building within this zone; and provide a stockpile of suitable renourishment material for use during storm conditions to protect critical areas.

(iii) Provide an initial beachfill to the area south of the Paterson groynes to restore these beaches to a more acceptable width.

(iv) 90 000m^3 of Cave Rock Bight material should be dumped annually on the beaches south of Somtseu Road, i.e. 60 000 $m^3/yr.$ on Addington and South Beach and 30 000 $m^3/yr.$ on North Beach.

(v) The Paterson groynes should be replaced by two low level structures. Subsequently, it can be decided whether further such structures should be constructed.

1.4 Action Taken by Council

The Council accepted (i) above and immediately put into effect (ii). It was decided in princple that (iv) should be handled by a conventional by-pass sand pumping scheme utilising the S.A.T.S. dredgers, as in the past. The technical feasibility of the construction of low level groynes is being investigated by a private firm commissioned by the Council.

Some 600 000 m^3 of beachfill was supplied by contract dredger to the Addington and South Beach areas during August and September 1982. This contract was negotiated with an overseas consortium working in Richards Bay at the time and the cost to the Council was about R2,3 m. This involved a trailer cutter suction dredger dredging material from an area seawards of the sand trap and pumping it ashore along a temporary pipeline from the S.A.T.S. dredger connection. Work was on a round-the-clock basis and usual output was about 20 000 m^3/day.

1.5 Programme for the Sand Pumping Scheme

The general conceptual design of the Durban beaches sand pumping scheme was finalised early in 1980 and immediately thereafter the detailed design work started. Tenders for the supply and installation of the mechanical/electrial equipment were invited in early 1981 and in April 1981 this contract was awarded on a "design and construct" basis, the City Engineer's Department having set out the technical concept of the scheme, the required output, concentrations, etc.

Shortly thereafter the civil and architectural contracts were put in hand and the commissioning of Stage I took place during August/September 1982. Commissioning of Stage II will take place in mid 1983.

2 Description of Scheme

2.1 Overall Concept and Modus Operandi

The focal point of the scheme is the hopper/administration site which lies near the North Pier. In this site are the tastefully designed administrative building which also houses the first booster station and the semi-circular reinforced concrete hopper which will receive and temporarily store sand from the S.A.T.S. dredgers. As stated previously the S.A.T.S. dredgers carry out maintenance dredging in the sand trap immediately to the south of the South Pier, generally dumping this material out to sea in a depth greater than 60 m. Alternatively, the vessel may tie up at the dredger connection at the North Pier and pump the sand through the "short line" to discharge into the Council's hopper.

Against the historical backdrop of the problem an agreement has been concluded with the S.A.T.S. in which they have undertaken to furnish 50 000 m^3 of sand per annum, free of charge. Any sand pumped in excess of this will be charged for at a rate of about R2,00/m^3.

Initial Beach Fill : Southern Beaches - Before

Initial Beach Fill : Southern Beaches - After

General View of Hopper/Administration Site.

Jet Water Station in Harbour Entrance.

The sand will then be re-dredged from the hopper by means of equipment housed on a mobile bridge by the injection of water pumped from the nearby jet water station, and delivered to the first booster station. From there the sand/water mixture will be boosted to four further stations with the final discharge point being near the Somtseu Road stormwater outfall. Sand can be discharged onto the beaches at a number of intermediate sites. The C.S.I.R. recommended that a minimum of 70 000-100 000 m^3 of sand is required on the beaches south of Somtseu Road annually to maintain the status quo and the scheme is designed to provide this quantity plus an anticipated 100 000 m^3 per annum to build up the beaches.

Booster stations are about 700 m apart to ensure unformity of equipment and the pumping main is a H.D.P.E. (high density polyethylene) pipe of 400 mm O.D., Class 6,3. The system has been designed to deliver a maximum concentration of 30% by volume. Total length of the pumping main is some 3,5 km and it should be noted that the entire scheme is automated and will be controlled from the hopper site. The power and signal cables run along the beach on the same route as the pumping main. The S.A.T.S. dredgers will deliver about 2000 m^3 of sand into the hopper at a time (total capacity 4 000 m^3), and this material will then be pumped onto the beaches (where required) at some 300 m^3 per hour in an 8 hour shift.

Total cost of the scheme, including the first two low level groynes and the initial fill is expected to be in the region of R10 000 000.

2.2 Mechanical and Electrical Equipment

2.2.1 Electrical supply and criteria

The supply in the area from the electrical grid is 11 kV and considering the stringent specification in relation to noise levels in residential areas it was decided to lay down that all motors were electric. The 11 kV supply is stepped down at the hopper site to 6,6 kV for the main booster station motor and to 400 V for the jet water pump motor, the dredge pump and other ancilliary equipment, for example drainage pumps, ventilation fan motors, etc. The remaining booster stations are all fed by landline from the hopper site (6,6 kV) with the respective ancilliaries at each station being catered for by separate 400 V feed.

Control of the scheme is by electrical signal transmitted by means of a "hard wire" system.

2.2.2 Mechanical data

2.2.2.1 Jet water station

The jet water pump is a vertical industrial turbine pump, the motor being rated at 150 kW and capable of delivering 1 800 m^3 of sea water per hour at a head of 18 m at 985 r.p.m. This is a mixed flow pump (nominal size 450 mm) and the impeller is manufactured from a special cast iron alloy known as Ni-resist. Other elements of the

View of Bridge Showing Control Cabin and Underslung Dredge Pump.

Jetting and Dredging Nozzles.

pump are also selected to resist corrosion, e.g. the column is Ni-resist, shaft stainless steel.

This pump station, as with all the other stations of the scheme, is force ventilated to dissipate heat generated.

2.2.2.2 Dredge pump unit

The dredge pump is underslung on the mobile bridge to ensure proper operation and is a centrifugal type slurry pump driven by a motor developing 185 kW, delivering 1 750 m^3 of sand/water mixture per hour at a head of 10-11 m at 390 r.p.m. The pump is belt driven and is identical to the main booster pumps.

2.2.2.3 Booster pump stations

The booster units (total of five) all consist of a centrifugal type slurry pump coupled to a motor rated at 450 kW, also delivering 1 750 m^3 of sand/water mixture per hour at a head of 30-35 m at 585 r.p.m. Here the motors drive the pumps through poly-vee drive belts. Nominal size of the pumps is 350 mm and materials of interest are:-

Impeller and casing - "MYTAK 1001"
Shaft - EN 8

Figure 2 shows a typical internal plan of a booster station.

3 DESIGN ASPECTS

3.1 Hydraulic Design

The design of the scheme is based on the calculation of critical velocity using the formula derived by Durand and the various parameters involved are dependent on the sand particle size and grading, the concentration to be pumped, the specific gravities of the solids and transporting fluids and the pipe diameter. The formula takes the following form:-

$$Vc = Fl\sqrt{2gD\,\frac{(S-Sl)}{(Sl)}}$$

where Vc = critical pipeline velocity.
Fl = factor dependent on particle size and concentration.
g = acceleration due to gravity.
D = pipe diameter.
S = S.G. of solids.
Sl = S.G. of transporting fluid.

The power requirement was then derived taking into consideration the various losses and safety margins.

In calling for tenders for the supply and installation of the mechanical and electrical plant, the City Engineer's Department specified broadly the criteria to be met by the scheme, amongst

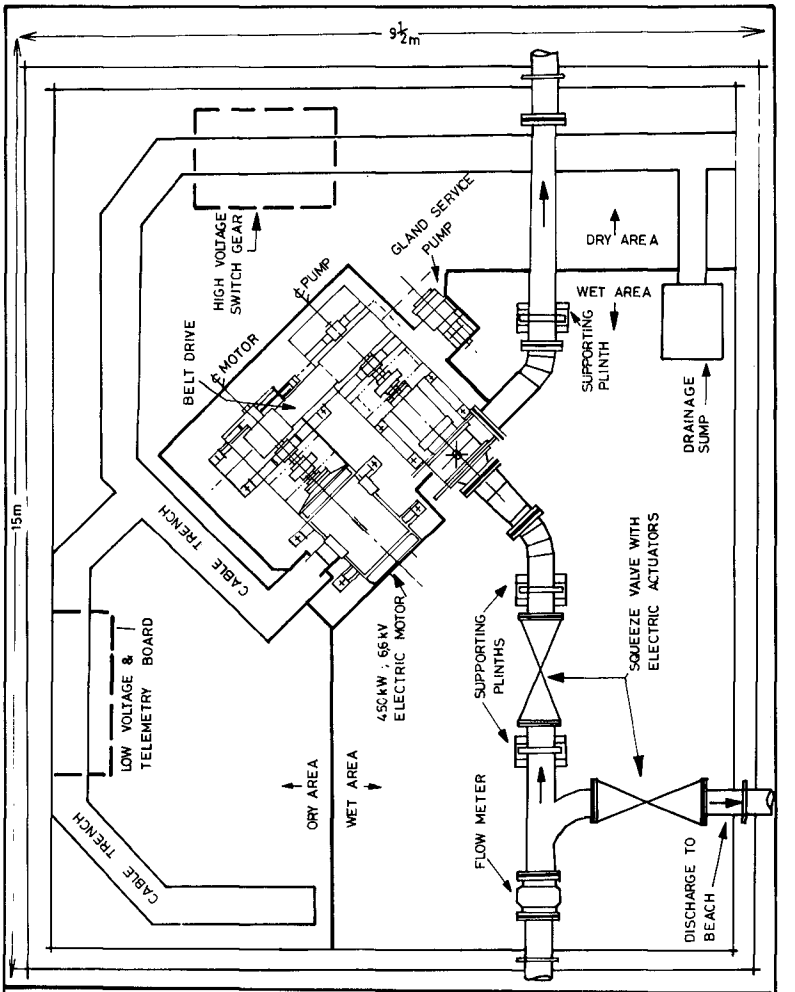

TYPICAL INTERNAL PLAN OF A BOOSTER STATION

FIG 2

View of Panel in Control Cabin.

Typical Booster Motor and Pump Set.

others that it should be capable of pumping concentrations of slurry from 0% to 30% of sand of volume. It was therefore the successful tenderer's responsibility to ensure that these criteria were met and that the scheme operated as designed.

3.2 Selection of Pipe Material

At the outset it was decided that the pipeline should be made of a material which had the following properties:-

(i) Extremely resistant to abrasion.
(ii) Robust.
(iii) Easy to handle.
(iv) Good cost/benefit.
(v) Resistant to corrosion.
(vi) Easily jointed.
(vii) Locally manufactured (availability).
(viii) Flexibility.

After an extensive literature survey and a study of a system already in operation at Richards Bay the choice of high density polyethylene was made. H.D.P.E. pipe scored high in all the above properties and although more expensive than, say, plain steel, was not by any means the most expensive material available and by all accounts appeared to have at least equivalent resistance to internal abrasion.

The valves on the line are all the squeeze type with butyl-type rubber sleeves with helicoil wire reinforcing and have remotely controlled, electrically driven actuators.

The pipe was generally heat welded into 39 m lengths which were then joined by means of stub ends and galvanised steel backing flanges. Stainless steel studs (grade 316) are used throughout for bolting the line together. The long term resistnce to corrosion of this jointing system in the beach environment will be closely monitored.

3.3 Architectural Treatment

Each of the buildings relevant to the scheme were handled separately and were designed to blend in with their individual surroundings. All were designed by the Architectural Branch of the City Engineer's Department except the hopper site building which was conceptually designed by the in-house architects, but owing to volume of work, a firm of private architects was commissioned to bring the project to completion.

Great care had to be taken with these structures to ensure that they would complement the Durban Beachfront Development Plan which is in the process of finalisation. The photographs of booster stations 1 and 2 and the figures 3 and 4 of booster stations 3 and 4 show the designs. Of particular importance was the choice of external finishes which had to combine ruggedness with an aesthetically pleasing product. Of interest is the architectural treatment of the outer wall of the hopper which sports abstract scenes painted with a highly resistant epoxy compound.

View of Booster Station No. 1

View of Booster Station No. 2

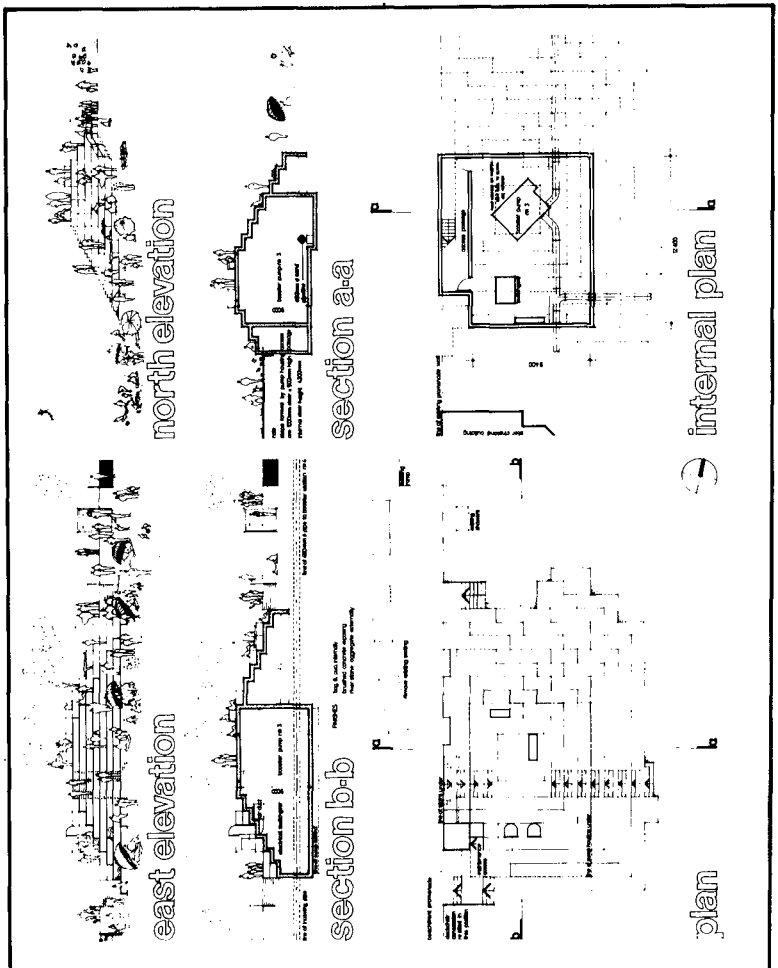

SKETCH PLAN OF BOOSTER STATION NO. 3

FIG 3

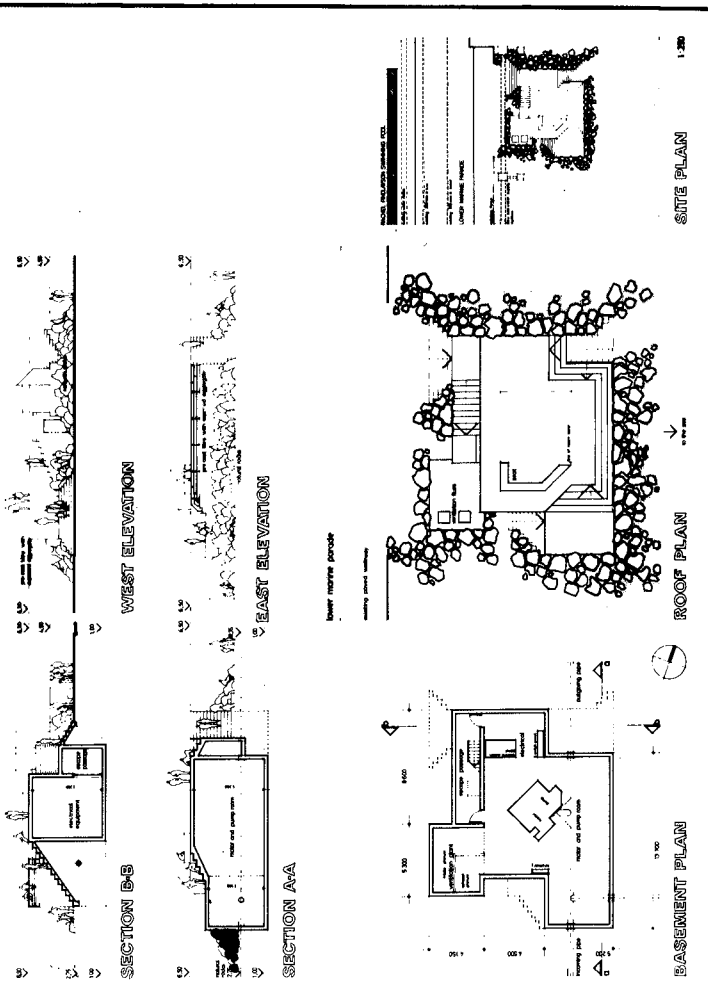

SKETCH PLAN OF BOOSTER STATION NO. 4

FIG 4

Special attention was paid to sound attenuation techniques as most of the etructures are in a seneitive locality being a combination of residential, hospital and recreational areas. It was also decided to make an attempt to reduce the transmission of vibration from the motor sets to the outer walls and roofs of the booster stations by providing completely separate foundations for the motor sets. Each motor pump base slab is on a separate pile group and the slab itself ie ieolated from the reet of the station floor slab. Noise levels were limited to 60 dB at 2 m from the structures.

To help reduce the noise levels outside the stations, walls and roofs are of reinforced concrete, solid wooden double doors are used and the ventilation inlets and outlets all pase through special muffler boxes to attenuate sound.

3.4 Civil Engineering Structures and Related Activities

The civil side of the booster stations and the hopper site building was handled by the Materials and Structures Division of the Roads Branch of the Depratment and included all reinforced concrete design as well as the requisite piling designs. The pile system of each building was designed to withstand a certain depth of scour resulting from abnormal sea attack, even though this is unlikely to occur.

The reinforced concrete sand storage hopper and the jet water station were implemented by "design and construct" contracts and had to match in with the architectural and/or mechanical/electrical requirements. The laying of the HDPE pipe and cables was handled Departmentally.

3.4.1 Sand storage hopper

This structure has a rectangular cross-section and is roughly a semi-circular annulus eubtending 152o at its centre. Centre line length of the hopper ie 109 m, depth ie 5,5 m, width 13 m and inside radius 34,15 m. The hopper can accommodate two loads from the SATS dredgers representing some 4 000 m^3 of material. Invert level of the hopper is at - 2,1 m msl and to resist buoyancy a system of tension piles was employed. In drastic instances of scour these piles can also easily double as normal compression piles to support the hopper. Static water level in the hopper is +2,4 m msl.

The hopper is simply filled by one inlet pipe at the one end, this being the discharge directly from the dredger. At full capacity the sand lies at a gradient of about 1/20 along the length of the hopper. The overflow is at the other end of the hopper and this is contained in a channel which routes the water directly back into the sea. Adequate scour protection is provided at the seaward end of the overflow channel.

Along the inner curve of the hopper is a water proof trough of 3,7m depth to accommodate the dredge pump which is mounted slung under the bridge. The top of the inner hopper wall is finished with an epoxy aggregate grout to a close tolerance to allow the bridge

wheels of bonded rubber to run smoothly and to give good operational life.

3.4.2 Jet water station

The conceptual design of this station was to give the effect of a submarine conning tower. The superstructure itself presented no problems but the founding on the North Pier was difficult as the pier was constructed some considerable tims ago and basically consists of a rubble core and loose stone pitched side slopes.

Finally, a portion of the side slope was fully grouted (under water) and the vertical column to house the pump was pre-casted and grouted into position. The superstructure was then cast on top of the column and fixed to the pier by means of grouted bars.

3.4.3 Pipe laying

To tie in with Phase I of the scheme, the jet water line from the jet water station to the hopper site (H.D.P.E., 450 mm, Class 4) and the pumping line (H.D.P.E., 400 mm, Class 6,3) from the hopper site to the West Street Jetty area was laid. Because of the high number of Contractors and sub-contractors already on site it was decided to lay the pipeline using Departmental labour. The gangs and equipment were more amenable to a "stop-start" work situation which resulted from tie-in to booster stations, beach area availability, etc.

By and large the pipe was laid in the highest part of the beach prism with approximately 600 mm to 800 mm of cover. The jointing system has been described under section 3.2. The supply Contractor welded the pipes into the 39 m lengths on site and these were then taken over in batches by the Department, and transported along the beach to the required laying area.

The laying operation was generally easy. It had been decided to lay the 6,6 kV main feed cable and the signal cable at the same time as the pumping main and in the same trench. After the trench was excavated (some 2 m bottom width) the services were merely laid at the requisite centres and the backfilling operation followed immdiately to ensure as little open trench as possible remained overnight on the beach. A laying rate of up to 100 m/day was commonly achieved. Finally the laid pipe was hydraulically tested to 1,5 times working pressure.

3.5 Control Systsm

The entire scheme is controlled by one man from the control cabin and is started merely by initiating one signal. Each booster station is started on flow, i.e. as it is recorded that there is flow just on the upstream side of a station, it starts. There is an intsrlocking system within each booster station which allows it to start up in a definite sequence as follows:-

(i) Inlet ventilation fan.
(ii) Extract ventilation fan.

(iii) Gland water pump.
(iv) Main motor.

Pressure starting devices were not used because of instrument sensitivity problems.

If any component breaks down the system shuts down automatically and if an overload should result an audible alarm sounds in the cabin. To stop the system the Superintendant only has to cancel the original signal.

4 MONITORING

4.1 History of Monitoring

Monitoring of the beaches was initiated by the C.S.I.R. in the early sixties and included the usual facets of this operation. The C.S.I.R. continued to organise and control all monitoring up until 1976 when their Coastal Engineering staff in Durban were transferred to Stellenbosch. It was considered logical, therefore, at the time, to hand over all monitoring functions to the City Engineer's Department as it was apparent that the City Council would be taking over control of the whole beach aspect progressively in the ensuing period.

Since 1976 virtually all monitoring functions have been controlled and organised by the Department and the scope of the programme has been widened considerably. A brief description of each aspect follows.

4.2 Visible Beach Survey

This is carried out each month by a firm of private surveyors. A total of 32 sections is surveyed and visible beach volume is calculated and recorded. Each section is defined by a co-ordinated beacon generally fixed at the upper part of the beach, the readings being taken from these beacons down to at least Chart Datum. The 32 sections cover the beaches from Addington to the mouth of ths Umgeni River. A plot of these volumes shows a long term degradation of the visible beaches.

Recently it was decided to establish six more sections north of the Umgeni mouth covering the beaches up to the northern City boundary. These sections are very widely spaced and are only read every 2 months at this stage to keep an overall check on the beaches there.

4.3 Nearshore Hydrographic Survey

Every month, between section 2 and 12 a shallow water survey is done covering from Chart Datum (approximately) to about 5 m of water. The survey team consists of the same private surveyors as above assisted by Departmental technicians and a motorised rubber dingy manned by 2 lifesavers from the Parks, Recreation and Beaches Department.

Soundings are taken by hand line and as all parties concerned are in radio contact, a simultaneous fix can be made. Rssults are plotted on a format, which, at a glance, shows the relative movsment of any particular contour.

Although this is a rather unsophisticated method and has only been done for about 2 years, practice and good teamwork has ensured acceptabls accuracy.

4.4 Offshore Hydrographic Survey

This survey basically covers the area from the surf zone to just seaward of the offshore mound. Originally these surveys were initiated by the construction of the mound and were all dons by the C.S.I.R., at first at frequent intervals but latterly every year only. In early 1981 this function was taken over by the Departmsnt and at pressnt the survey is being carried out quarterly again, partially to consolidate the team and also to satisfy all parties concerned of accuracy and consistency.

The Natal Anti-Shark Msasures Board hire the Dspartmsnt one of their boats and crew for the "water" side and once again the shore team consists of ths surveyors and Departmental Technicians. A sophisticated echo sounder is mounted in the boat and a continuous trace is produced on every run which co-incide with the sections mentioned in 4.2 (excluding those to the north of the Umgeni). Again, all are in radio contact and simultaneous fixes can easily be made. Additional sections are run over the northern end of the mound to assist the C.S.I.R. in their latest refraction studiss.

At this stage it is fslt that accuracy is within 250 mm either way and as this is improved so will the frequency of survey be dscreased, initially down to twice a year and possibly evsntually to once a year. The results are plotted as a contoured bathymstric chart.

4.5 Beach Sand Size Sampling

Sand samples are taken from the inter-tidal zone every month at each of the sections betwsen Addington and the Umgeni mouth. Four samplss are taken at each location, one from the high water mark, one from the low water mark and two from the third points (approximately) in between. These are not mixed together, but are analyssd separatsly, at present by a local soils laboratory, undsr annual contract.

It may be dscidsd in the future to mix the samplss from each section as there appears to be a trend towards this. Furthermore, the process will be speeded up by the use of a vsrtical tubs typs (water filled) rapid sand grader.

Figure 5 shows sand size distribution along the beaches.

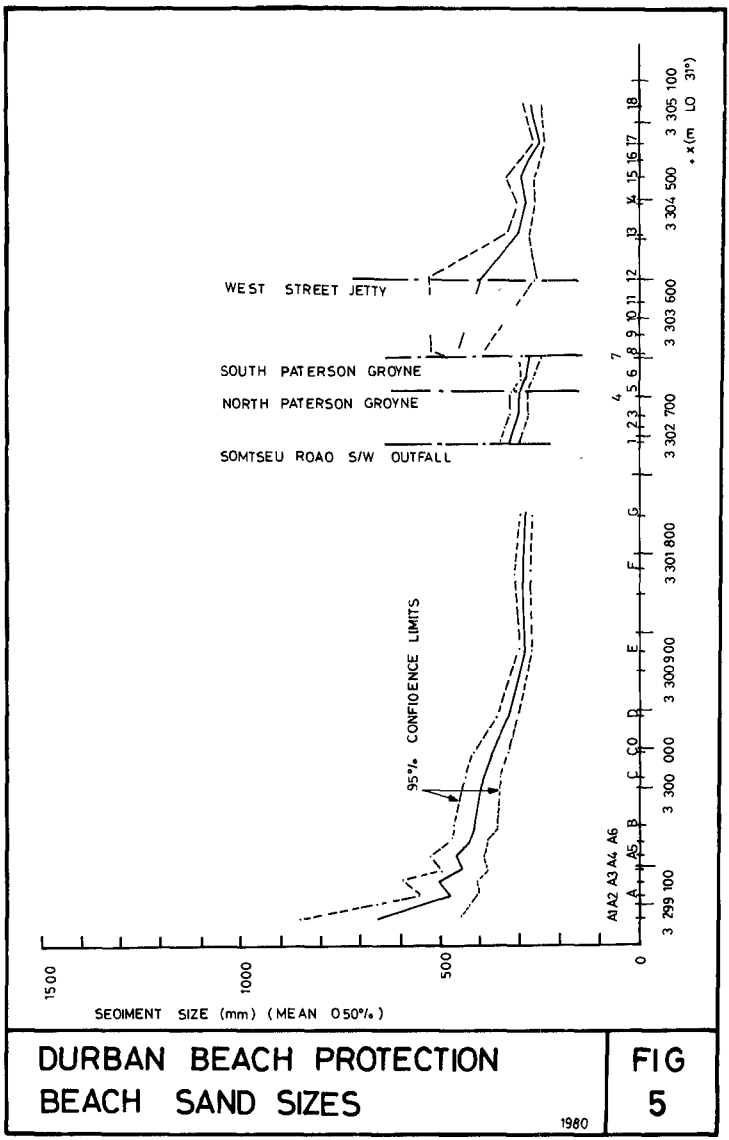
WEST STREET JETTY
SOUTH PATERSON GROYNE
NORTH PATERSON GROYNE
SOMTSEU ROAO S/W OUTFALL
95% CONFIDENCE LIMITS
SEDIMENT SIZE (mm) (MEAN 050%)
1500
1000
500
0
A1 A2 A3 A4 A5 A6
A B C D E F G
1 2 3 4 5 6 7 8 9 10 11 12 13 14 15 16 17 18
3 299 100
3 300 000
3 300 900
3 301 800
3 302 700
3 303 600
3 304 500
3 305 100
x (m LO 31°)
DURBAN BEACH PROTECTION
BEACH SAND SIZES
1980
FIG
5

4.6 Wave characteristics Recording

For many years the C.S.I.R. had a clinomster set up south of the harbour entrance to measure wave direction, height and period. This instrument was read by a private person who was trained for the work. When the Department took over the monitoring function this system was not interfered with and recently a second clinometer was installed in a tall hotel on the beachfront roughly oppoeite section 3.

The clinometer is a relatively simple instrument produced by the C.S.I.R. and is read 3 times a day. Although not the most accurate of instruments, it does provide a good and reliable insight into and data of wave direction, height and period.

In the middle of 1981, a wave rider bought by the University of Natal, Durban, was installed on the landward side of the mound. The monitoring side of this is handled by the Department whose staff make daily checks on the instruments and change and forward the magnetic and paper tapes to the relevant authorities. Periodically, checks on the wave rider itself are carried out from a boat and of course, every nine months it is uplifted for cleaning, checking, battery change, etc.

4.7 Deep Sea Sand Sampling

This operation will run hand in hand with the tracer sand aspect and samples will be taken on a grid pattern, initially every 3 months. It is thought that a grab-type sampler will be best and that a sea bed surface sample will be sufficient. However this may have to be modified in the light of experience when the schsme is undsr way.

4.8 Wave Refraction Analyses

Since the early sixties, the C.S.I.R. have done numerous wave refraction studies of the Durban Bight. Because of the techniques involved, the past studies were probably relatively "coarse" and recently the C.S.I.R. have developed, it is hoped, a much more reliable programme to handle areas such as Durban.

Previous studies showed that the old SATS dump helped to concentrate wave energy in the vicinity of the Paterson Groynes. The new study may confirm this and it may give pointers as to which are the best localities for dumping sand with the sand pumping echeme. Of particular interest will be the wave patterns around the northern end of the offshore mound as it is thought that certain wave directions will be so refracted as to give rise to undeeirable concentrations of energy on parts of the northern beaches.

4.9 Current Surveys

Attempts have been made to establish current patterns in the sea area landward of the mound. Floats with drogues some 4 m below the surface have been used but to date no significant results can be pressnted as the drogue movemente have not shown a sufficiently

reliable pattern. It has been proposed that the SATS dredgers dump material in the area landward of the mound but any peculiarities in current velocity here must be known beforehand.

4.10 Tracer Sand

At this point in time it is thought that the injection of 1 m^3 of tracer sand per load of 2 000 m^3 will be sufficient. A traditional paint-coated sand will be used but results of finds will have to be treated on a strictly qualitative basis. Depending on the results, a different type of tracer may have to be employed in the future.

5 RESULTS

At present, commissioning of Phase I is taking place. A few small problems have arisen but these are being rectified by the relevant Contractor or Sub-Contractor and it is expected that Phase I will shortly be taken over by the Department. The operation of the scheme appears to be very easy and maintaining a steady concentration presents no problems. Unfortunately, therefore, no results can be presented at this stage.

6 CONCLUSION

No conclusions or recommendations can be offered until the scheme has been operating for some time.

7 ACKNOWLEDGEMENTS

The author wishes to thank the City Engineer of Durban, Mr D.C. Macleod, for permission to publish this paper.

Thanks are also due to various members of the General Section of the Hydraulics Branch of the Department for their unflagging assistance, and especially to Mr R.B. Wicks who has worked "at the face" for more than 2 years now and who has been involved in every detail of the scheme, virtually from start to finish.

8 REFERENCES

SWART, D.H. (1976). Status Quo of the Durban Beach protection Investigation. Coastal Engineering and Hydraulics Division, National Research Institute for Oceanology, Council for Scientific and Industrial Research, Report C/SEA 7607. 27 pp.

SWART, D.H. (1977). Management of the Beaches in the Durban Bight. Volumes 1 and 2. Coastal Engineering and Hydraulics Division, National Research Institute for Oceanology, Council for Scientific and Industrial Research, Report C/SEA 7622. 73 pp.

FLOATING TYRE BREAKWATERS - A CASE HISTORY

ROBERT C. McGREGOR* and COLIN H.G. GILBERT**

1. INTRODUCTION

The problem of achieving a system of coastal protection which is cheap, effective and reliable has stimulated the minds of researchers and innovators for many years.

Although floating breakwaters have been written about since the 1840s, interest in them has increased rapidly in recent years. Over the last decade or so floating tyre breakwaters (FTBs) have received considerable attention. Several different designs have been proposed. Candle (1974) proposed what may be considered a nearly rigid mat of tyres where neighbouring tyres move relatively little with respect to one another whereas Noble (1976), Harms (1978) and Kowalski (1974,76) use breakwater flexibility in their wave-maze, PT and modular designs respectively. The breakwater described in this case history used the Kowalski or Goodyear design, which is made up of modules of eighteen tyres which are connected up to form a flexible mat (See Fig.1).

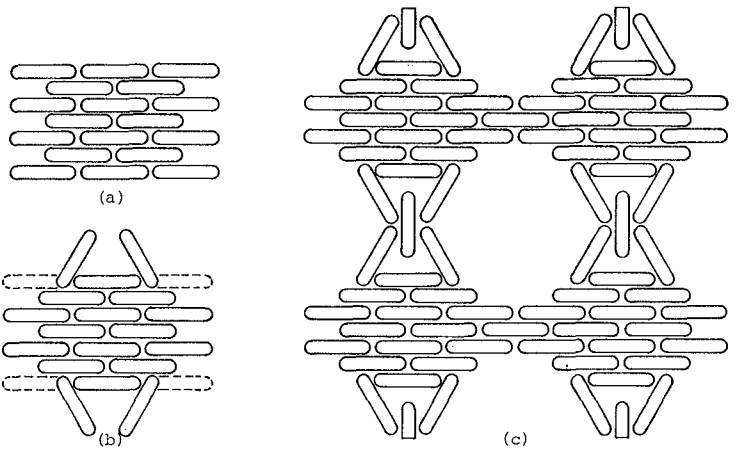

Fig. 1 - Floating Tyre Breakwaters
a) module as constructed on land
b) module ready for linking to others
c) four modules linked together

* Lecturer in Naval Architecture and Ocean Engineering, University of Glasgow, United Kingdom.
** Senior Engineer, Land Reclamation and Development Consultants, Haslemere, United Kingdom.

There is now an intense demand for increased recreational boating and the numbers of fish farms are growing rapidly. In both cases suitable sheltered water is scare and the mooring pontoons or fish cages require some protection to make marginal areas usable.

The FTB is a contender in these cases. An assessment needs to be made as to whether its advantages, or plus points, namely,

1. lower capital cost - since the main item the tyres themselves are scrap they are widely available in large numbers (e.g. in Britain alone 25 million tyres are discarded annually and only a small fraction are recycled) at very low unit cost,
2. simple and quick to build using unskilled labour (except for supervision) and a minimum of mechanical equipment - similarly mooring and any repairs are easily achieved with minimum interruption to the protection afforded,
3. adaptable to changing needs - the breakwater may be lengthened or broadened to provide more protection over a greater area if the needs of the site change, in addition the breakwater could be towed to another site and reformed to meet the different conditions,
4. ecologically safe with respect to
   i) toxicity - tyres are completely non-toxic in seawater and do in fact attract marine life to the extent that they have been used as submerged reefs and fishing islands,
   ii) impedance of of tidal currents which control sedimentation patterns and the regime of estuaries etc.
5. minimal hazards to boats because tyres are relatively soft in a collision,
6. not liable to catastrophic failure - failures within the module do not free part of the structure to float off to wreck boats or cages since the tyre, while it can be constrained to float vertically is bistable and will, if released, topple over and sink without causing damage or becoming a hazard; failures of moorings will lead to the situation where the breakwater wraps itself like a blanket around pontoons or cages and continues to afford some protection, and finally,
7. little wave reflection - the breakwater works by dissipating energy rather than by redirecting it and consequently undesirable standing wave conditions are not created in the access to the harbour,

outweigh the disadvantages of

1. higher maintenance cost - the breakwater is a dynamic structure and its composite parts are subject to abrasion and wear and so attention must be paid to the state of ties, moorings, buoyancy etc. at frequent intervals (to be discussed more fully later),

2. wave attenuation is partial - floating breakwaters act like filters absorbing the high frequency waves more efficiently than the larger ones but some wave energy will be transmitted or generated by the movement of the breakwater itself,
3. occupies more space - wave attenuation is linked to size of the breakwater, in particular the beam of the breakwater should be a substantial fraction of the wavelength of the waves which must be reduced,
4. relatively short service life - the materials used in the original construction will deteriorate over a few years and a point will be reached where maintenance is better achieved by a reconstruction, and
5. vulnerability to ice on lee side - this is a problem encountered mainly in fresh water sites in high latitudes but can be serious because the moorings may be overloaded.

The object of the design is to develop the situation where the disadvantages are reduced relative to the advantages. Essentially the breakwater is designed to have an adequate level of wave attenuation such that the risk of the damage is reduced to an acceptable level. If this can be achieved within the space limitations (and ice is not present) then the financial balance is the main consideration. Typically the annual maintenance cost is of the order of one third of the first cost. This is a high percentage but the first cost could be as low as 3% to 5% of that of a conventional breakwater, so the maintenance cost is less than servicing the capital involved in such a breakwater. Even with a reconstruction (costing 60% to 80% of the first cost) every three years (which is pessimistic) the life cycle costs compare favourably.

In the case under consideration there was plenty of room and wave conditions were such that an adequate design was possible within the bounds of existing FTB experience. However it is this experience which is rarely published, even though it may be communicated privately, that is presented here to justify the claim that FTBs are not only cheap and effective but can with proper handling be reliable.

2. BACKGROUND

Lothian Regional Council took over the former Royal Navy minesweeper base at Port Edgar on the south side of the Firth of Forth, Scotland.* The harbour at Port Edgar was well designed for its original purpose. Minesweepers are not troubled by waves of 0.6m or so. However yachts are. Consequently Lothian Region engaged Land Reclamation and Development Consultants (LRDC), a subsidiary of Grontmij, to review possible floating breakwaters with a view to establishing a marina as quickly as possible. LRDC recommended a floating breakwater and in association with the Department of Naval Architecture and Ocean Engineering at University of Glasgow** designed a breakwater which would provide

*The site lies in the shadow of the Forth Road Bridge and the Forth Rail Bridge is close by.

**This design service is now a function of Ostec Ltd.

adequate wave attenuation, planned its moorings, prepared detailed design documents and drawings and supervised the construction. The breakwater was made up from 3000 truck tyres and was completed in April 1979 within 5 weeks of the decision to proceed.

3. DESIGN

3.1 Site Assessment

The location of Port Edgar may be seen in Fig. 1. Fetches were measured for each of the relevant bearings and corrected for the effects of width of fetch. A shallow water correction was not considered appropriate.

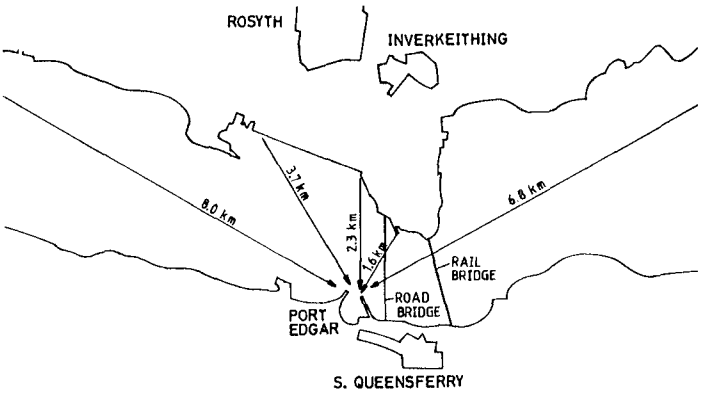

Fig. 2 - Firth of Forth near Port Edgar

Wind data was available from the Meteorological Office for a 20 year period and the mean hourly wind speeds which would have a return period of 10 years from each bearing were predicted.

Over short fetches the sea is quickly aroused to its full potential and the significant wave heights and periods were evaluated using a Bretschneider Chart (US Army, CERC, 1977). (Other methods were examined.) This predicted the sea conditions outside the harbour but in some cases diffraction by the piers of the existing harbour significantly reduces the height of the waves which would penetrate to the breakwater site. This leaves the bearings of 330° and 0° as those producing the only waves of sufficient height to justify attenuation. (In addition wave conditions from other headings are greatly ameliorated.)

This assessment is summarised in Table 1.

TABLE 1: Fetches, Wind and Wave Conditions near Entrance to Existing Harbour.

Bearing (Degrees)	275	285	330	0	30	60
Fetch (km)	7.4	16.7	3.7	2.3	1.5	6.8
Fetch (km)	5.0	7.4	3.7	2.3	1.5	5.1*
Wind Speed (ms^{-1})	26.8	17.4	14.3	14.3	14.3	14.3
Significant Wave Height (m)	1.60	1.15	0.70	0.55	0.45	0.75
Period(s)	4.4	4.0	3.0	2.7	2.4	3.3
Post Diffraction Height (m)	0.25	0.30	0.70	0.55	0.25	0.20

*Further reduced by effect of bridges.

3.2 Wave Attenuation

Extensive data on the performance of FTBs had been collected from experiments conducted on quarter scale car tyres in the Hydrodynamics Laboratory of the Department of Naval Architecture and Ocean Engineering at the University of Glasgow. This tank is 77m long, 4.6m wide and 2.4m deep and has a parabolic plunger wavemaker at one end which at that time could be programmed to generate a pseudo-random sea with wave heights up to 0.4m.

Twenty-five breakwaters fabricated of basic (Fig. 1) and deep modules were constructed and tested for wave attenuation and catenary mooring loads (McGregor 1978, McGregor and Miller 1978). In contrast with other tests on FTBs the breakwaters were tested in a broad band spectrum and analysis was by means of FFTs to generate the transmission function

$$C_T(f) = \left[\frac{S_A(f)}{S_F(f)}\right]^{\frac{1}{2}}$$

where $S_A(f)$ and $S_F(f)$ are the measured wave spectra aft and forward of the breakwater respectively. Sufficient runs were made to reduce the error in the spectral values to 4%.

Other tests described in Giles and Sorenson (1978), Harms and Bender (1978) and Kowalski (1976) have used monochromatic waves and achieved a transmission factor

$$\overline{C_T} = \left[\frac{\int_0^\infty S_A(f)\,df}{\int_0^\infty S_F(f)\,df}\right]^{\frac{1}{2}}$$

which is not useful in design.)

This different method of experimentation lead to different methods of

design. The monochromatic approach by establishing dependence on steepness implies the wave attenuation is non-linear which means that the storm sea spectrum must be idealised to a design wave. The spectral approach assumes wave attenuation can be approximated by a linear system employing a transfer function but can realistically represent the sea in spectral form.

Clearly neither of these approaches has a monopoly of truth but the authors believe that more useful information is ahcieved from a design calculation based on spectral methods. (This discussion is a superficial summary of a complex situation which merits further investigation.)

In this design study it was assumed that the sea could be represented by an ISSC spectrum. (The use of another form such as a modified JONSWAP would change the calculated values but not sufficiently to alter the design.) The evidence of the model tests was that the primary characteristic of a wave was its wavelength and so the transmission function was applied in the form $C_T(\lambda)$ (or even $C_T(^B/\lambda)$).

3.3 Breakwater Design

Figs. 3 and 4 show the predicted performance of a 3 row breakwater of truck tyres aligned east-west encountering waves from bearings of 330^o and 0^o respectively showing the difference in performance at high and low water.

From analysis of several beams and orientations this size of breakwater and orientation was judged to be satisfactory and is shown in Fig. 5. The orientation is a compromise between the extra wave attentuation available if the breakwaters western end is moved northwards and the shorter breakwater length achieved if it were moved south.

The breakwater length is determined by

a) the clearance between the breakwater and the boat moorings,
b) diffraction effects and the area to be protected, and
c) siltation problems.

The clearance was chosen to be 40m but the length is not sensitive to this value and after trying to avoid siltation problems near the east pier by as small a margin as possible it was seen that the diffraction considerations were most significant. The breakwater was designed to be 180m long.

3.4 Moorings

The peak pull on the moorings was calculated from a design wave analysis and was confirmed from extreme value statistics of the model mooring experiments (McGregor 1978) with appropriate scaling for tyre size and wave dimensions. The two methods were substantially in agreement in suggesting a probable maximum of 44 tonnes. The mooring arrangement is shown in Fig. 6.

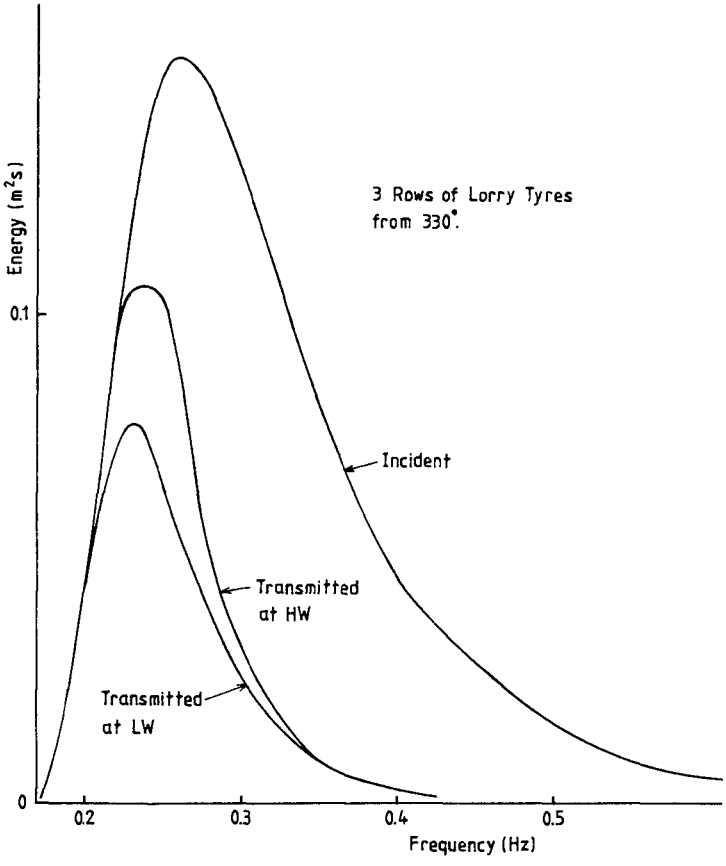

Fig. 3 - Breakwater Performance for 3 rows of lorry tyres with waves from 330°

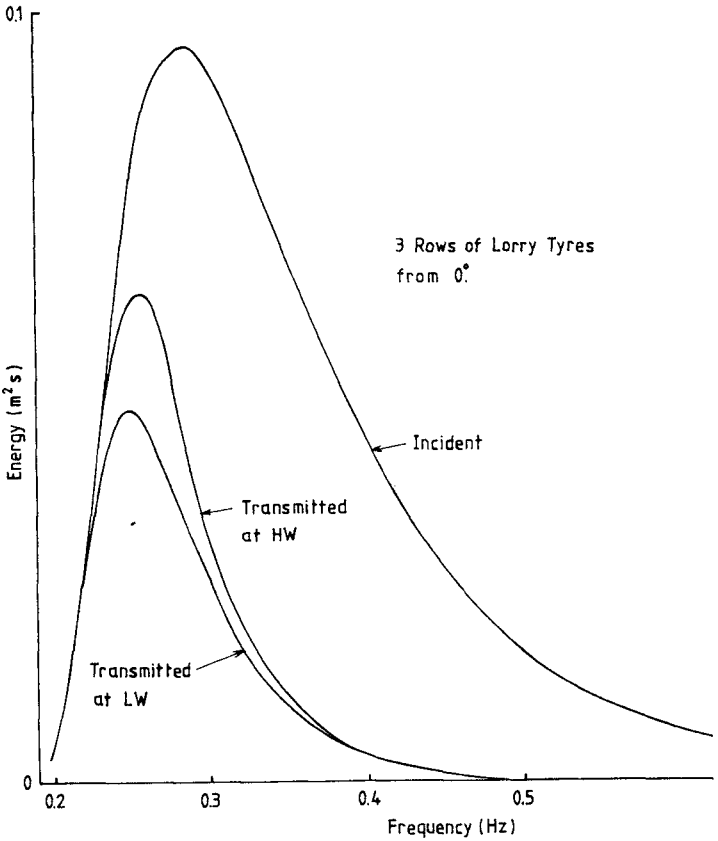

Fig. 4 - Breakwater Performance for 3 rows of lorry tyres with waves from 0°

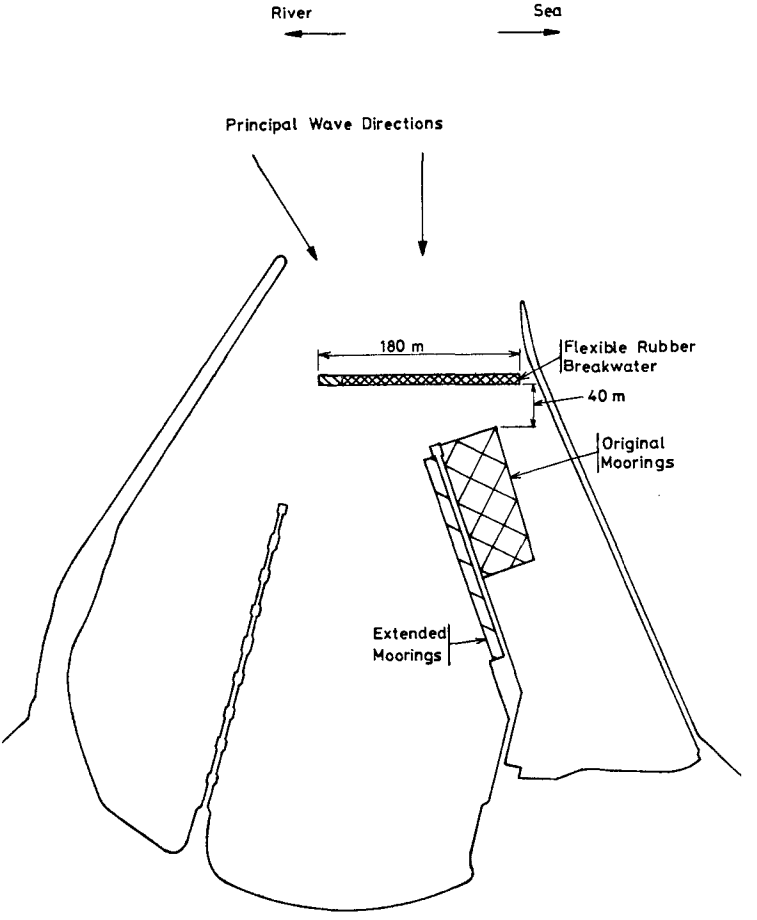

Fig. 5 - Breakwater location at Port Edgar Marina

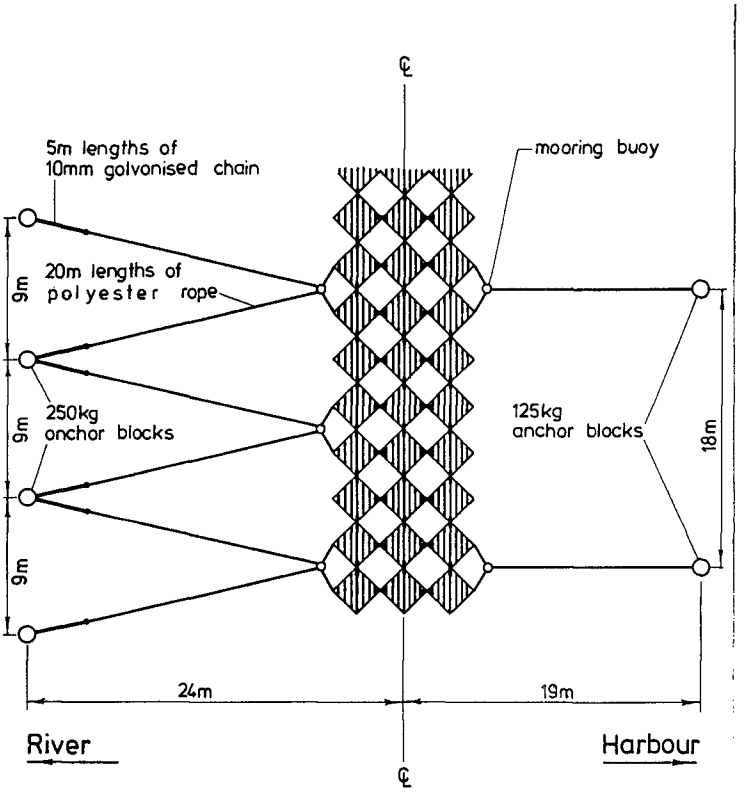

Fig. 6 - Mooring arrangement for floating tyre breakwater at Port Edgar

4. CONSTRUCTION

4.1 Timescale

One of the most attractive features of FTBs is that they can be assembled and installed very quickly. In this case following the initial order in February 1979 the breakwater was tendered for during March and the initial building phase took three weeks. An extension to the originally ordered length to provide protection for an increased area took a further two weeks and the breakwater was completed and operational by mid-April in good time for the marina to be in service and earning during that year's boating season.

Although there were some problems (see maintenance) the breakwater was a successful wave attenuator and the expected life was revised to five years. This coupled with growing suspicion of the status of many of the ties and the level of regular maintenance entailed by the decision that the original breakwater was constructed without additional buoyancy* led to a reconstruction in February and March 1980 carried out on a section by section basis thus maintaining complete protection.

A summary of key dates in the history of the Port Edgar Marina Breakwater are given in Table 2.

TABLE 2: History of Breakwater

1978	December	FTB proposal and design quotation.
1979	January	Report evaluating wave conditions and designing the breakwater was commissioned.
	February	Breakwater ordered as a temporary solution with an expected life of two years.
	March	Request for, assessment of and acceptance of tender Breakwater built to original specification within 3 weeks and then extended.
	April	Breakwater completed and marina becomes operable Some modules ground on silt and are held down.
	October	Breakwater partially sinks because of lack of maintenance but is refloated within 24 hours.
1980	Feb. & March	Breakwater is overhauled and fitted buoyancy since the expected life is increased to 5 years.
1982	November	Further FTB under consideration as means of enlarging marina.

* This was done to minimise first cost in the belief that maintenance over the 2 years of expected life would give a smaller life cost.

4.2 Materials

The main construction material is of course tyres. The choice lay between car and truck/tractor tyres. In this case truck tyres were chosen for the reasons below.

a) Scaling - although appreciable quantities of experimental data exist for tyres of different sizes the precise mechanism of wave attenuation is not certain and consequently appreciable uncertainty exists on the scaling laws. For the environment at Port Edgar truck tyres scaled relative to the model tyres in much the same way as the waves thus giving the two scaling factors a similar value and facilitating the scaling problem.
b) Constructional - the number of truck tyre modules required for comparable wave attenuation was very much less than would have been needed with car tyres.
c) Size - The truck tyre breakwater was less beamy than a car tyre design.

A significant price was paid for these advantages.

d) Buoyancy - most truck tyres are tubed and lack the butyl or chlorobutyl lining which is built into car tyres. This means air can leak through the tyre causing the tyre to sink lower in the water. Fig. 7 shows how this effects the breakwater.
e) Handling - truck tyres and truck tyre modules are appreciably heavier than their car tyre counterparts and this increases handling problems. This is offset to a degree by having fewer module connections to make in the water.
f) Abrasion - the extra steel in the beading of truck tyres makes them more abrasive to conveyor belting.

Although the tyre composition factors (d) and (f) were not appreciated prior to the original construction the choice of truck tyres was sound.

Plausible tying materials include nylon, dacron, polypropelene and (stainless steel) wire ropes, open or closed link chain and conveyor belting. All the ropes have overwhelming disadvantages and the choice lies between chain which is heavy and will wear inside the links and conveyor belting which is made of a material similar to the tyres and may be obtained as scrap. Conveyor belting was recommended by Davis (1977) and was chosen for the original breakwater. Belting was cut from used conveyor belts which were scrapped rather than edging of new belting which appears to have been available in America. Three makes of belting were used and two of them exhibited failures within six months. The remaining type appeared unscathed but in the reconstruction a complete transition to chain was made.

The choice of fastenings is determined by the typing material e.g. knots, splices or crimps for ropes, shackles or closing links for chain and stainless steel or black nylon bolts for conveyor belting. Initially stainless steel bolts were used with the belting and these were satisfactory. Later high tensile shackles were used in the reconstruction. A waterproof salt resistant grease is invaluable for use with the shackles when maintenance is necessary.

Fig. 7a - New section (with buoyancy) ready for installation

Fig. 7b - Modules with and without buoyance during refurbishing of breakwater

Rope, chain and belting have all been used alone or in combination for moorings. In this case nylon rope with spliced hard eyes and black chain were used.

The mooring loads are not in general very high and depending on the bed composition and the anchor handling capability available either small(ish) anchors or concrete blocks may be used. With a silt bed concrete blocks cast in half 50 gallon oil drums were used. The blocks buried well and gave no problems.

It is useful to provide a large number of buoys around the breakwater to provide mooring attachment points which have significant buoyancy to help support the mooring and mark the breakwater. The breakwater was also provided with low intensity intermittent battery powered lights.

(The materials available including floatation aids are discussed at length by Bishop (1980)).

5. MAINTENANCE

5.1 Basic Need

It is important in the context of FTB to appreciate that maintenance is an essential feature of the operation. The very low initial cost is to an extent offset by maintenance costs which will be high relative to the first cost, although only moderate in absolute terms.

Being a dynamic structure the FTB will inevitably be subject to wear and deterioration. It must therefore be inspected regularly and frequently as well as after each storm. It is recommended that at the time of initial construction the appointment of a maintenance contractor, with clearly defined responsibilities, should be considered. Any such contractor should attend to unscheduled maintenance or damage repair without delay. All maintenance should be carefully recorded.

5.2 Maintenance Problems

Several problems were experienced with the initial design which as has already been stated involved no additional buoyancy and relied on maintenance to ensure it floated with a reasonable freeboard. These problems are listed below.

a) Loss of buoyancy from tyres which was not replaced naturally by storms - buoyancy may be lost because of

   i) air dissolving - but seawater is fully saturated with gases and will dissolve no more,
   ii) air leaking through rubber (See 4.2),
   iii) air leaking through tyre faults - any local lightening will migrate to the top,
   iv) marine growth - weeds and crustacians,
   v) flotsam - small weight addition when beached on breakwater.

Once buoyancy is being lost reasons for lack of replenishment become important. These may include

i) shape of the tyre beading,
ii) tightness of the module - in a loosely fastened module individual tyres could heave sufficiently but loose modules are undesirable for other reasons,
iii) inertia of module to wave action - truck tyres with their higher virtual mass are less likely than car tyres to be lifted sufficiently,
iv) lack of freeboard caused by loss of buoyancy makes replenishment progressively more difficult.

Initially this difficulty was to have been tackled with an air line (operated from a boat) which although quite feasible is labour intensive. In addition during a period when there was a temporary lack of maintenance through staff leave an appreciable part of the breakwater sank. A wind of force 5 or 6 blew while the breakwater was down and some considerable damage was experienced. The breakwater was refloated within 24 hours by divers with an air hose. This led to the assessment of permanent floatation. The choice lay between sealed plastic containers for which various sources give evidence of cracking, crushing, escaping or leaking (Bushell (1978)) and foams. The foam may be moulded, rods or mixed in the tyre. The foam should be high density, resistant to crushing, abrasion and pollutants. Although polystyrene cannot be recommended both polyurethane and polyethylene appear to have been used successfull. In this case polyethylene rod was chosen.

Problems created by the belting chafing on the tyre beading were solved as stated by changing to chain.

Port Edgar proved to be an area with three other potential problems.

i) Silt - early in the breakwater's life modules near the east pier grounded at low spring tides and were held down by suction. They were refloated and the breakwater moved a little to the west.
ii) Biological and Zoological Growth - a prodigous growth of kelps (laminaria saccherina and laminaria digitata) which are indigenous to the area developed. These fruit in the coldest months i.e. December and January and should be cleared just before that period removing even the roots to avoid their own ecosystems being established. Mussels were the other major growth. These settle in April and should be cleared then.
iii) Accidental and malicious damage - although this could be serious observation, maintenance and responsible boat owners kept it to a minimum.

6. CONCLUSION

The breakwater has proved hydrodynamically successful in that no damage to boats at the moorings was experienced even when the winds reached

force 11 and waves up to 1.25m high were encountered. Without the breakwater, moorings could be untenable at wind forces as low as force 5 or 6. Early constructional problems have been overcome and develop ing biological problems contained by improved understanding of their causes. This has enabled the maintenance programme to be made more timely and more cost effective.

Overall acceptance is illustrated by the consideration of another FTB to provide further protection to the marina which is being extended.

7. ACKNOWLEDGEMENT

The authors are grateful to Lothian Regional Council and its servants for their co-operation, and to colleagues in LRDC and the University for helpful discussions.

8. REFERENCES

BISHOP, C. T. 1980 "Design and Construction Manual for Floating Tyre Breakwaters". Hydraulic Division, National Water Research Institute, Burlington, Ontario, Canada.

BUSHELL, J. B. 1978 "Experiences with Floating Tyre Breakwaters at Lyttelton Harbour, N.Z." Private Communication.

CANDLE, R. D. 1974 "Goodyear Scrap Tyre Floating Breakwater Concepts." Proc. 1974 Floating Breakwater Conf. 193-212.

DAVIS, A. P. 1977 "Evaluation of Typing Materials for Floating Tyre Breakwaters." Marine Tech. Rep. No. 54, U.R.I., Kingston, R.I.

GILES, M. L. and SORENSON, R. M. 1978 "Prototype Scale Mooring Load and Transmission Tests for a Floating Tyre Breakwater." Tech. Paper No. 78-3, U.S. Army Corps of Engineers, CERC, Fort Belvoir, Va.

HARMS, V. W. and BENDER, T. J. 1978 "Preliminary Report on the Application of Floating Tyre Breakwater Design Data." Water Resources and Environmental Engineering Rep. No. 78-1, Dept of Civil Eng., State University of New York at Buffalo.

HARMS, V. W. 1979 "Data and Procedures for the Design of Floating Tyre Breakwaters". Water Resources and Environmental Engineering Rep. No. 79-1, Dept of Civil Eng., State University of New York at Buffalo.

KOWALSKI, T. 1974 Ed. Proc. 1974 Floating Breakwater Conference.

KOWALSKI, T. 1976 "Scrap Tyre Floating Breakwaters for North Sea Operations." The Naval Architect, pp. 186-187.

McGREGOR, R. C. 1978 "The Design of Scrap Tyre Floating Breakwaters with Special Reference to Fish Farms." Proc. Roy.Soc. of Edin., 76B, 115-133.

McGREGOR, R. C. and MILLER, N. S. 1978 "Scrap Tyre Breakwaters in Coastal Engineering." Proc. 16th Coastal Engineering Conference, Hamburg, 2191-2208.

NOBLE, H. M. 1976 "Use of Wave-Maze Flexible Floating Breakwater to Protect Offshore Structures and Landings." Proc. 8th Offshore Technology Conference, Houston, Texas, 215-224.

U.S. ARMY COASTAL ENGINEERING RESEARCH CENTER 1977 "Shore Protection Manual." 3rd Edition, U.S. Govt. Printing Office, Washington D.C. 20402.

NON-LINEAR WAVE FORCES ON FLOATING BREAKWATERS

by C.T. Niwinski[1] and M. de St. Q. Isaacson[2], M. ASCE

ABSTRACT

A non-linear numerical method for calculating wave forces on floating bodies has been developed by Isaacson (1981). The time stepping procedure is programmed for a computer solution, and an incident wave train is time stepped past a fixed two-dimensional rectangular breakwater. The influence of various input parameters on the accuracy of results is investigated, and optimal values of the parameters are determined. The optimal numerical parameters are used to generate force and transmission coefficient results, which are compared to the results of other published studies. The method is shown to compare favorably with other results, with the non-linear nature of the method being clearly demonstrated by the different force curves produced by varying the wave height.

---

1) Coastal Engineer
Seaconsult Marine Research Ltd.
Vancouver, B.C.
Canada V6P 6G5

2) Associate Professor
Department of Civil Engineering
University of British Columbia
Vancouver, B.C.
Canada V6T 1W5

1. INTRODUCTION

The forces generated by waves on floating breakwaters or floating bridges are generally predicted on the basis of linearized potential theory. A nonlinear method for calculating the wave forces for the case of a fixed body has been developed by Isaacson (1981) and subsequently extended to floating bodies undergoing motions (Isaacson, 1982). The method employs the second form of Green's theorem, together with the usual governing equations, to time step an incident wave train past the body. In order to test the validity and range of the method, only the fixed body case is tested here. Although the method has been used on three-dimensional bodies, we apply it to the two-dimensional case and exploit that simplification to conduct a study of the incident wave conditions and numerical parameters used in the method. A comparison is made between force and transmission coefficient results generated by the method and those available from previously published studies.

2. GENERAL DESCRIPTION OF METHOD

For the two-dimensional case examined here, a body of rectangular cross-section with beam B and draught D is floating in water of uniform depth d. An x-z coordinate system is defined with x measured horizontally in the direction of incident wave propagation and z measured vertically upward from the still water level. The origin is located at the still water level midway along the beam of the body. Let η denote the free surface elevation above the still water level. A definition sketch is shown in Figure 1.

With the usual assumptions of an incompressible fluid and irrotational flow, the fluid motion is represented by the velocity potential ϕ which must safisfy the Laplace equation within the fluid region,

$$\frac{\partial^2\phi}{\partial x^2} + \frac{\partial^2\phi}{\partial z^2} = 0 . \qquad (1)$$

Assuming an impermeable seabed and body surface, the flow will be subject to the following boundary conditions,

$$\frac{\partial\phi}{\partial z} = 0 \qquad \text{at} \quad z = -d \qquad (2)$$

$$\frac{\partial\phi}{\partial n} = 0 \qquad \text{on} \quad S_b \qquad (3)$$

$$\frac{\partial\phi}{\partial n} = \frac{\partial\eta}{\partial t} n_z \qquad \text{on} \quad S_f \qquad (4)$$

$$\frac{\partial\phi}{\partial t} + g\eta + (\nabla\phi)^2 = \text{constant on} \quad S_f . \qquad (5)$$

Here, S_f and S_b are the free and body surfaces respectively, n is the direction normal to the surface, t is time, n_z is the direction cosine in the z direction of the vector $\underline{n}$, and g is the acceleration due to gravity. The equations given by (4) and (5)

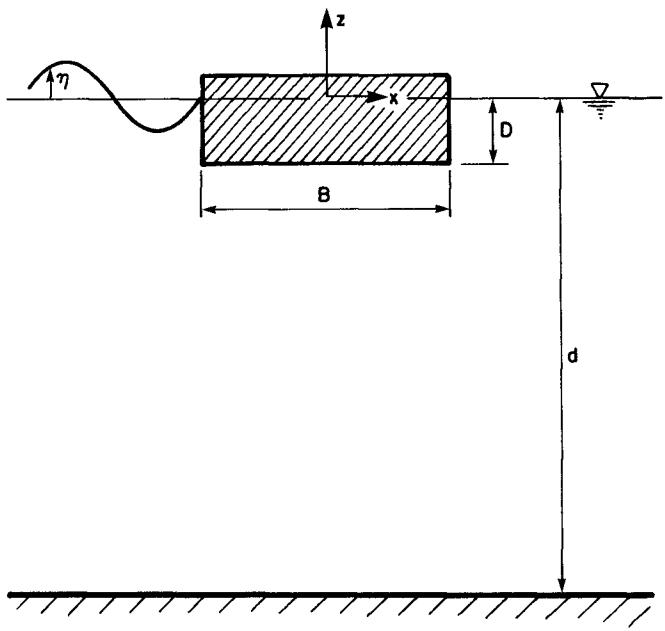

FIG. 1: DEFINITION SKETCH.

are the kinematic and dynamic free surface boundary conditions, with (4) being a form used by Isaacson (1981, 1982).

The second form of Green's theorem provides values of ϕ at any point $\underline{x} = (x,z)$ on the closed boundary in terms of ϕ and its normal derivative on the boundary:

$$\phi(\underline{x}) = -\frac{1}{\pi}\int_S \left[G(\underline{x},\underline{\xi})\frac{\partial\phi}{\partial n}(\underline{\xi}) - \phi(\underline{\xi})\frac{\partial G}{\partial n}(\underline{x},\underline{\xi})\right] dS \ . \qquad (6)$$

The point $\underline{\xi} = (\xi,\rho)$ is a point on the closed boundary in the x-z plane over which the integration is performed, dS is measured along the closed boundary, and G is an appropriate Green's function.

In order to consider a closed boundary over which the Green's identity can be integrated, vertical control surfaces extending from the free surface to the seabed are set at a chosen distance to either side of the body. The closed surface consists of the body surface, the free surface, and the control surfaces all reflected about the seabed. The control surfaces are set sufficiently distant so that the scattered potential due to the wave interaction with the fixed body will not reach the control surfaces throughout the time stepping procedure.

The closed surface on each side of the seabed is divided into N_b body segments, N_f free surface segments, and N_c control surface segments. This is shown in Figure 2. Values of ϕ and $\partial\phi/\partial n$ are assumed to be constant over each segment, and initial values of ϕ, $\partial\phi/\partial n$, and η are assigned to the midpoint of each segment according to a chosen wave theory defining the incident wave. The initial conditions require zero flow in the immediate vicinity of the body.

At a given time t, time stepping equations obtained from (4) and (5) are used to get N_f values of η and ϕ at $t+\Delta t$. A numerical integration of (6) at each body and free surface segment gives $N = N_f+N_b$ equations in N unknowns (N_b values of ϕ and N_f values of $\partial\phi/\partial n$), which are solved on the computer using conventional matrix solution techniques. Values of φ and $\partial\phi/\partial n$ on S_c are given at all times by the chosen incident wave theory. Thus, all values of ϕ, $\partial\phi/\partial n$, and η are obtained at $t+\Delta t$, and the process can be repeated as many times as necessary for the desired flow development.

With the velocity potential ϕ obtained for each segment at each time step, we can obtain the pressure distribution on the body surface using the unsteady Bernoulli equation,

$$p = -\rho\left[\frac{\partial\phi}{\partial t} + \frac{1}{2}(\nabla\phi)^2\right] . \qquad (7)$$

A numerical integration of Eq. (7) over the body surface yields the forces on the body at each time step. The numerical procedure described above is readily programmed for computer solution. The flow chart for such a solution is shown in Figure 3. A more complete

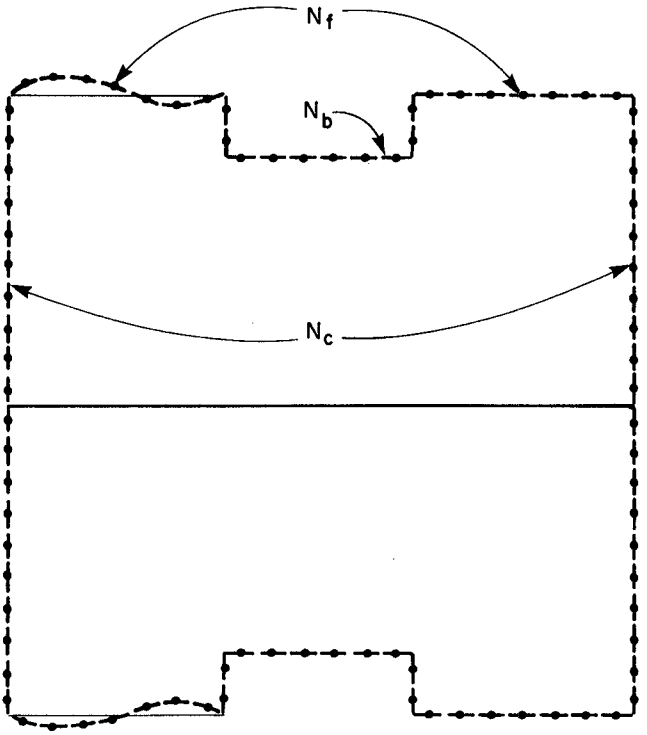

FIG. 2: SEGMENT GRID.

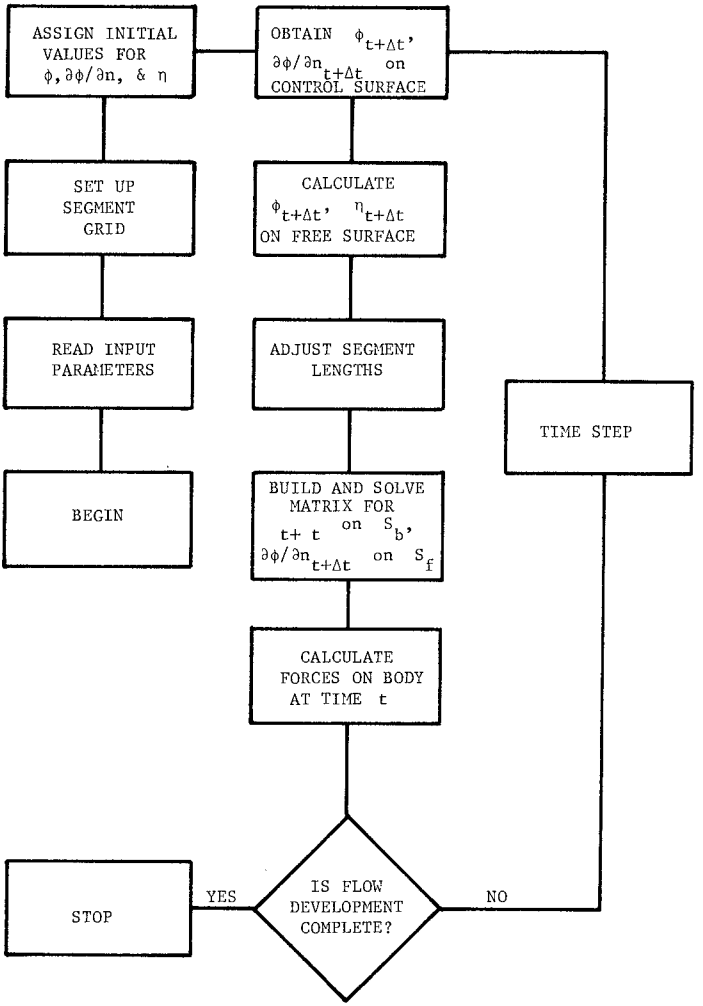

FIG. 3: FLOW CHART FOR COMPUTER SOLUTION.

derivation of the theory and numerical procedure is given by Isaacson (1981, 1982).

3. INCIDENT WAVE CONDITIONS

3.1. Incident Wave Decay Length

A harmonic wave predicted by either linear or Stokes's fifth order wave theory is used to prescribe the incident wave. To satisfy the condition that there initially be zero flow in the vicinity of the body, the incident flow is attenuated over a given decay length, L_d, as shown in Figure 4. When considering computing effort, a short decay length is desirable in order to reduce the length of the free surface and hence the number of segments needed on the free surface. A long decay length is expected to give smoother, more accurate flow development at the expense of much larger computing effort.

The program developed for this study is run with values of L_d varying from 0.25 up to 1.75 wavelengths, and the maximum forces on the body generated by the first fully developed wave to interact with the body are recorded. The results, shown in Figure 5, indicate that a decay length of about 0.75 wavelengths and less yields somewhat unreliable results, while a decay length of 1.25 and greater does not change the results significantly. A value of $L_d = 1.25$ or 1.50 is recommended for accurate results.

3.2. Group Velocity

Depending on the order of the time stepping procedure (see 4.2), the initial conditions along the entire boundary are specified at two or more time steps according to a chosen wave theory. The modulation envelope of the incident harmonic wave train travels at the group velocity c_g. For linear wave theory, c_g is given explicitly by

$$c_g = \frac{c}{2}\left[1 + \frac{2kd}{\sinh(2kd)}\right] . \qquad (8)$$

However, when using Stokes' fifth order wave theory, a reasonable value for the group velocity must be assumed since no explict expression for c_g exists.

To examine the effect of specifying different values of c_g, the program was run twice with an incident wave given by linear wave theory, the first time letting c_g equal its linear theory predicted value given by (8), and the second time setting c_g equal to the wave speed, c, which is about twice the predicted value of the group velocity. It was expected that specifying a value for c_g higher than that predicted by linear wave theory might lead to quicker flow development. However, the flow development results are found to differ only for the first few time steps, with subsequent flow development and force results being almost identical for both runs.

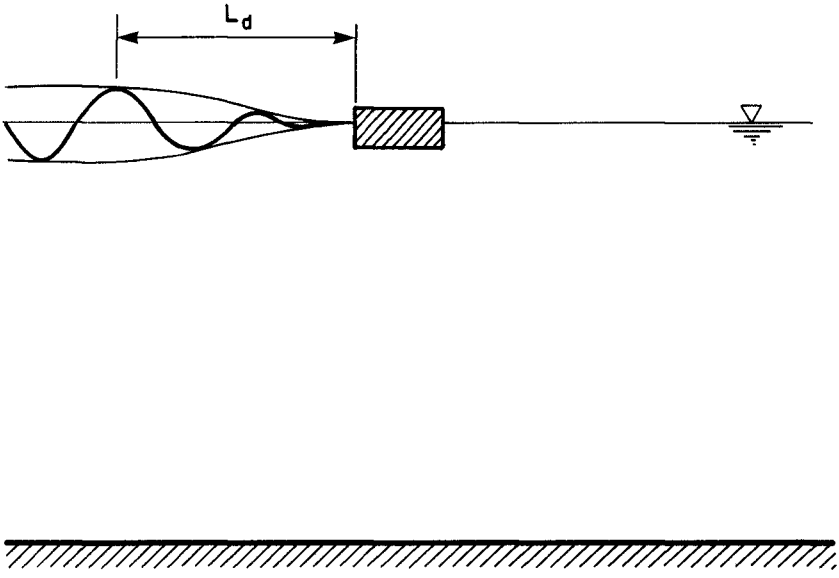

FIG.4: INCIDENT WAVE PROFILE.

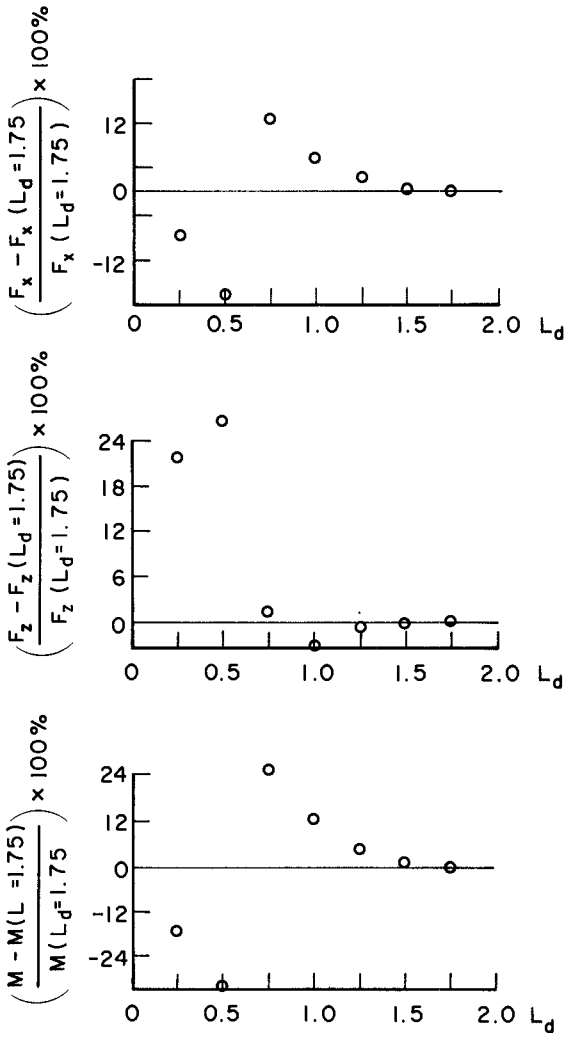

FIG. 5: EFFECT OF VARYING DECAY LENGTH, L_d.

We conclude that the method itself with its physical constraints expressed by the boundary conditions and the Green's identify very strongly defines the flow development and overrides any attempt to force a faster flow development in the vicinity of the body by setting the group velocity to a higher value.

When using Stokes' fifth order wave theory for the incident wave, the group velocity is now set equal to that predicted by linear wave theory.

4. NUMERICAL PARAMETERS

4.1. Time Step Size and Segment Length

Both the time step size and the segment length are required to be as large as possible in order to minimize the computing effort for the time stepping procedure. The time step parameter $\Delta t/T$ determines the number of cycles of the procedure for each wavelength, while the segment length parameter $\Delta S/L$ controls the size of the matrix that is solved at each time step. Here, Δt is the time step size, T is the incident wave period, ΔS is the segment length, and L is the wavelength.

If one considers the cyclical motion of the fluid particles over a wave period, it is readily apparent that the time step Δt must be sufficiently small to ensure that the motion of the particles is small compared to the segment length, and hence that $\Delta t/T$ should be less than $\Delta S/L$ for accurate flow development. Thus, for a given value of $\Delta t/T$, $\Delta S/L$ must be small enough to yield accurate results while being large enough to remain greater than the given $\Delta t/T$.

Since the body dimensions are significantly smaller than the wavelength for waves of longer period, the segment length parameter $\Delta S/L$ found to be appropriate on the free surface may not be very useful on the body surface if only one or two segments are needed to meet the specified global $\Delta S/L$ requirement. Recalling that ϕ and $\partial\phi/\partial n$ (and hence p) are constant over each segment, a minimum number of segments are needed on the body surface to adequately describe the pressure distribution over the body surface. The moment acting on the body is most likely to be sensitive to this consideration. For purposes of the body segments we define a parameter $\Delta S_b/L_b$, where ΔS_b is the body surface segment length, and L_b is the dimension of the body along which the segment lies (in our example, B or D).

Optimal values for $\Delta t/T$, $\Delta S/L$, and $\Delta S_b/L_b$ have been determined by letting each vary in turn while holding all other parameters constant and recording the force results.

It is found that as $\Delta t/T$ is decreased, the force results quickly converge to uniform values. Little increase in accuracy is gained by setting $\Delta t/T$ to values less than 0.05, and for $\Delta t/T = 0.04$ the results obtained are within 3% of the converged values.

The segment length parameter $\Delta S/L$ was set to values ranging from 0.05 to 0.25. The earlier discussion concerning upper and lower limits for $\Delta S/L$ is confirmed as the results remain relatively consistent when $\Delta S/L$ is in the vicinity of 0.1, diverging as $\Delta S/L$ is increased or decreased beyond a limited range. When $\Delta S/L$ is set to a value less than approximately twice the value of $\Delta t/T$, the results diverge to the point where the computer solution is unable to continue. It is concluded that $\Delta S/L$ should be at least two or three times greater than $\Delta t/T$, and that a value of 0.1 for $\Delta S/L$ will yield good results.

As previously discussed, a global limit on $\Delta S/L$ may not provide enough body segments to calculate the force results accurately. One should also check that the segment lengths on the body surface as defined by $\Delta S_b/L_b$ fall within the global constraints on $\Delta S/L$ determined above. Values of $\Delta S_b/L_b$ ranging from 0.1 to 0.25 have been tested. As with the global segment length parameter $\Delta S/L$, $\Delta S_b/L_b$ is found to be constrained by upper and lower bounds. A maximum value of $\Delta S_b/L_b = 0.2$ (five segments along each body dimension) is found to be necessary to adequately describe the pressure distribution on the body. More segments on the body, while desirable to define the pressure distribution more accurately, would potentially conflict with the requirement that $\Delta S/L$ be larger than $\Delta t/T$. It is recommended that for a particular body shape, a minimum of five segments be used along each body dimension and that the relationship of $\Delta S_b/L_b$ to $\Delta S/L$ and $\Delta t/T$ be checked to ensure that it falls within the required range.

4.2. Time Stepping Equation

As mentioned in Section 2, the time stepping equations for η and ϕ on the free surface are obtained from (4) and (5). Applying a central difference approximation to (4), we obtain

$$\eta_{t+\Delta t} = \eta_{t-\Delta t} + 2\Delta t \frac{1}{n_z}\left(\frac{\partial \phi}{\partial t}\right)_t .$$

A similar expression can be obtained for $\phi_{t+\Delta t}$ on S_f using (5).

For better accuracy, higher order time stepping methods are desirable. For our purposes, the Adams-Bashforth multistep methods are useful. These are described by Burden, Faire and Reynolds (1978).

The central difference method and the Adams-Bashforth two, three, four, and five step methods have each been tested with the same input parameters, and the forces at each time step recorded for each method. The plotted results are shown in Figure 6. It is found that the central difference method produces a slightly uneven plot, particularly for the first few time steps. The two, three, and four step methods give smoother results. The five step method produces highly erratic results which sawtooth about values coincident with the other plots.

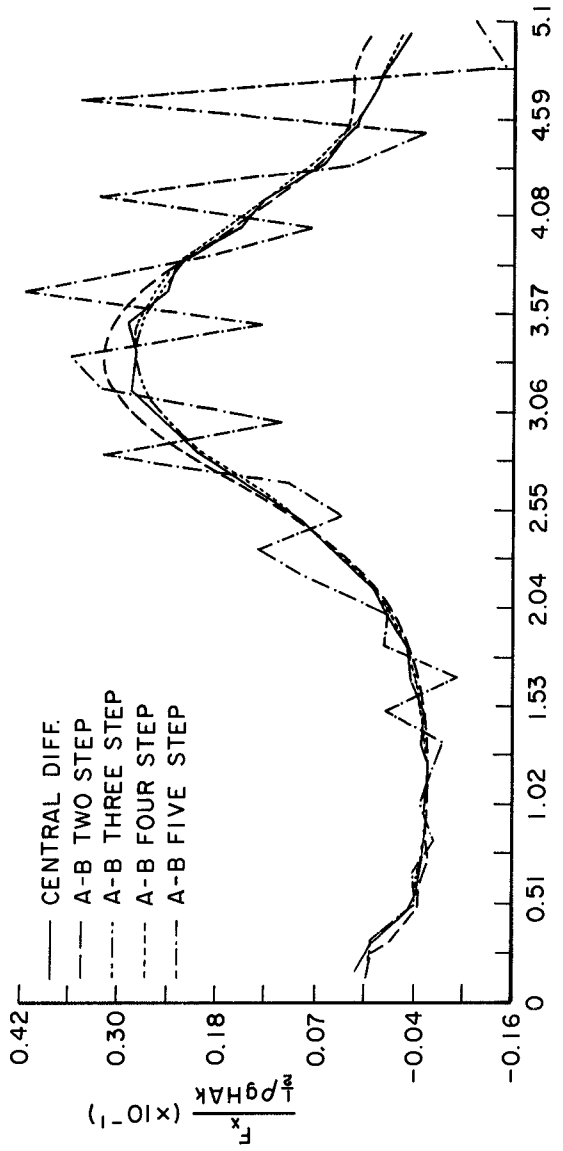

FIG.6: EFFECT OF VARYING TIME STEPPING METHODS.

The sawtoothed results of the five step method are probably caused by small perturbatlons from smooth results belng magnified by the fitting of a fifth order polynomial to previous points when projecting forward at each time step to values at $t+\Delta t$. Anticlpating that the same effect could occur for the four step method, the Adams-Bashforth two and three step methods have been adopted as the preferred time stepping techniques.

The program developed for this investlgation was also tested without a body present, using the optimal vaiues of the numerical parameters as determined above. The time stepping technique yielded a wave train progressing along the free surface as expected.

5. RESULTS

5.1. Exciting Forces

Using the method described in Section 2, the exciting forces on a two-dimensional rectangular cross-section were obtained for a range of lncident wave angular frequencies ω, and for different values of wave height to water depth ratios, H/d. An incident wave decay length of 1.25 wavelengths was used, with 25 time steps per wave period, 10 segment lengths per wavelength, and 5 segments along each body dimenslon. The Adams-Bashforth three step method was used as the time steppling technique for the equivalent of (4) and (5).

The force resuits for a beam to draught ratio, $B/D = 4.0$ are plotted in Figure 7, with Vugts' (1968) deep water experimental results and Fraser's (1979) linear finite element results shown for comparison. The results of Figure 7 clearly demonstrate the non-linearity of the method, with different force curves resulting from different values of H/D. The results show that the method used here has a fairly wide range of application, and that the magnitude of most of the force results compares well to previous experimental and theoretical results. While the results for the horlzontai exciting force coincide closely with Fraser's linear results, the non-iinear method produces curves for the vertlcal force and moment that dlffer significantly in slope from the linear predictions.

5.2. Transmisslon Coefficient

An interesting byproduct of the method is the capablllty to monitor the transmission coefficient for the fixed body case. Since the fixed case is used here only as an idealization to calculate exciting forces that can be used for a subsequent analysis of the actual response of a moored breakwater, the observed transmlssion coefficients are of little or practical value, but do provide a lower limit for the transmission coefflcient of a responding body.

The program was run with the same input parameters descrlbed in Section 5.1, but for $B/D = 2.0$, 4.0, and 8.0 in turn. The results for the transmission coefficient K_d are shown ln Figure 8 together with the results of Nece and Richley (1972) for $B/D = 5.0$. The experlmental results are for an incident wave of the same steepness for a given ω as for our results.

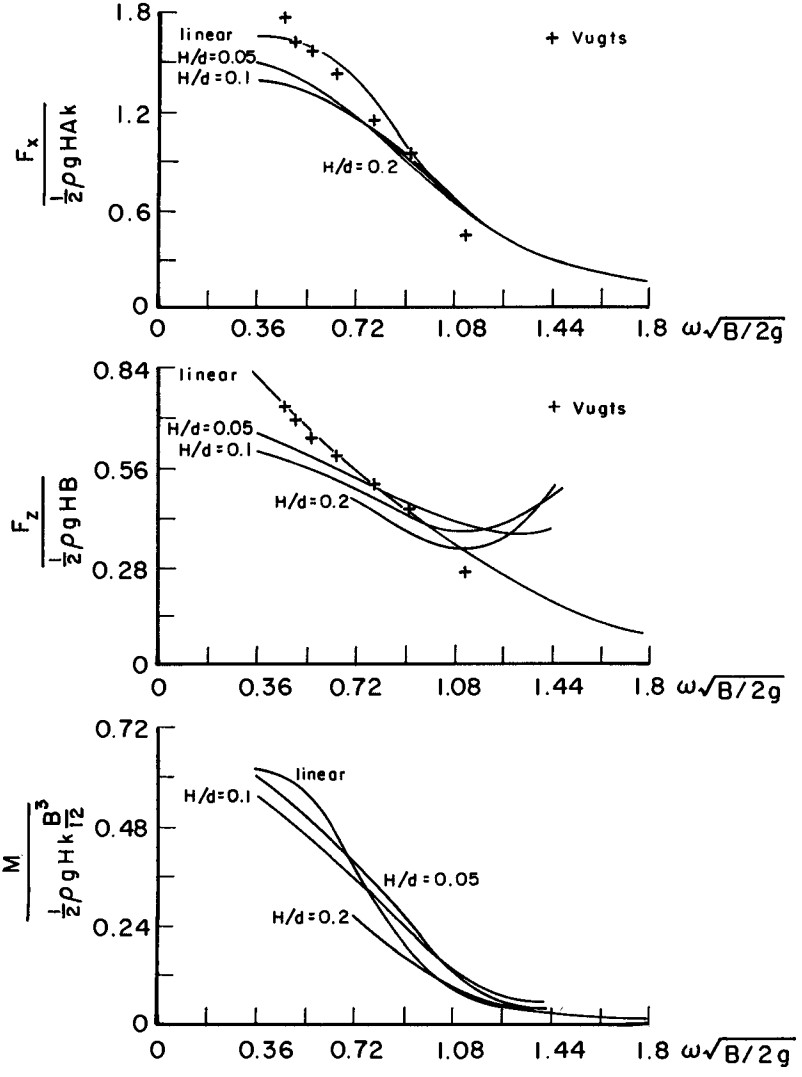

FIG. 7: FORCE RESULTS FOR B/D = 4.0 .

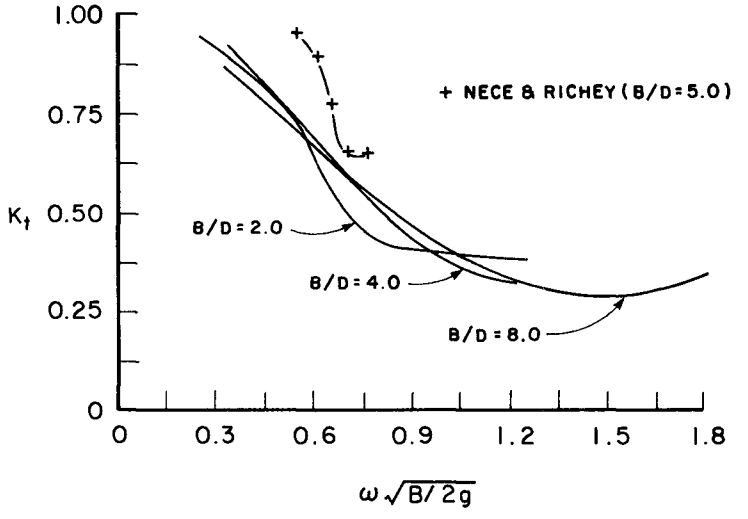

FIG.8: TRANSMISSION COEFFICIENT RESULTS.

The results obtained for the transmission coefficient are found to be relatively independent of water depth over the range tested. As expected, the present results for a fixed body give lower values for K_d than Nece and Richey's experimental results for a responding cable moored body, and thus appear to provide a reliable lower limit for K_d.

6. CONCLUSIONS

By testing a computer program based on the nonlinear numerical method described here, optimal values of the numerical parameters were determined. It was found that 25 or more time steps per wave period and at least 10 segments per wavelength were needed to obtain accurate flow development. There should also be at least 2 to 3 times as many time steps as segment lengths per wavelength. The decay length of the initial incident wave profile should be 1.25 or more wavelengths.

The method itself as defined by the physical conditions and boundary integral determines the group velocity of the flow development, and specifying a different value of the group velocity for the initial time steps changes the flow development of only the first few time steps.

Using a central difference time stepping equation produced a slight sawtooth effect in the force results, while using a four or five step method occasionally produced a divergent instability, probably due to the fitting of a higher order polynomial to the values at previous time steps. The recommended time stepping procedure is a two or three step Adams-Bashforth method.

Force results from the program were plotted in the appropriate dimensionless form over a range of frequencies. The results produced different force curves for different values of the wave height to water depth ratio, thus verifying the nonlinearity of the method. The force curves obtained compared well in magnitude to previous numerical and experimental results, although the slopes of the curves varied significantly. The transmission coefficient for the fixed rectangular breakwater over the range of frequencies tested appeared to provide a reliable lower bound for the transmission coefficient of responding bodies. It is concluded that the nonlinear method used here has a significant potential for improved accuracy in the prediction of forces on floating bodies and their transmission coefficients.

7. REFERENCES

FRASER, G.A. (1979). Dynamic response of moored floating breakwaters. M.Ap.Sc. Thesis, University of British Columbia, 90 pp.

ISAACSON, M. de St. Q. (1981). Steep wave effects on large offshore structures. Proc. 13th Annual Offshore Technology Conference, Vol. 1, pp. 21-29.

NECE, R.E. and RICHEY, E.P. (1972). Wave transmission tests of floating breakwaters for Oak Harbour. C.W. Harris Hydraulic Laboratory Technical Report 32, University of Washington.

VUGTS, J.H. (1968). The hydrodynamic coefficients for swaying, heaving, and rolling cyclinders in a free surface. International Shipbuilding Progress, Vol. 15, No. 167, pp. 251-276.

BURDEN, R.L., FAIRES, J.D., and REYNOLDS, A.C. (1978). Numerical Analysis, Boston, Prindle Weber & Schmidt Inc.

ISAACSON, M. de St. Q., (1982). Nonlinear wave effects on floating bodies. J. Fluid Mech., Vol. , pp.

DOLOS STABILITY
EFFECT OF BLOCK DENSITY AND WAIST THICKNESS

by

D J P Scholtz, J A Zwamborn and M van Niekerk*

ABSTRACT

Model tests were done with dolosse having the same shape and volume, but with different **block densities,** to determine the effect of block density on stability and to check whether the theoretical third-power relationship between block volume and relative block density is valid.

From these tests it can be concluded that the higher the density of the block material the greater the stability becomes. Although the individual scatter is appreciable, the average results indicate that the stability of dolosse is inversely proportional to a power of about 2,3 of the relative density, which is significantly less than the theoretical power of 3.

Model tests were also carried out on dolosse having the same mass and volume but with different **waist-to-height ratios** to determine the effect of waist-to-height ratio on the stability of a dolos armour.

From the results of these tests it can be concluded that the stability of the armour decreases with increasing waist thickness, particularly for relatively high waist ratios.

1. INTRODUCTION

The dolos armour unit has been used widely for harbour and shore protection works in various parts of the world (Zwamborn et al., 1980). Dolosse appear to provide an effective and economic means for protecting many small and medium-sized coastal structures, but, as these units are being used for increasingly larger projects in greater water depths and in more severe wave climates, serious doubts have emerged especially on, amongst other factors,

---

* Coastal Engineering and Hydraulics, National Research Institute for Oceanology, CSIR, Stellenbosch, Republic of South Africa

the structural behaviour of the units. The obvious answer to the more severe wave climates is to increase the unit size or mass. However, when the size of the dolos is increased, tensile stresses also increase which may result in breakages.

There are two possible solutions to this problem, namely, (1) reinforcing and (2) increasing the waist-to-height ratio of the units. This paper deals with model tests carried out to determine the effect on the stability of the dolos of increased waist thickness.

According to theoretical stability formulae, the mass of the armour block is inversely proportional to the third power of the relative block density (PIANC, 1976). It is, therefore, attractive and, in certain cases imperative (Standish-White and Zwamborn, 1978), to use a higher than normal block density. Some doubt has been expressed, however, about the validity of this proportionality as applied to dolosse (Zwamborn and Beute, 1972) and tests with regular non-breaking waves were, therefore, done to determine the effect of relative block density on the stability of dolosse (Zwambron, 1978 and 1980 and Zwamborn and Van Niekerk, 1982).

It is generally accepted that when the linear dimensions of a dolos block are increased to obtain a heavier block with better stability, the stresses in the block will increase if the shape of the block remains the same. To overcome this increase in stress the waist of a dolos must be thickened if reinforcing is not used. Zwamborn and Beute (1972) suggested that the following waist ratio for a dolos with a mass W be used:

$$r = 0{,}34 \sqrt[6]{W/20}$$

It was, however, uncertain what the effect of an increase in waist ratio would be on the stability of the armour; it was decided, therefore, to do tests to determine this effect.

2. TEST FACILITIES

Tests on both the block density and the waist thickness of the dolos were done in the 160 m long (effective length), 3 m wide and 1,1 m deep wind-wave flume in Stellenbosch (Figure 1). Only regular waves which were produced by a translatory wave board were used. Waves were recorded with temperature-compensated probes and wave height meters connected to standard chart recorders and/or an electronic microprocessor which processed the outputs from the probes to yield the heights of the incident and reflected waves and the reflection coefficient. During the wave calibration stage, the waves were measured at the place at which

the model slope would be positioned in the stability tests. During the actual tests, the waves were measured from a moving trolley in front of the model.

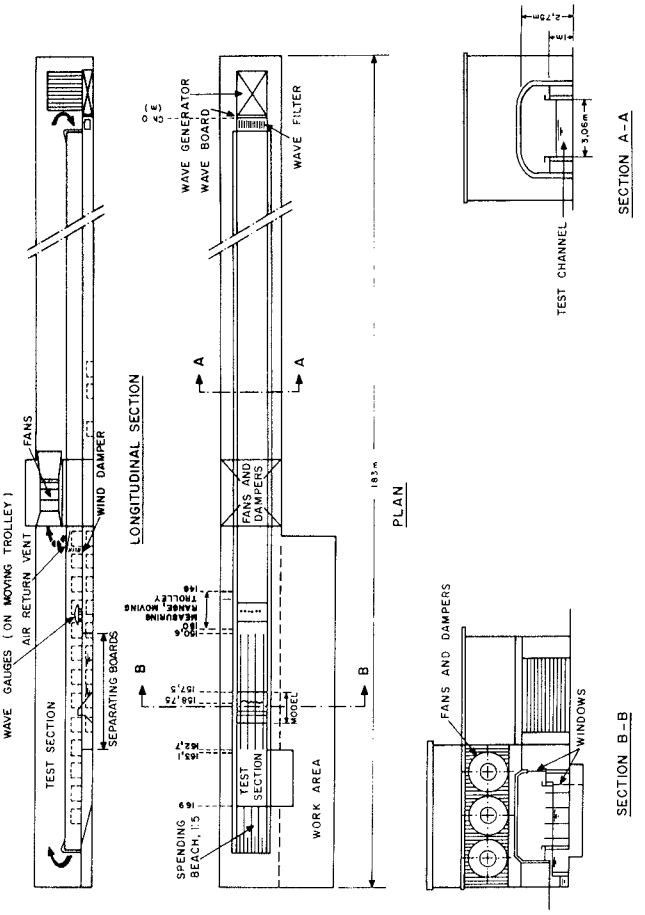

Figure 1 General layout of wind wave flume

3. MODEL LAYOUT

The flume was divided into three 0,75 m test sections leaving a dummy channel of about half that width on either side of the sections (Figures 2 and 3). The breakwater core was built of loose bricks and clean 6 mm stone. The underlayer consisted of 16,5 g sorted stone and the layer thickness was 43 mm. The top armour layer consisted of dolosse with a volume of about $35 \times 10^{-6} m^3$ during the block density tests and dolosse with a mass of about 81 g during the waist ratio tests. In both test series a 'mean' packing, $\phi = 1,00$ was used where (Zwamborn, 1980):

$$N_n = \phi_n V^{-2/3}$$

with N = number of dolosse per unit area
V = block volume
n = number of 'layers'.

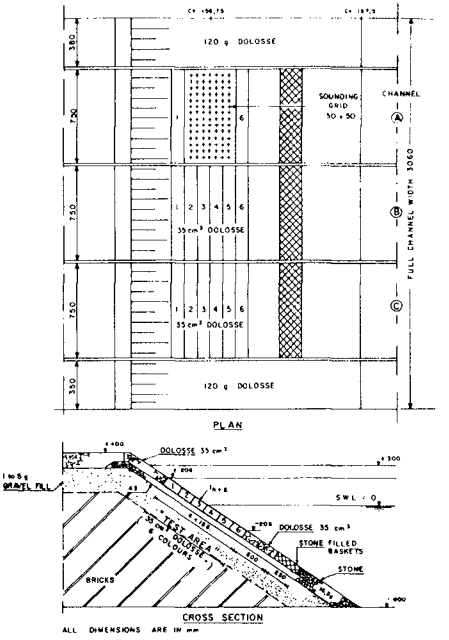

Figure 2 Model layout

Figure 3 General model view

The slope of the model was 1:1,5 and the depth of water was 0,8 m.

The test areas were 750 × 750 mm and the model dolosse were placed in six 125 mm (about 2 h, where h is the dolos height) wide bands of different colours, three above and three below still-water level, that is, 208 mm below to 208 mm above water (about 1,5 H_d, where H_d is the 'design wave height', Zwamborn, 1980).

4. TEST CONDITIONS AND PROCEDURES

All tests were done with regular waves of 1,75 s period, water depth of 0,80 m, and each test series consisted of 24 'bursts' of 2,5 min wave action for each wave height, namely, 49, 66, 83, 100, 117, 135, 152, 168, 185, 203, 221, 237 and 253 mm for the density tests and 75, 95, 115, 135, 146, 157, 173, 189 and 206 mm for the waist ratio tests. In the density tests the test series were repeated six to nine times and with the waist ratio tests nine repeat tests were done. During the repeat tests the test channels were alternated to eliminate the effects of the channels on the results.

With the above wave conditions the range of Ursell parameters used was 0,79 to 4,05 and of Iribarren number 2,9 to 6,6. Damage refers to the test section shown in Figure 2.

5. TEST RESULTS

5.1 Effect of Block Density

The initial tests with armour with block densities of 2,31; 2,41 and 2,57 indicated that increasing the density results in an increase in stability, but no clear relationship between dolos stability and block density could be established (Zwamborn, 1978 and 1980). Because of this, further tests were done with a much wider range of block densities, namely, γ_s = 1,81 to 3,02 (Zwamborn and Van Niekerk, 1982). The results of the latter tests will mainly be referred to in this paper.

Details of the model dolosse were as follows (based on 35 dolosse per density):

Model dolosse	W(g)	V($10^{-6}m^3$)	γ_s	h(mm)	r
Mean	62	34,2	1,81	59,6	0,32
Max deviation (%)	±1,45	±1,46	±0,83	±0,5	±1,5
Mean	83	34,8	2,39	59,2	0,33
Max deviation (%)	±3,25	±2,59	±2,15	±0,4	±5,3
Mean	106	35,1	3,02	60,1	0,32
Max deviation (%)	±2,55	±1,56	±1,10	±0,25	±1,7

The characteristics of the dolos armour for each test before wave action determined with the standard sounding technique (Zwamborn, 1978 and 1980), are given in the following table:

Test series D1,75		10	11	12	13	14	15	Mean
γ_s = 1,81	$t_{n=2}$ (mm)	75,6	68,5	72,2	70,0	68,6	71,3	71,0
	$C_{n=2}$	1,16	1,05	1,11	1,07	1,05	1,09	1,09
	P_f (%)	56,8	52,3	54,8	53,3	52,4	54,2	54,0
γ_s = 2,39	$t_{n=2}$ (mm)	73,4	69,2	68,9	71,1	66,7	70,5	70,0
	$C_{n=2}$	1,12	1,06	1,06	1,09	1,02	1,08	1,07
	P_f (%)	55,5	52,8	52,6	54,1	51,0	53,7	53,3
γ_s = 3,02	$t_{n=2}$ (mm)	71,1	73,8	67,2	71,5	67,1	70,8	70,3
	$C_{n=2}$	1,09	1,13	1,03	1,10	1,03	1,08	1,08
	P_f (%)	54,1	55,7	51,4	54,3	51,3	53,9	53,5

In the above tables:

W = dolos mass
V = dolos volume
h = dolos height
γ_s = specific block density
r = waist-to-height ratio
t_n = layer thickness
C_n = shape factor
= $\phi_n/n(1-P_f/100)$
P_f = fictitious porosity

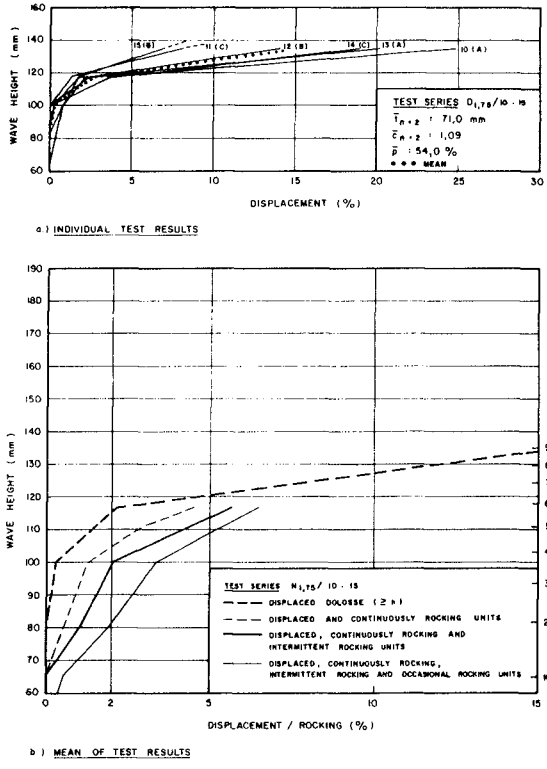

Figure 4 Test results with very light dolosse $\gamma = 1{,}81\ t/m^3$

The test results are plotted in Figures 4, 5 and 6 which show (a) the individual test results for displaced dolosse and (b) the mean results for displaced and rocking units. These figures show a considerable increase in 'damage' if the number of rocking units are included.

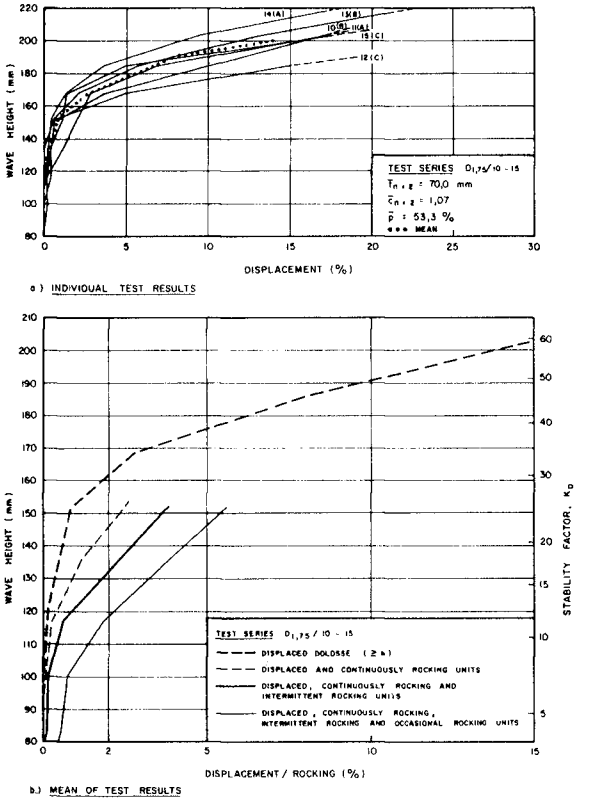

Figure 5 Test results with normal density dolosse $\gamma = 2,39\ t/m^3$

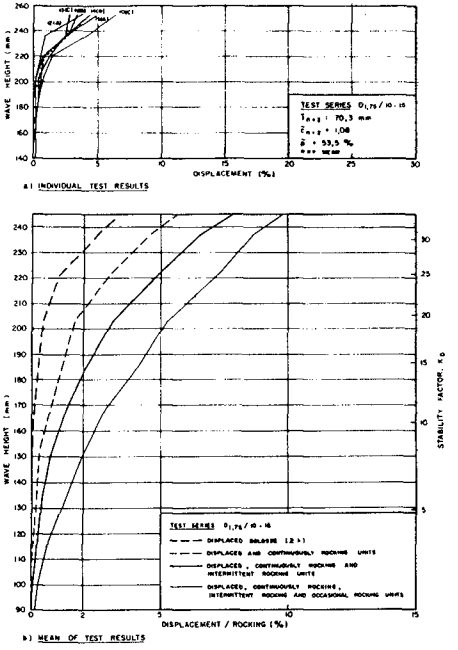

Figure 6 Test results with very heavy dolosse $\gamma = 3{,}02\ t/m^3$

The areal distribution of damage along the slopes is shown in Figure 7.

The mean and extreme values for displaced dolosse are compared in Figure 8. The mean values obtained in the initial tests are also shown in this figure from which it is clear that:

(i) initial and present test results compare reasonably well, particularly for the lower damage ranges;

(ii) there is a considerable increase in stability with increase in the density of the dolosse; and

(iii) an increase in damage from 1 to 5 per cent occurs for dolosse with

γ_s = 1,81 for a 13 per cent increase in wave height;
γ_s = 2,39 for a 15 per cent increase in wave height; and
γ_s = 3,02 for a 17 per cent increase in wave height.

The reserve stability for the heavier units is thus slightly greater but this is not considered to be very significant.

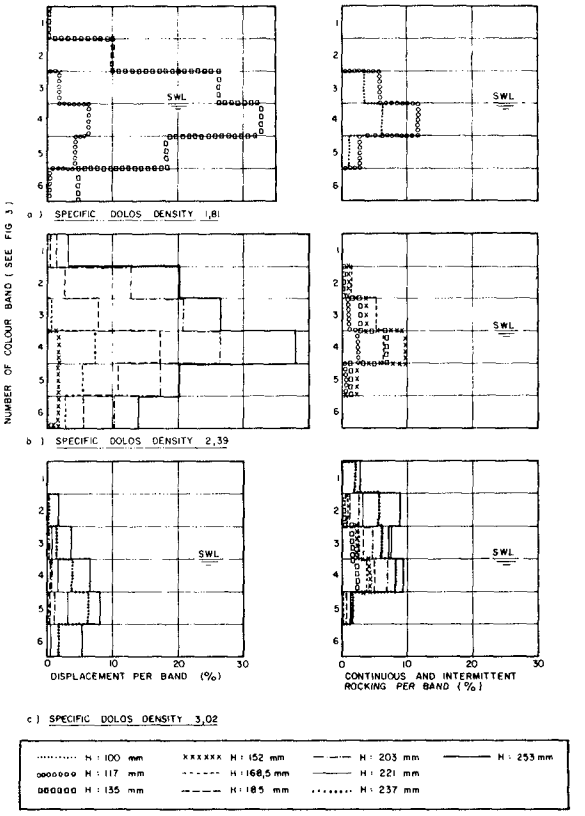

Figure 7 Block density tests - mean areal distribution of damage

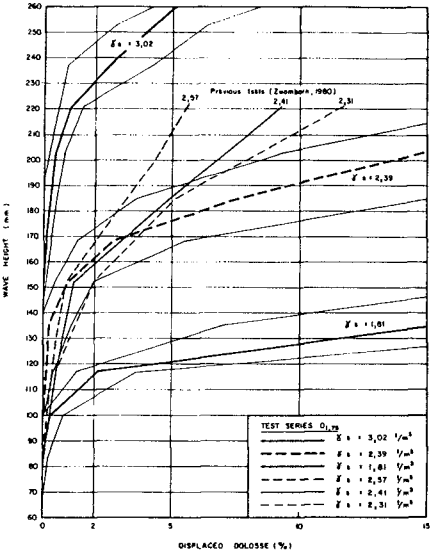

Figure 8 Comparison of mean and extreme test results for all unit densities tested

5.2 Effect of Waist to Height Ratio

Details of the model dolosse were as follows:

Model dolosse	W(g)	V($10^{-6}m^3$)	γ_s	h(mm)	r
Mean	80,9	34,50	2,34	59,3	0,33
Standard deviation	0,72	0,605	0,035	0,19	0,003
Mean	81,2	33,95	2,39	56,4	0,38
Standard deviation	2,30	0,785	0,047	0,18	0,004
Mean	80,4	33,47	2,40	52,9	0,43
Standard deviation	1,98	0,698	0,052	0,17	0,004

The characteristics of the dolos armour for each test before wave action, determined with the standard sounding technique, are given in the following table:

Test series R		1	2	3	4	5	6	7	8	9	Mean
r=0,33	$t_{n=2}$ (mm)	69,9	68,2	63,9	67,8	73,5	69,5	67,4	66,5	67,4	68,2
	$C_{n=2}$	1,07	1,05	0,98	1,04	1,13	1,07	1,03	1,02	1,03	1,05
	P_f (%)	53,4	52,3	49,0	52,0	55,7	53,2	51,7	51,0	51,7	52,2
r=0,38	$t_{n=2}$ (mm)	-	67,4	64,8	61,9	69,8	61,6	66,6	65,1	60,1	64,7
	$C_{n=2}$	-	1,04	1,00	0,96	1,08	0,95	1,03	1,00	0,93	1,00
	P_f (%)	-	52,0	50,0	47,7	53,6	47,4	51,4	50,3	46,1	49,8
r=0,43	$t_{n=2}$ (mm)	62,4	59,9	56,6	62,1	62,7	59,9	61,6	57,4	56,0	59,8
	$C_{n=2}$	0,97	0,93	0,88	0,96	0,97	0,93	0,96	0,89	0,87	0,93
	P_f (%)	48,3	46,2	43,1	48,1	48,6	46,2	47,7	43,9	42,4	46,1

The individual and mean test results of nine repeat tests for waist ratios r = 0,33; 0,38 and 0,43 are presented in Figures 9, 10 and 11.

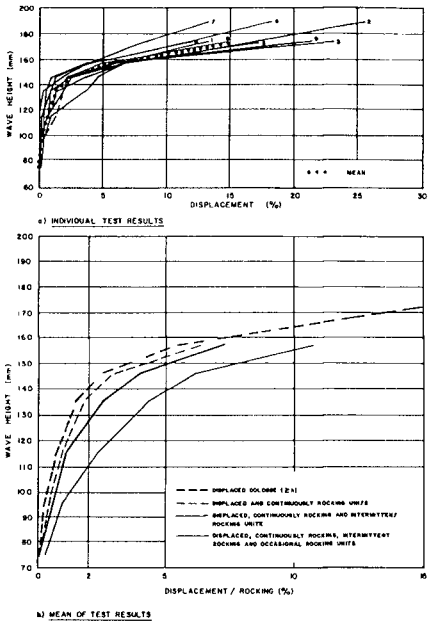

Figure 9 Test results with r = 0,33

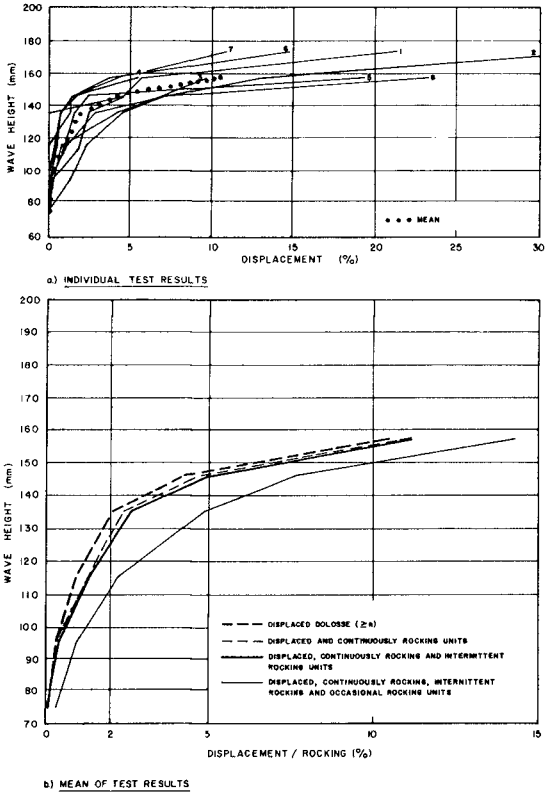

Figure 10 Test results with r = 0,38

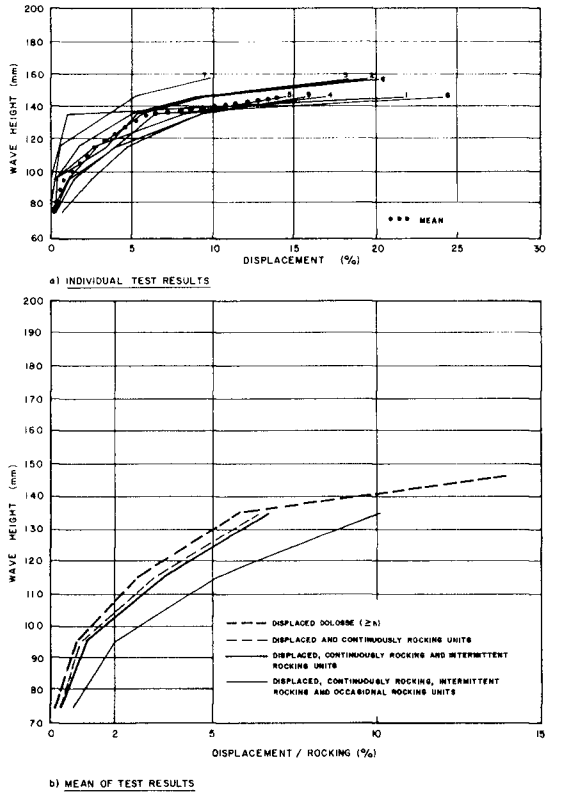

Figure 11 Test results with r = 0,43

The mean values for displaced dolosse for the three waist ratios tested are shown in Figure 12 for comparison. This figure indicates that there is a marked decrease in stability with r increased from 0,33 to 0,38 and a considerable decrease in stability with r increased from 0,38 to 0,43.

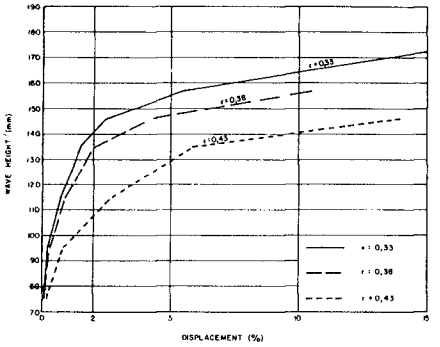

Figure 12 Comparison of mean test results for waist ratios tested

6. INTERPRETATION OF TEST RESULTS

6.1 Effect of Block Density

The basic stability equation may be written

$$\frac{V}{H^3} f(\alpha) = \frac{1}{K} \left(\frac{\gamma_s}{\gamma} - 1\right)^x = \frac{\Delta^x}{K} \quad \text{(Zwamborn, 1978 and 1980)}$$

This equation converts into the Hudson stability formula when $f(\alpha) = \cot \alpha$, $V = W/\gamma_s$, $x = -3$ and the constant $K = K_D$.

Since in the model tests the breakwater slope was always 1 in 1,5 ($\tan \alpha$), the effect of the slope, α, cannot be checked. By disregarding $f(\alpha)$ in the above equation, the tests with different γ_s values make it possible, however, to check the correctness of the remainder of the formula. Figure 13 shows the results of the initial tests (Zwamborn, 1978 and 1980) and of the new tests (Zwamborn and Van Niekerk, 1982) plotted as $V/H^3 \cot \alpha$ as function of $\gamma_s/\gamma - 1$ for 1, 2, 5 and 10 per cent damage (displaced dolosse).

Initially, curves were drawn through the test results excluding those for $\gamma_s = 1{,}81$ and these curves appeared to support the theoretical third power relationship, that is, $x \simeq -3$, for $\gamma_s > 2{,}3$ t/m^3 (Zwamborn and Van Niekerk, 1982). However, a statistical analysis of the test results showed that a significantly better fit was possible when

all test results are included, with the following resulting values for x and K (Figure 13):

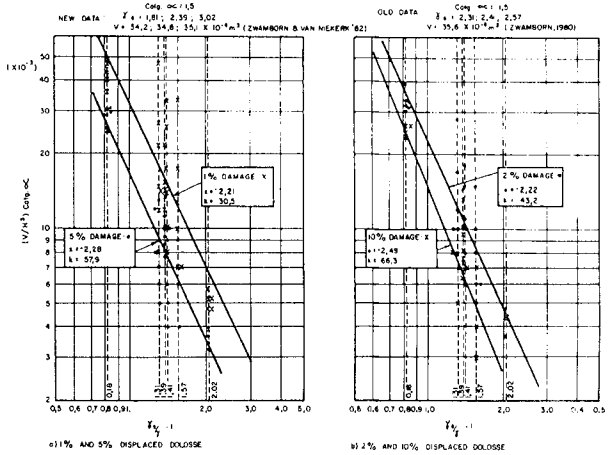

Figure 13 Relative dolos volumes versus relative density

Statistical values	Dolos displacements (%)			
	1	2	5	10
$-\bar{x}$	2,21	2,22	2,28	2,49
95% conf. lim.	1,18 to 3,24	1,78 to 2,66	1,92 to 2,64	1,87 to 3,11
$\bar{K}$	30,5	43,2	57,9	66,3

The mean value of the power x is therefore -2,30 (95% confidence limits 1,89 to 2,71) and not -3,0 and it thus appears that the theoretical equations (PIANC, 1976) and also Hudson's stability equation does not hold for dolosse, with respect to the effect of block density.

A comparison of earlier dolos tests (Zwamborn and Beute, 1972) also indicated a higher value of the power of the relative density (x > -3). Moreover, comprehensive tests on natural stone by Kydland and Sodefjed (Zwamborn, 1978) gave the following results (1 in 1,5 slope):

Power	Kydland		Sodefjed
	1% damage	4% damage	1% damage
-x	2,00	2,08	2,40

Thus the mean value for dolosse, $\underline{x = -2,30}$, compares reasonably well with the values for natural stone and it appears from this that the theoretical and Hudson's formulae **generally** overestimate the effect on stability of increased block density.

If the Hudson formula is adjusted for dolosse according to the above results, to determine the density effect, namely,

$$W = \frac{\gamma_s H^3}{K\Delta^{2,3} \cot \alpha}$$

corresponding values for K must be used and **not** the previous K_D values based on the Hudson formula. Values for K have been calculated for the test results and are plotted in Figure 14 as function of damage (per cent displacement). The data points for the different densities tested are all seen to fall in a relatively narrow band and the mean values can be used as first estimates for the 'stability factor', K.

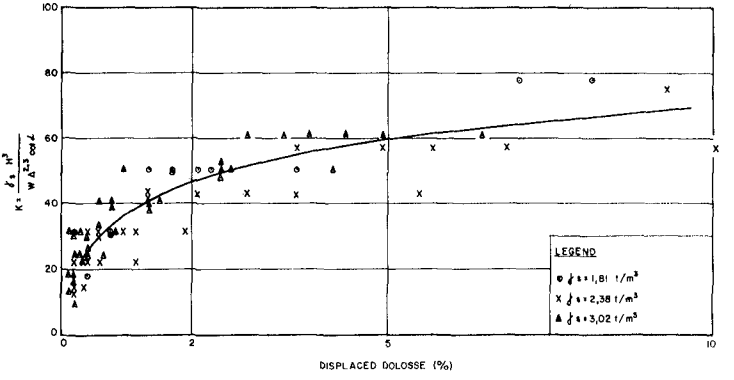

Figure 14 Comparison of stability factors, K, for different unit densities

6.2 Effect of Waist-to-height Ratio

The test results show two effects of an increase in waist ratio, first, on the layer thickness and porosity and, second, on the stability of the dolosse. The layer thickness, shape factor and fictitious porosity are seen to decrease slightly with an increase in waist ratio from 0,33 to 0,43 (see Section 5.2). Since all dolosse had the same volume, this reduction was expected. The layer thickness is defined by:

$$t_n = \tau_n V^{1/3}$$

where $\tau_n = nC_n$ = layer thickness for n layers. The following average values were found (see Figure 15a):

Waist-to-height ratio r	P_f (%)	$C_{n=2}$	$\tau_{n=2}$
0,33	52,2	1,05	2,10
0,38	49,8	1,00	2,00
0,43	46,1	0,93	1,86

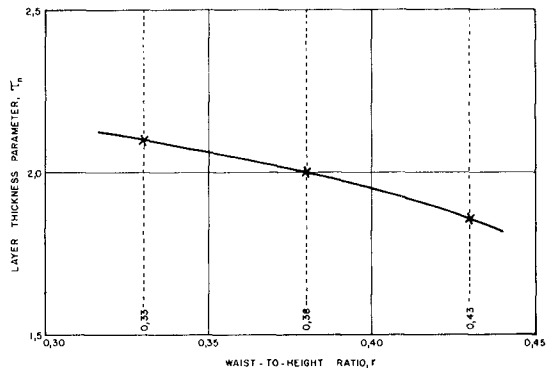

a.) LAYER THICKNESS PARAMETER.

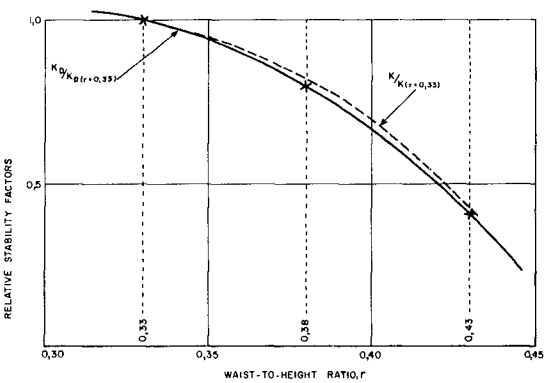

b) RELATIVE STABILITY FACTOR

Figure 15 Effect of increased waist ratio

Based on the test results, the relationship between the waist ratio (r) and the stability factors K_D and K are shown in Figure 15b. A marked decrease in stability occurs, especially when the waist ratio is increased to above 0,38. The reduction in stability is probably due to the loss in the interlocking ability of the units because of the thicker waist. If the waist ratio is increased further, the block will lose more of its interlocking ability and will ultimately resemble a cube which is totally dependent on its mass for stability.

Wave heights causing 2 per cent displacement in the model were converted to prototype values by adopting the waist ratio,

$$r = 0{,}34 \sqrt[6]{W/20}$$

suggested by Zwamborn and Beute (1972) and assuming γ_S = 2,40 and γ = 1,025. These results, presented in Figure 16, show that increasing the mass of dolosse above 40 t is much less effective in increasing stability then increasing the mass of dolosse below 40 t. It is also clear from this figure that the present data is insufficient to define the relationship between H and W and no attempt was therefore made to fit a curve through the data. To establish this relationship further tests will have to be done on dolosse with waist ratios of about 0,36 and 0,41.

Thus, when it is considered to use dolosse heavier than, say, about 40 tonnes it may well be more economical to use dolosse with reinforced thinner waists with correspondingly higher stability instead of a thick waist with lower stability. It must be stressed that Figure 16 is based on the relationship

$$r = 0{,}34 \sqrt[6]{W/20}$$

which was derived by accepting from prototype observations that 20-tonne dolosse with a waist ratio of 0,34 are strong enough to withstand stresses due to normal handling and design wave conditions. If, however, this would not be the case, for instance, a 15-ton dolos should rather have a 0,34 waist ratio, the W-H curve in Figure 16 will become lower.

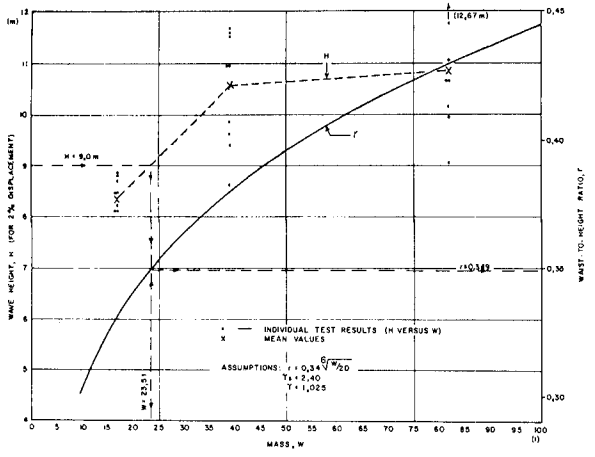

Figure 16 Relationship between H, W and r

7. CONCLUSIONS AND RECOMMENDATIONS

The initial tests with dolos armour with block densities of 2,31; 2,41 and 2,57 gave no conclusive results and further tests with dolosse with a larger range in block densities, namely, 1,81; 2,39 and 3,02 were done. These new test results showed clearly the effect of block density on the armour stability. The classic third-power relationship with regard to block density seems to over-estimate the effect of block density and a power of 2,3 was found to represent the test data better. The lower power agrees approximately with previous test results on natural stones and the theoretical stability equations, therefore, do not appear to represent the density effect correctly.

When high-density dolosse are used, care must be taken that they are at least as strong as the dolosse of normal density which can be achieved by increasing the waist-to-height ratio accordingly.

Test results showed that the stability of dolosse decreases as the waist ratio increases. Tests were done with dolosse with r = 0,33; 0,38 and 0,43 and K_D and K values for the latter two were found to be 20 and 60 per cent, respectively, smaller than the K_D value for dolosse with r = 0,33.

Further tests with waist ratios of about 0,36 and 0,41 would be needed to determine the reduction of stability more accurately.

Thus, when model tests are performed for a certain project, dolosse with the correct waist ratio must be used in the tests. If such dolosse are not available, the test results must be adapted to allow for the change in stability due to a different waist ratio tested.

To compensate for the larger tensile stresses in the heavier dolosse it has been suggested that the dolos waist ratio be increased according to the formula

$$r = 0{,}34 \sqrt[6]{W/20}$$

Because the stability decreases for the higher waist ratios, however, it was found that the stability of dolosse, designed accordng to this formula, increases very little when the mass exceeds about 40 t.

8. REFERENCES

PIANC (1976). Final report of the international commission for the study of waves. Annex to Bull. No. 25, Vol. III, Brussels.

STANDISH-WHITE, D W and ZWAMBORN, J A (1978). Problems of design and construction of an offshore seawater intake. Proc. XIth Coast. Eng. Conf., Hamburg.

ZWAMBORN, J A (1978). Dolos packing density and effect of relative block density. Proc. XVI Coast. Eng. Conf., Hamburg.

ZWAMBORN, J A (1980). Measuring technique, dolos packing density and effect of relative block density. CSIR Research Report 378, Stellenbosch.

ZWAMBORN, et al. (1980). Dolosse past, present, future? Proc. XVII Coast. Eng. Conf., Sydney.

ZWAMBORN, J A and BEUTE, J (1972). Stability of dolos armour units. ECOR Symposium S. 71, Stellenbosch.

ZWAMBORN, J A and VAN NIEKERK, M (1982). Additional model tests. Dolos packing density and effect of relative block density. CSIR Research Report 554, Stellenbosch.

IMPROVEMENTS IN MODELLING RUBBLE-MOUND BREAKWATERS

G.W. Timco and E.P.D. Mansard*

ABSTRACT

Physical modelling is a technique which is commonly used in the design procedure of rubble-mound breakwaters. For reliable results it is necessary that the model tests accurately represent the prototype situation. In this paper, two significant improvements in modelling of breakwaters are presented. They are the generation of realistic sea states at the test site, and the simulation of the breakage of the armour units by using units which have mechanical properties properly scaled from the prototype units. These techniques have been used to study the recent breakwater failure at Rivière-au-Renard, Canada.

1.0 INTRODUCTION

A common method of protecting harbours and in dissipating wave energy in both inland and ocean ports is by the use of rubble-mound breakwaters. These structures are built up from the sea floor with specific profiles and material layers. Usually the uppermost armour layer consists of large quarry stones or specially designed concrete units. Depending upon the wave climate at the site, armour units can weigh as much as 100 tons. Recently there have been a number of breakwater failures causing enormous financial and environmental losses. Some of these breakwaters failed due to the breaking of individual concrete armour units during storm conditions with an eventual collapse of the structure as a whole. The design of a stable breakwater is a challenging engineering problem.

Physical modelling is a method frequently used to aid an engineer in the design of a rubble-mound breakwater. For this, a model of the proposed breakwater is geometrically scaled in a laboratory flume and subjected to similarly scaled wave conditions. In order to obtain reliable information from these types of tests, it is necessary that certain scaling laws are met. In particular, it is important that geometric (linear), kinematic (velocities) and dynamic (forces) similitude be preserved. This entails maintaining in the model test system, the relative importance of each of the independent forces acting in the prototype system. If all forces are in the same ratio, then the equations of motion will be the same everywhere in the model and prototype. The model and prototype will behave, therefore, in the same dynamical fashion. In early model tests of breakwaters, a regular wave

*Hydraulics Laboratory, National Research Council, Ottawa, Ont. K1A 0R6 Canada

train was propagated onto a scale model of the breakwater and before-and-after profiles were used to define the stability of the structure. In recent years, several important improvements in the modelling techniques have been developed including the use of "random" waves simulating the variance spectral density, damage criterion in terms of the rocking motion of the armour units, and careful selection of materials which influence the hydraulic stability of the breakwater. Although these improvements have contributed to better model-prototype conformity, there still remains a number of important parameters to be considered.

This paper addresses itself to two important improvements achieved by the Hydraulics Laboratory of the National Research Council of Canada in the techniques of physically modelling breakwaters. They are:

(1) the generation of realistic sea states at the test section of the flume, and

(2) the simulation of the breakage of armour units by using a material which has properties scaled from those of prototype concrete units.

In this paper, the details and significance of these two improvements are discussed. In addition, these modelling techniques are applied to a model test study at a 1:25 scale of the dolosse-armoured breakwater at Rivière-au-Renard, Quebec, Canada.

2.0 REALISTIC SEA STATES

Most hydraulic laboratories now have the capability of generating irregular waves for their experimental investigations. The normal practice has been, however, to describe the sea state solely by a variance spectral density and then to reproduce it in the model. Recent studies [Johnson et al (1978), Burcharth (1979)] have shown that simulating just the spectrum is not sufficient because a certain sequence of high waves occurring as a wave group can induce greater damage on the structure than equally high waves occurring individually in a wave train. The large number of high waves present as a sequence in the grouped wave train cause a continuous rocking and eventual displacement or breakage of armour units. Because of this effect it is desirable that the frequency as well as the time domain characteristics of the natural sea states are reproduced in the model whenever possible.

The phenomenon of wave grouping is well known to the oceanographers since prototype waves often exhibit distinct wave group patterns in their records. Considerable research has therefore been carried out in the past particularly to relate the broadness of the spectrum to the wave group characteristics. In fact, the traditional concept of representing the sea state by just its variance spectral density was based on the assumption that the spectral width is an indication of the degree of grouping such that a narrow spectrum corresponded to higher grouping. However, in a recent study Funke and Mansard (1980) showed that there is no apparent relationship between the shape of the spec-

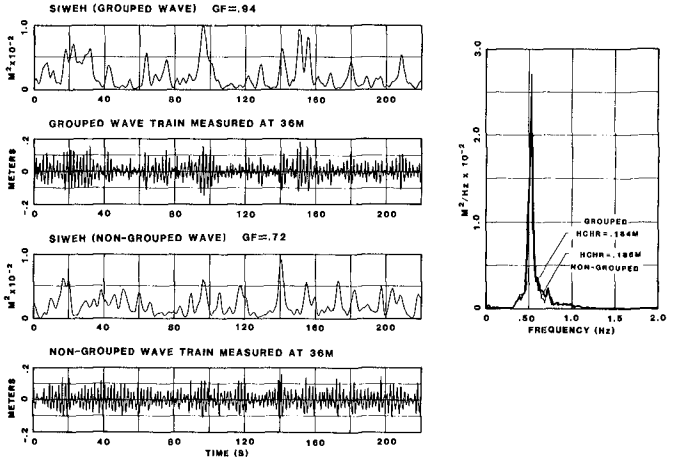

FIG.1 COMPARISON OF THE GROUPED AND NON-GROUPED WAVE TRAINS

trum and the amount of grouping in the wave train. Figure 1 presents two wave trains having a common variance spectral density but different degrees of grouping.

In order to have a physically meaningful description of wave group activity in a sea state, this Laboratory has developed the concepts of a Smoothed Instantaneous Wave Energy History (SIWEH) and a Groupiness Factor (GF). Both the SIWEH and the GF can be easily derived from the water surface elevations of the wave record (Funke and Mansard 1980). As illustrated in Figure 1, this SIWEH E(t) function, which represents the distribution of wave energy in the time axis, effectively describes the wave groups in a time series.

The concept of Groupiness Factor, developed as a tool to measure the degree of grouping in a sea state, is a dimensionless factor, describing the standard deviation of the SIWEH about its mean and normalized with respect to this mean.

The amount of wave grouping increases with increasing Groupiness Factor. Values of GF in the vicinity of 0.9 indicate highly grouped waves.

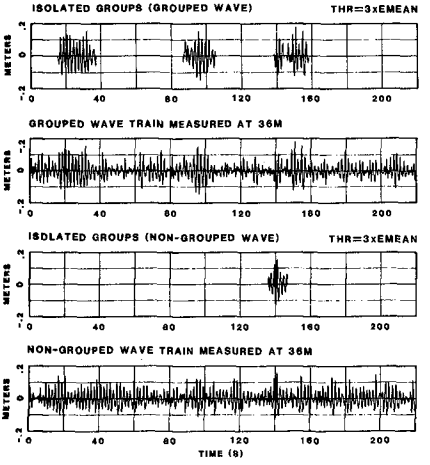

FIG.2 ISOLATION OF WAVE GROUPS

The SIWEH function can serve also as an effective tool to isolate wave groups in the time series. The groups shown in Figure 2 were isolated using a concept of threshold for the SIWEH. Any wave sequence which caused the SIWEH to exceed a given threshold (3*E in this case) was defined as a wave group event.

Because it is often not possible to obtain prototype wave records for a desired location of interest, this Laboratory has developed a synthesis technique to generate realistic sea states which include wave grouping. This technique, illustrated in Figure 3, provides the necessary tools for testing the stability of the various structures (be floating or fixed) for the wave grouping effects. The SIWEH spectral density shown in Figure 3 is a theoretical model often encountered in the linear dynamic system analysis. The expression for this SIWEH model is:

$$\varepsilon(\lambda) = \frac{1}{\sqrt{(1-\lambda^2)^2 + 4\zeta^2\lambda^2}} \cdot \frac{\lambda}{\sqrt{(1+\lambda^2)}}$$

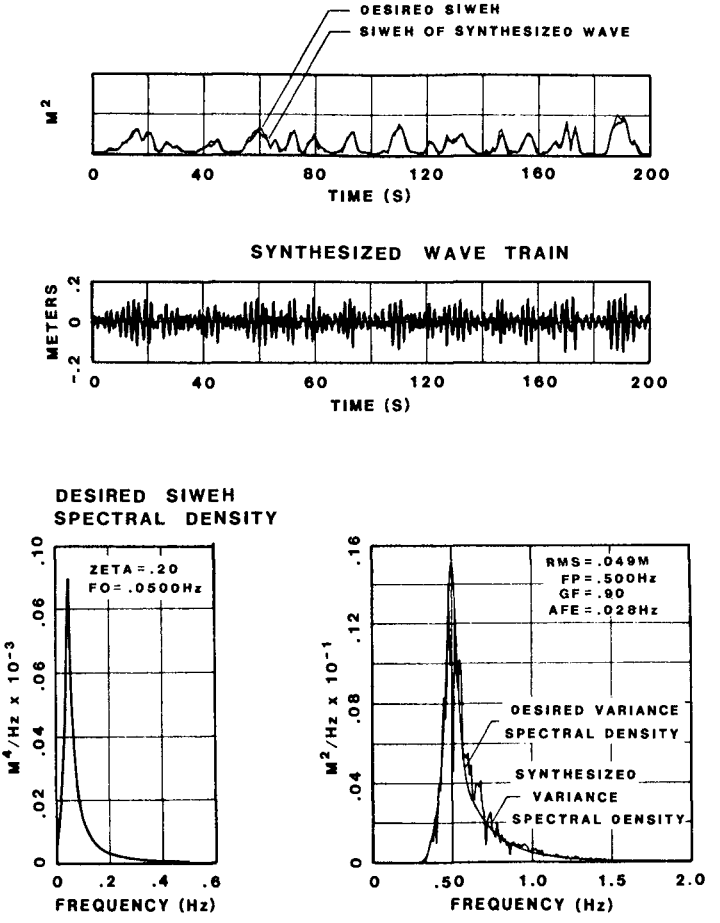

FIG.3 SYNTHESIS OF A GROUPED WAVE TRAIN

where $\varepsilon(\lambda)$ = SIWEH spectral density
λ = normalized frequency f/f_0
ζ = damping factor which controls the width of the spectral peak which occurs in the vicinity of $\lambda=1$. The smaller is ζ, the narrower is the spectral peak
f_0 = peak freguency for $\zeta=0$

The time history of SIWEH is derived from this spectral density through an Inverse Fourier Transform using random phases.

In the absence of prototype information on wave groups, this model could be used to synthesize time series with different grouping characteristics (GF) while maintaining a constant variance spectral density. The period of the groups can be changed by varying the peak frequency of this spectrum. The wave train shown in Figure 3 satisfies both the frequency domain characteristics of the desired spectrum and the time domain characteristics defined by the SIWEH function. This technique is well documented in Funke and Mansard (1980).

2.1 Reproduction of Wave Trains at the Test Section

When a time series (derived either from a prototype wave record or by synthesis technigue) is to be reproduced in the flume, it is necessary that it is realized at the test section rather than at the wave paddle. But in deep and intermediate water depths the various freguency components present in the sea state travel with their own celerities resulting in continually changing seguences of waves during propagation. However, it is found that these celerities can satisfactorily be described by the linear dispersion relationship. Hence, in order to achieve the desired time domain characteristics near the test section (which may be 30 to 50 m from the wave paddle), the inverse dispersion relationship is applied to the wave train, in order to account for the wave propagation. In addition to the propagation, it is found that important phase changes can occur in the various wave machinery components such as the servo hydraulics, wave paddle, analog filter, etc. Complex transfer functions (which include both the amplitude and phase compensations) are therefore applied to these various components while preparing the driving signal. This technique has been found to be quite successful in reproducing various sea states and even extreme waves in the Laboratory.

Figure 4 compares a prototype wave record with a wave record measured at 36 m from the wave paddle in the model. The severe seguencing of prototype waves has been well preserved in this reproduction of this time series in the wave flume.

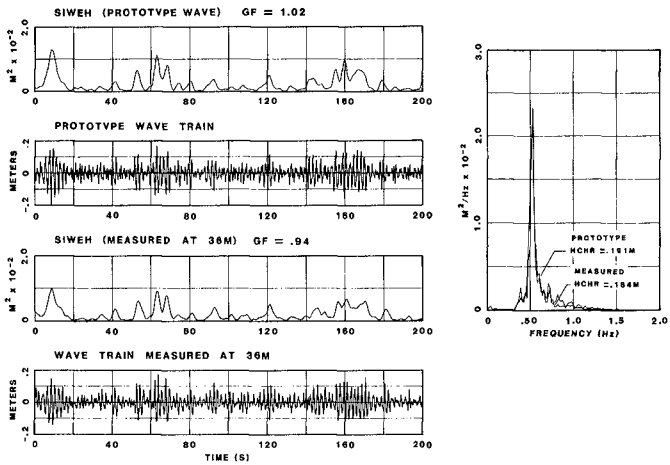

FIG.4 REPRODUCTION OF WAVE TRAIN IN THE FLUME

3.0 SIMULATION OF CONCRETE STRENGTH

In model testing of breakwaters, the interpretation of the results is very subjective. In early tests, the stability of a particular design was usually determined by a comparison of before-and-after storm profiles of a section of the structure. More recently, the stability has been defined subjectively as the onset of rocking of the armour layer. Neither of these techniques is satisfactory. This is so because a common failure mode of prototype breakwaters occurs through a deterioration of individual armour units with pieces breaking off and hammering against other larger units. In addition, the constant slight flexing and continual motion of the units during a storm result in a reduction in strength (and ultimately failure) due to slow propagation

of cracks. These two failure modes, although undoubtedly important in the prototype system, are not considered at all in geometrically scaled model tests. In order to simulate these conditions in a model test, it is important that some of the physical properties of the armour units scale by the linear scale factor (λ). In particular, the strength and strain modulus must be scaled whereas the density, Poisson's ratio and frictional factors must not. To date, this has not been done due to the lack of a material which would simulate homogeneously these properties of concrete on a reduced scale. Because of the many advantages of using strength-reduced armour units in model tests, a project was initiated to develop a material which would simulate the properties of concrete for this type of model testing. In this section, the development and properties of this material are briefly discussed.

3.1 Modelling Laws

The first step in developing the model material is to define the appropriate scaling laws and to define representative concrete (i.e. prototype) mechanical properties to which the scaling laws are applied. This defines the properties of the model material.

In model tests, the forces of interest are the gravity (weight), inertial, elastic and frictional (viscous). In order to maintain the relative importance of each of these in the model regime, it is necessary to maintain the Froude number (inertial forces/gravity forces), the Cauchy number (inertial forces/elastic forces), and the Reynolds number (inertial forces/viscous forces). Since it is not possible to simultaneously satisfy all three of these numbers, a compromise is made and the model tests are scaled according to Froude similitude. This is done since gravity and inertial forces predominate. As a consequence of this, the physical properties of the model armour units must meet certain well-defined requirements. In particular, the properties of the model (m) material must scale from the prototype (p) concrete values as

mass	$m_m = m_p/\lambda^3$
density	$\rho_m = \rho_p$
flexural strength	$\sigma_{fm} = \sigma_{fp}/\lambda$
tensile strength	$\sigma_{tm} = \sigma_{tp}/\lambda$
compressive strength	$\sigma_{cm} = \sigma_{cp}/\lambda$
elastic (Young's) modulus	$E_m = E_p/\lambda$
fracture toughness	$K_m = K_p/\lambda^{3/2}$
Poisson's ratio	$\mu_m = \mu_p$
friction	$f_m = f_p$

where λ is the scale factor of the test. For proper results in the model regime, the properties of the armour units must meet these requirements.

3.2 Mechanical Properties of Concrete: Prototype Values

Before it is possible to model the properties of concrete, representative values of the properties must be defined. However, concrete is a complex mixture of calcium silicates and aluminates cement, sand, stone and water. As such, by altering the relative proportions of each of these constituents, the properties of concrete can be varied over a wide range. Moreover, the properties of concrete are known to be affected by temperature, loading rate, moisture content, sample size, etc. This does not allow unique, unambiguous values to be defined. However, since the variation of the properties is reasonably systematic, such that conditions which lead to high compressive strength (say), also lead to high flexural and tensile strengths, representative values can be defined in this way. In the prototype system, usually high quality (35 MPa minimum compressive strength) concrete is used. Assuming a high quality concrete, the relevant properties of concrete, as determined from surveying the literature (Gonnerman and Shuman, 1928; Neville, 1977; Jayatilaka, 1979) as well as the required properties of the model material for two scale factors (λ=20 and λ=40) are

	Concrete	λ=20	λ=40
compressive strength (MPa)	31-38	1.6-1.9	.78-.95
flexural strength (MPa)	4.1- 4.7	.21-.24	.10-.12
tensile strength (MPa)	2.4-3.0	.12-.15	.06-.08
density (g/cc)	2.2-2.5	2.2-2.5	2.2-2.5
elastic modulus (static) (GPa)	29-32	1.5-1.6	.73-.80
elastic modulus (dynamic) (GPa)	43-47	2.2-2.4	1.1-1.2
fracture toughness (MPa-$m^{1/2}$)	.45-1.4	.005-.016	.002-.006
Poisson's ratio	.11-.21	.11-.21	.11-.21

3.3 General Consideration for Producing Strength-Reduced Armour Units

As a further restriction in defining the properties of model armour units, it would seem that in addition to the physical properties which the material must have, it must meet the following conditions:

(1) The material should be macroscopically homogeneous throughout.

(2) The material must be readily mouldable since armour units may have unusual shapes.

(3) The material must be able to be removed from the mould without breaking.

(4) The units made from the material should be relatively quick and easy to make since a large number would be required for a breakwater study.

(5) The material should be reasonably economical.

(6) The material should be non-toxic, non-corrosive and not break up into uncleanable debris.

(7) Since the tests are performed in water, the material must have relative stability in water over a reasonable time span.

In reviewing the properties which model armour units must have, it is clear that no "standard" material has these properties. Usually, for example, relatively weak materials have relatively low densities. As such, it was decided to try to develop a material which would meet as many of the properties as possible. Since one wants a structurally weak, yet dense material, this suggests that a reasonable approach to take would be to choose a binder (matrix) material which is filled with cohesionless inclusions. In this case, the strength of the material would be proportional to the volume porosity of the binder, i.e.

$$\sigma = \sigma_0 \ (1 - \psi)^n$$

where σ = strength of the material, σ_0 = strength of matrix material, ψ = volume of cohesionless material, and n is some exponent. In this way, the strength of the overall material can be decreased by decreasing the amount of matrix material, whereas the density of the overall material can be increased by increasing the density of the filler (inclusions) material. If the particle sizes are small enough, this will result in a homogeneous mix. Such an approach should allow enough flexibility for proper scaling of some strengths and density over a range of scaling factors.

In choosing a binder material for these tests, the general properties of the material (as discussed above) were considered. Although it is possible to choose any number of binder materials (such as waxes, cement, sulphur based binders, etc.), it was decided that a matrix of gypsum plaster ($CaSO_4 \cdot 1/2\ H_2O$) would best meet the requirements for a suitable matrix. This is so since it is economical, easily mouldable, fast setting, requires minimal equipment, etc. With regard to the filler, sand was chosen as a reasonable material to start with.

In setting up these experiments, it was decided that the density and flexural strength were two properties which were essential to scale properly. Clearly, if the density is incorrectly scaled, the armour units will not respond to the incident waves as they should. In observing failures of prototype armour units, it would seem that although there are undoubtedly several failure modes, crack propagation due to flexure (tensile) stresses is a predominate failure mode. This suggests that this failure mechanism must be properly scaled. To this end, a series of experiments were performed to measure the density and flexural strength of a number of different mixtures of plaster, sand, water and several other constitutents. This was done by weighing out the proper amount of each of the ingredients and mixing them to form a creamy paste. This paste was then poured into bar-shaped moulds 2.5 x 2.5 x 30 cm made out of aluminum and allowed to set overnight. A thin film of light oil was used as a parting agent. The bars were then removed from the mould and both the flexural strength and density of the bars were determined. In these tests, it was found that by decreasing

the amount of plaster in the mix, the strength of the resulting material could be reduced to the desired range; whereas by increasing the density of the aggregate mix (by adding iron ore ρ = 5.0 g/cm^3), the density could be increased to the proper range for concrete. Unfortunately, due to limitations in space, the complete details of the development and the variation of the properties of the model material with changes in constituent proportions, cannot be reported here. However, the recipe and complete information on the behaviour of the model material can be obtained from the senior author (Timco, 1981a).

3.4 Properties of Model Material

Before using this model concrete material in breakwater tests, it was necessary to know all of its mechanical properties. However, because of the mechanically weak nature of the material, testing of its mechanical properties is quite tricky. For example, at λ=50, a bar of this material 2.5 cm x 2.5 cm x 6 cm, if held at one of the square ends, would not support its own weight. In order to determine the properties, a series of tests were performed similar to those used to document the properties of "model ice" (Timco, 1981b). The full details and results of the tests on the model concrete will not be reported here. They can be found in Timco (1981a). Instead, only the salient features will be presented. In brief, for scale factors of $40>\lambda>20$, the properties of the model material can be summarized as follows:

Density - By properly choosing the ingredients in the mix, the density scales correctly for any scale factor.

Flexural Strength - Since the flexural strength is directly defined by the scale factor, it scales correctly for any scale factor.

Tensile Strength - The tensile strength is related to the flexural strength, and in testing using the ring-tensile test, it scales well for any scale factor.

Compressive Strength - Tests of the compressive strength were performed at two loading rates. In general, it is strain-rate independent and overscales (i.e. is too low) over the whole range of scale factors.

Elastic (strain) Modulus - Tests of the modulus were also performed at two loading rates. At very high rates (ultrasonic), the elastic modulus underscales; whereas at lower rates, the strain modulus overscales over the whole range of scale factors.

Fracture Toughness - The fracture toughness (i.e. resistance to fracture by crack propagation) scales correctly over the whole range of scale factors.

Frictional Properties - The frictional properties scale well over the range of scale factors.

Erosion - Because the amount of binder in the material is necessarily low (in order to produce the low strength), the material does not have good resistance to erosion. This limits the time span in which a model test can be performed (usually less than one hour).

Pourability - In the fluid state, before setting, the material has a low viscosity and can be cast in any shape (see Figure 5).

FIG.5 PHOTOGRAPH OF STRENGTH-SIMULATED MODEL DOLOS , CUBE D'ANTIFER AND TETRAPOD

Setting Time - The material has its initial set within 15 minutes of pouring. After this time, the unit can be removed from the mould.

Cost - The cost of the basic ingredients for these model armour units is extremely low (≈$0.10 each). However, the labour charge and non-reusability of the units significantly increases the overall cost of production.

Shelf-life - After making the armour units, they can be stored on the shelf for at least four months before testing in the flume.

In total, this material has all of the important mechanical properties correctly scaled. As such, if it is used conscientiously in

model testing of rubble-mound breakwaters, it should significantly improve the model results. Failures due to tensile cracking and flexing of the armour units due to both static and dynamic loads should be well simulated if the proper scale factor is chosen. The use of this material in model testing is a definite improvement in the physical modelling of rubble-mound breakwaters. Model tests using this material in the armour layer should give good insight into the structural stability of any proposed breakwater design.

4.0 RIVIERE-AU-RENARD BREAKWATER STUDY

In order to apply these two new modelling techniques to breakwater studies, a test was performed on a 1:25 scale of the breakwater at Rivière-au-Renard, Quebec, Canada. This breakwater was chosen since it has recently failed and new designs are currently being tested for its repair (Glodowski et al 1982). This breakwater is 0.5 km long with an armour layer primarily composed of 5 tonne dolos units. In failure, many of the dolosse have broken especially near the mean water level (MWL) resulting in a slumping of the structure in several locations. The water depth at the breakwater site is 6 m which represents a depth limited situation. Many wave spectra typical of that location were tested. Since it was a depth limited situation, there was considerable wave breaking near the structure. The results presented below correspond to a JONSWAP spectrum having a peak period of 11.6 s and a characteristic wave height of 4.9 m. In performing the tests, two different test set-ups were used. For the first test, a cross-section of the breakwater was built using regular (i.e. not strength-reduced) dolosse. During the storm conditions, there was some rocking of several of the dolos units. At the end of the storm, however, there was no change in the initial cross-section of the structure. Assuming that some rocking of these low mass dolos units is allowable without causing breakage, this test would suggest that this was a stable breakwater design. For the second test, the breakwater was rebuilt using the strength-reduced units. During the storm conditions in this test, there was a number of dolosse which were rocking and hammering on other units without intially breaking. As the storm progressed, as a result of the constant hammering, first one, and then a second unit, broke in the area of the centre of the flume. These breakages started an "unlocking" of the units such that at the end of the test, there were numerous broken units in this region and a large area of the underlayer was exposed (see Figure 6). After the storm, there were five features of the model test which were in agreement with the prototype: (1) the dolosse at the top were mostly intact and slightly pushed back; (2) there was dolosse breakage at the MWL; (3) the dolosse were pulled out of that region resulting in some exposure of the underlayer; (4) the units well below the MWL were intact without substantial movement from their original position; and (5) there was a general slumping of the breakwater as a whole. In addition to this, however, in some cases there were compression-type failures of the units evident which were not observed in the prototype. This results from an unavoidable overscaling of the compressive strength of the model material. The results of this test clearly showed the rapid deterioration of the breakwater as a whole once the individual dolos started to break due to the rocking under wave attack. Once breakage of the units occurred,

the stability and usefulness of the breakwater was substantially reduced. This test indicated that, as originally designed, the breakwater would fail under the severe storm conditions encountered in that region.

5.0 SUMMARY AND CONCLUSIONS

Two improvements in the techniques of modelling rubble-mound breakwaters have been discussed and applied to the study of a model of a dolosse-armoured breakwater. These improvements, the simulation of both realistic sea states and breakage of the armour units, if used conscientiously in model testing of rubble-mound breakwaters, should significantly improve the accuracy of the model test results.

FIG.6

PHOTOGRAPH SHOWING MODEL OF RIVIÈRE-AU-RENARD BREAKWATER AFTER STORM. THE HAND IS POINTING TO A UNIT WHICH BROKE IN THE TRUNK SECTION. NOTE THE REGION DIRECTLY BELOW THE HAND WHERE THERE ARE SEVERAL BROKEN DOLOSSE AND EXPOSURE OF THE UNDERLAYER.

6.0 REFERENCES

Burcharth, H.F. (1979): The effect of wave grouping on on-shore structures. Coastal Engineering, Vol. 2, pp. 189-199.

Funke, E.R. and Mansard, E.P.D. (1980): On the synthesis of realistic sea states. Proceedings of the 17th Conference on Coastal Engineering, Sydney, Australia.

Glodowski, C.W., Lajoie, D.L. and Ropars, Y. (1982): Repair to a dolos armoured breakwater. Proceedings of the 18th Conference on Coastal Engineering, Cape Town, South Africa.

Gonnerman, H.F. and Shuman, E.C. (1928): Compression, flexure and tension tests of plain concrete. Proceedings ASTM, Vol 28.

Jayatilaka, A.S. (1979): Fracture of engineering brittle materials. Applied Sci. Publishers Ltd., London, 1979.

Johnson, E.R., Mansard, E.P.D. and Ploeg, J. (1978): Effects of wave grouping on breakwater stability. Proceedings of the 16th Coastal Engineering Conference, Hamburg, Germany.

Neville, A.M. (1977): Properties of concrete. Pitman Publishers Ltd., London, England.

Timco, G.W. (1981a): The development, properties and production of strength-reduced model armour units. NRC/DME Report LTR-HY-92, Hydraulics Laboratory, National Research Council Canada, Ottawa, Ont., Canada.

Timco, G.W. (1981b): Invited commentary: On the test methods for model ice. Cold Regions Science and Technology, 4, pp. 269-274.

PROTOTYPE TESTING OF DOLOSSE TO DESTRUCTION

T. Terao[1], K. Terauchi[2], S. Ushida[3]
N. Shiraishi[4], K. Kobayashi[5], H. Gahara[6]

ABSTRACT

The Dolos, a type of armor unit, has been used widely for breakwater and shore protection works in the world. However, it has been reported that the armor layers of several breakwaters have been damaged by wave action, and it is probable that the breakage of Dolos has been the cause of that failure.

In this paper, static and dynamic tests using Dolosse units are described. 4t reinforced units and 4t, 0.4t and 0.04t unreinforced units were used.

In these tests, concrete surface and reinforcing bar stress of Dolos, and impact load were measured.

The results of these tests were as follows:
(1) From the both tests i.e. the static load test and the drop test, stress was greatest in the corner between the chamfer and the stem. Cracks occurred at this point.
(2) In the static load test, comparing the results of both units with reinforced and unreinforced chamfer, it became clear that the reinforcement of the chamfer could reduce the magnitude of the stress concentration.
(3) In the drop test, the drop height which made cracks was almost constantly independent of the weights of the units. And it could be considered that there was little influence of increasing the concrete strength as to the breakage of Dolos

1. INTRODUCTION

The Dolos is a type of concrete armor unit that has a high degree of interlocking capability. Dolosse have been

---

[1]Director of the 4th District Port Construction Bureau
[2]Special Assistant to the head of Naha Port Construction
[3]Deputy Special Assistant of Nagoya Port Construction Office
[4]Senior Managing Director of Nippon Tetrapod Co., Ltd.
[5]Manager of R & D section of Nippon Tetrapod Co., Ltd.
[6]R & D section of Nippon Tetrapod Co., Ltd.

used at many port and harbor locations (1, 2). However, recently, it has been reported that the armor layers of several breakwaters have been damaged by wave action (3), and it has been considered that the breakage of Dolos is one probable cause of this damage. Consequently, the problem related to the structual strength of Dolos has been discussed. O.J. Lillevang and W.E. Nickola (4) examined the stress distribution of Dolos model with some shapes of chamfers under static load by using the three-dimensional photoelastic stress analysis, and suggested the shape of the chamfer to reduce the concentration of the tention stress. H.F. Burcharth (5) did the drop and pendulum tests using 1.5t to 20t Dolosse, and proposed a method for the design of impact loaded Dolosse. C. Galvin and D.F. Alexander (6) proposed a theoretical relationship between wave height and concrete strength of armor units. And there were some papers of tests related to the breakage of Dolosse prior to using them to breakwaters, for example, S. Barab and D. Hanson, C.A. Walter and D.R. Clark (7, 8).

In the case of a composite type breakwater with armor layer which are filled completely with armor units of the same size, it is considered that the lowest units will be subject to the static load caused by the dead weight and the units of the exposed side will suffer from the impact load resulting from rocking.

As armor units in these two situations are prone to some damage, we made static load and drop tests using Dolosse and also measured the stresses in some parts of units.

2. TEST CONDITIONS AND PROCEDURE

Assuming the load conditions, two different types of tests were performed. The static load test was performed to simulate the condition of a dead load of units caused by settlement, and the drop test was instigated to simulate the impact resulting from rocking under wave action. Fig. 1 shows the test methods.

4t reinforced and 4t, 0.4t and 0.04t unreinforced units were used in these tests. The waist ratio was constant at 0.32. Table 1 shows the test program, Fig. 2 shows the geometry of units, and Table 2 shows the mix proportions of concrete. Tensil strength test results of steel bars and bar arrangement drawing are given in Table 3 and Fig. 3, respectively.

In the static load test, the vertical fluke of the unit was fixed by a support equipment. There were two different loading conditions. One was imposed on the mid point of the horizontal fluke and the other was on the tip point. A hydraulic jack was used for loading. Photo. 1 shows the

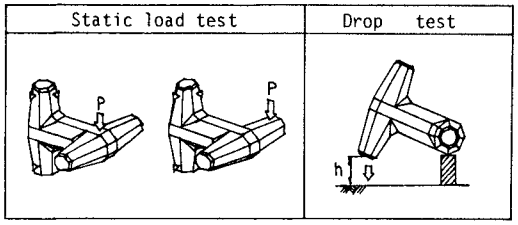

Figure 1 Test Method

Table 1 Test program

Test		Weight of unit (t)	Reinforcement (kgf/mm²)	Concrete strength (MPa)
Static load test	Imposed on the mid point of the horizontal fluke	4	75	20.6
			92	
			151	
			0	20.6
				29.4
				39.2
	Tip point		92	20.6
			151	
Drop test		4	92	20.6
			151	
			0	20.6
				29.4
				39.2
		0.4	0	20.6
		0.04	0	20.6

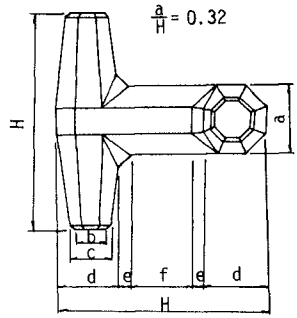

Weight (t)	H	a	b	c	d	e	f
4	2239	716	386	458	669	125	651
04	1038	332	178	212	310	58	302
0.04	482	154	82	98	144	27	140

(mm)

Figure 2 Geometry of units

Table 2 Concrete mixture

Concrete strength (MPa)	Slump (cm)	Max. diameter of agg. (mm)	W/C (%)	S/A (%)	Cement (kg/m³)	Water (kg/m³)	Sand (kg/m³)	Aggre-gate (kg/m³)	Additive (kg/m³)
20.6	10	25	55.5	38.5	251	139	743	1186	0.628
29.4	10	25	44.5	35.0	320	142	680	1184	0.800
39.2	10	25	34.5	34.5	421	145	612	1162	1.053

Table 3 Test results of reinforcing bar

Standard	Diameter (mm)	Strength	Results (MPa)
SR-24	13	Yield strength	294
		Ultimate tensile strength	428
	16	Yield strength	331
		Ultimate tensile strength	478

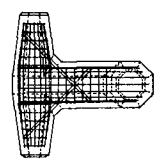

reinforcement: 13mm and 16mm bars
concrete cover layer: 65mm

Figure 3 Bar arrangement drawing

Photograph 1: The situation of the static load test

Photograph 2: The situation of the drop test

situation of the static load test.

In the case of the drop test, the horizontal fluke was supported in a way to keep the stem level. Then, the vertical fluke was lifted up to a predetermined height and dropped onto a concrete slab of 1 meter thickness by use of a quick release device. Drop height started at 2 cm and increased every 2 cm. Some of the drop test units were provided with load cells at the bottom of the vertical fluke to measure the impact load. Photo. 2 shows the situation of the drop test.

In both tests, several strain gauges were placed on the reinforcing bar and the concrete surfaces of each test unit in order to measure the strain.

3. TEST RESULTS

3-1 Static load test

3-1-1 In the case of imposing a load on the mid point of the horizontal fluke

Stress concentrated on the corner between the chamfer and the stem due to the bending force. Cracks occurred at this point. Photo. 3 shows the breakage of Dolos. From the results of unreinforced units shown in Table 4, it is considered that the ultimate imposed load which caused cracks increased slightly as the compressive strength of concrete increased. Fig. 4 shows the relationship between the concrete surface stress and static load.

In the case of reinforced units, cracks appeared in that corner under the static load which was almost as large as the results of unreinforced units. Fig. 5 and 6 show the stress distribution of the reinforcing bar using the units with the chamfer reinforced and unreinforced, respectively. Stress concentrated on the corner revealing themselves as corresponding cracks.

In the case where the chamfer was not reinforced, the reinforcing bars placed at the stem yielded under a smaller imposed load compared to that of the reinforced chamfer. It is apparent that reinforcement of the chamfer is effective.

3-1-2 In the case of imposing a load on the tip point of the horizontal fluke

The results of cracking were different between 92 kg/m^3 and 151 kg/m^3 reinforcement units.

In the case of the 92 kg/m^3 reinforcement unit, cracks occurred in the corner between the chamfer and the stem, and

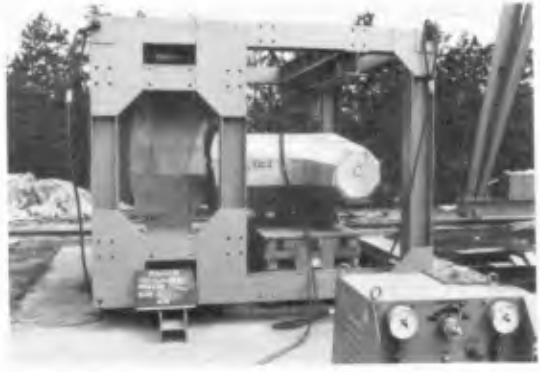

Photograph 3: The breakage of Dolos (Static loac test)

Photograph 4: The cracks of the stem (Static load test)

Table 4 Static load test results (unreinforced unit)

Weight (t)	Design compressive strength (MPa)	cracking static load (kN)	Breaking static load (kN)
4	20.6	61.7	73.5
	29.4	71.5	80.4
	39.2	80.4	93.2

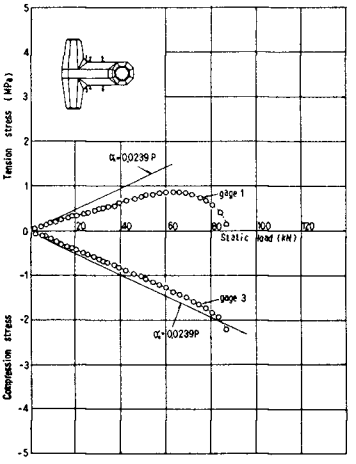

Figure 4 Relationship between concrete surface stress and static load

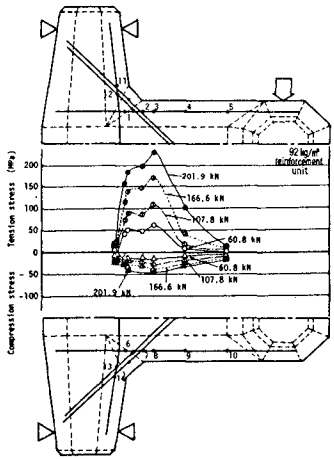

Figure 5 STRESS DISTRIBUTION OF REINFORCEMENT
(Imposed on the mid point of the horizontal fluke)

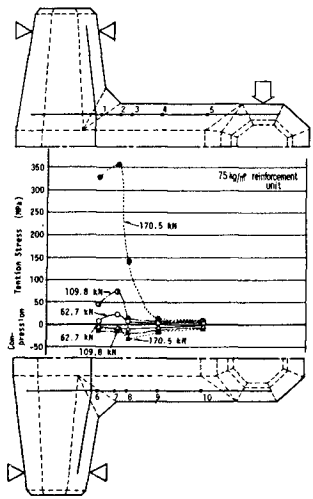

Figure 6 STRESS DISTRIBUTION OF REINFORCEMENT
(Imposed on the mid point of the horizontal fluke)

progressed toward the stem at 45°. Ultimate breakage was identified as shear rupture due to bending and torsion forces. Photo. 4 shows the cracks of the stem. Fig. 7 shows the stress distribution of the reinforcing bar. From the result of the relationship between the reinforcing bar and static load shown in Fig. 8, the stem and chamfer bars placed at the corner section ultimately yielded at about 170 KN.

While in the case of 151 kg/m^3 unit, cracks appeared in the corner with a small imposed load, and thereafter new cracks occurred and progressed inthe stem at 45°. Ultimate breakage was identified as sheer rupture due to tortion force. Fig. 9 and 10 show the stress distribution of the reinforcing and static load, respectively.

3-2 Drop test

Cracks occurred in the corner between the chamfer and the stem identical with the results of static load test.

From the results of unreinforced units shown in Table 5, it is considered that the drop height which crack occurs is almost constant independent of the weight of the units and concrete strength. Photo. 5 shows the broken unit.

In the case of the reinforced units, stress concentrated on the corner and cracks occurred at this point, too. But the units didn't separate into two pieces. The stress distribution of the reinforcing bar is shown in Fig. 11.

Impact load and impact time were also measured by using load cells. Fig. 12 shows the relationship between the impact time of the load and the drop height. Fig. 13 shows the relationship between the impact time of the load and the weight of the unit. From these results, it can be assumed that the impact time of the load is almost constant independent of the drop height while using the same weight of the unit, and the ratio of the impact times is almost equal to the ratio of their characteristic length i.e. Dolos height.

From the results of the relationship between the maximum impact load and drop height shown in Fig. 14, it is considered that the impact load is proportional to the square root of the drop height and the ratio of the impact loads is equal to the square of the ratio of their characteristic lengths under conditions of the same drop height.

As the ratio of the concrete surface strain is almost equal to the square of the reciprocal of the ratio of their characteristic lengths under conditions of the same impact

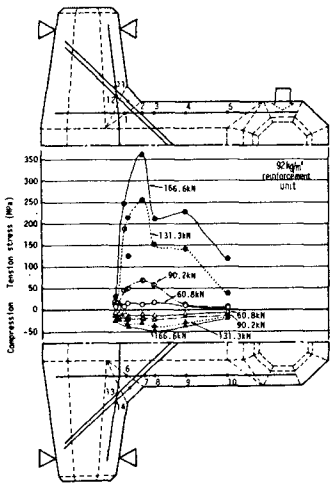

Figure 7 STRESS DISTRIBUTION OF REINFORECEMENT
(imposed of the tip point of the horizontal fluke)

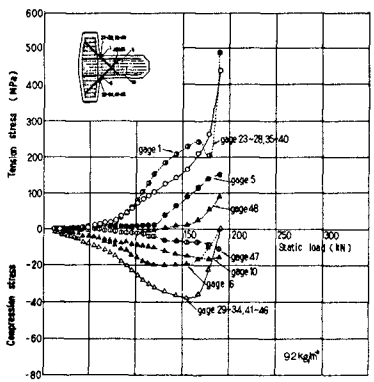

Figure 8 Relationship between reinforcing bar stress and static load

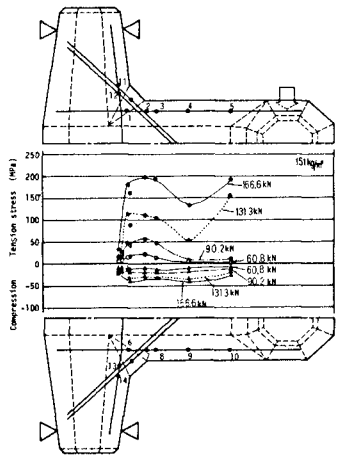

Figure 9 STRESS DISTRIBUTION OF REINFORCEMENT
(imposed on the tip point of the horizontal fluke)

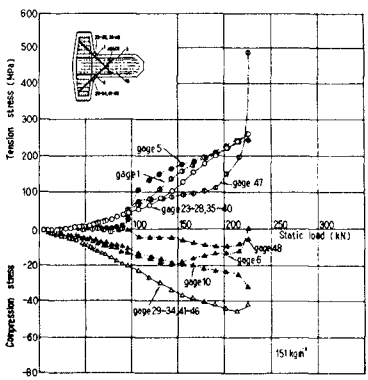

Figure 10 Relationship between reinforcing bar stress and static load

Table 5 Drop test results (unreinforced unit)

Weight (t)	Design compressive strength (MPa)	Cracking drop height (cm)	Breaking drop height (cm)
4	20.6	7	12
	29.4	10	14
	39.2	14	18
0.4	20.6	14	18
0.04	20.6	16	20

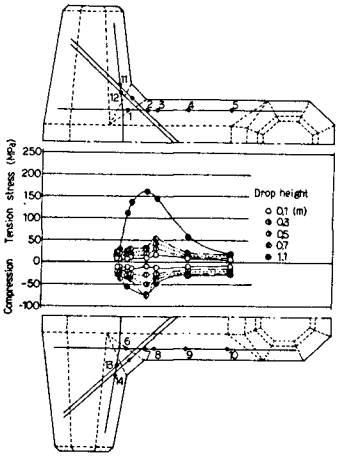

Figure 11 Stress distribution of reinforcement (Drop test)

Photograph 5: The breakage of Dolos (Drop test)

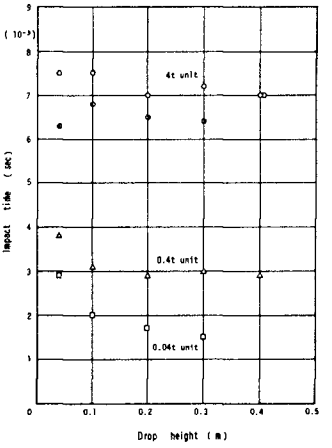

Figure 12 Relationship between impact time and drop height

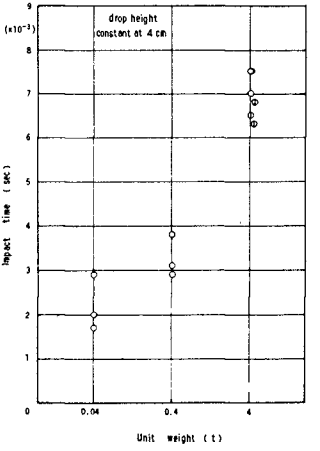

Figure 13 Relationship between impact time and unit weight

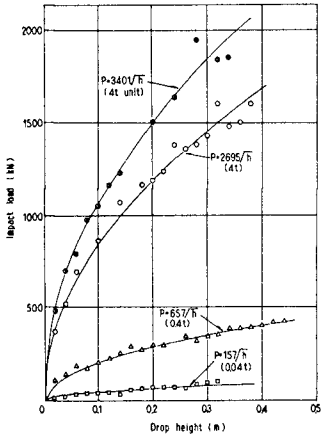

Figure14 Relationship between impact load and drop height

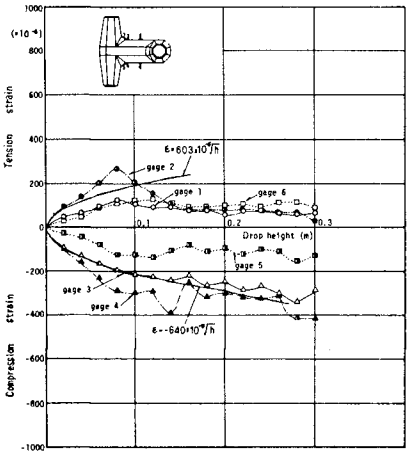

Figure 15 Relationship between concrete surface strain and drop height

load, the maximum strain on the concrete surface is proportional to the square root of the drop height as shown in Fig. 15. This results in the stress of the concrete surface being constant independent of the weight of the unit under conditions of the same drop height.

4. CONCLUSIONS

Stress distribution, the influence of the concrete strength and weight of unit for the breakage of Dolos, and impact load were obtained through these static load and drop tests.

The result of these tests were as follows:
(1) From the both tests, i.e., the static load test and the drop test, stress was greatest in the corner between the chamfer and the stem. Cracks occurred at this point.
(2) In the static load test, comparing the results of both units with reinforced and unreinforced chamfers, it became clear that the reinforcement of the chamfer could reduce the magnitude of the stress concentration.
(3) In the drop test, the drop height which made cracks was almost constant independent of the weights of the units. And it could be considered that there was little influence of increasing the concrete strength as to the breakage of Dolos.

5. REFERENCES

1 Zwamborn, J.A. Bosman, D.E. and Moes, J. (1980) "DOLOSSE: PAST, PRESENT, FUTURE ?", 17th ICCE, Sydney, Australia.
2 Sakou, T. Shiraishi, N. and Kobayashi, K. (1981) "JAPANESE PRACTICE WITH CONCRETE ARMOR UNIT", ASCE, New York, New York.
3 Magoon, O.T. Sloan, R.L. and Foote, G.L. (1974) "DAMAGES TO COASTAL STRUCTURES", 14th ICCE, Copenhagen, Denmark.
4 Lillevang, O.T. and Nikola, W.E. (1976) "EXPERIMENTAL STUDIES OF STRESSES WITHIN THE BREAKWATER ARMOR PIECE 'DOLOS'", 15th ICCE, Honolulu, Hawaii.
5 Burcharth, H.F. "A DESIGN METHOD FOR IMPACT-LOADED SLENDER ARMOUR UNIT" Bulletin NR. 18 Laboratoriet for Hydraulik OG Havnebygning, Aalborg, Danmark.
6 Galvin, C. and Alexander, D.F. (1981) "ARMOR UNIT ABRASION AND DOLOS BREAKAGE BY WAVE-INDUCED STRESS CONCENTRATIONS", ASCE, New York New York.
7 Barab, S. and Hanson, D. (1978) "INVESTIGATION OF FIBER REINFORCED BREAKWATER ARMOR UNITS" Proceedings, ACI, International Symposium: Fiber Reinforced Publication SP-44.
8 Walter, C.A. and Clark, D.R. (1981) "TESTING OF PRECAST CONCRETE DOLOSSE ARMOR UNITS", ASCE, New York, New York.

A NUMERICAL MODEL OF WAVE/BREAKWATER INTERACTIONS

D. Ian Austin, AM, ASCE*
Roger S. Schlueter*

Abstract

A numerical model has been developed to simulate breakwater response to wave impacts with special reference to armor unit behavior and breakwater stability. The model uses a finite difference hydrodynamic code to follow the wave impacts and determine wave forces upon the breakwater components. A discrete element code models the breakwater response and motions. The model rationale and numerical basis are followed by three examples used in this, the concept validation, stage of model development.

1. Introduction

Failures of rubble-mound breakwaters, particularly those built with artificial armor units, have been occurring over the last decade. The much publicized major breakwater failure at Sines, Portugal (Edge and Magoon, 1979) has highlighted the problem. Damage assessment of the Sines event (PSID, 1979) funded by the National Science Foundation demonstrated that the design methods and philosophies which were used may have been inadequate. These methods have included use of the empirical Hudson's stability formula which links the slope of the breakwater face with the weight and stability coefficient of the armor units.

With introduction of artificial breakwater armor shapes, in particular the dolos unit (Merrifield and Zwamborn, 1966), much lighter armor units than the equivalent quarried rock armor have been used. The artificial units have dramatically increased interlocking abilities and hence larger stability coefficients. Thus, for a given design wave, Hudson's formula predicts a lighter unit than if a low stability coefficient typical of natural rock had been used. However, recent studies have concluded that artificial armor units are particularly susceptible to dynamic motions imparted by the inertial and drag forces of waves impinging upon a breakwater structure. Specification of artificial armor units for breakwater design demands better understanding of the structural loading phenomena on individual elements and the limitations imposed by the concrete and reinforcing properties.

* Dames & Moore, Suite 1000, 1100 Glendon Avenue, Los Angeles, California 90024.

This paper presents a numerical technique for studying both the behavior and overall breakwater stability under a variety of wave loadings and the behavior of individual armor units. A discussion of the numerical approach is followed by examples using simplified armor unit shapes and breakwater geometries. While the ultimate aim of this line of research is to be able to model, in three dimensions, breakwaters constructed using both existing and proposed armor units, the object of this paper is to show the feasibility of the adopted approach using two-dimensional examples. The computer model is structured in a modular fashion which allows additions and enhancements to be included as they are developed.

2. Numerical Approach

Consider a generalized breakwater cross section consisting of a wave breaking on a multilayered armored breakwater (Figure 1). The wave breaking process is highly non-linear, consisting of inertial and viscosity induced forces. A complex energy dissipation and force reversal process follows in the armor unit, filter layer and core regions. The armor units are designed to resist the forces but they will rock and possibly break if overstressed or improperly positioned. Such breakages aid or initiate larger failures.

Rather than attempt to model the complete wave/breakwater interaction with one computer code, an approach has been adopted which is believed will allow both theoretical and numerical developments in wave breaking analysis to be incorporated with a minimum of program restructuring. The wave/breakwater interaction is modeled by two distinct codes, one describing the wave action and forces, the second describing the armor unit behavior. At this stage of concept development, it is being assumed that the interactions can be decoupled for time periods on the order of the time between subsequent wave impacts. This assumption implies that the short term response of the armor units does not significantly alter the wave force field within these intervals. For non-catastrophic failure, the assumption is valid as armor movement is on the order of centimeters. In failure situations, the assumption is no longer valid. However, the decoupling assumption reduced computation time considerably during this concept validation stage of the model development. As model development progresses, full coupling will be introduced.

In formulating an numerical approximation to the physical system it was realized that a complete description of the wave forces does not exist. However, simplified numerical approximations to the wave breaking process can be made. The classical equations describing stress within a structural unit are well known and have been applied in a number of studies of breakwater armor units (e.g., Lillevang and Nichola, 1976).

2.1 Wave Forces

The wave forces resulting from impacts upon a breakwater type structure are calculated using a version of the finite difference

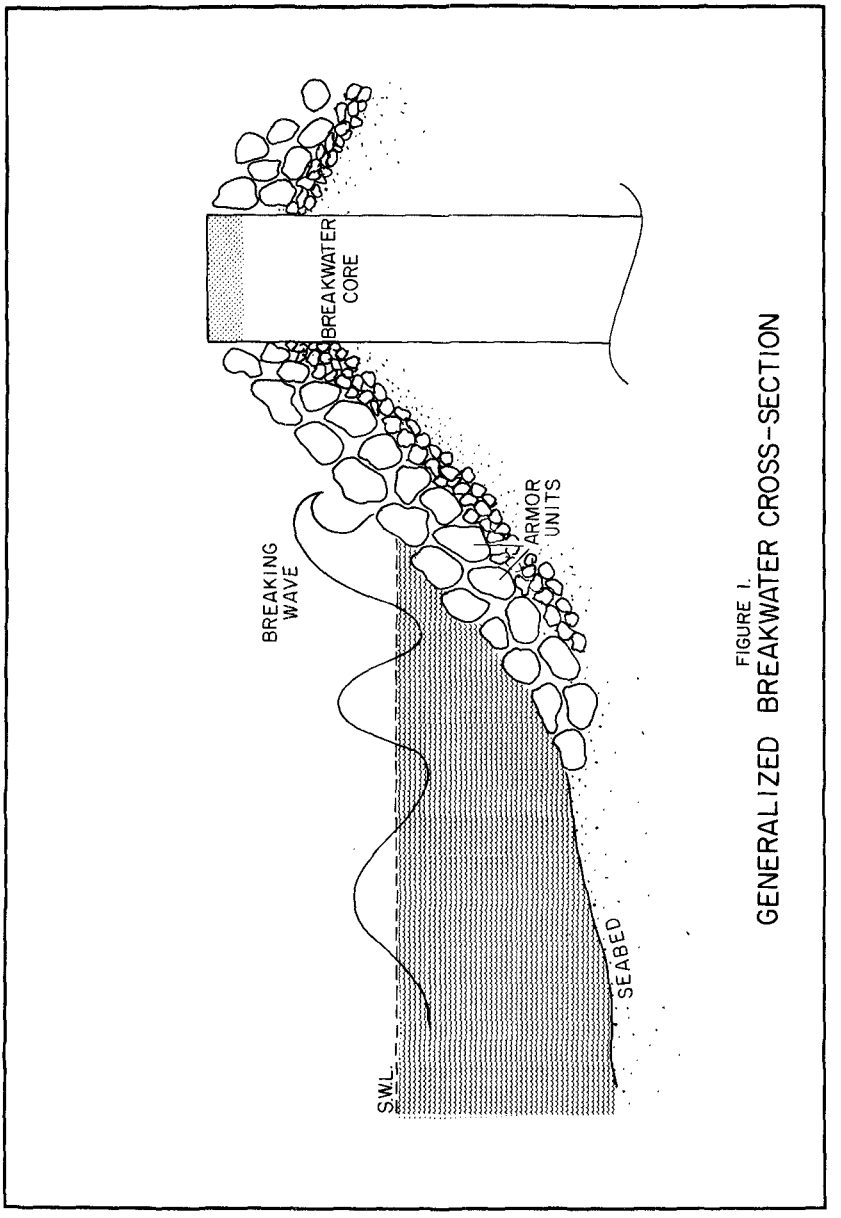

FIGURE 1.
GENERALIZED BREAKWATER CROSS-SECTION

computer code, SOLA-VOF, developed at Los Alamos Scientific Laboratories for solving transient fluid flow problems with multiple free boundaries (Nicholas et al., 1980). The constitutive equations used in the code are the Navier-Stokes equations and a form of the continuity equation which includes limited fluid compressibility (Figure 2). The feature of the program which makes it particularly useful in this application is the concept of the fractional volume of fluid (VOF). The "F" equation (see Figure 2) is used to describe the existence and position of a free surface within a finite difference cell. The value of F is zero in an empty cell and one in a full cell. A cell with a value between these limits indicates that a free surface (or boundary surface) exists in that cell. Because the free surface is defined in a cell by cell manner, multiple free surfaces can exist within a modeled region. As no a priori assumptions are necessary regarding the position of the free surfaces as it varies spatially or temporally, free surfaces can pass over or through a mound of obstacles.

At the current stage of development, obstacles to the water movement such as armor units are included as rigid zones within the modeling area. For non-failure conditions this approximation is reasonable. However in order to study the effects of rocking and failure, a more general movable description of the obstacles will be necessary. Forces on the obstacles are calculated by integrating the pressures around an obstacle. This method allows inertial effects to be included directly.

Wave loadings can be specified by a number of methods. In the examples to be shown, an initial water surface was defined with and without initial velocities. Alternatively, a pressure field can be used to initiate a wave response or a full description of internal velocities and surface elevations could be input. A random sea could be defined by the last method.

A simplified diagram of the program's operation is shown on Figure 3. The finite difference approximations to the momentum equations are first solved using the previous timestep values of velocity and pressure in the appropriate terms. After application of the boundary conditions, the continuity equation is solved in an iterative manner to obtain the new timestep values of velocity and pressure. Finally the F equation is solved for all cells. More explicit details of the scheme have been published previously (Nicholas et al., 1980).

2.2 Armor Units

The response and behavior of the breakwater armor units are modeled using a discrete element model originally developed for simulating jointed rock behavior (Cundall, 1980; Dames & Moore, 1981). The model calculates the individual armor unit (i.e., element) response to both the applied fores and the constraints of the surrounding units. The internal block stresses and inter-block fluid pressures can be calculated at each step in the armor unit

Navier-Stokes

$$\frac{\partial u}{\partial t} + u\frac{\partial u}{\partial x} + v\frac{\partial u}{\partial y} = -\frac{1}{\rho}\frac{\partial p}{\partial x} + g_x + \nu\left[\frac{\partial^2 u}{\partial x^2} + \frac{\partial^2 u}{\partial y^2}\right]$$

Continuity

$$\frac{1}{\rho c^2}\frac{\partial p}{\partial t} + \frac{\partial u}{\partial x} + \frac{\partial v}{\partial y} = 0$$

Volume of Fluid

$$\frac{\partial F}{\partial t} + u\frac{\partial F}{\partial x} + v\frac{\partial F}{\partial y} = 0$$

FIGURE 2. EQUATIONS USED IN FLUID CODE

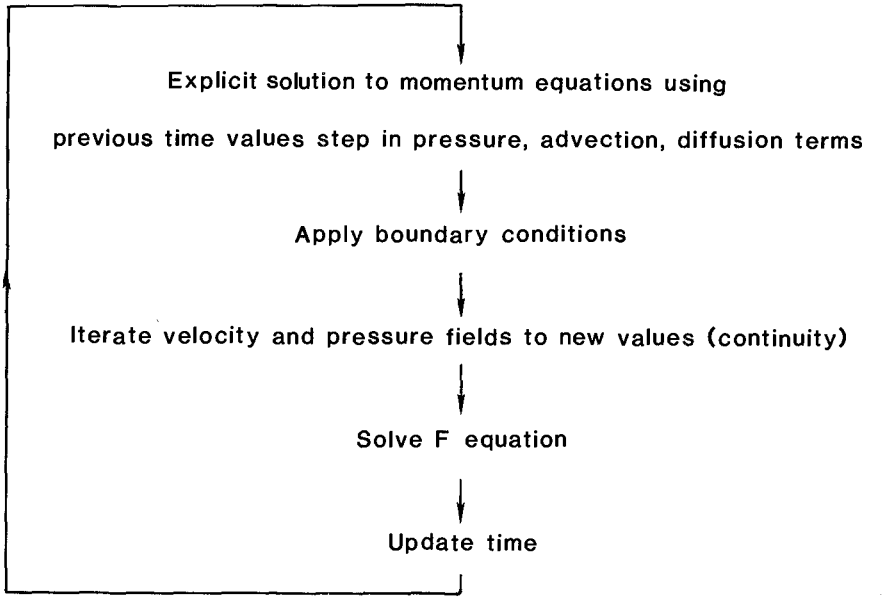

FIGURE 3. SIMPLIFIED CALCULATION CYCLE: SOLA-VOF

code. Joints between the units and corner-to-edge or corner-to-corner contacts are treated as boundary conditions between the units. Therefore the corner locking and frictional forces associated with breakwater unit interactions can be modeled correctly. By including fracturing and splitting within the discrete elements, failure of the armor units and/or the overall breakwater can simulated. The code uses a fully dynamic explicit scheme to solve the equations of motion thus allowing the true response of the units and the interactions to be followed. The basis calculation cycle is shown on Figure 4.

At the present stage of program development, armor unit shapes from discs to rectangles can be modeled. The discs are simulated by increasing the corner rounding, which is used to prevent elements "locking up", until a disc results. Further developments of the jointing or shaping aspects of the program, by which joints and hence blocks are defined, will allow more sophisticated armor shapes to be modeled.

3. Examples

Three examples of the current program configuration follow. The first two are essential revetment problems as a fully reflective boundary is assumed at the centerline of the "breakwater". In the third example, a breakwater is constructed by adding a "harbor" side to the revetment grid. In all cases, artificial spacing of the armor blocks in the fluid program is required to allow forces to develop around the blocks. The space is the result of modeling a three-dimensional problem in two dimensions. The breakwater geometries are extremely simplified - more so than the programs will allow - as these examples were aimed at concept validation rather than quantitative validation.

3.1 Revetment Example

The grid used in the fluid modeling is shown on Figure 5. The armor blocks are defined as rigid obstacles as is the revetment core. The armor units are 1.6 meters square. A wave loading is approximately by a 2.6-meter high "block" of water released in a manner similar to a dam break. One of the many verification cases of the fluid code included the reproduction of a laboratory dam break test. A no-flow boundary condition is used on all boundaries. As previously mentioned, the armor units are separated to allow fluid flow between the blocks. Snapshots of the fluid behavior are shown on Figure 6. This figure shows the initial block of water collapsing to form a "surging" wave.

The forces on the armor blocks developed during the wave impact and reversal are shown on Figure 7. Comparison of the force histories on Blocks 1 and 2 shows the expected force reduction on the second layer block afforded by the first layer block. A similar pattern can be seen in the force histories of Blocks 3 and 4. Blocks 1 through 4 show a smooth increase and decrease of forces as would be expected from submerged blocks. Blocks 5 through 7 show

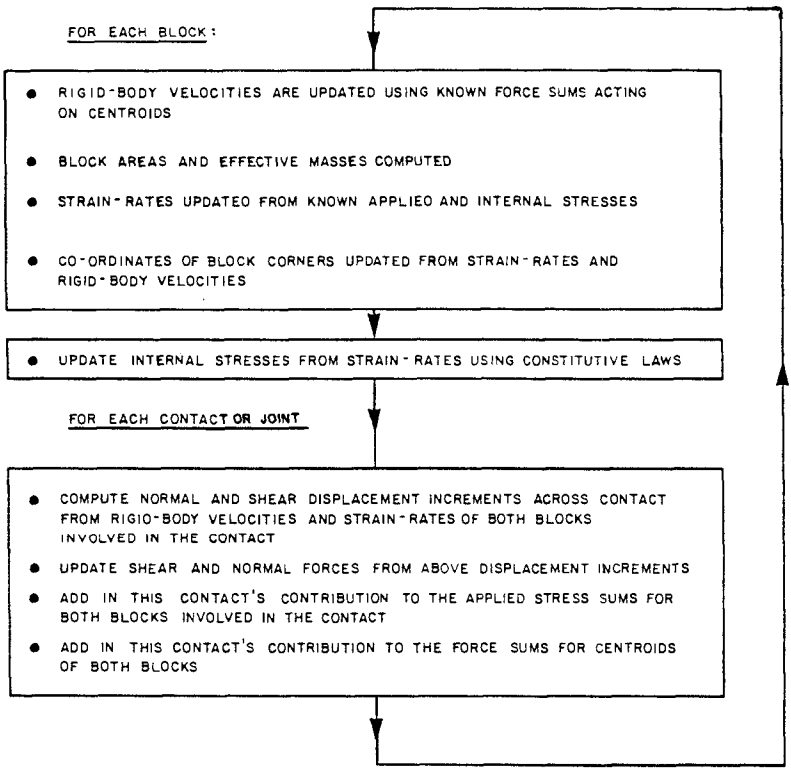

FIGURE 4. SIMPLIFIED CALCULATION CYCLE: RAGE

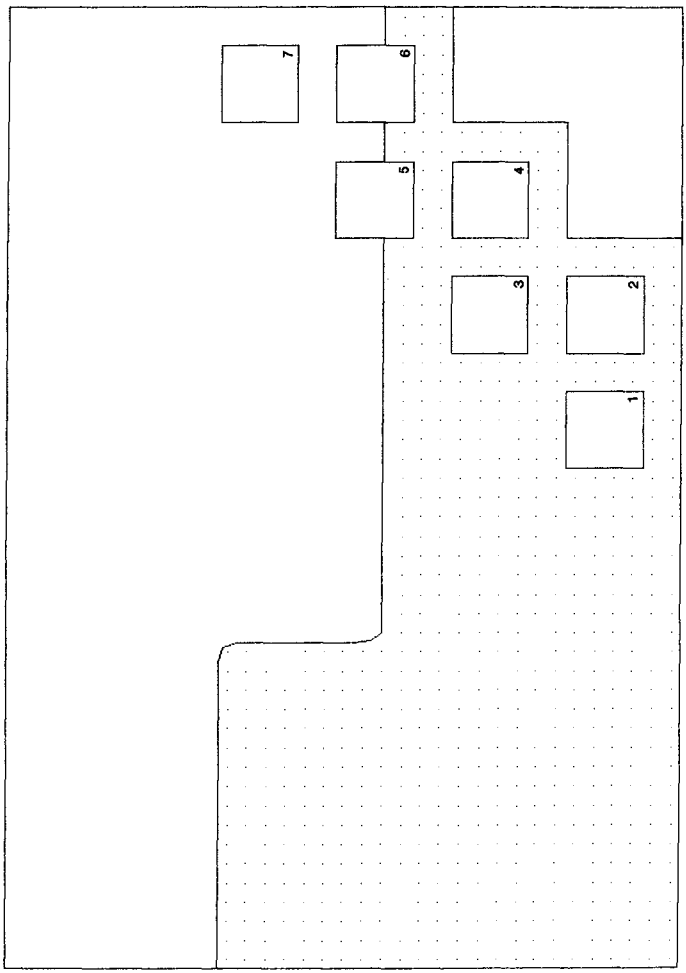

FIGURE 5. EXAMPLE 1: INITIAL WATER SURFACE

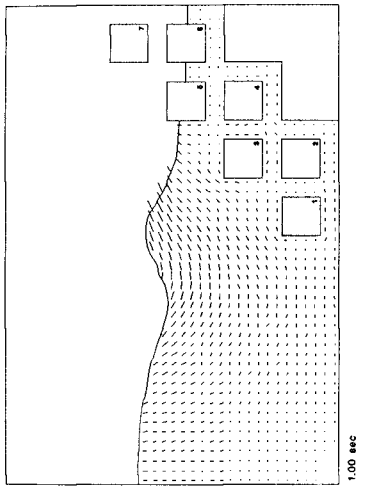

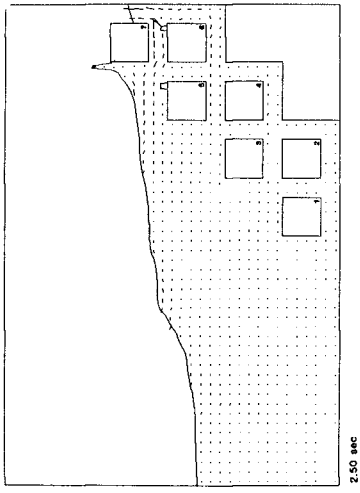

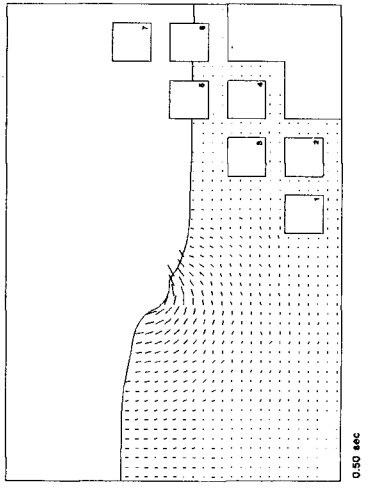

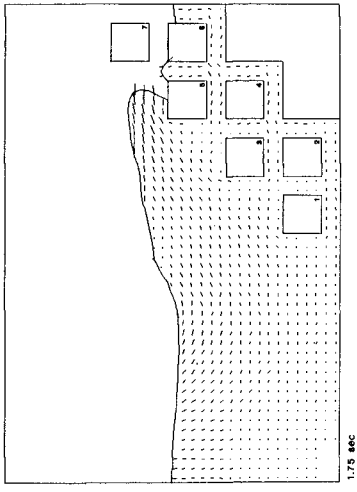

FIGURE 6. EXAMPLE 1: WAVE IMPACT

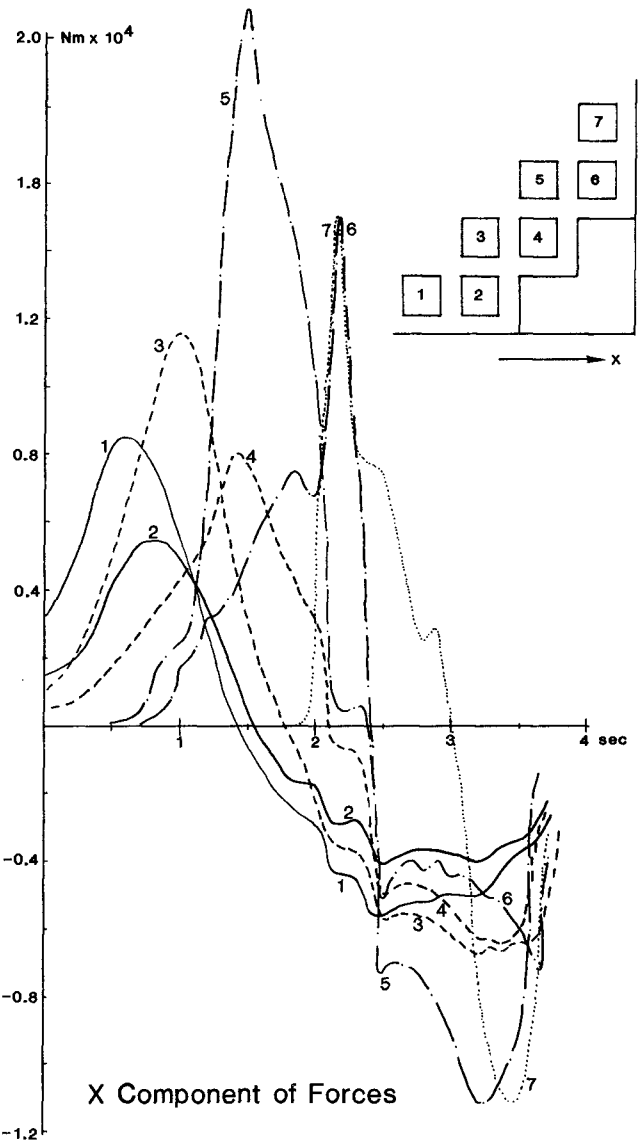

FIGURE 7. EXAMPLE 1: FORCES ON BLOCKS

much sharper peaks resulting from impacts upon the semi-submerged and free blocks. Block 5 shadows Block 6 as in the case of the submerged blocks.

The discrete element block model setup is shown on Figure 8.a. As the forces are applied at the block centers, no artificial spacing between the blocks is required or could be maintained as the blocks are free to move and are subjected to gravitational accelerations. The block movements resulting when the force histories are used is shown on Figures 8.a through 8.e. The displacements are exaggerated as the actual movements are very small (on the order of millimeters). The incoming wave (Figures 8.a, 8.b) has very little effect while the backwash (Figures 8.c, 8.d) causes the blocks to rock and hence the toe block to move outwards. Figures 8.e and 8.f show the return rocking of the blocks and the final pattern when the forces are removed. Reapplication of the same force history to the displaced blocks caused retightning during the incoming wave portion of the force history and redisplacing during the backwash. Repeated applications of the wave history did not cause a failure.

3.2 Revetment Modifications Example

The fluid grid was modified to include a "filter layer" of smaller blocks and four cases were run modifying the spacing between the blocks and the wave loading. Case 1 is the above "surging wave" example run again with the new grid, Case 2 is the same grid with the interblock spacing reduced from two grid cells to one grid cell. In the second two cases, a wave shaped block of water was defined with an initial velocity to form a "plunging" wave. Again, interblock spacings of two and one cells were used.

The histories of forces acting upon the small filter block marked with an X on Figure 9 are shown on Figure 10. As expected, the surging wave produces less force on the filter unit than the plunging wave. The larger spacings allow greater forces to develop in the interior of the breakwater.

3.3 Breakwater Example

To investigate the effect of replacing the revetment in the first example with a true breakwater, the grid was extended as shown on Figure 11. The figure shows snapshots of the wave passing through and over the breakwater. It is interesting to note that jetting through the breakwater (Figure 11.c) induces waves on the harbor side (right) of the breakwater. This jetting has been observed in real breakwaters.

In this example a "surging" type of wave was applied as in the first example. The x component of forces on two blocks are compared with the forces on the equivalent two blocks in the previous example, Case 2. Figure 12 shows the forces histories on the exposed Blocks 3 and 5. Block 3 is a submerged block, while Block 5 is initially only partially submerged. The impact histories for the blocks are identical with the exception that in the breakwater case

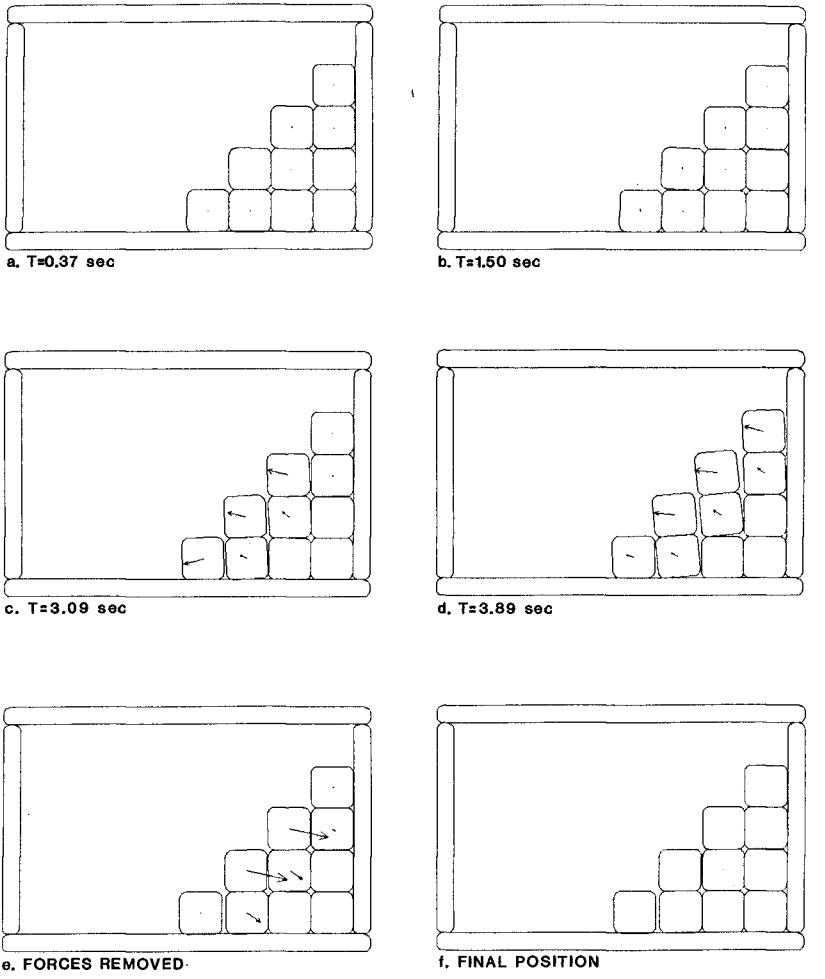

FIGURE 8. EXAMPLE 1: BLOCK MOVEMENTS

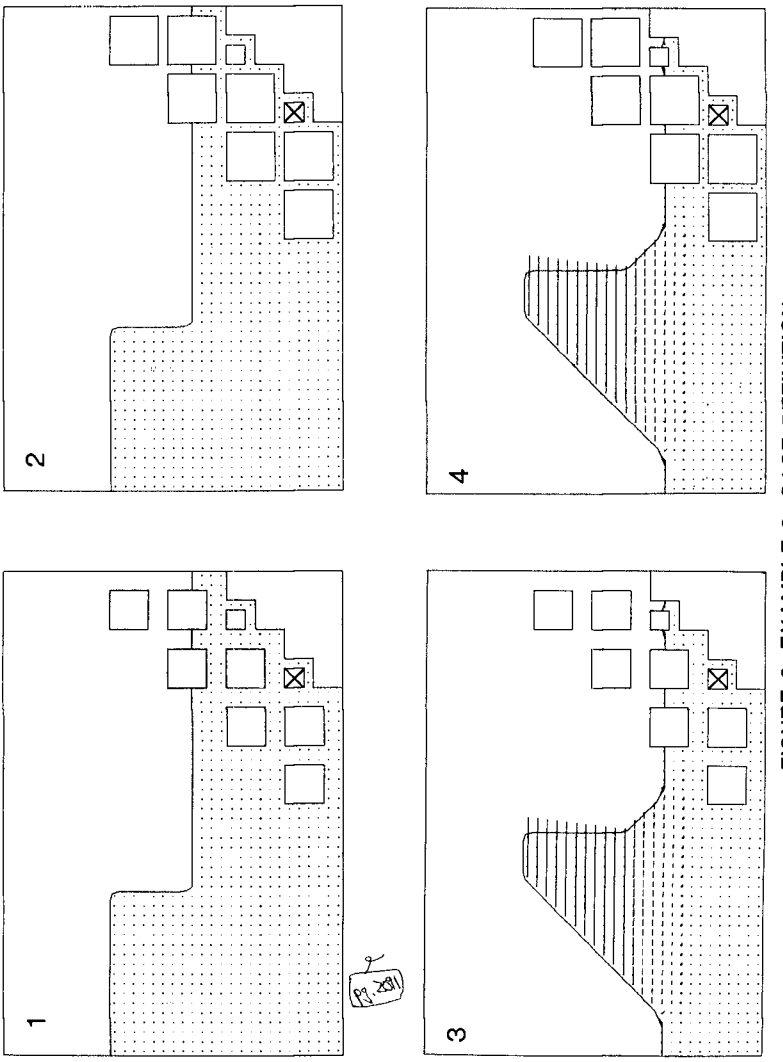

FIGURE 9. EXAMPLE 2: CASE DEFINITION

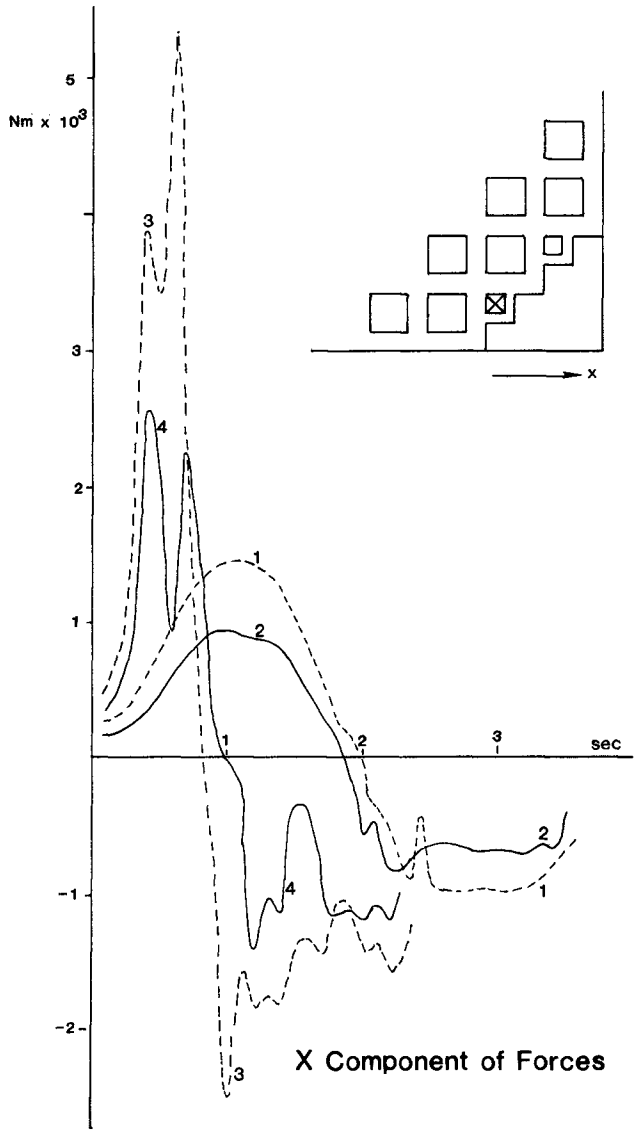

FIGURE 10. EXAMPLE 2: FORCES ON FILTER BLOCK

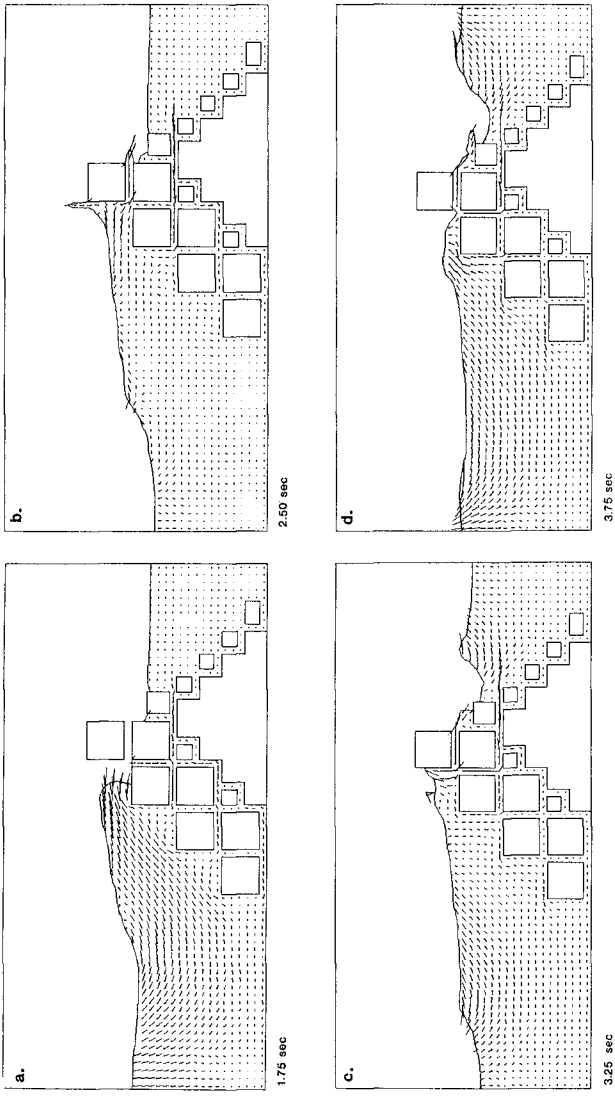

FIGURE 11. WAVE IMPACT ON BREAKWATER

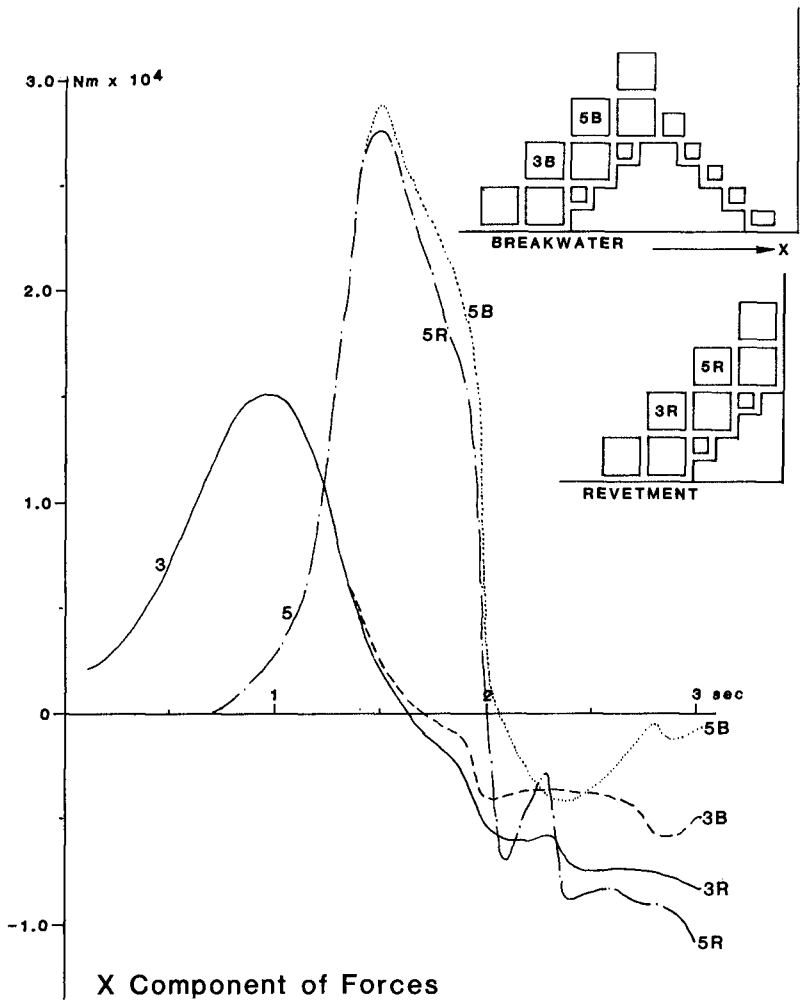

FIGURE 12. EXAMPLE 3: FORCES ON BLOCKS

a slightly greater maximum force is experienced on Block 5. This may be due to a reduction in the amount of water traveling up through the gap between Block 5 and its neighbor to the right in the breakwater case because of jetting through the breakwater. Consequently, an increase in the net impact force acting on the front face will result.

The backwash forces on both blocks are less in the breakwater case than those in the revetment case due to the flow through the breakwater. Block 5 shows a breater reduction than Block 3. This is probably because the backwash experienced by Block 5 in the revetment case is primarily due to wave runup caused by the revetment wall. The backwash experienced by the submerged Block 3 is due in greater part to the effects of the blocks to its right.

4. Conclusions

The results described above are encouraging and indicate the feasibility of the adopted approach. Considerable work needs to be done, such as introducing movement to units in the fluid program and conduting calibration tests, before the model can be used as a predictive tool. However, even in this relatively crude form, useful calculations can be made. Eventually, random placing of units matching that used in breakwater construction will be achieved by simulating the placing and settling processes.

Although the present model is two-dimensional, it is envisioned that in this form the model will provide a useful function in the design and stability analyses of present and future breakwaters. The jump from the current two-dimensional model to the three-dimensional model will eventually be made though at this time the additonal costs and complexity are not justifiable.

Acknowledgments

The authors are grateful for the help of Tony Hirt, Peter Cundall and Peter Carpenter in coaxing the model to its present state.

5. References

Cundall, P.A. (1980). UDEC - A generalized distinct element program for modeling jointed rock. Report PCAR-1-80, Peter Cundall Associates: Contract DAJA17-79-C-0548, European Research Office, U.S. Army.

Dames & Moore (1981). RAGE user's manual.

Edge, B.L. and O.T. Magoon (1979). A review of recent damages to coastal structures. Coastal Engineering 79.

Lillevang, O.J. and W.E. Nichola (1976). Experimental studies of stresses within the breakwater armor piece "Dolos". Proc. 15th Coastal Engineering Conference, Honolulu, Hawaii.

Nicholas, B.D., C.W. Hirt, and R.S. Hotchkiss (1980). SOLA-VOLA: A solution algorithm for transient fluid flow with multiple boundaries. Los Alamos Scientific Laboratory.

Port Sines Investigating Panel (1979). Failure of the breakwater at Port Sines, Portugal. Coastal Engineering Research Council, ASCE.

FACTORS OF SAFETY FOR THE DESIGN OF BREAKWATERS

*J.D. Mettam, M.A., C.Eng., F.I.C.E., F.ASCE., M.Cons.E.

**J.G. Berry, B.A., B.A.I., C.Eng., F.I.C.E., M.I.Struct.E.

ABSTRACT

This paper proposes to improve the safety of breakwaters by two important changes in the philosophy of design. When hydraulic model testing is used as a design tool the authors propose to reduce the specific gravity of the model breakwater to introduce a factor of safety in the prototype. They also recommend that the concept of testing for stability with the once in 50 year or once in 100 year wave should be replaced by a more rigorous statistical analysis to determine a design wave which has a probability of exceedence of no more than 5% in the lifetime of the structure.

INTRODUCTION

Severe damage to several breakwaters in recent years has focussed attention on current design methods, which appear in some circumstances to be unreliable. Most designers are aware of the inadequacy of present design formulae, and they therefore rely heavily upon hydraulic model tests. The use of conventional hydraulic models to check the design provides at best an uncertain safety margin against failure. The authors' view is that this is a major factor in the large number of breakwaters which fail.

Parallels are drawn from the design of building structures in which partial factors of safety are applied to the forces and to the properties of constructional materials in order to analyse the design of its ultimate limit state.

The introduction of quantified partial factors of safety in the design process for breakwaters is proposed, not only in theoretical analyses but also in hydraulic model testing procedures.

* Senior Partner, Bertlin and Partners, Consulting Engineers, Redhill, England

** Associate Partner, Bertlin and Partners, Consulting Engineers, Redhill, England

DAMAGE TO BREAKWATERS

During the winters of 1978, 1979 and 1980 several rubble mound breakwaters on the western seaboard of Europe and on the North African coast were severely damaged.

Possible causes of damage have been discussed by Brunn (1). Damage to caisson type breakwaters, used most frequently in the Far East, has also occurred in the past and has been summarised by Goda (2). Because of the bad record in service of large breakwaters, both of rubble mound construction and caisson construction, this paper has been prepared to consider improvements to our design philosophy with these two forms of construction chiefly in mind.

PRESENT DESIGN METHODS

The limitations of present design methods have been discussed in a previous paper (3). Present practice for the design of rubble mound breakwaters of the type shown in Fig. 1 is to prepare an outline design using Hudson's formula (4) and then test the cross-section in a hydraulic flume. The design is modified during the testing programme until predetermined damage criteria are satisfied.

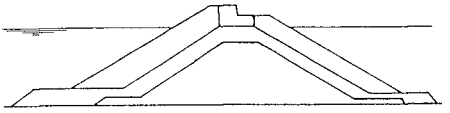

Figure 1 Rubble mound breakwater

In the case of natural rock armour the criterion may be expressed as a percentage loss of armour units over the exposed face, perhaps 1%. This is an inexact definition as "exposed" may have various conflicting meanings and for the same wave climate breakwaters at shallow and deep water sites have very different superficial areas of armour. Because the Hudson formula was developed for rock armour where breakage of units is not normally a problem, loss of armour in the model may have correctly represented the importance of damage in the prototype. Provided that it is relatively easy to mobilise the equipment to reposition armour stones (or provide extra armour) repair is not difficult but if plant is not available the problem of repair can be much more serious than is represented by the percentage of armour lost.

Although the Hudson formula is not strictly applicable to artificial armour units which depend for their stability on interlock, it is often used to obtain a first estimate of unit mass which is then checked by carrying out

flume tests. The acceptance criterion is the degree of rocking or movement of individual units. In cases where excessive movement leads to fracture of armour units, repair of damaged sections is quite a different matter from merely repositioning rock armour units.

Interpretation of the model test results should reflect this difference but there is no agreement on how to do this.

Irregular waves are now used in flume testing, except in laboratories which lack up-to-date wave making equipment and sophisticated control systems. The wave spectrum is usually based on JONSWAP or other spectra derived from instrumental recordings. The flume model is tested in stages by increasing the wave height until the armour layer becomes unstable, which gives an indication of the margin against failure.

Although vertical faced caisson type breakwaters of the type shown in Fig. 2 can be designed without tests by using wave pressure theory, it is usual to carry out hydraulic model tests in a flume to check the stability of the design. Failure can occur by either sliding or overturning, but Japanese experience (2) shows that sliding is the most common type of failure.

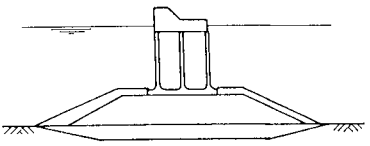

Figure 2 Caisson breakwater

The chief weakness of existing design and hydraulic model testing procedures is that there is no commonly agreed method of introducing a factor of safety against failure (however defined) for either type of breakwater nor is there an accepted set of definitions on which quantitive criteria and measurements are based.

The easiest way of providing a safety margin against failure of any type of breakwater is to increase the height of the design wave. Doing this increases the forces which the structure has to resist. For example in the case of Jubail east breakwater (5) completed in 1979, wave records were inadequate and the 1 in 100 year design wave height was assessed from wind records at 4.5m. Because no direct wave observations were available and because it was considered essential to provide a maintenance free

structure the consultants increased the design wave height to 6.5m. This represents a factor of 1.4 on the 1 in 100 year wave height.

For rubble mound breakwaters another simple way of increasing the margin of stability of the armoured slope is to use heavier armour in the prototype than the model tests, or calculations, indicate is required. If artificial armour units are used this does not necessarily lead to a corresponding increase in total volume of concrete used in the armour layer and it normally reduces the number of individual units to be placed. However, the feasibility and costs of producing and handling larger sized armour have to be taken into account. The increase in stability is not as great as it might appear as the wave height which can be resisted is in proportion to the cube root of the weight of armour unit. Doubling the weight of armour units therefore introduces a factor of about 1.26.

Measures such as these give a margin of safety but are purely arbitrary, and there is no generally accepted philosophy to guide the designer in applying them. When this lack of guidance is compared with the extensive use of codes of practice for the design of other types of structure the contrast is quite remarkable.

MODERN BUILDING DESIGN CODES

Consider, for example, the procedures for designing a building structure, in which (in contrast to breakwaters) the applied loads are reasonably known, the properties of the construction materials are strictly controlled and the workmanship is open to inspection at all stages. What is more the different phenomena such as bending, shear, bond etc., can be easily analysed separately; this is not at present the case with armour design, although the authors believe that further research would enable this point to be reached (3). There are however some useful concepts on factors of safety which could be applied to the design of breakwaters.

In the past, building structures have been designed on a "working stress" basis in which it is confirmed that the actual applied loads can be carried without exceeding allowable stresses. The allowable stresses are chosen to provide a margin of safety on stresses which would cause failure. This well established method is still used in many countries but it has weaknesses which have led to the introduction of a different method of design. The most serious weakness arises when the stability of a structure depends partly on its mass and partly on the strength of its members. Working stress analysis provides a margin of safety on the latter but not the former. Consider for example a quay wall design in which a relieving platform is supported on raking piles. The combined factor of safety against failure due to variations in applied load is not equal to the ratio between ultimate strength and working stress. To achieve this requires a different method of analysis.

The present design concept in UK, which was introduced for reinforced concrete structures by a code of practice published in 1972 (6) and is being introduced for other types of construction, is based on analysis of conditions at failure. The analysis, known as the limit state method of design, applies factors both to the values of the applied loads and to the strength of concrete and steel reinforcement. These factors, known as

partial safety factors, are chosen to ensure that when its stability has been analysed with appropriate partial factors of safety applied to loads and materials the structure will not become unfit for the use for which it is required, i.e. that it will not reach a limit state in service. In preparing the code of practice the drafting committee state that insufficient statistical data was available to enable a design method to be developed which is in complete accord with probability theory. The choice of partial factors of safety is admitted to be arbitrary but the intention is that as new knowledge of loads and strengths becomes available they can be amended. The factors applied will then vary according to the quality of data on loadings available to the designer, the accuracy of knowledge about material properties and the acceptable probability of failure.

The order of probability of failure which might be considered to be acceptable in the design of a building structure is 1 in 200,000 of failure leading to fatality during the working life of the building (7). This is achieved by adopting characteristic strengths of materials which have a 5% probability of being exceeded, and loadings which are intended to have a similar probability of being exceeded. The safety of the final structure depends upon the combination of events of low probability of occurence.

LIMIT STATE DESIGN OF BREAKWATERS

When designing breakwaters there are many areas of uncertainty where use of a partial safety factor would lead to a more logical design process.

These are:

(i) loadings

- wave heights
- wave periods
- wave form and grouping
- storm duration
- effects of wave refraction and diffraction

(ii) structure

- strength of materials
- specific gravity or bulk density of materials
- interlock achieved (for rubble mound breakwaters)
- accuracy of construction and general standard of workmanship
- breakage of elements

(iii) miscellaneous effects

- scale of model
- foundation settlement
- effectiveness of scour protection

Our present state of knowledge on breakwater design does not permit us to assign a partial safety factor to each of the variables outlined above. The two variables which are generally of the most importance are wave conditions and stability of armour layers or of caissons. Let us therefore consider the possible application of partial factors of safety to these two variables.

Wave conditions are usually assessed using graphical statistical methods to predict (for example) the once in 10, 20, 50 or 100 year wave height. Recorded data seldom fits the probability graph exactly and a judgement has to be made on precisely how the line on the graph should be extended to give the extreme wave heights, or which type of probability graph paper to use for this purpose.

If we then use one of these values for design of a breakwater, there is a high probability of thc design value being exceeded. Even if we know exactly what the once in 100 year wave is there would still be a 63 percent probability of it occurring or being exceeded once in 100 years, so this would not be a safe basis for design of a structure which we wish to have a 100 year life. But in fact our data and our methods of analysing it are far from perfect so the probabilities of exceedance may be much greater than 63%.

There is a strong case for adopting a more conservative design wave and also applying a partial factor of safety to the design.

A major consideration in applying factors of safety to wave heights is the length and type of records which determine the quality of our knowledge of the conditions. Perhaps the simplest case is when wave heights are depth limited. Before the concept of irregular waves was introduced it might have been argued that the maximum height of breaking wave was known, depending only on maximum depth of water (or highest water level), but we now know that combinations of waves of different periods are capable of producing "freak" waves even in shallow water. These cannot be predicted mathematically and even when they are reproduced in a hydraulic model we cannot be certain that there is not a more severe combination in nature. Some factor of safety is required to cover this uncertainty. When a final design depends upon model tests it will not be practicable in the depth limited case to provide this safety margin by increasing wave heights and it must be done in some other way. This is discussed later, but we should first consider the case when waves are not depth limited.

If wave heights are not depth limited it is logical to introduce a partial factor of safety by increasing the applied wave height.

By analogy with structural design we should be designing the breakwater to resist the most severe waves which have only a small probability of occurrence in the life time of the structure after making full allowance for the inadequacy of our basic data. It is common to use as a design wave the best estimates of the 1 in 50 year wave - or once in 100 year wave. As Tucker and Fortnum (8) have shown for Seven Stones Light Vessel there is a 63% probability that the 1 in 50 year wave height will be exceeded in a 50 year period. Clearly this is a much higher probability of exceedence than would be accepted in structural loadings. They also showed that there would be a 10% chance that the highest wave in 50 years would be more than 16% higher than the 1 in 50 year wave.

Another problem arises from the relatively short periods of observations which we have to use for projecting long term probabilities. All too often engineers have had to design breakwaters using significant wave heights

derived from only one or two years relevant wave records. Variations between individual years can be considerable; at Seven Stones light vessel the maximum 50 year wave height predicted from 12 months records in 1969 was 24.4m and from 12 months records in 1973/4 was 28.8m (8). Assuming a cubic relationship for armour weight, this represents an increase of 64% in weight of armour unit.

These relations depend upon local wave climate and require careful satistical analysis of specific records. The authors propose that statistical analysis to predict the wave height which has no more than 5% (or at most 10%) probability of exceedence during the life time of the structure should replace the use of once in 50 year or once in 100 year design waves.

As wave records are normally not available at the exact site of the structure, and wave heights may be affected by the presence of the structure, it would still be necessary to consider, as carefully as possible, the effects of refraction and diffraction on wave heights at the breakwater and to use increased waves to allow for these effects in the hydraulic model. The quality and duration of base data is also very important in assessing the possible range of variation in wave heights at the structure. Taking all aspects into consideration one would estimate the design wave heights which would have an acceptably low probability of being exceeded within the life time of any particular structure. These could then be used in theoretical analysis or in tests in a hydraulic flume.

We must also make allowance for uncertainties regarding the accuracy of hydraulic modelling of the wave spectrum and of the representation in a model of the true prototype stability.

Whether we are considering armouring of a rubble mound structure, a concrete capping on a rubble mound, or a deep caisson structure on a rubble base, the main disturbing force results from water pressure and the main stabilising forces derived from the weight of armouring, capping or caisson. In theoretical analysis using limit state design a factor of safety would be introduced by increasing the applied loads calculated from the design wave. In theory the same margin of safety could be achieved in model tests by increasing the specific gravity of the fluid used in the flume. This is however not a practicable method to usc in a hydraulic model; water is the only convcnient choice of fluid. The authors therefore propose instead that these uncertainties should be dealt with by a simple reduction in the specific gravity (in the model) of the main elements of construction. This has the same effect as increasing the wave forces.

Current modelling technique is based on the concept of reproducing the prototype as accurately as possible, and the main effort has been devoted to getting weights (specific gravities) correct. Precise reproduction of the prototype is no doubt an cxcellent aim in pure research intended to advance knowledge, say, of the type of collapse which can occur (or to reproduce a failure which has occurred) but in using hydraulic modelling as a design tool it would be much more helpful to the designer to model the structure deliberately with reduced specific gravities so as to incorporate a factor of safety in the prototype. In all the most

important failure conditions the critical masses are submerged. The factor of safety introduced by reducing specific gravity would therefore be in the ratio of submerged specific gravities in prototype and model.

A great advantage of doing this, rather than arbitrarily increasing the design wave height used in tests or altering the dimensions of, say, the armour units by testing for one size and building another larger size is that the geometry of the model and prototype would be the same. The hydraulic advantages of this will be obvious but correct geometrical relationship of the disturbing (wave) forces and stabilising (gravity) forces is no less important. Concentration in recent years on "correct" modelling of specific gravity has led to the use of armour units made from plastics rather than mortar. As a result it has not been possible to reproduce the coefficient of friction between units correctly and the geometry of the forces between units has also been wrong.

When modelling with reduced specific gravity, sand-cement mortar will again be a practical solution and it should be easier to produce units with surface friction close to prototype values.

Table 1 shows the effect on model specific gravities of introducing factors of safety of 1.2, 1.5 and 2.0 into tests of concrete armour units.

TABLE 1 - EFFECTS OF FACTOR OF SAFETY ON MODEL SPECIFIC GRAVITY

Factor of safety required	1.2	1.5	2.0
Specific gravity of prototype concrete	2.40	2.40	2.40
Prototype submerged specific gravity (sea water SG = 1.025)	1.38	1.38	1.38
Model submerged SG	1.15	0.92	0.69
Model SG in dry	2.18	1.95	1.72

A great advantage of introducing this concept of reducing specific gravities of breakwater units so as to provide a partial factor of safety in the prototype compared to the model is that in most types of breakwater, and in many different elements of, say, a rubble mound or caisson structure, weight in the final analysis provides all the stabilising forces. Even with interlocking units which derive stability partly from contact with their neighbours it is in the end the weight of a group of units which provides the stability of the structure. This method can therefore be applied consistently to a wide range of different forms of construction.

The exact choice of factor safety to be introduced in this way must be the subject of further research and therefore, another paper, but the authors would strongly advocate the adoption of partial factors of safety in

breakwater design and suggest the use of values in the above range in the meantime. The lower value of 1.2 might be adopted for rubble mound breakwaters armoured with rock, or with very robust concrete armour units such as cubes, where substantial movements can be accepted with no risk of breakage. A value of 1.5 might be adapted for caisson structures and for concrete armour units which are liable to break under excessive movement. A factor of 2.0 may be appropriate only where heavy loss of life could result from a failure. Factors of safety below 1.2 could be used for example, in rubble mound designs where the main armour is rock and where equipment could always be mobilised quickly for repair.

Conclusion

The authors' conclusion is that the large numbers of failures of breakwaters can and should be reduced in future by introducing the concept of partial factors of safety into the design philosophy.

When we have reliable mathematical methods of analysis we will be able to do this in exactly the same way as in limit state structural design codes.

Until then we much rely upon the use of hydraulic models to test and develop modifications to our ideas. Factor of safety can be provided by a deliberate reduction in the specific gravity of the elements of construction being tested. This would be the only way of introducing a factor of safety where waves are depth limited.

Where waves are not depth limited it is recommended that the use of design waves based upon return periods of once in 50 years or once in 100 years should be replaced by a more rigorous statistical analysis to determine the wave conditions which are likely to have a probability of occurence of not more than 5 percent during the intended lifetime of the structure.

If the authors' proposals are adopted they believe that there would be a long overdue improvement in the performance of breakwaters. Our choice between different design options would also be made on a more rational basis.

References

1. BRUNN,P. (1979). Common reasons for damage or breakdown of mound breakwaters. Coastal Engineering Vol.2, No. 3 pp 261-273.

2. GODA, Y. (1974). New wave pressure formulae for composite breakwaters. Proc. 14th Int.Conf. on Coastal Engineering pp 1702-1720.

3. METTAM, J.D. (1980). Can we develop new breakwater armour formulae? Proc.17th Int. Conf. on Coastal Engineering pp 2304-2322.

4. HUDSON, R.Y. (1959). Laboratory investigations of rubble mound breakwaters. Proc. ASCE Waterways and Harbours Div.

5. THORPE, W.R. (1982). The design and construction of an island breakwater at Jubail. Symp. on Engineering in Marine Environment, Koninklijke Vlaamse Ingenieursvereniging Technologisch Instituut, Bruges, Belgium pp 2.17-2.22.

6. BRITISH STANDARDS INSTITUTION (1972). Code of practice for the structural use of concrete. CP110, Part 1.

7. CONSTRUCTION INDUSTRY RESEARCH AND INFORMATION ASSOCIATION (1977). Rationalisation of safety and serviceability factors in structural codes. Report No. 63.

8. INSTITUTE OF OCEANOGRAPHIC SCIENCES (1977). Waves at Seven Stones light vessel. Report No. 39.

BREAKWATER STABILITY - BREAKING WAVE DATA

by

Robert D. Carver[1], M. ASCE, and D. Donald Davidson[2]

Abstract

The objective of the research presented is to furnish design information for stone and dolos armor on non-overtopping breakwater trunks that are subjected to severe depth-limited breaking waves. Since it would be a mammoth task to comprehensively investigate all the different types of existing armor, this particular research effort concentrated on stone, which is a natural and economical protection when it is of sufficient size and quality to meet design constraints, and on the dolos, which according to nonbreaking wave data is the best hydraulically stable concrete armor unit.

Introduction

A proposed rubble-mound breakwater may necessarily be designed for either nonbreaking or breaking waves depending on positioning of the breakwater and severity of anticipated wave action during its economic life. Some local wave conditions may be of such magnitude that the protective cover layer must consist of specially shaped concrete armor units in order to provide economic construction of a stable breakwater; however, many local design requirements are most advantageously met by quarry-stone armor. This paper addresses the use of quarry-stone and dolos armor on breakwater trunks subjected to breaking waves.

Previous investigations have yielded a significant quantity of design information for quarrystone (Hudson, 1958 and Carver, 1980) tetrapods, quadripods, tribars, modified cubes, hexapods, and modified tetrahedrons (Jackson, 1968), dolos (Carver and Davidson, 1977), and toskane (Carver, 1978). However, the studies conducted by Hudson, Jackson, Davidson, and Carver were limited in that test waves were always nonbreaking and the relative wave height (H/d) varied over a very limited range.

[1]Research Hydraulic Engineer, U. S. Army Engineer Waterways Experiment Station, Vicksburg, Mississippi 39180.

[2]Chief, Wave Research Branch, U. S. Army Engineer Waterways Experiment Station, Vicksburg, Mississippi 39180.

Purpose of Study

The purpose of the present investigation was to obtain design information for stone and dolos armor used on breakwater trunks and subjected to breaking waves. More specifically, it was desired to determine the minimum weight of individual armor units (with given specific weights) required for stability as a function of:

a. Type of armor unit.

b. The sea-side slope of the structure.

c. Wave period.

d. Wave height.

e. Water depth.

f. The sea-bottom slope on which the breakwater is constructed.

Dimensional Analysis

When short-period waves attack rubble-mound breakwaters, the interaction of the dislodging forces induced by the water motion and the resistive action of the armor units produces a complex dynamic phenomenon. Previous attempts to analyze this phenomenon to ascertain the magnitude of the dynamic forces involved by theoretical analyses have not been successful; however, hydraulic scale models of breakwaters can yield accurate design information that relates the required weight of individual armor units to breakwater geometry, local bathymetry, wave characteristics, etc.

An attempt will be made through the use of dimensional analysis to develop functional relationships between the primary variables affecting armor stability. The Buckingham Pi Theorem can be used to determine the number of dimensionless and independent quantities (Pi terms) required to express a relationship among the variables in any phenomenon. Dimensional analysis may then be used to obtain a suitable set of Pi terms.

Definitions and characteristic dimensions in terms of Force (F), Length (L), and Time (T) of the primary variables affecting armor stability are as follows:

γ_a = specific weight of an armor unit, F/L^3

W_a = weight of an armor unit, F

Δ = shape factor of the armor unit, dimensionless

γ_w = specific weight of water, F/L^3

H = wave height, L

L = wave length, L

d = water depth, L

g = acceleration due to gravity, L/T^2

h = height of breakwater crown, L

β = angle of wave attack, dimensionless

ν = kinematic viscosity, L^2/T

α = angle between the horizontal and the seaward face of the breakwater, dimensionless

θ = angle between the horizontal and the sea-bottom on which the breakwater is constructed, dimensionless

PT = technique used to place armor units in the cover layer, dimensionless

D = damage parameter, dimensionless

The present investigation addresses only waves normal to nonovertopping breakwater sections. Therefore, the variables, β and h, are eliminated. Also, since α is directly related to the seaward slope of the breakwater, this variable can be replaced by cot α where cot α is the reciprocal of breakwater slope. With these considerations, the list of variables is reduced to 13.

With 13 variables and 3 basic dimensions involved, the Buckingham Pi Theorem predicts that armor stability should be a function of 10 dimensionless Pi terms. One possible set of Pi terms is

$$\pi_1 = \frac{\gamma_a^{1/3} H}{(\frac{\gamma_a}{\gamma_w} - 1) W_a^{1/3}} \tag{1}$$

$$\pi_2 = H/d \tag{2}$$

$$\pi_3 = H/L \tag{3}$$

$$\pi_4 = L^2 H/d^3 \tag{4}$$

$$\pi_5 = \cot \alpha \tag{5}$$

$$\pi_6 = \Delta \tag{6}$$

$$\pi_7 = \theta \tag{7}$$

$$\pi_8 = \frac{(gH)^{1/2}\, \ell_a}{\nu} \tag{8}$$

$$\pi_9 = PT \tag{9}$$

$$\pi_{10} = D \tag{10}$$

Correlation of the test data will be attempted by the functional relationship

$$\pi_1 = f\,(\pi_2, \pi_3, \pi_4, \pi_5, \pi_6, \pi_7, \pi_8, \pi_9, \pi_{10}) \tag{11}$$

or

$$\frac{\gamma_a^{1/3} H}{\left(\frac{\gamma_a}{\gamma_w} - 1\right) W_a^{1/3}} = f\,(H/d,\ H/L,\ L^2H/d^3,\ \cot\alpha,\ \theta,\ \Delta,\ (gH)^{1/2}\, \ell_a/\nu,\ PT,\ D) \tag{12}$$

Stability Scale Effects

If the absolute sizes of breakwater materials and wave dimensions become too small, flow around the armor units enters the laminar regime; and the induced drag forces become a direct function of the Reynolds Number. Under these circumstances, prototype phenomena are not properly simulated and stability scale effects are induced. Hudson (1975) presents a detailed discussion of the design requirements necessary to ensure the preclusion of stability scale effects in small-scale breakwater models (critical $R_N = 3 \times 10^4$). For all tests reported herein, the sizes of model armor and wave dimensions were selected such that scale effects were insignificant (i.e., R_N was greater than 3×10^4).

Selection of Test Conditions

In planning a stability investigation, it is not possible to preselect exact values of H/L and H/d since the design-wave heights are unknown at the outset of the study. However, the widest possible range of these parameters can be insured by using various armor weights that range from just above the scale-effect regime at the lower limit up to the maximum weights that the test facility is capable of displacing. For the present investigation, armor weights ranged from 106 to 322 grams.

The wave flume was calibrated for depths from 12.2 cm to 29.0 cm in 1.5-cm increments at d/L values of 0.04, 0.06, 0.08, 0.10, 0.12, and 0.14. This range of depths and, consequently, breaking wave heights proved to be compatible with the selected armor weights and sea-side breakwater slopes.

All stability tests were conducted on sections of the type shown in Figures 1-3. Sea-side slopes of 1:1.5, 1:2, and 1:3 were investigated while the beach-side slope was held constant at 1:1.5. Structure heights of 30 to 50 cm were used. The height necessary to prevent wave overtopping was determined by the combination of structure slope, armor type and weight, and water depth being investigated.

Method of Constructing Test Sections

All model breakwater sections were constructed to reproduce as closely as possible results of the usual methods of constructing prototype breakwaters. The core material was dampened as it was dumped by bucket or shovel into the flume and was compacted with hand trowels to simulate natural consolidation resulting from wave action during construction of the prototype structure. Once the core material was in place, it was sprayed with a low-velocity water hose to ensure adequate compaction of the material. The underlayer stone was then added by shovel and smoothed to grade by hand or with trowels. No excessive pressure or compaction was applied during placement of the underlayer stone. Armor units used in the cover layers were placed in a random manner corresponding to work performed by a general coastal contractor, i.e., they are individually placed but are laid down without special orientation or fitting. After each test, the armor stones were removed from the breakwater, all of the underlayer stones were replaced to the grade of the original test section, and the armor units were replaced.

Test Equipment and Materials

All wave-action tests were conducted in a 1.5-m-wide, 1.2-m-deep, and 36.3-m-long concrete wave flume with test sections installed about 27.4 m from a vertical displacement wave generator. The first 3.0 m of flume bottom, immediately seaward of the test sections, was molded on a 1:10 slope while the remaining 24.4 m was flat. The generator was capable of producing sinusoidal waves of various periods and heights. Test waves of the required characteristics were generated by varying the frequency and amplitude of the plunger motion. Changes in water-surface elevation as a function of time (wave heights) were measured by electrical wave-height gages in the vicinity of where the toe of the test sections was to be placed and recorded on chart paper by an electrically-operated oscillograph. The electrical output of the wave gages was directly proportional to their submergence depth.

Rough hand shaped granitic stone (W_a) with an average length of approximately two times its width, average weights of 173 gr ($\pm$9 gr), 250 gr ($\pm$11 gr), and 322 gr ($\pm$14 gr), and a specific weight of 2.68 gr/cc was used to armor the stone sections. Dolos sections were armored with the following sizes of units.

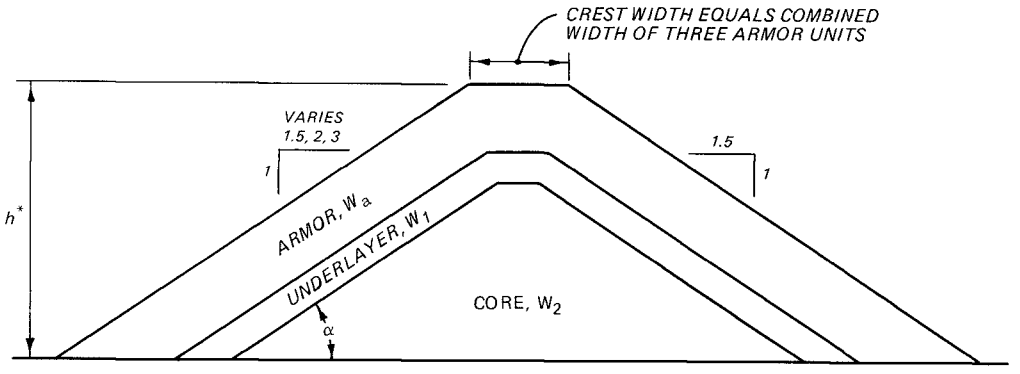

MATERIAL WEIGHTS, GRAMS

W_a	W_1	W_2	ARMOR TYPE
173	17	0.04 - 0.86	STONE
250	25	0.06 - 1.27	STONE
322	32	0.08 - 1.63	STONE
106	21	0.02 - 0.54	DOLOS
125	25	0.03 - 0.63	DOLOS
267	53	0.06 - 1.32	DOLOS

* TOTAL STRUCTURE HEIGHT (h) VARIED FROM 0.3 m TO 0.5 m DEPENDING ON THE COMBINATION OF STRUCTURE SLOPE, ARMOR WEIGHT, AND WATER DEPTH BEING INVESTIGATED.

Figure 1. General breakwater cross-section.

Figure 2. Cross-sectional view of typical stone section.

Figure 3. Cross-sectional view of typical dolos section.

W_a, gr	γ_a, gr/cc
106	2.21
125	2.28
267	2.26

Sieve-sized limestone (2.64 gr/cc) was used for the underlayer (W_1) and core (W_2) of both armor types.

Test Procedures

For a given wave period and water depth, the most detrimental breaking wave (i.e., the most damaging wave) was determined by increasing the stroke adjustment on the wave generator in small increments and observing which wave produced the most severe breaking wave condition on the model structures. Wave heights of lower amplitude did not form the critical breaking wave and wave heights of larger amplitude would break seaward of the test structures and dissipate their energy so that they were less damaging than the critically tuned wave.

A typical stability test consisted of subjecting the test section to attack by waves of a given height and period until stability was achieved. Test sections were subjected to wave attack in approximately 30-sec intervals between which the wave generator was stopped and the waves allowed to decay to zero height. This procedure was necessary to prevent the structures from being subjected to an undefined wave system created by reflections from the model breakwater and wave generator. Newly built test sections were subjected to a short duration (five or six 30-sec intervals) of shakedown using a wave equal in height to about one-half of the estimated no-damage wave. This procedure provided a means of allowing consolidation and armor unit seating that would normally occur during prototype construction.

Test Results

Breaking wave stability test results for stone and dolos armor are summarized in Tables 1 and 2, respectively. Presented therein are experimentally determined design wave heights, wave steepness, relative wave height, Ursell Number, and breakwater slope. All stability test results presented in Tables 1 and 2 were verified by at least one repeat test. Sea-side breakwater slopes of 1:1.5, 1:2, and 1:3 were used for both armor types. The following ranges of armor weights, water depths, wave periods and heights, relative depths, wave steepness, Ursell Numbers, and relative wave heights were investigated.

Variable	Range for Indicated Type of Armor	
	Stone	Dolos
armor weight, gr	173-322	106-267
water depth, cm	12.2-22.9	13.7-29.0

(continued)

TABLE 1

Values of $H_{D=0}$, d/L, H/L, H/d, L^2H/d^3, and N_s for Two Layers of Stone Armor Randomly Placed on Breakwater Trunks and Subjected to Breaking Waves with No Overtopping: W_a = 173, 250, and 322 gr; γ_a = 2.68 gr/cc; cot α = 1.5, 2, and 3

W_a, gr	d, cm	T, sec	$H_{D=0}$, cm	d/L	H/L	H/d	L^2H/d^3	N_s
			cot α = 1.5					
173	13.7	1.07	10.1	0.12	0.088	0.73	51.2	1.50
173	16.8	1.04	10.7	0.14	0.089	0.64	32.5	1.59
250	12.2	1.45	11.3	0.08	0.074	0.93	144.7	1.48
250	16.8	1.18	11.6	0.12	0.083	0.69	47.9	1.52
250	18.3	1.09	12.2	0.14	0.093	0.67	34.0	1.60
322	12.2	1.90	12.8	0.06	0.063	1.05	291.4	1.54
322	12.2	2.82	12.8	0.04	0.042	1.05	655.7	1.54
322	15.2	1.32	12.8	0.10	0.084	0.84	84.2	1.54
			cot α = 2.0					
173	15.2	1.13	12.5	0.12	0.098	0.82	57.1	1.86
173	16.8	1.18	11.6	0.12	0.083	0.69	47.9	1.72
173	18.3	1.09	12.2	0.14	0.093	0.67	34.0	1.81
250	12.2	2.82	12.8	0.04	0.042	1.05	655.7	1.68
250	15.2	1.32	12.8	0.10	0.084	0.84	84.2	1.68
250	18.3	1.24	13.7	0.12	0.090	0.75	52.0	1.80
250	19.8	1.13	14.0	0.14	0.099	0.71	36.1	1.84
322	13.7	2.02	14.0	0.06	0.061	1.02	283.9	1.69
322	19.8	1.29	15.5	0.12	0.094	0.78	54.4	1.87
			cot α = 3.0					
173	12.2	2.82	12.8	0.04	0.042	1.05	655.7	1.90
173	18.3	1.24	13.7	0.12	0.090	0.75	52.0	2.03
173	19.8	1.13	14.0	0.14	0.099	0.71	36.1	2.08
250	13.7	2.02	14.0	0.06	0.061	1.02	283.9	1.84
250	18.3	1.45	15.8	0.10	0.087	0.87	86.3	2.07
250	19.8	1.29	15.5	0.12	0.094	0.78	54.4	2.03
250	22.9	1.38	16.8	0.12	0.088	0.73	50.9	2.21

TABLE 2

Values of $H_{D=0}$, d/L, H/L, H/d, L^2H/d^3, and N_s for Two Layers of Dolos Armor Randomly Placed on Breakwater Trunks and Subjected to Breaking Waves with No Overtopping: W_a = 106, 125, and 267 gr; cot α = 1.5, 2, and 3

W_a, gr	d, cm	T, sec	$H_{D=0}$, cm	d/L	H/L	H/d	L^2H/d^3	N_s
			cot α = 1.5					
125	13.7	2.02	14.0	0.06	0.061	1.02	283.9	2.88
125	15.2	1.62	13.7	0.08	0.072	0.90	140.8	2.82
267	19.8	1.85	18.3	0.08	0.074	0.92	144.4	2.96
267	25.9	1.73	21.6	0.10	0.084	0.83	83.4	3.49
267	27.4	1.78	23.5	0.10	0.086	0.86	85.8	3.80
			cot α = 2.0					
106	13.7	2.02	14.0	0.06	0.061	1.02	283.9	3.18
125	16.8	1.70	16.5	0.08	0.079	0.98	153.5	3.39
125	25.9	1.30	17.1	0.14	0.092	0.66	33.7	3.52
125	25.9	1.47	19.2	0.12	0.089	0.74	51.5	3.95
125	29.0	1.37	18.6	0.14	0.090	0.64	32.7	3.83
			cot α = 3.0					
106	21.3	1.34	16.8	0.12	0.094	0.79	54.8	3.82
106	24.4	1.43	16.8	0.12	0.083	0.69	47.8	3.82
106	25.9	1.30	17.1	0.14	0.092	0.66	33.7	3.89
125	18.3	2.32	17.7	0.06	0.058	0.97	268.7	3.64
125	19.8	1.85	18.3	0.08	0.074	0.92	144.4	3.76
125	27.4	1.52	19.5	0.12	0.085	0.71	49.4	4.01
125	29.0	1.56	20.1	0.12	0.083	0.69	48.1	4.13

Variable	Range for Indicated Type of Armor	
	Stone	Dolos
wave period, sec	1.04-2.82	1.30-2.32
wave height, cm	10.1-16.8	13.7-23.5
relative depth	0.04-0.14	0.06-0.14
wave steepness	0.042-0.099	0.058-0.094
relative wave height	0.64-1.05	0.64-1.02
Ursell Number	34.0-655.7	33.7-283.9

The number of armor units per given surface area, A, was $N = 1.45\ \forall^{-2/3}$ and $N = 0.83\ \forall^{-2/3}$ for the stone and dolos, respectively. The variable, $\forall$, is defined as the volume of an individual armor unit. Figures 4 and 5 show typical after testing views of selected test sections.

As previously discussed, it was hoped that stability test results could be analyzed by the following functional relation for the stability number, N_s, where

$$N_s = \frac{\gamma_a^{1/3} H}{(S_a-1) W_a^{1/3}} = f(H/d,\ H/L,\ L^2H/d^3,\ \cot\alpha,\ \theta,\ \Delta,\ (gH)^{1/2}\ell_a/\nu,\ PT,\ D) \qquad (13)$$

For tests described herein θ, PT, and D were held constant; therefore, Equation 13 reduces to

$$N_s = f(H/d,\ H/L,\ L^2H/d^3,\ \cot\alpha,\ \Delta,\ (gH)^{1/2}\ell_a/\nu) \qquad (14)$$

Also, the sizes of model armor units and wave dimensions were selected such that turbulent flow was always obtained: therefore N_s was independent of Reynolds Number $[(gH)^{1/2}\ell_a/\nu]$ and Equation 14 becomes

$$N_s = f(H/d,\ H/L,\ L^2H/d^3,\ \cot\alpha,\ \Delta)$$

Plots of N_s versus H/d, H/L, and L^2H/d^3 are presented in Figures 6, 7, and 8, respectively. These data show a functional dependence of N_s on H/d, H/L, and the Ursell Number (L^2H/d^3) with the dependence being more pronounced for dolos armor. For both armor types it generally appears that minimum stability occurs for the larger values of H/d and L^2H/d^3 and for the intermediate range of H/L ($0.07 \leq H/L \leq 0.085$). Results of previous tests conducted on quarrystone by Hudson (1958) and

Figure 4. Typical sea-side view of stone section after wave attack.

Figure 5. Typical sea-side view of dolos section after wave attack.

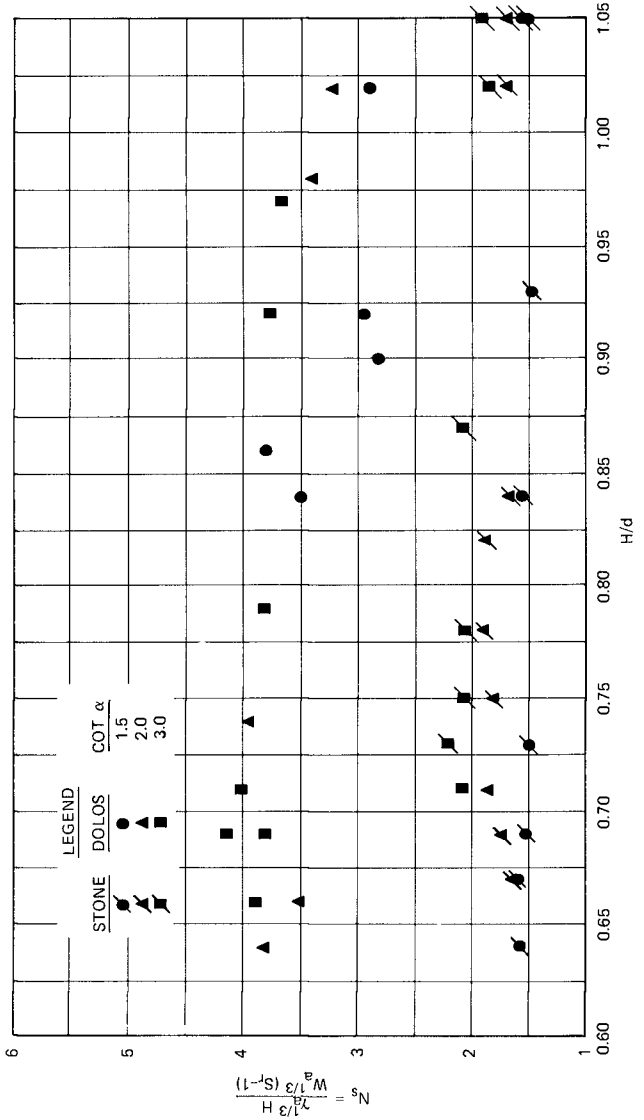

Figure 6. Stability number versus H/d.

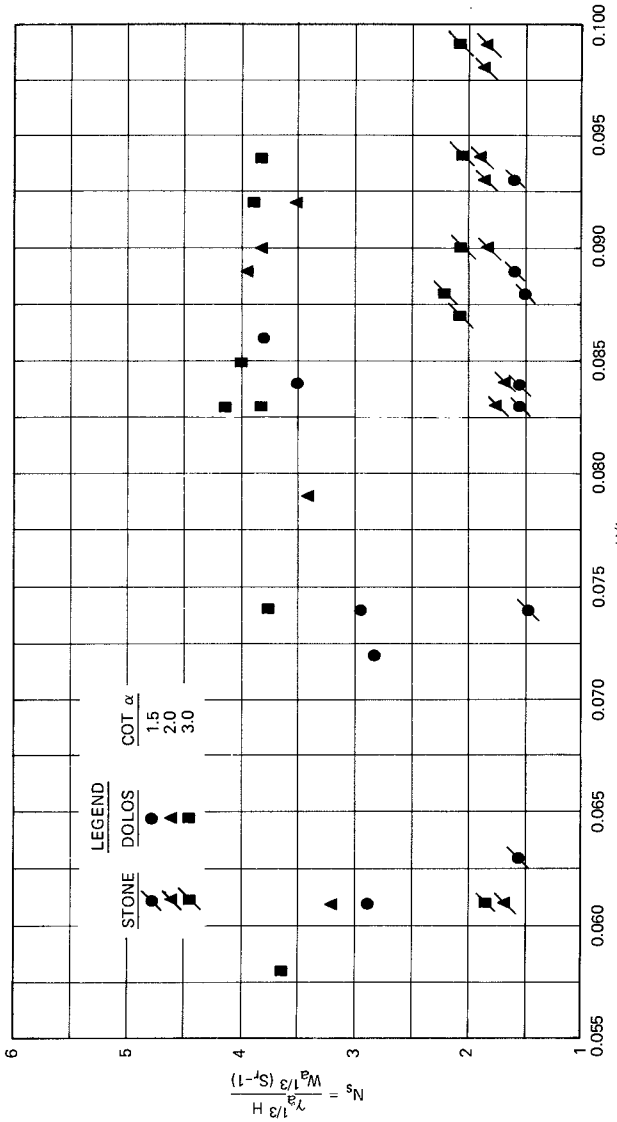

Figure 7. Stability number versus H/L.

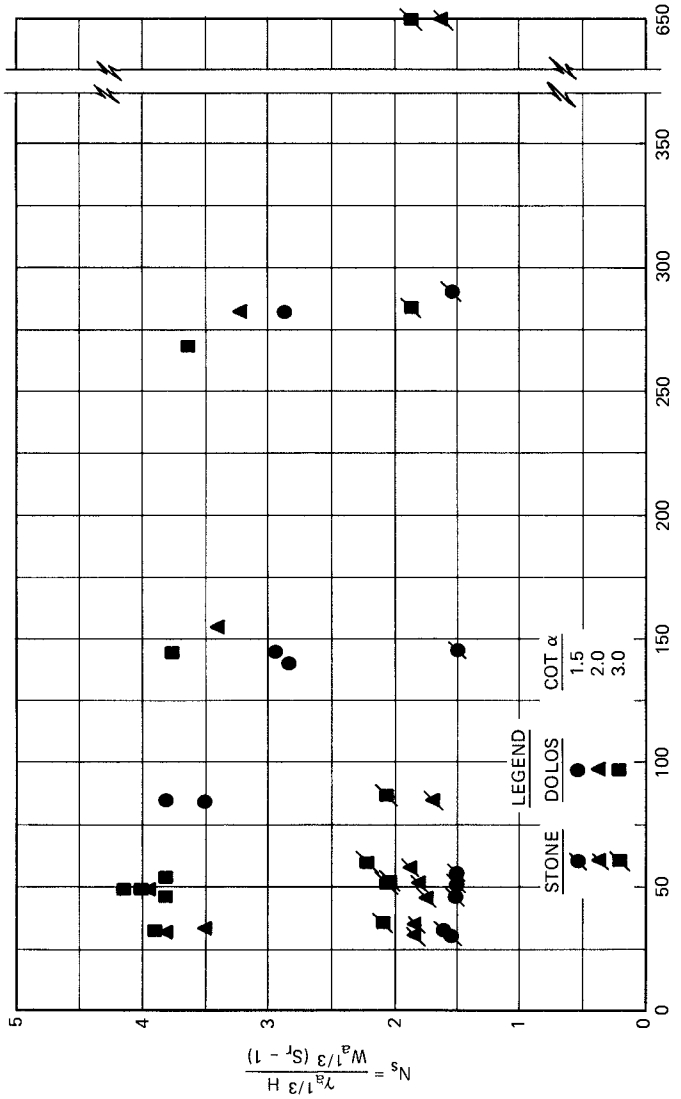

Figure 8. Stability number versus Ursell Number.

Carver (1980) for nonbreaking waves, $H/d \leq 0.32$, and $0.03 \leq H/L \leq 0.08$, do not show these trends. Also the trends are absent from earlier nonbreaking wave tests on dolosse (Carver and Davidson, 1977). The tests of Carver and Davidson were conducted with $H/d \leq 0.37$ and $0.031 \leq H/L \leq 0.083$.

Figure 9 presents a log-log plot of N_s versus cot α. Average and lower limit linear fits of the Hudson type, i.e., 1:3 slope linear fits, are also shown. Even though there is some data spread for each distinct value of cot α (due to variations of H/d, H/L, and L^2H/d^3) the linear fits generally give a reasonable approximation of N_s as a function of cot α, especially for the stone armor.

Conclusions

Based on the tests and results described herein, in which stone and dolos armor are used on breakwater trunks and subjected to breaking waves with a direction of approach of 90 deg, it is concluded that:

a. Armor stability is influenced by wave steepness (H/L), Ursell Number (L^2H/d^3) relative wave height (H/d), and breakwater slope.

b. Effects of H/d, L^2H/d^3, and H/L are more pronounced for dolos armor.

c. In general, minimum stability for each armor type occurred for the larger values of H/d ($H/d > 0.90$), intermediate values of H/L ($0.06 \leq H/L \leq 0.085$), and larger values of L^2H/d^3.

d. Linear Hudson-type data fits generally give a reasonable approximation of N_s as a function of cot α; however, the influences of H/d, H/L, and L^2H/d^3 are strong enough to merit their consideration in final selection of armor unit weight.

Acknowledgements

The data presented in this paper were extracted from model tests described in the Waterways Experiment Station (WES), Technical Report HL-83-____ , entitled "Stability of Stone- and Dolos-Armored, Rubble-mound Breakwater Trunks Subjected to Breaking Waves with No Overtopping," which is being reviewed for publication. The comprehensive study was conducted at WES for the Office, Chief of Engineers under the Corps of Engineers Civil Works Research and Development Program.

Grateful acknowledgement is extended to the Office, Chief of Engineers for granting permission to publish this paper.

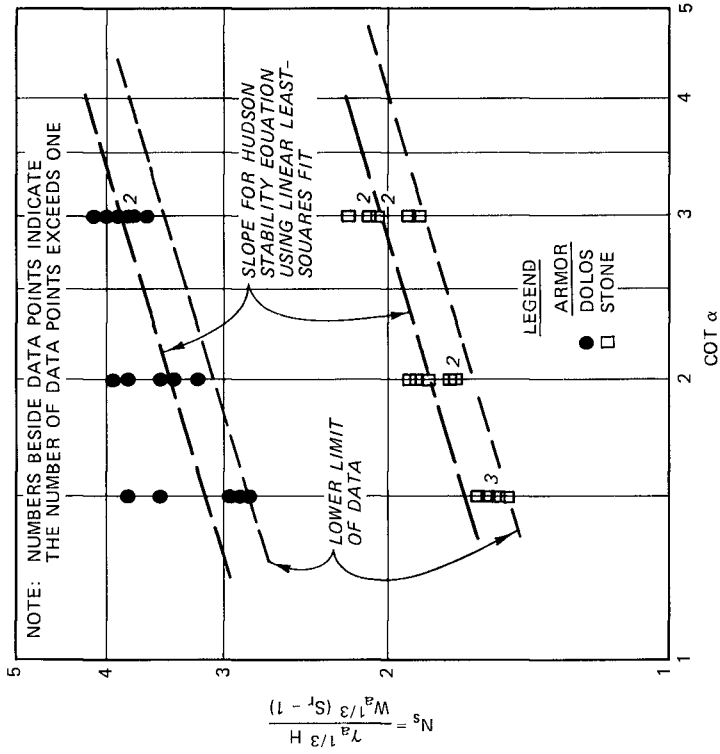

Figure 9. Stability number versus cot α.

REFERENCES

Carver, R. D., 1978. "Hydraulic Model Tests of Toskane Armor Units," ETL 1110-2-233, U. S. Army Engineer Waterways Experiment Station, CE, Vicksburg, MS.

_____. 1980. "Effects of First Underlayer Weight on the Stability of Stone-Armored Rubble-Mound Breakwater Trunks Subjected to Nonbreaking Waves with No Overtopping," Technical Report HL-80-1, U. S. Army Engineer Waterways Experiment Station, CE, Vicksburg, MS.

Carver, R. D., and Davidson, D. D., 1977. "Dolos Armor Units Used on Rubble-Mound Breakwater Trunks Subjected to Nonbreaking Waves with No Overtopping," Technical Report H-77-19, U. S. Army Engineer Waterways Experiment Station, CE, Vicksburg, MS.

Hudson, R. Y., 1958. "Design of Quarrystone Cover Layers for Rubble-Mound Breakwaters," Research Report No. 2-2, U. S. Army Engineer Waterways Experiment Station, CE, Vicksburg, MS.

_____. 1975. "Reliability of Rubble-Mound Breakwater Stability Models; Hydraulic Model Investigation," Miscellaneous Paper H-75-5, U. S. Army Engineer Waterways Experiment Station, CE, Vicksburg, MS.

Jackson, R. A., 1968. "Design of Cover Layers for Rubble-Mound Breakwaters Subjected to Nonbreaking Waves," Research Report No. 2-11, U. S. Army Engineer Waterways Experiment Station, CE, Vicksburg, MS.

NOTATION

A	Surface area, cm^2
β	Angle of wave attack
d	Water depth, cm
d/L	Relative depth
D	Damage parameter
f	Reads "function of"
g	Acceleration due to gravity, cm/sec^2
h	Height of breakwater crown, cm
H	Wave height, cm
H/d	Relative wave height
H/L	Wave steepness
ℓ_a	Characteristic length of armor unit, cm
L	Length, wavelength, cm
N	Number of armor units per surface area
N_s	Stability Number = $\gamma_a^{1/3} H/(S_a-1) W_a^{1/3}$
PT	Placement technique
R_N	Reynolds stability number = $(gH)^{1/2}\ell_a/\nu$
S_a	Specific gravity of an armor unit relative to water in which the breakwater is constructed
T	Wave period, sec
$\forall$	Volume of individual armor unit, m^3
W	Weight, gr
α	Angle of breakwater slope, measured from horizontal, deg
$\cot \alpha$	Reciprocal of breakwater slope
θ	Angle between the horizontal and the sea bottom on which the breakwater is constructed
γ	Specific weight, gr/cc

γ_a	Specific weight of an armor unit, gr/cc
Δ	Shape of armor unit or underlayer material
ν	Kinematic viscosity, ft^2/sec

Subscripts

a	Refers to armor unit
D	Refers to damage
s	Refers to stability
w	Refers to water in which the structure is located
1 and 2	Refer to underlayer and core, respectively

STABILITY ANALYSIS FOR A RUBBLE-MOUND FOUNDATION THROUGH IRREGULAR WAVE TEST

by

Masato Yamamoto* and Tsutomu Asakawa**

ABSTRACT

Irregular wave tests have been conducted to research into the stability characteristics of armor units for a rubble foundation of a composite breakwater.

A cover layer to protect the rubble foundation from erosion had two layers of tetrapods. Waves higher than $H_{1/10}$ (the average height of the highest 10% of all waves) caused damage to armor units at the point of critical stability. This suggested that wave height changes in the surf zone should be taken into consideration for design purpose.

1. INTRODUCTION

In Japan, composite breakwaters with superstructures resting directly on rubble foundations have been designed to be used even in areas of deep water. This is due to the fact that construction schedules of breakwaters can be shortened by adopting concrete caissons as a superstructure and damages during construction can be avoided. Many damages to breakwaters occur before completion of the construction.

These composite breakwaters are exposed to high design waves in areas of deep water and very large armor units are required to protect their rubble-mound foundations. Design wave heights sometimes exceed 10 meters in the southern districts of Japan e.g. Okinawa and Kogashima prefectures. Stones as foundations of composite breakwaters are unstable in such districts, especially in the surf zone. In such cases engineers have to use armor blocks like tetrapods to protect the foundations.

Stability analysis of vertical-faced superstructures such as concrete caissons have progressed remarkably. One example is Goda's (1974). To our knowledge some studies on rubble foundations have been reported but they are mostly based on regular wave test results.

---

* Engineer, Assistant Manager, Hydraulic Laboratory, Nippon Tetrapod Co., Ltd.

** Engineer, Manager, Hydraulic Laboratory, Nippon Tetrapod Co., Ltd.

The results using stones based on regular wave tests by Brebner and Donnelly (1963) have been very useful design criteria. But caution should be paid in selecting the design wave heights because of the irregularity of waves, especially in deep water areas and against high design waves.

This paper deals with model tests on the stability of rubble foundations to irregular waves and two layers of tetrapods as an armor layer were used.

2. TEST EQUIPMENT AND TEST PROCEDURE

2-1. Test equipment

The tests on rubble-mound foundations were carried out in a wave tank, 49.0 m long, 1.0 m wide and 1.0 m deep as shown in Figure 1 at the Hydraulic Laboratory, Nippon Tetrapod Co., Ltd.

The wave generator consisted of a flap type paddle which was operated by a hydraulic piston enabling it to make random waves.

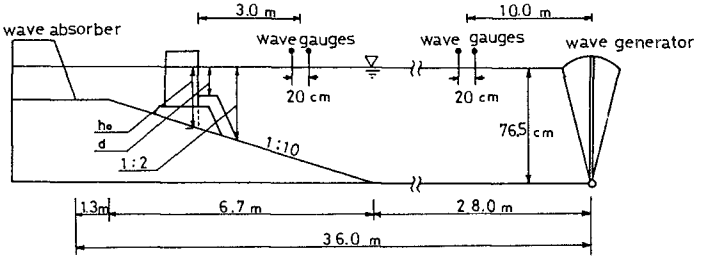

Figure 1 Wave tank and allocation of model

2-2. Test procedure

A simplified sketch of the allocation of model studies is also shown in Figure 1. The bottom slope was 1 in 10. Two pairs of wave gauges at a distance between them of 20 cm were set up at distances 10 m from the paddle of the wave machine and 3.0 m seaward from the model breakwater in order to separate incident and reflected wave heights using Goda's method (1976).

The test wave height was 10.8 cm at a point where the model breakwater was to be constructed. The wave periods were 1.3 sec and 1.8 sec in the model. These irregular waves of Bretschneider-Mitsuyasu spectrum presented by the following equation were simulated.

$$S(f)=0.257\ H_{1/3}^{2}T_{1/3}(T_{1/3}f)^{-5}\exp(-1.03(T_{1/3}f)^{-4})\text{---}(1)$$

where
S(f); power spectrum density function
$H_{1/3}$; significant wave height
$T_{1/3}$; significant wave period
f ; frequency

Two layers of tetrapods as armor blocks were used. The range of model tetrapod weight was from 14.7 g to 190.0 g.

A section of the model breakwater is shown in figure 2.

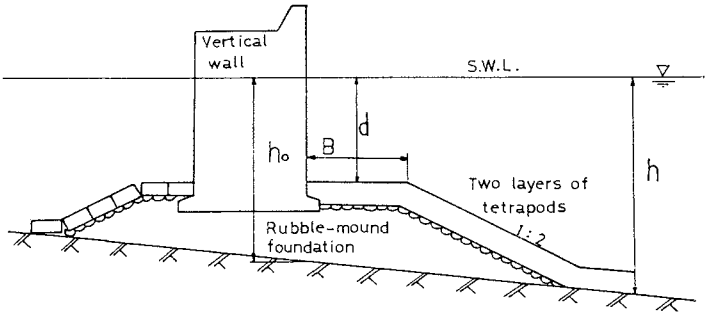

Figure 2 Sketch of cross section of model breakwater

where
h; water depth at the toe of breakwater
h_o; water depth at the structure site
d; depth at the crest of rubble-mound foundation
B; berm width of rubble-mound

B was fixed constant 15.0 cm. d values were 9.0 cm, 13.0 cm and 16.0 cm below the still water level in the cases where h_o=-28.0 cm and 9.0 cm, 11.0 cm and 14.0 cm were the d values in the case where h_o=-23.0 cm.

Wave duration time was 30 minutes in each case in the model.

3. TEST RESULT AND DISCUSSION

The conditions were classified. Three categories were decided on:

(1) Stable condition where the number of armor units which moved was zero and the number of rocking blocks was less than three.
(2) Unstable condition where more than two unis were moved by wave forces while more than four rocking units were discernable.
(3) Critical condition which is an intermediate state between the stable and unstable conditions.

The stability test results are shown in Figure 3 and 4. These figures show the relation between d/h and weights of tetrapods used. In these two figures black represents unstable, white is stable and black and white is the critical state respectively.

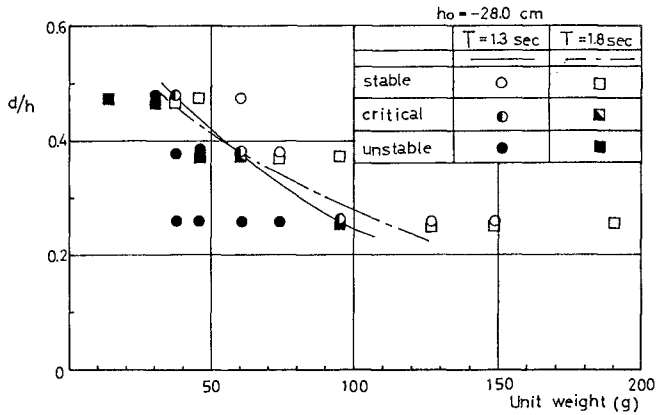

Figure 3 Test results (h_o=-28.0 cm)

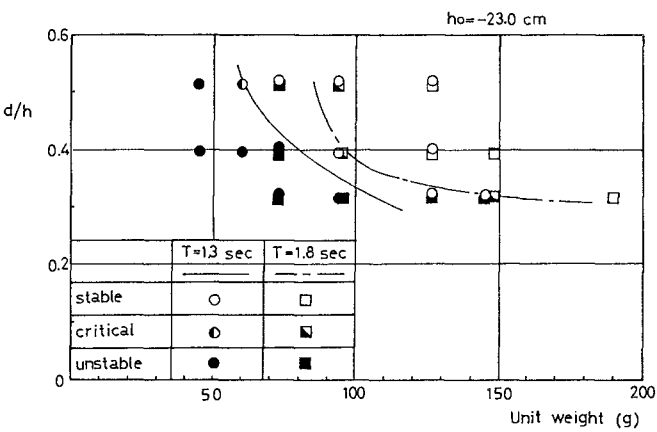

Figure 4 Test results (h_o=-23.0 cm)

Lines show the critical relation between d/h and the unit weight. As shown in Figure 3 and 4 the critical weights increase rapidly as d/h decreases indicating that d is smaller, the critical weight is required to be heavier if h is constant. In addition, it can also be seen that the critical weight is influenced by the wave period, especially in the case where h_o=-28.0 cm, the effects of the wave period are not so apparent. However as the water depth at the breakwater (h_o) increases, it becomes less apparent that the critical weight increases as the wave period increases.

Observation during the tests

In order to investigate how armor units had been damaged by a certain wave in the wave train, the wave action in front of the vertical wall and the movement of tetrapods were filmed by means of a video camera with a rotary shutter. The speed of the shutter was 1/60 seconds.

From this observation, as shown in Figure 5, armor unit suffered an up-lift force and rose up just after a large wave hit the site.

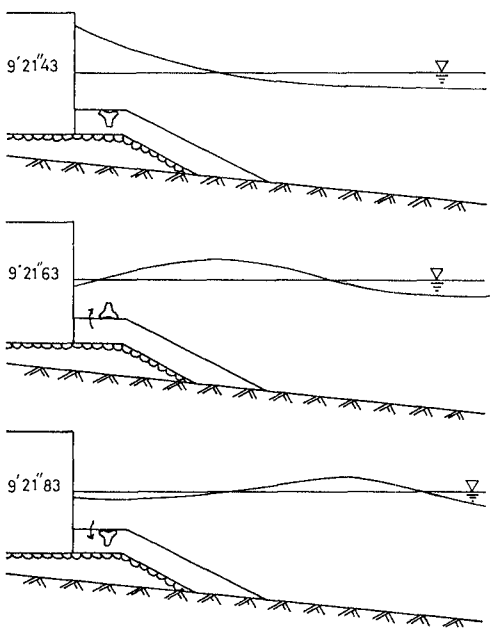

Figure 5 (a) Movement of tetrapod resulting from wave action

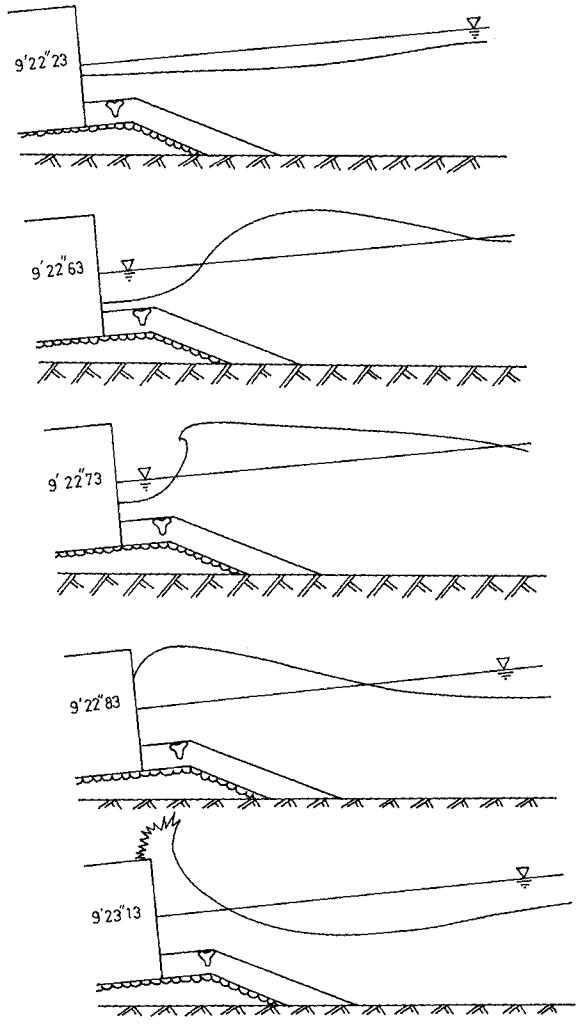

Figure 5 (b) Movement of tetrapod resulting from wave action

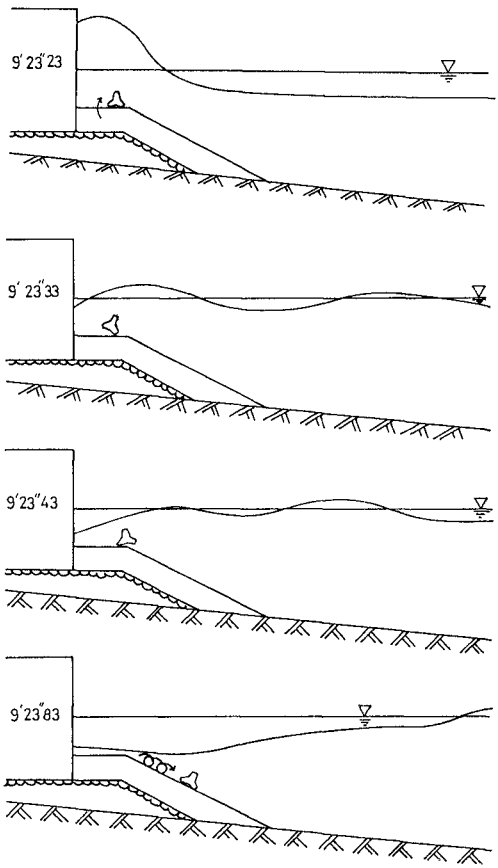

Figure 5 (c) Movement of tetrapod resulting from wave action

Subsequent run-down washed the units seaward. It could be seen that waves breaking on the mound were influenced by the previous run-down. It can be assumed that the magnitude of the lift force was influenced by the previous run-down meeting an incoming wave resulting in damage of the units. Damage in rubble foundations was observed to depend on how much of the top of the foundation was exposed above the water, especially when the troughs of waves near Hmax hit vertical faced structures.

Figure 6 shows an example of a surface elevation measured at a station at a distance of one wave length away from the site whereas Figure 7 shows a record of the waves without the breakwater measured at the point where the model breakwater was to be set up.

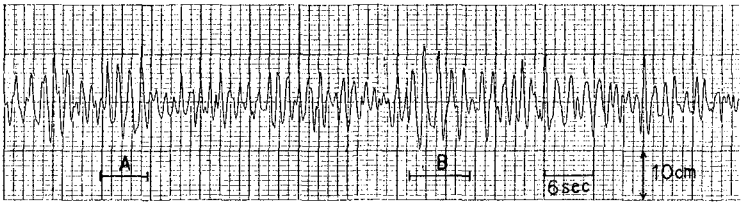

Figure 6 An example of a wave record at a distance of one wave length from the breakwater

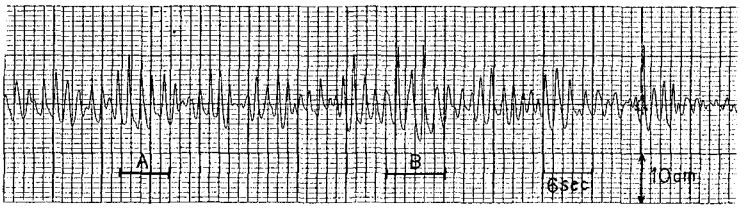

Figure 7 An example of a wave record at the breakwater

A few tetrapods moved due to waves in sections A and B (Figure 6 and 7).

Waves except those in sections A and B caused no movement to armor units. The damage of the armor units by waves in B section was greater than that in A. The maximum wave in this train appeared in section B and several large waves occured successively. These subsequent waves including the maximum wave struck the breakwater damaging the armor units. The consequtive wave heights including sections A and B are shown in Figure 8. The significant wave height and the one-tenth maximum wave height are illustrated in the same figure.

From the investigation using the video film, in critical cases, the movement of tetrapods was caused by those wave groups in sections A and B. Waves exceeding the one-tenth maximum wave height damaged the armor layer. Waves included in B section caused damage more sever than that in A section. Although the only maximum wave can damage, a group of waves exceeding the critical wave height (Hc) is more destructive.

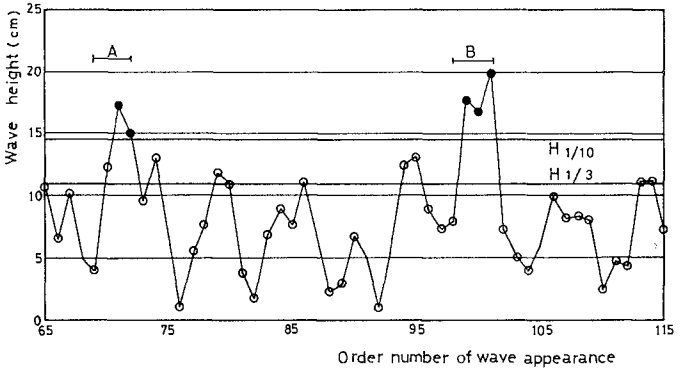

Figure 8 An example of wave group

Stability Number

Stability Number is presented by the following equation.

$$Ns = \frac{\gamma^{1/3} H}{W^{1/3} (Sr - 1)} \qquad \text{--------} \qquad (2)$$

where

Ns ; Stability Number
γ ; specific gravity of armor unit
W ; average weight of armor unit
Sr ; specific gravity of armor unit relative to water
H ; wave height

The relationships between d/h and Ns calculated by equation (2) using significant wave heights measured in the tests are shown in Figure 9 and 10.

Figure 9 shows the results in the case where h_o=-28.0 cm and Figure 10 is the results where h_o=-23.0 cm. In order to compare the test results with those obtained by Brebner and Donnelly(1963), their values of Ns are included using dashed lines in Figure 9 and 10. As it is not possible to compare directly with the results of Brebner and Donnelly(1963), their values of Ns were roughly revised using Kd values of quarry stones and tetrapods. Solid and dotted lines show the results of the cases where T=1.3 sec and T=1.8 sec respectively.

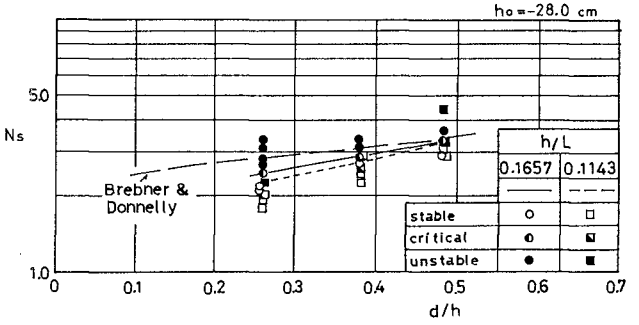

Figure 9 Stability Number as d/h ($H_{1/3}$ as H)

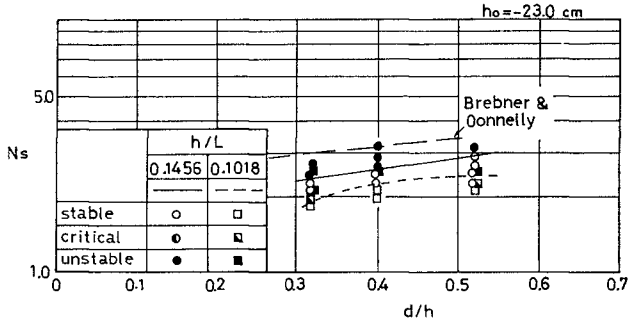

Figure 10 Stability Number as d/h ($H_{1/3}$ as H)

Stability Numbers show a tendency to increase as d/h increases. The rate of increase become smaller in the case where h_o=-23.0 cm.

Where h_o=-23.0 cm, if the wave period was 1.3 sec, the Stability Number is slightly smaller than that where T=1.8 sec. Hence the Stability Number seemed to be affected by the wave period.

The revised Stability number of Brebner and Donnelly(1963) dashed lines) is greater than that found in these test results which were obtained by substituting $H_{1/3}$ measured into equation(2).

Figure 11 and 12 show the Stability Number which was calculated using $H_{1/10}$ measured at the point of a site without a breakwater. In these figures the revised Ns found by Brebner and Donnelly(1963) is also included(by dashed lines). As shown in these figures, Their revised Ns has almost the same value as our results.

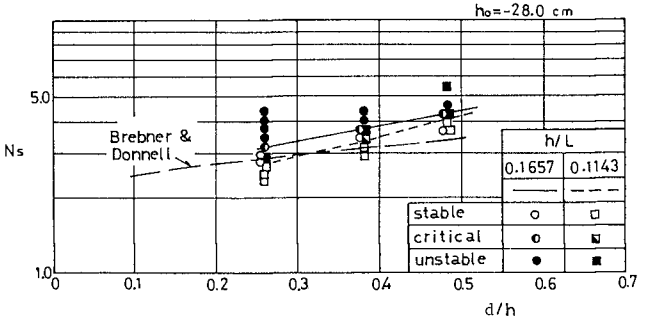

Figure 11 Stability Number as d/h ($H_{1/10}$ as H)

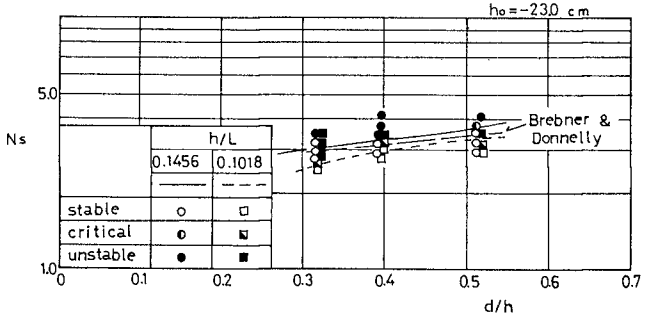

Figure 12 Stability Number as d/h ($H_{1/10}$ as H)

As mentioned above, if $H_{1/3}$ is used in the estimation of a critical unit weight using the revised Ns when the weight calculated is lighter than the required weight.

When the results obtained though regular wave tests are applied to evaluate a required weight of armor units, it seems that the one-tenth maximum wave height as a design wave height is appropriate.

There are no formulae for estimation of weights of armor units, like tetrapods, which protect the rubble-mound at present. Engineers have estimated the stable weight of the armor units as foundations referring to the results of Brebner and Donnelly(1963). However they have to select the design wave height with caution.

Critical weight

From the test results, the critical weight seemed to be a function as d/H where H is a representative wave height,e.g. $H_{1/3}$ and $H_{1/10}$, measured at a point on the site without a breakwater. The relationship between $Wc/w_oH_{1/3}^3$ (w_o: unit weight of water) and $d/H_{1/3}$ are shown in Figure 13 and 14.
Figure 13 shows the results of two cases where h_o=-28.0 cm and h_o=-23 cm at the fixed period of T=1.3 sec. Figure 14 shows similar results where the wave period was 1.8 sec.

From each figure, the boundaries of each case between stable and unstable results can be separated using one straight line, independent of the water depth at the site (h_o), on semilogarithmic graph paper.

Critical relationships are obtained as following equation in each case where T=1.3 sec and T=1.8 sec as a result of the lines drawn.

$$W/w_oH_{1/3}^3 = 0.284 \times 4.58^{-(d/H_{1/3})} \quad \text{(at T=1.3 sec)-----(3)}$$

$$W/w_oH_{1/3}^3 = 0.695 \times 6.55^{-(d/H_{1/3})} \quad \text{(at T=1.8 sec)-----(4)}$$

These two equations show the effect of the wave period.

Engineers have problems in making decisions about what wave height to use ($H_{1/3}$, $H_{1/10}$, Hmax) as design wave heights.

As mentioned before, the armor units were damaged by waves of heights exceeding the one-tenth maximum wave height under critical conditions. In addition, if the depth at the breakwater and the gradient of sea bottom change, the ratio $H_{1/10}$ to $H_{1/3}$ also changes. Then critical conditions would be presented more directly by $H_{1/10}$ than the significant wave height.

The relationship between $W/w_oH_{1/10}^3$ and $d/H_{1/10}$ is shown in Figure 15 and 16.

The empirical equations of the critical relationship are obtained as follows.

$$W/w_oH_{1/10}^3 = 0.125 \times 6.72^{-(d/H_{1/10})} \quad \text{(at T=1.3 sec)-----(5)}$$

$$W/w_oH_{1/10}^3 = 0.187 \times 7.56^{-(d/H_{1/10})} \quad \text{(at T=1.8 sec)-----(6)}$$

These results seem to have an application in estimation of the critical unit weight as suggested by Inagaki et al (1971). When these equations are applied, attention should be paid to the effects of the wave period because the wave with longer period are more destructive than those of shorter periods.

However, these equations were obtained through tests under conditions of a constant wave height, two values of wave period and a constant gradient sea bottom. The effects of these are not yet apparent. Some additional test will be tried.

The test wave height was not so longer in the model, therefore there still remains the problem of the scale effect.

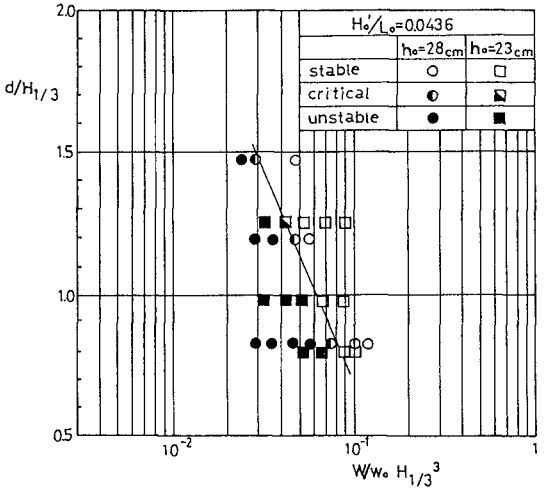

Figure 13 Critical weight as $d/H_{1/3}$ (T=1.3 sec)

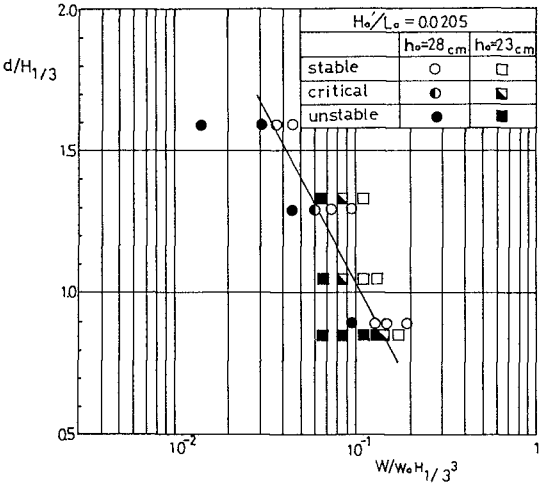

Figure 14 Critical weight as $d/H_{1/3}$ (T=1.8 sec)

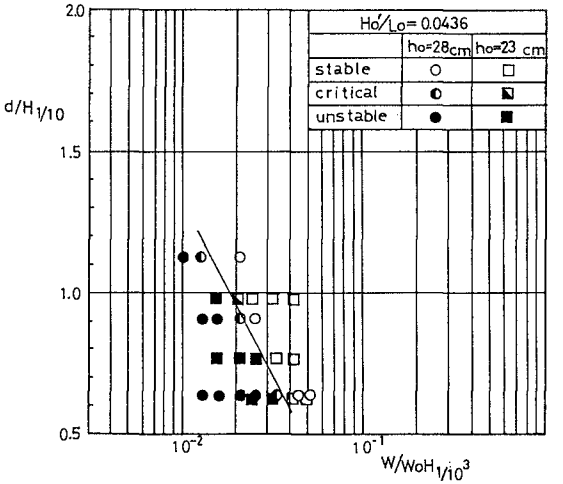

Figure 15 Critical weight as $d/H_{1/10}$ (T=1.3 sec)

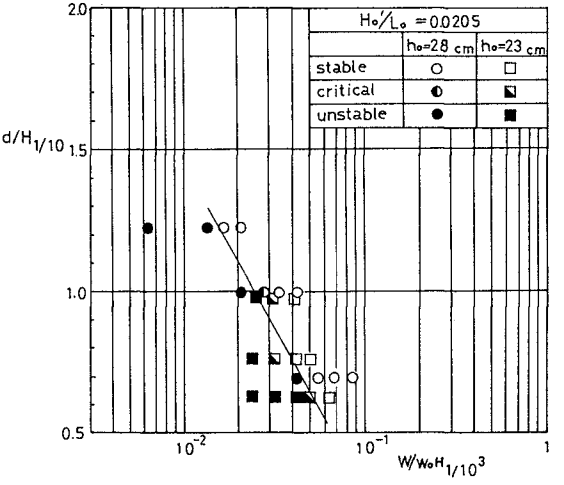

Figure 16 Critical weight as $d/H_{1/10}$ (T=1.8 sec)

Design wave heights are often greater than 7 m and 8 m in the southern area of Japan and the depths of foundations are around -10 m in many cases and as concrete armor units are used to protect such foundations. Figure 13 to 16 could be utilized when faced with this situation.

4. CONCLUSIONS

The conclusions obtained by the tests are summarized as follows.

1. The waves with longer periods were more destructive than shorter waves when h_o was small.
2. Under critical conditions, the tetrapods as a protection of the rubble-mound received damage by waves of height exceeding $H_{1\ 10}$.
3. The stability of the armor unit was affected by the wave group.
4. Critical weight was a function of d/H (H: representative wave height) and increased as the wave period became longer in our range of d/H. It is recommended to use $H_{1/10}$ for design, especially in the surf zone.

5. REFERENCES

Brebner, A., and P. Donnelly (1963). Laboratory study of rubble foundations for vertical breakwaters. Proc.8th coastal Engg. Conf., Mexico City, Mexico, pp.408-428.

Coda, Y. (1974). New wave pressure formulae for composite breakwaters, Proc. 14th Coastal Engg. Conf., Conpenhagen, pp.1702-1720.

Goda, Y. and Y. Suzuki (1976). Estimation of incident and reflected waves in random wave experiments, Proc. 15th Coastal Engg. Conf., Honolulu, pp.828-845.

Inagaki, H.and T. Katayama (1971). Analysis of damage to armor stones of mounds in composite breakwaters, Tech.Note of The Port and Harbor Reseach Institute, Ministry of Transport, Japan, No.127 (in Japanese)

IRREGULAR WAVE TESTS FOR COMPOSITE BREAKWATER FOUNDATIONS

Katsutoshi Tanimoto*, Tadahiko Yagyu**, Yoshimi Goda***

ABSTRACT

The stability of armor units for the rubble mound foundations of composite breakwaters has been investigated under the action of irregular waves. The tests establish that irregular waves are more destructive than regular waves, when the height of regular waves is set equal to the significant wave height.

The stability number, defined by Hudson, for quarry stones and concrete blocks with simple shapes is formulated on the basis of irregular wave tests. The stability number is expressed by two parameters of $h'/H_{1/3}$ and κ, where h' is the crest depth of the rubble mound foundation, $H_{1/3}$ is the design significant wave height, and κ is a parameter for the combined effects of the relative water depth and the relative berm width of the rubble mound foundation to the wavelength.

The design mass of armor units can be calculated by the stability equation with the stability number. The application of the proposed method to the results of the irregular wave tests demonstrates that the damage percent for the quarry stones is at most 3.5% at the design condition and the damage progresses rather gradually for the action of higher waves. On the other hand, the damage of the concrete blocks almost jumps beyond the design wave height. In particular, the drastic damage is often caused in the case of high rubble mound foundations. The proposed method is confirmed, however, to be applicable for the ordinary low mound foundations with a sufficient safety.

INTRODUCTION

Composite type breakwaters which are composed of upright sections and rubble mound foundations have several advantages over rubble mound breakwaters. They are more stable, faster in construction, and less in wave transmission than rubble mound breakwaters. Because of these advantages, they have been built in great length of extension in Japan without major mishaps in several scores of years in the past.

* Chief, Breakwaters Laboratory, Port and Harbour Research Institute, Ministry of Transport

** Deputy Director, Planning Division, Overseas Coastal Area Development Institute of Japan

*** Director, Hydraulic Engineering Division, Port and Harbour Research Institute, Ministry of Transport

Design practices of this type of breakwaters also have been improved continuously through theoretical, laboratory and field studies. In particular, much efforts have been maid to study wave forces on the upright sections. As a result of those studies, a general formula to calculate the design wave forces due to nonbreaking to postbreaking waves has been established by Goda (1974). This formula is being successfully applied to the design of composite breakwaters (Bureau of Ports and Harbours, 1980).

On the other hand, the armor layer of the foundation mounds are being designed on the basis of egineer's experiences, supplemented by informations obtained from laboratory studies: e.g. Brebner and Donnelly (1962). Those previous studies, however, were based on the regular wave tests and little information on the irregular wave attacks is available until now, although a number of studies on the stability of armor units for rubble mound breakwaters have been conducted using irregular waves. Consequently, design engineers are always puzzled how the results by regular wave tests should be applied to the actual action of irregular waves. A possible solution for this question is undoubtedly to investigate the stability of armor units for foundation mounds of composite breakwaters by irregular wave tests.

The authors have carried out the irregular wave tests for the stability of armor units in order to get better knowledges for the design of composite breakwaters. The present paper describes the results of the irregular wave tests and discusses the stability number, defined by Hudson (1959), to formulate it on the basis of test results. The study in the present paper is of two-dimensional and limitted to the action of waves of normal incidence to breakwaters.

STABILITY EQUATION

Figure 1 illustrates the typical cross section of the composite breakwaters and defines the symbols used in the present paper;

h : water depth at the structure site

h' : depth at the crest of rubble mound foundation excluding the armor layer

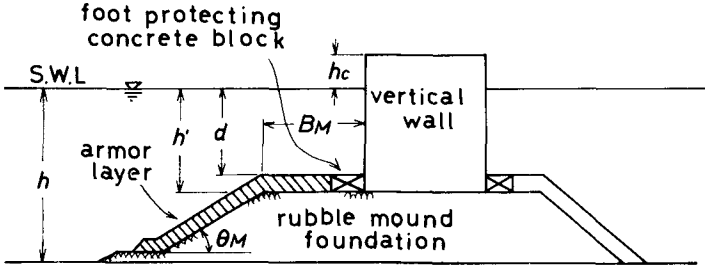

Figure 1 Definition sketch of cross section of composite breakwater

d : depth at the crest of rubble mound foundation
B_M : berm width of rubble mound foundation
θ_M : angle of the front slope measure from the horizontal plane
h_c : crest height of vertical wall above the still water level

Because these dimensions associated with the structure and the water depth as well as wave conditions influence on the stability of armor units for the rubble mound foundation, the problem is very complicated and inherently contains a number of parameters. In the present study, a simplified analytical consideration is made at first in order to find the principal parameters governing the stability of armor units.

In the ordinary conditions, the most critical position of the armor layer being subject to the initial damage may be assumed to be around the top of the slope or the seaward end of the berm crest. For this reason, the composite breakwater is replaced by the vertical breakwater on a hypothetical horizontal bottom having the water depth of h' and the stability of single rubble unit, which is placed at the position with the distance of B_M from the vertical wall, is considered under the action of standing waves as shown in Figure 2.

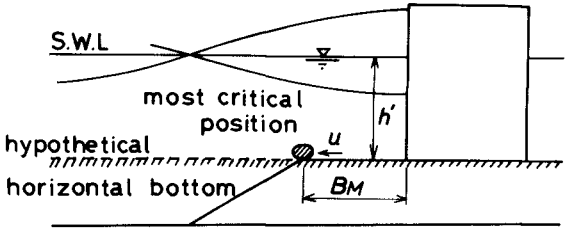

Figure 2 Simplified model for analytical consideration

As to wave forces on the unit, it is assumed that the drag forces predominate over the inertia forces. Then, the horizontal force (drag force, F_D) and the vertical force (lift force, F_L) on the unit are given by the following expressions:

$$F_D = \frac{\rho_w}{2} C_D u_{max}^2 k_A a^2 \quad (1)$$

$$F_L = \frac{\rho_w}{2} C_L u_{max}^2 k_A a^2 \quad (2)$$

where ρ_w is the density of fluid, C_D and C_L are the drag and the lift coefficients, u_{max} is the maximum horizontal velocity, a is the characteristic linear dimension of the unit such that the projected area of the unit perpendicular to the velocity is $k_A a^2$ and the volume of the unit is $k_V a^3$.

On the other hand, the mass of the unit, W, is expressed

$$W = \rho_r k_V a^3 \tag{3}$$

where ρ_r is the density of the unit. Then, the condition of limiting equilibrium against the horizontal displacement of the unit is

$$\mu\{g(\rho_r - \rho_w)k_V a - F_L\} = F_D \tag{4}$$

where μ is the friction coefficient, g is the acceleration of gravity. When Eqs.(1) and (2) are substituted into the above Eq.(4), the following relation is obtained:

$$a = \frac{1}{2g}\frac{k_A}{k_V}\frac{C_D/\mu + C_L}{S_r - 1}u_{max}^2 \tag{5}$$

where

$$S_r = \rho_r/\rho_w \tag{6}$$

Using Eq.(3), Eq.(5) is written as:

$$W = \{\frac{1}{2g}\frac{k_A}{k_V^{2/3}}(\frac{C_D}{\mu} + C_L)\}^3 \frac{\rho_r}{(S_r - 1)^3} u_{max}^6 \tag{7}$$

This relation indicates that the critical mass against the horizontal displacement is proportional to six powers of the maximum horizontal velocity.

When standing waves are formed in front of the vertical wall, the maximum horizontal velocity at the bottom can be expressed by the following equations according to the small amplitude wave theory:

$$u_{max} = \{\kappa \frac{H_I'}{h'} g H_I'\}^{1/2} \tag{8}$$

$$\kappa = \frac{4\pi h'/L'}{\sinh(4\pi h'/L')} \sin^2(2\pi B_M/L') \tag{9}$$

where H_I' is the incident wave height, L' is the wavelength at the depth of h'. The parameter κ represents the combined effects of the relative water depth and the relative distance from the vertical wall on the maximum horizontal velocity at the bottom.

Substituting Eq.(8) to Eq.(7), we get

$$W = \frac{\rho_r}{N_s^3 (S_r - 1)^3} H_I'^3 \tag{10}$$

$$N_s = \frac{2k_V^{2/3}}{k_A (C_D/\mu + C_L)} \frac{1}{\kappa} \frac{h'}{H_I'} \tag{11}$$

Eq.(10) is written in the form of the stability equation which was derived by Hudson (1959) for the armor units of rubble mound breakwaters and N_s is called as the stability number. According to Eq.(11), the stability number is in proportion to h'/H_I' and in inverse proportion to κ.

Because there are many assumptions in the above-mentioned derivation,

the relation given by Eq.(11) is not directly applicable to the armor units for the rubble mound foundations of composite breakwaters. For example, waves are deformed by the existence of the rubble mound foundation and breaking waves also act on the structure when incident waves are high enough. Therefore, in the present study, h'/H_I and K are simply considered as principal parameters governing the stability number, although the stability equation in the form of Eq.(10) is adopted as the basic equation. The wave height of progressive waves in the depth of h is applied to the wave height in the stability equation, and for the action of irregular waves the significant wave height, $H_{1/3}$, is selected as a representative wave height. Thus, the stability equation is defined by the following relation:

$$W = \frac{\rho_r}{N_s^3 (S_r - 1)^3} H_{1/3}^3 \qquad (12)$$

and the effect of the irregularity of individual waves becomes to be contained in the evaluation of the stability number.

The stability number may be expressed as:

$$N_s = f\left(\frac{h'}{H_{1/3}}, K ; \text{shape and placing method of armor units} \right) \qquad (13)$$

where f( ) indicates "function of". The parameter K is calculated for given values of h'/L' and B_M/L'. Figure 3 shows the K-value against B_M/L' when the value of B_M/h' is fixed. For the irregular waves, the wavelength corresponding to the significant wave period, $T_{1/3}$, is applied to L' in the calculation of K-value.

TEST CONDITIONS

Tests have been carried out in the wave flume of 163 m long, 1.0 m wide, and 1.5 m deep as sketched in Figure 4. The wave generator consists of a wave paddle of piston type driven by a linear electric motor with low inertia, the movement of which is controlled by an electric signal from a sine-wave generator (regular waves) or a magnetic tape (irregular waves). In front of the wave generator is a wave filter which absorbs, to some extent, waves reflected from the model structure. The bottom of the wave flume is mostly horizontal, but the test section is the sloping bottom formed as a fixed bed. In front of the model structure, a vertically sliding wall is prepared to avoid the unfavorable effect of transient waves which are caused in the wave flume when the motion of wave paddle is stopped. Glass windows are equipped in a side wall at the test site so that visual observation of the stability of armor units can be made from the side.

The water depth, h, at the site of model structure was selected to be 40 to 50 cm and the model of the composite breakwater was set up for four different thicknesses of the rubble mound foundation in the range of h'/h from 0.3 to 0.9. The front slope of the rubble mound was fixed to be constant at cot $\theta_M = 2$ for all the test cases. The relative berm width to the water depth, B_M/h, was fixed mostly to be 0.6, but, in case

of h'/h = 0.6, it was changed in the range from 0.4 to 1.4.

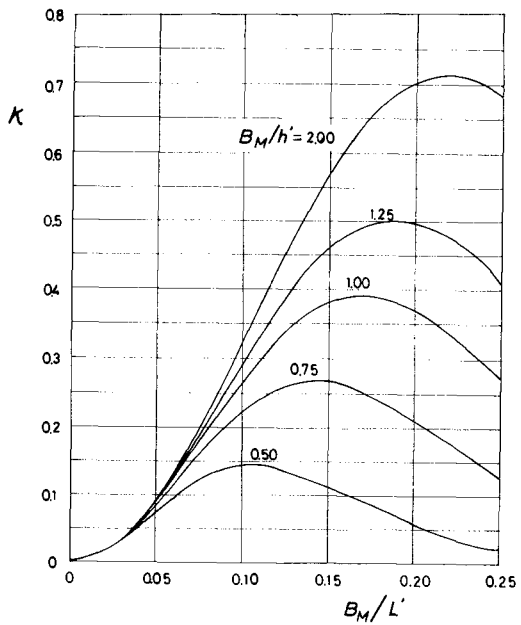

Figure 3 Value of K

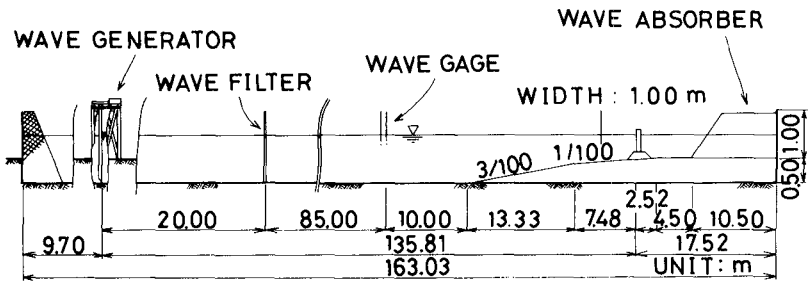

Figure 4 Wave flume

Quarry stones having five different graded sizes as shown Table 1 were tested. They were placed in two layers on the front slope and the crest berm of the rubble mound foundation. The foot of the vertical wall, however, was protected from scouring by placing concrete blocks of the rectangular solid with a sufficient mass.

Table 1 Mass and density of quarry stone

Grade	Mass W (g)		Density ρ_r (g/cm^3)
	average	standard deviation	
I	15.0	2.05	2.60
II	29.9	3.51	2.59
III	57.3	5.99	2.62
IV	105.5	12.5	2.64
V	250.0	27.9	2.75

The concrete block with a vertical hole as shown in Figure 5 was tested as well as the basic shape without a hole. Their masses are from 36.9 to 147.1 g for the basic shape and from 34.1 to 208.7 g for the shape with a hole. The densities are from 2.21 to 2.33 depending on the shape and the size. They were placed regularly in single layer on the rubble mound foundation.

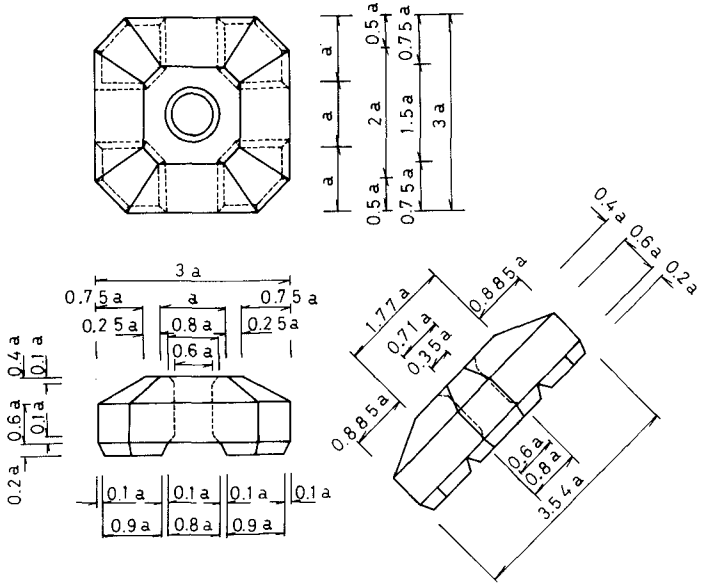

Figure 5 Concrete block with a vertical hole

Irregular waves having the following spectrum of Bretchneider type were simulated:

$$S(f) = 0.257 \ H_{1/3}^2 \ T_{1/3} \ (T_{1/3}f)^{-5} \exp\left[-1.03(T_{1/3}f)^{-6}\right] \quad (14)$$

where $S(f)$ is the spectrum density, and f is the frequency. The significant wave period was changed to give the range of relative water depth from 0.075 to 0.143. The effective duration of irregular waves was selected to be 900 seconds in most cases, but for the tests of the concrete blocks having a vertical hole it was determined so that about 500 zero-up cross waves act on the structure. During the tests, waves were recorded at two adjacent locations in the offshore, and the progressive wave height toward the structure was obtained by the resolution technique of incident and reflected waves from the composite waves (see Goda and Suzuki, 1976). Then, the incident wave height at the test section was estimated from the relation between the wave height at the offshore and the wave height at the test section, which had been measured preliminary without the model structure. The test range of relative wave height, $H_{1/3}/h$, is from 0.16 to 0.44 for the quarry stones and from0.14 to 0.61 for the concrete block having a vetical hole.

The crest height of the vertical wall, h_c, was changed according to the incident wave height so that the relative crest height, $h_c/H_{1/3}$, is kept to be constant value of 0.6. Therefore, the condition is that some extent of wave overtopping is caused for the all test cases.

TEST RESULTS AND DISCUSSIONS

Stability of quarry stones

Armor units of respective masses were tested for given conditions of h'/h, B_M/h and h/L by increasing wave heights, and the relationship between the average mass of armor units and the incident wave height at the equilibrium state between stable and unstable conditions was determined in order to evaluate the stability number. The typical results for the quarry stones are shown in Figure 6. The critical line between stable and unstable conditions is drawn so as to represent one percent damage on the distribution of damage percents which are defined as the percentage of armor units removed from the original position to the total number of armor units in the cover layer. When the critical wave height, Hc, for the respective average mass is determined, the stability number is evaluated by the relation of Eq.(12).

The stability number of quarry stones obtained by the above-mentioned procedure is plotted against $h'/H_{1/3}$ in Figure 7, in which the data are distinguished by the parameters h/L and h'/h, and linked by lines for the same conditions of them. The data indicate that the stability number is increased as $h'/H_{1/3}$ becomes large. It is also seen that the stability number is variated by the other parameters as h/L, and shorter waves are more destructive than longer waves if the value of $h'/H_{1/3}$ is the same. In particular, this tendency is apparently noticed, when the value of $h'/H_{1/3}$ is relatively large. These results establish, as predicted by the analytical considerations, that the stability of armor units for the composite breakwater foundations is greatly effected

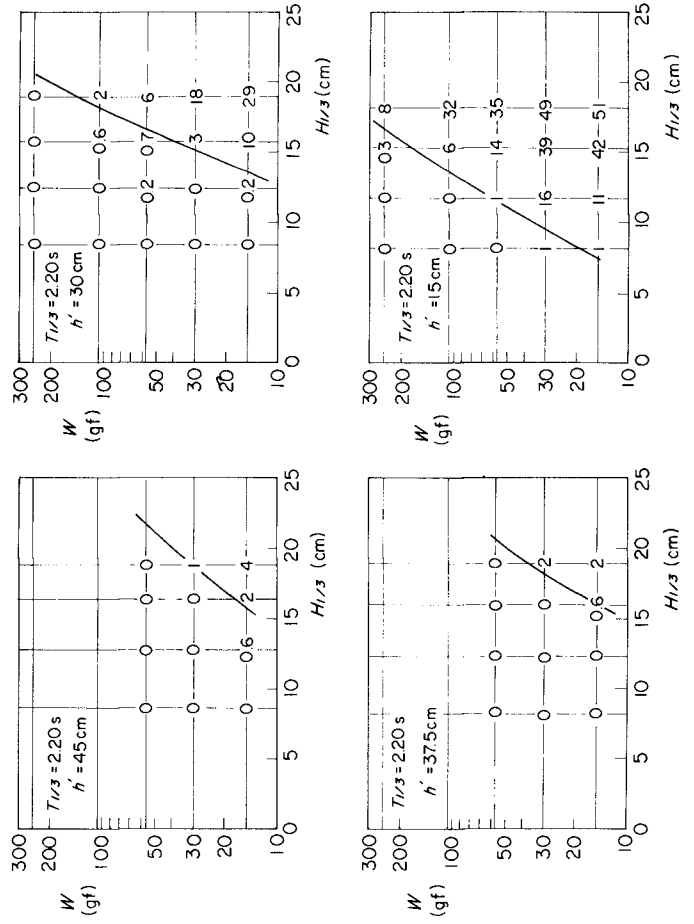

Figure 6 Example of test results for quarry stones (h = 50 cm, B_M = 30 cm)

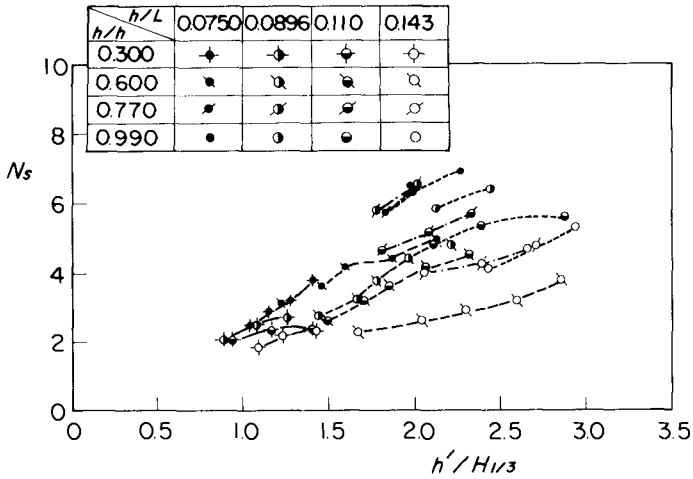

Figure 7 Effect of the crest depth and wave conditions (B_M/h = 0.6)

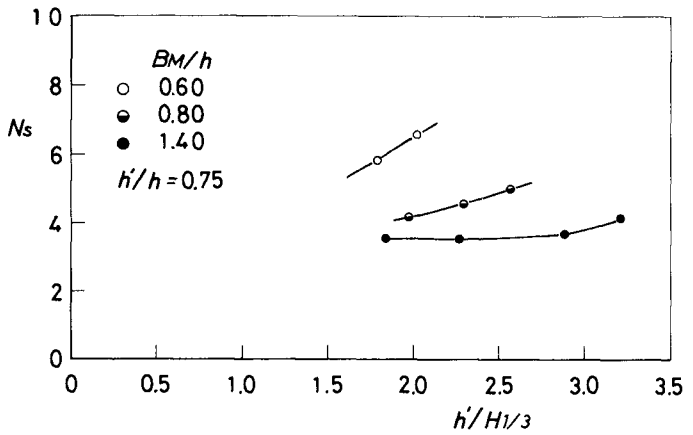

Figure 8 Effect of berm width (h'/h = 0.75)

by the wave height and the period, when the crest depth of the rubble mound becomes deep and standing waves are formed in front of the vertical wall. It is also observed that the stability number has a tendency to converge to a constant value when the value of $h'/H_{1/3}$ becomes small. This constant value must be the stability number of armor units for rubble mound breakwaters, since the extreme state of $h'/H_{1/3} = 0$ corresponds to the rubble mound breakwaters.

On the other hand, Figure 8 shows the stability number when the condition of B_M/h is changed. No data for the condition of $B_M/h = 0.4$ is plotted in the figure, because any damage was not caused at that condition. The results demonstrate that the stability number decreases as the value of B_M/h becomes large. This means that the armor units for the rubble mound foundation with a wide berm width are more subjected to damage than those for the rubble mound foundation with a narrow berm width.

Previous considerations based on the simplified model suggest that these effects of the wave period and the berm width on the stability number may be represented by the parameter K given by Eq.(9). For this reason, the data classified in the appropriate range of K-value are replotted in Figure 9. From these results the following remarks are pointed out:

(1) The stability number for the same rank of K-value increases almost linearly with $h'/H_{1/3}$, although the data are scattered.

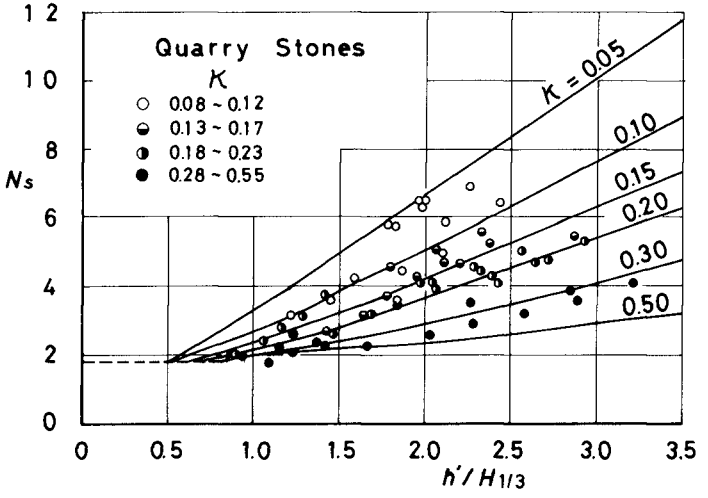

Figure 9 Stability number of quarry stones

(2) As the value of κ becomes large the stability number becomes small, but the difference is not large when the κ-value is larger than 0.3.
(3) When the value of $h'/H_{1/3}$ becomes small the stability number is not much different by the κ-value and has a tendency to converge to a constant value.

Thus, the stability number, N_s, may be formulated by a function of $h'/H_{1/3}$ and κ, so that $N_s = N_{s0}$ at $h'/H_{1/3}$ and N_s is increased in proportion to $h'/H_{1/3}$ when it is sufficiently large. In the present study, N_s is expressed as a sum of two terms as shown in Figure 10, the one is the term which increases linearly in proportion to $h'/H_{1/3}$ and the other is the term which decreases from the value of N_{s0} to infinitesimal at the large value of $h'/H_{1/3}$. After several trials, the following expression was selected:

$$N_s = A \frac{1-\kappa}{\kappa^m} \frac{h'}{H_{1/3}} + N_{s0} \exp\left[-B \frac{(1-\kappa)^2}{\kappa^m} \frac{h'}{H_{1/3}}\right] \qquad (15)$$

The constants of N_{s0}, A, B, m in the above equation are determined so that calculated results agree with test results as closely as possible. The following values were determined for the quarry stones:

$$N_{s0} = 1.8,\ A = 1.3,\ B = 1.5,\ m = 1/3$$

The stability number of $N_{s0} = 1.8$ corresponds to the K_D-value of 2.9 in the Hudson's formula for rubble mound breakwaters, when the value of $\cot\theta_M$ is set equal to 2.

However, Eq.(15) has a minimum value slightly less than N_{s0} at the

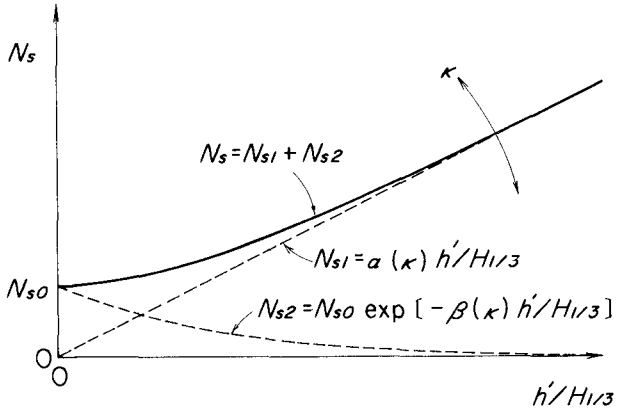

Figure 10 Formulation of stability number

small value of $h'/H_{1/3}$. Finally, the following empirical equation to calculate the stability number of quarry stones is proposed:

$$N_s = \max \{1.8,\ 1.3\ \frac{1-\kappa}{\kappa^{1/3}}\ \frac{h'}{H_{1/3}} + 1.8 \exp\left[-1.5\ \frac{(1-\kappa)^2}{\kappa^{1/3}}\ \frac{h'}{H_{1/3}}\right]\} \tag{16}$$

where max $\{a, b\}$ indicates the larger one of a or b. The curves in Figure 9 indicate the relationships between $h'/H_{1/3}$ and N_s which are calculated for the representative κ-values. It is seen that the calculated relations represent considerably well the tendency of test results.

The design mass of quarry stones can be calculated by applying the stability number obtained from Eq.(16) to the stability equation (12). The calculations were made for the all test conditions in order to compare with test results of damage percent. In Figure 11, the data of the damage percent realized in the tests are plotted against W/W_c. Here W is the average mass of quarry stones which were tested and W_c is the mass calculated by the above-mentioned method for the test conditions. In the theory, $W/W_c = 1.0$ indicates the equilibrium state between stable and unstable conditions, and the damage percent should be about one percent. Such ideal results, however, can not be expected, becuase the behaviours of armor units under the action of waves are essentially changeable due to the slight variations of conditions. The results shown in Figure 11 are satisfactory, although they are considerably scattered. It is also pointed out that the damge of quarry stones progresses rather gradually.

Stability of concrete blocks

Figures 12 and 13 show the test results of N_s for the concrete blocks with and without a vertical hole. The stability numbers for these concrete blocks are also formulated by two parameters of $h'/H_{1/3}$ and κ in the same way as the quarry stones. The curves in the figures indicate the relationships calculated for the appropriate κ-values. The constants in the empirical equation are as follows:

For the concrete block without a hole,

$N_{so} = 1.4$, $A = 1.0$, $B = 1.2$, $m = 1/3$

For the concrete block with a hole,

$N_{so} = 1.6$, $A = 0.82$, $B = 0.9$, $m = 1/2$

The stability number of concrete blocks having a vertical hole is generally higher than that of concrete blocks without a hole. Particularly, the advantages of having a vertical hole is noticed when the κ-value is relatively small.

The tests demonstrate that the damage of concrete blocks placed in single layer progresses drastically when the incident wave height exceeds the critical wave height. Therefore, it should be noted that slight overestimation in the stability number sometimes results in the serious damage. In particular, the drastic damage is often caused in the case of high rubble mound foundations. The results presented in Figure 14 show

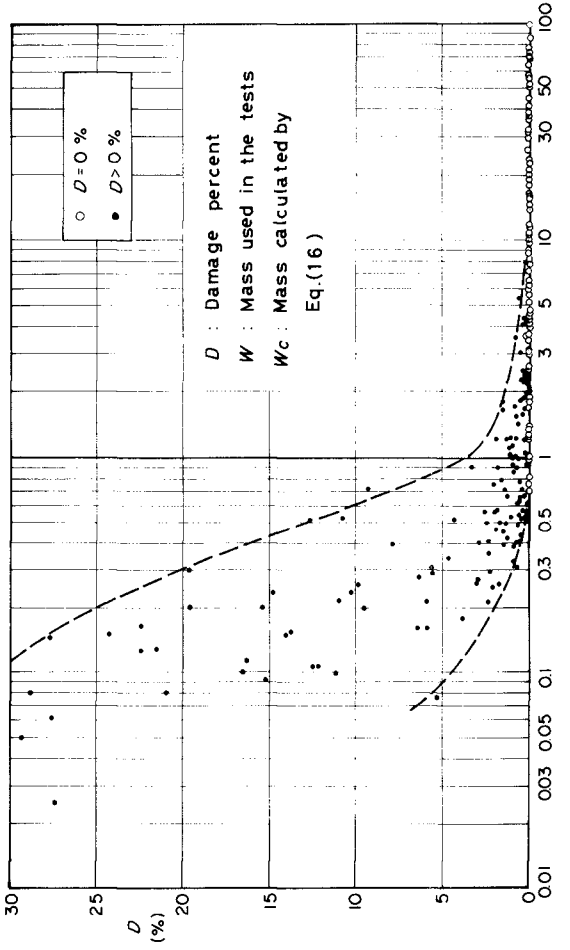

Figure 11 Damage percent of quarry stones

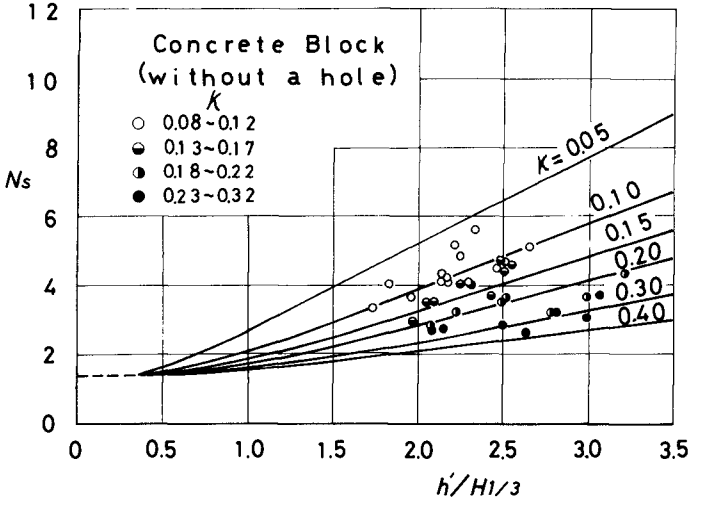

Figure 12 Stability number of concrete block without a hole

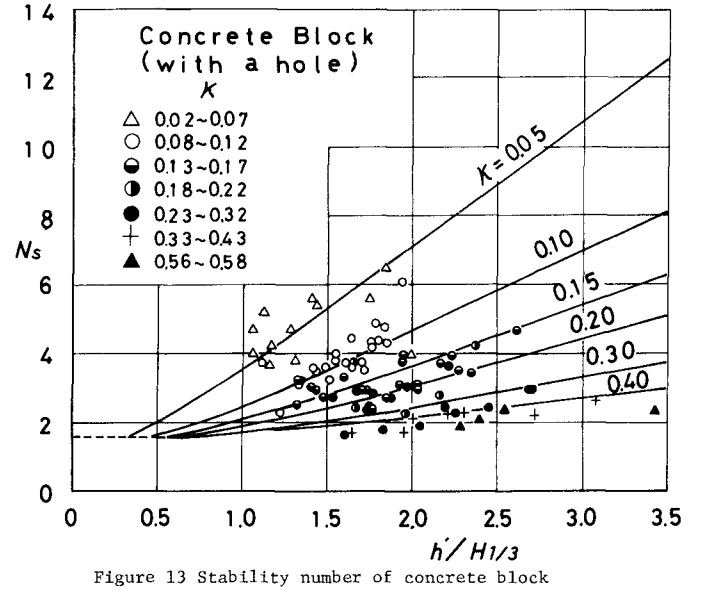

Figure 13 Stability number of concrete block with a vertical hole

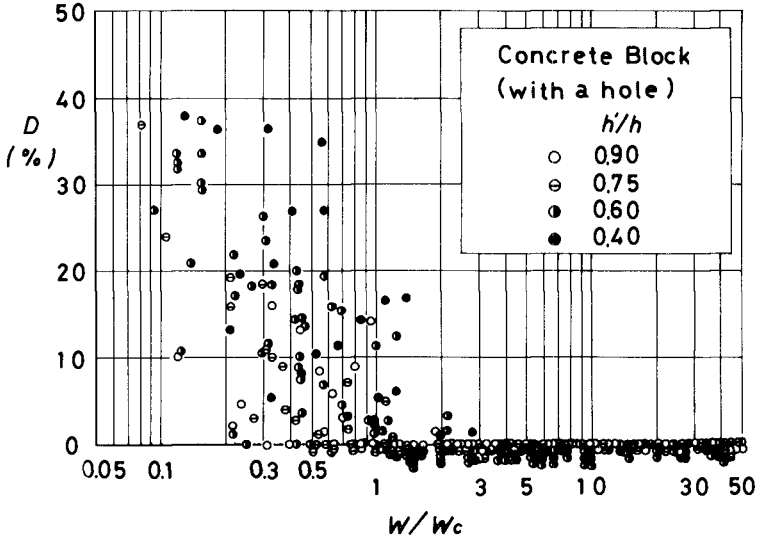

Figure 14 Damage percent of concrete block with a vertical hole

that the damage percent almost jumps beyond the critical conditions and the largest damage percent at W/W_c = 1.0 comes up to about 20 %. However, most data, which indicate the damage in the condition of $W/W_c \geqq 1.0$, are the cases of high rubble mound foundations of $h'/h \leqq 0.6$. For the ordinary low rubble mound foundations, the present method would be applicable with a sufficient safety.

Comparison with results of regular wave tests

Regular wave tests for the concrete block without a hole were carried out in order to make direct comparison with the results by irregular wave tests. The period of regular waves was selected so as to be equal to the significant wave period of irregular waves. The total duration of regular waves with a wave height of certain level, however, was shortened to one third of the duration of irregular waves and it was divided into several short runs so that no re-reflected waves from the wave paddle act on the structure. The tests were carried out by three different conditions of h'/h = 0.60, 0.75, and 0.90, but within the test range of wave heights no damage was caused by the action of regular waves for the case of h'/h = 0.90.

The tests establish that irregular waves are more destructive than regular waves, if the regular wave height is set equal to the significant wave height. Figure 15 shows the relation between the critical wave height of regular waves, H_{creg}, and the critical significant wave height of irregular waves, H_{cirreg}, at the equilibrium state. According to the

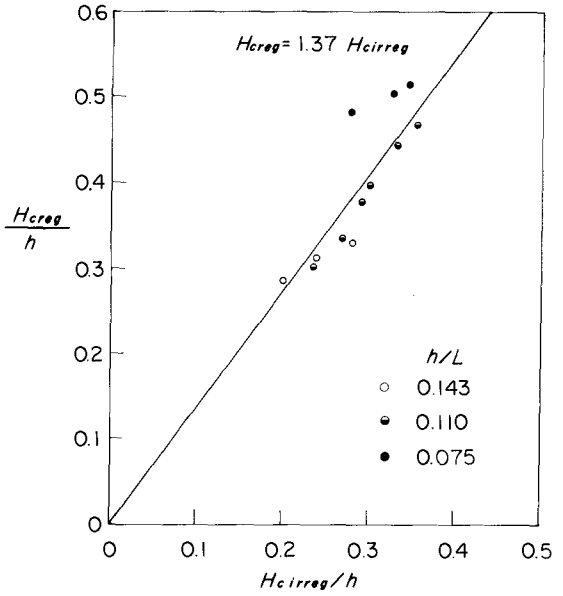

Figure 15 Relation between the critical significant wave height and the critical wave height of regular waves

results, the action of regular waves almost equivalent to that of irregular waves, when the height of regular waves is set equal to 1.37 times of the significant wave height on an average.

Examples of calculations

Examples of calculations of design mass of quarry stones will be given together with the results by two previous studies.

Brebner and Donnelly (1962) proposed the design curve of minimum stability number as a function of d/h. Although thier results were based on regular wave tests, they suggested that the design wave height used in the stability equation should be twice or one and half times of the expected significant wave height depenging on the importance of the structures. In the present calculations, however, the average wave height of the highest one percent of all waves, $H_{1/100}$ (= 1.67 $H_{1/3}$), and the average wave height of the highest of one tenth, $H_{1/10}$ (= 1.27 $H_{1/3}$), are applied according to the recommendation by CERC (1973). The regular wave height equivalent to the action of irregular waves, which was obtained for concrete blocks in the present study, corresponds to the average

wave height of highest one sixteenth, $H_{1/16}$, between $H_{1/10}$ and $H_{1/100}$.

The other previous study is made by Inagaki and Katayama (1971). They investigated the field data of damaged and non-damaged cases of armor stones and proposed the following empirical formula:

$$W = 0.08 \frac{1}{5^{d/H_{1/3}}} H_{1/3}^{3}$$

The conditions for calculations are as follows:

h = 20 m, h' = 15 m, B_M = 10 m

Wave conditions are selected so as to be $H_{1/3}/L$ = 0.045 for the range of the significant wave period from 8 to 16 seconds. Here, L is the wavelength corresponding to the significant wave period at the water depth of 20 meters. The cover layer for the rubble mound foundations is supposed to have a thickness of two armor units and densities of the rubble unit and the sea water are given to be 2.65 t/m^3 and 1.03 t/m^3, respectively.

The results are very different by the mothods as shown in Figure 16, where the absissa is taken as the significant wave height. Generally, the method by Brebner and Donnelly for the rubble mound as foundation results in a very large mass. On the other hand, the method by Inagaki and Katayama gives the minimum mass. The mass calculated by the authors' method is between them and close to the latter rather than the former. The calculated masses for the rubble mound as toe protection by Brebner and Donnelly are also shown in the figure. In this example, the results are very close to those by authors' method, when $H_{1/10}$ is applied. However, such relative relations by the different methods will be changed by the conditions of water depth and the configuration of the rubble mound foundation, since the parameters involved in the methods are different.

CONCLUDING REMARKS

The results of this study provide the design informations of armor units for rubble mound foundations of composite breakwaters. The stability number of the armor units are greatly influenced by the configuration of rubble mound foundation and wave conditions. The stability numbers for quarry stones and concrete blocks were formulated by two parameters of $h'/H_{1/3}$ and K on the basis of irregular wave tests. Generally, the damage of quarry stones placed in two armor layers progresses rather gradually. The application of the proposed method to the test results demonstrates that the damage percent of quarry stones is at most 3.5 % at the design condition. On the other hand, the damage of the concrete blocks placed regularly in single layer progresses drastically in the case of high rubble mound foundations. Therefore, it is not recommended to apply the concrete blocks in single layer to high rubble mound foundations.

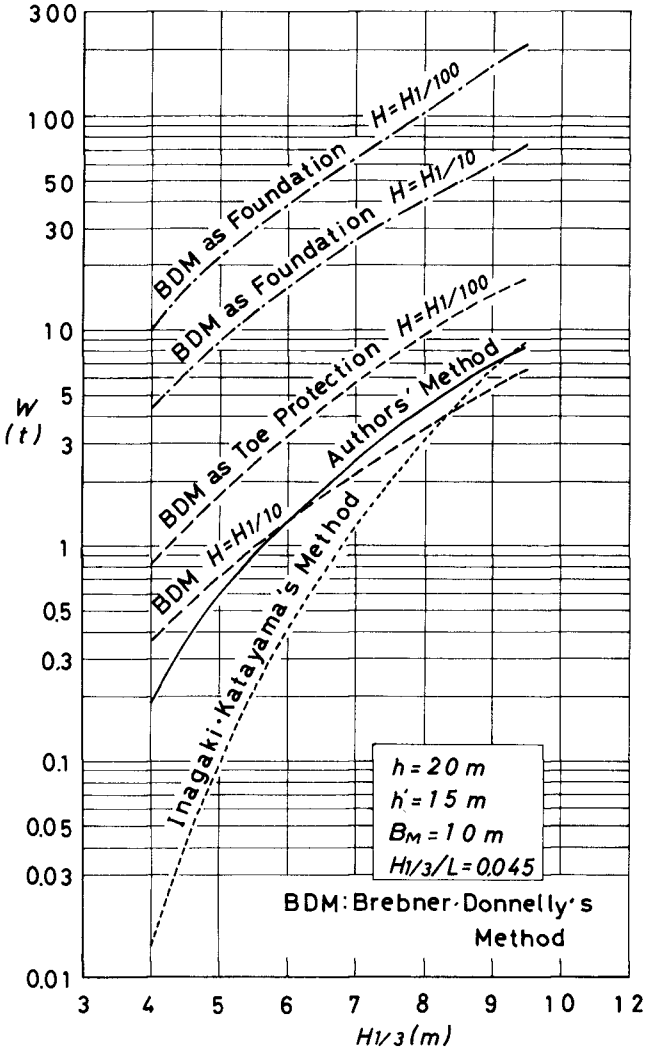

Figure 16 Design mass of quarry stones calculated by several methods

REFERENCES

Brebner, A. and D. Donnelly (1962) : Laboratory study of rubble foundations for vertical breakwaters, Proc. 8th Coastal Engg. Conf., New Mexico City, pp. 408 - 429

Bureau of Ports and Harbours, and Port and Harbour Research Institute, MOT (1980) : Technical standards for port and harbour facilities in Japan, 317p.

Coastal Engineering Research Center, U.S. Army (1973) : Shore protection manual, Volume II

Goda, Y. (1974) : New wave pressure formulae for composite breakwaters, Proc. 14th Coastal Engg. Conf., Copenhagen, pp. 1702 - 1720

Goda, Y. and Y. Suzuki (1976) : Estimation of incident and reflected waves in random wave experiments, Proc. 15th Coastal Engg. Conf., Honolulu, pp. 828 - 845

Inagaki, H. and T. Katayama (1971) : Analysis of damage to armor stones of mounds in composite breakwaters, Tech. Note of PHRI, No. 127, 22p. (in Japanese)

THE MONITORING OF RUBBLE MOUND BREAKWATER STABILITY USING A PHOTOGRAPHIC SURVEY METHOD

by

J W J Kluger*

ABSTRACT

A method of surveying the above-water slope of breakwaters by means of photography has been developed at the National Research Institute for Oceanology. The method is simple and inexpensive and yet capable of detecting movement or displacement of a single armour unit on a breakwater.

This poster paper describes the method and presents some examples of its application in the field.

1. INTRODUCTION

The long-term stability of, and the intermittent storm damage to, rubble mound breakwaters are of considerable interest to the designers, builders and authorities responsible for maintenance. A major disaster will obviously be noted immediately, whereas a gradual deterioration, settlement or breakage and movement of individual armour units can often pass unnoticed until major damage occurs. Early detection of cases of potential damage is therefore essential. Full breakwater surveys can become costly and time-consuming and often do not detect the finer details of damage.

A simple yet effective photographic method of surveying the above-water part of a rubble mound breakwater has been developed at NRIO to monitor effectively the movement, displacement and breakage of armour units on the slope. Since this method only records the above-water part of a breakwater it cannot reveal its overall condition, however, it will nevertheless give a reasonable indication of the condition of a breakwater since it is able to record damage in the above-water part of the zone where damage normally commences, that is, the zone with boundaries just above and below still water level (Zwamborn, 1980).

* Coastal Engineering Structures Division, National Research Institute for Oceanology, Council for Scientific and Industrial Research, Stellenbosch, Republic of South Africa

To determine the overall stability of a breakwater this method of survey should obviously be supplemented with an under-water survey method.

2. THE METHOD OF SURVEYING

The technique involves photographing the breakwater in sections from a distance such that individual armour units on the breakwater can be identified easily. A picture of the whole length of the breakwater is obtained by joining the photographs. The sections of the breakwater and the positions from which the photographs are taken are recorded so that subsequent photographs, taken of these sections from the set positions, when compared with the earlier photographs, permit damage to the breakwater to be detected and estimated.

The horizontal photographs taken at sea level can be complemented by photographs taken vertically from the air e.g. aerial survey photographs enlarged to the same scale as the horizontal photographs. These provide means for even closer examination of the condition of the breakwater.

The success of the method depends largely on the accuracy with which it is possible to identify and fix the positions from which the photographs are taken of the breakwater sections. However, no sophisticated position-fixing equipment is used in the surveys and the method is as follows:

Two large beacons are erected on shore to provide a fixed reference line parallel to the breakwater. By sighting and keeping the two beacons in line, the survey boat from which the photographs are taken can maintain a course parallel to, and at the required distance from, the breakwater.

Each breakwater section is identified by two marks painted on the breakwater, one on the top of the splash wall and the other on the land side of the breakwater deck. The line connecting these two marks is perpendicuar to face of breakwater. During a survey a large board with the number of the breakwater section and with a flag at its top is placed over the mark on the splash wall. A long staff, also with a flag at its top, is placed over the corresponding mark on the land side of the breakwater. These two markers, clearly visible from the survey boat, thus provided a reference line of sight to the breakwater section. The positioning of the survey lines and of breakwater sections is shown diagrammatically in Figure 1.

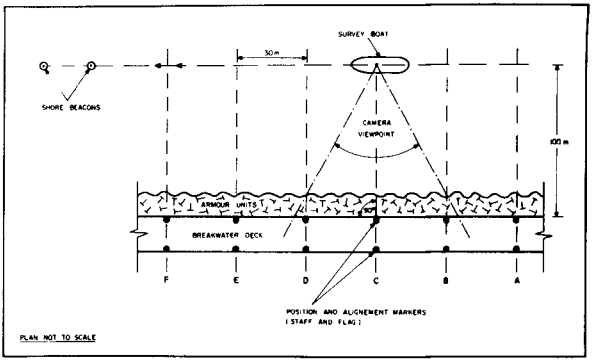

Figure 1 Method of photographic survey (diagrammatic)

The procedure for the survey is as follows:

The survey boat, using the two shore beacons as references, takes up a position on the line parallel to the breakwater, at a fixed distance from the breakwater section to be photographed. The identity board and the flagstaff are placed over the corresponding marks on the breakwater section. The survey boat then moves along the reference line and when the two markers on the breakwater coincide in the centre of the camera viewfinder the photograph is taken. In this way, the position from which the photograph is taken is fixed. This procedure is repeated at each section.

The camera used for the survey is a 6 × 7 single-lens reflex with a 90 mm focal length lens. Each photograph taken from a distance of 100 m provides a 74 m horizontal coverage of the breakwater.

Since the breakwater survey sections are normally marked at 30 m spacings each photograph covers more than two sections. This large overlap provides for the possibility of three-dimensional viewing under a stereoscope.

There are several ways in which the photographs can be analysed.

As mentioned earlier, the photographs can be viewed in pairs under a stereoscope to provide a three-dimensional image of the breakwater section.

For initial comparison of any two surveys, photographs of corresponding breakwater sections are enlarged to the same scale, usually 1:250, and the two photographs examined to detect any changes in the breakwater.

If any changes are noted, and if a closer inspection is needed, the photographs can be enlarged to a much higher degree. The photograph of the first survey (A) is printed in the normal way on photographic paper while the corresponding photograph from the second survey (B) is printed on a positive transparency sheet film. Changes in the positions of dolosse on the breakwater can be detected accurately when the transparency B is placed over the photograph A. If even more detailed analysis is warranted the photographs of only the damaged section can be enlarged further. Since lighting conditions, shadows, etc., are not likely to be the same in any two surveys, the outline of each dolos in the damaged section can be traced onto a film sheet to make the comparison easier. The two tracings overlaid can then be examined dolos by dolos.

When only one or two dolosse have been noted to have moved, the change in dolos position can be shown sufficiently well on an enlargement of the photograph of the relevant breakwater section.

Since damage to an armour slope normally occurs in a zone with boundaries just below and above still water level it is important to do the photographic survey during low water spring tide so that as much as possible of this zone is recorded.

3. SOME RESULTS OF SURVEYS

To date, the method has been used to monitor the stability of breakwaters at three sites, the western breakwater of the Table Bay harbour, the cooling water intake basin at the Koeberg power station and the harbour entrance breakwater at Richards Bay.

Table Bay harbour western breakwater is an old structure which in the course of time has been extended and modified. Because of this there are different types of construction and armour units along its length of about 1 km. These range from caissons to concrete blocks to dolosse. The breakwater is subjected to severe breaking wave action during the winter storms and some parts of the breakwater occasionally require repairs. Photographic surveys are

Figure 2 Loss of dolosse at section P10

used there to monitor the effectiveness of the repairs as well as the general stability of the breakwater. Examples of photographs of damage on the breakwater are shown in Figure 2.

The two breakwaters of the cooling water intake at Koeberg were completed recently (1980). Both breakwaters are rubble mound constructions overlaid with dolos armour units. Regular breakwater surveys have been undertaken as part of the post-construction monitoring programme. Very limited settlement of a few individual dolosse has been recorded on the two breakwaters. An example of settlement (two dolosse) on the head of the breakwater is shown in Figure 3.

Figure 3 Dolos settlement at section S2

Richards Bay harbour breakwaters, both of rubble mound construction with dolosse as the armour unit, were surveyed prior to the proposed improvements. Further surveys are planned to monitor the long-term stability of the breakwaters.

4. CONCLUSIONS

The method of photographic surveying of the above-water part of breakwaters has been found capable of detecting the movement and displacement of individual armour units on a breakwater slope. In spite of the fact that it can only record the above-water part of the zone about the still water level where damage normally commences it can be most valuable as far as giving an early warning of damage in that zone. The method is simple and inexpensive, involving a few people and a boat. A survey takes an average of

about one hour for a 1 km length breakwater. The time required for the analysis of results depends on the extent of change or damage on the breakwater recorded during the survey.

5. ACKNOWLEDGEMENTS

The development of the method was done as a basic research project of the National Research Institute for Oceanology. The assistance by South African Transport Services in the field trials and their permission as well as that of the Electricity Supply Commission to publish the field data is hereby acknowledged.

6. REFERENCE

ZWAMBORN, J A (1980). Measuring techniques, dolos packing density and effect of relative block density. CSIR Research Report 378, Stellenbosch.

COMBINED WAVE-CURRENT FORCES ON HORIZONTAL CYLINDERS

by

B.D. Chandler[1] and J.B. Hinwood[2]

ABSTRACT

Some early results are reported from an investigation of the forces exerted on horizontal cylinders by waves and currents. It appears that the values of the inertia coefficients decrease as U/u_o increases, and the drag coefficients decrease also, for values of U/u_o up to 0.7. Comparisons with measured data show that linear theory and the stream function theory satisfactorily describe the wave motion for the conditions investigated, and that velocity superposition can be used with either of these theories to describe conditions involving waves plus currents, with reasonable accuracy.

1. INTRODUCTION

There have been many theoretical and experimental investigations of the hydrodynamic forces that are exerted on submerged cylinders by wave action. Most have been aimed at deriving accurate values for the drag and inertia coefficients for use in the Morison force equation. The forces acting on a cylinder in a steady flow situation have also been investigated extensively, much of this work having been undertaken in wind tunnels. There has, however, been very little investigation of the forces that are exerted when there is a current present in addition to the waves.

Tung and Huang (1973) studied the importance of the presence of the current and the effects of wave-current interactions on the probability function, spectrum and peak distribution of the fluid loading on a cylinder. Since they were interested primarily in the effects of the current upon these statistical properties of the fluid

---

[1] Post Graduate Student, Department of Mechanical Engineering, Monash University, Clayton, Victoria, Australia.

[2] Associate Professor, Department of Mechanical Engineering, Monash University, Clayton, Victoria, Australia.

force, rather than in predicting actual force values for given situations, they assumed values for the Morison force coefficients. Dalrymple (1975) investigated the effects of combined waves and currents using field data obtained in the "Wave Project II" exercise. He concluded that the presence of a current must be taken into account in order to obtain accurate drag force coefficients. Knoll and Herbich (1980) conducted an experimental investigation of the simultaneous wave and current forces acting on a submerged pipeline. They found that the drag coefficients obtained from simultaneous measurement of the force and the velocity were less than those obtained when the velocity was computed by adding the wave velocity from Airy and Stokes third order wave theories to the current velocity. Recently, Kemp and Simons (1982) have undertaken an extensive experimental investigation of the wave/current kinematics. They found that the thickness of the steady flow boundary layer was reduced by the superposition of waves propagating with the current.

The purpose of the present study is to investigate the interaction that occurs between a known wave pattern and a known current; to determine the effects that this interaction has upon the hydrodynamic loading on a submerged, horizontal circular cylinder; and to relate the changes in loading to the detected flow pattern around the cylinder. Measurements were made of the water particle velocities in a combined wave-current flow condition. The wave-current interaction was investigated by comparing these measured values with the velocities obtained by vector addition of the individual wave and current components. One could thereby determine the accuracy achieved by representing the overall velocity field as the sum of the individual components. Measurements were also made of the forces acting on the cylinder; and these, together with the simultaneous velocity measurements, were used to calculate the force coefficients.

2. THEORY

2.1 Wave Theory

In this report, the principle of superposition is used for the theoretical prediction of fluid motion for conditions involving waves plus currents. The horizontal orbital velocities are therefore expressed as the sum of the current velocity and the orbital velocity predicted by the particular wave theory. For these calculations, the wave period used is the one measured in a frame of reference moving with the current. This period, denoted by T', is defined as:

$$T' = T\left(\frac{V}{V - U}\right) , \qquad (1)$$

where T = wave period in stationary frame
V = speed of propagation of wave crest in the flowing water
U = current velocity (the average value over the cross-section of the channel).

The measurements will be compared with the predicted results of two wave theories: the Airy linear theory, and the stream function

theory. The stream function results are obtained from the tables prepared by Dean (1974). Linear interpolation is used to correct for the small departure of the wave parameters from the tabulated results.

2.2 Force Equation

The Morison (1950) equation is normally used for determining the hydrodynamic forces acting on a submerged cylinder due to wave action. In this equation, the force is expressed as the sum of a velocity-dependent drag force and an acceleration-dependent inertia force, as follows:

$$F = C_d \frac{1}{2} \rho D u \left| (u^2 + v^2)^{1/2} \right| + C_m \rho \frac{\pi D^2}{4} \dot{u} \qquad (2)$$

where F = horizontal force per unit length
ρ = density of fluid
D = diameter of cylinder
u = horizontal wave-induced water particle velocity
v = vertical wave-induced water particle velocity
$\dot{u}$ = horizontal wave-induced water particle acceleration
C_d = drag coefficient
C_m = inertia coefficient.

The drag force term is commonly expressed as being proportional to $u|u|$; that is, independent of the vertical velocity. The definition given in eqn (2), however, more correctly describes the horizontal component of the total drag force acting on a horizontal cylinder.

Numerous investigations since 1950 have been aimed at determining the correct values to use for the drag and inertia coefficients. The results of these investigations show a considerable scatter in the derived values for the coefficients, and the coefficients have been shown to be dependent upon parameters such as the Reynolds number, the Keulegan-Carpenter period parameter, the surface roughness of the cylinder, and the vertical to horizontal velocity ratio, v/u .

The design codes (e.g. British Standards Institution (1978)) recommend that the velocities and accelerations be determined by using one of the commonly-used wave theories, such as the linear theory, the Stokes fifth order wave theory, or the stream function theory. The appropriate theory to use will depend upon the particular conditions at the site.

2.3 Force Equation for Simultaneous Waves Plus Current

For conditions involving waves as well as a current, the design codes recommend that the drag force term in the Morison equation be based upon the sum of the current velocity and the wave velocity which would be present in the absence of the current. For horizontal cylinders, the Morison equation should more accurately be written as follows:

$$F = C_d \frac{1}{2} \rho D(u + U)\left|((u + U)^2 + v^2)^{1/2}\right| + C_m \rho \frac{\pi D^2}{4} \dot{u} \qquad (3)$$

where U = current velocity at the depth at which u and $\dot{u}$ are being determined.

For the experimental analysis in this investigation, the term $(u + U)$ is replaced by the total, measured, horizontal velocity. Note that in eqn (3), F, u, v and $\dot{u}$ are functions of time, varying over the wave period.

3. EXPERIMENTAL PROGRAMME

3.1 Equipment

The tests were conducted in a wave channel measuring 15 m in length, 0.60 m in width, and 0.30 m in depth. The waves were generated using a paddle driven by a variable speed electric motor. Openings in and under the paddle permitted the current to flow through it. A specially designed beach was used which satisfactorily dissipated the wave energy, while at the same time allowing water to flow through it. The beach face consisted of parallel wooden slats, with gaps between the slats equal to about 25% of the slat width. A layer of nylon filter material was placed over the upper surface of the slats. The slope of the beach was approximately 1 in 10.

The aluminium test cylinders were 400 mm long, with phosphor bronze end plates fitted to each end. Two different cylinders were used; one having a diameter of 12.7 mm, and the other having a diameter of 25.4 mm. The hydrodynamic forces acting on the cylinder were measured with load-cell devices attached to each end of the cylinder. The load-cells employed semiconductor strain gauges arranged in a Wheatstone Bridge configuration, which had the advantages of increasing the signal output as well as rendering the devices insensitive to small temperature fluctuations. The load cells were tested and found to have negligible drift over a typical recording period of a few hours. Both the vertical and the horizontal forces acting on the cylinder could be measured and recorded simultaneously. To avoid possible errors, no mechanical damping was incorporated into the load cells. They were therefore vulnerable to external mechanical vibrations. To overcome this problem, a very rigid support was constructed for the test assembly, and the support was isolated from the parts of the laboratory building which could transmit vibrations.

A 2 W Argon-Ion laser-Doppler velocimeter was used to measured the water particle velocities. This enabled the horizontal and vertical velocity components to be measured simultaneously, at a point at the same relative depth as the test cylinder.

Two capacitance-type wave gauges were used to measure the water surface elevation directly above the velocity measurement point and above the test cylinder.

The laboratory's constant head tank was used to supply the water for the experiments requiring a current. The head tank was connected, via a control valve, to a reservoir behind the paddle. After flowing through the paddle, along the channel and through the beach, the water passed over a control weir into a weighing tank. It then flowed into the laboratory's sump, from which it was pumped back up to the head tank. The weighing tank was used to obtain an accurate measure of the mass flow rate of the current, from which one could easily determine the current velocity, averaged over the cross-section of the channel.

3.2 Procedure

The still water depth for all tests was 220 mm. The horizontal test cylinders were positioned at three different levels, namely 60, 100 and 150 mm above the floor of the channel. The lowest level was therefore 2.4 cylinder diameters above the floor of the channel, whilst the upper level was nearly 3 diameters beneath the still water level. These levels were set to ensure that no interference effects would occur as a result of the proximity of these boundaries.

The experiments involved generating waves of the same height and period on four different current velocities, ranging from 0 to approximately 100 mm/s. The experiments were repeated for waves of different heights and periods. Four different periods were used, ranging from 0.72 to 1.25 s, with two different heights, ranging from 40 to 74 mm, for each period.

In each experiment, six channels of data were recorded simultaneously. These were the horizontal and vertical forces acting on the cylinder; the horizontal and vertical velocities being measured by the laser-Doppler; and the water levels directly above the cylinder and the velocity measurement point. The velocity measurement point was normally about 150 mm upstream from the cylinder.

A sampling rate of 1000 Hz was used to record the six channels of data, and so each variable was sampled at approximately 167 Hz. The minimum number of measurements for each wave cycle was therefore 120. Data were sampled for approximately 30 seconds, corresponding to 24 to 43 successive wave cycles per sample. All measurements were immediately digitised and stored on magnetic disc for subsequent analysis on an HP21MX computer. The resolution of the analog to digital converter was 5 mV, which was satisfactory in view of the fact that the signal inputs were all of the order of a few volts.

Measurements were made of the time taken for the waves to travel 7.8 m along the channel. From this, one could determine the wave celerity, the wavelength (from knowing the period), and also the phase shift between the locations of the velocity measurement point and the test cylinder.

The load cells were calibrated each day, with the cylinder set up in the configuration being used for that day's experiments. The

calibration of the laser-Doppler was checked on several occasions throughout the course of the experiments; and the wave gauges were calibrated several times at the end of the experiments. No significant changes in the calibration factors were observed for any of the instruments.

3.3 Range of Parameters

The ranges of wave heights and periods, and the current velocities, have already been given in Section 3.2. The still water depth and the steady flow depth was 220 mm for all experiments.

The experiments covered the following ranges of dimensionless parameters:

$\frac{U}{u_o}$: 0 to 1.2

K : 2.1 to 14.2

Re : 9×10^2 to 5×10^3

$\frac{v_o}{u_o}$: 0.23 to 0.86

$\frac{H}{L_o}$: 0.015 to 0.069

$\frac{h}{L_o}$: 0.080 to 0.272

$\frac{H}{H_b}$: 0.23 to 0.43

where h = still water depth
H = wave height
H_b = breaker height = 0.78 h
u_o = horizontal velocity amplitude
v_o = vertical velocity amplitude
K = Keulegan-Carpenter number = u_oT/D
L_o = deep water wavelength
Re = Reynolds number (based on u_o).

3.4 Data Reduction

The drag and inertia coefficients, as defined in eqn (3), were determined by least squares curve-fitting over one whole wave cycle. The average values of the drag and inertia coefficients for each flow condition were obtained in two different ways. One method involved calculating the coefficients for each wave cycle sampled, and determining the average value of these 20 to 40 coefficients. The other method involved averaging the velocity, acceleration and force

data from the 20 to 40 wave cycles sampled, to obtain one representative cycle for each variable, for that particular flow condition. The drag and inertia coefficients were then determined from these averaged cycles of the velocity, acceleration and force. As would be expected, no significant differences were found between the values of the coefficients calculated by these two different methods. These averaged cycles of data were also used for all comparisons of profiles, velocities and accelerations with the wave theories.

4. RESULTS

4.1 Forces

One of the aims of this study is to investigate the effects that the introduction of a steady flow velocity component has upon the values of the drag and inertia coefficients. Figs. 1 and 2 show some of the results obtained by plotting the force coefficients against the current/wave velocity ratio U/u_o . The points lying on each series of lines have approximately the same values of K and v_o/u_o . The results shown are for the 25 mm diameter cylinder, for the levels 98 mm and 148 mm above the floor of the channel. The results for the 12.7 mm diameter cylinder showed similar trends to the larger cylinder, but there were unexpected inconsistencies between the three different levels. These experiments are presently being repeated, and so no results are yet available.

It can be seen in Fig. 1 that the values of C_m decrease steadily as U/u_o increases, such that when $U/u_o = 1.0$, the values of C_m are about 0.4 less than for $U/u_o = 0$. The values of K range from 2.3 to 7.6, and v_o/u_o ranges from 0.35 to 0.82. Both of these parameters appear to have had little influence on the value of C_m , over the ranges quoted.

In Fig. 2, the values of C_d decrease rapidly as U/u_o increases from 0 to about 0.7. Then the values increase rapidly as U/u_o increases from 0.7 to 1.1. The reasons for this dramatic change are not clear. It was observed, however, that, for conditions in which U/u_o was approximately 1.0, the force records displayed a periodic behaviour whose period was twice that of the wave period. This may have been caused by a regular, asymmetric vortex shedding pattern, and it is proposed to investigate this further with the assistance of hydrogen bubble flow visualisation. If a vortex shedding pattern is causing the two-period variation in the force records as well as the change in the C_d values, then it is surprising that it appears to have had negligible effect upon the values of C_m .

The ranges of K and v_o/u_o for the results shown in Fig. 2 are the same as those for Fig. 1, and once again these two parameters appear to have had little effect on the value of C_d .

The values obtained for both coefficients were compared with those reported by others for conditions involving waves alone. They

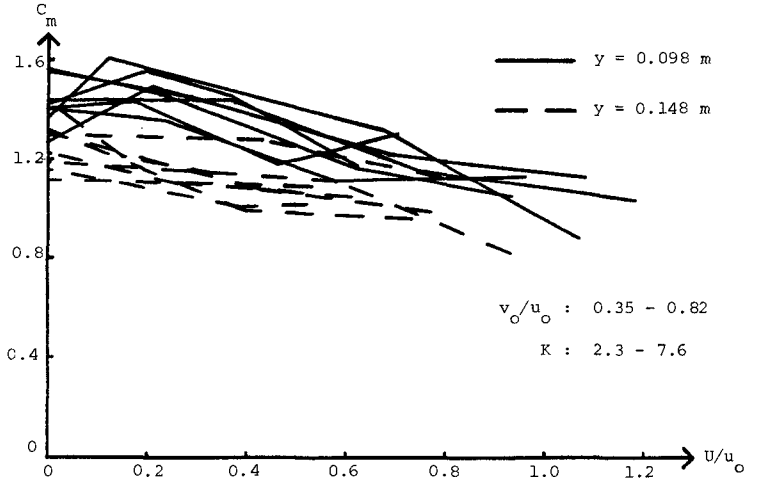

Fig. 1 C_m vs. U/u_o

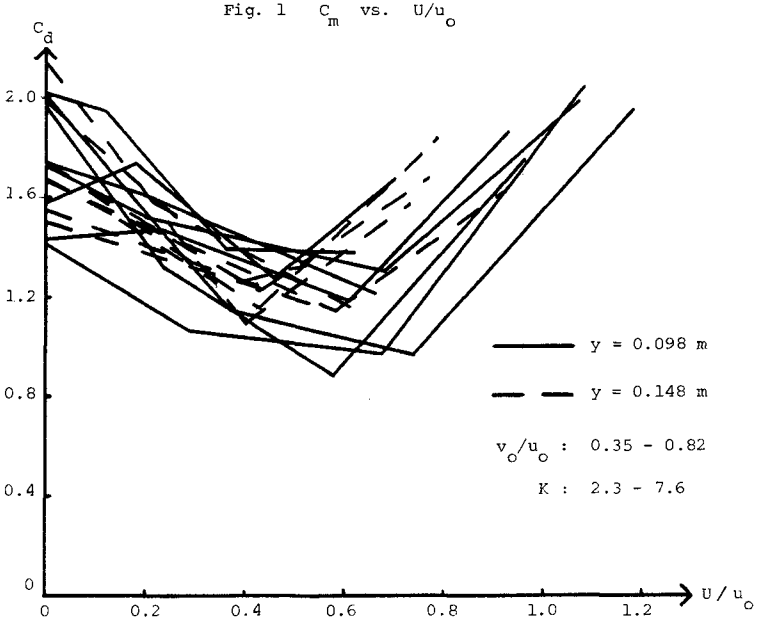

Fig. 2 C_d vs. U/u_o

were generally within the range bounded by the results obtained by Ramberg and Niedzwecki (1980), and the planar flow water tunnel results obtained by Sarpkaya, as reported by the previous authors. There was a slight tendency for the coefficients obtained for high values of U/u_o to be closer to Sarpkaya's results.

The error analysis technique developed by Dean (1976), and modified by Chandler and Hinwood (1981) to apply to conditions involving waves plus a current, was used to determine the suitability of the experimental data for determining the drag and inertia coefficients. Generally, the experiments involving waves alone were better suited for determining the inertia coefficients. As the current velocity was increased, the drag force became more dominant until, for the maximum current speeds investigated, the data had become better conditioned for determining C_d than C_m.

4.2 Wave Motion

4.2.1 Description of Wave Data

All of the experimental results presented in this section are averaged results, obtained by averaging the data from at least ten successive wave cycles. For the comparisons of experimental results with theoretical results, the phase-matching of the different curves was done subjectively to achieve the best general fit over the whole cycle, rather than just matching the curves at, for instance, the crests.

The same basic wave pattern was used for all of the comparisons presented. The main features of this wave pattern are as follows: $H = 0.073$ m ; $h = 0.220$ m ; $T = 0.83$ s (measured in the stationary reference frame); $L = 0.968$ m ; $C = 1.166$ m/s ; $h/L_o = 0.205$; $H/L_o = 0.068$; $H/H_b = 0.43$. For these conditions, Dean (1974) suggests that Stokes V would be the analytical theory providing the best fit to the dynamic free surface boundary condition, but that the stream function V theory would be the best theory overall. For the conditions involving waves plus current, the average current velocity across the channel was 101 mm/s for Figs. 3 and 4, and 61 mm/s for Figs. 5 to 8.

Similar comparisons have been done for a wave pattern with $H = 0.047$ m , $T = 1.03$ s and $L = 1.310$ m . The results are not shown in this report, but the observed trends and wave theory comparisons were found to be similar to those presented.

For the linear theory predictions for waves plus current, the calculations were based on the measured wave height, the measured wavelength, and the period measured in the frame of reference moving with the current, as described in eqn (1). The average current velocity (61 mm/s) was added to the calculated horizontal orbital velocity.

For the stream function predictions of waves plus current, the wave conditions were determined from the appropriate values of h/L_o

and H/L_o, where L_o was set equal to the speed of propagation of the wave in deep water multiplied by the period measured in the stationary reference frame. The speed of propagation was calculated as the sum of the deep water wave celerity for the wave period measured in the moving reference frame, and the average current velocity. Once again, the average current velocity (61 mm/s) was added to the calculated horizontal orbital velocity.

The measured velocities were all measured at a point 100 mm in from the side wall of the channel, and approximately 100 mm above the floor of the channel. The velocities were also measured 300 mm in from the wall, which is effectively in the middle of the channel, but these measurements were not used here since the laser-Doppler signals had higher noise levels than those obtained nearer the wall. Comparisons were made between data measured at these two locations, and it was found that there was no significant difference between them.

For the data presented in this report, the positive direction for the horizontal velocities is the direction of wave propagation. For the vertical velocities, positive is taken as being upwards. The surface elevations are also positive upwards.

4.2.2 Wave Profiles

Fig. 3 shows a comparison of the wave profiles for waves of identical height and period (measured in the stationary frame), one being for waves alone, and the other being for waves plus a current of 101 mm/s. The introduction of the current lowered the levels of both the trough and the crest by about 6% of the wave height, and the trough was not as flat and shallow as for the zero flow case. The current also made the leading face of the wave flatter, and the trailing face slightly steeper.

Figs. 5 and 6 show comparisons of the measured profiles with the linear theory and stream function theory profiles, for conditions involving waves alone and waves plus a current of 61 mm/s. For both flow conditions, the measured crests and troughs laid well above the linear theory predictions. For the zero flow case, the differences were about 8% of the wave height, while for waves plus current the differences were about 6%. The measured profiles had flatter troughs, and narrower, steeper crests than the sinusoidal profiles.

For waves alone, the stream function profile compared extremely well with the measured profile. The measured crest and trough were about 1% below the predicted levels, and the general shape of the wave was almost identical. For the wave plus current condition, the measured crest and trough were about 4% below the stream function levels, and there was still reasonably good agreement between the shapes of the two profiles.

The stream function profiles provided better predictions of the extreme water levels and water surface slopes than did the linear theory profiles, although the linear ones were still only about 8% to

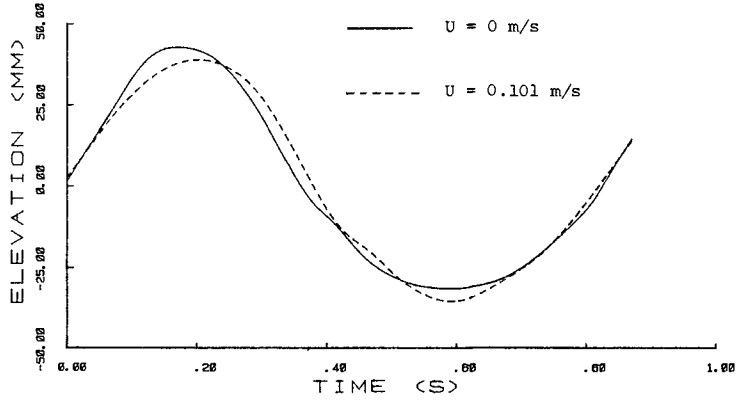

Fig. 3 Comparison of measured wave profiles
(H = 0.074 m, T = 0.83 s, y = 0.098 m)

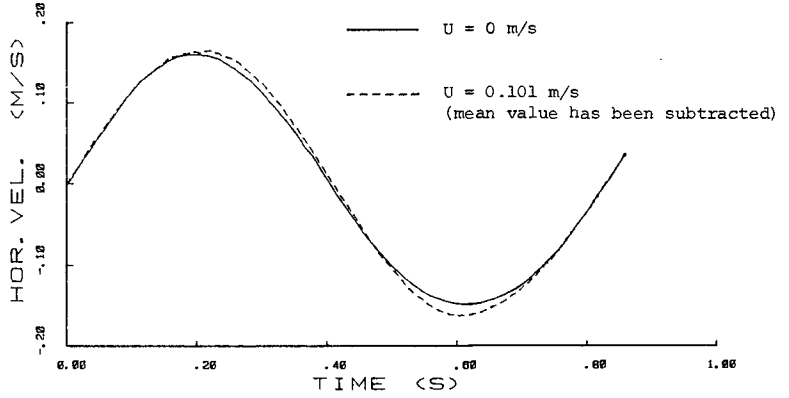

Fig. 4 Comparison of measured horizontal velocities
(H = 0.074 m, T = 0.83 s, y = 0.098 m)

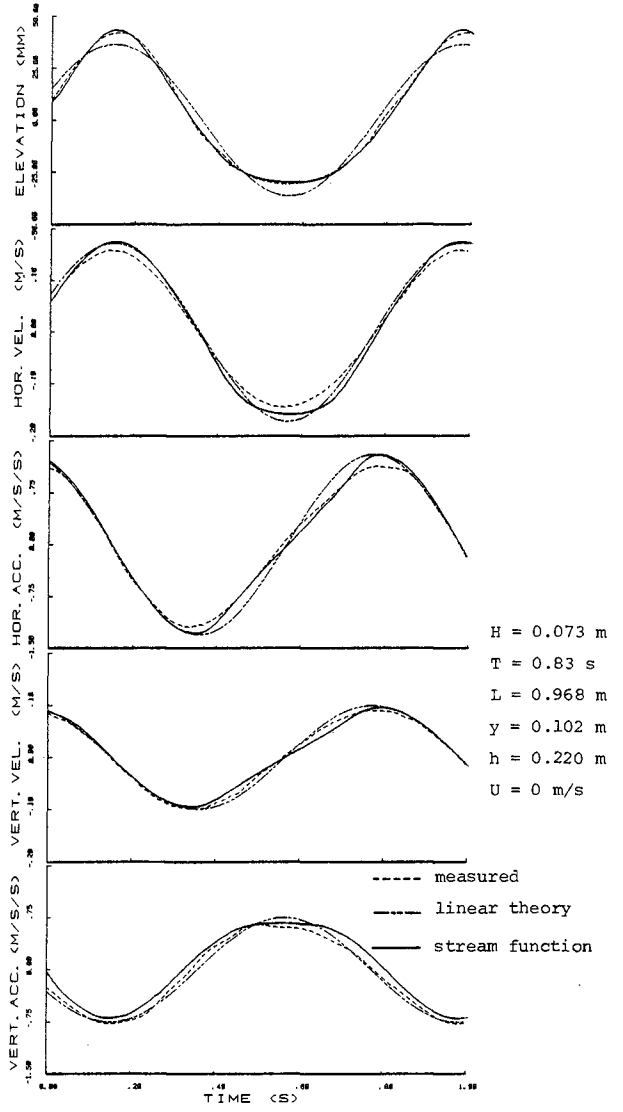

Fig. 5 Comparisons of measured and predicted values for waves alone

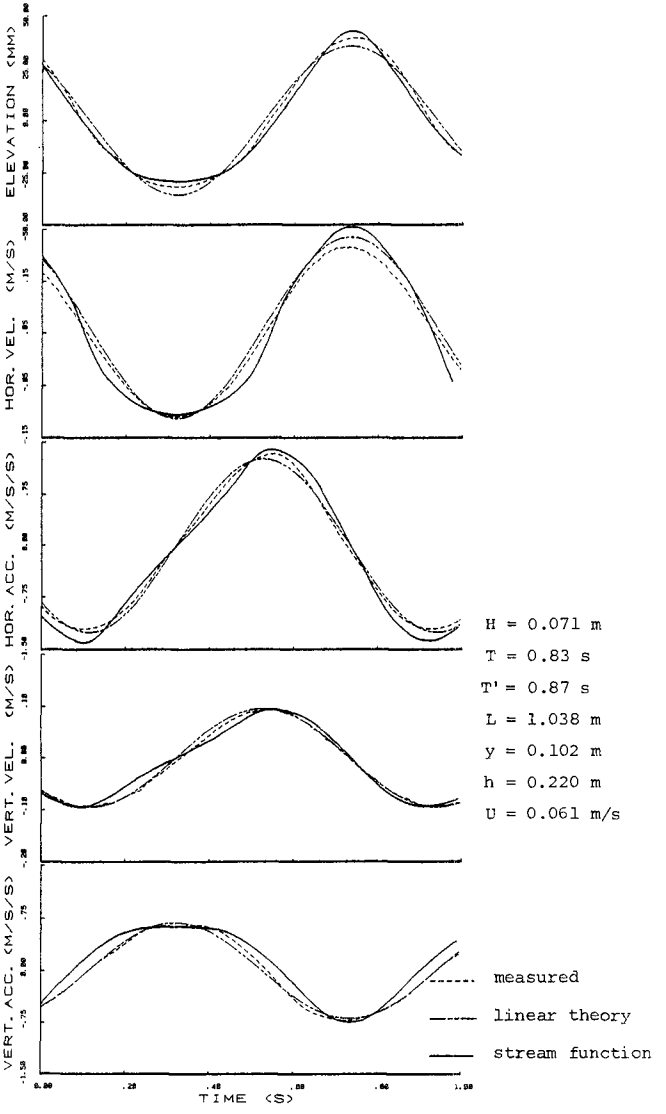

Fig. 6 Comparisons of measured and predicted values for waves plus current

10% of the wave height in error. The linear theory improved slightly for the waves plus current condition, whereas the stream function became slightly worse.

4.2.3 Velocities

Fig. 4 shows a comparison of the measured horizontal velocities for waves alone and for waves plus current. The average current over the cross-section of the channel was 101 mm/s, and the wave celerity for the zero flow condition was 1161 mm/s. The mean velocity over one cycle for the waves plus current condition at the point of measurement was 99 mm/s, and this has been subtracted from the velocities so that both curves have zero mean. The shapes of the two curves are very similar, but the waves plus current curve has a range about 6% greater than the waves only case. However, if linear theory corrections are applied to correct for the period measured in the moving reference frame and also the longer wavelengths of the waves on the current, then this reduces the waves plus current velocities by 6%, making the amplitudes of the two curves almost identical.

Figs. 5 and 6 show comparisons of the measured horizontal velocities with linear theory and stream function predictions. For waves alone, both theories gave similar velocity curves, and they both overestimated the peak velocities. The stream function theory overestimated the velocity range by about 10%, whilst the linear theory overestimated it by about 13%. For the waves plus current conditions, the stream function overestimated the range by about 10%, whereas the linear theory was only about 7% too great.

Figs. 7 and 8 show the variation with depth of the peak horizontal velocity, for y/h varying from 0 to 0.7, where y is the height above the floor of the channel. Due to limitations of the laser-Doppler traversing rig, velocity measurements could not conveniently be obtained at levels higher than $y/h = 0.7$. Fig. 7 indicates that for waves alone, both theories overestimated the velocity range, over most of the depth, by about 5% to 12%, with the stream function theory being generally slightly better. For the waves plus current conditions in Fig. 8, the mean values of the measured results became less than the average mean of 61 mm/s, as y/h increased. This suggests that there may have been a net circulation or drift set up in the channel, in addition to the steady flow. Looking at the velocity range, however, both theories once again overestimated the range by 5% to 15%. In this case the linear theory appears to have provided the better overall estimate.

Figs. 5 and 6 also show comparisons of measured vertical velocities with the theoretical estimates. Generally the agreement is very good. For waves alone, the peak downward velocities were predicted to within a few percent by both theories, and the peak upward velocities were overestimated by both theories, by up to about 5% for the linear theory. Overall, the stream function provided a better estimate. For waves plus current, the two predicted ranges were virtually the same as the measured range. The linear theory provided a slightly better fit at points between the peaks.

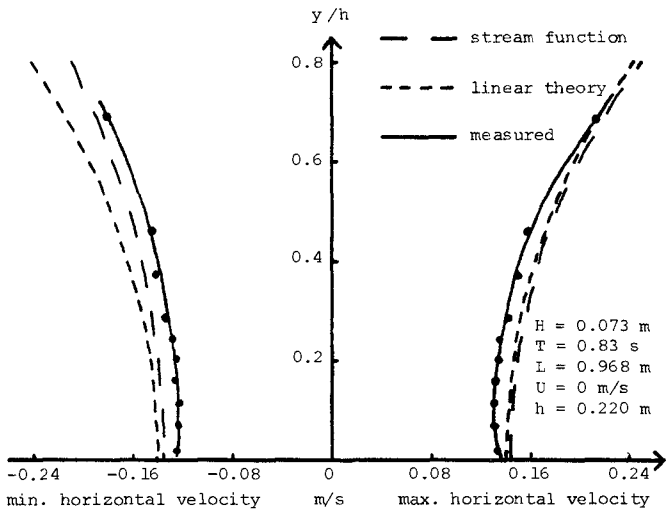

Fig. 7 Variation with Depth of Peak Horizontal Velocity - Waves Alone

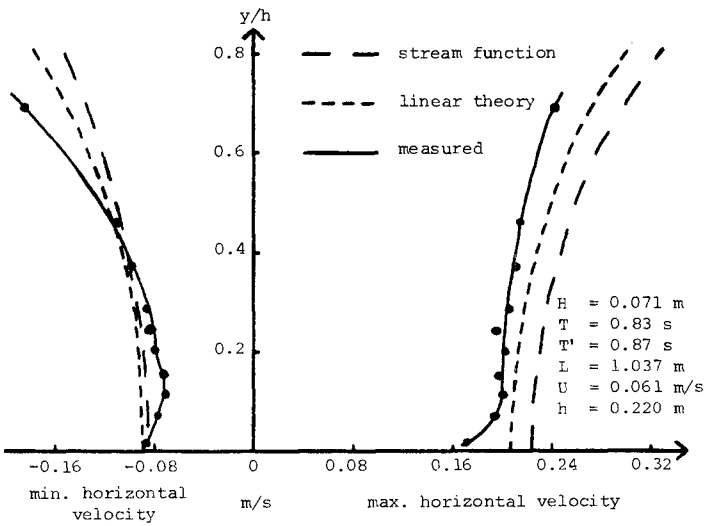

Fig. 8 Variation with Depth of Peak Horizontal Velocity - Waves Plus Current

4.2.4 Accelerations

Figs. 5 and 6 show comparisons of measured and predicted horizontal and vertical accelerations, for waves alone and waves plus current. In Fig. 5, for waves alone, both theories overestimated the peak horizontal accelerations. The linear theory overestimated the range by about 12%, and the stream function theory was about 10% too great. The stream function generally provided the better estimate.

For the case of waves plus current, (Fig. 6), the linear theory slightly overestimated the negative horizontal acceleration peak and underestimated the positive peak, so that its estimated range was only about 1% less than the measured range. The stream function theory overestimated the negative peak appreciably, and slightly overestimated the positive peak, so that its estimated range was about 9% greater than the measured range.

The linear theory's prediction of the vertical acceleration, for waves alone, slightly underestimated the downward accelerations at the wave crest, and overestimated the upward accelerations at the trough by about 7%. This is consistent with the fact that the measured wave profiles had wider, flatter troughs than the sinusoidal profile. The stream function slightly underestimated the crest accelerations, and overestimated the trough accelerations, such that its estimated range was approximately the same as the measured range.

For the vertical acceleration for waves plus current, both theories estimated the peaks and the range to within a few percent. The linear theory, however, provided the better estimate of the general shape of the acceleration curve.

5. CONCLUSION

This paper reports some of the early results obtained from a continuing investigation of the forces exerted on submerged horizontal cylinders by wave and current action. The range and conditions of the experiments were limited, with Keulegan-Carpenter numbers ranging from 2 to 14 and Reynolds numbers ranging from 900 to 5000, based on the orbital velocities. Due to the small scale of the experiments, it cannot be hoped to be able to use the experimental results to recommend coefficient values for prototype conditions. However, it is hoped to be able to provide a greater understanding of the forces exerted by interacting waves and currents, and in particular how these forces and the force coefficients compare with those for waves alone.

Early results from the force data analysis suggest that the values of the inertia coefficient decrease as the current velocity ratio U/u_o increases. Typically, the coefficients decrease from a value of about 1.4, at $U/u_o = 0$, to about 1.0 at $U/u_o = 1.0$. The drag coefficients initially decrease as U/u_o increases to about 0.7, and then they increase again, as U/u_o goes from 0.7 to 1.1. As already discussed, this change in behaviour may be attributable to a dominant vortex shedding phenomenon.

The measured water surface elevations, water particle velocities and accelerations for conditions involving waves alone and also waves plus current have been compared with the results predicted by the Airy linear theory and the fifth order stream function theory. The wave conditions, which extend to $H/H_b = 0.43$, are such that the linear theory would not be expected to be very accurate. It is found that the stream function theory provides better estimates of the elevation, velocities and accelerations, for conditions involving waves alone. Often, it is only marginally better than the linear theory, and the maximum errors associated with the linear theory are only about 10%. For conditions involving waves plus current, the linear theory generally provides a better estimate of the velocities and accelerations than does the stream function. The maximum errors for either theory are still normally less than 10% of the measured value. Both theories can therefore be used with reasonable accuracy for the types of wave conditions investigated here. It would also appear that velocity superposition is valid for both theories, for describing wave plus current conditions.

6. REFERENCES

BRITISH STANDARDS INSTITUTION (1978). Draft for development; fixed offshore structures.

CHANDLER, B.D. and HINWOOD, J.B. (1981). The hydrodynamic forces on submerged horizontal cylinders due to simultaneous wave and current action. Proc. 5th Aust. Conf. on Coastal and Ocean Eng., pp 108-115.

DALRYMPLE, R.A. (1975). Waves and wave forces in the presence of currents. Civil Engineering in the Oceans, Vol. 2, pp 999-1018.

DEAN, R.G. (1974). Evaluation and development of water wave theories for engineering application, Vols. I and II. U.S. Army, Corps of Eng., C.E.R.C.

DEAN, R.G. (1976). Methodology for evaluating suitability of wave and wave force data for determining drag and inertia coefficients. Proc. Behaviour of Offshore Structures, pp 40-64.

KEMP, P.H. and SIMONS, R.R. (1982). Wave and current interaction in the near bed region. Abstracts, 18th Int. Conf. on Coastal Eng., Cape Town, pp 240-241.

KNOLL, D.A. and HERBICH, J.B. (1980). Wave and current forces on a submerged offshore pipeline. 12th Offshore Technology Conference, 1980, Paper No. 3762.

MORISON, J.R., O'BRIEN, M.P., JOHNSON, J.W. and SCHAAF, S.A. (1950). The force exerted by surface waves on piles. Petroleum Transactions, AIME, Vol. 189, pp 149-154.

RAMBERG, S.E. and NIEDZWECKI, J.M. (1980). The sensitivity of wave force computations to common errors, uncertainties, and hydrodynamic approximations. NRL Memorandum Report 4206.

TUNG, C.C. and HUANG, N.E. (1973). Combined effects of current and waves on fluid force. Ocean Engineering, Vol. 2, pp 183-193.

DISSIPATION OF WAVE ENERGY IN A SEAWATER OUTFALL CHANNEL

K.G. WITTHAUS[1], G. DE F. RETIEF[2], G.K. PRESTEDGE[3]
AND L.R. HUSKINS[4]

ABSTRACT

This paper describes the investigation of means of reducing wave action reaching the shoreward end of a power station cooling water outfall channel without resulting in significant head loss to the outflowing water. A variety of conceptual methods of reducing wave action in the outfall channel was examined. A physical model of the outfall was constructed. It was found that a rubble mound wave energy dissipator located in the outfall channel dramatically reduced wave action at the discharge seal pit.

1. Partner, Watermeyer, Halcrow & Partners, R.S.A.
2. Professor of Ocean Engineering, University of Stellenbosch and Consultant to Watermeyer, Halcrow & Partners.
3. Principal Engineer, Watermeyer, Halcrow & Partners, R.S.A.
4. Project Engineer, Electricity Supply Commission, R.S.A.

1. INTRODUCTION

South Africa's first nuclear power station is located on the south west coast and will use seawater as a coolant. Up to 86 cumecs of seawater will be abstracted via an intake basin comprising two rubble mound breakwaters. The intake basin has an area of about 4 ha in which suspended sediments drawn into the basin through its 900 m offshore, 9 m deep entrance will settle before removal by maintenance dredging.

The warm return water will be discharged through a shallow outfall channel into the surf zone south of the intake basin.

The cooling water system is designed to operate as a syphon to minimise pumping costs. At the outfall, four low level 3 m diameter pipes discharge into a seal pit, over a weir and into a tapered concrete channel through the beach. The weir crest is 40 m long with a level of 0,0 m G.M.S.L. (Geodetic Mean Sea Level). The 150 m long outfall channel is curved in plan and tapers to 20 m at the seaward end. The level of the concrete floor is - 2,0 m. The capping beams to the concrete sheet piled walls have a top level of + 2,2 m. Mean sea level is at + 0,15 m G.M.S.L., Mean High Water Springs at 0,86 m and Mean Low Water Springs at - 0,56 m.

The outfall structure was designed to resist full wave action, but after construction of the outfall, the Electricity Supply Commission (ESCOM) requested the designers to investigate means of reducing wave action in the outfall channel. This decision was taken for several reasons but generally it was ESCOM's intention to research any improvements that might add to operating efficiency and safety of the station and thereby maintain the very high standard set by ESCOM for this project.

This paper describes the investigation of means of reducing wave action reaching the shoreward end of the outfall channel without resulting in significant head loss to the outflowing cooling water.

2. PHYSICAL MODEL

A variety of conceptual methods of reducing wave action in the outfall channel was examined. It was decided to construct a physical model of the outfall and foreshore in the vicinity of the outfall to examine wave action and to develop and test methods by which wave action could be reduced.

A fixed bed, 1:30 scale Froude model was built in the hydraulics laboratory of the University of Stellenbosch.

A general view of the modelled outfall and surrounding shoreline is shown on Photograph 1.

The seabed over the prototype distance of 150 m from the end of the channel was constructed at a level equivalent to - 2,0 m GMSL. Further offshore the water depth was gradually increased to provide the depth required for the mechanical generator.

PHOTOGRAPHS

1: GENERAL VIEW OF MODEL

2: CLOSE-UP VIEW OF MODEL OUTFALL STRUCTURE

In the prototype, jet action of the water discharged from the outfall is likely to scour the sandy bed in front of the channel exit, but further seaward, an offshore bar is likely to form. The sea bed level at the offshore bar is unlikely to be lower than the chosen fixed bed level in the model (- 2,0 m) and hence the resulting depth limited waves entering the channel in the model were considered to be a reasonable simulation of prototype conditions.

Regular waves generated in the model were controlled to approach the breaking limit close to the channel entrance in order to maximise the wave energy entering the channel. Wave periods between 6 and 16 seconds were used in the model. It was found that 10 second waves produced effects as severe as any other periods in the model.

This period, which is typical of a large proportion of waves recorded at the site was therefore used in the majority of tests.

Photograph 2 shows the model of the outfall structure with the modelled pipe transitions between the outfall structure and straight lengths of 3 m diameter (prototype) pipes connecting the structure to a reservoir. Water was pumped from the model into the reservoir (via a V-notch weir) to simulate the cooling water flow through the outfall. By means of varying the recirculating flow and capping off the pipes leading to the model C.W. structure, variable flows through any combination of the four C.W. ducts could be simulated. Model tests included no-flow, 40 cumec and 80 cumec flow conditions. Forty cumec flow conditions simulated the closure of either Reactor 1 or Reactor 2 by directing the flow through the northern (left hand side on photograph 2) or the southern pair of ducts respectively. The model C.W. outfall structure had removable perspex slabs to represent the temporary stoplogs. Various still water levels ranging from - 1,5 m to + 2,1 m were used in the model. Most of the tests were carried out with the S.W.L. at + 1,6 m as this was considered to be a realistic normal upper design condition and corresponded approximately to an event with a recurrence interval of 5 years. An extreme still water level of + 2,1 m was also tested. It had been calculated that the recurrence interval of this event, based on an extrapolation of the available records of water level fluctuations due to tide, surge plus long period (50 s to 300 s) wave action, will be in excess of 50 years. (This is the minimum recurrence interval resulting from the most pessimistic of the data using a Weibull population distribution.)

In order to record wave induced pressure surges in the pipes, manometer tubes were fitted to each of the four perspex pipe transitions entering the rear of the seal pit. In addition, pressure transducers were fitted diametrically opposite the manometers on the northern and southern ducts and linked to an analogue recorder.

Wave heights at the closed stoplogs were also measured.

The wave direction used in the model was 247,5 degrees (true bearing of wave orthogonal). This corresponded to the mode of the winter wave directional spectrum, (1,25 degrees north of the mode of the summer spectrum), was normal to the seabed contours between - 5 m

and - 10 m and was 9 degrees north of the C.W. channel centreline at its seaward end.

3. MODEL TESTS OF THE UNMODIFIED C.W. OUTFALL

3.1 No-Flow Conditions

A full range of tests was carried out to study the behaviour of the C.W. outfall without modification when subjected to various discharge flow rates and wave conditions.

Wave induced pressure surges in the ducts under no-flow and various flow conditions were measured and in addition, observations were made of the height to which the waves rose against the closed stoplogs. General wave action in the channel and over-topping of the channel walls was noted.

Model tests were carried out over a range of conditions including various wave periods, water depths, stoplog closure and flow rate conditions.

Photograph 3 shows the general pattern of wave action in the channel under conditions of no-flow. The waves which enter the seaward end of the channel are generally compressed against the southern wall of the outfall channel due to the curvature of the channel, resulting in a variation of wave height across the width of the outfall structure, with larger waves at the southern end.

Waves reflected off the vertical face of the stoplogs and walls of the structure were observed travelling seawards, resulting in increased wave height where the waves interact.

For still water levels higher than about + 1,6 m, an increasing proportion of wave crest overtopped the channel walls and hence wave action due to standing waves caused by the interaction of incident and reflected waves was reduced.

Photograph 4 shows a test carried out with the waterlevel at + 1,6 m and wave period of 10 seconds. During this test the wave height at the stoplogs on the most southern side of the structure was such that a spout of water was projected through the gap between the overhead bridge (+ 5,0 m) and the stoplogs. These test observations appeared to correspond closely with the observations on site and corresponded to the most severe conditions observed in the model.

Pressure surges in the ducts for the no-flow conditions and stoplogs removed were also recorded.

3.2 Half and Full Flow Conditions

Flow of cooling water in the channel resulted in reduced wave action in the channel and hence reduced pressure surges in the

3: TYPICAL WAVE ACTION IN CHANNEL
(SWL +1,6 m GMSL)

4: WAVE ACTION ON STOPLOGS-SOUTH BAY
(SWL +1,6 m GMSL)

ducts, as compared with the no-flow condition. The degree of reduction depends on flow velocity in the channel and therefore is greatest for large flow rates and shallow depths, (i.e. at low tide levels).

As a result of the variation of wave height across the outfall structure, (increasing from north to south i.e. left to right in photograph 4), a corresponding variation of pressure surges was recorded in the ducts.

Surges in the most southern duct, for the case of an extreme S.W.L. of + 2,1 m and 40 cumecs flow in the northern ducts was found to be 1,5 m.

Tests carried out under 40 cumec flow showed that wave action in front of the no-flow half of the structure and pressure surges in the corresponding no-flow ducts with the stoplogs removed were slightly less severe than for the complete shut-down condition.

4. POSSIBLE MEANS OF REDUCING WAVE PENETRATION

To reduce wave action at the outfall structure, a number of structural alterations or additions were considered. These fall into two basic categories, those than sought to prevent waves reaching the seaward end of the outfall and those that modified wave action within the outfall channel.

From preliminary evaluations of the various schemes that were considered, the following conclusions were reached. Some qualitative model testing was used to support conclusions drawn.

Offshore Structures

In this category an offshore rubble mound breakwater constructed either linked to or isolated from the southern breakwater of the intake basin was considered. Its position, orientation and length would have needed careful study but in any case it would have been very expensive. However, it would also have had potential disadvantages in its deflections of the discharge plume and the changes it would have imposed on siltation which may have been encouraged in its shadow.

Such a breakwater for a somewhat lower cost could have been attached to the north side of the channel thus retaining the continuity of the discharge jet, although the jet would have been deflected to the south with a potential loss of cooling efficiency. Scour at the base of the structure would have been a problem.

To retain the jet discharge direction two rubble mound breakwater arms could have been built on either side of the outfall, with spending beaches each side of the present outfall. This solution would also have been expensive, but it was nevertheless tried in the model. The brief trial indicated that very little protection

was afforded and that the outflow currents reduced the spending effects.

Despite the advantage that offshore structures could have been constructed during operation of the outfall, it was concluded that offshore structures would be investigated further only if high cost were justified and all other options were relatively unsuccessful. They were not therefore considered further and it was decided that solutions inshore of the sea end of the outfall should be persued as more likely to meet the requirements.

Outfall Channel Modifications

- Moveable Devices

  Moveable devices were considered as a possibility for insertion or operation during extreme wave conditions or under particular operating or shut down conditions. Such devices included for example gated structures, floating breakwaters or caissons but in all cases would have been attended by maintenance problems. Disadvantages would have varied with the particular arrangement and operating conditions but would have included problems of moving, maintenance, disruption of flow and flow back-up. It was concluded also that periodic floating-in or launching a structure would have been impracticable in this coastal environment. These solutions were therefore rejected.

- Reduction in channel entrance width

  Reduction of the outfall end width appeared attractive but of course higher discharge velocities at low levels would have caused flow back-up and consequent scour problems would have resulted. Nevertheless a trial was made on the model which indicated that significant wave action still penetrated the outfall channel.

- Increased roughness and/or canalising flow

  The addition of increased roughness to the sides and bottom of the outfall channel was mathematically investigated and found to have little effect. Even the use of a number of splitter walls with artificial roughness was found to offer only a modest reduction in wave height. It would, in any case, have been very difficult to construct such splitter walls.

  One new wall down the centre of the outfall channel was able to concentrate the 40 cumec flow over half the channel to equal the velocities of 80 cumec over the whole channel but did not reduce wave penetration in the no-flow condition. This solution would also have been somewhat difficult structurally and expensive to build.

- Change in Channel plan geometry

  More fundamental changes to the plan geometry of the outfall channel

were then considered. Resonator basins could have been used to damp out wave action travelling along the walls, particularly on the south side. Each resonator needed to be designed for a narrow band of wave period and a number would have been needed to cover sufficient of the wave spectrum.

Fairly fine tuning of the group would have been needed to optimise the result and hence they would have been less efficient when non-designed conditions occurred. Construction would have involved cutting down substantial lengths of the outfall piles and driving a longer indented length at high cost.

A simpler constructional approach would have been to build a combination of deflectors and wave breakers in the channel. A typical solution on these lines was modelled and showed that benefits might be obtained from the absorption but that the deflectors were less effective. Structural problems would have been similar to the central walls and probably expensive to overcome. An advance on the wave absorption theme could have been to cut off some of the side piling and produce a spending beach just outside the channel. The cut off level would have needed to be low, only the outer ends of waves would have been affected, and outflow would have been distorted.

To avoid expensive removal and reconstruction in the channel, isolated wave absorbing devices could have been placed in the channel, for example, shaped perforated blocks. These were tried in the model but the wave period was too long for their effect to be noticeable. These would, of course, have caused a restriction to outflow.

Many of the above solutions were found to have inherent cost or effectiveness disadvantages, however two promising solutions were a long slab spanning the entire width of the outfall at a relatively low level, and a rubble mound wave energy dissipator (WED) constructed inside the channel.

The first of these was sufficiently interesting to seek a degree of optimisation by model tests, from which it was concluded that, located near the downstream end of the channel and spanning 20 metres across it, an unbroken slab extending over about 18 metres length of the channel was needed. The level of the slab soffit had to be set at about 0,0 GMSL to prevent the passage of wave energy whilst allowing outflow of 80 cumecs beneath it. Large wave forces were involved, however, and the slab needed to be heavy. Its weight required separate support outside the sheet piling, which was not designed to support such loads.

There was sufficient head loss in the cooling water outflow across the slab (approximately 600 mm under the worst conditions). Wave resonance between the outfall structure and slab occurred under certain conditions which required the introduction into the channel of simple anti-resonance devices. The slab cut out wave overtopping at the inshore end of the channel and would have been virtually maintenance free. However, there could have been problems of

stability during construction and a lengthy model study would have been needed to optimise the design. The cost was estimated to be 50% more than the WED mound and therefore this alternative was carried no further.

The wave energy dissipator (WED) mound comprises a periphery of heavy precast concrete blocks in the centre of the outfall commencing at a point 25 m seaward of the crest of the seal pit weir and extending about half way down the channel. Inside the blocks, a rubble mound is constructed up to a peak level of + 3,0 m GMSL in the centre of the channel. The layout tested is shown in photographs 5 and 6.

During the course of testing the possibility of splitting the mound into two parts, one along each side wall of the channel, (for easier construction) was examined, but the result was far less effective hydraulically. Only the centre channel mound was therefore evaluated during the remaining model tests.

It quickly became apparent that the WED was not very sensitive to detailed adjustments in design, it was effective over a wide range of wave periods, and it eliminated resonance.

It achieved a significant reduction in wave action at the outfall structure under no-flow conditions and substantially reduced surge in the pipes when flow was present. It produced an insignificant loss in head in cooling water outflow.

The effectiveness of the WED in reducing wave penetration is due to three basic hydraulic phenomena:

(i) As a wave travels up the outfall it moves between the channel walls and the sloping rock bank. The latter causes wave refraction, so bending the wave front at that end and allowing its energy to be partly spent in the top of the rubble mound.

(ii) As the shoreward end of wave diffracts around the round head of the WED and the energy which remains is spread over a greater width of channel before reaching the outfall structure leading to a reduction in wave height.

(iii) During the half flow condition, the WED concentrates almost all the flow down one side of the channel, which effectively results in the same wave energy exclusion by current in that side of the channel as in the full flow condition over the full channel. The wave energy reaching the operating side of the outfall is thus further reduced.

The WED had one potential problem, namely how to construct it taking account of wave action and whilst still permitting outflow up to 40 cumecs in the channel. Further consideration, however, led to the conclusion that suitable temporary works could be devised to make the scheme entirely practicable.

5: MODELLED WAVE ENERGY DISSIPATOR (SWL -0,5 m GMSL, flow 80 cumecs)

6: MODELLED WAVE ENERGY DISSIPATOR (SWL +1,0 m GMSL, flow 80 cumecs)

5. MODEL TESTING OF THE RUBBLE MOUND WAVE ENERGY DISSIPATOR

Various preliminary tests were carried out to finalise the general arrangements of the WED concept and these included tests on a series of tall blocks projecting above the water surface around the perimeter of the mound to 'deflect' the wave towards the mound, additional V-walls along the length of the mound and a pier connecting the outfall structure with the shoreward end of the mound. These were found to have nominal benefit with respect to reducing the wave activity at the structure in relation to the cost of providing such refinements. A definite reduction in wave energy dissipation was noted for a reduced mound length.

Model testing of the WED has shown that it is capable of dissipating a large proportion of the incoming wave energy. There was also a significant reduction in wave activity and pressure surges on the no flow side of the structure under half flow conditions.

For the + 1,6 m design water level the maximum wave height recorded at the stoplogs was found to be 1,2 m for the no flow condition with all stoplogs in place - photograph 7.

It was found necessary to have 'toe' blocks to the rubble mound in order to ensure the stability of the rock in the mound under extreme low tide conditions when the velocity in the channel resulting from an average discharge of 86 cumec was greatest. An extreme low water level test equivalent to a water level of - 1,5 m (recurrence interval in excess of 1000 years) showed flow conditions to be acceptable and that the toe blocks would be stable.

Tests at the extreme high still water level of + 2,1 m indicated that the surge in the southern duct would be 0,6 m for the 40 cumec flow condition. The WED rock mound was also noted to be stable for the + 2,1 m water level and no flow condition.

6. APPLICABILITY OF MODEL RESULTS TO PROTOTYPE

Comparison of the roughness in the model channel with that in the prototype indicated that the model was marginally rougher than the prototype. For the 80 cumec flow and still water level at + 1,6 m the additional friction in the model could be expressed as an additional 10 mm of prototype head backup in the outfall chamber. The additional friction would result in very slightly lower channel velocities and correspondingly less wave reduction in the model, leading to conservative observations of surge.

With the WED in place the relative roughness of prototype and model are comparable.

The use of regular waves of equal height in the model represents the fairly severe condition of the wave train of maximum wave heights compared with a normal wave spectrum which would include a spread of wave height and wave periods.

7: WAVE ACTION ON STOPLOGS WITH WAVE ENERGY DISSIPATOR IN PLACE
(c.f. photograph No. 4)
(SWL +1,6 m GMSL)

8: TEMPORARY WEIR IN OUTFALL CHANNEL

9: COMPLETED WAVE ENERGY DISSIPATOR IN SERVICE

7. CONSTRUCTION

The WED was designed in such a manner that it could be constructed with minimum interference with the operation of the power station contractor. This was particularly important since cooling water pumping tests (40 cumecs) were scheduled to commence prior to completion of construction. Furthermore, these tests were likely to be intermittent and of unspecified duration.

A temporary weir (Photograph 8) had been built in the outfall channel ahead of construction of the WED to minimise C.W. flow velocities in the construction area and as far as possible to reduce the return of sand removed from the construction area of the channel. The weir would also afford a degree of wave exclusion.

The weir consisted of tubes made from anchovy fish net filled with 58 mm aggregate. Each tube had a mass of about 2 tonnes. This design successfully accommodated large settlements into the sand infill on which part of it was constructed and facilitated easy removal.

The rock mound consists of a 1 metre deep underlayer of 0 to 1 tonne quarry run rock placed within the precast concrete toe blocks and the remainder of rock is 1 to 3 tonne mass.

The completed structure is shown in Photograph 9.

8. CONCLUSION

It was found that a rubble mound wave energy dissipator located in the outfall channel dramatically reduced wave action at the discharge seal pit. Under maximum discharge the additional head loss in the channel due to the WED was found to be negligible. The authors believe that the rubble mound wave energy dissipator provides an economical and highly effective means of suppressing wave action in an outfall channel without creating impediment or head loss to the cooling water discharge.

TIDAL EROSIONAL EFFECTS ON A BULKHEAD SYSTEM

by
Ronald M. Noble[1], M. ASCE, Wolfgang H. Roth[2], M.ASCE
and Uday K. Patil[3], M.ASCE

ABSTRACT

In the design and construction of waterfront bulkhead systems, it is essential to consider the coastal effects of tides, waves, boat wakes, currents, bottom sediment movement and bottom scour. Many improperly designed bulkhead systems experience severe loss of backfill and toe materials with the bulkhead eventually failing if it is not corrected in time. Inadequate drainage, joint connections, and/or inadequate toe protection are typically the causes of failure.

This paper describes an investigation of a bulkhead system supporting a large waterfront development in southern California which was experiencing widespread sinkhole development in the bulkhead's backfill and was on the verge of losing toe material. The objective of this investigation was to determine the extent and cause of ongoing subsurface erosion, to evaluate its effect on the bulkhead stability, and to recommend and design mitigative measures. The cause of the erosion was determined to be piping of fine grained soils due to inadequate backfill drainage. A remedial drainage scheme was designed and field-tested, and several structural repair schemes were suggested for portions of the bulkhead where accumulated damage affected the integrity of the structure.

INTRODUCTION

The Channel Islands waterfront development in southern California consists of approximately 585 lots adjacent to artificial waterways connected to the Pacific Ocean. The lots are supported by concrete retaining walls or bulkheads completed in 1970. Two types of pile-supported bulkhead designs were used in this development: an L-shaped retaining wall without tie-back anchors and a precast panel and pilaster system with tie-back anchors. The latter was used for 231 lots and is the subject of this paper.

---

[1]President, R.M. Noble & Associates

[2]Associate, Dames & Moore

[3]Project Engineer, Dames & Moore, Los Angeles, CA

Within a period of 2 to 4 years after the completion of construction, several sinkholes and areas of subsidence were observed in various lots. The purpose of this investigation was to inspect the bulkheads and to assess their safety and stability. Following the initial assessment, the physical causes of the observed defects were investigated and, where necessary, recommendations for remedial measures were made.

BULKHEAD STRUCTURE

A typical cross section of the bulkhead is shown on Figure 1. The bulkhead is 9.5 feet high and consists of precast concrete panels, which are supported by precast concrete columns, 11 feet on center. The columns are tied back by anchors to a continuous concrete deadman and rest on a continuous 4-foot-wide by 2.5-foot-high poured-in-place footing which is supported by one row of batter timber piles. Two weepholes per panel, with wire mesh screens, are provided for drainage of the sand backfill.

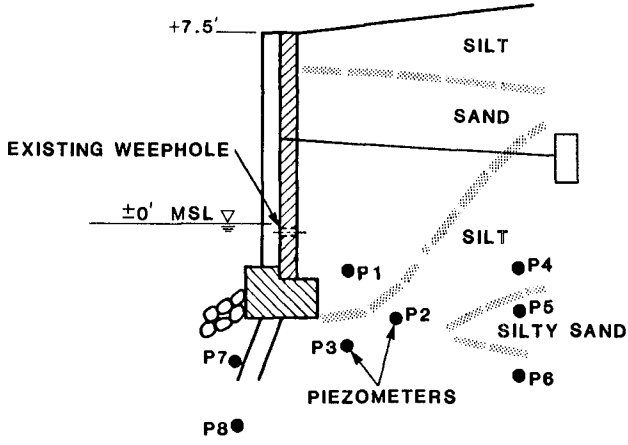

Note: MSL = Mean Sea Level

Figure 1. BULKHEAD CROSS SECTION

The waterway channel is dredged to a depth of approximately 6 feet below the bottom of the bulkhead footing. The underwater slope of 2(h):1(v) is protected by filter cloth and riprap. The elevation of the original ground surface was about 2 to 3 feet below the bulkhead top elevation. The construction of the waterfront development proceeded in three major steps: (1) excavation of channels with berms for bulkhead footing and concrete deadman; (2) construction of bulkhead; and (3) backfilling to existing grade, final grading and placing of slope protection.

INVESTIGATION

At the time of this investigation, approximately 50 percent of the waterfront lots were unimproved and accessible, while the rest were built on, and thus were not inspected. The investigation consisted of a visual inspection of all accessible lots, an exploratory drilling program on a few selected lots, a diving survey of selected underwater slopes, and a field testing program involving the installation of pore water pressure gauges on two selected lots for the purpose of measuring hydraulic gradients due to tidal movements within the backfill. Finally, one of the instrumented lots was selected to field-test remedial drainage measures.

Visual Inspection

During the visual inspection, numerous sinkholes measuring approximately 0.5 to 2 feet in diameter and 1 to 3 feet in depth were encountered immediately behind the wall. Such sinkholes were found mainly at the joints between the columns and wall panels and in a few cases at the locations of the weepholes in the center sections of the panels. In addition to the sinkholes, several areas (approximately 10 by 10 feet) with a subsidence on the order of 2 to 4 inches were encountered, usually at convex bulkhead corners.

Subsurface Investigation

Subsurface conditions were explored by drilling at least two borings each on seven selected lots, ranging in depth from 9 to 17 feet below the ground surface. Undisturbed soil samples were obtained at intervals of aproximately 2 feet. The emphasis of the laboratory testing program focused on grain-size analysis and determination of dry density, both considered to render data for evaluating the soil's potential for subsurface erosion (piping).

A typical subsurface profile in the immediate vicinity of the bulkhead is shown on Figure 1. A backfilled wedge of loose fine sand extends down to the footing base, which is underlain by soft natural sandy to clayey silts. The loose sand backfill is generally covered by a stiff silt layer of 3 to 4 feet in thickness. The soils behind the backfill wedge range from loose silty fine sands to dense sandy silts.

Underwater Slopes

The upper, riprap-covered portion of the underwater slope extends from an elevation of 1 foot below the top of the footing to 4 feet below the top, and slopes 2(h):1(v). After having reviewed preliminary data from the Phase I investigation and results of the bathymetric survey, several locations were explored qualitatively by divers. Generally, sandy silt deposits up to 8 inches in thickness were encountered on top of the footings, as well as on the riprap-covered slope extending downwards from the toe of the wall.

Judging qualitatively, the underwater slopes, seemed to be intact with the exception of the slopes at the convex corners of two lots. At one of these lots, the top of the slope had settled extensively, and a gap had developed between the footing base and soil. The gap was up to 17 inches high, and up to 4 feet deep. At the other lot, the top of the slope seemed to have settled also, however, without exposing a gap.

Pore Pressure Measurements

Pore pressures were measured in order to evaluate pressure gradients resulting from seepage toward the channel at low tide. Figure 1 shows the layout of the installed piezometers which consisted of instant-responding pneumatic pore pressure probes. After allowing a minimum of 7 days for stabilization of seepage conditions after installation, the piezometers were read hourly during one 24-hour cycle of extreme tidal movements. Relating the measured pore pressures to the free water level in the channel, it was possible to construct flow nets indicating areas of high hydraulic gradients in the backfill and bulkhead foundation which are especially endangered by piping.

The general trend of seepage gradients versus time in the backfill is shown graphically on Figure 2. The upper portion of the figure shows the pore pressure differentials, with reference to the free water level in the channel, at the locations of the installed piezometers. For instance, a pore pressure differential of +2 feet at a particular location and time would mean that the ground water in a hypothetical stand pipe installed at this location would rise 2 feet above the water table in the channel. The ground water seepage would thus be directed towards the water channel. From the standpoint of piping, the most severe conditions exist at the peak of positive pore pressure differentials. The lower portion of Figure 2 is a plot of the corresponding tide elevations versus time.

Flow nets were constructed at several critical times, making simplified assumptions, such as homogeneous soil conditions and two-dimensional flow conditions. The flow nets shown on Figure 3 represent two "snapshots" of a constantly changing flow pattern in the backfill. The indicated times (1 a.m. and 3 a.m.) for which the flow patterns are depicted correspond to the time scale of the graph on Figure 2.

The flow net at 1:00 a.m. indicates a zone of flow reversal moving away from the wall as the free water level in the channel moves down. The fact that this flow reversal condition, involving very small relative pressure differentials, could consistently be derived from actual pore pressure measurements increased confidence in the piezometer data.

The most critical flow condition in terms of underground erosion (piping) is demonstrated with the flow net at 3:00 a.m. The flow lines in this and subsequent "snapshot" flow nets (not shown here) suggest that the bulk of the seepage water escapes through the vertical panel/column joints above the footing.

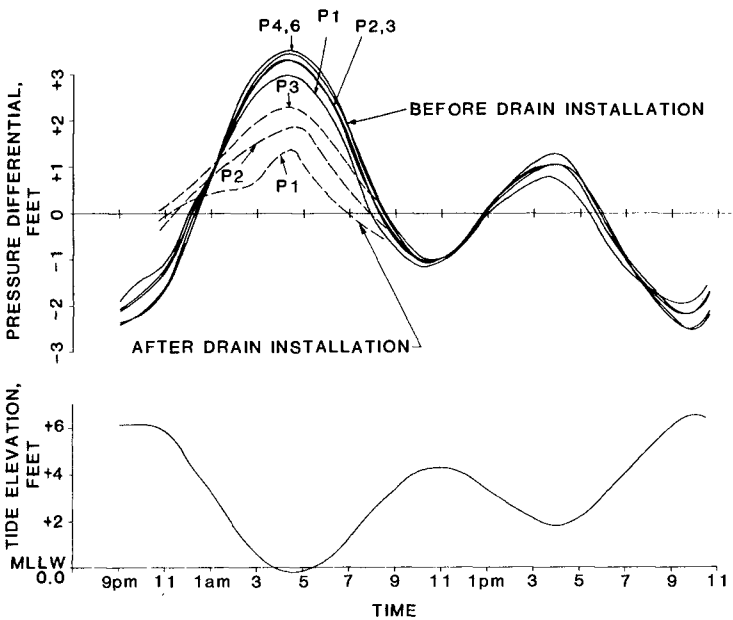

Note: MLLW = Mean Lower Low Water = -2.8' MSL

Figure 2. PORE PRESSURE MEASUREMENTS

Although the test results did not indicate significant seepage underneath the footing, a second test was performed with two additional piezometers (P-7 and P-8 in Figures 1 and 3) inserted on the waterside beneath the footing, with the objective to study the seepage in the foundation soils. It was observed that these two additional piezometers essentially fluctuate in phase with the free water level

a) 1:00 A.M.

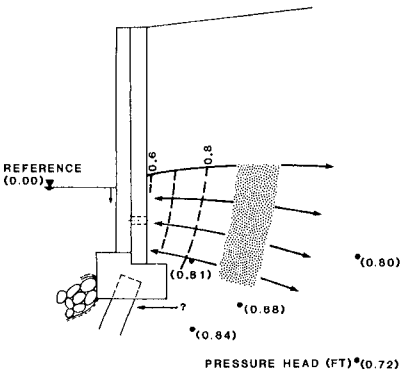

b) 3:00 A.M.

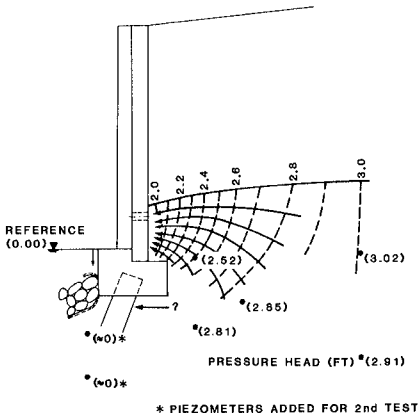

* PIEZOMETERS ADDED FOR 2nd TEST

Figure 3. FLOWNETS

in the channel. This indicates minimal seepage in the lower portions of the subsoil beneath the footing. However, it does not exclude the possibility of concentrated seepage through a gap or thin soil layer just beneath the footing base.

CONCLUSIONS

The primary cause for the development of sinkholes and subsided areas behind the bulkhead is loss of sand backfill through the panel joints caused by seepage forces (piping). Sinkholes and subsidence are initially of only cosmetic consequences. However, if such conditions were neglected for long periods, progressive failure involving the bulkhead footings and/or deterioration of the underwater slope could develop. Such conditions were actually encountered at some locations as described above.

Piping underneath the footing base does not appear to be a primary cause for loss of material. However, once a gap has developed between footing base and subsoil, migration of the sandy backfill progressively accelerates underneath the footing. Because the bulkhead rests on piles, the soil tends to settle away from the footing due to minor creep movements of the underwater slope. such creep movements are believed to have caused the slumping of the slope at some locations observed by the underwater survey.

Summarizing, there is evidence that cyclic seepage forces (piping) mainly due to tidal action, are responsible for existing subsidence, sinkholes and gaps. Therefore, the main objective of remedial measures discussed in the following sections is the reduction of these seepage forces. In addition, at selected locations where progressive undermining of the footings is already taking place, repair schemes for foundation and/or underwater slope will be discussed.

REMEDIAL MEASURES

Backfill Drainage

Consideration was given to various kinds of drainage systems, including vertical sand (or wick) drains, gravel drainage trenches, inclined wick drains, and horizontal well-point drains. A desk study narrowed the alternatives down to two: the inclined wick-drain system and the horizontal well-point system.

The schematic of the inclined wick-drain system is shown on Figure 4. A typical wick drain is 3 to 4 inches wide and consists of a corrugated plastic core wrapped in filter fabric. These drains are installed with a mandrill pushed into the ground with the wick drain attached to its point. Upon withdrawal of the mandrill, the drain stays in the ground acting as an effective drainage channel. The drains would be installed from the land side, aiming at a center location just above the footing. After installation of the drains, a gravel-filled filter-cloth pouch would be inserted, from the water side, through a hole drilled in the concrete panel.

Because access from the land side was judged to be quite difficult for the majority of the waterfront properties, the drainage method involving horizontal well-points (installed from the water side) was finally selected for a field test. No. 7 well points (0.007-inch-wide slots) 3/4-inch in diameter were used for this test.

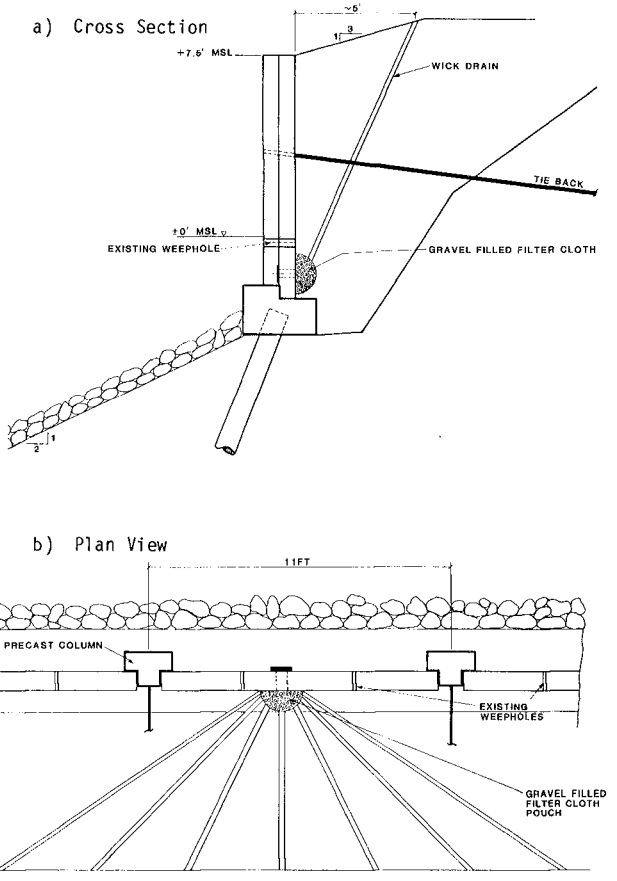

Figure 4. INCLINED WICK-DRAIN SYSTEM

The grain size distribution of the backfill material indicated that approximately 10 to 15 percent would pass the 0.007-inch sieve. While initially small amounts of the fine soils might pass through the well screens, rearrangement of the grains around the well screen will eventually develop a natural filter preventing further material loss. The field test was conducted at the location which was previously instrumented with piezometers, in order to compare hydraulic gradients before and after installation of the drainage system. Figure 5 shows the layout of the field test.

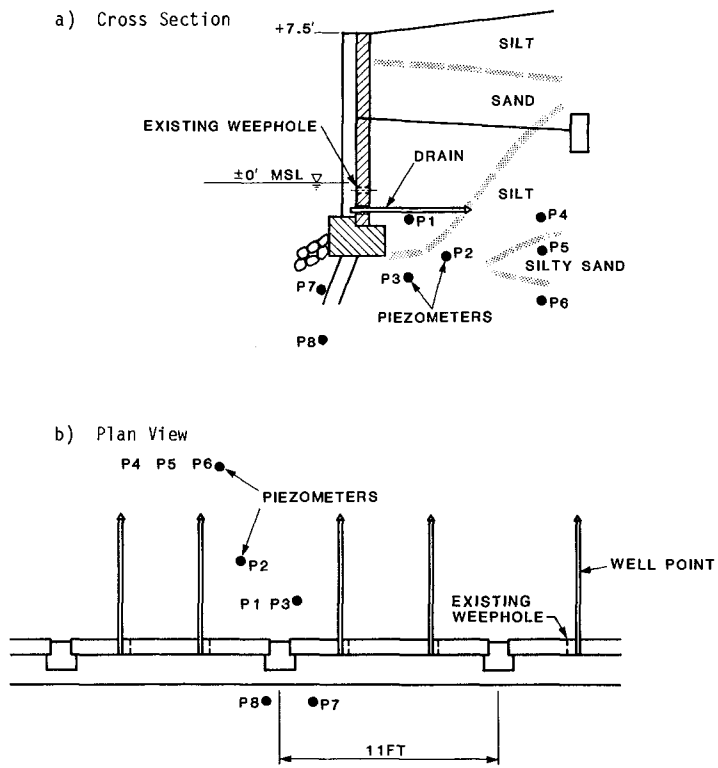

Figure 5. HORIZONTAL WELL-POINT SYSTEM

Based on experience with dewatering in similar soils, two drains per panel were estimated to be sufficient for significant drawdown of the water table in the backfill between the drains. A total of six horizontal drains, two per panel, were installed for the field test. Two well points are of plastic (PVC) and four are of stainless steel. While the material is insignificant for the functioning of the drains, it was found that the stainless steel well points were installed more conveniently than the plastic ones. The latter had to be driven with a mandrill acting on the pointed tip, and care had to be taken not to separate the tips during the driving procedure.

The evaluation of the drains' effectiveness relied on pore pressure measurements in the backfill before and after the installation. Figure 2 shows the pore pressure differential towards the free water level, measured during a critical tidal cycle before the drain installation, and during a similar cycle after the installation. Plotted pressure potentials (after installation) are those of locations P-1 through P-3, represented by the piezometers closest to the wall. Any potential piping which could lead to development of a gap would occur through seepage from the loose backfill at the footing/subsoil interface rather than through deeper zones of the underlying silty soils. The most important piezometer location is P-1 since it represents the conditions in the loose backfill just above the footing base. P-2 and P-3, on the other hand, were expected to record higher pore pressure differentials than P-1, because of the time lag caused by slower drainage of the natural silts in which they are embedded.

Piezometer P-1 shows a rather large reduction, due to the drains, of the maximum pressure potential towards the free water level (from 3 to 1.4 feet). The well points are approximately 1 foot higher than the minimum water level of the tidal cycle under consideration. Therefore, at the time of minimum water level, the ground water behind the wall forms a pool whose water table remains roughly at the well point outlet. Thus, the recorded pressure differential can not be smaller than 1 foot, even under perfect drainage conditions. Hence, the field test with horizontal well points was considered successful and this drainage system was recommended for remedial measure of the entire bulkhead system.

For the locations where apparent gaps beneath the footing base have already developed, repair measures for the footing and/or underwater slope protection were designed as described in the subsequent section.

Foundation Repair and Slope Protection

For lots where apparent gaps beneath the footing base had already developed, it was recommended that the gaps should be closed by grouting with provisions for proper formwork to retain the grout. The slope protection on these corner lots was to be upgraded to resist future erosion. Two schemes were developed for the foundation repair work. One scheme was to allow visual pile inspection at the pile-footing connection in case of marine borer attack on the piling. The potential for marine borers reaching exposed piling during extreme low

tides was considerable in areas with large gaps beneath the bulkhead footing. The second scheme only differed from the first in that it did not easily allow for visual pile inspection.

The two schemes are shown in Figures 6a and 6b. These schemes called for driving sheet piling several feet into the bottom in front of the bulkhead footing. The sheet piling would be secured to the footing and act as a protective curtain wall from bottom scour (erosion) exposing the pile-footing connection. The space between the footing and sheet pile wall would then be filled with concrete, and a grout pipe would be inserted behind the bulkhead to the base of footing to grout all void areas beneath the footing.

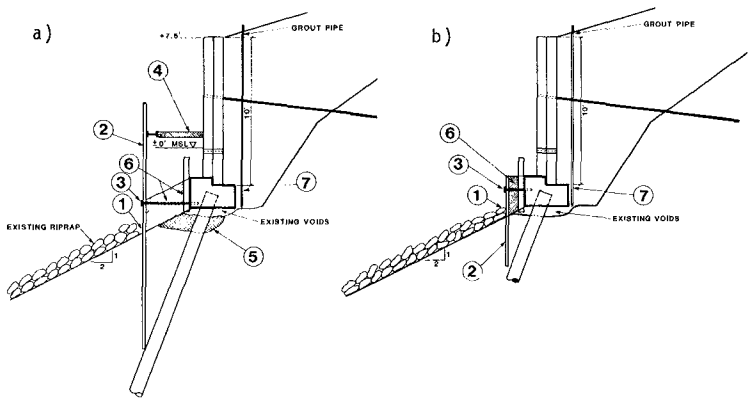

Figure 6. FOUNDATION REPAIR SCHEMES

(1) Remove rock slope protection.

(2) Drive sheet piles.

(3) Secure sheet piles to concrete footing.

*(4) Install support members and dewater.

*(5) Excavate and inspect pile.

(6) Fill with concrete and insert 4" pipes 3-5 feet on center, extending into the cavity (5).

(7) Pressure grout until grout extrudes from PVC pipe (6) (alternatively, pressure grout through PVC pipe).

(8) Cut off sheet pile at top elevation on concrete.

Note: Applies for Figure 6(a) only.

It was recommended that the slope protection for the corner lots be upgraded by use of either rock riprap and filter cloth or a concrete mattress and filter cloth as shown in Figures 7a and 7b. In addition, concentrated seepage of surface water into the backfill immediately behind the bulkhead was to be prevented by appropriate surface drainage.

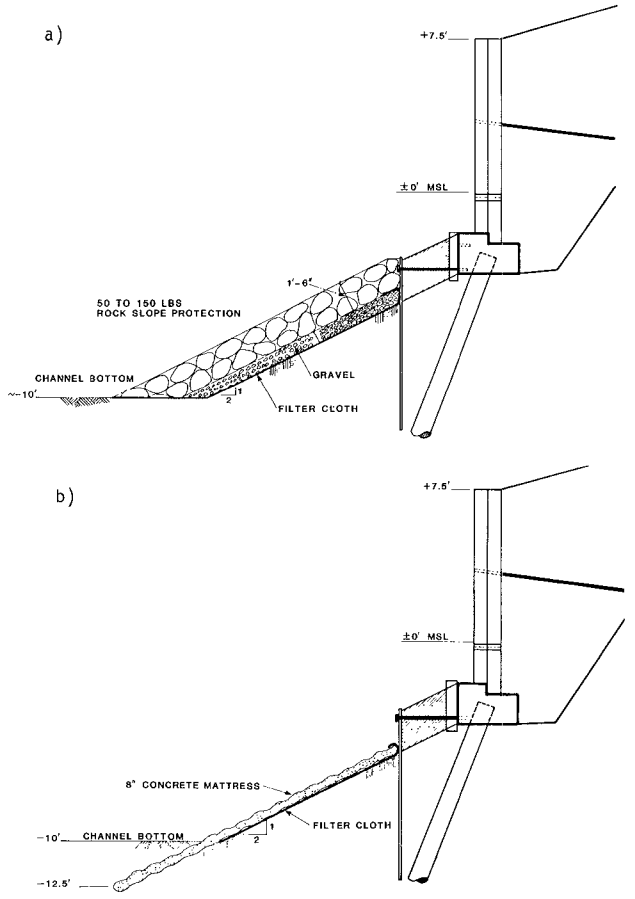

Figure 7. SLOPE PROTECTION

BREAKAGE OF CONCRETE ARMOR UNITS

by

Dennis G. Markle,[1] M. ASCE, and D. D. Davidson[2]

Abstract

A survey of existing Corps breakwaters with concrete armor units and hydraulic model tests of rubble-mound breakwater trunk sections protected with dolosse were conducted to determine the effects of broken armor units on breakwater stability and to establish some criteria by which decisions can be made as to when maintenance and rehabilitation work should be initiated on damaged concrete armor unit cover layers. The survey revealed that where good engineering designs were used, prototype breakage has been random and has not exceeded about 3 percent of the total number of units placed. The model tests, conducted with both breaking and nonbreaking waves with no overtopping, revealed the percent breakage can be quite a bit higher than 3 percent before the overall functional integrity of dolos cover layers is affected.

Introduction

In the past few years, the amount of breakage and the effect that broken concrete armor units have on breakwater stability have caused serious concern to designers and field engineers that are responsible for safe and reliable structures. Although concrete armor units have been and continue to be used extensively throughout the United States and the world (SPM, 1977), very little field performance data (Lillevang and Nickola, 1976; Zwamborn and Van Neikerk, 1981) and/or laboratory research (Davidson and Markle, 1976) are provided on the effect such breakage has on the stability of coastal structures. The need to determine prototype experience and to supplement these data with engineering research is of utmost importance.

Objectivies and Techniques

A field data survey (Markle and Davidson, 1982a) and experimental research investigation (Markle and Davidson, 1982b) were conducted to provide past prototype experience and to determine the effect broken

[1]Research Hydraulic Engineer, U. S. Army Engineer Waterways Experiment Station, Vicksburg, Mississippi 39180.

[2]Chief, Wave Research Branch, U. S. Army Engineer Waterways Experiment Station, Vicksburg, Mississippi 39180.

armor units have on breakwater stability against wave attack. This work consisted of both a survey of armor unit breakage that has occurred on existing Corps structures protected with concrete armor units and experimental model tests of rubble-mound breakwater trunk sections protected with dolosse. The survey of existing Corps structures was accomplished by field trips, letters, conferences, telephone conversations and a questionnaire to all Corps Districts and Divisions. The survey was restricted to Corps structures because preparation of plans and specifications, construction techniques and quality control are generally more uniform than non-Corps projects and access to more detailed cause-and-effect data was available. While data from non-Corps projects are important for learning purposes, it was surmized the efforts of collecting first-hand world-wide data and the uncertainies involved were not sufficiently warrented under this study. The experimental model tests involved various degrees of random and cluster breakage exposed to both nonbreaking and breaking wave conditions with no overtopping.

Prototype Case Histories

Crescent City Harbor, California, is located on the Pacific Coast about 17 miles (27.4 kilometres) south of the Oregon-California border, Figure 1. The existing outer breakwater is 4,670 ft (1,423.4 m) in length. The main stem and dogleg of the breakwater are approximately 3,670 (1,118.6 m) and 1,000 ft (304.8 m) in length, respectively. The original project did not call for the dogleg but intended for the main stem of the breakwater to extend out to Round Rock. The main stem of the original breakwater, beyond Sta 37+00, accrued severe damage and was reconstructed on two occasions. Finally, this portion of the main stem was abandoned and the 1,000-ft (304.8 m) dogleg, referred to above, was added. Two dimensional stability tests were conducted of the tetrapod breakwater designs proposed for the trunk portion of the 1,000-ft (304.8 m) dogleg (Hudson and Jackson, 1955 and 1956). In 1957, 1,836 25-ton (222,441 newtons), unreinforced tetrapods were placed on the sea-side slope from Sta 41+20 to the end of the dogleg (Sta 46+70) and 140 tetrapods (25 ton (222,441 newtons), unreinforced) were stockpiled on the sea-side slope of the first 200 ft (61 m) of the dogleg, adjacent to the main stem (Sta 37+00 to Sta 39+00). Model tests were not conducted for the severe breaking wave action that occurs around the elbow of the breakwater and, as of 1975, approximately 70 tetrapods placed in this area had been broken. To date, only 3 tetrapods placed on the last 550 ft (167.6 m) (Sta 41+20 to Sta 46+70) of the dogleg have been reported broken. In 1974, 246 40-ton (355,858 newtons), unreinforced dolosse were placed on the sea-side slope of the last 230 ft (70.1 m) of the breakwater's main stem (Sta 34+70 to Sta 37+00). Although there is some controversy as to the exact number of dolosse broken (reported values range from 38 to 70) a maximum number of 70 units has been reported. Of this number, it is certain that 22 were broken during placement and/or during storm conditions that occurred while construction was being completed. These units were not removed from the structure. Various portions of the breakwater were repaired with armor stone in 1979. With the completion of the latest repair work (1979), the breakwater is in relatively good repair and no major stability problems have been noted.

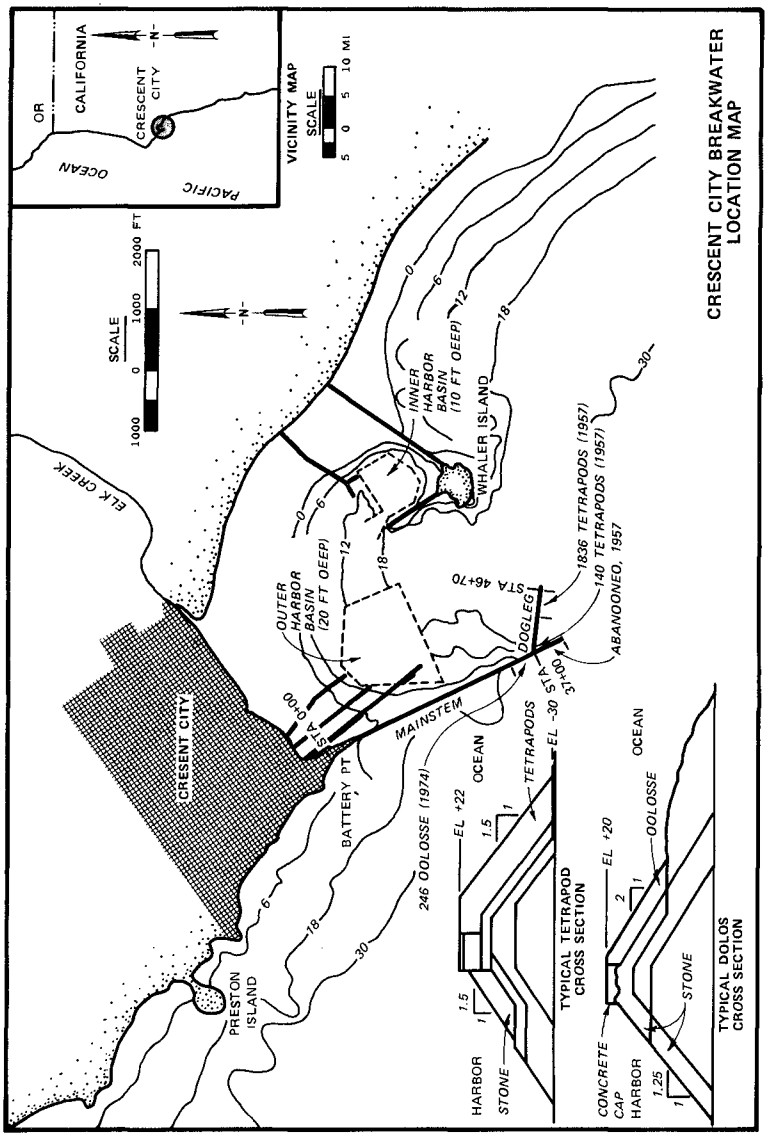

Figure 1. Location and vicinity maps of Crescent City Breakwater

Humboldt Bay is located on the Pacific Coast of northern California. The city of Eureka, about 280 miles (450.6 kilometres) north of San Francisco and about 80 miles (128.7 kilometres) south of Crescent City, California, is located on the northwest shore of Humboldt Bay, Figure 2. The Humboldt Bay entrance channel is protected by two rubble-mound jetties. Construction of the parallel north and south jetties, 4500- (1,371.6 m) and 5,100-ft (1,554.5 m) long, respectively, was initiated in 1889 and completed in 1899. The original jetty construction was rubble-mound armor stone. Severe damage to the heads and portions of the trunks has required numerous rehabilitations and reconstructions of both jetties. Between 1911 and 1970, parapet walls, concrete caps, 20- (177,929 newtons) and 100-ton (889,644 newtons) concrete blocks, concrete monoliths, armor stone, and 12-ton (106,757 newtons) tetrahedrons have been utilized on both jetties in an effort to stabilize the structures. The latest rehabilitation work, 1971 to 1972, consisted of rebuilding the concrete monoliths on both the north and south jetty heads. In addition to this, two layers of dolosse were placed around the heads and tapered into the trunks of both jetties approximately 400 ft (121.9 m) behind the heads. This repair work was model tested (Davidson, 1971). To date, 12 dolosse have been reported broken on the north jetty and 22 broken on the south jetty. About 5 of the total number of dolosse broken were supposedly left on the structure during construction. In any case, almost all of the breakage reported occurred in the first year after construction. At this time, the only noted effect is some settlement of the 42-ton (373,650 newtons) dolosse placed around the heads, but the structure does not appear to have any serious stability problems.

Santa Cruz Harbor is located on the northern end of Monterey Bay at the city of Santa Cruz, California. This area lies about 65 miles (104.6 kilometres) south of the entrance to San Francisco Bay, Figure 3. The 850-ft (259.1 m) and 1,125-ft (342.9 m) east and west jetties, respectively, were constructed in 1963 to protect the entrance channel and harbor from storm waves. The outer 400 ft (121.9 m) of the west jetty was constructed with 28-ton (249,100 newtons), unreinforced quadripods while the remainder of the jetties were constructed using armor stone. Based on available data, the structure has not as yet been exposed to the design storm conditions and no stability problems or breakage of armor units has occurred.

Pohoiki Bay is located on the southeast coast of the island of Hawaii, about 25 miles (40.2 kilometres) southeast of Hilo, Hawaii, Figure 4. In 1979 a 90-ft (27.4 m) breakwater was constructed to protect an existing boat launching ramp. The breakwater slopes and head were protected with two layers of 6-ton (53,379 newtons), unreinforced dolosse. The dolosse were placed from the toe of the structure to the concrete rib cap. Out of the 210 dolosse placed, 5 were broken and left on the structure during construction. Since its completion, the breakwater has been exposed to the design storm conditions on several occasions, and no dolos breakage or damage to the structure has been observed.

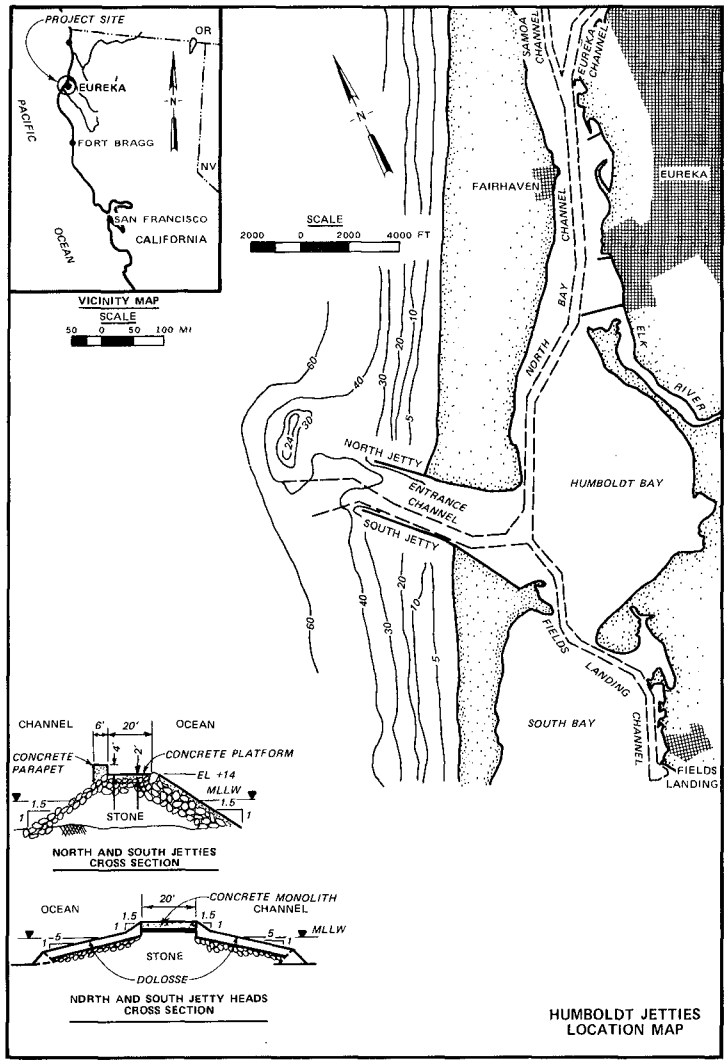

Figure 2. Location and vicinity maps of Humboldt Jetties

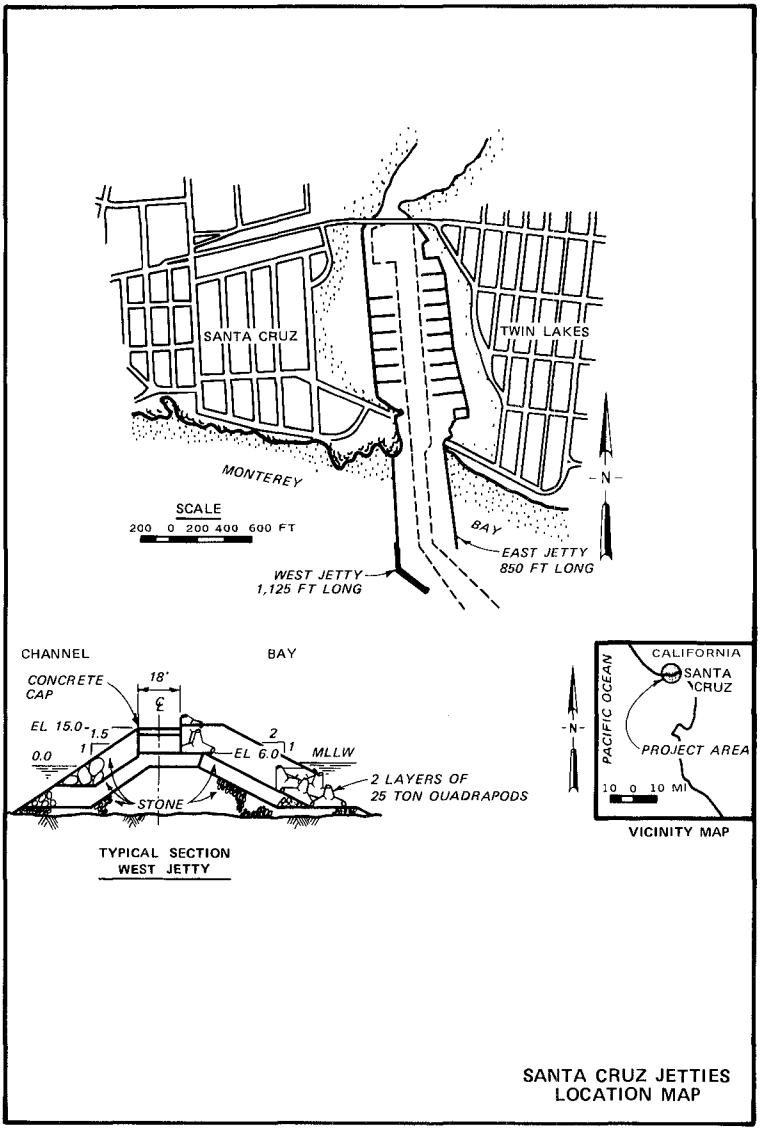

Figure 3. Location and vicinity maps of Santa Cruz Jetties

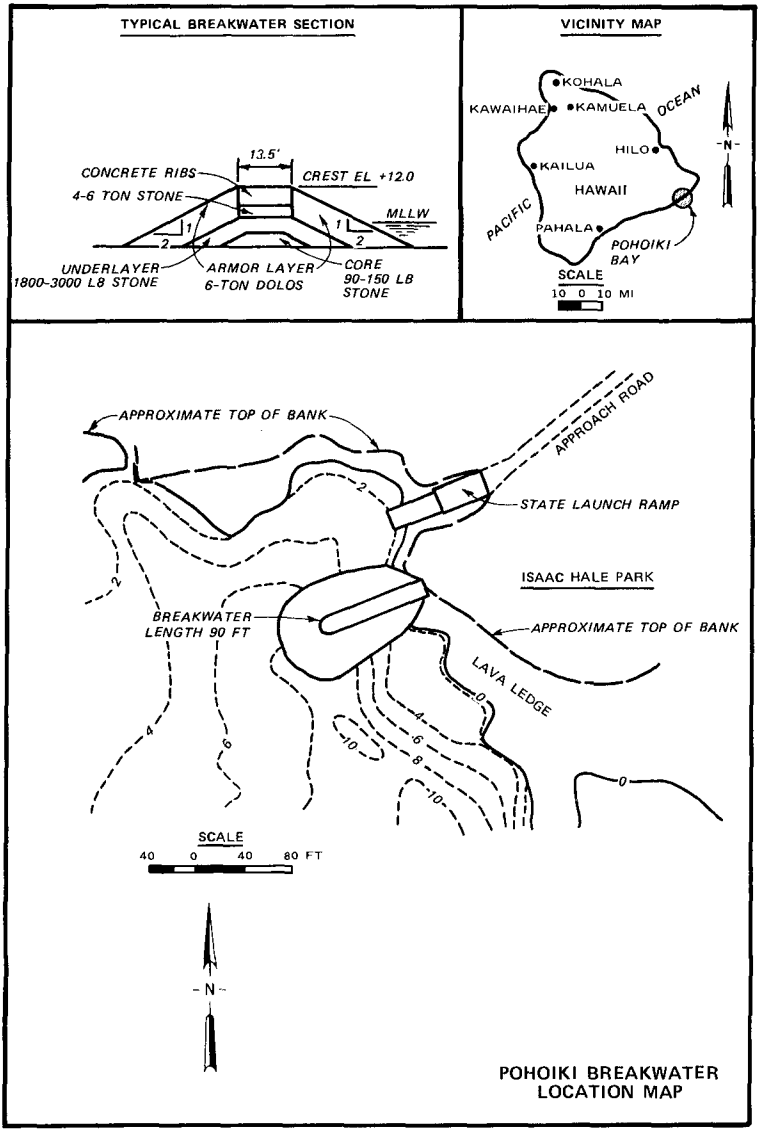

Figure 4. Location and vicinity maps of Pohoiki Breakwater

Kahului Harbor is located on the north coast of the island of Maui, Figure 5. Kahului, Hawaii is about 94 miles (151.3 kilometres) southeast of Honolulu, Oahu, Hawaii. The harbor is protected by two rubble-mound breakwaters. The 2,766- (843.1 m) and 2,315-ft (705.6 m) east and west breakwaters, respectively, were completed in 1931. The heads of both breakwaters were severely damaged by storm waves in 1947, 1952, and 1954. In 1956 the breakwater heads were repaired by casting concrete monoliths on the crowns. The slopes of both heads and 250 ft (76.2 m) of the west breakwater trunk (sea side only) were protected with a double layer of 33-ton (293,583 newtons), unreinforced tetrapods. A total of 400 units were placed. A major storm of 1958, approximately 34-ft (10.4 m) breaking waves at the breakwater heads, breeched the trunk of the east breakwater and caused major damage on both heads. Seven of the 33-ton (293,583 newtons) tetrapods were broken; 3 on the sea-side slope of the west breakwater trunk and 4 were among the 30 units that were displaced off the inside quadrant of the west breakwater head. A few units were also displaced off the east breakwater head, but no breakage of these units was observed. After the 1958 storm, emergency repairs were made on the east breakwater trunk using basalt-armor stones, and model tests were initiated at WES (Jackson, 1964) to determine the best methods of stabilizing the breakwaters. In 1966 a partial repair of the breakwaters was completed using 35 (311,375 newtons) and 50 ton (444,822 newtons), reinforced tribars. It is known that at least two units were broken and left on the structure during the 1966 repair work. Also during the 1966 repair, a concrete rib cap was added to the crest of the east breakwater trunk. In 1969, 260 19-ton (169,032 newtons), reinforced tribars and a concrete rib cap were added to the west breakwater trunk. This repair work was shoreward of the 33-ton (293,583 newtons) tetrapod area. This provided a partial repair of damages accrued by the structure during the storm of December 1967. None of the 19-ton (169,032 newtons) tribars used in the 1969 repair were broken during construction. In November 1970, high storm waves dislodged 25 of the shoreward end 19-ton (169,032 newtons) tribars and moved them toward the root of the west breakwater. Three units were reported broken during this event. Repair of the west breakwater trunk was initiated again in 1973 using 19- (169,032 newtons) and 35-ton (311,375 newtons) reinforced tribars: no construction breakage occurred. It was noted in the 1975 aerial photos that a total of 9 and 4, 33-ton (293,583 newtons) tetrapods were broken on the west and east breakwaters, respectively. A 1977 repair of the west breakwater included placing 30- (266,893 newtons) and 20-ton (177,929 newtons), reinforced dolosse over the damaged 33-ton (293,583 newtons) tetrapods areas. One of the 2 dolosse units broken during construction was left in place. Thirty, (266,893 newtons) 20- (177,929 newtons) and 6-ton (53,379 newtons) dolosse were used in the 1977 rehabilitation of the east breakwater. The 6-ton (53,379 newtons) dolosse were the only unreinforced units used in the repair work. During transporting and placement of the 6-ton (53,379 newtons) dolos units, 5 units were broken. This was the only construction breakage that occurred in the 1977 repair of the east breakwater and these units were either not used or were removed from the structure. On 28 March 1979 a survey was made of the east and west breakwaters to determine the amount of observable breakage. Table 1 lists all observed armor unit breakage to date. This breakage has not had an adverse effect on the functional integrity of the structure.

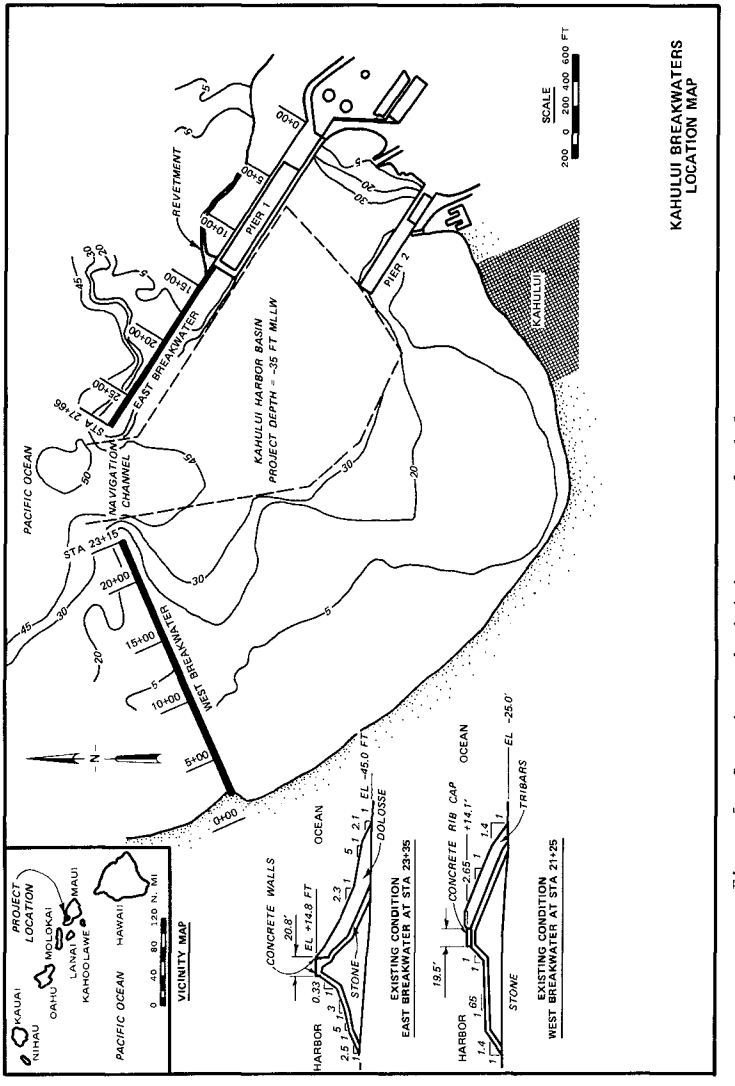

Figure 5. Location and vicinity maps of Kahului Breakwaters

TABLE 1

Armor Unit	Number Broken
Kahului West Breakwater	
33-ton (293,583 newtons), unreinforced tetrapods	9
19-ton (169,032 newtons), reinforced tribars	5
35- (311,375-) and 50-ton (444,822-newtons) reinforced tribars	2
20- (177,929-) and 30-ton (266,893-newtons) reinforced dolosse	14
Kahului East Breakwater	
33-ton (293,583 newtons), unreinforced tetrapods	4
35- (311,375-) and 50-ton (444,822-newtons) reinforced tribars	4
6-ton (53,379 newtons), unreinforced dolosse	6
20- (177,929-) and 30-ton (266,893-newtons) reinforced dolosse	2

Waianae Small Boat Harbor is located at the town of Waianae on the west coast of the island of Oahu, approximately 30 miles (48.3 kilometres) west of Honolulu, Hawaii, Figure 6. Model tests of the harbor geometry and stability of the 1,690 ft (515.1 m) main breakwater were conducted (Bottin, Chatham and Carver, 1976) and prototype construction was completed in January 1979. The first 350 ft (106.7 m) of the breakwater was constructed using armor stone only. The remainder of the structure was constructed with a double layer of 2-ton (17,793 newtons) unreinforced dolosse on the sea-side slope and around the breakwater head. Forty-seven of the 6,633 dolosse placed were broken and left on the structure during construction. To date, a total of 170 dolosse (including the 47 mentioned above) have been found broken and remain on the structure. Most of the post construction breakage occurred in the year following construction. During a field inspection of the breakwater in June 1980, it appeared that an unusually large number of the first layer dolosse had been placed with their vertical fluke downslope. Extensive stability tests conducted with dolos armor units (Carver, 1977) have indicated that pattern placement tends to reduce the stability of dolosse. Also several areas of the sea-side slope on the Waianae breakwater appear to be considerably steeper than the 1V:2H slope for which the structure was originally designed. These two

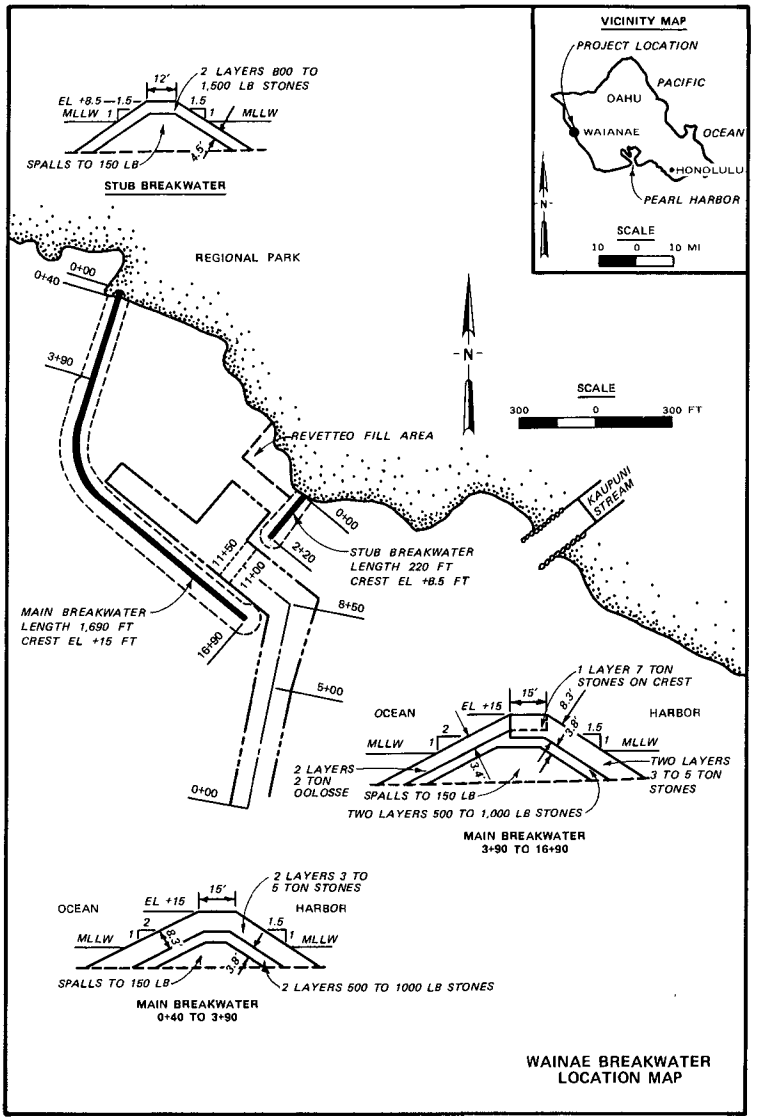

Figure 6. Location and vicinity maps of Waianae Breakwater

factors may have played a significant role in the dolos breakage that has occurred since the construction was completed. The breakage has caused no obvious stability problem to date but it is hoped the structure will be closely observed to see the long term effects of the existing or future breakage that may occur.

Nawiliwili Harbor is located on the southeast coast of the island of Kauai, about 100 nautical miles (185.2 kilometres) northwest of Honolulu, Hawaii, Figure 7. Construction of the 2,150 ft (655.3 m), rubble-mound breakwater was completed in 1930. Severe storms in 1954, 1956 and 1957 severly damaged the breakwater and model tests were conducted in 1958 (Jackson, Hudson, and Housley, 1960) to determine the best method of rebuilding the head and strengthening about 500 ft (152.4 m) of the seaward end of the breakwater. In 1959 the head and seaward 500 ft (152.4 m) of the sea-side slope of the trunk were rehabilitated with 17.8-ton (158,357 newtons) tribars and a concrete cap was poured on the crest of the breakwater. Of the 598 tribars placed, 351 were reinforced. One layer of tribars was uniformly placed on the trunk while a double layer of random placed tribars was used on the sea-side slope of the head. A survey of the breakwater in 1975 found major deterioration of about 1,000 ft (304.8 m) of the armor stone trunk and several slumped areas in the uniform placed tribars. Further inspection revealed that several of the tribar units (approximately 98) were broken and at that time model tests were initiated to determine the best method of rehabilitating the structure (Davidson, 1978). The rehabilitation work was completed in October of 1977. The one layer tribars were overlaid with 2 layers of 11-ton (97,861 newtons) unreinforced dolosse (485 dolosse). The dolos coverage extended from the toe of the slope to approximately +5.0 ft (+1.5 m) mllw. For 300 ft (91.4 m) shoreward of the tribar area, the sea-side slope of the trunk was rehabilitated with two layers of the 11-ton (97,861 newtons) dolosse. Four hundred forty-nine dolosse were placed in this area from the toe to the crown of the structure. Thirteen of the dolosse were broken during placement, but these were removed from the structure. No further stability problems or breakage have been observed since the 1977 rehabilitation work and the overall functional integrity of the breakwater appears to be good.

Manasquan Inlet is located on the Atlantic coast of New Jersey about 26 miles (41.8 kilometres) south of Sandy Hook in the boroughs of Manasquan and Point Pleasant Beach, Figure 8. The inlet forms the mouth of the Manasquan River and the northern most end of the New Jersey Intracoastal Waterway. In 1880, the previously unnavigable inlet was dredged to provide access to a safe harbor for small vessels navigating along the coast. At the same time, sand filled timber jetties were constructed out to 120 ft (36.6 m) beyond the low water line. The jetties proved to be ineffective in maintaining an open channel and no maintenance was provided. By 1887 the inlet was totally blocked by sand. In 1930 a 1,230-ft (374.9 m) North Jetty and a 1,030-ft (313.9 m) South Jetty were authorized. Both jetties were of riprap (rock) construction. Although the size of stone used is uncertain, the maintenance history (details not available) shows that the original and all subsequent repair and replacement stone have been inadequate. A reconnaissance in early 1977 found that the outer portion of both jetties had been destroyed and the sand accumulation in the inlet was accelerating

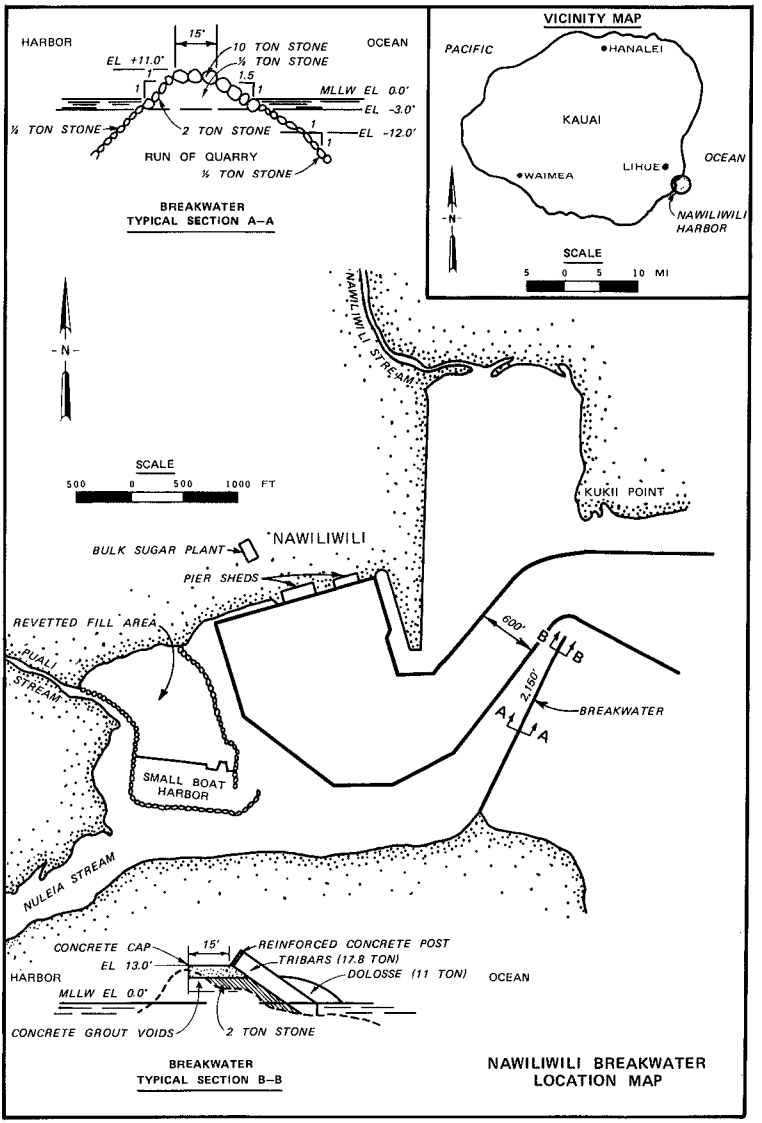

Figure 7. Location and vicinity maps of Nawiliwili Breakwater

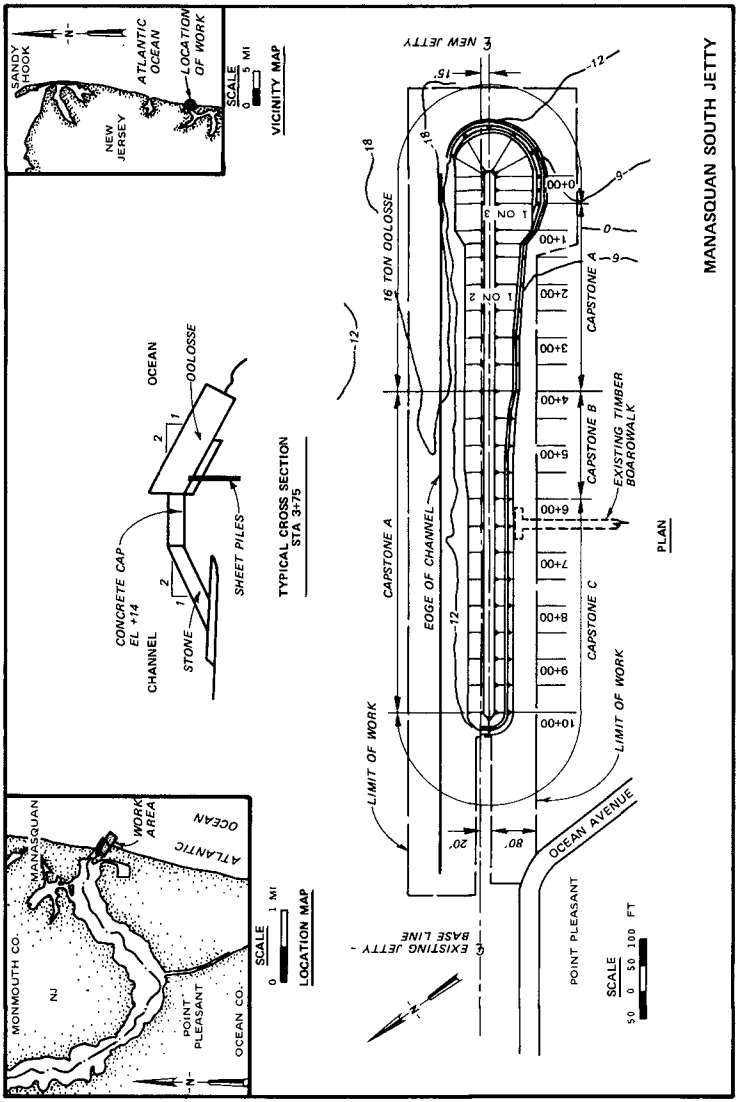

Figure 8. Location and Vicinity maps of Manasquan South Jetty

due to the damage accrued by the South Jetty. A rehabilitation of the South Jetty was carried out in 1980. A portion of the rehabilitation used reinforced, 16-ton (142,343 newtons) dolos armor units. One or two dolosse were broken during construction, but these units were removed. The structure has not been exposed to the design storm conditions and no dolos breakage has been observed since the rehabilitation was completed.

Cleveland Harbor is located on the southern shore of Lake Erie at Cleveland, Ohio, Figure 9. Cleveland is located about 110 miles (177 kilometres) east of Toledo, Ohio, and about 191 miles (307.4 kilometres) west of Buffalo, New York. The harbor is protected by a 20,970-ft (6,391.7 m) East Breakwater, 6,048-ft (1,843.4 m) West Breakwater and two 1,250-ft (381 m) arrowhead breakwaters. The arrowhead breakwaters are connected to the East and West Breakwaters at the main entrance to the harbor. The westerly 3,000 ft (914.4 m) of the East Breakwater is composed of a timber crib, constructed from 1887-1900, and a stone superstructure, constructed from 1917-1926. The remaining 17,970 ft (5,472.3 m) of the East Breakwater was constructed from 1903-1915. This portion of the breakwater is a rubble-mound structure with a keyed and fitted system of special shaped armor stone. Using construction similar to the original work, repairs were made on the East Breakwater in the years 1927, 1928, 1930, 1932-40 and 1946-78. During 1980, the eastern 4,400 ft (1,341.1 m) of the East Breakwater was rehabilitated. Two thicknesses of 2-ton (17,793 newtons) unreinforced dolosse were placed on the lakeside of the trunk, Figure 10, and around the head, Figure 11. Twenty-nine thousand seven-hundred dolosse were placed with a concentration of 161 dolosse per 25 linear ft (7.6 m) of the breakwater. Breakage of several dolosse occurred during the construction period and it was suspected that many of these were due to poor quality concrete and/or incorrect curing. Prior to completion of construction, but on a completed portion of the rehab, twenty two units (randomly located on the structure) were broken during a June 1980 storm. All units that were found broken after the 1980 storm were removed from the structure. Final construction on the dolos section was completed in November 1980, at which time a formal monitoring program to show armor unit movement and breakage on the rehab portion of the project was initiated. During the next year (primary period of consolidation and adjustment) ramdomly located breakage continued until by November 1981 the total number of broken dolosse observed was 329 (1.1 percent of the units placed). No adverse effect on the functional stability of the structure was noted during this time. On 6 April 1982, a particularly severe storm (hindcast waves of 12 ft (3.7 m) in height) occurred simultaneously with the highest lake level (+6.1 ft (+1.9 m) low water datum) ever recorded and caused damage to the rehabilitated dolos section. Although there was some displacement of dolosse over the crest of the trunk section, the primary damage was localized on the tip of the head section where a hole about 20 ft (6.1 m) in diameter at the armor surface penetrated to the underlayer stone. The exact cause of this localized damage is not known, but it is surmized by the authors that the combination of high water level, high wave action, and reflective characteristics of the Coast Guard tower monolith played a major role in the armor displacement. The number of units broken due to displacement from the damage hole was not available, but total breakage on the entire dolos section after the April 1982 storm was reported as 487 or 1.6 percent of the units placed.

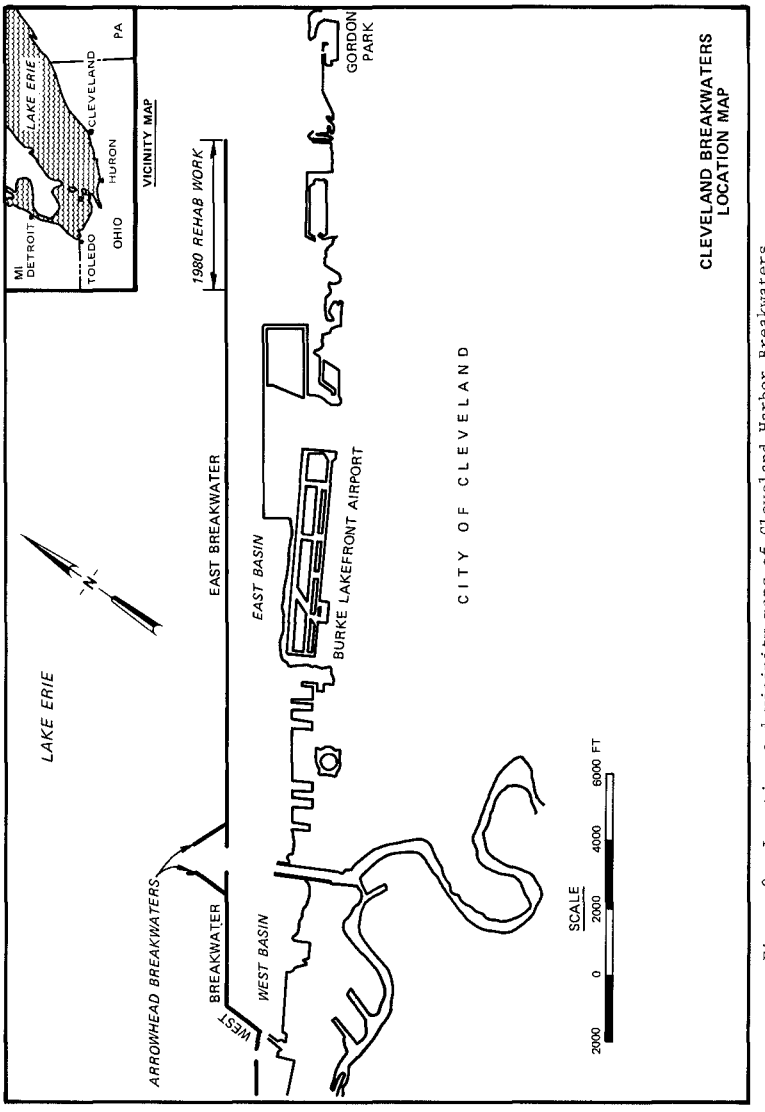

Figure 9. Location and vicinity maps of Cleveland Harbor Breakwaters

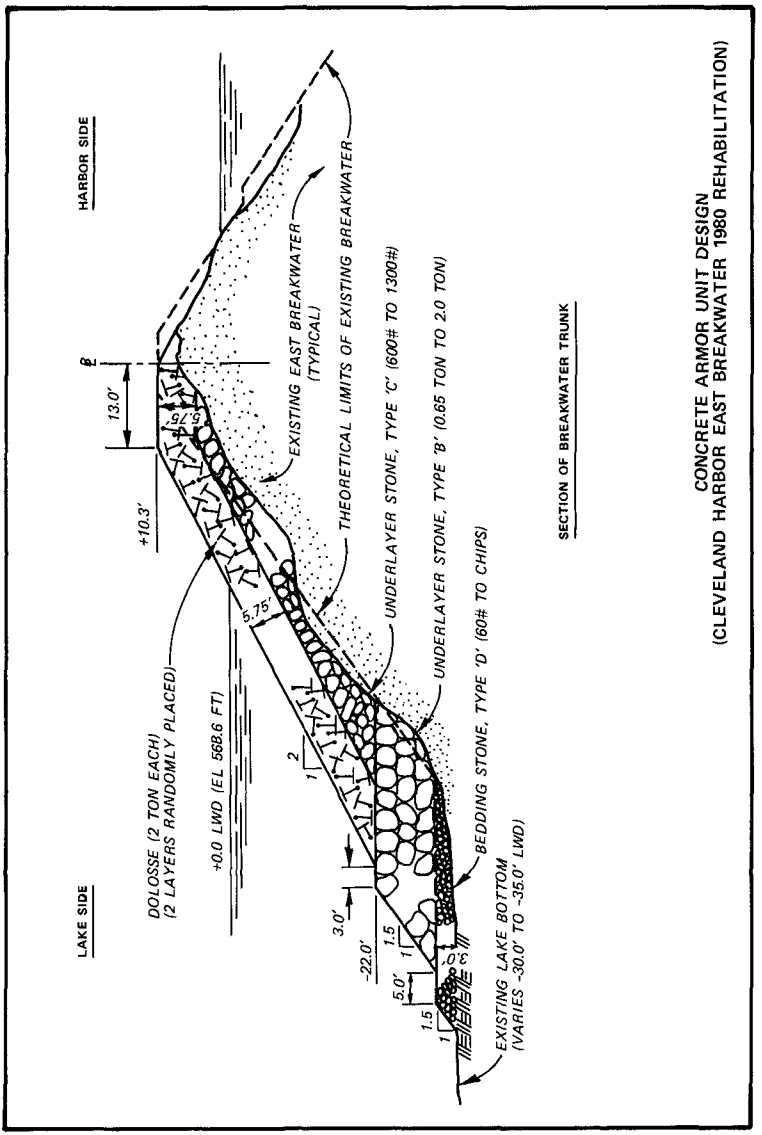

Figure 10. Cross section of Cleveland Harbor Breakwater Trunk

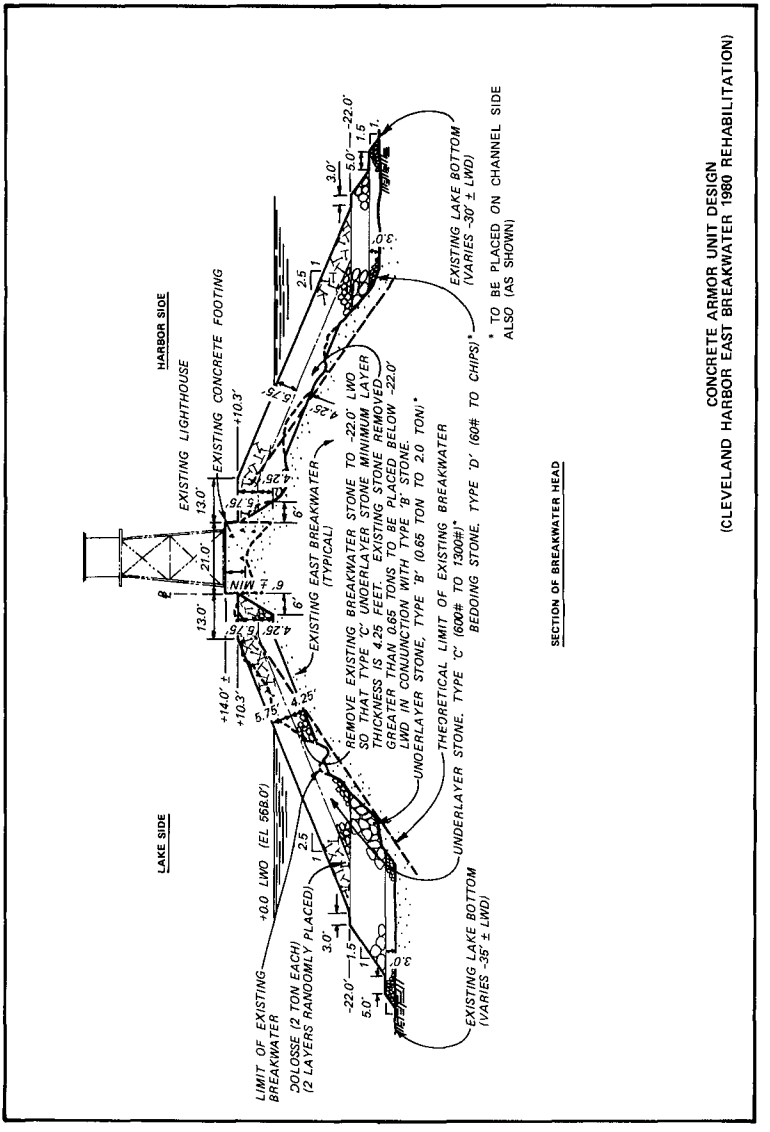

Figure 11. Cross section of Cleveland Harbor Breakwater Head

Diver's survey indicated that the broken dolosse are generally in a zone 4 (1.2 m) to 6 ft (1.8 m) above and below the water level. The head section is being repaired by placing approximately 200 dolosse in the localized damage area. The trunk section is not being repaired and does not appear to have any serious stability problems.

Discussion

Only 3 of the 9 existing Corps structures with concrete armor units were originally constructed using these units (Santa Cruz, Pohoiki and Waianae). The other 6 structures are old armor stone breakwaters or jetties that have been rehabilitated with one or more sizes or types of concrete armor units. Of the 9 structures discussed, only 2 have accrued any significant amount of known armor unit breakage and even these appear to have valid reasons for the breakage. All of the projects incurred breakage for one reason or another, but most of the breakage was <3 percent and has not had any adverse effect on the stability of the structures. Table 2 presents a summary of the breakage on each project. One of the two projects with significant breakage had been model tested for hydraulic characteristics (Nawiliwili) and one had not (Crescent City - the main tetrapod portion of this breakwater was model tested, but the areas where subsequent dolos and tetrapod breakage occurred was not).

When the initial model tests (Jackson, 1960) were conducted for the tribar rehabilitation portion of the Nawiliwili Breakwater, it was recommended that a row of large armor stone be placed along the breakwater toe to serve as a buttress for the tribars. Based on POD records this was not done during the prototype rehabilitation. It can not be stated conclusively, but this very well could have been part of the reason for the slippage and breakage that occurred in the one layer tribar area.

During addition of the 1,000-ft (304.8 m) dogleg at Crescent City in 1957, 140 tetrapods were not needed to complete the construction on the outer portion of the dogleg. Since it was already evident that the elbow area was receiving severe wave action due to remnants of the damaged breakwater extention toward Round Rock, the excess units were stockpiled in an incoherent manner on the sea-side slope of the dogleg adjacent to the main stem (about Sta 37+00 to Sta 39+00). Unlike the end of the dogleg, model tests were not conducted to check the adequacy of the 25-ton (222,411 newtons) tetrapods to withstand the severe breaking wave action that occurs in this area, thus it is not surprising that the tetrapods in this area have been subjected to high displacement and movement which would result in significant breakage and erosion.

As for the dolosse breakage at Crescent City, it has already been brought out that there is some controversy as to how many are broken. To date the numbers range from 38 to 70. It is fairly definite 22 were broken prior to completion of construction. Sixteen of the units were broken in a storm that occurred during construction when two rows of individual toe units had been placed ahead of the main body of dolosse. Six additional dolosse were reported broken immediately after construction was completed (1974-75 winter) and 6 units were reported broken

TABLE 2

Summary of Armor Unit Breakage
Reported on Prototype Survey

Location	Type of Unit and Date of Placement	Armor Unit Size (tons)	Was Reinforcement Used	Total No. of units Placed	Units Broken To Date No.	Units Broken To Date %
San Francisco District						
Crescent City Breakwater, Crescent City, CA.	Tetrapods (1957): Sta 41+20 to 46+70	25	No	1836	3	0.2
	Tetrapods (1957): Sta 37+00 to 39+00	25	No	140	70	50.0
	Dolosse (1974): Sta 34+70 to 37+100	40	No	246	70	28.5
Humboldt Jetties Eureka, CA	Dolosse (1971): South Jetty	42-43	Yes (2513) No (22)	2535	22	0.9
	Dolosse (1972): North Jetty	42-43	Yes (2255) No (4)	2259	12	0.5
Santa Cruz Jetties Santa Cruz, CA.	Quadripods (1963): West Jetty	28	No	900	0	0
Honolulu District						
Pohoiki Breakwater Pohoiki Bay, Hawaii, Hawaii	Dolosse (1979)	6	No	210	5	2.4
Kahului Breakwaters Kahului, Maui, Hawaii	Tetrapods (1956): West Breakwater	33	No	400	9 (13)	3.2
	East Breakwater	33	No		4	
	Tribars (1966): West Breakwater	35	Yes	181 (354)	2	0.6
		50	Yes	173		
	East Breakwater	35	Yes	827 (870)	4	0.4
		50	Yes	43		
	Tribars (1969): West Breakwater	19	Yes	260	5	1.9
	Tribars (1973): West Breakwater	19	Yes	80	0	0
		35	Yes	25	0	0
	Dolosse (1977): West Breakwater	20	Yes	291 (548)	14	2.6
		30	Yes	257		
	East Breakwater	6	No	455	6	1.3
		20	Yes	164 (774)	2	0.3
		30	Yes	610		
Waianae Breakwater Waianae, Oahu, Hawaii	Dolosse (1979)	2	No	6633	170	2.6
Nawiliwili Breakwater Nawiliwili, Kauai, Hawaii	Tribars (1959): Head	17.8	Yes(351)	351 (598)	98	16.4
	Trunk	17.8	No(247)	247		
	Dolosse (1977): Trunk	11	No	485	0	0
Philadelphia District						
Manasquan Jetty Point Plesant, NJ	Dolosse (1980): South Jetty	16	Yes	680	0	0
Buffalo District						
Cleveland Breakwater Cleveland, Ohio	Dolosse (1980)	2	No	29,700	487	1.6

during the winter of 1978-79. A survey conducted in mid-1982 indicated that total breakage could be as high as 70 units. More importantly, the fact that the original breakage was not removed and that the dolos section only extends to just below low water and is frequently subjected to very high depth limited breaking waves adds to the potential instability.

In summarizing the prototye experience that has been presented, it is generally found that where sound professional engineering practices were followed, prototype breakage has been random and has not exceeded about 3 percent of the total number of units placed. This amount of breakage does not appear to have had adverse effects on the overall functional and structural integrities of the breakwaters and jetties.

Experimental Tests

Previously conducted model tests to determine the number of dolosse which could be broken without having a detrimental effect on stability are reported by Davidson and Markle (1976). These tests were limited in scope in that it was a site specific project with limited wave conditions and the breakage investigated was limited to uniformly distributed units broken in the top layer or to specific sets of cluster breakage through both layers of units. Results of this study indicated that as long as the uniformly distributed breakage does not exceed 15 percent of the number of dolosse in the top layer and the cluster breakage does not exceed three dolosse, the functional stability of the breakwater would not be seriously affected.

More recent model tests by Markle and Davidson, (1982b) cover a much wider range of dolos breakage conditions and encompass both breaking and non-breaking wave conditions that produce little or no wave overtopping. Using a dolos armored no-damage trunk section (1V:1.5H slope) of unbroken units as a base condition, various degrees of uniformly distributed and cluster breakage were investigated. Wave conditions included a range of relative depths (d/L, where d denotes depth and L denotes wave length) from 0.08 to 0.25 and relative wave steepnesses (H/L, where H denotes wave height) ranged from 0.031 to 0.075. Dolos breakage conditions consisted of (1) uniform breakage in the top layer, (2) uniform breakage in the bottom layer, (3) uniform breakage in both layers, and (4) cluster breakage of both layers positioned at, above, and below the still water level. Results obtained from these tests were similar to the earlier work in that any one of the following breakage conditions can exist without having a detrimental effect on the functional stability of dolos armor layers. These conditions are: (1) 15 percent uniform breakage of either the top or bottom layer, (2) 7.5 percent uniform breakage of each layer, and (3) clusters of five broken units.

Conclusions

No firm guidance is available as to when, how much and what type of reinforcement, if any, should be used in concrete armor units. The survey showed that as a result of this lack of guidance, sporadic use of both normal and fiber steel reinforcement has occurred. This random

usage of reinforcement and the mixing of reinforced and nonreinforced units make it impossible to draw any definite conclusions as to possible benefits or problems derived from its use. Where sound professional engineering practices were followed, prototype breakage has been random and has not exceeded about 3 percent of the total number of units placed. This amount of breakage does not appear to have had adverse effects on the overall functional integrity of the breakwaters and jetties. Model tests substantiate that, depending on the type and location of dolos breakage, a significant amount of breakage can be tolerated without detriment to the overall stability of the structure.

Acknowledgements

The survey and model tests reported herein were extracted from parts of the Waterways Experiment Station (WES) Miscellaneous Paper HL-83-___, entitled "Breakage of Concrete Armor Units, Survey of Existing Corps Structures," and WES Technical Report HL-83-___, entitled "Effects of Dolos Breakage on Stability of Rubble-Mound Breakwater Trunks, Subjected to Breaking and Nonbreaking Waves With No Over-Topping," which are in the publication review stage. The comprehensive study was conducted by WES for the Office, Chief of Engineers under the Corps of Engineers Civil Works Research and Development Program.

Grateful acknowledgement is extended to the Office, Chief of Engineers for granting permission to publish this paper.

APPENDIX I: REFERENCES

Shore Protection Manual (1977). U. S. Army Corps of Engineers, Coastal Engineering Research Center, Fort Belvoir, Virginia.

Lillevang, O. J., and Nickola, W. E. (1976). "Experimental Studies of Stress Within the Breakwater Armor Piece 'Dolos'," Proceedings, Fifteenth Coastal Engineering Conference, Chapter 145, pp. 2519-2543.

Zwamborn, J. A., and Van Nickerk, M. (1981). "Survey of Dolos Structures," CSIR Research Report 385, National Research Institute for Oceanology, Stellenbosch, South Africa.

Davidson, D. D., and Markle, D. G. (1976). "Effect of Broken Dolos on Breakwater Stability," Proceedings, Fifteenth Coastal Engineering Conference, Chapter 146, pp. 2544-2563.

Markle, D. G., and Davidson, D. D. (1982 in preparation). "Breakage of Concrete Armor Units, Survey of Existing Corps Structures," M.P. HL-83-___ , U. S. Army Engineer Waterways Experiment Station, CE, Vicksburg, MS.

Markle, D. G., and Davidson, D. D. (1982b in preparation). "Effects of Dolos Breakage on Stability of Rubble-Mound Breakwater Trunks, Subjected to Breaking and Nonbreaking Waves with No Overtopping, T.R. HL-83-___ , U. S. Army Engineer Waterways Experiment Station, CE, Vicksbuarg, MS.

APPENDIX II: CONVERSION FACTORS, U. S. CUSTOMARY TO METRIC UNITS

Multiply	By	To Obtain
feet	0.3048	metres
miles (Nautical)	1.852	kilometres
miles (U. S. Statute)	1.693	kilometres
pounds (force)	4.44822	newtons
ton (2,000 pounds (force))	8896.44	newtons

Swartkops Estuary, Port Elizabeth

PART IV
COASTAL, ESTUARINE, AND ENVIRONMENTAL PROBLEMS

Palmiet Estuary, Caper Province

RESPONDING TO AN SOS - SAVE OUR SHORES

by
MG E. R. Heiberg III, M, ASCE[1]
L. A. Duscha, E, ASCE[2]
J. H. Lockhart, Jr, M, ASCE[3]

ABSTRACT

The rising sea level issue affecting U.S. coastal policy is reviewed, and the U. S. Army Corps of Engineers coastal role is summarized. Three case studies are provided to demonstrate the successful application of several structural devices available to solve different coastal problems. The coastal engineer, and other scientists, should contribute significantly to the information upon which society bases its decisions on use of the shoreline.

INTRODUCTION

The coastal zone represents the most rapidly growing region in the United States in terms of population and wealth. Forty-two percent of the population lives in this zone (U.S. Dept. Comm., 1978). Twelve of the 13 largest cities are located in the 30 coastal states. Increasing pressures of population and development are evident in the competition for use of the shoreline and coastal zone. Pressure is exerted for public access and use of the shore: for development of private residences and high-rise apartments; for construction of facilities for commercial, industrial, and transportation purposes; and for the preservation of aesthetic and natural values of shore and marsh areas (HD No. 93-121, 1973).

Prior to the mid-1800's, the sea usually provided the most convenient and economic means of transportation and communication, and cities grew in the vicinity of the ports. Industrialization and improved inland transportation brought increased population density to the coastal centers. Accommodating the expanding urbanization and the accompanying essential services required additional use of the estuaries and adjacent ocean shores. Harbor entrances and channels were improved and facilities to dispose of industrial and urban waste were constructed. However, very little of the outer coast was developed until the automobile and the airplane, together with a great increase in leisure time, made all coasts accessible and increased the demand for space.

[1]Deputy Chief of Engineers, Headquarters, Department of the Army, Corps of Engineers, Washington, D.C.

[2]Chief, Engineering Division, Headquarters, Department of the Army, Corps of Engineers, Washington, D.C.

[3]Civil Engineer, Hydraulic Design Section, Headquarters, Department of the Army, Corps of Engineers, Washington, D.C.

PRESSURES TO ABANDON THE SHORELINE

Many U.S. Citizens (individuals and groups) are lobbying publicly for abandonment of the shores and barrier islands of the United States. They reason that rising sea levels, an overly large government support system for protection, utility and transportation subsidies, and the potential devastation of development by coastal storms combine to justify this position. They explain that the barrier islands are transitory and that construction of permanent structures in such environments is futile. They conclude that the obvious solution is abandonment, to be achieved by prohibiting future development and circumscribing rehabilitation of damage. This stance is promoted through the media and through some elements of the scientific community as the only sensible means of saving our shorelines.

What has been overlooked in the debate regarding development in the coastal zone is that the desire for the enjoyment and habitation of the shore seems to be deeply ingrained in the nature of people. Furthermore, the satisfaction of this desire is now within the means of a large segment of the United States populace. The demand for space at the shore will likely be met, eventually, despite temporary obstruction by regulations, policies, or laws. Our objective should be to satisfy this demand without harming those features which make the coast attractive and without so limiting the available sandy shoreline as to make it economically unavailable to lower income families. Laws and policies which prohibit or strongly deter any increase in the shore areas open to development and public use will undoubtedly lead to an increase of land values in the already available coastal areas. Concomitant increases in the price of the facilities and services economically appropriate to those land values will increasingly restrict the number of people who can afford such recreation or who can afford to live there. Overcrowding and unacceptable environmental stress in the areas remaining open and easily accessible to the general public will soon lead to extension of restrictions to these areas. Clearly, some mechanism is required to determine the proper balance between development and preservation.

RISING SEA LEVELS

A basic rationale used to support the move to abandon the barrier islands and shores of the United States is that of rising sea level. The reasoning is that the sea level has been rising and will continue to do so in the near and long term. With the increasing sea level, the barrier islands are migrating, rolling over themselves like a caterpillar tractor tread, toward shore. All of man's efforts to stem or counter such eventualities are claimed to be futile and a waste of resources. Eustatic changes in sea level are a result of worldwide events which cause changes in either the capacity of the ocean basins or the volume of the ocean waters (Hands, 1977). The direct cause of this change is veiled in the passage of time, and only recently has man developed the technology and data with which to speculate as to the root cause or causes.

Various measurements indicate that sea level has been fairly stable over the past 2,000 years, probably within a range of about one meter

(O'Brien, 1982). Over the period of 1940 to 1975, tide gage data around the US. coast indicate a eustatic rise in the mean level of 1.15 dynamic mm per year (0.115 meter per century) (Hicks, 1978). This effect is frequently linked to melting of the polar ice caps, but also includes such factors as plate tectonics, changes in ocean temperatures and densities, climatic changes, underground withdrawal of liquids and gases, compaction, and other phenomena. The magnitude of long term mean sea level change due to various causes, observed at selected locations, is as follows.

Land Subsidence Due to Oil and Gas Production (Hands '77)

Location	Subsidence Rate (CM/YR)	Period (Yr)	References
Long Beach, CA	22	1926-67	Allen & Mayuga '69 Mayuga & Allen '69
Texas City and Galveston, TX	13	1964-73	Poland '73
San Jacinto Bay, TX	12	1917-25	Pratt & Johnson '26
Houston & Baytown, TX	6	1943-64	Gabrysch '69 Small '63
Lake Maracaibo, Venezuela	0.9	1930-75	Nunez & Escojiido '76
Niigata, Japan	0.14	1900-60	Comm. for Invest. of Earth Subsidence in Niigata '58

Land Subsidence Due to Excessive Ground Water Withdrawal (Hands '77)

Location	Subsidence Rate (CM/YR)	Period	Reference
Texas City & Galveston, TX	13	1964-73	Poland '73
Houston & Baytown, TX	6	1943-64	Gabrysch '69 Small '63
South Shore San Francisco Bay, CA	4	1934-67	Poland '73 Poland & Davis '69
Osaka Bay, Japan	3	1885-1928	Poland & Davis '69
New Orleans, LA	2	1938-64	Kazmann & Heath '68
Nobi Plain, Japan	2	1888-1973	Iida, et al '76

Venice, Italy	0.2	1926-42	Berghinz '71
	0.3	1942-52	
	0.5	1953-61	

Land Subsidence Due to Glacioisostatic Causes (Hands '77)

Location	Subsidence Rate (CM/YR)	Period	Reference
Netherlands	3-4	1880-1930's	Edelman '57
Great Lakes, US.	0.3	1878-1977	Hands '77

Subsidence can occure quite rapidly, as was the case at the Cook Inlet, Kodiak Island, Kenai Peninsula, Alaska, where the March 1964 earthquake lowered about 100,000 square kilometers about 1 meter (Stanley '68). On the Great Lakes, long term climatic cycles (10-30 yrs) can effect a relative subsidence of the land beneath the water (Hands '77). These areas of relatively rapid change require special attention for coastal activities.

A search of recent literature did not reveal that any of the investigations of mean sea level change have ventured a forecast of probable change during the next century (Keehn,1982). Considering the uncertainty associated with past eustatic sea level changes and the scientific uncertainty as to the predominant cause of change, it seems wiser to base public policy on the assumption that mean eustatic sea level will continue to rise during the next century at the same rate experienced over the past century. When more reliable predictive models exist, then public policy can be revisited.

While the physical consequences of mean sea level rise on sandy shores exposed to the open ocean may be significant, storms and their consequences are still the primary concern. Figure 1 illustrates the nature of shore change due to sea level rise and its caption explains the derivation of the formula, known as the Brunn rule (Brunn, 1962). Generally, the landward retreat of the shore (X), is many times the amount of the rise Z. The disproportionality of X to Z will vary from beach to beach, normally ranging hetween 10:1 and 100:1. The concept underlying the Brunn rule seems sound from the standpoint of the processes involved; measurements in the Great Lakes have confirmed this quantitative relationship.

Figure 2, showing profiles of the beach near the U.S. Army Corps of Engineers research pier at Duck, North Carolina during the year 1981, illustrates the difficulty of obtaining a direct measurement of the shore changes attributed to changes in mean sea level. The combined effects of waves and tides during the year were a horizontal movement of the high water line of 39.6 meters and a maximum change of profile elevation of 2.5 meters. Tide gages at Portsmouth, Virginia, north of the pier, and Charleston, South Carolina, south of the pier, had recorded a trend of mean sea level rise of about 3.9 mm per year (Hicks,1978). The Brunn rule indicates an average annual shoreline retreat of 0.15 meters per year. Although this change is unidentifiable in such a short period measurement, the effect, if continued over a

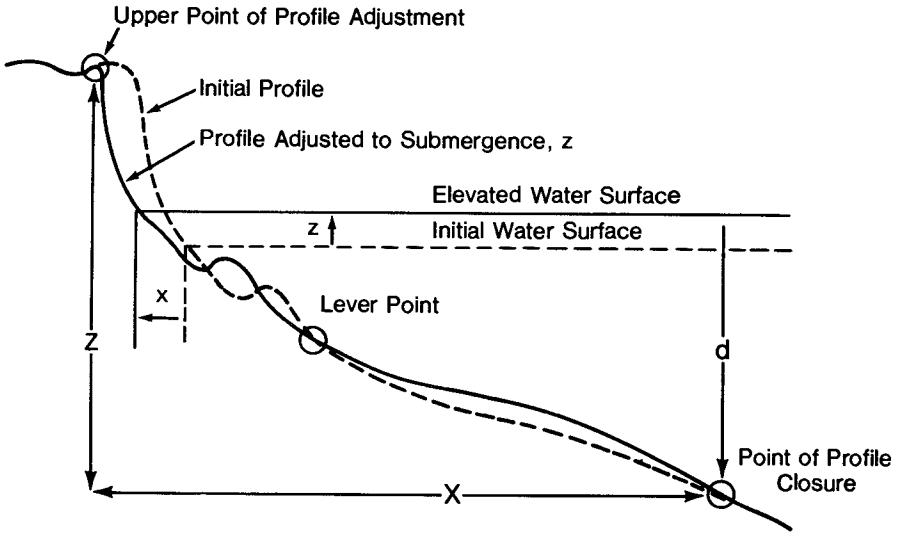

Use of Bruun Rule (Bruun, 1962). Sketch of Profile Measurements Required to Predict Shore Adjustment to a Change in Water Level Elevation. Providing There Is no Net Gain or Loss Outside the Control Volume, Constancy of Profile Shape Requires That the Ultimate Shore Retreat x Be Equal to zX/Z

FIGURE NO. 1

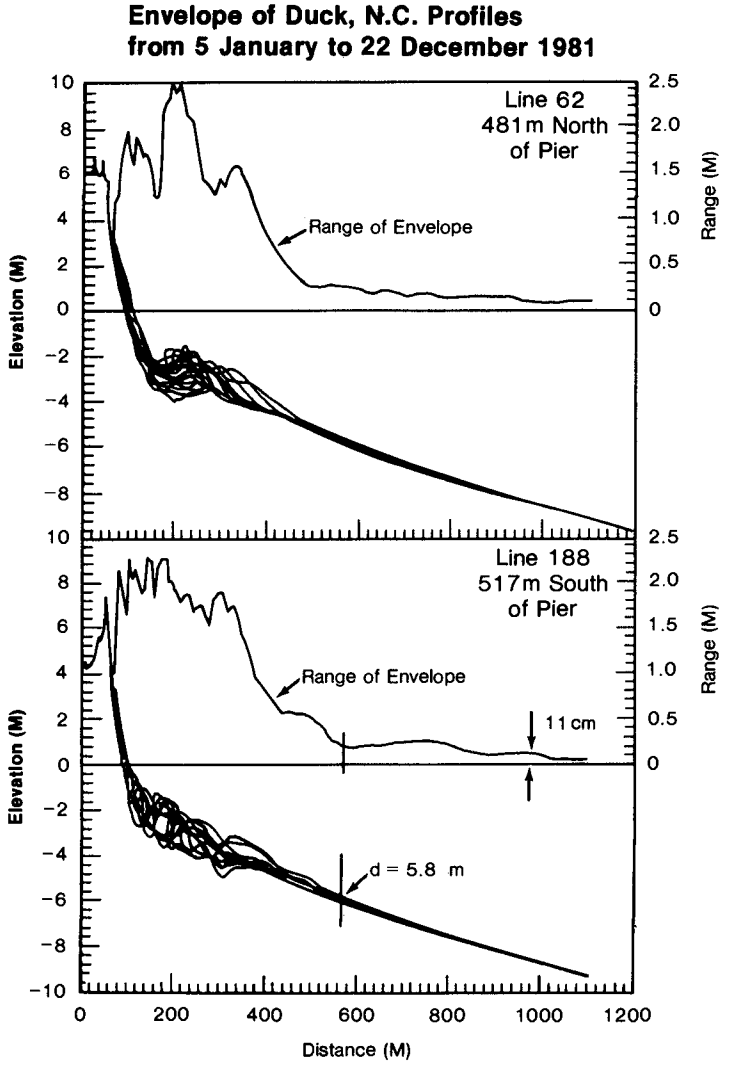

FIGURE NO. 2

(William A. Birkmeier Personal Correspondence, June, 1982)

century, is 15 meters of shoreline retreat. Shoreline change studies on Bodie Island south of the pier for the period 1937-1975 and on Hatteras Island for the period 1852-1946 indicate that actual shoreline retreat rates are 2 to 5 times greater than the 0.15 meter per year which may be attributed to sea level rise.

A trend noted in the comparison of the 1852 and 1946 maps of Hatteras Island was a general decrease in the total subaerial land mass of the barrier island, which indicated erosion on both the ocean and bay sides. In addition, the portion of the island that was marsh increased from approximately 26.6% in 1852 to 35.1% in 1946. This increase in marsh area occurred primarily as a result of seaward propagation of the marsh into low areas that were classified as upland in 1852. Overwash and aeolian processes were evident along the marsh line, but their effects on the island characteristics were minor compared to the ocean and bay shoreline erosion and marsh grass propagation seaward over the barrier island. These changes do not support the generalized theory of barrier island migration, at least within the time frame of several generations. (US Army Corps of Engineers, Wilmington, N.C. 1980)

The question at issue is not whether a rising sea level would cause erosion, hut rather what the prohahle course of sea level change will be over the next century. So far no one has been willing to make such a prediction. The National Academy of Sciences, through its Marine Board, has established a blue ribbon committee, chaired by Professor Rohert G. Dean of the University of Florida, to investigate the sea level change phenomena and to determine the efficacy of forecasting such changes.

RESOURCES MANAGEMENT

As indicated above, the growing population and growing demands for coastal vacations are providing for increased development pressure along our coastlines. The mechanisms used to balance these demands for coastal resources and to manage the utilization of coastal areas are incorporated within the governmental systems at all levels. As example, at the local level, zoning ordinances are used to regulate the type and density of development; at the state level, highway and bridge construction determines the accessability of coastal areas; and at the national level, significant historical, ecological, and scenic areas are preserved through acquisition and management or by withholding national subsidies. A law prohibiting the Federal Government from funding commercial and residential growth on undeveloped barrier beaches and islands was signed by the President on October 18, 1982. More than 190 pieces of land stretching through 16 states, incompasing 700 miles of coastal property are affected. The law specifies which portions of those islands should no longer receive Federal flood insurance or money for water and sewer systems.

The influence exerted on these barrier systems by changes in sea level will depend on the magnitude and direction (higher or lower) of future projected trends and the confidence in the projections exhibited by the scientific community and conveyed to the government decision makers. The shoreline and water level changes which accompany seasonal storms and variations in the along-shore littoral sand supply, as influenced hy nature and man, are normally much greater than the effects of mean sea

level change. These changes, and the attendant environmental consequences have influenced coastal resources management up to now. It is these changes, with the exception of some local areas such as those listed previously, rather than mean sea level changes, that cause the primary adverse effects with which rescue of the shore areas must deal.

THE CORPS ROLE

Nearly 100 years ago, the United States government, recognizing the need to maintain navigable waterways, gave the U.S. Army Corps of Engineers the mandate to develop and protect the Nation's waterways. At that time, the interests of navigation were considered paramount. Many of the affected beach areas were then undeveloped, and there had been little systematic study of the littoral processes involved.

The 1930 River and Harbor Act enacted by Congress provided a broader Federal role in shore protection. The Corps of Engineers was empowered to make studies of beach erosion problems at the request of, and in cooperation with, cities, counties, or states. In 1946, Federal contributions to construction costs were permitted when projects protected publicly-owned shores, or if such protection would result in public benefits. The Corps mission was expanded to include hurricane flood protection in 1955. Contained within the 1968 Federal legislation was the mission to prevent or mitigate shore damage attributable to Federal navigation works. An objective evaluation of the cost of Federal shoreline programs administered by the U.S. Army Corps of Engineers will show that a conscientious effort has been made to insure that public benefits substantially outweigh the public cost.

COASTAL STRUCTURES

Shoreline restoration and stabilization structures built with the assistance of Federal dollars and by the Corps of Engineers are tested by: (1) an economic analysis which indicates the benefit-to-cost ratio is greater than one; (2) an engineering analysis and an environmental assessment based on current technology, which has had the benefit of at least one and often two levels of review, usually including that of the Coastal Engineering Research Center; (3) a cost-sharing policy which reduces the Federal share--normally 50 percent--by the ratio of private to total benefits; and (4) a policy which requires public beach access and public beach use as a condition for Federal aid.

EFFECTIVENESS OF COASTAL STRUCTURES

The Corps of Engineers has constructed more than 800 jetties, breakwaters, and coastal groins. More than 80 beach fill projects have been constructed. Early coastal structures were mostly breakwaters to protect anchorages from wave action, jetties to stabilize the location of entrance channels, and sea walls to protect exposed port or urban areas. Most of these were built in support of navigation, and many have performed their intended functions for nearly a century. Structures to protect or stabilize sections of the open coast (groins, revetments, seawalls, and beach fills) are generally of more recent origin. Examples of long terms of effective service are understandably more limited. However, the record of coastal structures is generally one of

overall success, rather than of failure. It is, of course, true that coastal processes have become better understood in recent years and design techniques have improved correspondingly.

We have referred above to a large number of projects. If we had a huge number of failures, then we would have a national disaster. To list and comment on even the 100 or so projects constructed prior to 1900 is impractical for this presentation. We will instead focus on only three projects. One was an almost immediate success, one has evolved into a very successful project, and one is a recent project, which promises considerable success. The three projects perform different functions and illustrate a relatively wide variety of coastal structures.

GALVESTON, TEXAS, SEAWALL

At the turn of the century, Galveston, Texas, had a population of about 38,000. The first floors of residents and businesses were elevated as a safeguard against storm-induced flooding, which the city occasionally suffered. On September 8, 1900, a hurricane struck Galveston with a storm surge of 4.6 meters msl, accompanied by winds of up to 40.7 meters per second. The storm left in its wake 3,600 demolished buildings and about 6,000 people dead. The city rebuilt and protected itself with a seawall (See Figure 3). On August 16-17, 1915, another severe hurricane swept across Galveston. The winds exceeded 26.8 meters per second for over 19 hours and exceeded 31.3 meters per second for over 9 hours. By comparison the September 1900 hurricane winds had exceeded 26.8 meters per second for only about 7 hours, and its surge height was 8.9 centimeters less than the 1915 storm surge. In striking contrast to the less severe hurricane of 1900, there was comparatively small damage and few casualties (12) within the city in 1915. There was considerable scour along the toe of the seawall and the apron was undermined in places. However, the concrete section of the wall suffered no major damage. The seawall undeniably paid for itself during this one storm (Davis, 1961).

SANTA BARBARA HARBOR, CALIFORNIA

During the 1920's, the beaches of Santa Barbara, California, (Figure 4) and the communities to the east were developed with expensive public improvements and private beach homes. There was a demand for a protected harbor for small boats because severe storms and the open coastline made the Santa Barbara roadstead unusable as a safe moorage. During 1927-29, the city constructed a breakwater offshore to protect a harbor area of about 34 hectares. The breakwater was about 550 meters long and had a short arm at its western end which curved landward. A 183-meter gap to permit an unobstructed flow of sand along the beach was left between this arm of the breakwater and land.

On completion of the offshore section, the breakwater cast a "wave shadow" which caused the littoral transport to be deposited and sand began to shoal the harbor. Complete filling of the harbor was feared, and the breakwater gap was closed. Figure 5 shows the harbor shortly afterwards in 1930. By 1933, the beach had accreted to the bend in the breakwater and a shoal was building into the harbor from the eastern end of the breakwater. At the same time, the beaches to the east of the

FIGURE 3. Galveston Seawall. 1976.

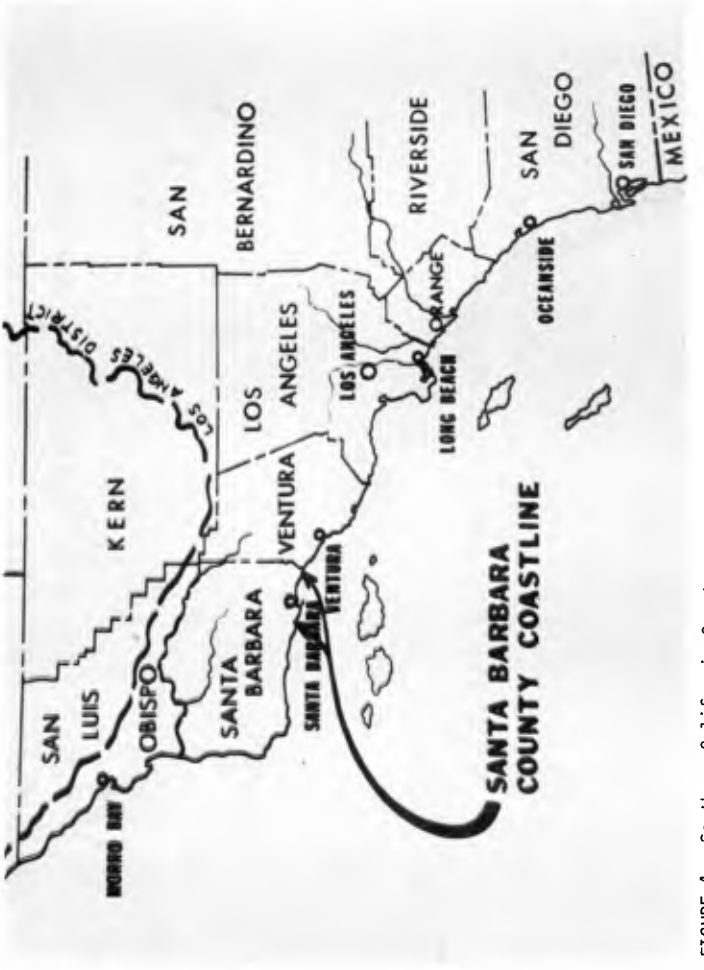

FIGURE 4. Southern California Coast

FIGURE 5. Santa Barbara Harbor, California - 1930.

FIGURE 6. Santa Barbara Harbor, California - 1938

FIGURE 7. Santa Barbara Harbor, California - 1970

harbor began to erode. Riprap walls and groins were constructed to protect the eroding areas. Ultimately, erosion proceeded eastward some 21 kilometers. In 1935, approximately 154,000 cubic meters of material were removed from the shoal by hopper dredge and placed as close to shore as possible. It was hoped that the sand would move shoreward and help replace the beach. The sand was placed in 6.1 meters of water, and very little, if any, reached shore. Years afterwards it was still possible to identify the disposal area when soundings were taken. Figure 6 is a 1938 photograph of the harbor. Initiation of periodic pipeline dredging of the shoal followed shortly thereafter. The material is placed east of the harbor beyond the wave shadow of the breakwater and the eastern beaches have recovered. Besides providing about 700 boat berths in an area of increasing demand (see Figure 7), the project has restored beach property values far in excess of expenditures and is now considered successful (Penfield, 1960).

This project was a first in "sand bypass" engineering. The processes involved were not as clear then as they are today, some 50 years later. The shoreline at Santa Barbara is shielded by the Channel Islands which shelter approximately 40 kilometers of the coast. Normal wave action enters the Santa Barbara Channel from the west and induces an eastward littoral transport through most of the year. However, storms may occasionally reverse the littoral transport for short periods. This situation was not clear when the breakwater was designed. Due to the limited wave exposure behind the Channnel Islands, the littoral drift at Santa Barbara is almost uni-directional and sand bypassing presents a relatively simple challenge. In other situations, where the littoral drift reverses over extended periods, as often is the case, the gross littoral transport quantity may be many times the net littoral transport quantity and the problems of designing a sand bypass system are an order of magnitude more difficult than the problems at Santa Barbara.

DADE COUNTY, FLORIDA

The beach erosion control and hurricane surge protection project for Dade County, Florida, provides a good example of the recent technology in beach fills.

Responding to public concern, the State of Florida, Dade County, and the Corps of Engineers cooperated in constructing the Dade County project, which is designed to withstand a hurricane similar to the 1926 hurricane, the maximum recorded at Miami, Florida. The project provides beach erosion control and hurricane surge protection by the initial placement of 10.7 million cubic meters of sand to form a protective and recreational beach and protective dune for 16.9 kilometers of Miami Beach shore. The project provides for a dune 6.1 meters wide at the crown at an elevation 3.5 meters above mean low water and a level berm 15.2 meters wide at an elevation of 2.7 meters above mean low water with a natural seaward slope (see Figure 8). The beach would be nourished, as needed, to compensate for erosion losses estimated at an annual rate of 161,000 cubic meters. All project fill came from borrow areas 1,800 to 3,700 meters offshore. The fill material was pumped ashore through a submerged discharge line hy a floating hydraulic dredge (US Army Corps of Engineers, Jacksonville, 1980).

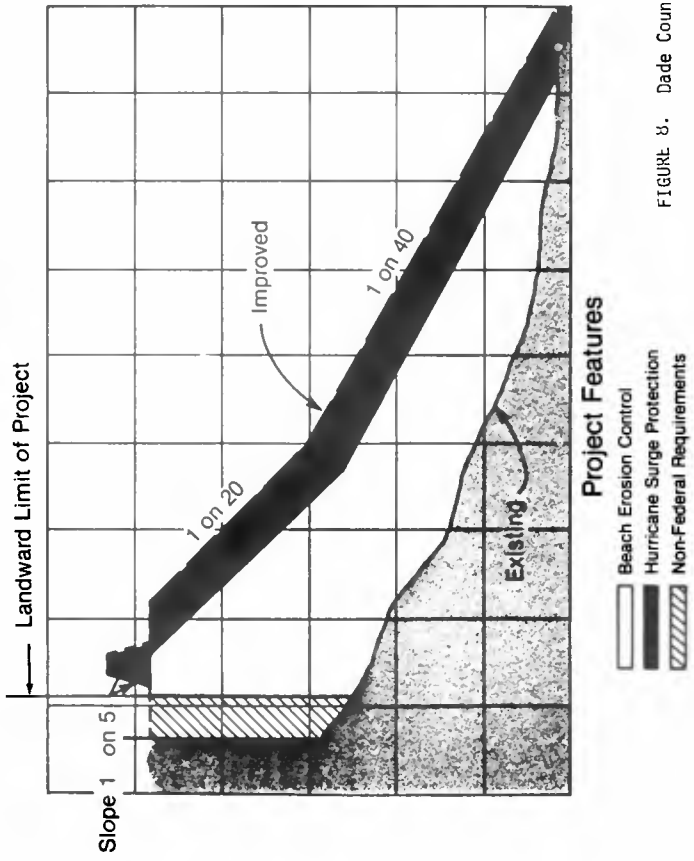

FIGURE 8. Dade County, Florida

FIGURE 9. Miami Beach, Dade County, Florida. Storm Wave Attack before project construction.

FIGURE 10. Miami Beach, Dade County, Florida, before project construction

FIGURE 11. Miami Beach, Dade County, Florida, after project construction.

What is the public receiving for the investment? To begin with, the beach (see Figures 9, 10 and 11), at a cost to date of $2.4 million per kilometer, is protecting property valued at $146 million per kilometer. Protection inherently enhances property by increasing its value on the market, by optimizing its income potential, and by increasing its tax contribution to government. Over one million international tourists visited the beach in 1980 and spent over $200 million, and combined with domestic tourist spending, this amount grows to $500 million, or $29.6 million per kilometer per year. All these factors account for a benefit to the public of $23.1 million per year. Miami Beach represents an excellent example of the merging of governmental functions, private investment, disparate interests, and puhlic demands in providing a high degree of protection and a recreation resource for the maximum use and enjoyment by the greatest number of people. By duplicating nature's own process, the beach fill remains in reasonable harmony with nature while protecting property and enhancing recreational opportunities (Adams, 1981).

This brief review illustrates that coastal erosion and catastrophic flooding can, in fact, be controlled. With proper mitigating actions, the coastal area can be utilized commercially and recreationally. Where circumstances warrant, the beach can be restored and maintained. The Corps of Engineers procedures insure that such efforts are only undertaken in cases that will produce greater economic efficiency than relocation, "no action," or other alternatives. Eurther, 1980's decision-making insures that social and environmental impacts are within acceptable limits. With almost 13,000 kilometers of the United States shoreline experiencing significant erosion, there are numerous areas where rescue of the shore is not only possible, but economically desirable (HD No.93-121,1973). At the same time, today's improved understanding of coastal processes makes it unlikely that costly mistakes will be made.

CONCLUSIONS

The processes active at the ocean's shores range in scale from granular to global and from seconds to centuries. Our planning, design, and construction in the coastal zone improves with an ever increasing understanding of this very dynamic environment. Society, through governmental, benevolent, and market-place mechanisms, makes the decisions on how the coasts will be used. Coastal engineers and other scientists must maintain a continuous, objective pursuit of factual information and make it available in an unbiased way for the judgment of society in arriving at the decisions that must be made. By supporting research and investigative efforts focused on better understanding the dynamic and wide range of processes present at the shore, and by utilizing this knowledge in guiding our activities, we can better plan and design to save our shores for ourselves and future generations.

ACKNOWLEDGEMENT

The authors wish to thank Dean M. P. O'Brien for his generous assistance and many helpful suggestions. We also wish to thank the other Corps of Engineers employees for their efforts in typing, editing, and illustrating the paper. Many constructive comments were provided by the

staff of the South Pacific Division, Galveston District, Jacksonville District, the Waterways Experiment Station, and the Coastal Engineering Research Center. The views expressed in the paper are our own and should not be construed as reflecting official U.S. Army Corps of Engineers policy.

BIBLIOGRAPHY

Adams, Colonel James W. R., 1981, "Florida's Beach Program at the Crossroads," Shore and Beach, Journal of the American Shore and Beach Preservation Association, V. 49, No. 2, Apr 81, pp. 10-14.

Allen, Dennis R. and Mayuga, Manuel N., 1969, "The Mechanics of Compaction and Rebound, Wilmington Oil Field, Long Beach, CA, USA", in Symposium of Tokyo, 1969-Land Subsidence, Vol. 2, International Association of Hydrologic Scientists, Pub. 89, pp. 410-422.

Berghinz, Carlo, 1971, "Venice is Sinking into the Sea," Civil Engineering, March 1971, pp. 67-71.

Bruun, P.,"Sea Level Rise as a Cause of Erosion," Journal of the Waterways and Harbors Division, American Society of Civil Engineers, V. WWI, Feb 1962, pp. 117-133.

Committee for Investigation of Earth Level Subsidence in Niigata, 1958, "On Subsidence of the Earth Level in Niigata Area, Report No. 1: Niigata, Japan," Bureau of 1st Harbor Construction, Ministry of Transportation, 50 p.

Davis, Albert B., Jr., 1961, "The Galveston Sea Wall," Shore and Beach, Journal of the American Shore and Beach Preservation Association, V. 29, No. 2, Oct 61, pp. 6-13.

Edelman, T., 1954, "Tectonic Movements as Resulting from the Comparison of Two Precision Levelings," Geol. in Mijnboww, V. 16, No. 6, pp. 209-212.

Gabrysh, Robert K., 1969, "Land-Surface Subsidence in the Houston-Galveston Region Texas," in Symposium of Tokyo, 1969-Land Subsidence, V. 1, Interna. Assoc. Sci. Hydrology, Pub. 88, pp. 43-54.

Global future: Time To Act, Council on Environmental Quality, United States Department of State, Superintendent of Documents, U.S. Government Printing Office, Washington, D.C. 20402, January 1981.

Hands, Edward B. (1977), Implications of Submergence for Coastal Engineers, Coastal Sediments '77 Proceedings, Fifth Symposium of the Waterways, Port, Coastal, and Ocean Division of the A.S.C.E., pp. 149-166.

Hands, Edward B., 1981, "Predicting Adjustments in Shore and Offshore Sand Profiles on the Great Lakes," Coastal Engineering Technical Aid No. 81-4, U.S. Army Corps of Engineers, Coastal Engineering Research Center, Ft. Belvoir, Virginia, Jan 81.

Hicks, Steacy D., 1978," An Average Geopotential Sea Level Series for the United States, Journal of Geophysical Research, V. 83, No C3, pp 1377-1379, Mar 20, 1978.

Holdahl, S. R. and Nancy L. Morrison, 1974, "Regional Investigations of Vertical Crustal Movements in the U.S., Using Precise Relevelings and Marograph Data," Tectonophysics, V. 23, pp. 373-390.

House Document No.93-121, 93d Congress, 1st session, National Shoreline Study, Vol.I, U.S. Government Printing Office, Washington, D.C., 1973. H.D. No.93-121

Iida, K., K. Sazanami, T. Kuwahara, and K. Ueshita, 1976,"Subsidence of the Nobi Plain, "Abstract., Proceedings of the 2nd International Symposium on Land Subsidence, Anaheim, California, Dec. 1976.

Kazamann, R. G., and M. M. Heath, 1968, "Land Subsidence Related to Ground-Water Offtake in the New Orleans Area,"Gulf Coast Assoc. Geol. Soc. Trans., V. 18, pp. 108-113.

Keehn, Stephen, 1982, "Can Mean Sea Level Changes be Predicted?", paper prepared for Prof. R.L. Wiegel, University of California, Berkeley, California, Winter 1982.

Mayuga, M. N. and D. R. Allen, 1969, "Subsidence in the Wilmington Oil Field, Long Beach, California, USA', Symposium of Tokyo, 1969-Land Subsidence, Vol. 1, International Association of Scientific Hydrology, Pub. 88, ppp. 66-79.

Nunez, O. and D. Escojido, 1976, "Subsidence in the Bolivar Coast," Abstract, Proceedings of the 2nd International Symposium on Land Subsidence, Anaheim California.

O'Brien, Murrough P., 1982, "The Shoreline Debate, "Shore and Beach, Journal of the American Shore and Beach Preservation Association, V.50, No.2, Apr 82, pp.3-8.

Penfield, Wallace C., 1960, "The Oldest Periodic Beach Nourishment Project," Shore and Beach, Journal of the American Shore and Beach Preservation Association, V. 28, No. 1, April 1960, pp. 9-15.

Poland and Davis, 1969, "Land Subsidence Due to Withdrawal of Fluids," in Varnes, D. Jr., and George kiersch, eds., Reviews in Engineerng Geology, V. 2, p. 187-269, Geol. Soc. Am., Boulder, Colorado.

Poland, J. F., 1973, "Subsidence in the United States Due to Ground-Water Overdraft-a Review," Proceedings of the ASCE Irrigation and Drainage Division Specialty Conference, August, Fort Collins, Colorado, pp. 11-38.

Pratt, W. E., and D. W. Johnson, 1926, "Local Subsidence of the Goose Creek Field," Jour. Geology, V. 54, No. 7, pp. 577-590.

Small, J. B., 1963, "Interim Report on Vertical Crustal Movement in the United States," U.S. Coast and Geol. Survey, pp. 14.

Stanley, Kirk W., 1968, "Effects of the Alaska Earthquake of March 27 1964 on Shore Processes and Beach Morphology," U.S. Geological Survey Professional Paper 543-J.

U.S. Army Corps of Engineers, Jacksonville District, Our New Beach, How It Works, Dade County Beach Erosion Control and Hurricane Protection Project Brochure, 1980.

U.S. Army Corps of Engineers, Wilmington District, Manteo (Shallowbag) Bay, North Carolina, General Design Memorandum Phase II, Design Memorandum 2, September 1980.

U.S. Department of Commerce, U.S. Ocean Policy in the 1970's status and issues. Government Printing Office, 1978.

ENVIRONMENT IN COASTAL ENGINEERING: DEFINITIONS AND EXAMPLES**

Cyril Galvin, M. ASCE*

ABSTRACT

In current usage, environmental aspects of coastal engineering design include aspects of ecology and aesthetics, as well as environment. In practice, the aspect of environment is a limited one, considering man's surroundings, with the works of man left out. The increased consideration of environmental aspects over the past 15 years has brought real benefits to the coastal engineering profession, as well as obvious problems. One problem is a mythology of coastal processes that has become widely accepted. Priorities in coastal engineering design remain a structure that will last a useful lifetime and perform its intended function without creating new problems. After satisfying these fundamental requirements, the structure should minimize ecological change, and fit pleasingly in its setting.

INTRODUCTION

Design and THE Environment. A coastal structure must remain standing when hit by the most severe waves, currents, and winds that can reasonably be expected during its intended lifetime. Waves, currents, and winds are basic elements of the physical environment. In this structural sense, good coastal engineering is always sensitive to the environment.

But the designer who creates a structure that doesn't fall down has not necessarily solved a coastal problem. The structure must also perform a function, without creating significant new problems. It must reduce beach erosion, prevent flooding, maintain a channel, provide a quiet anchorage, convey liquids across the shore, or serve other functions. There are groins standing out at sea after the beach has eroded away; jetties exist that enclose a deposit of sand rather than a navigable waterway; some seawalls are regularly overtopped by moderate seas; water intakes are silted in.

*Principal Coastal Engineer, Cyril Galvin, Coastal Engineer, Box 623, Springfield, Virginia 22150, USA.

** This paper is an overview of the papers discussed in the poster session on Environmental Aspects in Coastal Engineering Design. The papers discussed are presented in Chapters 136-137.

These functional failures are no less costly than structural failures. To design a structure to function as intended requires a thorough knowledge of the coastal processes affecting the site. These coastal processes are basic elements of the environment. So in the functional sense also, good coastal engineering is always sensitive to the environment.

But physical factors of the environment (waves, currents, sediment transport, etc.) are not the principal factors of THE environment, as that word is now used in discussing environmental aspects of coastal engineering. "Protect the Environment" does not mean protect the design wave height. Rather, "Protect the Environment" means protect a complex of factors including fish and wildlife, wetlands, scenic views, water quality, odors and sounds, low population density, and even the subjective imaginings of people who will never see the sight.

Intent of this Paper. This paper is about the relation between coastal engineering and the environment in the above contemporary sense. The occasion of the paper was a poster session "Environmental Aspects in Coastal Engineering Design" held on 15 November 1982 in Cape Town as a part of the 18th International Conference on Coastal Engineering. A poster session provides for the individual authors to publish abstracts of their papers and to display key illustrations from their papers at the meeting hall during the conference. The chairman of the session discusses the authors' papers and the general subject, and puts his ideas in a paper. This is the chairman's paper for the poster session on "Environmental Aspects in Coastal Engineering Design."

Given the occasion of this paper, it should serve two functions: review the work of the individual authors taking part in the session, and comment on the subject matter in general. There are 4 papers eligible for review, that is, 4 papers whose abstracts were published in the conference abstract volume and whose authors displayed their results at the conference. These are the works of Perry (1982), Clark (1982), Hoffman, Mussalli, and Taft (1982), and Geldenhuys (1982).

The next section of this paper defines and distinguishes the meanings of environment as they apply to this paper. Following these definitions, four sections review each of the poster papers. The final section presents opinions of the writer on environmental considerations in coastal engineering design.

DEFINITIONS

To a large extent, words mean whatever their users think they mean. This has been especially the case in discussing environmental questions. Nevertheless, it is useful to review the accepted meanings of key words that are a part of the discussion. There are three words particularly relevant here: Environment, Ecology, and Aesthetics.

The authoritative sources of meanings are dictionaries, and the most authoritative dictionary for the English language is the Oxford English Dictionary (OED), issued in corrected form in 1933 with later supplements. A more contemporary and concise dictionary is the Oxford American Dictionary (1980). These two dictionaries (the OED and the OAD) are the sources of the following definitions.

Environment. Environment, according to the 1933 OED, comes from a French word meaning to encircle. Two definitions are given, the first and most general being "the object or regions surrounding anything." The second definition is "the conditions under which any person or thing lives or is developed; the sum-total of influences which modify and determine the development of life or character." The 1980 OAD defines environment as "surroundings, especially those affecting people's lives."

The coastal engineer developing a design wave height for a structure considers the environment in the first sense of these dictionary definitions. Once it is built, the structure itself becomes part of the coastal environment in this sense. But the environment, as used in the phrase "Protect the Environment", implies a slightly different definition; environment in this usage corresponds roughly to animals, plants, and the natural landscape, with the works of man removed. As used in this environmental sense, the meaning approaches that of 'ecology'.

Ecology. The word, 'Ecology', as such, does not appear in the 1933 OED. At that time the accepted spelling was 'oecology', which is defined as "The science of the economy of animals and plants; that branch of biology which deals with the relations of living organisms to their surroundings, their habits and modes of life, etc." (The 1972 Supplement to the OED now accepts 'ecology' as the more usual spelling.)

The 1980 OAD shows the evolution in meaning of ecology that has accompanied recent usage. The first OAD definition of ecology is a concise restatement of the 1933 OED definition: "The scientific study of living things in relation to each other and to their environment". The second definition is simply "this relationship", i.e., the study of relationship among organisms which was the original meaning of ecology is now coming to be replaced by the relationship itself. The OAD editors also add a postscript to their definition: "Note that ecology does not mean environment."

Relationships among native species and their environment, i.e., the ecology, may be affected by coastal engineering works, and the works themselves may be affected by the ecology. As an example, improving an inlet to make it more navigable may also increase the tidal prism, and thus change the salinity of the bay waters. Changed salinity could increase or decrease the productivity of oyster beds in the bay, an effect of a structure on the ecology. It could also change the abundance of marine borers infesting timber piles and bulkheads in the bay, an effect of the ecology on those timber structures. Depending on the circumstances, the net effect of the changes may be beneficial or harmful, although the doubt is usually in favor of maintaining the status quo, since the individuals whose livelihood is most threatened by such changes often hold a potential veto over the approval of the project.

The practical effect of these considerations is the development of a new functional design requirement for a coastal structure: the structure should not cause any significant change in the existing ecology, except for changes (such as improved water quality) that are not strongly opposed by any element of the affected population.

Aesthetics. 'Environment' and 'ecology' are words that have become commonplace. Their meaning may be vague, and one is often confused with the other, but these two words undoubtedly connote good things that people are in favor of. It has been the writer's experience, however, that regulatory decisions made in the name of the environment or ecology are often based, not on ecological principles, but on the personal philosophy of the regulator about what is right, i.e., what contributes to beauty in the situation. Often, in fact, the regulator has relatively little ecological data to base a decision on.

In these decisions, personal aesthetics and not the environment or ecology, determines the outcome. Aesthetics is defined (1933 OED) as "The philosophy or theory of taste,

or of the perception of the beautiful in nature and art." The 1980 OAD defines aesthetics as "a branch of philosopohy dealing with the principles of beauty in art."

Few people, of course, formally sit down and write out their personal theory of what is pleasing and beautiful in nature, and then make decisions consciously following this formulation. It is more intuitive than that. Some things fit and others do not. Given the choice, wilderness is more appealing than development; clear water is preferred to turbid water; dunes are more natural than seawalls; and so on. Often it seems that these aesthetic judgements, with which almost everyone would agree, are made first and the ecological reasons to support the decision are brought up later. The net benefit of the structure to society runs a distant second in consideration.

Thus, while protecting the environment or the ecology may be the slogan, the practical application is often based on personal aesthetics. Aesthetic judgements are important and must be given weight. They are often intuitively correct. As an example, the selection of the site for the Field Research Facility of the Coastal Engineering Research Center located at Duck, North Carolina, was determined by a regulatory decision based on aesthetics. The site originally favored for that facility was Assateague Island, part of a National Seashore. The principal cogent objection to the facility at Assateague was the visual incompatibility of the pier superstructure with the setting. As a result of this objection, plans for the Assateague site were abandoned and the present site at Duck, North Carolina, was selected, a fortunate selection in the writer's view.

Sometimes, the basis for aesthetic decisions appears to automatically assume greater attractiveness of natural conditions. But the natural condition is not necessarily the most pleasing one, despite a strong predilection to assume so. The writer has had black California beach sand pointed out to him as evidence of oil spills. The sands in question were indeed visually unpleasing, but the blackness was entirely natural, due to naturally occurring dark minerals of the region.

In previous paragraphs, this section of the paper attempts to define and distinguish three terms applicable to what is called the environmental aspect of coastal engineering. The next sections get down to four concrete cases that were included in the poster session on Environmental Aspects of Coastal Engineering Design. These four cases are, in effect, a random sample of current coastal studies bearing on environmental aspects of design.

CLASSIFICATION OF NATAL ESTUARIES

Reference. The Estuaries of Natal: A Method of Classification, J.E. Perry, Abstracts volume, 18th International Conference on Coastal Engineering, Paper No. 17, pp. 33-34. (This abstract has been supplemented by selected data reports supplied by Mrs. Perry.)

Natal Estuaries. This report concerns the classification of 72 estuaries in Natal, South Africa. Classification is based on 6 sets of air photos covering the period from 1937 to 1980. Most of these photos were taken during the southern hemisphere winter. The photos are converted to a common 1:10,000 scale and landmarks used to locate changing features. A large number of measurements are made, most of which describe the geometry of the river and adjacent areas. Perhaps only 20% of these measurements concern coastal features directly, these being features associated with the river mouth. Table 1 identifies only the river mouth features measured in the classification.

The mouths of these estuaries often have spits from one or both sides, which frequently seal off the river mouth entirely. Rocks commonly occur in the vicinity of the mouth, and roads or rail bridges are also common. Data from the work of G.W. Begg (1978) and additional data supplied by J.E. Perry (received Dec 1982), show the following: The estuaries can be conveniently divided into north and south sets, with Natal Bay as the approximate dividing line (approximately $29^{o}53'$ south latitude). The majority of Natal estuaries are south of Natal Bay and most of these are usually closed. Spits commonly grow north to south in the south and south to north in the north. In the south about 43 of 53 estuary mouths have noticeable rocks in the vicinity, but in the north only 8 of 21 show rocks in the vicinity. The estuaries in the south commonly are crossed by road and/or rail bridges near the mouth, but in the north this is the case at only 4 estuaries.

In their present state, these data are still being tabulated and interpreted, but as indicated in the previous paragraph, they offer interesting information, for example, on longshore transport directions. Mrs. Perry reports that particularly for the coast north of the river Tugela ($29^{o}13'$ south latitude), there are long northward-directed spits. Some of these shores show prominent accretion, as shown by the shoreline changes in Figure 1, reduced from a supplement to the report by Selby and Perry (1982).

Table 1. RIVER MOUTH DATA, NATAL ESTUARIES

Characteristics*	Measurements*
open/closed	right bank breakwater length
natural/ artificial	left bank breakwater length
	rock sill level**
canalized	
	cliffs on right bank: height**
sandy	
	cliffs on left bank: height**
rocks on right bank	spit/bar: direction of growth in degrees
rocks on left bank	length of spit/bar
outer bar	stabilized length
silt plume (fluvial)	width
suspended sediment (marine)	

*taken from data form "Classification of the Lower Reaches of Natal Rivers"
**measured from MSL

Opinion. This study illustrates a necessary fundamental step in any proper environmental study: the description of what actually exists in the field. The use of aerial photos is ideal for this purpose, since they provide a uniform source of morphologic data at identifiable times in the past. Once finished, the availability of such a set of data will put future analysis and policy decisions on a much surer basis. The wider possibilities of these data are illustrated by the shoreline change information of Figure 1.

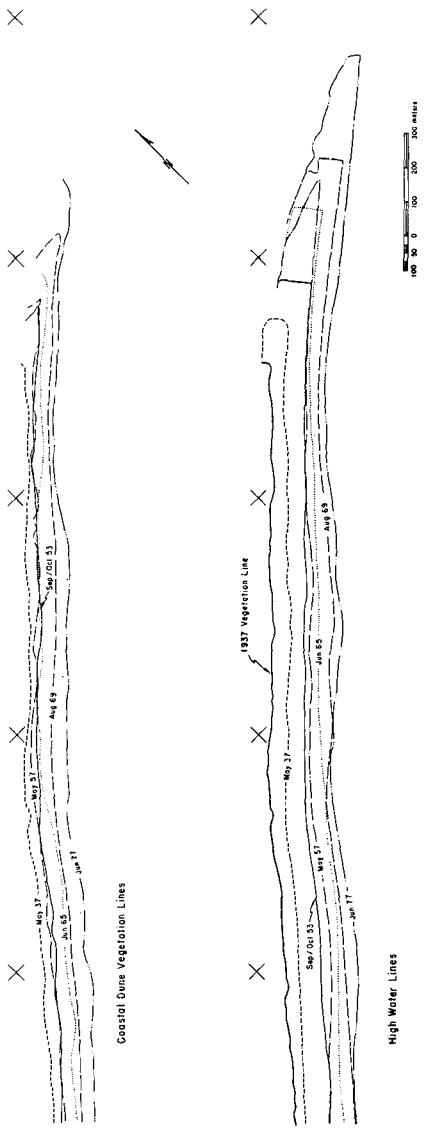

Figure 1. ACCRETION AT THE MOUTH OF SIALA RIVER, NATAL, SOUTH AFRICA (SELBY AND PERRY, 1982)

FLORIDA COASTAL CONSTRUCTION GUIDELINES

Reference. Coastal Construction Building Code Guidelines, Ralph R. Clark, P.E., editor, Florida Department of Natural Resources, Bureau of Beaches and Shores, Technical Report TR 80-1, Nov 1980, 52 pp.

Purpose. As explained in its introduction, this document is a product of the evolving state coastal management program in Florida. Since 1957, the Florida Department of Natural Resources (DNR) has held regulatory authority over building setback lines and coastal construction in the state. In recent years, Florida state legislation has encouraged delegation of this authority to the particular municipalities and counties, provided that the municipalities and counties have appropriate procedures to control coastal construction. The purpose of TR 80-1 is to provide local Florida governments with guidelines for a coastal construction building code.

(This delegation of regulatory authority to lower levels of government is an example of a nationwide trend. A similar effort in state coastal zone management is that taking place in California. Much of the permit jurisdiction formerly held by the California Coastal Commission is being assumed by the particular cities and counties within that state following completion of their local coastal programs.)

Building Code. This document (TR 80-1) consists of a one-page introduction, followed by two, nearly-identical modifications to existing building codes of approximately 24 pages each, and ending with 5 pages of references.

The body of the report (pages 1 thru 47) presents the building code guidelines recommended by DNR. These are in the form of supplements to the existing South Florida Building Code (pages 1 thru 23) and the existing Standard Building Code (pages 24 thru 47). The principal difference between the two supplements is the terminology used to subdivide and identify specific paragraphs.

As indicated by Clark (1982), three major concepts of coastal engineering design are incorporated into these building code guidelines:

a. Identification of a zone where major coastal construction is permitted, but where special coastal design criteria apply. The zone is three-dimensional, that is, it has both landward and seaward limits in plan, and vertical constraints in elevation.

b. Requirement that foundation design anticipate erosion occurring during the 100-year storm surge, or its cumulative equivalent.

c. Requirement that the structure be designed for loading expected during the 100-year storm surge.

Both supplements contain identical sections on definitions. The zone subject to these recommended building code supplements is defined as the Coastal Construction Building Zone. This zone is bounded on the seaward side by the Coastal Construction Conservation Zone, which is approximately the dunes and the beach as far as the mean high water line. Major structures cannot be constructed within the Conservation Zone. On the landward side, the Construction Zone is bounded by the Coastal Construction Control Line. This control line is defined by statute and plotted on official maps. It is intended to mark a landward limit to the effect of the storm surge with a 1% chance of occurrence in any year (the 100-year surge) or of a number of lesser storms which cumulatively have the same probability of occurrence. (The zoning is generalized for the purpose of this paper as Figure 2, drawn in part from the FEMA (1981) Coastal Construction Manual.)

Two types of erosion are distinguished under 'erosion' in the definitions: Horizontal Recession and Scour, based on whether or not the storm surge inundates the profile. This distinction appears unsatisfactory to the writer, because both horizontal recession and vertical scour can occur in the absence of storm surge, and because it appears to imply erosion due to onshore-offshore transport when much erosion is due to longshore transport. It would be better to define erosion within the concept of littoral sediment budget, erosion being the result when more sand is carried out of the area than is carried in by waves, currents, winds, and other processes.

The general load requirement is for all habitable buildings to be designed to withstand the forces accompanying the 100-year storm. These forces are defined to be "waves, hydrostatic, hydrodynamic, and wind loads". Wave loads are specified to be those required by appropriate Navy or Army Corps of Engineers Manuals (NAVFAC DM-26 or Shore Protection Manual, Volume II). Hydrostatic loads are given as the pressure resulting from the equivalent height of water. Hydrodynamic loads are given a lengthy discussion in the definitions section, but are discussed only briefly and in general terms under required loads. The wind load is

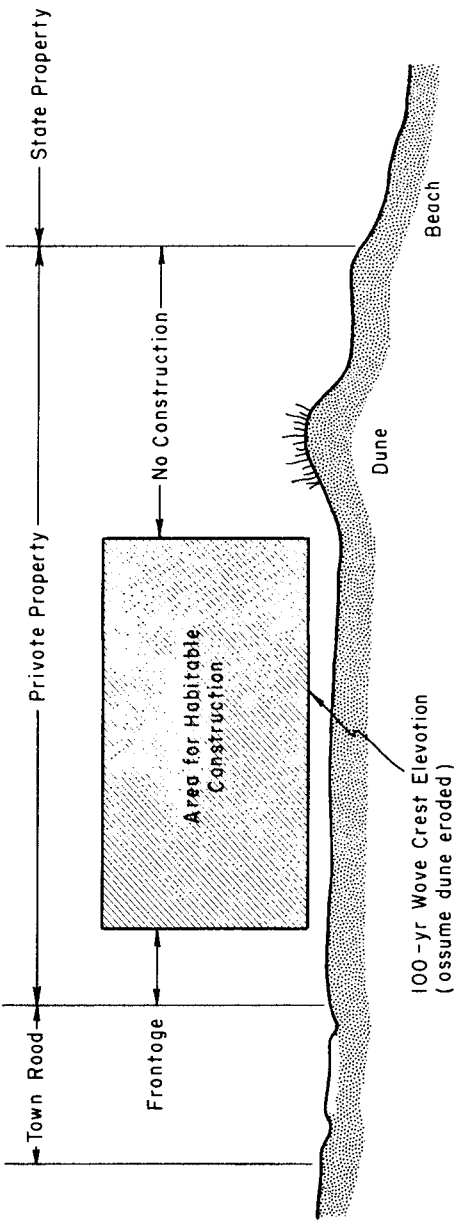

Figure 2. TYPICAL COASTAL CONSTRUCTION ZONE

specified by a table developed from the 2/7 power of elevation above grade, based on an assumed 140 mile per hour wind.

Although habitable structures must be designed for the 100-year storm, shore protection structures may have shorter design lifetimes, down to 10 years for bulkheads. Shore protection structures must be "designed for the minimum wave loads which are applicable for the design storm conditions which justify the structure."

Excavation in the Coastal Construction Building Zone is not recommended but is permitted, provided that excavated beach material is replaced or used elsewhere in the zone and provided that the excavation does not present potential danger during the 100-year storm design conditions.

The first floor must be above the expected wave crest elevation during the 100-year storm. This elevation is the higher of those determined by the DNR or the Federal Emergency Management Agency (FEMA), and is subject to revision.

A pile foundation is recommended for habitable structures, although soil-bearing foundations are permitted, if allowance is made for localized scour during the 100-year storm. The pile foundation is to have pile caps below the expected erosion surface during the 100-year storm. The pile foundation above grade is to have adequate spacing, defined as 8 feet or 8 times the pile diameter, which ever is greater.

Bibliography. The document contains a useful list of 65 references, almost all of which are not specifically listed in the building code guidelines. These 65 references identify about 13 national, county, and local building codes; 13 text books on a variety of subjects; 5 manuals; 6 reports related to FEMA's coastal flood insurance mapping; and at least 11 articles that might be called construction guidelines. The remaining 17 references deal mostly with coastal processes, sediment transport, and waves.

Opinion. Construction codes concern criteria based on the physical environment. The ecology of the environment is considered in the earlier steps defining the construction zone and granting the building permit. These Florida guidelines systematically reduce coastal engineering practice to terms applicable to the work of the building contractor, without overspecifying the criteria. The engineer still has to determine for the specific site the probable ground level during the 100-year surge and the forces exerted by this surge. Among the tougher questions to be determined is

whether the dune, which is usually pictured seaward of the construction zone (Figure 2), will survive the 100 year surge. The 5-page bibliography is a most useful addendum to the guidelines.

EXCLUDING ORGANISMS FROM COASTAL WATER INTAKES

Reference. Environmental Considerations in Designing Coastal Water Intakes, P. Hofmann, Y.G. Mussalli, and E.P. Taft, unpublished draft report, Stone & Webster Engineering Corporation, 1982, 14 pp. including 7 figures.

Fish Transfer Systems. Cooling water intakes to power plants may entrain organisms, resulting in high mortality to the entrained organisms and possible damage to the cooling water system. The problem of excluding organisms from the water intake without killing them is a sophisticated extension of the problem of excluding trash, which has occupied engineers for a longer time (Linsley and Franzini, 1979, p. 233). Design of a water intake usually requires consideration of a trash rack; exclusion of organisms from coastal water intakes adds to this standard design requirement the effect of a living organism capable of independent reaction to the environment, and the complications imposed by coastal processes. The authors describe solutions to the problem of organism entrainment which they have studied. Additional related studies are found in Taft and Mussalli (1978).

Physical constraints of the site usually will determine the overall plan of the cooling water system. Modifications to that system are then made to minimize organism entrainment. The principal modification recommended by the authors, based on their studies, is the use of screens angled at about 25° to the centerline of the upstream channel. Fish swept downstream sense these screens and in avoiding them, they are shunted into a bypass from which they are returned safely to open water. (The fish do not 'see' the screens, which are usually in the dark. Even if in a lighted conduit, the fish approach the screens tail first, so the sensing of the screens is presumably a reaction to the turbulent eddies shed by the screens.)

Louvers have been used for fish diversion in hydroelectric plant intakes, but the authors' studies show that the net efficiency, considering the cooling water system and fish mortality, makes screens the better choice. Mortality rates for fish vary considerably with the species tested. The 25° angle of the screen is an empirical result of their tests with live fish.

The use of these screens is further modified to minimize pumping requirements for the fish bypass system. To reduce this cost it is desirable to minimize the flow in the bypass. This is accomplished by making each screen a vertical conveyor belt with fish buckets which lift fish to a smaller return trough (Figure 3). The conveyor belts are equipped with low pressure sprays to transfer the fish into the fish trough and a high pressure spray to remove trash.

There is a further complication in one Florida power plant imposed by the requirement to remove small organisms from the flow. This requires reducing the screen mesh from the normal 9.5 mm to 0.5 mm, which results in unique operational and reliability problems.

Opinion. These modified solutions to the problem of avoiding organism entrainment appear to be still in the development stage. It will be useful to see statistics on their operational reliability after several years. Statistics concerning the net effect of the cooling water system on the local ecology would be useful in justifying the cost of the traveling screens. Presumably, the heat discharge and turbulent energy accompanying the operation of the cooling system contribute benefits, as well as losses, to the local ecology.

RICHARDS BAY OUTFALL

Reference. Richards Bay Marine Effluent Pipeline - Environmental Aspects, N.D. Geldenhuys, Abstracts volume, 18th International Conference on Coastal Engineering, Paper No. 20, Nov. 1982, p. 39.

Discussion. This abstract identifies salient factors of the outfall at Richards Bay, South Africa, intended to handle effluent resulting from future industrial and population growth. The pipeline is a 1 meter diameter plastic pipe which is to extend 4 to 5 kilometers out to sea. Buoyant effluent will be discharged at a depth of 28 meters; dense effluent at a depth of 25 meters. The effluent consists of 3 principal substances: dense waste from a phosphoric acid factory, including gypsum, fluorides, and heavy metals; buoyant paper and pulp mill effluent; and buoyant municipal sewerage.

The volume of effluent is expected to rise from 64,000 m^3/day in 1984 to 176,000 m^3/day by 2013. The volume of dense waste will be a relatively low percentage of the total initial discharge and will remain relatively constant in

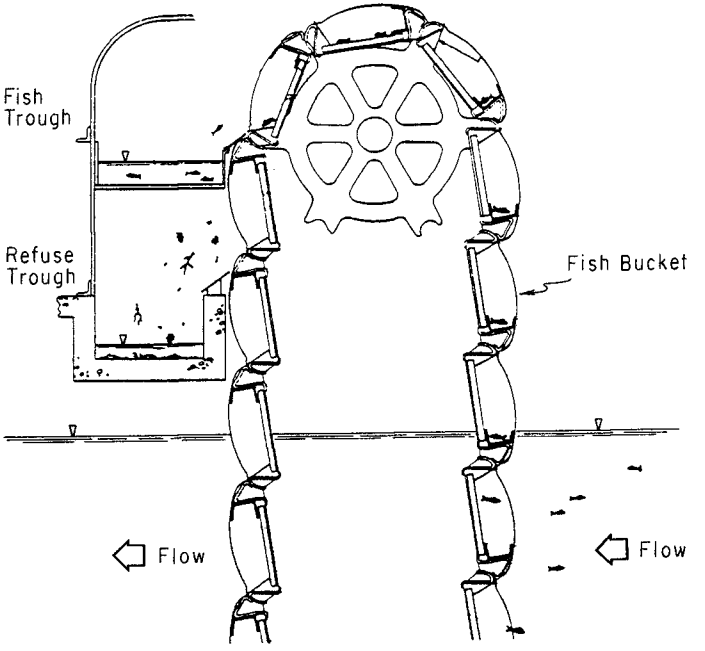

Figure 3. MODIFIED TRAVELING SCREEN WITH FISH BUCKETS (HOFMANN, MUSSALLI, AND TAFT, 1982)

absolute terms. The volume of buoyant waste is a large percentage of the initial total, and is expected to grow in absolute terms.

Some environmental deterioration is expected in the vicinity of the diffuser, particularly from deposition of the gypsum slurry which will eventually cover 4 square kilometers of bottom. Adverse effects may be reduced by inplant treatment, by searching for alternative use of the material, and by monitoring.

Bottom currents are estimated to be slight with median values between 7 and 10 cm/sec. Wave action is moderately severe with 90% of all wave heights between 0.5 and 2.0 meters. The available information does not provide data on the design criteria leading to the selected pipeline lengths, discharge point, and diameter. The design of outfalls based on physical and ecological criteria is discussed in detail by Grace (1978).

SELECTED ASPECTS OF ENVIRONMENT IN DESIGN

The previous sections of this paper indicate the range of environmentally related studies that now occupy coastal engineers and scientists, from basic description of the environment (Table 1) to design and testing of highly specialized fish handling mechanisms (Figure 3). The environmental concern that led to these studies has had a number of effects on coastal engineering design, some of them for the good. In this final section of this paper, three effects on the profession are discussed:

a. Benefits to coastal engineering practice
b. Fostering of coastal myths
c. Design priorities

Benefits of Environmental Concern. The environmental movement is blamed for delay and cancellation of projects; perversion of technical data; exaggerated concern over improbable outcomes; and many other errors of commission and omission. Most practicing coastal engineers will have their share of stories to tell, so they will not be reviewed here. Despite these real difficulties, however, the environmental movement has benefited the coastal engineering profession in significant ways.

On an economic level, environmental requirements have generated a lot of work for coastal engineers. On a technical level, environmental studies have significantly improved the profession's capacity to design for new environments.

The work done in planning for the Atlantic Generating Station in New Jersey provided much work for the profession and advanced its technical understanding considerably. There have been many other projects of smaller scope.

Preliminary studies required to satisfy environmental regulations probably have reduced net project costs in many cases by eliminating some of the uncertainty that faces a contractor in making up his bid. An Engineering News Record article ("Outfall bid $10 million under estimate", 9 Apr 1981) credits the low bid on the Southwest Ocean Outfall in San Francisco to preliminary studies which reduced the size of contingency allowances added to the bids.

Environmental requirements have forced coastal engineers to recognize the costs of unwanted ecological change. Although engineers retain strong suspicions that the ecological data on which these costs are calculated are often questionable, the requirement to consider the question has widened the view of the engineers, to the benefit of the profession.

The activity of coastal engineers on these environmental questions has also partially educated the regulators. There is now grudging recognition among environmentalists that some coastal engineers know what they are doing.

Myths. The environmental movement has fostered a pervasive mythology about coastal processes. These myths include logical impossibilities, highly improbable assertions, and dubious hypotheses. These are reviewed in reports and editorials published in Shore and Beach (see Adams, 1982; O'Brien, 1982; O'Brien, 1980) and in Proceedings of Coastal Zone '80 (see O'Brien and Johnson, 1982, Olsen, 1982). The following paragraphs start off with a brief statement of a myth, followed by a statement believed to more accurately represent the facts.

a. *All structures cause erosion.* Well designed structures retard or prevent erosion. As pointed out by O'Brien and others, few people would go to the expense of building a structure if erosion did not already exist at the site. Since many structures are separated from the water by a sand beach when they are built, this supposed causal action implies that waves are equipped with some sort of remote-sensing ability to perceive the structure behind the berm. To really evaluate the effect of the structure, compare the condition after construction with what would have been the condition had no structure been built.

b. *Seawalls cause unacceptable scour.* It has not been demonstrated that wave action at a seawall results in worse conditions than no seawall at all. Well designed seawalls are effective structures in sites that require them.

c. *Sea level rise is the cause of erosion.* The net effect of even rapid sea level rise is small compared to the effects of other coastal processes contributing to erosion (Galvin, 1983).

d. *The world's beaches are eroding almost everywhere.* Erosion probably does dominate, but accretion is not negligible. The writer believes that this myth is partly an artifact of the reporting system. The beaches most justifying study (and thus being reported) are those that are eroding. Accretion, such as that shown in Figure 1, gets noticed and reported only by accident. It is also true that both environmentalists and engineers may stand to gain from reports of widespread erosion, and this can subconsciously affect the reported prevalence of erosion.

e. *Erosion is inevitable.* Erosion is preventable, often by modest engineering efforts. A large sand fill at Ocean Beach, San Francisco, was maintained on the Pacific Ocean for half a century prior to current construction. A sand dike at the entrance to Fire Island Inlet, New York, has remained exposed to the Atlantic Ocean for over 20 years.

f. *Barrier islands are fragile.* Barrier islands have evolved in a tough environment, and they persist there. Barrier islands pictured on 18th century charts of the U.S. Atlantic coast are still in place, along with most of the important inlets between them. The seawall at Galveston, on a low barrier island in an area of subsiding land levels, is now about 80 years old and still functioning. Lighthouses from the 19th century and earlier exist today on Atlantic coast barrier islands.

Priorities in Coastal Engineering Design. It is difficult to design a structure that will last a useful lifetime and perform its intended function without introducing new coastal problems. The pressure of environmental concern tends to displace these design priorities. The ecological and aesthetic requirements of the design must be subordinate to these primary requirements. A suggested list of priorities for the responsible engineer are as follows:

a. Know the environment of the structure under design. This must be personal knowledge, adequate to establish the physical design criteria with confidence. This is a first requirement, before design can begin.

b. Design the structure to last a useful lifetime under the expectable extremes of the environment. This is the primary requirement of the design.

c. Design the structure to perform its intended function without introducing significant new problems. If this functional requirement is not satisfied, the structure will still be a failure, even if it lasts its intended design life.

d. Design the structure to minimize environmental change, particularly those aspects of the environment which are critical to the existing ecology. As indicated above, approval of the project may depend on this.

e. Within the constraints of the preceding priorities, make the structure fit the landscape in a pleasing way. A structure that is both physically adequate and functional is usually aesthetically pleasing as well.

REFERENCES

Adams, J.W.R., "Politics of Beach Nourishment," Shore and Beach, Vol. 50, No. 1, Jan 1982, pp. 3-5.

Begg, G.W., "Estuaries of Natal," Oceanographic Research Institute, Durban, 1978.

Bird, E.C.F., "Recent Changes on the World's Sandy Shorelines," from: Coastal Dynamics and Scientific Sites, E.C.F. Bird and Kazuyuki Koike, ed., Commission on the Coastal Environment, International Geographical Union, Department of Geography, Komazawa University, Tokyo, 1981, pp. 5-29.

Clark, R.R., "Structural Design Aspects of a Coastal Building Code," Abstracts Volume, 18th International Conference on Coastal Engineering, Paper No. 16, Nov 1982, pp. 31-32.

Clark, R.R., editor, "Coastal Construction Building Code Guidelines," Florida Department of Natural Resources, Bureau of Beaches and Shores, Technical Report TR 80-1, Nov 1980, 52 pp.

Federal Emergency Management Agency, "Design and Construction Manual for Residential Buildings in Coastal High Hazard Areas," FEMA Manual FIA-7, Jan 1981, 189 pp.

Galvin, Cyril, "Sea Level Rise and Shoreline Recession," Proceedings of Coastal Zone '83, American Society of Civil Engineers, June 1983 (in press).

Geldenhuys, N.D., "Richards Bay Marine Effluent Pipeline - Environmental Aspects," Abstracts Volume, 18th International Conference on Coastal Engineering, Paper No. 20, Nov 1982, p. 39.

Gordon, J.E., Structures, or Why Things Don't Fall Down, Penguin Books Ltd., Harmondsworth, England, 1978, 395 pp.

Grace, R.A., Marine Outfall Systems, Prentice-Hall, Englewood Cliffs, 1978, 600 pp.

Hofmann, P., Y.G. Mussalli, and E.P. Taft, "Environmental Considerations in Designing Coastal Water Intakes," unpublished draft report, Stone & Webster Engineering Corporation, 1982, 14 pp. including 7 figures.

--- "Environmental and Engineering Considerations in Designing Coastal Water Intakes," Abstracts Volume, 18th International Conference on Coastal Engineering, Paper No. 18, Nov 1982, pp. 35-36.

Linsley, R.K., and J.B. Franzini, Water Resources Engineering, 3rd ed., McGraw Hill, New York, 1979, 716 pp.

O'Brien, M.P., "Memorandum Covering a Document Entitled 'Saving the American Beach: A Position Paper by Concerned Coastal Geologists,'" Shore and Beach, Vol. 50, No. 2, Apr 1982, pp. 6-8.

O'Brien, M.P., and J.W. Johnson, "Structures and Sandy Beaches," Proceedings of Coastal Zone '80, Vol. IV, American Society of Civil Engineers, 1982, pp. 2718-2740.

O'Brien, M.P., "Editorial, Let's Look at the Record," Shore and Beach, Vol. 48, No. 3, July 1980, p. 2.

Olsen, E.J., "A Critique of the Draft HCRS 'Barrier Islands Document,'" Proceedings of Coastal Zone '80, Vol. IV, American Society of Civil Engineeres, 1982, p. 2741-2746.

Perry, J.E., "The Estuaries of Natal: A Method of Classification," Abstracts Volume, 18th International Conference on Coastal Engineering, Paper No. 17, pp. 33-34.

Selby, D., and J.E. Perry, "Hydrological/Hydraulic Study of Natal Estuaries: The Siaya Estuary," NRIO Memorandum 8134, National Research Institute for Oceanology, Stellenbosch, South Africa, January 1982, with later supplement, brief text with numerous figures and maps.

Taft, E.P., and Mussalli, Y.G., "Angled Screens and Louvers for Diverting Fish at Power Plants," Proc. Hydraulics Division, American Society of Civil Engineers, Vol. 104, No. HY5, May 1978, pp. 623-634.

STRUCTURAL DESIGN ASPECTS OF A COASTAL BUILDING CODE

by
Ralph R. Clark[1]

1 INTRODUCTION

Since 1957, the State of Florida, U.S.A., has witnessed the evolution of coastal regulatory concepts based upon coastal engineering design guidance. In 1978, the Florida Legislature encouraged counties and municipalities to adopt coastal construction zoning and building codes to supplement the existing minimum codes which include the Standard Building Code, the National Building Code and the South Florida Building Code. Subsequently, coastal building code guidelines were developed to provide statewide uniformity in the adoption of supplemental codes by coastal counties and municipalities.

It is the intent of this paper to present the structural design aspects required in a coastal building code using the code guidelines developed for and specifically applicable to Florida's coastal communities. These same design aspects and code guidance are applicable to most other state's or nation's developable sand shorelines which are subjected to coastal storm damage.

The purpose of a coastal building code in Florida communities is to supplement the existing minimum code by providing the structural design standards for construction within that portion of the beach and dune system which is subject to substantial scour, erosion, flooding, and loads accompanying the impact of a major hurricane. A coastal building code includes structural design standards for the construction of residential structures, enclosed commercial structures, coastal and shore protection structures, and other substantial structures of a semi-permanent nature. Although the few minimum codes currently in effect in the coastal communities are comprehensive for conventional construction, they do not adequately address the special structural design considerations identified for the Florida coast. Along a developable coast, special design considerations are necessary for the preservation of the beach and dune systems, as well as, for the structural adequacy of the construction.

The major concepts of coastal engineering design which are necessary in a coastal building code include:

1. Zone identification (horizontal and vertical).
2. Foundation design for erosion and scour.
3. Storm loading (including wind, waves, hydrostatic, and hydrodynamic loads).

---

[1] P.E., P.L.S., Chief of Bureau of Coastal Engineering and Regulation, Division of Beaches and Shores, Florida Department of Natural Resources.

2 ZONES

A coastal building code should identify the zone within which major construction should be designed for the physical environmental conditions accompanying a major storm event. The standard adopted by law in Florida is the zone of impact of a 100-year storm surge or of a number of lesser storms which cumulatively have an equivalent probability of occurrence. For coastal areas which are predicted to be flooded by the storm surge of a 100-year storm, a zone of impact is identified by the possible existence of breaking waves which are significantly large to cause structural damage. For coastal areas not overtopped by a predictable 100-year storm surge, the impact zone is identified by the wave runup and the erosion limits of that storm or of storms having impact with an equivalent cumulative probability.

Seaward of a coastal construction building zone, a coastal conservation zone should be identified within which no major habitable structures should be erected. The inland limits of this coastal conservation zone would coincide with the seaward limits of the coastal construction building zone and would identify the seaward-most dune and beach area in need of preservation from the impact associated with the construction of major habitable structures. Identification of the line of demarcation between a coastal construction building zone and a coastal conservation zone would have to result from a consideration of the existence and degree of existing development, as well as the predictable beach and dune response to high frequency (less than 20-year) storm events.

For developed coastal areas within which there exists a reasonably continuous line of rigid coastal protection structures, regardless of the design adequacy of these coastal protection structures, such a line should define the seaward limits of the coastal construction building zone. (See the following illustration.)

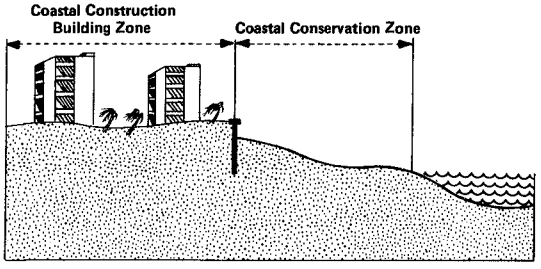

For developed and undeveloped coastal areas where there does not exist a line of rigid coastal protection structures, the dune system itself should be identified as a flexible coastal protection structure. Although guidance and rationale would vary in different locales, it is suggested that the inland limits of the coastal conservation zone be defined by the dune erosion limits of a 20-year storm event or the dune erosion which would be expected resulting from storms with an equivalent cumulative probability. (See the following illustration.)

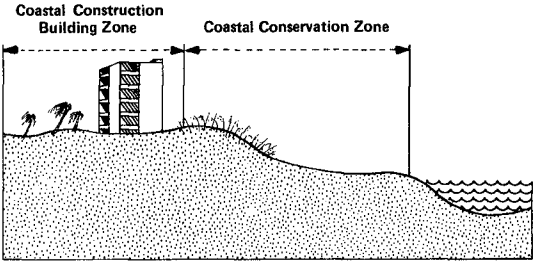

Although horizontal zonation, that is identification of the coastal construction building zone and coastal conservation zone, is of primary importance, vertical zonation should be included by identifying the elevation above which major habitable structures should be constructed. The standard adopted by the State of Florida is the requirement to elevate the habitable structure such that the structural soffit or the underside of the lowest supporting structural member, excluding the foundation piles, is above the design breaking wave crests or wave uprush as superimposed on the storm surge of a 100-year storm.

3 FOUNDATION DESIGN

Foundation design within the coastal construction building zone should consider the topographic changes which may be expected over the design life of the structure. Foundation design should consider the erosion, scour, and loads accompanying a 100-year storm event.

Soil bearing foundations are discouraged within the coastal construction building zone and should be prohibited above the design grade. The elevation of the soil surface to be used in the calculation of bearing capacities should not be higher than that which would result from the erosion of a design storm. Calculation of the design grade should account for localized scour due to the presence of structural components. The maximum elevation of a soil bearing foundation should be set below the design grade resulting from the erosion (including scour) of a 100-year storm event. Erosion computations for foundation design should account for all vertical and lateral erosion and scour producing forces.

All habitable structures within the coastal construction building zone are recommended to be elevated on and securely anchored to an adequate pile

foundation. The structure should be anchored in such a manner as to prevent flotation, collapse or lateral displacement. A pile foundation should be designed to withstand all anticipated loads resulting from a 100-year storm event including wave, hydrostatic, hydrodynamic, and wind loads acting simultaneously with live and dead loads.

Design ratio of pile spacing to pile diameter is not recommended to be less than 8:1 for individual piles; however, this would not apply to pile clusters located below the design grade. Pile caps should be set below the design grade (which includes localized scour), while the piles should be driven to a penetration which achieves adequate bearing capacity taking into consideration the anticipated loss of soil above the design grade.

In addition to normal foundation analysis, pile foundation analysis should consider piles in column action from the bottom of the supported structure to the design grade. Consideration should also be given to the degree of exposure to wave attack and the resulting impact loads on lateral or diagonal bracing between piles. Lateral bracing should be designed to minimize resistance to flow and to the entrapment of floating debris.

Within the coastal construction building zone, substantial walls and partitions constructed below the level of the first finished floor should be prohibited. It is recommended that such a prohibition exempt stairways, utilities, shearwalls perpendicular to breaking waves, wind/sand screens, light open wood lattice partitions, elevator shafts, and breakaway or frangible walls designed to collapse under wave forces. Any construction within the vertical zone of design storm wave impact should be designed in such a manner so as to minimize the release of destructive hydrodynamic missiles.

4 STORM LOADS

A coastal building code should require that all habitable major structures be designed for the loads accompanying a 100-year storm event, including wind, wave, hydrostatic, and hydrodynamic loads. Within the coastal construction building zone and the coastal conservation zone, minor structures need not meet specific structural requirements for wind and wave forces, but they should be designed to minimize the potential for generating aerodynamically or hydrodynamically propelled missiles. Minor structures should also be designed to produce a minimum adverse impact on the beach or dune system.

The wind load requirements of a coastal building code need to be established considering historical records of storm generated wind velocities over water in the specific region. The problem with the wind requirements of the existing minimum codes in Florida was the inland location of the data from which the wind requirements were derived. Following recommendations of the National Hurricane Center, the University of Florida, and the Florida Department of Natural Resources, the State of Florida increased the required wind velocity for load computations to a minimum of 140 mph (225 kilometers per hour) at a height of 30 feet (9 meters) above the ground. The designer of a habitable major structure

should be aware, however, that localized wind forces under design hurricane conditions may exceed this minimum wind load requirement.

The coastal building code should be flexible to invite a detailed analysis of structures whose dynamic properties allow for wind sensitivity. In designing for hurricane generated winds, consideration should be given to the frictional effects and induced vortices due to the influence of topographic roughness and other existing structures. Consideration should also be given to the internal pressures on interior walls, ceilings, and floors resulting from damaged windows or doors.

The water related loads accompanying a design coastal incident storm event provide a major area of deficiency in most building codes, with wind generated waves producing the most analytically complex yet the most critical of forces to which the coast and its structures are subjected. The coastal building code should require that major habitable structures be designed in consideration of the expected shore-propagating wave conditions upon the surge of a 100-year storm event. Breaking, broken, and non-breaking waves should be considered as applicable. Design wave loading analysis should consider vertical uplift pressures and all lateral pressures to include impact, as well as, dynamic loading and the harmonic intensification resulting from repetitive waves. Recommended sources from which to base minimum criteria and methodology in design wave computations are the Department of Navy, Naval Facilities Engineering Command Design Manual NAVFAC DM-26, the Department of the Army Corps of Engineers Shore Protection Manual, Volume II, Department of the Army Coastal Engineering Research Center Technical Papers and Reports, and Florida Department of Natural Resources, Division of Beaches and Shores Technical and Design Memoranda.

In addition to the wind and wave loads, a coastal building code should require that all major habitable structures be designed for the hydrostatic and hydrodynamic loads which would be expected under the conditions of maximum inundation associated with a 100-year storm event. Calculations for hydrostatic loads should consider the maximum water pressure resulting from a peaked breaking wave superimposed on the storm surge of a 100-year storm event. Both free and confined hydrostatic loads should be considered, while confined hydrostatic loads should be determined using the maximum elevation to which the confined water would freely rise if unconfined.

Vertical hydrostatic loads should be considered as forces acting both vertically downward and upward on horizontal or inclined surfaces of major structures (e.g. floors, slabs, roofs, walls). Lateral hydrostatic loads should be considered as forces acting horizontally above and below grade on vertical or inclined surfaces of major structures and coastal or shore protection structures. Hydrostatic loads on irregular or curving geometric surfaces may be determined in consideration of separate vertical and horizontal components acting simultaneously under the distribution of the hydrostatic pressures.

Calculations for hydrodynamic loads should consider the maximum water pressures resulting from the motion of the water mass associated with a

100-year storm event. A more detailed discussion of these loads may be found in the definitions which follow.

When considering water related loads, specialized loads of importance to the coastal building code are battering loads. Habitable major structures including the foundation should be designed to resist the battering loads which may reasonably be anticipated resulting from isolated floating or suspended objects during a 100-year storm event.

5 EXCAVATIONS

A major consideration of a coastal building code, excavation is generally not recommended within the coastal construction building zone and should be prohibited within the coastal conservation zone. Any proposed excavation design should consider the coastal topographic changes accompanying a 100-year storm event and those anticipated topographic changes which have an equivalent probability of occurrence. Upon consideration of these topographic changes, any excavation within the coastal construction building zone which have the potential for a negative impact or would accelerate erosion should be prohibited. Excavation associated with the construction of a major structure within the coastal construction building zone should be limited to that incidental to the construction of the foundation and necessary for utilities. Excavation required for swimming pool construction within the coastal construction building zone should be minimized, located as far inland as possible, and not result in a net loss of sediment in the immediate area. All beach compatible excavated material or an equivalent volume of beach compatible material should be used as fill to be placed generally seaward of the excavation.

6 COASTAL AND SHORE PROTECTION STRUCTURES

The coastal building code should address coastal and shore protection structures as a separate classification for design. In general, the construction or rehabilitation of flexible coastal and shore protection structures such as beach nourishment, dune construction and stabilization, and sand fencing should be encouraged over the construction of rigid coastal and shore protection structures (seawalls, bulkheads, revetments, rubble mounds, groins, etc.) if such beach and dune restoration activity is of acceptable coastal engineering design and is compatible with the existing coastal systems. The construction of isolated rigid coastal or shore protection structures on undeveloped property is not recommended nor should such structures be designed primarily to protect minor structures.

Seawalls and other rigid coastal protection structures are intended to protect upland structures and property and not to protect the beach. In fact, rigid coastal protection structures usually may be expected to have a long term adverse effect on the adjacent beach. In those instances in which a rigid coastal or shore protection structure is the only feasible means of protecting existing upland structures and property, then that rigid

coastal or shore protection structure should be located as far landward as possible, consistent with design and construction requirements. Any seawall or other rigid coastal protection structure should be designed to minimize its erosion impact. Sloping rock revetments, rubble mound structures, and toe-scour protection with rock in front of vertical bulkheads and seawalls are recommended over vertical or sloping solid walls which due to their reflective surface cause substantially greater erosion losses to the adjacent beach.

The major design considerations for coastal and shore protection structures should include structural siting, foundation (e.g. geotextiles), crest (or cap) elevation, toe elevation, structural slope(s), components as impacted by waves superimposed upon the design storm surge, expected scour, impact on the beach and dune system, and impact on the adjacent properties. Coastal and shore protection structures should be designed for the minimum wave loads which are applicable for the design storm conditions which justify the structures. Seawalls, revetments, and rubble mound structures are generally designed for a 20 to 50-year storm event. Recommended sources from which to base minimum criteria and methodology in the design of coastal and shore protection structures are the Department of the Army Corps of Engineers Shore Protection Manual, the Department of the Army Coastal Engineering Research Center Technical Papers and Reports, the Department of Navy, Naval Facilities Engineering Command Design Manual NAVFAC DM-26 and DM-7, and Florida Department of Natural Resources, Division of Beaches and Shores Technical and Design Memoranda.

The coastal building code should also address those cases where development is proposed upland of an existing seawall or other rigid coastal protection structure. Such development should be located a sufficient distance upland from the coastal protection structure to allow for the containment of partial failures and to provide adequate room for routine maintenance and future repair to the coastal protection structure. Wave and runoff induced seepage in fill behind coastal protection structures should be considered to avoid partial or complete failure due to piping of fill material under the structures.

7 CODE DEFINITIONS

The following definitions are recommended for inclusion within the coastal building code, in order to clarify the coastal engineering and construction terminology adopted.

BEACH: The zone of unconsolidated material that extends landward from the low water line to the place where there is marked change in material or physiographic form, or to the line of permanent vegetation. Unless otherwise specified, the seaward limit of a beach is the mean low water line. Beach is alternatively termed the "shore."

BREAK-AWAY WALL or FRANGIBLE WALL: A partition independent of supporting structural members that will withstand design wind forces but will fail under hydrostatic, wave and runup forces associated with the

design storm surge. Under such conditions, the wall should fail in such a manner that it dissolves or breaks up into components that will not act as potentially damaging missiles.

COASTAL AND SHORE PROTECTION STRUCTURES: Shore hardening structures, such as seawalls, bulkheads, revetments, rubble mound structures; groins and breakwaters; aggregates of materials other than beach sand used for shoreline protection; beach and dune restoration; and other structures which are intended to prevent erosion or protect other structures from wave and hydrodynamic forces. Coastal protection structures are intended for the protection of upland properties and structures, whereas, shore protection structures are intended for the protection of the beach or shoreline.

COLUMN ACTION: The elastic instability in piles or columns resulting from stresses due to axial and/or lateral loads.

DUNE: A mound or ridge of loose sediment, usually sand-sized, lying upland of the beach or shore, and deposited by any natural or artifical mechanism (e.g., a dune may also include a beach ridge, dune ridge, chenier, etc.).

EROSION: The wearing away of land or the removal of beach or dune material by wave action, tidal currents or deflation. Erosion includes but is not limited to:

(a) Horizontal recession, which is where the storm surge intersects but does not inundate the profile and where horizontal littoral activity due to waves, currents and runup erodes the profile.
(b) Scour, which is where the topography is completely inundated by the storm surge, and where wave and current forces erode the profile in the vertical direction.

EXCAVATION: Any mechanical removal of rock or unconsolidated material.

HYDRODYNAMIC LOADS: Those forces resulting from a mass of water in motion, e.g., the flow accompanying a storm surge. Hydrodynamic loads are generally lateral forces, but also include effects of the turbulence resulting from the interaction of the flowing water mass with a rigid structure. Hydrodynamic load computations for construction consider all predominant forcing functions responsible for the motion of the aquatic mass, which are the astronomical tide and the storm waves (including the orbital particle transport, longshore mass transport, and shore-normal mass transport), as well as the storm surge. Gravity and forced flow resulting from the inundation accompanying the storm surge of a 100-year storm event are considered. Hydrodynamic load computations consider the processes of mass transport, heat transport, and momentum transport, along with the corresponding natural laws which are the conservation of matter, the conservation of energy (first law of thermodynamics), and Newton's second law (the equation of motion). Hydrodynamic load computations also consider the various flow forms including forms referring to spatial variation (uniform and non-uniform flow), forms referring to variation in time (steady, quasi-steady, and non-steady flow), forms referring to the

nature of flow (laminar and turbulent flow), and forms referring to the type of flow energy (subcritical, critical, and supercritical flow). In addition, hydrodynamic load computations include the transformation of flow energy form from supercritical flow to subcritical flow, and vice versa, including all classifications of hydraulic jump. Hydrodynamic load computations consider hydraulic flow across both a fixed bed and a movable bed where applicable.

HYDROSTATIC LOADS: Those lateral and vertical (including uplift) forces resulting from a mass of water standing either above or below the soil surface. These loads are equal to the product of the water pressure at the centroid of the plane surface area on which the pressure acts times the area of that surface. The hydrostatic pressure is equal to the product of the unit weight of the water times the elevation of the water above the point of measurement. Hydrostatic loads which are confined may be determined using the elevation to which the confined water would freely rise if unconfined. Hydrostatic pressures at any point are equal in all directions and act normal to the applied surface and are passive in nature.

INUNDATE: To cover or overflow as with a flood.

MAJOR STRUCTURES: Houses, mobile homes, apartment buildings, condominiums, motels, hotels, restaurants, other types of residential or commercial buildings, towers, swimming pools, piers, pipelines, and other projects having the potential for substantial impact on the beach and dune systems. Major structures include any structure which is neither a "minor structure" nor a "coastal or shore protection structure."

MINOR STRUCTURES: Elevated dune and beach walkover structures, beach access ramps and walkways, stairways, pile-supported elevated viewing platforms, gazebos, boardwalks, lifeguard support structures, pile supported or cantilevered decks or porches on new or existing structures, slab patios, sidewalks, driveways, and other uncovered paved areas (e.g., parking areas, shuffleboard courts, tennis courts, etc.), earth retaining walls, sand fences, privacy fences, ornamental walls, ornamental garden structures, aviaries, subgrade utilities (e.g., wells, septic tanks, and drain fields) which require material alteration and restoration of topography, and ornamental projects. Usage is not the only criterion used to classify structures as minor. It is a characteristic of minor structures that they are considered to be expendable under wind and wave forces.

ONE-HUNDRED-YEAR STORM: A shore-incident hurricane or any other storm with accompanying wind and wave intensity having a one-percent chance of being equaled or exceeded in any given year during a 100-year interval.

PILE FOUNDATION: A system of piles providing the support of a structure, including those piles terminating below grade at pile caps and those piles extending above grade to superelevate a structure.

STORM SURGE: The rise above normal water level on the open coast due to a number of factors, including the action of wind stress on the water surface and the rise in level due to atmospheric pressure reduction.

UPLIFT PRESSURE: Any upward hydrostatic, hydrodynamic, or wind pressure on the soffit, base, deck or floor of a structure.

WAVE: A ridge, deformation, or undulation of the surface of a liquid. Storm generated ocean waves shore-propagating upon the storm surge are considered for design purposes. The wave forces are dependent upon the type of wave considered (i.e., unbroken, broken or breaking).

8 CONCLUSION

Special design standards are needed specifically for the construction of structures fronting on the open coast exposed to extreme storm events. Predicting waves, flooding, erosion and scour is a necessary requirement for the proper design of ocean front construction. By systematically identifying the special design aspects for coastal construction, a coastal building code may be developed to supplement the minimum design standards set forth in the current building codes.

9 REFERENCES

1. American Concrete Institute, ACI Standard Building Code Requirements for Reinforced Concrete, 1971.

2. American Institute of Steel Construction, Inc., Manual of Steel Construction Seventh Edition, 1970.

3. American National Standards Institute, 1977, ANSI Building Code, 1430 Broadway, New York, New York 10018.

4. Balsillie, James H., Design Hurricane Generated Winds, Florida Department of Natural Resources, Bureau of Beaches and Shores, Technical Report No. 78-1, October, 1978.

5. Balsillie, James H., "The Peaking of Waves Accompanying Shore-Breaking," Fifth Symposium on Coastal Sedimentology: Modern and Ancient Shores, Florida State University, Tallahassee, Florida, 1980.

6. Balsillie, James H. and R. W. G. Carter, "On the Runup Resulting from Shore-Breaking Wave Activity," Fifth Symposium on Coastal Sedimentology: Modern and Ancient Shores, Florida State University, Tallahassee, Florida, 1980.

7. Bowles, Joseph E., Foundation Analysis and Design, McGraw-Hill Book Company, 1968.

8. Chesnutt, C. B. and R. E. Schiller, Jr., Scour of Simulated Gulf Coast Sand Beaches Due to Wave Action in Front of Sea Walls and Dune Barriers, Texas A & M University, Sea Grant Report No. 207, May, 1971.

9. Christensen, B. A., "Sediment Transport," University of Florida, Department of Civil Engineering Course Notes, Spring, 1973.

10. Clark, Ralph R., et al, Coastal Construction Building Code Guidelines, Technical Report No. 80-1, Florida Department of Natural Resources, November, 1980.

11. "Coastal Construction Codes for that Area of Okaloosa County, Florida, Fronting the Gulf of Mexico, between Department of Natural Resources Monuments R31 and R50," Okaloosa County Ordinance No. 79-2, Florida, 1979.

12. "The Coastal Construction Code for the Barrier Islands of Pinellas County and its Municipalities," Chapter 39, The Coastal Construction Code, Pinellas County Construction Licensing Board, September, 1978.

13. "Coastal Construction Codes for Bonita Beach," Lee County Ordinance No. 76-10, Florida, 1976.

14. "Coastal Construction Codes for Captiva Island, Lee County, Florida," Lee County Ordinance No. 76-15, Florida, 1976.

15. "Coastal Construction Codes for Estero Island," Lee County Ordinance No. 76-3, Florida, 1976.

16. "Coastal Construction Codes for Gasparilla Island, Lee County, Florida," Lee County Ordinance No. 77-1, Florida, 1977.

17. Collier, Courtland A., Construction Guidelines to Minimize Hurricane Damage to Shore Area Homes, Florida Department of Natural Resources, November, 1976.

18. Collier, Courtland A., Seawall and Revetment Effectiveness, Cost and Construction, Florida Sea Grant Report Number 6, May, 1975.

19. Collier, Courtland A., et al, Guidelines for Beachfront Construction with Special Reference to the Coastal Construction Setback Line, Florida Sea Grant Report No. 20, February, 1977.

20. Commonwealth of Australia, Department of Transport and Construction, Structural Design of Cyclone Resistent Dwellings, Part A: Design, Part B: Construction, June, 1976.

21. Cyclone Building Construction Seminar Papers, Cyclone Building Research Committee, November, 1980.

22. Daily, James W. and Donald R. F. Harleman, Fluid Dynamics, Addison-Wesley Publishing Company, Inc., 1966.

23. Dean, R. G., "Beach Erosion: Causes, Processes, and Remedial Measures; CRC Reviews in Environmental Control," CRC Press, Inc., vol. 6, issue 3, 1976.

24. Dean, R. G., "Equilibrium Beach Profiles and Response to Storms," Proceedings of the 15th International Conference on Coastal Engineering, American Society of Civil Engineers, 1976.

25. Dean, R. G., "Heuristic Models of Sand Transport in the Surf Zone," Proceedings of Conference on Engineering Dynamics in Surf Zone, Sydney, New South Wales, 1973.

26. Dean, R. G., "Storm Characteristics and Effects," Proceedings, Seminar on Planning and Engineering in the Coastal Zone, Coastal Plains Center for Marine Development Services, Wilmington, N. C.

27. Department of the Navy, Naval Facilities Engineering Command, Design Manual, Harbor and Coastal Facilities, NAVFAC DM-26, July, 1968.

28. Department of the Navy, Naval Facilities Engineering Command, Design Manual, Soil Mechanics, Foundations, and Earth Structures, NAVFAC DM-7, March 1971.

29. Edelman, T., "Dune Erosion During Storm Conditions," Proceedings, 13th International Conference on Coastal Engineering, American Society of Civil Engineers, 1972.

30. Einstein, H. A., "Bed Load Function for Sediment Transportation in Open Channel Flows," U. S. Department of Agriculture, Soil Conservation Service, Technical Bulletin 1026, Washington, D.C., 1950.

31. Federal Emergency Management Agency, Federal Insurance Administration, Coastal Flooding Storm Surge Model: Part 1 - Methodology; Part 2 - User's Guide; and Part 3 - Codes, May, 1980.

32. Federal Emergency Management Agency, Federal Insurance Administration, Elevating to the Wave Crest Level, a Benefit : Cost Analysis, July, 1980.

33. Federal Insurance Administration, National Flood Insurance Program, Department of Housing and Urban Development, Elevated Residential Structures, Reducing Flood Damage Through Building Design: A Guide Manual, September, 1976.

34. Federal Emergency Management Agency, Flood Insurance Studies and Flood Insurance Rate Maps (for participating counties and municipalities), available from National Insurance Program, Post Office Box 34604, Bethesda, Maryland 20034.

35. Federal Emergency Management Agency, Federal Insurance Administration, User's Manual for Wave Height Analysis, June, 1980.

36. Florida Statutes, Chapter 161, "The Florida Beach and Shore Preservation Act."

37. Florida Statutes, Chapter 553, Part VI, State Minimum Building Codes, "Florida Building Codes Act."

38. Gee & Jenson, Engineers-Architects-Planners, Inc., "Coastal Construction Code for Arvida Properties, Longboat Key, Sarasota County, Florida," May, 1978.

39. Guidelines for the Testing and Evaluation of Products for Cyclone-Prone Areas, Technical Record 440, Experimental Building Station, Department of Construction, New South Wales, Australia.

40. Henderson, F. M., Open Channel Flow, The Macmillan Company, New York, 1966.

41. Home Building Code, Queensland, Appendix 4 to the Standard Building By-Laws 1975 (under the Building Act 1975-1979).

42. Ippen, Arthur T., ed. Estuary and Coastline Hydrodynamics, Engineering Societies Monographs, McGraw-Hill Book Company, Inc., New York, 1966.

43. Kamel, A. M., Water Wave Pressures on Seawalls and Breakwaters, Research Report No. 2-10, U. S. Army Corps of Engineers, Waterways Experiment Station, February, 1968.

44. Kinsman, Blair, Wind Waves, Their Generation and Propagation on the Ocean Surface, Prentice-Hall, Inc., Englewood Cliffs, New Jersey, 1965.

45. Lamb, H., Hydrodynamics (6th edition) 1932, Cambridge University Press, London (Reprinted by Dover Publications, Inc., New York, 1945).

46. Lambe, T. William and Robert V. Whitman, Soil Mechanics, John Wiley & Sons, Inc., New York, 1969.

47. McCormac, Jack C., Structural Analysis, Second Edition, International Textbook Company, Scranton, 1969.

48. Minor, Joseph E., and George R. Walker, "Advancements in Hurricane Resistent Housing: Research, Codes, Practice," Fourth U. S. National Conference on Wind Engineering Research, July 27-29, 1981, Seattle, Washington.

49. Northern Territory Cyclonic Areas Deemed to Comply Standards, 3rd Edition, Buildings Authority Branch, Department of Lands, Northern Territories, Australia, June, 1980.

50. Ordinance No. 80-5, Franklin County, Florida, May, 1980.

51. Panel on Wave Action Effects Associated with Storm Surges of the Science and Engineering Program on the Prevention and Mitigation of Flood Losses, Building Research Advisory Board, Commission on Sociotechnical Systems, National Research Council, Methodology for Calculating Wave Action Effects Associated with Storm Surges, National Academy of Sciences, Washington, D.C., 1977.

52. Reardon, G. F., and R. M. Aynsley, Houses to Resist Cyclone Winds-Construction Details, Information Bulletin No. 1, Cyclone Testing Station, James Cook University, Townsville, Queensland, August, 1979.

53. Rouse, Hunter, Engineering Hydraulics, First Edition, John Wiley & Sons, New York, 1954.

54. Saffir, Herbert S., Design and Construction Requirements for Hurricane-Resistant Construction, American Society of Civil Engineers, 1977.

55. Simiu, E., and R. H. Scanlan, Wind Effects on Structures, Wiley-Interscience, New York, 1978.

56. Sklarin, Joseph; Thomas G. Harmon; and C. Allin Cornell, Stochastic Analysis of Hurricane Wind Loads, R77-2, Massachusetts Institute of Technology, January, 1977.

57. Southern Building Code Congress International, Inc., Standard Building Code, 1979 Edition.

58. The South Florida Building Code, 1979 Broward County Edition.

59. State of Florida, Department of Natural Resources, Division of Marine Resources, Chapter 16B-33, Florida Administrative Code, "Rules and Procedures for Coastal Construction and Excavation."

60. Stoker, J. J., Water Waves, Interscience Publishers, Inc., New York, 1957.

61. Streeter, Victor L., Fluid Mechanics, Fourth Edition, McGraw-Hill, Inc., New York, 1966.

62. Terzagi, Karl, Anchored Bulkheads, Transactions, American Society of Civil Engineers, 1954.

63. Texas Coastal and Marine Council, Model Minimum Hurricane Resistant Building Standards for the Texas Gulf Coast, December, 1978.

64. U. S. Army Coastal Engineering Research Center, Shore Protection Manual, Volumes I, II, III, 1973.

65. U. S. Army Coastal Engineering Research Center Technical Papers and Reports, as listed: Andre Szuwalski and Linda Clark, Bibliography of Publications of the Coastal Engineering Research Center and the Beach Erosion Board June, 1980.

66. U. S. Steel, Steel Sheet Piling Design Manual, April, 1972.

67. Van de Graff, J., "Dune Erosion During a Storm Surge," Coastal Engineering, Volume 1, pages 99-134, 1977.

68. Walker, George R., "A Review of the Impact of Cyclone Tracy on Australian Building Regulations and Practice," Civil Engineering Transactions, 1980, The Institution of Engineers, Australia.

69. Walker, George R., and Joseph E. Minor, Applying Engineering to Housing through "Deemed to Comply" Standards, presented at the Spring Meeting of the Texas Section, ASCE, Ft. Worth, Texas, March 26, 1982.

70. Walton, Todd L., Jr., Hurricane-Resistant Construction for Homes, Florida Sea Grant Report No. SG-76-005, August, 1976.

71. Walton, Todd L., Jr. and Thomas C. Skinner, Beach Dune Walkover Structures, Florida Sea Grant Report Number SG-76-006, December, 1976.

72. Walton, Todd L. and T. Y. Chiu, Littoral Sand Transport on Beaches, University of Florida, Coastal and Oceanographic Engineering Laboratory, Technical Report-041, 1979.

73. Walton, Todd L., Jr. and William Sensabaugh, Seawall Design on the Open Coast, Florida Sea Grant Report No. 29, June, 1979.

74. Wang, Chu-Kia and Charles G. Salmon, Reinforced Concrete Design, International Textbook Company, July, 1969.

75. Weggel, J. Richard, "Maximum Breaker Height," Journal of the Waterways, Harbors and Coastal Engineering Division, Proceedings of the American Society of Civil Engineers, November, 1972.

76. Wilson, John D., Daniel L. Trescott, DeeEll Fifield, Vera McIntyre Hayes, Hurricane Hazard Mitigation at the Local Government Level: The Roles of the Building Code and Other Development Management Strategies, Bureau of Disaster Preparedness, Florida Department of Community Affairs, October, 1980.

THE ESTUARIES OF NATAL: A METHOD OF CLASSIFICATION

by

J E Perry

ABSTRACT

This poster paper describes a hydrological/hydraulic classification of the estuaries of Natal, based upon aerial photography. The modus operandi is outlined and although the study is in its early stages, some key factors (natural and man-made) are indicated together with the method by which they are quantified.

1. INTRODUCTION

A hydrological/hydraulic study, aimed at acquiring an understanding of the long-term functioning of the estuaries of Natal is being done by NRIO (CSIR) for the Natal Town and Regional Planning Commission. Special emphasis is given to the influence of man on the natural river régime. The investigation falls into three phases, namely, evaluation of available data, classification of the estuaries and examination of specific problems in particular estuaries. This poster paper is concerned with phase two, classification of the estuaries. As hydrological data are scarce, a method of study has been devised to make the maximum use of the main data source available which is aerial photography dating back to 1937.

2. PROCEDURE

2.1 Basis

For each of the 72 estuaries, a suitable reach of the river is selected to include at least the known estuarine area. The upstream limit is usually a road or railway bridge which provides a good control position but occasionally a river confluence has to be chosen. This reach is then identified on enlargements of six vertical aerial photographs from 1937 to 1980 and re-photographed. Prints are

* Sediment Dynamics Division, National Research Institute for Oceanology, CSIR, RSA

then made on a scale of 1:10 000 using tracings of permanent features from 1:10 000 orthophotos to obtain the best possible fit. The orthophoto itself is often used as one of the six photographs selected for study. Tracings of the river courses for the six years are made on transparent film (one for each year) and used to compile an envelope of mobility of the river. Within this envelope of mobility, lines of measurement are marked at regular 250 m to 300 m intervals from the upstream limit of the reach to the mouth together with a suitable datum line for measuring sand-spit lengths and directions. These items are transposed onto the six river course tracings together with an outline of the flood plain area (if present) which is assessed from the orthophoto. The remaining areas within the flood plain to be traced onto the six master river course film tracings are sand deposits, swamps and cultivation (from the 1:10 000 photographs).

2.2 Direct Observations and Measurements

The six aerial photographs are studied in detail with respect to:

(i) terrain above the valley,
(ii) valley characteristics,
(iii) river mouth,
(iv) flood plain, and
(v) the river course and its channel.

Several of the observations made are of a general descriptive and qualitative nature (e.g. terrain, land-use, settlement, relation of channel to valley bottom and sides, description of the river mouth, river pattern, lateral channel activity and man-made factors). Other observations require measurements. Some are done manually with a steel ruler or an opisometer, direct from the photographs: amongst these are vegetation and land-use on the valley sides and riverine vegetation. The remaining linear, areal and angular measurements are made using a flat-bed digitizer. These may be made direct from the photograph in the case of an orthophoto. Otherwise, for greater accuracy, they are made from the master film tracings - compilation of which is described in 2.1 above. Such linear and angular items measured include mid-valley lengths, thalwegs, valley widths, flood plain lengths and widths, wetted perimeters and sand-spit lengths, widths and directions. Areas measured on the digitizer include the flood plain, swamps, sand deposits, cultivation, open water and bars.

2.3 Indirect Measurements and Calculations

River widths are measured, averaged and the standard deviation calculated. If the channel widths (in this

context synonomous with bank-full conditions) are markedly different from the river widths and clearly seen on the aerial photographs, these are also measured (across the same lines of measurement, marked at 250 m to 300 m intervals). The sinuosity for the whole reach is calculated. In order to quantify the lateral stability, distances are measured from the maximum left bank position to mid-river (along the selected lines of measurement on the six master film tracings). From these measurements, an average lateral displacement and an average coefficient of lateral stability is calculated for the time period under review.

2.4 Recording of Data

A table has been compiled (Table I) to facilitate the observation and recording of salient points. The basic idea for this tabular classification was taken from Kellerhals et al. (1976). Modifications were made to the initial table as the study progressed to include:

(a) local features of Natal rivers,

(b) estuarine conditions (e.g. river mouth characteristics), and

(c) particular needs of the study (e.g. man-made influences).

Data reports are prepared for each estuary. These contain the basic tabular classification forms for each photograph studied and tables showing river widths and lateral stability. Thalweg displacement is graphed. Other features selected for graphing vary from estuary to estuary, depending upon what is found to be pertinent. These may include open water areas (often found to be decreasing with time), thalweg changes, sinuosity changes and bar areas. Copies of the photographs used for classification are reproduced in the data reports together with a most recent aerial photograph onto which is superimposed the 1937 river course. The latter give a good visual indication of changes occurring in the estuaries over a period of approximately 40 years. Brief notes and an abstract of results are also prepared for each estuary. Data will be codified later and stored on computer for further analyses.

3. BACK-UP DATA

Hydrological data are scarce but simulated run-off is now available for tertiary catchments in Natal (H.R.U. Report 9/81). These data are an invaluable aid to interpreting the aerial photographs because wet and dry phases together with antecedent soil moisture conditions can be defined.

TABLE I — CLASSIFICATION OF THE LOWER REACHES OF NATAL RIVERS — NRIO No 41

RIVER LOVU, 24 % ESTUARINE, REACH from Sugar Mill Bridge to Mouth, 3,8 km from mouth. REF. DEA 4 700 a

AERIAL PHOTO DATE 2-6-73 SCALE 1:10 000 CATCHMENT AREA 938 km², M.A.R. 115 m³x10⁶, No. of DAMS NIL

RIVER VALLEY AND RIVER MOUTH FEATURES

General Description of the Terrain above the Valley

Terrain	*Vegetation*	*Land-Use*
mountainous	✓ almost none	none
✓ hilly	grass	scattered cultivation
undulating	sparsely forested (0-25%)	partly cultivated
plains	moderately forested (25-75%)	✓ mainly cultivated
	heavily forested (75-100%)	scattered settlement
	swamp/bog	✓ partly built-up *
		urbanised

Valley Sides (~~Not~~ Well-defined)

Slumping	*Vegetation and Land-use*	*Left*	*Right*
✓ none	none		
occasional	grass	NIL	NIL %
frequent	trees	11	12 %
	cultivated	89	88 %
	built-up	NIL	NIL %

Comments * near coast

Valley Characteristics

Measurements	*Terraces*	*Relation of Channel to Valley Bottom (Vertical)*	*Relation of Channel to Valley Sides or Resistant Terraces (Lateral)*	*Surface Geology*
valley length 3600 m	none	not applicable	✓ not applicable (no valley or free)	bedrock
bottom width(av.) 880 m	indefinite	not obviously degrading	occasionally confined	lacustrine deposits
valley slope ± 1:900	✓ fragmentary	partly entrenched	frequently confined	✓ fluvial deposits
height at head	continuous	entrenched	entrenched	aeolian
of reach 4 m to MSL approx.		✓ aggrading		sand covered NIL % area

Comments

River Mouth

Characteristics	*Measurements*	
✓ open/~~closed~~	right bank breakwater length	m
✓ natural/~~artificial~~	left bank breakwater length	m
canalized	rock sill level	m to MSL
✓ sandy	cliffs on right bank: height	m to MSL
✓ rocks on right bank	cliffs on left bank: height	m to MSL
rocks on left bank	spit/~~bar~~: direction of growth 205	°
outer bar	length of spit/~~bar~~ 640	m
silt plume (fluvial)	length stabilized 510	m
✓ suspended sediment (marine)	width 110	m

Comments

FLOOD PLAIN AND CHANNEL FEATURES

Description of Flood Plain

Presence	*Extent*	*Vegetation*	*Forest Type*	*Land-Use*
none	none	almost none	not known/applicable	✓ ~~not cultivated~~, not built-up
indefinite	average width 735 m	grass	riverine:	✓ cultivated 53 % area
fragmentary	maximum width 1300 m	reed swamp 19 % area	main channel	✓ crop/s sugar cane
✓ continuous	aerial length 3419 m	sparsely forested	tributaries	partly built-up
	area 246 ha	moderately forested	✓ coastal dune/evergreen	mainly built-up
		heavily forested	mangroves	

Comments

Channel Description N.B. Estimate of flow stage: ~~LOW/NEAR LOW/~~MEAN/HIGH **

Pattern	*Measurements*		*Islands/Shoals*	*Type of Flow*	*Bar Type*
straight	thalweg	3817 m	none	stagnant/still	none
sinuous	*sinuosity	1,12	occasional	✓ uniform water surface	channel side bars
irregular	*open water area	15,7 ha	frequent	uniform with rapid in reach	✓ point bars
regular meanders	perimeter	9159 m	split	irregular	channel junction bars
✓ irregular meanders	lake/lagoon area	____ ha	braided	pool & riffle sequence	mid-channel bars
tortuous meanders	✓ river X-sections available				diamond bars
bifurcated	channel slope	____			diagonal bars
lake/s	channel width x	____ m	s = ____ m		sand waves/large dunes
lagoon	river slope	≈ 1:1388			
	river width x	37,4 m	s * 4,75 m		

Comments *whole reach

** Fairly high: Lower bars

Obstructions/Constructions

Natural	*Degree*
✓ none	none
logs	minor
boulders	major
vegetation	

Comments

Man-made	*Degree of Obstruction/Constriction for Each*	*Position (from head of reach)*
✓ road bridge/s	Sugar Mill + Naval Rd (NA) bridges	R. confined Head + 3km
✓ rail bridge/s		R. confined 3,8 km
✓ causeway	remains of 1959 causeway ? obstruction	± 3 km
weir/dam		
fish traps		
✓ embankment/s	(2) for NR + Hwy bridges	across L. flood plain
groynes		
✓ canal/s	making whole flow	0 - 1,2 km
✓ drainage furrows		widespread
✓ others		

Lateral Channel Activity

Lateral Activity	*Nature of Banks*	*Bank Vegetation*	*Lateral Stability*
not detectable	✓ alluvium (silt/sand)	none	stable
downstream progression	natural levées	✓ weak	slightly unstable
✓ progression & cut-offs	rock/boulders	good	✓ moderately unstable
mainly cut-offs	protected/stabilized	very strong	highly unstable
entrenched loop development	✓ cultivation to	left bank 8 %	
irregular lateral activity	channel edge	right bank NIL %	
avulsion			

Comments

Rainfall analyses of wet and dry periods, using exponentially filtered monthly rainfall data (Zucchini, 1975) are also very valuable - especially for smaller catchments for which no run-off data are available. When available, topographical surveys (for river gradients and cross-sections), physical model studies (for river flood behaviour), land-use studies for the whole catchment and archival data (old maps and cross-sections) are used to aid the study. For example, archival data has been used in one estuary to quantify river aggradation, making it possible to extend the period for which changes in the average river bed level could be calculated. At 21 estuaries, daily observations are made as to whether the mouth is open or closed. Water level stations are being established at 26 of the estuaries.

4. RIVER MOUTH AND SHORELINE FEATURES

Although this classification method highlights fluvial features which are dominant in the case of Natal's estuaries, the true quantitative picture of change is only revealed when viewed in conjunction with land-use and river mouth features. Table II gives a brief review of four important river mouth features:

(i) Mouth opening and closure is a dominant feature.

(ii) Rocks, rocky headlands and sills are very important because rocks to the south of an estuary afford protection from the dominant swell and allow a southerly extending spit to form where the general littoral drift is to the north.

(iii) Spits have an important effect on siltation. The prograding coastline north of the Tugela is dominated by long, northeasterly-extending spits causing river capture in one case and generally altering the courses of the rivers near the coast. For example the spit at Siaya has extended by 727 m in 40 years. South of the Tugela estuary the spits are generally southerly-extending.

(iv) Several man-made influences are apparent. Groynes affect littoral drift and the stabilization of spits inhibits the natural flood flows.

5. RESULTS

It has been found that major floods, riverine vegetation, swamp areas and sand-spits/bars at the mouth are the main natural factors influencing the behaviour of the estuaries. Man's influence is marked in land-use on the flood plain

TABLE II: SUMMARY OF MOUTH FEATURES

	Open/Closed			Rocks			Spit			Artificial
	Mostly									Including groynes, pipes, canals and spit stabilization
North Natal	O	C	O/C	→S	→N	N&S	→S	→N	Variable	
	10	7	3	7	0	1	8	7*	4	4
							* one shows spit →S after major floods			
South Natal	12	36	4	34	3	6	41**	7	3	36***
							** six - maybe more show spit →N after major floods			*** 30 of these have road/rail bridge embankments - often involving spit stabilization

The above table gives the number of estuaries to the north and south of Durban showing the features as itemized. It is based upon "The Estuaries of Natal" by G W Begg (1978) and a study of aerial photographs.

and in the whole catchment area, the construction of embankments and bridges, groynes and breakwaters, dams in the catchment, the drainage of swamps, the removal of riverine vegetation, canalization and the stabilization of formerly mobile sand-spit and bar areas. Instability is clearly shown by sinuosity index fluctuations, large lateral thalweg displacements with a high coefficient of variation and longer thalwegs (behind prograding sand-spits). The converse may not mean stability, however. "Apparently stable" estuaries often show marked deterioration through decreased open water areas, narrowing river widths, increased bar areas and general aggradation. Some examples of lateral stability are given below:

Estuary	Av. lateral displacement (m)	$\overline{V}$%	Notes
Mtamvuna	19	11	Stable
Mzumbe	122	40	Unstable
Mahlongwa	4	12	*Apparently stable
Mkomazi	22	17	*Apparently stable
Lovu	95	42	Unstable
Mgeni	53	16	*Apparently stable
Mdloti	62	42	Unstable
Tongati	30	35	Unstable
Zinkwasi	7	8	*Apparently stable
Siaya	14	47	Unstable (esp. 1953+)
Mhlatuze (Richards Bay)	1 255	66	Unstable

* These estuaries show instability in other ways e.g.

(i) loss of open water areas
(ii) aggradation with loss of tidal influence.

6. CONCLUSION

This interpretation of fluvial features, based upon aerial photographs over a period of 40 years, is expected to provide a key to the natural functioning of the estuaries of Natal and the estuarine responses to human influences. Thereby, this study will also facilitate conservation measures and/or planned development of estuarine resources by the Town and Regional Planning Commission, Natal.

7. FOOTNOTE

Readers are invited to contact the author direct for further information on specific estuaries.

ACKNOWLEDGEMENT

The author wishes to thank the Chief Planner, Natal Town and Regional Planning Commission, for permission to publish this paper.

REFERENCES

BEGG, G W (1978). The estuaries of Natal. Oceanographic Research Institute, Durban.

KELLERHALS, R K et al. (1976). Classification and analysis of river processes. Journal of the Hydraulics Division, ASCE, pp 813-827.

PITMAN, W V, MIDDLETON, B J and MIDGLEY, D C (1981). Surface water resources of South Africa, Vols V and VI. Hydrological Research Unit Report No 9/81.

ZUCCHINI, W (1975). Statistical models for droughts and floods. Lecture, 18th Annual Conference of the South African Statistical Association.

ENVIRONMENTAL AND ENGINEERING CONSIDERATIONS IN DESIGNING COASTAL WATER INTAKES

P. Hofmann, B.S., M.S., Ph.D., Assistant Chief -
Environmental Engineering Division
Stone & Webster Engineering Corporation

Y. G. Mussalli, B.S., M.S., Ph.D, Consultant
Stone & Webster Engineering Corporation
Boston, MA
E. P. Taft, B.S., Senior Ecologist
Stone & Webster Engineering Corporation

INTRODUCTION

Water intakes developed for coastal use often require special design considerations to ensure the incorporation of engineering features which are compatible with environmental protection. Due to the severity of the coastal zone environment, cooling water intakes for power generating facilities typically incorporate one of two possible designs:

1. A shoreline (surface) intake which could incorporate jetties, breakwaters, or inlet channels for wave protection and, when necessary, for retardation of sedimentary processes, or

2. An offshore, submerged intake connected via tunnel or pipeline to an onshore screen/pumphouse.

Naturally, protection of structural integrity is of primary concern in designing and locating such intakes. Therefore, physical or hydraulic conditions are required to enhance plant reliability which may be adverse from an environmental viewpoint. As a result, it is often necessary to integrate additional provisions into intake designs which will mitigate potential adverse impacts resulting from plant operation.

During the mid to late 1960s, as the size and number of power plants began to dramatically increase in the United States, various agencies responsible for protecting fish and wildlife were becoming increasingly alarmed that sport and commercial fisheries were being adversely affected by thermal discharges (Krenkel and Parker 1969). In response to this concern, various state and Federal regulations were promulgated to limit the effects of thermal discharges on aquatic biota. Various engineering options were developed to limit thermal effects. These options ranged from simply limiting the rise across the condenser, and therefore the ultimate temperature at the point of discharge, to employing various means of closed-cycle cooling, particularly at sites where water availability was limited (Parker and Krenkel 1969).

It became apparent in the early 1970s that, in addition to addressing the effects of thermal discharges on aquatic biota, consideration would have to be given to limiting the effects associated with withdrawing large quantities of water in cooling water intakes. In 1972, the Federal Water Pollution Control Act Amendments established requirements to ensure that large water withdrawals would not have significant impacts on various fish and invertebrate lifestages (e.g. eggs, larvae, and juveniles). Mortality of these organisms in circulating water systems may occur as a result of entrapment in intake structures, impingement (of larger lifestages) on screening equipment designed for condenser protection, or entrainment (of smaller life stages) through the system. Regulatory concern over the past decade has led to extensive research efforts in an attempt to resolve these problems. As a result, a variety of innovative technologies have been developed which can be integrated into the design of coastal intakes for organism protection without jeopardizing plant reliability (ASCE 1982). Three such designs are described in this paper.

INTAKE DESIGNS

The design of a coastal intake is largely dictated by site-specific physical, hydrologic, and environmental conditions. In areas of limited water depth, wave action, and littoral sediment transport, dredged canals protected by parallel jetties are often used to ensure an adequate water flow while minimizing problems resulting from sedimentation and wave forces. Where deeper water is available in near-shore areas, submerged intake structures connected to a shoreline pumping station via tunnels or pipes can offer protection from wave action and icing problems. In both cases, embayment areas are created which can cause mortality among aquatic organisms. Therefore, protection systems may be required to minimize organism losses.

Canal Intakes with Jetties

Engineering Design

A nuclear power plant in New York withdraws approximately 37 m^3s^{-1} from Long Island Sound for cooling and service water purposes. Initially, two alternatives were available for withdrawing water from Long Island Sound; a submerged offshore intake structure connected by pipeline to an onshore screenwell or an onshore intake structure.

For the offshore alternative, two locations were evaluated; 457 m and 1707 m offshore. These locations were selected on the basis of bottom topography and the fact that recirculation from an offshore discharge diffuser would be minimized. Based on a comparison of the offshore alternatives to an onshore location, the offshore locations were not selected. The offshore alternative operational and maintenance costs were substantially greater than an onshore location. Biofouling control in the long submerged inlet pipes would necessitate the use of large quantities of chlorine or a flow reversal scheme to elevate temperatures in the inlet pipe to 46°C for extended periods of time. It was deemed that utilization of these biofouling control methods for either of the offshore locations would present problems in complying

with environmental criteria. Another disadvantage of the offshore intake schemes is the inability to easily retrofit fish protection facilities to the system should an increased level of protection be required in the future.

On the basis of this evaluation, an onshore intake system was selected and is shown in Figure 1. It consists of the following:

(a) A 488 m long canal, 122 m of which extends beyond the mean low water (MLW) shoreline, with a 24 m bottom width at elevation -3.7 m MLW. It was not possible to select an onshore intake without a canal because of the rise and fall of the tide. It was also necessary to protect the canal with jetties to avoid the almost continuous dredging that would be necessary to prevent it from becoming filled with sand. The jetties are constructed to an elevation of 3 m MLW. The jetties were constructed of irregularly-shaped core stone blocks weighing from 1.8 to 7.2 MT. The canal sides are covered by a 0.8 m layer of core stone but the bottom consists of the naturally occuring sand, which will allow periodic dredging to remove accumulated sand.

    The canal has been designed to discourage fish entrapment by keeping the average velocity less than 0.3 ms^{-1} at MLW and 0.15 ms^{-1} at MHL.

(b) A screenwell, as shown in Figure 2, which is divided into four bays, with each bay supplying water to a service water (0.55 m^3s^{-1}) and a circulating water (9 m^3s^{-1}) pump. The flow passes through trash racks and traveling water screens which are designed for fish protection.

Organism Protection

Due to the need for jetties at this Long Island Sound site, an embayment resulted between open water and the cooling water intake screenhouse. The presence of this embayment raised regulatory concern that fish might become entrapped in the intake screenhouse and impinge on the traveling screens, a process which results in mortality unless protective measures are taken. For this reason, a novel fish collection system was incorporated into the screenwell design to allow for the safe removal and return of impinged fish to the Sound.

As shown in Figure 3, the collection system consists of a series of vertical, traveling water screens modified from the conventional design to include fish lifting buckets and a low-pressure spraywash to gently rinse collected fish into a trough for return to the Sound. The screens have the capacity to operate continuously to minimize the time of impingement, collection and removal.

Fish which enter the intake screenwell and impinge on a screen are carried by the screen to the water surface. At this point, they drop into a fish-lifting bucket containing approximately 5.0 cm of water. These buckets are attached to each screen panel at 0.61 m intervals.

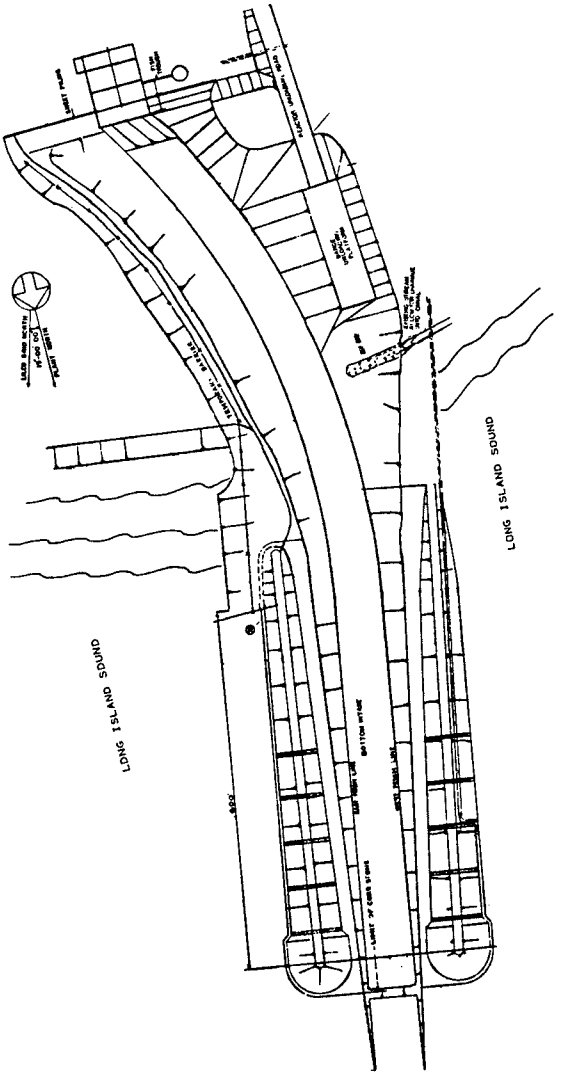

FIGURE 1 ONSHORE INTAKE SYSTEM WITH JETTIES

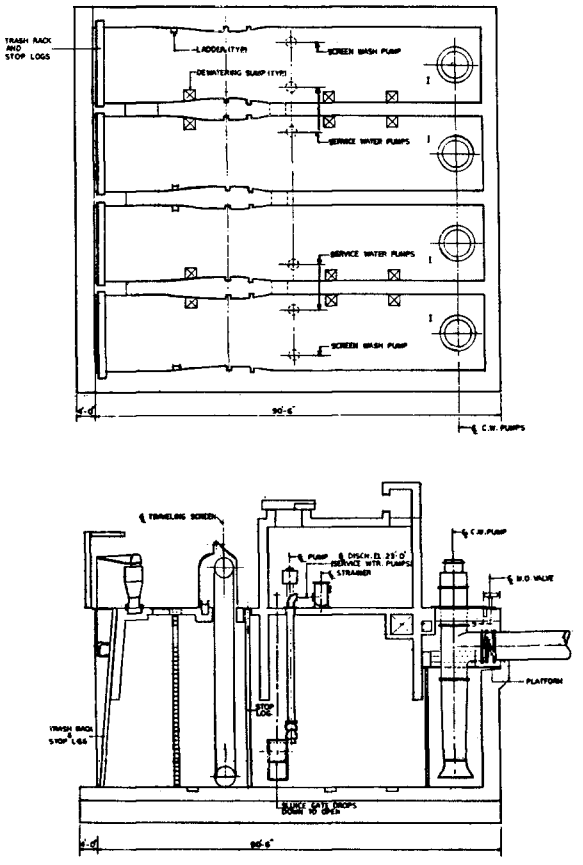

FIGURE 2 INTAKE SCREENWELL WITH MODIFIED, FISH PROTECTION SCREEN

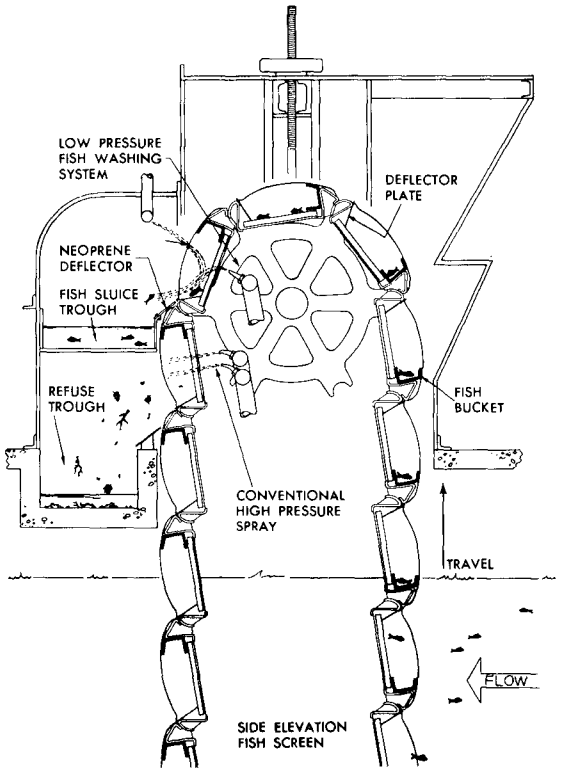

FIGURE 3 MODIFIED THROUGH-FLOW TRAVELING SCREEN WITH FISH BUCKETS

Containing the fish in water prevents them from flipping off the screen and becoming reimpinged on the submerged screen area.

At the operating deck level, a low-pressure spray (less than 1.4 kg cm^{-2}) rinses the contents of the lifting bucket into a return trough. A high-pressure spray is located above the low-pressure spray to rinse remaining debris from the screen mesh into a separate debris trough.

The fish trough transports recovered fish back to Long Island Sound at a suitable distance from the intake to minimize recirculation.

This system has only recently become operational and fish survival data is, unavailable at this time. However, other power plants incorporating this system have been in operation for several years. The biological data obtained at these sites clearly demonstrates the effectiveness of the modified screen concept.

The first collection screen system installed in the U.S. is at Virginia Electric Power Company's Surry Nuclear Station in Virginia. An 18 month biological evaluation of this system showed that the average initial survival of 58 species of fish after recovery from the screen was about 93 percent (White and Brehmer 1976).

Similar studies were conducted with a fish collection screen at Boston Edison Company's Mystic Station (Stone & Webster 1981). In these studies, all fish recovered from the screen were held for 96 hours after collection for observation of latent effects resulting from the collection and removal process. Initial survival rates were similar to those observed at the Surry Station for fish species common to both sites. However, latent survival varied by species, as expected. For example, the relatively hardy flounder showed nearly 100 percent survival under all conditions tested. On the other hand, fragile species, such as herring and smelt, displayed survival rates under optimal condition in the range of approximately 50 to 65 percent.

These studies, along with other studies conducted at power plants throughout the United States, indicate that the modified fish collection screen system is a viable and effective means of protecting fish entering intake screenwells.

Offshore, Submerged Intakes

Engineering Design

At a power plant on Lake Ontario, wave action and severe icing conditions that result in ice packing along the shore necessitated the withdrawal of cooling water (20.5 m^3s^{-1}) from a submerged (9.1 m) intake structure connected to an onshore screenhouse in a 305 m long tunnel.

As a result of regulatory requirements, provisions had to be incorporated into the design of this system to protect fish which may be drawn into the intake. In this case, the species of concern were fragile and could not survive collection on a screen. Therefore, an

innovative fish diversion system was incorporated into the design of the screenhouse. The design consists of primary and secondary fish diversion and pumping systems which together act to divert fish into a small bypass flow which ultimately returns the fish to Lake Ontario via a pipeline.

Figures 4 and 5 illustrate the screenwell arrangement incorporating angled flush mounted screens leading to the bypass. Fish entering the screenwell pass through 7.6 cm spaced trashracks and guide along the angled screens into a 15.2 cm wide bypass. Each bay is equipped with two 3 m wide screens angled 25° to the direction of the flow. The screens are separated by 1 m wide concrete piers and have been modified so that the screen baskets are flush with the piers and opening of the bypass to allow fish to easily guide along the face of the structure. Upon entering the bypass, fish are carried to a secondary angled screen and diverted to a pipeline which returns them to the lake.

Although debris loading tends to be low, the bypass was designed so that it can be manually cleaned by raking or, if necessary, flow can be reversed to free any material which passes through the trashracks and becomes lodged in the bypass. Bypass flow is designed such that the ratio of the screenwell approach velocity to the bypass entrance velocity is 1:1, a condition that yields high fish diversion efficiencies. Approach and bypass velocity is approximately 0.3 ms^{-1}, resulting in a 0.15 ms^{-1} velocity at the screenface. A jet pump provides the energy to induce the required bypass flow and return fish back to the lake in a submerged pipeline.

Organism Protection

The design of this system for fish protection was developed as a result of several years of investigation in the laboratory. (Taft and Mussalli 1978). These laboratory studies demonstrated that the angled screen system is 100 percent effective in diverting a wide variety of fish species to bypasses. Subsequent to diversion, test fish were held for 96 hrs for observation of delayed mortality. In all cases, mortality was low (less than 5 percent), thus yielding overall system efficiency values in excess of 95 percent.

The full-scale angled screen system on Lake Ontario has been in operation for over two years. Although published results are not presently available, ongoing studies indicate that diversion efficiencies are generally high for all fish entering the plant including species which had not previously been evaluated.

Intakes with Fine Screening

Organism Protection

In the previous two examples of coastal intake designs, engineering design requirements dictated the need for biological protection. At a power plant on the coast of Florida, the need for organism protection necessitated an engineering design study to develop an organism handling system. Due to regulatory concern over the loss of small

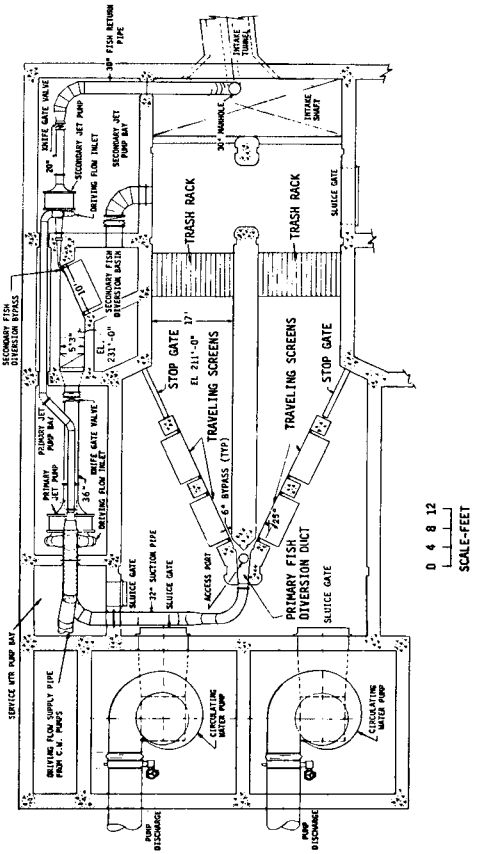

FIGURE 4 ANGLED TRAVELING SCREENS AT LAKE ONTARIO POWER PLANT

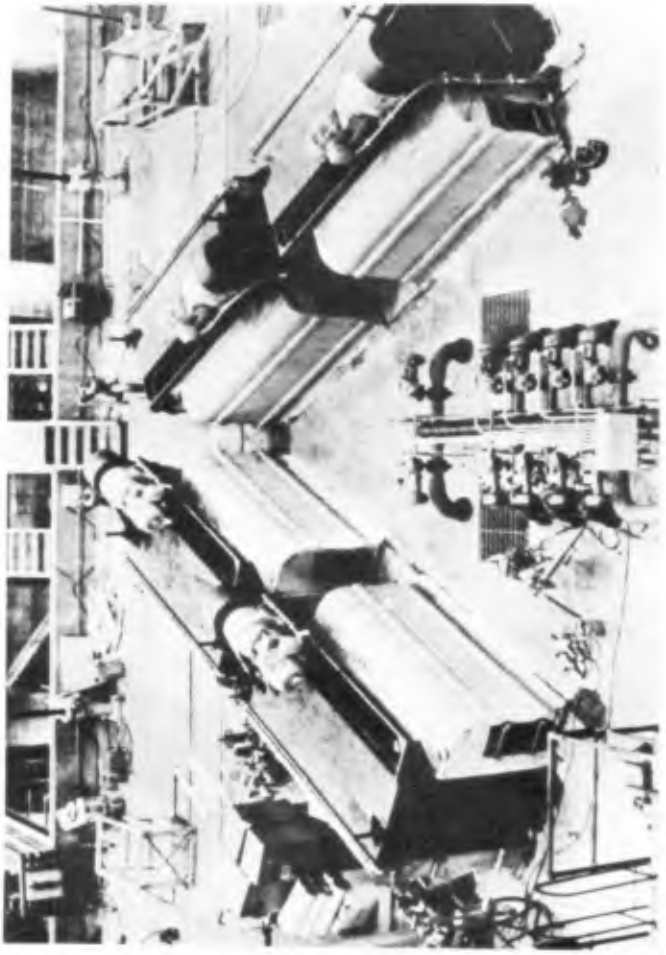

FIGURE 5
OSWEGO STEAM STATION - UNIT 6 ANGLED SCREEN INTAKE
DESIGNED AND CONSTRUCTED BY STONE & WEBSTER

organisms (the earliest life stages of various fish and invertebrate species) at this station, a major research program was conducted to optimize the design and operation of a unique collection screen system.

A full-scale, prototype system was constructed on site to permit both engineering and biological evaluations. The system consisted of a dual-flow (no-well) traveling screen, modified to incorporate 0.5 mm screen mesh (Figure 6) to exclude small life forms, special organism lifting lips and a very low-pressure spraywash system for rinsing collected organisms into a trough. Screens were also operated continuously to minimize the time that organsims would be impinged on the mesh.

Two years of research was conducted with the fine-mesh prototype screen. Results of biological studies indicated high survival rates for many of the organisms of concern at this site. For example, crab and shrimp larvae generally showed latent survival rates in excess of 85 percent, with many approaching 95 to 100 percent. Similarly, fish eggs collected from the screen showed hatching rates generally greater than 90 percent and subsequent, 48-hr larval survival rates ranging from about 82 to 100 percent (Taft, Horst, and Downing 1981).

Engineering Design

The field studies demonstrated a high biological efficiency of this organism collection system. As a result, two generating units are being equipped with fine-mesh screens (Figure 7). Each unit will be equipped with 3 screens to handle 15.3 m^3s^{-1}. The stringent design criteria required for organism protection (very small mesh size, continuous screen operations) necessitated detailed engineering design evaluations and studies to ensure reliable operation.

Due to the requirement for fine screening at this site, unique operation and reliability questions arose which had not previously been addressed. A major concern and focus of the developmental studies was the potential for greatly increased clogging due to the use of 0.5 mm mesh, and subsequently pressure drop, over that experienced with conventional 9.5 mm mesh. Consequently, a head loss monitoring program was conducted as part of the overall prototype system evaluation. The results of this program showed that, even under conditions of moderate loadings of jellyfish (ctenophores), head losses could be maintained at levels less than 10 cm.

In order to ensure reliable screen operation in actual application, features were incorporated to prevent clogging, including continuous operation capabilities and screen spray systems. The screens will be equipped with variable speed motors to accommodate various debris loadings and will be completely sealed to minimize organisms losses (Mussalli, et al 1981).

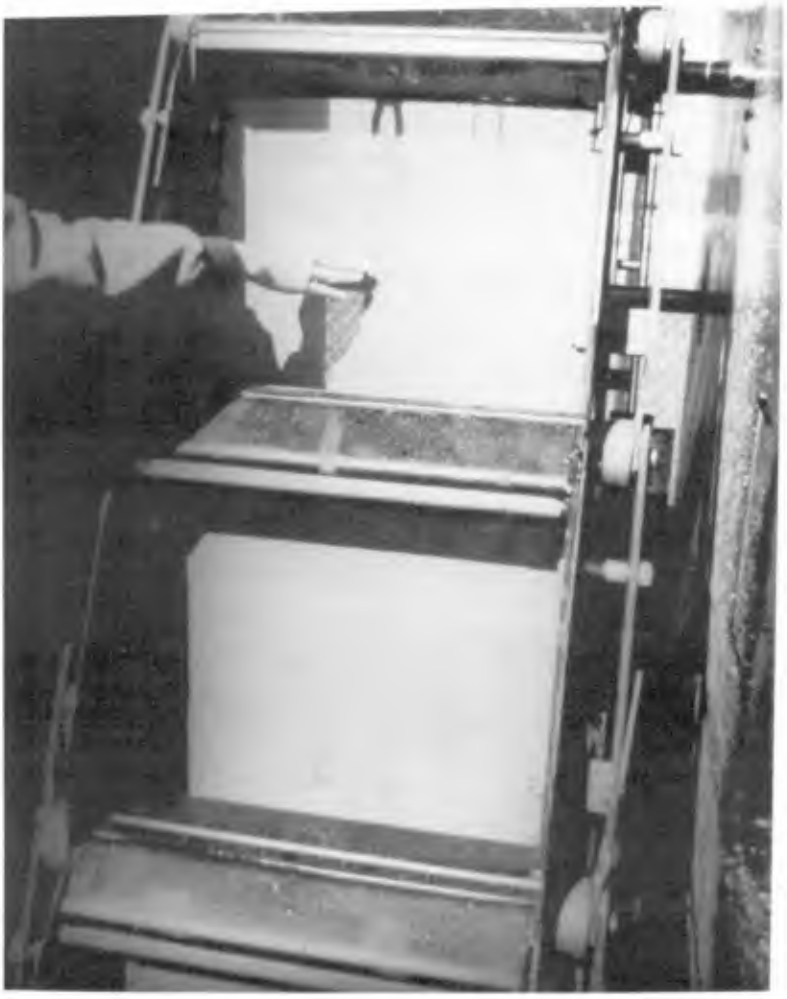

FIGURE 6 FINE-MESH SCREEN TEST FACILITY

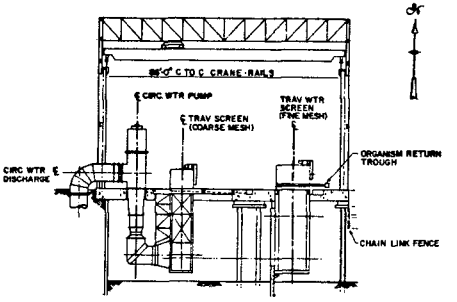

SECTION

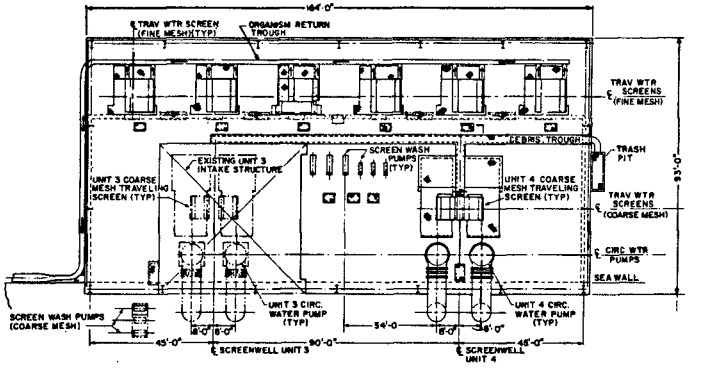

PLAN

FIGURE 7 FLORIDA FINE-MESH SCREEN INTAKE

CONCLUSIONS

The selection of a design for a coastal water intake depends on several factors. Consideration has to be given to the topography and geology at the site, severity of wave action and potential for icing, the types and quantities of debris that may be encountered, and regulatory concern as to the types of aquatic organisms that have to be protected.

These three cases demonstrate how environmental concerns related to the engineering of cooling water systems in coastal zones can be addressed and resolved through careful study and the development of innovative design concepts.

REFERENCES

AMERICAN SOCIETY OF CIVIL ENGINEERS (ASCE), Task Committee on Fish-Handling Capability of Intake Structures of the Hydraulics Division. Design of Water Intake Structures for Fish Protection. New York, NY, 1982.

KRENKEL, P.A. and PARKER, F.L. Biological Aspects of Thermal Pollution. Vanderbilt University Press, 1982.

MUSSALLI, Y.G.; TAFT, E.P.; KITCHING, B.D.; and HOLSAPPLE, J.G. The Development and Testing of New Fine-Mesh Screen Designs for Protecting Organisms at Power Plant Intakes. Proc. of the American Power Conference, Vol. 43, 1981, pp. 418-427.

PARKER, F.L. and KRENKEL, P.A. Engineering Aspects of Thermal Pollution. Vanderbilt University Press, 1969.

STONE & WEBSTER ENGINEERING CORPORATION. Alternative Intake Designs for Reducing Fish Losses - Mystic Station Unit 7. Prepared for Boston Edison Company. SWEC, Boston, MA, 1981.

TAFT, E. P. and MUSSALLI, Y. G. Angled Screens and Louvers for Diverting Fish at Power Plants. Proc. ASCE, Vol. 104, No. HY5, 1978, pp. 623-634.

TAFT, E.P.; HORST, T.J.; and DOWNING, J.K. Biological Evaluation of a Fine-Mesh Traveling Screen for Protecting Organisms. Proc. of Workshop on Advanced Intake Tech., San Diego, CA, 1981, pp. 159-168.

WHITE J.C. and BREHMER M.L. Eighteen-Month Evaluation of the Ristroph Traveling Fish Screens. Proc. Third National Workshop on Entrainment and Impingement, L.D. Jensen (ed.), Ecological Analysts, Inc., Melville, NY, 1976.

COASTAL ENGINEERINC IN SOUTH AFRICA

by

K S RUSSELL

1. INTRODUCTION

The paper presents a review of the historical movement of ships around the South African coastline, traces the evolution and development of the harbours of South Africa, describes the development of coastal engineering and summarises the organisations and their activities in both basic and applied research projects contributing towards coastal works.

2. HISTORICAL

The coastal currents and winds have played a major role in the historic exploration of the African coast. The earliest reference to a circum-navigation of Africa, although unconfirmed, was that by Herodotus who, in about 600 B.C. wrote that the Pharaoh Necho (Neco), then at war with the Syrians and wishing to combine his Mediterranean and Red Sea fleets, caused a fleet of ships manned by Phoenicians to sail from the Erythraean (Red) Sea and return through the Pillars of Hercules (Straits of Cibraltar). The journey is reputed to have taken three years; wind and currents make such a voyage in square-rigged boats a possibility.

Fig.1. Ocean currents in the Southern hemisphere. The Restless Seas.

Fig.2. The earliest navigations around Africa. Southern Land. A.R.Wilcox.

National Research Institute for Oceanology, Stellenbosch, South Africa

Accounts exist of voyages on the west coast by Hanno (c.500BC) who, with a fleet of 60 ships, explored as far as Cape Palmas (Liberia), and of Sataspes (c.475BC) who, in an attempt to sail around Libya (Africa) on the west and return by the Arabian Gulf (Red Sea), reached a similar destination. The limit to these voyages was dictated, no doubt, by the square-rigged ships which could not tack against the wind, and the extent of the NE trade winds off the West African coast, the doldrums being encountered at about latitude 5^{o} north.

Fig.3. Reconstruction of an ocean going Phoenician ship. Southern Land. A.R. Wilcox.

The Portuguese navigator Bartholomew Diaz in January 1488 rounded the Cape out of sight of land and subsequently landed at Mossel Bay. Because of his rough passage around the cape, Diaz named it "The Cape of Storms". On his return to Portugal it was renamed "The Cape of Good Hope" since it promised a sea route to the East Indies, so long a goal of the earlier explorers.

Fig.4. Diogo Cão caravel - 1483 AD. Southern Land. A.R. Wilcox.

The voyages of Diaz were followed by those of Da Gama (1497) and De Saldanha (1503), while the coast of Southern Africa was first surveyed by Perestrello (1576). On 18 July 1580, Sir Francis Drake rounded the Cape homeward bound on his circumnavigation of the world. The opening of this sea route led to extensive trade with the east coast of Africa and the Far East, but it was not until after the formation of the Dutch East India Company in the first half of the 17th century that a serious attempt was made to establish a permanent port of call at the Cape for the replenishment of supplies and repair of ships in preparation for the voyage to the Far East or return to Europe.

3. HARBOURS

The numerous bays and inlets along South Africa's 3 000 km of coastline provided convenient refuge for Portuguese, Dutch, English, French and Scandinavian vessels. Locations offering the best natural protection together with the opportunity to replenish water and food gradually emerged as potential harbours. These were Table Bay, Port Elizabeth, East London, Durban and Walvis Bay. Saldanha Bay, while providing ideal protection for anchorage, was without fresh water.

Numerous other shallow-draft harbours, most of which were located in river mouths, also developed along the coastline: Port Alfred, Port St. Johns, Port Shepstone and Port Nolloth. These harbours were important in the coaster trade active up to the 1930s until improvements in road and rail connections and the continuing increase in the size of freighters caused their gradual decline.

Major harbours developed at those locations which offered the maximum natural benefits and all have subsequently been improved by the construction of breakwaters and by dredging.

There are six major harbours along the coastline: Durban (the second largest port in Africa in terms of cargo handled), Richards Bay (190 km north of Durban, built especially to export coal but likely to become the country's biggest commercial port), East London (South Africa's only river port), Port Elizabeth (major mineral ore export harbour), Table Bay, Cape Town (its Sturrock "graving dock" is the largest in the southern hemisphere) and Saldanha Bay (110 km north of Cape Town, built especially to

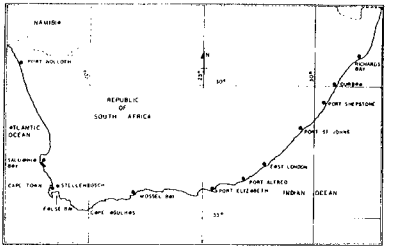

Fig.5. Location of South African Harbours.

export iron ore). Less significant are Mossel Bay (on the Cape south coast) and Walvis Bay (a South African enclave into South West Africa/ Namibia). These ports, administered by the South African Transport Services, annually handle 70 M tons of cargo and 12 500 ships with a gross tonnage of more than 300 M.

The fishing fleet consisting of 6 300 vessels of various sizes continues to utilise the several shallow draft harbours which are controlled by the Fisheries Corporation.

TABLE BAY - "TAVERN OF THE SEAS"

Fig.6. Aerial photograph of Table Bay Harbour and Cape Peninsula.

It was on 6th April 1652 that Jan van Riebeeck landed on the shores of Table Bay to set up a transit station for ships of the Dutch East India Company. The voyage - one way - from Holland to the Indies averaged about 6 months with appalling loss of men and ships. Although a number of jetties, dating from 1656, were originally built, the first significant coastal structure in South Africa was an uncompleted rubble mound breakwater. This breakwater, financed by taxing farmers delivering produce to the town through the use of their wagons to haul stone from the quarry to the breakwater, was started in 1743 but soon abandoned. Construction of a 546 m-long breakwater and excavation of a dock was inaugurated by H R H Prince Alfred on 17th September 1860. The dock, now Alfred Basin, was opened in 1870. Following the discovery of gold in the Transvaal, the breakwater was extended and the Victoria Basin was completed in 1905, with a water area of 27 hectares catering for ships up to 13 500 tons. No further development took place until after the First World War although ships of 18 500 tons were rounding the Cape regularly. In 1929 new quays were constructed which form part of Duncan Dock. Duncan Dock, developed between 1937 and 1945, provided an additional 195 hectares of water area 12 m deep and a total of 1 830 m of quay wall. A tanker basin was added in 1965, and by 1972, seven additional deepwater berths had been added. Construction of the Ben Schoeman Basin commenced in 1969 and it became fully operational in 1978.

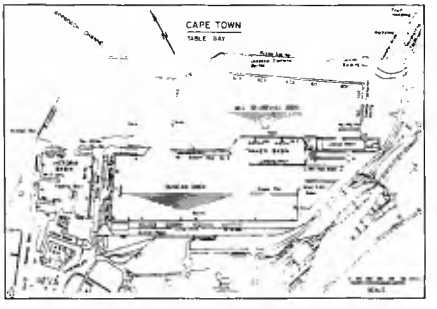

Fig.7. Lay-out of Table Bay Harbour.

DURBAN HARBOUR - "PORT NATAL"

Vasco da Gama sighted the coast, which he named Natal on Christmas Day, 1497. The Portuguese made no attempt to establish a settlement in Natal and there are many accounts by survivors of the many ships which foundered on the desolate coast and of their perilous journey to Lourenco Marques. In the later seventeenth century, survivors from the "Good Hope", together with survivors from the "Bonaventure" and "Stavinesse" built a boat and sailed to the Cape in 12 days. From descriptions of the bay and the rich trade in ivory the Dutch East India Company decided to develop the bay but changed their decision, as recorded in the Cape Town Archives.

"The East India Company would have taken possession of this fertile land (terra de Natal) years past, but for at the mouth of the port, a reef or sandbank that no galliot could get over without touching".

It was not until 1824 that the port began to develop; at that time the brig "Salisbury" was blown over the bar and grounded on what is now Salisbury Island. The first survey of the entrance was undertaken by Haure in 1831. Records of this and of subsequent surveys are still available in the Africana Museum.

In 1850, the first harbour engineer began to build two breakwaters designed to force the flow of the water down the channel and to scour the entrance. By 1854, a survey showed a depth of 6,4 m, but this was no permanent solution; in 1868 the depth had decreased to 3 m and by 1882 was reported to be 1,8 m. Sir John Coode in 1877 published a detailed description of the stability of the tidal entrance indicating the two opposing forces, the waves due to wind piling up sand in the entrance and the tidal currents and river flow scouring the entrance. He undertook an "estimate" of the tidal prism (quoting the tidal volume to be 18 794 737 yds^3) and by comparison with the entrance areas at Dunkirk, Calais, le Havre, Madras and Algiers suggested that the entrance width be reduced from 800 ft to 600 ft with a flow area between 1 300-1 400 yds^2 to produce a stable entrance. Many alternative schemes were proposed. In 1882 a new attempt at construction of piers was launched under a joint Milne and Coode scheme. Dredgers were purchased in 1889. By 1892 the sand bar was dredged to 4,4 m and the southern training wall extended by 474 m and by 1900 the depth of the bar had been increased to 5,9 m. Dredging thus far had been confined to the removal of obstructions after gales, in 1902 systematic dredging of the entrance and to provide a sand trap at Cave Rock updrift of the breakwater commenced.

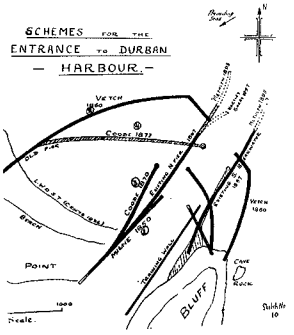

Fig.8. The numerous schemes suggested for the entrance to Durban Harbour.

This virtually solved the bar problem and by 1906 there was a depth of 10 m in the entrance. An average of 700 000 m^3/year

has been dredged in the entrance and sand trap since the early 1900s. Interception of this south to north sediment transport and development of the beach eventually led to severe erosion on the premier bathing beaches north of the harbour. In 1938 a sand by-passing scheme was introduced by which sand dredged from Cave Rock bight was transported by the dredger to a dolphin inside the entrance and pumped via a booster station onto the north beaches. In 1949, two pipes were laid under the harbour entrance through which sand, dredged from a jetty in Cave Rock bight, was syphoned directly to the booster station. This scheme was abandoned in 1954 and the scheme using the dredger re-introduced. At present some 100 000 m^3/year of dredged material is pumped from the dredger into a storage hopper loaded north of the north breakwater, for discharge at a number of intermediate sites along the beach.

The breakwaters have been considerably strengthened and improved over the years, the taper in the North Pier, due to Hartley and Barry, was removed during 1941 as it was considered to be a danger to shipping.

PORT ELIZABETH HARBOUR - "SETTLERS PORT"

Although visited by Diaz in 1488, Algoa Bay was little used since it provided scant shelter and little trade for ships. The 1820 settlers landed in Port Elizabeth by surf boat and sailing barges brought up to a warp secured to the beach. It was not until 1837 that the first jetty was begun using the remains of the wreck, as support for the deck of the jetty. This jetty, completed in 1841, measuring 147 m of timber jetty and 63 m of masonry approach, was totally destroyed in 1843 during a south-east storm. In the 1860s a 400 m-long solid breakwater was built at the mouth of the Bakens River; the work was a complete failure due to build-up of sand to the south of the structure and eventual shoaling in the lee.

The main breakwater was commenced in 1922 and completed in 1933. This breakwater was constructed from the top of an existing open piled Dom Pedro jetty which was filled with quarry material only after completion of the breakwater. A further expansion of the port commenced in 1975 included a 335 m curved extension of the breakwater and a 3 km-long approach channel 900 m wide, with a dredged depth of 14,5 m for the deeper-draught bulk carriers and container ships.

Fig.9. Buffalo River and East London Harbour.

EAST LONDON HARBOUR - "PIONEER PORT"

East London is the only South African river port and is located on the Buffalo River. A survey party, sent in 1689 by Simon van der Stel to explore from Table Bay to Delagoa Bay, found that the mouth of the Buffalo River formed a natural harbour but extensive

sandbars were located in the entrance - thus for centuries development of the port was prevented.

The town of East London was established in 1848.

By 1893 dredging had sufficiently deepened the entrance to allow ships of up to 8 000 tons to enter the port. In 1927 construction commenced of the present turning basin which was completed by 1937 and subsequently enlarged between 1959 and 1961.

RICHARDS BAY HARBOUR

Richards Bay is named after Rear Admiral Sir Frederick Richards who in 1879 landed troops during the Zulu War. During the early 1900s the British undertook hydrographic surveys along the coast to locate a possible bunker station, (to be linked by rail to an inland coal course) for the Royal Navy. In 1902, Richards Bay was surveyed by Cathcart Methven, the harbour engineer for Durban, who rated the bay to have more development potential than Durban Harbour. Methven proceeded to design and provide a cost estimate for the harbour at slightly more than £1M. The scheme was, however, never realised. Richards Bay was the first new South African harbour to be constructed since Union, at a total capital investment for the harbour works of some R200M.

Fig.10. Aerial photograph of Richards Bay Harbour.

The entrance channel, dredged on the alignment of an old submerged gorge, presently provides depths required for the handling of 150 000 t bulk carriers. The approach channel has a length of 3,5 km, width 400 m and depth -24m outside the breakwaters and 6,1 km, width 300 m and depths 24 m to 19 m inside the breakwaters. The main south breakwater extends 1,3 km offshore and the north breakwater 0,6 km offshore. The breakwaters are rubble-mound structures protected by dolos blocks. Dolos sizes range from 5 to 30 tons and a total of 42 200 blocks were used in the construction. Dredging of the entrance channel and harbour area involved a total volume of 160M m^3 of spoil material and a further 35M of dredge material used for reclamation.

As at Durban, the south to north sediment drift of 800 000 m^3/year is intercepted by a sand trap located adjacent to the south breakwater; some 400 000 m^3/year is by-passed by the dredger by being pumped onto the north beach while the remainder is dumped at sea. At present some 28M t of coal are exported per year and this is expected to increase to 44M t by 1987. Additional coal berths are presently under construction.

SALDANHA BAY

Saldanha Bay was named after Antonio de Saldanha - although he never visited it. The name was originally given by de Saldanha in 1503 to what is now Table Bay; the Dutch subsequently gave the name to the present Saldanha Bay.

Saldanha Bay provided the best natural anchorage along the entire coastline but was not developed since it totally lacked fresh water. The bay was the scene of major conflict between the Dutch/French and English exploiting the numerous seals and later guano (used as fertilizer). One report records that during August 1844 some 300 ships were concentrated in Saldanha Bay to mine guano and that Skaap Island had been divided into segments "like a cake" to avoid fighting between the different nationalities.

Saldanha Bay later became the centre for fishing and whaling along the productive west coast. The present harbour, developed for the export of iron ore, was constructed during the period 1973-76. Construction included an ore-loading jetty inside the bay protected from wave penetration from the open sea behind a sand breakwater linking an island (Marcus Island), with a headland (Hoedjies Punt). The entrance channel, located south of the island, can accommodate VLCs up to 250 000 tons although the jetties have been built to accommodate 350 000 ton vessels.

COASTAL ENGINEERING

Early harbour development in South Africa fell under the jurisdiction of the Colonial Office, with the result that the majority of the design and planning aspects were undertaken in England and local harbour engineers were responsible only for construction.

Coastal engineering is historically and essentially a branch of civil engineering and it was only following the creation, in 1919, of a department of civil engineering at the *University of Cape Town* that local expertise developed. An early staff member, Mr G Stewart in 1941 built what was probably the first coastal model in South Africa to study range action or harbour resonance in South Africa. Mr Basil Wilson continued the pioneering studies, and during the period 1941 to 1946 he extensively studied range action and the proposed harbour extension for Table Bay Harbour. The small 12 m by 15 m model built in the Cape Town docks was later replaced by a much larger model built by the South African Railways at Langlaagte (Johannesburg). Wilson also extended these studies to investigate mooring forces related to range action.

At the *University of Stellenbosch*, coastal engineering research was started in 1957 with a series of investigations on small-craft harbours and especially fishing harbours carried out in conjunction with the Fisheries Development Corporation of South Africa. Expansion of the hydraulic model facilities and in 1976 the formation of an Ocean Engineering Research Group has led to further work on armour units, breakwater stability, ocean dredging, devices for extraction of wave energy and the design of oil deflection booms.

Both the Universities of Stellenbosch and Cape Town offer study courses at postgraduate level towards a M.Eng. degree in Civil Engineering. The *University of Natal* (Durban) over the past few years has offered a specialist course in civil engineering as an honours thesis towards a B.Eng. degree.

The *Fisheries Development Corporation* is a State sponsored organisation responsible for the planning, construction and maintenance of fishing harbours. Model studies for proposed new fishing harbours or improvements to existing harbours are normally carried out in conjunction with the National Research Institute for Oceanology of the CSIR or with the University of Stellenbosch. Because of its requirements with regard to precise survey for demarcation of harbour boundaries, navigational aids, and hydrographic survey the Corporation's survey branch has developed expertise in seismic and side-scan surveys and aerial photography of the coastline.

The *Coastal Engineering and Hydraulics Division* of NRIO originated from a small Hydrodynamics Division established in 1956 as part of the National Mechanical Engineering Research Institute at Pretoria. The need for applied research in the field of coastal engineering increased rapidly, particularly because of the proposed construction of major harbours at Richards Bay and Saldanha Bay. The need for a suitable laboratory to house the usually large hydraulic models and the formation of a specialist group to undertake the studies became essential. These new buildings and facilities were created in Stellenbosch adjacent to the Faculty of Engineering to permit a close liaison with the University, and in 1969 the Hydraulic Research Unit was established.

The National Research Institute for Oceanology (NRIO) was formed in 1974 to take over and merge the ongoing CSIR activities in marine science and technology. The Institute now comprises four coastal engineering and hydraulic divisions, four marine science divisions, various service divisions, administrative back-up and the South African Data Centre for Oceanology. The staff numbers 165 (in 1982).

The Coastal Engineering and Hydraulics Divisions undertake basic and applied research (some 50 per cent of the projects are of an applied nature undertaken on a contract basis) required for the optimum design and operation of coastal works including major and 'small-craft' harbours, beach and estuary improvement and marine disposal works. A further objective is to develop and provide specialised expertise and consultancy services in coastal engineering with special reference to the needs in South Africa.

- Hydrodynamics Division
  - .. Numerical modelling of water flow and tidal circulation
  - .. Transport/dispersion of pollutants and water quality simulations
  - .. Harbour resonance
  - .. Wave data analysis (design wave condition)

. Sediment Dynamics	.. Coastal and estuarine sediment transport
	.. Estuary mouth dynamics
	.. Wave theory
. Ship Dynamics	.. Ship motions in entrance channels
	.. Moored ship dynamics
	.. Small craft harbours
. Structures	.. Breakwater design, dolos armour units
	.. Coastal structures, tidal swimming pools
	.. Ocean outfalls
	.. Laboratory facilities

SUMMARY

Despite a long history of shipping and considerable harbour construction along the coastline it was not until the early 1900s that "coastal engineering" emerged in South Africa. Prior to the Union of South Africa in 1910 all harbour development was under the jurisdiction of the Colonial Office and planning and design referred overseas. The establishment of a civil engineering department at the Univesity of Cape Town in 1919 provided a nucleus for gradual development of coastal engineering, which spread to the other universities with the formation of civil engineering faculties and particularly departments of hydraulic engineering. In the 1960s the proposed construction of major harbours at Richards Bay and Saldanha Bay dramatically emphasised the need for applied research in the field of coastal engineering and directly contributed to the development of the research facilities at the University of Stellenbosch and Coastal Engineering and Hydraulic Divisions of NRIO. The scope of work undertaken by the various organisations involved in coastal and ocean engineering research has expanded and now includes wave energy research, ocean outfalls and coastal management.

YACHT HARBOURS IN THE UNITED KINGDOM

*J.D. Mettam, M.A., C.Eng., F.I.C.E., F.ASCE., M.Cons.E.

**P.C.Mornement, M.A., C.Eng., F.I.C.E., F.I.Struct.E., F.C.I.Arb.

***J.G. Berry, B.A., BA.I., C.Eng., F.I.C.E., M.I.Struct.E.

ABSTRACT

The authors describe the introduction and development of commercial yacht harbours in the United Kingdom. In the case of the south and west coasts where there is a high mean spring tidal range of up to 8 metres, this has resulted in the provision of enclosed basins, provided with either some form of gate or sill to retain the water. These are described, with typical examples. Recent developments in the design of sector gates are reviewed.

INTRODUCTION

In this paper a yacht harbour means a harbour designed for yachts, and a marina means a yacht harbour combined with an integrated residential development, although these distinctions are not always observed. Yachts, in accordance with the PIANC definition, are taken to mean pleasure craft, either sale or powered, over 8 metres in length. Taken overall, about two thirds in U.K. are sailing yachts and one third are power boats. Few craft in U.K. exceed 12m to 15m overall length.

A yacht harbour provides protection from wave action, permanent access to berths and to adjacent deep water sailing or cruising areas, either the sea or a river/canal with sufficient navigable depth at all times. This is an ideal which is not always attainable because the costs involved may be unacceptable.

"Dry" yacht harbours, which provide land storage and launching facilities for small pleasure craft, are not discussed.

*Senior Partner
**Partner
***Associate Partner

Bertlin and Partners, Consulting Engineers, Redhill, England.

DEVELOPMENT OF YACHT HARBOURS

About twenty years ago the growth in recreational sailing led to a shortage of moorings in popular sailing areas along the south coast of England and the development of commercial yacht harbours. Fig. 1 shows that in 1966/7 there were 17 commercial yacht harbours with access to tidal waters, concentrated in the south-east of England. In 1979 there were 63, the locations being shown in Fig.2.

Fig.1 Yacht Harbour locations, 1966/7

Fig.2 Yacht Harbour locations, 1979

Yacht harbours tend to be located in the south-east of England, within reach of the London conurbation. Popular sailing areas along the south coast are shown in Fig. 3.

Some sheltered rivers, for example the Hamble River, are so crowded with moorings that the navigation authority has put a limit on numbers. Few berths are vacant in the yacht harbours shown in Fig. 3 and most have waiting lists. In other, less popular areas, this is not the case and occasionally berths are advertised as being vacant.

The number of berths in a yacht harbour averages about 250, except for the two biggest harbours at Chichester and Brighton, which provide about 1,000 and 2,000 berths respectively.

With the introduction of low maintenance, glass reinforced plastics (G.R.P.) hulls it is no longer essential for yachts to be taken ashore for winter

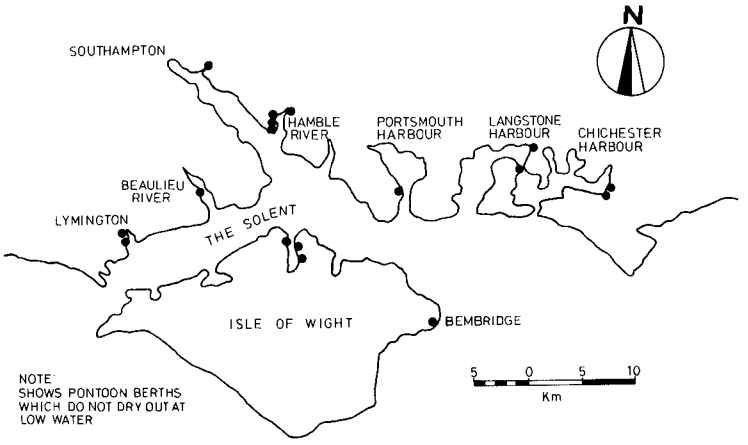

Fig. 4 Popular sailing areas - south coast

storage and most are kept afloat all year, apart from a scrub and application of anti-fouling in the spring.

BERTH CHARGES

There is no standard method of charging the yachtsman for his berth in a yacht harbour. In most cases the cost is expressed in pounds sterling per metre length per annum, on the assumption that the owner will keep his yacht in the marina all year. Typical rates, current in May 1982, are given in Table 1.

TABLE 1

TYPICAL BERTH CHARGES, MAY 1982

Location	Charge per metre
R. Hamble, Hampshire	£119
R. Thames, London	£53 to £66
R. Medway, Kent	£68
R. Crouch, Essex	£49 to £54
R. Orwell, Suffolk	£63
Poole Harbour, Dorset	£108
Falmouth, Cornwall	£75

COASTAL ENGINEERING ASPECTS

The first yacht harbours involved providing pontoons in a river, which replaced trot moorings, or mud berths, and gave sufficient depth for yachts to remain afloat at all stages of the tide.

When the river sites had been fully developed in popular sailing areas, it was necessary to look at coastal sites without natural wave protection. These can be developed either as tidal basins with surrounding breakwaters or as enclosed basins provided with a sill or a lock. All these solutions are expensive as they involve substantial civil engineering works as well as the basic pontoon accommodation provided at river sites; only a handful of yacht harbours come under this category at present because of cost constraints. They represent a challenge to the civil engineer because they present the same engineering problems as commercial ports but the investment is limited to a tenth (or less) of the cost. There are examples at Brighton and Poole, which have surrounding breakwaters with no entry restrictions, and at Chichester Yacht Basin and Ramsgate, which each have a locked entrance.

BREAKWATERS

Until recently the cost of infrastructure items, such as breakwaters, had to be borne by the developer. Grant aid is now available from EEC funds and from the British government for schemes in defined areas of Scotland. Two harbours have floating breakwaters but only one has been successful (1); the remaining few have fixed breakwaters. Examples from two ends of the scale are shown in Fig. 4. Fig. 4(a) is the breakwater at Brighton Marina, which is fully exposed to storm waves in the English Channel, whereas Fig. 4(b) is the one at Poole Harbour Yacht Club Marina, drawn to the same scale, which is in a relatively protected location.

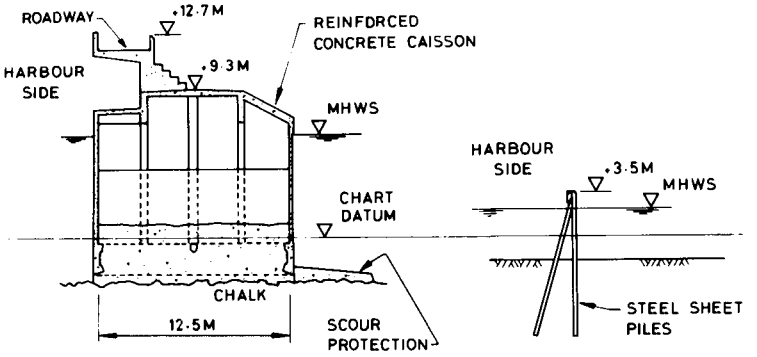

Fig. 4a Brighton Marina

4b Poole Harbour Yacht Club Marina

Fig. 4. Types of breakwater

The Brighton Marina breakwater, designed for about 5m waves, uses circular concrete caissons of the type used for Hanstholm harbour in Denmark. This type of construction was selected because the giant crane used for transporting and placing the caissons in Denmark was up for sale. The breakwater design was tailored to enable the crane to be reused at Brighton.

The Poole Marine breakwater, designed by the authors' firm, represents the other end of the scale. Although Poole Harbour is fully enclosed and land locked, apart from a narrow entrance from the sea, it is one of the largest natural harbours in the world. Wave action within the harbour from local fetches produces waves during the winter months approaching 1m, depending on the location. At the marina site the breakwater, which has a vertical face of continuous light steel sheet piling, was designed for a 50 year maximum wave height of 1.2m. Horizontal wave forces are resisted by inclined steel tube piles which are bonded to the sheet piling by means of a continuous reinforced concrete capping beam.

ENCLOSED BASINS

The need for enclosed basins arises from problems with tidal range and/or suspended silt load in the water. In the U.K. a mean spring range of about 4m can be considered as low, with 8m as a high value. This is not the highest; in the Channel Isles it reaches about 10m.

At coastal sites with a high tidal range the volume of material to be excavated or dredged to provide a basin is considerable. Capital costs can be reduced by partial or full control of water level in the basin. Set against this is the disadvantage that yachts do not have free access to the basin at all stages of the tide. There are however various means by which this disadvantage can be minimised and these are discussed below.

BASINS WITH FIXED SILLS

Partial control of water level can be achieved by providing a fixed sill around the basin so as to retain enough water at low tide to prevent yachts from grounding. Passage over the sill is only possible for an hour or two on each side of high water depending upon the tidal range. The principle is illustrated in Fig.5.

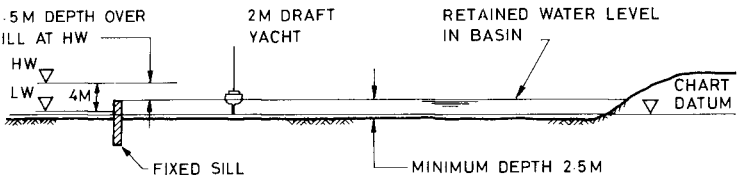

Fig.5. Basin with fixed sill

Where wave protection is needed the basin can be enclosed by an embankment with a gap in which the sill is installed. Emsworth Yacht Harbour with 250 berths is a typical example; its layout is shown in Fig. 6 (a). The basin is enclosed by banks of dredged spoil, the sill consisting of undisturbed material. Puddled clay is used as a watertight lining to the sill, which is shown in cross-section in Fig. 6 (b).

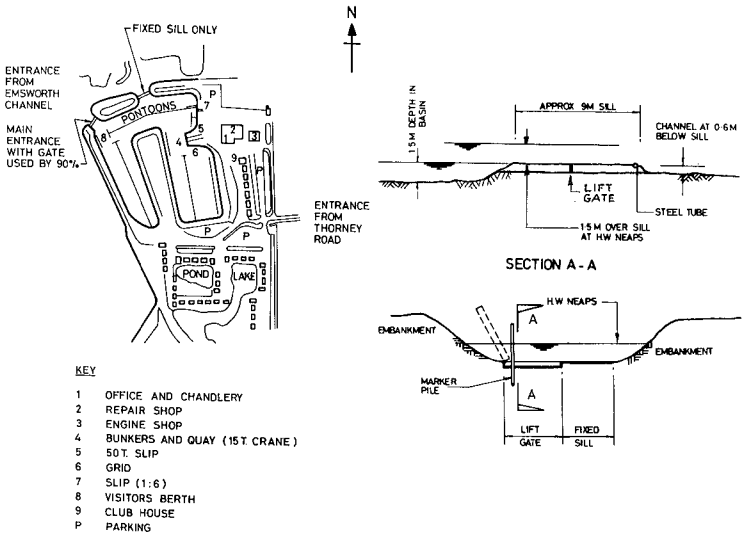

6a Layout 6b Sill Detail

Fig. 6 Emsworth Yacht Harbour

As the lifting gate, shown in Fig. 6 (b) is not working now, all the sill is fixed. The impounded depth is 1.5m.

The sill level was chosen to give 1.5m depth over the sill at lowest (i.e. neap) high water. Craft drawing only 0.9m can cross the sill for $2\frac{1}{2}$ hours each side of high water.

Another example, this time of a natural rock sill, is in Guernsey, at the Channel Islands Yacht Marina. The yacht harbour, which has pontoon berths for 150 craft, was made from a former 18m deep stone quarry by blasting a channel to the sea. The sill is undisturbed rock, and is shown in Fig. 7. The sill level has been chosen so that there is 2.8m of water at half tide, which gives a good duration of access. This is a consequence of the very high tidal range in the Channel, which accounts for use of basins with sills in several French yacht harbours in the area.

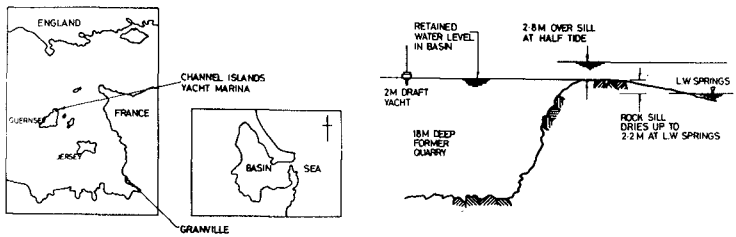

Fig. 7 Channel Islands Yacht Marina

This limitation leads to a fairly recent development - the use of a moveable sill - which goes some way to solving the problem. This arrangement is described below.

BASINS WITH MOVEABLE SILLS

Fig. 8 illustrates the principle of the moveable sill. When the level of the rising tide equals that of the retained water in the basin, the gate is lowered to give an immediate increase in depth. Movement of the sill is controlled automatically by a float system which responds to changes in tide level.

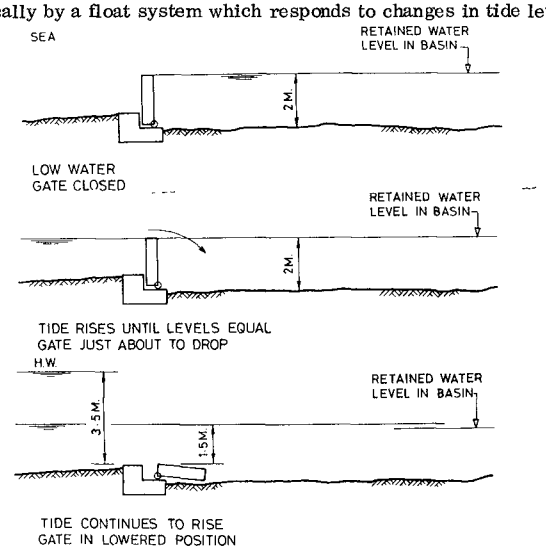

Fig. 8 Moveable Sill

Moveable sills represent a most useful facility for sites with high tidal ranges as they extend the time during which yachts can enter or leave the basin. They are cheaper than a lock and provided the resulting restrictions on yacht movements at mid tide and below are accepted, they should find further application in the U. K.

The first U. K. installation has been constructed at St. Helier Marina in the Channel Isles. An earlier example, but this time on the French coast, is at Granville (location shown in Fig. 7). The principle of the operating mechanism is shown in Fig. 9.

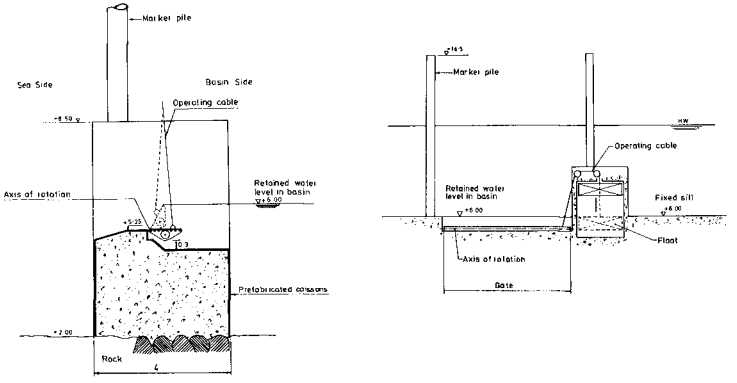

9 (a) Gate detail

9 (b) Operating principle

Fig. 9 Moveable sill - Operating Mechanism

BASINS WITH TIDAL GATES

There are a few yacht harbours, usually conversions of commercial docks, which have single gates which can be opened for an hour or so each side of high water. Although inconvenient this restriction is accepted. Ramsgate Yacht Marina in Kent, with 500 berths, is a good example. It is popular with yachtsmen because it gives the shortest crossing to France.

BASINS WITH LOCKS

A few former commercial docks with conventional lock access have been adapted for recreational use. The locks are of the mitre gate type illustrated in Fig. 10 (a), which are much longer than are needed for pleasure craft and slow to operate. The sector type of gate, illustrated in Figs. 10 (b) and 10 (c), has been developed in U. K. to reduce delays.

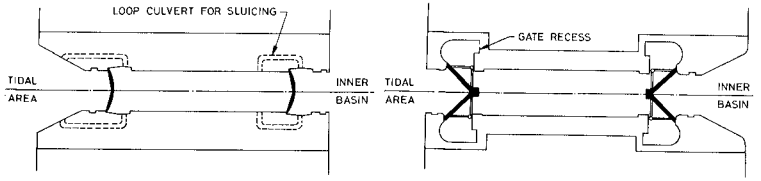

10 (a) Mitre gates

10 (c) Delta sector gates

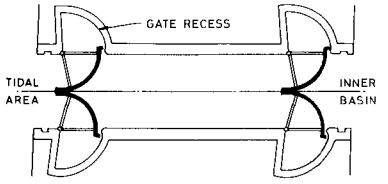

10 (b) Curved sector gate

Fig. 10 Types of Entrance Lock

DEVELOPMENT OF THE SECTOR TYPE LOCK GATE

At sites where the installation of a lock cannot be avoided, the provision of sector type lock gates gives rapid lock cycle times and, at suitable sites, a free-flow period when both sets of gates remain open. The first installation in U.K. was at Chichester Yacht Basin (1,000 berths) in 1966, shown in Fig. 10 (b), followed by Brighton Marina (2,000 berths) in 1978 shown in Fig. 10 (c).

Both installations were the responsibility of the authors' firm. The development of the cheaper flat faced "delta" gate from the curved type used at Chichester was carried out with the help of hydraulic model tests.

PONTOON LAYOUT AND CONSTRUCTION

Floating berths using pontoons are normal in U.K. Yacht harbours where craft moor end-on to a quay (i.e. Mediterranean fashion) are rare owing to tidal variations. Main piers are normally provided with "fingers", as illustrated in Fig. 11.

In the earlier marinas pontoons were constructed on a "do-it-yourself" basis using timber superstructures supported on oil drums or steel tanks. Current U.K. practice is to use expanded polystyrene as the buoyancy medium, in association with steel, timber or concrete superstructures.

Pontoons are located in position generally with vertical piles, but some are secured by chain moorings.

Increasing sophistication of services has meant that the provision of space for pipes and cables has come to dictate the design of pontoons. Electrical

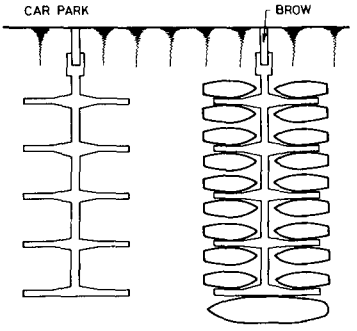

Fig. 11 Berth Layout

power outlets are a usual requirement in most new yacht harbours, as well as water and sometimes telephone services. Provision of firefighting equipment is extremely important.

Until recently no provision has been made for discharging sewage from holding tanks aboard. The first installation in U.K. was completed recently and with recent stricter legislation on pollution, more yacht harbours in U.K. will be providing this service.

References

1. McGregor, R.C. and Gilbert, C.H.G. (1983). Floating tyre breakwaters: a case history. Proc. 18th Int. Conf. on Coastal Engineering.

THERMAL IMPACT STUDIES

FOR FRENCH COASTAL NUCLEAR SITES

by

Y. COEFFE (1), P.M. CLIQUE (2), and B. MANOHA (2).

ABSTRACT :

The paper presents the different stages of the environmental studies performed at the Laboratoire National d'Hydraulique concerning some of the French coastal nuclear power plants using a once - through cooling system, and the different means used, in function of the proper caracteristics of the site, to come to an optimum inlet-outlet configuration leading to a minimum thermal impact and to a minimum recirculation of the heated waters at the intake.
The paper particularly describes the original studies performed for the Flamanville power plant where a special computer controlled tank has been used.

1. INTRODUCTION

The setting up of a coastal nuclear power plant using a once - through cooling system requires many environmental studies because of the importance of the coastal works leading to an important impact on the marine environment. For example the last generation of french coastal nuclear power plants (Paluel, Flamanville, Penly) are made of four units of 1300 MWe each, needing an intake and discharge flow of 180 m^3/s (corresponding to the average annual flow of the river Seine in Paris), with a discharge temperature elevation of 15°C.

So the thermal studies are particularly important as to :

- minimize the effect on the marine environment
- minimize the recirculation of the heated waters at the intake as to optimize the efficiency of the plant.

(1). Head of the maritime hydraulics division, Laboratoire National d'Hydraulique, E.D.F., Chatou, France.

(2). Research engineers, Laboratoire National d'Hydraulique, E.D.F., Chatou, France.

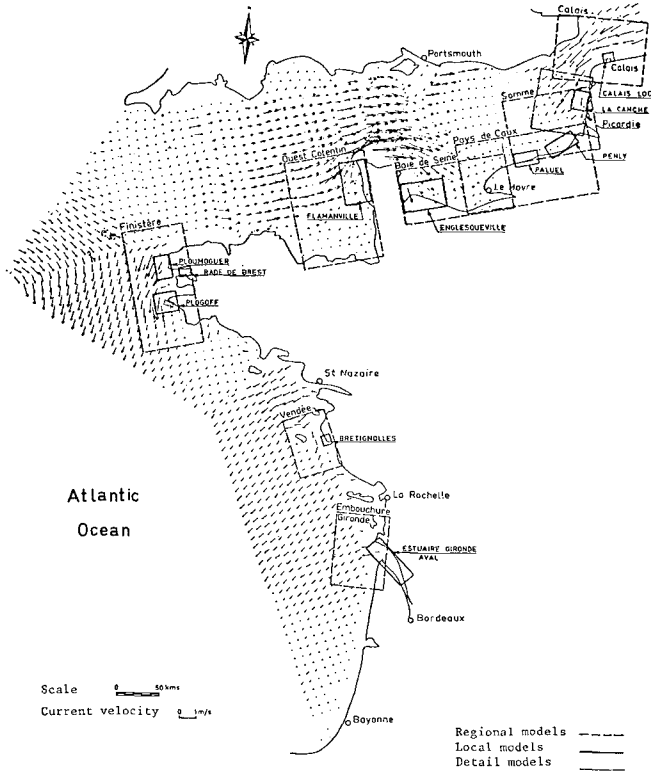

2 HOURS AFTER HIGH TIDE AT BREST

TIDAL CURRENTS COMPUTED ON THE FRENCH COAST

Fig.1

These two problems are of course closely connected and can be solved by way of numerical and physical models calibrated on many field measurements which are essential for a good knowledge of the medium where the calories will be diluted.

The paper presents the different stages of the studies performed at the Laboratoire National d'Hydraulique concerning some of the French coastal nuclear power plants, and the different means used, in function of the proper characteristics of the site, to come to an optimum inlet-outlet configuration leading to a minimum thermal impact and to a minimum recirculation of the heated waters at the intake.

The paper particularly describes the original studies made for the Flamanville power plant where a special computer controlled tank has been used.

2. DIFFERENT MEANS USED

2.1. Field measurements

The studies of the impact on the marine environment of the warm waters discharged by a nuclear power plant as Flamanville (4 x 1 300 MW needs 180 m^3/s of water with a discharge temperature elevation of 15°C) require a very good knowledge of the hydrometeorological characteristics of the site, and in particular of the tidal currents which are the main factor of dilution of the calories for the different french sites chosen up to now (cf. Flamanville). Therefore many drogue trackings and punctual current measurements by currentmeters are performed around the site as to evaluate the characteristics of the marine currents, and in particular the drift and the excursion of the waters.

Many other field measurements are performed, as the meteorological conditions (wind, air and water surface temperature) which are essential to estimate the exchange coefficient with the atmosphere which is the final sink of the calories, the waves (for the protection of the discharge and intake works), the salinity, the vertical profiles of water temperature (eventual possibility of thermocline), the bathymetry of the site, etc.

All these measurements enable then to evaluate the relative effects of the different parameters as to choose the most appropriate means to be used (different types of numerical or physical models), and to calibrate them as accurately as possible.

2.2. Numerical models

Many different numerical models can be used for the evaluation of the thermal impact ; they are mostly used for the intermediate and the far field, the near field being preferably studied by way of physical models.

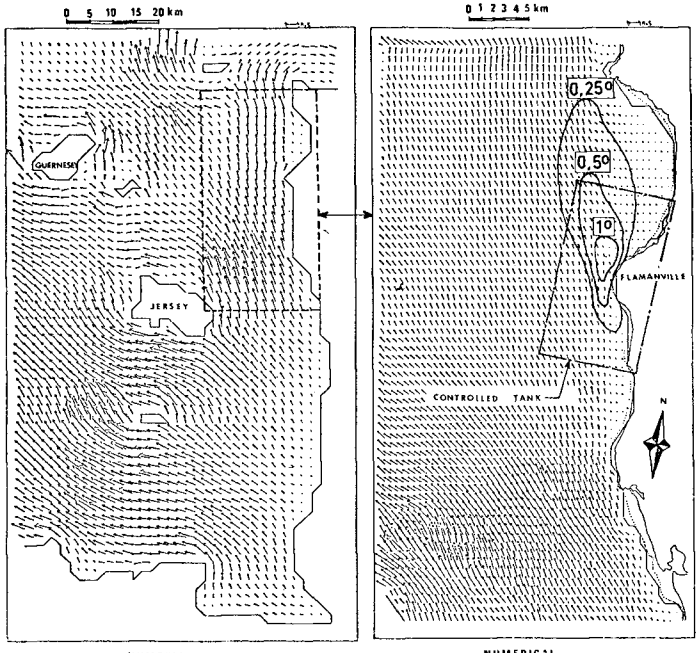

FLAMANVILLE
CALCULATED CURRENTS AND THERMAL IMPACT (3H AFTER HIGH WATER)

Fig. 2

2.2.1. Current models

The dilution of the calories is made by advection, diffusion and finally by exchange with the atmosphere ; different types of models can be used for the description of the current fields in which the calories will be diluted. For the nuclear power plants erected along the English Channel (ex : Flamanville), the currents are due to the tide and are nearly homogeneous along the vertical. Then bidimensional models of tidal currents, calibrated on field measurements, are used. A complete description of this type of numerical model, called CYTHERE ES, which can now take into account tidal flat flooding and drying, is presented in the ASCE paper : "New Method for Tidal Current Computation" (ASCE vol. 108, N° WW3, August 1982) ; let us just say that it is based on a fractional step method in which momentum advection is calculated using the method of characteristics, horizontal momentum diffusion is calculated using an implicit finite difference scheme, and wave propagation is calculated using an iterative alternating direction implicit algorithm. Many different zones, covering various areas, have then been studied (see figure 1) :

- "large models" (10 km gridmesh) cover the English Channel, the Bretagne, and the Atlantic coast ;

- "regional models" (2 to 2,5 km gridmesh) are then used for the far field ; their boundary conditions of flows and levels are given by the "large models" (additional calibrations and adjustments being performed if necessary) : Baie de Saint-Malo, baie de Seine, Finistère, etc.

- "local models" (about 500 m gridmesh) cover then the intermediate field (boundary conditions given by the regional models) : Paluel, Flamanville, Penly, etc.(figure 1) ;

- "detail models", with small and irregular gridmeshes can also be used for a finer description of particular zones in the near field (boundary conditions given by the local models).

The figure 2 presents the example of Flamanville where regional and local models of currents were built, each model using the results of its corresponding bigger sized model as boundary conditions.

2.2.2. Thermal models

The thermal impacts and their evolution during the tide, especially in the intermediate and far field, are then computed through bidimensional numerical models using the results of the above mentioned current models, where the equations of advection diffusion and exchanges with the atmosphere have been solved ; the order of magnitude of the dispersion coefficients used in these models are generally between 0,5 m^2/s (transversal) and 5 m^2/s (longitudinal), the exchange coefficients ranging between 30 and 100 $W/m^2/°C$; the intake and discharge zones are described by a refined gridmesh enabling a more precise evaluation of the near field impact.

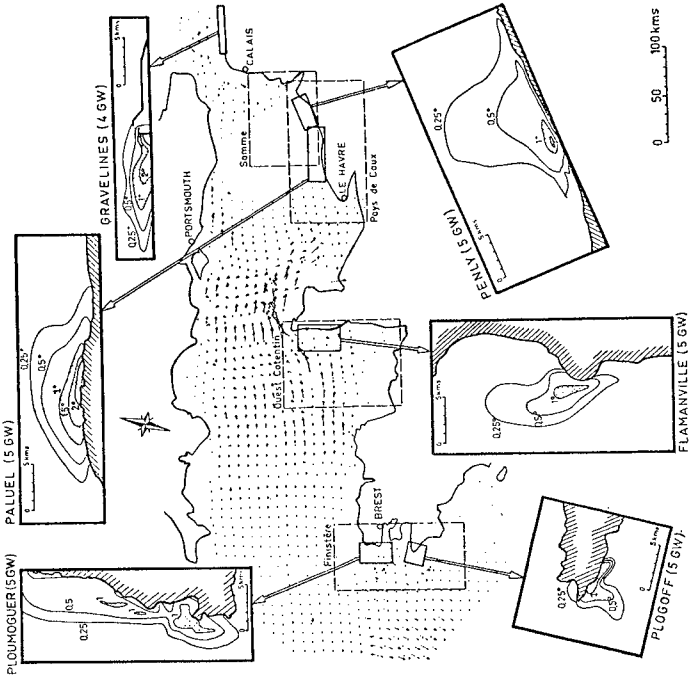

THERMAL IMPACTS CALCULATED FOR DIFFERENT COASTAL POWER PLANTS

Fig. 3

Some examples of results are shown on figure 3 where the thermal impacts calculated for different coastal nuclear power plants are presented :

- Gravelines : it was the first coastal nuclear plant, with an intake and an outfall made through free surface channels (intake inside the Dunkerque harbour, outfall outside the harbour).

- Paluel : as for Flamanville and Penly, the intake is erected along the shore (free surface channel), and the discharge is made through offshore submerged outfalls with high discharge velocities enabling a good initial dilution.

- Flamanville : this plant is erected on a cape with high current velocities contributing to a good dilution of the calories.

- Penly : on this site is a marine drift to the North East enabling a good renewal of the waters and thus a relatively small thermal impact.

- Ploumoguer : this project was situated inside a bay enjoining to make the discharge far away from the coast as to dilute the calories in the strong currents off the bay and to avoid a too important heating of the bay ; the difficulties of this project made it abandonned.

- Plogoff : this site, finally abandonned for political and ecological reasons, was very favourable from a thermal point of view because of the existence of an important dissymmetry between the ebb and the flood, leading to a big tidal drift to the West considerably reducing the thermal impact.

2.3. Physical models

In fact other numerical models can be used for the study of the near field, especially three-dimensional models, but usually most of the near field problems are studied by way of physical models taking into account more accurately and continuously the tridimensional aspects of the dilution : topography, density effects, turbulent mixing, vertical profiles of velocities and temperatures, etc...

As the boundary conditions on classical physical models are usually very long and hard to work up, we have recently built for the environmental studies a special test stand (first used for the Flamanville power plant) which is a hybrid model reducing those difficulties by using both numerical and physical techniques, i.e. a physical model whose boundary conditions are given by the numerical current models and automatically controlled by a computer.

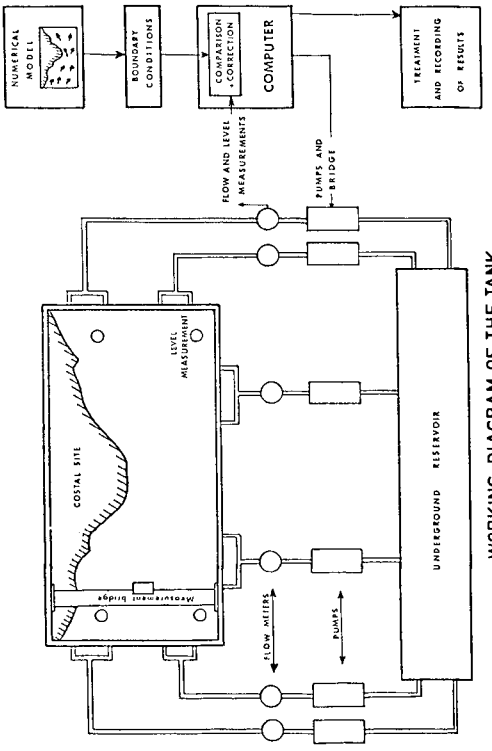

WORKING DIAGRAM OF THE TANK
CONTROLLED BY COMPUTER

fig.4

3. THE COMPUTER CONTROLLED TANK

3.1. Purpose of the model

The computer controlled tank developed by the L.N.H. allows to reproduce, without long manual adjustments, any configuration of non steady flow, for example tidal currents.

The large dimensions of the tank and of its whole equipment make the installation work as a testing stand allowing the study of successive sites one after the other, the only parameters to introduce being the topography and the boundary currents derived from field measurements or from a numerical model of larger area. If the boundary conditions are well known, they will be immediately reproduced whereas their reproduction with classical model equipments needs to proceed cautiously and tentatively during three months to one year, according to the complexity of the current field. If the boundary conditions are badly known, their determination by progressive adjustments in terms of the velocities obtained in the model will be possible within an iteration time of a few weeks, whereas the classical technology makes this research quite impossible because of the long iteration time. This automatic control by computer therefore induces an important gain of time.

3.2. Dimensions of the model.

The dimensions of the model are :

- Overall length : 54,50 m
- Useful length : 47,50 m
- Overall width ; 31,40 m
- Useful width : 28,40 m
- Overall depth ; 1,50 m
- Useful depth : 1,20 m

The underground associated storage capacity is about 1 200 m^3.

3.3 Simulation of the levels and currents

The working diagram of the tank is presented on figure 4.

The model is equipped at its three open boundaries with six water supply systems (2 for each boundary), each one being completely independent from the others and automatically controlled by a computer.

Three of them consist in reversible axial pumps dispatching the water from the underground reservoir to the model or from the model to the underground reservoir with a flow ranging between - 500 l/s (drainage of the model) and + 500 l/s (supply of the model). These pumps are equipped with direct current motors and thyristor speed variators.

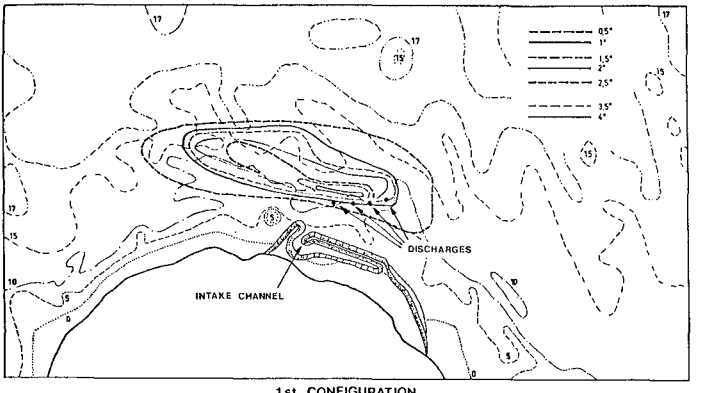

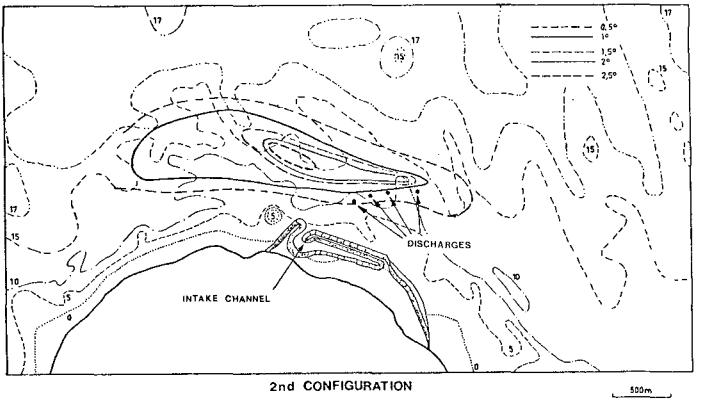

FLAMANVILLE NUCLEAR POWER PLANT
$\Delta T = 15°C$; DISCHARGE FLOW = 180 m^3/s
COMPUTER CONTROLLED TANK
SURFACE TEMPERATURE ELEVATIONS AT SPRING TIDE
6 H BEFORE HIGH WATER
Fig.5

The three others consist in constant-flow centrifugal pumps associated with flow partition valves ; according to the position of the valve, a part of the 500 l/s flow of the pump is recirculated in a closed loop, the other part going either to the model or to the underground reservoir.

The flow in each of the six supply circuits is measured by an electromagnetic flowmeter with an accuracy of about $\pm$ 0,5 %.

A minicomputer HP 2 100 S 32 Kbytes memory brings under control the flows of each water supply circuit, as to reproduce at the boundaries the flows and levels stored on a magnetic tape and previously calculated by a numerical model validated by field measurements.

3.4. Bottom topography

As to allow quick transitions from a site to another, the bottom topography is represented by removable moulded plastic caissons of 1,75 m x 2,50 m easily interchangeable.

3.5. Instrumentation of the model

The tank is equipped with a system of hot water and dye injection allowing to simulate thermal or polluted discharges and to study the diffusion of different types of pollutants.

The measuring equipment is composed of thermal probes, directional propeller currentmeters, 24 x 36 cameras for chronophotographies.

A measurement bridge, equipped with a probe holder trolley, whose movements in the three directions are controlled by the computer, allows automatic scanning of the model with temperature or current probes.

Moreover, a system of automatic treatment of float images by video camera connected to a computer is under progress for the acquisition of the current fields on the model.

3.6. Data acquisition

The acquisition of all the measurements of temperature, current velocities and directions, flows, levels, etc. is made by the HP 2 100 S computer during the experiments. All data are stored on a magnetic tape. Their treatment is made on large capacity computers equipped with quick and high-quality graphic display systems for final results edition.

3.7. - So this facility can be used to examine faster any problem involving tidal currents and diffusion processes, the dimensions and equipment of the tank allowing to treat the near field as well as the intermediate field, the far field being studied with mathematical modelling.

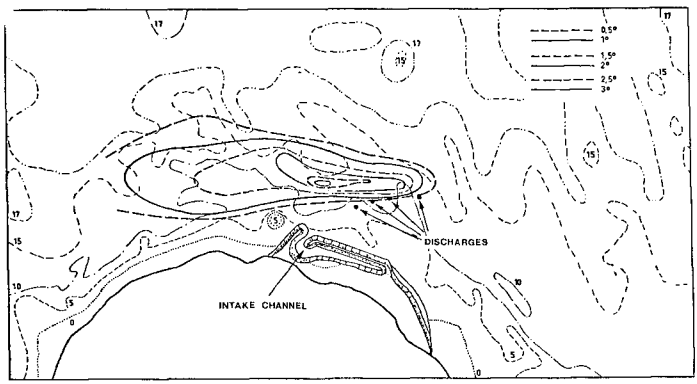

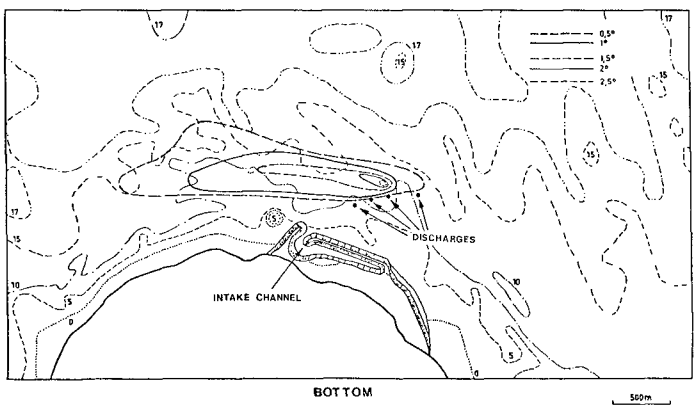

FLAMANVILLE NUCLEAR POWER PLANT
$\Delta T = 15°C$; DISCHARGE FLOW = 180 m^3/s
COMPUTER CONTROLLED TANK
TEMPERATURE ELEVATIONS AT SPRING TIDE
4 H BEFORE HIGH WATER
Fig.6 (2nd CONFIGURATION)

4. THE FLAMANVILLE POWER PLANT

The impact on the marine environment of the Flamanville nuclear power plant has been particularly studied in this model. Numerical regional and local models of currents have been first performed (figure 2). Then, they have been used for the thermal impact study in the far field by way of a numerical model (figure 3) ; this model gave, in particular, an estimation of the average area concerned by a temperature elevation of more than 1°C (about 5 km^2 during spring tide and 7 km^2 during neap tide), and an evaluation of the total recirculation peaks at the intake (maximum about 2°C during spring tide, 3°C during neap tide).

The results given by the numerical models of currents were then used for the currentological and thermal impact in the near and intermediate field by giving boundary conditions to the computer controlled tank here above described.

The model scales are 1/285e horizontal and 1/125e vertical, thus representing an area of about 15 km x 9 km ; once the bottom topography was set in place, the reproduction of the marine currents was quite immediate and showed the interest of the method which allowed to reproduce with a good accuracy the complex configuration of the currents existing North and South the Flamanville cape, which were poorly represented on the numerical model, though well known in the field and very important for the recirculation.

The study was directed on three main points :

- optimization of the positions of the four discharge outlets in order to minimize the recirculation,

- thermal impact in the near field (at different depths and in particular near the bottom),

- influence on the currents of the breakwaters protecting the intake works.

Some results of this study are presented on figures 5 to 7 :

- Figure 5 shows the effect of the relative positions of the 4 discharges (the second configuration was finally chosen) ;

- Figure 6 shows the thermal impacts measured in surface and at the bottom ;

- Figure 7 shows the effect of the tidal coefficient (neap and spring tide).

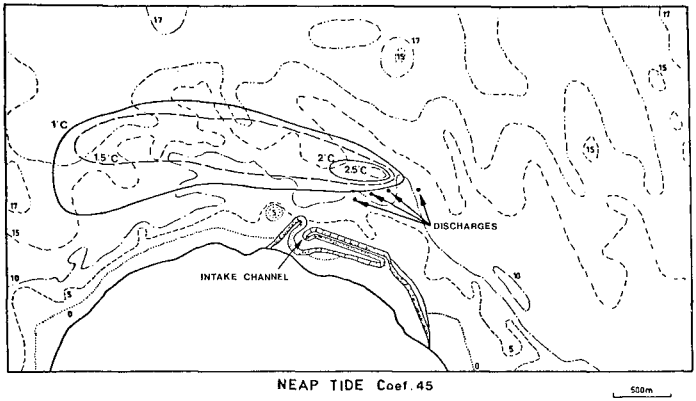

NEAP TIDE Coef. 45

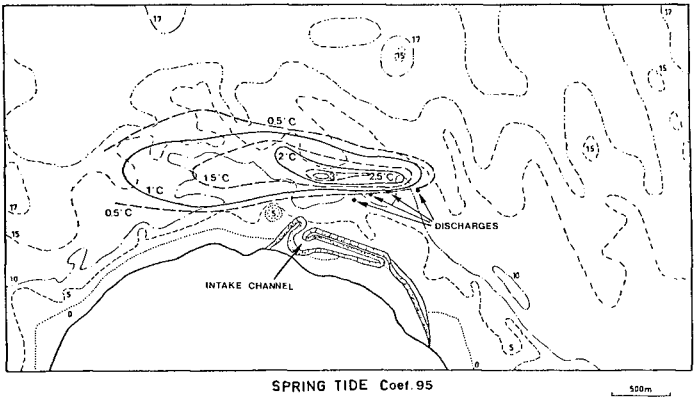

SPRING TIDE Coef. 95

FLAMANVILLE NUCLEAR POWER PLANT
$\Delta T = 15°C$; DISCHARGE FLOW = 180 m^3/s
COMPUTER CONTROLLED TANK
SURFACE TEMPERATURE ELEVATIONS AT SPRING TIDE
4 H BEFORE HIGH WATER
Fig. 7

5. CONCLUSION

Different types of means are used to study the thermal impact on the marine environment of french coastal power plants using a once-through cooling system. Both numerical and physical models are used depending on the problems. New hybrid models appear, as the computer controlled tank, using the complementarity of both techniques, giving then very interesting results in a much quicker studying time.

STUDY ON SEDIMENT TRANSPORT IN A POWER STATION HARBOR BASIN

By

Kohki Maruyama*, Ryoichi Kajima**

Akio Narihiro*** and Kosuke Kondo****

ABSTRACT

Extensive field investigations were carried out over a two-year period on the process of sand deposition in the cooling water intake basin in the harbor of a power station. The trapped bed load weight and mean suspended sediment concentration were found to have good correlations with the Shields Parameter corresponding to conditions of simultaneous waves and currents. A simple numerical model was developed to estimate the total net transport rate of the bed load and suspended load. Calculated results from the model were found to give a reasonable estimate of the sand deposition in the intake basin.

INTRODUCTION

In Japan, harbors for power stations are often built on the coast because of the availability of cooling water. Sediment deposition is one of the serious problems in designing harbor facilities which house water intakes and outfalls, since deposition around the harbor entrance can pose a danger to vessels. Fleming and Hunt (1976) investigated sediment deposition in a power station basin used for the intake of cooling water, and gave a brief description of the sedimentation occurring in the basin. In order to further our basic understanding of this problem, and to provide data for development of a predictive model of the deposition, comprehensive and intensive field investigations were carried out over a two-year period at Fukushima No. 1 Nuclear Power Station, Fukushima, Japan, beginning in the summer of 1979.

---

* Research Engineer, Civil Engineering Laboratory, Central Research Institute of Electric Power Industry (CRIEPI), 1646 Abiko, Abiko City, Chiba, 270-11 Japan.

** Manager of Coastal Hydraulics Section, CRIEPI.

*** Assistant Manager, Civil Engineering Division, Nuclear Power Construction Department, The Tokyo Electric Power Co., Ltd., Tokyo, Japan.

**** Senior Engineer, Design and Engineering Department, Penta-Ocean Construction Co., Ltd., Tokyo, Japan.

In addition to the data obtained from the intensive investigations, quarterly hydrographic surveys and daily incident wave observations have been performed at the site for more than 15 years. These measurements are useful for understanding the long-term tendency of sand deposition in the intake basin.

The objectives of this study were 1) to uncover the mechanisms of sediment transport around a harbor under conditions of simultaneous waves and currents, based on the results of extensive field investigations, and 2) to construct a simple numerical model useful for estimating the volume of sand deposited in a cooling water intake basin.

FIELD INVESTIGATION PROGRAM

Fukushima No. 1 Nuclear Power Station directly faces the Pacific Ocean as shown in Fig. 1(a). The harbor consists of two breakwaters, one to the north and one to the south. The basin in the harbor is used as a landing and for cooling water intake (Fig. 1(b)). At the present time, six B.W.R. generators are in operation with a total generating capacity of 4,696 MW. The maximum rate of cooling water intake is 270 m^3/sec. The width and the annually averaged water depth of the harbor entrance are 125m and 7.4m, respectively.

The field investigation program can be summarized as follows:

1) Periodic measurements of the waves and currents at the monitoring station at the harbor entrance (4 times/day).

2) Measurements of sediment transport using bed load traps at the harbor entrance (once/week). Measurements of suspended sediment concentration using pumps at the monitoring station and at the interior substation (twice/day). Grading analysis of sampled material (once/month).

3) Hydrographic surveys around the harbor entrance (700m by 700m; once/month).

4) Samplings and grading analysis of bed materials (50 locations in and around the harbor; once/month).

5) Measurements of wave height and current distribution in the basin using pressure wave gauges and electromagnetic current meters.

6) Measurements of sand movement using fluorescent dyed sand tracer.

The locations of both the monitoring station, substation, and hydrographic survey area are indicated in Fig. 1(b).

Figure 2 is a photograph of the monitoring station at the harbor entrance. Three electromagnetic current meters and one ultrasonic wave gauge were used for measuring the waves and currents. The intakes of the three pumps were set 0.5m, 1.0m and 5.5m above the sea bed. The pumps each sampled 200 liters of water for every measurement.

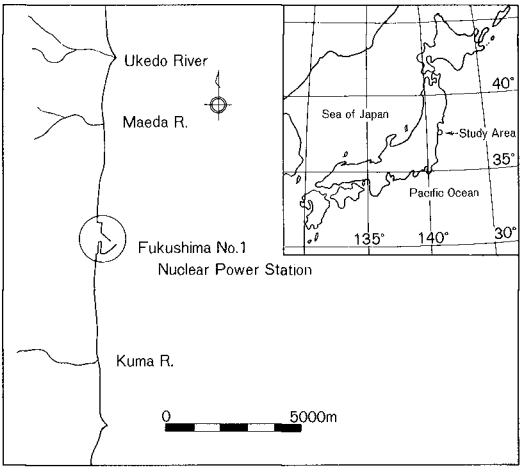

Fig. 1(a) Location of Fukushima No. 1 Nuclear Power Station.

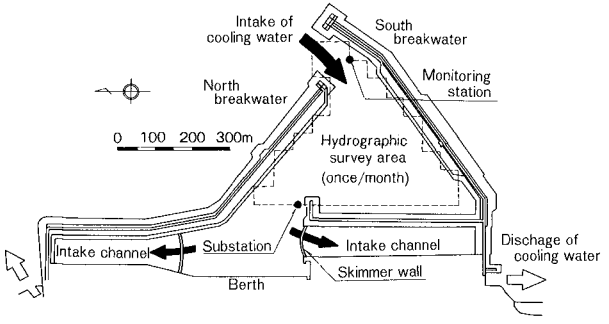

Fig. 1(b) Breakwater layout and the cooling water intake basin.

RESULTS OF FIELD INVESTIGATIONS

Long Term Tendency of Sand Deposition Around the Harbor

The topography, geology and wave climate of the coast at the Fukushima No. 1 Nuclear Power Station have been described in detail by Sasaki et al. (1980). A major characteristic of the area is the existence of coastal cliffs, some 30m high, which face the Pacific Ocean. These are constantly being eroded by wave action. It is estimated that 70% of the material supplied by such erosion consists of sand with the remaining 30% being silt and clay. The greater part of the sea bottom within the area having a water depth of 10m or less is covered with a sand layer of more than 1m. There are also partially exposed rocks along the bottom.

From comparisons of the locations of the cliffs measured on aerial photographs, it is estimated that a volume of material of about 176,000 m^3/year is supplied from the eroded cliffs which exist within a range of about 5 km north and south of the harbor. An additional amount of 35,000 m^3/year is estimated to be supplied from rivers within the range (Fig. 1(a)).

The cumulative sand deposition rate around the harbor (calculated from quarterly hydrographs) and the intake flow rate of cooling water (for the past 15 years) are shown in Fig. 3. Breakwater construction was completed in October, 1969, and the cumulative sand deposition rate was set to zero at that time. The deposition rate in the harbor (area III in Fig. 3) includes the dredged sand volume. From the figure, it is seen that the cumulative deposition rates in each area (I, II and III) are almost equal, and have reached about 500,000 m^3 in the past 10 years. The annual sand deposition rate in the habor (area III) tends to increase with increase of the intake flow rate, which has recently become 60,000 to 80,000 m^3/year.

Significant deposition outside the harbor also occurs up to 1,900 m north and 1,300 m south of the site. It can be roughly estimated that the volume deposited in the calculation area (I and II in Fig. 3) contains 60 to 70% of the total amount deposited outside the harbor. Taking this into account, the total amount of material deposited inside and outside the harbor is estimated to be about 200,000 m^3/year, an amount equivalent to that supplied by the cliffs and rivers within a range of 5 km from the harbor.

Table 1 shows the change in depth at the harbor entrance. The rate of bottom rise has also become greater with increase of the intake flow rate. The depth necessary for vessels to pass the harbor entrance safely is now maintained by dredging about twice a year.

An example of the median diameter distribution of sediment inside and outside the harbor is given in Fig. 4. The bed material in the vicinity of the harbor entrance consists of relatively coarse sand grains, whereas in the interior part of the basin, fine particles with diameters less than 0.1 mm are found.

Fig. 2 Monitoring station at the harbor entrance.

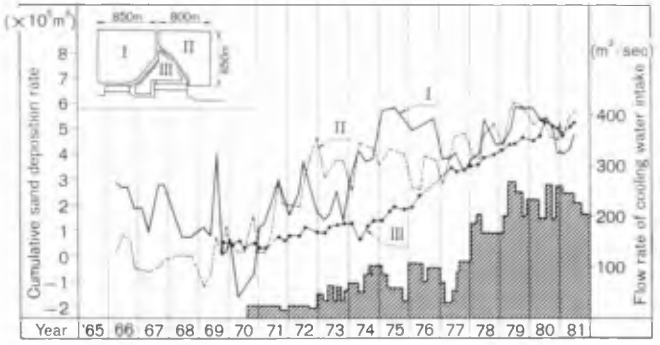

Fig. 3 Change of sand deposition rate around the harbor and flow rate of cooling water intake.

Table 1 Decrease in depth (bottom rising rate) at the harbor entrance.

Interval	Change in depth (m/year)	Average cooling water intake (m^3/sec)
1970—'74	0.5	30
'74—'76	1.0	70
'77—'78	2.0	100
'78—'79	3.0	170

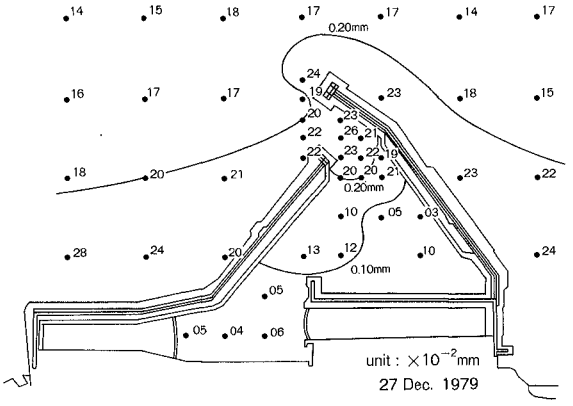

Fig. 4 Distribution of median diameters of the sediment inside and outside the harbor.

The gradings of the bed and suspended materials found at the harbor entrance are indicated in Fig. 5. Of the suspended material, more than 50% of the particles have a diameter less than 0.1 mm. Such sediment is scarce in the bed at the harbor entrance. The ratio of this fine material increases as the distance from the sea bed increases.

From the difference between levels of bottom surveys, and from the distribution of median diameters (see Fig. 4) measured every month, the total amount of sediment (from Jul. 1979 to Dec. 1980) deposited in the hydrographic survey area (see Fig. 1(b)) can be obtained for each diameter grading. The amount of suspended load for the same period entering through the harbor entrance can be estimated from the products of the cooling water intake rate and vertically averaged sediment concentration from the sea bed to the sea surface, which were measured at the monitoring station. In the calculation, the concentration at the sea bed was assumed to be three times that at the 0.5 m level above the bed, based on measurement of the vertical distribution of suspended sediment using suspended sediment traps set 0.5, 0.4, 0.3, 0.2 and 0.1 m above the bed. Moreover, the constituents by grade in the suspended load can also be calculated from the results of the monthly grading analysis, as shown in Fig. 5.

Figure 6 shows the estimated amounts of bed and suspended loads by sediment diameter step. In this figure, 'inflow rate' means the amount entering through the harbor entrance and 'net deposition rate' means the amount deposited in the hydrographic survey area. The amount for the bed load is the value obtained by subtracting the estimated net deposition rate of the suspended load from the total amount, for each sediment diameter step. From the figure, it is estimated that the contributions of each mode to the sand deposition, excluding fine material less than 0.1 mm in diameter, are about equal.

From Figs.4 to 6, it is concluded that the greater part of the fine material passes through the harbor entrance without settling, and that deposition only occurs in the interior part of the harbor where the wave height and current velocity are both low. Therefore, sand deposition just inside the harbor entrance, where the external forces decrease greatly, should depend upon the bed and suspended loads of sand grains with a diameter of more than about 0.1 mm.

Characteristics of Bottom Shear Stress Under Waves and Currents

In order to understand the characteristics of the bottom shear stress under simultaneous action of waves and currents, the bottom shear stress under waves only, τ_1 as presented by Jonsson and Carlsen (1976), and the bottom shear stress under waves and currents, τ_2 as presented by Tanaka and Shuto (1981), will be reviewed.

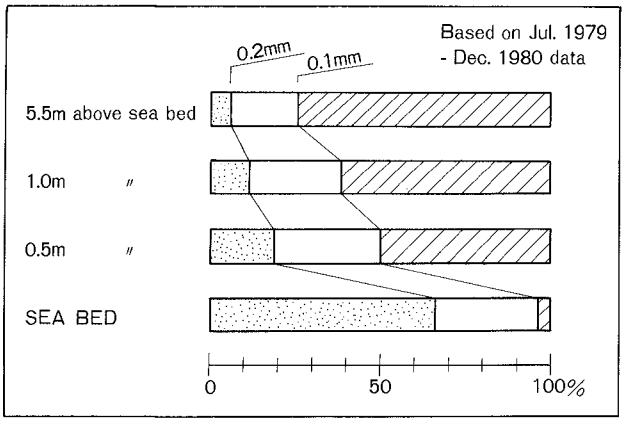

Fig. 5 Grain size constitution of the material deposited on the sea bed and the suspended load at the harbor entrance.

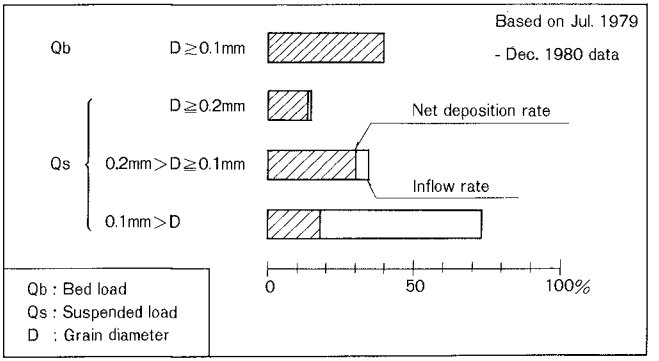

Fig. 6 Relative amounts of bed and suspended loads.

Jonsson and Carlsen gave an expression for the bottom friction factor under waves only, f_w, as follows:

$$f_w = 0.3 \qquad (a_o/z_o < 1.57)$$

$$\frac{1}{4\sqrt{f_w}} + \log \frac{1}{4\sqrt{f_w}} = 0.08 + \log \frac{a_o}{z_o} \qquad (a_o/z_o \geq 1.57) \tag{1}$$

Here a_o is the amplitude of bottom water particle movement, and z_o is the roughness length, ordinarily taken as the grain diameter, D. Using this friction coefficient, we can write the bottom shear stress under waves only, τ_1, as

$$\frac{\tau_1}{\rho} = \frac{f_w}{2} u_b^2 \mid \cos \sigma t \mid \cos \sigma t \tag{2}$$

in which ρ is the fluid density, u_b is the maximum bottom orbital velocity, and σ is the angular frequency of the waves.

On the other hand, Tanaka and Shuto introduced the following equations to express the bottom friction factor, f_{cw}, for the simultaneous existence of waves and current:

$$\frac{f_{cw}}{2} = B_1^2 \left(\frac{u_c}{u_w}\right)^2 + 2B_1C_1 \left(\frac{u_c}{u_w}\right) \cos \theta + C_1^2$$

$$B_1 = \frac{\kappa}{\ln (h/z_o) - 1}$$

$$C_1 = \frac{\kappa}{\pi} \{0.25 + 0.101 \left(-\ln \frac{u_w}{\sigma z_o} - 0.5 \ln f_{cw} + 2.42\right)^2\}^{-1/2} \qquad (50 < u_w/\sigma z_o) \tag{3}$$

and

$$C_1 = 0.728 f_{cw}^{-0.25} \left(\frac{u_w}{\sigma z_o}\right)^{-0.408} \qquad (10 < u_w/\sigma z_o \leq 50)$$

Here u_c is the current velocity, u_w is the amplitude of the bottom orbital velocity, θ is the angle between current direction and wave direction, κ is the Karman coefficient (= 0.4), h is the water depth, and z_o is the roughness length. It is noted that D/30 (D = grain diameter) must be used for the roughness length z_o in Eq. (3).

According to potential wave theory, u_w is given as

$$u_w = \frac{\pi H/L \ (L/T - u_c \cos \theta)}{\sinh (2\pi h/L)} \tag{4}$$

where H is the wave height, and L is the wavelength.

Using these equations, the bottom shear stress under waves and currents, τ_2, is given by Eq. (5), where the current direction and wave direction are assumed to be the same, i.e., $\theta = 0$.

$$\frac{\tau_2}{\rho} = (B_1 u_c + C_1 u_w) \ (B_1 u_c + C_1 u_w \cos \sigma t) \tag{5}$$

The maximum values of τ_1 and τ_2 divided by ρ, i.e., τ_{1m}/ρ and τ_{2m}/ρ, are compared in Fig. 7. In Fig. 7(a), the current velocity u_c (= 0.2 m/s) is fixed, and in (b), the wave height H (= 0.5 m) is fixed. For the calculations, it was assumed that D = 0.25 mm, h = 8m and $\theta = 0^o$, which would represent average topographical and hydrological conditions at the harbor entrance of the Fukushima No. 1 Nuclear Power Station. The two figures show the results for wave periods T of 10 sec and of 6 sec.

The distibution of current velocity u_c, i.e., the time-averaged value of the velocity measured by electromagnetic current maters, is shown in Fig. 8. The velocities 0.5 m above the sea bed are not uniform in the harbor entrance section, and the value near the north breakwater is usually 2 to 2.5 times that near the south breakwater. In addition, it was also found that the variation of the current velocity in the vertical direction is rather small, and that the current direction is almost parallel to the south breakwater. The waves diffracted by these breakwaters tend to propagate along the south breakwater; therefore, the angle θ can be regarded as zero.

It is readily seen from Fig. 7 that τ_{2m} is between 1.5 to 3 times τ_{1m} under ordinary environmental conditions at the harbor entrance of the investigation site, i.e., H = 0.5 m and u_c = 0.2 to 0.4 m/sec (see Fig. 8). It is also observed that τ_{1m} and τ_{2m} are almost equal when the wave height is about 2 m and u_c = 0.2 m/sec. However, such environmental conditions are rarely encountered at the harbor entrance.

Bed Load and Suspended Load Under Waves and Currents

A sketch and photograph of the trap used in measuring the bed load are shown in Fig. 9(a) and (b) respectively. A trap was placed at a given location for between 6 and 24 hr. Results from the traps for the area around the harbor entrance are tabulated in Table 2 with reference to sediment diameter, water depth, current velocity, and wave height and period. Figure 10 shows the relationship between trapped bed load weight, Q, and maximum Shields Parameter, ψ_m. The parameter ψ_m is

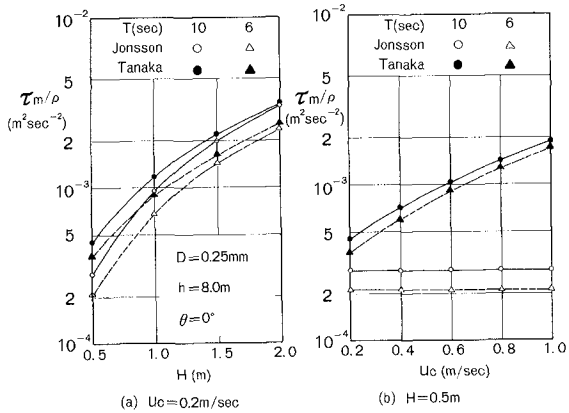

Fig. 7 Comparison between maximum bottom shear stresses; under waves only, (Jonsson and Carlsen, 1976); under simultaneous waves and currents, (Tanaka and Shuto, 1981), for D = 0.25mm, h = 8.0m, and $\theta = 0^{\circ}$. Current velocity is fixed (u_c = 0.2m/sec) in (a), and wave height is fixed (H = 0.5m) in (b).

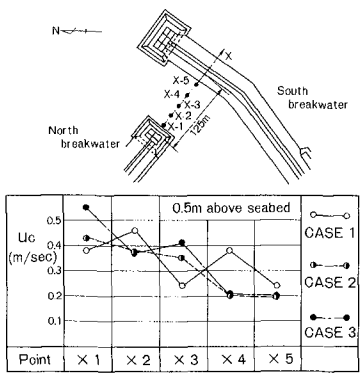

Fig. 8 Current velocity distribution at the level 0.5m above the sea bed.

defined as

$$\psi_m = \frac{\tau_m}{\rho g (s - 1) D} \tag{6}$$

in which s is the ratio of sediment density ρ_s to fluid density ρ, and g is the acceleration of gravity. The maximum shear stress τ_m was calculated from Eq. 5 for the condition of simultaneous waves and currents. Sand ripples were observed on the sea bed around the harbor entrance; however, it has been pointed out that the existence of ripples may not affect the bed load transport rate (Madsen and Grant, 1976). Therefore, the roughness length z_o in Eq. 3 was kept as D/30 even under ripple conditions.

From Fig. 10, it is seen that Q is proportional to $\psi_m^{3/2}$ for ψ_m greater than 0.1. In the region where ψ_m is smaller than 0.1, there is relatively wide scatter, and Q decreases rapidly. The critical value of the Shields Parameter is approximately 0.04. The trapped bed load weight corresponds to the to-and-fro rate of sand movement in the vicinity of the sea bed, and does not necessarily correspond to the net transport rate. Therefore, efforts to determine the functional relation between Q and ψ_m would not be fruitful as far as the net transport rate is concerned.

Examples of ten cases of measured vertical distributions of mean suspended sediment concentration, C, are shown in Fig. 11. The suspended load was measured by pumps at the monitoring station (Fig. 2) under relatively high wave conditions. The mean ratio of the concentration in the lower layer (0.5 m above the sea bed) to the concentration in the upper layer (5.5 m above the sea bed) is about 6:1. This ratio decreases as the wave height becomes smaller, and the mean ratio calculated from all data is about 3:1 (cf. Table 3, where the sediment diameter, water depth, current velocity, wave height and period are listed together with C). The mean ratio, however, is rather small compared to the estimate obtained by the well-known diffusion method (Rouse, 1937). One of the reasons for this is that fine materials, which occupy a considerable part of suspended sediment, flow into the harbor almost uniformly distributed in the water column.

The relationship between mean suspended sediment concentration 0.5 m above the sea bed, $C_{0.5}$, and ψ_m for selected representative values from Table 3 is shown in Fig. 12. It is noted that $C_{0.5}$ appears to be proportional to ψ_m over the entire region. The critical value of the Shields Parameter is not as clear as in the case of bed load.

The trapped bed load weight Q near the north breakwater, where the current velocities were comparatively large, was always greater than that near the south breakwater, whereas the suspended sediment concentration $C_{0.5}$ exhibited a rather uniform distribution at the entrance. The difference in distribution between Q and $C_{0.5}$ can be explained by the difference in terms of the coefficient of the exponent of ψ_m. That is, when the current velocity u_c varies in the harbor entrance section (Fig. 8), the deviation of $\psi_m^{3/2}$ ($\propto Q$) tends to become relatively larger than that of ψ_m ($\propto C_{0.5}$).

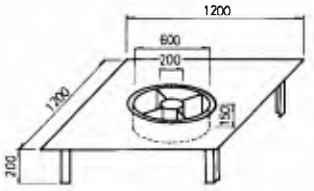

(unit : mm)

Fig. 9(a) Sketch of bed load trap.

Fig. 9(b) Bed load trap on the sea bed.

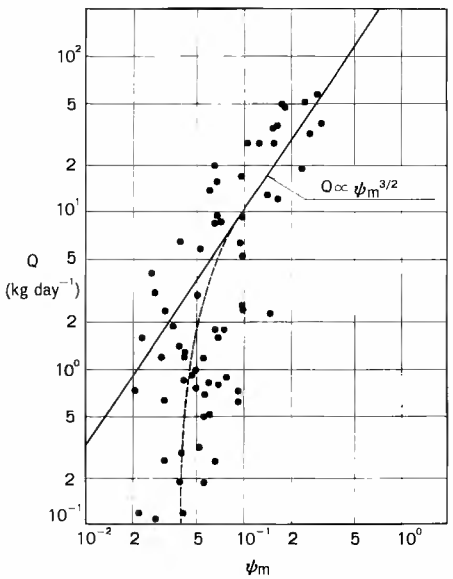

Fig. 10 Relationship between trapped bed load weight Q and maximum Shields Parameter ψ_m.

Table 2 Measurement results of trapped bed load weight presented in Fig. 10.

Case No.	Sediment Diameter D_{50} (mm)	Water Depth h (m)	Current Velocity Uc (m/sec)	Significant Wave Height $H_{1/3}$ (m)	Significant Wave Period $T_{1/3}$ (sec)	Maximum Shields Parameter ψ_m	Trapped Bed Load Weight Q (kg/day)
1	0.17	7.8	0.22	0.21	5.3	0.051	0.75
2	〃	8.0	0.24	0.22	3.6	0.033	1.21
3	〃	7.9	0.20	0.30	5.3	0.062	0.82
4	〃	7.9	0.19	0.16	4.8	0.033	0.26
5	〃	7.9	0.21	0.18	5.5	0.044	0.12
6	〃	7.9	0.16	0.18	5.1	0.029	0.11
7	〃	7.9	0.21	0.25	6.3	0.062	0.52
8	0.22	7.8	0.24	0.23	6.2	0.053	0.32
9	〃	7.7	0.19	0.35	6.5	0.070	1.84
10	〃	7.8	0.18	0.36	6.5	0.070	0.80
11	〃	8.0	0.18	0.37	4.7	0.051	1.04
12	0.20	8.1	0.19	0.36	7.8	0.080	0.92
13	〃	8.1	0.23	0.27	7.4	0.068	1.80
14	〃	8.0	0.17	0.24	5.4	0.040	0.19
15	〃	8.1	0.14	0.30	5.4	0.043	0.85
16	〃	7.9	0.16	0.61	7.6	0.15	2.29
17	0.13	7.9	0.11	0.55	4.8	0.065	0.62
18	〃	7.7	0.10	0.32	4.5	0.043	1.18
19	0.23	7.5	0.10	0.49	6.2	0.078	1.84
20	〃	7.5	0.14	0.71	7.8	0.17	12.47
21	0.21	7.7	0.26	0.79	9.3	0.27	4.08
22	〃	7.7	0.31	0.74	6.7	0.24	19.28
23	〃	7.7	0.27	0.34	8.0	0.10	2.38
24	〃	7.7	0.26	0.51	4.7	0.10	2.58
25	〃	7.7	0.22	0.22	5.2	0.044	1.30
26	〃	7.7	0.16	0.36	5.4	0.059	1.17
27	〃	7.7	0.16	0.17	4.6	0.021	0.73
28	0.24	7.6	0.14	0.33	5.2	0.067	0.26
29	〃	7.5	0.12	0.34	4.6	0.033	2.35
30	〃	7.5	0.12	0.52	7.2	0.095	0.71
31	〃	7.5	0.14	0.34	4.2	0.033	0.63
32	〃	7.5	0.15	0.51	7.7	0.10	5.27
33	〃	7.6	0.10	0.37	4.0	0.023	1.60
34	〃	7.6	0.13	0.44	5.4	0.062	14.38

Case No.	Sediment Diameter D_{50} (mm)	Water Depth h (m)	Current Velocity Uc (m/sec)	Significant Wave Height $H_{1/3}$ (m)	Significant Wave Period $T_{1/3}$ (sec)	Maximum Shields Parameter ψ_m	Trapped Bed Load Weight Q (kg/day)
35	0.24	7.5	0.09	0.44	5.6	0.067	19.56
36	〃	7.5	0.11	0.35	5.2	0.041	6.64
37	〃	7.2	0.14	0.40	6.0	0.067	8.54
38	〃	7.3	0.19	0.45	8.0	0.10	19.65
39	〃	7.5	0.14	0.36	5.9	0.054	2.97
40	0.26	7.4	0.14	0.28	5.1	0.040	1.38
41	〃	7.1	0.09	0.48	5.3	0.071	8.78
42	〃	7.2	0.12	0.32	4.5	0.037	1.87
43	0.24	6.8	0.23	0.78	9.0	0.25	51.17
44	〃	6.7	0.28	0.47	8.2	0.13	27.54
45	〃	7.1	0.21	0.31	7.4	0.070	15.88
46	〃	7.1	0.15	0.20	5.3	0.028	3.07
47	〃	7.1	0.25	0.24	5.3	0.054	5.90
48	〃	7.1	0.27	0.72	4.5	0.15	13.21
49	〃	7.0	0.25	0.23	6.3	0.057	0.50
50	〃	7.2	0.10	0.31	6.0	0.041	0.29
51	0.22	6.9	0.15	0.45	6.7	0.096	6.01
52	〃	6.9	0.18	0.31	5.4	0.059	0.69
53	〃	6.9	0.13	0.17	4.9	0.022	0.12
54	0.20	7.2	0.13	0.35	4.8	0.049	0.93
55	0.24	7.0	0.12	0.34	7.3	0.057	0.19
101	0.20	7.6	0.39	0.44	4.2	0.10	9.38
102	0.23	8.2	0.30	1.12	11.8	0.41	full
103	〃	8.2	0.29	0.94	6.7	0.27	32.72
104	〃	8.2	0.24	0.44	4.7	0.070	9.45
105	〃	8.2	0.37	0.80	5.4	0.16	28.10
106	0.26	7.4	0.31	0.68	5.4	0.16	35.15
107	〃	7.4	0.35	0.88	6.6	0.32	37.31
108	0.23	7.7	0.35	1.18	9.0	0.48	full
109	〃	7.8	0.23	0.68	6.2	0.17	38.33
110	〃	7.5	0.26	0.94	7.4	0.30	57.52
111	〃	7.6	0.39	0.62	5.3	0.18	50.53
112	〃	7.6	0.15	0.94	5.3	0.19	47.18
113	〃	7.7	0.28	0.62	4.5	0.11	28.20

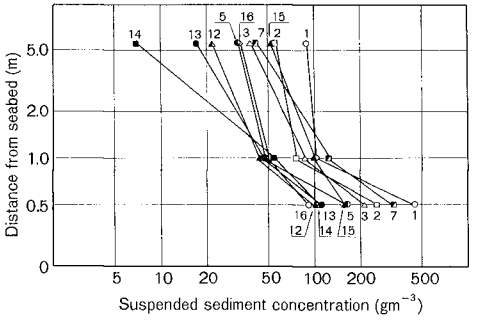

Fig. 11 Examples of vertical distributions of suspended sedimet concentration. The number above each line corresponds to the case number in Table 3.

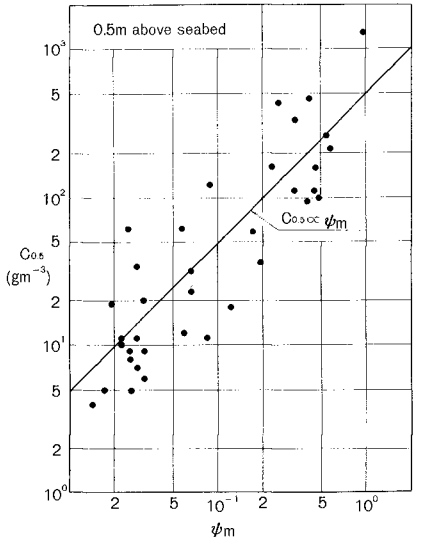

Fig. 12 Relationship between suspended sediment concentration $C_{0.5}$ and maximum Shields Parameter ψ_m.

Table 3 Mean suspended sediment concentration measured mainly using pumps. Specially developed suspended load samplers were used for Case No. 101 in order to obtain the concentration during severe wave conditions.

Case No.	Sediment Diameter D_{50} (mm)	Water Depth h (m)	Cunrent Velocity Uc (m/sec)	Significant Wave Height $H_{1/3}$ (m)	Significant Wave Period $T_{1/3}$ (sec)	Maximum Shields Parameter ϕ_m	Suspended Sediment Conc. (g/m³)		
							Distance 0.5m	above 1.0m	seabed 5.5m
1	0.20	7.1	0.18	1.16	6.7	0.41	456	103	89
2	0.24	6.8	0.44	1.00	7.6	0.53	261	77	56
3	〃	6.8	0.53	1.10	8.7	0.57	213	87	39
4	0.23	6.6	0.12	0.49	5.2	0.083	11	4	4
5	〃	7.3	0.16	0.88	6.6	0.23	163	48	32
6	〃	6.6	0.09	1.00	8.9	0.31	—	201	90
7	〃	7.1	0.07	1.11	8.6	0.33	332	126	43
8	0.24	7.2	0.16	0.53	5.1	0.088	118	79	5
9	〃	7.0	0.22	0.58	5.2	0.12	18	9	5
10	0.26	7.5	0.19	0.79	7.1	0.19	36	26	21
11	〃	7.6	0.20	0.73	7.3	0.17	58	33	14
12	0.20	7.2	0.17	1.22	8.0	0.47	101	44	22
13	〃	6.9	0.16	1.12	9.4	0.44	110	47	17
14	〃	6.9	0.14	0.94	9.8	0.33	109	55	7
15	〃	6.7	0.16	1.12	9.4	0.45	160	101	52
16	〃	6.6	0.17	1.00	9.2	0.39	93	50	33
17	〃	7.5	0.19	0.88	6.4	0.25	431	607	95
51	〃	7.1	0.10	0.41	5.6	0.065	31	28	29
52	〃	6.7	0.06	0.44	4.8	0.056	61	56	50
53	〃	7.2	0.14	0.34	3.3	0.019	19	21	11
54	〃	6.7	0.17	0.31	5.0	0.059	12	13	9
55	〃	7.1	0.11	0.26	4.5	0.028	11	12	13
56	〃	7.0	0.13	0.28	4.2	0.031	20	17	15
57	〃	7.1	0.10	0.20	4.9	0.022	10	11	7
58	〃	7.4	0.15	0.17	4.6	0.025	5	5	4
59	〃	6.9	0.12	0.26	3.9	0.025	61	84	45
60	〃	7.5	0.24	0.36	4.4	0.065	23	14	5
61	0.22	7.1	0.18	0.28	3.6	0.028	7	6	4
62	〃	7.1	0.15	0.28	4.1	0.031	9	6	6
63	〃	6.9	0.17	0.20	4.3	0.028	34	37	8
64	〃	7.3	0.11	0.21	3.9	0.014	4	4	2
65	〃	6.6	0.11	0.21	4.9	0.025	8	8	6
66	〃	7.4	0.09	0.21	5.6	0.022	10	10	5
67	〃	6.4	0.09	0.24	4.6	0.025	9	8	3
68	〃	7.4	0.10	0.19	4.6	0.017	5	4	4
69	〃	6.3	0.11	0.20	4.4	0.022	11	10	5
70	〃	7.4	0.16	0.20	5.5	0.031	6	3	1
101	〃	8.8	0.02	2.33	9.6	0.94	1273	—	—

HARBOR SAND DEPOSITION MODEL

This model for estimating sand deposition in a harbor is based on two assumptions.

(1) There is an inexhaustable supply of sand outside the harbor.

(2) The "wash load", consisting of fine materials with a particle diameter less than 0.1 mm (and which is difficult to relate to the external forces of the waves and the currents) can be neglected.

According to the results of the analysis in the previous section, the transport rates of bed load and suspended load are evaluated separately as:

transport rate of bed load $\sim \psi_m \cdot \psi_m^{1/2} \sim \psi \cdot u$

transport rate of suspended load $\sim C \cdot u \sim \psi_m \cdot u \sim \psi \cdot u$

Since ψ and u depend on time, both transport rates at given time are assumed to be proportional to the instantaneous power ($= \tau \cdot u \simeq \psi \cdot u$) exerted by waves and currents (Bagnold, 1963).

The following equations were then used to estimate the total "net" transport rate q (apparent volume) of the two modes:

$$\frac{q}{\sigma D^2} = \frac{\alpha}{1-\epsilon} \cdot \frac{1}{\sigma D} \cdot \overline{|\psi| \cdot u} \tag{7}$$

where

$$\psi = \tau / \rho g(s-1)D \tag{8}$$

and

$$u = u_c + u_w \cos \sigma t \tag{9}$$

Here ϵ is the sediment porosity, α is an empirical coefficient, and the overbar in Eq. 7 expresses an average for one wave cycle. The bottom shear stress τ is calculated by Eq. 3, which is modified for the coexistence of both waves and current. The sand deposition rate in the harbor can then be obtained by integrating Eq. 7 along the harbor entrance.

The critical value of the Shields Parameter is not included in Eq. 7 because it could not be clearly defined for the suspended load, and also because the contributions of bed load and suspended load to the sand deposition around the harbor entrance are about the same. Komar (1977) used an expression similar to Eq. 7 in estimating the longshore sand transport rate. Approximating the right side of Eq. 7 by $\psi^{3/2}$, an expression is obtained similar to that of Sleath (1978), whose result was based on detailed experiments dealing with sediment movement under waves.

A cumulative sand deposition rate was calculated using daily data of waves and current at the harbor entrance. The results were then compared to the measured bottom change around the harbor entrance and the empirical coefficient α was obtained as 0.92. The sediment diameter was assumed to be constant and equal to 0.22 mm, the annual mean value of median diameter D_{50} of the sediment at the harbor entrance. Figure 13 shows the estimated and measured sand deposition rates around the harbor entrance from July 1979 to November 1980, allowing for a possible scatter of $\pm$ 20%. The calculation is seen to give fairly good results throughout the simulated period.

A calculation was also made using the Brown formula, $q \sim \psi^3$ (Madsen and Grant, 1976) adapting the bottom shear stress under simultaneous waves and currents. However, the result for the total sand deposition rate over the same period as above was about 1/8 of the measured value. In an attempt to eliminate the discrepancy by modifying the procedure through a coefficient of proportionality, the maximum value of the deposition rates calculated for each month in Fig. 13, were found to reach about 50 times that of the minimum value, which deviates greatly from the actual observed phenomena.

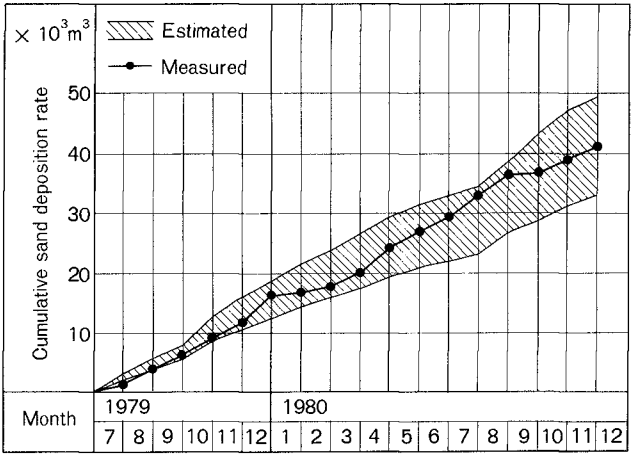

Fig. 13 Comparison between estimated and measured sand deposition rates.

CONCLUSIONS

Comprehensive field investigations were performed at the harbor of a power station, and a model for engineering use was developed to estimate the sediment transport rate based on the measurements. Calculated results of the model were found to give a reasonable estimate of sand deposition in the cooling water basin of the harbor. This model could be used in planning harbor facilities in order to minimize the dredging cost. Modification of the model is expected when the quantitative relationship between the transport rate of fine materials and external forces becomes known, on the basis of further investigations.

ACKNOWLEDGEMENTS

The authors extend their appreciation to Professor K. Horikawa, University of Tokyo, for valuable consultation and advice. We would also like to thank Dr. N. C. Kraus, Nearshore Environment Research Center, for critically reading and preparing the manuscript.

REFERENCES

Bagnold, R.A. (1963): Mechanics of marine sedimentation, in "The sea", Vol. 3, ed. M. N. Hill, Interscience, pp. 507-553.

Fleming, C.A. and J.N. Hunt (1976): Application of sediment transport model, Proc. 15th Conf. on Coastal Eng., ASCE pp. 1184-1202.

Jonsson, I.G. and N.A. Carlsen (1976): Experimental and theoretical investigations on an oscillatory turbulent boundary layer, Jour. of Hydraulic Research, Vol. 14, No. 1, pp. 45-60.

Komar, P.D. (1977): Beach sand transport, distribution and total drift, Proc. ASCE, Vol. 103, No. WW2, pp. 225-239.

Madsen, O.S. and W.D. Grant (1976): Quantitative description of sediment transport by waves, Proc. 15th Conf. on Coastal Eng., ASCE, pp. 1093-1112.

Sasaki, T.O., H. Igarashi and S. Harikai (1980): Nearshore currents on a partially rocky shore, Proc. 17th Conf. on Coastal Eng., ASCE, pp. 1071-1090.

Sleath, J.F.A. (1978): Measurements of bed load in oscillatory flow, Proc. ASCE, Vol. 104, No. WW4, pp. 291-307.

Tanaka, H. and N. Shuto (1981): Friction coefficient for a wave current coexistent system, Coastal Eng. in Japan, JSCE, Vol. 24, pp. 105-128.

Rouse, H. (1937): Modern conceptions of the mechanics of fluid turbulence, Transactions, ASCE, Vol. 102, Paper No. 1965, pp. 463-543.

SALINITY INTRUSION INTO MULTI-PORT SEA OUTFALLS

John A. Charlton, M.Sc., Ph.D., C.Eng., M.I.C.E., M.I.W.E.S., *

ABSTRACT

Sea water intrusion into the diffuser system of a long sea outfall is likely to reduce the efficiency of the outfall. Recent surveys have revealed outfalls with a significant proportion of their diffuser blocked, and others discharging through as few as 50% of their diffuser ports. It is suspected that intrusion is the cause of these malfunctionings. Intrusion may be encouraged by the design requirement of low efflux velocities to obtain optimum dilution, or by over-design to cater for future increases in discharge. Although intrusion can only commence at low discharge velocities, when a port Densiometric Froude number falls below about 1, once it has started sea water will continue to enter the diffuser system until a state of balance is reached. Subsequently a considerably greater flow will be required to purge the outfall of all sea water. Intrusion may also be prematurely triggered by wave action, currents, or by reduced flow through a damaged port.

Hydraulic model tests at the University of Dundee are leading to an understanding of the intrusion mechanism as it affects the various diffuser systems in current use. A continuing research and site survey programme is aimed at design recommendations to eliminate intrusion or reduce its effects.

* Department of Civil Engineering, and Tay Estuary Research Centre, University of Dundee, U.K.

1. INTRODUCTION

Long sea outfalls are being increasingly used to convey waste effluents away from the coastline into areas of the sea where currents are able to generate conditions favourable to rapid dilution and dispersion.

Most of these outfalls terminate in some form of multi-port diffuser designed to optimise the initial dilution of the effluent. The main design criteria for a diffuser system are:-

a) that the flow through the ports should be as equal as possible over the full discharge range of the system,

b) that head losses should be kept to a minimum, and,

c) that the initial or rising plume dilution should be as great as possible.

This is generally achieved by designing for low diffuser port flow efflux velocities, the limit being that the port Densiometric Froude number should remain greater than unity. (At values less than unity saline reverse flow will occur). (Abraham 1963, Brookes 1970)

Outfalls are frequently designed to cater for future population growth and consequent future increase in discharge. By their very nature, they also have to cope with wide ranges of discharge, particularly if they carry storm water. Thus it is likely, especially in the early life of an outfall, that it will occasionally operate under low flow conditions which are favourable to sea water intrusion.

Unfortunately, out of sight, out of mind, has too frequently been the dictum of many operators of sea outfalls, and it is therefore not too surprising that reduced performance of an outfall is rarely reported. However a number of observations have recently come to hand indicating that some outfalls have not been functioning in the manner that their designers envisaged. Noticeable failure is apparently rare, but reduced performance surprisingly common. A notable example in the UK, recently reported, is that of the Hastings sea outfall (type b, fig. 1). It was discovered that, although the outfall had been discharging its full load, a substantial portion of the seaward end of the diffuser was blocked by debris and marine growth. It is now accepted that this blockage resulted from continuous sea water intrusion due to over conservative design. (Bennet 1981, 1982) A similar case has been reported in 1982. Another case concerns a large UK tunnelled outfall (type c, fig. 1) in which only half of the diffuser risers are carrying effluent at the design D.W.F.

The problem of sea water intrusion is not new, but the realisation of the problem is comparatively new. It was at the ICE Conference on Sea Outfalls in London in October 1980 that the problem was privately discussed by a number of experts. One of the main difficulties on this occasion was conceptual, in that nobody had observed the intrusion problem, and its manifestation was largely conjectural, although a number of outfall designers had proposed mechanisms for the intrusion process.

1.1 Pilot model

A thorough literature search yielded virtually no references on the subject and no record of any relevant outfall model testing. Therefore in an attempt to elucidate the problem, a pilot model of a tunnelled outfall was constructed in the hydraulics laboratory at the University of Dundee. This model, entirely constructed in perspex, had a foreshortened tunnel and only two risers. For a typical outfall its modelling scale would be about 1:20. Despite difficulties in maintaining appropriate salinity levels in its small 'sea tank', this model convincingly demonstrated some of the intrusion mechanisms, and that intrusion problems could arise in existing outfalls. The opportunity to observe the intrusion process was extremely valuable and necessary before we could attempt to quantify the process by a theoretical approach.

1.2 The Aberdeen outfall model

We were very soon able to apply the lessons learnt on the pilot model when the Grampian Region's Department of Water Services, through their consultants D. A. Donald and Wishart of Glasgow, commissioned the building and testing of a section of the Aberdeen sea outfall, which was then under construction.

The Aberdeen outfall comprises a landward shaft and a 2.5 km tunnel of 2.5 m diameter, the last 270 m of which is a diffuser section. Ten diffuser risers are connected to the tapering tunnel invert on alternate sides at 30 m centres. (type d, fig. 1) The shaft, some 40 m of tunnel and the first 100 m of the diffuser section including four risers was modelled in perspex, to a scale of 1:18.9. The risers discharged into a 6 m^3 'sea tank' maintained at a density of 1025 kg/m^3, and flow behaviour was observed with the aid of a comprehensive dye injection system.

This model has now been superseded at Dundee by a multi-purpose outfall test facility built on very similar lines to the Aberdeen outfall model. This facility has been financed by the UK Science and Engineering Research Council as part of a 3 years laboratory and site investigation into the salinity intrusion problem. (Charlton 1982).

1.3 Sea water intrusion as a design parameter

It has become evident that the traditional approach to sea outfall design needs to be modified taking into account an appreciation of the intrusion phenomenon. It will be another 3 years before an analysed description of intrusion processes can be published from the Dundee research programme, but in the interim period it is considered that a broad description of these processes as they have been observed to date would be beneficial to those currently engaged in outfall design.

While not attempting to supply the answers, the following sections of this paper describe the intrusion process, and its consequences, as a current 'state of the art' document.

2. OUTFALL DESIGN

The criteria listed in section 1.2 are generally achieved, after appropriate hydrographic and dispersion surveys (Charlton 1980), by conveying the effluent seawards through a pipeline or tunnel to a diffuser section which is designed to maximise the initial dilution. Invariably the diffuser section comprises a number of ports close to the sea bed. The number and spacing of these ports is a function of the water depth, total effluent flow and the required surface dilution. The use of the Brookes and Abraham rules results in low port efflux velocities and consequent low differential pressures between the outfall pipe and the sea, particularly at low discharges. Outfalls frequently operate over wide ranges of flow and in trying to obtain maximum dilutions over the higher flows, designers sometimes reduce port Densiometric Froude numbers very close to unity, when intrusion is likely to occur. It will be shown in later sections that intrusion under these conditions can be triggered by other factors at flows corresponding to significantly higher Densiometric Froude numbers.

Clearly, if an outfall is being designed to cater for increased loadings in later life, this problem is exacerbated.

3. OUTFALL TYPES

To list the many variations of outfall design would be superfluous, but to simplify matters we may divide outfalls with diffuser sections into four main types.

a) Sea bed outfall pipes with the diffuser section being entirely above the sea bed. In this case the diffuser ports are usually in the side of the pipe. Fig. 1 (a).

b) Shallowly buried outfall pipes, the diffuser section consisting of a number of short riser pipes. Fig. 1 (b).

c) Tunnelled outfalls where the diffuser section consists of a number of shafts connecting the soffit of the tunnel to sea bed diffuser heads. Fig. 1 (c).

d) Tunnelled outfalls where the diffuser section consists of a number of staggered shafts connecting the invert of the tunnel to sea bed diffuser heads. Fig. 1 (d).

4. THE INTRUSION CONDITION

4.1 The intrusion condition in an outfall with a diffuser section entirely above the sea bed (Fig. 2).

This type of outfall tends to be self regulating, the amount of sea water remaining in the pipe at any given time depending on the gradient of the pipe and the location of the outlet ports.

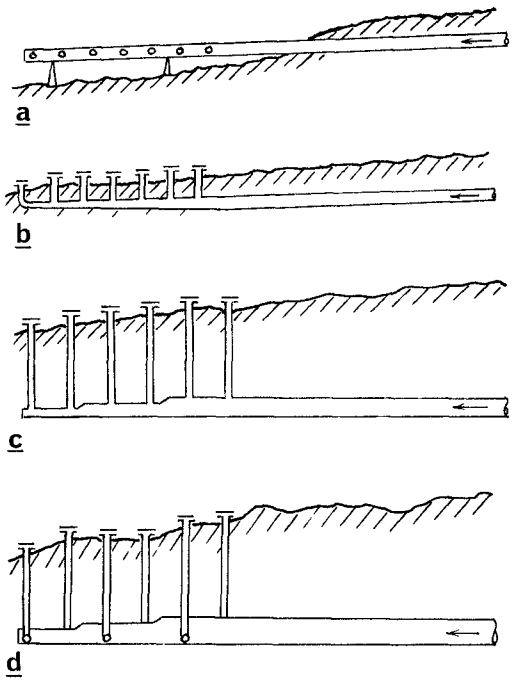

Figure 1 The four main types of outfall and diffuser configuration

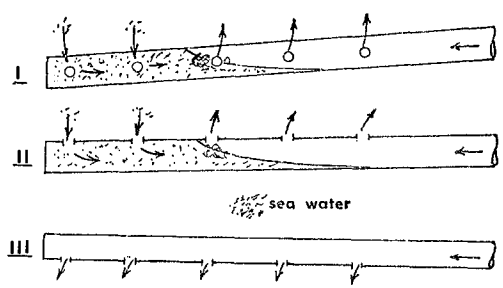

Figure 2 Intrusion processes in type *a* outfalls

Figure 2I shows how sea water intrudes into an inclined diffuser section. A similar interface configuration will occur whether the ports are on the side, top or bottom of the pipe.

The fresh-saline water interface will move downstream with increasing flow and vice-versa until an equilibrium position is reached. Mixing at the interface will be replenished by inflow through the sea water submerged ports.

As the diffuser pipe approaches a horizontal configuration there is a marked difference in performance between a diffuser with ports in the top or base of the pipe. (Figs. 2II and 2III) With top opening ports the flow patterns will be similar to case 2I, but with bottom ports there should be equal flow out of all ports at all times, particularly at low flows. (Any sea water within the pipe will be expelled with a horizontal interface inside the pipe until all sea water is cleared.)

4.2 The intrusion condition in a sea bed outfall with short vertical risers (type b), or a tunnelled outfall with longer risers (type c) both joined to the pipe/tunnel soffit.

These two cases are geometrically similar, the main difference being in the length of the riser pipes. (Fig. 3)

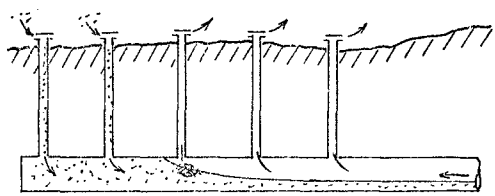

Figure 3 Intrusion process in type c outfalls

In this case the intrusive condition is very similar to that depicted in Figure 2II. However, the differential head created between a long riser full of sea water and another full of fresh water (effluent) increases with length and can generate considerable downward flow in those risers full of sea water. For equilibrium, mixing must take place at the interface as shown. Once again the interface will move to an equilibrium position.

4.3 The intrusive condition in a tunnelled outfall with invert connected risers.

This is the configuration that, to date, has been most closely studied (in the Aberdeen sea outfall model). (Fig. 4)

In this configuration the interface wedge is not so pronounced. The interface tends to form horizontally with a mixture of fresh and sea water being fed into the upward discharging risers. Under intrusive conditions some of the risers are full of sea water and flow downwards, thus maintaining the sea water layer in the tunnel.

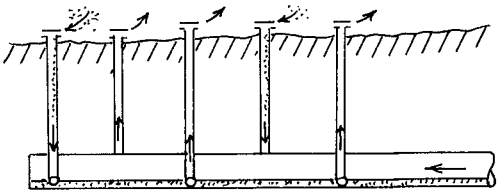

Figure 4 Intrusion process in type d outfalls

5. THE INTRUSION PROCESS

The conditions described in section 4 may be regarded as steady state conditions for a constant discharge. To arrive at this condition we may consider an outfall system full of sea water. This is a condition that would result from a cessation of effluent flow. If now a low flow of effluent commences, this flow will displace sea water with a clearly defined interface similar to that depicted in Figs. 2, 3 and 4. This interface will move downstream in types a, b and c with increasing effluent flow until the flow, and pressure differential, between the pipe and sea, is great enough to expel all the sea water. Once this condition is reached flow may be decreased again considerably before intrusion once again occurs. Intrusion will not recommence until the Densiometric Froude number of any orifice is reduced below unity. (See later for modifications to this condition.)

In the case of a type (d) outfall, with increasing flow from a fully saline start the horizontal interface in the tunnel is depressed until a mixture of sea and fresh water flows up the risers. At this stage, imbalances occur between adjacent risers and some actually go into reverse flow. This reverse flow maintains the saline layer in the tunnel and the upward flowing risers carry a mixture of fresh and saline water. With increasing effluent flow more risers come into the upward discharging state until eventually all are in this state and all sea water is expelled from the tunnel. As in the previous case intrusion cannot recommence until the outlet port Densiometric Froude Number reduces below unity. Once intrusion starts, it progresses to the full equilibrium condition described in section 4.3.

Flushing, which clears intrusive salt water with increasing fresh water flow tends to be a slow process as it depends on sea water entrainment by the fresh water, and there may be large volumes of sea water within the system.

Thus in most outfall configurations the intrusion process takes the form of a hysteresis loop, with an established intrusive condition persisting to fairly high flows, but once cleared, not starting again until a very low flow occurs. This is illustrated in Figure 5 where the total head loss through the outfall system is plotted against the total discharge. With intrusion the head required to discharge a given flow through a reduced number of ports is greater than it is without intrusion and discharge through all the ports.

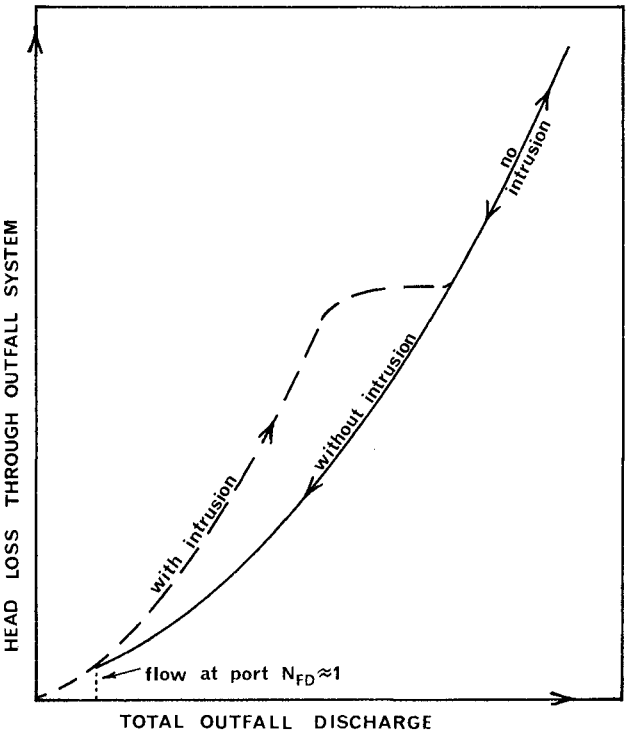

Figure 5 Diagram showing the effect of sea water intrusion on the head loss in a complete outfall system.

A number of factors may raise the commencement of intrusion above the nominal Densiometric Froude number unity condition. Wave action generating attenuated sea bed pressures will trigger this process, and varying levels of outlet port (usually due to sea bed slope) will generate unequal flows in tunnel diffuser risers at low flows. This latter condition will prematurely lower the flow in some outlets and make them vulnerable to intrusion.

6. THE SUSCEPTIBILITY OF OUTFALLS TO INTRUSION

By their very nature all outfalls are susceptible to intrusion to some degree at low flows. However some designs are more resistant than others. For example the configuration in Figure 2iii is almost proof against intrusion. Types b and c have proved to be most vulnerable as the flow needed to expel all sea water is often very close to their maximum discharge.

Outfalls which operate over a wide range of discharge can be designed to function above the intrusive condition, and outfalls which operate at high efflux velocities are naturally protected.

7. THE CONSEQUENCES OF SEA-WATER INTRUSION

If intrusion and sea water clearance take place regularly due to cyclic flow variations, little harm will come to an outfall system. It is expected that a large number of outfalls operate in this fashion. However, if the clearance condition is only occasionally reached and intrusion persists for long periods, those areas of an outfall which contain sea water may become subject to marine growth and debris collection. This can eventually lead to blockage.

Often tunnelled outfalls are driven up-hill in a seaward direction for ease of construction drainage. When working under intrusive conditions stratified sea water will migrate downhill towards the landward shaft and obstruct the stratified fresh water flow. Sedimentation will thus be encouraged in the tunnel.

8. CONCLUSION

While saline intrusion may often occur in outfall systems, it may not be persistent and by its self regulating nature may go unnoticed. However,there are many outfalls whose performance is being restricted by the phenomenon.

This paper, while not giving the remedies, does aim to describe the intrusion process, in the belief that for designers an awareness of a problem is nine tenths of the solution.

When our current research programme is completed we hope to present working design criteria and designs that will enable designers to avoid, or minimise,problems that might be caused by

saline intrusion.

Most of the observations made in this paper have come from hydraulic model investigations. While intrusion models are a new venture the principles on which they are operated are well proven, and prototype predictions based on their performance can be taken with confidence. We also have sufficient prototype case histories to back this confidence.

REFERENCES

Abraham G. "Jet diffusion in stagnant ambient fluid". Delft Hydraulics Col. Publ. No. 29 1963.

Bennett J.J. Initial dilution: a practical study on the Hastings long sea outfall. Proc. I.C.E. Vol. 70 Feb. 1981. Discussion:- Proc. I.C.E. Vol. 72 Feb. 1982.

Brookes N.H. "Conceptual design of submarine outfalls". II Hydraulic design of diffusers. California Inst. Tech. W.M. Kerr Lab. of Hyd. & W.R. Tech. Memo 70-2 Jan. 1970.

Charlton J.A. "The application of E.E.C. bathing water standards to the design of sea outfalls". Prog. Wat. Tech. Vol. 12, No. 1. Pergamon 1980.

Charlton J.A. "Hydraulic modelling of saline intrusion into sea outfalls." Int. conf. on Hydraulic Modelling of Civ. Eng. Structures. B.H.R.A. Coventry UK Sept. 1982.

Sharp J.J. & Chung-su Wang Arrested Wedge in Circular Tube. Proc. A.S.C.E. Hyd. Div. 100 HY7 Tech. note July 1974 pp 1085-1088.

DRIFT CURRENTS OF CLEAN AND SLICK SEA SURFACES

Jin Wu[1]

1 INTRODUCTION

Drift currents near sea surface govern movement and dispersion of man-made discharges near the sea surface, and influence design, deployment, and stability of offshore structures. The wind-induced drift currents and the wave-induced mass transports at the sea surface are separately estimated. The total surface drift current, the sum of wind- and wave-induced components, agree well with oceanic data (Hughes, 1956).

The mass transport of waves over slick surface is greater than that over clean surface due to dynamic interactions between the surface film and waves. On the other hand, the wind-stress coefficient of slick surface is smaller than that of clean surface, resulting in a smaller wind-induced drift current over the slick surface. Available laboratory results (Alofs and Reisbig, 1972) on slick movements are reanalyzed to provide basis for estimating movements of slicks of various sizes over waves of different lengths under different wind velocities.

2 DRIFT CURRENTS OF CLEAN SURFACE

2.1 Experiments in Laboratories

A slow forward motion of water particles under surface waves was theoretically predicted by Stokes (1847). The so-called Stokes transport at the water surface, V_v, can be expressed as

$$V_v = \sigma a^2 k \tag{1}$$

where σ, a, and k are the radian frequency, amplitude, and wave number of waves, respectively. Experimental observations of (1) were provided, among others, by Lange and Hühnerfuss (1978).

Studies on drift currents in a wind-wave tank have been conducted by Wu (1975). The difference between measured total drift current and estimated Stokes transport was considered as the wind-induced current. The wind-friction velocity was suggested (Wu, 1975) as the proper parameter for correlating this wind-induced component,

$$V_n/u_* = 0.53 \tag{2}$$

where V_n is the wind-induced surface drift current, and u_* is the friction velocity of the wind.

[1]Professor of Civil Engineering and Marine Studies, University of Delaware, Newark, Delaware 19711.

2.2 Estimations for Field

The Stokes surface transports at various fetches under different wind velocities can be obtained from (1) with wave data reported in Wu (1969),

$$V_v/U_z = 0.0186\ (gL/U_z^2)^{0.03} \qquad (3)$$

where g is the gravitational acceleration, L is the fetch, and U_z is the wind velocity at the elevation z above the mean sea surface.

In the meantime, the wind-induced shear current can be obtained from (2) with empirical wind-stress (Wu, 1980) and wave-drag coefficients. Combining wind- and wave-induced components, the ratio between the total surface-drift current and the reference wind velocity (V/U_z) decreases with increasing fetch at short fetches, and is independent of fetch at long fetches. The total surface drift current is about 3.1% wind velocity at very long fetches.

2.3 Comparison with Other Results

From the equilibrium wave spectrum (Phillips, 1977), Bye (1967) obtained an expression for the Stokes surface transport. Accepting the value of the spectral coefficient suggested by Longuet-Higgins (1969) for the open sea, we obtained from Bye's expression: $V_v/U_{10} = 0.0274$. This is in fair agreement with the present estimate of the mass transport. More recently, the spectral coefficient was found to vary with both fetch and wind velocity (JONSWAP). Coupling these results with Bye's expression, the mass transport at the sea surface decreases with fetch and increases with wind velocity, having the same trend as the present estimate.

An expression similar to (3) was proposed by Kondo (1976). The surface mass transports calculated from Kondo's and the present expressions for U_{10} = 10 m/s at various fetches are shown in Table 1. In comparison with the present as well as other results, such as those discussed above, Kondo's estimate appears to provide rather low values.

Fetch (km)	10	50	100	500	1000	5000
Kondo (1976)	1.63	1.68	1.70	1.75	1.77	1.82
Equation (3)	2.29	2.40	2.45	2.57	2.63	2.95

Table 1. Ratios (%) Between Estimated Surface Mass Transport and Wind Velocity for U_{10} = 10 m/s.

The drift currents at the sea surface were measured by Hughes (1956) with plastic envelopes floating close to the water surface. He found that the water within 1 cm or so of the surface drifted parallel to the wind. The drifting speeds of plastic envelopes were about 3.1% of the wind velocity. This value coincides with the present estimate.

3 DRIFT CURRENTS OF SLICK SURFACE

3.1 Increase of Surface Mass Transport

Experiments have been conducted by Alofs and Reisbig (1972) to investigate wave-induced drifts of simulated oil slicks in a wave tank. Floats made of

thin, flexible plastic sheets of various sizes were laid on the water surface before the experiment, and were found to conform with the wavy surface. The drift of floats due to waves, verified to be very similar to that of oil lens, was measured with waves of two different lengths and various steepnesses. For each experimental condition, we obtained an equilibrium drift velocity V_{max}, at which the drift current no longer increased with the float length, ℓ. Inasmuch as the mass transport over the clean surface in Alofs and Reisbig's experiments was found to be greater than V_v, we determined the additional movement due to the presence of float from $V_{max}-V_o$, where V_o is the velocity of the "float of zero length" found by extending their results obtained with floats of various lengths to $\ell = o$.

As discussed earlier, the leeway between the transports of slick and clean surfaces increases with the film length, and the maximum leeway is produced by the film with its length approaching the wavelength. Consequently, when the ratio between the measured and the maximum leeways is plotted versus the ratio between the float and the wave lengths, the movements of floats over waves of not only various steepnesses but also various lengths can be incorporated with a nondimensional relation expressed as

$$(V_f-V_o)/(V_{max}-V_o)=1-(3/4)\ \log\ (\ell/\lambda) \quad \text{for } \ell/\lambda < 1$$
$$(V_f-V_o)/(V_{max}-V_o)=1 \quad \text{for } \ell/\lambda < 1 \qquad (4)$$

where V_f is the measured float velocity, and λ is the wavelength.

The floats of monolayers were used by Lange and Hühnerfuss (1978) in their experiments. The length of floats was longer than the length of waves tested (20 cm < λ < 70 cm). They found no streaming effects with the drift velocity of floats following very closely the Stokes surface transport.

3.2 Decrease of Wind-Induced Surface Currents

Effects of the monolayer upon the wind structure have been studied in the field by Barger et al. (1970). Vertical wind profiles were measured over clean and slick surfaces, and were verified to follow the logarithmic distribution,

$$U_z/u_* = (1/\kappa)\ \ell n\ (z/z_o) \qquad (5)$$

where κ is the Karman universal constant, and z is the roughness length. Values of z_o and u_* for both the clean and slick surfaces were obtained by Barger et al. The presence of monolayer causes damping of small waves; consequently, the roughness length was drastically reduced. The transition of the wind boundary layer, therefore, occurred at a higher wind velocity, approximately 6 m/s. Below this wind velocity, the roughness length of the slick surface is about the same as that of the clean surface. The similarity in roughness lengths for clean and slick surfaces at high wind velocities is believed to be due to disruption of the surface film by wind.

As expected, the variation of the wind-friction velocity has similar features; for the same wind velocity the friction velocity for the surface covered with monolayers is much greater than that for the surface without.

Before the disruption of the monolayer, the wind velocity for the surface covered with the monolayer is about twice that for the clean surface having the same friction velocity. Because the wind-induced drift current is proportional to the wind-induced surface drift current, the wind velocity for the slick surface is, therefore, about one-half that for the clean surface.

No similar study has been reported with wind blowing over water surface covered by oil slicks.

4 ACKNOWLEDGMENT

I am very grateful to the sponsorship of this work provided by the Mechanics Division, Office of Naval Research under Contract N00014-75-C-0285.

5 REFERENCES

Alofs, D. J. and R. L. Reisbig, 1972. J. Phys. Oceanogr., 2, 439-443.

Barger, W. R., W. D. Garrett, E. L. Mollo-Christensen, and K. W. Ruggles, 1970. J. Appl. Meteor., 9, 396-400.

Bye, J. A. T., 1967. J. Geophys. Res., 74, 1515-1536.

Hughes, P., 1956. Q. J. Roy. Met. Soc., 82, 494-502.

Kondo, J., 1976. J. Phys. Oceanogr., 6, 712-720.

Lange, P. and H. Hühnerfuss, 1978. J. Phys. Oceanogr., 8, 142-150.

Longuet-Higgins, M. S., 1969. Proc. Roy. Soc., A310, 151-159.

Phillips, O. M., 1977. The dynamics of the upper ocean. 2nd ed., Cambridge University Press, Cambridge.

Stokes, G. G., 1847. Cambridge Phil. Soc., 8, 441-445.

Wu, Jin, 1969. J. Geophys. Res., 74, 444-455.

Wu, Jin, 1975. J. Fluid Mech., 68, 49-70.

Wu, Jin, 1980. J. Phys. Oceanogr., 10, 727-740.

LOCAL WIND FORCING AND SMALL SCALE UPWELLING

Cairns A.R. BAIN*

ABSTRACT

This study characterizes some wind stress effects on a coastal site which is a focus of small scale upwelling having a scale of the order of 10 km. Two time scales are considered. Firstly the seasonal character of wind stress with the associated sea temperature fluctuations is described. Secondly individual wind events of a few days duration are characterized by extent and rate of upwelling and offshore displacement of the thermocline front. Data on the thermocline displacement is fitted to Csanady's model of coastal upwelling, which leads to the prediction of upwelling parameters for given wind events.

INTRODUCTION

The occurrence of coastal upwelling induced by favourable alongshore winds is well known off Oregon, Northwest Africa, Peru and in the Southern Benguela region, (Huyer 1974); (Barber 1977); (Walsh 1971); (Andrews 1980). These upwellings are on a scale of 100's km alongshore and several tens of kilometer offshore. Less well known are the small scale localized upwellings with a length scale of about 10 km. These small scale upwellings are the result of orographic effects and changes in coastline orientation. Such sites are often embedded in the large scale upwelling regions, and have also been studied in the Great Lakes, (Csanady 1980) and in Gulf of Lions (Mediterranean), (Millot 1979).

Airborne radiation thermometry (ART) surveys have revealed several such areas of intense upwelling along the Cape Peninsula and adjacent west coast of South Africa, (Andrews 1969); (Bain 1976). The study site is a strong focus of localized upwelling with a scale of the order of 10 km^2 just north of the Melkboschstrand headland some 30 km north of Cape Town. (Fig. 1) Eight km north of Melkbosch is the site of South Africas first nuclear power station. A considerable amount of oceanographic and meteorological data has therefore been collected for this site (Loewy 1976) over several years by the Electricity Supply Commision of South Africa (ESCOM). This data provided an essential backup to the work reported here, which forms part of a more comprehensive study of wind stress effects on oceanographic parameters at the site.

* Principal Scientist, Nuclear Oevelopment Corporation, S.U.N.I. FAURE 7131, South Africa.

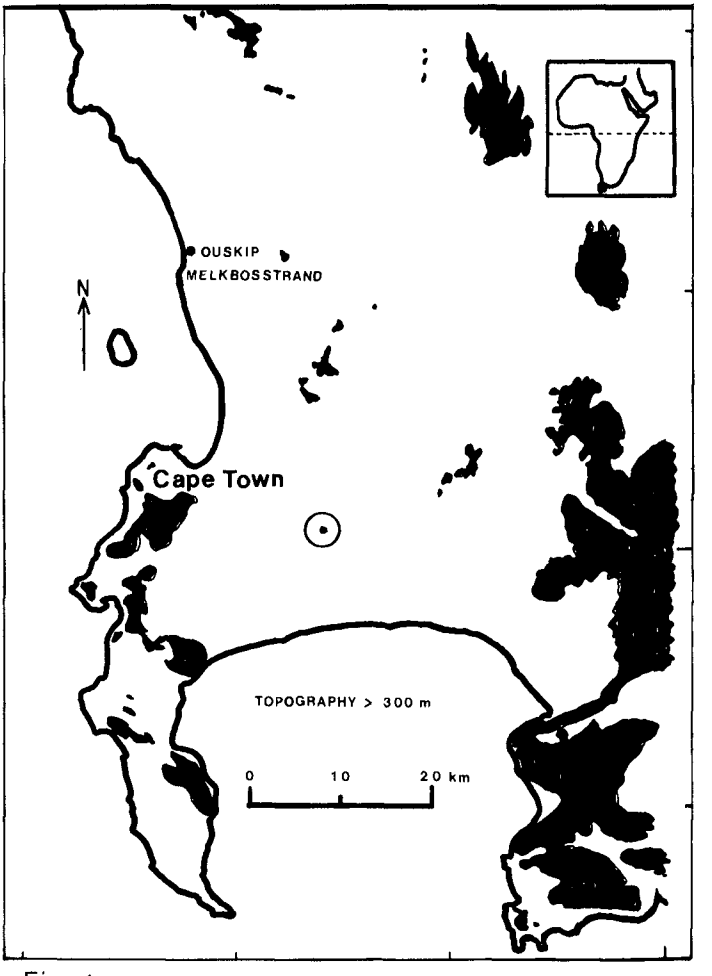

Fig. 1

In this report we discuss wind stress effects on two time scales. Firstly we characterize the seasonal wind pattern and the associated sea temperature fluctuations. Secondly we consider wind events of a few days duration, characterized by rate of upwelling and offshore displacement of the thermocline front. This displacement is compared with Csanady's model of coastal upwelling.

Factors about the site that are relevant to this report include: its position in the temperate zone which is subject to seasonal variations in the wind field as the semi-permanent south Atlantic anticyclone follows the solar incident. During summers, high pressure systems pass south of the country resulting in alongshore equatorward winds that are greatly influenced by the orography south and south east of the site. Strong thermal-diurnal mechanisms also feature at that time. In winter, low pressure systems skirt the southern corner of Africa and generate north-westerly onshore winds (Jury 1980). The temperature salinity properties of these coastal waters are such that temperature fluctuations are the main contributor to density changes and at a first approximation salinity changes can be ignored (Bang; 1973); (Gunn 1977). Temperature variations are therefore a good signature of upwelling processes in summer.

TECHNIQUES ANO OATA BASE USED

For the seasonal analysis use was made of ESCOM data. Their tabulations of hourly wind speed and direction at Ouskip (Lampbrecht anemometer situated on a tower ~ 20 m above sea level a few meters from the highwater mark) covering several years were coded for computer analysis. An ESCOM maintained sea tower one kilometer offshore in a depth of 11 meters was equipped with three temperature probes at 2 m, 5 m and 8,5 m depths. The temperature data was recorded continuously on a multipen chart recorder. A number of years of this raw chart data was digitized on an hourly basis and coded for computer analysis.

The event time scale study made use of the above data as well as bathythermograph temperature sections taken on a number of lines perpendicular to the coast and out to a distance of 6 to 10 km. The lines were run with a small ski boat with stations at 0,5 km intervals, on a number of consecutive days covering a wind event cycle.

There is a general lack of current data, particularly on a continuous time base. Lagrangian current trajectories and moored buoy current readings are available for the overall project but are not reported here.

ANALYSIS

The wind and temperature time series data were filtered with a twice applied 41 hour running mean filter (Chelton 1982) to suppress tidal and inertial oscillations and with a twice applied 23 day running mean filter (half power point of 50 days) to produce a very low passed time series. Simple statistical computations for standard deviations and

linear correlations between wind components and the different depth temperature records were computed for year long and seasonal sections of data.

The temperature section data was plotted and estimates made of the distance offshore that the thermocline intersected the surface to compare with (Csanadys 1977) model for full upwelling for a longshore wind impulse.

Assuming a two layer fluid with top layer having a thickness h_t and density ρ and the bottom layer having a thickness h_b and density ρ^1 the distance of the upwelled front from the coast is given by Csanady as:

$$Y_o = -R_i - \frac{I\, h_b}{f\, h_t\, (h_t + h_b)}$$

where $R_i = \frac{1}{f}\left(\frac{g\, \varepsilon\, h_t\, h_b}{h_t + h_b}\right)^{\frac{1}{2}}$, $\varepsilon = (\rho^1 - \rho)/\rho^1$

and I the wind impulse = $\int_o^{t_1} (\tau/\rho)dt$.

RESULTS

The study shows on a seasonal time scale that there are two major wind regimes. The southerly component dominates for on average about eight months over the spring/summer period, and the north component with a reduced amplitude dominates for about four months during winter. Fig. 2 for 1976 shows the main trends for very low passed filtered daily record but 1976 had a shorter than average winter regime and an anomously long duration northerly event at the end of November. Over a number of years the average duration of the transition between the summer and winter regime is only about 10 days; the winter to summer transition is longer about 30 days in duration.

The very low pass filtered temperature record shows a higher temperature during the winter months and generally lower temperature during the summer regime when active upwelling brings cold water to the surface. The 1976 data Fig. 3 shows this effect but also illustrates the marked rise in temperature during the anomolous onshore winds in November. In January 1976 the average monthly temperature was 10,7 ± 1,2 and 11,6 ± 1,3°C for the 8,5 m and 2 m depth probes respectively and in July 1976 the averages were 13,9 ± 0,9 and 14,1 ± 0,8°C for 8,5 and 2 m respectively. The mean annual temperatures for 1976 were 12,5 ± 2,0°C and 12,9 ± 1,9°C respectively.

The low pass filtered (41 hour running mean) time series for the wind data of 1976 Fig. 4 shows a good number of southerly wind events and only a few large northerly events. The associated temperature time series Fig. 5 shows a good correlation between temperature decreases during southerly (upwelling) events and increases during northerly or onshore winds. The temperature variability is most marked during the summer regime. A simple linear correlation between the N/S wind

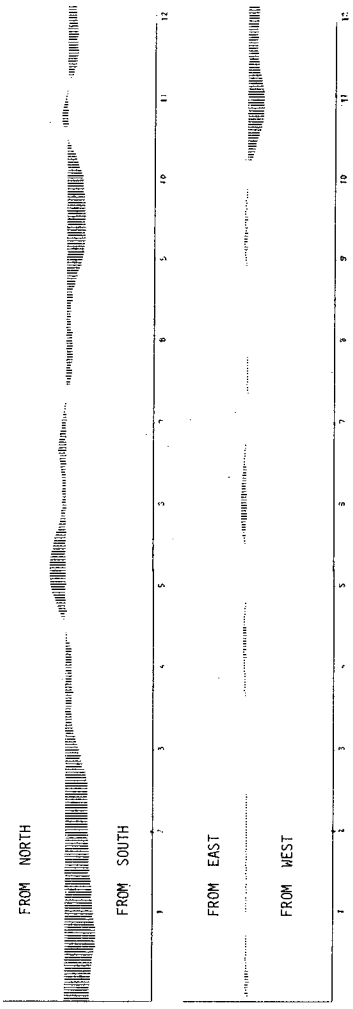

FIG 2 OUSKIP WINDS 1976 DAILY MEAN 2X23 DAY FILTER. TOP NORTH COMPONENT, BOTTOM EAST COMPONENT.

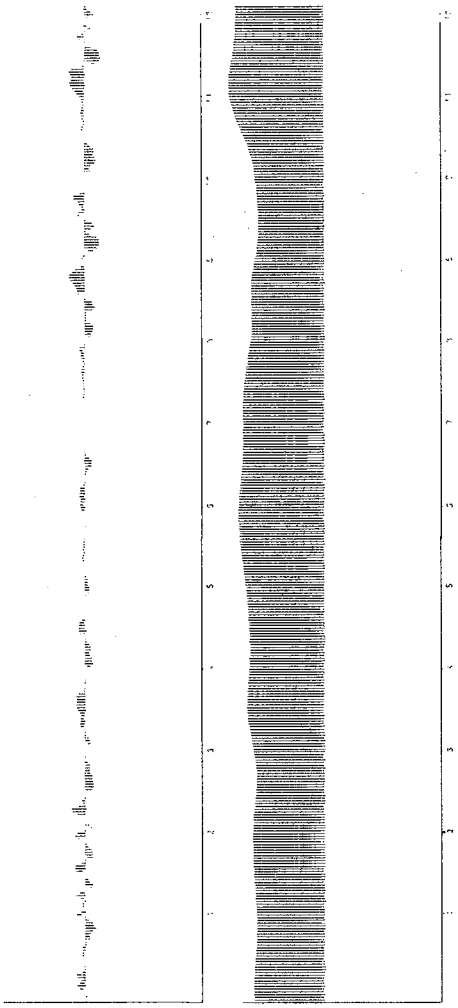

FIG 3 SEA TEMPERATURE 1976 2 METER DEPTH DAILY MEAN OF 2x23 DAY FILTER AND RESIDUALS

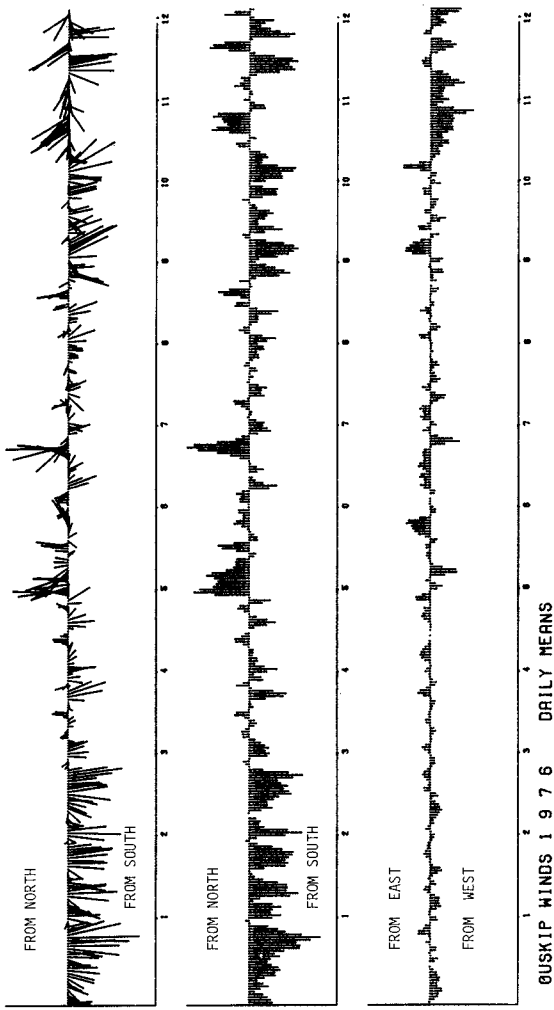
FROM NORTH
FROM SOUTH
FROM NORTH
FROM SOUTH
FROM EAST
FROM WEST
1
2
3
4
5
6
7
8
9
10
11
12
BUSKIP WINDS 1 9 7 6 DAILY MEANS
LLP 2X 41 HR FILTER. N COMPT, E COMPT, MEAN VECTOR

FIG 4

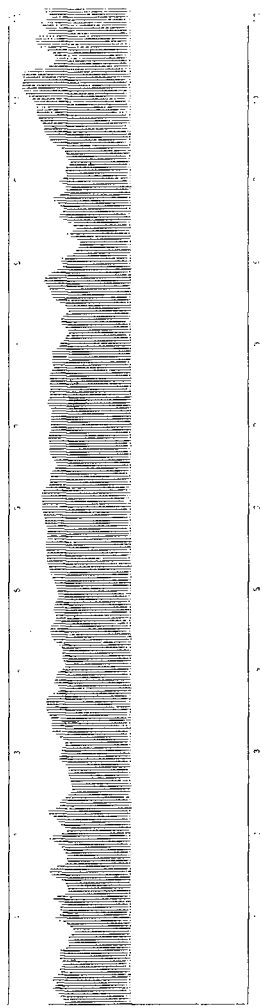

FIG 5 SEA TEMPERATURE 1976 2 METER DEPTH. DAILY MEAN 2X41 HOUR FILTER

component and the 2 m depth temperature low passed time series gave a correlation coefficient of 0,61 for January to April 1976 and of 0,11 for May and August. The significant correlation coefficient at the 95% confidence level is about 0,13. The explanation for the non significant correlation during winter is that the site, embedded in the larger scale Benguela upwelling region, has a more homogeneous water mass close inshore with the cold waters displaced offshore. In contrast during the summer regime, primed by the larger scale effects, stratified water comes close inshore and oscillates with the Ekman forcing of the wind event cycles.

The rapid responce of the thermocline to the onset of a wind event is shown in the bathythermograph temperature section data for 16 February 1978, Figs. 6 and 7. For the two days prior to these measurements the wind was light westerly veering to northerly causing the thermocline to be flattened. By the early hours of the 16th the wind had backed to strong SSE and veered to strong SSW at the time of the measurements. Within a few hours the 13°C isotherm is seen to be displaced a few kilometers offshore. In order to make comparisons with Csanadys model, events were chosen that had an initial sea condition approaching the ideal two layer system, followed by a wind impulse that lifted the thermocline. Table 1 shows reasonable agreement obtained between the theory and field observations.

TABLE 1

WIND EVENT	LAYER PROPERTIES				DISTANCE OF FRONT OFFSHORE			
					Predicted		Observed Y_o	
	h_t	h_b	T_t	T_b	Y_o	12^o	13^o	14^o
	m	m	C°	C°	km	km	km	km
12h00 77.01.26 till 10h00 77.01.27	15	25	16	12	0,94	1,2	1,8	-
till 10h00 77.01.28	15	25	16	12	1,98	~2	2,5	-
08h30 78.02.16 till 15h00 *	11	39	12,5	10,8	3,05	-	2,0	3.1
till 17h00 **	13	27	12,5	10,8	0,8	0,2	0,2	>5

* SECTION 2

** SECTION 1

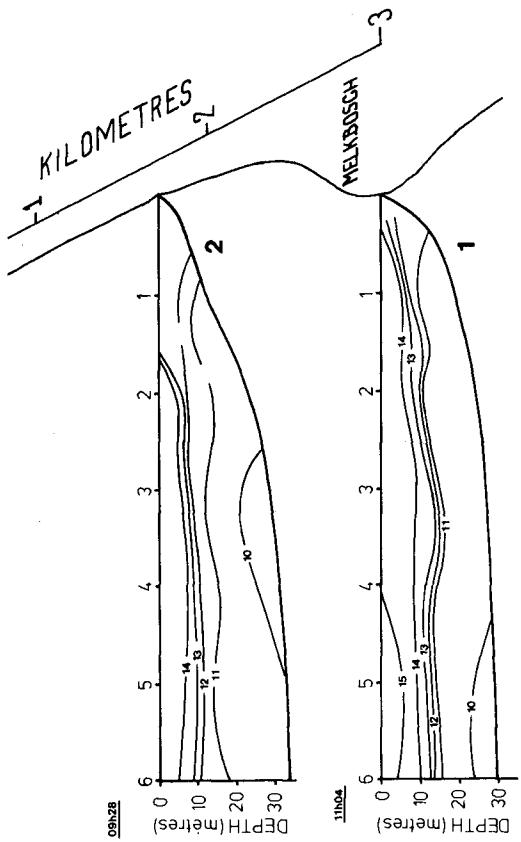

FIG 6 TEMPERATURE SECTIONS 78-02-16 AM

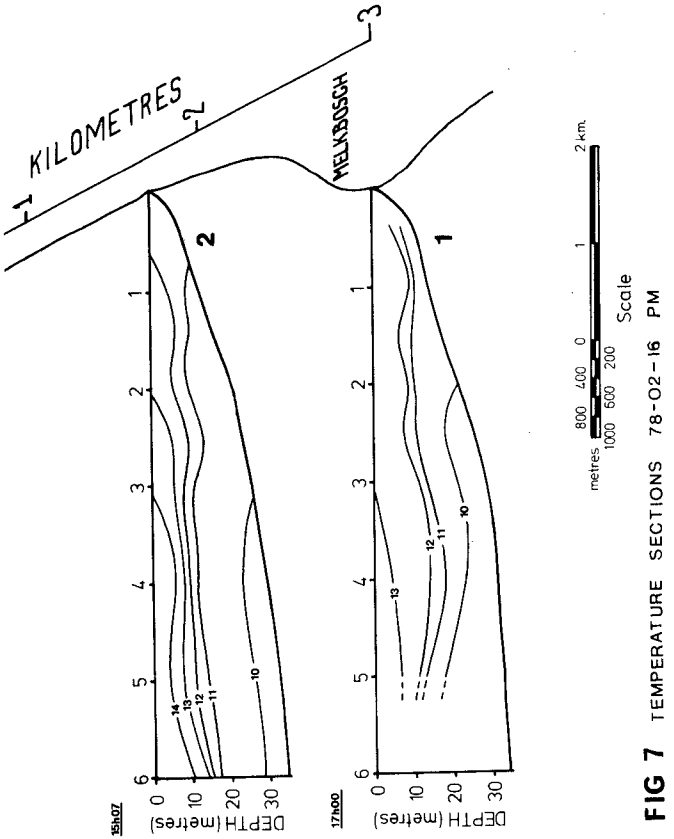

FIG 7 TEMPERATURE SECTIONS 78-02-16 PM

CONCLUSIONS

The study characterizes the wind stress and sea temperature response on a seasonal and event basis for a small scale coastal site. The displacement of the thermocline front from the coast is predicted for some wind conditions by the Csanady model. In the more comprehensive project of which this report forms part other aspects of Csanadys model including double wind impulses and current response are investigated. Initial rotary spectral analysis of the time series data indicate further potentially useful information for this small scale site. Useful 'edge effect' information for correlation with the much larger scale investigation of other workers of the Benguela upwelling program is obtained. Mans impact on the ocean occurs chiefly at the coast. The results of the complete study will provide needed background for both biological studies in the nearshore environment and dispersion studies of ocean outfalls and thermal water releases from power stations.

ACKNOWLEDGEMENTS

This project was funded by the Nuclear Development Corporation of S.A. (formerly Atomic Energy Board). We acknowledge with thanks; the use of the facilities of the Oceanography Department of the University of Cape Town and ESCOM for use of their field data.

REFERENCES

ANDREWS, W.R.H. and CRAM, D.L. (1969). Combined aerial and shipboard upwelling survey in the Benguela Current. Nature, Lond., Vol. 224 (5222), pp 902-904.

ANDREWS, W.R.H. and HUTCHINGS, L. (1980). Upwelling in the Southern Benguela current. Prog. in Oceanog., Vol. 9, pp 1-81.

BAIN, C.A.R. and HARRIS, T.F.W. (1976). Coastal water movement study report No. 2. University of Cape Town Oceanography Dept./Atomic Energy Board. Unpublished progress report.

BANG, N.D. (1973). Characteristics of an intense ocean frontal system in the upwell regime west of Cape Town. Tellus v 25 pp 256-265.

BARBER, R.T. (1977), The JOINT-I expedition of the Coastal Upwelling Analysis program. Deep-sea Research Vol 24, pp 1-6.

CHELTON, O.B. and DAVIS, R.E. 1982. Monthly mean Sea-level variability along West Coast of North America. Journ. of Physical Oceanog. v12 p 757-784.

CSANADY, G.T. (1977). Intermittent "Full" Upwelling in Lake Ontario. Jour. of Geophys. Res., Vol B2, pp 397-419.

CSANADY, G.T. and SCOTT, J.T. (1980). Mean Summer Circulation in Lake Ontario with the coastal zone. Jour. of Geophys. Res., Vol. B5 (C5), pp 2797-2818.

GUNN, B.W. (1977). The Nearshore Dynamics of Matroos Bay - Field and Theoretical Investigations. M.Sc. Thesis, University of Cape Town, S.A.

HUYER, A., SMITH, R.L. and PILLSBURY, R.D. (1974). Observations in a coastal upwelling region during a period of variable winds. Tethys, Vol. 6 pp 391-404.

JURY, M.R. (1980). Characteristics of Summer wind fields and air sea interactions over the Cape Peninsula.

MILLOT, C. (1979). Wind induced upwelling in the Gulf of Lions. Oceanol Acta., Vol. 2, pp 261-274.

WALSH, J.J. and DUGDALE, R.C. (1971). A simulation model of the Peruvian upwelling system. Investigation Pesquera, Vol. 35, pp 309-330.

MARINE PIPELINE PROTECTION WITH FLEXIBLE MATTRESS

Alan D. Crowhurst

Maccaferri Gabions, Inc.

Williamsport, Md. USA

Abstract

Development of oil and gas fields offshore presents new problems in the design of the civil engineering works since in many cases little is known about prevailing conditions on the bed of the sea over the considerable lengths involved. Movement of pipelines after construction, is, therefore, not uncommon and may result in the failure of the line. Consequent losses can be considerable.

Pipelines are also vulnerable to mechanical damage by anchors and by fishing activities, the latter giving rise to political problems where the pipelines are laid across existing fishing grounds. To give protection to oil and gas pipelines as well as to marine outfalls and cables a method of protection has been developed using the well known concept of rock filled wire mesh or gabions.

To adapt this method to use in underwater works another well proven material, sand mastic asphalt, has been combined with the gabion mattresses to give the required qualities of strength, durability, flexibility together with sufficient weight to restrain movement in the pipeline.

INTRODUCTION

Although pipelines have been built in the tidal zone and for short distances offshore for many years, earlier work has been largely in the sewage disposal and cooling water outfall sectors. In works of these types failures, although serious, are generally capable of repair by conventional means.

Offshore pipelines for oil and gas transmission have now been laid in much deeper water and for many miles at considerable depths. In addition, in areas such as the North Sea, work can only be carried out for a few months per year and failures therefore become extremely serious even before production losses are calculated.

Sea bed conditions over the lengths of these new pipelines are by no means uniform or consistent, nor is survey information as complete as the designers would like. Over undulating terrain pipelines laid on the surface may well bridge across many of the valleys.

Strong currents can lead to major movements of pipelines while in service, unless suitably anchored, and can also give rise to vibrations which may shorten the life of the pipes. Similar protection methods used to anchor pipelines may also be employed to protect against mechanical damage by trawls or by dragging anchors. Since pipelines may cross valuable fishing grounds it is necessary to ensure that these protective measures do not cause additional damage to the trawls and nets.

Although more familiar as a river defense system the use of wire-enclosed riprap, gabions, has been adapted to marine structures of many types. The main change is the addition of a PVC sleeve to the galvanized wire mesh to give resistance to corrosion in salt water. Gabions have been pre-filled and used for outfall protection, jetties in inshore waters and various coastal defense projects worldwide.

A method of protection and anchorage has been developed known as the Sarmac mattress which combines this ancient and well proven gabion method of construction with sand mastic asphalt grout to give a dense yet flexible mattress capable of being placed over a relatively small diameter pipe without failure. The units can be made with sufficient length on either side of the pipeline so as to give considerable protection against scour since they fold down to accommodate changes in bed levels over the service life of the pipeline.

Considerable care has to be taken in the design of the sand mastic asphalt mix since the required flexibility may have to be maintained over a large temperature range between that at the assembly yard and that at laying depth.

Methods of placing are also critical in view of the high cost of employing divers. For a recent project in the Mediterranean special lifting frames were developed by the subcontractor, Ing. Sarti Giuseppe S p A of Ravenna. This enabled placing to be carried out in deep water by remote control methods using a remote control vessel guided by television cameras. To date Sarmac mattresses have been placed satisfactorily at depths of up to 600 metres.

MATERIALS & METHODS

With the introduction of the Sarmac mattress into the offshore pipeline protection inventory there has been an interesting combination of ancient and very modern methods of construction.

Gabions are of considerable antiquity having origins in military uses several centuries ago and, it is thought, in hydraulic works in China, much, much earlier. Of course these early gabions were not made with metal but used wicker work filled with stones, soil and turf. From these origins gabions were developed using steel wire in the form of cylinders of mesh, filled with rock, used for emergency river protection. Later it was realized that it would be possible to manufacture the gabions in rectangular form thus enabling much larger and more uniform structures to be built.

A further development came in the use of woven mesh with a double twist for added security. From these rectangular forms were developed mattresses which were simply gabions with thicknesses relatively small compared with their length and width. Galvanized wire may have a limited life expectancy in highly corrosive conditions and the addition of a PVC sleeve extruded onto galvanized wire enable the mesh to be used in coastal and offshore locations.

For use in the tidal zone investigations have been carried out on the use of PVC coated woven wire mesh mattresses used as continuous revetments by a number of researchers in Canada, Australia and elsewhere, (2), with generally favorable results. In one case design rules have been formulated giving equations for eventual failure by downslope sliding, buckling and uplift (3).

For sloping revetments wire enclosed riprap or mattresses are not normally laid at inclinations greater than IV to 2H or 26° where downrush waves limit the stone size. This has been described by Stephenson who has listed comparisons with rounded rock, angular rock and also concrete units (4).

Proprietary concrete block systems have been tested in the wave zone along with other "low-cost" systems including gabions and mattresses in a comprehensive study by the U.S. Army Corps of Engineers (5).

FIGURE 1

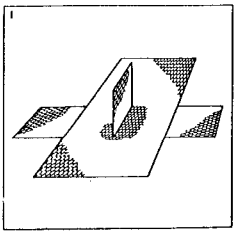

GABION BEFORE ASSEMBLY

FIGURE 2

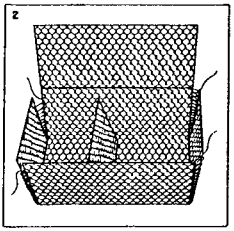

ASSEMBLY OF GABION

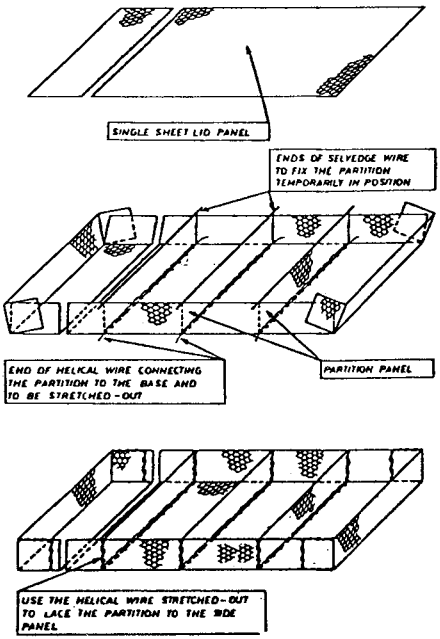

FIGURE 3 MATTRESS TYPE GABIONS

At one location, Ninilchik, in Alaska the gabions were filled by means of filter cloth bags which were themselves filled with a combination of beach gravel, cobbles and concrete rubble. However both this structure and a second at Kotzebue also in Alaska had a rock riprap toe protection which was displaced during the test period. In general this is not a good practice since the riprap can be thrown against the mesh causing damage. However the report on these trials and a third at Oak Harbor, Washington was very favorable.

Gabions and mattresses have also been used for many years to form groynes as a method of countering beach erosion in the United Kingdom, Italy and elsewhere (3). Sand mastic asphalt grouted riprap groynes have also been used with limited success in some locations but giving rise to problems when extended beyond the low water mark (6)(7).

These materials have been combined in revetments and groynes for coastal defenses and have been suggested for a number of related uses such as offshore breakwaters or headlands.

The use of pre-filled gabions for underwater structures had been developed over many years from the original use of cylindrical gabions to fill breaches in river defenses and scour holes around bridge piers and in similar emergency situations.

It was soon realized that modern rectangular gabions could be used in a similar fashion and gabions have subsequently been used pre-filled to form many types of structures (Fig.4). Examples included a large landing stage or jetty at Pula Langkawi in Malaysia, sea walls in Helsingfors Harbor, in Finland (Fig.5). A structure was built some five or six metres high to provide a quay for dhows at Ruweis in Qatar, the gabions having been pre-filled out in the desert and trucked to the site.

These structures employed cranes to place the units either from dry land or pontoons or barges but in recent years placing has even been carried out using helicopters.

However for offshore structures of some size other methods were adopted with gabions wired together into the form of a raft constructed above low water mark and subsequently floated into position using buoyancy supports of several types. Several outfall structures handling cooling water from nuclear power stations were so protected.

While methods of placement for standard gabions were being developed similar attention was being paid to enable Reno or Revet Mattresses to be pre-filled for placing underwater in river and canal projects. Although lifting frames similar to those used for placing filled gabions were employed, other methods were also initiated. These included launching from pontoons which at first were simple fixed decks (Fig. 6).

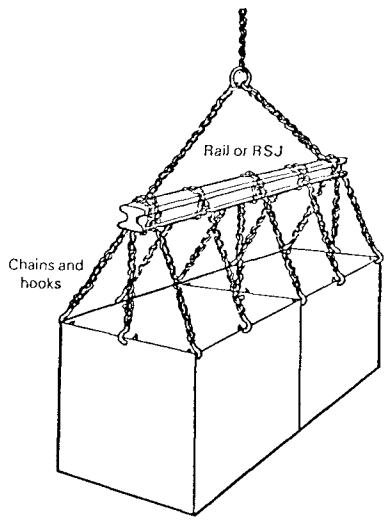

FIGURE 4
SIMPLE LIFTING METHOD

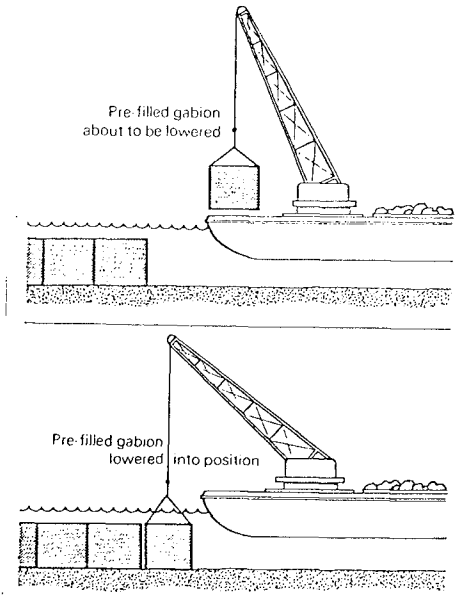

FIGURE 5
PLACING GABIONS BY CRANE

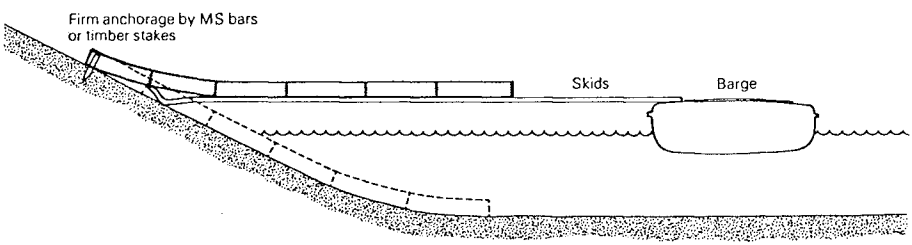

FIGURE 6

PLACING PREFILLED MATTRESSES FROM A SIMPLE PONTOON

Pontoons were then developed with tilting decks upon which mattresses could be built and then launched, the inshore ends being securely anchored to the bank.

This form of bank protection was also used in areas where impermeability was necessary. For this purpose, of course, gabion mattresses were unsuitable if used alone.

The addition of a sand mastic asphalt grout provided the necessary impermeability whilst retaining the essential flexibility of the revetments.

The use of pre-filled and grouted mattresses for underwater applications where construction in the dry was not feasible employed pontoons as developed for regular mattresses with the grouting operation actually carried out with the mattresses already in position on deck. When used with a grout the thickness employed could be reduced for some structures.

Pre-filled mattresses could also be placed by crane when grouted with sand mastic asphalt since the stone fill was held in place by the grout and not permitted to fall to the bottom of each cell as would happen if an ordinary mattress was so lifted (8)(9)(10). For offshore works gabion and Reno Mattresses had been used frequently since methods of placing were relatively expensive requiring the use of divers in many cases.

However protection was given to the cooling water outfall at a nuclear power station on the southern coast of England using a raft of Maccaferri Gabions floated into position and then lowered around the mouth of the outfall which was built in tunnel out from the power station, but this method was not applicable to most types of undwater structure.

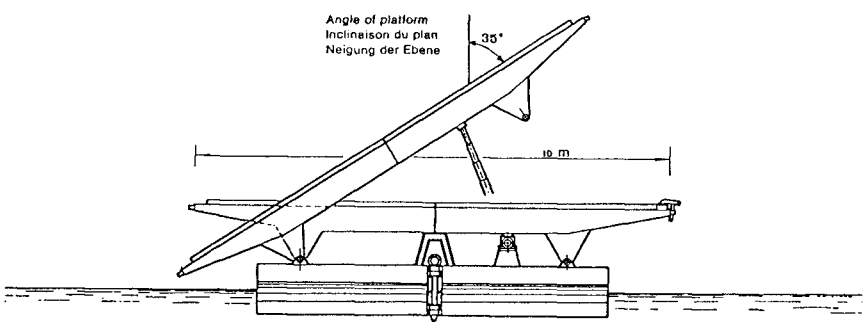

FIGURE 6

SAND MASTIC ASPHALT

Sand mastic asphalt has been used increasingly in gabion and mattress structures of various types ranging from canal linings, power station outfalls, protection of the upstream face of earth dams and for spillways. When used for canal linings the combination of the two products, gabion and sand mastic asphalt, enabled considerable reductions in thickness to be made in some cases. The design of the sand mastic asphalt mix varies according to the required design characteristics. Information on such applications is well documented (11).

TYPE	THICKNESS INCH	WEIGHT OF BITUMINOUS MASTIC: SURFACE GROUTING LBS/SQ. FT.	WEIGHT OF BITUMINOUS MASTIC: COMPLETE PENETRATION LBS./SQ.FT.
Revet Mattress	0' - 4"	14 - 15	22 - 26
	0' - 6"	16 - 18	26 - 28
	0' - 9"	20 - 25	28 - 30
Gabions	1' - 0"	27 - 30	37 - 40
	1' - 6"	30 - 40	50 - 60
	3' - 0"	50 - 70	80 - 120

TABLE 1 WEIGHTS OF GROUT

SARMAC MATTRESSES

From these origins was developed the Sarmac mattress which combined the strength and flexibility of the Reno or Revet Mattress form of construction with the addition of the weight and impermeability given by the addition of the sand mastic asphalt grout and while retaining the necessary flexibility of the mattress concept.

When used for hydraulic structures such as river and coastal defenses, dams and canals the design of the mastic asphalt mix was subject to rather less vigorous constraints than when applied to the Sarmac technique. It is only necessary that the asphalt can penetrate and flow through the gabions or riprap to the design depth and remain in place without further movement should ambient temperatures increase from those experienced during the construction period. The range of temperature during which such grouting takes place and to which the completed works are exposed is usually well documented and the range not too great to make additives necessary. When mastic grouted mattresses are placed from pontoons or by crane their thicknesses are relatively small and flexibility remains good.

With the new possibilities presented by the construction of offshore pipelines of considerable length and size, the techniques described in the preceding paragraphs were combined to give a material with the require characteristics and, as important, the ability to be placed economically at considerable depths.

At the design stage of such pipelines it has often been necessary to place reliance on climatic data and tidal information from available sources which was not always comprehensive enough for the purpose. In particular, although information might well be applicable for surface conditions, this did not apply to those existing on the sea bed where strong currents could be met. These could result in scouring around and under pipelines laid on the surface.

As a result of such scouring action pipelines may well become entirely unsupported and this can even occur where initial construction was as buried pipelines. The resulting effects arising from unsupported lengths on fatigue life have been assessed in a number of studies(1).

Experience gained in the design and construction of pipelines has resulted in the development of a method of both anchoring and protecting such pipelines. The method was also capable of use in the construction of supports under the pipes which could thus reduce the length of unsupported spans and could reduce vibratory effects.

Since the sea bed in the vicinity of the pipelines could vary considerably it was advantageous to develop the mattress used for its protection with capability to fold in service to adjust to the changing levels. Flexibility was also necessary to take up the curve of the pipe which could be as small as 500mm diameter.

Considerable weight was also called for in order to function as anchors and therefore the combination of sand mastic asphalt and gabions or mattresses already frequently used in combination in hydraulic structures of several types, was a logical development.

The Sarmac mattress was developed to address several of the problems experienced in the rapid construction of the massive net of oil and gas pipelines that now cross vast expanses of seas and oceans.

Reno or Revet Mattresses are used as the basis of a dense, flexible unit, using stone fill in the usual way but with stone size selected to permit the most suitable penetration by the sand mastic asphalt and to give the required finished weight. Choice of single or double thicknesses is made according to site conditions.

The sand asphalt mix is designed to give the required flexibility at the ambient temperatures in which it is to be placed, but at the same time must not be so soft as to deform or even flow during manufacture or transport to site. It is equally important that it should not become too hard thus losing flexibility in service and risking failure by brittleness. Since pipelines are currently being placed in conditions as diverse as the North Sea and the Indian Ocean, mix designs must be selected with care for each application.

	PENETRATION	R.& B. SOFTENINC POINT	DUCTILITY	VOLATILITY AFTER 5 HOURS AT 322° F
80/100 Pen	.314-.344	125 - 140°F	39,37 inch	0.5%
60/70	.234-.275	115 - 129°F	"	0.2%
40/50 Pen	.157-.196	124 - 136°F	"	0.2%

TABLE 2 BITUMEN SPECIFICATIONS

Having selected the correct mix design and thickness, overall dimensions are designed to suit the conditions of use, i.e. for mattresses used as protection against scour, as anchors where the pipeline is liable to move laterally, as deadweights to constrain the pipeline where it is not laid continuously on the ocean bed and as protection against mechanical damage.

For placing underwater in depths of up to 600 metres or more the use of divers to locate and place the Sarmac units may be impracticable or very expensive and methods have been developed by which the units can be located in position and released by remote control vessels whilst being monitored on close circuit television.

For such underwater structures temperature ranges are often even more restricted. Placing generally takes place during the warmer months although work was recently carried out on a project in Cumbria in North West England during a very cold period from November'81 to January '82 when the temperatures rarely rose above °Selsius and much of the grouting was carried out at much lower temperatures. This required that the temperature at the mixer was at or very near the maximum for the material in order that reasonable flows could be obtained in the very cold mattresses.

Earlier work had in fact been carried out by the French in Antartica many years ago and those experiences have been documented (12).

However initial studies were incorporated in projects sited in less intemperate areas and for the first full scale application this type of construction was used at points along the gas pipeline being built from Algeria to Italy which has 170 kilometres of its total length of 2500 kilometres on the bed of the Mediterranean. This project, which was initially proposed in 1971, was authorized in 1977 following negotiations between the Algerian authority SONATRACH and the Italian ENI company. Design work was carried out with the cooperation of both companies.

Across the Sicily Canal underwater construction was carried out by a consortium of Italian and Algerian companies under the title TMPC. However technical direction was the responsibility of SNAMPROGETTI. The depths at which pipes were laid in this sector exceeded 500 metres and the pipeline was divided into three separate lines for safety reasons.

The Sarmac units designed for this part of the project had overall dimensions of 4 metres by 3 metres. Each unit comprised two separate thicknesses of 200mm each giving an overall thickness of 400mm joined together with steel cables. Double twist mesh mattresses were used to give flexibility reinforced with steel wire ropes for lifting purposes. The units were wrapped in a non woven polyester filter cloth of weight 0.55 kilogrammes per square metre. Polyester was required as other fabrics are unable to withstand the temperatures at which the sand mastic asphalt is placed.

The total weight of the units was 12,000 kgs. or 1,000 kgs. per square metre and the specific gravity 2500 kgs. per cubic metre.

Manufacture took place at the SNAMPROGETTI yard in Trapani, Italy by the contractor, Ing. Sarti Guiseppe & Co. and then transported the short distance to the docks. Placing was made from the ship, Saipem Ragno 2, for most of the work.

The application for which the Sarmac units were required in this project was that of anchoring the pipes, by virtue of their weight, to the sea bed across areas where the bed was irregular.

A later use of Sarmac mattresses of similar size and construction but with overall thicknesses of 500mm is by Saipem in a British petroleum field in the North Sea. In this case the application is to protect one pipeline where it is crossed by new work and the total weight per unit and, of course, the specific gravity has been designed to be somewhat lower.

When the requirement is for thicker mattresses of the types used for Sarmac units, typically 40 or 50 cms thick, the composition of the mastic mix is much more difficult to design since the completed mattress must have excellent flexibility if it is to flex around small diameter pipes in deep water.

In addition the units may be manufactured in an area of fairly high ambient temperatures for placing in cold deep seas. If the required flexibility is not maintained, the unit could become brittle and not take up the required curvature in service.

To establish design criteria early experimental work was carried out in the United Kingdom by River and Sea Gabions, Ltd. but at an early stage the work was taken over by Officine Maccaferri S p A in Italy where there had been extensive work with sand mastic asphalt for a wide variety of hydraulic works.

This work proceeded jointly with Ing. Sarti Guiseppe with considerable assistance from Dr. V. Castagnetti of Industria Italiana Petroli of Genova. Much of this work was carried out simultaneously with the development of systems for use in the widening of the Suez Canal (13) (14)(15).

The experimental work not only concentrated on the design of the mix to achieve flexibility but also on completed thicknesses, density and application rates which were themselves variations on those already calculated and used in hydraulic works, see Table 1.

The Sarmac mattress concept also necessitated the development of methods to simplify lifting from the point of manufacture and transportation inland and by sea to the jobsite.

These were, of course, relatively minor problems since there was already a fund of knowledge based on previous uses of pre-filled and grouted mattresses and gabions. However placing underwater had previously involved the use of divers which was not impracticable when only a few units were to be placed in shallow seas.

For gas and oil pipelines the depths at which protection was to be carried out were such that effective diving time per shift would be very limited and costs accordingly very high. It was therefore necessary to develop underwater placing methods using remote control techniques and a lifting frame was devised which could be operated from a remote control vessel.

This has worked satisfactorily and has permitted relatively fast placing times although, unfortunately, detailed data remains confidential to the companies concerned.

A simplification of the construction technique, omitting both the filter cloth envelope and the lifting cables built into the body of the Sarmac units, has been employed for small scale pipeline protection in estuarial areas in the North Adriatic. These units, resembling the standard wire enclosed riprap mattresses used for river defenses, were grouted with a mix also being used to grout a riprap revetment several years old situated a few miles from the mixing plant. Since the application was close to normal water level, the range of temperatures under which the grouted mattresses were to be employed was very limited and the mix design was therefore not formulated specifically for that project.

It should be noted that few filter fabrics are suitable for use as envelopes for grouted mattresses since the melting point of most membranes is at or below the temperature at which the sand mastic is normally poured.

The final product, as used in offshore pipeline work, is very different to early underwater gabion structures such as that for a

nuclear power station in the United Kingdom where the gabions were assembled as a raft within Folkestone Harbor at a location between high and low water marks. The raft, supported by steel drums and fastened together by steel rails, was floated into position and sunk on top of the outfall position.

This type of simple construction has therefore evolved into a degree of sophistication not foreseen at that time but still offers a considerable scope for further development particularly in inshore areas and in the immediate vicinity of platforms where complex pipe layouts are to be found.

CONCLUSIONS

Use of these methods of construction to protect parts of the gas pipeline from Algeria to Italy and also a small application in the Magnus Project in the North Sea have shown the effectiveness of this method of construction. The experience gained in earlier underwater gabion work and in the design of sand mastic asphalt for hydraulic works has enabled challenges posed by the new applications to be met thus marrying old and very new techniques in the manufacture and use of the Sarmac Mattress.

ACKNOWLEDGEMENT

The author would like to express appreciation for assistance received over many years from Dr. Ing. R. Agostini, Officine Maccaferri S.p.A Bologna.

and

T A G Bristow, C. Eng. of River & Sea Gabions, (London) Ltd.

REFERENCES

(1) Tsahalis, D.T. and Jones, W.T. OTG Paper $4231 14th Annual O T G, Houston, Texas, May 1982

Bruschie, R.M. Gonter A., Matteelli R., & Mazzoli A., O T G Paper #4235 14th Annual O T G Houston, Texas, May 1982

(2) Kanphuis, W.J. Performance of light coastal structures under normal and high water conditions - Ganadian Journal of Givil Engineering, Vol. 2, No. 4, 1973

(3) Brown, C.T. Gabion Report or some factors affecting the use of Maccaferri Gabions and Reno Mattresses for Coastal Revetments Report No. 156, University of New South Wales, Water Research Laboratory, October, 1979.

(4) Stephenson, D. Rockfill in Hydraulic Engineering Elsevier Scientific Publishing Gompany, Amsterdam, 1979.

(5) Moffat & Nichol, Engineers. Low-Cost Shore Protection - Final Report on the Shoreline Erosion Gontrol Demonstration Program (Section 54) Office of the Ghief of Engineers, Washington, D.C. 20314, USA August 1981.

(6) Shore Protection Manual, U.S. Army Goastal Research Genter, Kingman Building, Fort Belvoir, Virginia, USA, 1973.

(7) Asphalt in Hydraulics, MS-12 The Asphalt Institute College Park, Maryland, USA November, 1976

(8) Officine Maccaferri S.p.A Notes on Mastic Grouted Gabions and Reno Mattress, Bologna, 1975

(9) Impiego dei Gabbioni e dei Materassi Reno bitumati nelle opere idrauliche - Note techniche, Shell Itaniani S.p.A, Genoa 21 February, 1982.

(10) Sand Mastic Grouted Gabions for Goast and River Bank Protection, Shell International Petroleum Co., Ltd. London, 1964

(11) Asphalt Institute 1976. Asphalt in Hydraulics Manual No 12 (MS-12) 68 pps.

(12) Lelu V., Bitumen in the Antartic. "Travaux", Issue #383, Paris, January 1967 and Shell Bitumen Review #24, Shell International, London

(13) Agostini, R., and Castagnetta V., "Nuovo tipo di Rivostimento Protettivo Flessibile Delle Sponde del Canale di Suez realizzato con i Mattrassi Reno" Bitumati. Bulletino d'informazione tecnoca No 280. I.I.P Genoa, Italy 1980.

(14) Sarti, G, "I Materassi Bituminos" II Franto, November 1975 Pava, Italy.

(15) Agostini R. & Della Luna G. New Methods of Countering Erosion generated by vessels in canals in Italy and other countries. 18 pps. Proceedings, XXVth International Navigation Congress P.I.A.N.C. Edinburgh, 1981.

SAN FRANCISCO'S SOUTHWEST OCEAN OUTFALL

by Y. Eisenberg[1], M.ASCE

and D. D. Treadwell[2], M.ASCE

ABSTRACT

The Southwest Ocean Outfall, with an overall length of 23,400 feet and a capacity of 450 million gallons per day, will be a major element of the Clean Water Program of the City and County of San Francisco, California, U.S.A. Offshore, the Outfall will cross one of the world's major active fault zones, the San Andreas.

Outfall construction started in 1981 and is scheduled to be completed by early 1985. The shoreward 3,000 feet is being built from a pile-supported trestle; offshore, the Outfall conduit sections will be placed using a barge designed and built specifically for the project. Oceanographic, coastal, geotechnical, and seismic conditions pertinent to design are presented along with discussions of specific Outfall design and construction features.

INTRODUCTION

The Southwest Ocean Outfall is part of an improved system of collection, transportation, treatment, and disposal of sanitary and storm wastewater flows for the City and County of San Francisco. After passing through a system of transport lines, treatment plants, and tunnels, these flows will reach the Outfall, where they will be dispersed at a diffuser section located in the Pacific Ocean approximately four miles southwest of Lake Merced (Figure 1). About 8,700 feet offshore, the Outfall will cross the San Andreas fault zone, one of the world's major active faults.

---

[1]Parsons Brinckerhoff, San Francisco, California.

[2]Woodward-Clyde Consultants, San Francisco, California.

The Outfall will be a single conduit composed of reinforced concrete pipe sections with an inside diameter of 12 feet extending about 23,000 feet offshore. The water depth at the Outfall terminus is about 80 feet. Throughout its length, the Outfall will be embedded in a trench excavated as much as 25 feet below the sea-floor. The design gravity flow rate of the Outfall system is 450 million gallons per day (about 700 cubic feet per second).

Starting in 1977, the project design team conducted various data acquisition and analysis programs (Belvedere et al, 1978; Treadwell et al, 1978; Murphy et al, 1979; Treadwell et al, 1980; Gilbert et al, 1981). The results of these studies were utilized in the planning, preliminary design, and final design efforts completed in late 1980.

The purpose of this paper is to describe the geotechnical, oceanic, coastal, and seismic conditions and their impact on the unique design features of this project. The first 18 months of Outfall construction are also described.

GEOTECHNICAL CONDITIONS

Prior to the studies and data acquisition programs associated with the Outfall project, very little information existed concerning geotechnical conditions offshore San Francisco. The offshore geotechnical investigations performed for the project included:

- surf zone borings using a truck-mounted rotary drill rig on a self-propelled shallow-water work platform

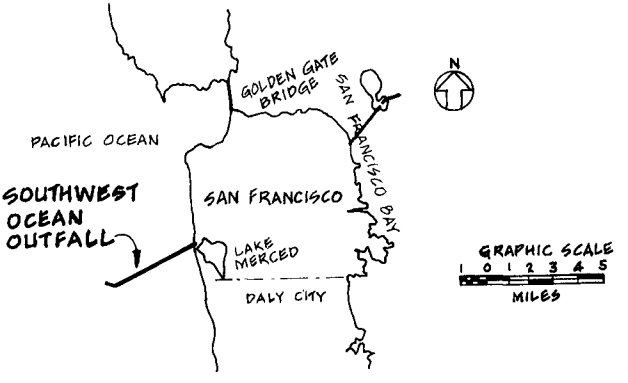

Figure 1 OUTFALL VICINITY MAP

- offshore borings, vibratory corings, and cone penetrometer tests using a specially-equipped and modified drillship
- marine geophysical surveys using an ocean survey vessel equipped with precision electronic navigation and fathometer systems as well as specialized seismic reflection, sonar, and magnetometer systems
- test pit construction and monitoring using a derrick barge clamshell dredge and an ocean survey vessel

Offshore Soil Conditions

The offshore soils along the Outfall alignment are primarily dense to very dense fine sands. Within the surf zone, extending to about 4,500 feet offshore, the seafloor generally consists of a loosely consolidated layer of sand 2 to 8 feet thick, underlain by hard clayey silts and silty clays. These cohesive soils are underlain by dense to very dense sands with occasional lenses of fine gravel.

A thin veneer of loose surface sands was encountered along the entire alignment. This layer is typically 2 to 4 feet thick, but in localized areas is as much as 6 to 8 feet thick. Beneath the surface layer, the sands increase in density with depth, from medium dense to very dense.

From about 11,000 feet offshore and westward, the surface sands are underlain by medium stiff to stiff, moderately overconsolidated silty clays which grade to clayey and sandy silts at greater depths. The top of the clays appears to vary from 15 to 35 feet below the seafloor, based on the borings and geophysical data. The relatively level surface of these cohesive soils apparently represents an ancient shoreline.

Offshore Faults

Offshore fault zones located in the project vicinity are the San Andreas, Pilarcitos, and Seal Cove (Figure 2). The latter were found to be westward of the Outfall, thus efforts were focused on defining the width and orientation of the San Andreas fault zone at the Outfall alignment.

Between the surf zone and the San Andreas fault zone is a series of tightly-folded, thinly-bedded sediments. These sediments may be correlative with similar outcrops seen on the shore. The limbs of the folds dip approximately 10 to 20 degrees; the fold axes plunge to the northwest, and the width of the geological structures decreases toward the fault.

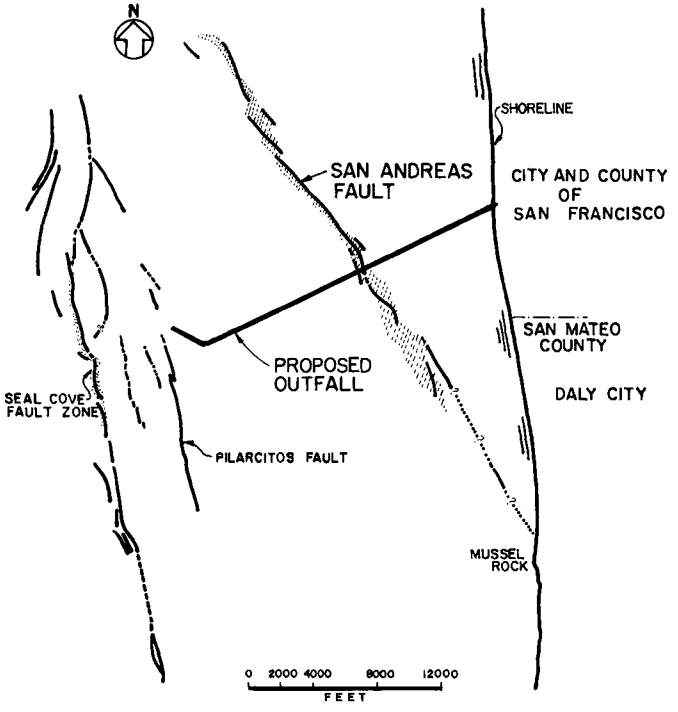

Figure 2 OFFSHORE FAULTS IN PROJECT AREA

In the vicinity of the Outfall alignment, the trace of the San Andreas fault is represented on the geophysical records by a blurred zone which does not show internal structure across the zone. This zone marks a transition between tightly-folded sediments to the east and relatively horizontally-bedded sediments to the west.

Along the Outfall centerline, the San Andreas fault zone was determined to be approximately 400 feet wide. The strike of the fault zone is approximately N39°W, which is 12 degrees west of perpendicular to the Outfall alignment.

OCEANOGRAPHIC CONDITIONS

A major factor in the design of the Outfall was the development of an understanding of the oceanographic conditions (e.g., wind, wave, current, tide, and water quality) likely to be encountered in the Gulf of the Farallones. These data were acquired and criteria developed through a variety of offshore sampling and analysis programs and reviews and evaluations of wave and storm records.

Monitoring Programs

A 13-month physical oceanographic monitoring program was conducted in 1977-78. Endeco current meters were installed and retrieved on a monthly basis from four fixed locations and two roving locations within the survey area (velocity and direction data were internally recorded every half hour by the meters). Density profiles and water quality samples were also taken on a monthly basis. In-situ measurements were taken of temperature and conductivity using an Inter-Ocean Model 513 CTD at selected depths and locations. The results of the measurements were converted to sigma-t (density) values.

Water quality samples were taken at selected locations and depths in the offshore project area. The water quality parameters analyzed were temperature, dissolved oxygen, conductivity pH, total coliforms, fecal coliforms, total suspended solids, settleable solids, turbidity, ammonia, nitrate, total phosphorous, chlorophyll, phaeophyton, and sulfide. The density profiling and water quality sampling programs were performed in cooperation with CH2M-Hill, Inc., the sanitary and hydraulic subconsultant to the design team.

On a less frequent basis, surface drifter and drogue studies were also performed. Surface drifters were plywood blocks painted a bright orange on both sides. Several drift block batches, from two to four in number (500 to 100 drift blocks each) were released in serial order during each drifter study. Ten-foot square windowshade drogues were also deployed, with releases during the three distinct

oceanic seasons, to measure current speeds and trajectories and eddy diffusivity.

Tides, Currents, and Wind

In the project area, tides vary over about an 11-foot range (about 8.05 feet above to 2.45 feet below MLLW), based on over 60 years of records at the Presidio tide gage near the Golden Gate Bridge. It is also expected that the sea level will rise about 6 inches in the 75-year design life of the Outfall.

Current velocity and direction were determined from the results of the oceanographic field data collection program. It was found that currents in the project area are dominated by the tidal influence and generally move toward the Golden Gate during a flood tide and away from the Golden Gate on an ebb. Currents greater than 1.0 knot occur less than one percent of the time.

Analyses of the current meter, drogue and drifter data indicated a net long term drift to the northwest (away from the shore). Winds are primarily from the west (toward the shore) and average 15 to 25 mph in warmer months and 10 mph in cooler months.

Waves

Determination of both normal and extreme wave conditions in the project area consisted of estimation of wave conditions offshore, in deep water, and transfer of these data to the nearshore. Extreme storm wave characteristics were developed based upon the selected design storm. The 8-hour design storm contained 3,141 waves with a significant wave period of 12 seconds; wave periods were expected to be primarily in the range of 7 to 14 seconds.

The design significant wave height at the diffuser location (80 feet of water) was predicted to be about 38 feet for the 100-year storm. For the 200-year storm, the significant wave height is expected to exceed 47 feet. The wave-induced currents at the seafloor are expected to be about 11 to 12 feet per second.

OUTFALL DESIGN

The Southwest Ocean Outfall is ultimately to be the terminus for all of San Francisco's sanitary and storm wastewater. Until recently, the existing combined wastewater disposal system caused severe pollution in San Francisco Bay and the surrounding shores. Every rainfall exceeding 0.02 inches per hour in intensity caused the system to overflow and discharge raw sewage into the Bay; on average, this used to happen about 80 times a year. The

Clean Water Program, of which the Outfall is an important part, is designed to remedy this condition.

The Outfall consists of a single 12-foot diameter pipe weighing about 3 tons per linear foot extending about 4.5 miles into the Pacific Ocean to a water depth of 80 feet. The Outfall's capacity is 450 million gallons per day by gravity; this capacity may eventually be increased to 590 million gallons per day by adding a pumping station. It is scheduled to be completed in the spring of 1985 and for the first 5 to 10 years will be utilized to only about 30 percent of its capacity, while the remainder of the system is completed.

The location of the Outfall was selected so as to carry the effluent into deeper water as quickly as possible within the otherwise relatively shallow continental-shelf. Also, the diffusers had to be placed at a sufficiently remote distance from the Golden Gate to avoid the likelihood of tidal currents carrying the effluent into San Francisco Bay.

The Outfall has been designed to resist or accommodate all environmental forces or displacements anticipated during the design life of the system. Where significant damage appears unavoidable, such as across the fault zone during a major rupture, provisions have been made to limit the extent of damage and to facilitate required repairs. Provisions have also been made to permit the operation of the Outfall system on an emergency basis during the repair period.

Seismic Design Criteria

The centerline of the Outfall lies across the San Andreas Fault, one of the world's most active and violent earthquake fault zones (Figure 2). Based on review of historical seismicity, a design Richter magnitude of 8+ was selected for the project with a peak ground acceleration of 0.6g, transient displacement of 20 inches, and a peak velocity of 30 inches per second.

Based on review of the famous 1906 event, it was concluded that the Outfall could be subjected to a relative horizontal displacement of 16 to 20 feet and a relative vertical displacement of 3 to 4 feet. Additionally, a relative fault creep movement of about 6 inches can be anticipated during the 75-year design life of the project.

Earthquake Joints

Conduit sections with special earthquake joints (Figure 3) will be placed longitudinally at 20 feet on center across the fault zone (400 feet) and the two bands on each side, a total length of 1200 feet. The earthquake joints were

designed to absorb the following anticipated transient forces and movements:

- o longitudinal pipe tension = 150 tons
- o total joint extension = 12 inches
- o total joint contraction = 5 inches
- o total joint deflection = 2.4 degrees
- o gasket pressure = 300 psi
- o internal water pressure = 10 psi

A joint consists of two neoprene gaskets sliding on teflon surfaces, the outer one being for testing purposes only. The locking device is made up of four Dywidag rods, fusion epoxy coated and encased in PVC conduit, with crushable closed cell urethane foam reinforced with nylon behind the rod washers. When the joint reaches its expansion or contraction capacity by crushing the urethane foam, it then transfers the force and movement through the pipe to the next joint, and then to the following joint(s) until the entire motion is absorbed.

Backfill Configuration

The backfill configuration (Figure 4) was designed to provide protection for the Outfall conduit for the design life of 75 years. The lowest layer of gravel (Type I) was selected to furnish proper bedding of highly pervious material providing rapid pore pressure redistribution during periods of earthquake-induced shaking and potential liquefaction. The second layer of gravel (Type II) is a graded filter course to minimize infiltration of the natural sands into the Type I backfill. The armour stone layers are for wave defense, with Type IV placed on top of Type III in the surf zone and diffuser areas only.

Diffusers and Manholes

At its outer extremity, the Outfall contains 85 diffuser units (Figure 5). Each diffuser consists of structural unit with a riser containing an 18-inch diameter conduit connecting the pipe invert to the diffuser riser cap which protrudes several feet above the seafloor. Each cap contains eight 4-inch diameter ports through which the effluent is diffused to the ocean. The risers are connected to the pipe bottom in order to minimize the likelihood of sediment accumulation and possible constriction of the pipe cross section and capacity. Surprisingly, the lateral forces caused by fishing nets dragged along the seafloor which may snag on the diffuser caps proved to be potentially far greater than the seismic

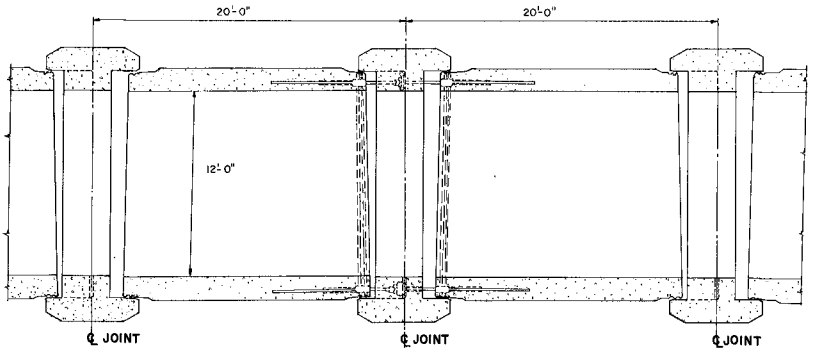

Figure 3 EARTHQUAKE JOINTS

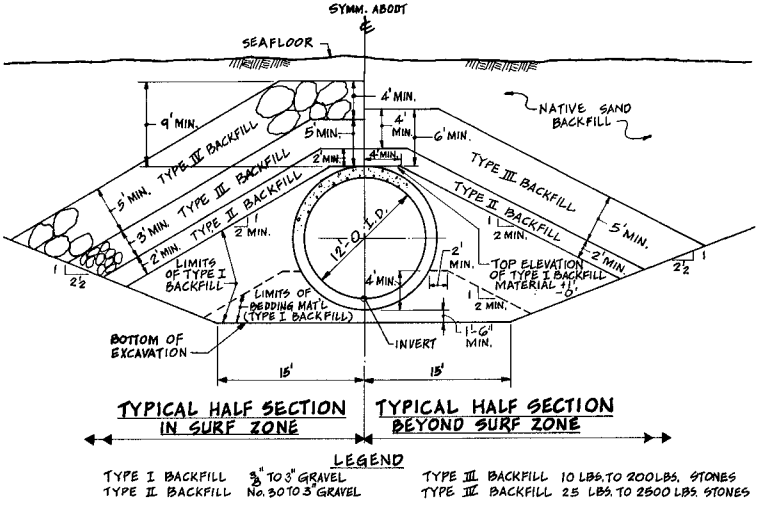

Figure 4 BACKFILL CONFIGURATION

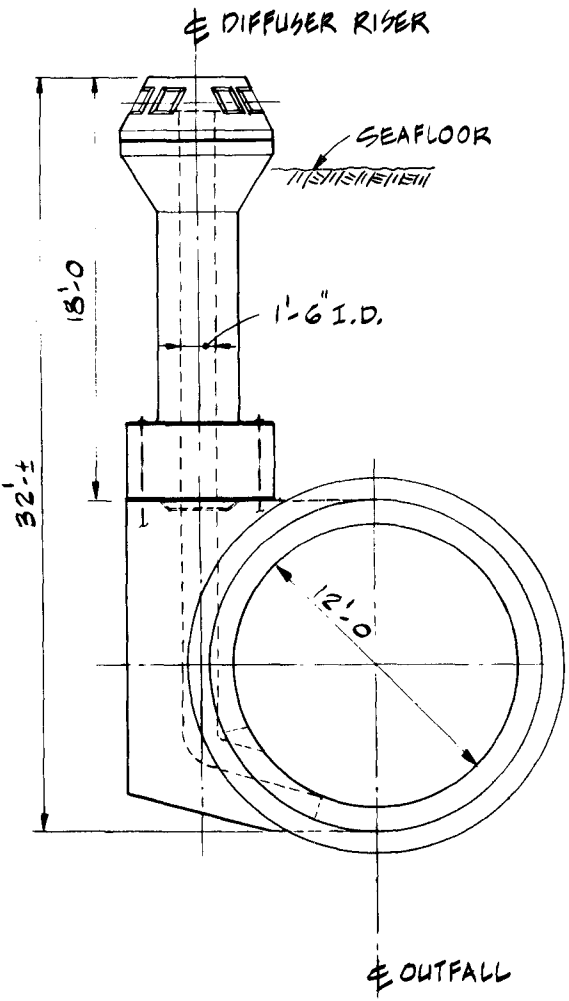

Figure 5 DIFFUSER UNIT

or wave forces and thus became the design load. Also, erosion or accretion of the seafloor in the diffuser area is not expected to exceed 3 feet in 75 years, based on historical records.

Access manholes were designed at a maximum center-to-center spacing of 500 feet. This spacing allows for the timely rescue of a tethered maintenance/repair diver inside the Outfall conduit. The manholes essentially consist of 42-inch diameter holes at the top of the Outfall pipe with reinforced concrete gasketed covers. A special marker is connected to the manhole cover and protrudes some 5 feet above the seafloor. The manhole cover is backfilled in a manner similar to the pipe itself. No access chimneys were designed to ease entry into the pipe, since it was felt that they were unlikely to survive the hostile seismic and wave environment. Access to the manholes will therefore require excavation and backfilling equipment in order to remove and later replace the backfill material above the manhole cover.

Emergency Features

Two emergency features have been incorporated into the Outfall design to respond to the possibilities of flows exceeding design capacity or a rupture of the conduit; these are the emergency overflow structure and several emergency diffuser units.

The emergency overflow structure consists of a 10-foot diameter pipe and spillway structure connecting the onshore headworks to Ocean Beach. It is anticipated that the emergency overflow structure would be used during rare periods of major flooding or in case the Outfall conduit should break near shore for any reason. The effluent discharge on the beach would continue until the flood flows abated or until repairs were completed.

Should a major slip occur along San Andreas fault zone in the project area, the Outfall conduit will almost certainly break. To mitigate the impact of this possibility, provisions have been made to excavate and expose two or more manholes on the shoreward side of the break, remove their covers, and then install emergency diffuser units (Figure 6). These units will act to diffuse the effluent about 1.5 miles offshore during the conduit repair operations.

OUTFALL CONSTRUCTION

The contractor has now (December 1982) finished the surf zone trestle (Figure 7) which extends about 3,000 feet into the ocean to a water depth of about 38 feet. The 32-foot wide deck of the trestle stands about 28 feet above the water. Its main supporting members are 24-inch diameter

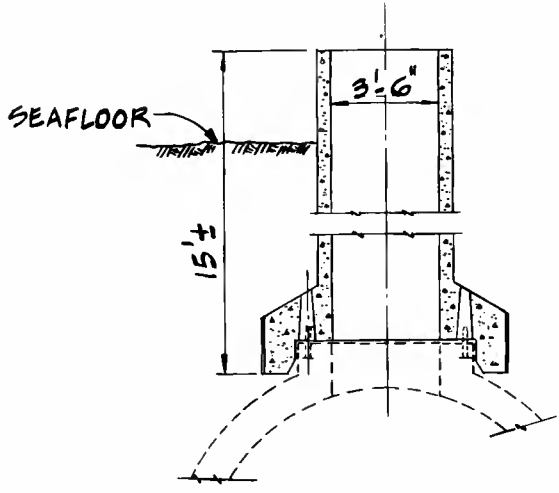

Figure 6 EMERGENCY DIFFUSER

Figure 7 SURF ZONE TRESTLE

pipe piles at 30 feet on center for the first 2,000 feet of trestle; 30-inch diameter piles were used for the outer 1,000 feet of trestle. The trestle carries tracks for movement of cranes, material carts, and a pipe laying gantry (Figure 8).

Surf Zone Construction

The Outfall pipe is presently being installed from the gantry in a protected trench (Figure 9). Ordinary interlocking sheet piles spaced 24 feet apart were used for the first four hundred feet; they were jetted and driven with some difficulty due to the hard material encountered just below the top loose sands. The contractor then employed three-legged wave barriers 20 feet long by 12 feet wide consisting of three pipes connected by steel plates with interlocking connections to the abutting wave barriers and weighing about 10 tons each (Figure 10). These are placed in position during relatively calm seas and pin piles are driven through the wave barrier piles to secure them in place. After the completion of the excavation, pipe laying, and backfilling in a given section, the pin piles are loosened and pulled and the wave barrier modules are transported to new positions (Figure 11). The present pipe laying rate is 2 to 3 units per day.

The pipe being installed from the gantry was produced in a pipe plant near the beach (Figures 12 and 13) and consisted of about 120 units weighing about 90 tons each. The other 900 or so conduit sections, including the special earthquake sections and the diffuser units, are being manufactured at Rio Vista, about 60 miles up the Sacramento River from San Francisco.

Offshore Construction

A 13,000 ton capacity barge (Figure 14) was built in Portland, Oregon specifically for this project at a cost of about U.S.$15 million. It was launched in mid-September 1982 and is presently being outfitted and rigged. It is scheduled to arrive at the site in early 1983 and to commence offshore operations beyond the end of the trestle shortly afterwards. The barge is 420 feet long, 98 feet wide and 25 feet high. It has a draft of 10 to 12 feet, depending on the weight of its cargo, and a 500-ton capacity crane with a 200-foot boom. Excavation, pipe laying, and backfilling will be performed off the barge at an anticipated rate of two pipe lengths (48 feet) during each 24 hour day.

ACKNOWLEDGEMENTS

The prime consultant for the Outfall is Parsons Brinckerhoff. Woodward-Clyde Consultants is principal subconsultant for geotechnical, seismic, coastal, and

Figure 8 PIPE GANTRY

Figure 9
PLACING CONDUIT IN
SHEETED TRENCH

Figure 10 WAVE BARRIERS

Figure 11 TRANSPORT OF WAVE BARRIERS

Figure 12 CASTING YARD

Figure 13 CONDUIT SECTIONS

Figure 14 BARGE DURING CONSTRUCTION

oceanographic aspects of the project. Principal subconsultant for hydraulic and sanitary design is CH2M-Hill, Inc. Cost estimates and special studies on constructibility are provided by H. V. Anderson Engineers.

In addition to the authors, the project management team includes P. H. Gilbert and G. J. Murphy of Parsons Brinckerhoff, G. E. Hervert of Woodward-Clyde Consultants, and P. B. Hall and L. E. Hanson of CH2M-Hill, Inc. The special joint system was designed by Robert Warshaw of Parsons Brinckerhoff; the senior geotechnical engineer was the late O. H. Gilbert, Jr. of Woodward-Clyde Consultants.

Guidance concerning seismic design and constructibility of the Outfall system was provided by the Seismic Advisory Board. This panel of consultants, under the chairmanship of T. R. Kuesel of Parsons Brinckerhoff, included H. B. Seed, B. C. Gerwick, Jr., B. A. Bolt, and J. W. Johnson of the University of California, Berkeley, G. W. Housner and N. H. Brooks of the California Institute of Technology, and the late N. M. Newmark of the University of Illinois.

The contractor, Ocean Beach Outfall Constructors, is a joint venture headed by Morrison-Knudsen of Boise, Idaho. R. R. Vlach is project construction director and W. Hirvela is project construction engineer. Construction management services are being provided by Deleuw-Greeley-Hyman under the direction of George Kline.

The cooperation and assistance of L. A. Vagadori, R. T. Cockburn, A. B. Kenck, and W. Tsai of the Clean Water Program of the City and County of San Francisco was instrumental to the success of the data acquisition, engineering, and design programs. The efforts of the staff of the State of California Water Resources Control Board are also gratefully acknowledged.

REFERENCES

Belvedere, J.A. et al (1978), "Southwest Ocean Outfall" Coastal and Offshore Considerations," Proceedings, Coastal Zone '78, ASCE, San Francisco, Volume III, pp. 1845-1861.

Gilbert, O. H., Jr., Y. Eisenberg, and D. D. Treadwell (1981), "Seismic Design of the San Francisco Ocean Outfall," Proceedings, International Conference on Recent Advances in Geotechnical Earthquake Engineering and Soil Dynamics, ASCE, St. Louis, Volume III, pp. 1133-1138.

Murphy, G. J. et al (1979), "Test Pit Program for San Francisco's Ocean Outfall," Proceedings, Civil Engineering in the Oceans IV, ASCE, San Francisco, Volume II, pp. 979-994.

Treadwell, D. D. et al (1978), "Southwest Ocean Outfall: Geotechnical and Oceanographic Predesign Studies," Proceedings, Coastal Zone '78, ASCE, San Francisco, Volume III, pp. 1862-1877.

Treadwell, D. D. et al (1980), "Offshore Faulting in the Gulf of the Farallones," Proceedings, 12th Offshore Technology Conference, Houston, Paper OTC 3916, Volume 4, pp. 611-616.

SEDIMENT TRANSPORT INVESTIGATIONS IN A NEW ZEALAND TIDAL INLET

K.P. Black & T.R. Healy
Department of Earth Sciences
University of Waikato
Hamilton, N.Z.

ABSTRACT

A study of sand and shell movement under the action of tidal flow was initiated in 1980 to ascertain the suitability of Whangarei Harbour at Marsden Point, New Zealand, for a proposed timber port. The aim was to assess the effects such a development may have on the sediment fluxes and the potential shoreline and channel instability that might be induced in the sandy inlet system.

Vertical water velocity profiles were analysed to determine bed friction coefficients which were subsequently broken into two component parts: one due to form drag and the other associated with the skin friction. It was shown that the Vanoni and Hwang (1967) equation for form drag can be extrapolated to include drag under tidal flow over megaripples. The skin friction component was obtained from the speed at 1m above the bed and the D_{65} grain size, by utilising the Karman-Prandtl equation. This was applied to analysis of bedload trap yields and bedform advance rates over megaripples and good agreement with the Yalin bedload equation for plane beds was obtained.

Suspended sediment transport was found to vary with $U_1^{7.75}$ and total load rates were in general agreement with the Engelund Hansen equation but deviations occurred due partly to expected form drag components being out of phase with the flow because of bedform hysteresis. Under tidal flow, the velocity at 1m was found to be a better predictor of sediment transport than the shear stress obtained from the velocity profile, thus methods presented in this paper use the 1m speed for determination of total load transport.

1. WHANGAREI HARBOUR HYDRAULIC CONDITIONS

Whangarei Harbour (Fig. 1) at high spring tide has a surface area of 98 x $10^6 m^2$ (Millar, 1980) and a tidal prism of 186 x $10^6 m^3$. At low tide exposed banks cover an area of 46 x $10^6 m^2$. Currents in the harbour mouth, in depths which exceed 30m attain a maximum vertically-averaged mean speed of approximately 1.3 ms^{-1} during Spring tides. The channel floors are depleted of sand by these erosive flows and a shell lag lines the bed.

Two flood tidal deltas, Snake and McDonald Banks, possess a high order of stability and the former supports commercial quantities of cockle (*Chione stutchburyi*).

Mair Bank is an ebb tidal delta with several shell beds (Venus and Beazley, 1982) and much of the surficial bank sediment is discarded shell. The bank is protected from ocean wave activity by Busby Head to the east, with generally only E-SE storm waves reaching it with any significant intensity.

Wave activity inside the harbour is mostly locally-generated (fetch ~5km near the port site) although some ocean swell refracts (Black and Healy, 1981) and diffracts to reach the port vicinity (Fig. 1).

Two continuous-recording tide gauges are located in the harbour; one at Marsden Point near the mouth and the other at Port Whangarei in the upper reaches. Analysis of these records over a seven month period from June to December 1981 revealed that the ebb at the mouth has a shorter average duration of 6 hrs 9 mins compared with the flood average half cycle of 6 hrs 16 mins. Mean tidal range was 1.87m and minimum and maximum ranges were 1.17 and 2.80m respectively.

2. COMPLEMENTARY INVESTIGATIONS

General stability of the subtidal deltas and channels was revealed when bathymetric surveys along transects in the lower harbour and across the Mair Bank ebb-tidal delta in 1981 were compared with an R.N.Z.N. survey completed 20 years earlier (1959-61). A complete bathymetric survey by the R.N.Z.N. in late 1981 revealed the same trends. The region of most significant change was on the western end of Mair Bank where sand was accreting. The source for this is most likely to be Bream Bay which has been subject to erosion (Tonkin and Taylor, 1979).

As a first stage in the investigation, some 70 sea floor sites were colour photographed with a still camera (Black et al., 1981) and large areas of shell lag were revealed. Much of the shell was algae-coated signifying bed stability. The photography aided the interpretation and analysis of data collected throughout the study.

A side-scan sonar survey of the inner harbour and Mair Bank region was undertaken in early 1982 (Black and Healy, in preparation, b). The side-scan allowed identification of shell-covered areas and "active" bedload transportation zones which were evident from the megaripples and/or sandwaves on the side-scan traces. Active regions (Fig. 1) flank the main channel where it discharges into Bream Bay. Others occur at Marsden Point and north of Mair Bank; off Pt Sinclair on the south side of the main shipping channel; along the northern side of Snake Bank towards Darch Point then to the west of Reotahi Bay; and finally from the sub-tidal extension south-east of Snake Bank across towards Marsden Point. The last "pathway" runs across the proposed port dredge zone and has been studied in some detail. Other smaller and some less active zones are present. Extensive areas of the harbour bed are covered with shelly lag including a large expanse at the proposed dredge zone. A better understanding of the inter-relationship between these regions is gained in the light of 2-dimensional numerical model results (Black, in preparation).

3. MEASURED CURRENT SPEEDS

During a four year period full-tidal cycle velocity measurements were made at 54 sites. These were made at several levels above the sea bed every half hour for a 13 hour period. Sites are shown on Fig. 1 and some were measured twice. This very detailed field program provided an unusually comprehensive specification of the prototype hydraulic conditions.

Using a Braystoke BFM 010 MkII multiparameter meter, the speed, direction, salinity and temperature were recorded at each level. Distance from the sea bed was obtained with a built-in sounder and the meter was winched between levels. At some of the earlier sites, mean velocity was found over a 50s time interval, but to average out the longer period turbulent fluctuations (Dyer 1973; Heathershaw & Simpson 1978) more completely, the recording time was extended to 100 seconds after field tests revealed significant differences (10-20%) in the speeds for two consecutive 50 second intervals.

In obtaining the velocity profile, speeds were measured consecutively, e.g. the speed at an upper level was measured perhaps 15 minutes after the first level. Under normal operation the speeds were measured at each level at half hourly intervals. Parabolae fitted through three such measurements gave velocity-time curves over a 1 hour period at each level. Instantaneous velocity profiles were determined from these curves.

Without further measurements, turbulent fluctuations with periods of the same order as the measurement time can only be considered as random and as such they cannot be corrected for. Errors introduced by turbulence, which are an integral part of measuring speeds consecutively, must remain in the data. The longer measurement time reduces the scatter considerably.

4. VELOCITY PROFILES

It is well accepted that the Karman Prandtl (K-P) equation describes the velocity profile near the sea bed in the majority of cases for fully rough, turbulent tidal flow. Sternberg (1968) found that a logarithmic profile was evident 62 to 100% of the time over low topography (ripples, gravel and shell). The profile applied in the inner boundary layer, which in fully developed tidal flow is the region from the bed up to about 15-20% of the total water depth. Komar (1976) reported that the outer boundary layer can be described by a velocity defect law (UVDL) of the following form.

$$\frac{U_\infty - u}{u_*} = -8.6 \log_{10} \left(\frac{z}{d}\right) \quad \ldots\ (1)$$

U_∞ is the free stream speed, u is the velocity at distance z above the bed, u_* is the friction velocity and d is the boundary layer thickness.

The Karman Prandtl equation can be represented as

$$\frac{u}{u_*} = 5.75 \log_{10} \left(\frac{z}{z_o}\right) \quad \ldots\ (2)$$

where the constant, 5.75, includes the von Karman constant $\kappa = 0.4$ for conditions of low suspended sediment levels (Soulsby and Oyer 1981) and z_o is the roughness length. From equations (1) and (2), the friction velocity u_*, can be found by linear regression. The measured profile gradient on a semi-log plot is 8.6 u_* for the UVDL, and 5.75 u_* for the K-P.

The question arises as to whether the bed shear stress is represented in the body of the flow, under tidal flow conditions. Smith and McLean (1977) state that at great distances from the boundary the velocity field is related "to the overall boundary stress, that is to the boundary stress averaged over a large region of the bed, form drag on the topographic features thus being included". The Whangarei data strongly support this, and values of the drag coefficient are shown to be related to the bed configuration over sand boundaries with megaripples.

Many of the measured vertical profiles spanned the inner and outer boundary layers. It has been shown by Black and Healy (1982b, in prep.) that there is a measurable change in gradient from the inner to the outer boundary layer under tidal flow conditions. At several sites the velocity gradients in the inner layer (taken as 0-20% of the depth) and in the outer layer (taken as 15-100% of the depth) were determined. Although there was considerable scatter for individual profiles, over a tidal cycle the average gradients in the two layers were nearly in the ratio suggested by the UVOL and K-P law of 8.6/5.75. Programming was written to fit the K-P law to the inner layer and the UVDL to the outer layer, then to average the value of the friction velocity obtained from each. This average value was used to calculate the bed shear stress and drag coefficient.

$$\tau_o = \rho u_*^2 \quad \ldots\ (3) \qquad C_1 = \left\{\frac{u_*}{u_1}\right\}^2 \quad \ldots\ (4)$$

where u_1 is the speed measured at 1m above the bed and ρ is the water density. Data were not used if fewer than 3 speeds were recorded in either layer.

5. SEDIMENT TRANSPORT EXPERIMENTS

Six full tidal cycle sediment transport experiments were conducted at 3 locations of significance to the harbour sediment circulation (Fig. 1). Measurements were made of water velocities, and both bed and suspended load, while the sea floor was observed on an underwater video camera. A velocity profile (0.5, 1.0,

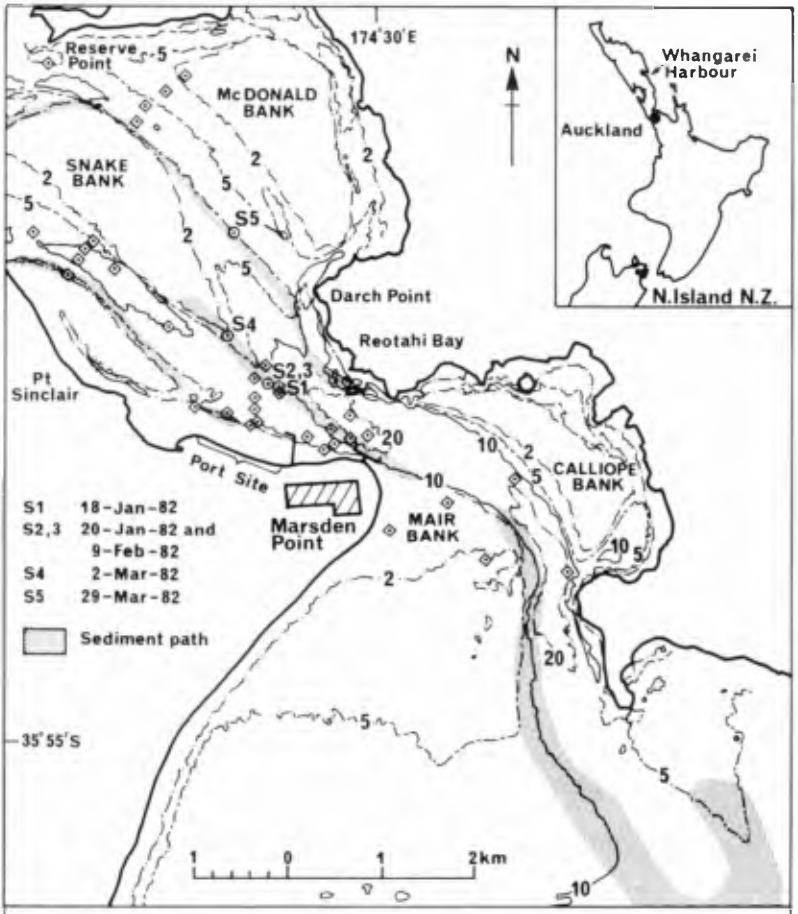

Fig. 1 Location of Whangarei Harbour, North Island, New Zealand and the field measurement sites. Active sediment transport paths are shaded.

2.0, 4.0, 6.0m above the bed) was recorded every half hour (e.g. Fig. 2). Speeds at 1m were measured every 15 minutes or more often on request during periods of interest on the video.

Bedload movement was obtained with two sediment traps of the VUV type (Graf, 1971 p. 363) and emptied every 1-2 hours. The trap is designed to be lowered by rope from the surface but experimentation revealed that a diver was needed to correctly align it on the bed, and to stabilise it in high flow on the way to the surface. Moreover to avoid sand being lost when the trap was raised, a door was fitted to the mouth which could be closed by a diver before retrieval. The traps have a rectangular mouth of size 260mm by 120mm.

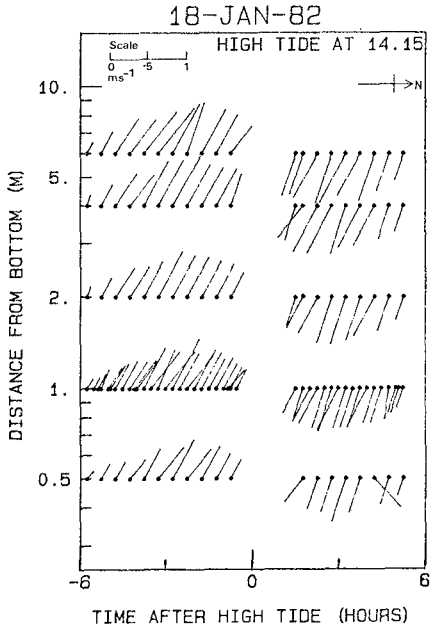

Figure 2: Velocities recorded on 18-Jan-82. True North is to the right.

During slack water, stakes were driven into the crests of 6 consecutive megaripples on the bed and crest advance was measured at the next two quiescent periods and during the tide.

Suspended load was sampled regularly at 0.1, 0.3 and 1.0m above the bed by pumping samples to the surface from nozzles mounted on a steel frame.

An underwater video camera mounted on a steel frame on the sea floor, supplied information on the sediment threshold, ripple advance rate and the behaviour of the sediment under tidal flow. Of the 6 experiments the video was used during the first two only.

6. SEDIMENT THRESHOLD

Of fundamental importance to the specification of sediment transport rates are the threshold conditions which initiate the movement of sediment. Many bedload equations use excess shear stress (Yalin 1963; Sternberg 1972; Bagnold 1963) and small errors brought about by inaccurate threshold conditions are magnified in the transport equations because of a high power dependence. For example, Gadd et al. (1978) modified the Bagnold equation to express the stream power in terms of the velocity at 1m. The bedload was assessed to be proportional to the cube of the difference between the water speed at 1m and the critical velocity.

A major difficulty associated with the determination of threshold in tidal flows is the effect of turbulent fluctuations. Sand moves in gusts, with sweeps and ejections (known as "bursting") occurring intermittently (Heathershaw 1974). When speeds are measured with an instrument such as the Braystoke to produce an average over a period of some 1-2 minutes, these high speed bursts are difficult to incorporate into the concept of a critical velocity. Grass (1970) defined a threshold by considering the overlap of the critical stress distribution associated with the placement of the grain on the bed and with the distribution of bed shear stresses due to fluid flow. Sternberg (1971) defined the threshold as a state of "general sediment movement". In tidal flow even at very low speeds there is still a chance of movement in a burst (Paintal 1971). Dyer (1980) interpreted the threshold as coinciding with the intercept of the regression line of sediment transport against water speed or friction velocity. A statistical approach is adopted in our paper.

6.1 Video Film Over a Sand Bed

The video tapes at Whangarei were analysed in a fashion similar to that undertaken by Dyer (1980). The film was viewed at 5 second intervals and a yes/no decision was made as to whether sandy sediment was moving anywhere in the frame of the camera (approximately a bed area of 12cm x 16cm). From

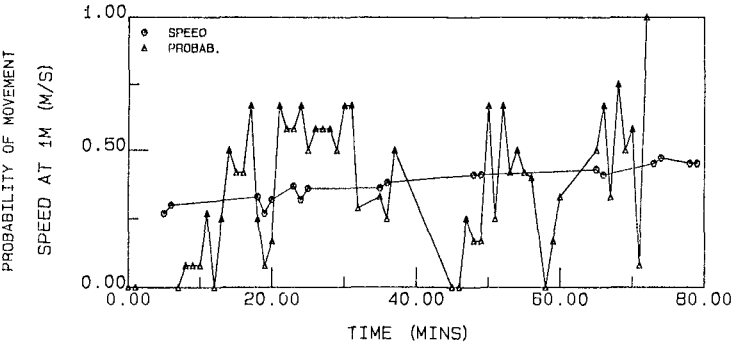

Figure 3: Sandy sediment threshold showing the probability that sand will move in a 1 minute interval with the speed at 1m, for 18-Jan-82 and based on analysis of video tapes.

12 consecutive answers a probability of movement was calculated for the one minute period.

Fig. 3 shows results for one tide during accelerating flood flow plotted with the speeds measured 1m above the bed. Initially below 0.3 ms^{-1} no movement was seen. Then firstly, as reported by Dyer (1980), shell fragments move randomly, appearing to "wobble" in the flow. These shell fragments were not considered for Fig. 3, which corresponds with the motion of sand grains only.

Grain size of the sediment viewed was found by sieving samples taken from nearby sediment traps, and off crests and troughs of the megaripples by divers. Median size D_{50} was coarsest in the troughs (0.35mm); finer in the trap (0.32mm); and finest on the crests (0.31mm). The sand in the trap was felt to best represent the population of sand that was being transported.

Initial motion - such that sand grains were moving more than 50% of the time - occurred when the speed at 1m was between 0.3 and 0.35 ms^{-1}. This was less than the corresponding threshold for grains over a plane bed (reported in Miller et al. 1977) and calculated to be 0.45 ms^{-1}.

The difficulty of assigning a threshold in tidal flow is highlighted by Fig. 3 where, after periods of activity and even with an increase in mean speed, there are still dormant times. Also the probability of movement shows no increase near time = 70 mins compared with time = 25 mins. This suggests that the threshold is increasing with increased flow velocity (Dyer 1980).

6.2 Laboratory Flume

In view of the effects on the threshold of the spread of the grain size distribution and the grain shape, experiments were conducted in a rectangular glass walled flume with sand taken from the port site at Marsden Point. The flume was 0.44m wide and 12.9m long, and shear stresses were determined by measuring vertical profiles on the centre line 9m from the top end of the flume with a mini flow meter. The impellor size was 9mms diameter. Observations of initial motion were made along the centre line and the bed was initially flattened before each run.

Grain size analyses from three sieved samples produced an average mean grain size of 0.24mm, D_{50} of 0.25mm and standard deviation of 0.41ϕ. These statistics were calculated by the moments method from the weight distribution in phi units.

The threshold obtained by curve fitting the vertical velocity measurements to the K-P equation was $u_* = 0.0148$ ms^{-1} or shear stress $\tau_o = 0.219$ N.m^{-2}. This is somewhat higher than an expected value of $u_* = 0.0133$ ms^{-1} (Yalin threshold curve modified by Miller et al. 1977) but is within the range of scatter on Fig. 3 in Miller et al. for quartz density sand of the same mean size, which includes values over the rather wide range of $0.0125 < u_* < 0.0161$ ms^{-1}.

6.3 Shell Bed

A coarse, shelly lag covers large areas of harbour floor and several experiments were conducted on the sea bed watching for the initiation of shell movement.

The difficulty encountered in these observations was due to the wide variety of shape and size of the shells. In summary, the general conclusions were that on a bed of total shell cover even in Spring tides the shells rarely move. Many of the beds have an aged appearance with the shells being covered by algae; a testimony to the stability of the sediment. Shells which were picked up by divers fell quickly to the sea bed and found a stable position with an orientation that depended on the configuration of their immediate neighbours. In contrast, on the sandy harbour floor pelecypod halves prefer to lie convex up but are more stable than surrounding sand.

7. ESTUARINE BED FRICTION ENERGY LOSSES

Tidal energy losses over a rough bed are complicated by many factors including flow accelerations and the mutual interaction of the fluid and the bed. Bedforms change with the stage of the tide, and moreover, the time-scale of bed inertia differs from that of the fluid (Allen 1973; Allen and Friend 1976; Nasner 1978). To estimate sediment transport rates under these conditions, the skin friction and form drag energy loss components must be isolated as only the former is effective in transporting sand (Einstein 1950). Whangarei velocity data were fitted by linear regression as described previously to determine the friction velocity (and the associated parameters: bed shear stress, drag coefficient and roughness length) and were then broken into component parts for application to sand transport under oscillatory tidal flow.

7.1 Average Bed Resistance

Fig. 4 shows the drag coefficient distribution for all sites (excepting sites discussed individually later) where the speed at 1m from the bed was greater than 0.3 ms^{-1}. The minimum speed limit ensures that the flow is fully rough (flow Reynolds Number greater than approximately 1.5×10^5 (Sternberg 1968)) and it is a natural cut-off being approximately the entrainment velocity for sandy sediment.

There is scatter of about 5 orders of magnitude in the flood values and 4 for the ebb. This compares with a similar spread found to occur in Chesapeake Bay by Ludwick (1975). Much of this is accounted for by variations in form drag over the wide range of bed types in Whangarei Harbour including sand bedforms, shell, gravel and marine flora.

The distribution peak during the flood lies between $1.0 \times 10^{-3} < C_1$ (flood) $< 3.2 \times 10^{-3}$ with the ebb maximum spanning a higher range $3.2 \times 10^{-3} < C_1$ (ebb) $< 1 \times 10^{-2}$. Also the correlation coefficient representing the goodness of fit of the measured profiles to the logarithmic shape was larger during the ebb than the flood (Table 1).

Ludwick (1975) noted a higher drag coefficient on the ebb using the same sort of experimental technique and Knight (1981) found that "in general the flood resistance coefficients were slightly less than the ebb values" in a tidal reach of the Conway estuary. Longitudinal density gradients may be partly responsible for the variations (McDowell and O'Connor, Fig. 1.10 1977).

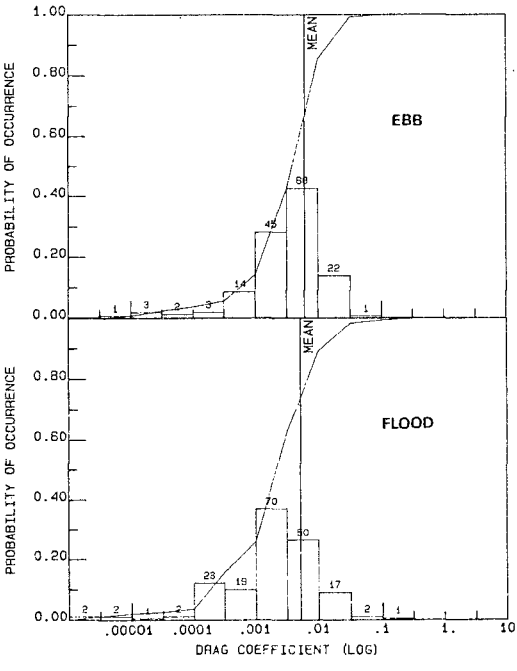

Figure 4: Distributions of ebb (upper) and flood drag coefficients for cases where $u_1 > 0.3$ m.s . Numbers above bars are the numbers of occurrences in each bin.

The shorter duration of the ebb flow and also the higher water speeds may be an influence.

Table 1 compiles mean statistics for (a) all sites, (b) sites with known shell beds and (c) sites with sand beds for all cases where the velocity at 1m exceeds 0.30 ms^{-1}. Mean and median C_1 values are supplied. Arguably, the mean is not the best statistic to describe a distribution which varies over several orders of magnitude. As with grain size analysis, the percentile sizes often represent the distribution and a physical process better than the mean; similarly median C_1 is a more stable statistic which is less affected by a few large C_1 values that may result from experimental error.

Over sand which is presumably bedformed, the increase of friction velocity due to form drag is reflected in a higher C_1 than over the shell sites. Median drag coefficients for cases where u_1 exceeds 0.3 ms^{-1} at Whangarei are then $C_1 = 3.0 \times 10^{-3}$ for all bed types

TABLE 1:

		$\bar{u}_1$ (ms^{-1})	$\bar{r}_{12}$	$\bar{u}_*$ (ms^{-1})	$\bar{C}_1$ ($\times 10^3$)	$\bar{R}$ ($\times 10^{-6}$)	Median C_1 ($\times 10^3$)	z_o $\times 10^2$ (m)
All Sites N = 513	Ebb	0.52	.80	.032	6.0	4.5	3.8	.15
	Flood	0.47	.55	.019	5.1	4.2	2.1	.02
	Both	0.49	.66	.025	5.5	4.3	3.0	.07
Shell Sites N = 132	Ebb	0.52	.73	.026	5.4	4.4	2.7	.05
	Flood	0.46	.31	.012	5.1	3.8	1.8	.01
	Both	0.49	.52	.019	5.2	4.1	2.3	.02
Sand Sites N = 238	Ebb	0.52	.81	.037	6.9	4.7	4.4	.24
	Flood	0.48	.50	.020	6.4	4.3	2.6	.04
	Both	0.50	.65	.028	6.7	4.5	3.5	.12

Mean values of velocity at 1 metre ($\bar{u}_1$), correlation coefficient of the velocities to the logarithmic profile ($\bar{r}_{12}$), friction velocity ($\bar{u}_*$), drag coefficient $\bar{C}_1$ and Reynolds Number

$R = \frac{u_1 z}{\nu}$, ν = kinematic viscosity, z = 1m.

Median C_1 is listed with the roughness length, z_o , calculated from the median C_1 using the K-P equation. N is the number of data points averaged.

(c.f. 3.1×10^{-3}, Sternberg 1972); $C_1 = 2.3 \times 10^{-3}$ for shell bed; and $C_1 = 3.5 \times 10^{-3}$ for non-cohesive sand bed.

By application of the Student's t test (Freund 1974), for the population correlation coefficient to be significantly different from zero, the sample correlation coefficient must exceed 0.81 for a typical case of 5 velocity measurements in the profile (0.99 for 3 levels) at the 0.05 level of significance. Only 57% of the profiles had $r_{12} > 0.8$ which is poorer correlation than that obtained by Sternberg (1968) and reflects that (i) the outer boundary layer is more subject to inertial variations than the inner layer and (ii) turbulent fluxes cannot be totally accounted for when speeds are measured sequentially.

7.2 Friction Losses Over Megaripples

Figs 5 and 6 show velocity at 1m and friction velocity for 5 of the sediment transport sites with megaripple beds. The friction velocity varies over a wider relative range than the speed at 1m. For example the friction velocity on the 9th February 1982 is about 5 times the value on the 20th January 1982. The explanation for this lies with the changing form drag, and sympathetic drag coefficient which is indicative of bed geometry. Dyer (1980) following Lettau (1969) suggests that the areal concentration of features is related to the flow roughness length as, $z_o = h.s/2S$ where h is the effective obstacle height, s is the cross-sectional area seen by the flow per unit horizontal area S.

For two dimensional megaripples, $z_o = \Delta^2/2\Lambda$, where Δ is the bedform height, and Λ is the wavelength.

Insertion of this into the K-P equation produces,

$$C_1 = 1/[5.75 \log_{10} \frac{2\Lambda}{\Delta^2}]^2 \quad \ldots.(5)$$

Average bedform heights and lengths were obtained from measurements at high and low water over 6 consecutive megaripples (Table 3). From this, the expected value of C_1 was calculated with (5) above and the median and mean values from the velocity profiles compared with it (Table 3). The agreement supports the suggestion of Smith and McLean (1977) that the profile reflects the average shear stress over a large region of the bed.

There is an overall correlation of the bedforms measured at slack water to the mean drag coefficient but the friction velocity varies widely throughout the tidal cycle. This compares with similar variations described by Dyer (1970) as "anomalously high and low", and assessed to be associated with the position relative to the megaripple crest at which the profile was measured. For the case at Whangarei where measurements were made largely in the outer boundary layer, the position of the megaripple crest is not as critical and the peak u_* is possibly related to the time when the megaripples turn around and generally occurs when the 1m speed is 0.5-0.55 ms^{-1}.

7.3 Form Drag and Skin Friction

In laboratory flumes a logarithmic relationship has been shown to exist which relates the form drag friction factor, c", to the geometry of the bed and flow depth (Vanoni and Hwang 1967; Pillai 1979).

The Vanoni and Hwang equation for a 2-dimensional bed can be written as

$$\frac{1}{\sqrt{f''}} = 3.3 \log_{10} \left[\frac{d\Lambda}{\Delta^2}\right] - 2.3 \quad \ldots. (6)$$

and $$f'' = \frac{8u_*''^2}{\bar{u}^2} = \frac{8}{c''^2} \qquad \text{i.e. } c = \frac{\bar{u}}{u_*} \quad \ldots. (7)$$

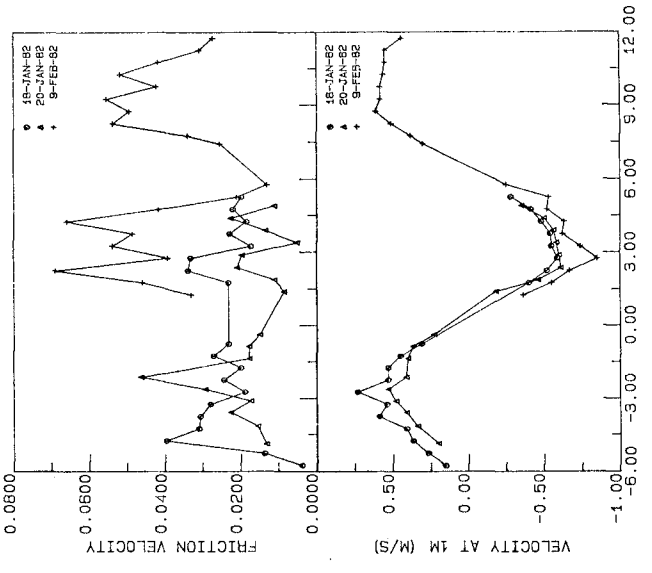

Figure 5: Friction velocity and velocity at 1m above the bed against time after high tide.

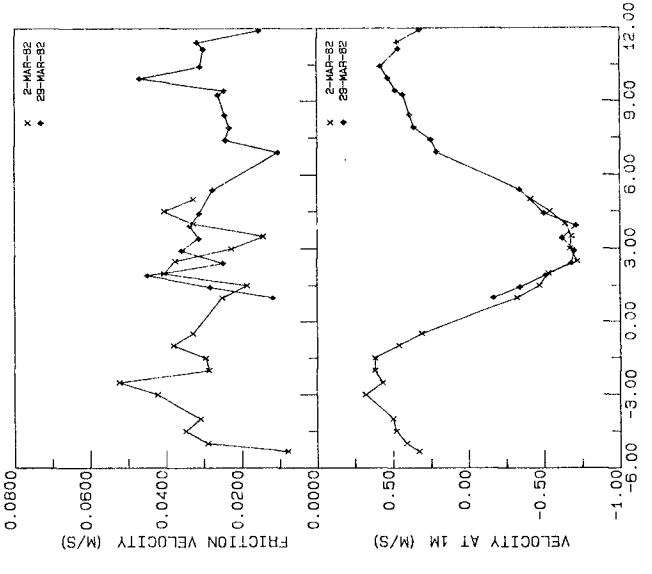

Figure 6: Friction velocity and velocity at 1m above the bed against time after high tide.

$\bar{u}$ is the mean water speed and $u_*"$ is the friction velocity associated with the form drag, and d is depth of flow.

As is usual the superscript (") will refer to form drag and the superscript (') will denote association with skin friction. Furthermore, the skin friction factor, c', may be derived using the K-P equation as

$$c' = \bar{u}/u_*' = 5.75 \log_{10} \frac{0.38d}{(k_s/30.2)} \quad \ldots\ (8)$$

where mean speed occurs at 38% of the depth, d, above the bottom and k_s is the Nikuradse roughness.

Over a moving bed, the roughness can be represented by $k_s = 2.0\ D_{65}$, where D_{65} is the grain size for which 65% is finer by weight. This assumes that the K-P equation is valid all the way to the surface, which has been shown to be strictly incorrect but will suffice for the sake of these calculations, (Mehta (1978) suggests that the K-P relationship can be used for determining mean speed in estuaries). If the total bed shear stress is partitioned in a fashion proposed by Einstein and Barbarossa (1952) such that the component due to form drag and that due to skin friction can be summed to give the total shear stress then,

$$u_*^2 = u_*'^2 + u_*"^2 \quad \ldots\ (9)$$

$$1/c^2 = 1/c'^2 + 1/c"^2 \quad \ldots.(10)$$

$$f = f' + f" \quad \ldots.(11)$$

This does not include a third component associated with energy lost by the flow when sediment is suspended (Yalin 1977).

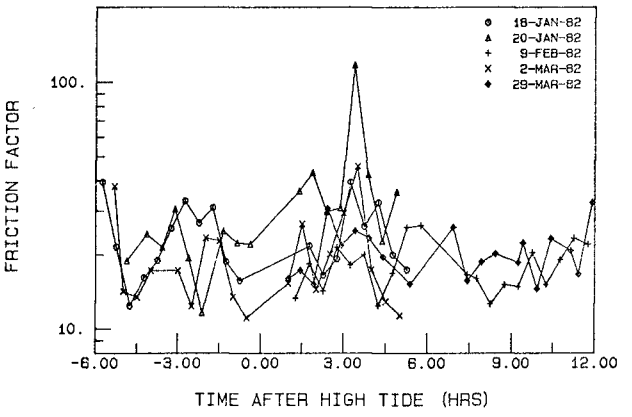

Figure 7: Friction factor ($\bar{U}/u_*$) against time after high tide.

Calculations to determine the combined friction factor from mega-ripple and grain sizes with eqns (6) and (8) respectively were compiled on Table 4 along with measured values of c (Fig. 7) found from the mean speed and friction velocity. Table 4 shows that the median measured friction factor is consistently 5-10% greater than the value obtained from the bed parameters. This consistency for average conditions is very encouraging even though several approximations were made including that (1) the bed geometry measured at slack water is representative of the bed during the tide; (2) a mean water depth taken as the depth at mid-tide is sufficient; (3) the megaripples are 2-dimensional; (4) the D_{65} grain size represents the bed grain roughness adequately; and (5) the K-P equation can be used to ascertain the skin friction. (Annambhotla et al. (1972) stated that Missouri River data were

TABLE 2:

	Mean depth (m)	D_{35} (mm)	D_{50} (mm)	O_{65} (mm)	D_{90} (mm)	T°C	θ'_{cr}	u'_{*cr}	u''_{*cr}	u_{*cr}
18-Jan-82	9.0	.28	.30	.32	.39	21	.042	.0140	.0160	.0213
9-Feb-82	8.5	.32	.34	.37	.48	20	.040	.0146	.0213	.0258
2-Mar-82	3.5	.30	.32	.34	.41	20	.041	.0143	.0198	.0244
29-Mar-82	8.5	.20	.24	.27	.44	19	.048	.0133	.0170	.0216

Mean depth, grain sizes, temperature and critical values at threshold of the Shield entrainment function (Yalin curve), skin friction velocity (Yalin curve), form drag friction velocity (Vanoni and Hwang) and the total critical friction velocity.

TABLE 3:

	$\bar{\Delta}$(m)	$\bar{\Lambda}$(m)	(a)$C_1 \times 10^3$	(b)$\bar{C}_1 \times 10^3$	(c)$C_1 \times 10^3$
18-Jan-82	.17	7.5	4.1	3.3	3.4
9-Feb-82	.25	3.7	7.0	6.5	6.3
2-Mar-82	.15	4.6	4.4	4.3	4.4
29-Mar-82	.16	4.2	4.6	4.4	4.1

Mean megaripple height ($\bar{\Delta}$) and wavelength ($\bar{\Lambda}$) with (a) predicted drag coefficient (b) measured mean drag coefficient (c) measured median drag coefficient. Data for 18-Jan-82 relies on only one measurement of Δ and Λ.

TABLE 4:

	C"	C'	$C_{calc.}$	Median C	Deviation
18-Jan-82	25.0	29.9	19.2	21.4	10%
9-Feb-82	18.7	29.4	15.8	17.5	10%
2-Mar-82	20.2	27.4	16.3	17.2	5%
29-Mar-82	23.3	30.2	18.5	19.8	7%

Form drag friction factor C"; skin friction factor C'; total friction factor C_{calc}, calculated from C" and C'; measured median friction factor; and percentage deviations between calculated and measured C.

TABLE 5:

Date	Time	Z	Z_m	x	u_*	$C_{1.0m}$	u_1	$\bar{u}$
9-Feb-82	10.35	1.38	.70	1.20	.0610	8.52	.77	.94
	12.06	1.53	.33	1.46	.0554	17.51	.68	.94
	17.20	1.52	.60	1.28	.0557	.91	.57	.80
	18.37	1.71	-.08	-	.0497	2.52	.61	.79
2-Mar-82	9.19	2.00	.94	1.21	.0394	2.63	.65	.73
	11.12	2.28	.68	1.35	.0346	4.62	.60	.61
	15.09	2.42	.84	1.31	.0326	13.81	.78	.72
29-Mar-82	13.20	1.47	.66	1.20	.0348	6.95	.71	.78
	15.11	1.65	.24	1.50	.0309	3.60	.62	.56
	21.31	1.73	.65	1.25	.0295	4.64	.47	.66

Suspended sediment statistics: defined as Z, calculated Rouse number (eqn 16); Z_m, regressed Rouse number; x, fall velocity power; u_* (ms^{-1}) friction velocity; $C_{1.0m}$ ($kg.m^{-3} \times 10^3$) concentration of sediment as mass per unit volume at 1m; u_1, (ms^{-1}) speed at 1m; $\bar{u}$, (ms^{-1}) mean speed.

"reasonably consistent" with the Vanoni and Hwang equation for a similar range of the function $\Delta^2/(\lambda d)$).

It appears that the form drag losses can be estimated adequately with the Vanoni and Hwang equation under tidal flow. Similar calculations made with the Engelund and Hansen (1967) development, which employs Carnot's equation for sudden flow expansions, produced unrealistically high values of the form drag friction factor in depths of 8-10m.

Furthermore, the Einstein-Barbarossa (1952) division of form drag and skin friction (Fig. 6.13, Raudkivi 1976), which relies on an implicit assumption that the mean flow and the bedforms are in equilibrium, was found to be unworkable for tidal flow where the bed hysteresis introduced a complicating factor, such that the bed geometry depends on the history of the bed as much as on the present conditions. Fig. 8 presents the Einstein-Barbarossa method in a site specific format. By entering this figure with the mean speed and friction velocity, the intersection of the two curves should supply the magnitudes of u_*'' and u_*'. In many cases with Whangarei data, it was found that the u_* and u curves did not intersect and no solution was possible especially near the beginning or end of the tide.

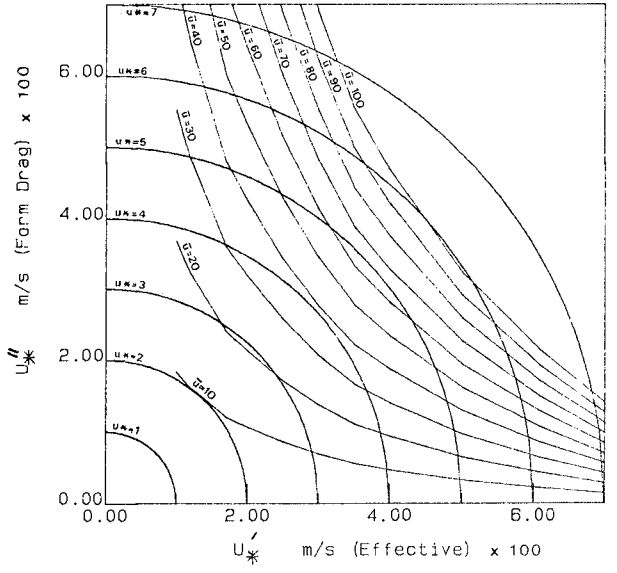

Figure 8: Einstein-Barbarossa division of form drag and skin friction for D_{35} =0.0002m, ρ_s =2650 kg.m^{-3}, ρ =1025 kg.m^{-3}.

8. BEDLOAD TRANSPORT OVER MEGARIPPLES

The bedload transport rates indicated by trap yields were compared with empirical equations derived from unidirectional flow data, to ascertain their applicability to the tidal environment in a megarippled region.

Of the six sediment transport experiments, three days were rejected (a) for wave interference or (b) because only one bedload trap was serviced. On the remaining three days, two traps were deployed simultaneously and the weights caught were averaged. This accounts in part for variations of transport rate with position on the bedform. Accepting Graf's (1970) assessment of work by Novak that VUV traps are about 70% efficient the trapped weights were scaled accordingly to compensate for systematic deficiencies.

In all cases, the bedload traps were placed for 1-2 hours and during this time both the friction velocity and 1m speed varied so that an "average" value had to be found. To do this, the area under the curves of velocity versus time was ascertained numerically by finding the area under continuously updated parabolae fitted to three values of velocity; the one nearest the time of interest

and the one before and after. Because bedload equations are non-linear in u_*, and vary as u_*^3 according to the Yalin equation, when a representative friction velocity was required, the interpolated values were cubed to ascertain the area under the cube of the function between the times that the traps were submerged. The resulting friction velocity was the cube root of the area divided by the elapsed time. With the cubed refinement, an improved correlation to the Yalin equation was obtained (Black, in preparation). By a similar method the Engelund Hansen predicted transport rate, was found from the area under the function $\overline{u^2}.u_*^3$.

It was necessary to introduce a critical friction velocity because often the traps were placed just after slack water in readiness for the next tide, and the total time that the trap was submerged included periods when the bed was dormant. The transport rates and mean friction velocities are more correctly estimated from the time that the bed was in motion. Critical skin friction velocity was found from the Yalin threshold curve (Miller et al. 1977). For cases dealing with total friction velocity, the threshold was the summation according to eqn (9) of the skin friction component from the Yalin curve and the form drag component, which in the light of the analysis in this paper, was calculated from the bedform geometry measured at slack water with the Vanoni and Hwang equation (6). The results of these calculations are compiled on Table 2. In all cases the D_{50} grain size was assumed to represent the bed sediment.

The data were compared with the Engelund Hansen total load equation for "duned" beds (Engelund and Hansen 1967). In mass per unit width of bed per unit time, q_m, this is

$$q_m = \frac{0.05\rho_s}{[g(\frac{\rho_s}{\rho} - 1)]^2} \cdot \frac{\overline{u}^2 . u_*^3}{D_{50}f} \quad \ldots.(12)$$

where ρ_s is sediment density, and g is the gravitational acceleration. After sieving sediment samples taken from the bedload traps (Table 2) the D_{50} fall velocity was obtained from the median diameter (Engelund and Hansen 1967, Table 2.2.1).

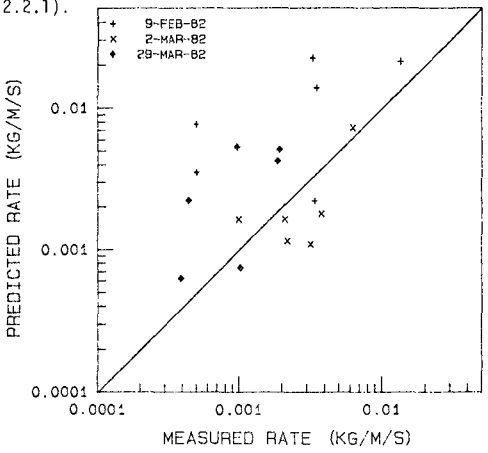

Figure 9: Transport rate according to the Engelund Hansen (1967) total load equation against the bedload trap measured rate.

Fig. 9 shows the predicted rate against the rate determined from the bedload catches. In general, the Engelund Hansen equation overestimates the bedload rate. This would be expected for a total load equation especially at the fastest site on 9th February 1982 where suspended loads which have not been included are likely to be significant. For some cases though (2nd March 1982 especially) there were greater catches in the bedload traps alone than predicted by the total load equation. This deviation is apparently systematic.

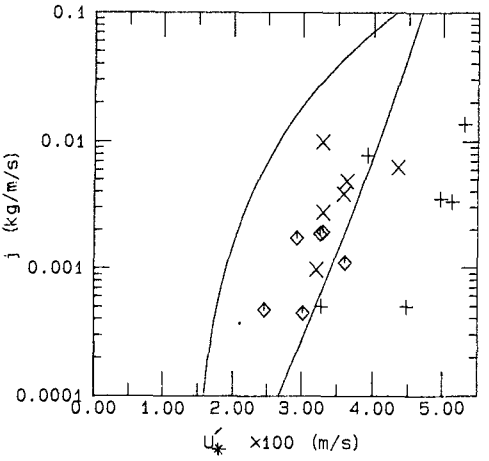

On Fig. 10, the transport rates plotted against u_* were compared with both the Yalin (1963) equation and the Sternberg (1972) modified Bagnold equation. The Yalin equation is for a plane bed and as the friction velocity includes the form drag, which does no effective work on the sediment, the equation overestimates the transport rate in all cases. The Sternberg formula which was partly derived from field data over ripples, approximates the Whangarei data better, but there is still a considerable scatter especially for the cases of high drag coefficient on 9th February 1982.

Figure 10: Measured bedload transport rate against the friction velocity, plotted with the Yalin and Sternberg bedload equations for D=0.0003m and u'_{*c} =0.014 m.s^{-1} .

Because of bedform hysteresis and site dependent form drag components, bedload equations which use total bed shear stress are susceptible to inaccuracies in tidal flow because there can be no way of guaranteeing that the effective shear will be represented in the total friction velocity which often has an over-riding form drag component. For this reason, it is felt that a better approach is to attempt to isolate the skin friction (Vittal et al. 1973) and revert to a bedload equation such as the Yalin curve.

Nasner (1978) states that "for water depth of approximately 10m ... the dune height is governed by the ... velocity over the dune crest". The sediment transport rate is similarly motivated, and further analysis revealed that the speed at 1m showed the best correlation with the bedload catches. Returning to the K-P equation, the skin friction was calculated as

$$u_*' = u_1/5.75 \log_{10} (\frac{30.2}{k_s}) \quad \ldots.(13)$$

with the roughness selected to be $k_s = 2.0\ D_{65}$. On Fig. 11 the bedload transport rate is plotted against the derived skin friction. The result is good correlation to the Yalin bedload equation with no apparent systematic deviations related to ebb or flood, or accelerating or decelerating flow (Gordon 1975). The remaining scatter in the data could be due to:

(i) Bedload trap deficiencies and too few sampling locations on the megaripples.

(ii) Turbulence at near bed levels which varies with megaripple geometry and is not accounted for by the analysis method. Turbulence over bedforms can affect transport levels especially at the point of flow reattachment (Raudkivi 1976). Turbulence can also reduce the critical friction velocity.

(iii) Experimental errors related to long term turbulence and the position of the current meter relative to the bedform crest when speeds were measured.

The Yalin bedload equation is:

$$q_m = 0.635\rho_s D u'_* [\tau_* - \frac{1}{a} \ell n(1 + \tau_* a)] \quad \ldots.(14)$$

$$\tau_* = \frac{u'^2_*}{u^2_{*cr}} - 1, \quad a = \frac{2.45\sqrt{\theta_{cr}}}{(\rho_s/\rho)^{0.4}} \quad \theta'_{cr} = \frac{\rho u'^2_{*cr}}{(\rho_s - \rho)gD}$$

τ_* is the dimensionless excess shear stress; u'_{*cr} is the threshold friction velocity to be ascertained from the Yalin threshold curve, and θ'_{cr} is the threshold Shields entrainment function, and D is grain size. The application of this equation has advantages in that the rate of transport depends on easily measured quantities, reducing fundamentally to a determination of the speed at 1m and the D_{50} and D_{65} grain sizes to specify the bedload rate. This compares with the modification of the Bagnold equation by Sternberg (1972) and by Gadd et al. (1977), for similar reasons. The correlation to the Yalin equation suggests that in oscillatory tidal flow over the short term (1-2 hours), the bedload transport rates approximate their counterparts under unidirectional currents.

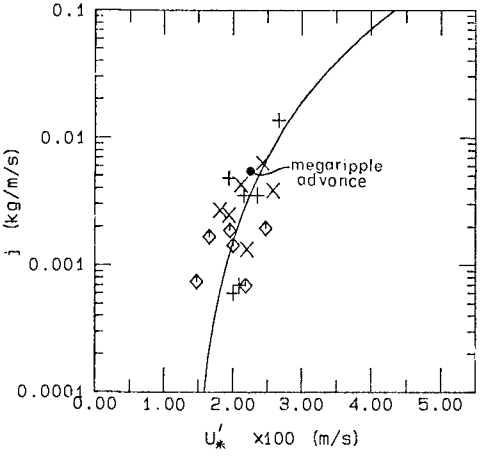

Figure 11: Measured bedload transport rate against the skin friction, plotted with the Yalin bedload equation for D=0.0003m and u'_{*c} =0.014 m.s

8.1 Megaripple Advance Rates

The experiments with staked megaripple crests were designed to measure nett bedload movement over a tidal cycle. For this reason, the crests were staked and generally measurements were taken at slack water only. It is evident that in reversing flow, it is difficult to estimate the bedload transport rate over a half cycle because when the megaripples turn around, the crest movement is often far in excess of the movement of the centre of mass of the feature, and the latter is required to specify the transport rate. A complete set of measurements over 6 megaripples were taken during the tide (i.e. after the crests had turned around) and then again at slack water when the features still faced the same way. Only this data is discussed here.

The bedload transport rate was found by application of the method with constants proposed by Engel and Lau (1981), which allows for reverse transport rates in the lee of the bedform crest, and under the assumption that the megaripples were triangular in form. The 6 megaripples (Table 2) moved an average of 0.3m in 1½ hours when the speed at 1m averaged 0.53 ms^{-1}. When plotted on Fig. 11 the megaripple advance rate compares favourably with both the Yalin bedload equation and the bedload trapping results. Skin friction was assessed with the K-P equation as described for the bedload traps.

9. SUSPENDED SEDIMENT LOAD

Suspended load concentrations have often been described by the Rouse (1937) formula

$$\frac{C}{C_a} = \left[\frac{d-y}{y} \cdot \frac{a}{d-a}\right]^z \quad \ldots.(15)$$

where C is the concentration ($kg.m^{-3}$) at y metres above the sea bed; C_a is the reference concentration at a metres; and d is the total water depth. The Rouse number z, is defined as

$$z = \frac{w}{\kappa u_*} \quad \ldots.(16)$$

where w is the fall velocity. Raudkivi (1976) suggests that for small values of z the formula gives "surprisingly" good results but for larger Rouse numbers there are deviations. Measured Rouse numbers are mostly less than the value calculated by eqn (16) (Fukuoka, Fig. 9.1 1978), signifying a more uniform sediment distribution than predicted by the Rouse formula. The formula could not be applied at Whangarei without modification to z.

Suspended sediment load was sampled at 0.1m, 0.3m, and 1.0m above the bed from three nozzles mounted on a steel frame. In megarippled regions, the definition of the zero bed level becomes important when sampling heights are comparable to the megaripple height. Also at low levels, the suspended load varies more markedly with distance from the crest. Practical difficulties prevented samples being taken along the length of the bedforms. The stand remained in place for the tidal cycle except to be turned around just after slack water to face into the next tide. For these reasons, the concentration at the highest level i.e. at 1m above the bed, was chosen as a reference.

Samples of approximately 2 litres were passed through a 70 micron filter. Material was washed to remove all fine suspended matter which was not of interest to this study. As no grain size analyses were performed, D_{35} from the samples out of the bedload traps was selected to represent the material in suspension.

With data from the three levels, the measured Rouse number, z_m, was found by linear regression, and in all cases (Table 5) it was less than the value from eqn (16), but was generally within the range of scatter in Fukuoka (1978). It was found that the observed concentrations could be predicted with the Rouse formula, when the Rouse number was redefined as,

$$z = \frac{w^x}{\kappa u_*} \quad \ldots.(17)$$

where x (Table 5) is any power. Average values of x were found to be

$\bar{x}$ = 1.31 9-Feb-82 N = 3
1.29 2-Mar-82 N = 3
1.32 29-Mar-82 N = 3

with overall mean of $\bar{x}$ = 1.31.

The suspended transport rate as mass per unit width of bed per unit time is equal to the integral over the depth of the concentration multiplied by the water speed. To evaluate this, the speeds at 0.1 and 0.3m were found from the gradient of the velocity profile and actual concentrations were used. In the upper levels where speeds had been measured, concentrations were derived from the Rouse formula with Rouse number defined by eqn (17) and x = 1.31 in all cases. The integral was evaluated from 0.12m above the bed (the height of the sediment trap mouth) up to the surface by numerical integration, assuming linear changes between measured levels.

Whereas suspended load showed scatter against u_* and $\bar{u}$, the calculated transport rate when plotted against the speed at 1m (Fig. 12) exhibited good correlation. The best fit equation was

$$q_{ss} = (2.03u_1)^{7.75} \times 10^{-3} \quad \ldots.(18)$$

where q_{ss} has units $kg.m^{-1}.s^{-1}$ and u_1 has units ms^{-1}.

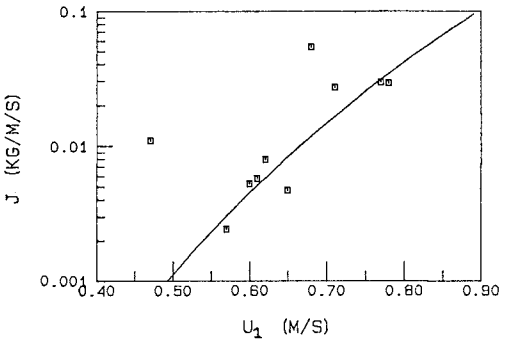

Figure 12: Suspended sediment mass transport rate against the speed at 1m with best fit curve.

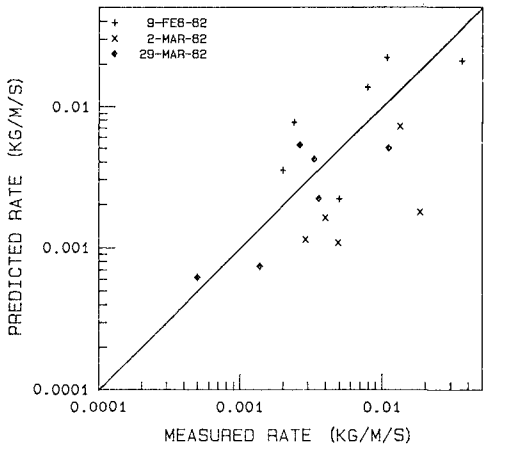

Figure 13: Predicted total load transport rate according to the Engelund Hansen equation against the measured total load transport rate.

The correlation coefficient was 0.94. This equation was obtained with 8 data points and did not include the two points furthest from the curve on Fig. 12. The high power dependence compares with a suspended transport rate proportional to the friction velocity raised to the seventh power found by Dyer (1980).

Applying error bars to the sample correlation of 0.94, with the Fisher Z transformation (Freund 1974, p. 428), the population correlation coefficient lies in the range $0.70 < R < 0.99$, at the $\alpha = 0.05$ level of significance. On the strength of this correlation, which includes data from three sites with different grain sizes, the suspended loads for the periods when the traps were on the bed were found: (1) from each measured velocity at 1m, the suspended sediment transport rate was determined with eqn (18), (2) the mean rates during the bedload trapping periods were found numerically, (3) these were added to the bedload trap rates and the total load was compared with the prediction of the Engelund Hansen equation on Fig. 13. The comparison is now adequate with data for 9-Feb-82 and 29-Mar-82 showing good correlation.

For the shallow site (2-Mar-82), there is a consistent trend for the measured rate to exceed the prediction by a factor of about 3. Raju et al. (1981) found that the Engelund Hansen equation underestimated the total load by an average factor of about 2 in unidirectional flow. At Whangarei, the deviation is associated with wide variations of friction velocity during the tidal cycle. The plotted point which deviates the most corresponds with an anomalously low friction velocity at about 3 hrs after high tide (Fig. 6). The form of Fig. 6 shows a strong resemblance to flood case (a) of Fig. 6 in Dyer (1970), which is typified by a steep peak ($u_* > 0.06$ ms^{-1}) then a sudden drop to an extremely low value of less than 0.02 ms^{-1}. Irrespective of whether these variations result from position relative to the megaripple crest or are associated with megaripple reversal, they make it more difficult to determine sediment transport with the bed shear stress obtained from the profile curvature. The

correlation of the 1m speed to the transport rates is pleasing because the former is an easier parameter to determine than either the bed shear stress or the mean velocity.

In summary, with the speed at 1m the suspended load was found from eqn (18), and the bedload with the Yalin equation (14) and skin friction from the K-P relationship (13) with $k_s = 2.0\ D_{65}$. The variation in grain size for the three sites discussed was $0.24^2 < O_{50}mm < 0.34$ with quartz density of 2650 $kg.m^{-3}$.

10. CONCLUSIONS

(1) Although the drag coefficient varies over several orders of magnitude, it centres on a peak between 0.001 and 0.01 with median value of 0.003 (c.f. 0.0031, Sternberg, 1972).

(2) In tidal estuaries, the form drag over megaripples can be described by the Vanoni and Hwang (1967) equation, and the skin friction by application of the K-P equation with the 1m speed, and the D_{65} grain size.

(3) As a result of the conclusions in (2), the bedload transport rate was estimated from the effective drag as represented by the skin friction. Bedload trap catches and megaripple advance showed good agreement with the Yalin (1963) bedload equation, which suggests a convenient way to ascertain the bedload transport rate in reversing flow.

(4) Suspended sediment transport rate varied with the 7-8th power of the speed at 1m (correlation of 0.94).

(5) The Engelund and Hansen total load equation adequately described the sediment transport over megaripples at two deeper locations but showed a systematic deviation at a shallower site. This is most likely due to megaripple hysteresis and difficulties associated with determination of effective bed shear stress from the friction velocity in tidal flow. The 1m speed showed better correlation with the transport rates. Use of the 1m speed overcomes the problems inherent in the estimation of τ_o from the velocity profile.

11. ACKNOWLEOGEMENTS

This research was undertaken on behalf of the Northland Harbour Board and their considerable assistance and logistic support is gratefully acknowledged. We are also indebted to the R.N.Z.N. for their assistance with the underwater video recording, photography and side scan sonar survey. Dr Alex Sutherland, Civil Engineering, University of Canterbury, kindly read a draft and provided helpful criticisms. A special thanks to our typist for handling a difficult manuscript.

12. REFERENCES

Allen, J.R.L. (1973): Phase differences between bed configuration and flow in natural environments and their geological relevance. Sedimentology, 20: 323-329.

Allen, J.R.L. and Friend, P.F. (1976): Relaxation time of dunes in decelerating aqueous flows. Jnl. Geol. Soc. Lond., 132: 17-26.

Annambhotla, V.S.S., Sayre, W.W. and Livesey, R.H. (1972): Statistical properties of Missouri River bedforms. Proc. A.S.C.E., 98 (WW4): 489-510.

Bagnold, R.A. (1963): Mechanics of marine sedimentation. In: M.N. Hill (Ed). The Sea, 3. Wiley-Interscience, New York. pp. 507-582.

Black, K.P. (in prep.): Ph.O. Thesis, University of Waikato.

Black, K.P. and Healy, T.R. (1981): Computer programs for wave analysis; wind wave generation; wave refraction diagrams; and fast Fourier analysis. Occasional Rept. No. 6, Dept. of Earth Sciences, University of Waikato. 76pp.

Black, K., Healy, T., Venus, G., Stoakes, J. and Hunter, M. (1981): Marsden Point Forestry Port Investigation, Sea Floor Photographic Survey. Northland Harbour Board. 149pp.

Black, K.P. and Healy, T.R. (in prep., a): Side-scan sonar survey of the entrance to Whangarei Harbour. Marsden Point Forestry Port Investigation.

Black, K.P. and Healy, T.R. (in prep., b): On the choice of a boundary layer velocity profile for estuaries.

Dyer, K.R. (1970): Current velocity profiles in a tidal channel. Geophys. Jnl. Royal Astro. Soc., 22: 153-161.

Dyer, K.R. (1973): Estuaries : a physical introduction. John Wiley & Sons. 140pp.

Dyer, K.R. (1980): Velocity profiles over a rippled bed and the threshold of the movement of sand. Est. Coast. Mar. Sci.,10: 181-199.

Einstein, H.A. (1950): The bedload function for sediment transportation in open channel flows. Tech. Bull. No. 1026, U.S. Dept. Agriculture.

Einstein, H.A. and Barbarossa, N.L. (1952): River channel roughness. Trans. A.S.C.E., 77: 1121-1146.

Engel, P. and Lau, Y.L. (1981): Bedload discharge coefficient. Proc. A.S.C.E., 107 (HY11): 1445-1454.

Engelund, F. and Hansen, E. (1967): A monograph on sediment transport in alluvial streams. Technisk Vorlag, Copenhagen. pp. 62.

Freund, J.E. (1974): Modern elementary statistics. (4th edn). Prentice/ Hall. 532pp.

Fukuoka, S. (1978): Interaction between turbulent fluid and suspended sediments. Chapter 9 in H.W. Shen and H. Kikkawa (Eds): Application of stochastic processes in sediment transport. Water Resources Publications, Colorado, U.S.A..

Gadd, P.E., Lavelle, J.W. and Swift, D.J.P. (1978): Estimates of sand transport on the New York shelf using near-bottom current-meter observations. Jnl. Sed. Pet., 48: 239-252.

Gordon, C.M. (1975): Sediment entrainment and suspension in a turbulent tidal flow. Mar. Geol., 18: M57-M64.

Graf, W.H. (1971): Hydraulics of sediment transport. McGraw-Hill, 513pp.

Grass, A.J. (1970): The initial instability of fine sand. Proc. A.S.C.E., 96 (HY2): 619-631.

Heathershaw, A.D. (1974): "Bursting" phenomena in the sea. Nature, 248: 394-395.

Heathershaw, A.D. and Simpson, J.H. (1978): The sampling variability of the Reynolds stress and its relation to boundary shear stress and drag coefficient measurements. Est. Coast. Mar. Sci., 6: 263-274.

Knight, D.W. (1981): Some field measurements concerned with the behaviour of resistance coefficients in a tidal channel. Est. Coast. & Shelf Sci., 12: 303-322.

Komar, P.D. (1976): Boundary layer flow under steady unidirectional currents. Chapter 7 in: D.N. Stanley and D.J.P. Swift (Eds): Marine sediment transport and environmental management. John Wiley. 602pp.

Lettau, H. (1969): Note on aerodynamic roughness - parameter estimation on the basis of roughness-element description. J. App. Met. 8: 828-832.

Ludwick, J.C. (1975): Variations in the boundary drag coefficient in the tidal entrance to Chesapeake Bay, Virginia. Mar. Geol., 19: 19-28.

McDowell, D.M. and O'Connor, B.A. (1977): Hydraulic behaviour of estuaries. Macmillan. 292pp.

Mehta, A.J. (1978): Flow dynamics and nearshore transport. Chapter 3 in P. Bruun: Stability of tidal inlets, Elsevier, pp. 83-203.

Millar, A.S. (1980): Hydrology and surficial sediments of Whangarei Harbour. M.Sc. Thesis, Univ. of Waikato, 212pp.

Miller, M.C., McCave, I.N. and Komar, P.D. (1977): Threshold of sediment motion under unidirectional currents. Sedimentology, 24: 507-527.

Nasner, H. (1978): Time-lag of dunes for unsteady flow conditions. Proc. 16th Conf. on Coastal Engineering, pp. 1801-1817.

Paintal, A.S. (1971): A stochastic model for bed load transport. Jnl. Hydraulic Research, 9: 527-553.

Pillai, C.R.S. (1979): Effective depth in channels having bed undulations. Proc. A.S.C.E., 105 (HY1): 67-81.

Raju, K.G.R., Garde, R.J. and Bhardwaj, R.C. (1981): Total load transport in alluvial channels. Proc. A.S.C.E.,107 (HY2): 179-191.

Raudkivi, A.J. (1976): Loose boundary hydraulics (2nd edn). Pergamon. 397pp.

Rouse, H. (1937): Modern conception of the mechanics of turbulence. Trans. A.S.C.E., 102: 463-505.

Smith, J.D. and McLean, S.R. (1977): Spatially averaged flow over a wavy surface. Jnl. Geophysical Res., 82: 1735-1746.

Soulsby, R.L. and Dyer, K.R. (1981): The form of near-bed velocity profile in a tidally accelerating flow. Jnl. Geophysical Res., 86: 8067-8074.

Sternberg, R.W. (1968): Friction factors in tidal channels with differing bed roughness. Mar. Geol., 6: 243-260.

Sternberg, R.W. (1971): Measurements of incipient motion of sediment particles in the marine environment. Mar. Geol., 10: 113-119.

Sternberg, R.W. (1972): Predicting initial motion and bedload transport of sediment particles in the shallow marine environment. In D.J.P. Swift, D.B. Duane and O.H. Pilkey (Eds): Shelf Sediment Transport. Dowden, Hutchinson and Ross, pp. 61-82.

Tonkin & Taylor Ltd, Consulting Engineers (1979): New Zealand Electricity Report on Foreshore Erosion Marsden Power Stations, Bream Bay, March 1979.

Vanoni, V.A. and Hwang, L.S. (1967): Relation between bed forms and friction in streams. Proc. A.S.C.E., 93 (HY3): 121-144.

Venus, G. and Beazley, M. (1982): The influence of shells on the stability on the north side of Mair Bank. Northland Harbour Board Rept., 41pp.

Vittal, N., Ranga Raju, K.G. and Garde, R.J. (1973): Sediment transport relations using concepts of effective shear stress. International symposium on river mechanics, Int. Assoc. Hydraulic Research, 1: 489-499.

Yalin, M.S. (1963): An expression for bedload transporation. Proc. A.S.C.E., 89 (HY3): 221-250.

Yalin, M.S. (1977): Mechanics of sediment transport (2nd ed.). Pergamon. 300pp.

ARTIFICIAL BREACHINGS OF BOT RIVER ESTUARY

by

G A W Fromme*

ABSTRACT

During the flood year of 1981 the "Bot River Vlei", one of the largest lagoons in the south-western Cape of the Good Hope was opened to the sea by two artificial breachings of the sand bar which were aimed at lowering the excessively high water levels in the lagoon, and at the re-establishment of estuarine conditions.

The Coastal Engineering and Hydraulics Division of the National Research Institute for Oceanology of the CSIR surveyed and monitored the hydrological and sedimentological events in the Bot River lagoon and at the mouth channels in an attempt to formulate a future viable management policy, which had to take into account the conflicting interests of the defenders of continued artificial breachings and of those who advocate conditions of a closed estuary which will eventually change into a coastal freshwater lake.

1. INTRODUCTION

Most South African tidal inlets are small or are closed for the greater part of the year because of relatively low run-off in the river catchment and high wave action resulting in strong sand movement along the coast. During the rainy season this situation may be temporarily reversed, when riverine floods lead to natural breaching of the sand bar at the mouth and to the scouring of an estuary inlet to many times its normal size.

The study area is the Bot River Vlei, a large shallow triangular lagoon, 7 by 2 km in extent, situated in a wide valley between the coastal townships of Kleinmond and Hermanus, about 100 km SE of Cape Town (Figure 1). Historical reports from the 19th century (Koop, 1982) indicate that the Bot River Vlei once was an open estuary

---

* Sediment Dynamics Division, National Research Institute for Oceanology, CSIR, Stellenbosch, RSA

which was used as a harbour for small vessels shipping grain from the fertile district of Caledon to Simonstown. At present the lagoon is separated from the sea by a massive dune belt which, because of a combination of artificial influences in the catchment as well as at the sea front, and a natural overflow system to an adjacent estuary, cannot be breached by natural forces.

At times, mainly during the rainy winter season, riverine run-off causes flooding of the Bot River Vlei which, although considered by scientists to be natural in the hydrology and ecology of such an estuary, causes concern to the users of the lagoon (property owners, yacht and fishermen and numerous visitors attracted by the recreational value of the lagoon). Reasons for this are:

(a) flooding of low-lying premises and bank erosion;

(b) desalination resulting in mass mortalities of marine and estuarine fish; and

(c) silt pollution rendering the waters and shore of the lagoon unsuitable for recreation.

To maintain its estuarine character and to augment the few natural breachings that occurred from time to time, the Bot River Vlei has been opened to the sea in the past 50 years by artificial breachings about every three years at a sufficiently deep section of the lagoon, namely, west of "Sonesta" (Figure 1). This caused the lagoon to be flushed and permitted seawater and fish to enter it, the salt water contributing at the same time to the flocculation and settling of the remaining mudload in the vlei so that clear-water conditions were re-established.

During the periods of two artificial breachings of the Bot River lagoon in 1981 the Coastal Engineering and Hydraulics Division of the National Research Institute for Oceanology of the CSIR monitored the cross-sectional variation of each of the two artificial mouths after breaching, as well as water levels, discharge and hydrological consequences of the openings on the Bot River system. The aim of this investigation was to provide hydraulic data on the behaviour of the system to be used in conjunction with biological studies, and to collect data on the post-breaching situation for application in mathematical models of estuary mouth dynamics presently being developed within the division.

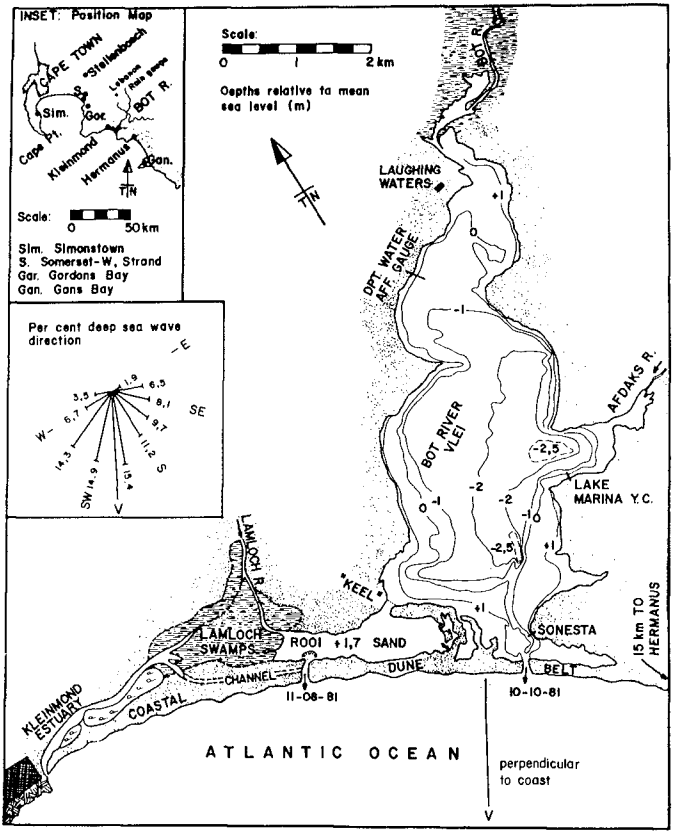

FIGURE 1: BOT RIVER LAGOON SYSTEM (Bathymetry after J. Willis, 1981)

2. PHYSICAL CHARACTERISTICS

2.1 General Setting, Geomorphology, Geology

Although the Bot River drains only a small catchment of about 900 km^2, which is situated in the winter rainfall area of the Cape, and has a mean annual rainfall of only 500 to 600 mm, it forms one of the largest lagoons in the south-western Cape. This is mainly due to the effective damming up of the lagoon waters by a large coastal dune belt along the sea front, 3 to 6 m high and partially vegetated, which is backed by a 100 to 200 m wide vegetated hummock dune hinterland (Figure 1).

The lagoon itself, 7 km long and 2 km wide at the seaward end, lies in a broad valley flanked by the mountains of Kleinmond to the north-west, and Hermanus in the south-west, both 450 m high on the average, and consisting of Table Mountain Sandstone (Ordovician). At the banks of the upper lagoon Bokkeveld shales (lower Carboniferous) outcrop, while the lower sections are surrounded by flats of drift sand and the above-mentioned dune belt on which shrubs grow (Koop, 1982).

2.2 Coastal Hydraulics and Sandbar Characteristics

Because it is exposed to the severe swells and storm waves of the open South Atlantic Ocean the coast at the Bot River mouth can be regarded as a **high-energy coastline.** Maximum wave heights of 8,7 m are recorded (Swart et al., 1982), while the average significant wave height is 3,5 m (Rossouw et al., 1982). As can be seen from the wave rose in Figure 1 the percentage occurrence of deep sea waves is the highest from the south-westerly sector, with a maximum of 15,4 per cent from SSW.

The wave rose in Figure 1 shows that 52,8 per cent of the incident waves arrive at the coast from the south-east. This, together with a number of visual observations such as the movement of turbid water masses flushed out of the lagoon during the artificial openings of mouth channels in 1981, indicates a **predominantly north-westerly longshore drift.**

The strong sand movement along this coastline causes relatively fast closure of any inlet openings by sand bars as soon as the fresh water flow from within the lagoon decreases, usually during the dry summer season.

In the coastal dune barrier there are two potential breaching sites which, according to cartographic evidence and local information, are opened by natural means only

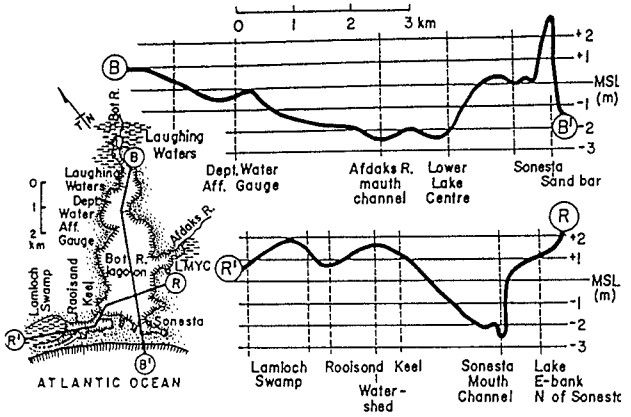

FIGURE 2: BOT RIVER LAGOON, Cross sections

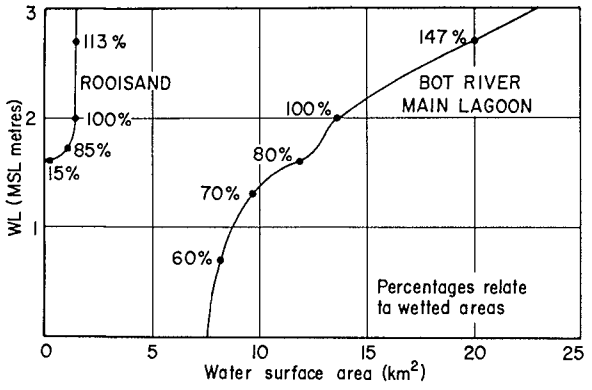

FIGURE 3: WATER LEVELS AND WETTED AREAS, Bot River main lagoon and Rooisand

every ten to twenty years, apparently under a combination of extreme conditions such as river floods and high spring tides.

The one site, at Sonesta, is indicated by a large syncline in the dune ridge, 250 to 300 m wide, and by a deep water channel leading from the shallow lagoon to the gap in the dunes (Figures 1 and 2). This has been formed by continuous, mostly artificial breachings every two to three years, but the mouth itself is usually closed a couple of months after a breaching. Conspicuous 8 to 10 m high bare transverse sand dunes are formed at the north-west bank of the breaching gaps by the strong south-easterly summer winds blowing across the large zone of unconsolidated sand produced by these breachings. From these dunes sand is also driven by wind action to an ever growing shoal at the north-westerly inner (lagoon) side of the mouth area.

In August 1981 another artificial opening was created in the Bot dune barrier at the westerly end of the shallow **"Rooisand"** lagoon, a westerly shallow side arm of the Bot River system (Figure 1). This mouth, which was about 50 m wide, was also closed by a sand bar only three months after the breaching.

There are also a number of natural, smaller transverse gaps in the dune barrier through which sea water washes occasionally. This happens only when equinox spring high tides coincide with high waves, onshore wind and a high water level in the lagoon.

2.3 Bathymetry and Hydraulics of the Lagoon

The isobaths in Figure 1 and two cross-sectional profiles in Figure 2 show that the lagoon is generally deeper along the easterly banks and that the deep-water areas are congruent with the thalweg of the ancient Bot River which existed when the valley was not yet flooded by the marine transgression to form the present lagoon ("Flandrian Transgression", about 18 000 years ago; Theron, Du Plessis and Rogers, 1981). The deepest parts of the main lagoon are at about MSL -2,5 m, but on average the lagoon bed is approximately only at MSL -1 m. The high elevation of the sandbar at Sonesta (nearly MSL +3 m) is also shown in Figure 2, cross-section BB^1. Some marginal low-lying areas of the lagoon are flooded only when the water level is high.

TABLE: RELATION WATER LEVELS AND WATER SURFACE AREAS (see Figure 3)

Water level MSL + (m)	Water surface area				Conditions
	Main lagoon		Rooisand		
	Km^2	%	Km^2	%	
2,7	20,0	147	1,44	113	Extreme high water level, July/August 1981
2,0	13,6	100	1,28	100	Average high water level
1,7	-	-	1,09	85	Elevation of Rooisand watershed
1,6	10,9	80	-	-	Water level Sep/Oct 1982
1,3	9,6	71	0	0	Water level December 1982
0,7	8,2	60	0	0	WL when lagoon is tidal (October/November 1981)

The relationship between water levels and submerged areas in the Bot River lagoon system is shown in the table above and in Figure 3. This demonstrates that a moderate decrease in water level in the range above MSL + 2 m will rapidly reduce the water surface area of the main lagoon, and vice versa; while decreases in water level below MSL + 2 m have a less radical effect on the water surface. This is due to the extensive shallow bank areas.

Because of the pan-like character of the adjacent Rooisand lagoon and a watershed elevated 1,7 m above MSL in the middle of the lagoon, the response to variations in water level is different, namely, that a slight drop in water level below MSL + 2 m will rapidly decrease the water area and cause complete depletion of the lagoon.

The above-mentioned Rooisand lagoon is of high hydraulic significance to the entire Bot system. This is because it forms an **overflow** from the main lagoon through a bottle-neck ("Keel") into the very shallow Rooisand lagoon (bottom elevation MSL + 1,7 m), and further westward through the "Lamloch swamps" into the Kleinmond estuary and, if this estuary is open, out to the sea. Comparison of cross-sections BB' with RR' (Figure 2) shows that a very high water level in the Bot River lagoon is required to overflow and breach the sand bar at Sonesta (approximately MSL + 3 m). Before this happens the flood water in the lagoon

will escape through the Rooisand-Lamloch overflow system (cross-section RR'). When the levels were very high in 1981 such excess water was even drained from the Rooisand lagoon to the Kleinmond estuary via an open channel through the slack behind the main dune ridge and the Lamloch swamps (Figure 1).

Although the Rooisand-Lamloch overflow represents a hydraulic link between the Bot River lagoon and the Kleinmond estuary it allows only a slow release of flood waters from the Bot system, while the influx of seawater from the Kleinmond estuary into the Bot lagoon is insignificant. **The Rooisand-Lamloch overflow can, thus, never fulfil the role of a fully functional tidal inlet for the Bot River lagoon.**

2.4 The Problem of Restricted Contact with the Sea

The hydraulics of the Bot River lagoon is governed by the seasonal character of the influent rivers (floods in winter, droughts in summer) and by the above-described overflow system from the main lagoon to the Kleinmond estuary (see pp 7, 8) which prevents the lagoon from breaking open naturally. This situation is aggravated by the extraction of water from the catchment for agriculture and forestry and by dune stabilization close to the potential breaching area at Sonesta.

Winter floods cause the water to rise to a very high level of about MSL + 2,7 m which is associated with a **freshening out of the lagoon water, mud pollution, exclusion of the flocculation effect** of saline water on mud-laden fresh water, and a **change from an estuarine to a fresh water lake-type of ecology** including mass mortalities of estuarine fish and increasing growth of limnetic weeds which, in turn, enhances deposition of sediment in the already shallow water body. Flooding of low-lying properties and undesirable bank erosion are other side-effects of high water levels in the lagoon.

The restricted "one-way" overflow system through the Rooisand lagoon and the Lamloch swamps to the Kleinmond estuary prevents discharge of mud-laden water from the main lagoon and the entry of seawater by tidal exchange, as well as the recruitment of fish from the sea.

3. FLOODING AND ARTIFICIAL BREACHINGS IN 1981

3.1 First Breaching at Rooisand in August 1981

After exceptionally high rainfalls in 1980 and 1981 the conditions in the Bot River Vlei became critical with regard to high water levels, mud pollution and desalination. By the end of July 1981 the water level in the Bot

River lagoon was very high at MSL + 2,69 m and the salinity was very low at 5 to 7 ppt at the beginning of August 1981 (Figure 6), while a large amount of mud was suspended in the water. In order to save low-lying properties from inundation, but also to minimize damage to the ecology of the lagoon, which apparently had already begun to adapt itself to near-freshwater conditions, the Department of Nature Conservation of the Province of the Cape of Good Hope decided on an opening at the western end of the very shallow Rooisand lagoon; this was done on 11 August 1981.

The most significant features of the breaching were:

(a) A spectacular increase of all dimensions of the initial channel cut by caterpillar within 24 hours from 11 to 12 August and the shaping of a wide flat erosion funnel into the lagoon bed by back-cutting erosion. The width of the channel increased from 5 to about 50 m, the length of the channel doubled from about 150 to 300 m, and the depth increased from 0,5 to 2,5 m. The erosion funnel was 165 m wide and 85 m long. By the end of August 1981 the scouring of the mouth appeared to have stabilized after the water level in the lagoon and the discharge through the mouth had subsided. The flow over the edge of the erosion funnel and over the steep "chute" down into the channel ceased between 8 and 9 October, the Rooisand mouth was found to have been closed on 4 November 1981 by a sandbar.

(b) A rapid increase in flow through the channel from about 1 to 40 m^3/s within the first two days after the opening and a decrease to 7,5 m^3/s on 25 August 1981. After a brief increase after heavy rainfalls to 26 m^3/s on 1 September the flow decreased steadily towards the beginning of October and ended on 9 October 1981, after which the mouth sanded up quickly from the sea side. Some typical cross-sections of the mouth channel during the breaching and a flow diagram of the Rooisand opening are shown in Figures 4 and 5.

(c) A lowering of the water level in the Bot River lagoon system as illustrated by the hydrograph in Figure 6. The maximum lowering was from MSL + 2,69 m before the opening (11 August) to MSL + 1,96 m (25 August), that is, 0,73 m. After the heavy rainfalls from the end of August to September the water level rose again to MSL + 2,15 m but fell slowly to below MSL + 2 m at the beginning of October 1981.

In contrast with the variations of water level in the main lagoon the drop in the water level at the Rooisand mouth (scour-edge) was more marked but the water level did not

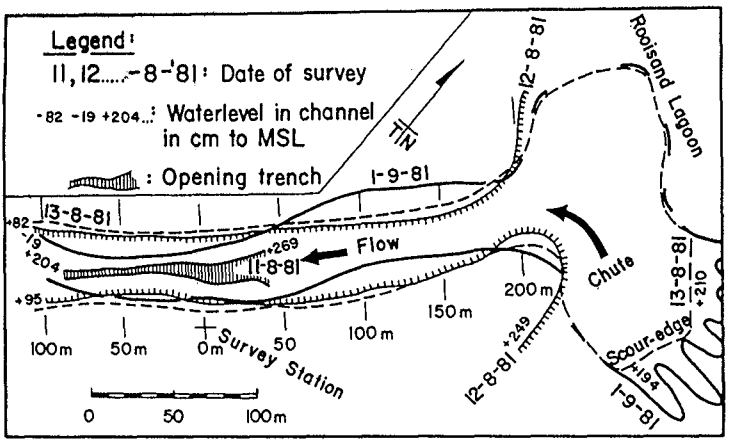

FIGURE 4: Breaching at "Rooisand", 11 August 1981

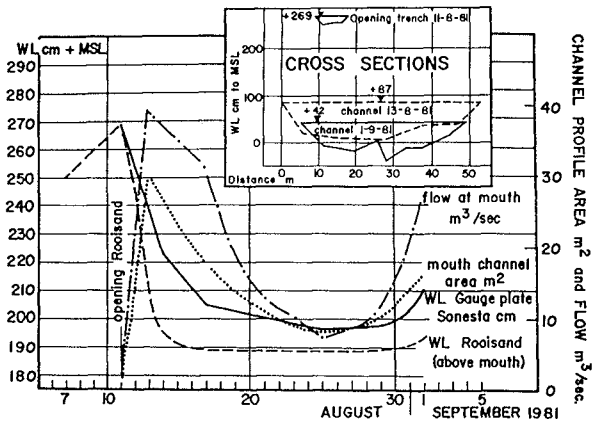

FIGURE 5: ROOISAND BREACHING, hydrograph and channel cross sections (inset)

rise after the heavy rainfalls at the same rate as it did in the main lagoon. This meant that any excess in flow into the Bot River Vlei reached the outlet at Rooisand only after being retarded considerably.

3.2 Second Breaching at Sonesta in October 1981

Although the opening at Rooisand on 11 August caused the desired lowering of the water level, no seawater could enter the main lagoon, because of the elevation of the bottom of Rooisand (MSL + 1,7 m). Subsequent to the above-mentioned rainfalls more flood water and mud entered the lagoon reducing the salinity to a mere 2 ppt and causing deterioration of the water quality. This resulted in a sudden mass mortality of adult estuarine fish at the beginning of October which necessitated a further breaching of the Bot on 10 October 1981, this time at the usual site west of Sonesta where a deep channel in the lagoon lends itself to effective breaching.

The conditions at the opening at Sonesta were different from those at Rooisand insofar as the water level had already been lowered by the Rooisand breaching. The deep water channel upstream of the Sonesta cutting, however, caused a similar behaviour of the cross-section of the mouth. The main difference was that, because of the deep water channel behind the cutting, this opening caused depletion of the lagoon from MSL + 1,88 m down to MSL + 0,7 m within one day of the breaching, that is, by 1,18 m. The lagoon became tidal immediately after the opening of the mouth, with a tidal range of about 0,15 m (see Figure 6). A side-effect of the lowering of the water level was the complete drying out of the shallow margins of the lagoon including Rooisand.

Although the mouth remained open only until 2 December 1981 this breaching can be considered as having been successful in terms of ridding the lagoon of decaying fish cadavers and of suspended mud which was flushed out to sea with every ebb tide. Also, the salinity increased to about 30 ppt, and the lagoon waters became clearer after one week. The disadvantage of the breaching was a substantial loss in water volume and water surface, the latter being reduced to about 60 per cent of the water surface prior to the Rooisand breaching; which had a severe impact on the ecology of the system, mainly because of the exposure of the shallow water habitats around the lagoon.

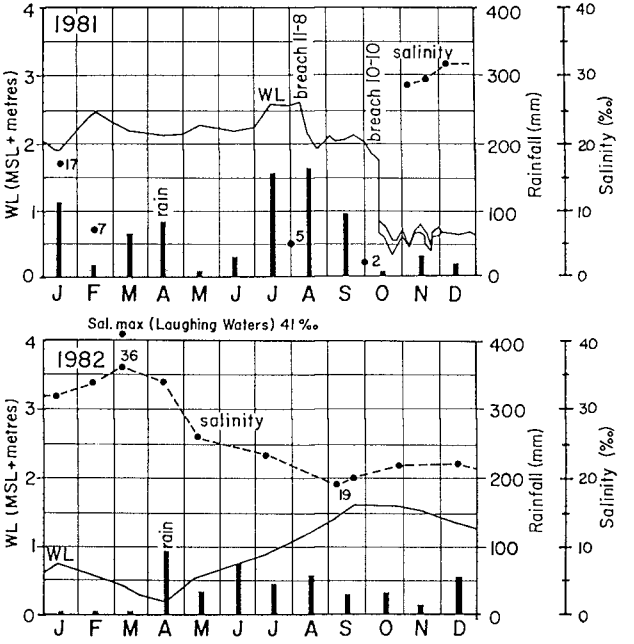

FIGURE 6: WATER LEVELS, RAINFALL AND SALINITIES, BOT RIVER LAGOON, 1981, 1982

Measuring Stations
- Water Levels: Dpt. Water Affairs Gauging Station
- Rainfall : Lebanon Forestry Station
- Salinity : Lake Marina Yacht Club

4. POST-BREACHING CONDITIONS IN 1982

4.1 Conditions in the Main Lagoon

The hydrograph in Figure 6 shows that the dry, hot summer season 1981-82 (December 1981 to April 1982) was marked by decreasing water levels and increasing salinities, which are typical for the summer conditions in the south-western Cape region. The lowering of the water level from the period when the lagoon had an open inlet and was tidal (October and November 1981) to the extreme low-water level in April 1982 was from MSL + 0,7 to MSL + 0,2 m, that is, 0,5 m; while the salinity increased from about 30 ppt (October/November 1981) to 36 ppt in March 1982, or even to 41 ppt at the inflow arm of Bot River Vlei at "Laughing Waters". This was caused by high evaporation rates and no inflow from the river.

The onset of the rainy winter season in April 1982 reversed this condition with the river flow increasing and the water level rising steadily in the main lagoon to a maximum of MSL + 162 cm, and an inverse proportional decrease in salinity to about 20 ppt in September 1982. With the increasing water levels most of the shallow marginal areas of the lagoon were submerged again (see table on page 7 and Figure 3).

Rainfall and run-off in 1982 were rather moderate, with low rains equally spread from April to December. Figure 6 shows that the hydrological reaction of the lagoon at the beginning of the dry summer season 1982/83 with regard to decreasing water levels and increasing salinities was mild. By the end of 1982 the water level was at MSL + 128 cm and the salinity 23 ppt (see table on page 7 and Figure 3).

4.2 Conditions at the Rooisand-Lamloch system

During the post-breaching period after October 1981 significant hydrological developments took place in the Rooisand-Lamloch-Kleinmond overflow area.

When that half of the Rooisand lagoon east of the low watershed in the centre of Rooisand (elevation MSL + 1,7 m; see Figure 1) became dry because of the Sonesta breaching, a confined little lagoon, 0,5 km long and 0,3 km wide, had formed in the westerly half of Rooisand by damming up behind the ever growing sandbar plugging the previous Rooisand inlet.

Being closed off from the saline waters of the Bot River lagoon by this watershed (which remains effective as long as the water level in the Bot River lagoon does not exceed MSL + 1,7 m), and receiving fresh water from the Lamloch

River during the winter season (2,9 m^3/s on 13 July 1982) the newly formed Rooisand-West lagoon changed into a small fresh-water lake, which showed all the attributes of a coastal fresh-water ecosystem, with regard to bird life, fish population and aquatic vegetation. The decrease in salinity in this lake was from 32 ppt in February 1982 to 18 ppt in April, 2 ppt in July and finally to zero salinity in September 1982.

Subsequently the water level in the Rooisand-West lake rose substantially so that the water started to **leak over from west to east** over the shallow watershed in the middle of Rooisand. Because the water level in the main lagoon was not able to keep pace with that in the Rooisand-West lagoon the unique situation arose in mid-winter 1982 that water from the Lamloch River freshened the water of the main lagoon (0 to 6 ppt salinity at the "Keel" in September 1982), and the usually **east-west orientated overflow** from the main lagoon into the Lamloch-Kleinmond system was **reversed** into an **overflow from west to east.** At this stage the entire Rooisand lagoon, including the extensive hummock dune area between the high sand dunes west of the previous Sonesta opening and Rooisand (Figure 1), was flooded with fresh water.

Only at the end of September and in October 1982, when the flow from the small Lamloch catchment subsided did this west-east overflow cease, while at the same time the level in the Bot River main lagoon rose to a maximum of MSL + 1,62 m, so that the "Keel" was filled rapidly with saline water (22 ppt on 28 October 1982).

Towards the end of the year, when the water level in the main lagoon decreased to about MSL + 1,3 m the water retreated from the area of the "Keel" leaving the entire Rooisand-East lagoon dry once again. At the same time, the fresh-water body at Rooisand-West had also decreased in extent and depth forming again a pool confined between the Rooisand watershed, the high sand bar at the previous Rooisand opening and the Lamloch swamp area, as happened shortly after the breaching at Sonesta during the summer of 1981/82.

5. SUMMARY AND DISCUSSION

During the present century the Bot River Vlei, having once been an open estuary (Koop, 1982), has changed character and has tended to become a coastal lake without an open connection to the sea. In such a stagnant water body increasing accretion of fluvial-terrestrial sediments will cause conversion into a marshland, similar to some marginal sections of the Bot River lagoon.

This is caused by extraction of water and soil erosion in the catchment by agriculture and forestry, and the stabilization of the barrier dune at possible sea inlet sites. A natural long-term trend of terrestrial sedimentation of low-lying coastal wetlands, together with the strong longshore sediment movement which closes inlets effectively, also contributes a great deal towards the closure of lagoon mouths and the formation of swampy fresh water lakes in estuaries.

In the case of the Bot River Vlei the local population have succeeded in counter-acting this trend by artificial breachings of the lagoon at Sonesta during winter flood conditions. Although such breachings remained open for only limited periods (up to half a year) they caused a re-establishment of estuarine conditions which lasted for periods of two to three years.

Recent (still incomplete) ecological studies have indicated that the ecosystem of the shallow water margins of the lagoon can be damaged by the abrupt drainage resulting from breachings. The argument which had arisen subsequently between ecologists and the defenders of regular artificial breachings shows the urgency of the establishment of a **scientifically supported management policy** to control the conditions in the Bot system.

The conditions in this respect were particularly critical during the flood year of 1981 because of the large extent of inundated shallow water areas during the relatively long period of more than half a year, which, after the artificial breachings in August and October 1981 were drained within hours.

It appears that the key to future decisions can be found in the bathymetry and the associated hydraulics of the lagoon (see Section 2.3). The Bot River lagoon consists of a deep-water zone in its central parts, and of marginal shallow water areas above a bottom level of approximately MLS + 1 m. These shallow water areas increase rapidly when the water rises to levels of higher than MSL + 1,6 m. Flooding with water levels of 2,7 m as recorded in 1981 will, therefore, abnormally increase the flat areas under water (see Figures 1 and 3). On the other hand, any lowering of such a high flood level must cause radical drainage of these flat areas, with an unavoidable impact on the ecology.

This suggests that from the point of view of hydraulics considerations, a viable proposal for the future management of Bot River Vlei would be **not to allow the water to flood the shallow margins of the lagoon, that is, not to rise to more than MSL + 2 m, and to breach the sand bar artificially before this happens.** In this way the establishment

of a shallow water ecology which will be destroyed by any slight or radical lowering of the water level, by artificial or natural breachings (the latter may still possibly occur!), or, by evaporation during the dry summer months, could be avoided. At the same time all the disadvantageous effects of flooding while the lagoon mouth is closed, such as mud-pollution, desalination, extermination of valuable marine/estuarine fish species and the damage to low-lying properties and bank erosion could be prevented.

The investigations on the Bot River Vlei are being continued with the aim of defining an optimum management policy based on all available information from hydraulic, hydrological, sedimentological and ecological research.

6. REFERENCES

KOOP, K (1982). Estuaries of the Cape, Part II; Synopsis of available information on individual systems, Report No 18, Bot and Kleinmond system. CSIR Research Report 417, pp 68, Stellenbosch, RSA.

ROSSOUW, J et al. (1982). Unpublished data from Slangkop Waverider. Dpt. Civil Eng., Univ. of Stellenbosch, RSA.

SWART, D H et al. (1982). Statistical analysis of visually observed wave data from voluntary observing ships for South African coast. Unpublished CSIR Report, Series T, Stellenbosch, RSA.

THERON, J N et al. (1981). Depositional history of the Bot River estuary. Summary notes: Worksession on the Bot/Kleinmond system. University of Cape Town, RSA.

INTERFACIAL AND BED SHEAR STRESSES IN SALINE WEDGES

by

Vassilios Dermissis[1], Member, Technical Chamber of Greece

and Emmanuel Partheniades[2], Member, A.S.C.E.

ABSTRACT

The shear stresses and the associated friction coefficients at the interface and at the bed of an arrested saline wedge have been studied experimentally together with the detailed flow structure. Interfacial stresses, evaluated from hot film anemometer measurements and actual velocity profiles, agree well with those based on the integration of the equations of motion while the simplified one-dimensional analysis gave considerably higher values. It was found that both the average interfacial friction coefficient, $\bar{f}_i$ and the average bed friction factor, $\bar{f}_o$ are best correlated with the dimensionless number, $ReFr^2$, where Re and Fr are the Reynolds number and the non-densimetric Froude number of the flow respectively, and with the relative density difference, $\Delta\rho/\rho$. The results are presented in two families of curves with $\Delta\rho/\rho$ as a parameter. The scattering of data points is minimal and the agreement with the results of some previous laboratory investigations and field data is good.

1. INTRODUCTION

Shear stresses at the interface and at the bed of arrested or quasi-stationary saline wedges develop as a result of the flow pattern which is generated by the dynamic interaction of fresh and salt water. These stresses, noted by τ_i and τ_o respectively, as well as the associated coefficients, f_i and f_o, have been extensively studied in the past not only for saline wedges but also for other types of two-layered stratified flows (3). In particular, the frictional resistance at the interface and the related flow dynamics constitute two of the most intricate and most important aspects of stratified flows. A reasonable evaluation of the interfacial friction may lead

---

[1] Lecturer, Dept. of Civil Engrg., Aristoteles University of Thessaloniki, Greece.

[2] Prof., Dept. of Civil Engrg., Aristoteles University of Thessaloniki, Greece; and Prof., Dept. of Engrg. Sciences, University of Florida, Gainesville, Florida, U.S.A.

to a quantitative model, since stratified flow systems are controlled by gravity, friction, and inertia forces; they can, therefore, be readily analyzed to various degrees of approximation provided that suitable expressions for the friction forces at the interface and at the solid boundary are introduced. Two typical examples of such models are the one-dimensional analyses for uniform density underflows (6) and for arrested saline wedges (13).

In an earlier paper the authors reviewed studies on stratified flows prior to 1978 (4, 10). It was found that results obtained through various theories and equations differed enormously, and that the scattering of experimental data points in certain studies was too wide for the formulation of any reliable universal law (7, 8). The discrepencies were attributed to the restricting assumptions and conditions of each study and to the limited range of variation of the governing parameters while the scattering of data points suggested either that an inadequate number of independent variables was taken into consideration or that these variables were not properly separated in the dimensionless correlation parameters for their effect on the friction coefficients to be sufficiently displayed. It, moreover, appears that turbulent exchange through the interface may take place to a degree sufficient for the generation of Reynolds stresses while the flow maintains its stratified appearance (11).

The authors, in their first attempt to derive a univeral functional relationship for the interfacial friction coefficient, conducted extensive experimental investigations in a closed rectangular duct where fresh water was flowing over a quasi-stagnant salt water layer at various salinities (4, 10). The analysis of the test data was based on a one-dimensional steady uniform flow model similar to that developed by Schijf and Schoenfeld for open channels (13). Attempts to correlate f_i with the Reynolds number, the densimetric Froude number, and the Keulegan number resulted, like in several earlier studies, in wide scattering with no consistent trend of variation. The Keulegan number is defined by the Eq.:

$$\theta = \frac{1}{V}\left(\nu\, g\, \frac{\Delta\rho}{\rho}\right)^{1/3} \qquad (1)$$

where V is the local average velocity in the moving layer, ρ is the density of the fresh water, $\Delta\rho$ is the density difference between fresh and salt water, g is the acceleration of gravity and ν is the kinematic viscosity assumed to be the same for both fluids.

The scattering was minimized and a consistent trend of variation was achieved when f_i was plotted against the parameter $ReFr^2$, where Re and Fr are the Reynolds number and the non-densimetric Froude number, with $\Delta\rho/\rho$ as an independent parameter. The family of curves, thus obtained, agrees reasonably well with reanalyzed data obtained by other investigators and with one data point from the Mississippi river. In the present study, a similar correlation was achieved for both $\overline{f}_i$ and $\overline{f}_o$ for saline wedges. The interfacial shear stresses were evaluated both directly from hot film anemometer measurements and from

an integration of the equation of motion over each layer along the same line used by Keulegan (7, 8).

2. THEORETICAL BACKGROUND

The interfacial friction coefficients, f_i, have been evaluated by the following four different approaches:

2.1 Direct Measurement Approach

This approach was based on directly measured velocity profiles and Reynolds stresses from which the interfacial shear stress was computed by the equation:

$$\tau_i = \mu \frac{du}{dy} - \rho\overline{u'v'} \tag{2}$$

In this equation, u is the local temporal mean velocity, y is the direction normal to the flow direction, x, u' and v' are the instantaneous turbulent velocity components in the x and y directions respectively, and μ is the dynamic viscosity. From Eq. 2 the local interfacial friction factor, f_i, is defined as:

$$f_i = \frac{8\tau_i}{\rho V_1^2} \tag{3}$$

where V_1 is the average fresh water velocity (Fig. 1).

2.2 Integration of the Equations of Motion

In this approach the equations of motion were integrated for each layer in the vertical and in the horizontal directions over the salinity intrusion length.

The general two-dimensional equations of motion and continuity for steady flow have the forms:

$$u\frac{\partial u}{\partial x} + v\frac{\partial u}{\partial y} = -g\frac{dz_o}{dx} - \frac{1}{\rho}\frac{\partial p}{\partial x} + \frac{1}{\rho}\left(\frac{\partial \tau_{zx}}{\partial z} + \frac{\partial \tau_{yx}}{\partial y}\right) \tag{4}$$

and

$$\frac{\partial u}{\partial x} + \frac{\partial v}{\partial y} = 0 \tag{5}$$

where, refering to Fig. 1, u and v are the local temporal mean velocities in the x and y direction respectively, z is the horizontal direction normal to x-y plane, z_o is the bed elevation and τ_{zx} and τ_{yx} are the shear stresses in the direction x, acting on planes normal to z and y directions repectively.

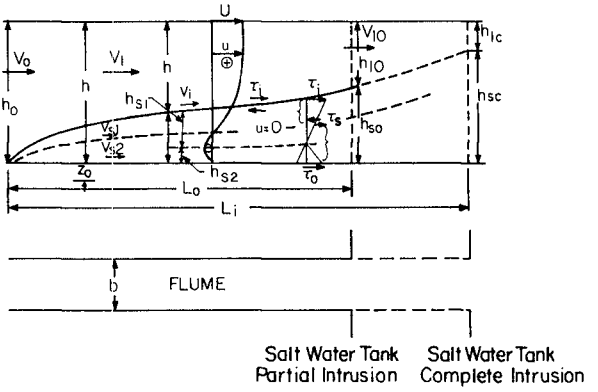

Fig. 1. Definition sketch of an arrested saline wedge.

A combinaton of Eqs. 4 and 5 leads to:

$$\frac{\partial u^2}{\partial x} + \frac{\partial (uv)}{\partial y} = -g \frac{dz_o}{dx} - \frac{1}{\rho} \frac{\partial p}{\partial x} + \frac{1}{\rho}\left(\frac{\partial \tau_{zx}}{\partial z} + \frac{\partial \tau_{yx}}{\partial y}\right) \qquad (6)$$

The last equation is first integrated over the cross sectional area of each layer separately and subsequently over the length of intrusion. In the second integration two cases had to be considered: 1) the case where the depth near the salt water basin is critical and the salinity intrusion length attains its maximum value, L_i and 2) the case where the fresh water depth near the basin is larger than critical, whereas the intrusion length, L_o, is less than L_i. In all experiments a layer of fresh water was formed over the salt water basin. As long as the depth of that layer was smaller than the critical depth of fresh water at the channel entrance, it had no effect on the salinity intrusion which attained its maximum length, L_i; otherwise, the actual intrusion length was equal to the distance from the toe of the wedge to the point where the fresh water depth is equal to that over the basin.

2.2.1. Complete intrusion.

2.2.1.1 Fresh water layer

The pressure distribution in that layer is given by

$$p = p_o + \rho g(h - y) \quad \text{for } y \geq h_s \qquad (7)$$

where $h = h_1 + h_s$ (Fig. 1) and where the vertical direction y is measured from the bottom. Eq. 6 is next integrated over the cross sectional area bh_1. Setting:

$$\alpha V_1^2 A_1 = \iint_{A_1} u^2 dA \tag{8}$$

where α is the momentum flux correction coefficient, neglecting the velocity variation in the z direction and taking into consideration the Leibnitz rule, integration of the first term of the left hand member yields:

$$\int_{-\frac{b}{2}}^{\frac{b}{2}} dz \int_{h_s}^{h} \frac{\partial u^2}{\partial x} dy = \frac{\alpha}{2} bh_1 \frac{dV_1^2}{dx} - bU^2 \frac{dh}{dx} + bV_i^2 \frac{dh_s}{dx} \tag{9}$$

where U and V_i are the velocities at the free surface and at the interface, respectively. Likewise:

$$\int_{-\frac{b}{2}}^{\frac{b}{2}} dz \int_{h_s}^{h} \frac{\partial (uv)}{\partial y} dy = bU^2 \frac{dh}{dx} - bV_i^2 \frac{dh_s}{dx} - bV_i v_s \tag{10}$$

where v_s is the net rate of salt water entrainment. The vertical velocity at the free surface is:

$$v_h = U \frac{dh}{dx} \tag{11}$$

and the same velocity at the interface was taken as:

$$v_{hs} = V_i \frac{dh_s}{dx} + v_s \tag{12}$$

The integrated terms of the right hand member of Eq. 6 are:

$$\int_{-\frac{b}{2}}^{\frac{b}{2}} dz \int_{h_s}^{h} g \frac{dz_o}{dx} dy = bh_1 g \frac{dz_o}{dx} \tag{13}$$

$$\frac{1}{\rho} \int_{-\frac{b}{2}}^{\frac{b}{2}} dz \int_{h_s}^{h} \frac{\partial p}{\partial x} dy = bh_1 g \frac{dh}{dx} \tag{14}$$

$$\frac{1}{\rho} \int_{h_s}^{h} dy \int_{-\frac{b}{2}}^{\frac{b}{2}} \frac{\partial \tau_{zx}}{\partial z} dz = -\frac{2h_1 \tau_w}{\rho} \tag{15}$$

$$\frac{1}{\rho}\int_{-\frac{b}{2}}^{\frac{b}{2}} dz \int_{h_s}^{h} \frac{\partial \tau_{yx}}{\partial y}\, dy = -\frac{1}{\rho}\, b\tau_i \tag{16}$$

where τ_w is the shear stress at the sidewalls. Eq. 6 obtains thus the form:

$$\frac{dH}{dx} + \frac{\alpha}{2g}\frac{dV_1^2}{dx} + \frac{1}{\rho g h_1}\left(\tau_i + \frac{2\tau_w h_1}{b}\right) + \frac{V_i v_s}{g h_1} = 0 \tag{17}$$

where H is the piezometric head, $z_o + h$, and $\frac{dH}{dx}$ is, therefore, the slope of the piezometric line. The entrainment velocity is equal to:

$$v_s = \frac{q_s}{b\bar{L}_i} \tag{18}$$

where q_s is the rate of salt water entrainment over the saline wedge. The latter has been given by Keulegan (8). In the analysis of data, the term $V_i v_s/gh_1$ was found to be of minor importance with a maximum effect of 5%. Because of this reason and of the fact that entrainment takes place not continuously over the interface, but at isolated spots in the form of breaking of interfacial waves, it was neglected in the subsequent analyses. Expressing, next, τ_w by:

$$\tau_w = f_w \frac{\rho V_1^2}{8} \tag{19}$$

the following equation for τ_i is obtained:

$$\frac{\tau_i}{\rho} = -g(h - h_s)\frac{dH}{dx} - \frac{\alpha}{2}(h - h_s)\cdot\frac{dV_1^2}{dx} - \frac{f_w(h - h_s)V_1^2}{4b} \tag{20}$$

which, integrated for $-L_i$ to 0, gives:

$$\frac{T_i}{\rho V_o^2} = -g\frac{h_o}{V_o^2}\overline{\frac{dH}{dx}}\, I_1 - \frac{\alpha h_o}{2L_i} I_2 - \frac{f_{wo} h_o}{4b} I_3 \tag{21}$$

where T_i and $\overline{dH/dx}$ are the average values of τ_i and of dH/dx over the wedge and where I_1, I_2 and I_3 are the following dimensionless functions:

$$I_1 = \int_{-1}^{0} \left(\frac{h}{h_o} - \frac{h_s}{h_o}\right) d\left(\frac{x}{L_1}\right) \tag{22}$$

$$I_2 = \int_{-1}^{0} \frac{1}{V_o^2} \frac{dV_1^2}{d\left(\frac{x}{L_1}\right)} \left(\frac{h}{h_o} - \frac{h_s}{h_o}\right) d\left(\frac{x}{L_1}\right) \tag{23}$$

$$I_3 = \int_{-1}^{0} \frac{f_w}{f_{wo}} \left(\frac{V_1}{V_o}\right)^2 \left(\frac{h}{h_o} - \frac{h_s}{h_o}\right) d\left(\frac{x}{L_1}\right) \tag{24}$$

For the evaluation of these integrals, the following dimensionless equations for the interface, developed by the authors and Mehta and based on Schijf and Schoenfeld's model (11, 13), was used:

$$\frac{x}{L_1} = \frac{\left(\frac{h_s}{h_{sc}}\right)^3 \left\{\left[4 - 2\frac{h_s}{h_{sc}}\left(1-(F_o')^{2/3}\right)\right]^2 + \left[4 + \frac{h_s}{h_{sc}}\left(1-(F_o')^{2/3}\right)\right]\right\}}{6(F_o')^{4/3} + 3(F_o')^{2/3} + 1} + \\ - \frac{10\left(\frac{h_s}{h_{sc}}\right)^2 \left[(F_o')^{4/3} + (F_o')^{2/3} + 1\right]}{6(F_o')^{4/3} + 3(F_o')^{2/3} + 1} + 1 \tag{25}$$

where $F_o' = V_o\sqrt{g(\Delta\rho/\rho)h_o}$ is the densimetric Froude number with V_o and h_o defined in Fig. 1. The three integrals obtain thus the form:

$$I_1 = \frac{2\left[5(F_o')^2 + 6(F_o')^{4/3} + (F_o')^{2/3} + 1\right]}{3\left[6(F_o')^{4/3} + 3(F_o')^{2/3} + 1\right]} \tag{26}$$

$$I_2 = 2\left[(F_o')^{-2/3} - 1\right] \tag{27}$$

$$I_3 = \frac{0.29\left[5 + 255(F_o')^{13/6} - 221(F_o')^2 - 39(F_o')^{17/6}\right]}{\left[1 - (F_o')^{2/3}\right]^3 \cdot \left[6(F_o')^{4/3} + 3(F_o')^{2/3} + 1\right]} \tag{28}$$

2.2.1.2 Salt water layer

A similar integration of Eq. 6 over the cross sectional area of the wedge, $A_s = bh_s$, with the pressure this time described by the equation:

$$p = p_o + (h - h_s)\rho g + g(\rho + \Delta\rho)(h_s - y) \tag{29}$$

gives:

$$\frac{\tau_i + \tau_o}{g(\rho + \Delta\rho)h_s} = \frac{\rho}{\rho + \Delta\rho} \cdot \frac{dH}{dx} + \frac{\Delta\rho}{\rho + \Delta\rho} \cdot \frac{d(h_s + z_o)}{dx}$$

$$+ \frac{\beta}{gh_s} \frac{d(V_i^2 h_s)}{dx} + \frac{V_i v_s}{gh_s} = 0 \tag{30}$$

where β is the momentum flux correction coefficient for the lower layer given in terms of V_i by:

$$\beta V_i^2 A_s = \iint_{A_s} u^2 dA \tag{31}$$

and where the sidewall friction has been neglected since, due to the reversal of flow direction, its overall effect is expected to be negligible . Integration of Eq. 30 from $-L_i$ to 0 gives:

$$\frac{T_i}{\rho V_o^2} + \frac{T_o}{\rho V_o^2} = \frac{gh_o}{V_o^2} \frac{\overline{dH}}{dx} I_4 + \frac{g\frac{\Delta\rho}{\rho}}{2V_o^2 L_i} h_{sc}^2 + \frac{\rho \frac{\Delta\rho}{\rho} h_o}{V_o^2} \cdot \frac{\overline{dz_o}}{dx} I_4$$

$$+ \beta\left(1 + \frac{\Delta\rho}{\rho}\right) \left(\varepsilon \frac{V_{ic}}{V_o}\right)^2 \cdot \frac{h_{sc}}{L_i} \tag{32}$$

where T_o is the average bed shear stress over the length of intrusion, $\overline{dz_o}/dx = -S_o$ is the average bottom slope, $h_{ic} = h - h_{sc}$ is the critical depth of the fresh water layer, and $\varepsilon = V_i/V_o$. The term $V_i v_s/gh_s$ has again been neglected for the aforementioned reasons while the integral I_4 is:

$$I_4 = \int_{-1}^{0} \frac{h_s}{h_o} d\left(\frac{x}{L_i}\right) \tag{33}$$

which, on the basis of Eq. 25, becomes:

$$I_4 = \frac{\left[1 - (F_o')^{2/3}\right] \cdot \left[10(F_o')^{4/3} + 4(F_o')^{2/3} + 1\right]}{3\left[6(F_o')^{4/3} + 3(F_o')^{2/3} + 1\right]} \cdot \qquad (34)$$

The analysis presented so far is similar to the one used by Keulegan (7, 8) with the following differences: 1) A more detailed analytical equation for the wedge profile has been used instead of one single experimental curve and, 2) the actual measured values of α and β for each experiment were used, instead of the constant values of $\alpha = 1.028$ and $\beta = 0.146$ used by Keulegan.

2.2.2 Partial intrusion

In several experiments, the fresh water layer at the downstream basin was larger than h_{1c} - in which case the salt water depth at the downstream end of the channel, h_{so}, was smaller than h_{sc} (Fig. 1). In these cases the following simplified form of Eqs. 21 and 32 was derived and used: First, Eqs. 20 and 30 are written in the form:

$$\frac{\tau_i}{\rho V_o^2} = -\frac{gh_1}{V_o^2}\frac{dH}{dx} - \frac{\alpha h_o}{V_o}\frac{dV_1}{dx} - \frac{f_w h_1 V_1^2}{4bV_o^2} \qquad (35)$$

$$\frac{\tau_i}{\rho V_o^2} + \frac{\tau_o}{\rho V_o^2} = \frac{gh_s}{V_o^2}\frac{dH}{dx} + \frac{(\frac{\Delta\rho}{\rho})gh_s}{V_o^2} \cdot \frac{dh_s}{dx} + \frac{\beta(1+\frac{\Delta\rho}{\rho})^2 \varepsilon^2}{V_o^2} \cdot \frac{d(V_1^2 h_s)}{dx} \qquad (36)$$

where dz_o/dx in Eq. 32 has been neglected as much smaller in comparison to dh_s/dx and where the wall friction coefficient f_w has been introduced by the Blasius equation:

$$f_w = \frac{0.316}{Re^{0.25}} \qquad (37)$$

where the Reynolds number, Re is:

$$Re = \frac{4V_1 R_{h1}}{\nu} \qquad (38)$$

and

$$R_{h1} = \frac{bh_1}{(b + 2h_1)} \qquad (39)$$

Eq. 35 obtains thus the form:

$$\frac{\tau_i}{\rho V_o^2} = -\frac{gh_1}{V_o^2}\frac{dH}{dx} - \frac{\alpha h_o}{V_o}\frac{dV_1}{dx} - \frac{0.0559}{b^{1.25}} h_o^2 \left(\frac{\nu}{V_o h_o}\right)^{0.25} \left[\frac{(b + 2h_1)^{0.25}}{h_1}\right] \qquad (40)$$

Averaging of Eqs. 36 and 40 over the actual length of salinity intrusion, L_o, as in the case of full intrusion, but considering h_1 and h_s constant and equal to their average values $\bar{h}_1$ and $\bar{h}_s$, leads to the following equations:

$$\frac{T_i}{\rho V_o^2} = -\frac{g\bar{h}_1}{V_o^2}\frac{d\bar{H}}{dx} - \frac{\alpha h_o}{h_{1_o}} \cdot \frac{h_{so}}{L_o} - \frac{0.0559}{b^{1.25}} h_o \left(\frac{\nu}{V_o h_o}\right)^{0.25} \left[\frac{(b + 2h_1)^{0.25}}{h_1}\right] \tag{41}$$

and

$$\frac{T_1}{\rho V_o^2} + \frac{T_o}{\rho V_o^2} = \frac{g\bar{h}_s}{V_o^2} \cdot \frac{d\bar{H}}{dx} + \frac{\left(\frac{\Delta\rho}{\rho}\right)g}{2V_o^2} \cdot \frac{h_{so}^2}{L_o} + \frac{\beta\left(1 + \frac{\Delta\rho}{\rho}\right)\varepsilon^2 V_{1_o}^2}{V_o^2} \cdot \frac{h_{so}}{L_o} \tag{42}$$

where bars indicate average values over the length L_o. For a direct evaluation of the average stresses T_1 and T_o, given either by Eqs. 21 and 32 or by 41 and 42, a reliable measurement of the average slope of the piezometric line, $d\bar{H}/dx$, is required - as was done earlier by Keulegan (7, 8). This has been found to be very difficult, since the head loss over the effective length of the flume is of the order of a few tenths of a millimeter. Attempts to measure that head loss optically through a laser beam required an excessively long time of measurement, due primarily to the slowness of achieving equilibrium in the two static tanks, and to the very long period of oscillation of the water level in these tanks. Moreover, the above equations are quite sensitive to $d\bar{H}/dx$ so that a measurement error of the order of 10% may cause an error in T_1 of the order of 50% (5). This difficulty was bypassed by introducing a linear relationship between τ_1 and τ_o. Indeed, the shear stress distribution within the wedge is given by the equation.

$$\frac{\partial\tau}{\partial y} = \frac{\partial}{\partial x}\left[p + g(\rho + \Delta\rho)z_o + (\rho + \Delta\rho)\frac{u^2}{2}\right] \tag{43}$$

The velocity head is very small and can be neglected. Eq. 29 then, for p gives:

$$\frac{\partial\tau}{\partial y} = \rho g \frac{dH}{dx} + (\Delta\rho)g \frac{\partial(h_s + z_o)}{\partial x} \tag{44}$$

The free surface slope, dH/dx, is very small, as discussed, and can be considered as constant. Also, apart from two relatively short segments around the wedge toe and the critical section, the interface is very nearly a plane surface, and $d(h_s + z_o)/dx$ is also very nearly constant. Therefore, it is reasonable to assume linear variation of τ with y within the wedge. It follows thus from Fig. 1 that:

$$\frac{\tau_i + \tau_o}{\tau_i} = \frac{h_s}{h_{s1}} = \lambda \tag{45}$$

where h_{s1} is the distance from the interface to the point of maximum velocity in the wedge. It was assumed next that λ is constant over the wedge - in which case Eq. 45 holds also for the average stresses T_i and T_o, that is:

$$T_i + T_o = \lambda T_i \tag{46}$$

Eliminating $d\bar{H}/dx$ from Eqs. 41 and 42 and using the last relationship, the following equation is obtained:

$$\frac{T_i}{\rho V_o^2} = \left\{ \frac{\left[\left(\frac{\Delta\rho}{\rho}\right) g h_{so} + 2\beta\left(1 + \frac{\Delta\rho}{\rho}\right)\varepsilon^2 V_{1o}^2\right] h_{1o}\bar{h}_1 - 2\alpha h_o \bar{h}_s V_o^2}{2V_o^2 h_{1o}(\lambda\bar{h}_1 + \bar{h}_s)} \right\} \frac{h_{so}}{L_o} +$$

$$- \frac{0.0559}{b^{1.25}} h_o^2 \left(\frac{\nu}{V_o h_o}\right)^{0.25} \cdot \left[\frac{(b + 2h_1)^{0.25}}{h_1}\right] \cdot \frac{\bar{h}_s}{(\lambda\bar{h}_1 + \bar{h}_s)} \tag{47}$$

All the terms of the right hand member of Eq. 47 are either known or can be directly measured. The maximum measurement error of λ was estimated to be about 15% (5). With T_i computed from Eq. 47, T_o is readily evaluated from Eq. 46. $d\bar{H}/dx$ could be eliminated in the same way from Eqs. 21 and 32, valid for complete intrusion. However, after a few trials for the latter case, it was found that Eqs. 41 and 42 could be used for both partial and complete intrusion. These equations have been used for the analysis of all data.

2.3 One-dimensional Energy Equation

This equation, developed by Schijf and Schoenfeld (13), is based on the energy conservation principle applied separately to each layer and on the assumptions of one-dimensional flow, infinite width, and negligible entrainment through the interface. For zero net flow within the wedge, the average velocity is also zero and, therefore, for the one dimensional approach, τ_o has to be taken also as zero. The final form of the equation is:

$$\bar{f}_i = \frac{2h_o}{L_i}\left[\frac{1}{5(F_o')^2} - 2 + 3(F_o')^{2/3} - \frac{6}{5}(F_o')^{4/3}\right] \tag{48}$$

which gives the average interfacial friction factor if the total intrusion length is measured. If the actual intrusion length, L_o, is less than L_i, the latter can be computed graphically from Eq. 25, where h_{sc} is known and equal to $h_o[1 - (F_o')^{2/3}]$ (11).

2.4 Simplified Equations of Motion

This is a combination of the last two approaches and its main objective was to investigate the effect of the assumption of zero bed shear stress and zero wall stress, used in the one-dimensional model, on the interfacial shear. For $\tau_o = 0$, $\lambda = 1$, $f_w = 0$ and $\beta = 0$, Eq. 47 reduces to the approximate form:

$$\frac{T_i}{\rho V_o^2} = \left[\frac{(\frac{\Delta\rho}{\rho}) g \bar{h}_1 h_{so}}{2V_o^2 h_o} - \frac{\alpha \bar{h}_s}{\bar{h}_{1_o}} \right] \cdot \frac{h_{so}}{L_o} \qquad (49)$$

3. BASIC RESEARCH EQUIPMENT

The experiments were conducted in a variable slope plexiglass flume 20 m long, 46 cm wide, and 46 cm deep, constructed at the Coastal Engineering Laboratory of the University of Florida. This flume, outlined in Fig. 2, discharges into a 3 m by 1.53 m tank supported on another 3 x 3 x 0.75 m^3 tank.

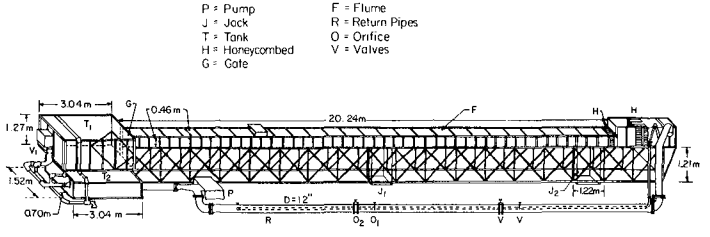

Fig. 2. Outline of basic experimental apparatus.

The channel is connected at its upstream end to a 2.31 m by 0.45 m head tank where the fresh water is pumped into from the fresh water tank and where turbulence dampens out through a honeycombed section. The water circulation system consists of an axial flow pump, of two pipes with either one or hoth in operation, depending on the required discharge, and of all the necessary orifice meters, valves, gates, pressure taps and manometers. The maximum discharge is ahout 115 l/sec.

The channel and head tank are supported on a steel frame 1.2 m high, which rests on two hydraulic jacks - one at the center and the other at the upstream end of the flume. Through a gear-chain system, the central jack could be moved up and down at a distance equal to $\frac{1}{2}$ that of the upstream jack. The $\frac{1}{2}$ -inch thich plexiglass wall of the flume forms a channel with its flanges, fortified with stiffeners, directed outwards. To this steel frame, rails have been placed on

each of the upper two flanges for the support and smooth movement of the instrument carriage. The downstream end of the channel is connected to the salt water tank through a five centimeter long thick rubber forming a flexible and waterproof hinge. A water-tight vertical plexiglass gate separates the flume from the salt water tank. That gate can be raised and lowered mechanically by a vertical threaded shaft and a circular threaded disc supported on an independently fixed frame. A second gate at the downstream end of the salt water tank regulates the water level in the latter. The outlined system of flume and tanks is supplemented with the necessary pipes and valves for proper operation and control.

The measuring instruments - that is, the hot film anemometers, a specially designed salinity probe, and the point gages - are supported on the aforementioned carriage, which is collapsable sidewise to permit its movement over the cross bars of the flume without removing the instruments.

4. EXPERIMENTAL RESULTS

After the necessary preparations and instrument calibration, each experiment was started and continued to a point where reasonable steady state conditions were established. Entrainment caused a gradual erosion of the salt water layer as a result of which salt water had to be periodically supplied from the preparation tank to the salt water basin. Space limitations do not permit a description of the detailed procedures of experimentation and calibration, which can be found in ref. (5) and in a forthcoming report. The measurements took place immediately after the steady state was achieved and lasted for about one-half hour, during which no measurable change in the flow conditions occurred. The primary measurements consisted of velocity and density profiles - with points more densely located around the interface. The instantaneous velocities were recorded on tapes from which the Reynolds stresses were subsequently computed. A total of 74 experiments were conducted with fully developed turbulent flows. The relative density difference, $\Delta\rho/(\rho + \Delta\rho)$, in these experiments ranged from 0.008 to 0.093. In such flows the velocity distribution in the neighborhood of the interface was found to be logarithmic and quite similar to that near solid boundaries. This is in general agreement with results from earlier studies (2, 9) but with major differences in certain important aspects. The velocity distribution laws and the flow structure around the interface is the subject of another forthcoming paper. It was found that the salinity distribution around the interface follows closely the law:

$$\frac{\rho_\ell - \rho}{\Delta\rho} = \frac{1}{2}\left[1 - \tanh\left(\frac{y - h_s}{\delta/2}\right)\right] \tag{50}$$

where ρ_ℓ is the local density, y is the distance from the bed, h_s is the depth of the density interface, and δ is the thickness of the interfacial zone, as defined in Fig. 3.

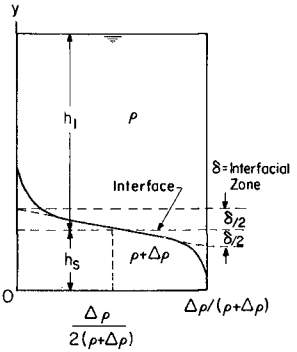

Fig. 3 Definition sketch for the interfacial zone.

As determined in an earlier study by the authors (4, 10), it was again found that the best correlation is obtained if f_i, determined by any one of the outlined four methods, is plotted against the dimensionless number $ReFr^2$ with $\Delta\rho/(\rho + \Delta\rho)$ as an independent parameter, where:

$$Re = \frac{4\overline{V}_1 R_h}{\nu}, \quad Fr^2 = \frac{V_1^2}{gR_h} \tag{51}$$

and where R_h is the hydraulic radius of the fresh water layer. The parameter $ReFr^2$ can be written in the form:

$$ReFr^2 = \frac{4\overline{V}_1^3}{g\nu} = \frac{4V_o^3 I_R}{g\nu} \tag{52}$$

where:

$$I_R = \frac{10}{\left[6(F_o')^{4/3} + 3(F_o')^{2/3} + 1\right]} \tag{53}$$

In Fig. 4 the results for four of the eight ranges of $\Delta\rho/(\rho + \Delta\rho)$ computed by all four approaches are shown with the average value of $\Delta\rho/(\rho + \Delta\rho)$ for each range indicated at the insert. The results from all four approaches can thus be compared. Here the interfacial friction coefficient is defined either as:

$$f_i = \frac{8\tau_i}{\rho\overline{V}_1^2} \tag{54}$$

or as:

$$\bar{f}_i = \frac{8T_i}{\rho \bar{V}_1^2} \tag{55}$$

with T_i computed from Eq. 47 for the second approach and from Eq. 49 for the fourth approach. In the third approach $\bar{f}_i$ was evaluated from Eq. 48. The comparison of these four sets of data leads to the following conclusions:

First, as in the earlier study by the authors (4, 10), the scattering of data points around each curve is minimal for a flow of this type. Secondly, there is a very good agreement between the data obtained from the first two approaches - that is, between the data based on direct shear stress measurements and those based on the integration of the equations of motion. These data constitute the lower family of curves. Thirdly, there is an equally good agreement between the results based on the two approximate approaches and which constitute the upper family of curves (dotted lines). Finally, a comparison of the two families of curves indicates that both approximate approaches give values of f_i considerably higher than the corresponding values obtained either by direct measurments or through the equations of motion. This difference is indicative of the effect of neglecting the bed shear stresses. It follows that $\bar{f}_i$, as determined from Eq. 48 through calibration, that is, by measuring L_i either in the laboratory or in the field (11), can be used as a convenient virtual friction coefficient for modeling purposes; it is not representative of the true shear stress at the interface, however.

The above conclusions hold also for the case of $\Delta\rho/(\rho + \Delta\rho)$ equal to 0.0225, 0.0355, 0.0485 and 0.082. For this reason the data for these cases are not reproduced in detail; instead, the summary of all eight curves based on the first and second approach is given in Fig. 5.

In Fig. 6 the curve corresponding to $\Delta\rho/(\rho + \Delta\rho) = 0.0225$ has been reploted together with reanalyzed laboratory data by Abraham and Eysink (1) and with one field data point from the Mississippi estuary (11). The agreement is quite good. This suggest that until the curves of Fig. 5 are implemented with field data, they can be tentatively extrapolated following the extrapolation of the 0.0225 curve of Fig. 6.

In Fig. 7, the results for $\Delta\rho/(\rho + \Delta\rho) = 0.0225$ are compared with resent results obtained by Powell for flow of fresh water over a semistagnant deep water layer in an open conduit and for a relative density difference close to 0.024 (12). When plotted against the Reynolds number only, these two sets of data deviate strongly (Fig. 7a); however, they appear to closely agree when they are plotted against $ReFr^2$. In fact, the drop of the curve for low values of $ReFr^2$ agrees with the trend observed in the authors' experiments. Thus, Powell's point for Re≈22000, which in his original diagram (Fig. 7a) seems to be in error, is in fact in agreement with the general law derived from this study.

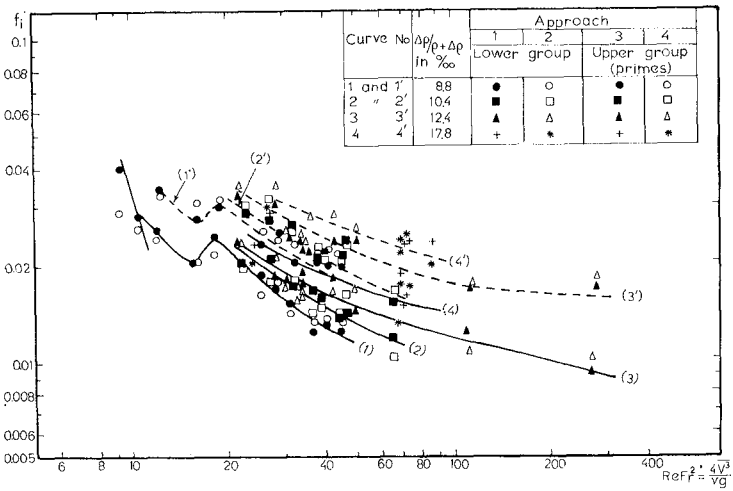

Fig. 4. Interfacial friction coefficients obtained from all four approaches.

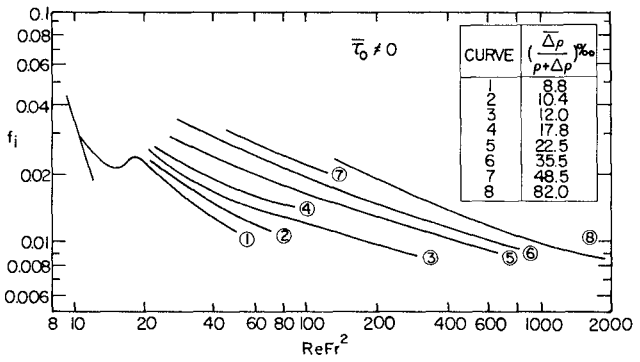

Fig. 5. Summary of interfacial friction coefficient curves based on approaches (1) and (2).

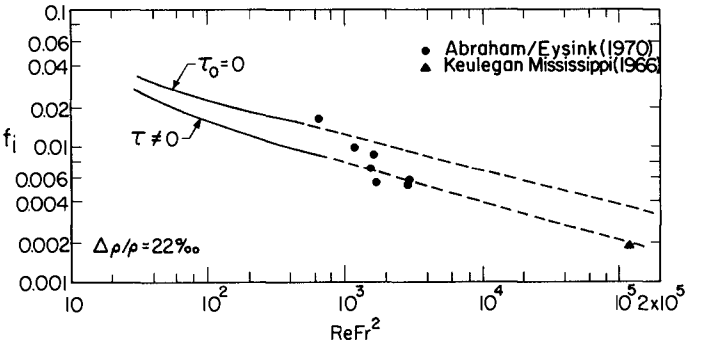

Fig. 6 Comparison of results of the present study with test data of previous studies.

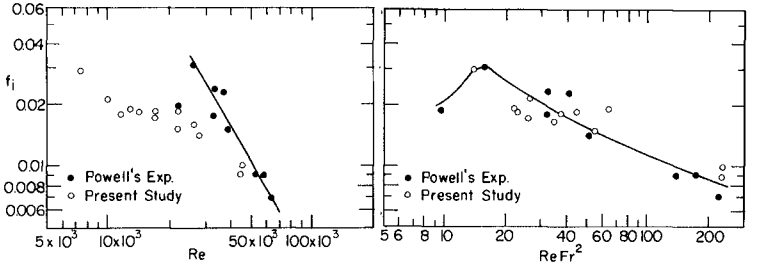

a. Plot vs Re b. Plot vs $ReFr^2$

Fig. 7 Comparison of results of present study with Powell's data (12).

The bed friction coefficient, f_o, defined as:

$$f_o = \frac{8T_o}{\rho \bar{V}_1^2} \tag{56}$$

has been determined from Eq. 46 where $T_1 = \tau_1$ was computed from Eq. 54 for values of f_1 taken from Fig. 5. The value of λ was determined for each experiment and the results are shown in Fig. 8. λ appears to be a function of the number $ReFr^2$ only while for values of the latter smaller than 100, it is essentially constant and equal to about 1.4. The results are plotted in Fig. 9 as a family of curves similar to the

one of Fig. 6. It is observed that, contrary to conclusions of earlier studies (7, 8), f_o is clearly smaller than the corresponding f_i.

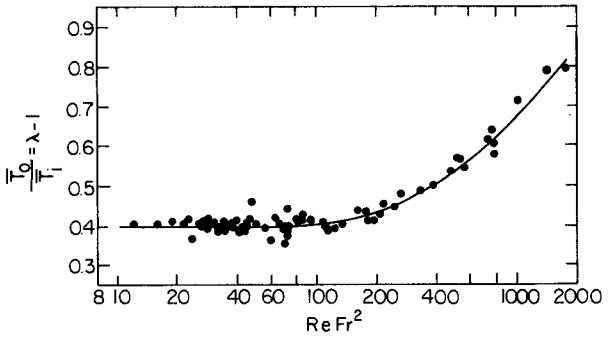

Fig. 8 Variation of $\lambda = \tau_i/\tau_o$ with $ReFr^2$.

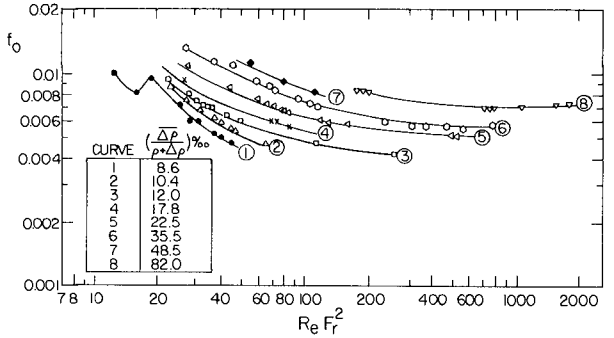

Fig. 9. Bed friction coefficients, f_o.

5. SUMMARY AND CONCLUSIONS

Laboratory experiments and theoretical analyses led to a new relationship linking the friction coefficients at the interface and at the bed of arrested saline wedges to the pertinent flow parameters and fluid properties. The relationships are presented graphically as a family of curves with $ReFr^2$ as an abscissa and the relative density difference, $\Delta\rho/(\rho + \Delta\rho)$, as an independent parameter. The scattering of data points was minimal and much lower than in earlier studies on the subject. In the present correlations the number $ReFr^2$ incorporates the friction, gravity, and inertia forces, which control the main flow, while the buoyant forces, which are responsible for the

density stratification and the asociated flow pattern have been separated and introduced through the parameter $\Delta\rho/(\rho + \Delta\rho)$.

This study indicated that values of f_i evaluated through an integration of the equations of motion closely agree with values based on measured velocity profiles and Reynolds stresses. Values of f_i obtained from the simplified and frequently used Schijf-Schoenfeld's one-dimensional analysis were shown to be higher than corresponding values based on the previous two methods.

ACKNOWLEDGEMENTS

This study has been supported by the U.S. National Science Foundation under Grant No. ENG 76-11537-A01. Travel funds were provided to the second author by the same institution under Grant No. CEE - 8214607 for presentation of this paper before the 18th International Conference on Coastal Engineering in Cape Town, South Africa. Both supports are gratefully acknowledged.

REFERENCES

1. Abraham, G. and Eysink, W.D., "Magnitude of Interfacial Shear in Exchange Flow," Journal of Hydraulic Research, I.A.H.R., Vol. 9, No. 2, 1971.

2. Csanady, G.T., "Turbulent Interface Layers," Journal of Geophysical Research, Vol. 83, No. C5, 1978, pp. 2329-2342.

3. Delft Hydraulics Laboratory, "Momentum and Mass Transfer in Stratified Flows," Report on Literature Study, R880, Delft, Netherlands, 1974.

4. Dermissis, V., "A Study of the Interfacial Friction Coefficient in a Two-layered Fluid System," (in Greek) Dissertation for the Degree of Doctor in Civil Engineering, School of Engineering, Aristotoles University of Thessaloniki, Greece, 1977.

5. Dermissis, V., "A Study of the Interfacial and Bed Shear Stresses in an Arrested Saline Wedge and of the Interfacial Flow Structure," (in Greek) Professorial (Dozent) dissertation, School of Engineering, Aristoteles University of Thessaloniki, Greece, 1982.

6. Ippen, A.T. and Harleman, D.R.F., "Steady State Characteristics of Subsurface Flows," Circular No. 521 "Gravity Waves", U.S. Dept. of Commerce National Bureau of Standards, 1952.

7. Keulegan, G.H., "Significant Stresses of Arrested Saline Wedges," Rept. No. 4267, National Bureau of Standards, August, 1955.

8. Keulegan, G.H., "The Mechanics of an Arrested Saline Wedge," Ch. 11, Estuary and Coastline Hydrodynamics, edited by A.T. Ippen, McGraw-Hill, 1966.

9. Lofquist, K., "Flow and Stress Near an Interface between Stratified Liquids," The Phys. of Fluids, Vol. 3, No. 2, 1960, pp. 158-175.

10. Partheniades, E. and Dermissis, V., "Interfacial Friction Coefficients in a Two-layered Stratified Flow," Proceedings, 16th Coastal Engineering Conference, Hamburg, Germany, Vol. 3, Ch. 170, pp. 2778-2797.

11. Partheniades, E., Dermissis, V. and Mehta, A.J., "On the Shape and Interfacial Resistance of Arrested Saline Wedges," Proceedings, 15th Congress of I.A.H.R., Sao Paulo, Brazil, Vol. I, 1975, pp. 157-164.

12. Powell, G.M., "The Structure of Velocity and Density Interfaces in a Weekly Turbulent Stratified Shear Flow," A dissertation presented in partial fulfillment of the requirements for the degree of Doctor of Philosophy, University of Florida, 1979.

13. Schijf, J.B. and Schoenfeld, J.C., "Theoretical Considerations on the Motion of Salt and Fresh Water," Proceedings, Minn. Intern. Hydr. Conv., 1953, pp. 321-333.

MORPHOLOGICAL REACTIONS OF TIDAL SYSTEMS DUE TO NEARSHORE CONSTRUCTION WORKS

by

R. DIECKMANN[1], H.W. PARTENSCKY[2], H. SCHWARZE[3]

1. INTRODUCTION

The nearshore region of the North German North Sea coast is characterised by a large area of tidal flats with a width of 10 to 30 km (Fig. 1).

The development of the structure of this coastal area in the past centuries was mainly determined by several severe storm surges, which have destroyed the formerly existing coastline. In its present state the coastal area is subdived into numerous tidal flats, islands and peninsulas of different size and more or less deep channels and small gullies.

Due to its historical development, this area cannot be expected to be morphologically stable. Once people learnt to build safe dikes, the coastline existing at the time was fixed whilst the islands in the shore belt were protected against flooding during storm surges.

However, the shore belt is furthermore exposed to waves and tidal currents which cause - apart from certain shiftings of gullies - extensive permanent erosion and sedimentation in parts of the shore belt with an increasing tendency in the last decades. The nearshore region at some places on the coast is extremely endangered in its function as part of the coastal protection system, consisting of the dike, the foreshore above MHW and the tidal flat area.

First attempts to achieve morphological stabilisation of the nearshore region consisted in the construction of dams normal to the coastline. However, the shore belt still remained morphologically unstable and could not yet be transformed into a stable system.

---

1) Senior Research Engineer, Dipl.-Ing.
2) Director, Professor Dr.-Ing. Dr.phys.
3) Chief Engineer, Dr.-Ing.

FRANZIUS-INSTITUT, University of Hannover,
Federal Republic of Germany

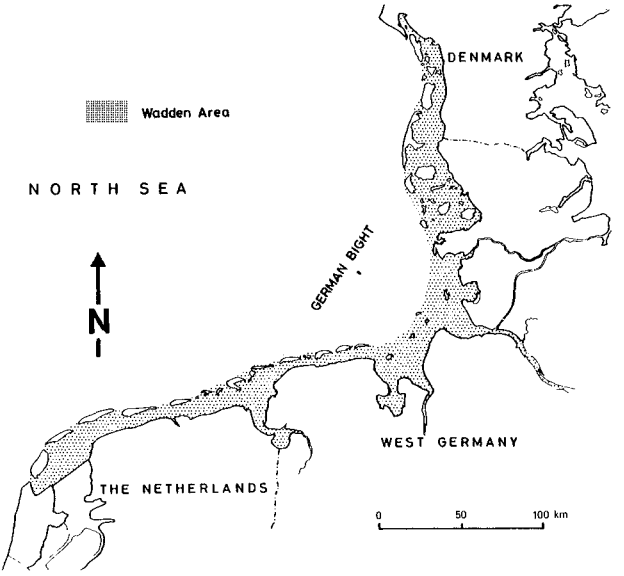

Fig. 1: Map of the North Sea with the German Bight

It was the aim of intensive investigations at the FRANZIUS-INSTITUT, together with the local authorities involved in these problems, to demonstrate the influence of artificial structures on the morphological reactions of well defined drainage areas, consisting of tidal flats and gullies, to a morphological stabilisation of the shore belt.

2. CONCEPT OF INVESTIGATIONS

On the basis of former investigations showing qualitative relationships between geometrical and hydrological parameters, investigations were performed in order to quantify morphological changes to be expected as a result of a variation of a drainage area due to dikes or reclamation works, or in other words, the artificial structures necessary to stabilise a morphologically unstable drainage area.

For instance, a stability criterion was determined for tidal systems, in which the ratio of the tidal prism upstream of a certain cross-section to the area of that cross-section at mean water level is a constant value. According to this criterion, if the tidal prism decreases, the cross-section will decrease proportionally.

In a more detailed investigation (RENGER and PARTENSCKY,1974), the evaluation of some 25 tidal systems, in which artificial constructions had not yet been carried out, showed a clear relationship between the tidal prism (water volume between Mean Low Water and Mean High Water Level) V_{TP} (in 10^6 m^3) and the corresponding drainage area E (in km^2), as follows (Fig. 2)

$$V_{TP} = 1.65 \cdot E^{1.036} \quad (1)$$

as well as between the volume of the tidal basin below Mean Low Water V_{MLW} (in 10^6 m^3) and the drainage area E (in km^2) (Fig. 3)

$$V_{MLW} = 4.39 \cdot 10^{-2} \cdot E^{1.643} \quad (2)$$

Certain scatter in the data may be explained by the fact that not all selected areas are in a true stable state.

The results of these investigations represent an important step towards solving the problem, since the possibility of generalising the results for all drainage systems has been demonstrated. However, deviations of calculated mean values from actual values for a certain drainage area using the above-mentioned equations provides only an approximate indication of the instability of the overall area. The distribution of erosion and sedimentation to be expected in different parts of the drainage area could not, however, be determined.

3. SUMMARY OF RECENT RESULTS

Recent investigations, carried out on approximately 50 tidal flat systems with different subsystems and subsubsystems along the Dutch, German and Danish coasts, have shown that the above criteria are also generally valid for parts of these basins.

Equations (1) and (2) can therefore be used in a stepwise determination of the increasing volume of the tidal basin from the origin of the main gully towards the sea.

For these evaluations, drainage areas are subdivided into portions as given by the distribution of gullies, branching more and more towards the coast line. Watersheds are determined on both sides of the gullies as boundaries of the drainage area belonging to the gullies (Fig. 4).

For each of these drainage areas, water volumes below MLW, as well as volumes of the tidal prism, are calculated and summarised for the whole drainage area.

The latter calculation results in a summation curve for the tidal volume relating to the surface area of the tidal basin. This curve describes the stable morphological and hydrological state of a drainage system.

This represents an important result of the investigations

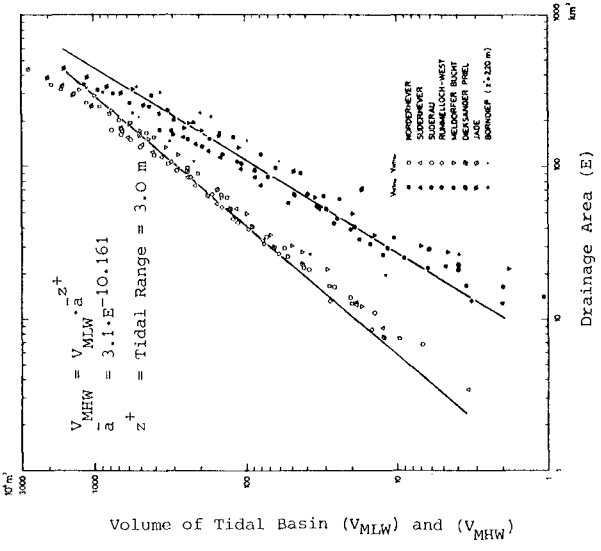

Fig. 3: Relationship between Volume below MLW/MHW and Drainage Area

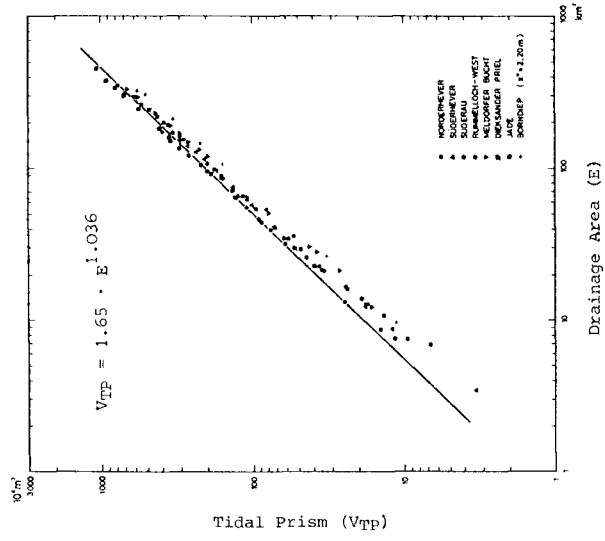

Fig. 2: Relationship between Tidal Prism V_{TP} and Drainage Area E

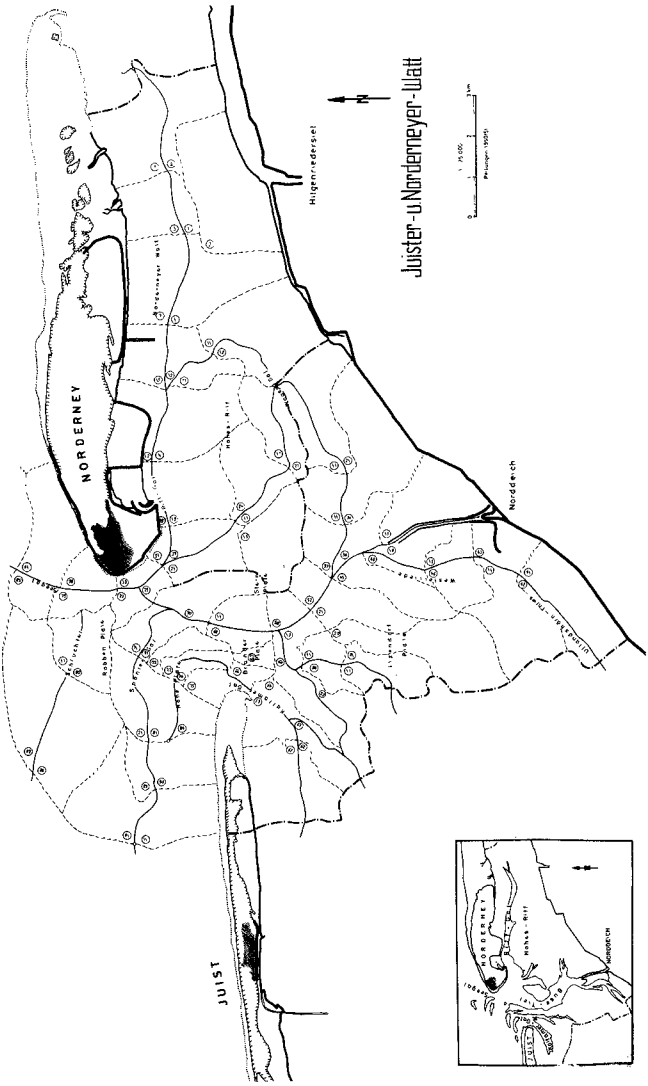

Fig. 4: Subdivision of a Drainage Area (Juister/Norderneyer Tidal Basin, Germany)

with respect to the description of the inner structure of a drainage area.

On the basis of the stability criteria for tidal systems, the stability of a certain area can be evaluated by comparing the measured tidal volume to that determined analytically from the volumetric summation curve based on equations (1) and (2). The deviation from the theoretical curve, which represents the equilibrium state, indicates the degree of instability of the tidal system and subsystems concerned.

In the case of a volumetric deficit, in which the calculated curve lies above the measured curve, erosion may be expected in the tidal basin. In the case of a surplus in tidal volume, a shrinkage of the tidal basin due to sedimentation will occur.

Fig. 5 illustrates a well-balanced tidal basin (Rummelloch-West). In Fig. 6, a tidal basin is presented in which sedimentation is present (Süderau).

The stability criteria show that a given drainage area is associated with a well-defined volume. This equilibrium can be disturbed by artificial measures such as nearshore constructions. The morphological reactions of the tidal system can be determined quantitatively from a comparison of the volumetric summation curves.

In addition, sedimentation in a nearshore region can be caused by the construction of offshore dikes and artificial dams.

Comparisons of water volumes, evaluated on the basis of hydrographic charts and soundings, with calculated volumes, have shown that some of the tidal basins on the northern coast of the Federal Republic of Germany are not in a state of equilibrium, but are rather subject to temporary erosion and sedimentation phases. The erosion of these areas significantly endangers the structural stability of the sea-dikes as well as of the islands in the vicinity of the coast.

For instance, in the last 50 years, increasing erosion has occurred in a gully between an island situated approximately 10 km from the coast and the shore line. In 1930 the water depth of this gully was only 0.5 m. Up to now the gully has deepened to nearly 12 m. The adjacent subdrainage areas are also in a state of erosion.

This problem can be overcome by constructing offshore dikes and control-dams between the mainland and the island concerned, thereby reducing the drainage area of the tidal basins. By this means, areas of erosion in a tidal basin may be influenced in such a way as to convert the deficit of volume into a surplus. Plans have been made to stabilise a coastal region of about 450 km^2 in this manner.

As an example, results of evaluations for a subsystem of the tidal system HEVER in the North Frisian shore belt are given

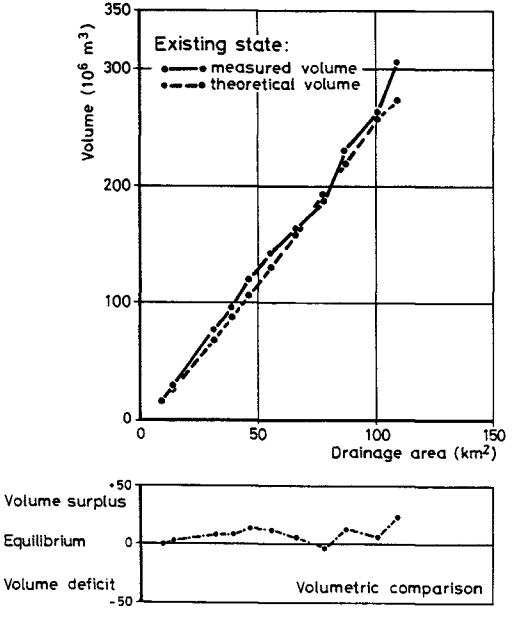

Fig. 5: Volumetric Comparison for Tidal Basin RUMMELLOCH as an Example of a well balanced Tidal Basin

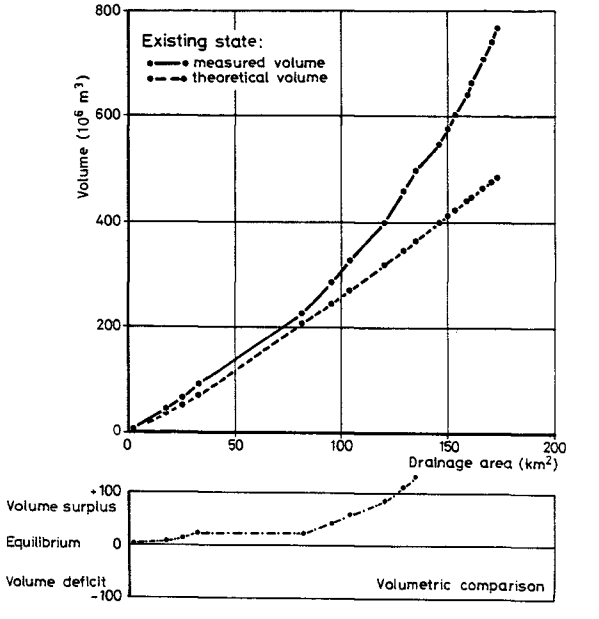

Fig. 6: Volumetric Comparison for Tidal Basin SÜDERAU as an Example of a Tidal Basin in which Sedimentation is Present

in Fig. 7. In this case, the summation curve for the water volume below MHW is plotted in relation to the length of the main gully of the subsystem HEVER. Calculations for the determination of the stability criterion were carried out using equations (1) and (2). The measured volume of water is determined on the basis of bathymetric plans.

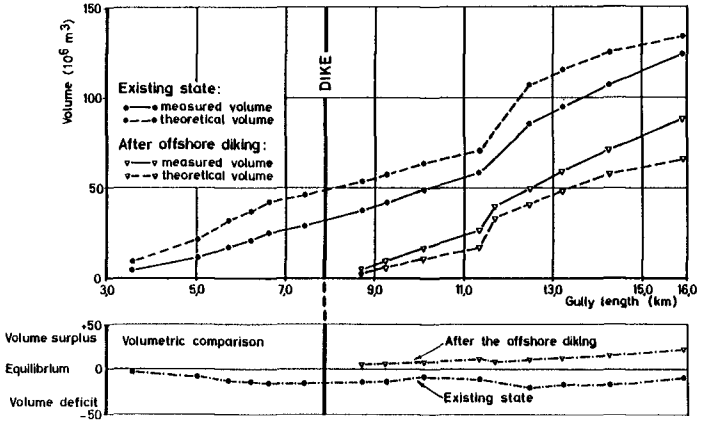

Fig. 7: Volumetric Summation Curves for Tidal Basin HOLMER FÄHRE at MHW before and after the Planned Offshore Diking Project

The comparison of both curves shows erosion throughout the entire system. The system is unstable and erosion must be prevented by an artificial construction, such as a dike, which reduces the drainage area.

By considering a certain dike, volumetric summation curves calculated both theoretically from equations (1) and (2), and evaluated on the basis of bathymetric plans for the reduced drainage area, are also plotted in Fig. 7. A comparison of the volumetric summation curves shows a change in the morphological behaviour of the system. The former volume deficit could be converted into a volume surplus, which means that sedimentation can be expected to stabilise the nearshore region in all cases.

4. APPLICATION OF THE RESULTS

Such investigations were carried out for all main drainage areas in the latter region of the German shore belt. An example of the results for one of the subareas is illustrated in Fig. 7.

On this basis of these results, a system of dams and dikes were planned in order to avoid further dangerous erosion of the nearshore flats (Fig. 8).

The conservation of the belt of foreshore and flats is vitally necessary to ensure stability of the islands distributed in the shore belt as well as the coastline. Nearshore reclamation works involving artificial groynes and trenches will be introduced in order to support and accelerate the natural morphological changes induced artificially.

The results of the investigations indicate the magnitude of volumetric changes to be expected in a tidal system until a morphologically stable state is achieved. The time dependent development of erosion or sedimentation, as well as the time necessary to establish a new final state following the construction cannot be predicted on the basis of the applied method at the present time.

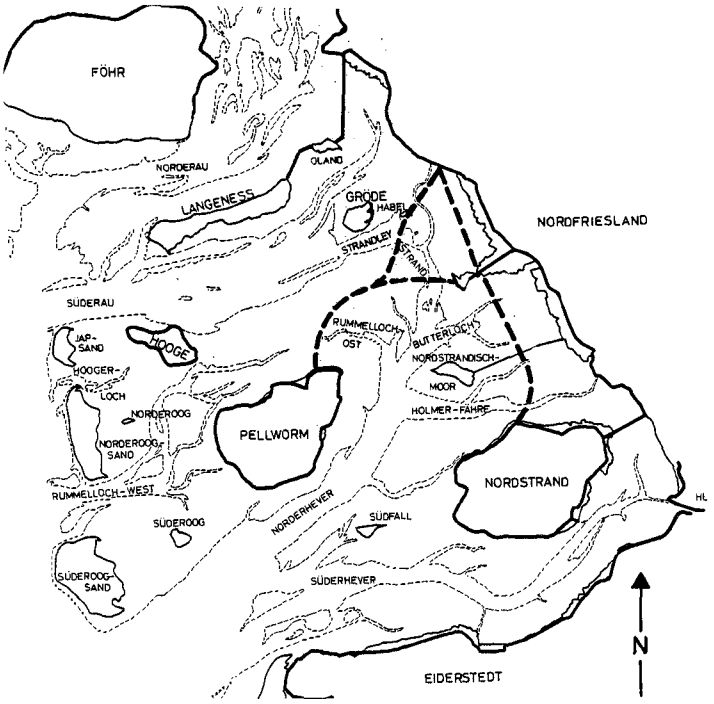

Fig. 8: Offshore Diking Project in the North Frisian Shore Belt

During the period of construction, and particularly after completing the system of dams and dikes, detailed measurements will be carried out in order to monitor morphological development. A minimum necessity is to provide confirmation of the empirically determined basis for estimating such a large impact on a tidal system.

5. REFERENCES

RENGER, E. and PARTENSCKY, H.W.: Stability Criteria for Tidal Basins. Proc. 14th International Conference on Coastal Engineering, Copenhagen, Vol.II, pp. 1605 - 1618, 1974

FRANZIUS-INSTITUT: Stabilitätsuntersuchungen für das südliche nordfriesische Wattenmeer. Report No. 422, 1979 Unpublished

PARTENSCKY, H.W. und SCHWARZE, H.: Wissenschaftliche Gutachten zu den hydrologischen und morphologischen Auswirkungen der geplanten Baumaßnahmen in der Nordstrander Bucht. Unpublished Report, 1980

PARTENSCKY, H.W.: Neue Erkenntnisse über das Stabilitätsverhalten und den Sedimenttransport in Watt-Priel-Systemen. Mitteilungen des Franzius-Instituts für Wasserbau und Küsteningenieurwesen der Universität Hannover, Heft 50, 1980

A SURVEY OF MAN-MADE TIDAL SWIMMING POOLS ALONG THE SOUTH AFRICAN COAST

by

D E BOSMAN*, D J P SCHOLTZ**

1. INTRODUCTION

A large number of man-made tidal swimming pools (two examples are shown in Figure 1) exist along the South African coast. They are usually situated on rocky outcrops in the close vicinity of popular sandy bathing beaches to provide protected bathing conditions in these areas mainly for children and elderly people. Some tidal pools, especially along rocky coast, provide the only safe bathing facilities. Besides affording protection against waves and surfzone currents the pools provide protection from sharks. A large number of tidal pools were built during the early 1950s along the Natal South Coast after the occurrence of a relatively large number of shark attacks on bathers on that coast.

The semi-diurnal tide with a range of about 1,5 m along the South African coast makes it possible for pools to be built such that water replenishment can occur during every high-water (approximately every 12 hours) during both neap and spring tide periods.

Presently, there exists a great need for more tidal pools as part of the demand for more recreational facilities along the South African coast. However, no information on design criteria could be found in the literature.

2. OBJECTIVES

Because of the existing lack of design guidelines for tidal pools it was decided to make a detailed survey of the existing pools. Data obtained from such a survey could then contribute to the first step in identifying factors which should be considered to ensure safe swimming conditions, effective operation of pools, minimum maintenance and minimum impact on the environment.

---

* D E BOSMAN: Geusteyn, Forsyth & Joubert, Inc., Republic of South Africa.

** D J P SCHOLTZ: National Research Institute for Oceanology, Republic of South Africa.

SUNSET BEACH TIDAL POOL

STRANDFONTEIN TIDAL POOL

FIGURE 1. EXAMPLES OF TIDAL POOLS

3. METHODS USED

Information on types, physical characteristics, maintenance, operation and usage was obtained from questionnaires sent to local authorities, followed up by discussions with the authorities and by making site visits to the pools.

Detailed observations such as of rate of overtopping versus tidal level were made at 13 of these pools.

Available aerial photographs of pools were also used as a source of information on the location and environment of the pools.

4. RESULTS

4.1 General

Data for 80 tidal pools (about 90 per cent of the existing pools along the 3 000 km coast) were obtained. Most of these pools are situated in the more highly developed coastal areas i.e. the Cape Peninsula, Natal South coast, Port Elizabeth and East London areas. The distribution of tidal pools along the South African coast is shown in Figure 2. It was found that tidal pools play an important role in providing safe bathing conditions. On rocky coasts and dangerous sandy beaches tidal pools provide, in many cases, the only safe bathing conditions, and where a safe bathing beach for adults exists, a tidal pool close to it can provide in the important need of safe bathing conditions for small children.

4.2 Types

Two basic types of pools could be distinguished:

(i) Pools which are partly enclosed by walls. The landward sides of these pools consist of sandy beaches.

(ii) Pools which are fully enclosed by walls. These are either attached to the shore or can become detached from the shore during the high water.

Figure 3 illustrates schematically the different types. The pools which are partly enclosed by walls are usually situated on beaches with relatively flat slopes. (See a, Figure 3). Their walls enclave part of the beach so that the depth in the pool varies from zero at the beach to the maximum depth of the pool at the seaward side. Wall crest levels of these pools are relatively low so that they usually do not significantly interrupt the longshore sediment movement in the beach zone. The pools which are fully enclosed by walls are usually situated on beaches with relatively steeper slopes. Pool b in Figure 3 illustrates the detached type and pool d the type attached to the beach with relatively high walls which exclude the beach from the pool and reach up to the primary dune. The semi-detached type (c, Figure 3) tends to intercept the longshore sediment transport on the beach with a consequent sand build-up next to the pool. The sand build-up can be of such an extent that large quantities of sand can eventually enter the pool.

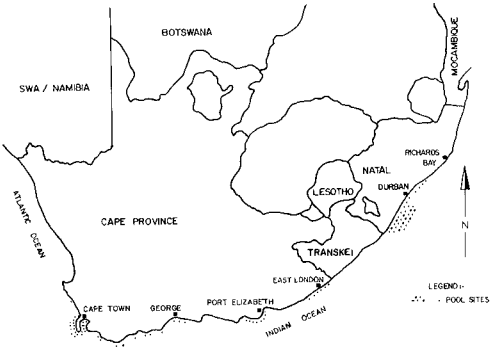

FIGURE 2: DISTRIBUTION OF TIDAL POOLS ALONG THE SOUTH AFRICAN COAST.

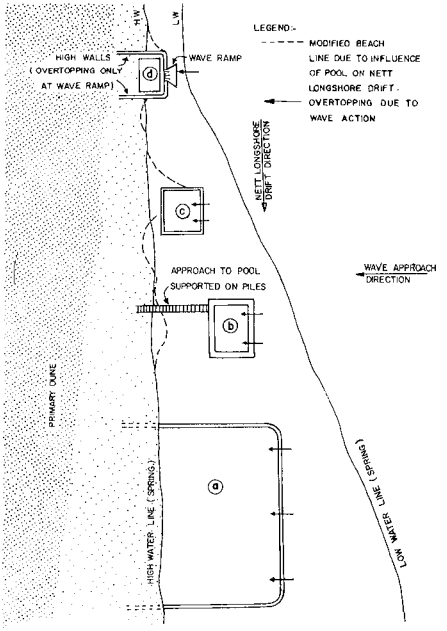

FIGURE 3: SCHEMATIZATION OF TYPES OF POOLS

4.3 Physical Characteristics

The walls of all pools (mostly of mass concrete) are founded on rock except in one case where the walls are partly founded on steel sheet piles driven 6 m into sand. (Besides serving as a foundation support to the wall the sheet piles also limit seepage of water from the pool). The foundation level of the walls are in most cases above the mean low spring tidal level.

Distributions of pool water area, wall crest level and maximum pool depth for the majority of the pools in Natal and Cape Province are shown in Figures 4, 5 and 6 respectively and the dominant ranges of these are summarized in the table below:

Parameter	Natal	Cape Province
Water area (m^2)	500 - 1 000	500 - 1 500
Wall crest level (m above mean sea level)	1,0 - 2,0	0,5 - 1,5
Maximum pool depth (m)	1,25 - 2,0	1,25 - 2,25

The wall crest levels of most of the pools are above the mean high water spring tidal level with the predominance of crest levels about 0,1 m to 0,5 m above mean high water spring level.

The majority of the pool walls facing the approaching waves have seaward slopes between 2:1 and vertical and crest widths between 0,4 m and 1,0 m.

Pool floors consist usually of either sand or rock or a combination of the two. Some pools have concrete floors.

All pools are provided with drain pipes at the lowest position in the pool to allow drainage during low water spring tides.

4.4 Operation

Detailed observations made of 13 pools showed that the rate of water inflow due to wave overtopping as well as the tidal level at which inflow commences is largely influenced by the location of the pool (namely, whether protected from wave attack by shallow rocky outcrops or whether exposed to large waves).

Other important factors influencing inflow are tidal level, wall crest level, offshore wave conditions and local wind conditions.

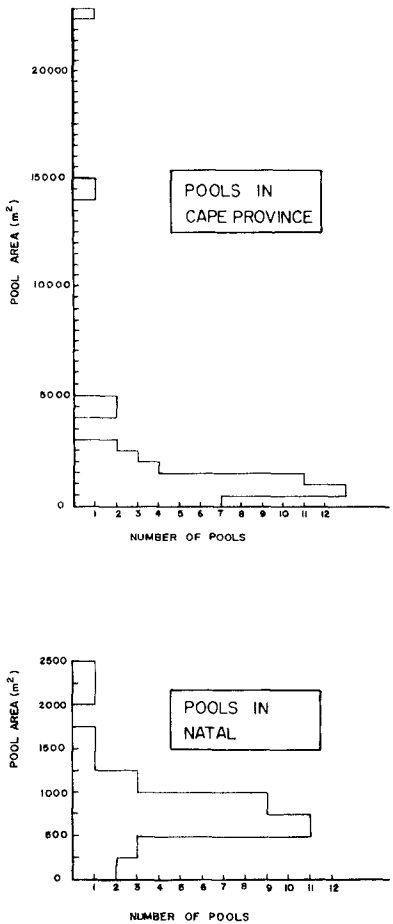

FIGURE 4: DISTRIBUTION OF POOL AREAS

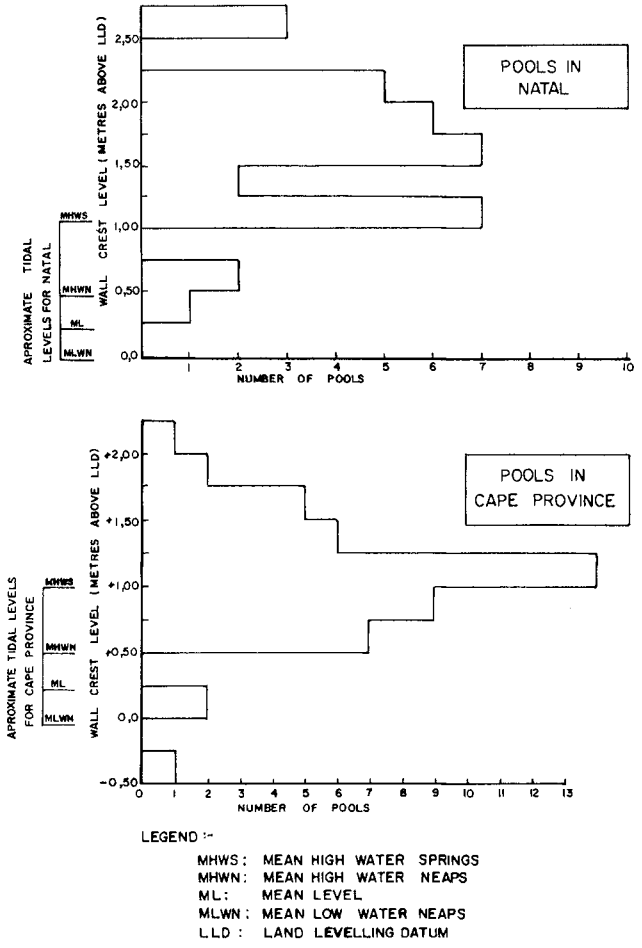

FIGURE 5: DISTRIBUTION OF WALL CREST LEVELS

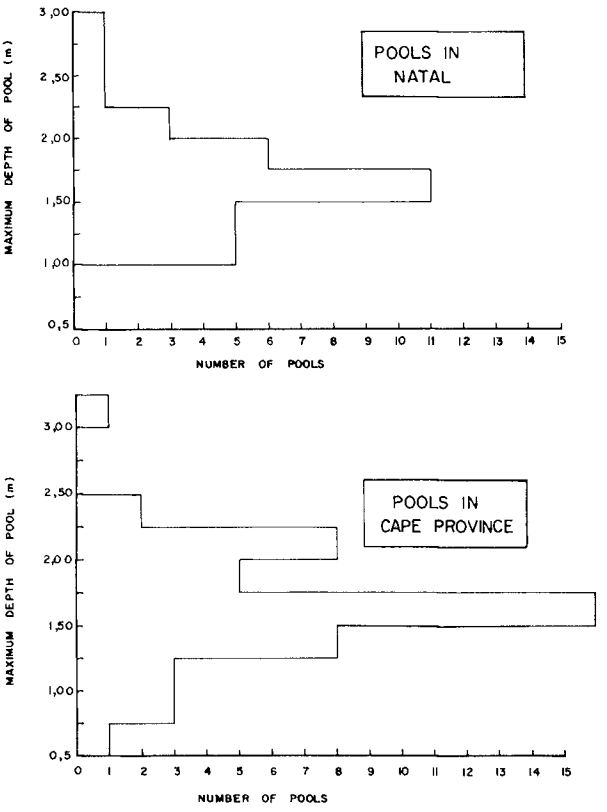

FIGURE 6: DISTRIBUTION OF MAXIMUM DEPTHS OF POOLS

Because of the above many factors, a large range in the water inflows during high water spring tide of between 20 and 650 m^3 per m length of wall was recorded.

4.5 Maintenance

A large number of pools are drained fortnightly to clean the pools, remove accumulated sand and to enable the rock and concrete surfaces to be washed with lime to control the growth of slippery algae. Other chemicals used to control algal growth are carbide and copper sulphate.

Several well-sited pools with low crest levels are self maintaining since inflow is frequent and sufficient to minimize the growth of algae and sand accumulation. These pools are usually submerged during high water spring tides.

4.6 Problems

A few pools are frequently sanded up due mainly to incorrect siting. Two of these are sanded up to such an extent that they are out of use.

Water replenishment at about eight of the pools is considered to be insufficient. This leads to stagnant water conditions and excessive algal growth.

Some of the pools are dangerous since bathers can be washed from side or back walls out to sea.

Parts of walls of three of the pools have been destroyed by waves. This was probably due to weak walls and improper bonding between wall and rock foundation.

5. DESIGN FACTORS TO BE CONSIDERED

The study indicated a number of factors which should be considered in the design of a recreational tidal swimming pool.

(a) The needs of the bathers: It should be established whether provision should be made for small children as well as adults and the type of bathing (e.g. swimming, diving, playing etc.) required by the bathers.

(b) The siting of the pool: The pool should preferably be situated so that the walls can be founded on rock where possible. Where no rock foundation is present sheet piling could be considered as a foundation for the walls. Seasonal variation of the beach profile as well as longshore sediment transport in the beach zone should be considered in the siting to prevent the pool from being sanded up.

Sufficient consideration should also be given to the aesthetic and ecological considerations to minimize the impact of the structure on the environment.

(c) Water replenishment by wave action: Sufficient quantities of

fresh sea water should enter the pool frequently enough and overflows should be situated so that adequate renewal of water throughout the pool is ensured. A general criterion for inflow would be to stipulate that inflow should occur at least during high water neap tides with dominant wave conditions. The walls should be built rather too low than too high since it will be easier to raise the walls if this is afterwards found to be necessary. The seaward slope of the wave-facing wall should be about 2 horizontally on 1 vertically or flatter since flatter slopes increase overtopping and stability.

(d) Safety: The pool floor should be even and if the pool is not of uniform depth the slopes should be gentle. Situations where overwash from walls to sea can occur which could be a danger to bathers should be prevented. Intakes of drain pipes should be covered with grids. Notice boards indicating water depths should be provided.

(e) Maintenance: The floor level of the pool should be above low water springs to allow drainage. It appears to be good practice to whitewash the walls with lime when the pool is cleaned as this apparently retards the growth of algae and shells and also gives the pool an attractive and tidy appearance.

DESIGN OF COASTAL STRUCTURES FOR RECREATIONAL PURPOSES
by G H O'CONNELL Pr Eng B.Sc C.E.

1. INTRODUCTION

1.1 Although the major aspect of this paper deals with a specific part of the South African coast line it is believed that certain fundamental parameters which emerge are applicable to the greater part of the Southern African coast line of 2954 km.

Typical of the African continent the nature of the Southern African coast line is regular and even with few bays or inlets and has long unprotected beaches subject to long- and off-shore current patterns.

The absence of barrier islands as well as the few in number of protected lagoons and inlets, requires the creation of artificial tidal enclaves or the protection of selected sections of beach to ensure safe bathing conditions where further extensions of existing areas is indicated both by an increase in the population as well as changing socio-economic conditions which place access to the coastal recreation areas, as an increasing facility, to a steadily growing number of people.

This need has been intensified in South Africa by the rapid urbanisation and socio-economic development of the rural population as well as the geographic dispersion of the population of which a high percentage lives at or near the coast.

It is unfortunately so that the need to provide additional access to the beach areas exists in such areas where maximum exploitation of the beach frontage has already taken place and where new development must take place accordingly in less favourable conditions and subject to various constraints imposed by existing development in these areas.

These constraints are inter alia the development of industrial areas right onto the beach front, urban area development on the beach front and sewage outfall works discharging raw sewage into the surf zone.

The absence of an adequate inland area contiguous to the beach, forces planners to absorb an increasing part of the primary dune area to accommodate parking areas and other facilities required for the accommodation of the mass migration to the beaches.

These very constraints imposed upon the planner as well as the capital limits to development, in itself creates a further concentration of people in the most vulnerable part of the beach environment.

1.2 The paper now laid before this congress seeks to evaluate various considerations and factors which lead to the adoption of certain design parameters which may satisfy the criteria of safety, user preference, health standards, beach stability and sympathetic environmental treatment.

The creation of a pleasing and sensible development of beach recreation areas may in turn be seen to create a need for a service infrastructure including access under peak conditions not dissimilar to those associated with a new and popular sports stadium.

The submissions made provide certain suggested standards for the service infrastructure for the accommodation of peak conditions. Notwithstanding that the objective of the submissions is to achieve a common philosophy in planning which may be applied generally, the analyses undertaken are relevant to particular sections of the coast line and are user orientated to that section of the population most likely to make use of the facilities thus created.

However, the successes attained as well as the errors incurred may hopefully stimulate sensible and responsible planning for the future.

1.3 Whereas the design of extensive coastal structures involves the complete spectrum of environmental, sociological, transport, future urbanisation and economic research, it is patently not within the terms of reference of this paper to deal with these other than in general terms when such have a direct bearing on the structure design and general arrangement being promoted.

The author expresses the opinion however that controlled and planned exploitation of selected portions of the coast to accommodate the needs of a growing and economically developing population is of greater overall environmental benefit than is a lack of planned development and a consequent concentration of human activity in the ecologically sensitive areas as an unlimited dispersion of temporary sojourners without a sense of permanent involvement.

2. USER CONSIDERATIONS AND PREFERENCES

2.1 Other than in the case of natural parkland areas where the emphasis is in the maintenance of the environment

and ecological system, the creation of artificial bathing areas is both to accommodate man and also to control his further exploitation of the coastal areas for recreation purposes.

In this regard no sensible planning can be undertaken without an indepth study of the user characteristics and preferences. User preferences vary from the east coast to the west coast over the length of the coast line of 2954 km. where the warm Mozambique-Agulhas current, which skirts the east and south coasts as far as Cape Point, is replaced by the Cold Benguela System flowing north along the west coast, with climatic conditions which vary from dominantly subtropical conditions on the North and East coast to generally cool temperate conditions of the South coast with the uninvitingly cold waters of the West.

These climatic as well as water temperature conditions determine the relative degree of emphasis on bathing or dry beach activity.

2.2 User preferences are also related to the heterogeneous character of the South African population and demographic considerations pertinent to the community involved. These in turn are affected by the degree of cultural and social heterogeniety prevalent as well as economic standards of different sections of the community.

Notwithstanding this complexity of influencing factors, man tends to adjust himself in his recreation to the circumstances and environment existing, provided such satisfies certain norms and in this regard the following is quoted from the report titled "Coastal Development Project - False Bay Coast - Cape Town". (Reference No 1).

"The relevant quality of bathing and beach enjoyment conditions, whether natural or man created, is of considerable but not sole importance, and are evaluated by the individual in terms of a number of other facets of his recreational pursuits and his decision to utilize a particular recreation area is the result of his assessment of all relevant factors in their inter-related importance, of which the accessibility of the beach area, provided that all other aspects are reasonably satisfied, may be of highest priority to the individual.

Under accessibility we consider that the actual point at which the motorcar is parked or where the bus delivers passengers, relative to the point where the individual may start 'doing his thing' is, in relative importance of equal value to the route and quality of access road from home to recreation destination.

It has been established that particularly in the case of the more affluent section of the total society, people will travel considerably further to reach a beach where they may step out of the vehicle onto the sand or where they may park their vehicle in the immediate vicinity of the beach and bathing area with good sight of beach activity and a continuous sense of involvement in the beach environment.

Throughout South Africa the significance of this aspect is revealed by the degree of preference given to those areas where parking is immediately adjacent to the beach, lagoon or bathing pool."

This inter-relationship between accessibility and quality of recreation, places an additional constraint on the selection of sites for development and requires the coastal engineer to be pleasingly creative under the most adverse physical conditions in order to create safe bathing conditions as near as practical to immediate access from motor vehicle parking areas which are served by arterial road systems.

The capital cost of the transport infrastructure synonomous with beach development schemes encourages the urban planner to create out of the area a grand terminus for all conceivable recreation as representing the optimum utilisation of capital resources.

The presence however in the vicinity of the beach area of other forms of entertainment such as park and playground development does not of necessity increase the popularity of the beach area but attracts generally a differently motivated recreation seeker whose presence in the area places a fresh complexity on the service infrastructure required and due to various factors adversely affects the comfort, safety and security of parents with young children.

The population age structure in respect of communities in the vicinity of which new beach recreation areas are being planned and which communities accordingly will be the dominant users of the facilities provided is particularly significant as will appear from the following figures applicable to the False Bay area.

Population Age Structure	
0 - 4 years	16,3 percent
0 - 9 years	32,1 percent
0 - 14 years	45,0 percent
0 - 19 years	55,5 percent
0 - 24 years	65,2 percent

For planning purposes, while giving the family factor due weight, the visitor population age structure is

likely to be :

3 - 9 years	45 percent
10 - 15 years	16 percent
16 - 24 years	14 percent
25 years and over	25 percent
Total :	100 percent

This reveals an important emphasis on the lower age group.

3. DEVELOPMENT OF DESIGN CRITERIA

3.1 All design, irrespective as to its nature, requires an evaluation of system loading and in the case of a tidal pool or bathing enclave with its related supporting infrastructure this is equally true, in as much as it is necessary to make a prediction of the visitor normal peak and the manner in which this may be accommodated in its occurence within the bathing area, on the beach, within the change rooms and ablution blocks and in terms of the transportation system.

There is no universal formula which can be applied and each particular set of circumstances requires its own evaluation based on, among others, the following factors and considerations :

1) The overall completeness and attractiveness of the beach recreation scheme and its immediate environs.

2) The relationship of parking areas and other transportation termini to the point where the individual may commence 'doing his thing'.

3) The capacity and quality of arterial road systems, their congestion factors and the distance to be travelled.

4) The socio-economic standards of the respective population.

5) The demographic structure of the relevant population.

6) The spatial relationship of urban residential areas and population densities.

3.2 In the studies and planning undertaken in the False Bay area of Cape Town the careful weighting and evaluation of the factors referred to, led to the preparation of a visitor projection graph for normal peak days of the form

$$p = k_1 - k_2 S^{\frac{1}{2}}$$

where p - resultant percentage of resident population who would visit the beach on a warm, sunny, low wind, vacation day.

k_1 - maximum effective percentage for people resident within walking distance of beach.

k_2 - spatial relationship - population dispersion factor.

S - best route travelling distance in kilometres.

The importance of the formula lies not solely in an assessment of visitor peak influx but also in the rational assignment of traffic flows to various routes and transportation modes.

The values adopted for the False Bay report are :

$K_1 = 40$; $K_2 = 5$

3.3 Notwithstanding the peak tendency, the facilities provided will have their own optimum capacity beyond which the user congestion factor acts to limit the abnormal peak and deflect the balance of visitors to other or adjoining areas.

For the planner however it is important that capacities throughout the system be consistent and compatible one with the other. In other words the overloading of the bathing enclave would be accompanied by an overload on the dry beach area, parking areas, toilet and ablution blocks, etc.

This requires the determination of a comfort level optimum capacity bearing in mind that man is gregarious in nature and beach crowding is part of the scene he loves.

Up to a water depth of 800 mm a loading of 20 people per square metres is acceptable; from 800 mm to 1500 mm the loading should not exceed 12 people per 100 square metres and over 1500 mm in depth the loading should be less than 8 persons per 100 square metres.

This would place the optimum capacity of the Strandfontein tidal pool at 5000 people whereas a peak of over 15000 has been experienced.

The probable ratio at peak hour of people in the water to people on the dry beach is 1 to 2.

3.4 A structural and geometric design philosophy for the attainment of favourable bathing conditions is functionally related to the measure of assurance of the

ordinary bather, when committing himself to the relatively strange environment, in his ability to predict changes in underwater topography as well as the dynamic forces to which he may be subjected.

In practical terms this design philosophy can be stated as ensuring that :

1) No localised changes of any serious consequence occur in the beach or tidal enclave topography in the design area.

2) The occurence of irregular and/or strong currents be eliminated.

3) That a beach gradient of good regularity and not exceeding 1 in 50 in the surf bathing zone between High Water Mark and Mean Sea Level - 3,0 metres should be aimed at.

4) That in the case of a tidal pool the floor gradient should not exceed 1 in 30.

5) That a sand area is to be preferred to a rock and sand area in the bathing zone.

3.5 Service To be Provided

The minimum number of plumbing fittings required for male and female changerooms should be in accordance with the applicable Building Regulations for places of public entertainment based on sixty percent of the assessed recreation area optimum capacity divided evenly between both sexes.

Changerooms should provide accommodation for peak usage at three percent of the optimum capacity at 2,5 square metres per person.

External showers should be provided on the ratio of ten percent of changeroom capita accommodation. An equal number of faucets is required within each changeroom block.

4. THE FALSE BAY RESEARCH AND CONSTRUCTION PROGRAMME

4.1 A report evaluating the need for development in the False Bay area and recommending further research was presented in 1979 and resulted in the construction of a tidal pool at Strandfontein Point as well as an extended research progamme in respect of protective works at Middlebank and Kapteinsklip.

4.2 The Strandfontein Tidal Pool Model Tests were carried

out at an early stage of the False Bay Model Studies and were directed at :

1) an examination of wave action under various wave conditions with a view to predicting the inflow of freshwater to the pool area for the geometric configration and full supply levels recommended by the Consultants

2) the determination of the stability of the toe armouring proposed

3) the determination of the overturning forces on the seawall due to wave action

4) a correlation between inflow and sediment transport into the pool.

Various tests for different wave conditions and tidal levels were undertaken by the C.S.I.R. the results of which in practice after completion of construction were found to be of a high order of accuracy of prediction.

The following limiting conditions of inflow from the model studies were ascertained for proto type crest level of seawall of R.L. 1,50 m M.S.L.

1) That inflow took place only during high tide conditions and when sea levels rose above R.L. 0,30 m M.S.L.

2) That no inflow under any conditions took place for wave heights (H_S) 0,40 m and less - which condition pertains for 16 percent of the time.

3) That during 50 percent of the high tides an inflow of more than 40 000 cubic metres could be expected.

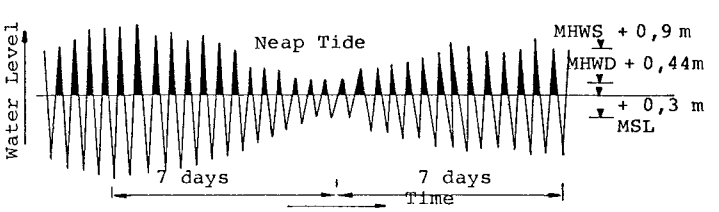

These results together with the structural stability results for armouring size and overturning moments were employed in the final design.

A good indication of sediment inflow probability was available from the correlation calculations and in all the use of the model was found to be completely

successful and fully justified and served to confirm the consultants recommendations. It is not possible in this paper to deal with the C.S.I.R. report in depth but to provide the following salient features.

Scales applicable to the model testing in accordance with the Froude laws were :

Geometrical	$1 : 15$
Velocity	$1 : 15^{\frac{1}{2}}$ (1 in 3,87)
Time	$1 : 15^{\frac{1}{2}}$ (1 in 3,87)
Force	$1 : 15^{3}$ (1 in 3375)

In view at that time of the early stage of the False Bay project research as well as the urgency of the tidal pool aspect of the research being undertaken, model calibration was based on wave directions determined from aerial photographs then available and field observations from survey rods located in accordance with the prototype geometrical configuration at 20 metre intervals.

4.3 The objective of the experimental measurements of inflow due to wave action was to optimize the height of the seawall so as to achieve a satisfactory fresh water replenishment rate without the occurrence of unduly rough conditions within the pool.

A full supply level of M.S.L. 1,50m based upon previous experience was adopted for experimental purposes and found to be the optimum level for geometric design.

The lowering of the crest level by 200 mm revealed in the experimental analysis virtually no change to the conditions of no-inflow but did affect quite appreciably the total inflow and bathing conditions.

A final crest level for construction purposes of 1,40 m M.S.L. was adopted.

The experimental mean inflow per tide was found to be 40 000 cubic metres with a maximum at sea level 0,90 m (M.S.L) at M.H.W.S.T. of 160 000 cubic metres.

In general it was established that the best sustained inflow conditions occur during the summer months and in particular December and January when incidentally the most severe visitor loading of the tidal pool takes place.

During December 1978 the sustained period of S.W.L. below M.H.W. was two days; for the same month in 1979 on no occasion; one day in January 1978 and two days in January 1979 as acertained from the S.A. Tide Tables for 1978 and 1979.

The occurrence during the remainder of the summer season of suitable water levels for wave actuated inflow needs however to be equated within the limiting parameter of minimum significant wave height of 0,40 metres in respect of which value waves lower in height occur for 16 percent of the time. The median inflow per tide for the adopted crest level of 1,40 m M.S.L. has been assessed as being 50 000 cubic metres.

Monitoring of water quality by examination of the faecal coli count under peak conditions has been undertaken by the City Engineer and found under all conditions to comply with acceptable standards for public swimming baths thus justifying the crest level adopted and the model analyses of wave inflow.

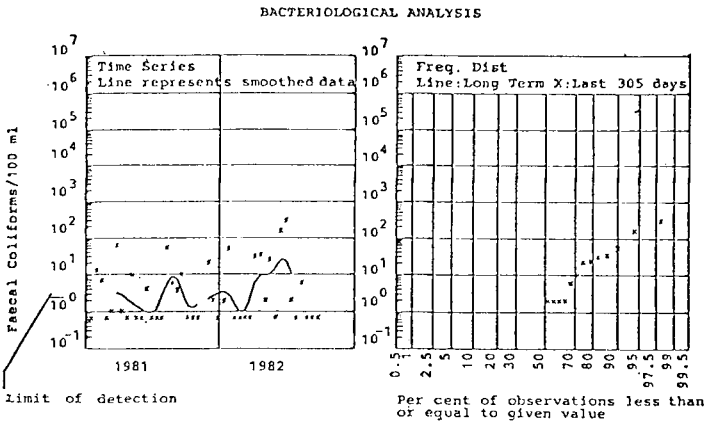

4.4 Siting of the pool was subject to geographic, environmental and foundation constraints. The extension of the residential suburbs in an easterly direction placed emphasis on coastal recreation development within easy reach of these areas while at the same time creating a new problem of environmental control consequent to the selective exploitation for recreation purposes for several hundreds of thousand of people of a part of the coast line as yet untouched in the False Bay area.

Foundation problems as well as the type of structure limited the choice of site in as much as the least exposure of the structure to the open sea was sought in view of the economic inaccessibility of bedrock which lies upto ten metres beneath the unconsolidated sediments.

From a regional planning point of view the City Engineer of Cape Town favoured the development of three nodal points in the study area and accordingly studies were directed at the establishment of a tidal pool complex at Strandfontein Point and groyne systems at Middle Bank and Kapteinsklip to cater for larger beach crowds. This planning concept was found to be compatible with the hinterland development, forming a sensible whole.

The location as primary objective of a large tidal pool at Strandfontein Point involving the daily movement in season of scores of thousands of visitors into the area made the removal of primary dune and fynbos environment and the provision of landscaped grassed areas and parking allotments an inescapable feature of the project development.

4.5 Pursuant to the preliminary report more extensive investigations of foundation conditions were undertaken. Although general uniformity of geological conditions pertain in the study area the occurrence of an extensive, albeit soft, calcarenite shelf at Strandfontein Point offered the most protected section of the coast for a minor structure.

In this respect the author suggests that the geometric limitations of the structure and the need to create a light and pleasing arrangement required a greater need for design sensitivity than might otherwise be the case.

Geological investigations of offshore conditions both in the field as well as from aerial photographs revealed discontinuous platforms of calcarenite in the surf zone. The calcarenite rock took the form of a surface layer overlying an extensive depth of unconsolidated sands.

Sites were selected for exploratory drilling and boreholes were advanced through unconsolidated sands by washboring methods using bentonite to support the sides of the holes.

Representative samples of the unconsolidated materials being penetrated were taken at intervals of 1,5 metres.

The calcarenite beach rock was penetrated using a diamond bit and NX size cores were recovered in this consolidated material.

Standard Penetration Tests were carried out in the unconsolidated materials at intervals of 500 mm i.e. with gaps of 200 mm followed by 300 mm of penetration over which the Terzaghy N-value was recorded.

The following is an abstract from the report prepared by Dr T Partridge on the geological investigation :

"The properties of the various materials, deduced from the four exploratory boreholes, augumented by Standard Penetration Tests in one case, are as follows :

a) Surface littoral sand : ranges in thickness from 1,3 to 6,0 meres. Usually a coarse, medium and fine shelly sand of loose consistency (N-value 4-8), which would correspond with an in situ dry density of 1450-1600 kg/m^3. Maximum allowable foundation pressure 50-100 kPa (Reference 1).

b) Calcarenite : ranges in thickness from 0,35 m to about 1,0 m. Usually a moderately weathered, medium textured soft rock material which becomes slightly softer towards the base. Joints are generally infrequent. This material is lenticular in its occurrence and may thicken and lens out sporadically under the surface.

c) Clayey sand : ranges in thickness from about 0,9 m to 3,0 m. Usually a clayey medium and fine sand of firm to stiff consistency (N-value 11-27). Maximum allowable foundation pressure 100 - 200 kPa. (Reference 1) May contain channels, as reflected by water losses during drilling of up to 35 litres per minute in this material and in underlying littoral sands. The material becomes progressively less clayey with depth and grades into underlying littoral sands; precise position of lower contact therefore uncertain.

d) Littoral sand : ranges in thickness from about 2,15 m to 4,55 m, but may be thicker in places. In the uppermost two metres it is usually a coarse, medium and fine shelly sand of very loose to loose consistency (N-value 1-70, which would correspond with an in situ dry density of about 1300-1500 kg/m^3. Maximum allowable foundation pressure about 50 kPa (Reference 1). The lower levels of this material are of similar texture, but have a medium dense to dense consistency (N-value 21-48), which would correspond with an in situ dry density of about 1600-1900 kg/m^3. Maximum allowable foundation pressure 200-400 kPa (Reference 1).

Horizons e, f and g are, in general, repetitions of horizons b, c and d respectively.

It should be noted that, in the tidal channels, horizon

(c) and the upper part of horizon (d) may be absent beneath the collapsed calcarenite slabs, depending on the depth to which scour has occurred locally."

Four principal factors emerge :

1) The relatively extensive depths of the unconsolidated littoral deposits.(In certain boreholes over ten metres)

2) The occurrence of two horizons of low N-values and related high porewater pressures.

3) The identification of a zone of firm to dense and stiff consistency of clayey medium and fine sand with N-values of 11 to 27. (Generally referred to in the report as the marl layer)

4) Marked lack of uniformity of foundation conditions over the length of the proposed wall.

4.6 From a structural point of view it was patent at the outset that in view of the previously referred to localised variations in foundation conditions a monolithic structure was desirable.

A semi-circular structure presented the following advantages :

1) A good natural geometric relationship between shallow and deep water relative to bather preference.

2) The most economical wall length per unit of surface area.

3) Certain dynamic load advantages in as much as that although a particular wave train could theoretically impose a simultaneous force system over the length of the wall, the maximum force acts over a limited length of the wall. In the structure under consideration the maximum force may be considered to act over a length of 60 metres i.e. over a 14 percent section of the wall.

It is a corollary that most of the wave inflow takes place over this section.

Beyond this section of wave frontal attack there is an appreciable progressive reduction in dynamic forces due to the effect of a changing angle of wave approach which decreases from a theoretical 90° for that portion of the structure at right angles to the wave direction to 0° at the diametral point.

From the model study photographs it may be observed that progessively away from the frontal attack section

the angle of wave approach tends to increase due to wave refraction over the shallow calcarenite reef. This is however accompanied by an appreciable refractive energy loss.

Disregarding wave refraction along the length of the wall the incident angle various linearly to length of wall and by applying the equation $R^1 = R\sin^2 \alpha$ the reduction factor for dynamic force calculation along the length of the wall becomes :

1) At frontal attack section	1,00
2) At three-quarter point	0,85
3) At half point	0,50
4) At quarter point	0,15
5) At diametral point	0,00

To satisfy the condition of simultaneous dynamic forces, the forces in their adjusted value for incident angle act radially resulting in an axial ring stress with secondary moments and shear forces due to load change along the length.

From the structural analysis it became apparent that the critical design condition is represented by an internal loading system comprising a pool filled with sand and water at L.W.S.T. tide state.

From the geological investigation it became apparent that in order to secure reasonable waterholding properties it was essential that the sheetpiling as curtain membrane be taken well into the dense clay sand layer. This depth as well as the minimum section required for driving the sheetpiling resulted in a fairly rigid simple cantilever and the effect of a ring beam apportionment of load was disregarded in the factor of safety analysis. This is illustrated by the low stress analysed in the ring beam when maximum stress is developed in the sheetpile in bending.

4.7 In order to determine the axial load resistance of the proposed sheetpiling a series of sheetpile driving and load tests were carried out employing six metre piles driven 4,40 metres into the substrata. Loading using 1,08 KN units took place five days after completion of driving and the following worst deflections recorded :

1) At working load 28,5 KN per metre,settlement 0,3 mm.

2) At test load 57,1 KN per metre,total settlement from unloaded level 0,6 mm.

3) At time zero plus 24h00 pile rose 1,0 mm.

4) At time zero plus 40h00 pile settled 1,0 mm.

5) At time zero plus 66h00 pile was unloaded.

6) At time zero plus 92h00 pile level was 0,4 mm above original unloaded position.

Spring tide conditions prevailed during the test period.

The geological section on the line of the sheet pile curtain membrane dictated the use of five metre and six metre piles driven to form an interlocking diaphragm to predetermined depths in accordance with the geological findings.

The pile section adopted was a BZ12 Arbed imported from Luxemborg.

Overturning moments transferred to the sheetpile are absorbed in passive resistance by the substrata in accordance with the deformation condition imposed by the sheetpile in bending deflection.

In the analyses the pile section adopted allows for loss of 50 % of steel section due to corrosion over a 40 year period. At the point where maximum bending moment occurs it is likely that anaerobic conditions prevail and that the assumption for reduced section modulus appicable at this point are conservative.

4.8 The following design considerations apply :

1) Worst possible internal load condition is pool full of sand submerged, at tide state L.W.S.T.

2) Worst possible external load condition occurs at maximum wave forces with pool empty.

3) The submerged sand and substrata mean angle of shearing resistance $\emptyset$, employed in the calculations, is 20°.

4) The solid weight of sand comprising quartzitic and shell particles is 20 KN/m^3.

5) The well compacted sand percentage voids is 30 %.

6) From the aforegoing the active pressure development factor K_p is 16,2 KN/m^2 per metre of depth.

7) The passive pressure development factor is 36,6 KN/m^2 per metre of depth.

8) Horizontal deflection of the superstructure results in a peripheral strain in the concrete section of where delta is the deflection and r the radius of the

pool.

4.9 Calculations are based on Terzaghi Theory for a Cantilever Sheetpile :

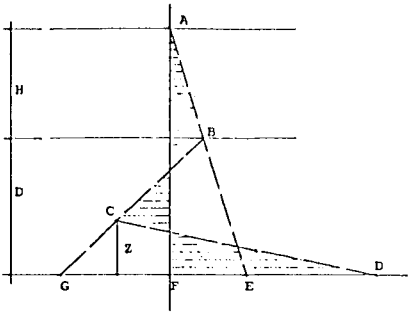

$$Z = \frac{D^2 Kp - (H + D)^2 Ka}{(H + 2D)(Kp - Ka)} \quad \ldots\ldots\ldots (1)$$

and

$$\left(\frac{D}{H}\right) + \frac{(Kp - 3Ka)}{Kp - Ka}\left(\frac{D}{H}\right)^2 - Ka\frac{(7Kp - 3Ka)}{(Kp - Ka)^2}\left(\frac{D}{H}\right)^2 - Ka\frac{(5Kp - Ka)}{(Kp - Ka)^2}\left(\frac{D}{H}\right) - \frac{KaKp}{(Kp - Ka)^2} = 0 \quad \ldots\ldots\ldots (2)$$

The following values of 'D' have been calculated compatible with the probable values of K_p and K_a.

Sand Level in Pool	Required 'D'
RL 01,40	4,86 m
RL 01,05	4,41 m
RL 00,70	3,92 m
RL 00,40	3,48 m
RL 00,00	3,13 m

'Z' for the extreme condition of 'D' = 4,86 m has been calculated to be 1,01 m, while developing a passive resistance of 55,9 KPa at a depth of 3,85 m equal to a linear rate of development of passive pressure = 14,5 KN/m^2 per metre of depth.

The 'D' value for the sheet piles installed is 5,40 m.

4.10 Seepage Losses

The substrata formation is as may be seen from the geological section complex and this together with a bedrock horizon of between four metres and eight metres below the lower limit of the sheet pile diaphragm places a low confidence level on the projection of seepage losses. Nevertheless actual observations of water loss conform well to the calculated values.

For the pool full at 01,40 m M.S.L. and tide state - 0,90 the maximum seepage hydraulic gradient is :

$$\frac{2,3}{(4,5 + 5,4)} \approx 0,23$$

and the critical gradient at which boiling displacement of the sand at L.W.S.T. on seaside can take place : $i_{cr} = \frac{\delta - \delta\omega}{\delta\omega}$

$$= \frac{20 - 9,8}{9,8} : 1,04$$

$$\text{Factor of Safety} : \frac{1,04}{0,23} : 4,52$$

Assuming the maintenance of a high pore pressure condition on the landward side of the pool which tends to stabilise water movement inland and secondly that the marl layer acts as a semi-pervious homogeneous blanket of effective thickness 1,80 metres as deduced from the geological reports, with permeability $K = 1 \times 10^{-4}$ cm/sec then the mean seepage gradient through the marl layer would be $\frac{1,4}{1,8} \approx 0,78$ and seepage rate 67 mm/day.

For a period of three days of no inflow the waterlevel would drop by a total of 200 mm.

This has been largely confirmed in the field.

4.11 Concrete Design

The reinforced concrete pile cap was designed to be sufficiently rigid for the structure to act monolithically so as to transfer localised foundation failure conditions to the remainder of the structure while at the same time providing a minimum cover on all steel of 100 mm.

A 30 MPa concrete was employed with 0,30 percent steel reinforcement.

A 0,25 to 1 seaface batter was adopted for wave induced inflow, reduction in dynamic forces and for aesthetic considerations.

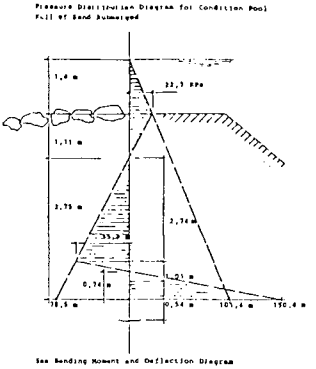

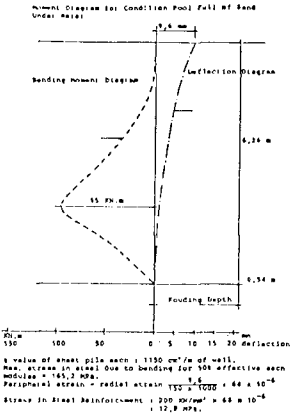

GEOMETRIC ARRANGEMENT OF STRANDFONTEIN TIDAL POOL

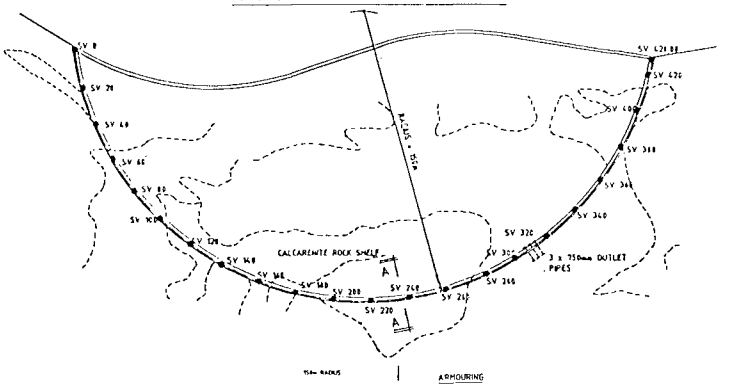

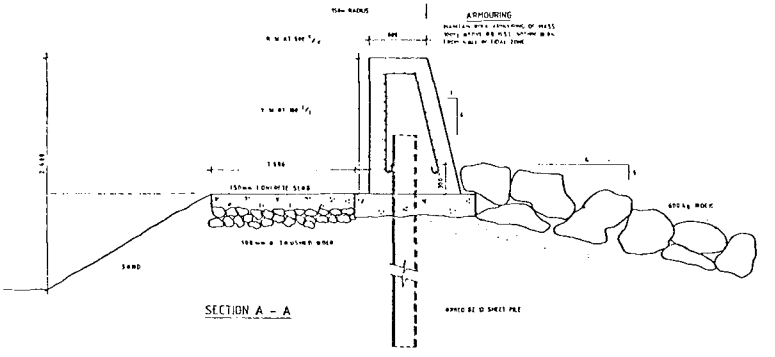

4.12 Armouring Design

It is essential to provide adequate toe armouring to prevent progressive scour in the seaface foundation area, while at the same time limiting the top reduced level of the armouring to the extent necessary to ensure retention of sufficient wave energy for wave induced inflow.

Reasonable assessments of the controlling levels based on experience were made but it is indubitably the case that the model experiments were essential to establish the adequacy of inflow.

Armouring size was determined by the Hudson Formula :

$$W = \frac{W_r H^3}{Kd(S_r - 1)^3 \cot \theta}$$

W_r = unit weight in lbs/ft³
= 156 lbs/ft³ (25 KN/m³)

H = Design wave height in feet
= 6,5 ft (2,0 m)

S_r = Specific gravity of armour unit
= 2,5

W_w = Unit weight seawater
= 64,0 lbs/ft³ (10 KN/m³)

θ = Structure slope angle in degrees
= 14°

K_D = Stability co-efficient
= 2,5

W = 1270 lbs (577 kg)

Say 600 kg.

4.13 Construction

The construction method adopted by the contractor involved the provision of a rubble mound as a sea cofferdam with a sand access road on the inside of the berm. The rubble mound was constructed to a height of 4,00 m M.S.L.

Sheet piles five to six metres in length were driven using a compressed air pile driver suspended from a 30 ton crawler crane off the access road.

The contractor successfully designed a system of driving to geometric configuration by use of steel

channel walers anchored to the previous piles and forward anchored to a transportable concrete block of some two tons mass.

A moveable shutter arrangement capable of being trimmed to the radius of curvature and hung from a gantry system on rails was a further successful innovation by the contractor.

The concrete was cast in alternate section of 7,5 metre length with continuity reinforcement but without waterstops.

On completion of construction the major portion of the rubble mound was employed to form the toe armouring.

The unavoidable inclusion in the armouring of undersize material resulted in an inflow of sharp rock fragments into the pool and future designs should provide particular attention to the temporary cofferdam in order to employ material which later may be utilized in the armouring zone.

ACKNOWLEDGEMENTS

1) The assistance of the City Engineer of Cape Town and his staff in the submission of this paper including the provision of results of pollution monitoring is gratefully acknowledged.

2) Research by the S.A. Institute of Oceanology of the S.A. Council of Scientific and Industrial Research has been fundamental to the submissions made and particular reference is made to the assistance of Dr D H Swart.

REFERENCES

1. False Bay Shore Improvements:
Model Study of Strandfontein Tidal Pool by the National Research Institution for Oceanology as submitted to O'Connell, Manthê and Partners Consulting Engineers.

2. False Bay Coastal Development Report by O'Connell, Manthê and Partners Consulting Engineers and the City Engineer of Cape Town Planning Department.

3. Various preliminary reports by the National Research Institution for Oceanology as submitted to O'Connell, Manthê Consulting Engineers.

4. Shore Protection Manual of U.S. Army Coastal Engineers Research Centre.

Multipurpose Gate Operation

by

Kazumasa Mizumura

Abstract

Predictions of time-varying salinity under arbitrary gate operations are presented of a tidal lake and its inlet. Particular regard is given to the modeling of salinity and gate operations and the applying the Markov process with Kalman filtering. In contrast to previous papers that predict only water levels the present paper also estimates salinity downstream the gate and of the tidal lake, simultaneously. It is postulated that present water level and salinity are expressed by the explicit linear functions of water levels, salinity, and gate operations at the other and the same positions in the past step. Using physically plausible estimate for these parameters in the functions the results of the predictions are in good agreement with observation.

Introduction

Gate operations at the inlet of tidal lakes have usually two purposes. First is to control the water surface level of the lake and second is to prevent from the intrusion of saline wedges. Considering the aspect of water quality and quantity, the existence of rice fields near the tidal lake requires precise gate operations. In this work, a method for estimating water level and salinity due to gate operations based on a combined estimation model including the Markov process and Kalman filtering theory is applied to control the gate at the inlet of Lake Kahokugata. Several applications of the Kalman filtering theory to water quality are found in (1, 2).

General

Lake Kahokugata (Fig.1) is located north of Kanazawa city and its length and width are almost 2.0 km and 1.0 km, respectively. The Ohno river connects the lake with the sea of Japan through the port of Kanazawa. A saline wedge intruded into the lake along the river before the construction of this gate. Therefore, this gate was constructed to prevent the lake from the intrusion of saline wedges and to control the water level of the lake. The simple illustration of

---

Professor of Civil Engineering, Kanazawa Inst. of Tech., 7-1, Ogigaoka, Nonoichimachi, Kanazawa, Ishikawa, Japan

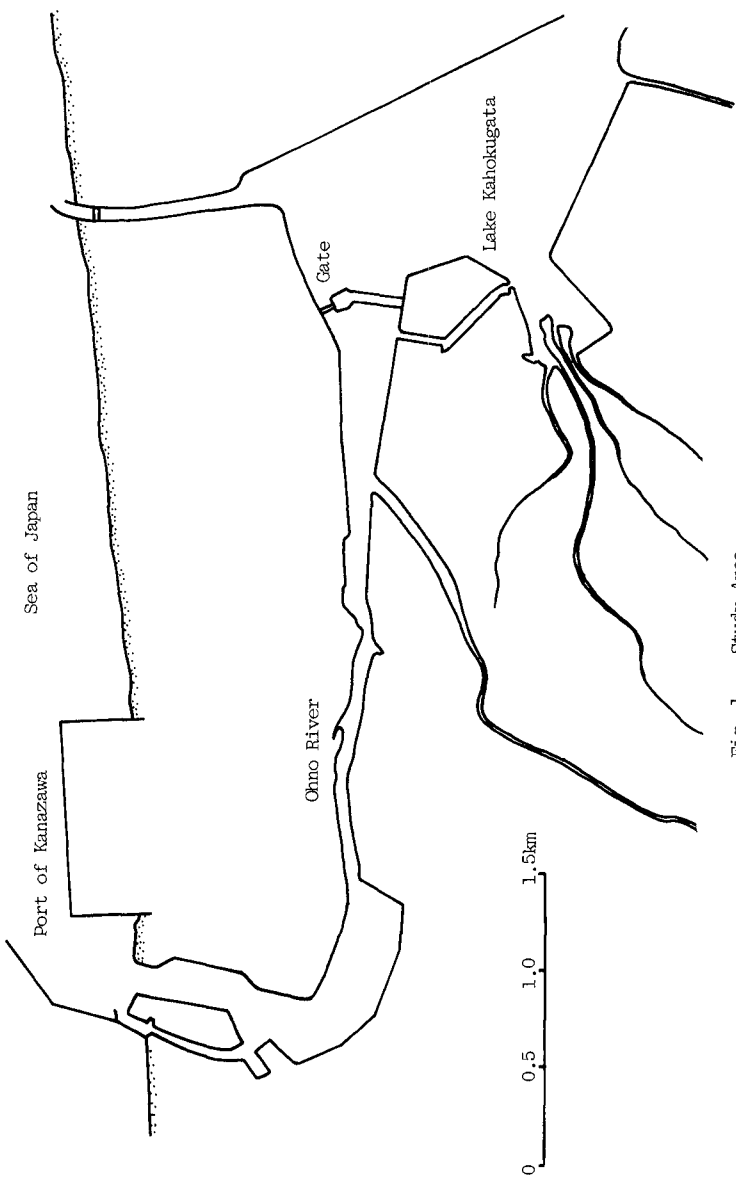

Fig. 1.— Study Area

the gate is given in Fig.2. Fig.3 represents the observed water levels at the sea, at the gate, and of the lake and the state of the gate operation every hour in May of 1980. There is another inlet and gate in this lake connecting to the sea. This gate is not considered in present study since this gate is not operated except during the typhoon season when the water level of the lake becomes remarkably high.

Prediction Techniques

For multipurpose gate operations we seek to predict the water levels and salinity at the position located downstream of the gate as a function of time. They are also considered to be the explicit functions of the sea level, the water level of the lake, and the state of the gate operation. If the sea level, the water level of the lake, and the salinity of the lake are not known, they are also predicted. Fig.4 and 5 show the effect of the gate operation on salinity at the gate and the relationship between the water level and the salinity of the lake. We consider that they may be expressed by the combination of the deterministic and the fluctuated part. That is,

$$y_k = \bar{y} + y'_k \tag{1}$$

$$T_k = \bar{T} + T'_k \tag{2}$$

$$d_k = \bar{d} + d'_k \tag{3}$$

$$c_k = \bar{c} + c'_k \tag{4}$$

$$s_k = \bar{s} + s'_k \tag{5}$$

in which k = time step, y_k = the water level at the gate, T_k = the sea level, d_k = the water level of the lake, c_k = the salinity of the lake, s_k = the salinity downstream the gate, and "–" and "'" mean the deterministic and the fluctuated part, respectively. By the physical consideration, the fluctuated parts are represented by the following forms.

$$y'_k = \alpha_1 y'_{k-1} + \alpha_2 y'_{k-2} + \cdots + \alpha_j y'_{k-j} + \beta_1 T'_{k-1} + \beta_2 T'_{k-2} + \cdots + \beta_j T'_{k-j} + \gamma_1 D_{k-1} + \gamma_2 D_{k-2} + \cdots + \gamma_j D_{k-j} + \delta_1 H_{k-1} + \delta_2 H_{k-2} + \cdots + \delta_j H_{k-j} \tag{6}$$

$$T'_k = a_1 T'_{k-1} + a_2 T'_{k-2} + \cdots + a_j T'_{k-j} \tag{7}$$

$$d'_k = b_1 d'_{k-1} + b_2 d'_{k-2} + \cdots + b_j d'_{k-j} \tag{8}$$

$$c'_k = \rho_1 c'_{k-1} + \rho_2 c'_{k-2} + \cdots + \rho_j c'_{k-j} + \sigma_1 d'_{k-1} + \sigma_2 d'_{k-2} + \cdots + \sigma_j d'_{k-j} \tag{9}$$

$$s'_k = \lambda_1 s'_{k-1} + \lambda_2 s'_{k-2} + \cdots + \lambda_j s'_{k-j} + \mu_1 T'_{k-1} + \mu_2 T'_{k-2} + \cdots + \mu_j T'_{k-j} + \nu_1 D_{k-1} + \nu_2 D_{k-2} + \cdots + \nu_j D_{k-j} + \pi_1 H_{k-1} + \pi_2 H_{k-2} + \cdots + \pi_j H_{k-j} \tag{10}$$

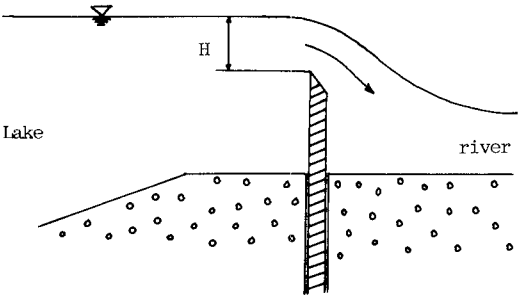

Fig. 2 (a)-- Lift Gate

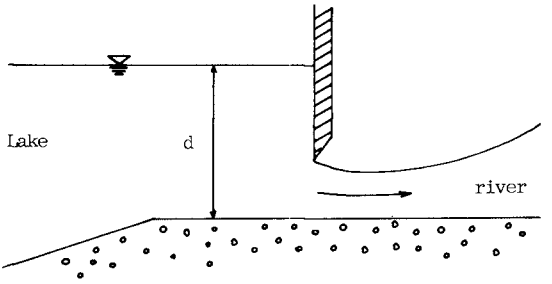

Fig. 2 (b)-- Lift Gate

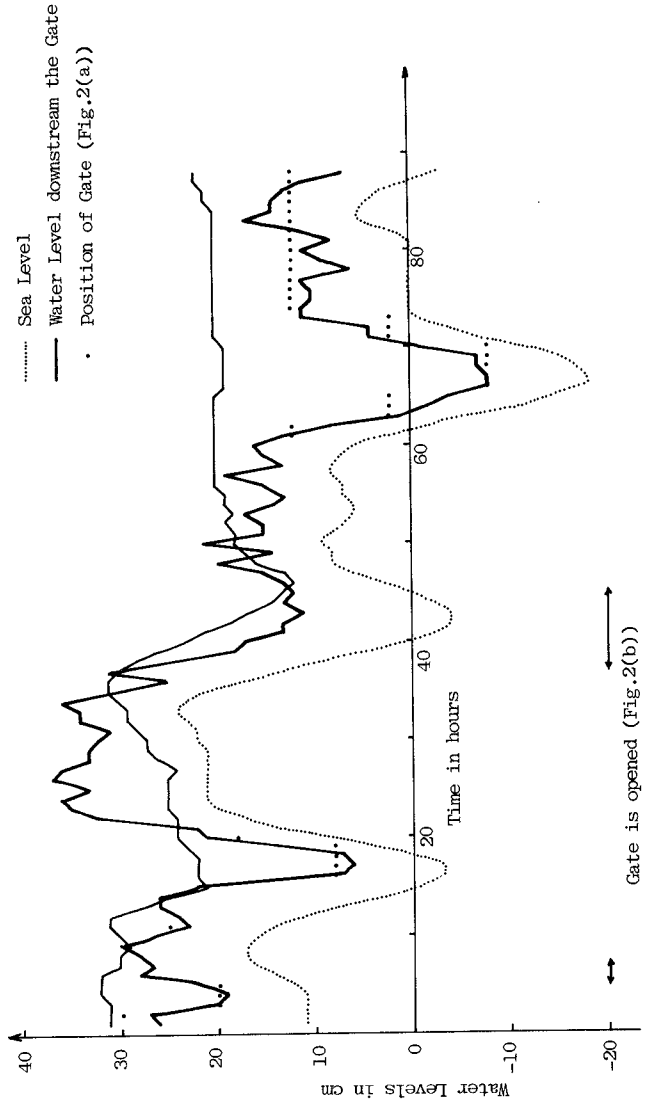

Fig. 3.— Observed water levels and gate operations

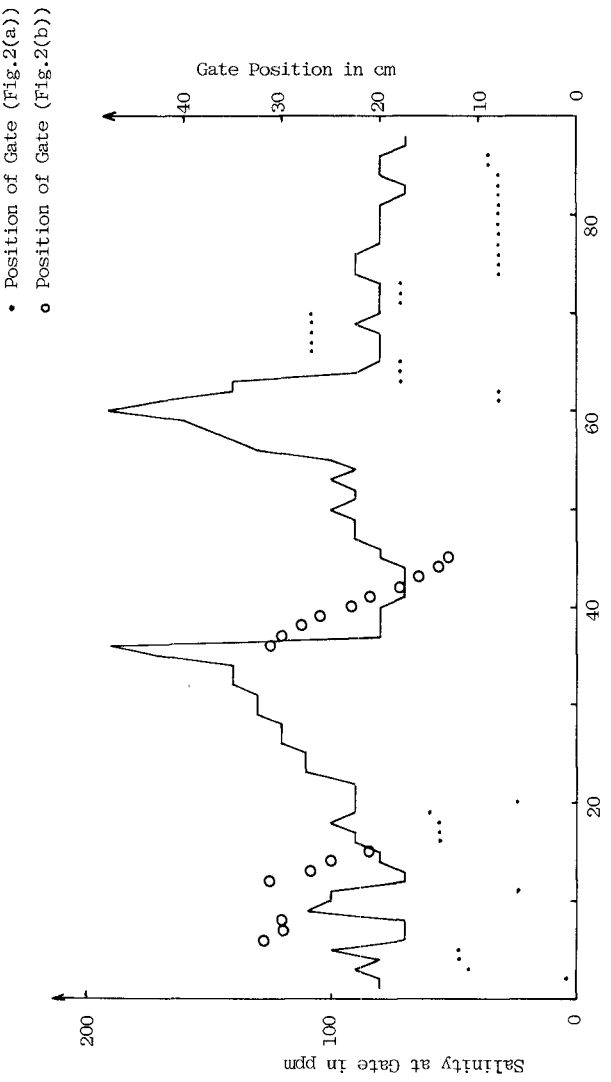

Fig. 4.— Effect of gate operation on salinity at gate

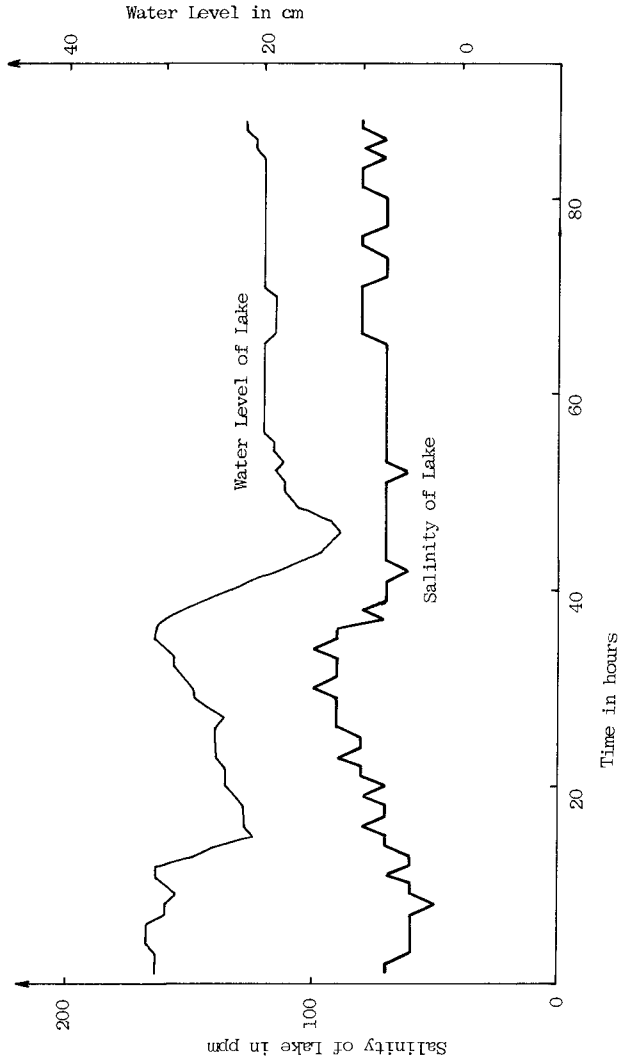

Fig. 5.— Relationship between water level and salinity of lake

in which α_i, β_i, γ_i, δ_i, a_i, b_i, ρ_i, σ_i, λ_i, μ_i, ν_i, and π_i = the constant parameters for $i = 1, 2, \cdots, j$, H_{k-j} = the water depth to determine the discharge through the gate (Fig.2(a)), and

$$D_{k-i} = \begin{cases} d_{k-j}, & \text{if the gate is opened (Fig.2(b))}, \\ 0, & \text{otherwise.} \end{cases}$$

Kalman Filtering Theory

The detailed discussion of the Kalman filtering theory is given in Gelb(3) or Sage and Melsa(6). By applying an appropriate transformation to the original formula (4, 5), the state equation for parameter identifications becomes

$$\underline{h}(k+1) = \underline{h}(k) + \underline{v}(k) \tag{11}$$

in which $\underline{h}^T = (\alpha_1, \alpha_2, \cdots, \alpha_j, \beta_1, \beta_2, \cdots, \beta_j, \gamma_1, \gamma_2, \cdots, \gamma_j, \delta_1, \delta_2, \cdots, \delta_j, a_1, a_2, \cdots, a_j, b_1, b_2, \cdots, b_j, \rho_1, \rho_2, \cdots, \rho_j, \sigma_1, \sigma_2, \cdots, \sigma_j, \lambda_1, \lambda_2, \cdots, \lambda_j, \mu_1, \mu_2, \cdots, \mu_j, \nu_1, \nu_2, \cdots, \nu_j, \pi_1, \pi_2, \cdots, \pi_j)$ and $\underline{v}$ = a noise vector (white Gaussian). The observation equation is represented by (Fig.6)

$$\underline{z}(k+1) = M(k)\,\underline{h}(k) + \underline{w}(k) \tag{12}$$

in which $\underline{z}^T(k+1) = (y'_{k+1}, T'_{k+1}, d'_{k+1}, s'_{k+1}, c'_{k+1})$, $\underline{w}(k)$ = a white Gaussian,

$$M(k) = \begin{bmatrix} \underline{m}_1^T(k) & & & & & 0 \\ & \underline{m}_2^T(k) & & & & \\ & & \underline{m}_3^T(k) & & & \\ & & & \underline{m}_4^T(k) & & \\ 0 & & & & & \underline{m}_5^T(k) \end{bmatrix}$$

$\underline{m}_1^T(k) = (y'_{k-1}, y'_{k-2}, \cdots, y'_{k-j}, T'_{k-1}, T'_{k-2}, \cdots, T'_{k-j}, D_{k-1}, D_{k-2}, \cdots, D_{k-j}, H_{k-1}, H_{k-2}, \cdots, H_{k-j})$, $\underline{m}_2^T(k) = (T'_{k-1}, T'_{k-2}, \cdots, T'_{k-j})$, $\underline{m}_3^T(k) = (d'_{k-1}, d'_{k-2}, \cdots, d'_{k-j})$, $\underline{m}_4^T(k) = (c'_{k-1}, c'_{k-2}, \cdots, c'_{k-j}, d'_{k-1}, d'_{k-2}, \cdots, d'_{k-j})$, and $\underline{m}_5^T(k) = (s'_{k-1}, s'_{k-2}, \cdots, s'_{k-j}, T'_{k-1}, T'_{k-2}, \cdots, T'_{k-j}, D_{k-1}, D_{k-2}, \cdots, D_{k-j}, H_{k-1}, H_{k-2}, \cdots, H_{k-j})$.

Illustrative Examples

By using the Kalman filtering algorithm, the water level and the salinity downstream the gate, the sea level, the water surface level

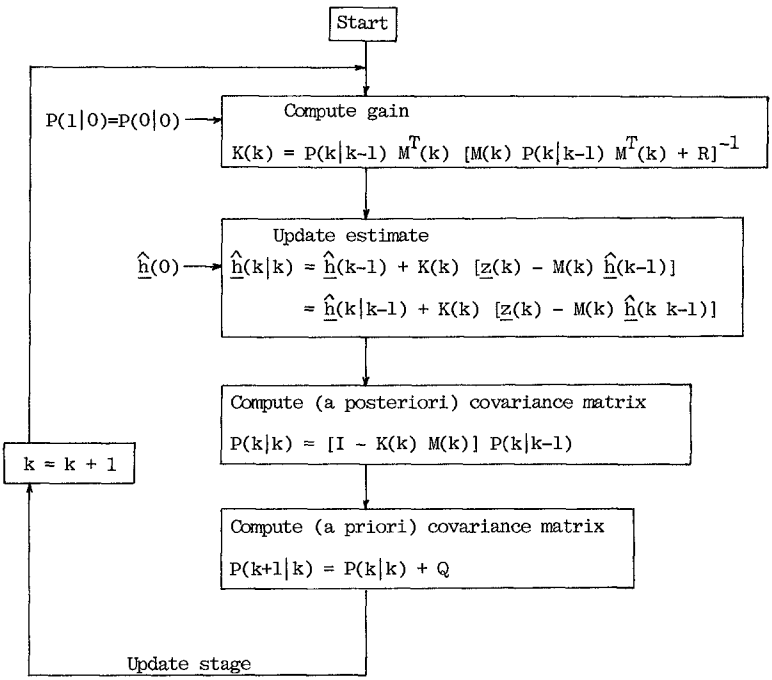

Fig. 6.— Algorithm of Kalman Filtering

and the salinity of the lake may be predicted step by step. Since we published the results on the prediction of water levels (5), we herein do not refer to them. The initial values of $\underline{h}$ and P are assumed as follows.

$$\underline{h} = \underline{0} \tag{13}$$

$$P = 0.1 \tag{14}$$

The initial values of each variable are used to represent the deterministic parts which are illustrated by "-". The predicted salinity downstream the gate an hour and three hours ahead of time is given in Fig.7 in the case of j=1. After 35 hours from the start the prediction an hour ahead of time almost coincides with the observation, but the prediction three hours ahead of time is not still in good agreement with the observation. Fig.8 shows the prediction of the salinity of the lake in the case of j=1. After 40 hours from the start the predicted salinity an hour ahead of time coincides with the observed data, but the prediction three hours ahead of time is not enough. The identified parameters by the Kalman filtering algorithm are illustrated in Fig.9. The severe fluctuations of the parameters are not found after 40 hours from the start. The time of 40 hours corresponds to the time when the reasonable prediction an hour ahead of time occurs. Fig.10 and 11 represent the predictions of the salinity downstream and of the lake during another time period which immediately follows to the period used in the previous analyses, respectively. These predictions are gradually improves as time passes. Fig.12 shows the erroes of the predicted salinity of the lake in the case of j=1 and j=2. In the early stage the prediction for j=2 is better than that for j=1. But after 40 hours the superiority decreases. That is, an appropriate prediction may be made by using the first order Markov process.

Summary and Conclusions

1. The prediction of the salinity and the water level is made by the Markov model with the Kalman filtering theory. The prediction an hour ahead of time is in good agreement with the observation.
2. To describe the phenomena in this paper the first order Markov process may be adequate, since the length of the river is short and the dimension of the lake is small. The modeling does not need to memorize much past information.
3. The prediction of future sea levels is usually calculated by the other method, but the prediction of the water level of the lake is not predictable. The limitation of the prediction model for the water level of the lake is made by using the simple Markov process (autoregressive process).

Appendix 1.- References

1. Chiu, C. L., Matalas, N. C., Dawdy, D. R., and Mizumura, K., " Applications of Estimation Theory to Hydraulic Problems," Proc. of 2nd IAHR Int. Sym. on Stochastic Hydraulics, Lund, Sweden, Aug., 1976, pp.167-183.
2. Chiu, C. L., ed., Application of Kalman Filter to Hydrology, Hyd-

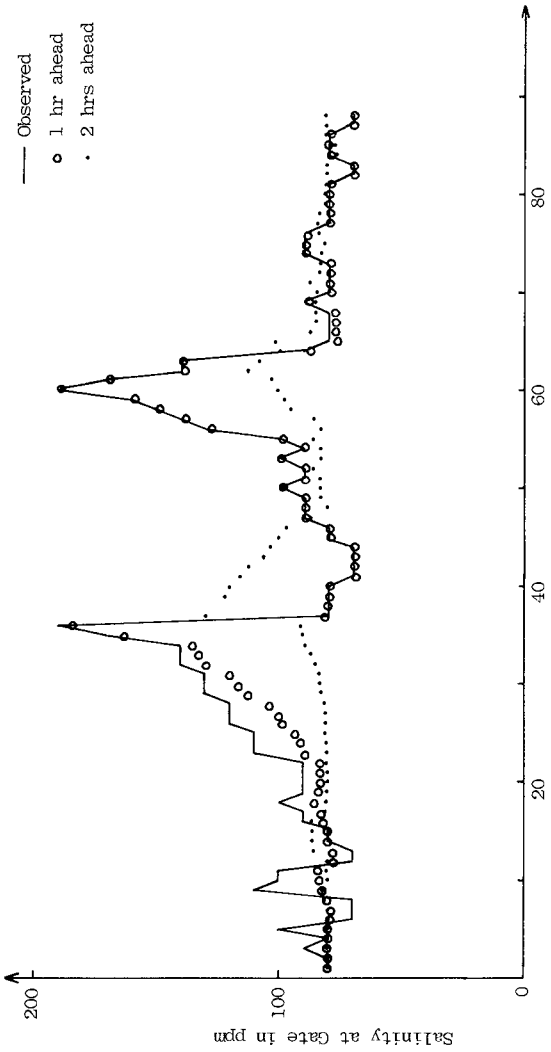

Fig. 7.-- Prediction of salinity downstream the gate

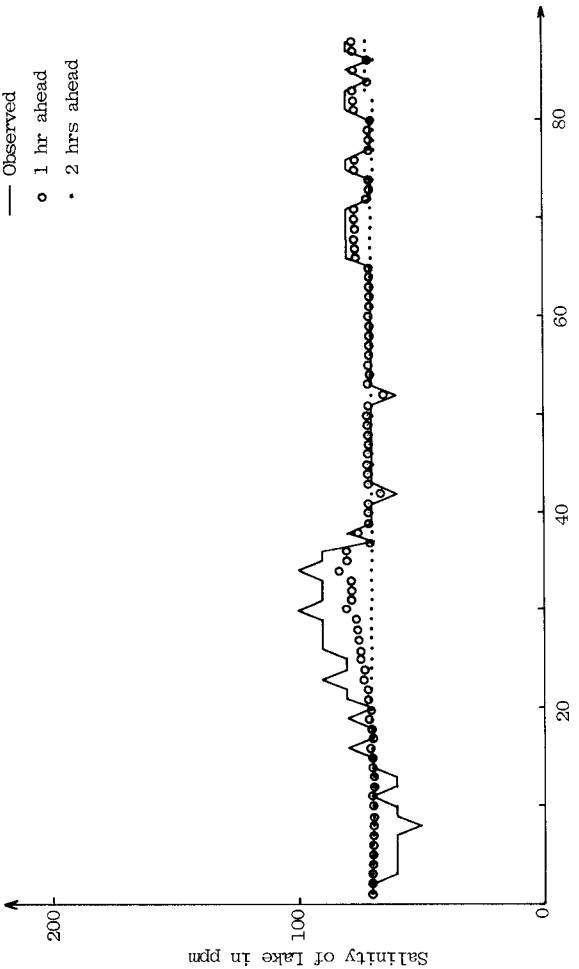

Fig. 8.-- Prediction of salinity of lake

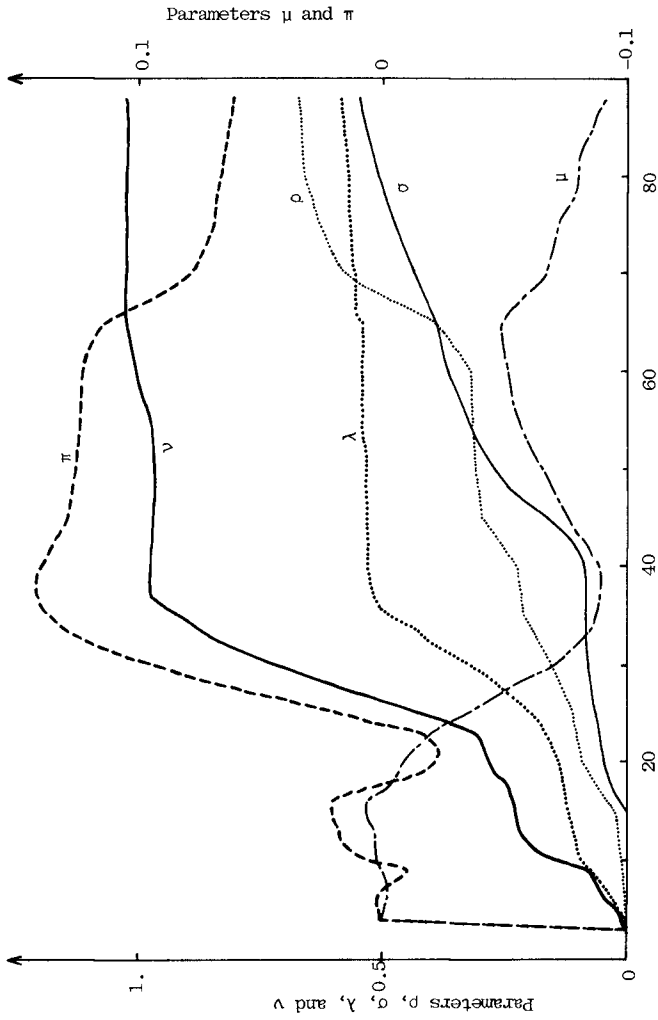

Fig. 9.— Parameters Identification

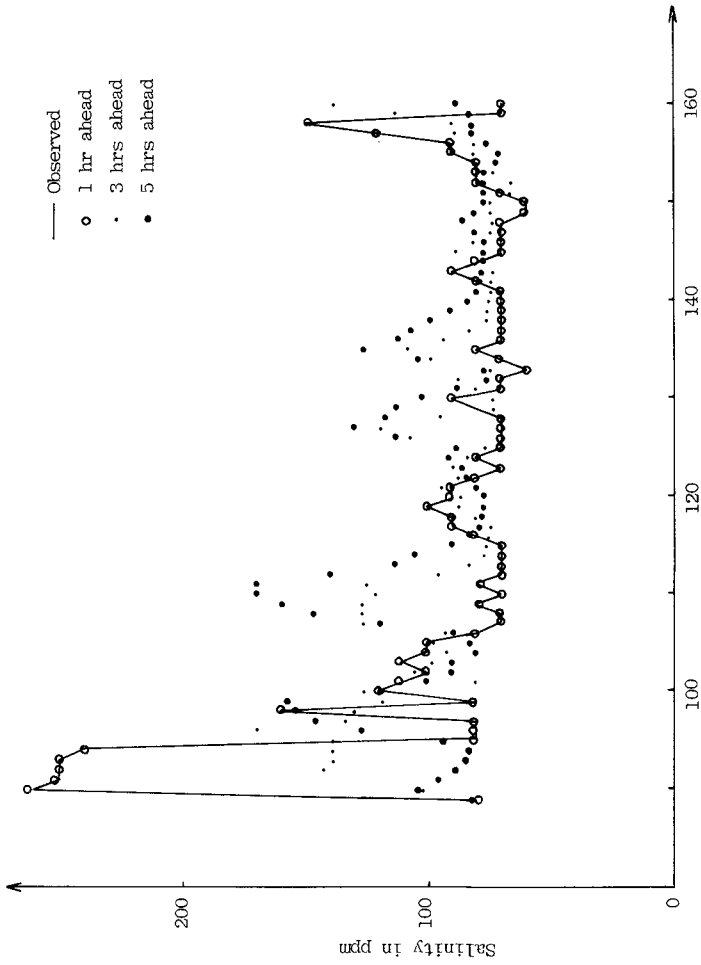

Fig.10.-- Prediction of Salinity downstream the Gate

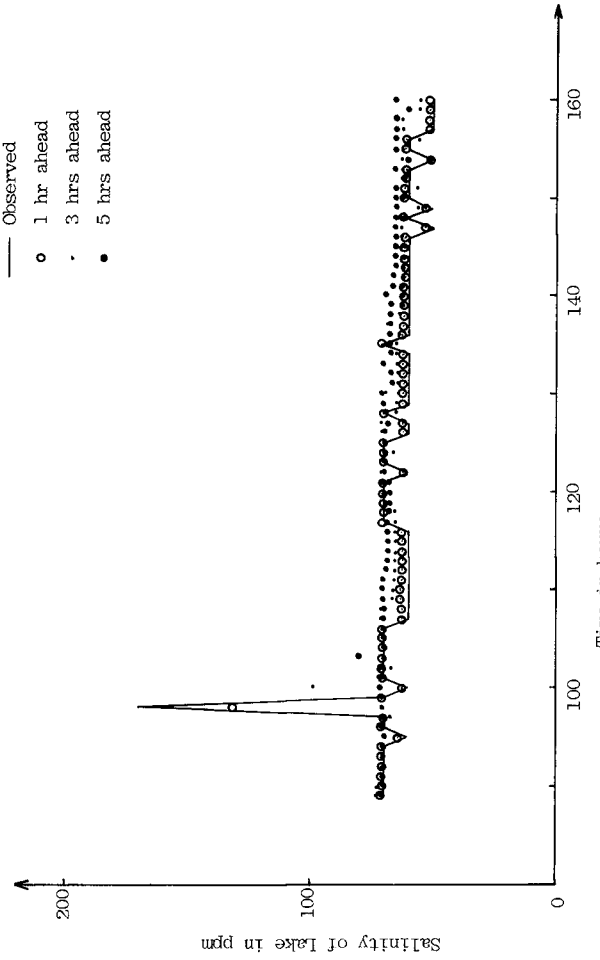

Fig.11.-- Prediction of salinity of lake

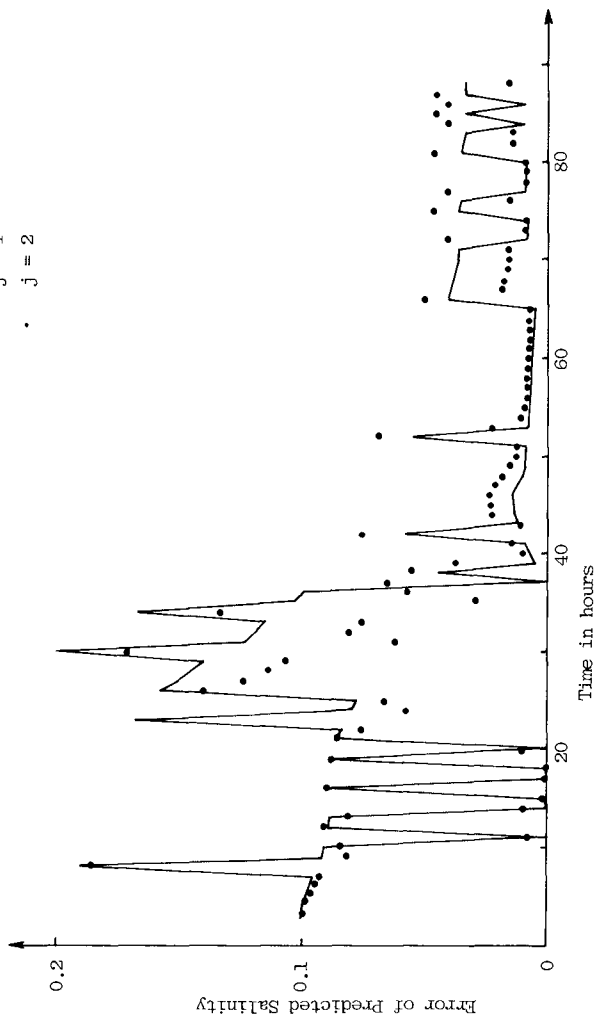

Fig.12.-- Absolute value of derivation of predicted salinity from observed salinity of lake

raulics, and Water Resources, 1st ed., Univ. of Pittsburgh, Pittsburgh, U.S.A., 1978.
3. Gelb, A., ed., Applied Optimal Estimations, The MIT Press, Cambridge, Mass., 1974.
4. Hino, M., "Prediction of Flood and Streamflow by Modern Control and Stochastic Theories," Proc. of 2nd IAHR Int. Sym. on Stochastic Hydraulics, Lund, Sweden, Aug., 1976, pp.115-140.
5. Mizumura, M., "Prediction of Water Level in the Tidal Inlet," Journal of the Waterways, Port, Coastal, and Ocean Division, ASCE, Feb., 1982, pp.97-106.
6. Sage, A. P. and Melsa, J. L., Estimation Theory with Applications to Communications and Control, 1st ed., McGraw-Hill, Inc., New York, U.S.A., 1971.

Appendix 11.- Notation

The following symbols are used in this paper:

a and b = constant parameters;
c_k = salinity of lake ($\approx c + c'_k$);
D_k = water depth, if gate is opened;
d_k = water surface level of lake ($= d + d'_k$);
H_k = vertical water depth between water surface level of lake and the upper part of gate (Fig.2(a));
$\underline{h}$ = parameter vector;
$\underline{K}$ = Kalman gain matrix;
j = order of Markov process;
k = time step;
M = observation transition matrix;
P = covariance matrix of estimation error;
Q = covariance matrix of $\underline{w}$;
R = covariance matrix of $\underline{v}$;
s_k = salinity of gate;
T_k = sea level;
$\underline{v}(k)$ = noise vector (white Gaussian);
$\underline{w}(k)$ = noise vector (white Gaussian);
$\underline{z}_k$ = observation state vector; and
α, β, γ, δ, λ, μ, ν, π, ρ, and σ = constant parameters.

THE COASTAL WIND FIELD OF THE SOUTHERN CAPE

by

Ian Tyrrell HUNTER

ABSTRACT

The coastal region of the South Cape is presented as a typical semi-developed coastal zone with a limited environmental dataset. The author places himself in the position of a coastal engineer requiring wind data for design purposes. The various sources of wind measurement are discussed. Time series are presented depicting responses at different sites to the same large-scale synoptic situation. Spatial variations, both across the coastal boundary and in the offshore region are emphasized. These variations are brought to the attention of those engineers who may have to extrapolate wind conditions to their site of interest.

1 INTRODUCTION

The Cape south coast extends from Cape Agulhas to Cape Padrone at the eastern extremity of Algoa Bay (Figure 1). The continental shelf widens considerably in this region to form the Agulhas Bank which has been chosen as the site of a multidisciplinary oceanographic research project. As part of the meteorological program for the project, existing sources of wind data were fully explored. They include:

(i) Long-term wind data from weather offices.
(ii) Synoptic reports from ships of opportunity.
(iii) Wind from offshore drilling platforms.
(iv) Estimated wind data from lighthouses.

An additional source was created in February 1982, when three automatic weather stations were erected at suitable coastal sites. A fourth station was periodically mounted on the *R V Meiring Naudé* and this provided invaluable offshore data. Figure 1 shows the distribution of the various sources of wind data along the coast.

The various types of wind observations are discussed in terms of their accuracy, representativeness and distribution. Justification for such a study, from a coastal engineering point of view, comes from the fact that a significant proportion of the wave energy on this coast is generated by the high-frequency, locally generated component.

2 WIND OBSERVATIONS AT FULLY FLEDGED WEATHER OFFICES

There are two weather offices in the study area, one at H F Verwoerd Airport, Port Elizabeth, and the other at George. Both have been

---

National Research Institute for Oceanology, Council for Scientific and Industrial Research, Stellenbosch, Republic of South Africa.

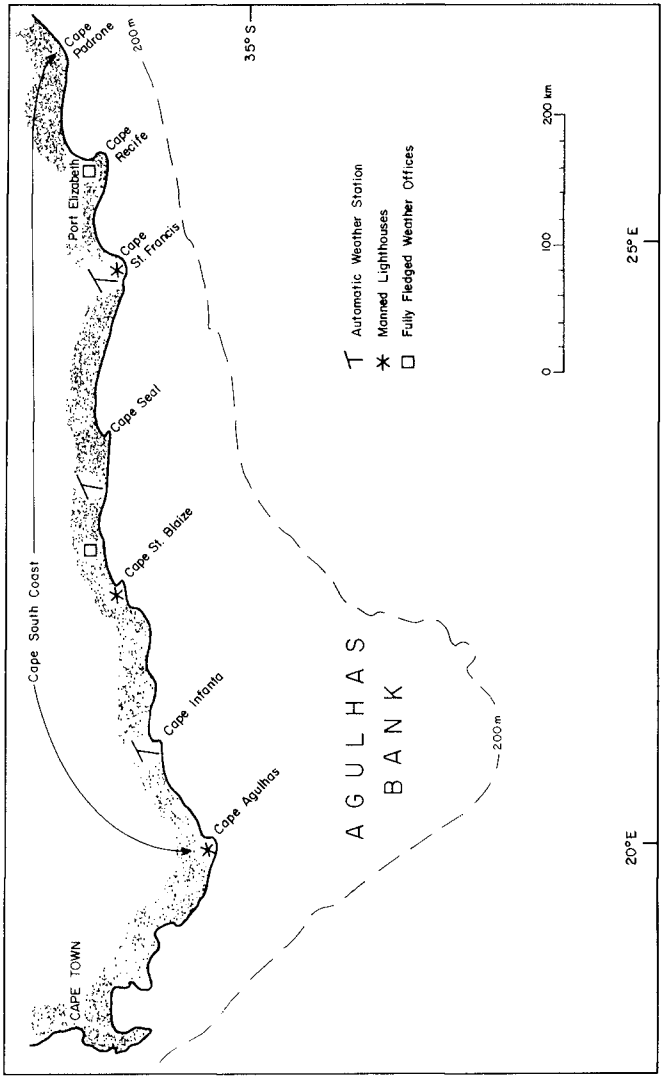

FIGURE 1: LOCATION OF WIND RECORDING STATIONS

recording hourly wind speed since 1951, using Dines pressure tube anemometers.

H F Verwoerd Airport (see inset Figure 2), is located 3 km from the coast with the anemometer at a height of 60 m a.s.l. The general terrain surrounding the airport is flat with no marked topographical features. Yet it can be shown that data collected here are not representative of coastal conditions.

During the period 1 to 3 September 1978, a series of intense low pressure systems resulted in high seas on the Agulhas Bank. In Figure 2 hourly wind data from H F Verwoerd Airport are compared with those from the oil rig Sedco-K, roughly 40 km to the south (See Section 5 for details of wind reduction to standard height).

It is evident that there was initially no coupling between air movement at the airport and that offshore. However, this situation improved as the boundary layer became more mixed, especially overnight. Nevertheless, if one compares the maximum values measured on the Sedco-K, with the 50-year return value of hourly wind speed for the airport (22,3 m/s), (South African Weather Bureau,1974), it is obvious that the airport is underestimating offshore conditions. This particular series of storms resulted in a significant wave height of 8,6 m (Shillington and Britten, 1979), at the Sedco-K site while an estimate of up to 15 m was received from a tanker within the Agulhas current further up the coast. The only other source of long-term, accurate wind data is the weather office at George. However, since this station is 221 m a.s.l. and more than 10 km from the coast it was considered to be unsuitable as a source of information on wind conditions.

Hsu (1980) has related mean monthly offshore wind conditions to those at a suitable coastal site. Unfortunately, insufficient data were available for such a study of conditions here. However, it is obvious from Figure 2 that the airport is not suitable for measuring coastal wind conditions.

3 WIND FROM OFFSHORE DRILLING PLATFORMS

The search for oil on the Agulhas Bank and the associated demand for environmental data, have provided researchers with invaluable offshore wind measurements. However, even this dataset presents problems:

(i) Although measurements began in 1978, the record is by no means continuous,
(ii) Measurements represent several well sites on the Agulhas Bank,
(iii) The anemometer is 73 m a.s.l. which poses a height reduction problem.

With regard to (ii), another drilling rig, the Sedco-708, was temporarily on the Agulhas Bank, drilling to the south of Sedco-K. While it was in a position roughly 78 km southwest of Sedco-K, wind speeds registered at Sedco-708 were significantly higher for much of the

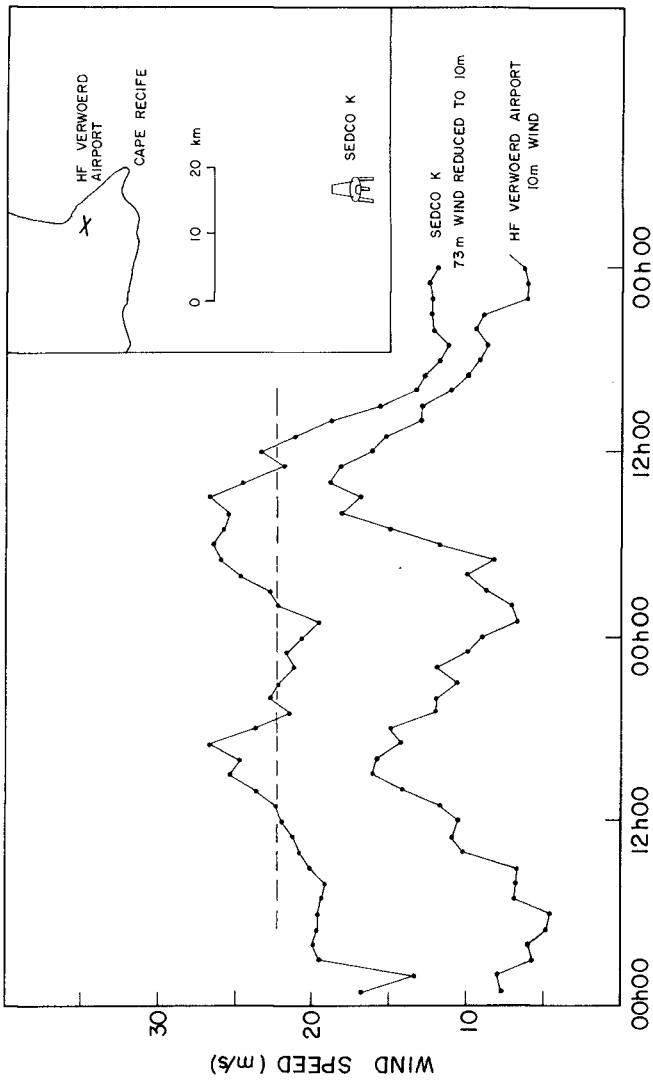

FIG. 2: VARIATION OF WIND SPEED OFFSHORE - HOURLY AVERAGES

time (Figure 3). However, the latter rig was later moved to a position roughly 74 km WSW of the Sedco-K and the comparison was greatly improved (Figure 4). It was significant that Sedco-708 was closer to the warm Agulhas Current when it was in the first position.

The reduction of wind speed from 73 m to the standard 10 m a.s.l. is a function of boundary layer stability, which may vary considerably in time and space. Whereas the wind power law has previously been applied with the exponent for a neutrally stable atmosphere, i.e.

$$U_{10} = U_{73} \cdot \left(\frac{10}{73}\right)^{,143}$$

subsequent wind measurements showed that this reduction may be too severe, especially under unstable, high-wind conditions. The hourly wind values plotted in Figure 2 were obtained using an exponent of 0,1 which effectively reduced the 73 m wind by 18%. It is felt that this reduction will, if anything, underestimate the 10 m wind, under extreme conditions.

In order to obtain a 50-year return period hourly wind for the Agulhas Bank, the method outlined by Katsiambirtas (South African Weather Bureau 1975), was followed. It should be noted that the chosen dataset of twelve months did not include the September 1978 storm (Figure 2). A value of 25,8 m/s was obtained. This value was exceeded on several occasions prior to the used dataset. This illustrates the folly of applying statistical methods to a relatively short wind record.

4 SHIPS OF OPPORTUNITY

Prior to the advent of offshore drilling operations, synoptic reports from merchant ships ('SHIP' reports) represented the only significant source of offshore wind data on the Agulhas Bank. The coastal engineer planning to utilise these data would have to bear in mind that :

1. Most vessels are 30 km or more from the coast in the region between Cape St Francis and Cape Agulhas (see Figure 5).
2. Reports are usually sent only on the main synoptic hour, i.e. every 6 hours.
3. Vessels will be trying to avoid extreme conditions if possible.
4. Observations are often neglected when the ship is within sight of land.
5. The majority of SHIP reports contain estimated wind speeds.

With regard to this last point, it must be borne in mind that most deck officers use state of sea to estimate wind speed. However, sea state is not purely a function of wind. Boundary layer stability and surface currents play an important role. Also it must be expected that wind estimates will decrease in accuracy as wind speeds increase. There is no simple solution to this problem, since an anemometer would measure relative wind speed and further errors may be introduced in the calculation of true wind speed. A height reduction problem also arises since anemometer height is not provided in the standard message and this will vary greatly from vessel to vessel.

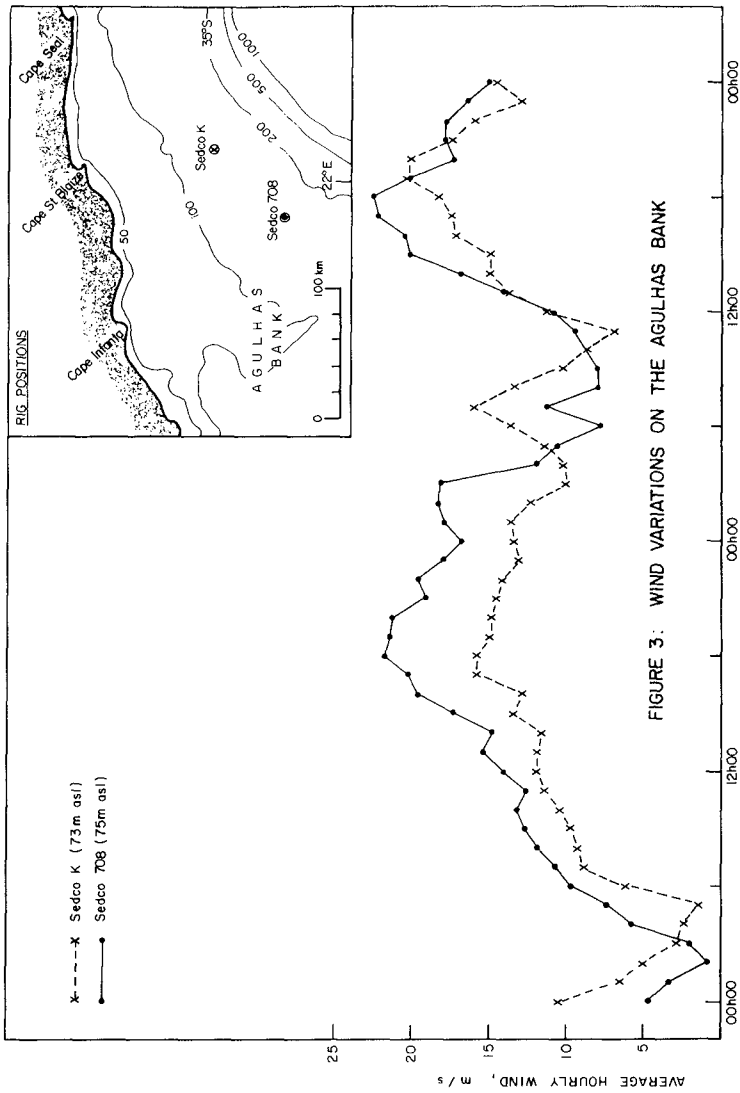

FIGURE 3: WIND VARIATIONS ON THE AGULHAS BANK

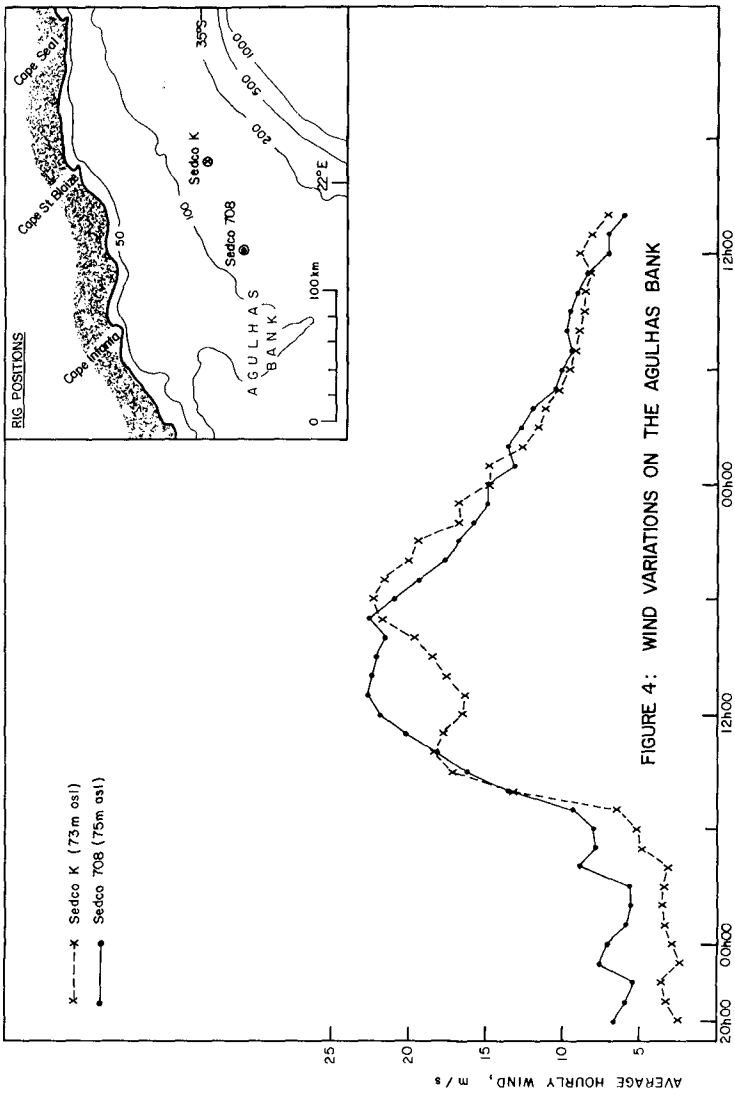

FIGURE 4: WIND VARIATIONS ON THE AGULHAS BANK

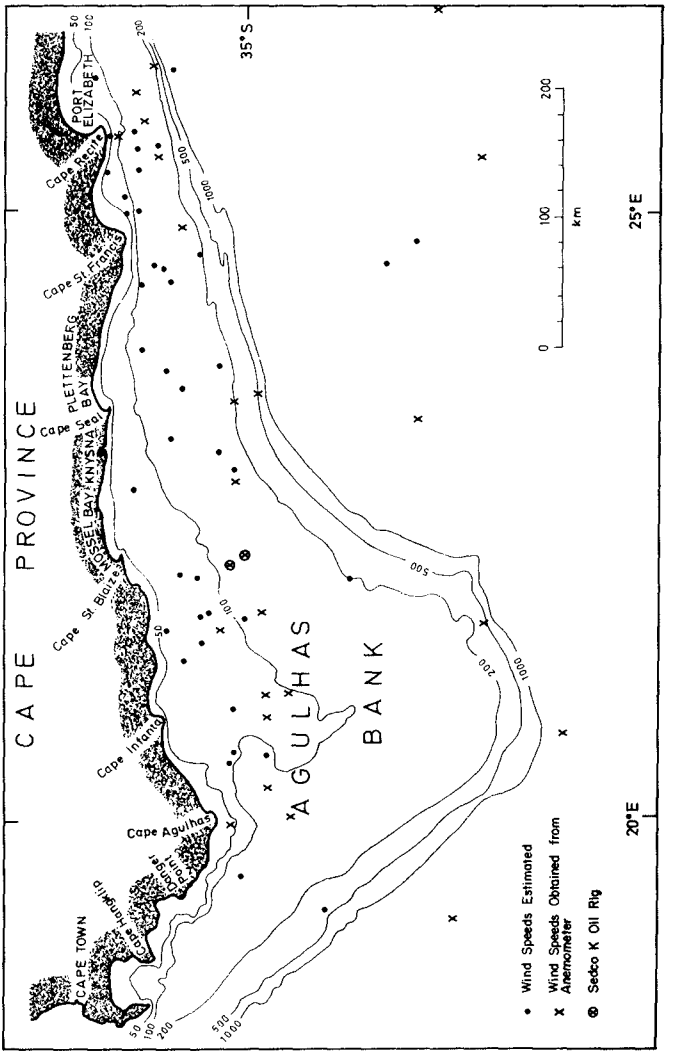

FIGURE 5: SHIPS' POSITIONS FOR MARCH AND APRIL 1982 AT 06h00 Z

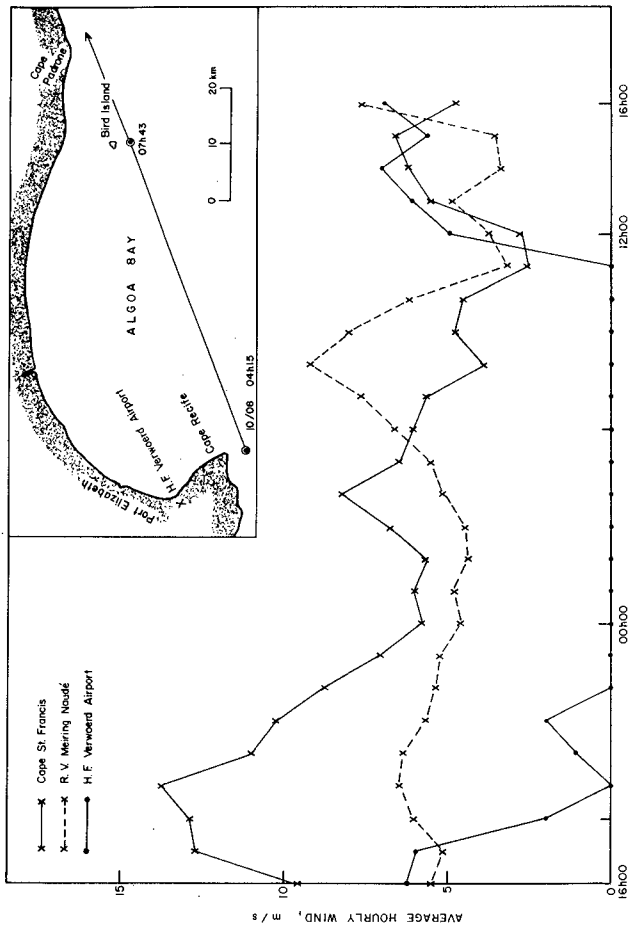

FIGURE 6: SPATIAL VARIATIONS

5 ESTIMATES OF HOURLY WIND FROM LICHTHOUSES

This represents the only source of long-term, truly coastal observations. There are now only three fully manned lighthouses on the Cape south coast (Figure 1). Of these three -

1 Cape St Francis is fitted with a pressure plate which is of no use under extreme conditions as it is almost horizontal at 15 m/s.
2 Cape St Blaize is badly positioned for wind observations, being sheltered from wind from certain directions.

Bearing in mind the limited accuracy of observations from these lighthouses, it has not been possible to determine their relationship to offshore conditions.

6 AUTOMATIC WEATHER STATIONS

Three permanent automatic weather stations were set up on the Cape south coast in February 1982. At all three sites, the prevailing winds have very limited stretches of coast to cross before reaching the anemometers. The surrounding terrain is also reasonably flat. The anemometers are all placed well above the internal boundary layer (IBL).

A fourth automatic weather station is mounted on the NRIO's research ship, R V *Meiring Naudé*, for those periods which she spends off the south coast. These wind data are invaluable in the study of offshore variation.

Figure 6 illustrates how nocturnal cooling may totally decouple the air flow on shore from that offshore. Early on 9 August, the R V *Meiring Naudé* was crossing Algoa Bay in the direction of Bird Island. A land breeze of about 5 m/s was blowing as the vessel passed within 15 km of H F Verwoerd Airport. At the latter site the establishment of the nocturnal inversion resulted in calm conditions from 22h00 until 11h00 the following day. In the vicinity of Bird Island the land breeze reached a peak of 9,2 m/s at 08h00, finally dying off at 11h00. The third curve in Figure 6 represents conditions at Cape St Francis (see Figure 1). The high wind speeds recorded there on 9 August are due to a frontal wave which was much weaker when passing the R V *Meiring Naudé* (the vessel was at that stage to the west of Cape St Francis). Note that the anemometer at Cape St Francis is above the nocturnal inversion with the land breeze there reaching a peak speed at 04h00.

7 CONCLUSIONS

This study has compared actual hourly wind averages as opposed to the comparison of long-term means. The following conclusions may be drawn:

(1) Although a simple relationship may, at times, exist between wind speed at a coastal site and one a few kilometres inland, the inland record may become completely decoupled due to excessive boundary layer stability.
Should extreme return period winds for such an inland site be applied to the coastal site, a severe underestimate may result.

(2) Extreme return period winds for an offshore site, based on a relatively short dataset (less than 10 years), may also underestimate the true condition.

(3) Offshore conditions may vary over relatively short distances (less than 100 km). This may be attributed, amongst other things, to sea surface temperature distribution and preferred locations for new synoptic developments.

8 ACKNOWLEDGEMENTS

Appreciation is expressed to the Southern Oil Exploration Corporation (Pty) Ltd., the Lighthouse Department of South African Transport Services, and the South African Weather Bureau for the valuable data which they provided.

REFERENCES

1 HSU, S A (1980) On the correction of land-based wind measurements for oceanographic applications. Proc. 17th Conf. on Coast. Eng. Sydney, Australia.

2 SHILLINGTON, F A and BRITTEN-JONES, A (1979) Features of surface waves off the southern Cape coast. S. Afr. J. of Sci.

3 SOUTH AFRICAN WEATHER BUREAU (1974). Climate of South Africa, Part 11, Pretoria.

4 SOUTH AFRICAN WEATHER BUREAU (1975). The estimation of extreme wind gusts from inadequate data. Technical paper No. 2.

TIDAL AND INERTIAL CURRENTS AROUND SOUTH AFRICA

by

E H SCHUMANN and L-A PERRINS

ABSTRACT

Limited information is available on currents in the semi-diurnal and diurnal frequency bands for the coastal ocean areas around Southern Africa. However, recently mooring data have become available from sites on the east, south and west coasts, and this paper analyses these results in an attempt to assess the importance of tidal and inertial currents.

It is clear that on the narrow shelf on the east coast the Agulhas Current dominates the energy spectrum, and tidal currents should be relatively unimportant at such sites. In the south on the Agulhas Bank the Current is still important, but comparable energy resides in inertial and tidal fluctuations. Modal analysis indicates the tides are primarily barotropic, with the inertial fluctuations mainly baroclinic.

In the absence of a major current on the west coast, most of the current variance occurs in the tidal and inertial bands; a complex vertical structure is also found. It is therefore clear that there are regions where such currents cannot be ignored.

1 INTRODUCTION

The most predictable forcing in the ocean is that due to the astronomical tides, with the tidal potentials associated with the various motions of the earth, moon and sun known to a high degree of accuracy. However, that does not mean that the response of the ocean to this forcing is necessarily predictable to the same degree of accuracy. Indeed, the ocean can respond in a variety of forms, dependent primarily on coastal and bottom topography, and the internal ocean structure.

The most obvious tidal motion is that of the surface of the ocean, with regular fluctuations in sea level ranging, in various parts of the world, from less than a metre to more than ten metres. Since such changes are of immediate interest to coastal communities, sea level tides have been known, studied, and predicted with various degrees of accuracy for many years. Prediction techniques have generally been

---

Physical Oceanography Division, National Research Institute for Oceanology, Council for Scientific and Industrial Research, P O Box 320, Stellenbosch, South Africa.

dependent on sea level measurements carried out over long periods at appropriate coastal sites. This is also so in South Africa, where regular tide tables are issued by the Naval Hydrographer.

By continuity, there must also be currents associated with such movements of the sea surface. The strength of the currents is dependent on topography, with the most apparent examples occurring in estuaries and on the wider continental shelf regions.

Internal tides, dependent on the density structures within the ocean, also occur. Wunsch (1975) reviewed the nature of these fluctuations, which may cause vertical deflections of 30 m or more in the constant density surfaces. As with the surface, or barotropic tides, there are also currents associated with such baroclinic motions, although phase changes take place with depth.

There are further fluctuations in ocean currents that will be discussed here, since the periods involved are in the range of the semi-diurnal and diurnal periods of the dominant tidal forcing. These are the inertial currents, the oscillations in water set in motion and then moving over a rotating earth. The major generating force is wind stress, but with the details of the motion dependent on topography and ocean density structure. The period of such inertial oscillations depends on latitude, being given approximately by the relation 12.04/ sin(latitude) hours.

Except where they are influenced by distinct coastal features such as estuaries, tidal currents around South Africa have been given little attention. To some extent this has been due to the lack of suitable measurements, but on the other hand it appears to be accepted that the effects of tidal currents should be negligible compared with currents generated by other forces. Reasons for such assumptions may be the generally straight coastlines, and the limited continental shelf areas.

This paper attempts to take a first look at tidal and inertial currents using data from moorings deployed on the east, south and west coasts of South Africa. These are distinctly different oceanic regimes, with the resulting currents also having different characteristics. It is clear that there are areas where such currents cannot be ignored, and where they may, in fact, constitute the most energetic part of the current spectrum.

2 OCCURRENCE OF TIDAL AND INERTIAL FLUCTUATIONS

The periods of astronomical tides cover a wide range, with the dominant components tending to fall into groups centered at semi-diurnal, diurnal and longer-period motions. Within these groups the frequencies are split by multiples of a cycle per fortnight, cycle per year, etc. Table 1 lists the major semi-diurnal and diurnal components of interest here.

Analyses have indicated that in many areas the tides propagate largely as Kelvin waves (e.g. Platzman, 1971; Munk, Snodgrass and Wimbush, 1970). This means that the tidal potentials can excite waves at

selected periods, and that the observed amplitudes and currents then occur as a result of the propagation of these waves. They are gravity waves modified by rotation, and propagate in the southern hemisphere with the coastline on the left in the direction of propagation.

The major portion of the tidal amplitude observed at a coastal site is generally due to a barotropic type of Kelvin wave. Such a wave does not depend on stratification, and for narrow shelf regions does not depend markedly on shelf topography. Around South Africa there are no great variations in the amplitudes of the semi-diurnal and diurnal barotropic tides, with spring tide amplitudes ranging from about 1.4 to 1.8 m, and neap tides from 0,5 to 0,6 m.

The offshore scales of the baroclinic tides are the corresponding Rossby radii of deformation, generally of the order of a few tens of kilometres or less. As such, smaller-scale topographic features on a continental shelf region can exert a considerable influence on their characteristics. Usually the buoyancy frequency due to the stratification is much less than the tidal frequencies, so that resonance does not occur. The patterns of baroclinic tides also show considerable variations with respect to the more stable barotropic tides. Thus the small wavelengths make them susceptible to Doppler shifting by more energetic currents, thereby changing the frequency with respect to a stationary observer. Moreover, if measured tidal current amplitudes are strong functions of time, it can be assumed with a fair degree of certainty that they are due to baroclinic tides.

Baines (1982) discusses the internal tide generation models, where the forcing is due to the barotropic onshore-offshore tidal currents. The analysis indicates that the amplitude of such forcing will be accentuated markedly at a shelf break; the generated internal tide should therefore be sensitive to variations in stratification in such a region.

Analyses, such as those by Torgrimson and Hickey (1979) and Huthnance and Baines (1982), indicate that the propagation of tidal signals and the associated currents are complex phenomena. If the details of their structures are to be elucidated, a knowledge of the ocean stratification, ambient currents and bottom topography is needed, not only in the region of interest, but also far enough alongshore to accommodate waves moving along the coast; this again brings with it factors such as frictional dissipation.

An important factor in tidal theory is the existence of so-called "inertial latitudes", where the inertial period at that latitude is equal to one of the tidal constituents (Wunsch, 1975). For the diurnal constituents this occurs at latitudes between 26,5° and 30°, while for the semi-diurnal constituents the inertial latitudes range between 71° and 90°. Initially it was in fact thought that inertial motions occurred primarily in resonance with tides. However, Webster (1968) reviewed existing literature on the subject and discounted the idea. In particular, it is now accepted that one of the prime generators of inertial period motions is wind stress (Wang and Mooers, 1977; Mayer, Mofjeld and Leaman, 1981).

By the nature of its dependence on the local vertical component of the earth's rotation, pure inertial motion is horizontally polarised. It is also a circular motion, with an anticlockwise rotation in the southern hemisphere.

In the South African context the inertial period is close to the diurnal tidal period, possibly giving rise to interactions and making the separation of the two motions more difficult. In particular, it is worth noting that in an earlier analysis Welsh (1964) found pronounced inertial currents on the Agulhas Bank.

3 DATA AND ANALYSIS

The current data analysed here were all recorded by Aanderaa RCM-4 meters. These utilise a Savonius rotor to give a mean value of current speed over the measuring period, while a large vane gives an instantaneous value of current direction; the size of the vane effectively eliminates high-frequency fluctuations. Water temperature was also measured.

One mooring was chosen on each of the east, south and west coasts, and Figure 1 depicts the approximate positions at which the moorings were deployed, while Table 2 gives further mooring details. The mooring off Natal formed part of the Shelf Dynamics Project, with the meter mounted on a rigid stand some 3 m off the bottom. The moorings on the Agulhas Bank and off the west coast were done as part of a contract for the Southern Oil Exploration Corporation (SOEKOR). These consisted of taut-wire moorings, with the one at site W1 deployed directly from an oil drilling platform. Four meters were included in the vertical array, although good data were obtained only from three meters at the S1 site.

The depth of the shallowest meters on all the moorings should have precluded excessive contamination of the current speed record by wave-induced motions (Halpern, 1977). The rigid stand deployment, the configurations off the oil drilling platforms, and the subsurface upper buoy deployment would also have stopped or limited "rotor pumping" caused by mooring motion (Halpern and Pillsbury, 1976). As a consequence, for present purposes the values of currents and temperatures registered will be assumed to be an accurate reflection of the conditions actually present in the ocean at the time.

For all meters the data interval was set at 15 minutes. The values of currents and temperatures thus obtained were subjected to standard processing and analysis procedures before being filtered and decimated to hourly values by the operation of a Cosine-Lanczos filter with 24 distinct weights and a half power point of 0,5 cycles/hour. The hourly values served as the basis for most of the subsequent analysis, although in some cases further filtering giving three-hourly values was also applied.

Standard spectral analysis techniques were utilised to obtain the power spectra of the measured currents and temperatures (Jenkins and Watts, 1968). The resultant of any periodic, orthogonal pair of velo-

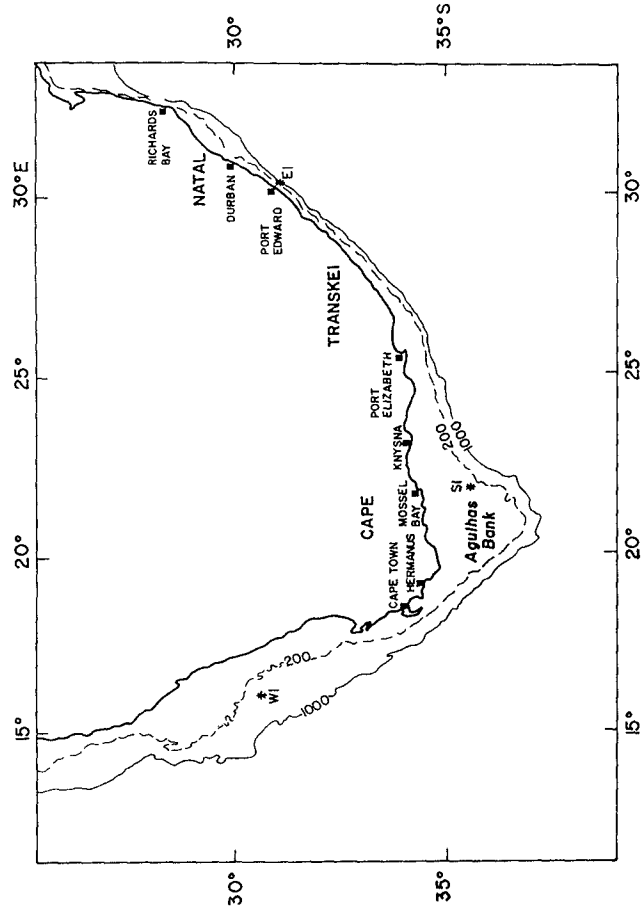

FIGURE 1. The Southern African coastline, showing bathymetry and indicating the positions of the moorings discussed in the text.

cities may also be represented as the combination of two vectors which rotate in opposite senses. Thus a velocity signal at a given frequency may be thought of as consisting of both clockwise and anti-clockwise portions. Such a decomposition can then be used to compute clockwise (S_-) and anti-clockwise (S_+) energy spectra, also referred to as rotary spectra (Gonella, 1972). The total spectrum S_t is then the sum of the two portions.

The rotary coefficient C is defined as

$$C = \frac{S_- - S_+}{S_t} = 1 - \varepsilon$$

and gives the partition of the energy S_t and the relationship with the normal ellipse eccentricity, ε. For pure circular motion the magnitude of C will be one, while it will be zero for linear fluctuations. Such an analysis is therefore important in distinguishing between inertial and Kelvin wave-type fluctuations. In the southern hemisphere inertial motion is anti-clockwise, that is, $S_+ >> S_-$, while for Kelvin waves $S_+ \sim S_-$.

Current ellipses can thus be determined at all frequencies of interest, with the orientation of the major axis giving the dominant direction for the current fluctuations.

A further parameter of importance in this analysis is the stability of orientation of the ellipse. This gives an idea of the isotropy of the wave field generated by tides and inertial motions in the ocean; in particular, the barotropic tides should be stable, with a greater variability inherent in the internal motions.

In order to obtain more information about the nature of the internal fluctuations, empirical orthogonal mode (eom) analysis can be performed (Kundu, Allen and Smith, 1975). In essence, this technique determines the subdivision of the variance of the current fluctuations into the possible modes of oscillation, as well as giving information on their depth structure. In this way it can be ascertained whether the motion was predominantly barotropic, first mode baroclinic, etc. Of course, with four meters in the vertical it is possible to investigate only the first three baroclinic modes, although even this depends on the position of the meters relative to the density structure.

The basic technique was extended by Wang and Mooers (1977) to enable modes to be determined at specified frequencies. This involves the determination of the co-spectra and quadrature spectra, and then finding the empirical modes as eigensolutions of the cross-spectrum matrix. These methods were used in the analysis of the results from moorings deployed on the south and west coasts.

4 EAST COAST - NATAL

As shown in Figure 1, the shelf here is narrow, with the off-shore region dominated by the influence of the Agulhas Current (Pearce, 1977). This is a major western boundary current flowing polewards along the coast. Schumann (1981) analysed the data from moorings deployed off Natal and concluded that markedly different regimes existed in the region. In particular, the subtidal currents measured at the site E1 were largely associated with the Agulhas Current.

Figure 2 shows the result of rotary spectral analysis at the site E1. It is clear that, at the diurnal O_1 and K_1 tidal frequencies, a fairly significant peak emerges. The stability and ellipticity are high, as would be associated with classical Kelvin wave propagation. The abrupt drop at the inertial frequency associated with a high ellipticity indicates limited inertial motion.

A peak also emerges at the M_2 semi-diurnal frequency. The ellipse stability is lower, with a lower ellipticity, indicating a more circular type of motion than that at the diurnal periods.

However, overall it is clear that the fluctuations at the diurnal and semi-diurnal periods play a relatively minor role in the energetics at the site. It is dominated by energy at much longer periods, probably associated with the Agulhas Current.

5 SOUTH COAST - AGULHAS BANK

The Agulhas Bank comprises the widest continental shelf around South Africa, with a maximum offshore extent of about 270 km (see Figure 1). The measurements to be discussed were made on the eastern side of the Bank in water depths of less than 150 m. The Agulhas Current plays an important part in the dynamics of the region, particularly in terms of the spin-off eddies on the inshore edge which can penetrate onto the Bank itself (Lutjeharms, 1981). The influence of the Current, and the variations over the shelf, is then also apparent from the results obtained at the mooring S1 (Figure 1), particularly at longer periods.

Figure 3 shows the results of rotary spectral analysis carried out at the site S1. It is clear that there are three main contributions to the current fluctuations observed there, namely, those occurring at periods longer than about three days, and then the diurnal/inertial and semi-diurnal fluctuations. Only the latter two are of interest here, although it is worthwhile noting that, at periods of longer than about ten days a clockwise rotation dominates; this is probably associated with the spin-off eddies.

A substantial, broad peak appears in the anti-clockwise spectrum covering the diurnal and inertial periods in the range from about 18,5 to 27 hours. This is not reflected in the clockwise spectrum, indicating the existence of a dominant anti-clockwise motion. This is as expected at or near the inertial frequency, and is confirmed by the relatively high ellipse stability and low ellipticity shown in Figure 3.

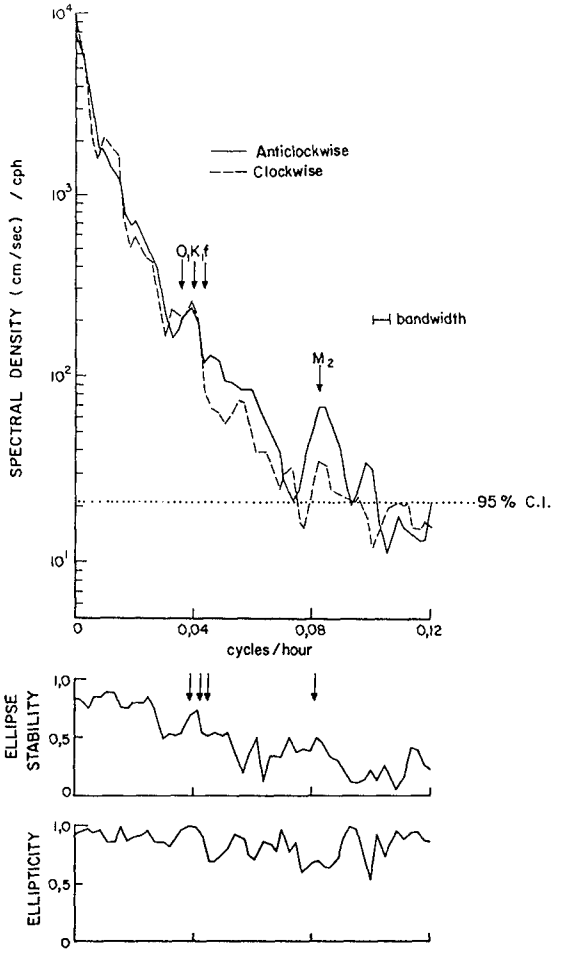

FIGURE 2. Clockwise and anticlockwise spectra for the measurements taken at site E1. Also shown are the ellipse stability and ellipticity, while the positions of the major tidal frequency bands are indicated, as well as the inertial frequency (f).

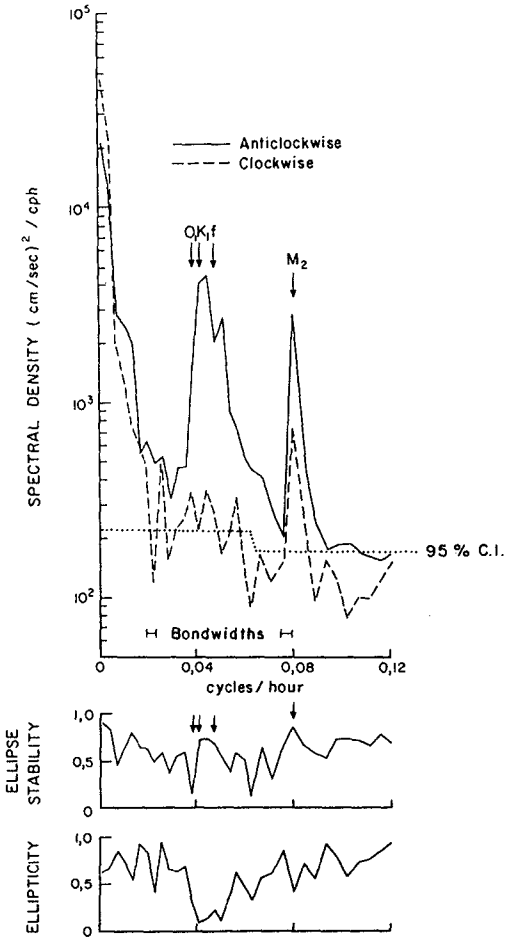

FIGURE 3. Clockwise and anticlockwise spectra and ellipse stability and ellipticity for the measurements taken at the topmost meter (depth 38m) at site S1.

A sharp, energetic peak occurs at the M_2 tidal frequency. Again the anti-clockwise spectrum dominates at this point, although there is nonetheless a substantial peak in the clockwise spectrum. A high ellipse stability is found, but with an intermediate value of the ellipticity.

The spectra determined from the measurements made at the two lower meters showed the same characteristics as those depicted in Figure 3 for the upper meter, although with slightly lower energies. However, this does not mean that the fluctuations observed were barotropic, since the analysis has merely indicated that the division of energy into the various frequency bands is similar.

Figure 4 shows the variations in coherence and phase between the east and north components of current at all three depths. It was not considered necessary to select any specific orientation for the current components, since Figure 3 did not reveal an exceptionally marked orientation for the current fluctuations.

It is clear that there is a major difference between the tidal and inertial period fluctuations. At the semi-diurnal and diurnal tidal periods a high level of coherence is found throughout the water column, with a minimal phase change with depth. At the inertial period a high level of coherence is also found, but with a phase change approaching 180° between the upper and middle meters. Calculation of the mean temperatures recorded at the three depths over the whole measuring period gives values of 16,6°C (38 m), 10,2°C (108 m) and 9,9°C (130 m). It is therefore clear that a major pycnocline existed between the upper and middle meters, giving favourable conditions for the existence of baroclinic fluctuations. On the other hand, only the inertial period fluctuations appear to respond, as indicated as well by the sharp dip in coherence between the diurnal tides and the inertial frequency in the upper meters of Figure 4.

The results of eom analysis are given in Table 3, and support the above conclusions. The vast majority of the fluctuation energy resides in the barotropic and first baroclinic modes, although there are some much smaller phase variations with depth in each of these modes; these may be associated with frictional effects or vertical propagation.

The difference between the long-period, tidal and inertial fluctuations is clear. The former are all essentially barotropic, with no more than about 10% of the energy distributed amongst the baroclinic modes. However, the inertial fluctuations are primarily dependent on the variations in density over the ocean depth, with less than 20% of the energy in the barotropic mode. This seems to be in agreement with the result that inertial oscillations in a coastal boundary or shelf region are essentially dependent on stratification (Pettigrew, 1981). It is also likely that there was considerable variability in the extent of the inertial fluctuations over the measuring period.

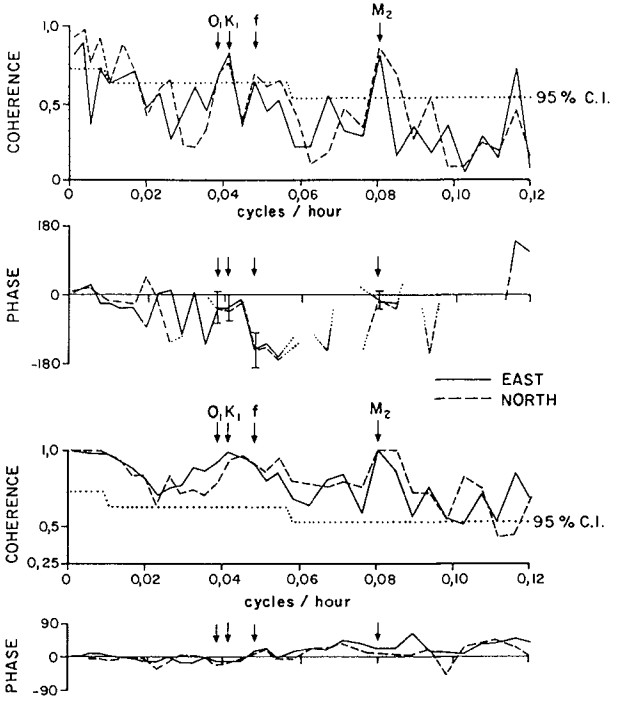

FIGURE 4. Coherence and phase between the east and north current components at site S1. The top section considers currents from the upper and middle meters (38 and 108 m), while the bottom section considers the middle and lowest meters (108 and 138 m). The 95% confidence limits are shown in the coherence, while for the upper meters the approximate error bars for phase are shown only at the indicated frequencies; for the lower meters the error in phase is less than 20°. Phase is only shown for relatively high coherence, while a positive value indicates that the lower of the two meters leads.

6 WEST COAST

The bottom topography is much more broken off this coast than either on the east or south coasts, with no well-defined shelf or slope. The Benguela Current flows northward here but should not be thought of as a well-defined current, but rather as a general movement of water northwards with eddies and current reversals.

The inertial period at this mooring is very close to the K_1 tidal period (Table 2). With the relatively short records, it was therefore not possible to resolve fluctuations at these two periods.

Figure 5 shows rotary spectral calculations at three of the four measuring depths. It is clear that the fluctuations at tidal and inertial frequencies contribute a major portion of the current energetics at the site. There is, moreover, a change with depth, with the diurnal/inertial peak highest at the upper meter, but then gradually being superseded by the semi-diurnal peak as the depth increases. However, it should be remembered that the time series at the upper meter covered only about four-fifths of that at the lower depths. The reason for the apparent emergence of a peak at about a 17-hour period is also not clear.

As expected, at the diurnal/inertial frequency the anti-clockwise peak contains most of the energy, with associated ellipticity values of less than 0,06 at all four depths. At the semi-diurnal peak the motion is also primarily anticyclonic, with ellipticity values of 0,42 at the upper meter and less than 0,28 at the deeper meters.

Figure 6 shows the coherence between adjacent meters on the mooring. Only the eastward components of the currents were considered, since again the low ellipticity values at the frequencies of interest show that any fluctuations will be reflected in all current components.

At the diurnal/inertial frequencies, there is a low coherence over the whole water column, while at the semi-diurnal M_2 frequency a very high coherence emerges. Inspection of the phase angles at the M_2 frequency shows values close to zero between all the measuring depths, that is, largely barotropic motion occurred with the semi-diurnal tidal propagation.

The eom results support these conclusions, with only the M_2 tidal fluctuations having a well-defined structure; here the barotropic mode dominated the energy partition with about 91%, with 8% in the first baroclinic mode. The long-period barotropic component comprised about 74% of that band's energy, although with more limited coherence especially near the surface. About 20% and 6% went into the first and second baroclinic modes, respectively. At the O_1, K_1 tidal and the inertial frequency bands the situation is much more confused, with little indication of barotropic motion, but with a limited vertical coherence in the baroclinic motions.

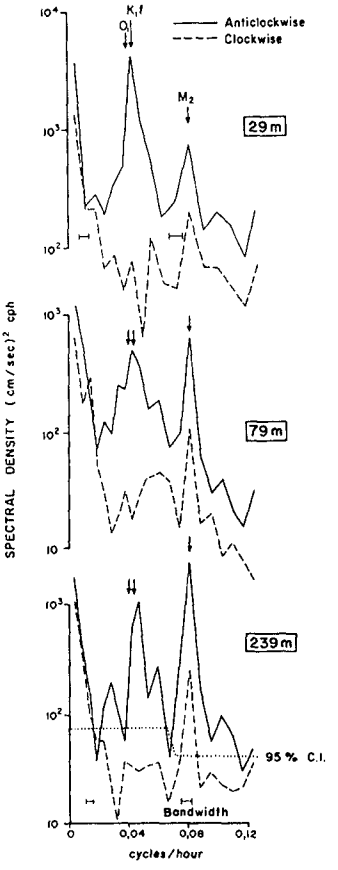

FIGURE 5. Clockwise and anticlockwise spectra from measurements at 29, 79 and 239 m depth at site W1. The 95% confidence limit shown for the bottom spectra applies to all three cases, while the bandwidths at the upper meter differ because of the shorter record.

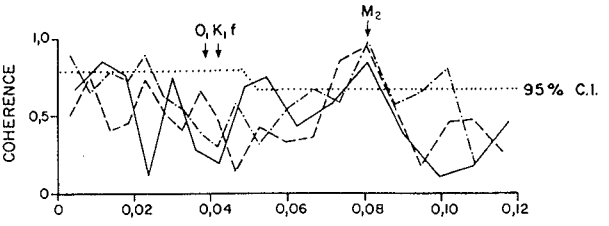

FIGURE 6. Coherence between adjacent meters on the mooring W1. Thus ———— considers the meters at 29 and 79 m, —·—·—· the meters at 79 and 159 m, while — — — — — is for 159 and 239 m depths.

7 CONCLUSIONS

The analysis that has been presented here has been limited by the small amount of current data available. As a result it was not possible to investigate the propagation of tidal and inertial signals, with only a limited analysis being possible of the vertical structure on the south and west coasts of South Africa.

Nonetheless, as a first look at the tidal and inertial currents, some very important differences between the coastal ocean regimes around South Africa have emerged. Moreover, it is clear that these currents cannot be ignored as a matter of course; indeed there are regions where they provide the dominant contribution to the total current variance.

Table 4 gives the comparison. The majority of spectra, particularly along the south and west coasts, have exhibited peaks at the semi-diurnal diurnal/inertial frequencies, as well as at the low-frequency limit. Consequently these peaks have been considered in the comparison; in some cases judging the extent of the peaks has been somewhat subjective, but in the majority of cases the error involved is small. The low frequency limit has included all frequencies less than about 0,014 cph (3 days).

On both the south and west coast sites the current ellipses at the tidal and inertial frequencies all rotate anti-clockwise. The ellipses themselves are not very eccentric, with the currents not showing the linear polarisation associated with the classic barotropic Kelvin wave. Nonetheless the indications are that at the M_2 semi-diurnal frequency the fluctuations were predominantly barotropic, also supported by the very consistent values found with depth in Table 4. Without more measurements the precise structure of the baroclinic fluctuations is not known, although the evidence for a strong first mode oscillation at the sharp thermocline at site S1 is clear.

The generation of the baroclinic fluctuation at tidal and inertial frequencies falls outside the scope of this paper, and indeed there are only limited data available to investigate this aspect. Nonetheless, given the proximity of the diurnal and inertial frequency bands, it is likely that some interaction occurred. Wind stress should also play a part, in which case a seasonal variation could be expected with the different seasonal winds. Changes in density structure would then markedly affect the response.

As a result, it is probable that considerable variability is likely to occur in the baroclinic fluctuations, that is, at times there may be minimal currents, but in order to achieve the mean values in Table 4, there must have been substantial currents at other times. Topographical variations and changes in ocean structure will also cause changes in the currents at the various frequencies; at present such variability across the shelf regions and with time is not known. It is nonetheless clear that in any construction or development in the ocean around South Africa, cognisance should be taken of the fact that tidal fluctuations may constitute the dominant portion of the currents actually encountered.

ACKNOWLEDGEMENTS

Much of the analysis presented here was done while one of us (EHS) was visiting the Woods Hole Oceanographic Institution. As such the PROSPECT series of programs were used, while Dr Bob Weller advised on aspects of the analysis. Acknowledgement is also given to Dr Ken Brink for the use of his eom programs, in addition to helping with the interpretation of results.

The data on the south and west coasts were collected under contract to the Southern Oil Exploration corporation, and acknowledgement is given here for permission to use the data in this analysis.

REFERENCES

BAINES, P G (1982). On internal tide generation models. Deep-Sea Research, 29, 307-338.

GONELLA, J (1972). A rotary-component method for analysing meteorological and oceanographic time series. Deep-sea Research, 19, 833-846.

HALPERN, D (1977). Review of intercomparisons of moored current measurements, Oceans '77 Conference Record, Marine Technology Society, Washington, DC, 46D1-46D6.

HALPERN, D and PILLSBURY, R D (1976). Influence of surface waves on subsurface current measurements in shallow water. Limnology and Oceanography, 21, 611-616.

HUTHNANCE, J M and BAINES, P G (1982). Tidal currents in the northwest African upwelling region. Deep-Sea Research, 29, 285-306.

JENKINS, G M and WATTS, D G (1968). Spectral analysis and its applications. Holden Day, 525 pp.

KUNDU, P K, ALLEN, J S and SMITH, R L (1975). Modal decomposition of the velocity field near the Oregon coast. Journal of Physical Oceanography, 5, 683-704.

LUTJEHARMS, J R E (1981). Features of the southern Agulhas Current circulation from satellite remote sensing. South African Journal of Science, 77, 231-236.

MAYER, D A, MOFJELD, H O and LEAMAN, K D (1981). Near-inertial internal waves observed on the outer shelf in the Middle Atlantic Bight in the wake of Hurricane Belle. Journal of Physical Oceanography, 11, 87-106.

MUNK, W H, SNODGRASS, F and WIMBUSH, M (1970). Tides offshore: transition from California coastal to deep-sea waters. Geophysical Fluid Dynamics, 1, 161-235.

PEARCE, A F (1977). Some features of the upper 500 m of the Agulhas Current. Journal of Marine Research, 35, 731-753.

PLATZMAN, G W (1971). Ocean tides and related waves. In: Mathematical problems in the geophysical sciences. Ed. W H Reid. Lectures in Applied Mathematics, 14(2), 239-291, American Mathematical Society, Providence, Rhode Island.

SCHUMANN, E H (1981). Low frequency fluctuations off the Natal coast. Journal of Geophysical Research, 86, 6499-6508.

TORGRIMSON, G M and HICKEY, B M (1979). Barotropic and baroclinic tides over the continental shelf and slope off Oregon. Journal of Physical Oceanography, 9, 945-961.

WELSH, J G (1964). Measurements of currents on the Agulhas Bank with an Ekman Current Meter, Deep-Sea Research, 11, 43-52.

WANG, D-P and MOOERS, C N K (1977). Evidence for interior dissipation and mixing during a coastal upwelling event off Oregon. Journal of Marine Research, 35, 697-713.

WEATHERLY, G L and NIILER, P P (1974). Bottom homogenous layers in the Florida Current. Geophysical Research Letters, 1, 316-319.

WEBSTER, F (1968). Observations of inertial period motions in the deep sea. Reviews of Geophysics, 6, 473-490.

WUNSCH, C (1975). Internal tides in the ocean. Reviews of Geophysics and Space Physics, 13, 167-182.

	Tidal Symbol (description)		Period (hrs)	Coefficient
Diurnal	O_1	(principal lunar)	25,82	0,415
	P_1	(principal solar)	24,07	0,194
	K_1	(lunisolar declinational)	23,93	0,585
Semi-diurnal	N_2	(elliptical to M_2)	12,66	0,192
	M_2	(principal lunar)	12,42	1,000
	S_2	(principal solar)	12	0,466
	K_2	(lunisolar declinational)	11,97	0,127

TABLE 1: The main diurnal and semi-diurnal tidal constituents. The coefficient gives a value of the appropriate tidal potential relative to the dominant M_2 tide.

Mooring (Period)	Water Depth (m)	Meter Depth (m)	Data (days)	Inertial Period (hrs)
East E1 (Oct.1976-Jan 1977)	29	26	91	23,25
South S1 (Nov.1978-Jan 1979)	144	38	93	20,75
		108	94	
		130	94	
West W1 (May-Jun 1981)	255	29	27	23,73
		79	35	
		159	35	
		239	35	

TABLE 2: Details of the data recovered from the moorings deployed on the east, south and west coasts of South Africa. Locations of the sites are given in Figure 1.

	Long Period	O_1K_1 Tidal	Inertial (F)	M_2 Tidal
Barotropic	94	89	18	91
First baroclinic	6	10	80	9

TABLE 3: Energy partition in the various frequency bands at the mooring site S1. Only the easterly current component was used in these calculations.

Site	Depth (m)	Mean Current (cm/s) Eastward	Northward	Current fluctuations (cm/s) Low Frequency	Diurnal/ Inertial	Semi-diurnal
S1	38	-11,2	-13,2	17,5	7,9	4,3
	108	-13,1	-5,5	13,3	6,8	4,0
	138	-12,6	-3,8	12,3	4,1	3,7
W1	29	-12,0	0,1	6,7	6,4	3,6
	79	-9,7	0,7	4,0	3,1	2,5
	159	-4,4	0,4	3,4	3,5	3,5
	239	-3,7	0,5	4,6	3,4	4,5

TABLE 4: Mean currents and the appropriate magnitude of current fluctuations over three frequency bands. These fluctuations have been calculated as the square root of the current variance over the bands shown.

THE RELINING OF SAICCOR'S EFFLUENT OUTFALL

BERNSTEIN, MARK
AHRENS, HUGH P.L. (MEMBER ASCE)
SMART, MICHAEL D.

ABSTRACT

This paper describes the method employed to refurbish an existing marine outfall which was deteriorating rapidly. It reviews the repair options that were available and how each was investigated and rejected until the best solution was obtained. Finally the execution of the project is described in detail through each stage to successful completion.

1.0 INTRODUCTION

The SAICCOR rayon pulp mill at Umkomaas on the east coast of South Africa was commissioned in 1954 with an initial capacity of 100 tons of pulp per day and is currently producing 1 200 tons of pulp per day.

During 1964 and 1965, investigations into the provision of a sea outfall were carried out and in 1967, a rubber lined steel pipeline of 914 mm internal diameter designed to discharge a little over 100 000 m^3 per day of effluent at 50°C into the Indian Ocean through a diffuser system located 2500 m offshore in 20 to 25 m of water was commissioned. The outfall consisted of a landline delivering effluent from a pumping station on the south bank of the river to a sealine which was located north of the Umkomaas River mouth.

The landline was made up of three separate sections as follows:

(a) Pumphouse to bridge

This was a 117 m long section of buried pipe terminating in a 9 m high vertical leg discharging into a bend on a bridge over the Umkomaas River.

(b) Bridge section

This consisted of 8 No 25 m long self supporting pipes spanning between the existing bridge piers.

Bernstein, M. Consultant to Campbell, Bernstein & Irving
Ahrens, H. Partner of Campbell, Bernstein & Irving, Overport, South Africa
Smart, M. Engineer with Campbell, Bernstein & Irving

(c) Bridge to the sea outfall

This consisted of a 200 m length of buried pipe from the end of the bridge to a 90° bend at the beach which is the start of the sealine.

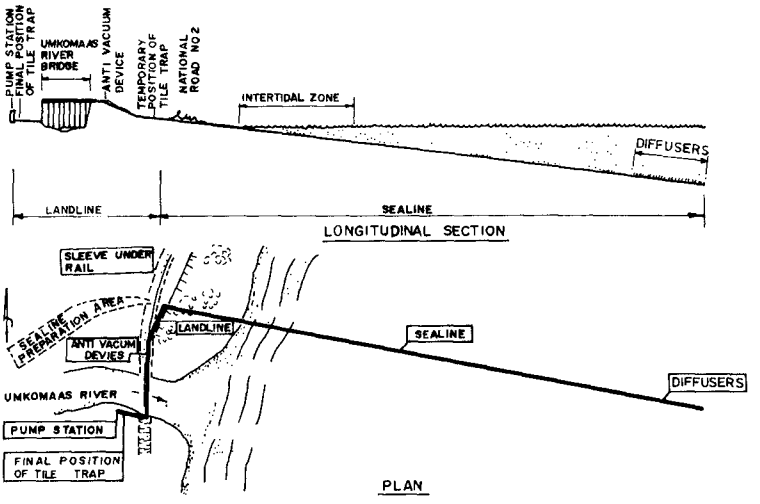

FIGURE 1

The 2000 m long sealine was made up of 97,5 m flanged lengths with a 100 mm thick concrete weightcoat. It terminated in a 300 m long diffuser section containing 48 No vertical outlets ranging in diameter between 100 mm and 137 mm.

An examination of the pipeline at the end of 1971 revealed some deterioration of the rubber at the invert and there were also signs of blistering up to 25 mm diameter under the pulp scale which had built up to a thickness of about 25 mm. It was considered that most of this deterioration was caused by the passage of heavy grit in the effluent and equipment to reduce this was installed.

Further inspections at regular intervals revealed a reduction in the rate of deterioration. Although the friction factor was building up at a rapid rate, it was decided not to attempt to remove the scale because this was undoubtedly offering protection to the lining.

An inspection in 1978 revealed that tiles from the pump station sump lining had broken away and entered the pipeline through the pumps. These 150 x 150 x 37 clay tiles accumulated at the bottom of the 9 m high riser to the bridge until they broke roughly in half and were carried up the riser and through the main pipeline.

Following reports of further deterioration and damage to the lining within the pipeline as a result of the movement of tiles, a series of shut-downs was arranged and inspections of the accessible sections of the pipe were made during early 1981.

Photographs were taken which revealed that the build-up of pulp was severe and, in certain areas, debris mainly in the form of broken tiles had built up and become cemented by the pulp. Attempts to clear away the debris mechanically proved largely ineffective because of the lack of suitable facilities to transport the debris over any distance in the time available.

Later in that year, leaks were detected on the land section of the pipe north of the bridge and these were sealed using external clamps. A further internal inspection using television equipment was made of that section of the pipe and the resulting picture was not encouraging. It was realised that the repair or replacement of the pipe was a matter of urgency and SAICCOR, working with its Consultants, pressed ahead with investigations into various alternatives.

2.0 ALTERNATIVE SOLUTION

Investigations revealed that the following were the only alternatives available:

(a) a new pipeline estimated to cost more than R10 million requiring 15-18 months for construction,

(b) relining of the existing pipeline with 800 mm OD plastic pipes estimated to cost R2,5 million but requiring only a few days to construct once pipes were available and site preparations completed.

The latter alternative which had obvious attractions also had attendant risks of blockage due to:

(i) pulp accumulated on pipe walls,
(ii) rubber lining which may have been loosened by debris passing through the pipeline,
(iii) accumulations of cemented debris which had been observed during inspections,
(iv) the configuration of the existing pipeline which was known to have been moved into a flat S-curve shortly after laying.

A study of each of these problems revealed that they were not insuperable and it was agreed that there were emergency measures which could be taken provided that a jam did not occur within the surf zone which was inaccessible to divers.

3.0 RELINING

3.1 PHILOSOPHY

A simple philosophy was evolved in which the existing pipeline would be regarded as a "hole in the ground or in the sea" which could be exploited for either the receipt of a new internal liner or as an anchor for a new pipeline if this had to be laid external to the existing pipeline in the event of a jam.

The following main factors emerged from the ensuing study:

(i) that the gap between an existing 914 mm internal diameter rubber-lined steel pipe and an 800 mm external diameter plastic pipe should be adequate to prevent jamming as a result of pulp accumulations,

(ii) that, if jamming did occur outside the surf zone, the causes could either be removed by divers who would cut holes under water in the existing pipeline or alternatively, a large hole would be cut to permit a connection to be made between the section of liner already completed and a new pipeline which would be clamped to the extension of the existing pipeline,

(iii) that an experiment would be carried out by lining the short landline section before embarking on the more formidable task of lining 2 000 m of underwater sealine.

It was obvious that the entire operation was primarily dependant upon the passage of the liner through the 500 m long surf zone which was inaccessible to divers and it was accordingly decided to carry out an inspection of this section and clear any debris before proceeding further with the project.

The hot dark coloured effluent in the surf zone section was displaced by cold seawater and divers traversed the entire surf zone in order to inspect the interior of the pipe. This was a formidable task requiring great physical endurance and courage but it was completed without incident and divers reported that there was no loose rubber or piles of debris in this section of the pipeline. It is also of interest to note that two heavy stainless steel props which had been used to secure plates internally over leaks had also disappeared having been carried away by the pumped

effluent. As a result of the favourable report by divers, it was decided to proceed with the re-lining proposal.

3.2 MATERIALS

It was apparent that only semi-rigid pipes could be used particularly in the case of the sealine where the liner had to be introduced in one continuous length of 2100 m. Jointing was therefore of prime importance because, in addition to constructional requirements, the liner could only be anchored at the shore end which would result in the full frictional force of about 20 tonnes being transmitted by tension through the joints.

Many relining materials were investigated including the following:

(i) Stainless Steel

Stainless steel had proved reliable against chemical attack but was extremely costly and inflexible so that the use of this material would be restricted to use on the land only.

(ii) Glass Reinforced Plastic (GRP)

Although this material had been successfully used in relining operations, it was considered that the jointing procedure was too slow and could not be rigidly controlled to obtain uniformity and reliability. The local cost was also somewhat high and production capacity limited.

(iii) Polypropylene (PP)

This material which was manufactured locally would have been capable of withstanding the chemical attack and could meet the temperature requirements. The wall thickness proposed by the manufacturers was however considerable and some concern was expressed regarding the reliability of welding such thick walled pipes in the field.

(iv) High Density Polyethylene (HDPE)

These pipes could also be manufactured locally but were unsuitable for the high temperature of the effluent.

(v) Ultra high molecular weight high density polyethylene (UHMWHDPE)

This material was only available from the United States of America. At that time there was only one

manufacturer with the expertise, equipment and experience of re-lining existing pipes of the size under consideration. Although more expensive than

local products, the reduced wall thickness permitted greater flexibility and the use of a proven welding technique. The supplier also offered the services of an experienced technician to carry out the fusion welding of the pipes and to supervise the handling of the pipe on site.

3.3 DIAMETER AND CAPACITY

Ultra high molecular weight high density polyethylene was therefore selected for the material of the liner and 800 mm was chosen as the outside diameter. This allowed a 57 mm annular space which would provide adequate flexibility during relining and would ensure a somewhat better capacity than the existing pipeline in its "aged" condition.

The coefficient of friction for new rubber lined steel pipes would be about 0,013 in the Manning formula but, as a result of pulp adhering to the internal surface, the existing pipeline had a measured co-efficient of 0,023.

It was considered however that a co-efficient of 0,020 could be achieved by light pigging and this figure was used for comparative calculations of capacity.

The Manning co-efficient for new plastic pipes was given as 0,007 and it was assumed that, if pulp built up on the plastic surface, it could be easily dislodged with regular pigging. It was nevertheless decided to use a conservative 0,010 for comparative calculations.

Table 1 shows comparative friction heads per 1 000 m of the existing pipeline and of a new 800 OD plastic liner for flows of 3 000, 3 500 and 4 000 m^3/h.

TABLE 1 : FRICTION HEADS PER 1000 m

TYPE OF PIPELINE	NETT INTERNAL DIAMETER	FRICTION HEAD in m per 1000 m at		
		3000 m^3/h	3500 m^3/h	4000 m^3/h
Rubber-lined steel	914 mm	4,60	6,27	8,19
Plastic Pipe 800 OD	738,8 mm	3,59	4,89	6,39

Allowing for a possible 500 m extension of the pipeline for a new diffuser at a later date, total heads for various flows would be as shown in Table 2.

TABLE 2 : TOTAL FRICTION HEADS

TYPE OF PIPELINE	TOTAL FRICTION HEAD in m at FLOWS of		
	3000 m^3/h	3500 m^3/h	4000 m^3/h
Rubber-lined steel	13,43	18,28	23,88
800 OD Plastic Pipe	10,64	14,49	18,93

It will be seen from TABLE 1 that the smaller plastic pipe has a lesser unit frictional head than the larger rubber-lined steel pipe whilst TABLE 2 shows that, even with an additional length of diffuser, the total head in the new smaller diameter plastic pipe would be less than that in the existing larger pipe because of the reduced friction.

It was concluded therefore that the lined pipeline would have a better capacity than the original pipeline.

PRESSURE DIAGRAM

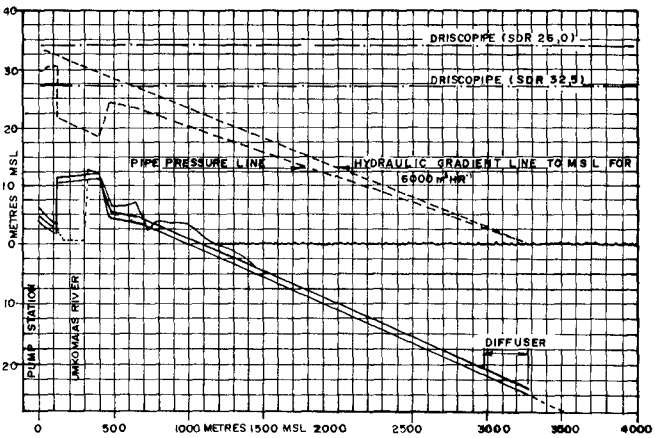

FIGURE 2

3.4 TIME FACTOR

It was important to minimise the times of stoppages because of the considerable loss of production involved and the difficulty of stopping and restarting operations at the pulpmill.

The construction work was therefore designed and planned to have stoppages of only 21 hours for the landline and 34 hours for the sealine.

4.0 CONSTRUCTION

4.1 PREPARATION FOR PROJECT

The preparatory work required in order to achieve the least possible stoppage of factory operation was a most important part of the project and required several months of intensive effort and the massing of considerable resources. Everything that could be done without causing interference with the flow of effluent was completed well in advance of the relining operations. Main items requiring special attention were as follows:-

4.1.1 The sea end of the pipeline was opened and the diffuser ports were blanked off. Pumping at maximum flow rates was then used periodically to flush debris from the pipeline. Divers made frequent inspections at the outlet and reported considerable discharges of debris and pulp.

4.1.2 Wherever relaying was possible as an alternative to relining, this work was completed well in advance of the relining operation.

4.1.3 Specials were manufactured and anchor blocks and foundations were constructed in advance.

4.1.4 Scaffolding was erected at the south end of the bridge where the lining operations would take place at a height of some 9 m above the roadway.

4.1.5 Where connections were to take place below ground level sheet piling was driven to ensure safe access.

4.1.6 A large site was prepared for the receipt and storage of the 12 m long pipes and a welding machine was set up on that site to enable the pipes to be welded into 500 m lengths in readiness for the relining operation. Arrangements were made for the welded joint between the 500 m long sections to be carried out speedily during the relining operation.

4.1.7 As this site was on the side of a main railway line away from the sea, a 2 m diameter concrete culvert was jacked under the railway in order that the stored lining could be fed into the existing sealine.

4.1.8 A system of winches mounted on tracks was set up so that the new liner could be pulled through the concrete sleeve and pushed into the pipeline.

4.1.9 Divers and fully equipped vessels were commissioned to standby during the operation in order to open the pipeline and clear any jam should this occur or alternatively, to lay the new pipes alongside the existing pipeline in the event of it not being possible to insert the entire liner. A pinger was purchased for installation in the end of the pipe to assist with location of the pipe end in the event of a jam.

4.1.10 Food kitchens, emergency power equipment, and a mass of special tools and equipment was assembled in case of need.

4.1.11 Rigid timetables and lists of duties were established in order to implement a number of alternative plans in case problems should arise.

4.1.12 Special equipment and protection was set up to cope with inclement weather.

In effect, the whole exercise was planned as an emergency operation with plans to meet any contingency and it was significant that no contingency arose during the operations for which there was not a plan prepared well in advance.

4.2 PRELIMINARY WORKS

4.2.1 The section from the bridge to the sea outfall was constructed first and this involved the laying of a plastic pipe in a new position adjacent to the existing pipe. The north end of this new pipe was connected to a tile trap combined with a pig port adjacent to the 90° bend at the start of the sealine. This tile trap remained in this temporary position to trap any further debris which might find its way into the line after commissioning of this section of pipes so as to avoid further accumulations of broken tiles in the sealine.

Each end of this new pipeline was restricted by means of heavy anchor clamps. Details of the anchor clamps are shown in Figure 3 and a feature of these clamps was the arrangement provided to allow for adjustment of lengths and location should this be necessary. The holding down plate

was drilled with oversize holes and large rectangular washers were fitted. These large washers allowed reasonable movement within the bolt holes and, after final tightening of the bolts, the washers were welded in position.

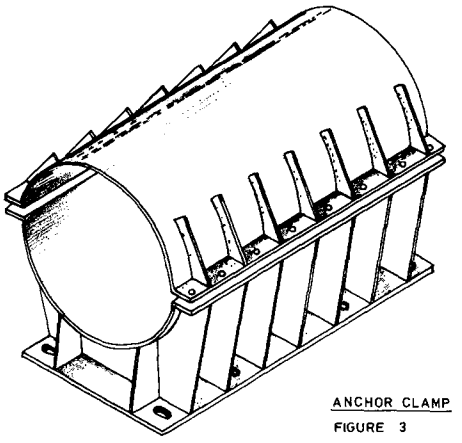

ANCHOR CLAMP
FIGURE 3

The whole of this section, except for the two ends, was backfilled before the first mill shut so as to hold the pipe in place and to provide a platform on which the liner pipe could be laid out in readiness for winching into the bridge section.

At the south end of this section, provision was made for the connection to the bridge section after relining by sheetpiling a portion of the existing line which had to be removed later to provide a gap for the insertion of the liner. All necessary preparatory work for connecting the liner to the newly laid pipeline was thus prepared in advance.

4.2.2 The section of the landline from the pumphouse to the bridge was constructed between the two mill shuts. Due to the complexity of the route, part of the pipeline was replaced using a plastic pipe buried adjacent to the existing pipe with stainless steel fabricated fittings being used to tie in at the pumphouse and bridge ends. The final connections were made during the second mill shut.

4.2.3 During the landline operations, the liner for the sealine was being made up into approximately 500 m lengths ready for introduction into the sealine.

As the liner was to be pushed into the sealine by using a system of clamps and winches, preparations were made to receive a hydraulic clamp mounted on rails and two sets of winches for moving the clamp backwards and forwards.

4.3 MILL SHUT NO. 1

4.3.1 The bridge section was relined during the first mill shut by pulling the liner into the existing pipes which were retained as structural beams. The liner was pulled from the south end of the bridge using a system of winches which would pull against the southern most flange of the pipeline and not introduce any load on to the bridge structure itself. The liner was introduced at the north end once an existing air valve, bend and length of pipe had been removed.

A sample length of plastic pipe was pulled through as a sizing piece to confirm that the liner could negotiate a 4° bend which was known to exist in that section of the pipeline. Once this test had been cleared, the new liner was pulled into position. The actual pulling operation was completed in about 1,5 hours.

The front end of the line being pulled was notched to form a conical nose while the tail end was fitted with a stub-end and loose flange. This flange was pulled hard up against the flange of the existing steel pipe. A new flanged stainless steel air valve tee was bolted to this and was then anchored to a concrete base so that the north end of the liner was effectively locked into position.

The gap between the air valve tee and the previously laid plastic pipeline was closed with a section that comprised a length of plastic pipe, a specially designed stainless steel anti-vacuum fitting and an adjustable stainless steel closure piece to ensure an accurate fit.

This closure piece is shown in Figure 4 and comprised a temporary stuffing box which was welded up after commissioning. The anti-vacuum device consisted of a NORVAL type reflux valve with a stainless steel screen and diaphragm designed to allow air to enter the pipeline and prevent the creation of an air vacuum which could cause collapse of the plastic pipes.

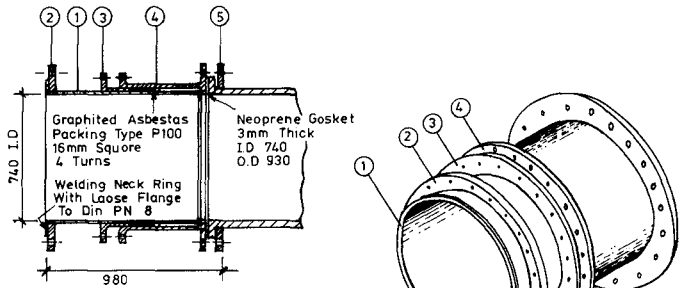

ADJUSTABLE CLOSURE PIECE (FULLY CLOSED)

LEGEND

1. 10mm thick stainless steel pipe with welding neck ring
2. Loose carbon steel flange
3. Stainless steel packing compressor
4. Stainless steel outer sleeve
5. Loose carbon steel flange

FIGURE 4.

To achieve a seal at the south end of the bridge, the notched end of the pipe was cut off square and a specially designed sleeve was inserted and bolted between the steel pipe flanges. Once the pipe was commissioned, the plastic liner would expand and seal itself against a neoprene ring around the sleeve.

4.3.2. The divers' inspection of the 500 m surf zone section was carried out during the relining of the bridge section. Water which had been stored in a dam on the beach was pumped into the sealine via a manhole on the beach. Once the pipeline had cooled sufficiently, three divers entered the pipe and began the inspection. Only one diver traversed the full 500 metres, the other two divers stopping off en route to assist in handling the air lines, communication cable and safety lines necessary for the lead diver. This magnificent team effort was completed in about 6 hours, and the information obtained from the survey enabled the decision to proceed with the second mill shut to be made with confidence.

4.4 MILL SHUT NO. 2

4.4.1 When the time for the second mill shut arrived, it was necessary to carry out two preliminary operations before the relining could commence. First the tile trap was disconnected and physically removed from its temporary foundations. This exposed the open end of the pipe entering the sleeve under the national road.

Rails for the winch assembly designed to pull the liner pipe into the sea outfall were bolted to the concrete foundation of the tile trap so that the task of winching the pipe from the assembly yard, through the railway culvert and into the sealine, could commence. This winch assembly consisted firstly of a hydraulic clamping device which was mounted on rails and which gripped the pipe with sufficient force to transmit the winch pulling force to the pipe. The hydraulic clamp had a travel of 12 m and was pulled by two winches capable of exerting a total pull of 40 tonnes. On completion of its 12 m travel, a return winch, mounted over the culvert under the railway pulled the hydraulic clamp, which was now in the open position, back to its starting position. The clamp would then be closed and the main winches would repeat the cycle and pull the hydraulic clamp back over the 12 m track.

Next an existing bend and portion of an adjoining length of steel pipe were uplifted on the beach side of the road as the bend was too sharp for the passage of the semi-flexible liner. In order that the total anchoring force required to restrain the completed liner would not be restricted to a single flange at the beginning of the section, an additional anchor block was constructed in advance on the beach side of the main road. This was provided with a clamp to which the liner could be bolted when completed.

The first 500 m of liner moved into the pipe with ease and a speed approaching 10 m per minute was initally achieved. This rate gradually decreased and, towards the end of the operation, the speed had reduced to about 1,5 m per minute whilst the force induced by the winches had gradually increased to a maximum of 16,3 tonnes.

Including brief stoppages to weld the 500 m lengths together, the lining operation continued for 21 hours until the end flange of the liner was set against the flanged end of the existing sealine as the first anchor. The liner was then clamped to the anchor block previously provided on the beach to act as a second anchorage. The sea end of the liner was left loose to accommodate the 18 m of expansion anticipated when hot effluent was re-introduced into the pipeline.

4.4.2 Whilst the sealine was being relined, the tile trap was moved to its new and final position adjacent to the pump station and the new pipeline laid between pumphouse and the south end of the bridge was connected into the system.

The gap between the relined sea outfall and the new pipe previously laid up to the tile trap during the first mill shut was closed with a stainless steel bend anchored to the tile trap foundation and connections made by using the same adjustable closure piece described previously.

5.0 CONCLUSION

The operation was carried out with relative ease largely because of the advance planning of the exercise. Although not all precautions taken in anticipation of problems were required, they were necessary in order to minimise the heavy risks involved in a major operation of this type.

The system has been in successful operation for over 12 months and the pumps are handling the total effluent quantity effectively at a reduced pumping head.

It is believed that this is the longest large diameter pipe relining ever attempted and it was completed in a total shutdown time of less than 60 hours at a cost of about 25% of a replacement pipeline. Its success heralds opportunities for the renewal of many ageing pipelines which would otherwise require costly and disruptive replacement.

6.0 ACKNOWLEDGEMENTS

The contributions made by SAICCOR and its engineers during the project, the expertise and experience of working with large bore plastic piping provided by Maskell-Robbins Inc of Oregon USA, and the co-operation and dedication of all the staff of the main contractor, Murray and Roberts, associated with this project, are acknowledged.

The authors wish to thank SAICCOR for permission to publish this paper.

CIRCULATION OF TWO MULTIPASS ESTUARIES IN THE GULF OF MEXICO

by

Donald Steven Graham[1] A.M. ASCE

1. Introduction

An important class of estuaries which has received relatively little attention is the barrier-island-contained multi-inlet one. Cases range in scale from the tidal rivers common along the S.E. coast of the U.S.A. to the very extensive embayments found on the Gulf of Mexico. A sound knowledge of the dynamics of the type of estuary is important for enlightened management of the resource. In the Gulf of Mexico region these estuaries tend to be significant spawning areas for marine fishes, and also support important local fisheries and oyster beds. Fortunately (or not) they are also geomorphically associated with coasts underlain by nearly-horizontal sedimentary rocks which often yield petroleum. Finally, in the Gulf of Mexico area of the U.S.A. the relatively attractive setting and climate of the barrier islands induces dense human development. (Surprisingly this attraction does not seem to occur in Latin America where the Gulf Coast is relatively unpopular and sparsely populated). Petroleum extraction and residential development, and the civil appurtenances needed to support them, can pose significant threats to the water quality, and hence marine life, of these estuaries. Local economic and social impacts can be severe since the fishing economy is usually marginal and traditional (even in the U.S.), while the oil and real estate businesses are usually strongly linked to wealthier portions of the exogenous economies. Because of this, regulation is probably necessary to prevent excessive adverse impacts, and sound knowledge is required for proper and enforceable water quality regulation.

As occurs in many disciplines from time to time, Carter, Najarian et al. (1, p. 1586) pointed out that rigorous estuarine analysis has suffered from the nature of its origin in Chesapeake Bay:

> "One of the most extensive and most thoroughly analyzed set of observations for any estuary was that of Pritchard ... taken in the James River in 1950. ..Although this set of measurements and their analysis by Pritchard resulted in vastly improved understanding of estuarine physical (sic) processes, it so influenced subsequent estuarine studies that measured circulation patterns that were at variance, at least for part-

1 Assistant Professor, Dept. of Geography, Scarborough College, University of Toronto, West Hill, Ontario, Canada, M1C 1A4

> ially mixed estuaries, were viewed as measurement artifacts, which they were not rather than .... real events, which they probably were"

A particular mental constraint resulting from the notion of the classical estuary (i.e., James River, VA) was that tidally-averaged water flux equals freshwater inflow and tidally-averaged salt flux is zero, under steady state conditions. Further, tidal motion was considered to be the most important variable affecting estuarine dispersion, and the source of most of the ambient turbulence available for mixing. A review of the literature indicates these notions only came to be questioned, disproved, and then incorporated into more sophisticated models after about 1975. Two significant papers appeared around that time. Weisberg (2, also 3) showed that meteorological forcing caused a significant portion of the total turbulent energy even in a narrow tidal river. It has subsequently been realized that wind forcing can almost completely overwhelm tidal effects in broad shallow embayments of the Gulf of Mexico which has minimal tidal amplitude (of the order of a foot). (In all honesty it appears that this may have been appreciated by field biologists before coastal engineers and oceanographers).

The second significant paper was that of van de Kreeke and Dean (4) (followed later by 5, 6, 7), in which the principles of Stokes velocity, as discussed in an earlier theoretical paper by Longuet-Higgins (8), were applied to the engineering analysis of circulation of shallow bays with 2 inlets. The essence of the paper was that nonlinear flux terms resulting from periodic tidal motion do not disappear upon tidal averaging (even for single inlet estuaries(9)) and residual flows will typically occur. This will be discussed in more detail anon.

The environmental engineering and biological implications of these results are extremely significant, and, in the author's opinion, almost totally unappreciated by workers in these fields despite some efforts by van de Kreeke (5, 7) to point them out. The effect of net nontidal residual flows caused by wind or nonlinear tidal residuals is to induce an advective component which can greatly reduce the flushing time of the estuary, and change distributions of water quality parameters (7). Since coastal engineering projects can change these renewal rates (10), or at least require them to be evaluated for EIS's, it follows that they should be studied in detail so that adverse environmental impacts can be avoided wherever possible by engineers working in these estuaries.

2. Scopes of Apalachicola and Terminos Projects

Apalachicola Bay is a large (550 km^2) 4-inlet embayment on the Florida Panhandle. Laguna de Terminos, the largest (2000 km^2) estuary on the Gulf of Mexico, is a 2 inlet-embayment located at the base of the Yucatan Peninsula. See Figures 1 and 2. Both support significant local fisheries. Apalachicola is being impacted by nonpoint pollution from silvicultural activities near its head (11-15), and by residential development in St. George Island. Terminos is being affected by intensive petroleum exploration offshore in the Gulf of Campeche and by associated growth of the barrier island city of C. de Carmen. There

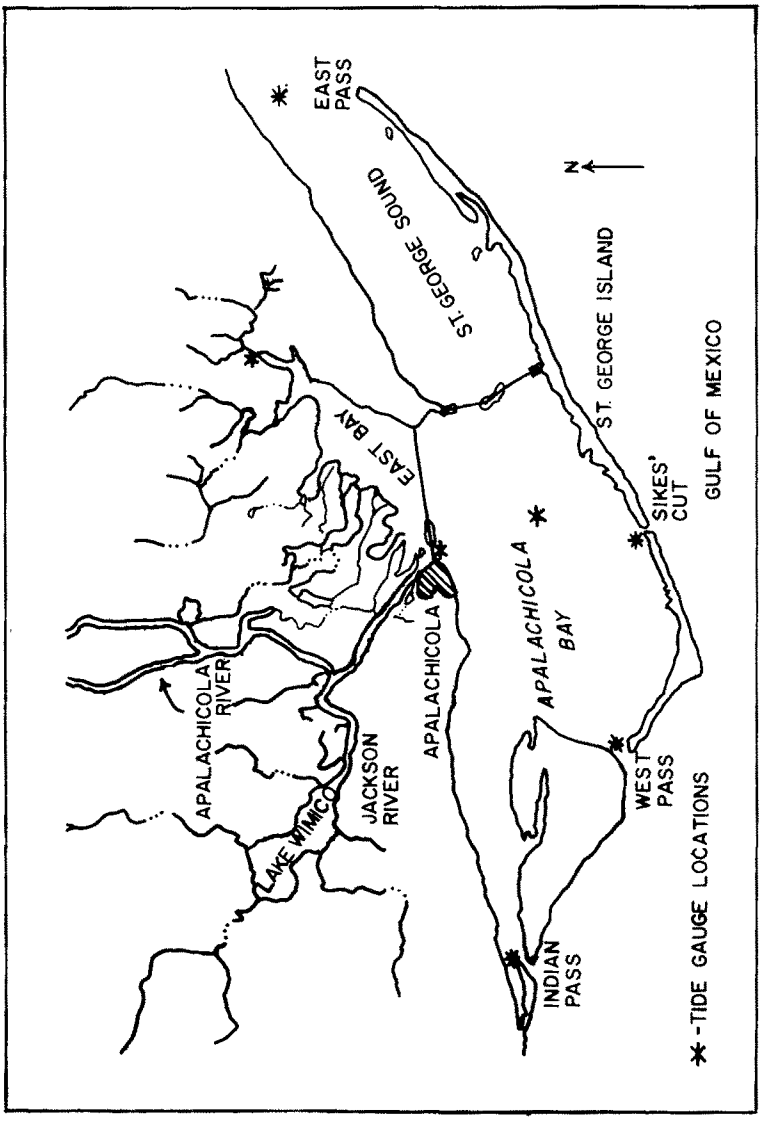

Figure 1 GEOGRAPHY OF APALACHICOLA BAY

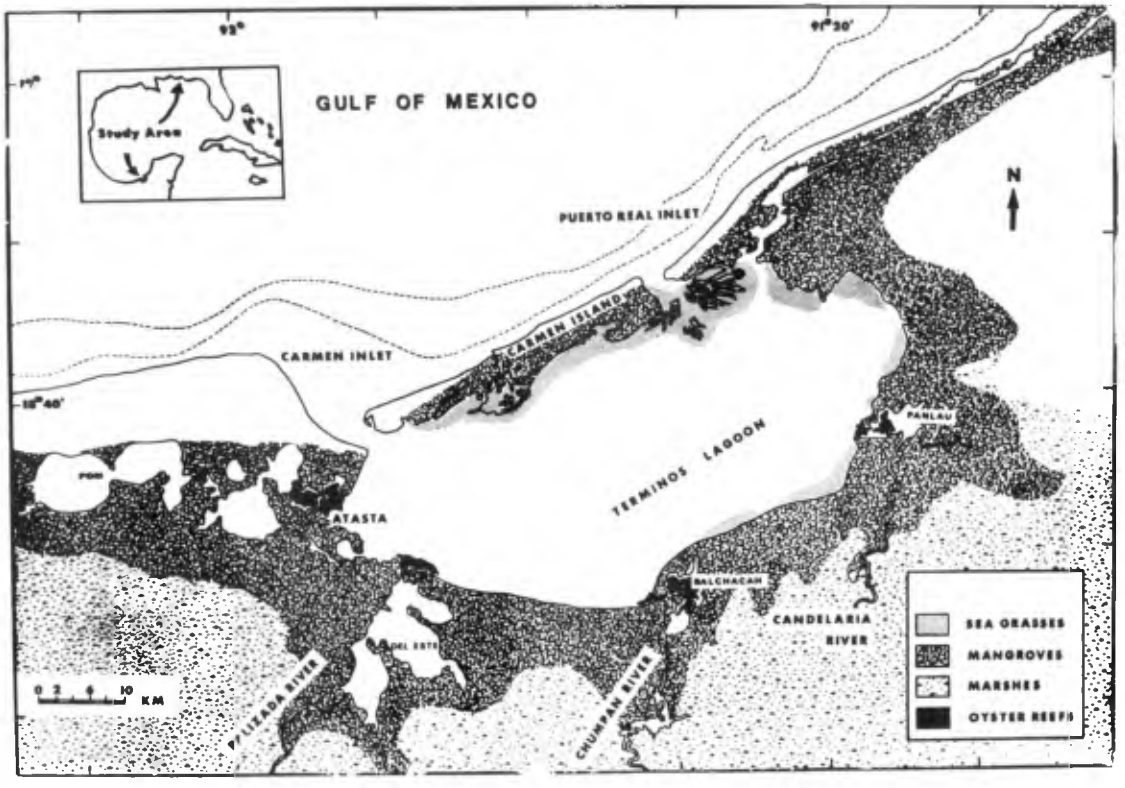

Figure 2 Geography of Laguna de Terminos, Mexico

is concern over the fate of another large oil spill or blowout. In both cases the vertically-averaged 2-dimensional real-time finite-element circulation model CAFE-1 (16) was applied to provide information about the macro-circulation features of the estuaries. Both projects were consulting jobs essentially in support of biological studies and hence were limited in scope and funding. Some field data for model verification were obtained for Apalachicola Bay, none was specifically available for Terminos. The purpose of the paper is to discuss the general results of the two model applications to geomorphologically and dynamically similar estuaries on the Gulf of Mexico, and the relate these to the comments made in the introduction. It is emphasized that these were engineering projects limited in scope and not exhaustive scientific programs.

3. Discussion of Significance of van de Kreeke's Results

Numerical model outputs for both Apalachicola Bay (10, 17) and Laguna de Terminos (18, 19, 20) both showed residual nontidal flows with windless conditions. Frankly, we thought that either the model results might be erroneous or that we had discovered something new, particularly since drowning victims and loose boats at Apalachicola were known to drift west. Dr. Tavit Najarian kindly brought van de Kreeke's work to the attention of the author. This material appears to be germane, although it does not seem to have been applied to such large systems before. It will be compared to numerical results herein.

In terms of unit discharges the equations of motion used by van de Kreeke (4, 6) were

$$\frac{\partial \eta}{\partial t} + \frac{\partial q}{\partial x} = 0 \qquad 1.$$

$$\frac{\partial q}{\partial t} + gh\frac{\partial \eta}{\partial x} + g\eta\frac{\partial \eta}{\partial x} + \frac{2}{h} q \frac{\partial q}{\partial x} + \frac{gh^2}{\rho 2} * \frac{\partial \rho}{\partial x} = - Fr \qquad 2.$$

$$\text{where } Fr = \frac{F_1 \, q \, |q|}{(h + \eta)^2} \quad \text{quadratic} \qquad 3.$$

$$\text{or} \quad Fr = \frac{F_2 q}{h} - \frac{F_2 q \eta}{h^2} \quad \text{quasi-linear to second order} \qquad 4.$$

where η - tidal were amplitude, q - unit discharge, h - mean depth, ρ - density, Fr - bottom friction term, F_1 - constant and F_2 - constant.

In comparing these with the basic equations in the CAFE-1 model (see 16, or 14, 17, 19) the primary differences are i) the dimensionality, ii) the exclusion of Coriolis and wind-stress terms, and iii) the inclusion of a baroclinic term. A 2-D analog of equations 1-4 is given by van de Kreeke in (7), but ii) still holds. The quadratic resistance relation, eq. 3, is used in CAFE, while van de Kreeke uses the quasi-linear form (4) for his illustrations. As shown in (4) the differences are great enough to warrant using full quadratic formulation, but the results are similar and of the same order. Substituting eq. 4 in

eq. 2, a tidally-averaged form of eq. 2 can be derived in which second-order terms are retained as residuals and are balanced by the net bottom stress (see 4, 5, 6, 7). Assigning boundary conditions at each inlet of the channel of

$$\eta = a_0 + a_1 \sin\sigma t \text{ and } \rho = \rho_a \text{ at } x = -L/2 \qquad 5.$$

$$\text{and } \eta = b_0 + b_1 \sin(\sigma t - \delta) \text{ and } \rho = \rho_b \text{ at } x = +L/2 \qquad 6.$$

and denoting the tidally averaged unit discharge as q_*, it is shown (4, 6) that

$$\frac{q_* T}{hL} = P\left(\frac{\lambda}{L}, \frac{F_2 L}{C_0 h}\right) \frac{a_1 b_1}{h^2} \sin\delta + Q\left(\frac{\lambda}{L}, \frac{F_2 L}{C_0 h}\right) \frac{a_1^2 - b_1^2}{h^2}$$

$$+ \frac{C_0 h \lambda}{F_2 L L} \frac{a_0 - b_0}{h} - \frac{C_0 h}{F_2 L} \frac{\lambda}{L} \frac{\rho_a - \rho_b}{\rho_0} \qquad 7.$$

where T - wave period, λ - wave length, $C_0 = \sqrt{gh}$, P and Q are functions (see 4). Eq. 7 is given in (6), while only the first two terms on the rhs appear in (4). The contributions represent, respectively, net flow induced by phase differences, amplitude differences, differences in mean water level, and baroclinic effects. The nature of the latter is reasonably well known and will not be given further consideration here. Also, $\partial\rho/\partial x$ effects are not used in CAFE. Note that terms in the rhs of eq. 7 are of order a^2/h^2, so q_* would be expected to be largest in shallow lagoons, such as Apalachicola and Terminos.

In other words, if the tidal wave at each inlet has a different amplitude and phase lag, caused by differences in offshore shelf topography, then a net nontidal flow will be set up in shallow multi-inlet estuaries. Further, if the mean sea level varies along the coast, a net-flow will be induced, as expected. The latter is not uncommon and van de Kreeke (6) found this to be the largest contribution at Marco Island, Florida. Unfortunately we did not have the capability of finding mean sea level at either Apalachicola or Terminos, although we expect there is a difference at Apalachicola since superior model results were obtained by inputting a gradient of mean sea level.

A final comment is made that van de Kreeke and Chiu (7) found similar residual currents with a 2-D finite-difference model. Residual flow eddies were also present but it could not be readily determined to what extent these were real or numerically-induced. Tee (21) claimed residual eddy currents computed for the Minas Basin, NS, were real. At the April 1980 AGU convention in Toronto van Zant and Hsueh (see 22) presented a finite difference Leendertse-type model of Apalachicola Bay which they had developed contemporaneously, but independently, from our own CAFE application. Using similar boundary conditions, but cruder boundary representation, they computed residual eddies near East and West Passes. CAFE, on the other hand did not (although a (real) residual eddy can appear near East Bay under some circumstances). Further, our field work and satellite images showed no

evidence of such eddies existing under these conditions. Consequently, residual eddies in numerical models must be viewed with skepticism until proven. As shown in (19), satellite images confirmed the existence of the central eddy in Terminos calculated by CAFE.

4. Selected Apalachicola Results

Since most of the Apalachicola and Terminos material has been published, only selected results germane to the foregoing comments will be presented. Interested readers are referred to the original papers for more details.

As shown in Figure 3, a strong east to west net nontidal velocity was calculated for windless conditions with T = 44640s; at West Pass $a_0 = 0$, $a_1 = 0.21$ m; at East Pass $b_0 = 0$, $b_1 = 0.40$ m; $\delta = 3780$ sec (see eq. 5, 6) from the tide tables. In this case then, L = 39 km, h = 3 m approximately, $C_0 = 5.4$ mps, $\delta = 30.48^0$, $\sin\delta = .507$, $\lambda = 242$ km. n = 0.018 in the model, so

$$F_1 = \frac{n^2 g}{h^{1/3}} = \frac{.018^2(9.81)}{3^{1/3}} = .00220 \qquad 8.$$

and letting $F_1 \doteq F_2$ (rather than eq. 22 in (4)) we get, from eq. 7, 9.

$$q_* = 2.62\,[P(6.21,\ 5.30)(.008)(.507) + Q(6.21,\ 5.30)(-.014)] \qquad 10.$$

$$P \doteq 1.8, \quad Q \doteq 1 \quad \text{from (4)} \qquad 11,\ 12.$$

$$\text{so } q_* \doteq 2.62\ (.007 - .014) = -.019 \qquad 13.$$

$$\text{so } v_* = q_*\, h = -0.019 * 3 = 6 \text{ cm/s westward} \qquad 14.$$

Typical values computed (10) are about 20-30 cm/s westward for 3 m depths, hence the results are reasonable and comparable, considering the approximations of eq. 9, 11, 12, lack of Coriolis terms in (4), and the suspicion that $a_0 \neq b_0$ on the average. Hence the net westward flux in Apalachicola Bay can be ascribed to nonlinear interaction of tidal waves. This net flux is surmised to be responsible for the high quality of Apalachicola Bay water, and it was demonstrated in (10) that construction of a mid-Bay island for bridge abutments had probably resulted in an increase in flushing time.

In November 1979 we placed tide gauges at each inlet to Apalachicola Bay and in the Bay center (see Figure 1). Records were correlated by superposing Doodson-filtered signals of mean surface water levels (17). The magnitude of wind-induced (5-10 kt maxima) fluctuations in amplitude and "mean" sea level in this type of estuary is evident in Figure 4. Wind forcing can readily dominate tidal motion. As shown in Figure 5, CAFE produced reasonably good results. It can be seen however that relatively long-term records are needed to establish that $a_0 = b_0$ in eq. 5 and 6.

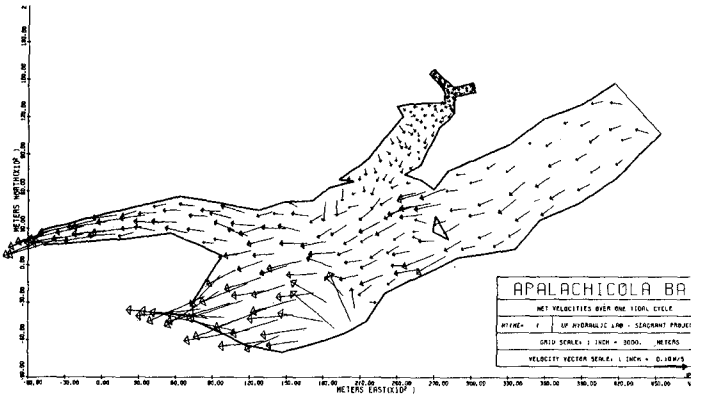

Figure 3 Net Residual Apalachicola Bay Velocities

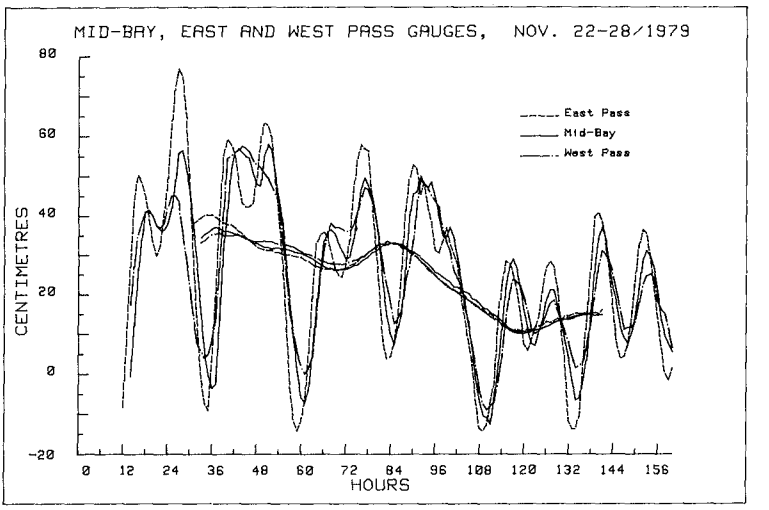

Figure 4 Measured and Doodson- Filtered Tide Records

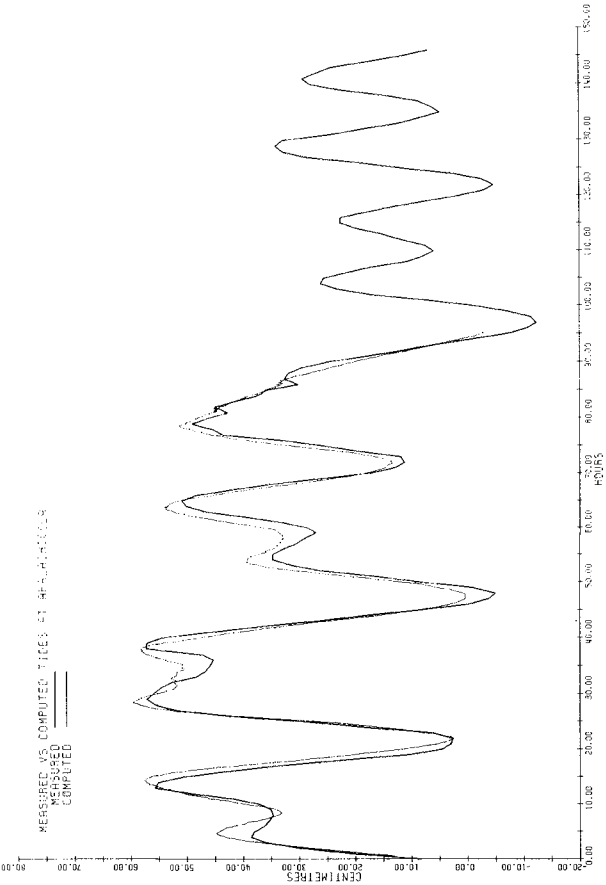

Figure 5

MEASURED VS. COMPUTED TIDES AT APALACHICOLA

5. Selected Terminos Results

Because Laguna de Terminos is morphologically and dynamically similar to Apalachicola, we were asked to apply the CAFE model to it in support of a UNAM - LSU biological assessment. No data were available to us except those in standard tide tables. A crude bathymetry of Terminos was provided by LSU. Terminos lies in Trade Wind zone so that it enjoys a constant breeze from the NE of about 2-5 mps for much of the year. This is surmised to cause the net westward flow , as discussed by Mancilla and Vargas (23), and evidenced by the prominent flood-tidal delta at Puerto Real inlet.

The cases simulated for Terminos are listed below

	Amplitude			Lag			Wind	
	E	m	W	E	s	W	Speed mps	Direction from
1	.24		.24	0		0	0	-
2	.24		.30	+120		0	0	-
3	.24		.24	0		0	5	NE
4	.24		.24	0		0	10	NW

where E - Puerto Real inlet, W - Carmen inlet. The LSU field biologist said he suspected there was no difference in tidal properties between the two inlets. The differences in Case 2 were the greatest that could be expected by interpolation and extrapolation from the few stations in Tide Tables. The results showing net velocities are depicted in Figure 6. The large eddy for Case 4 also appears in winter satellite images.(19)

Subsequent work by M. C. Julio Candela P. (24) and Crivel et al. (25) appears (to the extent the author understands the Spanish) to yield the following information on the tidal properties. According to Candela the dominant tides at Carmen are O_1(amp = 11.23 cm, period = 25.82h, phase = 317.25°), K_1 (amp. = 11.04 cm, period = 23.93 h, phase = 321.32°), and M_2 (amp = 7.51 cm, period = 12.42 h., phase = 88.58°). This results in a mixed tide with Band 1 dominant. Taking mean values of $O_1 + K_1$ of amp = 22 cm, phase = 319.3° for Carmen, the comparable values for Isla Aguda in Puerto Real are, for Band 1, amp. = 22 x 0.92 = 20.2 cm and phase = 319.3° + 6.7° = 326°. Crivel et al. (25) find the same phase difference, i.e. 6.7° or 27 minutes, to exist.

In summary the Band 1 amplitude difference is 1.8 cm and the phase difference is 27 minutes with Carmen leading. These are of the same order as those used by Craham in Case 2, but not close. An analysis using van de Kreeke and Dean's (4) eq. 7 for $a_o = b_o$ (25) with the values: T = 25h = 90000s, h = 3.5 m (24), L = 38.5 km between the inlets (24), C_o = 5.9 mps, λ = CT = 527 km, a1 = 20.2 cm, b1 = 22 cm, δ = 6.7°, sinδ = .117, F = F_2 = .0022, then

$$q_* = 1.5\,[P(13.7,\ 4.1)(.0036)(.117) + Q(13.7,\ 4.1)(-.00062)] \quad 15.$$

$$P \doteq 0.6,\ Q \doteq 1.8 \text{ from (4)} \quad 16.$$

so $q_* = 1.5\ (.00025 - .00112)$

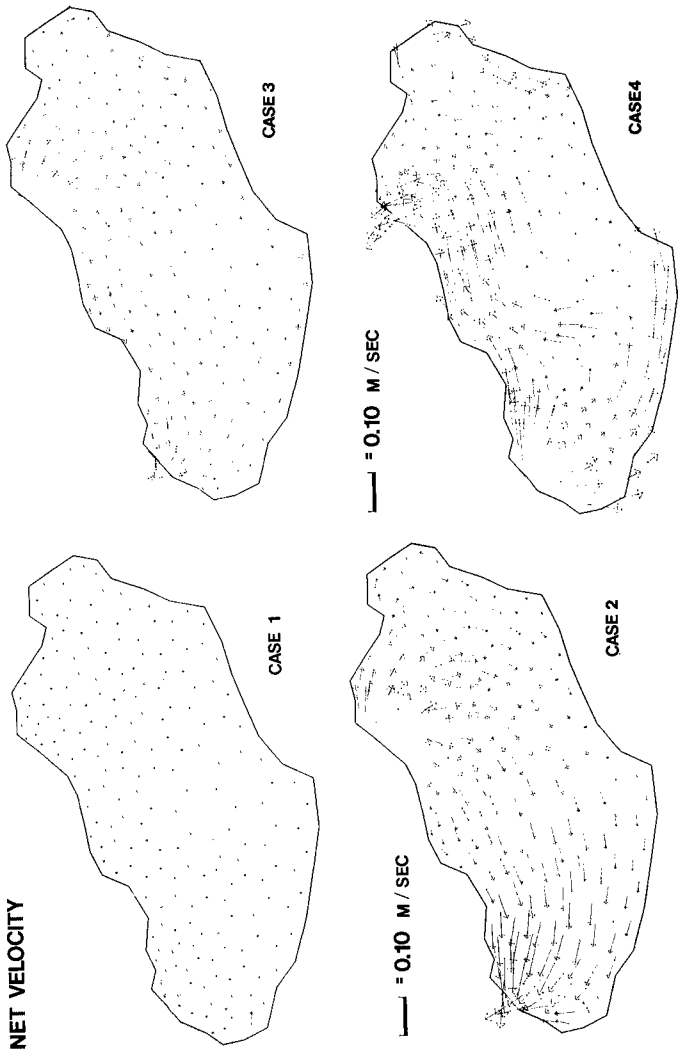

Figure 6 Net Residual Terminos Velocities

$$q_* = -.00082 \qquad 17.$$

$$\text{so} \quad V_* = q_* \, h = -.003 \text{ m/s} = -.30 \text{ cm/s} \qquad 18.$$

eastward. This does not correspond to the computed results of Figure 6 because the phase is lagged in the opposite direction. It also suffers the same caviats as mentioned earlier for Apalachicola. It may be concluded that the net westward drift in Terminos likely occurs because of the steady trade winds and in spite of the nonlinear tidal wave flux. Modification or filling of Puerto Real inlet could severely alter the flushing rate of the Laguna. Conversely, oil spills near Carmen might enter Terminos under windless conditions. It is hoped further cooperative work on Terminos can be done.

6. Summary

The flushing and water quality of shallow multi-inlet estuaries in the Gulf of Mexico appears to be dominated by nonlinear wave flux advection and wind forcing, rather than advection from river inflow and tidally enhanced dispersion. Understanding and managing these systems requires detailed knowledge of their tidal characteristics and response to wind shear. Coastal engineering works could significantly alter the properties of the circulation of these estuaries.

7. Acknowledgements

John Daniels performed much of the CAFE modeling and his assistance is gratefully acknowledged. Jack Hill supplied satellite images. Julio Candela P. furnished information on Terminos and interesting discussions. The Apalachicola work was sponsored by NOAA, Office of Sea Grant (Florida) under Grant No. 04-158-44046, and by the Engineering and Industrial Experiment Station of the University of Florida. Assistance was provided by the Departments of Environmental, Civil and Industrial Systems Engineering of UF. The Terminos work was funded through the Center for Wetland Resources, LSU by International Sea Grant, and by UNAM. The Estacion de Investigacion Oceanographica and CICESE at Ensenada provided some assistance and gracious hospitality. The University of Toronto has provided clerical support.

8. References

1. Carter, H. H., T. O. Najarian, D. W. Pritchard, and R. E. Wilson, "The Dynamics of Motion in Estuaries and Other Coastal Water Bodies", Reviews of Geophysics and Space Physics, Vol. 17, No. 7, Oct. 1979, pp. 1585 - 1590.

2. Weisberg, R. H., "The Nontidal Flow in the Providence River of Narragansett Bay: A Stochastic Approach to Estuarine Circulation," Journal of Physical Oceanography, Vol. 6, No. 5, Sept. 1976, pp. 721 - 734.

3. Ibidem, "A Note on Estuarine Mean Flow Estimation", Journal of Marine Research, Vol. 34, No 3, 1976, pp. 387 - 394.

4. van de Kreeke, J. and R. G. Dean, "Tide-Induced Mass Transport in Lagoons", Journal of the Waterways, Harbors and Coastal Engineering Division, ASCE, Vol. 101, No. WW4, Nov. 1975, pp. 393 - 402.

5. van de Kreeke, J., "Tide-Induced Mass Transport: A Flushing Mechanism For Shallow Lagoons", Journal of Hydraulic Research, IAHR, Vol. 14, No. 1, 1976, pp. 57-61.

6. Ibidem, "Mass Transport in a Coastal Channel, Marco River, Florida," Estuarine and Coastal Marine Science, Vol. 7, 1978, pp. 203 - 214.

7. Ibidem and A. A. Chiu, "Tide-Induced Residual Flow in Shallow Bays", Journal of Hydraulic Research, IAHR, Vol. 19, No. 3, 1981, pp. 231 - 249.

8. Longuet-Higgins, M. S., "On the Transport of Mass by Time-Varying Ocean Currents," Deep-Sea Research, Vol. 16, 1969, pp. 431 - 447.

9. Pritchard, D. W., "A Note on Stokes Transport in Tidal Estuaries", Chesapeake Bay Institute Contribution No '68, The Johns Hopkins University, Baltimore, MD, undated, 16 pp.

10. Craham, D. S., J. P. Daniels and B. A. Christensen, "Predicting Circulation Changes From Bathymetric Modification", in Proceedings of ASCE Hydraulics Division Specialty Conference Civil Engineering in the Oceans IV, Vol. 1, held Sept. 10-12, 1979 at San Francisco, CA, pp. 531 - 549.

11. Craham, D. S. and B. A. Christensen, "Development of an Estuarine Model for Apalachicola Bay, Florida", in Proceedings of ASCE Hydraulics Division Specialty Conference Coastal Zone '78, held March 14 - 17, 1978 at San Francisco, CA, pp. 621 - 633.

12. Craham, D. S., J. M. Hill and B. A. Christensen, "Verification of an Estuarine Model for Apalachicoa Bay, Florida," in Proceedings of ASCE Hydraulics Division Specialty Conference Verification of Mathematical and Physical Models in Hydraulic Engineering, held Aug. 9-11, 1978 at College Park, MD, pp. 237 - 245.

13. Graham, D. S. and J. M. Hill, "Field Study for Landsat Water Quality Verification", in Proceedings of Aerospace Division Specialty Conference on Civil Engineering Applications of Remote Sensing, held 11 - 12 August 1980 at Madison, WI, pp. 101 - 117.

14. Hill, J. M., and D. S. Graham, "Using Enhanced Landsat Images For Calibrating Real-Time Estuarine Water Quality Models", in Proceedings of AWRA - USGS Pecord Symposium, Satellite Hydrology, held June 1979 at Sioux Falls, SD, 1981, pp. 603 - 614.

15. Graham, D. S. and J. M. Hill, "Landsat and Water Quality Model Verification", accepted for publication in Journal of the Transportation Engineering Division, ASCE, late 1982.

16. Wang, J. D. and J. J. Connor, "Mathematical Modeling of Near Coastal Circulation", Report No. 200, Ralph, M. Parsons Laboratory, Dept. of Civil Engineering, MIT, April 1975, 272 pp.

17. Daniels, J. P. and D. S. Graham, "Application and Calibration of CAFE-1 Model to Apalachicola Bay, Florida", in Proceedings of 5th Canadian Hydrotechnical Conference, held 26 - 27 May 1981 at Fredericton, NB, pp. 515 - 536.

18. Graham, D. S., and J. P. Daniels "CAFE-1 Hydrodynamic Simulation of Laguna de Terminos, Mexico", Report submitted to LSU, International Sea Grant and Government of Mexico - UNAM, April 1980, 15 pp. plus figures.

19. Graham, D. S., et al., "A Preliminary Model of the Circulation of Laguna de Terminos, Campeche, Mexico", Annales de Instituto de Ciencias del Mar y Limnologica, UNAM, Vol. 3, No. 1, 1981, pp. 51 - 62.

20. Dressler, R., "Investagación sobre mareas y efectos del viento en la Laguna de Terminos (México). Mediante un modelo Hidrodinámico-Numérico", Informe Tecnico OC-82:01, Centro de Investigacion Cientifica y de Educacion Superior de Ensenada, Dec. 1981, 19 pp. plus figures.

21. Tee, K. T., "Tide-Induced Residual Current, A 2-D Nonlinear Numerical Tidal Model", Journal of Marine Research, Vol. 34, No. 4, 1976, pp. 603 - 628.

22. Graham, D. S., "Tidal Hydrodynamics of Apalachicola Bay, Florida", Abstract in EOS, Vol. 61, No. 17, 1980, p. 272, Number 0 - 199. That of van Zant and Hsueh appears on the same page as Number 0 - 198.

23. Mancilla P., M. and M. Vargas F., "Los Primeros Estudios Sobre el Flujo Neto de Agua à Través de la Laguna de Terminos, Campeche", Annales de Instituto de Ciencias del Mar y Limnologia, UNAM, Vol. 7, No. 2., 1980, pp. 1 - 14.

24. Candela P., M. C. J., "Estudio de la Dinamica de la Laguna de Terminos, Campeche", Reporte Num. 1, Estacion de Investigacion Oceanografica de la Direccion General de Oceanografica de le Secretaria de Marina, August 1982, 42 pp.

25. Grivel, F., J. T. Guzmán and H. Cepeda, "Estudio Mareografica de la Laguna de Terminos", undated and unreferenced reprint, obtained from Candela P., 10 pp.

This paper was prepared for the 18th International Conference on Coastal Engineering, 14 - 19 November 1982, Capetown, South Africa.

AUGMENTATION OF URBAN WATER BY ANTARCTIC ICEBERGS

by J.D. Lawson, M.ASCE.[1] and D.S. Russell-Head [2]

ABSTRACT

The indigenous water resources of the south west of Australia are under increasing stress. One solution to this problem may be water importation in the form of Antarctic icebergs. This possibility is discussed in this paper. To be cost effective, an iceberg water scheme needs to provide water at less than A$ 0.14 kl^{-1} from the reservoir, and at yearly volumes of the order of 10^8 m^3. A number of analyses of the selection and towing of icebergs have been given in the past but the offshore processing of icebergs has been somewhat neglected. A conceptual solution to the processing problem is given in this paper and cost estimates for the acquisition and processing of icebergs are given. Our analysis indicates that iceberg water may be a feasible and economical urban water augmentation system for yearly volumes greater than 2 x 10^8 m^3. Further work on iceberg water augmentation is warranted.

1 INTRODUCTION

The water resources, especially for urban use, in the south western region of the Australian continent are under increasing stress and augmentation alternatives and demand management strategies have been examined closely during the last decade. Serious interest in the use of icebergs for water has been shown since 1973. This paper examines the process of water supply augmentation by icebergs and focuses on the largely undiscussed problem of iceberg processing. A conceptual solution to the problem of processing icebergs in the coastal zone is offered and, as the cost of water is the most important basis of comparing various methods of augmentation, indicative iceberg water costs are given.

2 URBAN WATER COSTS

A water resources study for Metropolitan Adelaide in 1978 (Engineering and Water Supply Department, 1978) included indicative costs of water supply augmentation. Table 1 has been adapted from the report of the study.

1. Professor, Dept. of Civil Eng., University of Melbourne, Australia
2. Research Fellow, Faculty of Eng., University of Melbourne.

Method	Indicative cost cents per kilolitre
Present cost including treatment	29
Mount Lofty Ranges evaporation control	36
Adelaide groundwater basin/surface supply	37 - 42
River Murray/Mount Lofty Ranges storage	40
River Murray - direct pumping	42
Mount Lofty Ranges - new storage	51
Iceberg (cost excludes harvesting uncertainties)	71
Desalination of seawater	78
Sewage effluent re-use	78
River Murray - flood cropping	93
Water tankering	101
Urban runoff	101
Rainwater tanks	144

Table 1. Cost of water supplied to Adelaide by various methods (June 1977 A$ cost levels)

The costs in Table 1 include treatment and reticulation costs.

Cost analyses have also been carried out for Perth where particular emphasis has been placed on the utilization of extensive groundwater resources present in that region of Western Australia (Metropolitan Water Supply, Sewerage and Drainage Board, 1981). For urban Perth, the ex-reservoir price of iceberg water needs to be about A$0.14 kl^{-1} for iceberg importation to be competitive with other augmentation methods.

An alternative (or complementary) strategy to water supply augmentation is to exercise demand management and improve the efficiency of water use. Demand management tends to gain recognition by water supply authorities only in times of severe drought.

Management options considered in the Adelaide study included

- Changing community attitudes to water use. (One major area of water wastage in Australia is the watering of urban gardens. Half the annual water use in some cities is for the maintenance of exotic gardens and lawns.)
- Alternative pricing. (Higher water prices could be charged during the hot dry summer.)
- Technical changes. (Toilets could be fitted with reduced discharge flushing devices.)

It is against this background of water augmentation and management alternatives that consideration should be given to Antarctic icebergs as a source of urban water.

Figure 1. Tabular Antarctic iceberg 1200 m by 400 m by 27 m freeboard. (R. Wills)

3 ICEBERG TECHNOLOGY BASICS

There are three distinct phases to the business of getting urban water from icebergs

- iceberg selection
- iceberg towing
- iceberg processing

In this paper, we shall refer to iceberg selection and towing as iceberg "acquisition".

3.1 Iceberg Acquisition

The papers which first discussed the use of Antarctic icebergs as a source of water (Weeks and Campbell, 1973 and Hult and Ostrander, 1973) were mostly concerned with iceberg acquisition. The proceedings of two subsequent international conferences on icebergs (Husseiny, 1977 and International Glaciological Society, 1980) contain further detail on the characteristics of icebergs and methods of propulsion and protection.

At present, the general consensus seems to be that an iceberg of suitable size (Fig. 1) can be transported to southern areas of continents in the Southern Hemisphere, but protection from melting and break-up will be necessary for transportation to the Northern Hemisphere. A review paper by Schwerdtfeger (1979) gives a good overview of the acquisition phase.

3.2 Iceberg Processing

After an iceberg has been delivered, it then remains to turn it into water for urban reticulation. This is not a trivial task. When delivered, an iceberg of an economic size is likely to be of the order of 100 m draft and will ground on the continental shelf several kilometers from shore. The iceberg will melt at its base and sides at a rate of between 1 and 3 m per day (Russell-Head, 1980). The energy required to process ice by various techniques has been discussed by Weeks and Mellor (1978). DeMarle's (1980) paper is another of the relatively few to deal in some detail with the processing phase. In it, he discusses an iceberg processing scheme for Saldanha Bay in South Africa and provides subjective target estimates for the costs of implementing the scheme.

Our approach was to devise a harvesting scheme based as much as possible on existing technology, and then to cost the processing component of iceberg water using the best estimates applicable to that known technology. The total augmentation cost of iceberg water is the sum of the acquisition and processing costs. We were particularly interested to find out the relationship between iceberg size and total augmentation cost.

3.2.1 Processing techniques

The main aim of the processing phase is to land a high proportion of the iceberg mass as fresh water. Unless the iceberg is totally enclosed with an impermeable wrapping, sea water will melt ice from the berg and mix with the melt water. An important function of the harvesting scheme then is to separate melting ice from sea water.

Some of the proposed (Husseiny, 1977) processing methods are

- Skirt collection
- Mechanical cutting
  - saws
  - high pressure jets
  - dredging
  - blasting
- Electrothermal cutting
  - heated cables
  - laser beam

and these will now be briefly discussed.

Skirt entrapment of fresh water does not seem feasible (Huppert and Turner, 1978) due to the substantial mixing of saline and melt water during the iceberg melting process.

Mechanical methods of harvesting are efficient from an energy expenditure viewpoint but all suffer from the problems of the transfer of mechanical power to the cutting face. It would be undesirable to instal large equipment on an iceberg to be processed and therefore dredging and high pressure jets are not favoured methods. Blasting is energetically efficient but control and secondary processing of the blasted ice would be difficult. Sawing appears to be the most attractive of the mechanical methods. A type of bladeless chain saw that cut over the entire width of the iceberg could probably be developed.

Electrothermal methods are not as energetically efficient as mechanical ones but they do possess the ability to easily transfer power to the cutting face. Laser methods offer the possibility of transferring energy without physical contact with the iceberg, however their overall thermal efficiency is only about 10%. Cutting with heated cables is probably the processing method easiest to implement and is the one we have adopted for costing purposes in this paper.

4 ICEBERG WATER COSTS

The cost of iceberg water is the sum of the acquisition and processing costs. We shall use the results of other studies for an estimation of acquisition costs. A processing method will be described and costed.

4.1 Acquisition Costs

Weeks and Campbell (1973) have provided costs of towed ice delivered to offshore processing sites. Table 2, applying to Western Australia, was derived from their analysis.

Initial volume 10^6 m^3	Delivered volume 10^6 m^3	1972 cost cents m^{-1}	1982 cost cents m^{-1}
1200	840	0.3	2.1
600	390	0.5	3.5
300	180	0.8	5.6
150	75	1.5	10.5

Table 2. Cost in A$ of delivering icebergs to Western Australia.

The 1972 costs have been increased by a factor of seven to update to 1982 A$. Allowances have been made for inflation, increases in oil prices and, on the other hand, improvements in towing technology.

4.2 Processing Costs

The processing system that is costed here contains six functional elements:

iceberg + MOOR + SLICE + TUG + LOCK + POND = POWER + water

The moored iceberg is cut by heated electrical cables into slices which are towed into a lock. The lock serves to separate the ice from sea water and to pass it into a freshwater cooling pond used by a power station. The lower condenser temperature provided by the ice melting in the pond increases the thermal efficiency of the power station and thus provides some offset to the other costs. Table 3 provides a breakdown of the indicative costs.

The unit costs of mooring, slicing and tugging are independent of iceberg volume as is the return from power generation. The largest costs are for the provision of a lock and pond. The unit cost of locking is proportional to the throughput of ice and so it could be reduced if more than one iceberg per year were processed. The unit cost of providing a pond to accommodate the processed ice reduces with increasing volume.

Further discussion on the details of the cutting process, block sizes, locking and ponding schemes, as well as a consideration of the environmental impact of the presence of a large low-temperature heat sink, is to be the subject of a further paper.

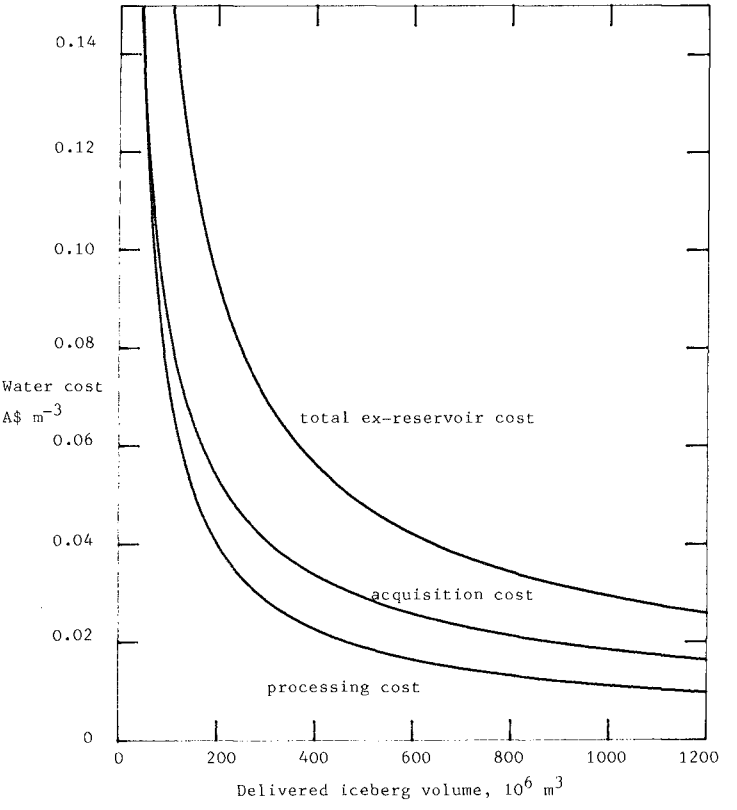

Figure 2. Ex-reservoir iceberg water costs for Western Australia.

Iceberg size 10^6 m^3	COSTS (cents kl^{-1}) Moor	Slice	Tug	Lock	Pond	Power	Water
1000	0.01	0.17	0.22	0.57	0.53	-0.45	1.0
500	0.01	0.17	0.22	1.13	0.76	-0.45	1.8
200	0.01	0.17	0.22	2.84	1.20	-0.45	4.0
100	0.01	0.17	0.22	5.67	1.69	-0.45	7.3

Table 3. Indicative costs of iceberg processing (1982 A$ prices).

4.3 Total Costs

The sum of the harvesting and processing costs are shown in Figure 2. For a yearly augmentation demand of 2 x 10^8 m^3 or more, the indicative ex-reservoir unit cost is less than 14 cents kl^{-1}.

5 CONCLUSIONS

A generalized estimate of an iceberg water augmentation scheme for the Perth region of Western Australia has been given in this paper. The costs of processing icebergs through the coastal zone appear to be about half the cost of bringing an iceberg to the offshore site. There are economies of scale applicable to both the acquisition and processing phases of iceberg water augmentation and it seems that the augmentation demand perceived by the water authorities in south western Australia may be economically fulfilled by iceberg water.

At this stage it seems that a system can be implemented using fairly conventional technology and that the cost may not be prohibitive. The use of icebergs as a supply of urban water is a concept that warrants further serious enquiry.

6 ACKNOWLEDGEMENTS

We thank the water supply authorities of both Perth and Adelaide for the availability of their reports. Professors Bill Budd and Peter Schwerdtfeger are also thanked for their discussions with us on this topic.

7 REFERENCES

DeMarle, D.J. 1980. Design parameters for a South African iceberg power and water project. Annals of Glaciology, Vol.1, p.129-31.

Engineering and Water Supply Department, South Australia. 1978. Metropolitan Adelaide water resources study.

Hult, J.L. and Ostrander, N.C. 1973. Antarctic icebergs as a global fresh water resource. Rand Corporation, Santa Monica. Report No. R-1255-NSF. 83 pp.

Huppert, H.E. and Turner, J.S. 1978. On the melting of icebergs. Nature. Vol. 271, No. 5640, p.46-48.

Husseiny, A.A.(ed). 1978. Iceberg Utilization. Proceedings of the First International Conference, Ames, Iowa, 1977. Pergamon Press, New York. 759 pp.

International Glaciological Society. 1980. Proceedings of the Conference on the Use of Icebergs. Annals of Glaciology, Vol. 1. 136 pp.

Metropolitan Water Supply, Sewerage and Drainage Board, Western Australia. 1981. Development Plan 1981-1986.

Russell-Head, D.S. 1980. The melting of free-drifting icebergs. Annals of Glaciology, Vol. 1, p.119-22.

Schwerdtfeger, P. 1979. Review on icebergs and their uses - a report to the Australian Academy of Science. Cold Regions Science and Technology, Vol. 1, No. 1, p.59-79.

Weeks, W.F. and Campbell, W.J. 1973. Icebergs as a fresh-water source: an appraisal. Journal of Glaciology, Vol. 12, No. 65, p.207-233.

Weeks, W.F. and Mellor, M. 1978. Some elements of iceberg technology. In Hussieny, A.A. (ed) Iceberg Utilization. Proceedings of the First International Conference, Ames, Iowa, 1977. Pergamon Press, New York. p.45-98.

Observing Ship Motions of Ship leaving Richards Bay Harbour

PART V

Ship Motions

Observed Ship Motions, Ship leaving Richards Bay Harbour

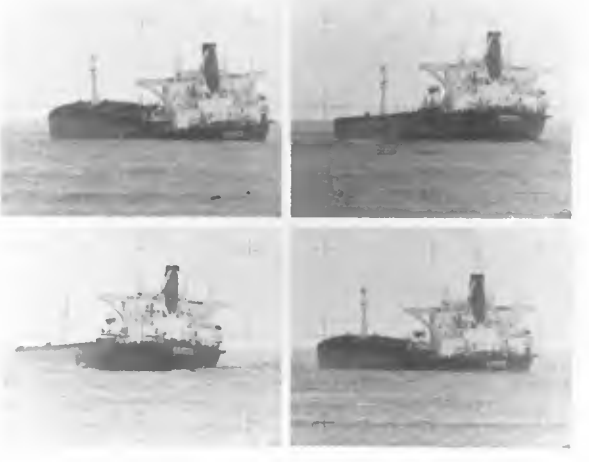

MOORED SHIP RESPONSE IN IRREGULAR WAVES

E.P.D. Mansard and B.D. Pratte

ABSTRACT

The traditional concept of representing a "random" sea state by just a variance spectral density has been found to be insufficient for modelling the slow drift oscillations of large moored ships. This paper illustrates, through experimental investigations, the importance of including wave grouping as an additional design parameter. A special technique called SIWEH, developed by the Hydraulics Laboratory of the National Research Council Canada, for the generation of realistic wave climates which include wave grouping, is presented. However, when generating the grouped sea state, one also has to properly create the group-bound long wave components. The effect of proper compensation for the spurious free wave components is illustrated by the test results on the moored vessel response.

1.0 INTRODUCTION

It has been observed, in physical model studies, that the response of moored vessels, in terms of motions and mooring loads, is far greater in irregular waves than in regular waves of equivalent wave height. This is due to the non-linearities found in irregular waves which give rise to slowly varying forces which over time are able to build up large oscillations of the vessel, leading to high mooring forces.

A vessel floating in regular waves experiences a steady force, while in the case of irregular waves, since the wave height is not constant, the force will vary with the wave envelope. This results in a slowly varying force on the vessel with a period equal to that of the wave groups.

The horizontal oscillations, such as surge, sway and yaw, for a large vessel have natural periods in the range of 20 seconds to a few minutes, far greater than the wind generated waves. The largest response of the vessel would be expected to occur when the period of the groups, which is often in the low frequency range, is equal to or lies in the vicinity of these natural periods. Although considerable research work has been carried out [Remery and Hermans (1972), Rye et al (1975), Van Oortmerssen (1976), Faltinsenen and Loken (1978), Pinkster (1979), Spangenberg (1980)], to investigate these slowly varying forces, there exists no suitable technique to simulate wave groups in terms of their periodicity and energy content. Recently the Hydraulics

National Research Council, Hydraulics Laboratory, Ottawa, Ontario K1A 0R6, Canada

Laboratory of the National Research Council Canada has developed a synthesis technique to generate realistic sea states which include wave grouping [Funke and Mansard (1980)]. This technique, which can generate varying amounts of grouping and group periods, was used in the present study in order to illustrate the importance of these slowly varying forces.

Longuet-Higgins and Stewart (1964), using the concept of radiation stress, have shown that in irregular waves, a set-down of mean water level (MWL) occurs under wave groups with a corresponding set-up between the groups. This results in a long wave variation of mean water level, with a period equal to that of the wave group in question, interacting with the vessel.

This variation of MWL, known as group-bound long wave or Bounded Long Wave, is of second order and therefore cannot be reproduced correctly with classical first order wave generation. Currently, many investigations are being carried out to establish the importance of these second order wave components in the assessment of the dynamics of structures (fixed or floating).

This paper will also illustrate, through experimental investigations, the importance of reproducing this MWL variation in order to have a realistic response of the vessel.

2.0 LOW FREQUENCY COMPONENTS IN IRREGULAR WAVES

Figure 1 presents a definition sketch of the frequency components present in irregular waves, which result in slow drift oscillations of the vessel. The Smoothed Instantaneous Wave Energy History (SIWEH) shown in this figure, serves as a useful tool to define the wave group characteristics present in a sea state. This function, developed at the National Research Council Canada [Funke and Mansard (1980)], can be computed from the water surface elevations by using the following equation:

$$E(t) = \frac{1}{T_p} \int_{\tau=-\infty}^{\infty} \eta^2(t+\tau) \cdot \phi_K(\tau) d\tau$$

where $E(t)$ = SIWEH function
$\eta(t)$ = water surface elevation
ϕ_k = smoothing window function
T_p = peak period of the spectrum

A measure of the wave group activity, known as the Groupiness Factor GF can be computed using the following expression:

$$GF = \sqrt{\frac{1}{T_n} \int_0^{T_n} (E(t)-\bar{E})^2 dt} \Big/ \bar{E} = \frac{\sqrt{m_{\epsilon_0}}}{m_0}$$

where T_n = length of wave record
$\bar{E}$ = mean value of E(t)
m_{ε_0} and m_0 = zeroth moments of the SIWEH and the variance spectral densities

The SIWEH describes the distribution of wave energy in the time axis while the GF represents the standard deviation of the SIWEH about its mean and normalized with respect to its mean.

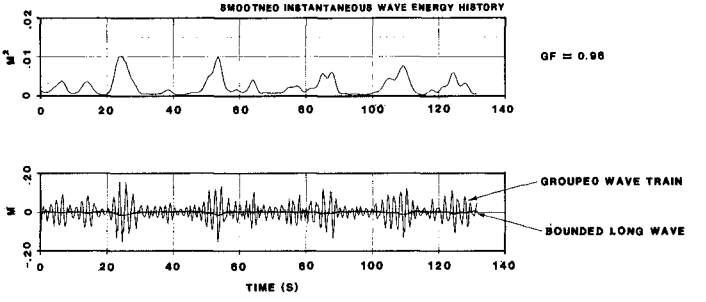

FIG.1 GROUPED WAVE TRAIN AND ITS LOW FREQUENCY COMPONENTS

Figure 1 also illustrates the long period oscillation of the MWL generated by the wave groups. This oscillation, known as Bounded Long Wave (BLW) is 180° out of phase to the SIWEH function. It can be shown that the amplitude of this oscillation is directly related to the Groupiness Factor GF.

As discussed above, the Bounded Long Wave cannot be correctly reproduced in the model by first order wave generation since the boundary condition required at the paddle to generate it cannot be satisfied directly (Ottensen-Hansen et al 1980, Bowers 1980). This results in the generation of certain spurious long wave components (shown in Figure 2), which in turn lead to a vessel response which is not realistic. The two main sources which contribute to these spurious long waves are:

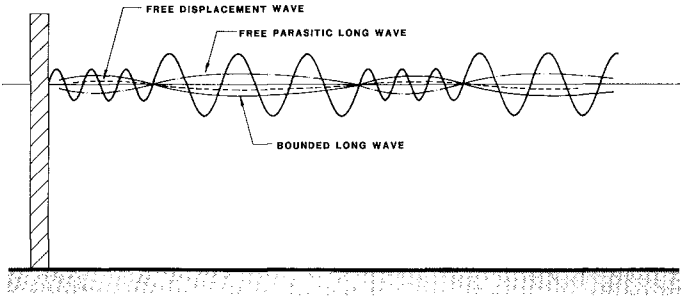

FIG.2 DEFINITION SKETCH OF LONG WAVE COMPONENTS IN A GROUPED WAVE TRAIN

1. free parasitic long wave, which is opposite in phase to the BLW, generated at the paddle since the particle motions from the group induced long waves cannot pass through the solid paddle;

2. free displacement waves generated due to the moving boundary of the paddle.

These spurious long waves are called free waves since they travel with their own celerity, while the Bounded Long Wave travels with the group velocity since it is bound to the wave groups. The free long waves can travel back and forth along the flume corrupting the incident wave system, since the reflection coefficient of these long waves is often very high (50 to 60%) even from beaches with mild slopes. However, the free long waves can be eliminated by including proper suppression terms in the wave generation. Under a cooperative program between the Danish Hydraulic Institute, the Delft Hydraulics Laboratory and the National Research Council Canada, techniques for the correct reproduction of the Bounded Long Wave were developed by verifying the various long wave terms and the effectiveness of the suppression. A joint publication by the three laboratories (Barthel et al 1983), describing the various techniques involved, is being submitted to Ocean Engineering. The present paper, therefore, only deals with the application of this technique in the assessment of the vessel response.

3.0 WAVE GENERATION TECHNIQUES

The effect of wave grouping on the dynamics of floating or fixed structures can be investigated in laboratory models by the wave synthesis technique illustrated in Figure 3. This technique, developed at the National Research Council Canada, can be used to synthesize time series with different wave grouping characteristics, keeping however the variance spectral density of the sea state constant. Because of

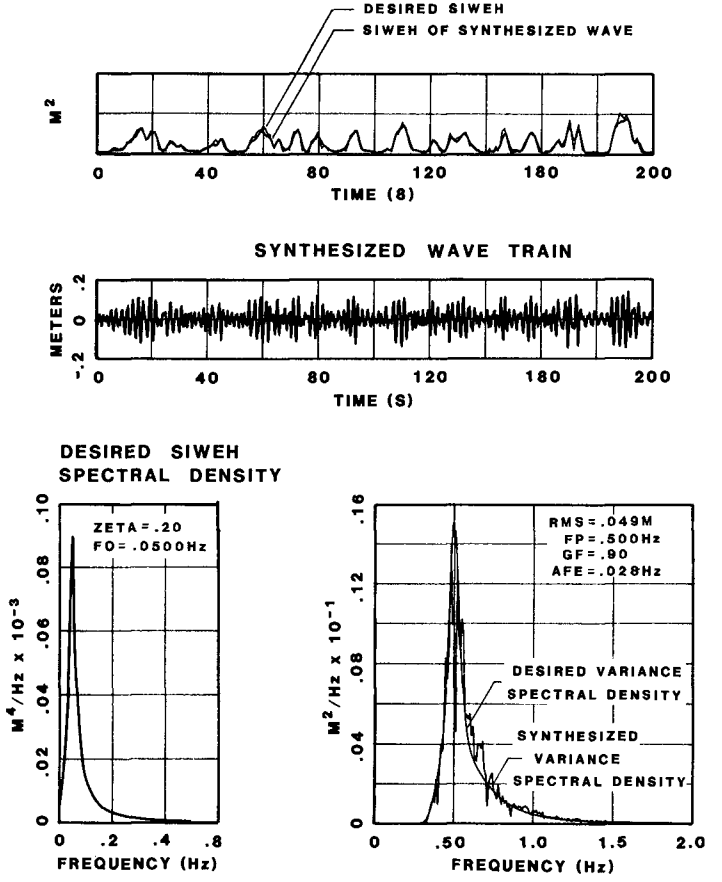

FIG.3 SYNTHESIS OF A GROUPED WAVE TRAIN

the high correlation which exists between the wave groups and the slow drift oscillations, this technique is particularly useful to evaluate their relationships in a given sea state.

In the absence of sufficient analysed prototype records of wave groups, a theoretical model of the SIWEH spectral density is used in this synthesis. The parameters of this model can effectively be varied to generate SIWEH functions having different characteristics. Since, $GF = \sqrt{m_{\varepsilon_0}}/m_0$, the area under the SIWEH spectrum, shown in Figure 3, can be varied to achieve different Groupiness Factors with the same variance spectral density. On the other hand, different period and distribution of the groups can be obtained by varying the peak frequency and the width of the spectrum.

As shown in Figure 3, the synthesized wave train satisfies the frequency domain characteristics of the desired variance spectral density as well as the time domain characteristics defined by the SIWEH function. Details of the various steps involved in this synthesis technique are well documented in Funke and Mansard (1980).

4.0 EXPERIMENTAL SET-UP

The investigations in the physical model were carried out to a scale of 1:100 using a model of a 227000 DWT tanker in a wave basin approximately 67 m long and 7.7 m wide. The flume, Figure 4, was equipped with a hydraulically-driven wave generator controlled by an on-line computer. The model tanker, located midway between the wave paddle and the beach, was moored at about a 30° angle between the bow and the incident wave direction. Greater angles could not be tested due to the relative narrowness of the flume. A mild sloped stone beach (1:25) ensured good dissipation of the incident energy.

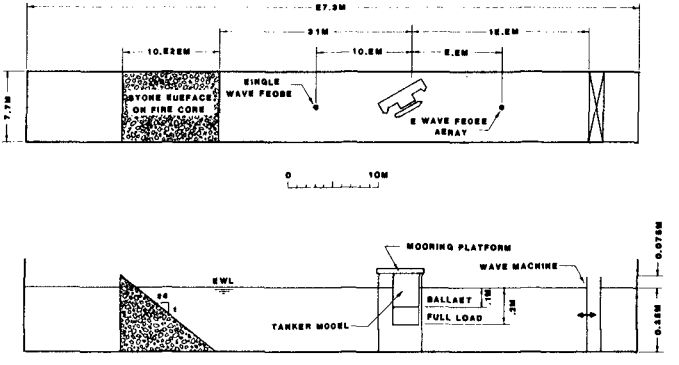

FIG.4 SHIP MOORING BASIN LAYOUT

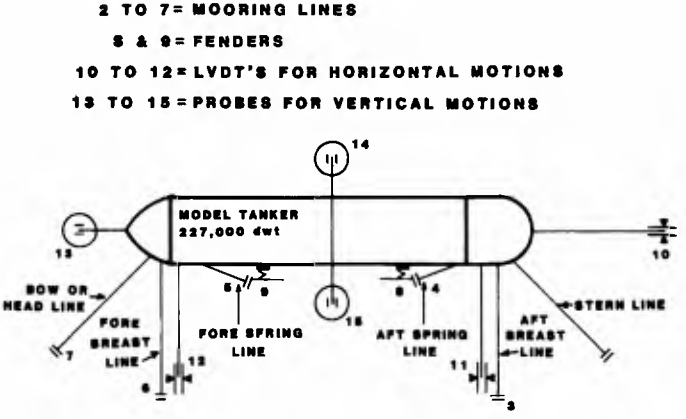

FIG.5 GENERAL LAYOUT OF MOORING CONFIGURATION

FIG.6 PHOTOGRAPH SHOWING A GENERAL VIEW OF THE PHYSICAL MODEL

The water surface elevations were monitored using twin wire capacitance probes located midway between the vessel and the wave paddle. An array of five probes was used to establish the reflection characteristics of the vessel and of the beach.

The model tanker was moored, as shown in Figures 5 and 6, by six mooring lines (representing four prototype nylon lines each with a pretension of 30 t and two steel spring lines with nylon tails with 10 t pretension). Two fenders, placed symmetrically, absorbed the impacts of the vessel on the mooring jetty. The jetty was supported on thin piles, and presented no obstruction to the waves. Since a direct measurement of the six degrees of freedom of the vessel motions (surge, sway, heave, roll, pitch and yaw) was not feasible, the approach used was to monitor the motions at the six locations (10 to 15) shown in Figure 5 and then to relate them to the six degrees of freedom. Accordingly, the vertical motions were measured by capacitance type probes while the horizontal movements were monitored by using Linear Variable Displacement Transducers (LVDT).

In model studies it is not easy to simulate the non-linear load elongation characteristics of the mooring lines by just varying their elasticity. Therefore, non-stretching mooring lines were used and the elasticity of the prototype mooring lines were simulated by the device shown in Figure 7. This simulator, developed at the Hydraulics Laboratory of the National Research Council Canada, consists of a cantilevered blade spring of rectangular cross-section mounted on a plate. The desired non-linear load-elongation characteristics of the mooring line can be achieved by varying the positions of the spring contact points so that as the spring is pulled down onto them an effective shortening of the length of the spring and consequently a stiffening effect results. Mailhot et al (1982) have recently developed a computer method for determining these contact positions.

Stainless steel is a spring material well suited for this device since it combines very low permanent deformation with high elasticity. The choice of the width and thickness of the spring can be used to vary the stiffness to a certain extent. The frequency response of this simulation was found to be high, on the order of 5 to 10 Hz.

While the elasticity of the prototype mooring line is simulated by the above device, the loads on the different lines are monitored by using Direct Current Displacement Transformers (DCDT) in a force transducer. The DCDT has a moving core, suspended from a pair of spring blades, and connected to the mooring line. As the core moves through the electromagnetic field within the DCDT windings, a voltage output is produced which is calibrated to the displacement of the core and thus to the force required to achieve that displacement.

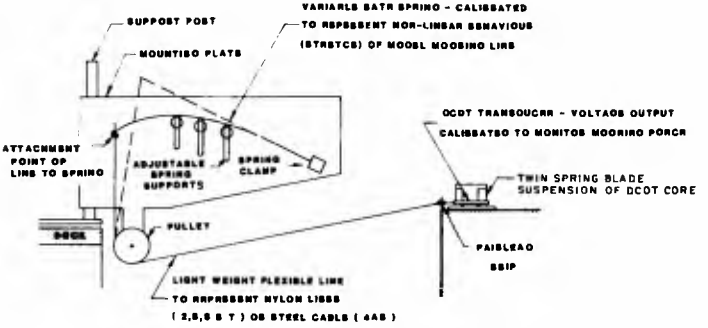

FIG.7 NON - LINEAR CANTILEVER SPRING MOORING SYSTEM

FIG.8 PHOTOGRAPH SHOWING THE CANTILEVER SPRING, FENDER, AND MOORING FORCE TRANSDUCER

5.0 EFFECT OF LONG WAVE COMPENSATION ON VESSEL RESPONSE

In order to establish the effect of the correct reproduction of the Bounded Long Wave (BLW) on vessel response, tests were carried out using two different cases of wave generation: with and without compensation for spurious long waves. The BLW components measured in these two cases are presented in Figure 9 along with the grouped wave trains. In the same figure, a comparison between the expected (theoretical) and the measured BLW is also shown (to a larger scale) for these two cases.

The measured BLW was extracted from the total grouped wave train by applying a low pass filter whereas the expected BLW was computed by theoretical relationships, from the measured wave train using a cut-off frequency which excludes the measured long wave.

In the first case, where proper compensation accounted for the spurious long waves, the agreement between the measured and expected values of BLW is satisfactory: the set-down under each group is well reproduced and the small discrepancies found in amplitude are only in the order of millimetres in the model. On the other hand, where no compensation is done, the amplitudes and especially phases of the BLW are different from the theoretical predictions. The change in phases results in an improper set-down (or cross-over from a set-up to a set-down) under the wave groups. This is mainly due to the standing wave pattern caused by the free long waves.

The correct reproduction of the BLW can also be checked by its propagation characteristics. Figure 10 shows an example of the propagation of the Bounded Long Wave in a flume, for three distances from the waveboard. With compensation, the set-down under the groups is well maintained during propagation, while with no compensation important amplitude and phase changes can be detected. This means that, in tests where no suppression of the spurious components is made, the response of the vessel could be quite different (high or low) depending upon the position of the test structure in the flume.

The vessel response, in terms of mooring line forces and vessel movements, for the two wave trains presented in Figure 9, is summarized in Table 1.

The two wave train records had similar time and frequency domain characteristics. The peak frequency of the SIWEH spectrum and the groupiness factor were the same as well as the peak period and the characteristic wave height. The results show, that both the RMS and maximum values of the mooring line forces (in tonnes) and vessel motions (meters, radians) were generally higher when the spurious long waves were properly suppressed (WC). This is possibly due to the proper timing of the set-down, causing an increase in velocity due to the slightly shallower water conditions, resulting in a larger response of the vessel with the higher waves of the groups. With no compensation (NC) for spurious long waves, the set-down is less, resulting in less vessel response. Table 1 for motions shows that with compensation the main component excited is sway for this particular wave input and incidence angle.

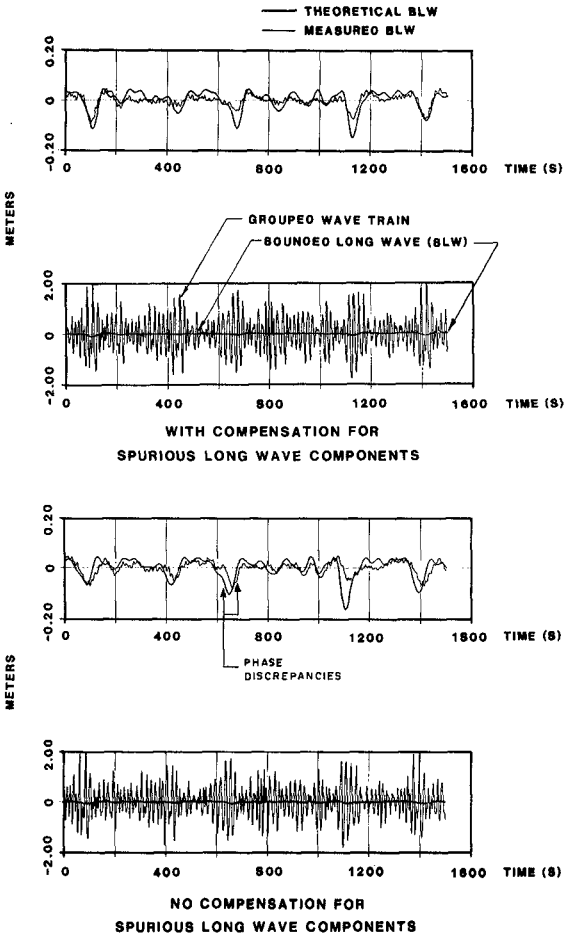

FIG.9 BOUNDED LONG WAVE COMPONENTS IN THE FLUME (WITH SHIP)

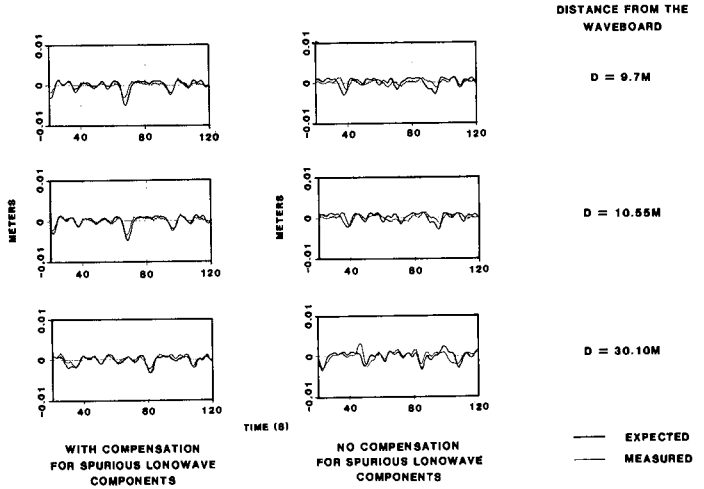

FIG.10 BOUNDED LONGWAVE COMPONENTS ALONG THE FLUME

(NO SHIP)

(MODEL UNITS)

When considering the response of a moored structure, the heave exciting force may be assumed to be:

$$F_e = \beta_1 \eta(t) + \beta_2 \eta^2(t)$$

where β_1 and β_2 are coefficients and η is the water surface elevation [NAESS (1978)]. This means that the heave motion of the vessel is related to the square of the water surface elevation $\eta^2(t)$, or in this case to the SIWEH function. This relationship is well illustrated in Figure 11 where the second order heave motion was extracted from the measured response by low pass filtering. Figure 11 also presents a comparison of the heave response between the two cases of wave generation discussed. In the first case, the long wave component of the heave response is well correlated to the SIWEH (i.e. amplification under the groups, whereas a cross-over phase shift occurs for the non-compensated free long waves. The RMS heave motions are much the same in either case.

CHAR. WAVE HEIGHT HCHR (M)	GROUPINESS FACTOR G.F	STERN (T)	STERN BREAST (T)	STERN SPRING (T)	BOW SPRING (T)	BOW BREAST (T)	BOW (T)	STERN FENDER (T)	BOW FENDER (T)	
2.53	0.81	57.2	86.3	54.9	198.1	147.7	61.1	657.2	1210.5	N.C
		8.1	12.1	6.0	17.4	20.4	7.4	107.1	197.0	
2.55	0.60	71.4	112.1	71.1	215.5	146.5	85.6	982.9	1273.1	W.C
		7.05	14.1	9.2	22.0	23.3	8.2	130.2	202.3	

FORCES

CHAR. WAVE HEIGHT HCHR (M)	GROUPINESS FACTOR G.F	SURGE (M)	SWAY (M)	HEAVE (M)	ROLL (RAD)	PITCH (RAD)	YAW (RAD)	
2.53	0.81	2.53	3.85	.78	.022	.019	.025	N.C
		.64	.72	.21	.006	.005	.010	
2.55	0.80	2.50	5.10	.76	.018	.018	.029	W.C
		.88	.87	.21	.006	.005	.011	

MOTIONS

MAX
RMS

N.C - NO COMPENSATION FOR SPURIOUS LONG WAVES
W.C - WITH COMPENSATION FOR SPURIOUS LONG WAVES

TABLE 1

EFFECT OF LONG WAVE COMPENSATION ON VESSEL RESPONSE

$f_{p\ (SIWEH)} = 0.004Hz$

$f_p = 0.05Hz$

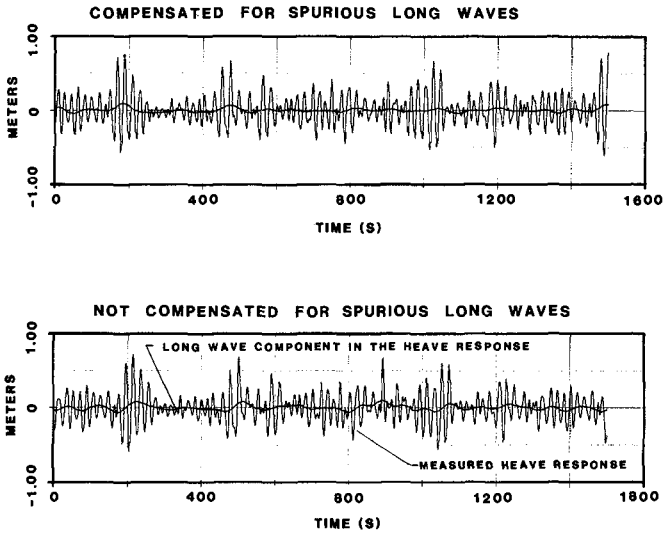

FIG.11 MEASURED HEAVE MOTION

Since the above results indicate that the response of the vessel is a function of the long wave components, it appears that proper compensation for spurious long wave components is required, in model studies, in order to determine realistic mooring line forces and vessel movements.

The results presented in the next section, on the relationship of the SIWEH to the slow drift oscillations of the vessel, were therefore investigated using proper suppression for the free long waves.

6.0 EFFECT OF WAVE GROUPING ON SLOW DRIFT OSCILLATIONS OF THE VESSEL

In order to investigate the relationship between the wave grouping present in a time series and the resulting slow drift oscillations of the vessel, three sets of wave conditions were generated in the flume using the technique previously described. These wave trains, measured in the flume, had identical variance spectral densities but different SIWEH spectra. Since the Groupiness Factor GF is directly related to the SIWEH spectrum GF = $\sqrt{m_{\epsilon_0}}/m_0$, these three wave records, shown in Figure 12, had different groupiness factors ranging from 0.46 to 1.03.

The maximum and the RMS values of the vessel movements and the resulting mooring loads, measured under the three wave conditions, are summarized in Table 2. These results indicate that the response of the vessel increases with increasing groupiness factor in spite of the fact that the characteristic wave height and the peak period of the sea state were similar. The horizontal oscillations, surge, sway and yaw, which are sensitive to excitation by long wave components, increase when the amplitude of the long waves generated by the groups increases, resulting in increased mooring line forces.

The results of these investigations are illustrated in Figures 13 and 14 in the form of spectral plots. Figure 13 presents the spectra of mooring line forces for three typical mooring lines while the spectra of horizontal motions are shown in Figure 14.

The results indicate that a distinct correlation exists between the wave grouping and the vessel response. Therefore, in model studies, a sea state cannot be represented solely by its variance spectral density, peak period and significant wave height without considering its time domain characteristics. In other words, the wave grouping is an important parameter to be taken into account in the assessment of vessel response.

It should be mentioned that the experimental results were somewhat limited due to the narrowness of the flume to small angles of heading (30°) of the vessel relative to the waves. Further work in a wider basin may well yield more dramatic response comparisons for other heading angles, under-keel clearances, and vessel loading conditions.

In a recent study, Spangenberg (1980), was able to show a similar correlation between the wave grouping and the slow drift oscillation of a semi-submersible. The synthesis technique used in that work does not, however, allow an easy control of wave grouping characteristics (well defined periods and groupiness factors). Furthermore, no compensation was done for the spurious long wave components.

The concept of SIWEH can also be used in numerical models as input excitation functions for the slow drift oscillations.

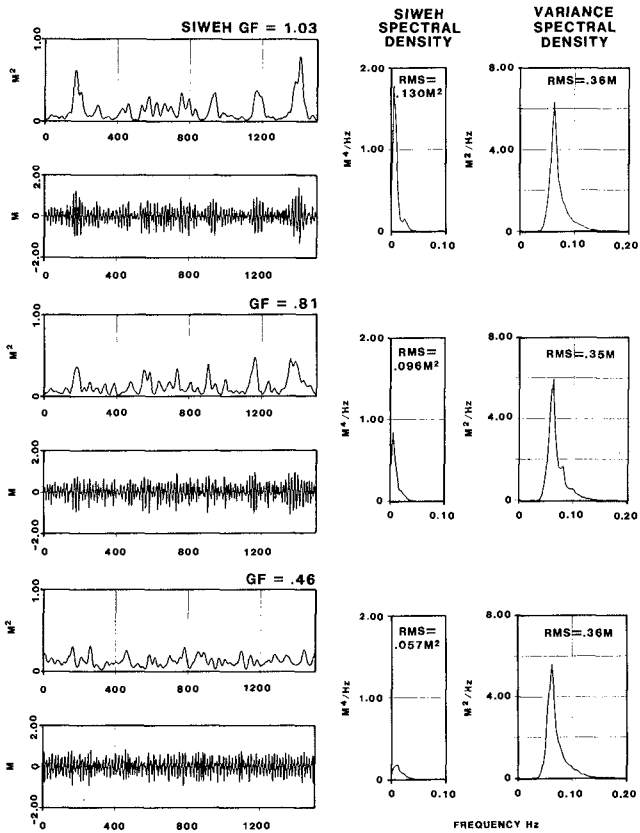

FIG.12 WAVE TRAINS WITH COMMON VARIANCE SPECTRAL DENSITIES BUT DIFFERENT GROUPINESS FACTORS

CHAR. WAVE HEIGHT HCHR (M)	GROUPINESS FACTOR G.F	STERN (T)	STERN BREAST (T)	STERN SPRING (T)	BOW SPRING (T)	BOW BREAST (T)	BOW (T)	STERN FENDER (T)	BOW FENDER (T)
1.44	1.03	49	99	93	39	71	52	990	949
		2.99	7.49	9.58	4.59	9.45	3.74	120.24	128.99
1.40	0.91	44	57	37	39	93	45	756	722
		2.74	9.99	4.44	4.37	9.09	3.22	119.79	125.79
1.42	0.46	43	52	33	34	97	49	721	919
		2.38	9.94	3.79	3.39	9.32	3.92	115.29	142.32

FORCES

CHAR. WAVE HEIGHT HCHR (M)	GROUPINESS FACTOR G.F	SURGE (M)	SWAY (M)	HEAVE (M)	ROLL (RAD)	PITCH (RAD)	YAW (RAD)
1.44	1.03	1.80	3.14	0.33	0.014	0.010	0.018
		0.491	0.440	0.077	0.004	0.003	0.004
1.40	0.91	1.39	1.90	0.33	0.013	0.009	0.015
		0.409	0.319	0.079	0.004	0.003	0.004
1.42	0.49	1.04	1.93	0.29	0.013	0.019	0.014
		0.305	0.357	0.075	0.004	0.003	0.004

MAX
RMS

MOTIONS

TABLE 2

EFFECT OF GROUPINESS FACTORS ON VESSEL RESPONSE

$f_{p\ (SIWEH)} = 0.004$ Hz

fp = 0.06 Hz

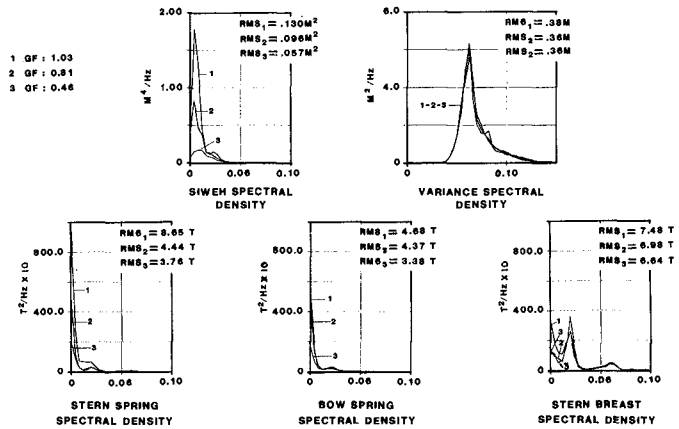

FIG.13 EFFECT OF GROUPINESS FACTORS ON MOORING LINE FORCES

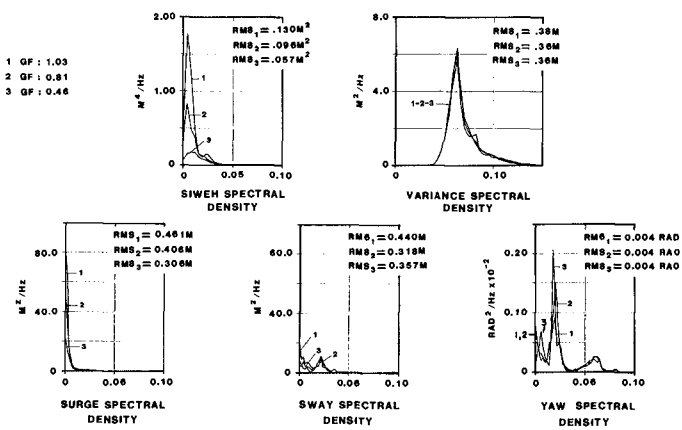

FIG.14 EFFECT OF GROUPINESS FACTORS ON VESSEL MOTIONS

7.0 CONCLUSIONS

Representing a sea state solely by its variance spectral density has been found to be insufficient for modelling the slow drift oscillations of the vessel.

The synthesis technique, used to generate realistic sea states in the model, has successfully illustrated the correlation between the slow drift oscillations and the wave grouping.

The results show that the wave grouping, present in irregular waves, is an important parameter to be taken into account in the assessment of vessel response.

It has been shown that a correct reproduction of Bounded Long Wave Components is required, in model studies, in order to have a realistic response of the vessel.

8.0 ACKNOWLEDGEMENTS

The authors wish to thank Mr. E.R. Funke, who developed the cantilevered mooring line simulator, for his invaluable suggestions during this study. Thanks are also due to Mr. J.R. Clarke for his technical assistance.

9.0 REFERENCES

1. Barthel et al (1983): "Group Bounded Long Waves in Physical Models". Joint Research Project by Danish Hydraulic Institute, Delft Hydraulics Laboratory and National Research Council Canada. Paper to be submitted to Ocean Engineering.

2. Bowers, E.C. (1980): "Long Period Disturbances Due to Wave Groups". Proc. XVII Conf. on Coast. Eng., Sydney, Australia.

3. Faltinsen, O.M. and Loken, A.E. (1978): "Drift Forces and Slowly Varying Forces on Ships in Irregular Waves". J. App. Res. 1.

4. Funke, E.R. and Mansard, E.P.D. (1980): "On the Synthesis of Realistic Sea States". Proc. XVII Conf. on Coast. Eng., Sydney, Australia.

5. Longuet-Higgins, M.S. and Stewart, R.W. (1964): "Radiation Stresses in Waver Waves, a Physical Discussion with Application". Deep Sea Res., No. 11.

6. Mailhot, G. and E. Dunberry (1982): "A Computerized Calibration for a Mooring Line Simulator". Proj. Rep. Dept. of Civil Eng., McGill University, Montreal, Quebec.

7. Naess, A. (1978): "On Experimental Prediction of Low-Frequency Oscillations of Moored Offshore Structures". Norwegian Marine Research, No. 3, pp. 30-37.

8. Ottensen-Hansen, N.E., Sand, S.E., Lundgren, H., Sorensen, T. and Gravesen, H. (1980): "Correct Reproduction of Group-Induced Long Waves". Proc. XVII Conf. on Coast. Eng., Sydney, Australia.

9. Pinkster, J.A. (1979): "Mean and Low Frequency Wave Drifting Forces on Floating Structures". Ocean Eng., Vol. 6, pp. 593-615.

10. Remery, G.F. and Hermans, A.J. (1972): "The Slow Drift Oscillations of a Moored Object in Random Seas". Jour. Soc. Pet. Engrs.

11. Rye, H., Rynning, S. and Moshagen, H. (1975): "On the Slow Drift Oscillations of Moored Structures". Paper No. OTC 2366, Offshore Tech. Conf., Houston, U.S.A.

12. Spangenberg, S. (1980): "The Effect of Wave Grouping on Slow Drift Oscillations of an Offshore Structure". Meddelelse, Bulletin No. 46, Danish Ship Research Laboratory.

13. Van Oortmerssen, G. (1976): "The Motions of a Moored Ship in Waves". NSMB, Pub. No. 510.

MEASUREMENT TECHNIQUES FOR MOORED SHIP DYNAMICS

by

J Moes and S G Holroyd*

ABSTRACT

Problems arise during adverse sea conditions with ships moored to the ore loading jetty at Saldanha Bay. Under certain wave conditions moored ships undergo large motions which cause breakage of mooring lines. In order to obtain a quantitative insight into the problem an extensive measurement system was installed at Saldanha Bay. This system comprises instrumentation for the measurement of short and long waves, currents and wind, mooring line and fender forces and the motions of the moored ships. Preliminary results show that during storm conditions long waves with periods between 50 and 150 s occur at the jetty. These periods fall within the same range as the observed natural periods of horizontal oscillation of the moored ships.

1. INTRODUCTION

The increase in the size of tankers and bulk carriers during the last decades has led to a tendency to build cargo-handling jetties for these ships close to deep water in order to reduce the costs of dredging navigation channels. As a result of this development, the mooring locations are, in general, more exposed to wave action. This requires careful design and operation of the mooring equipment to assure the safety of ships and jetty structures and to reduce downtime in loading or unloading of the ships.

A loading jetty has been built in Saldanha Bay, a natural bay on South Africa's west coast, about 150 km north of Cape Town, for the export of iron ore (see Figure 1 and Photograph 1). The main harbour construction, which was completed during 1976, consists of a sand breakwater between Hoedjies Point and Marcus Island, an ore handling plant, a causeway, a jetty and a navigation channel, dredged to a depth of between -23,0 and -23,7 m CD (Chart Datum) in order to allow ships of up to 250 000 dwt to be

* National Research Institute for Oceanology, CSIR, Stellenbosch, Republic of South Africa

PHOTOGRAPH 1:

General view of ore jetty at Saldanha Bay

PHOTOGRAPH 2:

Attachment of strain gauges onto mooring hook (see arrow)

PHOTOGRAPH 3:

Coiled cable connection for fender measurements

PHOTOGRAPH 4:

Digital data acquisition system

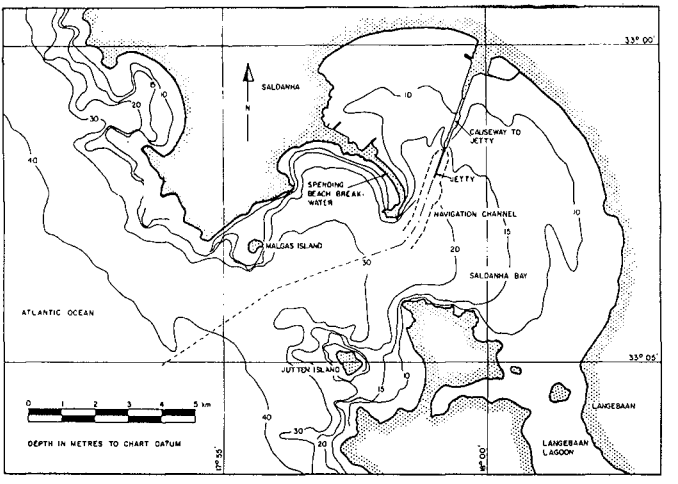

FIGURE 1:

Layout of Saldanha Bay Harbour

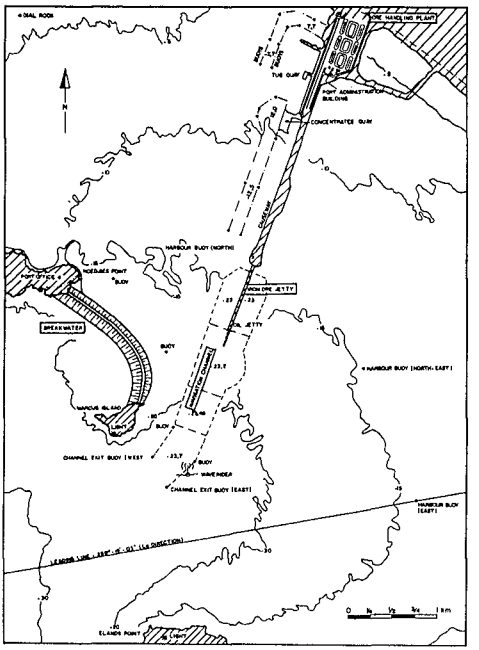

FIGURE 2:

Saldanha Bay Harbour Structures

loaded at the jetty (see Figure 2). Since 1977 up to 18 million tons of iron ore have been exported annually.

2. MOORING PROBLEMS

At Saldanha Bay problems have arisen with moored iron ore carriers. Under certain wave conditions, the moored ships undergo large horizontal motions which have, on occasions resulted in the breaking of mooring lines. This in turn has led to interruptions of the loading of iron ore and even necessitated in some isolated instances the removal of ships from the jetty.

The South African Transport Services requested CSIR to assist in investigating these problems and to advise on possible steps to minimize or eliminate their occurrence.

3. STUDY APPROACH

In order to investigate the nature of the problems NRIO initially carried out a feasibility study. This study comprised a literature survey on possible similar problems experienced elsewhere, long-wave measurements at the jetty and discussions with the operational staff at Saldanha Bay on the characteristics of the mooring system, the behaviour of the moored ships and the environmental conditions during the occurrence of problems.

From the literature it was found that similar problems were encountered elsewhere, as reported by Wilson (1954), Keith and Murphy (1970), Bowers (1975) and Nagai *et al.* (1977). Most problems were caused by the occurrence of relatively long waves with periods between 50 and 150 s, which is in the same range as the natural periods of horizontal oscillation of the moored ships. These long waves may be penetrating into the harbour from the ocean or may be caused by harbour resonance.

During the design of the harbour Wilson was asked to investigate the occurrence of harbour resonance at Saldanha Bay. He concluded (Wilson, 1972) that the natural periods of wave oscillation in the bay would be much larger than the resonance period of the moored ships.

From discussions with the operational staff at Saldanha Bay it appeared that the mooring pattern of the ship is always rather similar, using an average of about 16 mooring lines of various materials and thicknesses (see Figure 3). The jetty consists of a concrete deck supported by caissons and is about 60 per cent open. The jetty is equipped with Yokohama pneumatic fenders with a diameter of 3,3 m and a length of 6,5 or 10,6 m. In almost all cases when problems with moored ships occurred heavy swell was reported. This

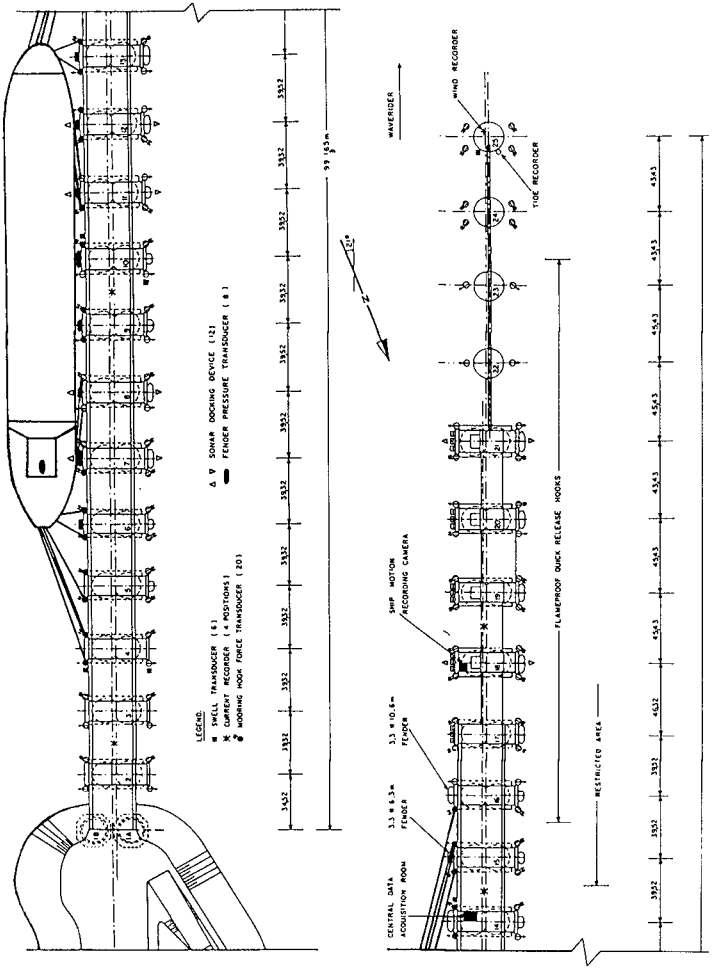

FIGURE 3: Ore jetty, position of instrumentation and typical mooring layout

was determined using a Datawell Waverider, positioned at the entrance of the navigation channel (see Figure 2).

On the basis of this information the first aim of the study was therefore to determine quantitatively the relationship between any low-frequency wave energy and the resulting ship motions and mooring forces. For this purpose an extensive measurement program was undertaken, involving a wide variety of instruments. On the basis of the results of the field measurements preliminary recommendations will be made in order to alleviate the problems. However, physical and mathematical model studies may be necessary to determine the effect of various alternative mooring conditions. These models may be calibrated with prototype data obtained from the field measurements.

4. MEASUREMENT SYSTEM

In order to collect the data required for the investigation, a data-logging system was designed to monitor and record the environmental conditions as well as the motions of the moored ship and of the forces involved. The following were therefore measured:

(a) Long swell at six points along the jetty.

(b) Two components of current from at least one point along the jetty.

(c) Forces in up to 20 mooring lines.

(d) Pressures in eight fenders. The pressure data could be processed to determine forces.

(e) Ship motions.

The above measurements are made only during the presence of a ship in adverse conditions. To obtain general historic data, the following environmental observations are made continuously:

(f) Wind speed.

(g) Wind gust speed.

(h) Wind direction.

(i) Long swell at one point along the jetty.

(j) Waves.

(k) Tides.

For the measurement of the ship motions and of the forces involved it was decided that monitoring the conditions at one of the ore berths would yield sufficient data for the study. The eastern side of the jetty was chosen (see Figure 3), since the largest ships are usually moored at this berth.

5. WAVE MEASUREMENTS

5.1 General

A waverider buoy is anchored at the entrance of the navigation channel (see Figure 2). This buoy can record waves with periods of only between about 1 and 25 s. This is below the range of wave periods expected to be critical for the moored ships, namely, 50 to 150 s. Therefore, long-wave recorders had to be installed to record the waves with periods of between 25 and 150 s.

5.2 Short Waves

To establish a possible relationship between the energies of long and short waves it was decided to use also the waverider data. To facilitate spectral analysis of the data a data logger was installed which sampled the wave-rider signal at 0,5 s intervals during a period of about 20 min., four times a day. Provision was also made to allow continuous recording during severe ship motions.

5.3 Long Waves

During the feasibility study a pressure recorder was in operation at caisson No 14, east side (see Figure 3) from August 1979 to January 1981, except during the winter months of 1980 when the transducer failed. In order to determine the variation of long-wave energy along and across the jetty it was later decided to deploy six pressure recorders, distributed along the jetty (see Figure 3). To be able to obtain a wave period resolution of between 5 and 500 s the sampling rate of the pressure recorders was set at 2 s while the recording period was about 120 min. The transducers measured the instantaneous water pressures two to five metres below the water surface, where they were fixed onto the caissons by means of stain-less steel brackets. One swell recorder (at caisson No 14) was set to record automatically twice a day, while the others could be switched on as required.

5.4 Tides and Very Long Waves

Very long waves with periods of at least 300 s could be determined from the tide recorder installed at caisson No 25 (see Figure 3).

5.5 Wave Correlations

The pressure transducer data were spectrally analysed, and a typical storm sequence is shown in Figures 4a to d.

The spectral analysis is performed for four period ranges, namely, for the wave period ranges 5 to 50 s, 30 to 100 s, 70 to 150 s and 90 to 250 s. Figures 4a to d show that low-frequency energy between 30 and 150 s occurs only during the peak of the storm (Figure 4c). Figures 5a and b show a comparison of characteristic wave heights for the specific wave period ranges. It appears that the low-frequency wave height for both the period ranges 30 to 100 s and 70 to 150 s is about 20 per cent of the wave height in the period range 5 to 50 s.

From visual inspection of the spectral plots such as Figures 4a to d, those plots showing a clear low-frequency energy content, such as in Figure 4c, were selected. These occurrences are related to the observed short-term maximum wave heights H_M at the waverider position, as shown in Figure 6. It can be seen that low-frequency wave energy almost always occurs when the observed wave height H_M at the waverider is larger than 2 m.

6. CURRENT MEASUREMENTS

The most severe motions of the moored ships were reported by the operational staff to be in a horizontal plane, namely, surge, sway and yaw. Therefore, the horizontal water motions are probably a major cause of the problems. These motions can be estimated from the heights and periods of the waves and from the local water depth. In order to provide a check for these estimates as well as to determine a possible existence of cross-currents at the jetty a current meter was installed. Initially only one current meter was used. This could be installed at various positions along the jetty (see Figure 3). In this way possible cross-currents could be measured during various wave conditions, while it was hoped that a correlation with the swell data could be established. A reported strong marine growth at Saldanha Bay prohibited the use of a propeller type current meter, while the large amounts of moving iron ore and steel structures would render an electro-magnetic current meter useless. Therefore, an ultrasonic current meter was used (see Figure 7). The instrument was suspended between two adjacent caissons by means of four stainless steel wires. Because of corrosion problems these were later replaced by polypropylene lines (see Figure 8).

7. WIND MEASUREMENTS

Because wind as well as water motions contribute to ship motions, an Aanderaa anemometer was installed at the top of

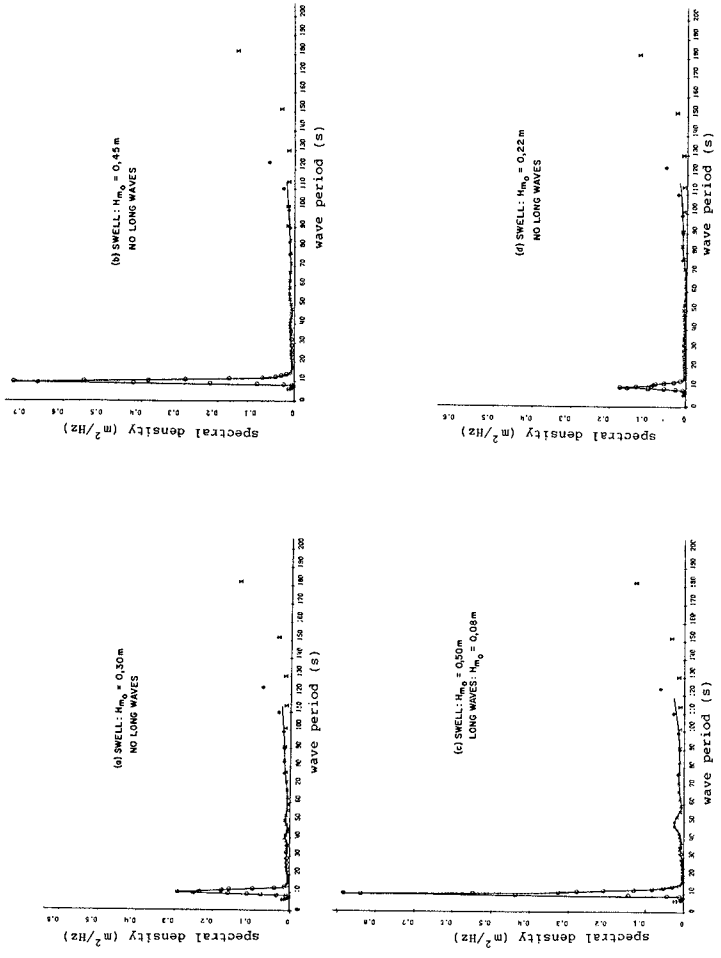

FIGURE 4: Spectral density estimates for a typical storm

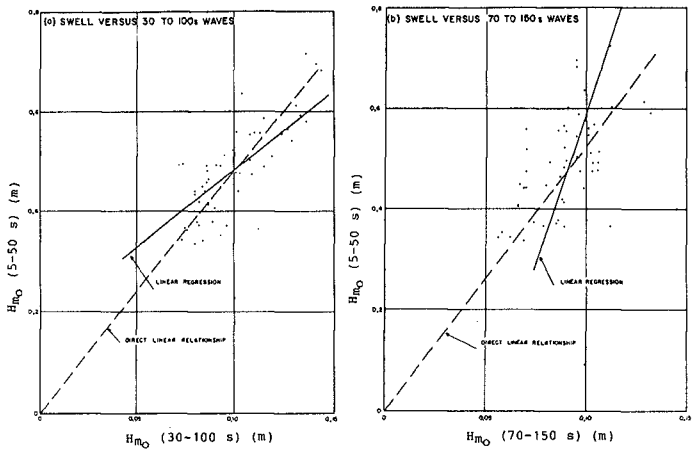

Figure 5: Relationship between characteristic wave heights based on various wave period bands

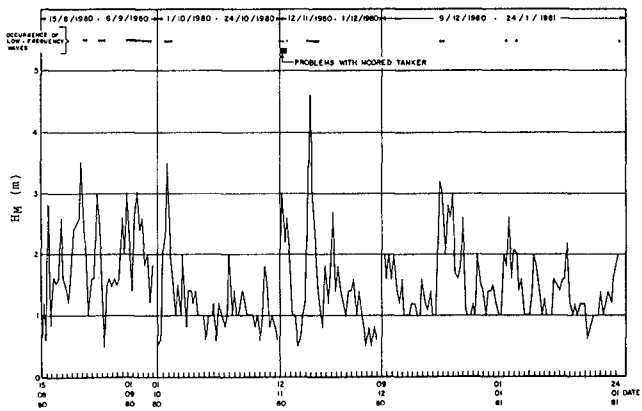

Figure 6: Relationship between short-term maximum wave height H_M and the occurrence of low-frequency waves

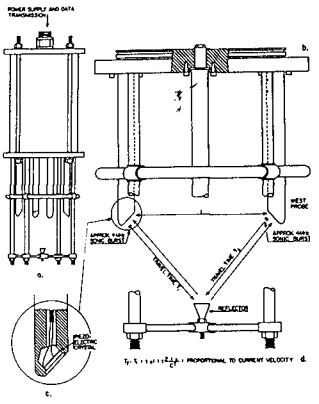

Figure 7: Simrad HC-100 ultrasonic current meter

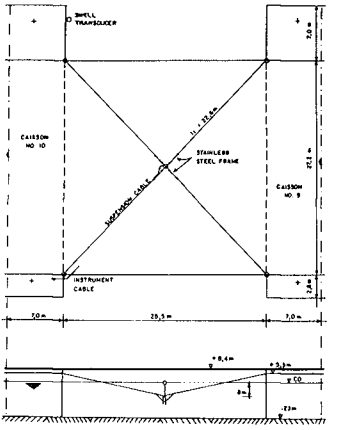

Figure 8: Typical position of current meter

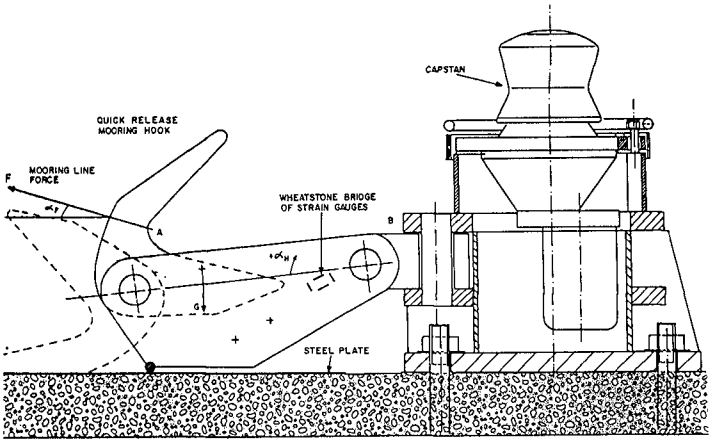

Figure 9: Mooring hook equiped with strain gauges

a light mast at caisson No 25 (see Figure 3). This anemometer monitored continuously wind speed and direction,and every 15 minutes the following data were recorded:

(a) The average wind speed during each 15 min. interval.

(b) The average wind direction during each 15 min. interval.

(c) The maximum wind gust during each 15 min. interval.

8. MOORING LINE FORCE MEASUREMENTS

Forces in the mooring lines can be determined either by monitoring the tensions in the ropes or those in the mooring hooks. Four methods of doing this were considered:

(a) Use of a load cell fitted to the mooring hook and onto which the mooring line could be hooked. The sheer mass of such a device as well as its relative complexity made this impracticable. Its use would also mean the loss of the advantages of the quick-release mechanism of the hook.

(b) Use of a mooring line "forerunner" incorporating a load cell. This offered a technically sound solution but in the given situation would have been difficult to use. The danger of loss of these forerunners, either by their being left attached to the ship's mooring lines or by their falling off the jetty into the water seemed too great to make this method feasible. Further, use of the quick-release mechanism of the hook would almost certainly have resulted in loss of the forerunner. As with method (a) this device would have had to be tested regularly to ensure that mechanical failures did not occur. Further, the long flexible electrical connections would be fairly vulnerable to damage and therefore unreliable.

(c) Monitoring strain in one of the pivot pins of the quick-release mooring hooks, using strain gauges mounted onto these pins. A disadvantage of such a system would have been the complexity of retrofitting such pins in hooks which were in regular use.

(d) Monitoring strain in the mooring hook side plates. This offered a neat solution to the problem, provided that the stability, reproducibility and system inaccuracies were within the required specifications. Also, calculations predicted that the stress in the side plates at the selected point of measurement would have been almost linear with respect to force on the hook (see Figures 9 and 10).

To investigate the feasibility of this method preliminary tests were done on one hook. Strain gauges were fitted to one side plate (see Figure 9) and the hook was taken

through a number of load cycles. This test was repeated after three weeks and again after a further two weeks. During these tests the following points were examined:

(a) Reproducibility of observations, both in the short-term and in the long-term.

(b) Temperature stability, particularly with regard to irregular heating of the hook, such as heating up of one side of the hook only by the sun.

(c) Linearity.

The results of these tests showed that the system would meet the required accuracies, namely, that the hooks could be used to monitor forces up to 800 kN (about 80 ton-force) with a resolution and accuracy of 10 kN (about 1 ton-force). Greater inaccuracies would occur at the lower forces but these could be neglected since they were not in the area of interest. At the higher forces the linearity and repeatability improved, giving adequate accuracies.

On the strength of these tests, 20 mooring hooks were instrumented using strain gauges mounted on the side plates of the hooks (see Figure 3 and Photograph 2). The strain gauges are covered with an epoxy-coated aluminium die-cast box which apart from affording protection to the gauges, also houses the local electronics and line drivers.

The hooks are calibrated by means of an hydraulic jack, together with a calibrated load cell, various attachments and spacers. The jack applies a force between the bollard and the curve of the hook (between point A and B as shown in Figure 9). By taking into account the bending moment introduced about the rear pivot axis of the hook, a sufficiently accurate calibration curve was obtained.

9. FENDER FORCE MEASUREMENTS

Since tables are available which give the relationship between pressures in, and forces applied to, the fenders, it seemed that the monitoring of pressure in the fenders would provide the simplest method of determining the forces on the fenders. Tables are also available giving the relationship between fender deflection and force against the fender. Photographic measurements of fender deflection could therefore also be correlated with pressure measurements.

The attachment of the pressure transducer was simple, as a suitable outlet plug was available on the headplate of the fender and required only the insertion of an adaptor and throttle valve. Coupling the transducer to the jetty was a greater problem as the cable had to be flexible enough to

allow for the continuous movement of the fender due to wave and swell actions as well as the movement due to tidal variations. The problem was solved by using the coiled flexible cables used between trucks and trailers. Two such lengths joined together provided a sufficient extension to cater for the movements encountered.

The pressure transducer used is a Bell and Howell type with a range of 300 kPa absolute pressure. This provided a range of close to 200 kPa above atmospheric pressure. The fenders are maintained at a pressure of about 75 kPa gauge and the safety release operates at 175 kPa. Eight fenders were equipped with these pressure transducers (see Figure 3 and Photograph 3).

A local pressure transducer amplifier and line driver is mounted on the edge of the jetty in a protective housing. This converts the pressure transducer signal into one suitable for driving down a long line to the recording station. When fenders are being serviced or replaced, it is a relatively simple matter to remove the pressure transducer and the coiled cable from one fender and install it in the replacement fender.

10. SHIP MOTION MEASUREMENTS

10.1 Photographic Technique

Various methods were considered for measuring the motions of the moored ships. This can be done mechanically by attaching an instrument onto the ship, e.g. by a set of lines connected to potentiometers (see Stammers et al., 1977). Another possibility, which was chosen for Saldanha is a remote-sensing method. In this case a camera was installed at a fixed position to take photographs of the ship at 2 s intervals.

A relatively suitable vantage point for the installation of a camera was found at the top of the chimney at caisson No 18 (see Figure 3). From this position it was possible to determine the most important sway and yaw motions of the ship accurately, as well as the vertical motions of heave, roll and pitch. Only the surge motions could not be determined accurately from this position.

It is necessary to photograph fixed points behind the ship as well as fixed points on the jetty (see Figure 11). Furthermore, the forward mast, bridge and funnel of the ship must be included as target points on the ship. To include all these points for a large ship a lens with a focal length of about 100 mm was required. The large number of photographs to be taken required a camera with a large magazine and an automatic recording system. On the basis of these considerations a Robot Motor Recorder was chosen,

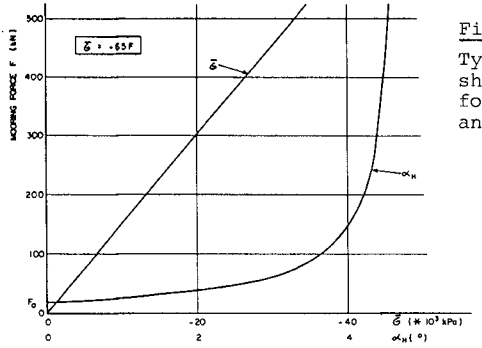

Figure 10:
Typical relationship between mooring force F, stress σ and lift angle α_H

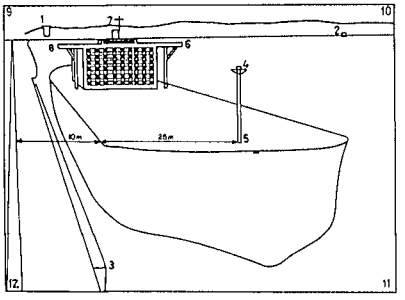

Figure 11:
Sketch of photograph of moored ship

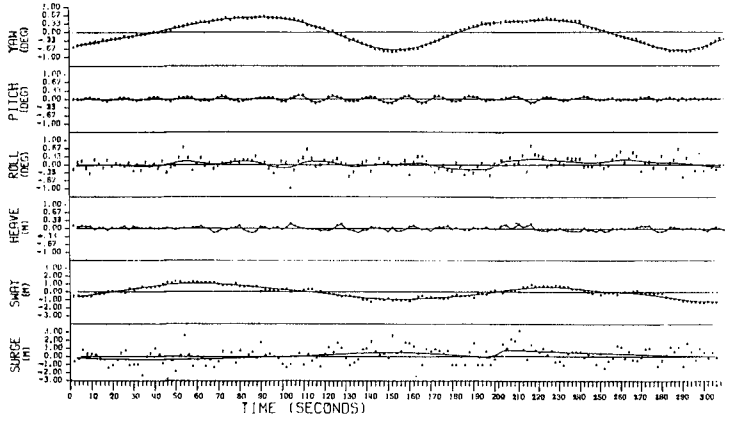

Figure 12: Results of analysis of digital moored ship photographs (run No SM003)

with a lens of 75 mm focal length and a magazine which could contain film for 1 600 frames of 18 by 24 mm.

10.2 Sonar Docking Device

The ore jetty is equipped with an Elac sonar docking device installed by the harbour authority for use by pilots during docking operations. The device makes use of two independent horizontally-looking ultrasonic echo sounders, one for the bow and the other for the stern of the ship. Each system has two transducers mounted in the water on the side of the jetty (see Figure 3). The decision as to which of the two transducers to use, was based on the size of the ship and the position of the ship alongside the jetty.

Measurements of speed of the bow and stern are made as well as of the distance of the bow and stern from the jetty. It was decided that since the device was available, its outputs should be recorded to provide some back-up for and a check on the photographic recording system.

11. DATA ACQUISITION

11.1 Central Data Acquisition System

Most data acquisition is done at the central recording station at caisson No 14 (see Figure 3). This therefore means that all signals have to be transmitted from the various sensors to the recording station. It was decided to use a frequency-modulated system for the transmission of all signals to the recording station and this therefore led to the design of a general-purpose amplifier module to interface the sensors to the cabling system. The module includes an amplifier, voltage-to-frequency convertor and line driver. The amplifier stage can be adjusted to suit the output of the particular sensor, and the voltage-to-frequency convertor is set to suit the range required. Conventional 25-pair telephone cables are installed along the length of the jetty with junction boxes at each caisson. The amplifier modules are installed as close to the sensors as possible and are connected via two-pair telephone cables to the junction boxes on the respective caissons. At the recording station all the frequency modulated signals are fed via phase-locked loops (for filtering and signal conditioning) to the recording system.

The data-acquisition system, DAS (see photograph 4), is an exact copy of the data-acquisition system used in the NRIO coastal engineering model hall (Holroyd, 1980). It is based on the NRIO microcomputer system (Holroyd, 1982) and, in line with the general approach of the Institute, uses digital cassettes as the storage medium. The DAS is split between the continuous monitoring section and the section which operates only when ship monitoring is being done.

The continuous monitor is permanently on power and automatically logs data from the wind sensors and the swell sensor at caisson No. 14. Wind data include the average wind speed, the average wind direction and the highest gust speed for each 15-minute interval. These data are accumulated in the computer's memory over a 12-hour period and are written onto the cassette at 06h00 and 18h00 as a complete data file covering the past 12 hours. At noon and midnight swell data files are recorded for a two-hour period with a two-second sampling interval.

The ship monitoring section of the DAS includes the central control unit, with keyboard and VDU, and five data logging units all connected to and controlled from the central control unit. The central control unit is used to initiate a monitoring run, insert header information, such as the ship's name, and generally acts as a communication link for commands to and prompts from the data-logging units. It was decided to use five data logger units because of the volume of data being collected during a monitoring run. This has the added advantage that the data from each group of sensors are stored on a different cassette, therefore simplifying the subsequent sorting of the data during the analysis stage. All inputs are synchronously sampled at two second intervals and a direct measurement is made of the frequency from the sensor amplifiers.

All data are stored onto digital cassettes in a properly file organised format with headers giving real-time, the type of data, the data format as well as information entered by the operator during initialization. The data are allocated to the logging units as follows:

Unit 1 - sonar docking device, bow and stern, speed and distance from jetty
Unit 2 - six long swell sensors
Unit 3 - X and Y current speed from Simrad HC100 current meter
Unit 4 - eight fender force sensors plus six mooring hook force sensors
Unit 5 - fourteen mooring hook force sensors.

The DAS includes a cassette reader and a printer which permits **in situ** checking of the system's performance. Another important built-in maintenance aid permits the display of the sensor line frequencies on the VDU, simplifying checks on sensor performance and calibration.

11.2 Other Data

It was not feasible to store all recorded data at the central data-acquisition system on Memodyne cassettes. The waverider data logger is already an automatic recording system with an accurate time base. Besides graphical

recording of the wave history, the signal is sampled every 0,5 s and the values written onto Memodyne cassette four times a day, namely, at 00h00, 06h00, 12h00 and 18h00 GMT. These tapes are spectrally analysed at NRIO using a standard FFT program.

The data from the tide recorder are recorded only graphically. However, any long period oscillations can be easily noticed. Also the actual water levels during the presence of a ship can be read off directly. Both the waverider data logger and the tide recorder are installed at the Port Administration Building (see Figure 2), where they are also used to provide normal harbour operational data.

12. DATA PROCESSING AND ANALYSES

12.1 Digital Data

The in-house data processing system has extensive facilities for reading cassette tapes. Quick look and edit programs are available for checking the data on cassettes, scaling the data according to the calibration values for each sensor and transferring the data onto nine-track magnetic tapes in a standard ASCII-coded file format.

These data are then read from the tape and stored on high-density archive tape at the CDC Cyber 170/750 computer at the Centre for Computing Services of the CSIR. The data from each channel will be spectrally analysed using programs based on the autocovariance method. Directly related spectra can be analysed further using cross-correlation techniques, while also time-history plots of the various signals may show any correlation by visual inspection.

12.2 Photographic Data

12.2.1 Digitizing technique

After the films of the moored ship have been developed, the negatives are projected onto a digitizing tablet where the coordinates of three fixed shore points, of five points on the ship and of the corners of the frame are determined and stored on cassette tape.

The coordinates of the fixed shore points (1 to 3 in Figure 11) relative to those of the corner points of the frame (9 to 12) are used to compute the orientation of the camera and a coordinate system with its origin at the camera position is defined. Also the fixed points 1 to 3 are used to compute the scale of the projection. The projected height of the forward mast (from points 4 and 5) relative to the real height is used to compute the instantaneous distance of the ship relative to the camera, which yields the surge motion of the ship after projecting the

distance to the camera to a horizontal plane. The top of the forward mast (point 4), the bridge tip (either point 6 or 8) and the top of the funnel or radar mast (point 7) are used to compute the motions of the ship relative to the camera-based coordinate system. After this system has been transformed to a horizontal coordinate system the instantaneous motions of sway, heave, roll, pitch and yaw can be determined.

The process of digitising is controlled by a Tektronix 4051 desk top calculator. After the digitizing is completed the data files on tapes are transfered to disc storage at NRIO's in-house HP 21 ME minicomputer and from there transformed into ASCII code and written onto nine-track magnetic tape. From here the data are treated in the same way as the digital data described in Section 12.1 are.

12.2.2 Analysis program and ship motion results

A computer analysis program has been developed to compute the motions of the ship in six degrees of freedom, using the coordinates determined with the digitizing tablet. A typical raw result of this analysis is shown in Figure 12. It can be seen that the surge motion has the largest scatter, while sway and yaw show a very smooth variation with periods of about 100 s and almost in phase. Heave and pitch show oscillations with periods of about 16 s, which is slightly above the dominant swell period of about 14 s.

13. PROBLEMS

A number of problems were encountered during the installation period and some are still present. As already mentioned in Section 6 it was known that very active marine growth occurs at Saldanha Bay, especially barnacles, red bait and black mussels. These animals grow so rapidly that they can choke the aperture of pressure gauges. Although copper gauze was used to protect apertures, this toxic metal proved to be ineffective and regular mechanical cleaning by divers has to be performed to keep the instruments functioning.

Another problem is strong corrosion of the metals in the sea water. Initially, copper was used in order to control the marine growth at the instruments. Stainless steel was also used because copper is not a very strong and elastic material. Therefore, initially stainless steel Hilti bolts were used to fasten clamps, brackets and instruments under water. Some instruments were made of stainless steel, such as the Simrad current meter. However, serious galvanic corrosion occurred between copper and stainless steel, as well as mutually between stainless steel when parts of the surface became active due to lack of oxygen. Even the

application of zinc anodes did not prevent galvanic corrosion.

The system of sensors along the jetty requires many long lengths of cables which carry signals to the main telephone cables or directly to the recording station. Many of these cables are in fairly vulnerable positions and can easily be damaged during normal mooring operations. Even though cable damage is less than expected, it is still necessary to inspect cables regularly for wear or damage.

Iron ore dust is everywhere and is hostile to electronic circuitry. Keeping the electronic units such as the remote amplifiers clean during installation, repair or calibration is not easy. This task is often made more difficult by unfavourable weather conditions. On some occasions the presence of strong winds, swell and sea spray make repair work impossible.

The scatter of the surge motion results is very large. Attention should be given to determining surge more accurately.

14. CONCLUSIONS

On the basis of the results obtained so far it can be concluded that the various instruments are effective in yielding the required quantitative data for the moored ship investigations. The strain-gauged mooring hooks do not show a significant drift during short periods of measurements; regular recalibration checks are, however, necessary. The flexible coiled cable has also proved to be an adequate connection between the continuously moving fenders and the caissons.

The most important motions of the moored ship, namely, sway and yaw which form the most serious problem, are effectively and accurately determined by using the Robot Motor Recorder and computer analysis system. The central data acquisition system, particularly is very useful in recording the monitored data on a mutual time base.

Preliminary results of the analysis of long-wave data and ship motion data show that wave energy is present at periods between 50 and 150 s, while natural periods of horizontal oscillations of moored ships have been shown to be in this same range. It is expected that further correlation of environmental and ship dynamics data will permit the determination of firm relationships between cause and effect of the moored ship problems, when a sufficient number of problem cases have been monitored.

Acknowledgements

The authors wish to thank the South African Transport Services for their cooperation in the installation, maintenance and operation of the monitoring equipment, as well as for permission to publish this paper.

REFERENCES

BOWERS, E C (1975). Long period oscillations of moored ships subjected to short wave seas. The Royal Institution of Naval Architects, Transactions, Paper W4.

HOLROYD, S G (1980). Coastal engineering model hall data-acquisition system. CSIR Research Report 383.

HOLROYD, S G (1982). NRIO microcomputer system. CSIR Technical Report T/SEA 8134.

KEITH, J M and MURPHY, E J (1970). Harbor study for San Nicolas Bay, Peru. Journal of the Waterways and Harbors Division, ASCE, Vol 96, No WW2.

NAGAI, S, ODA, K AND LEE, T T (1977). Impact forces, mooring forces and motions of super-tankers at offshore terminals subjected to wave actions. Proc. 24th Congress of PIANC, Leningrad.

STAMMERS, A J, BROCKBANK, R AND WENNINK, C J (1977). Investigation of vessel mooring subject to wave action. The Dock and Harbour Authority, Vol 57, No 677.

WILSON, B W (1954). The mechanism of seiches in Table Bay Harbour, Cape Town. Proc. 4th Conference on Coastal Engineering, Chicago.

WILSON, B W (1972). Sishen-Saldanha Project. Iron ore loading terminal, Saldanha Bay, oceanographic engineering evaluation. Pasadena.

SHIP MOTIONS RELATED TO DEEP DRAFT CHANNEL DESIGN

By Scott Noble, [1] A.M. ASCE

ABSTRACT: This paper discusses the investigation that the U.S. Army Corps of Engineers, Portland District undertook for possible modifications to the Columbia River entrance channel. Because of the characteristically high sea conditions at this location, wave induced ship motions were considered an important criteria to be evaluated. Phototype ship motion measurements were obtained along with wave data. The data and preliminary results are summarized. Emphasis is given to the analysis of a relationship between environmental conditions and vertical excursions, and the subsequent use of the relationship to determine a new channel depth.

INTRODUCTION

In 1972, a resolution was adopted by the Public Works Committee of the United States Senate directing the Corps of Engineers to investigate the feasibility of modifying the entrance channel to the Columbia River, especially with regard to providing deeper depths. The Columbia River Port authorities, who lobbied for the resolution, felt that a deeper channel was necessary to bring the entrance channel in-line with the river channel as well as to allow larger ships to transit the system in the future. In the early phases of the investigation it was determined that insufficient data were available to permit an accurate design of the channel. This was especially true since sea conditions in this area are notoriously rough and analytic procedures to determine channel depths where wave induced ship motions are a primary design factor are scarce. Therefore, a prototype ship motion monitoring program was initiated that was to provide the criteria with which to base the modifications. References (4,5,6) contain detailed discussions of the field work, data results and initial analyses. The present paper will discuss further analysis of the data and its application

---

[1]Vice Pres., Noble Coastal & Harbor Engineering, Ltd., Tiburon, CA., U.S.A., during study Project Engr., U.S. Army Corps of Engineers, Portland Dist., Portland, OR, U.S.A.

to the determination of modified channel dimensions. Previously presented information will however be summarized.

The Columbia River rises on the west slope of the Continental Divide in British Columbia and flows approximately 1,200 miles (1,900 km) to the Pacific Ocean, approximately 745 miles (1,200 km) in the United States. As shown in Figure 1, the river also forms the natural border between the states of Oregon and Washington. The river is a major artery for the transportation of goods to domestic and international markets. An annual average of about 23 million tons (21 million m tons) are transported past the mouth of the river by roughly 2,000 vessels.

Congress has delegated to the Corps of Engineers the responsibility for construction and maintenance of Federal navigation projects. Portland District has those responsibilities for over 40 seperate projects in Oregon and Washington. The project at the entrance, shown in Figure 2, provides for a channel 48 ft (14.6m) deep, measured from the plane of mean lower low water (mllw), 2,640 ft (805 m) wide and about 5 miles (8 km) long. The channel is to be secured by two rubble-mound jetties, a spur jetty, Jetty A, on the north shore and by dredging. Maintenance dredging is primarily performed by the hopper dredge BIDDLE, which historically has averaged about 4.5 million cu yd (3.4 million m^3) annually. The deep-draft river channel then proceeds from the mouth to the Portland-Vancouver area some 102 miles (165 km). The primary dimensions of this project are 40 ft (12.2 m) deep by 600 ft (183 m) wide. Annual maintenance dredging of this project is roughly 5 million cu yd (3.8 million m^3).

DATA COLLECTION

The monitoring program involved acquiring ship motion and wave data. This was done so that a correlation between environmental conditions and ship motions could be investigated.

Ship Motion Measurements - During the periods of May - June 1978, October 1978 - March 1979, and October 1979 - March 1980 a total of 53 deep-draft vessels were monitored. The field work was accomplished through a contract with Tetra Tech, Inc. Basically, a two-man field team boarded the vessels at the point of departure and recorded measurements during the approximately half hour necessary to transit the entrance. Measurements were made of vessel vertical acceleration (heave), pitch, roll, heading, and position continuously. The data were then reduced and analyzed to generate time histories and distributions of bow, stern and side excursions, vessel

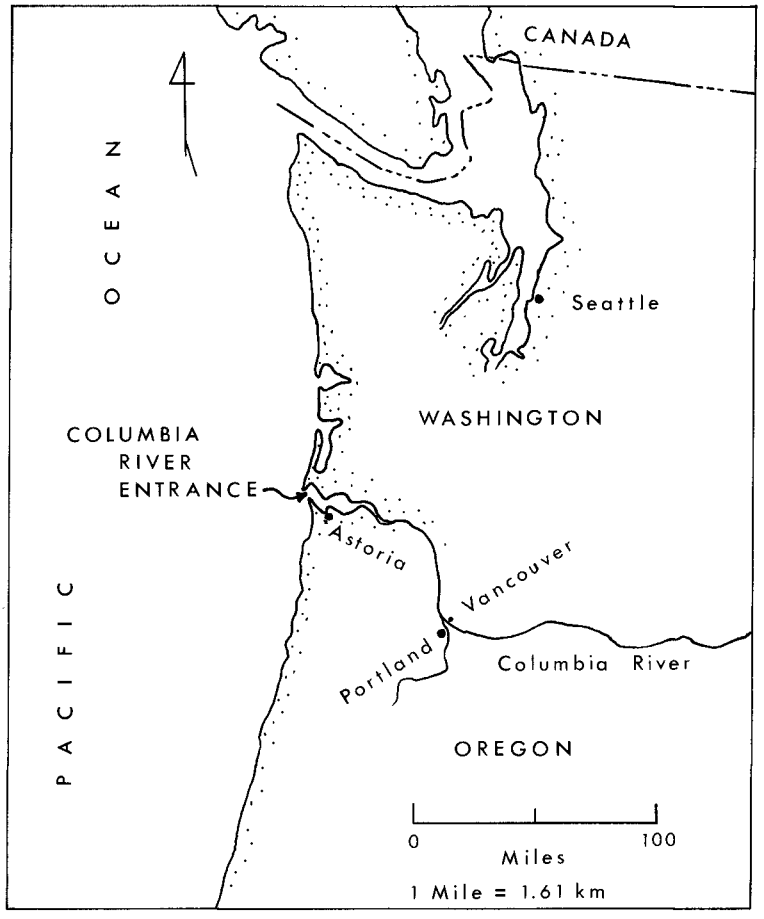

FIG. 1- VICINITY MAP

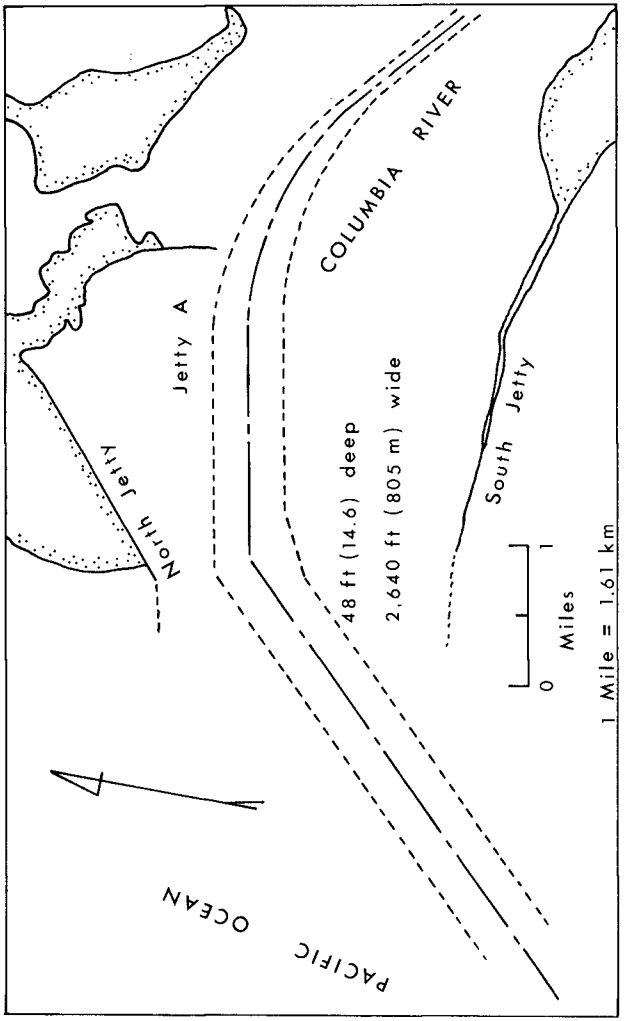

FIG. 2- COLUMBIA RIVER ENTRANCE

heading and yaw, as well as of the recorded motions. - The excusion is the vertical movement of a particular point on the vessel relative to its still water position.

With the aid of the Port of Portland, arrangements were made to monitor Chevron tankers, Weyerhaeuser bulk carriers, Japanese and Matson line container carriers, and an auto carrier. Table 1 gives the principal dimensions for the vessels monitored. The monitored vessels resemble the distribution of vessels that transit the Columbia River.

Wave Data Gathering

Under the guidance of the Corps of Engineers Coastal Engineering Research Center waverider buoys were deployed in the entrance area and offshore to measure wave height and period, and a wave imaging radar unit was used to obtain wave direction, length and transformation characteristics over a broad region. Numerous difficulties were experienced in getting the equipment operating properly and maintaining the operation. The buoys were hard to keep on station because of the rough sea conditions experienced there and the high density of commercial and pleasure craft. Other sources of data were also utilized to provide information on wave conditions throughout the monitoring period. These included visual observations of sea conditions made by the two man field crew aboard the instrumented ships; and, wave measuring instrumentation placed on the Columbia River entrance navigation buoy just outside the entrance. A comparison of the visual observations with coincidently recorded significant wave heights indicated that the observations were a reliable source of information.

DATA RESULTS

Although the study was concerned with both vertical and horizontal motions, this paper will deal with just the vertical motion results and the implication to channel depth design.

Ship Motion Results - Out of the 53 voyages monitored, 51 complete sets of vertical motions were obtained. Equipment failure occurred during two of the crossings. Table 2 is a tabulation of the cumulative percent frequency of occurrence for the average and maximum heave, roll and pitch values. The table indicates the magnitude of motion that is exceeded by a certain percentage of the crossings. For instance the table shows that 25 percent of the voyages had a maximum heave, roll and pitch value of at least 6.0 ft (1.8 m), 5.7 deg and 2.1 deg, respectively.

TABLE 1. - Monitored Vessel Dimensions

	Vessel Type (1)	Length overall, in feet (2)	Beam, in feet (3)	Design Draft, in feet (4)	Dead Weight Tonnage, in tons (5)
	Oil Carriers				
1.	Chevron Gas Turbines	651	96	34	35,000
2.	HILLYER BROWN	523	68	32	18,000
	Container Carriers				
3.	ALASKA MARU	685	98	34	23,000
4.	BEISHU MARU	697	98	34	24,000
5.	GOLDEN ARROW	616	82	35	19,000
6.	HIKAWA MARU	700	101	34	23,000
7.	LION'S GATE BRIDGE	718	102	36	27,000
8.	MAUNA LEI	630	71	32	18,000
	Bulk Carriers				
9.	HOEGH M CLASS	695	101	33	36,100
	Auto Carriers				
10.	WORLD WING	566	90	29	23,000

Note: 1 ft = 0.305 m; 1 ton = 1.016 Kg

The next step in the preliminary analysis was to convert the preliminary motions into vertical excursions. This was done by combining the heave and pitch to determine bow and stern excursion, and combining the heave and roll to determine side excursion. In the analysis the center-of-gravity was assumed to be the point-of-rotation. Table 3 is a tabulation of the cumulative percent frequency of occurrence for the average and maximum bow, stern and side excursions. The table shows that 25 percent of the voyages had an average bow, stern and side excursion of at least 5.3 ft (1.6 m), 2.6 ft (0.8 m) and 2.6 ft (0.8 m), respectively. Similarly, 25 percent of the voyages had a maximum bow, stern and side excursion of at least 15.0 ft (4.6 m), 7.4 ft (2.3 m) and 7.1 ft (2.2 m). The table indicates that the bow and stern excursion are the critical excursions to consider in the channel design.

Wave Data - As mentioned previously, wave data was gathered from a few sources. During the monitoring program 5 percent of the voyages had waves in excess of 15 ft (4.6 m) high. Most of the waves were however below 10 ft (3 m). Wave periods were generally 10 seconds but ranged between about 6 to 17 seconds. Wave directions near the Columbia River are predominantly from the west to northwest but storms generally come from the southwest. The wave directions observed during the monitoring program also tended to follow this pattern.

DATA ANALYSIS

After the initial data reduction and analysis, the object of the study was to relate the ship motions to the environmental conditions. If a satisfactory relationship could be obtained, then an appropriate channel depth could be determined based upon a design wave condition.

As a design procedure, we were interested in the maximum motions, although the best relationship did not occur with the maximum values. The reason for this is that the maximum motion is dependent on the wave height, length and direction at the time and location that the maximum motion occurs. Since we did not obtain this detailed wave data, nor did we attempt to, and since wave conditions at the Columbia River vary greatly throughout the entrance area, a relationship other than with the maximum motion was sought. Since basic wave conditions, as obtained during the field study, should be indicative of average conditions, a relationship between average motions and wave conditions was investigated. Then, as shown by Wang (5) the maximum motion, or a motion with some other cumulative percent frequencey of occurrence, could be determined utilizing the Rayleigh distribution. For example, the motion with a 90 percent cumulative frequency of occurrence during a particular voyage could be determined from the average

TABLE 2. - Summary of Heave, Roll and Pitch Motions

Cumulative Percent Frequency Occurrence (1)	Heave, in feet Avg (2)	Max (3)	Roll, in degrees Avg (4)	Max (5)	Pitch in degrees Avg (6)	Max (7)
75	0.8	2.0	0.8	2.3	0.4	0.9
50	1.3	3.6	1.3	3.8	0.5	1.3
25	2.2	6.0	2.2	5.7	0.7	2.1
10	2.8	8.4	3.1	13.0	1.2	2.9
5	3.1	9.7	5.1	13.4	1.7	4.9
maximum	4.1	12.4	5.5	17.5	2.2	6.0

Note: 1 ft = 0.305 m

TABLE 3. - Summary of Bow, Stern and Side Excursions

Cumulative Percent Frequency Occurrence (1)	Bow Excursion, in feet Avg (2)	Max (3)	Stern Excursion, in feet Avg (4)	Max (5)	Side Excursion, in feet Avg (6)	Max (7)
75	1.8	4.8	1.2	3.0	1.4	3.6
50	2.9	9.0	1.7	4.5	2.0	4.8
25	5.3	15.0	2.6	7.4	2.6	7.1
10	7.9	19.4	4.5	12.1	3.8	10.4
5	9.5	20.3	9.8	21.9	4.0	12.7
maximum	11.2	22.9	10.8	25.7	4.9	16.1

Note: 1 ft = 0.305 m

motion.

To begin the investigation into a possible relationship between average motions and environmental conditions use was made of Lundgren (1). In his general report to the 1965 PIANC Congress on the subject of ship motions due to waves, he listed 5 dimensionless parameters as principal variables. These variables were:

1. Wave height to ship draft ratio (H/D)
2. Encounter period of ship to natural response period of ship ratio (Te/Tp:Tp for the case of pitch period)
3. Relative wave length in direction of ship to ship length ratio (Lr/LOA)
4. Depth of water to ship draft ratio (d/D)
5. Wave direction relative to ship.

As the initial results showed, and later analysis clarified, the critical motions occurred at the bow or stern of the ship, and these motions were most dependent on the wave height and encounter period. The wave height, as would be expected, has the most influence on the magnitude of the motions. From the initial results, it was apparent that the outbound voyages generally exhibited greater motions than inbound voyages, indicating that shorter encounter periods cause greater bow/stern motions than longer periods. Following through with this thinking, a "best fit" relationship was determined using the independent variables wave height, natural pitch period, and encounter period of the ship. The dependent variable was the average bow or stern excursion. In the statistical analysis the greater of the 2 excursions was used. The relationship, as shown in Figure 3 is:

$$E\ (avg) = 0.57 + 0.99\ (HTp/Te)....(Ft)....(1)$$

The 95 percent confidence limits are also shown in the figure. The correlation coefficient (r^2) for the relationship is 0.86. The values used to derive the relationship are listed in table 4, with vessel type being referred back to table 1.

As the above equation shows, average excursion increases as wave height increases and/or the ratio of ship's natural pitch period to encounter period increases. While the excursion is predominantly related to wave height, the period ratio accounts for additional variance in the excursion. Of the two period variables, the encounter period has a much wider range than the natural pitch period, and thus is the dominant component of the ratio. The following

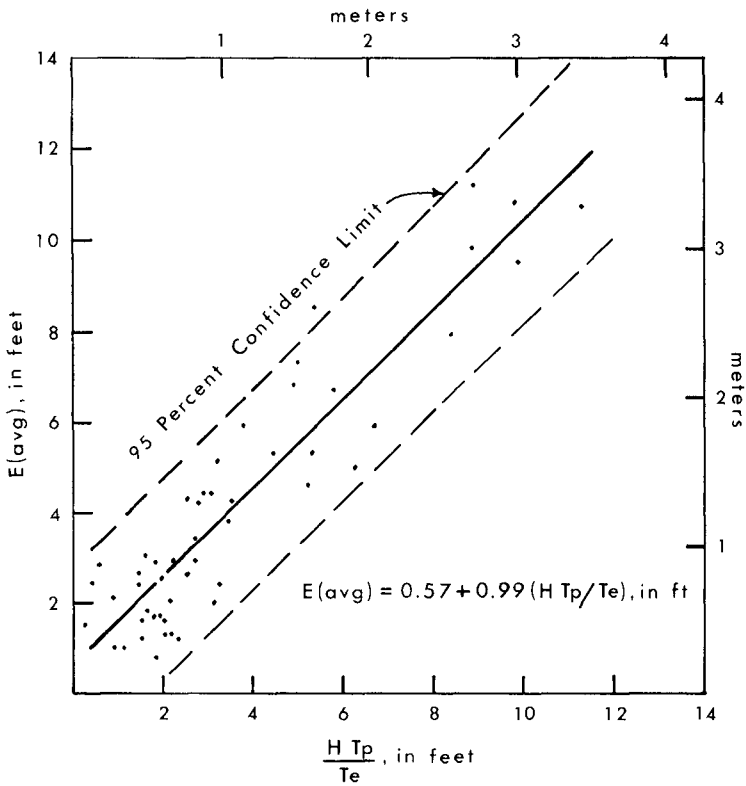

FIG. 3 - SHIP EXCURSION REGRESSION RELATIONSHIP

TABLE 4. - Primary Ship Motion Variables

Voyage no. (1)	Vessel[a] type (2)	Average[b] excursion, in feet (3)	Wave height, in feet (4)	Encounter period, in seconds (5)	Natural pitch period in seconds (6)
1	1	7.3	7.0	8.0	5.7
2	1	4.2	6.0	12.5	5.8
3	9	2.6	4.0	13.5	4.9
4	9	2.8	2.0	17.0	5.0
5	1	4.6	9.0	10.2	5.9
6	9	2.0	5.0	8.3	5.2
7	9	3.4	3.0	5.8	5.3
8	1	5.3	10.0	11.0	5.8
9	1	5.9	11.0	8.7	5.3
10	1	5.3	6.0	7.8	5.8
11	1	4.4	5.0	7.9	4.8
12	3	2.4	6.0	20.2	4.8
13	1	2.4	1.0	14.1	5.8
14	1	8.5	9.0	7.7	4.6
15	2	9.8	18.0	10.4	5.1
16	2	10.7	15.0	6.8	5.1
17	3	1.5	1.0	16.8	4.7
18	8	2.6	5.0	9.9	5.0
19	8	10.8	17.0	8.9	5.1
20	6	2.5	8.9	21.0	4.7
21	5	4.4	10.7	18.1	4.9
22	3	4.2	10.6	14.8	4.9
23	7	2.9	10.0	18.8	5.1
24	4	1.8	6.0	17.8	4.8
25	5	2.1	4.0	22.3	5.2
26	3	1.6	7.0	23.2	5.0
27	4	3.0	5.0	15.3	4.9
28	1	4.3	6.0	12.1	5.2
29	1	5.1	5.0	7.8	5.0
30	1	1.3	3.8	10.7	5.8
31	1	11.2	20.1	11.6	5.1
32	3	2.9	7.0	16.7	5.4
33	9	1.2	3.9	14.8	5.8
34	9	5.0	7.2	6.8	5.9
35	8	6.7	9.8	9.3	5.5
36	5	1.7	7.4	22.0	5.4
37	9	1.2	7.8	18.0	5.4
38	9	N.A.	12.6	5.4	5.6
39	1	0.8	4.3	13.6	5.8
40	1	7.9	12.9	8.0	5.2
41	6	1.0	4.0	22.4	5.0
42	5	1.3	5.3	13.7	5.5
43	10	1.6	7.5	20.3	5.4
44	10	9.5	14.3	7.7	5.3
45	9	1.7	5.5	16.9	5.9

TABLE 4. - Continued

(1)	(2)	(3)	(4)	(5)	(6)
46	9	6.8	5.0	5.9	6.0
47	8	2.0	6.3	16.2	5.6
48	7	2.9	7.9	22.6	5.2
49	9	N.A.	9.6	16.9	N.A.
50	9	5.9	8.0	12.7	6.0
51	5	2.4	9.9	16.8	5.5
52	3	3.8	9.0	14.1	5.4
53	9	1.0	3.0	15.1	5.6

[a]See table 1 for dimensions of vessels

[b]Average excursion at bow or stern whichever is greater

Note: 1 ft = 0.305 m

paragraphs briefly describe the independent variables.

The wave height used in the formulation of the equation was the measured significant wave height closest to the time of transit, when measurements were made. Precedence was given to channel measurements, and then to measurements made off the entrance. For the remainder of the transits visual observations by monitoring crew were used. Observations were taken as indicative of the significant wave height.

The natural pitch period is a function of vessel length, beam, and loaded condition (draft, displacement, and center of gravity). The method described in Myers (2) was used to determine the natural pitch period of the 51 vessel crossings for the regression analysis. The natural pitch period was calculated by:

$$Tp \triangleq 1.108\ Kxx/GM\ (L)^{\frac{1}{2}} \quad \ldots. \text{ (U.S. Customary Units)} \ldots. (2)$$

The position of the center of gravity (cg) needs to be known to calculate GM(L). The natural pitch period ranged between 4.6 and 6.0 seconds for the vessels monitored. In the design the distance from the center of buoyancy to the metacenter is used as an estimator of GM(L).

The encounter period is the wave period relative to the moving ship and is a function of wave period and direction, and ship speed and course. The equation to determine encounter period is,

$$Te = Tw/\ (1 - 2\ \pi\ (1.689\ VcosB)gTw). \text{(U.S. Customary Units)} (3)$$

CHANNEL DESIGN

In the case of the Columbia River most of the deep draft traffic travels the approximately 102 miles (165 Km) to the Portland-Vancouver area. The river channel is therefore an important aspect of the movement of commerce. For this reason the primary assumption in the design of the entrance channel was to determine a depth that would bring the entrance channel in-line with the river channel. In other words, the design vessel for the river channel would also be used as the design vessel for the entrance channel. Specifically, the design vessel for the entrance channel was chosen to be that vessel which could transit the river channel approximately 95 percent of the time. It was also decided to consider the largest grain vessel that could transit the river channel (grain being the greatest commodity moved on the system); and, the largest vessel that could call at the Port of Astoria, which is located near the entrance where a vessel could play the tides. Table 5

lists the dimensions of the vessels considered in the study.

TABLE 5. - Dimensions of Design Vessel and Others

Vessel (1)	Draft, in feet (2)	Length overall, in feet (3)	Beam, in feet (4)	Dead weight tonnage, in tons (5)
Design Vessel	35	650	90	40,000
Largest-Grain	39	700	100	50,000
Largest-Astoria	43	780	105	70,000

Note: 1 ft = 0.305 m; 1 ton = 1,016 kg

The basic equation used in the design of the channel depth was:

$$d + T = D + E + t + C \quad \ldots\ldots \quad (4)$$

or,

$$d = D + E + t + C - T \ldots \quad (5)$$

A few points need to be made about the equation and its specific application to the Columbia River entrance. The design of the channel was predicated on a design excursion that is exceeded only 5 percent of the time when waves are less than or equal to about 10 ft (3 m) high. The reason for this was that when waves are higher than this level other factors come into play; e.g., the pilot can slow the vessel to minimize motions, or higher tide levels can be played. Vessel squat was not specifically designated in equation (4). The 2 reasons for this are that the measurement technique indirectly accounted for squat by measuring any movement, whether long term or short term; and, the 2 mile (3.2 km) wide opening will not induce much of a squat phenomenon. The last comment is that for the design the tidal elevation was taken as 0 mean lower low water, the vessel trim was assumed to be 1 ft (.3 m), and the minimum clearance was assumed to be 2 ft (0.6 m).

As stated earlier, the distribution of excursions on an individual voyage follows the Rayleigh distribution. For the case of ship motions this distribution can be stated as:

$$p = 1 - \exp\left(- (E(p)/E(\text{rms}))^2 \right) \ldots\ldots\ldots \quad (6)$$

The equation can be rearranged to read,

$$E(p) = E(rms) (-\ln (1-p))^{\frac{1}{2}} \quad \ldots\ldots\ldots (7)$$

Since the cumulative Rayleigh distribution results in,

$$E(rms) = 1.13\ E(avg) \quad \ldots\ldots\ldots\ldots\ldots (8)$$

then,

$$E(p) = 1.13\ E(avg) (-\ln (1-p))^{\frac{1}{2}} \quad \ldots\ldots (9)$$

It was also assumed that the critical excursion for a particular voyage would be E(95) as opposed to either the average or the maximum excursion. Therefore, the critical excursion would be

$$E(95) = 1.13\ E(avg) (-\ln (1-.95))^{\frac{1}{2}} \quad \ldots (10)$$

or,

$$E(95) = 1.96\ E(avg) \quad \ldots\ldots\ldots\ldots\ldots (11)$$

The upper 95 percent confidence level was used in the determination of E(avg).

Instead of designing the channel based on a particular wave condition, it was decided to base the design on the distribution of all waves below the 10 ft value mentioned previously. The basic wave data were obtained from a National Marine Consultants (3) wave hindcast study. Use was then made of a 1978 refraction study of the Columbia River entrance performed by the Waterways Experiment Station for the Portland District. The refraction results were used to obtain a distribution of swell characteristics just outside the entrance. A comparison was then made between wave data collected in the entrance and data collected outside the entrance during the ship motion study. It was determined that on the average, waves are approximately 10 percent higher in the entrance than outside the entrance. This factor was used to modify the hindcasted annual wave distribution for the design analysis. By considering the frequencey of occurrence of each wave condition, a distribution of the critical excursion (critical excursion being the E(95) of a voyage under a particular set of conditions) was obtained for a particular vessel. Figure 4 is the resulting distribution of E(95) for the design vessel. The meaning of Figure 4, for example, is that over a long period of time 50 percent of the transits of the design vessel during the year will have an E(95) that will not exceed approximately 9.5 ft (2.9 m).

As stated previously, the channel was to be designed so that passage is available 95 percent of the time under

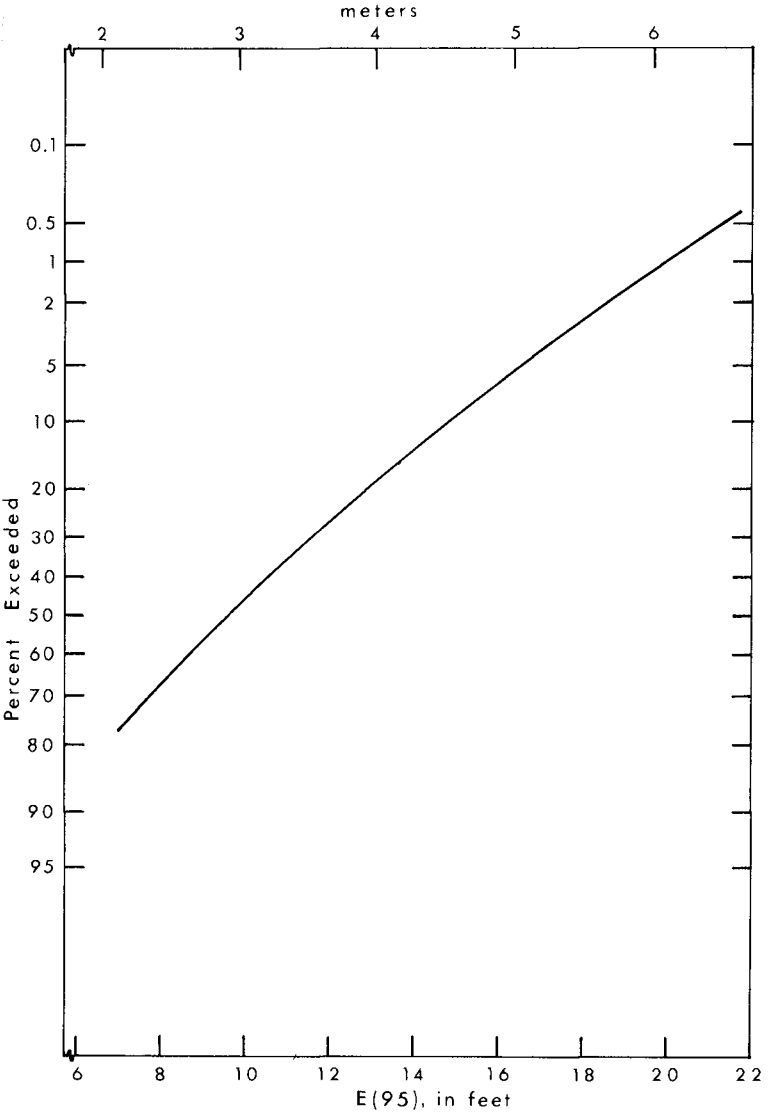

FIG. 4 - DISTRIBUTION OF E(95) FOR THE DESIGN VESSEL

certain wave and tide conditions. Therefore, from Figure 4 the design excursion (E) was determined to be 16.5 ft (5.0 m). From equation (5) the design depth is determined to be

$$d = 35.0 + 16.5 + 1.0 + 2.0 - 0 \approx 54.5 \text{ ft } (16.6 \text{ m}) \quad (12)$$

Therefore, an entrance channel of at least 54.5 ft (16.6 m) is necessary to bring the entrance channel in-line with the river channel.

The same procedure is followed to determine a depth associated with the other vessels. Table 6 is a summary of the design excursion and channel depth required for all vessels assuming a mllw tide level.

TABLE 6. - Channel Depth Requirements

Vessel (1)	Draft, in feet (2)	Excursion, in feet, (3)	Channel Depth, in feet, mllw (4)
Design Vessel	35	16.5	54.5
Largest Grain	39	16.8	58.8
Largest - Astoria	43	17.0	63.0

Note: 1 ft = 0.305 m

SUMMARY AND CONCLUSIONS

Since the completion of the ship motion study a feasibility report recommending an entrance channel depth of 55.0 ft (16.8 m) has been forwarded from Portland District Office of the Corps of Engineers. It is anticipated that this depth will provide a channel that can be utilized by the design vessel essentially all the time. Vessels larger than the design vessel, or vessels with higher motion response functions, may have to modify their operating procedures at times to transit the entrance. This may require reducing speed to minimize motions, playing the tides, or waiting for calmer conditions.

The equation (eqn 1) relating average bow or stern excursion to wave height, encounter period and natural pitch period can be utilized at other coastal entrances to aid in channel design. Other sources of information should also be consulted when ships much larger or differthan those considered in this particular study are the

primary design vessels. Hopefully in the future enough information will be analyzed from various sources to propose design guidelines bracketing all possibilities.

ACKNOWLEDGEMENTS

The work described in this paper was accomplished while the author was employed by the Portland District, Corps of Engineers. The author wishes to thank Mr. Gene Pospisil, his immediate supervisor at that time, for permission to present this material.

APPENDIX I. - REFERENCES

1. Lundgren, H., General Report - Section II Subject 2, Proceedings of XXI Congress, Permanent International Association of Navigation Congresses, Stockholm, 1965.
2. Myers, J.J. et al., Handbook of Ocean and Underwater Engineering, McGraw-Hill Book Co., 1969.
3. National Marine Consultants, "Wave Statistics for Three Deep Water Stations Along the Oregon-Washington Coast," for U.S. Army Corps of Engineers. Seattle and Portland Districts, May 1961.
4. Noble, S. and Herndon, H., "Prototype Ship Motion Measurements and Modeling Techniques Applied to a Channel Design," Proceedings of WODCON IX, WORLD Dredging Association, Oct. 1980, pp 403-415.
5. Wang, S. et al., "Columbia River Entrance Channel Deep-Draft Vessel Motion Study, Final Report," Tetra-Tech Report No. TC-3925, for U.S. Army Corps of Engineers, Portland District, September 1980.
6. Wang, S. and Noble, S., "Columbia River Entrance Channel Ship Motion Study," Journal of the Waterway, Port, Coastal, and Ocean Division, ASCE, Vol. 108, No. WW3, Aug. 1982, pp 291-305.

APPENDIX II - NOTATION

B = ships heading relative to wave direction
C = minimum underkeel clearance
D = vessel draft
d = channel depth
E = design vertical excursion
E(avg) = average vertical excursion
E(p) = vertical excursion with p percent of excursions less than value
E(rms) = root-mean-square vertical excursion
GM(L) = longitudinal metacentric height
g = gravitational acceleration
H = wave height
Kxx = radius of gyration about the transverse axis through the center of gravity
LOA = vessel length overall
Lr = wave length relative to ship heading
p = cumulative probability (less than or equal to)
r^2 = correlation coefficient
T = tidal elevation
Te = encounter period
Tp = natural pitch period
Tw = wave period
t = vessel trim (mean draft to bow or stern draft)
V = vessel speed

WAVE-INDUCED SHIP MOTIONS IN HARBOUR ENTRANCES - A FIELD STUDY

by

A C van Wyk*

ABSTRACT

Extensive field monitoring programmes were implemented to study the behaviour of deep-draught ships in the entrance channels to two major South African ports. These programmes form part of a study to assess the future accessibility of these ports to ships of greater draught.

This paper describes briefly the monitoring techniques and methods of data analysis used, and reviews the results with regard to the environmental conditions during the monitoring operations.

The prototype results on ship response to waves will provide valuable data for the calibration and validation of both mathematical and physical models. The results are also used to establish allowance criteria based on safe underkeel allowances for ships presently using these harbours.

1. INTRODUCTION

In 1978 the Ship Dynamics Division of the National Research Institute for Oceanology started an extensive study, on behalf of the South African Transport Services, to determine criteria for optimum use by deep-draught ships of the entrance channels to the two major South African export harbours under adverse sea conditions.

The coal harbour at Richards Bay on the east coast presently handles bulk carriers of up to 150 000 dwt (17 m draught in an outer channel depth of -24,0 m CD (Chart Datum)) while the ore harbour at Saldanha Bay on the west coast frequently accommodates vessels of up to 270 000 dwt (21 m draught in an outer channel depth of -23,7 m CD).

---

* Ship Dynamics Division, National Research Institute for Oceanology, Council for Scientific and Industrial Research, Stellenbosch, RSA

Safe use of the entrances with respect to underkeel allowance during adverse sea conditions has become a matter of considerable importance in the light of demands for handling larger ships and of the high costs involved in deepening the channels.

As part of the overall study, field monitoring programmes were implemented at these harbours to record the behaviour of the larger ships using the entrance channels under various environmental conditions. The data are needed to calibrate and validate the mathematical and physical models to be used in future studies and, also to update the provisional allowance criteria used at present which were based on limited results of earlier model studies.

This paper describes briefly the monitoring techniques and methods of data analysis (covered in detail by Zwamborn and Van Wyk, 1981) and reviews the results with regard to the wave conditions during the monitoring operations. Since the emphasis is entirely on wave-induced vertical motions, horizontal behaviour of the ship is considered only in order to determine the direction of wave approach relative to the ship.

2. FIELD MONITORING

Ship behaviour is recorded by a method of discrete time-interval photography. The monitoring technique, basically, comprises taking photographs, from a land-based station, at 2 s intervals, of each ship during her transit of the entrance channel. The photographic equipment consists of a motorized 35 mm camera fitted with a telephoto lens which enables behaviour of the ship to be monitored over a distance of roughly 2 km in the channel. Recording is therefore limited to daylight hours and when visibility is satisfactory.

The environmental conditions recorded during each event comprise the wind, the tide and, particularly, the waves. A waverider system provides, during monitoring, a continuous record of the waves in the vicinity of the entrance channel while the dominant wave direction is obtained from clinometer observations, radar wave images or pilot boat observations.

Each ship is also visited after arrival or before departure to obtain essential geometric details of the ship as well as the loading condition at the time of sailing.

Since August 1978 just over 200 different shipping events have been monitored, about 90 per cent of them at Richards Bay. These events were rated according to the severity of the wave climate as well as quality and extent of the records.

3. DATA PROCESSING AND ANALYSIS

3.1 Film Processing

To date the photographic records of the 70 top-rated events (all of which were recorded at Richards Bay) have been processed using a simple photogrammetric technique. The procedure consists of digitizing target points on the images of the ship on each film negative relative to a fixed coordinate system.

These coordinates, together with the geometry of the ship, are used to compute:

(i) the vertical motions of the target points on, and

(ii) the route, heading and speed of each ship.

The motions of the target points are used to derive:

(a) the three principal motions, namely, roll, pitch and heave, and

(b) the vertical wave-induced motions at the perpendiculars, shoulders and quarters of the ship due to roll, pitch and heave.

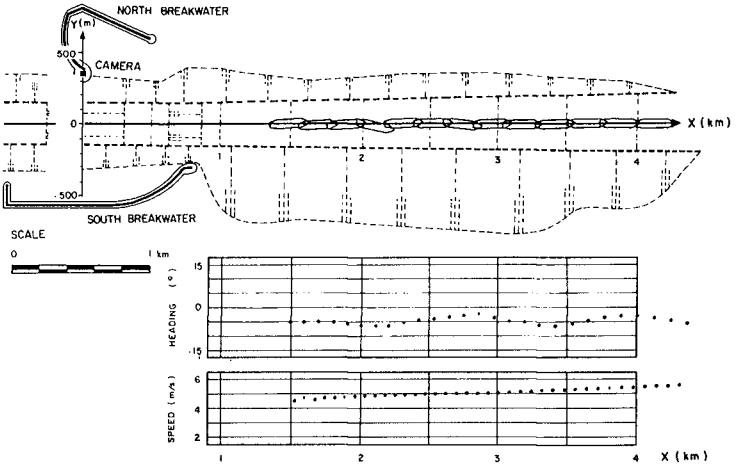

Figure 1.1 Ship trajectory for event R065

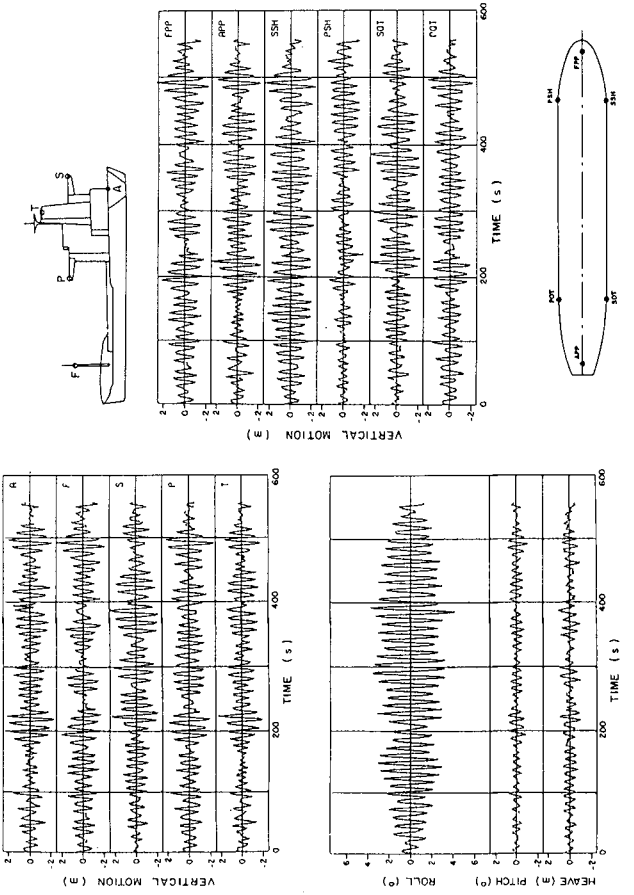

Figure 1.2 Sample motion time series for event R065

Examples of the results for a typical case study (event R065) are shown in Figures 1.1 and 1.2. Ship positioning relative to the channel coordinate system is believed to be accurate to within 50 m longitudinal and 10 m transverse. Heading angles relative to the channel orientation are accurate to about 1,5° and the speed of the ship averaged over intervals of 14 s is accurate to about 0,05 m/s. The vertical motions are subject to random measuring errors of about 0,1 m to 0,3 m depending on the distance from the camera to the ship (1 000 m to 3 000 m).

Since certain target points, particularly those chosen on the bow of departing ships, were frequently obscured from view, all three principal motions, and, consequently, the combined motions at the perpendiculars and shoulders of the ships, could not always be calculated. For the majority of the events the motions of only the port and starboard tips of the bridge superstructure and the stern of the departing ship could be obtained. The bridge motions, however, could be taken as approximately those of the ship's quarters since the bridge tips more or less coincide with the hull quarter points, the bridge width being equal to the beam of the ship.

3.2 Probabilistic Analysis

The motion time series, being, on average, of about 8 min duration, were accepted to be representative samples of a stationary random process so that the standard deviation of motion, s, could be used to characterise each record.

Normalized distributions of motion amplitude were derived for the motions at each target point and were compared with the well-known Rayleigh distribution given by

$$P(a) = \exp\left(-\tfrac{1}{2}\left(\frac{a}{s}\right)^2\right) \qquad \ldots 1$$

where a is the apparent amplitude of motion.

The calculated distributions were found to fit the Rayleigh distribution very well as is shown, for example, by the exceedence distribution of motion amplitudes at the port quarters of 70 different ships in Figure 2.

Longuet-Higgins (1952) postulated that the expected maximum amplitude, $E\{a_{max}\}$, in a given sample record with known standard deviation, s, and with Rayleigh-distributed apparent amplitudes, depends only on the record duration (number of oscillations, N) and is found from the relationship

$$E\{a_{max}\}/s = 2\left[(\ln N)^{1/2} + \tfrac{1}{2}\nu(\ln N)^{-1/2}\right] \qquad \ldots 2$$

with $\nu = 0{,}5772$ (Euler's constant).

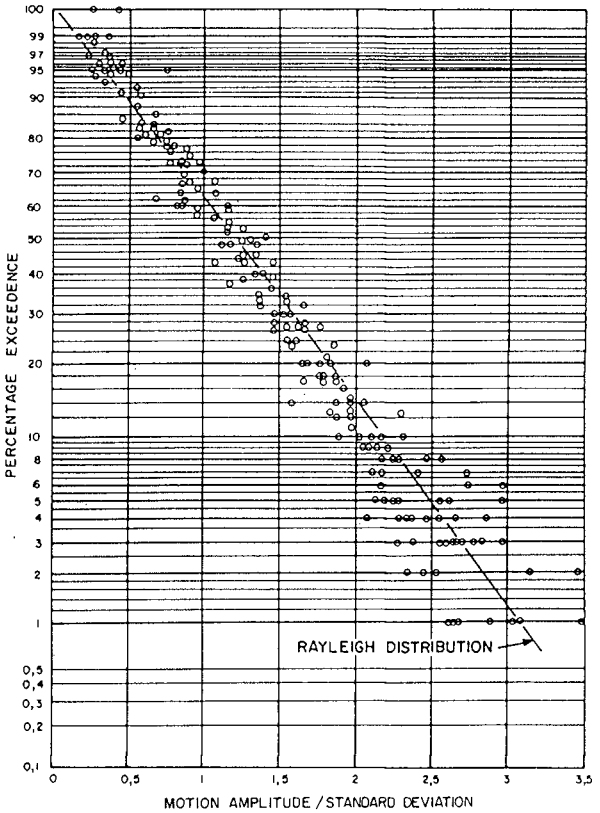

Figure 2 Distribution of motion amplitudes at port quarter

Using Equation 2, expected maximum motion amplitudes were calculated for 35 different records of from 20 to 50 oscillations and were compared with the recorded maxima as shown in Figure 3. Since Equation 2 apparently predicts the maximum motion amplitude well even for records of short length, this approach was adopted to estimate maxima from the sample standard deviations of motion and assuming that on average the ship underwent 100 oscillations for the period that she remained in the channel. Equation 2 then becomes

$$E\{a_{max}\} = 3{,}22\ s \qquad \ldots 3$$

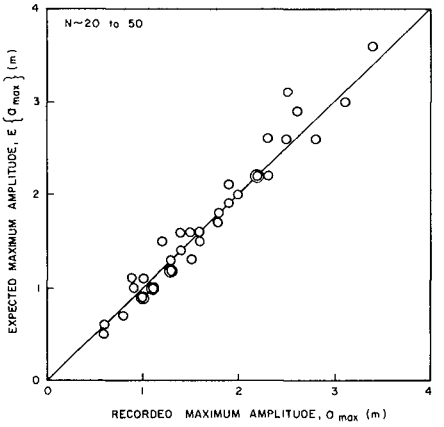

Figure 3 Expected versus recorded maximum motion amplitudes

3.3 Frequency Domain Analysis

For a selected number of events the incident wave records and ship motion records were spectrally analysed using a frequency resolution of 0,005 Hz.

The incident wave spectrum, S(f), was transformed to an apparent wave spectrum, $S_e(f_e)$ the wave spectrum encountered by the ship, using the relationships

$$S_e(f_e) = S(f) \frac{df}{df_e} \quad \ldots 4a$$

and

$$f_e = f - \frac{V}{\lambda} \cos\alpha \quad \ldots 4b$$

where V is the ship's speed, λ is the incident wavelength and α is the angle of wave incidence relative to the ship.

The incident and apparent wave spectra for event R065 are shown in Figure 4. The incident waves show a typical 1,7 m swell peaking at 15,4 s. With the dominant angle of wave incidence of 220° and taking the average speed of the ship to be 5 m/s (the ship in fact increased speed from 4,3 m/s to 5,5 m/s over a distance of roughly 2 km) the ship would have encountered the peak of the swell at about 12,2 s.

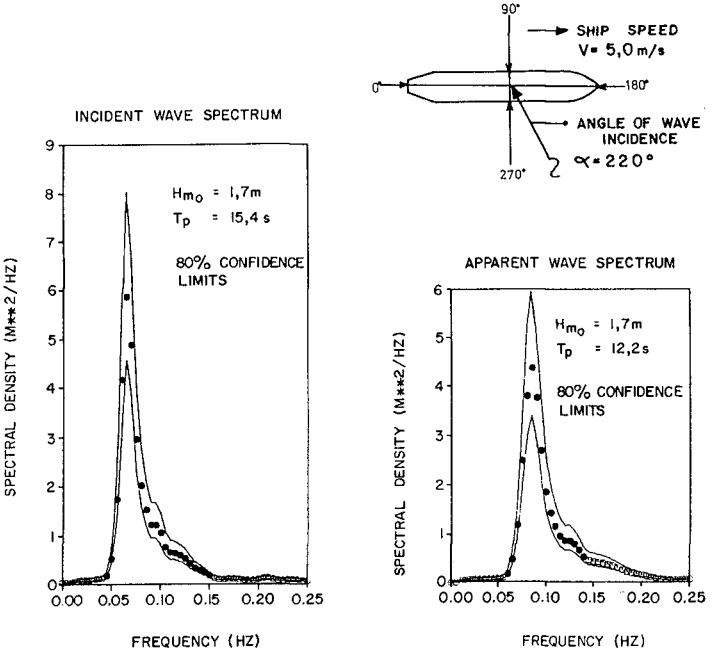

Figure 4 Incident and apparent wave spectra for event R065

Figure 5 illustrates the motion spectra of the ship, $S_S(f_e)$, for roll, pitch and heave and the combined motions were converted to translatory vertical motions at the ship's quarters.

From the assumption that a ship can be regarded as a linear system, the amplitude response function, $R(f_e)$, for each of the motions was calculated using the relationship

$$R(f_e) = [S_S(f_e)/S_e(f_e)]^{1/2} \quad \ldots 5$$

The amplitude response functions for roll, pitch and heave and for the combined vertical motions at the quarters for the ship monitored during event R065 are shown in Figure 6.

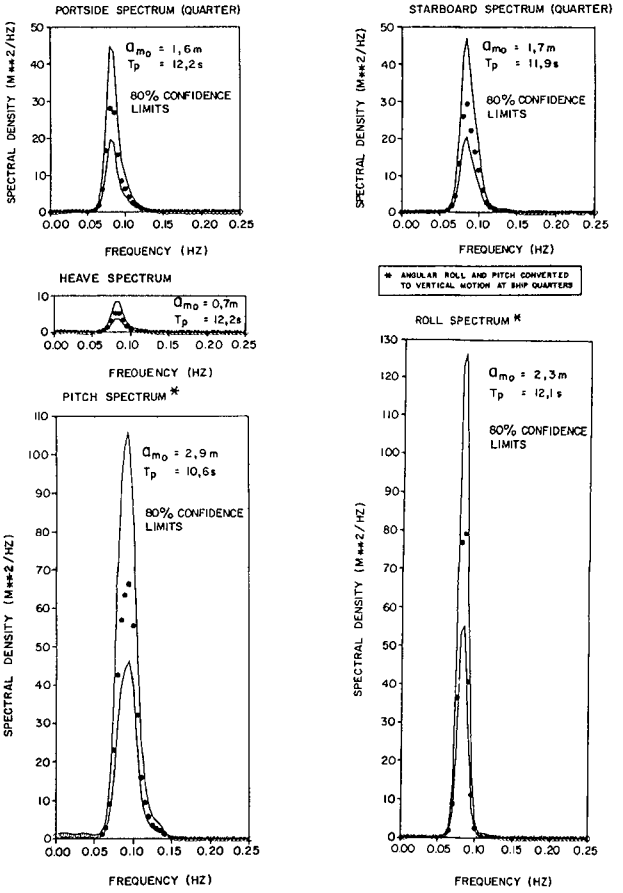

Figure 5 Sample ship motion spectra for event R065

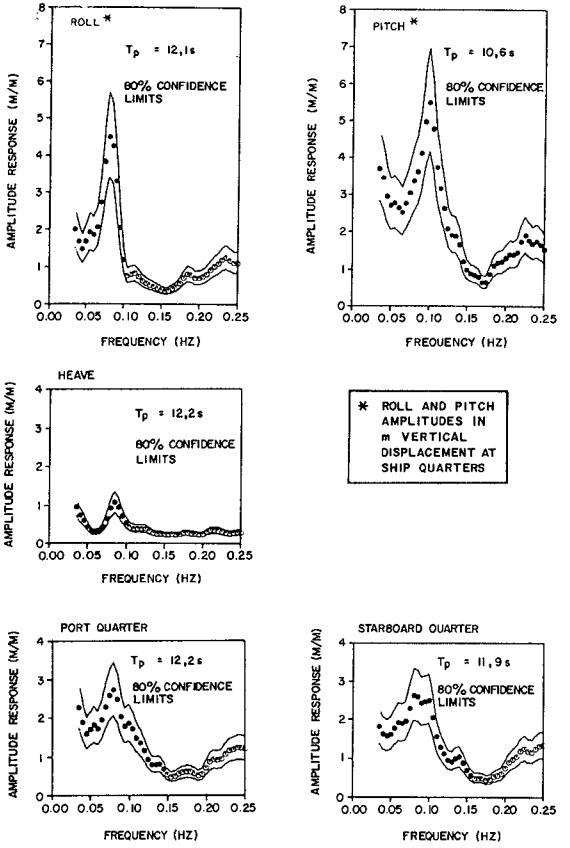

Figure 6 Sample amplitude response functions for event R065

4. DISCUSSION AND INTERPRETATION OF RESULTS

4.1 Maximum Ship Motions Versus Significant Wave Height

The expected maximum motion amplitudes calculated from the records with the largest standard deviations for each of the 70 processed events are shown plotted against significant wave height, H_{m_o} in Figure 7. The 18 events labelled with run numbers all took place under particularly adverse wave conditions.

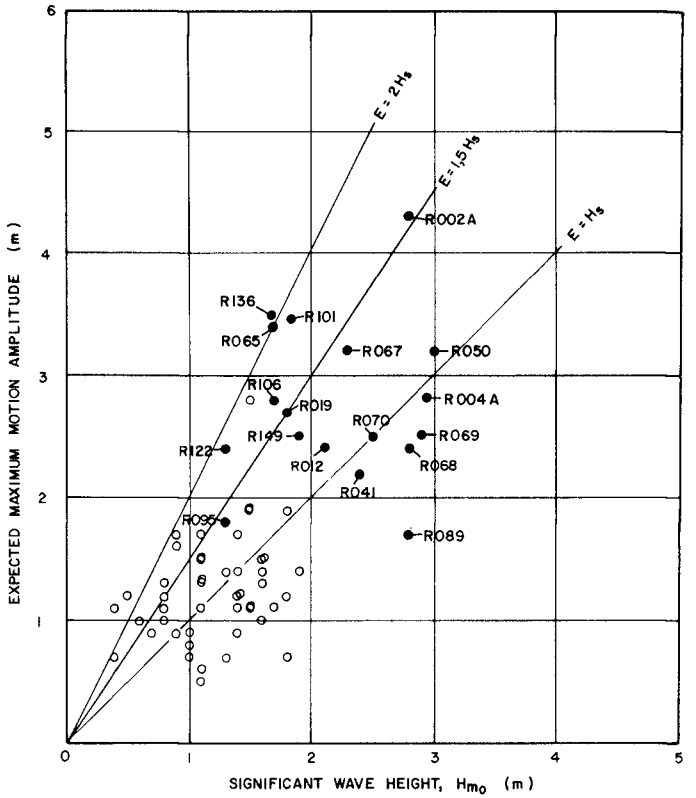

Figure 7 Maximum motion amplitude versus significant wave height

Gradients of 1:1, 3:2 and 2:1 were included showing that about 24 per cent of the data falls above the 3:2 gradient with significant wave heights generally less than 2 m. For larger wave heights the data always remained below the 3:2 gradient.

Inspection of the data enables the large variation in ship response to be attributed to a number of possible causes:

(i) **Variability of incident wave fields:** The wave spectra showed various stages of wind-generated seas and swells and were often composed of both. Swells approaching the channel varied in direction by as much as 70° and peaked at periods ranging from 11 s to well over 16 s. Heavy seas resulting from strong local winds were either beam-on or parallel to the channel line of orientation. The wind fields were, at times, of sufficient duration and strength to generate appreciable wave energy at periods of up to 12 s.

(ii) **Variations in ship's speed and heading:** Speeds ranged between 3 m/s (6 kn) and 6 m/s (12 kn) while ships, on leaving port, often increased speed by about 1 m/s to 2 m/s over a distance of 2 km. Angles of wave incidence relative to the ship also varied considerably due to variations in the ship's course. Figure 8 summarizes ship speed and angle of wave incidence for the 70 events considered in Figure 7.

(iii) **Differences in ship geometry and size:** The ships ranged in size from 95 000 dwt to 160 000 dwt and showed large variations in principal dimensions even for ships of equal displacement. Lengths between perpendiculars ranged from 240 m to 290 m and beams ranged from 37 m to 45 m.

(iv) **Differences in ship loading:** Ships leaving port were carrying from 100 000 t to just over 150 000 t of coal and had draughts ranging from 14 m to just over 17 m. The occasional entering ship was either in ballast or partly loaded.

Table I summarizes the principal ship dimensions and loading conditions for 18 of the 70 events (those numbered in Figure 7).

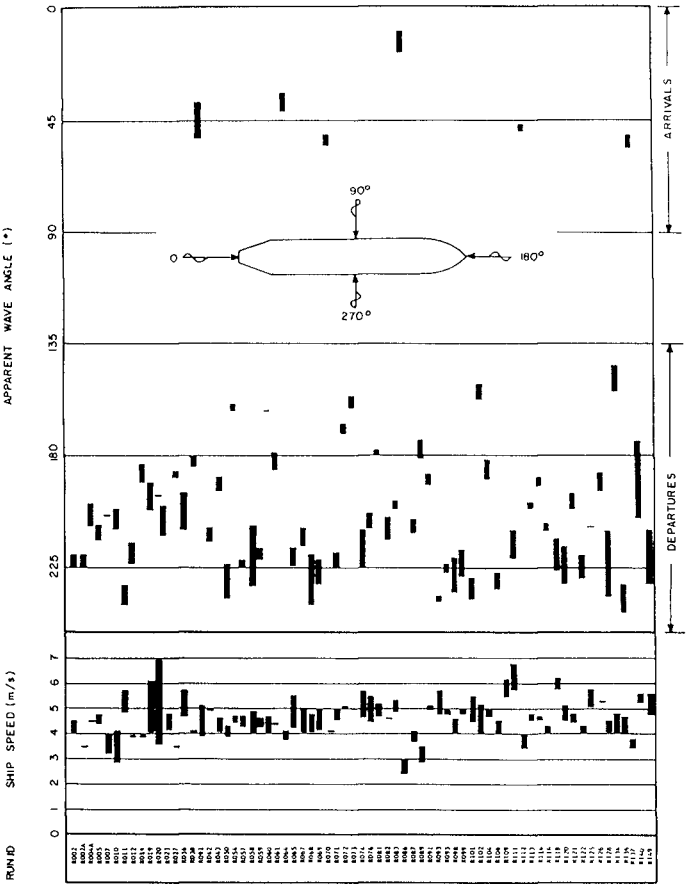

Figure 8 Range of apparent wave angles and ship speeds

TABLE I: SHIP PARTICULARS

Event	Ship code	Principal dimensions						Loading conditions						
		LOA (m)	LPP (m)	BEAM (m)	DRAFT (m)	LSW (t)	DWT (t)	Drafts (m) FWD	MID	AFT	DWT (t)	XG (m)	KG (m)	GM (m)
R002A	F(I)	260,0	248,0	41,6	16,81	19 819	125 103	16,55	16,80	16,61	123 125			
R004A	PP	259,8	249,0	39,6	15,78	20 180	112 731	15,36		15,83	109 437			
R012	NN	261,0	250,0	40,8	16,20	20 181	119 500	14,82	15,30	15,68	109 336			
R019	Q(II)	283,3	270,0	42,5	16,42	22 942	140 440	15,60	16,14	16,46	136 434	6,7	12,9	4,7
R041	V	250,1	237,0	38,9	14,68	20 189	95 357	9,14	9,94	10,74	42 208	-7,3	13,5	3,7
R050	F(I)	260,0	248,0	41,6	16,81	19 819	125 103	16,53	16,81	16,83	124 796	-5,8	10,7	6,1
R065	C(II)	266,0	251,5	38,4	15,78	19 910	110 338	15,39		15,93	110 318	1,9	8,1	7,5
R067	Q(II)	283,3	270,0	42,5	16,42	22 942	140 440	15,72	16,08	16,28	120 000	6,5	12,8	4,7
R068	OO	269,0	256,0	42,7	16,77	20 488	139 720	15,19	15,56	15,83	120 000			
R069	U(II)	303,0	287,0	43,0	16,64	28 854	148 200	16,26	16,59	16,15	144 964		13,1	4,5
R070	R(I)	261,0	247,0	40,6	17,61	20 739	129 629	12,30	12,50	12,80	74 000			
R089	E	292,0	280,4	42,7	17,30	24 276	154 483	17,06	17,06	17,06	152 267	2,5	12,7	4,9
R095	LL	268,0	259,0	39,0	16,08	18 407	123 000	15,70	16,00	16,00	122 800	-1,4	12,4	3,9
R101	EE(II)	261,0	249,0	39,6	16,45	20 407	118 712	15,39	15,77	16,08	112 210	5,8	12,2	3,7
R106	T	262,0	247,0	40,8	17,58	23 525	129 537	17,07		17,09	122 045	7,1	8,8	7,7
R122	MM	280,0	266,5	43,4	16,61		153 322	16,23		16,84	133 081	7,3		
R136	E	292,0	280,4	42,7	17,30	24 276	154 483	17,25	17,15	17,22	147 863			
R149	PP(I)	267,6	259,0	39,0	16,09	18 311	123 125	13,90	14,30	14,70				

4.2 Hull Points of Maximum Vertical Motion

The wave-induced vertical motions at the perpendiculars, shoulders and quarters of the ships could be calculated from the measured target motions for 25 of the 70 processed events.

For these events expected maximum motion amplitudes at both starboard shoulders and starboard quarters (thus, on the weather side of the ship) were, at times, up to about 50 per cent larger than the motions at their port-side counterparts (Figures 9a and b). A comparison of the starboard motions at the quarters and shoulders of these ships (Figure 9c), however, showed no tendency for motions at one point to be consistently larger than those at the other point.

Motions at the forward perpendiculars (resulting purely from heave and pitch), moreover, were of the same order of magnitude as those at the shoulders and quarters (which also include roll), Figure 9d. This emphasizes the fact that, in the majority of cases, wave encounter was such as to also stimulate ship motions in the pitch mode.

4.3 Ship Response Functions

Ship response functions were calculated from the motion spectra and wave spectra for the 18 events identified in Figure 7. The ship particulars are listed in Table I and the wave and ship response data are summarized in Table II.

Observations of dominant wave directions were often limited to visual clinometer measurements only and could, sometimes, be very misleading, particularly with strong winds which caused very confused sea states. Thus, verification of the primary wave fields was obtained by relating incident wave spectra to meteorological conditions prior to and during these events. The synoptic weather charts were found to be useful for delineating the primary sources of wave generation and to confirm the deep-sea swell directions. These were then converted to wave directions in and around the channel by means of appropriate refraction diagrams, and the results were checked against the local observations.

The extreme swells recorded during these events can be seen to have propagated from three primary directions, these being SSW/SW'ly, S'ly and SSE'ly. The peak swell periods ranged from 11,7 s to as long as 17,8 s and significant wave heights ranged from 1,2 m to 3,0 m.

These swells were refracted considerably while approaching the channel because of the coastal bathymetry and this

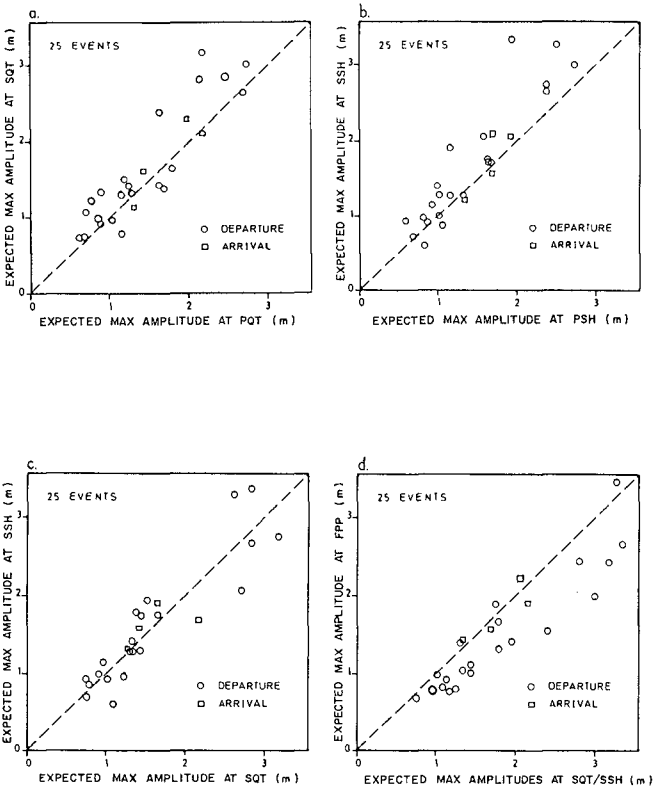

Figure 9 Hull motion relationships

TABLE II: WAVE AND SHIP RESPONSE DATA

Event	Incident waves				Ship/wave encounter				Ship response									
									Roll		Pitch		Heave		P.qrt		Stb.qrt	
	H_{m_0} (m)	T_p (s)	θ_o	$\theta_{channel}$	D/A*	V (m/s)	α ($^\circ$)	T_e (s)	T_p (s)	R_{max} (m/m)	T_p (s)	R_{max} (m/m)	T_p (s)	R_{max} (m/m)	T_p (s)	R_{max} (m/m)	T_p (s)	R_{max} (m/m)
R002A	2,7	14,5	SSW/S	140÷150	D	3,5	210	12,0	12,2	3,5	11,9		12,1		12,2	2,3	11,8	2,0
R004A	2,7	17,8	SSW	135÷155	D	4,5	220÷210	14,5÷14,0	13,0	2,0					13,4	1,6	13,3	1,4
R012	1,8	12,5	SW/SSW	150÷160	D	3,9	215÷225	10,0÷10,5	11,1	3,4					11,3	2,0	11,0	2,0
R019	1,8	11,7	S	145÷155	D	4,1÷6,1	215÷220	9,5÷9,0	11,2	3,3	11,4		11,3		11,5	2,5	11,1	2,3
R041	2,4	14,1 (8,0)	SW/SSW (SE)	145÷155 (130÷135)	A	3,9÷5,1	35 (15÷20)	18,0÷19,5 (12,0÷13,5)	11,5	0,6	14,9 (10,2)				13,6 (17,0)	1,5	11,8	1,0
R050	3,0	15,4	SW/SSW	140÷155	D	3,9÷4,2	190÷210	12,5	12,0	4,0					12,5	2,6	11,5	2,8
R065	1,7	15,4	SW/SSW	140÷155	D	4,3÷5,5	215÷230	12,5÷13	12,1	4,5	10,6	5,5	12,1	1,0	12,5	2,6	11,9	2,6
R067	2,3	14,3	S	140÷150	D	4,1÷5,0	210÷225	11,5	11,7	2,5	10,7	3,5	12,2		12,1	1,0	10,9	2,0
R068	2,8	12,5	S	145÷155	D	4,1÷4,8	205÷220	10,0	11,1	2,4					11,1	1,5	10,1	1,7
R069	3,0	14,2	SSE	135÷140	D	5,0÷4,2	205	10,5÷11,5	11,0	1,0	11,1		11,1		11,1	0,9	11,1	0,6
R070	2,6	14,2	SSE	135÷140	A	4,1	35÷25	18,5	12,2	2,0	15,4		14,7 (19,0)		15,1	1,0	15,4 (12,3)	1,0
R089	2,8	11,7	SSW/S	145÷160	D	2,9÷2,5	220÷225	10,0÷10,5	11,5	2,7					10,6	1,3	11,1	2,3
R095	1,2	13,2	S	145÷150	D	4,8	215÷220	10,5	11,0	4,5	10,1	3,0	11,1	0,7	11,0	3,1	10,8	2,3
R101	1,7	15,5	SW/SSW	140÷155	D	4,5÷5,5	210÷220	12,5÷12,0	11,8	4,0					12,1	2,7	11,6	2,8
R106	1,7	13,4	SW	150÷160	D	4,1÷4,5	215÷235	11,0÷11,5	12,2	4,4	11,0	7,0	11,2	0,8	12,0	2,4	11,2	3,0
R122	1,4	13,0 (11,0)	SW/SSW (S/SSE)	150÷160 (145÷150)	D	4,3÷4,0	215÷220	10,5 (9,0)	11,4	5,3					11,8	2,6	11,2	3,9
R136	1,6	13,8	SW/SSW	145÷160	D	4,7÷4,1	220÷225	11,0÷11,5	11,8	2,7	11,9		12,1		12,2	2,8	11,4	2,6
R149A	1,8	13,8	SSW	145÷155	D	4,8÷5,6	195÷220	10,5	10,5	4,0					10,7	2,6	10,5	2,6

* D - departure
A - arrival

resulted in channel wave directions being confined to a narrower sector ranging from 130° to 160° TN.

When allowance was made for the ship's heading relative to the channel orientation, the angles of wave incidence to the ships while leaving port ranged from about 190° to 235° (bow waves) and depended both on the directions and periods of the swells. The periods of wave encounter thus were shorter than those of the incident waves. Both ships entering port (events R041 and R070) encountered quartering waves with the resultant periods of wave encounter being much longer than those of the incident waves.

The motion amplitude response functions for the ships are characterised by the maximum amplitude response and corresponding period in Table II.

Maximum response ranged between 2,5 and 5,3 for roll at periods of wave encounter between 11 s and 12 s. Pitch and heave response could be assessed only for a limited number of these ships. Pitch resonance seemed to occur at periods between 10 s and 11 s. Maximum response factors at these periods were usually large, a value of 7 having been recorded at one occasion. Heave response, however, showed little, if any, gain at the normal periods of wave encounter.

Maximum amplitude response at the port and starboard quarters of the ships showed values of up to 4, but generally remained below 3.

Motion amplitude response due to combined roll, pitch and heave motions were much less than would have resulted from simply adding the contributions algebraically. This indicates strong phase dependence between the three principal motions.

5. CONCLUSIONS

The field monitoring programmes have been successful in providing useful data on wave-induced vertical ship motions as well as on ship speeds and ship trajectories under a variety of wave conditions.

The data, particularly the amplitude response functions, will prove valuable for the calibration of both mathematical and physical models which are presently being developed and which will be deployed to assess harbour accessibility for future deeper-draught ships. The measurements are also useful in verifying and updating existing allowance criteria based on limited earlier model tests.

Since vertical wave-induced ship motions are intrinsically narrow-banded and amplitudes are found to be Rayleigh-distributed, maxima can be estimated well by means of the Longuet-Higgins approach.

Though plots of expected maximum motion amplitude versus significant wave height showed large variations due to differences in both the wave conditions and ship characteristics, maximum amplitudes were shown to **never exceed twice the significant wave height** in magnitude.

Starboard motions were frequently **larger** than port side motions while motions at the perpendiculars of the ships were often of the same order of magnitude. It became evident that both pitch and roll contributed largely to the vertical hull motions while a strong phase dependence exists between all three principal motions.

The longer period swells (14 s to 16 s) proved to be most critical with regard to vertical ship motions for ships leaving port since these ships tended to encounter the waves at periods close to their natural resonance periods. These swells, however, would have less effect on ships entering port since the periods of wave encounter would then be far removed from their own natural periods of oscillation.

Acknowledgements

The author is grateful to the South African Transport Services for their permission to publish this paper.

REFERENCES

ZWAMBORN, J A and VAN WYK, A C (1981). Monitoring of ship motions in the Richards Bay harbour entrance channel. Proceedings of the XXVth International Navigation Congress, PIANC, Edinburgh.

LONGUET-HIGGINS, M S (1952). On the statistical distribution of the heights of sea waves. Jnl. of Marine Research, Vol XI, No 3.

OPERATIONAL PROCEDURES RICHARDS BAY HARBOUR

by

J A Zwamborn* and P J Cox**

ABSTRACT

The new port of Richards Bay on the east coast of South Africa (Figure 1), was officially opened in April 1976 and was mainly built for the export of bituminous coal. Exports increased from an initial 2,5 million tons per annum to 26,5 million tons per annum in 1981. Extensions are now under way to increase this further to 44 million tons per annum by 1987.

Fig. 1 Richards Bay Harbour

* Ship Dynamics Division, Coastal Engineering and Hydraulics, National Research Institute for Oceanology, South African Council for Scientific and Industrial Research

** Port Captain, Cape Town (previously Richards Bay), South African Transport Services

Because near-beam long swells occur frequently at Richards Bay, special care was taken with the design of the entrance channel. These swells cause much greater vertical ship motions than normally occur in other ports around the world and a 24 m deep outer channel was therefore provided for the 17 m draught design ship (40 per cent underkeel allowance, based on physical model tests).

Vertical motions recorded at Richards Bay as part of a comprehensive research project into ship motions in shallow water confirmed that this large underkeel allowance is realistic. Experience with ship manoeuvring also indicated that the channel width (300 to 400 m) and the stopping length (6,1 km) are adequate, probably for ships up to about 250 000 dwt.

To assist the port operating staff in deciding whether a particular entry or departure of a loaded vessel under adverse conditions is safe, particularly with regard to underkeel clearance, a **Port Operation Manual, Mark I,** was prepared. This manual describes the procedures for collecting ship and environmental data and contains diagrams from which the limiting wave height or the minimum required tide level can be read off as function of wave direction and the ship's draught.

This manual has been in use since October 1981 and has already been found very valuable in the operation of the port. As the research into ship motions progresses, the manual will be updated.

INTRODUCTION

Richards Bay harbour was officially opened to traffic on 1 April 1976. The harbour was built for the handling of bulk cargoes, initially, mainly the export of bituminous coal. Situated on the Zululand coast between Durban and Maputo, it was the nearest suitable site to the Transvaal and the Orange Free State coal fields. Total cargo handled during 1981 was 29,4 million tons of which 26,5 million tons was coal.

A detailed description of the design and construction of the harbour was given by Campbell and Zwamborn (1977).

Layout

The overall harbour layout is shown in Figure 2. The relevant dimensions of the **entrance channel** are as follows:

length,	outer channel	~ 3,5 km
	inner channel	6,1 km (available stopping length)
width,	seaward end	400 m
	tapering to	300 m (inside breakwaters)

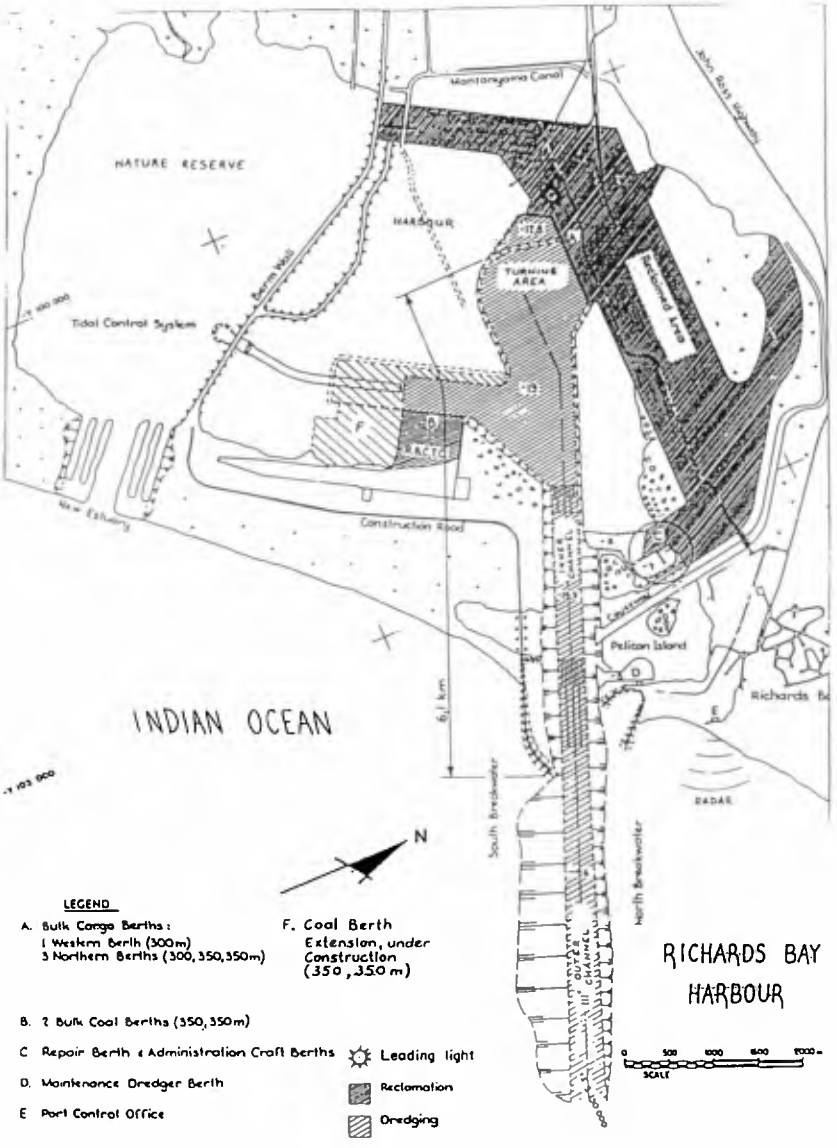

Fig. 2 Harbour layout

depth, outer channel - 24 m CD (Chart Datum ≈ LWOST)
transition area - 22 m CD
inner channel - 19,5 m CD
turning and
mooring area - 19 m CD.

The foundation level of the coal quays was set at -23 m CD. A turning area with a diameter of 1000 m was provided.

Design Criteria

The channel dimensions were originally determined to allow the entry and departure of 17 m draught ships (about 150 000 dwt) for 99 per cent of the time, with a tide level assumed to be at 0,0 CD (Campbell and Zwamborn, 1977). However, the possibility of handling larger ships, up to 20 m draught (about 250 000 dwt), was taken into account throughout the design stage. For this reason, the coal quays were founded at -23 m, to allow for possible future dredging to -22 m CD and the breakwaters were placed in such a way that the entrance channel could be widened and/or deepened if necessary.

Design Studies

The harbour design was assisted by a detailed programme of field measurements, sediment model studies, breakwater stability tests, wave penetration studies and physical ship model tests (Campbell and Zwamborn, 1977; Zwamborn and Grieve, 1974).

The latter were undertaken to assist in the determination of the entrance **channel dimensions.** They were carried out in the 1 in 100 scale wave penetration model using a self-propelled radio-controlled model of a 150 000 dwt, 17 m draught bulk carrier (Hoppe, 1972). Most tests were carried out with near-beam regular waves of near-resonance frequencies, conditions, which occur frequently at Richards Bay. The test results indicated that:

- a maximum overdraught ('sinkage') of 6 m is to be expected for the 1 per cent occurrence SSW'ly swell, indicating a minimum channel depth of 24 m, allowing 1 m underkeel **clearance** (thus underkeel **allowance** is 7 m or 40 per cent of the design draught);

- a channel width of 300 to 400 m would be sufficient for single-lane traffic during all but the SSW design waves for **entry** speeds of 3,5 to 4 m/s (7 to 8 kn) and for ships **leaving** under design conditions at a speed of 3,5 to 4,5 m/s (7 to 9 kn);

- an approximately 150 m wider entrance channel would be necessary for **entry** under the SSW'ly design wave con-

dition, alternatively the entry speed would have to be increased to 4,8 m/s (9,5 kn) to avoid transgression of the 300 to 400 m wide channel bounderies.

Based on information on **stopping distances** available at the time, it was accepted that 150 000 to 250 000 dwt loaded ships entering the harbour at $\leq$ 4 m/s (8 kn) could be stopped within the available 6,1 km stopping length, provided powerful tugs could attach and assist when the ship was moving at a speed of $\leq$ 2 m/s (4 kn).

A group of 20 pilots who were also asked to operate the model concluded that the handling of the model ship was generally realistic but they thought that its movements were somewhat excessive and initially they were reluctant to enter at speeds much in excess of 1,5 to 2 m/s (3 to 4 kn).

Future Expansion

The first-phase development at Richards Bay was mainly based on a 2,5 million tons per year export contract of bituminous coal and anthracite, as from April 1976. As a result of the oil crisis in the early seventies, the demand for coal increased dramatically and the export rate increased rapidly to the present (1981) figure of 26,5 million tons per year.

Extensions to the coal berths and loading facilities (Figure 2) are under way at present to increase the export capacity to 44 million tons per year. These extensions are scheduled to be completed by 1987. Moreover, the South African Government has approved export permits up to a total of 80 million tons per year and further extensions to the harbour must therefore be expected in the future.

The harbour was originally designed for 17 m draught ships. From the start the official draught restriction was 17,1 m (10 per cent underkeel clearance in the inner harbour) although draughts up to 17,3 m were allowed at certain times to assist with the ship motion monitoring programme. Shipping agents approached the harbour authority during 1980 for use of 17,6 m draught ships for early 1983 (about 185 000 dwt). This increase of draught to 17,6 m could be achieved by using the tide, but any further increase would require a certain amount of dredging in the turning/mooring areas and in the inner channel.

Finally, as mentioned above, allowance was made in the foundation level of the coal quay for 20 m draught ships (250 000 dwt) and studies are underway at present to determine the dredging depths in the outer and inner entrance channels required to accommodate these ships for 99 per cent accessibility.

EXPERIENCE IN THE OPERATION OF THE PORT

A maximum degree of flexibility was aimed at in the design of the entrance channel because it was realised that, as experience was gained in the operation of the port, particularly with regard to negotiating the entrance channel, adjustments in the channel dimension or in the limiting operational conditions might have to be made at a later stage. It was, therefore, important to gather any information on possible problems experienced during operation related to the channel depth, width and length.

Ship Statistics

Because Richards Bay is mainly an export port for coal, large bulk carriers normally enter the port light (about 10 to 12 m draught) and leave loaded (up to 17,1 m draught). This reduced the entry problem for this traffic because light ships are much easier to stop than a fully loaded ship although the ship's larger freeboard could cause additional manoeuvring problems during strong SW or NE wind (a 150 000 dwt bulk carrier has a displacement of about 180 000 t when fully laden but only 110 000 t when in full ballast).

However, there are occasions on which fully or near-fully laden bulk carriers come in to 'top up' their coal load or for bunkers and these occurrences were of particular interest in checking the design.

The use of the port by VLC's in excess of 100 000 dwt can be summarised as follows (1981 data):

Ship size (dwt)	< 50 000	50-100 000	100 - 150 000	> 150
Number of ships	367	106	160	29

This gives a total of 662 ship movements (compared with 522 in 1979 or a growth rate of 13,5 per cent per year).

The deepest draught for a **sailing** VLC in 1981 was 17,37 m.

During the year eight ships **entered** in almost fully loaded condition (to 'top up') with a deepest draught of 16,8 m.

Port Control

Apart from the usual lights on the ends of the breakwaters the centre line of the channel is marked by leading lights situated at 6,7 and 9,2 km from the end of the main breakwater at 27 and 50 m above CD, respectively (Figure 2). The lights consist of sealed beam units with the following light power:

- front light, red: 4 800 000 candelas during the day (fixed) and 57 200 candelas at night (flashing);
- rear light, white: 3 600 000 candelas during the day (fixed) and 57 200 candelas at night (flashing).

Radar Responder Beacons (Racons) have been provided on the leading light towers to mark the channel centre line on the ship's radar should the leading lights become obscured by rain or mist (radar particulars: 9 300 to 9 500 MHz, 72 s sweep, 360° coverage, 20 km range, continuous transmission).

The port control office is situated 1,5 km north of the harbour entrance at 55 m above sea level. Apart from the usual radio equipment, 30 and 100 mm wavelength **radar** sets are installed in the operating room. The pilots and the Assistant Port Captain are also stationed at the port control office (Figure 2, E).

Tugs and Pilotage

The following **tugs** are available at Richards Bay to assist with entry/departure manoeuvres:

Type	Number	Power HP/kW	Bollard Pull (t)	
			Ahead	Astern
Kort-Nozzle	2	4400/3200	52	28/32
Voith-Schneider	1	4000/2940	40	34

Compulsory pilot service is provided by the South African Transport Services, at present only during daylight hours, extended to 21h00 on special request for unberthing loaded coal vessels.

For entry, the pilot boards 5 to 9 km offshore, depending on whether the ship is light or fully laden. A 21,5 m long pilot boat is used for this purpose; it goes alongside the ship which makes a lee from the wind and sea. It is virtually always possible for the ship to provide a lee to the pilot boat but during heavy swell and sea conditions (winds

exceeding about 40 kn or 20 m/s) the pilot boat itself becomes difficult to handle.

For departing ships, the pilot boards at the coal quay and normally disembarks just before the ship leaves the protection of the main breakwater. Thereafter, further advice is provided by port control on the basis of the ship's radar image which is carefully monitored as the ship passes through the outer channel.

Entry Manoeuvres

Typically, an entry manoeuvre of a VLC at Richards Bay goes as follows (Figure 3, a):

- pilot boards 7 to 9 km offshore
- ship lines up with leading lights, speed 6 to 8 kn
- approaches entrance with engines slow to dead slow, speed 5 to 7 kn
- enters between breakwaters with engines dead slow to stopped, speed 4 to 6 kn
- tugs attach in inner channel, one or two for'd and one aft
- ship turns to port towards coal quay, reverse power
- starboard turn, reverse towards coal quay
- pilot leaves the ship at the coal quay.

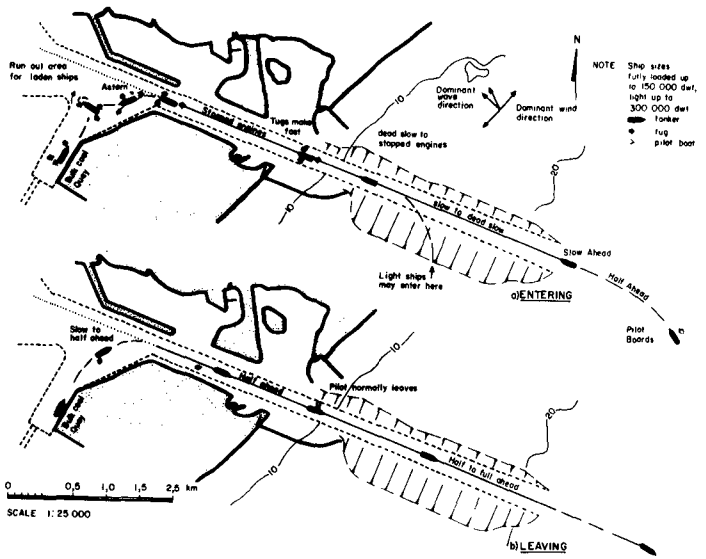

Fig. 3 Typical manoeuvres

Departure Manoeuvres

Normally, the departure manoeuvre goes as follows Figure 3, b):

- pilot boards at the coal quay
- ship lifts off and turns into inner channel, slow to half ahead, one tug in attendance
- ship moves through inner channel, half ahead, speed 5 to 8 kn
- pilot leaves ship between breakwaters
- ship moves through outer channel half to full ahead, speed $\geq$ 9 kn
- progress and position is monitored on radar at port control from where advice is given on course adjustments, if necessary.

Discussion and Comparison with Model Predictions

Ships enter Richards Bay at minimum speeds of between 4 to 6 kn (2 to 3 m/s), depending on the conditions. Entering at these speeds allows, mostly, light ships of the 150 000 dwt class to be stopped and turned in the coal berth area which means a stopping length of 4 to 4,5 km. Further data on the entry of laden vessels under near-design conditions will be collected but, based on present experience, there is little doubt that the 6,1 km available stopping length will be sufficient for up to 250 000 dwt loaded vessels entering at speeds of up to 8 kn (4 m/s), perhaps even 9 kn (4,5 m/s).

Also, tugs can make fast at virtually any manoeuvring speed but only tractor-type tugs can start to assist with **steerage** at speeds of 4 to 5 kn (2 to 2,5 m/s); conventional tugs cannot 'open-up' at speeds above 2 to 3 kn (1 to 1,5 m/s) and can thus only assist a little by reducing the ship's speed. Thus, when tractor tugs are available (at present there is only one tractor tug, the Voith-Schneider tug), relatively higher entry speeds will be possible, if required, for the control of the ship during adverse conditions; alternatively, larger ships could probably be stopped within the available stopping length.

Finally, the available channel width was found to be adequate in most circumstances. However, it is imperative that under southerly wind and wave conditions (near-beam conditions) sufficient speed be maintained to ensure control of the ship, as indicated by the model tests (that is, 7 to 8 kn for entry and 7 to 9 kn for departure). This is borne out by an occurrence where a departing loaded VLC was forced over the north channel bank under these conditions while travelling at only 5 kn (2,5 m/s) and two recent occurrences where similar ships leaving at a speed of about 9 kn were able to remain in the channel although leaving

under near-design conditions (measured wave height, $H_S \simeq$ 2,7 m, wave period, T_Z = 10 s, wave directions, $\emptyset$ = 160°, 25 kn, SSW wind). Both ships first took a sharp turn to port (north) just outside the breakwaters, probably due to a local northbound current. After nearly 'locking' into the waves (heading parallel to the waves) the ships took a very strong 'sheer' to starboard. Although these manoeuvres included course changes of + and -15°, the ships remained in the channel.

SHIP MOTION STUDIES FOR RICHARDS BAY HARBOUR

A programme of free moving ship motion studies has been undertaken for Richards Bay, including prototype measurements, mathematical modelling and physical modelling. The diagram given in Figure 4 shows all the elements of the studies, and also the various interactions between the 'three-legged' approach (the moored ship studies are done for Saldanha Bay harbour and are not discussed here).

Purpose of Studies

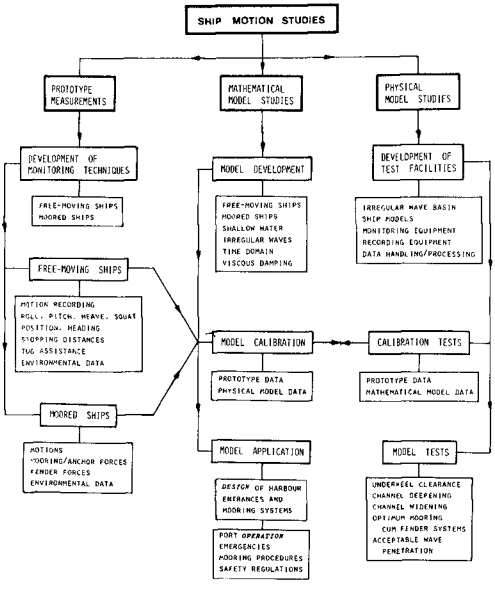

Fig. 4 Ship motion studies flow diagram

The above studies were undertaken for Richards Bay:

(a) to confirm the predictions based on the original hydraulic model tests,

(b) to determine the conditions under which 18 m draught ships could use the present entrance channel safely,

(c) to determine minimum required dredging depths to allow 20 m draught ships to use the port with a maximum downtime of 1 per cent (regarding underkeel clearance), and

(d) to develop guidelines to assist with the safe operation of the port, particularly with regard to required underkeel allowance under various conditions.

Prototype Measurements

A photographic technique has been developed which enables the accurate monitoring of the course, speeds and vertical motions of all ships using Richards Bay harbour (Zwamborn and Van Wyk, 1981). Since August 1978, 175 ships with a dead weight tonnage exceeding 100 000 dwt have been monitored and some of the results are presented in another paper to this conference (Van Wyk, 1982). The results of these measurements provided valuable data with regard to entry and departure speeds vis-à-vis stopping distances and ship handling (discussed above) and they indicated that the adopted underkeel allowances are of the right order.

More data on near-design conditions (small underkeel clearances) are, however, required and arrangements have been made to charter loaded bulk carriers when these conditions occur, to carry out special monitoring runs.

Mathematical Modelling

To determine the required channel depths for ships larger than those using the port at present, a mathematical model will be used. This model will first be calibrated against available prototype data obtained from the measurements. A deep-water strip-theory model was tried first but the results were not satisfactory. A shallow-water version and a shallow-water three-dimensional source technique model are therefore being used at present.

Once properly calibrated, the mathematical model will be invaluable in the operation of the port.

Physical Modelling

As soon as a fully-irregular wave basin becomes available, model runs will be made reproducing typical prototype

measuring runs, to check possible scale efffects. Thereafter, the physical model will be used to provide additional **calibration data** for the mathematical model, particularly regarding different wave directions, as well as for a final check on the required dredging depths to accommodate ships up to 250 000 dwt.

APPLICATION OF SHIP MOTION STUDIES TO PORT OPERATION

The large underkeel allowances at Richards Bay, reducing from 7 m in the outer channel to 2 m inside (at low water), were dictated by the regular occurrence of long waves with near-beam directions. These long waves cause considerably greater sinkages than those due to the squat and trim, which are determinative in many other ports. It was therefore considered necessary to use available information on ship motions due to waves, to determine the expected overdraught during the passage of the ship through the outer and inner entrance channels in order to decide under what heavy weather conditions vessels would be permitted to negotiate the channel. This procedure also requires knowledge of the environmental conditions at or near the time of passage.

Wave Directions

Vertical ship motions are greatly influenced by wave direction and it was therefore necessary to determine the wave directions,preferably those in the entrance channel. This is done by using radar, wave clinometer or by pilot boat observations.

Wave direction in the channel can be read off the **radar** screen, provided there is sufficient backscatter from the water surface,that is, a wind chop superimposed on the swell. For better definition, the short wave length (3 cm) or X band is used. Wave direction is observed in the channel about 1 to 2 km out to sea.

If no radar direction can be observed, a **wave clinometer** direction reading is used. The wave clinometer is an inclined (3°) graduated telescope directed onto a buoy anchored in 13 m water depth at about 800 m offshore and 1600 m north of the entrance channel.

If both methods were to fail or when conditions are such that confirmation is advisable, the **pilot boat** can be used to record/check the swell directions in the channel by heading into the swell and reading the compass direction.

Wave Height

Vertical ship motions are generally assumed to be proportional to wave height. Preferably, the wave heights should

again be measured in the entrance channel but this is impracticable. The measurements are normally made with a **waverider buoy,** anchored in 20 m water 1 km south of the channel and about 1,5 km out to sea, and with a receiver at the port control station.

Available data on ship motions, that is, the maximum expected sinkage during passage through the channel is related to the significant wave height, H_S. A quick estimate of H_S can be made by reading off the waverider chart the maximum wave heights for three consecutive 3 min records and calculating the mean, that is, $H_S \approx H_{rep} = \frac{H_1+H_2+H_3}{3}$. This wave height, H_{rep}, is a conservative value. Assuming Rayleigh wave height distribution and considering that a ship will on average be 20 min in the channel, $H_{rep} \approx H_{S\text{-}20\ min}$ (Longuet-Higgins, 1952).

In the event of waverider failure, an estimated wave height is obtained from the **wave clinometer.** The average vertical movements of the anchored buoy, relative to fixed graduations in the telescope, is determined over a period of three to five minutes.

Wave Period

Vertical ship motions are also very dependent on the **wave periods.** Because of the regular occurrence of long-period swells, near-resonance conditions normally occur, particularly under moderate to heavy swell conditions. Although wave period records are available from the waverider and the wave clinometer, these are not used in the present operational procedures, which assume that most of the wave energy is concentrated near the natural roll/pitch periods of the ships.

Tide Levels and Water Depths

The lowest tide level, Z_O, during the passage of a ship through the channel (on average 20 min) must be used to determine available water depth relative to the proclaimed channel bottom level (taking into account possible siltation, ΔZ).

Tide levels are read from an automatic **tide recorder** or, in the absence thereof, from the tide tables.

Ship Motions in the Outer Channel

Because of the lack of sufficient directional spread in the conditions during prototype monitoring, the first version of an 'operational model' was based on the results of model

tests with a 200 000 dwt tanker (Koelé and Hooft, 1969) and a 150 000 dwt bulk carrier (CSIR, 1976).

Figure 5 gives the expected maximum sinkages as functions of wavedirection for a 18,9 m draught ship, proceeding at 4 m/s (8 kn) in a 10 km long channel of various depths, under irregular swell with H_S = 1,5 m and T_Z = 10 s (zero-crossing wave period). The sinkages also include squat, linearly extrapolated for greater underkeel clearances (CSIR, 1979).

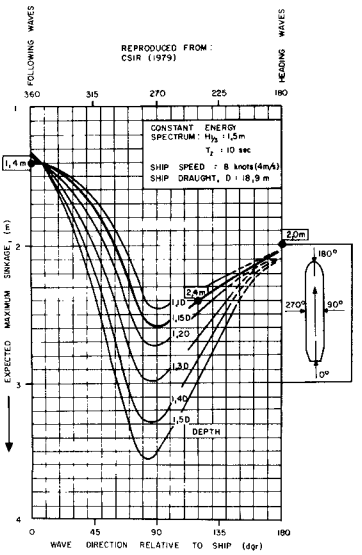

Fig. 5 Sinkage of 200 000 dwt model tanker as function of wave direction and water depth

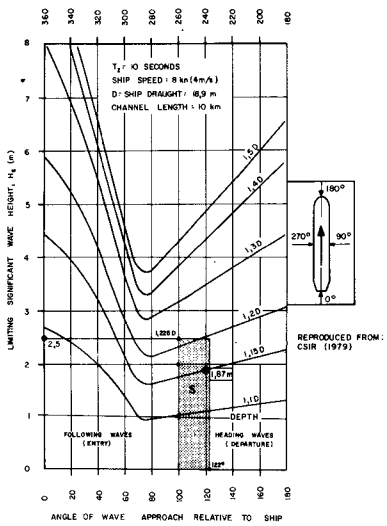

Fig. 6 Limiting significant wave height for which a ship may touch the bottom

Figure 5 was converted into Figure 6 giving the limiting significant wave heights as functions of wave direction and underkeel allowance. In this conversion, linearity was assumed between (a) sinkage due to waves and wave height and (b) sinkage due to squat and trim and underkeel allowance; the latter reduces from 0,7 m for 10 per cent to 0,0 m for 50 per cent underkeel allowance. For example, for a wave direction of 240° and 15 per cent underkeel

allowance, Figure 5 gives a total sinkage of 2,4 m of which 0,65 m is due to squat and trim. The limiting H_S then follows from $0,15\ D = \frac{H_{S-lim}}{1,5}\ (2,4 - 0,65) + 0,65$ or, since D = 18,9 m, H_{S-lim} = 1,87 (see Figure 6).

Using Figure 5 and assuming linearity between sinkage and wave height the expected maximum sinkages for the 200 000 dwt model ship in the Richards Bay channel are compared with the maximum sinkages measured in the original Richards Bay tests using a 150 000 dwt model in Figure 7 (CSIR, 1979). The results are seen to be compatible with a maximum sinkage for beam waves of about 6 m and Figures 5 and 6 were therefore considered to be a safe basis for determining maximum sinkages for bulk carriers up to about 250 000 dwt passing through the Richards Bay outer entrance channel.

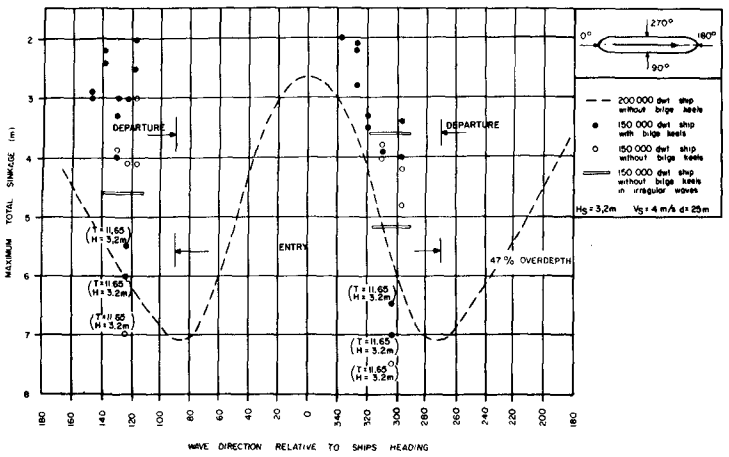

Fig. 7 Comparison of maximum sinkages of 150 000 dwt and 200 000 dwt ships

Ship Motions in the Inner Channel

The waves entering the harbour will run parallel to the channel axis and will therefore be either following (0°) or heading (180°) waves for entering and leaving, respectively (see Figure 6). To determine the ship motions in the inner channel the local wave heights must be known. These were obtained from the results of the Richards Bay physical model tests which showed maximum wave penetration for the

deep-sea wave direction of 146° and very low penetration for ESE, the direction parallel to the channel axis (Zwamborn and Grieve, 1974).

Two specific areas were chosen for ship motions determination, namely, the 'top of slope', where the channel depth changes from -22 m to -19,5 m CD and 'Sandy Point', just before the channel widens into the coal berth area (-19,5 m CD). Figure 8 shows the relationships between wave penetration and wave direction for these two areas using wave refraction data to convert deep-sea to entrance channel wave directions (Moes and Van Niekerk, 1981). Accepted penetration values for the entrance channel directions are also shown in this figure. For example, for the direction sector SE, the penetration factor is 0,6 at 'top of slope' and 0,2 at 'Sandy Point'.

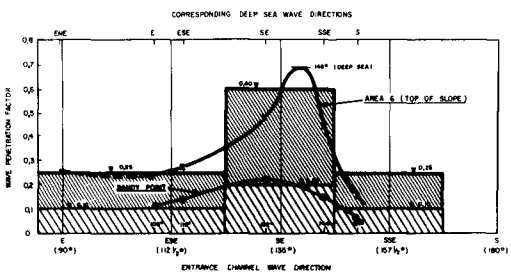

Fig. 8 Wave penetration at 'top of slope' and 'Sandy Point' versus wave direction

On the basis of the above and using Figure 5 (following and heading waves), the limiting wave heights at the positions in the inner channel could be found. For example, taking the available depth at the 'top of slope'at -20 m CD and allowing a minimum underkeel clearance of 1 m, the available depth at low water in this area is 19,0 m. For a ship **entering** under SE'ly waves, the wave penetration factor is 0,6 while the total sinkage for 1,5 m high waves is 1,4 m. Assuming 0,5 m squat and trim the sinkage due to waves is thus 0,9 m. Now the maximum permissible sinkage Z_{max} = $19,0 - D = 0,5 + \frac{0,9}{1,5} \times 0,6\ H_{s-lim} = 0,5 + 0,36\ H_{s-lim}$ or $H_{s-lim} = \frac{18,5-D}{0,36}$, which is a linear relationship between draught D and H_{s-lim}. For a ship **leaving** under SE'ly waves, the total sinkage for heading waves must be used, namely, 2,0 m for 1,5 m high waves. Thus the sinkage due to waves is 1,5 m (0,5 m squat). This leads to the following relationships:

$$Z_{max} = 19,0 - D = 0,5 + \frac{1,5}{1,5} \times 0,6\ H_{s-lim} = 0,5 + 0,6\ H_{s-lim}$$

$$\text{or } H_{s-lim} = \frac{18,5-D}{0,60}.$$

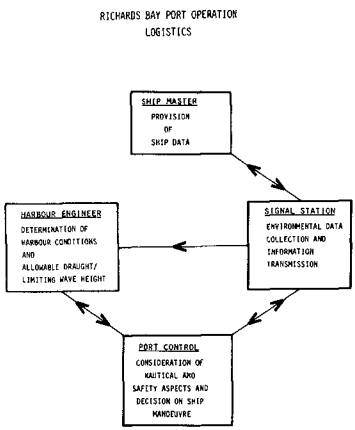

Fig. 9 Port operation logistics

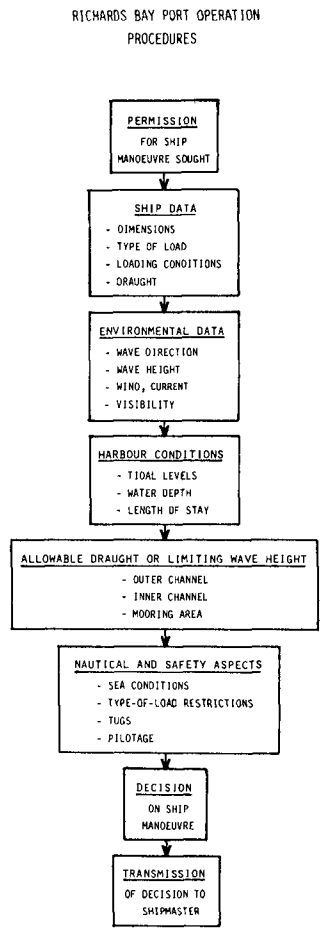

Fig. 10 Port operation procedures

PORT OPERATION MANUAL, MARK I

The first version of a port operation manual (CSIR, 1981) was drawn up on the basis of the data and assumptions discussed above. It is realised that the data are limited and that the problems have been over-simplified; this is the reason for a conservative approach throughout. The main purpose of Operation Manual, Mark I was to provide the nautical operating staff at Richards Bay with a first tool to assist in their decision making, with regard to under-keel clearance, on acceptable conditions for entry/departure of VLC's under severe conditions.

Logistics and Procedures

Port operation logistics are shown diagrammatically in Figure 9. Although for routine operations Port Control can apply the operation manual directly, it is the Harbour Engineer's responsibility to ensure that the manual is correctly interpreted, kept up to date and amended when necessary. The Harbour Engineer should also be consulted on special cases (e.g. emergency entry of larger then design vessels) and he is responsible for providing up-to-date information on possible channel siltation.

Operation procedures are shown diagrammatically in Figure 10. Operation Manual, Mark I, forms an important part of these general procedures. It contains the following steps/instructions:

(i) Obtain details on the ship's draught, D (maximum stationary value), from the ship's master;

(ii) record environmental conditions, including wave direction, $\emptyset$, wave height, H_{rep}, and tide level, Z_o;

(iii) check available water depths in the area concerned and calculate the equivalent draught ($D_{eq} = D - Z_o$); and

(iv) determine the limiting wave height, $H_{rep,lim}$, for a ship with equivalent draught D_{eq} and angle of wave approach, $\emptyset$, and check whether the recorded wave height is equal to or smaller than the limiting wave height, that is, $H_{rep} < H_{rep,lim}$;
alternatively
determine the minimum tide level, $Z_{o,min}$, required for a ship with a draught, D, angle of wave approach, $\emptyset$, and wave height, H_{rep}, and check whether the actual tide is equal to or higher than the limiting tide level, that is, $Z_o > Z_{o,min}$.

Specific instructions on how to determine the environmental and other data are included in the Manual (CSIR, 1981).

Draught Allowance Criteria

To facilitate step (iv) above, easy-to-read coloured draught allowance diagrams were prepared and are also included in the manual, one for entry and one for departure (the latter is shown in Figure 11). These diagrams allow for a minimum underkeel clearance of 1 m anywhere in the harbour or entrance channel. The straight lines in Figure 11 represent the conditions in the inner channel (example equations derived in the above), the dotted vertical line is the limit for the turning and mooring area (see Figure 11, maximum D_{eq} = 19 - 1 = 18 m) and the curved lines represent the limiting conditions in the outer channel.

The latter are obtained from Figure 6. For example, taking the S direction sector (169° to 191°), the wave angles relative to a leaving ship travelling on the channel centre line (111° to north, corresponding to 180° relative to the ship) will be 122° to 100°. Considering the limiting wave height of 2,5 m, the largest required depth for this wave height in the S direction sector is 1,225 D (Figure 6). With a channel depth of 24 m and 1 m underkeel clearance, the allowable draught follows from 1,225 D = 24 - 1 or D = 18,7 m. This gives one point of the curve for S'ly waves (see Figure 11).

It is clear from Figure 11 that a ship with D = 18,7 m would be able to be in the port only when its equivalent draught, D_{eq} = 18 m or with a minimum tide of 0,7 m. This brings out the interesting point that, with the present channel depths, the inner channel forms a greater limitation to large draught ships than the outer channel, particularly for SE'ly waves (see Figure 11).

Example Applications

Example 1: Loaded carrier to leave port

Ship draught	D	=	17,0 m
Recorded wave direction	Ø	=	169°
Recorded representative wave height	H_{rep}	=	3,8 m
Tide level at time of manoeuvre	Z_o	=	0 m

Can this ship leave the port?
Determine $D_{eq} = D - Z_o = 17,0 - 0 = 17,0$ m.
For S direction sector, Figure 11 yields $H_{rep,lim}$ = 3,45 m.

Since this is 0,35 m less than the recorded value, the ship cannot leave the port.

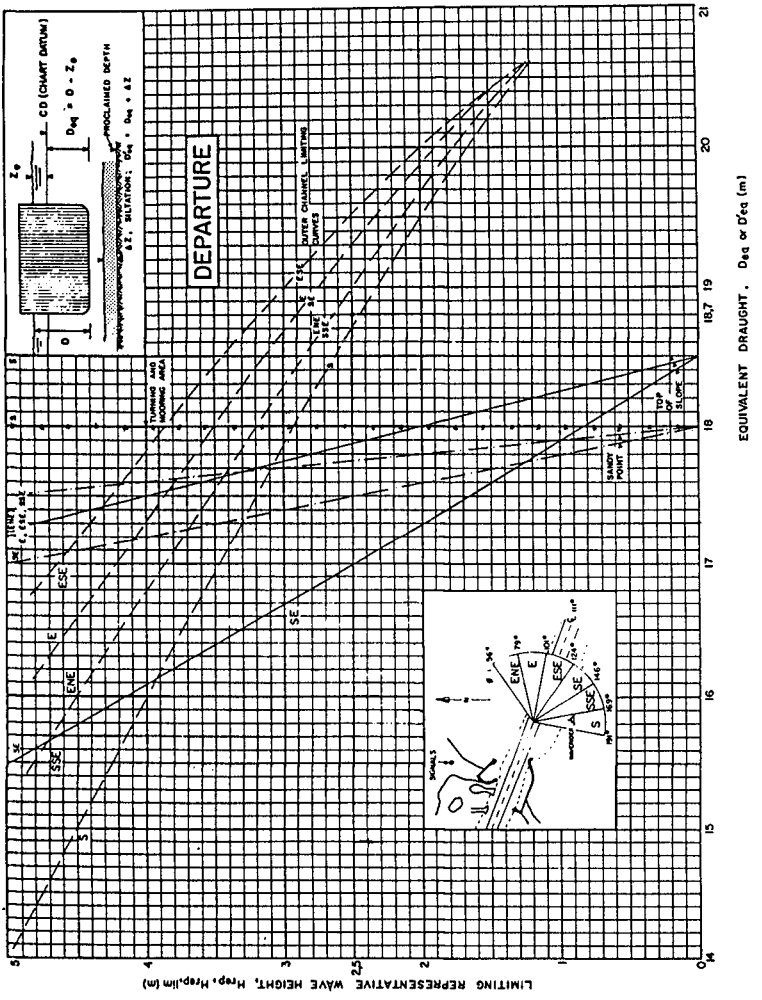

Fig. 11 Allowable draughts during departure

Example 2: Loaded carrier to leave port
Taking the same ship as in Example 1 and assuming that the sea conditions remain the same, what is the minimum tide required for the ship to leave?

For H_{rep} = 3,8 m, D_{eq} = 16,4 m (Figure 11, S direction sector).
Thus, $Z_{o,min}$ = 17,0 - 16,4 = 0,6 m.

Under these severe conditions this ship will thus have to wait until a minimum tidal level of + 0,6 m CD is reached.

Practical Experience in Using the Manual

The "Richards Bay Harbour Port Operation Manual, Mark I" has been in use since October 1981. Records of ships in excess of 100 000 dwt which enter or leave the port under fairly rough conditions are kept on special record sheets provided to 'port control'. These records include information on the ship, its loaded condition, recorded wave direction and height during passage through the channel and tide records. The calculated equivalent draught (D_{eq}) and the limiting wave height ($H_{rep,lim}$) read from the draught allowance diagrams and the decision taken are also recorded on these sheets.

So far (August 1982), 97 departures and one entry of loaded coal carriers between 101 600 dwt and 169 080 dwt have been recorded on the special record sheets (maximum draught up to 17,3 m). Of these there were six occasions on which ships had to be held back, either for the high swell to subside or until the tide level had increased. In one case, the swell height was more than 1 m too high.

Future Improvement to the Manual

It is expected that the manual will be improved in two ways, firstly, by improving the recording system of the environmental data and, secondly, by improving the techniques for determining maximum expected vertical motions.

Wave heights are already recorded on magnetic tape and it is intended to replace the present graphic technique to determine H_{rep} by a spectral analysis technique. Provided the response functions of the ships are known (these will be determined from the prototype measurements), the effect of wave period can then also be included. Since ship motions are very dependent on wave direction, it is also expected that an automatic wave direction recording system will be used in the future.

The results of the present prototype measurements of vertical ship motions and additional physical model tests will be used to calibrate available mathematical ship motion

models. The final aim would be to replace the present draught allowance diagrams by a simplified version of such a model, which would predict the maximum expected vertical motions for a given ship under various wave and tide conditions.

CONCLUSIONS

The main cargo through Richards Bay harbour consists of coal exports using bulk carriers up to about 170 000 dwt, loaded to 17,1 m draught (in certain cases, 17,3 m was allowed).

Experience with the operation of the port indicates that the available stopping distance (6,1 km) is more than adequate for ships, presently calling at Richards Bay, entering at 6 to 8 kn (3 to 4 m/s) although further data on loaded design ships is still needed. Provided outer channel speeds of at least 7 to 8 kn (3,5 to 4 m/s), indicated by the hydraulic model test, are maintained, there is no serious problem in holding the ships in the 300 to 400 m wide channel.

Ship motion research is aimed at determining the minimum required dredging depths for ships up to 20 m draught (about 250 000 dwt) and at developing guidelines to assist in the safe operation of the port. The results of the prototype measurements showed that the underkeel allowance of 7 m accepted in the original design is of the right order of magnitude.

Because of the lack of sufficient direction coverage in prototype data, the Port Operation Manual, Mark I, was based on physical model tests with a 200 000 dwt and a 150 000 dwt model ship. Data on these test results were used to draw up easy to apply draught allowance diagrams which relate equivalent draught and limiting wave height for various wave directions. These diagrams allow for a minimum underkeel clearance of 1 m in the outer channel, the inner channel and the turning/mooring areas. To apply these diagrams to port operation, reliable data on wave heights and directions, tide levels and channel depths must be available.

The manual has been in use at Richards Bay port control since October 1981 and has been found to be of great value in assisting in the safe operation of the port.

The success of this project depended largely on the **understanding and co-operation of the various disciplines** involved, namely, those of the harbour engineers (civil engineering), the nautical staff and the research engineers (civil and mechanical/naval engineering).

Acknowledgement

The permission from the South African Transport Services to publish this paper is gratefully acknowledged.

REFERENCES

CAMPBELL, N P and ZWAMBORN, J A (1977). Special features in the design and construction of the new harbour for bulk cargoes at Richards Bay, Republic of South Africa. Proc. 24th PIANC Congress, Leningrad.

CSIR (1976). Manoeuvring tests with a 150 000 dwt model ship in the recommended final Richards Bay harbour entrance. CSIR Report C/SEA 7603, Stellenbosch.

CSIR (1979). Conditional allowance criteria for deeper draught ships using Richards Bay harbour. CSIR Report C/SEA 7906, Stellenbosch.

CSIR (1981). Richards Bay Harbour Port Operation Manual, Mark I. CSIR Report C/SEA 8104, Stellenbosch.

HOPPE, K G (1972). Scale effects in manoeuvring tests with small ship models. Proc. ECOR Symposium, S71, Stellenbosch, RSA.

KOELé, L A and HOOFT, J P (1969). The behaviour of a 200 000 dwt tanker in shallow water. Rijkswaterstaat Report No. W69-074, Wageningen.

LONGUET-HIGGINS, M S (1952). On the statistical distribution of the heights of sea waves. Journal of Marine Research, Vol. XI, Number 3.

MOES, J and VAN NIEKERK, M (1981). Refraction studies for Richards Bay using the Wale program. CSIR Report T/SEA 8105, Stellenbosch.

VAN WYK, A C (1982). Wave induced motions in harbour entrances: a field study. Proc. 18th International Coast. Eng. Conf., Cape Town.

ZWAMBORN, J A and GRIEVE, G (1974). Wave attenuation associated with harbour approach channels. Proc. 14th International Coast. Eng. Conf., Cophenhagen.

ZWAMBORN, J A and VAN WYK, A C (1981). Monitoring of ship motions in the Richards Bay harbour entrance channel. Proc. 25th PIANC Congress, Edinburgh.

THE RESPONSE OF SMALL CRAFT TO WAVE ACTION

by

M. ISAACSON[1], M.ASCE and A.G. MERCER[2], M.ASCE

ABSTRACT

A comprehensive study has been conducted for the Small Craft Harbours Branch, Department of Fisheries and Oceans Canada, to provide improved criteria for acceptable wave climate in small craft harbours (Ref. 3). An important part of the study was directed to model tests of vessel response to waves, and comparisons of these to field measurements and to simplified analytical predictions.

The objective of the present paper is to describe these specific comparisons and present the corresponding results in the context of improving harbour entrance designs. The model tests results and theoretical predictions are adequate to show quantitatively the dependence of a sailboat's response to different wave lengths with sufficient accuracy for wave periods, heights and directions to be selected as variables in formulating the required wave criteria.

INTRODUCTION

A commonly accepted criterion used in the design of small craft harbours is that wave heights within the harbour should not exceed 0.3 m (1 ft). However, it is clear that such a criterion is inadequate to take account of the many variables which give rise to vessel damage within a harbour. Consequently, a comprehensive study has been conducted for the Small Craft Harbours Branch, Department of Fisheries and Oceans Canada, to provide improved criteria for acceptable wave climate in small craft harbours (Ref. 3).

An important part of the study was directed to model tests of vessel response to waves, and comparisons of these to field measurements and to simplified analytical predictions. The model tests were carried out with a 0.8 m long model of a moored, fin-keel sailboat subjected to head and beam seas. The field measurements were carried out with a 7 m long boat similar to the model. The

[1] Dept. of Civil Engineering, Univ. of British Columbia, Vancouver, B.C., Canada.

[2] Northwest Hydraulic Consultants Ltd., North Vancouver, B.C., Canada.

analytical predictions were made for four categories of hull shape using different simplified analytical methods.

The objective of the present paper is to describe these specific aspects of the project and to present the corresponding results. A description of the overall project including the recommended criterion of acceptable wave conditions, is given in a companion paper (Ref. 1).

MODEL TEST PROCEDURE

Tests were carried out in a wave basin with a 0.76 m long model of a high performance fin-keel sailboat. Some of the basic specifications of the model are given in Table 1, and the fundamental configuration of the model is sketched in Fig. 1(a).

The boat was moored to a walkway (dock) which could be either fixed or floating. To arrive at appropriate model characteristics a typical wooden dock, 1.5 m wide and 12.2 m long, was replicated. When the walkway was allowed to float, it was constrained against lateral action by four vertical model piles. For fixed dock tests, the ends of the dock were constrained from vertical motion.

For all tests the model was moored with four lines, bow and stern breast lines set slack and bow and stern spring lines set at a small initial steady state tension. The lines were modelled to represent the elasticity of 1.3 cm braided nylon line commonly used for moorage.

The wave basin at the University of British Columbia used for the tests is approximately 13.7 m long, 4.9 m wide and could take water depths up to 0.6 m. The basin was provided with a wave absorbing beach along the end opposite to the wave generator. The wave generator was a hinged paddle with controls to vary the frequency up to 2 Hz and amplitude of motion up to 0.24 m. Only regular waves could be produced.

The wave height was measured with a capacitance-type wave gauge. A motion transducer was designed to record the three appropriate components of boat motion: heave, surge, pitch for head seas, or heave, sway, roll for beam seas. This comprised of a hinged arm which operates as three parallel systems capable of measuring the three required component motions of the vessel. The weight of the transducer was counterbalanced by a low tension spring or a counterweight in order to eliminate the effective weight of the transducer. In addition, movie film was shot of the vessel's motion with and without the transducer connected in order to establish the importance of the transducer in affecting the vessel motion. The transducer was calibrated over its range of application at the beginning of the tests and checked each day against a single reference point for each motion.

In the series of the tests, measurements were also made of the rise and fall of the dock and of peak hawser forces. Numerous photographs were taken and approximately 300 feet of 16 mm movie film

TABLE 1

PRINCIPAL CHARACTERISTICS OF BOAT HULLS ANALYSED

	Hull #1 Model Fin Keel Sailboat	Hull #2 Full Keel Sailboat	Hull #3 Planing Powerboat	Hull #4 Non-Planing Powerboat
Basic Specifications				
Length Overall (m)	0.76	12.50	12.80	10.87
Length Waterline (m)	0.67	10.67	11.18	10.16
Beam (m)	0.24	3.96	4.34	3.66
Draft (m)	0.15	1.45	1.07	1.14
Displacement (kg)	2.24	11,000	13,000	8,000
Ballast in Keel (kg)	1.27	4,500	-	-

TABLE 2

LIST OF CASES TREATED IN ANALYSIS

CASE	WAVE DIRN.	MOORING CONDITION	DEGREES OF FREEDOM	ANALYSIS METHOD	COMMENTS
1	Head	Free Floating	Surge, Heave Pitch	LWA, SBA	
2	Head	Linear Surge Stiffness	Surge, Heave Pitch	LWA, SBA	Heave, pitch as in Case 1
3	Head	Slack/Elastic Surge Spring	Surge, Heave Pitch	SBA	Heave, pitch as in Case 1
4	Head	Stern Hinge Links	Heave, Pitch	LWA, SBA	Heave, pitch as in Case 1
5	Beam	Free Floating	Sway, Heave Roll	LWA, SBA	
6	Beam	Stern Hinge Links	Heave, Roll	LWA, SBA	Heave as in Case 5

LWA: Long Wave Approximation
SBA: Modified Slender Body Approximation

Fig. 1. Hull Configurations Analysed

(a) Fin keel sailboat (model).

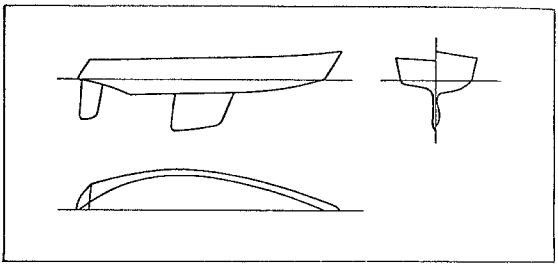

(b) Full keel sailboat.

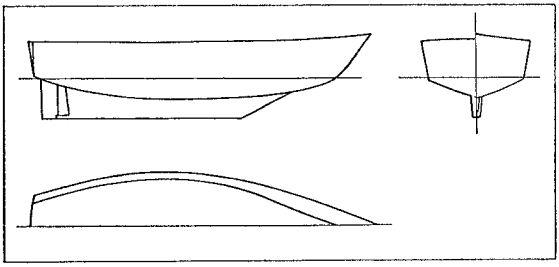

(c) Planing powerboat.

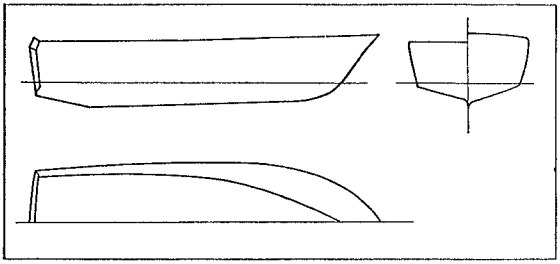

(d) Non-planing powerboat.

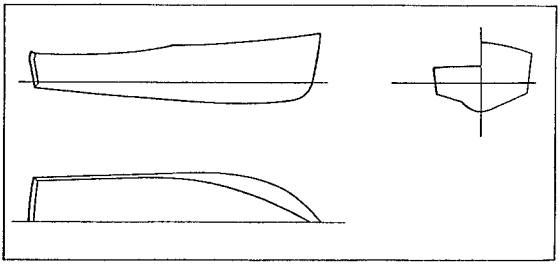

were shot to provide some documentation of the motions involved.

Preliminary tests were first conducted to measure the vessel's natural periods in roll and pitch, and its static stability characteristics. The curves of pitch and roll angles against applied moment were used to obtain the corresponding hydrostatic stiffnesses and are given in Fig. 2. Subsequently, a series of 148 tests, in which wave period, wave height and wave direction varied, were run and documented. The ranges of conditions for which the tests were carried out were as follows (prototype values for 1:10 scale model are given in parentheses):

water depth:	0.30 and 0.46 m (3.0 and 4.6 m)
water period:	0.5 - 2.0 sec (1.6 - 6.3 sec)
wave height:	0.01 - 0.07 m (0.08 - 0.71 m)
wave direction:	head and beam seas
dock motion:	fixed and floating

FIELD TEST PROCEDURE

The field measurement program, carried out at Fisherman's Cove near Vancouver, developed into several short term activities including:

(i) Calm water tests mostly on a Swiftsure 24 sailboat to obtain data for comparison with the model.

(ii) Wave tests on a Swiftsure 24 and a Bayfield 25 for comparison with model response data.

Measurements were first made of the static moment vs. roll or pitch angle relationships for the Swiftsure 24, and the corresponding curves are compared to those obtained with the model in Fig. 2. Natural periods in roll were measured for a number of vessels using the marina, and these ranged from 2.1 sec to 3.7 sec.

For the wave response tests, the Swiftsure 24 sailboat was moored alongside a gasoline service barge with taut springs and loose breastlines as in the model tests. Wave measurements for the period during testing indicated a significant wave height of 0.37 m and a peak period of 2.4 sec. Measurements of the vessel motions were taken for both head and beam sea conditions, and were carried out with the use of surveying equipment and by photography.

HYDRODYNAMIC ANALYSIS

The hydrodynamic analysis of a freely floating vessel responding to wave action is well known and has been reviewed, for example, by Newman (2). In a linear analysis the vessel is taken to oscillate harmonically in six degrees of freedom with displacements given as $\mathrm{Re}\{\xi_j e^{i\omega t}\}$, with $j = 1$ coresponding to surge, $j = 2$ to heave, $j = 3$ to sway, $j = 4$ to roll, $j = 5$ to yaw and $j = 6$ to pitch, and ω is the wave angular frequency.

Fig. 2. Model prototype static test results.

(a) Roll

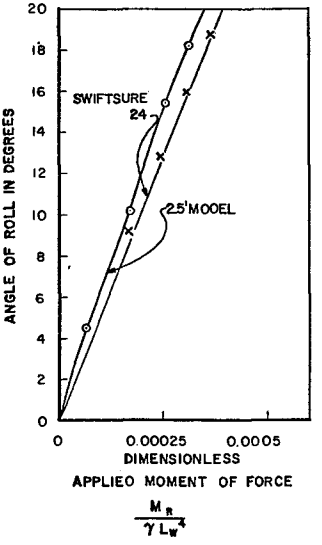

(b) Pitch

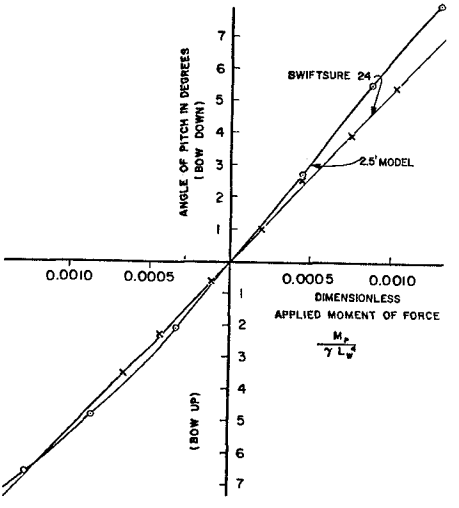

The equations of motion of an unrestrained floating body can be expressed in terms of the complex amplitudes ξ_j by a matrix equation:

$$\{-\omega^2 ([M] + [A]) + i\omega [B] + [C]\} (\xi) = (F) \quad (1)$$

where [M] is the mass matrix, [A] the added-mass coefficient matrix, [B] the damping coefficient matrix, [C] the stiffness matrix, and (F) the exciting force vector. In this notation the components F are the exciting force complex amplitudes, with corresponding time varying forces given as $Re\{F_j e^{i\omega t}\}$. The mass matrix components and stiffness matrix components are simply derived for a given vessel configuration and weight distribution.

In the case of a moored body, the various terms in the equation of motion, Eq. (1), may be extended to reflect the influence of the moorings on the body's motion. In the usual case, the moorings may be treated as linear springs with constant coefficients and the stiffness matrix can be modified to incorporate these.

In a complete hydrodynamic anlaysis, the matricies [A] and [B], and the vector (F) are obtained from a solution to the governing radiation/diffraction boundary value problem. This usually derives from the assumptions of a linear motion (small amplitude waves) and an irrotational flow (flow separation effects neglected). An assumption often made in a motion response analysis of a moored vessel is that the mooring system affects the low frequency (drift) oscillations only, but is too light and flexible to affect the vessel oscillations at higher wave frequencies. However, this assumption is unrealistic in the case of light boats with slack moorings.

In the present study, a complete hydrodynamic analysis of a moored vessel with six degrees of freedom has been considered unwarranted because many of the common assumptions generally made are considered unrealistic in relation to the additional effort and cost entailed in a full three-dimensional analysis. For example, for small craft complicating effects may include flow separation, particularly around a keel in beam seas, asymmetric motions for a nominally symmetric condition (e.g. yaw in head seas), nonlinear mooring conditions (e.g. slack/elastic moorings), wave nonlinearities, etc. The intention has been instead to investigate simplified analytical procedures which would adequately predict measured responses over specific ranges of conditions. These analyses are restricted to head seas (with only surge, heave and pitch motions occurring) and to beam seas (with only heave, sway and roll motions occurring).

Long Wave Approximation (LWA)

When the wave length to vessel length ratio is large, a long wave approximation may be made, whereby the exciting force components can be expressed directly in terms of the added-mass the damping

coefficients and the vessel's hydrostatic characteristics. The underlying theory is given by Newman (2) and appropriate expressions for the exciting force complex amplitudes may thereby be derived. These may be written in terms of $F' = 2F/H$, where H is the wave height, as follows:

Head Seas:

$$F'_1 = \frac{ik}{\omega^2}\left[-\omega^2(m + a_{11}) + i\omega b_{11}\right] \tag{2a}$$

$$F'_2 = S - \omega^2(m + a_{22}) + i\omega b_{22} + kS_1 \tag{2b}$$

$$F'_6 = S_1 + ikmy_B + ikS_{11} \tag{2c}$$

Beam Seas:

$$F'_2 = S - \omega^2(m + a_{22}) + i\omega b_{33} \tag{2d}$$

$$F'_3 = -\frac{ik}{\omega^2}\left[-\omega^2(m + a_{33}) + i\omega b_{33}\right] \tag{2e}$$

$$F'_4 = ik(my_B + a_{34}) + ikS_{33} + \frac{k}{\omega} b_{34} \tag{2f}$$

These equations for the exciting force can be substituted into the RHS of the corresponding equation represented by Eqs. (1) to obtain expressions for peak displacements which can then be solved. Since some terms appear on both sides of the equations considerable simplification arises in many cases.

In the above $k(= 2\pi/\lambda)$ is the wave number, y_B is the vertical ordinate of the centre of buoyancy, S is the waterplane area, and S_1, S_{11} and S_{33} are the waterplane area moments defined as follows:

$$S_1 = \int x\, b(x)\, dx \tag{3a}$$

$$S_{11} = \int x^2\, b(x)\, dx \tag{3b}$$

$$S_{33} = \int \frac{1}{12} b^3(x)\, dx \tag{3c}$$

where $b(x)$ is the sectional beam of the waterplane profile, the integrals are taken over the waterplane length L_ω of the vessel, and x is the horizontal coordinate measured towards the bow.

As part of the approximations carried out in the present analysis, estimates of a_{ij} and b_{ij} (frequency dependent) have been obtained by using published data of the coefficients for related reference configurations. All cross coefficients have been taken equal to zero except a_{34}, b_{34} which couple roll and sway in beam seas. Viscous effects are known to alter the damping coefficients from the predicted potential theory values, particularly for roll motions, and available experimental and theoretical results of drag

coefficients in an oscillatory flow past a flat plate have been used to estimate corresponding values of viscous damping coefficients for vessels (including the model) containing deep keels.

Slender Body Approximation (SBA)

The slender body approximation provides an alternative approximation procedure which is valid for shorter wave lengths of the order of the boat length. This depends on the beam/length ratio being small so that certain terms in the equations of motion which are proportional to higher orders of this ratio may be neglected. In this approximation, the actual Froude-Krylov forces are used in the RHS of Eqs. (1), rather than using Eqs. (2). Simplifications are made by neglecting certain terms in the LHS of Eqs. (1). The method is outlined by Newman (2).

Since mass or stiffness terms are neglected for various modes of motion, resonance behaviour is not predicted for most cases: that is, the resonant frequencies are assumed to occur outside the wave length (frequency) range considered. In order to predict the resonance features found for most modes of motion, an attempt has been made to include additional mass and stiffness terms beyond those used in the formal approximation.

Slack/Elastic Mooring Line Approximation

The non-linear analysis required for a slack/elastic mooring line can be idealized as that pertaining to a spring-mass-dashpot system with non-linear spring characteristics and subjected to a known (exciting) force. The spring constant due to the moorings is approximated to be a constant value (depending on the elasticity of the mooring) for positive vessel displacements and zero otherwise. The corresponding non-linear ordinary differential equation can be approximated as:

$$m\ddot{\xi} + r\dot{\xi} + s\xi = Fe^{i\omega t} \tag{4}$$

where m is the body mass (including added-mass), r is the damping constant, $s = 0$ for $\xi < 0$ and $s = c$ for $\xi > 0$, and c is the elastic constant of the mooring. This non-linear ordinary differential equation can be solved by a Ritz approximation procedure which is particularly simple when extracting the fundamental harmonic of the vessel displacement. The results may be expressed as

$$\xi = Xe^{i\omega t} \tag{5a}$$

with the amplitude of the motion given by:

$$|X| = F\left\{\left(\frac{c}{2} - m\omega^2\right)^2 + r^2\omega^2\right\}^{-1/2} \tag{5b}$$

and the phase relative to that of F given by:

$$\text{Arg}(X) = \tan^{-1}\left[\left(\frac{c}{2} - m\omega^2/r\omega\right)\right] \qquad (5c)$$

These equations have been used to compute the vessel's surge and sway response to a slack/elastic moorage.

Moorage Conditions Analysed

Application of the different approximations described to different moorage arrangements has been accomplished by considering a series of specific cases, including head and beam seas, a freely floating boat, a linear mooring restraining surge only, a slack/elastic mooring for surge or sway only, and stern hinge links which restrain fore-and-after motions but allow the stern to move vertically. These cases are listed in Table 2. The computations have been carried out for four hull configurations corresponding to a deep fin sailboat, a full keel sailboat, a planing power boat and a displacement type power boat, as indicated in Fig. 1, and their principal characteristics are given in Table 1.

RESULTS

Model Test Results

The model test results are presented in Figs. 3 and 4 showing the response amplitude operators (RAO's) as functions of the wave length to vessel length ratio. The response amplitude operators are defined here as:

$$\text{RAO} = \begin{cases} \dfrac{\text{motion amplitude}}{\text{wave amplitude}} & \text{for surge, heave, sway} \\ \dfrac{\text{roll amplitude (rads)}}{2\ H/B} & \text{for roil} \\ \dfrac{\text{pitch amplitude (rads)}}{2\ H/L_w} & \text{for pitch} \end{cases}$$

where H is the wave height, B the beam and L_w the water plane length.

Results for both fixed and floating dock cases are given in Fig. 3 for head seas, and in Fig. 4 for beam seas.

There is some spread of the experimental data points which indicates either non-linear effects, a lack of consistency in the phenomena, or the degree of data taking and instrumentation accuracy. Evidently all three effects were present to some degree.

As mentioned previously, movie footage was taken of several tests with the transducer in place and with it removed. This data has also been plotted in Fig. 3(b) and it fell within the scatter of the transducer data indicating that the transducer did not grossly misrepresent the model motions. A complete discussion of the various trends indicated in the figures is given in Ref. 3.

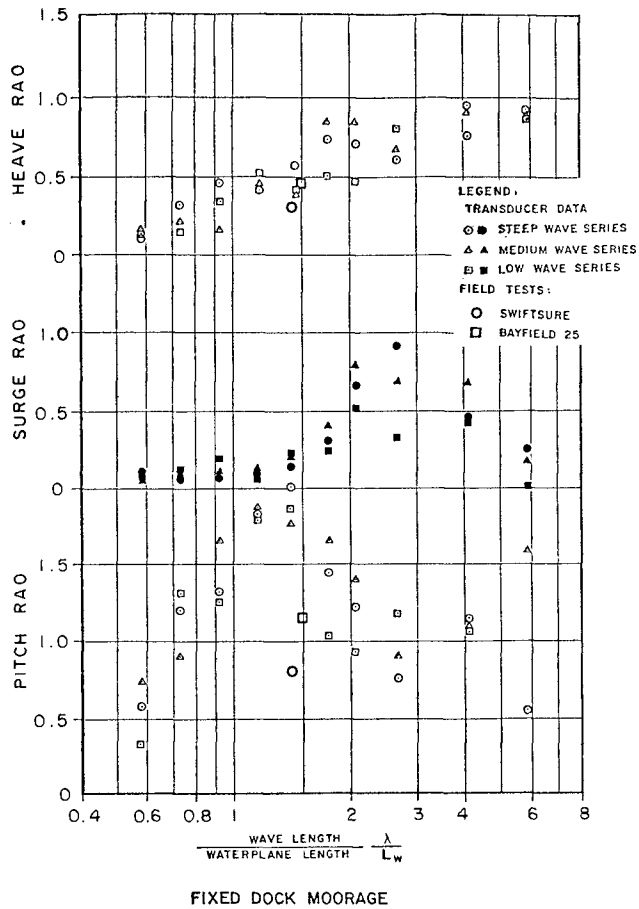

Fig. 3(a). Dimensionless model test results for head seas - Fixed dock moorage.

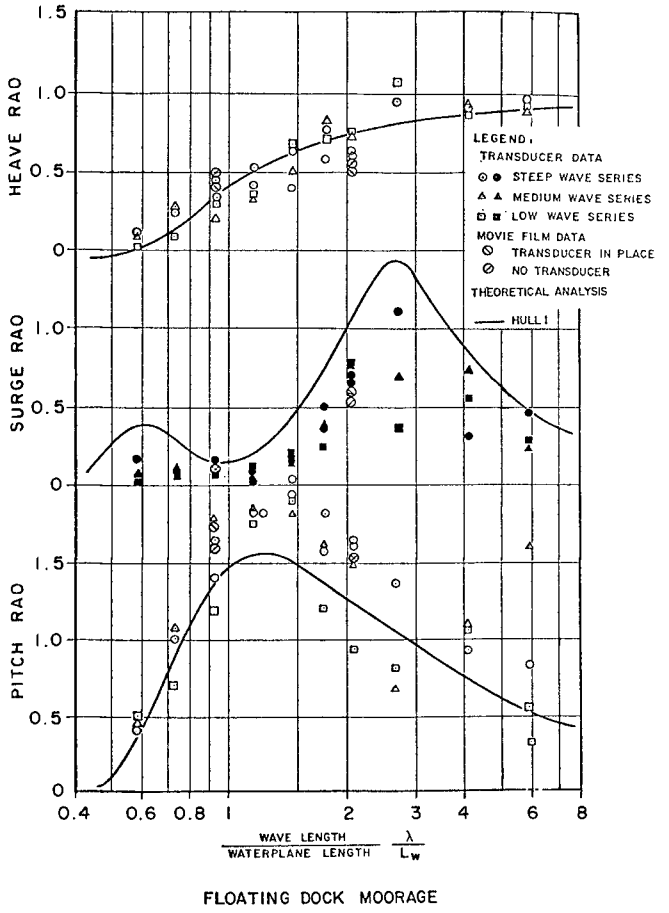

Fig. 3(b). Dimensionless model test results for head seas - Floating dock moorage.

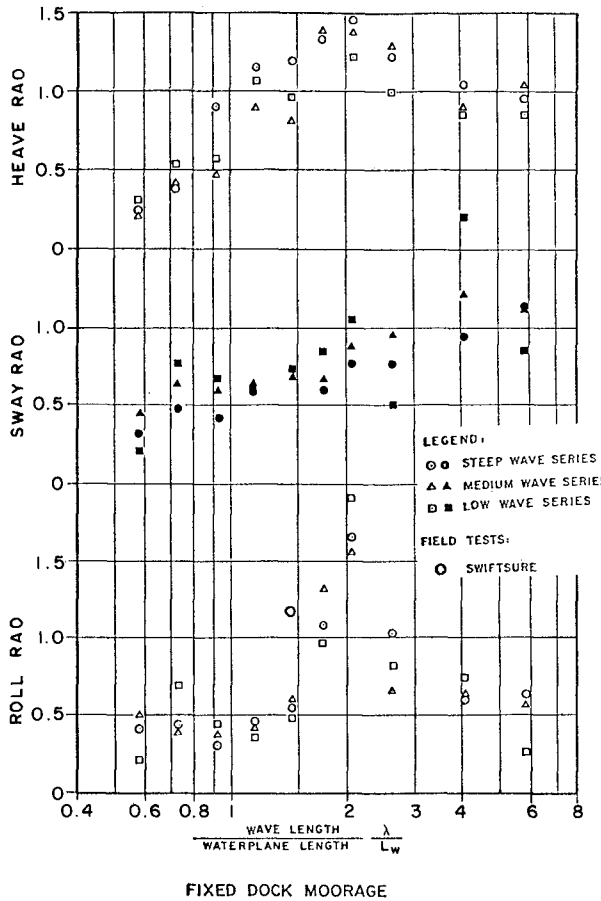

Fig. 4(a). Dimensionless model test results for beam seas - Fixed dock moorage.

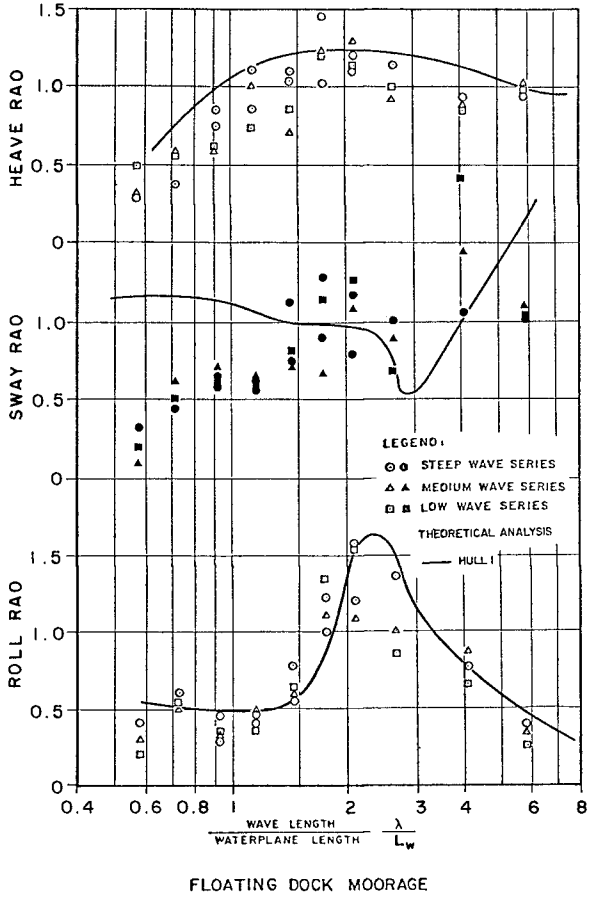

Fig. 4(b). Dimensionless model test results for beam seas - Floating dock moorage.

Field Test Results

The corresponding results for the Swiftsure and Bayfield vessels are superposed with the model test results in Figs. 3(a) and 4(a). The results for pitch are relatively low while those for heave and roll show good agreement with the model data.

Analytical Results

The analytical results for Hull 1 (the model vessel) based on the alternative approximations adopted are given in Fig. 5 for head and beam seas. For head seas, both heave and pitch equations are coupled so that the results are interdependent. For both heave and pitch the LWA produces results close to the SBA for longer waves but they diverge rapidly for shorter waves. In beam seas, sway and roll are also closely coupled and must be treated together. Although moorage constraint is important to sway and roll, the coupling make the constraint difficult to handle so that only free response curves are shown here.

For both head and beam seas, the SBA (modified) is found to provide a better representation of response than the LWA when compared with model results. Thus the SBA analytical results for Hull 1 are compared to the experimental data points in Fig. 3(b) for head seas and in Fig. 4(b) for beam seas. For head seas, the SBA plots will be seen to agree very closely with the measured data over the full range of wave lengths tested. Heave response is shown to be equal to the wave height for longer waves (greater than 5 times boat length) but diminishes for shorter waves until it reaches zero for wave lengths approxiamtely one-half the boat length. Pitch response for longer waves (greater than 4 times the boat length) follows the pitch (slope) of the wave surface. It diminishes for shorter waves approaching zero for wave lengths about one half the boat length. Neither heave or pitch have a resonant condition in head seas under the SBA and this is supported by model data. The response in surge is more complex because surge is heavily constrained by the moorage lines, and free floating response results are expected to be grossly excessive.

For beam seas, the SBA also provides a better representation of response than does the LWA. The roll reaches at least 3 times the equivalent slope of the water surface. The frequency of roll at resonance is very close to the natural period of roll noted in still water. As with surge in head seas, the (free floating) analytical sway results are quite invalid because of the influence of the moorings. Heave response in a beam sea shows a broad resonance condition with boat response as much as 25 percent greater than the wave height. However, as with head seas the heave response ratio approaches unity for long waves and approaches zero for short waves.

Finally, Fig. 6 shows the analytical results based on the SBA for the four hull types indicated previously (Table 1 and Fig. 1). The curves show that responses are very similar except for those

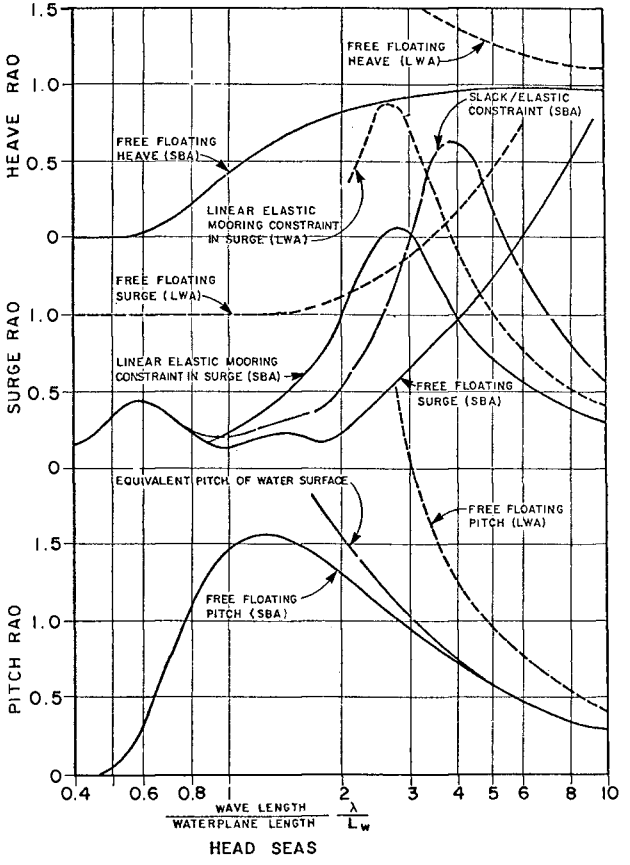

Fig. 5(a). Analytical evaluations of vessel response for Hull 1 - Head Seas.

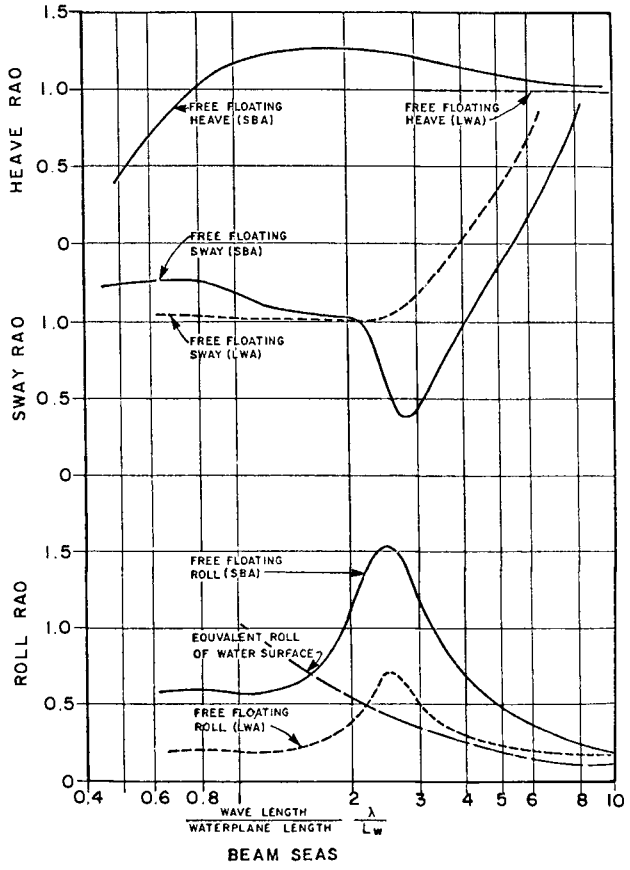

Fig. 5(b). Analytical evaluations of vessel response for Hull 1 - Beam Seas.

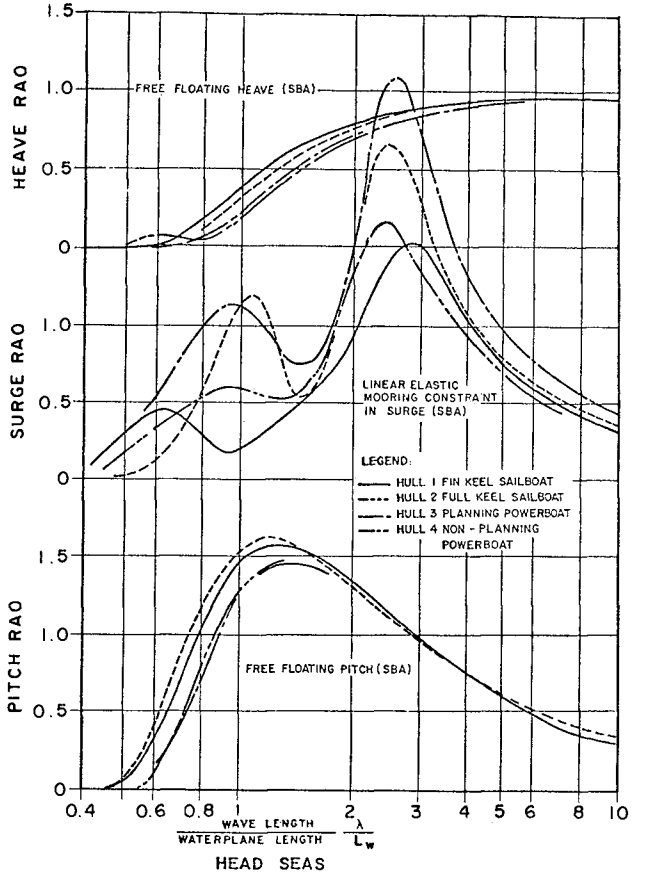

Fig. 6(a). Analytical evaluations of vessel response for four hulls - Head Seas.

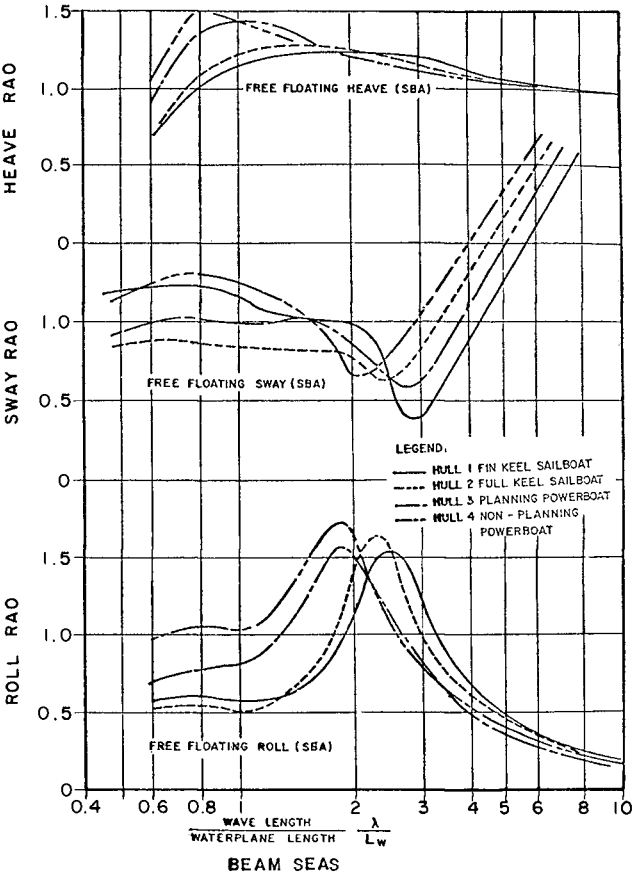

Fig. 6(b). Analytical evaluations of vessel response for four hulls - Beam Seas.

responses involving resonances which include heave in a beam sea and surge with linear elastic constraint. (Sway with moorage constraint also is subject to strong resonances but is not included here.) The resonance in heave is not strong so that the differences between hull types is not large. Nonetheless they are large in surge. Also the response values at the resonant peaks are not too reliable because they vary greatly with amount of damping that is present. As a result, the responses in heave, pitch and roll appear to be reasonably predictable but the responses in surge and sway can only be predicted with a sizeable degree of uncertainty.

CONCLUSIONS

The model test and analytical results have been compared and are generally quite adequate to show quantitatively the dependence of vessel response on wave height, period and direction with sufficient accuracy to enable improved criteria of acceptable wave climate for small craft to be established.

REFERENCES

1. Mercer, A.G., Isaacson, M. and Mulcahy, M.W. (1982). Design Wave Climate in Small Craft Harbours. Proc. 18th International Conference on Coastal Engineering, Cape Town, South Africa.
2. Newman, J.N. (1977). Marine Hydrodynamics, MIT Press.
3. Small Craft Harbours Branch, Fisheries and Oceans Canada (1980). Study to Determine Acceptable Wave Climate in Small Craft Harbours. Prepared by Northwest Hydraulic Consultants Ltd., Vancouver.

THE MOTIONS OF A MOORED SHIP IN A HARBOR BASIN

T. Sawaragi, Dr. of Eng., Professor,Dept. of Civil Eng., Osaka Univ., Osaka, Japan.
M. Kubo, Dr. of Eng., Associate Professor, Kobe Univ. of Mercantile Marine, Kobe, Japan.

ABSTRACT

In harbors affected by ocean swells,cargo handlings are often interrupted and mooring lines are broken as a result of severe ship motions[1]. In order to decrease such accidents, the moored ship motions in a harbor basin must be studied. In this paper the ship motions in the harbor basin are investigated by using three dimensional Green's function and close agreement between theoretical and experimental results can be found. New methods to reduce moored ship motion are also proposed. The efficiency of these methods is verified theoretically and experimentally.

1. INTRODUCTION

At the initial stage of harbor planning, the hydraulic experiment with respect to stillness in a harbor is usually carried out and the degree of stillness in the harbor has been traditionally evaluated by the wave height. In the field, however, the limits of cargo handling in rough sea condition are judged by the ship movements. Therefore, lately, an analysis of moored ship motions in a harbor basin has become major interest for harbor planning.

As for the ship motions, there are short-period ones induced by wind waves and swells such as surge, sway, heave, roll, pitch and yaw, and long-period ones such as surge, sway and yaw whose natural periods are decided by the moored system. Many studies concerning long-period motions of a moored ship along the quay wall in beam sea have been done. The authors have also presented a paper about the long-period ship motions induced by the harbor oscillations in an arbitrary geometry basin[2]. Therefore, in this paper, the short-period ship motions are investigated by three dimensional method.

The three dimensional analyses are divided into two methods, one is the singularity distribution method[3] and the other is the joining method of divided region[4]. The latter method is used in this paper in order to analyze the ship motions along a straight quay wall and in a slip and these results are verified by the experiments.

On the other hand, Joglekar and Kulkani[5] have proposed the mooring system with the dash-pots in order to reduce the long-period ship motion in bore tide. However, the effects of these dash-pots on the short-period ship motions was not clarified yet. In this paper, the new mooring system with dash-pots is also analyzed theoretically and experimentally.

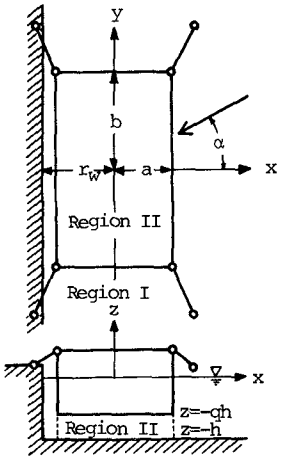

Fig.1 Definition of the coordinate system

2. THEORY OF SHIP MOTIONS

2.1 Motions of Moored Ship Along the Straight Quay Wall.

The authors will try to develop the joining method of divided region into that which can be applied to the ship motions along a straight quay wall. Since very large memory size and a great deal of cost are required in three dimensional analysis, the method of images are applied to decrease memory and cost.

Fig. 1 shows the moored ship and the coordinate system. The amplitudes of ship motions and waves are supposed to be small, and fluid around the ship is assumed to be ideal and irrotational. The coordinates of the center of gravity of the moored ship are given by $(0,0,\bar{Z}_0)$ in still water and by (X_0, Y_0, Z_0) in waves. δ_1, δ_2 and δ_3 show the rotation of the center of gravity of the moored ship around X, Y and Z axis, respectively. Then, the ship motions are expressed by:

$$X_0=\xi^* e^{-i\sigma t} \text{ (sway)}, \quad Y_0=\eta^* e^{-i\sigma t} \text{ (surge)}, \quad Z_0-\bar{Z}_0=\zeta^* e^{-i\sigma t} \text{ (heave)}$$
$$\delta_1=\omega_1^* e^{-i\sigma t} \text{ (pitch)}, \quad \delta_2=\omega_2^* e^{-i\sigma t} \text{ (roll)}, \quad \delta_3=\omega_3^* e^{-i\sigma t} \text{ (yaw)} \tag{1}$$

where ξ^*, η^*, ζ^*, ω_1^*, ω_2^* and ω_3^* are the amplitudes of ship motions, $i=\sqrt{-1}$, $\sigma=2\pi/T$, T is the wave period and t is the elapsed time. The water region is divided into two parts as shown in Fig. 1. The velocity potential in region I is given by:

$$\phi_I^w = \frac{g\zeta_0}{\sigma}[\{f_0(x,y)+f_1(x,y)\}\frac{\cosh k(h+z)}{\cosh kh} + \sum_{n=1}^{\infty} f_2^{(n)}(x,y)\frac{\cos k_n(h+z)}{\cos k_n h}] \tag{2}$$

where g is the gravitational acceleration, ζ_0 is the amplitude of incident waves, h is the water depth and the superscript w means the velocity potential along the quay wall. k and kn satisfy the following equation:

$$\sigma^2 h/g = kh \tanh kh = -k_n h \tan k_n h, \quad (n=1,2,\ldots) \tag{3}$$

The wave function f_0 corresponding to the incident and the reflected waves is given by:

$$f_0(x,y) = -i \exp\{-ik(x\cos\alpha + y\sin\alpha)\} - i\exp[-ik\{(-2\gamma_w - x)\cdot \cos\alpha + y\sin\alpha\}] \tag{4}$$

where γ_w is the distance between the quay wall and the center line of the ship, α is the angle of wave incidence. The functions $f_1(x, y)$ and $f_2^{(n)}(x, y)$ are the terms corresponding to the evanescent modes and they are expressed as Eq.(5) by using the Green's formula:

$$f_1(x,y) = -\frac{1}{2}\sum_{j=1}^{q}\{\bar{A}_{xj} f_1(j) - A_{xj}\bar{f}_1(j)\}$$

$$f_2^{(m)}(x,y) = -\frac{1}{2}\sum_{j=1}^{N}\{\bar{B}_{xj}f_2^{(m)}(j)-B_{xj}\bar{f}_2^{(m)}(j)\} \tag{5}$$

where over bars indicates the normal derivative to the boundary, namely, $\bar{f}_1(j)=\partial f_1(j)/k\partial\nu$, $\bar{f}_2^{(m)}(j)=\partial f_2^{(m)}(j)/k\partial\nu$, N is the number of segments of the boundary of ship and A_{xj}, $\bar{A}_{xj}$, B_{xj} and $\bar{B}_{xj}$ are given by:

$$A_{xj}=-\frac{i}{2}\int_{\Delta s_j}\{H_0^{(1)}(k\gamma_S)+H_0^{(1)}(k\gamma_I)\}k\,ds,\quad \bar{A}_{xj}=-\frac{i}{2}\int_{\Delta s_j}\frac{\partial}{\partial\nu}\{H_0^{(1)}(k\gamma_S)+H_0^{(1)}(k\gamma_I)\}ds,$$

$$B_{xj}=-\frac{1}{\pi}\int_{\Delta s_j}\{K_0(k_n\gamma_S)+K_0(k_n\gamma_I)\}k\,ds,\quad \bar{B}_{xj}=-\frac{1}{\pi}\int_{\Delta s_j}\frac{\partial}{\partial\nu}\{K_0(k_n\gamma_S)+K_0(k_n\gamma_I)\}ds,$$

$$\gamma_S=\sqrt{(x-\xi_j)^2+(y-\eta_j)^2},\quad \gamma_I=\sqrt{(2\gamma+x+\xi_j)^2+(y-\eta_j)^2} \tag{6}$$

where the coordinates (ξ, η) correspond to the boundary of ship, j is the number of segments of boundary of ship and the coordinates (x, y) express the internal point.

On the other hand, the velocity potential in region II is given by:

$$\left.\begin{aligned}\phi_{II}^{W}=&\frac{g\zeta_0}{\sigma}\,[\psi_0(x,y)+\sum_{s=1}^{\infty}\psi_s(x.y)\cos\bar{s}\,(z+\bar{q}h)\\&+i\,\frac{1}{2\bar{q}}\,\frac{\sigma^2h}{g}\{(-\frac{\zeta^*}{\zeta_0}-\frac{\omega_1^*y}{\zeta_0}+\frac{\omega_2^*x}{\zeta_0})((1+\frac{z}{h})^2-\frac{\bar{q}^2}{3})\\&+\frac{1}{4}(\frac{2\zeta^*}{\zeta_0}+\frac{\omega_1^*y}{\zeta_0}-\frac{\omega_2^*x}{\zeta_0})(\frac{x^2+y^2}{h^2})\}],\end{aligned}\right\} \tag{7}$$

where $\bar{s}=s\pi/\bar{q}h$, $\bar{q}=1-q$ and qh is the draft of the ship. When Ps are the wave forces, Ts are the moments of wave forces, Fs are the mooring forces and Ms are the moments of the mooring forces, the equations of motions of moored ship are given by:

$$\left.\begin{aligned}M\frac{d^2X_0}{dt^2}&=Px+Fx,\quad M\frac{d^2Y_0}{dt^2}=Py+Fy,\quad M\frac{d^2Z_0}{dt^2}=Pz+Fz,\\I_x\frac{d^2\delta_1}{dt^2}&=Tx+Mx,\quad I_y\frac{d^2\delta_2}{dt^2}=Ty+My,\quad I_z\frac{d^2\delta_3}{dt^2}=Tz+Mz,\end{aligned}\right\} \tag{8}$$

where M and Is are the mass and moments of inertia of the ship.

The continuity conditions of fluid particle velocity and pressure at the imaginary boundary shown in Fig. 1 are given by:

$$\left.\begin{aligned}\frac{\partial\phi_I^W}{\partial x}&=-i\sigma\{\xi^*-\omega_3^*y+\omega_2^*(z-\bar{z}_0)\},\ (\xi=\pm a,\ 0>z>-qh),\\\frac{\partial\phi_I^W}{\partial y}&=-i\sigma\{\eta^*+\omega_3^*x-\omega_1^*(z-\bar{z}_0)\},\ (\eta=\pm b,\ 0>z>-qh),\\\frac{\partial\phi_I^W}{\partial\nu}&=\frac{\partial\phi_{II}^W}{\partial\nu},\ (-qh>z>-h),\quad \phi_I^W=\phi_{II}^W,\ (-qh>z>-h)\end{aligned}\right\} \tag{9}$$

where a=B/2, B the breadth of the ship, b=Ls/2, Ls the length of the ship. From Eq.(1) to Eq.(9), the amplitudes of ship motions ξ^*, η^*, ζ^*, ω_1^*, ω_2^* and ω_3^* and the unknown functions f_1, $f_2^{(m)}$, $\partial f_1/\partial\nu$, $\partial f_2^{(m)}/\partial\nu$ are obtained.

2.2 Motions of Moored Ship in a Slip

2.2.1 Wave Height Distribution in a Slip

Since the ship motions in a slip are naturally induced by waves in a slip, it becomes important to investigate the accuracy of wave height distributions in advance of the analysis of moored ship motions in the slip. Moreover, the three dimensional analysis of the ship motions especially in a slip requires very large memory size and a great deal of cost, so the method of images are also applied to decrease memory and cost.

The region around the slip is divided into two parts, as shown in Fig. 2. The velocity potential in each region is given by:

$$\left.\begin{aligned}\phi_I &= \frac{g\zeta_0}{\sigma}\{f_0(x,y) + f_1(x,y)\}\frac{\cosh k(h+z)}{\cosh kh}\\ \phi_{II} &= \frac{g\zeta_0}{\sigma} f_2(x,y)\frac{\cosh k(h+z)}{\cosh kh}\end{aligned}\right\} \quad (10)$$

when the incident waves into the slip are given by:

$$\zeta = \zeta_0 \exp\{-i(kx\cos\alpha + ky\sin\alpha + \sigma t)\} \quad (11)$$

the wave function f_0 is expressed by:

$$f_0(x,y) = -2i\cos(ky\sin\alpha)\exp(-ikx\cos\alpha) \quad (12)$$

Using the Green's formula, the wave function f_1 and f_2 are given by:

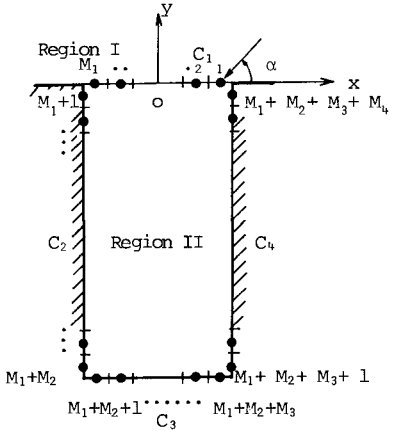

Fig.2 Division of the region around a slip and segmentation of the boundary. The angle of wave incidence is measured anti-clockwise from x-axis.

$$\left.\begin{aligned}f_1(x,y) &= -\varepsilon\sum_{j=1}^{M_1}\{\bar{A}_{xj}f_1(j) - A_{xj}\bar{f}_1(j)\}\\ f_2(x,y) &= -\varepsilon\sum_{j=1}^{N_s}\{\bar{A}_{xj}f_2(j) - A_{xj}\bar{f}_2(j)\}\end{aligned}\right\} \quad (13)$$

where M_1 is the number of segments at the entrance and Ns is the total number of segments of the slip. When (x, y) are on the boundary, ε=1/2, and when (x, y) are in the slip, ε=1.0 . It is not convenient to apply the method of images to the parallel boundaries, because the number of images amounts infinity and the times of computation becames long[6]. So the Green's functions are chosen so as to satisfy the following relations:

$$\bar{A}_{xj} = 0 \quad \text{on } C_2 \text{ , } C_3 \quad (14)$$

As the following equation is satisfied on the boundary,

$$\bar{f}_2(j) = 0 \qquad \text{on } C_2,\ C_3,\ C_4\ , \tag{15}$$

the number of segments in Eq.(13) is reduced from Ns of Lee's method to M_1+M_4. Then the Green's function A_{ij} which satisfies Eq.(14) can be obtained by the method of images as shown in Fig. 3:

$$\left.\begin{aligned}
&A_{xj}=\int_{\Delta s_j}-\frac{ik}{2}\sum_{p=1}^{4}H_0^{(1)}(k\gamma_p)\,ds,\quad \bar{A}_{xj}=\int_{\Delta s_j}\frac{ik}{2}\sum_{p=1}^{4}H_1^{(1)}(k\gamma_p)\frac{\partial\gamma_p}{\partial\nu}\,ds,\\
&\gamma_1=\sqrt{(x_j-x)^2+(y_j-y)^2}, && \frac{\partial\gamma_1}{\partial\nu}=-(y_j-y)/\gamma_1\\
&\gamma_2=\sqrt{(-x_j-2\ell_s-x)^2+(y_j-y)^2}, && \frac{\partial\gamma_2}{\partial\nu}=-(y_j-y)/\gamma_2\\
&\gamma_3=\sqrt{(-x_j-2\ell_s-x)^2+(-2ds-y_j-y)^2}, && \frac{\partial\gamma_3}{\partial\nu}=-(2ds+y_j+y)/\gamma_3\\
&\gamma_4=\sqrt{(x_j-x)^2+(-2ds-y_j-y)^2}, && \frac{\partial\gamma_4}{\partial\nu}=-(2ds+y_j+y)/\gamma_4
\end{aligned}\right\} \tag{16}$$

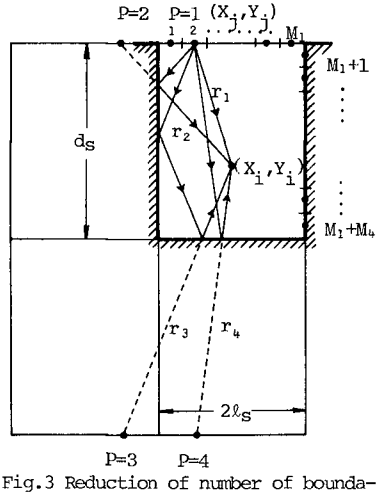

Fig.3 Reduction of number of boundary points by applying the method of images

Besides the above alternations, the computation is carried out in much the same way as the Lee's method[7]. The memory size and cost in this case is one quarter of those in the Lee's method.

Figure 4 shows the response of wave height to the wave period T. The coincidence of numerical and experimental results is fairly well. So the wave height distributions in the slip can be obtained exactly by the above method.

2.2.2 Ship Motions in a Slip

The region around the slip is divided into three parts, that is, the outer part of the slip region I, the under part of the ship region III and the rest part in the slip region II. The velocity potential in the region I is equal to Eq.(2) and is given by:

$$\phi_I^s=\phi_I^w \tag{17}$$

where the superscript s means the velocity potential in the slip. The velocity potential in the region II corresponds to the one which is lacking in $f_0(x, y)$ in Eq.(2) and is given by:

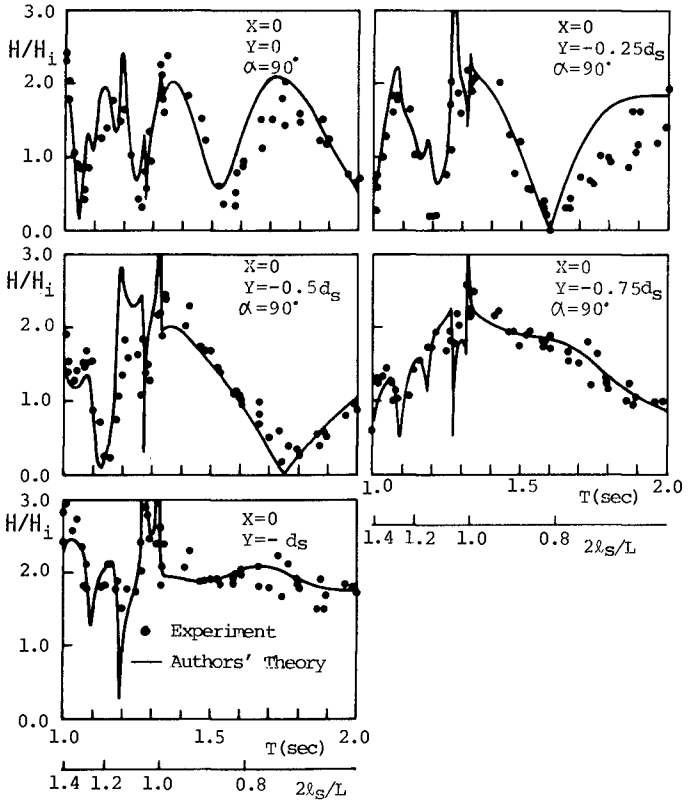

Fig.4 Amplification factor of wave height H at the typical point in the slip, where H_i is the incident wave height.

$$\phi^{s}_{II} = \frac{g\zeta_0}{\sigma}\left[\{f_2^{(0)}(x,y)\frac{\cosh k(h+z)}{\cosh kh} + \sum_{n=1}^{\infty} f_2^{(n)}(x,y)\frac{\cos k_n(h+z)}{\cos k_n h}\right] \quad (18)$$

The velocity potential in region III is the same as Eq.(7)

$$\phi^{s}_{III} = \phi^{w}_{II} \quad (19)$$

As shown in Figure 5, boundaries are chosen as follows: the entrance C_1, the quay walls surrounding the slip C_2, C_3, C_4 and the ship sides C_5. They are divided into M_1~M_5 segments.

At the entrance the following conditions must be satisfied:

$$\phi_I^S = \phi_{II}^S \ , \quad \frac{\partial \phi^S}{\partial \nu} = \frac{\partial \phi^S}{\partial \nu}, \text{on } C_1 \qquad (20)$$

Substituting Eqs.(17) and (18) into (20) and multiplying each term of above equations by cosh k(h+z) and cos kn(h+z), and integrating from z = -h to z = 0, following relations are obtained.

$$\left.\begin{aligned} f_0(i) + f_1^{(0)}(i) &= f_2^{(0)}(i), \\ f_1^{(n)}(i) &= f_2^{(n)}(i), \\ \frac{\partial (f_0(i)+f_1^{(0)}(i))}{\partial \nu} &= \frac{\partial f_2^{(0)}(i)}{\partial \nu}, \\ \frac{\partial f_1^{(n)}(i)}{\partial \nu} &= \frac{\partial f_2^{(n)}(i)}{\partial \nu}, \end{aligned}\right\} \qquad (21)$$

on C_1

where the symbol i shows the i-th position of segment instead of x,y axes. If the coastal line is straight, one of the boundary conditions is simplified as follow:

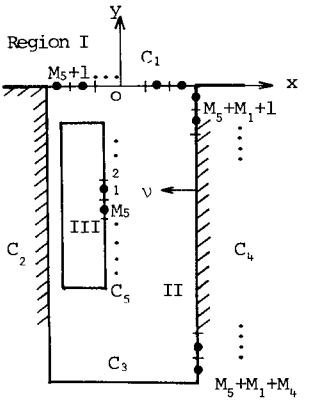

Fig.5 Definition of the coordinate system of the moored ship in the slip

$$\frac{\partial f_1^{(0)}(i)}{\partial \nu} = \frac{\partial f_2^{(0)}(i)}{\partial \nu} \ , \text{ on } C_1 \qquad (22)$$

Since the normal to the boundary is directed outward in region I, the wave function $f_1^{(0)}(i)$ is given from the Green's formula as

$$f_1^{(0)}(i) = -\frac{i}{2} \sum_{j=M_5+1}^{M_5+M_1} \{f_1^{(0)}(j) \frac{\partial H_0^{(1)}(k\gamma)}{\partial \nu} - H_0^{(1)}(k\gamma) \frac{\partial f_1^{(0)}(j)}{\partial \nu}\} \, ds \qquad (23)$$

Substituting Eqs.(21), (22) into Eq.(23), the boundary conditions for $f_2^{(0)}(i)$ is obtained:

$$f_2^{(0)}(i) = f_0(i) + \frac{i}{2} \sum_{j=M_5+1}^{M_5+M_1} H_0^{(1)}(k\gamma) \; k\bar{f}_2^{(0)}(j) \, ds \ , \quad \text{on } C_1 \qquad (24)$$

where $\bar{f}_2^{(0)}(j) = \partial f_2^{(0)}(j)/k\partial\nu$. In the same way, the next condition can be obtained.

$$f_2^{(n)}(i) = \frac{1}{\pi} \sum_{j=M_5+1}^{M_5+M_1} K_0(k_n\gamma) \; k\bar{f}_2^{(n)}(j) \, ds \ , \text{ on } C_1 \qquad (25)$$

where $\bar{f}_2^{(n)}(j) = \partial f_2^{(n)}(j)/k\partial\nu$.

Applying the Green's formula to the boundaries C_1, C_4,C_5, the next equations can be obtained:

$$\left.\begin{aligned} f_2^{(0)}(i) &= -\sum_{j=1}^{M_5+M_1+M_4} \{\bar{A}_{ij} f_2^{(0)}(j) - A_{ij} \bar{f}_2^{(0)}(j)\} \\ f_2^{(n)}(i) &= -\sum_{j=1}^{M_5+M_1+M_4} \{\bar{B}_{ij}^{(n)} f_2^{(n)}(j) - B_{ij}^{(n)} \bar{f}_2^{(n)}(j)\} \\ & \qquad \text{on } C_1, C_4, C_5 \end{aligned}\right\} \qquad (26)$$

where A_{ij}, $\bar{A}_{ij}$, $B_{ij}^{(n)}$, $\bar{B}_{ij}^{(n)}$ are given as follows:

$$A_{ij} = -\frac{i}{2} \int_{\Delta s_j} \sum_{p=1}^{4} \{H_0^{(1)}(k\gamma_p)\} k \, ds, \quad \bar{A}_{ij} = -\frac{i}{2} \int_{\Delta s_j} \sum_{p=1}^{4} \{\frac{\partial}{\partial \nu} H_0^{(1)}(k\gamma_p)\} ds,$$

$$B_{ij}^{(n)} = -\frac{1}{\pi}\int_{\Delta s_j} \sum_{p=1}^{4} \{K_0(k_n\gamma_p)\}k\, ds, \quad \bar{B}_{ij}^{(n)} = -\frac{1}{\pi}\int_{\Delta s_j} \sum_{p=1}^{4} \{\frac{\partial}{\partial n}K_0(k_n\gamma_p)\}ds \qquad (27)$$

where γ_p and $\partial\gamma_p/\partial\nu$ are equal to those given by Eq.(16).

Since the particle velocity normal to the boundary C_4 is zero, the following boundary condition is added:

$$\frac{\partial f_2^{(0)}(j)}{\partial\nu} = \frac{\partial f_2^{(n)}(j)}{\partial\nu} = 0 \text{ , on } C_4 \qquad (28)$$

The above equations from (23) to (28) can be written in the matrix form:

$$\left.\begin{aligned} \mathbf{e}^{(n)} &= \mathbf{G}^{(n)} + \mathbf{H}^{(n)}\bar{\mathbf{e}}^{(n)} \\ \mathbf{f}^{(n)} &= -\bar{\mathbf{A}}^{(n)}\mathbf{f}^{(n)} + \mathbf{A}^{(n)}\bar{\mathbf{f}}^{(n)} - \bar{\mathbf{B}}^{(n)}\mathbf{e}^{(n)} + \mathbf{B}^{(n)}\bar{\mathbf{e}}^{(n)} - \bar{\mathbf{P}}^{(n)}\mathbf{X}^{(n)} \\ \mathbf{e}^{(n)} &= -\bar{\mathbf{C}}^{(n)}\mathbf{f}^{(n)} + \mathbf{C}^{(n)}\bar{\mathbf{f}}^{(n)} - \bar{\mathbf{D}}^{(n)}\mathbf{e}^{(n)} + \mathbf{D}^{(n)}\bar{\mathbf{e}}^{(n)} - \bar{\mathbf{Q}}^{(n)}\mathbf{X}^{(n)} \\ \mathbf{X}^{(n)} &= -\bar{\mathbf{R}}^{(n)}\mathbf{f}^{(n)} + \mathbf{R}^{(n)}\bar{\mathbf{f}}^{(n)} - \bar{\mathbf{S}}^{(n)}\mathbf{e}^{(n)} + \mathbf{S}^{(n)}\bar{\mathbf{e}}^{(n)} - \bar{\mathbf{T}}^{(n)}\mathbf{X}^{(n)} \end{aligned}\right\} \quad , \ n=1,2\ldots \qquad (29)$$

where

$$\mathbf{G}^{(0)} = \begin{pmatrix} f_0(M_5+1) \\ f_0(M_5+2) \\ \\ f_0(M_5+M_1) \end{pmatrix}, \quad \mathbf{G}^{(n)} = \mathbf{0} \qquad (30)$$

and $\mathbf{f}^{(n)}$, $\mathbf{e}^{(n)}$ and $\mathbf{X}^{(n)}$ are the vectors of the wave functions $f_2^{(n)}$ on the boundaries C_5, C_1 and C_4, respectively. $\mathbf{A}^{(n)}$, $\bar{\mathbf{A}}^{(n)}$, $\mathbf{B}^{(n)}$, $\bar{\mathbf{B}}^{(n)}$, $\mathbf{C}^{(n)}$, $\bar{\mathbf{C}}^{(n)}$, $\mathbf{D}^{(n)}$, $\bar{\mathbf{D}}^{(n)}$, $\bar{\mathbf{P}}^{(n)}$, $\bar{\mathbf{Q}}^{(n)}$, $\mathbf{R}^{(n)}$, $\bar{\mathbf{R}}^{(n)}$, $\mathbf{S}^{(n)}$, $\bar{\mathbf{S}}^{(n)}$, $\bar{\mathbf{T}}^{(n)}$ are the known matrices.

Rearranging the expression (29), the wave functions $\mathbf{f}^{(n)}$ and $\bar{\mathbf{f}}^{(n)}$ (n=1,2,...) on the ship boundary can be transformed into:

$$\bar{\mathbf{f}}^{(n)} = \bar{\mathbf{U}}^{(n)}\mathbf{f}^{(n)} + \mathbf{u}^{(n)} \ , \qquad (31)$$

where $\bar{\mathbf{U}}^{(n)}$ is the known matrix and $\mathbf{u}^{(n)}$ is the known vector.

Once the relation between $f_2^{(n)}$ and $\bar{f}_2^{(n)}$ on the ship boundary is obtained, the procedure of the calculation hereafter is the same as that of ship motions along the straight quay wall.

3 EXPERIMENTAL VERIFICATION

3.1 Experimental Apparatus and Procedure

The experimental setup in cases of the quay wall and the slip are shown in Figure 6 (a) and (b), respectively. The wave basin of 30 m long, 20 m wide and 0.6 m deep was used in the experiment. A rectangular floating body of 2.4 m long, 0.455 m wide and 0.098 m deep was used as a ship model. The other dimensions of this ship model are shown in Tables 1 and 2. The ship model was moored by coiled springs whose spring constant was 67 gf/cm. The ship motions were measured by the 6-component measuring instrument.

3.2 Results and Discussion

3.2.1 Ship Motions Along the Quay Wall

The kinds of experiments of the ship motions are carried out under the following conditions. In one group, the wave period is varied and

the angle of wave incidence was kept constant and vice versa in the other group.

(a) Ship motions in beam seas

In Figure 7, the ship motions measured in experiments are compared with the theoretical results. As can be seen in the rolling motion, the calculated period of resonance is little bit smaller than that of the experiment. The reason of this difference is the effect of eddy-making which is not taken into account in this analysis. While experimental results of heaving and swaying motions seem to be predicted fairly well by this theoretical analysis.

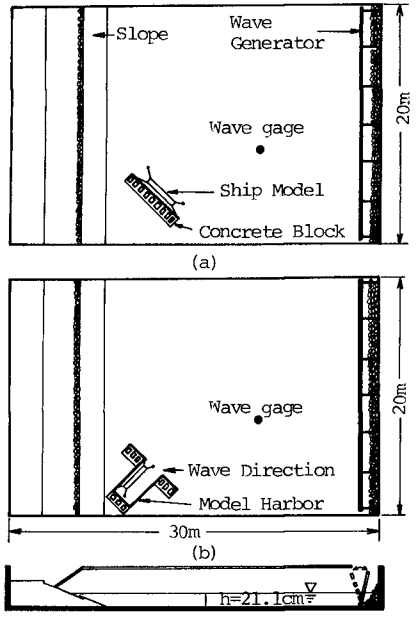

Fig.6 Arrangement of moored ship in the wave basin

If the floating body is symmetric with respect to the x-axis in beams seas, pitching, surging and yawing motions should not occur in the potential theory. Although the solid lines in Fig. 7 in these ship motions show the results considering the difference of the center of gravity from the center of figure in y-direction, there is wide division between theoretical and experimental results especially in yawing motion. The asymmetry of waves and the effect of eddy shedding may account for this discrepancy.

Table 1 Dimensions of moored ship along the quay wall

Natural period (sec)	
Sway 8.2 ,Surge 5.5 ,Heave 1.22	
Pitch 1.7 ,Roll 1.34,Yaw 3.8	
Moment of inertia	
Pitch	$486 \times 10^6 (g \cdot cm^2)$
Roll	$313 \times 10^5 (g.cm^2)$
Yaw	$497 \times 10^5 (g.cm^2)$

Table 2 Dimensions of moored ship in the slip

Natural period (sec)	
Sway 7.7 ,Surge 5.0 ,Heave 2.08	
Pitch 2.5 ,Roll 1.38,Yaw 3.89	
Moment of inertia	
Pitch	$569 \times 10^6 (g.cm^2)$
Roll	$432 \times 10^5 (g.cm^2)$
yaw	$593 \times 10^5 (g.cm^2)$

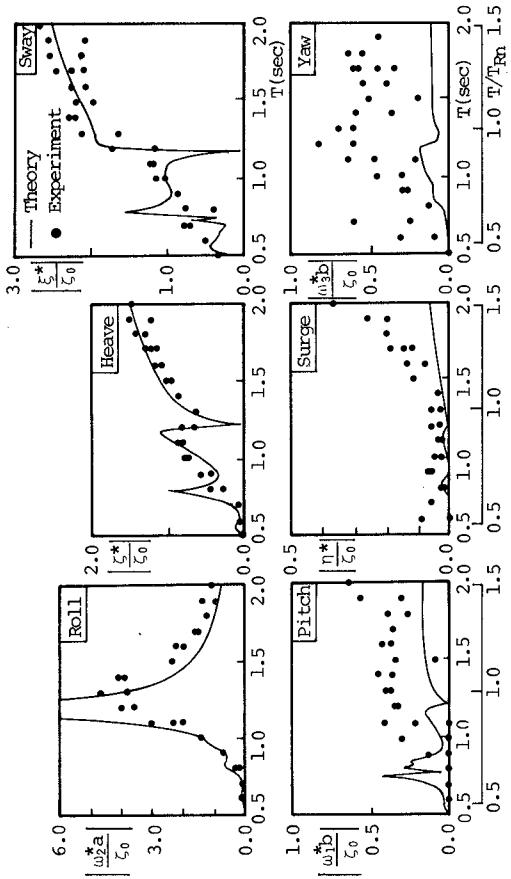

Fig.7 Motions of moored ship along the straight quay wall in beam seas

(b) Ship motions in waves of arbitrary angle of wave incidence

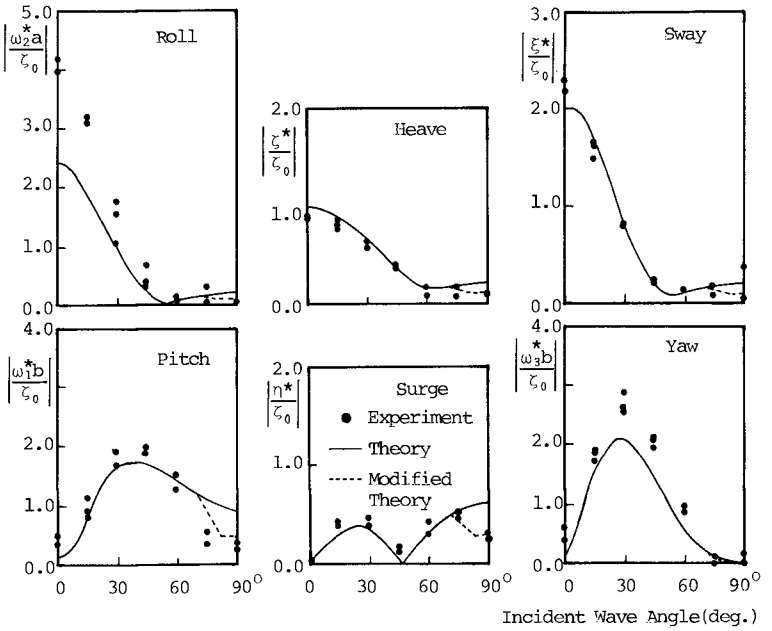

Fig.8 Relationship between ship motions and angle of wave incidence

Figure 8 shows the comparison of the experimental results with the theoretical results when the angle of wave incidence is changed from 0 to $\pi/2$. Both results show fairly good agreement. However, the theoretical results of rolling motions become smaller than the experimental ones at the small angle of wave incidence. The cause of this disagreement seems to be the difference between the numerical resonance period and the experimental resonance period as shown in Figure 7. The yawing motion in the experiment becomes larger than the theoretical one. This enlargement is thought to be caused by the eddies induced at the both ends of the ship. Finally, experimental values of almost all ship motions decrease by one-half of theoretical ones near $\alpha = 90^0$. Figure 9 schematically shows the straight quay wall of finite length and the floating body. The all reflected waves from the quay wall affect the floating body when $\alpha < \alpha_1$ but the effects of the reflected waves on the floating body become small when $\alpha_2 \geq \alpha \geq \alpha_1$, and the effects vanish entirely when $\alpha > \alpha_2$. But the reflected waves always affect the floating body in the theoretical analysis, because the quay wall is assumed to be infinity. This is the reason that experimental

results become smaller than theoretical ones near $\alpha = 90^0$. By the way, as the angle θ_{ir} shown in Fig. 9 becomes small when α approaches 90^0, the effects of the incident waves and reflected waves on the ship motions can be considered nearly equal. From the above facts, the incident wave hieght is considered one half when $\alpha > \alpha_2$ and it is considered to decrease from one to one half when $\alpha_2 \geq \alpha \geq \alpha_1$. The dotted lines show the results conducted by the above modified theory. The experimental results indicate the validity of the above way of thinking.

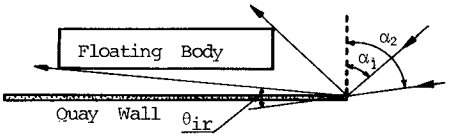

Fig.9 Reflected wave by the quay wall of finite length

3.2.2 Ship Motions in a Slip

Figure 10 shows the ship motions for three angles of wave incidence, $\alpha = 30^0$, 60^0, 90^0. It is clear from these figures that the resonance periods in a slip are different from the natural periods at the open sea. For example, the natural period in heave at the open sea is 0.8 seconds which is represented by T^O_{Hn}, but the natural period in the slip is 2.08 seconds which is expressed by T^S_{Hn} as shown in Figure 10 (b). And the natural period of the rolling motion in the slip is 1.38 seconds which is expressed by T^S_{Rn}, but the resonance periods are 1.15 seconds which are represented by T^T_{Rn} and 1.35 seconds as shown in Figure 10 (c). The resonance at T^T_{Rn} seems to be induced by the lateral oscillation which is the second mode harbor oscillations having loops at the boundaries C_2 and C_4 in Figure 5. Though T^T_{Rn} and T^S_{Rn} do not coincide each other in this experiment, the rolling motion should become large when the both resonance periods coincide.

Another important characteristics of the ship motions are the coupled resonances among mutual ship motions. Namely, as the ship is surrounded by three quay walls, the waves induced by predominant ship motions in one mode affects the other mode of ship motion. And many peaks of ship motions can be seen in Figure 10 in comparison with the ship motions along the straight quay wall or in an open sea. For example, the resonance of heaving motions at $T = T^O_{Hn}$ and T^S_{Hn} induces the new resonance in swaying and rolling motions at the same wave periods. And the resonance of rolling motions at $T = T^T_{Rn}$ and T^S_{Rn} produce the ones of swaying motions at $T = T^S_{Rn}$ and of heaving motions at $T = T^T_{Rn}$ and T^S_{Rn}. The same phenomena can be seen in the other ship motions, though they are not shown in Figure 10. By the way, since the damping forces due to eddy-shedding which will be obtained from free oscillation test are not considered in this analysis, the theoretical peaks of ship motions are fairly larger than the experimental ones. These disagreements should be improved by considering the

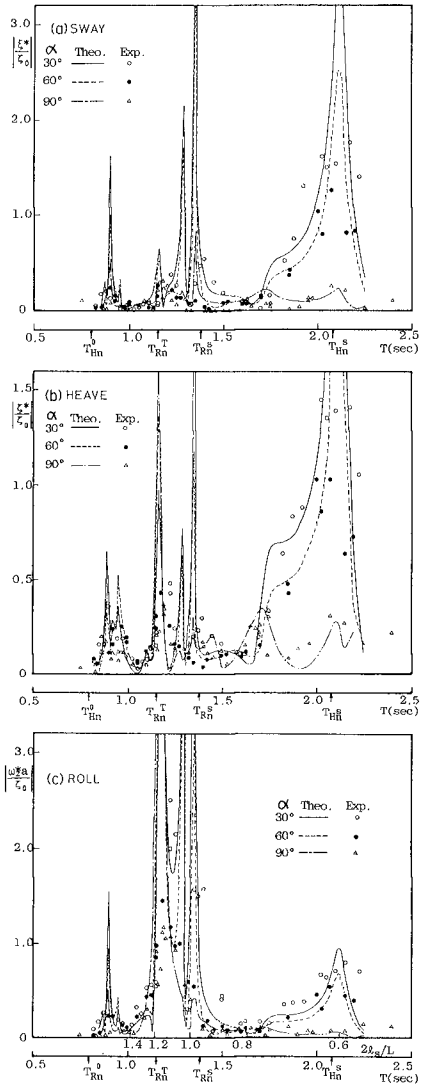

Fig.10 Ship motions in the slip

damping forces in Eq.(8). But it is clarified that the theoretical and experimental results show fairly good agreement except near the resonance periods. So it can be concluded that the short-period ship motions in the slip can be predicted by using the above potential theory.

4 MOORING SYSTEM WITH DASH-POT

The authors have already discussed the effect of the perforated quay wall[8] on the ship motions, but it was found that all ship motions along the perforated quay wall were not always smaller than those along the ordinary quay wall. So the dash-pot system is considered as the another damping system of moored ship motion[9]. In this section, the damping effect of dash-pot system on the short-period ship motion is analyzed.

4.1 Theory of Ship Motions with the Damping System

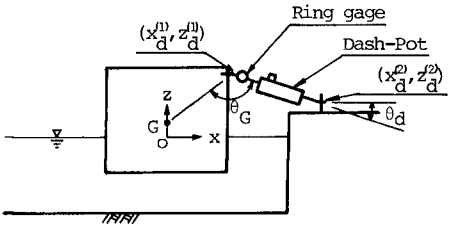

Fig.11 Arrangement of dash-pot(θ_d is measured anti-clockwise from positive x-axis)

In order to simplify the problem, it is analyzed by the two dimensional theory in the simulation. The coordinate system is shown in Figure 11. One end of the dash-pot on the ship has the coordinate $(x_d^{(1)}, z_d^{(1)})$ and the other end on the quay wall has the coordinate $(x_d^{(2)}, z_d^{(2)})$. These ends can rotate freely by universal joints. The length between both ends ℓ_d is expressed by:

$$\ell_d = \sqrt{(x_d^{(2)} - x_d^{(1)})^2 + (z_d^{(2)} - z_d^{(1)})^2} \tag{32}$$

When the ship starts to move, the end of the dash-pot on the ship moves with the ship movements, but the other end on the quay wall does not move. The change of the length of mooring line $\Delta\ell_d$ is approximated by:

$$\Delta\ell_d = \left[\frac{x_d^{(2)} - x_d^{(1)}}{\ell_d}\{\xi^* - (z_d^{(1)} - \bar{z}_0)\omega_2^*\} + \frac{z_d^{(2)} - z_d^{(1)}}{\ell_d}(\zeta^* + x_d^{(1)}\omega_2^*)\right] e^{-i\sigma t} \tag{33}$$

Since the damping force caused by dash-pot can be considered to be proportional to the velocity, the damping force F_{dp} can be given by:

$$F_{dp} = -k_d \frac{d(\Delta\ell_d)}{dt} = \hat{F}_{dp}\, e^{-i\sigma t} ,$$

$$\left.\begin{aligned}\hat{F}_{dp} = &\frac{-i\sigma k_d(x_d^{(2)} - x_d^{(1)})}{\ell_d}\{\xi^* - (z_d^{(1)} - \bar{z}_0)\omega_2^*\} \\ &\frac{-i\sigma k_d(z_d^{(2)} - z_d^{(1)})}{\ell_d}\{\zeta^* + x_d^{(1)}\omega_2^*\}\end{aligned}\right\} \quad (34)$$

where k_d is the damping coefficient. In the case of orifice with constant area, k_d is given as follow[10]:

$$k_d = \frac{8\pi\mu\ell_p A_d}{\{(a_0 + a_p)C_d\}^2}, \quad (35)$$

where μ is the coefficient of molecular viscosity, ℓ_p is the length of the orifice, A_d, a_0 and a_p are the cross-sectional areas of cylinder, orifice and piston clearance, and C_d is the coefficient of discharge. Using $\hat{F}_{dp}$, the forces $\hat{F}x$ in x-direction and $\hat{F}z$ in z-direction and the moment $\hat{M}$ are given by:

$$\left.\begin{aligned}\hat{F}_x &= -\hat{F}_{dp}\cdot\frac{x_d^{(2)} - x_d^{(1)}}{\ell_d}, \quad (36)\\ \hat{F}_z &= -\hat{F}_{dp}\cdot\frac{z_d^{(2)} - z_d^{(1)}}{\ell_d}, \quad (36)\\ \hat{M} &= -\hat{F}_x\cdot(z_d^{(1)} - \bar{z}_0) + \hat{F}_z\cdot x_d^{(1)},\end{aligned}\right\}$$

If above forces and moments caused by dash-pot are substituted into the equations of ship motions (8), the amplitudes of ship motions can be easily obtained by the same method as that of section 2.

4.2 Hydraulic Experiment

In order to verify the short-period motions of ship equipped with dash-pot, the hydraulic experiments are carried out. The arrangement of the experiment is shown in Figure 12. The sketch of the dash-pot is shown in Figure 13, and the characteristics are described in Table 3.

Both results of the ship motions with and without dash-pot are shown in Figure 14. It is found from these figures that the ship motions in every mode with the dash-pot is smaller than those without the dash-pot. Therefore, the new mooring system with dash-pot seems effective to reduce the ship motions.

Furthermore, the theoretical and the experimental results have good agreement each other. So it is clarified that the ship motions with dash-pot can be explained by the above mentioned theory. The force acting on the axis of the dash-pot is measured and is compared with the theoretical results. Both results show the same tendency, however, the theoretical one is larger than the experimental one. One reason of this difference comes from the inaccuracy of the measurement of compressive force by ring gauge. So the method of measurement should be improved hereafter.

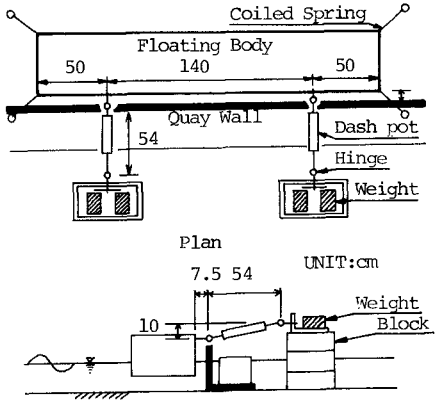

Fig.12 Experimental arrangement

Table 3 Dimensions of dash-pot

$x_d^{(1)}$	0.303m
$z_d^{(1)}$	0.197m
$x_d^{(2)}$	0.843m
$z_d^{(2)}$	0.297m
A_c	9.62cm^2
ℓ_p	10mm
a_0	14.1mm^2
a_{LR}	4.0mm^2

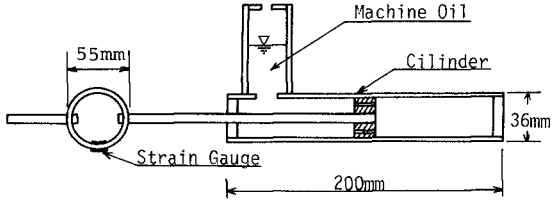

Fig.13 Dash-pot used in the experiment

4.3 Optimum Design of Dash-Pot by Numerical Simulation

Using the above mentioned theory, the optimum design of dash-pot system is investigated. Figure 15 shows the calculated ship motions and axial forces acting on the dash-pot in case of various installed angle of dash-pot θ_d. From these figures, it is found that rolling motions are significantly affected by θ_d and become smallest when $\theta_d = -57^0$, however, θ_d does not affect another nodes. On the other hand, the axial force F is the least when $\theta_d = -57^0$. As it is not favorable that the axial force which is the force acting on the bits on the ship and the quay wall is large, the angle $\theta_d = -57^0$ is the most suitable one to reduce the ship motions by dash-pot. Let θ_G be the angle as shown in Figure 11, $\theta_d = -57^0$ corresponds to $\theta_G = 90^0$. This fact shows that the dash-pot should be equipped so as to make the damping moment maximum and to suppress the rolling motion.

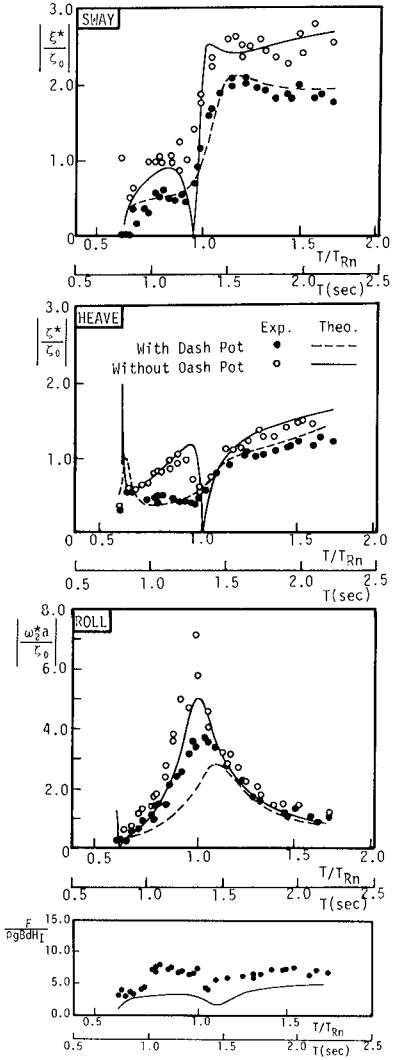

Fig.14 Comparison of ship motion with and without dash-pot, and the axial force of the dash-pot

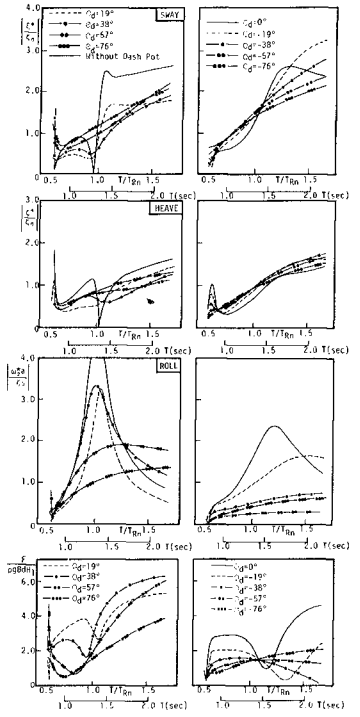

Fig.15 Ship motions and axial force of dash-pot obtained by numerical simulation

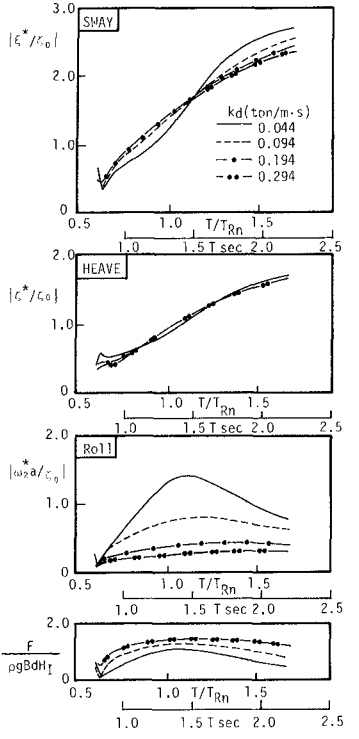

Fig.16 Relationship among ship motions, axial force and damping coefficient when $\theta_G = 90^0$

Figure 16 shows the effects of damping coefficient k_d on the ship motions and the force acting on the dash-pot when $\theta_G = 90^0$. It is noticed that the swaying and heaving motions are not heavily influenced by k_d, but the rolling motion is reduced satisfactorily with the increase of k_d.

The resonance of roll can be seen in the region when $k_d < 0.094$ ton f/(m.sec), but the resonance disappears when $k_d > 0.094$ ton f/(m.sec). The larger k_d becomes, the smaller the roll becomes. While the axial force acting on dash-pot increases. So the smallest value of k_d where the resonance of roll disappears is regarded as the optimum damping coefficient which is expressed as k_{d_0}. Though it is obtained

from the above numerical model, it can be also estimated by the following simple method.

Now, the equation of rolling motion of free oscillation is expressed by:

$$I\ddot{\delta}_2 + k_d \ell_1^2 \dot{\delta}_2 + M \cdot g \cdot GM \cdot \delta_2 = 0 \quad , \tag{38}$$

where I is the virtual moment of inertia in roll, ℓ_1 is the length between the center of gravity of the ship and the one end of the dash-pot on the ship, GM is the metercentric height. Let the natural period of roll be T_{Rn}, and define ε_R and define η_R by:

$$2\varepsilon_R = \frac{k_d \ell_1^2}{I}, \quad \eta_R^2 = \frac{M \cdot g \cdot GM}{I} \fallingdotseq \left(\frac{2\pi}{T_{Rn}} \right)^2 . \tag{39}$$

Then it can be said from the theory of mechanical vibration that the resonance of roll disappears when the following equation is satisfied [10].

$$\frac{\varepsilon_R}{\eta_R} = \frac{1}{\sqrt{2}} \tag{40}$$

The damping coefficient k_d which satisfies the above condition is also the optimum damping coefficient k_{d_0} , so by arranging the expression, k_{d_0} is obtained as follow:

$$k_{d_0} = \frac{1}{\sqrt{2}} \cdot \frac{M \cdot g \cdot GM \cdot T_{Rn}}{\pi \ell_1^2} \quad , \tag{41}$$

Since $T_{Rn} = 0.8B/\sqrt{GM}$ [11] , Eq.(41) is rewritten by:

$$k_{d_0} = \frac{0.8}{\sqrt{2}} \cdot \frac{M \cdot g \cdot B\sqrt{GM}}{\pi \ell_1^2} \tag{42}$$

Now, for example, substituting experimental conditions M = 0.455*0.093 ton/m, GM = 0.13 m, T_{Rn} =1.3 seconds and ℓ_1 = 0.36 m into Eq.(42), k_{d_0} = 0.124 ton f/(m.sec) which is between 0.094 ton f/(m.sec) and 0.194 ton f/(m.sec) is obtained. From this, it is clear that the optimum damping coefficient can be estimated by Eqs.(41) or (42).

5 CONCLUSIONS

The motions of a moored ship in a harbor basin and the mooring system with dash-pots are investigated. The conclusions are summarized as follows:

1) The ship motions along the quay wall and in the slip can be analayzed by the three dimensional analysis.
2) Wave height distribution in the slip can be estimated by the method of images which is suitable to save cost of computation.
3) In order to reduce the short-period ship motions, a new mooring system with dash-pot is proposed. It is clarified that the system is very useful for reducing the rolling motion. Furthermore, it is clear from the numerical simulation that the angle θ_G should be

adjusted to $\pi/2$ and the optimum damping coefficient of the dash-pot is given by Eq. (42).

ACKNOWLEDGEMENT

This study is supported in part by the Research Fund of the Ministry of Education of Japan. The authors also wish to express their gratitude to Mr. S. Aoki, postgraduate student of Osaka University, who assisted us in the experiment.

REFERENCES

1) For example, Wilson,B.W.: Ship responce to range action in harbor basins, Trans. A.S.C.E.,Vol. 116,pp. 1129 - 1157, 1951.
2) Sawaragi,T. and M.Kubo: Long-period motions of a moored ship induced by harbor oscillations. Coastal Engineering in Japan, (in printing).
3) Oortmerssen,G.Van: The motions of a moored ship in waves, Publication No.510, Netherlands Ship MOdel Basin, Wageningen, The Netherlands, 1976.
4) Ijima,T.,A.Yoshida and Y.Yumura:On the motions of elliptical or rectangular floating body in waves of finite water depth, Proc. J.S.C.E.,Vol.244,pp.91 - 105, 1975 /12. (in Japanese).
5) Jogleka,D.V. and P.K.Kulkani: Mooring problems in harbors subject to seiches and tidal bores, XIXth International Navigation Congress, section II, pp. 95 - 117, 1957.
6) Sawaragi,T. and M.Kubo: Computation on wave height distribution in a slip by the method of images, The Journal of Japan Institute of Navigation, Vol. 65, pp.107 - 113, Sept.,1981. (in Japanese)
7) Lee,J.J.: Wave-induced oscillations in harbors of arbitrary geometry J.Fluid Mech. Vol. 45, pp. 375 - 394, 1971.
8) Sawaragi,T.,M.Kubo and T.Kyotani: Motions of a moored ship along the perforated quay wall, Coastal Engineering in Japan,Vol.23, pp. 277 - 286, 1980.
9) Sawaragi,T.,M.Kubo and S.Aoki: Some considerations on the method to reduce the short-period motions of moored ship by dash-pots, The Journal of Japan Institute of Navigation, Vol.66, pp. 127 - 135, 1981. (in japanese).
10) Taniguchi,O.et al.: Handbook of mechanical oscillation, Yokendo Book Company, pp. 851 - 865, 1976. (in Japanese).
11) Ohgushi,M.: Theory of ships, Vol.III, Kaibundo Book Company,Inc., pp. 25 - 30, 1961. (in Japanese).

Study of Ship's Track and Motions at Port Taranaki

G. Greenstreet

ABSTRACT *This paper describes a study carried out at Port Taranaki, New Plymouth, New Zealand to determine ship's track and motions at the port entrance. The results of the study being used to establish the extent (plan area) and optimum depth of proposed capital dredging works. The time lapse photographic technique, incorporating reference levels and bearings in each frame, used to record vessels entering and leaving the port is described. Maximum increases in ship's draft due to sea conditions are given.*

1. INTRODUCTION

Port Taranaki, located in New Plymouth on the West Coast, North Island, New Zealand (Fig.1) is undergoing major development to handle, by 1987 a threefold increase in trade brought about by the utilization of the Maui (off shore) and Kapuni gas and oil fields.

As part of the port development, capital dredging including the port entrance is required to allow for deeper draft vessels (up to 11.0m) and a greater tidal 'window' for arriving and departing ships. The present dredged depth is 9.0 - 10m below chart datum.

This paper describes the work carried out to determine:-
(i) the extent (plan area) or port entrance to be dredged by plotting the tracks taken by vessels at the entrance.

(ii) the optimum increase in dredge depth for vessels using the port by measuring the magnitude of ship's motions (as they effect draft) caused by wave action.

Due to budgetary restraints the study had to be carried out at minimal cost.

*Bruce Wallace & Partners, Auckland, New Zealand.

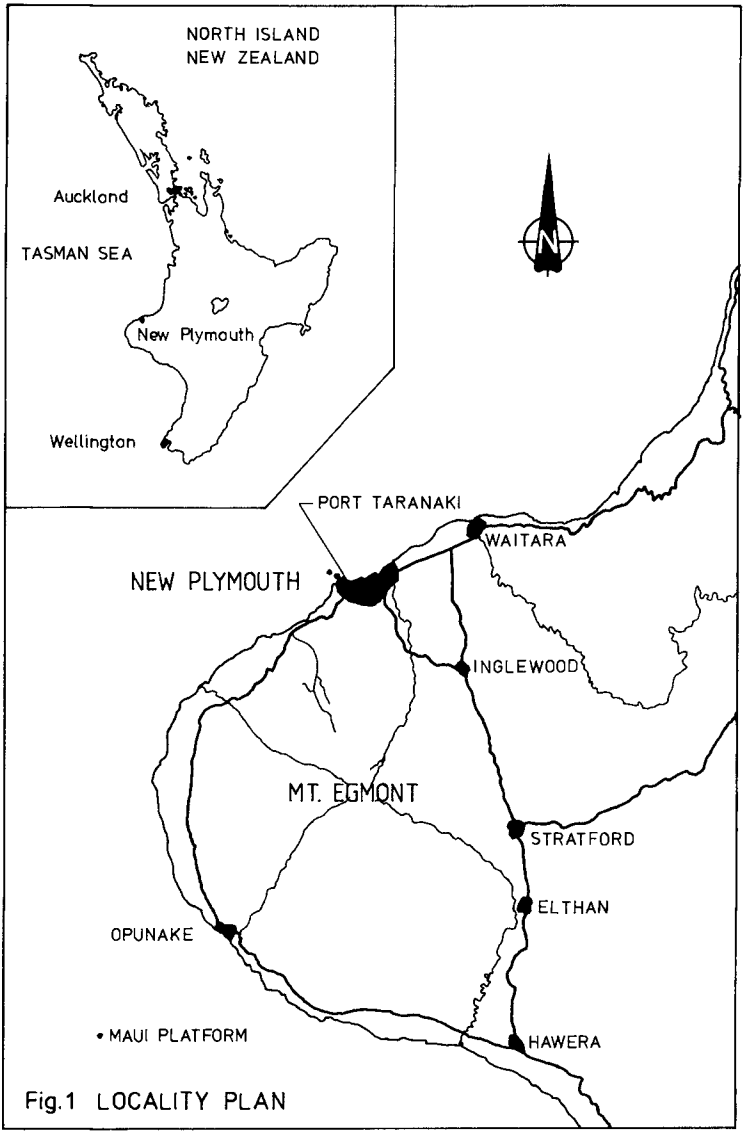

Fig.1 LOCALITY PLAN

2. SEA CONDITIONS

Vessels entering or leaving the port are subject to quarter or beam seas from the prevailing westerly/southwesterly swells and storm waves generated by low pressure systems in the south Tasman Sea.

Significant wave height projections *(1)* for the sea off the port are:

Significant Wave Ht (m)	Average Frequency
0-1.2	49.3%
1.2-2.4	29.5%
2.4-4.6	16.5%
over 4.6	4.7%

3. METHOD

A single camera photographic method was chosen for the recording of the track and motions of ship's at the port entrance after a number alternatives had been investigated. These included:

*Mounting portable measuring equipment on each ship and recording motions. Apart for difficulty in obtaining suitable equipment, its transfer to and from a pilot vessel in storm conditions would have proved difficult and required staff, additional to the pilot, on board.

Based on the experience of Columbia River Entrance Study *(2)* delays of 2-3 hours to set up and calibrate equipment on board a vessel could be expected. This length of delay could not be justified particularly as the average transit time through the entrance was between 5 and 10 minutes. Position fixing equipment was not available at the port.

*Photographic methods using two remotely located cameras syncronised to film simultaneously would have given an accurate fix of ships' position. However, this method would have required more manpower and equipment than the system chosen.

The method employed used a super 8mm cine camera, with time lapse and zoom capabilities, mounted at the end of an existing wharf on a permanent stand. A gradulated horizontal sight board was constructed in front of the camera at a constant 20.0m radius from the camera position.

This radius was approximately the minimum focusing distance when the camera was at full zoom.

Levels (above datum) of the sight board and camera lens were determined (approx 300mm difference) together with co-ordinates of the camera position and a true bearing from the camera to a point on the sight board.

The main area of interest, at the port entrance, was between 500mm and 1500mm from the camera position. The nature of the ship's tracks meant that vessels were photographed from either the bow or stern quarter.

The cameras zoom capability was used to ensure the largest possible image of a vessel was obtained in each frame. Filming was at a rate of a frame every two seconds.

The still water draft (bow and stern) of the berthed vessels was recorded and a copy of the ship's plans obtained for the vessel. Wind speed and direction were recorded together with a visual estimate of wave heights and direction at the port entrance.

4. FILM ANALYSIS

With the incorporation of the sight board, each photographic frame contained a reference scale and bearing together with a reference level datum. Film frames were viewed for analysis by back projection on to a screen faced with plate glass (approx.650mm x 450mm). Distances between various points on the ship and between these points and the sight board were measured in terms of the graduated scale on the sight board (Fig.2). Horizontal distances from the reference bearing to points were also recorded (Fig.3).

Using the measured distances and the fixed references incorporated in each frame, together with the vessels dimensions, the ship's positions (2 co-ordinated points) and the reduced level of three points on the vessel were calculated by trigometric functions using a purpose written computer program. As the orientation of the vessel in relation to the camera was not known, plan dimensions could not be used to determine the distance of ship from the camera. Therefore a vertical dimension which gave a true rather than apparent height in the frame was used. (h1 in Fig.2). The image height focal/length relationship of the camera could not be used to determine distance as the focal length varied with the adjustment of the zoom lense.

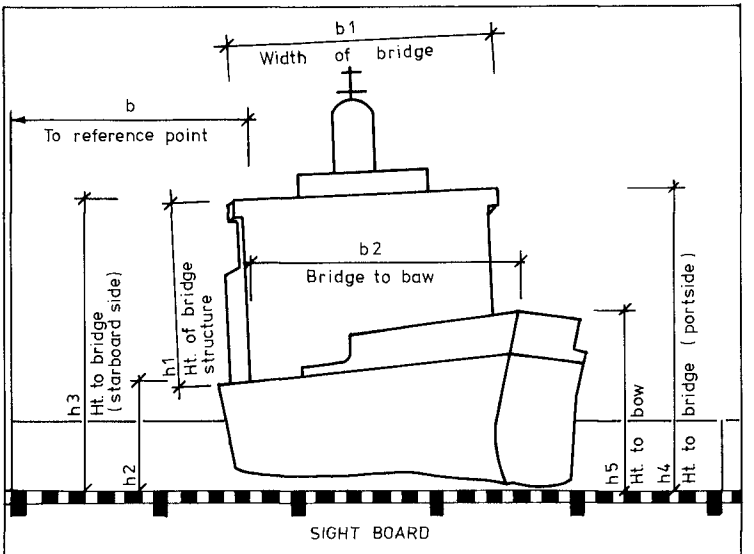

Fig.2 ELEVATION - SHIP MEASUREMENT POINTS

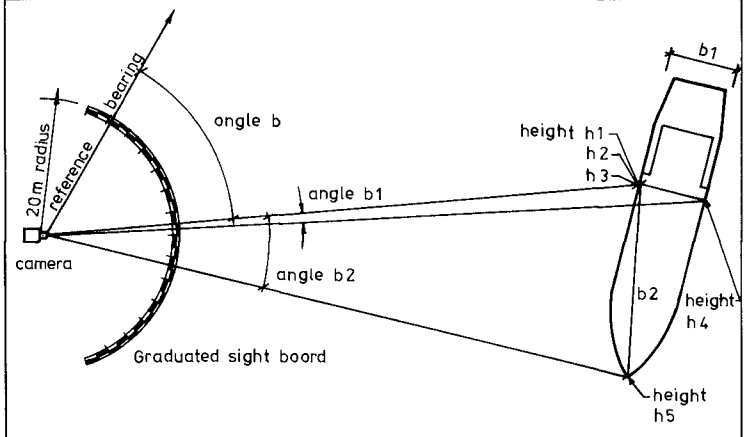

Fig. 3 PLAN - SHIP MEASUREMENT POINTS

Where track only was required, every 10th frame was analysed (i.e. ship's position every 20 seconds) with vessels with significant motion (i.e. rolls over 5^{o}) having additional frames analysed.

From the three calculated levels and the previously recorded still water draft, ship's motions (pitch, roll and heave) were calculated together with the change in draft caused by these motions.

A major factor in the accuracy of the results was the definition of the image obtained, particulary the sight board to which all measurements are related. Based on the limits to which measurement could be taken, errors in position (at approx 1000m from the camera) were estimated to be in the order of $\pm$ 7m with levels of points on the vessel varying $\pm$ 300mm.

5. RESULTS

To date, some 100 vessel movements have been photographed over an 18 month period of which some 20 have been analysed. Of the remainder, light conditions (i.e. dawn, dusk) did not give sufficient definition for accurate measurements or there was no significant ship's motion.

5.1 Ships' Track

A plot of ships' tracks was made (Fig.4) to determine the extent of the port entrance traversed by vessels. Once in port and prior to berthing, ships are turned to starboard (towards the main breakwater) and reversed with the aid of a tug into their berth. Consequently the tracks of arriving ships are closer to the lee breakwater to allow a greater turning radius within the port.

5.2 Ship's Motions

Rolling motions caused by beam or quarter seas were the most significant cause of increase in ship's draft. Rolls over 5^{o} were recorded by eight vessels with two of these being over 10^{o}. The maximum roll observed was in the order of 17^{o} but this was in deep water outside the area of interest.

The most significant results were obtained from two vessels on the same day when an estimated 1.5-2m swell was running at the port entrance with 15-20 knot winds gusting to 30 knots from the southwesterly direction.

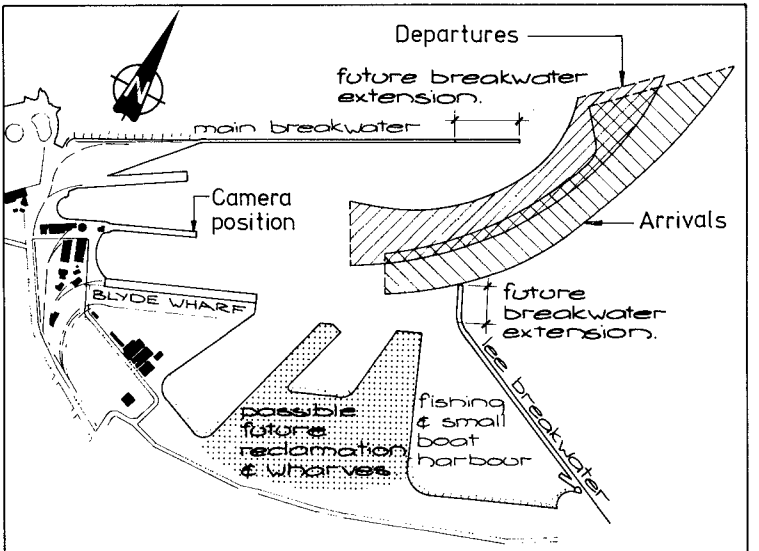

Fig. 4 PLAN - ENVELOPE OF SHIPS TRACKS

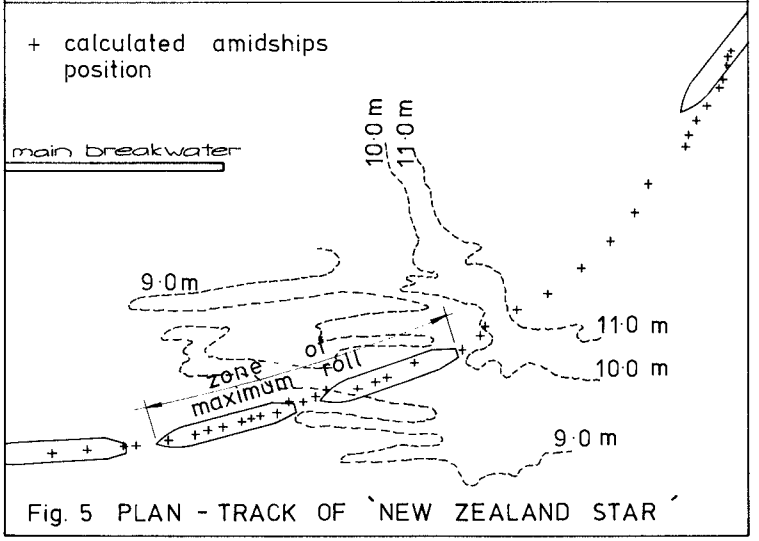

Fig. 5 PLAN - TRACK OF 'NEW ZEALAND STAR'

"New Zealand Star" - 7.0m draft; 170m o/a length (Fig.5) - consistently rolled 10-12° with a 12.8° roll combined pitch and heave (downwards) to give an increase in draft of 3.5m over still water draft. The rolling motion with a period of approx 16 sec increased from 2-3° to over 10° and this amplitude was maintained over 6 or 7 cycles before reducing to the previous figure. This increase was observed twice during the film run.

"Columbus Louisiana" - 9.0m draft; 168m o/a length - a pitching motion (with 2-3° rolls) to give a maximum increase in draft of 2.5m. It was observed, when running the film of the departure at a fast speed (9 frames/sec), that longitudinal flexing of the vessel may also have occured.

The remainder of the vessels analysised gave draft increases of between 0.5m and 1m.

6. EXTENT OF DREDGING

Based on the results of the study the extent and depth of dredging at the entrance to the port was determined.

A dredge depth of 13m below chart datum has been decided for the entrance. Except in servere sea conditions this depth will allow all but the deepest draft vessels to enter the port over the whole tidal range (3.0m at Mean Spring Tides). Depending on sea conditions,movement of large vessels will be governed by the state of the tide.

7. DISCUSSION

Merits of the system employed include:-
-ease of operation. Once the camera and sight board have been set up only one person is required to photograph the vessels and collect tidal and vessel draft data.

-each photographic frame contains all data (except ship dimension and draft) necessary for analysis.

- no on-board equipment is required

- the capital cost of the equipment employed was low

Limitations of the method are:-

-it is dependant on lighting conditions. That is, poor images were obtained at dawn and dusk and sometimes during the day when sunlight reflecting off the sea gave only a silhouette of the vessels. Ideally the camera should have its back to the sun.

- film analysis is time consuming

- data processing and calculation requires computer assistance Initally this was carried out using a programmable desk top calculator and latera micro computer.

Improvements to the system could include increasing the distance of the sight board from the camera (30 to 50m radius) and the use of a larger film size (i.e. 16mm or 35mm) to improve the quality of the enlarged image used for analysis.

Having established the requirements for dredging the port entrance it is intended to continue the study to provide the port's pilots with guidelines as to the likely increase in ship's draft for various sea conditions. To this end, a wave recorder will be installed at the port entrance later in 1983 and a further series of runs recorded. It should then be possible to establish a relationship between ship motions and sea conditions.

8. SUMMARY

The photographic technique employed in the study gave a low budget means of determining ship's track and motions and allowed the dredged area and depth of dredging at the port entrance to be determined.

Significant increases in draft due to ship's motions were recorded (3.5m maxm). These were greater than the normal empirical allowances made for keel clearance. All three types of motion (roll, pitch and heave) contributed to the draft increase.

The accuracy of the method was considered to be within acceptable limits but could be improved by more sophisticated photographic equipment and by increasing the distance between the camera and the reference sight board.

9. ACKNOWLEDGEMENTS

This study was carried out for the Taranaki Harbours Board and the author wishes to thank the Board's Chief Engineer, Mr P.D.L. Holmes, for permission to publish this paper.

Thanks also to the Bruce Wallace & Partners staff members who, due to vagaries of shipping time-tables, spent countless hours, often in adverse conditions, waiting to film the vessels.

10. REFERENCES

1. Glen & Associates "Meteorological & Oceanographic Conditions Affecting Design and Operation of Offshore Tanker Terminal Facilities, New Plymouth Power Station Project" for Ministry of Works and Development, Wellington, 1972.

2. Tetra Tech "Columbia River Entrance Channel Deep-Draft Vessel Motion Study, Final Report-Phase 1 "Tetra Tech Report No. TC3925, for U.S. Army Corps of Engineers, Portland District, September 1979.

SUBJECT INDEX

Page numbers refer to first page of paper

Aerial photography, 2300
Armor units, 1733, 1745, 2026, 2047, 2062, 2079, 2107, 2129, 2164, 2216, 2444

Barrier beaches, 1008, 1219
Barrier islands, 1062, 1219
Bars, 941, 1094
Beach erosion, 903, 1326, 1873
Beaches, 903, 923, 1161, 1181, 1369, 1385, 1405, 1439, 1837, 1970
Bed load, 1199
Bed load movement, 1353
Bed ripples, 282, 312
Boundary layer, 282
Breakwaters, 1119, 1248, 1716, 1733, 1745, 1765, 1873, 1893, 1930, 2062, 2079, 2097, 2129, 2216, 2444
Building codes, 2285
Bulkheads, 2204

Case reports, 1078, 1992, 2241
Channel design, 2662
Channels, waterways, 1199, 2662, 2681
Classification, 2300
Coastal engineering, 745, 2264, 2322
Coastal management, 2241
Coastal morphology, 1028, 1459, 2494
Coastal processes, 1008, 1857, 1950, 2264
Coastal structures, 523, 1800, 1857, 2285, 2494, 2504, 2514
Cohesive sediment, 1569
Composite structures, 2129
Computer models, 384
Construction, 1786
Construction methods, 1765, 2418
Construction procedure, 1219, 1248
Cooling water, 2308, 2342, 2357
Critical velocity, 1555
Currents, 404, 413, 1677, 2171
Cylinders, 1522, 2171

Data collection, 598
Deep water, 1522, 2129
Design, 2097
Design criteria, 1745, 1786
Design waves, 2097, 2129
Dikes, 804, 1873
Dredging, 1514, 2763

Earthquakes, 765
Ecology, 2264
Energy conversion, 245
Energy dissipation, 473, 2189
Environmental effects, 2342
Environmental factors, 1745, 2264
Erosion, 804, 1569, 2204
Erosion control, 1326
Estuaries, 136, 2300, 2458, 2595

Failures, 1733
Field investigations, 598, 785, 923, 1369, 2357
Fills, 1219
Finite difference method, 635, 652
Finite element method, 617
Floating breakwaters, 2009
Floating tire breakwaters, 1992
Flow rates, 312
Flumes, 1385
Foundations, 2129, 2444
Frequency distribution, 58
Friction coefficient, hydraulic, 2474

Gabions, 2403
Gates, 2534
Gravity waves, 129, 413
Great Barrier Reef, 219

Harbor facilities, 2700, 2723
Harbors, 172, 439, 454, 1119, 1514, 1716, 1765, 1970, 2026, 2322, 2332, 2681, 2700, 2743
Hurricanes, 77, 108, 357, 1459
Hydraulic models, 297, 745, 2216
Hydrodynamics, 573, 598
Hydrographs, 108

Icebergs, 2610
Incipient motion, 1555
Inlets, waterways, 1062, 1078, 1094, 1479, 1496, 2436

Laboratory tests, 3, 725
Lagoons, 2458
Lagrange's equations, 652
Lagrangian functions, 887
Laminar flow, 1589

Littoral current, 219, 1149, 1640, 1659
Littoral deposits, 969
Littoral drift, 1028, 1046, 1288, 1305, 1326, 1369, 1405, 1496, 1620, 1640, 1950
Longshore deposits, 954, 989

Marinas, 2332
Mass transport, 328, 652, 2386
Mathematical models, 745
Meteorological data, 2551
Modal analysis, 2562
Model tests, 1305, 2047, 2216
Monitoring, 1600, 2164, 2681
Mooring, 2621, 2641, 2743
Morphology, 941
Multi-port diffuser, 2376

Navier-Stokes Equations, 832
Navigation, 1231
Nuclear power plants, 2342
Numerical calulations, 172
Numerical models, 203, 439, 454, 617, 635, 846, 1659, 2079

Ocean bottom, 543
Oceanographic surveys, 87
Offshore drilling, 598
Offshore pipeline, 2403
Offshore structures, 172, 677, 1786, 1837
Outfall sewers, 2418, 2581
Overtopping, 270, 804

Photogrammetry, 695
Photography, 2164
Piles, 1699, 1800
Ports, 2700, 2763
Predictions, 823
Pressure gages, 129
Probability density functions, 342
Progressive waves, 811
Prototype tests, 1820, 2062

Reclamation, 1970
Recreation facilities, 1161, 2504, 2514
Repairing, 2581
Resonance, 439
Revetments, 1914
Riprap, 1820
Risk analyses, 598
Rubble-mound breakwaters, 1745, 2026, 2047, 2079, 2107, 2129, 2164, 2216, 2444

Safety factors, 2097
Saline water intrusion, 2376, 2474
Salinity, 2534
Sand, 1181
Scour, 1522

Sea floor, 543, 1149
Sea level, 2241
Sea walls, 1873
Sediment load, 1028, 1555
Sediment transport, 282, 404, 555, 923, 954, 969, 1046, 1094, 1127, 1161, 1181, 1268, 1288, 1326, 1335, 1353, 1369, 1419, 1439, 1479, 1555, 1589, 1600, 1620, 1930, 2357, 2436
Sedimentation, 1119, 1231
Seismic design, 2418
Seismic waves, 765
Shallow water, 58, 203, 485, 617, 486, 1127, 1268
Shear stress, 2474
Ship motion, 2621, 2641, 2662, 2681, 2723, 2743, 2763
Shipping, 2322
Shoaling, 22, 38, 384, 523, 1199, 1496
Shore protection, 1078, 1857, 1893, 1901, 2026, 2062, 2241
Shoreline changes, 923, 989, 1028, 1369, 1385, 1405, 1893, 1950
Simulation, 582
Simulation models, 297
Site investigation, 1231
Slopes, 555, 1820
South Africa, 87, 2322
Spatial distribution, 58
Stability, 2164, 2444
Stability analysis, 2129
Standing waves, 811
State-of-the-art reports, 1992
State-of-the-art reviews, 192, 1857
Storm surges, 785, 823, 1459
Structural design, 2285
Surf zone, 38, 58, 154, 485, 1677, 1699
Surveys, 2164
Suspended sediments, 282, 404, 1199, 1288, 1569, 2436

Temperature distributions, 485
Thermal factors, 2342
Tidal currents, 454, 573, 582, 635, 2562
Tidal effects, 2204
Tidal flats, 2494
Tidal waters, 2534
Tides, 192, 203, 823
Transport rate, 1305, 1335, 1589, 2357
Tropical cyclones, 370
Tsunamis, 765
Tubes, 1901
Turbulence, 3, 282, 370
Turbulent flow, 1589
Two-dimensional flow, 832

Velocity distribution, 1640
Vessels, ships, 2621, 2641

Water depth, 862, 2662
Water intakes, 2308, 2357
Water level, 2534
Water levels, 108
Water quality, 573, 2595
water resources, 2610
Water surface, 485, 811, 2386
Water surface profiles, 505
Water temperature, 2390
Water waves, 832, 846
Wave action, 505, 887, 1149, 2062, 2107, 2171, 2189, 2723
Wave climatology, 87
Wave diffraction, 172, 1930
Wave dispersion, 154
Wave energy, 245, 473, 765, 887, 1288, 2189
Wave forces, 677, 804, 1699, 1800, 2009, 2079, 2171, 2621, 2641, 2662, 2681
Wave generation, 710, 725
Wave height, 38, 58, 136, 270, 342, 357, 473, 523, 695
Wave measurement, 38, 129, 203, 261, 357, 505, 695, 1677
Wave propagation, 811
Wave reflection, 228, 543
Wave refraction, 384, 1930
Wave runup, 785, 804
Wave spectra, 77, 261, 765
Waves, 3, 22, 270, 862, 2621, 2641
Wind, 635, 2551
Wind forces, 2390
Wind loads, 370
Wind speed, 1181

AUTHOR INDEX

Page number refers to first page of paper

Ackers, P., 1820
Ahrens, H.P.L., 2581
Alach, D., 1522
Anima, R.J., 1268
Arenillas, M., 989
Asakawa, T., 2129
Austin, D.I., 2079
Ayoub R.N.M., 1589

Bailard, J.A., 1419
Bain, C.A.R., 2390
Barnett, K.A., 1970
Barthel, V., 136
Benque, J.P., 582, 823
Berek, E.P., 954, 1620
Bernstein, M., 2581
Berry, J.G., 2097, 2332
Biesel, F., 129
Black, K.P., 2436
Blackman, D.R., 261, 370
Bleach, G.P., 887
Bosman, D.E., 2504
Botes, W.A.M., 439
Bowman, D., 941
Bownass, T.M., 270
Burdick, B., 941
Burg, M.C., 635
Busching, F., 154
Butler, H.L., 1127, 1659
Byrne, A.P., 1514

Cahouet, J., 832
Carver, R.D., 2107
Chandler, B.D., 2171
Chapman, D.M., 1914
Charlton, J.A., 2376
Chen, Y.Y., 505, 811
Chenin, M.l., 582
Chiu, M-H., 77
Clark, R.R., 2285
Clique, P.M., 2342
Coakley, J.P., 1288
Coeffe, Y., 635, 823, 1149, 2342
Coetzee, L.W., 87
Converse, H., 1008
Cooper, C.K., 384
Cordes, H., 297
Cox, P.J., 2700
Cross, R.H., 1353
Crowhurst A.D., 2403
Crowley, J.B., 384

Daemrich, K-F., 297
Daubert, O., 832
Davidson, D.D., 2107, 2216
Dean, R.G., 954, 1199, 1620
Dermissis, V., 2474
Dieckmann, R., 2494
Diez, J.J., 989
Dingler, J.R., 1268
Draper, L., 270
Du Toit, C.G., 312
Duscha, L.A., 2241

Edge, B.L., 1893
Eggert, W-D., 297
Eisenberg, Y., 2418
Escalante, R.S., 1231

Falconer, R.A., 454
FitzGerald, D.M., 1094
Fleming, C.A., 384, 1640
Foster, D.N., 1857
Fromme, G.A.W., 2458
Funke, E.R., 710, 725

Gable, C.G., 954
Gahara, H., 2062
Gaillard, P., 172
Galvin, C., 1496
Galvin, Cyril, 2264
Gilbert, C.H.G., 1992
Glodowski, C.W., 1733
Goda, Y., 2444
Goldsmith, V., 941
Gonsalves, J.W., 328
Goto, S., 22
Graham, D.S., 2595
Grass, A.J., 1589
Greenstreet, G., 2763
Greenwood, B., 1677
Grune, J., 785

Harley, R.B., 1199
Hashimoto, H., 1369, 1405

Hattori, M., 923
Hauguel, A., 582, 617, 832, 846
Hayes, M.O., 1479
Headland, J., 523, 1800
Healy, T.R., 2436
Heathershaw, A.D., 543
Helberg, E.R., III, 2241
Hendry, R.W., 1765
Henry, R.F., 203
Herbich, J.B., 413
Hinwood, J.B., 261, 2171
Hofmann, P., 2308
Holroyd, S.G., 2641
Horikawa, K., 969, 1181, 1335, 1439
Hotta, S., 38, 1181
Hou, H-S., 357
Housley, J.G., 1893
Houston, J.R., 1659
Huizinga, P., 439
Hunter, I.T., 2551
Huntsman, S.R., 1353
Huskins, L.R., 2189
Hwung, H.H., 811, 862

Igarashi, H., 969
Imberger, J., 1522
Inada, Y., 3
Isaacson, M., 2723
Isaacson, M. de St Q., 2009
Isobe, M., 38, 969
Iwagaki, Y., 58

Juang, J.-T., 342

Kajima, R., 1385, 2357
Kamphuis, J.W., 1305
Kana, T.W., 903
Katori, S., 1335
Kemp, P., 1459
Kemp, P.H., 404
Kiley, K., 941
Kilner, F.A., 695
Kitamura, T., 282
Kjeldsen, S.P., 677
Kluger, J.W.J., 2164
Kobayashi, K., 2062
Kohlhase, S., 804
Kondo, K., 2357
Kraus, N.C., 969
Kubo, M., 2743
Kubota, S., 1181
Kuo, S.C., 357

Labadie, G., 617
Lajoie, D.L., 1733
Latteux, B., 617
Lawson, J.D., 2610
Leendertse, J.J., 573, 598
Lehan, G.R., 1219
LeMehaute, B., 1800
Lencioni, P., 823
Lenhoff, L., 1555
Li, Y-C., 413
Liu, S-K., 573, 598
Lleonart, G.T., 261
Lockhart, J.H., 2241

Ma, C.-M., 1353
Mangarella, P.A., 1353
Manoha, B., 2342
Mansard, E.P.D., 710, 725, 2047, 2621
Markle, D.G., 2216
Mart, Y., 941
Maruyama, K., 1385, 2357
Mase, H., 58
Maynard, A.K., 1459
McCarthy, M.J., 1062, 1219
McGregor, R.C., 1992
Mehta, A.J., 1569
Melbourne, W.H., 370
Mercer, A.G., 2723
Mettam, J.D., 2097, 2332
Miranda, F.C.C., 1950
Mizuguchi, M., 485
Mizumura, K., 2534
Moes, J., 2641
Moller, J.P., 1161
Mornement, P.C., 2332
Moutzouris, C.I., 1028
Muller, F.P.J., 245
Muraca, A., 1078
Mussalli, Y.G., 2308
Muzuguchi, M., 38

Narihiro, A., 2357
Nelson, R.C., 555
Nersesian, G., 1062
Niedorada, A.W., 1353
Nihoul, J.C.J., 745
Nir, Y., 1837
Niwinski, C.T., 2009
Noble, R.M., 2204
Noble, S., 2662
Nummedal, D., 1459

O'Connell, G.H., 2514
Ochi, M.K., 77
Oliveira, I.B.M., 1950
Ouyang, Y.C., 505

Partenscky, H.W., 804, 2494
Partheniades, E., 1569, 2474
Patil, U.K., 2204
Pechon, P., 846, 1149
Perrins, L-A., 2562
Perry, J.E., 2300
Petroni, R.V., 1231
Pitt, J.D., 1820
Ploeg, J., 1119
Pos, J.D., 695
Power, H., 228
Pratte, B.D., 1119, 2621
Prestedge, G.K., 245, 2189

Retief, G. de F., 245, 1716, 2189
Riedel, H.P., 1514
Rogan, A.J., 1028
Ronday, F.C., 745
Ropars, Y., 1733
Rosen, D.S., 1930
Rossouw, J., 87
Roth, W.H., 2204
Russell, K.S., 439, 2322
Russell-Head, D.S., 2610

Saito, S., 1385
Sakai, T., 3
Sandanbata, I., 3
Sasaki, T., 969
Savoie, M.A., 652
Sawamoto, M., 282
Sawaragi, T., 2743
Sayao, O.F.S.J., 1305
Schepis, J., 1522
Schlueter, R.S., 2079
Schmeltz, E.J., 1062, 1219
Scholtz, D.J.P., 2026, 2504
Schoonees, J.S., 1161
Schumann, E.H., 2562
Schwartz, S., 582
Schwarze, H., 2494
Serman, D.D., 1231
Sexton, W.J., 1479
Seymour, R.J., 954
Shah, V.K., 1901
Sheng, Y.P., 1127
Sherman, D.J., 1677
Shibayama, T., 1439
Shillington, F.A., 473
Shimizu, T., 1385
Shimoni, J., 1786
Shiraishi, N., 2062
Simons, R.R., 404
Skafel, M.G., 1288
Smart, M.D., 2581
Smith, A.W., 1914
Sobey, R.J., 108
Sofer, S., 941
Sorensen, R.M., 1062
Suter, J.R., 1459
Svetlichny, M., 903
Swart, D.H., 328, 1640

Taft, E.P., 2308
Tang, F.L.W., 342, 505
Tanimoto, K., 2444
Tautenhain, E., 804
Terao, T., 2062
Terauchi, K., 2062
Timco, G.W., 2047
Toyoshima, O., 1873
Treadwell, D.D., 1353, 2418
Tsai, C.P., 862
Tseng, R.S., 357
Tsuchiya, Y., 22, 1326
Tzachar, C., 1786

Uda, T., 1369, 1405
Ushida, S., 2062

Vajda, M., 1930
Valle, A.J.S.F., 1950
Van Damme, L.V., 1745
van de Kreeke, J., 652
van Dijk, W.S., 1716
van Niekerk, M., 2026
van Wyk, A.C., 2681
Van't Hoff, J., 1248
Vemulakonda, S.R., 1659
Visser, C.J., 87
Vonk, A.P.M., 1716

Walker, J., 523, 1800
Walton, T.L., 1046
Wang, J., 1800
Warluzel, A., 635
Watanabe, A., 1335

Weggel, J.R., 1046
Wiegel, Robert L., 1699
Willis, D.H., 1119
Wilson, B.W., 765
Witthaus, K.G., 2189
Wolanski, E., 219
Wu, J., 2386

Yagyu, T., 2444
Yamamoto, M., 2129
Yamashita, T., 282
Yaron, S.L., 1786
Yasuda, T., 22

Zacks, J., 1600
Zetler, B.D., 192
Zwamborn, J.A., 2026, 2700
Zwemmer, D., 1248, 1786